MICROPHYSICAL STRUCTURE OF A NIMBOSTRATUS OVER JILIN PROVINCE PROVIDED BY AIRBORNE OBSERVATIONS

Zhen Zhao[1] and Heng-chi Lei[1]
[1] Institute of Atmospheric Physics, Chinese Academy of Sciences

1. INTRODUCTION

The cold vortex is a major rain-bearing circulation system that can exist over northeastern China and can lead to severe convective weather and floods, especially in summer. Nimbostratus (Ns) clouds occur extensively in cold vortices and are known to cause stratiform precipitation, generating long periods of light precipitation. Previous studies have not addressed cloud structure or crystal growth in stratiform rainfall associated with the cold vortex however. The evolution of ice crystals in nimbostratus is thought to begin with depositional growth in the upper regions of the cloud, followed by aggregation after a sufficient number of large particles have formed (Field, 1999; Gordon and Martwitz, 1986; Lo and Passarelli, 1982). Evidence for this sequence of particle formation was derived by observations from aircraft that determined ice crystal size spectra in frontal clouds to explore the processes responsible for precipitation. These physical processes are summarized by previous authors (e.g., Mitchell, 1988).

The dominant processes of particle formation in nimbostratus are relatively simple and provide a good basis for generalized descriptions of this type of cloud. However, specific characteristics of a given precipitation event have not been documented. This study uses airborne observations of a nimbostratus cloud to investigate the relationship between cloud structure, particle size spectra parameters, and ice crystal evolution.

2. OBSERVATIONS AND METHODS

Between 2000 LST 20 June and 2000 LST 21 June 2005, a synoptic scale northeast cold vortex generated a wide distribution of light and moderate rainfall in the center of Jilin Province, with heavy precipitation in a localized small area. The vortex appeared to have passed maximum strength and turned into the depression stage. The aircraft data was obtained from flights around the Yitong (43.35°N, 125.28°E, sea level elevation of 249 m) in an Ns cloud associated with moderate to heavy stratiform precipitation on 21 June 2005. Most of the measurements reported in this study were collected from instruments mounted on the Y-12 aircraft.

Three Particle Measuring Systems (PMS) instruments were available to measure the cloud microphysical properties. The two-dimensional cloud and precipitation probes (hereafter ‘2D-C’ and ‘2D-P’) nominally measure ice-phase and precipitation hydrometeors with diameters ranging from 25–800 μm and 200–6400 μm, respectively, and provide an array resolution of 50 μm and 400 μm, respectively (see Knollenberg, 1970). The PMS Forward Scattering Spectrometer Probe (FSSP)-100 was used to detect and count cloud particles in the diameter range of 2–47 μm (Cerni, 1983). The King probe (King et al., 1978) uses a heated wire to measure liquid water content (LWC). This instrument is relatively simple and accurate for samples with high LWC. While droplets between 5 and 40 μm diameter are

Corresponding author: Zhen Zhao, zhaozhen@mail.iap.ac.cn

efficiently sampled by the King probe (King et al., 1981), ice particles do not adhere and are not detected.

Drops smaller than or equal to 125 μm in diameter detected in the first two channels of the 2D-C instrument were discarded because of the significant sizing errors that occur in these channels (Korolev et al., 1991, 1998). Also, we note that only the 2D-C and 2D-P data (with the minimum particle size of 125 μm) were used in quantitative evaluations of particle spectral characteristics.

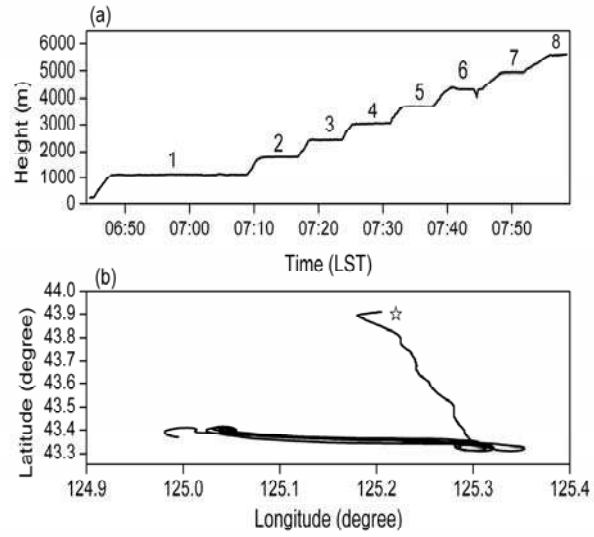

Figure 1 (a) Time series of aircraft altitude and (b) horizontal projection of the aircraft flight track on 21 June 2005. The star denotes the location of Changchun.

The flight pattern shown in Fig. 1a was designed to obtain the vertical distribution of microphysical properties in the cloud. The stepwise route included repeated ascents and horizontal-level (labeled in Fig. 1a); the total ascent from ~1 to 5.6 km was nearly 70-min in duration. The following discussion focuses on the vertical distribution data obtained during this ascent. The data were averaged in sequential 30-s intervals, corresponding to a mean horizontal length scale of 1.8 km. The 30-s averaging scale was chosen to provide a short averaging scale and to allow sufficient PMS measurements for statistical significance.

Particle spectra are approximately exponential in form such that

$$n(D) = N_0 e^{-\lambda D}$$

where n is particle number concentration per unit size interval, N_0 is the intercept, and λ is the distribution slope controlling the shape of the curve. Here D is the actual particle size measured by the 2D probe.

3. RESULTS

3.1 HYDROMETEOR DATA

The vertical profile of LWC is plotted in Fig. 2. LWC was highest in the middle of the cloud near 3 km, with a maximum 0.48 g m^{-3}. LWC was concentrated in the warm region, averaging about 0.23 g m^{-3}. There were several spikes in LWC observed in this region of the rainband, in which values exceeded 0.40 g m^{-3}, indicating active upward motion in this part. In regions that were below 0°C, there was a thick layer of supercooled cloud where LWC ranged from 0.06 to 0.3 g m^{-3}, averaging about 0.13 g m^{-3} with an LWC maximum near -2°C. As shown in Fig. 2, droplets with diameters greater than 24 μm were more concentrated in regions below 0°C.

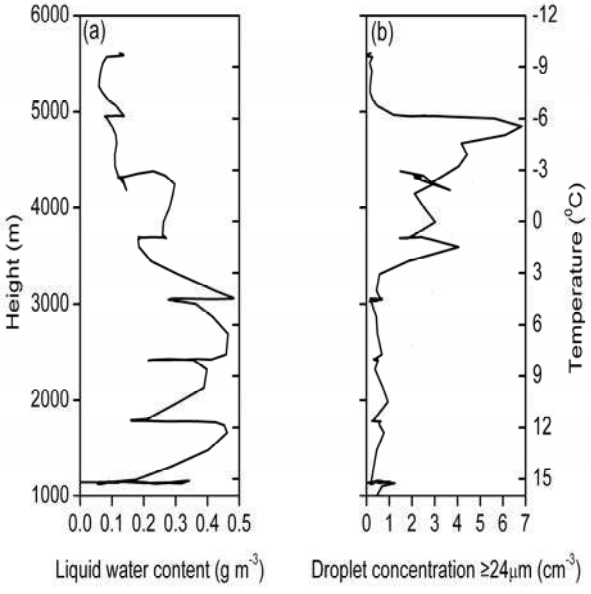

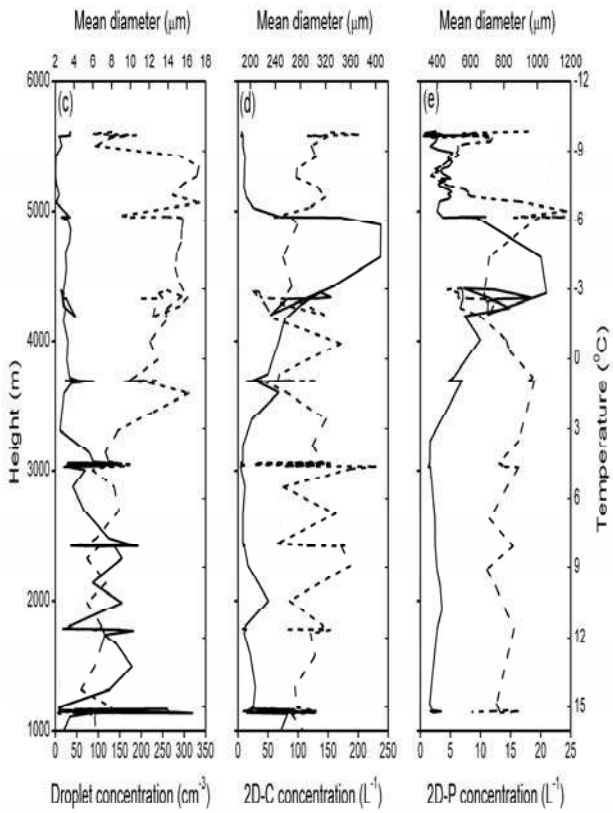

Figure 2 Vertical profiles of (a) liquid water content measured by King liquid water probe, (b) FSSP concentration of drops larger than 24 μm, particle concentration and mean diameter (dashed line) measured by the (c) FSSP, (d) 2D-C and (e) 2D-P probe during the ascent.

Particle concentration and mean diameter are also shown in Fig. 2. At temperatures below 0°C, the mean in-cloud FSSP concentrations were on the order of 0.7-47 cm^{-3}, with an average of 21 cm^{-3} and a mean diameter that ranged from about 7 to 16 μm. A relatively large region of concentrated supercooled cloud drops (up to 36 cm^{-3}) with LWC up to 0.14 g m^{-3} was observed near the top of the cloud (about -10°C). The most substantial region of cloud droplets was observed in the warm layer, with a mean of 77 cm^{-3} and a mean diameter that was generally smaller than 10 μm.

Mean concentrations from the 2D-C probe varied from 4 to 238 L^{-1}, corresponding to a mean diameter in the range 195-400 μm. Droplets detected by the 2D-P probe were in the range of 0.7-21 L^{-1} and ranged in mean diameter from 317 to 1175 μm. A very high concentration (~238 L^{-1}) of ice particles was observed in the region that ranged from -3°C to -6°C. Maximum ice particle concentrations were recorded in the layer near -6°C, where needle crystals and aggregates were detected as observed in 2D-C images. The maximum concentration measured by 2D-P reached 21 L^{-1} at a temperature of about -3°C. Raindrop concentrations below the melting layer were <7 L^{-1}.

The observed increase in ice crystal concentrations (with maximum values up to 238 L^{-1}) with increasing altitude suggests the possibility that active ice enhancement was occurring. The FSSP recorded supercooled cloud droplets larger than 24 μm in diameter at concentrations ranging from 3 to 7 cm^{-3} when the aircraft passed through the temperature region -3°C and -6°C (Fig. 2b). The conditions for Hallett-Mossop (H-M) rime-splintering ice multiplication mechanism (Hallett and Mossop, 1974; Mossop, 1985) were satisfied in the -3°C to -6°C region, assuming that the FSSP only responded to water drops. However, the occurrence of the H-M mechanism under these conditions is speculative given the time and space variations of natural cloud characteristics that escape detection by in situ measurements.

Between altitudes of 4.3 and 5.5 km (-10 to -2°C), ice particle concentrations measured by 2D-C and 2D-P (averaged over 0.6 km horizontal distances, corresponding to 10s) gradually decreased with increasing altitude (Fig. 3). Ice particle concentration was highly variable, with mean concentrations ranging from 7-130 L^{-1} and 3-14 L^{-1} for the 2D-C and 2D-P probes, respectively.

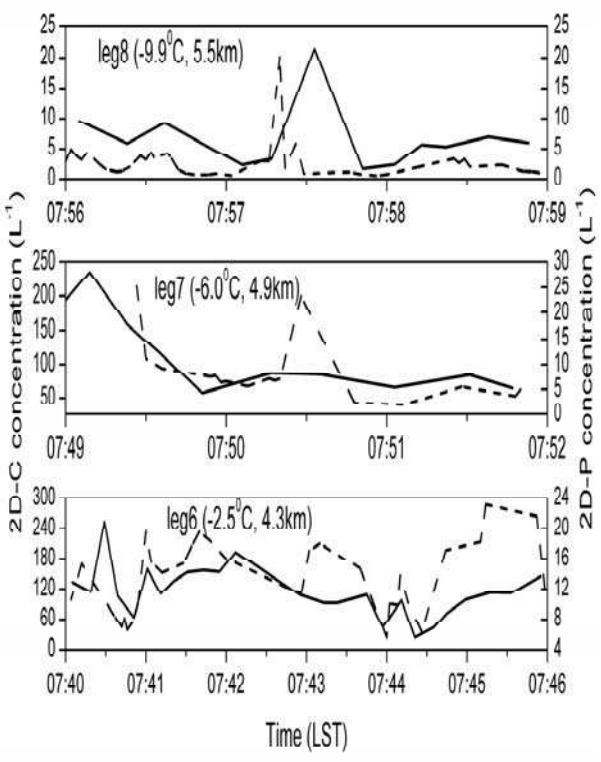

Figure 3 Particle number concentrations measured by the 2D-C (solid line) and 2D-P (dashed line) probes across the horizontal legs. Temperature and altitude of the horizontal flight legs are also indicated.

3.2 PARTICLE SPECTRA

In accordance with earlier studies (Gordon and Martwitz, 1986; Lo and Passarelli, 1982), particles >125 μm exhibited ice particle spectra that were adequately described by an exponential relationship. Figure 4 shows a logarithmic plot of N_0-λ for 2D-C and 2D-P data collected during the spiral ascents. There is a high correlation between λ and N_0 that is best described by a power law; however, there is scatter about this relationship and it is not clear if individual N_0-λ relationships are defined by environmental conditions.

The ability to assess growth processes and the evolution of ice crystals was limited by the flight pattern used in this study, which was not designed to follow particles developing at the top of the cloud. As Lo and Passarelli (1982) have proposed, particle aggregation results from decreases in both λ and N_0 in exponential size distributions. Growth by deposition would tend to increase only N_0; λ would remain relatively constant. In the data set described here, a strong correlation was found between λ and N_0 (see Fig. 4), which is consistent with the pattern expected for aggregation.

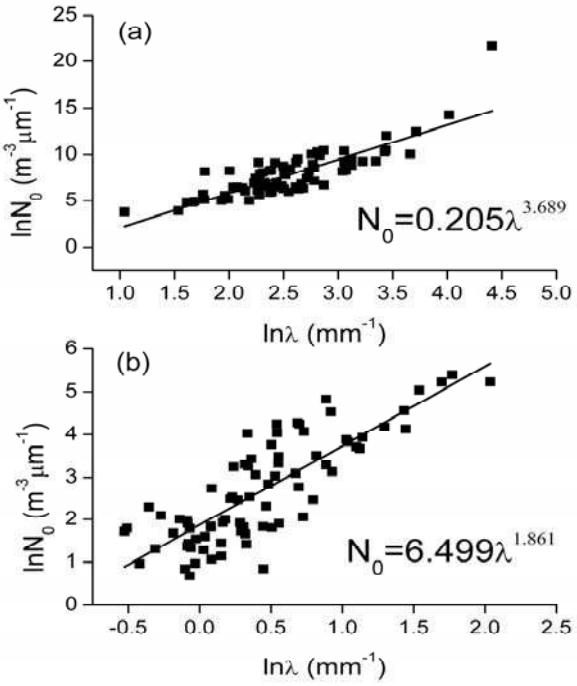

Figure 4 A log-log plot of slope parameter (λ) and intercept parameter (N_0) during the ascent on 21 June 2005 by (a) 2D-C, (b) 2D-P.

4. CONCLUSIONS

In situ measurements were performed in a nimbostratus precipitation band which was associated with the depression of northeast cold vortex in Jilin Province. Aircraft observations indicated large LWC and droplet concentration in the warm layer. There was a thick layer of supercooled cloud that had a LWC as high as 0.3 g m^{-3}, whereas the number concentration was small. High ice particle concentrations were observed at temperatures ranging from about -3°C to -6°C, which was explained by the Hallett-Mossop ice multiplication process. Ice particle concentrations varied

on a relatively small scale for different horizontal legs. Ice particle spectra were exponentially correlated and a power law expression described the relationship between N_0 and λ parameters. These data suggest that aggregation of the crystals led to the final shaping of the precipitation size spectra.

5. BIBLIOGRAPHY

Cerni, T. A., 1983: Determination of the size and concentration of cloud drops with an FSSP, *J. Appl. Meteor.*, 22, 1346-1355.

Field, P. R., 1999: Aircraft observations of ice crystal evolution in an altostratus cloud, *J. Atmos. Sci.*, 56, 1925-1941.

Gordon, G. L., and J. D. Martwitz, 1986: Hydrometeor evolution in rainbands over the California valley, *J. Atmos. Sci.*, 43, 1087-1100.

Hallett, J., and S. C. Mossop, 1974: Production of secondary ice particles during the riming process, *Nature*, 249, 26-28.

King, W. D., D. A. Parkin, and R. J. Handsworth, 1978: A hot-wire liquid water device having fully calculable response characteristics, *J. Appl. Meteor.*, 17, 1809-1813.

King, W. D., C. T. Maher, and G. A. Hepburn, 1981: Further performance tests on the CSIRO liquid water probe, *J. Appl. Meteor.*, 20, 195-202.

Knollenberg, R. G., 1970: The optical array: An alternative to scattering or extinction for airborne particle size determination, *J. Appl. Meteor.*, 9, 86-103.

Korolev, A. V., S. V. Kuznetsov, Y. E. Makarov, et al., 1991: Evaluation of measurements of particle size and sample area from optical array probes, *J. Atmos. Oceanic Technol.*, 8, 514-522.

Korolev, A. V., J. W. Strapp, and G. A. Isaac, 1998: Evaluation of the accuracy of PMS optical array probes, *J. Atmos. Oceanic Technol.*, 15, 708-720.

Lo, K. K., and R. E. Passarelli, 1982: The growth of snow in winter storms: An airborne observational study, *J. Atmos. Sci.*, 39, 697-706.

Mitchell, D. L., 1988: Evolution of snow-size spectra in cyclonic storms. Part I: Snow growth by vapor deposition and aggregation, *J. Atmos. Sci.*, 45, 3431-3451.

Mossop, S. C., 1985: Secondary ice particle production during rime growth: The effect of drop size distribution and rimer velocity, *Q. J. R. Meteorol. Soc.*, 111, 1113-1124.

Acknowledgements

This research was supported by the National Natural Science Foundation of China (Grant No. 41175120) and the Knowledge Innovation Program of the Chinese Academy of Sciences (Grant No. KZCX2-EW-203).

ICE MULTIPLICATION, HEAVY SNOWFALL, AND HIGH ELECTRIFICATION OF HOKURIKU WINTER SNOW CLOUDS - VIDEOSONDE OBSERVATION

Tsutomu Takahashi[1], Soichiro Sugimoto[2], and Kenji Suzuki[3]
[1] Honolulu, Hawaii
[2]Central Research Institute of Electric Power Industry
[3] Yamaguchi University

1. INTRODUCTION

A prominent unsolved problem in Cloud Physics is the observation in some clouds of a much higher concentration of ice crystals than would be expected from ice nucleation, alone (Hobbs and Rangno, 1985). This suggests that extra-nucleation processes contribute to the high concentrations of ice crystals required for heavy snowfall and high cloud electrification. Hallett and Mossop (1974) proposed that secondary ice particles are produced during riming at temperatures between -3°C and -8°C and that this process contributes to the high ice crystal concentrations observed in certain Florida clouds (Hallett et al., 1978). However, Hobbs and Rangno (1990) found it difficult to use this mechanism to explain their observations of a high rate of ice crystal production in winter maritime cumuli near the Washington state coast.

In Hokuriku winter clouds, ice crystal production was especially high when both large and small graupel were present, as observed using an aircraft-mounted, video-based, particle counter (Takahashi, 1993). Consistent with this, in cold room experiments, colliding two ice spheres with different growth modes produced very large numbers of ice particles (Takahashi et al., 1995). Here, we present an improved description of graupel and ice crystal distributions in Hokuriku winter clouds based on extensive videosonde observations. These data also increase our understanding of the precipitation processes which generate heavy snowfall in these clouds, including ice multiplication.

2. OBSERVATIONS

a. INSTRUMENTS

The principal instrument used was the videosonde, a balloon-borne surveyor of precipitation particle morphology and charge (Fig. 1, Takahashi, 1990). Particles entering through an aperture at the top, first pass through an induction ring which measures particle charge. Signals are logarithmically amplified (0.1-200 pC). Particles next pass through a video recording system. An infrared light is mounted above a video camera with its beam parallel to the camera's line of sight. Interruption of the beam by any particle larger than 0.5 mm in diameter triggers a flash lamp mounted just above the camera lens. Very small particles (below ~ 0.2 mm), fall below the resolution limit of the camera. As a result, the particle concentrations which we report here probably underestimate the actual totals by an order of magnitude**.** Only the observed, uncompensated counts are reported here. An LED array is positioned at the bottom of the camera's field of view. The first two LEDs indicate the sign of the electric charge and

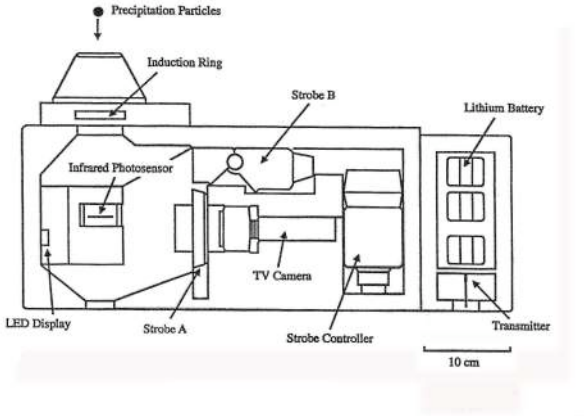

Fig. 1. Videosonde

the rest indicate its magnitude (refer Fig. 3). Video is transmitted to the ground on a 1680 MHz carrier wave, its frequency modulated between 10 Hz and 1 MHz according to image signal intensity. The received video signal is recorded on tape and displayed on a monitor. Particle shape and charge were analyzed by frame-by-frame inspection. Particle size was measured as pixel count in jpeg frame-captures .

b. OBSERVATION SITE

In typical winter monsoons, strong northerly winds transport cold, Siberian air over the warm Japan Sea, forming cloud bands 5-6 km high, a process most active near the coast (Fig. 2). These bands often produce heavy snowfall and lightning near the coast. In Jan-Feb 2010, and Dec 2010-Jan 2011, 55 videosondes were launched into snow clouds ~3 km inland from the coast at Kashiwazaki in Hokuriku, Japan. Videosondes were launched during strong winds into cloud centers guided by radar images provided by the Japan Meteorological Agency.

Fig. 2. Winter monsoon clouds in Japan

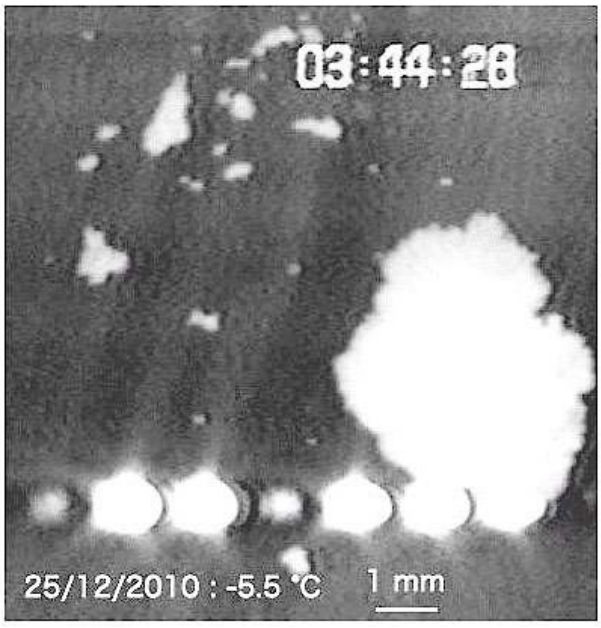

Fig. 3 Graupel and ice particles of # 16 sonde

3. RESULTS

In-cloud videosonde images displayed brittle-looking graupel, often in the midst of small ice particles (Fig. 3). In the course of cloud development, as peak graupel concentration exceeded 100 m^{-3}, peak ice crystal concentration increased sharply and became very high (Fig. 4).

Peak graupel number concentration and peak ice crystal number concentration were observed least frequently at around –10°C.

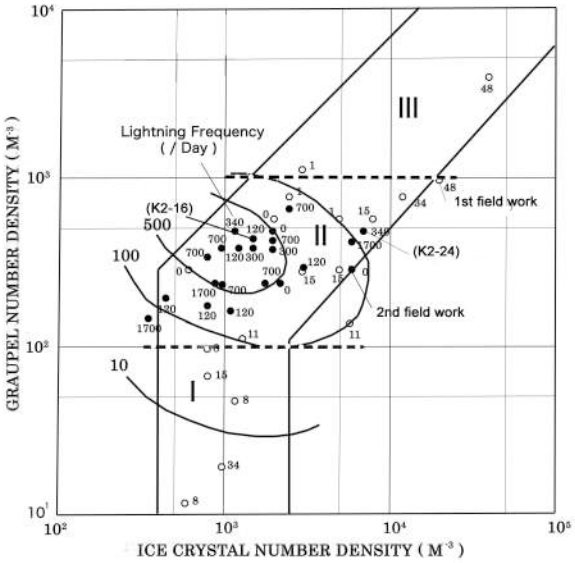

Fig. 4. Peak ice crystal and graupel numbers, and lightning activities

When peak graupel concentration was plotted against peak ice crystal concentration for each videosonde launch, the sampled areas could be grouped into three basic types (Region I-III in Fig 4).

In Region I, graupel concentration was less than 100 m^{-3}. Here, graupel size was small, and the graupel size distribution was narrow.

In Region II, graupel concentration was 100-1000 m^{-3}. The graupel size distribution was broad, suggesting an active riming process (Fig. 5). This region exhibited the highest conversion rate of rimed ice crystals to graupel, the highest precipitation (>30mm/day), and the most frequent lightning activity (>40 events/day). Interestingly, snowflake formation was also very active here at all altitudes (Fig. 6).

In Region III, graupel concentration was >1000 m^{-3}. Ice crystal concentration was also relatively high. The graupel size distribution was dominated by two peaks: small and large.

4. DISCUSSION

Graupel imaged in-cloud were highly brittle in appearance. As graupel concentration exceeded 100 m^{-3}, ice crystal concentration

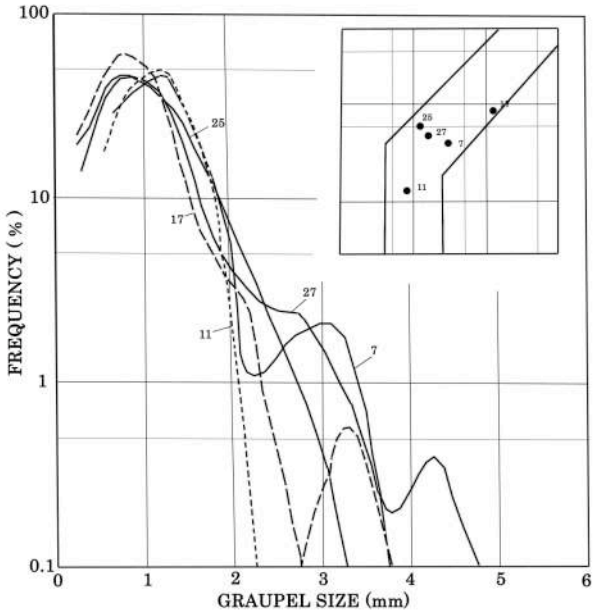

Fig. 5 Graupel size distributions

increased sharply; it is at this critical graupel concentration that 1-mm diameter graupel falling through a 3 km cloud depth are expected to begin to collide with each other. In these clouds, ice branches growing from the surface of small graupel, probably by deposition, are likely to be broken during graupel-graupel collisions, ejecting new ice particles (Takahashi et al., 1995). In our observations, peak graupel and peak ice crystal numbers were least frequently observed at around – 10°C. This may correspond to the minimum ice crystal growth rate at -10 °C in the laboratory (Ryan et al., 1976), suggesting the importance of ice branch growth for ice ejection.

In the active riming area (Region II), both lightning and precipitation processes are active. This is consistent with the theory that the riming electrification process is the main charge separation mechanism in thunderstorms (Takahashi, 1978, and others). Rimed ice particles are the main precipitation particles during heavy snowfall (Meteorological Research Institute, 2005).

Surprisingly, in Region II, high snowflake formation was observed throughout the entire cloud depth regardless of temperature where ice crystal concentration exceeded 1000 m^{-3}. High snowflake formation suggests the presence here of the cloud droplets important to this process.

We propose that Hokuriku snowfall is generated as follows (Fig. 7): In small convective clouds over the ocean, cloud droplets freeze and grow ice crystals. Through riming, they develop into rimed ice crystals and then into graupel. As these clouds approach the coast, clouds grow taller. Graupel within the increased height through which they fall, increases the probability of graupel-graupel collisions. These collisions eject new ice particles. Ice crystals also agglomerate, aided by supercooled drops, and form snowflakes. Graupel tend to be charged negatively and ice crystals positively above -10 °C level while graupel changed sign below -10 °C level. The area of high ice crystal and graupel concentration is where electric

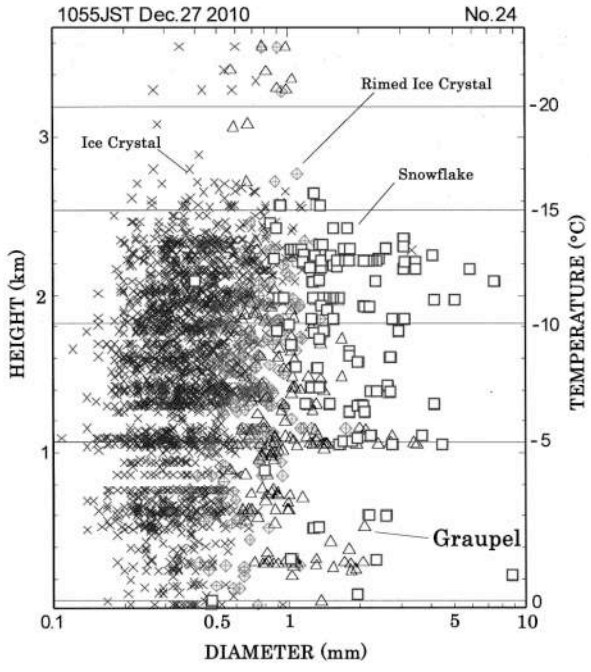

Fig 6. Precipitation particle distribution of # 24 sonde.

charge separation is most active. Because of intense wind shear, graupel and snowflakes separate horizontally in space and fall adjacent to each other.

REFERENCES

Hallett, J., and S. C. Mossop, 1974: Production of secondary particles during the riming process. Nature, 49, 26-28.

Hallett, J., R. I. Sax, D. Lamb, and A. S. R. Murty, 1978: Aircraft measurements of ice in Florida cumuli. Quart. J. Roy. Meteor. Soc., 104, 631-651.

Hobbs, P. V., and A. L. Rangno, 1985: Ice particle concentrations in clouds. J. Atmos. Sci., 42, 2523-2549.

Hobbs, P. V., and A. L. Rangno, 1990: Rapid development of high ice particle concentrations in small polar maritime cumuliform clouds. J. Atmos. Sci., 47, 2710-2722.

Meteorological Research Institute Japan, 2005: Study of precipitation mechanisms in snow clouds over the sea of Japan and feasibility of their modification by seeding. Technical Note 48, 1-221.

Ryan, B. F., E. R. Wishart, and D. E. Shaw, 1976: The growth rates and densities of ice crystals between -3 °C and -21 °C. J. Atmos. Sci., 33, 842-850.

Takahashi, T., 1978: Riming electrification as a charge generation mechanism in thunderstorms. J. Atmos. Sci., 35, 1536-1548.

Takahashi, T., 1990: Near absence of lightning in torrential rainfall producing Micronesian thunderstorms. Geophys. Res. Lett., 17, 2381-2384.

Takahashi, T., 1993: High ice crystal production in winter cumuli over the Japan Sea. Geophys. Res. Lett., 20, 451-454.

Takahashi, T., Y. Nagao and Y. Kushiyama, 1995: Possible high ice particle production during graupel-graupel collision. J. Atmos. Sci., 52, 4523-4527.

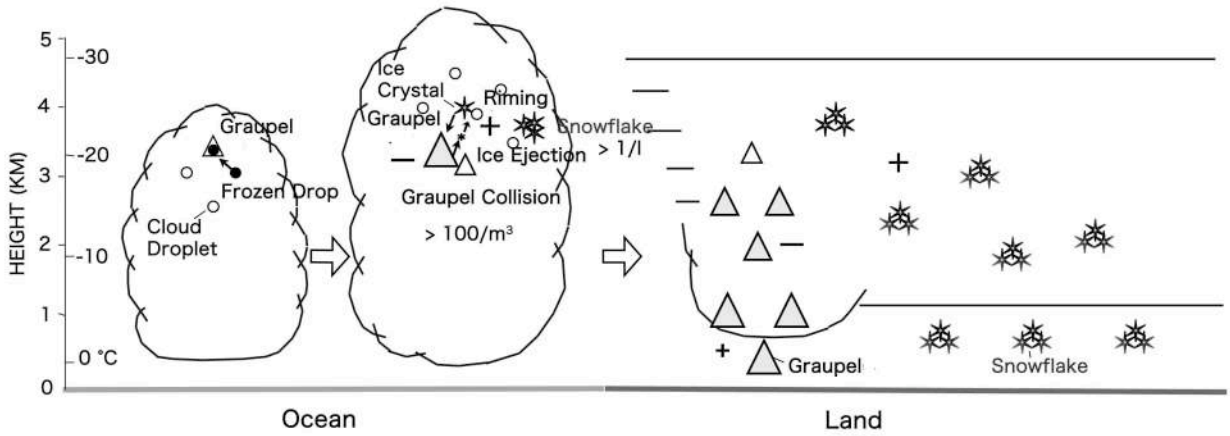

Fig. 7. Hokuriku snowfall microphysics model.

ICE NUCLEI CONCENTRATION AT THE SOUTH POLE STATION, ANTARCTICA

Zev Levin[1,2], Karin Ardon Dryer[1,3] and Paul Lawson[4]

[1]Department of Geophysics and Planetary Science, Tel Aviv University, Israel
[2]Energy, Environment and Water Research Center, The Cyprus Institute, Cyprus
[3]The Porter School of Environmental Studies, Tel Aviv University, Israel
[4]SPEC Incorporated, Boulder, Colorado, USA

ABSTRACT:

The effectiveness of aerosols as immersion freezing nuclei in the South Pole station was investigated during a campaign that took place in January and February 2009. Twelve samples were collected, nine from the rooftop and three from a balloon. The effectiveness of the sampled aerosols as immersion freezing was measured using the drop freezing technique in the FRIDGE-TAU (FRankfurt Ice-nuclei Deposition freezinG Experiment, the Tel Aviv University version). The freezing nuclei (FN) were found to be effective from -19 to -26ºC and their concentrations varied from $0.1L^{-1}$ to $53L^{-1}$, respectively, with a concentration of $1L^{-1}$ observed at -23ºC. The strongest correlation of FN concentration was found with wind speed. FN concentrations were almost five to nine times higher when the wind increased from 4.4 to 9 ms^{-1}.

1. INTRODUCTION:

Much attention has been given to condensation nuclei (CN) characteristics in the Antarctic continent (Saxena, 1983; Gras et al., 1985; DeFelice et al., 1997), yet the characteristics of ice-forming nuclei, their origin, composition and concentrations have only seldom been studied (Bird et al., 1961; Bigg and Hopwood, 1963; Kumai, 1976; Saxena and Weintraub, 1988; Junge and Swanson, 2008). Most of the above studies were conducted along the coast of Antarctica and only a very few reported on measurements at the South Pole (e.g. Kumai, 1976).

Bigg and Hopwood (1963) reported on ice nuclei concentrations at McMurdo station located near the coast of Antarctica. They found that freezing occurred between -14 to -26°C, with concentrations of 0.5-$13L^{-1}$ of active nuclei at -20ºC. Most of the nuclei had a diameter of around 0.01µm, while some had a diameter of 0.1µm. Bigg (1973) measured IN concentrations at -10, -15 and -20°C with mean concentrations of 1-$5^{x}10^{-3}$, 10-$20^{x}10^{-3}$ and 0.1 (L^{-1}) respectively. Saxena and Weintraub (1988) used drop freezing measurements at Palmer station over the temperature range of -5ºC to -17ºC. They reported on the presence of high concentrations of IN (0.01 to $10L^{-1}$) even at temperatures as high as -5 to -7ºC. They also reported finding good correlation between ice nuclei concentrations and the presence of

Potassium, Silicon and Zinc. Carpenter et al. (2000) and Warren and Hudson (2003) reported on the existence of bacteria in the South Polar snow. However, their effectiveness as IN is still unclear. Junge and Swanson (2008) suggested that immersion-freezing of marine psychro-active bacteria and viruses would not be important for heterogeneous ice nucleation processes in polar clouds nor for the formation of sea ice, because they would nucleate ice at temperatures very close to the homogeneous nucleation temperature (-42.2±0.3ºC). The present report is a short summary of the paper by Ardon-Dryer et al (2011).

2. METHODS:

The measurements were conducted during January and February 2009 at the Amundsen-Scott station at the geographical South Pole (Latitude 89°59.77′S, Longitude 92°1′E, Fig. 1) on a polar plateau at an altitude of 2850m (for more information about the campaign see Lawson et al., 2011).

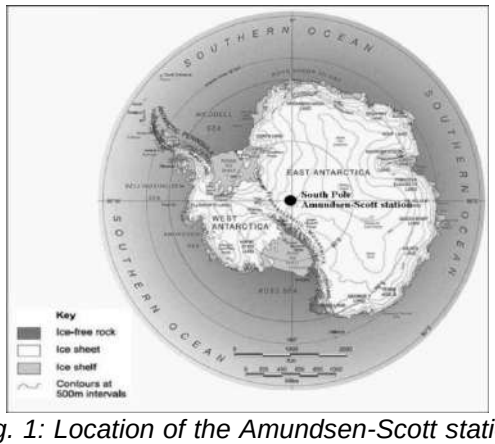

Fig. 1: Location of the Amundsen-Scott station at the South Pole, in Antarctica, marked in black circle (Geology, 2010 with modification).

Twelve filter samples (Nitrocellulose Membrane Black filters of 47mm diameter and 0.45µm pore size) were collected; nine from the rooftop and three from a balloon (see Table 1) the inlet of the filter holder was positioned with the wind to its back. The effectiveness of the sampled aerosols as immersion-freezing was measured using a drop freezing technique, based on Vali (1968). In this technique the collected aerosols were removed into a test-tube containing 10ml of double distilled water by placing the tube in an ultrasonic bath for 30 min. The resulting mixture of water and aerosols was the source of the drops tested for immersion-freezing. Each test consisted of about 120 drops (1µl; 0.8mm diameter) that were placed on the temperature controlled stage in the FRIDGE-TAU (see Fig. 2), A thin layer of vacuum oil was first put on the stage in order to prevent ice from forming on the surface during cooling, thus affecting the measurements. The temperature of the cooling stage was lowered at a constant rate of $1^{\circ}min^{-1}$ and the numbers of drops that froze at each temperature were recorded by the CCD camera.

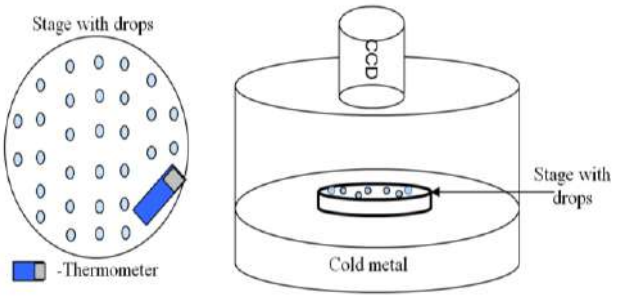

Fig. 2: Schematic diagram of the immersion-freezing method.

Two unexposed filters were tested under identical procedures as reference for comparison with the exposed filters.

Table 1: Description of sampled filters.

Filter #	Filter Location	Volume of air sampled (L)	Time of measurement (UTC)
1	Rooftop	344	28.01.09
2	Rooftop	327	28.01.09
3	Rooftop	319	29.01.09
4	Rooftop	450	29.01.09
5	Balloon	327	29.01.09
6	Balloon	245	29.01.09
7	Balloon	245	29.01.09
8	Rooftop	499	30.01.09
9	Rooftop	1317	30.01.09
10	Rooftop	1579	31.01.09
11	Rooftop	1873	01.02.09
12	Rooftop	2495	02.02.09

In order to estimate the concentrations of immersion Freezing Nuclei (FN) in the air we converted Vali's (1971) equation taking into account the amount of air that had been sampled in each measurement. The equation is composed of two parts: the first is an integration of the differential probability that a drop will freeze at temperatures between θ and $\theta - \Delta\theta$ due to the presence of a single active nucleus in it over the temperature range from 0ºC to θ. The result of the integration is the cumulative nucleus concentration K'(θ), which represents the number of nuclei active at all temperatures warmer than θ. In order to obtain the actual concentrations of ice nuclei in the sampled air, consideration must be given to the total air sampled. This is presented in the last part of the equation:

$$K'(\theta) = \frac{1}{V} \times \left[\ln(N_0) - \ln(N(\theta)\right] \times \frac{x}{y} \qquad (1)$$

K'(θ) - Cumulative concentration of FN in the air active at temperature θ (L^{-1})

V - Volume of drop (L)

N_o - Total number of drops measured

N (θ) - Number of unfrozen drops at temperature θ

x - The volume of water used to remove the aerosols from the filter (L)

y - The volume of air sampled through the filter (L)

3. RESULTS AND DISCUSSION:

Twelve samples containing a total of 1459 drops were analyzed. The analysis was carried out between 0 to -27ºC within which all the drops froze (see Fig. 3). Most drops in most samples began to freeze only at -18ºC. The freezing occurred at warmer temperatures as compared to water drops taken from pure water. It is apparent that although freezing of drops started at -18ºC most froze at temperatures lower than -20ºC. 50% of the drops in all the samples froze between -23 to -24.5ºC. The average temperature in which 50% of the drops froze occurred at -24ºC, much warmer than reported by Junge and Swanson (2008) where near homogeneous freezing temperatures were observed for specific bacterial isolates.

Drop freezing experiments using water with blank filters revealed that most of the

drops froze at temperatures well below those from the exposed filters. However, there was a small overlap between the blank filters and the others from -23ºC to -27ºC (see Fig. 3). In order to calculate the concentrations of FN in the air the fraction of drops from the blank that froze at each temperature was deducted from the corresponding frozen drops on the sampled filters. The effect on the calculated concentrations was minimal (from ~0.06 to 5.9% over the temperature range in the experiment).

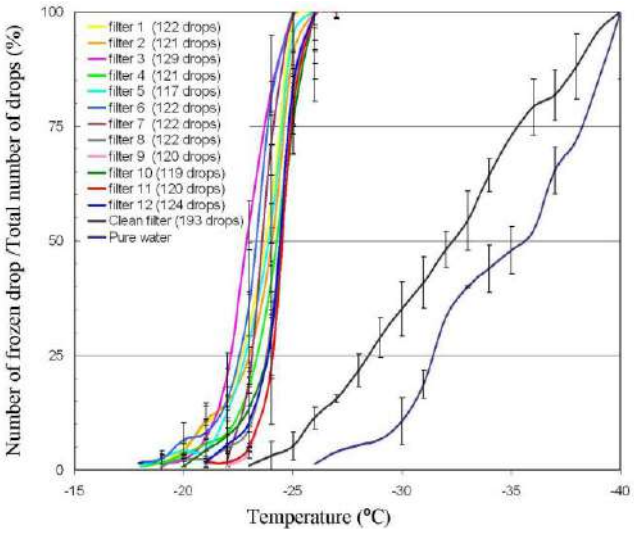

Fig. 3: The cumulative freezing spectrum of all the South Pole samples and the average spectrum of freezing temperature from clean (blank) filters and pure water. The bars represent the standard deviation.

The concentrations of FN in the sampled air were calculated using Eq. 1. The concentration of freezing nuclei in the air calculated for the different samples between -19 to -26ºC varied from $0.1L^{-1}$ to $53L^{-1}$, respectively, as can be seen in Fig. 4. As expected, the number of active nuclei increases as the temperature decreases. A concentration of $1L^{-1}$ was observed in all the filters between -21ºC to -25ºC.

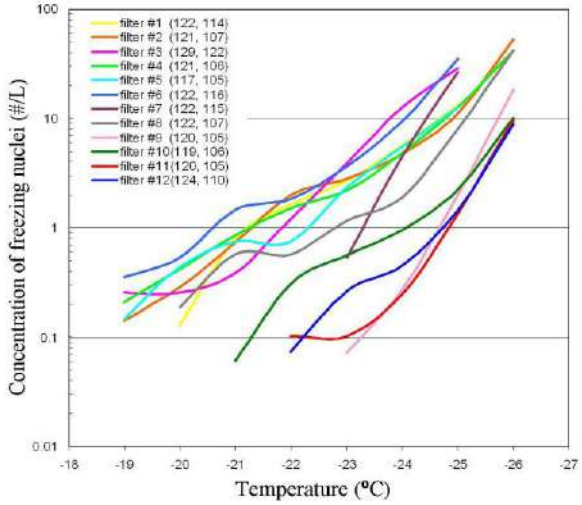

Fig. 4: Concentration of FN in the air for the different samples calculated from Eq. 2.2. The first number in the parenthesis represents the number of drops used in the experiment and the second is the one used for the present calculations after subtracting the drops that froze on the blank filters (see text for explanation).

Based on the meteorological data collected at the measuring site, it appears that the aerosols samples were collected under different meteorological conditions. Wind speed was found to be a dominating factor in the measured concentrations of FN. Each filter sample was collected under different wind speeds, as can be seen in Table 2. High correlation between wind speed and FN was found for all measured temperatures (Fig. 5a). Similarly, the correlation of wind speed with total aerosol concentrations was high also (Fig. 5b). It should be noted that the aerosol concentrations shown in Table 2 refer to total aerosols greater than 0.01μm

(measured by the TSI CPC 3760). Most of these aerosols may not be so relevant for the FN measurements because they are much smaller than the expected size of the IN (e.g. DeMott et al., 2010), however, this was the only reliable and available data on aerosol size and concentration.

Table 2: Average surface meteorological conditions during sampling period.

Filter nu	Aerosol number concentration >0.01µm (cm^{-3})	RH in the air (%)	Wind direction (deg)	Wind speed (m/s)	Ambient pressure (hPa)	Temp (deg C)
1	1864.3	98.5	5.5	9.7	680.2	-25.0
2	1996.3	98.9	5.0	10.3	680.0	-25.2
3	1978.0	97.9	10.4	8.6	680.0	-26.5
4	1748.5	98.2	16.2	7.5	679.9	-27.0
5	1464.7	98.3	21.0	6.5	679.5	-27.2
6	1757.7	97.9	23.3	8.0	679.0	-26.6
7	1704.2	96.3	28.1	6.4	678.8	-26.8
8	335.4	97.1	353.4	4.7	680.4	-31.3
9	545.3	98.1	76.0	5.4	683.4	-32.6
10	520.6	97.4	92.5	4.1	682.9	-33.1
11	1152.2	97.4	59.3	5.6	685.0	-27.5
12	1308.5	82.7	298.9	2.4	689.1	-30.6

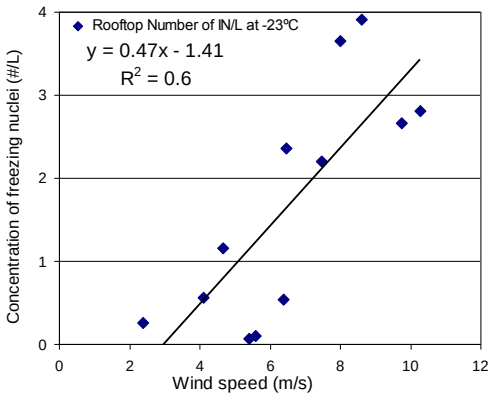

Fig 5a: Concentration of freezing nuclei at -23ºC as a function of wind speed

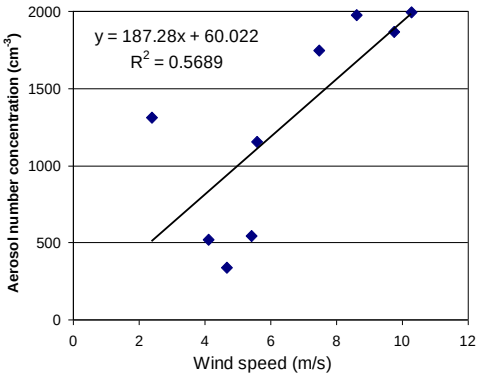

Fig. 5b: Concentration of aerosols > 0.01µm as a function of wind speed.

Lawson et al. (2006) reported that at the South Pole Station blowing snow is observed when the wind speed exceeds about $4ms^{-1}$. Knuth et al. (2010) measured a threshold of between 6.6 to $7.5ms^{-1}$ at 10m height for blowing dry snow at the Ross Ice Shelf. The threshold for blowing wet snow was higher at 8.5 to $9.6ms^{-1}$. Threshold for blowing snow on the Ross Ice Shelf is likely to be different than at the South Pole since the type of precipitation is quite different. For our purpose here $6ms^{-1}$ was chosen as a threshold for blowing snow. Based on that, our filter samples were divided into two groups, above and below the wind speed of $6ms^{-1}$. For example, filters 1-4 were exposed to higher wind speed (average of $9ms^{-1}$) and had $2.9L^{-1}$at -23ºC. Filters 8-12, which were exposed to lower average wind speeds of about $4.4ms^{-1}$ had only $0.4L^{-1}$ at -23ºC. One explanation for this observation was based on the suggestion by Hogan (1979) who showed that strong winds in the South Pole increased the mixing of air near the surface, leading to higher concentration of larger particles at higher elevations, implying higher

concentrations of FN. During the sampling time of filter 9-11, the station was affected by falling ice crystals and broken clouds that occurred from 30 January 2009 to 1 February 2009 (see decrease in FN concentration in Fig. 4.31). These falling ice crystals undoubtedly scavenged aerosols in the lower atmosphere, thus reducing the measured FN concentrations. The possibility that sublimated ice crystals in the air affected the IN measurements was ruled out because the relative humidity was far above ice saturation. The only possible effects could be the collection of some of the ice crystals on the filters, which sublimated later, leaving the ice nuclei on the filters. However, the chance for this to happen was considered low because of (a) the sampler was facing away from the average wind direction, thus making it difficult for the ice crystals to enter the inlet and (b) the inlet air speed was about 5.6ms^{-1}, which implies that we under-sampled the large particles (see Su and Vincent, 2004) and reduced the potential for collecting blowing ice crystals. However, we cannot rule out the possibility that on the balloon ice crystals were collected. This is because the position of the inlet could not be fixed with respect to the wind direction.

An average parametric equation for FN concentrations was calculated, for this remote site, something that could be helpful in numerical models. For this purpose all the rooftop measurements were combined and a best fit line was calculated (Fig. 6). The resulting best-fit line is:

$$N_{FN} = 3\times10^{-7} e^{0.66\Delta T} \qquad (2)$$

Where N_{FN} represents the number concentrations of FN (L^{-1}) and ΔT represent supercooling in ºC (0–T).

.

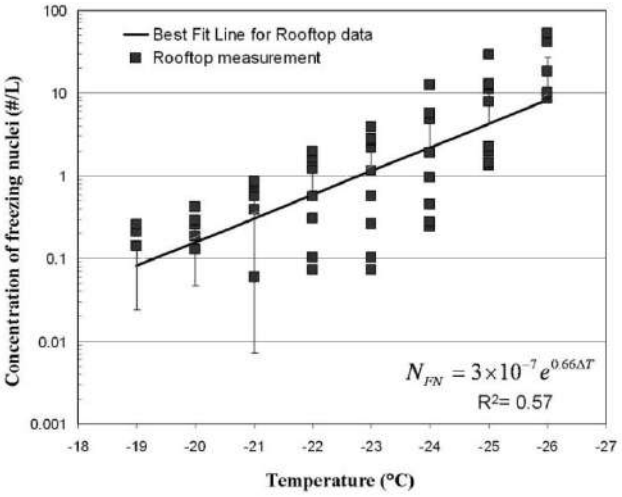

Fig. 6: The FN concentrations of all rooftop samples in the air. The equation represents the best fit line to the rooftop data.

From the figure one can see that FN concentration of ~1L^{-1} is found at -23ºC, which is a little lower than what Bigg and Stevenson (1970) reported as average concentrations at higher latitudes (~1L^{-1} at -20ºC). The FN concentrations obtained from Eq. 2 are slightly lower than those reported by Bigg (1973) for measurements near the coast of Antarcticaat -15ºC (~0.015L^{-1}). Eq. 2 also gives lower concentrations than those reported by Saxena and Weintraub (1988) for measurements at Palmer Station. These differences are not surprising since in the

past 37 years the anthropogenic activity in and around Antarctica have increased dramatically, leading to more pollution from ships and other activities next to the sea shore (Graf et al., 2010).

Overall the IN concentrations that were found in the South Pole station are in agreement with other IN concentrations that were measured in other locations around the globe, as can be seen in Fig.7. The parametric equation we obtained gives lower FN concentrations than any of the other parametric equations of Fletchers (1962), Cooper (1986) or Meyers (1992), but it falls well within the data points presented in Fig 7.

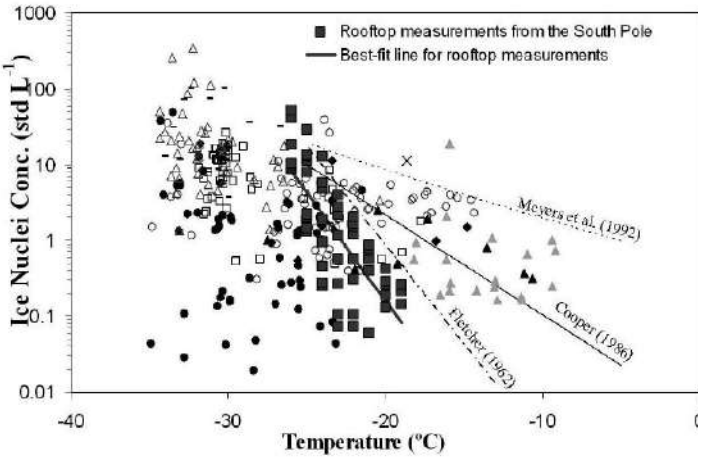

Fig. 7: Ice nuclei concentrations as a function of temperature from DeMott et al. (2010) with the present measurements shown in black squares.

4. CONCLUSIONS:

Immersion Freezing Nuclei were measured from samples collected at the South Pole station during late January early February 2009. FN was found to be effective from -18ºC down to -27ºC, with concentrations ranging from 0.1 to 53 L^{-1}. The temperature at which 50% of the drops froze occurred at -24ºC. Concentration of 1 L^{-1} was observed at -23ºC.

The meteorological conditions, such as wind speed appear to have affected the FN concentrations at the South Pole station. A strongest correlation of FN concentration was found with wind speed. FN concentrations were almost five to nine times higher when the wind increased from 4.4 to 9ms^{-1}.

Using the data, a parametric equation was calculated for the mean concentrations of FN as a function of temperature for a remote location such as the South Pole station. Since the measurements vary with meteorological conditions, more measurements under different conditions are needed to improve the parametric equation derived here.

5. ACKNOWLEDGMENT

We want to thank Patrick J. Sheridan, from NOAA, Dr. Alexei Korolev from Environment Canada, Dr. Chris Roden and Pat Zmarzly of SPEC Inc. for their support in collecting the data. The analysis of thedata was carried out with partial support from the Virtual Institute on Aerosol-Cloud Interactions, supported by the Helmholtz-Gemeinschaft (HGF) and by the German Israeli Foundation (GIF) grant number 1-860-27. The South Pole field project was sponsored by Grant OPP-

0337876 to SPEC Incorporated from the U.S. National Science Foundation.

6. REFERENCES:

Ardon-Dryer, K. Levin, Z. and Lawson, R.P.: Characteristics of immersion freezing nuclei at the South Pole station in Antarctica, Atmos. Chem. Phys., 11, 4015-4024, 2011.

Bigg, E.K.: Ice nucleus measurements in remote areas, J. Atmos. Sci., 30, 1153-1157, 1973.

Bigg, E.K. and Hopwood, S.: Ice Nuclei in the Antarctic, J. Atmos. Sci., 20, 185-188, 1963.

Bigg, E.K. and Stevenson, C.M.: Comparison of ice nuclei in different parts of the world, J. Rech. Atmos., 4, 41-58, 1970.

Bird, I. Cresswell, G. Humble, J. Norris, I.D. and Bigg, E.K.: Atmospheric Ice Nuclei in high southern latituder, J. Meteor., 18, 563-564, 1961.

Carpenter, E.J. Lin, S. and Capone, D.G.: Bacterial activity in South Pole, Appl. Environ. Microbiol., 66, 4514-4517, 2000.

Cooper, W.A.: Ice initiation in natural clouds. Precipitation Enhancement-A Scientific Challenge, Meteorology Monographs, Amer. Meteor. Soc, 43, 29-32, 1986.

DeFelice, T.P. Saxena, V.K. and Yu, S.: On the measurements of cloud condensation nuclei at Palmer Station, Antarctica, Atmos. Environ., 31, 4039-4044, 1997.

DeMott, P.J. Prenni, A.J. Liu, X. Kreidenweis, S.M. Petters, M.D. Twohy, C.H. Richardson, M.S. Eidhammer, T. and Rogers D.C.: Predicting global atmospheric ice nuclei distributions and their impacts on climate, Proc. Natl. Acad. Sci. USA., 107, 11217-11222, 2010.

Fletcher, N.H.: The Phys. of Rainclouds, Cambridge University Press, Cambridge, U.K, 1962.

Geology.: Map of Antarctica and Southern Ocean, landsat image mosaic of Antarctica (LIMA) project. Retrieved April 17, 2010, from: http://geology.com.

Graf, H.F. Shirsat, S.V. Oppenheimer, C. Jarvis, M.J. Podzun, R. and Jacob, D.: Continental Scale Antarctic deposition of sulphur and black carbon from anthropogenic and volcanic sources, Atmos, Chem. Phys., 10, 2457-2465, 2010.

Gras, J.L. Adriaansen, A. Butler, R. Jarvis, B. Magill, P. and Lingen, B.: Concentration and size variation of condensation nuclei at Mawson, Antarctica, J. Atmos. Chem., 3, 93-106, 1985.

Hogan, A.W.: Meteorological transport of particulate material to the South Polar Plateau, J. Appl. Meteor., 18, 741-749, 1979.

Junge, K. and Swanson, B.D.: High-resolution ice nucleation spectra of sea-ice bacteria: implications for cloud formation and life in frozen environments, Biogeosciences. 5, 865-873, 2008.

Knuth, S.L. Gregory, J.T. Jonathan E.T. and George, A.W.: The Influence of Blowing Snow and Precipitation on Snow Depth Change across the Ross Ice Shelf and Ross Sea Regions of Antarctica, J. Appl. Meteorol. Clim., 49, 1306-1321, 2010.

Kumai, M.: Identification of nuclei and concentrations of chemical species in snow crystals sampled at South Pole, J. Atmos. Sci., 33, 833-841, 1976.

Lawson, R.P. Baker, B.A. Zmarzly, P. O'Connor, D. Mo, Q. Gayet, J.F. and Shcherbakov, V.: Microphysical and optical properties of ice crystals at South Pole Station, J. Appl. Meteor., 45, 1505-1524, 2006.

Lawson, R.P., Stamnes, K., Stamnes, J., Zmarzly, P., Koskuliks, J., Roden, C., Mo, Q., and Carrithers, M.: Deployment of a Tethered Balloon System for Cloud Microphysics and Radiative Measurements at Ny-Ålesund and South Pole, J. Atmos. Ocean. Tech., 28, 656-670, 2011.

Meyers, M.P. DeMott, P.J. and Cotton, W.R.: New primary ice nucleation parameterizations in an explicit cloud model, J. Appl. Meteor., 31, 708-721, 1992.

Saxena, V.K.: Evidence of biogenic nuclei involvement in Antarctic coastal clouds, J. Phys. Chem., 87, 4130-4134, 1983.

Saxena, V.K., and Weintraub, D.C.: Ice forming nuclei concentrations at Palmer Station, Antarctica In: Wagner, P.E. and Vali, G. (Eds): Atmospheric Aerosols and Nucleation, Springer-Verlag, New York, 1988.

Su, W.C. and Vincent, J.H.: Towards a general semi-empirical model for the aspiration efficiencies of aerosol samplers in perfectly calm air, J. Aerosol Sci., 35, 1119-1134, 2004.

Vali, G.: Filter - Elutriation experiments for the measurement of airborne freezing nuclei, J. de Rech. Atmos., 3, 175-177, 1968.

Vali, G.: Quantitative evaluation of experimental results on the heterogeneous freezing nucleation of supercooled liquids, J Atmos. Sci., 28, 402-409, 1971.

Warren, S.G. and Hudson, S.R.: Bacterial Activity in South Pole Snow Is Questionable, Appl. Environ. Microbiol., 69, 6340-6341, 2003.

NEW EVIDENCE FOR LIQUID AMORPHOUS WATER IN COLD CLOUDS

Anatoly N. Nevzorov

Central Aerological Observatory. Dolgoprudny 141700, Russsia
Email: an-nevzorov@yandex.ru; Website: www.anevzorov.com

●*The world-wide measurements with the high-sensitive Nevzorov LWC probe actually indicate that a liquid fraction is permanently present in virtually every piece of ice-containing stratiform clouds, thereby convincingly signifying its being in condensational equilibrium with ice. To argue against A-water conception by supporting the conventional Vegener – Bergeron – Findeisen mechanism of cloud phase formation, some authors assign this important data to a residual effect of ice on the LWC's cylinder-shaped hot sensor. This explanation proves to be inadequate as it is based on speculative, physically invalid quantitative estimation of this effect, wittingly meant only to achieve the preset result of "zero LWC".* ●*A comparison in various properties between a natural glory in clouds, theoretical models of glory formation on droplets with n=1.33 (ordinary water), and this with n=1.81 (liquid amorphous water, or A-water) evinces that the version with n=1.33 is inherently erroneous, while the true natural glory is actually produced by A-water droplets of >20 μm in diameter. Hence the presence of A-water droplets in clouds with T < 0°C appears as common as the occurrence therein of a colored ring around a shadow cast by a sun-lit airplane.* ●*Every like failure to negate the cloud A-water conception can thus be considered as an auxiliary convincing argument in favor of its validity.*

1. INTRODUCTION

In the current knowledge of the physics of cold (with temperatures below 0°C) clouds, the problems connected with the presence of a liquid water fraction in ice-containing clouds (ICC) remain both the least investigated and the most disputable. This concerns its nature, repeatability, and physical role in cloud processes. The conventional notions based on Vegener – Bergeron – Findeisen principles consider supercooled liquid water in mixed-phase clouds to be an unstable, short-lived substance. Meanwhile, more and more world-wide experimental data on the liquid fraction behavior in the ICCs furnishes increasingly more solid arguments against this conventional approach. Namely, they as a rule are clearly indicative of an abnormally steady coexistence of liquid and ice disperse phases. Moreover, in mixed-phase clouds most of liquid water tends to be contained in much larger droplets (>30 μm) than in purely water clouds (<30 μm).

Initially, similar data was referred to occasional ("case study") observations, whose results were only considered as an exception from the general rule, applicable to very rare situations. The results would then be explained by possible spatial isolation of each of the two phases, or by vapor super saturation over water, *e.g.* in ascending or turbulent air, and even by the specific chemistry of cloud water. The abnormally big sizes of ICC droplets – up to hundreds micrometers – were conventionally explained in terms of their coalescence growth. Theoretical researches in this area, *e.g.* by Korolev *et al.* (2006b, 2007), are as well concerned with specific dynamical processes, strictly time-limited by their relaxation, and is far from being able to explain the permanent character of a mixed-phase structure of usually quiet, long-live stratiform clouds.

In our aircraft measurements (Nevzorov, 1992, 2000), the large-droplet liquid fraction was found in practically all stratiform ICCs at temperatures from 0°C down to, at least, –55°C (in *Cirrus*). A thorough analysis of complex microphysical measurements and literary data available concerning insufficiently investigated problems of the physics of water and clouds at T<0°C, has led us to the following conclusion. The ICC liquid water considerably differs in its properties from the universally known ordinary water (hereinafter *water-1*), and is in a specific, amorphous phase, named *A-water*. The details of the analysis, a discussion of the properties of A-water, its nature, and its role in the physics of cold clouds are presented in the papers of Nevzorov (1993, 2006b, 2009). Most importantly, A-water is in stable condensation equilibrium with ice phase, and can directly condense and remain in its metastably liquid state even at temperatures below -40°C. Its refractivity, as specified by the value of n = 1.81÷1.82 for yellow light, corresponds to H_2O substance density of about 2.1 g.cm^{-3}.

Its specific evaporation heat is estimated to be approximately 5 times less than that of water-1.

The essentially novel and unusual results above were hard to obtain and remain hard to reproduce for technology reasons, all the more needing independent confirmation. So far the conception of cloud A-water is far from being generally acknowledged, and instead arouses open discussions and counterarguments (Korolev *et al.*, 2003a; Mayer and Emde, 2007; Romanov and Doubnichenko, 2010). The ideas put forward by these opponents are critically considered below.

2. LIQUID WATER OR ICE?

Numerous measurements in cold stratiform clouds using the IVO device, best known as Nevzorov TWC/LWC probe (Korolev *et al.*, 1998), invariably indicate the presence of a liquid phase in practically any ICC. Paradoxically, the data regularly obtained the world over contradicts Wegener – Bergeron – Findeisen principles those deny the possibility of ubiquity and permanent presence of liquid water droplets in clouds at T <0°C owing to physically proved processes of their freezing and recondensation on ice particles with the formation of stable purely ice clouds. This paradox still needs realistic explanation.

In the paper of Korolev *et al*. (2003a) and in consequent papers of same and other authors sharing the traditional notion of a single liquid state of water, that “anomaly” is considered as a residual effect of ice particles on the LWC’s hot collector. The estimation of “share of ice” in LWC readings W_L was made from measurements in clouds *a priory* taken as purely ice. In data of (Korolev *et al*., 2003a), the relation W_L / W_T where W_T is the TWC output, in instant readings showed a spread from 0 up to 1 often in the same cloud, while the cloud-averaged values varied between 0.1 and 0.5.

Such a significant and variable effect of ice particles on the streamline-shaped LWC collector can only be accounted for by no other reason than the assertion the authors of proceed from, and cannot be physically feasible. Indeed, in contrast to the surface-film mechanism of liquid droplet evaporation on colliding with the collector, any ice particle rises over its surface like a sail, and is instantly swept away by an air flow. This effect is promoted by the repulsion action of a thinnest layer of vapor formed between the contact spot of ice particle and the hot collector surface.

As early as in 1980s, we followed another approach to estimating the residual effect of ice on the LWC collector. On hundreds meters of visual records made at a rate of 2.5 mm/sec., the sites or sections with W_L = 0 at W_T > 0 were selected. For each of them the relation $R_0 = \Delta W_L / W_T$ was determined, where ΔW_L is possible absolute error caused by a "dry" drift of the LWC output. The minimal value R_0 = 0.03 thereby obtained implies that the real ice effect is at least less than the measurement error caused by the output drift.

Fortunately, in typical ICCs the main contribution to liquid A-water content (LAWC) is generally made by droplets of a large enough size and density (Nevzorov, 2009) to result in collection efficiencies close to unity for both sensor-collectors. This circumstance extremely simplifies the calculation of the cloud disperse phases content from the IVO outputs:

$$LWC = W_L\,, \tag{1}$$

$$IWC = \frac{E_I}{E_W}(W_T - W_L)\,, \tag{2}$$

$$LAWC = \frac{E_W}{E_{AW}}W_L\,. \tag{3}$$

Here E_x is the specific energy of evaporation of phase x. Based on own experience, we confidently assert that these working formulas are not only quite simple and obvious, but, in essence, the most adequate.

The experimental corroboration of the view shared by the authors of (Korolev *et al*., 2003) by means of comparing synchronous outputs of the IVO and the icing sensor RICE cannot be correct because of the essential difference in their threshold sensitivity to liquid phase. As theoretically evaluated by Mazin *et al.* (2001), the RICE sensitivity threshold must be about 10 mg^{-3}, while actually it is much higher, as can be seen from the example taken from (Korolev *et al.* ,2003) and shown in Fig. 1.

In Fig.1, the characteristic intervals of the records of both devices are positioned between the vertical lines. The intervals Nos 1, 3 and 5 correspond to the events where RICE indications (increase of icing of its sound pin) denote the presence of liquid water. It can be seen that they occur only when W_L values surpass 0.08÷0.1 g.m^{-3} (horizontal line). This value does be the true sensitivity threshold of RICE in the water-1 scale. It implies that RICE provides no information on the liquid phase at W_L less than ~0.1 g·m^{-3} and according to (3), at LAWC values less than 0.5 g·m^{-3}, i.e. in most of cold stratiform clouds (Nevzorov, 2009).

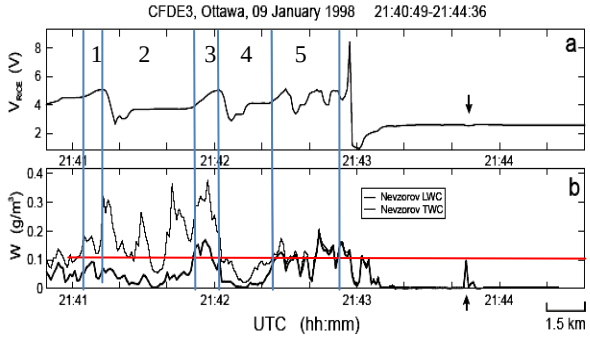

***Fig.1**. An example of simultaneous records of RICE (a) and IVO (b) probes. Copied from (Korolev et al., 2003)* and lined as in the text.

Note that the highest peaks within interval #2 in the IVO TWC record do not affect the behavior of the LWC record, which directly contradicts the declared “ice effect” on the LWC sensor.

Thus, only a single example of other similar ones seems to be enough to show the groundlessness of the speculative idea of distorting LWC measurement by the “ice effect”.

3. A-WATER AND GLORY

The most convincing confirmation of the existence and specific properties of A-water in the ICCs has been acquired from the analysis of an optical phenomenon of glory on cold clouds (Nevzorov, 2006, 2009). However in the papers by Mayer and Emde (2007) and Romanov and Doubnichenko (2011) our conclusion about glory formation on of A-water droplets is criticized on the main ground that its formation on water-1 droplets has already been proved. Really, a number of papers beginning from that by Hulst (1957), do consider this problem. They all follow similar methodologies and present similar results, which makes it possible to consider them together within a united virtual model of glory on spheres with n = 1.33.

This model is based on the notion that the glory always consists of several concentric rings. The theoretical descriptions of this phenomenon are largely focused on the relative position of the rings. Having failed to find any realistic explanations of the physical nature of secondary rings, van de Hulst (1957) has put forward an idea of “superficial waves” which supposedly deflect the beams tangentially incident onto a spherical surface, by a small discrete angle. Despite the absence of a sound proof, and for lack of any alternative approach, this idea is still supported by some authors.

In fact, all observations of natural glory (see *e.g.* photos in Internet) show that far not always the external rings do accompany the ring of the glory itself. If occurring, their number rarely reaches a mere two; they are much weaker and successively decreasing in brightness, In other words, the abstract notion of secondary rings as an integral attribute of the glory is not true in fact, and thus the hypothesis of "superficial waves” does not actually make sense.

Calculations by Mie theory of a backscattering indicatrix at n = 1.33 yield ambiguous results. In (Mayer and Emde, 2004) as well as in papers of some other authors, harmonic oscillations are revealed in the form of attached "ripple", adjacent to the peak on the indicatrix as shown in Fig.2 copied from the cited paper. Their peaks are interpreted as belonging to glory rings. Meanwhile, in our calculations with similar conditions no such oscillations have arisen as shown in Fig.3.

This distinction allows an explanation such as follows. The rigorous Mie theory solution for each combination of the scattering angle θ, the diffraction parameter x, and the refractivity n of glory-forming particles is the sum of infinite and weakly convergent sign-variable series. In common real practice, the number, N, of the summands in a series is limited. When N value is fixed, the residual series Δ (the difference between the sums of truncated and infinite series) is naturally harmonically de-

pendent on all the parameters, including the scattering angle θ. The dependence of both amplitude and period of Δ fluctuations on the angle θ and droplet size range (Fig.2) is nothing but a purely mathematical effect. Thus the theoretical glory model under consideration does not build upon Mie theory alone, but also allows for a sign-alternative computational error.

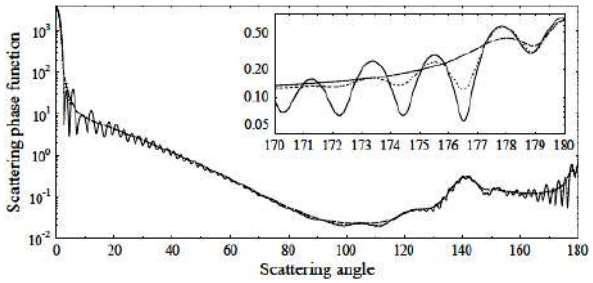

***Fig.2**. Full indicatrix of light scattering by 12 μm sphere as calculated by Mayer et al. (2004). The "ripples" on the graph result from the truncation of Mie series, i.e. are in fact the calculation error.*

Our Mie calculations were made with the computer program developed by Petrushin (1989), where the number N of summands in every point of θ is not fixed, but increases until the residual Δ becomes less than the desired low value. This algorithm permits model results to be as close to rigorous Mie theory as possible.

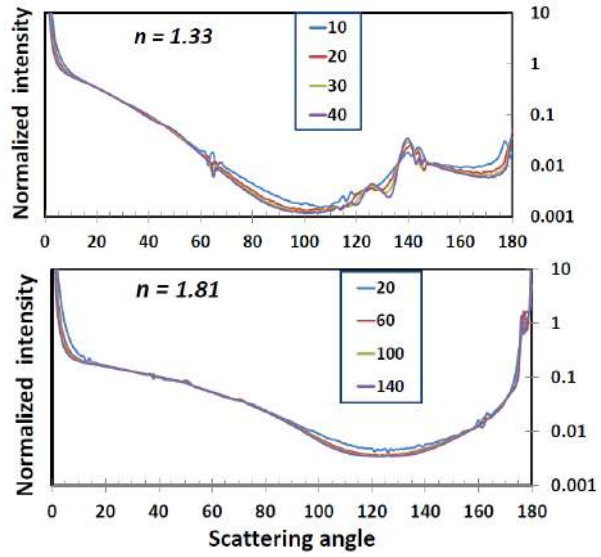

***Fig.3**. Scattering indicatrixes for spheres with n=1.33 (top) and n=1.81 of diameters (μm) given in the legends. Calculated by the Petrushin program.*

In Fig.3 the results of the calculation of full scattering indicatrixes for monodisperse droplets with n = 1.33 and n = 1.81 are shown. The absence of the characteristic "ripples" as in Fig.2 on the graphs of Fig.3 confirms their abovesaid “artificial” nature.

All the functions of relative scattering intensity in Fig.3 are normalized to the light flow per a droplet optical section, and plotted on the same logarithmic scale.

It is important that a distinct visual image of the backscattering phenomenon is formed not in the whole depth of cloud body, where diffuse (multiple) scattering suppresses directed beams, but in its frontier layer with effective optical thickness of no more than an unity. This implies that the droplet collectives directly responsible for the image formation are of identical total cross-section areas irrespective of droplet refractivity, size, and concentration. Hence it follows from Fig.3 that the glory on A-water in ICCs must be almost two orders brighter than on water-1 clouds.

Note that on the scattering indicatrixes for n=1.33 (Fig.3) the rainbow peak at θ~140° is not less in height than that at θ~180° with droplet diameter being of more than 5 ÷ 10 μm. This implies that glory if occurring on a cloud containing water-1 droplets must be accompanied by a concentric luminous ring with its angular radius of about 40°. In fact, the natural glory is extremely rarely accompanied by such a ring which, when occurs, informs of the temporary simultaneous presence of both liquid disperse phases in a cloud.

The details of the indicatrixes of yellow (λ = 0.58 μm) light scattering by the droplets of different nature and size within the angle range, adjacent to 180° and including the glory peaks, are plotted in Fig.4 and Fig.5 on same linear scale for both models. The experimental limits are marked of variability by Nevzorov (2006a) of the radial angles of natural glory. As before, no peak corresponding to additional ring around a natural glory was found on the indicatrixes for both models. In view of their incidental occurrence, variability in brightness, and certain geometric features, it is inferred in (Nevzorov, 2006a) that they are created by the peaks of secondary forward scattering of glory-forming beam by cloud ice crystals of specific shapes.

The calculations reveal a great difference between the two virtual models. First

of all, it is in unlike dependence of the peak angle on droplet diameter.

The model with n=1.33 (Fig.4) is essentially restricted in feasibility by the requirement that a cloud consists only of almost monodisperse droplets of ~8 to ~16 μm modal diameter. In fact, as follows from a great number of experimental data available, the probability of occurrence of such tropospheric clouds is at least quite negligible as compared with the natural glory on high clouds.

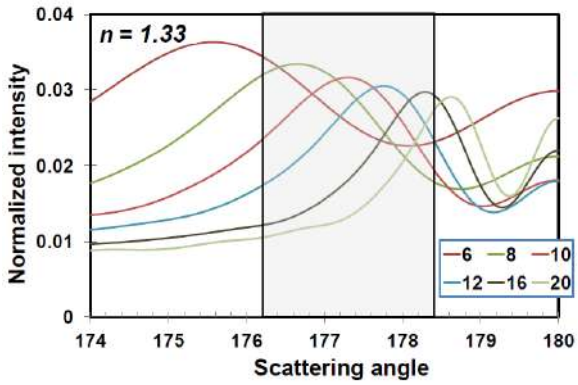

Fig. 4*. Zoom pieces of backscattering indicatrixes for sphere diameters as in the legend, at n = 1.33.*

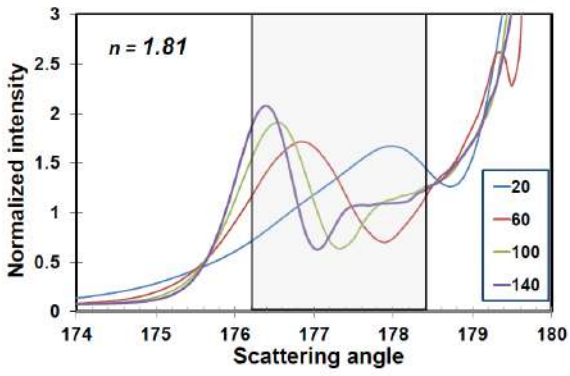

Fig 5*. As in Fig.4, for n=1.81.*

At n=1.81 (Fig.5) a single backscattering peak of an indicatrix appears with droplet diameter exceeding somewhat less than 20 μm. All peaks of >20 μm droplets go into the angle variability range of natural glory, By their absolute height over the background, these peaks surpass the peaks in the 1.33-model by as much as almost two orders. With droplet size increasing, the peak becomes narrower and higher, its scattering angle decreasing. In addition, the presence of droplets <20 μm and ice crystals in a glory-forming cloud layer is able to noticeable obscure the image. Indeed, smallest natural glories look as a rule much more pallid. All this is why the visible (angular) size, brightness, and color contrast of the natural glory as observed are in general directly correlated.

Unlike this, the n=1.33 model doesn't follow those natural glory features as well.

In the nature, only a single type of glory occurs as respect to its definition and properties. And it is only in cold clouds where even a portion of liquid droplets can steadily coexist with the ice fraction, the conditions favor the formation of the optical phenomenon called "glory". Thus the glory phenomenon is intimately connected with A-water, signifying its presence in a cloud. The experimental example presented in (Mayer et al., 2004) cannot be sufficient to prove the opposite, because of cloud temperature and phase structure omitted, whereas the brightness contrast and spatial stability of the phenomenon described fitting the inherent features of glory on a cold stratiform cloud.

It seems obvious that the presence of A-water droplets in ICCs appears as common as the occurrence of a colored ring around a shadow cast by a sun-lit airplane..

4. CONCLUSION

The problem of the occurrence, dynamics and properties of a liquid disperse phase in cold (with $T < 0^{o}$C) and especially ice-containing clouds is one of the most important, but at the same time the least studied and the most disputable of all topical problems in cloud microphysics. The lack of key experimental data required for its solving gives rise to speculative conceptions and theories. In spite of the fact that such abstract reasoning builds upon the commonly assimilated utilitarian knowledge of water properties and classical ideas of Vegener – Bergeron – Findeisen in the physics of phase-mixed clouds, it fails to explain even more frequently observed anomalies of liquid phase behavior in cold stratiform clouds. In any event, our high-sensitive measurements of cloud phase components have managed not only to detect such anomalies, but also to prove that practically all cold clouds are of mixed phase.

Logically, the futility of the attempts to explain the nature of such anomalies on an

aprioristic classical basis must lead one to dismiss habitual dogmas and seek for new solutions. Our recent research has revealed specific properties of liquid disperse phase in ICC that distinguish it from the ordinary supercooled water. In particular, its condensation equilibrium with ice is a true reason of stable coexistence of liquid and ice fractions in a cloud. The established set of physical properties of the substance of amorphous water (A-water) droplets helps, on the physical basis alone, to fill almost every gap in the ICC microphysics without sophisticated theoretical reasoning.

We have considered the most notable arguments against our finding of the existence of liquid amorphous water in natural cold clouds. These arguments refer to different aspects of the phenomenon, but follow the same logic, proceeding from such assumptions that wittingly lead to expected orthodox results, thus supposedly supporting a preconceived position of the opponents. Unfortunately, this artificial approach (*apropos*, not so infrequent in science) builds upon dogmatic statements that may actually be or prove objectively wrong.

Here we tried to prove that every failure to negate or ignore the A-water conception in the microphysics of cold clouds can thus be considered as an auxiliary convincing argument in favor of its validity.

To finalize, the author is hopeful that the critical analysis presented above is sufficiently justified, objective and convincing.

5. REFERENCES

Hulst, van de, H.C., 1957. Light scattering by small particles. John Wiley: New York, US,

Korolev A.V., Strapp J.W., Isaac G.A., Nevzorov A.N., 1998. The Nevzorov airborne hot wire LWC/TWC probe: principle of operation and performance characteristics. – J. Atm. and Oceanic Techn., 15, No 6, 1495–1510.

Korolev, A. V., G. A. Isaac, S. Cober, J. W. Strapp, J.Hallett, 2003a. Microphysical characterization of mixed phase clouds. Quart. J. Roy. Meteorol. Soc.,129, 39-66.

Korolev, A. V., G. A. Isaac, 2003b. Phase transformation in mixed phase clouds. Quart. J. Roy. Meteorol. Soc.,129, 19-38.

Korolev, A V., Field P., 2007. The effect of dynamics on the formation of mixed phase clouds (theoretical considerations). J. Atm. Sci.,65,

Mazin, I. P., A.V. Korolev, A. Heymsfield, G.A. Isaac, and S.G. Cober, 2001. Thermodynamics of icing cylinder for measurements of liquid water content in supercooled clouds. J. Atmos. Oceanic Technol., 18, 543-558.

Mayer B., Schröder M., Preusker R., Shüller L., 2004: Remote sensing of water cloud dropletlet size distribution using the backscattering glory: a case study. Atmos. Chem. Phys. 4, p. 1255–1263

Mayer B., Emde K., 2007: Comment on "Glory phenomenon informs of presence and phase state of liquid water in cold clouds" by Anatoly N. Nevzorov. Atmos. Res., 84, No 4, p. 410-419.

Nevzorov A. N., 1992. Permanence, properties and nature of liquid phase in ice-containing clouds. – 11th Int. Conf. on Clouds and Precipitation, Montreal, Canada, p. 270–273.

Nevzorov A. N., 1993. Researches on physics of a liquid phase in ice-containing clouds. Meteorology and hydrology, No 1, 55-68.

Nevzorov A.N., 2000: Cloud phase composition and phase evolution as deduced from experimental evidence and physico-chemical concepts. – 13th Int. Conf. on Clouds and Precipitation, Reno, Nevada, USA, p. 728–731.

Nevzorov A. N., 2006a: Glory phenomenon informs of presence and phase state of liquid water in cold clouds. – Atm. Res., 82, Nos 1–2, p. 367–378.

Nevzorov A. N., 2006b: Some properties of metastable states of water. – Phys. of Wave Phenomena, № 1, p. 45–57.

Nevzorov A.N.,2009. Liquid-state water bimorphism in cold atmospheric clouds. In: "Atmospheric Science Research Progress", New York, Nova Sci. Publ., 15–58.

Petrushin A.G., 1989. Transformation matrix for components of an electric field of radiation scattered by a dielectric sphere at angle of θ= 90°. Trudy Inst. Exp. Meteor., issue 139, 59-63 (in Russian).

Romanov, N.P., Doubnichenko S.O., 2010. The physics of forming and analytical description of glory properties. Optika Atm. Okeana, 23, No 7, 549-560 (in Russian).

ASSESSMENT OF THE EFFECTS OF ACID-COATED ICE NUCLEI ON THE ARCTIC CLOUD MICROSTRUCTURE, ATMOSPHERIC DEHYDRATION, RADIATION AND TEMPERATURE DURING WINTER

E. Girard[1], G. Dueymes[1], P. Du[1], A.K. Bertram[2]

[1]Department of Earth and Atmospheric Sciences, University of Quebec at Montreal, Montreal, Quebec, Canada
[2]Department of Chemistry, University of British Columbia, Vancouver, British Columbia, Canada

1. INTRODUCTION

Wintertime cloud cover in the troposphere over the Arctic ranges between 40 to 50% (Wyser *et al.*, 2008), and low-level mixed phase clouds and optically thin ice clouds dominate. Thin ice clouds are difficult to detect by passive imagery and this results in a substantial underestimation of cloud cover (Curry *et al.*, 1996; Wyser and Jones, 2005; Karlsson and Dybbroe, 2010). Grenier *et al.* (2009) have shown that there are two types of optically thin ice clouds. The first one is formed by a large concentration of small ice crystals and the second one is formed by larger precipitating ice crystals in smaller concentration. The latter cloud type is correlated with aerosol concentration (Grenier et al., 2009). These results suggest that there might be a relationship between the second type of thin ice clouds and large aerosol concentrations possibly of anthropogenic sources.

The Arctic is highly polluted during the cold season with high concentrations of aerosols often observed (Schnell, 1984, Yli-Tuomi *et al.*, 2003, Law and Stohl, 2007). These aerosols, which are mainly emitted over northern European cities, China, and Siberia (Shaw, 1995), are transported from the mid-latitudes to the Arctic by large-scale atmospheric circulations (Bourgeois and Bey, 2011, Fisher *et al.*, 2011, Barrie *et al.*, 1989, Shaw, 1995). This transport is favoured by the southward progression of the polar front during winter in the Northern Hemisphere. Anthropogenic aerosols are emitted north of the front in an environment with little precipitation, resulting in limited loss of aerosols by wet deposition. The aerosol component consists of a significant fraction of highly acidic sulphate, and previous work has shown that most of the submicron aerosol particles are coated with this highly acidic sulphate (Bigg, 1980, Cantrell et al., 1997).

Laboratory experiments and field observations suggest that acid coatings on ice nuclei (IN) can have an important effect on heterogeneous ice nucleation, which can occurs either in the deposition, condensation-freezing, immersion and contact modes (Pruppacher and Klett, 1997). In the immersion mode, ice nucleation occurs on a solid particle immersed in either an aqueous solution in subsaturated air with respect to liquid water or in an activated cloud water droplet. In the condensation-freezing mode, ice nucleation occurs on a solid particle immersed in an aqueous solution and above liquid water saturation. In the deposition mode, ice nucleation occurs on a solid particle or a solid particle only partially immersed in an aqueous solution. Finally, in the contact mode, ice nucleation occurs on a solid particle in contact with a water droplet.

Archuleta *et al.* (2005) have shown that the decrease of ice nucleation at temperatures below -40^0C by immersion and condensation modes due to sulphuric acid coating is variable and depends on the IN chemical composition. Other laboratory experiments performed at temperatures ranging between –10 and -40^oC also show that the heterogeneous freezing temperature

initiated by immersion of various mineral dust particles decreases as the percentage by weight of sulphuric acid in the particle increases (Ettner *et al.*, 2004). More recently, Eastwood *et al.* (2009) have shown that deposition ice nucleation on kaolinite particles is considerably altered at temperatures below 243K, requiring an additional 30% ice supersaturation for ice nucleation to occur when compared to uncoated particles. According to Sullivan *et al.* (2010a), the de-activation effect of sulphuric acid on dust particle is irreversible and is still active once the acid has been neutralized with ammonia. Chernoff and Bertram (2010) have shown that other coatings such as ammonium bisulphate also increases the onset relative humidity for ice nucleation when compared to uncoated dust particles but to a lesser extent than sulphuric acid coating. Other laboratory experiments on coated and uncoated mineral dust particles have been performed by Knopf and Koop, (2006), Salam *et al.* (2007), Cziczo *et al.* (2009), Niedermeier *et al.* (2010), and Sullivan *et al.* (2010b). The coating effect on ice nucleation was also indirectly observed during the Arctic Gas and Aerosol Sampling Program (AGASP) by Borys (1989). In this study the authors showed that the IN concentration is decreased by 3 to 4 orders of magnitude during highly polluted (Arctic haze) events (Borys, 1989). While deposition ice nucleation seems strongly affected by acid coating, immersion freezing of activated cloud water droplets does not seem to be affected (Sullivan et al., 2010b).

Blanchet and Girard (1994; 1995) were the first to hypothesize that the ice nucleation inhibition effect of acid coatings on aerosols can have an important effect on cloud microstructure and on the surface energy budget during winter in the Arctic. According to their hypothesis, the decrease of the IN concentration leads to the formation of fewer but larger ice crystals. This process leads to the formation of optically thin ice clouds recently identified by Grenier *et al.* (2009). Acid coating on IN and the resulting larger ice crystals dehydrate the troposphere by increasing the precipitation over large areas. This results in the decrease of the greenhouse effect due to the strong effect of water vapour, primarily in the broad rotational band in the far infrared. The reduced greenhouse effect further promotes dehydration and cooling (Blanchet and Girard, 1995; Curry *et al.*, 1995). This hypothesis is referred to as the dehydration-greenhouse feedback.

This process was first evaluated by Girard *et al.* (2005) using a single-column model. They simulated 4 cold seasons over Alert (Canada) using observed aerosol composition and concentration. The acid aerosol scenario shows a tropospheric cooling ranging between 0 and 2K when compared to an uncoated aerosol scenario. Girard and Stefanof (2007) have used a regional climate model with prognostic aerosols to evaluate the effect of acid aerosols on the Arctic surface radiative budget for February 1990. They have assumed 2 aerosol scenarios: (1) an acid scenario in which the reduction of the IN concentration depends on the sulphate concentration and (2) a natural aerosol scenario in which the IN concentration is unaltered. Their results show an increase of precipitation and dehydration of the troposphere and up to 3K in cooling in the coldest part of the Arctic.

In these previous investigations, the acid aerosol scenario was treated rather subjectively and crudely since few laboratory studies on the effects of coating on ice nucleation were available. The decrease of IN concentration due to acid coating was a function of the sulphate concentration using an exponential function and was based on Borys (1989) observations of IN decrease in polluted events. The choice of an exponential function was made to produce substantial IN reduction for cases where the sulphate concentration was large. Furthermore, it was assumed that all ice nucleation modes were altered equally by the presence of acid coatings. Finally, the one-moment microphysics scheme used in

the Girard and Stefanof (2007) investigation was relatively simple with no detailed representation of the ice crystal sedimentation process.

This research aims to refine the representation of the effects of acid coating on IN to get a more realistic evaluation of the potential effect of anthropogenic aerosols on arctic wintertime clouds and radiation budgets. Laboratory data from Eastwood *et al.* (2008; 2009) on ice nucleation properties of uncoated and sulphuric acid-coated kaolinite particles are used to develop a more physically-based and refined parameterization of ice nucleation in sub-saturated air with respect to liquid water. This new treatment of heterogeneous ice nucleation is implemented into an elaborate two-moment cloud microphysics scheme.

2. MODEL DESCRIPTION

The limited-area version of the Global Environmental Multiscale (GEM) Model is used in this study. A detailed description of GEM can be found in Côté et al. (1998). The microphysics scheme used in this study is from Milbrandt and Yau (2005). Two versions of this scheme are available in GEM-LAM (single and double moments). In this study, we use the two-moment version. The scheme includes the following prognostic variables: the mixing ratio and the number concentration of cloud liquid water, cloud ice water, rain, snow, hail and graupel. The description of the various microphysical processes is available in Milbrandt and Yau (2005). In this section, the emphasis is put on the parameterization of ice crystal nucleation due to the importance of this microphysical process in this investigation.

Homogeneous freezing of cloud liquid droplets is based on the parameterization of DeMott *et al.* (1994) in which the ice nucleation rate is a polynomial function of temperature. The fraction of cloud droplets that freeze homogeneously gradually increases from 0 at -30^{o}C to 1 at -50^{o}C. Therefore, both homogeneous and heterogeneous freezing processes can occur simultaneously in this temperature range. Contact freezing is parameterized following Young (1974), in which the number concentration of contact IN is parameterized as a function of temperature. Immersion freezing of activated rain and cloud water droplets follows the parameterization of Bigg (1953). The representation of heterogeneous ice nucleation by water vapour deposition and condensation freezing is particularly important in this investigation. In the original version of the Milbrandt and Yau (2005) microphysics scheme, deposition and condensation freezing depends on the ice supersaturation following the empirical relationship of Meyers *et al.* (1992). This parameterization for deposition ice nucleation has been modified to distinguish ice nucleation on sulphuric acid-coated IN from ice nucleation on uncoated IN.

The new parameterization for ice nucleation in subsaturated air with respect to liquid water is based on the classical theory of heterogeneous ice nucleation of Fletcher (1962). The new parameterization can represent both deposition nucleation on uncoated IN and immersion freezing of haze droplets in subsaturated air with respect to liquid water which will be referred to as the deposition-immersion nucleation mode in this study. It is assumed that the surface of the ice nuclei is energetically uniform for ice nucleation. The only additional unknown parameter is the contact angle (Θ) between the ice embryo and the IN. Following the single contact angle approach (Chen et al., 2008; Chernoff and Bertram, 2010; Eastwood et al., 2008, 2009; Fornea et al., 2009; Hung et al., 2003), the contact angle has been derived using the results of the laboratory experiments of Eastwood *et al.* (2008; 2009) for uncoated kaolinite particles ($\Theta_{uncoated}$=12^{o}) and for kaolinite particles

coated with sulphuric acid (Θ_{coated}=27°). The following equation is then used to determine the number of ice crystals (N_{ice}) nucleated in a given time step (Dt):

$$N_{ice}(\Delta t) = N_{kaolinite}\left[1 - \exp(-JA_{kaolinite}\Delta t)\right] \quad (1)$$

where $A_{kaolinite}$ is the surface area of the kaolinite particles, $N_{kaolinite}$ is the total concentration of kaolinite particles and J is the nucleation rate of ice embryo per unit area of the particle and is defined as:

$$J(cm^{-2}s^{-1}) = B\exp\left(\frac{-\Delta G*}{kT}\right) \quad \text{where}$$

$$\Delta G* = \frac{16\pi\sigma_{iv}^3 f(\cos\Theta)}{3\left(\rho_i R_v T \ln S_i\right)^2}$$

where B is the pre-exponential factor (Pruppacher and Klett, 1998), ΔG* is the critical Gibbs free energy for the formation of an ice embryo, k is the Boltzman constant, σ_{iv} is the surface tension between ice and water vapour, r_i is the bulk ice density, R_v is the gas constant for water vapor, T is the temperature and S_i is the saturation ratio with respect to ice. $f(\cos\Theta)$ is a function that depends on the contact angle as defined by Pruppacher and Klett (1998) for an infinite plane surface.

3. DESIGN OF THE EXPERIMENT

The months of January and February 2007 are simulated. This choice was motivated by the fact that the transport of aerosols was particularly effective during this time period with the presence of a series of uncommon strong extra tropical storms over the North Atlantic and Northern Europe (Fink *et al.*, 2009). These storms have contributed to enhance the transport of pollution emitted over Northern Europe and Siberia to the Arctic. Two aerosol scenarios are considered. In the first scenario (hereafter aerosol scenario A), it is assumed that dust particles are uncoated. In the second aerosol scenario (hereafter aerosol scenario B), dust particles are coated with sulphuric acid. The appropriate contact angle for deposition-immersion ice nucleation (see previous section) is used in each aerosol scenario. Note that the same parameterizations for contact freezing and immersion freezing of activated cloud water droplets are used for both aerosol scenarios. Since the model does not simulate explicitly the aerosol composition and concentration, it is assumed that the concentration of dust particles is constant in time and space with a value of 0.38 cm^{-3}. This value is based on observations taken during field experiments in the Arctic, which shows variable dust mass concentrations ranging between 50 ng m^{-3} and 3000 ng m^{-3} (Winchester *et al.*, 1984; Franzén *et al.*, 1994) depending on the air mass origin. The assumed number concentration of dust particles ($N_{kaolinite}$) and surface area of kaolinite particles ($A_{kaolinite}$) in our simulations corresponds to a mass concentration of 500 ng m^{-3} and a diameter of 0.5 μm. The chosen concentration is representative of the dust concentration over the Arctic during winter (Quinn *et al.*, 2007).

The integration domain is centred over the Arctic and covers all areas north of 50° N, which include most of Europe, North Asia, Northern Canada, Siberia, and the North Atlantic and Pacific Oceans. The simulation domain has 364 by 304 grid points with a horizontal resolution of 0.25°. There are 53 vertical levels with the highest resolution in the lower troposphere. Initial and boundary conditions for atmospheric fields are provided by the European Centre for Medium-range Weather Forecast (ECMWF) ERA-Interim reanalysis on a 2.5° by 2.5° longitude/latitude grid. Monthly mean sea surface temperature and sea ice concentration are from the Atmospheric Model Intercomparison Project (AMIP II) (Hurrel et al., 2008) reanalysis on a 1° by 1° grid. These values are interpolated on the grid used for our simulations.

4. RESULTS

4.1 Cloud microstrucutre

Figure 1 shows the JF mean liquid and ice water path anomaly (an anomaly is defined as the difference between aerosol scenarios

B and A). Over the Arctic, the ice water path is generally slightly smaller in aerosol scenario B compared to aerosol scenario A except for small isolated areas where it is larger. Over the mid-latitudes and sub-Arctic regions, the ice water path anomalies are also negative and larger (absolute values). The increase of the liquid water content is the largest in the lower troposphere at about 850 hPa. This is the height corresponding to the highest occurrence of mixed-phase clouds (discussed at the end of this section). However, the increase of the liquid water path is also positive higher in the troposphere up to 600 hPa. The decrease of the ice water content in aerosol scenario B spreads over the whole troposphere from the surface to 300 hPa with a maximum at 500 hPa.

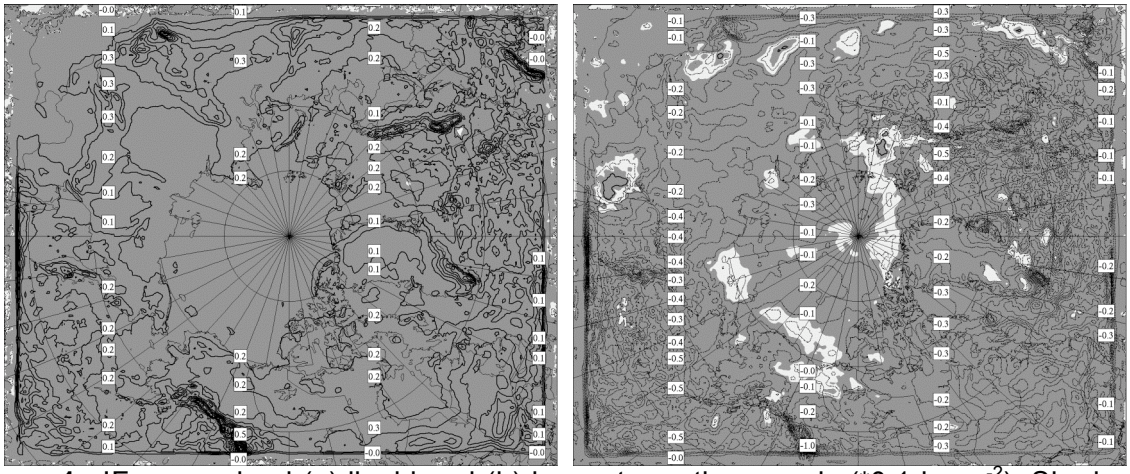

Figure 1: JF mean cloud (a) liquid and (b) ice water path anomaly (*0.1 kg m^{-2}). Shadowed areas indicate that anomalies are statistically significant with a confidence level of 95%. (after Girard et al., 2012)

Figure 2 shows the spatial and temporal average of the vertical profile of the ice crystal number concentration and mean diameter. Below 500 hPa, the ice crystal number concentration is smaller and the ice crystal mean diameter is larger in aerosol scenario B. This result is consistent with the hypothesis formulated in the previous section. However, above 500 hPa, the ice crystal number concentration increases and the mean diameter of ice crystals decreases in aerosol scenario B.

The different effects of acid coating on cloud microstructure above and below 500 hPa is related to temperature. At the upper levels, above 500 hPa, temperatures are generally below -40^{o}C. At these temperatures, the homogeneous freezing rate of cloud water droplets is relatively large. In these conditions, the decrease of ice nucleation in the deposition-immersion mode in aerosol scenario B leads to the formation of more water droplets. A large fraction of them freeze homogeneously as soon as they are nucleated. This results in an increase of the ice crystal concentration and a smaller mean ice crystal diameter in aerosol scenario B. In aerosol scenario A, the nucleation rate of ice crystals in the deposition mode prevents the saturation ratio to reach the saturation point with respect to liquid water as often as in aerosol scenario B. The concentration of ice crystals remains smaller when compared to aerosol scenario B since the contribution of homogeneous freezing of water droplets is much smaller in this scenario.

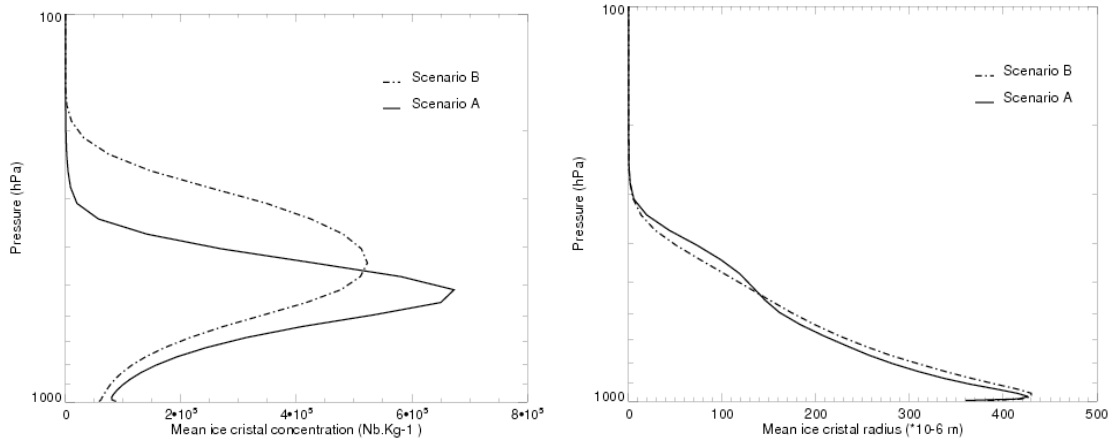

Figure 2: Vertical profiles of cloud ice crystal (a) number concentration (kg^{-1}) and (b) mean radius (mm) for aerosol scenarios A and B averaged over time and spatially averaged over a mask delimited by sea ice boundaries (after Girard et al., 2012).

Below 500 hPa, the JF mean air temperature remains mostly above -40°C over much of the Central Arctic. The homogeneous freezing of water droplets is not dominant at these temperatures. The Central Arctic is characterized by the presence of either anticyclones or cold decaying low-pressure systems in which very weak ascents or subsidence of air prevail. In such an environment, deposition ice nucleation can be significant since the air mass slowly cools by infrared radiation and thus can stay long periods of time oversaturated with respect to ice but sub-saturated with respect to liquid water. In aerosol scenario A, the nucleation rate of ice crystals by water vapor deposition is larger than in aerosol scenario B. Ice crystals are therefore smaller compared to aerosol scenario B since more ice crystals can absorb the available water vapor.

In aerosol scenario B, the heterogeneous ice nucleation rate is much smaller when the atmosphere is sub-saturated with respect to liquid water. This results in a smaller concentration of larger ice crystals as shown in **Figure 2**. The reduced concentration of ice crystals in this scenario has also a consequence on the mean relative humidity with respect to ice (RHi). The total flux of water vapor onto the existing ice crystals is smaller, thus allowing the relative humidity to increase. **Figure 3** shows the JF mean relative humidity with respect to ice (RHi) anomaly at 850 hPa.

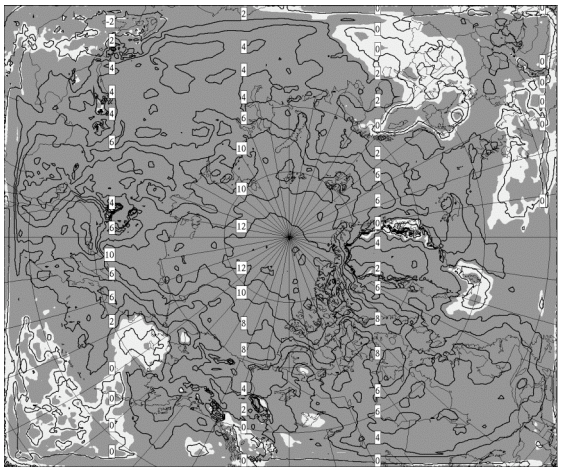

Figure 3: JF mean relative humidity with respect to ice (%) at 850 hPa anomaly. Shadowed areas indicate that anomalies are statistically significant with a confidence level of 95% (after Girard et al., 2012)

The RHi increase in aerosol scenario B is the largest over the Arctic, Siberia and Northern Canada where the temperatures are the coldest. The JF RHi anomaly at 850 hPa reaches values up to 14% in the Canadian and Central Arctic. Although smaller, a RHi increase is also

obtained higher in the troposphere (not shown). It is noteworthy to mention that the positive RHi anomaly covers more or less the Arctic air mass, characterized by the persistence of cold decaying lows and anticyclones. This suggests that weak cooling rate associated to either weak air ascent and/or infrared radiative cooling is a necessary condition for acid coating on IN to have an effect on cloud microstructure through RHi increase. At lower latitudes, synoptic systems are more active and air ascent velocity is larger. In these conditions, the air cooling rate is much larger when compared to the Arctic air mass. Consequently, ice nucleation in sub-saturated air with respect to liquid water is not as important since the ice crystal concentrations are typically not large enough to deplete the available water vapor. Therefore, in both aerosol scenarios, large RHi values are reached and the cloud microstructure is similar. This explains why the RHi anomalies are close to 0 south of the Arctic front.

Figure 4 shows the JF mean frequency of mixed-phase clouds for both aerosol scenarios at 850 hPa and the difference between scenarios B and A (the anomaly). In both aerosol scenarios, the frequency of mixed-phase clouds is very large over Northern Europe and Northeastern Asia, where the Icelandic and Aleutian lows respectively are predominant. These baroclinic zones are characterized by the development of low-pressure systems with strong vertical ascents. Therefore, the effect of deposition ice nucleation is negligible. This is why the differences between both aerosol scenarios over these two areas are relatively small. However, differences are much larger in the Arctic air mass, which corresponds to the region where the RHi increase in aerosol scenario B is the largest. In aerosol scenario A, the frequency of mixed-phase clouds in the Arctic air mass varies between 0 and 20% compared to a frequency ranging between 30% and 50% for aerosol scenario B. The mixed-phase cloud frequency anomaly is positive at all levels between 600 hPa and the surface (not shown).

4.2 Radiation and temperature

The energy budget at the surface and at the top of the atmosphere (TOA) is mostly driven by terrestrial radiation owing to the quasi-absence of solar radiation during January and February. The net infrared radiation at the surface or at the TOA strongly depends on the presence of clouds and their microphysical properties. According to Shupe and Intrieri (2004), the downward longwave radiation at the surface can increase by as much as 40 Wm^{-2} if liquid water is present in low-level arctic clouds compared to an ice cloud. Modeling studies have also shown a large sensitivity of infrared radiation fluxes to cloud microstructure (e.g. Du *et al.*, 2011, Simjanovski *et al.*, 2011). It is therefore expected that changes induced by acid coating on the cloud microphysical properties in aerosol scenario B will have an impact on the energy budget both at the surface and at the TOA.

To estimate the effect of clouds on the radiation budget, cloud radiative forcing (CRF) was proposed by Ramanathan *et al.* (1989) to characterize the cloud effect on the net radiation either at the surface or at the TOA. CRF is defined as the difference between the net radiative flux in the presence of clouds and the net radiative flux without the presence of clouds. It can also be separated into its longwave and shortwave components. **Figure 5** shows the JF mean CRF anomaly at the TOA. In our analysis, only the longwave componennet of the CRF is discussed since the shortwave radiation is quasi absent during winter. In both aerosol scenarios, the CRF is positive with smaller values varying between 0 and 20 W m^{-2} over the Arctic and higher values of up to 60 W m^{-2} south of the Arctic air mass (not shown). The CRF anomaly at the TOA is negative over most of the Arctic with

values ranging between 0 and -6 W m^{-2}. Relative to the CRF absolute values of about 20 W m^{-2}, the CRF anomalies represent a substantial reduction of the CRF at the TOA.

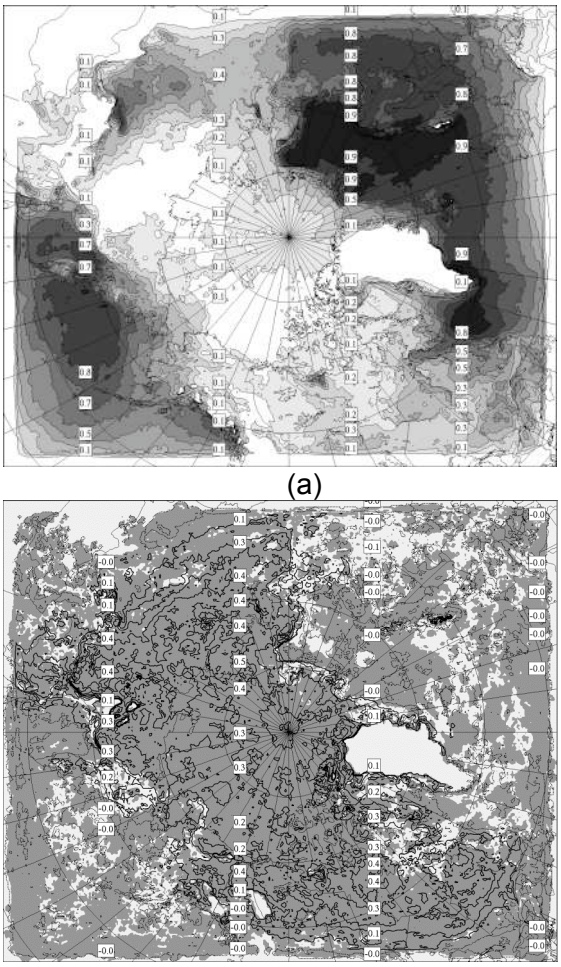

(a)

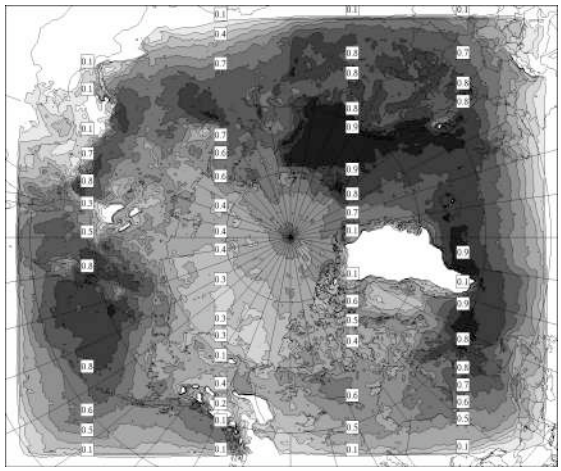

(b)

(c)

Figure 4: JF mean mixed-phase cloud frequency at 850 hPa in aerosol scenarios (a) A, (b) B and (c) the anomaly. In (c), shadowed areas indicate that anomalies are statistically significant with a confidence level of 95% (after Girard et al., 2012).

Mixed-phase clouds are mostly located in the lower troposphere. Their temperatures are warmer than the surface skin temperature. Therefore, the presence of these clouds leads to an increase of upward longwave radiation emission when compared to the surface. Assuming the same amount of mid and upper level ice clouds, the increase of low-level liquid (or mixed) phase clouds will enhance the CRF at the TOA.

In aerosol scenario B, the increased frequency and optical thickness of mixed-phase clouds combined to the reduced cloud optical thickness in the mid and high troposphere contribute to increase the upward infrared radiation fluxes at the TOA.

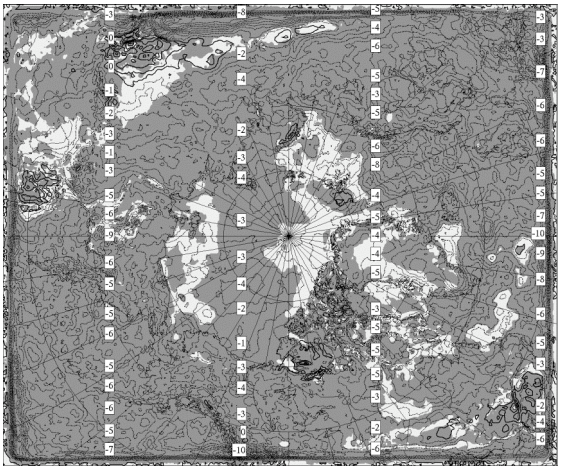

Figure 5: JF mean cloud radiative forcing (W m^{-2}) at the TOA anomaly. Shadowed areas indicate that anomalies are statistically significant with a confidence level of 95% (after Girard et al., 2012).

Figure 6 shows the JF mean air temperature anomaly at 1000, 850 and 500 hPa. The Central Arctic is colder in aerosol scenario B with a decrease of the temperature by up to -3K near the surface. This cooling, which spreads over much of the Arctic air mass, is also obtained higher in the troposphere with values ranging from -2K to -4K at 850 and 500 hPa . Enhanced atmospheric cooling in aerosol scenario B also leads to a decrease of the vertically integrated water vapor (not shown) owing to the decrease of the saturated water vapor pressure with temperature. This also contributes to the cooling of the surface by a decrease of the water vapor greenhouse effect.

SUMMARY AND CONCLUSIONS

In this study, the effects of acid-coated IN on the Arctic cloud microstructure and radiation is investigated for January and February 2007. A new parameterization for heterogeneous ice nucleation is implemented into the 2-moment microphysics scheme of the Canadian Global Environmental Multiscale (GEM) model. The main objective of this study is to assess the impact of the wintertime long-range transport of anthropogenic sulphate on Arctic clouds and energy budget.

Results show that acid coatings on IN have an important effect on ice nucleation with the coatings modifying both ice and mixed-phase cloud microstructures. The primary effect of acid coating on IN is to significantly decrease the nucleation rate at a given ice supersaturation. The consequences of this change are a function of temperature as illustrated in **Figure 7**.

In the upper part of the troposphere the temperature is often below -40^{o}C and homogeneous nucleation is the dominant freezing mechanism. .In this case, the inhibition effect of acid coatings on deposition ice nucleation leads an increased concentration of water droplets, which freeze homogenously.. In the uncoated aerosol scenario, larger heterogeneous ice crystal nucleation rates in sub-saturated air with respect to liquid water prevents liquid water saturation more often than in the coated aerosol scenario. As a result, the ice crystal concentration is lower and their size is larger when compared to the coated aerosol scenario. Since a very high ice supersaturation is needed to nucleate ice crystals in the acid coated aerosol scenario, the JF mean ice water content is lower than the uncoated aerosol scenario at these levels.

In the mid and lower part of the atmosphere, heterogeneous ice nucleation dominates over homogeneous freezing. In the uncoated aerosol scenario, larger ice crystal nucleation rates by deposition nucleation more oftenprevents the atmosphere from becoming saturation with respect to liquid water compared to the coated aerosol scenario. This leads to the an increased frequency of mixed-phase clouds in the coated-aerosol scenario with an increase of the liquid water content and a decrease of the ice water content when

compared to the uncoated aerosol scenario. This effect, associated with warmer temperatures, peaks at 850 hPa.

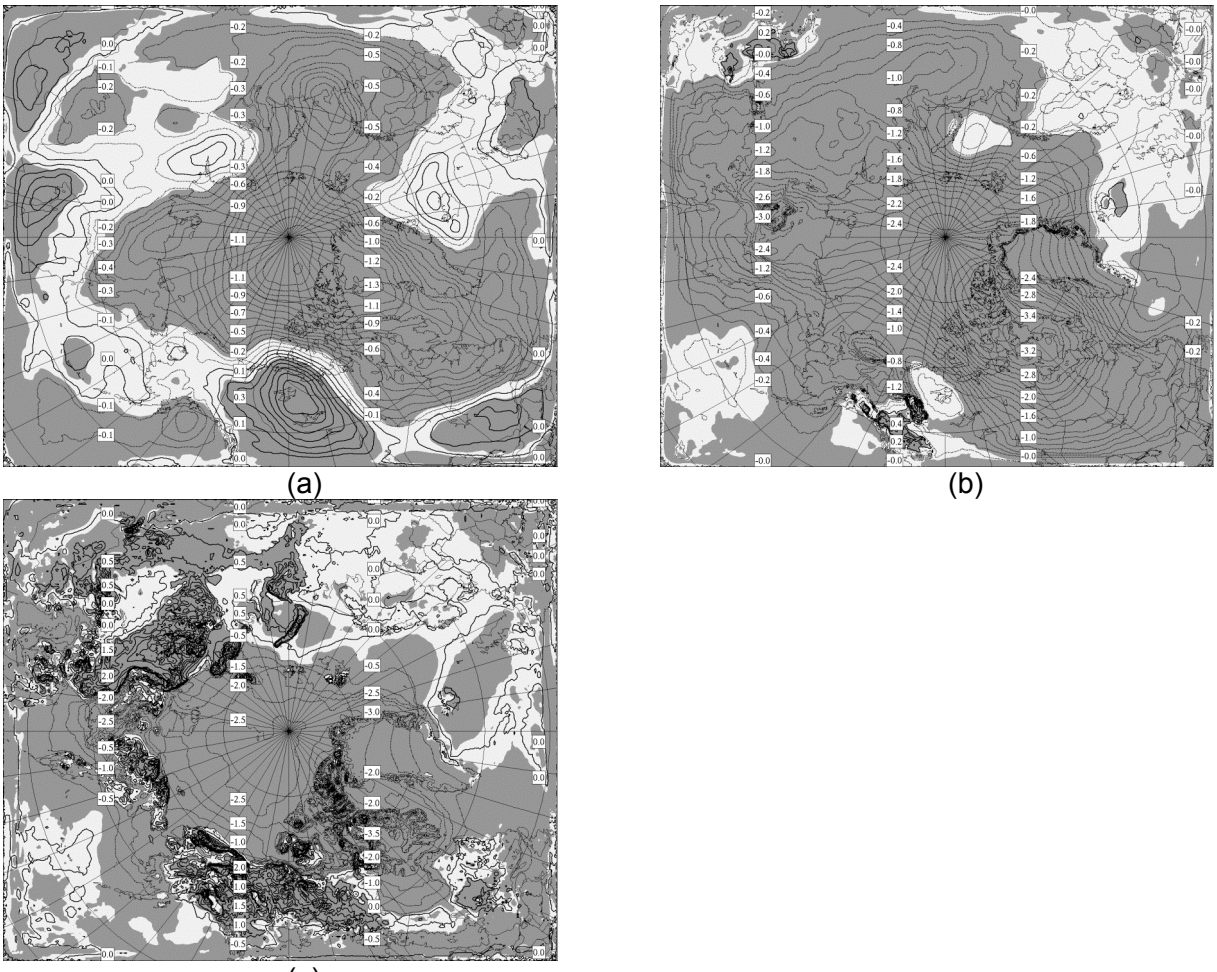

(a) (b) (c)

Figure 6: JF mean temperature anomaly (K) at (a) 500 hPa, (b) 850 hPa and (c) 1000 hPa. Shadowed areas indicate that anomalies are statistically significant with a confidence level of 95% (after Girard et al., 2012).

These two different effects have a common impact on the infrared radiative budget at the top of the atmosphere. Optically thinner mid to upper ice clouds in the coated aerosol scenario increase the atmospheric transmissivity of terrestrial radiation. At the same time, the upward infrared radiation flux is increased in the coated aerosol scenario due to optically thicker and more frequent mixed-phase clouds when compared to the uncoated aerosol scenario. The end result is a decrease of the cloud radiative forcing at the top of the atmosphere ranging between 0 and -6 Wm^{-2}. This leads to an atmospheric cooling that varies between 0 and -4K. The atmospheric cooling further promotes the formation of clouds in the coated aerosol scenario leading a decrease in the water vapor greenhouse effect and precipitation for January and February. . Results show that this Arctic cooling is large enough to strengthen the large-scale tropospheric circulation associated with the polar front through the intensification of the baroclinic zone.

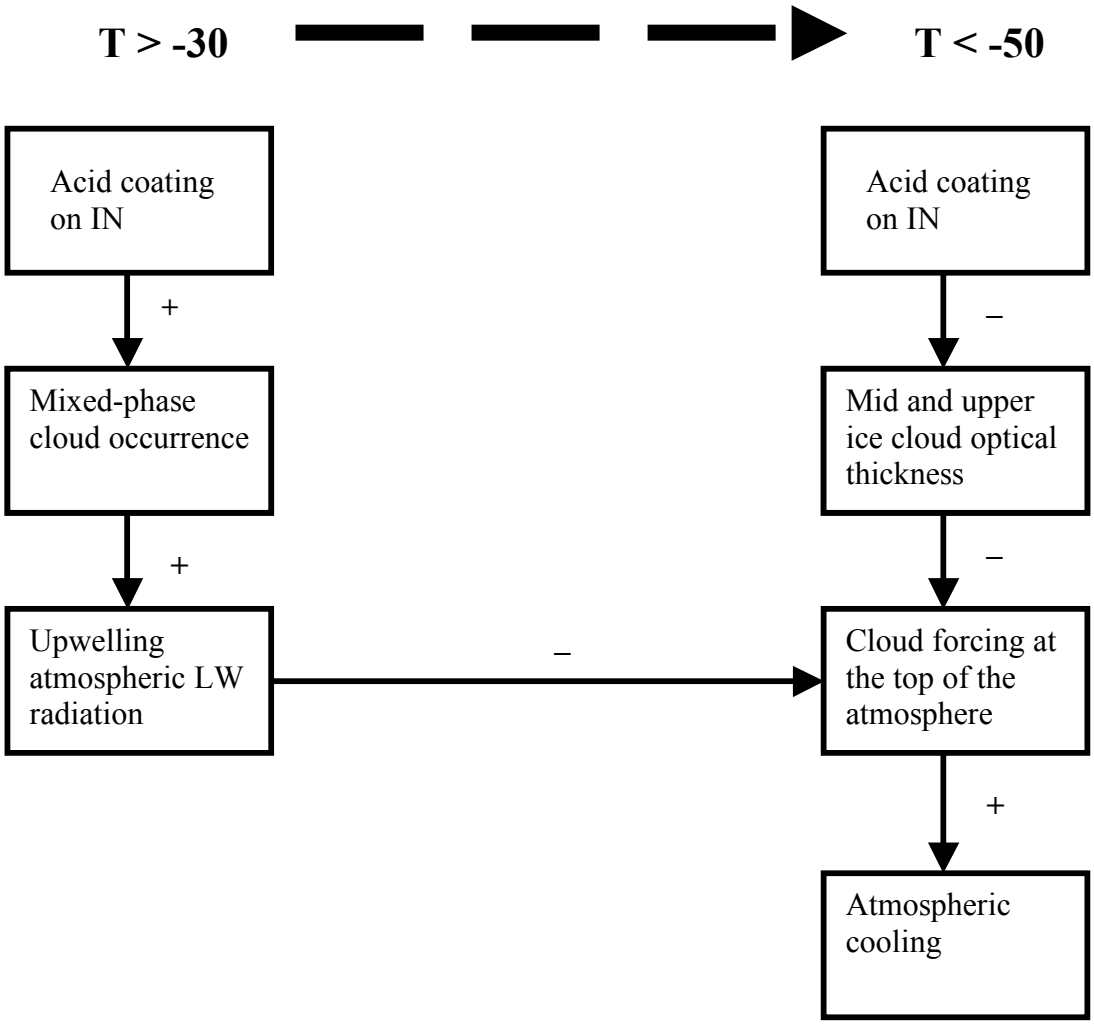

Figure 7: Flowchart showing the linkage between acid coating on ice nuclei, cloud microstructure, temperature and radiation at the TOA (after Girard et al., 2012).

The results obtained in this study show that ice nucleation plays an important role for both mid and upper ice clouds and low-level mixed-phase clouds in the Arctic, which in turn has an effect on radiation and atmospheric circulation. Quite interestingly, acid coatings have little effect on cloud and radiation south of the arctic air mass. This suggests that deposition ice nucleation is important mainly in stable air masses that cool slowly, thus preventing the relative humidity from reaching liquid water saturation rapidly.

The tropospheric cooling resulting from acid coatings on IN obtained in this study may be conservative. In our study, ice nucleation in the contact mode is assumed to be un-altered by acid coating. Hoose *et al.* (2008) and Storelvmo *et al.* (2008) in their modeling studies have assumed that acid coating on dust particles inhibits contact ice nucleation.

Such an alteration of contact nucleation by acid coating can only enhance the cloud microstructure changes obtained in our study, that is an increase of the cloud liquid water and a decrease of the ice crystal number concentration.

Using a refined treatment of the IN de-activation effect based on laboratory experiment, this research has confirmed the results obtained in previous modeling investigations (Girard *et al.*, 2005; Girard and Stefanof, 2007) on the effect of acid coating on the Arctic clouds and radiative budget during winter. This indirect effect of acid aerosols on arctic clouds and the resulting atmospheric cooling could explain, at least in part, the unexpected observed cooling trend of surface air temperature over the Arctic Ocean during winter in the period 1979-1999 as observed by boys (Rigor *et al.*, 2000) and by satellite remote sensing (Wang and Key, 2003).

5. References

Archuleta, C.M., DeMott, P.J., Kreidenweis, S.M., 2005. Ice nucleation by surrogates for atmospheric mineral dust and mineral dust/sulfate particles at cirrus temperatures. *Atmospheric Chemistry and Physics* **5:** 2617-2634.

Barrie, L.A., 1986. Arctic air pollution: an overview of current knowledge. *Atmospheric Environment* **20:** 643- 663.

Barrie, L.A., Olson M.P., Oikawa, K.K., 1989. The flux of anthropogenic sulphur into the Arctic from mid-latitudes. *Atmospheric Environment* **23:** 2502-2512.

Bigg, E.K., 1980. Comparison of aerosol at four baseline atmospheric monitoring stations. *Journal of Applied Meteorology* **19:** 521-533.

Blanchet, J.-P., Girard, E., 1994. Arctic greenhouse cooling. *Nature* **371:** 383.

Blanchet, J.-P., Girard, E. 1995. Water-vapor temperature feedback in the formation of continental Arctic air: Implications for climate. *Science of the Total Environment* **160/161:** 793-802.

Borys, R.D., 1989. Studies of ice nucleation by arctic aerosols on AGASP-II. *Journal of Atmospheric Chemistry* **9:** 169-185.

Bourgeois, Q. and I. Bey, 2011. Pollution transport efficiency toward the Arctic: Sensitivity to aerosol scavenging and source regions. *Journal of Geophysical Research* **116:** D08213, doi:10.1029/2010JD015096.

Chernoff, D.I., Bertram, A.K., 2010. Effects of sulfate coatings on the ice nucleation properties of a biological ice nucleus and several types of minerals. *Journal of Geophysical Research* **115:** D20205, doi:10.1029/2010JD014254.

Côté, J., Gravel,S., Méhot,A., Patoine,A., Roch,M., Staniforth,A., 1998. The operational CMC-MRB Global Environmental Multiscale (GEM) Model. Part I. Design considerations and formulation. *Monthly Weather Review* **126:** 1373-1395.

Curry, J.A., Meyers, F.G., Radke, L.F., Brock, C.A., Ebert, E.E., 1990. Occurrence and characteristics of lower tropospheric ice crystals in the Arctic. *International Journal of Climatology* **10:** 749-764.

Curry, J.A., Schramm, J.L., Serreze, M.C., Ebert, E.E., 1995. Water vapor feedback over the Arctic Ocean. *Journal of Geophysical Research* **100:** 14 223-14 229.

Curry, J.A., Randall, D., Rossow, W.B., Schramm, J.L., 1996. Overview of arctic cloud and radiation characteristics. *Journal of Climate* **9:** 1731-1764.

Cziczo, D.J., Abbatt, J.P.D., 1999. Deliquescence, efflorescence, and supercooling of ammonium sulfate aerosols at low temperature: Implications for cirrus cloud formation and aerosol phase in the atmosphere. *Journal of Geophysical Research* **104:** 13 781-13 790.

Cziczo, D.J., Froyd, K.D., Gallavardin, S.J., Moehler, O., Benz, S., Saathoff, H., Murphy, D.M., 2009. Deactivation of ice nuclei due to atmospherically relevant surface coatings. *Environmental Research Letters* **4:** doi:10.1088/1748-9326/4/4/044013.

DeMott, P.J., Meyers, M.P., Cotton, W.R., 1994. Parameterization and impact of ice initiation processes relevant to numerical model simulations of cirrus clouds. *Journal of Atmospheric Sciences* **51:** 77-90.

DeMott, P.J., Sassen, K., Poellot, M.R., Rogers, D.C., Brooks, S.D., Prenni, A.J., Kreidenweis, S.M., 2003. African dust aerosols as atmospheric ice nuclei. *Geophysical Research Letters* **30:** 1732.

Du, P., Girard, E., Bertram, A.K., Shupe, M.D., 2011. Modeling of the cloud and radiation processes observed during SHEBA. *Atmospheric Research* **101:** 911-927.

Dymarska, M., Murray, B.J., Sun, L.M., Eastwood, M.L., Knopf, D.A., Bertram, A.K., 2006. Deposition ice nucleation on soot at temperatures relevant for the lower troposphere. *Journal of Geophysical Research* **111:** D04204

Eastwood, M.L., Cremel, S., Wheeler, M., Murray, B.J., Girard E., Bertram, A.K., 2008. Ice nucleation on mineral dust particles: onset conditions, nucleation rate and contact angles. *Journal of Geophysical Research* **113:** doi:10.1029/2008JD010639.

Eastwood, M.L., Cremel, S., Wheeler, M., Murray, B.J., Girard E., Bertram, A.K., 2008.The effect of sulphuric acid and ammonium sulfate coatings on the ice nucleation properties of kaolinite particles. *Geophysical Research Letters* **36:** doi:10.1029/2008GL035997.

Ettner, M., Mitra, S.K., Borrmann, S., 2004. Heterogeneous freezing of single sulfuric acid solution droplets: laboratory experiments utilizing an acoustic levitator. *Atmospheric Chemistry and Physics* **4:** 1925-1932.

Fink, A.H., Brücher, T., Ermert, V., Krüger, A., Pinto, J.G., 2009. The European storm Kyrill in January 2007: synoptic evolution, meteorological impacts, and some considerations with respect to climate change. *Natural Hazards and Earth System Sciences* **9:** 405-423.

Fletcher, N.H., 1962. Physics of Rain Clouds. Cambridge University Press, London, PP. 396.

Frenzén, L.G., Hjelmroos, M., Kallberg, P., Brorström-Lundén, E., Juntto, S., Savolainen, A.L., 1994. The yellow snow episode of northern Fennoscandia, March 1991 – A case study of long-distance transport of soil, pollen and stable organic compounds. *Atmospheric Environment* **28:** 3587-3604.

Girard, E., Bekcic, B., 2005. Sensitivity of an arctic regional climate model to the horizontal resolution during winter: implications for aerosol simulation. *International Journal of Climatology* **25:** 1455-1471.

Girard, E., Blanchet, J.-P., Dubois, Y., 2005. Effects of sulphuric acid aerosols on wintertime low-level atmospheric ice crystals, humidity, and temperature at Alert, Nunavut. *Atmospheric Research* **73:** 131-148.

Girard, E., Stefanof, A., 2007. Assessment of the dehydration-greenhouse feedback over the Arctic during February 1990. *International Journal of Climatology* **27:** 1047-1058.

Girard, E., Dueymes, G., Du, P., Bertram, A.K., 2012. Assessment of the Effects of Acid-Coated Ice Nuclei on the Arctic Cloud Microstructure, Atmospheric Dehydration, Radiation and Temperature during Winter. *International Journal of Climatology* (in press) doi: 10.1002/joc.3454

Grenier, P., Blanchet, J.-P., Munoz-Alpizar, R., 2009. Study of polar thin ice clouds and aerosols seen by CloudSat and CALIPSO during mid-winter 2007. *Journal of Geophysical Research* **114:** doi:10.1029/2008JD010927.

Hoose, C., Lohmann, U., Stier, P., Verheggen, B., Weingartner, E., 2008. Aerosol processing in mixed-phased clouds in ECHAM5-HAM: Model description and comparison to observations. *Journal of Geophysical Research* **113:** doi:10.1029/2007JD009251.

Karlsson, K.-G., Dybbroe, 2010. Evaluation of arctic cloud products from the EUMETSAT climate monitoring application facility based on CALIPSO-CALIOP observations. *Atmospheric Chemistry and Physics* **10:** 1789-1807.

Knopf, D.A., Koop, T., 2006. Heterogeneous nucleation of ice on surrogates of mineral dust. *Journal of Geophysical Research* **111:** doi:10.1029/2005JD006894.

Li, J., Barker, W., 2005. A radiation algorithm with correlated-K distribution. Part I: Local thermal equilibrium. *Journal of Atmospheric Sciences* **62:** 286-309.

MacFarquar, G.M., Ghan, S., Verlinde, J., Korolev, A., Strapp, J.W., Shmid, B., Tomlinson, J.M., Wolde, M., Brooks, S.D., Cziczo, D., Dubey, M.K., Fan, J., Flynn, C., Gultepe, I., Hubbe, J., Gilles, M.K., Laskin, A., Lawson, P., Leaitch, R.W., Liu, P., Liu, X., Lubin, D., Mazzoleni, C., Macdonald, A.-M., Moffet, R.C., Morrison, H., Ovchinnikov, M., Shupe, M.D., Turner, D.D., Xie, S., Zelenyuk, A., Bae, K., Freer, M., Glen, A., 2010. Indirect and semi-direct aerosol campaign (ISDAC): the impact of arctic aerosols on clouds. *Bulletin of the American Meteorological Society* (in press).

Meyers, M.P., DeMott, P.J., Cotton, W.R., 1992. New primary ice-nucleation parameterizations in an explicit cloud model. *Journal of Applied Meteorology* **31:** 708-721.

Milbrandt, J.A., Yau, M.K., 2005. A Multimoment Bulk Microphysics Parameterization. Part I: Analysis of the Role of the Spectral Shape Parameter. *Journal of Atmospheric Sciences* **62:** 3051-3064.

Noilhan, J., Planton, S., 1989. A simple parameterization of land surface processes for meteorological models. *Mon. Wea. Rev.* **117:** 536-549.

Pruppacher, H.R., Klett, J.D., 1997. Microphysics of Clouds and Precipitation. Kluwer Academic Publishes, Dordrecht, 1997.

Quinn, P.K., Kapustin, V.N., Bates, T.S., Covert, D.S., 1996. Chemical and optical properties of marine boundary layer aerosol particles of the mid-Pacific in relation to sources and meteorological transport. *Journal of Geophysical Research* **101:** 6931-6951.

Ramanathan, V., Cess, R.D., Harrison, E.F., Minnis, P., Barkstrom, B.R., Ahmas, E., Hartman, D., 1989. Cloud-radiative forcing and climate: Results for the Earth Radiation Budget Experiment. *Science* **243:** 57-63.

Rigor, I.G., Colony, R.L., Martin, S., 2000. Variations in surface air temperature observations in the Arctic, 1979-1997. *Journal of Climate* **13:** 896-914.

Rinke, A., Dethloff, K., 2000. On the sensitivity of a regional Arctic climate model to initial and boundary conditions. *Climate Research* **14:** 101-113.

Rinke, A., Dethloff, K., Fortmann, M., 2004. Internal variability in arctic regional climate simulations: Case study for the SHEBA year. *Climate Research* **27:** 197-209.

Rinke, Dethloff, A.K., Cassano, J., Christensen, J.H., Curry, J.A., Du, P., Girard, E., Haugen, J.-E., Jacob, D., Jones, C.G., Køltzow, M., Lynch, A.H., Pfeifer, S., Serreze, M.C, Shaw, M.J., Tjernström, M., Wyser, K., Zagar, M., 2006. Evaluation of an ensemble of Arctic regional climate models: Spatial patterns and height profiles. *Climate Dynamics* **26:** 459-472.

Salam, A., Lohmann, U., Lesins, G., 2007. Ice nucleation of ammonia gas exposed montmorillonite mineral dust particles. *Atmospheric Chemistry and Physics* **7:** 3923-3931.

Schnell, R.C., 1984. Arctic haze and the Arctic Gas and Aerosol Sampling Program (AGASP). *Geophysical Research Letters* **11:** 361-364.

Shaw, G.E., 1995. The Arctic haze phenomenon. *Bulletin of the American Meteorological Society* **76:** 2403-2413.

Shupe, M.D., Intrieri, J.M., 2004. Cloud radiative forcing of the Arctic Surface: the influence of cloud properties, surface albedo, and solar zenith angle. *Journal of Climate* **17:** 616-628.

Simjanovski, D., Girard, E., Du, P., 2011. An evaluation of arctic cloud and radiation processes simulated by the limited-area version of the Global Multiscale Environmental Model (GEM-LAM). *Atmosphere-Ocean* **49:** 219-234.

Storelvmo, T., Kristjansson, Lohmann, U., 2008. Aerosol influence on mixed-phase clouds in CAM-Oslo. *Journal of the Atmospheric Sciences* **65:** 3214-3230.

Wang, X., Key, J.R., 2003. Recent trends in Arctic surface, cloud, and radiation properties from space. *Science* 5613: 1725-1728.

Winchester, J.W., Li, S.M., Fan, S.M., Schnell, R.C., Bodhaine, B.A., Naegele, S.S., 1984. Coarse particle soil dust in arctic aerosols, Spring 1983. *Geophysical Research Letter* **11:** 995-998.

Wyser, K., Jones, C.J., 2005. Aerosol and clouds – Modeled and observed clouds during SHEBA. *Journal of Geophysical Research* **110:** doi 10.1029/2004JD004751.

Yli-Tuomi, T., Vanditte, L., Hopke, P.K., Shamasuzzoha Basunia, M., Landsberger, S., Viisanen, Y., Paatero, J., 2003. Composition of the Finnish Arctic aerosol: collection and analysis of historic filter samples. *Atmospheric Environment* **37:** 2355-2364.

Young, K.C., 1974. The role of contact ice nucleation in ice phase initiation in clouds. *Journal of Atmospheric Sciences* **31:** 1735-1748.

Wyser, K., Jones,C.G., Du,P., Girard,E., Willén, U. , Cassano, J. , Christensen, J. H., Curry, J.A., Dethloff, K., Haugen,J.E., Jacob,D., Koltzow,M., Laprise,R., Lynch,A., Pfeifer,S., Rinke,A., Serreze,M., Shaw, M.J., Tjernström,M., Zagar, M., 2008. An evaluation of Arctic cloud and radiation processes during the SHEBA year: simulation result from eight Arctic regional climate models. *Climate Dyn.* **30:** 203-223.

Acknowledgments
The authors would like to thank the Canadian Foundation for Climate and Atmospheric Sciences (CFCAS), the Natural Sciences and Engineering Research Council of Canada (NSERC) and the Fonds Québécois de la Recherche sur la Nature et la Technologie (FQRNT) for support funding.

PHORETIC FORCES ON AEROSOL PARTICLES SURROUNDING AN EVAPORATING DROPLET IN MICROGRAVITY CONDITIONS

F.Prodi[1], G.Santachiara[1], F.Belosi[1]
A.Vedernikov[2], D.Balapanov[2]

[1] Institute of Atmospheric Science and Climate (ISAC), National Research Council, Bologna, Italy
[2] Université Libre Bruxelles, Microgravity Research Center, Avenue Roosevelt 50, 1050 Brussels, Belgium

1. INTRODUCTION

Aerosol particles may be scavenged in- and below-cloud by water drops and ice crystals via impaction scavenging, including impaction, Brownian diffusion, thermophoresis, diffusiophoresis, and, in the presence of charges, electric effects. Thermophoresis is the phenomenon whereby a small particle suspended in a gas with a temperature gradient, experiences a force called thermophoretic force and moves towards the region of lower temperature. Diffusiophoresis is the movement of particle due to the gas momentum transfer process in an isothermal gas mixture with concentration gradients of chemical species. In the case of a binary mixture in a steady condition (pure diffusiophoresis), the aerosol particle should move in the direction of the diffusive flux of the heavier gas molecules (Waldmann, 1959).

A case of great interest in the atmosphere occurs when vapour molecules evaporate or condense from or to a surface, diffusing through the resting air. The average mass and molecular velocities are then different from zero and a hydrodynamic flow (the Stefan flow) necessary to maintain a uniform total pressure, comes into existence (Stefan, 1881).

In the case of diffusiophoresis with Stefan flow, the direction of motion of the particulate should be the same as that of the water vapour flux (Waldmann and Schmitt, 1966). In clouds or during the fall of hydrometeors, when growth or evaporation of droplets and ice crystals occur, there is the simultaneous presence of thermo- and diffusiophoretic forces, which act in opposite ways.

Theoretical models agree that Brownian diffusion appears to dominate scavenging of aerosol in the size range $r<0.1$ μm (r is the radius of the aerosol particles), while inertial impaction dominates scavenging in the size range $r>1$ μm. Thus, there is a minimum collection efficiency for particles in the approximate range of 0.1μm - 1 μm, where phoretic and electric effects are felt.

Concerning the contribution of phoretic forces in the scavenging process, it is important to evaluate the strength of thermophoretic and diffusiophoretic forces, in order to assess which force is prevalent. Phoretic forces strongly depend on the thermal and water vapour concentration gradients between the drop or ice crystal surfaces and the ambient air. Theoretical and experimental papers have addressed the problem of the contribution of phoretic forces to the aerosol scavenging process in- and below-clouds, but the results are contradictory.

The prevalent goal of this research is to evaluate experimentally whether there is a prevalence of thermo- or diffusio-phoretic force on aerosol particles, during the evaporation of water drop in stationary conditions. The presented experiments were performed in microgravity conditions. In such conditions the problem is less complex, as the motion of particles due to gravitational force is removed.

2. EXPERIMENTAL ARRANGEMENT

The microgravity experiments were carried out in the Bremen Drop Tower facility, which provides a weightless stage of about 4.7 s under free fall conditions with residual acceleration of about $10^{-5}g_0$. The Drop Tower system consists of a 110 m high drop tube with an internal diameter of 3.5 m, and a 10 m high shaft deceleration chamber at its foot. The drop tube and the deceleration chamber form a vacuum system with a volume of 1700 m^3, which can be evacuated down to a residual pressure of 1 Pa in about 2.5

hours. The drop tube is built into a tower of 146 m height.

The experimental apparatus was housed within a special pressurized capsule. The temperature and pressure inside the capsule were continuously monitored. A specially constructed tank filled with fine-graded polystyrene was used to decelerate the capsule. The complete electronic system of the Bremen Drop Tower (ground station computer system, telemetry- telecommand-transmission line and capsule computer system inside the capsule itself) allows the control and automatization of the experiment.

The small cell used here in the Bremen Drop Tower for experiments concerning evaporating drops consisted of two flat plates at a fixed distance, one at the top and one at the bottom of the square mono-block vessel of optically polished Pyrex. The distance between the plates was 7 mm and the internal dimension of the cell was 20x20x9 mm^3.

A needle (D_{inter}=0.20 mm; D_{ext}=0.30 mm) was inserted in the top plate penetrating into the cell by 0.9 mm. The generation of drop occurred through a micro-litre syringe (Hamilton company, USA) connected to the needle. The plunger of the syringe (d= 0.15 mm) was moved by a motor, set by an electronic device (EL-MO electronic, Milan) which allows the variation of drop diameter. Liquid water was used (Milli-Q, resistivity ~ 18 MΩ cm), previously degassed in order to avoid bubbles.

The bottom plate of the cell had a square cavity of the same area as the cell, filled with silica gel, and covered with a net. Silica gel adsorbs water vapour, causing the evaporation of the generated water drop, due to the water vapour gradient inside the cell. The problem may be considered equivalent to the evaporation of a stationary drop into a still atmosphere.

Paraffin aerosol was generated by a new generator (MINIMAGE), a modified version of MAGE (Prodi, 1972). A sintered plate imbued with paraffin is heated, and the vapours condense heterogeneously. Nitrogen was used as carrier gas. The aerosol diameter can be varied by changing the temperature of the sinterized plate. Calibration of the system was performed preliminarily in a ground laboratory by sampling the generated aerosol on Nuclepore filters and by examining them with an electronic microscope.

The inlet and the outlet of the aerosol occur through two small holes located on the bottom plate, which shut immediately after the introduction of the aerosol, assuring a good seal. Using the electronic system of the Bremen Drop Tower, the aerosol in nitrogen carrier gas was automatically injected into the cell until 11 s before the capsule free fall (beginning of microgravity). The drop was produced after the introduction of the aerosol and shutting of the cell. The drop generation started 5 s and stopped 4.4 s before the start of the fall. The relaxation time of the aerosol, measured by examining the images stored at the beginning of microgravity, was about 0.25 s.

A red light laser (wavelength of 650 nm, 10 mW) was used to light the aerosol, which was observed throught an optical device (Tamron lens, AF 70-300 mm, MACRO mod.372D, field of view 3.2x2.5 mm^2). Images were recorded (15 frames s^{-1}) by an Allied Vision Technologies, AVT-D1 digital video-camera, controlled during drops by means of a computer installed within the capsule.

The goal of the experiments performed in the Bremen Drop Tower was to evaluate whether there is a prevalence of thermo- or diffusio-phoretic force during the evaporation of the water drop, for the considered aerosol diameter.

3. RESULTS AND DISCUSSION

Table 1 shows the results of the tests performed by changing the diameter of the water drop (D) and of the aerosol (d), i.e. the measured aerosol velocity (V_{aer}) and the standard deviation (S.D.), the temperature of the nitrogen gas inside the cell (T_a), and the calculated equilibrium temperature reached by the drop due to evaporation (T_{equil}). The tests were limited in number, as each run involved the complex procedure shown in the experimental part.

Fig. 1 a-b shows a picture of the test no. 7, showing the water drop (D=2.15 mm) and the aerosol particles (d=1.9 μm) a few frames after the beginning of the

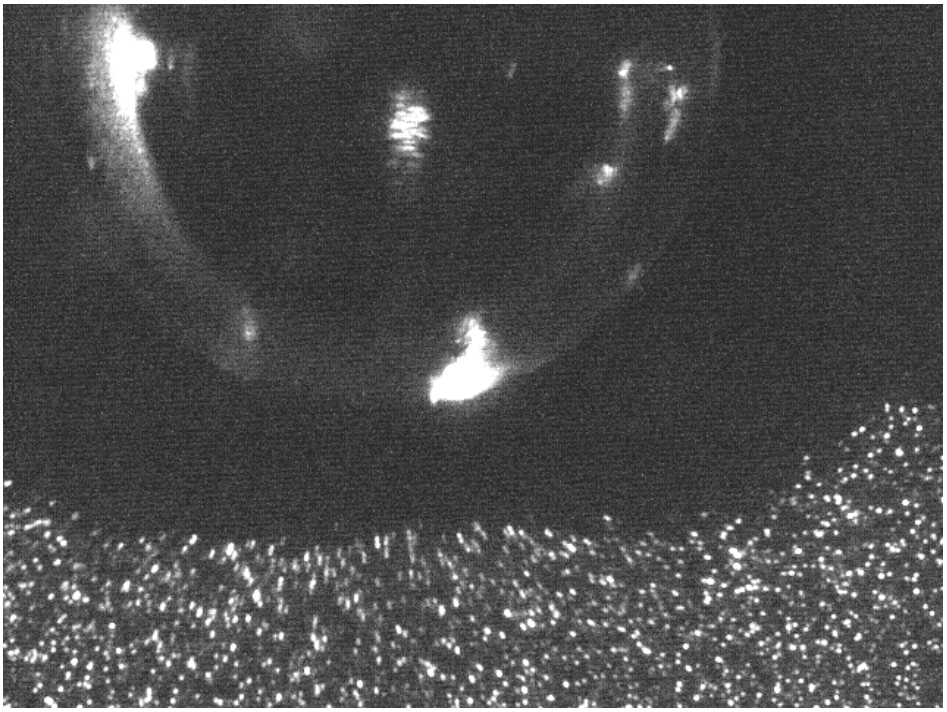

(a)

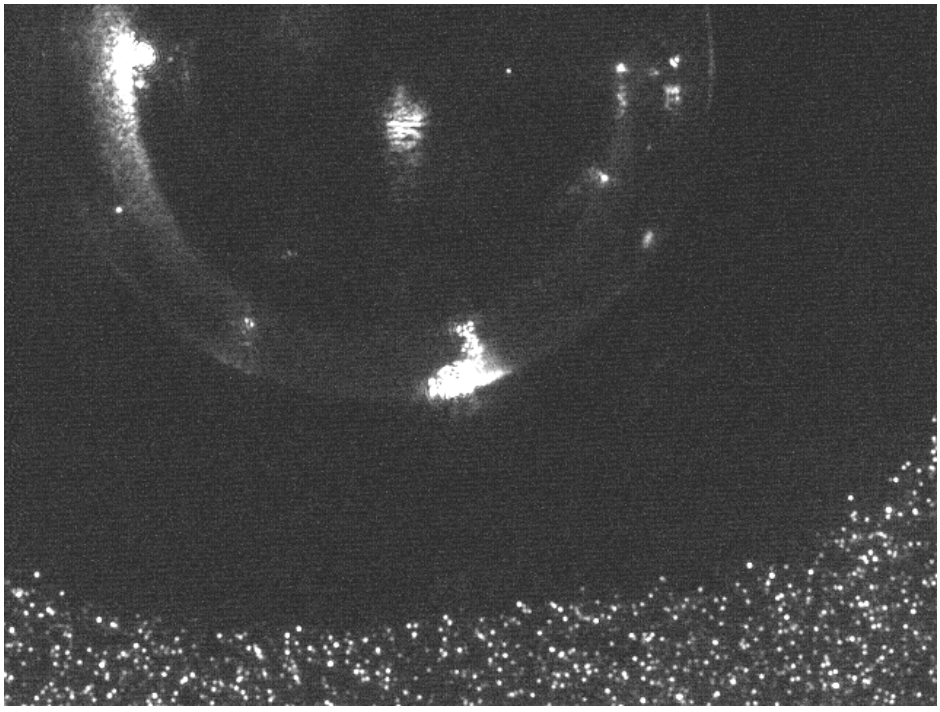

(b)

Fig. 1. Water drop and aerosol at the beginning (a) and at the end of the microgravity (b).

Test no.	Drop D, mm, ±0.01	Aerosol, d, μm ±0.05	V_{aer}, μm s^{-1}	S.D. μm s^{-1}	T_{cell}, °C	$T_{equil.}$ °C	dp/dx, mbar cm^{-1} ± 0.3
1	1.11	0.80	53.7	9.4	20.4±0.2	8.8	12.7
2	0.48	0.40	18.1	4.9	22.5±0.2	10.1	12.1
3	1.07	0.40	25.9	6.5	23.2±0.2	10.6	13.6
4	1.07	1.00	54.5	7.8	21.1±0.2	9.3	12.8
5	1.16	1.00	50.9	9.5	23.7±0.2	10.9	14.0
6	1.16	2.00	73.4	9.5	20.3±0.2	8.7	12.8
7	2.15	1.90	97.7	10.6	27.5±0.2	13.3	19.0
8	0.96	1.90	57.0	10.6	27.4±0.2	13.2	14.9
9	1.35	1.20	45.9	8.0	24.0±0.2	11.1	14.6

Table 1. Results of the microgravity experiments

microgravity, and at the end of the capsule free fall. It is evident that the aerosol is moving away during the drop evaporation.

The water vapour pressure gradient inside the cell (dp/dx) was theoretically evaluated by assuming a linear variation of the water vapour pressure between the surface of the drop and the bottom of the cell, where a hollow filled with silica gel is placed.

The initial temperature of the water drop is considered to be equal to the measured temperature of the nitrogen in the cell. The equilibrium temperature reached by evaporating liquid drop was calculated by assuming that the drop reaches a steady state, in which the heat loss due to the latent heat of evaporation balances the heat gained by the drop from the gas. Due to the small area of contact between drop and the needle, the heat transmission between the drop and the capillary during the period of the capsule fall (4.7 s) was considered to be negligible.

The drop temperature in a steady state can be calculated by solving the following equations: (Pruppacher and Klett, 1997).

$$T_d = T_a + (L/ 4 \pi k_g) * dm/dt \qquad (1)$$

$$dm/dt = 4 \pi r D (\rho_{v,\infty} - \rho_{v,R}) \qquad (2)$$

where: T_d is the drop temperature; T_a, is the nitrogen temperature in the cell; L, latent heat of vaporization of water; k_g, thermal conductivity of nitrogen; D, bulk molecular diffusivity of water in nitrogen; $\rho_{v,\infty}$ and $\rho_{v,R}$, water vapour density at the bottom of the cell and at the surface of the water drop; dm/dt, rate of change of the drop mass m.

Equation 1) assumes a uniform temperature of the drop, since thermal diffusivity in water is much higher than gas thermal diffusivity. The time constant τ_T that characterizes the time required for droplets to reach the thermal equilibrium in air is about 20 times greater than the time required to reach a uniform temperature. In addition, as the time constant for thermal exchange τ_T is much lower than the one for moisture exchange (τ_r), the drop temperature reaches equilibrium with air long before the droplet radius does (Andreas, 1989). Water vapour density at the bottom of the cell, where silica gel absorbing water vapor was located, was calculated by assuming a 20% r.h. The variation in drop radius during the fall, both theoretically calculated and measured from the recorded images, turned out to be lower than 10 μm.

The most important outcome of the experimental runs performed was a prevalence of the diffusiophoretic with respect to thermophoretic force, for the considered aerosol (diameter in the range 0.4 – 2 μm).

Additional outcomes should be mentioned. By considering runs which show similar values of estimated vapour

gradient, i.e. test no. 1-2-3-4-5-6, and the same for runs 8-9, it appears that the measured values of particle velocity increase with increasing aerosol diameter. This result agrees with theoretical and experimental approaches, which evidence an increase of aerosol thermophoretic velocity by decreasing the aerosol diameter (Talbot et al., 1980; Yamamoto and Ishihara, 1988; Prodi et al., 2006), while diffusiophoretic velocity has a small dependence on the aerosol diameter (Schmitt and Waldmann, 1960; Chernyak et al., 2001, Prodi et al., 2006). From runs 7-8 performed with a constant aerosol diameter, an increase appears in the measured velocity with increasing vapour pressure gradient.

REFERENCES

Andreas, E.L., 1989:Thermal and size evolution of sea spray droplets. CRREL Report 89-11.

Chernyak, V.G., S.A. Starikov, and S.A. Beresnev, 2001: Diffusiophoresis of an aerosol particle in a binary gas mixture. *J. Applied Mechanics Technical Physics*, **42**, 445-454.

Prodi, V. , 1972: A condensation aerosol generator for solid monodisperse particles. In: *Assessment of airborne particles.* Edited by T.T. Mercer, P.E.Morrow & W. Stober.,169-181.

Prodi, F., G. Santachiara, S. Travaini, A. Vedernikov, F.Dubois, J.C. Legros, 2006: Measurements of phoretic velocities of aerosol particles in micrograviy conditions. *Atmos. Res.*, **82**, 183-189.

Pruppacher, H. R. and J.D. Klett, 1997: Microphysics of Cloud and Precipitation, Kluwer Academic Publishers, Dordrecht, 954 pp.

Schmitt, K.H. and L. Waldmann, 1960: Untersuchungen an Schwebstoffteilchen in diffundierendem Gasen. *Z.Naturforsch*, **15A**, 843-851.

Stefan, J., 1881: Über die Verdampfung aus einem kreisförming oder elliptisch begrenzten Becken, *Wien. Ber.*, **83**, 943-949.

Talbot, L., R.K. Cheng, R.W. Schefer, and D. R. Willis, 1980: Thermophoresis of particles in a heated boundary layer, *J. Fluid Mechanics*, **101**, 737-758.

Waldmann, L., 1959: Über die Kraft eines inhomogenen Gases auf kleine suspendierte Kugeln. *Z.Naturforsch*. **14a**, 589-599.

Waldmann, L. and K.H. Schmitt, 1966: Thermophoresis and diffusiophoresis of aerosol," Aerosol Science (Edited by Davies, C. N.), Academic Press, London, 163-194.

Yamamoto, K. and Y.Ishihara, 1988: Thermophoresis of a spherical particle in a rarefied gas of a transition regime, *Phys. Fluids*, **31**, 3618-3624.

THE CLOUD STRUCTURE AND PRECIPITATION MECHANISM OF A FRONTAL STRATIFORM CLOUD SYSTEM

Yan-Chao Hong [1], Hong-Yu Li [2]
1 Institute of Atmospheric Physics, Chinese Academy of Sciences
2 Beijing Weather Modification Office

1 INTRODUCTION

In China, frontal stratiform cloud precipitus is the main object of artificial precipitation. Understand the structure of the cloud system, especially structures and precipitation mechanism of "seeding-feeding" is the key to choose artificial precipitation conditions. Research shows that, distribution of cloud water resources in "seeding-feeding" cloud can be helpful precipitation form, also be helpful for artificial precipitation enhancement, is an important element of the potential of artificial precipitation [1]. Research shows on temperate cyclones that precipitation from the warm front cloud system is mainly formed by "seeding-feeding" mechanism, in which super-cold water drops and ice crystals coexist and ice crystals in this layer rapid growth[2-4], and the layer may have been the key of precipitation formation[5].The cloud concept model in the northern region of China shows that "seeding -feeding" cloud is the most typical characteristics of stratiform cloud precipitus[6].

The transformation conditions of cloud water are related to distribution of cloud water resources, i.e. cloud structure. In the pure cold cloud process or pure warm cloud process, the cloud water hard to transform into rain. This shows that formation mechanism of precipitation is related to distribution characteristics of cloud water resources. The "seeding-feeding" cloud is a distribution system of cloud resource, it actually represent a typical physical mechanism of the precipitation formation.

This paper attempts to analysis cloud structure and precipitation mechanism of a stratiform cloud system produced by a low trough and a cold front (hereinafter referred to as 0405 cloud system) on 5 April 4, 2002,using the observed data and the numerical simulation result [7,8].

2 STRUCTURE IN THE FRONT AREA OF 0405 CLOUD SYSTEM

2.1 The Weather Situation

The large range precipitation happened in Henna province on 4-5 April 4, 2002.There is a trough line At 500 hpa and 700 hpa levels respectively and a cold front on ground. The cold front reached Zhengzhou station at 05:00, April 5. The rainfall is from 05:00 to 15:00 at Zhengzhou station.

2.2 Layered Structure of the Cloud

According to observed, there are two cloud layers (table 1) over zhengzhou station on 20 April 4. Among them, top height of the high cloud of about is 13.3 km, and it corresponding temperature is 49.2 ℃, its bottom high 7.4 km; The top height of lower cloud layer of is about 7.0 km, corresponding temperature is 16.7 ℃ and the cloud base height is 1.5 km and the temperature of 11.5 ℃. The cloudless area between two clouds less than 400 m thickness. At 08:00 on April 5, the cold front pass through Zhengzhou station and the high cloud and low cloud connected into one, height of the cloud base is close to the ground, only about 100 m, at this time the cloud produces precipitation. Statistics indicate that low through and cold front cloud system two over two layer cloud is 69.1% in spring of henna area.

Table 1 Height and temperature of cloud top and cloud base at Zhengzhou station.

Time	Height (m) of cloud top	Height (m) of cloud base	Tem. (°C) of cloud top	Tem. (°C) of cloud base
20:00 on April 4	13313/7016	7000/1500	-49.2/-16.7	-18.4/11.5
08:00 on April 5	12077	100	-14.6	13.6

2.4 Microphysical Structure

Distribution of water content in the simulated cloud system [8] is given in Fig.1. It can be seen that structure vertically of cloud is different in different position of the cloud system.

(1) Near by 300 hpa level, there is a wide range of clouds which should be mainly composed by ice crystals. For example there are the ice cloud in area with 106° E~108° E in figure 1 b2 and area with in 35° N~39° N in fig.1b3, with horizontal scales of hundreds of kilometers, larger thickness and 0.2 g/kg the water content.

(2) Below 300 hpa level, there is cloud body which continuous on the vertical direction, water content center is located in 600-650 hpa layer, as shown in 35° N ~37° N range in figure 1b3.

(3) In the some part of the cloud system, there is only mid –low cloud and do not exist high cloud (ice clouds), as shown in range of 108° E~111° E in figure 1 b2 and area with 30 ° N~32° N in figure 1b3.

(4) In the some part of the cloud system, there is only warm cloud.

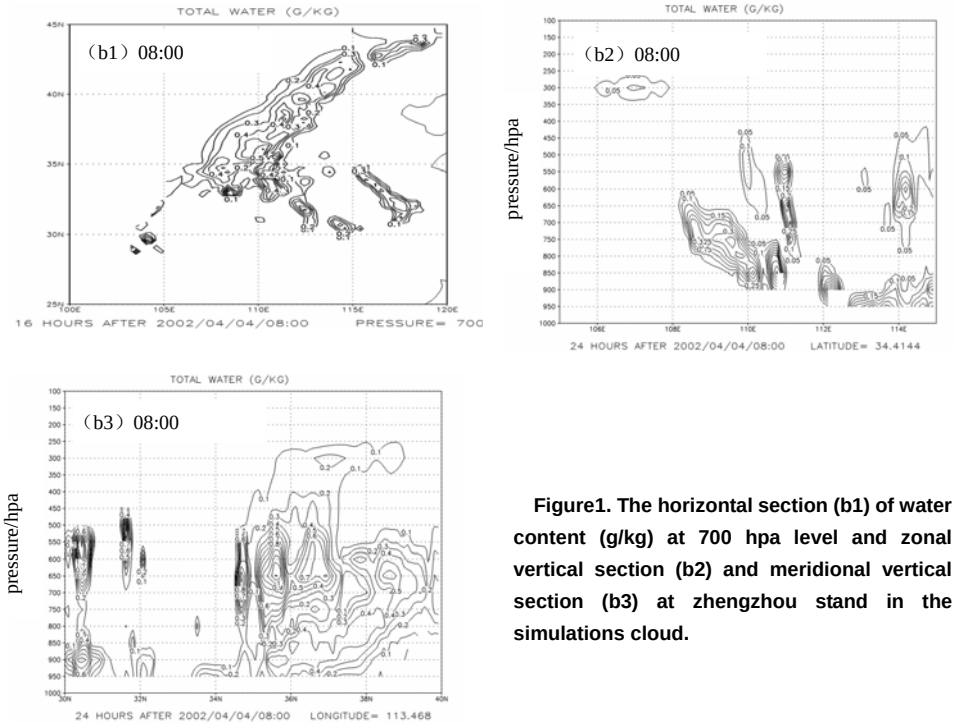

Figure1. The horizontal section (b1) of water content (g/kg) at 700 hpa level and zonal vertical section (b2) and meridional vertical section (b3) at zhengzhou stand in the simulations cloud.

General look, the cloud system can be divided into 3 levels of the high, medium and low. In some parts of the cloud system, there are the two levels and in some other parts three levels; there is a cloudfree area between some cloud layers; three cloud layers are connected into one body in other part of the cloud system which is "seeding-feeding" cloud. Water content center of upper cloud layer is at 300 hpa level, water content center of middle cloud layer is located

600-650 hpa level and low cloud layer is between 800-900 hpa levels. Figure 2 shows vertical distribution of atmospheric condensation rate calculated by NCEP data. From 20:00 4April to 14:00 5April, in high, middle and low atmospheric layers, the lager condensation rates are mainly in 300-400hpa level, 500-600hpa level and 700-800hpa level, respectively. The lager values of condensation rate correspond to the water content centers.

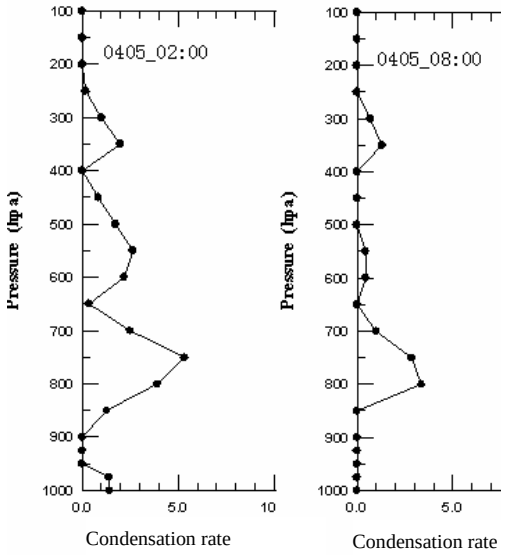

Figure 2 Vertical distribution of atmospheric condensation rate (mm/100h) on 5 April .

The microphysical features of the multilayer cloud can be seen from fig.3.Combined with figure 1 and figure 3, according to cloud physical structure and height of the water content center, the vertical ranges (see dotted line in fig.3) of the three layers are determined. The upper layer of cloud, consisting of ice crystal and snow, located mainly above 500 hpa level; the middle layer cloud is located in range from 500hpa level to 0° C layer, where exist snow, graupel, cloud droplet and raindrop. The low cloud layer to be in below 0° C layer consists of cloud droplet and raindrop. Isoline with 0.01 g/kg of water content of graupel close to 0° C layer level, so low-level of clouds also contain a small amount graupel particles. The upper layer of the cloud is called ice phase layer of "seeding-feeding" cloud and the middle layer, mixing layer with ice and water, and the low layer of the cloud, liquid water layer or warm layer.

It can be shown from the structures analysis that the multilayer cloud is macro structure features of the cloud system. There is "seeding-feeding" cloud in the front area and this system is the main precipitation mechanism. Because the structure is different in different parts of the cloud system and transformation condition of the cloud water resources is different, so that the condition and potential for artificial enhancement precipitation are also different. But certainly, "seeding-feeding" cloud is beneficial to transformation of cloud water resources and cloud type producing precipitation.

3 WATER TRANSFER AND PRECIPITATION MECHANISM FOR THE CLOUD SYSTEM

3.1 Water Transfer

As for 0405 cloud system [7], 71% of the vater vapor inputted in the cloud system transforms to hydrometeor by condensation and sublimation process, and efficiency of the hydrometeor to produce precipitation is about 43%. 29% of the cloud droplets is converted into precipitation particles, in which about 55% are due to ice phase process, and accretion growth by ice particles is the main processes for cloud water converting into precipitation. About 49% of ice crystals are transformed into snow and graupel, converted ice crystals are almost become snow and ice crystal is main source of snow. About 92% of the snow becomes graupels. 96% of the graupels are melted into rainwater that accounting for 57% of the total amount of rain water. Finally, rainfall amount on ground is 7.6 kg/m2 and the precipitation efficiency 60%. The ice water of 2.5 kg/m2 is detained in the cloud.

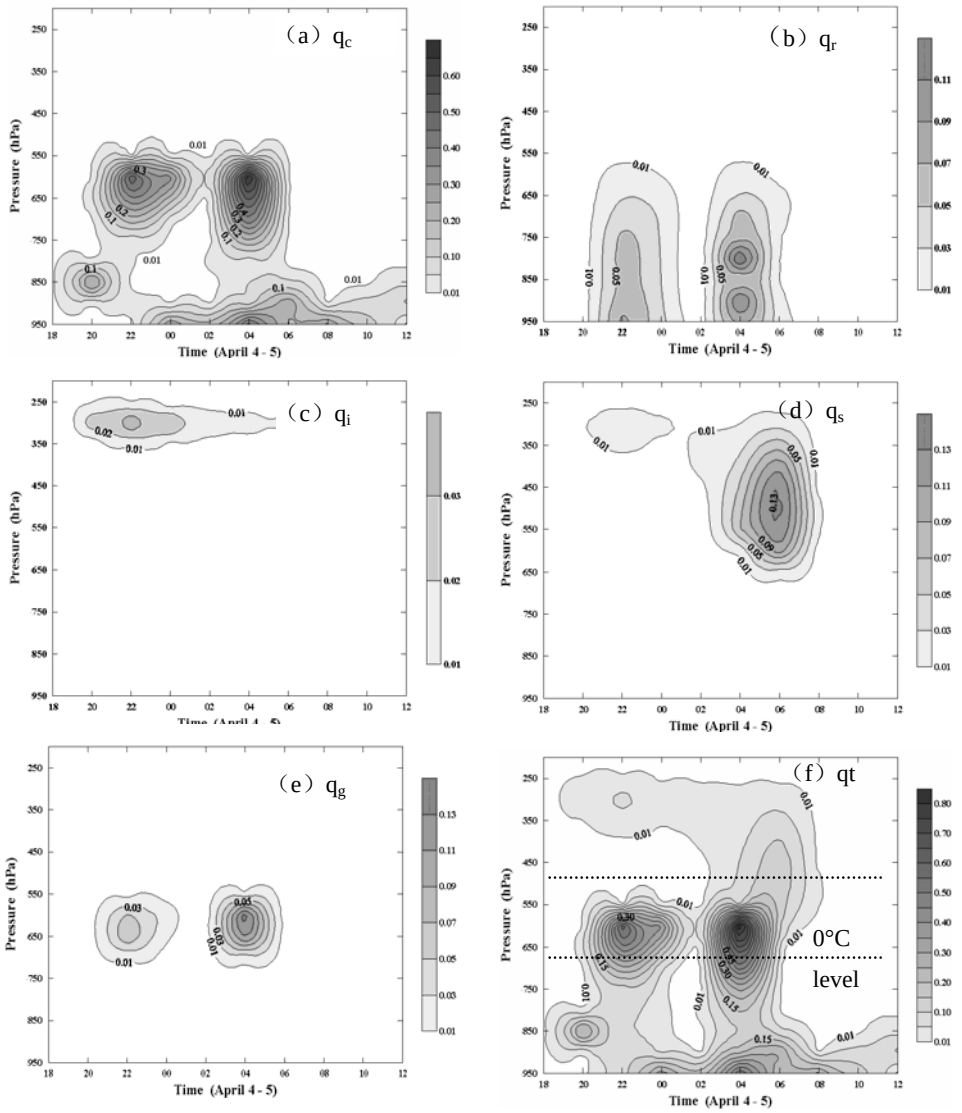

Figure3. Time-height section of water content of the rain (qr), ice crystals (qi), snow (qs), graupel (qg) and their total water content (qt) in the simulation cloud from April 4 to 5 at Zhengzhou station.

3.2 Precipitation Formation Mechanism in Different Position of the Cloud System

At 20:00, April 4, yinchuan station is the back area far away from the cold front, zhengzhou station is located in the front of the cold front. At 05:00, April 5, zhengzhou sation is in the front area. The precipitation mechanism in the front area has been studied[7].

Parameters of the simulation clouds in different positions of the cloud system are given in Table 3. It can be seen from these parameters that the precipitation formation mechanisms may be different in the frontal different parts. MLxr in the table is accumulative rainwater amount formed by melting of ice particles at 300th min of the cloud development and Qr represents the rain accumulate quantity. The ratio MLxr/Qr can indicate importance of the cold cloud processes in formation of rain water. The data in the table show that, precipitation in the back area far away from the cold front is formed by the cold cloud process and condensation-coalescence process is a very small role process. As for formation and growth way of the particles, snows in the back area far away from the front are mainly sublimation

process (VDvs) and growth process (CLcs) by accretion is weak, and in other parts of the cloud system, accretion growth process is stronger; graupels is formed mainly by frozen of small raindrops (CLrig) and in the other positions mainly by auto-conversion of snow (CNsg). 50% or more of the precipitations in the front area is formed by the cold cloud process, namely the cold cloud process advantage in the formation of precipitation. And in the front of the cold frontal cloud system, precipitation is formed mainly by warm cloud process. In addition, there is higher water vapor condensation rate in the front area and lower in the front of the cold front and extremely low in the back area of the front.

In other words, in the back part to be far away from the front，snow is mainly grown by sublimation process and can not be converted into graupel. Graupel is formed by freezing little raindrop and grown by collecting snow. Sublimation growth on the ice particles has a significant contribution to mass of the ice particle, precipitation mainly is formed by melting of ice particles. Compared with the front area, in the front area of the cold front, the warm cloud process has a larger contribution to rain water and 60% of the rain is produced by the warm cloud process; and contribution of cold cloud process to the formation of rain is significant. It follows that in different parts of the frontal cloud system, precipitation formation mechanisms are different and contributions of the cold cloud and warm cloud process to precipitation are different.

Table3. Precipitation formation characteristics in different parts of 0405 cloud system.

station	MLxr/Qr	Generation and growth of snow	Generation and growth of graupel	Condensation rate
Back area of front	100.0	CNis VDvs CLcs CLis	CLrig CLsg	1.5
Front area	57.1	CLis VDvs CLcs	CNsg CLsg CLcg	56.4
Front area of cold front	39.5	CLis CLcs VDvs	CNsg CLcg CLsg	32.1

4 ANALYSIS ON CONDITIONS OF ARTIFICIAL PRECIPITATION

Conditions for artificial precipitation of the stratiform cloud are discussed from research results of cloud structure and precipitation mechanism. It has been shown from analysis about vertical structure of the "0405" cloud system that the cloud water resources is layered, precipitation is formed by the "seeding-feeding" mechanism and cold cloud process plays an important role, melting of the ice particles has an important contribution for rainfall. Pure cold cloud or warm clouds do not produce larger precipitation and they have small precipitation enhancement. Therefore, "seeding-feeding" cloud is basic structure conditions for artificial precipitation of stratiform cloud.

In 040505 "seeding-feeding" clouds at zhengzhou, ice crystals are elementary particles to initiate precipitation, nearly 50% of ice crystals are transformed into snows and snow of 90% into graupels. The cold cloud precipitation is mainly formed by graupel melting. It is can be seen from generating process of the snow and graupel that ice crystals are the precipitation source, so the number of snow and then graupel is directly effected by the number of cloud ice. Ice crystals transformed into snow are almost entirely grown by sublimation, so in the area producing ice crystals, water vapor supersaturated with respect to ice is rich; In the snow region, there is must rich super-cooled water, snow transformed into graupel must be grown by accreted; Snows are grown mainly by the sublimation and collection; The growth of graupel depends on snow and super-cooled water. Thus, ice crystal concentration, water vapor supersaturated with respect to ice and super-cooled water content are main conditions

conducive to produce rainfall.

Research shows that [7], in the stratiform cloud, in which ice phase physical process has a significant contribution to precipitation, contributions of the vapor and super-cooled water to precipitation are almost same. Therefore, not only super cloud water is an operation parameter for artificial enhancement precipitation, but also water vapor supersaturated with respect to ice an important parameter.

In addition, as for descendent ice particles in the feeding cloud, they can be grown by collecting cloud water and have notable contribution to precipitation. So that as part of “seeding-feeding" cloud, cloud water content and cloud thickness of the warm cloud is also important factor for artificial enhancement precipitation.

In "seeding-feeding" cloud system, the precipitation is formed by the warm cloud and cold cloud processes, but they have different contributions in different cloud system, different positions and different developing stages of a cloud system. At present， artificial ice nucleus is generally seeded in stratiform cloud to increase precipitation, only cloud in which contribution of cold cloud process on natural precipitation is larger, artificial seeding has effect. So only cold cloud mechanism play an important role in precipitation formation, the "catalytic-supply" cloud just have seeding conditions.

5 BRIEF SUMMARY AND DISCUSS

By using the observed data and the numerical simulation, macro and micro structure, conversion of moisture and precipitation transformation mechanism for a low trough and cold front cloud system in henna area are analyzed, and on that Basis, seeding conditions for the artificial precipitation.

(1) Vertical stratification structure appears in stratiform cloud in the frontal area and there are high, medium and low three clouds, "seeding-feeding" cloud is a main structure characteristics. In different parts of the cloud system, compound mode of multilayer cloud is different, large condensation rate corresponds to the center of the moisture content.

(2) It can be seen from analysis of conversion of cloud water that 43% of water vapor input into cloud is transformed rainwater, i.e., rain efficiency is about 43%, 29% of the cloud droplets are transformed into precipitation particles, in which that transformed by ice phase process accounted for 55%. The growth of ice particles by accretion is the main process to convert cloud water into precipitation. About 49% of ice crystals are transformed into snow and ice crystal is the main source of snow formation. About 92% of the snow become graupel and 96% of graupels transformed into rain water by melting, rain water formed by the melting accounts for 57% of total amount of rain formation.

(3) Formation mechanisms of precipitation are quite different in the different parts of the cloud system. In the back area far away from the front area, the precipitation is almost entirely formed by the melting of the ice particles. Compared to the front area, warm cloud process has large contributions to precipitation in the front area of the cold front; And cold cloud process in the front area.

(4) On basis of over research, conditions of artificial precipitation are analyzed. The "seeding-feeding" cloud structure, precipitation mechanism, super-cooled water content, ice crystals concentration and water content in the warmer area and water vapor amount saturated with respect to ice can be used to judge the seeding condition for artificial precipitation.

REFERENCE

[1] Hong Yanchao, Zhou Feifei，2006:The study

of evaluation of potential of artificial precipitation enhancement in stratiform cloud system. Chinese Journal of Atmospheric Sciences, **30**(5)，913-926.

[2] Hobbs P V，1978:Organization and structure of clouds and precipitation on the mesoscale and microscale in cloud stroms. Rev. Geophys. Spcae Phys., **16**: 741—755.

[3] Hobbs P V, Matejka T J, Herzegh P H, et al. ,1980: The mesoscale and microscale structure and organization of clouds and precipitation in midlatitude cyclones. I: A case study of a cold front. J. Atmos. Sci., **37**,568—596.

[4] Herzegh P H, Hobbs P V, 1980: The mesoscale and microscale structure and organization of clouds and precipitation in midlatitude cyclones. II: Warm-frontal cloud. J. Atmos. Sci., **37**: 597-611.

[5]WANG Yang-feng , LEI Heng-chi , FAN Penga , WU Yu-xia , LU Zhong-yan,2007: Analyses on microphysical characteristic and precipitation mechanism on stratiform cloud in Yan an. Plateau Meteorology, **26**(2):388-395.

[6] You Laiguang, 1991: Progress in the study of cloud physics and weather modification in field experiment, Ann. Rep. Advances in Research of AMS, 1986-1990, China Meteorological Press, 89—100.

[7]Hong Yanchao, Zhou Feifei, 2005:A numerical simulation study of precipitation formation mechanism of “seeding-feeding”cloud system.Chinese Journal of Atmospheric Sciences, **29**(6), 885-896.

[8]Li Hongyu ,Wang Hua, Hong Yanchao,2006: A numerical study of precipitation enhancement potential in frontal cloud system. Chinese Journal of Atmospheric Sciences, **30**(2):341-350.

A NEW PARAMETERISATION FOR THE SEDIMENTATION OF HYDROMETEOR ENSEMBLES USING A FINITE MAXIMUM PARTICLE DIAMETER

Corinna Ziemer and Ulrike Wacker

Alfred Wegener Institute for Polar and Marine Research, Bremerhaven, Germany

1 INTRODUCTION

The parameterised treatment of the sedimentation of a drop ensemble still is a demanding task. Recently, several studies [Wacker and Lüpkes, 2009, Milbrandt and Yau, 2005, Mansell, 2010, Milbrandt and McTaggart-Cowan, 2010] have pointed out problems in the representation of physically relevant quantities when using the parameterisation of sedimentation as is. The latter three studies circumvented these problems with empirical corrections of the moment's mean fall speeds.

The authors present a new parameterisation with two prognostic moments, based on a more physical definition of the integral which constitutes the moments: while conventional methods employ an upper diameter limit of infinity for the sake of easy calculation, here a finite maximum drop diameter D_{max} is introduced. This corresponds to the non-existence of huge particles in nature.

2 PARAMETERISATION

We solve the equations for the drop number density N and the liquid water content L:

$$\partial_t N + \partial_z (\bar{v}_0(D_{max})\, N) = 0, \quad (1a)$$

$$\partial_t L + \partial_z (\bar{v}_3(D_{max})\, L) = 0, \quad (1b)$$

where $\bar{v}_i$ are the moments' mean falls speeds:

$$\bar{v}_i(D_{max}) = 1300 \int_0^{D_{max}} D^{i+0,5} f(D)\, dD / M_i, \quad (2)$$

given in cgs-units.

M_i denotes the i-th moment of the drop size spectrum f, so $N = M_0$ and $L \sim M_3$. The spectrum is assumed as $f(D) = n_0 D^{\mu} e^{-\lambda D}$ with $\mu = 0$ (Marshall-Palmer).

For the $\bar{v}_i$, the parameters of f (n_0 and λ) have to be calculated from N and L. In contrast to the conventional parameterisation with $D_{max} = \infty$, the slope parameter λ can be negative. This requires a special integration technique for Eq. (2) (see Ziemer and Wacker [2012] for details).

The initial configuration is a homogenous 'cloud' between two height layers. The initial mean mass L/N is termed x_{init}.

3 RESULTS

Fig. 1 shows the solution of (1) for various D_{max} and the spectral reference solution, which uses the fall speed of Beard [1976] and a maximum drop diameter of 0,75 cm.

D_{max} has a systematic influence on the results. For decreasing D_{max}, the N-signal speeds up, while the L-signal slows down. Furthermore, the spread of the L-signal decreases.

In the standard case of $D_{max} = \infty$, the N-signal is the same as for D_{max} = 1,00 cm. The L-signal, however, is much more damped and its forefront travels much faster.

The sensitivity of the results on changes in

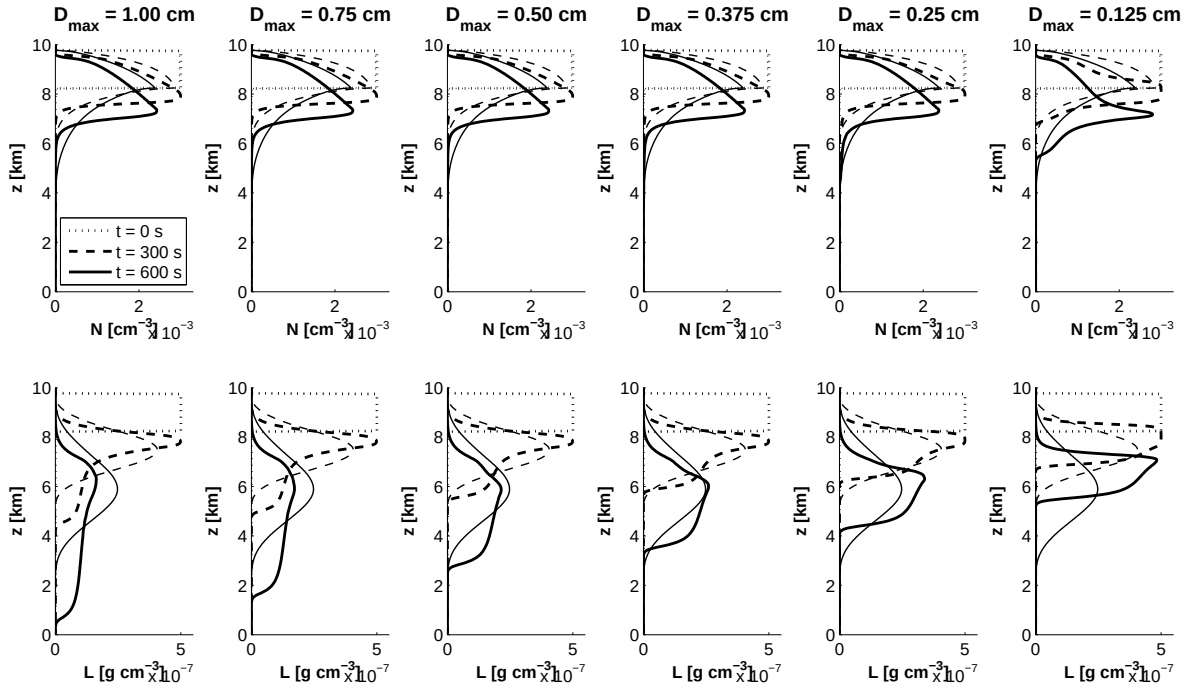

Figure 1: Results for the prognostic moments N and L with variable D_{max} (thick lines) and the reference solution (thin lines). $x_{init} = x_0 = 1{,}67 \cdot 10^{-4}$ g.

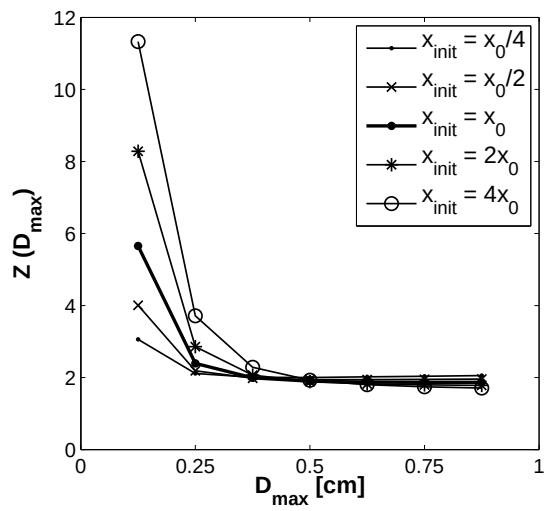

Figure 2: Sensitivity vs. D_{max}.

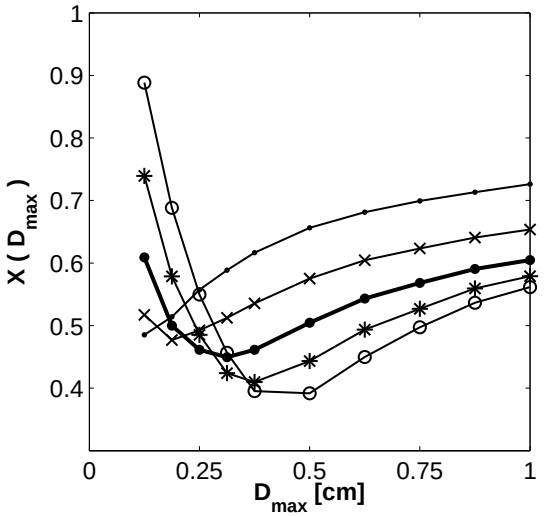

Figure 3: Error vs. D_{max}.

D_{max} for a quantity $\mathcal{M}$ is measured with

$$Z_{\mathcal{M}}(D_{max}) = \sum_{t_i} \left(\sum_{z_n} \left(\frac{\mathcal{M}_{i,n}(D_{max,2}) - \mathcal{M}_{i,n}(D_{max,1})}{\mathcal{M}_{init}(D_{max,1})\, \Delta D_{max}\, \mathcal{N}} \right)^2 \right)^{1/2}, \tag{3}$$

where $\Delta D_{max} = D_{max,2} - D_{max,1} > 0$ and $\mathcal{N}$ ist the number of timesteps t_i. A combination of this measure for $\mathcal{M}$ = N, L, M_6, RR, L/N gives the overall sensitivity Z (Fig. 2). It decreases with increasing D_{max}, giving low values for typical maximum drop diameter values of 5 to 10 mm.

The difference to the spectral reference so-

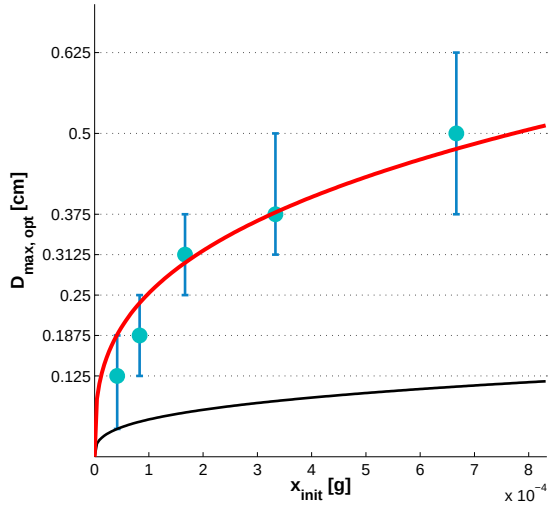

Figure 4: Data (blue points, error bars) and fit (red line) for $D_{max,opt}$. Black line: $\bar{D}(x_{init})$.

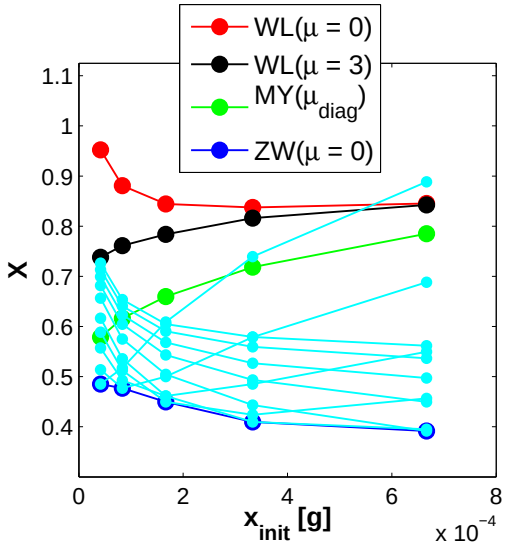

Figure 5: Error X vs. x_{init} for four different parameterisations (see text). •: ZW-Parameterisation for different values of D_{max} (0,125 to 1,00 cm).

lution can be measured with

$$X_{\mathcal{M}}(D_{max}) = \sum_{t_i} \left(\sum_{z_n} \left(\frac{\mathcal{M}_{i,n}^{param}(D_{max}) - \mathcal{M}_{i,n}^{spek}}{\mathcal{M}_{init}^{spek}\,\mathcal{N}} \right)^2 \right)^{1/2} . \quad (4)$$

The mean error X (Fig. 3) as a combination of the $X_{\mathcal{M}}$ is a quality criterion for the parameterisation. Its minimum gives an optimal D_{max}, termed $D_{max,opt}$. It depends on x_{init} and is lower than the physical maximum drop diameter. Fig. 4 shows a fit for $D_{max,opt}$.

Last, in Fig. 5, the new parameterisation (abbr. ZW(μ = 0)) is compared with the parameterisations of Wacker and Lüpkes [2009] (abbr. WL(μ = 0), WL(μ = 3)) and Milbrandt and Yau [2005] (abbr. MY(μ_{diag})). ZW(μ = 0) with its optimized D_{max} ranks lowest for all considered x_{init} and even non-optimal D_{max} have a comparably low error score.

With the help of an error score, an optimal D_{max} can be found, depending on x_{init}. The fact that $D_{max,opt}$ is smaller than the maximum drop size in nature makes its physical interpretation difficult.

The dependency of D_{max} on x_{init} implies: when simulating clouds in the tropics, where the mean drop mass is high, the use of a high D_{max} would yield good results in most cases. In mid-latitudes, however, a smaller D_{max} should be chosen, as in general the mean drop mass is lower.

The new parameterisation is computationally more expensive than the existing parameterisations. However, in exchange, the proposed parameterisation with a finite maximum drop diameter is closest to the reference, when comparing the results with existing parameterisations.

4 CONCLUSIONS

A new parameterisation for the sedimentation of drop ensembles was presented, which uses a finite upper drop diameter limit in the calculation of the moments.

The upper diameter limit D_{max} influences the results in a systematic way. The sensitivity decreases for higher D_{max}.

5 BIBLIOGRAPHY

K. V. Beard. Terminal velocity and shape of cloud and precipitation drops aloft. *J. Atmos. Sci.*, 33(5):851–864, 1976.

E. R. Mansell. On sedimentation and advection in multi-moment bulk microphysics. *J. Atmos. Sci.*, 67:3084–3094, 2010.

J. A. Milbrandt and R. McTaggart-Cowan. Sedimentation-induced errors in bulk microphysics schemes. *J. Atmos. Sci.*, 67:3931–3948, 2010.

J. A. Milbrandt and M. Yau. A multimoment bulk microphysics parameterization. Part I: Analysis of the role of the spectral shape parameter. *J. Atmos. Sci.*, 62(9):3051 –3064, 2005.

U. Wacker and C. Lüpkes. On the selection of prognostic moments in parameterization schemes for drop sedimentation. *Tellus*, 61A:498 – 511, 2009.

C. Ziemer and U. Wacker. Parameterisation of the sedimentation of raindrops with finite maximum diameter. *Mon. Weather Rev.*, 140(5):1589–1602, 2012.

Acknowledgments

This work was funded by the Deutsche Forschungsgemeinschaft grant WA 1334/8-1 within the framework of SPP 1276 MetStröm.

ASSESSMENT OF AEROSOL HYGROSCOPIC GROWTH USING AN ELASTIC LIDAR AND A RAMAN LIDAR IN URBAN METROPOLITAN AREAS.

P. F. Rodrigues[1], E. Landulfo[1], B.B. Demoz[2], D.D. Venable[2], M. Walker[2], R. Connell[2], D.N. Whiteman[3].

1 – Center for Lasers and Applications, Nuclear and Energy Research Institute, Sao Paulo, Brazil, E-mail:patricia.ferrini.rodrigues@usp.br

2 –Department of Physics and Astronomy, Howard University, Washington, D.C. 20059, USA

3 – NASA Goddard Space Flight Center, Greenbelt, Maryland 20771, USA

ABSTRACT

The extent to which aerosol particles have affinity for water vapor is a property that depends on chemical composition and atmospheric parameters, such as availability of water vapor, and is known as hygroscopic growth factor.

The size increase of aerosol particles resulting from water vapor uptake has important implications for the direct scattering of radiation and cloud droplets formation.

We used a single-wavelength backscatter LIDAR (532 nm) and relative humidity profiles obtained by radio sounding to study the growth of particles over the Sao Paulo metropolitan region, Brazil, on 13 September 2011, under different conditions of water vapor. On this day we had an ocean breeze onset and cloud formation over the metropolitan area, potentially bringing marine aerosols and humidity from the Atlantic Ocean. In order to infer the hygroscopic growth factor, we developed a fitting model algorithm, already proposed in the literature, calculating the 20-minute average backscattering coefficient at 532 nm during the breeze onset. We compared this average backscattering values from various altitude levels to a reference backscattering at the lowest relative humidity level.

Also, as a contrast to the Sao Paulo study, we used data from a Raman LIDAR (355 nm), to study the relation between the changes in backscatter with the changes in relative humidity over the metropolitan region of Washington D.C, United States. The values of water vapor mixing ratio and backscattering were determined using the Raman LIDAR instrument. For that purpose we used cloud caped days and clouds as point of reference, selecting periods with clouds and performing the calculations of changes in backscattering based on the water vapor mixing ratio and the relative humidity. Both results were compared.

1. INTRODUCTION

1.1. Hygroscopic Growth

The size increase of aerosol due the water uptake is a property known as hygroscopic growth. It depends on the chemical nature, size and shape of aerosol and on the water vapor availability and has important effects on direct radiation scattering (direct effect) and on indirect effects, related to the capacity of one aerosol population to work as CCN (cloud condensation nuclei to form cloud droplets). Acting as a CCN is common in more hygroscopic aerosols[1,2]. As clouds contribute to the enhancement of the albedo from earth, the indirect effect leads to a radiative cooling of the global system. As discussed by Twomey [3], an increase in antropogenic sources of aerosol would increase the number of CCNs, leading to a higher cloud droplets number and consequently to more reflection of solar radiation by clouds. But, as shown by Wulfmeyer and Feingold [4], if these aerosols are non hygroscopic, the increase in their number would not mean more cloudiness and could even result in reduction of cloud droplets. For this reason, understanding the hygroscopic properties of aerosols is important in the determination and their relation to cloud formation and the radiative balance.

LIDAR has several advantages over other methods on measuring hygroscopic growth. Foremost, the fact that this remote sensing system is able to measure changes in backscattering under unperturbed atmospheric conditions, besides the fact that the range of measurements can be extended to very close to saturation.[5] The increase in the liquid water absorbed by particles leads to an increase of their size (hygroscopic growth) and also causes changes in the refractive index. Therefore, significant variations in the aerosol backscattering signal detected with a LIDAR are expected when changes in RH are observed. This is particularly true for high RH levels, where hygroscopic growth of aerosols is more pronounced.[6]

In this work, we investigated and compare hygroscopic growth of aerosols over Washington, D.C., U.S, using data obtained from a Raman LIDAR operating at 355nm (Howard University Raman LIDAR - HURL), with data obtained with an elastic LIDAR over São Paulo, Brazil (IPEN – Nuclear And Energy Research Institute LIDAR)

For this purpose, we selected backscattering and relative humidity data for one day of measurement during the DISCOVER-AQ experiment (*www.nasa.gov/**discover-aq**/*) in the US and one day of data obtained in São Paulo, aiming at evaluating differences in backscatter signal of aerosol population with changes in relative humidity at the two sites.

1.2. DISCOVER-AQ

The DISCOVER-AQ project (Deriving Information on Surface Conditions from COlumn and VERtically Resolved Observations Relevant to Air

Quality) is a collaboration between U.S. Environmental Protection Agency (EPA) and NASA aimed at improving satellite capability to interpret air quality conditions near the earth's surface. DISCOVER-AQ employs NASA aircraft to make series of flights with instruments on board to measure gaseous and particulate pollution in targeted metropolitan areas. The research is expected to provide a greater understanding on how satellites can be used to understand pollutant concentrations and distributions near the earth's surface. The first segment of the project's data collection ran from July 1-31 (14 flights), when two NASA airplanes flew over the Baltimore-Washington Interstate-95 corridor collecting data on ozone, nitrogen dioxide, formaldehyde, aerosols, and sulfur dioxide.

1.3. Howard University Raman Lidar

A Raman Lidar system was developed at the Howard University Atmospheric Observatory in Beltsville, MD (HURL), to provide nighttime and daytime measurements of water vapor, aerosols, and cirrus clouds. Signals at three wavelengths, the Rayleigh-Mie for aerosol scattering at 354.7 nm, Raman scattering for nitrogen at 386.7 nm, and water vapor at 407.5 nm are analyzed. The transmitter is a triple harmonic Nd: YAG solid state laser. The receiver is a 40 cm Cassegrain telescope.

1.4 The IPEN elastic LIDAR

The elastic LIDAR system employed in this work, located at the Nuclear and Energy Research Institute (IPEN), in São Paulo, is a single-wavelength backscatter system pointing vertically to the zenith and operating in the coaxial mode. The light source is based on a commercial Nd:YAG laser (Brillant by Quantel SA) operating at the second harmonic frequency (SHF), 532 nm, with a fixed repetition rate of 20 Hz. The emitted laser pulses have a divergence of less than 0.5 mrad after expansion. A 30 cm diameter telescope (Focal length =1.5m) is used as receiver. The telescope's field of view (FOV) is variable (0.5 mrad) by using a small diaphragm. The system is currently used with a fixed FOV of 1mrad, which permits a full overlap between the telescope FOV and the laser beam at heights around 300m above the ground level. This FOV value, in accordance with the detection electronics, permits the probing of the atmosphere up to the free troposphere (12-15 km). The backscattered laser radiation is then sent to a photomultiplier tube (PMT) coupled to a narrowband (1nm FWHM) interference filter to assure the reduction of the solar background during daytime operation and to improve the signal-to-noise ratio (SNR) at altitudes greater than 3 km. The PMT output signal is recorded by a transient recorder in both analog and photoncounting mode. Data are averaged between 2 and 5 min and then summed up over a period of about 20 min, with a spatial resolution of 3.75 m. [8]

2. METHODOLOGY

We choose 1 day from the DISCOVER-AQ data archive in which we could verify and characterize cloud cap using the LIDAR and data from radiosondes launched at the same site. The Raman LIDAR provided data for water vapor mixing ratio and aerosol scattering ratio, and the radiosondes data for temperature and pressure.

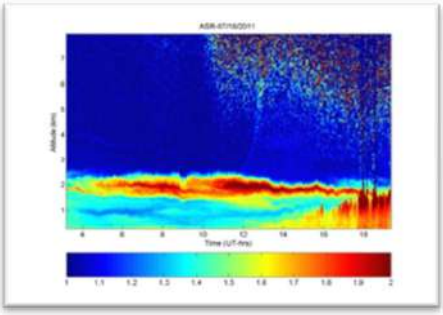

Figure 1 – Aerosols Scattering Ratio for 18 September 2011. It´s possible to see the cloud cap around 18UTC, at the top of the fast increasing of backscatter signal.

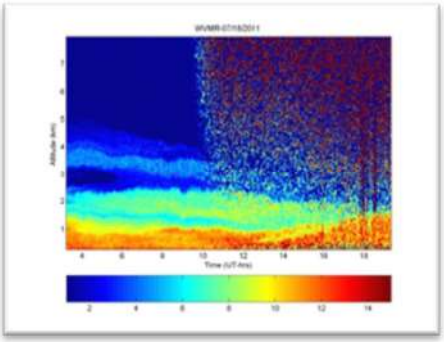

Figure 2 – Water Vapor Mixing Ratio for 18 September 2011. The cloud cap is possible to identify due the high noise above 1.2 km around 18UTC

We selected 25 minutes data around the time when the radiosonde was launched, and calculated relative humidity using water vapor mixing ratio from LIDAR and temperature and pressure using radiosonde. The aerosol scattering ratio provided by the LIDAR was used to derive the backscattering in the same sample were the RH was calculated. After obtaining the backscattering and the relative humidity, we calculated the hygroscopic growth factor, where is the backscattering value for aerosol subjected to a RH value higher than the reference one, and is a reference backscattering value for a chosen level of RH. In this work we used the particular value of of 42% for 07/18/2011 (data from Washington D.C.) and 72% for 09/13/2011 (data for São Paulo). Those reference levels were the lowest value of the relative humidity for the data studied. In sequence, we fitted a curve to the data, in the form [7]:

— **(1)**

were **a** represents the total light scattering for the dry aerosol and **b** is a fitting parameter that can be used to describe the variation of the data set.

For data obtained in São Paulo using an elastic LIDAR, we selected one day of Atlantic Ocean breeze onset over the metropolitan region, when we could verify also a cloud cap formation around 22 UTC (09/13/2011). A radiosonde was launched at 00UTC in Campo de Marte Airport, 10 km away from the place where the LIDAR was located.

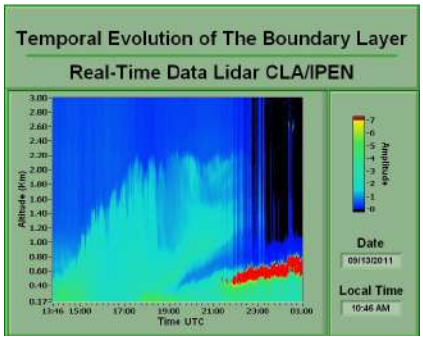

Figure 3 – Evolution of the boundary layer for 09/13/2011 showing the breeze onset around 19 UTC and the cloud cap formation around 22 UTC

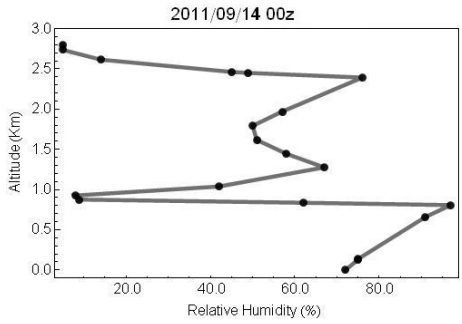

Figure 4 – Relative humidity profile obtained by the radiosonde launched at 00 UTC. It´s possible to see the increasing of the relative humidity with altitude from 0 to 900 meters.

For this Brazil data, we took three periods of twenty minutes each and calculated the hygroscopic growing factor using a lowest level of relative humidity of 72% and taking the cloud base as the stop point. The results were fitted to the curve described by equation 1. As the radiosonde is launched 10 km far from the LIDAR and showed an increasing pattern of relative humidity in the altitudes of interest, we used an interpolation function to obtain the relative humidity at the same heights of the LIDAR. Also, we performed a simulation using BRAMS (Brazilian developments on the Regional Atmospheric Modelling System) to follow the trajectory of the air parcel coming from the Atlantic Ocean at the same time of the breeze onset over Sao Paulo (data not shown) [9]. The breeze is assumed to transport humidity and marine aerosols from the ocean, contributing for the cloud formation.

3. RESULTS AND DICUSSION

The results for the parameters **a** and **b** are shown in the figures 5 and 6.

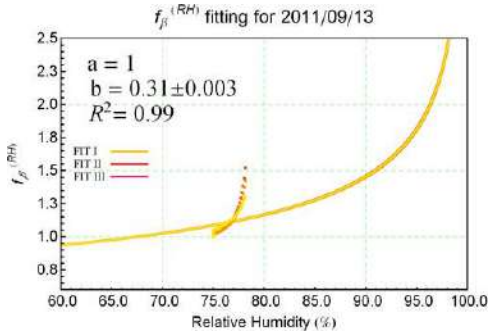

Figure 5 – Fitting curve for 09/13/2011 for the three periods considered for analysis. Data from São Paulo.

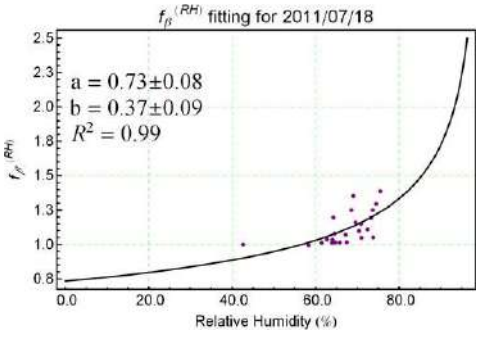

Figure 6 – Fitting curve for 07/18/2011. Data from Washington, D.C.

The highest point to be considered for 09/13/2011 was chosen using the images of the backscattering pattern for

this day, combining with the relative humidity obtained by the radiosonde. The maximum RH in altitude for 09/13/2011 is 95%, and then we have a ratio ——. As the cloud cap formation is about 400m to 500m from the ground, only few points could be used for analysis. With these few available points, we fixed the value of **a** equal to one and adjusted **b**, as done by Im [2].

As we consider only a few points above the cloud basis, it was difficult to conclusively derived the backscattering pattern. Thus, we used points when we had clear sky during the cloud period as reference point for Klett analysis.

The highest point to be considered was chosen using the images of Aerosol Scattering Ratio for this 07/18/2011, and an algorithm to derive cloud base is needed and is still being constructed for these analysis, combining the relative humidity calculated from the water vapor mixing ratio and the peak in the backscattering. The maximum RH in altitude for 07/18/2011 is 78%, and then we have a ratio —— . The adjustment for **a** and **b** were done without using a fixed value by **a**, as done by Tardif [7].

Im et al. [2] encountered, for one experiment made in western North Carolina, the values for **b** to be equal to 0.38 ± 0.03 with an $R^2=0.94$ for polluted continental air masses, 0.37 ± 0.05 with an $R^2 = 0.84$ for continental air masses, and 0.38 ± 0.05 with an $R^2 = 0.85$ for marine air masses and the hygroscopic growth factor was calculated to be 1.61 for polluted continental air masses, 1.61 for marine air masses, and 1.59 for continental air masses, indicating that the hygroscopic growth factor is nearly constant for the three different air masses unlike our values here. They used a ratio from —— in their work, maintaining a constant and equal to 1 [7]. Our results showed agreement with the results found by Im. The differences between the two places considered, São Paulo and Washington D.C. may be due to the distance from the radisonde to the LIDAR place in São Paulo, implying in data collected from different air parcels. But even if the radiosondes were lauched at the LIDAR site, differences are expected because of variations of the aerosol population.

Further developments of this work include, besides the algorithm to retrieve cloud base, error analysis, modeling of the origins of aerosol population and comparisons of lidar data to data obtained from other instruments.

BIBLIOGRAPHY

1. Dubovik, O., Holben, B., Eck, T. F., Smirnov, A., Kaufman, Y. J., King, M. D., Tanre, D., and Slutsker, I. 2002: Variability of absorption and optical prop-erties of key aerosol types observed in worldwide locations. J. Atmos. Sci., 59, pp. 590-608.

2. Im, J.-S., Saxena, V. K., and Wenny, B. N. 2001: An assessment of hygroscopic growth factors for aerosols in the surface boundary layer for computing direct radiative forcing Journal of Geophysical Research, 106, pp. 20213-20224.

3. Twomey, S. 1974: Pollution and the planetary albedo Atmospheric Environment, 8, pp. 1251-1256.

4. Wulfmeyer, V. and Feingold, G. 2000: On the relationship between relative humidity and particle backscattering coefficient in the marine boundary layer determined with differential absorption lidar Journal of Geophysical Research, 105, pp. 4729-4741.

5. Feingold, G. and Morley, B. 2003: Aerosol hygroscopic properties as measured by lidar and comparison with in situ measurements Journal of Geophysical Research, 108, pp. 4327.

6. MacKinnon, D. 1968: The Effect of Hygroscopic Particles on the Backscattered Power from a LaserBeam. Journal of The Atmospheric Sciences, 26, pp.500-510.

7. Tardif, R. 2002: Boundary layer aerosol backscattering and its relatioship to relative humidity from a combined raman-elastic backscattering LIDAR.

8. Landulfo, E., Papayannis, A., Freitas, A. Z., Vieira Junior, N. D., Souza, R. F., Gonçalves, A., Castanho, A. D. A., Artaxo, P., S´anchez-CCoyllo, O. R., Moreira, D. S., and Jorge, M. P. M. P. 2005. “Tropospheric aerossol observations in Sao Paulo, Brazil using a compact lidar system,” Int. J. Rem. Sens. 13, 2797–2816.

9. Rodrigues, P. F., Lopes, F. S., Costa, R. F., Nakaema, W., and Landulfo, E., 2010. “Indirect aerosol hygroscopic growth observations with a backscatter LIDAR,” in [Proceedings of SPIE], 7832, 78320F, SPIE Digital Library.

LABORATORY SIMULATION OF SPONTANEOUS BREAKUP OF POLLUTED WATER DROPS IN THE HORIZONTAL ELECTRIC FIELD

Rohini Bhalwankar, Subashini Subramanian and A K Kamra

Indian Institute of Tropical Meteorology, Pune, India

ABSTRACT: A laboratory simulation experiment to study the spontaneous breakup of distilled and polluted water drops suspended in horizontal electric field of 0, 100, 300, 500 kV m^{-1} has been performed in a small vertical wind tunnel. Water drops are formed from distilled water and from 100 ppm solution of ammonium sulphate and potassium nitrate. Results show that the life time of the suspended water drops decreases with the increase in electric field. The decrease in life time is sharper when the water drops are polluted. Water drops formed from both distilled and polluted water become more oblate as the electric field is increased. The results have been interpreted in terms of enhanced instability of water drops due to dramatic increase in the conductivity of water drops when pollutants are added in the distilled water. The changes in surface tension, viscosity and hydro-dynamics of the water drop due to addition of pollutants in them are also discussed. Significance of the results is discussed in view of the possible modification of drop size distribution and consequent growth of raindrops and lightning activity due to the combined effect of pollutants and electrical forces in clouds formed over big cities.

1. INTRODUCTION

Spontaneous breakup of raindrops is an important process in the evolution of drop spectra and development of precipitation by collision–coalescence processes in convective clouds. Langmuir [1948] first proposed the formation of rain in warm cloud by a chain reaction i.e. fragmentation of large drops due to aerodynamic breakup and growth of smaller drops by collision-coalescence which determines drop size distribution of raindrop in convective clouds. Since then many experimental and theoretical studies showed the importance of the raindrop breakup in evolution of their size distribution. The overwhelming cause of drop breakup which governs the drop evolution in larger size range is collision with smaller droplets [McTaggart–Cowan and List, 1975 b; Low and List,1982a, b; Feingold et al., 1988]. However, discussing the relative importance of spontaneous breakup of raindrops, Blanchard [1949]; Komabayasi [1964]; Beard and Pruppacher [1969]; Reisin et al.[1998] showed that it restricts the formation of giant drops with diameter > 4mm. Recently, Villermaux and Bossa [2009] described the breakup of large single drops (d > 6mm) with a laboratory demonstration of bag breakup. Moreover, in a model, they proposed the importance of spontaneous breakup than that of the collisional breakup as the time scale for distortion and spontaneous breakup for a single drop is much shorter than the typical collision time between the drops. In addition to spontaneous breakup and collisional breakup, the third conceivable cause for the drop breakup is the strong electrical forces present in thunderclouds [Latham, 1965; Richards & Dawson, 1971; Levine, 1971; Kamra et al., 1991, 1993; Coquillat et al., 2003, Bhalwankar and Kamra, 2007].

In most of the previous theoretical and experimental studies pure water has been considered to form the drops. In recent decades, however, impact of anthropogenic aerosols on cloud microphysical processes have become increasingly important as these aerosols pollute the raindrops in clouds either by nucleation or scavenging processes. Incidences of acid rain in big cities show a great impact of pollutants on cloud and raindrops. Further, analysis of rain water and cloud water samples show that there are several chemical compounds in the rain water and their concentrations vary over many orders of magnitude. [Huff and Changnon,1973; Pruppacher and Klett, 2000]. The polluted water drops and strong electric fields coexist in the thunderstorms which develop over big cities. Thus, the change in surface tension, viscosity, density and electrical conductivity of polluted drops will significantly affect the collision-coalescence

and breakup mechanisms which in turn influence the formation of rain in thunderclouds [Boussaton et al., 2005; Bhalwankar and Kamra, 2009]. Moreover, recently it has been suggested by many investigators that presence of these polluted drops in thunderclouds not only modify the size distribution of raindrops but also influence the occurrence and nature of the lightning activities over cities [Westcott,1995; Steiger et al., 2002].

The present work extends our earlier results to include the effect of pollutants on breakup of water drops in presence of horizontal electric fields. We present here, results of laboratory simulation experiments performed in a small vertical wind tunnel to study the combined effect of pollutants and horizontal electric field on the probability of breakup of large drops.

2. EXPERIMENTAL PROCEDURE

Experiments were conducted in a small, low turbulence vertical wind tunnel by suspending the uncharged water drops of known volume [Kamra et al., 1991,1993]. Water drops of equivalent diameter of 6.6 mm are freely suspended in a velocity well created in the airflow. The details of measurements and profiles of the vertical velocity and intensity of turbulence in the tunnel are reported earlier by Kamra et al. [1991]. These measurements show that even in presence of electrodes, the turbulence level in the center of test section where drops are suspended is less than 0.8 %.

Uncharged water drops of 6.6 mm diameter formed from distilled water and 100 ppm solution of ammonium sulphate /potassium nitrate were suspended in the wind tunnel in presence /absence of electric fields of 0, 100, 300 and 500 kV m^{-1}. The values of surface tension, viscosity and density of the solution at 20^0C for sulphate/nitrate solution, interpolated from tables (Lange and Forker, 1967) show an increasing trend than that of distilled water. However, the electrical conductivity of solutions of ammonium sulphate /potassium nitrate measured by a conductivity meter is 149 µS cm^{-1} and 110.6 µS cm^{-1} which is higher by 2 order of magnitude than that of distilled water which is 1.10 µS cm^{-1}.

To generate horizontal electric field, two flat, circular, aluminium electrodes of 15 cm diameter with edges suitably rounded are mounted vertically above the test section. Detailed description of the experimental arrangement is given in Kamra et al.[1993]. These two electrodes are separated by 12 cm distance. So by raising one of the electrode to 60 kV, an electric field of up to 500 kV m^{-1} can be generated without any measurable corona from the electrodes.

3. EXPERIMENTAL RESULTS

A. LIFE TIME OF DROPS

Raindrops break up immediately after they attain a critical size. The stability and the critical size for break up of the falling drop is determined by the surface tension, hydrostatic, aerodynamic and electrostatic forces and the forces due to drop's internal circulations. Level of turbulence in the airflow also influences the value of critical diameter at which spontaneous breakup is initiated. It has been observed that the uncharged water drops of < 6.6 mm diameter do not break up in our wind tunnel [Kamra et al.,1991]. In the present experiment, we take only uncharged water drop of 6.6 mm diameter. These drops were formed from distilled water as well as aqueous solution of sulphate /nitrate salts. Drops were suspended between the two electrodes placed vertically above the test section and then the electric field was quickly raised to a desired value within 2 to 3 sec. The time interval from raising the electric field to the spontaneous breakup was measured with a stop watch. The idea of spontaneous breakup of large drops was taken from the concept of disintegration of radioactive matter due to its random nature. Therefore, the time period from the suspension to breakup of a drop was termed as lifetime of the drop as defined by Komabayasi et al. [1964] and in our earlier experiment [Kamra et al., 1991]. The lifetime of individual drop was different even when the size of the drop, electric field value and the solution are same. 10 drops of distilled water and each solution were suspended in horizontal electric fields of 0,

100, 300 and 500 kV m^{-1} and the life time of individual drop was measured.

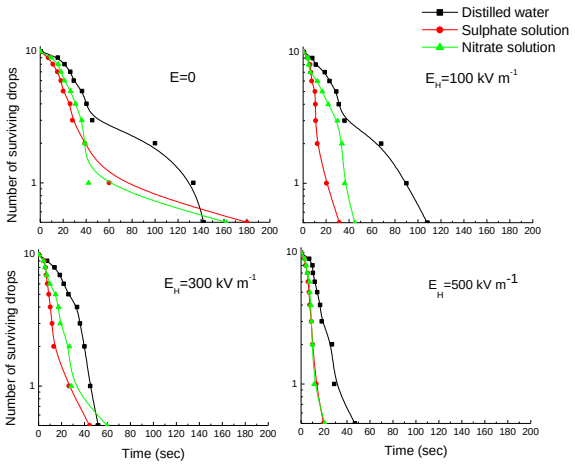

Figure 1.Number of water drops surviving spontaneous breakup at different times when drops are formed from distilled water and aqueous solution of sulphate /nitrate salt and suspended in different horizontal electric fields

Figures 1 shows the number of drops surviving without breakup at a particular time for drops of 6.6 mm diameter formed from distilled and polluted water drops (aqueous solution of sulphate and nitrate salts) suspended in presence of horizontal electric fields of 0, 100, 300 and 500 kV m^{-1}. Figure 1 shows that lifetime of drops decreases as electric field increased from 0 to 500 kV m^{-1} In the absence of electric field, the data for both polluted and distilled water show that some of the drops can be suspended for relatively much longer times giving rise to a tail in the curve. This tail is not observed when the drops are suspended in horizontal electric fields. Results show sharp decrease in number of surviving drops when they are suspended in high electric field region i.e. 500 kV m^{-1}. Figure 1 also shows the effect of pollutants on their lifetime. In all electric field values, lifetime of the drops formed from sulphate/nitrate solution is less than those formed from distilled water. However, with increase in electric field, lifetime of the polluted drops decreases sharply and the difference between the lifetime of drops formed from sulphate and nitrate solution decreases. Thus, the combined effect of chemical impurities and electrical forces in polluted drops feedback each other for drop break up to occur more readily than that of unpolluted drops.

B. HALF LIFE OF THE DROPS

As in case of radioactive matter, the spontaneous breakup of water drops is considered as a random phenomenon. Thus, the time at which the number of surviving drops remains half of the initial number can be termed as half-life of the drop. Figure 2 shows half-life for drops of distilled water as well as polluted solution of 6.6 mm diameter in different electric fields. The half-life of the drop decreases with the increase in the electric field values from 0 to 500 kV m^{-1} and with the addition of pollutants. This shows that conductivity, density, surface tension forces due to addition of pollutants and the electrical forces play an important role in destabilizing the water drops. The difference between the half life of the drops with distilled water and pollutants reduces as electric field increases.

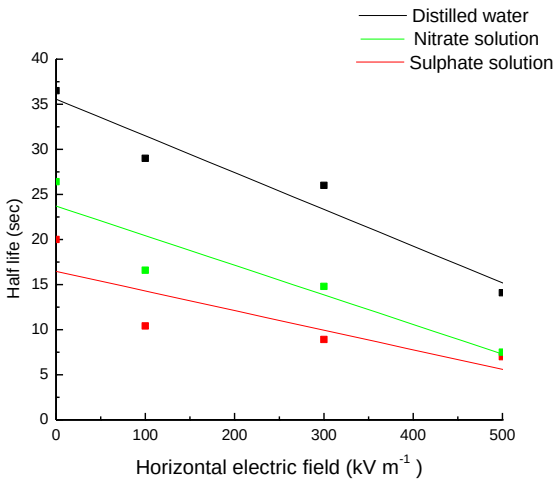

Figure 2. Half-life of drops formed from distilled water and aqueous solution of sulphate / nitrate salt suspended in different horizontal electric fields.

4. DISCUSSION

With the increase in drop diameter, there is gradual increase in the instability of the drop and after attaining a critical size, drops become hydrdynamically unstable and break up in smaller fragments. However, raindrops in thunderstorms which develop over big cities, industrial area are polluted with chemical impurities and also located in high electric fields. Results of our laboratory experiment show that in addition to spontaneous and collisional breakup, the breakup of polluted drops due to the electrical forces may be important in thunderstorms.

Addition of inorganic salts in water drops increases the surface tension, viscosity, density, and electrical conductivity of water [Pruppacher and Klett, 2000] and the forces due to these modified parameters interact in a complex way to determine the equilibrium shape of the drop. Change in electrical conductivity is likely to play an important role in distorting the drop. Salts added in water get dissolved in it and their dissociation in water produces cations and anions. In presence of horizontal electric fields these ions get attracted towards positive or negative electrodes. The enhanced distortion of polluted drops with horizontal electric field is the combined effect of the enhanced induced charges on the surface of water drops and the attraction of cations and anions along the direction of electric field. Enhancement in drops distortion is more in higher horizontal electric fields since the electrical forces due to induced charges on the drop and acting on anions and cations are proportional to the square of the electric field. The effect of horizontal electric field will be to make it more oblate and to increase the probability of its breakup in electric field. The systematic decrease in half life of the drops with increase in electric field and with addition of salts observed in our experiments, are in accordance with such effects. The enhanced breakup of drops will narrow down the drop size distribution in regions of horizontal electric field in clouds as also concluded by *Bhalwankar and Kamra* [2007]. The enhanced drop distortion will increase the probability of corona discharge from drop which may initiate the lightning discharge inside the clouds formed over polluted cities.

5. CONCLUSIONS

Our observations of the breakup of water drops suspended in a vertical wind tunnel shows that probability of drop breakup increases with increase in horizontal electric field and addition of inorganic salts. The observed changes in drop's instability are likely to be a consequence of the enhanced electrical conductivity of the water polluted with sulphate/nitrate salts. The results are significantly important in interpreting the modification of the size distribution, rate of growth of raindrop and lightning activity in the clouds formed over big cities. Analysis of breakup characteristics of drops with high speed photography revealing more details of the drop breakup will certainly improve our knowledge of the phenomenon.

REFERENCES

Beard K. V. and H. R. Pruppacher (1969), A determination of the terminal velocity and drag of small water drops by means of a wind tunnel, J. Atmos. Sci., 25,1066-1072.

Bhalwankar and Kamra (2007), A wind tunnel investigation of the deformation of water drops in the vertical and horizontal electric fields, J. Geophys. Res., 112, D10215, doi:10.1029/2006JD007863.

Bhalwankar, R. V., and A. K. Kamra (2009), A wind tunnel investigation of the distortion of polluted water drops in the horizontal electric fields, J. Geophys. Res., 114, D10205, doi:10.1029/2008JD011102.

Blanchard, D. C. (1949), Experiments with water drops and the interactions between them at terminal velocity in air, Occas. Rep. 17, Proj. Cirrus, Gen. Electr. Res. Lab., Schenectady, N.Y., 29.

Boussaton, M. P., S. Coquillat, S. Chauzy, and J. F. Georgis (2005), Influence of water conductivity on micro-discharges from raindrops in strong electric fields, Atmos. Res., 76, 330– 345, doi:10.1016/j.atmosres.2004.11.017.

Coquillat, S., and S. Chauzy (1993), Behavior of precipitating water drops under the

influence of electrical and aerodynamical forces, J. Geophys. Res., 98,10,319–10,324, doi:10.1029/93JD00389.

Feingold, G., S. Tzivion, and Z. Levin (1988), The evolution of raindrop spectra, Part I, Stochastic collection and breakup, J. Atmos. Sci., 45, 3387-3399,

Kamra, A. K., R. V. Bhalwankar, and A. B. Sathe (1991), Spontaneous breakup of charged and uncharged water drops freely suspended in a wind tunnel, J. Geophys. Res., 96, 17,159–17,168, doi:10.1029/91JD01475.

Kamra, A. K., R. V. Bhalwankar, and A. B. Sathe (1993), The onset of disintegration and corona in water drops falling at terminal velocity in horizontal electric fields, J. Geophys. Res., 98, 12,901 – 12,912,doi:10.1029/93JD00625.

Komabayasi, M., T. Gonda, and K. Isone (1964), Life time of water drops before breaking and size distribution of fragment droplets, J. Meteorol. Soc. Jpn., 42(II), 330-340.

Latham, J. (1965), The mass loss of water drops falling electric fields, Q. J. R. Meteorol. Soc., 91, 87-90.

Lange, N. A., and G. M. Forker (1967), Handbook of Chemistry, McGraw Hill, New York.

Langmuir I. (1948),The production of rain by a chain reaction in cumulus clouds at temperature above freezing, J. Meteorol., 5, 175-192.

Levine, N. E. (1971), Disruption of charged water drops in an external electric field, J. Geophys. Res., 76, 5079-5100.

Low, T. B., and R. List (1982a), Collision, coalescence and breakup of raindrops, Part I, Experimentally established coalescence efficiencies and fragment size distribution in breakup, J. Atmos. Sci., 39, 1591-1606.

Low, T. B., and R. List (1982b), Collision, coalescence and breakup of raindrops, Part II, parameterization of fragment size distribution, J. Atmos.Sci., 39, 1607-1618.

McTaggart –Cowan, J. D., and R. List (1975), Collision and breakup of water drops at terminal velocity, J. Atmos. Sci., 32, 1401-1411.

Pruppacher, H. R., and J. D. Klett (2000), Microphysics of Clouds and Precipitation, Kluwer Acad., Dordrecht, Netherlands.

Reisin T. G., Yan Yin, Z. Levin, and S. Tzivion (1998), Development of giant drops and high-reflectivity cores in Hawaiian clouds: numerical simulations using a kinematic model with detailed microphysics, Atmos. Res. 45,275-297.

Richards, C. N., and G. A. Dawson (1971), The hydro-dynamic instability of water drops falling at terminal velocity in vertical electric fields, J. Geophys Res., 75, 3445-3455.

Steiger, S. M., R. E. Orville, and G. R. Huffines (2002), Cloud-to-ground lightning characteristics over Houston, Texas: 1989–2000, J. Geophys. Res., 107(D11),4117, doi:10.1029/2001JD001142.

Villermaux, E. and B. Bossa (2009), Single-drop fragmentation determines size distribution of raindrops, Nature Physics 5, DOI:10.1038/NPHYS1340, 697-702.

Westeott, N. E., (1995), Summertime cloud-to-ground lightning activity around major Midwestern urban areas, J. Appl. Meteorol., 34, 1633-1642.

PHYSICAL PROCESSES AND CHANGES IN CB CHARACTERISTICS DUE TO FEEDER CLOUD MERGING

Andrei A. Sinkevich[1] and Terrence W. Krauss[2]
[1]Main Geophysical Observatory, St.Petersburg, Russia, 194021, sinkev@email.com
[2]Weather Modification Inc., 3802 20th Street, Fargo, ND 58102,USA, twkrauss@gmail.com

1.INTRODUCTION

Cloud mergers become the subject of numerous observational and numerical modeling studies (Dennis et al, 1970, Westcott, 1984, Farley, 1987, Cheng and Rogers, 1988). Cumulus (Cu) merging is a complex dynamical and microphysical process in which two convective cells merge into a single cell. Previous radar observations and numerical simulations show a substantial increase in the maximum area, maximum echo top and maximum reflectivity as a result of the merging process (e.g., Simpson and Woodley 1971; Changnon 1976; Wiggert et al. 1981; Woodley et al. 1982; Turpeinen , 1982, Krauss et al. 2007a,b, Krauss et al. 2011b,c,d, Sinkevich et al. 2009). In Florida, Simpson et al. (1980) noted that the merging of two moderate-sized cumulonimbus (Cb) produced a ten to twenty-fold increase of rainfall, and that merged cells were responsible for 86% of the rainfall over the area even though 90% of the cells were unmerged. Case studies of seeding experiments carried out in Russia, using aircraft data and numerical modeling, showed that seeding of feeder clouds can impact Cb development (Dovgaljuk et. al 1990, Sinkevich 2001). Krauss et al. (2010) attempted to evaluate the precipitation enhancement by cloud seeding in southwest Saudi Arabia, however, the results were complicated by several cloud mergers that dominated the results.

Although the qualitative aspects of merging have been well-documented, the quantitative effects on stom properties remains less defined. Most of the mentioned investigations deal with a few case studies, therefore, a statistical assessment of changes in storm characteristics due to merging is of high importance. Further investigation into the effects of cloud merging provided the motivation for this study.

The main objective of this study is to investigate in a statistical manner the changes in storm characteristics derived from radar measurements before and after merging takes place.

2. BRIEF CLIMATOLOGY OF THE STUDY REGION and TYPICAL METEOROLOGICAL CONDITIONS

Measurements were carried out in Asir region of the Kingdom of Saudi Arabia (KSA). The Asir (southwest) region receives annual rainfall > 300 mm, primarily due to the interaction of the nearby escarpment and the advection of warm, humid conditionally unstable air in the lower atmospheric layer from the Red Sea, a trough of low pressure in Sudan, and the extension of the Indian monsoon low centered over Asia (Abdullah and Al-Mazroui, 1998, Ghulam, A.S., 2007). The precipitation in summer has a strong diurnal cycle due to a sea breeze circulation from the Red Sea and the rapidly rising terrain of the escarpment. The escarpment consists of a rugged western face with mountains exceeding 2,400 meters in several places with some peaks topping 3,000 meters to the west of Abha. The rugged western face of the escarpment drops steeply to a coastal plain along the Red Sea. For this study, thunderstorms were analyzed during June to September 2008. A total of 68 cases involving merging were investigated.

A typical atmospheric sounding at Abha during summer time is shown in Fig. 1. As in most cases, a parcel of air at the surface with temperature 27 C and dew point 17 C, produces a lifted condensation level (cloud base) at 3.35 km MSL with temperature 14.7 C, and convective available potential energy (CAPE) of 4306 J/kg.

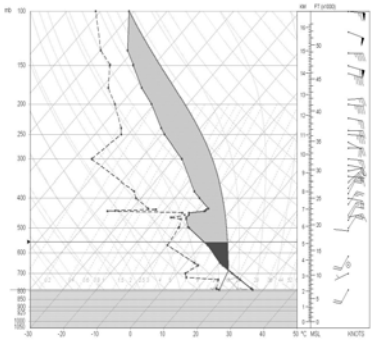

Fig. 1. A typical SKEWT vertical profile of temperature, humidity, and wind at Abha on July 4, 2008 at 12UTC (1500 local time). The shading represents a CAPE of 4306 J/kg. Cloud base is at 3.35 km and 14.7 C.

The typical atmosphere is conditionally unstable. It is usually very dry above approximately 6 km MSL due to the presence of a quasi-stationary sub-tropical High above 400 hPa. The upper winds are prevailing easterlies above 500 hPa. An afternoon southwesterly or westerly wind in the lower atmosphere below 3 to 4 km MSL forms due to a sea breeze circulation between

the Red Sea and the escarpment. The sea breeze increases the humidity in the lower atmosphere and releases the instability, causing tall cumulonimbus clouds to form along the escarpment. All the clouds in this study formed by this process.

CAPE values were computed using the 12UTC sounding from Abha (WMO station OEAB) for the 31 days of this study. The mean CAPE was 4969 J/kg and the standard-deviation was 1383 J/kg. The median value was 4864 J/kg. The minimum and maximum CAPE values were 1916 J/kg and 7264 J/kg respectively. Only 10% of the cases had CAPE less than 3000 J/kg. Large CAPE and an extremely unstable atmosphere are characteristics of days with storm mergers in this study. The directional and speed wind shear with altitude contributes to the formation of long-lived storms and the possibility to form hail (Marwitz, 1972; Bibilashvili et al, 1981). Hail is a common phenomena during the summer in the Asir region.

3. WEATHER RADAR CHARACTERISTICS

The radar used in this study is located at Abha (18.2286^{o} N, 42.6607^{o} E, elevation 2105 m). It is a C-band (5.35 cm wavelength) radar, manufactured by Gematronik. The nominal output power is 250 kW and the beam width is 0.9 deg. The minimum detectable signal equals approximately 0 dBZ at 100-km. The radar was operated 24 hr per day during the operational period. A complete volume scan was performed every 5 min.

The radar data for this study was processed using the software system called TITAN (Thunderstorm, Identification, Tracking, Analysis and Nowcasting). TITAN was set to objectively identify and track cells defined by radar reflectivity >30 dBZ, with volume >10 km^3, above 2 km MSL.

A “Storm” is defined as a thunderstorm that persisted for a long time (typically more than 1 hour), produced a TITAN radar cell and merged with a new developing cell (feeder). A “Feeder” is defined as a cumulus–congestus cloud that developed nearby a larger storm, existed less time than a storm, formed a TITAN radar cell, and then merged with another, pre-existing larger storm. Both storms and feeders formed TITAN cells in this study, and only the merging processes of these types of cells were under consideration. Only one feeder merged in the cases analyzed in this study.

The following radar derived characteristics were analyzed in this paper: precipitation flux (Pflux), cell top height, cell mass, maximum radar reflectivity (Zmax), and height of maximum reflectivity.

All of the mentioned data was obtained according to the following radar scans: “zero” time is defined as the time of the scan just before the merging took place. Two scans were analyzed prior to “zero” time i.e.; -5 and -10 min; and 4 scans were analyzed after merging took place i.e., 5 min (first scan after merging), and the following +10, +15, +20 min). This procedure allowed the possibility to study the storm evolution or dynamics. If any additional merging or splitting took place during these scans the data from these scans was omitted. The same radar characteristics were analyzed for the feeder clouds, but only one scan just prior to merging is discussed.

4. EXAMPLES OF MERGING

Figure 2 is presented to illustrate merging process which took place on September 6 2008 70 km west of Abha. Vertical cross sections of the investigated storm for 4 time periods are presented. Relative time in accordance with our definition is also presented in the Figure. Feeder cloud is located at the right part of the Figure (0 min). Storm is rather developed cloud with a top at 16 km. Feeder cloud is still developing but high reflectivity region can be fixed near 7 km high. Cloud bridge with 40dBZ reflectivity is located at a rather low high between merging clouds (10 min). Next figure (20 min) illustrates final stage of merging when supercell Cb appeared. The last figure shows further vertical development of new formed Cb when cloud top reached 16 km. Some of the large particles which were formed during storm development had chances to be transferred to the new merged Cb and to continue their growth in this new developing cloud, this can be an important mechanism for precipitation and hail development.

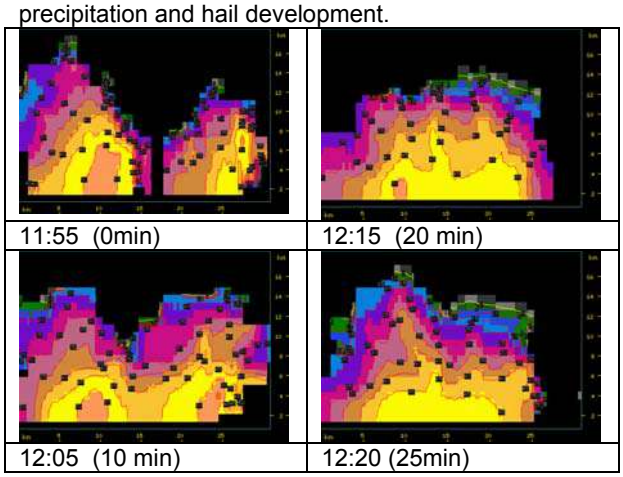

Fig.2. Vertical radar cross section (west-east) of the investigated clouds during merging for 4 time periods (6 September 2008)

Satellite data can also contribute significantly to our understanding of the physical processes which take place during clouds merging. Figure 3 presents serious of images obtained and derived

from Meteosat measurements. A case study, when merging between several cells took place, on July 4 2008 was analyzed in details by Krauss, et al. 2011a. 3-D images are presented in the first column. Infrared atmospheric window channel centered near 10.8 μ was used to build 3-D images of the investigated clouds. A vertical axes is a pixel temperature (less than -40C). Cloud images obtained with a high resolution visual channel of Meteosat 9 are presented in the second column. Cb2 –storm and Cb3 – feeder clouds were under consideration in this case study. Cb2 – long living storm started to decay, at the same time Cb3 – a new growing cell developed significantly near the main cell, merging took place and a new supercell appeared (Cb2 -15 min).

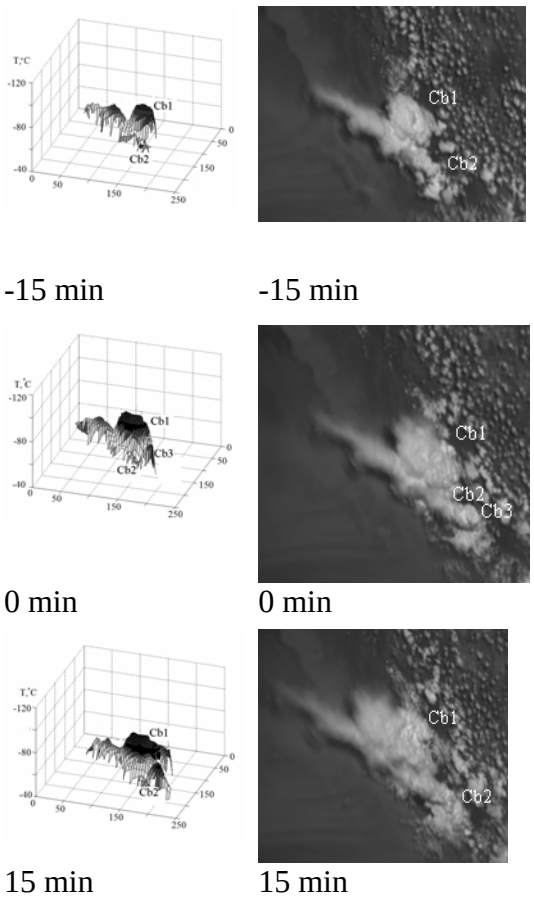

Fig3. 3D cloud images (left column, vertical axes – temperature, horizontal axes-km) and images obtained with a high resolution visual channel of Meteosat 9 (right column)

5. DATA ANALYSIS

5.1 Storm and Feeder Cloud General Characteristics

A statistical summary of storm characteristics is given in Table 1, calculated from the 3 radar scans before merging, plus 4 scans after merging when the data were available. The time period for these characteristics is 35 min for a maximum of 7 radar scans. The storm data set consists of the TITAN software processing of 417 scans. The storm data set always included one scan before the merging and one scan after the merging. However, if secondary splits or mergers occurred within 3 scans, then those data were excluded.

A statistical summary of characteristics of the associated feeder cells, using the single time-scan just before merging, is given in Table 2. There were 68 scans with feeder cloud characteristics.

Table 1: Statistical characteristics of the investigated storms (calculated from the 3 radar scans before merging, plus 4 scans after merging. The time period is 35 min for 7 radar scans.

Storms	N	Mean	Median	Maximum
Top (km)	417	13.5	14.1	18.6
ZMax (dBZ)	417	54.4	56.5	64.5
Mass (ktons)	417	1268	707	10068
Ht of max dBZ (km)	417	5.8	5.5	10.7
Precip flux (m3/s)	417	1428	980	8034

Table 2: Statistical characteristics of the investigated feeders (at the time just before merging)

Feeders	N	Mean	Median	Maximum
Top (km)	68	10.4	9.6	17.8
ZMax (dBZ)	68	46.4	46.1	61.5
Mass (ktons)	68	173	51.1	1314
Ht of max dBZ (km)	68	6.1	6.2	13.7
Precip flux (m3/s)	68	249	86	2047

Storm Zmax was rather high. The median Zmax was 56.5 dBZ, and the maximum Zmax was 64.5 dBZ. Feeder cells had lower values of Zmax; the median was 46.1 dBZ and the maximum was 61.5dBZ. The height of maximum reflectivity was similar for both groups and the mean and median values were located at 5.5 and 6.3 km respectively.

The median Pflux for storms (980 m^3/s) was approximately an order of magnitude greater than the Pflux produced by feeder cells (86 m^3/s). The significant difference between storm and feeder

Pflux is illustrated in the probability plot shown in Fig 4.

The cell top heights of the investigated storms ranged between 6.6 and 18.6 km. The mean cell top height was 13.5 km. Cell tops were >10 km in 85% of the analyzed cases. The maximum values of cloud top heights could be overestimated due to the presence of high reflectivity cores in the storms and the effects of antenna beam side lobes as discussed by Krauss, et al. (2011b). Some of the feeder cells were also rather intense clouds, with maximum top height equal to 17.8 km. Some feeder cells developed significantly during the period of observation, but they were smaller than storms on average. The mean feeder cell top height was 10.4 km. The feeder cell tops did not exceed 12 km in 72% of cases, and the median top height was 9.6 km.

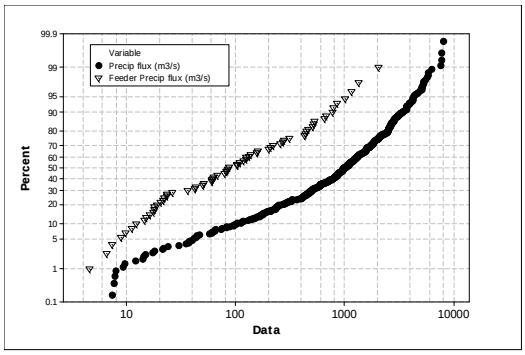

Figure 4: The probability plot of precipitation flux (Pflux) for 417 storm observations and 68 feeder cell observations.

The mass of the investigated storms was significantly bigger than that of feeder cells. Mean storm mass was equal to 1268 ktons and mean feeder cell mass was 173 ktons.

5.2 Time Dependence of Storm Characteristics

Changes in storm characteristics before and after merging of the feeder cells were investigated. A statistical summary of the storm parameters as a function of time is given in Table 3.

The biggest changes as a result of merging were observed with Pflux, Mass, and Zmax. It is reasonable to expect the mass to increase significantly as two clouds merge, and this was found to be the case. The mean storm mass increased from 938 ktons to 1375 ktons (147% change) and the median storm mass increased from 385 to 801 ktons (208% change). Precipitation flux was stable during the 3 scans prior to merging (median was equal to ~475 m^3/s). The Pflux increased to 1047 m^3/s (212% change) 5 min after merging, and increased up to 1446 m^3/s (an additional 138% change) at 10 minutes after merging.

Table 3: Mean and median values of the storm characteristics as a function of time. Time Zero refers to the radar scan just before merging. The merging of a feeder cell is included in the radar scan at Time = 5 min.

Time (min)	Top (km), mean	Zmax (dBZ), mean	Mass (ktons), mean	Ht of MaxZ (km), mean	Precip flux (m3/s), mean
-10	11.8	50.4	732.6	5.7	898.9
-5	12.1	50.9	684.3	5.8	819.6
0	13.0	53.0	938.4	5.8	1071.3
5	14.0	56.1	1375.0	6.0	1584.8
10	14.4	56.9	1624.1	6.0	1816.0
15	14.4	56.7	1702.9	5.4	1860.0
20	14.4	56.0	1747.6	5.5	1858.6

Time (min)	Top (km), median	Zmax (dBZ), median	Mass (ktons), median	Ht of MaxZ (km), median	Precip flux (m3/s), median
-10	11.5	55.1	325.3	5.5	476.7
-5	11.8	53.2	237.9	6.2	450.6
0	13.3	53.6	385.5	6.2	495.1
5	14.1	56.4	801.2	6.2	1047.4
10	14.8	57.8	1091.1	5.5	1446.5
15	14.8	57.6	981.8	5.5	1363.0
20	14.8	57.8	1032.8	5.5	1334.5

The median Zmax showed some increase after merging took place. It decreased in the period -10 to 0 minute, but increased during 5-10 min after merging. The increase was equal to 4.2 dBZ. The height of maximum reflectivity (mean and median) was stable during -5 to +5 min and started to decrease later, which is consistent with the rainfall descending in the cloud and falling from the base of the cloud.

The data also show that there was some increase in the height of storms tops with time. The mean and median values of Top height increased significantly during the period of -5 to +10 min (from 12km up to ~15 km), then they stabilized. On average, clouds started to grow before merging and finished 10 minutes after merging.

6. DISCUSSION AND CONCLUSIONS

This study has documented the radar derived characteristics of cumulonimbus clouds during merging with feeder cells over the Asir region of

southwest Saudi Arabia. The period analyzed was June to September 2008. A total of 68 cases of merging were investigated on 31 days. The atmospheric thermo-dynamics characteristics, observed for the days with merging, were studied. The storms were observed when CAPE had very large values. CAPE (mean and median) equaled 4800-4900 J/kg respectively. On 90% of the days, CAPE exceeded 3000 J/kg when merging was observed. A statistical summary of the storm observations was presented and discussed. Storms tops exceeded 10 km in 85% of the analyzed cases. Storm maximum reflectivity was rather high at 65 dBZ. Feeders had smaller values of reflectivity; the maximum was 61 dBZ. Precipitation flux for storms exceeded several times the precipitation flux produced by feeders. The mean Pflux for storms was 1428 m3/s, and 249 m3/s for feeders.

A method to study the merging process was developed; it was based on statistical analysis of storm characteristics prior to and after merging. Such an approach provided the possibility to derive changes in cloud characteristics and to filter them from trends which were the result of cloud development. It also provided the possibility to quantify changes in storm characteristics due to merging.

It was confirmed that merging has a strong effect on storm development. The data analysis shows that an increase in the median of the distribution of maximum reflectivity was observed just after merging and was equal to 4.2 dBZ. The storm mass and precipitation flux also increased significantly. The median mass increased from 385 to 1091 ktons (283%), and Pflux increased from ~475 m^3/s to ~1400 m^3/s (290%).

7. BIBLIOGRAPHY

Addullah, M.A., and M.A. Al-Mazroui, Climatological study of the southwestern region of Saudi Arabia. I. Rainfall analysis. Climate Research, 1998, 9, p.213-223.

Bibilashvili N.Sh, I.I. Burcev, Yu.A. Seregin. Manual on Organization and Providing of Hail Suppression Operations. Hydrometeoizdat, 1981, Leningrad, 167pp.

Changnon, S. A., Jr. Effects of urban areas and echo merging on radar echo behavior. J. Appl. Meteor., 1976, 15, p.561–570.

Cheng L., and D. C. Rogers. Hailfalls and hailstorm feeder clouds – an Alberta case study. J. Atmos. Sci., 1988, 45, p.3533-3544.

Dennis, A.S., C.A. Schock, and A. Koscielski. Characteristics of hailstorms of western South Dakota. J. Appl. Meteor. 1970, 9, p.127-135.

Dovgaljuk Yu.A., A.D. Egorov, A.A. Sinkevich, E.N. Stankova , V.D.Stepanenko, L.I. Shumakov. Investigation of the Cu cong Transforming into Cb after Seeding. Collection: Modification of Hydrometeorological Processes. Gidrometeoizdat, Proceedings of the All-Union Conference, Leningrad, 1990, p.265-270.

Farley, R.D. Numerical modeling of hailstorms and hailstone growth. Part III: Simulation of an Alberta hailstorm – natural and seeded cases. J. Climate Appl. Meteor,1987, 26, p.789-812.

Ghulam, A.S. The Development of a Heavy Thunderstorm Climatology in Saudi Arabia Based on Observations, Analyses and Numerical Simulations. PhD thesis, University of East Anglia, Norwich, England. 2007, 381 pp.

Krauss T.W., A. A. Sinkevich, N. E. Veremey, Y. A. Dovgaluk, V. D.Stepanenko. Investigation of Large Vertical Depth Cb in India. 4th European Conference on Severe Storms 10 - 14 September 2007a - Trieste - ITALY .

Krauss T.W., A.A. Sinkevich, N.E. Veremey, Yu. A. Dovgaluk, V.D.Stepanenko . Investigation of the large vertical depth Cb (Andhra Pradesh province, India, 2004, September 28). Meteorology and Hydrology, 2007b, N1, p. 30-42.

Krauss, T.W., A. A. Sinkevich, and A. S. Ghulam. Precipitation Characteristics of Natural and Seeded Cumulus Clouds in the Asir Region of Saudi Arabia. Journal of Weather Modification, 2010, v.42, p.61-77.

Krauss T.W., A.A. Sinkevich, R.P. Burger, N.E. Veremey, Yu. A. Dovgaluk, V.D.Stepanenko. Investigation of the impact of dynamic factors on Cb development in Saudi Arabia. Russian Meteorology and Hydrology, 2011a, N10, p.5-19.

Krauss T.W., A.A. Sinkevich, N.E. Veremey, Yu. A. Dovgaluk, V.S.Makitov, V.D.Stepanenko. Complex investigation of cumulonimbus characteristics developed over the Arabian peninsula in a very dry atmosphere. Part 2, Analysis of METEOSAT data. Russian Meteorology and Hydrology, 2011b, N3, p.36-47.

Krauss T.W., A.A. Sinkevich, N.E. Veremey, Yu. A. Dovgaluk, Makitov V.S.,V.D.Stepanenko. Complex investigation of cumulonimbus characteristics developed over the Arabian peninsula in a very dry atmosphere. Part1: in situ observations and numerical modeling. Russian Meteorology and Hydrology, 2011c, N2, p.44-59.

Krauss T.W., A. A. Sinkevich and A. S. Ghulam. Effects of Feeder Cloud Merging on Storm

Development in Saudi Arabia. JKAU: Met., Env. & Arid Land Agric. Sci., Vol. 22, No. 2, p. 23-39 (2011d A.D./1432 A.H.) DOI: 10.4197/Met. 22-2.2

Marwitz, J.DThe structure and motion of severe hailstorms. Part III: Severely sheared storms. J. Appl. Meteor., 1972, 11, p.189-201.

Simpson, J.,, and W. L. Woodley, Seeding cumulus in Florida: New 1970 results. Science, 1971, 172, p.117–126.

Simpson, J., N. E. Westcott, R. J. Clerman, and R. A. Pielke. On cumulus mergers. Arch. Meteor. Geophys. Bioklim., 1980, 29A, p.1–40.

Sinkevich A.A. Cu of North-West of Russia. Hydrometeoizdat, St. Petersburg. 2001, 106 p.

Sinkevich A.A., T. W. Krauss, V.D.Stepanenko, Yu. A. Dovgaluk, N.E. Veremey, A.B.Kurov, L.V.Pivovarova. Investigation of the anvil dynamics of a large vertical depth Cb. Russian Meteorology and Hydrology, 2009, No. 12, p. 5-17.

Turpeinen, O. Cloud interactions and merging on day 261 of GATE. Mon. Wea. Rev., 1982,110, p.1238–1254.

Westcott, N. E. A historical perspective on cloud mergers. Bull. Amer. Meteor. Soc., 1984, 65, p.219–227.

Wiggert, V. G., J. Lockett, and S. S. Ostlund, 1981: Rainshower growth histories and variations with wind speed, echo motion, location and merger status. Mon. Wea. Rev., 109, p.1467–1494.

Woodley, W. L., J. Jill, A. Barnston, J. Simpson, R. Biondini, and J. Flueck. Rainfall results of the Florida Area Cumulus Experiments, 1970–1976. J. Appl. Meteor., 1982, 21, p.139–164.

9. Acknowledgements

The authors wish to thank the Presidency of Meteorology and Environment (PME) of the Kingdom of Saudi Arabia under the leadership of Prince Turki bin Nasser bin Abdul Aziz for funding the program.

VALIDATION OF SURFACE DOWNWARD SHORTWAVE RADIATION OF THE JAPAN METEOROLOGICAL AGENCY MESO-SCALE MODEL FOR THE FORECAST OF PHOTOVOLTAIC POWER PRODUCTION

Hideaki Ohtake[1]*, K.Shimose[1], Y. Yamada[2], Joao Fonseca [1], T. Takashima[1] and T. Oozeki[1]

[1]Research Center for Photovoltaic Technologies National Institute of Advanced Industrial Science and Technology, Tsukuba, Japan

[2]Meteorological Research Institute, Tsukuba, Japan

1. INTRODUCTION

In a photovoltaic (PV) system, a power production of PV is dependent on a weather condition. A forecast of meteorological elements, which have a large variability in both the temporal and spatial scales, is necessary for the forecast of PV power production and stabilization of an electric power system with other power generation systems.

Recently, forecasts of PV power production using an engineering model based on the Japan Meteorological Agency (JMA) mesoscale numerical model (MSM; e.g., Saito et al. 2007) grid point value (GPV) data sets has been also studied (Fosenca Jr et al. 2011). In their study, the indirect meteorological elements are used as an input data to their engineering model to forecast the surface downward shortwave radiation (DSW) and/or PV power production. However, the more accurate forecast of PV power production used the DSW forecast by MSM has been expected.

To forecast the PV power production for one-day ahead (next day) using the DSW forecast outputs of MSM, it is necessary to understand the forecast accuracy of the DSW forecast based on the ground-observed DSW data sets. JMA have investigated the forecast errors of DSW forecast for the whole area around the Japan Islands using the surface observed DSW data during the three years (from spring 2004 to autumn 2007), and reported that the DSW forecast tend to have the negative bias for summer (Nagasawa, 2006, 2008).

In this study, regional characteristics of forecast errors of DSW in JMA MSM forecast are investigated based on the ground-observed solar irradiance data sets at the whole stations of JMA. Furthermore, this study investigate that what kind of cloud types could be observed when the forecast errors of the DSW forecast by MSM is large.

2. SOLAR IRRADICANCE DATA

Solar irradiance (i.e., DSW), which observed at JMA operational meteorological observational stations in Japan (a total 52 stations), has been measured with a pyranometer (Kipp & Zonen CM3 and CM21 or EIKO MS62). At Tsukuba station, the direct and diffuse solar irradiances were measured from the direct sunlight measurement with a pyrheliometer (Kipp & Zonen CH1) and a pyranometer (Kipp & Zonen CM21) shaded with an automatically sun-tracking shadowing-disk to avoid the direct solar beam. The total component of the solar irradiance (i.e., DSW) was determined by the sum of direct and diffuse solar irradiances. Hourly averaged DSW are recorded in an archive. The locations of ground observation stations in Japan are shown in Figure 1.

At these JMA stations, cleaning of a glass dome of the pyranometers has been routinely conducted by a feather brush and a soft cloth to remove dust, drops of dew, ice (snow) particles etc., since an accuracy of the measurements may be greatly affected by these dusts. Data during the period including a thunderbolt or the maintenance of observational equipment was removed. Surface observed DSW data was used in this analysis to validate the DSW forecast, since the observed DSW data sets measured and calibrated by JMA has the highest quality data sets in Japan.

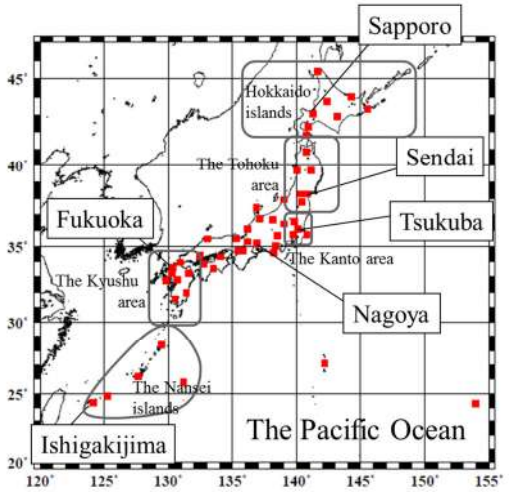

Fig. 1. (a) Map of the area over the whole Japan. The red squares indicate JMA operational observation stations (a total of 52 stations) in Japan.

3. NUMERICAL MODEL

The model domain of MSM is a region surrounding the Japan Islands and its domain size is 3600 km × 2900 km × 21.8 km in the x, y, and z directions, respectively. The horizontal grid spacing is 5km. For its initial condition, a four-dimensional variational data assimilation analysis is given in MSM. Lateral boundary condition is supplied by JMA global spectral model (GSM) whose horizontal resolution is 20 km. MSM is run every three hours (8 times per day). Four forecasts per day of MSM are 15 or 33 h forecasts (the local standard time in Japan; LST = UTC + 9 hours). To forecast the PV power production for one-day ahead, the relative large forecast outputs (33 h forecast) in MSM is

useful for the forecast. Thus, the results of 33 h forecast in MSM were used in this analysis. The period from 2008 to 2010 is selected in our analysis.

The substantial horizontal grid size of radiative transfer process is 10 km to reduce the calculation cost. The radiative transfer calculations are conducted with a time interval of 15 minutes. Shortwave radiative transfer scheme in MSM is based on the 22-band model which includes the parameterizations of optical absorptions of Briegleb (1992) for water vapor and Freidenreich and Ramaswamy (1999) and cloud optical parameters (Slingo, 1989; Briegleb 1992; Ebert and Curry, 1992; Freidenreich and Ramaswamy 1999;). As for the calculation of the radiative transfer processes, a sub-grid scale condensation scheme proposed by Sommeria and Deardorff (1977) is also introduced in MSM in order to treat the effect of the sub-grid scale clouds.

4. RESULTS

4.1. REGIONAL CHARACTERISTICS OF FORECAST ERRORS OF DSW FORECAST

A regional characteristic of forecast errors of an accumulated daily DSW were investigated. Here the Japan islands area divided into six rough climatic regions in this study. Figure 2a shows the comparison between the DSW forecast and the observed for the winter (January) of 2010 for Sapporo, Sendai, Tsukuba, Nagoya, Fukuoka and Ishigakijima, respectively. In the northern and eastern areas (Sapporo and Sendai), the correlation coefficients are relatively low. The correlation coefficients in the western and southern areas are relatively high. However, the forecast errors of DSW forecast for summer (July) of 2010 tend to be larger than those for the winter (Fig. 2b). At Sapporo, the variations of forecast errors are large. Particularly, the underestimations of DSW forecast over the area on the side of the Pacific Ocean for summer are significant. Similar tendency are found in the cases of the other two years (not shown).

To estimate the forecast errors of the DSW forecast , the evaluations are conducted by the mean error (ME) and the root mean square error (RMSE) of the DSW forecast based on the JMA operational observation data sets (a total of 52 stations). Figure 3 shows the time series of monthly ME and RMSE during the three years (from 2008 to 2010). The ME is within ± 50 W m^{-2}. The overestimations (underestimations) of DSW forecast for winter (summer) are found cyclically. The forecast errors of DSW forecast over the Nansei islands (located in the southwestern part in Japan (e.g., at Naha and Naze JMA stations) are large (not shown). Furthermore, it is found though the time series of RMSE that the RMSE has a

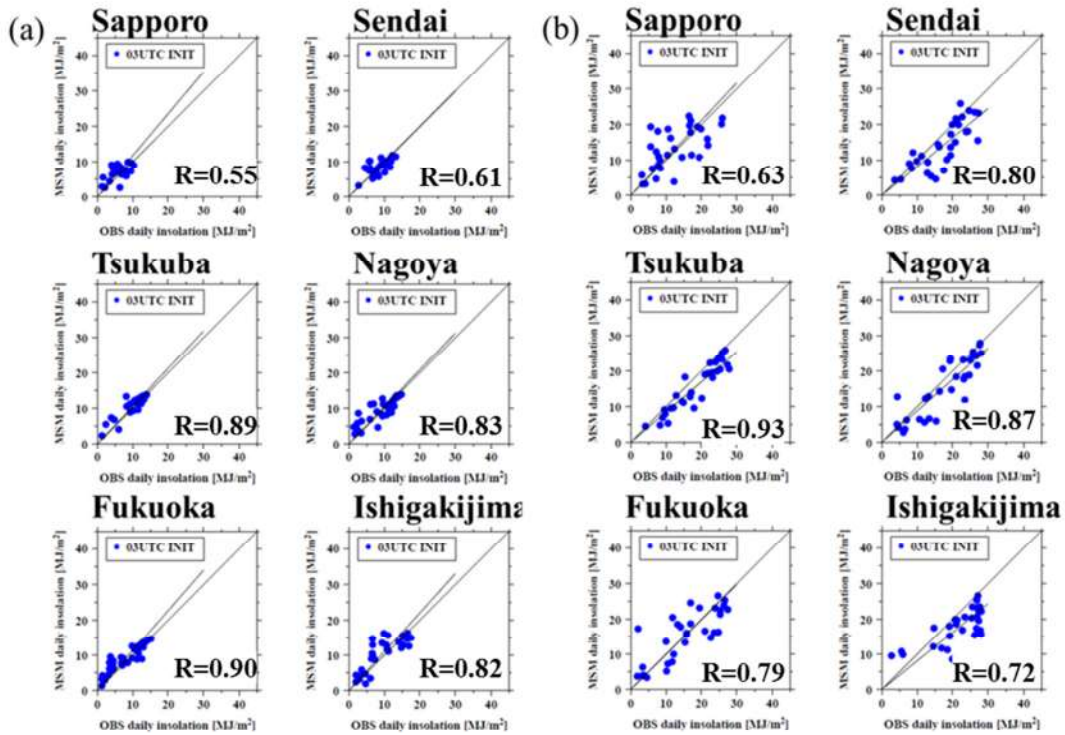

Fig.2 . Daily accumulated DSW energy of both DSW forecast and the observations during 2010 for (a) Sapporo, (b) Sendai, (c) Tsukuba, (d) Nagoya, (e) Fukuoka and (f) Ishigakijima stations, respectively. Each location is shown in Fig. 1. Lines show least squares linear fits every month. The letter “r” denotes a correlation coefficient.

range from 90 to 180 W m^{-2} and the forecast errors for summer (from June to August) are relatively large.

Next, a forecast error mapping of annual ME of DSW forecast at the all of the JMA stations (a total of 52 stations) in Japan is shown (Figure 4). From the results, the locations of the overestimations and/or underestimations of DSW forecast vary every observational station over the area from the northern part of Japan to the western part (i.e., the Kyusyu area). It is noted that the underestimation of DSW forecast is significant over the area from the Kanto area to the Kyusyu area on the side the Pacific Ocean. Particularly, the underestimation of DSW forecast is significant on the Nansei islands and the area over the sea of the south in Japan.

In the same way as Fig. 4, the forecast error mapping of annual RMSE are shown in Figure 5. As for the regions from the Hokkaido islands to the Kyusyu area, the RMSE at many of the JMA stations is < about 140 W m^{-2}. Particularly, the RMSE is relatively larger (exceed 140 W m^{-2}) in the relatively lower latitude (subtropical) regions of Japan islands (i.e., particularly the Nansei islands and the area over the sea of the south in Japan). The north-south change of RMSE is clear.

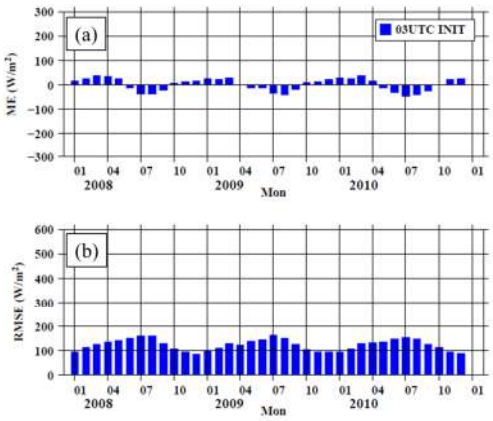

Fig. 3. Time series of monthly forecast errors of DSW forecast in comparison to ground measured values. (a) Mean errors (ME) and (b) root mean square errors (RMSE) of the MSM model are shown, respectively.

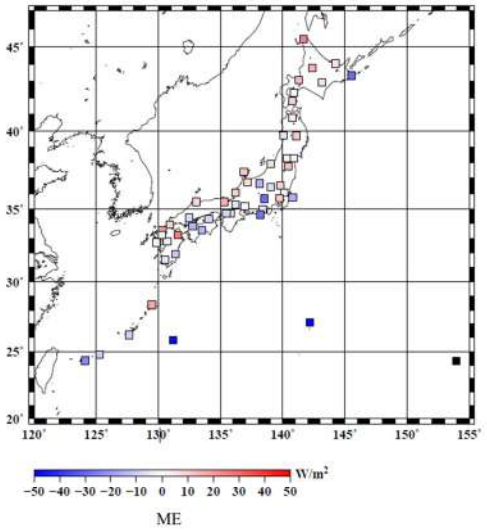

Fig. 4. Mapping of ME of DSW forecast in Japan. ME were computed during one year of 2010 (annual values).

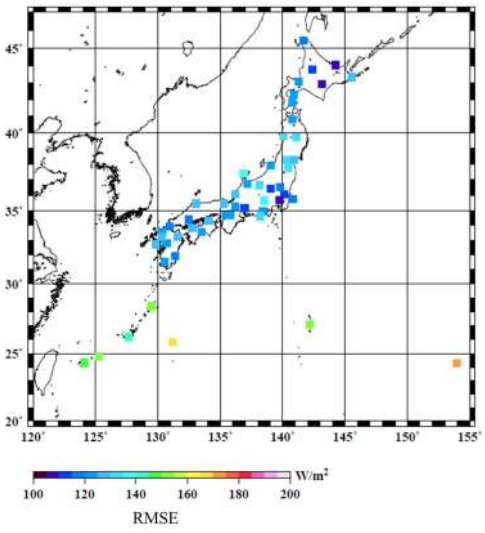

Fig. 5. As in Fig. 4, but for RMSE.

4.2 APPEARANCE FREQUENCY OF CLOUD TYPES IN THE CASE OF A RELATIVELY LARGE FORECAST ERROR

To detect a relatively large forecast errors case, the relatively forecast errors normalized using the extraterrestrial solar irradiance is defined by the following parameter.

$$\left|\frac{I_{model} - I_{obs}}{I_{top}}\right|$$

Where, I_{model} is the DSW forecast at the ground and I_{top} is the extraterrestrial incident solar irradiance at the top of the atmosphere, respectively. I_{obs} indicate the observed DSW at the JMA operational stations. Here, we set 0.2 for the Kanto area as a threshold of the normalized forecast errors to define as the relatively large forecast error case. The total of 75 cases during the period of three years (from 2008 to 2010) were selected by the threshold as the relatively large forecast errors cases over the Kanto area and analyzed in this study. Surface observation of cloud types have been conducted by an eye monitoring at JMA stations.

Appearance frequency of observed

cloud types in the large forecast cases at Tsukuba JMA station during the three years are summarized in Table 1. The results at Tsukuba show that cirrus (Ci) clouds are often found at the high level (48.3% at maximum). At the middle level, the altocumulus (Ac; 70.6% at maximum) clouds is observed. Particularly, stratocumulus (Sc; 48.3% at maximum) and status (St; 13.8% at maximum) clouds, nonprecipitating clouds, are often found at the low level. Cumulus (Cu) clouds are often found at the low-level (76.5% at maximum), although the observed cumulus clouds often include nonprecipitating clouds. However, appearance frequency of precipitating clouds (Cb and Ns) is low. Such a tendency is seen at Choshi and Tokyo JMA stations over the Kanto area (not shown). The forecast errors of DSW forecast seem to be large in the case of nonprecipitating stratiform and/or cumulus clouds.

5. SUMMARY

Regional characteristics of forecast errors of DSW forecast in MSM were investigated for the whole extent of Japan islands in this study. Generally, the forecast errors for summer tend to be large compared with those for winter. It is found though the mapping of forecast errors (ME and RMSE) that there are the regional characteristics of the forecast accuracy in MSM. The underestimation of DSW forecast is significant over the region from the Kanto area to the Kyusyu area on the side of the Pacific Ocean. Particularly, the underestimation of DSW forecast is significant on the Nansei islands (in the southwest part of Japan)

TABLE 1: Appearance frequency of cloud types for the case of the relative large forecast errors at both 09LST and 15LST for Tsukuba stations during the three years (from 2008 to 2010). The ten cloud types: convective clouds such as cumulus (Cu), cumulonimbus (Cb), stratiform clouds at the low level clouds (stratocumulus, Sc; stratus, St), and middle level (altocumulus, Ac; Altostratus, As; Nimbostratus, Ns) and high level (cirrus, Ci; cirrocumulus, Cc; and cirrostratus, Cs) are shown, respectively.

2010	Case:29	High-level clouds			Middle-level clouds			Low-level clouds		Convective clouds	
Location	OBS Time Cloud types	Ci	Cc	Cs	Ac	As	Ns	Sc	St	Cu	Cb
Tsukuba	09LST	24.1%	0.0%	0.0%	37.9%	10.3%	0.0%	48.3%	10.3%	58.6%	0.0%
	15LST	27.6%	0.0%	3.4%	37.9%	10.3%	0.0%	48.3%	6.9%	58.6%	0.0%
2009	Case:29	High-level clouds			Middle-level clouds			Low-level clouds		Convective clouds	
Location	OBS Time	Ci	Cc	Cs	Ac	As	Ns	Sc	St	Cu	Cb
Tsukuba	09LST	27.6%	0.0%	3.4%	51.7%	6.9%	0.0%	37.9%	13.8%	62.1%	0.0%
	15LST	48.3%	0.0%	0.0%	55.2%	10.3%	0.0%	31.0%	3.4%	75.9%	3.4%
2008	Case:17	High-level clouds			Middle-level clouds			Low-level clouds		Convective clouds	
Location	OBS Time	Ci	Cc	Cs	Ac	As	Ns	Sc	St	Cu	Cb
Tsukuba	09LST	23.5%	0.0%	0.0%	58.8%	0.0%	5.9%	35.3%	5.9%	70.6%	0.0%
	15LST	23.5%	0.0%	0.0%	70.6%	0.0%	0.0%	29.4%	5.9%	76.5%	0.0%

and the area over the sea of the south in Japan. The results suggest that it is difficult to forecast DSW in the lower latitude (subtropical) regions of Japan islands compared with the mid-latitude regions. These results of this study has a useful information to improve both the radiative transfer processes and the microphysical processes in MSM that is relevant to the forecast of both the DSW and/or PV power production using an engineering model.

As for the cases of relatively large forecast errors, one of the reasons of forecast errors might be caused from the interaction between the cloud processes and radiation transfer processes. It will be necessary to investigate a three dimensional analysis of cloud distributions in MSM for such as a case of a relatively large forecast error in detail.

ACKNOWLEDGMENTS

We are grateful to the personnel in the Forecast Research Department of the Meteorological Research Institute, Tsukuba Aerological Observatory and the Numerical Prediction Division of Japan Meteorological Agency for their helpful comments in this study. This study was supported by NEDO (New Energy and Industrial Development Organization, Japan).

REFERENCES

Briegleb, B.P., 1992. Delta-Eddington Approximation for Solar Radiation in the NCAR Community Climate Model. J. Geophys. Res., 97, 7603–7612.

Davy, R.J., Troccoli, A., 2011. Interannual variability of solar energy generation in Australia. Solar Energy, doi:10.1016/j.solener.2011.12.004

Ebert, E. E., J. A. Curry, 1992. A parameterization of ice cloud optical properties for climate models, J. Geophys. Res., 97, 3831-3836.

Freidenreich, S.M., V. Ramaswamy, 1999. A new multiple-band solar radiative parameterization for general circulation models. J. Geophys. Res., 104, 31 389–31 409.

Fonseca Jr., J.G.S., Oozeki, T., Takashima, T., Koshimizu, G., Uchida, Y., Ogimoto, K., 2011. Use of support vector regression and numerically predicted cloudiness to forecast power output of a photovoltaic power plant in Kitakyushu, Japan. Prog. Photovolt: Res. Appl., doi: 10.1002/pip.1152.

Nagasawa, R., 2006. Improvement of a radiation process for the non-hydrostatic model. *In 12th Conference on Atmospheric Radiation. American Meteorological Society*, P2-10, URL http://ams.confex.com/ams/pdfpapers/113356.pdf.

Nagasawa, R., 2008. Radiation process. *Suuchiyohoka Houkoku Bessatsu*, **54**, 149-165, (in Japanese).

Saito, K., Ishida, J., Aranami, K., Hara, T., Segawa, T. , co-authors, 2007. Nonhydrostatic atmospheric models and operational development at JMA. *J. Meteor. Soc. Japan*, **85B**, 271–304.

Slingo, A., 1989. A GCM parameterization for the shortwave radiative properties of water clouds. J. Atmos. Sci., 46, 1419-1427.

Sommeria, G., J., Deardorff, W. 1977. Subgrid-Scale Condensation in Models of Nonprecipitating Clouds. J. Atmos. Sci., 34, 344–355.

MIXTURE OF OVERSHOOTING AIR IN THE LOWER STRATOSPHERE

S. Iwasaki[1], T. Shibata[2], H. Kubota[3], H. Okamoto[4], and H. Ishimoto[5]
[1]National Defense Academy, Japan.
[2]Nagoya University, Japan.
[3]Japan Agency for Marine-Earth Science and Technology, Japan.
[4]Kyushu University, Japan.
[5]Meteorological Research Institute, Japan.

1. Introduction

Since water vapor is a greenhouse gas, it influences temperatures in the stratosphere. Stratospheric water vapor is transported from lower to higher latitudes by Brewer–Dobson circulation [Brewer, 1949], accurate estimation of the water budget in the tropical tropopause layer (TTL) is important for understanding the global stratospheric climate.

Overshoot, defined as cloud intrusion through the level of neutral buoyancy above deep convection, is believed that it plays one of the mechanisms that control the transfer of water vapor from the troposphere to the stratosphere. However, its role is not understood. Danielsen [1993] conducted airborne observations during the Stratosphere – Troposphere Exchange Project (STEP) in Darwin, Australia and showed that the overshooting air dehydrated the lower stratosphere. Conversely, during the Tropical Convection, Cirrus, and Nitrogen Oxides Experiment (TROCCINOX) in Sao Paulo, Brazil, and the Stratosphere-Climate Links with Emphasis on the Upper Troposphere and Lower Stratosphere (SCOUT-O3) project in Darwin, Australia, Corti et al. [2008] used an airborne hygrometer to show that the overshooting air hydrated the lower stratosphere. Thus, further research is necessary to resolve this debate.

2. Data

The CloudSat data utilized were 2B-GEOPROF, ECMWF-AUX, and MODIS-AUX data where the 2B-GEOPROF, ECMWF-AUX, and MODIS-AUX data include the attenuated radar reflectivity factor, pressure and temperature estimated by ECMWF, and brightness temperatures measured MODIS, respectively. We also used level 1b of CALIOP, which contains 532-nm attenuated backscattering coefficients. Note that these data are synergy observational, since CloudSat, MODIS, AIRS, and CALIOP measure the same point within 1 min. We analyzed those data between 20°S and 20°N recorded from September 2006 to December 2010.

3. Results

Jensen et al. [2007] simulated overshooting and showed that the coldest temperature of overshooting is 21 K colder than that of the environment because overshooting air is adiabatically expanded owing to updraft. However, the ratio of pixel numbers between overshooting whose CloudSat echo top height is higher than the level of cold-point temperature (CPT) and the same overshooting but also satisfying colder 11μm brightness temperature than CPT is 0.11. That is, 89% of overshooting air is not adiabatically

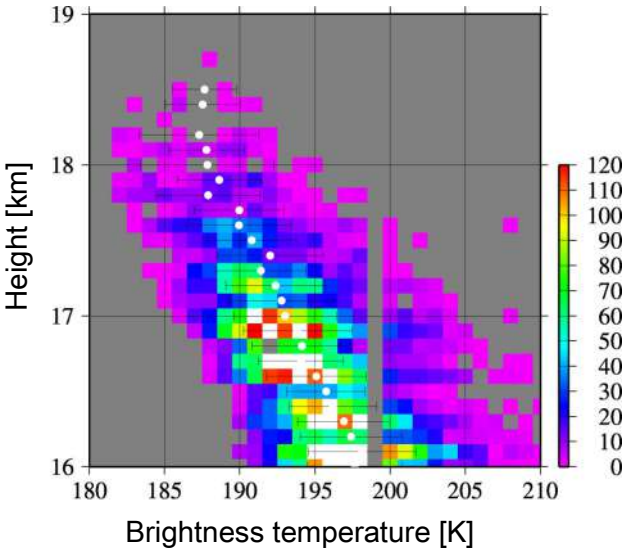

Figure 1. Occurrence number of overshooting whose brightness temperature is warmer than CPT. The color denotes occurrence number of pixels. (From Iwasaki et al. [revised].)

expanded. Figure 1 shows occurrence number of overshooting whose MODIS brightness temperature is higher than CPT. The figure suggests overshooting air above 17.5 km is not adiabatically expanded.

The radar-lidar algorithm [Okamoto et al., 2003] assuming the ice cloud particle size distribution as a log-normal distribution with a standard deviation of 1.5 shows the mode of averaged ice water content of the overshoot above the CPT height is 6.3–10 mg/m^3 (Fig. 2). 1 mg/m^3 of IWC is approximately 10 ppmv of water vapor in the TTL if all the ice particles are sublimated. The water vapor mixing ratio in the lower stratosphere is 3–4.5 ppmv [e.g., Fig. 11 of Fujiwara et al., 2010]. Therefore, if 5% or more of ice particles are sublimated and mixed into the lower stratospheric air, overshooting would result in a hydrated lower stratosphere.

4. Summary

Synergy spaceborne observations of overshooting air, defined as cloud intrusion through the level of neutral buoyancy above deep convection, are analyzed.

Most of overshooting brightness temperature is higher than CPT; the lapse rate of overshooting is lower than that of an adiabatic expansion. It would be because the overshooting air is locally warmed by a mixture of warmer stratospheric air. Analysis of CALIOP and CloudSat data by using a radar-lidar algorithm shows that the mode of averaged ice water content of the overshoot above the CPT height is 6.3 – 10 mg/m^3. Therefore, if 5% or more of ice particles in overshooting are sublimated and mixed into the lower stratospheric, the lower stratospheric air would be hydrated.

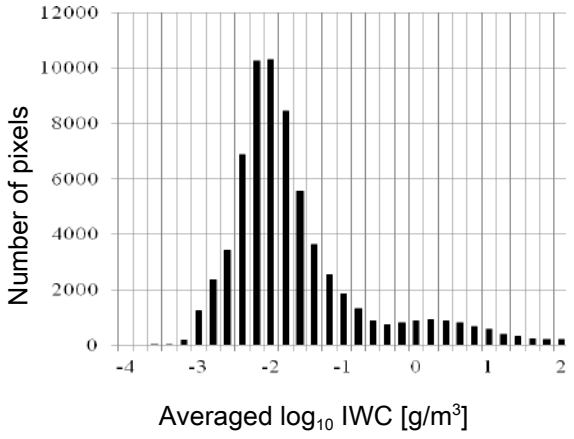

Figure 2 Histograms of ice water content [g/m^3] of which cloud top is higher than CPT height. (From Iwasaki et al., [revised].)

5. Bibliography

Brewer, A. (1949), *Q. J. R. Meteorol. Soc., 75*, 351–363, doi:10.1002/qj.49707532603.

Corti, T., et al. (2008), *Geophys. Res. Lett., 35*, L10810, doi:10.1029/2008GL033641.

Danielsen, E. F. (1993), *J. Geophys. Res., 98(D5)*, 8665 – 8681, doi:10.1029/92JD02954

Fujiwara, M. et al. (2010), *J. Geophys. Res., 115*, D18304, doi:10.1029/2010JD014179.

Iwasaki, S., T. Shibata, H. Okamoto, H. Kubota, H. Ishimoto (revised), *J. Geophys. Res.*.

Jensen, E. J., A. S. Ackerman, and J. A. Smith (2007), *J. Geophys. Res.*, *112*, D11209, doi:10.1029/2006JD007943.

Okamoto, H., S. Iwasaki, M. Yasui, H. Horie, H. Kuroiwa, and H. Kumagai (2003), *J. Geophys. Res., 108(D7)*, 4226, doi:10.1029/2001JD001225.

Acknowledgements

This work was supported by the Japan Society for the Promotion of Science, Grant-in-Aid for Scientific Research (A) 22241004 and Grant-in-Aid for Young Scientists (B) 24710024. H. Okamoto and H. Ishimoto were supported by the Japan Society for the Promotion of Science, Grant-in-Aid for Scientific Research (B) 22340133. Data from AIRS – AMSU, MODIS, CloudSat, and CALIOP were obtained from the NASA Goddard Earth Sciences Data and Information Services Center (GES DISC), the Level 1 and Atmosphere Archive and Distribution System (LAADS), the CloudSat Data Processing Center, and the Atmospheric Sciences Data Center (ASDC), respectively.

MEASUREMENTS OF ICE NUCLEI IN THE EASTERN MEDITERRANEAN

Karin Ardon Dryer[1,2], Zev Levin[1,3] and Amit Teller[4]

[1]Department of Geophysical, Atmospheric and Planetary Science, Tel Aviv University, Israel

[2]The Porter School of Environmental Studies, Tel Aviv University, Israel

[3]Energy, Environment and Water Research Center, The Cyprus Institute, Cyprus

[4] Rafael, Haifa, Israel

ABSRACT:

The aim of this research was to study the temporal variations of Ice Nuclei (IN) in the Eastern Mediterranean and relate them to the characteristics of the atmospheric aerosols in that region. For this purpose, we carried out daily measurements of ice nuclei concentrations using the FRIDGE-TAU chamber for a period of two years (2009-2010). The measurements were carried out in Tel Aviv, Israel. The results show a strong dependence of ice nucleation on the supersaturation with respect to ice or water and a weaker dependence on temperature. concentrations measured at different temperatures (-8ºC to -23ºC) and saturation ratios (S_w of 0.88–1.0, S_i of 1.0–1.25) ranged from 0.5 L^{-1} (measured at -13 °C for S_w of 0.88) to 267.3 L^{-1} (measured at -18°C at water saturation) and the values of the Activation Fraction (for aerosol 0.11–3µm) ranged from $1.2x10^{-7}$ up to $5x10^{-4}$ (measured at -13°C for S_i of 1 and at -18°C for S_i of 1.19, respectively). From the data we developed new parameterizations that combined the effects of temperature, saturation ratio and total aerosol concentrations on ice nuclei concentrations and activation fraction values. These parameterizations were introduced into the TAU-2D cloud model with detailed microphysics and the results were compared with those obtained by using other parameterizations of ice nuclei concentration (Meyers et al., 1992 and DeMott et al., 2010). It was found that Bigg (1953) parameterization of immersion-freezing process contributes much more ice than other ice formation mechanisms. Removing Bigg's parameterization of immersion-freezing from the simulation helped us study and compare the effects of Meyers et al. (1992), the, DeMott et al. (2010) and the present parameterizations on the cloud microphysics and precipitation processes.

The Meyers et al. (1992) parameterization produces higher concentrations of ice crystals than either DeMott et al. (2010) or our parameterization, mostly in the upper parts of the cloud. On the other hand, our new parameterization produces more ice crystals at warmer temperatures at lower altitudes than either DeMott et al. (2010) or Meyers et al. (1992). DeMott et al. (2010) parameterization, which forms the smallest concentrations of ice crystals produces the highest precipitation amount

as compared to the other two parameterizations.

1. INTRODUCTION:

The Eastern Mediterranean region is characterized by air masses arriving from different sources and containing a variety of aerosol types, such as anthropogenic aerosols originated from local industrial pollution or distant origin such as Europe (Levin and Lindberg, 1979; Graham et al., 2004), dust from the Sahara desert (Ganor, 1994), marine aerosol (Levin et al., 1990) and biogenic material from land or marine sources (Ganor et al., 2000).

There are very few measurements of Ice Nuclei (IN) in the Eastern Mediterranean (e.g. Gagin, 1975; Levi and Rosenfeld, 1996). These measurements showed concentrations that vary between about 0.3 L^{-1} at -10 °C to about 3.8 L^{-1} at -20 °C. All these measurements were performed using the filter method which we found to significantly underestimate the IN concentrations due to the deactivation of the particles by the petroleum jelly used underneath the filters for enhanced thermal contact (Klein et al., 2010a).

2. METHODS:

2.1. ICE NUCLEI MEASUREMENTS:

The ice nuclei were collected at the Tel Aviv University campus, which is located at the north part of Tel Aviv, Israel (32°6'46.7"N 34°48'22.9"E) (Fig.1), in the Eastern Mediterranean region. The sampling was performed on the roof top of the Department of Geophysical, Atmospheric and Planetary Science about 20 m above ground, 60 m above sea level and about 2.5km from the seashore. The aerosols were collected on a daily bases for the period of 2009–2010.

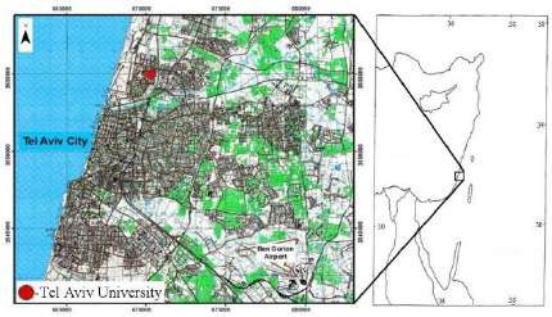

Fig. 1: Location of the sampling station at Tel Aviv University (marked in red).

The aerosols were sampled on silicon wafers (Wacker-Siltronic, 0.7 mm thickness, 45 mm diameter) using the Electrostatic Aerosol Collector (EAC). In the EAC (Klein et al., 2010a) the aerosols are charged by a shower of electrons and a strong electric field created by a 15000 V potential. The aerosols are then impacted onto the surface of a silicon wafer by the strong electric field. The aerosols collected on the silicon wafers are then analyzed for deposition and condensation-freezing modes using the FRIDGE-TAU (FRankfurt Ice-nuclei Deposition freezinG Experiment, the Tel Aviv University version) chamber, a newly developed IN-Counter (see Bundke et al., 2008 and Klein et al., 2010a for more details). In the FRIDGE-TAU (Fig 2) the aerosols are exposed to the desired and known vapor pressures at different temperatures. In this work the measurements were performed from a

temperature of around -8°C down to -23 °C, with a number of different values of vapor pressure at each temperature, from ice saturation to water saturation (S_w of 0.88–1.0, S_i of 1.0–1.25), The ice crystals that are formed are recorded with a computer controlled CCD camera.

During the aerosol collection, a total aerosol concentration (Nt) in the size range of 0.11–3µm was also measured using the TSI (CPC) 3010 and was used to calculate the activation fraction values of the ice nuclei (# of IN/Nt).

It should be noted that the aerosols collected by the EAC include particles that could be larger than 3 µm. In that case the values of activation fraction obtained here may be a slight overestimation of the real values.

In addition PM_{10} and $PM_{2.5}$ (Particulate Matter with aerodynamic diameter of less than 10 µm and 2.5 µm, respectively) were measured as well as different meteorological data including air temperature (°C), wind direction (degree), wind speed (m/sec), visibility (km), relative humidity (%) and rain amount (mm).

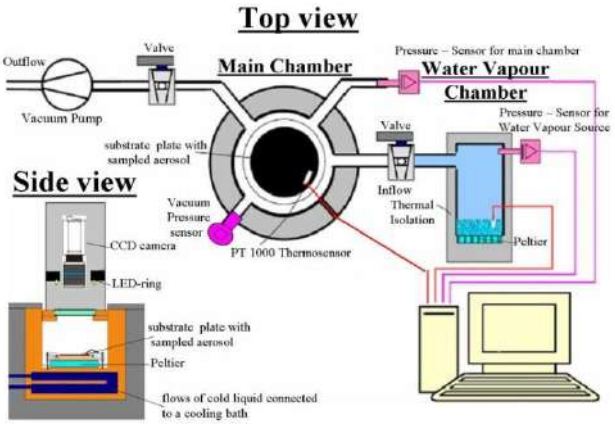

Fig. 2: Schematic diagrams of the FRIDGE-TAU method.

2.2. DESCRIPTION OF TAU-2D MODEL:

The Tel Aviv University 2D numerical cloud model (TAU-2D) with detailed treatment of cloud bin-microphysics was used (Yin et al., 2000 and references therein). The model simulates the evolution of precipitation in mixed-phase clouds starting from cloud condensation nuclei. The ice microphysical processes included were drop freezing and ice nucleation. The algorithm of ice nucleation by immersion-freezing is based on Bigg (1953), named Bigg in this work, while deposition and condensation-freezing is based on the parameterization of Meyers et al. (1992). Interactions of ice-ice and ice-drop (aggregation, accretion and riming), melting of ice particles, and sedimentation of both drops and ice particles are included in the model. All the microphysical processes have been formulated using kinetic equations and solved using the method of multi-moments (Tzivion et al., 1987; Reisin et al., 1998). More details about this model can be found at Yin et al. (2000).

In this study, the initial conditions (temperature and humidity profiles) were similar to those of Levin et al. (2005) and Teller and Levin (2006). The temperatures at sea surface and at cloud base (about 1000m) were 19°C and 7°C, respectively. This profile represents average thermodynamic conditions of winter convective clouds in the Eastern Mediterranean region. Wind shear was not included in the simulations discussed here. The simulations use 300 m height and 300 m lateral resolutions and a 2 s time step for a 90 minute period.

In the simulations, the CCN concentrations are characterized on the basis of the fractions of CCN (soluble aerosols) in fine (diameter <0.5 μm) and coarse (diameter >0.5 μm) modes, based on the measurements of Levin et al. (2005) during the MEditerranean Israeli Dust EXperiment (MEIDEX) campaign. From these data the concentration of potential active IN can be calculated by subtracting the CCN concentration from the total aerosol concentration in each size mode.

3. RESULTS AND DISCUSSION:

3.1. IN MEASUREMENTS:

A total of 328 samples were measured from January 2009 to December 2010 for IN concentration (#/L) and Activation Fraction (AF) for deposition and condensation-freezing (depending on the saturation ratio value). The lowest number concentration and AF value of 0.5 L^{-1} and $1.2^{x}10^{-7}$ respectively, were measured at -13°C at S_w of 0.88 while the highest number concentration and AF value of 267.3 L^{-1} and $5^{x}10^{-4}$ respectively were measured at -18°C at water saturation .

The samples were separated based on clean or dusty conditions. Dust events were defined as cases in which (1) the daily average of PM_{10} or the values of PM_{10} during the aerosol sampling exceeded 100 μg/m^3 (Ganor et al., 2009) and (2) the air mass trajectory in the previous 72 hours had originated or passed over a dust source. Samples were defined as clean when (1) PM_{10} daily average values and the PM_{10} value during the aerosol sampling were below 50 μg/m^3 (Ganor et al., 2009) and (2) the air mass trajectory in the previous 72 hours had not passed over a source of dust.

Most of these samples arrived at the measuring station from the north-west direction. Days with PM_{10} values between 50 and 100 were not included in the present evaluation because of the difficulty of classifying them as dusty or clean.

A total of 40 samples were categorized as dust conditions (see orange lines in Fig. 3). Out of all dust conditions, only 20% reached the measuring station by only passing over land (named continental), and the remaining 80% were transported, at least for part of the time over the Mediterranean Sea, or the Red Sea. A total of 104 samples were categorized as clean (see blue lines in Fig. 3). Most clean

samples were define as maritime, because in more than half of them (54%) the air mass spent more than 60 hours over the Mediterranean Sea before reaching the station.

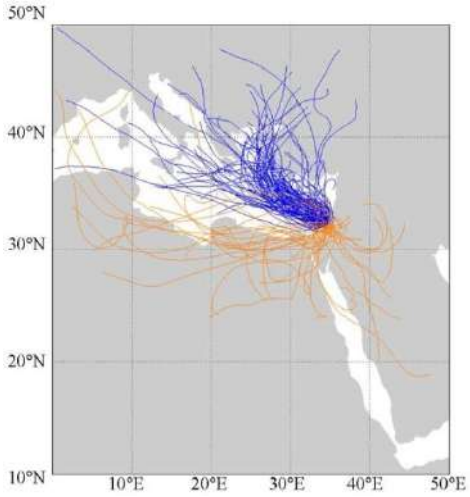

Fig. 3: Back trajectory history of air masses showing passage of air prior to reaching the sampling station. Each line represents a 72 hour trajectory at 500 m altitude. The back trajectories were taken from http://www.arl.noaa.gov *website. The orange lines represent dust conditions and the blue lines represent clean conditions.*

IN concentrations of clean and dust conditions were calculated based on the volume sampled on the silicon wafer. The average IN concentrations of the clean and dust conditions were calculated for all temperatures and saturation ratios with respect to water (Fig. 4A) and ice (Fig. 4B). The average IN concentrations of the dust conditions ranges from 24.4 L^{-1} (at -13ºC for S_w of 0.89 corresponding to S_i of 1.01) up to 84.8 L^{-1} (at -18ºC for water saturation corresponding to S_i=1.19). The average IN concentrations of the clean events range from 10.3 L^{-1} (at -13ºC for S_w of 0.89 corresponding to S_i of 1.01) up to 37.8 L^{-1} (at -23ºC for water saturation corresponding to S_i of 1.25). Average concentrations of the dust conditions were 2.4 times higher than those of the clean conditions. This difference ranges from a low value of 2.1 for -8ºC at water saturation (S_i of 1.08) up to 2.8 (the highest difference) at -18ºC at water saturation (S_i of 1.19). Similar increases by the same factor were found by Bowdle et al. (1985) and Levi and Rosenfeld (1996). On the other hand, Castro et al. (1998) found smaller differences in their measurements. DeMott et al. (2003) who measured the IN concentrations while flying in a dust layer that was transported from Africa to Florida found that the concentrations were about 20 to 100 times higher than those measured at lower altitudes in a non-dusty environment at the same location. Higher increases were also found by Klein et al. (2010b), who measured at a Central European mountain site during an episode of dust transport from the Sahara. The smaller increase of IN in our measurements as compared to those from Central Europe and Florida, agrees with previous measurements (e.g. Levin and Lindberg, 1979) indicating that in the Eastern Mediterranean the atmosphere always contains some dust particles, even in the absence of dust storms. On the other hand, in many other locations, such as Central Europe and Florida, the presence of mineral dust particles under clean conditions is less common.

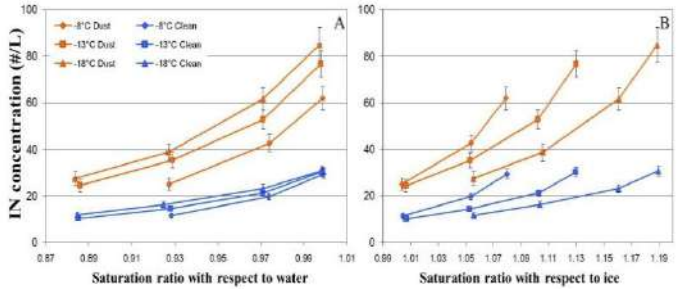

Fig. 4: Average values of IN concentrations for clean (blue) and dust conditions (orange), for different temperatures and saturation ratios, (A) as a function of Sw and (B) as a function of Si. The error bars represent the standard errors. Due to the small number of dust measurements at -23 ºC, the concentration of this temperature were not shown or taken into account.

The average Activation Fraction (AF) values of dust and clean conditions were also calculated, as can be seen in Fig. 5A (for S_w) and 5B (for S_i). The average AF values of the dust were 1.4 times higher than those of the clean conditions. This difference ranges from 1.2 (at -8ºC for water saturation corresponding to S_i of 1.08) up to 1.6 (for -18ºC at S_w of 0.97 corresponding to S_i of 1.16).

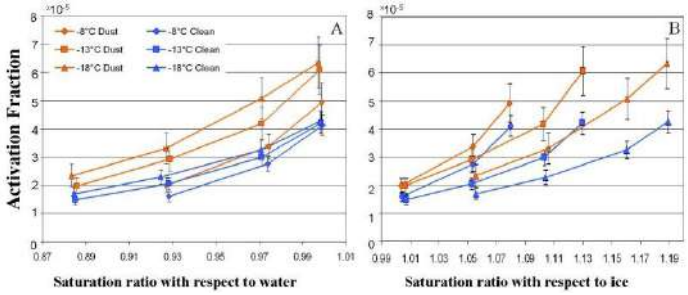

Fig. 5: Average Activation Fraction (AF) values for dust (orange) and clean (blue), for different temperatures and saturation ratios, (A) a function of Sw and (B) as a function of Si. The error bars represent the standard errors. Due to the small number of dust measurements at -23ºC, the values of this temperature were not shown or taken into account.

3.1.1. PARAMETERIZATION OF CLEAN AND DUSTY CONDITIONS

With the present distribution of clean and dusty conditions, we developed new parameterizations that combine the effects of temperature, saturation ratio and total aerosol concentrations on IN concentrations and AF values. The parameterizations were developed using a multiple regression analysis of the independent values of temperatures, saturation ratios (with respect to water or ice) and the dependent values of IN concentration or AF values. The values of the coefficient of the multiple regression ranged from 0.69 to 0.81 (the values were statistically significant). The values of the coefficients were higher for the dust than for the clean conditions. Since it was impossible to separate the nucleation modes between deposition and condensation-freezing, the parameterizations we developed combine both modes. The parameterizations refer to the temperature range from -8°C to -18 °C for dust cases and from -8°C to -23°C for clean cases. Saturation ratios for all parameterizations range from S_w=0.88–1.00 corresponding to S_i=1–1.19 for -18°C and S_i =1–1.25 for -23°C. In agreement with our observations, the parameterizations show a strong and significant connection to changes of saturation ratio but smaller dependence on changes in temperature.

The parameterization equations based on IN concentration values for clean and dusty conditions are the following:

$$IN_{\_clean} = -142.8 - 0.1 \times T + 144 \times S_i \quad (1)$$

$$IN_{\_clean} = -168.4 - 1.6 \times T + 169.8 \times S_w \quad (2)$$

$$IN_{\_dust} = -345.7 - 1.3 \times T + 341.7 \times S_i \quad (3)$$

$$IN_{\_dust} = -392.6 - 4.9 \times T + 389.1 \times S_w \quad (4)$$

Where IN represents the IN concentration (#/L), T is Temperature (°C), S_w represents the saturation ratio with respect to water and S_i represents the saturation ratio with respect to ice. The above equations are shown in Fig. 6A for S_w and B for S_i.

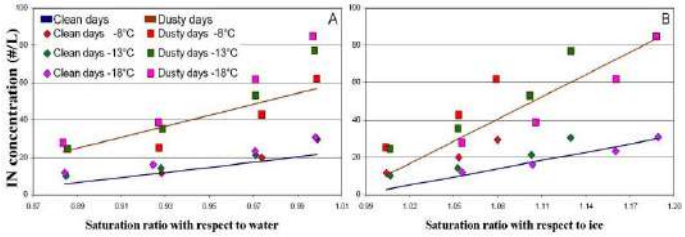

Fig. 6: Average IN concentrations of clean (diamond) and dust (square) conditions, for different temperatures and saturation ratios, (A) as a function of Sw and (B) as a function of Si. The lines represent the parameterization equations for the clean (blue) and dust condition (brown) from Eq.1 to 4.

The parameterization equations based on AF values for clean and dusty condition are the following:

$$AF_{\_clean} = -1.8*10^{-4} - 1.1*10^{-7} \times T + 1.8*10^{-4} \times S_i \quad (5)$$

$$AF_{\_clean} = -2.1*10^{-4} - 2.1*10^{-6} \times T + 2.2*10^{-4} \times S_w \quad (6)$$

$$AF_{\_dust} = -2.6*10^{-4} - 1.2*10^{-6} \times T + 2.6*10^{-4} \times S_i \quad (7)$$

$$AF_{\_dust} = -2.9*10^{-4} - 3.8*10^{-6} \times T + 2.9*10^{-4} \times S_w \quad (8)$$

Where AF represents the activation fraction values for aerosol with diameter of 0.11-3 μm. The above equations are shown in Fig. 7A for S_w and B for S_i.

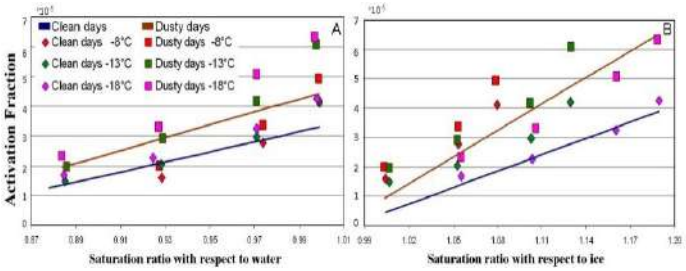

Fig. 7: Similar to Fig. 4.11 except for the activation fraction values (x10^{-5}) and the parameterizations from Eq.5 to 8.

As the saturation ratio increases, the number of activated particles increases much more rapidly under dusty conditions than for cases where the dust particles are absent or exist in low concentrations. Rosinski and Lecinski (1983) who also evaluated the concentrations of IN as a function of the nature of the aerosol particles, supersaturation with respect to ice and temperatures had a much steeper line then those presented here. The reason for that could also be the fact that in the Eastern Mediterranean, dust particles are present even when the atmosphere is clear.

3.2. USE OF THE NEW PARAMETERIZATION IN TAU-2D MODEL:

The new parameterization (Eq. 7, from here on define as Ardon) were compared with those obtained by using Meyers et al. (1992) (define as Meyers in this work) which depends on temperature and saturation ratio and DeMott et al. (2010)

parameterizations (define as DeMott in this work), which depends on temperature and aerosol concentrations with sizes larger than 0.5 μm.

Using a case with initial CCN concentration of 900 cm^{-3}, we calculated the **potential number** concentrations of IN based on the above parameterizations (see Fig. 8). In this calculations only the temperature, ice supersaturation (assuming water saturation at each temperature) and the aerosol concentrations were used without any effects of dynamics. As can be seen from Fig. 8, at warmer temperatures the parameterization of Meyers and Ardon produces similar concentrations of IN and they are both higher than those produced by DeMott parameterization. At temperatures lower than -20ºC, Meyers parameterization produces the highest IN concentrations, while from -26.5ºC IN concentrations by DeMott parameterization exceeds that of Ardon. It is also shown that there is a smaller dependence on temperature of IN formation using Ardon's parameterization as compared to the other two.

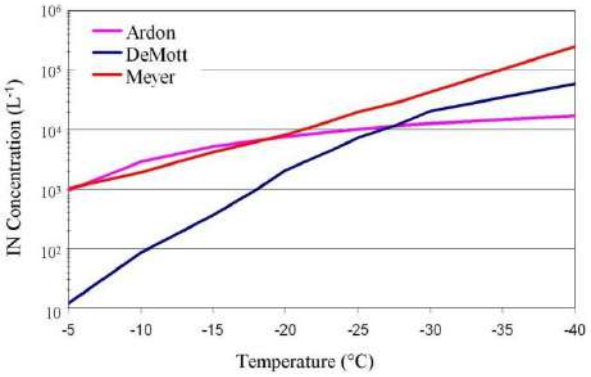

Fig. 8: Comparison of Ardon (in pink), DeMott (in blue) and Meyers (in red) IN concentration (L-1) based on their parameterization used in the 2D model as a function of temperature for water saturation measurements.

The comparisons between the three parameterizations have been made for CCN concentrations of 900 cm^{-3}. While Meyers parameterization calculates the concentration of IN based on the changes of saturation ratios without considering the available aerosols, DeMott and Ardon parameterizations take into account the temperature and the aerosol concentration (but for different size ranges). Ardon also added the dependence on saturation ratio with respect to ice. For DeMott and Ardon parameterizations the fraction of IN particles from the total aerosol concentrations was calculated. Table 1 summarizes the three different tested scenarios.

Table 1: The IN parameterizations scenarios used in the simulations.

Case	Ice Nuclei paramet.	Aerosol Conc. (cm^{-3})	CCN Conc. (cm^{-3})	IN Fraction for fine particles (0.11-0.5 μm) (%)	IN Fraction for coarse particles (0.6-32 μm) (%)
1	Meyers et al. (1992)	1019	900	-	-
2	DeMott et al. (2010)	1019	900	10	50
3	Ardon 7Eq.	1019	900	10	50

It was found that the Bigg parameterization of immersion-freezing overshadows all the other ice parameterizations in the development of ice in the cloud model. In other words, when Bigg was used in the model hardly any difference could be detected by using the other three parameterizations. Therefore in order to compare Meyers, DeMott and Ardon we removed the mechanism of drop freezing based on drop size (Bigg) from the model runs that are presented here. These runs are summarized in Table 1.

A comparison of the model results for rain rate and total rain amounts using the three parameterizations are shown in Fig. 9. The figure reveals that DeMott parameterization produces 30% more precipitation and similar higher maximum rain rate than Ardon and 60% higher than Meyers. Ardon's total precipitation and rain rate were 30% higher than Meyers. These results agree with the conclusions reached by Teller and Levin (2006), which showed that when more ice crystals are formed in the upper parts of the clouds, more of this ice does not take part in the development of precipitation because it remains as small ice crystals, which are blown away to the anvil (see Fig 10 - compare the ice concentrations of Meyers and the other two). In other words, the fact that in DeMott less ice crystals are formed, allows the warm precipitation development to be more effective. In Meyers on the other hand, the high concentrations of ice in the upper parts of the cloud reduces the precipitation efficiency, leading to less total precipitation and lower precipitation rates.

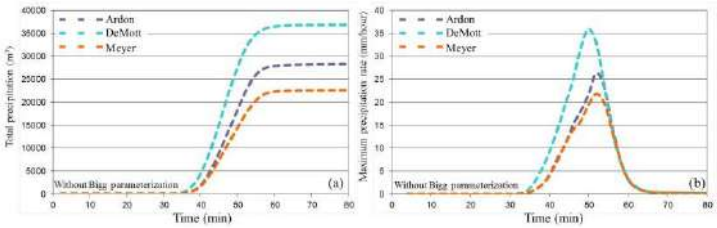

Fig 9: Amount of precipitation (in m^3) as a function of time for different IN parameterizations (different colors) when Bigg parameterization is omitted. (a) Represents the total precipitation on the ground; (b) represents the precipitation rate (mm/hour).

The vertical distribution of water droplets, ice crystal and graupel particles for the three parameterizations were compared (see Figure 10). Ardon producing larger masses of graupel particles than DeMott, but similar to those produced in Meyers. On the other hand, the ice mass concentrations are much greater in Meyers than in the other two and it covers a larger volume above 3000 m.

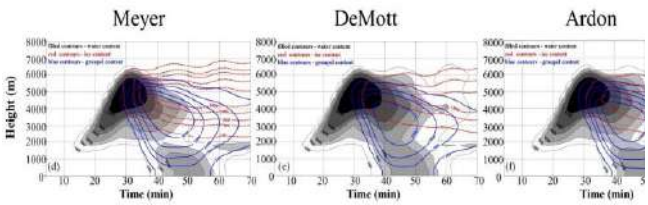

Fig 10: Vertical distribution of mixing ratio paths (gm^{-2}) of water (in grey), ice (in red) and graupel (in blue) as a function of time, height without Bigg's parameterization for immersion-freezing. The left figure is the results of Meyers parameterization, the center figure is the results of DeMott parameterization and the right figure is the results of Ardon parameterization.

An effective way of comparing the effects of the different ice nucleation parameterization on the development of the cloud formation is to evaluate the variations between these parameterizations as a function of height and time. For that purpose the concentration of ice crystals for each parameterization was calculated for three chosen heights (3, 4.5 and 6 km) in two minute steps for the entire cloud lifetime (from the first formation of ice crystals to the end of simulation at 90 min). Each value at a certain time and height represents the sum of all ice crystal number concentrations, which were formed in the cloud at this same height.

The values of ice crystal concentration from DeMott and Meyers were subtracted from those calculated in Ardon (at the same height and time) see Fig. 11. The difference in ice crystal concentrations between Ardon and DeMott (Fig. 11a) shows that Ardon produces higher concentrations of ice crystals at lower altitudes, while the picture reverses at higher altitude. Meyers produces a much higher concentration of ice crystals at higher altitudes than either Ardon (Fig. 11b) or DeMott (not shown). These results support the observations of Gultepe et al. (2001) and Prenni et al. (2007) who state that Meyers parameterization overestimates the rate of ice formation in clouds. The results of Ardon's parameterization also agrees with the measurements of Levin et al. (1996) who observed high concentrations of ice crystals at temperatures as high as -10°C in winter convective clouds in Israel.

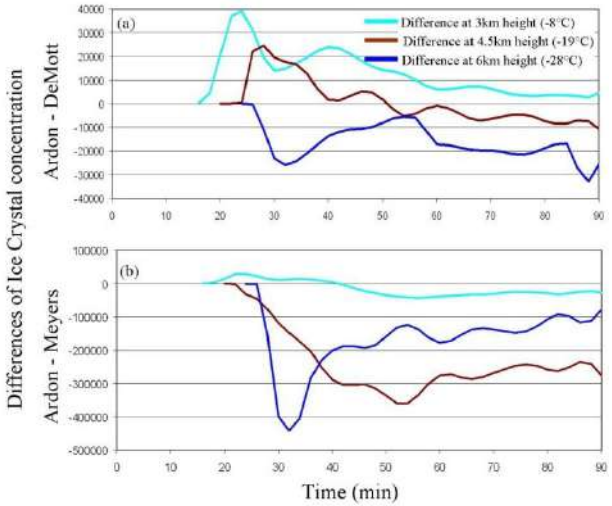

Fig 11: The differences in ice crystal number concentrations using the difference between Ardon and DeMott (Ardon-DeMott) (a) and Ardon with Meyers (Ardon-Meyers (b), for three different heights: 3 km (light blue), 4.5 km (brown) and 6 km (blue) for the entire time period of the model run.

4. CONCLUSION:

Ice nuclei concentrations were 2.4 times higher while AF values were 1.4 times higher in dust conditions compared to those measured in clean conditions. IN concentration was strongly dependent on

saturation ratio and less dependent on temperature.

New parameterizations that combine the effects of temperature, saturation ratio and total aerosol concentrations on IN concentrations and activation fraction values were developed and implemented in TAU-2D model. It was found that the parameterization of Bigg for the immersion freezing process overshadows all the other ice formation processes in the development of ice crystals in the cloud model. Removing the immersion-freezing parameterization by Bigg helped us identify the different effects of the parameterizations of Meyers, DeMott and Ardon.

Meyers parameterization produced higher concentrations of ice crystals compared to either DeMott or Ardon and mostly in the upper parts of the cloud. On the other hand, Ardon produced ice crystals at warmer temperatures at lower altitudes compared to either DeMott or Meyers. DeMott parameterization, which formed the smallest concentrations of ice crystals produced the highest precipitation amount (total precipitation and maximum rate) as compared to Meyers or Ardon.

The type of IN parameterization used in cloud models could have an effect on the formation of water, ice and graupel particles and could affect all the subsequent processes that lead to precipitation formation. Therefore, in order to validate model results and decide on the appropriate IN parameterization, more measurements of ice concentrations and mixing ratios as a function of height are needed. In addition, it should be emphasized that these conclusions apply to winter convective clouds affected by mineral dust in the Eastern Mediterranean. In these clouds the warm microphysical processes seem to be strong. It is therefore important to also test the parameterizations in clouds that are colder, where the ice processes dominate the precipitation development.

5. ACKNOWLEDGMENT

We would also like to acknowledge the German Israeli Foundation (GIF) grant number 1-860-27 for their support and to Dr. Heinz Bingemer for all his help.

6. REFERENCES:

Bigg, E.K.: The formation of atmospheric ice crystals by the freezing of droplets Quart. J. Roy. Meteor. Soc., 79, 510-519, 1953.

Bowdle, D.A., Hobbs, P.V. and Radke, L.F.: Particles in the Lower Troposphere over the High Plains of the United States. Part III: Ice Nuclei, J. Climate Appl. Meteor., 24, 1370-1376, 1985.

Bundke, U. Nillius, B. Jaenicke, R. Wetter, T. Klein, H. and Bingemer, H.: The fast ice nucleus chamber FINCH, Atmos. Res., 90, 180-186, 2008.

Castro, A. Marcos, J.L. Dessens, J. Sanchez, J.L. and Fraile, R.: Concentration of ice nuclei in continental and maritime air masses in Leon (Spain), Atmos. Res., 48, 155-167, 1998.

DeMott, P.J., Sassen, K., Poellet, M.R., Baumgardner, D., Rogers, D.C., Brooks, S.D., Prenni, A.J. and Kreidenweis, S.M.: African dust aerosols as atmospheric ice nuclei, Geophys. Res. Lett., 30, 1732, doi:10.1029/2003GL017410, 2003a.

DeMott, P.J. Prenni, A.J. Liu, X. Kreidenweis, S.M. Petters, M.D. Twohy, C.H. Richardson, M.S. Eidhammer, T. and Rogers D.C.: Predicting global atmospheric ice nuclei distributions and their impacts on climate, Proc. Natl. Acad. Sci. USA., 107, 11217-11222, 2010.

Gagin, A.: The Ice Phase in Winter Continental Cumulus Clouds, J. Atmos. Sci., 32, 1604-1614, 1975.

Ganor, E.: The Frequency of Saharan Dust episods over Tel-Aviv, Israel, Atmos. Environ., 28, 2867-2871, 1994.

Ganor, E., Foner, H.A. Bingemer, H.G. Udiste, R. and Setter I..: Biogenic sulfate generation in the Mediterranean Sea and its contribution to the sulfate anomaly in the aerosol over Israel and eastern Mediterranean, Atmos. Envir., 34, 3453– 3462, 2000.

Ganor, E. Stupp, A. and Alpert P.: A method to determine the effect of mineral dust aerosols on air quality, Atmos. Envir., 43, 5463-5468, 2009.

Graham, B. Falkovich, A.H. Rudich, Y. Maenhaut, W. Guyon, P. and Andreae, M.O.: Local and regional contributions to the atmospheric aerosol over Tel Aviv, Israel: a case study using elemental, ionic and organic tracers, Atmos. Envir., 38 1593-1604, 2004.

Gultepe, I., Isaac, G.A. Cober, S.G.: Ice crystal number concentration versus temperature for climate studies, Internat. J. Climatology, 21, 1281-1302, 2001.

Klein, H. Haunold, W. Bundke, U. Nillius, B. Wetter, T. Schallenberg, S. and Bingemer, H.: A new method for sampling of atmospheric ice nuclei with subsequent analysis in a static diffusion chamber, Atmos. Res., 96, 218-224, 2010a.

Klein, H. Nickovic, S. Haunold, W. Bundke, U. Nillius, B. Ebert, M. Weinbruch, S. Schütz, L. Levin, Z. Barrie, L.A. and Bingemer, H.: Saharan dust and ice nuclei over Central Europe, Atmos. Chem. and Phys., 10, 10211-10221, 2010b.

Levi, Y. and Rosenfeld, D.: Ice nuclei, rainwater chemical composition, and static cloud seeding effects in Israel, J. Appl. Meteorol., 35, 1494-1501, 1996.

Levin, Z. and Lindberg, J.D.: Size distribution, chemical composition, and optical properties of urban and desert aerosol in Israel, J. Geophys. Res., 84, 6941-6950, 1979.

Levin Z. Price C. and Ganor E.: The contribution of sulfate and desert aerosol to the acidification of cloud and rain in Israel, Atmos. Envir., 24, 1143-1151, 1990.

Levin, Z., Teller, A., Ganor E. and Yin, Y.: On the interactions of mineral dust, sea salt particles and clouds - A Measurement and modeling study from the MEIDEX campaign, J.

Geophys. Res., 110, D20202, doi:10.1029/2005JD005810, 2005.

Meyers, M.P. DeMott, P.J. and Cotton, W.R.: New primary ice nucleation parameterizations in an explicit cloud model, J. Appl. Meteor., 31, 708-721, 1992.

Prenni, A.J. Harrington, J.Y. Tjernstrom, M. DeMott, P.J. Avramov, A. Long, C.N. Kreidenweis, S.M. Olsson, P.Q. and Verlinde J.: Can ice-nucleating aerosols affect arctic seasonal climate?, Bull. Am. Meteorol. Soc., 88, 541- 550, 2007.

Reisin, T.G. Yin, Y. Levin, Z. and Tzivion, S.: Development of giant drops and high reflectivity cores in Hawaiian clouds: Numerical simulation using a kinematic model with detailed microphysics, Atmos. Res., 45, 275-297, 1998.

Rosinski, J. and Lecinski, A.: Temperature-supersaturation relation for natural sorption ice-forming nuclei, J. Atmos. Sci., 14, 49-63, 1983.

Teller, A. and Levin, Z.: The effects of aerosols on precipitation and dimensions of subtropical clouds; a sensitivity study using a numerical cloud model, Atmos. Chem. and Phys., 6, 67-80, 2006.

Tzivion, S. Feingold, G. and Levin, Z.: An efficient numerical solution to the stochastic collection equation, J. Atmos. Sci., 44, 3139-3149, 1987.

Yin, Y. Levin, Z. Reisin, T.G. and Tzivion, S.: The effects of giant condensation nuclei on the development of precipitation in convective clouds - a numerical study, Atmos. Res., 53, 91-116, 2000.

ESTIMATION OF THE EFFECT OF CLOUD LIQUID WATER CONTENT ON CALCULATIONS OF THE SPECTRAL CHARACTERISTICS OF HORIZONTAL TURBULENT EXCHANGE BETWEEN A CUMULUS CLOUD AND AMBIENT ATMOSPHERE BASED ON AIRCRAFT OBSERVATIONS

Post grad. stud. Alexander M. Strunin[1] and
Post grad. stud. Dmitriy N. Zhivoglotov[1]

[1] Federal State Budgetary Institution "Central aerological observatory", 3, Pervomayskaya, 141700 Dolgoprudny Moscow Region, Russia

1. INTRODUCTION

One of the main mechanisms of cumulus clouds development is the turbulent energy exchange across the clouds boundaries. The modern aircraft instruments allows measuring wind speed and temperature fluctuations that gives possibility to calculate turbulent heat fluxes in cumulus zone, i.e. inside the cloud and in the ambient area under cloud effect. However, correct temperature measurements inside the cloud with liquid droplets are troubled due to evaporating of cloud water from sensitive element of thermometer. This leads to appearance of false temperature fluctuations, which named as "wetting effect" of thermometer. According to previous estimations (*Cumulus clouds* …, 1977) the value of cloud droplet influence on aircraft thermometer readings can be about 1 ^{o}C or even more. There are a few methods to take into account the droplet affect on temperature measurements using aircraft instruments.

Supposing that sensitive element of thermometer is completely wetted it is possible to evaluate psychometric effect, i.e. influence of evaporation from the sensor surface on measured temperature. One of the ways is the using of special designed thermometer (thermometer-psychrometer), which is always fully wetted (Telford, Warner, 1962). In this case wetting correction for the thermometer ΔT is defined as (*Cumulus clouds* …, 1977):

$$\Delta T = \Delta T^{*}(1-\beta_0) \qquad (1)$$

where $\Delta T^{*} = 0{,}2rM^2$ is the dynamic heating of thermometer, and $\beta_0 = \dfrac{1}{1+\dfrac{1550}{p}\dfrac{dE}{dT}}$ is the factor for completely wetted thermometer (M is Mach number, r is the recovery factor of aircraft thermometer, p is the pressure at the flight level, E is the pressure of saturated vapor).

If aircraft thermometer is not fully wetted the wetting coefficient β for this

thermometer can be defined as (*Cumulus clouds* …, 1977):

$$\Delta T = \Delta T^{*}(1-\beta) \qquad (2)$$

Since the value of β is the constant for the thermometer the magnitude of wetting correction is also practically constant for a cloud (changing of flight velocity is not significant affect on the correction). Thus, this method allows correcting only the average value of air temperature in a cloud and it is not useful for compensation for fluctuation temperature error and calculation turbulent heat fluxes in clouds.

2. INVESTIGATIONS OF HIGH-FREQUENCY AIRCRAFT THERMOMETER IN SPECIAL WIND TUNNEL

A high-frequency aircraft thermometer HFAT was designed in Central aerological observatory (CAO, Russia) for measuring turbulent fluctuations of air temperature from aircraft-laboratory. Initial design of the thermometer was suggested by A. Nevzorov and V. Shugaev (*Cumulus clouds* …, 1977). Later the sensor HFAT was modified and investigated (*Strunin. and Hiyama, 2004b*) and at the present time it became the basic instrument for temperature measurements at aircraft-laboratories using CAO. The common view of the HFAT is presented in ***Fig. 1***. Sensitive element of the thermometer is a platinum hot wire with 30 mkm in diameter, coiled on the x-frame. Teflon cone is prevented the ice accumulation on the front part of the sensor and short-time heating element provide removing the ice from the holder of the sensor. Special water proof prevents damage of the wire.

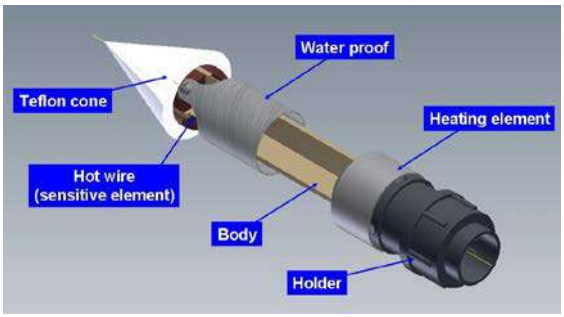

Fig. 1. Aircraft high-frequency air temperature sensor designed in CAO

Laboratory and flight tests of the HFAT, which were fulfilled in earlier time (Strunin and Hiyama, 2004b), showed that the time constant of the sensor was 0.012 s (that was correspondent to spatial scale about 1.5 m for typical civil aircraft speed) and recovery factor of the sensor was $r = 0.72 \pm 0.04$.

Calculations of air flow over the thermometer made through the computer program FlowVision, showed that air stream in the area of the sensitive element had direction, which was opposite to the main flow. This allowed us suggesting that

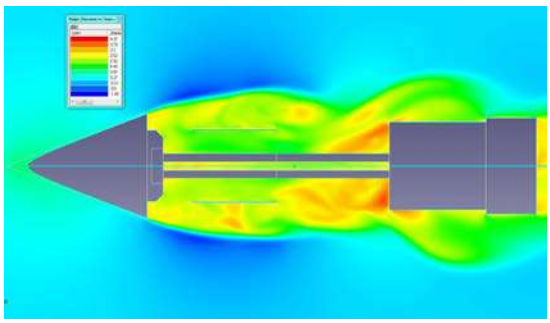

Fig. 2. Temperature distribution in the flow over the HFAT calculated through FlowVision computer program

cloud droplets did not impact directly at the sensor wire. However, the process of air cooling due to droplets evaporation could take place on the protecting parts of the sensor. Distribution of calculated temperature in the area of sensitive element (***Fig. 2***) demonstrated that recovery factor of HFAT was $r = 0.715$, that was practically coincided with the value, obtained earlier in flight tests.

Special wind tunnel SWT with the precision bridge circuit and analog-to-digital converter and registration system. True air temperature T was calculated through well-known gas dynamic equation:

$$T = \frac{T_i}{1 + 0{,}2rM^2} \qquad (3)$$

where T_i is the HFAT-measured temperature.

It is known that in common view recovery factor of a thermometer depends on Mach number, Reynolds and Prandtl

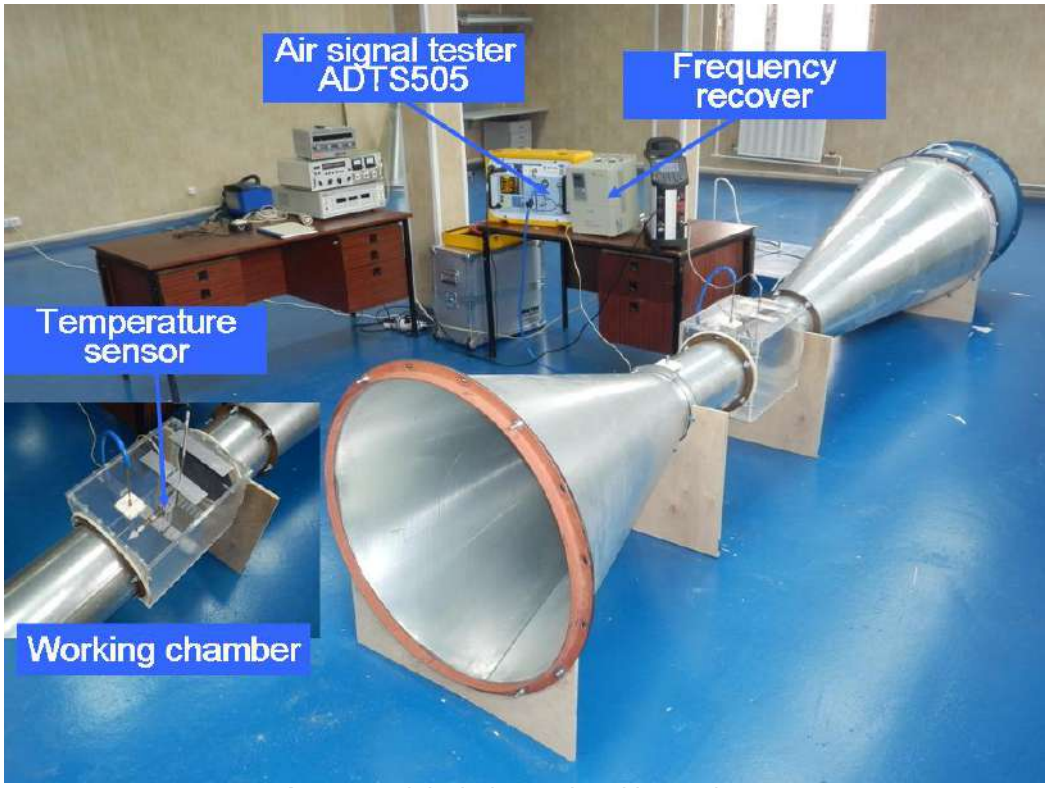

Fig 3. Special wind tunnel and its equipment

flow speed up to 80 ms^{-1} was created for laboratory testing aircraft temperature and liquid water sensors (***Fig. 3***). System of atomizer supplied in air flow controlled liquid water content with values up 5 gm^{-3}. Pressure measurements fulfilled with high accuracy air signal tester ADTS-505 with error not more than ± 5 Pa. Tested temperature sensor was inserted in numbers. (Strunin and Hiyama, 2004b). Depending on Reynolds and Prandtl numbers for our temperature sensor can be treated as negligible. Testing made in our wind tunnel allowed us defining the dependence of recovery factor on the Mach number (***Fig. 4***) in the range from 0.1 up to 0.25. As well-known that in Mach number range typical for civil airplanes

(from 0.3 to 0.7) recovery factor is practically constant, thus fitting curve was being seek in the form of $r = r_0 - Ae^{-aM}$.

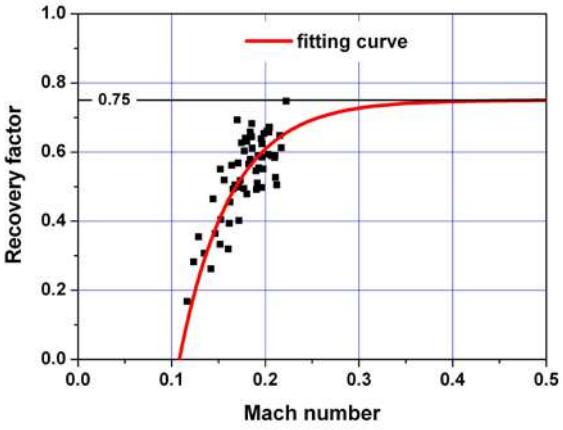

Fig. 4. Recovery factor of HFAT vs Mach number

Our calculations showed that coefficients of the fitting curve were a=1.69, A=6.21*10^7. Extrapolation of the curve to typical Mach numbers for aircraft-laboratory gave us possibility to define asymptotic value of recovery factor r_0=0.75±0.05. Thus, value of recovery factor for temperature sensor HFAT, defined through wind tunnel testing was close to the one calculated as through computer program so based on the flight experiments. We use for the further temperature calculation the value of recovery factor r=0.72.

Special instruments for wind tunnel was designed for testing aircraft thermometers and estimating influence of liquid water content in the flow on aircraft temperature sensor readings. System of injectors created the flow in wind tunnel with controlled water content. Example of testing HFAT in wind tunnel with liquid water content is presented in ***Fig. 5.***

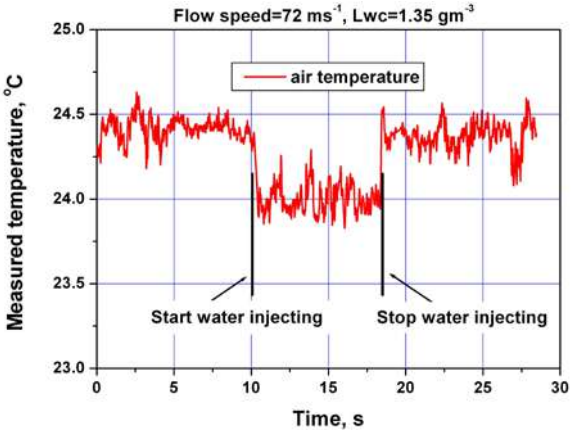

Fig 5. Influence of liquid water content in air flow on temperature sensor readings

Simultaneous air temperature and liquid water content measurements in wind tunnel and in clouds allowed us creating a method of correcting temperature readings on droplet influence. As the sensor HFAT had construction protected its sensitive element from direct impacting of droplets the process of droplet evaporation was moved to protect elements of the sensor. It was clear that the sensor was wetting in part and correction was depended on the value of liquid water content. Introducing the coefficient of temperature correction on liquid water content k_w it was possible to calculate true air temperature as:

$$T' = T_i' + k_w \Delta T^* Lwc \qquad (4)$$

where T_i' was measured air temperature fluctuations in a flow with water and Lwc was instantaneous value of liquid water content.

Liquid water content in wind tunnel flow was defined based on measurement of water discharge through injector and estimating volume of created droplets. Water discharge controlled based on high-accuracy balance (up to 0.3 g). Droplet

volume was defined by flow visualizer with colored water.

Thus, wind tunnel experiment allowed us estimating value of k_w based on measurement of liquid water content Lwc and dynamic heating of thermometer ΔT^*. Estimations of five wind tunnel tests showed that values of k_w were from 0.10 up to 0.19 m^3g^{-1}. Important, that temperature of injecting water, which varied from 25 up to 50 ^oC, did not effect on the test results. The average value of k_w was 0.145 m^3g^{-1}, thus for further calculations we use the value of 0.15.

3. AIRCRAFT OBSERVATIONS OF CUMULUS CLOUDS

Aircraft observations of cumulus clouds were fulfilled in August – September 2007 in the frame of Russian-Cuban experiment over the Camaguey meteorological sampling area (***Fig. 6***). In particular instruments designed in Central aerological observatory for measurements of horizontal wind speed fluctuations u' and air temperature fluctuations T' were installed aboard the Antonov-26 aircraft of Cuban airline «Aerogaviota» (***Fig. 7***). Simultaneously, liquid water content in clouds Lwc was measured using Nevsorov's cloud water content sensor. All data were recorded with the frequency of 20 Hz on aboard computer.

All measurements were made at special horizontal parts of the steady flight called as "sampling legs". At the sampling leg variations of wind speed, pitch and roll angles and flight height should not exceed $\pm$20 kmh^{-1}, $\pm5^o$ and $\pm$20 m respectively. Lengths of all sampling legs were from 5 to 10 km. At the sampling leg aircraft crossed the cumulus, including area before and after the cloud, which named as cumulus zone. In period from August to October 2007 13 research flights were fulfilled and measurement at the 60 sampling legs (which corresponded to 60 Cu) were made.

At the sampling legs (where variations of aircraft speed, pitch and roll

Fig 6. Location of the meteorological testing area over Cuba Island near Camaguei-City.

angles were small) turbulent fluctuations were defined as:

$$u' = -U + U_p + U \sin\Delta\alpha \sin\Delta\theta + U \sin\Delta\alpha \quad (5)$$

where $\Delta\alpha$ was variation of attack angle, $\Delta\theta$ was variation of pitch angle at the horizontal sampling leg. Variation of attack

Fig. 7. Aircraft-laboratory An-26 during experiment over Cuba in 2007

angle was calculated based on increment of acceleration of the aircraft center of gravity. Ground speed of the aircraft U_p was defined based on aboard GPS system. Fluctuations of true air temperature were calculated through the equation (3) with correcting on the flight level changing:

$$T' = T - \overline{T} + \tau\Delta h_b \quad (6)$$

where τ was vertical temperature gradient at the flight level, $\overline{T}$ was average air temperature at the flight level and Δh_b was variation of barometric height of the flight. Temperature gradient was defined empirically for every sampling leg. Absolute square-average errors of measured fluctuations were

$$\delta u' = \pm(\gamma_{u_0} + \gamma_u u');$$

$$\delta T' = \pm(\gamma_{T_0} + \gamma_T T'),$$

where γ_{u_0}=0,1 ms^{-1}, γ_{t_0}=0,02 K were initial sensitivity of wind speed and temperature fluctuations respectively, γ_u=0,07, and γ_t=0,08 were square-average relative errors of u' и T'.

Turbulent (eddy) horizontal kinematic heat fluxes H were calculated through the formula:

$$H = \overline{u'T'} \quad (7)$$

where averaging was made along the measuring line (track of aircraft flight).

4. EVALUATION OF WATER CONTENT CORRECTING COEFFICIENT FOR THE AIRCRAFT THERMOMETER BASED ON AIRCRAFT OBSERVATIONS OF CUMULUS CLOUDS

Data obtained during aircraft observations over Cuba give us possibility to estimate the value of k_w. Investigations of temperature readings during entering to the cloud and exiting from it showed that fronts of temperature increasing and decreasing with wetting correction were not conflicted with common conception of temperature behavior in atmospheric turbulent zones.

Table 1

Thermodynamic characteristics in cumulus cloud zones (**Date** is the date of experiment; **Time** is the Greenwich time of the beginning and end of the sampling leg; Lwc is the average value of liquid water content in the cumulus cloud; T_b is the air temperature before the cloud; T_c is the air temperature inside the cloud; T_a is the temperature after the cloud; H_1 and H_2 are the kinematic horizontal heat fluxes in the first and second parts of cumulus zone correspondently.

DATE	TIME	Lwc, gm^{-3}	k_w, m^3g^{-1}	T_b, °C	T_c, °C	T_a, °C	H_1, K ms^{-1}	H_2, K ms^{-1}
24/08/07	18:10:17-18:11:48	0.53	0	-6.29	-6.50	-6.27	0.049	-0.136
			0.15		-5.97		0.057	-0.340
17/09/07	18:40:49-18:42:35	0.82	0	-7.89	-8.30	-8.01	-0.207	0.075
			0.15		-7.48		0.262	-0.093
22/09/07	18:48:57-18:49:50	1.64	0	-7.68	-7.89	-7.89	-0.048	-0.035
			0.15		-6.02		0.055	-0.223

According to common conception of turbulent transport in atmosphere turbulent heat fluxes depends on temperature gradient and coefficient of turbulence. It was evident that if the cloud was warmer than an ambient air the horizontal heat flux through the side boundary of the cloud should be directed outside the cloud. Calculations of average air temperature and horizontal heat fluxes in Cu zones were made based on formula (4) for the parts of zone before clouds, inside Cu and after clouds. Calculations were made both without and with liquid water corrections at that with different value of k_w. Results of estimations for the three Cu zones are presented in ***Table 1*** (time was

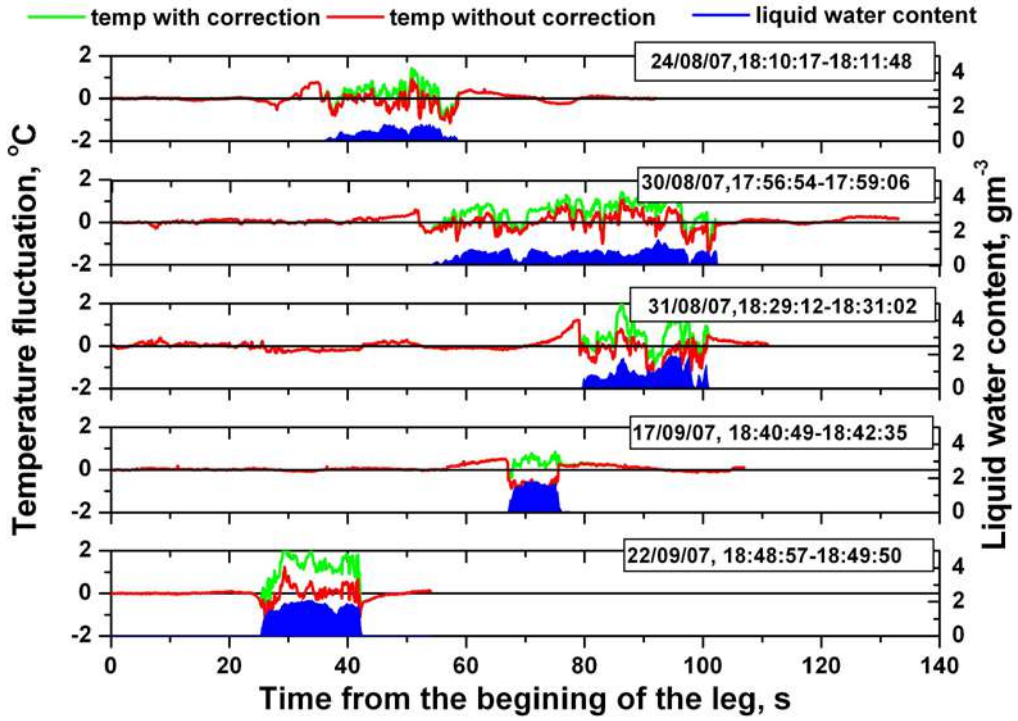

Fig. 8. Temperature realizations in cumulus zones (without and with the wetting corrections)

Greenwich). Important that in some cases liquid water correcting changed not only value of calculated heat fluxes, but also the sign of the fluxes. Analysis showed that non-contradictory fluxes distributions for all concerned cases could be observed at the value k_w=0.15 m^3g^{-1}. In that case average air temperature in the cloud was higher than in ambient air and heat fluxes directed outside the cloud. Important that value of k_w=0.15 m^3g^{-1} was close to the values obtained during wind tunnel tests. Thus, value of coefficient k_w=0.15 m^3g^{-1} used for calculating spectra of true air temperature and spectral structure of heat fluxes.

In ***Fig. 8*** examples of temperature realizations in Cu zones with and without liquid water corrections are presented. As clear seen from the picture corrections was essentially changed temperature distributions inside clouds and therefore influence of liquid droplet should be take into account during investigations of fine structure temperature and heat fluxes fields. Note that in the most cases so called "warm jackets", i.e. layers near clouds with temperature at 0.3 - 0.5 ^oC higher than ambient air were observed around Cu. Different authors pointed to the existing of warm "jacket" (see, for example, Shmeter, 1970). One of the reasons of a warm "jacket" appearance could be horizontal heat flux from the relative warm cloud to cold ambient air. However, in some cases there were cold "jackets" around Cu, but clouds were also warmer than ambient air (see, for example, bottom panel in ***Fig. 8*** for sampling leg on 22/09/07, 18:48:57 – 18:49:50). The reasons of arriving warm and could "jackets" around cumulus clouds call for additional research.

5. ESTIMATING LIQUID WATER AFFECT ON THE SPECTRAL STRUCTURE OF AIR TEMPERATURE AND HEAT FLUXES FIELDS IN CUMULUS ZONES

Numerous aircraft investigations showed that cumulus clouds essentially distorted thermodynamic fields and especially the temperature field. As well-known distortion zone of Cu could be more than in two times wider than the horizontal size of Cu (Vinnichenko et. al., 1980). Therefore researching of spectral structure of air motions in cumulus needs considering so called Cu zone including both a cloud and area around it. During aircraft observations this took into attention and measurements at all sampling legs starting a long before clouds and ending rather after it.

Turbulence in Cu zone was very non-homogeneous thus the wavelet transform $Wf(a,b)$ was used for studying spectral structure of air motions. Wavelet transform of a random function $f(x)$ (in our case they were air temperature and horizontal wind speed fluctuations) was defined as the integral transform with a family wavelet functions $\Psi(t)$ and was

given as (Kumar and Foufoula-Georgiou, 1994):

$$Wf(a,b)=\frac{1}{|a|^{1/2}}\int_{-\infty}^{+\infty}\Psi\left(\frac{x-b}{a}\right)f(x)dx \quad (8)$$

where a was a scale parameter and b was a shift (location) parameter, x was the distance along the flight path. Function $\Psi(x)$ was Morlet's wavelet with frequency of ω_0=6 s^{-1}. Matrixes of values $|WT(a,b)|^2$ were calculated and defined as wavelet scalogram of function $T'(x)$, and in analogy real part of the product $Wu(a,b)\overline{WT(a,b)}$ can be called as a cross-scalogram $Co_{uT}(a)$ for horizontal heat fluxes $u'T'$ (where $\overline{WT(a,b)}$ was the complex conjugate wavelet transform of random function $T'(x)$). Physical meaning of scalogram was the distributions of turbulent energy or variances and covariances of different parameter in the space of wave numbers $k=\frac{1}{\lambda}$ (where λ was the eddy size). Scalograms allowed identifying the location of an event at the same distance and wave numbers with respect to the cloud.

Matrixes $|WT(a,b)|^2$ allowed getting so-called wavelet spectrum, which was analog of Fourier spectrum and should fully coincident with it:

$$S_T(a)=C_\Psi^{-1}\int_{-\infty}^{+\infty}|WT(a,b)|^2db \quad (9).$$

Wavelet coefficient matrixes $Wu(a,b)\overline{WT(a,b)}$ were used for calculating function, which was reasonable

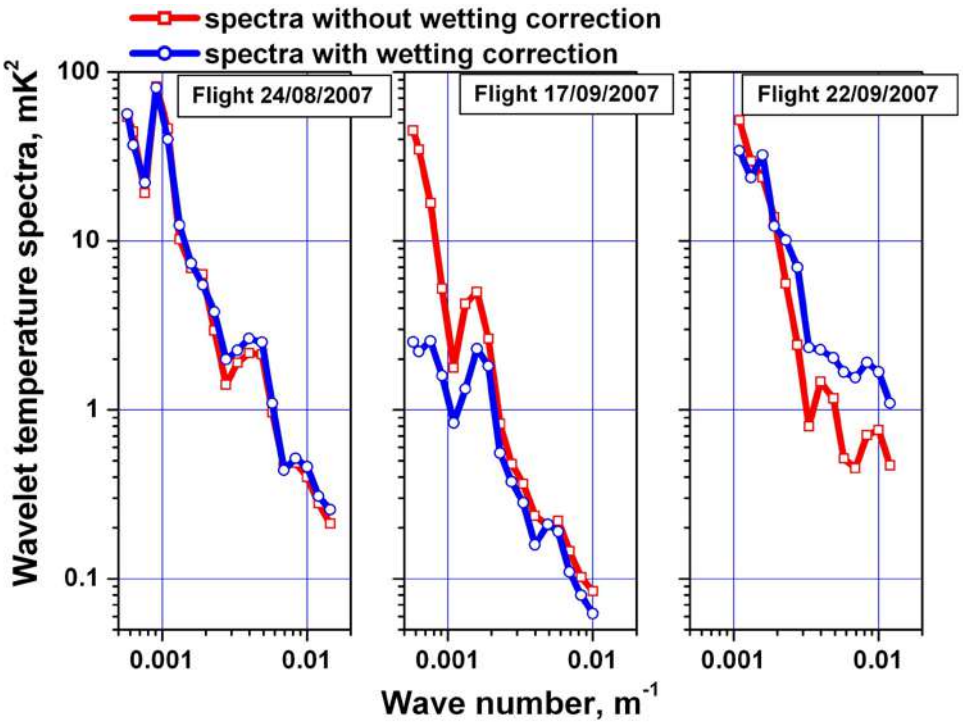

Fig. 9. Wavelet temperature spectra in cumulus zones (without and with the wetting corrections)

named as “wavelet cross-spectrum”:

$$Co_{uT}(a) = C_{\Psi}^{-1} \int_{-\infty}^{+\infty} Wu(a,b)\overline{WT(a,b)}db \quad (10)$$

where C_{Ψ} =1.062 was the constant for base Morlet’s wavelet.

Applying wavelet procedure to the turbulent wind speed and air temperature fluctuations in Cu zones gave the following results. In ***Fig. 9*** wavelet spectra of air temperature fluctuations for different sampling legs, calculated through the formula (9) without and with water content corrections (k_w =0.15 m^3g^{-1}). As it seen from the pictures water content affect could be different. In first case (left panel) correcting did not give essential changing to the spectrum, all differences were in the limits of spectra stability (Vinnichenko et. al., 1980). In other case spectrum was changed in low-frequency part (middle panel), and in third case all differences were observed in high-frequency of the spectra (right panel).

Water content correction was essentially affected at the results of heat fluxes cospectra calculations. ***Fig. 10*** presents cross-scalograms of horizontal heat fluxes, calculated for sampling leg on 22/09/07, 18:48:57-18:49:50 without water content correction (top panel) and with correction with coefficient of k_w =0.15 m^3g^{-1} (middle panel). Intensity of the fluxes was marked by colors, blue colors corresponded fluxes directed along the flight and brown color denoted the fluxes against the flight direction. Distribution of water content, demonstrated cloud

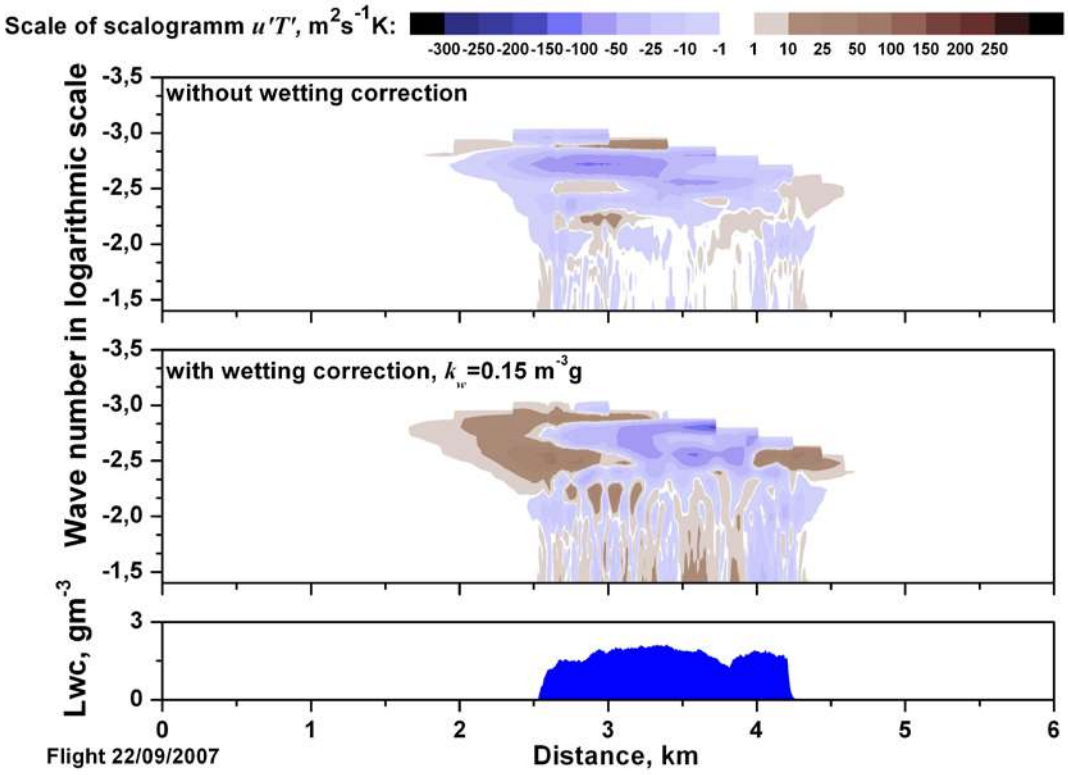

Fig. 10. Wavelet cross-scalogramms of kinematic horizontal heat fluxes in cumulus zone (without and with the wetting corrections)

boundaries was also presented in the picture (bottom panel).

Note that the main mechanism of heat exchange between a cloud and ambient area was meso-scale eddies with

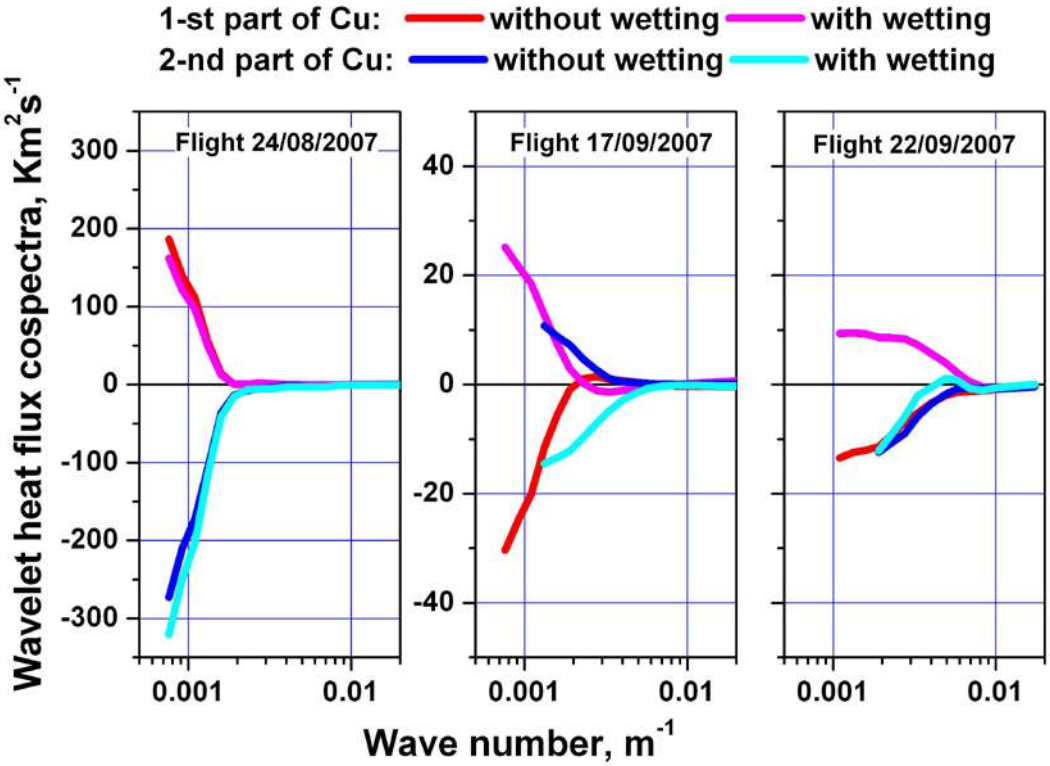

Fig. 11. Wavelet cross-spectra of kinematic horizontal heat fluxes for different parts of the cumulus clouds (without and with the wetting corrections)

sizes more than 500 m. Role of pure turbulent fluctuations was only in mixing inside the cloud. Fluxes, calculated without water content correction were directed only along the flight line, i.e. fluxes were directed to the cloud at the first part of Cu zone and outside of the cloud in its second part. It was contradicted to the modern view about turbulent exchange, since the cloud was warmer than ambient atmosphere. Water content correction removed this contradiction and spectral structure of heat fluxes in Cu zone became correspondent to the local horizontal temperature gradients.

Cross-spectra of horizontal heat fluxes calculated with and without water content corrections also verified this statement (see ***Fig. 11***).

Water content correction did not essential changed the spectra, calculated for sampling leg on 24/08/07 (left panel). Cospectra for first and second parts of Cu zone had opposite sign, which mean that fluxes were directed thought the side boundaries out of the cloud to the ambient area practically at all eddy scales.

In other cases cospectra transformations were more significant.

At the sampling leg on 17/09/07 (middle panel) cospectra showed that fluxes without correcting were directed

inside the cloud, which was abnormal flux distribution. Cospectra calculated with water content correcting had true sign that corresponded to fluxes directed outside the cloud.

Cospectra calculated for sampling leg on 22/09/07 for first and second parts of Cu zone had the same sign that mean abnormal fluxes calculations. After temperature correcting cospectra had opposite signs that corresponded to a view of heat fluxes structure through side boundaries of cumulus clouds.

6. CONCLUSIONS

Special wind tunnel was designed for testing aircraft thermometers and estimating influence of liquid water content in the flow on temperature readings. Investigations of high-frequency aircraft thermometer for measuring atmospheric turbulence and, especially turbulence in clouds, were made. Recovery factor of the sensor was defined based on wind tunnel tests and through computer program FlowVision. Investigations provided the correction coefficient for temperature on liquid water content, which defines the degree of influence of droplets.

Another way of estimating droplets effect was based on the analysis of the horizontal heat fluxes co-spectra calculated inside and around cumulus, temperature and water content distributions in clouds. Aircraft observations of cumulus clouds made over a meteorological testing site in Cuba have allowed investigating the spectral structure of horizontal heat exchange between clouds and the ambient atmosphere based on wavelet analysis. It is known that cloud droplets can distort temperature measurement, which leads to errors in calculated heat fluxes and intern abnormal flux distributions. The investigations have allowed building up a consistent picture of horizontal heat flux distribution in cumulus zone, depending on wave number and cloud location. Meso-scale eddies (extending the 500 m length) were the main factor of heat exchange between clouds and the ambient space. The role of turbulence was only the mixing inside the cloud.

Bibliography

Cumulus clouds and meteorological fields distortion connected with them, 1977, Edd. by I.P. Mazin and S.M. Shmeter, TsAO, **134**, 128 p. (in Russian).

Strunin M.A. and Hiyama T.: 2004a, 'Applying wavelet transforms to analyse aircraft-measured turbulence and turbulent fluxes in the atmospheric boundary layer over eastern Siberia', *Hydrol. Proc.*, **18**, 3081 - 3098.

Strunin M.A. and Hiyama T.: 2004b, 'Response properties of atmospheric turbulence measurement instruments using Russian research aircraft', *Hydrol. Proc.*, **18**, 3099 - 3117.

Kumar P. and Foufoula-Georgiou E., 1994: 'Wavelet analysis in geophysics: An introduction', In: *Wavelet in geophysics,*

Academic Press, Inc., San Diego, New York, Boston, London, Sydney, Tokyo, Toronto, 1 - 43.

Shmeter S.M. 1970: 'S tructure of fields of meteorological elements in a cumulonimbus zone', Trudy Central aerological observatory, Translation from Russian, Jerusaliem, 117 p.

Telford J.W., Warner J., 1962: 'On the measurement from an aircraft of buoyancy and vertical air velocity in cloud', *Journ. Atm. Sci*., **19**, 5, 415-423.

Vinnichenko N.K., Pinus N.Z., Shmeter S.M, Shur G.N., 1980: *Turbulence in free atmosphere*, Consultants Bureau, New York and London, 310.

NUMERICAL SIMULATION OF SILVER IODIDE DIFFUSION

Yilin Wang* and Shijun Li

Shandong Institute of Meteorology, Jinan, 250031,China

1. INTRODUCTION

In previous studies, Abshaev et al. (2003) analyzed the diffusion of catalyzer in convective clouds. Shen et al. (1983,1994) studied the diffusion of catalyzer regarding exploded cannon shots as point-sources. The diffusion in seeding was also discussed by Yu et al. (2002). However, much work still needs to be done for application. In order to improve rocket precipitation enhancement operations, the rocket precipitation enhancement scheme of practical use is brought forward based on a great number of numerical simulations. The scheme takes into account not only diffusion and transportation from line-sources, but also maximum affected areas with multiple shots at different azimuth and elevation angles. Sensitivity tests have been conducted for parameters of large variability, providing a reference value for practical use. The scheme has been coded in the Rocket Precipitation Enhancement Operation Command System, which can determine automatically the optimum azimuths, elevation angles, proper number of shots and other operation parameters. The method of determining the effective seeding area has also been used in rocket precipitation enhancement assessment.

2. DEFINED OF EFFECTIVE SEEDING AREA

In recent years, cold cloud observation experiments using Particle Measuring System (PMS) probes have been carried out in China. Results show that the number of ice crystals in clouds is mostly at the rank of 10^0-$10^1 L^{-1}$. Based on previous studies, for effective seeding, the number of artificial ice crystals should be equal to that of natural ice crystals. Through the simulation in wind conveying, rocket diffusion area changes with the launch time. When K =60 $m^2 \cdot s^{-1}$, v=15$m \cdot s^{-1}$, elevation=60° and time are 20, 40, 60, 80, 100, 120 and 130 second respectively, fig.1 is three rockets projection of instantaneous diffusion zone that concentration of AgI is q>=10 L^{-1}. Over time, the projection would change from small to big, and then narrowed to disappear. A total area of the projection area can be obtained by time integration. The total area is the effective seeding area. The effective seeding area can be defined as the vertical ground projection of the accumulated area where AgI-generated crystals should exceed 10L^{-1} after diffusion of rocket bombs.

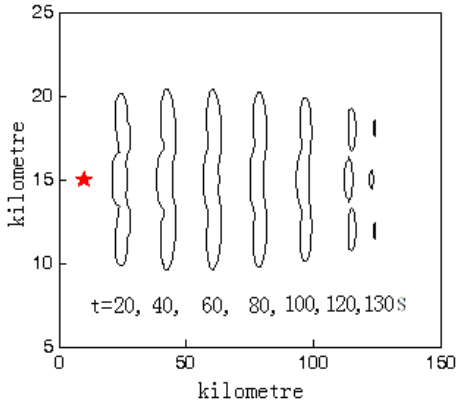

Fig.1 Schematic diagram of the diffusion area at different times (The five-pointed star position is the rocket launching position.)

*Corresponding author's address: Yilin Wang, Shandong Institute of Meteorology, Jinan, 250031,China; E-Mail:qxwyl@sohu.com

3. LINE-SOURCE DIFFUSION

To demonstrate the effect of different turbulent diffusivity coefficients (*K*), we simulated diffusion radius of AgI concentration (q>=10 L^{-1})，assuming *K* =20, 40, 60, 80, and 100 m^2s^{-1}. Single apex curves of maximum diffusion radius are shown for each *K* value in Fig.2. The diffusion radius increases with time firstly, then decreases after reaching its maximum, and ultimately disappears. For *K* = 20, 40, 60, 80 and 100 m^2s^{-1}, the maximum value of diffusion radius are 839.8 m, 1045.0 m, 1181.0 m, 1284.0 m and 1367.0 m respectively, the time of maximum diffusion radius are 52'40", 43'19", 40'00", 37'40" and 35'00" respectively, and the time that the diffusion radius disappear are 109'59", 94'59", 86'38", 81'40", and 76'41" respectively.

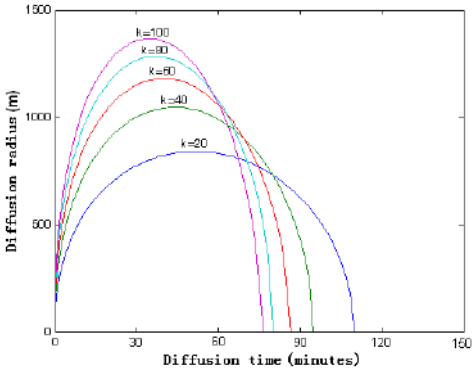

Fig.2 The changes of diffusion radius under different eddy diffusion coefficients.

4. OPERATION HEIGHT

The Tab. 1 is parameter of rocket. The bigger elevation angle is, the higher start seeding height is. For safety, the elevation is between 45°- 85°. The operation height is determined by radar echoes.

5. OPERATION AZIMUTH

In order to get the largest effective seeding area and save shots in rocket precipitation enhancement, Fig.2 shows a new operation method that named upwind shooting. The angles (α) are equivalent and decided by simulations according to the principle that no gap area is left between rocket bombs after diffusion. The numerical value of α is listed in Tab.2. From the table 2, we can see that the range of emission angle is between 22°- 90°. The α increases with the elevation angle increasing. When the turbulent diffusion coefficient is 20 and elevation is 45°, α is 22°. When emission elevation angle up to more than 70°, the α is maximum, or launching three rockets, they are perpendicular to each others.

Tab.1 Rocket parameter

Elevation angle	Start seeding		Seeding end	
	Height /km	Distance /km	Height /km	Distance /km
45°	2.870	4.407	2.306	6.978
50°	3.357	4.087	3.174	6.450
55°	3.805	3.725	3.970	6.076
60°	4.208	3.307	4.881	5.504
65°	4.547	2.836	5.506	4.795
70°	4.836	2.323	6.060	3.987
75°	5.068	1.775	6.523	3.089
80°	5.238	1.199	6.874	2.111
85°	5.342	0.605	7.095	1.073

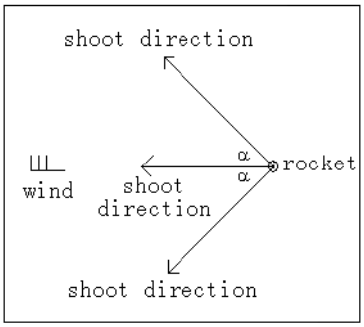

Fig. 2 Sketch of rockets operation.

Tab. 2 Relationship α with turbulent diffusion coefficient and elevation (unit: degrees)

K	Elevation angle								
/$m^2 \cdot s^{-1}$	85°	80°	75°	70°	65°	60°	55°	50°	45°
20	90	90	71	46	36	31	27	24	22
40	90	90	90	64	48	39	34	31	28
60	90	90	90	90	56	46	39	35	32
80	90	90	90	90	65	51	44	39	36
100	90	90	90	90	75	56	47	42	38

6. EFFECTIVE SEEDING AREA

The Fig.4 show isolines of the diffusion area and number 10 are silver iodide concentration of $10L^{-1}$, they are the effective seeding area. The diffusion equation (omission) shows that the turbulent diffusion coefficient increases, the diffusion area increases, when the environmental wind and the elevation is the same (Fig.4 a and b). The effective seeding area is 698.6 km^2 (Fig.4 a) and 768.4 km^2 (Fig.4 b) respectively. The environmental wind increases, the diffusion area also increases, when the turbulent diffusion coefficient and the emission elevation is the same (Fig.4 b and c). The effective seeding area is 768.4 km^2 (Fig.4 b) and 1529.2 km^2 (Fig.4 c) respectively.

Multiple simulations were conducted with a combination of different elevation angles, turbulent diffusivity coefficients, and wind speeds. The areas of effective seeding are listed in Table 3. For example, with K=20 m^2s^{-1}, u=20 $m{\cdot}s^{-1}$ and the elevation of 60º, the effective seeding area is 1395.4 km^2.

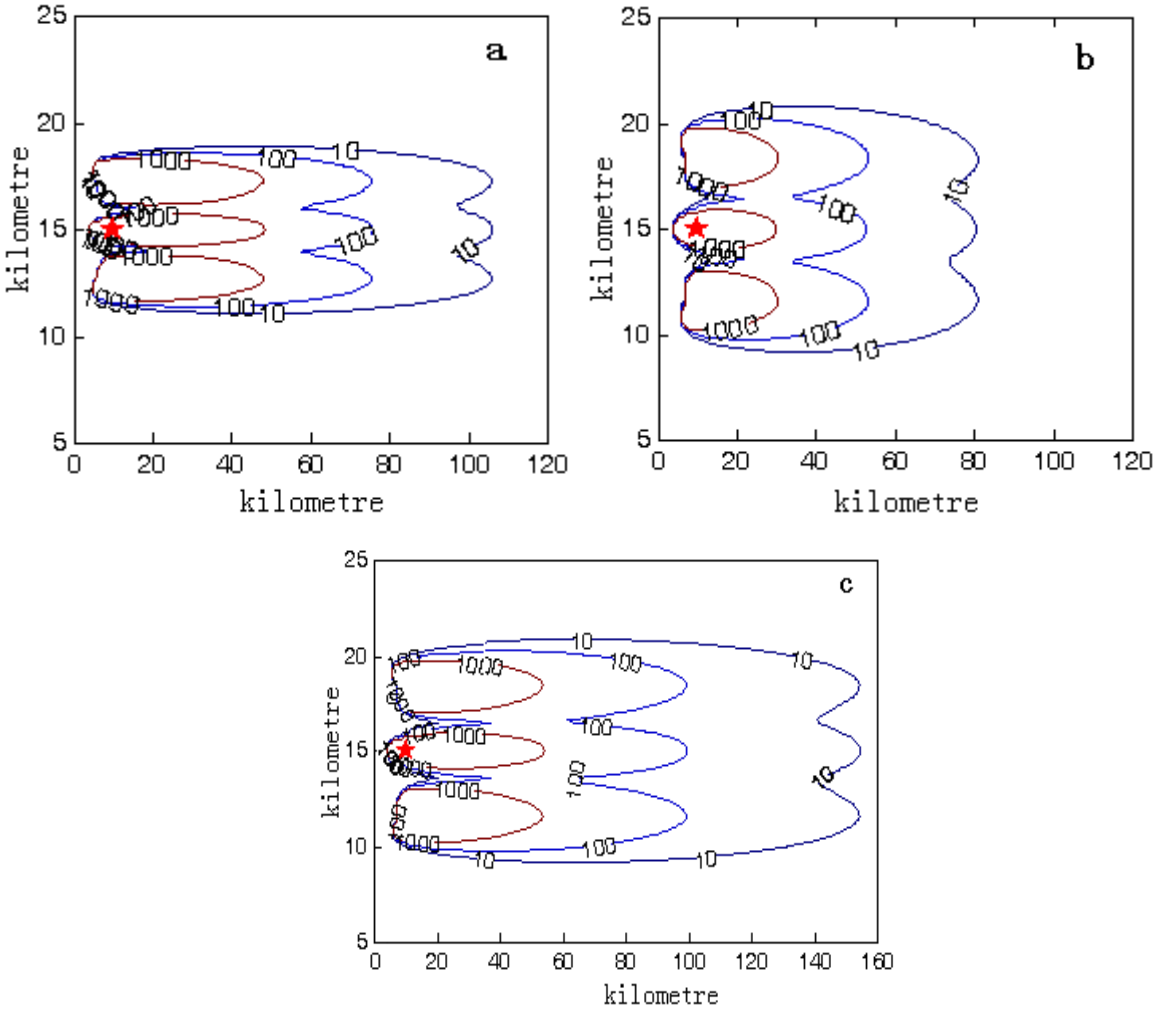

Fig. 4 When elevation is 60°, isolines map of the diffusion area.
（a: K =20$m^2{\cdot}s^{-1}$， u=10$m{\cdot}s^{-1}$. b: K =80$m^2{\cdot}s^{-1}$， u=10$m{\cdot}s^{-1}$. c: K =80$m^2{\cdot}s^{-1}$， u=20$m{\cdot}s^{-1}$）

7. CONCLUSIONS

(1) Based on the principle that the number of artificial ice crystals should be equal to that of natural ice crystals, the vertical ground projection of the

accumulated area where AgI-generated crystals exceeds $10L^{-1}$ after diffusion is calculated and can be defined as the effective seeding area.

(2) Operation azimuth is decided based on a new method that each round fire three rockets upwind and the angle between rocket bombs is equivalent. The angle is decided by simulations according to the principle that no gap is left after diffusion. Operation elevation angle is decided based on operation height.

(3) Precipitation enhancement should be operated with multiple rounds.

ACKNOWLEDGEMENTS

The authors thank professor Yu kangyuan to provide some material.

REFERENCES

Abshaev, A.M., M.T. Abshaev, and Ya. A. Sadykha, Diffusion of artificial aerosol in cu cong clouds. J. *Russian Meteorology and Hydrology*, 2003, 9, 18-24.

Shen Yiming, Liu Guixiang, Xu Huanbin et al., The problem of diffusion of point source in the convective clouds. J. *Acta Meteorologica Sinica* 1983, 41(4), 415-425.

Shen Yiming, The Diffusion of Activators in Cloud. Beijing: *China Meteorological Press,* 1994, 48-51.

Yu Xing, Wang Xiaoling and Dai Jin, Research on simulation of effective range for cloud seeding by aircraft within super-cooled stratus. J. *Acta Meteorogica Sinic,* 2002, 60(2), 205-214.

Table 3 Different factors corresponding to the effective seeding area with three rounds （unit: square kilometers）

K	**Wind**	**Elevation**								
/m^2·s^{-1}	**/m·s^{-1}**	**85º**	**80º**	**75º**	**70º**	**65º**	**60º**	**55º**	**50º**	**45º**
20	10	332.4	531.6	677.4	692.0	696.2	698.6	690.6	668.8	663.6
	15	498.6	799.0	1017.6	1036.8	1044.6	1047.4	1033.4	1003.6	993.4
	20	664.8	1064.4	1355.6	1381.0	1390.6	1395.4	1376.2	1336.4	1323.8
40	10	318.2	500.0	648.8	734.4	746.6	737.2	735.2	724.6	712.6
	15	478.4	753.0	974.0	1099.0	1117.4	1103.6	1100.2	1085.6	1064.8
	20	636.6	1001.8	1299.2	1465.2	1488.4	1469.0	1466.6	1445.2	1419.4
60	10	310.8	479.8	620.4	729.8	758.0	761.8	753.6	738.2	735.2
	15	465.2	719.0	929.8	1095.2	1134.6	1141.4	1128.0	1103.0	1098.2
	20	620.8	960.4	1242.0	1461.8	1510.6	1518.0	1504.0	1468.2	1464.8
80	10	301.6	470.2	602.6	707.4	768.4	768.4	765.2	754.4	755.4
	15	449.4	700.8	899.0	1057.6	1149.0	1148.2	1143.6	1128.2	1127.4
	20	600.0	933.4	1199.2	1410.4	1529.2	1529.2	1521.0	1501.2	1500.4
100	10	297.6	456.4	584.8	682.2	766.4	772.8	769.2	754.8	752.6
	15	444.6	681.8	872.0	1020.8	1148.2	1151.0	1147.8	1129.4	1122.0
	20	592.4	905.6	1158.6	1359.2	1529.2	1533.2	1527.8	1502.4	1492.0

THE EFFECTS OF THE VALLEY ON VORTICAL CHARACTERISTICS OF A HAILSTORM

Mladjen Ćurić and Dejan Janc

Institute of Meteorology, University of Belgrade, Belgrade, Serbia

1. INTRODUCTION

Internal vortical motions are important features common to the majority of hailstorms. Numerical models and Doppler radar observations reveal that a vortex (Markowski et al., 2008) or a counter-rotating vortex pair is formed within a hailstorm. A vortex pair formation is frequently explained by the convective tilting of mean flow horizontal vorticity mechanism produced by the strong directional low-level wind shear. Such a storm splits into cyclonic (moving to the right of the shear vector) and anticyclonic (moving to the left) as pointed by Robert Davies-Jones (2002) and van den Heever and Cotton (2004). Observational evidence shows that right-moving hailstorms are favored in environments characterized by clockwise-turning hodographs (Grasso and Hilgendorf, 2001). More model studies of hail vortex pair evolution are performed over flat terrain.

The relationship between hailstorm vortex pair evolution and complex terrain were investigated by Ćurić et al. (2007) and Ćurić and Janc (2012) in their model and observational studies. Their investigations are targeted at the intense hailstorms in the valley area in vicinity of their source. The main effect of a valley side is the lateral mean wind shear affected by friction or differential heating. The resulting effect is stronger weakening of the left-moving (anticyclonic) hailstorms than their cyclonic counterpart. In addition, the stretching is also expressed in the presence of the valley.

Due to its importance the rotational characteristics of hailstorms were analyzed theoretically by Davies-Jones (2004), Davies-Jones (2006) and others. The model and observed split hailstorm characteristics under influence of complex terrain therefore requires more detailed theoretical framework of the most influential factors that determine the hailstorm vortex pair behavior. For this reason, we shall perform the detailed analysis of the vorticity equation by introduction of the additional terms that appears in the valley.

2. VORTICITY EQUATION

For the purpose of this study the vertical vorticity component equation (Houze, 1993) is used in the form as follow

$$\frac{d\zeta}{dt} = \zeta \frac{\partial w}{\partial z} + \xi \frac{\partial w}{\partial y} + \eta \frac{\partial w}{\partial x}, \qquad (1)$$

where η, ξ and ζ are vorticity components in x, y and z directions, respectively. In our analysis the Coriolis parameter is neglected. We also use the continuity equation as

$$\nabla \cdot \boldsymbol{V} = \frac{1}{\alpha}\frac{d\alpha}{dt}, \qquad (2)$$

where **V** is the velocity vector and α the specific volume.

The vorticity equation (1) can be linearized about a mean flow in the x direction, U = U(y, z), while the mean values of the other two velocity components (V and W) are zero. By using (2) the linearized form of (1) becomes

$$\frac{\partial \zeta'}{\partial t} + U\frac{\partial \zeta'}{\partial x} = \frac{\partial U}{\partial z}\frac{\partial w}{\partial y} + v\frac{\partial}{\partial y}\left(\frac{\partial U}{\partial y}\right) + w\frac{\partial}{\partial y}\left(\frac{\partial U}{\partial z}\right) - \frac{\partial U}{\partial y}\frac{\partial w}{\partial z} + \frac{\partial U}{\partial y}\frac{1}{\bar{\alpha}}\left(U\frac{\partial \alpha'}{\partial x} + w\frac{\partial \bar{\alpha}}{\partial z}\right), \qquad (3)$$

where ζ' is the vertical vorticity perturbation, while $\bar{\alpha} = \bar{\alpha}(z)$ and α' are mean and perturbation values of the specific volume. Under assumption that U is a function of z only (3) is the same as that analyzed by Houze (1993). For analysis of the vortex pair evolution, it is useful to use the vorticity equation in a coordinate system moving with the storm (Davies-Jones,1984; Kanehisa, 2002) where a cloud velocity is

$$\boldsymbol{V}_c = u_c \boldsymbol{i} + v_c \boldsymbol{j} \,. \tag{4}$$

We propose that $U \approx u_c$. The terms on the left-hand side of the vorticity equation (3) then become

$$\frac{\partial \zeta'}{\partial t} - v_c \frac{\partial \zeta'}{\partial y} \,. \tag{5}$$

By integrating (3) we obtain the approximate form of the vertical vorticity perturbation for a steady-state condition as

$$\zeta' = A + B + C + D + E \,,$$

where

$$\begin{aligned}
A &= -\frac{1}{v_c}\frac{\overline{\partial U}}{\partial z} w, \\
B &= -\frac{\overline{v}}{v_c}\mathrm{sgn}(y)\left(\left.\frac{\partial U}{\partial y}\right|_y - \left.\frac{\partial U}{\partial y}\right|_2 \right), \\
C &= -\frac{\overline{w}}{v_c}\mathrm{sgn}(y)\left(\left.\frac{\partial U}{\partial z}\right|_y - \left.\frac{\partial U}{\partial z}\right|_2 \right), \\
D &= \frac{1}{v_c}\mathrm{sgn}(y)\frac{\overline{\partial w}}{\partial z}\left(U_y - U_2\right), \\
E &= -\frac{1}{v_c}\frac{\overline{w}}{\overline{\alpha}}\frac{\partial \overline{\alpha}}{\partial z}\mathrm{sgn}(y)\left(U_y - U_2\right).
\end{aligned} \tag{6}$$

where subscripts 2 and y relate to the center of the valley (Fig. 1) and sites in y direction, while $\overline{X}$ represents the mean value in y direction. For reason of further analysis the terms on the right-hand side of (6) are denoted by A, B, C, D and E, respectively.

3. ANALYSIS OF PARTICULAR TERMS

The x, y and z directions in a valley are oriented as in Fig. 1. In this case, U as a function of y near the ground is presented in Fig. 2. Its change with height for three sites (denoted by 1, 2 and 3 in Fig. 1) is shown in Fig. 3. Hereafter we shall analyze each term in corresponding subsections.

3.1 The term A

Only the tilting term A exists if U is a function of z as pointed by Rotunno (1981). This term is widely elaborated by Houze (1993) or Ćurić and Janc (2012). Its impact on vertical vorticity perturbation in y direction is essential.

It is well-known that the mean velocity, U, at a low-level grows with height (Fig. 3). Its mean vertical change in a direction perpendicular to the valley axis must be also positive so that $\overline{\partial U}/\partial z > 0$. At site 1 (sunward side of the valley, Fig. 1), the extra warming implies greater vertical velocity and thus greater negative vorticity. An analysis performed by Ćurić and Janc (2012) shows that the mean vertical wind shear takes smaller values over the sunward side of the valley than over the sunshade one. The resulting effect of the term A to the vertical vorticity perturbation is a stronger increase of positive vorticity (associated with a right-moving storm).

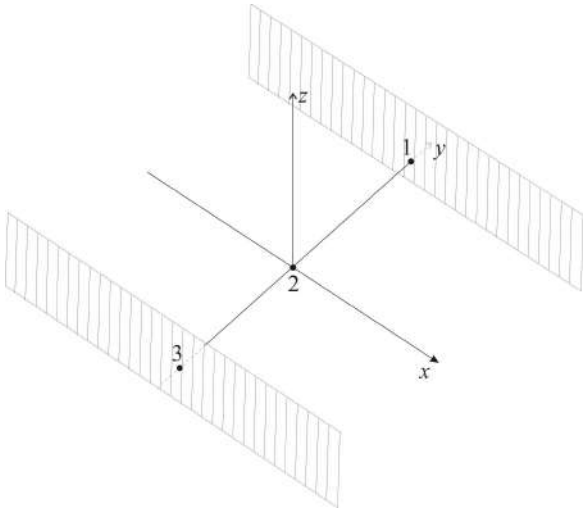

Fig. 1. Coordinate axis in the valley. The sites over the sunward and sunshade sides of the valley as well as at the valley center are denoted by 1, 3, and 2, respectively.

3.2 The term B

The typical horizontal mean wind shear in the valley is shown in Fig. 2. As noted, U decreases towards the sunward (a greater rate, f_1) and sunshade sides (a smaller rate, f_2) of the valley. But the change of the horizontal wind shear is small (its value is zero for the linear profile). On the other hand, the rotational motion within the vortex at both sides of the valley (although not mirror images of each other) also implies the small magnitudes of this term. The term B may be neglected.

3.3 The term C

The importance of the term C will be recognized from the following discussion. As shown in Fig. 3, the vertical wind shear is typically weaker over the sunward side of the valley (line 1) than over the sunshade one (line 3), but both rates are smaller than that along the valley-axis (line 2) according to Ćurić and Janc (2012). In such a way, this term contributes to a decrease of the anticyclonic vortex (the sunward side of the valley) and an increase of its cyclonic counterpart (the sunshade side of the valley).

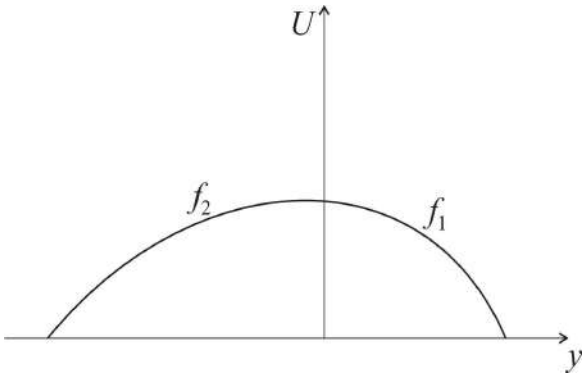

Fig. 2. The horizontal wind shear in the valley.

3.4 The term D

For the sunshade side of the valley (1, Fig. 2), an U value is smaller than that over the sunshade side (3, Fig. 2). The term $\overline{\partial w}/\partial z$ is typically positive over the valley and may be greater over its sunward side due to the extra warming. On the other hand, the greater value of U is over the sunshade side of the valley (3, Fig. 1) while $\overline{\partial w}/\partial z$ may be smaller. The resulting effect is an increase of vertical vorticity perturbation over both sides of the valley. But the vertical vorticity perturbation change depends on the factor $U\,\overline{\partial w}/\partial z$.

3.5 The term E

The divergence term exists in the vorticity equation due to the horizontal wind shear. This term may be transformed by using the relation

$$\frac{1}{\bar{\alpha}}\frac{\partial \bar{\alpha}}{\partial z} = \frac{\gamma_h - \gamma}{\bar{T}},$$

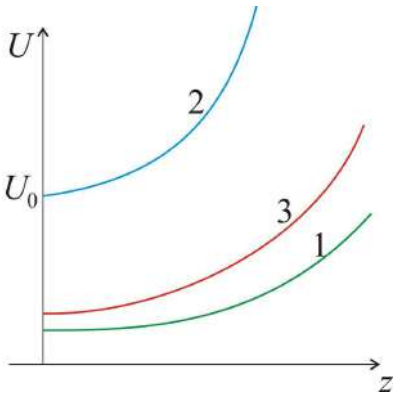

Fig. 3. Vertical wind shear in the valley over sites defined in Fig. 1.

where γ_h and γ are temperature lapse rates of the homogenous and real atmospheres, while $\bar{T}$ is the mean temperature. Over the sunward side of the valley $v_c > 0$ and $U_y - U_2 < 0$ and then its term implies an increase of the vertical vorticity over the sunward side of the valley. Same trend occurs over the sunshade side of the valley. Fig. 2 demonstrates that $\left|U_y - U_2\right|$ is greater over the sunward side of the valley, while $\bar{w}$ may be also greater due to the extra warming. On the other hand, the main updraft is more frequently placed to the right with respect to a mean vertical wind shear vector. For this reason, the magnitudes of this term may be different.

We must emphasize that our analysis is performed in the coordinate system moving with the storm in which the storm center moves roughly with the mean wind velocity. This is not fully consistent with the divergent flow assumption. However, we believe that this analysis represents the good estimate of the factors that determine the vortex-pair evolution in the valley. This statement is based on facts that the divergent term is smaller than the terms A and D and comparable with the C term for typical conditions associated with a storm motion along the valley. We must always take in mind that only linear effects are discussed. Among nonlinear ones, the stretching seems to be important for the valley condition as pointed by Ćurić and Janc (2007).

4. CONCLUDING REMARKS

The main intent of this article was to investigate the factors determining the vortex-pair evolution over a valley area. We analyze an approximate version of the vertical vorticity equation linearized about a mean westerly wind which increases with height and decreases towards the sunward and sunshade sides of the valley. Mean wind profile is chosen to approximate the typical environmental condition associated with a storm motion along the valley. Our principal findings are as follows:

- A valley terrain contributes essentially to an increase of the cyclonic vortex intensity and decrease of its anticyclonic counterparts due to the vertical velocity, the vertical wind shear as well as its change in a direction perpendiculat to the valley axis. Such scenario is primarily influenced by differential heating of the sunward and sunshade sides of the valley.
- A term that depends on the mean wind change in y direction as well as the vertical velocity change with height may produce smaller or greater increase of both vortices. The same trend produces the divergent term.

These findings tell us that the valley terrain does not impact on the vortex-pair intensity likewise. However, the dominant factors supports the cyclonic storm (over the sunshade side of the valley). Within our investigation we consider only linear terms in the vertical vorticity equation. Former results obtained with the numerical model shows clearly that the stretching is also very important during a storm evolution in the valley.

Despite performed approximations we think that this investigation represents the good basis for full insight in interaction of a storm and complex terrain. In either case the development of storm rotation is not drastically different that discussed here, hence we believe the present results are generally relevant.

Acknowledgements. This research was supported by the Ministry of Science of Serbia. We gratefully acknowledge Dragomir Bulatović for technical preparation of the figures.

REFERENCES

Ćurić, M., Janc, D., and V. Vučković, 2007: Numerical simulation of Cb cloud vorticity. Atmos. Res., 83, 427-434.

Ćurić, M. and D. Janc, 2012: Differential heating influence on hailstorm vortex pair evolution. Q.J.R. Meteorol. Soc., 138, 72-80.

Davies-Jones, R.P.,1984: Streamwise vorticity: The origin of updraft rotation in supercell storms. J. Atmos. Sci.,41, 2991-3006.

Davies-Jones, R.P., 2002: Linear and nonlinear propagation of supercell storms. J. Atmos. Sci., 59, 3178-3205.

Davies-Jones, R.P., 2004: Growth of circulation around supercell updrafts. J. Atmos. Sci., 61, 2863-2876.

Davies-Jones, R.P., 2006: Integrals of the vorticity equation. Part I: General two- and three-dimensional flows. J. Atmos. Sci., 63, 598-610.

Grasso, L.D. and E. R. Hilgendorf, 2001: Observations of a severe left moving thunderstorm. Wea. Forecasting, 16, 500-511.

Houze, R.A. Jr., 1993: Cloud Dynamics. Academic Press.

Kanehisa, H., 2002: A nonlinear extension of the helicity formula for convective storms. J. Meteor. Soc. Japan, 80, 1301-1306.

Markowski, P., Rasmussen, E., Straka, J., Davies-Jones, R.P., Richardson, Y., and R.J. Trapp, 2008: Vortex lines within low-level mesocyclones obtained from pseudo-dual-Doppler radar observations. Mon. Wea. Rev.,136, 3513-3534.

Rotunno R., 1981: On the evolution of thunderstorm rotation. J. Atmos. Sci., 109, 577-586.

van den Heever, S.C. and W.R. Cotton, 2004: The impact of hail size on simulated supercell storms. J. Atmos. Sci., 61, 1596-1609.

Analysis of Large-scale Precipitation Process in Spring in Tianjin area

Jin Ruijun Song Wei Wang Zhaoyu

Tianjin Weather Modification Office, Tianjin, 300074,China

Abstract: Based on Doppler Weather Radar data, weather graph and satellite inversive cloudy products, A large-scale precipitation process on April 18th 2009 in Tianjin was analyzed.Three main conclusions were reached from the results of this study.(1)It was a stratocumulus mix cloud precipitation process, which was affected by Hetao low trough and Jianghuai cyclones.(2)The reflectivity of Doppler-radar presented the characteristics of newborn, developing, maintaining and weakening.(3)During the MODIS satellite transit time, the cloud particle effective radius was above 15 μm ,and the value of highest appearance frequency was 25-27 μm .The maximum value area of atmospheric precipitable water was consist with the precipitation of hourly automatic weather station.

Key Words: precipitation, circulation pattern, Doppler-radar products, MODIS cloud parameters

1. Introduction

Nowadays，the Doppler-radar network improved gradually, The Doppler-radar had the characteristics of high power, high precision and phase-coherent, It provided high temporal resolution volume-scanning data. The Doppler-radar could pursue the development and evolvement of precipitation cloud, and could also understand the intensity and scale of precipitation.There were plenty of precipitation characteristics research using Doppler-radar data(Wang et al.2006;Zhang 2010;He et al.2010;Wang et al.2009;Wu et al.2009).

In this paper,a large-scale precipitation

process in Tianjin area was analyzed .The paper discussed the characteristics of Doppler-radar product and spatial distribution of MODIS cloud parameters, which could help to revolve the mechanism of precipitation and forecast the large-scale spring rainfall process in Tianjin.

2. The Precipitation Situation and Synoptic System

2.1. The Precipitation Situation

During April 18th to April 19th of 2009, a large-scale rainfall process was appeared in Tianjin area, the precipitation lasted for 16 hours. The daily precipitation of Tianjin urban area reached 34.3mm,which reached the extremum in the same historical period. On the precipitation distribution chart, the precipitation were less in north area and more in southeast area. The data of automatic weather station（AWS）showed that, the precipitation of 122 stations were between 25.0-49.9mm.

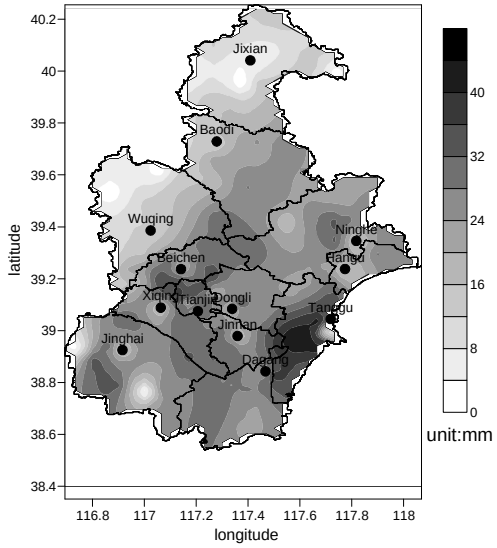

Figure1. The distribution chart of cumulative precipitation from Apr.18th to Apr.19th，2009

2.2. The Synoptic System

The circulation pattern(figure2a) was two troughs and one ridge in east-Asia area of 500hpa at 12:00(Universal Time) on April 18th. North China area was affected by Hetao low trough, the southwest airflow gathered ahead of the trough. The low-level shear line maintained in the center of Hebei province at 850hpa.The southwest jet stream transported warm-wet airflow to North China area. The relative humidity exceeded 90％ at low layer, the relative humidity of high layer also reached 70％-80％.

At surface pressure field(figure2b), Jianghuai cyclone system provided plenty of water vapor for precipitation process. The centre of cyclone located at 28.41℃N，116.26℃E at 21:00 on April 18th,the pressure value was 1002.5hpa.With the motion of Jianghuai cyclone, the precipitation maintained and strengthened. After 06:00, the precipitation weaken gradually.

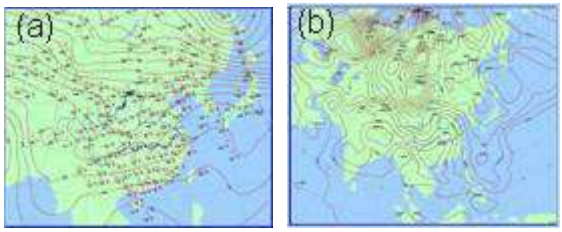

Figure2. The weather graph of precipitation process((a)500hpa circulation pattern at 12:00 on Apr.18th,2009 (b)Surface pressure field at 21:00 on Apr.18th,2009)

3. Analysis of Radar Echo Characteristics

The Doppler-radar reflectivity products presented echo characteristics of newborn, developing, maintaining and dissipating in the precipitation process.

(1) The echo newborn stage. Before 12:30 of April 18th, the precipitation cloud moved in the area where radar could detect,the small-scale precipitation echoes was appeared in southwest of Tianjin at 11:00. Later, the precipitation echoes appeared in east of Jinghai and Wuqing(figure3(a)),the echoes intensity was between 15-30dbz.When the radar echoes moved towards to northeastward, the scale and intensity of echoes increased gradually.

(2) The echo developing stage. From 13:00 to 21:00, many new radar echoes were born around Qingxian and Dacheng area, which moved northeastward. At the same time, the radar echo intensity of Baodi area increased, while the echo shape also changed. The edge of echo was not clear. Some convective echo mixed in it, and the intensity was below 45dbz.The echo top (figure 3(c)) was about 3-5km, some exceeded 9km.

(3) The stable maintaining stage. With the establishment of southwest jet stream,the

warm and wet flew was transported northward. This stage lasted for several hours. On radar reflectivity images, Tianjin area was covered with precipitation cloud at 00:00(figure3(b)).The echo intensity gradient reduced. The image of reflectivity profile(figure3(d)) showed that the echo intensity was not more than 30dbz,while the echo top height was below 5km.

(4)The echo dissipation stage. With the eastward movement of Hetao low trough, the relative humidity diminished. The radar echo intensity weakened gradually and the echo removed far away from Tianjin.The precipitation process which lasted for 16 hours finished.

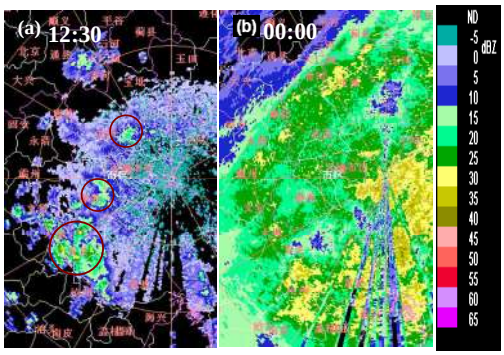

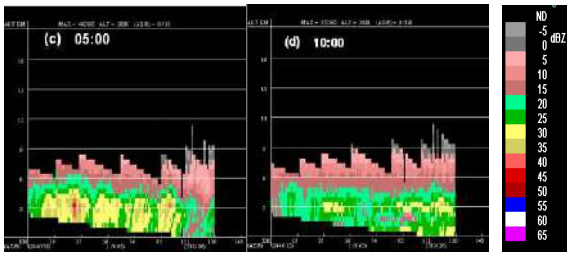

Figure3. The charts of reflectivity and cross section of the reflectivity of Doppler-radar

4.The Relationship between Cloud Micro-physical Parameters of MODIS Satellite and Precipitation of automatic weather station(AWS)

The transit time of TERRA/MODIS satellite was 03:35 on April 19th, 2009. Figure4a showed that the average cloud particle effective radius of Tianjin area was 15 μm. Some research presented, the cloud particle effective radius should reach at least 12 μm, the effective precipitation would come into being. From the result of value statistics, the most common value was 25-27 μm.These larger particles might play an important part in precipitation. In figure4a, the cloud particle effective radius were larger in north of Ninghe, east of Hangu, north of

Baodi and urban districts of Tianjin.

Based on the reflectivity of MODIS 1B data, the atmospheric precipitable water vapor(PWV) of 19 channel could retrieved. The value were larger in Jinghai and Baodi. At the same time, The hourly precipitation of AWS showed the average value was 3.95mm.Compareing with figure4b and figure4c,it could be found the large value area of atmospheric precipitation corresponded well with the precipitation of AWS, especially in middle and north of Jinghai, junction area between Beichen and districts of Tianjin.

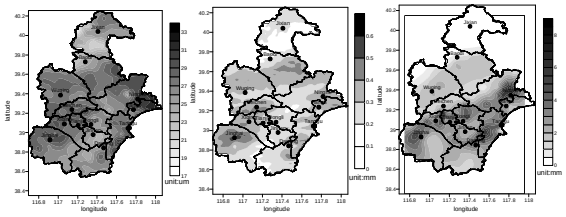

(a) (b) (c)

Figure4. Distribution charts of cloud parameters and hourly surface precipitation

（(a)The distribution of the cloud particles effective radius at 03:35.(b)The distribution of the PWV of 19channel of MODIS at 03:35(c)The distribution of precipitation in Tianjin area from 03:00 to 04:00）

5. Conclusion

(1)The precipitation process was affected by Hetao low trough, coordinating with the northward motion of Jianghuai cyclone. The southwest jet stream transported plenty of water vapor to North China area.

(2)This precipitation process was stratocumulus mix cloud precipitation. The Doppler-radar reflectivity products presented obvious characteristics of newborn, developing, maintaining and dissipating.

(3)The cloud particle effective radius of Tianjin area was above 15 μm at MODIS satellite transit time. The most common cloud particle effective radius was 25-27 μm ,which might play an important part in precipitation. The large value area of precipitable water corresponded well with the precipitation of AWS, especially in middle and north of Jinghai, junction area

between Beichen and districts of Tianjin.

Acknowledgements

The work was supported by National Science and Technology Ministry (2006-BAC12B01-01-04) and Key Laboratory for Cloud Physics and Weather Modification of China Meteorological Administration (2009Z00310)

Reference

He Bingwen,Ge Wenzhong,Gao Yuchun,et al. Analysis of a local extraordinary rainstorm in northwestern Hunan [J]，Meteorological Science and Technology.2010,38(2):193-196.

Wang Lirong,Tang Dazhang,Zhang Yangang. Analysis of characteristics of Doppler Weather Radar images during a precipitation process in spring[J]. Meteorological Science and Technology.2006,34(1)：88-92.

Wang Weitai,Li Zhaorong,Xu Qiyun,et al. Characteristics of new generation Doppler Weather Radar echoes for a severe vortex rainstorm[J], Meteorological Science and Technology.2009,37(5)：533-537.

Wu Zhifang,Ye Aifen,He Ruyi，et al. Application of Doppler-radar products in analyzing spring weather characteristics and conditions for rain enhancement in Guangdong province[J]. Meteorological Science and Technology.2009, 37(2): 224-229.

Zhang Xiaodong.Radar features and simulation analysis of a heavy rainfall event[J],Meteorological Science and Technology.2010,38(5)：550-557.

EXPLORING THE 2nd INDIRECT AEROSOL EFFECT WITH REMOTE SENSING, GEOSTATISTICS AND THE WEATHER RESEARCH FORECASTING MODEL

Michael Hewson[1,2], Hamish McGowan[1], Stuart Phinn[2]

[1]Climate Research Group, [2]Centre for Spatial Environmental Research,
School of Geography, Planning and Environmental Management,
The University of Queensland Brisbane Q Australia 4072
m.hewson@uq.edu.a

1. INTRODUCTION

In their Fourth Assessment Report, the Inter-Governmental Panel on Climate Change [1] summarized direct and indirect aerosol effects on cloud properties and rainfall. The second indirect aerosol effect suggests rain is suppressed in warm phase clouds. Using satellite images, Rosenfeld [2] suggested that cloud droplet coalescence is inhibited in polluted clouds. Further studies have contributed to an emerging consensus that urban and industrial aerosol may inhibit stratiform cloud system rainfall but may enhance cumuliform cloud system rainfall.

To date most aerosol effect on rainfall studies have used remotely sensed estimates of atmospheric properties over multiple years or global climate modelling. Investigations of aerosol impacts on a local rain event scale (city environs at a given time, 100's km^2 in an hour) are rare. The subtropical city of Brisbane on the east coast of Australia was the focus of a study that suggested anthropogenic emissions might inhibit rainfall around the city [3].

Here we present preliminary results of a geo-statistical comparison of modelled aerosol size distribution with satellite remotely sensed cloud drop size and ground based radar rain rate for a single rain event.

Because remote sensing of aerosol from passive imaging sensors is not possible due to cloud cover associated with rainfall, the chemistry transport version of the Weather Research and Forecasting model (WRF-Chem) [4] is used to prepare maps of aerosol size and single aerosol species distribution during rain events.

Besides, cloud, rain and aerosol parameters, two atmospheric properties need to be measured in a study comparing aerosol effect on rainfall - atmospheric stability and precipitable water content [5] since both influence rain processes. Accordingly, the geo-statistical spatial analysis was also applied to copies of the statistical sample grid segmented for: (1) average vertical air mass movement – a proxy for atmospheric stability; and (2) cloud water path – a proxy for atmospheric column water content.

The satellite images and model output to be used in the study are described next, followed by an account of the study methods. The results of the geo-statistic data exploration; variograms, cross-variograms and cross-correlograms, comparing the spatial correlation of aerosol, cloud and rain parameters, are presented and discussed. The paper concludes that, while correlation values are low, the form of the graphs indicates a potential effect from anthropogenic aerosol on rainfall, in this study area for this chosen rain event.

At the conference further spatial analysis results will be presented from additional configurations of WRF-Chem gas phase chemistry and aerosol transport schemes as well and comparing cumuliform and stratiform rain systems on different days.

2. STUDY AREA AND RAIN EVENT

The study area, shown in Figure 1 is centred close to the geographic middle of the city of Brisbane at 153ºE and 27.5ºS.

On Saturday the 25th September 2010, a surface trough extended across inland Queensland directing a humid and unstable air mass over Brisbane as shown in the Figure 2 synoptic weather chart provided by the Bureau of Meteorology (BoM). Matching a MODIS satellite overpass of Brisbane at 03:42 UTC, the scattered rainfall distribution around Brisbane is shown in Figure 1.

A 03:46 UTC CloudSat image (Figure 3 provided by the Collaborative Institute for Research in the Atmosphere CIRA) indicates alto-cumulous (Ac) and alto-stratus (As) cloud systems in the area. The Cloudsat ground-track was approximately 90 km to the east of Brisbane parallel to the coast and, despite the distance, the CloudSat image is at least indicative of the cloud structure around Brisbane because the rain bearing system was being driven by high level westerly winds. The As cloud layer is also evident in Figure 4, while Figure 1(b) shows the two cloud layer system over Brisbane. Two distinct cloud layers were visible to remote sensing in the study area. Observations noted that the Ac cloud base was at 750 m above mean sea level.

Figure 2: *Mean sea level pressure chart 25Sep10 06:00 UTC - source: BoM.*

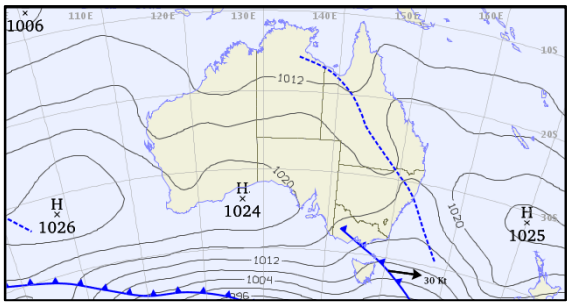

Figure 3: *Cloudsat images 25Sep10 03:46 UTC Brisbane due west at the yellow line (a) cloud classification and (b) radar reflectivity (red–most cloud water) - source: CIRA.*

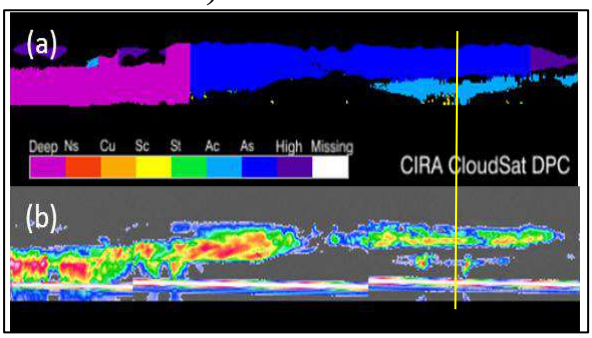

Figure 4: *Brisbane ceilometer cloud base 25Sep10 03:46UTC was 3000m above mean sea level (y-axis altitude km; x-axis 15 minute "window" of time) – source: UQ.*

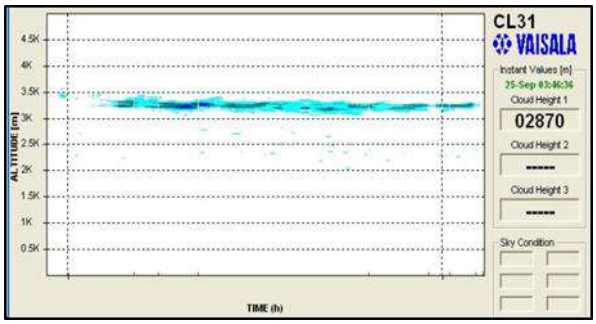

Figure 1: *The study area (a) Australia, (b) monochrome MODIS image (c) superimposed with Doppler radar rain rate (legend – see Figure 5) for 25Sep10 03:42 UTC - source: NASA and BoM.*

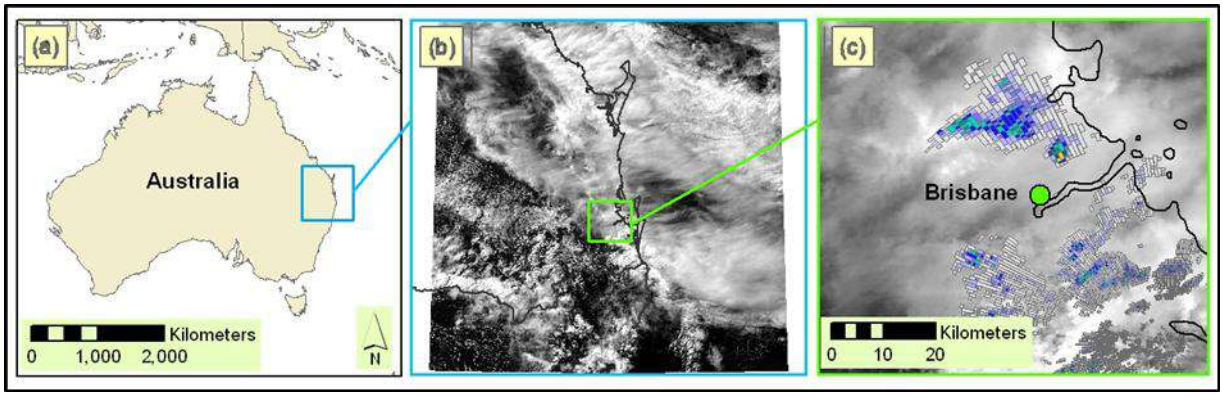

3. DATA

The study sourced rain rate from the Bureau of Meteorology (BoM), cloud properties from the NASA Moderate-Resolution Imaging Spectroradiometer (MODIS) satellite; and aerosol size distribution from WRF-Chem.

MODIS on the AQUA platform overflew Brisbane, at 03:42 UTC providing derived cloud properties: cloud effective radius (cer); and cloud water path (cwp). At 1 km spatial resolution, cer is a weighted mean of the size distribution of cloud droplets [6] and is used in this study to delineate cloud droplet size generally. MODIS cwp, also at 1 km spatial resolution, is the column amount of water in the cloud and is derived from the cloud optical thickness and cer parameters [7]. Cloud top pressure (ctp) at 5 km spatial resolution was also collected for reference only – it was not used in the geo-statistics.

The BoM Doppler rain radar site is at Staplyton, 33 km to the south-east of Brisbane. The 03:42 UTC rain rate, chosen to match the MODIS overflight time, was provided in ESRI ArcGIS shape-files. The integer value rain intensity parameter was processed by the BoM from radar reflectivity echo images of water droplet size hydrometeors. The intensity parameter corresponds to rain rate values in mm/hr using a lookup table provided by the BoM.

WRF-Chem models for 04:00 UTC, centered on Brisbane were configured with nested domains - a 3 km outer domain and a 1 km inner domain. The model spatial resolution was chosen to match that of the MODIS cloud property images.

WRF-Chem provided the vertical air movement parameter, aerosol optical depth at two wavelengths for the calculation of aerosol size distribution and sulphur-dioxide (SO_2) plume concentrations used in the geo-statistics.

WRF-Chem allows combinations of schemes for atmospheric physics, aerosol transport, gas phase chemistry as well as options for anthropogenic, biogenic and background aerosol emission sources. The MOSAIC (Model for Simulating Aerosol Interactions and Chemistry) 8 bin sectional aerosol transport scheme and CBMZ (Carbon Bond Mechanism - Zaveri) gas phase chemistry schemes [8] were chosen for this study because advice [9] indicates this scheme combination improves model algorithms for gas phase species conversion to the particle phase, the aging of secondary organic aerosol from primary anthropogenic aerosol sources and represents aerosol size distribution into 8 bins.

WRF-Chem meteorological boundary conditions were updated every six hours by weather observations used in the US National Centre for Environmental Prediction, Global Forecast System. The model aerosol boundary conditions were established from global databases of background and anthropogenic emissions: (1) RETRO global chemical composition of anthropogenic emissions over 40 years as at year 2000; spatial resolution of 0.5 degrees [10]; (2) GOCART global anthropogenic and background emissions as at year 2006; spatial resolution of 1 degree [11]; (3) EDGAR global anthropogenic emissions as at year 2005; spatial resolution of 0.1 degree [12]; and (4) MEGAN biogenic aerosol emissions as at 2003; spatial resolution of 1 km [13].

4. METHODS

The aim of the study was to examine aerosol effect on rainfall in the context of atmospheric parameters for individual rain events around Brisbane. Atmospheric parameters are distributed in space and time and a statistic is needed to provide some quantitative measure of the spatial correlation of atmospheric parameters. Geo-statistics provides such tools: (1) the variogram, a measure of dissimilarity, shows the degree of spatial autocorrelation at set distances for individual variables; (2) the cross-variogram, a measure of the joint

variability of two parameters at set distances; and (3) the cross-correlogram, a unit free standardised form of covariance which indicates the spatial correlation coefficient for two variables at increasing lag distance [14]. Geo-statistical packages provided in the open source statistics software application "R" [15] were used to generate geo-statistical graphs - "gstat" [16] for cross-variograms and "ncf" for cross-correlograms.

Data collection started with acquiring the MODIS images and using Exelis ENVI image analysis software to extract, geo-reference and sub-set cer, cwp and ctp parameters.

Three WRF-Chem runs were made with different aerosol emission configurations: (1) All aerosol sources (background, biogenic, anthropogenic emissions); (2) without biogenic emissions; and (3) anthropogenic emissions only.

The dimensionless Angstrom exponent (α), a suitable proxy for aerosol size distribution [17], was calculated in ESRI ArcGIS from WRF-Chem generated aerosol optical depth maps at two wavelengths; 300 and 1000 ηm, where λ is wave length:

$$\alpha_{\lambda 1/\lambda 2} = - \mathrm{Ln}(AOD_{\lambda 1} / AOD_{\lambda 2}) / \mathrm{Ln}(\lambda_1 / \lambda_2)$$ [18]

A higher value of α at a point in the map indicates a smaller mean aerosol size in the atmospheric column at that location.

WRF-Chem output included SO_2 concentration, which was used here to further test the correlation of anthropogenic aerosol to rain-fall. The mean vertical air movement (avW) was produced in WRF-Chem as were wind speed and direction at 10 metres and 7.4 km above ground level. WRF-Chem parameters were integrated from the model vertical levels below the tropopause; the location of which was determined from a BoM aerological diagram.

A 62 * 53 km statistical sampling grid of 1 km resolution was selected from the study area encompassing an area in Brisbane from which anthropogenic SO_2 emissions were evident as well as a band of rain-fall downwind to that source.

ESRI ArcGIS mapping software was used to aggregate the variables to grid point text files suitable for the "R" geo-statistics processing. The variable names are those used in Figures:

(1) in - rain rate (intensity);
(2) Ae - aerosol size distribution ;
(3) so2 - SO_2 concentration (ppmV);
(4) cer - cloud effective radius (μm);
(5) cwp - cloud water path (gm^{-2}); and
(6) avW - mean vertical air speed (ms^{-1}).

Similarly four further text files were created – each one a selection of grid points as follows:

case (1) - all points;
case (2) - avW <= 0;
case (3) - avW > 0;
case (4) - cwp <= mean of cwp case (1);
case (5) - cwp > mean of cwp case (1).

Case (2) represents areas of atmospheric subsidence; case (3) represents air being lifted; case (4) represents cwp less than, or equal to, the cwp mean; and case (5) represents cwp greater than the cwp mean.

5. RESULTS

During a review of model data output it was found that the all-aerosol and no-biogenic aerosol model outputs produced similar geostatistic graphs - accordingly, the model runs omitting biogenic emissions are not shown further here. Similarly, since it has been established that the cloud structure in the study area has two distinct layers any correlation of cer with α or rain intensity may be misleading. Accordingly geo-statistical graphs with cer are not included here either. Ideally the sample grid should have included a single height cloud structure – something not possible on this occasion.

Maps of the MODIS cer, cwp, ctp and the radar rain rate superimposed on the band 1 monochrome image; all sized to the geo-statistics grid extent, are shown in Figure 5. Figure 6 shows maps of WRF-

Figure 6: *Extracts from MODIS images: (a) band 1 and Doppler radar rain rate; (b) cloud effective radius(cer); (c) cloud water path (cwp; and (d)cloud top pressure (ctp) - source: NASA, BoM.*

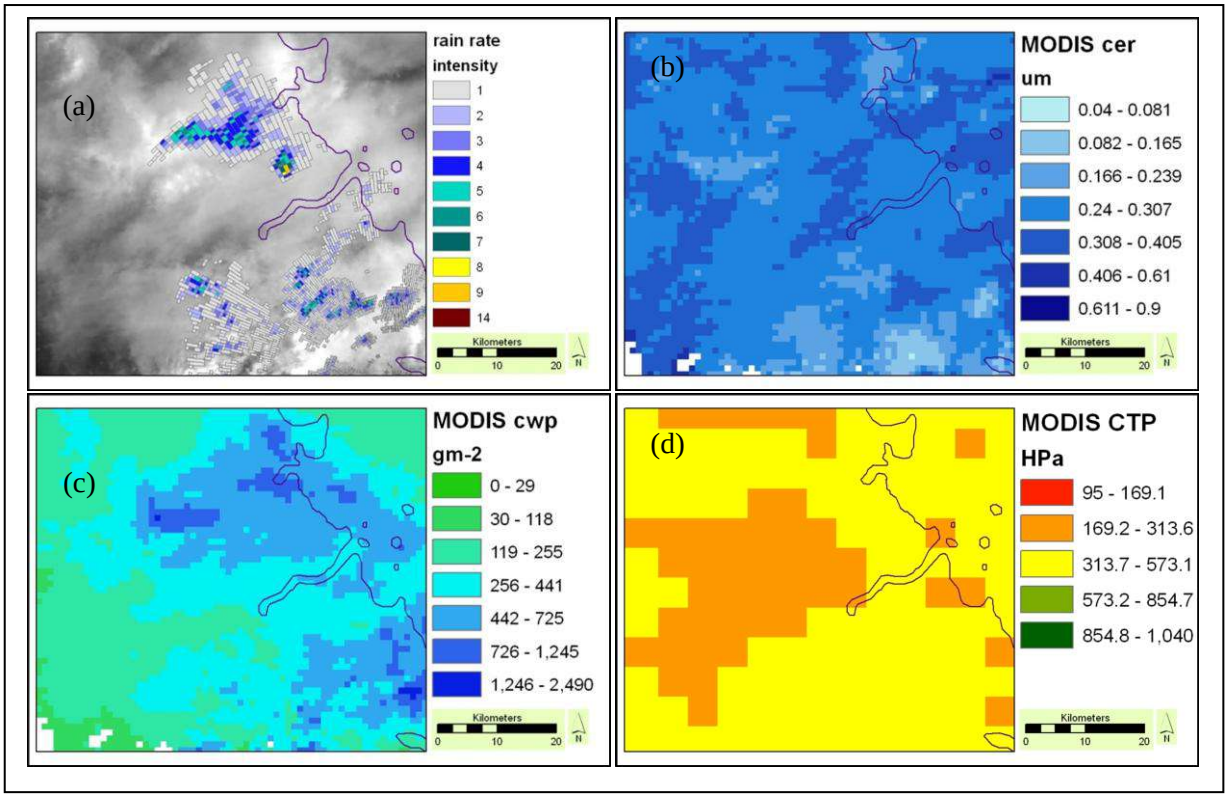

Chem provided variables also sized to the geo-statistics grid - α, so2 and avW. Output for the all aerosol model are shown in Figure 6 (a) to (c), while Figure 6 (d) to (e) are the output for the anthropogenic emissions only model run. Figure 7 is the WRF-Chem winds at 10 metres and 7.4 km above ground level, both used to indicate aerosol and rain movement.

The five data sets for both model runs had a sufficient number of grid points for geo-statistics as shown in Table 1. Table 2 presents the mean value of each variable for the 5 data sets for the all aerosol model run as does Table 3 for the anthropogenic aerosol only model run.

Table 1: *Number of grid points of five data sets for two WRF-Chem model outputs.*

Case	All aerosol	anthro-only
1	3286	3286
2	1227	1129
3	2059	2157
4	1891	1891
5	1395	1395

Table 2: *Mean of atmospheric variables for the five data sets for the all aerosol WRF-Chem model run.*

#	cwp	avW	Ae	in	cer	so2
1	367.6	0.044	1.171	0.367	0.283	0.00205
2	418.1	-0.053	1.071	0.57	0.279	0.00209
3	337.5	0.102	1.23	0.246	0.285	0.00203
4	243.2	0.069	1.447	0.133	0.281	0.00202
5	536.1	0.01	0.797	0.683	0.285	0.0021

Table 3: *Mean of atmospheric variables for the five data sets for the anthropogenic only aerosol WRF-Chem model run.*

#	cwp	avW	Ae	in	cer	so2
1	367.6	0.059	2.504	0.367	0.283	0.00211
2	380.8	-0.058	2.534	0.493	0.285	0.00215
3	360.7	0.12	2.489	0.301	0.282	0.0021
4	243.2	0.086	2.682	0.133	0.281	0.00213
5	536.1	0.021	2.264	0.683	0.285	0.0021

Table 2 indicates that for the all-aerosol model output, average rainfall intensity is maximized when average cloud water content is high. Table 2 shows that average rain intensity values are high when

the data set is constrained to subsiding air mass. This is also seen in Table 3 – for the anthropogenic only aerosol model run. This unexpected result may be explained by the 18 minute time difference between the model output and the rainfall observation. From Figure 6, the extent of discrete areas of rising or subsiding air are a few kilometres in size, modelling air flow associated with Ac cloud systems. In the indicated wind conditions, clouds would move far enough in an 18 minute period for the rain rate and model data sets to misalign. Correlating atmospheric parameters constrained by vertical air movement is probably not valid for this case study. Accordingly geo-statistical graphs for cases (2) and (3) – data sets constrained by positive or negative air movement, are not shown further.

For the remaining three data sets for both model runs, a Moran's I calculation on each variable in each data set indicated that similar values cluster together and at 99% certainly, the clustering is not by chance.

The geo-statistic graphs comparing α and rain rate spatial correlation for all grid points of both model outputs are in Figure 8. Similarly, geo-statistic graphs comparing SO_2 distribution and rain rate spatial correlation are in Figure 9.

Figure 6*: WRF-Chem output comparing model runs: (1) all aerosol emissions - (a) aerosol size distribution Ae, (b) sulphur dioxide concentration so2; and (c) mean vertical air speed avW; with (2) anthropogenic aerosol emissions only - (d) Ae, (e) so2 and (f) avW.*

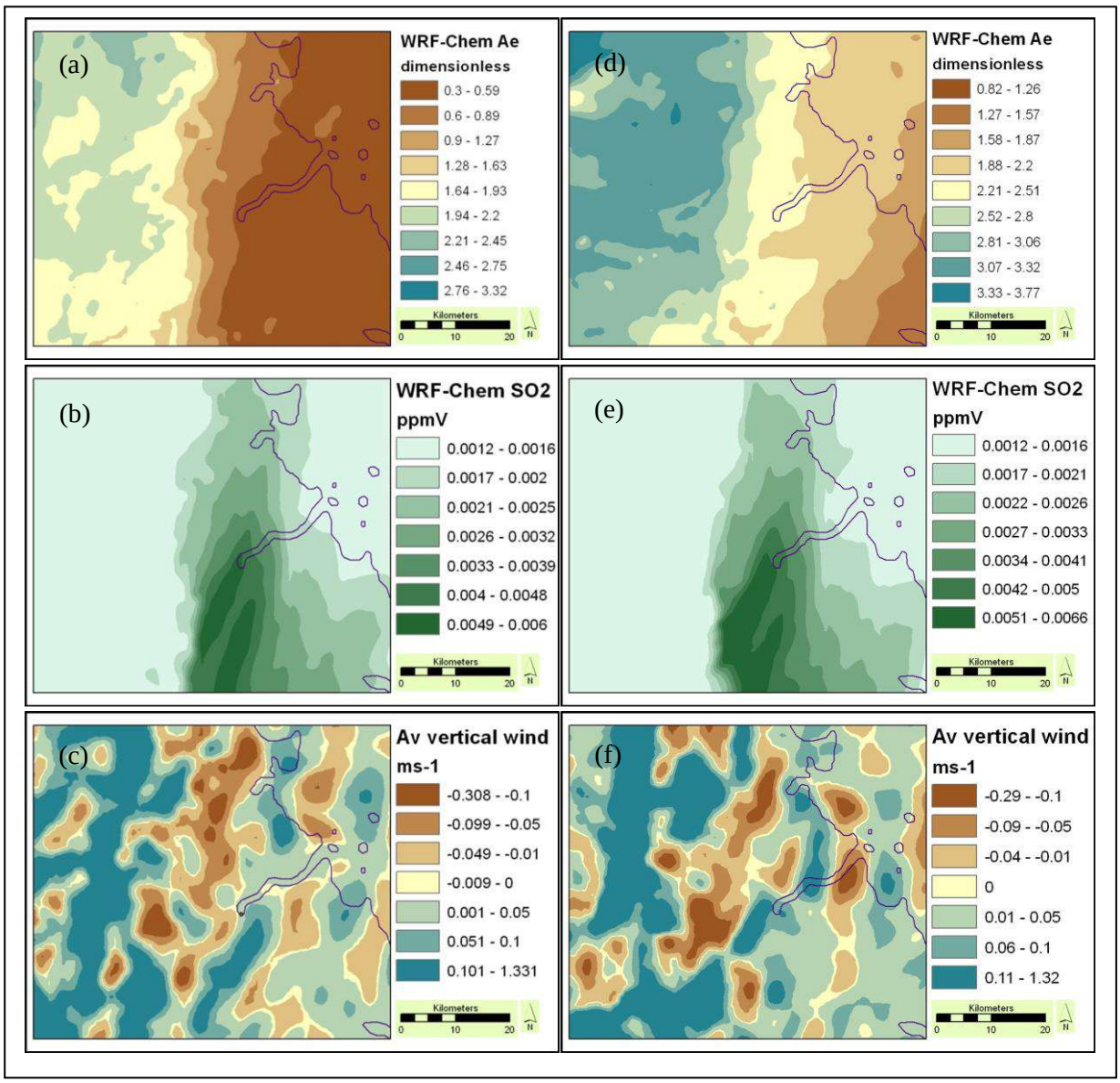

Figure 7*: WRF-Chem above ground winds for 25th September 2010, 04:00 UTC: (a) 10 metres and (b) 7.4 km.*

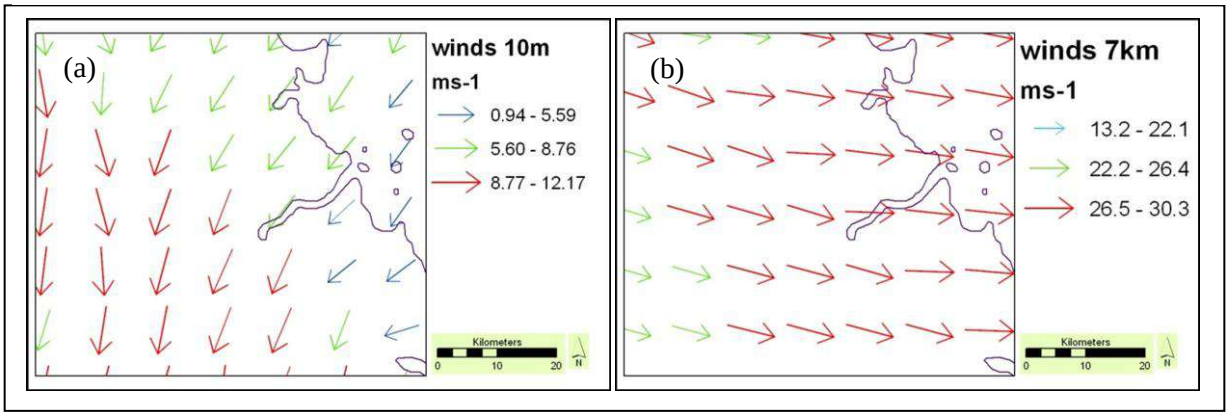

Figure 8*: Geo-statistic spatial relationship graphs of aerosol size and rainfall rate for* ***case (1); all data****: [(a), (b)] –all aerosol emissions; and [(c), (d)] – anthropogenic only emissions.*

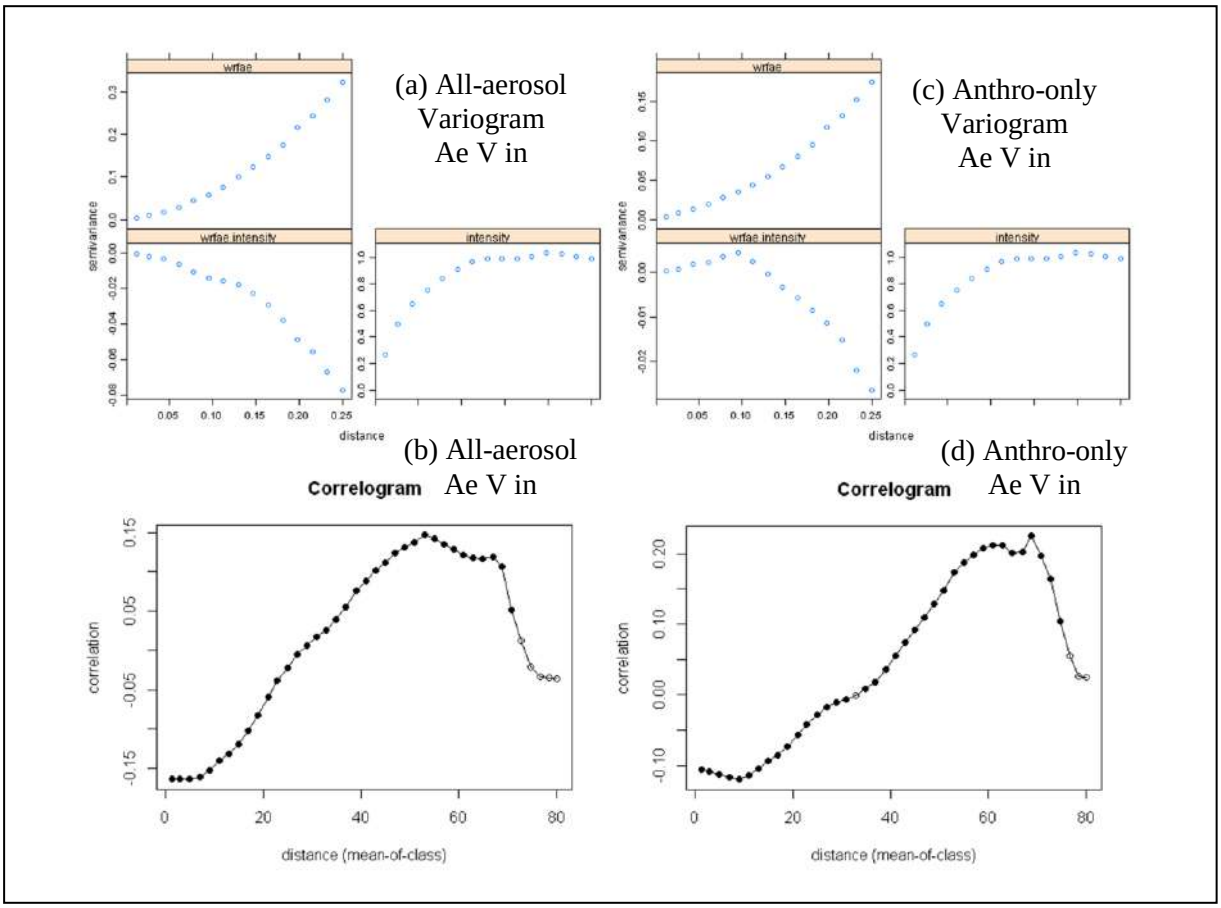

Figure 9*: Geo-statistic spatial relationship graphs of SO2 concentration) and rainfall rate for* ***case 1 (all data):*** *[(a), (b)] – no biogenic emissions; and [(c), (d)] – anthropogenic only*

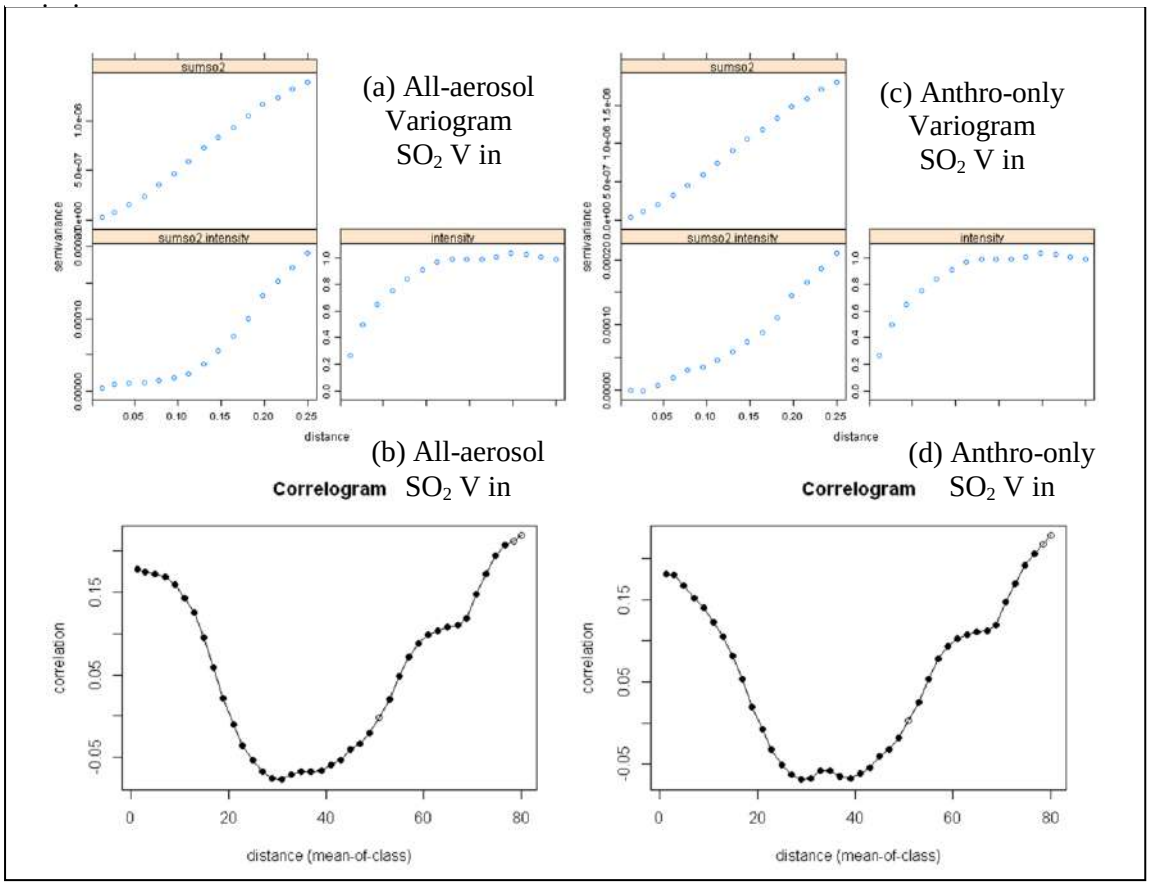

Figure 10*: Geo-statistic spatial relationship graphs of aerosol size and rainfall rate for* ***case (4): cwp <= mean cwp****: [(a), (b)] –all aerosol; and [(c), (d)] – anthropogenic only.*

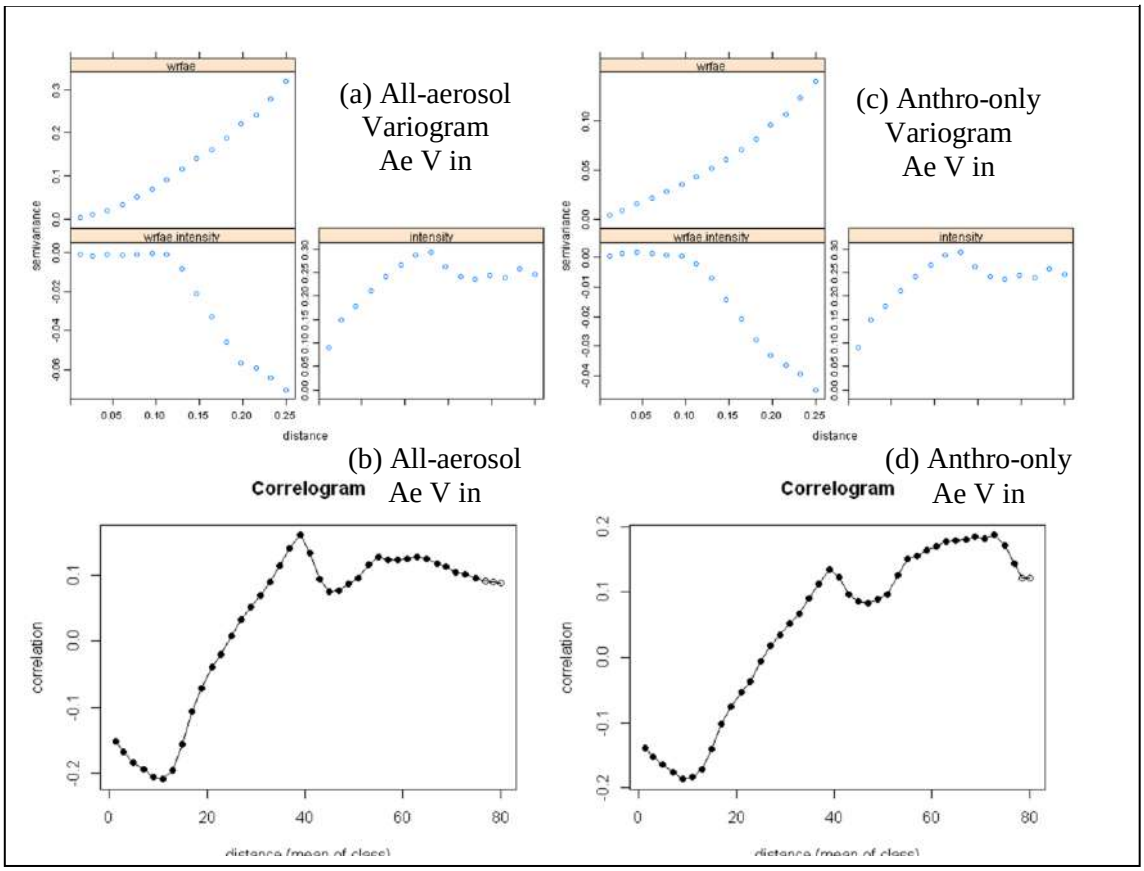

Figure 11*: Geo-statistic spatial relationship graphs of aerosol size and rainfall rate for* ***case (5); cwp > mean cwp****: [(a), (b)] –all aerosol; and [(c), (d)] – anthropogenic only.*

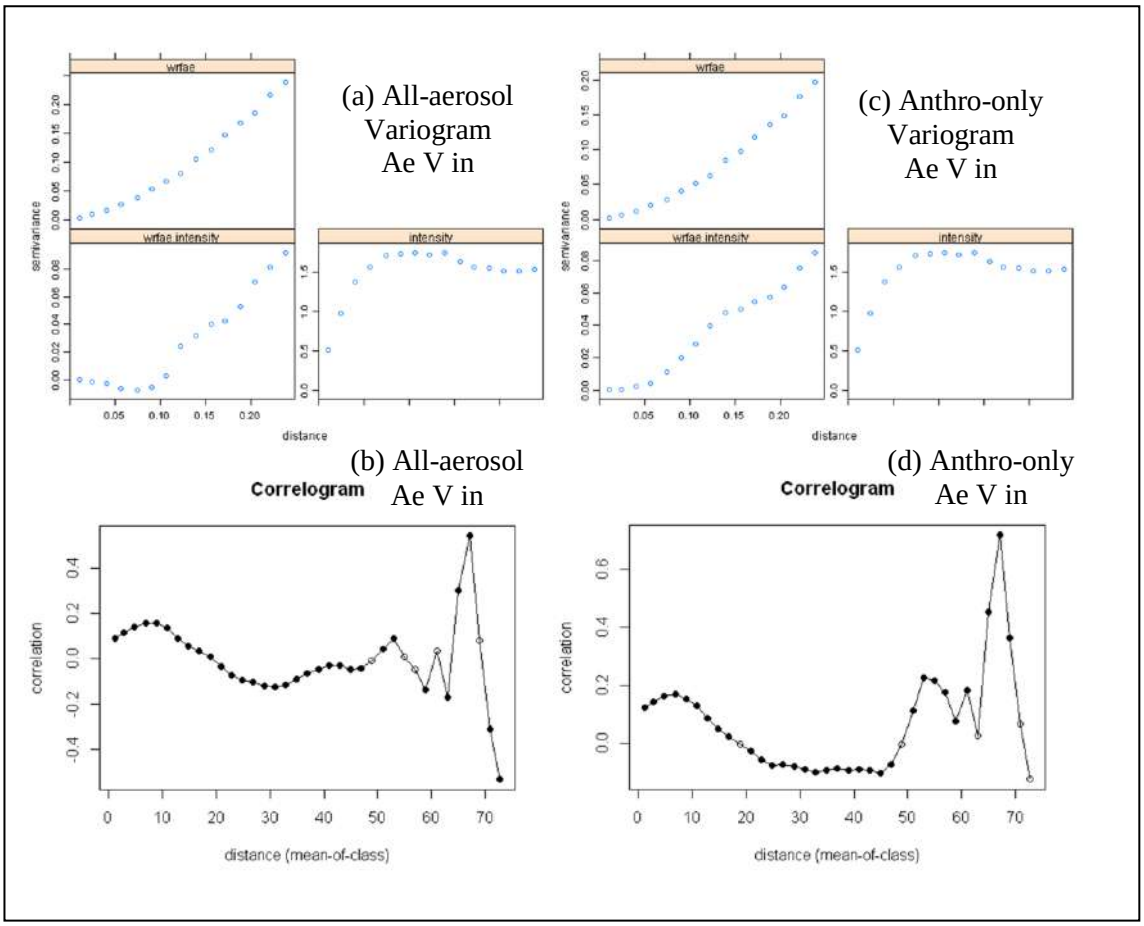

Figure 10 contains the geo-statistic graphs comparing α and rain rate spatial correlation where the data is stratified for cwp less than, or equal to, the mean cwp. Similarly, Figure 11 is graphs for data stratified for cwp greater than the mean cwp.

6. DISCUSSION

The differences in the mean α values between Table 2 all aerosol emission and Table 3 anthropogenic emissions only, are consistent with the choice of model configurations. The larger average α values in Table 3 indicate the smaller particle size of pollution compared with the smaller α, therefore larger particles, when background aerosol (dust etc) is included in the aerosol distribution. Interestingly for case 4, α is highest, or the aerosol size smallest, in both model outputs where cwp is less than, or equal to, the mean cwp. This is possibly explained by the model aerosol size distribution in high cwp areas attaining hygroscopic growth.

None of the experimental variograms for α, and to some extent SO_2 reach a firm variogram sill by any range which indicates both distributions have strong trends in the sample grid extent. Applying a logarithmic transformation to the variables did not change the experimental variograms. Since this study is merely using the variograms to explore the spatial correlation; and no further co-kriged variable prediction is being done, the lack of stationarity in the aerosol distributions is simply accepted and no further data manipulation is thought necessary. The open circles in the correlograms of following figures indicate correlation values at that lag distance not significant at the 5% level. The “gstat” package did not show different variograms when evaluating anisotropy specifying

direction of lags, and so the distributions are taken to be isotropic.

From Figure 8 for case (1), the full data set, rain intensity values become unrelated to each other at about the 12 km sample point separation distance. The cross-variogram for all-aerosol emissions shows that rain rate and α varies negatively – that is, as one parameter increases the other decreases, out to 25 km lag distance. The Figure 8(b) correlogram shows that a weak negative correlation between rain rate and α becomes uncorrelated at around 18 km and then becomes increasingly positively correlated, albeit weakly, out to 50 km. The strength of the correlation decreases past 60 km – this being the maximum lag distance possible for the sample grid extent – and so not considered important.

The key result of the study is shown in the differences of the correlogram structure for the WRF-Chem all aerosol emissions model output (Figure 8(b)) compared with the anthropogenic aerosol only model output (Figure 8(d)). Both models show a constant and slight negative correlation of aerosol size distribution with rain rate to 10 km. This initial negative correlation is very slightly less significant for the anthropogenic aerosol case. Importantly the negative correlations for both model configurations becomes zero at significantly different lag distances; around 30 km for anthropogenic aerosol only and 18 km for all-aerosol emissions. This suggests decreasing rain rate is correlated with increasing aerosol size to a longer distance for anthropogenic aerosol for the specific atmospheric conditions studied. Put another way - pollution only particles remain correlated with lower rainfall values at a longer distance between sample points.

Figure 8 correlograms go on to show that α becomes positively correlated for lag distances greater 18 and 30 km for all-aerosol and pollution only aerosol respectively. The anthropogenic aerosol reaches a higher positive correlation peak (0.22) at 60 km than the all-aerosol case (0.14) at 46 km. Although the correlation trends past 60 km are less significant due to sample size, this may suggest that anthropogenic only aerosol does eventually correlate with increasing rainfall, but at a greater distance and slightly stronger, than the all-aerosol case; for these particular study conditions.

Figure 9 shows that the WRF-Chem output for anthropogenic SO_2 emissions are very similar whether the model is configured for all-aerosol or anthropogenic only aerosol emissions. The SO_2 correlation illustrated in the correlograms reflects the spatial distribution of SO_2 with respect to the rainfall pattern and indicates the all-aerosol model configuration suitably represents anthropogenic aerosol in its distribution.

Figure 10 indicates for the all-aerosol model constrained to grid points were cwp is less than, or equal to, the mean cwp, that α and rain rate are increasingly slightly negatively correlated to 16 km, losing any correlation at about 25 km lag distance between sample points and thereafter become slightly positively correlated to 40 km. The pollution only aerosol case is very similar, with less strength in the slight negative correlation at 10 km probably indicative of less aerosol contributing to the size distribution. In low cloud water path areas there is little difference in the way the aerosol size distribution of the two aerosol configurations affect rain rate.

The geo-statistical graphs for cwp greater than the mean cwp in Figure 11(a) tell a different story. Going out to 50 kms, the correlograms are similar for both aerosol configurations the α and rain rate correlation are slightly positive to 10 km, losing correlation at 20 km lag distance and remaining insignificantly correlated to 50 km.

There is clear difference in the α and rain rate spatial correlation relationship in low and high cloud water path environments. Given the MODIS cwp is in part derived from cer – and noting the two cloud types in this study; further discussion will be deferred until more study cases are processed.

The study to examine the spatial correlation of aerosol size distribution and rain rate at local rain event scales has some limitations. Model output time should be as close as possible to the satellite and radar rain rate data acquisition times in order to constrain geo-statistical data sets for vertical air movement. Selecting rain events of a single cloud structure is important to add the cloud droplet size into the geo-statistics. Other limitations include the coarse spatial resolution, and collection age of the aerosol emission data sources and the necessary column integration of atmospheric quantities means a level of abstraction is being unavoidably introduced into the study.

7. CONCLUSION

The study, while not yet complete, indicates that the spatial correlation characteristics of rain fall compared with aerosol size distribution can be shown using geo-statistics. Further work to refine the process, and further case studies in different cloud systems, is required.

For the Ac/As rain bearing system in the early afternoon of 25th September 2012 around Brisbane Australia, smaller pollution particles remain correlated with rain rate at greater distances between sample points than that for all-aerosols. Initially smaller aerosol correlates with less rainfall to grid point separation of 30 km whereas the same relationship for all-aerosols runs out at 18 km. At 50 km smaller aerosols correlate with higher rain rates to a slightly higher degree for pollution only aerosol than for all aerosol. The result suggests anthropogenic aerosol potentially affects rainfall possibly delaying the onset of rain for this particular study.

At the conference, further rain events comparing three aerosol emission configurations with geo-statistical fitted models of linear co-regionalisation, to more accurately compare the cross-variogram properties will be presented. Further events will be chosen such that cloud droplet size can be added into the geo-statistics process as well as data sets constrained by atmospheric stability. It is expected that the correlation of aerosol size distribution, cloud droplet size and rain rate will vary between cumuliform and stratiform cloud systems comparing different emission configurations.

8. ACKNOWLEDGEMENTS

The authors thank:

- Dr. Georg Grell, Dr. Steven Peckham for hosting a NOAA WRF-Chem visit.
- Dr. Terry Clark for configuring WRF-Chem on UQ's Research Computing Centre.
- The Bureau of Meteorology for Doppler radar rain rate data.
- NASA mission scientists and personnel for MODIS data.
- CIRA at CSU Fort Collins CO USA for a CloudSat image.
- The UQ Graduate School for a travel award to fund the NOAA visit.

9. REFERENCES

[1] Forster, P, Ramaswamy, V, Artaxo, P, Berntsen, T, Betts, R, Fahey, DW, Haywood, J, Lean, J, Lowe, DC, Myhre, G, Nganga, J, Prinn, R, Raga, G, Schulz, M & R. Van Dorland 2007, *Changes in Atmospheric Constituents and in Radiative Forcing*, Intergovernmental Panel on Climate Change, Cambridge, United Kingdom and New York, NY, USA.

[2] Rosenfeld, D 2000, 'Suppression of Rain and Snow by Urban and Industrial Air Pollution', *Science*, vol. 287, no. 5459, pp. 1793-6.

[3] Bigg, EK 2008, 'Trends in rainfall associated with sources of air pollution', *Environmental Chemistry*, vol. 5, no. 3, pp. 184-93.

[4] Grell, GA, Peckham, SE, Schmitz, R, McKeen, SA, Frost, G, Skamarock, WC & Eder, B 2005, 'Fully coupled "online" chemistry within the WRF model', *Atmospheric Environment*, vol. 39, no. 37, pp. 6957-75.

[5] Ayers, G 2009, 'Air pollution and precipitation suppression over SE Australia: critical review of evidence presented by Rosenfeld (2000) and Rosenfeld (2006)', *Tellus*, vol. 61B, pp. 685-93.

[6] NASA 1997, *Cloud Retrieval Algorithms for MODIS: Optical Thickness, Effective Particle Radius, and Thermodynamic Phase*, by King, MD, Tsay, S-C, Platnick, SE, Wang, M & Liou, K-N, NASA.

[7] Otkin, JA & Greenwald, TJ 2008, 'Comparison of WRF Model-Simulated and MODIS-Derived Cloud Data', *Monthly Weather Review*, vol. 136, no. 6, pp. 1957-70.

[8] Zaveri, RA, Easter, RC, Fast, JD & Peters, LK 2008, 'Model for Simulating Aerosol Interactions and Chemistry (MOSAIC)', *J. Geophys. Res.*, vol. 113, no. D13, p. D13204.

[9] Kazil, J & Ahmadov, R 2011, *Aerosol in WRF-Chem*, Powerpoint Lecture NCAR WRF-Chem Tutorial, 18 July 2011.

[10] Schultz, MG, Backman, L, Balkanski, Y, Bjoerndalsaeter, S, Brand, R, Burrows, JP, Dalsoeren, S, Vasconcelos, Md, Grodtmann, B, Hauglustaine, DA, Heil, A, Hoelzemann, JJ, Isaksen, ISA, Kaurola, J, Knorr, W, Ladstaetter-Weißenmayer, A, Mota, B, Oom, D, Pacyna, J, Panasiuk, D, Pereira, JMC, Pulles, T, Pyle, J, Rast, S, Richter, A, Savage, N, Schnadt, C, Schulz, M, Spessa, A, Staehelin, J, Sundet, JK, Szopa, S, Thonicke, K, Bolscher, Mvh, Noije, Tv, Velthoven, Pv, Vik, AF & Wittrock, F 2007, *REanalysis of the TROpospheric chemical composition over the past 40 years (RETRO) — A long-term global modeling study of tropospheric chemistry Final Report*, Max Planck Institute for Meteorology, Hamburg, Jülich/Hamburg, Germany.

[11] Chin, M, Ginoux, P, Kinne, S, Torres, O, Holben, BN, Duncan, BN, Martin, RV, Logan, JA, Higurashi, A & Nakajima, T 2002, 'Tropospheric Aerosol Optical Thickness from the GOCART Model and Comparisons with Satellite and Sun Photometer Measurements', *Journal of the Atmospheric Sciences*, vol. 59, no. 3, pp. 461-83.

[12] Olivier, JGJ, Van Aardenne, JA, Dentener, FJ, Pagliari, V, Ganzeveld, LN & Peters, JAHW 2005, 'Recent trends in global greenhouse gas emissions:regional trends 1970–2000 and spatial distributionof key sources in 2000', *Environmental Sciences*, vol. 2, no. 2-3, pp. 81-99.

[13] Guenther, A, Karl, T, Harley, P, Wiedinmyer, C, Palmer, PI & Geron, C 2006, 'Estimates of global terrestrial isoprene emissions using MEGAN (Model of Emissions of Gases and Aerosols from Nature)', *Atmos. Chem. Phys.*, vol. 6, no. 11, pp. 3181-210.

[14] Goovaerts, P 1997, *Geostatistics for Natural Resources Evaluation*, Applied Geostatistics Series, Oxford University Press.

[15] Venables, WN, Smith, DM & R-Development-Core-Team 2009, *An Introduction to R*, 2nd edn, Network Theory Limited.

[16] Pebesma, EJ 2004, 'Multivariable geostatistics in S: the gstat package', *Computers & Geosciences*, vol. 30, pp. 683-91.

[17] Yu, X, Zhu, B & Zhang, M 2009, 'Seasonal variability of aerosol optical properties over Beijing', *Atmospheric Environment*, vol. 43, pp. 4095-101.

[18] Radhi, M, Box, MA, Box, GP, Mitchell, RM, Cohen, DD, Stelcer, E & Keywood, MD 2010, 'Optical, physical and chemical characteristics of Australian continental aerosols: results from a field experiment', *Atmos. Chem. Phys.*, vol. 10, no. 13, pp. 5925-42.

A NUMERICAL STUDY OF AEROSOL EFFECTS ON CLOUD MICROPHYSICAL PROCESSES OF HAILSTORM CLOUDS

Hui-Ling YANG, Hui XIAO, and Yan-Chao HONG
Laboratory of Cloud Precipitation Physics and Severe Storms (LACS), Institute of Atmospheric Physics, Chinese Academy of Sciences, Beijing 100029, China

1. INTRODUCTION

Aerosols acting as cloud condensation nuclei (CCN) can significantly impact the efficiency of hydrometeor growth and the resulting precipitation (Rosenfeld, 1999; Yin et al., 2000; Saleeby and Cotton, 2005; Flossmann and Wobrock, 2010). Some numerical simulations and observations reveal that greater concentrations of CCN result in the production of many more small cloud droplets, narrower cloud-droplet spectra, and reduced collision efficiencies, all of which act to inhibit precipitation processes (e.g., Warner and Twomey, 1967;Jirak and Cotton, 2006). However, some other studies have shown increases in precipitation in some heavily polluted cities (e.g., Tokyo, Houston, etc.) (Ohashi and Kida, 2000; Shepherd and Burian, 2003). As reviewed in the 2007 Intergovernmental Panel on Climate Change (IPCC) report, a great deal of uncertainty about the role of aerosols in modifying clouds and precipitation remains.

In this study, numerical simulations were conducted in an attempt to shed some light on these problems. The regional atmospheric modeling system (RAMS) mesoscale model was used to investigate the effects of varied CCN concentrations on microphysical processes of spring hailstorm clouds in a semiarid region. Special effort was made to investigate the effects of CCN on the hydrometeor particle character and the characteristics and distributions of the sources of hail particles (i.e., microphysical transfer processes).

2. MODEL AND EXPERIMENTAL SETUP

The improved RAMS model (version 4.3; Saleeby and Cotton, 2004; Saleeby and Cotton, 2005) was utilized in this study to perform sensitivity simulations. Two-way nesting with a three-grid arrangement was used for all simulations conducted in this study. The outer grid 1 covered most of North China and Northeast China with a horizontal grid resolution of 10 km (160×200 grid points). Grid 2 covered northern Hebei and Shanxi Provinces, and the middle-eastern region of Inner Mongolia of North China, with 2.5-km grid spacing (250×242 grid points). Grid 3 covered the major hail precipitation area, with a 0.5-km grid spacing (227×215 grid points; Fig. 1). A total of 42 vertical levels with variable grid spacing were employed, and the model top extended to ~20.5 km aboveground.

For these simulations, we focused on the impacts of CCN on microphysical processes of hailstorm clouds. The background GCCN concentrations were initialized as three-dimensional (3D) homogeneous, with the value of 0.00001 cm^{-3} for all simulations. The CCN concentrations were initialized, horizontally homogeneous, with vertical profiles that decreased linearly with height up to 4 km AGL. Such distribution

of CCN approaches some in situ observations (Van den Heever et al., 2006). Three simulations were performed using the same vertically decreasing CCN concentration profile with height. The surface CCN concentration was initialized with maximum values of 300 cm^{-3} (C1), 1000 cm^{-3} (C2), and 5000 cm^{-3} (C3), respectively. The minimum initial concentration of CCN allowed at any grid point was 100 cm^{-3}. C1 represents clean clouds, C2 represents polluted clouds, and C3 represents heavily polluted clouds.

A large range of hailstorms occurred on 23 April 2009 in the semiarid areas of northern Hebei Province; and observation data from these storms comprised the simulation case. The model was initialized with real-time NCEP (National Centers for Environmental Prediction) reanalysis data from 23 April 2009 (1°×1°, 6–h intervals). For all simulations, the model started at 0000 UTC and ran for 18 h. Hail precipitation in the simulations occurred between 0550 UTC and 0930 UTC and covered most of area A (40.7–41.5°N, 114.3–115.8°E).

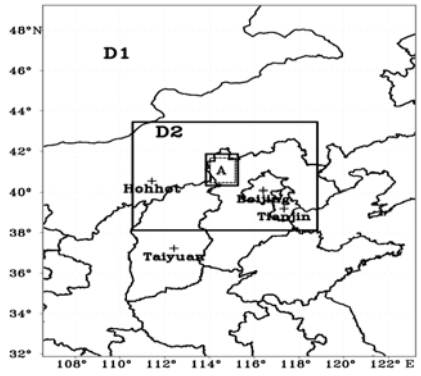

Fig. 1. The locations of three nested grids. D1 and D2 represent grid 1 and grid 2, respectively. The innermost solid line box for grid 3 and the dotted line area is area A, which is the major hail precipitation region.

3. OBSERVATIONS AND MODEL COMPARISON

Observational comparison was not the primary focus of this study. Model outputs were briefly compared with observations to make a broad assessment of the forecast ability in this case. The comparison between the model analysis data and the observations show that the simulation generally performed well in forecasting the precipitation and pressure field as well as the radar reflectivity.

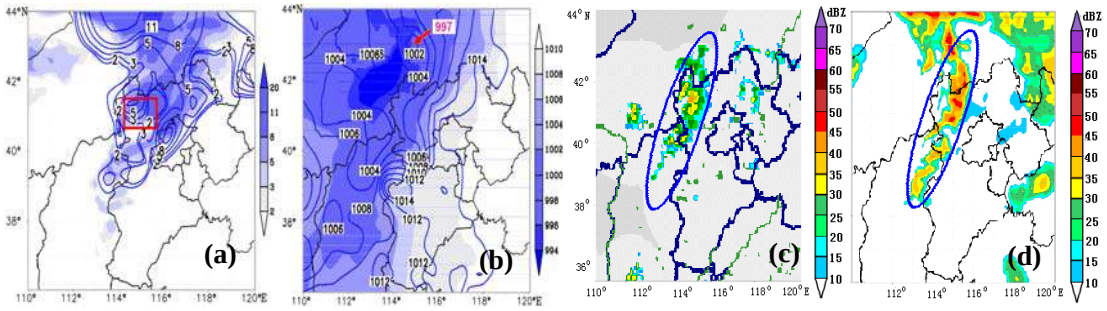

Fig. 2. Six hours (0600 UTC–1200 UTC) of (a) surface accumulated precipitation (units: mm) and (b) 0600UTC sea level pressure (units: hPa) for the observations and simulations. Solid lines represent observations, and shading represents simulations; (c) radar reflectivity (units: dBZ) at 0730 UTC of meteorological observation, and (d) model simulation; (The simulation was for experiment C2).

Table1. Change of hydrometeor characteristics in the three experiments (the data in the table are the spatial-time averaging values).Only grid points with hydrometeor mixing ratio>0.0001 g

kg-1 were considered.

Note: Q stands for mixing ratio, N = concentration and D = mean diameter; Subscript Cld1 = cloud1 and Cld2 = cloud2. Subscripts r = raindrop, i = ice crystal, s = snow, a = aggregate, g = graupel, and h = hail.

Hydrometeor parameters	The parameter values			increased percentage(%) relative to Case1		
	C1	C2	C3	C1	C2	C3
Q_{cld1} (10^{-1}g kg^{-1})	1.86	2.20	2.92	—	18.3	57.0
N_{cld1}(cm^{-3})	48	139	522	—	189.6	987.5
D_{cld1}(μm)	9.8	7.00	4.76	—	-28.6	-51.4
Q_{cld2} (10^{-3}g kg^{-1})	3.5	1.1	1.2	—	-68.6	-65.7
N_{cld2}(10^{-3}cm^{-3})	12.6	3.73	3.65	—	-70.4	-71.0
D_{cld2}(μm)	65.2	65.1	63.4	—	-0.15	-2.76
Q_r(10^{-3}g kg^{-1})	6.20	2.24	1.09	—	-63.9	-82.4
N_r(m^{-3})	272	43	6	—	-84.2	-97.8
D_r(10^{-1}mm)	2.59	4.5	7.7	—	52.5	197.3
Q_i(10^{-3}g kg^{-1})	8.37	7.45	5.09	—	-11.0	-38.7
N_i(m^{-3})	29984	53838	23834	—	79.6	-20.5
D_i (μm)	69.7	64.8	59.9	—	-7.0	-14.1
Q_s(10^{-2}g kg^{-1})	2.12	1.98	1.77	—	-6.6	-16.5
N_s(m^{-3})	5787	4802	3318	—	-17.0	-42.7
D_s(10^{-1}mm)	5.63	5.64	5.81	—	0.2	3.2
Q_a(10^{-2}g kg^{-1})	12	14	16	—	16.7	33.3
N_a(m^{-3})	1340	1482	1189	—	10.6	-11.3
D_a(mm)	1.37	1.38	1.52	—	0.73	10.9
Q_g(10^{-3}g kg^{-1})	3.83	7.93	6.74	—	107.0	76.0
N_g(m^{-3})	2.56	3.97	4.93	—	55.1	191.6
D_g(mm)	2.03	1.83	1.96	—	-20.4	-3.45
Q_h(10^{-2}g kg^{-1})	5.32	3.74	3.70	—	-29.7	-30.5
N_h(m^{-3})	54.7	17.6	0.55	—	-86.1	-99.0
D_h(mm)	0.84	1.05	2.58	—	5.8	46.6

Table 2. Domain-averaged (area A) and time averaged (C1and C2: 0500UTC to 1020UTC and C3: 0500UTC to 0950UTC) quantities for hail particles.

Note: $\overline{Q_h}$ = hail mixing ratio; $\overline{N_h}$ = hail concentration; $\overline{D_h}$ = hail mean diameter; $\overline{Q_{melt}}$ = melting mixing ratio. IN = hydrometeor characteristics in cloud. SURF = hydrometeor characteristics at the point where they reached the surface of the earth. OUT = hydrometeor characteristics between the surface of the earth and the cloud base height.

Expt	$\overline{Q_h}$ (10^{-2}g kg^{-1})	$\overline{N_h}$ (m^{-3})	$\overline{D_h}$ (mm)	$\overline{Q_{melt}}$ (10^{-3}g kg^{-1})
	IN/SURF	IN/SURF	IN/SURF	IN /OUT
C1	5.32/2.8	54.7/7.1	0.84/1.2	7.31/43.3
C2	3.74/3.3	17.6/4.5	1.05/1.4	4.14/33.4
C3	3.70/1.7	0.55/1.2	2.58/1.9	1.02/7.8

Table 3. Transfer amount (g kg-1) averaged over time over area A of each particle in the cloud to hail in the three experiments.

Note: C = transfer amount (g kg-1) of each particle to hail. Subscript Cld1 = cloud1 and Cld2 = cloud2. Subscripts r = raindrop, i = ice crystal, s = snow, a = aggregate, g = graupel. Total = Ca + Ccld1 + Ccld2 + Cg + Ci + Cr + Cs.

Expt	C_{Cld1}	$C_{Cld2}(10^{-2})$	C_a	C_g	$C_i(10^{-5})$	C_r	$C_s(10^{-2})$	Total
C1	19.7	67	9.0	2.72	358	2.68	138	36.15
C2	11.2	11	8.7	3.89	67.8	1.68	69	26.27
C3	1.25	0.52	2.15	0.79	5.41	1.72	2.37	8.29

4. RESULTS

4.1. Effects of CCN on microphysical structures of a hailstorm cloud

The hydrometeor characteristics of different CCN backgrounds are shown in Table 1. All of these quantities were time averaged and domain averaged in clouds. There were some differences in storm duration among the three cases.

The CCN concentration influenced the characteristics of hydrometeor particles. As CCN concentrations increased, mixing ratios of small liquid particles (i.e., cloud1) increased, while that of large liquid particles (i.e., cloud2 and rain) decreased. Mixing ratios of small ice-phase particles (i.e., pristine ice and snow) decreased, while that of the large ice-phase hydrometeor particles (i.e., aggregates and graupel) increased. Hail number concentration, mixing ratio, and melting mixing ratio tended to decrease, but the mean diameter of hail increased with greater CCN concentrations.

4.2. Effects of CCN on hail particle characteristics

Table 2 shows that the mixing ratio and number concentration of hail were greatest in clean conditions (C1) in clouds, while they were greatest in polluted conditions (C2) on the surface. The minimum values appeared in heavily polluted conditions (C3) both in clouds and on the surface. These results demonstrate that the surface precipitation of hail in polluted clouds was greater than that in clean clouds or heavily polluted clouds. With greater CCN concentrations, hail number concentration, mixing ratio, and melting mixing ratio tend to decrease, but the mean diameter of hail increased. The surface precipitation of hail in polluted clouds was greater than that in clean clouds and heavily polluted clouds.

4.3. Aerosol impact upon microphysical processes of hail particles

The contributions of each hydrometeor species to hail were altered with different aerosol backgrounds. For liquid water, cloud water played a great role in C1 and C2, but the contribution of rain to hail in C3 was significantly greater than in C1 and C2. For ice-phase hydrometeors, aggregates made the greatest contributions to hail formation in the three experiments. The contribution of liquid hydrometers to hail formation was greater than that of the ice-phase hydrometeor particles in C1. However, in C2 and C3, the contributions of ice particles to hail were close to that of liquid particles to hail. Higher CCN concentrations leading to the contribution of cloud1 to hail formation decreased, while the contribution of aggregates to hail increased.

4.4. Effects of CCN on rain production

Domain averaged, surface accumulated, total precipitation, rain, hail, and graupel during the hail precipitation time of the sensitivity tests are shown in Fig.3. Increasing CCN

concentrations reduced the total surface precipitation. Increasing CCN concentration resulted in a decrease of rain. The contribution of ice-phase precipitation to total accumulated precipitation increased with increasing CCN concentrations (C1: 6.88%; C2: 18.80%; C3:25.15%).

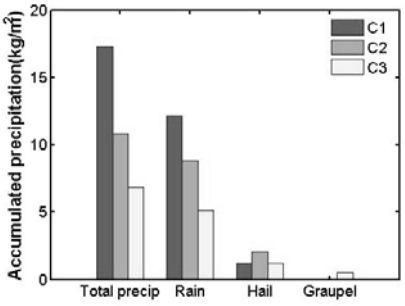

Fig.3.Domain-averaged,surface-accumulated, total precipitation, rain, hail, and graupel of the three experiments (units: kg m-2) during the hail precipitation time (0550 UTC–0930 UTC).

5. SUMMARY AND CONCLUSIONS

The results demonstrate that CCN concentrations have a significant impact on the cloud microphysical processes, as well as on the surface hail precipitation. The following is a summary of key findings:

1. CCN concentration influenced the characteristics of hydrometeor particles. As CCN concentrations increased, mixing ratios of small liquid particles (i.e., cloud1) increased, while the concentration of large liquid particles (i.e., cloud2 and rain) decreased. Mixing ratios of small ice-phase particles (i.e., pristine ice and snow) decreased, while that of the large ice-phase hydrometeor particles (i.e., aggregates and graupel) increased.

2. Hail number concentration and mixing ratio tended to decrease, but the mean diameter of hail increased with greater CCN concentrations. The surface precipitation of hail in polluted clouds was greater than that in clean clouds and heavily polluted clouds.

3. The contributions of each hydrometeor species to hail changed with different aerosol backgrounds. For liquid water (i.e., cloud1, cloud2, and rain), cloud1 played a great role in both clean clouds and polluted clouds, but rain made more of a contribution to hail in heavily polluted clouds. For ice-phase hydrometeors (i.e., aggregates, graupel, snow, and pristine ice), aggregates make the greatest contribution to hail formation in all cases. The contribution of liquid hydrometers to hail formation was greater than that of the ice-phase hydrometeor particles in clean clouds. However, in polluted and heavily polluted clouds, the contributions of ice-phase particles were close to that of liquid particles to hail.

4. Higher CCN concentrations caused the contribution of cloud1 to hail formation to decrease while the contribution of aggregates to hail increased.

5. The addition of CCN concentrations led to the decrease of total surface accumulated precipitation. However, the contribution of ice-phase precipitation to the total precipitation increased with greater CCN concentrations.

ACKNOWLEDGMENTS

This work was partially supported by the National Natural Science Foundation of China (Grant No. 40875080, 40875002) and Ministry of Science and Technology of China (Grant No.2006BAC12B01-01). The authors also wish to thank Stephen M. Saleeby for providing RAMS model code.

REFERENCES

Flossmann, A.I., Wobrock, W., 2010. A review of our understanding of the aerosol–cloud interaction from the perspective of a bin resolved cloud scale modelling. Atmos.Res. 97,478-497.

Jirak, I., Cotton, W., 2006. Effect of air pollution on precipitation along the Front Range of the Rocky Mountains. J. Appl. Meteorol. 45(1), 236-245.

Ohashi, Y., Kida, H., 2000. Effects of Urban Renewal in the Keihanshin Region on local meteorological conditions: Numerical experiments. Proceedings of Annual Meeting of Enviromental Systems Research. 28,339-344

Rosenfeld, D., 1999. TRMM observed first direct evidence of smoke from forest fires inhibiting rainfall. Geophys. Res. Lett. 26(20), 3105-3108.

Saleeby, S. M., Cotton, W. R., 2004. A large-droplet mode and prognostic number concentration of cloud droplets in the Colorado State University Regional Atmospheric Modeling System (RAMS). Part I: Module descriptions and supercell test simulations. J. Appl. Meteorol. 43(1), 182-195.

Saleeby, S. M., Cotton, W. R., 2005. A Large-Droplet Mode and Prognostic Number Concentration of Cloud Droplets in the Colorado State University Regional Atmospheric Modeling System (RAMS). Part II: Sensitivity to a Colorado Winter Snowfall Event. J. Appl. Meteorol. 44, 1912-1929.

Shepherd, J.M., Burian, S.J., 2003. Detection of urban-induced rainfall anomalies in a major coastal city. Earth Interactions. 7, 1-17.

Van den heever, S.C., Carrió, G.G., Cotton, W.R., DeMott, P.J., Prenni, A.J., 2006. Impacts of nucleating aerosol on Florida storms. Part I: mesoscale simulations, J. Atmos. Sci. 63, 1752-1775.

Warner, J., Twomey, S., 1967. The production of cloud nuclei by cane fires and the effect on cloud droplet concentration. J.Atmos.Sci. 24(6), 704-706.

Yin, Y., Levin, Z., Reisin, T., Tzivion, S., 2000. The effects of giant cloud condensation nuclei on the development of precipitation in convective clouds—a numerical study. Atmos.Res. 53(1-3), 91-116.

A NUMERICAL STUDY OF THE SENSITIVITY OF TORNADOGENESIS IN SUBTROPICAL SUPERCELL STORMS TO MICROPHYSICAL DROP SIZE DISTRIBUTION

Dr. Kailin Zheng , Dr. Baojun Chen
Nanjing University, School of Atmospheric Sciences, 22 Hankou Road, Nanjing, 210093 China

1. INDRODUTION

Significant progress has been made in our understanding of supercell storms and tornadogenesis in the past few decades (e.g., Rotunno and Klemp 1985; Wicker and Wihelmson 1995; Markowski 2002; Straka et al. 2007; Makowski et al. 2008). However, Markowski and Richardson (2009) have pointed out that the importance of microphysical differences among various supercells and how those differences arise is still a poorly understood aspect which should be paid more attention to. Using the U.S. National Center for Atmospheric Research (NCAR)/National Centers for Environmental Prediction (NCEP) reanalysis data with grid spacing of 200 km and at 6 h interval, Brooks et al. (2003) examined the atmospheric environments associated with significant severe thunderstorms and tornadoes at the global scale. Their results showed that the subtropical southeastern China area was also a potential region favorable for the formation of tornadoes. As we know, supercell clouds developing over different regions with different climate characteristics are expected to have different microphysical characteristics. Thus, considering the different microphysical characteristics of supercells developed in U.S. Great Plains and subtropical regions in China and the reality that little is knew about tornadogenesis in Southeastern China, Various idealized simulations using a single sounding as initial background for storm are performed to determine the sensitivity of tornadogenesis in subtropical supercell storms to the microphysical drop size distributions (DSDs).

2. SOUNDING

The storm environment for the present study is defined by a sounding associated with the 8 July 2003 Anhui supercell storm. This storm developed over northern Anhui province, eastern China, and intensified into a supercell around 1500 UTC 8 July. After then, a tornado occurred in Wuwei County around 1520 UTC. Considering the availability of a proximity sounding, the sounding used for the idealized experiments was generated by the ARPS 3-km simulation. Following Dawson et al. (2010), the model sounding was extracted at 1200 UTC in simulated time at a grid point that was determined to be more representative of the unstable inflow region of the storms during the early stages of their tornado-producing phase. As shown in Fig. 1b, this extracted sounding has a similar temperature and wind profiles to the observed sounding of Anqing (Fig.1a) at 1200 UTC 8 July 2003, the nearest upper air observation station available in this area, about 150 km southwest of Wuwei, but the dew-point and moisture profiles are significantly different. Compared with the observed sounding, the extracted sounding has a drier warm layer at the middle and low levels. The mixing ratio of water vapor at 600 hPa is 6 g kg^{-1} for the observed sounding versus 3.3 g kg^{-1} for the extracted sounding, and corresponding relative humidity is 65% and 40%, respectively. In our simulations, the presence of the mid- and low-level dry air plays a very important role in determining cold pool strength and

storm development. With the absence of this dry layer, the sounding was found to be unable to sustain tornadogenesis in the model.

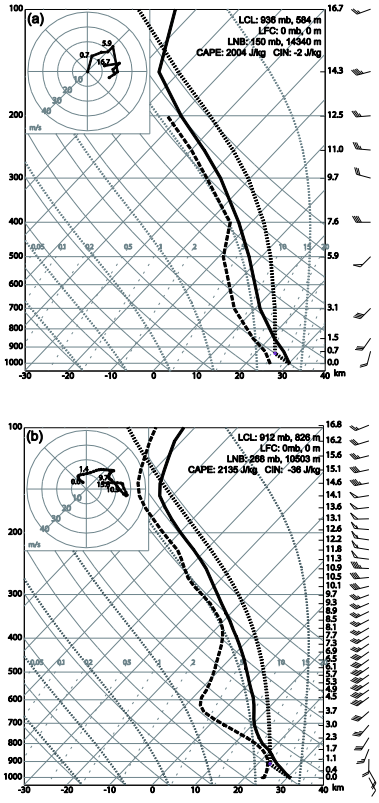

FIG. 1. (a)Observed sounding at Anqing on 8 July 2003 at 1200 UTC; (b) model extracted sounding at 1200 UTC from the 3-km experiment in the inflow region of the simulated supercell storms.

3. EXPERIMENT DESIGN

Snook and Xue (2008, hereafter SX08) showed that supercell tornadogenesis was very sensitive to the intercept values of rain and hail DSDs. Here, we further investigate the role of these two intercept parameters in determining tornadogenesis in subtropical supercells. Table 1 shows the specifications of the intercept parameters for all experiments. Note that the configurations for the first seven runs are similar to SX08 except for the intercept values of snow that are set to 3×10^6 m^{-4} based on LFO83. Case S8 is added here to test effects of snow DSDs, in which the intercept of snow is set to 8×10^6 m^{-4} referred to SX08. The last two runs are performed to assess effects of large hailstones and small raindrops (H2R7) and small hailstones and large raindrops (H6R5) on tornadogenesis. And these two runs have not been performed in SX08.

TABLE 1. Summary of Sensitivity Experiments

Experiment Name	Intercept Parameter (m^{-4})		
	Rain	Hail	Snow
CNTL	8×10^6	4×10^4	3×10^6
H2	8×10^6	4×10^2	3×10^6
H6	8×10^6	4×10^6	3×10^6
R5	8×10^5	4×10^4	3×10^6
R7	8×10^7	4×10^4	3×10^6
H2R5	8×10^5	4×10^2	3×10^6
H6R7	8×10^7	4×10^6	3×10^6
H2R7	8×10^7	4×10^2	3×10^6
H6R5	8×10^5	4×10^6	3×10^6
S8	8×10^6	4×10^4	8×10^6

Previous studies (e.g., Lerach et al. 2008; SX08) have shown that tornadoes within a supercell storm can be simulated successfully using the horizontal grid spacing of ~100 m. For all experiments in this work, the horizontal grid spacing is 100 m and the vertical grid is stretched from 10 m near the ground to roughly 500 m at the model top. The domain is $64\times64\times20$ km^3 in size with 81 vertical levels. Free-slip lower boundaries and radiative lateral boundaries conditions are adopted. Convection was initialized with a warm thermal bubble of 4 K maximum perturbation centered 1.5 km above the ground, with horizontal and vertical radii of 10 and 1.5 km, respectively. Before initialization, a constant wind of u=10 m s^{-1} and v=6 m s^{-1} is subtracted from the sounding to keep the simulated storm within the domain. All simulations were run out to 3 h. The large and small time step sizes are 0.2 s and 0.1 s, respectively.

4. PRELIMINARY RESULTS

4.1 Storm Evolution

From the plots of storm (radar reflectivity and horizontal winds at 2km level) at every time step (not shown here), it is easy to find that before 1800s the storms simulated in

various runs present quite similar structure and intensity. The initial storm forms and then splits into a right-mover and a left-mover as observed from radar figures. Then, significant differences develop quickly between experiments. Simulated storm in CNTL is quite like what we observed (Fig.2 and Fig.3a). It presents a typical classic supercell structure and characteritics. Results in S8 (Fig.3b) turn out to be qualitatively similar with those of CNTL (Fig.3a), though the storm simulated in S8 takes more time to evolve into its mature phase, and its duration is longer. It's identical with what SX08 has pointed out: the change of DSD of snow does not affect the simulation results qualitatively.

From a detailer view of the structures of simulated storms in other experiments when they are in their mature phase (Fig.3), obvious "hook" echoes with "V" shape inflow region to their southeast are easily found in various simulations. However, initiated in a same horizontal homogeneous environment, the shape and evolution of these "hook" echoes are quite different among various simulations(Fig.3). Thus, the structure of supercell storm simulated is sensitive to various DSDs. Compared with the structures in H2 (Fig. 4c), R7 (Fig. 4f) and H2R7 (Fig. 5h), it is very interesting that the shape of storm in H2R7 is more similar with the result of R7. It might imply that the structure and intensity of storms simulated are more sensitive to DSDs of rain.

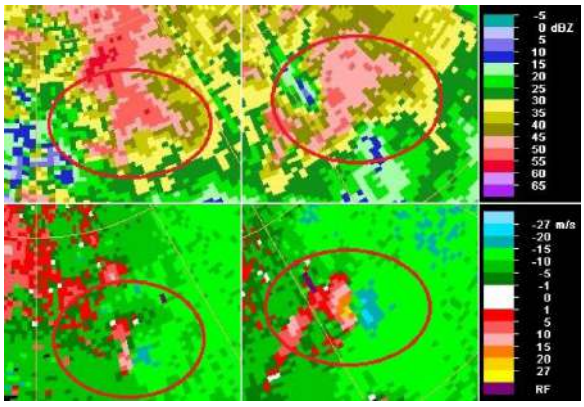

FIG. 2. The 0.5°-tilt radial velocity (m s^{-1}) (top) and reflectivity (dB*Z*) (bottom) from the Hefei radar at 1455 UTC (left) and 1529 UTC (right). North is up. Radar is situated at the northwest direction of the image. Stronger regions of cyclonic shear are shown within the white circles. The inflow region of the storm and the location of the tornado are roughly denoted by the black solid circle and dashed circle, respectively.

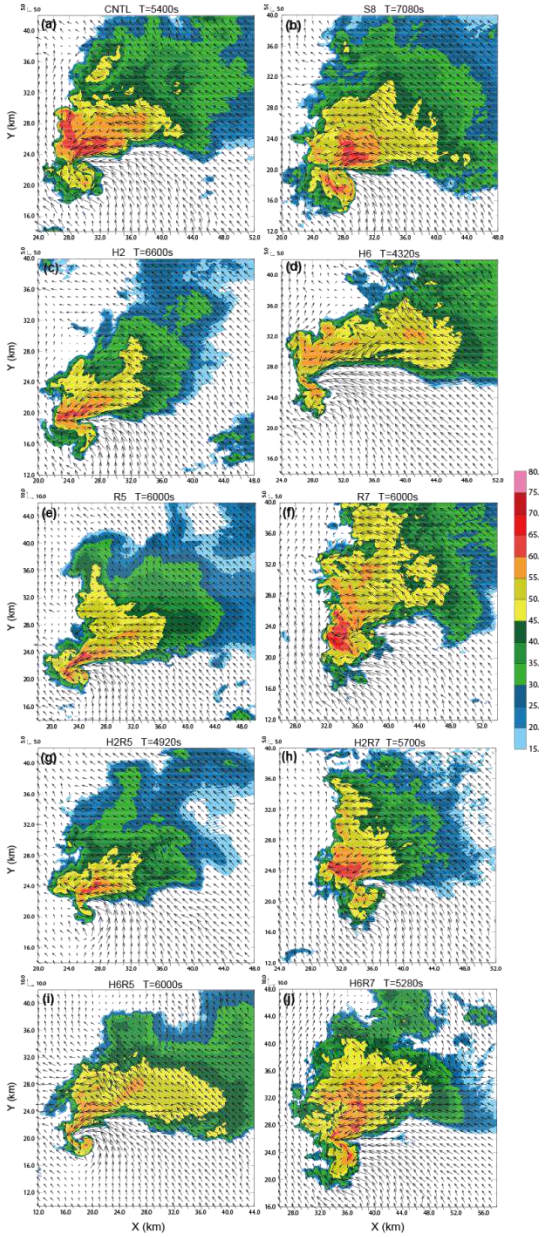

FIG. 4. Radar reflectivity (color shaded, dB*Z*) and horizontal storm-relative winds at 2 km AGL (vectors, m s^{-1}) for (a) CNTL, (b)S8, (c) H2, (d) H6, (e) R5, (f) R7, (g) H2R5, (h) H2R7, (i) H6R5, and (j) H6R7 at the time when the simulated storm is at mature phase. Notice that the wind scales of R5, H6R5 and H6R7 are different from those of others.

4.2 Precipitation Pattern

Accumulated surface rain fall integrated over the first 2 h of simulation are show (Fig. 4). Contours are shown in 25mm increments beginning at 25mm. Maximum values are more than 300 mm for both R5 and H2 runs and are more than twice the maximum content for the H6R7 run. The largest accumulated surface rain contents for R7 and H6 are also much less than those of R5 and H2. The rain falls for CNTL and S8 are moderate. A conclusion can be drawn here that in simulations where DSDs favor large hydrometers may result more rain falls at surface. Moreover, with further analyses of the results of H2R5 and H2R7, the maximum values of these two runs are both a little less than 300mm, larger than that of R7 run. Obviously, the location of surface precipitation is determined by the evolution of the storm which has been shown to vary with various microphysical PSDs as well.

4.3 Cold Pool

Past studies have shown that the microphysical DSDs can affect the intensity of cold pool and then the interaction between the cold pool and the updraft is very important to the development of the storm, so efforts are also made to explore the characteristic of cold pools of various simulated storms in our study. Time series of total cold pool areas (Fig.5a), minimum perturbation potential temperature (Fig.5b) and mean perturbation potential temperature at surface (Fig.5c) are shown. Total surface cold pool area is defined as the sum of the area of all grid squares with $\theta_e' < -1K$. Total surface cold pool area for each run increases after 1800 s. However, the increase rate is much greater in R7 and H6R7, and by the end of 2 h simulation, the cold pools in R7 and H6R7 are almost 2.5 times the size of that in R5 and H6R5, and roughly 3 times the size of that in H2R5. Besides of larger areas the cold pool of simulated storms in R7 and H6R7 cover, the strengths of their cold pools are also much stronger than those in R5 and H2R5. Evidently from Fig.5b and Fig.5c, the minimum and mean surface θ_e' within cold pool of R7, and H6R7 is more than 4 K colder than those for R5 and H2R5 runs. These results make physical sense as smaller raindrops with larger surface areas can result more evaporation cooling.

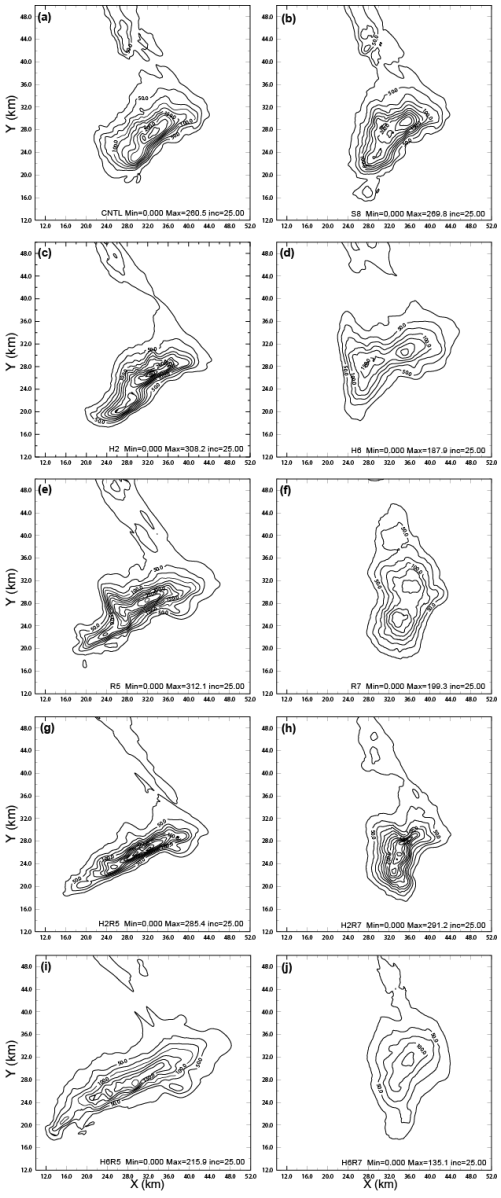

FIG. 4 Accumulated surface rain fall integrated over the first 2 h of simulation for (a) CNTL, (b)S8, (c) H2, (d)H6, (e) R5, (f) R7, (g) H2R5, (h) H2R7, (i) H6R5, (j) H6R7.

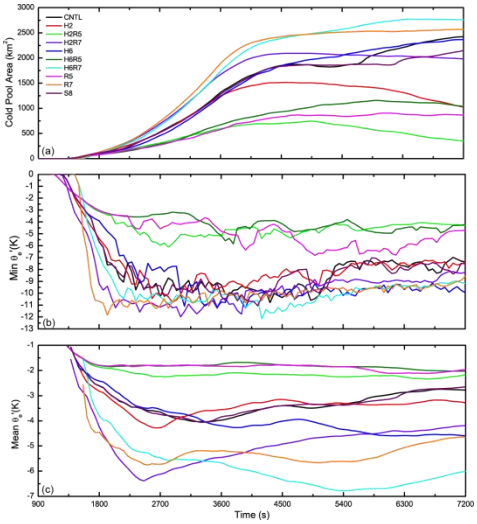

FIG. 5. Time series of (a) total surace cold pool ares, (b) minimum pertubation potentail temperature at surface, and (c) mean pertubation potential temperature within cold pool for each simualtion of various micophysical PSDs.

4.4 Microphysical Effects

In SX08, they have also pointed out that the major causes of the differences of cold pool strength among various experiments are by the processes of melting of hails and the evaporation of rain drops. Similar budget analyses as in SX08 are also performed in our study. The area below 5 km AGL and where vertical velocity w is < -0.5 m s^{-1} is chosen as downdraft region for this budget analysis and it is performed from 3600s to 7200s. The total mass converted from one species to another is calculated at each time step and multiplied by the latent heat corresponding to these various microphysical processes then outputted every 15s. This budget analysis is performed among all sensitivity experiments above except S8 since it is quite similar with the results of CNTL.

Referring to results of budget analyses, we find two main microphysical processes which contribute to cold pool formation most. Similar with SX08, the largest contribution comes from the evaporation cooling and the second largest is from the hails/graupel melting. Contributions from other processes are negligible since they are more than one order of magnitude smaller than those of two main terms mentioned. These two main terms of eight sensitivity experiments are divided by those of CNTL to explore the DSDs effects on these two terms and then the strength of cold pool. Time series of these two terms and the total amount are shown in Figure 6.

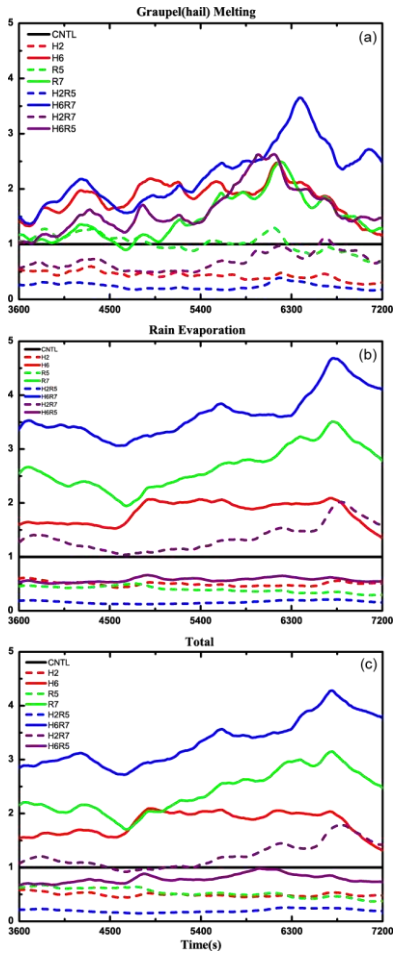

FIG. 6. Contributions of melting of hail/graupel (a), evaporation of rain drops (b) to cold pool formation and then the ratio of total amounts compared with CNTL (c). Y-axes of these plots are all unitless ratio.

Similar with the results in SX08, differences of melting cooling among various simulations (Fig.6a) are less pronounced than evaporation cooling (Fig.6b). The ratios are under 1, which means the total amounts of hail melting are less in H2, H2R5 and H2R7 than that in CNTL run whereas more melting cooling result in H6, H6R5 and H6R7. And little change in the melting

cooling is obtained by various DSDs of rain (R5 and R7). However, melting cooling in our study differs more significantly among experiments than those in SX08, with the ratio is more than 3 when approaching 6300 s in H6R7. Thus, the melting cooling is more sensitive to DSDs in our study.

In simulations where DSDs favor smaller raindrops (such as R7, H6R7 and H2R7), evaporation cooling is much stronger than that of CNTL and the increasing range is larger in our study than those in SX08 as well. From Fig. 6b, the maximum ratio of evaporation cooling in H6R7 in our study is even more than 4.5, roughly twice of the maximum ratio in SX08. The increasing range of evaporation cooling in R7 and H6 are both larger the corresponding ratios in SX08 as well. This might be related with the moister condition where the storms evolved in our study. More evaporation cooling in H6 is because more hails melt into raindrops. The evaporation cooling of H2R7 is just a little more than that of CNTL. Similar with SX08, the evaporation cooling of H2 and R5 are only about half of that in CNTL. The evaporation cooling of H2R5 is even less. Two reasons could explain this reduction: one is that larger raindrops fall out of the storm faster which limit the time for evaporation; the other is that with the same total amount of water, few larger raindrops form then less total surface areas result which reduce the rate of evaporation.

Seen from the Fig.6c, it is easy to explain why storms in simulations where DSDs favor smaller hydrometeors produce colder cold pools. And evaporation cooling plays more important part in cold pool formation (seen from the curves of melting and evaporation of H6R5). However, there might be other reasons which are not the main concern in our study, thus we pay less attention to them here.

4.5 Tornado Activity

From the analyses above, we check every figure of the simulated storms at 10 m level (radar reflectivity and horizontal wind) during the period when there is a drastic increase in vertical vorticity and correspondingly an abrupt decrease in pressure field at low levels (below 2 km). We make sure the center of the target vortices at 10 m level every minute during this period firstly, then take this location as the horizontal center to find the maximums of both the vertical vorticity and horizontal wind in a 3km×3km area under 2 km level. The maximums are summarized to determine the existence of the sustained tornadic vortices in every simulation. Vortices match the following requirements are considered as sustained tornadic vortices: 1) it is related with a middle-level mesocyclone; 2) the low-level maximum vertical vorticity is larger than 0.3 s^{-1}; 3) the related low-level horizontal wind is stronger than 29 m s^{-1}(>= EF0). Sustained tornadic vortices are found in three simulations: CNTL, R5 and S8. General information is summarized in Table 2. The duration, dimension and intensity of these tornadic vortices are summarized. The horizontal size at 10m AGL is about 1.5km~2km, the maximum vertical vorticity of these tornadic vortices near ground is > 0.3 s^{-1} which is pretty intense. The locations of these tornadic vortices in various runs are not exactly same, but they all locate along their gust fronts which are formed because of the interaction between cold pools and the warm inflows which is in accord with what others found in early studies. Tornadic vortices are only found in the experiments where weak (R5) to moderately intense (CNTL and S8) cold pool is formed. In H6R7 and R7, surface vortices are weak and short lived because of the strong cold pools.

TABLE 2. Summary of tornadic vortices of various sensitivity experments

Experiments

	CNTL	R5	S8
Duration(min)	14	6	14
Horizontal D_{max} (km)	~1.5	~1.8	~1.8
Maximum low-level vertical vorticity (1/s)	0.39	0.35	0.37
Maximum low-level winds (m/s)	45.7	38.8	37.9

Note: Low-level: under 2 km

The tornadic vortex in CNTL begins at 5160s and lasts for about 14 minutes with a maximum low-level wind speed of 45 m s^{-1}, corresponding to EF1 intensity. The maximum vertical vorticity is about 0.39 s^{-1} during this time. And the near-surface vortex in R5 lasts for 6 minutes, a little shorter than that in CNTL, starting at 6600s and the low-level maximum vertical vorticity exceeds 0.35 s^{-1}. However, the maximum low-level wind is weaker in R5 than in CNTL, only about 34 m s^{-1}(EF0). The duration and intensity of this tornadic vortex in R5 are much shorter and weaker than those in SX08, which makes it very interesting to figure out how these differences of results in R5 are formed between SX08 and our study. This might be because of the different initial background where the storm develops. The structure of tornadic vortex in S8 is quite like that in CNTL. The structures of tornadic vortices in CNTL and R5 are shown in Figure 7. The structures and intensities of these vortices are quite different at 10 m AGL in these two simulations.

The trajectories of particles which form these near-surface vortexes are also analyzed. The time of peak tornado intensity is chosen as the reference time. One particle is located at the center of the vortex at 100m AGL and 29 particles are evenly distributed along the circle with the vortex center as the center and the radius of 500m. Then trajectories of these particles are traced back about 20 minutes to find out where these particles are from and how they act to form the near-surface tornadic vortex.

The horizontal cross-sections at 100m for CNTL and R5 are shown in figure 7b and figure 7d. Trajectories for CNTL are from two major sources. One is along the black lines; particles originate at about 3km AGL, and then descend cyclonically to surface to form the near-surface vortex. The other is along the dark gray lines. Particles initially locate at about 0~1km AGL, and then also cyclonically descend to surface to form the vortex. However, things for R5 are a little complicated than CNTL. There are three kinds of trajectories which are distinguished using black, dark gray and light gray lines, respectively: 1) Particles along black lines originate near 100m AGL then travel along a complicate line into the vortex; 2) Particles along the dark gray lines initially locate a little far from the target vortex near the surface then move cyclonically into the vortex; 3) Particles (light gray) from about 3km AGL descend cyclonically to surface to form the vortex. It's easy to find, trajectories to form tornadic vortexes in CNTL and R5 are not identical though quite similar. That makes us to consider, if we want to know better that the formation of tornadic vortex, more efforts should be made to gain more information.

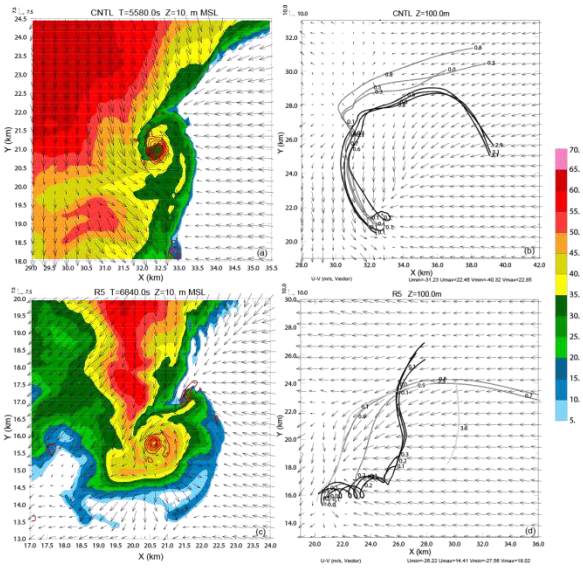

FIG.7. Comparison of CNTL (a) and R5 (c) at the time of peak tornado intensity, plotted are radar

reflectivity (shaded, dBz), wind vectors and vertical vorticity (contours, s^{-1}, minimum value of 0.05s-1). (b) and (d) are the trajectory for particles which form the tornadic vortex of CNTL and R5.

5. SUMMARY AND DISCUSSION

In this work, we have performed high-resolution idealized simulations of the 8 July 2003 Anhui tornadic supercell thunderstorms over the eastern China. This study extended the work of Snook and Xue (2008) to subtropical cases and aimed to further test the impact of microphysical DSD parameters on tornadogenesis in supercell thunderstorms that developed in various climatic regimes. The simulated storm structure, intensity, and cold pool characteristics in response to various intercept values of the DSD in LFO83 single moment scheme have been investigated.

Similarly to existing studies (e.g., Gilmore et al. 2004; van den Heever and Cotton 2004; Snook and Xue 2008), we found that the structure, dynamics, precipitation and evolution of simulated storms developed in subtropical thermodynamic conditions were also highly sensitive to various DSD parameters. When the DSD parameters favor larger (smaller) hydrometeors, weaker (stronger) cold pools result. The reduction in total hydrometeor surface area associated with larger raindrops/hailstones leads to less evaporation and melting, which are the dominant processes affecting the cold pool intensity. In addition, the faster-falling larger hydrometeors reduce the areal coverage of precipitation and the coverage and intensity of the cold pool.

Compared with the CNTL run, evaporation and melting cooling which are considered to be two major processes in cold pool formation and dominant to its intensity differ dramatically among simulations. Generally, when the DSD parameters favor larger (smaller) hydrometeors, weaker (stronger) cold pools result because of the smaller (larger) total hydrometeor surface area which leads to less (more) evaporation and melting. Moreover, through similar budget analyses of microphysical processes in cold pool area as in SX08, it is found that the supercell storm developed in this initial condition is more sensitive to the MP DSDs than those occurred in U.S. Great Plains. Thus MP DSDs have strong influences on the tornadogenesis through their effects on the cold pool. .

Moreover, in practical, various measurements of rain and hail carried out around the world have shown that DSDs vary spatially over a wide range (e.g., Bringi et al. 2003; Rosenfeld and Ulbrich 2003; Sánchez et al. 2009). From observation results, DSD of hail could be approximately considered as an inverse-exponential function, however, the intercept parameters of HSD exist spatial differences. This is because the intercept parameter depends highly upon the thermodynamics of storm: the higher the cloud base temperature of the storm, the larger the N_0 of HSD (Cheng et al. 1985). With warmer cloud base of summer storms in subtropical regime than those in U.S. Great Plains, the HSD is more likely to favor small hydrometeors. For DSD of rain, an inverse-exponential or gamma distribution is usually considered. And the intercept parameter of RSD is also various spatially. Past DSD observations of rain in convections during summer in east China has shown that the DSD of rain in this area has larger intercept and smaller mean diameter (D_m) than those in continental convection in U.S. Great Plain. The PSD of rain is also found different between continental and marine convections (e.g., Bringi et al. 2003). Considering the real situation of DSDs of rain and hail in summer storms in east China, combined with the simulation results above, thus it might be explained why though past work have

showed that the subtropical southeastern China area is potentially a favorable region for tornadoes (Brooks et al. 2003), the frequency of sever tornado broken out and observed is much lower than in the U.S Great Plain. It is practically less favorable for tornadogenesis in southeast China because of the larger intercept parameter of PSDs of rain and hail which favor smaller hydrometeors, and storms develop in this area is more sensitive to DSDs variations.

There are still other reasons which have not been taken into account here, such as the aerosol conditions which are considered as active CCN to change the DSDs. And the pollution conditions are obviously different among different regions. Thus, more work is still needed to gain a further and better understanding of sensitivity of supercell tornadogenesis to MP DSDs. This is our future plan.

6. BIBLIOGRAPHY

Bringi, V. N., V. Chandrasekar, J. Hubbert, E. Gorgucci, W. L. Randeu, and M. Schoenhuber , 2003: Raindrop size distribution in different climatic regimes from disdrometer and dual-polarized radar analysis. *J. Atmos. Sci.*, **60**, 354–365.

Brooks, H. E., J. W. Lee, and J. P. Craven, 2003: The spatial distribution of severe thunderstorm and tornado environments from global reanalysis data. *Atmos*. *Res*., *67–68*, 73–94.

Dawson, D. T., II, M. Xue, J. A. Milbrandt, M. K. Yau, 2010: Comparison of evaporation and cold pool development between single-moment and multimoment bulk microphysics schemes in idealized simulations of tornadic thunderstorms. *Mon. Wea. Rev*., **130**, 1692–1721.

Gilmore, M. S., J. M. Straka, and E. N. Rasmussen, 2004a: Precipitation and evolution sensitivity in simulated deep convective storms: Comparisons between liquid-only and simple ice and liquid phase microphysics. *Mon.Wea. Rev*., **132**, 1897–1916.

Lerach, D. G., B. J. Gaudet, and W. R. Cotton, 2008: Idealized simulations of aerosol influences on tornadogenesis. *Geophys. Res. Lett*., **35**, L23806, doi:10.1029/2008GL035617.

Markowski, P. M., 2002: Hook echoes and rear-flank downdrafts: a review. *Mon. Wea. Rev.*, **130**, 852-876.

—, Y. P. Richardson, E. N. Rasmussen, J. M. Straka, R. P. Davies-Jones, and R. J. Trapp, 2008: Vortex Lines within Low-Level Mesocyclones Obtained from Pseudo-Dual-Doppler Radar Observations. *Mon. Wea. Rev.*, **136**, 3513–3535.

—, and —, 2009: Tornadogenesis: Our current understanding, forecasting considerations, and questions to guide future research. *Atmos. Res*., **93**, 3–10.

Rosenfeld, D., and C. W. Ulbrich, 2003: Cloud Microphysical Properties, Processes, and Rainfall Estimation Opportunities. *Meteorol. Monogr*., **30**, 237–258.

Rotunno, R., and J. B. Klemp, 1985: On the rotation and propagation of simulated supercell thunderstorms. *J. Atmos. Sci.*, **42**, 271-292.

Sánchez, J. L., B. Gil-Robles, J. Dessens, E. Martin, L. López, J. L. Marcos, C. Berthet, J. T. Fernández, and E. García-Ortega, 2009: Characterization of hailstone size spectra in hailpad networks in France, Spain, and Argentina. *Atmos. Res*., **93**, 641–654.

Snook, N., and M. Xue, 2008: Effects of microphysical drop size distribution on tornadogenesis in supercell thunderstorms. *Geophys. Res. Lett*., **35**, L24803, doi:10.1029/2008GL035866.

Straka, J. M., E. N. Rasmussen, R. P. Davies-Jones, and R. P. Markowski, 2007: An observational and idealized numerical examination of low-level counter-rotating vortices toward the rear flank of supercells. *E. J. Severe Storms. Met.* **2(8),** 1-22.

van den Heever, S. C., and W. R. Cotton, 2004: The impact of hail size on simulated supercell storms. *J. Atmos. Sci*., **61**, 1596–1609.

Wicker, L.J., and R. B. Wihelmson, 1995: Simulation and analysis of tornado development and decay within a three-dimensional supercell thunderstorm. *J. Atmos. Sci.*, **52**, 2675-2703.

Acknowledgments

Thank Dr. Xiaoding Yu for providing radar data. We also thank Dr. Kun Zhao and Mr. Long Jin for their assistance with analysis of radar data. This work was primarily supported by the National Natural Science Foundation of China under Grants 41175118 and 40775005. Research results presented in this paper were partially supported by the R&D Special Fund for Public Welfare Industry (meteorology) by Grants GYHY200906003 and GYHY201006004. Simulations were performed on the IBM Blade cluster system in the High Performance Computing Center (HPCC) of Nanjing University.

INVESTIGATION OF LOCAL, MEAN SHEAR EFFECTS AT THE STRATOCUMULUS TOP USING DIRECT NUMERICAL SIMULATIONS

Juan Pedro Mellado[1], Bjorn Stevens[1] and Heiko Schmidt[2]
[1]Max Planck Institute for Meteorology, Hamburg 20146, Germany
[2]Brandenburg University of Technology, Cottbus 03046, Germany

1 INTRODUCTION

The role that the local dynamics of the cloud top play in the transition from the stratocumulus to the shallow cumulus regimes is still uncertain and parametrizations thereof need to be improved [1]. The problem is complex, it combines turbulence, moist convection, stable stratification, radiation and microphysical processes, and it can be studied from different points of view [2–6]. We approach it here from the fluid-dynamics perspective of turbulent mixing across a density interface, which is in itself still a matter of active research [7, 8]. We investigate the interaction between the buoyancy reversal caused by the evaporative cooling and the local turbulent mixing, specifically the possibility of the so-called cloud-top entrainment instability [9, 10].

Recent work using direct numerical simulations of the cloud-top mixing layer have shown that buoyancy reversal *alone* cannot be responsible for the cloud-top break-up and regime transition because the turbulence created by this process is too weak [11]. Equally, the corresponding mean entrainment rates are too small, about 0.2 mm s^{-1}, less than one order of magnitude smaller than the range $3-5$ mm s^{-1} measured in field campaigns [3]. It indicates that turbulent mixing driven by other mechanisms should be investigated.

In this paper, we study the interaction between a steady, horizontal mean shear and buoyancy reversal in the cloud-top mixing layer. We use direct numerical simulations to faithfully represent the difference between the shear-free case, dominated by molecular processes, and the inviscid, shear-dominated case. We use the first research flight RF01 from the DYCOMS-II field campaign as reference. As explained below, results show that turbulence intensities, although stronger than in the shear-free case, are still weak and the cloud top is not broken. The inversion remains thin, between a fraction of a meter and several meters depending on the velocity difference across the inversion, and the entrainment velocities remain substantially below 1 mm s^{-1}.

2 FORMULATION

The idealized numerical experiment is sketched in figure 1 and explained there.

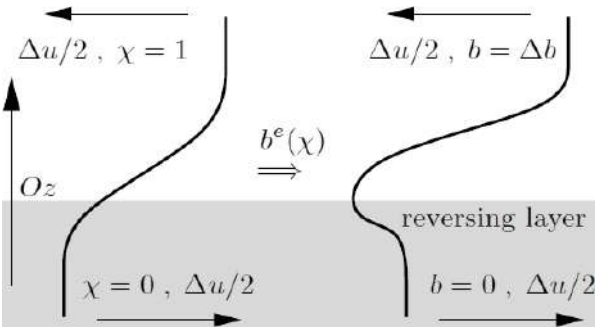

Figure 1: The cloud-top mixing layer consists of a region of dry, warm air, representing the free-atmosphere, on top of a region of moist, relatively cold air, representing the cloud (gray area). The mean vertical structure of the system in terms of the mixture fraction χ (equal to the normalized enthalpy and total water content) and the buoyancy b is shown here. Each of the two layers is assumed to have a well-defined homogeneous state far enough from the cloud boundary. The buoyancy difference Δb across the inversion measures the strength of the stratification. The velocity difference Δu across the inversion is created, for instance, by large-scale circulations.

We use a two-fluid (or bulk) formulation based on a continuum description of the liquid phase under equilibrium conditions. Despite this strong simplification of the cloud bound-

ary, this formulation provides a leading-order solution to the problem of the cloud-top entrainment instability, and an upper bound to the entrainment velocity that might be caused by buoyancy reversal alone. Corrections due to the settling velocity, which moves the droplets away from the dry air above inducing their evaporation, and corrections due to finite evaporation rates, which slow down the formation of cold, heavy parcels of fluid mixture, tend to weaken the strength of the buoyancy reversal; hence, the conclusion that evaporative cooling effects are too weak to break the cloud remains valid. The two-fluid formulation leads to the Boussinesq equations with a buoyancy term b that is given by an analytical, non-linear function $b^e(\chi)$ (see figure 1). The mixture fraction χ is equal to the normalized enthalpy and total water content, obeys the standard advection-diffusion equation, and can be defined, without loss of generality, to be 0 inside of the cloud and 1 in the upper, cloud-free region [12]. The set of parameters defining the problem are $\{\Delta u\,, \Delta b\,, \kappa\,, \nu\,, b_s, \chi_s\}$. The Prandtl number ν/κ, the ratio between the kinematic viscosity and the scalar diffusivity, is set to one. The last two parameters characterize the buoyancy reversal in terms of the saturation anomaly $b_s < 0$ at saturation conditions χ_s. The thermodynamic state of the RF01, DYCOMS-II case yields $b_s/\Delta b = -0.031$ and $\chi_s = 0.09$ [3]. The third and last non-dimensional parameter is

$$Re_0 = (\Delta u)^3/(\nu \Delta b)\ , \qquad (1)$$

a reference Reynolds number. The value that we can reach, based on our computational resources, is $Re_0 \simeq 3.3 \times 10^4$, which correspond to a velocity difference of about 0.5 m s^{-1} for the DYCOMS-II case, where $\Delta b \simeq 0.25$ m s^{-2}. These values of Δu, though moderate, do cover part of the range found in the cloud top, where velocities up to 1 m s^{-1} are typical, and more importantly, are shown to be large enough to describe major aspects of the interaction between evaporative cooling and steady, mean shear.

3 RESULTS

Given a dry, stably stratified shear layer with an initial thickness small enough for the Kelvin-Helmholtz instability to develop, a state is finally reached in which turbulence dissipates and molecular diffusion dominates thereafter (they are self-limiting). This final state is characterized by a bulk Richardson number

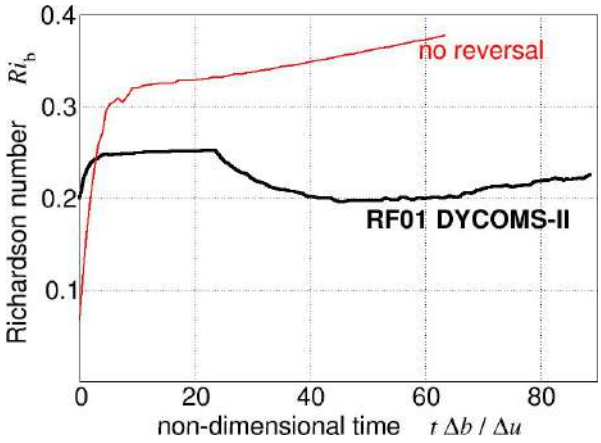

Figure 2: Evolution of the bulk Richardson number, equation (2), for the thermodynamic state of the RF01, DYCOMS-II case. The time scale is $\Delta u/\Delta b \simeq 2$ s.

$$Ri_b = \delta_\omega \Delta b/(\Delta u)^2 \qquad (2)$$

about 1/3, having defined the vorticity thickness as usual by $\delta_\omega = \Delta u/(\partial\langle u\rangle/\partial z)_{\max}$ (see figure 2 and, e.g., Ref. [13] and references therein). In the moist system that we investigate here, the buoyancy reversal will modify this scenario. However, buoyancy reversal effects are known to be small compared with the stratification ($|b_s|/\Delta b \ll 1$) and, hence, it is appropriate to conjecture a characteristic thickness

$$h_S = (\Delta u)^2/(3\Delta b) \qquad (3)$$

for the inversion. Since $\delta_w/h_S = 3Ri_b$, it can be inferred form figure 2 that indeed the sheared cloud-top develops an inversion with a depth $\delta_\omega \simeq 0.6 - 0.8 h_S$ after a relatively short transient of about $10\Delta u/\Delta b$. The difference between the dry and the moist cases is that the latter, because of the buoyancy reversal, develops a turbulent convective boundary layer inside the cloud that continuously perturbs the inversion on top. Such a state is shown in figure 3, as obtained from the direct numerical simulations. We are interested in the evolution of the system during this stage.

Qualitatively, the vertical structure of the system shown in figure 3 is very similar to that of the shear-free case discussed in Ref. [11],

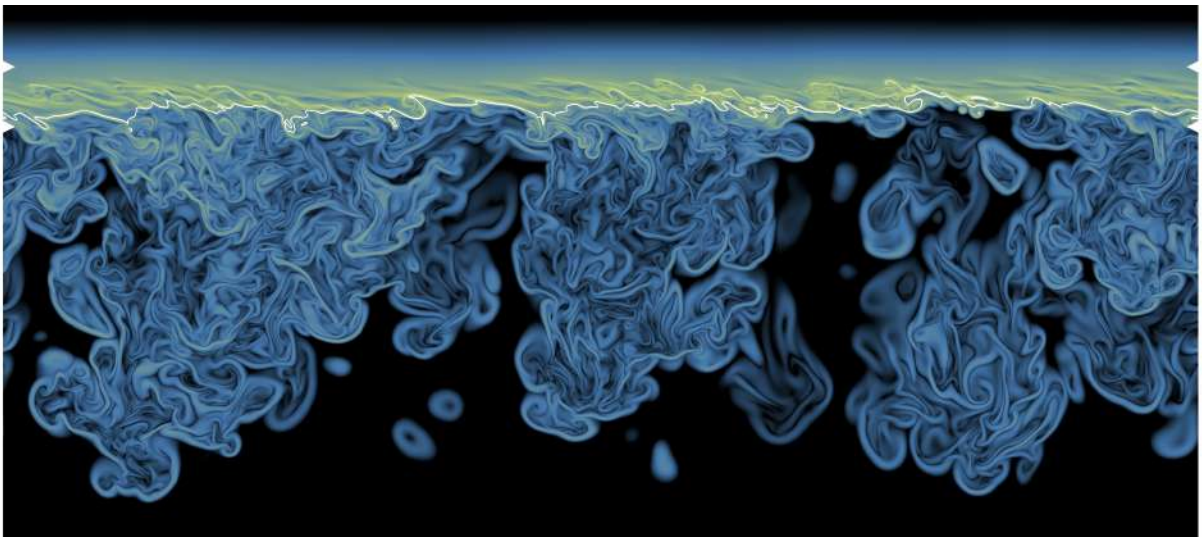

Figure 3: Logarithm of $|\nabla\chi|^2$ inside a vertical plane. Color code varying in the sequence black-blue-white between the values $10^{-4}/h_S^2$ and $10^4/h_S^2$, where h_S is defined by (3). The side triangular marks correspond to $z = \pm h_S/2$ with respect to the point of maximum shear production, providing therefore a measure of the inversion thickness. The thin, convoluted white line indicates the saturation surface $\chi(\mathbf{x}, t) = \chi_s$. The grid is $2048 \times 2048 \times 1664$ and the physical size is 6.6 m in the two horizontal directions.

in particular the cloud-top remains flat and does not break. Quantitatively, however, there are differences. The non-dimensional parameter controlling those differences is the Reynolds number Re_0 defined by (1). Once Re_0 is large enough, the mean shear, instead of the molecular transport, dominates the system. This is observed for instance in a strong peak of the shear production term $-\langle u'w'\rangle\partial\langle u\rangle/\partial z$ forming next to the inversion, significantly larger than the maximum of the buoyancy production term $\langle b'w'\rangle$ (not shown).

However, this transition of regimes from molecularly to mechanically dominated with increasing Re_0 occurs somehow slowly. As already mentioned above, the values that we can reach, based on our computational resources, are $\Delta u \simeq 0.5$ m s^{-1}. We find that there is still a contribution from molecular transport to the entrainment velocity w_e of about 10%. The reason is that the inversion remains relatively thin, h_S is about 0.33 m, and this thickness, instead of the turbulent integral scale within the cloud, controls the local mixing inside the inversion. This relatively limited effect of Δu is also manifest in the magnitude of the entrainment velocities, about 0.3 mm s^{-1} for the cases $\Delta u = 0.5$ m s^{-1} considered here. This is about twice the entrainment velocity obtained in the shear-free case, and scaling laws suggest that w_e grows proportionally to Δu, but it is still one order of magnitude smaller than measurements at the stratocumulus top.

4 Conclusions

The results summarized above show that, for typical atmospheric conditions, turbulence generated locally by evaporative cooling in the presence of a steady, horizontal mean shear is stronger than in the shear-free case but still small compared to measurements, and in particular too weak to break the cloud top. The inversion remains relatively thin and therefore the molecular transport remains relevant for a non-negligible interval of Δu. A crossover value around 0.5 m s^{-1} is found, for which 10% of the entrainment velocity is due to molecular effects; lower values of Δu lead to larger contributions and *vice versa*. These results suggest that turbulent mixing induced by other processes (e.g. unsteadiness, radiatively driven turbulence or large-scale dynamics) are more likely to control the evolution of the cloud top.

Partial financial support was provided by the Deutsche Forschungsgemeinschaft, SPP

1276 Metström program, and by the National Science Foundation under Grant No. NSF PHY05-51164. Computational time was provided by the German Climate Computing Centre in Hamburg.

5 BIBLIOGRAPHY

[1] B. Stevens. Entrainment in stratocumulus-topped mixed layers. *Q. J. Roy. Meteorol. Soc.*, 128:2663–2690, 2002.

[2] S. K. Krueger. Linear eddy modeling of entrainment and mixing in stratus clouds. *J. Atmos. Sci.*, 50:3078–3090, 1993.

[3] B. Stevens, D. H. Lenschow, I. Faloona, C.-H. Moeng, D. K. Lilly, B. Blomquist, G. Vali, A. Bandy, T. Campos, H. Gerber, S. Haimov, B. Morley, and C. Thorton. On entrainment rates in nocturnal marine stratocumulus. *Q. J. Roy. Meteorol. Soc.*, 129(595):3469–3493, 2003.

[4] M. J. Kurowski, S. P. Malinowski, and W. Grabowski. A numerical investigation of entrainment and transport within a stratocumulus-topped boundary layer. *Q. J. Roy. Meteorol. Soc.*, 135:77–92, 2009.

[5] T. Yamaguchi and D. A. Randall. Cooling of entrained parcels in a large-eddy simulation. *J. Atmos. Sci.*, 69:1118–1136, 2011.

[6] H. Siebert, R. A. Shaw, and Z. Warhaft. Statistics of small-scale velocity fluctuations and internal intermittency in marine stratocumulus clouds. *J. Atmos. Sci.*, 67: 262–273, 2010.

[7] H. J. S. Fernando. Turbulent mixing in stratified fluids. *Annu. Rev. Fluid Mech.*, 23:455–493, 1991.

[8] G. N. Ivey, K. B. Winters, and J. R. Koseff. Density stratification, turbulence, but how much mixing? *Annu. Rev. Fluid Mech.*, 40:169–184, 2008.

[9] J. W. Deardorff. Cloud top entrainment instability. *J. Atmos. Sci.*, 37:131–147, 1980.

[10] D. A. Randall. Conditional instability of the first kind upside-down. *J. Atmos. Sci.*, 37:125–130, 1980.

[11] J. P. Mellado. The evaporatively-driven cloud-top mixing layer. *J. Fluid Mech.*, 660:1–32, 2010.

[12] J. P. Mellado, B. Stevens, H. Schmidt, and N. Peters. Two-fluid formulation of the cloud-top mixing layer for direct numerical simulation. *Theor. Comput. Fluid Dyn.*, 24:511–536, 2010. doi: 10.1007/s00162-010-0182-x.

[13] K. A Brucker and S. Sarkar. Evolution of an initially turbulent stratified shear layer. *Phys. Fluids*, 19(105105):1–18, 2007.

SIZE-RESOLVED WATER-SOLUBLE IONIC COMPOSITIONS OF AEROSOL PARTICLES AT A HIGH MOUTAIN IN SOUTHEAST CHINA

Y. Qin, Y. Yin, B. Wen and K. Chen
Nanjing University of Information Science & Technology, Key Laboratory for Atomspheric Physics and Environment of China Meteorological Administration, 219 Ningliu Road, Nanjing 210044, China

1. INTRODUCTION

Over the past few decades, rapid development of industrialization and urbanization process in China leads to a significantly increase in atmospheric aerosol particles. Atmospheric aerosol particles can influence climate directly by modification the income solar radiation and indirectly by interact with cloud microphysical properties [1-3]. In recent years, the size distribution of aerosol particles and the constituent components of source apportionment are always a focus of atmospheric chemistry research. Amazon basin aerosol inorganic and organic constituents of the mass concentration in the period of the different seasons, and with the distribution characteristics of particle size change are closely related to the weather conditions [4]. A large number of observation and analysis of aerosol composition in domestic mainly concentrated in big cities [5, 6], less reports on the Alpine atmospheric aerosol composition. Alpine atmospheric aerosol samples collected are with a regional representative [7], because of atmospheric environment less affected by the surrounding local pollution. This paper selects Mt. Huang (1840 m above mean sea level) to analysis the aerosol composition, size distribution characteristics and background sources of pollutants. It help further study the aerosols on cloud formation and microphysical characteristics.

2. MATERIAL AND METHODS

2.1 .SAMPLING SITES

As shown in Fig.1, Mt. Huang is located in the mountainous area of southern Anhui Province (30°08′N,118°09′E), north-south length of about 40km, from east to west 30km, mountain range an area of 1200 km^2, Mt. Huang Scenic area of about 154 km^2. Due to the altitude, the location and the corresponding atmospheric circulation, the climatic characteristics at Mt. Huang is both the Chinese northeast subtropical monsoon characteristics and characteristics of vertical changes in the mountain climate[7]. Observation site is located at the Bright Summit of Mt. Huang (1840m above mean sea level, Fig.1b), during May 23 to September14, 2011. Conventional meteorological element (temperature, pressure, wind speed, wind direction and relative humidity, etc) were measured by Automatic weather station during the observation period.

Fig.1 The sampling location (Mt. Huang, a) and the Bright Summit of Mt. Huang (b)

2.2 AEROSOL SAMPLING AND ANALYSIS

Size-resolved aerosol particles were collected using a MOUDI cascade impactor (MSP Corporation), a flow rate of 10 L/min, Teflon membrane used (47mm). The total 238 effective membrane were collected when the non-rainy aerosol sampling (June 26-July 5), with each time collected about 24h. Membranes were weighed by electronic balance (BSA224S, sartorius) before and after sampling. Aerosol water-soluble ions（cation: Na^+、NH_4^+、K^+、Ca^{2+}、Mg^{2+}，anion：F^-、Cl^-、NO_2^-、NO_3^-、SO_4^{2-} and organic acid: formic acid, acetic acid, oxalic acid）were analyzed with ion chromatography instrument (Metrohm 850).

2.3 TRAJECTORY MODEL

In order to analyze the sources of pollutants, the air mass which affects the sample aerosol was analyzed by the trajectory model. The model is an Eulerian and Lagrangian hybrid computing model (http://www.arl.noaa.gov/HYSPLIT_info.php, Hysplit 4.9) [8]。Trajectory model use the National Centers for Environment Prediction (NCEP) reanalysis meteorological data. Cluster analysis of 17 trajectories is to further study the impact of the different character of the air mass on aerosol composition.

3 RESULTS AND DISCUSSION

Figure 2 shows the total aerosol mass concentration spectrum distribution during the observation period. Aitken nuclei mode has a small peak in diameter of 0.01-0.018μm, which are from the combustion process to produce original aerosol particles and gas molecules by a chemical reaction homogeneous nuclear conversion into secondary aerosol particles. The maximum peak appears in the diameter range of 0.32-0.56μm in accumulation mode with the smaller size range, called “droplet mode”, taking place in non-precipitation clouds or fog [9]. High relative humidity and high frequent clouds lead to the higher aerosol mass concentration of the particle size segment at the Bright Summit of Mt. Huang. The other peak in 1.0-1.8μm was resulted from that high relative humidity (most of RH>80%) could make high concentration of soluble hygroscopic ions (such as sulfate) in “droplet mode” particles grow up [10]. Another reason is that in the relative humidity above 80% particle size cut of percussive sampling will cause some error due to the hygroscopic components, making hygroscopic small particles grow up and collected in the greater size [11]. Besides, there is a small peak in the the diameter range of 10-18μm in coarse particle mode with greater size range.

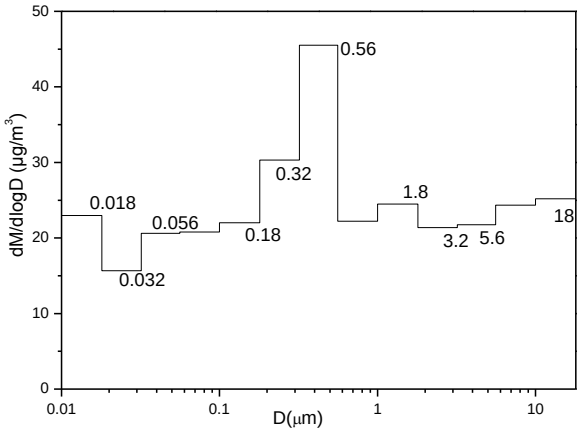

Fig.2 The total aerosol mass distribution during the observation period

The water-soluble ion is the important chemical composition of aerosol. In the mainland, the water-soluble components increase with the particle size decreases. The aerosol water-soluble ions are hygroscopic. It is easy to form fog droplet by hygroscopic growth. The droplet diameter change as the relative humidity varies, thus affecting the optical properties and visibility of the atmosphere, which led to the earth-atmosphere system energy balance. The water-soluble components are the main component of cloud condensation nuclei (CCN) which can influence cloud lifetime and optical properties.

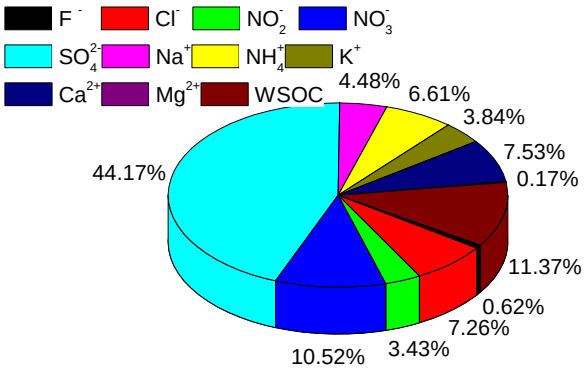

Fig.3 The proportion distribution of the aerosol soluble ions

The aerosol water-soluble ion accounts for 34.2% of the total mass concentration (Fig.3). The average SO_4^{2-} anion concentration (12.3μg/m^3) is the highest, followed by NO_3^- (2.9μg/m^3). The average cation concentration is Ca^{2+} and NH_4^+ were 2.1μg/m^3 and 1.8μg/m^3 respectively. Organic acid accounts for 11.37% of the water-soluble composition.

The ratio of $(NH_4^+ + Ca^{2+})/(NO_x + SO_4^{2-})$ in aerosol particles is 0.65, which indicates that most of the particles are of acidic nature, probably due to the existing a plenty of acidic precursor, such as SO_2 and NO_X in the air. The NO_3^- and SO_4^{2-} mass ratio （NO_3^-/SO_4^{2-}） in the aerosols can be used to compare the contribution to the amount of sulfur and nitrogen in the atmosphere from the stationary sources(such as coal) and mobile source(such as car exhaust)[12]. In this observation period this ratio is 0.89 in the spring and 0.15 in the summer, which indicating that the characteristics of Mt. Huang atmosphere belong to the pollution of coal-burning sulfur oxides. However, in spring the contribution to SO_2 and NO_X from mobile source is higher than in summer, because that an increase in the flow of people and more car emissions around Mt. Huang in the holiday, led to SO_2 and NO_X concentration more.

To understand the mechanisms behind the different nature the particles presented, the aerosol samples obtained during the observation period were categorized into four different types of airflow trajectory which affect the Mt. Huang region (Fig.4). Combined with the weather situation, the long distance transport northern continental air mass (class1 and 2) of high pressure control (weather map omitted) account for 35% in the whole. The track of Class 2 reaches the way ocean before the Mt. Huang region.

The track of Class 3 has shorter transport distance, accounting for 47%. It occurred in the low pressure system, mainly reflecting the impact of local pollution. However, the track of class 4 is mostly in low pressure system affected by the long distance transport southwest continental air mass, up to 18% of the total number of trajectories.

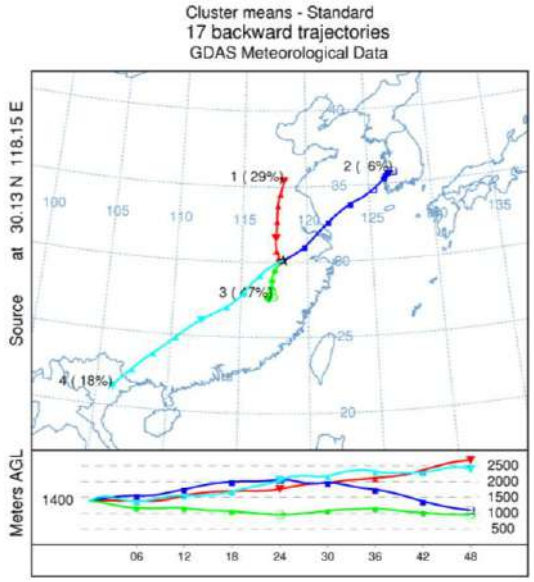

Fig.4 The back trajectory of the air masses during the sampling periods

The arithmetic mean value of soluble ions mass concentration corresponding to each type of tracks reflects the impact of different air massed on the atmospheric aerosol composition at Mt. Huang (Fig.5). It is found that the concentrations of the anthropogenic chemical compositions originated from the local pollution are highest among the three cases. The reason is that under low-voltage system control,

sustained easterly winds continue to transport the pollutant of the Yangtze River Delta and the eastern coast, coupled with stable boundary layer and low surface wind speed, easily lead to pollutant accumulation. As shown in Fig.5, aerosol soluble components generally increased, mainly as SO_4^{2-}、NH_4^{2+} and organic acids. The soluble component mass concentration of PM_{10} is 33.6μg/cm^3. The mass concentration of organic acids is higher, mainly from plant emissions and natural fire [13], because of more vegetation in the eastern coastal than inland.

Influenced of high pressure and the northern continental air mass (N for short), the weather is clear and wind speed is more than 4m/s. It is favor to long distance transmission of the northern sand. Due to the coarse particle deposition on the way, element enrichment factor in fine particles is higher [14] after arrival at Mt. Huang, especially the Ca^{2+}, NO_3^- mass concentration increase.

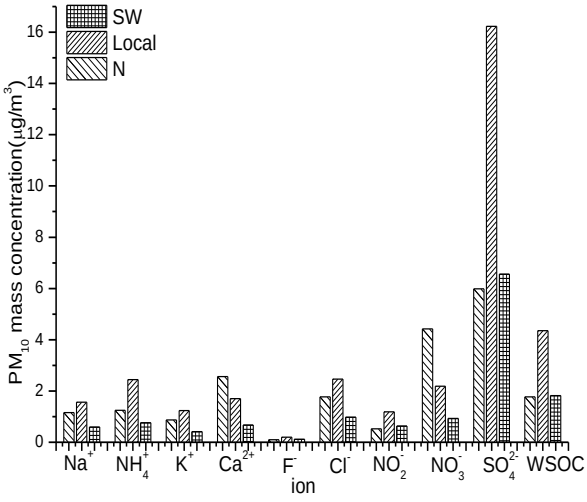

Fig. 5 The mass concentration of ions under different air masses

In contrast, the southern continental air mass (SW for short) causes the lowest soluble aerosol mass concentration (13.5μg/cm^3). Heavy industrial pollutant emissions are less in southwest provinces than the eastern, with the average wind speed more than 6m/s, which led to the low aerosol concentration.

In different weather situation soluble aerosol species mass concentration with particle size changes are in a bimodal distribution (Fig.6). Aerosol mass concentration affected by local pollution air mass (Local) is much higher than the other two cases. The peak in accumulation mode appears in the diameter range of 0.32-0.56μm and 1.8-3.2μm in coarse particle mode. However, the peaks are in the diameter range of 0.18-0.32μm and 5.6-10μm when aerosol affected by northern continental air mass (N) and the southern continental air mass (SW). Different sources of pollutants lead to the proportion of soluble aerosol and the main ion change.

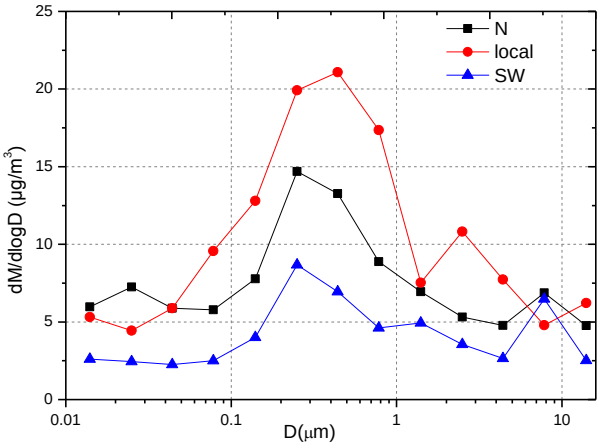

Fig.6 The aerosol concentration distribution of water soluble component under different weather situation

4. CONCLUSIONS

To characterize the chemical and physical properties of aerosol particles and their effects on cloud and precipitation at highly elevated locations of Southeast China, size-resolved aerosol particles were collected using a MOUDI cascade impactor at the Bright Summit of Mt. Huang (1840 m above mean sea level), southeast China, during May to September 2011. The mayor results are as follows:

A bimodal distribution is shown for the total aerosol mass, with one mode

appearing in the diameter range of 0.32-0.56 μm and the other in 1.0-1.8μm. It is also found that sulfate, nitrate, calcium, ammonia and organic acids are the dominant components of water-soluble ions, accounting for up to 80% of the water-soluble ions in particles and 34.2% of the total mass of particles. The pH values indicate that most of the particles are of acidic nature, probably due to the existing a plenty of acidic precursor, such as SO_2 and NO_X in the air.

To understand the mechanisms behind the different nature the particles presented, the aerosol samples obtained during the observation period, were categorized into three groups (the northern continental air mass, the local pollution air mass and the southern continental air mass) by back trajectory analysis, using the Hybrid Single-Particle Lagrangian Integrated Trajectory (HYSPLIT) model, and it is found that the concentrations of the anthropogenic chemical compositions originated from the local pollution are highest among the three cases, which can affect the air quality under favorable meteorological conditions associated with stable boundary layer and low surface wind speed.

5. BIBLIOGRAPHY

[1] Friedman B., Herich H., Kammermann L. et al. Subarctic atmospheric aerosol composition:1. Ambient aerosol characterization. Journal of Geophysical Reserch, 2009,114(D13): D13203.

[2] Lohmann U., Feichter J. Global indirect aerosol effects: a review. Atmospheric Chemistry and Physics, 2005,5(3): 715-737.

[3] McCormick R A, Ludwig J H. Climate modification by atmospheric aerosols. Science (New York, NY), 1967,156(780): 1358.

[4] Fuzzi S, Decesari S, Facchini MC et al. Overview of the inorganic and organic composition of size-segregated aerosol in Rondônia, Brazil, from the biomass-burning period to the onset of the wet season. Journal of geophysical research, 2007,112(D1).

[5] Yin Y, Tong YQ, Wei YX et al. The analysis of chemistry composition of fine-mode particles in Nanjing(in chinese). Transactions of Atmosperic Sciences, 2009,32(06): 723-733.

[6] Gao J. Study on aerosol number concentration, size distribution and the particle formation and growth process(in chinese). Shangdong University Doctoral Dissertation. 2008.

[7] Yin Y, Chen C, Chen K et al. An observational study of the microphysical properties of atmospheric aerosol at Mt.Huang(in chinese). Transactions of Atmosperic Sciences, 2010, 33 (02): 129-136.

[8] Zhao H, Wang TJ, Jiang F et al. Investigation into the source of air pollutants to Hong Kong by using backwark trajectory method during the Trace-P campaign(in chinese). Journal of tropical meteorology, 2009,25(02): 181-186.

[9] Kerminen VM, Wexler AS. Growth laws for atmospheric aerosol particles: An examination of the bimodality of the accumulation mode. Atmospheric Environment, 1995,29(22): 3263-3275.

[10] Hu M, Zhao YL, He LY, et al. Mass size distribution of Beijing particulate matters and its inorganic water-soluble ions in winter and summer(in chinese). Environmental Scinence, 2005,26(04): 1-6.

[11] Fang CP, McMurry PH, Marple VA et al. Effect of flow-induced relative humidity changes on size cuts for sulfuric acid droplets in the microorifice uniform deposit impactor (MOUDI). Aerosol Science and Technology, 1991,14(2): 266-277.

[12] Huebert B J., Wang M X, LÜ W X Atmospheric nitrate, sulfate, ammonium and calcium concentrations in China. Tellus B,

1988,40(4): 260-269.
[13] Tang XY, Zhang YH,Shao M, et al. Atmospheric Environmental chemistry(in chinese). Beijing: Higher Education Press, 1990: 311.
[14] Odabasi M, Muezzinoglu A, Bozlaker A. Ambient concentrations and dry deposition fluxes of trace elements in Izmir, Turkey. Atmospheric Environment, 2002,36(38): 5841-5851.

Acknowledgements
This study is jointly sponsored by the National Science Foundation of China (Grant No. 41030962), the graduate Education Innovation Project of Jiangsu Province through Grant No. CX10B_294Z, and the Priority Academic Program Development of Jiangsu Higher Education Institutions (PAPD).

NEW RUSSIAN AIRCRAFT-LABORATORY YAK-42D «ATMOSPHERE» FOR ENVIRONMENTAL RESEARCH AND CLOUD MODIFICATION

Dr. Yuri Borisov [1], Dr. Victor Petrov [1], Prof. Mikhail Strunin [1], Dr. Viacheslav Khattatov [1], Dr. Bagrat Danelyan [1], Dr. Alexander Azarov [1], Prof. Boris Fomin [1], Vasiliy Martanov [2], Prof. Valeriy Stasenko [2], Prof. Sergey Vakulovskiy [3], Prof. Andrey Sinkevich [4], Lyudmila Sokolenko [4], Boris Lepukhov [5]

[1-]Federal State Budgetary Institution “Central aerological observatory”, 3, Pervomayskaya, 141700 Dolgoprudny Moscow Region, Russia;

[2-]The Federal Service for Hydrometeorology and Environmental Monitoring, 12, Novovagankovsky, 123995 Moscow, Russia;

[3-] Research and Production Association "Typhoon", 4 Pobeda str., 249038 Obninsk, Russia;

[4-]Federal State Budgetary Institution "Main geophysical observatory", 7, Karbysheva str., 194021 St.-Petersburg, Russia;

[5-]Joint Stock Company "Myasishchev Design Bureau", 7, Narkomvod str., 140180 Zhukovsky, Russia

1. INTRODUCTION

Investigations and control of environment are indispensible to provide with the human life and vital activity of humanity. Resent events, such as convolution of nature of volcano Eyjafjallajokudl in Iceland on 2010, catastrophe in the atomic station Fukushima in Japan on 2011, or earlier Chernobil atomic crush on 1986 demonstrated necessity of efficient reacting with the goal of defining possible dangers and with active actions on atmospheric processes for minimizing consequences. A special instrumented aircraft-laboratory could be very effective mean for atmospheric observations and weather and clouds modifications (Hiyama et. al., 2003).

Aircraft-laboratory (or special instrumented airborne platform) has a set of advantages making it effective instrument for environmental research, which give possibility:

- To fulfill simultaneous measurements of different parameters of atmosphere and underlying surface;
- To get meridian, latitudinal and altitude distributions of atmospheric parameters in given region with high spatial and temporal resolvability;
- To integrate ground-based and remote control data in common informational picture;
- To make clouds modification and control it in any given area;
- To provide observation over difficult of access regions.

2. THE MAIN GOALS OF NEW AIRCRAFT LABORATORY

The aircraft-laboratory Yak-42D “Atmosphere” created in Central aerological observatory of Russian Federal Service for Hydrometeorology and Environmental Monitoring is intended for measuring the following parameters of atmosphere and underlying surface:

- Thermodynamic parameters of atmosphere (air temperature, pressure, density and humidity, wind speed, turbulence and turbulent fluxes);
- Gas and aerosol structure of atmosphere;
- Radiation in atmosphere and from surface, radiation balance in atmosphere;
- Radioactive pollution of atmosphere and underlying surface;
- Microstructure of atmospheric clouds and participation;
- Atmospheric electricity.

The aircraft-laboratory Yak-42D “Atmosphere” is also equipped with instruments for clouds modification.

The main objectives of the aircraft-laboratory Yak-42D “Atmosphere” are the following:

- Investigations and monitoring atmospheric pollutants;
- Remote control of underlying land surface and ocean;
- Control of the climate factors in free atmosphere;
- Fulfilling scientific and applied investigations in physics and dynamics of clouds, atmospheric fronts and cyclones, planetary boundary;
- Validation of satellite observations of atmosphere and underlying surface;
- Fulfilling research and special works on clouds modification for regulation of atmospheric participations.

3. BASE CIVIL AIRCRAFT YAK-42D FOR CREATING MULTIPURPOSE AIRCRAFT-LABORATORY

Russian civil aircraft Yak-42D is used for the base of new aircraft-laboratory. The common view of bought aircraft Yak-42D # 42440 and its interior is presented in ***Fig. 1.***

The main technical parameters of Yak-42D are as follows:

- Sky crew – 2 (3) members.
- Maximum flight level – 9600 m;
- Maximum commercial load - 12000 kg;
- Flight distance with the load of 5000 kg – 4100 km;
- Air speed rang – from 350 up to 700 kmh^{-1};
- Maximum take-off weight – 57 500 kg.

The decision # РЭ-69/5.9-23 of Ministry of aviation sets for airplanes Yak-42D the following restored life:

Fig. 1. Base Yak-42D Russian civil aircraft

- Up to 40000 flight hours, up to 18000 flights and period of life up to 35 years.

Residual life of Yak-42D # 42440 aircraft is:

- 38500 flight hours, 17500 flights, 25 years.

Aircraft Yak-42D is fully equipped for flying using international lines. Aboard Yak-42D the following facilities are installed:

- Global navigation system GPS KLN-90 BRNAV;
- Token collision aircraft system TCAS-II Honeywell with the special system of signals S(EHS);
- System of earlier warning of collision with the land SRPB3;
- Oxygen equipment KSP-42;
- Automatic radio beacon ARM-406;
- Electronic altimeter VBE-1.

Aircraft Yak-42D # 42440 is permitted for the flights with precise echelement RVSM.

4. MEASURING SYSTEM OF AIRCRAFT-LABORATORY YAK-42D "ATMOSPHERE"

The measuring system of aircraft-laboratory Yak-42D "Atmosphere" includes three levels.

The first level consist of different kind of sensors and measuring systems of instruments complexes (temperature and pressure sensors, navigation systems, spectrometers, radars, radiometers, particles counters and others).

The second level is the set of hardware-software complexes which unite sensor and measuring systems through special computer programs. These complexes produce measurements of navigation parameters, thermodynamic characteristics of atmosphere, different gases and aerosol concentrations and common content of the gases, solar radiation and radiation balance in atmosphere, radioactive pollutants, and

microphysical characteristics of clouds, electric characteristics, and radars.

The third level is the integration of hardware-software complexes to common aboard measuring system of the aircraft-laboratory Yak-42D “Atmosphere”. This system contains Data Acquisition System (DAS), facilities for cloud modification, satellite channel for fast transmission data from the aircraft to ground-based centers and means for providing control of local experiment from the special ground center. At this level processing, recording and reservation of all data, data exchange between complexes, control of experiment and transmission of data to ground-based centers are provided.

Each complex included to integrated information aircraft system can operate independently thus has the own DAS. Refusal of one of complexes (except of the thermodynamic and onboard DAS) does not lead to refusal of all measuring system of aircraft-laboratory Yak-42D " Atmosphere ".

The common structure of aircraft measuring system of Yak-42D “Atmosphere” is presented in ***Fig. 2*** and ***Fig. 3*** demonstrates scheme of the aircraft Data Acquisition System.

5. HARDWARE-SOFTWARE COMPLEXES OF AIRCRAFT-LABORATORY YAK-42D “ATMOSPHERE”

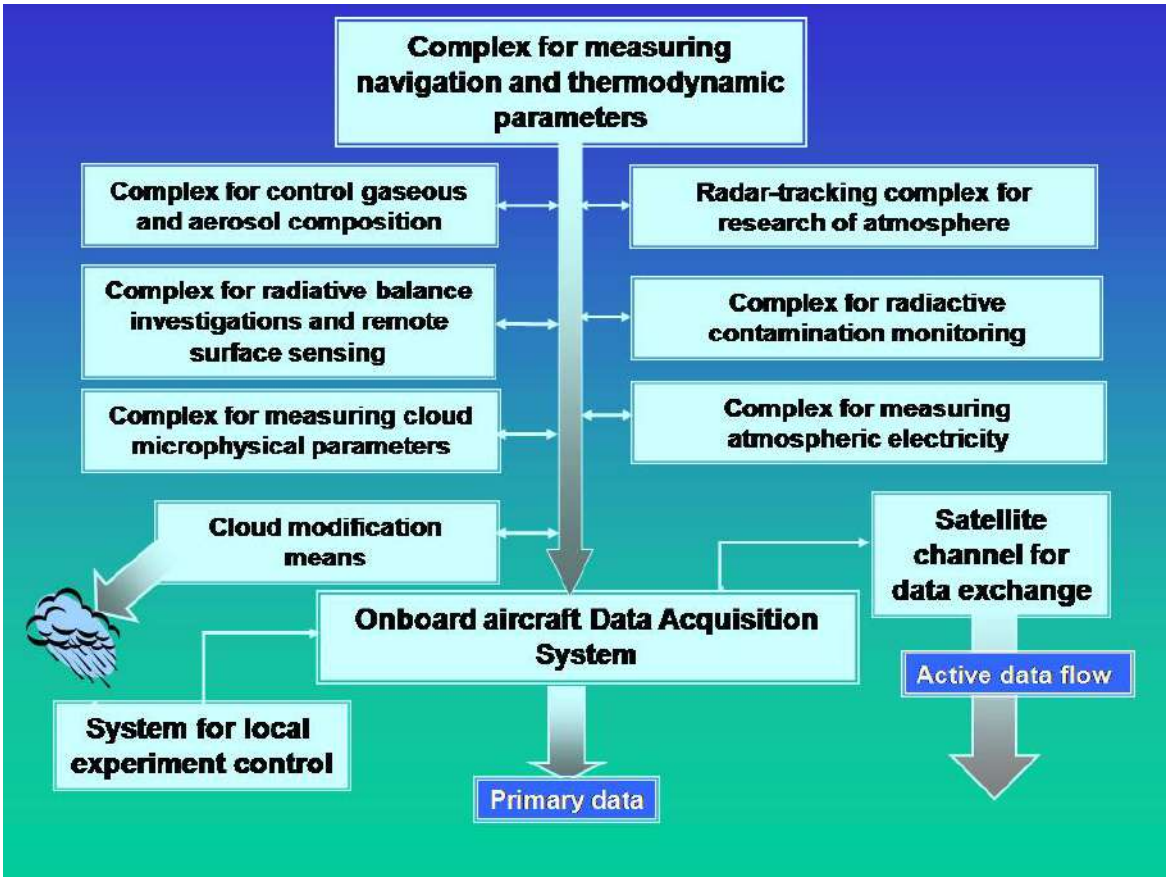

Fig. 2. Common structure of aircraft-laboratory Yak-42D measuring system

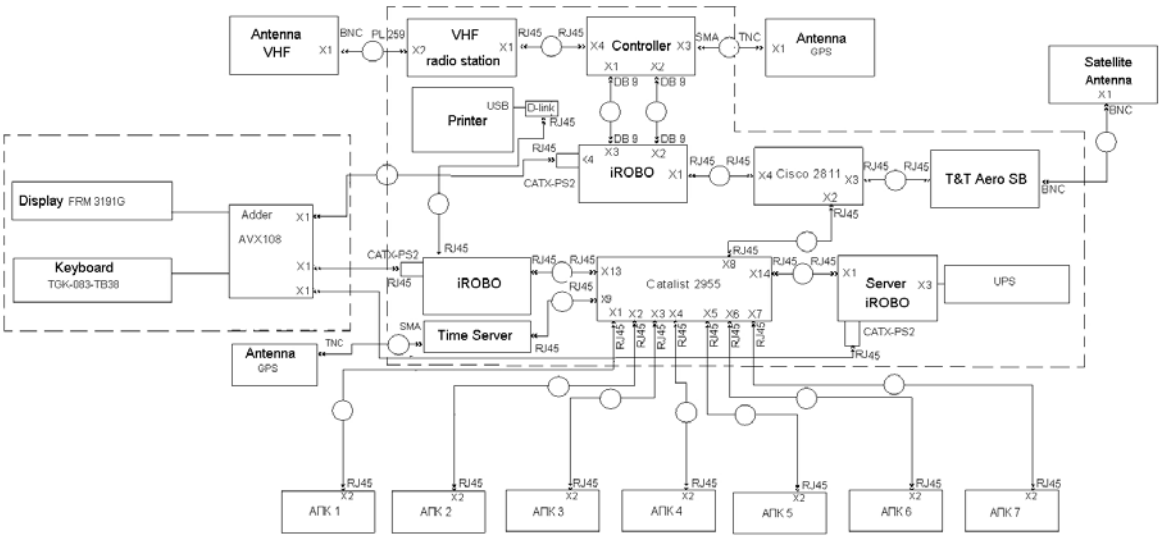

Fig. 3. Scheme of the aircraft Data Acquisition System

5.1. HARDWARE-SOFTWARE COMPLEX FOR MEASURING NAVIGATION PARAMETERS AND THERMODYNAMIC PARAMETERS OF ATMOSPHERE

This complex provides measurements of parameters, characterized precise aircraft attitude and thermodynamic structure of the atmosphere (Strunin, 2010). Data of this complex are the base for building up meteorological fields or spatial-temporal distributions of thermodynamic parameters. Navigation parameters (coordinates, heights, speed of aircraft, attitude angles) and wind speed, air temperature and humidity, atmospheric turbulence data are also necessary for presentation and analyzing data of others measuring complexes.

The following sensors and measuring systems are installed aboard aircraft-laboratory Yak-42D “Atmosphere”:

- Global position system GPS and GLONASS BPSN-2, Russia;
- Inertial reference system IRS Honeywell Laseref VI, USA;
- Radio-altimeter of high levels A-075, Russia;
- Radio-altimeter of low levels A-053, Russia;
- Half-spherical 5-points pitot-static heads Rosemount 858AJ and 858Y, USA;
- Pressure probe PVD-30, Russia;
- Air data transducers Rosemount MADT 2016B, USA;
- Dynamic pressure sensor Rosemount 1221F2AF7B1B, USA;
- Differential pressure sensors Rosemount 1221F2VL7B1A, USA;

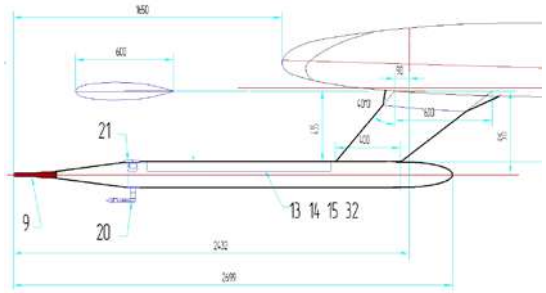

Fig. 4. Scheme of under-wing boom for thermodynamic sensors

Fig. 5. Inertial reference system Laseref VI

Fig. 6. Global position system

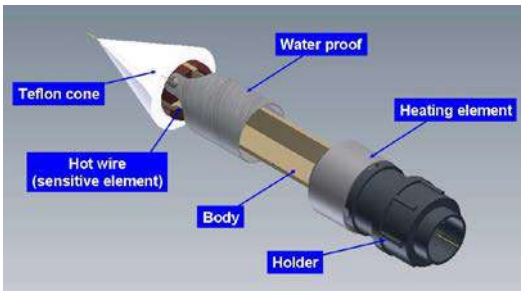

Fig. 7. High-frequency aircraft thermometer CAO

- Sensors interface units SIU, CAO, Russia;
- Temperature sensors Rosemount 102CT2D6, USA;
- Temperature sensor Rosemount 102LA2AG, USA;
- Temperature sensor Rosemount 102LA2AG, USA;
- High-frequency aircraft thermometer HFAT CAO, Russia;
- Inertial measuring unit AIST-350, Russia;
- Condensation hygrometer General Eastern 1311XR, USA;
- Aircraft condensation hygrometer ACH, CAO, Russia;
- Ultra-violet hygrometer UVH, CAO, Russia.

Some of these sensors and systems are installed in the special boom under the wing (***Fig. 4***). These sensor and systems provide measurement of so call primarily parameters, which than used for calculating all necessary thermodynamic characteristics of atmosphere. Common views of some sensors and systems from the above list are presented in ***Fig. 5 – 8.***

Listed sensors and measuring systems are united to the hardware-software complex through the special

Fig. 8. Ultra violet hygrometer CAO

computer program. The complex produces data processing for defining thermodynamic parameters of atmosphere, recoding the data, and data transmission to the aircraft Data Acquisition System:

- Latitude and longitude, geometric height of aircraft-laboratory flight;
- True height (radio-height) and barometric height of the flight level;
- Components of ground speed of the aircraft;
- Attitude angles of the aircraft (roll, pitch and heading angles);
- True air speed of aircraft and true air temperature;
- Components of wind speed in geographic coordinate system;
- Dew-point/frost point temperature and absolute air humidity;

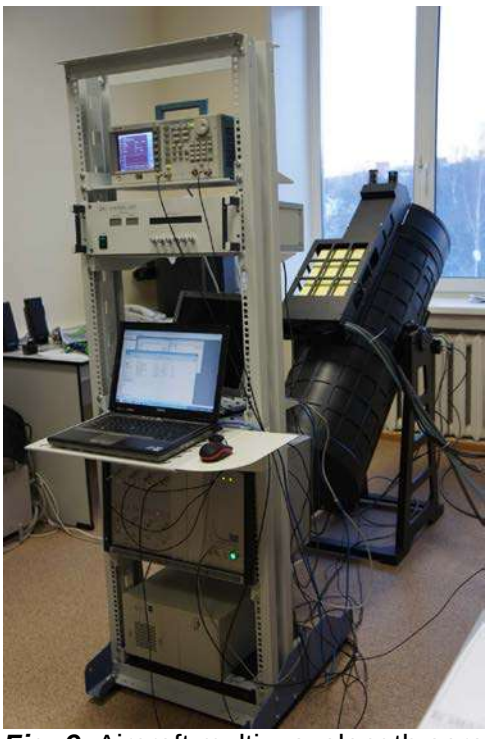

Fig. 9. Aircraft multi-wavelength aerosol lidar ML-375-A

- Turbulent fluctuations of wind speed, air temperature and absolute air humidity.

5.2. HARDWARE-SOFTWARE COMPLEX FOR THE CONTROL OF GASEOUS AND AEROSOL COMPOSITION OF THE ATMOSPHERE

This complex allows monitoring of changes in chemical composition, including the monitoring of pollutants and greenhouse gases in the atmosphere control of the stratospheric aerosol layer

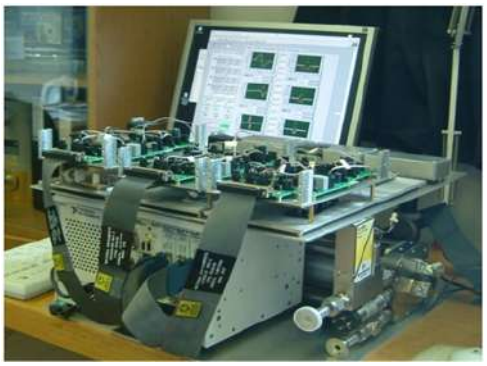

Fig. 10. Aircraft tunable diode laser spectrometer

and the ozone layer of the atmosphere. To solve these problems requires systematic airborne measurements of spatial and temporal distributions of gases and aerosols on various scales, and altitudes in the free atmosphere. Airborne sensing of gaseous and aerosol composition of the atmosphere will identify as early as possible climate factors that may lead to changes in regional and global scales, and are associated either with the natural fluctuations in climate-parameter, or by anthropogenic influences.

- Aircraft multi-wavelength aerosol lidar ML-375-A (***Fig. 9***) is designed

to measure the backscattering coefficient and the aerosol extinction in the spectral range 355 nm - 1064 nm. Based on the data made assessment of the main physical characteristics of aerosols, such as size, density and complex refractive index.

- Aircraft tunable diode laser spectrometer (***Fig.10***) for measurement of the concentration of greenhouse gases (water vapor, carbon dioxide, methane) and their isotopic composition in the atmosphere, CAO, Russia. Airborne spectrometer consists of the electronics module (1), which supports the work of six diode lasers, and 3 measuring channels for H_2O (2), CH_4 (3), CO_2 (4).

Fig.11. NO-analyzer ECOPHYSICS

- Spectrometer, ultraviolet and visible range Shamrock SR-303i Andor Technology for measurements of the total content of O_3, NO_2, BrO, OClO in the atmosphere.
- Ozone Analyzer Model 205 (2B Tech, Inc., USA) and chemiluminescent ozonometer, CAO, Russia for measuring the concentration of ozone and its fluctuations in the range from 1.0 to 1000 ppb.
- Chemiluminescent instruments for nitrogen oxides, ECOPHYSICS, Switzerland for measuring concentrations of NO (***Fig.11***), NOx, NOy in the range from 0.3 to 500 ppb.
- High-frequency pulsation measuring chemiluminescent nitrogen dioxide, CAO, Russia for measuring Ripple-NO2 concentrations in the range from 0.1 to 100 ppb.
- Greenhouse Gas Analyzer G2301-mc (Picarro, Inc., USA).
- Non-dispersive infrared analyzer SO2/N2O air LI-7500ADP, USA;
- Gas chromatograph Agilent-7820A with a device for sampling air Hermes, Germany. Whole air samples (NMHC, alkyl nitrates, long lived tracers like halocarbons), CO2, N2O, CO, CH4.
- High-precision fluorescence aircraft hygrometer, CAO, Russia. Fluorescent aircraft hygrometer

designed to measure spatial and temporal distributions of the relative volume concentration of H_2O in the range from 1 to 2000 ppm (m^{-1}).

5.3. HARDWARE-SOFTWARE COMPLEX FOR THE RADIATIVE BALANCE INVESTIGATIONS AND REMOTE SENSING OF CLOUDINESS AND UNDERLYING SURFACE

This complex measures the upward and downward integral fluxes of solar and thermal radiation for the radiative transfer and radiative heat exchange investigations. The net shortwave fluxes, being measured at the aircraft and at the underlying surface, gives a possibility to define absorption of solar radiation by the atmospheric layers below and above the aircraft, respectively. Along with the similar measurements of the thermal radiation it gives a possibility to evaluate influence of the natural and anthropogenic aerosols and greenhouse gases on the radiative balance. The high-resolution measurements of the shortwave spectral reflectance by a hyper-spectral viewer allows investigating the influence of the natural and anthropogenic factors on the surface. Maps of the surface brightness temperatures obtained using the 4-channel IR radiometer also may be useful for investigations of the surface. For example they give a possibility to evaluate the soil moisture as well as to found sources of carbon dioxide and methane.

Fig.12. Pyranometers CMP22, Pyrgeometers CGR4 and UV-radiometer UV-S-B-T/C

Additionally such maps of cloudiness contain information about cloud structure and radiative properties. The McW radiometer, which the water vapor channel centered at 6.2 μ, is applied to get information on in-cloud temperature. Radiometer will work in horizontal direction in this case. This information is free from typical errors of immersion type thermometers due to their (or their shield) wetting or icing in clouds

Thus on board of the aircraft there are the following instruments:

- Pyranometers CMP22, Kipp&Zonnen, Germany;

- Shortwave integral (0.2 -3.6 μm) hemispherical fluxes.

- Pyrgeometers CGR4 Kipp&Zonnen, Germany;

-Longwave integral (4.5 – 42.0 μm) hemispherical fluxes.

- UV-radiometer UV-S-B-T/C Kipp&Zonnen, Germany;

- UV hemispherical fluxes in (0.28 – 0.315 μm) and (0.315 – 0.400 μm) spectral range.

Common view of these sensors is presented in ***Fig. 12***.

- Shortwave hyper-spectral viewer (NIR and VIS spectral regions), NPO «LEPTON», Russia (***Fig. 13***);

- Pictures of the underlying surface in 150 channels from 0.420 to 0.900 μm.

- Longwave 4-channel viewer 4КСР(Т) , Main Geophysical Observatory, Russia;

- Pictures of the underlying surface in 4 channels from (1.8 – 12.5 мкм).

- McW two-channel radiometer, MGO, Russia;

Fig. 13. Shortwave hyper-spectral viewer

- Two channels (22 and 37 GHz) for retrieval of the water vapor content in the atmosphere and liquid water in clouds.

5.4. HARDWARE-SOFTWARE COMPLEX FOR RADIOACTIVE CONTAMINATION MONITORING

This system enables assessing a degree of radioactive pollution of the air (air volumetric activity) and underlying surface based on gamma radiation dose rate and isotopic composition. Measurements of volumetric activity of radon decay products, given detection of various man-made impurities in the air, permit identifying a possible source of pollution and direction of impurities with respect to the source. By measuring space neutrons a source of such particles can be

Fig. 14. Gamma spectrometer with scintillation and high purity germanium detector GEM 40-86 «ORTEC»

Fig. 15. Space neutron counter

identified (on request from Institute of Applied Geophysics). Data obtained about volumetric activity of short-lived decay products of radon-222 at different heights can be used as a tracer of air masses. The system includes:

- Radiometer-dosimeter DMG-01 for detecting radioactive clouds in the atmosphere and radioactive footprints on the ground - SI RPA "Typhoon". The range of gamma radiation dose rate measurements: 10 nGy hr^{-1}-10 Gy hr^{-1} (1 μR hr^{-1}-1000 R hr^{-1}).
- Gamma spectrometer (***Fig. 14***) with scintillation and high purity germanium detector GEM 40-86 «ORTEC», USA, pulse analyzer DSPEC Pro «ORTEC», USA, and collimator screen - SI RPA "Typhoon". Gamma radiation from the underlying surface,

  -range of detected gamma quanta energy: 0.1-3.0 MeV;

  -range of measuring ^{137}Cs contamination density of the area, with a flight at 50 m height: 2 104 –2 107 Bqm^{-2}
- Setup "Vega-1M" for measuring radon-222 concentration in the troposphere (aerosol sampler "Vega-1M" radiometric system "RUS-2B") - SI RPA "Typhoon". Atmospheric concentration of radon-222 is the air mass tracer.
- Space neutron counter (***Fig. 15***) (neutron detector LB-6411 and datalogger unit UMo LB 123) "Berthold Technologies", USA)

Range of measuring neutron energy: up to 20 MeV

Range of measured doses: 30 nSv hr^{-1} - 100 mSv hr^{-1}.

5.5. HARDWARE-SOFTWARE COMPLEX FOR MEASURING CLOUD MICROPHYSICAL PARAMETERS AND COMPLEX OF CLOUD MODIFICATION MEANS

This complex provides measurements of atmospheric aerosols of different origin in a wide range of sizes at the level of the flight of aircraft-laboratory. Monitoring of atmosphere transparency, concentrations and size spectra of atmospheric aerosol will give opportunity to evaluate the degree of natural and anthropogenic disturbances due to emissions of particles from different sources.

Fig. 16. Nevzorov LWC/TWC probe

The microphysical complex of aircraft-laboratory includes following devices:

- Nevzorov LWC/TWC probe (Russia) liquid and total water content (***Fig. 16***) 0,003 gm^{-3} - 4 gm^{-3};

- Cloud Extinction Probe (Russia) extinction factor 1 – 200 km^{-1};
- The analyzer of a phase and structure of clouds AFSO (Russia) particle size spectra 10 – 400 mkm;
- Super-large particles sizes probe (Russia) large particle size spectra 200 – 6000 mkm;
- Cloud Condensation Nuclei Counter, Dual Column, CCN-200 (DMT, USA) Condensation Nuclei concentrations. The air flow to devices UHSAS, CCN200 and SP2

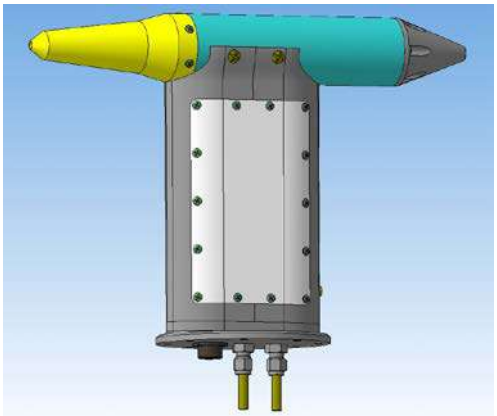

Fig. 17. The aircraft sample inlet for UHSAS, CCN200 and SP2

is brought with the help aerodynamic inlets, installed on a fuselage apart 1,2 - 2 m from devices (***Fig. 17***);

- Ultra High Sensitivity Aerosol Spectrometer – UHSAS (DMT, USA) aerosol particle spectra 0.055 – 1 μm;
- Passive Cavity Aerosol Spectrometer Probe, PCASP-100X (DMT, USA) aerosol particle spectra 0.1 – 3.0 μm;

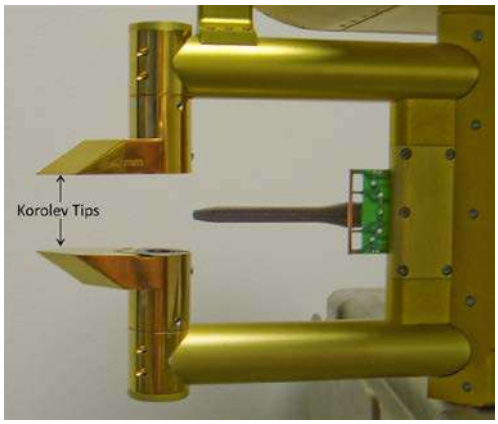

Fig. 18. Cloud Imaging Probe CIP DMT

- Single Particle Soot Photometer, SP2 (DMT, USA) black carbon mass in particles, number concentration up to 5000 particles cm^{-3};
- Cloud Droplet Probe, CDP (DMT, USA) cloud particle spectra 2 – 50 μm;
- Forward scattering spectrometer probe FSSP-100ER (DMT, USA) cloud particle spectra 2 – 50 μm;
- Cloud Imaging Probe CIP DMT (DMT, USA) 2-Dimensional Images of particles from 25-1550 μm with

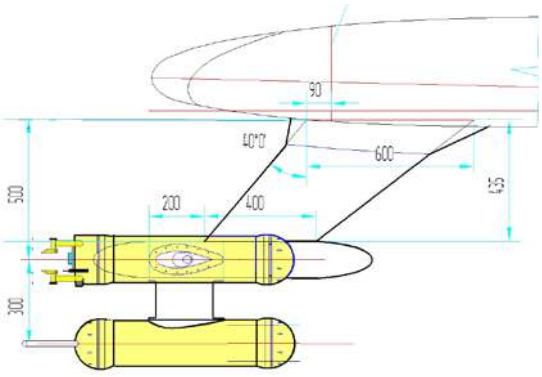

Fig. 19. PMS/DMT canisters under the wing

new type of tips (***Fig. 18***);

- PMS Optical Array Probe OAP-2DC (PMS, USA) 2-Dimensional

Images of particles from 25-1550 μm;

- Precipitation Imaging Probe PIP (DMT, USA) 2-Dimensional Images of particles from 100 -6200 μm;
- Cloud Particle Imager SPI (SPECinc., USA) -Resolution 2,3 μm, up to 1000 particles s^{-1},
- Local Data Acquisition System M300 (SEA inc., USA).

PMS/DMT canisters and SPI are installed on the pylons located underneath the wings (***Fig.19***).

Fig. 20. The set of pyrotechnic means UV-26

Fig. 21. The small ice particle generator SIPG-A

For expansion of opportunities to use aircraft-laboratories, the latter are equipped with the cloud seeding means, allowing performing weather modification activities.

To perform cloud seeding by ice-forming, hygroscopic, and cooling agents on the aircraft will be put the appropriate technical means.

In order to seed clouds with the help of ice-forming and hygroscopic agents the aircraft will be equipped with two sets of UV-26 mean to release pyrotechnic flares of type PV-26 in the amount of 1024 cartridges. ***Fig. 20*** shows a set of UV-26.

For cloud seeding by cooling agents (liquid nitrogen) the aircraft is equipped with the small ice particle generator SIPG-A (***Fig. 21***) permitting to seed clouds in the range of dosages of 0, 5 kg min^{-1} up to 10 kg min^{-1}.

All microphysical data are saved on the disk of local DAS M300.

5.6. THE HARDWARE-SOFTWARE RADAR-TRACKING COMPLEX FOR RESEARCHES OF ATMOSPHERE

This complex provides reception of cuts of clouds and precipitations with measurement of structures of their radar-tracking reflectivity and values of radial projections of speeds of movements of particles in clouds, detection of zones of turbulence, three-dimensional fields of

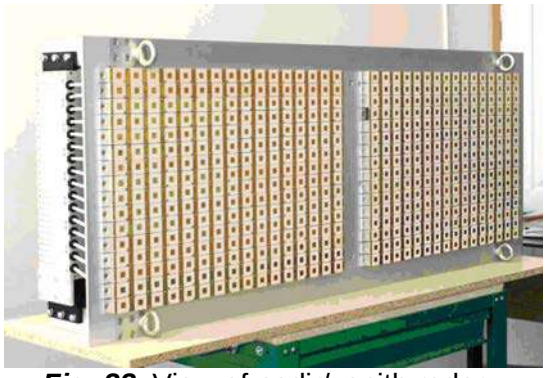

Fig. 22. View of nadir/zenith radar

radar-tracking reflectivity, a map of height of cloud tops; a map of weather phenomena; a map of precipitation

intensity; a map of visibility in precipitation zones.

The radar-tracking radar complex of aircraft-laboratory is equipped with coherent X-ray wavelength radar with vertical sector field of view. Radar is based on active phased array (APAA). The complex consists of two radars – one pointed towards zenith and another towards nadir - with ability to control the position of an electron pattern 5x4 degrees within 60 degrees in the plane transferring the direction of flight (***Fig. 22***). To improve the detection and to allow a study of meteorological objects with weak reflectivity in X-band (such as layered cloud forms) the radar is using complex sounding signals, which is based on nonlinear frequency modulation and phase shift keying. A radiated power of transmitting APAA is 1200 W. The ratio of radiation to the pause is equal to 10. The system has overall potential sufficient to detect hydrometeors with reflectivity up to -35 dbZ at a distance of 10 km. In radar pointed towards the nadir, there is a provision for a mode of lateral view of the earth's surface, which in implemented using the synthesis of a radiation pattern.

Radars use a design with separate transmit and receive phased arrays based on the printed micro strip radiators. The control system of an APAA allows you to create up to 64 positions of a radiation pattern.

5.7. HARDWARE-SOFWARE COMPLEX FOR MEASURING ATMOSPHERIC ELECTRICAL CHARACTERISTICS

This complex provides possibility to measure electrical characteristics of the atmosphere including clouds and other atmospheric phenomena which obtain electrical charge (Begalishvily et al. 1993).

Fig. 23. Aircraft electrical field mill SPNP-011

Potential of ionosphere and its changes due to natural reasons and artificial

Fig. 24. Aircraft air conductivity probe SAIV-011

modification can be derived from the measurements. The complex can be used also to discover electrical charges in troposphere associated with aerosol layers and clouds. Electrically charged layer clouds which are dangerous phenomena

for aircrafts can be studied with the mentioned instruments. Another important possibility to use the complex is a possibility to assess seeding results, as electrical cloud characteristics usually change after seeding. Our early investigations have also shown that radioactive emissions and their temporal and spatial variations can be also detected with the help of presented complex.

This complex includes the following instruments.

- Active compensator of an aircraft charge (AKZS).

An instrument is used to regulate aircraft electrical charge. The principle of such regulation is based on regulation of corona discharge from the aircraft. Special discharge rods are installed on aircraft wings.

- Aircraft electrical field mill (SPNP-011).

The instrument (***Fig. 23)*** is used to measure electrical field strength E at the position where the probe is installed. Six probes SPNP-011 are installed at different parts of the aircraft fuselage. Processing of the data provides possibility to derive electrical field vector E and aircraft charge Q.

- Aircraft air conductivity probe (SAIV-011).

The probe (***Fig. 24)*** is used to measure air conductivity of both polarities. Aspiration method is used for measurements.

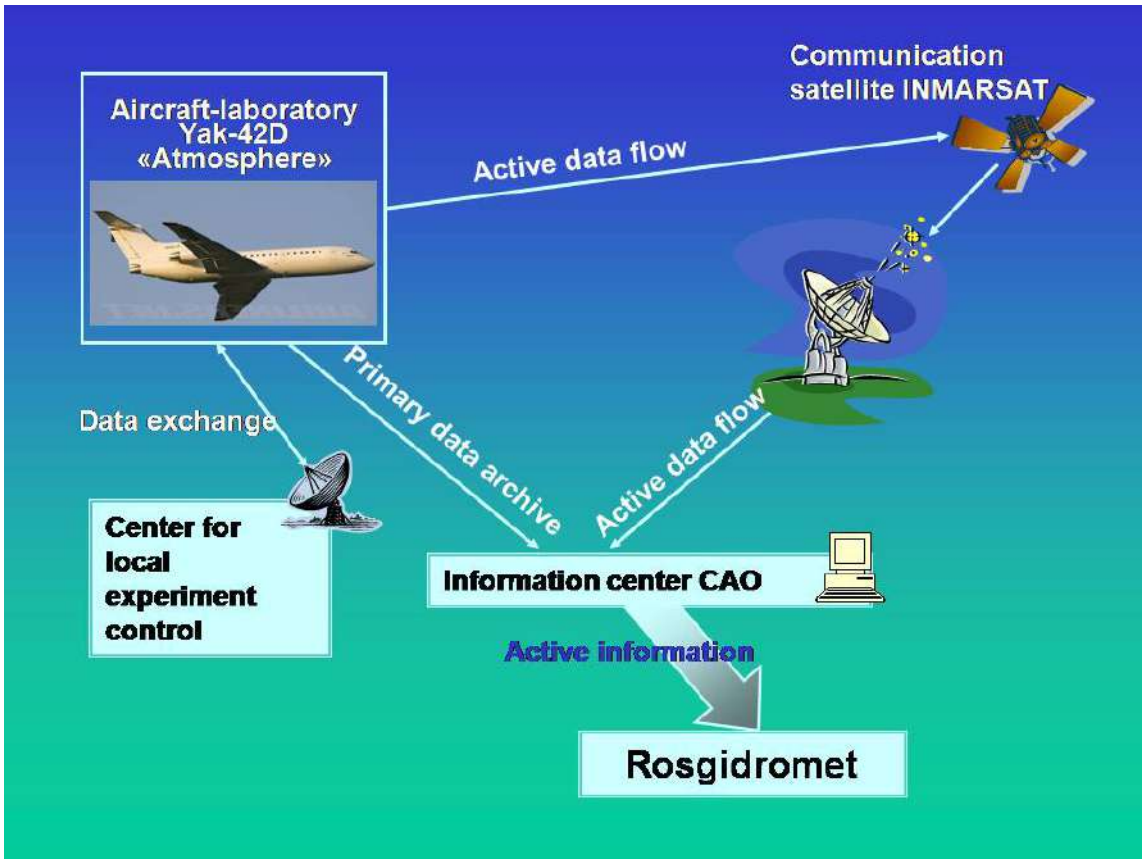

Fig. 25. The structure of information interaction between aircraft-laboratory Yak-42D "Atmosphere" and ground-based centers

5.8. ONBOARD AIRCRAFT DATA ACQUISITION SYSTEM (OA DAS)

OA DAS provides collecting and archiving of data from measuring devices and the systems which are included in all hardware-software complexes.

OA DAS carries out the following functions:

- Initial data collecting and processing on workplaces;
- Collecting and storage of processed results in Onboard archive;
- Displays of results from uniform onboard archive;
- Exchange of current data between measuring complexes;
- Data transmission on liaison channels;
- Internal monitoring of measuring system and the control of its integrity;
- Export of results of flight to ground archive of data;
- Storage of results of flight experiments in Ground archive.
- Managements of local experiment on updating clouds from ground command center.

Onboard Aircraft Data Acquisition System is constructed on the basis of industrial computers of type “iROBO”, network equipment CiscoCatalyst, Satellite communication System “T&T Aero SB Lite”, radio data transmission system “Land – Aircraft – Land” (Petrov et al., 2007).

The structure of information interaction between aircraft-laboratory

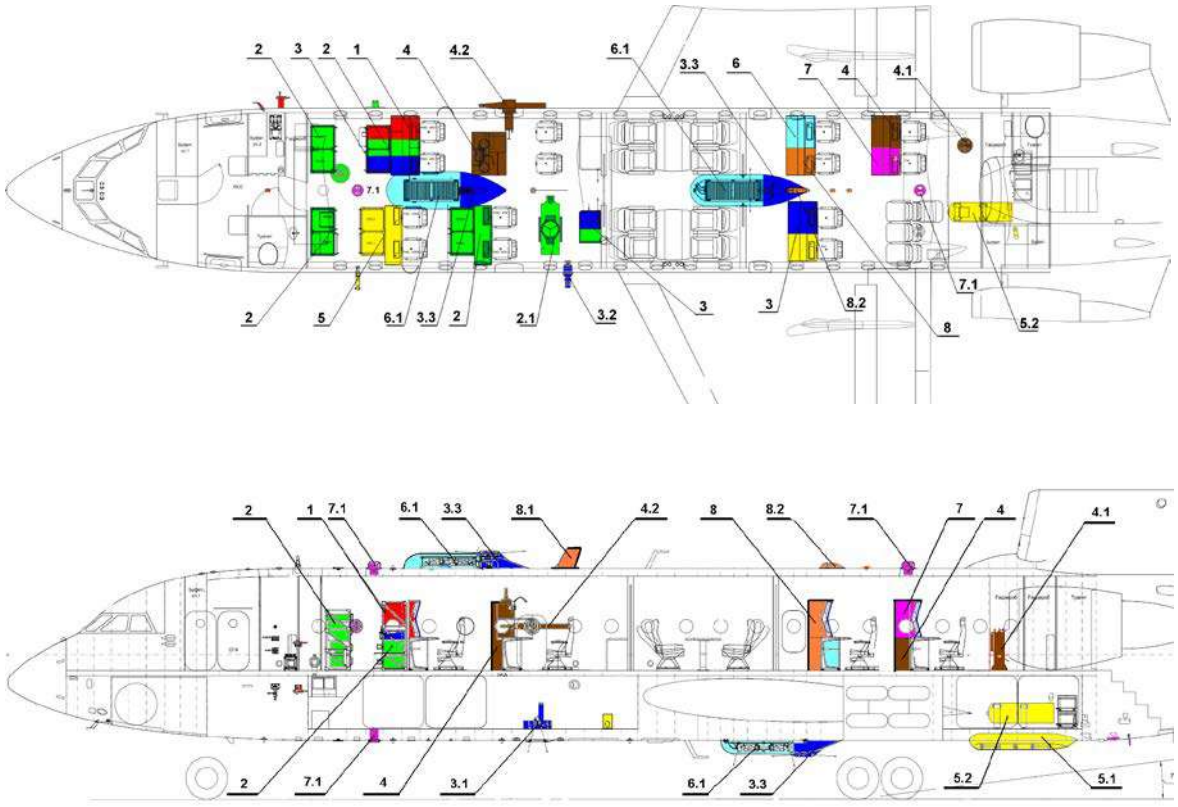

Fig. 26. The common view of aircraft-laboratory Yak-42D “Atmosphere” layout

Yak-42D “Atmosphere” and ground-based center for local experiment control and information center CAO is presented in ***Fig. 25***.

6. EQUIPMENT LAYOUT OF AIRCRAFT-LABORATORY YAK-42D “ATMOSPHERE” AND CONDITION OF ITS DEVELOPMENT

The common view of equipment layout aboard Yak-42D (vies from the side and from above) is presented in ***Fig. 26***.

We use the following denotes in the figure:

1. Complex for researches of Thermodynamic parameters of atmosphere;
2. Complex for researches of Gas and aerosol structure of atmosphere;

2.2. Aircraft multi-wavelength aerosol lidar ML-375-A;

3. Complex for researches of Radiation in atmosphere and from surface, radiation balance in atmosphere;

3.1. Hyper-spectral viewer;

3.2. Long wave 4-channel viewer 4KCP(T);

3.3. Thermal radiation sensors;

4. Complex for researches of Radioactive pollution of atmosphere and underlying surface;

4.1. Gamma spectrometer with scintillation and high purity germanium detector GEM 40-86 «ORTEC»;

4.2. Aerosol sampler “Vega-1M”;

5. Complex for researches of Microstructure of atmospheric clouds and participation;

5.1. The set of pyrotechnic means UV-26;

5.2. The small ice particle generator SIPG-A;

6. Radar-tracking complex for researches of atmosphere;

6.1. Coherent X-ray wavelength radar;

7. Complex for researches of Atmospheric electricity;

7.1. Aircraft electrical field mill SPNP-011;

8. Central server of DAS and data transmission system;

Fig. 27. A model of aircraft-laboratory Yak-42D “Atmosphere”

8.1. VHF antenna;

8.2. Satellite communication system antenna.

In the front part of the aircraft fuselage different kind of gas proves are located (pitot-static heads, air temperature and humidity sensors, air sampling probes for number of measuring systems, cloud particle probes and others). At the top and the bottom parts of fuselage there are a number of special fairings of radar antennas, pyranometers and pyrgeometers sensors. Aircraft-laboratory also has a set of special windows for upward view and downward view lidar, spectrometer, ultraviolet and visible range

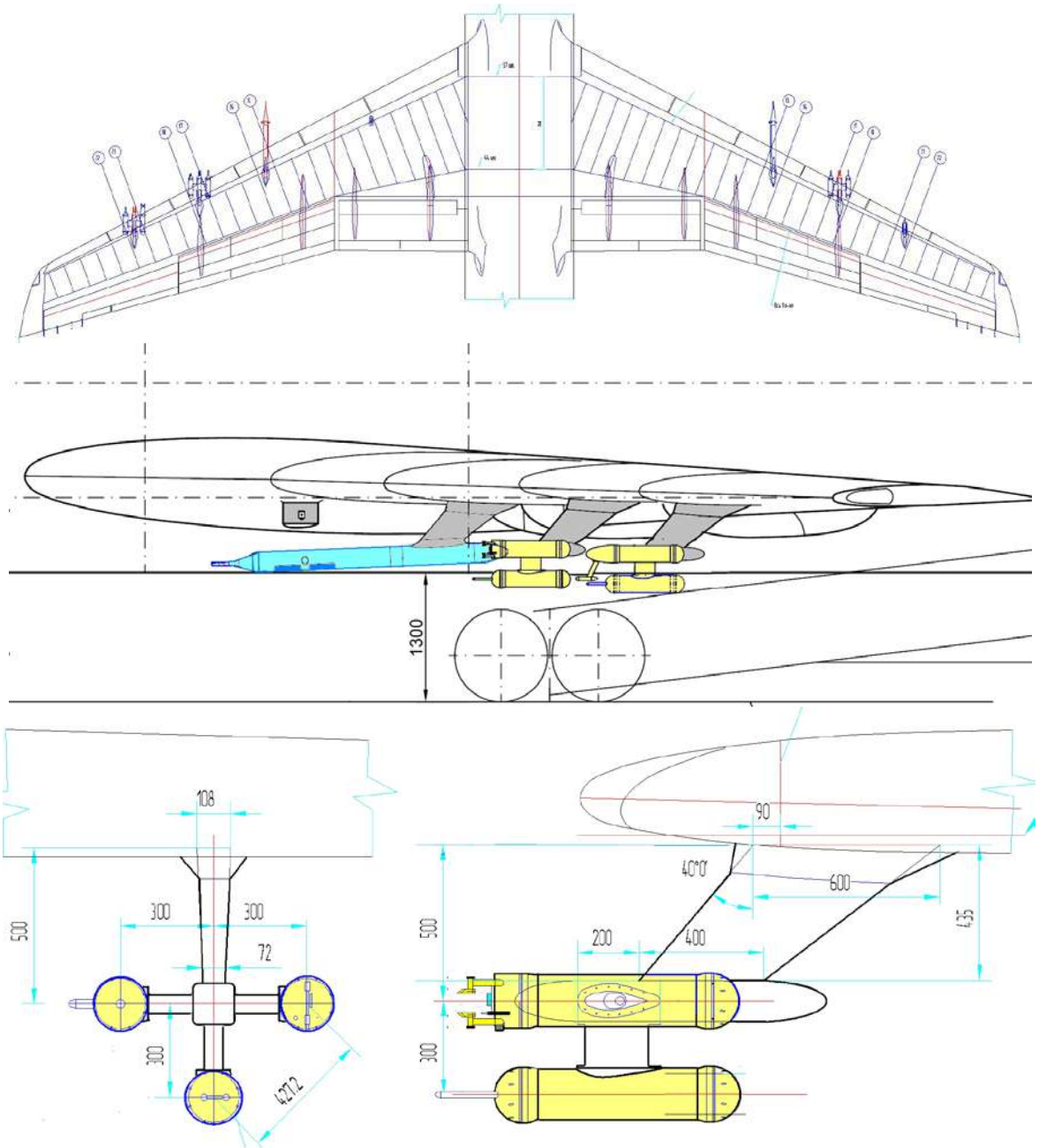

Fig. 28. Location of sensors under the wings

Shamrock, microwave radiometers, hyper-spectral viewer, long-wave 4-channel viewer, cloud extinction probe. A lock-chamber for collecting samples of radon-222 measuring is also installed at the right side of the fuselage. Six sensors for measuring electricity field of atmosphere are located along the fuselage. Several fuselage hard points and aperture plates are also installed for deployment of new instruments as needed.

The 3-D view of future aircraft-laboratory is presented in photo of aircraft model (***Fig. 27***).

Six pylons for carrying two remote bars for thermodynamic and microphysical sensors and 9 canisters of PMS/DMT type with microphysical instruments are located underneath the wing.

PMS/DMT canisters and SPI probe are installed at the pylons located underneath the wings (***Fig. 28***). There are three additional places on the pylons for further installations of canister type devices.

Aboard Yak-42D “Atmosphere” there are 8 working places for 10 operators maximum, including scientific head of the flight. It is possible to place 4 seats for additional members of experiments. The scientific instruments are located in a cabin of the aircraft using standard 19-inch racks. The model view of working place aboard aircraft-laboratory Yak-42D “Atmosphere” is presented in ***Fig. 29***.

In order to gain some insight about the current situation with creating of

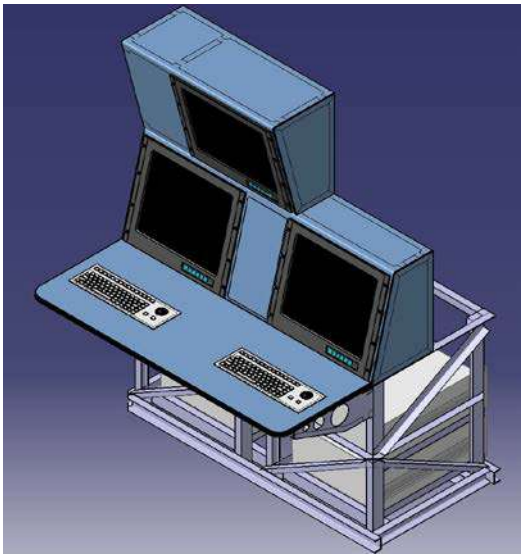

Fig 29. The model view of working place aboard the aircraft-laboratory

Fig. 30a. Current situation with the aircraft-laboratory creating

Fig. 30b. Current situation with aircraft-laboratory creating

aircraft-laboratory a few pictures of the aircraft in hangar under working are presented in ***Fig. 30a*** and ***b***. According to working plan all jobs should be completed in the first part of the 2013 and after this the aircraft-laboratory could fulfill special flight tests.

BIBLIOGRAPHY

Hiyama T., Strunin M.A, Suzuki R., Asanuma J., Mezrin M.Y., Bezrukova N.A. and Ohata T. 2003: 'Aircraft observations of the atmospheric boundary layer over a heterogeneous surface in Eastern Siberia', *Hydrol. Proces.*, **17**, 2885 – 2911.

Begalishvily N.A., Ponomaryov Yu.F., Sinkevich A.A., Stepanenko V.D., 1993: Aircraft Laboratory Yak-40, Russian Meteorology and Hydrology, N4, p.102-108.

Petrov V., Egorov O., Melnik S. and Skuratov S., 2007: "Land – Aircraft – Land" data transmission system, *Proc. of 9th WMO Conf. on Wea. Mod., 22-24 October, 2007, Antalia, Turkey.*

Sinkevich A.A., 1984: Investigation of Thermal Characteristics of Cu cong Using IR Radiometer, Russian Meteorology and Hydrology, No.1, p.40-46.

Sinkevich A.A., Lawson P. A., 2005: Survey of Temperature Measurements in Convective Clouds, Journal of Applied Meteorology, Vol. 44, No. 7, p. 1133–1145.

Strunin M.A., 2010: *Scientific-methodology base of study thermodynamic structure of the atmosphere based on aircraft observations*, Reference textbook, Moscow, 96 p. (in Russian).

MOISTENING PROFILE OF THIN CLOUDS IN THE AMAZON DERIVED WITH UV RAMAN LIDAR

Henrique M. J. Barbosa[1], **D. A. Gouveia**[1], **T. Pauliquevis**[2], **P. Artaxo**[3]

[1]*Instituto de Física, USP, São Paulo-SP, Brazil*
[2]*Depto. de Ciencias Exatas e da Terra, UNIFESP, Diadema, São Paulo-SP - Brazil*
[3]*Instituto de Física, USP, São Paulo-SP, Brazil*

ABSTRACT

Since mid-2011 a Raman-Lidar is being used to perform night time measurements of the vertical distribution of water vapor mixing ratio in the Amazon forest. The instrument is installed 30 km up-wind from Manaus-AM, in a low impacted site, and remotely senses the troposphere with a 95 mJ Nd-Yag laser at 355 nm from 350m up to 12km. The elastic backscattered and inelastic signals due to the Raman crossection of N_2 (387 nm) and H_2O (408 nm) were recorded yielding the determination of the vertical profile of vapor mixing ratio. Further it was calibrated with collocated soundings. In this paper we report on a set of measurements across thin clouds ($< 300\ m$) in the lower and mid-troposphere ($< 6\ km$) for which the signal to noise ratio of the water vapor channel is still acceptable. From 110 nights of measurements, 7 cases were selected. The profiles before and after each cloud overpass were considered to be a reference of the cloud-free environment. A large systematic enhancement (reduction) of about 5 g/kg (-1 g/kg) in the vapor mixing ratio was observed up to 150 m above (within/below) the cloud layer for these very thin clouds.

1. INTRODUCTION

The concentration of water vapor in the tropics is highly variable in both time and space. Its vertical distribution above the boundary layer depends on slow advection and on deep convection, which serves as the free troposphere's water vapor source. In the Amazon basin shallow warm clouds that form during the morning and early afternoon have an important role on regulating the diurnal cycle of temperature and humidity. The vertical redistribution of sensible and latent heat exchanged at the surface prepares the environment for the development of deep convection latter during the day [1; 2]. At the same time, deep convection itself is sensitive to the distribution of humidity in the free troposphere, developing more vigorously in humid environments. Moreover, recent modeling studies [3; 4] have shown that representing this diurnal cycle in atmospheric models is extremely important because it is the injection of energy in such high frequency that excites slower modes in the atmosphere (e.g. El Nino, Maden-Julian Oscilation or Pacific Decadal Oscilation).

Since mid-2011, a new experimental site was implemented near Manaus-AM, in the Brazilian Amazon Forest. The ACONVEX (*Aerosols, Clouds, cONVection EXperiment*) site will run continuously during the next years applying a synergy of different instruments, as described in section 2.1. This paper focus on the Raman-Lidar system used for measurements of water vapor and aerosol optical properties vertical distributions. Further details about the system is given in section 2.2. For reliable water vapor measurements, Lidar profiles were calibrated with collocated soundings launched during an intensive campaign between in September 2011, as described by [5]. In this paper we report on a set of measurements across thin clouds ($< 300\ m$) in the lower and mid-troposphere ($< 6\ km$) for which the signal to noise ratio of the water vapor channel is still acceptable. Section 4 presents the results and discussions.

2. ACONVEX

ACONVEX intends to fill in the gap of a long time series of measurements with high spatial and temporal resolution necessary for understanding the interactions and feedback mechanisms between humidity, convection, clouds and aerosols. It was initially implemented by a partnership between different research projects: AEROCLIMA (Direct and indirect effects of aerosols on climate in Amazonia and Pantanal), CHUVA (Cloud processes of tHe main precipitation systems in Brazil: A contribUtion to cloud resolVing modeling and to the GPM) and Amazonian Dense GNSS Meteorological Network [6].

2.1. Site Description

The ACONVEX site is located up-wind from Manaus-AM, Brazil, inside the campus of Embrapa Amazônia Ocidental, on 2.89^oS 59.97^oW. Figure 1 gives an overview of the area which is partially impacted by land use change. Instruments installed include: a meteorological weather station, a disdrometer, a multi filter shadow band radiometer, a cimel sun photometer (AERONET), a 24 Ghz micro rain radar, a ceilometer, a Trimble GNSS Receiver/Vaisla met. station and an UV Raman Lidar.

2.2. UV Raman Lidar

The UV Raman Lidar is operational on the ACONVEX site since July 2011. It uses a Quantel CFR-400 Nd-YAG laser at 355 nm with 95 mJ per pulse and 10 Hz repetition rate. Beam is expanded by 3 and final laser divergence is 0.25 mrad. The optical system uses a bi-axial setup with a 400 mm separation between the cassegrain telescope and the laser axis. The telescope's primary mirror has 400 mm diameter, while the secondary has a diameter

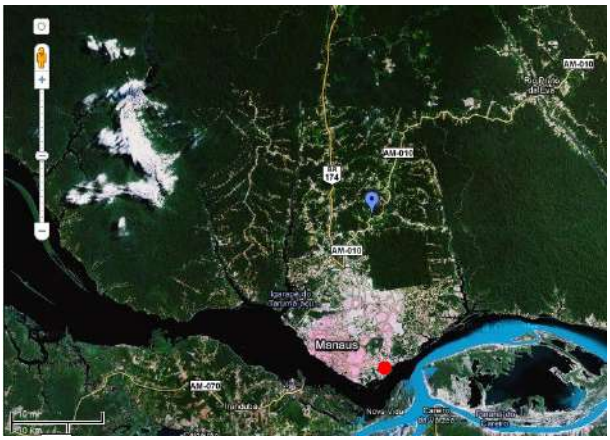

Figure 1: The location of ACONVEX site up-wind from Manaus-AM, Brazil, is indicated by the blue balloon. The red dot marks the position of the operational soundings.

of 90 mm. Focal length is 4000 mm resulting in a f/10 system. An iris is used at the focal plane which gives a field of view of 1.75 mrad and an initial overlap at 85 m and full overlap at 450 m.

No fiber optics are used and light passing through the iris goes directly in the optical detection box. Interferometric filters separate the elastic backscattered signal and the inelastic signals due to the Raman cross-section of N_2 (387 nm) and H_2O (408 nm) which are read collected in different photo-multiplier-tubes. Signals from 355 and 387 nm were recorded in analog and photon-count modes, while 408 nm only in photon count. The optical system was designed to give an uniform signal on the cathode surface almost independent of height of the detected signal. A neutral density filter is used to attenuate the elastic signal avoiding saturation, and a good signal to noise ratio (S/N) is found above 15 km depending on the atmospheric conditions. The N_2 channel, 1-min average signals have good S/N up to 15 km but only during night time. For the H_2O channel, 1-min average signals have good S/N only up to 6 km during night time.

3. METHODS

3.1. Water vapor measurement

The Raman Lidar equation for a pulse of wavelength λ returning at a Raman wavelength λ' can be written as

$$P(z,\lambda,\lambda') = P_0 \frac{c\Delta T}{2} A_{tel} \eta_{eff}(\lambda') \frac{O(z)}{z^2} \beta(z,\lambda,\lambda') \; exp\left[\int_0^z (\alpha(z',\lambda)+\alpha(z',\lambda'))dz'\right]$$

where P_0 is the pulse energy, $c\Delta T/2$ is its length, α is the volumetric attenuation coefficient, $\beta(z,\lambda,\lambda')$ is the Raman backscatter coefficient, A_{tel} is the telescope effective area, $\eta_{eff}(\lambda')$ is the detection quantum efficiency, and $O(z)/z^{-2}$ is a geometric factor.

As the atmospheric mixing ratio of N_2 is constant, it is possible to measure the mixing ratio of H_2O by taking the ratio of both background corrected signals. As shown by [5] this results in the following expression

$$w_{H_2O} = C\Gamma_A\Gamma_M \frac{\overline{S_{H_2O}} - \overline{BG_{H_2O}}}{\overline{S_{N_2}} - \overline{BG_{N_2}}}$$

where the constant Γ_A and Γ_M are the differential aerosol and molecular transmission between 387 nm and 408 nm and the over bars denote temporal and spatial averages. This smoothing is necessary for obtaining a good signal to noise ratio, but care was taken not to smooth too much and remove real variations in the water profile.

To obtain the term $C\Gamma_A\Gamma_M$, [5] did least square fits between the uncalibrated Lidar profiles and eight independent collocated soundings, performed during an intensive campaign between August 30^{th} and 5^{th} September 2011. The largest correlations were found at +8 min (i.e. $\sim$2 km height) when using 5 min and 30 m averages.

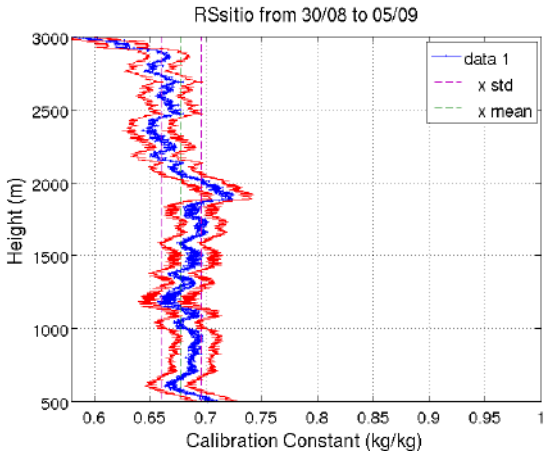

Figure 2: Ratio between uncalibrated Lidar profiles and reference water vapor measurements for collocated soundings. Data shown is the average of 8 sounding between August 30^{th} and September 5^{th} 2011.

Figure 2 shows the vertical variability of the calibration constants. The valued used in the current study corresponds to the vertical average, which was found to be 0.681±0.045 g/g [5].

3.2. Vapor profiles across clouds

From 110 nights of measurements, a visual inspection of night-plots of range correct signals led to the selection of 7 cases were single shallow clouds crossed the field of view of the instrument. The number of events selected is rather low because: (1) only thin clouds (¡300m), (2) with bases below ¡6 km (3) and good signal to noise ratio were considered.

The water vapor profiles before or after each cloud overpass were considered to be a reference of the cloud-free environment. The time-slice of the environment

and cloud portions always had the same length of about 20 min, and were separated by 10-15 min to avoid contamination steaming from the time-averages. A direct comparison of the environmental and cloudy water vapor vertical profiles was performed, and their difference calculated.

4. RESULTS AND DISCUSSION

Figure 3 show the results for four of the seven selected events. The first column shows the range and background corrected signal (RCS) with no normalization. The second column shows the water vapor field (g/kg). The dashed vertical lines indicate the region for averaging the environmental portion, while the continuous vertical lines indicated that of the cloudy portion. The last column shows the difference between the cloudy and free atmospheres, hereafter called moistening profile, where the horizontal dot-dashed line indicates the cloud base. Each row corresponds to a different date with cloud base increasing downwards: 13 Jul 2h46 / 2.75 km, 19 Jul 2h30 / 2.91 km, 11 Sep 0h30 / 4 km, 13 Jul 3h15 / 5.15 km. In all panels, time is the local Amazon time.

For all cases, the moistening profile, shown in the third column, reaches a maximum about 200 m above the cloud base, and a minimum between 200-500 m below it. The third case shows a vertical profile very similar to those obtained by shallow cumulus parametrizations [7] with a large drying up to 1 km below the cloud base. From all seven cases analyzed, however, this was the only one found. For instance, the first case in Fig.3 shows a stable layer below cloud base, while the last case shows alternating drying and moistening regions. In all cases, the maximum drying below the cloud reaches only -0.5 to -1.5 g/kg.

For the first three cases shown, there is a large amount of water vapor above the cloud. Maximum in second column is reached around 200 m above cloud base, and values of 8-10 g/kg were found even at heights above 3 km. The moistening profile reach values of about 2-5 g/kg. These results, however, must the considered with extra care, since no correction has been made for the differential scattering of the N_2 and H_2O Raman wavelengths, i.e., Γ_A and Γ_M. Moreover, multiple scattering inside the cloud was not considered.

This can be investigated by comparing the last case with the previous three. The range corrected signal in the last case is not so different inside and outside the cloud (note the orange background instead of blue), which means a very low optical depth. At the same time, the second column shows no high value of water vapor mixing ratio on the cloud top edge. This is clearly a strong indication that multiple scattering is indeed important.

5. CONCLUSIONS AND FUTURE WORK

A large systematic enhancement of about 5 g/kg in the vapor mixing ratio was observed up to 150 m above the cloud layer for these very thin clouds. At the same time, a reduction of about -1 g/kg below the cloud base was also found. Only 4 cases were analyzed, out of 7 found, but the current implementation of an automatic algorithm to detect cloud layers [8] should allow for and increased statistics.

Results above the cloud base must the considered with extra care, since no correction has been made for the differential scattering of the N_2 and H_2O Raman wavelengths and multiple scattering inside the cloud was not considered. A simple comparison of optically thin and thick clouds have shown that multiple scattering correction is indeed important.

Currently work is being done to calibrate the water vapor profiles with explicit corrections for the differential molecular and aerosol scattering of the N_2 and H_2O Raman wavelengths. The following step will be to try to correct for multiple scattering inside the cloud what should allow for the evaluation of the moistening profile in the entire column.

ACKNOWLEDGMENTS

Author's acknowledge FAPESP's support under different research grants. Institutional support from EMBRAPA and LBA was fundamental. Dr. Barbosa is thankful for the instruments shared by AEROCLIMA, CHUVA and GNSS Dense Meteorologial Network projects.

REFERENCES

1. Houze 1993: Cloud Dynamics. International Geophysics Series, **53**, Academic Press
2. Dai, Trenberth and Karl 1999: Effects of Clouds, Soil Moisture, Precipitation, and Water Vapor on Diurnal Temperature Range. *J. Climate*, **12**, pp. 2451.
3. Raupp and Silva Dias 2009: Resonant Wave Interactions in the Presence of a Diurnally Varying Heat Source. *J. Atmos. Sci.*, **66**, pp. 3165.
4. Raupp and Silva Dias 2010: Interaction of equatorial waves through resonance with the diurnal cycle of tropical heating. *Tellus A*.
5. Barbosa, et al. 2012: Intercomparison of water vapor calibration constants derived from in-situ and distant soundings for a Raman-Lidar operating in the Amazon Forest *26^{th} International Laser Radar Conference*, Athens, Greece.
6. Adams K. et al. 2011: A dense GNSS meteorological network for observing deep convection in the Amazon *Atmos. Sci. Let.*.
7. Siebesma et al. 2003: A large eddy simulation intercomparison study of shallow cumulus convection. *J. Atmos. Sci.*, **60**(10), pp. 1201.
8. Wang and Sassen 2001: Cloud Type and Macrophysical Property Retrieval Using Multiple Remote Sensors em Journal of Applied Meteorology, **40**(10), pp. 1665.

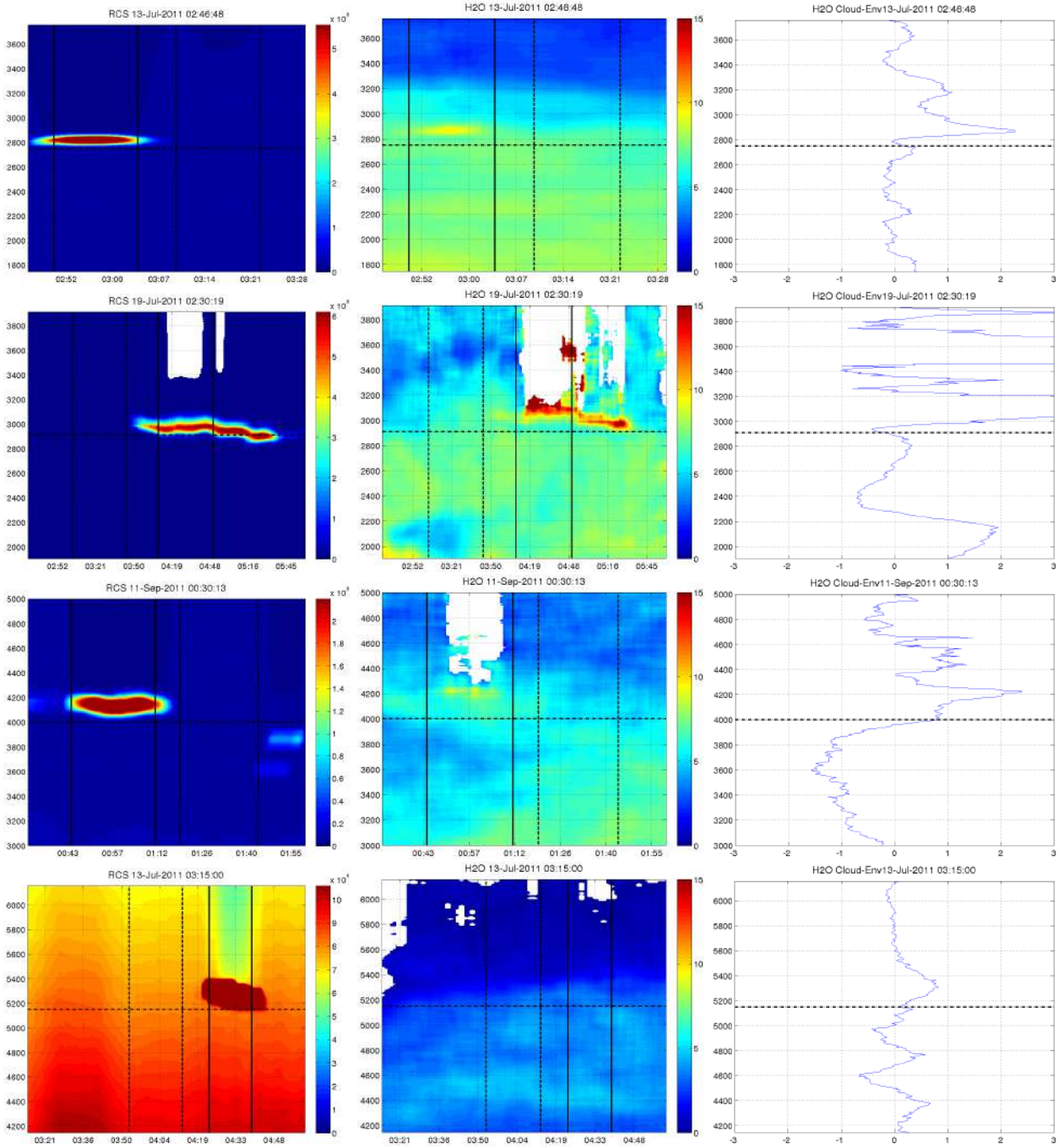

Figure 3: Range corrected elastic signal @355 nm (left), water vapor mixing ratio (g/kg, center) and difference between cloudy and environmental averages are shown. Vertical dashed lines indicated the environmental portion, while continuous lines the cloudy portion. Horizontal line indicates the cloud base altitude. From top to bottom, different cases are shown, with increasing cloud base downwards: 13 Jul 2h46 / 2.75 km, 19 Jul 2h30 / 2.91 km, 11 Sep 0h30 / 4 km, 13 Jul 3h15 / 5.15 km. Time is given as local Amazon time.

Observation of Liquid-Water Content in Precipitation in Melting Layer

Ryohei Misumi[1], Hiroki Motoyoshi[2], Satoru Yamaguchi[2], Sento Nakai[2],
Masaaki Ishizaka[2] and Yasushi Fujiyoshi[3]

[1]*National Research Institute for Earth Science and Disaster Prevention, Tsukuba, Japan*
[2]*Snow and Ice Research Center, National Research Institute for Earth Science and Disaster Prevention, Nagaoka, Japan*
[3]*Institute of Low Temperature Science, Hokkaido University, Sapporo, Japan*

1. INTRODUCTION

Numerical modeling of melting process of snowflakes is very important for forecasting of precipitation types as well as estimation of precipitation intensity in melting layer by remote sensing. However, verification of such models is still difficult, because the measurement of liquid-water amount in melting layer is not easy, especially for the liquid water held inside of individual snowflakes.

Nakamura (1960) collected falling snowflakes by dye-treated filter papers and estimated the mass fraction of liquid water in the snowflakes by measuring the spot areas just after the fall of snowflakes. However, there were two problems in Nakamura's method. One was that melting or freezing occurs immediately after a snowflake touches the filter paper unless the paper was kept exactly at 0°C. Another problem was that all the liquid water held inside of snowflakes does not always move onto the filter paper, thus the measured values would be underestimated.

Sasyo et al. (1991) improved the method of Nakamura (1960) by developing a new instrument which collects snowflakes on the filter paper kept at 0°C by a cooling unit. They discussed the dependency of liquid-water content of snowflakes on their size, but their discussion was limited in their qualitative characteristics, because the problem of the underestimation was not solved even in their study. In addition, the instrument developed by them was too expensive to be widely used by other researchers. Therefore, the observation of liquid-water content of melting snowflakes is still insufficient.

In the present study, we observed liquid-water content of melting snowflakes with the instrument developed by Sasyo et al. (1991) to provide the verification data for numerical models of melting process. In order to reduce quantitative errors, a calibration was carried out using an imitated snowflake made of polyurethane sponge. Some empirical relationships are proposed about the liquid-water amount of precipitation in melting layer and that about the liquid water soaked in individual melting snowflakes. The proposed relationships are compared with the results of a simple numerical simulation of melting snowflakes.

2. OBSERVATION

a. Instrument

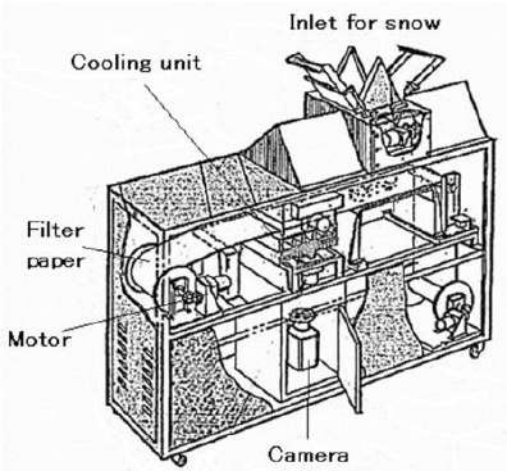

Fig 1. The instrument to measure the liquid-water content of individual snowflakes.

Figure 1 shows the instrument used in this study. It was originally developed by Sasyo et al. (1991) and produced by Suga Test Instruments Co., Ltd. The process for the measurement is as follows: 1) Snowflakes falling into the inlet are caught by the dye-treated filter paper being kept at 0°C with the cooling unit. After waiting two minutes for the water to soak into the paper, the spots on the filter paper are photographed by the camera. 2) Then the snowflakes are warmed until they completely melts, then the spots on the paper are photographed again. 3) By an image analysis, the area of a spot just after the

fall (A_1) and that after the melt (A_2) are measured. The ratio A_1/A_2 indicates the mass fraction of liquid water of the snowflake. This image analysis was carried out using software called ImageJ developed at the National Institutes of Health of the US. If $A_1/A_2 > 1$, the particle was regarded as a raindrop. The mass and the melted diameter of each snowflakes can be easily estimated by the spot area-mass relationships. Precipitation intensity is calculated by the total mass of water on the filter paper divided by the area and the time.

Here we define following three parameters in the analysis.

- Mass fraction of liquid water in precipitation.

$$F_L = R_L/R \quad . \tag{1}$$

- Mass fraction of raindrops in precipitation.

$$F_R = R_R/R \quad . \tag{2}$$

- Mass fraction of liquid water in individual snowflakes

$$W = M_L/M \quad , \tag{3}$$

Here, R_L, R_R and R are precipitation intensity of liquid water, raindrops and all hydrometeors, respectively. M is the mass of a snowflake and M_L is the mass of liquid water held inside of the snowflake.

b. Calibration

In the above measurement, it is assumed that all the melted water inside of snowflakes moves onto the filter paper. However, a part of the melted water might remain in the snowflake. As a result, the evaluated liquid-water content would be underestimated. To reduce such errors, a calibration was carried out with imitated snowflakes made of polyurethane sponge. The mass of the water contained in the imitated snowflakes and snowflakes themselves were measured accurately with an electronic balance (Shimadzu AUW120). Then the imitated snowflakes were dropped from 80 cm in height to a dye-treated filter paper, and the liquid-water content was also measured with the spot area on the paper. Figure 2 compares the mass fraction of liquid-water of individual snowflakes measured with the filter paper (W_F) and the electronic balance (W_E). W_F shows smaller values than W_E especially when the liquid-water fraction is small. As a result, the following calibration curves were obtained.

$$W_E = W_F^{0.41} \tag{4}$$

All the measured values were corrected using (4).

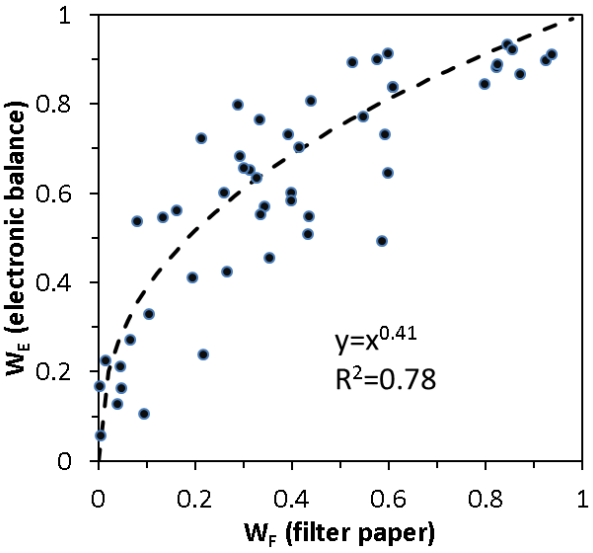

Fig.2 Plots of mass fraction of liquid-water content in imitated snowflakes made of polyurethane sponge measured by the filter paper (W_F) and the electronic balance (W_E). Broken line indicates the best-fit curve.

c. Observation

The observation was performed at the Snow and Ice Research Center in Nagaoka City, Japan (37.4260°N, 138.8867°E). Table 1 shows the date of observation, range of temperature and relative humidity, and the number of samples (number of sheets of filter papers).

Table 1 Observation cases

Time (JST)	Temperature (°C)	Relative humidity (%)	Samples
3:20-7:56 26 Mar 2011	0.27-1.58	88.1-96.2	23
15:11-18:51 9 Dec 2011	0.10-1.79	93.6-97.9	19
23:42-0:11 22-23 Dec 2011	0.62-0.85	95.6-96.8	4
16:05-18:45 24 Dec 2011	0.17-1.31	82.7-95.1	6
9:13-12:14 12 Mar 2012	1.23-1.72	79.5-94.1	2

During the observation, microscopic

photographs of precipitating particles were taken to confirm the type of hydrometeors. Figure 3 shows the photographs taken on 26 March 2011. There were snowflakes in various melting stages; some particles remained their crystal structure while others completely melted. These types of hydrometeors fell together. Most of the original snowflakes were rimed aggregates of dendrites.

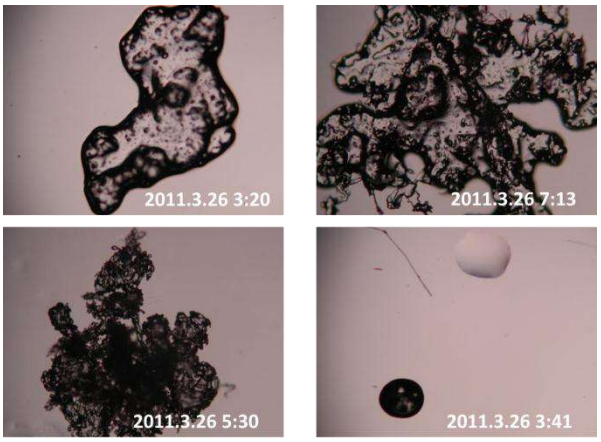

Fig.3 Photographs of melting snowflakes sampled on 26 March 2011

3. RESULTS

a. Relationship between F_L and F_R

Figure 4 shows the plots of the mass fraction of raindrops (F_R) as a function of mass fraction of liquid water in precipitation (F_L).

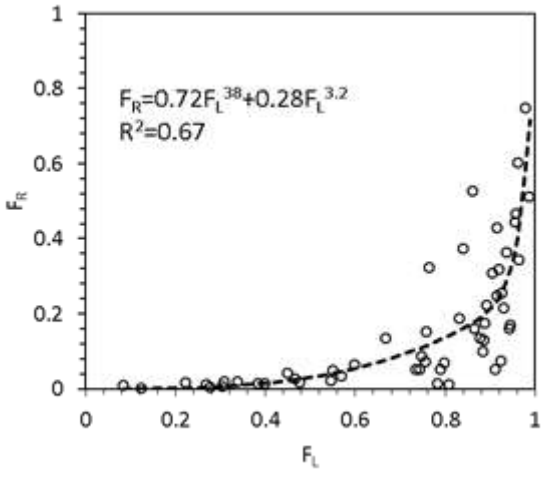

Fig. 4 Relationship between mass fraction of liquid water in precipitation (F_L) and that of raindrops (F_R). Broken line indicates the best fit.

From the above plots, the relationship between F_L and F_R is approximated as:

$$F_R = 0.72F_L^{38} + 0.28F_L^{3.2} \quad (5)$$

According to this empirical formulation, most of the melted water is kept inside of snowflakes when $F_L < 0.9$. For instance, $F_R=0.14$ when $F_L=0.8$, which indicates the mass fraction of raindrops is only 14% even when liquid water occupies 80% of the precipitation. This information would be very important for validation of numerical models of melting layer, which treat snowflakes and raindrops separately. As will be shown later, this relationship is not strongly dependent on the precipitation intensity.

b. Liquid-water fraction of individual snowflakes

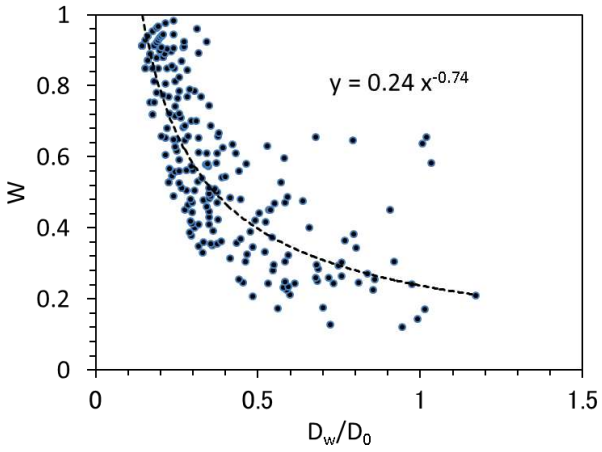

Fig. 5 Relationship between the mass fraction of liquid water in individual snowflakes (W) and their melted diameter normalized by D_0 sampled at 16:01 JST on 9 December 2011.

In each sample, we found the tendency that the liquid-water fraction of each snowflake (W) becomes small as its size was large (Fig.5). We approximated the relationship between W and the melted diameter (D_W) as follows:

$$W = \alpha\left(\frac{D_W}{D_0}\right)^{\beta} \quad (6)$$

Here, D_0 is the median volume diameter in each sample calculated by assuming the size distribution of Gunn and Marshall (1957). If we applied the expression (6) to all the samples, α and β were found to be functions of F_L:

$$\alpha = 0.90F_L + 0.11 \quad (7)$$

$$\beta = 1.02F_L - 0.98 \quad (8)$$

Empirical formulations (6)-(8) reproduced W of each snowflake in our observation with 0.09 in averaged error.

c. Particle size distribution

In order to see the variation of particle size distribution according to the melting process, we divided the samples into four classes with the value of F_L and calculated the averaged size distribution in each class. Because the fall speed of individual snowflakes was unknown, we used N_H ($cm^{-3}s^{-1}$) as the vertical axis. Figure 6 shows the size distribution averaged in $F_L < 0.25$ and $0.5 < F_L < 0.75$.

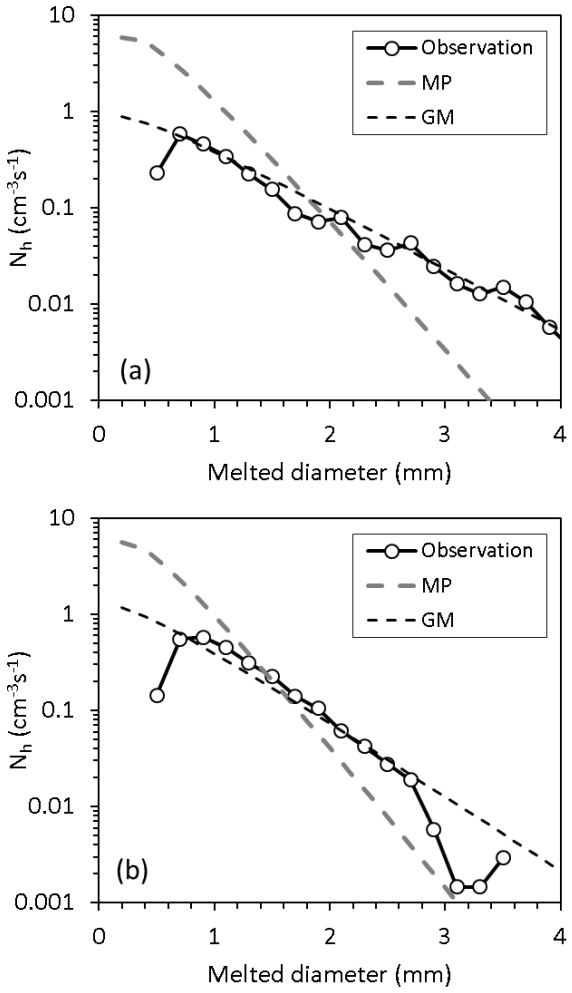

Fig. 6 Size distribution of precipitation particles averaged in the samples with (a) $F_L < 0.25$ and (b) $0.5 < F_L < 0.75$. The Gunn-Marshall (GM) and the Marshall-Palmer (MP) distributions are shown by the black and the gray broken lines, respectively.

In both classes, the size distribution agrees well with that of Gunn and Marshall (1957). However, the number of snowflakes bigger than 3 mm in melted diameter decreased when F_L is large. We cannot conclude if such difference was due to the melting breakup of snowflakes or simply due to the difference of precipitation systems.

4. NUMERICAL SIMULATION

A simple numerical simulation assuming spherical snowflakes was carried out to discuss if a melting model of snowflakes can explain the observational results. In the simulation, following assumption was made: 1) Shape of snowflakes is sphere. 2) Bulk density of snowflakes follows the empirical formulation of the A-type aggregates in Ishizaka (1995). 3) Melting of snowflakes occurs from their surface, and the melted water soaks internally. That is, the diameter of snowflakes becomes small by the melting. 4) Surface temperature of melting snowflakes is 0℃. 5) The effect of deposition and sublimation during melting is not taken into account. This assumption is justified by the fact that the humidity was close to the saturation at 0°C in our observation. 6) The particle size distribution follows the Gunn-Marshall distribution. 7) The fall speed of snowflakes was calculated by the formulation of Bohm (1989).

Melted diameter of snowflakes were divided into 40 bins from 0.1 mm to 8.1 mm. Snowflakes fall from the 0°C level in the air with lapse rate 5 K/km. We used a constant height step (0.1 m) instead of a constant time step in order to calculate F_L, F_D and W at the same height levels. Precipitation intensity was assumed as 1, 5 and 10 mm/h.

Figure 7 shows the relationship between calculated F_R and F_L. It shows that the relationship is not strongly dependent on the precipitation intensity. Some flip-flops in the graph are caused by the discrete bins. The calculated relationships agree well with the observation, which suggests that a spherical-snowflake model without breakup or shedding can explain the raindrop rate in melting layer.

Figure 8 shows the mass fraction of liquid water of snowflakes (W) versus normalized diameter (D_0/D_w) when F_L=0.5. Results of the simulation agree well with the empirical formulation given in (6)-(8), although there is slight underestimation for snowflakes with large diameter. However, the difference is not

significant because the calculation results are within the variance of observational data.

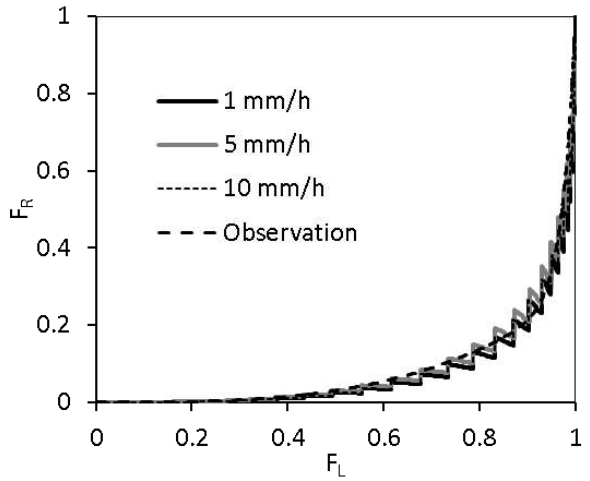

Fig.7 Mass fraction of liquid water in precipitation (F_L) and that of raindrops (F_R) simulated with the numerical model. Broken line indicates the empirical formulation (5) obtained from the observation.

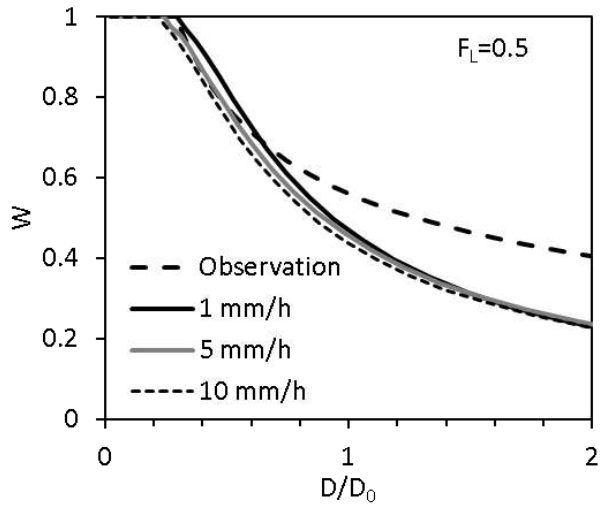

Fig. 8 Relationship between mass fraction of liquid water of individual snowflakes (W) and melted diameter normalized by median-volume diameter (D_w/D_0) when F_L=0.5. Broken line indicates the empirical formulation (6)-(8).

5. SUMMARY

Liquid-water content of melting snowflakes was measured with filter papers which kept at 0°C by a cooling unit. By a calibration using imitated snowflakes, quantitative errors were reduced. From the results, we proposed the empirical relationships on the mass fraction of raindrops (F_R) and liquid water (F_L) in precipitation in melting layer, and also for the mass fraction of liquid water in individual snowflakes. The proposed relationships agreed well with a simple numerical simulation assuming spherical snowflakes. The proposed relationships are expected to be used for validation of numerical models of melting snowflakes.

ACKNOWLEDGMENTS

The authors express their hearty thanks to Suga Test Instruments Co., Ltd. for providing us the instrument developed by Sasyo et al. (1991).

REFERENCES

Bohm, H. P., 1989: A general equation for the terminal fall speed of solid hydrometeors. *J. Atmos. Sci*., 46, 2419-2427.

Gunn, K. L. S. and J. S. Marshall, 1957: The didtrubution with size of aggregate snowflakes. *J. Meteor*. 15, 452-561.

Ishizaka, M. 1995: Measurement of falling velocity of rimed snowflakes. *Seppyo*, 57, 229-238 (in Japanese with English abstract).

Nakamura, T. 1960: On the method of measuring the liquid water content of falling snowflakes. *Seppyo*, 22, 145-146 (in Japanese with English abstract).

Sasyo, Y., T. Mori and O. Onozaki,1991: Observation of liquid water content of melting snowflakes with a new instrument. *J. Meteor. Soc. Japan,* 69, 83-90.

HAMMOCK EFFECT OF ATMOSPHERIC BOUNDAR LAYER FOR DOWNDRAFT ASSOCIATED WITH NEW-TYPE OF ORGANIZED TURBULENT AIR MOTION

Yasushi FUJIYOSHI[1], Akihito UMEHARA[2], Chusei FUJIWARA[2]
[1] Inst. Low Temp. Sci., Hokkaido Univ., Sapporo, JAPAN
[2] Graduate School of Environmental Science, Hokkaido Univ., Sapporo, JAPAN

1. INTRODUCTION

Since layer clouds are formed near the discontinuous layer of air density and wind shear, such kinematic and thermo-dynamic instabilities as Kelvin-Helmholtz Instability (KHI) Wave, Gravity Wave and Mammatus would be expected to occur. However, there have been a limited number of studies on the organized disturbances formed near the cloud base (e.g., Hlad, 1944; Kikuchi et al., 1991; Martner, 1995; Kollias and Albrecht, 2005; Schultz et al., 2006, Wang and Sassen, 2006, Kanak et al., 2008).

Using a 3D-scanning Coherent Doppler Lidar (3DCDL), we found a new-type of organized turbulent air motion below cloud base. This turbulence often caused strong downdraft in the free atmosphere like the “Heat Burst” (e.g., Johnson, 2001). This downdraft, however, was not able to reach the ground surface because of the hammock effect of the atmospheric boundary layer (ABL) like the cushion stage of stationary microburst (Fujita,1981).

2. ORGANIZED CURLY PATTERN FORMED WITHIN THIN LAYER CLOUD

Figure 1 shows time-series of RHI images of a thin layer cloud observed by the 3DCDL at Sapporo, Japan, on 1 May 2007. The cloud changed from layer to curly type within 10 minutes. Figure 2 shows vertical cross sections of S/N ratio, Doppler velocity and estimated vertical velocity of the curly type of clouds. Like anvil mammata, this pattern shows smooth and cauliflower-like protube-rance. However, this turbulence did not develop below anvil-clouds. The mean

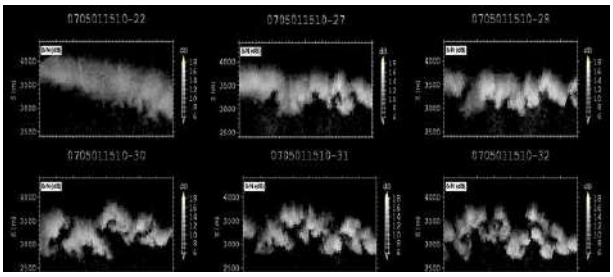

Fig. 1 Change with time of RHI images of a thin layer cloud from 15:32 to 15:42 JST on 1 May 2007.

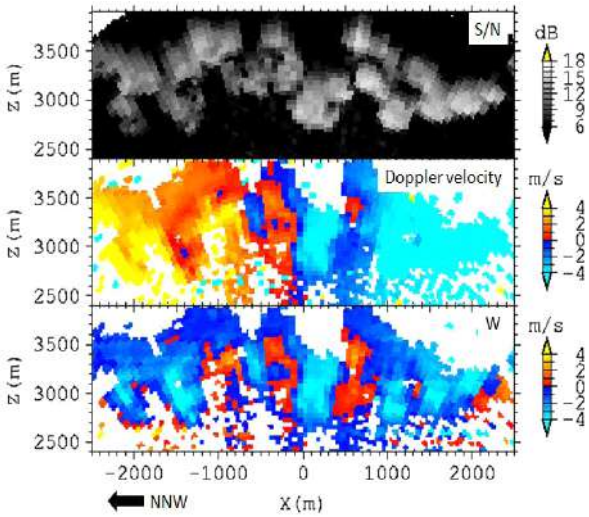

Fig. 2 Vertical cross sections of S/N ratio, Doppler velocity and estimated vertical velocity of the curly pattern.

horizontal scale, depth and aspect ratio are 0.6 km, 0.45 km and 1.6, respectively. Estimated vertical velocity ranged from -4.5 m/s (downdraft) to 1.5 m/s (updraft).

3. STRONG DOWNDRAFT ASSOCIATED WITH THE CURLY PATTERN

The curly pattern was also observed by the 3DCDL on 3 June 2005. Figure 3 shows time series of vertical cross sections of S/N ratio, Doppler velocity and estimated vertical

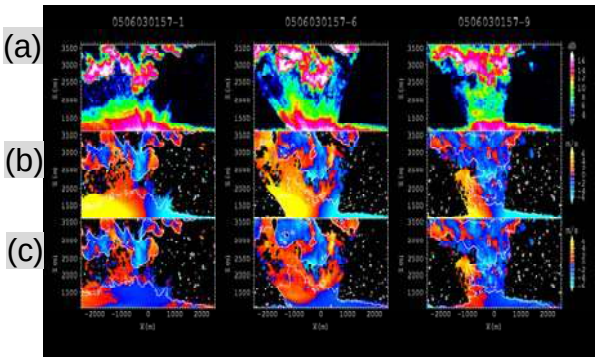

Fig. 3 Time series of vertical cross sections of S/N ratio (a), Doppler velocity (b) and estimated vertical velocity (c) from 01:57 to 02:10 JST.

velocity from 01:57 to 02:10 JST. As seen in the figure, strong downdraft (about 8 m/s) is

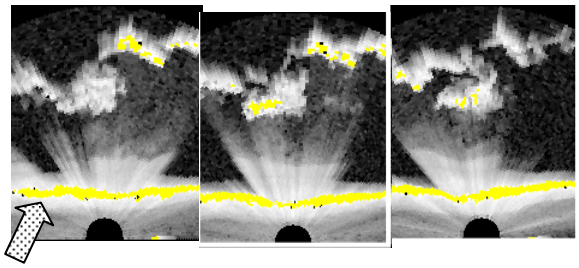

Fig.4 Time series of vertical cross section of S/N when the strong downburst approached to the top of ABL (indicated by an arrow)

found just below the curly pattern. However, no strong winds (gusts) were detected on the ground surface.

Figure 4 shows the time series of vertical cross section of S/N when the strong downburst approached to the ground surface. As seen in the figure, top boundary of the atmospheric boundary layer showed convex surface when the downdraft reached to there.

4. DISCUSSION AND SUMMARY

This strange curly pattern began to develop near the base of optically thin cirro- or altostratus cloud. Since vertical wind shear was not large, thermodynamic effects (entrainment and evaporation) would play an important role in formation of this pattern. This organized pattern often caused strong downdraft (about 8 m/s) in the free atmosphere. This downdraft, however, was not able to reach the ground surface because of the hammock effect of the atmospheric boundary layer. This process is the good contrast with rising thermals that cannot overshoot the top boundary of the atmospheric boundary layer.

References

Fujita, T. T., 1981: Microburst as an Aviation Wind shear Hazard, AIAA 19th Aerospace Sciences Meeting, January 12-15, St. Louis, Missouri.

Hlad, C. J., Jr., 1944: Stability-tendency and mammatocumulus clouds, Bull. Amer. Meteor. Soc., 25, 327–331.

Johnson, R. H., 2001:Surface mesohighs and mesolows, Bull. Amer. Meteor. Soc., 82,13-31.

Kanak, K. M., and Coauthors, 2008: Numerical Simulation of Mammatus, J. Atmos. Sci., 65, 1606-1621.

Kikuchi et al., 1991: The cloud base structure of stratocumulus clouds, J. Met. Soc. Japan, 69, 701-708.

Kollias, P., I. Jo, and B. A. Albrecht, 2005: High-resolution observations of mammatus in tropical anvils, Mon. Wea. Rev.,133, 2105–2112.

Martner, B. E., 1995: Doppler radar observations of mammatus, Mon. Wea. Rev., 123, 3115–3121.

Schultz, D. M., and Coauthors, 2006: The mysteries of mammatus clouds: Observations and formation mechanisms, J. Atmos. Sci., 63, 2409–2435.

Wang, L., and K. Sassen, 2006: Cirrus mammatus properties derived from an extended remote sensing dataset, J. Atmos. Sci., 63, 712–725.

A REVIST TO MARSHALL-PALMER SIZE DSITRIBUTION OF RAINDROPS

Yasushi FUJIYOSHI[1], Nobuhiro NAGUMO[2], Ikuyo YAMAMURA[2], Atsushi AOKI[2]
[1] Inst. Low Temp. Sci., Hokkaido Univ., Sapporo, JAPAN
[2] Graduate School of Environmental Science, Hokkaido Univ., Sapporo, JAPAN

1. INTRODUCTION

Based on the long-term (more than several years) measurements of raindrop size distribution (RSD) with two-dimensional video disdrometers (2DVD) in different climatic regimes: subarctic (Sapporo and Kanazawa, Japan), subtropical (Okinawa, Japan) and tropical (Sumatra, Indonesia) regions, we reported “The maximum size of raindrops” (Fujiyoshi et al., 2008).

In this paper, we will statistically confirm that large raindrops fell in short periods with exceptionally high concentration numbers, and propose a new RSD based on the statistical analysis of the degree of closeness of two raindrops with the same size bin.

2. METHOD OF ANALYSIS

2DVD can record the time (t_i) and position (X_i,Y_i) of a raindrop when it fall into the sampling area of 2DVD (10cmx10cm). We defined the measure of closeness (MC) of two raindrops with the same size bin (d～d+δd) as follows:

MC≡Number-density(i)/Number-density(MP)

Here,

(a) Number-density (i) = 2/Volume

Volume = H(Height) x S(Area)

H = V(Terminal velocity of raindrop) x (t_i-t_{i+1})

t_i= Time when a raindrop with the size bin (d～d+ δ d) is observed.

S = (X_i-X_{i+1})x(Y_i-Y_{i+1})

(X_i,Y_i)= Sampling position of a raindrop

(b) Number density(MP) is calculated by using Marshall-Palmer (M-P) RSD.

Therefore, MC>1, MC=1, and MC<1 mean that measured number density is higher, equal, lower than that of M-P RSD, respectively.

3. RESULTS

Figure 1 shows the appearance frequency of MC for raindrops with d=1.5 – 1.75 mm of all raindrops observed in four climatic regimes. The highest appearance frequency appears a little bit larger than MC=1.

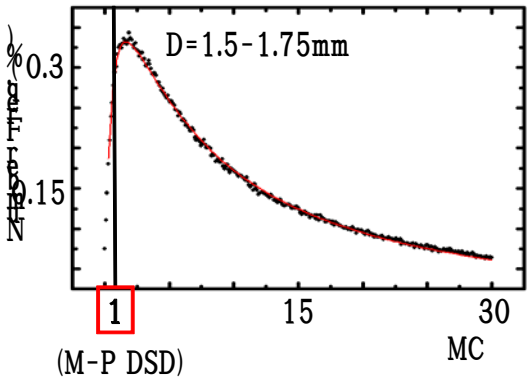

Fig. 1 An example of appearance frequency (%) of MC. MC=1 means that observed number density is the same with that of M-P RSD.

Appearance frequency of MC can be approximated by the Log-Normal distribution. Using the approximated Log-Normal distribution function, we can calculate an expected value of MC for each size bin of raindrops (Fig. 2). As shown in Fig. 2, the expected value of MC exponentially increases with increasing size of raindrops. This result clearly shows that two raindrops fell much higher concentration than M-P RSD.

Changing rainfall intensity (R ; 10 minutes mean) and the size bin of raindrops, we made the same figures with Fig. 1. Then we

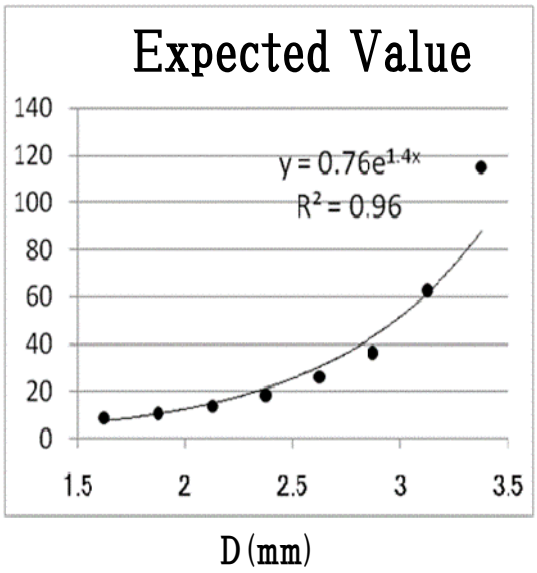

Fig. 2 Size dependency of the expected value of MC.

identified the highest MC(peak) for each rainfall intensity and size bin. If we know MC(peak), we can calculate the Number-density(i)(peak). Figure 3 shows RSDs using the Number-density (i) (peak). As seen in Fig.3, number densities are very close to M-P RSD when d<3mm. On the contrary, they deviate largely from M-P RSD when d>3 mm, that is, large raindrops fell much higher concentration than that of M-P RSD. It is also noted that the critical size of raindrops at which the Number-density (i)(peak) begins to deviate from M-P RSD increases with the size of raindrops.

4. DISCUSSION AND SUMMARY

Based on many 2DVD data measured at different climatic regimes, we statistically confirmed that the number densities of raindrops with d>3mm are much higher than those of M-P RSD.

Following processes would explain the observed results:

1) The melting of large graupels and snowflakes can produce large raindrops.
2) Melting particles and raindrops are sorted during their fall depending on their fall velocities.
3) Raindrops larger than 9 mm in diameter experience spontaneous break-up during their fall.
4) Large raindrops can survive a fall when the concentration of small raindrops is low enough.
5) Most of smaller raindrops found at the beginning of rainfall events or after a pause in rainfall are originated from break-up of larger raindrops.
6) Most of raindrops found during the intense rainfall events are formed by the collision-coalescence and collision-breakup processes of raindrops.

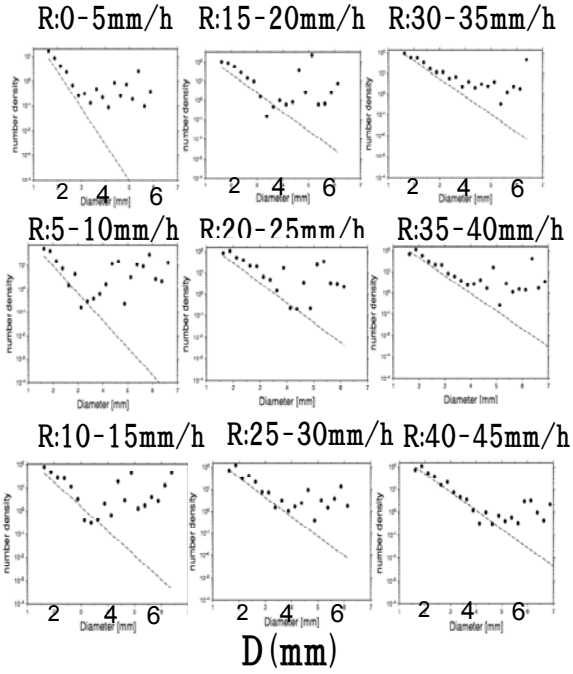

Fig. 3 Distribution of Number-density(i) (peak) with size of raindrops.

Reference

Fujiyoshi, Y., I.Yamamura, N. Nagumo, K. Nakagawa, K. Muramoto, T. Shimomai, 2008: The maximum size of raindrops — Can it be a proxy of precipitation climatology? Int. Conf. Clouds and Precipitation, Cancun, Mexico, 7–11 July, Poster P1.31.

INVESTIGATION OF THE SIGNIFICANT RADIATION ERROR CASE OF THE JAPAN METEOROLOGICAL AGENCY MESO-SCALE MODEL FOR THE FORECASTING THE PHOTOVOLTAIC POWER PRODUCTION

Ken-ichi Shimose[1], Hideaki Ohtake[1], Yoshinori Yamada[2], Joao Gari da Silva Fonseca Junior[1], Takumi Takashima[1] and Takashi Oozeki[1]

[1] Research Center for Photovoltaic Technologies, National Institute of Advanced Industrial Science and Technology, Tsukuba, JAPAN
[2] Meteorological Research Institute, Japan Meteorological Agency, Tsukuba , JAPAN

1. INTRODUCTION

Power production of a photovoltaic (PV) power plant varies according to weather conditions. Therefore, in association with the stabilization of the electric power system which takes account of varying PV power, it is important to predict the PV power production in a few days. The prediction of the PV power production is often executed by the engineering model. The input of the engineering model is from the output of the weather forecasting model so that the accuracy of the weather forecasting model affects the prediction of the PV power production. In particular, the forecast value of solar irradiance, which is calculated as downward shortwave radiation (DSWR) flux at surface in the weather forecasting model, is one of the major factors for the PV power production so that it is necessary to assess the accuracy of its value.

In our research group, the output of the Japan Meteorological Agency Meso-Scale Model (hereafter JMA-MSM) is used for the input of the engineering model (Fonseca et al., 2011). JMA-MSM is a non-hydrostatic and regional model (Saito et al., 2007). There are several studies that validate the value of DSWR of JMA-MSM (e.g., Nagasawa, 2006; Ohtake et al., 2011). These studies only mentioned about two-dimensional features of accuracy of forecast DSWR. The accuracy of the forecast DSWR is greatly associated with the forecast cloudiness so that it is necessary to analyze the error cause of the individual case using the three-dimensional feature of the forecast cloud.

The purpose of this study is the investigation of the significant error cause of the forecast DSWR in JMA-MSM. In this study, because of the limitation of the radiation data set, we focus on the analysis area around Tsukuba, Japan.

2. DATA AND METHODS UTILIZED

The output of JMA-MSM is the grid point value. The horizontal resolution of JMA-MSM data is 5 km. The computational domain (Fig. 1a) is covering around Japan with 721 x 577 x 50 points (3600 km x 2880 km x 21.8 km). The radiation scheme of JMA-MSM is based on Kitagawa (2000). The partial condensation scheme is used to diagnose cloud fraction (Nagasawa, 2008). In order to reduce the computational cost, the calculation of the radiation process is conducted at 10 km and 15 minutes intervals. The forecasting cycle of JMA-MSM is every 3 hours, in UTC time, providing forecasts for the next 15 or 33 hours, depending on the forecast time. In this study, JMA-MSM 33 hour forecasts started at 03UTC (the local standard time, LST, of Japan is plus 9 hours) are used for analysis. The output interval is every 1 hour.

The observational DSWR data which is used for the validation is measured by the JMA using a pyranometer at Tsukuba observation station (about 50 km northeast of Tokyo, Fig. 1b). The forecast DSWR is represented by the average of the nearest grid point and its neighbor points (total 9 grid points). The analysis period is from 2008 to

2010.

In order to extract the significant error case, given threshold of error amount is set as follows: | (forecast DSWR) − (observational DSWR) | ／ (DSWR at the top of atmosphere) > 0.2. The extracted cases are categorized as overestimate or underestimate and investigated weather conditions using the weather map, satellite image, visual observation of cloud condition at Tsukuba (09LST and 15LST) and JMA-MSM three-dimensional cloudiness.

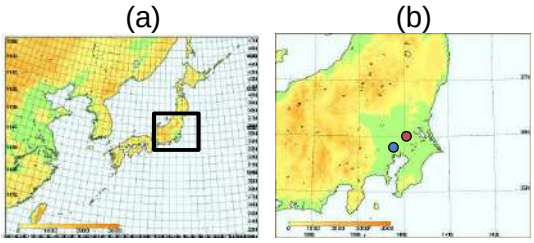

Figure 1: (a) Computational domain of JMA-MSM. (b) Topography around Tsukuba inside the rectangle of (a). Blue point: Tokyo, Red point: Tsukuba.

3. RESULTS

3.1 Error characteristic

The error cases which exceed the threshold described above are 89 cases: 53 of them are overestimate case, 36 cases are underestimate case. Figure 2 shows the seasonal distribution of the error cases. The underestimate cases mainly occurred during the summer season. In another season, error cases were mainly overestimate. The tendency of under/over estimate is corresponding to the result of large area analysis (Ohtake et al., 2011; Nagasawa, 2008).

Figure 3 shows the classification of synoptic weather conditions for each case. For the overestimate case (Fig.3a), it is found that 25 overestimate cases occurred after the passage of the low pressure and cold front and 23 cases occurred after the passage of the high pressure. For the underestimate case (Fig.3b), it is found that 9 overestimate cases occurred after the passage of the high pressure, 7 cases were associated with typhoon and 9 cases were related to Baiu front. This information is possible to be associated with air flow information so that it is necessary to investigate the property of wind direction at Tsukuba, but it is future work.

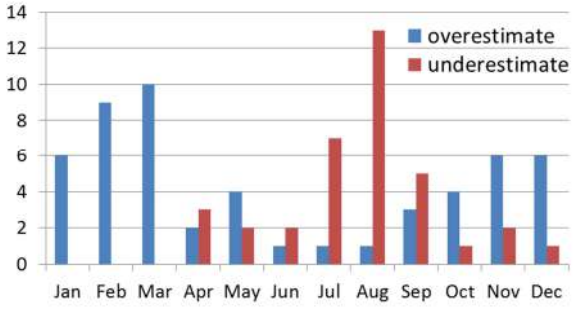

Figure 2: Seasonal distribution of the error cases.

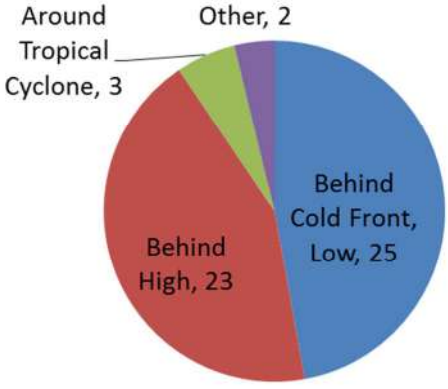

(a) Overestimate case

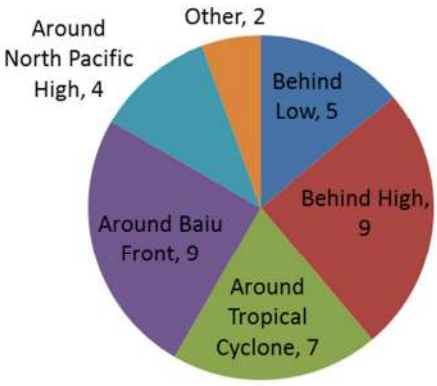

(b) Underestimate case

Figure 3: Classification of synoptic weather conditions. (a): overestimate case and (b): underestimate case.

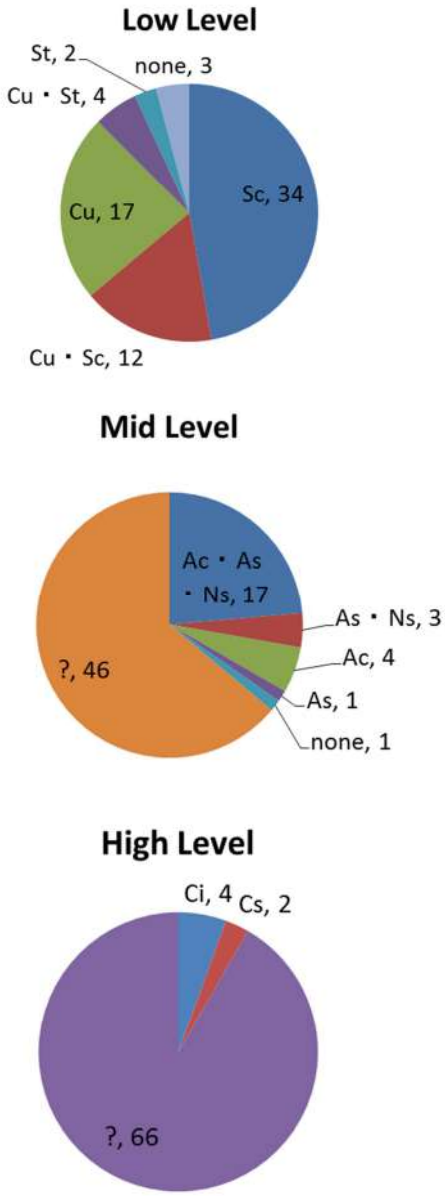

Figure 4: Classification of the visual observation of cloud conditions for the overestimate case at Tsukuba.

Figure 4 shows the classification of the visual observation of cloud conditions at Tsukuba. The visual observation data only exists at 09LST and 15LST so that cases are classified only when the over/ underestimate occurred that time. For the overestimate case, there were thick clouds (80% of them were associated with stratocumuli or stratus) at the low level (850 hPa below) so that the conditions of the mid level (850 hPa – 500 hPa) and high level (500 hPa – 100 hPa) were not visible. For the underestimate case (Fig.5), in the case of 90 %, there were cumuli at the low level. About 80% mid level clouds were associated with altocumulus and about 60% high level clouds were cirrus. There were thin clouds at the mid level and high level and the sun could be identified from the ground.

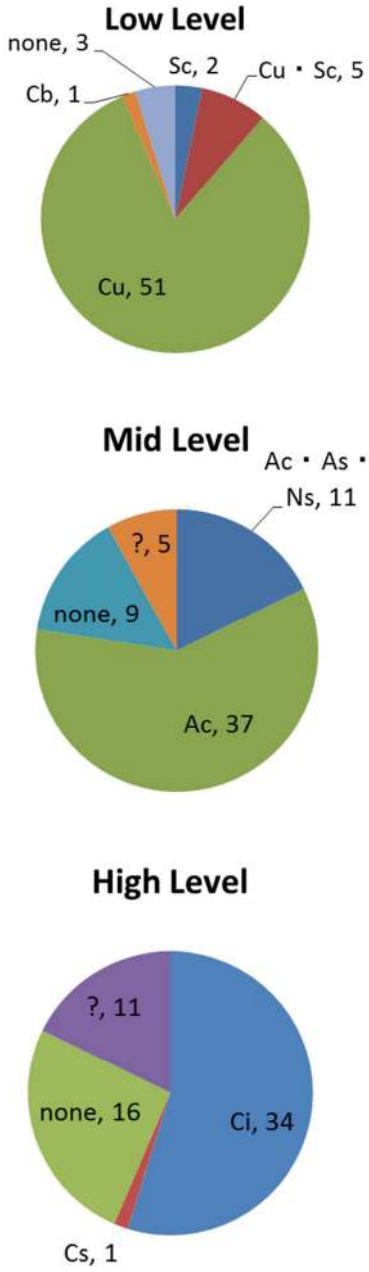

Figure 5: Same as Fig. 4 except for the underestimate case.

3.2 Case study

(a) Overestimate case

Figure 6 shows the time series of the DSWR at the represent overestimate day,

16 Feb. 2010. All grid point value of forecast DSWR in the region of 100^2 km^2 centered Tsukuba are also shown in Fig. 6. In this case, the forecast DSWR is overestimated all day and the maximum error is about 200 W m^{-2}. The spread of each grid point value of forecast DSWR is small so that this tendency covered large region around Tsukuba. Figure 7 shows the weather map at 09LST. This case was associated with the cold front. Figure 8 shows the satellite image around Tsukuba at 15LST. There were widespread clouds at the behind of the cold front around Tsukuba. Table I shows the visual observation of cloud condition at Tsukuba. There was thick stratocumulus at the low level all day.

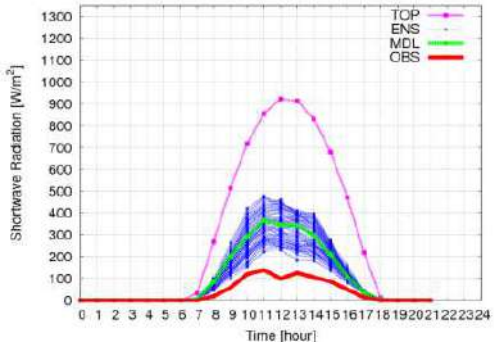

Figure 6: Time series of the solar irradiance at Tsukuba on 16 Feb. 2010. Red line: observation, Green line: forecast, Blue lines: forecasts around Tsukuba (within 100^2 km^2 centered Tsukuba), Pink line: solar irradiance at the top of atmosphere

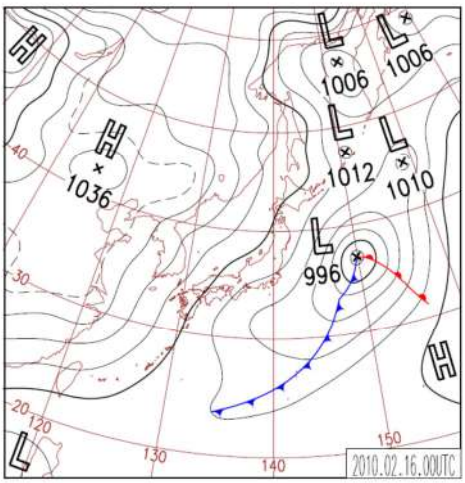

Figure 7: Weather map around Japan at 09LST (00UTC) 16 Feb. 2010.

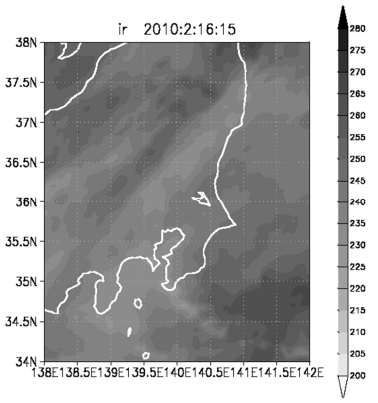

Figure 8: Satellite image (infrared radiation) around Tsukuba at 15LST (06UTC) 16 Feb. 2010.

Table I: Visual observation of the cloud condition at Tsukuba on 16 Feb. 2010.

	09LST	15LST
high level	unknown	unknown
mid level	unknown	unknown
low level	stratocumulus	stratocumulus

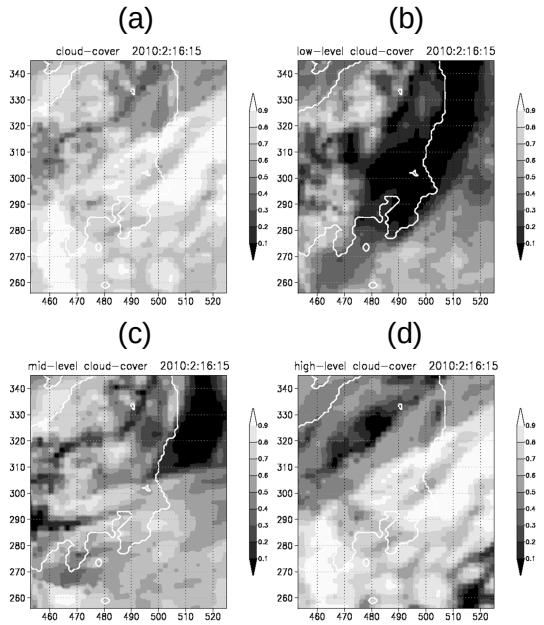

Figure 9: Forecast cloudiness around Tsukuba at 15LST 16 Feb. 2010. (a): total, (b):low level, (c):mid level, (d):high level.

Figure 9 shows the JMA-MSM forecast cloudiness data around Tsukuba at 15LST 16 Feb. 2010. The total cloudiness of the JMA-MSM forecast (Fig. 9a) appears similar distribution as the satellite image (Fig. 8).

However, at the low level, there is few forecast cloudiness (Fig. 9b). Although the visual observations indicated the thick stratocumulus at the low level, the JMA-MSM fails to simulate low level clouds. This false is the one of error cause for the forecast DSWR.

(b) Underestimate case

Figure 10 shows the time series of DSWR at the represent underestimate day, Aug. 11, 2010. All grid point value of forecast DSWR in the region of 100^2 km^2 centered Tsukuba are also shown. In this case, the forecast DSWR is underestimated all day and the maximum error is about 500 W m^{-2}. The spread of each grid point value of forecast DSWR is small, same as the represent case of overestimate. Figure 11 shows the weather map at 09LST. This case was associated with the typhoon. Figure 12 shows the satellite image around Tsukuba at 15LST. There were no thick clouds near Tsukuba. Table II shows the visual observation of cloud condition at Tsukuba. There was cumulus at the low level, thin altocumulus at the mid level and cirrus at the high level all day.

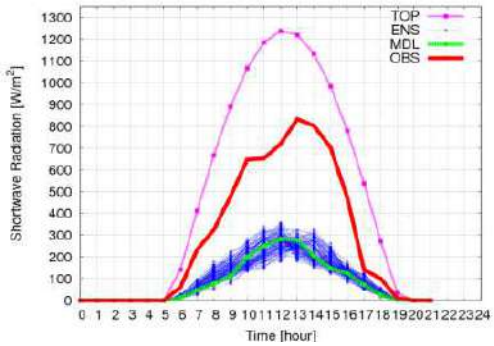

Figure 10: Same as Fig. 6 except for 11 Aug. 2010.

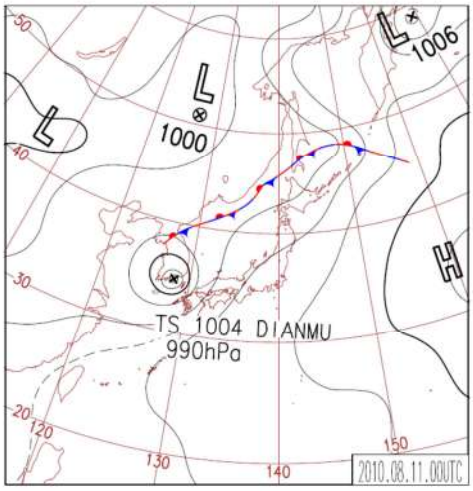

Figure 11: Weather map around Japan at 09LST (00UTC) 11 Aug. 2010.

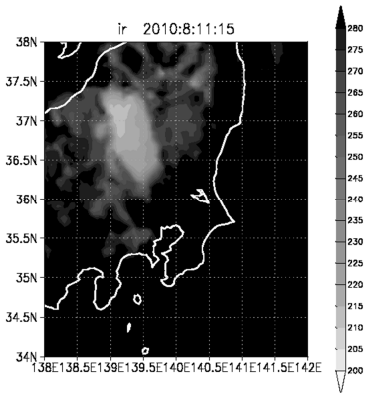

Figure 12: Satellite image (infrared radiation) around Tsukuba at 15LST (06UTC) 11 Aug. 2010.

Table II: Visual observation of cloud condition at Tsukuba on Aug. 11, 2010.

	09LST	15LST
high level	cirrus	cirrus
mid level	thin altocumulus	thin altocumulus
low level	cumulus	cumulus

Figure 13 shows the JMA-MSM forecast cloudiness data around Tsukuba at 15LST 16 Feb. 2010. The total cloudiness of the JMA-MSM forecast (Fig. 13a) appears excess and widespread comparing with the satellite image (Fig. 12). In particular, the forecast cloudiness is excess at the mid level and high level (Fig 13c,d) so that the

JMA-MSM fails to simulate these levels clouds. This false is the one of error cause for the forecast DSWR.

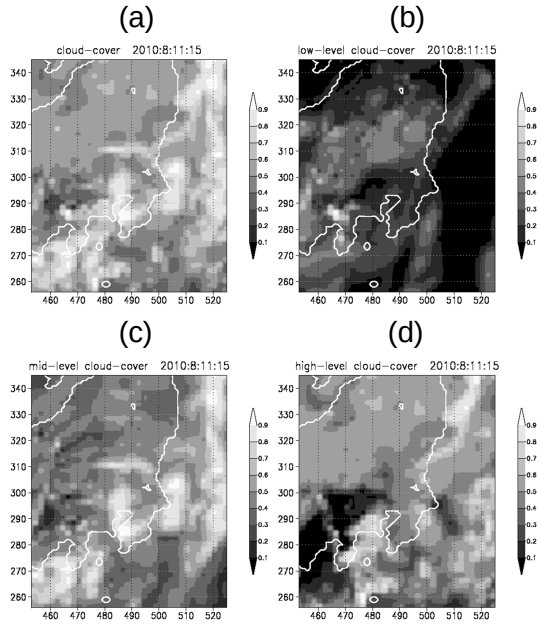

Figure 13: Same as Fig. 9 except for 11 Aug. 2010.

4. CONCLUSIONS

In order to validate solar irradiance of the JMA-MSM, the significant error cause of the forecast downward shortwave radiation (DSWR) in JMA-MSM is investigated at Tsukuba, Japan. The extracted 89 cases are categorized as overestimate or under-estimate and investigated weather conditions.

For the case of overestimate, when the thick stratocumulus appears at the low level, the JMA-MSM fails to simulate the low-level cloud. This is the one of the reason why the forecast DSWR becomes overestimate. For the case of underestimate, when the thin clouds appear through the all levels, the JMA-MSM fails to simulate the mid-level and high-level clouds. This is the one of the reason why the forecast DSWR becomes underestimate.

Acknowledgements. This work was supported by NEDO (New Energy and Industrial Development Organization, Japan). The authors wish to thank the member of Numerical Prediction Division of the Japan Meteorological Agency, Forecast Research Department of the Meteorological Research Institute and Aerological Observatory, whose suggestions helped us.

REFERENCES

Fonseca, J. G. S., T. Oozeki, T. Takashima, G. Koshimizu and Y. Uchida, 2011: Forecast of power production of a photovoltaic power plant in Japan with multilayer perceptron artificial neural networks and support vector machines, 26th EU PVSEC, Hamburg, Germany

Kitagawa, H., 2000: Radiation scheme, Report of Numerical Prediction Division, 46, 16-31 (in Japanese), 2000

Nagasawa, R., 2006: Improvement of a radiation process for the non-hydrostatic model, 12th Conference on Atmospheric Radiation, Madison, USA

Nagasawa, R., 2008: Radiation scheme, Report of Numerical Prediction Division, 54, 149-165 (in Japanese)

Ohtake, H., Y. Yamada, A. Hashimoto, S. Hayashi, T. Kato, T. Hara and T. Oozeki, 2011: Prediction accuracy of shortwave radiation of the Japan Meteorological Agency Meso-Scale Model in the Kanto region, Japan, ICEM 2011, Gold Coast

Saito, K., J. Ishida, K. Aranami, T. Hara, T. Segawa, M. Narita and Y. Honda, 2007: Nonhydrostatic atmospheric models and operational development at JMA. J. Meteor. Soc. Japan, 85B, 271–304.

STRUCTURE OF PRECIPITATION SYSTEM ENHANCED AROUND MT. HALLA, JEJU ISLAND, KOREA ON 6 JULY 2007

Keun-Ok LEE[1], Hiroshi UYEDA[1], Shingo SHIMIZU[2] and Dong–In LEE[3]

[1]*Hydrospheric Atmospheric Research Center, Nagoya University, Japan*

[2]*Dept. of Storm, flood and landslide Research, National Research Institute for Earth Science and Disaster Prevention, Japan*

[3]*Dept. of Environmental Atmospheric Sciences, Pukyong National University, Korea*

1. INTRODUCTION

Jeju Island frequently suffers from severe rainfall system during the rainy season. A previous study (Lee et al., 2010) reported the localized heavy rainfall occurred at the lateral side of Jeju island (Mt. Halla; h=1,950m) was generated by orographically induced convergence in low altitude with a moist environment during the rainy season. In this article, dual–Doppler radar analysis and cloud resolving numerical experiment with high resolution (1.0 km in horizontal) investigated the 3-dimensional structure of an orographically–enhanced precipitation system passing on the northern side of an isolated elliptical mountain of Jeju Island, Korea on 6 July 2007.

2. OBSERVATIONAL DATA AND NUMERICAL MODELS

2.1 Observational data and analysis method

Two operational S–band Doppler radars of Korea meteorological administration (KMA) at Gosan (GSN) and Seongsan (SSN) across Jeju Island (white circles, Fig. 1), which each cover a radius of 250 km and together cover all of Jeju Island, record sets of volume scans of reflectivity and Doppler velocity every 10 min. The dual–Doppler radar data are interpolated into a Cartesian coordinate system with the vertical and horizontal grid intervals of 0.25 and 1.0 km, respectively. A Cressman–type weighting function (Cressman, 1959) is used for the interpolation with the fixed horizontal and vertical effective radius of influence of 1.5 and 1.0 km, respectively. To determine the 3–dimensional wind field, variational method (Gao et al., 1999) was employed. The three Cartesian components of wind are calculated within the dashed circles, except in the intersection area specified in Fig. 1 (intersection angle less than 35°).

KMA also conducts upper-air soundings at GSN, from the same site as the radar.

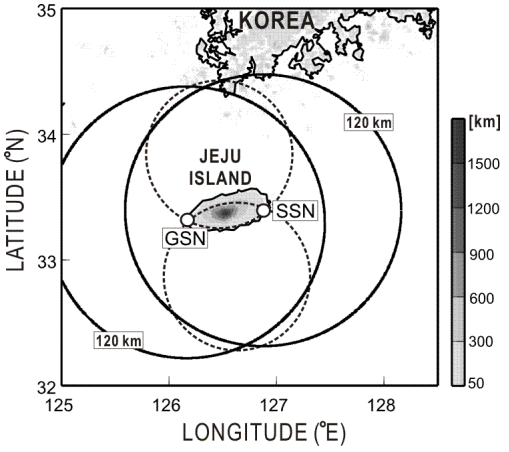

Fig.1. Elevation map of Jeju Island and observational range (120 km; black circles) of the dual–Doppler radars installed at Gosan (GSN) and Seongsan (SSN). The GSN and SSN radar sites are indicated by small open circles. Dual–Doppler radar analysis is conducted within the two dashed circles, except for within the area of intersection.

2.2 Model description

To clarify the 3-dimensional evolution of the system and the related moist inflow, the numerical simulations using a cloud-resolving storm simulator (CReSS Ver. 3.4, Tsuboki and Sakakibara, 2007) developed by Nagoya university was conducted in 1.0 km resolution. For the initial and lateral boundary conditions of the numerical simulations, we used the output data of the meso-scale model of Japan Meteorological Agency at 12 LST on 6 July 2007. For the simulation, the vertical grid contained 38 levels with variable grid intervals (Δz = 150 m near the surface and 340 m at the top level, at 8.6 km). The horizontal domain had 850 $\times$ 740 grid points, with a time step of Δt = 3.75 s.

CReSS model includes a bulk cold rain parameterization and a 1.5-order closure with a turbulent kinematic energy prediction (Tsuboki and Sakakibara, 2001; see Table 1 for a detailed description of the model). The prognostic variables in microphysics are the mixing ratios of water vapor (q_v), cloud water (q_c), rain (q_r), cloud ice (q_i), snow (q_s), and graupel (q_g) and number concentrations of cloud ice (N_i), snow (N_s), and graupel (N_g). The microphysics in CReSS is based on Lin et al. (1983), Cotton et al. (1986), Murakami (1990), Ikawa and Saito (1991), and Murakami et al. (1994).

3. RESULTS

3.1. Precipitation system on 6 July 2007

An intense precipitation system passed on the northern side of Jeju Island on 6 July 2007. Figure 2 shows the accumulated rainfall amount (dots) from 0000 to 0130 LST (local standard time; LST = UTC + 9 h) recorded by 17 rain gauges on the island. Only 5 mm of accumulated rainfall was recorded on the west of the island, while 24 and 34.5 mm was recorded on the north and the east of the island, respectively. With a good agreement with rain gauges, CReSS simulated the intense rainfall on the north side of the island. Regions of the simulated accumulated-rainfall amount (shades in Fig. 2) exceeding 50 mm (contoured by white line every 5 mm) were apparent on the north coastal region and eastern side of the island. From the upper-air sounding, Froude number (*Fr*) was calculated to be 0.2. The height of 0 ℃ was apparent 4.5 km ASL.

Table 1. Specifications of CReSS.

Model feature	Description
Basic equation	Quasi-compressible nonhydrostatic Navier–Stokes equations with a map factor
Projection	Lambert conformal conic
Vertical coordinate	Terrain-following
Grid	Staggered Arakawa C type in the horizontal and Lorenz type in the vertical
Advection scheme	Antiflux form with fourth-order central differential
Diffusion scheme	Fourth-order central differential method
Turbulent closure	1.5-order closure scheme
Time splitting	Horizontally explicit and vertically implicit for sound waves
Precipitation scheme	Bulk cold-rain scheme (predicting q_v, q_c, q_r, q_i, q_s, q_g, N_i, N_s, and N_g)
Surface layer	Bulk method similar to Segami et al. (1989)

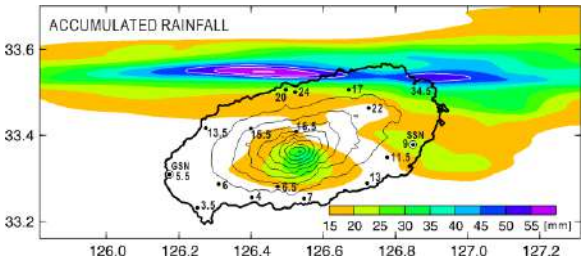

Fig. 2. Accumulated rainfall recorded by 17 rain gauges (dots) on Jeju Island from 0000 to 0130 LST on 6 July 2007. Simulated accumulated-rainfall for entire calculating time (2.5 hours) by CReSS is shown by shades. The white contour lines indicate the accumulated rainfall exceeding 50 mm with interval of 5 mm. The locations of the two radar sites (GSN and SSN) are indicated by small open circles.

Horizontal distributions of reflectivity at 2 km ASL (above sea level) are shown for every 10 minutes during 0000-0130 LST in Fig. 3. Region having reflectivity stronger than 40 dBZ is contoured every 5 dBZ. From 0000 to 0030 LST (Fig. 3a-d), as an elongated precipitation system moved from the offshore to northwestern side of the island, horizontally-enhanced convective region (area with reflectivity larger than 45 dBZ) was found. The farther eastward-moving convective region reached to the northern island and the preserved convective region was observed at 0040 and 0050 LST (Fig. 3e-f). At 0100 LST when the precipitation system located at the northeast island (Fig. 3g), the convective region around 20-30 km north of GSN was persistently shown. In Contrast, relatively dissipated convective region was found around 30-50 km north of GSN. In subsequence, during 0110-0120 LST (Fig. 3h-i), the preserved convective region moved to the eastern island showing the relatively expanded convective region on the eastern slope of the island, whereas barely discernible convective region off the northern shore. At 0130 LST (Fig. 3j), the relatively-dissipated convective region was observed off the eastern shore of the island.

To show the horizontal evolution of the convective region depending on the relative location to the island, four analysis domains were selected within a 40 × 10 km area north of GSN that includes the convective region. These domains are referred to as **N1** (10–20 km north of GSN, over the mountainous area; depicted in Fig. 3b, d, f, and h), **N2** (20–30 km north of GSN, over the northern coast), **N3** (30–40 km north of GSN, just off the northern coast), and **N4** (40–50 km north of GSN, over open sea). The time variation of horizontal area of the convective region at 2 km ASL is illustrated in Fig. 4. Two significant enhancement of the horizontal area of the convective region: 1) at **N2** area during 0000-0040 LST and 2) at **N1** area during 0100-0130 LST were characterized. We focused on the 3-dimensional structure of the reflectivity and wind of the convective region on the two significant enhancement stages.

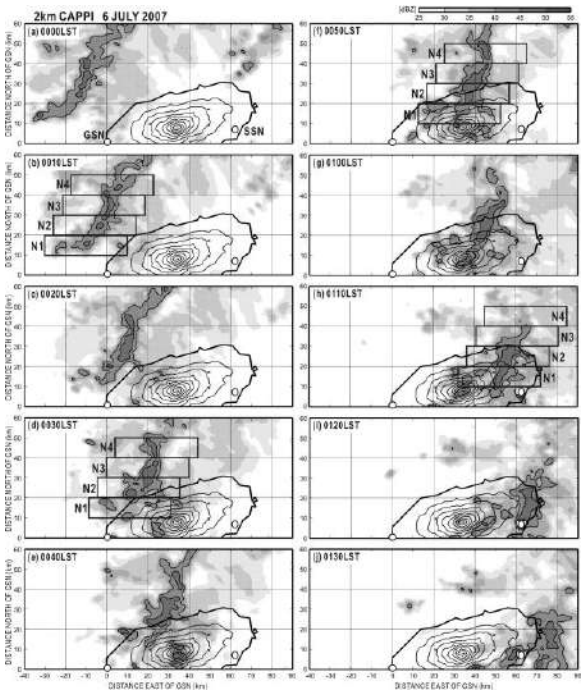

Fig. 3. Horizontal distributions of reflectivity at 2km ASL for (a) 0000 LST, (b) 0010 LST, (c) 0020 LST, (d) 0030 LST, (e) 0040 LST, (f) 0050 LST (upper right), (g) 0100 LST, (h) 0110 LST, (i) 0120 LST, and (j) 0130 LST on 6 July 2007.

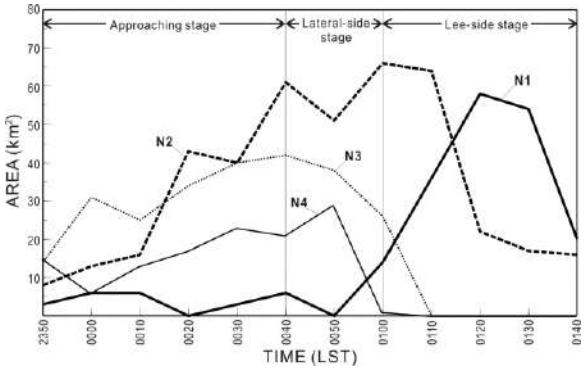

Fig. 4. Time variations of the horizontal area of the convective region (area with reflectivity larger than 45 dBZ) at 2 km ASL within the analysis boxes of **N1** (thick solid line), **N2** (thick dashed line), **N3** (thin dotted line) and **N4** (thin solid line) which were depicted in Fig. 3.

3.2. Structure of convective region in **N2**

3.2.1. Horizontal structure

The horizontal evolution of reflectivity (contour lines from 35 dBZ with interval of 5 dBZ) and wind from 0000 to 0050 LST are illustrated in Fig. 5. As shown in Fig. 5a-b, relatively strong westerly (20 m s^{-1}) and weak southwesterly (7 m s^{-1}) winds were found at the west and the east of the elongated precipitation system at 2 km ASL. Simultaneously, an elongated updraft region (oriented southwest-to-northeast, red shade for updraft > 1.5 m s^{-1}) became obvious on the west side of the system. As the system approached the northwestern coast of the island at 0020 LST (Fig. 5a-b), the southwesterly winds accelerated to around 20 m s^{-1} in the southern part of the system, and the related an updraft region was shown between the southern part of the system and the northwestern coast of the island. During 0020-0030 LST, the convective region expanded horizontally at 2km ASL in the northwestern coastal area (Fig. 5b-c).

Related to the updrafts and enhanced convective region, the simulated horizontal distributions of the relative humidity (RH, shadings) and wind at 599 m ASL, and the reflectivity (broken contours) at 1919 m ASL are shown in Fig. 6. When the convective region is apparent in the northwestern open sea (Fig. 6a), the high RH over 98 % was concentrated around the northwest coastal region with southwesterly wind blowing around the mountain (10 m s^{-1}). In 20 minutes, the eastward-moving system located in the high RH region showing the horizontally-expanded region of reflectivity over 40 dBZ (Fig. 6b).

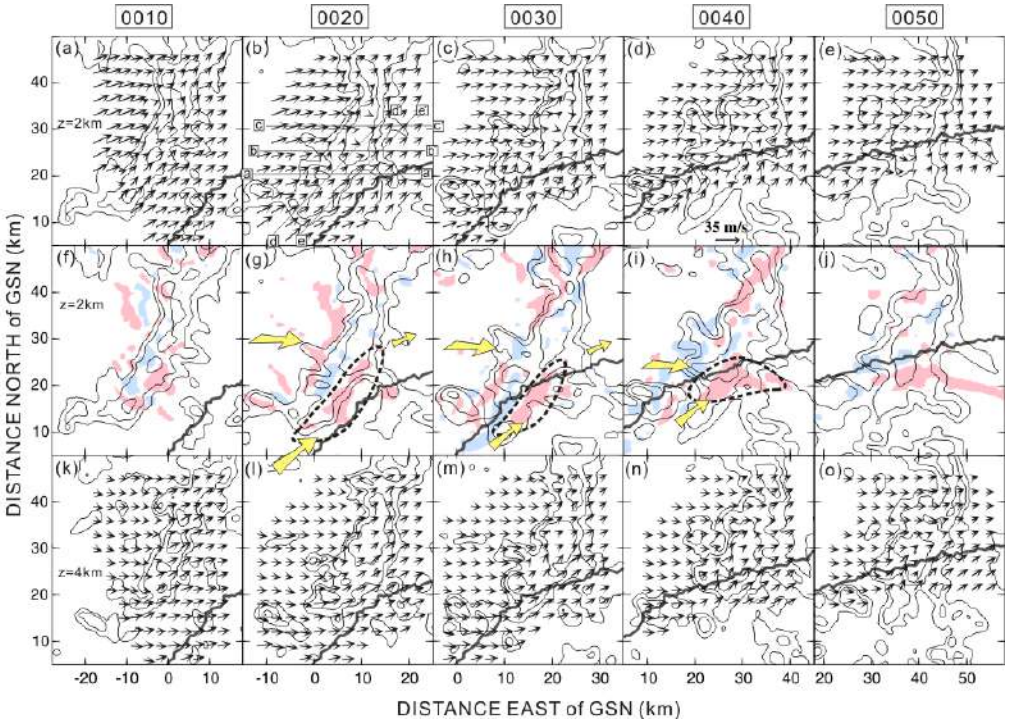

Fig. 5. Horizontal sections of reflectivity and cell-relative wind fields during 0000-0050 LST. The first row (a)-(e) and the third row (k)-(o) show horizontal wind vectors and reflectivity (contour from 35 dBZ at 5 dBZ interval) at 2 km and 4 km ASL, respectively. The second row (f)-(j) shows vertical wind (shadings) at 2 km ASL. Regions of updraft larger than 1.5 m s^{-1} and those of downdraft less than -1.5 m s^{-1} are shaded by red and blue, respectively. Thick contour line in each panel represents coastal line of Jeju Island.

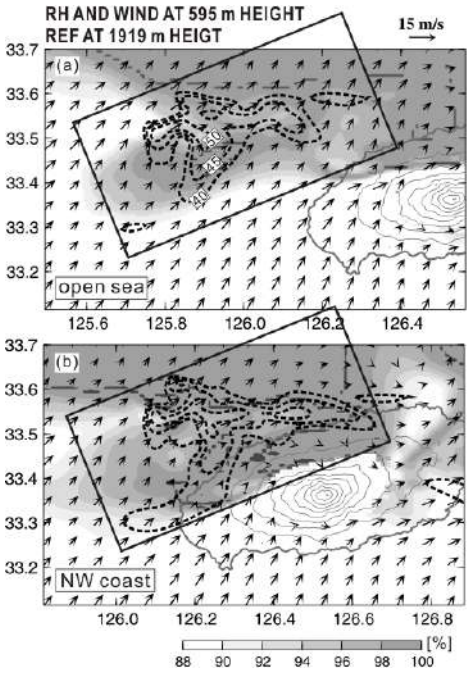

Fig. 6. Horizontal distribution of simulated RH (shade) and wind at 595 m ASL, and reflectivity (contours every 5 dBZ from 40 dBZ) at 1919 m ASL when system located on the northwest open sea (a) and coastal region (b).

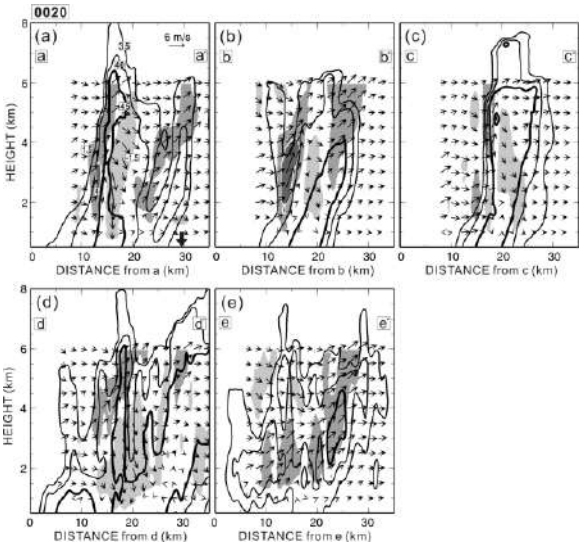

Fig. 7. Vertical cross-sections of reflectivity and system-relative wind fields at 0020 LST. Regions of updrafts in excess of 1.5 m s^{-1} are shown as dark shading and regions of downdraft less than –1.5 m s^{-1} are shown as light shading. The regions of intense updrafts (greater than 4 m s^{-1}) are indicated by the darkest shading.

As shown in Fig. 5c-e, the enhanced convective region in the coastal region (**N2**) was continuously observed in 0030-0050 LST with the convergence of westerly and southwesterly winds on the northern part of the island.

3.2.2. Vertical structure

Several vertical cross-sections have been selected from the regions depicted in Fig. 5b to illustrate the vertical structure of the updraft region and the accelerated southwesterly winds that were generated off the northwestern coast of the island, to the south of the precipitation system. Figure 7 shows vertical cross-sections of radar reflectivity (contouring every 5 dBZ from 35 dBZ with thick lines from 45 dBZ) and wind along the transect lines a–a', b–b', c–c', d–d', and e–e' at 0020 LST. The transect lines a–a', b–b', and c–c' were selected from around the **N2** analysis domain.

Along the a–a' transect, the convective region had a maximum height of 6.5 km ASL and a maximum width of 6 km (Fig. 7a). A region of paired updrafts (dark shading) and the downdrafts (light shading) was located near this convective region, extending from 1 to 6 km ASL at 10–20 km. Another updraft region is apparent to the east of this coastline (thick downward arrow), between the convective region and the island. This updraft region extended from 1.5 to 6 km ASL at 20–30 km, with reflectivity in excess of 35 dBZ up to 6 km ASL. Along the b–b' transect (Fig. 7b), as similarly, a region of paired updrafts and downdrafts is apparent along this transect at 10–20 km, including an area of intense updrafts (stronger than 4 m s^{-1}; depicted by the darkest shading) between 2 and 4 km ASL. To the east side of the downdrafts, an additional updraft region (20–30 km, Fig. 7b) can be identified above 3 km ASL, with the extended convective region up to 4 km ASL.

Along the c–c' transect (Fig. 7c), the convective region extended from the surface to 6 km ASL with a maximum width of 10 km. The updraft region can be found adjacent to the convective region, from 1.5 to 6 km ASL, and the downdraft region can be found below 5 km ASL to the east of the updraft region. The additional updraft region identified to the east of the downdraft along the a–a' and b–b' transects (Fig. 7a–b) is not apparent along the c–c' transect (Fig. 7c). The updrafts between the convective region and the island were generated locally by the convergence of the strong westerly wind and the enhanced southwesterly wind.

The vertical transects d–d' and e–e' (Fig. 7d–e) are oriented parallel to the enhanced southwesterly wind. Along the d–d' transect (Fig. 7d), the convective region extended from the surface to 6 km ASL over a relatively wide horizontal range (5–35 km). An updraft region was located adjacent to the convective region (10–20 km) from 3 to 6 km ASL, with a downdraft region below. The convective region was relatively small along the e–e' transect (Fig. 7e), in the region of accelerated southwesterly winds (Fig. 5b) and updraft region (Fig. 5g), extending only from 2 to 4.5 km ASL. A relatively wide updraft region is apparent along this transect at 10–28 km. This updraft region tilted from lower–southwest to upper–northeast, and extended from 1.5 to 6 km ASL.

The accelerated southwesterly between the southern part of the system and the island at 0020 LST and the related enhanced convective region were reflected in Fig. 8b. Figure 8 shows a time-height cross-section of maximum reflectivity from 0000 to 0120 LST in the 4 analysis domains (**N1**, **N2**, **N3**, and **N4**) depicted in Fig. 3. The heights of reflectivity in excess of 44 dBZ increased gradually from 0000 to 0020 LST in the **N2** (Fig. 8c), **N3** (Fig. 8b), and **N4** (Fig. 8a) analysis domains. In **N2** (Fig. 8c), reflectivity in excess of 40 dBZ was observed up to 8 km ASL, and the area of reflectivity greater than 48 dBZ extended from the surface to 6 km ASL above level of 0 ℃ (4.5 km ASL) in 0010-0030 LST. The strong southwesterly wind between the system and the island at 0020 LST, and the enhanced convective region were reflected as the reflectivity exceeding 50 dBZ was apparent around 4 km ASL in **N3** (Fig. 8b).

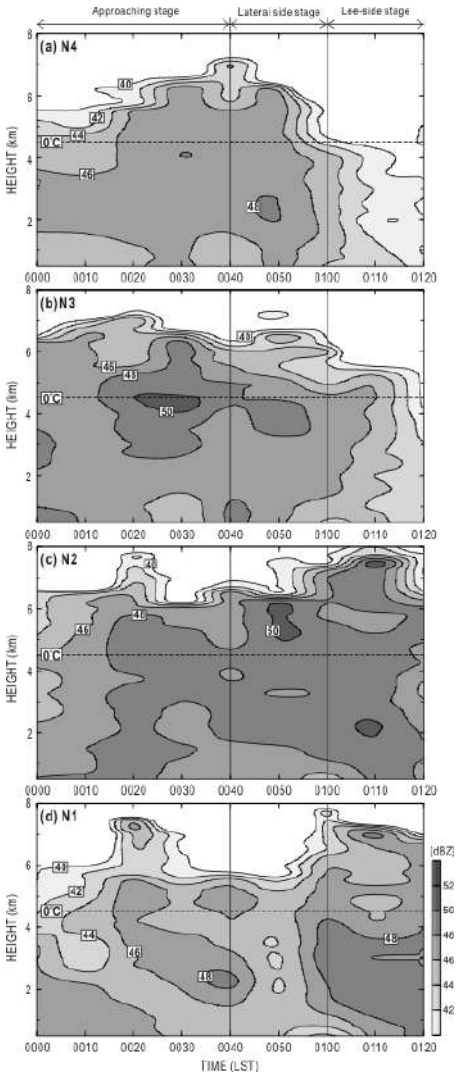

Fig. 8. Time-height cross-section of maximum reflectivity from 0000 to 0120 LST in the analysis domains (a) **N1** (over land), (b) **N2** (coastal), (c) **N3** (offshore), and (d) **N4** (open sea). The boundaries of the analysis domains are depicted in Fig. 3. Contours and shading show reflectivity at intervals of 2 dBZ starting from 40 dBZ.

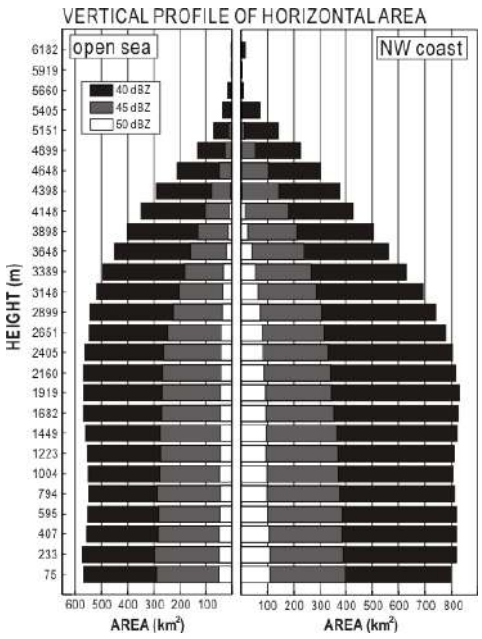

Fig. 9. Vertical profile of the simulated horizontal area of reflectivity exceeding 40 dBZ (black bar), 45 dBZ (grey bar), and 50 dBZ (white bar) at 0040 LST (left panel) and 0110 LST (right panel) on 6 July 2007.

Simulated profile of horizontal area of the convective region is shown in Fig. 9. For this analysis, a domain was selected within an 80 km × 40 km area that includes the convective region (depicted by a rectangle in Fig. 6a-b). The horizontal expansion of the area of the convective region was clearly shown as the system approached from the open sea (left panel of Fig. 9) to the northwestern coastal area of Jeju Island (right panel). Especially, the area expansion below 2 km ASL was significant as the horizontal area of reflectivity exceeding 40 (black bar), 45 (grey bar), and 50 dBZ (white bar) was increased around 144, 131 and 200 %, respectively during the period.

3.3. Structure of convective region in **N1**

3.3.1. Horizontal structure

Related to the enhanced convective region at **N1**, the horizontal evolution of the reflectivity and wind from 0100 to 0130 LST is illustrated in Fig. 10. At 0100 LST (Fig. 10a) when the convective region located at the northeast island, predominant westerly wind (13 m s^{-1}) was found around the convective region. At the same time, the strong southwesterly wind (16 m s^{-1}) and its associated updraft were found in the eastern slope of the island at 2 km ASL (Fig. 10d). In subsequence, at 0110 LST (Fig. 10b), the convective region moved to the eastern slope of the island passing over the updraft region, than it significantly enhanced (Fig. 10e). Constantly, the local updraft region was apparent on the eastern slope of the island. At 0120 LST, the enhanced convective region was still found around eastern coastal area (Fig. 10c).

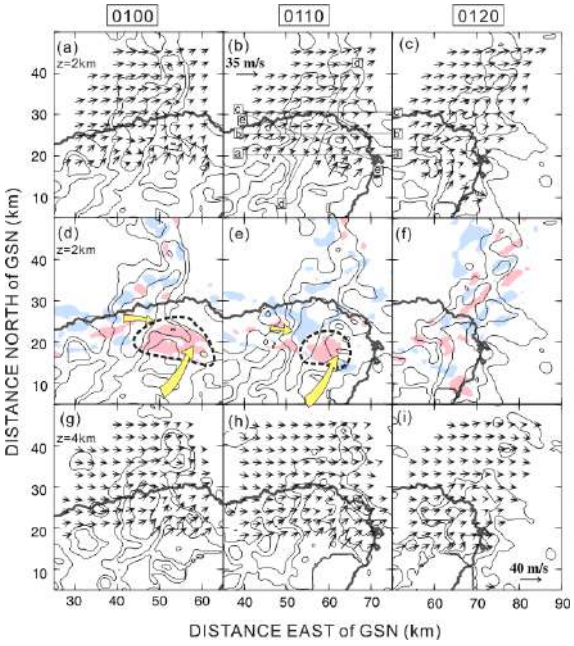

Fig. 10. Same as Fig. 5 but for 0100-0120 LST.

Horizontal distributions of the simulated RH and wind at 599 m ASL, and reflectivity at 1919 m ASL are shown in Fig. 11. When the convective region located on the north slope of the island, high RH over 98 % was apparent on the northern side of the island (Fig. 11a) with weak westerly wind (6 m s^{-1}). In 20 minutes, the convective region moved on the eastern slope where the weak westerly from the northern island was converged with the southwesterly from the

southern island (Fig. 11b). Simultaneously, on the southeastern slope of the island, region of high RH higher than 98 % was apparent with southwesterly wind.

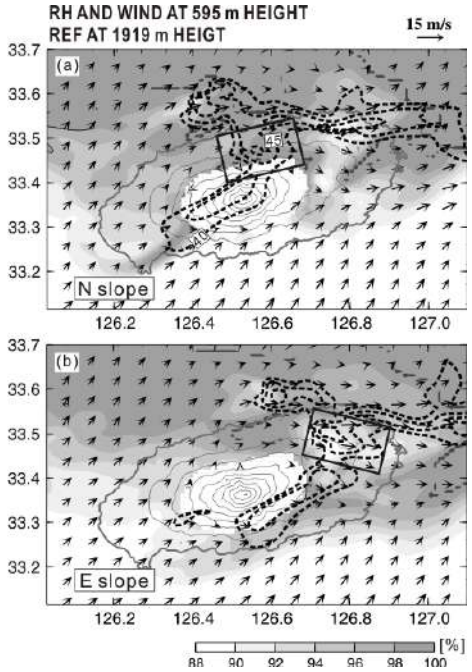

Fig. 11. Same as Fig. 6 but for the time when system located on the northern slope (a) and the eastern slope (b).

3.3.2. Vertical structure

Several vertical cross-sections have been selected to see the vertical structure of the southwestward-expanded convective and the related updraft region on the eastern slope of the island at 0110 LST.

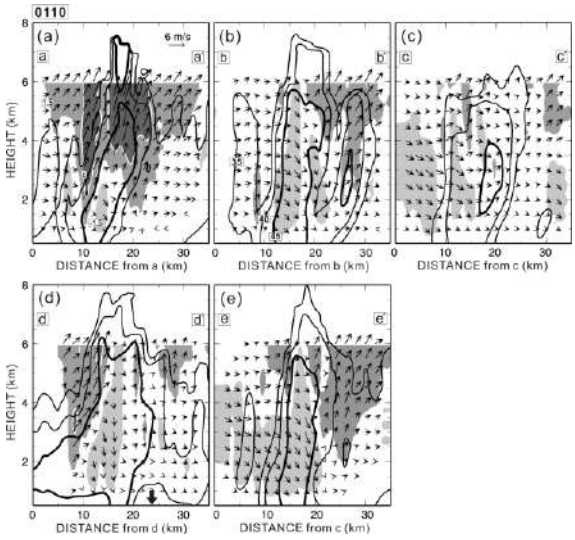

Fig. 12. Same as Fig. 7 but for 0110 LST.

Figure 12 shows the vertical cross-sections of radar reflectivity and wind along the transect lines a–a', b–b', c–c', d–d', and e–e' at 0110 LST. The a–a', b–b', and c–c' transects are oriented parallel to the horizontal axis of Fig. 10b and spaced at 5 km interval from the eastern slope (**N1**) to the northeastern coastal area of the island.

Along the a–a' transect (Fig. 12a), the convective region was tilted from lower–west to upper–east, and extended from the surface to 7.5 km ASL at 10–20 km along the transect. Updrafts were predominant within the convective region, including two regions of intense updrafts (stronger than 4 m s^{-1}; depicted by the darkest shading).

One intense updraft region was located above 2 km ASL, at the west side of the convective region near 8–15 km. Another intense updraft region was located above 3.5 km ASL near 15–25 km, and included a relatively tall convective region that extended up to 7.5 km ASL. Along the b–b' transect (Fig. 12b), 5 km north of a–a', the convective region was dominated by downdrafts. A narrow updraft region was located at 8–10 km along the transect with a vertical extent from 1 to 3.5 km ASL. To the east of this narrow updraft region, the convective region extended from the surface to 6 km ASL with a maximum width of 7 km. To the east of this convective region, another updraft region was located at 20–32 km above 2 km ASL, including a short convective region between 2 and 4 km ASL. The maximum height of 40 dBZ reflectivity in this updraft region was 5.5 km ASL. Along the c–c' transect (Fig. 12c), 5 km north of b–b', the convective region was even further diminished. This convective region extended from 2 to 4 km ASL with maximum width of 4 km, and was dominated by downdrafts. The updraft region was very small, and is barely discernable in Fig. 12c.

The d–d' transect (Fig. 12d) oriented parallel to the strong southwesterly wind and passes through the center of the convective region. The convective region was horizontally extensive along this transect, with a maximum width of 20 km. A relatively short convective region (1 to 3 km ASL) was located at 0–10 km, over the eastern slope of the island. Updrafts were prevalent in this region above 2 km ASL, including an area of intense updrafts between 3 and 4 km ASL. This updraft region extended upward and northeastward, with another area of intense updrafts above 5.5 km ASL at 12–13 km. A relatively tall convective region (6 km ASL) was located adjacent to this area of intense updrafts. Another narrow updraft was located in 4–6 km ASL at 20 km, coincident with another peak in the height of the convective region (6 km ASL). Downdrafts were prevalent below 6 km ASL in the convective region at 10–17 km (Fig. 12). The e–e' transect (Fig. 12e) is oriented perpendicular to the convective region. Downdrafts dominated the convective region below 6 km ASL along the e–e' transect. A relatively wide updraft region (15 km) was located above 2 km ASL to the southeast of the convective region.

Figure 8d reflects the enhancement of the horizontal area of the convective region on the eastern island at 2 km ASL, as the height of the reflectivity exceeding 40 dBZ increased up to 8 km ASL. The area of the reflectivity over 48 dBZ was identified from below 4 km ASL from 0100 to 0120 LST. The region of the intense updrafts was extended to the northeastern slope of the island by the strong southwesterly winds, as evidenced by the area of high reflectivity (greater than 50 dBZ) located at relatively high altitude (7 km ASL) in the northeastern coastal area of the island (**N2**, Fig. 8c).

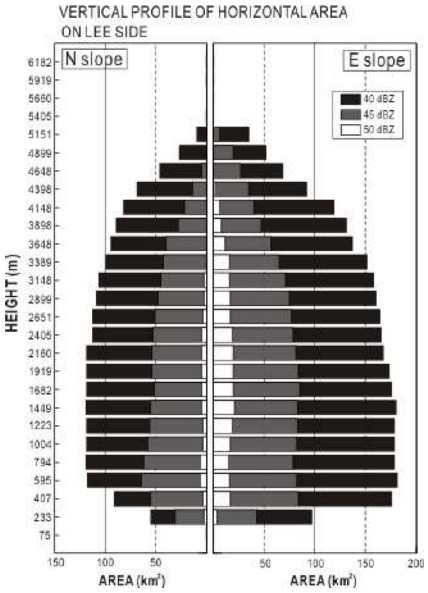

Fig. 13. Same as Fig. 9 but for the evolution of the convective region on the north (left panel) and east (right panel) slope of the island.

The enhancement of the convective region on the eastern slope of the island was shown in detail in the vertical profile of the horizontal area (Fig. 13). The analysis domain was selected within a 15 km × 12 km area that includes the convective region on the northern slope and the eastern slope of the island (depicted by a rectangle in Fig. 13). When the system located on the northern island (left panel of Fig. 11a-b), average of the horizontal area of reflectivity exceeding 45 dBZ (grey bar) in 595-1919 m ASL was calculated to be less than 60 km^2. In 20 minutes, as the system moved on the eastern slope, the average increased to around 80 km^2. During this period, the area of reflectivity exceeding 50 dBZ (white bar) increased from less than 10 to around 35 km^2.

4. SUMMARY

An elongated precipitation system strengthened significantly on the northern lateral and lee sides of an isolated mountain (height of 1,950 m) on Jeju Island on 6 July

2007. In focus on the enhancements of the system, detailed 3-dimensional structure of rainfall, wind and moist were revealed by dual-Doppler radar analyses and numerical simulation with high resolution of 1.0 km horizontal resolution.

As the system approached near to northwestern coastal region, southwesterly winds accelerated and induced regional updrafts between the southern part of the system and the island. These updrafts were a crucial component in the initial significant enhancement of the convective region. Furthermore, the isolated and elliptical terrain of Jeju Island modified the low-level wind blowing around the terrain with a relatively low *Fr* of 0.2. This modification of the low-level winds brought a steady supply of moist air to the convective region. By this favor condition for system enhancement, the the convective region was increased up to 8 km ASL above freezing level (4.5 km).

After this intensification, the convective region moved to the northern lateral side of the island. The modification of the prevailing winds by the terrain was consistently supply the moist air to the northern lateral side of the island; this configuration of the moist low-level wind allowed the convective region to retain its intensity.

The convective region then moved to the lee-side of the island, where it again intensified significantly. Weak westerlies from the northern lateral side of the island and stronger, moist southwesterlies from the southeastern slope of the island induced a local updraft region over the lee-side of the island. The second enhancement of the convective region occurred as it passed over these locally generated moist updrafts.

Analyses result indicates that the isolated mountain and elliptical shape of Jeju Island modified the prevailing winds containing moist, generating local updrafts. These local updrafts and local moist regions played an important role in intensifying the southern part of an elongated precipitation system as it passed the northern side of the mountain in a moist ambient environment.

Further analyses on the evolution of the microphysical parameters such as the evaporation, sublimation, or melting rates would be interesting to see how the mountain-generated local moist updraft played a role on growth of the precipitation cloud around the isolated mountainous slope.

REFERENCES

Cressman, G.P., 1959: An operational objective analysis system. *Mon. Wea. Rev.*, **87**, 367-374.

Cotton, W.R., G.J. Tripoli, R.M. Rauber, and E. A. Mulvihill, 1986: Numerical simulation of the effects of varying ice crystal nucleation rates and aggregation processes on orographic snowfall. *J. Climate Appl. Meteor*., **25**, 1658-1680.

Gao, J., M. Xue, A. Shapiro, and K.K. Droegemeier, 1999: A variational method for the analysis of three-dimensional wind fields from two Doppler radars. *Mon. Wea. Rev*., **127**, 2128-2142.

Ikawa, M., and K. Saito, 1991: Description of a nonhydrostatic model developed at the Forecast Research Department of the MRI. *MRI Tech. Rep.* **28**, Meteorological Research Institute, 238 pp. [Available online at http://www.mri-jma.go.jp/Publish/Technical/DATA/VOL_28/28_en.html.]

Lee, K.-O., S. Shimizu, M. Maki, C.-H. You, H. Uyeda, and D.-I. Lee, 2010: Enhancement mechanism of the 30 June 2006 precipitation system observed over the northwestern slope

of Mt. Halla, Jeju Island, Korea. *Atmos. Res*., **97**, 343-358.

Lin, Y.-L., R.D. Farley, and H.D. Orville, 1983: Bulk parameterization of the snow field in a cloud model. *J. Appl. Meteor*., **22**, 1065-1092.

Murakami, M., 1990: Numerical modeling of dynamical and microphysical evolution of an isolated convective cloud – The 19 July 1981 CCOPE cloud. *J. Meteor. Soc. Japan*, **68**, 107-128.

Murakami, M., T.L. Clark, and W.D. Hall, 1994: Numerical simulations of convective snow clouds over the Sea of Japan; Two-dimensional simulations of mixed layer development and convective snow cloud formation. *J. Meteor. Soc. Japan*, **72**, 43-62.

Segami, A., K. Kurihara, H. Nakamura, M. Ueno, I. Takano, and Y. Tatsumi, 1989: Operational mesoscale weather prediction with Japan Spectral Model. J. Meteor. Soc. Japan, 67, 907-923.

Tsuboki, K., and A. Sakakibara, 2001: CReSS User's Guide, 2nd edition, 210 pp. [available from http://www.rain.hyarc.nagoya-u.ac.jp/~tsuboki/cress_html/src_cress/CReSS2223_users_guide_eng.pdf].

Tsuboki, K., and A. Sakakibara, 2007: Numerical prediction of high-impact weather systems: The textbook for seventeenth IHP training course in 2007. [available from http://www.rain. hyarc.nagoyau.ac.jp/~tsuboki/cress_html/src_cress/CReSS2223_users_guide_eng.pdf]

Acknowledgment

This research was funded by the Korea Meteorological Administration Research and Development Program under Grant CATER 2012-2072. This work is also partially supported by Grant-in-Aid for Scientific Research defrayed by the Ministry of Education, Culture, Sports, Science and Technology of Japan (24253006). One of the authors (Keun-Ok Lee) is supported by the Ministry of Education, Culture, Sports, Science, and Technology, Japan, as a doctoral student in the Graduate School of Environmental Studies, Nagoya University, Japan.

THE TEMPORAL AND SPATIAL DISTRIBUTION CHARACTERISTICS OF THE WATER RESOURCES IN CLOUD IN TIANJIN PRELIMINARY ANALYSIS

Hui Meng , Wei Song , Xiaojun Guo , Wan Wang
Tianjin Weather Modification Office, Tianjin, 300074, China

1. INTRODUCTION

TianJin is located in the northeast of the north China plain,north to yanshan mountain, east to the BoHai sea,in the HaiHe river basin in the lower reaches,is the important trading ports and business and financial center city in the north,has the construction of the international metropolis favorable conditions.TianJin is located in the east of mid-latitude of Eurasia,belong to half dry continental monsoon climate,is one of the dry areas in the north. Per capita water quantity of about 159m^3, Only for the national average of 1/16. The climate characteristics is four distinct seasons.The precipitation is extremely uneven distribution in the year. 85% of the precipitation focused on 6-9 months, and mainly in late July and early August. By topography, climate and other factors,the temporal and spatial distribution of precipitation decrease trend from the north to the south. A shortage of water resources,water resources the distribution has severely restricts economic and social development in TianJin.The artificial precipitation which developed the water resources in air is to alleviate the shortage of water resources of a important way.

Some domestic provinces analyses each province or regional air water resources situation and artificial precipitation enhancement potential. But the most of the provinces are applied atmosphere sounding data to calculate PWV of the whole atmosphere. Due to the lack of sounding station,the method that is applied atmosphere sounding data to calculate PWV can not be used in TianJin,so this paper using ground humidity parameters analysis.

Although artificial rainfall in TianJin has been conducted for several years,the city's natural rainfall cloud system,development and distribution of knowledge has to some extent, but the distribution of water resources in cloud has been the lack of comprehensive research and scientific computing.Used of the ground water vapor pressure and precipitation data in 30 years (during 1981 to 2010) in 13 meteorological stations in TianJin,application experience the formula to calculate the amount of water resources in air of TianJin and precipitation efficiency and analyzes their temporal and spatial distribution characteristics.For rationally develop and utilize the water resources,improve the ability of drought disaster mitigation provide theoretical and technical support.

2 DATA AND METHOD

2.1 Data source

We selected the ground water vapor pressure and precipitation data by the period of ten-days from January to December in 30 years(during 1981 to 2010)in 13 meteorological stations in TianJin.

2.2 The calculation method of PWV in the whole atmosphere

Precipitable Water Vapor (PWV) in the whole atmosphere (also called water resources in cloud) refers to the vertical column contained in the total water vapor, assumed that all water vapor condensation, and build up in a column on the underside is the liquid water depth, it represents the precipitation potential, is the important basis

of water resources evaluation.

We use the empirical formula which is used the ground humidity parameters to deduce by Yangjingmei and other people to calculate the PWV:

$$W = a_0' + a_1' e \quad (1)$$

In this formula, W is represented for the PWV (the unit is cm), e is represented for the ground water vapor pressure (the unit is hpa), a_0' and a_1' is experience coefficient.

The coefficient of experience outside of the qinghai-tibet plateau areas:

$$a_0' = \begin{cases} 0.03\exp(-1.39H^2 + 2.74H + 0.15) \\ 0.04\exp(0.6H) - d_1 + d_2 \quad (j < 33°) \end{cases} \quad (2)$$

$$a_1' = \begin{cases} 0.17 + d_3 \quad (j \geq 33°) \\ (0.20 - d_3)d_4 \quad (j < 33°) \end{cases} \quad (3)$$

$$d_1 = 0.05/\left[(j - 25.0)^2 + 0.25\right];$$

$$d_2 = \begin{cases} 0 \quad (j > 20°) \\ -0.9 \quad (j \leq 20°) \end{cases};$$

$d_3 = 0.066/\left[(j - 33)^2 + 4.41\right]$; $d_4 = 1.0$; In this formula, j is represented for the geographic latitude, H is represented for the altitude of the stations.

2.3 Natural rainfall rate

Atmospheric natural rainfall rate (precipitation efficiency) is defined as the rate of the actual precipitation and PWV in the whole atmosphere,it reflects the atmospheric natural rainfall efficiency.

3.THE SPATIAL DISTRIBUTION CHARACTERISTICS OF THE PWV AND THE ACTUAL PRECIPITATION IN TIANJIN

3.1 The spatial distribution of the PWV

Figure 1 shows the spatial distribution of the average annual PWV.The maximum of PWV is 7603mm which appeared in HanGu in the eastern coastal area and the minimum of PWV is 7003mm which appeared in JiXian in the northern mountains.The average annual PWV is 7371mm in TianJin. The spatial distribution characteristics of the water resources in air of TianJin is more of the southeast coast,less of the northern mountains,middle of the plains center.

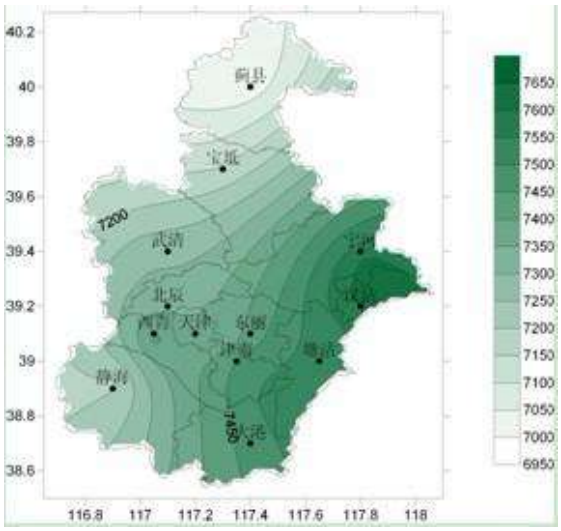

Fig.1 distribution of average annual PWV over Tianjin from 1981 to 2010

3.2 The spatial distribution of the actual precipitation

Figure 2 reflects the regional distribution of practical annual precipitation in 30 years (during 1981 to 2010) in TianJin city. In figure 2, the high value of 30 years average of annual precipitation is 615mm where is located in JiXian area and the low value is 515mm where is located in XiQing area. The space distribution general characteristics of precipitation is that the northern mountains is more then the southern plains; the eastern coastal is more then the western.

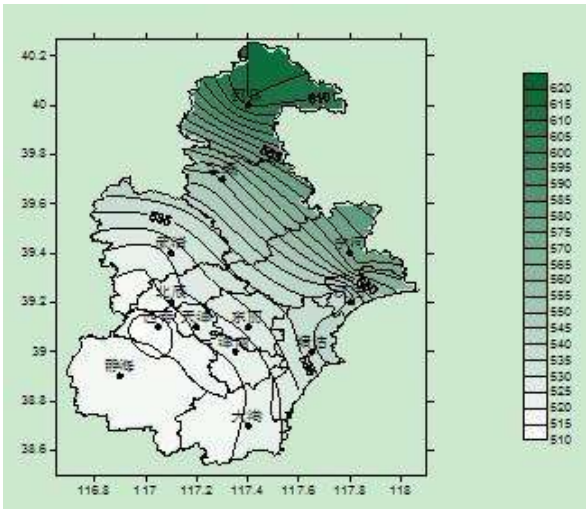

Fig.2 The average precipitation distribution form 1981 to 2010 in Tianjin (unit: mm)

3.3 The spatial distribution of the actual precipitation

The above analysis results show that the spatial distribution of the actual precipitation and PWV is inconsistency. The high value of PWV is corresponding to the middle value of precipitation, and JiXian has the lowest PWV, the precipitation is the highest in TianJin. Therefore, we introduce the natural rainfall rate to analysis the artificial precipitation potential.

According to the calculation, nearly 30 years average precipitation rate in TianJin is only 5.4%, lower than other provinces and municipalities of the country (such as Heilongjiang province and JiLin province are 7% and 11%). The calculation results show that the lowest efficiency is the main reason that is caused by the less natural precipitation and high frequent drought. Figure 3 shows the space distribution of the average efficiency of precipitation. In the northern JiXian, the highest efficiency of precipitation is 6.4%. In BaoDi where is close to JiXian, it was 5.7%. The lowest efficiency of the precipitation only 5.1% appeared in the XiQing district. In the southern, JingHai have a 5.45% of the high value area. The spatial distribution of rainfall efficiency is high in the north and south and low in the middle. There is high efficiency of the precipitation in the northern.

The results of the study show that the water resources quantity in cloud is enough in TianJin, but the efficiency of precipitation is low. It is the great potential for development of water resources in cloud in Tianjin.

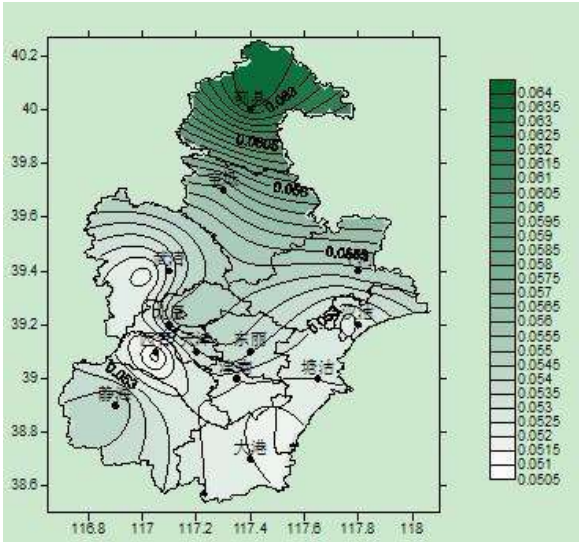

Fig.3 distributions of natural precipitation efficiency over Tianjin

4 .PWV AND PRECIPITATION EFFICIENCY WITH THE CHANGE OF TIME

Figure 4 shows the inter-monthly variation of precipitation,PWV and natural precipitation efficiency. The distribution characteristics of three curves present agreement type which has one peak. It increases gradually from January to July and decreases gradually after August. The PWV is the most in July, was 1392.1mm, while the precipitation and precipitation efficiency reached a high value, was 153.6 mm and 11%, August followed. The lowest of PWV and precipitation appeared in January, only 147.9 mm and 3.3 mm, precipitation efficiency was only 2.2%. The lowest of precipitation efficiency appeared in January, only 1.9%. The PWV and precipitation efficiency are bigger than annual average value between April and September, it has potential precipitation enhancement. The precipitation is less in wintry and spring (during January and April,

during October and December), because PWV and precipitation efficiency are low. So the less PWV is the main reason that is caused by the high frequent drought in winter and spring in TianJin.

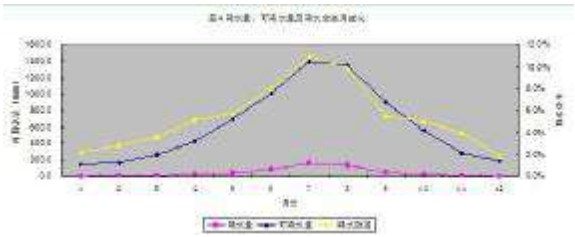

Fig.4 The inter-monthly variation of precipitation,PWV and natural precipitation efficiency.

5. CONCLUSION

1)The annual average PWV is between 7002mm and 7616mm, the precipitation efficiency is between 6.0% and 8.1% in TianJin. It is suggested that the water resources in cloud are very rich, but the efficiency of precipitation is low, therefore it has a very good potential precipitation enhancement.

2) The spatial distribution characteristics of the PWV in TianJin is more of the southeast coast, less of the northern mountains, middle of the plains center. Precipitation efficiency, the space distribution features from the north to the south is gradually reduced. The development potential of water resources in cloud in the south is greater than the north.

3) The PWV and precipitation efficiency are bigger than annual average value between April and September, it is the key time to the reasonable development of water resources in cloud in TianJin. The PWV is less in winter and spring, lack of sufficient moisture in the atmosphere, which is unfavorable for the precipitation formation.

Acknowledgements

1. Liu Shi-xiang, Wang Sui-chan, Chen Xue-jun,etc, A Climatic Research Of Artificial Precipitation Prtentiality In Gassu,Journal of Gansu Sciences, 2005,(17):44-47.

2. Tang Lin, Wang Zhiping, Ding Yueqiang, etc, Water Vapor Resource and Potentiality of Increasing Rain Artificiallyin Zhexi Reservoir and Its Drainage Area of Hunan Province, Meteorplogical Monthly, 2006, (32): 29-34.

3. Sun Li, Spatial and temporal variation of atmospheric Water-Vapor Resources over Northeast China, Scientia Geographica Sinica, 2007, (27): 2-9.

4. Yang Jingmei, Qiu Jinhuan, A Method For Estimating Preeipitable Water and Effective Water Vapor Content from Ground Humidity Parameters, Chinese Journal of Atmosphere Sciences, 2002,(26):9-22.

5. Zhang Miao-miao etc, Temporal and Spatial Distribution Characteristics of Water Resources in the Air in Heilongjiang Province, Journal of Anhui Agri. Sci, 2010,(38):15169-15171.

6. LIAO Fei,HU Ya-min,HONG Yan-chao, Numerical Study for the Influences of Orographic Dynamic on Cloud and Precipitation in North China, Plateau Meteorology, 2009, (28):115-126.

OBSERVATIONAL STUDY OF MICROPHYSICS AND DYNAMICS IN ENTRAINMENT-MIXING PROCESSES IN CUMULUS DURING RACORO

Chunsong Lu[1, 2], Yangang Liu[2], Shengjie Niu[1], Seong Soo Yum[3], Andrew Vogelmann[2], Satoshi Endo[2], Gunnar Senum[2] and Haflidi Jonsson[4]

1. School of Atmospheric Physics, Key Laboratory of Meteorological Disaster of Ministry of Education, Nanjing University of Information Science and Technology (NUIST), Jiangsu, China 210044
2. Atmospheric Sciences Division, Brookhaven National Laboratory (BNL), New York, USA 11973
3. Department of Atmospheric Sciences, Yonsei University, Seoul, Korea 120-749
4. Center for Interdisciplinary Remotely Piloted Aircraft Studies, Naval Postgraduate School, Monterey, California, USA 93943

1. INTRODUCTION

Entrainment of dry air into clouds is essential to many cloud-related processes, for example, warm-rain initiation [e.g., *Beard and Ochs*, 1993; *Su et al.*, 1998; *Liu et al.*, 2002; *Lasher-Trapp et al.*, 2005; *Yum and Hudson*, 2005], cloud feedbacks in climate models [e.g., *von Salzen and McFarlane*, 2002; *Grabowski*, 2006], aerosol indirect effect [e.g., *Kim et al.*, 2008] and radar retrieval of cloud liquid water content [e.g., *Liu et al.*, 2008].

Turbulent entrainment-mixing processes have been studied in the framework of the so-called homogeneous/ inhomogeneous model, but the understanding is still far from complete. *Lehmann et al.* [2009] pointed out that it is unclear whether the entrainment-mixing process is predominantly homogeneous, inhomogeneous, or in-between, and what the controlling factors are and how they interact. This incomplete understanding of the entrainment-mixing processes calls for further state-of-the-art observations.

Coordinated by the Atmospheric Radiation Measurement (ARM) Aerial Facility (AAF), the Routine AAF CLOWD Optical Radiative Observations (RACORO) campaign was carried out at the Southern Great Plains (SGP), USA in 2009 [*Vogelmann et al.*, 2012]. The data collected during RACORO provide a great opportunity to investigate entrainment-mixing processes occurring in mid-latitude continental cumulus clouds.

2. DATA

The cloud droplet size distributions were observed with Cloud and Aerosol Spectrometer (CAS) deployed on the Twin Otter aircraft. The CAS probe sizes and counts aerosol and cloud particles in 20 bins with bin centers from 0.29-25.05 μm in radius. In this study, only the cloud part with bin centers from 1.01-20.25 μm in radius is used. Temperature and water vapor mixing ratio were observed with Rosemount and Diode Laser Hygrometer, respectively. Dissipation rate is calculated with true air speed based on the method introduced by *Chan et al.* [1998]. The 10 Hz data are used in this study.

3. RESULTS

For every horizontal aircraft penetration, a number of single cumuli were often observed. To focus on entrainment-mixing processes and reduce effect of other factors (e.g., meteorological and aerosol conditions),

cumuli from one aircraft flight (26 May 2009) are analyzed. There were 44 cumuli along the two horizontal penetrations, and these cumuli are further filtered based on Figure 1. First select the maximum number concentration (N_{max}) and cubic volume mean radius (r_{vmax}^3) along every horizontal penetration, then normalize the number concentration (N) and cubic volume mean radius (r_v^3) in every cumulus along that horizontal penetration with N_{max} and r_{vmax}^3, respectively. The lines representing the ratio of liquid water content (LWC) to the maximum liquid water content (LWC_{max}) are also plotted (Figure 1 shows three examples: LWC/LWC_{max} = 0.2, 0.5, 0.8). If 1/3 of the data points in one cumulus are along one of the LWC/LWC_{max} lines, then this cumulus is thought to have a center close to adiabatic cloud, which is less affected by entrainment-mixing processes. These clouds are excluded in the analysis. In the 44 cumuli, 11 had such adiabatic centers, so 33 cumuli are used here to study entrainment-mixing processes.

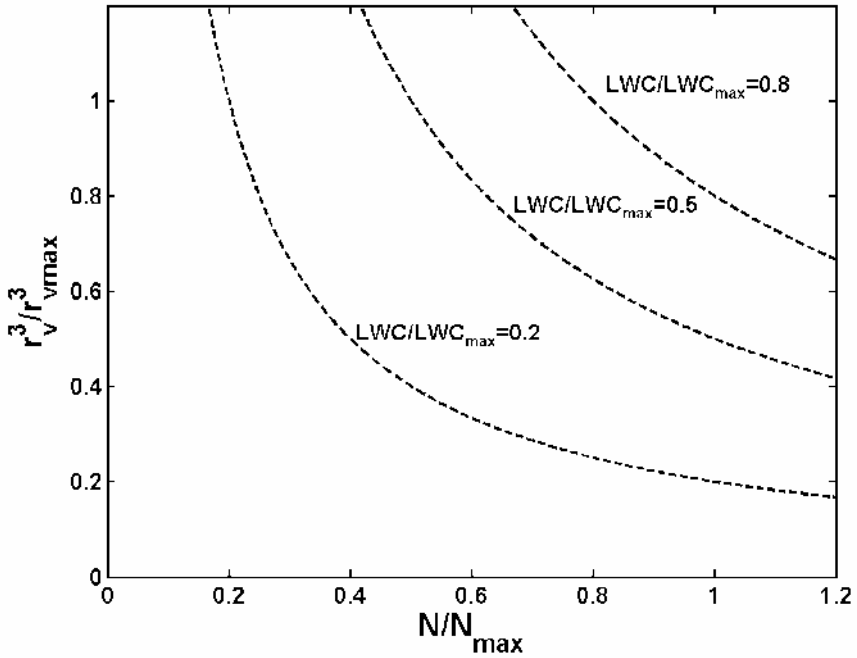

Figure 1 Normalized cubic volume mean radius (r_v^3) as a function of droplet number concentration (N); r_{vmax} and N_{max} are the maximum volume mean radius and number concentration along one horizontal penetration, respectively. The dash lines represent the ratio of liquid water content (LWC) to maximum LWC (LWC_{max}), 0.2, 0.5 and 0.8, respectively.

The entrainment-mixing processes are studied in the framework of homogeneous/inhomogeneous entrainment-mixing model which was built on the classical work presented by *Baker and Latham* [1979] and *Baker et al.* [1980]. According to this model, the microphysical relationship associated with different entrainment-mixing processes can be classified into three major types, which are briefly discussed below.

The first type is the homogeneous entrainment-mixing mechanism. Under this mechanism, all cloud droplets are exposed to the same environmental conditions and evaporate at the same time. Thus r_v and N are anticipated to be positively correlated. The second type is the so-called extreme inhomogeneous entrainment-mixing mechanism. It proceeds in two-steps: all

droplets surrounding the entrained dry air parcel first evaporate to saturate the parcel; then, mixing between this parcel and the remaining part of cloud dilutes the cloud. Under such conditions, r_v changes slightly as N decreases due to evaporation. The third type is inhomogeneous entrainment-mixing with subsequent ascent. If the diluted parcel after the extreme inhomogeneous entrainment-mixing process is lifted upward again, the big droplets in this parcel are expected to grow faster than those in other undiluted parcels due to less competition for water vapor. Under such conditions, r_v is negatively correlated to N.

In the 15 cumuli along the first horizontal penetrations, 14 cumuli were mainly affected by homogeneous entrainment-mixing process and only one cumulus was mainly affected by extreme inhomogeneous entrainment-mixing process. Similarly, in the 18 cumuli along the second horizontal penetration, 13 were mainly affected by homogeneous entrainment-mixing process and 5 were mainly affected by extreme inhomogeneous entrainment-mixing process. Figure 2 shows the relationships between r_v and N in four typical cumuli along the two horizontal penetrations. Thus homogeneous entrainment-mixing process was the main entrainment-mixing mechanism in the cumuli. *Yum and Hudson* [2001] found similar phenomena. But in stratocumuli at the same observation site in 2000, extreme inhomogeneous entrainment-mixing process was dominant [*Lu et al.*, 2011].

To further examine entrainment-mixing process, transition scale number (N_L) is calculated; N_L was defined by *Lu et al.* [2011]:

$$N_L = \frac{L^*}{\eta} \tag{1}$$

where η is Kolmogorov microscale, and L^* is transition length introduced by *Lehmann et al.* [2009]. The expression of L^* is

$$L^* = \varepsilon^{1/2}\tau_{react}^{3/2} \tag{2}$$

where ε is dissipation rate and τ_{react} is defined as either the time when the droplets have completely evaporated or the time at which the relative humidity has reached 99.5% (s > -0.005). A larger value of N_L indicates a higher probability of homogeneous mixing process. See the appendix in *Lu et al.* [2011] for a more detailed explanation of N_L.

Figure 2 shows the average N_L in the four typical cumuli and Figure 3 shows the mean values of N_L in every cumulus. Along the first horizontal penetration, the cumulus mainly affected by extreme inhomogeneous entrainment-mixing process had the smallest N_L. Along the second horizontal penetration, the cumuli mainly affected by extreme inhomogeneous entrainment-mixing process generally had smaller N_L than the cumuli mainly affected by homogeneous entrainment-mixing process; however, cumuli # 3-7 had similar N_L values and are mainly affected by different entrainment-mixing processes. The reason is that N_L or L^* is not the only factor that determines entrainment-mixing mechanisms; the other factor is the size of dry air blob (L) in cumuli. Thus, even if N_L or L^* are the same in two cumuli, the entrainment-mixing mechanism could be different, homogeneous or inhomogeneous, depending on L. If $L/\eta < N_L$, mixing is more likely homogeneous; otherwise, mixing is more likely inhomogeneous. In cumuli # 3-7, L might be different; as a result, although N_L values were similar, the entrainment-mixing mechanisms were different.

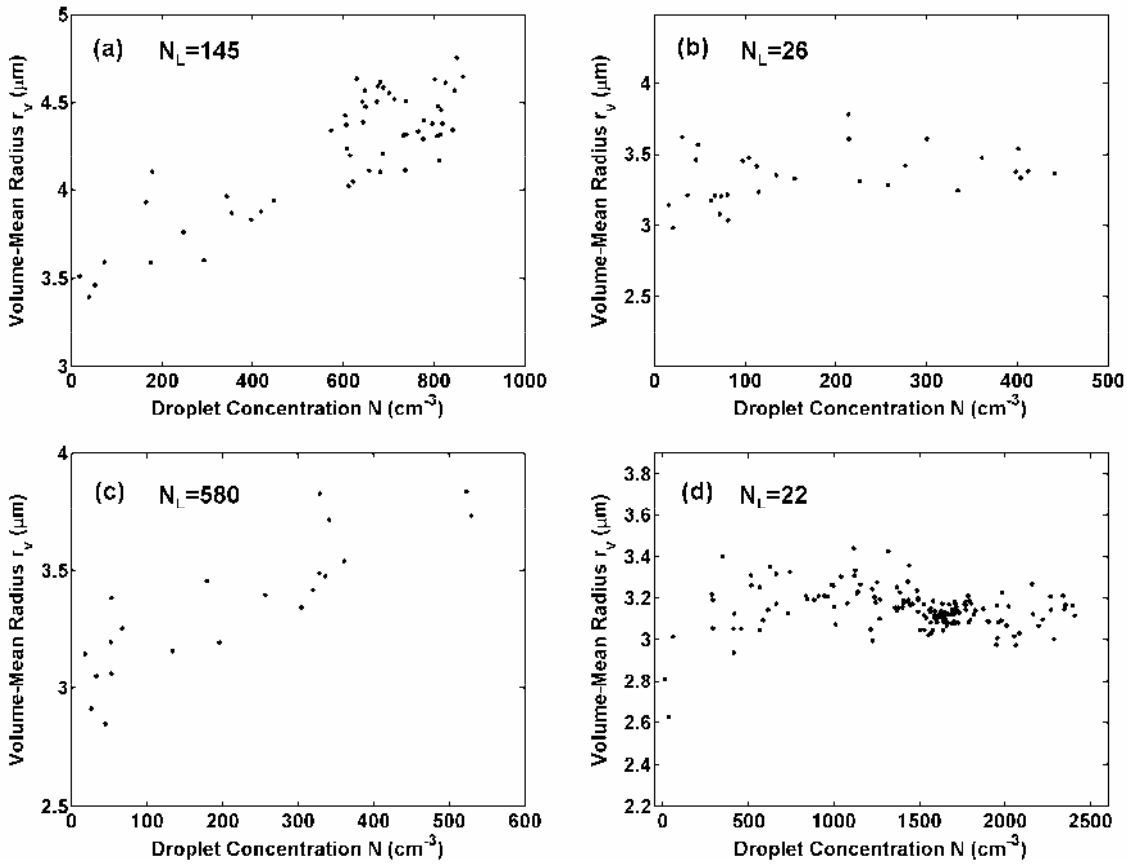

Figure 2 Volume mean radius (r_v) as a function of number concentration (N) in 4 typical cumuli at the Southern Great Plains site, US, on 26 May 2009. (a) A cumulus affected by homogeneous entrainment-mixing process along the first horizontal penetration and (b) a cumulus affected by extreme inhomogeneous entrainment-mixing process along the first horizontal penetration; (c) and (d) are as for (a) and (b), respectively, but for the cumuli along the second horizontal penetration. Average transition scale number (N_L) in every cloud is also shown.

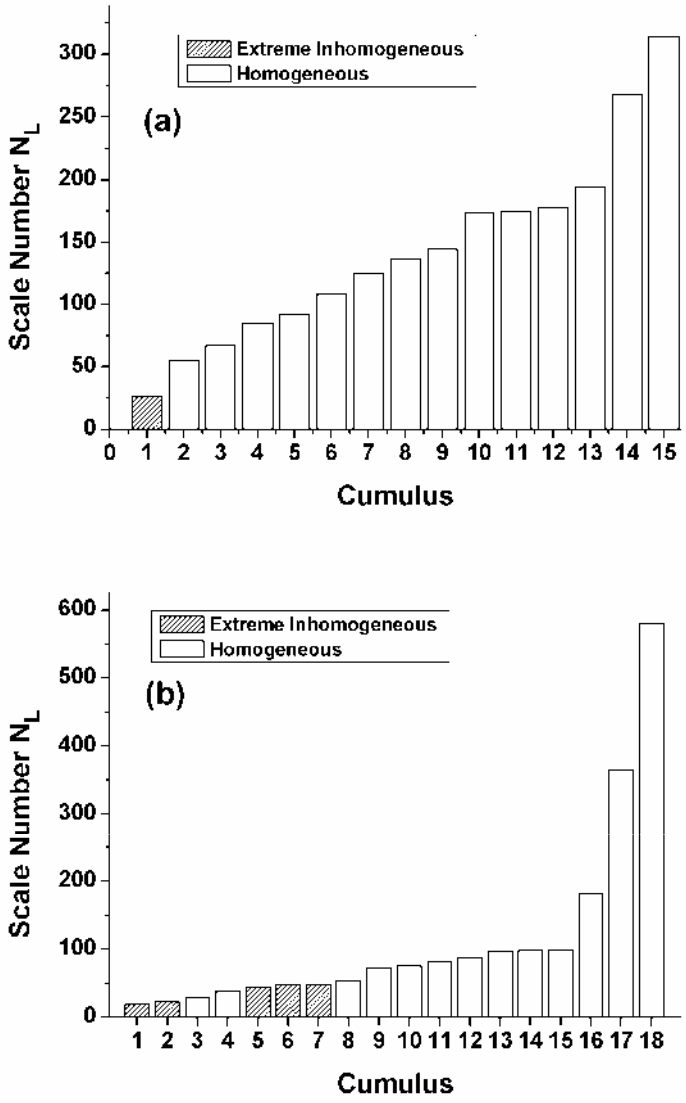

Figure 3 Average transition scale number (N_L) in every cloud of (a) 15 cumuli along the first horizontal penetration and (b) in 18 cumuli along the second horizontal penetration at the Southern Great Plains site, US, on 26 May 2009. White bars represent the cumuli mainly affected by homogeneous entrainment-mixing process; black stripes represent the cumuli mainly affected by extreme inhomogeneous entrainment-mixing process.

4. CONCLUSIONS

Entrainment-mixing mechanisms are analyzed in 33 cumuli along two horizontal penetrations in one case from RACORO in terms of microphysics and dynamics. (1) The microphysical relationship between volume mean radius (r_v) and number concentration (N) was mainly positive; thus homogeneous entrainment-mixing mechanism was dominant in the cumuli, whereas extreme inhomogeneous entrainment-mixing mechanism was the main mechanism in the stratocumuli at the same site in 2000 [*Lu et al.*, 2011]. (2) Transition scale number (N_L), the dynamic measure of homogeneous entrainment-mixing mechanism [*Lu et al.*, 2011], is calculated for every cumulus. Generally speaking, along the two horizontal penetrations, the cumuli mainly affected by extreme inhomogeneous entrainment -mixing mechanism had smaller N_L than the

cumuli mainly affected by homogeneous entrainment-mixing mechanism, consistent with the theoretical analysis of N_L. However, in the second horizontal penetration, some cumuli were mainly affected by different entrainment-mixing mechanisms but had a similar N_L, likely due to the effect of the size of dry air blob in the clouds.

5. BIBLIOGRAPHY

Baker, M. B., and J. Latham (1979), The evolution of droplet spectra and the rate of production of embryonic raindrops in small cumulus clouds, *J. Atmos. Sci.*, *36*(8), 1612-1615, doi:10.1175/1520-0469(1979)036<1612:TEODSA>2.0.CO;2.

Baker, M. B., R. G. Corbin, and J. Latham (1980), The influence of entrainment on the evolution of cloud droplet spectra: I. A model of inhomogeneous mixing, *Q. J. Roy. Meteor. Soc.*, *106*(449), 581-598, doi:10.1002/qj.49710644914.

Beard, K. V., and H. T. Ochs (1993), Warm-rain initiation: An overview of microphysical mechanisms, *J. Appl. Meteorol.*, *32*(4), 608-625, doi:10.1175/1520-0450(1993)032<0608:WRIAOO>2.0.CO;2.

Chan, K. R., J. Dean-Day, S. W. Bowen, and T. P. Bui (1998), Turbulence measurements by the DC-8 Meteorological Measurement System, *Geophys. Res. Lett.*, *25*(9), 1355-1358.

Grabowski, W. W. (2006), Indirect impact of atmospheric aerosols in idealized simulations of convective-radiative quasi equilibrium, *J. Climate*, *19*(18), 4664-4682, doi:10.1175/JCLI3857.1.

Kim, B.-G., M. A. Miller, S. E. Schwartz, Y. Liu, and Q. Min (2008), The role of adiabaticity in the aerosol first indirect effect, *J. Geophys. Res.*, *113*(D5), D05210, 10.1029/2007jd008961.

Lasher-Trapp, S. G., W. A. Cooper, and A. M. Blyth (2005), Broadening of droplet size distributions from entrainment and mixing in a cumulus cloud, *Q. J. Roy. Meteor. Soc.*, *131*(605), 195-220, doi:10.1256/qj.03.199.

Lehmann, K., H. Siebert, and R. A. Shaw (2009), Homogeneous and inhomogeneous mixing in cumulus clouds: dependence on local turbulence structure, *J. Atmos. Sci.*, *66*, 3641-3659, doi:10.1175/2009JAS3012.1.

Liu, Y., P. H. Daum, S. K. Chai, and F. Liu (2002), Cloud parameterizations, cloud physics, and their connections: An overview, *Recent Res. Devel. Geophysics*, *4*, 119-142.

Liu, Y., P. H. Daum, S. S. Yum, and J. Wang (2008), Use of microphysical relationships to discern growth/decay mechanisms of cloud droplets with focus on Z-LWC relationships, paper presented at 15th International Conference on Clouds and Precipitation, Int. Comm. on Clouds and Precip., Cancun, Mexico.

Lu, C., Y. Liu, and S. Niu (2011), Examination of turbulent entrainment-mixing mechanisms using a combined approach, *J. Geophys. Res.*, *116*, D20207, doi:10.1029/2011JD015944.

Su, C.-W., S. K. Krueger, P. A. McMurtry, and P. H. Austin (1998), Linear eddy modeling of droplet spectral evolution during entrainment and mixing in cumulus clouds, *Atmos. Res.*, *47-48*, 41-58.

Vogelmann, A. M., G. M. McFarquhar, J. A. Ogren, D. D. Turner, J. M. Comstock, G. Feingold, C. N. Long, H. H. Jonsson, A. Bucholtz, D. R. Collins, G. S. Diskin, H. Gerber, R. P. Lawson, R. K. Woods, E.

Andrews, H.-J. Yang, J. C. Chiu, D. Hartsock, J. M. Hubbe, C. Lo, A. Marshak, J. W. Monroe, S. A. McFarlane, B. Schmid, J. M. Tomlinson, and T. Toto (2012), RACORO extended-term, aircraft observations of boundary-layer clouds, *B. Am. Meteorol. Soc.*, (In press), 10.1175/bams-d-11-00189.1.

von Salzen, K., and N. A. McFarlane (2002), Parameterization of the bulk effects of lateral and cloud-top entrainment in transient shallow cumulus clouds, *J. Atmos. Sci.*, *59*(8), 1405-1430, doi:10.1175/1520-0469(2002)059<1405:POTBEO>2.0.CO;2.

Yum, S. S., and J. G. Hudson (2001), Microphysical relationships in warm clouds, *Atmos. Res.*, *57*(2), 81-104.

Yum, S. S., and J. G. Hudson (2005), Adiabatic predictions and observations of cloud droplet spectral broadness, *Atmos. Res.*, *73*(3-4), 203-223, doi:10.1016/j.atmosres.2004.10.006.

ACKNOWLEDGEMENT

Liu and Lu are supported by the Department of Energy (DOE) Earth System Modeling (ESM) program via the FASTER project (www.bnl.gov/esm) and Atmospheric System Research (ASR) program. Niu is supported by the Qing-Lan Project for Cloud-Fog-Precipitation-Aerosol Study in Jiangsu Province, China, a Project Funded by the Priority Academic Program Development of Jiangsu Higher Education Institutions. Yum is funded by the Korea Meteorological Administration Research and Development Program under Grant CATER_2012-3051.

SHAPES OF GRAUPEL OBTAINED FROM VIDEOSONDE OBSERVATION DURING THE RAINY SEASON IN OKINAWA

Kenji Suzuki[1], Kosei Yamaguchi[2], and Eiichi Nakakita[2]
[1]Yamaguchi University, Yamaguchi, 753-8515, Japan
[2]Disaster Prevention Research Institute, Kyoto University, Kyoto, 611-0011, Japan

1. INTRODUCTION

The videosonde has been developed to reveal the vertical distribution of hydrometeors (Takahashi, 1990). The main component of the device is a video camera used to record images of precipitation particles. Since the first videosonde soundings at Ponape (Takahashi and Kuhara, 1993), several hundred videosondes have been launched into the clouds in climatologically different areas and have contributed to better understanding into cloud microphysics (Takahashi et al., 1995a, 1995b; Takahashi et al., 1999; Keenan et al., 2000; Takahashi et al., 2001; Takahashi and Keenan, 2004; Takahashi, 2006; Takahashi and Suzuki, 2010; Takahashi, 2010).

The videosonde is a useful tool for giving important information for remote sensing techniques such as polarimetric radar. Polarimetric radar can estimate cloud microphysics, such as raindrop size distributions and classification of cloud hydrometeors, and improve the accuracy of quantitative rainfall estimation with using appropriate combination of polarimetric parameters. To investigate the relationship between the polarimetric parameters and hydrometeors, simultaneous observations by videosondes and polarimetric radar are essential. Nakakita et al. (2008, 2009) conducted an in-situ observation campaign with synchronization of videosondes and COBRA, which is a C-band polarimetric radar (Nakagawa et al., 2003) at the National Institute of Information and Communications Technology (NICT), Okinawa Electromagnetic Technology Center.

In this study, we focus on the shape of graupel obtained from videosonde observations during the Baiu monsoon clouds. Graupel is generally observed as a cone-like shape in clouds as a result of riming. However, we often observed nearly round graupel. We evaluated it quantitatively using videosonde images.

Corresponding author address: Kenji Suzuki, Yamaguchi University, Yamaguchi 753-8515, Japan; E-mail: kenjis@yamaguchi-u.ac.jp

2. OBSERVATION

The videosonde (Fig.1) used in the present study was an improved version of that designed by Takahashi (1990), being lighter and less expensive while providing the same level of performance. Videosonde is a balloon-borne radiosonde that acquires images of precipitation particles via a CCD camera. The videosonde system consists of a CCD camera, a video amplifier, an infrared sensor, a transmitter, batteries, and a control circuit. The system has a stroboscopic illumination that provides information on particle size and shape. Interruption of the infrared beam by particles triggers a flash lamp and particle images are then captured by the CCD camera. Images of particles were converted to frequencies between 10 Hz and 1 MHz and transmitted by a 1680 MHz carrier wave (bandwidth 4 MHz, transmission power 0.5 W) to the receiving system at surface before being displayed and recorded onto videotapes and DVDs. Recorded precipitation particles were classified as either raindrops, frozen drops, graupel, ice crystals, or snowflakes on the basis of transparency and shape, as described by Takahashi and Keenan (2004). Information concerning atmospheric pressure, temperature, humidity, and wind was obtained from a Vaisala RS-92 radiosonde attached to the videosonde.

Figure 1. Videosonde (left) and launching balloon (right). Videosonde used in this study was an improved version of that designed by Takahashi (1990). 450(L)x150(W)x 220(H), 1.7kg.

Videosonde observations of Baui Monsoon clouds were conducted as part of the in-situ campaign observation by a C-band polarimetric radar synchronized with videosonde (Nakakita et al., 2009), which were carried out at Okinawa Electromagnetic Technology Center of National Institute of Information and Communications Technology (26°29'N ,127° 50'E). After the launch of a videosonde, the Range Height Indicator (RHI) scans by the C-band Okinawa polarimetric radar (COBRA) was continuously performed every minutes, targeting the videosonde in the precipitating cloud. During the campaign observation in 2008 and 2009, we launched 21 videosondes into the Baiu monsoon clouds. In this study, five cases were chosen for analysis (Table1).

Table 1. List of videosonde soundings

#	Date (JST)	Remarks
2008#2	0036 June 4	Convective rain, Cloud top 7km
2009#10	1941 June 12	Convective rain, Cloud top 11km
2009#12	1757 June 11	Convective rain, Cloud top 13km
2009#11	0629 June 12	Convective rain, transit to stratiform above 0 ° C, Cloud top 13km, No bright band
2009#3	0235 May 27	Stratiform rain, Cloud top 9km, Clear bright band

3. RESULTS AND DISCUSSION

Five videosonde soundings were classified into four different developing stages of clouds according to the COBRA radar images; a shallow convective cloud, a deep convective cloud, a transition cloud to stratiform, and a stratiform cloud. Figure 2 shows the precipitation particle size-height diagrams obtained from videosonde soundings. On June 4, 2008, we launched a videosonde into the shallow isolated convective cloud. Graupel images transmitted from videosonde 2008#2 were nearly round and showed that the particle size was smaller and flatter with altitude (Fig.3a). Videosonde 2009#10 and 2009#12 were classified into the deep convective cloud type. As shown in Fig. 3d, the shape of graupel was not cone-like but nearly round. The shape of aggregate in Fig. 3c was not flake-like but with rounded outlines. It is different from snowflakes consisting of ice crystals in deep stratiform cloud case (2009#3). In the case of 2009#3, the clear bright band was observed. According to the COBRA radar images, the videosonde 2009#11, classified into the transition stage, was launched into a convective cloud, and then it had changed to be stratiform.

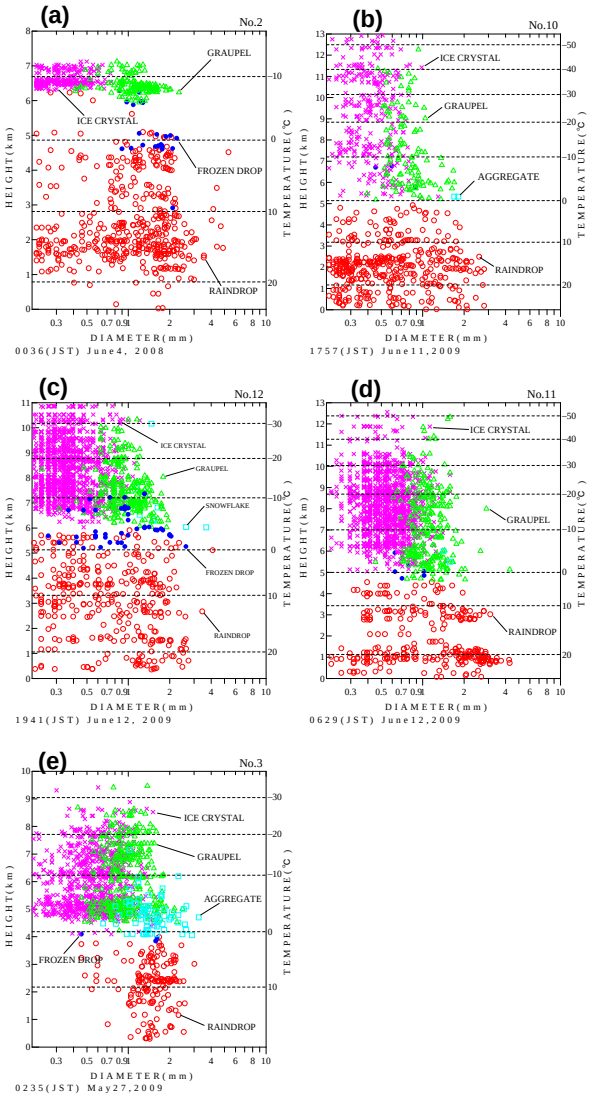

Figure 2. Precipitation particle size-height diagram of videosonde (a) 2008#2, (b) 2009#10, (c) 2009#12, (d) 2009#11, and (e) 2009#3. Open circle (raindrop), triangle (graupel), cross (ice crystal), and square (aggregate).

To evaluate the graupel shapes quantitatively, we define two parameters; flattening of graupel (f) and ratio of cross sections of graupel against the ellipsoid-assumed cross sections (r). If f=0, the shape of graupel is a circle (a sphere), and r=1 means an oval (or a circle). Figure 4 shows f-r diagram of four different developing stages. It is found that r was decreasing and f increasing as the cloud type changed from convective to stratiform.

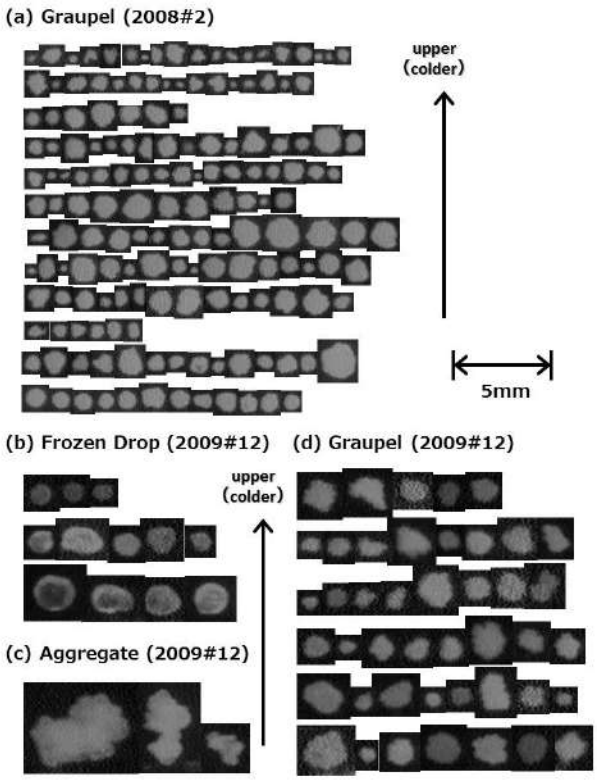

Figure 3. Precipitation particle images of (a) graupel obtained from videosonde 2008#2 sounding, (b) frozen drops, (c) aggregates, (d) graupel from videosonde 2009#12.

This indicates that graupel formation process is different in cloud developing stages. Nearly round graupel were likely to be observed in the shallow convective clouds and more irregular-shape graupel in the stratiform clouds. Harimaya (1976) showed the embryo and formation mechanism of graupel, and concluded that both snow crystals and frozen drops can become graupel embryo. The origin of nearly round graupel is supposed to be dendrite crystals or frozen drops. In the case of a shallow convective cloud observed in this study, because of the low concentration of ice crystals, the origin of the nearly round graupel goes back to the frozen particle lifted by the updraft, which is quite different from the case of the stratiform clouds where graupel originated in ice crystals.

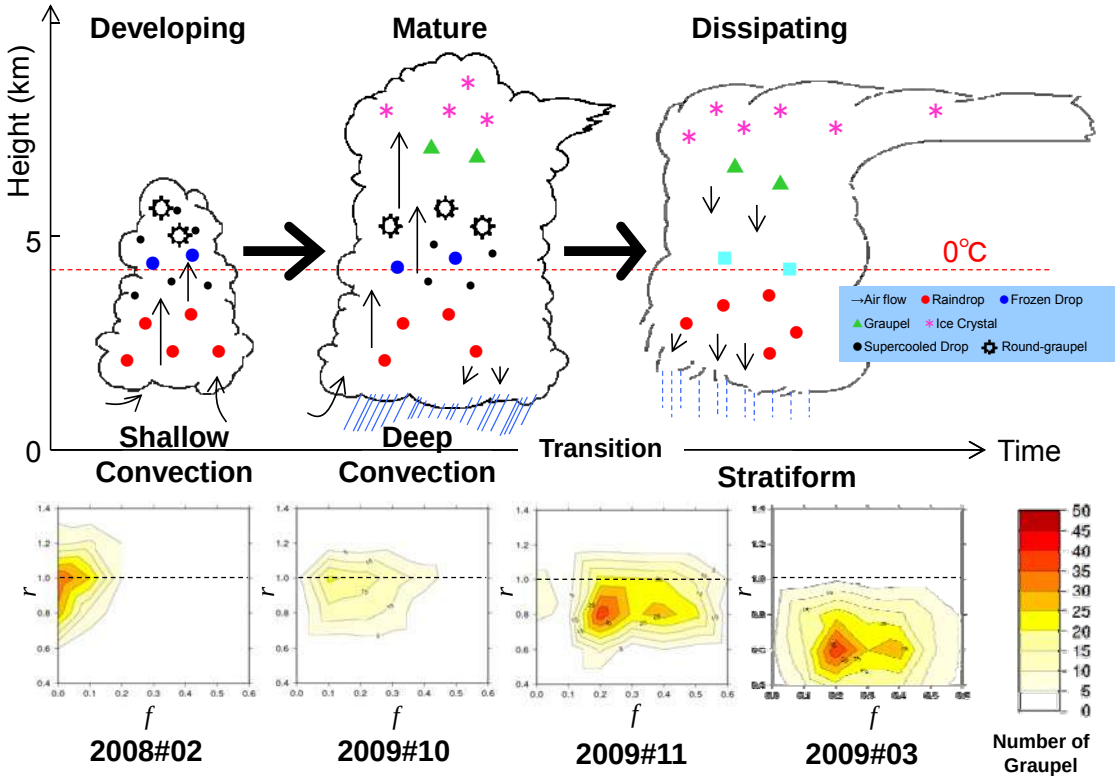

Figure 4. Schematic diagram of nearly-round graupel formation process (top) and f-r diagram of four different developing stages (bottom).

Acknowledgements

The present study was supported by a Grant-in-Aid for Scientific Research from the Japan Society of the Promotion of Science (19206054). The authors would like to thank the staff of Okinawa NICT and the many students who helped to conduct the field observations in Okinawa for their assistance in conducting the balloon launches and performing COBRA operations.

References

Harimaya, T., 1976: The embryo and formation of graupel, J. Meteor. Soc. Japan, **54**, 42-51.

Nakakita E., K. Yamaguchi, Y. Sumida, H. Takehata, K. Suzuki, K. Nakagawa, S. Oishi, Y. Shusse, and K. Tsuboki, 2008: Classification of hydrometeors using a C-band polarimetric radar and validation by in-situ campaign observation synchronized with video-sonde. *Annuals of Disas. Prev. Res. Inst., Kyoto Univ.*, **51**, 519-533.

Nakakita E., K. Yamaguchi, Y. Sumida, H. Takehata, K. Suzuki, K. Nakagawa, S. Oishi, Y. Shusse, K. Tsuboki, and T. Ohigashi, 2009: Development of hydrometeor classification system using polarimetric radar measurements synchronized with the video-sonde observation. *Annual Journal of Hydraulic Engineering*, *JSCE*, **53**, 361-366

Nakagawa, K., H. Hanado, S. Satoh, N. Takahashi, T. Iguchi, and K. Fukutani, 2003: Development of a new C-band bistatic polarimetric radar and observation of typhoon events. *Proc. 31st Conf. on Radar Meteor.*, *Seattle*, *Amer. Meteor. Soc.*, 863-866.

Pruppacher, H. R. and J. D. Klett, 1997: Microphysics of clouds and Precipitation, Kluwer Academic Publishers, 954pp.

Suzuki, K., Y. Shigenaga, T. Kawano and K. Yoneyama, 2006: Videosonde Observation during the R/V Mirai MR04-08 Cruise. J. Marine Meteor. (Umi to Sora), **82** (2), 29-38.

Suzuki, K., K. Shimizu, T. Ohigashi, K. Tsuboki, S. Oishi, S. Kawamura, K. Nakagawa, K. Yamaguchi and E. Nakakita, 2012: Development of a New Videosonde Observation System for In-situ Precipitation Particle Measurements. SOLA, **8**, 1-4.

Takahashi, T. 1990: Near absence of lightning in torrential rainfall producing Micronesian thunderstorms. Geophys. Res. Lett., **17**, 2381 -2384.

Takahashi, T. and K. Kuhara, 1993: Precipitation mechanisms of cumulonimbus clouds at Pohnpei, Mirconesia. J. Meteor. Soc. Japan, **71**, 21-31.

Takahashi, T., K. Suzuki, M. Orita, M. Tokuno and R. de la Mar, 1995: Videosonde observations of precipitation processes in equatorial cloud clusters. J. Meteor. Soc. Japan, **73**, 509-534.

Takahashi, T. and T. D. Keenan, 2004: Hydrometeor mass, number, and space charge distribution in a “Hector” squall line. J. Geophys. Res., **109**, D16208, 10.1029/2004 JD004667.

Takahashi, T.,2006: Precipitation mechanisms in east Asia monsoon: Videosonde study. J. Geophys. Res., **111**, D09202, 10.1029/2005 JD006268.

Takahashi, T, and K. Suzuki, 2010: Development of negative dipoles in a stratiform cloud layer in a Okinawa “Baiu” MCS system, *Atmos. Res.*, doi:10.1016/j.atmosres.2010.07.013.

Takahashi, T., 2010: The videosonde system and its use in the study of East Asian monsoon rain. *Bull. Amer. Met. Soc.*, doi:10.1175/2010BAMS2777.1.

A UNIQUE CUMULONIMBUS PRODUCING A LOCALIZED HEAVY RAINFALL IN TOKYO METROPOLITAN DURING TOMACS

Yoshinori YAMADA
Meteorological Research Institute, Japan Meteorological Agency
1-1, Nagamine, Tsukuba, 305-0052, Japan

1. INTRODUCTION

The vulnerability to sever weather events such as heavy rainfall and strong winds seems to be inherent in large cities of dense population, where human activities are supported by highly developed communication and transportation networks. Since the large cities consist of concrete buildings and paved roads, heavy rainfall would give rise to flush floods and submersion, resulting in loss of lives in some cases, for example. Recently, sudden localized heavy rainfall sometimes occurs from vigorous cumulonimbi in Tokyo Metropolitan, producing severe damages. Accordingly, needs for the accurate detection and forecast of such severe weather events are increasing in Japan.

In such background, a five-year project named “Tokyo Metropolitan Area Convection Study for Extreme Weather Resilient Cities” (hereafter “TOMACS”) has started from 2010. This project includes three sub-themes: (a) elucidation of mechanisms of severe weather based on a dense observation network, (b) development of monitoring and prediction systems of severe weather, and (c) social experiment concerning the efficient dissemination and use of information on severe weather in order to mitigate disasters. This study is made in the sub-theme (a), in which active cumulonimbi occurring in and around Tokyo are main targets of research.

The understanding of the structures of cumulonimbi based on observations through their whole lifetime is not sufficient yet in Japan. Such understanding is indispensable to the improvement of the forecasts accuracy of precipitation and winds associated with cumulonimbi. This paper presents a structure of a unique cumulonimbus observed on Jul. 5, 2010, in the first year of TOMACS, based mainly on C-band Doppler radar data. Its uniqueness lies in a high potential of producing heavy rainfall regardless of the relatively low-cloud top height and weak updrafts compared to summertime active deep cumulonimbi often observed in and around Tokyo Metropolitan.

2. DATA AND WIND SYNTHESIS

Three-dimensional wind fields in cumulonimbi were derived from MUSCAT formalism (Bousquet and Chong 1998) using data from three C-band Doppler radars at Narita and Haneda Airports and Kashiwa, which are routinely operated by Japan Meteorological Agency. An additional constraint (Chong and Bousquet 2001; Bousquet et al. 2008) was also employed. MUSCAT provides the accurate determination of the wind components than does the conventional approach by Ray et al. (1980) as shown in Yamada (2011). No adjustments of the vertical winds were made. The wind recovery was made in Cartesian common grids, whose origin was set at the position of the Narita radar (Fig. 1). In this figure, the locations of the three radars are also shown. The horizontal and vertical resolutions of common grids were 1 km and 0.5 km, respectively, with the lowest height of 0.5 km above ground level. The Doppler radars at Haneda and Narita collect data at a spatial resolutions in the radial and azimuthal directions of 0.125 km and 0.7°, respectively. Their maximum detecting range is 128 km. Each of these two radars is operated in one of the two observation modes consisting of conical scannings at predetermined elevation angles, depending on the location of echoes relative to each radar. Each mode completes in several minutes. On the other hand, available data from the Kashiwa radar data are at the resolutions of 0.5 km and 0.7°in the radial and azimuthal directions, respectively. Its maximum detection range in Doppler mode is 150 km. Operation mode of this radar is also conical scanning, and a predetermined observation sequence including volume scan in Doppler mode is repeated at ten-minute intervals. Number of conical scans in Doppler

mode of the Kashiwa radar was, however, reduced from Jul. 1st, 2009 according to the change in the antenna scan sequence in order to observe more frequently rain rates near the surface. One of the limitations of the use of the operational radar data is relatively sparse scanning at higher elevation angles. Thus, the wind components at higher heights would became less accurate in some cases.

Even though the three Doppler radars collect volume scan data independently, dual-Doppler wind recovery can be made at about 5 – 7 minute-intervals using the Haneda and Narita radar data. At this time, the difference in the start time of each of volume scans of these two radars was less than about three minutes. For the triple-Doppler analysis, time difference in the start time of volume scans from the three radars was also within about ± 3 minutes with respect to the standard time of the wind synthesis. A profit of the triple-Doppler synthesis is a better wind determination at higher heights by mutual compensation of their sparse scannings at higher elevation angles.

Other than Doppler radars, routine sounding at Tateno and the meso-surface network operated by the Japan Meteorological Agency and so on were also used.

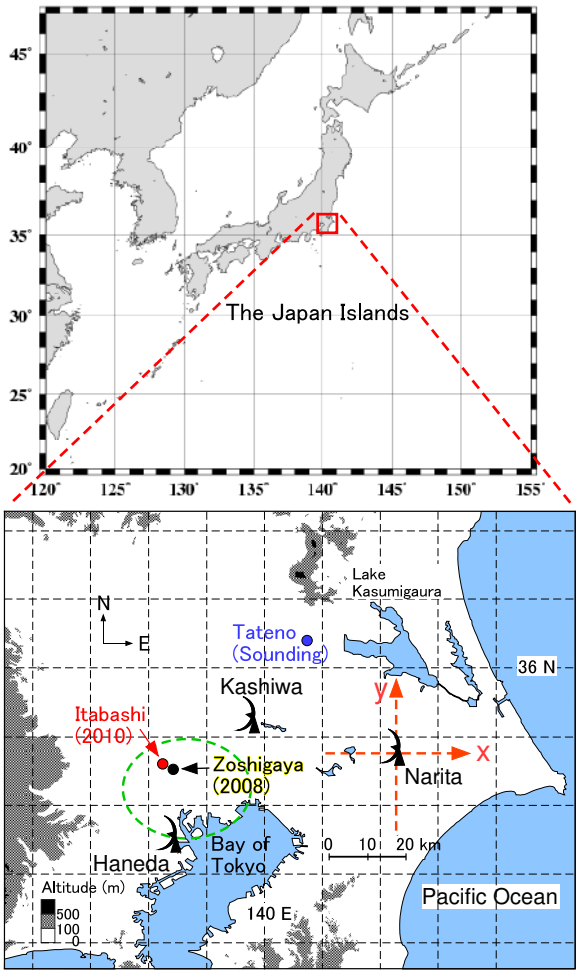

Fig. 1: The location of the experimental region is shown by an open rectangle in red color in the upper panel. Its enlarged map is presented in the lower panel, where positions of three Doppler radars, and two locations of heavy rainfall (Itabashi and Zoshigaya) described in this paper are also indicated. The Tokyo Metropolitan lies approximately in the dashed green oval. The x- and y-axes of the common grids for the wind recovery are in the east-west, and north-south directions, respectively. Longitude and Latitude are shown by thin dashed lines at 10-degree intervals. Altitudes are also indicated by shading.

3. THE UNIQUE CUMULONIMBUS ON JUL. 5, 2010

A shallow cumulonimbus produced an hourly rainfall reaching 95 mm at Itabashi, Tokyo. This heavy rainfall resulted in inundation and submersion. It may have been triggered by the low-level interaction between the sea breeze and a pre-existing rain region. Wind recovery was made by means of dual-Doppler synthesis employing Haneda and Narita radar data for this case.

a. ATMOSPHERIC CONDITIONS

The unique cumulonimbus appeared in a convective precipitation region at around 1900 JST[1], and it persisted at least for one hour and forty minutes. The surface weather maps on this day showed that a Baiu-front was located to the far south of Tokyo, over the Pacific Ocean. At the 500-hPa level, no appreciable cold air was present and west-southwesterly winds prevailed. The cloud environment seemed to be moist because mean relative humidity of lower atmosphere below 700-hPa height was 87% from the 0900-JST sounding at Tateno. Sounding data at Tateno also showed that LCL was at 0.52 (0.24) km at 0900 (2100) JST, and that LNB was located at about 650-hPa (570-hPa) height at 0900 (2100) JST. These data implied that no deep convection was ex-

[1]Japan Standard Time. JST = UTC + 9 hours

pected. Convectively unstable stratification was observed from the surface up to about 4-km height at 0900-JST sounding. Convective Available Potential Energy (CAPE) for the air below the 900-hPa height was very small to be about 55 and 60 J kg^{-1} from the 0900-JST and 2100-JST sounding, respectively.

b. MEAN PPI IMAGE AND 10-MINUTE PRECIPITATION

Figure 2 shows a mean reflectivity of the Haneda radar. Itabashi is located in a small region of a high reflectivity between 45 – 52 dBZ. In a snaps shot of PPI images, maximum reflectivity larger than 59 dBZ was observed in a very small region at some observation times. No hail report was made. In addition, k_{DP} data from multiparameter radars operated by Ministry of Land, Infrastructure, Transport, and Tourism suggested that the precipitation particles from this cumulonimbus were in the form of rain. The time change in 10-minute rain amount is shown in Fig. 3. Associated with high reflectivity, hourly precipitation from 1940 to 2040 JST reaching as much as 95 mm hr^{-1} was observed. This heavy rainfall appeared to be brought about the shallow cumulonimbus.

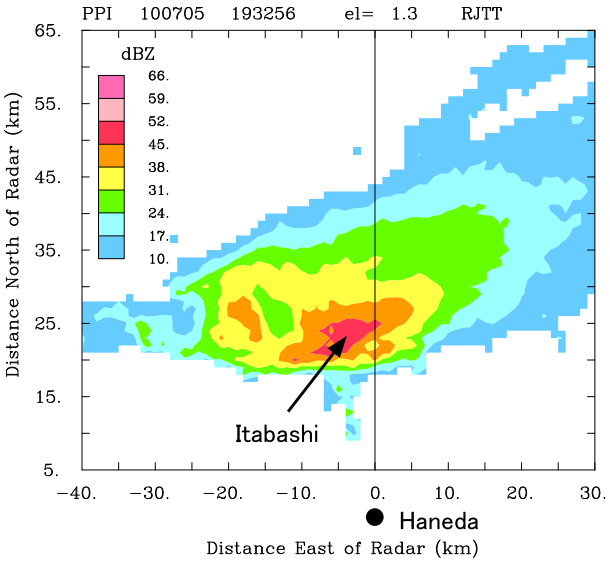

Fig. 2: Mean reflectivity in PPI mode of the Haneda radar at an elevation angle of 1.3°between 1932 and 2033 JST. Reflectivity is shown by shading at a 7-dBZ intervals, starting from 10 dBZ. The position of the Haneda radar is indicated by a solid circle, and the location of Itabashi is also pointed by an arrow.

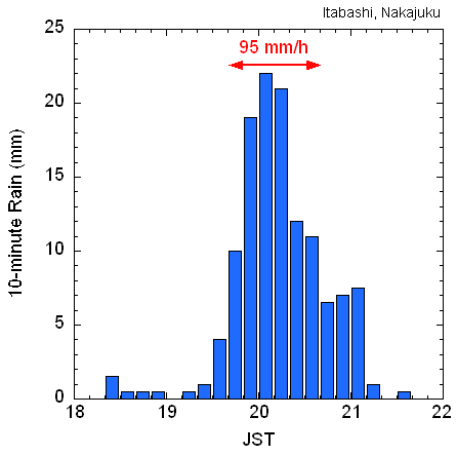

Fig. 3: 10-minute precipitation observed in Itabashi at an observation point (Toshima) of the Tokyo Metropolitan Government. This point was almost located under the cumulonimbus.

c. AIRFLOW STRUCTURES

Figure 4 shows wind fields in horizontal cross-sections at the 0.5- and 4.5-km heights at 1945 JST, at which maximum updrafts in the cumulonimbus were analyzed. The echo region including the cumulonimbus traveled at a mean speed of 3 m s^{-1}to the east-northeast between 1905 and 2024 JST. At the 4.5-km height, an updraft core in the cumulonimbus is identified as a circular shape of 6-m s^{-1}contour, embedded in regions with relatively weak vertical winds, whose magnitudes were less than 3 m s^{-1}. The horizontal dimension of the updraft core was about 5 km. As is clearly shown in the cross-section at the 0.5-km height, there was a system-relative airflow directing to the cumulonimbus; it produced a low-level convergence at around the cloud. This low-level airflow is regarded as sea breeze from the Bay of Tokyo, and might have been responsible to activation and maintenance of this cloud. In fact, the decay of this cumulonimbus seemed to correspond to the slight shift of this low-level wind direction, which was detected by the meso-surface network. The temperature deficit of the cold pool beneath the precipitation echoes in this figure was estimated to be about 1 – 2 ° C from surface temperature fields observed by this network.

Airflow and reflectivity fields in a vertical

cross-section along a line AB in Fig. 4 are exhibited in Fig. 5. The reflectivity field demonstrates that the cumulonimbus was shallow such that its echo top height was about 6 km, at which air temperature was about -6° C from the 0900JST-sounding at Tateno. In this cumulonimbus, a narrow reflectivity core $>$ 54 dBZ was identified below 2-km height at a horizontal distance of about 26 km, and a region of high reflectivity $>=$ 47 dBZ directed almost vertical. The southeasterly low-level inflow was present below the 2.5km height. In addition, updrafts slightly tilted into the upshear direction (see Fig. 12). The airflow structure resembled, to some extent, to that in squall lines reported so far. In this case, however, the precipitation system was almost at rest in this cross-section.

Figure 6 displays time change in the mean updrafts in the updraft core of the cumulonimbus. The mean value at each height was computed using five updrafts from the largest. This figure shows that the maximum updrafts were at most 6 – 7 m s^{-1}confided to in a height interval between 3 and 4.5 km, and that these large updrafts persisted about 30 minutes. Figures 5 and 6 indicate that the localized heavy rainfall was bring about by a shallow cumulonimbus characterized by relatively weak updrafts.

4. A VIGOROUS DEEP CUMULONIMBUS ON AUG. 5, 2008

This example of a vigorous deep cumulonimbus, which also formed over the central Tokyo, will highlight the uniqueness of the cumulonimbus described in the foregoing section even though its occurrence was prior to the start of TOMACS. It was regarded as an isolated heat thunderstorm, and produced a localized intense precipitation at around Zoshigaya in the central Tokyo, resulting in a sudden increase in the flow in sewerage to kill five workers in it. It propagated at a very small mean speed of ~ 0.9 m s^{-1}toward the northeast between 1139 and 1255 JST.

For this deep case, triple-Doppler wind retrieval was made from 1139 to 1255 JST, except for at 1217 and 1236 JST, at which wind fields were derived from dual-Doppler recovery as in section 3.

a. ATMOSPHERIC CONDITIONS

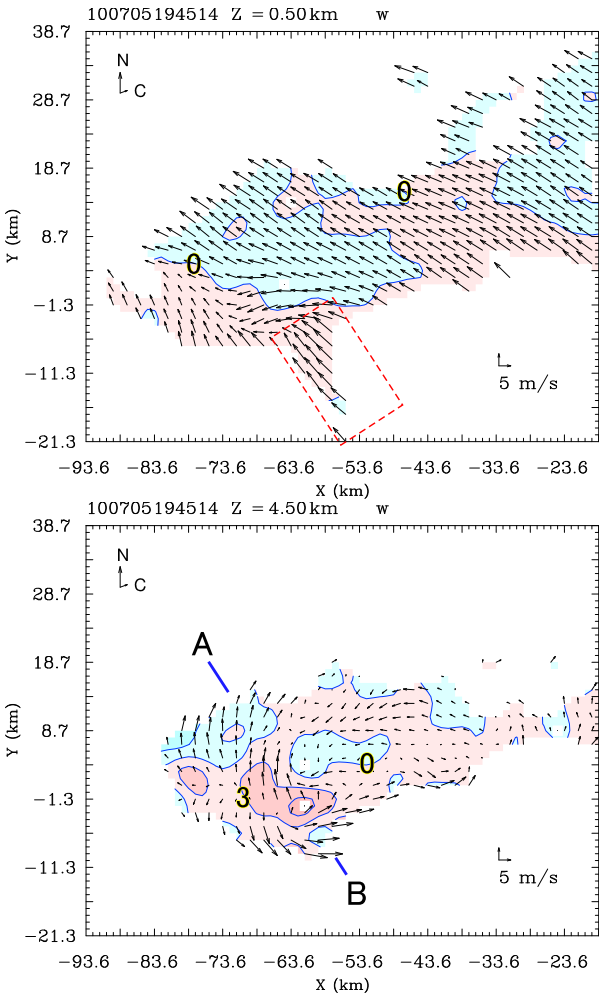

Fig. 4: System-relative airflow (arrows) and vertical wind fields (shading) at the 0.5-km (upper panel) and 4.5-km (lower panel) heights at 1945 JST. Wind vectors are plotted every other grid points. Vertical wind fields are contoured at 3 m s^{-1}intervals, and updraft and downdraft regions are shown in red and blue, respectively. The arrows labeled “C” and “N” indicate the system motion and the direction of north, respectively. A rectangle of red dashed line is the portion, where mean wind shown in Fig. 12 is computed. A line AB in the 4.5-km height is the position of a vertical cross-section in Fig. 5.

The active cumulonimbus occurred over the central Tokyo under high pressure. The surface wind analysis based on the meso-surface network data indicated that the central Tokyo was located in a weak convergent zone at larger scale because a stationary front passing around the Bay of Tokyo was analyzed in surface weather maps from 0300 to 1800 JST

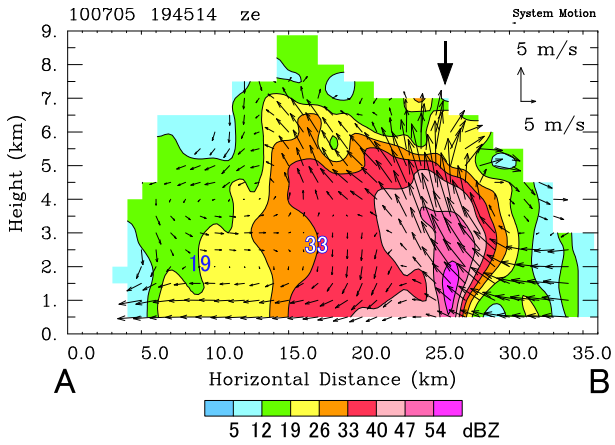

Fig. 5: Structure of airflow and reflectivity in a vertical cross-section along line AB in Fig. 4. Arrows are vector representation of system-relative horizontal and vertical wind components, and are drawn such that each arrow is parallel to the stream line at each point. Reflectivity is indicated by shading at 7-dBZ intervals. The system motion in this vertical cross-section is close to 0 m s^{-1}. The position of the cumulonimbus is indicated by a solid bold arrow.

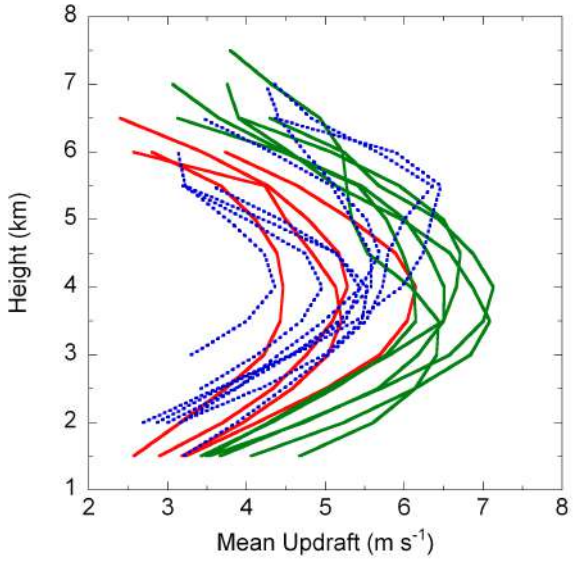

Fig. 6: Time changes in vertical profiles of mean updrafts in the updraft core of the cumulonimbus from 1905 to 2042 JST. The red, green, and blue lines are for the developing (from 1905 to 1922 JST), mature (from 1927 to 1956 JST) , and decaying stages (from 2002 to 2042 JST), respectively.

on this day. The sounding data at 0900 JST at Tateno indicated that a convectively unstable layer extended from the surface to about 2-km height. From this sounding data, LNB was located at about 170-hPa height, LCL was at about 0.2-km height, and CAPE was about 1400 J kg^{-1} . No presence of cold air at 500-hPa height was shown in a weather map.

b. MEAN PPI IMAGE AND 5-MINUTE PRECIPITATION

Figure 7 shows a mean reflectivity field in PPI image. It depicts that a heavy rainfall is very localized as indicated by a small extent of large reflectivities in red color corresponding to 45 – 52 dBZ. Indeed, surface precipitation recorded at an observation point by the Tokyo Metropolitan Government near the accident point in the sewerage shows a large amount of rainfall (Fig. 8). This figure implies an occurrence of a very intense rain rate in a short period of time because rainfall amount between 1145 to 1200 JST was turned into hourly rainfall of as much as 84 mm.

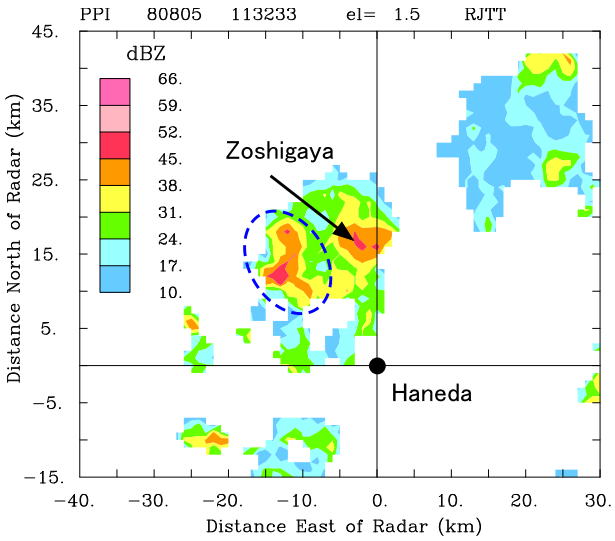

Fig. 7: As in Fig. 2, except for PPI of the Haneda radar at an elevation angle of 1.5°between 1133 and 1236 JST. The location of Zoshigaya is pointed by an arrow. Echoes enclosed by a dashed blue oval are associated with daughter cells.

c. AIRFLOW STRUCTURES

Figure 9 exhibits system-relative and vertical wind fields in the horizontal cross-sections at 0.5- and 8.5-km heights at 1205 JST, at which the cumulonimbus was considered to be in mature stage, and had maximum updrafts at middle heights. At the 0.5-km height, con-

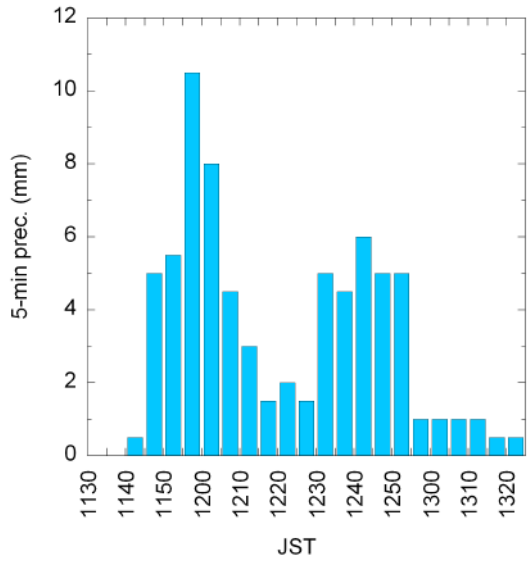

Fig. 8: 5-minute precipitation observed at Toshima observation point. Accumulated rainfall was 42 mm from 1145 to 1230 JST. These data are extracted from the accident report published by the Tokyo Metropolitan Government (2008).

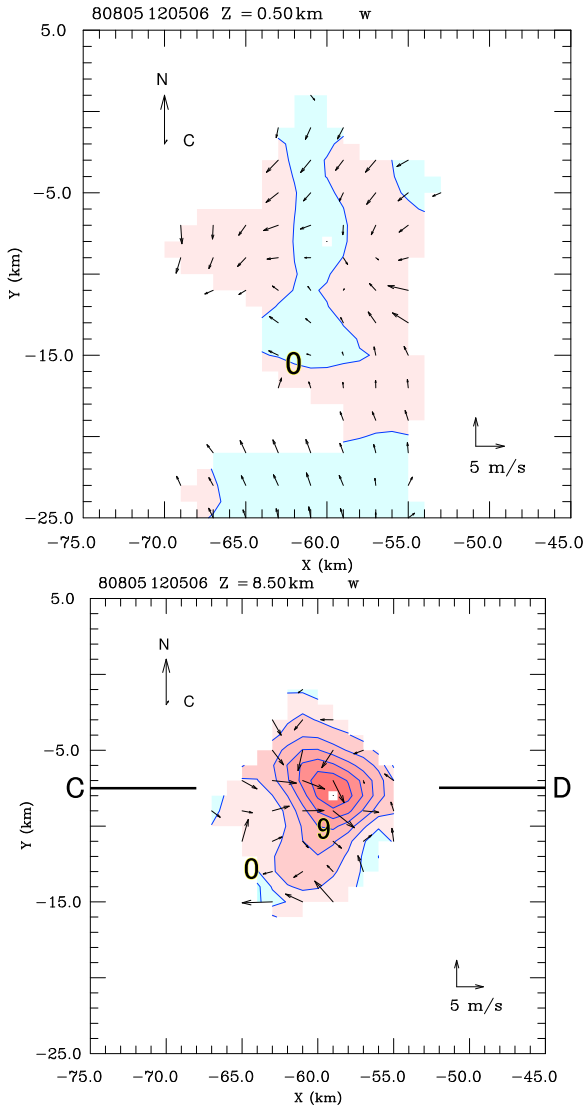

Fig. 9: As in Fig. 4, except for the cumulonimbus on Aug. 5, 2008 at the 0.5-km (upper panel) and 8.5-km (lower panel) at 1205 JST. A line CD in the lower panel is the position of a vertical cross-section in Fig. 10.

vergent flow pattern is identified. This airflow pattern was observed up to the 3-km height. At the 8.5-km height, the updraft region dominated in the cumulonimbus, and an updraft core was well analyzed. The horizontal dimension of the updraft core was about 5 km. Airflow and reflectivity fields in a vertical cross-section along a line CD in this figure are shown in Fig. 10. The echo top reached about 15-km height, and very large updrafts are confined in a narrow region in the cloud. The easterly inflow toward the cumulonimbus was present at low levels below the 3-km height. Reflecting weak vertical shear, the majority of updrafts directed almost vertically.

Figure 11 shows time change in the mean updraft in the updraft core of the cumulonimbus. The mean value was computed in the same manner as in the previous shallow case. The updrafts at heights ≥ 10 km may be contaminated relatively large errors. In contrast to the shallow cumulonimbus, maximum updrafts were very large to be 15 – 20 m s^{-1}between 7- and 10-km height interval. This figure also implies a rapid development of updrafts from 1150 to 1205 JST. The intense updrafts did not last long time, unlike the shallow case, and it weakened soon after 1211 JST. The decay of updrafts began from lower heights. Even in the decaying stage, however, intense updrafts exceeding 10 m s^{-1}were found at from 1217 to 1236 JST at upper heights between 7 and 9 km.

5. Discussion

The cumulonimbus on Jul. 5, 2010 was characterized by shallowness, relatively weak updrafts, and large reflectivities. It produced a large amount of precipitation in the form of rain in a limited area. This cumulonimbus lasted at least for one hour and forty minutes. This

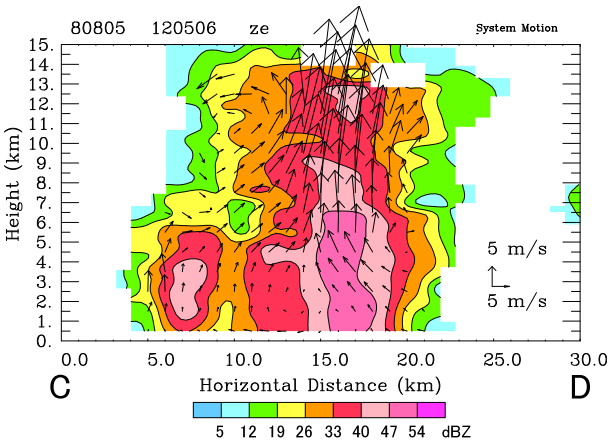

Fig. 10: As in Fig. 5, except for the Aug. 5, 2008 cumulonimbus along a line CD in Fig. 9. The arrows are plotted every other grid points in the vertical direction.

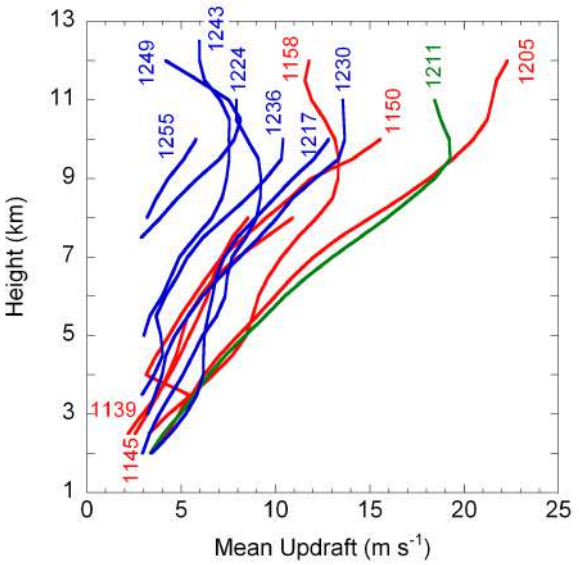

Fig. 11: As in Fig.6, except for the Aug. 5, 2008 cumulonimbus. Numbers in the figure show the time of wind recovery in JST. Wind fields at upper heights at 1139 and 1145 JST are not well determined because the cumulonimbus was in early developing stage.

long lifetime may be, in part, attributed to the upshear tilting of updrafts as depicted in Fig. 5 and continuous low-level inflow of the Bay of Tokyo. Upshear tilting updrafts are shown from Figs. 5 and 12. The mean magnitude of vertical shear from these two profiles in a height interval between 2 and 5 km was 3.7×10^{-3} s^{-1}.

Its shallowness and weak updrafts are very different character relative to those of the very

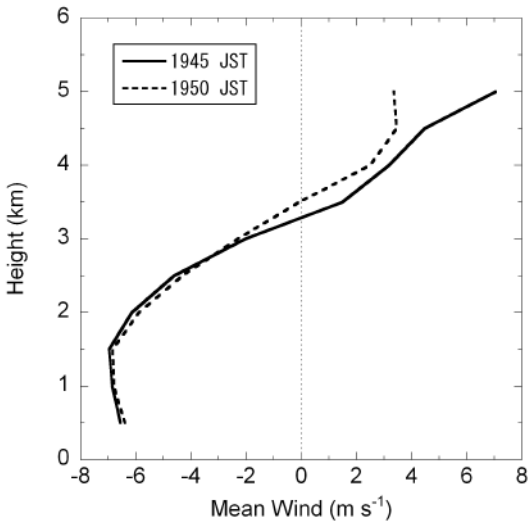

Fig. 12: Vertical profiles of Doppler-derived mean horizontal wind component in the direction parallel to the system-relative wind direction at the 0.5-km height at 1945 and 1950 JST in the domain depicted in Fig. 4. Nagative values indicate the wind components toward the northwest.

active deep cumulonimbus on Aug. 5, 2008 characterized by strong updrafts exceeding 10 m s^{-1}at middle heights. Such strong updrafts seem to be a common character to most of vigorous deep cumulonimbi because Doppler wind synthesis of several cumulonimbi, in and near Tokyo Metropolitan, producing high rain rates exceeding 30 mm per 30 minutes or hail revealed that all of them had strong updrafts exceeding 10 m s^{-1}at a 1-km horizontal resolution. Based on the results of the present study, the magnitude of updrafts at middle heights in the updraft core may be used as a measure for diagnosing vigorous cumulonimbi for most cases, it is, however, not applied to the unique cumulonimbus on Jul. 5, 2010.

6. Conclusion

A unique cumulonimbus, occurring on Jul. 5, 2010, observed during a project “TOMACS” was analyzed, mainly by means of multiple-Doppler wind synthesis using data from routinely operated Doppler radars by the Japan Meteorological Agency. It was unique in the aspect that it produced a localized large amount of rainfall regardless of its character of shallowness and less intense updrafts when compared to commonly observed active cumulo-

nimbi in and around Tokyo Metropolitan. Since the occurrence frequency of this type of cumulonimbus seems to be very rare in Japan, further studies are needed for better understanding of their structures and precipitation mechanisms.

REFERENCES

Bousquet, O., and M. Chong, 1998: A multiple-Doppler synthesis and continuity adjustment technique (MUSCAT) to recover wind components from Doppler radar measurements. *J. Atmos. Oceanic. Technol.*, **15**, 343-359.

Bousquet, O., P. Tabary, and J. P. Châtelet, 2008: Operational multiple-Doppler wind retrieval inferred from long-range radial velocity measurements. *J. Appl. Meteor. Climatol.*, **47**, 2929-2945.

Chong, M. and O. Bousquet, 2001: On the application of MUSCAT to a ground-based dual-Doppler radar system. *Meteor. Atmos. Phys.*, **78**, 133-139.

Ray, P. S., C. L. Ziegler, W. Bumgarner, and R. J. Serafin, 1980: Single- and multiple-Doppler radar observations of tornadic storms. *Mon. Wea. Rev*, **108**, 1607-1625.

Yamada, Y., 2011: Characteristics of MUSCAT-derived wind fields. submitted to *J. Meteor. Soc. Japan*. *In revision*.

Acknowledgments

TOMACS is supported by the Strategic Funds for the Promotion of Science and Technology of the Science and Technology Agency. The author would like to thank Dr. M. Maki at National Research Institute for Earth Science and Disaster Prevention for providing us information from multiparameter radars for the case on Jul. 5, 2010. Doppler radar data are provided from the Japan Meteorological Agency.

BLACK CARBON EFFECTS ON AMAZON PRECIPITATION

Weber Andrade Gonçalves[1], Luis Augusto Toledo Machado[2]

[1,2]National Institute for Space Research (INPE)

ABSTRACT

The relationship between precipitation and anthropogenic aerosols (black carbon), in the largest Amazon City (Manaus in Brazil), was studied using one year of data from a S-Band ground radar combined with measurements of black carbon and atmospheric thermodynamic profiles. The principal result found was a strong indication that the black carbon influence on precipitation is dependent on the atmospheric stability degree. Depending on the combination between the period of the year (with higher or lower black carbon concentration) and the stability degree, it was possible to separate the microphysical and the radiative effects.

1. INTRODUCTION

Biomass burning, as occurs in the Amazon Forest, releases to the atmosphere a great amount of black carbon, which could potentially influence the cloud formation, precipitation and the radiation budget (LIN et al., 2006). The knowledge of the aerosol influence on cloud and precipitation is extremely important and has been strongly explored in the last years. Two main effects are well known: Radiative or direct and microphysical or indirect. The characteristic of absorption in the visible part of the electromagnetic spectrum enables the heating of the atmospheric layer and inhibits the cloud formation (KOREN et al., 2004), which is the radiative effect, caused due to atmospheric stabilization (KOREN et al., 2008). The microphysical effect is linked to the possibility of black carbon particles become cloud condensation nuclei (ACKERMAN et al., 2000; ROBERTS et al., 2001). Then, it's expected that the amount of cloud droplets increase with the number of particulate material.

Accordingly to the results found in the literature the radiative and microphysical effects could affect the nebulosity depending on the cloud type. For warm clouds it´s believed that both effects act together in a way to decrease precipitation and cloud amount. The microphysical effect increases the small droplets formation (ROSENVELD, 1999; RAMANATHAN et al., 2001), affecting the coalescence (KAUFMAN et al., 2005). This small droplets could evaporate easily (ARTAXO et al., 2006), decreasing the cloud amount (KOREN et al, 2004) and precipitation (ROSENFELD, 1999). In other hand, the aerosol influence on convective clouds seems to be different. In addition to an increase of cloud fraction and precipitation (LIN at al., 2006, DUSEK et al., 2006), the electrical activity is also strengthened (GRAF, 2004, ALTARARZ et al., 2010). This behavior occurs mainly due to the microphysical effect. In this case the small droplets could ascent to high level of the atmosphere, reaching the freezing level and releasing more latent heat, which increase the updrafts and

strengths the convection (LIN et al., 2006; ROSENFELD et al., 2008).

The objective of this research was to start to explore a year of a radar dataset for a city located in the core of the Amazon Forest, Manaus-AM in Brazil, combined with *insitu* measurements of black carbon. This combination, associated with thermodynamic profiles, enabled us to start figuring out what is the effect of the pollution on precipitation in the forest.

2. DATA AND METHODOLOGIES

We used a dataset from a Band-S Doppler Radar located in the city of Manaus-AM. A Vertical Profiles of Reflectivity (VPR) technique was applied for a total of 6248 radar samples, following Kirstetter et al. (2010). By the use of this technique it was possible to fix the bright band and extrapolate the radar reflectivity to a plan at the same elevation of the radar, which was named as Constant Altitude Plan Position Indicator-Ground (CAPPI-Ground).

In order to determine the general behavior of precipitation in the study area, as well as its relationship with the presence of aerosols, an index was determined as follows:

$$Rain\_Fraction = \left(N_{20dBZ} / N_{TOTAL} \right) * 100$$

Where,

N_{20dBZ} is the amount of CAPPI-Ground pixels with a reflectivity equal or higher than 20 dBZ, and N_{TOTAL} is the total of pixels in the area.

The black carbon database was obtained from the experiment European Integrated Project on Aerosol Cloud Climate and Air Quality Interactions (EUCAARI) in the city of Manaus-AM during 2009, totaling 15162 samples. Atmospheric soundings data collected twice a day during 2009 in the city of Manaus-AM were also used. In order to obtain the stability degree of the atmosphere the Convective Available Potential Energy (CAPE) was calculated, following the equation below:

$$CAPE = \int_{NCE}^{NPE} g\left(\frac{Tv_p - Tv_a}{Tv_a} \right) dz$$

The last dataset to be described was the topography one. This data was obtained from the Shuttle Radar Topography Mission (SRTM) with an original resolution of 90 meters (RODRIGUES et al., 2005).

3. RESULTS

The first results to be commented are related to two important characteristics of precipitation in the region: seasonality and topographic. The more intense precipitation rates were found in the second semester (dry to wet period), which coincides with the higher CAPE values (Figure not shown). Although the region do not presents high topography variation (maximum around 160 m), some interesting features were observed. It was found that during the dry period most of the precipitation occurs in elevated areas, in other hand, for the first semester (rainy period) the precipitation occurs nearly homogeneously around the region (Figure not shown).

For the analysis of the black carbon influence over precipitation two main considerations were made. The first one was the year division in two periods, one with lower and the other with higher aerosol concentrations (which coincides with rainy and dry

periods, first and second semesters respectively). The second consideration was to analyze the black carbon influence for different atmospheric instability degrees. CAPE values were used to achieve this purpose. When the atmosphere presented a value less than 1400 J/kg it was considered stable and unstable when values greater than 2600 J/kg were observed. Between all possible combinations the aerosol effect is to decrease the rate and intensity of the precipitation (Figure 1), except during the dry period when atmosphere is unstable (Figure 2). In this situation, the black carbon concentration influenced the increase of precipitation, what can be associated with the microphysical aerosol effect. For the other combinations, the radiative affect was dominant reducing precipitation.

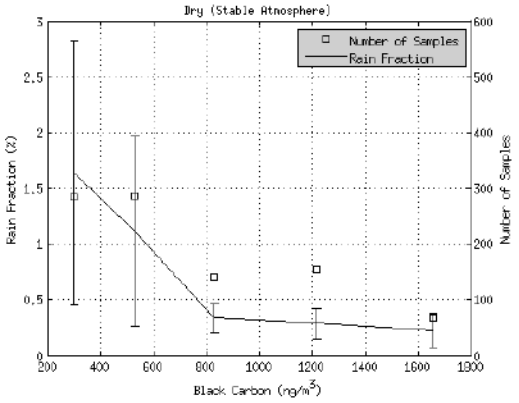

Figure 1 - Mean, standard deviation and number of samples of Rain Fraction for each black carbon bin, during the dry season for a stable atmosphere. The wet season curve is similar but with smaller values of black carbon.

4. CONCLUSIONS

The results presented in this research are an indication that a higher concentration of black carbon can´t determinate itself the increase of decrease of the precipitation in the Amazon. The stability degree of the atmosphere, represented by CAPE in this research, plays an important role in this relationship. In atmospheres with low potential to convection the larger number of small droplets can´t ascend to elevated atmospheric levels and evaporates, decreasing the precipitation. The opposite behavior happens in the case of an unstable atmosphere, where the convection is enhanced by a presence of a high black carbon concentration. It´s important to comment that this result is a first attempt to infer the relation between aerosol and precipitation in the Amazon with the presented radar and insitu black carbon dataset. Another approaches can and will be done to reach more details.

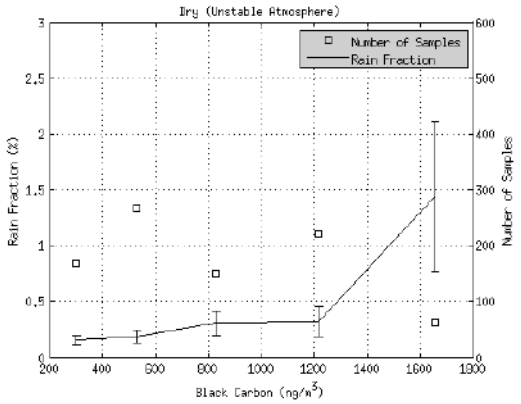

Figure 2 - Mean, standard deviation and number of samples of Rain Fraction for each black carbon bin, during the dry season for a unstable atmosphere.

5. REFERENCES

ACKERMAN, A. S.; TOON, O. B.; STEVENS, D. E.; HEYMSPELD, A. J.; RAMANATHAN, V.; WELTON, E. J. Reduction of tropical cloudiness by soot. Science, V.288, 2000.

ALTARATZ, R.; KOREN, I.; YAIR, Y.; PRICE, C. Lightning response to smoke from Amazonian fires. Geophysical Research Letters, V.37, 2010.

ARTAXO, P.; OLIVEIRA, P. H.; LARA, L. L. PAULIQUEVIS, T. M.; RIZZO, L. R. JUNIOR, C. P.; PAIXÃO, M. A. Efeitos climáticos de partículas de aerossóis biogênicos e emitidos em queimadas na Amazônia. Revista Brasileira de Meteorologia, V. 21, n.3a, p.168-189, 2006.

DUSEK, U.; FRANK, G. P.; HILDEBRANT, L.; CURTIUS, L.; SCHNEIDER, J.; WALTER, S.; CHAND, D.; DREWNICK, F.; HINGS, S.; JUNG, D.; BORRMAN, S.; ANDERAR, M. O. Size matters more than chemistry for cloud-nucleating ability of aerosol particles. Science. p.1375-1378, 2006.

GRAF, H. F. The complex interaction of aerosols and clouds. Science, V.303, 2004.

KIRSTETTER, P. E.; ANDRIEU, H.; DELRIEU, G.; BOUDEVILLAIN, B. Identification of vertical profiles of reflectivity for correction of volumetric radar data using rainfall classification. Journal of Applied Meteorology and Climatology. 2010.

KOREN, I.; KAUFMAN, Y, J.; REMER, L. A.; MARTINS, J. V. Measurement of the effect of Amazon smoke on inhibition of cloud formation. Science, V.303, 2004.

KOREN, I.; MARTINS, J. V.; REMER, L. A.; AFARGAN, H. Smoke invigoration versus inhibition of clouds over the Amazon. Science, V.321, 2008.

LIN, J. C.; MATSUI, T. PIELKE, R. A.; KUMMEROW, C. Effects of biomas-burning-derived aerosol on precipitation and cloud in the amazon basin: a satellite-based empirical study. Journal of Geophysical Research, V.111, 2006.

RAMANATHAN, V.; CRUTZEN, P.J.; KIEHL, T.; ROSENFELD, D. Aerosols, climate, and the hydrological cycle. Science, V.294, 2001.

RODRIGUEZ, E.; MORRIS, C. S.; BELZ, J. E.; CHAPIN, E. C.; MARTIN, J. M.; DAFFER, W.; HENSLEY, S. An assessment of the SRTM topographic products. Technical Report JPL D-31639. Jet Propulsion Laboratory, 2005.

RODRIGUEZ, E.; MORRIS, C. S.; BELZ, J. E.; CHAPIN, E. C.; MARTIN, J. M.; DAFFER, W.; HENSLEY, S. An assessment of the SRTM topographic products. Technical Report JPL D-31639. Jet Propulsion Laboratory, 2005.

ROSENFELD, D. TRMM observed first direct evidence of smoke from forest fires inhibiting rainfall. Geophysical Research Letters, V.26, n.20, p.3150-3108, 1999.

SIZE-RESOLVED AND BULK ACTIVATION PROPERTIES OF AEROSOL AT HIGHLY ELEVATED LOCATION IN SOUTHEAST CHINA

Kui Chen[1], Yan Yin[1*], Zhenhua Hu[1], Guxue Song[1], Haobo Tan[1], Bin Yang[2] Yongze Wu[2]

[1] Open Key Laboratory for Atmospheric Physics and Environment of China Meteorological Administration, Nanjing University of Information Science & Technology, Nanjing, 210044, China

[2] Huangshan National Basic Meteorological Observatory, Huangshan, 242709, China

*Corresponding author, Tel.: +86-25-58731207, Fax: +86-25-58731207

E-mail address: ch_k@163.com (Kui Chen); yinyan@nuist.edu.cn (Yan Yin)

1. INTRODUCTION

Aerosol particles act as cloud condensation nuclei (CCN) at water vapor supersaturations S (percentage of relative humidity minus 100%) that are relevant for atmospheric conditions(Dusek, Frank et al. 2006). They could indirectly force climate through modification of cloud radiactive properties and precipitation efficiency (Albrecht 1989; Dusek, Frank et al. 2006). The perturbation of this balance by anthropogenic aerosols is currently one of the largest uncertainties in estimating global climate change (Furutani, Dall'osto et al. 2008) (IPCC 2007).

In order to a better understanding and produce more accurate predictive models of the global climate system, it is required for understanding of CCN activation properties. CCN activation of aerosols is therefore being studied intensively in laboratory and field experiments (Roberts, Andreae et al. 2001; Giebl, Berner et al. 2002; Broekhuizen, Kumar et al. 2004; Lohmann, Broekhuizen et al. 2004; Dusek, Frank et al. 2006). Several earlier and recent studies have reported laboratory experiments of the CCN activity of aerosols consisting of relatively simple model chemical species such as $(NH_4)_2SO_4$, NaCl, and organic molecules commonly detected in atmospheric aerosols (Giebl, Berner et al. 2002; Snider, Guibert et al. 2003; Matsunaga, Mochida et al. 2004; Zhang, Canagaratna et al. 2005; Wang,

Collins et al. 2006; Shrestha, Barros et al. 2010). In recent years, anthropogenic emissions of aerosol particles and precursors from Asia have increased significantly (Giebl, Berner et al. 2002; Snider, Guibert et al. 2003; Matsunaga, Mochida et al. 2004; Zhang, Canagaratna et al. 2005; Wang, Collins et al. 2006; Shrestha, Barros et al. 2010), and several researchers consider that anthropogenic aerosol particles have changed cloud microphysical and radiative properties (Anderson and Ogren 1998; Xu 2001; Liu, Xu et al. 2004; Zhang, Qin et al. 2004; Qian, Kaiser et al. 2006; Sorooshian, Brechtel et al. 2006; Li, Xia et al. 2007; Deng, Tie et al. 2008; Rose, Nowak et al. 2010; Muller, Laborde et al. 2011). To obtain an understanding of CCN-active atmospheric aerosols, field studies have been carried out. However, only few CCN measurements have been performed in Asia. No research has been carried out on CCN activation measurements at the top of Southeast China's mountain, which altitude is the height of the cloud.

Mts. Huangshan located in the southern part of the Anhui province, at the southern edge of the North China Plain. The air particulate matter from the Yangtze River Delta metropolis clusters (about 200 km to the northeast) is also easily transported to the site with the prevailing northeast wind (Pan, Kanaya et al. 2011). Within the "Program of Integrated Experiments of the Interactions between Aerosols and Cloud over the Southeast China", we measured and characterized the CCN properties of aerosol particles in different height of Huangshan. In this manuscript, we focus on the results of the aerosol number size distributions and the size-resolved activation ratios.

2. METHODS

2.1 SAMPLING SITE

From Aug. 20 to Sep 14 2011, measurements had been performed at the summit of Mt. Huang of the south of Anhui province, China (30.13^{o}N, 118.15^{o}E, 1840 m a.s.l.), about 380 km away from the East China Sea. Mt. Huangshan has a subtropical monsoon climate, which summit covered with cumulus or orographic cloud in rainy season. In addition to the measurements described here, the site is Huangshan National Reference Climatological Station.

2.2 INSTRUMENTAL

Size-resolved CCN efficiency spectra (CCN activation curves) were measured with a Droplet Measurement Technologies (DMT) streamwise thermal-gradient CCN counter (Roberts and Nenes 2005) coupled to Aerosol Generator and Monitor (AGM™ Model 1500) of MSP Corporation (http://www.mspcorp.com). The MSP's DMA (Differential Mobility Analyzer) and CPC (Condensation Particle Counter) are similar to TSI's instrument that reported by paper (Rodrigue, Dhaniyala et al. 2007). The CCN Counter (CCNC) was operated at a total flow rate of 0.5 L min^{-1} with a sheath-to-aerosol flow ratio of 10.

Aerosol number size distributions were obtained by a scanning mobility particle size (AGM™ Model 1500) with a time resolution of three minutes. Prior to introduction into the AGM, ambient aerosol was dried using two dryers containing silica gel and a molecular sieve (mixture of 13X and 4A), then charged by an Electrical Ionizer and introduced into the DMA. The relative humidity (RH) inside instruments was below 20%. The Electrical Ionizer (Model 1090, MSP Inc.) is similar to that produced by a radioactive ionizer, but without the use of radioactivity (http://www.mspcorp.com). The DMA sheath and sample flows were 3 lpm and 0.3 L min^{-1}, respectively. The systems were carefully calibrated using Polystyrene Latex standards.

The nearly mono-disperse dry aerosol particles with a diameter $D_{p,0}$ are selected by the differential mobility analyzer, subsequently measured number concentration of particle and cloud condensation nuclei, respectively. The N_{CCN}/N_{CN} ratios after the corrections above were fitted with the following equation (Rose, Gunthe et al. 2008).

3 RESULTS AND DISCUSSION

3.1. SIZE DISTRIBUTION MEASURED

Figure 1 shows averaged number, surface area and volume size distributions for the entire sampling period. The surface area and volume distributions are computed assuming unit density spherical particles. The diameter range 0.15-0.95 μm for the number distribution is shown as an inset. The number size distributions present a unimodal shape. The max value of aerosol number concentration is appeared in the accumulation mode (133nm).

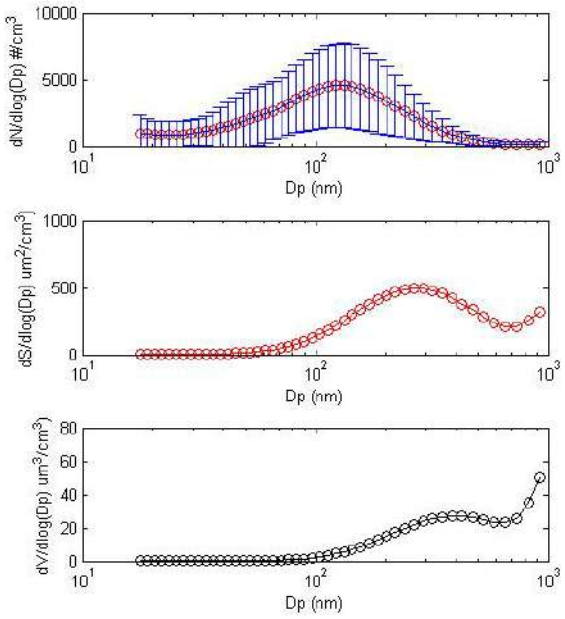

Figure 1 Size distribution of particle number, surface and volume averaged over the sampling campaign at the Huangshan.

Hourly average size distribution of number concentrations was used in the comparison. The diurnal variations of size distribution of number concentrations of particles during sampling period were presented in figure 2. In one day, the minimum number concentrations were appeared at 0:00-3:00, and then gradually increase. For main particles in Aitken nuclei mode from 0:00 to 11:00, while main peak of 11:00 to 23:00 occurred at accumulation mode and higher number concentration, because that the transport of anthropogenic pollutants of terrestrial surface (TS) was responsible for the vertical uplifting of air masses from TS to the atmospheric boundary layer (ABL). The dynamical processes of transport has delayed, therefore, the maximum appeared around 13 o'clock.

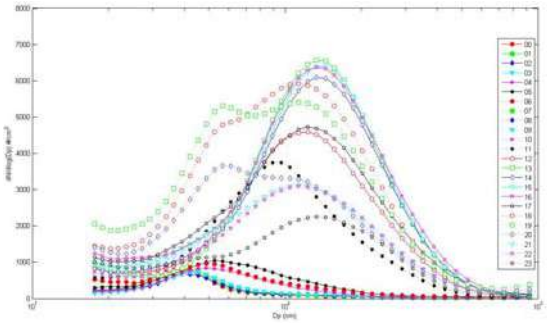

Figure 2 Average daily pattern of particle number concentration

Summary statistics for the distribution of 24-h average particle number concentration were showed in Figure 3. The number concentrations of all samples were in the orders of 10^3 cm^{-3}. There were two times evidently change processes of variation of number concentration from high to low under different meteorological background conditions. The first higher value was appeared in August 20-24 while lower value from August 25 to September 2; the second higher value began in September 3 and ending at 6 then in September 9-12 lower value. In the second process, we had measured of the particle chemical composition and aerosol activation in the

same period.

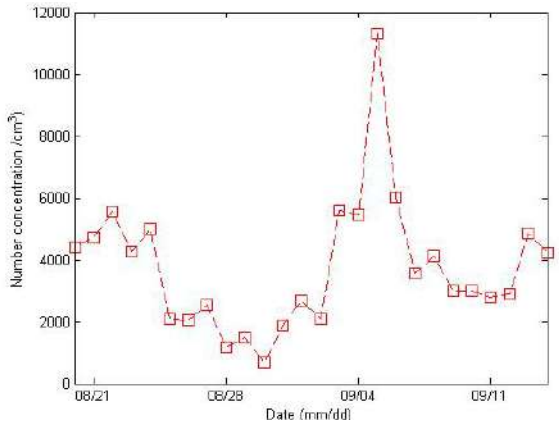

Figure 3 Daily number concentrations during sampling period

There was a high-pollution periods (September 3-6) and a clean periods (September 9-12), see figure 3. Analysis of the wind direct associated with “polluted” and “clean” periods indicate prevailing winds from north during polluted periods, while clean periods were associated with winds predominantly from the southeast (see figure 4). On a regional scale, northly winds are coming from the North China Plain, a heavily industrialized region with many plants to cause significantly anthropogenic emissions. The relative impact of local sources in the vicinity of the measurement site will vary with wind direction, but most significantly in terms of these ‘‘clean’’ versus ‘‘polluted’’ scenarios.

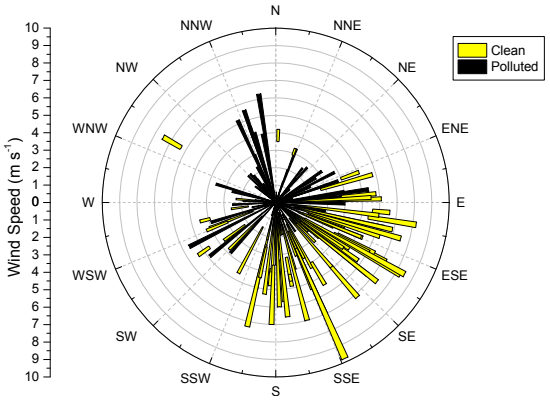

Figure 4 wind direction diagram rose in “polluted” and “Clean”

3.2 CCN ACTIVATION

Figure 5 shows a representative example of averaged CCN efficiencies. The activation curves at different supersaturations are distinct. Particles smaller than 150 nm are rarely activated at supersaturation 0.1%, while 50 nm particles have activation ratios of 0.6 at 0.7% supersaturation. Most 150 nm particles activate more than 60% at all measured supersaturations.

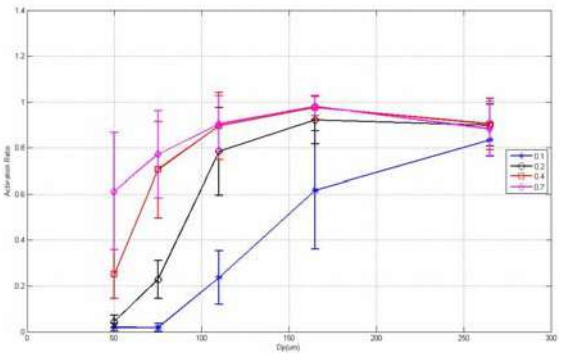

Figure 5 Average activation curves for different supersaturations

Figure 6 shows the time series of the activation ratios for 50, 75, 110, 165 and 260 nm particles at different supersaturations. At lower supersaturations and for smaller particles (<100nm), the activation ratios are close to 0, because the particles are too small to be activated. Particles larger than 75 nm are mostly activated at supersaturations above 0.4%. It can be seen in figure 6 that the activation ratios is more 50% for 265 nm particles at all supersaturations.

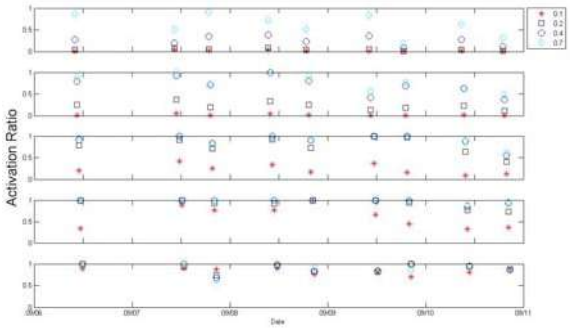

Figure 6. Time series of the activation ratio during September 2011

We selected pollution case on September 6, while clean case on September 10. In figure 6, the aerosol activation rations were roughly the same for all particles at lower supersaturations above 0.1%, while higher activation ratios of pollution at other supersaturations and for smaller particles, e.g. 50, 75 and 110nm. Particles larger than 150 nm are mostly activated for pollution and clean at supersaturations above 0.2, 0.4 and 0.7%.

4. CONCLUSIONS

An investigation of activation properties of aerosol at a high elevation site of Huangshan was performed from August to September, 2011. The average of number size distributions presented a unimodal shape in submicron particle at the top of huangshan. Because of the vertical uplifting of air masses from TS to the ABL, the diurnal variations of size distribution of number concentrations of particles, appeared higher number concentration after noon, during sampling period. CCN activation spectra presented activation ratio increased, accompanied by particle size and supersaturation increased. A variety of air mass types were sampled; polluted air coming from North China Plain tends to have higher concentrations of particles and contains significant amounts of anthropogenic matter and higher activation fraction (CCN/CN).

5 BIBLIOGRAPHY

Albrecht, B. A. (1989). "AEROSOLS,

CLOUD MICROPHYSICS, AND FRACTIONAL CLOUDINESS." Science **245**(4923): 1227-1230.

Anderson, T. L. and J. A. Ogren (1998). "Determining aerosol radiative properties using the TSI 3563 integrating nephelometer." Aerosol Science and Technology **29**(1): 57-69.

Broekhuizen, K., P. P. Kumar, et al. (2004). "Partially soluble organics as cloud condensation nuclei: Role of trace soluble and surface active species." Geophysical Research Letters **31**(1).

Deng, X. J., X. X. Tie, et al. (2008). "Long-term trend of visibility and its characterizations in the Pearl River Delta (PRD) region, China." Atmospheric Environment **42**(7): 1424-1435.

Dusek, U., G. P. Frank, et al. (2006). "Size Matters More Than Chemistry for Cloud-Nucleating Ability of Aerosol Particles." Science **312**(5778): 1375 - 1378.

Furutani, H., M. Dall'osto, et al. (2008). "Assessment of the relative importance of atmospheric aging on CCN activity derived from field observations." Atmospheric Environment **42**(13): 3130-3142.

Giebl, H., A. Berner, et al. (2002). "CCN activation of oxalic and malonic acid test aerosols with the University of Vienna cloud condensation nuclei counter." Journal of Aerosol Science **33**(12): 1623-1634.

Li, Z. Q., X. G. Xia, et al. (2007). "Aerosol optical properties and their radiative effects in northern China." Journal of Geophysical Research-Atmospheres **112**(D22).

Liu, B. H., M. Xu, et al. (2004). "Taking China's temperature: Daily range, warming trends, and regional variations, 1955-2000." Journal of Climate **17**(22): 4453-4462.

Lohmann, U., K. Broekhuizen, et al. (2004). "How efficient is cloud droplet formation of organic aerosols?" Geophysical Research Letters **31**(5).

Matsunaga, S., M. Mochida, et al. (2004). "Variation on the atmospheric concentrations of biogenic carbonyl compounds and their removal processes in the northern forest at Moshiri, Hokkaido Island in Japan." J. Geophys. Res. **109**(D4): D04302.

Muller, T., M. Laborde, et al. (2011). "Design and performance of a three-wavelength LED-based total scatter and backscatter integrating nephelometer." Atmospheric Measurement Techniques **4**(6):

1291-1303.

Orsini, D. A., Y. Ma, et al. (2003). "Refinements to the particle-into-liquid sampler (PILS) for ground and airborne measurements of water soluble aerosol composition." Atmospheric Environment **37**(9–10): 1243-1259.

Pan, X. L., Y. Kanaya, et al. (2011). "Correlation of black carbon aerosol and carbon monoxide in the high-altitude environment of Mt. Huang in Eastern China." Atmospheric Chemistry and Physics **11**(18): 9735-9747.

Qian, Y., D. P. Kaiser, et al. (2006). "More frequent cloud-free sky and less surface solar radiation in China from 1955 to 2000." Geophysical Research Letters **33**(1).

Roberts, G. and A. Nenes (2005). "A continuous-flow streamwise thermal-gradient CCN chamber for atmospheric measurements." Aerosol Science and Technology **39**(3): 206-221.

Roberts, M. C., M. O. Andreae, et al. (2001). "Cloud condensation nuclei in the Amazon Basin: "Marine" conditions over a continent?" Geophysical Research Letters **28**(14): 2807-2810.

Rodrigue, J., S. Dhaniyala, et al. (2007). "Performance Comparison of Scanning Electrical Mobility Spectrometers." Aerosol Science and Technology **41**(4): 360-368.

Rose, D., S. Gunthe, et al. (2008). "Calibration and measurement uncertainties of a continuous-flow cloud condensation nuclei counter (DMT-CCNC): CCN activation of ammonium sulfate and sodium chloride aerosol particles in theory and experiment." Atmospheric Chemistry and Physics **8**(5): 1153-1179.

Rose, D., A. Nowak, et al. (2010). "Cloud condensation nuclei in polluted air and biomass burning smoke near the mega-city Guangzhou, China – Part 1: Size-resolved measurements and implications for the modeling of aerosol particle hygroscopicity and CCN activity." Atmospheric Chemistry and Physics **10**(7): 3365-3383.

Shrestha, P., A. P. Barros, et al. (2010). "Chemical composition and aerosol size distribution of the middle mountain range in the Nepal Himalayas during the 2009 pre-monsoon season." Atmospheric Chemistry and Physics **10**(23): 11605-11621.

Sioutas, C., P. Y. Wang, et al. (1996). "Laboratory and field evaluation of an improved glass honeycomb denuder/filter pack sampler." Atmospheric Environment

30(6): 885-895.

Snider, J. R., S. Guibert, et al. (2003). "Aerosol activation in marine stratocumulus clouds: 2. Kohler and parcel theory closure studies." Journal of Geophysical Research-Atmospheres **108**(D15).

Sorooshian, A., F. J. Brechtel, et al. (2006). "Modeling and characterization of a particle-into-liquid sampler (PILS)." Aerosol Science and Technology **40**(6): 396-409.

Wang, J., D. Collins, et al. (2006). "Temporal variation of aerosol properties at a rural continental site and study of aerosol evolution through growth law analysis." J. Geophys. Res. **111**(D18): D18203.

Xu, Q. (2001). "Abrupt change of the mid-summer climate in central east China by the influence of atmospheric pollution." Atmospheric Environment **35**(30): 5029-5040.

Zhang, Q., M. R. Canagaratna, et al. (2005). "Time- and size-resolved chemical composition of submicron particles in Pittsburgh: Implications for aerosol sources and processes." J. Geophys. Res. **110**(D7): D07S09.

Zhang, Y. L., B. Q. Qin, et al. (2004). "Analysis of 40 year records of solar radiation data in Shanghai, Nanjing and Hangzhou in Eastern China." Theoretical and Applied Climatology **78**(4): 217-227.

Acknowledgments

This study was jointly funded by the National Natural Sciences Foundation of China through Grant No. 41030962, the graduate Education Innovation Project of Jiangsu Province through Grant No. CX10B_294Z, and the Priority Academic Program Development of Jiangsu Higher Education Institutions (PAPD).

A NEW ICE NUCLEATION PARAMETERIZATION SCHEME BASED ON OBSERVATIONS FOR MONSOON SEASON OVER INDIA

Pradeep Kumar Pallath[1]*, Sachin Patade[2], Thara Prabhakaran[2], and RS Maheshkumar[2]
[1]University of Pune, Department of Atmospheric & Space Sciences, Pune 411007, India
[2]Indian Institute of Tropical Meteorology, Pashan, Maharashtra, Pune 411008, India

1. INTRODUCTION

The heterogeneous nucleation involving ice nuclei (IN) has a pivotal role in the precipitation formation and radiation balance. IN directly impact the ice number concentration. IN is particularly important in mixed phase clouds where balance between the ice and liquid phase is sensitive to the presence of ice number concentration (Korolev and Field, 2008). Ice nuclei representation in the GCMs is based on temperature (Fletcher, 1962) for predicting ice nuclei concentration or using an empirical relationship between ice nuclei concentration and ice supersaturation (Meyers et al., 1992) or based on hybrid formulation as proposed by Cotton et al. (1986). Based on the data obtained from continuous flow diffusion chamber (CFDC), Meyers et al. (1992) established an exponential relationship between ice nuclei concentration (activated by deposition-condensation freezing mode) and ice supersaturation which is reasonably independent of temperatures between -7^{O}C and -20^{O}C. Predicted ice nuclei concentration from these measurements exceeds values predicted by the Fletcher's approximations by as much as one order of magnitude at temperature warmer than -20^{o}C. The impact of changing from modified Fletcher's approximation to the new deposition-condensation-freezing model of nucleation produced higher concentrations and more mass of pristine ice at temperatures warmer than -20^{o}C. Meyers parameterization for ice nucleation is widely used in the cloud models.

DeMott et al (2010) has shown that the concentration of ice nuclei active in mixed-phase cloud conditions can be related to the temperature and the number concentration of particles larger than 0.5 µm in diameter. When implemented in global climate models, the new parameterization strongly altered cloud liquid and ice water distributions compared to the simple, temperature-only parameterizations.

Current study is oriented towards better understanding of role of ice nucleation in monsoon clouds by developing and implementing new parameterization scheme based on unique observations of ice nuclei over Indian region during the monsoon season. Ice nuclei samples were collected onboard the aircraft used for Cloud Aerosol Interaction and Precipitation Enhancement Experiment (CAIPEEX). Based on ISCCP observations, Pai and Rajeevan (1998) showed that cloud radiative forcing is strongly correlated with changes in high clouds over tropical Indian Ocean. The presence of large amount of high clouds and large optical depth of these clouds results in large negative net cloud radiative forcing in the Asian monsoon region during June to September (Rajeevan and Srinivasan 2000; Sathiyamoorthy et al 2004). High clouds are predominant over Indian monsoon region (Tang and Chen, 2006). The recent reanalysis products over the Indian region also illustrate that the high clouds impose a significant cloud radiative forcing over the monsoon region (Urankar et al., 2012).

2. OBSERVATIONS

A Thermal Gradient Diffusion Chamber (TGDC) was designed and built for operation inside the cold room (see Figure 1a). Ice nuclei can be activated (Figure 1b) by deposition-condensation-freezing mode inside the chamber depending on the processing temperature and supersaturation w.r.t. water and ice. Aerosol samples were collected on hydrophobic filters (Sartorius PTFE- filters,

pore size of 0.45 µm) onboard the CAIPEEX instrumented aircraft over different geographical locations and altitudes. The TGDC is used to determine the IN concentrations from samples collected during CAIPEEX. An empirical relationship can be built between ice nuclei concentration and ice superstation. Detailed information on the CAIPEEX experiment and sample of first results has been presented by Prabha et al (2011) and Kulkarni et al (2012). The aircraft was instrumented with several cloud physics and aerosol instruments, such as cloud droplet probe (CDP; Droplet Measurement Technologies DMT for cloud droplet size distributions in 30 bins between 2 and 50 µm, and derived parameters include liquid water content (LWC), droplet effective radius, cloud droplet number concentrations (CDNC), mean volume radius, etc), Aircraft Integrated Meteorological Measurement System **(**AIMMS for air temperature, relative humidity, and winds), DMT CCN Cloud condensation nuclei (CCN) counter for CCN concentration, Passive Cavity Aerosol Spectrometer Probe (PCASP for size distribution, effective radius and concentration).

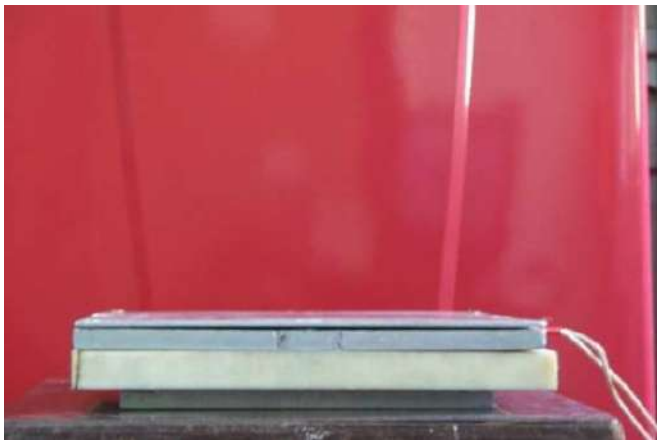

Figure 1a. TGDC

Figure 1b. Activated Ice Nuclei on the filter paper

The ice nuclei concentration is highly variable spatially as well as temporally. Meyers(1992) parameterization scheme is based on the observational data over specific geographical location and does not contain any observations over the monsoon region. No intensive observations of ice nuclei are available over India which is having large geographical variation and spatial distribution of aerosol particles. CAIPEEX provided a good platform to make such observations.

3. MODEL SETUP

Advanced Research Weather Research and Forecasting model (ARW) version 3.3 (Skamarock et al. 2007) is used in our study. ARW is a nonhydrostatic mesoscale model. We have followed similar configuration for the ideal case setup as used by Morrison and Milbrandt (2010) and similar to the standard ideal case of super cell storm, where no radiative transfer and surface fluxes parameterization were used. Horizontal and vertical turbulent diffusion is based on 1.5 order turbulent kinetic energy scheme. This case uses open boundary condition at lateral boundaries. The grid spacing is 2 km and has a domain size of 84 km x 84 km and 41 vertical levels. Initialization sounding used is same as the one of Weisman and Klemp (1982; 1984) and the shear layer extends to 7 km. The precipitable water is 4 cm, CAPE is 2758 Jkg^{-1}, LCL pressure is 854 hPa and temperature is 16 ^{O}C. The convection is triggered with a thermal/bubble and integration is carried out for a period of 6 hours. In all the simulations we use Milbrandt and Yau (2005a, b) scheme implemented with some modifications in the recent ARW 3.3. We have chosen this scheme, after comparing different double moment schemes for a real case of deep convection. This scheme predicts both mixing ratio and number concentration and has hydrometeor categories of cloud liquid, ice, graupel, snow, ice and hail. The scheme does nucleation of droplets in strong updrafts which lead to the production of cloud liquid water at elevated layers of deep convective cases. Our emphasis was to test the ice nucleation scheme in such an environment where there is also cloud liquid water present at elevated layers. The presence of supercooled liquid in the deep convective clouds over Indian region during CAIPEEX was illustrated by Prabha et al (2011). Supercooled liquid was noted in deep convective clouds down to temperature of -37.5 ^{o}C in continental mixed phase clouds (Rosenfeld and Woodley, 2000).

4. RESULTS AND DISCUSSION

4.1 ICE NUCLEI SAMPLES DURING CAIPEEX

Samples were collected over several geographical locations as illustrated in Figure 2a and in Table I. These samples were analyzed in the TGDC.

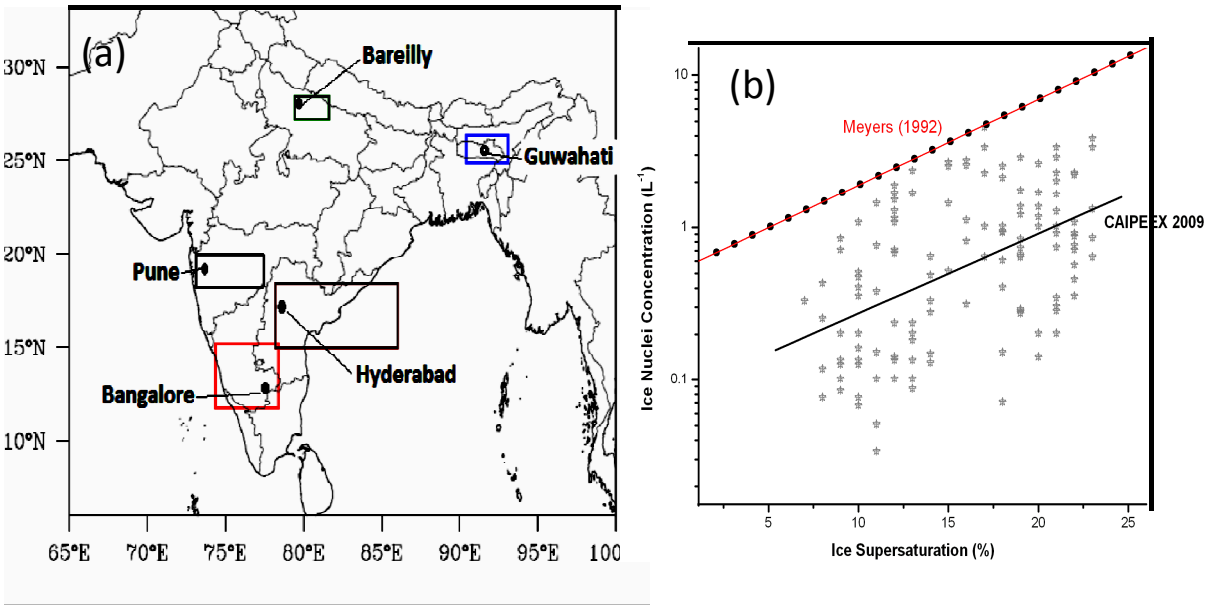

Figure 2. CAIPEEX IOP base locations during 2009 where ice nuclei observations are made (a) and ice nuclei observations during CAIPEEX compared with Meyers (1992) (b)

Table I Location, coordinates and dates of sample collection during CAIPEEX 2009

Location	Coordinates	Dates of sample collection
Hyderabad	17.22 ^{o} N , 78.29 ^{o} E	June- 10,11,16,17,18,19,20,21, August –14, 15, 16,18 September-27, 28.
Bangalore	12.59 ^{o} N, 77.40 ^{o} E	June- 3,28; 2009 July – 6,7,8,13
Pune	18.29 ^{o} N, 73.5 ^{o} E	September – 16,17,23,24
Bareilly	26.18 ^{o} N, 81.2 ^{o} E	July – 16,17,18,22,August – 20,23,24,25.
Guwahati	26.1 ^{o} N, 91.45 ^{o} E	August – 27, 29, 30

Figure 2b shows the ice nuclei observations over various locations over Indian region during monsoon. These observations showed relatively less values compared to the reported values in the literature (Demott et al., 2010)

4.2 SIMULATION OF A SUPER CELL STORM

The supercell simulation (default) was carried out for the default case with ARW model configurations and specifications as described above. The new ice nuclei parameterization was derived from the TGDC analysis of samples collected onboard the CAIPEEX aircraft. This parameterization is used in the ARW model and simulation (named as new scheme) is carried out for exact same configurations and initial conditions. Both simulations (default and new) showed no difference in the accumulated rainfall until 250 min of integration. Differences started appearing after that period and enhanced with time. The spatial distribution of rainfall (Figure 4) and reflectivity (Figure 5) at 240 min and at 360 min showed that there are differences in the spatial distribution of

rainfall and reflectivity. These differences increase as integration progresses. One important aspect to note is that at 240 min, though there is no difference in the accumulated rainfall, the spatial distribution of rainfall and reflectivity are quite different. These differences are apparently contributed by the changes in the ice nucleation.

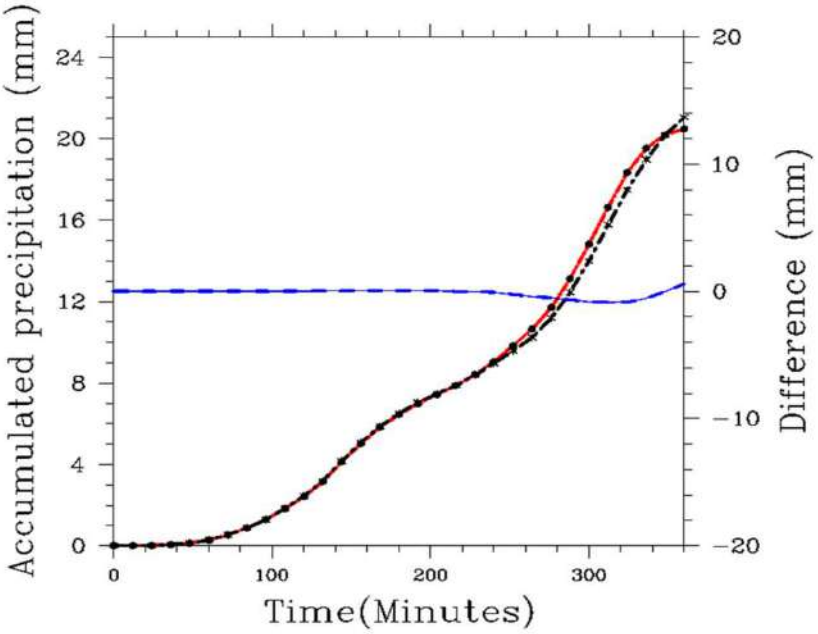

Figure 3. Accumulated surface rainfall using the default and new ice nucleation schemes. Difference between the two simulations is also indicated.

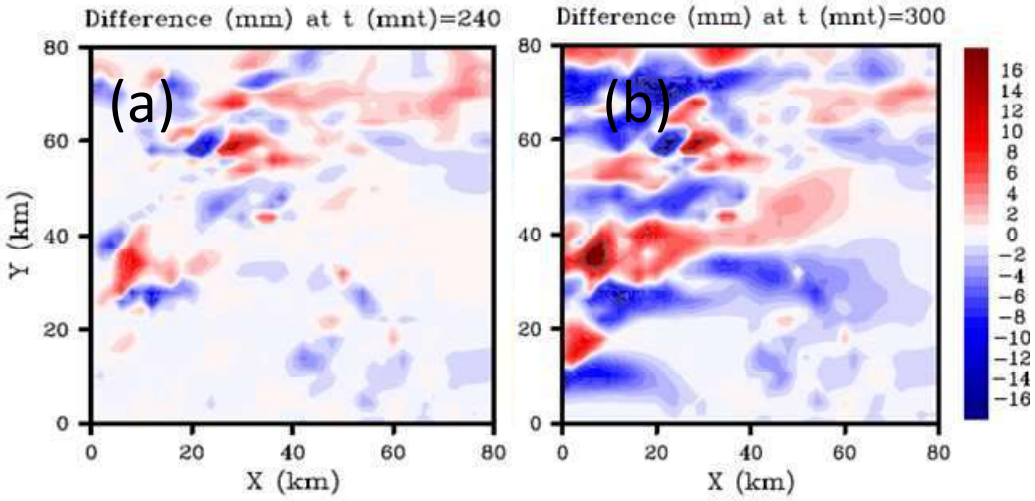

Figure 4. Spatial distribution of difference (in mm) in the surface rainfall between the new and old ice nucleation parameterization. The simulated fields at 240 min (a) and 360 min (b) of the super cell simulation are shown.

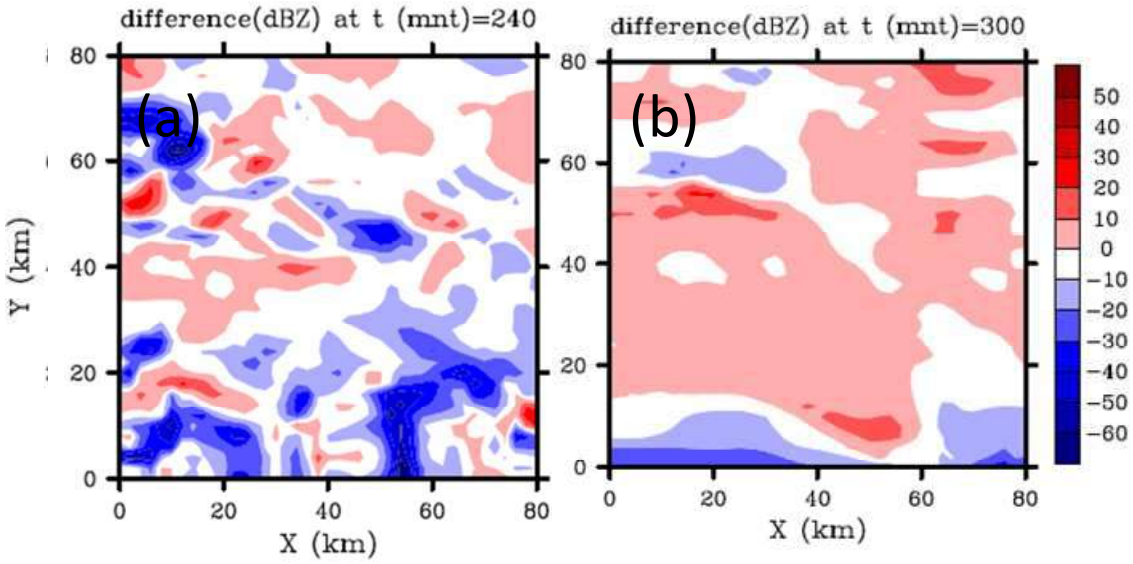

Figure 5. Same as in Figure 3, but for difference in the simulated maximum reflectivity at 240 min (a) and at 360 min (b)

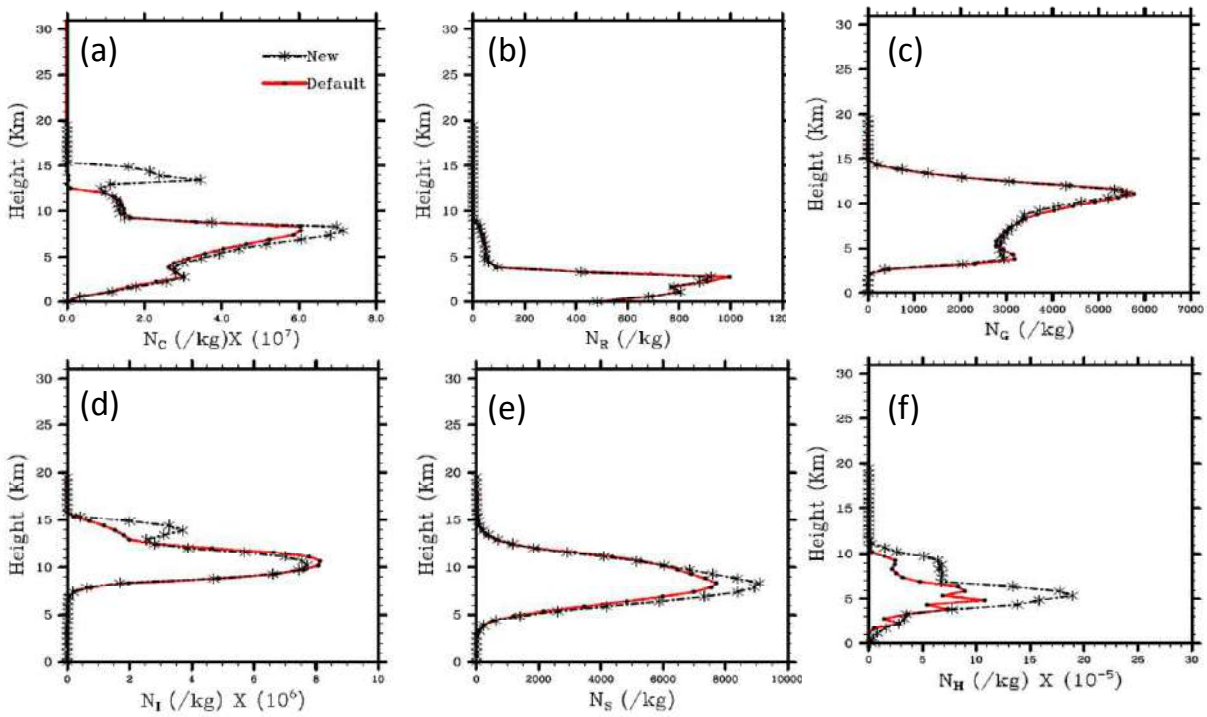

Figure 6. Time averaged vertical distribution of number concentration of hydrometeors; cloud (N_C), snow (N_S), rain (N_R), graupel (N_G), ice (N_I) and hail (N_H) from default and new scheme for super cell storm

The new scheme introduced an increase in the number concentration of cloud droplets, ice, snow and hail (Figure 6). Above 12 km there is an increase in the cloud liquid water, ice. Below this level, there is increase in hail number concentration, indicating that the production of supercooled liquid and ice crystals situated above produced hail. The increase in supercooled liquid in the upper

levels (>12 km) is primary factor for increased hail in the new scheme. Thus it is clear that a change (decrease) in the ice nucleation can cause a significant change in the upper levels of super storm.

Figure 7a, 7b and 7c gives time height distribution of cloud liquid, ice and hail water mixing ratio. These results show that the storm matures at 125 minutes of integration. After 160 min storm weakens and the cloud liquid water and ice water in the new scheme is slightly higher (on average) than the default scheme.

Ice water is noted only above 12 km. Production of more hail coincides with the joint presence and increase in supercooled liquid and ice at high levels of the storm.

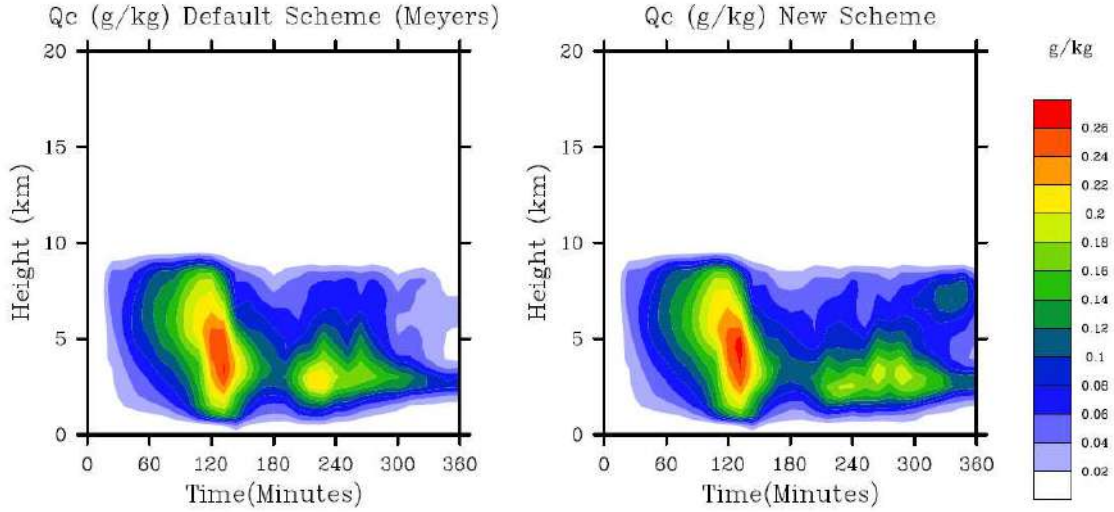

Figure 7a. Time height distribution of cloud water mixing ratio in the default and new scheme based simulations

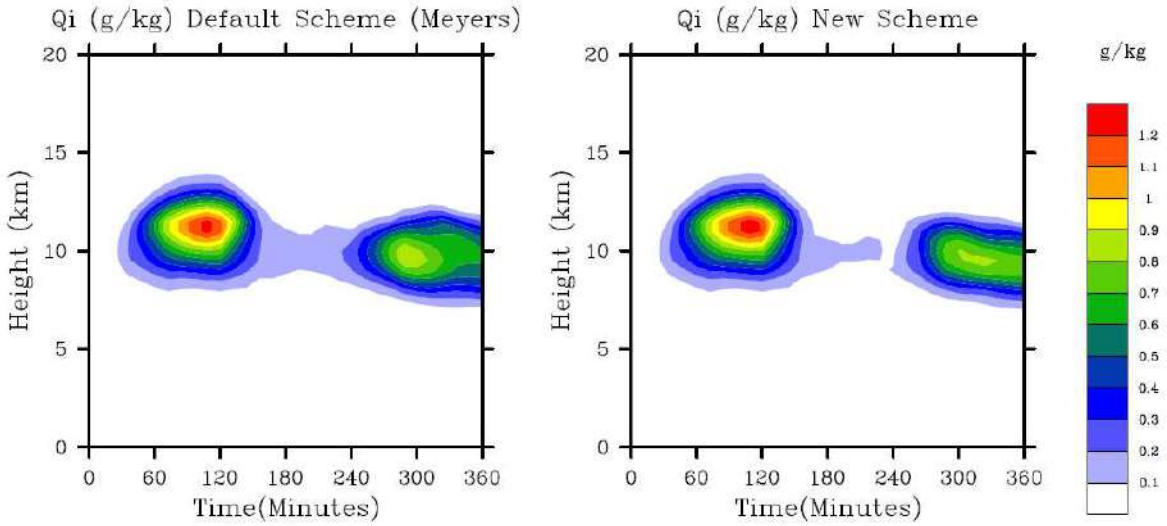

Figure 7b. Time height distribution of ice water mixing ratio in the default and new scheme based simulations

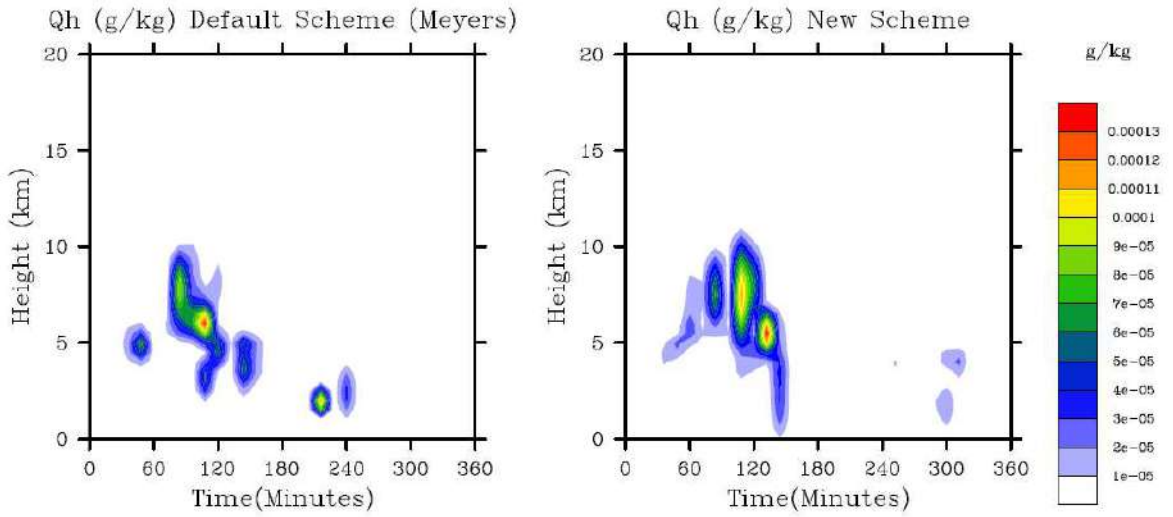

Figure 7c. Time height distribution of hail mixing ratio in the default and new scheme

Our results lead to similar conclusions as Lebo and Seinfeld (2011) on the effect of IN on the development deep convective clouds. In that study, increase in the IN number concentration on the dynamics of deep convective clouds is very small. The decrease in domain averaged cumulative precipitation was not statistically significant; however spatial distribution of precipitation was affected by small changes in ice nuclei concentration. This is an important result in regard to the effect of new parameterization on deep convection. Especially the stratiform part of the cloud is influenced significantly. In the new scheme, graupel decreased and rainwater decreased subsequently in the decaying stage of the storm unlike in the default simulation. Morrison and Milbrandt (2010) showed that different approaches in treating graupel and hail in two different microphysical schemes produce distinct differences in storm structure, precipitation, and cold pool strength. The IN parameterization can indeed influence these processes indirectly in the mixed phase region.

5. CONCLUSIONS

A new parameterization was developed for the ice nucleation in the deposition-condensation-freezing mode for Indian region. First time unique observations of IN over the Indian continent during monsoon season are presented. These observations are used to develop ice nucleation scheme in mixed phase clouds which are abundant over the Indian region and contribute to precipitation.

When the storm is well developed (especially in the convective part of the storm), supercooled liquid was enhanced in the upper regions (above 12 km). The accretion of supercooled water and production of more hail is seen in the simulation with new parameterization. The hail enhancement is a result of increased supercooled liquid at higher levels. In the warm region of the cloud, there is also an increase in cloud droplet number concentration. However, the net effect of these microphysical changes was not reflected in the surface rainfall.

In the stratiform part of the storm, significant difference in the spatial distribution is noted as in several earlier studies emphasising that aerosol effects impact the spatial distribution rather than the precipitation amount (Khain et al., 2004; Teller and Levin, 2006; Khain and Lynn, 2009; Lee and Feingold, 2010), depending on the type of cloud, thermodynamical conditions, etc.

The importance of this work is paramount due to the fact that monsoon clouds principally high clouds contribute to the precipitation and cloud radiative forcing over Indian region. The dimming observed over the Indian region is largely explained by high cloud cover and unless these cloud processes (involving primarily ice) are understood, cloud-precipitation feedback will be erroneous in the numerical models used for monsoon rainfall prediction.

REFERENCES

Cotton, W. R., G.J. Tripoli, R. M. Rauber, and E. A. Mulvihill (1986), Numerical Simulation of the effect of varying ice crystal nucleation rates and aggregation and processes on orographic snowfall, J. Appl. Meteorology, 1658-1680.

DeMott, P., J, A., J., Prenni, X., Liu et al., 2010: Predicting global atmospheric ice nuclei distributions and their impacts on climate, PNAS, VOL. 107, No. 25.

Fletcher, N.H., 1962: Physics of Rain clouds: Cambridge University Press, 386 pp.

Khain A. P., A. Pokrovsky, M. Pinsky, A. Seifert, and V. Phillips (2004): Simulations of effect of atmospheric aerosols on deep turbulent convective clouds using a spectral microphysics mixed phase cumulus cloud model. Part-1: Model description and possible applications, J. Atmos. Sci., 161, 2963-2982, 2004.

Khain, A., and B. Lynn (2009), Simulation of a supercell strorm in a clean and dirty atmosphere using weather research and forecasting model with spectral bin microphysics, J. Geophys. Res., 114, doi:10.1029/2009JD011827.

Kulkarni J.R, Maheshkumar R.S., Morwal S.B., Padma kumari B., Konwar M., Deshpade C.G., Joshi R.R., Bhalwankar R.V., Pandithurai, Safai P.D., Narkhedkar S.G., Dani K.K., Nath A., Sathy Nair, Sapre V.V., Puranik P.V., Kandalgaonkar S.S., Mujumdar V.R., Khaladkar R.M., Vijaykumar R., Prabha T.V., and Goswami B.N. (2012), Cloud Aerosol Interaction and Precipitation Enhancement Experiment (CAIPEEX): overview and preliminary results, current science, 102, February 2012, 413-425.

Korolev A, P. R. Field, 2008: The effect of dynamics on Mixed-Phase clouds: Theoretical considerations.

Lee, S. S. and Feingold, G. (2010): Precipitation cloud-system response to aerosol perturbations, Geophys. Res. Lett., 37, L23806, doi: 10.1029/2010GL045596.

Lebo, Z., J. and Seinfeld, J.H.: Therotical basis for convective invigoration due to increased aerosol concentration (2011), Atmos. Chem. Phys., 11, 5407-5429, doi: 10.5194/acp-11-5407-2011.

Meyers MP, DeMott PJ, Cotton WR (1992) New primary ice-nucleation parameterization in an explicit cloud model. J Appl Meteorol 31:708-721

Milbrandt, J. A., and M. K. Yau, 2005a: A multimoment bulk microphysics parameterization. Part I: Analysis of the role of the spectral shape parameter. J. Atmos. Sci., 62, 3051–3064.

Milbrandt, J. A., and M. K. Yau, 2005b: A multimoment bulk microphysics parameterization. Part II: A proposed three-moment closure and scheme description. J. Atmos. Sci., 62, 3065–3081.

Morrison H. and Milbrandt J., 2010, Comparison of Two-Moment Bulk Microphysics Schemes in idealized Supercell Thunderstorm Simulations, Monthly Weather Review doi:10.1175/2010MWR3433.1.

Pai, D., S., and M.,Rajeevan, 1998: Clouds and cloud radiative forcing over tropical

Indian ocean and their relationship with sea surface temperature. Curr. Sci., 75, 372-381

Prabha T.V., Khain A., Maheshkumar R.S, Pandithurai G., Kulkarni J.R, Konwar M.,Goswami B.N. (2011), Microphysics of pre-monsoon and monsoon clouds as seen from in situ measurements during CAIPEEX, J, Atmos, Sci., doi:10.1175/2011 JAS3707.1,1-60.

Rajeevan, M., and J., Srinivasan, 2000: Net cloud radiative forcing at the top of the atmosphere in the asian monsoon region, Journal of Climate,Vol 13.

Rosenfeld D. and W. L. Woodley (2000): Deep convective clouds with sustained supercooled liquid water down to -37.5 ^{O}C, Nature, 405, 440-442.

Sathiyamoorthy, V., P., K., Pal, and P., C., Joshi (2004): Influence of the upper-tropospheric wind shear upon cloud radiative forcing in the Asian Monsoon region, J. Clim., 17, 2725-2735.

Skamarock, W. C., J. B. Klemp, J. Dudhia, D. O. Gill, D. M. Barker, W. Wang, and J. G. Powers, 2007:Adescription of the Advanced Research WRF version 2. NCAR Tech. Note NCAR/TN-4681STR, 88 pp.

Tang, X., and B. Chen (2006), Cloud types associated with the Asian summer monsoons as determined from MODIS/TERRA measurements and comparison with surface observations, Geophys. Res. Lett., 33, L07814, doi: 10.1029/2006GL026004.

Teller, A. and Z. Levin, 2006: The effect of aerosols on precipitation and dimensions of subtropical clouds: a sensitivity study using a numerical cloud model, Atmos. Chem. Phy., 6, 67-80.

Urankar, G., T. V. Prabha, G. Pandithurai, P. Pallavi, D. Achuthavarier, and B. N. Goswami (2012), Aerosol and cloud feedbacks on surface energy balance over selected regions of the Indian subcontinent, J. Geophys. Res., 117, D04210, doi: 10.1029/2011JD016363.

Weisman, M. L., and J. B. Klemp, 1982: The dependence of numerically simulated convective storms on vertical wind shear and buoyancy. Mon. Wea. Rev., 110, 504–520.

Weisman, M. L., and J. B. Klemp, 1984: The structure and classification of numerically simulated convective storms in directionally varying wind shears. Mon. Wea. Rev., 112, 2479–2490

EFFECT OF HYGROSCOPIC SEEDING ON WARM RAIN CLOUDS

- Numerical study using a hybrid cloud microphysical model -

N. Kuba[1] and M. Murakami[2]

[1]Atmosphere and Ocean Research Institute (AORI), The University of Tokyo,

Kashiwa, Japan

[2] Meteorological Research Institute (MRI), Tsukuba, Japan

Correspondence to: N. Kuba (kuba@aori.u-tokyo.ac.jp)

1 Introduction

The purpose of the present study is to quantitatively evaluate the effect of hygroscopic seeding on surface rainfall from warm rain clouds. We developed a hybrid cloud microphysical model that incorporates a Lagrangian CCN (cloud condensation nuclei) activation model, a semi-Lagrangian droplet growth model, and an Eulerian spatial model for advection and sedimentation of droplets (Kuba and Fujiyoshi, 2006).

This model can simulate the CCN activation process precisely so that the effect of a slight change in the initial cloud droplet size distribution due to hygroscopic seeding can be evaluated in detail. The model can also accurately calculate the consequent droplet growth through condensation and collision-coalescence as well as advection, size sorting, collision-breakup, and sedimentation of drops in clouds, leading to a reliable estimate of the seeding effect on surface precipitation. The simulations for shallow convective and stratiform clouds with moderate continental background CCN were performed in Kuba and Murakami (2010).

In this study, the simulations for shallow and deep convective clouds were performed to estimate the effect of cloud thickness on hygroscopic seeding.

And this model was improved to simulate the field experiments. A hygroscopicity parameter κ introduced by Petters and Kreidenweis (2007) was adopted to simulate the observed background CCN and seeding particles (salt micro-powder and hygroscopic flare) in real atmosphere. The results showed that hygroscopic seeing can be effective to increase rainfall amount in the limited cases (cloud thickness, background CCN, amount and chemical component of seeding particles). And relationship between changes in number concentration of cloud droplets and in surface rainfall amount due to hygroscopic seeding was studied in detail.

2 Model description

The hybrid microphysical cloud model was developed to accurately estimate the number concentration and size distribution of cloud droplets and the effect of CCN on cloud microstructures (Kuba and Fujiyoshi, 2006). The activation of CCN and initial condensational growth are computed in a Lagrangian particle framework using a parcel model. The solute effect of CCN is taken into account even after the

activation. Because the maximum supersaturation experienced by an air parcel is estimated accurately, the number of cloud droplets that can be activated is also estimated accurately. This method precludes numerical diffusion of the droplet size distribution. A time step of 0.05 s is adopted for the parcel model to calculate CCN activation and the consequent condensational growth of droplets. This hybrid cloud microphysical model also uses a two-moment bin method based on that of Chen and Lamb (1994) to calculate condensation and coalescence growth with a semi-Lagrangian particle framework and to calculate sedimentation and advection with an Eulerian spatial framework. The cloud droplet size distribution estimated by the parcel model is used as the initial cloud droplet size distribution for the two-moment bin method. This method to provide the initial cloud droplet size distribution seems to be preferable to previously used methods in which activated droplets were added to the first bin (Morrison and Grabowski, 2007; Grabowski and Wang, 2009) or distributed to bins assuming some size distribution shapes (Tzivion et al., 1994; Reisin et al., 1996). Details of the model have been reported by Kuba and Fujiyoshi (2006).

The present study made the following improvements to the hybrid microphysical cloud model of Kuba and Fujiyoshi (2006). To properly estimate multi-coalescence in one time step, two schemes are used. One is a general stochastic coalescence scheme for rare lucky coalescence between droplets, and the other is a continuous coalescence scheme for frequent coalescence of a large drop and numerous small droplets (numerous small droplets are evenly shared by large drops) following the method reported in the doctoral dissertation of Dr. Jen-Ping Chen (1992). We distinguish rare lucky coalescence and frequent coalescence using the predicted frequency of collision in one time step. If the predicted frequency of collision between one particle in the i-th bin and smaller particles in the k-th, (k+1)-th, ..., and i-th bins in one time step is 1 or less, a general stochastic coalescence scheme is used to calculate the growth of particles in the i-th bin by coalescence with particles in the k-th, (k+1)-th, ..., and i-th bins. If the predicted frequency of collision of one particle in the i-th bin and smaller particles in the first, second, ..., and i-th bins in one time step is larger than 1, a continuous coalescence scheme is used to calculate the growth of particles in the i-th bin by coalescence with particles in the first, second, ..., and (k-1)-th bins. If only the general stochastic coalescence scheme is used, a very short time step such as 0.01 s is needed to avoid underestimation of coalescence growth caused by the neglect of multiple coalescences. This method using both continuous and stochastic schemes with a time step of 3.0 s leads to the same results as the method using only the stochastic scheme with a time step of 0.01 s (not shown here). However, in this study, a 0.5 s is adopted for the time step of bin method considering other conditions. We use 73 bins to express a range of radii (from 1 μm to 4 mm) for activated cloud droplets and raindrops. In addition, we adopt the coalescence efficiency proposed by Seifert et al. (2005) and a breakup scheme based on that of Feingold et al. (1988) to estimate the collision-breakup of raindrops.

3 Numerical experiments

The kinematic framework of this study is based on that proposed by Szumowski et al. (1998) to test the warm rain microphysical model. The kinematic cloud model prescribes an evolving flow and performs 2-D advection of temperature and water variables (domain: 9 km x 3 km, dx and dz: 50 m, dt: 3 s). The flow pattern shows low-level convergence, upper-level divergence, and a narrow updraft located in the center of the domain. The magnitude, vertical structure, width, and tilt of the flow through the central updraft are all prescribed using simple analytical functions. This kinematic framework with a microphysical scheme predicts temporal and spatial evolution of water vapor, hydrometeors, and potential temperature

explicitly by using the prescribed flow field and initial and boundary conditions of water vapor content and potential temperature. The advection scheme is a modified version of that of Smolarkiewicz (1984). The bulk microphysical scheme incorporated in Szumowski's original model is replaced with our hybrid microphysical model (Kuba and Fujiyoshi, 2006). This simple model cannot estimate the effect of microphysical processes (hydrometeor loading and latent heat release due to condensation and evaporation) on dynamics. The effect of change in microphysical processes caused by differences in CCN will be studied in future work. However, the model can estimate the effects of CCN on the cloud microstructure and raindrop formation. Therefore, this model is suitable for estimating the effect of hygroscopic seeding on warm rain formation from the microphysical viewpoint. Figure 1 shows the wind field at the time of peak updraft velocity for the shallow convective cloud case (a) and the deep convective cloud case (b). Figure 2 shows the vertical profile of updraft velocity at each time for the shallow convective cloud case (red line) and the deep convective cloud case (green line).

Kuba and Takeda (1983), Cooper et al. (1997), Feingold et al. (1999), and Saleeby and Cotton (2004) showed that giant CCN have the greatest effect on the precipitation efficiency of warm rain clouds in cases with numerous small background CCN.

When low concentrations of smaller-sized CCN are present, adding giant CCN results in a slight decrease in rainfall, suggesting that almost all rainwater is produced by coalescence among cloud droplets formed on smaller-sized CCN. On the other hand, when high concentrations of small CCN are present, adding giant CCN leads to a modest increase in rainfall amount, suggesting that rainwater is produced mainly from coalescence between small cloud droplets formed on smaller-sized CCN and large droplets formed on giant CCN (Kuba and Fujiyoshi, 2006). Preliminary numerical experiments using our hybrid microphysical cloud model also suggested that hygroscopic seeding cannot increase warm rain when the number concentration of background CCN is low (the size distribution of maritime background CCN used in preliminary numerical experiments is shown by the red line in Fig. 3). Therefore, it is assumed that CCN for the non-seeded case (reference case) consist of high concentrations of small particles like a continental case or polluted case. To clearly estimate the role of seeding particles, the number concentration of giant CCN is assumed to be very small (e.g., the number concentrations are 2.0 e-5 cm^{-3} for CCN larger than 1 μm in radius and 5.0 e-7 cm^{-3} for CCN larger than 5 μm in radius). The chemical composition of these CCN is assumed to be NaCl. The CCN size distribution for the non-seeded case (background CCN) is shown by the green line in Fig. 3. We use 181 classes to express the range of radii from 0.009 to 9 μm for background CCN. Figure 4 shows cloud water in the non-seeded case for shallow and deep convective clouds at 15 min. Seeding is assumed to begin 5 min after cloud initiation below the cloud base. Seeding durations are 10 min. Seeding material is assumed to micro-powder (NaCl) with a log-normal size distribution. Mode radius of the size distribution is 0.5 μm or 2 μm (mode radius of blue line in Fig. 3 is 2 μm).

4 Results of numerical experiments

Figure 5 shows temporal change in accumulated surface rainfall averaged over the domain for the shallow convective cloud case. Mode radius of seeding particles is 0.5 μm (Fig.5a) or 2 μm (Fig.5b). A black solid line shows non-seeded case with continental backgrond CCN. For seeded cases, micro-powder with five different amounts are seeded. For reference, non-seeded maritime cloud case is also shown by a black broken line. For cloud seeding with 0.5μm-mode-radius micro-powder (Fig.5a), black (non-seeded), red (amount of seeding particles is 5.5e-4 gm^{-3},180 cm^{-3}) and green (1.1e-3 gm^{-3},

360 cm^{-3}) lines show that rainfall increases with increasing the amount of seeding particles. But blue (2.8e-3 gm^{-3} , 900 cm^{-3}), pink (5.5e-3 gm^{-3} , 1800 cm^{-3}) and light blue (1.1e-2 gm^{-3}, 3600 cm^{-3}) lines show that larger amount of seeding particles make rainfall amount smaller. On the other hand, for cloud seeding 2μm-mode-radius micro-powder (Fig.5b), rainfall increases with increasing amount of seeding particles (see red line; 5.5e-4 gm^{-3} and 2.5 cm^{-3}, green line; 1.1e-3 gm^{-3} and 5.0 cm^{-3}, blue line; 2.8e-3 gm^{-3} and 12.5 cm^{-3}) and saturates at the seeding amount of 5.5e-3 gm^{-3} (25 cm^{-3}) shown by pink line.

Figure 6 is the same as Fig. 5 but for deep convective cloud. Note that scale of vertical axis is four times as large as that of Fig. 5 because deep convective cloud produces much larger rainfall amount than shallow convective cloud does. Black solid and broken lines show non-seeded background case and maritime CCN case. The difference is small and it means that rainfall efficiency of deep cloud is not sensitive to CCN number concentration. Red, green and blue lines show seeded case. They show that seeding is not effective to increase rainfall from deep convective cloud.

Figure 7 shows relationship between the changes in accumlated surface rainfall averaged over the domain for 60 minutes and in cloud droplet number concentration near the cloud base due to micro-powder seeding for shallow convective cloud (a) and deep convective cloud (b). Cloud droplet number concentration near the cloud base for non-seeded case (●) is about 500 cm^{-3} at 6 minutes and about 800 cm^{-3} at 12 minutes. Mode radius of seeding particles is 0.5 μm (○) or 2.0 μm (●). When particles with 0.5 μm-mode radius are seeded for shallow convective cloud (Fig.7a), cloud droplet number concentration decreases and rainfall increases with increasing the amount of seeding particles (1 ⟶). It suggests that competition effect works. But too much seeding leads to an increase in cloud droplet number concentration and a decrease in rainfall (2 ⟶). When particles with 2.0 μm-mode-radius are seeded, small decrease in cloud droplet number concentration and an increase in rainfall (⟶) suggest that raindrop embryo effect works. Seeding a large number of ultra giant particles leads to very low number concentration of cloud droplets and a large increase in rainfall. It seems that both rain drop embryo effect and competition effect work. Even for the heavily seeded cases where cloud droplet number concentrations are less than those for maritime CCN case, rainfall amount is smaller than maritime CCN case. In these cases, almost all cloud droplets are fomed on seeded giant particles. This situation does not have an advantage over maritime CCN case in rainfall production. This is discussed by using Fig.8 in detail.

For deep convective cloud case (Fig.7b), rainfall amount is not sensitive to cloud droplet number concentration. It means that hygroscopic seeding is not effective for deep convective clouds.

In Fig.7a, the cloud seeded with 2μm-mode-radius micro-powder, which has almost the same cloud droplet number concentration as maritime cloud has (surrounded by red circle), has smaller rainfall than maritime case. Figure 8 shows cloud droplet size distributions in these cases. Cloud droplet number concentration of seeded case shown by green line (backgroud CCN + 2μm-mode-radius seeding particles) is smaller than background CCN case shown by red line, and almost the same as maritime case shown by purple line. For reference, the case of maritime CCN without giant particles (it means a part of red line up to 1μm in Fig.3) is shown by blue line. In cases shown by green, purple, ane blue lines, the cloud droplet number concentrations and mode radii are almost the same. At 1200m above the cloud base (Fig.8a), seeded case has largest number concentration of small rain drops (about 50 μm in radius) because of large number of giant seeding particles. Difference between blue and purple lines is caused by the difference in number concentration of giant CCN. At later time and higher level (Fig.8b), number concentration of rain drops larger than 200 μm is smallest

in the seeded case. Small number of CCN leads to many rain drops even if there are not giant CCN. Too many small rain drops can not produce large rain drops because of severe competition for coalescence growth with smaller cloud droplets. These results suggests that not only cloud droplet number concentration but also cloud droplet size distribution is important for rain drop production

5 SUMMARY

This study examined the effects of hygroscopic seeding on warm rain clouds using a hybrid cloud microphysical model combining Lagrangian, semi-Lagrangian, and Eulerian frameworks. The hybrid cloud microphysical model can accurately estimate the effect of CCN on cloud microstructure. The simulation results suggest the following conclusions regarding hygroscopic seeding of warm rain cloud in moderate continental air masses.

1. Appropriate amount of micro-powder with 0.5μm-mode-radius to increase rainfall from shallow convective cloud is about 1.1e-3 gm^{-3} (360 cm^{-3}). Decrease in cloud droplet number concentration due to competition effect leads to an increase in raifall amount. Seeding more particles decreses rainfall.
2. Appropriate amount of micro-powder with 2.0μm-mode-radius to increase rainfall from shallow convective cloud is about 5.5e-3 gm^{-3} (25 cm^{-3}). Both competition effect and raindrop embryo effect make rainfall amount larger.
3. For deep convective cloud case, rainfall amount is not sensitive to cloud droplet number concentration, and hygroscopic seeding is not effective to increse surface rainfall.
4. Seeding a large amount of micro-powder with 2.0μm-mode-radius cannot make rainfall amount larger than that from maritime shallow convective cloud even though cloud droplet number concentrations of seeded shallow convective cloud become less than those in the maritime cloud

Acknowledgements

The authors sincerely thank Ryohei Misumi of the National Research Institute for Earth Science and Disaster Prevention (NIED), who supplied FORTRAN code for the breakup process. This study was carried out as a part of the Japanese Cloud Seeding Experiments for Precipitation Augmentation (JCSEPA) funded by the Ministry of Education, Culture, Sports, Science and Technology, Japan, under the Special Coordination Funds for Promoting Science and Technology.

References

Chen, J. -P.: Numerical simulation of the redistribution of atmospheric trace chemicals through cloud processes, Ph.D. dessertation, The Pennsylvania State University, 343 pp., 1992.

Chen, J. -P. and Lamb, D.: Simulation of cloud microphysics and chemical processes using a multicomponent framework. Part I Description of the microphysical model, J. Atmos. Sci. 51, 2613-2630, 1994.

Cooper, W. A., Bruintjes, R. T., and Mather, G. K.: Calculations pertaining to hygrospic seeding with flares, J. Appl. Meteor., 36, 1449-1469, 1997.

Feingold, G., Tzivion, S., and Levin, Z.: Evolution of raindrop spectra. Part I: Solution to the stochastic collection / breakup equation using the method of moments, J.Atmos.Sci., 45, 3387-3399, 1988.

Feingold, G., Cotton, W. R., Kreidenweis, S. M., and Davis, J. T.: The impact of giant cloud condensation nuclei on drizzle formation in stratocumulus: implications for cloud radiative properties, J. Atmos. Sci., 56, 15, 4100-4117, 1999.

Grabowski, W. W. and Wang, L. -P.: Diffusional and accretional growth of water drops in rising adiabatic parcel: effects of the turbulent collision kernel, Atmos. Chem. Phys., 9, 2335-2353, 2009.

Kuba, N. and Takeda, T.: Numerical Study of the effect of CCN on the size distribution of cloud droplets. Part II. Formation of large droplets, J. Meteor. Soc. Japan, 61, 3, 375-387, 1983.

Kuba, N. and Fujiyoshi, Y.: Development of a cloud microphysical model and parameterizations to describe the effect of CCN on warm cloud, Atmos. Chem. Phys., 6, 2793-2810, 2006. http://www.atmos-chem-phys.net/6/2793/2006/ .

Kuba, N. and Murakami, M.: Effect of hygroscopic seeding on warm rain clouds – numerical study using a hybrid cloud microphysical model, Atmos. Chem. Phys., 10, 3335-3351, 2010. http://www.atmos-chem-phys.net/10/3335/2010/

Morrison, H. and Grabowski, W. W.: Comparison of bulk and bin warm rain microphysics models using a kinematic framework, J. Atmos. Sci., 64**,** 2839-2861, 2007

Petters, M. D. and S. M. Kreidenweis: A single parameter representation of hygroscopic growth and cloud condensation nucleus activity. Atmos. Chem. Phys., 7, 1961-1971, 2007.

Reisin, T., Tzivion, S., and Levin, Z.: Seeding convective clouds with ice nuclei or hygroscopic particles: A numerical study using a model with detailed microphysics, J. Appl. Meteorl., 35, 1416-1434, 1996.

Saleeby, S. M. and Cotton, W. R.: A large-droplet mode and prognostic number concentration of cloud droplets in the Colorado State University Regional Atmospheric Modeling System (RAMS). Part I: Module descriptions and supercell test simulations, J. Appl. Meteor., 43, 182-195, 2004.

Seifert, A., Khain, A., Blahak, U., and Beheng, K. D.: Possible effect of collisional breakup on mixed-phase deep convection simulated by a spectral (bin) cloud model, J. Atmos. Sci., 62, 1917-1931, 2005.

Smolarkiewicz, P.K.: A fully multidimensional positive definite advection transport algorithm with small implicit diffusion. J.Comput.Phys., 54, 325-362, 1984.

Szumowski, M. J., Grabowski, W. W., and Ochs III, H. T.: Simple two-dimensional kinematic framework designed to test warm rain microphysical models, Atmos. Res., 45, 299-326, 1998.

Tzivion, S., Reisin, T., and Levin, Z.: Numerical simulation of hygroscopic seeding in a convective cloud, J. Appl. Meteor., 33, 252-267, 1994.

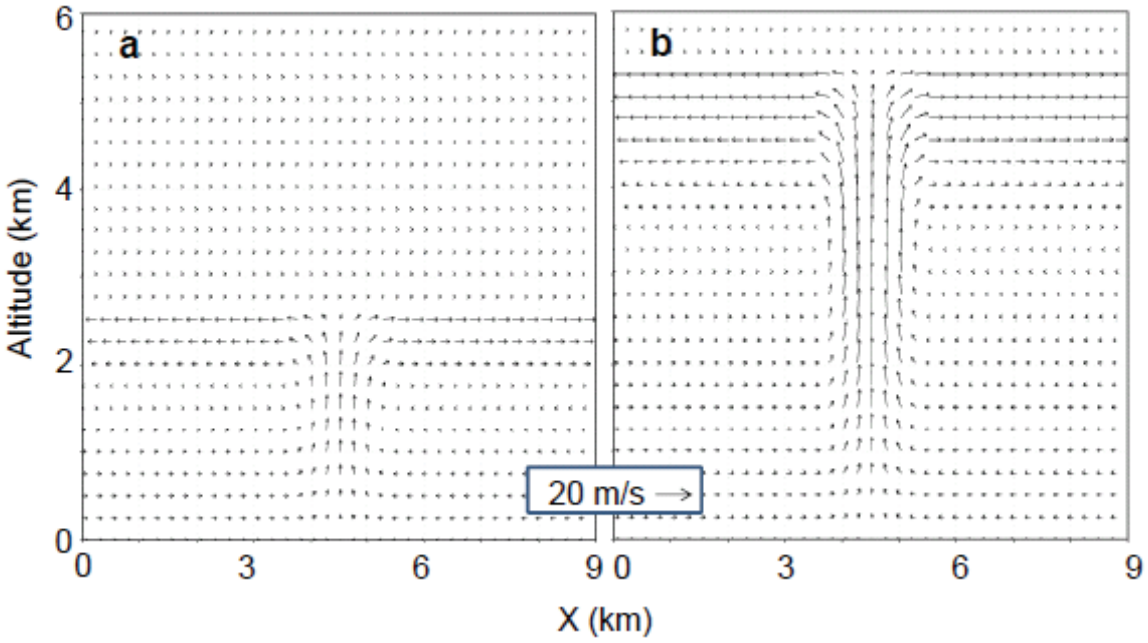

Figure1. The wind field at the time of peak updraft velocity at 15 min for the shallow convective cloud case (a) and for the deep convective cloud case (b).

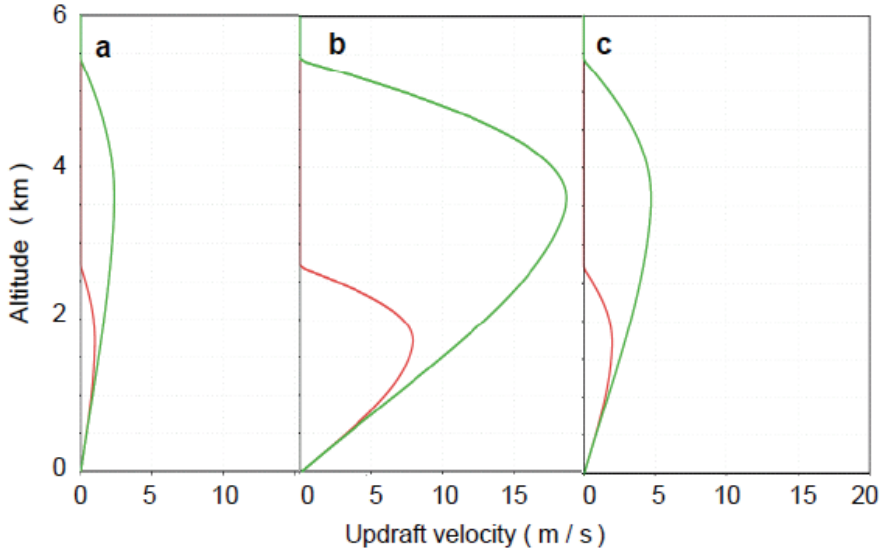

Figure 2 Vertical profile of updraft velocity at 5 min. (a), 15 min. (b), and 25 min. (c) for the shallow convective cloud case (red line) and the deep convective cloud case (green line).

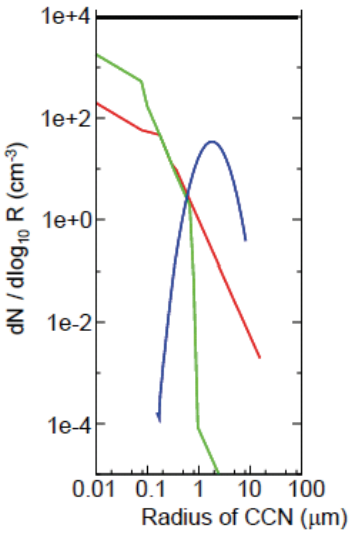

Figure 3. Size distributions of the background CCN (green line), salt micro-powder with 2μm-mode-radius (blue line), and maritime CCN (red line). Total number concentrations of background CCN and maritime CCN ($r > 0.01$ μm) are 1000 and 100 cm^{-3}.

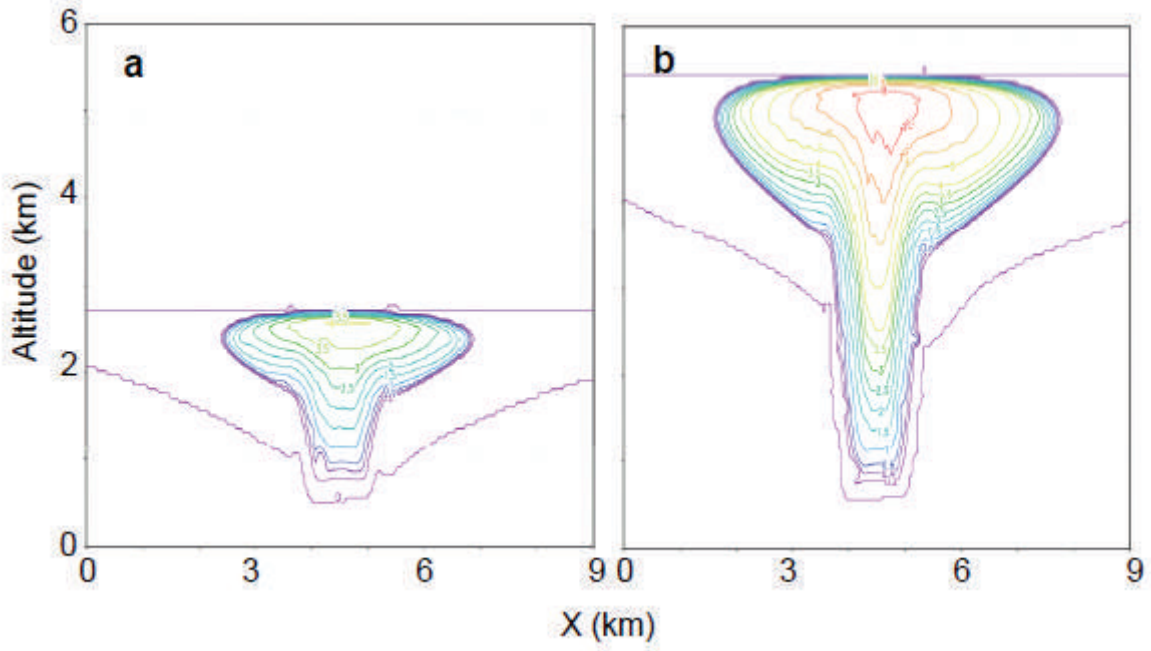

Figure 4. Cloud water content (g kg^{-1}) at 15 min. for non-seeded cases. (a) Shallow convective cloud. (b) Deep convective cloud.

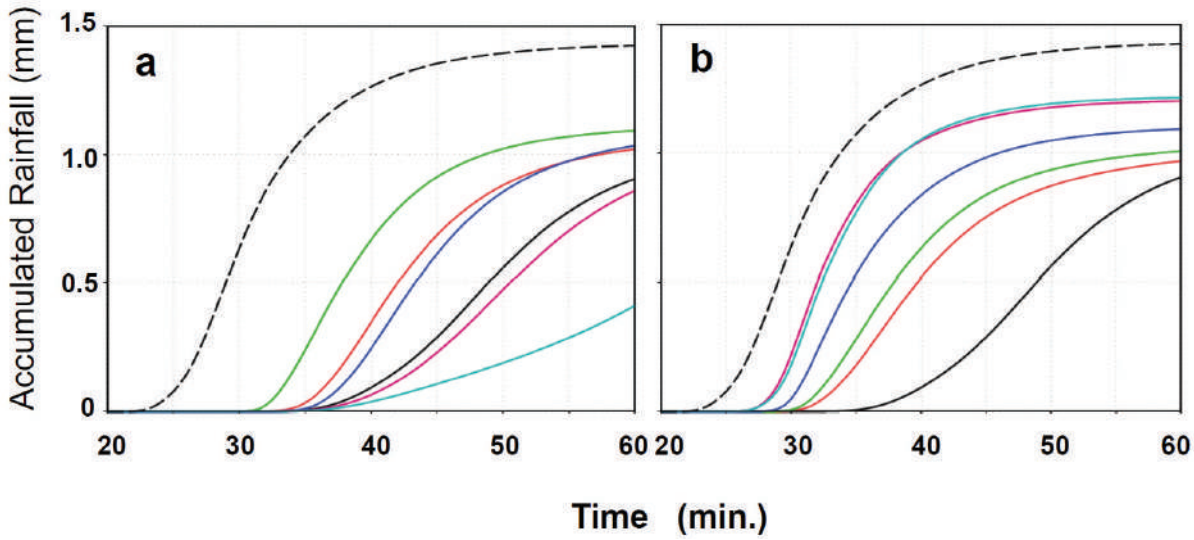

Figure 5. Temporal change in accumulated surface rainfall averaged over the domain for the seeded and unseeded shallow convective clouds. Mode radius of seeding particles is 0.5 μm (a) or 2 μm (b). A black solid line shows unseeded case with continental background CCN. For seeded cases, five different amounts of salt micro-powder are seeded: 5.5e-4 (red), 1.1e-3 (green), 2.8e-3 (blue), 5.5e-3 (pink), and 1.1e-2 (light blue) gm^{-3}. For reference, unseeded maritime cloud case is also shown by a black broken line.

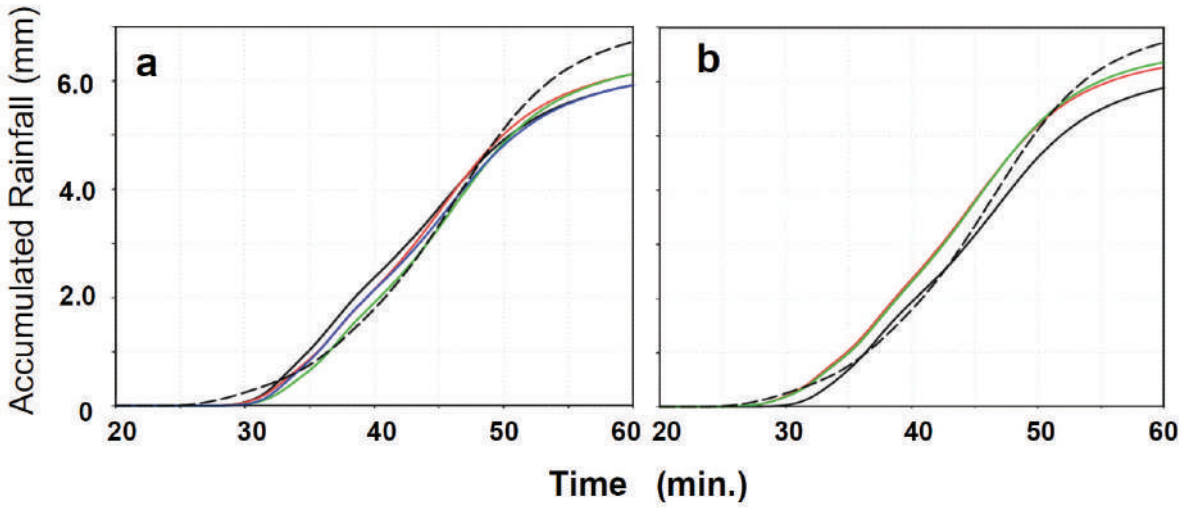

Figure 6. Same as Fig.5 except for deep convective cloud case.

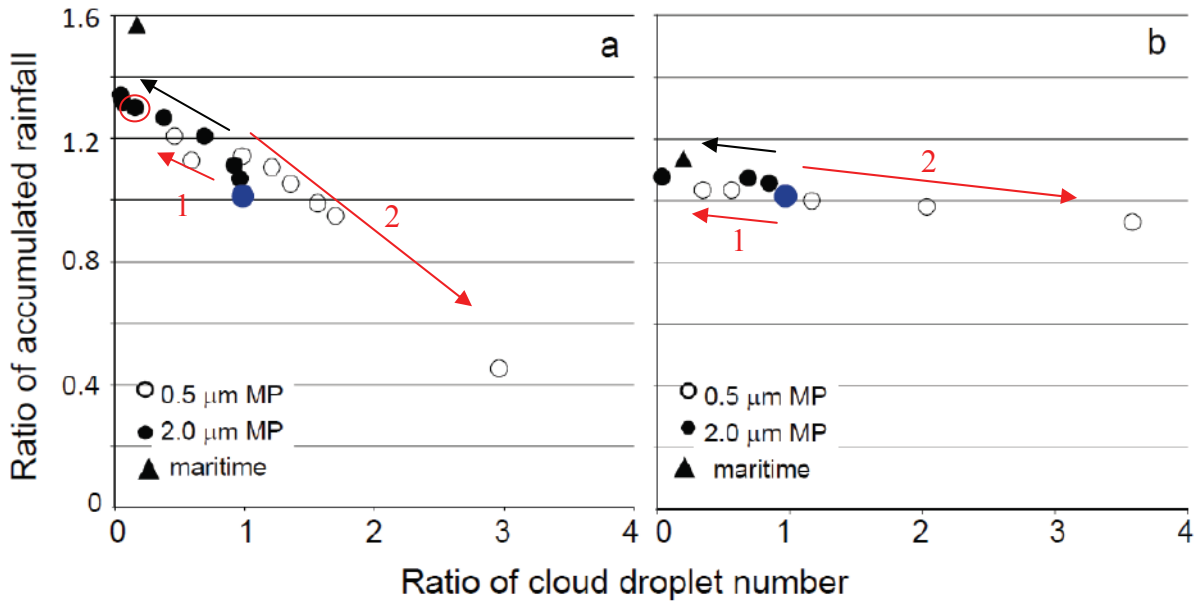

Figure 7. Relationship between the changes in accumulated surface rainfall averaged over the domain for 60 minutes and in cloud droplet number concentration due to micro-powder seeding for shallow convective cloud (a) and deep convective cloud (b).

● shows non-seeded case . ○ shows seeded case with 0.5μm-mode-radius particles.

● shows seeded case with 2.0μm-mode-radius particles. ▲ shows non-seeded maritime CCN case.

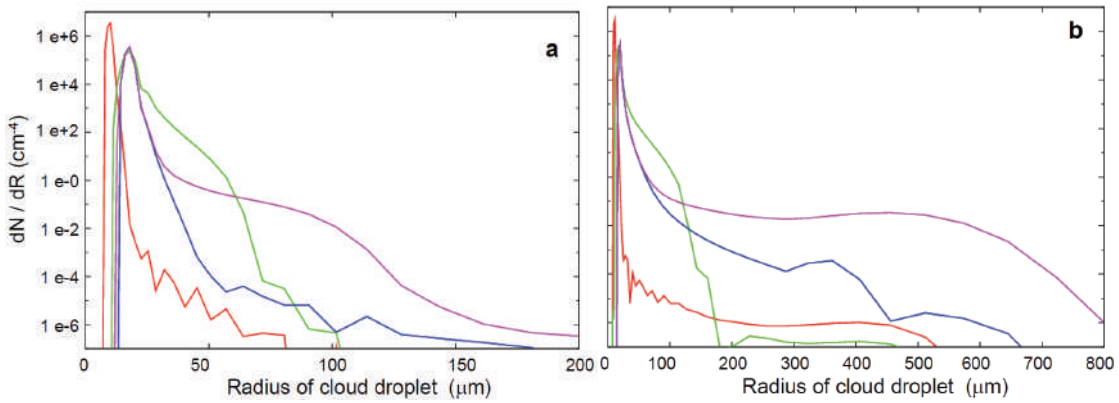

Figure 8. Cloud droplet distributions at 1200 m above cloud base at 15 min.(a), and at 1700 m above cloud base at 16 min. (b).

Red line; unseeded case (background CCN)

Green line; seeded case (mode radius of seeding particles is 2 μm)

Purple line unseeded maritime case

Blue line unseeded maritime case without giant particles.

HOLE-PUNCH CLOUDS OVER HELSINKI, FINLAND: A CASE STUDY

Hirsikko[1], A., E. J. O'Connor[1,2], P. Jokinen[1], J. Kotro[1], D. Moisseev[3] and J. Leinonen[1]

[1]Finnish Meteorological Institute, P.O. BOX 503, FI-00101, Helsinki, Finland
[2]Meteorology Department, University of Reading, Reading, UK
[3]Department of Physics, University of Helsinki, P.O. BOX 64, 00014 Univ. of Helsinki, Finland

1. ABSTRACT

Several hole-punch clouds were observed simultaneously over Helsinki, Finland on 5th November, 2011, in a supercooled liquid layer at an altitude of 7.5 km. Based on the observations by vertically-pointing Doppler cloud radar, Doppler lidar and scans from the Dual-polarisation C-band weather radar at the Kumpula campus, we posit a mechanism that can provide ice nuclei in sufficient quantities: intermittent fallstreaks from higher cirrus layer. Interaction between a higher cirrus layer (8-11 km) and a lower mixed-phased layer 1 km deep (supercooled layer at 7.5 km with ice falling up to 1 km below) was noted in the cloud radar Doppler velocity spectra, where the velocity distribution of the falling ice from the cirrus layer broadened, then shifted to faster falling velocities after encountering the supercooled liquid layer.

2. INTRODUCTION

Formation of holes in the clouds is a result of glaciation (e.g. Pedgley, 2008): the presence of ice nuclei in a super-cooled liquid layer can produce large numbers of ice crystals which grow rapidly by deposition of water vapour in the supersaturated conditions. This growth is maintained at the expense of evaporation of liquid droplets, causing a gap to form in the cloud, and the heavier ice crystals falling in visible streak below the liquid layer. However, ice nuclei are not normally present in high enough concentrations in the atmosphere to cause glaciation. It is thought that ice nuclei originate via rapid freezing of water when an aircraft passes through the liquid layer (Westbrook and Davies, 2010; Heymsfield et al., 2010, 2011). However, our observations with Doppler and weather radars, accompanied by Doppler lidar and radiosounding profiles, suggest another mechanism that can provide ice nuclei in sufficient quantities; intermittent fallstreaks from cirrus layers above, analogous to the seeder-feeder mechanism for enhanced orographic precipitation.

3. METHODS

The observations were obtained from vertically-pointing Doppler cloud radar (Mira 35 GHz, METEK GmbH), 1.5 µm wavelength Doppler lidar (Halo Photonics, Pearson et al., 2009) and scans from the Dual-polarisation C-band weather radar at the Kumpula campus (60.12°N, 25.58°E) 5 km north-east from the city centre of Helsinki, Finland. Radiosounding profiles at Jokioinen, ca. 110 km north of Helsinki, and satellite images from NOAA AVHRR, provided supporting evidence. In addition, several human observers took photos of hole-punch clouds in and around the Helsinki Metropolitan area.

4. RESULTS AND DISCUSSION

The Doppler cloud radar and Doppler lidar indicate the existence of three cloud layers on 5th of November (Fig. 1): a) a liquid stratocumulus cloud layer with a base at 0.5 km (visible in both radar and lidar), b) a mixed-phase altocumulus cloud between 6.3-7.3 km with the supercooled liquid layer at the top, and c), a cirrus layer at 8-11 km.

The radiosounding profile suggests that conditions for cirrus-ice formation were suitable at about 10 km (relative

humidity close to 100% with respect to ice), as seen in the cloud radar reflectivity factor and Doppler velocity image (Fig. 1). Initially, evaporation of falling ice limited the layer-depth to a kilometer or so, later on the fallstreaks began to extend to 3 km or more.

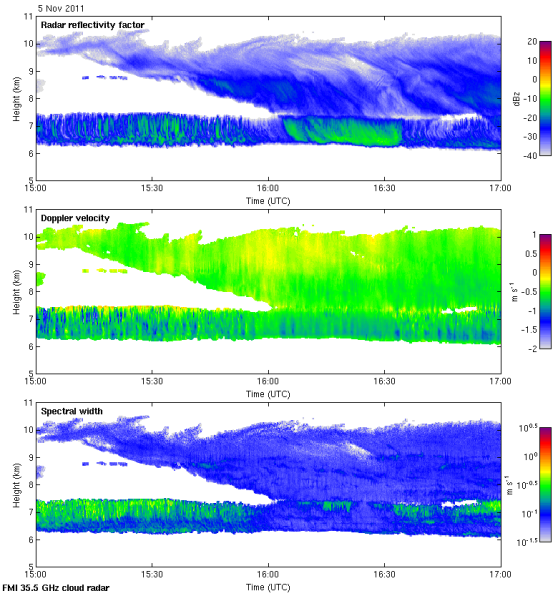

Figure 1. Doppler cloud radar profiles of reflectivity factor (upper panel), Doppler velocity (middle panel) and spectral width (lower panel) measured on 5th of November in Helsinki, Finland.

The radiosounding also displayed a region at about 7.3 km with almost 100% relative humidity with respect to water. A liquid layer was present at this level throughout much of the day, with ice virga precipitating below to about 6.3 km. Small amounts of ice were continuously produced, but the liquid layer was stable and continually replenished, until the increasing intensity of ice produced in the cirrus layer above provided a new direct source of ice nuclei. Rapid glaciation took then place, as seen in Fig. 1 from 16.00-16.30 UTC. By late evening, the cirrus layer was producing enough ice to cause complete glaciation of any liquid.

The glaciation mechanism was clearly evident in the Doppler velocity spectra of the radar at and below the liquid layer at 7.3 km. The vertical velocity distribution seen in the ice falling from the cirrus layer broadened considerably, before shifting towards larger terminal fallspeeds, on passing through the supercooled liquid layer.

In addition, images from the NOAA AVHRR satellite captured small holes in the cloud deck above southern Finland. Members of the public also observed several simultaneous holes in the supercooled liquid layer in locations where the low-level stratocumulus layer was broken or had dissipated, as in Helsinki city center. Photos of the phenomenon were also published in local newspapers (e.g. blogit.hs.fi/saa/2011/11/05/aukkoja-pilvessa/).

5. REFERENCES

Heymsfield, A. J., et al.: Aircraft-induced hole punch and canal clouds, BAMS, 91, 753-766, 2010.

Heymsfield, A. J., et al.: Formation and Spread of Aircraft-induced Holes in Couds, Science, 333, 77, doi: 10.1126/science.1202851, 2011.

Pearson, G., Davies, F., Collier, C.: An Analysis of the Performance of the UFAM Pulsed Doppler Lidar for Observing the Boundary Layer J. Atmos. Ocean. Tech., 26, 240-250, 2009.

Pedgley, D. E.: Some thoughts on fallstreak holes, RMetS-Wether, 63, 12, 356-360, 2008.

Westbrook, C. and O. Davies: Observations of a glaciating hole-punch cloud, RMetS-Weather, 65, 7, 176-180, 2010.

CCN ability of soot and mineral dust particles

Katsuya Yamashita, Takuya Tajiri, and Masataka Murakami
Meteorological Research Institute, Tsukuba, Japan

1. INTRODUCTION

Aerosol particles with soluble and insoluble materials produce ice crystals through homogeneous and heterogeneous freezing nucleations in upper troposphere. Their physicochemical nature and number concentration affect the properties of ice cloud, such as albedo, coverage and life time, which have an effect on the radiative forcing of ice cloud.

The variety of different IN types and their scarcity complicates the measurement and simulation of heterogeneous ice nucleation. In addition, heterogeneous nucleation can occur via several different mechanisms (deposition, immersion, condensation, and contact freezing). Although some of the mechanisms have been investigated with numerical models (e.g., Khain et al., 1999), our knowledge of them is still not sufficient.

Contact, immersion, and condensation freezing involve liquid droplets and are therefore the most commonly accepted ice nucleation mechanisms in supercooled liquid clouds. According to Hoose et al. (2010), immersion freezing by mineral dust is found to be the dominant ice formation process, followed by immersion and contact freezing by soot from a global climate model implemented with an ice nucleation parameterization based on classical nucleation theory.

In order to fully understand immersion and condensation freezing of soot and mineral dust, it is important to know the ability of the aerosol particles as not only IN but also CCN. We investigated size distribution, activated fraction of CCN, hygroscopicity parameter (κ), and activated fraction of IN (as a function of temperature and supersaturation with respect to water) of the artificially generated pure soot and mineral dust particles in our laboratory. In this paper, we report on the CCN ability of the soot and mineral dust particles, and present the simulation results using a parcel model implemented with the κ-Köhler theory and using the measured values (CCN size distribution and hygroscopicity parameter (κ)) which are the initial value for the model. The results of IN ability will be also reported in a companion presentation by Tajiri et al. in this conference.

Corresponding author: Katsuya Yamashita, Meteorological Research Institute, 1-1 Nagamine, Tsukuba, Ibaraki 305-0052, Japan.

E-mail: kayamash@mri-jma.go.jp

2. EXPERIMENTAL METHOD

The CCN abilities of soot and mineral dust particle were investigated by measuring the activation spectrum, hygroscopicity parameter (κ), and droplet size distribution (DSD) activated on particles in a cloud condensation nuclei counter (CCNC).

The soot particle was generated by graphite spark type generator (PALAS Inc., Model GNP2000). The morphology, organic carbon to elemental carbon ratio, and optical properties of the same type generator were comprehensively analyzed in AIDA studies (Saathoff et al., 2003; Schnaiter et al., 2003)

Certified Asian mineral Dust (CAD) and Arizona Test Dust (ATD) were dispersed by the rotating brush type disperser (PALAS Inc., Model RBG1000). The CAD was produced by Nishikawa et al. (2000) to reference Asian mineral dust. Detailed information was provided by their paper. They demonstrated that the

mineral composition of the CAD particles and Asian mineral dust aerosols collected in Japan (Osaka Pref., Kagoshima Pref., and Yamaguchi Pref.) were very similar in elemental composition and claimed that CAD is an appropriate reference material for Asian mineral dust aerosol particles. The ATD is available from Powder Technology Inc. (Minesota, USA) as a reference material, which can be used in other labs for comparison of results and methods of IN measurements. Detailed information was presented in Möhler et al. (2006).

The generated and dispersed particles were stored in an aerosol buffer tank (1.4 m^3 volume) via two cyclones (50% cutoff diameter 2.5 μm and 1.0 μm), and then supplied to aerosol instruments.

The activated fractions of the soot, CAD, and ATD were determined by measuring CCN concentrations with the CCNC (DMT Inc., Model CCN-200) and CN concentrations with Condensation Particle Counter (CPC). The CCNC is a continuous-flow thermal-gradient diffusion chamber for measuring aerosols that can act as cloud condensation nuclei. Particles (Dp > 0.75 μm) large enough to be detected by built-in optical particle counter (OPC) of the CCNC are counted as CCN. The CCNC measured CCN number concentrations and size distributions of droplet from 0.75 μm to 10 μm.

A differential mobility analyzer (DMA, TSI Inc., Model 3080), CCNC, and CPC were used for measuring hygroscopicity parameter (κ). The particles classified by DMA were simultaneously measured with CPC and CCNC. The activated fraction of the particles (Nccn/Ncn) was calculated from the concentrations of CN (Ncn) and CCN (Nccn), and the supersaturation was increased in a stepwise manner, the critical supersaturation was then determined to be the supersaturation at which a minimum of 50% of the particles activated as cloud droplets. The critical supersaturation as a function of dry particle diameter was obtained from each classification for particle diameter. Details of this procedure have been described by Koeler et al. (2007) and Rose et al. (2008).

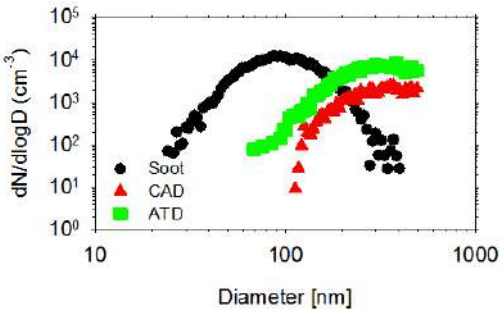

Figure 1 Size distributions of the soot, CAD, and ATD particles measured with SMPS.

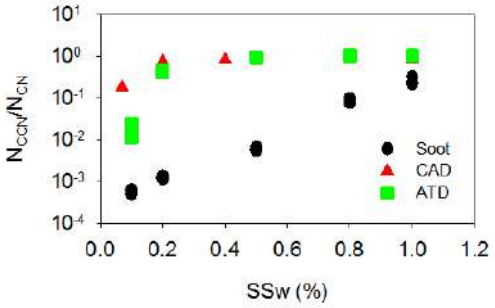

Figure 2 Activation spectra of the soot, CAD, and ATD particles as a function of supersaturation with respect to water. Each dot indicates the mean value averaged over 1min.

3. RESULTS

The size distributions of the dispersed soot, CAD, and ATD particles are shown in Fig. 1. These size distributions were measured with a scanning mobility particle sizer (SMPS, TSI Inc., Model 3936). The soot, CAD, and ATD particles prepared for the present experiments have a peak diameter of 100, 350, and 300 nm, respectively.

Figure 2 depicts the activation spectra of the soot, CAD, and ATD particles. The ratios of Nccn/Ncn were 0.001, 0.8, and 0.5 at SS = 0.2% and 0.4, 0.9, and 1.0 at SS = 0.8%, respectively. The soot particle prepared for the present experiments was

not efficient as CCN. The CAD and ATD particle were efficient as CCN.

Figure 3 indicates the relationship between critical supersaturation and the dry diameter for soot, CAD, and ATD particles. The mean κ-value of soot, CAD, and ATD was 0.006, 0.014, and 0.017, respectively.

In the κ-Köhler theory, the κ-value of the particle indicates its hygroscopicity. Once the κ-value was known, the activation and subsequent condensation growth of the particle could be calculated. To simulate such processes, the parcel model of Chen and Lamb (1994) was modified to include the κ-Köhler theory instead of the classical Köhler theory (Yamashita et al. 2011). Figure 4 show that DSDs activated and grown in the supersaturation column of the CCNC, where SS are set to 0.4 (soot and CAD) and 0.5% (ATD). In the case of soot (κ=0.006), there was a difference between the calculated and measured DSDs. The difference was especially large at large diameters. Although the reason of the difference is not clear, a possible reason is considered to be an uncertainty in the size measurement with for the soot particles. As the morphology of the soot particles is an aggregate made of finer particles, the size of them may be underestimated by the SMPS. For the CAD (κ=0.014) and ATD (κ=0.017), the calculated DSDs were consistent with the measured ones. Although the model needs to be improved, it shows a reasonable performance.

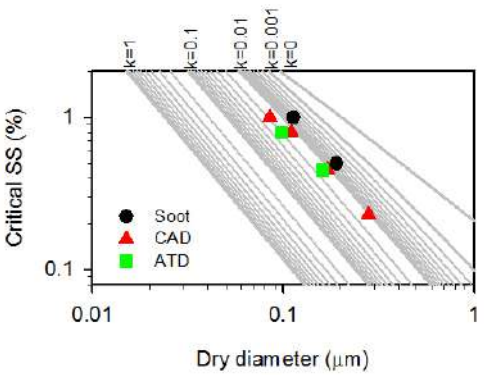

Figure 3 Theoretical (solid lines) and measured (marks) critical supersaturation as a function of dry diameter for soot, CAD, and ATD.

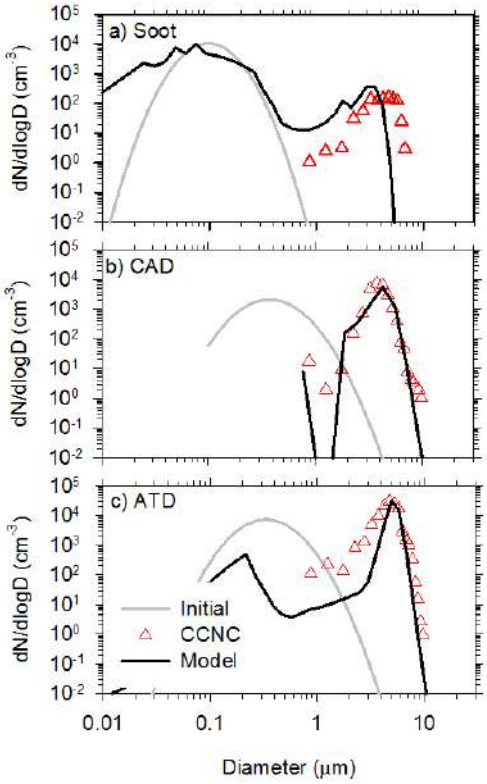

Figure 4 DSDs activated and grown in the supersaturation column of CCNC, where SS are set to 0.4 (soot and CAD case) and 0.5% (ATD case). The grey line is the lognormal distribution fitted to the measured dry size distribution. Triangles are DSDs measured with CCNC, black lines are DSDs calculated by the parcel model implemented with the κ-Köhler theory.

4. MODEL SIMULATION OF ADIABATIC EXPANSION FOR THE SOOT AND MINERAL DUST PARTICLE

This section presents the results of the parcel model simulation where the measured value (CCN size distribution and hygroscopicity parameter (κ)) are used as the initial value.

In the simulation, the initial air temperature and pressure were set to 15 °C

and 1000 hPa, respectively. The parcel is adiabatically lifted at 1 ms^{-1}. The initial CCN size distribution was the lognormal distribution fitted to the measured dry particle size distribution (see Fig. 4). The total concentration was set to constant (300 cm^{-3}).

Figure 5 shows time series of pressure, temperature, RHw, RHi, and droplet number concentration. The temperature at the lifting condensation level (LCL) is -10.3 °C. The maximum RHw for soot, CAD, and ATD simulation was 101.9, 101.3, and 101.2%, respectively. Since the water vapor was not efficiently consumed through the condensational growth of the low hygroscopicity particles until the onset of droplet activation, the maximum supersatuartion for the soot particles (lowest hygroscopicty in this study) was the highest. The RHi at LCL was about 111%, and then gradually increased.

The droplet number concentrations at the maximum supersaturation for soot, CAD, and ATD cases were 180, 265, and 265 cm^{-3}, respectively. About 60, 88, and 88% of soot, CAD, and ATD particles, respectively, were activated.

We also conducted some other simulations when the total CCN concentration was 1000 cm^{-3} and other parameters were same as those mentioned above. Although results are not shown here, the temperature at LCL is -10.3 °C, and the maximum RHw for soot, CAD, and ATD simulation was 101.5, 101.0, and 100.9%, respectively. These values are lower than those for lower CN concentration (300 cm^{-3}) case because of competition effect. The droplet number concentration at the maximum supersaturation for soot, CAD, and ATD case was 481, 803, and 813 cm^{-3}, respectively. About 48, 80, and 81% of soot, CAD, and ATD particles, respectively, were activated. These values are also lower than those for the lower CN concentration (300 cm^{-3}) case. These results are reasonable results reflecting cloud microphysical effects.

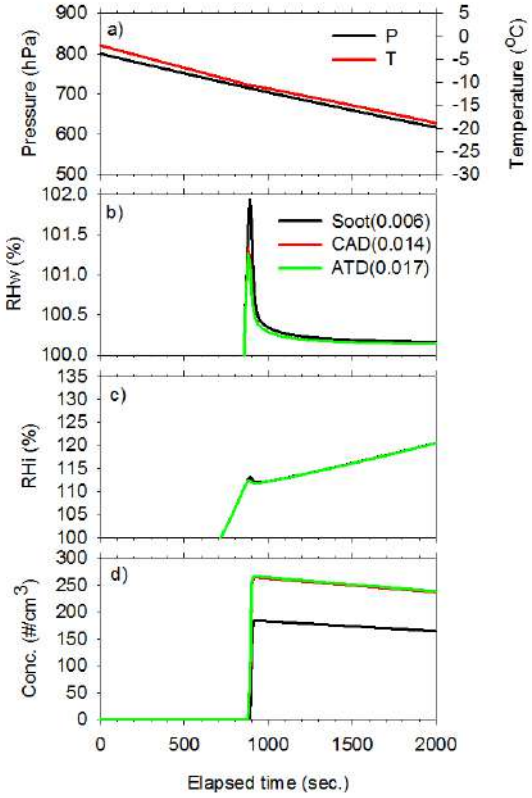

Figure 5 Time series of (a) pressure and temperature, (b) relative humidity for water, (c) relative humidity for ice, and (d) number concentration of droplets between 5.0 μm and 100 μm in diameter.

5. SUMMARY

Investigations of the CCN ability of the artificially generated soot and mineral dust particles were conducted. The mean hygrosocopic parameter κ for soot, CAD, and ATD is 0.006, 0.014, and 0.017. Using the mean hygroscopic parameters, their activation and subsequent condensational growth in the supersaturation column of the CCNC were simulated by the validated parcel model. Although there was a difference between the calculated and measured DSDs for soot case, the model shows a reasonable performance. Model simulations for adiabatic expansion were also conducted. From the simulation results, the model implemented with the κ-Köhler theory could simulate the liquid phase microphysics reflecting cloud microphysical

effects.

REFERENCES

Chen J. –P. and D. Lamb, 1994: Simulation of cloud microphysical and chemical processes using a multicomponent framework. Part 1: Description of the microphysical model. *J. Atmos. Soc.*, 51, 2613-2630.

Khain A., A. Pokrovsky, and I. Sednev, 1999: Some effects of cloud-aerosol interaction on cloud microphysics structure and precipitation formation: Numerical experiments with a spectral microphysics cloud ensemble model. *Atmos. Res.*, 52, 195-220.

Koehler, K. A., S. M. Keidenweis, P. J. DeMott, A. J. Prenni, and M. D. Petters, 2007: Potential impact of Owens (dry) Lake dust on warm and cold formation, *J. Geophys. Res.,* **112**, D12210, doi:10.1029/2007JD008413.

Möhler, O., Field, P. R., Connolly, P., Benz, S., Saathoff, H., Schnaiter, M., Wagner, R., Cotton, R., Krämer, M., Mangold, A., and Heymsfield, A. J. 2006: Efficiency of the deposition mode ice nucleation on mineral dust particles, *Atmos. Chem. Phys.*, 6, 3007-3021, doi:10.5194/acp-6-3007-2006.

Nishikawa, M., Q. Hao, and M. Morita, 2000: Preparation and evaluation of certified reference materials for Asian mineral dust. *Global Environ. Res.*, 4, 102–113.

Hoose, C., J. E. Kristjánsson, J. –P. Chen, A. Hazra, 2010: A Classical-Theory-Based Parameterization of Heterogeneous Ice Nucleation by Mineral Dust, Soot, and Biological Particles in a Global Climate Model. *J. Atmos. Sci.*, **67**, 2483–2503.

Saathoff, H., O. Möhler, U. Schurath, S. Kamm, B. Dippel, and D. Mihelcic 2003, The AIDA soot aerosol characterisation campaign 1999, *J. Aerosol Sci*., 34(10), 1277– 1296.

Schnaiter, M., H. Horvath, O. Möhler, K. H. Naumann, H. Saathoff, and O. W. Schöck 2003, Uv-vis-nir spectral optical properties of soot and soot-containing aerosols, *J. Aerosol Sci.*, 34(10), 1421– 1444.

Rose, D., S. S. Gunthe, E. Mikhailov, G. P. Dusek, M. O. Andreae, and U. Poschl, 2008: Calibration and measurement uncertainties of a continuous-flow cloud condensation counter (DMT-CCNC): CCN ammonium sulfate and sodium chloride aerosol particles in theory and experiment, *Atmos. Chem. Phys.,* **8***,* 1153-1179.

Yamashita, K., M. Murakami, A. Hashimnoto, and T. Tajiri, 2011: CCN Ability of Asian Mineral Dust Particles and Their Effects on Cloud Droplet Formation. *J. Meteor. Soc. Japan*, 89, 581–587.

DO ANOMALOUS ZONES OF NON-INDUCTIVE CHARGING INFLUENCE THE ELECTRICAL STATE OF THE THUNDERSTORMS: NUMERICAL EXPERIMENTS WITH MESONH

Boryana Tsenova[1], Jean-Pierre Pinty [2], Rumjana Mitzeva [3], Christelle Barthe [4]

[1]National Institute of Hydrology and Meteorology, 66 Tsarigradsko Chaussee, 1784 Sofia, Bulgaria

[2]Laboratoire d'Aerologie, 14, Avenue E. Belin, 31400 Toulouse,

[3]University of Sofia, Faculty of Physics, 5, J. Boucher, 1164 Sofia, Bulgaria

[4]Laboratoire de l'Atmosphere et des Cyclones, 15 avenue Rene Cassin, 97715 Saint Denis Reunion, France

1. INTRODUCTION

It is accepted that the electrification of thunderstorms results from a charge separation process during rebounding collisions between ice particles in the presence of supercooled droplets (non-inductive charging process). Based on their laboratory results, Saunders et al. (1991) proposed empirical equations for the sign and magnitude of the separated charge as a function of the effective water content *EW* and temperature *T*. During their laboratory experiments, the so-called 'anomalous zones' were established where for a given cloud temperature, the polarity of ice particles charging at low effective water content was opposite to the polarity at higher *EW*. Furthermore, in these zones the charge magnitude is considerably higher in comparison to the remainder of the charge separation domain. In Helsdon et al. (2001), due to the dominating role of the positive and negative anomalous zones on the overall charge structure of their simulated cloud case, it is proposed to diminish the charge magnitude in these regions by a certain percentage to reduce their effect on the results. Mansell et al. (2005) reduced also the magnitude of separated charge at low *EW.*

In Brooks et al. (1997) modifications of the equations in Saunders et al. (1991) for the separated charge to be presented as a function of cloud temperature and rime accretion rate *RAR* = *EW.V,* instead of *EW* are proposed. However, in their parameterization, the authors do not mention about the ‘anomalous zones’. Preliminary results in Tsenova et al. (2011) where the electrification of an idealized cloud case is simulated with the different existing parameterizations of non-inductive charging showed that the inclusion of the ‘anomalous zones’ at low *EW* (or *RAR*) affect significantly the cloud charge structure. In the present study numerical simulations of an idealised cloud case are performed with MésoNH model with and

without the ‘anomalous zones’, using parameterizations based on the effective water content *EW* (Saunders et al., 1991) and on the rime accretion rate *RAR* (Brooks et al., 1997) with the aim to determine to what extent including or not the anomalies may affect the simulated charge structures.

2. NUMERICAL SIMULATIONS AND RESULTS

The MésoNH code is a non-hydrostatic mesoscale model which results from a joint development of Laboratoire d'Aérologie and Météo-France. In the model, the charge separation mechanisms are entirely due to non-inductive processes. Charges are separated during collisions between graupel and pristine ice crystals, graupel and snow/aggregates and between snow/aggregates and pristine ice crystals. The electric charges carried by each of the five hydrometeor categories (cloud and rain drops, ice crystals, snow, and graupel) are transported along the airflow and are exchanged according to the various microphysical mass transfer rates. A power law distribution of the individual charges as a function of the particle size is assumed. All the charging rates are obtained after integration over the particle size distributions.

The parameterizations are based on laboratory data for the non-inductive charge transfer between rebounding ice crystals and graupel in the presence of cloud droplets. The charge separation values are calculated in the temperature range [−40°C, 0°C], i.e. no charging is assumed below −40°C. The considered parameterizations are:

- SAUNa — the parameterization based on the equations presented in Saunders et al. (1991), thereafter referred to SKM. According to these equations the charge transfer Q per separation event for graupel/ice crystal collision depends on crystal size d and relative velocity V following the equation:

$$Q = A\, d^a V^b q(EW,T) \qquad (1),$$

where *A*, *a*, and *b* are constants depending on crystal size and graupel velocity and are tabulated in SKM, *q* is the charge determined from the experimentally derived equations linking *EW* and *T* for the positive and negative charging cases. There is no reduction of the magnitude of separated charge in the anomalous zones charging.

- SAUNn – same as SAUNa, but without taking into account the charge in “anomalous zones” at low *EW*; instead, the charge is calculated by linear interpolation of data from closest zones.

- BSMPn — the parameterisation is based on the equations presented in Brooks et al. (1997). According to these equations the charge transfer Q per separation event is given by:

$$Q = A\, d^a V^b q(RAR,T) \qquad (2),$$

- BSMPa – same as BSMPn with

included equations for the charge transfer in the “anomalous zones” as a function of RAR, with no reduction of the charging in these zones.

The model was run using temperature and moisture profiles observed on July 19, 1981 during the Cumulus Co-operative Precipitation Experiment near Miles city, Montana. The simulated cloud forms at 3.5 km AGL (about 5^{o}C) and rises up to 12 km altitude (about -55^{o}C). Charging in the simulated cloud occurs at 40 min model time (MT), about 5 minutes after the first graupel particles formation in the cloud. Figures 1 and 2 show the temporal evolution of the height of the maximum positive and negative total charge density obtained with SAUNa and SAUNn (Fig.1) and BSMPa and BSMPn (Fig.2). From the two figures it is visible that when the ‘anomalous zones’ are excluded from the two parameterizations (based on *EW* and on *RAR*) for non-inductive charging, the simulated maximum negative total charge density is achieved above the maximum positive one (see bottom panels of the two figures), which is contrary to the conceptual picture of the distribution of charge based on the measurements in the real CCOPE cloud Dye at al., 1986.

Considering the temporal evolution of the maximum positive and negative total charge densities obtained with the four parameterizations (figures 3 and 4), one can see that exclusion of the ‘anomalous zones’ leads to considerably lower values of maximum total charge densities.

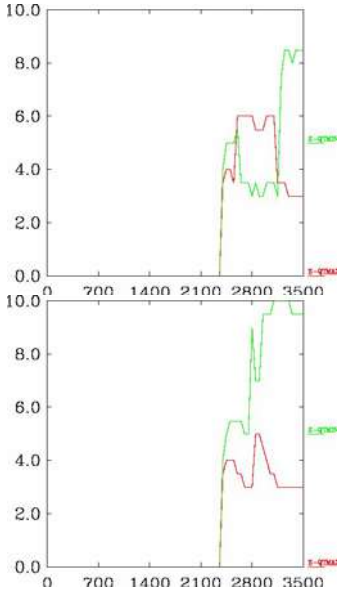

Fig.1. Temporal evolution of the height (in km) of the maximum positive (in red) and negative (in green) total charge density obtained with SAUNa (top panel) and SAUNn (bottom panel)

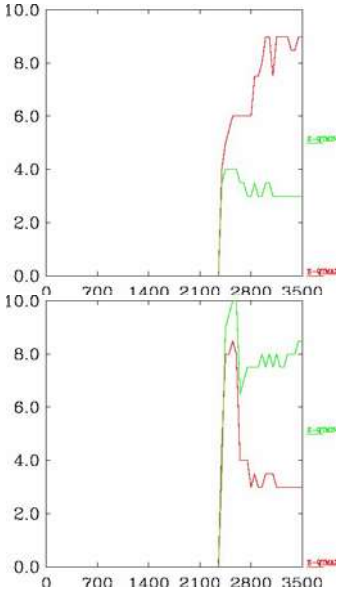

Fig.2. Temporal evolution of the height in km of the maximum positive (in red) and negative (in green) total charge density obtained with BSMPa (top panel) and BSMPn (bottom panel)

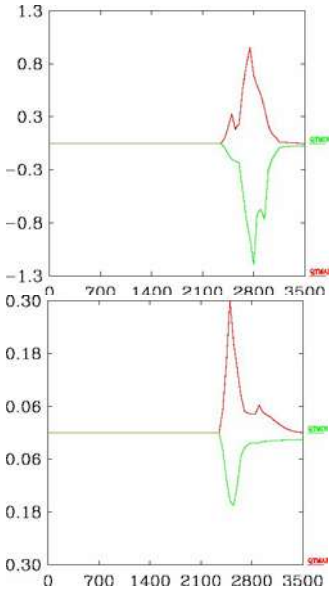

Fig.3. Temporal evolution of the maximum positive (in red) and negative (in green) total charge density in nC/m^3 obtained with SAUNa (top panel) and SAUNn (bottom panel)

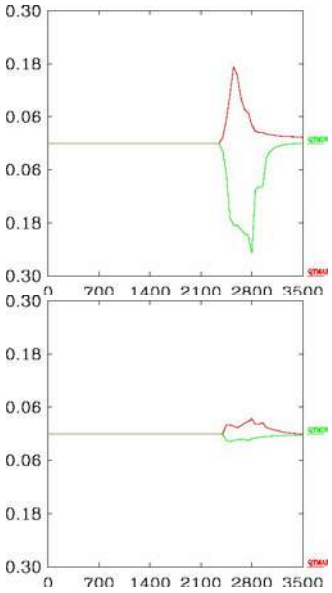

Fig.4. Temporal evolution of the maximum positive (in red) and negative (in green) total charge density in nC/m^3 obtained with BSMPa (top panel) and BSMPn (bottom panel)

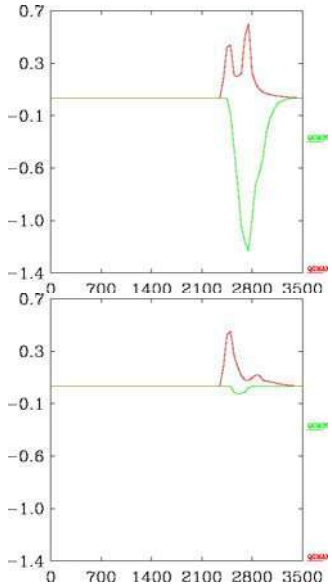

Fig.5. Temporal evolution of the maximum positive (in red) and negative (in green) carried by graupel charge density obtained in nC/m^3 with SAUNa (top panel) and SAUNn (bottom panel)

Figure 5 shows that when SAUNn is used the graupel negative charging is much smaller when compared to the SAUNa case. It is the opposite for the positive charge density of snow particles which becomes considerably large when SAUNa is used instead of SAUNn (Fig. 7). When Brooks et al. (1997) equations are used, the inclusion of the ‘anomalous zones’ reverses graupel charging, i.e. graupel particles carry a negative charge in the BSMPa case and positive charge in BSMPn case (Fig. 6). By symmetry, snow particles carry a positive charge when BSMPa is used but a negative one when BSMPn is used. The pristine ice crystals are charged positively when SAUNa is used, while in the SAUNn case, these particles are charged negatively during the

whole simulation (Fig. 9). The same is true when the BSMPn, versus BSMPa, parameterization is used (Fig.10).

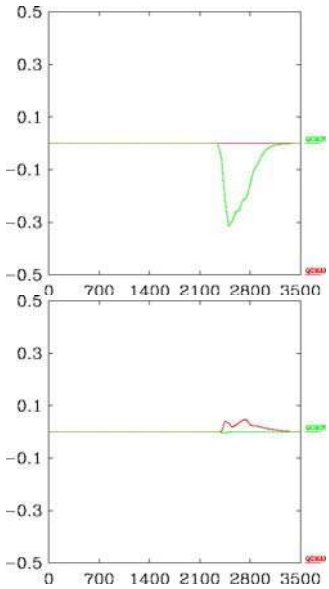

Fig.6. Temporal evolution of the maximum positive (in red) and negative (in green) carried by graupel charge density in nC/m^3 obtained with BSMPa (top panel) and BSMPn (bottom panel)

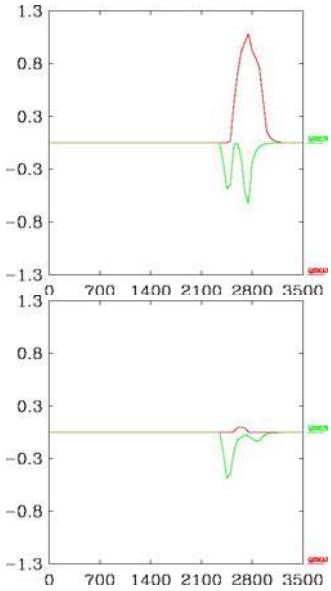

Fig.7. Temporal evolution of the maximum positive (in red) and negative (in green) carried by snow particles charge density in nC/m^3 obtained with SAUNa (top panel) and SAUNn (bottom panel)

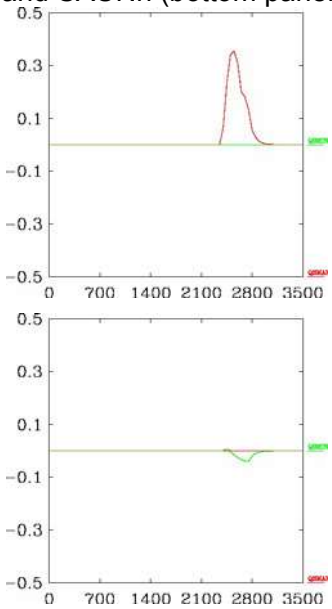

Fig.8. Temporal evolution of the maximum positive (in red) and negative (in green) carried by snow particles charge density in nC/m^3 obtained with BSMPa (top panel) and BSMPn (bottom panel)

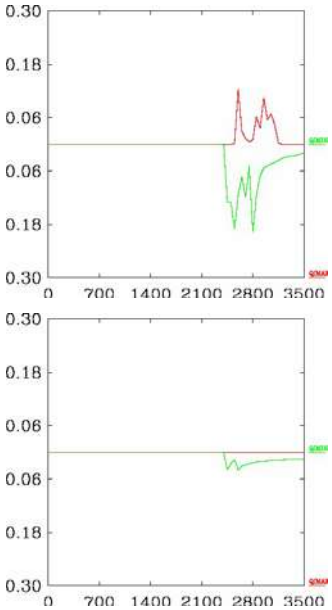

Fig.9. Temporal evolution of the maximum positive (in red) and negative (in green) carried by ice particles charge density in nC/m^3 obtained with SAUNa (top panel) and SAUNn (bottom panel)

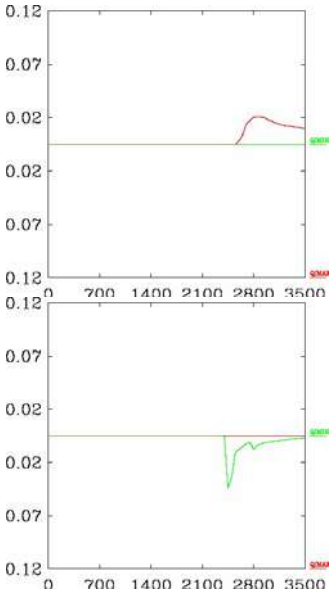

Fig.10. Temporal evolution of the maximum positive (in red) and negative (in green) carried by ice particles charge density in nC/m^3 obtained with BSMPa (top panel) and BSMPn (bottom panel)

3. CONCLUSIONS

The present study reports numerical simulations of an electrified deep convective case performed with MésoNH model. The simulations differ by considering or not, the 'anomalous zones' of the SKM charging diagram. Two types of parameterizations are used; they are based on the effective water content *EW* (Saunders et al., 1991) and on the rime accretion rate *RAR* (Brooks et al., 1997). Preliminary results show that the inclusion in the parameterization of the magnitude and sign of charge transfer rate at temperatures and EW (or RAR) corresponding to the 'anomalous zones':

- tends to favour the formation of a positive dipole or 'normal cloud charging' in agreement with the field data analyses when SAUNa or BSMPa are used, while the dipole structure is inverted when SAUNn or BSMPn are used,

- leads to an increase of the total charge density in the SAUNa and BSMPa cases in comparison to SAUNn and BSMPn respectively.

Based on this one can conclude that the charge separation rate in the so-called "anomalous zone", established by SKM has to be considered in the parameterization of the non-inductive charging rate in numerical models of electrified thunderstorms.

4. REFERENCES

Brooks, M., C. Saunders, R. Mitzeva, R. Peck, 1997, The effect on thunderstorm charging of the rate of rime accretion by graupel, J. Atmos. Res., 43, 277-295

Dye, J.E., Jones, J.J, Winn, W.P., Cerny, T.A., Gardiner, B., Lamb, D., Pitter, R.L., Hallett, J., Saunders, C.P.R.,1986. Early electrification and precipitation development in a small isolated Montana thunderstorm. J. Geophys.Res. 91, 1231–1247.

Helsdon, J. Jr, W. Wojcik, R. Farley, 2001, An examination of thunderstorm-charging mechanisms using a two-dimensional storm electrification model, J. Geophys. Res., 106, 1165-1192

Mansell, E., D. MacGorman, C. Ziegler, J. Straka, 2005, Charge structure and lightning sensitivity in a simulated multicell thunderstorm, J. Geophys. Res.,

Saunders, C., W. Keith, R. Mitzeva, 1991, The effect of liquid water content on thunderstorm charging, J. Geophys. Res., 96, 11007-11017

Tsenova, B., C. Barthe, R. Mitzeva, J.-P. Pinty, 2011, Numerical Simulations of a Thunderstorm with MésoNH using Different Non-Inductive Electrification Schemes, Proceedings of XIV International Conference on Atmospheric Electricity, August 08-12, Rio de Janeiro, Brazil

PHENOMENON of "WARM THUNDERSTORM"

L.V. Kashleva[2] , V.Yu. Mikhalovsky[1], Yu.P.Mikhalovsky[2]

1 Russian State University, S. Petersburg, Russia

2. Russian Hydrometeorological University, S. Petersburg, Russia

ABSTRACT.

Analysis of the works that corroborate the existence of the warm storms (WS) shows that there are no enough reliable instrument observations of the WS. Moreover, even instrumental measurements carried by the great researchers in this sphere (D.R.Fitzgerald, H.R.Byers, B.Vonnegut, C.B.Moore, I.M.Imyanitov, I.M.Shwarts) that showed high values of the electric fields in warm clouds give rise to doubts, because the question of accuracy of aircraft measurements of electric field, particularly inside clouds, has not been solved till now. On the other hand we have carried a great number of aircraft experiments on the beginning of the convective cloud electrification. The experiments were carried in various climatic zones (from the north-west of Russia till subtropical zone of the Caucas and in Cuba), in different seasons and over different surfaces (plain, sea, mountains) [Mikhailovsky,1992]. We have established that till the cloud top have not exceeded the isotherm minus 8^0 C (Russia) and minus 6^0 C (Cuba) any indication of charged particles in the cloud could not be recorded (field strength over cloud could not be distinguished from the back-ground values on the same altitude). Furthermore electrification wasn't recorded till large particles inside supercooled part of the cloud could be recorded by the radar. Thus, the results our experiments and analysis of the articles about the "warm storms" bring us to conclusion that the thunderstorm processes in the clouds without ice particles - is a myth.

1.INTRODUCTION

The phenomenon of warm thunder-storms is one of paradoxes of modern physics of clouds. Today most of all contributors consider that the main role in electrifying clouds is played by an ice phase of a cloud. Alongside with it the possibility of existence of thunder-storms in clouds where are no conditions for existence of ice phase, is not denied by anybody, at least in publications, and till now is meat on pages of textbooks and monographs. When the authors in 70's started in researches of electrifying the convective clouds, they following their teachers were sure that WS was though very rare, but the substantial phenomenon. Having worked in this area almost 30 years and having flown for this time more than 3000 hours on various airplanes – labs the authors consider that this phenomenon is

similar to riddles of “Bermuda triangle”, i.e. pseudo-scientific myth.

One of the earliest testimonies of existence of a WS is the message by Foster, 1950. He wrote, that from aside of an airplane he observed rather frequent (interval of 9 -11 sec) discharges in completely exotic clouds of diameter 100 - 150 meters and vertical extent about 1600 m. When the zero isotherm at a level 4500 m, the isotherm of 6^0C was on the altitude of 2400 m, i.e. mean gradient about 3 degrees on kilometer was observed. One more example of the testimony of the eyewitness is the article by Pietrowski, 1960. He, on the contrary, in thick (diameter 3км) cumulous clouds without rain (top was on the level of 3300 m, top temperature was 2^0C and vertical extent was 2500 m) also out of an airplane observed discharges with an interval 3 - 4 sec. Michnowski, 1963 visually observed two lightning with an interval 3 minutes in a warm, on his sight, orographic cloud in mountains of Northern Vietnam. The vertical extent of the cloud was by his own estimation less than 1 km.

These and other visually-subjective testimonies of existence of a WS cause many questions about 1) accuracy of definition of top boundary of a cloud and its temperature, 2) belonging of discharges to these small warm clouds, specially accounting the circumstance, that the observations were carried in twilights or even at the night. It’s very important to understand in what stage the clouds discharges were observed – on the stage of growing or, on the contrary, on the stage of destroying of normal thunderstorm clouds. Gunn, 1956 on the basis of such separate testimonies of the random spectators has declared existence of WS. And despite of objections of some scientists [Appelman, 1957], this hypothesis began to be represented as established fact. The very large contribution in strengthening of positions of this hypothesis has been introduced by Moor C.B., Vonnegut B., 1960. But also after reading the papers by these undoubtedly great contributors of cloud physics, the same questions arise – how they determined the level of the top boundary of a cloud that was located on the distance of 50 km from them? As follows from our experience, in any version (by the radar or visually) the error of 1 - 2 km is rather probable.

Generalizing the above, we should state, that there is not any experiment on research of warm thunder-storms that was in detail described and used instrument methods of control. Moreover, since the seventies with increase of technical accuracy of experiments and requirements to reliability in general the papers on observations of a WS have not appeared. Despite of existing technical facilities of control of clouds and discharges the carrying out of observations of a WS was not serious problem. These investigations would either prove the possibility of WS without the ice phase or would state that

WS is the consequence of experimental errors or differences in terminology. For example, large dissipating thundercloud on the decay stage could be taken as "warm cloud". Or "warm cloud" could be seeded with the ice particles out of anvil of a neighboring thunderstorm.

As it will be in detail shown below, during detailed and careful researches of warm convective clouds we did not manage to detect even their slight electrifying. There was an inconsistency with previous results by I.M.Imyanitov, 1972, etc. The joint efforts made it possible to install that the high values of electrical fields in warm cumulus are a consequent of errors of measurements E inside clouds. And it happened in the case when Imyanitov, was one of the best experts of that time in the world in measuring the parameters of atmospheric electricity. The measurements were carried out with the help of a system of aircraft flux meters, the deformation factors for sensors were determined in the flat electrostatic condenser and other methods. But even in these conditions the level of errors has remained to be very high. The technical and methodical support of aircraft measuring of E carried by the other contributors (D.R.Fitzgerald, H.R.Byers, 1958, B.Vonnegut, C.B.Moore, 1961) at that time was even less reliable. It is enough to indicate that Moore and B.Vonnegut have utilized a collector method of measuring E. And its limitations in comparison with measurements by flux meters are well-known. Allowing these circumstances it is necessary, apparently to recognize that high (about 1000 V/m) values of E in warm cumulus, measured above mentioned contributors, are, most likely, consequent of errors of measurements [Mikhailovsky, 1992].

Thus it turns out that we have no the authentic testimonies even of gentle electrifying of warm convective clouds, the more so of discharges. And on the contrary, as it will be shown below, we have the authentic testimonies of that absence.

2.EXPERIMENTAL EQUIPMENT AND OBSERVATIONAL TECHNIQUE

Studies in Russia were carried on board of aircraft meteorologic laboratories (AML) IL-14, IL-18, AN-12, AN-26 and YaK-40. However, principal results were obtained in flights of the "Cyclone" AN-12 (see Fig.1).

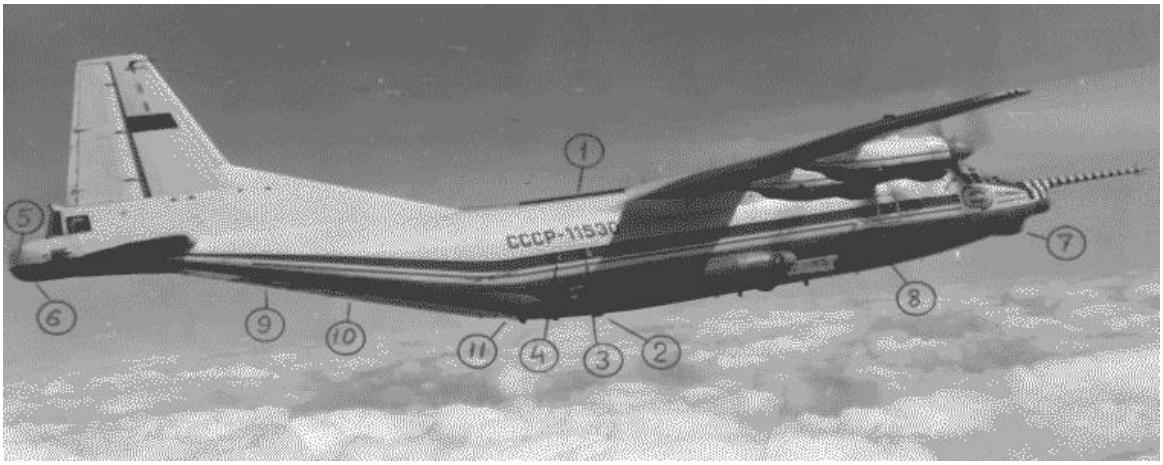

Figure 1. Equipment's layout on the aircraft-lab AN-12 "Cyclone" #11530. 1,2,3,5 – top, down, lateral and rear sensors of airplane electrical field meters, correspondently, 4 - tip of active airplane charge compensator, 6- on-board meteorological locator 7 – on-board meteorological radar "Groza"(BMR), 8 - aircraft meteorograph, 9,10 – devices for explosive charges fifing, 11 – roller conveyer for free-flowing reagents.

AML outfitted with: 4 field mill sensors to measure the vector of electric field tension (E) and the plane self-charge (Q); an on-board meteorologic radar (BMR) sighting to nadir and yielding vertical radar cross-sections of cloud from above; instrumentation to measure temperature and humidity, and other instruments. Calibration of the field mills sensors was carried out in the laboratory standard condenser. Amplifier sensitivities were routinely controlled during the experiments using particular plates inside the sensors. Form factors were derived from the aircraft model, confirmed thereafter (by flights in the electrical fields of the earth or cloud or another aircraft, as well as from aircraft charge variations etc.). To reduce Q to zero special discharges were used. The sensitivity was controlled with special devices in the course of the experiments [Mikhailovsky,1992].

The aircraft radar calibration was also confirmed by results from experiments and by ground locators MRL-2 and MRL-5 meteorological polygon in Turgoshi.

A positive direction of the vertical E component was chosen to be the one coinciding with the "fair weather E", that is from plus to minus downward.

Flying outside clouds and applying specially designed special techniques field mills were capable of measuring E within 10 to 250000 V/m. Signals from top and down field meters were summarized by the analogue device using appropriate coefficients. Values Ez, Q, Eside, and Etail were tape recorded. The changing of E over a small isolate convective cloud was simple and smoothed and similar to those

over a monopole charge or a dipole. Visual observations of clouds and their photographic imaging were also taken from board the AML. Visually the state of the top VST was defined to correspond to: 1 - no crystallization, the top was completely water droplet - bright and brilliant, "gloria" was observed; 2 - start of crystallization, separate "jets" were observed; 3 - crystallization intensely developed, numerous jets were observed, the top was "torn" and "tousled"; 4 - completely crystallized top - dull, flat, "false sun" was observed. Observation technique foresaw tracking of cloud during the whole of its life-span. Observations commenced at the Cu cong or Cu med stage, when the temperature at top of clouds was Tt > 0^o C, Z < 0 dbZ, E=0 and ended when the cloud disintegrated. Single cell separate clouds were mainly chosen for such observations. We conducted measurements during successive step by step flies over the center top, 10 to 50 m above it, depending on the cloud development stage and its top height.

Thus the process of ECC is characterized by the E vector above cloud, formation of large ice particles (precipitation) - by cloud radar reflectivity Z. Having Tt and VST one may estimate the process of crystallization in the cloud, and by the increase of its top height, Ht judge on the cloud dynamics. A technique was specifically designed to measure charge structure inside the cloud by measuring vector E, but the first attempt of its application indicated that it should be further upgraded, and that the accuracy of measurements of the E vector should be additionally analyzed. The vertical component Ez appeared to be sufficient to provide the answers to questions stated above, that's why for this task we used Ez to characterization the electric field of the cloud.

Investigations of electrification of the convective clouds (ECC) at Cuba were carried out in July - August 1991 by means of aircraft AN-26 and radar MRL-5 at meteopolygon Camaguey (Cuba) [Mikhailovsky,1996,2000]. The aircraft was equipped with 2 field mills and microwave radiometer. It measured the vertical component of electric field E, beside the cloud on the level of zero isotherm, and liquid-water-content of the cloud W in the layer 0÷-15^0C. Two field mills were installed at the top and at the bottom of fuselage near the centriplain. They measured the vertical component Ez of the electric field and the charge of the aircraft Q. Form factors were defined using the shape similarity of aircrafts AN-26, AN-24, IL-14 and the special technique[Mikhailovsky,2000].

Liquid-water- content W in a tilted section of a cloud was determined by microwave radiometer with wavelenght 8 mm. It was maintained in a window on the left side of aircraft at an angle of 30 degrees. The technique of investigation of clouds with radiometer was described earlier

(Koldaev, 1990). Radar MRL-5 with wavelenght 5 cm equipped with automatic system of processing information was placed in the center of meteopolygon (airport Camaguey). We could receive spase-and-time variations of reflectivity Z and select separate convective cells.

The technique was in step-by-step passes beside a cloud on the altitude of zero isotherm and in control of E,W. The studies began on the earlier stages of cloud's development ($T_t > 0^o$ C, E = 0 V/m, Z < 0 dbZ). The level of top Ht was determined visually on the earlier stages and by radar when Z > 0 dbZ.

3.RESULTS AND DISCUSSION

The experiments were conducted at various latitudes (from Batumi up to the Leningrad area, Cuba), in a various season (since March till November), above various underlying surface (plains, sea, mountains). For the analysis the results more than 50 experiments above territory of the USSR (2 – over the Black Sea) and 14 above territory of Cuba were utilized (4 – over Caribbean Sea).

As it was indicated above our study technique in Russia envisaged observing the cloud through the whole of its life span. It was taken flies-over 10-50 m above the cloud top during the initial stages of its development. Under these conditions we took that the initial moment of ECC coincided in time with that fly-over, during which significant values of E were observed over the cloud, (E over the cloud exceeded the value of fair weather E on the same altitude by the factor of 3-5). A precondition to this was that no such values of E were recorded during the previous fly-over. Since we tried to start our observations during the stage when E= 0, such a regime was indeed available for most of the clouds. In experiments we established, that while the top of a cloud has not exceeded the isotherm –8 ^{0}C there were not observed the values of electrical field 10÷100 meters above the clouds that could be distinguished from background values at the same altitude and at the same accuracy of measurements. Moreover, the fields were not marked till in the supercooled part of a cloud there were no large particles that could be found out by an meteorologic radar (Z > 0 dbZ). Cloud parameters fixed in that fly-over were assumed to yield those of the start of ECC.

We received that:

- ECC is not observed till Tt remains above -8^{0}C and is always observed if Tt drops below -22^0 C (see fig.2);
- it is never observed if precipitation reflectivity below the cloud is lower than 0 dbZ (Zr < 0 dbZ) while it is always observed if Zr > 40 dbZ.

Similar relations are found to relate ECC to the thickness of its supercooled part (dH) (see fig.3). As it follows from those relations the organized ECC starts only when the cloud reaches the stage of its development, at which large ice

particles may appear inside the cloud (T_t < -8^0 C, Z > 0 dbZ, dH > 1.4 km) (see fig.2,3).

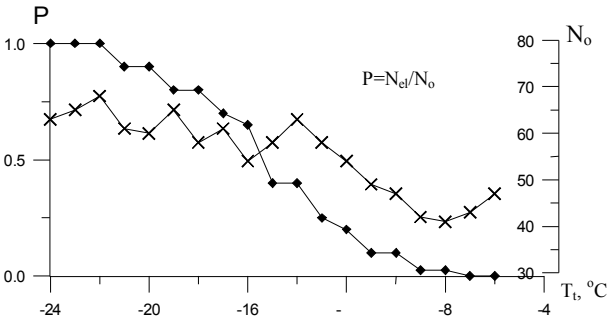

Image 2. Experimental curve shows organized ECC probability (P) dependence of temperature of top boundary of cloud(T_t). Crosses(x) show overall number of flights (N_o) over the cloud with current T_t.

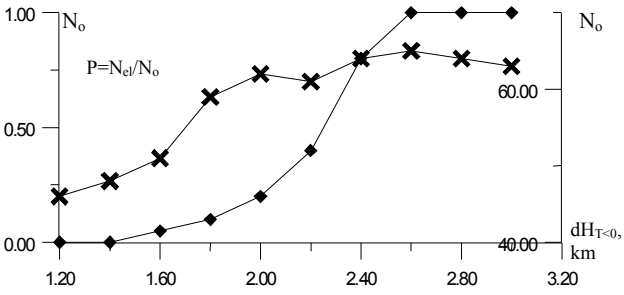

Image 3. Experimental curve shows organized ECC probability (P) dependence of temperature of thickness of superecooled part of cloud($dH_{T<0}$). Crosses(x) shows overall number of flights(N_o) over the cloud with current $dH_{T<0}$.

Investigations of the early stage of ECC in the tropics (Cuba) showed that the necessary conditions for onset of these clouds electrification were also the conditions for appearance of ice particles. We can see that the electrification of convective tropical clouds didn't occur until Tt > - 6^0 C, Z < 0 dbZ, dH < 1.0 km (see fig.4).

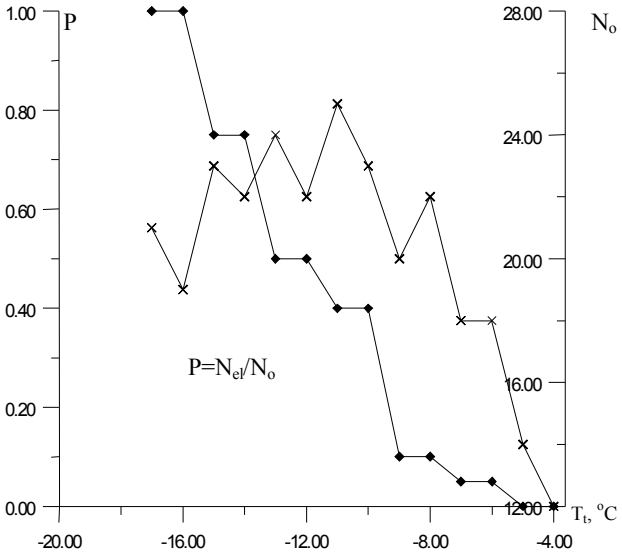

Image 4. Experimental curve shows organized ECC probability (P) dependence of temperature of top boundary of cloud (T_t) in Cuba area. Crosses(x) show overall number of flights (N_o) over the cloud with current T_t.

These conditions are similar to those obtained above for convective clouds in the former USSR and didn't verify the hypothesis of "warm thunderstorm". It should be marked that the electrification starts earlier in convective clouds over the sea then over the land. For example, according to the previous data the conditions for ECC in continental clouds for the territory of the former USSR are the following: Tt < -12 ^{0}C, Z > 0 dbZ, dH > 1.8

km, and for Cuba: Tt <-8^{0}C, Z > 0 dbZ, dH > 1.4km [Mikhailovsky,2000].

CONCLUSION.

Thus, results of own experiments (first of all!), the analysis of studies by the supporters of existence of warm thunderstorms, own experience and intuition cause us to think that thunderstorm processes or even simply the organized elecrification in clouds where is no ice phase is nothing but myth.

REFERENCES

Appelman H. Comments on “Initial electrification process in thunderstorms” J. Met., 1957,v. 14, no. 1,p. 89.

Chalmers J.A. Atmospheric electricity . Leningrad, Gidrometeoizdat, Russia, 420 pp.,1974.

Faster H. An unusual observation of lightning, Bull.Amer. Met.Soc., 1950, v.31, No. 4, p.140-141.

Gunn R., Initial electrification process in thunderstorms, J. Met., 1956,v. 13, No. 1,p. 21-29.

.Imyanitov I.M.,Chubarina E.V.,Shwarts J.M. Electricity of clouds. -L. Gidrometeoisdat, 1972.-94 c.

Koldaev A , Melnichuk Yu., Mironov A., Agapov Yu., Dmitriev V., Nicolski A. (1990), The Application of Aircraft Microwave Radiometric Tomografy in Weather Modification Expiriments. Proc, of 20th European microwave coference, Budapest, Hungary, 1402 -1407

Mikhailovsky, Yu.P., L.V.Kashleva and V.D.Stepanenko (1992). Aircraft investigation of the convective clouds electrification. Proc. of the 9th Conf. of the Atm. Electricity, St.Petersburg, Russia, 193-197.

Yu.Mikhailovsky,Yu.Agapov,B.Koloskov Electrification of the tropical clouds. Proc. of the 9th Conf. of the Atm. Electricity, St.Petersburg, Russia, 1992,193-197.

Mikhailovsky Yu. P. " About the phenomena of the warm thunderstorms". Proc.Int. lightning detection conf/ Tucson, Arizona, USA, 2000

Mikhailovsky Yu. P. " Errors during aircraft measurements of the electric field and ways to reduce them". Proc.Int. lightning detection conf/ Tucson, Arizona, USA, 2000

Michnowski S. On the observation on lightning in warm clouds, Indian J. Met. Geophys., 1963, v. 14, No. 3, p. 320-322.

Moor C.B., Vonnegut B., Stein B.A.,Survilas H.J. Observations of electrification and lightning on warm cloud, J. Geoph. Res.,1960,v. 65,No. 7,p.1907-1910.

Pietrowski E. L. An observation of lightning in warm clouds, J. Met., 1960,v.17,No. 5,p.562-563

Vonnegut B., Moore C.B., Apparatus using radioactive probes for measuring the vertical component of atmospheric potential gradient from am airplane, Bull. Amer. Met. Soc.,1961, v. 42, No. 11, p. 773-792.

SATELLITE IDENTIFICATION OF INDIRECT AEROSOL EFFECTS OVER SEMI-ARID AND ARID LAND REGIONS

Lars Klüser[1] and Thomas Holzer-Popp[1]

[1]German Aerospace Center (DLR), German Remote Sensing Data Center (DFD)

1. INTRODUCTION

Multiannual aerosol and cloud observations from different satellite instruments are used to assess the impact of aerosols on convective cloud regimes over several semi-arid and arid land regions in Africa and Arabia. Satellite observations are from the MODIS on the Aqua satellite (including the "Deep Blue" aerosol retrieval), from SCIAMACHY and AATSR on ENVISAT (Kriebel et al., 2003; Holzer-Popp et al., 2008) and from IASI on Metop (Klüser et al., 2011, 2012), all gridded into 1°x1°. The analysis regions cover the West-African Sahel, the Maghreb, the Karoo-Kalahari region of Southern Africa, the Arabian Peninsula (Fig. 1) and observations include the years 2004-2009 (MODIS: all, ENVISAT: 2004-2008, IASI: 2009).

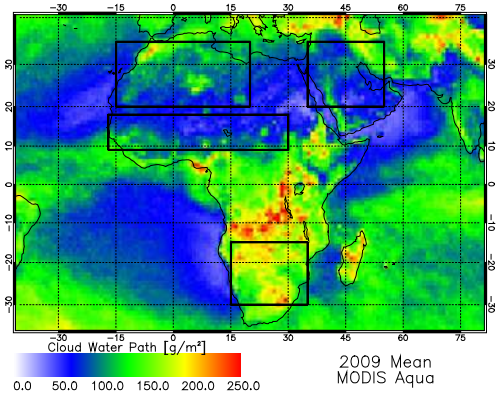

Figure 1: Analysis regions and annual mean cloud water path for 2009 from MODIS.

2. METHODOLOGY

From these observations histograms of cloud microphysical properties are derived for different aerosol classes (background, moderate and heavy aerosol for total aerosol, mineral dust and fine mode aerosol). The IASI retrieval is sensitive to mineral dust only and also only ice cloud properties are derived, thus this sensor provides information about dust influence on ice clouds only.

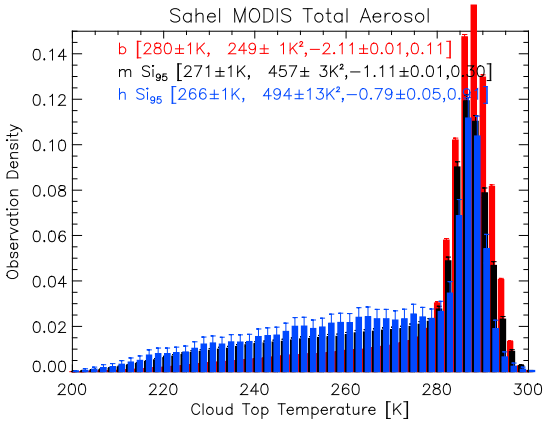

Figure 2: Cloud top temperature histograms from MODIS for Sahel total aerosol.

Using cloud water path respective cloud top temperature (Fig. 2) of the background observations the cloud property histograms are projected to the respective background cloud state by calculating two-dimensional histograms as estimates of the probability density functions. This method allows for analysing histogram deviations from the background observable histogram without any additional seasonal subsetting, which would reduce the sample sizes for individual analysis.

3. RESULTS

For most regions and most aerosol types the so-called "Twomey-Effect" (Twomey, 1974) is clearly visible in the

observations: droplet sizes are reduces under aerosol influence resulting in higher optical depth (Fig. 3).

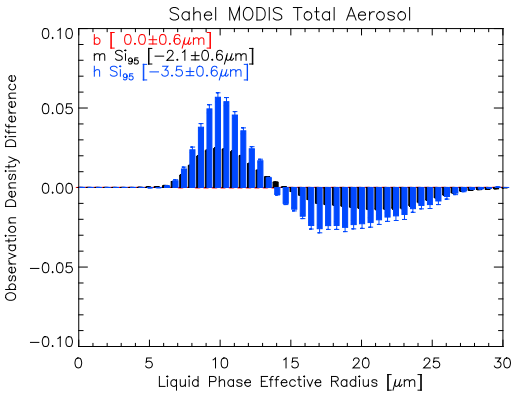

Figure 3: Deviation of liquid phase cloud effective radius from projected background conditions (for MODIS, Sahel total aerosol).

This effect is observed for both, liquid water and ice fraction of the clouds. Also reduced cloud top temperatures and increasing cloud cover with decreasing droplet radius is observed in the majority of cases (the so-called “Albrecht-Effect”). Moreover the ice fraction is increased under aerosol influences significantly in almost all regions and for all aerosol types (Fig. 4). The magnitudes of effects differ partly with aerosol type, although MODIS aerosol type identification has been shown to have very large uncertainties over land (Levy et al., 2010).

The relative decrease of droplet sizes is more effective in the liquid water fraction, reaching mean effective radius differences of down to -6.9±0.2 µm. For those cases mean cloud optical depth is increased by up to 7.2±0.2.

On the other hand in the Karoo-Kalahari region also increased droplet sizes under aerosol influence are observed.

From the histogram analysis it is evident that the fraction of mid-level cloud is strongly increased in aerosol episodes (potentially plume top convection) while the large fraction of boundary layer clouds with very small droplets dominates the background sample.

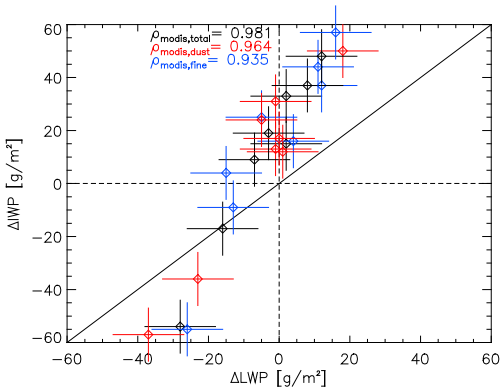

Figure 4: Regional mean deviations of ice water path versus liquid water path from background conditions for different aerosol subsets (MODIS observations).

Detailed analysis of these results provides a mostly stable effective radius - optical depth deviation relationship, thus the majority of deviation magnitudes from different regions shows a very consistent picture. The same is true for the mean deviations from background observations of optical depth and cloud top temperature. For cloud cover and ice fraction (fraction of ice cloud cover to liquid phase cloud cover) the picture is not as clear, the observed aerosol effects of these variables show a strong scattering.

4. CONCLUSIONS

From the analysis of three different satellite datasets (MODIS, ENVISAT, IASI) in four semi-arid and arid land regions (Maghreb, Arabia, Sahel and Karoo-Kalahari), divided into three aerosol subsets (total, biomass burning, mineral dust) and three cloud subsets (liquid water, ice, total) the Twomey effect has been identified for both, liquid water and ice clouds. But it has also been shown that the cloud optical depth deviation from background conditions is widely

controlled by cloud water path rather than only by a change in cloud droplet size. The aerosol effect on cloud cover could not as clearly be attributed to a specific mechanism. Changes in cloud phase (i.e. the ice phase fraction) are strongly pronounced in cloud water path but not as clearly in cloud cover. In the current satellite datasets also some limitations have been identified, which have to be addressed in the future: the aerosol type retrieval from MODIS has very large uncertainty, from AATSR effective radius and cloud water path have to be derived and from IASI the (ice) cloud optical depth and ice water path retrieval has to be revised.

5. BIBLIOGRAPHY

Holzer-Popp, T., Schroedter-Homscheidt, M., Breitkreuz, H., Martynenko, D., and Klüser, L.: Improvements of synergetic aerosol retrieval for ENVISAT, Atmos. Chem. Phys., 8, 76551-7672, 2008.

Klüser, L., Martynenko, D., and Holzer-Popp, T.: Thermal infrared remote sensing of mineral dust over land and ocean: A spectral SVD based retrieval approach for IASI, Atmos. Meas. Tech., 4, 757-773, 2011.

Klüser, L., Kleiber, P.D., Holzer-Popp, T., and Grassian, V.H.: Desert dust observations from space – Application of measured mineral component infrared extinction spectra, Atmos. Env., 54, 419-427, 2012.

Kriebel, K.T., Gesell, G., Kästner, M., and Mannstein, H.: The cloud analysis tool APOLLO: improvements and validations, Int. J. Remote Sensing, 24, 2389-2408, 2003.

Levy, R.C., Remer, L.A., Kleidman, R.G., Mattoo, S., Ichoku, C., Kahn, R., and Eck, T.F.: Global evaluation of the Collection 5 MODIS dark target aerosol products over land, Atmos. Chem. Phys., 10, 10399-10420, 2010.

VERTICAL DISTRIBUTIONS OF SUPERCOOLED LIQUID WATER ON WINTER STRATIFORM CLOUDS IN NORTHERN JAPAN

Tadayasu Ohigashi, Kazuhisa Tsuboki, Mariko Oue, and Ryuhi Furihata

Hydrospheric Atmospheric Research Center, Nagoya University, Nagoya, Japan

1. INTRODUCTION

Supercooled liquid water (SLW) is widely seen from −40°C to 0°C (e.g. Rosenfeld and Woodley 2000). SLW has important roles on precipitation formation and radiative transfer in cloudy atmospheres. Tsushima et al. (2006) conducted a intercomparison of cloud water in AGCMs run for control and doubled carbon dioxide climates and showed that there is large variability among models in the difference of cloud water between two experiments at mid and high latitudes. Therefore, information about SLW profiles contributes to improvements in the representations of clouds in numerical models, especially in climate models. In addition, detection and forecast of SLW are important for aviation safety because SLW is concerned with aviation accidents.

Some recent studies used remote-sensing instruments on the space shuttle and satellites to estimate quantitative characteristics of SLW and information of cloud-top phase (Hogan et al., 2004; Hu et al., 2010; Morrison et al., 2011). There are a lot of observations of SLW in the Arctic clouds (e.g. Hobbs and Rangno 1998; Pinto 1998). In contrast, fewer observations of SLW have been reported in mid-latitudes. In the present study vertical distributions of SLW in precipitating stratiform clouds were observed using hydrometeor videosondes (HYVIS) at Hokkaido, which is located in northern Japan in mid-latitudes, in February 2011.

2. OBSERVATION

We performed a special observation for winter clouds from 8 to 28 February 2011 in the inland part of Hokkaido (Fig. 1a). The hydrometeor videosonde (HYVIS) observation was performed at Rikubetsu (143.76°E, 43.46°N; Fig. 1b). In addition, two Nagoya-Univsersity X-band (9 GHz) polarimetric radars were placed at Rikubetsu and Kunneppu to observe precipitating particles.

HYVIS was developed at the Meteorological Research Institute of Japan (Murakami and Matsuo, 1990; Orikasa and Murakami, 1997) and is made by Meisei Electric Co.,

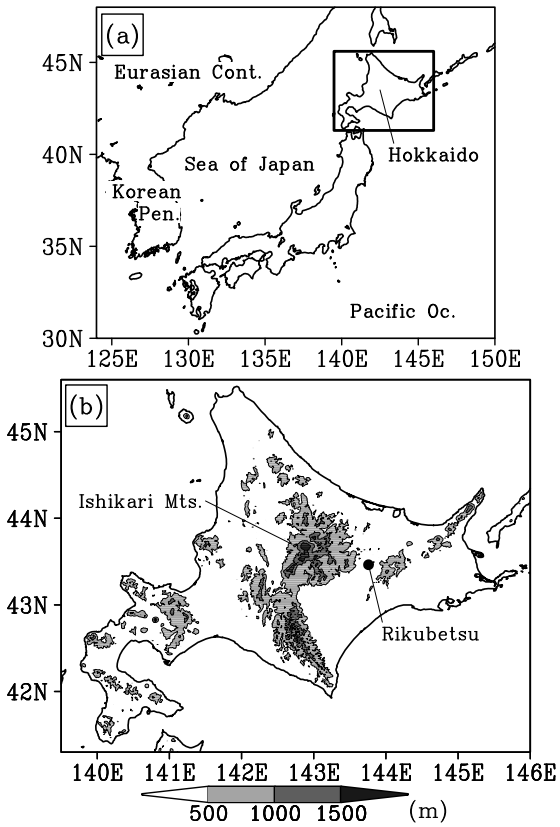

Fig. 1 (a) Map around Japan. (b) Map and altitude of topography (gray scale, m) around Hokkaido, Japan in a region shown by a square in Fig. 1a. A filled circle indicates the Rikubetsu site where hydrometeor videosondes were released.

Corresponding author address: Tadayasu Ohigashi, Hydrospheric Atmospheric Research Center, Nagoya University, Furo-cho, Chikusa-ku, Nagoya 464–8601, Japan
E-mail: ohigashi@rain.hyarc.nagoya–u.ac.jp

Ltd. in Japan. HYVIS collects particles on a transparent film coated with silicon oil and takes a movie using two video cameras: microscopic and closeup cameras. Widths of views of microscopic and closeup cameras are 1.4 mm and 7-9 mm, respectively. Particles more than about 10 μm can be recognized using a microscopic camera. A radiosonde is attached to HYVIS to measure temperature, humidity, and horizontal wind. A HYVIS with a radiosonde is released using balloons. Movie taken by HYVIS is transmitted to the surface using a radio wave with a frequency of 1680 MHz and is recorded on a recording medium. HYVISs have been utilized to observe warm frontal clouds (Murakami et al., 1992), snow clouds developing during cold-air outbreaks (Matsuo et al., 1994; Murakami et al., 1994; Kusunoki et al., 2004), and cirrus clouds (Mizuno et al., 1994; Uchiyama et al., 1999; Uchiyama and Fukabori, 1999; Sakai et al., 2006).

In this special observation, nine HYVISs were released and eight vertical profiles except for one failure were obtained. Three vertical profiles were obtained for frontal stratiform clouds and the remaining five ones were for non-frontal stratiform clouds. In all cases, snow precipitation was seen at surface.

3. VERTICAL DISTRIBUTION OF SUPERCOOLED LIQUID WATER

SLW was visually confirmed in movies taken using microscopic cameras. In all three HYVISs released in frontal clouds and three profiles of five soundings in non-frontal clouds, SLW layers were present. For the frontal clouds, surface temperature, cloud top height, height and temperature ranges in which SLW was present are summarized in Table 1. Surface temperatures were between -4.7°C and -2.8°C. Therefore, all liquid water observed by HYVISs was considered as SLW. Cloud top heights determined from images of HYVISs were above about 7000 m, which is considerable higher than those of snow clouds developing around the Sea of Japan during cold-air outbreaks in winter. SLW layers are present in the relatively lower levels between heights of 770 m and 1770 m as compared with the cloud

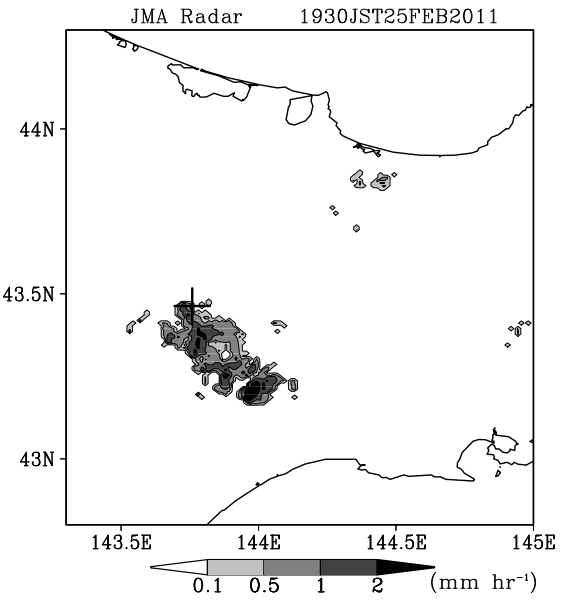

Fig. 2 Precipitation intensity (gray scale, mm hr^{-1}) derived from the Japan Meteorological Agency radar at 1930 JST, 25 February 2011. A mark of + indicates the observation site at Rikubetsu.

top heights. The temperature range that SLW was present is between -13.1°C and -7.2°C.

The non-frontal clouds, that HYVISs were released, were stratiform precipitating clouds with the maximum radar reflectivities were about 30 dBZ. Characteristics of SLW layers for the non-frontal clouds is summarized in Table 2. Surface temperatures are between -4.7°C and -3.2°C. Cloud top heights are present around heights of 3000 m, which is considerably lower than those in the frontal clouds. Three SLW layers are present in the case of 11 February and one SLW layer in the other two cases. As a common feature in the three profiles, SLW layers were present just below the cloud top. These are referred to as cloud-top SLW layers hereafter. The thicknesses of the cloud-top SLW layers are between 60m and 230m and the temperature range is between -25.5°C and -21°C.

As an example of the cloud-top SLW layers in the non-frontal clouds, a profiles released at 1933 JST (Japan Standard Time), 25 is examined. In 25 February, Hokkaido was located far south of a synoptic-scale extratropical cyclone. Over the Sea of Japan off the western coast of Hokkaido, northwest and west-northwest winds were predominant. Be-

Table 1 Characteristics of frontal clouds in February 2011 observed by hydrometeor videosondes and radiosondes at Rikubetsu. Ts and SLW indicates surface temperature and supercooled liquid water, respectively.

Release Time (JST)	Ts (℃)	Cloud Top (m)	Height Range of SLW (m)	Temperature Range of SLW (℃)
1152, 12	−4.7	7420	770-1290	−13.1-−9.6
2111, 12	−4.7	6970	805-890	−9.8-−8.9
1732, 17	−2.8	at least 7000	1675-1770	−7.5-−7.2

Table 2 Same as in Table 1, but for non-frontal clouds.

Release Time (JST)	Ts (℃)	Cloud Top (m)	Height Range of SLW (m)	Temperature Range of SLW (℃)
1945, 11	−4.7	2880	745-830	−7.5-−7.0
			1790-1815	−15.1-−15.1
			2660-2860	−23.3-−21.5
1933, 25	−3.2	2785	2580-2640	−21.8-−21.0
1802, 27	−3.2	3205	2975-3205	−25.5-−23.8

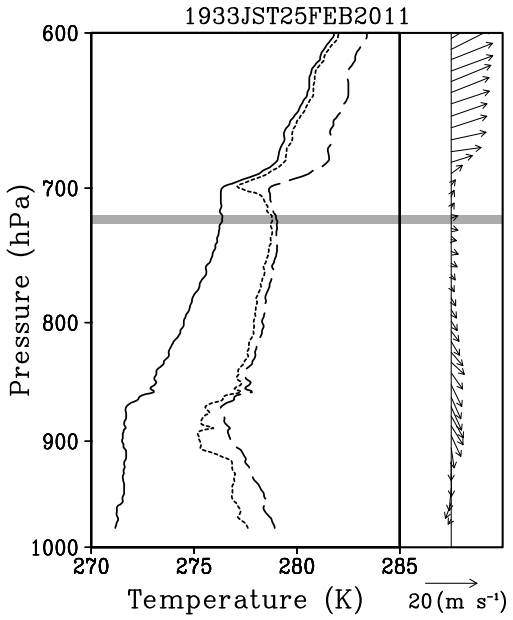

Fig. 3 Vertical profiles of potential temperature (solid line, K), equivalent potential temperature (dashed line, K), saturation equivalent potential temperature (broken line, K), and horizontal wind (vectors, m s^{-1}) at 1933 JST, 25 February 2011 at Rikubetsu. A shaded part indicates a layer of supercooled liquid water.

hind the Ishikari Mountains, that is located in central Hokkaido, as much as 2000 m high, northerly component is large in the lower levels.

In the low-level northwesterly or northerly winds, a lot of scattered precipitation regions with a horizontal scale of less than 100 km developed and moved toward the south or the southeast. Figure 2 shows the precipitation intensity at 1930 JST, 25. One of the scattered precipitation region with a horizontal scale of a few tens of kilometers crossed over the Rikubetsu observation site from the northwest to the southeast. Precipitation intensity is 1-2 mm hr^{-1}

A HYVIS was released at 1933 JST, 25 in the north edge of the scattered precipitation region. Figure 3 shows a vertical profile of stability and humidity. A shaded portion in Fig. 3 indicates a SLW layer. Largely stable layer with dry air is present above 700 hPa. This is located just above the SLW layer. Between 920 hPa and the lower limit of the stable layer (700 hPa), the stability is more neutral and relative humidity is larger as compared with the stable layer. The potential temperature is almost constant with height, which indicates absolutely neutral, in a thickness of 200 m from the SLW layer top to the lower limit of the stable layer. In the absolutely neutral layer, equivalent potential temperature decreases with height, which indicates convective instability is locally formed.

4. COMPARISON OF THE CLOUD-TOP SUPERCOOLED LIQUID WATER LAYERS WITH OTHER STUDIES

A lot of literatures report that SLW was present at the cloud top of stratiform clouds

in the Arctic (e.g. Hobbs and Rangno 1998; Pinto 1998). Recent literatures showed cloud-top SLW layers existed in the Antarctic (Lawson et al., 2011) and mid-latitudes (Carey et al., 2008). Carey et al. (2008) showed from vertical observations in altocumulus clouds using aircraft that SLW was present at cloud tops in two third of the vertical cloud observations. They also showed that the temperature range was between $-26°$C and $-13°$C, and the thicknesses of the layers were between 80 m and 1000 m, with an average thickness of about 350 m. The thicknesses and temperature ranges in the northern Japan obtained in the present study was within the ranges shown in Carey et al. (2008).

Morrison et al. (2012) showed using a lidar observation that a SLW layer was continuously present at the cloud top for more than 5 days in the Arctic. They explained that frequent appearances of SLW layers at the cloud top seen in intermittent observations are probably caused by continuous formation of SLW at the cloud top. They also reviewed the previous literatures and showed the basic structures and primary processes of the Arctic mixed-phase clouds with SLW at the cloud tops. One of the characteristic structures is small-scale weak turbulence at the cloud top. They explained the turbulence is driven by radiative cooling of SLW at the clout tops. A absolutely neutral layer seen at the cloud top in the present study probably indicates local overturning at the cloud top.

5. SUMMARY

In February 2011, winter stratiform clouds formed over inland Hokkaido, which is located in northern Japan, were observed using hydrometeor videosondes (HYVISs) and the Nagoya-University polarimetric radars. Eight HYVISs attached with radiosondes obtained vertical profiles of particle images and kinematical structures.

Three HYVISs were released in frontal clouds and the remaining five ones in non-frontal clouds. In all the three HYVISs in frontal clouds and three of five HYVISs in non-frontal clouds, supercooled liquid water (SLW) is visually confirmed. All the SLW layers in non-frontal systems were present at the cloud top. The thicknesses of the cloud-top SLW layers are between 60 m and 230 m, and the temperature ranges is $-25.5°$C and $-21°$C. There is a strong stable layer with dry air above the cloud top. Around the SLW layer, absolutely neutral layer was present. This implies local overturning in the cloud top. The characteristics of the SLW layers in non-frontal clouds corresponds to those in stratiform mixed-phase clouds seen in the polar and mid-latitude regions.

In inland Hokkaido, weak snowfall contributes to total snow accumulation in addition to those associated with frontal systems in winter. It is inferred that ice crystals formation in the high-concentration SLW at the cloud top and subsequent growth is one of the major snowfall formation processes in winter in this region. Appearance frequency of SLW layers and formation mechanisms around northern Japan remain to be studied.

ACKNOWLEDGMENTS

This study was supported by Grant-in-Aid for Scientific Research B (22340136) of the Ministry of Education, Culture, Sports, Science and Technology, Japan and the program "Virtual Laboratory for the Earth's Climate Diagnostics."

REFERENCES

Carey, L. D., J. Niu, P. Yang, J. A. Kankiewicz, V. E. Larson and T. H. Vonder Haar, 2008: The vertical profile of liquid and ice water content in midlatitude mixed-phase altocumulus clouds. *J. Appl. Meteor. Climatol.*, **47**, 2487–2495.

Hobbs, P. V. and A. L. Rangno, 1998: Microstructures of low and middle-level clouds over the Beaufort Sea. *Quart. J. Roy. Meteor. Soc.*, **124**, 2035–2071.

Hogan, R. J., M. D. Behera, E. J. O'Connor and A. J. Illingworth, 2004: Estimate of the global distribution of stratiform supercooled liquid water clouds using the LITE lidar. *Geophys. Res. Lett.*, **31**, L05106, doi:10.1029/2003GL018977.

Hu, Y., S. Rodier, K. Xu, W. Sun, J. Huang, B. Lin, P. Zhai and D. Josset, 2010: Oc-

currence, liquid water content, and fraction of supercooled water clouds from combined CALIOP/IIR/MODIS measurements. *J. Geophys. Res.*, **115**, D00H34, doi:10.1029/2009JD012384.

Kusunoki, K., M. Murakami, M. Hoshimoto, N. Orikasa, Y. Yamada, H. Mizuno, K. Hamazu and H. Watanabe, 2004: The characteristics and evolution of orographic snow clouds under weak cold advection. *Mon. Wea. Rev.*, **132**, 174–191.

Lawson, R. P., K. Stamnes, J. Stamnes, P. Zmarzly, J. Koskuliks, C. Roden, Q. Mo, M. Carrithers and G. L. Bland, 2011: Deployment of a tethered-balloon system for microphysics and radiative measurements in mixed-phase clouds at Ny-Ålesund and South Pole. *J. Atmos. Oceanic Tech.*, **28**, 656–670.

Matsuo, T., H. Mizuno, M. Murakami and Y. Yamada, 1994: Requisites of graupel formation in snow clouds over the Sea of Japan. *Atmos. Res.*, **32**, 55–74.

Mizuno, H., T. Matsuo, M. Murakami and Y. Yamada, 1994: Microstructure of cirrus clouds observed by HYVIS. *Atmos. Res.*, **32**, 115–124.

Morrison, A., S. T. Siems and M. J. Manton, 2011: A three-year climatology of cloud-top phase over the southern ocean and north Pacific. *J. Climate*, **24**, 2405–2418.

Morrison, H., G. de Boer, G. Feingold, J. Harrington, M. D. Shupe and K. Sulia, 2012: Resilience of persistent Arctic mixed-phase clouds. *Nat. Geosci.*, **5**, 11–17.

Murakami, M. and T. Matsuo, 1990: Development of the hydrometeor videosonde. *J. Atmos. Oceanic Tech.*, **7**, 613–620.

Murakami, M., Y. Yamada, T. Matsuo and H. Mizuno, 1992: Microphysical structure of warm-frontal clouds –The 20 June 1987 case study–. *J. Meteor. Soc. Japan*, **70**, 877–895.

Murakami, M., T. Matsuo, H. Mizuno and Y. Yamada, 1994: Mesoscale and microscale structure of snow clouds over the Sea of Japan. Part I: Evolution of microphysical structures in short-lived convective snow clouds. *J. Meteor. Soc. Japan*, **72**, 671–694.

Orikasa, N. and M. Murakami, 1997: A new version of hydrometeor videosonde for cirrus cloud observations. *J. Meteor. Soc. Japan*, **75**, 1033–1039.

Pinto, J. O., 1998: Autumnal mixed-phase cloudy boundary layers in the Arctic. *J. Atmos. Sci.*, **55**, 2016–2038.

Rosenfeld, D. and W. L. Woodley, 2000: Deep convective clouds with sustained supercooled liquid water down to $-37.5°$C. *Nature*, **405**, 440–442.

Sakai, T., N. Orikasa, T. Nagai, M. Murakami, K. Kusunoki, , K. Mori, A. Hashimoto, T. Matsumura and T. Shibata, 2006: Optical and microphysical properties of upper clouds measured with the Raman lidar and hydrometeor videosonde: A case study on 29 March 2004 over Tsukuba, Japan. *J. Atmos. Sci.*, **63**, 2156–2166.

Tsushima, Y., S. Emori, T. Ogura, M. Kimoto, M. J. Webb, K. D. Williams, M. A. Ringer, B. J. Soden, B. Li and N. Andronova, 2006: Importance of the mixed-phase cloud distribution in the control climate for assessing the response of clouds to carbon dioxide increase: a multi-model study. *Clim. Dyn.*, **27**, 113–126.

Uchiyama, A. and M. Fukabori, 1999: Ground-based cirrus observation: II. Spectral properties of cirrostratus clouds in the 8-12 μm. *J. Meteor. Soc. Japan*, **77**, 533–552.

Uchiyama, A., S. Asano, M. Shiobara and M. Fukabori, 1999: Ground-based cirrus observation: I. Observation system and results of frontal cirrostratus clouds on June 22 and 30, 1989. *J. Meteor. Soc. Japan*, **77**, 513–532.

SUPER-DROPLET APPROACH TO SIMULATE PRECIPITATING TRADE-WIND CUMULI – COMPARISON OF MODEL RESULTS WITH RICO AIRCRAFT OBSERVATIONS

Sylwester Arabas*[1] and Shin-ichiro Shima†[2]

[1]Institute of Geophysics, Faculty of Physics, University of Warsaw, Poland

[2]Graduate School of Simulation Studies, University of Hyogo, Kobe, Japan

1. INTRODUCTION

In this study we present a series of Large Eddy Simulations (LES) employing the Super-Droplet Method (SDM) for representing aerosol, cloud and warm-rain microphysics (Shima, 2008; Shima et al., 2009). SDM is a particle-based and probabilistic Monte-Carlo type model. The particle-based formulation helps to overcome the problem of parameterisation of processes occurring at single-particle scale (micro- to millimetres) as source/sink terms in the LES equations solved on grids with cell dimensions of the order of tens of metres. The aim of this paper is to showcase the capabilities and point out the limitations of SDM in context of simulation of a field of precipitating clouds.

2. THE SUPER-DROPLET METHOD

The framework of the method consists of two mutually coupled simulation components: (i) a fluid flow solver computing (in an Eulerian sense) the evolution of fluid velocity field and evolution of the thermodynamic scalar quantities, and (ii) a particle-tracking logic computing (in a Lagrangian sense) evolution of physical coordinates and physicochemical properties of a population of particles. The coupling between the Eulerian and Lagrangian components is bi-directional. The Lagrangian component feeds on the fluid velocity field in order to update the positions of super-droplets, and the thermodynamic fields to compute the condensational growth or evaporation rates. The Eulerian component feeds on the water vapour and heat source/sink rates resulting from condensation and evaporation of water on the particles. Although mutually coupled, the Eulerian and Lagrangian computations are decomposed, in the sense that they happen sequentially and the state vectors of one component are constant from the standpoint of the other (within a time-step).

The model does not differentiate between aerosol particles, cloud droplets, drizzle or rain drops. Each particle in the model (referred to as super-droplet) represents a multiplicity of real-world particles of the same size and of the same chemical composition. From the standpoint of the Lagrangian component, the super-droplets are subject to three processes besides advection: (i) gravitational settling, (ii) condensational growth/evaporation and (iii) collisional growth. Consequently, the model covers representation of such cloud-microphysical processes as: cloud condensation nuclei (CCN) activation; drizzle formation by collisions of cloud droplets (autoconversion); accretion of cloud droplets by drizzle drops and raindrops, as well as coalescence of these larger hydrometeors (self-collection); and precipitation of drizzle and rain including aerosol wet deposition. Analogous particle-based techniques were recently used in context of simulations of precipitation-forming clouds e.g. by Andrejczuk et al. (2010) and Franke and Raasch (2010); what distinguishes SDM however, is the probabilistic Monte-Carlo type representation of the particle coalescence process. Probabilistic representation of particle coalescence has also been recently used in atmospheric modelling studies; however, to authors' knowledge, none of these models were bi-directionally coupled with LES – see e.g. Jensen and Lee (2008) for description of an adiabatic parcel model with Monte-Carlo coalescence or Riemer et al. (2009) for description of particle-resolved aerosol transport model with Monte-Carlo coalescence but working off-line from the flow dynamics).

3. MODELLING SET-UP

All simulations in the present study were carried out using the Nagoya University Cloud-Resolving Storm Simulator (CReSS: Tsuboki, 2008, chapter 9.2 and references therein). CReSS is a non-hydrostatic compressible flow LES-type solver. Two types of moist processes representations were used: the SDM and a bulk microphysics model (Kessler-type parameterisation implemented following Klemp and Wilhelmson, 1978, section 2b). The simulations are carried out using a set-up based on the RICO composite case defined in van Zanten et al. (2011) and corresponding to atmospheric state measured and modelled in context of the Rain in Cumulus over Ocean (RICO) field project (Rauber et al., 2007). The set-up defines initial profiles of po-

*Correspondence to: Sylwester Arabas, Pasteura 7, 02-093 Warsaw, Poland. E-mail: sarabas@igf.fuw.edu.pl

†Affiliation at the time of research: Japan Agency for Marine-Earth Science and Technology, Kanagawa, Japan

Paper presented at the 16th International Conference on Clouds and Precipitation ICCP-2012, Leipzig, Germany
Submitted to arXiv on 2012-05-15 (http://arxiv.org/)

Table 1: List of model runs discussed in the paper. The run label denotes whether bulk (blk) or SDM (sdm) microphysics was used, as well as which grid resolution (coarse, middle or high) and super-droplet number density was chosen. Coarse resolution corresponds to a quarter of the domain from the original RICO set-up (i.e. grid box size of 100×100×40 m with 64×64×100 grid points); the middle and high resolutions denote settings resulting in halved and quartered grid box dimensions, respectively (with the domain size kept constant). For each simulation there are five time-steps defined: long and short time-step of the Eulerian component (the short one used for sound-wave terms), the time-step used for integrating the condensational growth/evaporation equation, the time-step used for solving collisional growth using the Monte-Carlo scheme, and the time-step for integration of particle motion equations.

run label	grid	dx=dy	dz	time-steps [s]	sd density [cm^{-3}]
blk-coarse	64 × 64 ×100	100m	40m	1.00/0.100 n/a	n/a
sdm-coarse-8	64 × 64 ×100	100m	40m	1.00/0.100/0.25/1.0/1.0	2.0×10^{-11}
sdm-coarse-32	64 × 64 ×100	100m	40m	1.00/0.100/0.25/1.0/1.0	8.0×10^{-11}
sdm-coarse-128	64 × 64 ×100	100m	40m	1.00/0.100/0.25/1.0/1.0	3.2×10^{-10}
sdm-coarse-512	64 × 64 ×100	100m	40m	1.00/0.100/0.25/1.0/1.0	1.3×10^{-09}
sdm-middle-8	128×128×200	50m	20m	0.50/0.050/0.25/1.0/1.0	1.6×10^{-10}
sdm-middle-32	128×128×200	50m	20m	0.50/0.050/0.25/1.0/1.0	6.4×10^{-10}
sdm-middle-128	128×128×200	50m	20m	0.50/0.050/0.25/1.0/1.0	2.6×10^{-09}
sdm-high-8	256×256×400	25m	10m	0.25/0.025/0.25/1.0/0.5	1.3×10^{-09}

tential temperature, specific humidity and wind characteristics for the trade-wind boundary layer following RICO observations (see Nuijens et al., 2009). This set-up was previously used in several modelling studies including: (Stevens and Seifert, 2008; Jiang et al., 2009; Seifert et al., 2010; Matheou et al., 2011; Grabowski et al., 2011). Here the only exception from the original set-up is the domain size – a quarter of the original domain was used (i.e. 6.4×6.4×4 km instead of 12.8×12.8×4 km), and the grid cell sizes – several settings were used. Tests with full domain size (not discussed herein) revealed that quartering the domain enlarges the fluctuations in time of cloud macroscopic properties; however, not to a level significant for the presented discussion.

For simulations using SDM, the initial coordinates and sizes of particles are chosen randomly with uniform distribution in physical space and bi-modal lognormal distribution in particle-size space (size spectrum as specified in van Zanten et al., 2011, section 2.2.3). All particles are initially put in equilibrium with ambient humidity assuming that all are composed of ammonium sulphate solution. The mean number of super-droplets per LES grid box varied from 8 to 512 in different simulations (see Table 1). In all calculations discussed in the paper the probability of collisions and coalescence was defined following Hall (1980, section 3d, and references therein) hence no effects of small-scale turbulence on the drop collision efficiency was taken into account.

4. SIMULATION RESULTS

A list of model runs and their corresponding labels used in the paper is given in Table 1. The SDM simulations were carried with different grid resolutions and different super-droplet number densities. The table also lists different time-steps used in the simulations - in SDM the time-steps used for the Eulerian and Lagrangian computations differ as the corresponding numerical stability constraints differ.

Following the methodology of van Zanten et al. (2011) the analyses are restricted to the last four hours of the 24-hour model runs. Presented results are based on the LES grid data output every minute simulated time and super-droplet data (particle positions and sizes) output every 10 minutes simulated time.

4.1 CLOUD MACROSTRUCTURE

Figure 1 presents time-series of scalar quantities characterising domain-wide cloud field features: cloud cover (cc), liquid water path (LWP), rain water path (RWP) and cloud top height (zct). All quantities are labelled and defined following van Zanten et al. (2011, section 2.4.2 and Table 4 therein, and caption of Figure 1 herein). Presented time-series cover the first and the last four hours of simulations corresponding to the spin-up, and the relatively steady-state stages of the simulation, respectively. The figure is intended for comparison with analogous plots from modelling studies employing the RICO set-up: Fig. 2 in Stevens and Seifert (2008), Fig. 5 in Seifert et al. (2010), Fig. 3 in van Zanten et al. (2011), Figs 1-3,7 in Matheou et al. (2011) and Fig. 6 in Grabowski et al. (2011).

The cloud-cover (cc) plots reveal considerable dependence of cc on the choice of grid resolution, with a significant increase of cloud cover for higher-resolution simulations. This is, at least partially, caused by the definition of cc which includes an arbitrary threshold value for the cloud water mixing ratio (e.g. in a hypothetic 2x2 chessboard water content distribution with cc of 50%, downsampling to a single grid point could result in a zero cc). Furthermore, since the formation of convective clouds is triggered by vertical air motion and since refinement of the grid resolution helps to resolve in more detail the dynamics, an increase in the number of (smaller) clouds may be expected (Matheou et al., 2011, Sect. 3.2).

Liquid water path (LWP) plots show that the increase of cc with increased resolution is correlated with increase of LWP. The values of LWP obtained in middle-resolution SDM simulations (blue lines) fall within the range of values obtained with other LES from the study of van Zan-

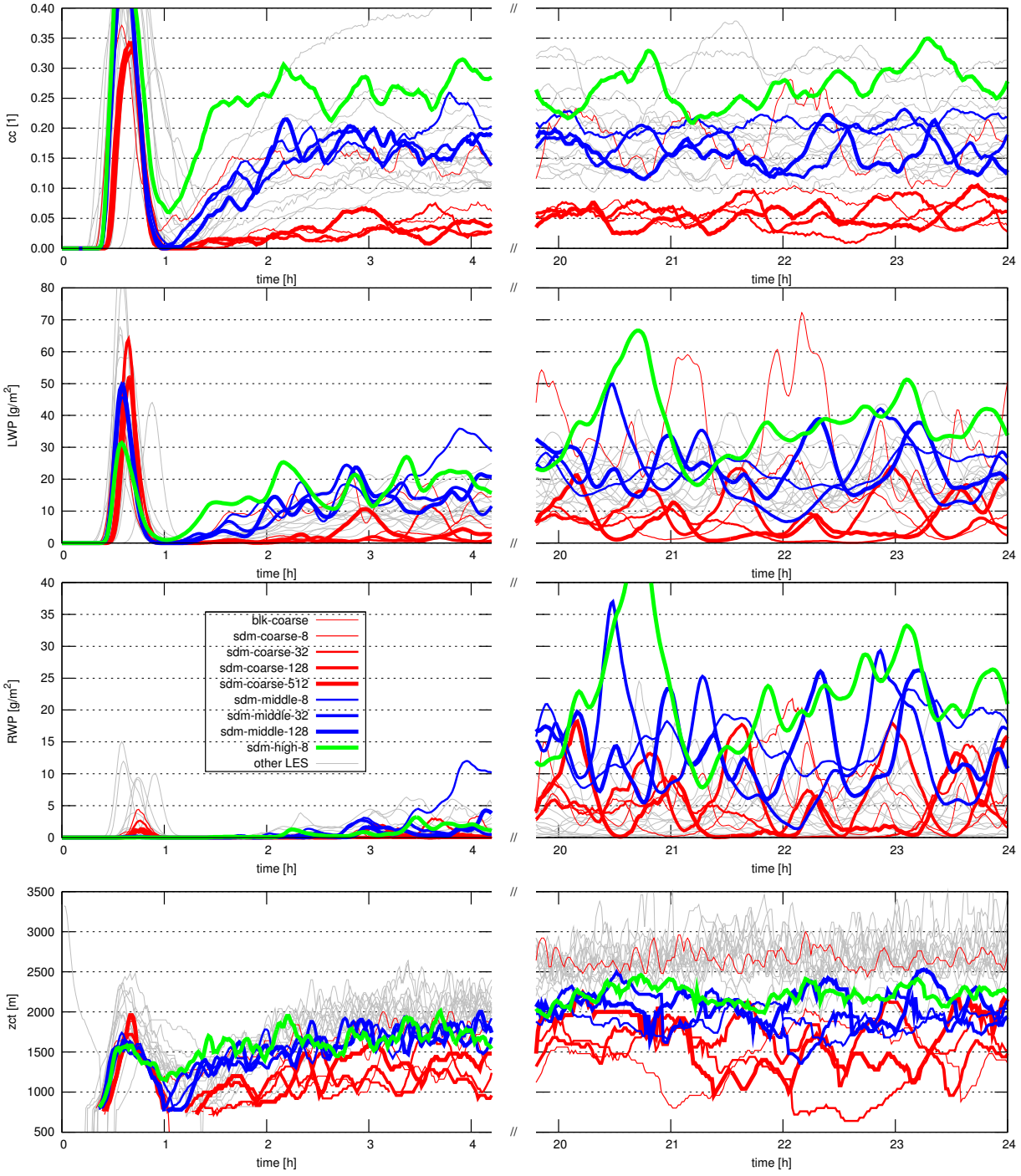

Figure 1: Time-series of cloud macrostructure characteristics defined following van Zanten et al. (2011, section 2.4.2 and Table 4 therein): (i) cloud cover "cc" is defined as the fraction of columns with at least one cloudy grid cell (a grid cell is defined as cloudy if the cloud water mixing ratio exceeds 0.01 g kg^{-1}); (ii) liquid water path "LWP" is the mean over all columns of column-integrated liquid water content (density of both cloud and rain water); (iii) rain water path "RWP" is calculated in the same manner using rain water only; (iv) the cloud top height "zct" is the height of the top of the highest cloudy grid cell. For SDM simulations the cloud and rain water mixing ratios are diagnosed by summing over the population of particles with radius smaller and larger than 40 μm, respectively. In the foreground there are plots depicting data from the nine simulations listed in Table 1. In the background (plotted with thin grey lines) there are the results from LES simulations described in van Zanten et al. (2011, data obtained at: http://knmi.nl/samenw/rico/). See section 4.1 for discussion.

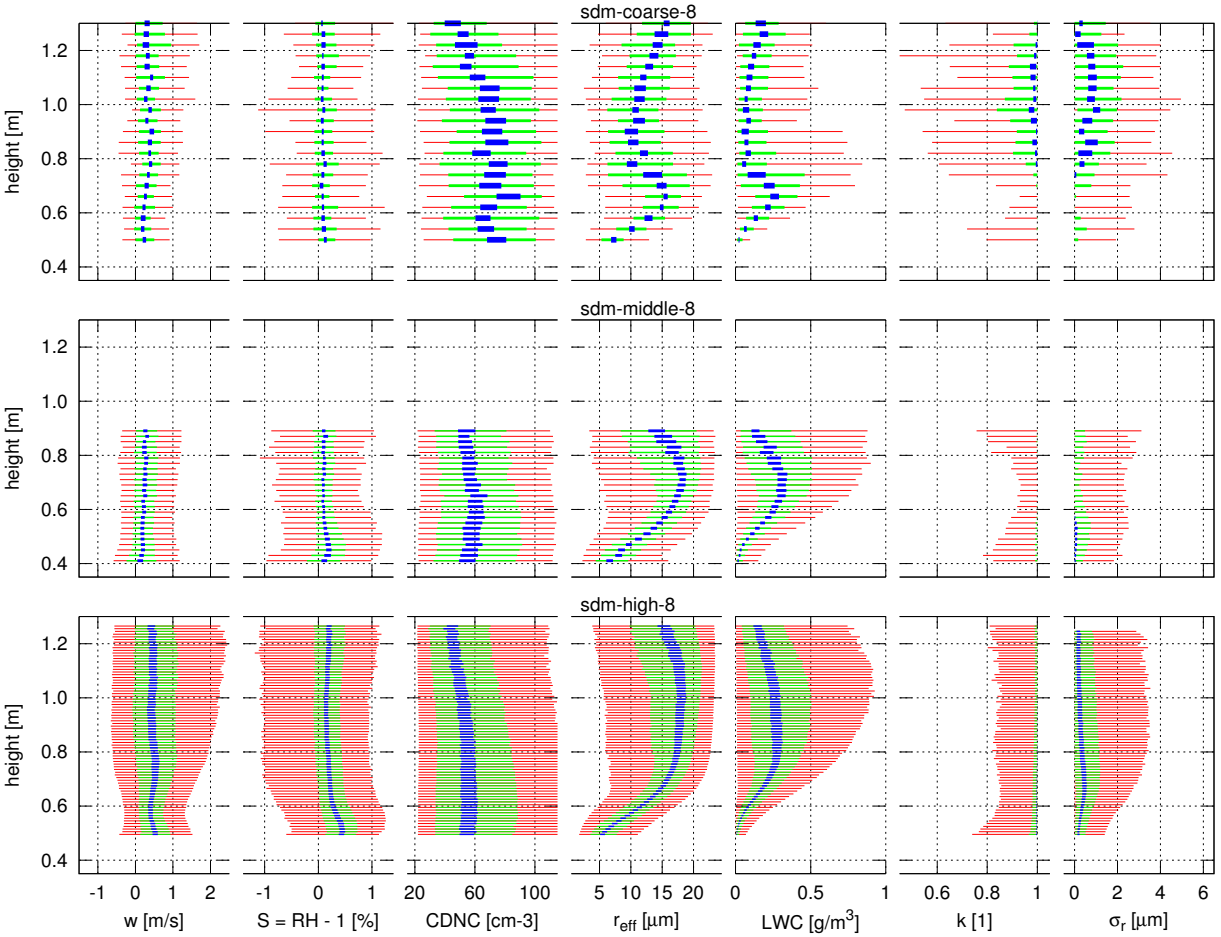

Figure 2: Height-resolved statistics of cloud droplet spectrum parameters derived from SDM simulation data. All plots in a row share the same y-axis representing height above sea level. See section 4.2 for discussion and plot construction method description.

ten et al. (2011, grey lines in Fig. 1 herein) for most of the simulated time. The high-resolution run (green line) features highest fluctuations of values of both LWP and RWP which likely corresponds to the low super-droplet density, and hence the low spectral resolution of the microphysics model.

The rain water path was one of the quantities that varied most from one simulation to another in the study of van Zanten et al. (2011, Sect. 3.2). Similarly, the hereby presented results exhibit both significant variations in RWP with simulation time as well as significant departures from one simulation to another (i.e. when changing grid resolution or super-droplet density). A notable feature is the high correlation of RWP with both LWP and cc.

The plots of cloud-top evolution with time clearly show that the SDM-simulated cloud field is shallower than the one obtained with bulk microphysics or in other LES. While the employed definition of cloud-top height does not allow direct comparisons with measurements, arguably the SDM-predicted heights for middle- and high-resolution seem more comparable to those observed during RICO (e.g. Rauber et al., 2007; Genkova et al., 2007, Fig. 1). In general, the significant inhibition of convection in all coarse resolution runs suggest that the 100×100 meter resolution is not enough when coupled with a Lagrangian model which, among other factors, relies on LES-predicted supersaturation field directly coupled with the vertical motions.

4.2 CLOUD MICROSTRUCTURE

Figures 2,3 and 4 present height-resolved statistics of the vertical velocity w, the supersaturation S, cloud droplet concentration CDNC, droplet effective radius $r_{eff}=<r^3>/<r^2>$, liquid water content LWC, the cubed ratio of mean volume radius to effective radius $k=<r^3>/r_{eff}^3$, and the standard deviation of cloud droplet radius σ_r. The plots are intended for comparison with the analysis presented in Arabas et al. (2009, Figs. 1 and 2) where the data from aircraft measurements during the RICO campaign using the Fast-FSSP optical cloud droplet spectrometer (Brenguier et al., 1998) were analysed. The herein analysis of SDM simulation data is constrained to in-cloud regions defined as the grid boxes having CDNC> 20 cm^{-3} where CDNC is derived by summing over the super-droplets representing particles of radius between 1 and 24 mi-

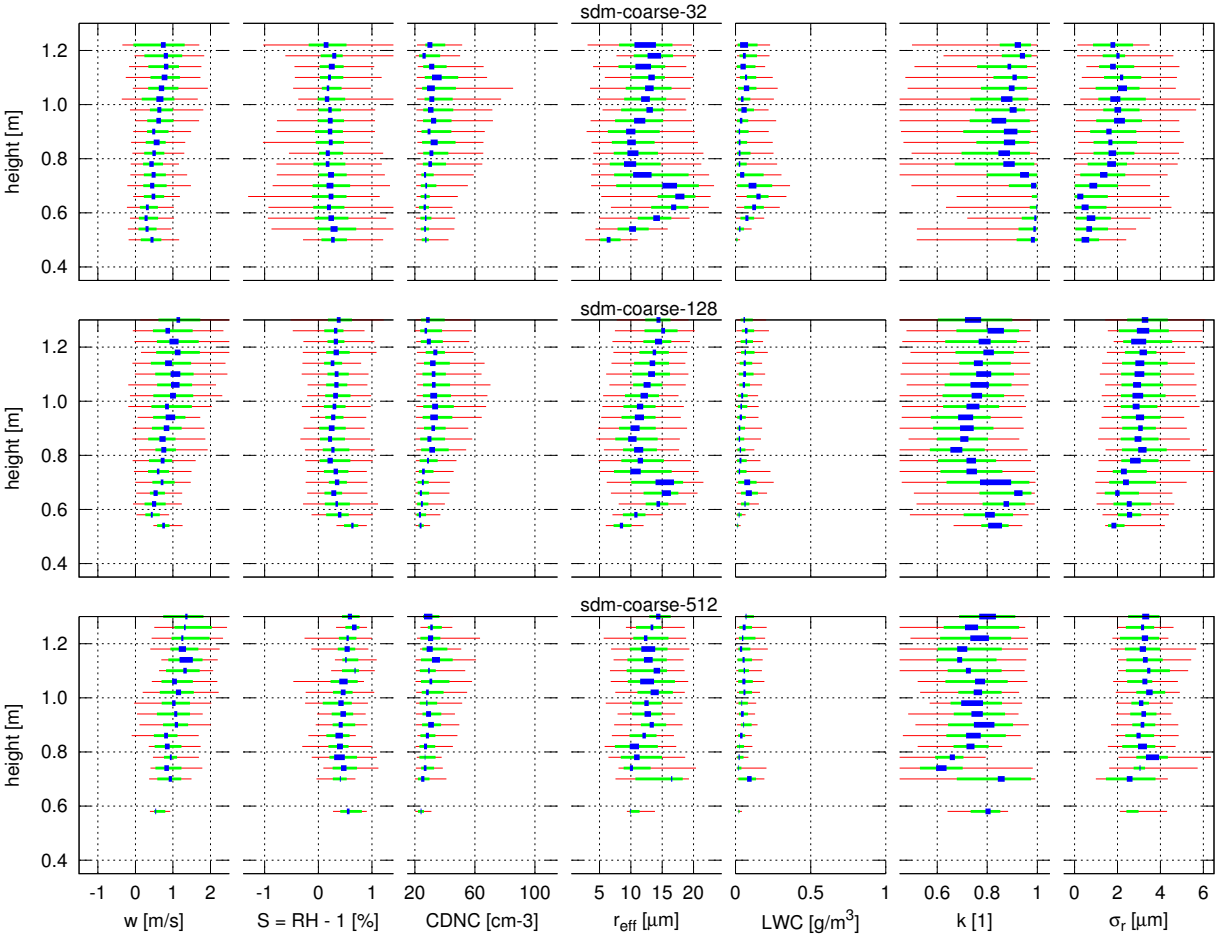

Figure 3: Same as Fig. 2 for model runs: sdm-coarse-32, sdm-coarse-128 and sdm-coarse-512.

crometers. The choices of the CDNC threshold and the spectral range correspond to those characteristic of the Fast-FSSP probe.

Plot construction method was chosen following the methodology of Arabas et al. (2009). For each level of the model grid and each plotted parameter a list of values matching the in-cloud criterion is constructed, sorted and linearly interpolated to find the 5th, 25th, 45th, 55th, 75th and 95th percentiles. The lists are constructed from the LES-grid values (w, S) or super-droplet statistics calculated for each grid cell (CDNC, r_{eff}, LWC, k and σ_r). The sample volumes are therefore defined by grid cell sizes and are of the order of $10^4 - 10^5\, m^3$, while the sample volume for the $10\, Hz$ Fast-FSSP dataset used in Arabas et al. (2009) is of the order of $10^{-6}\, m^3$ – a thing one has to bare in mind. The vertical extent of the measurement sample volume of ca. $10\, m$ is comparable to the grid cell size, though. Levels with less than $0.1 \cdot N_{max}$ data-points, where N_{max} is the number of data-points at the level with the highest number of data-points, are discarded from the analysis. Finally, the 5th – 95th percentile, the interquartile, and the 45th – 55th percentile ranges are plotted as a function of height using red, green and blue bars, respectively. The profiles composed of the 45th 55th percentile range bars are referred to as median profiles hereinafter.

VERTICAL VELOCITY Profiles of the vertical velocity generally show a gradual increase of the spread of values with the increasing grid resolution. It is consistent with the fact that the grid acts as a spatial filter in the LES. The median profiles resemble each other regardless of the resolution suggesting that the macroscale dynamics of the simulated cloud layer are robust to both the LES grid choice and the super-droplet density choice (however, the differences in cloud-top heights plotted in Fig. 1 and evident in Figs. 2–4 reveal that this robustness is limited). The slight increase of the vertical velocities with height visible in some of the profiles, and noted in the RICO observations analysis (Gerber et al., 2008, Table. 2), may correspond to the fact that only the more vigorous updraft regions were able to produce clouds reaching the upper part of the cloud field.

SUPERSATURATION The profiles of supersaturation, especially for the high and middle resolution, show the characteristic cloud-base maxima. This confirms that the model formulation, and the time resolution used allows to capture the influence of CCN activation kinetics on the

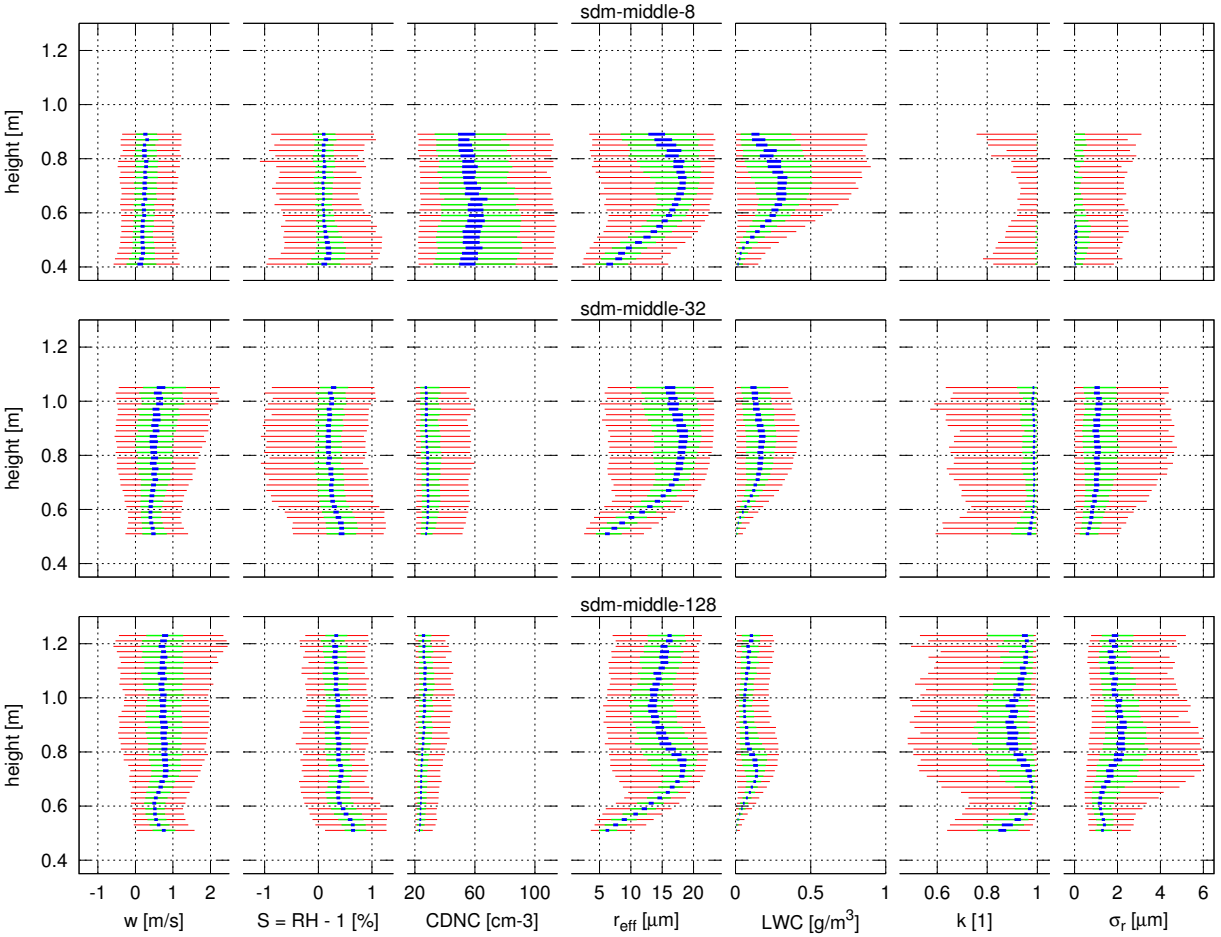

Figure 4: Same as Fig. 2 for model runs: sdm-middle-8, sdm-middle-32 and sdm-middle-128.

evolution of supersaturation. Both the values of maximal supersaturation (ca. 1%), as well as a roughly estimated supersaturation relaxation time (ca. 100s assuming ≈ 1 m/s vertical velocity, and an ≈ 100m height scale over which the supersaturation falls off to an asymptotic value) correspond to those reported in modelling studies that employed supersaturation-predicting models (e.g. Morrison and Grabowski, 2008; Khvorostyanov and Curry, 2008). Comparison of the supersaturation prediction in the model with measurements is not viable as direct measurements of supersaturation in clouds are virtually unavailable (Korolev and Mazin, 2003). In none of the runs there is any other maximum of supersaturation visible along the profile. This suggests that the employed Lagrangian technique for representing water condensate inhibits the spurious production of cloud-edge supersaturation inherent in Eulerian models. (see Sec. 1 in Grabowski and Morrison, 2008, and references therein). The reason for it is likely (as noted as well in Andrejczuk et al., 2008, par. 10) that such coupled Eulerian-Lagrangian approach does in fact cover representation of fractional cloudiness within a grid cell.

DROPLET CONCENTRATION The range of drop concentration values obtained in the simulations does roughly correspond to the values observed during RICO and presented in Arabas et al. (2009, figure 1a), Gerber et al. (2008, figure 4) and Colón-Robles et al. (2006, figure 3). The discrepancies in the median values and the spread of CDNC among different model runs show, however, that the prediction of drop concentration is sensitive to the super-droplet density (Fig. 4). Furthermore, the higher concentrations obtained with low super-droplet densities (i.e. low spectral resolution) are closer to the observed values. The observed invariability of CDNC with height is robustly reproduced suggesting that the discrepancies are solely related to the treatment of CCN activation in the model.

EFFECTIVE RADIUS The effective radius profiles are generally robust to both grid and super-droplet density choices, and they do resemble the profiles observed with the Fast-FSSP instrument during RICO (Arabas et al., 2009, fig. 2). The profiles show a gradual increase in cloud droplet sizes from the cloud base up to the altitude of 700–800 metres where the median values of r_{eff} reach 15–20 micrometres. Above, the profiles differ more from one model run to another but still the flattening of the r_{eff} profile slope is a robust feature. The reduced slope of the median

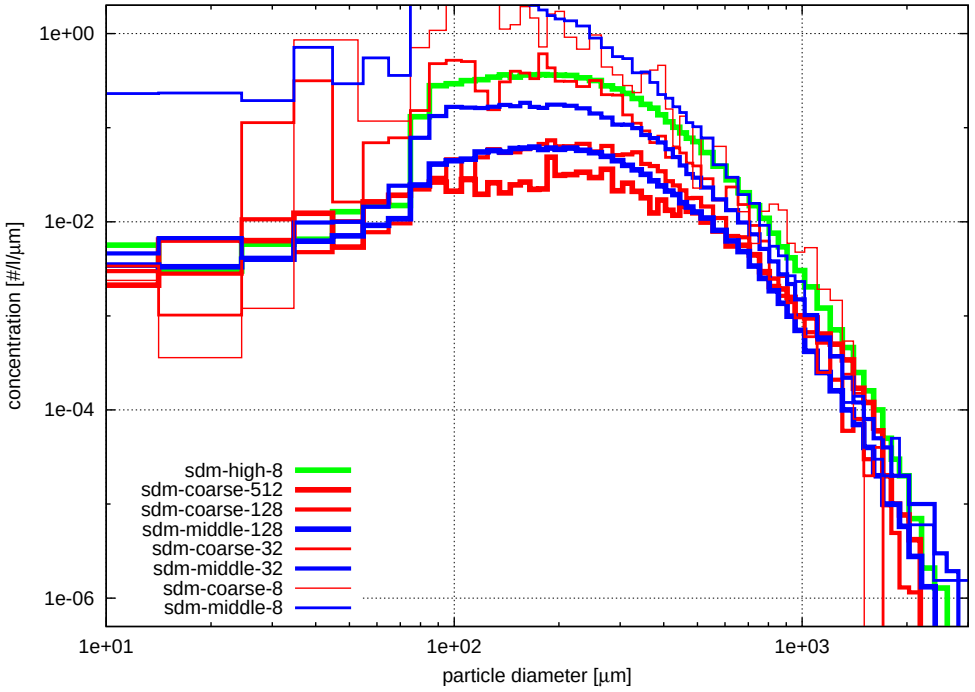

Figure 5: Comparison of model-predicted spectra for particles within size range of the OAP-2DS instrument, within grid cells with rain water mixing ratio $q_r > 0.001$ g/kg and within an altitude range of 183 ± 100 m. Figure intended for comparison with Fig. 4 in Baker et al. (2009), see section 4.3 herein for details.

profiles of r_{eff} reflects (i) the chosen drop radius range (1–24 μm – emulating the Fast-FSSP instrument range), (ii) the decreased efficiency, in terms of radius change, of the condensational growth for larger droplets, and (iii) the increased efficiency of drop collisions reached after the initial condensational growth stage (see e.g. section 3.1 in Zhang et al., 2011, for discussion of influence of precipitation on effective radius profiles). The spread of r_{eff} values high above cloud base indicates presence of smaller droplets even near cloud top. The present analysis (and the corresponding choice of data output rate during simulations) does not provide an answer to the question of the origin of these small particles – e.g. if they were activated at cloud edges above cloud base or not (see e.g. Slawinska et al., 2012).

LIQUID WATER CONTENT The LWC profiles do show considerable departures from one another when altering the super-droplet density (Fig. 4), but behave robustly when changing the grid resolution (Fig. 2). As LWC is approximately proportional to the product of CDNC and r_{eff}^3, this reflects in fact the sensitivity of the drop number prediction to the super-droplet number choice discussed above. Consequently, the simulations with the lowest super-droplet densities produce the most credible LWC profiles comparable with the ones observed during RICO (e.g. Gerber et al., 2008, Fig. 1, 1 Hz data-points). In all simulations the 95$^{\text{th}}$ percentile profiles (right ends of red bars) are sub-adiabatic (not shown, LWC approximately linear with height increasing from 0 to 1 g/m^3 within 500 metres). In SDM the condensational growth and evaporation is computed using values of supersaturation interpolated to super-droplet positions, hence when a cloudy air volume mixes with clear air the mixing scenario is not strictly homogenous. The difference between the median and maximal values of LWC suggests that the model does reproduce the influence of mixing on the dilution of cloud and the decrease of water content (see e.g. the discussion of the adiabatic fraction profiles in Fig. 2 in Arabas et al., 2009).

PARAMETER K Most GCMs employ a parameterisation of the effective radius when diagnosing the cloud optical depth of clouds from predicted liquid water content and drop number concentration (see e.g. section 2 in Brenguier et al., 2000, and references therein). Typically, the cubed ratio of the mean volume radius to the effective radius $k = < r^3 > / r_{eff}^3$ (or a similarly defined scaling coefficient) is assumed to be constant or to depend solely on drop concentration (e.g. Peng and Lohman, 2003). Value of $k = 0.8 \pm 0.07$ based on aircraft observations in maritime clouds using an FSSP-type instrument reported in Martin et al. (1994) is often used in climate models.

As shown in Figure 2, all simulations with the mean value of 8 super-droplet per LES grid cell predict values of k hardly different from unity. This means that the effective radius is in most cases equal to the mean volume radius, as it should be, taking into account that the 8 super-droplets (which may be thought of as size bins) are used to represent a wide spectral range of

particles: aerosol, cloud, drizzle and rain; while the statistics presented in the plot cover a narrow spectral range. Consequently, cloud water is likely represented by a single super-droplet (bin) in each grid cell, a situation in which all of the cloud droplets would have the same size and $k = 1$ by definition. The values of the k parameter calculated in the model runs with mean super-droplet density of 128 range from approximately 0.6 to 0.9. There is no significant difference when the super-droplet density is increased to 512 suggesting that the density of 128 per cell is enough to resolve the relevant cloud droplet size spectrum features.

DROP RADIUS STANDARD DEVIATION

In consistency with the aforementioned behaviour of k for low super-droplet density, the drop radius standard deviation σ_r hardly differs from zero when a mean of 8 super-droplets per cell is used, and it still goes down to zero at some levels with a mean of 32 super-droplets per grid cell. For all higher spectral resolution simulations the 5$^{\text{th}}$ percentile of σ_r is greater than zero at all levels, and the increase of mean super-droplet density from 128 to 512 does not influence the profile shape. In general agreement with RICO observations, the standard deviation ranges from 1 to 6 micrometres. The profiles of σ_r show a slight increase with height (best captured in the sdm-middle-128 run); however, the observed inclination of the σ_r profiles resembles more the 95$^{\text{th}}$ percentile profile derived from SDM simulations. The fact that the values of σ_r are larger than those obtainable in adiabatic drop growth process (see e.g. Yum and Hudson, 2005, and references therein) suggests that the model does capture to some extent the mixing-induced broadening of the cloud droplet spectrum. However, since the mixing in SDM is limited to LES-resolved motions with characteristic length scales constrained by grid cell dimensions, the level of agreement with observations is, as expected, limited.

4.3 PRECIPITATION MICROSTRUCTURE

The analysis depicted in Figures 2, 3 and 4 concerned the cloud-droplet region of the particle size spectrum. A comparison of model-predicted spectra for larger particles is depicted in Figure 5. The figure is intended for comparison with Fig. 4 in Baker et al. (2009) based on measurement data obtained with the OAP-2DS instrument (Lawson et al., 2006) during RICO research flights. During RICO the OAP-2DS instrument was set to classify particles into 61 size bins spanning the 2.5 μm – 1.5 mm size range in radius. In the analysis of Baker et al. (2009) a mean size spectrum was derived from 237 spectra measured within rain-shafts below the cloud base at the altitude of about 183 metres (600 ft). In order to derive comparable quantities from the SDM simulation results, the super-droplets in each grid cell were classified into size bins of the same layout as used by the OAP-2DS instrument, an altitude range of 183 ± 100 m was chosen, and only grid cells with rain water mixing ratio $q_r > 0.001$ g/kg were taken into account (q_r being derived from summation over super-droplets representing particles with radii greater than 40 μm). A comparison of Figure 5 with Fig. 4 from Baker et al. (2009) (both plots share the same axis ranges) reveal that the model results, regardless of the grid-resolution or super-droplet density choice, show fair agreement with the measurement results for drop diameters greater than 0.1 mm. The spectrum from the sdm-coarse-512 run (with the highest spectral resolution and the best Monte-Carlo sampling density) resembles most closely the measurements having the lowest concentrations in the 0.1–0.4 mm diameter range. All simulations disagree markedly with the measurements within the 10–20 μm diameter range. These measured particles within this range were "most likely deliquesced aerosols" (Baker et al., 2009) and since there are no aerosol sources in the model, this disagreement is still a plausible result. The drop breakup process was identified as another possible source of droplets smaller than 100 μm, and this process is also not included in the present version of the model. Moreover, it was the lack of hydrometeors smaller than 100 μ in diameter that was considered as the primary highlight of the observations reported in Baker et al. (2009), and this feature of the spectrum is in fact hinted in the simulation results.

5. SUMMARY

The salient features that distinguish SDM from bulk and bin warm-rain microphysics models are:
(i) diffusive error-free computational scheme for both condensational and collisional growth;
(ii) particle spectrum representation allowing straightforward comparison with experimental data obtained with particle-counting instruments;
(iii) persistence of arbitrary number of scalar quantities assigned to a super-droplet (e.g. chemical properties);
(iv) scalability in terms of sampling error (i.e. super-droplet density);
(v) parameterisation-free formulation of the key processes involved in cloud-aerosol interactions.

The last feature, in particular, does not come without its challenges. Explicit treatment of aerosol microphysics implies taking care of their budget within the simulation domain, including modelling their sinks (wet and dry deposition) and sources, the latter not being represented in the present study.

The other two processes not represented in the discussed simulations are: (i) the impact of turbulence on drop collisions (see e.g. Devenish et al., 2012), and (ii) the influence of drop breakup on the size spectrum of precipitation particles (see e.g. Villermaux and Bossa, 2009). Yet, the arguably fair level of agreement of the simulation results reported herein and the previously published in-situ measurement results from RICO,

suggest that the set of processes represented in the present set-up of SDM includes at least the key players involved in determining the features of the size spectra of cloud and precipitation particles. One has to bare in mind that a direct comparison of RICO measurement data with LES results of the type presented herein is not possible due to different time- and space- scales associated with the model variables and the measurements, as well as due to the nature of the "composite" modelling set-up. (typical atmospheric conditions, with the diurnal cycle neglected in particular).

The SDM modelling approach offers the unique possibility to mimic in the analysis the particle-counting process inherent in the principle of operation of most airborne aerosol, cloud and precipitation probes. As a result, it becomes meaningful to analyse such model-predicted cloud droplet size spectrum parameters as e.g. k or σ_r, not taken into account in previous comparisons of RICO LES results with aircraft observations (Abel and Shipway, 2007; van Zanten et al., 2011). What militates in favour of pertinence of the obtained results is that the present model employs fewer parameterisation (in comparison with bulk or bin models) and more basic principles to describe processes occurring at the microscale (e.g. description of the Köhler curve shape as opposed to employment of such parameters as the exponent in Twomey's formula for CCN activation parameterisation in bin models, or the autoconversion threshold in Kessler-type bulk models).

The key conclusion from the presented analysis is that while the convergence of the macroscopic cloud parameters do not seem to get any better than in the other LES simulations using the RICO set-up, the SDM is able to provide more detailed insight into cloud microstructure, and thus indirectly into its optical properties.

Acknowledgements

All simulations were carried out on "The Earth Simulator 2" operated by the Japanese Agency for Marine-Earth Science and Technology (JAMSTEC) in Kanagawa, Japan. JAMSTEC supported a month-long research visit of SA to Japan, and provided computer time on the ES2. Thanks are due Hanna Pawlowska (University of Warsaw) and Kanya Kusano (JAMSTEC, Nagoya University) for their support throughout the project; and Kozo Nakamura (JAMSTEC) for his help with implementing the RICO set-up in CReSS.

References

Abel, S. and Shipway, B.: A comparison of cloud-resolving model simulations of trade wind cumulus with aircraft observations taken during RICO, Quart. J. Roy. Meteor. Soc., 133, 781–794, doi:10.1002/qj.55, 2007.

Andrejczuk, M., Reisner, J., Henson, B., Dubey, M., and Jeffery, C.: The potential impacts of pollution on a nondrizzling stratus deck: Does aerosol number matter more than type?, J. Geoph. Res., 113, D19 204, doi:10.1029/2007JD009445, 2008.

Andrejczuk, M., Grabowski, W., Reisner, J., and Gadian, A.: Cloud-aerosol interactions for boundary layer stratocumulus in the Lagrangian Cloud Model, J. Geoph. Res., 115, D22 214, doi:10.1029/2010JD014248, 2010.

Arabas, S., Pawlowska, H., and Grabowski, W.: Effective radius and droplet spectral width from in-situ aircraft observations in trade-wind cumuli during RICO, Geophys. Res. Lett., 36, L11 803, doi:10.1029/2009GL038257, 2009.

Baker, B., Mo, Q., Lawson, R., O'Connor, D., and Korolev, A.: Drop size distributions and the lack of small drops in RICO rain shafts, J. Appl. Meteor. Climatol., 48, 616–623, doi:10.1175/2008JAMC1934.1, 2009.

Brenguier, J.-L., Bourrianne, T., Coelho, A., Isbert, J., Peytavi, R., Trevarin, D., and Weschler, P.: Improvements of droplet size distribution measurements with the Fast-FSSP (Forward Scattering Spectrometer Probe), J. Atmos. Oceanic Technol., 15, 1077–1090, doi:10.1175/1520-0426(1998)015<1077:IODSDM>2.0.CO;2, 1998.

Brenguier, J.-L., Pawlowska, H., Schüller, L., Preusker, R., F., J., and Fouquart, Y.: Radiative properties of boundary layer clouds: droplet effective radius versus number concentration, J. Atmos. Sci., 57, 803–821, doi:10.1175/1520-0469(2000)057<0803:RPOBLC>2.0.CO;2, 2000.

Colón-Robles, M., Rauber, R., and Jensen, J.: Influence of low-level wind speed on droplet spectra near cloud base in trade wind cumulus, Gephys. Res. Lett., 33, L20 814, doi:10.1029/2006GL027487, 2006.

Devenish, B., Bartello, P., Brenguier, J.-L., Collins, L., Grabowski, W., IJzermans, R., Malinowski, S., Reeks, M., Vassilicos, J., Wang, L.-P., and Warhaft, Z.: Droplet growth in warm turbulent clouds, Quart. J. Roy. Meteor. Soc., doi:10.1002/qj.1897, 2012.

Franke, T. and Raasch, S.: Large-eddy simulation of convective clouds with explicit simulation of cloud droplets via Lagrangian particles, in: 13th Conference on Cloud Physics, p. P1.52, Amer. Meteor. Soc., Portland, OR, 2010.

Genkova, I., Seiz, G., Zuidema, P., Zhao, G., and Di Girolamo, L.: Cloud top height comparisons from ASTER, MISR, and MODIS for trade wind cumuli, Remote Sens. Environ., 107, 211–222, doi:10.1016/j.rse.2006.07.021, 2007.

Gerber, H., Frick, G., Jensen, J., and Hudson, J.: Entrainment, mixing, and microphysics in trade-wind cumulus, J. Meteorol. Soc. Jpn., 86A, 87–106, 2008.

Grabowski, W. and Morrison, H.: Toward the mitigation of spurious cloud-edge supersaturation in cloud models, J. Atmos. Sci., doi:10.1175/2007MWR2283.1, 2008.

Grabowski, W., Slawinska, J., Pawlowska, H., and Wyszogrodzki, A.: Macroscopic impacts of cloud and precipitation processes in shallow convection, Acta Geophysica, 59, 1184–1204, doi:10.2478/s11600-011-0038-9, 2011.

Hall, W.: A Detailed Microphysical Model Within a Two-Dimensional Dynamic Framework: Model Description and Preliminary Results, J. Atmos. Sci., 37, 2486–2507, 1980.

Jensen, J. and Lee, S.: Giant sea-salt aerosols and warm rain formation in marine stratocumulus, J. Atmos. Sci., 65, 3678–3694, doi:10.1175/2008JAS2617.1, 2008.

Jiang, H., Feingold, G., and Koren, I.: Effect of aerosol on trade cumulus cloud morphology, J. Geoph. Res., 114, D11 209, doi:10.1029/2009JD011750, 2009.

Khvorostyanov, V. and Curry, J.: Kinetics of cloud drop formation and its parameterization for cloud and climate models, J. Atmos. Sci., 65, 2784–2802, doi:10.1175/2008JAS2606.1, 2008.

Klemp, J. and Wilhelmson, R.: The simulations of three-dimensional convective storm dynamics, J. Atmos. Sci., 35, 1070–1096, doi:10.1175/1520-0469(1978)035<1070:TSOTDC>2.0.CO;2, 1978.

Korolev, A. and Mazin, I.: Supersaturation of water vapor in clouds, J. Atmos. Sci., 60, 2957–2974, doi:10.1175/1520-0469(2003)060<2957:SOWVIC>2.0.CO;2, 2003.

Lawson, R. P., O'Connor, D., Zmarzly, P., Weaver, K., Baker, B., Mo, Q., and Jonsson, H.: The 2D-S (stereo) probe: design and preliminary tests of a new airborne, high-speed, high-resolution particle imaging probe, J. Atmos. Oceanic Tech., 23, 1462–1477, doi:10.1175/JTECH1927.1, 2006.

Martin, G., Johnson, D., and Spice, A.: The measurement and parameterization of effective radius of droplets in warm stratocumulus clouds, J. Atmos. Sci., 51, 1823–1842, doi:10.1175/1520-0469(1994)051<1823:TMAPOE>2.0.CO;2, 1994.

Matheou, G., Chung, D., Nuijens, L., Stevens, B., and Teixeira, J.: On the fidelity of large-eddy simulation of shallow precipitating cumulus convection, Mon. Wea. Rev., 139, 2918–2939, doi:10.1175/2011MWR3599.1, 2011.

Morrison, H. and Grabowski, W.: Modeling supersaturation and subgrid-scale mixing with two-moment bulk warm microphysics, J. Atmos. Sci., 65, 792–812, doi:10.1175/2007JAS2374.1, 2008.

Nuijens, L., Stevens, B., and Siebesma, A.: The environment of precipitating shallow cumulus convection, J. Atmos. Sci., 66, 1962–1979, doi:10.1175/2008JAS2841.1, 2009.

Peng, Y. and Lohman, U.: Sensitivity study of the spectral dispersion of the cloud droplet size distribution on the indirect aerosol effect, Geophys. Res. Lett., 30, 1507, doi: 10.1029/2003GL017192, 2003.

Rauber, R., Stevens, B., Ochs III, H., Knight, C., Albrecht, B., Blyth, A., Fairall, C., Jensen, J., Lasher-Trapp, S., Mayol-Bracero, O., Vali, G., Anderson, J., Baker, B., Bandy, A., Burnet, F., Brenguier, J.-L., Brewer, W., Brown, P., Chuang, P., Cotton, W., Di Girolamo, L., Geerts, H., Gerber, H., Gke, S., Gomes, L., Heikes, B., Hudson, J., Kollias, P., Lawson, R., Krueger, S., Lenschow, D., Nuijens, L., O'Sullivan, D., Rilling, R., Rogers, D., Siebesma, A., Snodgrass, E., Stith, J., Thornton, D., Tucker, S., Twohy, C., and Zuidema, P.: Rain in shallow cumulus over the ocean – the RICO campaign, Bull. Amer. Meteor. Soc., 88, 1912–1928, doi: 10.1175/BAMS-88-12-1912, 2007.

Riemer, N., West, M., Zaveri, R., and Easter, R.: Simulating the evolution of soot mixing state with a particle-resolved aerosol model, J. Geoph. Res., 114, D09 202, doi: 10.1029/2008JD011073, 2009.

Seifert, A., Nuijens, L., and Stevens, B.: Turbulence effects on warm-rain autoconversion in precipitating shallow convection, Quart. J. Roy. Meteor. Soc., 136, 1753–1762, doi: 10.1002/qj.684, 2010.

Shima, S.: Estimation of the computational cost of Super-Droplet Method, RIMS Kokyuroku, 1606, 110–118, 2008.

Shima, S., Kusano, K., Kawano, A., Sugiyama, T., and Kawahara, S.: The Super-Droplet Method for the numerical simulation of clouds and precipitation: A particle-based and probabilistic microphysics model coupled with a non-hydrostatic model, Quart. J. Roy. Meteor. Soc., 135, 1307–1320, doi: 10.1002/qj.441, 2009.

Slawinska, J., Grabowski, W., Pawlowska, H., and Morrison, H.: Droplet activation and mixing in large-eddy simulation of a shallow cumulus field, J. Atmos. Sci., 69, 444–462, doi: 10.1175/JAS-D-11-054.1, 2012.

Stevens, B. and Seifert, A.: Understanding macrophysical outcomes of microphysical choices in simulations of shallow cumulus convection, J. Meteorol. Soc. Jpn., 86A, 143–162, 2008.

Tsuboki, K.: High-resolution simulations of high-impact weather systems using the cloud-resolving model on the Earth Simulator, in: High resolution numerical modelling of the atmosphere and ocean, edited by Hamilton, K. and Ohfuchi, W., pp. 141–156, Springer, doi:10.1007/978-0-387-49791-4_9, 2008.

van Zanten, M., Stevens, B., Nuijens, L., Siebesma, A., Ackerman, A., Burnet, F., Cheng, A., Couvreux, F., Jiang, H., Khairoutdinov, M., Lewellen, D., Mechem, D., Noda, A., Shipway, B., Slawinska, J., Wang, S., and Wyszogrodzki, A.: Controls on precipitation and cloudiness in simulations of trade-wind cumulus as observed during RICO, J. Adv. Model. Earth Sys., 3, M06 001, doi:10.1029/2011MS000056, 2011.

Villermaux, E. and Bossa, B.: Single-drop fragmentation determines size distribution of raindrops, Nature Phys., 5, 697 – 702, doi:10.1038/nphys1340, 2009.

Yum, S. S. and Hudson, J. G.: Adiabatic predictions and observations of cloud droplet spectral broadness, Atmos. Res., 73, 203–223, doi:10.1016/j.atmosres.2004.10.006, 2005.

Zhang, S., Xue, H., and Feingold, G.: Vertical profiles of droplet effective radius in shallow convective clouds, Atmos. Chem. Phys., 11, 4633–4644, doi:10.5194/acp-11-4633-2011, 2011.

MEASUREMENT AND COMPARISON OF THE AEROSOL-CLOUD INTERACTION USING GROUND BASED IN-SITU MEASREMENT AND MODIS DATA

I. Ahmad[1], T. Mielonen[2], H. Portin[1,2], A. Arola[2], S. Mikkonen[1] A. Leskinen[2], M. Komppula[2], K.E.J. Lehtinen[1,2], A. Laaksonen[1,3], S. Romakkaniemi[1]

[1]Department of Applied Physics, University of Eastern Finland (Kuopio).

[2]Finnish Meteorological Institute, Kuopio Unit (Finland).

[3]Finnish Meteorological Institute, Helsinki (Finland).

1. INTRODUCTION

The complex and dynamic mixture of solid and liquid particles in the atmosphere (aerosol) influence clouds and consequently earth's radiation budget. Aerosol can produce climate variability, haze (visibility degradation), health problems and change cloud microphysics. Aerosol acts as cloud condensation nuclei and hence can affect cloud's life time, cloud's cover and cloud optical thickness (*COT*) (Twomey, 1974; d'Almeida, 1991), which means aerosol can also affect liquid water path *(LWP*), cloud droplet effective radii (R_{eff}) and cloud droplet number concentration (N_d) (Platnick et al., 2000; Schreier et al., 2007). The dynamic nature of aerosols and its affect on clouds produces large uncertainties in the estimates of global radiation budget (IPCC report, 2007).

The studies regarding the aerosol modification of clouds shows that an increase in the aerosol concentration lead to an increase in N_d (Snider et al., 2003; Komppula et al., 2005; Romakkaniemi et al., 2009; Portin et al., 2009). N_d is a key parameter changing clouds microphysical and optical properties (Gultepe and Isaac, 2004), e.g. rain formation efficiency and ultimately enhance cloud fraction, this process has been termed as a second indirect effect (2nd AIE) (Albrecht,1989).

To increase the scientific knowledge and reduce uncertainty in the complex process of aerosol cloud interaction some work has already been done using, ground based measurement, remote sensing tools, such as instruments onboard of satellites, airborn measurement and combination of them (e.g. Dong et al., 2002 and 2008; McComiskey et al., 2009; Nakajima et al., 2001; Quaas et al., 2009; Rathke et al, 2000; Gultepe et al, 2001b). Some studies have used ground based data for aerosol properties and satellite data for cloud properties (e.g. Boers et al., 2006; Lihavainen et al., 2010; Janssen et al., 2011), and in some cases satellite retrievals have been validated with airborne measurements (e.g. Schuller et al., 2003; Painemal and Zuidema 2011). Results of cloud response to aerosol are often different for different measurement methods (Quaas et al., 2009; Lihavainen et al., 2010; McComeskey and Fiengold., 2012).

In this work we studied the aerosol modification of cloud properties using ground based measurements station and MODIS instruments onboard Aqua and Terra satellites (remote sensing). We used the ground based in-situ data from our Puijo measurement station (SMEAR IV station) and MODIS derived cloud properties to analyze the Aerosol-Cloud Interaction (ACI) (effect of aerosol concentration on N_d, *COT* and R_{eff}) (i.e. first aerosol indirect effect or 'Twomey effect'). The impact of accumulation mode aerosol from ground based measurements on cloud radiative properties like, *COT*, R_{eff} and N_d from MODIS was analyzed. We also calculated ACI values for both ground based and satellite measurement.

Corresponding author's address: Irshad Ahmad Aerosol Physics Group, Department of Applied Physics, University of Eastern Finland, Kuopio. P.O Box: 1627, 70211 Kuopio. Email: irshad.ahmad@uef.fi

2 METHOD

2.1 GROUND BASED DATA

Puijo measurement station (SMEAR IV) is located on top of Puijo tower (62º54'34" N, 27º39'19" E, 224 m above the surrounding lake) in Kuopio (Finland). The station is providing aerosol particle, cloud droplet and meteorological data since June, 2006 (Leskinen et al. 2009; Portin et al. 2009).
In this study we used accumulation mode (100nm−800nm) particle number concentration (N_{acc}) and cloud droplet number concentration data from Differential Mobility Particle Sizer (DMPS) system and, Cloud Droplet Probe (CDP), respectively (Leskinen et al. 2009; Portin et al. 2009) placed at Puijo measurement station to see the effect of aerosol burden on cloud physics.
For the comparison of ground based in-situ measurements and MODIS data only single layer cloud events is selected. Vaisala CT25K Ceilometer from Finnish Meteorological Institute (FMI) research station was used for the detection of single, and multi layered cloud events. The site is located in the campus area of UEF, Kuopio and around 2 km southwest from Puijo, and 5m above the lake level. To make sure clouds are in the boundary layer it was limited that the cloud base must be less than 800m from the lake level. To select warm (liquid water) and non precipitating clouds we kept limits for some weather parameters like temperature (*T*), pressure (*P*) and rain intensity (*RI*) from Puijo weather station and/or MODIS data. This was done so that our analysis of aerosol-cloud interaction is not affected by precipitation and ice phased clouds. We limit temperature, pressure, rain intensity and visibility to (>265 K), (>700 hpa), (<0.2 mm/h) and (<200 m) respectively, to be assured that we are analyzing low level cloud. For our task we used one hour averages of N_{acc} and N_d from Puijo for analyses and to compare with the MODIS data.

2.2 SATELLITE DATA

For analyzing *ACI* using remote sensing technique, we used MODIS instruments onboard Aqua and Terra polar synchronous orbiting satellites for clouds optical and microphysical parameters like *COT*, R_{eff}, *and LWP* and N_d. Collection 5.1 from atmosphere level 2 data was selected from LAADS WEB website. For the data-analysis we have used 1^0x1^0, 5x5 km^2 and 1x1 km^2 spatial resolution data. High resolution data (1x1 km^2) was used for MODIS Quality Assurance Flags to exclude low quality data and to compare with the cloud retrieval for larger area. MODIS Level 3 cloud with 1^0x1^0 resolution data was taken from the Giovanni website.

3 DATA ANALYSIS

We have selected single layer boundary level water clouds using Puijo (weather data); FMI (Ceilometer CT25K) stations and MODIS cloud top temperature and pressure data. Our analysis of aerosol cloud interaction is over a period of 2006 to 2011, as the CDP and DMPS system on Puijo start measurement from July, 2006. For comparing and analyses of the effect of aerosol on cloud properties we have used one hour average N_{acc}, N_d and weather data from Puijo station, and R_{eff}, *COT*, *LWP* and N_d derived from MODIS instrument onboard Aqua and Terra satellites.
From the measured parameters R_{eff} and *COT* it is possible to calculate N_d as well as *LWP* (Bennartz et al., 2007).

$$N_d = \frac{2^{-2.5}}{k}[COT]^3\left[\frac{LWP}{C_F}\right]^{-2.5}\left[\frac{3}{5}\pi Q\right]^{-3}\left[\frac{3}{4\pi\rho_w}\right]^{-2}C_w^{0.5} \quad (1)$$

Where $k = \frac{R_{vol}}{R_{eff}}$ is the ratio between the volume mean radius and the effective radius usually varying from 0.5 to 0.9 (Lu and Seinfeld, 2006) and given here a constant value of 0.80, *COT* and *LWP* is cloud optical thickness and liquid water path respectively. C_F is the cloud fraction which is 1 for cloudy pixels. For stratus/stratocumulus clouds we assumed C_F to be 1. *Q* is scattering efficiency whose value is approximately 2 (Lu and Seinfeld, 2006). ρ_w is density of water and the constant $C_w = 0.8\frac{1}{R_{H2O}T}\frac{de_{sat}(T)}{dT}\frac{dT}{dz}$ is the condensation rate that depends on temperature (*T*) and the available excess

water, R_{H2O} is the gas constant, e_{sat} is saturation vapour pressure and *z* is the height.

Aerosol-Cloud Interaction (*ACI*) values were calculated using equation 2 (Feingold, et al., 2001; Lihavainen, et al., 2010; McComiskey et al., 2009; Romakkaniemi, et al., 2012) below;

$$ACI = \frac{1}{3}\frac{dln(N_d)}{dln(N_{acc})} \qquad (2)$$

Here N_d is cloud droplet number concentration; N_{acc} is aerosol number concentration in accumulation mode.

4 RESULTS AND DISCUSSION

Our data for the period over 2006 to 2011 gave us around 750 cloud events for analysis using MODIS level 3 (1^0x1^0) cloud properties and ground based measurements. In Figure 1 we can see that on average the R_{eff} and *COT* have values of 11.5 µm and 13.5 respectively. Our results here are almost the same to the values by Jansen et al (2011) derived over larger area (2^0x2^0) above the Hyytiälä measurement station (SMEAR II) 200km southwest of Puijo station. The average value range of N_d derived from MODIS data using equation 1 is usually around 90 – 110 cm^{-3}, with mean value of 100 cm^{-3}.

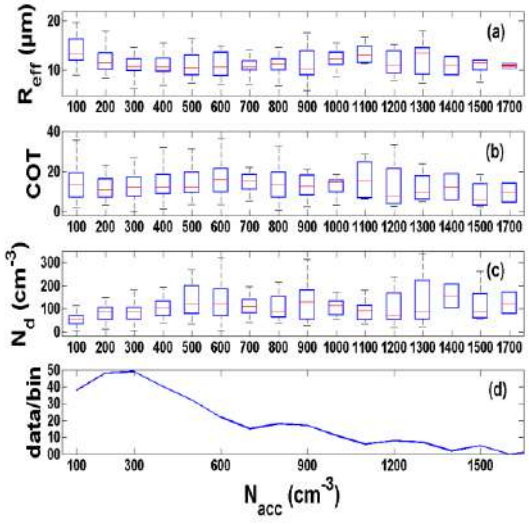

Fig. 1. Effect of accumulation mode particle number concentration on cloud droplet effective radii, cloud optical thickness and cloud droplet number concentration retrieved from MODIS over 2006-2011. Panel d shows effect of N_{acc} is clear for small value and where we have adequate amount of data per bin in the beginning. Panel (a), (b) and (c) represent effect of aerosol on effective radii, cloud optical thickness and cloud droplet number concentration from MODIS. Panel (d) represents data points per bin.

Figures 1 shows comparison of ground based measurement of N_{acc} to MODIS retrieved R_{eff}, *COT* and N_d for 1^0x1^0 data, it can seen that for lower concentrations of aerosol (N_{acc}); the Twomey effect can be seen i.e. an increase N_{acc} decreases R_{eff} and increases N_d gradually, but in case of *COT* this trend starts for N_{acc} higher than 100 cm^{-3}. For larger N_{acc} concentrations there is no correlation found for all the MODIS parameters. The calculated *ACI* value here is 0.25. We did the similar analysis to in situ measured cloud properties and dependence of N_d on N_{acc} is shown in Figure 2. From this measurement the *ACI* value is 0.30, being slightly higher than the one from satellite retrieved cloud properties. These values are comparable to Lihavainen et al. 2010 for similar kind of area.

However, as expected the effect of N_{acc} on N_d is more visible when compared to MODIS data. As in direct measurements the cloud droplets and aerosols are measured from the same place (Puijo measurement station). The average ground based value of N_d is around 280 cm^{-3}.

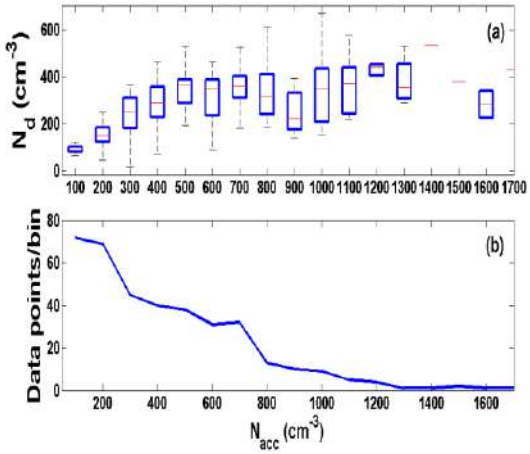

Fig. 2. Illustration of the effect of accumulation mode aerosol number concentration on cloud droplet number concentration using Puijo staion data.

AKNOWLEDGMENT: This work was supported by Maj and Tor Nessling Foundation, Academy of Finland (through the Centre of Excellence program (project

no 1118615)), and by the strategic funding of the University of Eastern Finland. The MODIS level 2 and level 3 atmosphere data used for this work is taken from LAADS WEB (Goddard Space Flight Centre) and Analyses and visualizations used in this study were produced with the Giovanni online data system, developed and maintained by the NASA GES DISC**.** Giovanni online data system developed and maintained by the NASA GES DISC.

REFERENCES

Boers, R., Acarreta, J. R., and Gras, J. L., (2006): Satellite monitoring of the first indirect aerosol effect: Retrieval of the droplet concentration of water clouds, J. Geophys. Res., 111, D22208, doi:10.1029/2005JD006838.

d'Almeida, G. A., Koepke, P. and Shettle, E. P., Atmospheric aerosols: global climatology and radiative characteristics. A. Deepak Publishing, 1991.

Dong, X., Minnis, P., Mace, G. G., Smith Jr., W. L., Poellot, M., Marchand, R. T. and Rapp, A. D., (2002): Comparison of Stratus Cloud Properties Deduced from Surface, GOES, and Aircraft Data during the March 2000 ARM Cloud IOP, J. of the Atm. Sci., Vol. 59, No. 23, 2002.

Dong, X., Minnis, P., Xi, B., Sun-Mack, S. and Chen, Y., (2008): Comparison of CERES MODIS stratus cloud properties with ground-based measurements at the DOE ARM Southern Great Plains site. J. of Geophy. Res, 113, D03204, doi:10.1029/2007JD008438.

Gultepe, I., Isaac, G. A. and Strawbridge, K. B., (2001b): Variability of cloud microphysical and optical parameters obtained from aircraft and satellite remote sensing measurements during RACE. Int. J. Climatol. 21: 507–525. DOI: 10.1002:joc.582

IPCC Report 2007, Climate Change 2007: Synthesis Report. Contribution of Working Groups I, II and III to the Fourth Assessment Report of the Intergovernmental Panel on Climate Change [Core Writing Team, Pachauri, R.K and Reisinger, A.(eds.)]. IPCC, Geneva, Switzerland, 104 pp.

Janssen, R. H. H., Ganzevald, L. N., Kabat, P., Kulmala, M., Niemenen, T., and Roebeling, R. A., (2011): Estimating seasonal variations in cloud droplet number concentration over the boreal forest from satellite observations. Atmos. Chem. Phys., 11, 7701–7713, 2011. doi:10.5194/acp-11-7701-2011

Komppula M., Lihavainen H., Kerminen V.-M., Kulmala M. and Viisanen Y. (2005): Measurements of cloud droplet activation of aerosol particles at a clean subarctic background site. J. Geophys. Res. 110, D06204, doi:10.1029/2004JD005200.

Lihavainen H., Kerminen., V, M., and Remer, L. A., (2010): Aerosol-cloud interaction determined both in situ and satellite data over a northern high-latitude site. Atmos. Chem. Phys., 10, 10987-10995, doi:10.5194/acp-10-10987-2010.

McComiskey, A., Feingold, G., Frisch, A. S., Turner, D. D., Miller, M. A., Chiu, J. C., Min, Q. and Ogren, J. A., (2009): An assessment of aerosol- cloud interactions in marine stratus clouds based on surface remote sensing, J. Geophys. Res., 114, D09203, doi:10.1029/2008JD011006.

Nakajima, T. Y., Higurashi, A., Kawamoto, K. and Penner, J. E., (2001): A possible correlation between satellite- derived cloud and aerosol microphysical parameters, Geophys. Res. Lett., 28(7), 1171–1174, doi:10.1029/2000GL012186.

Painemal, D., and P. Zuidema (2011): Assessment of MODIS cloud effective radius and optical thickness retrievals over the Southeast Pacific with VOCALS-REx in situ measurements, J. Geophys. Res., 116, D24206, doi:10.1029/2011JD016155.

Platnick, S., Durkee, P. A., Nielsen, K., Taylor, J. P., Tsay, S. C., King, M. D., Ferek, R. J., Hobbs, P. V. and Rottman**,** J. W., (2000): The Role of Background Cloud Microphysics in the Radiative Formation of Ship Tracks. J. Atmos.

Sci., 57, 2607–2624. doi: 10.1175/1520-0469.

Portin, J. H., Komppula, M., Leskinen, A.P., Romakkaniemi, S., Laaksonen, A., and Lehtinen, K. E. J., (2009): Overview of the aerosol-cloud interaction at the Puijo semi-urban measurement station. Boreal Env. Res., 14: 641-653.

Quaas, J., Ming, Y., Menon, S., Takemura, T., Wang, M., Penner, J. E., Gettelman, A., Lohmann, U., Bellouin, N., Boucher, O., Sayer, A. M., Thomas, G. E., McComiskey, A., Feingold, G., Hoose, C., Kristjansson, J. E., Liu, X., Balkanski, Y., Donner, L. J., Ginoux, P. A., Stier, P., ´ Grandey, B., Feichter, J., Sednev, I., Bauer, S. E., Koch, D., Grainger, R. G., Kirkevag, A., ˚ Iversen, T., Seland, Ø., Easter, R., Ghan, S. J., Rasch, P. J., Morrison, H., Lamarque, J.- F., Iacono, M. J., Kinne, S., and Schulz, M. (2009): Aerosol indirect effects – general circulation model intercomparison and evaluation with satellite data. Atmos. Chem. Phys., 9, 8697– 8717, doi:10.5194/acp-9-8697-2009.

Rathke, C., Armbruster, W., Fischer, J., Becker, E., Notholt, J., (2000): Comparison of stratus cloud properties derived from coincident airborne visible and ground-based infrared spectrometer measurements. Geophys Res Lett, vol. 27, NO. 17, PP. 2641-2644, doi:10.1029/1999GL010942.

Romakkaniemi, S., McFiggans, G., Bower, K. N., Brown, P.,Coe, H. and Choularton, T. W., (2009): A comparison between trajectory ensemble and adiabatic parcel modeled cloud properties and evaluation against airborne measurements. J. Geophys. Res. 114 D06214. doi:10.1029/2008JD011286.

Romakkaniemi, S., Arola, A., Kokkola, H., Birmili, W., Tuch, T. M., Kerminen, V. M., Räisänen, P., Smith, J., Korhonen, H. and Laaksonen, A., (2012): Effect of aerosol size distribution changes on AOD, CCN and cloud droplet number concentration: case studies from Erfurt and Melpitz, Germany, *J. Geophys. Res.*, doi:10.1029/2011JD017091, in press.

Schreier, M., Mannstein, H., Eyring, V and Bovensmann, H., (2007): Global ship track distribution and radiative forcing from 1 year of AATSR data. *Geophysical Research Letters*, 34, 2007.

Snider, J. R., Guibert, S., Brenguier, J.-L. and Putaud, J.-P., (2003): Aerosol activation in marine stratocumulus clouds: 2. khler and parcel theory closure studies, J. Geophys. Res., 108 (D15), doi:10.1029/2002JD002692.

Twomey, S., (1977): The influence of pollution on the shortwave albedo of clouds., J. Atmos. Sci., 34, 1149–1152.

MICROPHYSICAL CHARACTERISTICS OF LOW-LEVEL CLOUDS AND FOGS IN A MOUNTAINOUS REGION OF SOUTH KOREA

Jin-Yim Jeong[1], Chulkyu Lee[1], Ki-Ho Chang[2], Joo-Wan Cha[3], and Young-Jean Choi[1]
[1]Applied Meteorology Research Lab., National Institute of Meteorological Research/KMA
[2]National Typhoon Center, Korea Meteorological Administration
[3]Weather Radar Center, Korea Meteorological Administration

1. INTRODUCTION

Clouds play a decisive role in climate because of their important impact on radiative transfer in the atmosphere (Arking, 1991). In order to quantify this influence detailed measurements not only of integral cloud microphysical parameters but also of the drop size distribution of the clouds are required (Wendisch, 1998).

National Institute of Meteorological Research (NIMR) in South Korea has recently taken the initiative to encourage cloud physics research activities. NIMR established the Cloud Physics Observation System located at Daegwallyeong on the northeastern mountainous region of South Korea and carried out measurements of microphysical characteristics of low-level clouds and fogs by the Forward Scattering Spectrometer Probe (FSSP).

The aim of this study is to analyze the influence of the proposed cloud condensation nuclei (CCN) type on the size and the number of cloud droplets and to compare the parameters in this study with those in previous research.

2. DATA AND METHOD

The microphysical characteristics are presented through analyzing number concentration (N_d), mean diameter (D_m), liquid water contents (LWC), and size distribution of cloud particles sampled with the ground-based FSSP. The FSSP is an optical spectrometer measuring the count and size of cloud droplets for the 15 size bins (0.5 to 47 μm in diameter). The FSSP measurements had been conducted from November 29, 2003 to October 9, 2004 except for the ice clouds and fogs in winter. During this period, the total number of cases is 46.

Observational cases are classified 5 sectors according to 72-hour backward air mass trajectories from the NOAA/ARL HYSPLIT (Hybrid Single Particle Lagrangian Integrated Trajectories) model coupled with NCEP Reanalysis climate data. Clean continental cloud is characterized by sector #1 trajectories and contaminated continental cloud is by sector #2. Clean maritime cloud is by sector #3 and contaminated maritime cloud is by sector #4. Sector #5 trajectories are undefined air masses (Fig. 1).

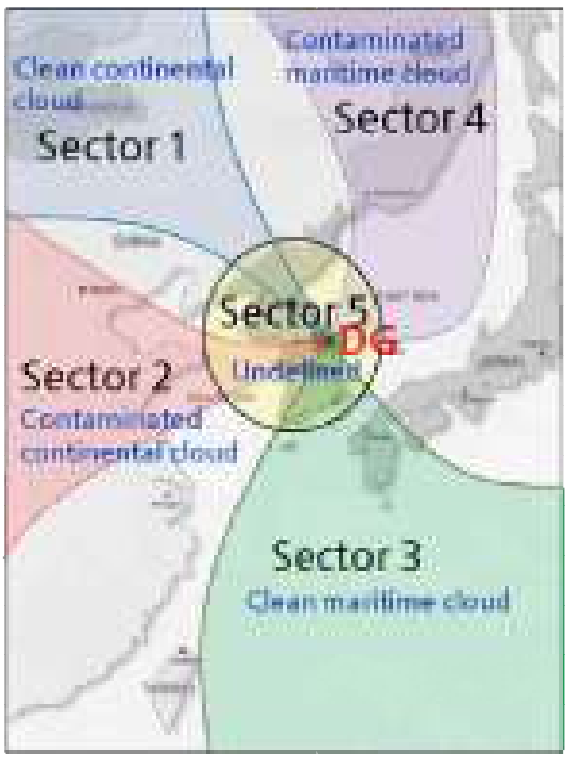

Fig. 1. Five sectors of proposed cloud type according to 72-hour backward trajectories starting from Daegallyeong (DG). The height is at 842 m.

3. RESULTS

It shows that the microphysical parameters separated by cloud type are presented in Table 1. On average, the total droplet number concentrations (N_d) in marine clouds are lower than for continental clouds, while the mean diameters (D_m) for marine clouds are larger than for continental clouds. There are 60 cm^{-3} and 0.9 μm differences between the two. Also, the number concentrations (N_d) in clean air masses are lower than for contaminated them while the mean diameters (D_m) are larger than for continental clouds. There are 50 cm^{-3} and 0.5 μm differences between the two. But, there is not much difference in liquid water content between the two.

Table 1. The number of cases, average total droplet number concentration (N_d), mean diameter (D_m), and liquid water content (LWC) by the individual sector. In this table, *S denotes the sector.

Values	*S1	S2	S3	S4	S5
No. cases	7	4	17	12	6
N_d, cm^{-3}	146	227	115	138	204
D_m, μm	4.2	4.7	6.1	4.6	4.5
LWC, gm^{-3}	0.11	0.20	0.22	0.11	0.13

Fig. 2 presents the cloud droplets size distribution for sector 1, 2, 3, and 4 divided by contamination of air. Contaminated clouds have more narrow size distribution than clean clouds. The cloud droplet spectra width of sector 3 is wide by comparison with the sector 1. However, there is not much difference in spectra width between sector 2 and 4 except for having large number concentrations of 2 to 5 μm of sector 2.

In table 2, the microphysical characteristics measured in this study are compared with those measured in Miles et al. (2000) and Garcia et al. (2002).

a)

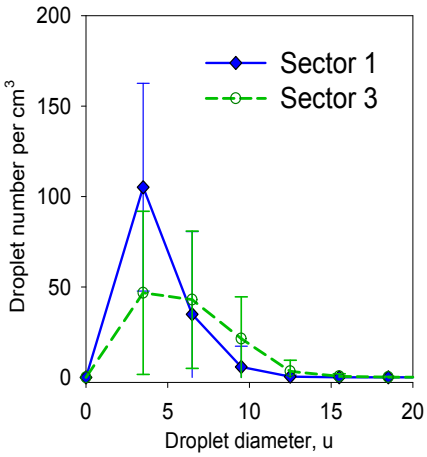

b)

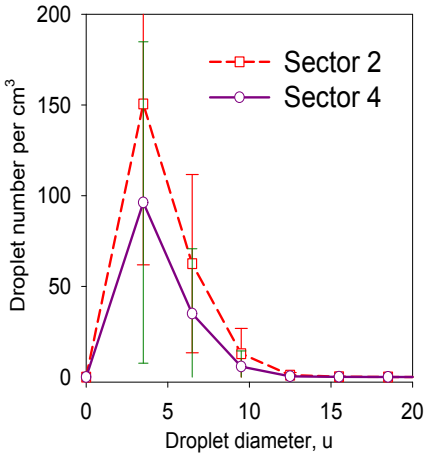

Fig. 2. The droplets size distributions of (a) clean clouds and (b) contaminated clouds.

Table 2. The total droplet number concentration (N_d), mean diameter (D_m), and liquid water content (LWC) in this study in comparison with other measurements from previous research. In this table, "A" denotes the results from Miles et al. (2000) and "B" denotes the results from Garcia et al. (2002). "C" refers to the results in this study.

Source / Values	Marine			Continental	
	A	B	C	A	C
N_d, cm^{-3}	5~182	80~120	45~185	12~693	53~239
D_m, μm	7.1~22.5	6.6~9.0	4.5~7.7	1.0~6.3	3.4~5.0
LWC, gm^{-3}	0.01~0.6	0.1~0.2	0.02~0.4	0.00~0.7	0.01~0.2

Our observed number concentration (N_d) and liquid water contents (*LWC*) for marine clouds are similar to the reported values from previous studies. However, the mean diameter (D_m) in this study is a little smaller than them from other measurements. About continental clouds, the values of the liquid water contents (*LWC*) and mean diameter (D_m) are similar. But, the number concentration (N_d) is quite smaller than that in results from previous measurements.

4. CONCLUSION

The microphysical droplet properties are important for investigating the cloud and fog growth process. We investigate microphysical characteristics in 5 types of clouds and fogs (clean maritime clouds, contaminated maritime clouds, clean continental clouds, contaminated continental clouds, and undefined clouds) based on ground-based FSSP measurements and trajectories calculated using NOAA/ARL HYSPLIT model. It seems that the maritime cloud condensation nucleus (CCN) is an effective factor in broadening the size distribution. In comparison of their microphysical parameters with previous research, the number concentration in this study is slightly larger and the mean diameter is slightly smaller. This results needs the further investigation.

5. BIBLIOGRAPHY

Arking, A., 1991: The radiative effects of clouds and their impact on climate. *Bull. Amer. Meteor. Soc.*, 72, 795-813.

Garcia, F., U. Virafuentes, and G. Montero-Martinez, 2002: Fine-scale measurements of fog-droplet concentrations: a preliminary assessment. *Atmos. Res.,* 64, 179-189.

Miles, N. L., J. Verlinde, and E. E. Clothiaux, 2000: Cloud droplet size distribution in low-level stratiform clouds. *J. Atmos. Sci.,* 57, 295-311.

Wendisch, W., 1998: A quantitative comparison of ground-based FSSP and PWM measurements. *J. Atmos. Oceanic Technol.*, 15, 887-900.

Acknowledgements

This work was supported by the NIMR/KMA project ‘Development of meteorological resources for green growth”, and “Hydrometeorology research for the test-bed region”.

EVALUATION OF SIMULATION RESULTS OF A CLOUD-RESOLVING MODEL USING SATELLITE DATA AND A SATELLITE SIMULATOR

Taro Shinoda[1], Hirohiko Masunaga[1], Munehisa K. Yamamoto[2,3], Masaya Kato[1], Atsushi Higuchi[2], Kazuhisa Tsuboki[1] and Hiroshi Uyeda[1]

[1] Hydrospheric Atmospheric Research Center, Nagoya University
[2] Center for Environmental Remote Sensing, Chiba University
[3] Graduate School of Science, Kyoto University

1. INTRODUCTION

Cloud resolving models (CRMs) explicitly resolve isolated convective clouds and precipitation systems in fine spatial and temporal scales, thus they are useful tools to analyze the structure of the systems. However, CRMs are still subject to many uncertainties, in particular, in cloud microphysical processes. To confirm the accuracy of the CRM simulation, it is useful to compare the results of the simulation with satellite observations.

To validate the CRM simulation in previous studies, data obtained by satellite observations were converted to physical parameters; e.g., surface precipitation amount and latent heating profile. These retrieved physical parameters were compared with those simulated by CRMs (e.g., Blossey et al. 2007, Zhou et al. 2007). However, the retrieved physical parameters obtained by satellite observations could contain their own biases due to uncertainties in retrieval (inversion) algorithms. Thus, it was difficult to make a detailed evaluation of the CRM simulation using satellite-retrieved physical parameters.

To avoid this situation, it is preferable to estimate satellite-consistent radiances from the model-generated microphysical distributions using radiative transfer calculations; that is a forward model. Direct satellite measurements (radiances) should have much less uncertainties than retrieved physical parameters. The method of these measurements is called as a "satellite simulator." Several satellite simulators (Matsui et al. 2009, Masunaga et al. 2010) have been developed recently. This study examines the evaluation by comparing brightness temperature (T_{BB}) of infrared (T_{BB}-IR) and microwave (T_{BB}-MW) bands and radar reflectivity calculated using Satellite Data Simulator Unit (SDSU: Masunaga et al. 2010) applied to the daily simulation results by Cloud Resolving Storm Simulator (CReSS: Tsuboki and Sakakibara 2002, Tsuboki 2008) with those obtained from satellite observations around the Taiwan-Okinawa region during the Meiyu/Baiu season in 2008 and 2010.

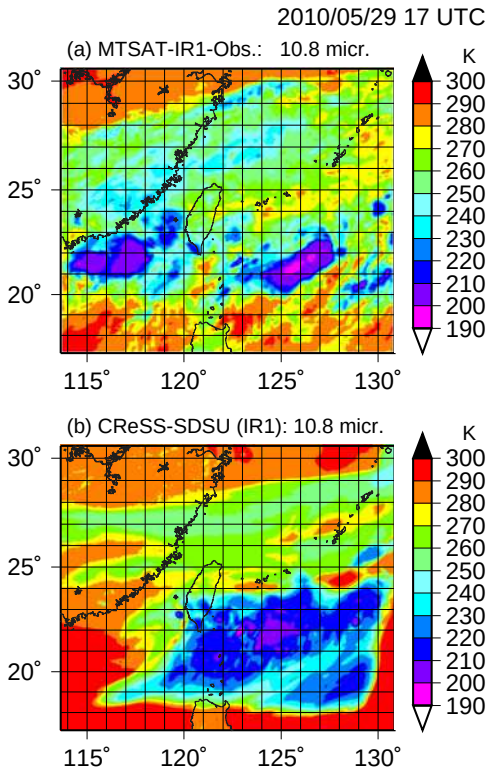

Fig. 1 Horizontal distributions of T_{BB} for infrared band (IR-Ch1) obtained from (a) the satellite observation (MTSAT) and (b) the simulation (CReSS-SDSU) at 17 UTC on May 29, 2010.

2. DAILY SIMULATIONS USING CRESS, SATELLITE DATA, AND

SDSU

CReSS is formulated on the basis of the nonhydrostatic and compressible equation system with terrain-following coordinates. A cold rain parameterization developed by Murakami (1990) and Murakami et al. (1994) is used. No convective parameterization is included. A 1.5-TKE closure scheme is applied for subgrid-scale parameterization. The prognostic variables includes 3-D velocity components, perturbations of pressure and potential temperature, subgrid-scale turbulent kinetic energy (TKE), mixing ratio of water vapor and water substances (i.e., cloud water, rain, cloud ice, snow, and graupel), and number concentrations of solid water substances (cloud ice, snow, and graupel). The surface fluxes of the momentum and the energy, and the surface radiation processes are included using the parameterization described by Louis et al. (1981).

Daily simulations using CReSS with horizontal grid resolution of 4.0 km were conducted every day for 36 hours from May 14 to June 24, 2008. Those with 2.5 km resolution were carried out from May 13 to June 30, 2010. A whole of the simulation domain in 2010 is shown in Fig. 1. The simulation domain in 2008 was almost same that in 2010. The Global Spectral Model (GSM: horizontal grid resolution is approximately 50 km) and Merged satellite and in situ data Global Daily Sea Surface Temperature provided by the Japan Meteorological Agency (JMA) were used as the initial and boundary conditions. Simulations started at 18 UTC every day and continued for 36 hours. The most important difference between in 2008 and 2010 simulations was the cloud ice sedimentation process. In 2008 simulations, cloud ice did not have its fall velocity. However, cloud ice had fall velocity of 0.1 m s^{-1} in 2010 simulations.

Data of infrared T_{BB} (Ch-1: 10.8 μm) with horizontal resolution of 4 km are obtained every hours by Multi-functional Transport Satellite (MTSAT). Data of microwave T_{BB} of 89.0 GHz with horizontal resolution of 5.9 km $\times$ 3.5 km are obtained about two times in a day by Advanced Microwave Scanning Radiometer for EOS (AMSR-E) loaded

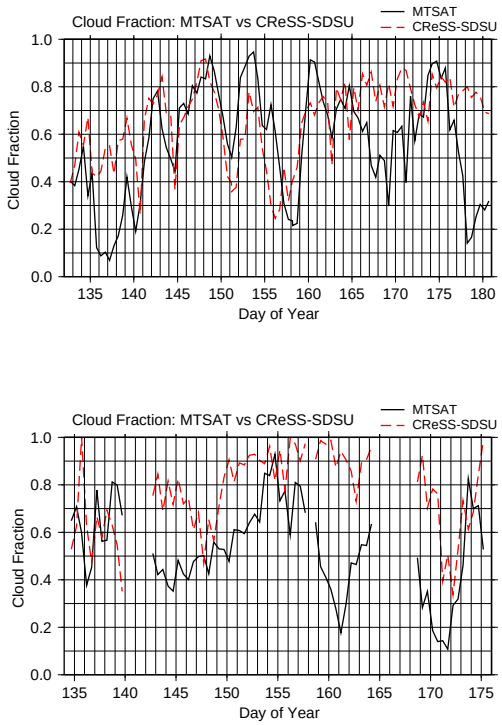

Fig. 2 Time series of cloud fractions obtained from the satellite observation (MTSAT: black solid lines) and the simulation (CReSS-SDSU: red broken lines) only over the sea columns of the simulation domain (a) from May 13 (DOY = 132) to June 30 (DOY = 180) in 2010 and (b) from May 14 (DOY = 134) to June 24 (DOY = 175) in 2008.

on the Aqua. Data of three-dimensional reflectivity with horizontal resolution of 4.3 km are obtained by Precipitation Radar loaded on Tropical Rainfall Measuring Mission (TRMM-PR).

SDSU designs to simulate visible radiance, infrared T_{BB} (e.g., for MTSAT), microwave T_{BB} (e.g., for AMSR-E), and radar reflectivity (e.g., for TRMM-PR). Input parameters into SDSU are those from CRM outputs; temperature, mixing ratio and number concentrations of water substances, and several surface parameters. Since the hourly simulation results by CReSS were archived every day, data of the nearest time passing the Aqua over the simulation domain were selected. Horizontal distributions of T_{BB}-IR and T_{BB}-MW were calculated using SDSU applied to the simulation results and compared with those obtained from MTSAT and AMSR-E. Three-dimensional reflectivity fields at the time when TRMM passed over the simulation

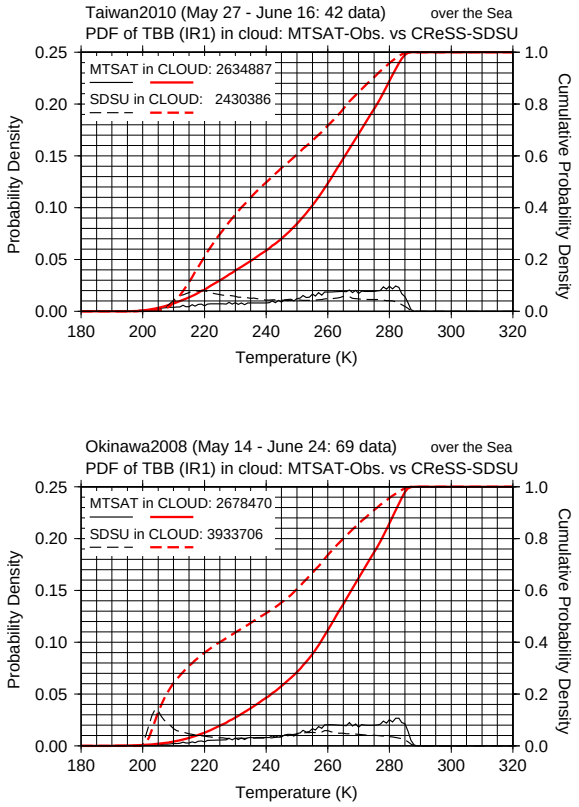

Fig. 3 Probability densities of T_{BB} for infrared band in the cloud column for all data obtained in (a) 2010 and (b) 2008. Black solid and broken lines show probability densities of T_{BB} obtained from the satellite observations (MTSAT) and the simulation (CReSS-SDSU), respectively. Red solid and broken lines show cumulative probability densities of them.

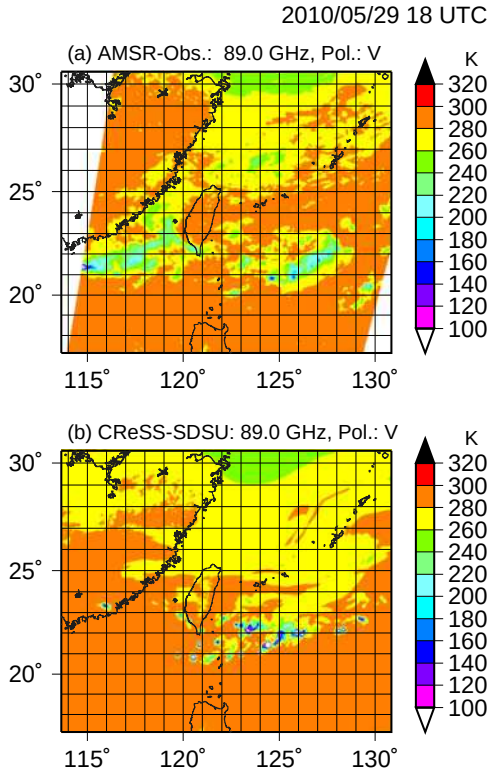

Fig. 4 Horizontal distributions of T_{BB} for 89.0-GHz microwave band obtained from (a) the satellite observation (AMSR-E) and (b) the simulation (CReSS-SDSU) for the vertical polarization at 18 UTC on May 29, 2010.

domain were also calculated using SDSU applied to the simulation results and compared with those obtained from TRMM-PR.

3. RESULTS

Figure 1 shows horizontal distributions of T_{BB} for infrared band obtained from the satellite observation and the simulation at 17 UTC on May 29, 2010. In the satellite observation, well-developed mesoscale convective systems (MCSs) whose minimum T_{BB} was less than 200 K (cloud-top height was approximately 17 km) developed over the southeast and southwest far from Taiwan Island. The location and its minimum T_{BB} of the southeastern MCS were well reproduced in the simulation. However, the southwestern MCS could not be reproduced, a cloud free region appeared there in the simulation. The cloud cover less than approximately 280 K was seen over the almost all of the simulation domain in the satellite observation and was reproduced in the simulation.

Figure 2 shows time series of cloud fractions obtained from the satellite observations and the simulations only over the sea columns in the simulation domain from May 13 to June 30 in 2010 and that from May 14 to June 24 in 2008. The cloud column was defined by the difference between obtained infrared T_{BB} and simulated SST of greater than 15 K over the sea column. And the cloud fraction is defined by a ratio of total cloud columns to all of the sea columns of the simulation domain. In the MTSAT observation, the cloud fraction was high on May 28-30 (DOY = 149-151), June 2-4 (DOY = 154-156), June 9-10 (DOY = 161-162), and June 13-15 (DOY= 165-167) in 2010. The difference of cloud fractions was almost small less than 10%, although sometimes it exceeded 30%. The variation of the cloud fraction was well repro-

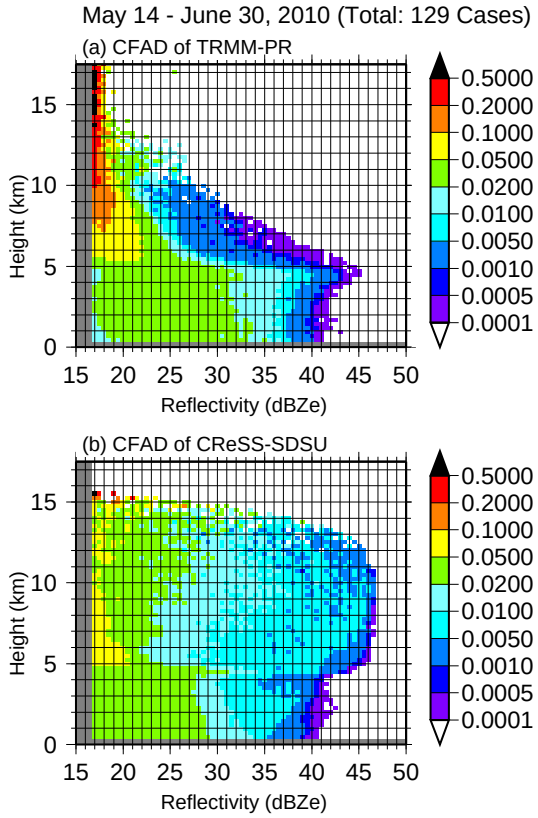

Fig. 5 CFADs obtained from (a) the satellite observations (TRMM-PR) and (b) the simulations (CReSS-SDSU) for the total 129 paths from May 14 to June 30, 2010. Color shows the frequency.

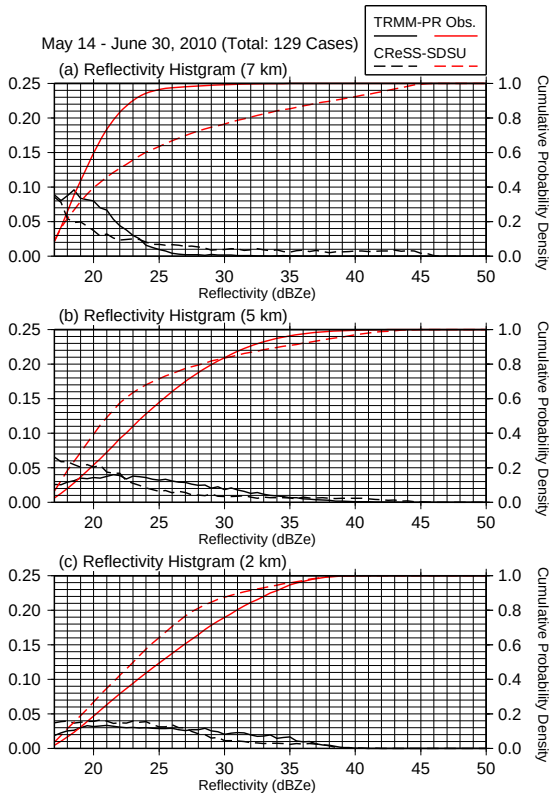

Fig. 6 Probability densities of reflectivity obtained from the satellite observations (TRMM-PR) and the simulations (CReSS-SDSU) for the total 129 paths at heights of (a) 2 km, (b) 5 km, and (c) 7 km. Black solid and broken lines show probability densities of reflectivity obtained from the satellite observations and the simulations, respectively. Red solid and broken lines show cumulative probability densities of them.

duced in the simulations in 2010. However, the simulated cloud fraction was quite larger than the observed one in 2008, thus the cloud fraction in 2008 was not reproduced.

Figure 3 shows probability densities of T_{BB} for infrared band in the cloud column for all data obtained in 2008 and 2010 simulations. Frequency of upper clouds (T_{BB} was less than 240 K) of the simulation both in 2008 and 2010 was larger than that of the satellite observation. On the other hand, frequency of middle and lower clouds (T_{BB} was greater than 240 K) of the simulation was smaller than that of the satellite observation. In addition, the difference of the frequency of upper clouds in 2010 was reduced a little than that in 2008. This should be attributed to the inclusion of cloud ice sedimentation. Cloud ice in the upper layer should fall to the middle layer by its sedimentation in 2010, but this process was not included in 2008. Thus, the inclusion of the cloud ice sedimentation contributed a better reproducibility of the cloud-top height, however, there would be additional room for improvement of reproducibility to sophisticate the cloud ice sedimentation.

Figure 4 shows horizontal distributions of T_{BB} for 89.0-GHz microwave band obtained from the satellite observation and the simulation for the vertical polarization at 18 UTC on May 29, 2010. This frequency is sensitive to solid precipitation particles in the upper troposphere. If large amount of ice particles exist, T_{BB} shows small values (e.g., less than 220 K). In the satellite observation, low T_{BB} areas were seen over southeast and southwest far from Taiwan Island, corresponding to the well-developed MCSs observed by the in-

frared band (Fig. 1). For the southeastern MCS, low T_{BB} areas were reproduced in the simulation. However, minimum T_{BB} of the simulation (less than 100 K) was quite lower than that of the satellite observation. This suggested that the simulation reproduced the excessive existence of solid hydrometeors in the precipitation cells in the MCS. On the other hand, the area of moderate T_{BB} ranged between 200 and 260 K of the simulation was quite smaller than that of the satellite observation. This suggested that the simulation cannot reproduce the expansion of dense stratiform region formed by solid hydrometeors in the MCS.

Figure 5 shows contoured frequency by altitude diagrams (CFADs: Yuter and Houze 1995) obtained from the satellite observations and the simulations for the total 129 paths from May 14 to June 30, 2010. Distributions of reflectivity below the melting level was reproduced very well in the simulations. However, large reflectivity above the melting level appeared in the simulations.

Figure 6 shows probability densities of reflectivity obtained from the satellite observations and the simulations at heights of 2 km, 5 km, and 7 km. Above the melting level (7 km), frequency that was greater than 24 dBZ in the simulations was quite large in comparison with the satellite observations. This suggested the excessive existence of hydrometeors in the limited area that should be the convective cores. Around the melting level (5 km), frequency between 23 and 35 dBZ in the simulations was less in comparison with the satellite observations. Below the melting level (2 km), frequency of reflectivity obtained from the satellite observations and the simulations was quite similar, but that was greater than 28 dBZ of the simulations was underestimated. These suggested the less expansion of the stratiform region in the simulations.

4. SUMMARY

An evaluation method for a CRM using satellite data and SDSU are presented. This study shows the comparison T_{BB}-IR, T_{BB}-MW, and radar reflectivity calculated using SDSU applied to the daily simulation results with those obtained from the satellite observations around the Taiwan-Okinawa region during the Meiyu/Baiu season in 2008 and 2010. The reproducibility of cloud fraction is improved in 2010. Frequency of upper (middle/lower) clouds of the simulation was larger (lesser) than that of the satellite observation. The inclusion of the sedimentation process of cloud ice should contribute to the improvement of distribution of T_{BB}-IR. The excessive existence of solid hydrometeors in the MCSs and less expansion of dense stratiform region should be presented in the simulation.

Using the evaluation method shown in the present study, we can visualize the bias of the microphysical processes in the current CReSS model. Thus, we can fix the indicator and return point when we try to improve the microphysical processes (snow-graupel conversion process in CReSS) in near future.

References

Blossey, P. N., C. S. Bretherton and J. Cetrone, 2007: Cloud-resolving model simulations of KWAJEX: Model sensitivities and comparisons with satellite and radar observations. *J. Atmos. Sci.*, **64**, 1488–1508.

Louis, J. F., M. Tiedtke and J. F. Geleyn, 1981: A short history of the operational PBL parameterization at ECMWF. *Proc. ECMWF Workshop on Planetary Boundary Layer Parameterization, Reading, United Kingdom, ECMWF*, 59–79.

Masunaga, H., T. Matsui, W.-K. Tao, A. Y. Hou, C. D. Kummerow, T. Nakajima, P. Bauer, W. S. Olson, M. Sekiguchi and T. Y. Nakajima, 2010: Satellite Data Simulator Unit (SDSU): A multi-sensor, multi-spectral satellite simulator package. *Bull. Amer. Meteor. Soc.*, **91**, 1625–1632.

Matsui, T., X. Zeng, W.-K. Tao, H. Masunaga, W. S. Olson and S. Lang, 2009: Evaluation of long-term cloud-resolving model simulations using satellite radiance observations and multi-frequency satellite simulators. *J. Atmos. Oceanic Technol.*, **26**, 1261–1274.

Murakami, M., 1990: Numerical modeling of dynamical and microphysical evolution

of an isolated convective cloud: the 19 July 1981 CCOPE cloud. *J. Meteor. Soc. Japan*, **68**, 107–128.

Murakami, M., T. L. Clark and W. D. Hall, 1994: Numerical simulations of convective snow clouds over the Sea of Japan; two-dimensional simulations of mixed layer development and convective snow cloud formation. *J. Meteor. Soc. Japan*, **72**, 43–61.

Tsuboki, K., 2008: High-resolution simulations of high-impact weather systems using the cloud-resolving model on the Earth Simulator. K. Hamilton and W. Ohfuchi, Eds., *High Resolution Numerical Modelling of the Atmosphere and Ocean*, Springer, 141–156.

Tsuboki, K. and A. Sakakibara, 2002: Large-scale parallel computing of Cloud Resolving Storm Simulator. H. P. Zima and et al., Eds., *High Perfomance Computing*, Springer, 243–259.

Yuter, S. E. and R. A. Houze, 1995: Three-dimensional kinematic and microphysical evolution of Florida cumulonimbus. Part II: Frequency distributions of vertical velocity, reflectivity, and differential reflectivity. *Mon. Wea. Rev.*, **123**, 1941–1963.

Zhou, Y. P., W.-K. Tao, A. Y. Hou, W. S. Olson, C.-L. Shie, K.-M. Lau, M.-D. Chou, X. Lin and M. Grecu, 2007: Use of high-resolution satellite observations to evaluate cloud and precipitation statistics from cloud-resolving model simulations. Part I: South China Sea Monsoon Experiment. *J. Atmos. Sci.*, **64**, 4309–4329.

Acknowledgements

This study is performed by the Formation of a Virtual Laboratory for Diagnosing the Earth's Climate System (VL) and the Innovative Program of Climate Change Projection for the 21th century (KAKUSHIN) project "Cloud Modeling and Typhoon Research" funded by the Ministry of Education, Culture, Sports, Science and Technology (MEXT).

3D-VISUALIZATION OF LUNAR VARIATION OF PRECIPITATION AND CLOUDINESS

L. Hejkrlík
Czech Hydrometeorological Institute, 400 11, Ústí nad Labem, Czech Republic

1. MOTIVATION

Linkages between lunar synodic cycle and select types of meteorological parameters have been suggested in previous studies, especially by *Bradley et al. (1962)* in the USA and by *Adderley and Bowen (1962)* in Australia. It was demonstrated that extreme precipitation events occur more frequently on the third to fifth day after syzygies; the effect is sometimes called Bowen's signal. Similar lunar or semi-lunar modulation was later found also in ozone concentrations *(Adderley, 1963)*, sunshine *(Lund 1964)*, thunderstorm frequencies *(Lethbridge 1970)* and in global temperatures observed by polar orbiting satellites *(Balling and Cerveny 1995)*.

In our earlier papers we tried to analyse the possibility that the effect is transient in relation to solar activity (see *Fett 2008)*. We confirmed the long-term quasi-periodical nearly-parallel changes in expression of lunar signal in 100-year long series of daily precipitation amounts at 14 European stations *(Hejkrlík 2009),* in subseries of one element divided by climatological seasons *(Hejkrlík 2010)* and recently also for two different meteorological parameters at one single station *(Hejkrlík 2011)*. The prevailing periods seemed to be similar to 22-year Hale solar magnetic cycle but there was no clear evidence and other similar celestial cycles could not be excluded *(Andrlík and Brůžek 1967).*

2. DATA

A unique set of uninterrupted daily precipitation data from Prague-Klementinum since 1804, published by the Czech Hydrometeorological Institute, was available. In this study we also made use of a related dataset of daily mean cloudiness that dates back as far as 1775. The cloud cover has been observed in a subjective way but we think its reliability is relatively good. In the case of precipitation we also examined the days with daily amount exceeding 10 mm.

3. METHOD

The data were analysed by superposed epoch technique with the date of new moon as the null day. The data were divided into epochs of synodic months and superposed for 5 or 11 years with a step of one year. We get six sets of mean 29-day synodic signals containing 198-204 records (individual mean courses of given element for specific year) for precipitation and 227-233 records for cloudiness.

The mean synodic graphic representations of every single year were displayed stepwise year-by-year by Golden Software Surfer 10.4. The resulting 3D surface map was smoothed by local polynomial grid to produce visual perception of gradual development of synodic variation and of presence of Bowen's signal.

The temporal occurrence of lunar variation was also quantified by correlation coefficient ψ between semi-lunar cosine function (period 4π/29.53), emulating the Bowen's signal, and the mean signals.

The graphs of ψ exhibit quasi-periodic behaviour with periods similar to solar magnetic cycle of about 22 years. In order to detect the predominant frequencies we applied the process from *Takahashi et al. (2009)*. After removing from ψ both short and long-term variations using a band-pass filter (cut-off periods 4 and 64 years) the power spectra of ψ were calculated by FFT and afterwards smoothed with a running mean of 3 data points.

4. RESULTS

3D surface maps for six different series of daily precipitation and cloudiness data from Prague-Klementinum in periods 1804 to 2011 (precipitation) or 1775 to 2011 (cloudiness) were created by above mentioned method (Figures 1. to 6.). All the maps demonstrate the ever-changing picture of lunar synodic variation that only in some periods resemble the classic Bowen's signal. The correlation coefficients ψ exhibit in all cases a quasi-periodicity with many frequencies. The power spectra of ψ

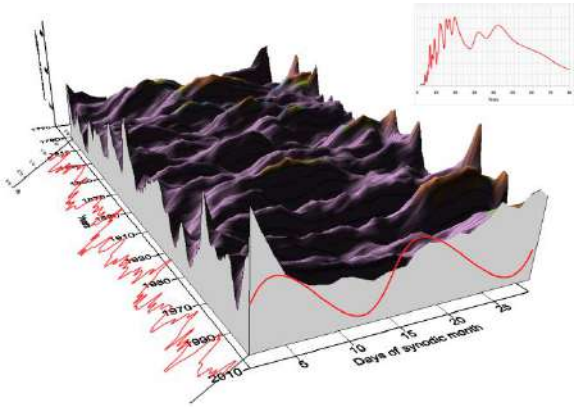

Figure 1. 3D-visualization of long-term development of synodic signal of precipitation, superposed for 5 years. Parameter ψ is drawn along y axis, the model Bowen's signal along x axis. The embedded graph is power spectrum of ψ.

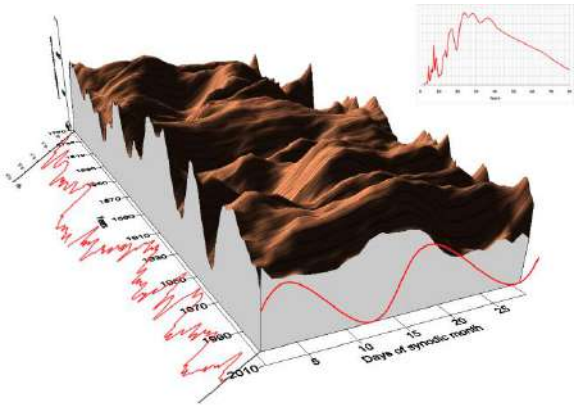

Figure 2. 3D-visualization of long-term development of synodic signal of precipitation, superposed for 11 years. Parameter ψ is drawn along y axis, the model Bowen's signal along x axis. The embedded graph is power spectrum of ψ.

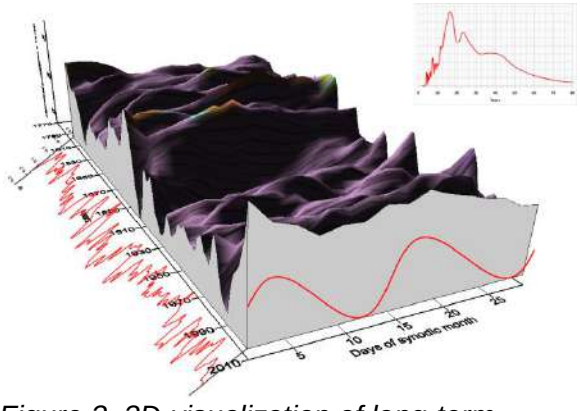

Figure 3. 3D-visualization of long-term development of synodic signal of ppt ≥ 10 mm, superposed for 5 years. Parameter ψ is drawn along y axis, the model Bowen's signal along x axis. The embedded graph is power spectrum of ψ.

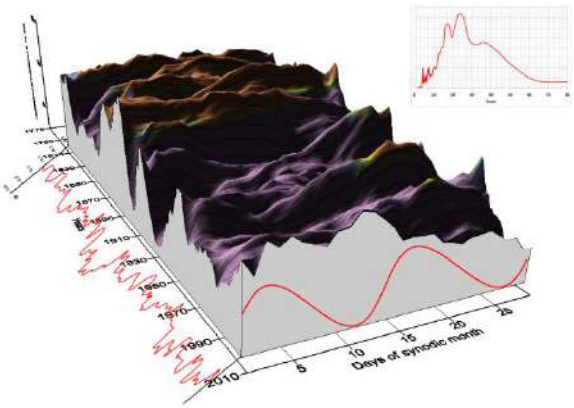

Figure 4. 3D-visualization of long-term development of synodic signal of ppt ≥ 10 mm, superposed for 11 years. Parameter ψ is drawn along y axis, the model Bowen's signal along x axis. The embedded graph is power spectrum of ψ.

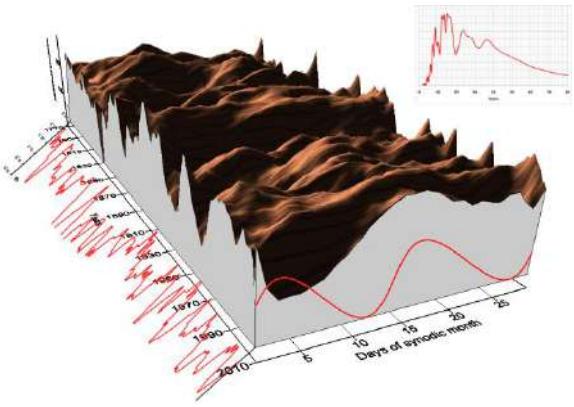

Figure 5. 3D-visualization of long-term development of synodic signal of cloudiness, superposed for 5 years. Parameter ψ is drawn along y axis, the model Bowen's signal along x axis. The embedded graph is power spectrum of ψ.

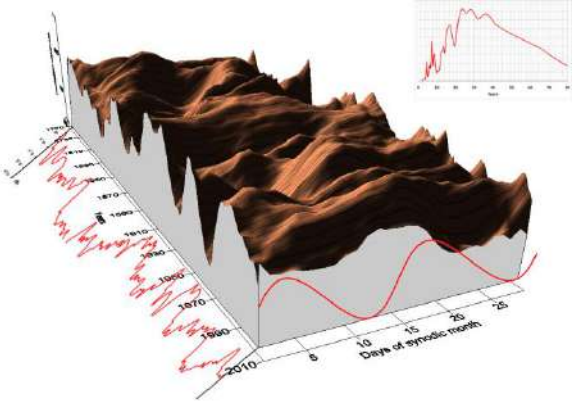

Figure 6. 3D-visualization of long-term development of synodic signal of cloudiness, superposed for 11 years. Parameter ψ is drawn along y axis, the model Bowen's signal along x axis. The embedded graph is power spectrum of ψ.

of particular series show maxima mainly near periods about 20 years but are unfortunately quite dissimilar. The most important periods after which the signals are cyclically comparable with the Bowen's signal are listed in Table 1.

Element	Superposition	1st max	2nd max
Precipitation	5 years	12-23 yrs	43 years
Precipitation	11 years	20 years	32-43 yrs
Ppt ≥ 10 mm	5 years	16 years	23 yers
Ppt ≥ 10 mm	11 years	17 years	23 years
Cloudiness	5 years	12-17 yrs	23 years
Cloudiness	11 years	17 years	23-32 yrs

Table 1. Main periods in power spectra of ψ for various series

5. CONCLUSION

We tried to verify the hypothesis about possible temporal displacement of the semi-lunar signal of various meteorological elements so that only in some periods it equals Bowen's signal. The visual representation of 3D surface maps give the impression of extremely changeable picture of mean synodic variation.

The spectral analysis of a parameter ψ that characterizes the occurrence of classic Bowen's signal gives no good chance to distinguish between comparable natural periods from solar system like heliomagnetic Hale cycle (22 years) or lunar Saros cycle (18.6 years) or their multiples.

6. BIBLIOGRAPHY

Adderley, E. E. - Bowen, E. G.: Lunar component in precipitation data. Sci., 137, 1962, p. 749-750

Adderley, E. E.: The Influence of the Moon on Atmospheric Ozone. J. Geophys. Res., 68 (5), 1963, p. 1405-1408

Andrlík, L. - Brůžek, V.: Effect of the Moon on the rainfall course (in Czech). Meteorol. Zpr., 20, 1967, No 3-4, p. 102-103

Balling R. C. – Cerveny R. S.: Impact of lunar phase on the timing of global and latitudinal trophospheric temperature maxima. Geophys. Res. Lett. Vol. 22, No. 23, 1995, p. 3199-3201,

Bradley, D. A. et al.: Lunar synodic period and widespread precipitation. Sci., 137, 1962, p. 748-749

Fett, W: Sonne, Mond und Regen. Beilage zur Berliner Wetterkarte, Berlin 2008

Hejkrlík L.: Luni-solar interaction in precipitation over Europe. European Aerosol Conference 2009, Karlsruhe, Abstract T044A04

Hejkrlík L.: Quasi-persistency of lunar synodic signal of precipitation in different parts of year. EGU General Assembly 2010, Vienna, Abstract No EGU2010-3865

Hejkrlík L.: Lunar signal in cloudiness is stronger than in precipitation. EGU General Assembly 2011, Vienna, Abstract No EGU2011-2877

Lethbridge M. D.: Relationship between Thunderstorm Frequency and Lunar Phase and Declination. J. Geophys. Res., 75, 1970, p. 5149-5153

Lund, I. A.: Indications of a Lunar Synodical Period in United States Observations of Sunshine. Journ. of the Atmospher. Sci., 22, 1964, p. 24-39

Takahashi et al.: 27-day variation in cloud amount and relationship to the solar cycle. Atmos. Chem. Phys. Discuss., 9, 2009, p. 15327-15338

REAL-CASE STRATOCUMULUS-TOPPED PLANETARY BOUNDARY LAYER IN THE BAY OF BISCAY SIMULATED BY A LIMITED-AREA MODEL

Anna Possner[1], Elias Zubler[1], Oliver Fuhrer[2], Ulrike Lohmann[1], Christoph Schaer[1]
[1]Institute for Atmospheric Sciences, ETH, Zürich, Switzerland
[2]MeteoSwiss, Zürich, Switzerland

1 MOTIVATION AND MODEL DESCRIPTION

Simulating stratocumulus-topped planetary boundary layers (PBL) with strong temperature inversions aloft poses a major problem in the atmospheric modelling community. Most models struggle to capture complex PBL profiles and, in particular, sharp inversions. During this study a setup of the limited-area model COSMO-CLM was developed to simulate the case from the 26th to 27th of January 2003 in the Bay of Biscay. This case was characterised by a strong inversion (up to 12 K within 100 m centred at 500 m a.s.l.), as was observed at the 4 nearby radiosonde stations (Brest, Bordeaux, Santander and La Coruña), as well as by extensive marine stratocumuli with embedded ship tracks. Here we present a model setup with which we successfully simulated sharp temperature inversions over large parts of the marine domain and significantly improved cloud cover. We will proceed to use this setup in future studies to simulate ship tracks.

In order to test the dependency on horizontal resolution on the PPL profiles as well as for the purpose of the future ship track studies a nesting procedure was used. A reanalysis-driven simulation with 12 km horizontal resolution (coarse) forces a 2-km simulation (fine) over the Bay of Biscay. The applied COSMO-CLM model version consists of the standard Runge Kutta core (*Wicker and Skamarock*, 2002; *Foerstner and Doms*, 2004), the radiation scheme by *Ritter and Geleyn* (1992) with the relative humidity criterion for determining subgrid-scale cloud cover, as well as a semi-Lagrangian scheme for the positive definite advection of moisture variables. Furthermore, the sub-gridscale turbulence is parameterised by the second order closure scheme based on Mellor and Yamada (1974;1982). The model's 1-moment cloud microphysics scheme was replaced by a 2-moment scheme (*Seifert and Beheng*, 2006; *Zubler et al.*, 2011). This scheme parameterises the droplet nucleation, based on the CCN concentration, the vertical saturation gradient and the vertical velocity, as well as the processes of accretion and autoconversion, self-collection, rain-droplet break-up and rain sedimentation for the warm-phase cloud microphysics on the grid-scale.

Applying the operational MeteoSwiss setup in the COSMO-CLM simulations leads to too shallow temperature inversions between 300 to 600 m and too little cloud cover, in spite of the captured large-scale subsidence. During this study we attempted to improve the model's performance by changing the resolution (vertical and horizontal), as well as changing the tuning parameters influencing the vertical mixing.

2 RESULTS

This study showed, that changes in both, vertical (max. 100 m, 50 m and 10 m in first kilometre) and horizontal resolution (12 km and 2 km), lead to no significant improvement of the temperature gradient at the inversion height as well as the spatial stratocumulus distribution.

Based on the continued absence of the inversion during these initial test simulations, we aimed to reduce the vertical mixing at the PBL top. To this end the surface fluxes were increased and decreased in some simulations by setting the tuning parameters rat_sea and rat_lam to the limiters of their allowed ranges (1–100 and 0.1–10 respectively). Rat_sea provides an overall scaling of both the moisture and heat fluxes from the surface, whereas rat_lam changes the ratio of heat to moisture fluxes emitted into the atmosphere. Again no significant improvements of the PBL struc-

ture were observed.
These results suggested that the vertical mixing at the PBL top was too strong independently of the vertical and horizontal resolution and independently of the magnitude of the surface fluxes. For this reason, the turbulence parameterisation of the PBL based on Mellor and Yamada was investigated. In this parameterisation the equations of motion for the turbulent parts of the flow are proportional to the product of $K_M \times \partial U_i/\partial z$ for momentum and $K_H \times \partial \Theta/\partial z$ for heat respectively. K_M and K_H are the diffusion coefficients for momentum and heat, which are the product of the turbulent kinetic energy, the stability functions of Mellor and Yamda as well as an assumed fundamental length scale of turbulence. For numerical stability a limiter is applied to these diffusion coefficients in the COSMO-CLM model which imposes a lower bound of at least 1 m^2/s.
Buzzi et al. (2011) showed in idealised studies that this limiter leads to artificial vertical mixing under very stable stratiform conditions, as they are present in the Bay of Biscay. Based on their results, we decreased the $K_{M,min}$ and $K_{H,min}$ values, which are the minimum values for the momentum and heat diffusion coefficients respectively, to 0.01 m^2/s and set the asymptotic length scale of turbulence to 150 m (default: 500 m for 12-km and 250 m for 2-km simulations).
The resulting model profiles for potential temperature and relative humidity are shown in Fig. 1 for Brest together with the observed radiosonde profiles at 00 UTC 27.01.2003. The figure shows how a clear decoupling of the moisture fluxes between the boundary layer and the free atmosphere is achieved by allowing the vertical diffusion to decrease to lower values, which is a direct result of the model's ability to simulate the inversion correctly.

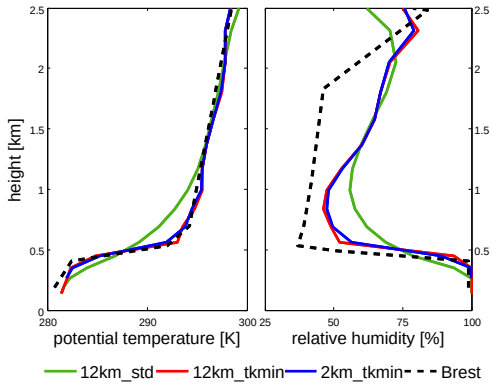

Figure 1: *Comparison between PBL potential temperature and relative humidity profiles at 00 UTC 27.01.2003 for the 12-km and 2-km simulations with reduced diffusion coefficients (*_12km_tkmin and *_2km_tkmin respectively) and the 12-km standard setup simulation (*_std) with the Brest sounding.*

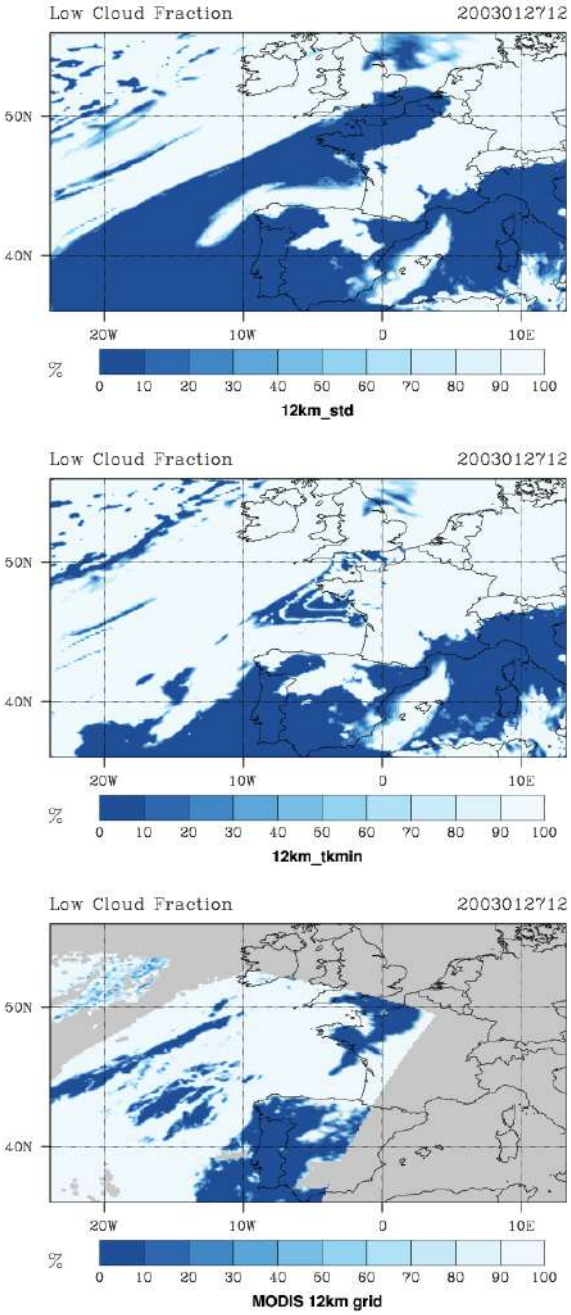

Figure 2: *Low cloud fraction (cloud fraction below 800 hPa) for the standard setup simulation (12km_std) in comparison to the reduced diffusion coefficient simulation (12km_tkmin) and the MODIS satellite at 12 UTC 27.01.2003. In the MODIS plot grey areas are either outside the satellite's imaging range, or obscured by higher level clouds.*

Although only the Brest profile is shown here, the strengthening of the inversion between 300 – 600 m was not only restricted to that particular location, but was observed over large areas of the marine domain to the West of the Bay and Portugal. The increase of potential temperature between 300 m to 600 m doubled from the standard setup simulation (∼4 K) to the reduced diffusion coefficient simulation (∼8 K – ∼10 K). The stronger capping of the PBL also had a tremendous effect on the spatial distribution of low cloud coverage (see Fig. 2), which was significantly increased and is now in better agreement with the observed MODIS satellite cloud cover for this time period.

3 CONCLUSIONS AND OUTLOOK

In this study it was shown that the regional COSMO-CLM model is able to simulate a realistic marine, shallow, cloud-topped boundary layer with the important changes to the default setting, in which the limiters of the diffusion coefficients of momentum and heat were reduced from their default value of 1 m^2/s to 0.01 m^2/s. With this setup, we will proceed to simulate the impact of ship emissions on the cloud-microphysical properties and their meteorological feedbacks in 2-km simulations for the real case.

BIBLIOGRAPHY

Buzzi, M., M. Rottach, M. Raschendorfer, and A. Holstag (2011), Evaluation of the COSMO-SC turbulence scheme in a shear-driven stable boundary layer, *Meteorol. Z.*, *20*(3), 335–350.

Foerstner, J., and G. Doms (2004), Runge-kutta time integration and high-order spatial discretization of advection - a new dynamical core for the LMK, *Model Development and Application*, COSMO *Newsletter*, No. 4 [Available online at http://www.cosmo-model.org/content/model/documentation/newsLetters/newsLetter04/chp9-6.pdf.].

Mellor, G., and T. Yamada (1974), A hierachy of turbulent closure models for planetary boundary layers, *J. Atmos. Sci.*, *31*, 1791–1806.

Mellor, G., and T. Yamada (1982), Development of a turbulence closure model for geophysical flow problems, *Rev. Geophys. and Space Phys.*, *20*, 851–875.

Ritter, B., and J. Geleyn (1992), A comprehensive radiation scheme for numerical weather prediction models with potential applications in climate simulations, *Mon. Wea. Rev.*, *120*, 303–325.

Seifert, A., and K. Beheng (2006), A two-moment cloud microphysics parameterization for mixed-phase clouds. part 1: Model description, *Meteorol. Atmos. Phys.*, *92*, 45–66.

Wicker, L., and W. Skamarock (2002), Time-splitting methods for elastic models using forward time schemes, *Mon. Wea. Rev.*, *130*, 2088–2097.

Zubler, E., D. Folini, U. Lohmann, D. Lüthi, A. Mühlbauer, S. Pousse-Nottelmann, C. Schär, and M. Wild (2011), Implementation and evaluation of aerosol and cloud microphysics in a regional climate model, *J. Geophys. Res.*, *116*(D02211), doi:10.1029/2010JD014572.

4 ACKNOWLEDGEMENTS

I would like to acknowledge the COSMO-CLM community for providing and maintaining the code, C2SM for source code support, as well as the CSCS (Swiss Center for Scientific Computing), where the simulations were carried out on a CRAY-XE6 system. I would also like to thank Dr. Dani Lüthi for his help on data handling.

QUANTIFYING DUST'S IMPACT ON THE ICE GENERATION IN SUPERCOOLED STRATIFORM CLOUDS BY COMBINING REMOTE SENSING AND IN SITU MEASUREMENTS

Damao Zhang[1], Zhien Wang[1], Jefferson Snider[1], Min Deng[1], Ming Zhao[1], Andrew Heymsfield[2], Dong Liu[3], Jiwen Fan[4]

[1]University of Wyoming, Department of Atmospheric Science, Laramie, WY, USA

[2]NCAR MM, Boulder CO, USA

[3]Key Laboratory of Atmospheric Composition and Optical Radiation, CAS, Hefei, China

[4]PNNL, Richland, WA, USA

1. INTRODUCTION

Ice generation in the atmosphere has profound impacts on the cloud radiative properties and precipitation generation. However, the primary ice generation in clouds is poorly understood. Among many aspects of ice generation in the atmosphere that need to be advanced, understanding the linkages of aerosols and ice generation is a critical step [*Cantrell and Heymsfield*, 2005]. Dust particles have widely been recognized as the most important ice nuclei (IN) sources [*DeMott et al.*, 2010]. To improve our understanding of the effectiveness of dust particles as IN, this presentation provides an update on using four-year (2006-2010) collocated CloudSat and CALIPSO measurements to quantify dust's impact on ice generation in supercooled stratiform clouds. The results highlight an important contribution of space-based active remote sensing measurements to the investigation of primary ice generation processes.

2. IDENTIFICATION OF SSCs AND DUST LAYERS

Supercooled stratiform clouds (SSCs) are ideal targets because of their less complex dynamic environments for ice growth (e.g., limited vertical extent). The SSCs have a thin supercooled liquid-dominated mixed-phase layer at the top. The ice particles are presumed to form within that layer, grow and fall out [Wang et al. 2004; *Westbrook and Illingworth*, 2011]. The resulting ice virga or precipitation has depth up to 2.5 km [*Fleishauer et al.*, 2002].

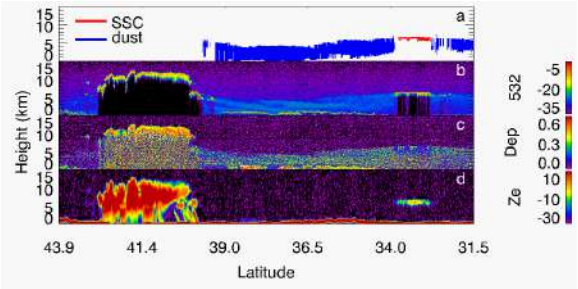

Figure 1. *(a) Identified SSCs and dust layers; (b) CALIOP lidar TAB at 532nm; (c) CALIOP lidar depolarization at 532nm; (d) CloudSat CPR radar reflectivity.*

The collocated CloudSat and CALIPSO measurements provide unique dataset for studying ice generation in SSCs and the aerosol impacts. The SSCs could be reliably detected from space-borne lidar measurements because of the strong lidar backscattering and also the strong attenuation of lidar signal by the liquid dominated layer at the top [*Zhang et al.*, 2010]. In this study, the radar reflectivity factor (Z_e) from CloudSat were used to detect ice particle occurrence in SSCs [*Stephens et al.*, 2008], while CALIPSO measurements can detect dust layers around the clouds [*Winker et al.*, 2010]. Fig.1 shows an example of an identified SSC and contrasts it with a deeper cloud system from collocated CALIPSO and CloudSat measurements. The SSC has a liquid-dominated layer with tops at ~5 km and cloud top temperatures (CTT) of ~ -11 ^{o}C. Ice virga is detectable below cloud top as indicated by the CloudSat Z_e measurements. In addition, CALIPSO lidar measurements also provide high vertical

resolution profiles of backscattering and depolarization ratio for identifying major aerosol types [*Winker et al.*, 2010]. For example, the dust layer top and base can be detected by using lidar total attenuated backscattering (TAB) and depolarization for cloud free profiles [*Liu et al.*, 2008]. In Fig.1, the dust layer is evident with a top and base at about 5 km and 1 km, respectively, on both sides of SSCs.

3. QUANTIFYING DUST IMPACTS ON ICE GENERATION IN SSCs

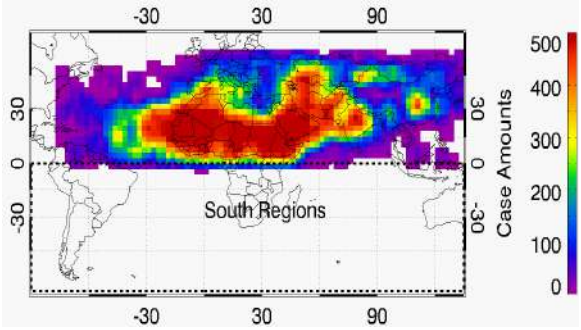

Figure 2. Global distribution of dusty SSCs based on four year CloudSat and CALIPSO measurements.

We relied on dust layer detected between or surrounding clouds to infer whether SSCs are impacted by dust, or not. If dust layers are detected close to either one side or both sides of SSCs, it is believed that the SSC layer is affected by dust particles and referred as a dusty SSC (Fig.1). Fig.2 shows the global geographical distribution of the dusty SSCs. Dusty SSCs cases are mainly located at northern Africa, Saudi Arabian and East Asia regions – the so called 'dust belt'. For non-dusty SSCs in the 'dust belt', they might still be influenced by dust aerosol present at concentrations and sizes that produce a signal less than the detection limit of the CALIPSO lidar. Therefore, we also included SSCs in the same longitude and latitude ranges in the Southern Hemisphere for comparison and referred it as the 'South Regions', as shown in Fig. 2.

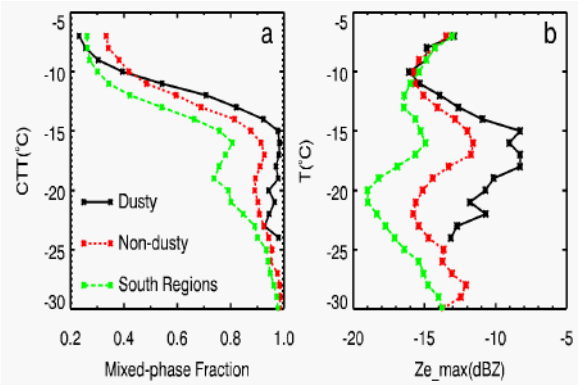

Figure 3. (a) Mixed-phase fractions relative to all SSCs for dusty, non-dusty and 'South Regions'; (b) for mean Z_e_max (calculated within 500m of SSC top).

When ice particles are detected based on the temperature-dependent Z_e thresholds (Zhang et al 2010), the SSC is then regarded as in mixed-phase state. The dusty SSCs have ~20% higher mixed-phase fractions at CTT colder than -10 °C as indicated in Fig 3 (a). About 98% of the dusty SSCs are mixed-phase at CTT ~-15 °C, while the non-dusty and 'South Regions' cases only reach the dusty SSC's magnitude of mixed-phase fraction at CTT values ≤ -30 °C. From Fig. 3b, the dusty SSCs have larger mean Z_e_max at CTT colder than -10 °C. At ~-20 °C, the dusty SSCs have mean Z_e_max about 4 dBZ higher than non-dusty SSCs in the same region and up to 8 dBZ higher than the 'South Regions'. Due to similar ice crystal growth history in SSCs with comparable CTT and liquid water path, it is fair to assume that ice concentration is the main reason for the observed Z_e_max difference. Thus, statistically speaking, an 8 dBZ Z_e_max difference indicates that dust can enhance the ice concentration in SSCs by a factor of up to 6.3.

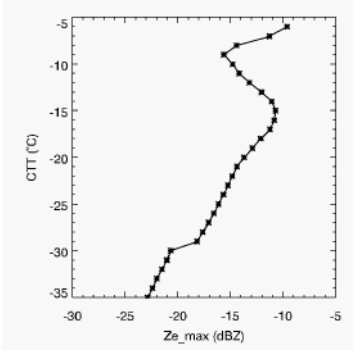

Figure 4. Calculated Z_e_max from 1-D ice growth model for ice concentration of 1/L.

On the other side, if we can model the ice crystal growth trajectory, the ice crystal number concentrations could be estimated from Z_e_max. Recent developments in ice crystal diffusional growth studies showed that strong dependence of ice growth rate on the temperature and growth habits can be modeled [*Chen and Lamb*, 1994; *Westbrook and Heymsfield*, 2011]. A 1-D ice growth model based on *Chen and Lamb [1994]*, using ice particle inherent growth ratio, which allows for both the a-axis and c-axis evolution during growth process, was developed to simulate the ice mass growth along with time. *Westbrook and Heymsfield [2011]* showed that the simulated growth is in reasonable agreement with cloud chamber measurements made between -2.5 °C and -22 °C. To obtain the ice growth along the trajectory, the terminal velocity of the particle was estimated based on parameterizations from *Heymsfield and Westbrook [2010]*. The Ice particle's initial size distribution was formulated as a gamma distribution and, initially, their shape was assumed to be spherical. The Z_e averaged over the top 500 m of cloud (corresponding to the CloudSat vertical resolution) at each CTT and for a broad range of crystal concentration. One of the simulations is shown in Fig. 4. The Z_e maxima at around -5 °C and -15 °C are caused by column-needle, dendrite growth habits, respectively. The minimum, at -8 °C, is for isometric growth.

By combining the observed Z_e_max values with the 1-D ice growth model, we retrieved the ice particle concentration at specified meteorological conditions in terms of CTT and LWP.

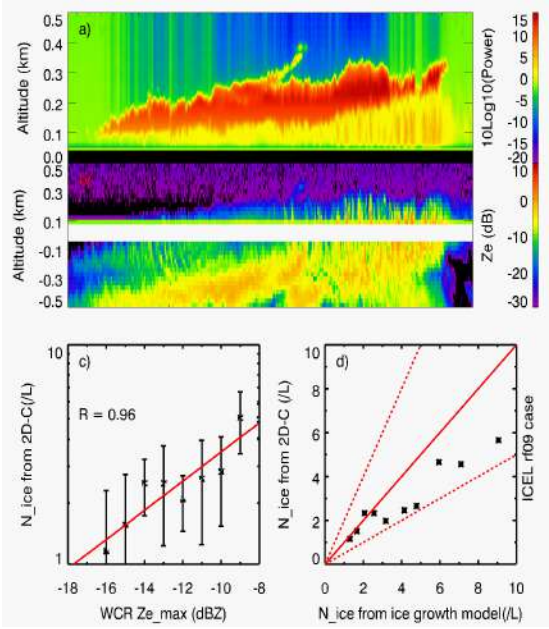

***Figure 5**. a) SSC detected by Wyoming Cloud Lidar during ICE-L (RF09). b) Z_e structure from Wyoming Cloud Radar. c) The correlation between ice number concentrations measured from 2D-C and the Z_e_max. d) The relationship between ice number concentrations measured from 2D-C and retrieved from Z_e_max.*

To validate the retrieved crystal concentrations, we compared the retrieval with in situ measurements, and with a 3-D cloud resolving model simulation. An SSC layer case observed during ICE-L is shown in Fig. 5. The CTT was -27 °C and ice virga was detected from Z_e measurements. As shown in Fig. 5 d), the ice concentrations from 2D-C correlated well with Z_e_max and the estimated ice crystal number concentration is within uncertainties; about a factor of 2.

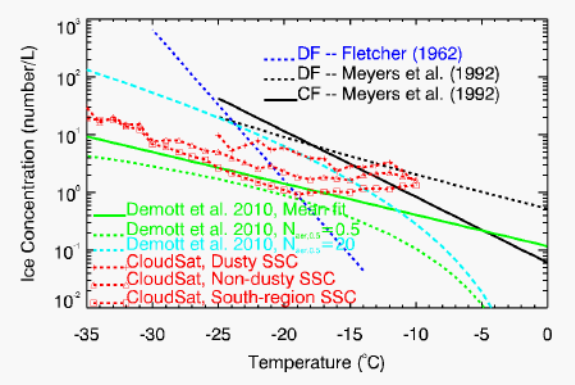

Figure 6. *The retrieved ice concentration in SSCs and comparison with different parameterizations for dusty, non-dusty and 'South Region' cases. CF and DF mean contact freezing and deposition freezing, respectively.* $N_{aer,0.5}$ *is the coarse mode aerosol (with diameter > 0.5 μm) number concentration.*

The retrieved ice concentrations, binned by temperature for dusty, non-dusty and 'South Region' SSCs shown in Fig. 6. Also presented are crystal concentrations base on ice-nucleation parameterizations [*DeMott et al.*, 2010; *Meyers et al.*, 1992]. In the case of values derived using the DeMott et al. [2010] parameterization, a range of coarse mode aerosol particle concentrations is assumed.

Fig. 6 demonstrates that dusty SSCs have higher ice concentrations, but this difference diminishes with increasing temperature. Compared to what we retrieve, Fletcher's deposition scheme underestimates at warm temperatures and vice versa. Meyers's deposition and contact freezing schemes overestimate the ice concentrations compared with non-dusty and 'South Regions' cases, while fit the dusty cases better at CTT warmer than ~ -25 °C. DeMott's parameterizations compare well with non-dusty and 'South Region' cases, but a little bit underestimate the ice concentration compared with dusty SSCs for N = 0.5 cm^{-3} and mean fit. While for N = 20 cm^{-3}, DeMott's parameterizations overestimate the ice concentration compared with non-dusty and 'South Region' cases, but compare well with dusty cases.

4. SUMMARY

Satellite remote sensing was used to evaluate dust impacts on ice generation in SSCs. We showed that ~98% of dusty SSCs contain ice, provided the cloud top temperature is less -15 °C, while the non-dusty SSCs, in the same geographical region, only reach this magnitude of mixed-phase occurrence at temperatures colder than -30 °C. Using a suite of airborne sensors, deployed to sample a SSC, we also validated the retrieval algorithm used to derive the crystal concentration. Based on that case study, we conclude that ice concentration in mixed-phase stratiform clouds can be estimated within about a factor of 2. Overall, we conclude that ice concentrations in dusty SSCs, compared to non-dusty SSCs, can be 2 to 5 times larger, for results binned by cloud top temperature. Our ongoing researches are refining the approach to better link dust concentration with ice generation in SSCs with CloudSat and CALIPSO measurements.

Acknowledgements

This research was funded by NASA grant NNX10AN18G, and also partially supported by DOE DE-SC0006974 as part of the ASR program. We thank CALIPSO PI Dave Winker, CloudSat PI Graeme Stephens and the CALIPSO/CloudSat data group. Many thanks to J.P.Chen (National Taiwan University) and K.J. Sulia (Penn State University) for providing ice growth model data.

References:

Cantrell, W., and A. Heymsfield (2005), Production of ice in tropospheric clouds - A review, *Bull. Amer. Meteorol. Soc.*, ***86*****(6),** 795-807.

Chen, J. P., and D. Lamb (1994), The theoretical basis for the parameterization of ice crystal habits-

growth by vapor-deposition, *J. Atmos. Sci.*, ***51*****(9),** 1206-1221.

DeMott, P. J., et al., (2010), Predicting global atmospheric ice nuclei distributions and their impacts on climate, *Proc. Natl. Acad. Sci. U. S. A.*, ***107*****(25),** 11217-11222.

Fleishauer, R. P., V. E. Larson, and T. H. Vonder Haar (2002), Observed microphysical structure of midlevel, mixed-phase clouds, *J. Atmos. Sci.*, ***59*****(11),** 1779-1804.

Liu, D., Z. Wang, Z. Y. Liu, D. Winker, and C. Trepte (2008), A height resolved global view of dust aerosols from the first year CALIPSO lidar measurements, *J. Geophys. Res.-Atmos.*, ***113*****(D16)**.

Meyers, M. P., P. J. Demott, and W. R. Cotton (1992), New primary ice-nulceation parameterizations in an explicit cloud model, *J. Appl. Meteorol.*, ***31*****(7)**, 708-721.

Stephens, G. L., et al. (2008), CloudSat mission: Performance and early science after the first year of operation, *J. Geophys. Res.-Atmos.*, ***113*****(D23),** D00A18, doi:10.1029/2008JD009982.

Wang, Z., K. Sassen, D. Whiteman, and B. Demoz 2004: Studying altocumulus plus virga with ground-based active and passive remote sensors. *J. Appl. Meteor.,***43**, 449-460.

Westbrook, C. D., and A. J. Illingworth (2011), Evidence that ice forms primarily in supercooled liquid clouds at temperatures >-27 degrees C, *Geophys. Res. Lett.*, ***38,*** L14808, doi:10.1029/2011GL048021**.**

Westbrook, C. D., and A. J. Heymsfield (2011), Ice Crystals Growing from Vapor in Supercooled Clouds between-2.5 degrees and-22 degrees C: Testing Current Parameterization Methods Using Laboratory Data, *J. Atmos. Sci.*, ***68*****(10),** 2416-2429.

Winker, D. M., et al. (2010), THE CALIPSO MISSION A Global 3D View of Aerosols and Clouds, *Bull. Amer. Meteorol. Soc.*, ***91*****(9),** 1211-1229.

Zhang, D. M., Z. Wang, and D. Liu (2010), A global view of midlevel liquid-layer topped stratiform cloud distribution and phase partition from CALIPSO and CloudSat measurements, *J. Geophys. Res.-Atmos.*, ***115,*** D00H13, doi:10.1029/2009JD012143**.**

ANALYSES OF LIGHTNING AND RADAR DATA FOR SUMMER THUNDERSTORMS OVER NORTHEAST BULGARIA AND BLACK SEA

Rumjana Mitzeva[1], Boryana Markova[1,2], Savka Petrova[1], Nikolai Bratkov[3], Vassiliki Kotroni [4]
[1] Faculty of Physics, University of Sofia, Sofia, Bulgaria,
[2]National Institute of Meteorology and Hydrology – Varna, BAS, Bulgaria,
[3] Air Traffic Services Authority, Burgas, Bulgaria
[4] Institute for Environmental Research and Sustainable Development, National Observatory of Athens, Athens, Greece

1. INTRODUCTION.

In the scientific community there is a general consensus that the so-called non-inductive mechanism plays the major role in the electrification of thunderstorms, culminating in lightning. This mechanism is based on laboratory experiments (Reynolds et al., 1957; Takahashi, 1978; Saunders et al., 1991, and others) showing that substantial charge is transferred during rebounding collisions between ice crystals and graupel pellets (of millimetric dimensions) growing by the accretion of supercooled cloud droplets. The magnitude of the charge transfer per collision increases rapidly with increasing velocity of impact and (especially) the size of ice particles, so it is expected that there should be a correlation between different in-cloud characteristics related to the size of ice particles and lightning activity in thunderstorms. Due to this in the last decade there has been extensive study of the relation between different lightning characteristics, radar reflectivity, cloud dynamic and different aspects of precipitation to the ground. Most of the works are based on the combined analyses of radar data (maximum radar reflectivity, radar cloud top, height of proper radar reflectivity) and lightning characteristics (flash rate, flash density, multiplicity, polarity). Some of the studies concentrate to establish if the electrification of thunderstorms is a direct consequence of the development within them of ice, both non-precipitating (crystals) and precipitating (graupel) (Petersen and Rutledge, 1998; Blyth et al., 2001; Deierling et al., (2005, 2008)). Several works are directed to the search for correlation between flash rate (density) and precipitation amount (Soula et al., 1998; Tapia et al., 1998; Soula and Chauzy, 2001; Rivas Soriano et al., 2001; Seity et al., 2001; Ezcurra et al., 2002; Zhou et al., 2002; Underwood et al., 2004; Gungle and Krider, 2006; Price and Federmesser, 2006; Jayaratne and Kuleshov, 2006; Katsanos et al., 2007, Petrova et al,. 2009, etc.), other – to the relation between lightning activity and severe events (Kane et al., 1991; Williams et al., 1999; Lang et al., 2000; Soula et al., 2004; Moriah et al., 2011; Price et al., 2011a; Price et al., 2011b ,etc). Rivas Sorriano et al. (2001) and Soula et al. (2004) assumed that the variability of

lightning parameters is linked to several factors, especially the latitude, the season, and the climatic conditions, which could be the reason for the contradictory conclusions based on the studies conducted in different geographical areas. There are only a limited number of studies (Dimitrova et al., 2009, 2011, Mitzeva et al., 2011) concerning lightning activity of thunderstorms developed over central and northwest Bulgaria. They showed that there is a significant difference between lightning characteristics in thunderstorms, producing hail, heavy and weak rain.

The results from analysis of lightning and radar data related to summer convective thunderstorms that have been developed over northeast Bulgaria and the Black sea are presented here. The present work is devoted to the study of the relationship between flash rate and thunderstorm development, estimated by available radar information. Special attention is paid on the moment of first detection of lightning regarding thunderstorms development. Statistical analyses is performed to estimate if there is a correlation between flash rate and some radar characteristics.

2. DATA

Thirteen summer thunderstorms, that developed during 2006 over northeast Bulgaria in a 100 km radius around Varna town are selected for the analysis.

The lightning data are provided from the ZEUS network operated by the National Observatory of Athens (NOA). Radar information is obtained by the C-band Doppler radar METEOR – 360 AC, which is located close to Varna airport.

The data are grouped in time intervals of 15 minutes (hereafter named events), in accordance with the period of radar volume scan. The number of flashes is integrated with radar products for each interval and selected thunderstorm area (the border of cell was outlined by radar reflectivity 15 dBZ). Several radar characteristics (maximum radar reflectivity, Z max, radar cloud top height (height of 15 dBZ), H15, heights of 30 dBZ, H30, of 40 dBZ, H40 and of 45 dBZ, H45) are extracted from the radar information. As a result the number of events with lightning for the analysis 13 thunderstorms is 123.

The height of the zero isotherm, of -10 ^{0}C -15 ^{0}C, -20 ^{0}C and -40 ^{0}C isotherms are estimated using proximity sounding, obtained by the numerical model GFS (http://www.arl.noaa.gov/ready/cmet.html). The depth of thunderstorms above -40^{0}C isotherms is included in the analyses. The temporal evolution of lightning and available radar information is examined too.

3. RESULTS

To obtain the idea for the studied thunderstorms, their life time, time with lightning, average flash rate (aveFR) for each thunderstorm and maximum flash rate are presented in Table 1. The rows are arranged in accordance with the

ascending values of the average flash rate.

Table 1. Date of the studied thunderstorms, their life time and duration of time with lightning, average (for each thunderstorm) flash rate (aveFR), maximum flash rate (FR max).

Date	life time [min]	time with flashes [min]	ave FR flashes per 15min	FR max flashes per 15min
LFR				
22/08/06 II	90	75	6	15
27/06/06	90	45	14,3	36
19/06/06 II	105	75	8,17	11
05/08/06	120	90	31,9	72
22/08/06	135	120	26,3	49
24/06/06	180	60	6,8	11
HFR				
19/06/06	150	105	174	442
20/06/06	180	165	44,5	116
20/06/06 II	180	120	65,5	170
19/06/06III	225	195	48,7	110
28/07/06	225	210	209,9	587
05/08/06 II	255	195	57	213
21/08/06	270	195	166,7	273

The analysis reveals that the studied thunderstorms are vigorous with maximum of their cloud tops H15≥ 11 km AGL and with maximum radar reflectivity Zmax between 45 and 65 dBZ. Their life time varies between (90 - 270) minutes with the duration of lightning detection between (45 – 210) minutes. There are 6 thunderstorms (37 events) with average flash rate aveFR≤ 32/15 min (~2/min) and 7 thunderstorms (86 events) with the corresponding higher values of aveFR. Our analysis (F- and t-tests with significant level 0.05) shows that there is statistical significant difference between mean values of FR and duration of time with lightning in the above mentioned groups (see Fig. 1 and Fig. 2 respectively). For this reason the analysis is performed separately for two samples. The sample with aveFR ≤ 32/15 min (~2/min) is denoted hereafter as a LFR (**L**ow **F**lash **R**ate) and the sample with aveFR > 32/ 15 min (~2/min) is denoted hereafter as HFR (**H**igh **F**lash **R**ate).

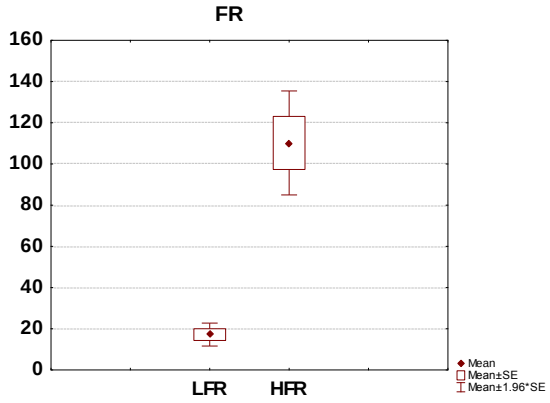

Fig. 1 Box and Whiskers plot for average flash rate (number of flashes per 15 min) for LFR and HFR

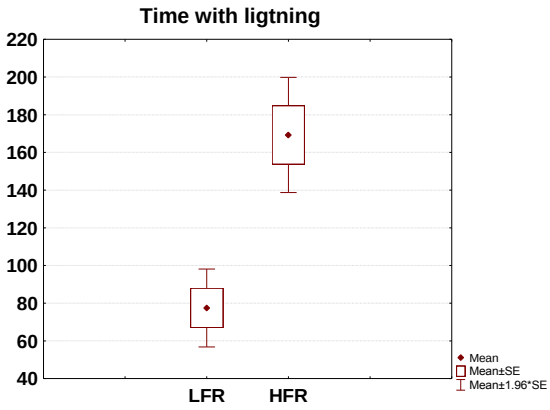

Fig. 2 Box and Whiskers plot for time with lightning for LFR and HFR

The results show that mean values of H15, H30, H40 and H45 are significantly larger for thunderstorms in HFR sample in comparison with the corresponding values in the thunderstorms from LFR sample, which indicates that as an average the flash rate is higher in more vigorous thunderstorms. The Box and Whiskers

plots for H15 and H40 are presented in Fig.3.

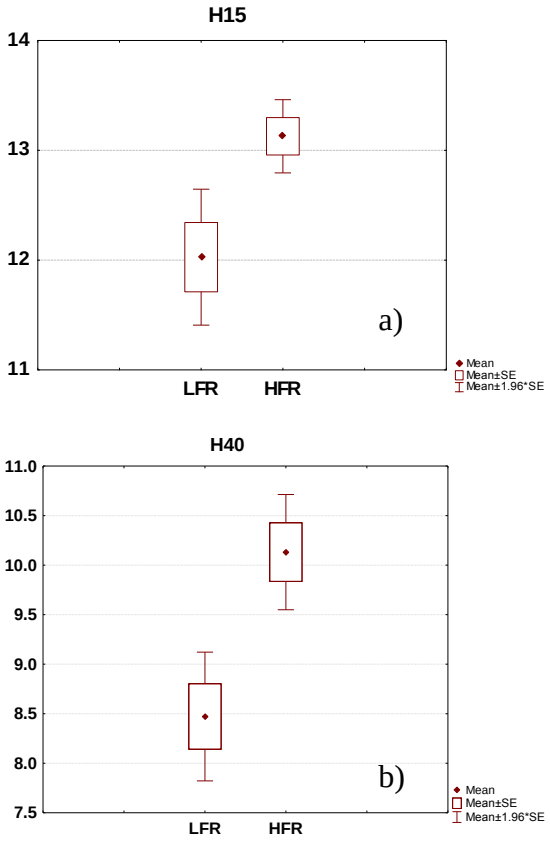

Fig. 3. Box and Whiskers plot for a) the radar cloud top H15 and b) the height of radar reflectivity 40 dBz, H40 for thunderstorms in LFR and HFR samples

The depths of the regions without cloud droplets, H15-H(-40^{0}C) in both samples are compared. The results presented in Fig. 4 show that the mean values of cloud depth above -40 ^{0}C is significantly larger in thunderstorms from HFR sample than in thunderstorm from LFR. Based on these results one can assume that the rebounding collisions between graupel and ice crystals at the absence of cloud droplets (above -40^{0}C) contribute also significantly to the charging of thunderstorms. Thus, one can conclude that the regions of the clouds where the charge separation mechanisms are active, are larger than previously thought. This is in accordance with the numerical simulations in Mitzeva et al., 2006, as well with the recent laboratory study by Avilla et al., 2011 showing that significant charge is transferred at very low temperatures.

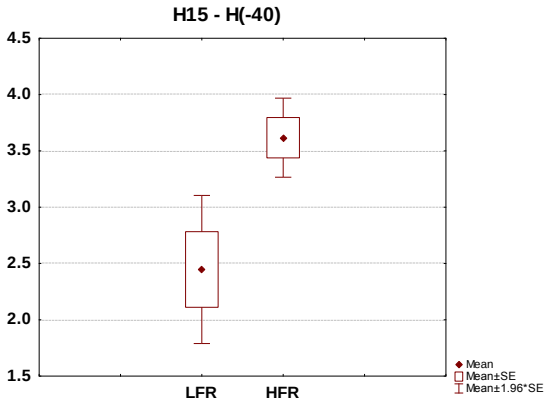

Fig. 4. Box and Whiskers plot for depth above -40 ^{0} C isotherm in thunderstorms from LFR and HFR samples

In all thunderstorms (with the exception of the thunderstorm developed on 20/06/06) the first flashes are detected when echo - height of 40 dBZ, H40 is above 6-7 km AGL at the temperatures lower than -15 ^{0}C. In this moment the radar cloud tops are above 10 km AGL at temperatures lower than -35 ^{0}C (see Table 2) In the thunderstorm developed on 20/06/06 the first flashes are detected when radar cloud top reaches 12 km AGL (temperature -54 ^{0}C) and the maximum radar reflectivity is 30 dBZ with H30 =9 km AGL (temperature -37^{0}C). It is clear from Table 2 that there is a high variability between the proper values of H15 and H40 and the corresponding temperatures in all thunderstorms at the first moment of flash detection. The absence of flashes before a certain threshold of high values of

H15 and H40 (with the exception of one thunderstorm) and low values of the temperatures at the corresponding levels is in accordance with the results obtained by other authors. For example it is found by Martinez (2001) that in all analyzed 12 storms with lightning during STEPS, the radar echoes of at least 40 dBZ had to exist at altitudes greater than 7 km MSL in order for lightning to occur.

Table 2. Radar cloud top height, H15, temperature at H15, height of 40 dBz , H40, temperature at H40 at the first moment of flash detection

.

Date	H15 [km]	T H15 [^{0}C]	H40 [km]	T H40 [^{0}C]
LFR				
22/08/06 II	10	-41	10	-41
24/06/06	15	-56	8	-26
19/06/06 II	16	-58	12	-55
27/06/06	12	-49	7	-19
22/08/06	11	-46	9	-34
05/08/06	10	-44	8	-30
HFR				
20/06/06	12	-54		
19/06/06 III	12	-54	7	-22
05/08/06 II	10	-44	6	-15
20/06/06 II	12	-54	8	-29
21/08/06	12	-48	11	-43
19/06/06	13	-53	10	-46
28/07/06	10	-45	7	-21

The more detailed analyses of the evolution of FR and radar parameters for thunderstorms reveal that during the growth stage of the studied thunderstorms there is an increase in FR after a sharp increase of H40 above isotherm -20 ^{0}C, and H15 above isotherm -40^{0}C (Fig.5 and Fig.6). The similar behavior is established in the study of Rigo et al., (2005) and Pessi and Businger (2009).

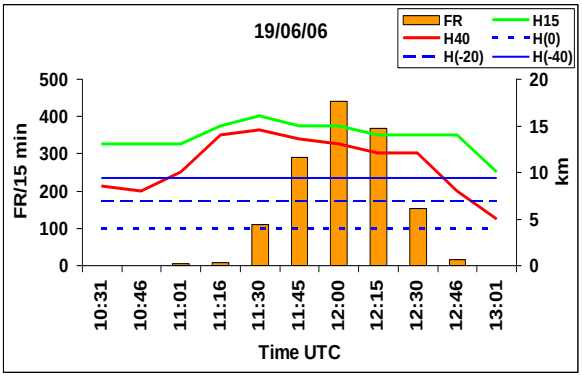

Fig. 5 Number of flashes for 15 minutes, FR and radar information as a function of time for the thunderstorms developed on 19/06/06.

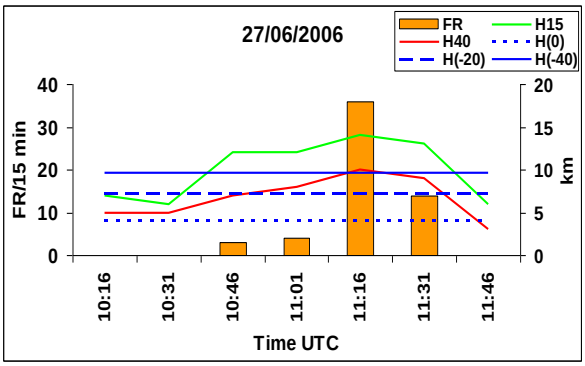

Fig. 6 Number of flashes for 15 minutes, FR and radar information as a function of time for the thunderstorms developed on 27/06/06.

The scatter plots between flash rate and several radar parameters (not shown here) indicate that there is no pronounced relation between flash rate and analysed radar parameters in both samples (HFR and LFR). However, for thunderstorms from HFR sample logarithmic correlation is established between FR averaged in 1 km bin, $\overline{FR}$ and H15, H30, H40 (see Fig. 7 a,b.c). No such correlation exists for thunderstorms from the LFR sample. The

sharp increase of $\overline{FR}$ with the increase of cloud top height is obtained by other authors (e.g Pessi and Businger, 2009) and can be linked to the intensification of the updraft which favours electrification.

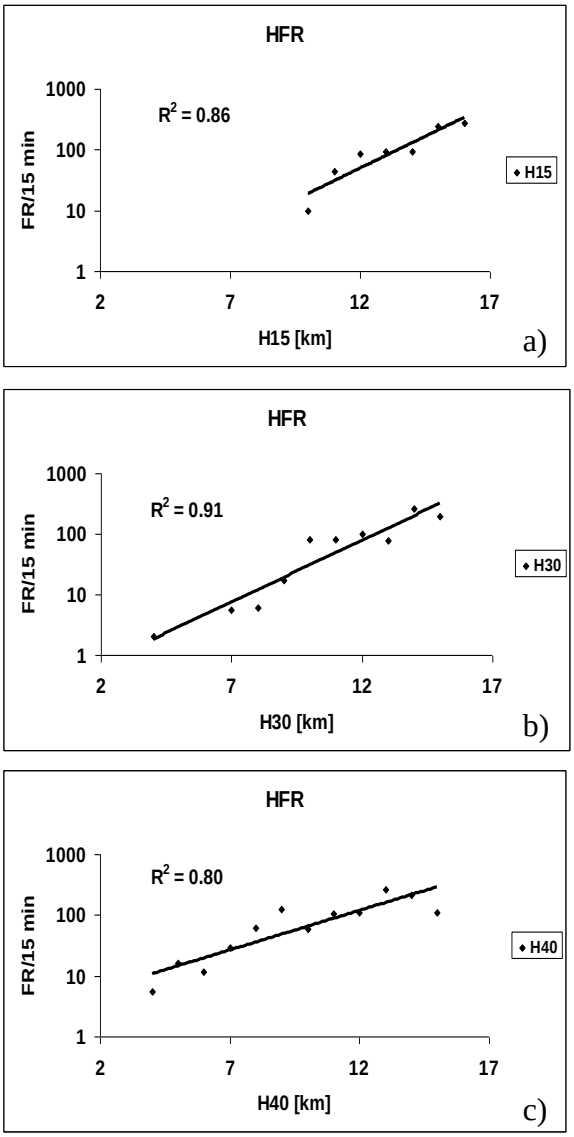

Fig. 7 Scatter plot of flash rate $\overline{FR}$ (averaged in 1 km bin) for HFR sample, as a function a) of H15; b) of H30 ; c) of H40

4. CONCLUSION

A combined analysis of lightning and radar data for thirteen summer convective thunderstorms that have been developed over northeast Bulgaria are presented.

The data are grouped in time intervals of 15 minutes in accordance with the period of radar volume scan. The analysis is performed for two samples of thunderstorms: HFR (High Flash Rate) and LFR (Low Flash Rate) with aveFR> 2/ min and aveFR ≤ 2/ min respectively. The main results are:

- In all thunderstorms (with one exception) the first flashes are detected when echo-height of 40 dBZ, H40 is above 6-7 km AGL (temperatures lower than -15 ^{0}C) and radar cloud top is above 10 km AGL (temperatures lower than -35 ^{0}C) .
- In most of the thunderstorms there is an increase in FR after a sharp increase of H40 above isotherm -20 ^{0}C, and H15 above -40^{0}C.
- The mean values of H15, H30, H40 and H45 are significantly larger for thunderstorm in HFR sample in comparison with the corresponding values in thunderstorms of LFR sample, which indicates that as an average the flash rate is higher in more vigorous thunderstorms.
- The mean value of thunderstorm depth above -40 ^{0}C is significantly larger in thunderstorms from HFR sample than in thunderstorm from LFR. Based on this results one can speculate that the rebounding collisions between graupel and ice crystals at the absent of cloud droplets (above -40^0 C) contribute also

significantly to the charging of thunderstorms.

- A logarithmic correlation is established between FR averaged in 1 km bin, $\overline{FR}$ and heights of radar reflectivity H15, H30, H40, for thunderstorms from HFR sample.

The present study reveals that most of lightning features of the studied thunderstorms over northeast Bulgaria are similar to those in other geographical regions. Some comparisons are given in the previous section.

Acknowledgements

The authors are grateful to Air Traffic Services Authority in Bulgaria for radar information.

BIBLIOGRAPHY

Avila E .E, R. E. Bürgesser, N. E. Castellano, R. G. Pereyra, and C. P . R. Saunders, 2011. Charge separation in low temperature ice cloud regions. Journal of Geophysical Research, vol. 116, D14202, doi: 10.1029/2010JD015475

Blyth, A. M., Christian, H. J., Driscoll, K., Latham, J. 2001. Determination of precipitation rates and thunderstorm anvil ice contents from satellite observations of lightning. Atmos. Res., 59-60, 217-229.

Deierling, W., Latham, J., Petersen, W., Ellis, S., Christian, H. 2005. On the relationship of thunderstorm ice hydrometeor characteristics and total lightning measurements. Atmos. Res., 76, 114 – 126.

Deierling, W., Latham, J., Petersen, W., Ellis, S., Christian, H. 2008. The relationship between lightning activity and ice fluxes in thunderstorms, J. Geophys. Res., 113, D15210

Dimitrova, Ts., Mitzeva, R., Todorova, A., 2009: Lightning activity in rain and hail bearing thunderstorms over Bulgaria, Preprints 5th European Conference on Severe Storms, Landshut,Germany, 12 - 16 October 2009, 239-240

Dimitrova Ts, R. Mitzeva, H. D. Betz, Hr Zhelev, S. Diebel, 2011: Lightning behaviour during the lifetime of severe thunderstorms, Procceding of 6th Europian Conference of Severe Storms (ECSS-2011), 3-7 October 2011, Palma de Mallorca, Balearic Islands, Spain..

Ezcurra, A., Areitio, J. and Herrero, I. 2002. Relationships between cloud to ground lightning and surface rainfall during 1992-1996 in the Spanish Basque Country area. Atmospheric Research, 61, 239-250.

Gungle, B. and E. P. Krider, Cloud-to-Ground Lightning and Surface Rainfall in Warm-Season Florida Thunderstorms, Geophys. Res.Lett., 111, D19203, 2006.

https://www.arl.noaa.gov/ready/cmet.html NOAA Air Resources Laboratory.

Jayaratne, R and Kuleshov, E., 2006. Geographical and seasonal characteristics of the relationship between lightning ground flash density and rainfall within the continent of Australia. Atmospheric Research 79(1):pp. 1-14

Kane, R. J., 1991. Correlating lightning to severe local storms in the northeastern United States, Wea. Forecasting, 6, 3–12.

Katsanos D., Lagouvardos, K., Kotroni, V., Argiriou, A. 2007. Combined analysis of rainfall and lightning data produced by mesoscale systems in the Central and Eastern Mediterranean. Atmospheric Research, 83, 55-6.

Lang, T.J., Rutledge, S.A., Dye, J., Venticinque, M., Laroche, P., Defer, E., 2000. Anomalously low negative Cloud-to-ground lightning flash rates in intense convective storms observed during STERAO-A, Mon. Wea. Rev., 128, 160-173

Lang, T.J, Miller, L.J, Weissman, M., Rutledge S.A., Barker III, L.J., Chandrasekar, V., Detwiler, A., Doesken, N., Helsdon, J., Knight, C., Krehbe, P, Lyons, W.A., MacGorman, D., Rasmussen, E., Rison, W., Rust, W., Thomas, R.J.,2004. The severe thunderstorm electrification and

precipitation study, Bull Am. Meteorol. Soc.,85, 1107-1125.

Martinez, M, 2001: The Relationship Between Radar Reflectivity and Lightning Activity at Initial Stages of Convective Storms

Mitzeva R., C. Saunders and B.Tsenova, 2006: Parameterisation of non-inductive charging in thunderstorm regions free of cloud droplets, Atmos. Res., vol.82, p.102-112

Mitzeva, R., Dimitrova, Ts., Betz, H.-D., Pisarova, Y, Combined Analysis of Lightning and Radar Data for Thunderstorm-Produced Rain over Bulgaria, XIV International Conference on Atmospheric Electricity, August 08-12, 2011, Rio de Janeiro, Brazil

Moriah K., Galanti E., Price C., Lagouvardos K. and Kotroni V. 2011. Nowcasting thunderstorms in the Mediterranean region using lightning data. Atmospheric Research, 100, 489-502.

Pessi A. and S. Businger, 2009: Relationships among Lightning, Precipitation, and Hydrometeor Characteristics over the North Pacific Ocean, Journal of Applied Meteorology and Climatology, v. 48, p.833-848.

Petrova S., R. Mitzeva, V. Kotroni, J. Latham and E. Peneva, 2009. Analyses of summer lightning activity and precipitation in the Central and Eastern Mediterranean , Atmospheric Research 91,453-458.

Petersen, W.A., Rutledge, S.A. 1998. On the relationship between cloud-to-ground lightning and convective rainfall. J.Geophys. Res ., 103, 14025-14040

Price C., Federmesser, B. 2006. Lightning-rainfall relationships in Mediterranean winter thunderstorms. Geophys Res. Lett.,vol. 33, L07813, 4 PP.

Price, C., Y. Yair, A. Mugnai, K. Lagouvardos, M.C. Llasat, S. Michaelides, U. Dayan, S. Dietrich, E. Galanti, and L. Garrote, 2011a. The FLASH Project: using lightning data to better understand and predict flash floods, Environmental Science and Policy, 14(7), 898.

Price, C., Y. Yair, A. Mugnai, K. Lagouvardos, M. C. Llasat, S. Michaelides, U. Dayan, S. Dietrich, F. Di Paola, and E. Galanti, 2011b. Using Lightning Data to Better Understand and Predict Flash Floods in the Mediterranean, Surveys in Geophys, 32(6), 733

Rigo T., J. Bech, N. Pineda, A. Sairouni, J. R. Miró, Combining lightning and radar data to improve the nowcasting of summer thunderstorms, 2005, World Weather Research Program Symposium on Nowcasting and Very Short Range Forecasting; Toulouse France, 5-9 september 2005

Rivas Soriano, L., de Pablo, F., Garcia Diez, E. 2001. Relationship between convective precipitation and cloud-to-ground lightning in the Iberian Peninsula. Monthly Weather Review, 129, 2998-3003.

Saunders, C.P.R., 1993. A review of thunderstorm electrification processes, J. Appl. Meteorol., 32, 642–655.

Saunders, C.P.R., Keith, W.D., Mitzeva, R.P., 1991. The effect of liquid water on thunderstorm charging. J. Geophys. Res. 96, 11007– 11017

Seity, Y., S. Soula and H. Sauvageot, 2001. Lightning and precipitation relationship in coastal thunderstorms, J. Geophys. Res., 106, no.d19, 22801-22816

Soula, S., Sauvageot, H., Molini´e, G., Mesnard, F., and Chauzy, S., The CG lightning activity of storm causing a flashflood, Geophys. Res.Lett., 25, 1181–1184, 1998.

Soula, S. and S. Chauzy, Some aspects of the correlation between lightning and rain activities in thunderstorms, 2000, Atmospheric Res.,56, 355-373,

Soula S., Seity Y., Feral L., Sauvageot H., 2004. Cloud-to-ground lightning activity in hail-bearing storms, J. Geophys. Res., 109, D02101, 1-13.

Takahashi, T., 1978. Riming electrification as a charge generation mechanism in thunderstorms. J. Atmos. Sci.35, 1536–1548.

Tapia, A. and J.A. Smith, Estimation of Convective Rainfall from Lightning Observations, Appl. Meteorol., 37, 1497–1509, 1998.

Underwood, S. J. and M.D. Schultz , Patterns of Cloud-to-Ground Lightning and Convective Rainfall Associated with Postwildfire Flash Floods and Debris Flows in Complex Terrain of the Western

United States, Journal of hydrometeorology, 5, 989-1003, 2004.
Zhou, Y., Qie, X., Soula, S., A study of the relationship between cloud-to ground lightning and precipitation in the convective weather system in China, Annales Geophysicae, 20, 107-113, 2002.
Williams, E..R., Boldi, B., Matlin, A., Weber, M., Hodanish, S., Sharp, D., Goodman, S., Raghavan, R., Buechler, D., 1999. The behavior of total lightning activity in severe Florida thunderstorms, Atmos. Res., 51, 245-265.

Analysis of Hailstone Characteristics in Tianjin during Recent Years

Song Wei[1,2], Jin Ruijun[1], Meng hui[1], Guo Xiaojun[1]

1.Tianjin Weather Modification Office, Tianjin, 300074, China

2. Key Laboratory for Semi-Arid Climate Change of the Ministry of Education , Lanzhou University, Lanzhou, 730000, China

Abstract: Based on the hailstone data of 13 meteorological observation stations, the article analyzed the spatial and temporal distribution characteristics of hailstones in Tianjin. The results showed:(1)The annual mean hailstone-days was 13 during the recent 20 years, the hail days in Jixian district was most(105 days). The hailstone weather often appeared in spring, summer and autumn. (2) Based on hailstone data from 1990 to 1999,hailstone duration which exceed 30 minutes occupied high proportion.From 2000 to 2009, the hail duration between 1 to 10 minutes occupied the highest proportion, the value was 64.5 %.(3) The hail weather appeared between 05:00 and 15:00 mostly, the proportion reached 79.7%.

Key Words: hailstone temporal and spatial distribution hail duration

Introduction

Hail is a form of precipitation which consists of balls or irregular lumps of ice (hailstones).Hail is only produced by cumulonimbi, usually at the front of the storm system. Hailstones on the earth usually consist mostly of water ice and measure between 5 and 50 millimeters in diameter. They would lead to disaster and huge economic losses in agriculture, forestry, industry, communications and transportation.

Tianjin is located in the eastern part of the North China Plain, it is often affected by polar generated air[1]. The encounter of cold air with warm moist air from Bohai Sea often causes hailstone in summer and autumn. Those researches of hailstones concentrated on now-forecasting techniques, diagnostics on weather, and convective clouds formation mechanisms[2-5],while the analysis of developing and changing characteristics of hailstone, would not only reveal the rules of emergence, but also provide some scientific

evidence for hail suppression researches.

Using the data of hailstone events from 13 meteorological observation stations , the article analyzed the spatial-temporal distribution and variation characteristics in Tianjin.

1. Data Description

The research data included hailstone data of 13 meteorological observation stations in Tianjin from 1990 to 2009. By statistical analysis, it could obtain the spatial and temporal distribution characteristics of hailstone, and moving paths of heavy convective clouds. These results would provide some basis for hail suppression works and disaster prevention and reduction.

2. The Hail-falling Characteristics in Tianjin from 1990 to 2009

2.1 The Temporal and Spatial Characteristics of Hail-falling Days

The annual mean hail days was 13 during the recent 20 years in Tianjin, which occurred at a high frequency in 1990s, and the average number was 16. The year with the most hail days out of the years studied was 1990, with 29 hail days(Figure 1). The number of annual mean hail days decreased after 2000,which was 9. From the hail spatial distribution chart(Figure 2)，It could be found that the hail days in Jixian district was the most(about 105 days),Jinghai and Baodi were also the heavy hail regions， The account hail days were 50 and 49. While the hail-days in Dagang district were only 11 days.

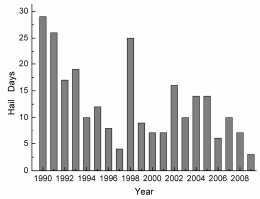

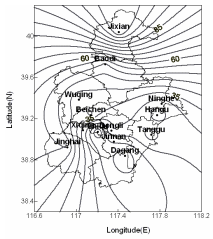

Figure 1.The changing characteristics of hail-falling days in Tianjin between 1990-2009; Figure 2.The spatial distribution of hail-falling days in Tianjin

2.2 Characteristics of Monthly Cumulative Hail Days from 1990 to 2009

The hail appearance presented significant seasonal changes and unimodal distribution. From the spatial distribution chart of monthly cumulative hail days(Figure3),It could be found that hailstone weather often appeared in spring, summer and autumn. The most frequent hail-falling month was June. There were no hail days in January， February and December. It might be related to atmosphere

unstable stratification.

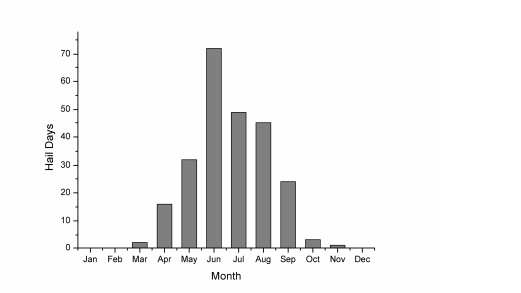

Figure 3. The chart of monthly cumulative hail days distribution from 1990 to 2009

2.3 The Characteristics of Hailstone Duration

The duration of hail-falling process vary with synoptic situation, atmosphere stability conditions and convective cloud structure. Table 1 showed hailstone duration in 1990 to 1999 and 2000 to 2009. There were some differences. Based on the hailstone data in 1990's. Hailstone duration which exceeded 30 minutes occupied high proportion, It was 49.2％. Hailstone duration between 1 and 10 minutes occupied high proportion. It reached 30.3 ％.The proportion which hailstone duration exceeded 30 minutes was only 7.9 ％ from 2000 to 2009.

Hailstone Duration	Emergence Frequency	
	1990-1999	2000-2009
1-10minutes	20.5％	64.5％
10-30minutes	30.3％	27.5％
＞30minutes	49.2％	7.9％

Table 1. The statistical table of hailstone duration in 1990 to 1999 and 2000 to 2009

Based on figure 4，it could be found that the hail-falling time presented obvious diurnal variation. The hail weather appeared between 05:00 and 15:00(coordinated universal time, UTC) mostly，the proportion reached 79.7 ％.The hail appearance probabilities were low from 20:00 to 22:00 and 01:00 to 03:00，the proportion was only 1.4％.

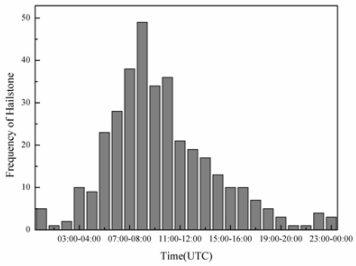

Figure 4. The chart of hail-falling time in Tianjin between 1990 and 2009

3. Conclusion

(1)Between 1990 and 2009，the annual mean hailstone-days were 13.The appearance frequency was high in 1990's. After 2000，the hail days reduced gradually. The accumulative hail days in Jixian were most(105 days).

(2)Thehail appearance presented significant seasonal changes and unimodal distribution. Hailstone weather often appeared in spring, summer and autumn. The most frequent

hail-falling month was June.

(3)Based on hailstone data from 1990 to 1999,hailstone duration which exceed 30 minutes occupied high proportion, the number was 49.2％.From 2000 to 2009, the hail duration between 1 to 10 minutes occupied the highest proportion, the value was 64.5％.

(4) The hail weather appeared between 05:00 and 15:00 mostly，the proportion reached 79.7％.

Acknowledgments

These researches were supported by foundation of Key Laboratory for Cloud Physics and Weather Modification of China Meteorological Administration and foundation of Key Laboratory for Semi-Arid Climate Change of the Ministry of Education in Lanzhou University.

Reference

[1]Wen K.,Z.Wang.2008,China Meteorological disasters-Tianjin, China Meteorological Press,Beijing,142-143.

[2]Liu Y.,S.Shou,Y.Xie.2011,Diagnostic Analysis of the Effect of Thermal Inhomogeneous Field on the Hail，Plateau Meteorology,30(1):226-233.

[3] Wang L.,R.Yang,Z.Li.2009,Application of CINRAD 3D mosaic products in strong convective weather, Journal of Meteorology and Environment,25(5):18-23.

[4]Liao X.,X.Yu,B.Yu.2008, Analysis on Infrequent Big Hail Event in Beijing Area, Meteorological Monthly,34(2):10-17.

[5]ChenX.,Y.Hao,H.Zhou.2007,Using Convection Parameters to Analyze a Peculiar Hail Weather. Meteorological Science and Technology,27(3):335-341.

#630 Effects of Marine Cloud Brightening on Polar Regions and Meridional Heat Flux

Ben Parkes [1] Alan Gadian [1] John Latham [2,3]

[1] NCAS, SEE, University of Leeds, UK. [2] MMM, NCAR, USA. [3] University of Manchester, UK

Abstract:

Marine cloud brightening (MCB) is one of several proposed solar radiation management geoengineering schemes designed to enhance the albedo of marine stratocumulus clouds, with concomitant overall cooling, and the intention of averting some of the undesirable effects of climate change (Latham et al. 2008, 2012). Such changes include ice loss, desertification and increased sea levels. Polar sea ice fraction has been recorded by satellite data for the last 40 years. This data shows a general long term reduction in sea ice thickness and area and this reduction has been attributed to climate change. Changes in climate have been reported to be disproportionately larger in polar regions.

The HadGEM1 (UK Met Office Climate Model, V6.1) is a fully coupled climate model. It is used to project changes in polar ice cover and temperatures as a result of increasing carbon dioxide and the deployment of MCB geoengineering. The meridional heat flux is the mechanism for moving energy from the tropics to the polar regions. The results show that for a comparison between a control (~ 2020 carbon dioxide concentrations) and a double pre-industrial carbon dioxide simulation, the maximum meridional heat flux is found to change from 5.8 PW to 6.1 PW. With three-region MCB seeding of marine stratocumulus, this is reduced to 5.7 PW. Application of a three region seeding scenario, results an increase in sea ice cover to 0.20 million sq km above the initial values. (Parkes et al. 2012)

Methodology:

The HadGEM1 fully coupled climate model (Latham et al 2012 and Parkes et al. 2012) were used for the climate simulations. More information is available in these papers and in the presentation. The droplet number concentrations wer modified to 375/cc in the MCB simulations.

Four simulations were used in the calculations to examine the effects of MCB on the meridional heat flux

Experiment name	Carbon dioxide fraction (ppm)	Seeding scheme
CON	440	None
2CO2	440 + 1%/year, held at 560	None
MCB3	440 + 1%/year, held at 560	Three regions
MCBA	440 + 1%/year, held at 560	All ocean

Table 1. Simulations carried out to investigate MCB (Parkes et al. 2012)

The control run (CON) was compared with the results of Wunsch (2005) and these can be seen in Figure 1.

The second simulation was used to simulate a double CO2 atmosphere, and examine the consequences for the meridional heat flux.

The two final simulations were carried out to examine the effects when only a three small region seeding (5% of the maritime stratocumulus clouds, MCB3) was implemented and when all the maritime stratocumulus clouds (MCBA) were seeded.

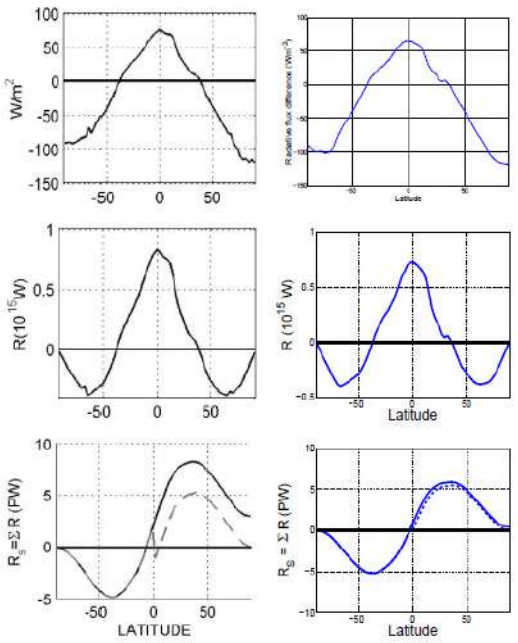

Figure 1*. Calculation of the MHF from radiative balance values in the ERBE dataset (left) and HadGEM1 (right). Panels (a) and (b) show the annual average radiative balance. Panels (c) and (d) multiply (a) and (b) by the area in each latitude band. Panelss (e) and (f) sum these values from 90^0 S to 90^0 N to give the MHF. Dotted lines in Figures (e) and (f) show the result from 90^0 N to 90 ^{0} S. Panels (a), (c) and (e) are copied from Figure 2 (a) ,(b) and (c) of Wunsch 2005 { Parkes et al. 2012 }*

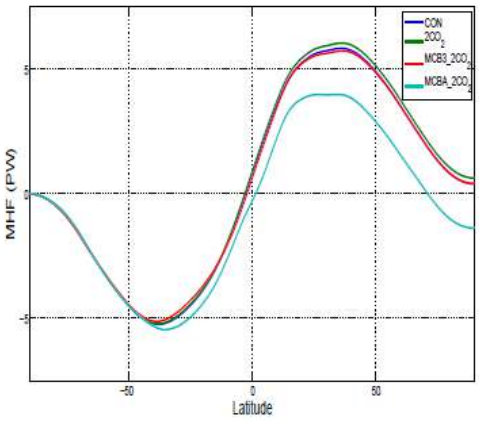

Figure 2. *Meridional Heat Flux for the simulations described in Table 1 (Parkes et al. 2012)*

Results and Discussion:

For brevity, the plots of the change in ice coverage and surface temperatures are not included in this extended abstract, but can be found in Parkes et al. 2012). Figures 1(a) and 1(b) show the annual average radiative balance at the top of the atmosphere from the ERBE dataset and our computed HadGEM1 results. These values are multiplied by the area in each latitude band to give the contribution of each band to the total MHF. To produce Figures 1(d) the data from Figure 1(b) was regridded from the HadGEM1 model grid to the 2.5^0 square grid used by the ERBE dataset. The regridding enables a direct comparison between the results in Figures 1(c) and 1(d) . Figure 1(e) shows the summation of the results in Figure 1(c) from the South pole to the North pole. Figure 1(f) is generated using the same method as Figure 1(e) with data that has not been regridded to the lower ERBE resolution. It can be seen that the MHF values derived from HadGEM1 compares well with the dataset and shows less of an imbalance when the calculation direction is reversed from the North to the South.

We present the first analysis of changes to a MHF as a result of simulating the deployment of MCB in a double carbon dioxide concentration atmosphere. The maximum MHF, in the northern hemisphere, is generally found close to 40 degrees N and the maximum value from the control, CON is found to be 5.8 PW. The heating from doubling carbon dioxide raises the maximum to 6.1 PW while three region seeding in MCB3 reduces this to 5.7 PW. In MCBA the maximum MHF is reduced to 4.0 PW. These results demonstrate how MCB, even when seeding is applied in three relatively small maritime regions, can cause an appreciable change in the global MHF.

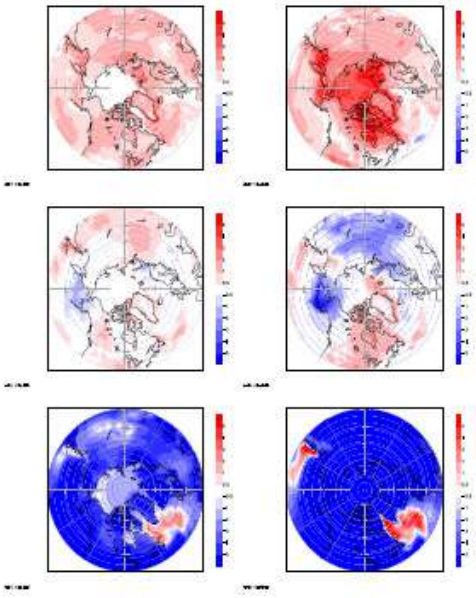

Figure 3. *Comparison of summer (let) and winter (right) polar surface temperatures (K) for the engineering simulations. The upper panels (a) and (b) show the differences between 2CO2 and CON. Panels (c) and (d) show the differences between MCB3 and CON and panels (e) and (f), the lower panels show the differences between MCBA and CON.*

In the presentation plots of sea ice extent and surface temperatures will be produced as in Parkes et al (2012). The surface temperatures are shown in Figure 3 and indicate that indeed these simulations do reduce the size of the Surface Temperatures.

The results from our four climate simulations including two MCB scenarios show a strong connection between sea ice fraction and sea surface temperatures. These two quantities are influenced by a sea ice - albedo feedback loop which in turn is influenced by the MHF, which transports heat energy polewards. Furthermore our control simulation (CON) is in good agreement with previous work on the MHF using the ERBE dataset (Wunsch05). Polar amplification leads to a polar heating and thus a reduction in sea ice which then possibly starts the positive feedback resulting in further heating and sea ice loss. Thus MCB may be able to target polar regions more effectively than other geoengineering methods (Latham et .al 2008) . In particular, in the double carbon dioxide scenario, MCB produces a significant reduction in sea ice loss.

References:

Latham J. et al (2008) Global temperature stabilization. Phil Trans Ro Soc A. dou 10.1098/rsta.2008.0137

Latham J. et al. (2012) Marine Cloud Brightening, Phil Trans. R. Soc. A. July, 2012.

Parkes B. et al. (2012) The effects of Marine Cloud Brightening on Seasonal Polar Heat Temperatures and Meridional Heat Flux. ISRN Geophysics. Doi: 10.5402/2012/142872.

Wunsch C. (2005)Total meridional heat flux and its ocean and atmospheric transports. J.O.C 18, 4374-80

OBSERVATION OF AEROSOL AND CCN ACTIVATION SPECTRA ON THE SEMI-ARID REGION OF NORHTEAST BRAZIL (NEB)

Gerson Paiva Almeida (gerson.almeida@uece.br)
Antônio Geovan de Araújo Holanda Guerra, João Bosco Verçosa Leal Junior
Universidade Estadual do Ceará

1. INTRODUCTION

The CCN plays a crucial role in precipitation development, particularly in warm shallow clouds. Those results are emphasized by the studies (Breon et al., 2002) who pointed out that cloud droplet sizes are the largest over remote tropical oceans and smallest over highly polluted continental areas.

In recent years many studies have drawn attention to the tropical Amazon rain forest biome (Roberts et al., 2001; Gunthe et al., 2009, Chen et al., 2009) in the northern region of Brazil, while the Brazilian large semiarid area continues to be the least studied, although the most susceptible to weather variations (Oyama and Nobre, 2004). NEB has a population of more than 47 million people, about 19 million of which live on its semi-arid portion and depends strongly on the annual cycle of precipitation. As warm clouds are the main responsible for the total precipitation in NEB, the impact of CCN in the precipitation efficiency is potentially larger than in the Amazon region, what indicate the importance of this kind of studies to this particular region.

2. THE CEAREX PROJECT

The CEAREX, CEara AeRosol EXperiment, was planned and executed by Ceara State University (Universidade Estadual do Ceará, Uece) in cooperation with the Max Planck Institute (MPI, Mainz, Germany) to study the variability of the aerosol size distribution and CCN activation spectra in the Brazilian semi-arid region. One of the secondary goals of the study was to evaluate the viability of a larger field campaign on the Brazilian Northeast semi-arid region.

2.2. THE AEROSOL AND CCN iNSTRUMENTATION

Three instruments were used during the field observations: **(1.) The optical particle counter (OPC)** is a Grimm Model 1.109 (Grimm Aerosol Technik) and covers a particle size diameter range from 0.25 to 34 µm in 31 channels (Heim et al., 2008). **(2.) The electric aerosol charger (EAC)** is a Grimm Model 1.365 for measuring total aerosol number concentration within the size range from 25 nm to 400 nm and also the mean aerosol diameter distribution assuming a lognormal distribution with σ = 1.7. **(3.) A Cloud Condensation Nuclei Counter (CCNC),** designed and built at UECE (Pinheiro et al., 2011).

2.3. THE LOCATION FOR FIELD OBSERVATION

The coastal observations were performed at Fortaleza, as indicated in Figure 1. While UECE's campus can be considered as embedded in the urban pollution, the second observation point for the most part is free from pollution since the trade wind direction is almost constantly from East in Fortaleza.

Figure 1. Map of Brazil, with magnification to investigated region of investigation. Ceará State is shown in more detail along with the Quixadá city and Fortaleza Metropolitan Region. The Fortaleza city map highlights the two sites used to measure aerosol and CCN concentration in the coastal region.

Inland observations were performed on the Urucum hill, situated at 5.038231 S, 39.009331 W, with an elevation of about 490 m above sea level. The observation point is about 10 km from the city of Quixadá, and 180 km south of Fortaleza. The hill is located on a place very representative of the semi-arid Northeast region of Brazilian.

The first inland observation period was performed during 4 days from 17 to 20 December 2010. During that period, a few rain events were observed and vegetation was turning green due to previous rain events.

The second inland observational period was performed from 31 October 2011 to 06 November 2011. Although October and November coincide with the dry season of the region, during this specific year considerable amount or rain was observed prior and during this experiment, and vegetation was unusually green. If there is any influence of vegetation on aerosols, both inland observational periods can be considered as having the same vegetation cover.

2.4 THE METEOROLOGICAL CONDITION DURING CEAREX

Analysis on meteorological data in Fortaleza indicated that wind speed is larger during the day, increasing at sunrise and decreasing systematically after noon. The wind direction can change depending on the hour of day during the year, but it tends to always come from easterly directions (90 degrees E) at 18 hours local time. In Figures 2a and 2b the back trajectories are illustrated for the air masses that arrive on the coastal observation point. Under all situations air masses pass over the ocean, but they reach observational site from different directions depending on the prevailing circulation. In Figure 2a some of the air mass trajectories are influenced by local winds, like the sea and land breezes, which cause air masses to reach the observational site under angles lower than 90 degrees, especially after 18 hours local time as demonstrated by Teixeira

(2008).

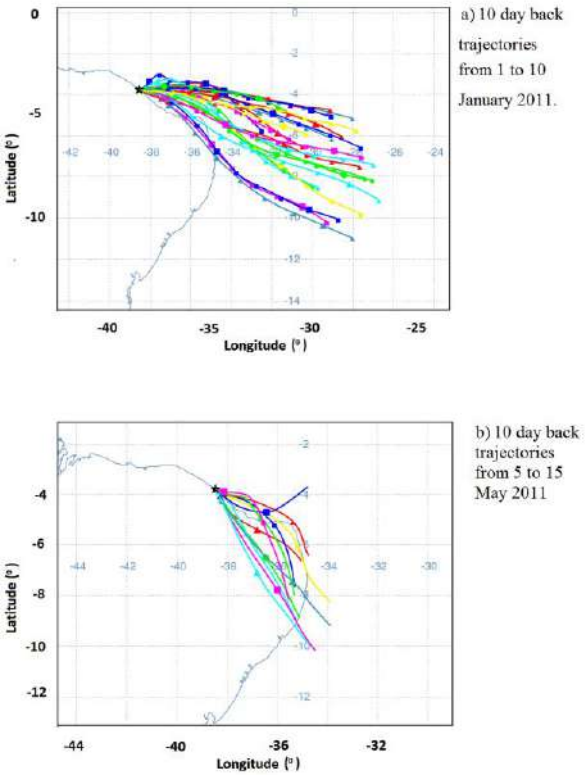

Figure 2. location of the coastal measurement site in the semiarid region of the Brazilian Northeast. Trajectories indicate the large scale airflow during measurements, calculated by HYSPLIT (NOAA-ARL, GDAS1 model).

Figure 3a illustrates the back trajectories of the air masses that arrive on the observation point during the first period of inland observations. Most of the lines come from east to southeast, and across large continental areas, spending more than one day to reach the site. Figure 3b illustrates the air masses trajectories during the second inland observation. Most of the lines now come from northeast to east and across shorter continental areas than the first continental observation period.

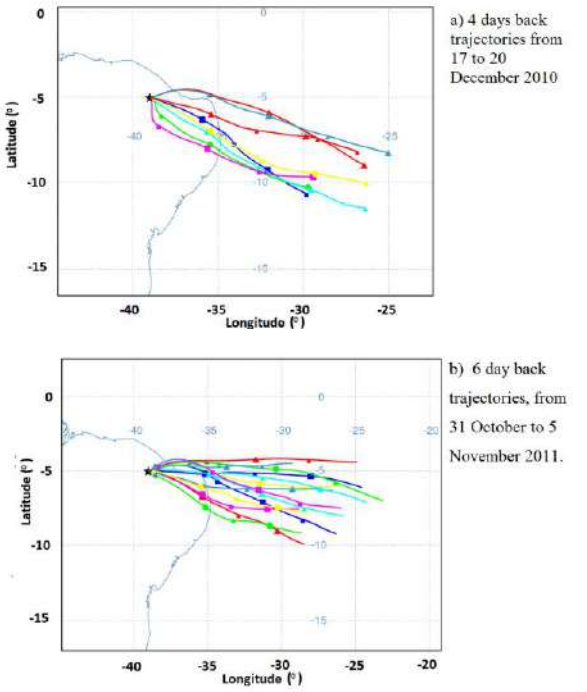

Figure 3. Same as Figure 2, but for remote inland measurement location, 180 km south of Fortaleza (start height 500 m, start time 11:00 local time).

Figure 4a depicts the observations performed on Uece's campus in December 2010 and January 2011, while Figure 4b shows observations performed during the months of April and May at observation point closer to the ocean. Both Figures 4a and 4b depicts the same tendency: during the afternoon the CCN concentration have an approximately constant value, but it tends to increase in the early evening.

Observations suggest that coastal concentration of CCN is always high in Fortaleza and does not depend on the point of observation neither on the month of the year.

Figure 5 shows the mean hourly aerosol concentration of sizes from 25 to 400 nm observed on Fortaleza in December

2010 and January 2011. We can observe that aerosol concentration is most of the time very high. After 15 hours concentration increases continuously until 19 hours, when it reaches values of about 5000 cm^{-3}. Although there is a decrease after 20 hours, mean values during the evening tends to be higher than those observed during the day.

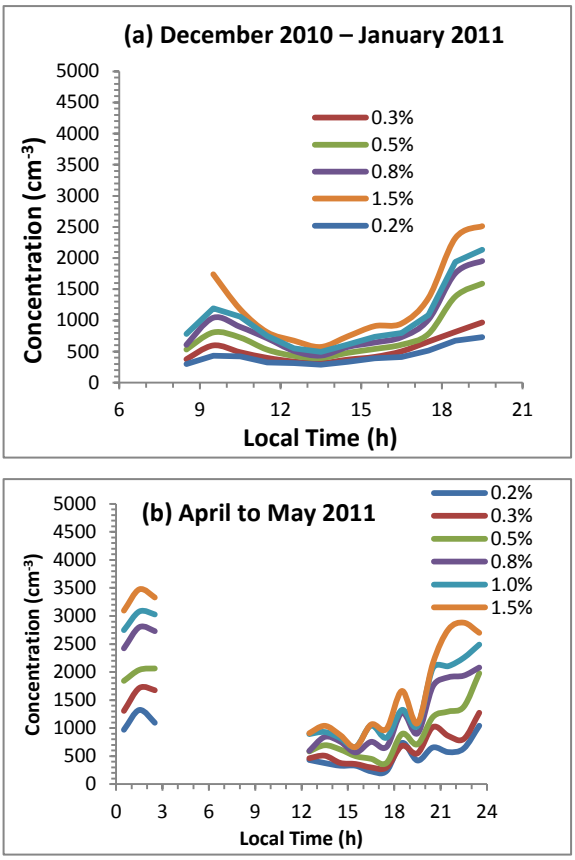

Figure 4. Mean hour cloud droplet concentration as measured with the CCNC as result of activation at supersaturations of 0.2%, 0.3%, 0.5%, 0.8%, 1.0 % and 1.5% in Fortaleza during (b) December 2010 – January 2011 and (c) April to May 2011.

Figure 6 illustrates the size distributions of days 5, 6, 15, and 20 April 2011. In general concentrations do not vary significantly from one hour to the other for particulates larger than 250 nm, and are close to each other during observations.

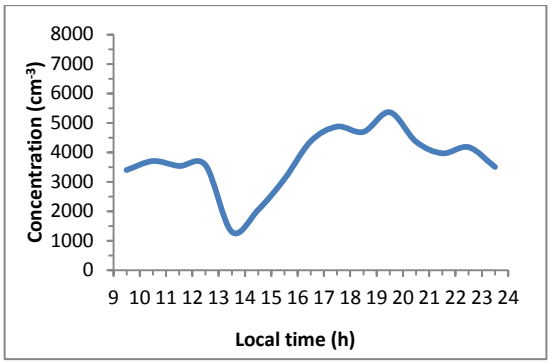

Figure 5. Mean aerosol concentration from 25 nm to 400 nm in Fortaleza measured with EAC.

Figure 7 illustrate the aerosol concentration observed during the first inland data collection. As it can be seen, the total aerosol number concentration was observed to have values between 2000 cm^{-3} to about 3000 cm^{-3} during the first day of observation on the continent, as illustrate in Figure 7a,but the mean number concentration during this period was 1818 cm^{-3} ± 1158 cm^{-3}.

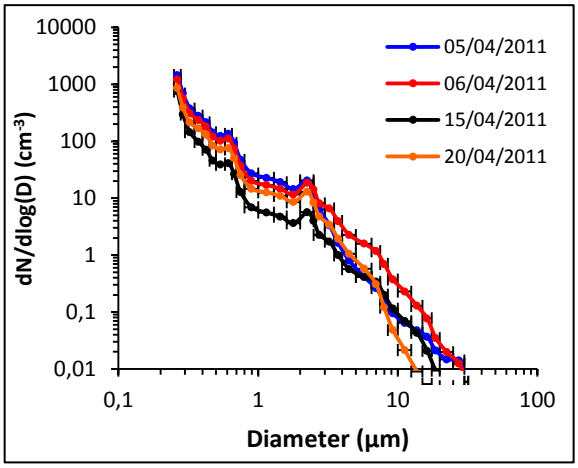

Figure 6. Observations of Aerosol size distribution in Fortaleza measured with OPC, April 2011.

Figure 8 depicts values of the observed aerosol distribution. There is large variability in the smallest size channel, but in general concentration values were observed

to be low. Spectra density is observed to diminish after rain events, as the red line, observed after rain events.

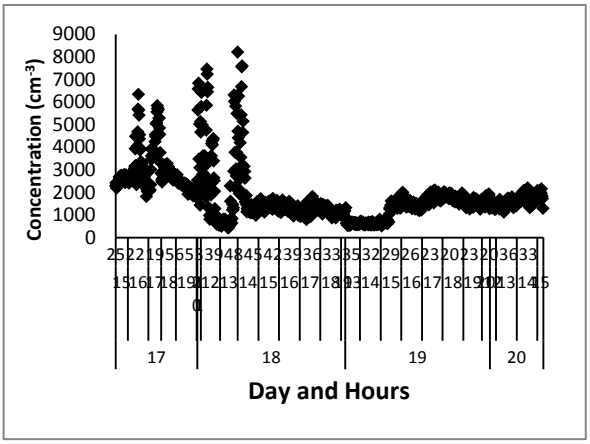

Figure 7. Aerosol concentration measured with EAC during the first inland observation period for days 17 to 20 December 2010. Hours are indicated as local time.

Figure 9 shows the observed CCN spectra activation. Number concentration values of activated CCN are relatively low, approximately 150 cm^{-3} even at 1.5% supersaturation.

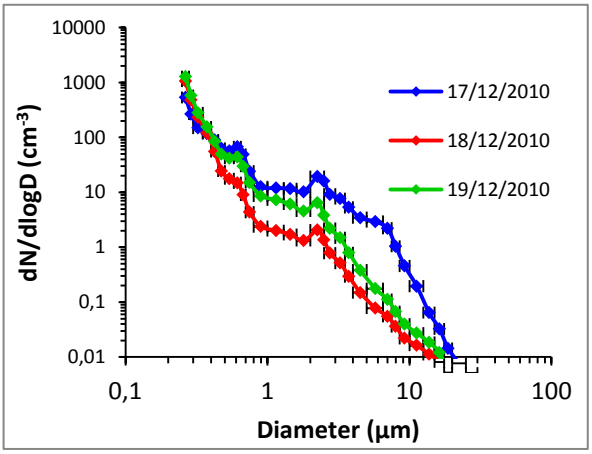

Figure 8. Same of Figure 6, but for the first continental observation period, December 2010. Standard deviation for day 17/12/2010 are not shown because they are too large on the largest size of the spectra.

During the second period of inland observation, number concentration was still relatively high, as was observed in Figure 10a. The aerosol mean concentration during the second continental observation was 1901 cm^{-3} ± 634 cm^{-3}.

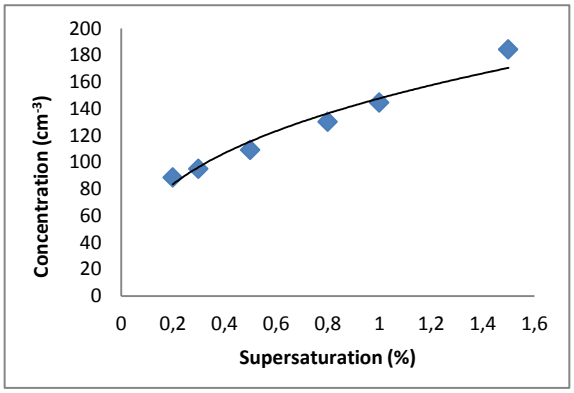

Figure 9. CCN number concentration plotted against water vapor supersaturation (%) measured on continent from 17 to 20 December 2010. The data points are mean values for the observational period. The black line is a power law fit of the form $N=Cs^k$, with the best fit parameter C=147 cm^{-3} and k=0.35.

The aerosol size distribution (Figure 11) was not seen to vary largely at small sizes, as was observed previously, and was not also severely affected after the rain event observed during November 1st.

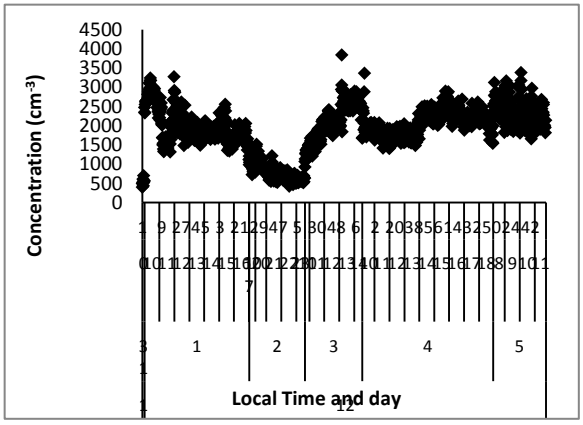

Figure 10 Same as Figure 7a), but for the second inland observational period.

Figure 12 depict the mean averaged CCN concentration observed from October 31st to November 3th. The CCN activation spectra were different from that observed previously (Figure 12). While in the former observation concentration values activated at 1.0% was only about 150 cm^{-3}, the later values reached 950 cm^{-3} at the same supersaturation.

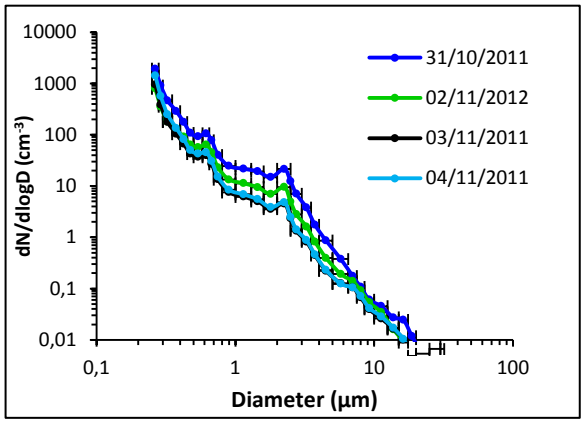

Figure 11 Same of Figure 6, but for the second period of inland observations, November 2011.

4. CONCLUSION

This work describes observations of aerosol and CCN activation spectra in the Brazilian Northeast semi-arid region (NEB). The observations were performed using an Electric Aerosol Charger (EAC), an Optical Particle Counter (OPC) and a CCN counter (CCNC). Those instruments were able to determine aerosol number concentration and mean aerosol size distribution from 25nm to 400 nm, aerosol size distribution from 250 nm to 32 µm in 32 sizes channels, and CCN activation spectra. Three places were used as observational points. One was at Ceara State University campus, located at 3.794542 S, 38.557606 W, and a second closer to the coast, at 3.785958 S, 38.461289 W. The third point was about 180 km from the coast at 5.038231 S, 39.009331 W, representing remote inland site.

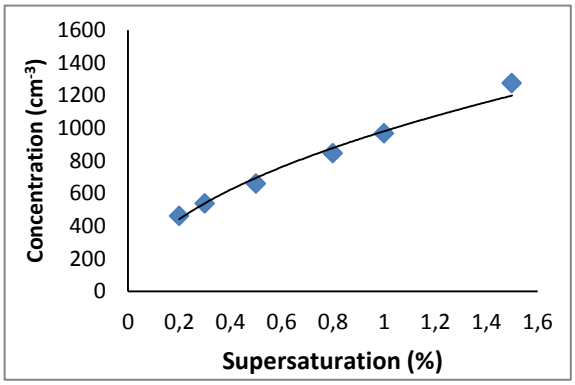

Figure 12. Same as Figure 9, but for 31 October to 05 November 2011. The best fit parameter C= 980 cm^{-3} and k=0.50.

The observations show that aerosol concentration on the NEB is usually high. For example, coastal particle number concentrations are above 3000 cm^{-3} on average, exhibiting concentration peaks that depend on the time of the day. Inland concentrations were about 1800-1900 cm^{-3}, which also is high, but the data do not show much diurnal variation.

A remarkable difference between inland and coastal cloud condensation nuclei (CCN) concentration regimes was found. While in the coastal environment the CCN concentration activated at 1.0% supersaturation was above 1000 cm^{-3} on average, the inland observations presented regimes that apparently depend strongly on the back trajectory of the air masses. When air masses arrived at the point of observation which previously had crossed large continental areas, the average concentrations were below 200 cm^{-3} at 1.0%

supersaturation. When the air masses originated from marine environment, passing only over a shorter stretch of land surface, the concentration levels of CCN were about 950 cm^{-3}.

As a perspective to new measurements it would be important to include more instruments on the investigation. Under this perspective it would be important to evaluate chemical composition to determine chemistry sources involved on the aerosol sampled and also equipments able to show lower size particles distribution.

5. ACKNOWLEDGMENT

This work was supported by FUNCAP (Fundação Cearense de Apoio ao Desenvolvimento Científico e Tecnológico). We wish to thank Funceme for the access to its meteorological data.

6. REFERENCE

Ayers, G. P., J. P. Ivey, and R. W. Gillett (1991), Coherence between seasonal cycles of dimethyl sulfide, methanesulfonate and sulfate in marine air, Nature, 349(6308), 404– 406.

Breon, F. M., Tanre, D., & Generoso, S. (2002). Aerosol effect on cloud droplet size monitored from satellite. *Science*, *295*, 834–838.

Chen, Q., Farmer, D., Schneider, J., Zorn, S., Heald, C., Karl, T., Guenther, A., Allan, J., Robinson, N., Coe, H., Kimmel, J., Pauliquevis, T., Borrmann, S., Poschl, U., Andreae, M., Artaxo, P., Jimenez, J., and Martin, S.: Mass spectral characterization of submicron biogenic organic particles in the Amazon Basin, Geophys. Res. Lett., 36, L20806, doi:10.1029/2009GL039880, 2009.

Frank, G. P., Dusek, U. and Andreae, M. O. (2006). Technical note: Characterization of a static thermalgradient ccn counter, *Atmospheric Chemistry and Physics* **6**: 2151–2174.

Gunthe, S. S., S. M. King, D. Rose, Q. Chen, P. Roldin, D. K. Farmer, J. L. Jimenez, P. Artaxo, M. O. Andreae, S. T. Martin, and U. Pöschl. Cloud condensation nuclei in pristine tropical rainforest air of Amazonia: size-resolved measurements and modeling of atmospheric aerosol composition and CCN activity, Atmos. Chem. Phys., 9, 7551–7575, 2009.

Heim, M., B. J. Mullins, H. Umhauer, G. K., 2008: Performance evaluation of three optical particle counters with an efficient “multimodal” calibration method. Aerosol Science, **39**, 1019–1031.

Liu, P. S. K., W. R. Leaitch, J. W. Strapp, and M. A. Wasey, 1992: Response of PMS airborne ASASP and PCASP to NaCl and latex particles. *Aerosol Sci. Technol.*, **16,** 83–95.

Oyama, M. D, and C. A. Nobre, 2004: Climatic Consequences of a Large-Scale Desertification in Northeast Brazil: A GCM Simulation Study. Journal of climate, v. 17, 3203 – 3213.

Pinheiro, F. G. M.; Cortez , P. C. e Mota, J. C. M., 2011: Automatic System for Measuring the Concentration of Clouds Condensation Nuclei by Computer Vision (in

protuguese). Revista Controle & Automação, 22, n. 3, p. 296 – 307.

Roberts, G.C., M. O. Andreae, J. Zhou, P. Artaxo, 2001: Cloud condensation nuclei in the Amazon Basin: “Marine” conditions over a continent? G. Res. Letters, 28, 14, 2807-2810.

Ross, K. E., S. J. Piketh, R. T. Bruintjes, R. P. Burger, R. J. Swap, and H. J. Annegarn: Spatial and seasonal variations in CCN distribution and the aerosol-CCN relationship over southern Africa, J. Geophys. Res., 108(D13), 8481, doi: 10.1029/2002JD002384, 2003.

Teixeira, R. F. B., 2008: The breeze phenomenon and its relationship with the rain over Fortaleza-CE. Brazilian Journal or Meteorology (In Portuguese) , V.23, n.3, 282-291.

AEROSOL EFFECTS OF THE CONDENSATION PROCESS ON A TROPICAL SQUALL LINE SIMULATION

Tatsuya Seiki[1], Masaki Satoh[2,3], Teruyuki Nakajima[1], Hirofumi Tomita[1,3]
1. RIKEN Advanced Institute for Computational Scinece
2. Atmosphere and Ocean Research Institute, The University of Tokyo
3. Japan Agency for Marine-Earth Science and Technology

1. INTRODUCTION

There remain many uncertainties in cloud radiative forcing involving aerosol indirect effects. In particular, the impact of aerosols on convective cloud systems in the climate system is not well known since general circulation models (GCMs) employ cumulus parameterization to represent sub-grid convections. Therefore, this study newly developed a double-moment bulk cloud microphysics scheme (NDW6) on a non-hydrostatic atmospheric model NICAM (Satoh et al., 2008), and investigated the impact of aerosols on a tropical squall line system.

In past, warm phase collisional processes have been investigated as a microphysics of the aerosol lifetime effect (Albrecht, 1989): aerosol loading prevents cloud water from growing into rain by providing many tiny cloud droplets by activation. Following the fact, preceding studies have stressed importance of the collisional processes for convective cloud system using cloud resolving models (Khain et al., 2008). In contrast, this study aimed to isolate the aerosol effects to various cloud microphysics, and evaluated the effect of aerosols to the condensation and evaporation processes with feedback processes.

2. EXPERIMENTAL DESIGNS

NDW6 is based on Seifert and Beheng (2006). In this study, we considered aerosols only as precursors of cloud droplets and gave the their activating spectra as follows,

$$N_{\mathrm{ccn}} = C_{\mathrm{ccn}} s_{sw}^{\kappa_{\mathrm{ccn}}},$$

where s_{sw} % is supersaturation ratio, and C_{ccn} cm^{-3} and κ_{ccn} are spectral constants given by observations. To evaluate this effect, an explicit condensation scheme was used instead of the saturation adjustment method. (Khvorostyanov and Sassen, 1998). The tendency of supersaturation δ_{liq} within a model time-step is given as,

$$\frac{d\delta_{\mathrm{liq}}}{dt} = -\frac{\delta_{\mathrm{liq}}}{\tau_{cnd,c}} + A_{cnd},\ \tau_{cnd,c} \equiv \left\{ \frac{1}{\rho q_{vs}} 2\pi G_{\mathrm{liq}} D_c F_{va} N_c \right\}^{-1}.$$

Here, the first term is the reduction term by vapor consumption due to condensation, and the second term is the production term by other processes. It's found that supersaturation changes with the timescale of $\tau_{cnd,c}$, and the timescale is inversely proportional to the number concentration of cloud water N_c (Fig. 1). This means that condensation and evaporation rates depend on aerosols through N_c (hereafter the aerosol condensational effect). In a maritime aerosol condition (N_c ~ 50 cm^{-3}), the timescale is about several tens of seconds when supersaturation cannot be adjusted with a model timestep longer than several seconds. On the other hand, in a continental aerosol condition (N_c~1000 cm^{-3}), supersaturaton could be adjusted at once.

We performed a set of sensitivity experiments with C_{ccn}=100, κ_{ccn}=0.462 as the control experiment (CTL), and polluted experiments with C_{ccn} = 200, 400, 400, and 800 cm^{-3} (CCN2, CCN4, and CCN8). In addition, to evaluate only the aerosol condensational effect, we performed experiments with accelerated condensation and evaporation by factors of 2, 4, and 8 (TAU2, TAU4, and TAU8).

We choose the case of a tropical squall line system by GEWEX-GCSS model inter comparison (Redelsperger et al., 2000). The horizontal resolution is 1km at the center of a stretched grid system (Tomita, 2008). The vertical layer is divided by 44, and the top of the atmosphere is 20km. We performed 7-hours integration with the model timestep of 6 s.

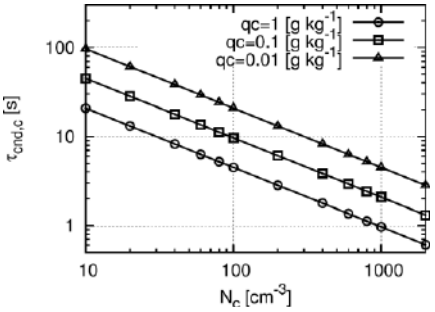

Fig.1. The dependency of the time-scale of condensation on the cloud droplets number concentration with q_c = 1g kg^{-1} (circle), 0.1 g kg^{-1} (rectangle), and 0.01 g kg^{-1} (triangle) under the condition of T = 273 K, p = 800 hPa.

3. RESULTS

In the initial stage of the squall system, the aerosol effect is dominated by the condensation process. Particularly, the role of latent heat is important for development of convection in terms of dynamical feedbacks. In

addition, this study showed that the aerosol condensational effect intensifies convective core and accelerate evaporation on the lateral boundary of convective clouds. The analysis of two-dimensional vorticity equation proposed by Weisman and Rottuno (2004) showed that this contrast produces the buoyancy gradient across to the leading edge of squall line and intensifies the cold-pool-shear interaction (Fig. 2).

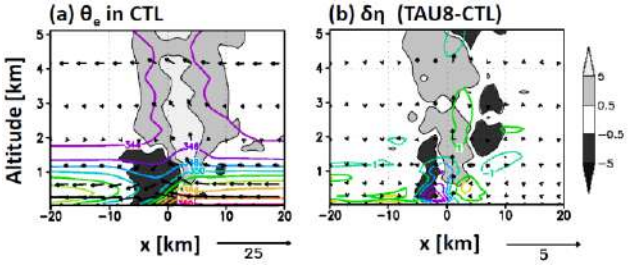

Fig.2. (a) The time-line-averaged vertical profile of the equivalent potential temperature [K] (contour), the heating rate [K hr^{-1}] (shade), and wind vector [m s^{-1}] for the first two hours. (b) The time-line-averaged vertical profile of the departures of the along-line vorticity [s^{-1}], the heating rate [K hr^{-1}], and the wind vector [m s^{-1}] in TAU8 from those in the CTL for the first two hours. In these figures, the *x*-axis is the distance from the leading edge, and the vertical wind is scaled by multiplying by 10.

4. BIBLIOGRAPHY

Albrecht, B. A., 1989: Aerosols, cloud microphysics, and fractional cloudiness. *Science*, 245, 1227–1230.

Khain, A. P., N. BenMoshe, and A. Pokrovsky, 2008: Factors Determining the Impact of Aerosols on Surface Precipitation from Clouds: An Attempt at Classification. *J. Atmos. Sci.*, 65, 1721–1748.

Khvorostyanov, V. I. and K. Sassen, 1998: Cirrus Cloud Simulation Using Explicit Microphysics and Radiation. Part I: Model Description. *J. Atmos. Sci.*, 55, 1808–1821.

Redelsperger, J.-L., P. R. A. Brown, F. Guichard, C. How, M. Kawasima, S. Lang, T. Montmerle, K. Nakamura, K. Saito, C. Seman, W-K. Tao, and L. J. Donner, 2000: A gcss model intercomparison for a tropical squall line observed during toga-coare. I: Cloud-resolving models. *Quart. J. Roy. Meteor. Soc.*, 126: 823–863.

Satoh, M., T. Matsuno, H. Tomita, H. Miura, T. Nasuno, and S. Iga, 2008: Nonhydrostatic icosahedaral atmospheric model (NICAM) for global cloud resolving simulations. *J. Comput. Phys.*, 227, 3486-3514.

Seifert, A., and K. D. Beheng, 2006: A two-moment cloud microphysics parameterization for mixed-phase clouds. Part I: Model description. *Meteor. Atmos. Phys.*, 92, 45–66.

Tomita, H., 2008: A stretched icosahedral grid by a new grid transformation. *J. Meteor. Soc. Japan*, 86A, 121-142.

Weisman, M. L., and R. Rotunno, 2004: “A Theory for Strong Long-Lived Squall Lines” Revisited. *J. Atmos. Sci.*, 61, 361–382.

5. ACKNOWLEDGEMENT

The authors wish to thank Dr. Masaki Satoh, Dr. Hirohumi Tomita, and the NICAM development team for providing us with helpful discussions. The numerical experiments were performed using the HITACHI SR11000 at the Information Technology Center, the University of Tokyo. This study was partly supported by the Core Research for Evolutional Science and Technology program (CREST) of the Japan Science and Technology Agency and the Innovation Program of Climate Projection for the 21st Century of the Ministry of Education, Culture, Sports, Science, and Technology (MEXT). One of the authors was supported by the Research Program on Climate Change Adaptation of MEXT.

STUDIES OF THE OPTICAL PROPERTIES OF WARM CLOUDS BY A DETAILED MICROPHYSICAL SCHEME

Eszter Lábó[1], István Geresdi[2]
[1]OMSZ-Hungarian Meteorological Service, Address: H-1024 Budapest, Kitaibel P. u.1., Tel.: +36-1-346-4664, Fax: +36-1-346-4665, E-mail: labo.e@met.hu
[2]University of Pécs, Faculty of Sciences, Address: H-7624 Pécs, Ifjúság útja 6. Tel.: +36-72-503-600, Fax: +36-72-501-527, E-mail: geresdi@gamma.ttk.pte.hu

1. INTRODUCTION

Clouds have important effect on the radiation budget of the atmosphere (Arking, 1991). Similarly to greenhouse gases, they absorb the longwave radiation, thus contribute to the warming of the Earth's atmosphere. The extent of cloud forcing produced by interaction between longwave radiation and cloud particles can be of 31 W/m^2 (Gregory and Morris, 1996). As a contrary cooling process, clouds reflect the shortwave radiation of the Sun (Corti and Peter, 2009). The overall effect of the clouds is an average cooling of the atmosphere by 13.2 W/m^2 (Ramanathan et al., 1989).

For numerical weather prediction purposes, there is a need to describe the cloud-radiation interactions adequately, due to the considerable impact clouds have on the radiation budget and on the evolution of the weather system consequently (Fouquart et al., 1990). Radiation exchange is the driving force of temperature changes, which creates atmospheric flows and cloud formation processes (Liu et al., 2009). The longwave radiation at the surface can be altered by 40 W/m^2, depending on the radius size of cloud droplets, and the radiation at the top of the atmosphere changes by 5 W/m^2 if the cloud droplet characteristic size is reduced (Harrington and Olsson, 2001). Similar results have been presented by Hongqi and Zhao, 2002. In our studies, we will only study the optical properties of clouds against infrared radiation.

In case of infrared radiation, the interaction between cloud particles and radiation is dominated by the absorption, to which scattering can be neglected (Stephens, 1984). Extinction coefficients of the water droplets are usually calculated depending on the Liquid Water Content (LWC), which is one of the main parameters for the definition of optical properties of clouds (Ritter and Geleyn, 1992; Chou et al., 1990). In order to reduce computational costs, operational numerical weather prediction models do not take into account the water droplet size distribution. Instead, they define a characteristic radius of the droplet size distributions, and use this radius in the parameterization of extinction coefficients besides the LWC (Lindner and Li, 2000, Walko et al., 1995). The drawback of this approach is that size distributions resulting from complex microphysical processes, which are different from the idealized gamma-size distribution, cannot be included (Geresdi, 1998).

Detailed microphysical schemes can only be introduced in the radiative transfer of numerical weather prediction models if the calculation of optical properties of cloud droplets is based on bin-microphysical schemes. The bin microphysical schemes divide the radius spectrum of water droplets in small intervals, in which the number of droplets can be chosen independently (Lynn et al., 2005). Thus, arbitrary droplet-size distribution can be achieved.

In our studies, a new scheme for the calculation of extinction coefficients of water droplets in the infrared region has been developed. It is based on the work of Harrington and Olsson, 2001, who have provided extinction coefficients in function of spherical droplet radius and wavelengths. Pre-calculated kernel functions have been defined for use to reduce the computational costs in model applications. The research focuses only on the longwave radiation.

In this paper, we present the results of the newly developed parameterization scheme. The extinction coefficients obtained by using bin microphysics have

been compared to the extinction coefficients of bulk microphysics (Hu and Stamnes, 1993) in case of Gamma size distributions. It has been found for effective radius smaller than 13μm that the bin scheme provides smoother dependence of the extinction coefficients on the wavelengths than the bulk scheme. At bigger effective radius, the bin scheme is underestimating the extinction coefficients. Further investigations of the newly developed scheme are needed in case of non-Gamma size distributions. Collisions and the evolution of the microphysical properties of clouds are intended to be taken into account.

2. METHODOLOGY

Radiative transfer in the atmosphere is coupled to microphysical models by the preceding computation of the cloud optical properties. The optical properties describing the scattering, the extinction, and the absorption of radiation in clouds consist of the single scatter albedo (ω_0), which is the proportion of scattering in total extinction processes, the optical depth (δ), which is the product of the extinction coefficient and the cloud depths, and the asymmetry parameter (g), which characterizes the angle-dependence of the scattering. These parameters can be computed for each band of the radiative transfer.

As scattering is a negligible effect at infrared wavelengths, we have to calculate the optical depths of the clouds. For this, we use the parameter Q_{ext} extinction cross section (Roach and Slingo, 1979). Extinction coefficient is an average over a given radiative band, and over a given n(D) size distribution function.

$$\bar{\beta}_{\mathrm{ext}} = \int_{\Delta\lambda}\left[\int_0^{\infty} A(D)\,Q_{\mathrm{ext}}(D, m\lambda)\,n(D)\,\mathrm{d}D\right] E_\lambda\,\mathrm{d}\lambda \Big/ \int_{\Delta\lambda} E_\lambda\,\mathrm{d}\lambda,$$

$$E_\lambda = B(\lambda, T_s) \qquad (1)$$

where A(D) is the cross-sectional area of the water droplets, m is the complex index of refraction, E_λ is the infrared energy density, and T_s=273 K is the reference value used for the Planck function.

The Lorentz-Mie theory describes the radiation-droplet interactions; however, it cannot be analytically solved. Instead, we have chosen to use the Modified Anomalous Diffraction Theory (ADT) which describes the optical properties of water drops with only small errors associated (Mitchell, 2000). According to this theory, the extinction can be defined as a sum of two different components: the corrected Q_{ext}, and Q_{edge}:

$$Q_{\mathrm{ext},m}(D,\lambda,m) = \left(1 + \frac{C_{\mathrm{res}}}{2}\right) Q_{\mathrm{ext}} + Q_{\mathrm{edge}}, \qquad (2)$$

The dependence of Q_{ext} on the droplet diameter (d), on the wavelength (λ), and on the index of refraction (m) can be described as follows:

$$Q_{\mathrm{ext}}(D,\lambda,m) = 2K(tD) \qquad (3)$$

$$t = \frac{2\pi}{\lambda}\left[n_i + i(n_r - 1)\right], \qquad m = n_r - in_i$$

$$K(x) = 1 + 2Re\left[\frac{e^{-x}}{x} + \frac{e^{-x} - 1}{x^2}\right] \qquad (4)$$

The correction parameter C_{res} is as follows:

$$C_{\mathrm{res}} = r_a \frac{k^m e^{-\epsilon k}}{k_{\max}^m e^{-m}}, \qquad (5)$$

where $r_a = 0.7393 n_r - 0.6069$, and (6)

$$m = \frac{1}{2}, \quad k = \frac{D}{\lambda}, \quad k_{\max} = \frac{m}{\epsilon},$$

$$\epsilon = \frac{1}{4} + 0.6\left\{1 - \exp\left[-\frac{8\pi n_i}{3}\right]\right\}^2. \qquad (7)$$

The Q_{edge} component is defined as:

$$Q_{\mathrm{edge}} = 2(\pi k)^{-2/3}\left[1 - \exp(-0.06\pi k)\right] \qquad (8)$$

Refractive indexes defined in Refractive index database (http://refractiveindex.info/?group=LIQUIDS&material=Water) have been applied.

The bin scheme applied is a numerical scheme which has a radius ranging from r_0=1.5625 μm to r_{36}= 5.07968 cm. It consists of 36 bin intervals, the edges of which defined as $r_k = r_0 * 2^k$. In each of the intervals, an A(k) and B(k) constant is determined, to describe n(D) distribution in the interval as linear:
$n_k(D) = A(k) + D * B(k)$.

We have implemented the above linear approximation bin-scheme into the (1) equation, by replacing the integral over the D diameter by summa over the bin intervals. As a result, we have the coefficients for A(k) and the coefficient for B(k) for each of the bins, and for arbitrary wavelengths. We have also calculated the coefficients for A(k) and the coefficient for B(k) for each of the bins for the whole infrared spectra (3.33 μm – 1000 μm).

3. RESULTS

Extinction coefficients obtained with the newly developed bin-microphysical scheme have been compared to the extinction coefficients obtained with a commonly used parametrization method in numerical models, which is parametrized by the effective radius and the Liquid Water Content. This method is fully described in Hu and Stamnes, 1993, the basic equation is as follows:

$$\beta_{ext}/LWC = a_1 * r_1^{b1} + c_1 \qquad (9)$$

The a_1, b_1, c_1 coefficients are defined for three wavelengths intervals: 2.5 μm-12 μm; 12 μm -30μm; and 30 μm -60 μm. this schemes is based on Mie-scattering calculations; however, the size distribution cannot be included.

We have produced several gamma-size distributions with the same LWC=10^{-3} kg/m^3, but with different water droplet concentrations. Table 1 summarizes the concentrations used, and the relevant effective radiuses.

N (*10^6)	r_{eff} (*10^{-6}) m
1000	7,92
500	9,98
300	11,83
250	12,57
50	21,5
20	29,18
15	32,12
5	46,33

Table 1: Number of concentrations and effective radius for different gamma-distributions for LWC=1 g/m^3

Comparison of the extinction coefficients from both bulk and bin-microphysical schemes are presented in Figure 1-3.

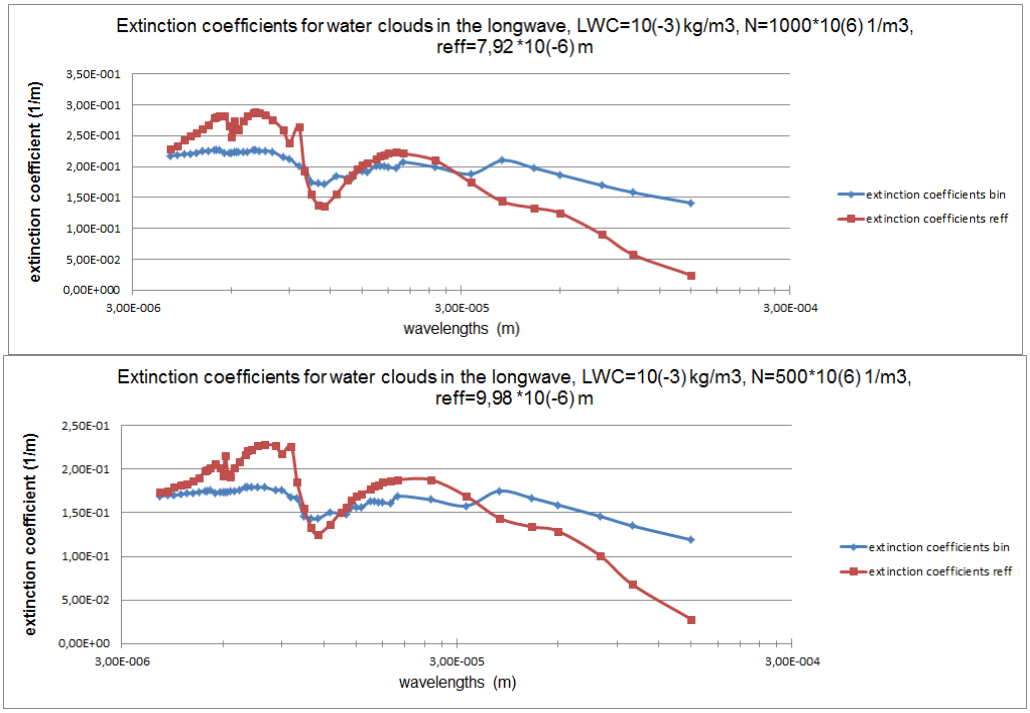

Figure 1: Extinction coefficients for water clouds in the longwave spectrum, LWC=1 g/m^3, N=1000*10^6 1/m^3 and N=500*10^6 1/m^3

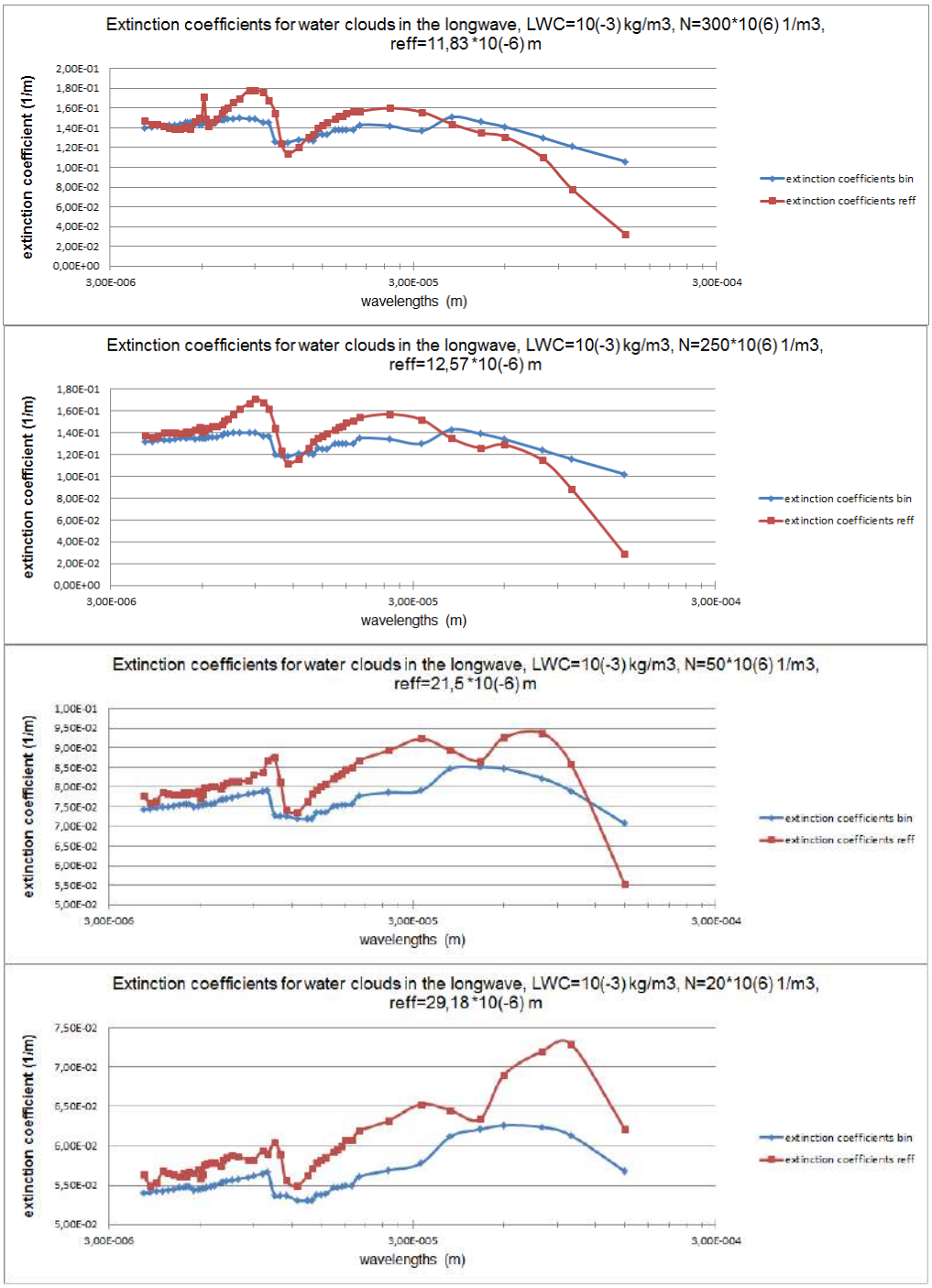

Figure 2: Extinction coefficients for water clouds in the longwave spectrum, LWC=1 g/m^3, N=300*10^6 1/m^3, N=250*10^6 1/m^3, N=50*10^6 1/m^3 and N=20*10^6 1/m^3

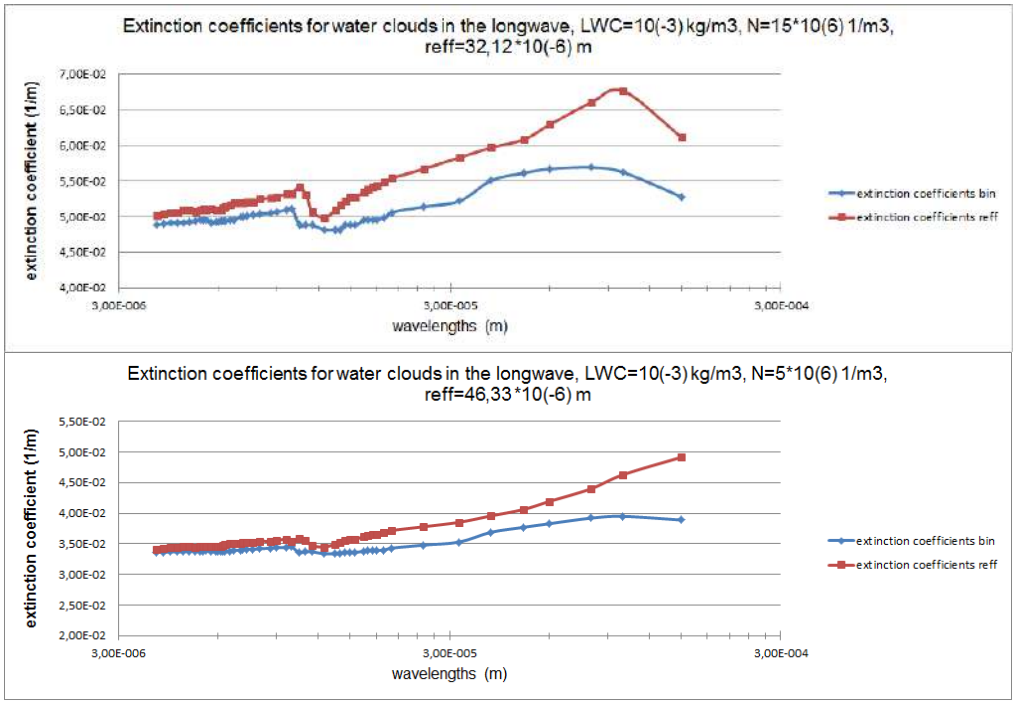

Figure 3: Extinction coefficients for water clouds in the longwave spectrum, LWC=1 g/m^3, N=15*10^6 1/m^3 and N=5*10^6 1/m^3

4. DISCUSSION

For the relatively small effective radiuses (r_{eff}=7.92 μm, and r_{eff}=9.98 μm), the extinction coefficients for the bin-scheme are smoother, they do not vary with the wavelengths as the parametrization in case of a bulk microphysical scheme using r_{eff} as input parameter. The difference is the highest at small wavelengths (can reach 25%), and is relatively low at wavelengths of 10^{-5} m. However, in the whole longwave spectrum, the band-averaged extinction coefficient for the two methods is very similar (differences are compensated).

For r_{eff}~12 μm, there is no significant difference in the extinction coefficients at small wavelengths (5 μm), and at λ~30 μm, the difference is also reduced to 15%. For r_{eff}>20 μm, the difference between the two schemes is also smaller at small wavelengths (λ~5 μm), and become higher (13%) at λ~30 μm. The extinction coefficients calculated from the r_{eff} are always higher than those calculated from the newly developed bin-scheme at r_{eff}>20 μm.

The impact of the change in the size distribution needs to be investigated in the future. We will investigate superposed gamma size-distributions with the same effective radius as a single gamma-size distribution. The effect of the simplification of using only r_{eff} as size-parameter will then be assessed.

For the continuation of the work, we will use detailed description of microphysical processes as e.g. collision in our bin-model, and calculate extinction coefficient for these cases as well. Later on, 2D cloud models will be used to describe cloud processes. The newly developed radiation scheme will be coupled to these cloud models.

The newly developed microphysical scheme is to be implemented in the Rapid Radiative Transfer (RRTM) code (Mlawer et al., 1997), which is currently using the Hu and Stamnes parametrization for defining optical properties of clouds. With the inclusion of the bin-scheme in the RRTM code, it will be possible to account for detailed microphysical processes, which can be important in low stratus situations and fogs in numerical weather prediction modelling. The present form of RRTM code is used in several numerical models, as e.g. the WRF model.

5. CONCLUSION

A new parametrization has been developed for calculating optical properties of water clouds in the longwave region, which is capable to take into account the variations in the size distribution of water

droplets. The newly calculated extinction coefficients are compared to bulk microphysical scheme, which is widely used in current operational numerical weather prediction models.
The results are encouraging as differences between the two schemes are usually smaller than 15% for single wavelengths, and the difference between the wavelengths band-averaged values are even smaller than this. Further research is planned on the implementation of the new code in the radiative transfer model RRTM. Coupling of the radiation code with cloud microphysical models is also planned. Low-stratus and fog cases are believed to be sensitive to the description of detailed microphysics in the radiation scheme.

6. BIBLIOGRAPHY

Arking, A. 1991: The Radiative Effects of Clouds and their Impact on Climate, Bulletin of the American Meteorological Society, vol. 72, Issue 6, pp.795-953.

Chou, M.D., Kratz, D.P. – Ridgway, W., 1990: Infrared Radiation Parameterizations in Numerical Climate Models, Journal of Climate, vol. 4, Issue 4, pp. 424-437.

Corti, T., Peter, T. 2009: A simple model for cloud radiative forcing. – Atmos. Chem. Phys. Discuss., 9, pp. 8541-8560.

Fouquart, Y., Buriez, J.C., Herman, M., Kandel, R.S. 1990: The Influence of Clouds on Radiation: A Climate-Modeling Perspective, Rev. Geophys., 28(2), pp. 145–166.

Geresdi, I., 1998: Idealized simulation of the Colorado hailstorm case: comparison of bulk and detailed microphysics., Atmospheric Research, Volume 45, Issue 4, pp. 237-252.

Gregory, D. and D. Morris, 1996: The sensitivity of climate simulations to the specification of mixed phase clouds. Climate Dyn. 12, pp 641-651.

Harrington, J., Olsson, P.Q., 2001: A method for the parameterization of cloud optical properties in bulk and bin microphysical models. Implications for arctic cloudy boundary layers, Atmospheric Research, Vol. 57, No. 1., pp. 51-80. doi:10.1016/S0169-8095(00)00068-5

Hongqi W., and Gaoxiang, Z., 2002: Parametrization of longwave optical properties for water clouds, Advances in Atmospheric Science, Vol.19, .n.1, pp 25-34, DOI: 10.1007/s00376-002-0031-y

Hu, Y. X., and K. Stamnes, 1993: An accurate parameterization of the radiative properties of water clouds suitable for use in climate models. J. Climate, Vol. 6, pp. 728-742.

Lindner, T. H., Li, J., 2000: Parameterization of the Optical Properties for Water Clouds in the Infrared. J. Climate, 13, pp. 1797–1805.

Liu, M., Nachamkin, J.E., Westphal, D.L., 2009: On the Improvement of COAMPS Weather Forecasts Using an Advanced Radiative Transfer Model, Weather and Forecasting, vol. 24, issue 1, pp. 286.

Lynn, B.H., Khain, A.P., Dudhia, Rosenfeld, D.J., Pokrovsky, A., Seifert, A., 2005: Spectral (Bin) Microphysics Coupled with a Mesoscale Model (MM5). Part I: Model Description and First Results. Mon. Wea. Rev., 133, 44–58.
doi: http://dx.doi.org/10.1175/MWR-2840.1

Mitchell, D.L., 2000: Parameterization of the Mie extinction and absorption coefficients for water clouds. J. Atmos. Sci. 57, pp. 1311–1326.

Mlawer, E. J., Taubman, S. J., Brown, P. D., Iacono, M. J., Clough, S. A., 1997: Radiative transfer for inhomogeneous atmospheres: RRTM, a validated correlated-k model for the longwave, J. Geophys. Res., 102(D14), pp. 16,663–16,682, doi:10.1029/97JD00237.

Ramanathan, V., Cess, R.D., Harrison, E.F., Minnis, P., Barkstrom, B.R., Ahmad, E., Hartmann, D., 1989: Cloud-Radiative Forcing and Climate: Results from the Earth Radiation Budget Experiment, Science, New Series, Vol. 243, No. 4887., pp. 57-63.

Ritter, B., Geleyn, J. –F., 1992: A Comprehensive Radiation Scheme for Numerical Weather Prediction Models with Potential Applications in Climate Simulations, Monthly Weather Review; Vol.120, Issue 2, pp 303-325.

Roach, W.T., Slingo, A., 1979: A high resolution infrared radiative transfer scheme to study the interaction of radiation with cloud, Quart.J.R.Met.Soc., 105, pp. 603-614.

Stephens, G.L., 1984: The parameterization of radiation for numerical weather prediction and climate models, Monthly Weather Review, 112, pp. 826-867.

Walko, R.L., Cotton, W.R., Meyers, M.P., Harrington, J.Y., 1995: New RAMS cloud microphysics parameterization:
Part I. The single moment scheme. Atmos. Res. 38, pp. 29–62.

Acknowledgements
Special thanks to my tutor, István Geresdi from the University of Pécs, Faculty of Sciences for his guidance and orientation in the research, and for his attention and availability at all times. The work was financially supported by the Hungarian grant of Developing Competitiveness of Universities in the South Transdanubian Region (SROP-4.2.1.B-10/2/KONV-2010-0002).

SYNOPTIC INFLUENCE ON SHALLOW CUMULUS CLOUDS

Heiner Matthias Brueck[1,2], Louise Nuijens[1] and Bjorn Stevens[1]

[1] *Max Planck Institute for Meteorology, Hamburg, Germany*

[2] *Universtity of Hamburg, Meteorological Institute, Hamburg, Germany*

1 ABSTRACT

This study explores the interaction of the large scale meteorological situation in the Atlantic trade wind region with the variability in cloudiness.

The main questions are: (1) What is the characteristic seasonal cycle of the marine boundary layer structure in the western part of the Atlantic trade wind regime? (2) Is it possible to find simple bulk quantities derived from the large scale meteorological environment which can explain cloudiness on timescales ranging from days (synoptic) to weeks (seasonal)?

To answer these questions ECMWF ERA Interim reanalysis data, satellite observations (MODIS level 2) and local point measurements from the "Barbados cloud observatory" (by the Max-Planck Institute for Meteorology) are compared. Barbados, clear offshore the Caribbean islands, is located downstream in the undisturbed Atlantic trade wind flow and therefore an appropriate site for trade wind cumulus observation. Cloud observations are gathered since April 2010 and for the first time they are seen in a large scale context. We identify the different characteristics in cloudiness and explore how these relate to measures of the large-scale environment, such as humidity, temperature structure, stability, subsidence, tradewind inversion height and mean winds.

Within the the north atlantic trade wind regime low level winds is generally defined by the subtropical Atlantic pressure distribution and the converging movement of low level winds into the Intertropical Convergence Zone (ITCZ). The atmospheric stability in the lower Troposphere is primarily defined by large scale subsidence from the descending branch of the Hadley cell and sea surface temperature (SST). The most dominant signal of the seasonal cycle is the latitudinal oscillation of the ITCZ when the belt of maximum upsidence and humidity is moving into the summer hemisphere. Furthermore, low level winds depend on the location and intensity of the Azores high and Bermuda high which are triggered by the SST distribution and the associated sensible and latent heat flux into the lower troposphere. The anticyclonic trade wind circulation is strong when the horizontal SST gradients are maximal (June-July) and weak after homogenization (fall). As a first-order approximation the annual variability of cloudiness in the western Atlantic trade wind region can be split into a dry season (January - May) and a wet season (June - December). During the wet season the cloud development is heavily triggered by synoptic-scale disturbances such as cold fronts, tropical easterly waves or upper level troughs. However throughout the relatively undisturbed dry season, records of cloudiness at the observatory show that the variability in cloudiness is just as large as during the wet season and cloudiness on average tends to be larger.

Making use of the MODIS imagery we analyze to what extent this variability in cloud fraction and structure is associated with small variations in the generally assumed steady synoptic regime.

ARE RAINDROP SIZE DISTRIBUTIONS OBTAINED WITH ELECTRO-MECHANICAL DISDROMETERS REAL?

Guillermo Montero-Martínez and Fernando García-García

Centro de Ciencias de la Atmósfera, Universidad Nacional Autónoma de México

1. INTRODUCTION.

Raindrop size distribution (DSD) is a key parameter in many cloud physics studies, so its actual knowledge is worthy in most meteorological applications. On the other hand, it is well known that DSD varies both spatially and temporally, not only across different storm types but also within a specific storm (Jameson and Kostinski, 1998; Bringi *et al*. 2003).

Nowadays several instruments are used to obtain DSDs, one of the most common ones being the Joss-Waldvogel disdrometer (JWD – Joss and Waldvogel, 1967). This impact-type, electro-mechanical device is widely accepted as a reference for rain spectra measurements at the ground, although its precise operating physical principle remains unclear. As stated by Joss and Waldvogel (1977), and according to its manufacturer, "the device transforms the vertical momentum of the impacting drop into an electrical pulse whose amplitude is a function of the drop diameter." However, a laboratory study by Kinnell (1976, 1977) showed the influence of both fall velocity and drop shape on the measured drop size from the impact. This suggests that the electrical pulse is more likely proportional to the force acting on the transducer integrated over the impact time interval, that is, the impulse rather than the momentum. In addition, several studies have shown a number of limitations on the performance of the Joss-Waldvogel disdrometer (see, for example, Sheppard, 1990; McFarquhar and List, 1993; Tokay *et al.*, 2005; Islam *et al.*, 2012).

An important shortcoming of the JWD is that it cannot measure the actual speed of a falling drop and thus the terminal velocity is usually assumed from semi-empirical relationships such as those developed by Gunn and Kinzer (1949). Several authors (Kinnell, 1976; Sheppard, 1990; Salles and Creutin, 2003) have studied the effect of the fall velocity on the assignment of the drop size, and concluded that the JWD cannot properly determine drops larger than 5 mm in diameter and that there is a shift in the DSD towards smaller sizes.

Recent findings have shown important deviations of actual drop fall-speeds with respect to their theoretical terminal velocities within the JWD lower measurement range (Montero-Martínez *et al.*, 2009). In the case of drops with sizes smaller than 0.8-mm in diameter, there is a large number of so-called super-terminal drops falling faster than their terminal speeds. Because these super-terminal drops have an "enhanced" vertical momentum, the JWD may detect them erroneously. In the present study, raindrop fall speed measured during actual rain events with two optical array probes deployed in a fixed, vertical fashion, are used to explore the effect on the estimation of the DSD for various rainfall episodes.

2. INSTRUMENTATION AND METHODOLOGY

Raindrop spectra were measured in the southern end of Mexico City during the rainy seasons of 2002, 2004 and 2007. The data were obtained using two two-dimensional Particle Measuring Systems Optical Array Spectrometer Probes – an OAP-2D-C and an OAP-2D-P (Knollenberg, 1981) – fixed on the ground and vertically oriented. Briefly, an OAP uses a photodiode array with 32 active elements and associated photodetection electronics to achieve two-dimensional information from particles passing through a laser beam at the sampling area. The image data were analyzed with a software routine specifically developed for the particular sampling conditions (Álvarez and Torreblanca,

Corresponding author's address:
Fernando García-García.
Centro de Ciencias de la Atmósfera.
Universidad Nacional Autónoma de México.
Circuito de la Investigación Científica,
Ciudad Universitaria. Del. Coyoacán.
04510 México, D.F. México.
e-mail: ffgg@unam.mx

1992). The reconstruction algorithm uses a center-in technique and is capable of taking into account the slanting of the images. The drop sizing nominal ranges for the 2D-C and 2D-P devices are 0.02 to 0.8-mm and 0.2 to 6.4-mm, respectively. For details on the size and drop fall speed determinations, the reader is referred to Montero-Martínez *et al.* (2010). Once the size and actual fall speed data were obtained, the vertical momentum and kinetic energy for each drop were estimated. Based on these data, the drops were redistributed by size considering the same number of bins and size limits used in the optical devices.

Environmental conditions were monitored and recorded with a weather station located besides the OAPs. Temperatures recorded during the field observations ranged from 15 to 25°C and ambient pressure was around 780 mb. Rainfall rates were derived from the precipitation water content of the measured spectra and compared well with those measured with the rain gauge.

3. RESULTS AND DISCUSSION

For analysis purposes, data were stratified in terms of rainfall rate, R, during periods of steady rain (R constant) according to the rain gauge data. The horizontal wind speed was also considered in order to look for its possible effects on the drop fall speed as detected by the probe. Although both OAPs – especially the 2D-C – are capable of detecting drops smaller than the lower limit of the JWD measuring range, the results shown here refer only to those obtained with the 2D-P. These data clearly show the effects on the spectra estimations due to considering either the actual drop fall speed, v_f, or the theoretical terminal speed, v_t.

Spectra obtained with the methodology mentioned above during a period of moderate rain (R = 12 mm h^{-1}) and for raindrops with diameters larger than 0.3 mm are shown in Figure 1. As it can be observed, high values of v_f (super-terminal drops) cause increments in the vertical momentum and redistribute the size assignment for the drops within smaller bins: even drops outside the nominal detection range are included in the first two bins due to their large v_f. This is the main reason for the increment on the number of drops with diameters between 0.3 and 0.8 mm in the estimated "momentum" DSD. The wind during the sampling period was calm (maximum instantaneous draft of 0.9 m s^{-1}), so the changes in the number of drops in each bin can be attributed to discrepancies in v_f. The rest of the spectrum (drop diameters larger than 1 mm) shows a minor tendency in drop undercounting. In spite of these variations, rain rate estimations are very similar (11.4 and 10.5 mm h^{-1} for the OAP and momentum DSD, respectively) because the small drops do not considerably contribute to the amount of rain and, thus, the differences in R can be considered within the instrumental error.

It is expected for the wind to affect the vertical movements of raindrops. Preliminary results (not shown here) indicate that the number concentration of super- and sub-terminal drops (drops with smaller values of actual fall speeds than their calculated terminal speeds) varies between calm-wind and windy periods. Observations with optical disdrometers have also shown that large drops fall slower than their expected v_t (Tokay *et al.* 2005). Figure 2 displays the DSDs obtained during a moderate rain period under windy conditions (mean and maximum values of 2.9 and 4.9 m s^{-1}, respectively). The "momentum" DSD shows larger amounts of drops less than 1.0 mm in diameter and similar counts for the other bins, except for those of drop sizes larger than about 2.5 mm. The R differences between the obtained DSDs and the rain gauge are almost 30% (8.6 and 8.1 mm h^{-1} for the spectra, 12 mm h^{-1} for the rain gauge). However, the difference in the estimation of R for drops smaller than 1.0 mm in diameter in the "momentum" DSD is three times larger with respect to that of the OAP spectrum. Nevertheless, this is meaningless when calculating the value of R over the whole drop-size range due to the fact that the largest drops are those which contribute the most to the total amount of water during a rainfall event.

Yet another case under windy conditions (mean and maximum values of 2.1 and 3.1 m s^{-1}, respectively), but for twice the rainfall rate than in the previous cases, is shown in Figure 3.

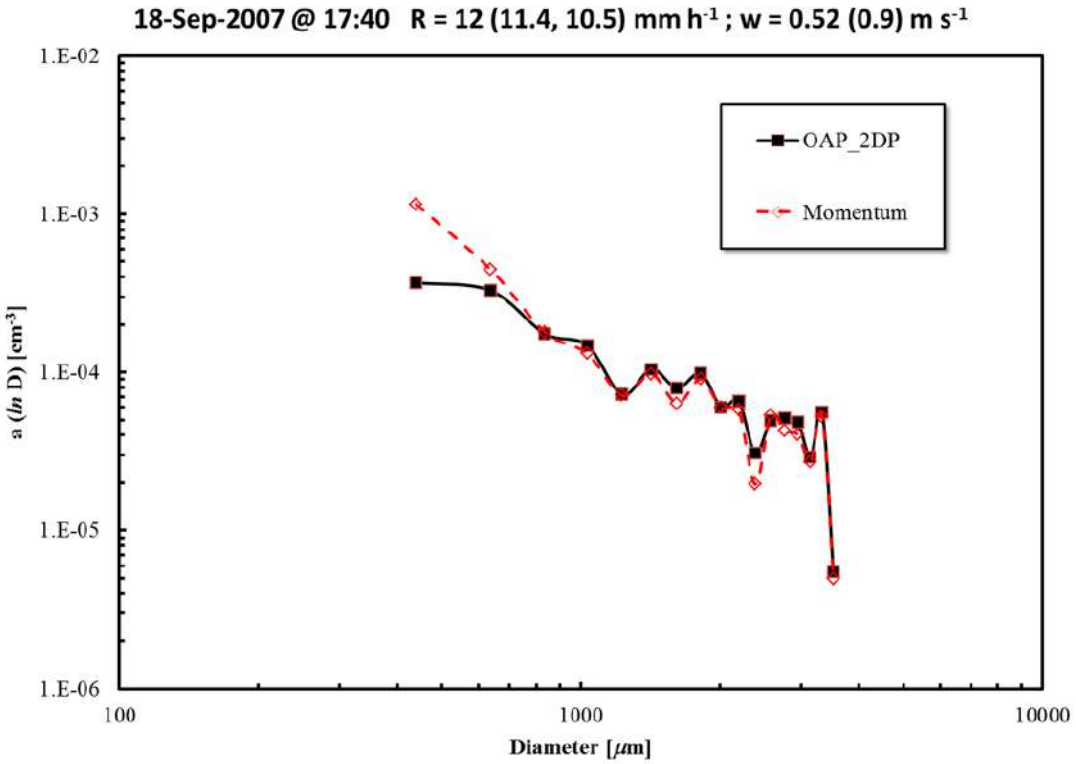

Figure 1. Raindrop spectra determined with the OAP-2D-P and estimated from the drop momentum of the impact. Calculations were made using the measured fall speed of each raindrop. This event (R = 12 mm h^{-1}) occurred in Mexico City under calm-wind conditions on September 18th, 2007.

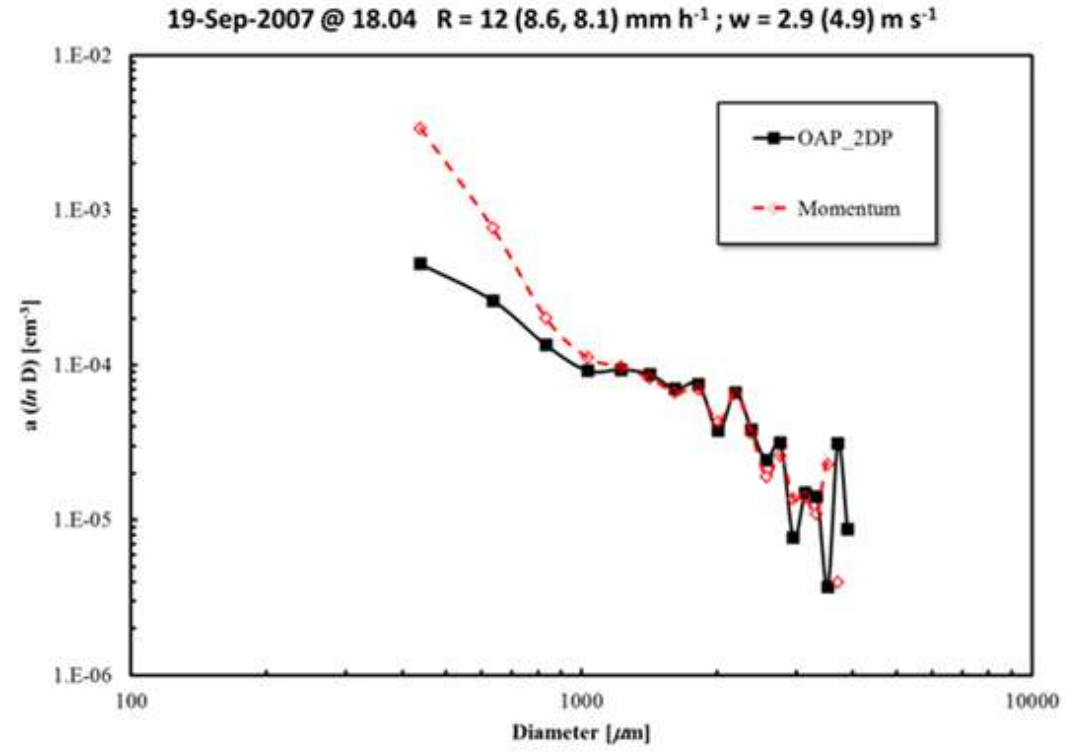

Figure 2. As in Figure 1, but for windy conditions. This event (R = 12 mm h^{-1}) occurred in Mexico City on September 19th, 2007.

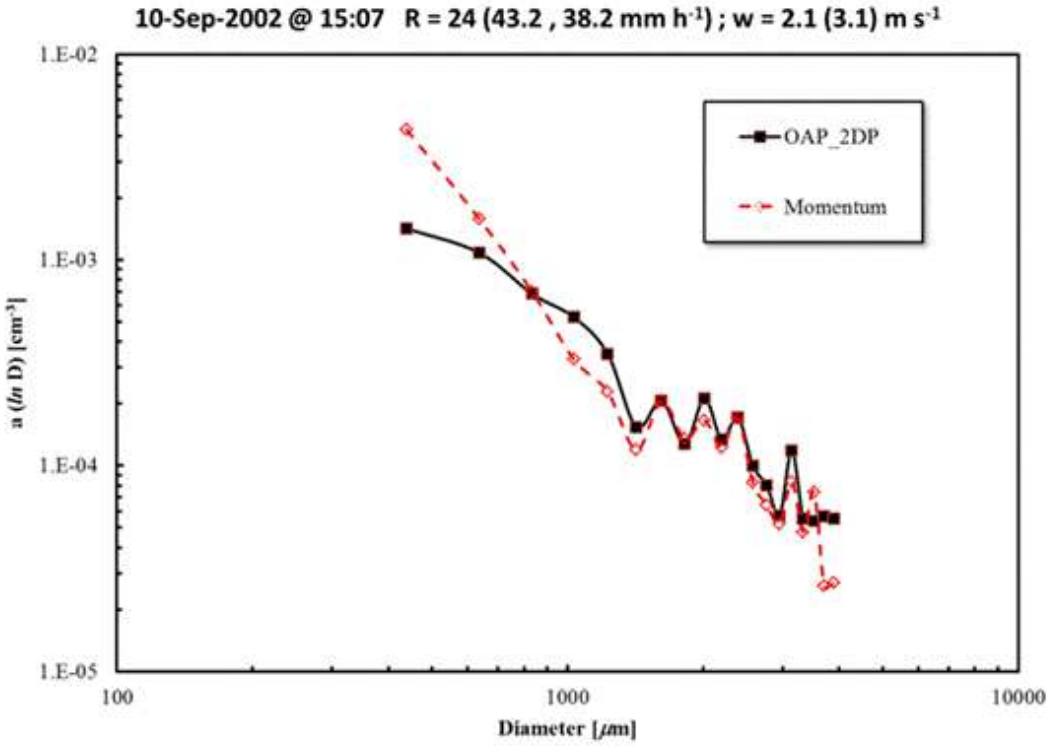

Figure 3. As in Figure 2, but for R = 24 mm h^{-1}. This event occurred in Mexico City on September 10th, 2002.

As in the two previous cases, the estimated number of smaller drops is larger in the "momentum" DSD, and also the variation in number concentration in the other bins is more pronounced (notice the large variations in the 1.0 to 1.4 mm range). These variations may be the cause, amongst others, of the major differences in R estimations: 43.2 and 38.2 mm h^{-1} for 2D-P and "momentum" DSD, respectively; whereas the value obtained with the rain gauge was 24 mm h^{-1}.

In order to evaluate the redistribution of drops in the different bins, the ratio of the number concentration of drops in each size category estimated from the momentum of the impact, $N_{Momentum}$, to that assigned by the OAP based on the number of covered photodiodes, $N_{2D\text{-}P}$, was calculated. The results for the cases selected for this work are presented in Figure 4.

There are two main aspects to notice. First, the number concentration in the smaller size-categories is generally larger for the case of momentum assignment than for that of the normal mode used by the optical instruments (number of photodiode elements covered). This was an expected result, given that super-terminal drops are more common for diameters smaller than 0.8 mm (Montero-Martínez *et al.*, 2009). Besides, the fall speeds of these super-terminal drops are large enough to modify the momentum of some drops that should not (theoretically) be "observed" by an electromechanical device and, thus, increase the number of counts in the bins corresponding to the smaller drops. The second aspect has to do with the dispersion of values for the large drops, i.e., those with diameters larger than 2.5 mm: there are reports about these drops falling at velocities slower than their calculated terminal speeds. In this sense, it would be necessary to determine if some of these large drops should be considered sub-terminal and how their detection by different instruments, especially the JWD, would be affected. From the results presented here, it seems that there would be a tendency to assign less drops larger than 3.5 mm in diameter to the corresponding bins, but further studies are necessary to confirm this. Finally, the results shown in Figure 4 indicate that drop assignment in categories corresponding to the smaller sizes is highly dependent on the wind conditions.

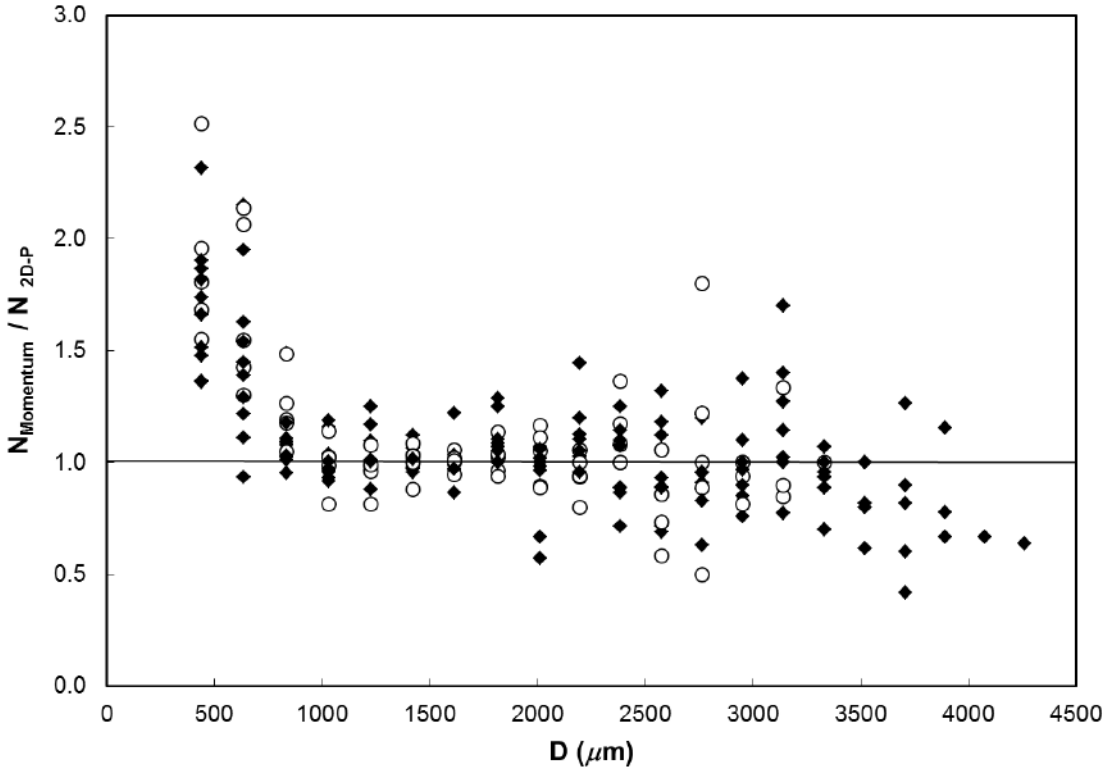

Figure 4. Ratio of the number concentration of drops in each size category estimated from the momentum of the impact to that assigned by the OAP based on the number of covered photodiodes, $N_{Momentum}$ / N_{2D-P}, as a function of bin size. Solid and open symbols refer to periods of calm-wind and of mean horizontal wind values larger than 2 m s^{-1}, respectively.

4. SUMMARY AND CONCLUSIONS

Raindrop size distributions (DSD) from natural events were measured at the ground in Mexico City using optical array probes in a fixed, vertical fashion. With this methodology, the actual drop size and fall speed are measured as the particle crosses through the sampling area. Making use of these data, it is possible to redistribute the raindrops in a new DSD based on their momentum, such as an electromechanical disdrometer would do it. The findings here presented indicate that a JWD would overestimate the number of small drops (diameters less than 1 mm), even during calm-wind periods, due to the presence of super-terminal drops. Also, a different size redistribution in the range of large raindrops (diameters larger than 2.5 mm) seems to occur. Furthermore, the measurements during windy conditions show a tendency to a larger overestimation on the counting of small drops when the momentum calculation is used to obtain the DSD.

Based on these results, it is concluded that these effects not only affect the rainfall rate estimations, but also the plausible considerations based on the DSD shapes assumed in various fields, such as meteorological radar, hydrology and soil erosion. Given the fact that the Joss-Waldvogel disdrometer is considered a reference instrument, widely used in cloud physics and weather research, it is necessary to attain a better knowledge of the operating principle on which the instrument is based in order to reduce the errors in DSD estimations.

Acknowledgements.

The authors appreciate the continuous technical support provided by Messrs. L.M. García, W. Gutiérrez, A. Rodríguez and V. Zarraluqui.

5. REFERENCES

Álvarez P., J.M., and J. Torreblanca B., 1992: *Desarrollo de un Sistema de Software para Interpretación y Análisis de Datos de Espectrómetros de Gotas*. Tesis de Licenciatura. Departamento de Computación, Facultad de Ingeniería, Universidad Nacional Autónoma de México. 150 pp.

Bringi, V. N., V. Chandrasekar, J. Hubbert, E. Gorgucci, W.L. Randeu and M. Schoenhuber, 2003: Raindrop size distribution in different climatic regimes from disdrometer and dual-polarized radar analysis. *J. Atmos. Sci*., **60**, 354-365. doi: http://dx.doi.org/10.1175/1520-0469(2003)060<0354:RSDIDC>2.0.CO;2

Gunn, R., and G.D. Kinzer, 1949: The terminal velocity of fall for water droplets in stagnant air. *J. Meteor*., **6**, 243–248. doi: http://dx.doi.org/10.1175/1520-0469(1949)006<0243:TTVOFF>2.0.CO;2

Islam, T., M.A. Rico-Ramirez, D. Han and P.K. Srivastava, 2012: A Joss-Waldvogel disdrometer derived rainfall estimation study by collocated tipping bucket and rapid response rain gauges. *Atmos. Sci. Lett*., **13**, 139-150. doi: 10.1002/asl.376

Jameson A.R., and A.B. Kostinski, 1998: Fluctuation properties of precipitation. Part II: Reconsideration of the meaning and measurement of raindrop size distributions. *J. Atmos. Sci*., **55**, 283-294. doi: http://dx.doi.org/10.1175/1520-0469(1998)055<0283:FPOPPI>2.0.CO;2

Joss, J., and A. Waldvogel, 1967: Ein Spektrograph für Niederschlagstropfen mit automatischer Auswertung. *Pure Appl. Geophys*., **68**, 240-246. doi: 10.1007/BF00874898

Joss, J., and A. Waldvogel, 1977: Comments on “Some observations on the Joss-Waldvogel rainfall disdrometer”. *J. Appl. Meteor*., **16**, 112-113. doi: http://dx.doi.org/10.1175/1520-0450(1977)016<0112:COOOTJ>2.0.CO;2

Kinnell, P.I.A., 1976: Some observations on the Joss-Waldvogel disdrometer. *J. Appl. Meteor*., **15**, 499-502. doi: http://dx.doi.org/10.1175/1520-0450(1976)015<0499:SOOTJW>2.0.CO;2

Kinnell, P.I.A., 1977: Reply to Joss and Waldvogel (1977). *J. Appl. Meteor*., **16**, 113–114. doi: http://dx.doi.org/10.1175/1520-0450(1977)016<0113:R>2.0.CO;2

Knollenberg, R.G., 1981: Techniques for probing cloud microstructure. In: *Clouds: Their Formation, Optical Properties, and Effects*, P.V. Hobbs and A. Deepak (Eds.), Academic Press, 15-91.

McFarquhar, G.M., and R. List, 1993: The effect of curve fits for the disdrometer calibration on raindrop spectra, rainfall rate, and radar reflectivity. *J. Appl. Meteor.*, **32**, 774-782. doi: http://dx.doi.org/10.1175/1520-0450(1993)032<0774:TEOCFF>2.0.CO;2

Montero-Martínez G., A.B. Kostinski, R.A. Shaw and F. García-García, 2009: Do all raindrops fall at terminal speed? *Geophys. Res. Lett.*, **38**, L11818. doi: 10.1029/2008GL037111

Montero-Martínez G, R.A. Shaw and F. García-García: 2010: What is producing super-terminal drops? *Proc. 13th Conf. Cloud Phys.* Amer. Meteor.Soc., Boston, Mass., USA. P12.3, 6 pp. http://ams.confex.com/ams/pdfpapers/170888.pdf

Salles, C., and J.-D. Creutin, 2003: Instrumental uncertainties in Z–R relationships and raindrop fall velocities. *J. Appl. Meteor.*, **42**, 279–290. doi: http://dx.doi.org/10.1175/1520-0450(2003)042<0279:IUIZRR>2.0.CO;2

Sheppard, B.E., 1990: Effect of irregularities in the diameter classification of raindrops by the Joss-Waldvogel disdrometer. *J. Atmos. Oceanic Technol.*, **7**, 180-183. doi: http://dx.doi.org/10.1175/1520-0426(1990)007<0180:EOIITD>2.0.CO;2

Tokay, A., P.G. Bashor and K R. Wolff, 2005: Error characteristics of rainfall measurements by collocated Joss-Waldvogel disdrometers. *J. Atmos. Oceanic Technol.*, **22**, 513–527. doi: http://dx.doi.org/10.1175/JTECH1734.1

ICE FOG (POGONIP) AND FROST IN ARCTIC DURING FRAM-IF PROJECT: AVIATION AND NOWCASTING APPLICATIONS

I.Gultepe[1], T. Kuhn[2], M. Pavolonis[3], C. Calvert[4], J. Gurka[5], G. A. Isaac[1], A. J. Heymsfield[6], P. Liu[1], B. Zhou[7], R. Ware[8], and J. Sloan[9], J. Milbrandt[10], and B. Bernstein[11]

[1] *Cloud Physics and Severe Weather Research Section, Environment Canada, Toronto, Ontario, Canada*
[2]*Lulea University of Technology, Division of Space Technology, PO Box 812, 981 28 Kiruna, Sweden*
[3]*NOAA/NESDIS Madison, Wisconsin, US*
[4]*CIMSS, University of Wisconsin, Madison, Wisconsin, US*
[5]*NOAA/NESDIS, Greenbelt, Maryland, US*
[6]*NCAR Boulder, Colorado, US*
[7]*IMSG/EMC/NCEP/NOAA, Springfield, MD US*
[8]*Radiometrics Corporation, Boulder, Colorado, US*
[9] *University of Waterloo, Department of Earth and Environmental Sciences, Waterloo, Ontario, Canada*
[10]*RPN, CMC, Environment Canada, Dorval, Quebec, Canada*
[11]*Leading Edge Atmospherics,Longmont, Colorado, US*

1. INRODUCTION

Ice fog (Pogonip as a Native American definition) occurs usually at temperatures (T) less than -15°C and consists of only ice crystals; it affects aviation and transportation in northern latitudes significantly because of low visibilities (Vis) and ice accumulation on the surface of structures that include aircraft, power lines, and roads. Ice fog (IF) may also be called a radiation fog consisting of ice crystals, formed under conditions of clear skies, very low temperatures, and little or no wind (McGraw Hill Dictionary of Aviation). The fog may cause a halo and is sometimes called a *frost fog*. The IF forecasting is usually very difficult (Gultepe et al., 2009; 2012) and cannot be predicted because of limited resources available for surface and satellite observations, and limitations in the ice microphysics (Gultepe et al., 2001) and anthropogenic effects of operational numerical weather prediction (NWP) models. During FRAM-IF project IF occurred approximately 14 times during 2 months-time period (0<Vis<10 km) over the Yellowknife International Airport, NWT, Canada. Its intensity was usually much higher in the town compared to the project site because of anthropogenic aerosol contributions (Gultepe and Isaac, 2002) from the heating systems and automobiles.

IF and frost occur commonly (~at least 27% of time) in the northern latitudes and Arctic regions during winter at temperatures (T) less than about -15°C. IF is strongly related to frost formation, a major reason for aircraft deicing in the northern latitudes: in fact, it may be considered as a more dangerous event than snow because of stronger aircraft surface adhesion compared to snow particles. The Fog Remote Sensing and Modeling-IF (FRAM-IF) project took place near Yellowknife International Airport (YZF), NWT, Canada during winter 2010-2011 (Nov 25 to Feb 5). IF studies over the Arctic regions can help us to better understand ice microphysical processes, including ice nucleation, extinction, parameterizations, and energy budget because IF conditions act like a natural ice cloud chamber.

2. PROJECT AND OBSERVATIONS

The FRAM-IF field project took place nearby the Yellowknife International Airport (YZF at 62°27'46" N and 114°26'25" W), Yellowknife, NWT, Canada, during winter of 2010-2011 (from Nov 25 to Feb 5). The YZF site was at the northern section of the airport, away from take offs and landings. The flight paths were usually in the E-W direction. Figure 1 shows the instruments deployed at the site. These instruments were selected to obtain visibility,

snow rate and accumulated amount, solar and infrared broadband fluxes, 3D wind components at 1Hz and 16Hz sampling rates, snow reflectivity, vertical profile of T, vapor mixing ratio (q_v), and liquid water content (LWC). The four Vis sensors used during the project were the Vaisala FD12p, Sentry Vis sensor, Metek HSS SWS-200, and LS OFS. Details on the sensors can be found in Gultepe et al (2009; 2012).

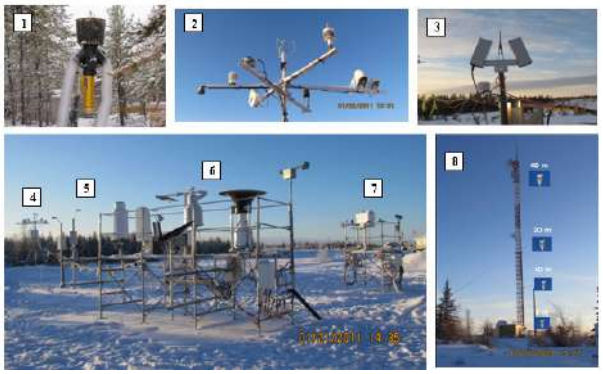

Figure 1: Instruments deployed at the YK International airport, NWT, Canada. The # represents the sensors or towers. The Jack Fish Tower (#8) is used for obtaining meteorological parameters (T, relative humidity with respect to water (RHw), Wind speed and direction, precip rate, pressure) over 1 min intervals from WXT520s mounted at 2 m, 10 m, 20 m, and 40 m levels.

During the 2010-2011 winter, mean hourly temperature values were much below the 47 and 10 year averages of minimum temperature (1953-2000 and 2000-2010, correspondingly). The RH_w for 2010-2011 was also lower than other time periods (not shown). The cold high pressure systems with clear skies were one of main reasons for IF and frost formation during the FRAM-IF project. In many cases, clear skies or radiative cooling were not sufficient for IF formation likely due to lack of IN and moisture.

Particle spectra and/or shape were measured by optical sensors such as the Climatronic Aerosol Profiler (CAP), the Ultra High Sensitivity Aerosol Spectrometer (UHSAS), a fog measuring device (FMD), a ground cloud imaging probe (GCIP), a laser precipitation monitor (LPM), and OTT and POSS distrometers. The images of ice crystals were taken by a microscope, a Canon camera with macro capability, and an ice crystal imager (ICI). The GCIP sensor (Fig. 1) adapted from an aircraft instrument called the DMT CIP probe has been developed for ground based measurements of fog and light precipitation. The small ice crystals size distributions of fog and snow particles over 62 channels were obtained at 1 s intervals. The resolution of the spectra is 15 µm, and min and max size are about 7.5 and 930 µm, respectively. The smallest image obtained represents particles less than about 10 µm.

The LPM sensor (Thies Clima Inc. Manual) uses a parallel laser-light beam (0.780 µm, not visible) to detect the ice crystals and snow particles (also for droplets). A photo diode with a lens is situated on the receiver side in order to measure the light intensity by transforming it into an electrical signal. When a precipitation particle falls through the light beam over the measuring area of 45.6 cm^2 (sampling volume: 20 mm (width), 228 mm (length), and 0.75 mm (depth)), the receiving signal is reduced. The diameter of particle is calculated from the duration of the reduced signal. The measured values are processed by a signal processor and then, intensity, quantity, and type of precipitation, and spectra are calculated. T is also included in precipitation type detection (<-4ºC for ice, >9ºC for liquid, and between any type).

The four WXT520 instruments were mounted along a 40 m tower (called Jack Fish Tower) at levels of 2 m, 10 m, 20 m, and 40 m (Fig. 1) to obtain T and RH profiles within the boundary layer. Each WXT520 provided T, RH, 2D wind speed and direction, and precipitation type. These measurements will be used to validate PMWR profiles and model validations at the low levels (<40 m).

The ICI from Luleå University of Technology is designed to sample ice and snow particles. Main components of ICI are inlet and microscope systems. The microscope imaging system is mounted underneath the sampling

inlet that consists of a funnel tapering from a 25 mm id tube to a 8 mm id nozzle, and also a 12 mm id co-centric sampling tube below the nozzle acting as a virtual impactor. A flow of about 11 L min^{-1} is pumped through the nozzle of which only 3 L min^{-1} continues through the sampling tube to the imaging system, the rest is pumped away from the space between nozzle and sampling tube entrance. A laser beam traverses the sampling volume in a direction orthogonal to the axis of this imaging set-up and is used to detect particles and trigger the imaging system. The pixel resolution is given by the choice of microscope objective and tube lens; here it is 4.2 µm/pixel so that particles between about 20 µm and 2 mm can be imaged and their size and shape determined. The CCD camera is interfaced to a laboratory PC that records the images.

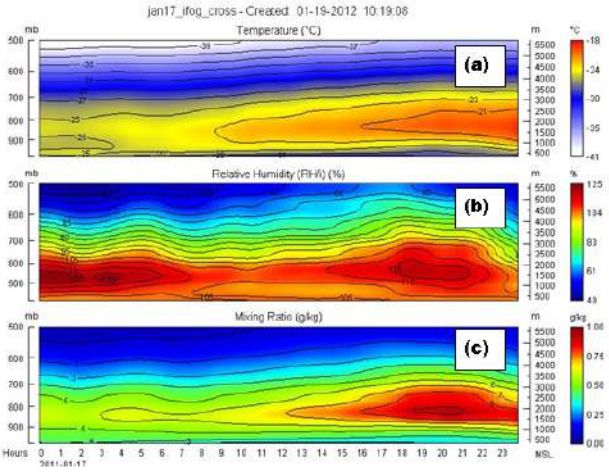

Figure 2: Time-height cross-section of T (a), Relative humidity with respect to ice (RH_i) (b), and q_v (c) measurements from PMWR during Jan 17 IF event

The measurements from Radiometrics PMWR (Figs. 2a,b,c) were used to retrieve T, RH_i, and q_v (and LWC, not shown). Figure 2b shows that relatively high RH_i were observed below 3 km level where T (Fig. 2a) was between -20 and -35°C. IF was observed below about 700 mb where q_v (Fig. 2c) reached up to 0.8 g kg^{-1}.

3. SATELLITE OBSERVATIONS

FRAM-IF measurements will also be used to validate and characterize satellite derived fog/low cloud products developed for the first of the next-generation series of Geostationary Operational Environmental Satellites (GOES-R), which is scheduled for launch in the 2015 time frame. The Advanced Baseline Imager (ABI) on GOES-R will offer more spectral bands, higher spatial resolution, and faster imaging than does the current GOES Imager (Schmit et al. 2005; 2008). The ABI has 16 spectral bands compared to 5 on the current series of GOES Imagers (Schmit et al., 2001; Menzel and Purdom, 1994). As such, algorithms for characterizing cloud properties such as cloud phase and cloud base height were developed (e.g. Pavolonis, 2010a; Pavolonis 2010b; Calvert and Pavolonis, 2011).

i) Cloud phase determination

The ABI cloud phase algorithm utilizes a series of infrared-based spectral and spatial tests to determine cloud phase (liquid water, supercooled water, mixed phase, ice). In lieu of brightness temperature differences, effective absorption optical depth ratios are used in the spectral tests. As shown in Pavolonis (2010a), effective absorption optical depth ratios allow for improved sensitivity to cloud microphysics, especially for optically thin clouds. Using the MODerate Resolution Imaging Spectroradiometer (MODIS), the GOES-R cloud phase algorithm was tested during the FRAM-IF. Figures 3a and 3b shows the false color image and cloud phase a nighttime overpass of *Aqua* MODIS on December 18, 2010, indicating the presence of mixed phase and ice clouds at the vicinity of Yellowknife, which is consistent with surface observations. Figures 3c and 3d are for ceiling and explained in the next section.

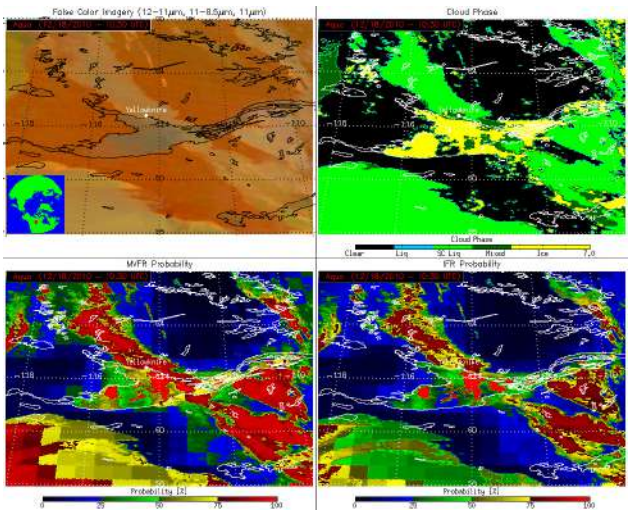

Figure 3: An *Aqua* MODIS overpass at 10:30 UTC on December 18, 2010 is used to demonstrate cloud phase and low cloud base detection algorithms developed for GOES-R. A false color image is shown on (a). The GOES-R cloud phase product is shown on (b). The GOES-R probability of MVFR ceilings and probability of IFR ceilings are shown on (c) and (d), respectively.

ii) Identifying hazardous low clouds

The GOES-R low cloud base identification algorithm determines the probability that the cloud base (ceiling) is lower than 914 m above ground level (AGL) and the probability that the cloud base is 305 m AGL. These conditions correspond to the Marginal Visual Flight Rules (MVFR) and Instrument Flight Rules (IFR) categories, respectively. A naïve Bayesian classifier (e.g. Kossin and Sitowski, 2008) is used to objectively determine the probability of MVFR and IFR conditions. Both satellite and Numerical Weather Prediction (NWP) model data are used as predictors and ceilometer based surface observations of cloud ceiling are used to train the classifier. Figures 3c and 3d show the probability of MVFR cloud ceilings and IFR cloud ceilings, respectively, that are consistent FRAM-IF measurements. Additional comparisons will be performed to assess the accuracy of the GOES-R algorithms for detecting FF and IF conditions.

4. PRELIMINARY RESULTS

Radiosonde measurements were only available from Fort Smith which was about 100 km south of the project site. Vertical profiles of T and T_d over the entire Jan 2011 for 0000 UTC and 1200 UTC, two times a day, are shown in Fig. 4a. This shows that there was usually an inversion layer below 900-850 mb. This inversion layer usually breaks down when a large scale frontal system moved in or a subsidence of cold air comes from the higher levels. Time-height cross section of radiosonde measurements of T and RH_i during Jan 15-22 is shown in Fig. 4b. The numbers in the x axis represents the number of sounding from day 1 at 0000 UTC. Three IF events (Jan 16, 17, and 21; between x=25 and x=43) which were observed during this time period occurred at T<-30°C where RH_i was close to 100%. Note that a cold air mass subsidence is seen above 700 mb and a shallow cold layer with relatively moist air is seen below 900 mb. The warm regions at about -15°C have relatively high moistures e.g. q_v~1 g kg^{-1}.

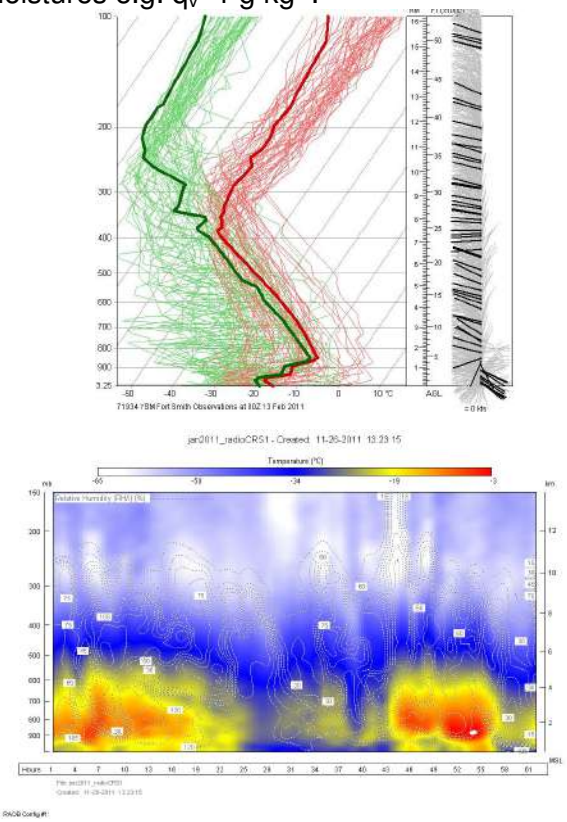

Figure 4: T (red) and Td (green) profiles from radiosonde measurements for entire January of 2011 (top); thick lines are for Jan 13 on 0000 UTC, and the RH_i contours overlaid on T image for entire Jan 2011 are shown in (bottom); vertical scale is height in km or mb.

Based on in-situ observations at the surface, the occurrence of the IF, frost, LSN, and other important meteorological events are summarized in Table 1

Table 1: Summary of significant weather events over 67 days occurred during FRAM-IF project (Nov. 24 2010-Jan 31 2011). IF: ice fog; LSN: Light snow; SNH: Heavy snow; FR: Frost; DD: Diamond dust (precipitating ice crystals); CA: Clear air; BS: Blowing snow; IC: Ice crystals; CLD: Cloudy. Note that CLD means no precipitation but cloudy. Numbers do not represent the days but any event lasted more than about 30 minutes. The occurrence of IF and frost is about 27%.

IF	LSN	SNH	FR	DD	CA	BS	IC	CLD
14	23	8	12	10	13	2	7	8

This table shows that IF occurred about 14 times (Vis<10 km) during the FRAM-IF project. LSN conditions were very common during the project and occurred almost every day. The information on de-icing conditions obtained from the First Air flights suggested that IF and frost conditions (occurred at least 14 and 12 times, respectively). Figures 5a, 5b, and 5c are for the FRAM-IF project that took place at YZF showing the frost on electrical wires, Vaisala T/RH sensor, and icing sensor, respectively. Figure 5d shows a heavy frost occurred during the FRAM-IF project at DOE NSA site. The maximum frost thickness over 12 hrs time period during an IF event was 2-3 cm on Apr 9-12 2008. If the sensors were not heated, measurements would have been severely compromised.

The dry aerosol spectra time series were measured by the UHSAS that was located in the trailer where the T was heated nominally to about 15ºC. The particles measured were dry as opposed to those measured by the CAPS which was located out in the ambient environment. During fog free conditions the spectra from both sensors indicated a smooth continuation (not shown) but during FF conditions, the CAP spectra shifted to the right over larger size ranges (size>0.5 µm), indicating the fraction of aerosols particles growing to FF particles.

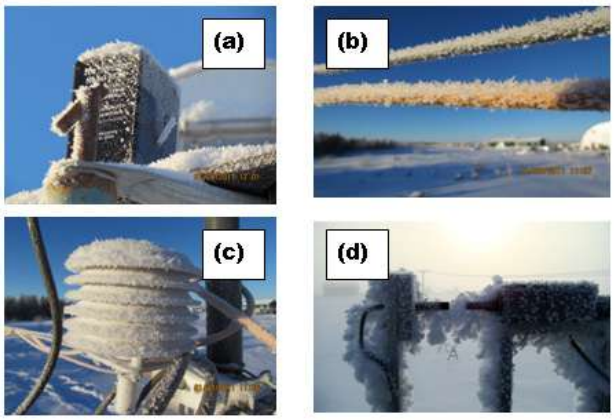

Figure 5: IF leading frost on several events: over T/RH sensor (a), over the electrical cable (b), and over the Maser icing sensor (c) on Jan 20 2011 at T=-13°C. A heavy frost occurred after an ice fog event on the ice particle sensor for April 10 2008 during ISDAC project at the DOE NSA site (-17°C) (d).

For larger particle sizes (>10 µm), the GCIP images and spectral measurements during the project clearly indicated IF existence but fog crystal shapes could not be clearly discriminated. The FMD suggested that their numbers were more than 1000 L^{-1} usually. Overall, IF and frost occurred early morning after a clear sky night during periods of high pressure. Winds were usually calm and less than 1 m s^{-1}. This was required but was not sufficient for IF formation on several days. IN and availability of moisture were also critical parameters for the IF formation and maintenance. Single precipitating (pristine) ice crystals (<500 µm) usually happened when strong inversion layers with tops at about 1-1.5 km were present (Fig. 4). Figure 6a shows that there were many small ice crystals with sizes less than 100 µm during Jan 16 case. Occasionally, particles were present at sizes greater than 1000 µm size. These particles were collected over a piece of cloth and then their picture taken with a Canon camera with macro capability. Because of a resolution issue, small ice particles are seen as spherical. Figure 6b also shows many small ice crystals

with sizes<50 µm. Figures 6c and 6d show IC pictures taken with a Barska Microscope with 40 times magnification. The size of these ice crystals at -35°C were about 5-10 µm and their shape were not spherical, but instead were column, plates, and some other shapes. Figure 6e shows that the ice particle images collected during Jan 16 have sizes <100 µm.

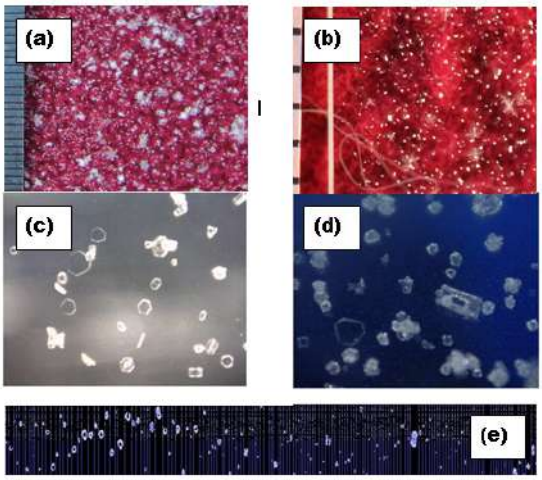

Figure 6: Ice crystal pictures: small ice crystals and light snow particles (Jan 16) (a); small ice crystals with sizes less than 50 µm (Jan 16) (b); Ice crystals with sizes less than 10 µm (Jan 18) (c), and another view of small ice crystals (Jan 18) (d). A GCIP particle image with crystal sizes less than 10 µm and up to 150 µm on Jan 18 (e).

Figure 7 shows the ICI sensor (a) and various particle types imaged with the probe (b-d). Fig. 7c shows two images of the same ice particle that were taken for IC fall velocity (V_f) calculation directly from in-situ measurements. This technique with increased size resolution may give an estimate of particle fall velocity directly and can allow us its parameterization as function of particle shape that can be used for model applications. Figure 7d shows a stellar IC with maximum dimension of about 1.7 mm taken on Jan 4. The PR estimated from the FD12P suggested that PR for IF can be up to 0.05 mm hr^{-1}.

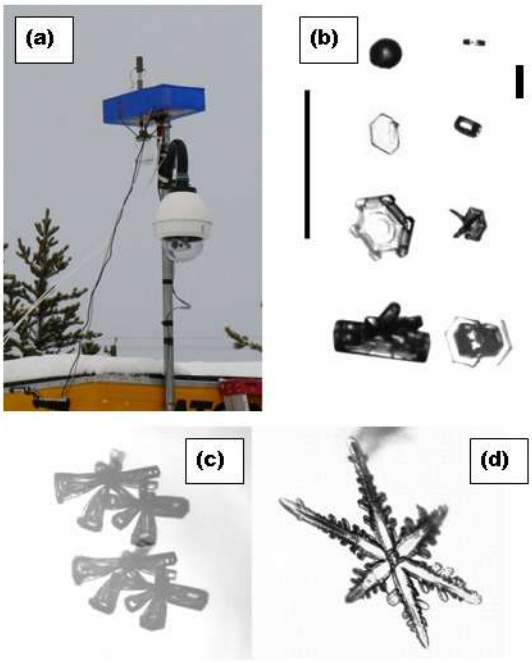

Figure 7: The ice crystal imaging sensor (ICI) is shown on the left (a) in its location mounted above the trailer. The inlet and the box containing the optical set-up can be seen. A few images taken by ICI are shown for on (b) with a reference scale of 100 µm. Two images of the same bullet rosette are shown on (c) and a rimed stellar ice crystal with 6 branches is shown on (d).

5. ICE FOG PREDICTION

In this section, possible use of the two forecasting models to predict ice fog is given below.

i) GEM LAM Model

Environment Canada (EC) currently runs the GEM (Cote et al., 1998) mesoscale model in a limited-area model (LAM) configuration over various domains in Canada with 2.5-km horizontal grid spacing. In this model configuration, clouds and precipitation are predicted by the 2-moment version of the Milbrandt and Yau (2005a,b) bulk microphysics parameterization (hereafter, "MY2"). In this scheme, ice crystals are represented by two

categories, "ice" representing pristine crystals and "snow" representing larger crystals (D> 250 µm) and/or aggregates, each of whose particle size distributions (PSDs) are represented by complete gamma functions whose parameters evolve along with the two prognostic variables (for each category x), the total number concentration, Nx, and the mass mixing ratio, qx. Currently, MY2 includes this process using the parameterization of Meyers et al. (1992). This parameterization, however, is based on limited aircraft and laboratory measurements that do not represent the Arctic conditions. Therefore, IF visibility parameterization developed based on measurements of N_i and IWC, using the current MY2 scheme may be problematic. However, the new measurements will be used to constrain the scheme for the prediction of N_i in these conditions, and thus ultimately improve the prediction of visibility in IF in the model.

ii) North American Mesoscale (NAM) model

For operational applications, NCEP's 12-km NAM model (Rogers et al. 2009; Ferrier et al., 2002) is used for regular weather guidance over Continental US (CONUS), Alaska, Hawaii and Puerto Rico. The NAM is run 4 times per day (00, 06, 12 and 18 UTC), providing forecast guidance over all of North America with hourly products out to 36 h and 3-h output at longer ranges out to 84 h. The NAM post processor calculated visibility reduction using a method that assumes the extinction is a function of cloud IWC (Stoelinga and Warner, 1999); however, this tended to underestimate the intensity of the IF (i.e., the amount of visibility reduction). Because this algorithm may not have been appropriate for IF, several alternative methods were tested. The first used surface parameters from the NAM (Zhou and Du, 2010), but it only predicted the occurrence of IF and not its intensity. The second method included the effects of moisture advection (Zhou and Ferrier, 2008; Zhou, 2011), which significantly improved the prediction of IF for one of the cases. But since IF can occur within the boundary layer in conditions not dependent on moisture advection, more research is needed

iii) Ice fog parameterization

IF (also LSN conditions) can be parameterized assuming that Vis is a function of IWC (ice water content) and N_i (~1000 L^{-1}) at sizes usually less than 200 µm. In this size range, particle terminal velocity (V_t) can be about 1 cm s^{-1} depending on its shape. If we assume that (as shown earlier) their sizes are usually less than 100 µm, V_t can be about 1 cm s^{-1}. This suggests that IF crystals can fall in the air about 36 m over 1 hr time period. However, if their V_t is about 1 mm s^{-1}, then they fall only about 4 m. This shows that for any model to correctly predict IF visibility it should be sensitive to low IWC and high N_i values (Ohtake and Huffman, 1969; Gultepe et al., 2008; 2012).

Visibility is strongly related to particle shape, density, N_i, and IWC. Therefore, the extinction coefficient (β_{ext}) can be obtained as a function of N_i and cross-section surface area (A_c) of ice crystals. If A_c is related to a crystal mass e.g. $m_i=aA_c^b$ (Lawson et al., 2011), then $\beta_{ext,}$ using in-situ 2DS probe measurements from Arctic clouds collected during ISDAC can be written as a function of IWC and total N_i (similar to Gultepe et al., 2007). Then, using an equation between Vis and β_{ext}, Vis is written for ice particles between 10-1000 µm as

$$Vis = 1.19(IWC \bullet N_i)^{-0.5066} \quad (1)$$

If IWC and N_i are known from a forecasting model at the each time step, then Vis (or β_{ext}) is obtained. The current observations of ice microphysical observations will allow for Vis estimation from the current forecasting models.

iv) Modeling issues

The current forecasting models were not designed for IF and LSN conditions occurring over the Arctic areas. In fact, IF occurrence in various space and time scales in a 3D volume can complicate its accurate prediction. The major issues are related to prediction of small ice crystals N_i and IWC, and limitations in the ice microphysical processes in the cold temperatures. Clearly, deposition nuclei and radiative processes in the clear Arctic boundary

layer conditions and existence of a weak or strong inversion needs to be predicted accurately for obtaining IF visibility and related ice microphysical parameters.

6. DISCUSSIONS AND CONCLUSIONS

IF occurs very often in the northern latitudes when temperatures go down below -15°C. In fact, IN can be found at T as high as -8°C (Gultepe et al., 2008). When T is very low, RH_i can easily be saturated with little moisture in the air. Its effect on aviation and local weather can be very significant and affect the aviation industry severely by delaying flights and increasing accidents because of low visibilities and icing on the planes. When IF does occur, it may also lead to frost formation but frost formation may not always be related to IF occurrence. Table 1 suggests that both IF and frost usually occur more often than other weather events in the Arctic. IF and frost may also affect power lines which can lead to disruptions in electrical energy distribution.

IF crystals can be as small as 5-10 μm, and usually have sizes less than 200 μm. Depending on their shape and density, they can be suspended in the air for a long time and may generate a very low PR compared to LS and SN conditions. They may play an important role in controlling heat loss to the sky in clear air conditions and balancing further cooling dependent on their optical properties. Preliminary conclusions can be listed as:

- IF crystal number concentrations can be more than 1000 L^{-1}.
- Visibility measurements can be highly variable during the cold T below -20°C, especially close to -40°C.
- Particle type from FD12P measurements should be used cautiously and it may only be only used as light, medium, and heavy snow types. Other particle types may not be representative of the real environmental conditions.
- IF can be considered as a cold cloud. Studying IF helps us to better study ice clouds and their microphysical and optical properties.
- IF Vis can be obtained from IWC and N_i that are obtained prognostically from a forecasting model. Models usually get N_i less than 100 L^{-1} based on microphysical parameterizations obtained from the aircraft observations; therefore, its prediction becomes questionable and N_i needs to be adjusted for specific environmental conditions.
- Accurate prediction of IF Vis and IWC, and frost conditions can be used advantageously to help plan for the use of aircraft de-icing fluids in northern latitudes.
- Vis-PR relationships for LSN conditions can be very sensitive to the instrument type. Optical sensors (e.g. FD12P) can be superior against the weighing gauges and hot plate type sensors (e.g. TPS and Geonor). Especially, during the strong wind conditions, measurements from the latter two sensors cannot be accurate for LSN conditions.
- Satellite-based nowcasting of IF over Arctic regions can be done if future operational satellites can be launched such as the PCW (Polar Communication and Weather) satellite because current satellites do not provide adequate time and space resolution over the Arctic regions.

Overall, the observations and model simulations from this project will be used to better understand the IF and frost predictions and their microphysical parameterizations. Detail analysis of the observations is in progress and results will be presented in the future meetings and publications. It is believed that IF studies will be a major step to improve our understanding of Arctic and cold cloud systems, and forecasts of these events.

7. BIBLIOGRAPHY

Calvert, C. and Pavolonis, M. J., 2011: *GOES-R Advanced Baseline Imager (ABI) Algorithm Theoretical Basis Document for Fog and Low Cloud Detection*, Version 2.0., 67 pp.

Côté, J., S. Gravel, A. Méthot, A. Patoine, M. Roch, and A. Staniforth, 1998: The operational CMC-MRB Global Environmental Multiscale (GEM) model. Part I: Design

considerations and formulation. *Mon. Wea. Rev.*, **126**, 1373-1395.

Ferrier, B. S., Y. Jin, Y. Lin, T. Black, E. Rogers, and G. DiMego, 2002: Implementation of a new grid-scale cloud and precipitation scheme in the NCEP Eta model. Preprints,15th Conf. on Numerical Weather Prediction, San Antonio, TX, Amer. Meteor. Soc., No: 10.1.

Gultepe I., G. A. Isaac, P. Joe, P. A. Kucera, J. Theriault, and T. Fizico, 2012: RND mountain top research site: Measurements and uncertainties for extreme weather conditions. J. Pure and Applied Geophysics. Accepted.

Gultepe, I, P. Minnis, J. Milbrandt, S. G. Cober, L. Nguyen, C. Flynn, and B. Hansen, 2008: The Fog Remote Sensing and Modeling (FRAM) field project: visibility analysis and remote sensing of fog n Remote Sensing Applications for Aviation Weather Hazard Detection and Decision Support. Edited by Wayne F. Feltz; John J. Murray, ISBN: 9780819473080, Proceedings of SPIE Vol. 7088-2, 12 pages (SPIE, San Diego, CA), 204 pp.

Gultepe, I., and Coauthors, 2007: Fog research: A review of past achievements and future perspectives. *Pure Appl. Geophys.*, **164**, 1121–1159.

Gultepe, I., G. A. Isaac, and S. G. Cober, 2001: Ice crystal number concentration versus temperature for climate studies. *Inter. J. of Climatology*, **21**, 1281-1302.

Gultepe, I., and G. A. Isaac, 2002: The effects of air-mass origin on Arctic cloud microphysical parameters during FIRE.ACE. *J. Geophys. Res.* –Ocean, 107, No. C10, SHE 4-1 to 4-12.

Gultepe, I., G. Pearson J. A. Milbrandt, B. Hansen, S. Platnick, P. Taylor, M. Gordon, J. P. Oakley, and S.G. Cober, 2009: The fog remote sensing and modeling (FRAM) field project. *Bull. Of Amer. Meteor. Soc.*, **90,** 341-359.

Kossin, J.P. and M. Sitkowski, 2008: An Objective Model for Identifying Secondary Eyewall Formation in Hurricanes. *Mon. Wea. Rev.,* **137,** 876-892.

Lawson, R. P., 2011: Effects of ice particles shattering on optical cloud particle probes. *Atmos. Meas. Tech. Discuss.*, **4,** 939-968.

Menzel, W.P., and J.F.W. Purdom, 1994: Introducing GOES-I: The first of a new generation of geostationary operational environmental satellites. *Bull. Amer. Meteor. Soc.,* **75,**757-781.

Meyers, M. P., P. J. DeMott, and W. R. Cotton, 1992: New primary ice-nucleation parameterizations in an explicit cloud model. *J. App. Meteor.*, **31**, 708-721.

Milbrandt, J. A. and M. K. Yau, 2005a: A multimoment bulk microphysics parameterization. Part I: Analysis of the role of the spectral shape parameter. *J. Atmos. Sci.*, **62**, 3051-3064.

Milbrandt, J. A. and M. K. Yau, 2005b: A Multimoment Bulk Microphysics Parameterization. Part II: A Proposed Three-Moment Closure and Scheme Description. *J. Atmos. Sci.*, **62**, 3065-3081.

Ohtake, T., and P. J. Huffman, 1969: Visual range in IF. *J. Appl. Meteor.*, **8**, 499-501.

Pavolonis, M. J., 2010a: Advances in extracting cloud composition information from spaceborne infrared radiances: A robust alternative to brightness temperatures Part I: Theory, *J. Applied Meteorol. And Climatology*, **49**, 1992-2012.

Pavolonis, M. J., 2010b: *GOES-R Advanced Baseline Imager (ABI) Algorithm Theoretical Basis Document for Cloud Type and Cloud Phase*, Version 2.0., 86 pp.

Rogers E., G. DiMego, T. Black, M. Ek, B. Ferrier, G. Gayno, Z. Janjic, Y. Lin, M. Pyle, V. Wong, W.-S. Wu, and J. Carley, 2009: The NCEP North American Mesoscale Modeling System : Recent Changes and Future Plans. Proc. 23rd Conference on Weather Analysis and Forecasting/19th Conference on Numerical Weather Prediction, American Meteorological Society, Omaha, NE.

Schmit, T.J., E.M. Prins, A. J. Schreiner, and J.J. Gurka, 2001: Introducing the GOES-M imager. *Natl. Wea. Assoc. Digest*, **25**, 28-37.

Schmit, T.J., M.M. Gunshor, W.P. Menzel, J. Li, S. Bachmeier, and J.J. Gurka, 2005: Introducing the next- generation Advanced Baseline Imager (ABI) on GOES-R. *Bull. Amer. Meteor. Soc*., **86**, 1079-1096.

Schmit, T.J., J. Li, J.J. Gurka, M.D. Goldberg, K.J. Schrab, Jinlong Li, and W.F. Feltz, 2008: The GOES-R Advanced Baseline Imager and the continuation of current sounder products. *J. Appl Meteor,* **47**, 2696-2711.

Stoelinga, T. G. and T. T. Warner, 1999: Non-hydrostatic, mesobeta-scale model simulations of cloud ceiling and visibility for an east coast winter precipitation event. *J. Apply. Meteor*. **38**, 385-404.

Zhou, B. and J. Du, 2010: Fog prediction from a multimodel mesoscale ensemble prediction system. *Wea. Forecasting*, **25**, 303-322.

Zhou, B. and B. S. Ferrier, 2008: Asymptotic analysis of equilibrium in radiation fog. *J. Appl. Meteor. and Clim*., **47**, 1704-1722.

Zhou B. 2011: Introduction to a new fog diagnostic scheme. NCEP Office Note 466, NOAA, pp 32

ACKNOWLEDGMENTS

Funding for this work was provided by the Canadian National Search and Rescue Secretariat and Environment Canada. ISDAC was supported by the Office of Biological and Environmental Research of the U.S. Department of Energy (Grant No. DE-FG02-08ER64554) through the Atmospheric Radiation Measurement (ARM) program and the ARM Aerial Vehicle Program with contributions from the DOE Atmospheric Sciences Program (ASP), and Environment Canada and the National Research Council of Canada.

ESTIMATION OF MAXIMUM PRECIPITATION FOR DIFFERENT CATCHMENT AREAS IN SAXONY

Manuela Barth[1], Ludwig Schenk[1,2] and Armin Raabe[1]

[1]University of Leipzig, Institute for Meteorology, Stephanstr. 3, 04103 Leipzig, Germany
[2]Leibniz Institute for Tropospheric Research, Permoserstr. 15, 04318 Leipzig, Germany

ABSTRACT

Estimates of area-averaged maximum possible precipitation (AMPP) for different water catchment areas in a typical region of Central Europe, the Erzgebirge (Saxony), are presented. Calculations are based on a physical concept which considers the forced elevation of water vapor saturated air masses. The vertical structure of this air mass is determined by climatological observations for those situations where very large amounts of precipitation are observed in Saxony. Apart from vertical profiles of temperature and dew point, only average flow velocities in 925 hPa are necessary for calculations. The results of computation supply averaged rainfall for specific areas, without taking into account any processes which could reduce this amount of rain.
The concept also allows to determine the input data (profiles and velocity) from climate model calculations (ECHAM5/MPI-OM), so that statements about future extreme precipitation events in an area can be deduced. Generally, this concept is not restricted to the central mountain regions of Saxony, though here it is used as a starting point for the control of hydrological dams.

1. INTRODUCTION

Climate models provide valuable information about possible future changes in climate based on assumptions about the global demographic and economic development (SRES: Special Report on Emission Scenarios, see Nakicenovic et al., 2000). Climate changes also affect derived parameters such as water availability in the catchment areas of dams.
In this contribution a method is described which enables an estimation of area-averaged maximum possible precipitation (AMPP) from vertical profiles and near ground atmospheric data. Results are given exemplarily for two catchment areas in the Erzgebirge (Saxony, Germany) as representatives for the typical mid-mountain ranges of Central Europe.
The precipitation model used for calculations bases on a physical concept which considers the forced elevation of water vapor saturated air masses. The vertical structure of this air mass is obtained from measurements (radiosonde data) and climate model calculations (vertical profiles of temperature, humidity).

2. METHOD

Calculations of AMPP are not only based on analyses of measured or modeled precipitation data, but in addition on the structure of the atmosphere. Estimated AMPP consists of a synoptic scale portion and an orographically induced part, which are treated separately, while convective precipitation is excluded.

Orographic precipitation (OP) is induced by the flow of air over a mountain region (the topography of a typical region of Central Europe, the Erzgebirge, is used here), which forces the air to rise. The vertical transport of air causes an adiabatically cooling. After temperature falls below dew point temperature, clouds are formed. To estimate maximum orographically induced precipitation it is assumed that most of the cloud water rains off at the slope of the mountain. In accordance with Kessler (1969) the remaining cloud water content in air is set to 0.5 g/kg.

Calculations of maximum orographic precipitation on the basis of aerologic data (vertical profiles of temperature, humidity

and wind) and topography are described by Tetzlaff and Raabe (1999). The aerologic data are statistically analyzed in order to find a vertical profile of humidity for which maximum precipitation events can be expected in Central Europe.
To estimate the vertical motion at the mountain region the boundary condition for flows over a mountainous topography is used. In this case, the vertical wind component at the surface w_0 is given by

$$w_0 = \mathbf{v}_{h\ 0} \cdot \nabla h$$

where $(\mathbf{v}_h)_0$ is the horizontal wind at the surface and h is the height of the terrain (Houze, 1993).
Furthermore, it is taken into account that the vertical velocity w, which is induced by topography, is damped with increasing height z exponentially

$$w\ z = w_0 \exp\left[-\frac{z}{11000\ \mathrm{m}}\right].$$

Precipitation on synoptic scale (SSP) is linked to an estimation of large-scale vertical transport of moist air. To estimate the synoptic lifting modeled pressure changes in 700 hPa (GFS, grid size about 100 km) have been analyzed. From these data, the vertical velocity was estimated, which, in turn, was used to calculate synoptic scale precipitation based on atmospheric conditions.

3. BASE DATA

3.1 TOPOGRAPHY

The estimation of vertical wind speeds requires the knowledge of the terrain profile h. Area-averaged maximum possible precipitation is exemplified for two dams in Saxony (Germany), one representing the conditions in the lowlands (LLD: low-level dam, height of catchment area up to approx. 300 m) and the other representing the conditions in a higher elevated region (HLD: high-level dam, height of catchment area up to approx. 800 m).
The terrain profiles were taken from “Digitales Geländemodell 25” (DGM25, spatial resolution of 25 m). It was ensured that the selected profiles (figure 1) cover a large part of the catchment areas on the one hand and that a maximum slope is achieved on the other hand. The latter is a precondition for maximum lifting velocities $w(z)$, which, in turn, leads to maximum precipitation.

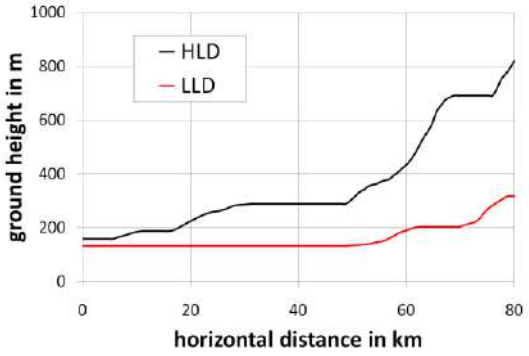

Figure 1: Terrain profiles with maximum slope for the catchment areas of a low-level dam (LLD) and a high-level dam (HLD) in Saxony (Germany).

3.2 AEROLOGIC DATA

Calculation of AMPP bases on an analysis of vertical atmospheric profiles. Such profiles may be gathered from measurements (radiosonde soundings) as well as from climate models. From the available data sets vertical profiles were chosen for which the wind in 925 hPa was blowing from northern directions (300 … 50 degrees), because for such conditions maximum orographically induced precipitation due to a lifting of air at the mountain region (Erzgebirge) is expected. Furthermore, only vertical profiles were considered for which the content of precipitable water was at least 30 mm (radiosonde data) or the daily amount of modeled precipitation exceeded 10 mm (climate model data). Moreover, maximum wind speeds for different duration periods (6 h, 12 h, 24 h, 48 h) were estimated from wind data in 925 hPa.
For those profiles that met the selection criteria, maximum dew points have been estimated on different pressure levels (ground/1000[1], 925, 850, 800/775[1], 700, 600, 500, 400, 300, 250 hPa, additionally for the model data: 200, 150, 100 hPa). In the lower levels (up to about 750 hPa/ 2400 m) this profile has been adjusted such that no convective processes occur if the air is forced to lift, because otherwise large area covering and long-lasting rain-

[1] for radiosonde/model data. If no alternative is given, the indicated pressure level is valid for both, radiosonde and model data.

fall would be prevented. Temperature profiles belonging to the dew point temperature profiles have been adjusted according to observed spreads (dew point differences) for heavy rainfall events.
A measure to distinguish between convective and non-convective precipitation is the amount of energy which is released due to the vertical lifting of moist air. Considering the whole troposphere, this energy (known as CAPE) must not exceed an amount of 300 J/kg. Temperature and dew point profiles developed here were adjusted to satisfy CAPE $\leq$ 10 J/kg. Furthermore, only cases with a stable atmospheric layering are considered. Thus, convective precipitation is strictly excluded.

3.2.1 CLIMATE MODEL DATA

Analyses of climate model calculations refer to the global climate model ECHAM5/MPI-OM, which is operated by the Max-Planck-Institut für Meteorologie (Hamburg, Germany). Data are available from the CERA database of the World Data Center for Climate, Hamburg (CERA, 2012).
Model calculations (first run) with a temporal resolution of 6 hours were used to represent the present time (January 1960 - December 1989, see Roeckner, 2005) and the future (January 2070 – December 2099) for SRES A2, B1, and A1B (Roeckner, 2006a-c). For estimation of maximum precipitation, nine model grid cells in the range of 11.25 E–15.01 E and 49.39 N–53.21 N were considered. For each climate projection, vertical profiles of relative humidity and temperature were used to calculate the dew point profiles.

3.2.2 RADIOSONDE DATA

For analyses of measured data, radiosonde profiles were used. To estimate the temperature and dew point profiles radiosonde data from station Dresden, Germany (10486) were analysed. Wind data are estimated from radiosonde data of station Lindenberg, Germany (10393). Analyses refer to data from January 1971 till September 2000 (for Dresden) and till December 2000 (for Lindenberg) (Quelle: Deutscher Wetterdienst)

3.2.3 DATA ASSIMILATION

Due to the different basic data (point measurements for radiosonde data, area-averaged values for climate model data) vertical profiles of temperature and dew point differ between radiosonde and model data for present time. In order to derive statements about future changes of AMPP from climate model data it has to be ensured, that measurements and simulations of present time correspond to each other. Therefore, simulations are adapted to measured data. Subsequently, an adjustment of modeled data for the future is performed based on the adjustment of the data of present time.
To adjust the maximum wind speeds for the different duration periods, a mean difference between measured and modeled data was calculated for present time. This difference was used to adjust the model data for present and future time (figure 2).

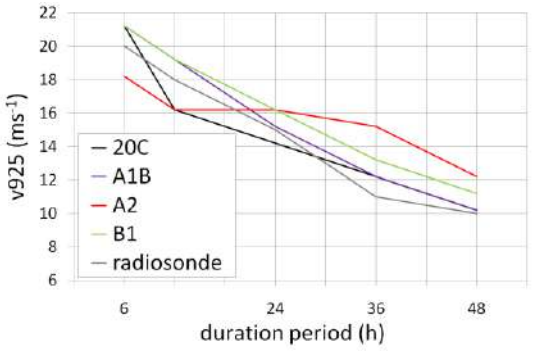

Figure 2: Maximum wind speeds in 925 hPa for different duration periods of present time (radiosonde: measurement data, 20C: adjusted model data) and adjusted model data for SRES A1B, B1, and A2 (2070-2099).

The adjustment of dew point profiles is based on differences between measured and modeled data for present time in the considered pressure levels. These differences were used to correct the modeled data (for present time and future) to fit the measured profiles (figure 3). Temperature profiles have been adapted to the accordant dew point profiles as described in section 3.2 (figure 4).

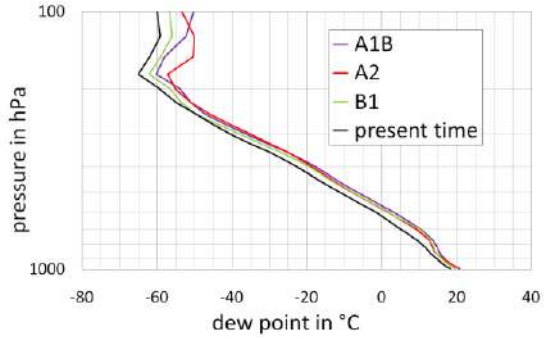

Figure 3: Dew point profiles for calculations of AMPP for present time (measurement and adjusted model data) and adjusted model data for SRES A1B, B1, and A2 (2070-2099).

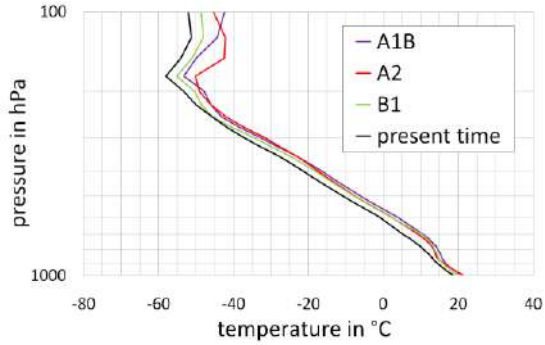

Figure 4: Temperature profiles for calculations of AMPP for present time (measurement and adjusted model data) and adjusted model data for SRES A1B, B1, and A2 (2070-2099).

4. RESULTS/ CONCLUSIONS

The synoptic scale portion of AMPP is the same for all catchment areas in Saxony and does not depend on the location. For different duration periods, values for SSP are given in table 1.

Table 1: Synoptically induced precipitation in mm for different duration periods

6 h	12 h	24 h	48 h
68 mm	109 mm	163 mm	215 mm

The results for analyses of the orographically induced part of AMPP for radiosonde and model data for the two catchment areas of the dams in the low-land and in the high-land are shown in table 2 and 3, respectively.

It turns out that, combined with a rise of temperature and wind speeds, the orographically induces part of AMPP increases especially for longer duration periods (24 h, 48 h) independently from the SRES in future. However, it has to be differentiated. On the one hand the increase of AMPP for shorter duration periods is smaller than for longer ones. On the other hand the increase of AMPP at higher elevations (HLD) is more evident than in lower situated catchment areas (LLD).

Independently from the location of the catchment area, a maximum increase of orographically induced precipitation at the end of the 21st century is calculated for SRES A2. Generally, this scenario is regarded as the one which represents the most extreme case of global warming due to anthropogenic trace gas emissions. It is linked with a maximum increase of wind speeds for long duration periods (24 h, 48 h) of more than 2 m/s and a temperature increase of up to 4 K at the lower troposphere.

For the catchment area of HLD a maximum increase of orographically induced precipitation at the end of the 21st century was estimated to be ca. 140 mm for a duration period of 48 h and SRES A2. For the lowland catchment area, the maximum increase of OP for SRES A2 and a duration period of 48 h amounts to only about 10 mm.

Table 2: Low-level dam (LLD): Orographically induced precipitation in mm for radiosonde data (radio), model data for present time (20C) and scenario calculations (A1B, A2, B1) for 2070-2100.

	6 h	12 h	24 h	48 h
radio	13	24	40	54
20C	13	21	38	55
A1B	15	27	44	59
A2	12	22	46	68
B1	14	27	46	64

Table 3: High-level dam (HLD): Orographically induced precipitation in mm for radiosonde data (radio), model data for present time (20C) and scenario calculations (A1B, A2, B1) for 2070-2100.

	6 h	12 h	24 h	48 h
radio	92	169	285	382
20C	98	152	270	390
A1B	114	211	337	454
A2	94	170	346	523
B1	110	203	346	480

All modeled climate scenarios analyzed here hypothesize an increase of extreme (non-convective) precipitation events for all duration periods. The increase of precipitation differs dependent on the emission scenario. Assuming a more moderate increase of greenhouse gas concentrations

in the atmosphere (SRES B1) a rather moderate increase (16 %) of AMPP is expected for the future compared to the present. For larger increases of greenhouse gas concentrations (SRES A2), a maximum increase of AMPP of 24 % is expected (for the HLD catchment area).

6. BIBLIOGRAPHY

CERA, 2012: http://www.dkrz.de/daten-en/cera/portal (last visited: May 2012).

Houze, R.A., 1993: Cloud Dynamics. Chapter 12: Orographic Clouds. Academic Press, Inc., San Diego, California.

Kessler, E., 1969: On the distribution and continuity of water substances in atmospheric circulations. Meteor. Monogr. 27, 1-84, Amer. Meteor. Soc.

Nakicenovic, N., J. Alcamo, G. Davis, H.J.M. de Vries, J. Fenhann, S. Gaffin, K. Gregory, A. Grubler, T.Y. Jung, T. Kram, E.L. La Rovere, L. Michaelis, S. Mori, T. Morita, W. Papper, H. Pitcher, L. Price, K. Riahi, A. Roehrl, H-H. Rogner, A. Sankovski, M. Schlesinger, P. Shukla, S. Smith, R. Swart, S. van Rooijen, N. Victor, and Z. Dadi, 2000: Special Report on Emissions Scenarios. Intergovernmental Panel on Climate Change, Cambridge University Press, Cambridge. (URL: http://www.grida.no/publications/other/ipcc_sr/?src=/climate/ipcc/emission/)

Roeckner, E., M. Lautenschlager, H. Schneider, 2005: IPCC-AR4 MPI-ECHAM5_T63L31 MPI-OM_GR1.5L40 20C3M_all run no.1: atmosphere 6 HOUR values MPImet/MaD Germany. World Data Center for Climate. DOI: 10.1594/WDCC/EH5-T63L31_OM-GR1.5L40_20C_1_6H.

Roeckner, E., M. Lautenschlager, H. Schneider, 2006a: IPCC-AR4 MPI-ECHAM5_T63L31 MPI-OM_GR1.5L40 SRESA2 run no.1: atmosphere 6 HOUR values MPImet/MaD Germany. World Data Center for Climate. DOI: 10.1594/WDCC/EH5-T63L31_OM-GR1.5L40_A2_1_6H.

Roeckner, E., M. Lautenschlager, H. Schneider, 2006b: IPCC-AR4 MPI-ECHAM5_T63L31 MPI-OM_GR1.5L40 SRESA1B run no.1: atmosphere 6 HOUR values MPImet/MaD Germany. World Data Center for Climate. DOI: 10.1594/WDCC/EH5-T63L31_OM-GR1.5L40_A1B_1_6H.

Roeckner, E., M. Lautenschlager, H. Schneider, 2006c: IPCC-AR4 MPI-ECHAM5_T63L31 MPI-OM_GR1.5L40 SRESB1 run no.1: atmosphere 6 HOUR values MPImet/MaD Germany. World Data Center for Climate. DOI: 10.1594/WDCC/EH5-T63L31_OM-GR1.5L40_B1_1_6H.

Tetzlaff, G., A. Raabe, 1999: Räumliche und zeitliche Verteilung maximaler Niederschläge. In: Extreme Naturereignisse und Wasserwirtschaft – Niederschlag und Abfluss, Intern. Symp., Bayr. Landesamt f. Wirtschaft, Informationsheft Nr. 5, S. 57-64.

NUMERICAL SIMULATIONS OF MELTING OF GRAUPEL PARTICLES AND SNOWFLAKES

Sarkadi Noémi, Dr. Geresdi István

1. INTRODUCTION

This paper presents results of numerical simulations of melting of graupel particles and snowflakes. The proper simulation of this process near to the surface or above the surface in the melting region is necessary for the correct simulation of the type of the precipitation (e.g. snow, rain, freezing rain etc.). Also the size distribution of the rain drops formed due to the melting affects the formation of the cold pool related to thunderstorms. In most of the numerical models this process is described by using bulk schemes, which can be one-moment, two-moment or multimoment parameterization (Milbrandt-Yau, 2005a,b). In this type of the microphysical scheme and even in most of the detailed microphysical models the basic idea about the melting is that melted water sheds immediately from the surface of the ice core (e.g. Reisin et al. 1996) This assumption is far from the real process. Observation shows that the melted water remains on the surface of both snowflakes (Mitra et al, 1990) and on that of the graupel particles (Rasmussen et al, 1984a,b), and shedding can occur only in the case of the hail/graupel if the size of these particles is above about 1 cm. A numerical model was developed to simulate the melting in the atmosphere.
Verifying of the results of numerical models able to use radar images, where we can discern the different hydrometeor types. Battan and Bohren (1982) noted that when the melting layer was treated like a mixture of water and ice the melting associated with the rapid increases of radar reflectivity.

2. MODEL DESCRIPTION

The calculation was made by using a one-dimensional numerical model. The three different types of the particles (snow, graupel, water drops) are allowed to fall with their terminal velocities.

Two-moments, detailed microphysical scheme (Tzivion et al, 1987) was used to simulate melting, collision between the particles and diffusional growth of the particles. Beside the number concentrations and mixing ratios of the above mentioned parameters, the amount of the melted water in each bin was prognostic variable for both melted snow flakes and graupel particles. The melting rate of the particles was affected by the heat conduction and by the released latent heat of diffusion as it is given in Pruppacher and Klett (2004). Besides these physical processes the heat given by the collected warmer water drops is also taken into consideration (Geresdi, 1992). It is supposed that while the characteristics (shape, density, terminal velocity) of the graupel particles are hardly affected by the melting, these parameters change significantly as the amount of the liquid water increases on the surface of the snow flakes (see eg. Mitra et al, 1990). Because the melting ice particles generally feel high supersaturation in the precipitation zone their diffusional growth can significantly increase the masses of the falling solid precipitation elements. It is supposed that condensed water increases the mass of the melted water.
In our model we considered the following interaction and physical processes: melting of snowflakes, and graupel particles, condensation, deposition, break up of water drops. If the melting rate has exceeded 95%, the melted snowflakes and graupel particles, were transferred to the water drop category.

3. NUMERICAL EXPERIMENTS

In the numerical experiments we examined how melting of snowflakes and graupel particles occurs at different initial conditions. In the first case we analyzed the melting processes at a temperature profile which was given by wet adiabatic lapse rate. In the second case the melting process of graupel particles was simulated at similar environmental conditions as in

the case of the snowflakes. Finally the formation of freezing drizzle was simulated when an inversion layer formed above the surface.
The sensitivity of the melting for the saturation of the environment was investigated in every cases.
At the top of the melting layer a constant flux of the precipitation elements (snowflakes, graupel particles) have been provided.

4. RESULTS OF SIMULATIONS

4.1. MELTING OF SNOWFLAKES

The results show that (i) the relative humidity strongly affects the type of the surface precipitation. In the case of low humidity the melting layer is deeper. (ii) In the positive temperature region the vapor condense on the melted particle, but due to the temperature decrease and the evaporation of the water drops formed by complete melting of the snow the relative humidity increases in the melting region.
(iii) The melting layer getting deeper during the simulation (Fig 1. and Fig 2.). Initially it was about 400 m, and by the end of the simulation it was near to 600 m. The temperature change from the melting at the beginning is the highest at the top of the melting layer (Fig. 3.). The water mixing ratio is changed because of the melting of snowflakes. This change was rapidly, and significant at the first 10 minutes, this can be seen on Fig. 4. The water vapour mixing ratio has also been changing, the change is consistent with the temperature change (Fig. 5.). Fig 6. shows the size distribution of the water drops on the surface at different times. Likewise Fig. 7. shows the size distribution of the melting snowflakes and the size dependence of fraction of the melted water at top of the melting region. While the particles of less than 200 μm melt almost completely, the particles with sizes above one mm remain almost dry.

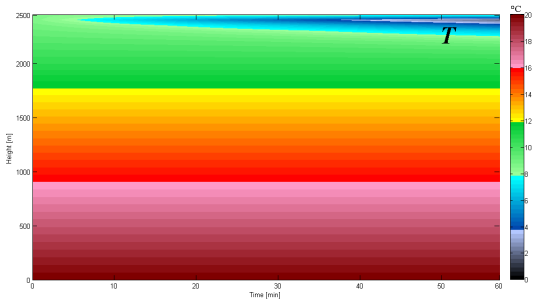

Fig. 1.: Temperature change, y-axis represents the height, x-axis represents the time

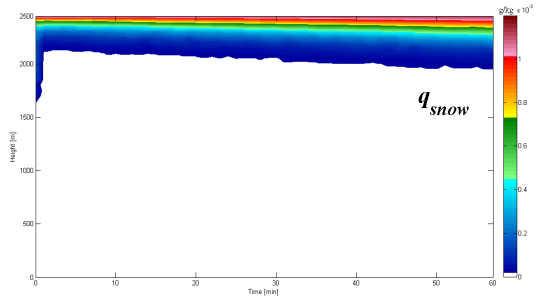

Fig. 2.: Snow mixing ratio change, y-axis represents the height, x-axis represents the time

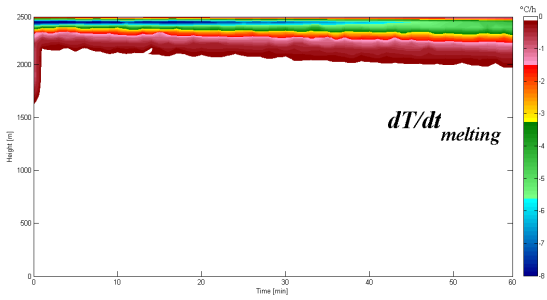

Fig. 3.: Temperature change due to melting, y-axis represents the height, x-axis represents the time

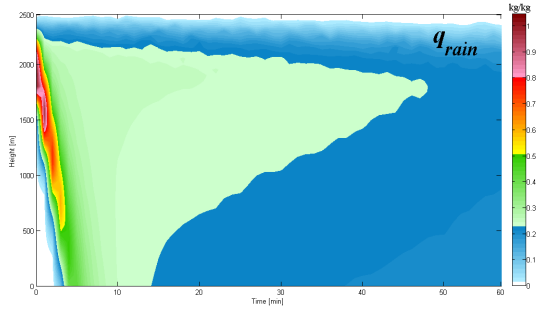

Fig. 4.: Water mixing ratio change, y-axis represents the height, x-axis represents the time

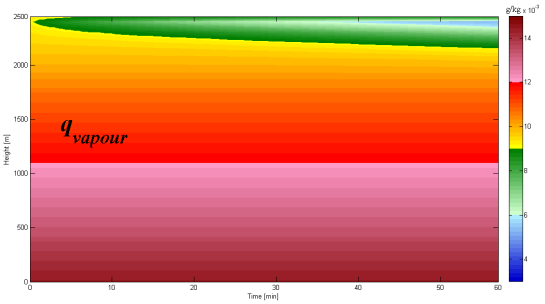

Fig. 5.: Water vapour mixing ratio change, y-axis represents the height, x-axis represents the time

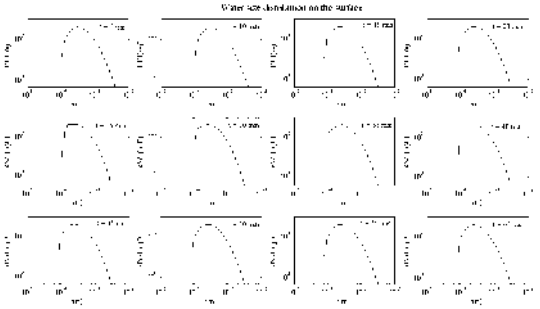

Fig. 6.: Water size distribution on the surface, y-axises represent logarithmic number concentration, x-axises represent the logarithmic radius of water droplets

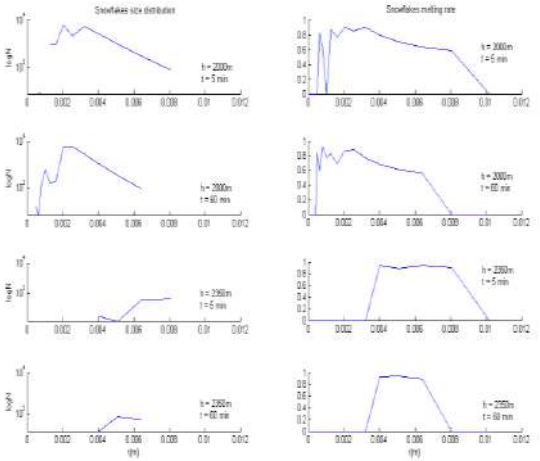

Fig. 7.: Snowflakes size distribution and melting rate on different heights, at different time, y-axises represent logarithmic number concentration, x-axises represent the radius of snowflakes

4.2. MELTING OF GRAUPEL PARTICLES

Because of the higher terminal velocity the melting process of the graupel particles and its effect on the environmental condition is different from that of the snow flakes. Except of the small graupel particles (< 0.8 mm) all the particles reach the surface. The melting fraction also depends on the size of the particles. The evolved water droplets are smaller than in the case of the melting of snowflakes (Fig. 8.,9.).

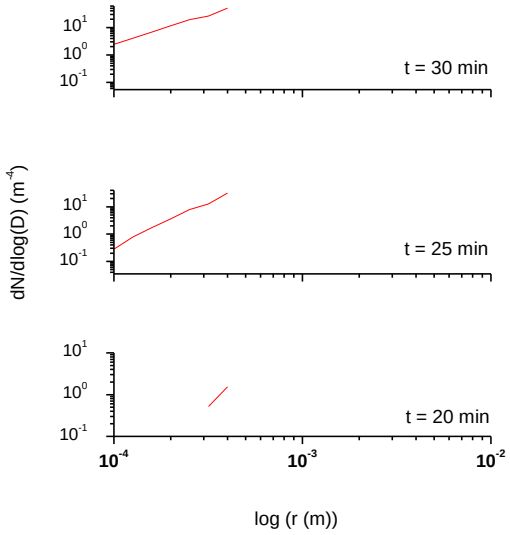

Fig. 8.: Water size distribution on the surface

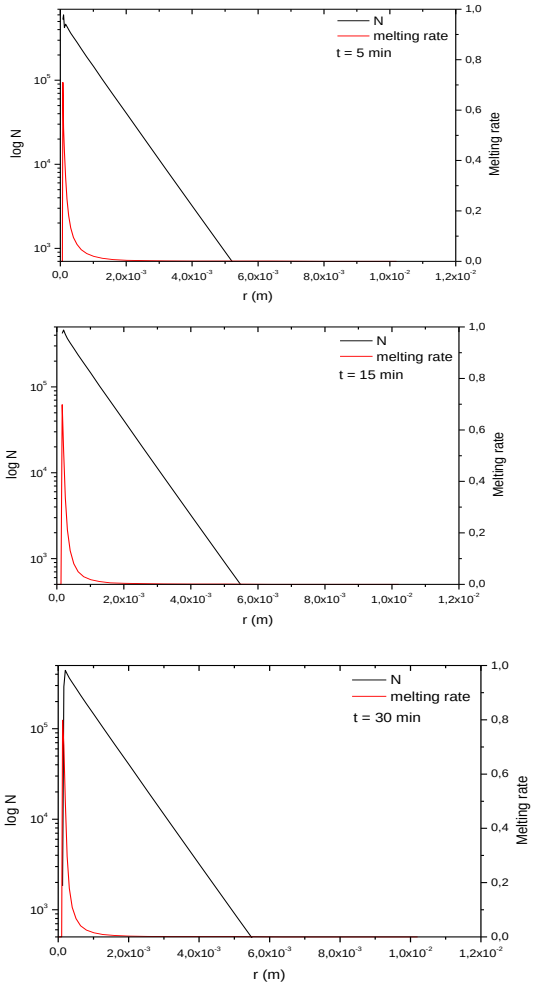

Fig. 9.: Graupel particles size distribution and melting rate, at 2500 m height

4.3. MELTING OF SNOWFLAKES IN THE CASE OF INVERSION LAYER

Studies show that the freezing rain and sleet formation are significantly affected by initial conditions: (i) temperature profile (e.g. max. temperature and depth of the melting layer), (ii) relative humidity.

5. SUMMARY AND CONCLUSIONS

In our studies a detailed microphysics technique is applied to simulate how the snow flakes and graupel particles melt. Numerical experiments were made to investigate how the different environmental conditions affect the melting of the snow flakes and graupel particles.
The calculation shows: (i) The falling precipitation elements can significantly modify the environmental conditions which feedbacks to the melting process. (ii) The new description of melting process (melted water is retained on the surface of the particles) allows to give more correct simulation of the freezing rain formation. (iii) The results are sensitive to the relative humidity in the melting layer.

6. BIBLIOGRAPHY

1. BATTAN, L. J. – BOHREN, C. F., 1982: Radar backscattering by melting snowflakes, *Journal of Applied Meteorology*, Vol. 21. pp. 1937-1938.
2. MITRA, S. K. et al., 1990: A Wind Tunnel and Theoretical Study of the Melting Behavior of Atmospheric Ice Particles. IV: Experiment and Theory for Snow Flakes, *Journal of Atmospheric Sciences*, Vol. 47. No. 5. pp. 584–591.
3. MILBRANDT, J. A. – YAU, M. K.,2005a: A multimoment bulk microphysics parameterization. Part I: Analysis of the Role of the Spectral Shape Parameter, *Journal of Atmospheric Sciences*, Vol. 62. pp. 3051–3064.
4. MILBRANDT, J. A. – YAU, M. K.,2005b: A multimoment bulk microphysics parameterization. Part II: A proposed three-moment closure and scheme description, *Journal of Atmospheric Sciences*, Vol. 62. pp. 3065–3081.
5. PRUPPACHER, H. R. – KLETT, J. D., 2004: Microphysics of Clouds and Precipitation, *Kluwer Academic Publishers*, New York/Boston/Dorbrecht/London/Moscow, 2004.
6. RASMUSSEN, R. M. – LEVIZZANI, V. – PRUPPACHER, H. R., 1984a: A Wind Tunnel and Theoretical Study of the Melting Behavior of Atmospheric Ice Particles. II: A Theoretical Study for Frozen Drops of Radius < 500 μm, *Journal of the Atmospheric Sciences*, Vol. 41. No. 3. pp. 374–380.
7. RASMUSSEN, R. M. – LEVIZZANI, V. – PRUPPACHER, H. R., 1984b: A Wind Tunnel and Theoretical Study of the Melting Behavior of Atmospheric Ice Particles. III: Experiment and Theory for Spherical Ice Particles of Radius > 500 μm, *Journal of the Atmospheric Sciences*, Vol. 41. No. 3. pp. 381–388.
8. REISIN et al, 1996: Rain production in convective clouds as simulated in an axisymmetric model with detailed microphysics. Part I: Description of the model, *Journal of the Atmospheric Sciences*, Vol. 53. No. 3. pp. 497–519.
9. TZIVION, S. – FEINGOLD, G. – LEVIN, Z., 1987: An Efficient Numerical Solution to the Stochastic Collection Equation, *Journal of the Atmospheric Sciences*, Vol. 44. No. 21. pp. 3139–3149.

Acknowledgements

The research was supported by the grant of Developing Competitiveness of Universities in the South Transdanubian Region (SROP-4.2.1.B-10/2/KONV-2010-0002)

AN OBSERVATION STUDY OF HAILFALL DISTRIBUTION CHARACTERISTICS OF A SPRING HAILSTORM EVENT BY USING AN X-BAND DUAL-POLARIZATION RADAR SYSTEM

Hui XIAO*, Qi TANG, Chun-Wei GUO, Hui-Ling YANG,
Liang FENG, Ya-Nan LIU, Ai-Xun LI, and Jia-Yan YANG
Laboratory of Cloud-Precipitation Physics and Severe Storms, Institute of Atmospheric Physics, Chinese Academy of Sciences, Beijing 100029, China
* Corresponding author: XIAO, Hui, hxiao.2008@163.com

1. INTRODUCTION

Severe hail shooting is a worldwide meteorological disaster. It is a combined result of dynamic, thermodynamic, micro-physical and electrical processes in convective clouds. The use of weather radar to identify precipitation particles of storm cloud is an important topic in meteorological radar field (Huang et al. 1980; Gong and Cai 1992; Xiao et al. 2002). However, there is a big uncertainty to correctly identify precipitation particles from a mixing cloud by use of single-polarized weather radar. In recent decade, with successful application of the dual-polarization Doppler weather radar, it becomes possible to identify cloud particle through detection by radar (Seliga & Bringi 1976; Bringi et al. 1984; Aydin et al. 1986; Tuttle 1989; Liu et al. 1993; Kennedy & Rutledge 1995; Zhang et al. 2001). A dual-polarization Doppler radar can provide more radar parameters than the new generation of Doppler radar. These polarimetric parameters have different relations to precipitation hydrometeors on the size, shape, arrangement, distribution, spatial orientation, density, and dielectric constant (Bringi & Chandrasekar 2000). Thus, it is possible to identify precipitation particles using these polarimetric parameters. In this regard, there are a lot of research results around the world (Seliga & Bringi 1976; Bringi et al. 1984; Hall et al.1984; Bringi et al.1986; Liu 2002; Qi et al. 2002), for instance, the fuzzy logic algorithm has been gradually formed and wide applied.

In China, some dual-polarimetric Doppler weather radars in X-band and C-band have been developed in recent years. At the same time, some studies on classification and identification of precipitation particles were also carried out, but there is little identification research combined with *in situ* high time-resolution observational data of precipitation particle spectra.

In this paper, a fuzzy logic algorithm applying to identification of precipitation particles was developed for X-band polarimetric observational data, and the features of radar echo and hailfall

microphysical structure of a springtime hailstorm system were analyzed.

2. THE DATA SITUATION

Zhangbei County is located in a semiarid area of the north of Hebei Province, China.

During the time period through April to August 2009, a field observation campaign was conducted to study typical precipitating cloud physical structures and precipitation processes using a vehicle-borne X-band dual-polarization Doppler advanced radar system with two channels (X-PARS) in Zhangbei, Zhangjiakou City. Table 1 shows the main characteristics of the X-PARS radar system. The XDPARS radar was set up by the Institute of Atmospheric Physics of Chinese Academy of Sciences, and Chengdu Jinjiang Electronic System Engineering Company Limited in 2005. The radar was placed in the north beach of Huanggainao Reservoir in Zhangbei. The radar observational site located at 21.2km north of Zhangbei town. Its altitude of the radar is 1350m. At the same time, an OTT Parsivel laser-based optical disdrometer located at Zhangbei County Weather Station (the altitude is 1395m) was used to do the observation of precipitation particles. The disdrometer can detect and identify eight different precipitation types as drizzle, mixed drizzle/rain, rain, mixed rain/snow, snow, snow grains, ice pellets and hail.

Table 1 Performance parameters of the X-PARS dual-polarization Doppler radar with two channels

System characteristics	Detail description
Transmit system	Wave-length: 3.2cm; Total transmitting power: ≥75KW, Single transmitting power: ≥ 35KW; Selectable pulse width: 0.5,1.0, 2.0μs
Polarization diversity	Transmit horizontal and vertical polarized waves simultaneously
Antenna system	antenna diameter: 2.4m; 3-dB beam width:1.0°; antenna speed: 20°/sec
Antenna control system	PPI, RHI,VOL (volume scan) and sector scan modes, can customize parameters such as azimuth, elevation angle etc; solar calibration
Radar measurands	Horizontal polarization reflectivity (Z_H), Doppler velocity (V), Spectrum width (W), Differential propagation phase shift (Φ_{DP}), specific differential propagation phase shift (K_{DP}), differential reflectivity (Z_{DR}), cross-correlation coefficient (ρ_{HV})
Radar calibration	Calibrate antenna gain using signal generator, calibrate Radar position and orientation using solar method and GPS

On the afternoon of April 23, 2009, a severe convective weather system moved into the semiarid area and caused the first hailfalling of the year 2009 in Zhangbei area. According to the sounding data observed by the closest Zhangjiakou sounding station on the morning of April 23, 2009, the freezing level was about the altitude of 2.7km above sea level (corresponding altitude above the X-PARS radar level was 1350m). In the radar detection range (150km), the precipitation occurred during the time from 1500 to 1800. There were two hailstorms which passed respectively through the XDPARS radar station and the Parsivel disdrometer observation site. At that time, the dual-polarization radar was measuring the hailstorms.

3. WEATHER PROCESS AND OBSERVATIONAL DATA

According to the analysis of weather maps, the hail process on the afternoon of April 23, 2009, occurred in a favorable situation of the circulation and interaction of upper trough and ground cyclones. Affected by the cold air going southward from Mongolia region, Zhangbei, Shangyi, and Huai'an counties of Zhangjiakou City in the semiarid area were suffered by hail shooting and strong winds on the afternoon of April 23. According to real-time measurement, the hailstones falling at the X-PARS radar site had a maximum size of 12mm, the density of hail and graupel particles was large, approximately 60 to 80 per 100cm^2. Most of the hail and graupel particles were of irregular shape and their surfaces were wet. Therefore, it was a precipitation process of wet hail and wet graupel.

The radar observation showed that the hailcloud system had the characteristics of multi-cell structure on the weather radar echo. The multi-cell storm system went into the west side of the radar coverage (150km in radius) at 1300 and went out the east side of the radar coverage at 1800, it maintained about five hours.

It should be noted that before using the X-band radar polarimetric data, the quality control of data, like attenuation correction of Z_H and Z_{DR}, back-propagation effect (i.e. δ effect) on differential propagation phase Φ_{DP}, the elevation effect on Z_{DR} observation, has been done (He et al. 2009a, b; Ryzhkov et al., 2005,).

4. RADAR ECHO CHARACTERISTICS

The X-band radar observation show that, on the morning of April 23, 2009, some convective cloud cells appeared in succession in the radar observation area, and they moved from southwest to northeast. At 0934 BJT, a stronger echo appeared at 57km southwest of the radar station, the maximum reflectivity is generally about 35dBZ. In the next one hour, the convective echo repeatedly merged with other cells to strengthen, the maximum reflectivity achieved 50 - 55 dBZ, and the maximum echo top reached 8 km, but the strong convective clouds became weakened

quickly after soon. Till 1250 BJT, a band-type echo composed by a number of convective clouds was entering the radar detection range (150km) from the southwest, and the echo band moved from west to east, but the movement direction of the strong echo cells in the band deviates about 45° relative to the movement direction of the echo band, that is, moved from southwest to northeast. In the process of move eastward, the echo band continued to strengthen, its maximum reflectivity achieved above 50 dBZ. The length of the echo band exceeds 250km. At 1406 BJT when the echo band eastward shifted to 50km west of the radar station, it broken into two parts (south part and north part), the south part moved eastward quickly. And at 1509 the south part of the echo band went through the radar station, but the northern section still connected with a weaker echo band located in the southwest of the radar and formed another organized strong echo band,. The new strong echo band continually moved to the eastward.

Figure 1 shows the PPI echo intensity and polarization parameters of the hail cloud system observed at 1522 April 23, 2009, with a 0.5° elevation. There were two southwest - northeast direction convective echo band at 1522 April 23, one of them passed just through the radar station and Parsivel disdrometer observation site, the length reached above 200km, the maximum width reached 50km, and the maximum strength achieved 50~55dBZ. Looked from the structure, it was composed both by convective cloud echoes and by degraded convective cloud echoes. According to the RHI scan (Figure 2), the northeast part of the echo band was composed still by convective cloud echoes, the top of the convective clouds reached 6 km height, and the maximum reflectivity achieved 55-60 dBZ, but the southeast part of the band was consisted in some degenerating convective clouds, and the horizontal distribution of the echoes was more evenly, the area was larger, the echoes were higher and the top of echoes still reached 6.0km, but a bright band on freezing-level appeared in the 1.3~1.4 km level above the ground. The height of the bright band was consistent with the height detected from Zhangjiakou sounding data of 0800 Beijing time on that day. The emergence of a freezing-level bright band is an important symbol of stratifying convective clouds and stratiform clouds.

There was another radar echo band in the west of the radar station (see Figure 2). The radar echo band was about 40km west of the radar station at 1534 BJT and the band was constructed by strong convective cloud echoes, whose length was about 150km and width was 20km only. The maximum reflectivity of the convective clouds was up to 55 dBZ and the maximum height of echo was 6.0km. The strong echo centers moved, followed this band, to the

east and some convective clouds has developed into strong storm clouds, whose maximum of the reflectivity is 57dBZ. The top of the cloud raised significantly, especially the 45dBZ echo top extended to 4.5km height. It was very close to the cloud top, indicating that the strong cloud should be a hail cloud and have a hail shooting the ground would fall hail.

As seen from Figure 2, the vertical Z_{DR} was not very big (only about -0.5dB ~ 0.5dB) while Z_H was very strong. This is mainly because the irregular graupel and hail particles fallen in stumbling state and they did not have specific orientation arrange. In result, Z_{DR} was small, and K_{DP} was also small with -0.5 - 0.5 deg·km^{-1} only. Therefore, the corresponding area would have graupel and hail falling down. Figure 2 also shows that the hail fell from stronger echo area of the hail storms. When precipitation occurred at the radar site, the field observer took photographs of precipitation particles on the ground at the same time and checked out

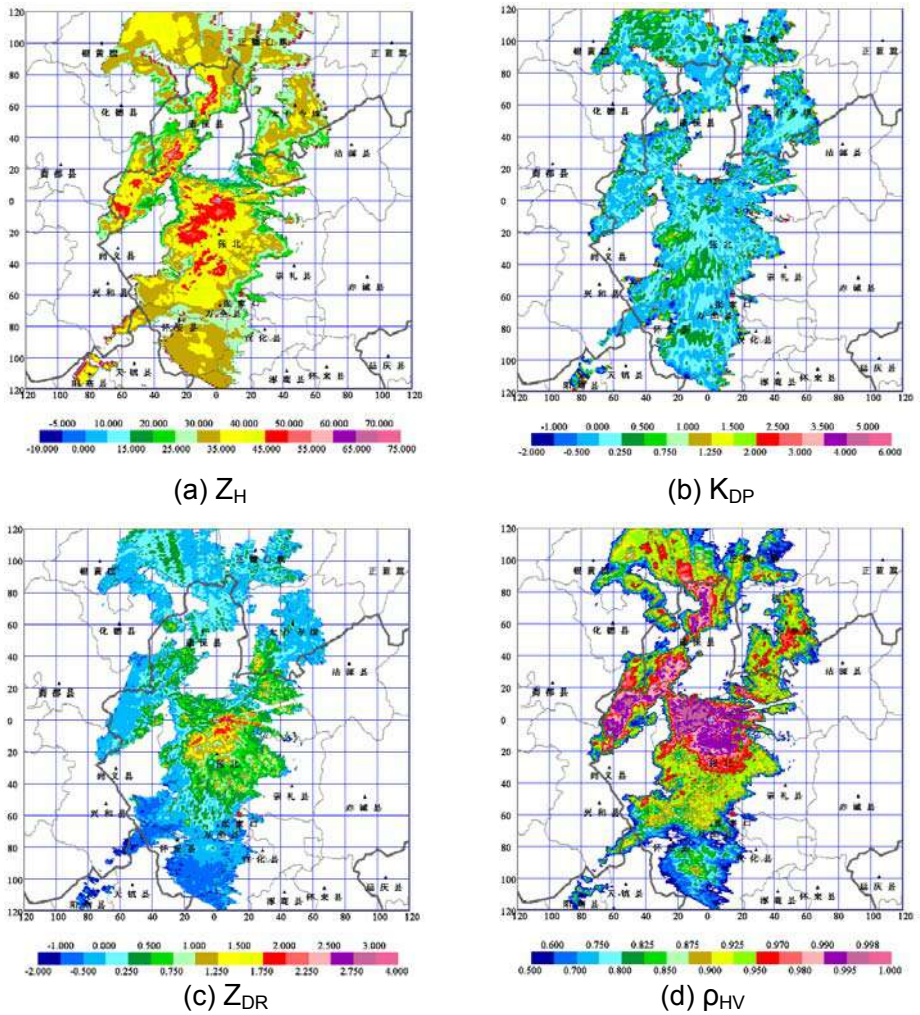

(a) Z_H (b) K_{DP}

(c) Z_{DR} (d) ρ_{HV}

Fig.1 PPI reflectivity and polarimetric data at 1522 BJT April 23, 2009 (elevation:0.5°)
(a) horizontal reflectivity (Z_H, dBZ), (b) specific differential propagation phase (K_{DP}, deg·km^{-1}), (c) differential reflectivity (Z_{DR}, dB), (d) cross-correlation coefficient (ρ_{HV})

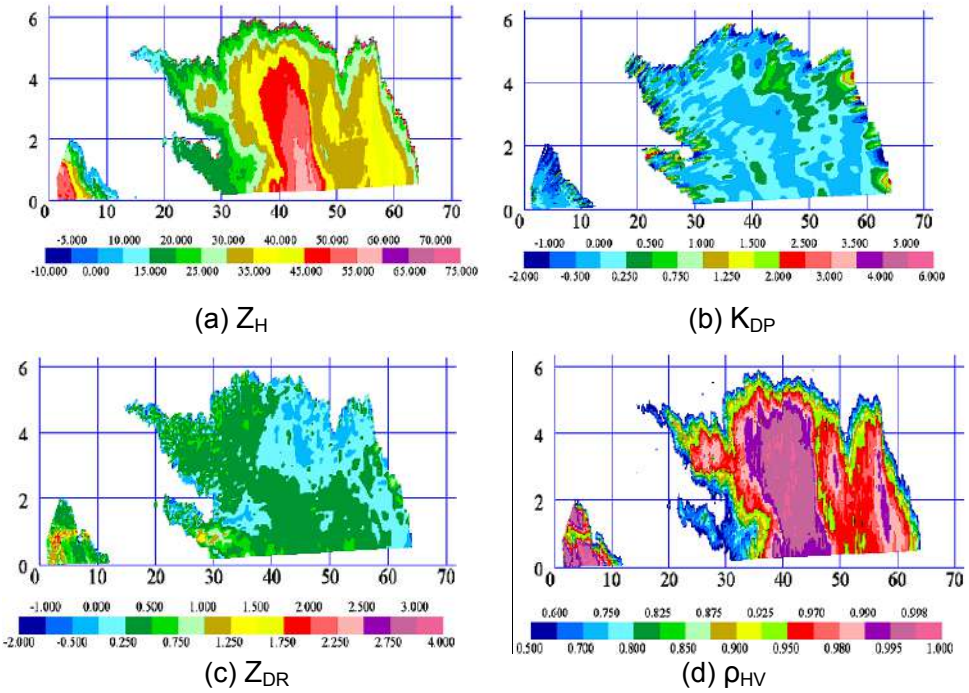

(a) Z_H (b) K_{DP}

(c) Z_{DR} (d) ρ_{HV}

Fig.2 RHI reflectivity and polarimetric data at 1534 BJT April 23, 2009 (azimuth: 270°)

their types and number density. The result shows that the solid precipitation particles were mainly graupel and hail with sizes less than 12mm.

5. IDENTIFICATION OF HAILFALL

5.1 Fuzzy logic identification method

In this paper, a fuzzy logic classification algorithm has been developed for X-band polarimetric radar data. The model has five input variables with four polarimetric measurands: Z_H, Z_{DR}, K_{DP}, ρ_{HV} and one environmental temperature T. The output result from the model are ten different hydrometeor types: drizzle, rain, wet graupel, dry graupel, small hail, large hail, rain and hail mixture, wet snow, dry snow, and ice crystals. Table 2 gives the values of polarimetric parameters of X-band dual-polarization radar and the ranges of environmental temperature for various hydrometeors. The ranges of these parameters in Table 2 are comprehensively given by referring to Straka et al. (2000), Zrnic et al. (2001), Keenan (2003), and He et al. (2010), and considering the characteristics of X band polarimetric radar as well. Therefore, there is some physical basis for the selection of these polarimetric parameter ranges. Because ambient temperature is an important parameter affecting the phase types of hydrometeors, it has been taken as an input variable of fuzzy logic classification algorithm in this paper. And the weight coefficient of temperature is set to 0.3. In addition, a quality control of the polarimetric radar data has been carried out by a processing as shown in Section 3 before their application.

Table 2 Values of polarimetric measurands and corresponding temperature ranges for various precipitation particle types

precipitation particle		parameter				
type	symbol	Z_H (dBZ)	Z_{DR} (dB)	K_{DP} (deg·km^{-1})	$\rho_{HV}(0)$	T (°C)
Drizzle	DZ	10 ~ 25	0.0 ~ 0.8	0.0 ~ 0.1	>0.97	-5 ~ 40
Rain	RN	25 ~ 60	0.5 ~ 4.0	0.0 ~18.0	>0.95	-5 ~ 40
Wet graupel	WG	30 ~ 50	-0.5 ~ 2.0	0.0 ~ 5.3	>0.95	-15 ~ 5
Dry graupel	DG	20 ~ 35	-0.5 ~ 1.0	0.0 ~ 1.7	>0.95	-15 ~ 0
Small hail (<2cm,wet)	SH	45 ~ 60	-0.5 ~ 0.5	-1.8 ~ 1.8	0.92 ~ 0.95	-15 ~ 5
Large hail (>2cm,wet)	LH	55 ~ 70	-1.0 ~ 0.5	-1.8 ~ 3.5	0.90 ~ 0.92	-40 ~ 25
Rain & hail	RH	45 ~ 75	-1.0 ~ 6.0	0.0 ~ 13.0	0.70~ 0.95	-20 ~ 20
Wet snow (melting)	WS	20 ~ 45	0.5 ~ 3.0	0.0 ~ 1.8	0.5 ~ 0.95	0 ~ 5
Dry snow (low density)	DS	-10 ~ 35	-0.5 ~ 1.0	-0.9 ~ 1.4	>0.95	-15 ~ 0
Ice crystal (high density)	IC	-10 ~ 25	0.1 ~ 5.0	0.3 ~ 2.0	>0.96	-50 ~ -5

5.2 Fuzzy logic identification and comparison with in situ observation

Figure 3 shows the radar PPI reflectivity observed respectively at 1625, 1632, and 1640 on April 23 and the corresponding identification results of precipitation particles by the fuzzy logic classification method mentioned above.

At 1625 there were two strong convective echoes appearing at the distance of 15km southwest and northeast of the radar station (Figure 3a),. In addition, a band echo of stratiform cloud appeared in the range of 25~60 km southeast of the radar station and removed from the radar station. Here we just discuss the band system in the west side of the radar. The maximum intensity of the radar echoes in the southwest reaches 55 dBZ, and the average values of corresponding Z_{DR} and K_{DP} are -0.36dB and -0.04 deg·km^{-1} respectively (figures omitted). Meanwhile, the maximum intensity of the radar echoes in the north is slightly smaller, reaching 50 dBZ, and the average values of Z_{DR} and K_{DP} corresponds to -0.23 dB and -0.10 deg·km^{-1}. According to these values of the polarimetric parameters, the two areas will appear hail shooting (Table 2). And the high reflectivity and low differential reflectivity also indicate an existence of tumbling hail. The types of the precipitation particles are indentified by the fuzzy logic classification method. The strong echo areas in the southwest appear a

hail-and-rain mixture (see the area within a red circle in Figure 3b), and outside of these areas is surrounded by wet graupel. The identification results in the northeast were to exist in a small area of hail-and-rain mixture and some wet graupel particles. And a rare content of wet graupel appeared outside of this region. Rainfall and dry graupel only existed in the other cloud area, without graupel and hail.

At 1632, as the echo band in the southwest of the radar station moved eastward, the forefront of the strong echo had reached the station. The average intensity of the strong echoes was 50 dBZ and the maximum reached 60 dBZ. At the time, it began to fall hail, graupel and rain at the radar station, and the hailfall lasted about five minutes. Maximum size of the landing hailstones achieved to 12 mm, the density of graupel and hail was about 60 to 80 per 100cm^2 by in situ measurement. The strong convective clouds accompanied by thunder and lightning were also observed during this time period. According to the fuzzy logic identification model, the ground in this area appeared a hail-and-rain mixture and small hail particles in size less than 2cm, and a small amount of wet graupel and rain as well. This is very consistent with the in situ observational results. Meanwhile, there was a zone of small hail particles appeared at the distance of 20~30 km in the northeast.

At 1640, the strong echoes had removed from the radar station and reached about 10 km distance in the east. The maximum echo intensity of the storm was still 58 dBZ after the hail shooting. And at this time the average values of Z_{DR} and K_{DP} corresponds to -0.6 dB and -0.01 deg·km^{-1}. Therefore, there were still wet graupel, dry graupel, and small hail on the ground. Based on the phase identification procedures, the region has been determined by small hail particles less than 2cm in size, little wet graupel and rain as well. The classification showed that identification results are consistent with the theoretical analysis.

Comparing the radar echo intensity with identification distribution of graupel and hail, we can clearly find that the landing locations of graupel and hail agreed with the position of radar strong echo intensity values very well. And the position mainly located in the front of the storm clouds.

These results suggest that the developed X-PARS radar can observe the exact zones of hydrometeor particles of hail clouds, especially the size and the landing location of hail through the fuzzy logic classification algorithm. The results are in good agreement with in situ ground truth observations, indicating that the X-PARS radar system can play an important application in hail suppression of hail cloud.

5.3 Comparisons of polarimetric classification to disdrometer observation

It has been carried out to compare the observation of the X-PARS radar combined with the fuzzy logic classification algorithm for the situation when the hail clouds passed through the radar site. The following

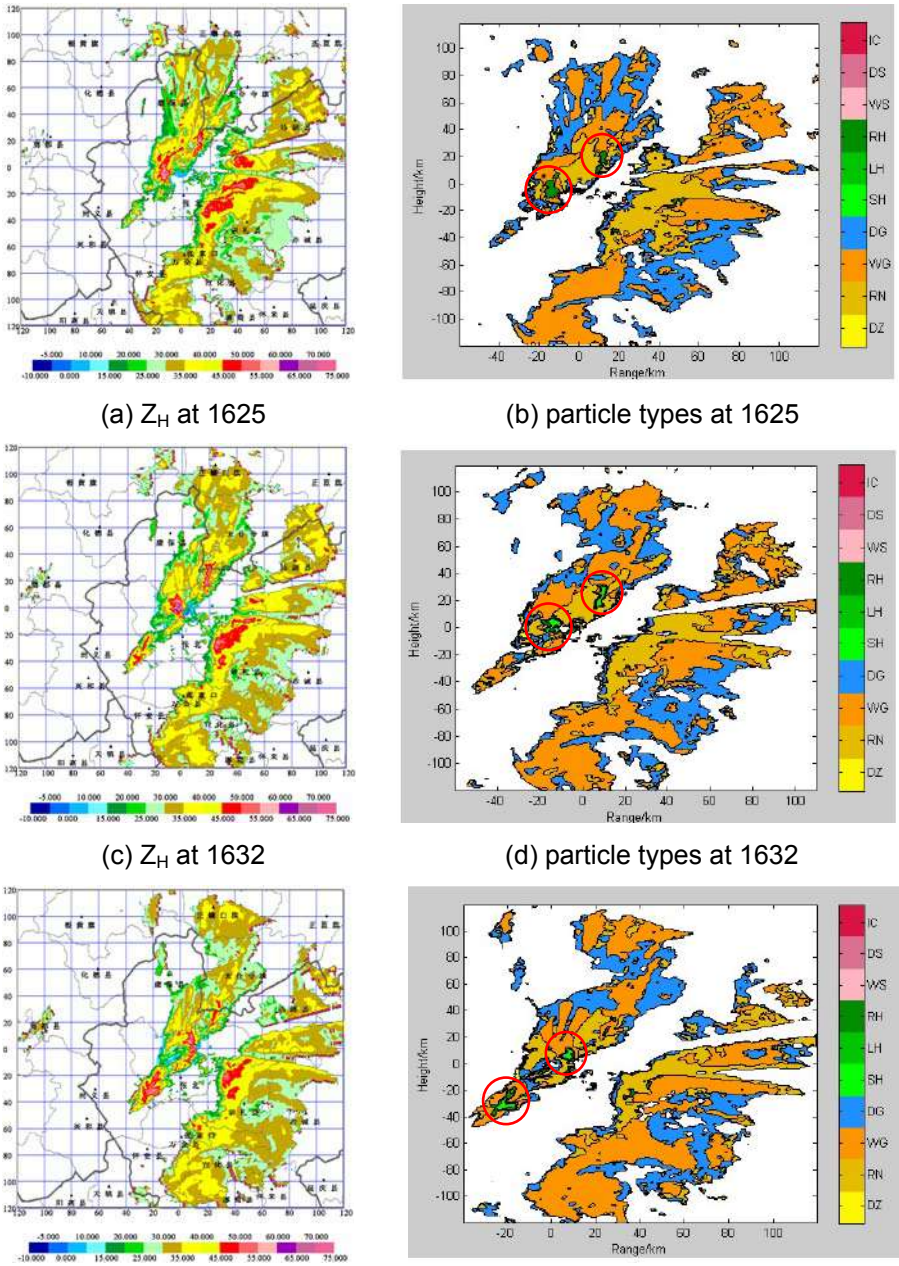

(a) Z_H at 1625 (b) particle types at 1625

(c) Z_H at 1632 (d) particle types at 1632

(e) Z_H at 1640 (f) particle types at 1640

Fig. 3 PPI reflectivity of X-band polarization radar observation on April 23, 2009, and the corresponding precipitation particle types by fuzzy logic classification algorithm (elevation: 0.5°) (a) at 1625, (b) at 1632, (c) at 1640

comparison is for the observations of another hailstorm which occurred in the southwest of the radar. The hailstorm moved also northeastward and through the observation site of the Parsivel disdrometer during the time period from 1650 to 1710, April 23. And the comparison will give further analysis of the hail cloud structure.

The X-PARS radar made twice RHI scans along the direction of the Parsivel disdrometer (the azimuth was 180°) at 1658 when a hailcloud just passed through the Zhangbei town on the afternoon of April 23, 2009. It was suited to compare the radar

observations with the in situ particle spectra data measured by the disdrometer.

Figure 4 shows the RHI echo intensity distributions made along the azimuth of 180° at 1658 and the corresponding precipitation particle types based on the fuzzy logic classification method. The location of the disdrometer was just under the severe convective clouds.

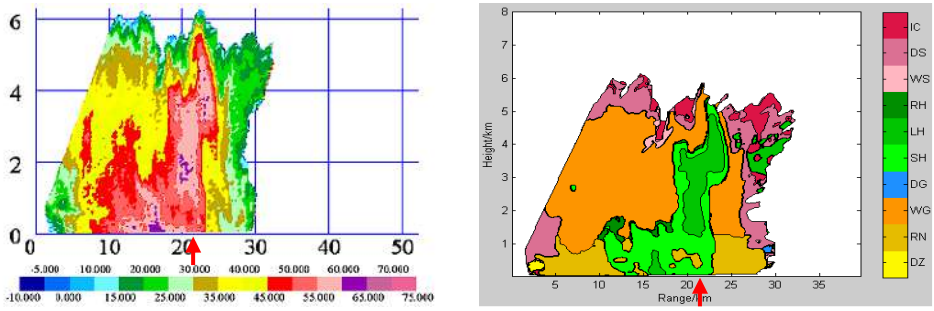

(a) Z_H at 1658 (b) particle types at 1658

Fig. 4 RHI reflectivity of X-band polarization radar observation on April 23, 2009, and the corresponding precipitation particle types by fuzzy logic classification algorithm (azimuth: 180.0°, the red arrow marks the location of the Parsivel disdrometer which is 21.2 km far from the radar station)

The storm clouds were strengthened at 1658 and the top of 45 dBZ stretched up to the height of 5.5 km. The maximum values of Z_H, Z_{DR} and K_{DP} are 60 dBZ, -0.66 dB and -0.36 deg·km^{-1} respectively. According to the classification results based on the fuzzy logic classification method, the hail clouds had a lot of large hail particles with size larger than 2 cm appeared in the layer of 1.3-5.0 km height over the Parsivel disdrometer site. There were small hail particles in the layer below 1.3km height. These results suggest that the sizes of larger hail particles in the high altitude reduced in the fall process. This may be related to partly melting below the freezing level (at 1.35km height).

The measurements of the Parsivel disdrometer show that the maximum diameter of the hail particles is 8.0 mm with two peaks, and the second peak appears around 5 mm at 1658 on April 23. The precipitation intensity was 14.53mm·h^{-1} corresponding to radar echo intensity 50.35 dBZ given from the disdrometer. Furthermore, a hail weather phenomenon was determined by the disdrometer. At the results indicate that the fuzzy logic classification results from the X-band polarimetric radar observation were consistent well with the actual measurement.

In summary, the results of the X-PARS radar observations combined with the fuzzy logic classification method are agreed with the particle spectrum observations on the ground. This further proves that the classification results which are based on the

developed X-band dual-polarimetric radar and fuzzy logic classification method are accurate.

6. CONCLUSIONS

In this paper, the X-band dual-polarimetric radar with two channels was used to make a following-up observation for the features of radar echo and hail particles of a springtime hailstorm system. The radar echo structure and the hail particle characteristics of the hail clouds were analyzed, and the classification results of hail particles by using the fuzzy logic classification method are compared with artificial observations and precipitation particle disdrometer measurements on the ground. The conclusions are drawn as follow:

(1) The large-scale hail process was caused by the different hailstorm clouds in a springtime multi-cell hailstorm system. The maximum height of the storm echoes was only 6.0 km and the thickness of the supercooled layer was 4.7 km in hailfall zones, which are all much lower than those of hailstorms in summertime; the maximum radar echo intensity after attenuation correction was 55-60 dBZ, and the corrected differential reflectivity and specific differential phase shift both were not large. These characteristics indicated that the hail particles were in the state of rolling during their falling process and did not have a fixed orientation arrangement.

(2) The ground observations show that wet graupel particles, small-size hailstones, and hail-and-rain mixture took the lead among the precipitation particles on the ground, the maximum particle sizes were 12 millimeters.

(3) According to the principle of fuzzy logic, a classification model of precipitation particles based on the dual-polarimetric observation data can identify the location, the sizes and the state of hail and graupel particles in hail clouds. And the classification results show that the particles from the springtime hailstorms were mainly wet graupel, small hail, and the hail-and-rain mixture, and the sizes of precipitation particles were less than 2 cm. The classification results coincide well with the in situ field observations of a precipitation particle disdrometer and artificial measurements.

ACKNOWLEDGEMENTS

This work was supported by National Natural Science Foundation of China (Grant No. 40875080), Project of the Ministry of Science and Technology of China (Grant No. 2006BAC12B01-01), and China National commonweal Science (Meteorology) Special Project (Grant No. GYHY201006031).

REFERENCES

Aydin, K., T.A. Seliga, V. Balaji, 1986. Remote sensing of hail with a dual-linear polarization radar. J. Climate Appl. Meteor., 25, 1475–1484.

Bringi V N, Chandrasekar V. 2000. Polarimetric Doppler Weather Radar: Principles and Applications. Cambridge University Press, 256-312.

Bringi V N, Seliga T A and Aydin K, 1984. Hail detection with a differential reflectivity radar. Science, 225: 1145-1147.

Bringi V N, Vivekanandan J, Tuttle J D, 1986. Multiparameter radar measurements in Colorado convective storms, Part II: Hail detection studies. J. Atmos. Sci, 43:2564~2577.

Gong Naihu, Cai Qiming, 1992. Characteristics and identification of hail cloud based on radar observations]. Plateau Meteorology (in Chinese), 1(2):43-52.

Hall P M, Goddard J W F, Cherry S M. 1984, Identification of hydrometeors and other targets by dual-polarization radar. Radio Sci, 19:132-140.

He Yuxiang, Lü Daren, Xiao Hui, et al. 2009a. Attenuation correction of reflectivity for X-band dual polarization radar. Chinese J. Atmos. Sci., (in Chinese), 33 (5):1027-1037.

He Yuxiang, LüDaren, Xiao Hui, et al. 2009b. Attenuation correction of radar differential reflectivity for X-band dual polarization radar. Plateau Meteorology (in Chinese), 28 (3):607-616.

He Yuxiang, Xiao Hui, Lu Daren, 2010. Analysis of hydrometeor distribution characteristics in stratiform clouds using polarization radar. Chinese J. Atmos. Sci., 34(1):23-34.

Huang Meiyuan, Wang Angsheng, et al., 1980. Introduction to Hail Suppression (in Chinese). Beijing: Science Press, 138-141.

Keenan, T. 2003. Hydrometeor classification with a C-band polarimetric radar. Aust. Met.Mag. 52:23-31.

Kennedy P C, Rutledge S A, 1995. Dual−Doppler and multiparemeter radar observations of a bow−echo hailstorm . Mon. Wea. Rev., 123(4):921−949.

Liu H., Chandrasekar V., 2000. Classification of hydrometeor type based on polarimetric radar measurements: Development of fuzzy logicand neuro-fuzzy systems, and in situ verification. J. Atmos. Oceanic Technol, 17, 140-164.

Liu Liping, Zhang Hongfa, Wang Zhijun, et al., 1993. Method of hail identification with dual-linear polarimetric radar observations. Plateau Meteorology (in Chinese), 12(3):333-337.

Liu Liping. 2002. A theoretical study of estimations of rain and hail rates in mixed-phase areas with dual linear polarization radar. Chinese J. Atmos. Sci., 26(6):761-772.

Qi Liangbo, Xiao Hui, Huang Meiyuan, et al., 2002. A numerical study of hail identification using dual-polarization radar. J. Atmos. Sci., 26(2):230-240.

Ryzhkov, AV, Giangrande SE, Melnikov VM, et al., 2005, Calibration issues of dual-polarization radar measurements. J. Atmos. Oceanic Technol, 22, 1138–1155.

Seliga T A, Bringi V N. , 1976. Potential use of radar differential reflectivity measurements at orthogonal polarizations for measuring precipitation.

J. Appl. Meteor., 15 (1): 69-76.

Straka J M, Zrnic D S. 2000. Bulk hydrometeor classification and quantification using polarimetric radar data:Synthesis of relations. J. Appl. Meteor. 39:1341-1372.

Tuttle.J. D., 1989. Multiparameter radar study of a microburst: Comparison with model results. J. Atoms. Sci., 46: 601-620.

Xiao Hui, Wu Yuxia, Hu Zhaoxia, et al. , 2002 Early identification and numerical simulation of hail clouds in Xunyi region. Plateau Meteorology (in Chinese). 21(2): 159-166.

Zhang Hongfa, Qie Xiushu, Wang Zhijun, et al., 2001. Observations of severe convective hail storm cloud with polarization radar. Chinese J Atmos Sci, 24(1):38-48.

Zrnic D S, Ryzhkov A, Straka J, et al., 2001. Testing a procedure for automatic classification of hydrometeor types. J. Atmos. Ocean. Technol., 18, 892-913.

SYNERGETIC USE OF POLARIMETRIC DOPPLER RADARS AT KA- AND C- BAND FOR RETRIEVAL OF WATER DROP AND ICE PARTICLE SIZE DISTRIBUTIONS

Kersten Schmidt[1], Martin Hagen[1]

[1]Deutsches Zentrum für Luft- und Raumfahrt (DLR), Institut für Physik der Atmosphäre (IPA), Oberpfaffenhofen, Germany

1. ABSTRACT

A retrieval method to derive size distributions from synergetic use of vertical pointed Ka-band and polarimetric C-band radar is introduced. The method is based on using the full height-resolved Doppler spectra instead of mean values of reflectivity and radial velocity inside the radar bin volume. Within a Mie based radar forward operator, Doppler spectra were simulated from assumed size distributions, taking into account the attenuation at Ka-band. In an iterative way, the parameters of distributions were varied until differences between simulated and observed Doppler spectra could minimized. First results were achieved from a case study of 23 July 2007 during the Convection and Orographically Induced Precipitation Study (COPS).

1. INTRODUCTION

The verification of radar retrieval results like hydrometeor type, quantity, and dynamics of clouds is an essential requirement for assimilating observation data into Numerical Weather Prediction (NWP) models. Field campaigns were executed to enrich the observational data base. One of the aims of Convection and Orographically Induced Precipitation Study (COPS) in 2007 – took place in south-west Germany and eastern France - was to improve the Quantitative Precipitation Forecast (QPF) in mountainous areas (Wulfmeyer et al., 2007). For this purpose, a huge amount of different observation instruments were concentrated in the region around Black Forest, Vogues and Rhine valley, especially at so-called supersites. The current study focus on comparison between polarimetric C-band and vertically pointed Ka-band radar, to retrieve profiles of hydrometeor content and quantity.

2. DATA

A vertical pointing Doppler research radar, MIRA-36, was operated at supersite Achern during the COPS period. From measured spectra, the radar moments: reflectivity, mean Doppler velocity and depolarization ratio (LDR) were estimated every 10 seconds with altitude resolution of 30 m. The DLR C-band radar POLDIRAD was located during the COPS period 36 km away from Achern supersite. Every 10 min a profile was taken by scanning as range height indicator (RHI).

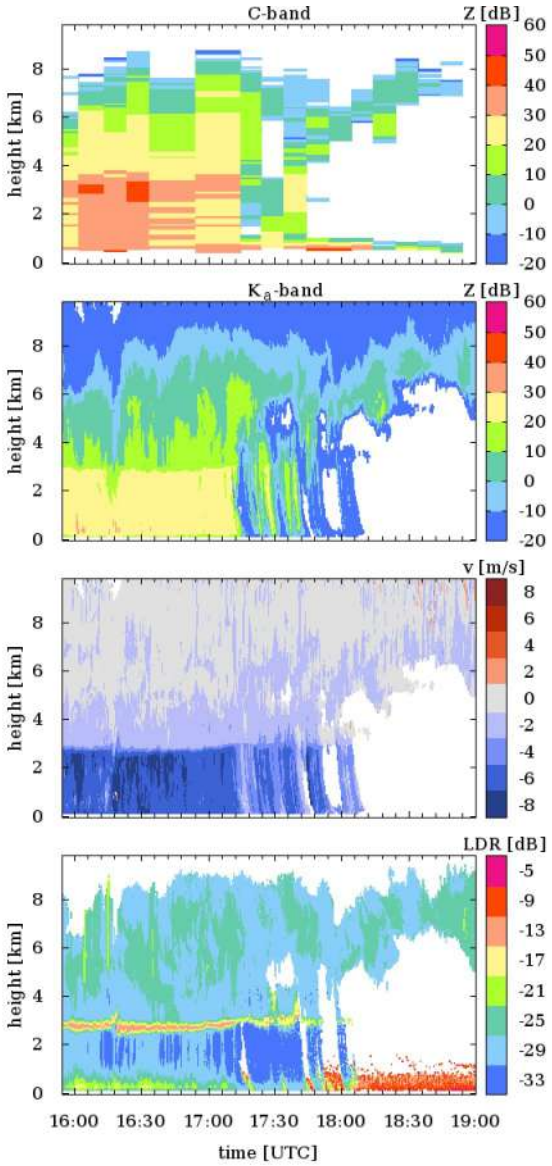

Figure 1: *Radar observations above Achern supersite at 23 July 2007 from 16 to 19 UTC. C-band reflectivity (top) taken from RHI scans every 10 min were compared with reflectivity, mean Doppler velocity and depolarization ratio (LDR) with 10 sec time resolution from vertically looking Ka-band radar.*

3. METHOD

As a first step, spatial and temporal correlated reflectivity profiles from Ka and C-band radar were compared. Generally, two different effects could be observed in the reflectivity profiles with raising altitude:

- an increasing of reflectivity differences below the melting layer in rainfall regions and
- a decreasing of reflectivity differences above the melting layer in regions dominated by small ice crystals and snow.

The first effect is caused by the rain drop attenuation which is stronger at the Ka- as at the C-band, the latter by the higher sensitivity of Ka-band for small particles.

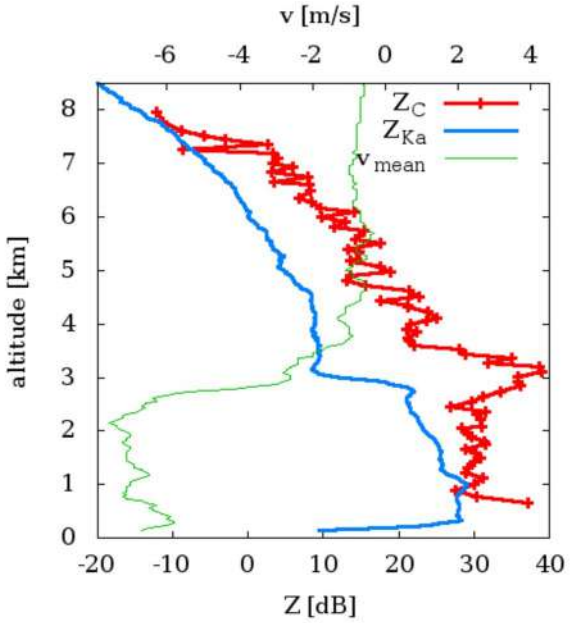

Figure 2: *Measured profile at 23 July 2007 16:38 UTC of C-band radar reflectivity from POLDIRAD with corresponding Ka-band cloud radar reflectivity and mean velocity.*

By evaluating the cloud radar Doppler spectra and comparing the profiles of reflectivity, water drop and ice particle size distributions could be quantified by executing the following steps:

1) scaling of measured cloud radar spectra by using retrieved reflectivity after Bauer (2007),

2) fitting of parameters of an exponential particle size distribution to measured spectra by using radar forward operator (Haynes et al, 2007),

3) recalculating of Ka-band reflectivity profile considering rain attenuation, and

4) simulating C-band reflectivity and comparing with measured profile.

For the rain drop size distribution (RDSD) an exponential size distribution *N(D)* with two independent parameters (N_0, D_0) is used.

$$N(D) = N_0 \; e^{-3.67 \; D/D_0}$$

4. FIRST RESULTS

4.1 Scaling of measured spectra

Cloud radar Doppler spectra are available for the co- and the cross (cx) channel. While for the co channel the reflected and transmitted waves are at the same plane, for the cx-channel the planes are rotated by 90°. The ratio between co- and cx- channel is called linear depolarization ratio (LDR) and useful for instance for estimating the melting layer height and extension.

From vertical upward looking point of view, water drops are predominantly spherical and in this case LDR has no import evidence. Therefore it was tested to taking into account co- as well as cx-channel for the scaling of measured spectra. Because of strong reflectance, for many cases the co-channel was frequently saturated and the uses of scaled cx-channel is suggested instead (Figure 3).

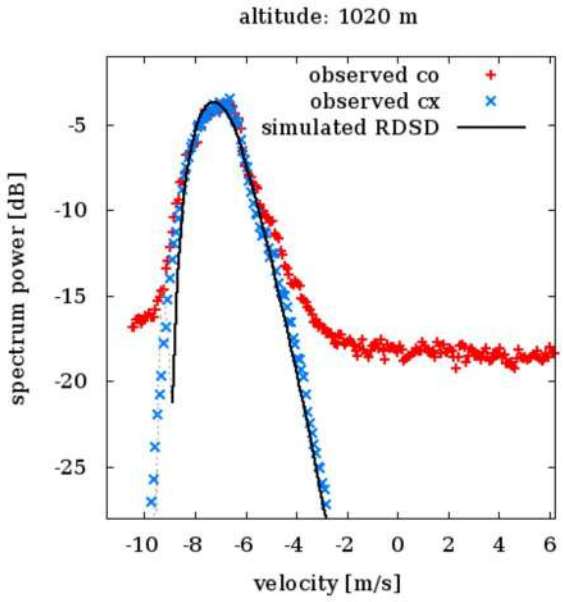

Figure 3*: Scaled Doppler spectra by using co- and cross- (cx) channel to reach the reflectivity of 29 dBZ from profile at 16:38 UTC at 1 km altitude. Because of saturation effects, noise level for co channel is higher as for cx-channel. Exponential size distribution parameters N_0, D_0 were fitted to linear scaled spectra power of co and cx-channel.*

Both channels were scaled until the reflectivity reached the same value calculated by using the radar moment procedure after Bauer (2007). The main errors are expected due to estimating of noise level.

4.2 Relationship between Doppler velocity and rain drop size

The drop sizes required for the simulation could be derived from measured cloud radar Doppler velocities by using relation between fall velocity *v* and drop diameter *D* after Atlas (1973).

$$v(D)[m/s] = 9.65 - 10.3\ e^{-0.6\ D[mm]}$$

Restrictions have to take into account for the reverse function *D(v),* first a maximum velocity of 9.65 m/s will be reached for increasing diameter and second the minimum velocity have to limited to -0.65 m/s to prevent negative drop sizes.

Because of water drop collapsing effects, in practice drop sizes are limited to 6-8 mm diameter, corresponding to fall velocities of 9.37 and 9.57 m/s, respectively. Higher Doppler velocities are supposed to related to additional vertical air motion and spectral broadening because of turbulence effects.

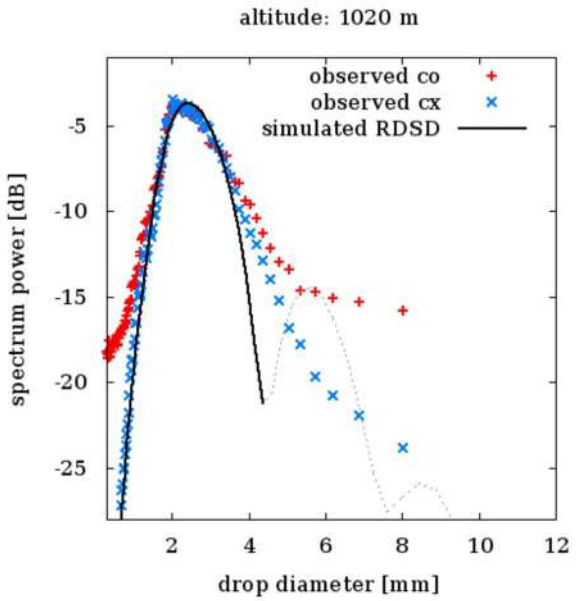

Figure 4*: Scaled measured and simulated Doppler spectra as in Figure 3 plotted with corresponding drop size diameter after Atlas (1973). The rain drop size distribution (dotted line) were limited to 4.2 mm (black line) for calculating corresponding Ka- and C-band reflectivity.*

For the current study, all drop size distributions were cut at 4.2 mm (8.8 m/s), related to the first minimum of mie backscattering (dotted line in Figure 4). An extended drop size range (up to 6 mm) with a small amount of larger drops does'nt effect the Ka-band reflectivity, but the corresponding C-band reflectivity would achieve unrealistic high values.

4.3 Fitting of size distribution parameters

A spectral bin radar forward operator was developed, based on routines from radar simulator Quick-Beam (Haynes, 2007). By using the forward operator, the spectrum power for each diameter range were calculated for an assumed drop size distribution. Further the reflectivity, attenuation and mean fall velocity were estimated from given size distribution.

For the liquid phase, the parameters of exponential size distribution (N_0, D_0) were fitted to the measured power spectra in a least square sense. To prevent the noise level effect, datasets were compared at linear instead of displayed logarithmic scale.

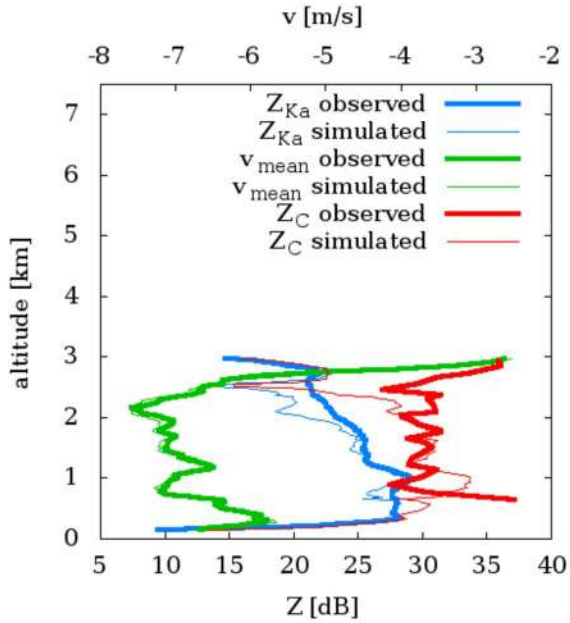

Figure 5: *Juxtaposing of measured and simulated reflectivity as well as mean fall velocity below the melting layer (3 km) by using exponential RDSD for 16:38 UTC.*

4.4 Simulated and observed reflectivity

The retrieval method was tested for a rainfall event at 23 July 2007 for the liquid water column below the melting height (< 3 km). While the

simulated mean fall velocity matched well with measured values for the whole liquid phase profile, the simulated Ka-band and C-band reflectivity matched only below 1.8 km (Figure 5). In the upper part (above 1.8 km) reflectivity at both bands were underestimated by the simulation due to not considered part of Doppler spectra with velocities above 8.8 m/s (Figure 6). Further the shape of the spectrum contains multimodale peaks which is not consistent to the assumed exponential size distribution. The additional peak at -9.5 m/s could be explained by a strong downward wind (> 1 m/s) caused by embedded convection below the melting layer.

The retrieved Ka band attenuation (not shown) was used to adjust the cloud radar reflectivity profile. The attenuation reached maximum values around 0.4 dB/km and were be used for estimating the liquid water content (LWC).

A similar radar intercomparison C/Ka band study by Matrosov (2010) (there Figure 2) shows lower Ka-band reflectivity (0 to 10 dBZ) with similar C-band reflectivity (~30 dBZ) compared to our samples. The discrepancy to our study could be caused by a different size distribution in the liquid part.

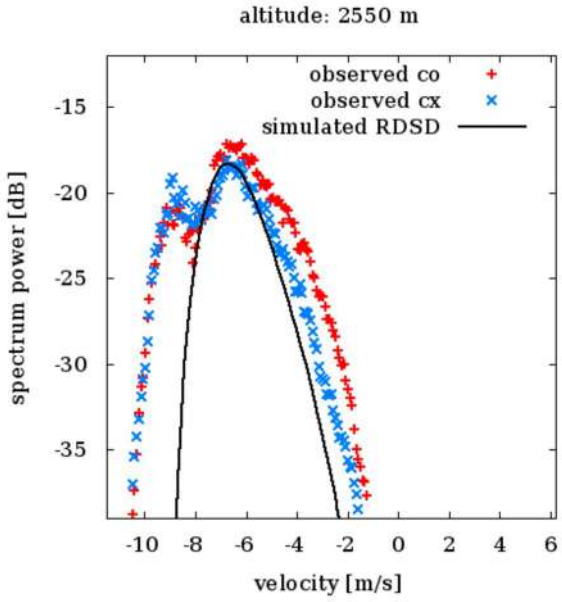

Figure 6: *Measured Doppler spectra and best fitted RDSD at 2.5 km altitude where the reflectivity is strongly underestimated by the simulation due to the limited spectrum at -8.8 m/s.*

5. SUMMARY AND OUTLOOK

Radar data from vertical pointed Ka-band and synchronized range height indicator scans (RHI) from C-band were compared during the COPS-field campaign. A new method was introduced for retrieving parameters of exponential size distribution from measured Doppler spectra. Derived Ka-band attenuation were used to adjust the profile. First results show good agreements between simulated and measured C- and Ka- band reflectivity in the lower part as well as mean fall velocity in the whole profile below the melting layer. The discrepancies were caused due to spectrum signal at Doppler velocities below -9.5 m/s which were suppressed by the evaluating procedure.

In a further step, the procedure will also tested above the melting layer in cases of ice and snow with adjusted relation between particle size and terminal velocities. Furthermore, additional data e.g. from sounding and SODAR wind profilers will be used to estimate and minimize the relevant error sources expected from vertical air motion and turbulence.

BIBLIOGRAPHY

Atlas, D., R.C. Srivastava, and R.S. Sekhon, 1973: Doppler radar characteristics of precipitation at vertical incidence. Rev. Geophys. 11(1), 1-35.

Bauer, M.R., U. Goersdorf, 2007: Target separation and classification using cloud radar Doppler-spectra. – In: 33rd AMS Conference on Radar Meteorology, Cairns, Australia.

Haynes, J.M., R.T. Marchand, Z. Luo, A. Bodas-Salcedo, and G.L. Stephens, 2007: A multipurpose radar simulation package: Quick-Beam. Bull. Amer. Meteor. Soc., 88, 1723-1727.

Matrosov, S. Y., 2010: Synergetic use of millimeter- and centimeter-wavelength radars for retrievals of cloud and rainfall parameters. Atmos. Chem. Phys., 10, 3321–3331

Wulfmeyer, V., Behrendt, A., Kottmeier, C., Corsmeier, U., Barthlott, C., Craig, G., Hagen, M., Althausen, D., Aoshima, F., et al.: The convective and orographically-induced precipitation study (COPS): The scientific strategy, the field phase, and research highlights, Quarterly Journal of the Royal Meteorological Society, 137, 3–30, doi:10.1002/qj.752, 2011.

Acknowledgements

The authors thank Prof. Dr. Felix Ament from University of Hamburg for providing spectra data of cloud radar during the COPS period.

ICE SELECTIVE INLET (ISI): A NOVEL TOOL FOR ICE NUCLEATION MEASUREMENTS

Piotr Kupiszewski[1], Paul Vochezer[2], Martin Schnaiter[2], Ernest Weingartner[1]

[1]Laboratory of Atmospheric Chemistry, Paul Scherrer Institute,
CH-5232 Villigen PSI, Switzerland
[2]Institute for Meteorology and Climate Research, Karlsruhe Institute of Technology (KIT),
D-76021 Karlsruhe, Germany

1. INTRODUCTION

Uncertainties in climate projections are largely due to an insufficient understanding of aerosol-cloud interactions. One particularly poorly understood process is formation of mixed-phase clouds, where ice nuclei (IN), a small but important sub-population of aerosol particles, facilitate heterogeneous ice nucleation. IN abundance influences the ice mass fraction, strongly affecting cloud radiative properties (Sun and Shine, 1994). Furthermore, increased IN concentrations have been found to enhance precipitation formation, thus causing a decrease in cloud lifetime and cloud cover. Meanwhile, the physical and chemical characteristics of IN in ambient mixed-phase clouds are not well known. Moreover, the anthropogenic contribution to IN, in particular the role of black carbon (BC) as an IN, is uncertain. Should BC be found to be an effective IN, a glaciation indirect effect would take place, leading to increased absorption of shortwave radiation by the Earth-atmosphere system (Lohmann, 2002). Field studies of IN aiming to shed light on the aforementioned issues are hampered by difficulties with sampling the chemically complex ice residuals and separating them from liquid droplets.

2. INSTRUMENTATION

The Ice Selective Inlet (ISI) aims to overcome sampling issues, separating small ice particles (their residuals are considered representative of original IN) from cloud droplets, interstitial particles and potentially contaminated large ice crystals.

The instrument (Figure 1) is based on the existing Ice-CVI design (Mertes et al., 2007). The key improvement in the operating principle is separation of supercooled droplets from ice crystals via evaporation in the airborne state, as opposed to physical impaction. This would minimize potential artifacts e.g. resulting from ice-crystal breakup.

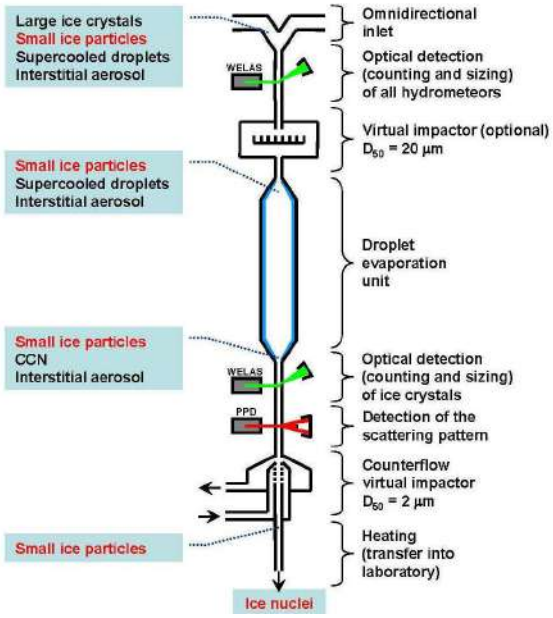

Figure 1. A schematic of the Ice Selective Inlet (ISI).

The core of the ISI is an evaporation unit with ice-covered inner walls, removing droplets using the Wegener-Bergeron-Findeisen process: Due to different water vapor pressures over liquid water and ice, the relatively large ice wall surface area will induce the desired evaporation of the super-cooled droplets while the ice crystals remain

unimpaired. The design is based on model calculations (Figure 2) solving mass transfer equations and Köhler theory, ensuring sufficient residence time for evaporation of droplets. Cloud droplets with diameters of <20 µm (the upper size limit of particles entering the evaporation chamber) should be evaporated within 20s in the temperature range where mixed phase clouds exist (-35<*T*<-5℃). Particles smaller than 2 µm, namely interstitials (un-activated particles) and cloud condensation nuclei (released during the droplet evaporation process) are removed downstream of the evaporation chamber by a pumped counterflow virtual impactor (Boulter et al., 2006).

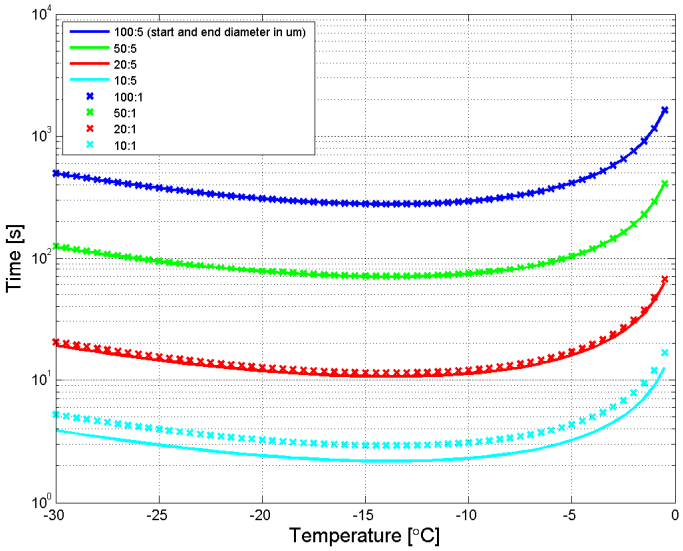

Figure 2. Evaporation times of cloud droplets in the evaporation unit for different droplet start and end diameters (in µm) as a function of temperature at a pressure of p=65kPa.

Droplet and ice crystal number size distributions are measured before and after the evaporation unit using Welas white light optical particle counters (OPC). The use of white light is important in order to avoid the strongly non-monotonic relationship between intensity of scattered light and particle diameter experienced when using a laser spectrometer (Spiegel et al., 2012). A further important feature of the OPCs is a light source decoupled from the measuring volume, preventing heat transfer to the ISI system.

The PPD-2, an improved version of the Particle Phase Discriminator (Kaye et al., 2008), acquires high resolution scattering patterns of individual particles in a size range of 1 – 100 µm. The setup and the generated results of the PPD-2 are equivalent to the in situ cloud probe Small Ice Detector mk. 3 (SID-3). The scattering patterns contain detailed information about the microphysical properties of individual cloud particles such as habit and surface roughness. Analysis of the PPD-2 data enables unambiguous distinction between water droplets and ice particles (Figure 3).

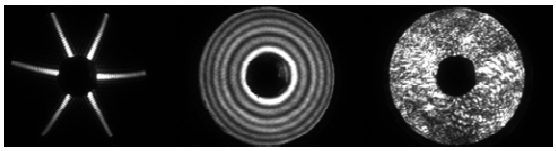

Figure 3. Scattering patterns obtained with SID-3. Hexagonal ice plate of a pure ice cloud (left); droplet (middle); irregularly shaped mixed-phase cloud ice particle (right).

By including the PPD-2 downstream of the droplet evaporation unit in the ISI setup the working principle of this unit can be continuously checked. Furthermore, the detection of the scattering patterns of ice crystals selectively transferred through the droplet evaporation unit by the PPD-2 will help to illuminate ice related cloud microphysics. In addition to the scattering images the PPD-2 generates a particle number size distribution based on the forward scattering signal which is a valuable cross-check opportunity for the OPC.

The SID-3 instrument will be operated next to the ISI inlet within the same cloud. The simultaneous operation of the PPD-2 (probing only the ice fraction) and the SID-3 (probing all cloud particles) will further enhance the prospects of our work.

Downstream of the ISI, the physical and chemical properties of the extracted ice residuals are analyzed with state of the art instrumentation (eg. AMS, SP2, SMPS).

3. MEASUREMENTS

The ISI will be tested at the AIDA cloud chamber of KIT. The AIDA chamber is capable of generating mixed-phase clouds under well-defined conditions.

Subsequently, a field campaign (CLACE 2013) will be conducted at the high alpine Jungfraujoch site (3580 m.a.s.l) in order to characterize IN in ambient mixed-phase clouds considered representative of the European background.

REFERENCES

Boulter, J. E. et al. (2006) Design and Performance of a Pumped Counterflow Virtual Impactor, *Aerosol Science and Technology*, 40(11), 969-976.

Kaye, P. et al. (2008) A light scattering instrument for investigating cloud ice microcrystal morphology, *Eleventh Conference on Electromagnetic & Light Scattering*, 235-238.

Lohmann, U. (2002) A glaciation indirect aerosol effect caused by soot aerosols, *Geophysical Research Letters*, Vol. 29, 1052, 4 pp.

Mertes, S. et al. (2007) Counterflow Virtual Impactor Based Collection of Small Ice Particles in Mixed-Phase Clouds for the Physico-Chemical Characterization of Tropospheric Ice Nuclei: Sampler Description and First Case Study, *Aerosol Science and Technology* 41(9), 848-864.

Spiegel, J.K et al. (2012) Evaluating the capabilities and uncertainties of droplet measurements for the fog droplet spectrometer (FM-100), *Atmos. Meas. Tech. Discuss*., 5, 3333–3393.

Sun, Z. and Shine, K. P. (1994) Studies of the radiative properties of ice and mixed-phase clouds, *Q. J. R. Mereorol. Soc*., 120, 111-137.

ACKNOWLEDGEMENTS

This work is funded by the Swiss National Science Foundation and the German Research Foundation.

SIMULATION OF CHEMICAL SPECIES IN CLOUDS

Dragana Vujović[1] and Vladan Vučković[2]

[1,2]*University of Belgrade, Faculty of Physics, Department of Meteorology, Dobračina 16, Belgrade, Serbia*

[1]dvujovic@ff.bg.ac.rs, [2]vvladan@ff.bg.ac.rs

1. ABSTRACT

To understand how clouds affect chemical constituents and their distributions, numerical modeling the chemistry in clouds is an active area of research. In recent years there is considerable interest in the roles that clouds and precipitation play in cycles of various troposphere chemical species, especially sulfur. Sulfur dioxide is the dominant anthropogenic pollutant in air that contains sulphur. Its presence in the troposphere is the result of direct anthropogenic emissions, i.e. combustion of fossil fuels.

In this paper, transport and redistribution of sulfur dioxide from thermal power plant is simulated. To do this, an aqueous chemistry module is created and included in nonhydrostatic 3D cloud-resolving ARPS model. The chemistry module comprises of five chemical species: sulfur dioxide, sulfate ion, ammonium ion, hydrogen peroxide and ozone. A real, complex orography is included in the model. Prognostic fields from nonhydrostatic regional prediction NMM model initialize the model. Chemical reactions of sulfur dioxide in cloud are researched. Wet deposition of sulfates, as an important way of cleaning of the atmosphere, is included in the paper. As a result, redistribution of sulfur dioxide and sulfate in troposphere and spatial and temporal distribution of acid precipitation on surface are given.

2. INTRODUCTION

Deep convective clouds play an important role in troposphere chemistry. First of all, clouds droplets and raindrops are a suitable liquid environment for chemical reactions of gases that exist in the atmosphere. Namely, although the liquid phase occupies only a very small fraction of the total volume of air, it is recognized that it is very important in atmospheric chemistry (Graedel and Weschler, 1981). Furthermore, microphysical processes into the clouds redistribute chemical species from one water category to other; strong convection can rapidly transports chemical species from the atmospheric boundary layer to the upper troposphere (Chatfield and Crutzen, 1984; Dickerson et al., 1987; Yin et al., 2005); wet deposition is efficient way to clean the atmosphere.

3. MODEL DESCRIPTION

Here we used a comprehensive 3D cloud-resolving mesoscale ARPS (Advanced Regional Prediction System) model developed in the Center for Analysis and Prediction of Storms (CAPS) at the University of Oklahoma (Xue at al., 2000, 2001) to simulate a Cumulonimbus (Cb) life cycle in conditions of a real orography. It was already shown the ARPS model with complex terrain of western Serbia was able to reproduce development and life cycle of a Cumulonimbus cloud (Ćurić et al., 2003a, b). The model numerically integrates time-dependent, nonhydrostatic and fully compressible equations. The model uses Lin's (Lin et al., 1983) bulk-water microphysical scheme and represents six water categories: water vapor, cloud water, cloud ice, rain, snow, hail. Rain, hail and snow are each represented by Marshall-Palmer distribution (Marshall and Palmer, 1948). Cloud droplets and nonprecipitating cloud ice are supposed to be monodispersing. Turbulence is treated by 1.5 order turbulent kinetic energy formulation. The advection of momentum and scalars is treated with 4th-order scheme in the horizontal direction and 2nd-order scheme in the vertical direction. Radiating (open) conditions are used for lateral boundaries. Rigid-wall boundary conditions were applied for the top and on the bottom of domain. The large time step was 6 s, and the small step (for acoustic waves) was 1 s.

The authors develop a chemistry module and coupled it with the ARPS model. A detailed description of the chemistry module is given in Vujović and Vučković (2011). The chemistry module contains five chemical species: SO_2, H_2O_2, O_3, SO_4^{2-} and NH_4^+. There are six prognostic continuity equations for mixing ratios of each chemical species for each of water categories. After dissolution, the chemical species were transferred from one water category to another by microphysical reactions. Oxidation of S(IV) by H_2O_2 and O_3 in cloud droplets and raindrops were included in the module due to their being very important sulfate production processes. pH values for cloud droplets and raindrops were calculated in every time step.

4. THE EXPERIMENT

We modeled a severe convective episode developed on 5th July 2010 in north part of Serbia (called Vojvodina). The clouds gave a large amount of precipitation in all area with significant hail damage. That day Novi Sad received 36 mm of rain, where the mean precipitation in July for the period 1961-1990 is 61.2 mm. The total damaged area in Novi Sad was 350 ha, with a 20-30% degree of damage. We initialize ARPS model with a 3D prognostic fields of WRF-NMM nonhydrostatic regional prediction model (Janjić et al., 2001), so we have nonuniform horizontal meteorological fields on the start of the integration. The centre of the domain is

45.5°N, 20°E; the domain size is 155 km×155 km×16 km. Space resolution in the model is 1000 m in the horizontal and 250 m in vertical direction. Two hours of integration is made. It is assumed that initial concentration of the chemical fields fall off exponentially from the given values of mixing ratios at the lowest model level. We have measurements of sulfur dioxide emission from thermal power plant and use that for simulation in the model.

5. RESULTS

Two experiments are conducted: with emission (WE) of sulfur dioxide and without it (NE). The observed radar reflexivity by Doppler radar at 13pm local time is given in Fig. 1. Also, the real 30'' topography of Serbia is given in Fig. 1. Radar is in the center of the Fig.1 with radius of 250 km. The drawn square denotes the domain of integration.

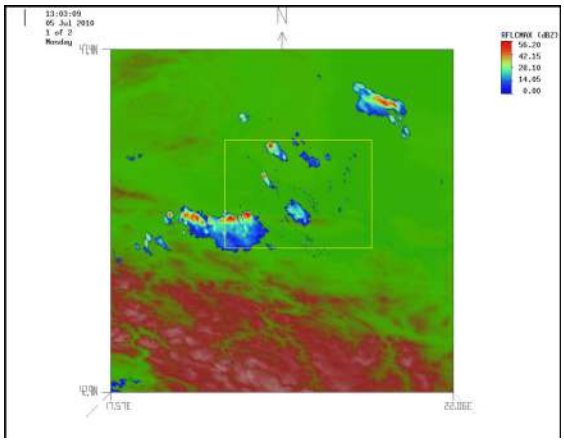

Fig. 1 Radar reflectivity on 5th July 2010. The drawn square denotes the domain of integration.

The modeled radar reflectivity isosurface of 50 dBz, also at 13 pm local time, and real topography are given in Fig. 2. There is a similar cell structure as in Fig. 1 and clouds move from northwest direction.

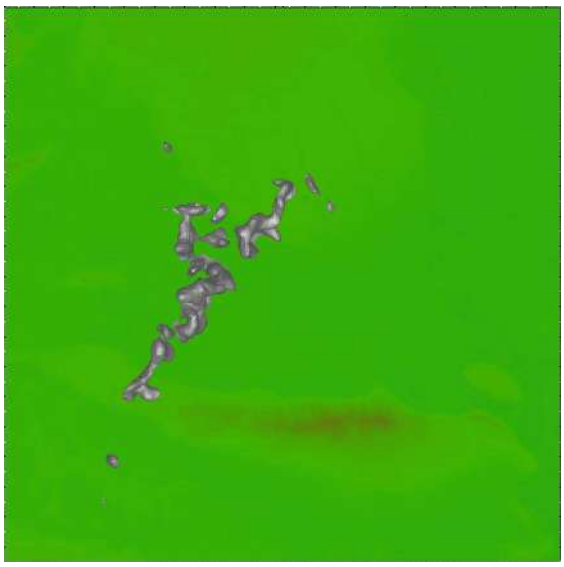

Fig. 2 The modeled radar reflectivity isosurface of 50 dBz.

Figure 3a, b gives cross section of SO_2 mixing ratio field into cloud water (q_{SO2_c}) in the experiment NE and the experiment WE, respectively. Isoline of cloud water mixing ratio (q_c=0.1 g kg^{-1}, white line) is also shown. The difference in q_{SO2_c} between these experiments is obvious and expected: q_{SO2_c} is larger in the WE experiment. Also, the place of q_{SO2_c} maximum values is different: in WE sulfur dioxide in cloud water is transported faster and reached greater heights, because of potential temperature perturbation on the top of the emission source. Also, convective current and microphysical processes into the cloud play significant role in redistribution of SO_2 from

atmospheric boundary layer to upper troposphere.

a)

b)

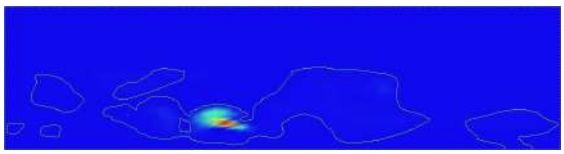

Fig. 3 Cross section of isoline of cloud water mixing ratio (q_c=0.1 g kg^{-1}, white line) and SO_2 mixing ratio field into cloud water in the experiment: a) without emission, b) with emission. q_{SO2_c} is given in μg kg^{-1}.

Wet deposition in a very effective way cleans the atmosphere from polluted species, in this case sulfur. Spatial distribution of accumulated precipitation of sulfate ion (SO_4^{2-}) in experiments NE and WE is shown in Fig. 4a, b, respectively. Looking at the area affected by the rain, there is a small difference between them. The amount of the precipitation is more significant. Namely, in NE experiment there is 298.76 kg of deposited sulfur in all domain of integration. In WE experiment mass of sulfur is greater: 315.49 kg. That means that the emission gives 5% more deposited sulfur on the surface and the model can capture it.

a)

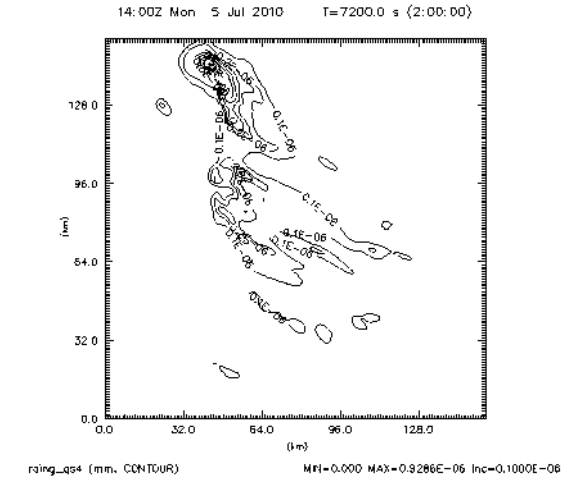

b)

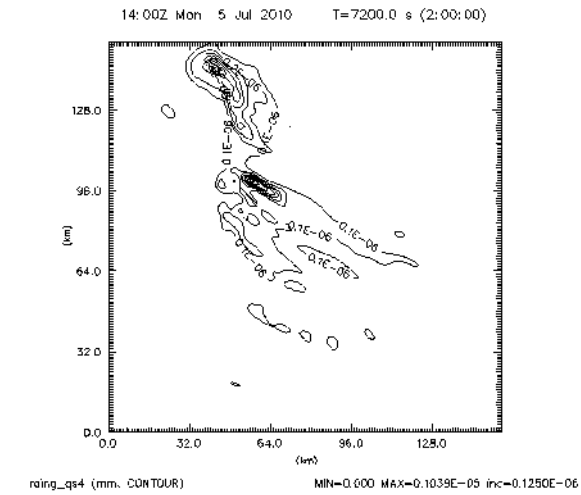

Fig. 4 Accumulated precipitation of SO_4^{2-} (mm) ion in: a) experiment NE and b) experiment WE.

6. CONCLUSION

We modeled a severe convective episode with the chemistry module coupled with 3D nonhydrostatic prognostic ARPS model. The model was initialized with 3D prognostic meteorological fields. In integration the source of emission of SO_2 was included. The model gave a good

direction of cloud movement and structure of clouds. In experiment with emission of SO_2 sulfur dioxide in cloud water is transported faster and reached greater heights, because of potential temperature perturbation on the top of the emission source. We had 5% more deposited sulfur on the surface in entire domain in the case when emission was included.

Our chemistry module coupled with comprehensive ARPS model is a powerful tool for foreseeing chemical species in the case when clouds were developed. Also, we can predict spatial and temporal distribution of chemical species from some particular emission source.

ACKNOWLEDGEMENT

The work was supported by Serbian Ministry of Education and Science under Grant 176013. We appreciate data from Hydrometeorological Service of Serbia, from radar center Fruska gora (courtesy of Ms Julijana Nadj).

BIBLIOGRAPHY

Chatfield RB and PJ Crutzen, 1984: Sulfur dioxide in remote oceanic air: Cloud transport of reactive precursors. *J. Geophys. Res.*, **89**, 7111-7132.

Ćurić M, D Janc, D Vujović and V Vučković, 2003a: The effects of a river valley on an isolated cumulonimbus cloud development. *Atmospheric Research*, **66**, 123-139.

Ćurić M, D Janc, D Vujović and V Vučković, 2003b: 3-D model characteristics of a Cb cloud which moves along a valley. *Meteorol. Atmos. Phys.*, **84**, No. 3-4, 171-184.

Dickerson RR, GJ Huffman, WT Luke, LJ Nunnermacker, KE Pickering, ACD Leslie, CG Lindsey, WGN Slinn, TJ Kelly, PH Daum, AC Delaney, JP Greenberg, PR Zimmerman, JF Boatman, JD Ray and DH Stedman, 1987: Thunderstorms: An important mechanism in the transport of air pollutants. *Science*, **235**, 460-465.

Graedel TE and CJ Weschler, 1981: Chemistry within aqueous atmospheric aerosols and raindrops. re. *Geophys. Space Phys.*, **19**, 505-539.

Janjić ZI, JP Jr Gerrity and S Ničković (2001) An alternative approach to nonhydrostatic modeling. Mon Wea Rev 129: 1164-1178

Lin L, RD Farley and HD Orville, 1983: Bulk parameterization of the snow field in a cloud model. *J. Appl. Meteor.*, **22**, 1065-1092.

Marshall JS and WM Palmer, 1948: The distribution of raindrops with size. *J. Meteor.*, **5**,165-166.

Vujović D and V Vučković, 2011: An aqueous chemistry module for a three-dimensional cloud resolving model: sulfate redistribution. J. Serb. Chem. Soc., doi: 10.2298/JSC111010218V.

Xue M, KK Droegemeier and V Wong, 2000: The Advanced Regional Prediction System (ARPS)-A multi-scale nonhydrostatic atmospheric simulation and prediction model. Part I: Model dynamics and verification. *Meteor. Atmos. Physics*, **75,** 161-193.

Xue M, KK Droegemeier, V Wong, A Shapiro, K Brewster, F Carr, D Weber, Y Liu, DH Wang, 2001: The Advanced Regional Prediction System (ARPS)-A multi-scale nonhydrostatic atmospheric simulation and prediction tool. Part II: Model physics and applications. *Meteor. Atmos. Physics*, **76**, 143-165.

Yin Y, KS Carslaw and G Feingold, 2005: Vertical transport and processing of aerosols in a mixed-phase convective cloud and feedback on cloud development. Q. J. R. Meteorol. Soc., 131, 221-245.

NUMERICAL SIMULATION OF HEAVY SNOWFALLS

G. Pirnach , T. Romash

Ukrainian Hydrometeorological Institute, Nauki 37, 03028 Kyiv, Ukraine

1. INTRODUCTION

Present work continues theoretical studies of heavy precipitation of cold season. Numerical simulation of heavy snowfalls connected with atmospheric fronts and their cloud systems that caused the damages in economy have been fulfilled for investigation of conditions of their formation on the territory of Ukraine caused by Mediterranean cyclones in December 2009. For comparison situation on January, 2004 was chosen.

Theoretical interpretation of atmospheric state by diagnostic numerical models and cloud evolution modeling by forecasting models were conducted and inner structure of modeled cloud at different stages of their development were investigated (more detailed in Palamarchuk and Pirnach, 1992; Pirnach and Krakovskaya, 1994; Pirnach, 1998).

2. SYNOPTIC SITUATION

During 15-21 December 2009 there were such dangerous events as heavy snowfalls, strong wind and snowstorms on the great part of Ukraine. According to weather stations data there was 20-36 mm per 10-12 h of snow, wind was near 25-28 m/s, durations of snowstorms were from 13 till 14 hours.

The reason of such dangerous events in Ukraine was moving of three active Mediterranean cyclones to the Black Sea and their blocking by powerful cold anticyclone with its centre in Moscow (Fig. 1).

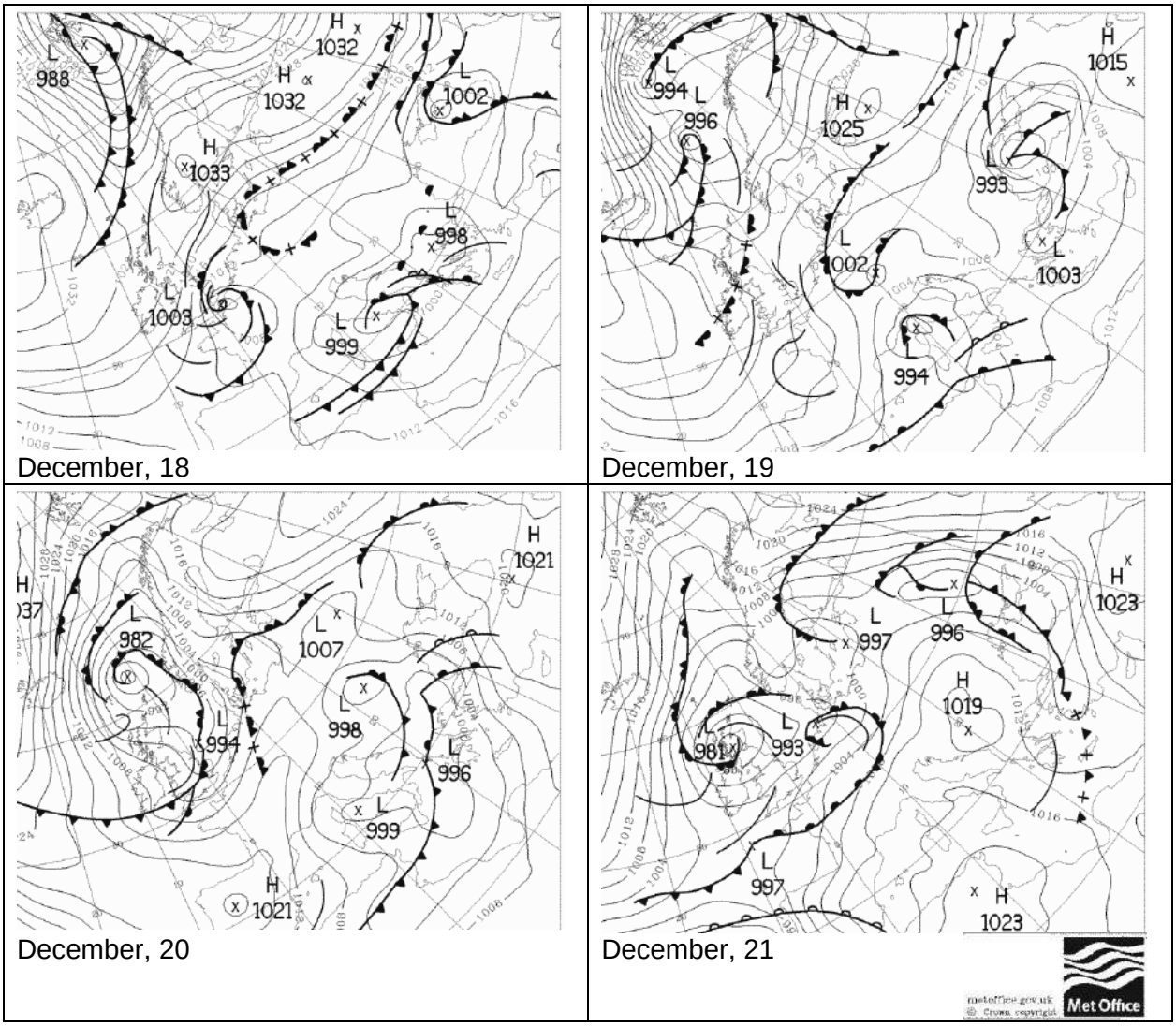

Fig 1. Synoptic situation during snowfall period on December 2009

More detail description of synoptic situation see in (Pirnach et al., 2011, Romash, 2011).
Snowfall in Odessa and Bilhorod-Dnistrovsky on December, 16 was analysed in detail. Near these cities zones with large amount of precipitation were observed.
For comparison situation on the 6-7th of January, 2004 was chosen. The reason of heavy snowfalls on the southern part of Ukraine were 2 active cyclones moving from Turkey to the Azov and the Black Sea and caused heavy snowfalls. 23-32 mm of snow per 10-12 h was fixed on the 6th of January in the Crimea and Kherson region (32 mm per 9.5 h in Feodosiya).

3. DIAGNOSTIC SIMULATION

Cases of these heavy snowfalls in different parts of Ukraine have been investigated by numerical simulation. Three-dimensional diagnostic models for complex and plain relief developed in UHMI have been used for investigation of inner state of cloud systems at the radiosounding time during heavy snowfall formation on the territory of Ukraine.
On Fig. 2 there are results of diagnostic simulation of horizontal characteristics of cloudiness for two different grids: 1) main grid with horizontal step 20 km; 2) nested grid with horizontal step 5 km on December, 16. Vertical step was equal to 200 m. Central point was Kyiv.
Using of nested grid gave the opportunity to analized in detail the distribution of main meteorological parameters during snowfall formation. Initial conditions on December 18-19 see in (Romash, 2011).
.

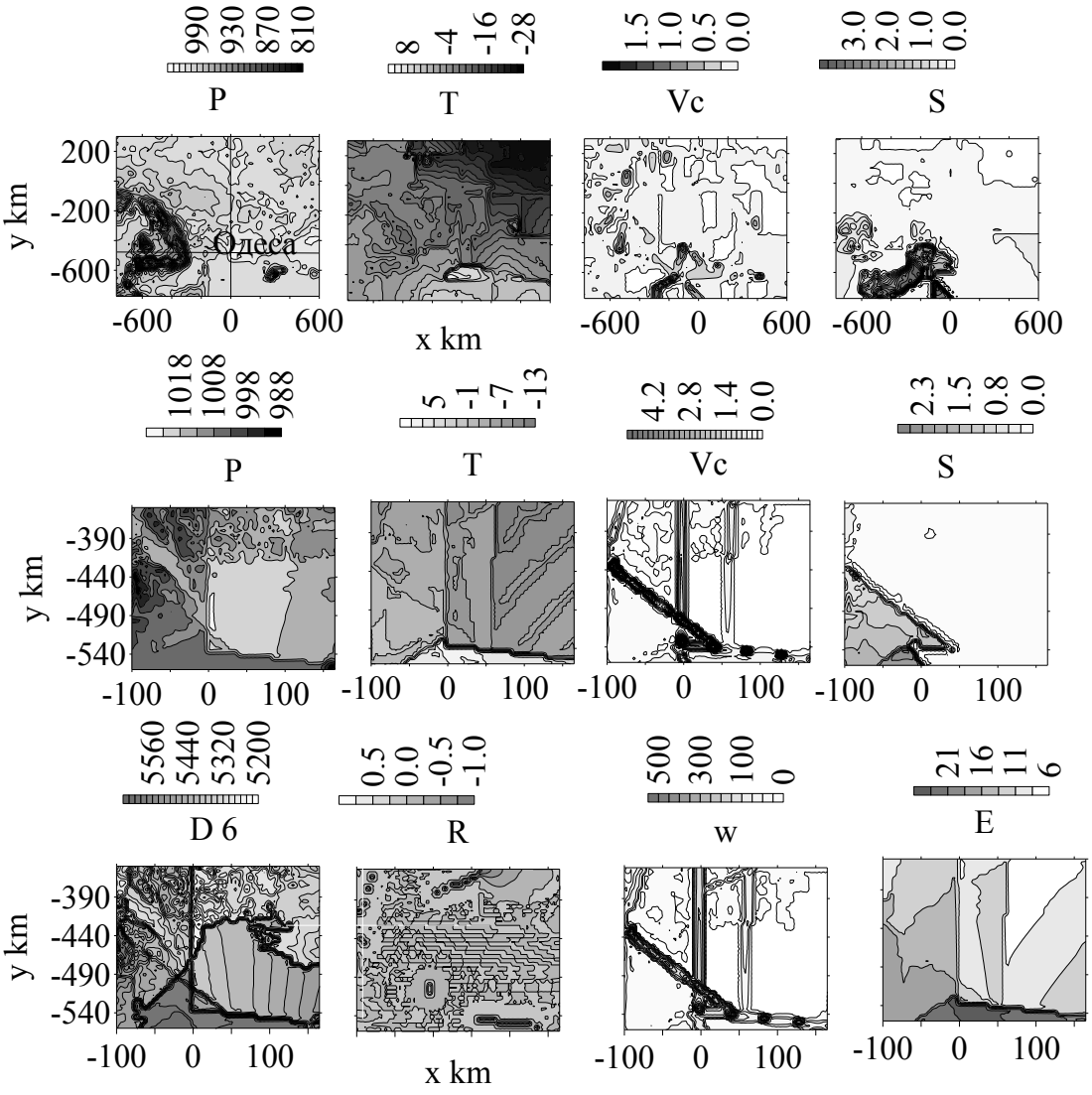

Fig. 2 Horizontal characteristics of cloudiness on December, 16
1st row – step is 20 km; 2nd row and 3rd – nested grid with step 5 km. P – pressure, hPa; T – temperature,°C; Vc – z-integral condensation rate, mm/h; S – z-integral ice supersaturation, mm. D6 – difference between isobaric surfaces 1000 and 500 hPa; R – whirlwind 1/s; w – maximum of f updrafts, cm/s; E – entropy

Region near to the south of Odessa was characterized by high values of z-integral ice supersaturation, condensation rate and upward movements. Areas of high gradients of temperature and pressure were prior to the accumulation of moisture here and rainfall. It also was shown by the low band entropy values, which emphasized the existence of organized structures in the area, including bands of clouds and precipitation.

For comparison initial conditions of snowfall on January 5-6, 2004 were simulated by diagnostic numerical models (Fig. 3-4). The central point for this simulation was Simferopol. Region with heavy snowfalls (east part of Crimea) was also characterized by high values of ice supersaturation and condensation rate in both cases of simulation (for complex and plain relief).

4. EVOLUTION OF HEAVY SNOWFALLS

The three-dimensional prognostic models have been used for numerical simulation of the evolution of the most interesting cases to find out key parameters caused heavy snowfall. Numerical experiments have been carried out with different relationships between ice particles and drops. Relationships varied by including or excluding from calculations of different mechanisms of cloud and precipitation formation.

The series of numerical experiments were carried out in *Z*-sigma coordinate system for different ice nuclei concentration (INC).

INC is defined by relationship:

$$N_s = A_s e^{0.56 T_S}, \quad (1)$$

$T_S = T_0 - T$, T_0=0°C, T is air temperature, °C; A_s is empirical parameter (Hobbs et al., 1975).

Series of numerical experiments were fulfilled by variation *a*-parameter (*a* = log A_s in (1)) that regulated INC distribution during cloud development.

Table 1 shows the calculated maximum three-hour amounts which were modeled in the investigated period for different variants of calculation, with varying intensity mechanisms of ice and precipitation formation. They are close in value to those observed at meteorological stations, with the possible exception of precipitation, which are calculated after 18 h of calculation time when weather conditions can change quickly. Lack of coagulation processes did not cause large differences with the measurements even in the long-term calculation. Including of coagulation rain drops with cloud drops approaches time of precipitation maximum, increased the size of precipitation core and oscillation intensity.

Table 1

Maximum amount of precipitation, mm / 3 hours, 16 December 2009

№	Time, h (GMT)							
	3	6	9	12	15	18	21	24
	Maximum amount of precipitation, mm / 3 hours							
1	2	9	12	16	16	22	94	180
2	2	11	18	15	31	58	24	29
3	3	12	21	19	18	29	126	183
4	3	27	14	17	19	35	45	59
5	4	16	20	18	24	28	30	46
6	4	7	9	18	22	28	39	33
7	1	1	4	5	7	7	8	11

1 – Maximum amount of precipitation with *a* = -5, including coagulation ice particles with drops(riming) ; 2 – riming and coagulation large and small drops; 3 – riming and *a* = -3; 4 – riming and coagulation large and small drops, *a* = -3; 5 – without coagulation, a = -3; 6 – precipitation near Bilhorod-Dnisrovsky; 7 – precipitation near Odessa

Fig. 5 shows that the usage of various combinations of precipitation and ice formation mechanisms does not lead to radical changes in the behavior of the precipitation band in the Odessa region, slightly changing the band configuration and intensity of precipitation. Precipitation is more expressive when both mechanisms of coagulation (case 2, 4, Table 1) are involved.

In the simulation of snowfall on December, 19 near Komsomolske (Kharkiv region) runs show that the largest intensity corresponds to mean INC values. If the INC number is small (*a* = -5) oscillation intensity is small and there are maximum at first and finish stage of snowfall. At first intensity of snowfall increase with the INC increasing. But if INC reached of too high values (*a* = -2) water vapour is absorbed very fast and values of precipitation intensity decreased. At *a* = -4 the maximum snowfall sums (1.9 mm) was found in period from 6 to 9 hour (Tab. 2) and they decreased to the 15 hour of simulation.

Combinations of physical processes and *a*-parameter correspond to such ones on Fig. 6. When *a* = -3 all values were higher

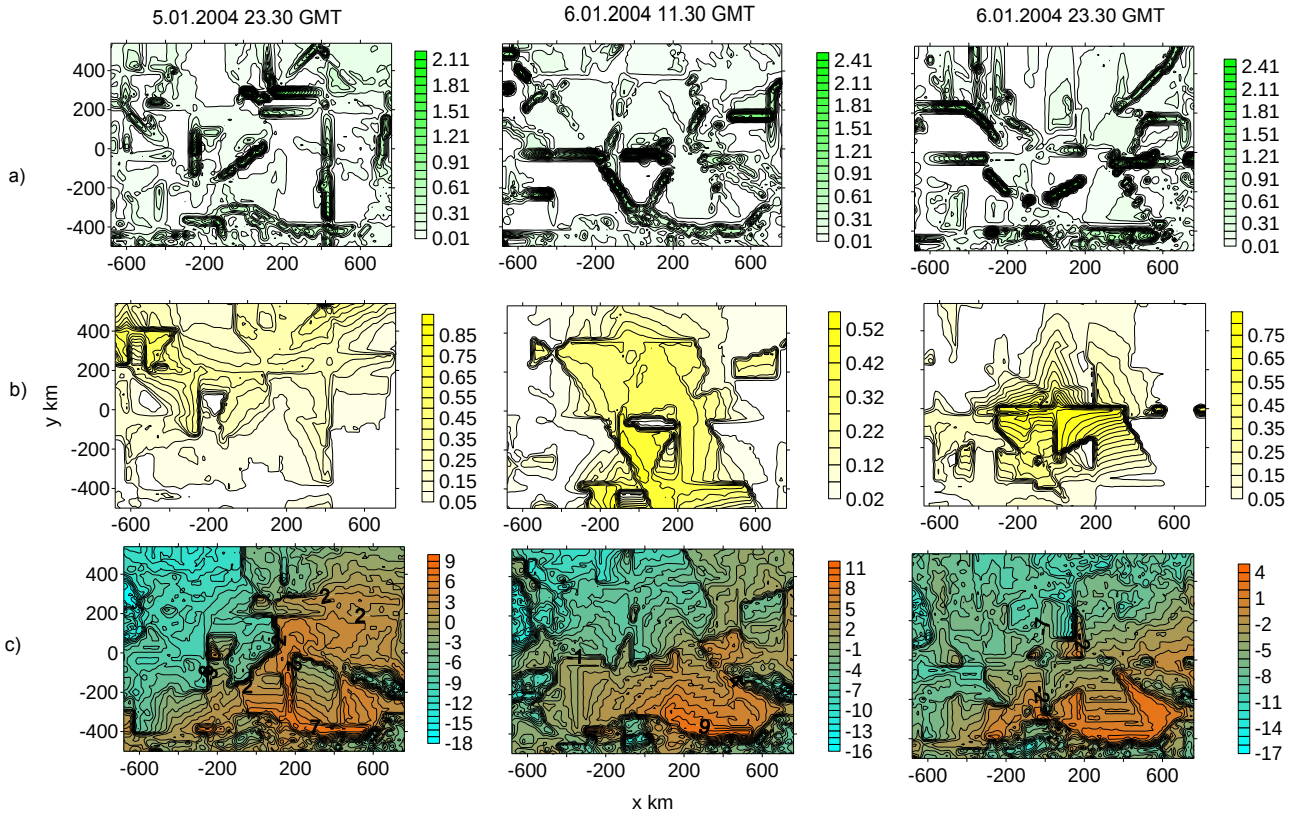

Fig. 3 Initial conditions on January 5-6, 2004; a)z-integral condensation rate, mm/h; b) z-integral ice supersaturation, mm; c)surface pressure, hPa; d)surface temperature, °C (Central point was Simferopol)

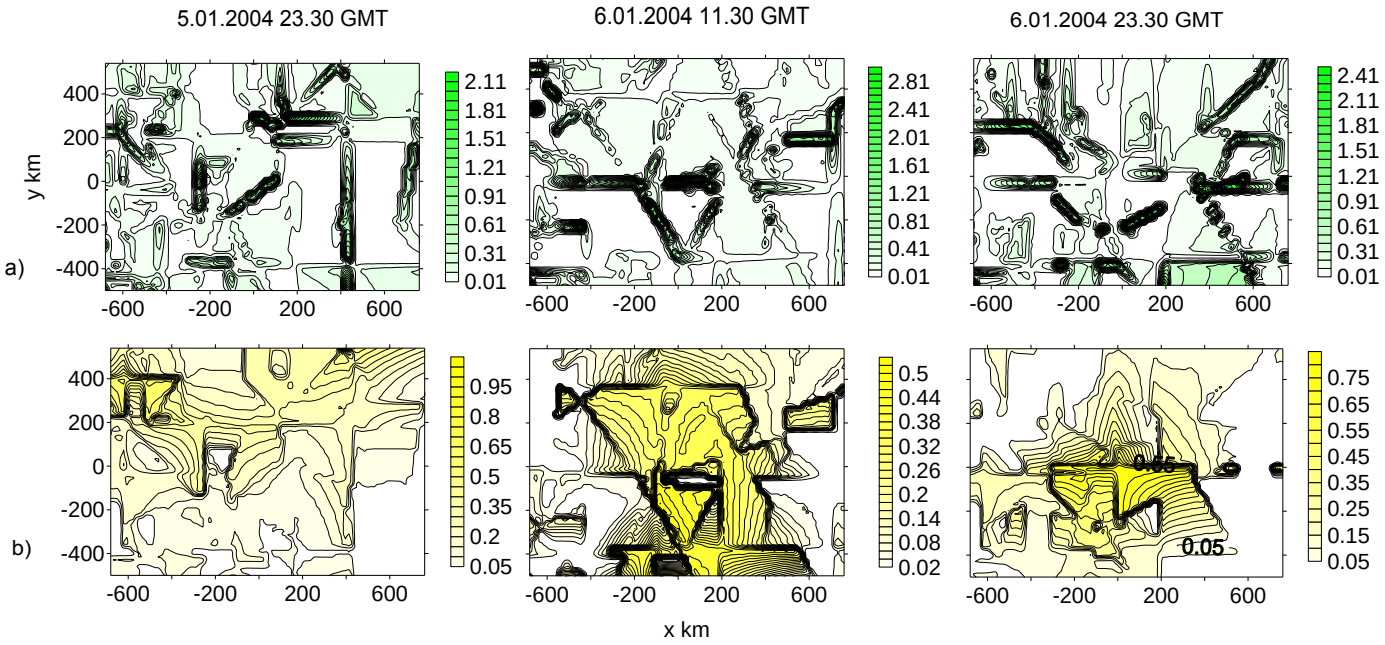

Fig. 4 Initial conditions on January 5-6, 2004 calculated without orography. a)z-integral condensation rate, mm/h; b) z-integral ice supersaturation, mm

and maximum precipitation amount was the largest. It was equal 8.8 mm from 9 to 12 h. Snowfall practically stopped till 15 h. In the last case (*a* = -2) total maxima amount was the largest. But the precipitation intensity wasn't so much as in Case 3 in certain time. High maximum values were observed from 3 to 12 h of simulation. More realistic results corresponded to observation data were obtained using *a* = -3.

Table 2

Maximum precipitation amount with different a in domain

Time,h *a*	3	6	9	12	15	Total, mm
-5	0.3	0.3	1.2	2.7	0.5	5.0
-4	0.6	0.7	1.9	0.5	0.3	4.0
-3	2.4	1.3	3.3	8.8	0.2	16.0
-2	1.8	4.3	4.4	5.6	0.4	16.5

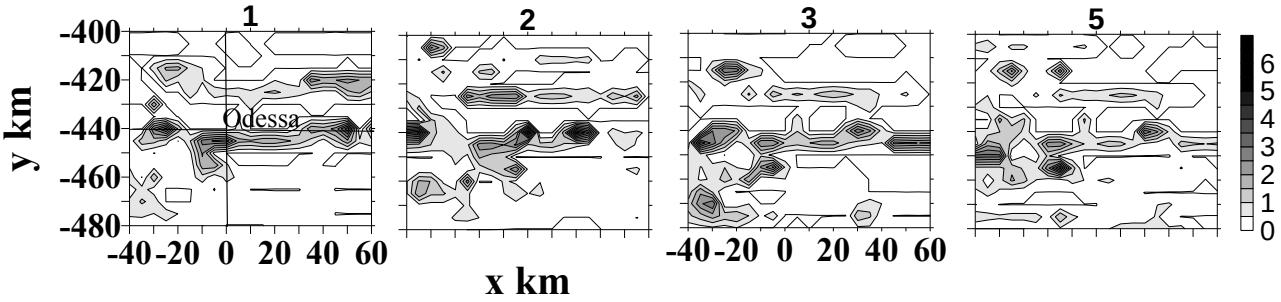

Fig. 5 Three-hour amount of precipitation for t = 9 hours in the region of Odessa. The numbers at the top pictures correspond to numbers in table 1.

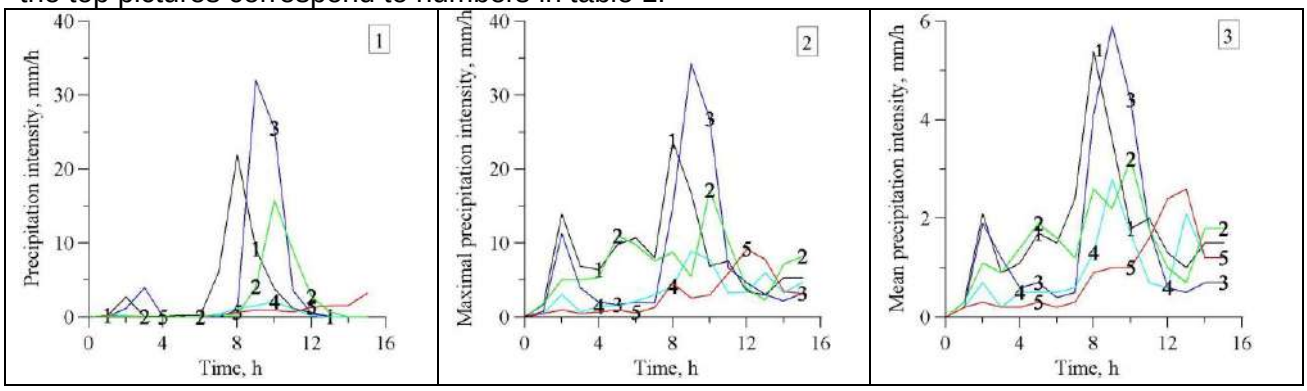

Fig. 6 – Evolution of precipitation intensity. Numbers in tops: 1) precipitation intensity in a target point (x; y) = (450; -50 km); 2) maximal precipitation intensity in precipitation core; 3) mean precipitation intensity. Numbers near lines: 1) case calculated with riming and coagulation of large and small drop and parameter a= -2; 2) riming and parameter a= -2, 3) a= -3, 4) a= -4, 5) a= -5

Evolution of precipitation intensity with different INC is shown on Fig. 6. Case 1 (line 1) was calculated with riming and coagulation of large and small drops. In this case precipitation intensity is high.

Oscillation of snowfall intensity was depicted for all *a*-parameter. The highest maxima of precipitation intensity, and its both the mean and maximal values were got up in different time for different *a*. At small *a*-parameter snowfall cores maintained longer time and its highest precipitation falling down later (excepting *a* = -3). Mean sums increased in finish time reason why the area of precipitation core decreasing. It is found that optimal *a* for maximum sum and intensity in precipitation core (*a* = -3 in this situation) existed.

5. CONCLUSIONS

Including of coagulation rain drops with cloud drops approaches time of precipitation maximum, increased the size of precipitation core and oscillation intensity.

It is found, the optimal ice nuclei concentrations that caused the highest snowfall intensity existed. Optimal $A_s \approx 10^{-3}$. At the end of cloud existence stage decreasing of total area of precipitation and increasing of their mean sums were obtained. Oscillation of snowfall intensity in precipitation cores occurred in all cases but if INC approached to optimal the amplitude was the highest.

6. BIBLIOGRAPHY

Hobbs P.V., Houze R.A., Mateika T.J., 1975. The dynamical and microphysical structure of the occluded front and its modification by orography. J. Atmos. Sci., 32(8) 1542-1562.

Palamarchuk L.V., Pirnach A.M., 1992. Study of an internal structure of frontal zone with the help of three-dimensional numerical models. Trudy UHRI, 243 107-125 (in Russian).

Pirnach A.M., 1998. The construction and application of numerical models to the study of cloud dynamics and the structure of winter frontal rainbands. Atmos. Res., 45-47 355-376.

Pirnach A.M., Balabukh V.O., Romash T.A., 2011. Numerical simulation of thermodynamic conditions of heavy snowfall formation. Nauk. pr. UHMI, 260 28-45 (in Ukrainian).

Pirnach A.M., Krakovskaya S.V., 1994. Numerical studies of dynamics and cloud microphysics of the frontal rainbands. Atmos. Res., 33 333-365.

Romash T.A., 2011. Synoptic analysis and numerical simulation of condition of heavy snowfall formation during Mediterranean cyclones moving. Nauk. chasopys Drahomanov NPU., 14 (26) 118-125 (in Ukrainian).

STUDYING THE AEROSOL-CLOUD-PRECIPITATION INTERACTION IN THE TRANSITION FROM CLOSED TO OPEN MESOSCALE CELLULAR CONVECTION USING AIRCRAFT OBSERVATIONS

Christopher R. Terai and Robert Wood
Department of Atmospheric Sciences, University of Washington,
Seattle, WA USA <terai@atmos.washington.edu>

1. BACKGROUND

The transition from closed-to-open mesoscale cellular convection in stratocumulus over the southeast Pacific can be typically found at the edges of pockets of open cells. Pockets of open cells, or POCs, are regions of open cellular convection embedded in a much larger region of closed cellular convection. Observed in past field campaigns (Stevens et al., 2005; vanZanten and Stevens, 2005; Sharon et al., 2006; Wood et al. 2008; Wood et al., 2011a) and modeled in high resolution large eddy simulations (Wang and Feingold, 2009; Berner et al., 2011; Kazil et al., 2011), POCs have been found to have some common features. As is evident from satellite images of POCs, cloud cover is lower inside POCs and the LWP is more variable, owing to a difference in the organization of cloud convection. In POCs, the concentrations of accumulation-mode aerosols and cloud drops are also very low, which is largely attributed to higher loss rates in the POCs from collision-coalescence processes associated with higher drizzle rates (Stevens et al., 2005; Petters et al., 2006; Kazil et al., 2011; Wood et al., 2011a). In this study we analyze five aircraft-observed case studies of POCs to closely examine this loss mechanism of cloud drops and see whether observations support the hypothesis that higher loss rates largely explain the differentials in aerosol concentration between POCs and surrounding regions.

In October and November of 2008, the VAMOS Ocean Cloud Atmosphere Land Study Regional Experiment (VOCALS REx) was conducted over the southeast Pacific Ocean (Wood et al., 2011b). During VOCALS REx, six research flights flown by the NSF/NCAR C-130 sampled the atmospheric conditions across transitions from closed-to-open cellular clouds. This study reports on the observed microphysical gradient across those transitions. In addition, we will examine aspects of the drop size distribution, with the aim to identify any consistent characteristics that are observed across different POC cases and to glean the relative importance, if any, of the microphysical processes (self-collection of cloud drops, autoconversion, and accretion) in maintaining the observed microphysical differences across the closed-to-open cell transition.

2. METHODS

Five of the six research flights flown by the C-130 with flight strategies to intercept POCs are used in this analysis, since the closed-to-open cell transition in one of the cases (RF14) was difficult to distinguish (see below for how we distinguish the different regions of the transition). Each research flight is considered a different POC case. The flight strategy consisted of profile legs through the depth of the atmospheric boundary layer and level flight legs below cloud (~150 m), incloud (~1000 m), and above cloud (~1500 m). This study uses data collected aboard the C-130 during the incloud flight legs to compare the conditions across the POC boundary. Note that for RF06 and RF13 a second incloud legs was flown.

Incloud measurements of the cloud and drizzle properties are obtained from a Cloud Droplet Probe (CDP), which measures drops with radius between 1 and 23.5 μm, and a 2DC optical array probe for drops with radius larger than 30 μm (Wood et al, 2011b). Unless otherwise stated, all measurements are analyzed at 1 Hz time resolution.

To calculate estimates of the mass conversion rates and cloud drop loss rates from autoconversion, accretion, and self-

collection, we calculate the stochastic collection equations using a solver based on Bott (1998) as described by Wood (2005). Unless otherwise noted, process rates are calculated on drop size distributions averaged over 1-km segments. In the calculations, cloud drops correspond to CDP-measured drops with radius < 20 μm, and drizzle drops correspond to 2DC-measured drops. No attempt was made to interpolate the gap between the CDP and 2DC measurements.

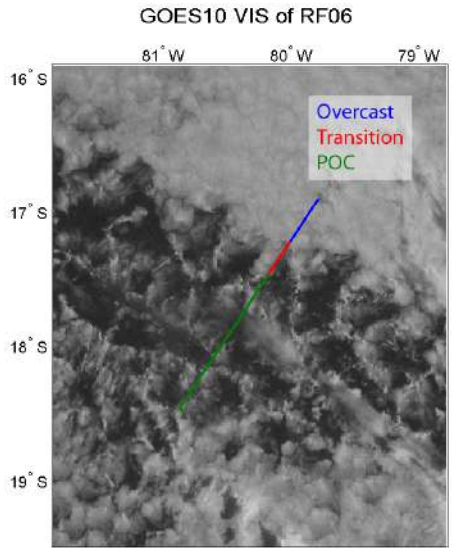

Figure 1: Incloud flight leg from RF06 and a coincident GOES 10 visible image at 12:28 (UTC) 28 Oct. 2008. The flight leg is divided into the overcast (blue), transition (red), and POC (region).

An incloud flight leg from Research Flight 06 (RF06) is overlaid on a GOES visible satellite image taken around the time of flight in Fig. 1. All flight legs are divided into segments corresponding to inside the POC (POC), outside of the POC (overcast), and the region between the POC and the overcast regions (transition), as in Fig. 1. We can then compare the microphysical characteristics in the POC and the overcast regions. The POC represents conditions in open cellular convection, and the overcast region, conditions in closed-cellular convection. Since we wish to apply the same method to flight legs flown at different levels and at different times of the day, GOES-10 infrared imagery is used to divide the flight segments into the different regions. Visual inspection was used to differentiate the different regions. Although in some cases measurements were also made in the overcast regions to the south of the POCs, for this study we only investigate the differences between the POC and the overcast regions to the north of the POC.

3. MACROPHYSICAL DIFFERENCES

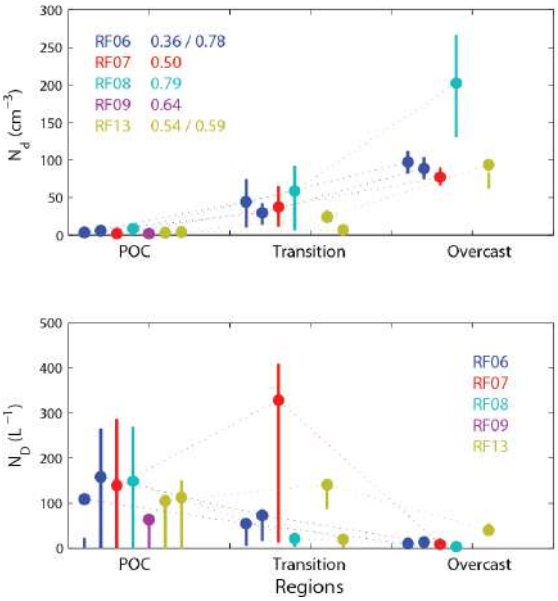

Figure 2: (top panel) Mean values (dots) and middle 50th percentile values (vertical bars) of cloud drop number concentration, N_d, as measured by the CDP in the POC, in the transition, and in the overcast region. Different colors represent different research flights. To disregard clear air when calculating the mean concentrations, the means are taken over portions where either condition $N_d > 0.1$ cm^{-3} or $N_D > 0.1$ L^{-1} is satisfied. The fraction of the POC segment that satisfied either condition is shown for each flight leg in the top left. (bottom panel) Same as above, but with drizzle drop number concentration, N_D, as measured by the 2DC.

The first noticeable difference across the POC boundary in Fig. 2 is the drastically lower cloud drop number concentration, N_d, inside the POC. Despite variability in the overcast region across the different cases, the segment mean N_d inside the POC is consistently below 10 cm^{-3}. On the other hand, the drizzle drop number concentration, N_D, increases more than an order of magnitude from the overcast region to the POC. Based on our

current understanding of aerosol-cloud-precipitation interaction, the low N_d and high N_D inside the POC are consistent, if we hypothesize that with decreased N_d, cloud drops tend to be larger, which speeds up collision-coalescence rates and increases drizzle drop production. In Fig. 2, we have calculated concentrations over portions where $N_d > 0.1$ cm^{-3} or $N_D > 0.1$L^{-1} to obtain concentrations only in cloudy or precipitating portions of the leg. The differences across the POC boundary nonetheless hold regardless of whether non-cloudy portions are included in calculating the mean N_d and N_D.

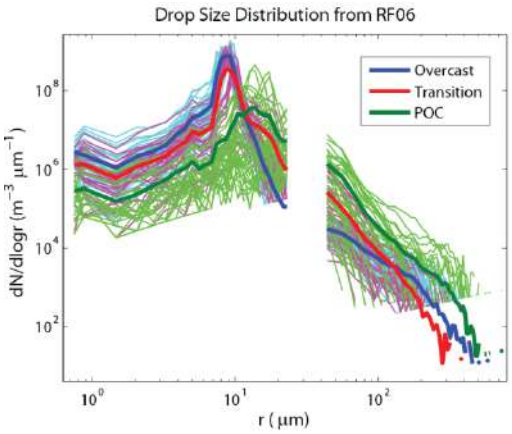

Figure 3: Drop size distribution of cloud and drizzle drops from a cloud-level flight leg during RF06, as measured by CDP and 2DC. Thinner lines represent distributions averaged over 1 km, while thicker lines represent distributions averaged over the POC (green), transition (red), or overcast (blue) segment. The gap represents drop sizes for which neither the CDP nor 2DC measured concentrations.

A more detailed picture of the differences in cloud and drizzle number concentrations can be obtained from the drop size distributions of cloud and drizzle drops across the three regions (Fig. 3). Note the log-scale along the y-axis. We can see that the concentrations of cloud drops are significantly higher in the overcast region across all sizes, except for the largest of cloud drops. The cloud drop distribution in the overcast region is also narrower and the concentrations peak around 8 μm, with a sharp drop off around 10 μm. Compare this to the wider distribution of cloud drops inside the POC, which has a peak around 14 μm. We also note that concentrations of drizzle drops are higher in the POC across all drizzle drop sizes, with the largest relative differences found for small drizzle drops with radii < 100 μm.

5. SELF COLLECTION, AUTOCONVERSION, AND ACCRETION

From Fig. 2 and 3, it is evident that N_d is lower and N_D is higher inside the POCs compared to the overcast region. We now examine the differences in microphysical process rates that exist due to the differences in drizzle and cloud drop distribution inside and outside of the POCs. By examining the process rates, we hope to verify whether cloud drop loss rates and drizzle drop production rates are consistent with the low N_d and high N_D that are observed inside the POC.

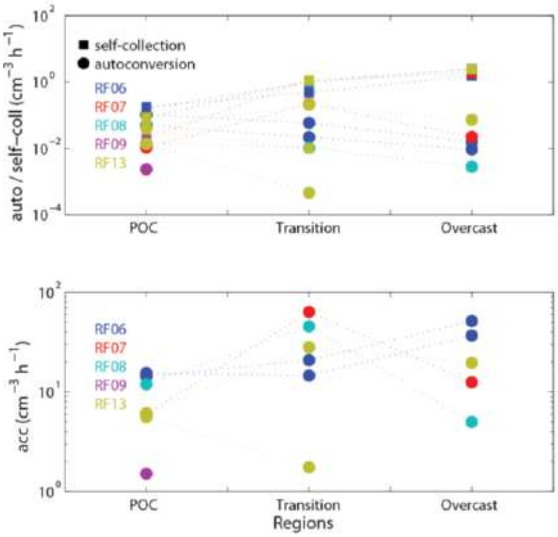

Figure 4: Loss rates of cloud drops from autoconversion (circle) and self-collection (square) in the top panel, and from accretion in the bottom panel across the overcast-to-POC transition. Autoconversion, self-collection, and accretion rates are calculated based on applying the stochastic collection equation solver (as described in the text) to the 1-km averaged drop size distributions, as measured by the CDP and 2DC. Different colors represent different research flights.

Typically, the mass conversion of cloud water into drizzle water is

distinguished between the process by which two cloud drops coalesce (autoconversion) and the process by which existing drizzle drops collect cloud drops (accretion). If we assume that each flight leg is representative of POC-wide behavior, a natural question would be whether the production rate of drizzle drops through autoconversion is substantially larger inside the POC, which would explain the high N_D values inside POCs. In Fig. 4, the cloud drop loss rates (in cm^{-3} h^{-1}) are plotted for self-collection, autoconversion, and accretion. The production of drizzle drops can be obtained from the cloud drop loss rate due to autoconversion by dividing the value by two, since two cloud drops coalesce to form a drizzle drop. For the RF06 and RF08 case, the production of drizzle drops from autoconversion increases inside the POC by roughly a factor of five, while for RF07 and RF13, the production decreases inside the POC. The autoconversion rates do not appear from this analysis to explain the large changes in N_D concentrations across the POC boundary. Perhaps condensation plays a role at creating the small drizzle drops. It must be noted that these process rate estimates are based on one or two flight legs for each case. In assessing differences between POC and overcast conditions, we assume that they are representative of the average conditions inside the POC and overcast region in each case, which may not necessarily be the case. In Fig. 4, we can also see the importance of self-collection as a sink of N_d in the overcast region. It appears that even in the absence of drizzle, self-collection of cloud drops can represent a substantial sink of N_d.

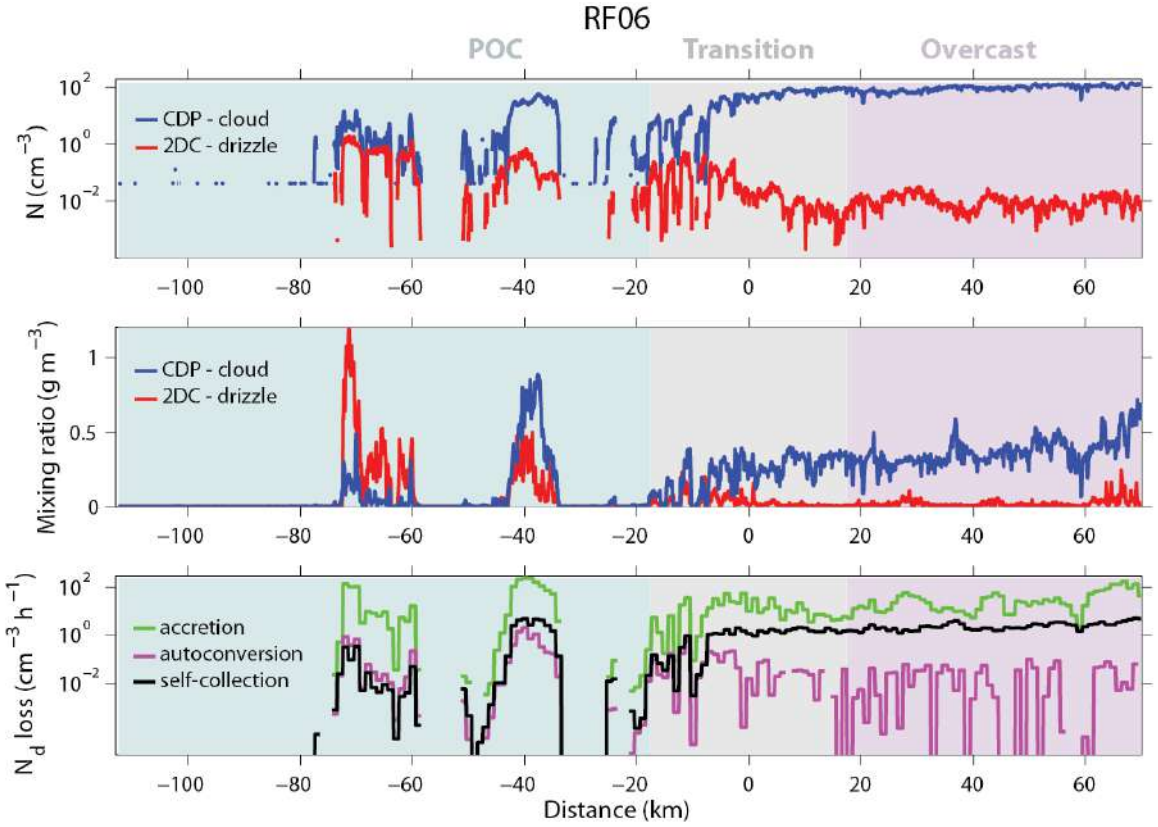

Figure 5: Cloud leg flight leg across the overcast-to-POC transition from RF06. The flight leg is divided up into POC, transition, and overcast regions based on looking at flight leg overlaid onto coincident GOES IR images. The top panel shows the number concentration of cloud drops (blue) and drizzle drops (red) as measured by the CDP and 2DC. The middle panel shows the liquid water liquid water content as measured by the CDP (blue) and the 2DC (red). The third panel shows the N_d loss rates calculated using the stochastic collection equations, based on 1km averaged cloud and drizzle drop spectra.

We take a more detailed look at how the process rates vary across a flight leg that traverses the three regions in Fig. 5. The top panel shows N_d and N_D along the flight leg. In the overcast region N_d is four orders of magnitude larger than N_D. In certain portions of the POC, N_D is within an order of magnitude of N_d, which can be inferred from Fig. 2, but is more clearly seen in Fig. 5. The second panel of Fig. 5 shows how cloud and drizzle water content varies across the three regions. In the overcast region, cloud water dominates the total liquid water content, while in the POC, drizzle water dominates the total liquid water content. The drastic change appears to mark a distinct difference in microphysics between the POC and the overcast region. Yet despite these differences, accretion remains the dominant sink of cloud drop number in both regions, as can be seen in the third panel. The third panel also shows the importance of self-collection in reducing cloud drop number across the overcast region and in one of the cells inside the POC. Autoconversion, on the other hand, acts as a smaller and more variable sink of cloud drops. Self-collection and autoconversion are expected to be higher towards cloud top, since it is largely controlled by the liquid water content, whereas accretion will be at a maximum in the cloud center where the aircraft mainly sampled the clouds.

6. DISCUSSION AND CONCLUSIONS

From analyzing the cloud level legs flown through the overcast-to-POC transition in multiple cases, we see consistent differences and similarities in the overcast and POC regions. Beginning with the differences, we confirm results from previous studies (Wood et al., 2011a) that N_d and N_D are vastly different in the two regions, such that the N_d:N_D ratio decreases three orders of magnitude when going from the overcast to POC region. A closer look at the drop size distribution shows that in the POC, the concentration of large cloud drops and small drizzle drops is largely increased. We expect that the differences in the size distribution to substantially influence different cloud microphysical processes inside and outside of the POCs. We, however, find that in both POC and overcast regions accretion is the dominant process by which cloud water is converted into drizzle water, as well as the major sink of N_d. Production of rates drizzle drops due to autoconversion also do not appear to be substantially higher inside the POC, which is intriguing in light of the high concentration of drizzle drops inside the POC.

Future work will further investigate the interaction of the processes between self-collection, autoconversion, and accretion to look at what characteristics inside the POC help to create and maintain the high values of N_D. We will also look at the variations in N_d, N_D, and cloud dynamics in both observations and large eddy simulations of POCs to determine the important processes that help to keep the accumulation-mode aerosol concentrations so low inside the POCs.

7. REFERENCES

Berner, A. H., Bretherton, C. S., & Wood, R. (2011). Large-eddy simulation of mesoscale dynamics and entrainment around a pocket of open cells observed in VOCALS-REx RF06. Atmospheric Chemistry and Physics, 11(20), 10525-10540. doi:10.5194/acp-11-10525-2011

Bott, A. (1998). A Flux Method for the Numerical Solution of the Stochastic Collection Equation. Journal of the Atmospheric Sciences, 55(13), 2284-2293. doi:10.1175/1520-0469(1998)055<2284:AFMFTN>2.0.CO;2

Kazil, J., Wang, H., Feingold, G., Clarke, a. D., Snider, J. R., & Bandy, a. R. (2011). Modeling chemical and aerosol processes in the transition from closed to open cells during VOCALS-REx. Atmospheric Chemistry and Physics, 11(15), 7491-7514. doi:10.5194/acp-11-7491-2011

Petters, M. D., Snider, J. R., Stevens, B., Vali, G., Faloona, I., & Russell, L. M. (2006). Accumulation mode aerosol, pockets of open cells, and particle

nucleation in the remote subtropical Pacific marine boundary layer. Journal of Geophysical Research, 111(D2), 1-15. doi:10.1029/2004JD005694

Sharon, T. M., Albrecht, B. A., Jonsson, H. H., Minnis, P., Khaiyer, M. M., van Reken, T. M., Seinfeld, J., et al. (2006). Aerosol and Cloud Microphysical Characteristics of Rifts and Gradients in Maritime Strato-cumulus Clouds. Journal of the Atmospheric Sciences, 63(3), 983-997. doi:10.1175/JAS3667.1

Stevens, B., Vali, G., Comstock, K., Wood, R., Van Zanten, M. C., Austin, P. H., Bretherton, C. S., et al. (2005). Pockets of Open Cells and Drizzle in Marine Stratocumulus. Bulletin of the American Meteorologi-cal Society, 86(1), 51-57. doi:10.1175/BAMS-86-1-51

VanZanten, M. C., & Stevens, B. (2005). Observations of the Structure of Heavily Precipitating Marine Stratocumulus. Journal of the Atmospheric Sciences, 62(12), 4327-4342. doi:10.1175/JAS3611.1

Wang, H., & Feingold, G. (2009). Modeling Mesoscale Cellular Structures and Drizzle in Marine Stratocu-mulus. Part II: The Microphysics and Dynamics of the Boundary Region between Open and Closed Cells. Journal of the Atmospheric Sciences, 66(11), 3257-3275. doi:10.1175/2009JAS3120.1

Wood, R. (2005). Drizzle in Stratiform Boundary Layer Clouds. Part II: Microphysical Aspects. Journal of the Atmospheric Sciences, 62(9), 3034-3050. doi:10.1175/JAS3530.1

Wood, R., Comstock, K. K., Bretherton, C. S., Cornish, C., Tomlinson, J., Collins, D. R., & Fairall, C. (2008). Open cellular structure in marine stratocumulus sheets. Journal of Geophysical Research, 113(D12), 1-16. doi:10.1029/2007JD009371

Wood, R., Bretherton, C. S., Leon, D., Clarke, a. D., Zuidema, P., Allen, G., & Coe, H. (2011a). An aircraft case study of the spatial transition from closed to open mesoscale cellular convection over the Southeast Pacific. Atmospheric Chemistry and Physics, 11(5), 2341-2370. doi:10.5194/acp-11-2341-2011.

Wood, R., Mechoso, C. R., Bretherton, C. S., Weller, R. A., Huebert, B., Straneo, F., Albrecht, B. A., et al. (2011b). The VAMOS Ocean-Cloud-Atmosphere-Land Study Regional Experiment (VOCALS-REx): goals, platforms, and field operations. Atmospheric Chemistry and Physics, 11(2), 627-654. doi:10.5194/acp-11-627-2011

EVALUATION OF INSTABILITY INDICES COMPUTED USING ALADIN-BG OUTPUT AND THEIR RELATIONSHIP WITH THE THUNDERSTORM ACTIVITY OVER BULGARIA

B. Tsenova and A. Bogatchev
National Institute of Meteorology and Hydrology, Bulgaria

1. INTRODUCTION

The precise prediction of thunderstorms, is still a demanding activity for the operational weather forecasting. The atmospheric instability is the major determinant in order to estimate the possibility of thunderstorm development. Even if the advances of regional scale numerical models enables thunderstorm forecasting, it is still worth to estimate the atmospheric instability with some known instability indices additionally. The determination of atmospheric instability with the use of instability indices generally requires computation based on several thermodynamic parameters (Showalter, 1953; George, 1960; Boyden, 1963; Jefferson, 1963a, b; Miller, 1967; Litynska et al., 1976; Peppler, 1988; Peppler and Lamb, 1989). All instability indices describe the potential of convection development, but the referred threshold values are not definite, and vary with geographical location, season and synoptic situation. Markova et al., 2010 tested the ability of some instability indices to be used as an indicator of lightning from convective clouds over the Eastern Bulgaria. Their study showed that thunderstorms in Bulgaria are developing at lower values of the indices selected, than in other regions (i.e. the USA). Similar conclusions for the lower threshold values of the instability indices were obtained in Tsenova and Kolev, 2008, where preconditions of thunderstorm initiation over Bulgaria were studied based on vertical sounding data.

In the present study several instability indices: (K index, Lifted Index, Sweat index, Cross Totals index, Vertical Totals index, Total Totals index) over Bulgaria were computed from ALADIN forecast production (obtained twice daily - at 06:00 and 18:00 UTC, with a forecast range of 72 h), for the warm half of the last two years, 2010 and 2011. Their relationship with the observed data for thunderstorms, obtained from the 46 synoptic stations in Bulgaria was evaluated.

The aim of the study is the improvement of severe weather forecast, determining the threshold values of predicted by the operational model instability indices at thunderstorm development over Bulgaria.

2. AVAILABLE DATA AND RESULTS

The considered K index (KINX), Lifted Index (LIFT), Sweat index, Cross

Totals index (CTOT), Vertical Totals index (VTOT), Total Totals (TTOT) index are calculated as:

KINX = (T850 – T500) + TD850 – (T700 – TD700)

LIFT = T500 – Tparcel

CTOT = TD850 – T500

VTOT = T850 – T500

TTOT = CTOT + VTOT

SWEAT = 12TD850 + 20max(TTOT – 49) + 2SKT850 + SKT500 + 125[sin(DIR500 – DIR850) + 2]

where T850, T700 and T500 are the environment temperature in ^{o}C at 850, 700 and 500 hPa; TD850 and TD700 are environment dew point temperature in ^{o}C at 850 and 700 hPa; Tparcel is the temperature in ^{o}C at 500 hPa of a lifted parcel with the average pressure, temperature and dew point of the layer 500 m above the surface; SKT850 and SKT500 are wind speed in knots at 850 and 500 hPa; DIR500 and DIR850 are wind direction at 500 and 850 hPa.

The parameters needed for the calculation of the instability indices are taken from ALADIN forecast production for the territory of Bulgaria (longitude from 21.6 E to 29.2 E and latitude from 40.7N to 44.6N) at a 0.1x 0.1 deg LALON grid. The forecast is produced twice daily, at 06:00 and 18:00 UTC and the forecast range is 72 hours at 3 hours post processing frequency. For the purpose of the study only the first 12 hours of the forecast were considered. The observed data for thunderstorm (lightning) were taken from the 46 synoptic stations (see Fig.1) where in-situ observations are also with 3 hours frequency.

Fig.1. Synoptic stations (red points) in Bulgaria

In Table 1 are shown number of cases without (second column) and with (third column) observed lightning over the stations during the last 2 years for the different months.

Table 1. Number of observations at synoptic stations during 2010 and 2011.

Month	Cases without Lightning	Cases with Lightning
April *	13143	62
May	25842	1262
June	24727	1497
July	25423	1681
August	26528	576
September	26603	325

(*only data from 2011 are considered).

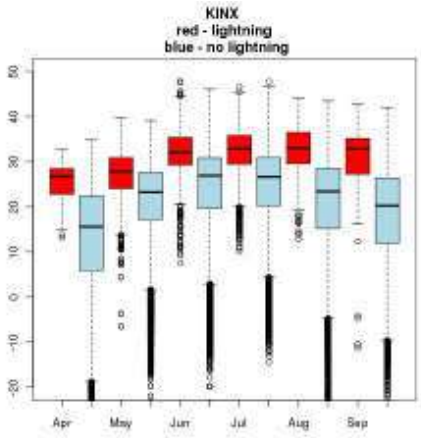

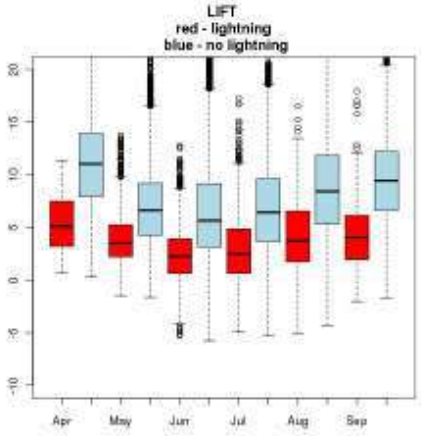

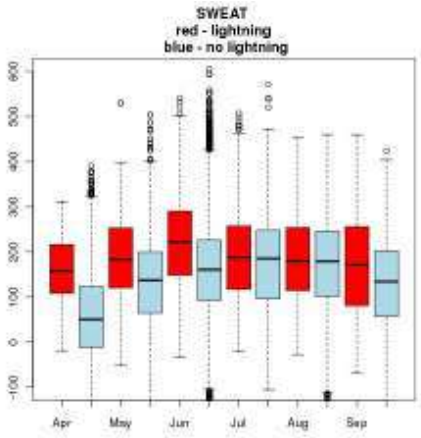

Fig.2a. Box and whisker plots of the computed KINX, LIFT and SWEAT indices for the observed cases with (in red) and without (in blue) lightning.

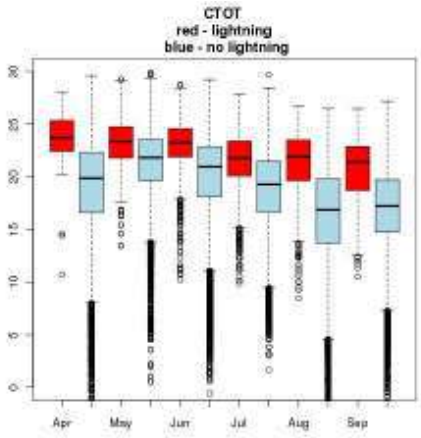

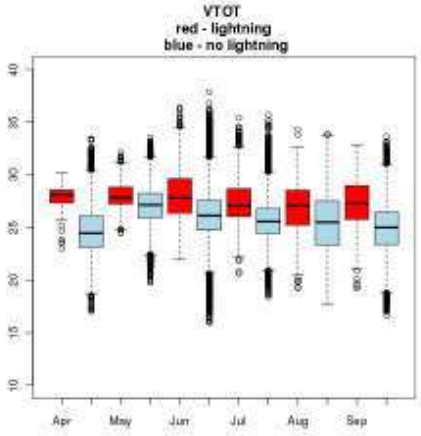

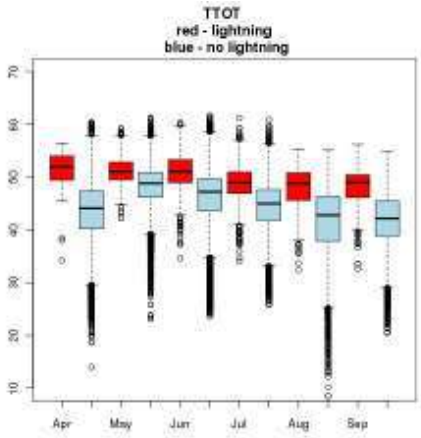

Fig.2b. Box and whisker plots of the computed CTOT, VTOT and TTOT indices for the observed cases with (in red) and without (in blue) lightning.

In Fig.2 box and whisker plots of the computed indices for the cases with and without lightning observed at the synoptic stations are shown. From the figure it is visible that there is a relatively good separation of KINX and LIFT indices at cases with lightning from those without. The mean values of computed from ALADIN forecast data KINX are higher and dispersions - smaller for cases with lightning in comparison to cases without lightning. On the analogy, mean values of LIFT are lower for cases with lightning comparing to cases without lightning. CTOT, VTOT, and TTOT are also relatively well separated for the cases with and without lightning. However, there is no visible tendency for SWEAT index at case with and without thunderstorm, especially for the months of July, August and September.

K-means clustering of all computed indices is performed for 2, 3 and 4 number of clusters. Here are presented the results from the statistical partitioning of data for two of the considered instability indices (KINX and LIFT) for the different months in 4 clusters and their comparison with the observed cases with and without thunderstorm.

From Table 2 one can see that for all months almost all observed cases with lightning are within the first two clusters (groups 1 and 2), especially for April and August, where 0% for the cases with observed lightning the calculated KINX are in ranges of the groups with low values (groups 3 and 4). Also, it is visible that the highest value of KINX (47.88) was obtained during June, while the lowest monthly maximum of K index was during April (34.85).

Table2. Results from cluster analysis of computed KINX and comparison with observations

Month	gr	Min	Max	% case with lightning	% case without lightning
April	1	19.84	34.85	84.2	34.4
	2	9.60	19.83	15.8	32.4
	3	-2.8	9.61	0	22.6
	4	-31.8	-2.8	0	10.5
May	1	25.45	39.71	67	37.5
	2	16.76	25.45	28.1	38.8
	3	4.46	16.76	4.4	16.4
	4	-25.8	4.44	0.5	7.3
June	1	28.9	47.88	77.2	37.8
	2	20.4	28.9	20.1	35.4
	3	8.55	20.4	2.7	18.9
	4	-23.5	8.53	0.1	7.9
July	1	29.78	47.75	73.1	31.8
	2	21.89	29.78	21.7	38.2
	3	11.59	21.89	5	23
	4	-14.4	11.58	0.2	7
August	1	24.48	44.06	93.6	45.4
	2	11.49	24.47	6.4	35.9
	3	-8.1	11.48	0	15.1
	4	-51.7	-8.1	0	3.7
September	1	25.73	42.71	78.7	27.7
	2	16.42	25.72	19.1	35.8
	3	5.0	16.42	0.6	23.4
	4	-35.9	4.9	1.5	13.2

Table3. Results from cluster analysis of computed LIFT and comparison with observations

Month	gr	max	min	% cases with lightning	% cases without lightning
April	1	7.36	0.27	73.7	21
	2	11.05	7.36	22.8	29.1
	3	14.7	11.05	3.5	31.2
	4	25.19	14.7	0	18.7
May	1	4.33	-1.65	64.5	25.4
	2	7.5	4.33	23.3	33.4
	3	11.39	7.5	9.22	29.2
	4	23.52	11.4	3	12
June	1	3.34	-5.75	66.9	27.1
	2	7.22	3.35	26.6	35.5
	3	11.87	7.22	6.4	25.7
	4	30.38	11.87	0.2	11.8
July	1	3.5	-5.25	61.1	23.5
	2	7.3	3.5	29.3	34.0
	3	11.62	7.3	8.3	29.3
	4	22.666	11.63	1.4	13.2
August	1	4.78	-5.07	59	20.4
	2	8.88	4.71	30.9	33.3
	3	13.29	8.88	9.2	29.4
	4	24.82	13.29	0.9	16.9
September	1	5.94	-2.04	72.9	20.4
	2	9.62	5.94	20.6	31.5
	3	13.36	9.62	4.9	30.5
	4	24.28	13.36	1.5	17.6

Table 3, shows the results from cluster analysis of computed LIFT and comparison with observations. It is visible, that although Lifted index would predict thunderstorms slightly worse than K index (the total percent of cases with lightning in the groups 1 and 2 are lower for LIFT in comparison to KINX in Table 2), the % of “false alarm” cases is slightly lower with lifted index, i.e. total percent of cases without lightning fallen in groups 1 and 2 is lower with LIFT in comparison to KINX.

To generalise, all statistical analyses show that the considered instability indices are able to predict thunderstorm correctly. However, the high percent of “false alarms” with the different indices indicates that their use for the correct thunderstorm forecast should be considered in a non-trivial way.

3. CONCLUSION

In the present study some instability indices over Bulgaria were computed from ALADIN forecast production for the warm half of the last two years - 2010 and 2011. Their relationship with the observed data for thunderstorms, taken from the 46 synoptic stations in Bulgaria is evaluated, with the aim to determine threshold values of the predicted by the operational model instability indices at thunderstorm development. Results show that all considered instability indices predict thunderstorm formation correctly. However, the percent of “false alarms” with the different indices is also relatively high. Therefore a “non-trivial” procedure of using the instability indices for thunderstorm forecast is in a test operational mode.

4. REFERENCES

Boyden, C. J., 1963. A simple instability index for use as a synoptic parameter, Meteorological Magazine, 92, 198–210

George, J. J., 1960. Weather forecasting for Aeronautics, Academic Press, New York, 409–415

Jefferson, G. J., 1963. A modified instability index, Meteorological Magazine, 92, 92–96

Jefferson, G. J. 1963. A further development of the instability index, Meteorological Magazine, 92, 313–316

Litynska, Z., Parfiniewicz, J., and Pinkowski, H. 1976. The prediction of air mass thunderstorms and hails, W.M.O., No. 450, 128–130

Markova, B., R. Mitzeva, A. Todorova, 2010. Instability indices as an indicator of thunderstorms in East Bulgaria - preliminary results based on discriminant analyses, Geophysical Research Abstracts, Vol. 12, EGU2010-6883

Peppler, R. A., A review of static stability indices and related thermodynamic parameters, Illinois State Water Survey Misc. Publ. 104, (Illinois State Water Survey, 2204 Griffith Drive, Champaign, IL 61820), 87 pp.,1988.

Peppler, R. A. and Lamb, P. J. 1989. Tropospheric static stability and central North American growing season rainfall, Mon. Wea. Rev.,117, 1156–1180

Showalter, A. K.: A stability index for thunderstorm forecasting, Bull. Amer. Meteorol. Soc., 34, 250–252, 1953.

B. Tsenova, S. Kolev, 2008, Climatical study of the relationships between thunderstorms lightning activity and the environmental conditions over western Bulgaria, 15th International Conference of Clouds and Precipitation, Cancun-Mexico, July 7-13

CLOUD PROCESSING OF AEROSOL PARTICLES: CONSEQUENCES FOR PRECIPITATION?

Andrea I. Flossmann[1,2] and Wolfram Wobrock[1,2]

[1]Clermont Université, Université Blaise Pascal, Laboratoire de Météorologie Physique, F-63000 Clermont-Ferrand, France

[2]CNRS, INSU, UMR 6016, LaMP, F-63177 Aubière, France

1. INTRODUCTION

One of the greatest uncertainties in current climate models is connected to aerosol particles through their direct and indirect effect. In addition, the increased drop concentration is suspected to modify cloud properties resulting in modified lifetimes and precipitation (second indirect effect). Some groups suggest that pollution can, thus, be at the origin of droughts in a future climate, as the numerous small drops will prevent the formation of precipitation-sized particles.
This concept seems in contradiction to the fact that the capacity of the atmosphere to hold water (vapour or condensed) is limited and even simple forecast models that don't consider the effect of aerosol particles on hydrometeor formation and treat water in a bulk form are able to roughly reproduce precipitation quantities.

The topic of this presentation is to discuss in which way precipitation potentially depends on aerosol particle properties and suggest pathways to link these two concepts. The key hypothesis here is that the capacity of drops and ice crystals to process and modify aerosol particles during a cloud passage will be the regulating process.
Thus, the following questions need to be addressed: Are clouds able to modify the ambient aerosol particle spectrum so that the number concentration is reduced and the size and chemical composition of the particles are changed? Can they do it in such a way that the cloud forming on these particles will finally be able to precipitate and remove the water and pollution from the atmosphere?

2. THE MODEL

The 3D model with detailed (bin) microphysics used herein couples the 3D non-hydrostatic model of Clark and Hall (1991) with the Detailed Scavenging Model DESCAM (Leroy et al., 2009; Flossmann and Wobrock, 2010) for the microphysical package. It follows 5 density distribution function: the number distribution function for the aerosol particles $f_{AP}(m_{AP})$, for drops $f_d(m)$ and for the ice particles $f_i(m_i)$, as well as the mass density distribution function for aerosol particles in the drops $g_{AP,d}(m)$and in the ice crystals $g_{AP,i}(m_i)$.

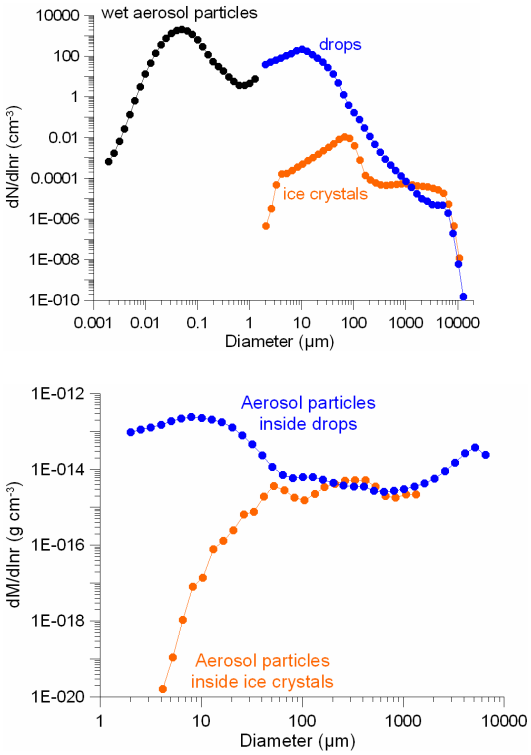

Fig.1: the grid resolution of the different distribution functions treated by DESCAM 3D.

A discussion of the different processes considered in the microphysics code can be found in Flossmann and Wobrock

(2010), and the coupling with the 3-D code is discussed in Leroy et al (2009).

3. RESULTS

a) cloud-aerosol-interaction

Leroy et al (2009) have shown in a 3-D simulation of an individual cloud that the aerosol particle spectrum in the boundary layer can influence precipitation formation :

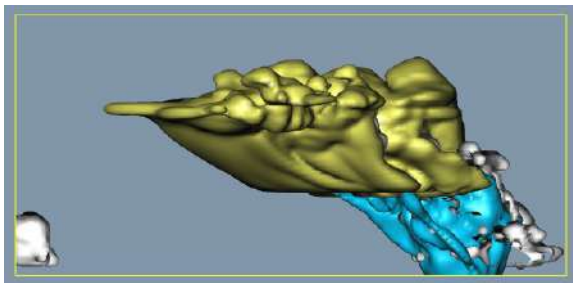

Fig. 2a. Clean boundary layer: $N_{AP} \approx$ 400 cm^{-3}; Cloud drops (grey): 0.01 g m^{-3}; Raindrops (blue): 1 g m^{-3}; Ice crystals (yellow) : 0.01 g m^{-3}

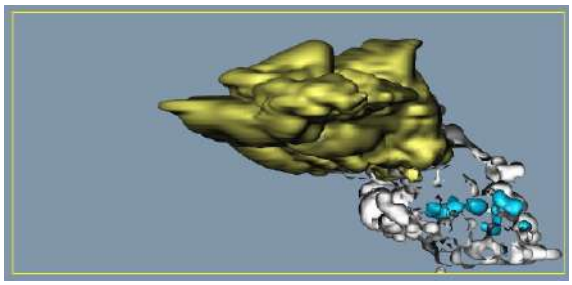

Fig. 2b. Polluted boundary layer: $N_{AP} \approx$ 6500 cm^{-3}; Cloud drops (grey): 0.01 g m^{-3}; Raindrops (blue): 0.03 g m^{-3}; Ice crystals (yellow) : 0.01 g m^{-3}

We note that in the polluted case (2b) almost no rain (blue) is formed. This result is in agreement with other studies from the literature. However, its interest is limited as normally clouds appear in fields and influence each other on larger space and time scales.

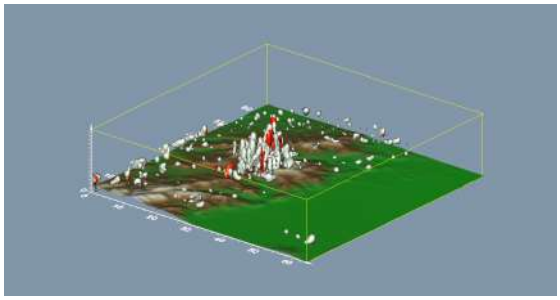

Fig. 3a. Cloud field over complex terrain; white: cloud water, red: rain water

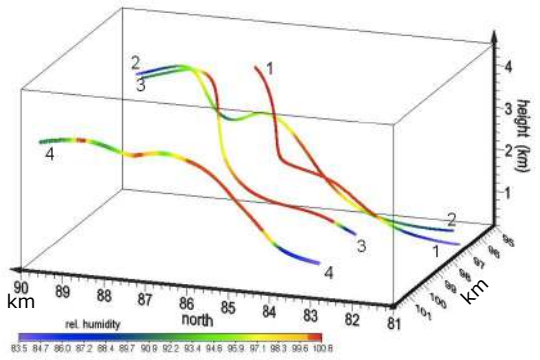

Fig. 3b. Red: supersaturated; blue: outside cloud; green: still in cloud

Recently, we have applied our model to entire cloud fields (Planche et al, 2010) and found that most individual air parcels in 3-D clouds run through a number of subsequent activation and deactivation periods, as can be seen in Fig.3b for four examples of trajectories.

We noted that in the complex cloud field about 85% of the parcels experience one, two, three, or more periods of subsaturation, while only 15% of the parcels stay always supersaturated (color red in Fig.3b) after passing cloud base, as is suggesting a modeling approach by a rising air parcel concept.

The complex dynamics of a 3-D cloud field result in a broad spectrum of super-saturations present inside the cloud region.

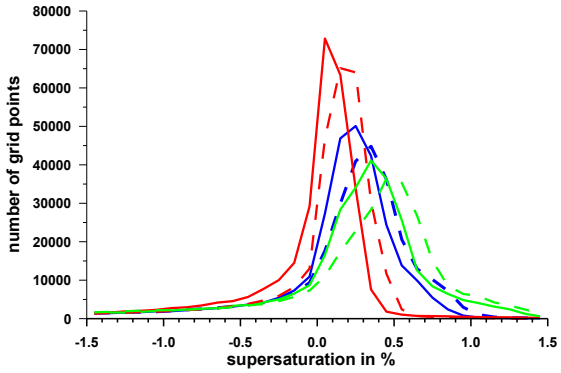

Fig. 4. Distribution of the supersaturation inside the cloud for grid points with LWC>0.1gcm^3; red: polluted case; blue: continental case; green: clean case; solid line: all soluble particles (ε=1); dashed line: ε=0.01

Overall, in these cases we noted that an increasing particle number concentration and increasing solubility reduced overall precipitation. For cloud fields and longer simulations times, we noted however also

a strong temporal and spatial variability and that some locations showed an inverse behavior from the overall trend at some time. Furthermore, the differences of the impact of the particle number concentration on precipitation seemed to decrease in the course of time

b) cloud processing of particles

In order to be able to quantify the amount of processing during a cloud event, we have extended our bin resolved microphysics model to fully consider two types of aerosol particle spectra (Flossmann and Wobrock, 2010). The first type holds the initial particle spectrum on which the cloud forms. The second type is initially empty and is filled up only by deactivated and cloud-processed particles. This approach will allow quantifying for the first time the amount of particles concerned by cloud processing.

We have tested this approach first in the simple context of a 1.5D cloud model, in the framework previously used by Leroy et al (2006). The model is initialized with their CCOPE case and a continental aerosol particle spectrum, which is assumed constant in the boundary layer and above, decreases exponentially. The simulated 1-D cloud produces rain readily and the simulation is stopped after 1h when the system dissipates and the rain stops.
In Fig.4, the time evolution of the two aerosol particle types in the cloud water and in the air are shown.
Fig. 4a and b show the initial (pristine) aerosol particle mass concentration in the air (a) and activated into liquid water (b).

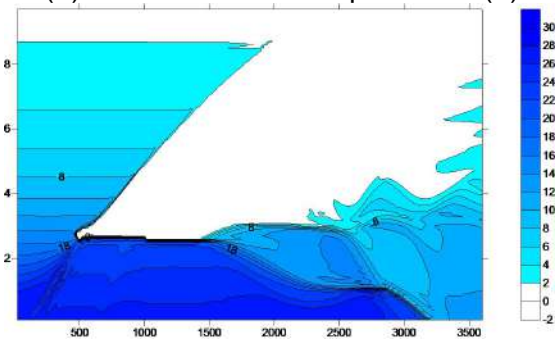

Fig.4a: pristine aerosol mass concentration in μg/m3 in the air as a function of x:time (sec) and y:height (km)

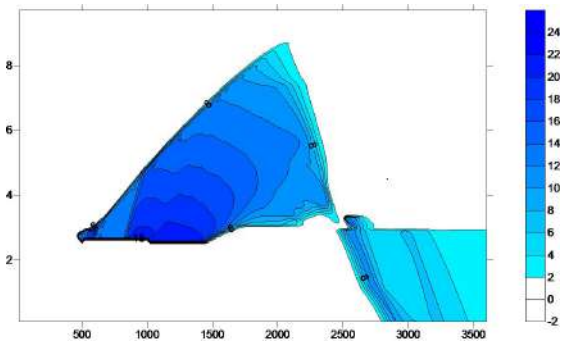

Fig.4b: pristine aerosol mass concentration in μg/m3 in the liquid water as a function of x:time (sec) and y:height (km)

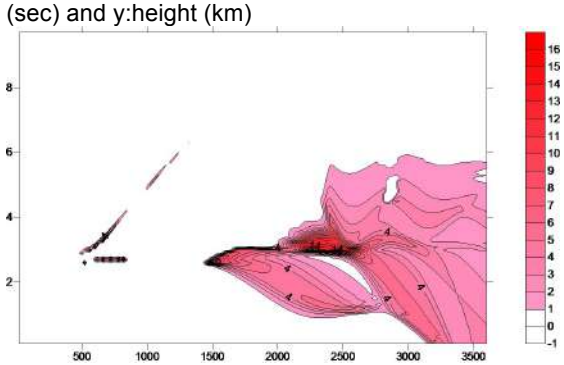

Fig.4c: aerosol mass concentration released after evaporation in μg/m3 in the air as a function of x:time (sec) and y:height (km)

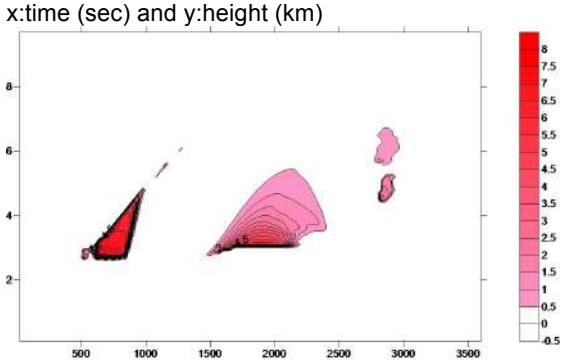

Fig.4d: previously released aerosol mass concentration in μg/m3 re-incorporated in the liquid water as a function of x:time (sec) and y:height (km)

Fig.4c shows the aerosol particle mass in the air resulting from the complete evaporation of the hydrometeors. We note that the mass concentrations are highest below cloud base during the onset of precipitation. The maxima approach the values of the pristine particle mass at the same location (compare Fig.4a). These recycled particles can be reactivated, as is shown in Fig. 4d.
Fig. 5a and b show the aerosol particle number concentrations at an altitude of 2km for the pristine particles (a) and the recycled particles (b).

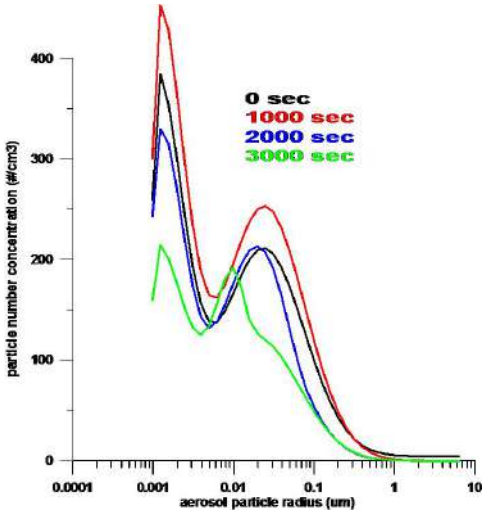

Fig.5a: number concentration of pristine particles for different times as 2km.

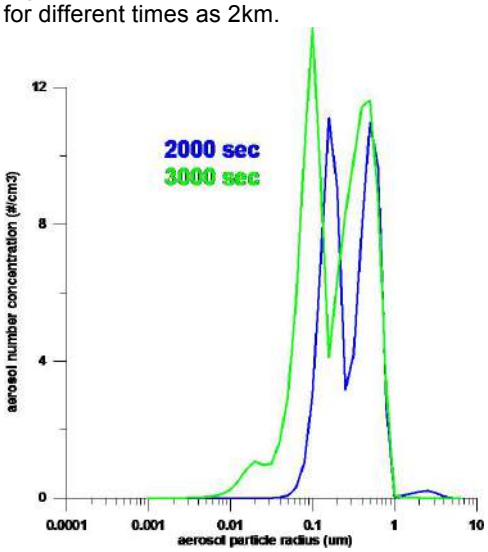

Fig.5a: number concentration of recycled particles for different times as 2km.

We note that the particles that form after complete evaporation of the hydrometeors are generally between 0.1 and 1um in radius.

4. CONCLUSION

We have been able to successfully study the fate of the aerosol particle number and mass that is activated into cloud, processed by the microphysical processes and released back into the air during complete evaporation of the hydrometeors. We note that in the 1.5D framework a significant amount of the aerosol particles are concerned by cloud processing.

However, in the ground precipitation, only 0.4 mg/m^2 were resulting from processed particles while 22.6 mg/m^2 were pristine particles.

Currently, we are incorporating the two types of aerosol particles into the 3D dynamic framework. Only in a complete dynamic framework we will be able to quantify the overall processing of aerosol particles by clouds and its impact on precipitation. Here, it is assumed that the fraction of the processed particles also in the surface rain will increase and finally dominate precipitation.

5. ACKNOWLEDGEMENTS

The calculations for this study have been done on computer facilities of IDRIS, CNRS at Orsay and CINES in Montpellier, under the project 940180. The authors' acknowledgement with gratitude the hours of computer time and the support provided.

6. REFERENCES

Clark, T.L. and W.D. Hall, 1991: Multi-domain simulations of the time dependent Navier-Stokes equation: benchmark error analysis of some nesting procedures. J. Comput. Phys., 92, 456-481.

Flossmann, A. I. and W. Wobrock, 2010: A review of our understanding of the aerosol – cloud interaction from the perspective of a bin resolved cloud scale modelling, Atmos. Res. doi:10.1016/j.atmosres.2010.05.008

Leroy, D. Monier, M. ; Wobrock, W. ; Flossmann, A. I. 2006: A numerical study of the effects of the aerosol particle spectrum on the development of the ice phase and precipitation formation, Atmos. Res. Vol. 80 , No. 1 , p. 15-45 DOI 10.1016/j.atmosres.2005.06.007

Leroy, D., W. Wobrock and A. I. Flossmann, 2009: The role of boundary layer aerosol particles for the development of deep convective clouds: a high-resolution 3D model with detailed (bin) microphysics applied to CRYSTAL-FACE , Atmos. Res.; *DOI: 10.1016/j.atmosres.2008.06.001*

Planche, C., Wolfram Wobrock, Andrea I. Flossmann, Frédéric Tridon, Joël Van Baelen, Yves Pointin et Martin Hagen, 2010: The influence of aerosol particle number and hygroscopicity on the evolution of convective cloud systems and their precipitation: A numerical study based on the COPS observations on 12 August 2007; Atmos. Res. doi.:10.1016/j.atmosres.2010.05.003

Pruppacher H. R. and J.D. Klett, 1997 : *Microphysics of clouds and precipitation*. 2nd ed. Kluwer Academic, 954p.

AIRCRAFT MEASUREMENTS OF AEROSOL, CLOUD DROPLET AND CCN DISTRBUTION CHARACTERISTIC OVER NORTHERN CHINA

Duan Ying[1], *Duan Jing*[2] ,*Yin Yan*[3]

[1]*Weather Modification Office of Hebei Province, 050021, China*
[2]*Chinese Academy of Meteorological Sciences, Beijing, 100081, China*
[3]*Nanjing University of Information Science & Technology, Atmospheric Physics, Nanjing, 210044, China*
Presenting author email: hbwmo@heinfo.net;duany2011@126.com

1. INTRAOUCTION

Hebei province is located in the north of China, Beijing and Tianjin is surrounded with it, the Bohai sea gulf is in the east of Hebei province. In this study, the data from the Piper Cheyenne twin urbo-prop aircraft was used to observe the clouds and precipitation, since 2005 year. The aerosol was measured by a PMI Aerosol Spectrum Probe (size range 0.1～3.0 micron). The cloud droplet was measured by a FSSP probe (size range set up as 2 ~ 47μm). The 2D – C (25 ~ 800μm) and 2D - P (150 ~ 9300μm) probes can provide two-dimensional particle image. In addition, the aircraft is also equipped with other devices to obtained corresponding data. CCN were measured by a DMT continuous flow streamwise thermal gradient CCN counter. The supersaturation is set at S=0.3% in observed period.

The concentration and size with spatial and temporal distribution of aerosol particles ,CCN and cloud droplet over Hebei area, northern China, are analyzed. The preliminary results show that the distribution of them are very different during the precipitation in stratiform. Synthetical research results show that the aerosols played an important role in formation of clouds and precipitation processes.

2. INSTRUMENT AND METHODOLOGY

In this study, the data from A Piper Cheyenne ⅢA twin urbo-prop aircraft was used to observe the clouds and precipitation. The aerosol was measured by a PMI (Particle Metrics Inc, USA) Aerosol Spectrum Probe (size range 0.1 ～ 3.0 micron). The cloud droplet was measured by a FSSP-100ER probe (size range 1～95 micron). Two-dimensional gravity-scale probe OAP-2D-GA2 (25 ~ 800μm) and OAP-2D-GB2 (150 ~ 9300μm) were used, they are the 2D - C and 2D - P probes can provide two-dimensional particle image. In addition, the aircraft is also equipped with a thermometer, dew point, pressure sensors, GPS and other devices.

In this sduty, the measurement range of FSSP-100ER probe set up as 2 ~ 47μm (range “1”) , so that get the cloud particle concentration, liqiud water content, average particle diameter data, corresponding. CCN were measured by a DMT continuous flow streamwise thermal gradient CCN counter.CCN measuring principle with a chemical gradient diffusion chamber (Twomey and Squires, 1959).Since that time, nearly all measurements have used the thermal gradient diffusion chamber. All early measurements were made with static photographic instruments that used batch processing of the samples. In other words, continuous flow chambers using optical particle counters. The supersaturation is set at S=0.3% in observations of this sduty.

Weather Modification Office of Hebei province bought airborne cloud physical instruments from USA and modified a Cheyenne IIIA aircraft in 2004. The instrument for CCN measurement is DMT (Droplet Measurement Technologies, USA) CCN counter.

Specially modified aircraft and airborne equipment for the detection of cloud physics are shown in figure 1.

Fig.1 specially modified aircraft and airborne equipment

3. RESULTS AND DISCUSSIONS

Figure 2 shows that the aerosols and cloud condensation nuclei (CCN) with spatial and temporal distribution in the aircraft detection time at May 27, 2010. The vertical left axis indicates the aerosol and cloud condensation nuclei concentration, the units is cm^{-3}. The vertical right axis indicates height of aircraft flight, its units is meter.

The results shown in the figure 2, light blue curve shows the altitude change with time, the red solid point is the temporal and spatial distribution of aerosol concentration, the black solid point is the spatial and temporal distribution of CCN concentration.

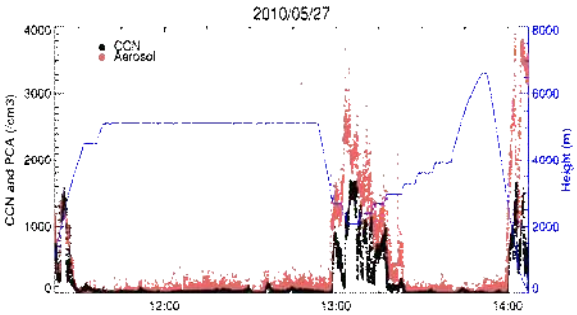

Fig. 2 the temporal and spatial distribution of aerosol and CCN concentration

In the above analysis, the concentration of aerosols and CCN changes are analyzed in the cloud base and inside the cloud. The results show that there is very difference in both cases（figure 3）.

The results shown in the figure 3, light blue curve shows that flight altitude change with time, the red curve is the distribution of aerosol concentration with time, the black curve is the distribution of CCN concentration with time, the green curve is the distribution of cloud droplet concentration with time by FSSP-100ER dada.

Compare of three curves in figure 3, the concentration of aerosols and CCN changes greatly within the cloud base level. Combination of macro-record dada analysis showed that the aircraft detect from 13:20 at the cloud base height of about 3000 meters to 13:24, horizontal flight lasted four minutes, the flight speed is 360 km / h, this flights continued 24 km straight distance. During this time, aerosols and cloud condensation nuclei concentration variation trend is consistent, but their values were the larger of difference between in them, in which aerosol concentration range is 200-600 cm^{-3}, the range of cloud condensation nuclei concentration is 50-150 cm^{-3}.To compare these two values, aerosol concentration is four times with CCN concentration.

On the other hand, the aircraft into to the altostratus cloud at 13:24, the flight height is about 3300 meters , horizontal flight lasted four minutes to 13:28, the flight speed is 360 km / h, the flight continued about 24 km horizontal distance too. During this time, although aerosols and cloud condensation nuclei concentration variation trend is consistent, but compared with the cloud outside (cloud base), their values were less then inside the cloud, in which aerosol concentrations range from 200-600 cm^{-3} reduced to less than 100 cm^{-3} quickly, the range of cloud condensation nuclei concentrations from 50-150 cm^{-3} quickly reduced to less than $10^{1}cm^{-3}$. Cloud droplet (see the green curve) appeared at same time, the results show that the aerosol is heavy consumed in cloud. Because converted to CCN and cloud droplets partly, the concentration of cloud condensation nuclei is reduced quickly.

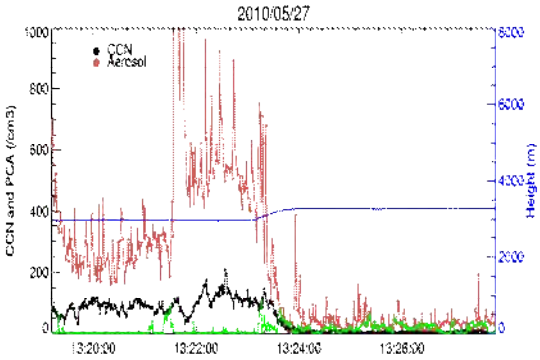

Fig.3 aerosol and CCN concentrations comparison in cloud outside (bottom) and in cloud

In order to analyze aerosols, cloud condensation nuclei and cloud droplets in cloud base and cloud inside, the corresponding concentration and scale distribution between the spectra shown in figure 4. The results showed that the aerosol concentration and cloud condensation nuclei are very different, in two different conditions of inside and outside of cloud.

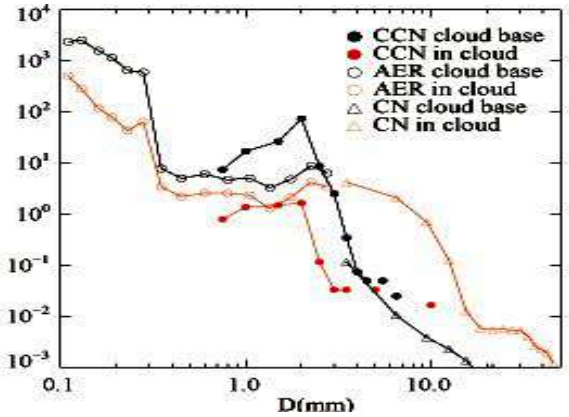

Figure 4. aerosol and CCN spectra comparison inside and outside of cloud

In order to further study the distribution and variation of cloud droplets and aerosols in precipitation process, two flights sounding data getting from airborne PMS system on October 4, 2008 were analyzed. The precipitation in that day is stratiform precipitation.The results show that the distribution of aerosol particles in Shijiazhuang is very different before and after precipitation. Before the precipitation, weather conditions is cloudy and foggy, the average concentration of aerosol particles is $10^3 cm^{-3}$, the maximum concentration is 5.2 × $10^3 cm^{-3}$, the minimum concentration is $39.3 cm^{-3}$, aerosol particles average diameter is 1.06μm. When it is rainy, the average concentration of aerosol particles is $10^2 cm^{-3}$, the maximum concentration is 2.1 × $10^3 cm^{-3}$, an order of magnitude of aerosol concentration is smaller than that of previous of precipitation, minimum particle concentration is 16.7 cm^{-3}, average particle diameter is 1.28μm. Scouring effect by precipitation, after precipitation the aerosol particle concentration less than the before precipitation, decreases is very obviously.

Cloud droplets average concentration is $10^1 cm^{-3}$ on before and after at precipitation, the cloud droplets concentration maximum is $2.7\times10^2 cm^{-3}$, the minimum is $12.2 cm^{-3}$. Cloud droplet concentration is smaller than the 1-2 amount of aerosol particles level.

Above results show that the aerosols played an important role in formation of clouds and precipitation processes. It is considered that part of the aerosol particles went into cloud in which they played cloud condensation nuclei through the activation of nuclear, and then formed cloud particles.

The analysis results of vertical distribution of cloud particle concentration are shown in figures 5.

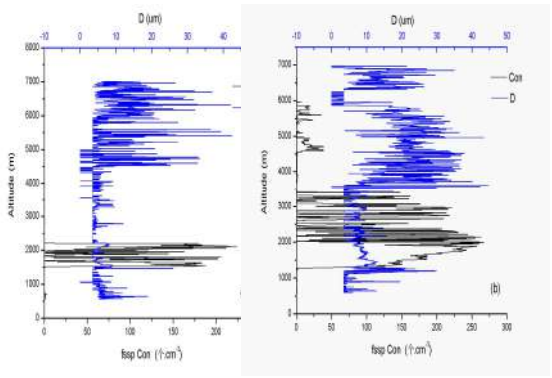

Fig.5 vertical distribution of cloud particle concentration
（a．morning of October 4；b．afternoon of October 4）

BIBLIOGRAPHY

Duan, J., and J. T. Mao（2009）, Influence of aerosol on regional precipitation in North China, Chinese Science Bulletin, 54(3), 474-483, doi: 10.1007/s11434-008-0447-6.

Duan ying et.al（2000）, an Analysis of the Evolution Characteristics and Physical Cause of Formation about Forty Years Natural Rainfall in Hebei Province .13th Internatoinal Conference on Clouds and Precipitation Proceeding-Volume 1,:395-397, Reno ,Nevada USA ,14-18.

Shi L. X., Y. Duan(2008), Observations of Cloud Condensation Nuclei in North China ,Acta Meteorologica Sinica, 22(1) , 97-106.

Yin yan et al, Airborne measurements of the spatial and spectral distributions of aerosol particles over Hebei area, northern China, PIAGENG 2009: Intelligent Information, Control, and Communication Technology for Agricultural

Acknowledgements

This research was Jointly funded by National Natural Science Foundation of China (Grant No. 40905058), the social commonweal research program (GYHY(QX)2007-6-36) funded by the Ministry of Science and Technology of the People's Republic of China.

A REFINED STATISTICAL CLOUD CLOSURE USING DOUBLE-GAUSSIAN PROBABILITY DENSITY FUNCTIONS

Ann Kristin Naumann[1], Axel Seifert[2] and Juan Pedro Mellado[1]

[1]Max Planck Institute for Meteorology, Hamburg, Germany
[2]Hans-Ertel Centre for Weather Research, Deutscher Wetterdienst, Hamburg, Germany

May 16, 2012

1 INTRODUCTION

The cloud fraction and cloud liquid water content in a given volume in thermodynamic equilibrium depend on the variability of temperature and moisture within that volume as characterised by the probability density function (PDF). Diagnostic schemes that are based on single-Gaussian PDFs go back to Sommeria and Deardorff (1977) and Mellor (1977). Refining the approach of Larson et al. (2001) who assumed a double-Gaussian distribution, we introduce a PDF-based scheme to parameterize cloud fraction, average liquid water mixing ratio and liquid water flux in large-scale numerical weather prediction (NWP) and global circulation models (GCM). We develop this parameterization from, and test it against, cloud resolving large-eddy simulation (LES) data of different case studies.

2 METHOD

a. LES

For our study we use the UCLA-LES (Stevens et al. 1999, 2005) adapted to four different case studies which span over a range of different cloud regimes. Shallow cumulus over ocean (RICO; see Rauber et al. 2007) and over land (ARM; see Brown et al. 2002) are considered as well as stratocumulus (DYCOMS; see Stevens et al. 2003) and the transition from stratocumulus to cumulus (ASTEX; see Albrecht et al. 1995). Domain sizes and resolutions of the different LES cases are given in Tab. 1.

b. THEORETICAL BACKGROUND

Following Sommeria and Deardorff (1977), Mellor (1977) and Lewellen and Yoh (1993), we define the extended liquid water mixing ratio, s, in terms of the approximately conserved liquid water potential temperature, θ_l, and the total water mixing ratio, q_t, by

$$s = \frac{q_t - q_s(T_l)}{1 + \alpha L/c_p}, \tag{1}$$

where $q_s(T_l)$ is the saturation mixing ratio at a given value of $T_l = \theta_l T/\theta$ and α is the slope of the saturation mixing ratio at T_l, giving $\alpha = Lq_s(T_l)/(R_v T_l^2)$. T is the temperature, θ the potential temperature, L the latent heat of vaporization, c_p the specific heat at constant pressure and R_v the gas constant for water vapour. For $s > 0$, s is approximately equal to the liquid water mixing ratio, q_l, but for subsaturation s is negative. Note that the ratio of the mean of s, $\overline{s}$, to the standard deviation of s, σ, can be approximated by the normalized saturation deficit, Q_1, which is defined as the bulk value of s, s_{bu}, divided by σ (Lewellen and Yoh 1993, ζ therein).

If the PDF of s was known for each grid box in a NWP model or GCM, the cloud fraction and average liquid water could be calculated by integration over the PDF of s (see Eq. (3) and (4) for the formulation of the integral). Unfortunately, only the first moments of the PDF of s can usually be predicted. We are using high resolution LES data to learn about the behaviour of the distribution of s on the subgrid scale.

	RICO	ARM	DYCOMS	ASTEX
L	20 km	12 km	10 km	10 km
H	4.0 km	5.1 km	1.4 km	3.2 km
Δx	40 m	50 m	20 m	40 m
Δz	20 m	40 m	5 – 52 m	20 m

Table 1: Horizontal and vertical domain size, L and H, and horizontal and vertical resolution, Δx and Δz, of the different LES cases.

Corresponding author's address: Ann Kristin Naumann, Max Planck Institute for Meteorology, Bundesstraße 53, 20146 Hamburg, Germany.
E-mail: ann-kristin.naumann@zmaw.de

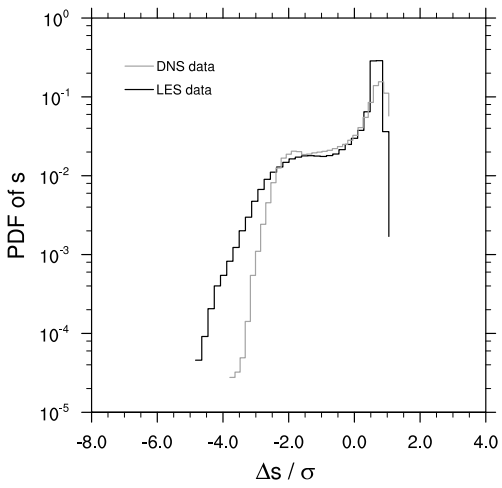

Figure 1: PDF of s from DNS data (grey) and LES data from DYCOMS (black). The PDF is calculated from the respective model level where the variance of the horizontal wind is maximum. It is $\Delta s = s - \overline{s}$.

Considering the PDF of s from each model level in the LES data, we find that the PDF of s can be highly skewed in the cloud layer. In Fig. 1 the PDF of s, calculated from the respective model level where the variance of the horizontal wind is maximum, is shown to compare the distribution of s from direct numerical simulation (DNS) and LES model results. The DNS data corresponds to a local study of turbulent mixing at the cloud top, due solely to evaporative cooling (Mellado et al. 2010). We find that the skewness of the distribution of s is not a unique feature of LES but can also be found on much smaller scales of DNS.

From the different LES cases, we identify positively skewed PDFs of s for shallow cumulus and negative skewness for stratocumulus. The tail of the PDF is representing the cloudy and the non-cloudy part of the cloud layer for cumulus and stratocumulus, respectively. Therefore the success of a scheme diagnosing the cloud fraction and the average liquid water depends crucially on the ability to quantify the tail of the distribution.

We hence choose to represent the PDF of s by a double-Gaussian distribution following Larson et al. (2001)

$$\begin{aligned} P(s) &= aP_1(s) + (1-a)P_2(s) \\ &= \frac{a}{\sqrt{2\pi}\sigma_1} \exp\left[-\frac{1}{2}\left(\frac{s-s_1}{\sigma_1}\right)^2\right] \\ &+ \frac{1-a}{\sqrt{2\pi}\sigma_2} \exp\left[-\frac{1}{2}\left(\frac{s-s_2}{\sigma_2}\right)^2\right], \quad (2) \end{aligned}$$

where P_1 and P_2 are single-Gaussian distributions, a is the relative amplitude of the two single Gaussians and s_1, s_2, σ_1 and σ_2 are the mean and the standard deviation of the two single Gaussians, respectively. By convention, we choose $s_1 > s_2$.

To calculate the best fit of the five parameters of the double Gaussian (a, s_1, s_2, σ_1, σ_2) to each level of our LES data, we first do χ^2-tests in the relevant region. Because this procedure gets computationally expensive easily (at least if five parameters are to be fitted like it is done here), we only search for a coarse estimation of the best fit for the five parameters and then use this best fit as input for Nelder-Mead downhill simplex method (Press et al. 1992) to find the absolute minimum.

3 CLOSURE EQUATIONS

Even if we assume that the first three moments of the PDF of s can be predicted, e.g. from a higher-order closure boundary layer model, the number of parameters has to be reduced from five to three, i.e. two closure equations are necessary. In Fig. 2 the closure equations suggested by Larson et al. (2001) are shown along with our LES data and our new closures equations which fit the LES data.

Because we defined $s_1 > s_2$ by convention, large values for σ_1/σ represent the cloudy tail in shallow cumulus, where the skewness of the distribution of s has high positive values. Vice versa, large values for σ_2/σ represent the non-cloudy part of the cloud layer in stratocumulus, where the skewness is negative. While Larson et al. (2001) suggested an antisymmetric behaviour for σ_1/σ and σ_2/σ depending on skewness, we find that in the cumulus regime σ_1/σ has higher values than σ_2/σ in stratocumulus. This is consistent with the physical understanding that cloudy updrafts in shallow cumulus are more vigorous than non-cloudy downdrafts in stratocumulus. The tail of the distribution of s is therefore heavier in the cumulus regime than in the stratocumulus regime.

4 DOUBLE-GAUSSIAN CLOUD SCHEME

Assuming a double-Gaussian distribution of s, the cloud fraction and the average liquid water can be

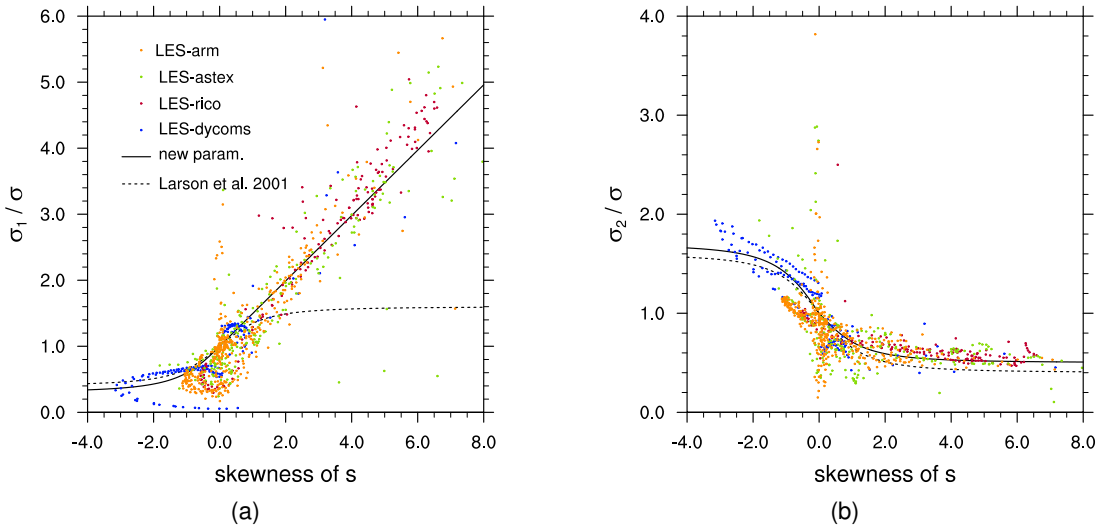

Figure 2: LES data of RICO, ARM, DYCOMS and ASTEX along with closure equations suggested by Larson et al. (2001) (dashed lines) and our new closure equations (solid lines) relating (a) σ_1/σ and (b) σ_2/σ to the skewness of s. The legend in (a) also applies to (b).

found analytically. For the cloud fraction, C, we find

$$\begin{aligned} C &= \int_0^\infty P(s) \\ &= \frac{a}{2}\left(1+\mathrm{erf}\left(\frac{s_1}{\sqrt{2}\sigma_1}\right)\right) \\ &\quad + \frac{1-a}{2}\left(1+\mathrm{erf}\left(\frac{s_2}{\sqrt{2}\sigma_2}\right)\right) \end{aligned} \tag{3}$$

which is equal to Eq. (23) in Lewellen and Yoh (1993). For the average liquid water, $\overline{q}_l$, we find:

$$\begin{aligned} \overline{q}_l &= \int_0^\infty P(s) s ds \\ &= s_1 \frac{a}{2}\left(1+\mathrm{erf}\left(\frac{s_1}{\sqrt{2}\sigma_1}\right)\right) \\ &\quad + s_2 \frac{1-a}{2}\left(1+\mathrm{erf}\left(\frac{s_2}{\sqrt{2}\sigma_2}\right)\right) \\ &\quad + \frac{a}{\sqrt{2\pi}}\sigma_1 \exp\left(-\frac{s_1^2}{2\sigma_1^2}\right) \\ &\quad + \frac{1-a}{\sqrt{2\pi}}\sigma_2 \exp\left(-\frac{s_2^2}{2\sigma_2^2}\right) \end{aligned} \tag{4}$$

In Fig. 3a und 3b the new parameterization of C and $\overline{q}_l/\sigma$ using our new closure equations (see Fig. 2) are shown as a function of the normalized saturation deficit, Q_1, together with the LES data of the ASTEX case. Note that the parameterizations depend on the skewness of s and that zero skewness equals the case of a single-Gaussian distribution of s (like assumed in Sommeria and Deardorff 1977; Mellor 1977). The LES data compares very well with the new parameterizations, except for a few data points representing the cloud top of the stratocumulus deck.

In contrast to C and $\overline{q}_l$, the liquid water flux, $\overline{w'q_l'}$, cannot be found analytically from s because it depends also on the vertical velocity. When calculating e.g. the buoyancy flux, $\overline{w'q_l'}$ has to be known. Therefore Cuijpers and Bechtold (1995) suggest that

$$\overline{w'q_l'} = FC\overline{w's'} \tag{5}$$

where F is a nondimensional function depending only on Q_1. From our LES data we find that F is not only a function of Q_1 but also depends on the skewness of s (see Fig. 3c).

5 PROFILES

While we chose to show ASTEX data for the double-Gaussian cloud scheme presented in the last section to cover the whole relevant parameter space, we now focus on the data of RICO with comparatively low cloud cover. In Fig. 4 the profiles of C, $\overline{q}_l$ and $\overline{w'q_l'}$ from LES data of RICO are shown together with the results of different parameterizations. Considering the profiles of C and $\overline{q}_l$, the new parameterization is built by applying the cloud closure using double-Gaussian PDFs and the new closure equations.

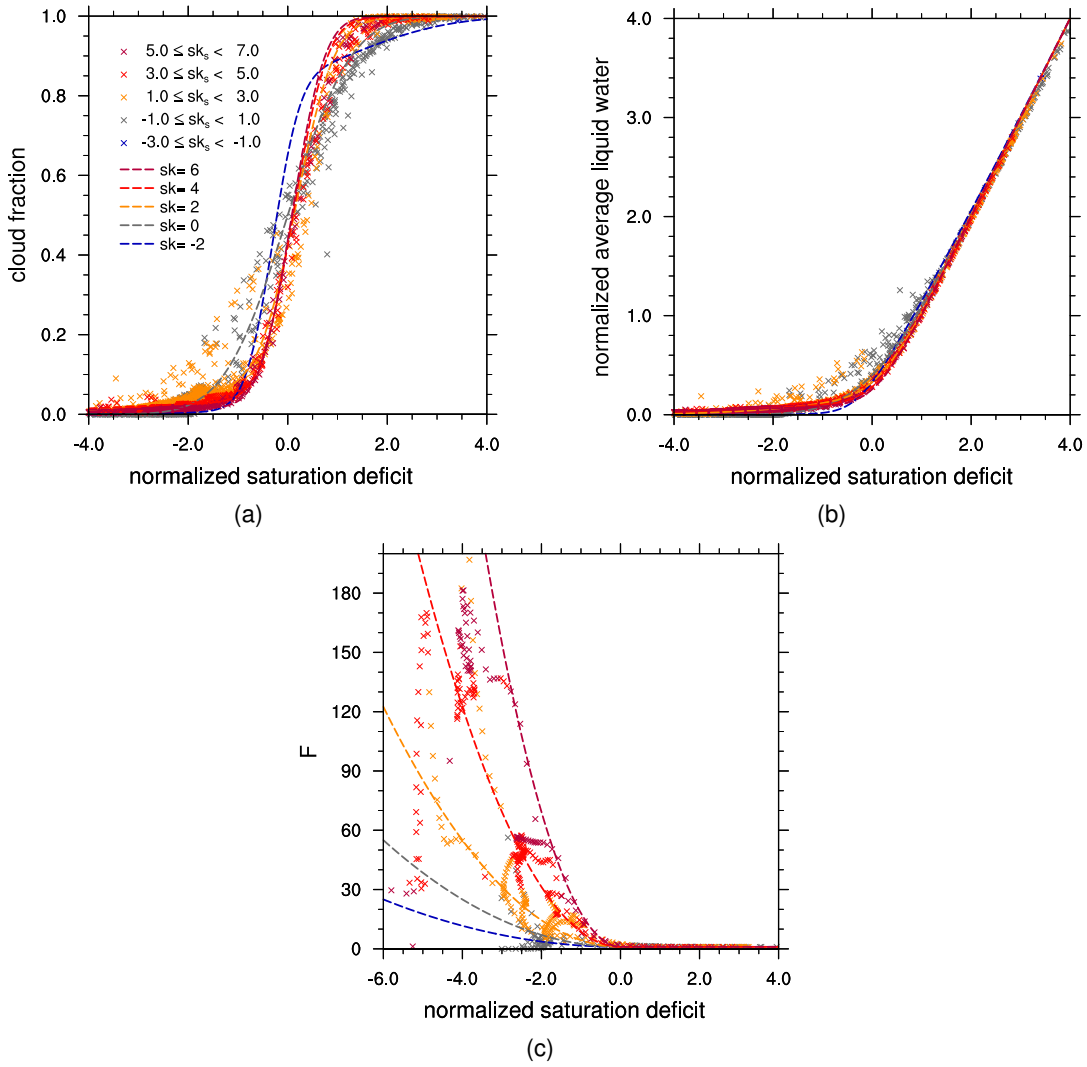

Figure 3: Our new parameterization (dashed lines) as a function of the skewness of s, sk_s for (a) the cloud fraction, C, (b) the normalized average liquid water, $\overline{q}_l/\sigma$, and (c) the flux factor F as defined by Eq. (5) shown together with the corresponding LES data from the ASTEX case (crosses). The legend in (a) also applies to (b) and (c).

The new parameterization is able to reproduce the profiles of C and $\overline{q}_l$ a little better than the parameterization using the closure equations from Larson et al. (2001). Both cloud schemes are clearly superior compared to a single-Gaussian cloud closure, which is severely underestimating especially $\overline{q}_l$.

For the profiles of $\overline{w'q'_l}$, Eq. (5) is used with F parameterized like shown in Fig. 3c to calculate $\overline{w'q'_l}$ from $\overline{w's'}$. For comparison with this new parameterization, the exponential fit of F by Cuijpers and Bechtold (1995) is also shown in Fig. 4c. Although the absolute values are overestimated, the new parameterization is able to reproduce the shape of the profile of $\overline{w'q'_l}$.

6 SUMMARY AND CONCLUSION

We introduced a refined statistical cloud closure using double-Gaussian PDFs. Starting from the work of Larson et al. (2001), who provided an elegant framework for a diagnostic parameterization of the cloud fraction and the average liquid water, we were able to improve their parameterization especially in the case of strong positive skewness of the distribution of the extended liquid water mixing ratio, s. The introduced double-Gaussian closure (relying on the first three moments of s as input parameters) is shown to be clearly superior to a single-Gaussian approach in diagnosing the cloud fraction and average liquid water profiles from the subgrid variability of s.

For the liquid water flux, we introduced a new

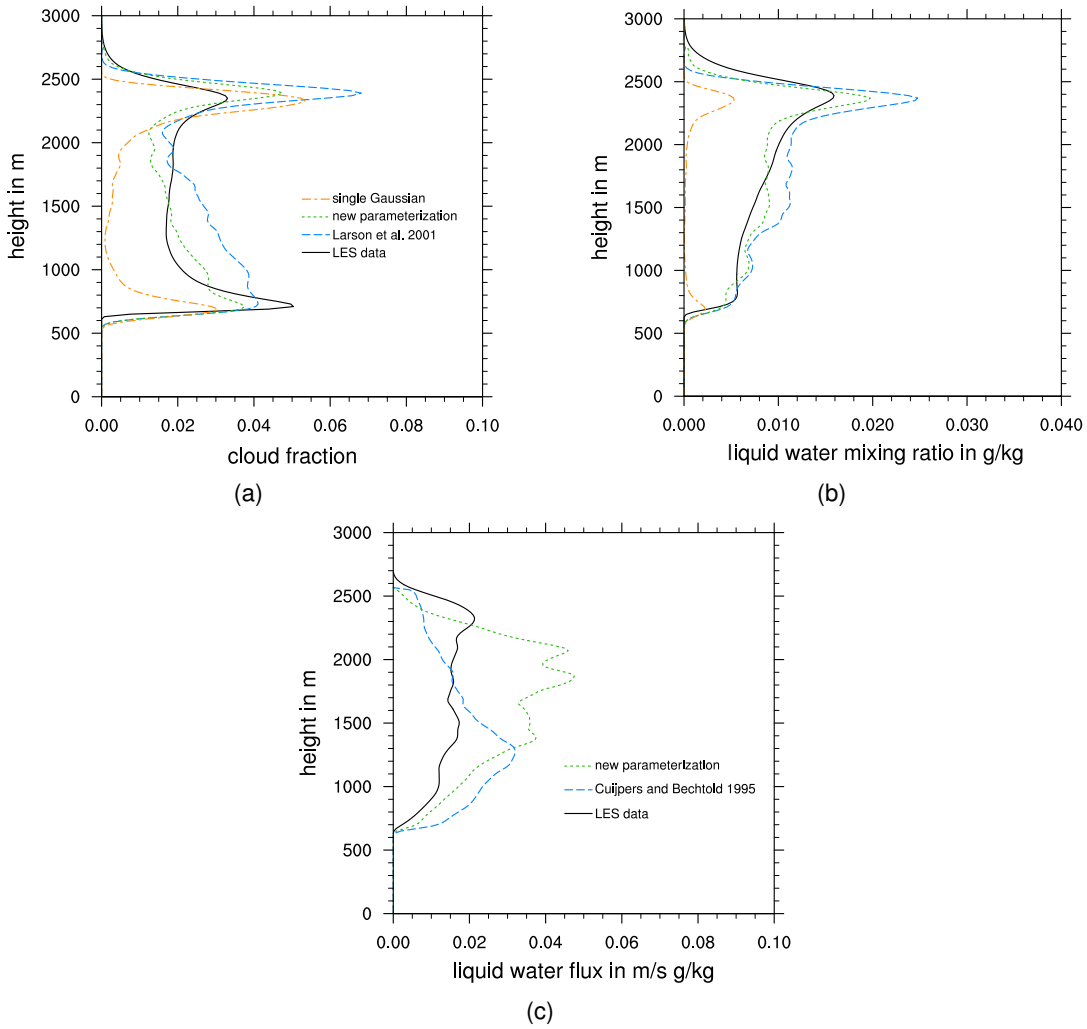

Figure 4: Profiles of (a) the cloud fraction, C, (b) the average liquid water, $\overline{q}_l$, and (c) the liquid water flux, $\overline{w'q'_l}$. All data is from the RICO case after 36 hours of simulation. Shown are the "true" values from LES and different kinds of parameterizations. The legend in (a) also applies to (b).

parameterization of the factor F, which is relating the liquid water flux to the flux of s. This parameterization is depending on the skewness of the distribution of s and although it overestimates the absolute values, we are able to reproduce the shape of the profiles of the liquid water flux.

References

Albrecht, B. A., C. S. Bretherton, D. Johnson, W. H. Scubert, and A. S. Frisch, 1995: The Atlantic stratocumulus transition experiment – ASTEX. *Bull. Am. Met. Soc.*, **76**, 889–903.

Brown, A. R., R. T. Cederwall, A. Chlond, P. G. Duynkerke, J.-C. Golaz, M. Khairoutdinov, D. C. Lewellen, A. P. Lock, M. K. MacVean, C.-H. Moeng, R. A. J. Neggers, A. P. Siebesma, and B. Stevens, 2002: Large-eddy simulation of the diurnal cycle of shallow cumulus convection over land. *Quart. J. Roy. Met. Soc.*, **128**, 1075–1093, doi:10.1256/003590002320373210.

Cuijpers, J. W. M. and P. Bechtold, 1995: A simple parametrization of cloud water related variables for use in boundary layer models. *J. Atmos. Sci.*, **52**, 2486–2490.

Larson, V. E., R. Wood, P. Field, J. Golaz, T. H. V. Haar, and W. Cotton, 2001: Small-scale and mesoscale variability of scalars in cloudy boundary layers: One-dimensional probability density functions. *J. Atmos. Sci.*, **58**, 1978–1994.

Lewellen, W. S. and S. Yoh, 1993: Binormal model of ensemble partial cloudiness. *J. Atmos. Sci.*, **50**, 1228–1237.

Mellado, J. P., B. Stevens, H. Schmidt, and N. Peters, 2010: Probability density functions in the cloud-top mixing layer. *New J. Phys.*, **12**, doi:10.1088/1367-2630/12/8/085010.

Mellor, G. L., 1977: The Gaussian cloud model relations. *J. Atmos. Sci.*, **34**, 356–358.

Press, W. H., S. A. Teukolsky, W. T. Vetterling, and B. P. Flannery, 1992: *Numerical Recipes in FORTRAN*. Cambridge University Press, Cambridge.

Rauber, R. M., B. Stevens, H. T. Ochs, III, C. Knight, B. A. Albrecht, A. M. Blyth, C. W. Fairall, J. B. Jensen, S. G. Lasher-Trapp, O. L. Mayol-Bracero, G. Vali, J. R. Anderson, B. A. Baker, A. R. Bandy, E. Burnet, J. L. Brenguier, W. A. Brewer, P. R. A. Brown, P. Chuang, W. R. Cotton, L. D. Girolamo, B. Geerts, H. Gerber, S. Goke, L. Gomes, B. G. Heikes, J. G. Hudson, P. Kollias, R. P. Lawson, S. K. Krueger, D. H. Lenschow, L. Nuijens, D. W. O'Sullivan, R. A. Rilling, D. C. Rogers, A. P. Siebesma, E. Snodgrass, J. L. Stith, D. C. Thornton, S. Tucker, C. H. Twohy, and P. Zuidema, 2007: Rain in shallow cumulus over the ocean - the RICO campaign. *Bull. Am. Met. Soc.*, **88**, 1912+.

Sommeria, G. and J. W. Deardorff, 1977: Subgrid-scale condensation in models of nonprecipitating clouds. *J. Atmos. Sci.*, **34**, 344–355.

Stevens, B., D. Lenschow, G. Vali, H. Gerber, A. Bandy, B. Blomquist, J. Brenguier, C. Bretherton, F. Burnet, T. Campos, et al., 2003: Dynamics and chemistry of marine stratocumulus – DYCOMS-II. *Bull. Am. Met. Soc.*, **84**, 579–594.

Stevens, B., C. Moeng, A. Ackerman, C. Bretherton, A. Chlond, S. De Roode, J. Edwards, J. Golaz, H. Jiang, M. Khairoutdinov, M. Kirkpatrick, D. Lewellen, A. Lock, F. Muller, D. Stevens, E. Whelan, and P. Zhu, 2005: Evaluation of large-eddy simulations via observations of nocturnal marine stratocumulus. *Mon. Wea. Rev.*, **133**, 1443–1462.

Stevens, B., C.-H. Moeng, and P. P. Sullivan, 1999: Large-eddy simulations of radiatively driven convection: sensitivities to representation of small scales. *J. Atmos. Sci.*, **56**, 3963–3984.

Acknowledgements: We thank Thijs Heus for providing the LES data of the ARM case. This research was carried out as part of the Hans-Ertel Centre for Weather Research. This research network of Universities, Research Institutes and the Deutscher Wetterdienst is funded by the BMVBS (Federal Ministry of Transport, Building and Urban Development).

A COUPLED OBSERVATION - MODELING APPROACH FOR STUDYING ACTIVATION KINETICS FROM MEASUREMENTS OF CCN ACTIVITY

T. Raatikainen[1], T. L. Lathem[1], R.H. Moore[2], and A. Nenes[1,2]

[1]School of Earth and Atmospheric Sciences, Georgia Institute of Technology, Atlanta, Georgia, USA

[2]School of Chemical and Biomolecular Engineering, Georgia Institute of Technology, Atlanta, Georgia, USA

1. INTRODUCTION

Changes in cloud droplet growth kinetics may considerably impact droplet number (e.g. Nenes et al., 2002), but remain largely unconstrained for ambient aerosol. Different definitions exist for describing possible limitations beyond those from water vapor mass transfer, but the effective water vapor uptake coefficient (α_c) is widely used in cloud microphysics models. The general view is that α_c is close to unity or at least larger than 0.1 for pure water droplets (e.g. Kolb et al., 2010; Davidovits et al., 2006). Ambient particles, on the other hand, may have values from ~0.001 to 1.0 (e.g. Ruehl et al., 2008 & 2009).

Cloud droplet activation and growth kinetics can be studied experimentally by using cloud condensation nuclei (CCN) counters such as the Droplet Measurement Technologies (DMT) CCN counter (e.g. Lance et al., 2006), which measure droplet size distributions. Ideally, changes in observed droplet size would indicate changes in droplet growth kinetics. However, droplet size depends strongly on instrument operating conditions (e.g. supersaturation), aerosol properties (hygroscopicity and dry particle size) and concentration; therefore, a detailed numerical model is required to unravel these dependencies and enable a quantification of the effective kinetic parameters (α_c).

We address the above need by developing a comprehensive instrument and CCN growth model which is computationally efficient, stable and incorporates all major sources of instrument variability mentioned above. Model accuracy is first assessed through comparison of measured and model predicted droplet sizes for ammonium sulfate calibration experiments. The modeling framework is then applied to numerous *in-situ* CCN data sets.

2. CCN MEASUREMENTS

The DMT CCN counter (e.g. Lance et al., 2006) is a continuously operating instrument where aerosol flow is exposed to a selected supersaturation (from 0.1 % up to 2 %) in the continuous-flow streamwise thermal gradient cloud condensation nuclei chamber (Roberts and Nenes, 2005), and the resulting droplet size distribution is measured by an optical particle counter (OPC). The OPC is able to detect 1-10 μm droplets, which are assigned to 20 bins with 0.5 μm size resolution.

3. CCN COUNTER MODEL

The fully coupled CCN counter and droplet growth model, which simulates aerosol activation and growth in the instrument, was first introduced by Roberts and Nenes (2005). The latest model version described by Raatikainen et al. (2012) contains the core elements of the original CCN counter and droplet growth codes, but the coupling part of the code is completely revised. The new model version is significantly faster, more reliable, and easier to use.

The CCN counter model computes supersaturation and flow velocity profiles from instrument operation parameters such as total flow rate and calibrated maximum supersaturation. Particle trajectories and corresponding supersaturation profiles are used in the droplet growth model to calculate droplet size development and the droplet size at the chamber exit. The instrument and droplet growth models are coupled, because droplets are a condensation sink for water vapor. High CCN concentrations (>1000 cm^{-3}) are required to cause a detectable effect on the maximum supersaturation, but droplet size, which depends on the full supersaturation profile, is more sensitive to water vapor depletion effects (Lathem and Nenes, 2011).

4. MODEL VERIFICATION

Model accuracy in predicting calibration aerosol droplet size was verified in a comparison with standard calibration data covering a wide range of instrument operation parameters (Raatikainen et al., 2012). Specifically, the experiments were designed to test if the model can predict droplet size using a constant water uptake coefficient (α_c). Because accurate droplet sizing is important when finding numerical values for α_c, the optical particle counter (OPC) was calibrated using glass spheres with known sizes. Two different approaches were used in introducing particles into the OPC, but the results are fairly similar (Figure 1); on average, the real droplet size is 17 % larger that the observed size.

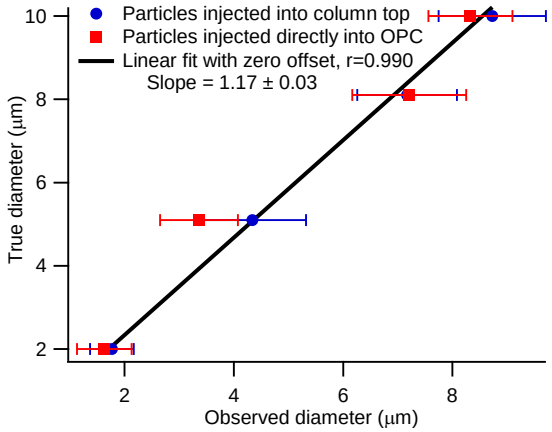

Figure 1: OPC calibration results using glass particles and the fitted calibration line (Raatikainen et al., 2012).

When the OPC sizing bias is corrected, observed and simulated droplet sizes are in good agreement when using water vapor uptake coefficients between 0.1 and 1.0. The influence of pressure and flow rate variability on droplet growth is only through changes in the supersaturation (i.e., other effects are much weaker), so a constant α_c equal to 0.2 is found to reasonably predict the calibration aerosol droplet sizes. Figure 2 shows an example of simulated and (OPC bias corrected) observed droplet sizes (Raatikainen et al., 2012). The narrow shaded region indicates the range of droplet sizes resulting in using α_c values from 0.1 to 1.0.

The simulations are based on two model versions: the detailed model and a model version with simplified instrument geometry (no inlet section) and assuming constant flow velocity profiles. The model predictions are quite similar especially for the atmospherically relevant <1 % supersaturations, but the simplified model is about 100 times faster; this makes it more suitable for large data sets.

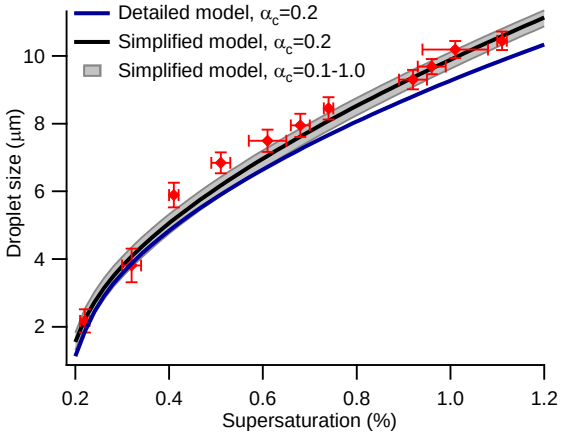

Figure 2: Experimental (markers) and simulated (lines) droplet size for 90 nm ammonium sulfate particles as a function of instrument supersaturation. Flow rate and pressure are 0.5 L/min and 963 mbar, respectively (Raatikainen et al., 2012).

When applying the model to ambient data, the simplified model version with α_c=0.2 gives the droplet size for fast kinetics. If the observed droplet size is smaller than this, the water vapor uptake coefficient is likely to be smaller than 0.2. The main limitation for this approach is that the OPC must be carefully calibrated, which is not possible when analyzing non-contemporaneous data from previous field campaigns. Alternatively, the model can be used to explain changes in droplet size. This is the recommended approach for most data sets.

5. THE FIRST RESULTS

The updated model was first applied to an airborne CCN data set collected from Deepwater Horizon oil spill (Moore et al., 2012). The model could explain observed droplet size variability by changes in aerosol hygroscopicity and water vapor depletion effects while having a constant water vapor uptake coefficient. The model was also applied to airborne data collected from forest fire plumes in Canada (Raatikainen et al., 2012). As shown in figure 3, the

model can explain most of the droplet size variability (width of the gray boxes in figure 3b) when accounting for water vapor depletion effects. The figure also shows the two most typical limitations related to the analysis. First, the observed droplet size is significantly smaller than the simulated one. OPC calibration is one explanation, but it is also possible that there are some differences between the instruments. This difference is not related to droplet growth kinetics, because a similar difference is seen in calibration aerosol droplet size (black square markers). The second limitation is that there are always some unexplainable variations in the observed droplet size. These variations are among the highest observed, but common for non-size resolved airborne sampling where aerosol properties can change within the time required for size distribution measurements.

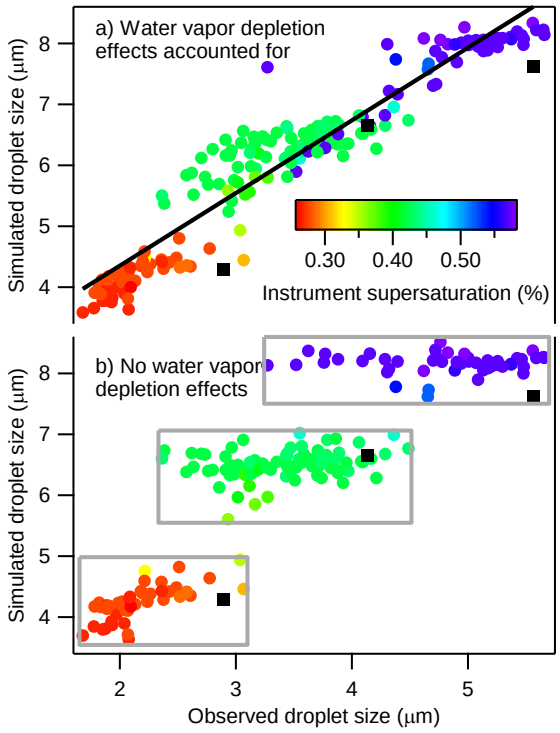

Figure 3: Correlation between observed and simulated (with and without water vapor depletion effects) droplet size for the ARCTAS 2008 campaign data (Raatikainen et al., 2012). The black squares represent calibration data.

6. CONCLUSIONS

The fully coupled instrument (the DMT CCN counter) and droplet growth model was updated and model accuracy for calibration aerosol was verified. When analyzing ambient data, model simulations provide droplet size representing fast activation and growth kinetics while fully accounting for water vapor depletion effects, changes in instrument operation parameters, and changes in dry particle properties. If these cannot explain observed droplet size, it is likely that water vapor uptake coefficient (α_c) is changing, in which case, model simulations can be used to obtain numerical values for α_c.

The model has been applied to two ambient data sets where it showed that the observed droplet size variations were caused by water vapor depletion effects and changes in dry particle properties (hygroscopicity). Without the model, these variations might have been incorrectly attributed to slow activation kinetics.

Currently, several field data sets are being analyzed by using the model predicted droplet size as the reference (Raatikainen et al., manuscript in preparation, 2012). The data sets include boreal forests (Hyytiälä, Finland), arctic areas (Alaska, USA; Canada; Greenland, Denmark), biomass burning plumes (Canada), and polluted and biogenically influenced urban areas (Mexico City, Mexico; Houston, Texas, USA; Atlanta, Georgia, USA; Los Angeles, California, USA). So far the model has been able to explain the observed droplet size variations by water vapor depletion effects and changes in dry particle hygroscopicity and size. This indicates that a high water vapor uptake coefficient (~0.1-1.0) is common for ambient droplets.

There are few previous studies (e.g. Ruehl et al., 2008 & 2009) where slowly growing droplets have been observed, but the majority of the studies have found growth kinetics similar to that of pure water (e.g. Bougiatioti et al., 2011; Cerully et al., 2011). One explanation for this is that kinetic limitations may be observable only at certain atmospheric conditions such as low temperature and humidity. This motivates continued field measurements and data analysis in order to properly quantify the spatial and temporal distribution of cloud droplet kinetic limitations.

7. BIBLIOGRAPHY

Bougiatioti, A., Nenes, A., Fountoukis, C., Kalivitis, N., Pandis, S. N., and Mihalopoulos, N.: Size-resolved CCN distributions and activation kinetics of aged continental and marine aerosol, Atmos. Chem. Phys., 11, 8791–8808, 2011.

Cerully, K. M., Raatikainen, T., Lance, S., Tkacik, D., Tiitta, P., Petäjä, T., Ehn, M., Kulmala, M., Worsnop, D. R., Laaksonen, A., Smith, J. N., and Nenes, A.: Aerosol hygroscopicity and CCN activation kinetics in a boreal forest environment during the 2007 EUCAARI campaign, Atmos. Chem. Phys., 11, 12369–12386, 2011.

Davidovits, P., Kolb, C. E., Williams, L. R., Jayne, J. T., and Worsnop, D. R.: Mass Accommodation and Chemical Reactions at Gas-Liquid Interfaces, Chem. Rev., 106, 1323–1354, 2006.

Kolb, C. E., Cox, R. A., Abbatt, J. P. D., Ammann, M., Davis, E. J., Donaldson, D. J., Garrett, B. C., George, C., Griffiths, P. T., Hanson, D. R., Kulmala, M., McFiggans, G., Pöschl, U., Riipinen, I., Rossi, M. J., Rudich, Y., Wagner, P. E., Winkler, P. M., Worsnop, D. R., and O'Dowd, C. D.: An overview of current issues in the uptake of atmospheric trace gases by aerosols and clouds, Atmos. Chem. Phys., 10, 10561–10605, 2010.

Lance, S., Medina, J., Smith, J. N., and Nenes, A.: Mapping the Operation of the DMT Continuous Flow CCN Counter, Aerosol Sci. Tech., 40, 242–254, 2006.

Lathem, T. L., and A. Nenes: Water vapor depletion in the DMT continuous-flow CCN chamber: Effects on supersaturation and droplet growth, Aerosol Sci. Tech., 45, 604-615, 2011.

Moore, R. H., Raatikainen, T., Langridge, J. M., Bahreini, R., Brock, C. A., Holloway, J. S., Lack, D., Middlebrook, A. M., Perring, A. E., Schwarz, J. P., Spackman, J. R., and Nenes, A.: CCN Spectra, Hygroscopicity, and Droplet Activation Kinetics of Secondary Organic Aerosol Resulting from the 2010 Deepwater Horizon Oil Spill, Environ. Sci. Technol., 46, 3093–3100, 2012.

Nenes, A., Ghan, S., Abdul-Razzak, H., Chuang, P. Y., and Seinfeld, J. H.: Kinetic limitations on cloud droplet formation and impact on cloud albedo, Tellus B, 53, 133–149, 2001.

Raatikainen, T., Moore, R. H., Lathem, T. L., and Nenes, A.: A coupled observation-modeling approach for studying activation kinetics from measurements of CCN activity, Atmos. Chem. Phys., 12, 4227-4243, 2012.

Roberts, G. C. and Nenes, A.: A Continuous-Flow Streamwise Thermal-Gradient CCN Chamber for Atmospheric Measurements, Aerosol Sci. Tech., 39, 206–221, 2005.

Ruehl, C. R., Chuang, P. Y., and Nenes, A.: How quickly do cloud droplets form on atmospheric particles? Atmos. Chem. Phys., 8, 1043–1055, 2008.

Ruehl, C. R., Chuang, P. Y., and Nenes, A.: Distinct CCN activation kinetics above the marine boundary layer along the California coast, Geophys. Res. Lett., 36, L15814, 2009.

Acknowledgements

We would like to thank funding support from the Finnish Cultural Foundation and Emil Aaltonen Foundation. We also acknowledge support from a NSF Graduate Student Fellowship, an NSF CAREER award, DOE Global Change Education Program, the DOE program STTR, NASA Earth and Space Science Graduate Research Fellowship, and NOAA. We thank G. Kok and R. Drgac from Droplet Measurement Technologies for their support and advice on calibration of the OPC. S. Lance and C.A. Brock are acknowledged for their help with the MIE calculations. We also thank the Langley Aerosol Group for their work on the ARCTAS campaign.

MODELING ATMOSPHERIC AEROSOLS, CHARACTERIZED AT THE PUY DE DOME STATION (FRANCE)

Christelle BARBET, Laurent DEGUILLAUME and Nadine CHAUMERLIAC [1,2]

[1] Clermont Université, Université Blaise Pascal, Laboratoire de Météorologie Physique (LaMP) 63000 Clermont-Ferrand, France
[2] CNRS, UMR6016, 63177 Aubière, France

1. INTRODUCTION

Since several years, a significant increase in the emissions of gases and aerosol particles has been observed. Thus, efforts have been made by the scientific community to better understand the atmospheric chemistry. Therefore, one of the main actor of the atmospheric chemistry is aerosol particles. These ones are classified into two categories according to their production mechanism: primary particles which are directly emitted into the atmosphere and secondary particles which are formed from gaseous precursors through gas-particle conversion. Aerosols can modify the Earth's radiative budget. In fact, they can absorb or diffuse solar and terrestrial radiations which lead to a warming or a cooling of the atmosphere (direct effect). Moreover, they can have a significant radiative impact via their interactions with clouds (indirect effect).

Modeling studies attempt to correctly represent atmospheric environment. For this, chemistry mechanisms are increasingly introduced in transport models. Chemical species are exposed to various reaction pathways and their changes between gas, aerosol and cloud phases are studied. Interactions between microphysical, chemical, radiative and dynamical processes are also considered. In addition, observational data are essential to make comparisons with model outputs in order to improve all the processes taken into account.

2. MODEL DESCRIPTION

WRF-chem model results from the coupling of the WRF (Weather Research and Forecast) with a chemistry module. This coupling between dynamics, radiation and chemistry allows for simulating gases, aerosols and cloud chemistry.

A double-moment microphysical scheme module, developed by Morrison et al. (2009) and predicting both the number concentration of cloud droplets and their number concentration and the mixing ratio of rain, ice, snow and graupel is used.

The chemical mechanism, RADM2 (2nd generation Regional Acid Deposition Model; Stockwell et al., 1990) includes 26 stable species and 16 peroxy radicals for organic species and 14 stable species, 4 reactive intermediates and 3 abundant stable species (oxygen, nitrogen and water) for inorganic species. In order to limit number of model groups, some similar organic compounds are grouped together based on the principle of reactivity weighting. Aggregation factors, computed by Middleton et al. (1990), are used for VOC (Volatil Organic Compounds).

RADM2 chemical mechanism is coupled with MADE (Modal Aerosol Dynamic Model for Europe; Ackermann et al.,, 1998). Moreover, secondary organic aerosols are simulated due to the incorporation of SORGAM into MADE (Secondary Organic Aerosol Model; Schell et al., 2001). Thereby, the size distribution of aerosols is represented by 3 modes (Aitken, accumulation and coarse mode). Each mode is represented by a log-normal distribution. The dynamical processes include condensation, coagulation, size-dependent dry deposition and sedimentation, advective and diffusive transport and aerosol-cloud interaction. Particle formation is treated by two

processes: direct particle emission and secondary formation by nucleation.

Moreover, chemical initial and boundary conditions extract from MOZART-4 (Model for OZone and Related chemical Tracers ; Emmons et al., 2009) coupled with GEOS-5 (Goddard Earth Observing System Model, version 5) with a time resolution of 6 hours and a time resolution of 1.9°x2.5°, are used.

3. EMISSIONS DATA SETS

Three types of emissions data sets are necessary to correctly initialize chemical species in the model: anthropogenic, biogenic and biomass burning (wildfire) emissions data.

Anthropogenic emissions come from two different data sets: TNO-MACC (Kuenen et al., 2011) and MACCity (Lamarque et al., 2010). TNO-MACC emissions are available from 2003 to 2007 with a yearly temporal resolution and spatial resolution of 0.5° per 0.5°. Chemical species emissions used are: NMVOC, PM10 and PM2.5. MACCity provides information about some gases but also about BC and OC emissions. Data are available from 1990 to 2010 with a monthly temporal resolution and a spatial resolution of 0.5° per 0.5°.
Table 1 and Table 2 represent the emitted species (for gases and aerosols) considered into the inventories and the corresponding WRF species.

Biogenic emissions are provided by MEGAN with estimations for gas and aerosols emissions from terrestrial ecosystems into the atmosphere (Guenther et al., 2006). Its temporal resolution is around 1km.

Biomass burning emissions are derived from the Fire Inventory from NCAR version 1.0 (FINNv1). As described by Wiedinmeyer et al. (2011), global estimates of gas and particle emissions from open burning of biomass (wildfire, agricultural fires and prescribed burning) are provided with a daily resolution and a spatial resolution close to 1km.

Table 1. Emitted gases and the corresponding WRF species. (■: extracted from MACCity inventory, ■: extracted from TNO-MACC)

Emissions species	WRF species
CO	E_CO
NOx	E_NO, E_NO2
SO_2	E_SO2
Ethane (C_2H_6)	E_ETH
Propane (C_3H_8)	E_HC3
Ethene (C_2H_4)	E_OL2
Propene (C_3H_6)	E_OLT
Methanol (CH_3OH)	E_HC3
Other alcohols	E_HC3, E_HC5
Formaldehyde (HCHO)	E_HCHO
Others aldehyde	E_ALD
Acetone (C_3H_6O)	E_KET
Other ketones	E_KET
NMVOC	E_HC3, E_HC5, E_HC8, E_TOL, E_XYL, E_ORA2

Table 2. Emitted aerosols and the corresponding WRF species. (■: extracted from MACCity inventory, ■: extracted from TNO-MACC)

Emissions species	WRF species
EC	E_ECI, E_ECJ
OC	E_ORGI, E_ORGJ
PM2.5	E_P25I, E_P25J, E_SO4I, E_SO4J, E_NO3I, E_NO3J
PM10	E_PM10

4. MODEL OUTPUTS AND MEASUREMENTS

In order to compare model outputs and observations, measurements performed at the puy de Dôme monitoring site are used. This latter is located in central France (45°46N 2°57E) and is equipped with

probes to characterize meteorology as well as gases and aerosol particles. One of them is the Aerodyne ToF-AMS (Canagaratna et al., 2007) which provides information about chemical composition and mass concentration of the particulate matter (Freney et al., 2011).

Concerning the simulation, a domain (Figure 1) is defined by 360 grid points in the west-east direction and 390 grid points in the south-north direction with a resolution of 30 km. The center of the domain is 52.5° latitude and 15.0° longitude. The 3 simulation's days are 16-17-18/09/2008 during which a Mediterranean air mass was observed and sampled.

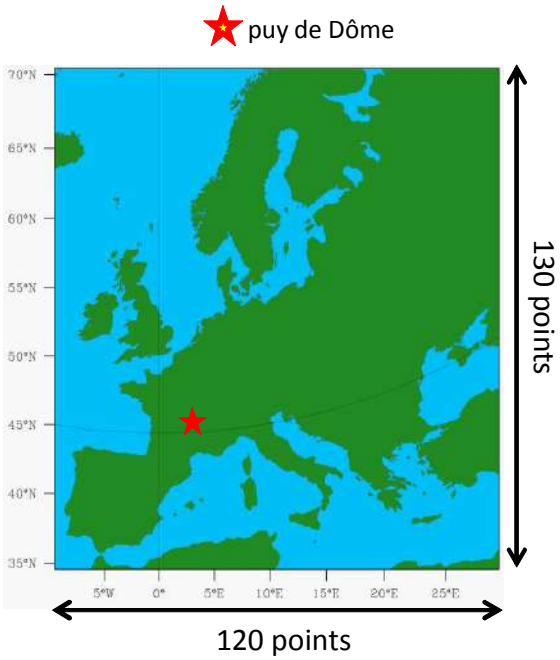

Figure 1. Simulation domain and location of the puy de Dôme

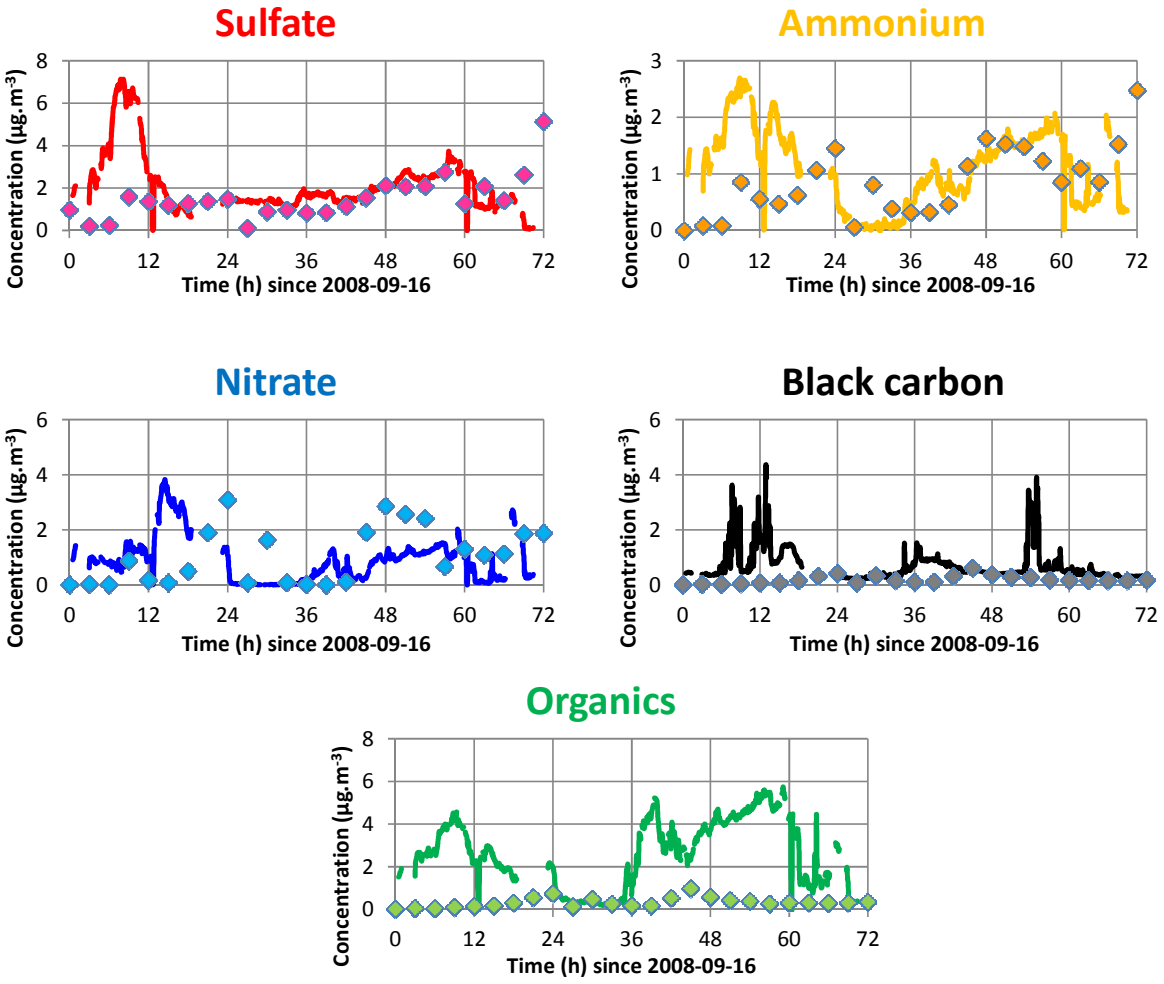

Figure 2. Temporal evolution of sulphate, ammonium, nitrate, black carbon and organics compounds concentrations. Solid lines = observations, markers = model outputs

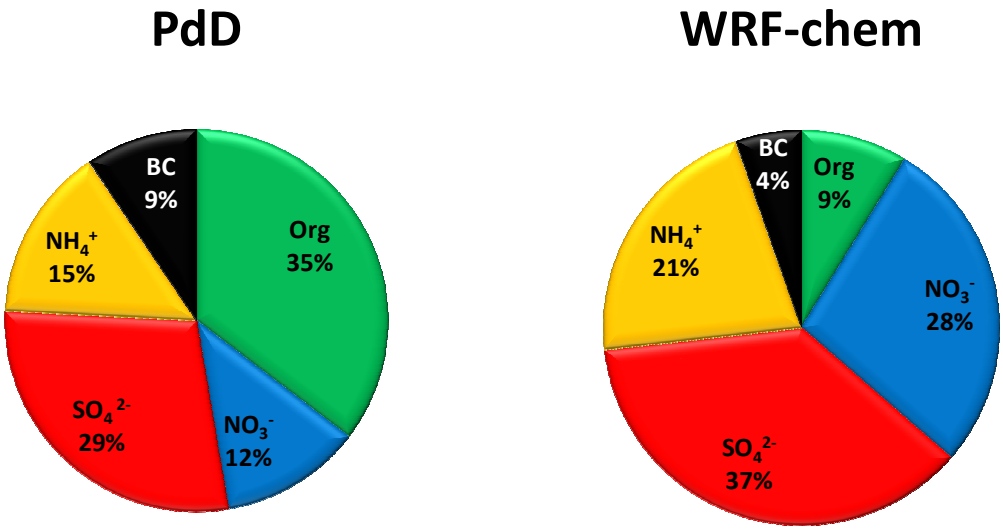

Figure 3. Chemical composition of aerosols at the puy de Dôme (left) & in the model (right)

Time evolution of the concentrations of sulphate, ammonium, nitrate, black carbon and organic compounds of the particulate matter for both observations and model outputs are represented in Figure 2. In addition, chemical composition of aerosols at the top of the puy de Dôme and in the model results are presented in Figure 3.

Firstly, these results show that organic compounds are under-estimated by the model. This can be due to the fact that the model hasn't taken into account local sources of volatile organic compounds (VOC). These ones can condense on aerosol particles explaining that organic compounds contribute to 35% of the particulate matter at the puy de Dôme and contribute only to 9% in the model outputs.

Secondly, black carbon seems to be under-estimated too but the peaks of concentration in the observations (between 48h and 60h for example) may come from local pollution.

Finally, if the 24 first hours of the simulation are considered to be influenced by model spin-up, later on sulphate, ammonium and nitrate concentrations follow quite well the observations.

Differences observed between observations and model outputs can be due to the complex topography around the puy de Dôme for which an altitude of 750m is observed while the real altitude of the puy de Dôme is 1465m.

In order to improve these results, a more detailed topography with a finer spatial topography, less than 30km, will be tested over a variety of situations with contrasted seasons and air pollution conditions. To do this, the model will be run with nested domains, with a spatial resolution of about 3km around the puy de Dôme.

5. BIBLIOGRAPHY

Ackermann, I.J., Hass, H., Memmesheimer, M., Ebel, A., Binkowski, F.S., Shankar, U.: Modal aerosol dynamics model for Europe: development and first applications. Atmos. Anviron., 32 (17), 2981-2999,1998.

Canagaratna, M. R., Jayne, J. T., Jimenez, J. L., Allan, J. D., Alfarra, M. R., Zhang, Q., Onasch, T. B., Drewnick, F., Coe, H., Middlebrook, A., Delia, A., Williams, L. R., Trimborn, A. M., Northway, M. J., DeCarlo, P. F., Kolb, C. E., Davidovits, P., Worsnop, D. R.: Chemical and microphysical characterization of ambient aerosols with the aerodyne aerosol mass spectrometer, Mass Spectrom. Rev., 26, 185-222, 2007.

Freney, E. J., Sellegri, K., Canonaco, F., Boulon, J., Hervo, M., Weigel, R., Pichon, J. M., Colomb, A., Prévôt, A S.H., Laj,P.: Seasonal variations in

aerosol particle composition at the puy-de-Dôme research station in France. Atmos. Chem. Phys., 11, 13047-13059, 2011.

Emmons, L. K., Walters, S., Hess, P. G., Lamarque, J.-F., Pfister, G. G., Fillmore, D., Granier, C., Guenther, A., Kinnison, D., Laepple , T. Orlando, J., Tie, X., Tyndall, G., Wiedinmyer, C., Baughcum, S. L. and Kloster, S.: Description and evaluation of the Model for Ozone and Related chemical Tracers, version 4 (MOZART-4). Geosci. Model Dev., 3, 43-67, 2010.

Guenther, A., Karl, T., Harley, P., Wiedinmyer, C., Palmer, P. I., Geron, C.: Estimates of global terrestrial isoprene emissions using MEGAN (Model of Emissions of Gases and Aerosols from Nature), Atmos. Chem. Phys., 6, 3181-3210, 2006.

Kuenen, J., Denier Van der Gon, H., Visschedijk , A., Van der Brugh ,H.: High resolution European emission inventory for the years 2003- 2007. TNO report, Utrecht, 2011.

Lamarque, J.F., Bond, T., Eyring, V., Granier, C., Heil, A., Klimont, Z., Lee, D., Liousse, C., Mieville, A., Owen, B., Schultz, M. G., Schindell ,D., Smith, S., Stehfest, E., VanAardenne, J., Cooper, O., Kainuma, M., Mahowald, N., McConnell, J., Naik, V., Riahi, K.,Van Vuurent, D.: Historical (1850-2000) gridded anthropogenic and biomass burning emissions of reactive gases and aerosols: methodology and application. Atmos. Chem. Phys., 10, 7017-7039, 2010.

Middleton, P., Stockwell, W. R., Carter, W. P. L.: Aggregation and analysis of volatile organic compound emissions for regional modeling. Atmos. Environ., 24A, 1107-113, 1990.

Morrison, H., Thompson, G., Tatarskii, V.: Impact of Cloud Microphysics on the Development of Trailing Stratiform Precipitation in a Simulated Squall Line: Comparison of One- and Two-Moment Schemes. Mon. Wea. Rev., 137, 991-1007, 2009.

Schell, B., Ackermann, I.J., Hass, H.: Modeling the formation of secondary organic aerosol within a comprehensive air quality model system. J. Geophys. Res., 106, 28275-28293, 2011.

Stockwell, W.R., Middleton, P., Chang, J.S., Tang, X.: The second generation regional acid deposition model chemical mechanism for regional air quality modeling. J. Geophys. Res., 95, 16343-16367, 1990.

Wiedinmyer, C., Akagi, S.K., Yokelson, R. J., Emmons, L. K., Al-Saadi, J. A., Orlando, J. J., Soja, A. J.: The Fire INventory from NCAR (FINN) – a high resolution global model to estimate the emissions from open burning. Geosci. Model Dev. Discuss., 3, 2439-2476, 2010.

HELICOPTER-BORNE OBSERVATIONS OF GIANT NUCLEI AND THEIR IMPACT ON MICROPHYSICAL PROPERTIES OF SHALLOW CUMULUS CONVECTION

Tina Schmeissner, Holger Siebert, Heike Wex
Leibniz Institute for Tropospheric Research, Leipzig, Germany

1 INTRODUCTION

The process of rain formation in warm shallow cumulus clouds, such as trade wind cumuli, is still connected with a lack of knowledge. Ludlam (1951) stated that a small number of droplets with initial radii of about 20 μm could already lead to the onset of the collision/coalescence process, which is the first step in the formation of rain. For maritime air masses large sea-salt particles are supposed to provide such large droplets if suitable meteorological and thermodynamical conditions are present. Woodcock (1952) stated that for large sea-salt particles, which were found at cloud levels in marine air, their weight and number concentration agree in part with the assumption that each sea-salt particle becomes a rain drop. These particles are called Giant Nuclei (GN, diameter range 1 - 20 μm) or UltraGiant Nuclei (UGN, diameter $>$ 20 μm), see Beard and Ochs (1993). It is the purpose of this paper to present an analysis of GN measured in marine air masses and their impact on marine shallow cumulus convection.

2 EXPERIMENTAL

In November 2010 and April 2011 the Cloud Aerosol Radiation and tuRbulence of Trade wInd cumuli over BArbados (CARRIBA) field campaign took place over the coastal area east of the Caribbean Island Barbados. Measurements were performed with the helicopter-borne payload ACTOS (Airborne Cloud Turbulence Observation System). The payload performed high resolution measurements of thermodynamical and meteorological parameters (Siebert et al. 2006). A Phase Doppler Interferometer (PDI) was installed to derive microphysical cloud properties such as droplet size and droplet velocity. The measurement range of the PDI instrument is 1 - 180 μm.
Droplets need to fulfill certain criteria to be detected by the PDI instrument: they have to be optically homogeneous at a length scale small relative to the size of the droplets and they have to be close to spherical (Chuang et al. 2008). For correct size determination the refractive index has to be known (for cloud drop measurements refractive index of water). The PDI instrument is capable to detect GN particles, since sea-salt goes into a dissolved state at relative humidities (RH) above approximately 80%, and once diluted only would go back to its dry state at RHs below about 40%. As these low RHs are unlikely to be encountered in the marine boundary layer (MBL, lowest part of the troposphere ranging from sea surface to about 500 m in height) in the Caribbean area, it is safe to assume that the GN are in a dissolved state. Moreover, dissolved sea-salt particles exhibit a refractive index which is relatively close to that of water, if RH is sufficiently high.

3 RESULTS AND DISKUSSION

During the first CARRIBA campaign in 2010 the PDI instrument was part of the measurement setup during 9 flights. During all these flights, it not only detected cloud droplets, but also “droplets” which were dispersed in the cloud-free air. Because of their relatively small size range and the fact that they were detected in areas with RH well below 100% (therefore consequently in absence of clouds) and also nearby ground level, we assume that these “droplets” are GN. In the following sections, one measurement flight is presented and some statistics about GN are performed using all 9 measurement flights.

Corresponding author’s address: Tina Schmeissner, Leibniz Institute for Tropospheric Research, Germany
Permoser Straße 15, 04318 Leipzig
tinas@tropos.de

3.1 Measurement Example: November 24, 2010

In Fig. 1(a) a time series of the droplet diameter measured by the PDI is shown. It becomes obvious that the droplets cover a wide range of sizes. Moreover, two regimes can be distinguished - marine shallow cumulus clouds (drop size range 1 - 140 μm) and droplets outside of these clouds which are assumed to be GN (smaller drop sizes up to 30 μm).
In Fig. 1(b) a histogram depicts the size distribution of the same flight with a separation into GN detected in the MBL (here only height range 0 - 400 m to ensure that measurements are performed below cloud base, which is located at a relatively constant height of approximately 500 m) and cloud droplets. The separation between cloudy and non-cloudy regimes was based on a threshold in liquid water content (LWC). If LWC exceeded a value of 0.02 g m^{-3} the data was regarded as in-cloud data. Moreover, events with potential GN which were one second before or after a cloud droplet event, were rejected to ensure that no edges of clouds are regarded as GN.
The drizzle tail of the size distribution of the cloud droplets, which is a common feature of trade wind cumuli, ranges up to 70 μm (other flights show even longer drizzle tails ranging up to 100 μm). There are only few counts of droplets with diameters of about 130 μm. This is amplified by the rather poor counting statistics of the PDI, since it is a single drop detection instrument and the chance for one of the rather sparsely distributed very large droplets to pass the measurement volume is rather low. Therefore, it is to assume that there are also some droplets in the size range 70 - 130 μm, which did not pass through the probe area of the PDI.
There is a kind of plateau in the size distribution designating the highest number of drops in the size range of 10 - 25 μm, and the median diameter is located at 15.7 μm. The size distribution for the GN in contrast, is much more narrow (1 - 25 μm) with a median diameter of 4.9 μm. The number concentrations of the GN in the MBL (not shown here) are approximately 0.1 cm^{-3}, i.e. about 10^3 times lower compared to that of the cloud droplets.

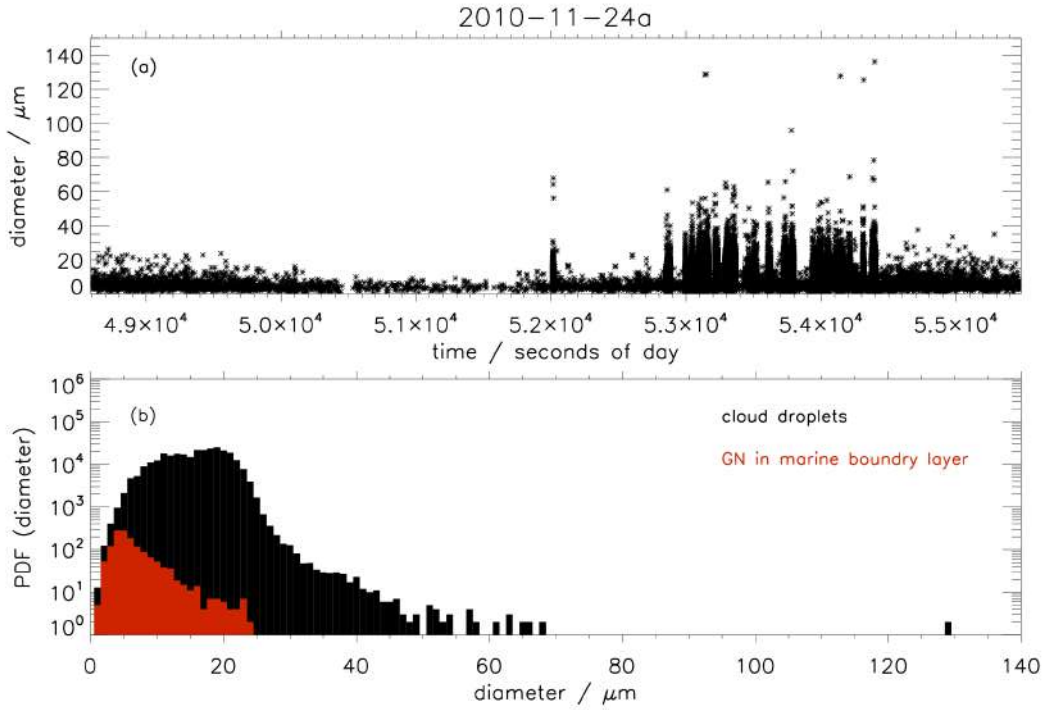

Figure 1: (a) Time series of droplet diameters for the measurement flight on November 24, 2010 and (b) respective probability density function (PDF) for cloud droplets and marine boundary layer Giant Nuclei.

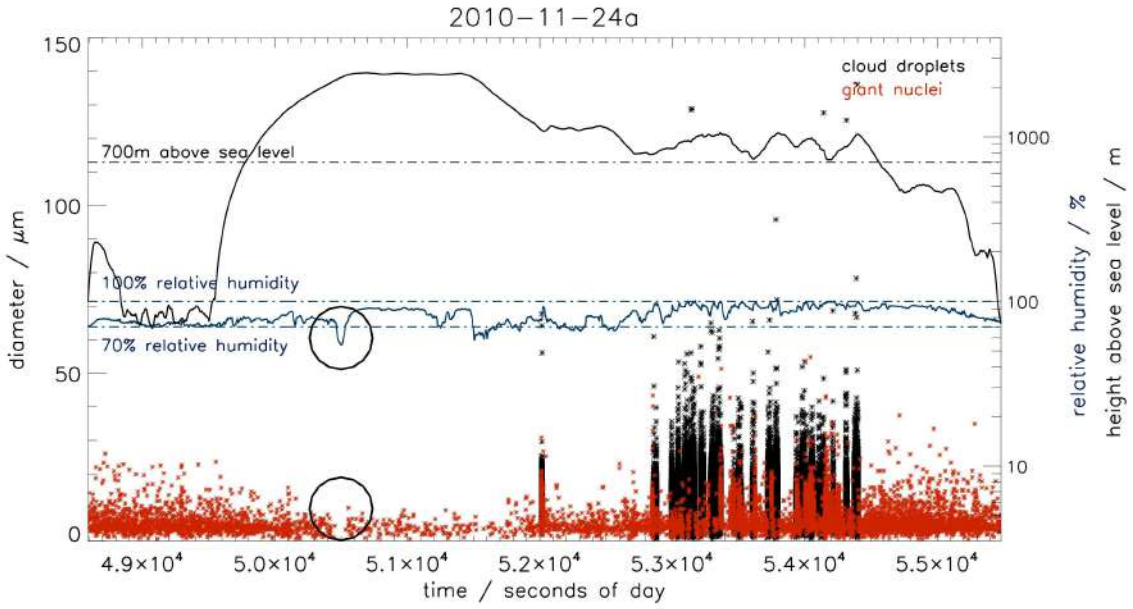

Figure 2: Time series of droplet diameters for the measurement flight on November 24, 2010 as well as flight height and relative humidity. Only droplet data for measurements over sea are shown. Black circles highlight correlation between RH and detection of GN.

In Fig. 2 the GN data and cloud droplet data is shown for measurements performed only over sea in order to avoid influence from the land. Besides the size of the detected droplets, the flight height and the measured RH is shown. GN (depicted in red color) are present in the MBL as well as in the adjacent conditionally unstable layer. Moreover, a dependency of the GN on the RH becomes obvious - at a time of 50500 s RH decreases below 70% and simultaneously the amount of detected GN decreases significantly (see black circles in Fig. 2). The dissolved sea-salt particles are in equilibrium with the RH of the surrounding air, i.e. they decrease in size with a decrease in RH. At a certain RH, which is obviously nearby 70%, the GN will be to small to still be detectable for the PDI.

Figure 3(a) shows a vertical profile of the GN size, as well as the potential temperature and RH for the first ascent of the flight. A decrease in size with increasing height is on the one hand due to the fact that RH decreases with height as long as measurements are performed outside of clouds. On the other hand it might be possible that larger GN do not get transported up to greater heights du to their mass and thus greater terminal velocity. Moreover, an intense decrease in size occurs at about 2200 m, where RH starts to decrease strongly. It can clearly be seen here that for RHs below about 70% no GN are detected anymore. The same can be seen in Fig. 3(b) where the number concentration of the GN is plotted versus the height. Relatively heigh number concentrations of 0.6 - 0.7 cm^{-3} occur between ground level and about 1700 m. Above, the concentration of GN decreases and reaches locally a value of 0 when RH is as low as 55%. The observed number concentrations agree with former findings by Woodcock and Gifford (1949), who found sea-salt particle concentrations of up to 2 cm^{-3}. Mason (2001) also found similar concentrations but remarked, that these values increase if the measurement threshold is set below 1 μm.

3.2 Dependency on RH and horizontal wind speed

As shown in Fig. 2 and Fig. 3, there is a correlation between the size and subsequently the number concentration of the GN and RH. Wright (1940) already stated that the visibility increased at RH smaller 70%, because less particles dispersed in the air grow to larger sizes and cause an extinction of light. These observations go along quite well with our findings (see Fig. 2, no detection of GN where RH decreases strongly below 70%).

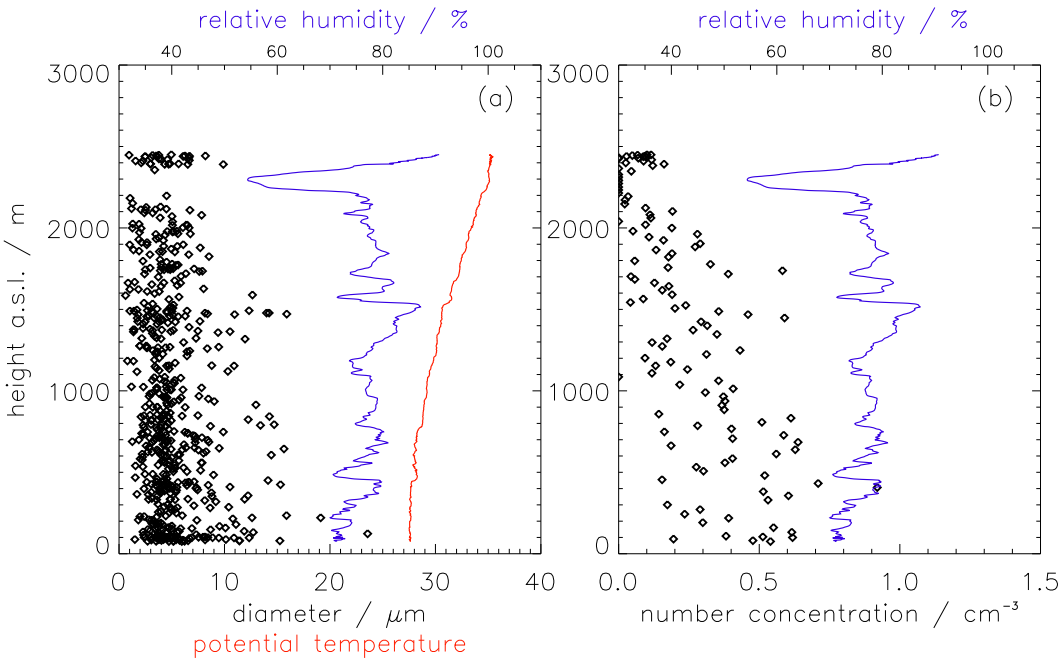

Figure 3: Vertical profile of (a) diameter of the Giant Nuclei, as well as the relative humidity and potential temperature. (b) Number concentration of Giant Nuclei (in 10s means) and the relative humidity.

In Fig. 4(a) this dependency of the number concentration of the GN on RH is shown for all 9 measurement flights. For RH less than 60% the number concentration is almost zero. With increasing RH the number concentration increases as well. This is due to the fact that with increasing RH the GN take up more water to still be in equilibrium with the surrounding air. Therefore, with increasing RH more of the smallest dissolved sea-salt particles can grow into a size range which can be detected by the PDI.

Figure 4(b) shows the correlation between the GN and the horizontal wind speed. The horizontal wind speed measured by ACTOS is used and thus

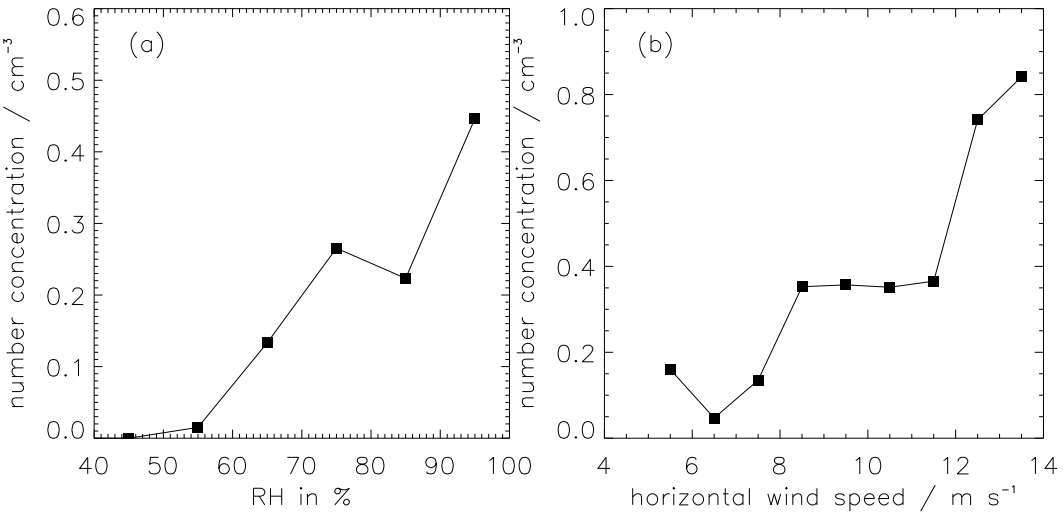

Figure 4: Relationship between number concentration of GN in marine boundary layer and (a) relative humidity and (b) horizontal wind speed.

covers the whole height range of our measurement flights. For the range of 5 - 8 m s^{-1} the number concentration of the GN increases, followed by an almost constant number concentration of 0.35 cm^{-3} for 8 - 11 m s^{-1}, and a strong increase for higher wind speeds. Woodcock (1952) also found a strong relationship between the detected mass of sea-salt and the horizontal wind speed. Looking at the Beaufort wind scale, 12 m s^{-1} belong to Beaufort 6 where the sea is characterized by frequent white foam crests. At Beaufort 7 some foam from the breaking waves is blown into streaks along with the wind direction and a moderate amount of airborne spray is present. Thus, the observed increase in GN number concentration with increasing wind speed can be explained by a higher production of white caps and sea spray at higher Beaufort scales.

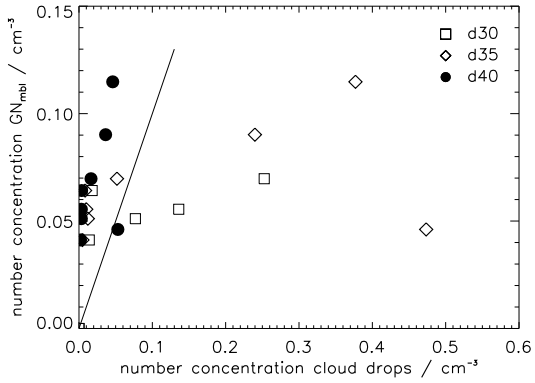

Figure 5: Mean number concentration of large cloud drops (lowest drop size 30 μm, 35 μm and 40 μm) versus mean number concentration of GN in marine boundary layer. The solid line shows the 1:1 line.

3.3 Relation Between GN and Drizzle

It is assumed that there is a correlation between the number concentration of GN and the amount of drizzle in warm shallow cumulus clouds. GN are expected to represent the first droplets large enough to cause the onset of collision and coalescence processes and thus the production of larger droplets having diameters above approximately 50 μm. As a first outlook on this topic, Fig. 5 shows the number concentration of a fraction of cloud droplets as a function of the number concentration of GN detected in the MBL. The fraction of cloud droplets is specified by a predefined lower size threshold (30 μm, 35 μm and 40 μm) and an upper limit defined by the measurement conditions. The number concentration of droplets larger than 40 μm resembles the one of the measured GN the most. This could be an indication for the fact that the amount of GN has an impact on the development of larger droplets in warm clouds.

For further work the information on GN for each measurement flight will be compared to simultaneously taken filter probes with respect to mass of sea-salt. Also, the results from our measurements will be used as input for a numerical model. The goal is to examine whether the size and number concentration of the observed GN can, under given turbulence conditions, cause an efficient collision and coalescence processes leading to the production of drizzle drops and later to the formation of rain.

Acknowledgements. Thanks go to D. Schell and C. Claus from enviscope GmbH for their support during the measurement campaign, B. Stevens and L. Nuisens from MPI Hamburg for the successful collaboration and the Caribbean Institute for Meteorology and Hydrology.

References

Beard, K. V. and Ochs, H. T.: 1993, Warm-rain initiation: an overview of microphysical mechanisms, *J. Appl. Meteor.* **32**, 608–625.

Chuang, P. Y., Saw, E. W., Small, J. D., Shaw, R. A., Sipperley, C. M., Payne, G. A. and Bachalo, W. D.: 2008, Airborne phase doppler interferometry for cloud microphysical measurements, *Aerosol Sci. Technol.* **42**(8), 685–703.

Ludlam, F. H.: 1951, The production of showers by the coalescence of cloud droplets, *Quarterly Journal of the Royal Meteorological Society* **77**, 402–417.

Mason, B. J.: 2001, The role of sea-salt particles as cloud condensation nuclei over the remote oceans, *Q. J. R. Meteorol. Soc.* **127**, 2023–2032.

Siebert, H., Franke, H., Lehmann, K., Maser, R., Saw, E. W., Schell, D., Shaw, R. A. and Wendisch, M.: 2006, Probing finescale dynamics and microphysics of clouds with helicopter-borne measurements, *Bull. Amer. Meteorol. Soc.* pp. 1727–1738.

Woodcock, A. H.: 1952, Atmospheric salt particles and raindrops, *Journal of Meteorology* **9**, 200–212.

Woodcock, A. H. and Gifford, M. M.: 1949, Sampling sea-salt nuclei over the ocean, *J. Mar. Res.* **8**, 177–197.

Wright, M.: 1940, Atmospheric Opacity at Valentia, *J. R. Met. Soc.* **66**, 66–77.

WHEN DO INSOLUBLE PARTICLES ACT AS GOOD CCN?

Nenes A.[1,2], Kumar P.[2,3], Karydis V.A.[1], and Sokolik I.N.[1]
[1]School of Earth and Atmospheric Sciences, Georgia Institute of Technology
[2]School of Chemical and Biomolecular Engineering, Georgia Institute of Technology
[3]SABIC innovative plastics, Selkirk, NY, USA

1. INTRODUCTION

The ability of dust particles to serve as CCN under atmospherically relevant supersaturations depends on their mineralogy, size, morphology, and atmospheric processing. Most studies to date focus on the soluble fraction of aerosol particles when describing cloud droplet nucleation, and overlook the interactions of the hydrophilic insoluble fraction with water vapor. A new approach to include such interactions is presented, by combining multilayer Frenkel-Halsey-Hill (FHH) physical adsorption isotherm and curvature (Kelvin) effects.

The importance of adsorption activation theory (FHH-AT) is demonstrated by measurements of CCN activity of mineral aerosols generated from clays, calcite, quartz, and desert soil samples from Northern Africa, East Asia/China, and Northern America. Based on the dependence of critical supersaturation (S_c) with particle dry diameter (D_{dry}), it is found that the FHH-AT is a better framework for describing fresh (and unprocessed) dust CCN activity than classical Köhler theory (KT). Ion Chromatography (IC) measurements performed on fresh regional dust samples indicate negligible soluble fraction, further supporting FHH-AT.

The results presented reshapes the conventional model of CCN activity, as it demonstrates that dust particles do not require deliquescent material to serve as atmospheric cloud nuclei. A droplet parameterization framework for large scale models that includes the new CCN activation physics is also developed and constrained by laboratory measurements. The framework is augmented to account for aging of dust (via deposition of hygroscopic material), and included within a global model framework to assess the impact of dust on warm cloud droplet number.

2. MODEL DESCREPTION

The NASA GMI, used in this study, is a state-of-the-art modular 3-D chemistry and transport model (CTM), with the ability to carry out multi-year simulations for impact assessment studies. The detailed description of the framework can be found in Considine et al. (2005). The GMI aerosol model was contributed by Liu et al. (2005) and coupled to the GMI-CTM advection core. The meteorological fields used in the simulations were taken from the Goddard Institute for Space Studies version II' (GISS II') GCM which includes a slab (Q-flux) ocean model to represent the ocean-atmospheric coupling. The horizontal resolution is 4° latitude by 5° longitude. The vertical resolution is 23 vertical layers.

The concentration of particles that can experience hygroscopic growth, is given as an input from the aerosol module to the cloud droplet formation parameterization and is distributed in four aerosol types: fossil fuel (sulfate, organic mass, and black carbon), biomass burning (organic mass and black carbon), marine (natural sulfate and sea salt), and mineral dust. Fossil fuel, biomass burning, and marine aerosols are assumed to follow the KT for CCN activation whereas mineral dust is assumed to follow the "unified dust activation framework" of Kumar et al. (2011) based on the FHH-AT. Particles within each aerosol type are internally mixed and assumed to follow a prescribed number size distribution shape following the recommendations of Karydis et al. (2011). Parameters used by the cloud droplet formation parameterization also include the accommodation coefficient of 0.06, the updraft velocity representative of typical stratocumulus clouds, V = 0.3 m s^{-1} over land, and V = 0.15 m s^{-1} over ocean, and "basecase" FHH adsorption parameters, AFHH = 2.25 and BFHH = 1.2 (Kumar et al. 2011).

Calculation of CDNC is carried out in two conceptual steps, one involving the determination of the "CCN spectrum", which is the number of CCN that can activate to form droplets at a certain level of supersaturation (Kumar et al., 2009), and

another one determining the maximum supersaturation, s_{max}, that develops in the ascending cloudy parcels used to represent droplet formation in the GCM (Fountoukis and Nenes, 2005). The CDNC is then just the value of the CCN spectrum at s_{max}.

3. RESULTS AND DISCUSSION

Figure 1 shows data (symbols) of s_c as a function of D_{dry} (Koehler et al., 2009; Sullivan et al., 2009) for different dust types and individual mineral particles generated in the lab either with the use of a dry fluidized bed, or via wet atomization from an aqueous suspension of dust particles. The CCN activity data are fitted to a power law expression, $s_c = C(D_{dry})^x$, from which the ''experimental'' exponent, x, is determined. A_{FHH} and B_{FHH} and the corresponding exponent, x_{FHH}, were determined from fitting the FHH-AT model (Figure 1, colored lines) to the experimental data via least squares minimization. The KT fits to the data are expressed in terms of hygroscopicity, κ (Figure 1, black lines). Based on the dependence of S_c with particle D_{dry} it is found that the FHH-AT is a better framework for describing fresh (and unprocessed) dust CCN activity than classical KT(Kumar et al., 2009b).

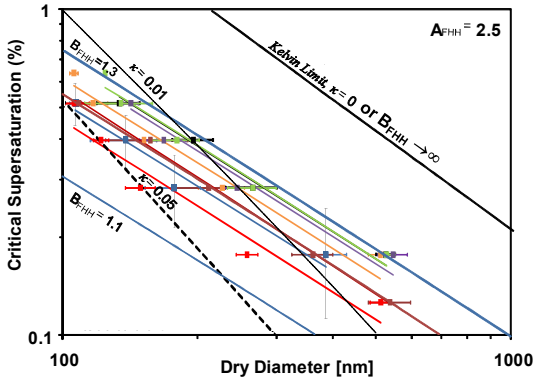

Fig. 1. FHH adsorption activation fits (lines) to the observed CCN activity (points) for dust aerosols generated from clays, calcite, quartz, and desert soil samples from Northern Africa, East Asia/China, and Northern America.

Figure 2 shows the predicted contribution of cloud droplets formed from the activation of both soluble and insoluble aerosols on total CDNC. Even if the contribution of dust to the predicted CDNC is not significant on a global scale, it can be regionally important as it can affect not only the local air quality but also the nearby and long distance regions due to its ability to remain aloft for several days and travel thousands of kilometers (e.g. the transport of Saharan dust to the tropical Atlantic Ocean). The contribution of dust particles to the predicted CDNC on areas close to mineral dust sources (i.e. deserts) is up to 90 cm^{-3} (Fig. 2). Mineral dust also has a small contribution on the annual average predicted CDNC across the Atlantic Ocean, as far as the Caribbean Sea (up to 50 cm^{-3}). Nevertheless, this effect can be even more important in specific dust storm episodes.

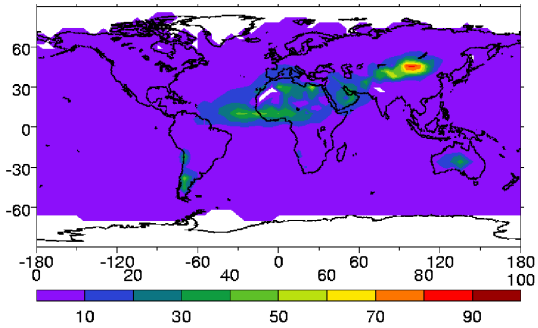

Fig. 2. Predicted annual mean mineral dust fractional contribution on CDNC at 920 mb.

4. BIBLIOGRAPHY

Considine DB, Bergmann DJ, Liu H (2005) Sensitivity of Global Modeling Initiative chemistry and transport model simulations of radon-222 and lead-210 to input meteorological data. Atmos Chem Phys 5: 3389-3406. doi:10.5194/acp-5-3389-2005

Fountoukis C, Nenes A (2005) Continued development of a cloud droplet formation parameterization for global climate models. J Geophys Res 110(D11): D11212. doi:10.1029/2004JD005591

Karydis V, Kumar P, Barahona D, Nenes A (2011) On the effect of insoluble dust particles on global CCN and droplet number. J Geophys Res 116: D23204. doi:10.1029/2011JD016283.

Koehler, KA, Kreidenweis SM, DeMott PJ, Petters MD, Prenni AJ, and Carrico CM (2009), Hygroscopicity and cloud droplet activation of mineral dust aerosol, Geo-

phys. Res. Lett., 36, L08805, doi:10.1029/2009GL037348.
Kumar P, Sokolik IN, Nenes A (2009a) Parameterization of cloud droplet formation for global and regional models: including adsorption activation from insoluble CCN. Atmos Chem Phys 9(7): 2517-2532. doi:10.5194/acp-9-2517-2009
Kumar P, Nenes A, Sokolik IN (2009b) Importance of adsorption for CCN activity and hygroscopic properties of mineral dust aerosol. Geophys Res Let 36: L24804. doi:10.1029/2009GL040827
Kumar P, Sokolik IN, Nenes A (2011) Measurements of cloud condensation nuclei activity and droplet activation kinetics of wet processed regional dust samples and minerals. Atmos Chem Phys 11(4): 8661-8676. doi:10.5194/acp-11-8661-2011
Liu XH, Penner JE, Herzog M (2005) Global modeling of aerosol dynamics: Model description, evaluation, and interactions between sulfate and nonsulfate aerosols. J Geophys Res 110(D18): D18206. doi:10.1029/2004JD005674
Sullivan, RC, Moore MJK, Petters MD, Kreidenweis SM, Roberts GC, and Prather KA (2009), Effect of chemical mixing state on the hygroscopicity and cloud nucleation properties of calcium mineral dust particles, Atmos. Chem. Phys., 9, 3303 – 3316.

Acknowledgments We would like to acknowledge support from NASA-ACMAP, CONOCO-Phillips, and NOAA.

ELUCIDATING THE RELATIVE SIGNIFICANCE OF AEROSOL CHARACTERISTICS AND UPDRAFT VELOCITY ON CLOUD DROPLET AND ICE CRYSTAL NUMBER THROUGH THE USE OF CLOUD PARAMETERIZATION ADJOINTS

Athanasios Nenes[1,2], Shannon L. Capps[2], Vlassis A. Karydis[1], Donifan Barahona[3], Prashant Kumar[4]

[1]School of Earth and Atmospheric Sciences, Georgia Institute of Technology
[2]School of Chemical and Biomolecular Engineering, Georgia Institute of Technology
[3]USRA GESTAR, Columbia, Maryland, United States
[4]SABIC innovative plastics, Selkirk, NY, USA

1. INTRODUCTION

Aerosols affect properties of warm clouds by acting as cloud condensation nuclei and contributing cloud droplet number concentration (CDNC). In cirrus clouds, aerosols affect the concentration of ice crystals (ICNC) largely through their ability to act as ice nuclei. Within global models, these aerosol-cloud links are represented by physically-based parameterizations. Understanding the relative importance of all parameters affecting CDNC and ICNC in a 3D simulation is an important but daunting task. Inverse modeling by means of model adjoints is an ideal approach to accomplish this, as it efficiently produces gradients of CDNC and INDC to all model inputs with analytical accuracy and in a single model execution.

We present the adjoints of the Kumar et al. (2009) and Barahona and Nenes (2010) parameterizations, which are state-of-the-art schemes which consider cloud droplet and ice crystal formation within an ascending air parcel containing a diverse mixture of aerosol. The adjoints are used to study the effects of aerosol number and chemical composition, modal characteristics of each population, updraft velocity, and particle type on CDNC and ICNC within a year-long execution of the NASA Global Modeling Initiative (GMI) Chemical Transport Model (CTM) using wind fields generated by NASA GISS GCM Model II'. Seasonal, regional and global sensitivities presented unravel when and what is important for CDNC and ICNC.

2. MODEL DESCREPTION

The NASA GMI, used in this study, is a state-of-the-art modular 3-D CTM, with the ability to carry out multi-year simulations for impact assessment studies. The detailed description of the framework can be found in Considine et al. (2005). The GMI aerosol model was contributed by Liu et al. (2005) and coupled to the GMI-CTM advection core. The meteorological fields used in the simulations were taken from the Goddard Institute for Space Studies version II' (GISS II') GCM which includes a slab (Q-flux) ocean model to represent the ocean-atmospheric coupling. The horizontal resolution is 4° latitude by 5° longitude. The vertical resolution is 23 vertical layers.

The predicted mass concentrations of aerosols from GMI are given as an input to the cloud droplet formation parameterization. Aerosols are distributed in four aerosol types: fossil fuel (sulfate, organic mass, and black carbon), biomass burning (organic mass and black carbon), marine (natural sulfate and sea salt), and mineral dust following a prescribed in-cloud number size distribution (Karydis et al., 2011). Fossil fuel, biomass burning, and marine aerosols are assumed to follow the Köhler theory for CCN activation whereas mineral dust is assumed to follow the FHH adsorption activation theory (Kumar et al., 2009). Other important parameters for CDNC calculations include an effective water vapor uptake coefficient of 0.06; FHH adsorption parameters, A_{FHH} = 2.25 and B_{FHH} = 1.2; updraft velocities, V = 0.3 m s^{-1} over land, and V = 0.15 m s^{-1} over ocean.

Calculation of CDNC is carried out in two conceptual steps, one involving the determination of the "CCN spectrum", which is the number of CCN that can activate to form droplets at a certain level of supersaturation (Kumar et al., 2009), and another one determining the maximum supersaturation, s_{max}, that develops in the ascending cloudy parcels used to represent droplet formation in the GCM (Fountoukis and Nenes, 2005). The CDNC

is then just the value of the CCN spectrum at s_{max}.

The adjoint of the cloud droplet formation parameterization efficiently determines the sensitivity of the CDNC with respect to each input value (updraft velocity, uptake coefficient, aerosol number, hygroscopicity of soluble aerosol species, adsorption parameters of insoluble aerosols). After calculation of the forward model at the specified parameter values, the derivative of CDNC with respect to each intermediate variable in the code is computed and passed through the augmented code in reverse order by applying the chain rule of derivative calculus. The result is the efficient, simultaneous calculation of the local adjoint sensitivities of CDNC with respect to the parameterization inputs.

3. RESULTS AND DISCUSSION

CDNC sensitivity to updraft velocity is low in areas where the activation fraction of aerosols into droplets is high (i.e. Southern Oceans), as most of the aerosols are already activated. Therefore, the CDNC sensitivity to updraft velocity in these areas is predicted to be as low as 0.2 (Figure 1). When the activation fraction is low (i.e. polluted marine and continental environments), CDNC sensitivity to updraft velocity is higher, especially close to coasts, with values up to 1.3 over W. Europe (Figure 1). Over the continents, the sensitivity is larger over Eastern Asia, Central Europe, and Eastern North America (up to 1) where the activation fraction is predicted to be low (between 1% and 6%).

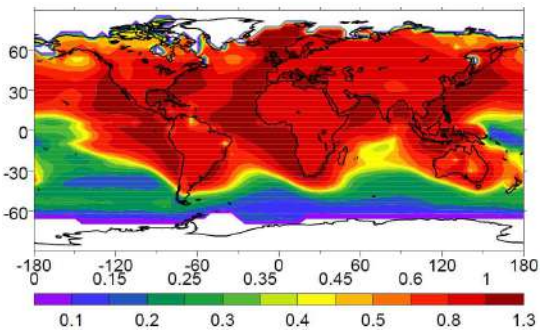

Fig. 1. Predicted annual mean CDNC sensitivity to updraft velocity for the lowest cloud-forming level.

The sensitivity of CDNC to water uptake coefficient is negative and larger over the polluted environments of the Northern Hemisphere (Figures 2). The largest sensitivity is predicted over the west coasts of Europe and North Africa (up to -0.6).CDNC sensitivity to uptake coefficient is also large (~ -0.4) over Eastern Asia, Europe, Eastern US, as well as over the biomass burning areas of South America and Central Africa, due to the low droplet activation fractions. Over more pristine environments, such as the Southern Oceans, uptake coefficient has a lower impact on CDNC, (~ -0.1).

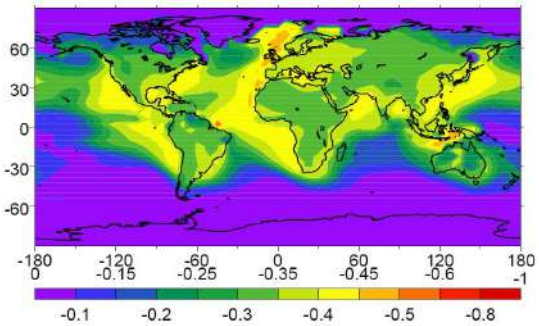

Fig. 2. Predicted annual mean CDNC sensitivity to water uptake coefficient for the lowest cloud-forming level.

The sensitivity of CDNC to anthropogenic aerosol concentrations is low over polluted areas as both the s_{max} and the droplet activation fraction are low (Figure 3). On the other hand, clean areas are characterized by high s_{max} and droplet activation fractions, resulting in large CDNC increases when aerosol concentration is increased. Consequently, GMI predicts a moderate influence (up to 0.2) of aerosol concentration on CDNC over East Asia, Europe, and Eastern Northern America. On the other hand, the sensitivity of CDNC to aerosol concentration is moderate along the polluted coasts (~ 0.4) and increases as we move to more pristine environments such as the tropical Pacific and Atlantic Oceans (up to 0.7). The CDNC sensitivity to anthropogenic aerosol concentration over the southern oceans is not large given that CDNC is most sensitive to sea salt, the main aerosol component in the area.

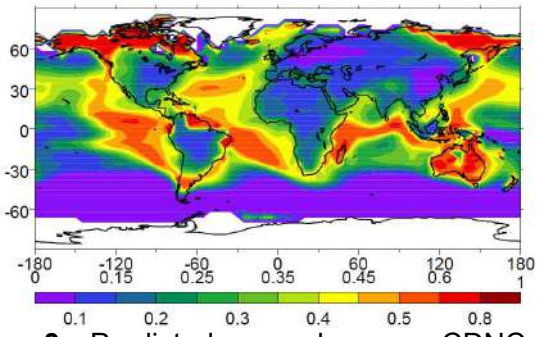

Fig. 3. Predicted annual mean CDNC sensitivity to anthropogenic aerosol concentration for the lowest cloud-forming level.

Over areas with high aerosol load, increasing the hygroscopicity of the aerosols will have a very small impact on CDNC (less than 0.1) as the tendency to increase the activation fraction will be compensated by a decrease in s_{max} due to the increasing competition for water vapor. Over moderately polluted areas (i.e. over north Atlantic and Pacific Oceans) the droplet activation fraction is moderately high (~ 15%). Increasing the hygroscopicity of the aerosols will lead to a notable increase in the droplet activation fraction without a compensating decrease on s_{max} as the competition for water is less intense. GMI predicts that over Atlantic and Pacific Oceans, the CDNC sensitivity to anthropogenic aerosol hygroscopicity is up to 0.4 (Figures 4).

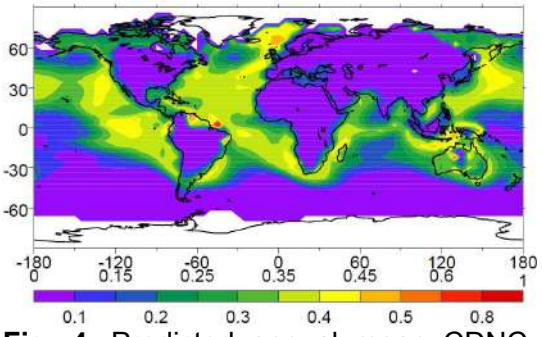

Fig. 4. Predicted annual mean CDNC sensitivity to anthropogenic aerosol hygroscopicity for the lowest cloud-forming level.

4. BIBLIOGRAPHY

Barahona, D, Rodriguez J, and Nenes A (2010) Sensitivity of the global distribution of cirrus ice crystal concentration to heterogeneous freezing, *J. Geophys. Res.*, *115*, doi:10.1029/2010JD014273

Considine DB, Bergmann DJ, Liu H (2005) Sensitivity of Global Modeling Initiative chemistry and transport model simulations of radon-222 and lead-210 to input meteorological data. Atmos Chem Phys 5: 3389-3406. doi:10.5194/acp-5-3389-2005

Fountoukis C, Nenes A (2005) Continued development of a cloud droplet formation parameterization for global climate models. J Geophys Res 110(D11): D11212. doi:10.1029/2004JD005591

Karydis V, Kumar P, Barahona D, Nenes A (2011) On the effect of insoluble dust particles on global CCN and droplet number. J Geophys Res 116: D23204. doi:10.1029/2011JD016283.

Kumar P, Sokolik IN, Nenes A (2009) Parameterization of cloud droplet formation for global and regional models: including adsorption activation from insoluble CCN. Atmos Chem Phys 9(7): 2517-2532. doi:10.5194/acp-9-2517-2009

Liu XH, Penner JE, Herzog M (2005) Global modeling of aerosol dynamics: Model description, evaluation, and interactions between sulfate and nonsulfate aerosols. J Geophys Res 110(D18): D18206. doi:10.1029/2004JD005674.

Acknowledgments We would like to acknowledge support from NASA-ACMAP, CONOCO-Phillips, and NOAA.

HIGH-RESOLUTION WIND-PROTECTED OBSERVATIONS OF WINTER PRECIPITATION PARTICLES AND PRECIPITATION INTENSITY

Sento Nakai[1], Manato Fuzita[2], Takahumi Katsushima[3],
Hiroki Motoyoshi[1], Toshiro Kumakura[2], Masaaki Ishizaka[1],
Kotaro Yokoyama[4], Shigeki Murakami[5]

[1] Snow and Ice Research Center, National Research Institute for Earth Science and Disaster Prevention (NIED)
[2] Department of Civil and Environmental Engineering, Nagaoka University of Technology
[3] Toyama National College of Technology
[4] Hokuriku Research Center, National Agricultural Research Center (NARC)
[5] Tohkamachi Experimental Station, Forestry and Forest Products Research Institute (FFPRI)

1. INTRODUCTION

The shape of solid and melting precipitation particles varies significantly, leading to the difficulty of the quantitative precipitation estimation (QPE) from ground and space-borne radars. In order to derive good estimation based on the appropriate relations, we have to understand the microphysical processes including change of particle shape and liquid water content. Detailed and continuous observations of ground precipitation particles, by combining with radar observations, will supply a basic data to clarify the microphysical processes. It is also important for constructing the Global Precipitation Measurement (GPM) standard algorithms. We have started three-year observations of precipitation particles and high-resolution precipitation intensity as part of a field experiment to obtain a basic data for GPM algorithm. The observations were made within the range of a polarimetric Doppler radar. The specifications of the observation site and some preliminary results are described in this manuscript.

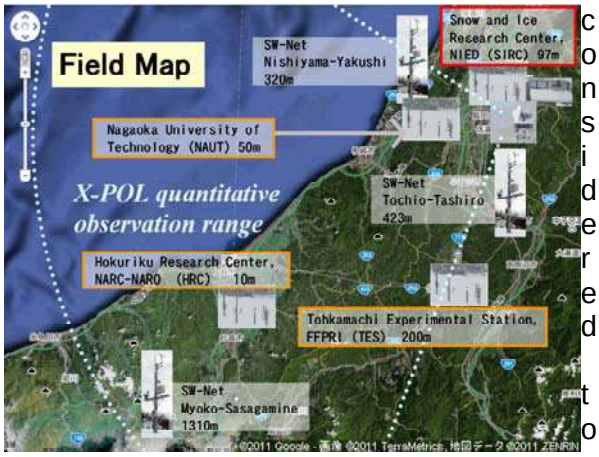

Fig. 1. Field map of the observation area. Snow and Ice Research Center, NIED (SIRC), Hokuriku Research Center, NARC (HRC), Tohkamachi Experimental Station, FFPRI (TES), and Nagaoka University of Technology (NAUT) are the research institutions at which snow particle observation stations (SPOS) were installed. Surface stations of SIRC SW-Net (Yamaguchi et al. 2007), Nishiyama-Yakushi (NY), Tochio-Tashiro (TT), and Myoko-Sasagamine (MS) are also shown. Altitude of each station is indicated after the station name.

2. BRIEF DESCRIPTION OF FIELD EXPERIMENT

A field experiment composed of several items is conducted in the Niigata region, a heavy snowfall area facing the Japan Sea (Fig. 1). This region have a lot of snowfall and precipitating days during winter season (Fig. 2). Moreover, a large part of the precipitation in this region is brought under temperature around 0 ^{0}C (Yamaguchi et al., 2007). Hence, the Niigata region is be an optimal location for the effective research observation project to acquire the data set and knowledge on solid and melting precipitation particles. Several research organizations have been conducted observations of snowfall intensity, snowfall particles on the ground, radar Ze, as well as related meteorological observations during winter seasons. This

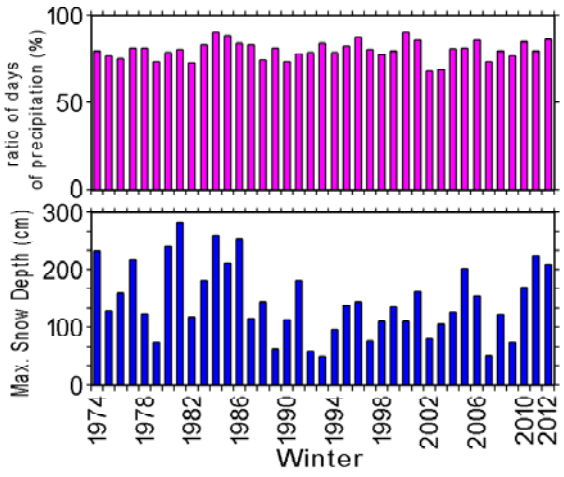

Fig. 2. Seasonal maximum snow depth and ratio of days of precipitation > 0.5 mm at SIRC.

Table 1. Sampling area size and resolution of snow particle observation facilities used in this study.

Facility / sampling area size	Element	Resolution
SPOS		
PARSIVEL W30 x D180 mm^2	particle size fall speed	0.2 to 25 mm 32 classes 0.2 to 20 ms^{-1} 32 classes
SPOS, SW-Net		
SR-2A / 14000 mm^2	precipitation intensity	0.0052 mm
HRC, TES, SIRC, SW-Net		
RT-3,4 / 38000 mm^2	precipitation amount	0.5 mm
SIRC		
FSO / W160 x D200 mm^2	particle size fall speed	0.25 mm 0.03 ms^{-1}

means that the region has the high potential for obtaining high-quality winter precipitation data. We conducted Intensive observations of the field experiment in this region in 2010/2011 and 2011/2012 winter seasons. Observations are scheduled also in 2012/2013 winter season.

This field experiment is composed of the following items:

1) Automatic observations of solid precipitation particles to obtain the distribution of the kind, size, and fall speed of the particles.
2) High-frequency precipitation intensity observations to obtain the precipitation intensity verification data.
3) X-band radar observations to obtain horizontal and vertical changes of Ze and mesoscale cloud system classification using the Ze.
4) The analysis of the precipitation-particle-type dependency of Z-R, Z-M relationship by comparison with the observed data.

The snowfall particle observation stations (SPOS) were installed at four institutions: SIRC (Seppyo-ken site), HRC (Jo-etsu site), TES (Tokamachi site), and NAUT (Gidai site) (See caption of Fig. 1 on abbreviation). Other than the SPOS sites, SR-2A was operated at some of the Snow and Weather Observation Network (SW-Net) stations deployed by SIRC (Yamaguchi et al. 2007) without wind shield fence. The RT-3/4 type JMA (Japan Meteorological Agency) standard raingauges with attached wind shield were operated at SIRC, HRC, and TES. The observation elements, sampling volumes, resolutions of these facilities are summarized in Table 1.

The data obtained by the Falling Snow Observatory (FSO, Ishizaka et al. 2004) and an X-band polarimetric Doppler radar (X-POL, Iwanami et al. 1996) will be used for comparison with the data obtained by SPOS observations. All SPOS sites and SW-Net stations locate within or near the observation area of the X-band radar XPOL installed at SIRC (Fig. 1). The arrangement of the SPOS sites and SW-Net stations cover from coastal to mountainous areas and enable us to carry out surface observations of various snowfall in the X-POL observation range.

3. SPECIFICATIONS OF SPOS

An SPOS is composed of a PARSIVEL (OTT Hydromet GmbH) for observations of precipitation particltes of item 1, an SR-2A (Tamura Seppyo Keisoku Laboratory) for high-frequency precipitation intensity observations of item2, a Web camera system (Panasonic BB-HCM581 and an LED lamp) for monitoring of snow accretion on PARSIVEL and SR-2A, and wind shield fence. Photographs of the Tokamachi

Fig. 3. Tokamachi SPOS site installed in the observation field of TES. PARSIVEL and SR-2A is set up in a 5-meter high wind shield (left panel). They are monitored by a Web camera with an LED lamp for lighting (right upper panel). These facilities are controlled by PCs in a observation hut (right middle panel). They are connected by protected cables of 50 meters long (right lower panel).

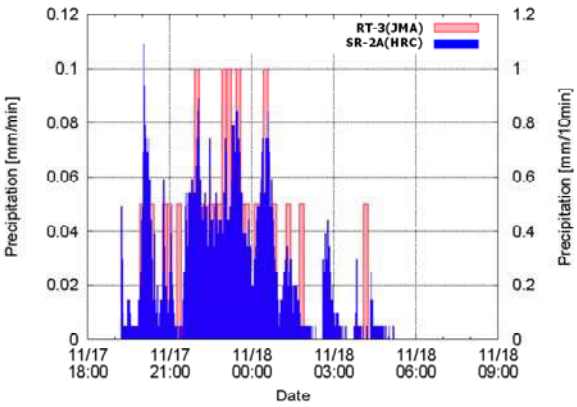

Fig. 4. Sample data obtained by a SR-2A at Jo-etsu SPOS site (HRC) and the JMA operational RT-3 data (Takada, a station close to HRC.)

SPOS site is shown in Fig. 3.

A comparison of SR-2A and RT-4 is shown in Fig. 4. It is apparent that high size and time resolution of SR-2A (Table 1) is more suitable for the comparison with PARSIVEL and radar data.

A 2-dimensional histogram of falling snow particle spanned by particle diameter and falling velocity is obtained in 1-minute intervals by PARSIVEL. An example of time series of accumulated histogram is shown in Fig. 5. The shape of 2-d histogram at 0700-0800 JST indicates rain. Large particles with low falling speed gradually dominated hour by hour, and finally, particles with falling speed about 1-1.5 ms^{-1}, indicating snow aggregates, dominated at 1100-1200 JST. The time series clearly indicate the change from rain to solid precipitation. Temperature at 0700

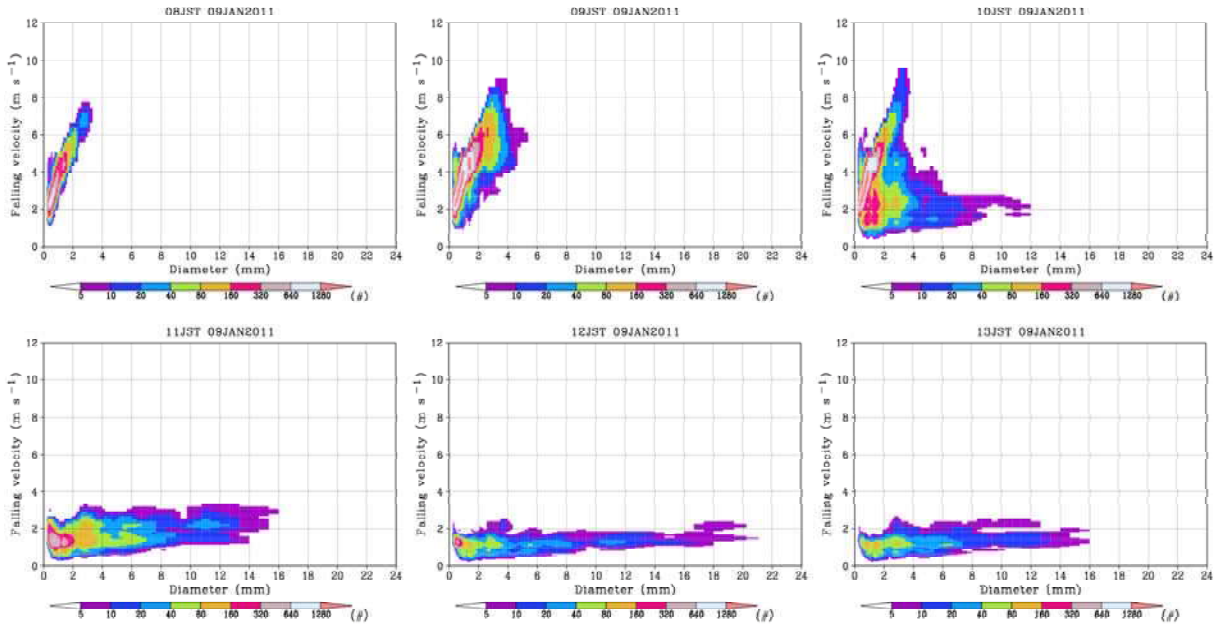

Fig. 5. An example of hourly 2-dimensional histogram of precipitation particles obtained by a PARSIVEL at Seppyo-ken SPOS site. Particle count during 1 hour ending at the time indicated on the top of each panel is shown. Note that bin intervals are variable through observation range.

Fig. 6. Example of monitoring images of the Tokamachi SPOS site.

JST and 1000 JST were 2.6 ^{o}C and 0.2 ^{o}C, respectively. Relative humidity was more than 90% from 0700 JST to 1300 JST. Hourly precipitation amount from 1.5 mm to 8.0 mm were recorded. These suggest that the precipitation was wet snow after 1000 JST and consistent with PARSIVEL observations. Ishizaka et al. (2010) pointed out that a PARSIVEL has a negative bias in the measured particle size distribution. It may be caused by the small sampling volume of a PARSIVEL. We are developing a database for correction of PARSIVEL data using FSO observations.

It is important to eliminate data including errors caused by snow accretion to the observation facilities. An SPOS site has a Web camera which views the facilities and wind shield fence from above. Monitoring images in 10-minute intervals (Fig. 6) are automatically recorded. These images are used for checking snow accretion on the facilities and the wind shield fence. The LED lamp is turned on for 24 hours, as it can be dark when it snows heavily even in the daytime. The whole site works by a single 100V/15A power supply, and are battery backuped.

4. EXAMPLE OF 10-MINUTE INTERVAL DATA AT TOKAMACHI SITE

We made a comparison of data observed at Tokamachi SPOS site (200 m above mean sea level) during 11-20 January 2011. Daily mean temperature of this period was often below 0 ^{o}C suggesting that most precipitation was in solid phase. We used the SPOS data and temperature observed by TES. The interval of observed data was 1 minute. Ten-minute mean or sum was calculated using these data. The number of 10-minute interval data was 1440. A 10-minute mean diameter D_{FC} and falling velocity V_{FC} weighted by water flux of each particle was derived from 2-dimensional (size and falling velocity) particle histogram obtained by PARSIVEL in 1-minute intervals using the method of Ishizaka et al. (2012).

A nearby grid point of X-POL polar coordinate at elevation of 1.9^{o} was selected for comparison considering beam blocking. Ze was observed by X-POL radar in 10-minute intervals. The distance between this point and Tokamachi SPOS site was

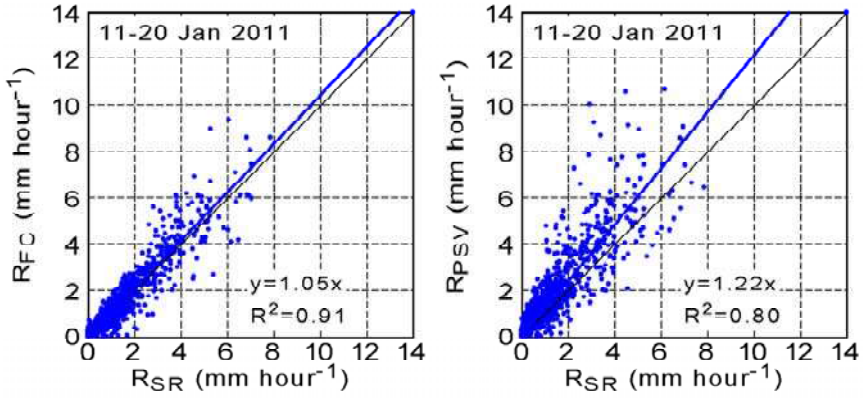

Fig. 7. Comparison of precipitation intensity measured by SR-2A (abscissa) and that derived from PARSIVEL observation (ordinate). An algorithm of Ishizaka et al. (2012) was used to derive precipitation intensity from particle diameter and falling speed (left panel). That derived by built-in algorithm is also shown (right panel).

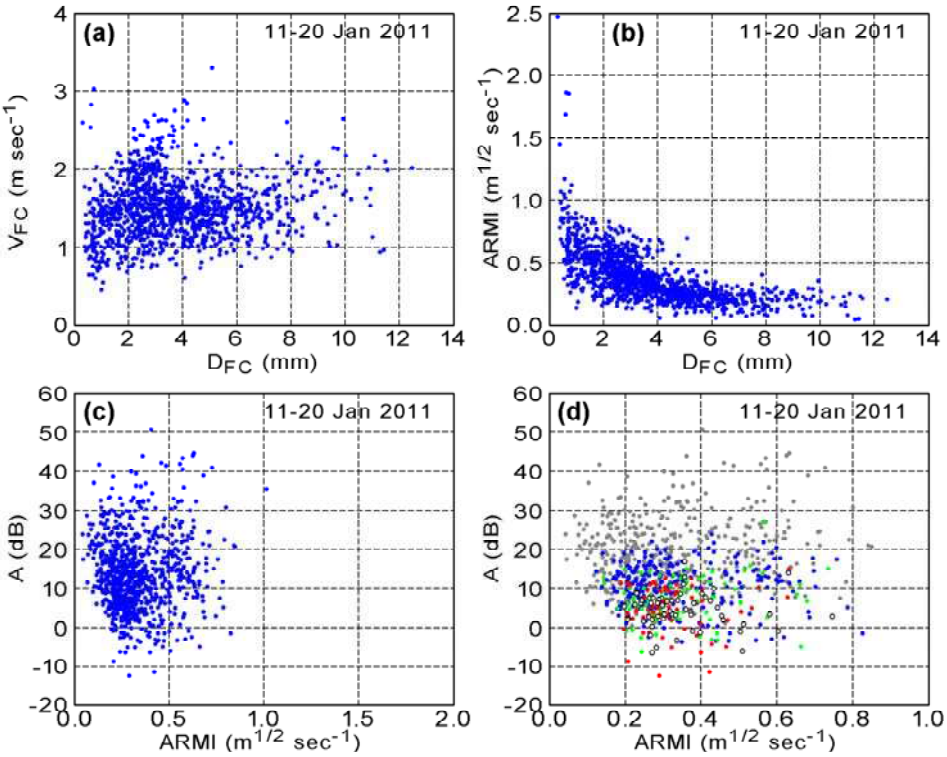

Fig. 8. Scatterplot of (a) D_{FC} and V_{FC}, (b) D_{FC} and ARMI, and (c)(d) ARMI and A. Colors in (d) indicates precipitation intensity measured by SR-2A: 0-1 mm hour^{-1} (gray), 1-2 mm hour^{-1} (blue), 2-3 mm hour^{-1} (green), 3-4 mm hour^{-1} (red), and >4 mm hour^{-1} (open circle). See text for abbreviations.

1056 m in altitude and 2.34 km in horizontal distance in a direction of 289^{o}. The grid point was located upwind of the Tokamachi SPOS site. The beam width of X-POL is 1.16^{o}, that is, the radar beam spread in a width of about 700 m at a distance of 34.4 km between TES and X-POL.

The method of Ishizaka et al. (2012) yielded precipitation intensity from PARSIVEL 2-dimensional particle histogram larger than SR-2A measurement by 5% in average. The coefficient of determination was more than 0.9 (Fig. 7). The intensity of PARSIVEL built-in output was much larger and the coefficient of determination was lower (Fig. 7). In this case, the method of Ishizaka calculated more accurate solid precipitation intensity from particle histogram data.

PARSIVEL data was also compared with radar Ze. Precipitation particles in this period were mainly composed of snow aggregates and graupel was mixed only partially (Fig. 8a). Small particles with diameter less than 3 mm was dominated in part of the period. A parameter named Aerodynamical Riming and Melting Index (ARMI) was defined to describe conveniently the characteristics of a precipitation particle expressed using D_{FC} and V_{FC} .

$$ARMI = V_{FC} / D_{FC}^{0.5}$$

When D_{FC} >3 mm, ARMI in ranges of approximately 0.1-0.5, 1-2, and 2-4 correspond to, respectively, snow aggregates, graupel, and rain. The data of current analysis show ARMI of 0.1-0.5 corresponding to the particles dominated by snow aggregates. No ARMI >1, that corresponds to graupel, was found when D_{FC} >3 mm (Fig. 8b).

Rasmussen et al. (2003) showed that the Ze-R relations of solid precipitation can be expressed by $Ze=aR^{1.67}$. Modifying this equation yields

$$A = dB(Ze) - 16.7\log(R) .$$

Figure 8c is a scatterplot of A and ARMI. If these two variables showed a good relationship, We can derive a variable Ze-R relationship of solid and melting

precipitation using ARMI as a parameter. However, Fig. 8c does not indicate a clear relationship. Magnifying a part of Fig. 8c with dots colored by precipitation intensity (Fig. 8d), it was indicated that A became smaller as the precipitation intensity was larger. To derive good Ze-R relations, it is necessary to analyze variable A using much larger amount of data.

5. CONCLUDING REMARKS

Four SPOS observation sites were constructed at HRC, TES, NAUT and SIRC within the observation range of an X-band polarimetric Doppler radar, X-POL. An SPOS is composed of a PARSIVEL, an SR-2A, a Web camera, an LED lamp and wind shield fence. Size- and falling-velocity-distribution of snow particles, and high-resolution snowfall intensity were measured automatically.

A preliminary analysis using 10-day data was conducted. Weighted-mean diameter D_{FC} and falling velocity V_{FC} was calculated from 2-dimensional (size and falling velocity) particle histogram obtained by PARSIVEL using an algorithm developed by Ishizaka et al. (2012). Precipitation intensity R_{FC} calculated using the same algorithm showed 5% larger values compared with SR-2A intensity in average. The R_{FC} was much closer to the SR-2A direct measurement than precipitation intensity of facility built-in output. A parameter ARMI was defined to describe conveniently the characteristics of a precipitation particle. The effect of ARMI on the Ze-R relation was examined, though, clear relationship was not found in the preliminary analysis.

It is expected that this research supply the fundamental data on parameter setup in the development of the GPM standard algorithms, and that the data can be used for the algorithm verification. The results also have important meaning in providing correct snowfall data with respects to quality and to quantity to the snow and ice disaster occurrence prediction. This research can contribute towards establishment of the ground-based quantitative precipitation estimation in the winter seasons.

6. BIBLIOGRAPHY

Ishizaka, M., T. Shiina, K. Muramoto, S. Nakai and A. Sato, 2004: An automated system for identifying types of solid precipitation by image processing, *Proceedings, 14th International Conference on Clouds and Precipitation*, 1103-1106.

Ishizaka, M., M. Murakami, H. Motoyoshi, S. Nakai, S. Orikasa, A. Saito, T. Tajiri, T. Shiina and K. Muramoto, 2010: Snow particle observations by optical disdrometer -A comparison with CCD-camera imaging-. *Proceedings, 2010 autumn semi-annual meeting of the Meteorological Society of Japan*, D207.

Ishizaka, M., H. Motoyoshi, S. Nakai, T. Kumakura, T. Shiina and K. Muramoto, 2012: A method for identifying types of hydrometeors mainly contributing to precipitation. *16th International Conference on Clouds and Precipitation*, July 30-August 3, 2012, Leipzig, P.12.7.

Iwanami, K., M. Maki, T. Sato and M. Higashiura, 1996: Distribution of precipitation parameters estimated from observations with a Doppler radar and a polarimetric radar: Part 2, Results from polarimetric radar observation. *Proceedings, 12th International Conference on Clouds and Precipitation*, 190-192.

Rasmussen, R., M. Dixon, S. Vasiloff, F. Hage, S. Knight, J. Vivekanandan and M. Xu, 2003: Snow nowcasting using a real-time correration of radar reflectivity with snow gauge accumulation. J. Appl. Meteor., **42**, 20-36.

Yamaguchi, S., O. Abe, S. Nakai, A. Sato, 2007. Recent snow cover fluctuations in the mountainous areas of Japan. *Glacier Mass Balance Changes and Meltwater Discharge, IAHS Publ. No. 318*, 116-125.

Acknowledgments

This research is supported by the Japan Aerospace Exploration Agency (JAXA) as part of Precipitation Measuring Mission (PMM) Science 6th Research Announcement (RA), and a project of the National Research Institute for Earth Science and Disaster Prevention (NIED) "Research on advanced snow information and its application to disaster mitigation."

HOMOGENEITY OF SUBGRID-SCALE TURBULENT MIXING IN A LARGE-EDDY SIMULATION OF BOUNDARY-LAYER CLOUDS

Dorota Jarecka*[1], Wojciech W Grabowski[2], Hanna Pawlowska[1], and Hugh Morrison[2]

[1]Institute of Geophysics, Faculty of Physics, University of Warsaw
[2]National Center for Atmospheric Research, USA

1 INTRODUCTION

Turbulent entrainment and mixing between a cloud and clear air from its immediate environment is an important processes affecting macrophysical (e.g., cloud depth) and microphysical (e.g., spectrum of cloud droplets) properties of boundary layer clouds such as the shallow tropical cumulus and subtropical stratocumulus. (e.q., Warner, 1973; Siebesma, 2003, among many others). Entrainment of clear unsaturated air leads to evaporation of cloud water with associated cooling affecting cloud buoyancy field and leading to buoyancy reversal (e.g., Grabowski, 1993). However, entrainment-related evaporation and cooling do not happen instantaneously because turbulent mixing involves stirring and gradual filamentation of cloudy and cloud-free volumes down to the microscale homogenization scale. In this process, spatial scales of scalar fields (the temperature, moisture, and cloud water) decrease as time progresses due to the development of smaller and smaller eddies, and the microscale homogenization (i.e., evaporation of cloud water) takes place once scales close to the Batchelor and Kolmogorov scales are reached (e.g., Jensen and Baker, 1989; Grabowski, 1993; Malinowski and Zawadzki, 1993; Andrejczuk et al., 2004, 2006). Scales at which microscale homogenization occurs in clouds are much smaller than the typical gridlength of a large eddy simulation (LES) cloud model (below 1 cm versus tens or hundreds of meters). It follows that the homogenization is significantly delayed in nature, but there is no representation of this subgrid-scale process in traditional LES models.

As entrainment and mixing leads to the reduction of the liquid water content (LWC), the additional issue is whether the evaporation of cloud droplets results in the reduction of only the droplet size (as in the homogeneous mixing), only the droplet concentration (as in the extremely inhomogeneous mixing), or both the concentration and the size (as in the inhomogeneous mixing). This paper extends an approach for modeling subgrid-scale processes associated with entrainment and mixing proposed in Grabowski (2007) and Jarecka et al. (2009). In Grabowski (2007) and Jarecka et al. (2009), the discussion was limited to the bulk representation of cloud microphysics. Here, the approach is extended to the double-moment bulk microphysics scheme of Morrison and Grabowski (2007, 2008) to locally *predict* the homogeneity of mixing.

2 DELAY OF CLOUD EVAPORATION DUE TO THE TURBULENT MIXING

The standard thermodynamic grid-averaged equations for the 2-moment bulk advection-diffusion-condensation problem are as follows (Morrison and Grabowski, 2007):

$$\begin{aligned}
\frac{\partial \theta}{\partial t}+\frac{1}{\rho_o}\nabla\cdot(\rho_o \mathbf{u}\theta) &= \left(\frac{\partial \theta}{\partial t}\right)_{act}+\frac{L_v\theta_e}{c_pT_e}C+D_\theta \\
\frac{\partial q_v}{\partial t}+\frac{1}{\rho_a}\nabla\cdot[\rho_a q_v \mathbf{u}] &= \left(\frac{\partial q_v}{\partial t}\right)_{act}-C+D_{q_v} \\
\frac{\partial q_c}{\partial t}+\frac{1}{\rho_a}\nabla\cdot[\rho_a\,(\mathbf{u}-V_{q_c}\mathbf{k})\,q_c] &= \left(\frac{\partial q_c}{\partial t}\right)_{act}+C+D_{q_c} \\
\frac{\partial N_c}{\partial t}+\frac{1}{\rho_a}\nabla\cdot[\rho_a\,(\mathbf{u}-V_{N_c}\mathbf{k})\,N_c] &= \left(\frac{\partial N_c}{\partial t}\right)_{act}+\left(\frac{\partial N_c}{\partial t}\right)_{evap}+D_{N_c}
\end{aligned} \tag{1}$$

*Correspondence to: Dorota Jarecka, Pasteura 7, 02-093 Warsaw, Poland. E-mail: dorota@igf.fuw.edu.pl

where θ, q_v, q_c and N_c are the potential temperature, the water vapor mixing ratio, the cloud water mixing ratio, and the cloud droplets number concentration, respectively; $\rho_o(z)$ is the base state density profile; $V_{N/q}$ is the number-/mass-weighted mean particle fall speed; $\theta_e(z)$ and $T_e(z)$ are the environmental potential temperature and temperature profiles; $\mathbf{u}$ is the wind velocity vector; L_v and c_p denote the latent heat of condensation and specific heat at constant pressure, respectively; C is the condensation rate; $(\partial N_c/\partial t)_{evap}$ is the source term that describes changes of the cloud droplets number concentration due to the evaporation; $(\partial * /\partial t)_{act}$ are the source terms representing activation/deactivation of cloud condensation nuclei (CCN); and D terms represent subgrid-scale turbulent transport terms.

To simulate the entrainment-related delay of cloud water evaporation, Grabowski (2007) and Jarecka et al. (2009) suggested a relatively simple approach by including two additional variables: the scale (or width) of a filament λ, which characterizes the progress of turbulent stirring (Broadwell and Breidenthal, 1982; Jensen and Baker, 1989) and the fraction of the gridbox containing cloudy air β. The evolution of λ is supposed to represent the progress of subgrid-scale turbulent mixing toward the microscale homogenization (e.g., Broadwell and Breidenthal, 1982; Jensen and Baker, 1989). Local values of the cloudy-air fraction β are affected by resolved advection and subgrid-scale diffusion, and by the subgrid-scale homogenization. When extended into the multi-dimensional framework and written in the conservative (flux) form, the equation for λ and β are:

$$\begin{aligned}\frac{\partial \lambda}{\partial t} + \frac{1}{\rho_o}\nabla\cdot(\rho_o \mathbf{u}\lambda) &= -\gamma(\epsilon\lambda)^{1/3} + S_\lambda + D_\lambda \\ \frac{\partial \beta}{\partial t} + \frac{1}{\rho_o}\nabla\cdot(\rho_o \mathbf{u}\beta) &= S_\beta + D_\beta \end{aligned} \qquad (2)$$

where the first term on the right-hand side of first equation describes the decrease of λ as the turbulent mixing progresses [ϵ is the local dissipation rate of the turbulent kinetic energy (TKE) and $\gamma \sim 1$ is a nondimensional parameter taken as $\gamma = 1.8$; (see Grabowski, 2007; Jarecka et al., 2009)], S_λ, S_β are the source/sink terms, and D_λ, D_β are the subgrid transport terms. The source/sink terms S_λ and S_β consider three processes that affect the scale λ and the cloudy-air fraction β: (a) initial formation of a cloudy volume due to grid-scale condensation, (b) removal of a cloudy volume due to complete evaporation of cloud water, and (c) homogenization of a cloudy volume. A uniform cloudy gridbox is characterized by $\lambda = \Lambda$ and $\beta = 1$, where $\Lambda \equiv (\Delta x\ \Delta y\ \Delta z)^{1/3}$ (Δx, Δy, Δz are model gridlength in x, y, and z direction, respectively). A cloud-free gridbox has $\lambda = 0$ and $\beta = 0$. It follows that the source/sink term S_λ resets the current value of λ to Λ in cases (a) and (c), or resets λ to 0 in the case (b). Similarly, the source/sink term S_β resets the current value of β to 1 in cases (a) and (c), or resets β to 0 in the case (b). Microscale homogenization of a cloudy gridbox is assumed once the scale predicted by eq. 2 falls bellow the threshold value λ_0 taken as 1 mm (note that $\lambda_0 = 1$ cm was used in Grabowski (2007) and Jarecka et al. (2009)).

Adding to the model new variables λ and β allows representing the chain of events characterizing turbulent mixing and to include a corresponding delay of evaporation in the model. In the bulk $\lambda - \beta$ model discussed in Jarecka et al. (2009) and in Grabowski (2007), the evaporation of cloud water due to the turbulent mixing was delayed until the predicted filament scale λ reached the scale of molecular homogenization λ_0. However, one might anticipate a gradual increase of the evaporation as the scale of λ_0 is approached instead of an abrupt transition from zero to finite evaporation. This is supported by simulations using the DNS approach (Andrejczuk et al., 2004, 2006, 2009) and simulations using the linear eddy model (e.g., Krueger, 1993; Krueger et al., 1997, S. Krueger, personal communication). This is also consistent with a heuristic argument that, during the turbulent stirring, complete evaporation of cloud droplets is anticipated near the edges of the filaments, while droplets away from the interface should not experience any evaporation at all (except due to resolved vertical motions). To include a gradual increase on the evaporation due to the turbulent mixing, we postulate that the amount of cloud water Δq_c^* that evaporates at the filament edges is a fraction of the cloud water mixing ratio Δq_c that would evaporate during model time step in the traditional model, that is, when the microphysical adjustment is applied without any subgrid-scale considerations (i.e., applying model-predicted values of θ, q_v, q_c, and N_c). Heuristic arguments following

ideas discussed in Sreenivasan et al. (1989); Malinowski and Zawadzki (1993) and considering the increase of the surface area of the cloud-clear air interface during turbulent stirring suggest that:

$$\Delta q_c^* = \frac{\lambda_0}{\lambda} \Delta q_c \tag{3}$$

As expected, eq. 3 implies almost no evaporation when $\lambda >> \lambda_0$ and the correct evaporation $\Delta q_c^* \rightarrow \Delta q_c$ when $\lambda \rightarrow \lambda_0$. Note that the above considerations apply only for gridpoints affected by the entrainment and mixing, that is, when $\Delta q_c < 0$ and $\lambda_0 < \lambda < \Lambda$.

The key differences between traditional cloud models and the model with delayed entrainment-related evaporation of cloud droplets are illustrated in Figure 1.

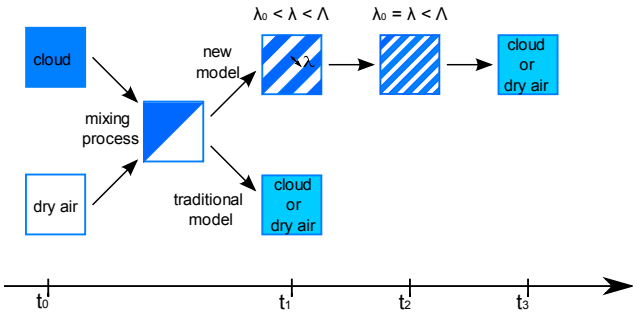

Figure 1: Evaporation of cloud water as a result of turbulent mixing between cloudy and cloud-free gridboxes. The horizontal axis represents time. The two gridboxes are shown on the left hand side of the figure, at time t_0. During a model time step, from t_0 to t_1, parametrized turbulent mixing creates a gridbox containing both cloudy and cloud-free air. The traditional model immediately homogenizes the gridbox, resulting in either a saturated and cloudy or subsaturated and cloud-free gridbox at time t_1. In the modified model, homogenization is only possible once turbulent stirring reduces the filament width λ from the initial value $\sim \Lambda$ to the value corresponding to the microscale homogenization λ_0. This process may take several model time steps. Before homogenization, the condensation rate is calculated using eq. 3.

3 DROPLET SPECTRUM CHANGES DUE TO THE TURBULENT MIXING

Mixing of cloud air with dry environmental air changes also the spectrum of cloud droplets. In general, microscale homogenization may result in the reduction of only the mean droplet size without changing the number of droplets. This is typically referred to as the homogeneous mixing. In contrast, the size may remain unchanged and only the number of droplets may be reduced. This is the extremely inhomogeneous mixing. In practice, both the size and the number of droplets may change as a result of the microscale homogenization.

On theoretical grounds, homogeneity of mixing depends on the relative magnitude of the time scales for droplet evaporation and turbulent homogenization. If the turbulent homogenization time scale is much shorter than the droplet evaporation time scale, the subsaturated air dilute the cloud fast enough that all droplets experience the same subsaturated conditions. In that situation sizes of all droplets decrease, so the homogeneous mixing is thought to take place. In the opposite limit, when the droplet evaporation time scale is much shorter than the turbulent homogenization time scale, droplets which are in the vicinity of the subsaturated air evaporate so fast that there is no time to uniformly dilute the cloudy air. In that case only some droplets evaporate completely and the rest does not experience any change, so the extremely inhomogeneous mixing is thought to take place.

In the Morrison and Grabowski (2008) double-moment scheme, the mixing scenario is determined by a single parameter α. This parameter is used to calculate the final droplet concentration after entrainment and turbulent mixing according to:

$$N_c^f = N_c^i \left(\frac{q_c^f}{q_c^i} \right)^{\alpha} \tag{4}$$

where N_c^f is the final droplet concentration after microphysical adjustment due to the evaporation, N_c^i is the droplet concentration after advection and turbulent mixing (i.e., the initial value for the microphysical adjustment), and q_c^i and q_c^f are the initial and final cloud water mixing ratios (i.e., before and after the microphysical adjustment). Note that, in the Morrison and Grabowski (2008) scheme, the microphysical adjustment of the cloud water mixing ratio q_c takes place before adjusting N_c, and it is dictated by the predicted supersaturation and characteristics of the cloud droplet population (i.e., the droplet

concentration and size). Thus, q_c^i and q_c^f in eq. 4 are already known, and eq. 4 predicts the corresponding microphysical adjustment of the droplet concentration N_c once α is known. The parameter α varies from 0 for the case of the homogeneous mixing (i.e., no change to N_c) to 1 for the extremely inhomogeneous mixing (i.e., when N_c changes in the same proportion as q_c and thus the mean volume radius remains unchanged). In simulations presented in Morrison and Grabowski (2008), α could only be assumed constant in space and time during the simulation. The same applies to simulations discussed in Slawinska et al. (2012).

To predict the local value of α, we take advantage of the direct numerical simulations (DNS) results reported in Andrejczuk et al. (2009). Andrejczuk et al. (2009) performed 72 simulations of decaying moist turbulence mimicking turbulent mixing and microscale homogenization of cloudy and clear air using detailed (bin) microphysics. They analyzed DNS results in terms of the instantaneous change of microphysical characteristics versus the ratio between the turbulent mixing and droplet evaporation time scales, τ_{mix} and τ_{evap} respectively. The change in the microphysical characteristics was measured by the slope δ of the line depicting the evolution of the total number of droplets plotted against the mean volume radius cubed, both normalized by the initial values, the $r - N$ diagram, applied in Andrejczuk et al. (2004, 2006). In this diagram, the homogeneous mixing corresponds to the horizontal line (i.e., changing droplet size without changing the number of droplets; $\delta = 0$). The vertical line (reduction of the number of droplets without changing the size; $\delta \to \infty$) implies extremely inhomogeneous mixing. The simulations suggested approximately one-to-one relationship between the ratio of the two time scales and the slope of the mixing line, that is, $\delta \sim \tau_{mix}/\tau_{evap}$ (see Fig. 2 in Andrejczuk et al. (2009)).

The slope δ is related to the parameter α in eq. 4. Since $q_c \sim N_c r^3$, eq. 4 implies that $N_c \sim (r^3)^{\alpha/(1-\alpha)}$. It follows that the slope $\delta \equiv dN_c/d(r^3)$ equals $\alpha/(1-\alpha)$ which leads to

$$\alpha = \frac{\delta}{1+\delta} \tag{5}$$

The turbulent homogenization time scale is calculated following Andrejczuk et al. (2009) as

$$\tau_{mix} = \lambda/u(\lambda) \tag{6}$$

where $u(\lambda)$ is the characteristic velocity at spatial scale equal to the filament scale λ. It can be related to the model-predicted TKE as

$$u(\lambda) = (TKE)^{1/2}(\lambda/\Lambda)^{1/3} \tag{7}$$

This relationship assumes inertial range scaling for subgrid-scale turbulence and considers TKE to be dominated by the eddies of scale Λ [i.e., $u(\Lambda) \sim (TKE)^{1/2}$]. The droplet evaporation time scale is estimated as

$$\tau_{evap} = \frac{r^2}{A\,(1 - RH_d)} \tag{8}$$

where r is the mean volume radius of cloud droplets (predicted by the double-moment microphysics scheme), RH_d is the relative humidity of the cloud-free portion of the gridbox, and $A \approx 10^{-10}$ m^{2}s^{-1} is the constant in the droplet diffusional growth equation (i.e., $dr/dt = AS/r$, where $S = RH - 1$ is the supersaturation). RH_d can be estimated using the mean (model-predicted) relative humidity of a gridbox RH, and assuming that $RH = 1$ for the cloudy part of the gridbox. These lead to

$$RH_d = \frac{RH - \beta}{1 - \beta} \tag{9}$$

Once the values of the two time scales are derived, their ratio provides a prediction of the slope δ using the relationship suggested in Andrejczuk et al. (2009), and the parameter α can be calculated from eq. 5 and subsequently applied in eq. 4.

4 APPLICATION OF THE LES MODEL TO THE STRATOCUMULUS CASE

The subgrid-scale microphysics model described above was included in the anelastic semi-Lagrangian /Eulerian cloud model EULAG doc-

umented in Smolarkiewicz and Margolin (1997; model dynamics), Grabowski and Smolarkiewicz (1996; model thermodynamics), and Margolin et al. (1999; subgrid-scale turbulent mixing). The double-moment microphysics scheme of Morrison and Grabowski (2007, 2008) was recently added to the model; simulations using the scheme and *prescribed* values of the parameter α were reported in Slawinska et al. (2012). Eulerian version of the model is used. For simulations of the stratocumulus case data from the EUCAARI-IMPACT were used (Kulmala et al., 2011). Model initial profiles were derived from the aircraft data taken during flight on May 15th (RF51). Computational domain was 6.4×6.4 km^2 in the horizontal (with periodic lateral boundary conditions) and 3 km deep. The gridlength was 50 m in the horizontal and 20 m in the vertical. All simulations were run for 6 hrs and data from last 3 hrs are used in the analysis.

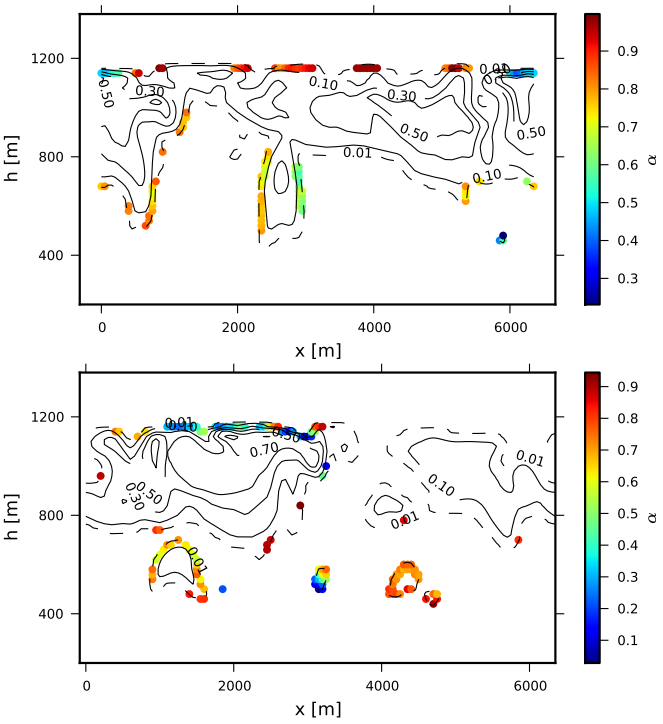

Figure 2: Vertical cross section through selected cloud fields. Cloud boundaries are marked with the dash contour of $q_c = 0.01g/kg$. The colored points mark the local values of the α parameter in places where model predicts cloud evaporation due to the turbulent mixing.

Figure 2 shows the vertical cross section through selected cloud fields. There is a layer of shallow cumuli beneath the stratocumulus growing into the stratocumulus deck. Similar double-layer structure seemed to be present in aircraft observations (not shown). The colored points mark the local values of the α parameter in places where model predicts cloud evaporation due to the turbulent mixing. There is significant number of points where evaporation occurs in the cumulus cloud layer with the α parameter values close to 1, implying mixing close to extremely inhomogeneous. In the stratocumulus layer, mixing occurs mostly near the top of the cloud, and broad spectrum of mixing scenarios is predicted by the model.

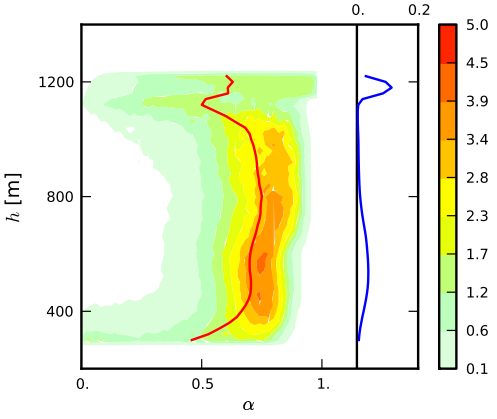

Figure 3: CFAD of the values of the α parameter. Profiles of mean values is shown using red line. Blue line shows the percentage of points at one domain level, where model predict evaporation due to the turbulent mixing and calculate the values of the α parameter.

Figure 3 shows the contoured frequency by altitude diagram (CFAD) of values of the α parameter that defines the mixing scenario. The figure highlights wide range of mixing scenarios that occurs in simulated clouds, especially near the top of the stratocumulus layer and in the lower part of the cumulus layer.

More extensive analysis of the model results will be presented at the meeting. We will try to explain the behavior of the α values and the mixing scenarios in the simulated clouds.

ACKNOWLEDGEMENTS

IMPACT data were provided by CNRM Meteo-France (Fred Burnet, Bruno Piguet and Vincent Puygrenier). Authors would like to thank all people involved in the EUCAARI-IMPACT campaign.

In addition, the lead author thanks Andrzej Wyszogrodzki and Joanna Slawinska for their assistance with the EULAG model and the double-moment microphysics scheme.

This work was done within the European Union 6 FP IP EUCAARI (European Integrated Project on Aerosol Cloud Climate and Air Quality Interactions) No. 036833-2 and the Polish MNiSW grant 396/6/PR UE/2007/7. Additional support was provided by the Polish MNiSW grant N N307 128038, the NOAA grant NA08OAR4310543, DOE ARM grant DE-FG02-08ER64574, and by the NSF Science and Technology Center for Multi-Scale Modeling of Atmospheric Processes (CMMAP), managed by Colorado State University under cooperative agreement ATM-0425247. Computer time was provided by NSF MRI Grant CNS-0421498, NSF MRI Grant CNS-0420873, NSF MRI Grant CNS-0420985, NSF sponsorship of the National Center for Atmospheric Research, the University of Colorado, and a grant from the IBM Shared University Research (SUR) program.

References

Andrejczuk, M., Grabowski, W. W., Malinowski, S. P., and Smolarkiewicz, P. K.: Numerical Simulation of CloudClear Air Interfacial Mixing, Journal of the Atmospheric Sciences, 61, 1726–1739, 2004.

Andrejczuk, M., Grabowski, W. W., Malinowski, S. P., and Smolarkiewicz, P. K.: Numerical Simulation of CloudClear Air Interfacial Mixing: Effects on Cloud Microphysics, Journal of the Atmospheric Sciences, 63, 3204–3225, 2006.

Andrejczuk, M., Grabowski, W. W., Malinowski, S. P., and Smolarkiewicz, P. K.: Numerical Simulation of CloudClear Air Interfacial Mixing: Homogeneous versus Inhomogeneous Mixing, Journal of the Atmospheric Sciences, 66, 2493–2500, 2009.

Broadwell, J. E. and Breidenthal, R. E.: A simple model of mixing and chemical reaction in a turbulent shear layer, Journal of Fluid Mechanics, 125, 397–410, 1982.

Grabowski, W. W.: Cumulus entrainment, fine-scale mixing, and buoyancy reversal, Quarterly Journal of the Royal Meteorological Society, 119, 935–956, 1993.

Grabowski, W. W.: Representation of Turbulent Mixing and Buoyancy Reversal in Bulk Cloud Models, Journal of the Atmospheric Sciences, 64, 3666–3680, 2007.

Jarecka, D., Grabowski, W. W., and Pawlowska, H.: Modeling of Subgrid-Scale Mixing in Large-Eddy Simulation of Shallow Convection, Journal of the Atmospheric Sciences, 66, 2125–2133, 2009.

Jensen, J. B. and Baker, M. B.: A Simple Model of Droplet Spectral Evolution during Turbulent Mixing, Journal of the Atmospheric Sciences, 46, 2812–2829, 1989.

Krueger, S. K.: Linear Eddy Modeling of Entrainment and Mixing in Stratus Clouds, Journal of the Atmospheric Sciences, 50, 3078–3090, 1993.

Krueger, S. K., Su, C.-W., and McMurtry, P. A.: Modeling Entrainment and Finescale Mixing in Cumulus Clouds, Journal of the Atmospheric Sciences, 54, 2697–2712, 1997.

Kulmala, M., Asmi, A., Lappalainen, H. K., Baltensperger, U., Brenguier, J.-L., Facchini, M. C., Hansson, H.-C., Hov, Ø., O'Dowd, C. D., Pöschl, U., Wiedensohler, A., Boers, R., Boucher, O., de Leeuw, G., Denier van der Gon, H. A. C., Feichter, J., Krejci, R., Laj, P., Lihavainen, H., Lohmann, U., McFiggans, G., Mentel, T., Pilinis, C., Riipinen, I., Schulz, M., Stohl, A., Swietlicki, E., Vignati, E., Alves, C., Amann, M., Ammann, M., Arabas, S., Artaxo, P., Baars, H., Beddows, D. C. S., Bergström, R., Beukes, J. P., Bilde, M., Burkhart, J. F., Canonaco, F., Clegg, S. L., Coe, H., Crumeyrolle, S., D'Anna, B., Decesari, S., Gilardoni, S., Fischer, M., Fjaeraa, A. M., Fountoukis, C., George, C., Gomes, L., Halloran, P., Hamburger, T., Harrison, R. M., Herrmann, H., Hoffmann, T., Hoose, C., Hu, M., Hyvärinen, A., Hõrrak, U., Iinuma, Y., Iversen, T., Josipovic, M., Kanakidou, M., Kiendler-Scharr, A., Kirkevåg, A., Kiss, G., Klimont, Z., Kolmonen, P., Komppula, M., Kristjánsson, J.-E., Laakso, L., Laaksonen, A., Labonnote, L., Lanz, V. A., Lehtinen, K. E. J., Rizzo, L. V.,

Makkonen, R., Manninen, H. E., McMeeking, G., Merikanto, J., Minikin, A., Mirme, S., Morgan, W. T., Nemitz, E., O'Donnell, D., Panwar, T. S., Pawlowska, H., Petzold, A., Pienaar, J. J., Pio, C., Plass-Duelmer, C., Prévôt, A. S. H., Pryor, S., Reddington, C. L., Roberts, G., Rosenfeld, D., Schwarz, J., Seland, Ø., Sellegri, K., Shen, X. J., Shiraiwa, M., Siebert, H., Sierau, B., Simpson, D., Sun, J. Y., Topping, D., Tunved, P., Vaattovaara, P., Vakkari, V., Veefkind, J. P., Visschedijk, A., Vuollekoski, H., Vuolo, R., Wehner, B., Wildt, J., Woodward, S., Worsnop, D. R., van Zadelhoff, G.-J., Zardini, A. A., Zhang, K., van Zyl, P. G., Kerminen, V.-M., S Carslaw, K., and Pandis, S. N.: General overview: European Integrated project on Aerosol Cloud Climate and Air Quality interactions (EUCAARI) - integrating aerosol research from nano to global scales, Atmospheric Chemistry and Physics, 11, 13 061–13 143, 2011.

Malinowski, S. P. and Zawadzki, I.: On the Surface of Clouds, Journal of the Atmospheric Sciences, 50, 5–13, 1993.

Morrison, H. and Grabowski, W. W.: Comparison of Bulk and Bin Warm-Rain Microphysics Models Using a Kinematic Framework, Journal of the Atmospheric Sciences, 64, 2839–2861, 2007.

Morrison, H. and Grabowski, W. W.: Modeling Supersaturation and Subgrid-Scale Mixing with Two-Moment Bulk Warm Microphysics, Journal of the Atmospheric Sciences, 65, 792–812, 2008.

Siebesma, A. P. e. a.: A large eddy simulation intercomparison study of shallow cumulus convection, Journal of the Atmospheric Sciences, 60, 1201–1219, 2003.

Slawinska, J., Grabowski, W. W., Pawlowska, H., and Morrison, H.: Droplet activation and mixing in large-eddy simulation of a shallow cumulus field, Journal of the Atmospheric Sciences, 2012.

Sreenivasan, K. R., Ramshankar, R., and Meneveau, C.: Mixing, Entrainment and Fractal Dimensions of Surfaces in Turbulent Flows, Proceedings of the Royal Society of London. Series A, Mathematical and Physical Sciences, pp. pp. 79–108, 1989.

Warner, J.: The Microstructure of Cumulus Cloud: Part IV. The Effect on the Droplet Spectrum of Mixing Between Cloud and Environment, Journal of the Atmospheric Sciences, 30, 256–261, 1973.

OVERVIEW OF PUIJO CLOUD EXPERIMENT (PuCE) 2011

Portin, Harri[1,2], Leskinen, Ari[1], Brus, David[3], Neitola, Kimmo[3], Hyvärinen Antti-Pekka[3], Kortelainen Aki[2], Hao, Liqing[2], Miettinen, Pasi[2], Jaatinen, Antti[2], Lihavainen, Heikki[3], Romakkaniemi, Sami[2], Laaksonen, Ari[2,3], Lehtinen, Kari E.J.[1,2] and Komppula, Mika[1]

[1]Finnish Meteorological Institute, Kuopio Unit, P.O.Box 1627, FI-70211, Kuopio, Finland
[2]University of Eastern Finland, Department of Applied Physics, P.O.Box 1627, FI-70211, Kuopio, Finland
[3]Finnish Meteorological Institute, Climate Change, P.O.Box 503, FI-00101 Helsinki, Finland

Keywords: atmospheric aerosols, cloud droplet activation, aerosol-cloud interactions, chemical composition

1. INTRODUCTION

Indirect effect of aerosol particles is the largest source of uncertainty when predictions about future climate are made (IPCC, 2007). The indirect effect originates from the ability of particles to act as cloud condensation nuclei (CCN). As human activities have increased the CCN number concentration, more and smaller droplets are formed. This leads to Twomey effect: higher cloud albedo and increased reflection of solar radiation (Twomey, 1977). Another consequence is the Albrecht effect: since droplets are smaller, precipitation development is weaker and clouds are more persistent (Albrecht, 1989).

To reduce the uncertainty in the estimation of the indirect effect, the process of CCN activating into cloud droplets must be understood in more detail. It is already known that size and chemical composition are the most important particle properties affecting cloud droplet activation (Dusek et al. 2006). The effect of CCN size on cloud droplet activation is already well-known but the knowledge about the role of chemical composition is still lacking and more experimental observations are necessary to improve the level of understanding.

2. MEASUREMENT SITE

The Puijo station was established in summer 2006 by the Finnish Meteorological Institute and the University of Kuopio (now University of Eastern Finland) and since then it has provided continuous data on aerosol-cloud interactions. The station resides on the top floor of the Puijo observation tower (62°54'32'' N, 27°39'19'' E, 306 m above sea level, 224 m above the surrounding lake level), which is located in the city of Kuopio (97000 inhabitants), in a semi-urban environment. An overview of the station and the surrounding area can be found in Leskinen et al. (2009). The top of the tower is covered by cloud about 15 % of the time, offering perfect conditions for studying aerosol-cloud interactions. Besides the normal measurements, also several intensive measurement campaigns with a wider measurement setup (Puijo Cloud Experiments, PuCE), have been arranged during autumns, when the occurrence of clouds is most frequent.

3. INSTRUMENTATION

At Puijo station, aerosol measurements are performed with a special twin-inlet setup (total and interstitial inlets). Total inlet has a cutoff size of approximately 40 μm and it is

heated. When the tower is covered in cloud, this inlet samples both cloud droplets and unactivated, interstitial aerosol particles. Water from the droplets evaporates because of the heating, leaving only the core particles. This way it is possible to observe the aerosol size distribution as it would be outside of the cloud. Interstitial inlet has a PM_1 impactor to prevent cloud droplets from entering the sampling line. When a cloud is present, this inlet samples only the interstitial aerosol. Between the main sampling lines and measurement equipment is a valve system which is used to switch measurement devices between the sampling lines in six-minute intervals.

Aerosol particle size distribution from 7 to 800 nm is measured with a twin differential mobility particle sizer (DMPS) which is connected to the twin inlet system. By comparing the size distributions from total and interstitial inlets, it is possible to observe size dependent cloud droplet activation of particles.

Cloud droplets are observed with a cloud droplet probe (CDP, Droplet Measurement Technologies) which is mounted on the roof of the tower. CDP measures cloud droplet size distribution in the size range of 3-50 µm. As the device is located only a few meters away from the aerosol inlets, it is possible to compare the cloud droplet data with the aerosol data from the DMPS (Portin et al. 2009). Droplet data can be also used to calculate cloud liquid water content (LWC). Other continuous measurements at Puijo include scattering and absorption of aerosols, particulate matter, basic weather parameters including vertical wind component and concentration of some climatically relevant gases (NO_x, SO_2, O_3, CO_2, CH_4).

During PuCE 2011 campaign, the station was equipped with some additional measurement devices. Aerosol chemical composition was observed with aerosol mass spectrometer (AMS) and Single Particle Soot Photometer (SP-2). These were both connected to the twin inlet setup, providing data about the effect of particle chemical composition on cloud droplet activation. Other instruments included Hygroscopic Tandem Differential Mobility Analyzer (HTDMA) for particle hygroscopicity measurements. Potential CCN in different supersaturations were measured with two CCN counters (CCNC). The other CCNC was operated with a Differential Mobility Analyzer (DMA) to obtain size selected CCN spectra.

4. DATA PROCESSING

The results presented here are from the latest measurement campaign (PuCE 2011). During this campaign, 20 cloud events were observed, providing in total 105 hours of cloud data. A cloud event is considered to take place when the visibility drops below 200 meters. We also remove rainy cloud events, since rain drops remove unactivated aerosol particles and would disturb activation calculations. As a limit for rain, we use rain intensity of 0.2 mm/h. One more limiting factor is temperature: the CDP has a tendency to freeze when temperature drops below 0 °C, so we only consider data with temperature above this limit. After leaving out all rainy and low-temperature observations, we still have 70 hours of cloud data.

5. RESULTS

An example of the particle size distribution and size-dependent activation data during a cloud event is shown in figure 1. A pronounced accumulation mode can be seen in the size distribution observed from the total line around 200 nm, whereas data from interstitial line shows that this mode has in large part activated into cloud droplets.

Activated fraction of particles as a function of size is shown in figure 2. Also shown is the diameter where 50% of particles are activated, D_{50}. In this case D_{50} is 135 nm. This is somewhat smaller than the average D_{50} during PuCE 2011, 164 nm.

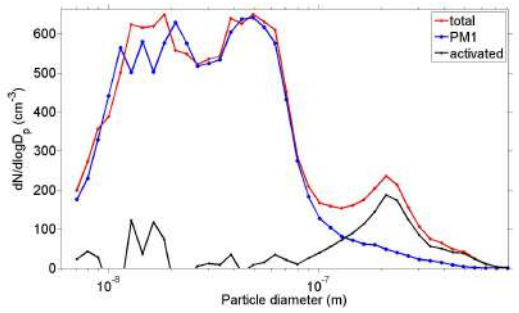

Figure 1. Average size distributions for total and interstitial aerosol observed with the DMPS during a cloud event taking place on 23th of October. Also shown is the average size distribution of activated particles (total-interstitial).

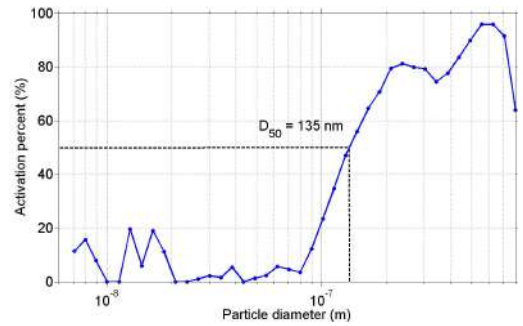

Figure 2. Average activated fraction of particles as a function of particle diameter during a cloud event taking place on 23th of October. Also shown is the diameter of 50% activation, D_{50}.

The use of AMS together with the twin-inlet system provides interesting data about how different chemical constituents behave in cloud droplet activation. In figure 3 a time series of activated fraction of chemical components measured by the AMS is shown. This time period included a long, almost continuous cloud event, which started around 9 a.m. on 22nd of October lasting until 5 a.m. on 24th of October. The starting and ending times can be seen clearly from the activated fractions. Two clearer periods, in the evening of 22th and in the afternoon of 23th of October, can also be spotted as the activated fractions drop. When looking at the behaviour of different components, it seems that ammonium is most hygroscopic, with on average 70% in the activated fraction. However, it is possible that this high fraction is caused by the partitioning of ammonia from gas to cloud droplets. From the other constituents, organics are somewhat hydrophobic with an average fraction of 44%. Sulphate and nitrate fall between ammonium and organics, (both 57%).

Future work with PuCE 2011 data will include a more detailed analysis of DMPS, CDP and AMS data, to find out how particle concentration, size distribution and chemical composition affect the properties of the cloud droplet population. Also vertical wind speed, HTDMA and CCNC data will be included in the analysis.

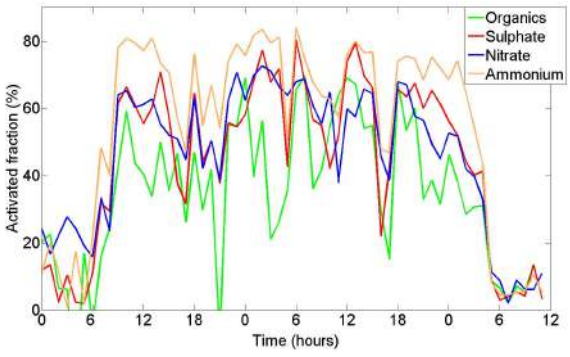

Figure 3. Activated fraction of chemical components measured by the AMS during a cloud event between 22th and 24th of October.

REFERENCES

Albrecht, B.A., 1989. Aerosols, cloud microphysics, and fractional cloudiness. Science, 245, 1227-1230.

Dusek, U., Frank, G.P., Hildebrandt, L., Curtius, J., Schneider, J., Walter, S., Chand, D., Drewnick, F., Hings, S., Jung, D., Borrmann, S., Andreae, M.O., 2006. Science, 312, 1375-1378.

IPCC 2007. Climate change 2007: The physical science basis. Intergovernmental panel on Climate Change, Cambridge University Press, New York.

Leskinen, A., Portin, H., Komppula, M., Miettinen, P., Arola, A., Lihavainen, H., Hatakka, J., Laaksonen, A., Lehtinen, K.E.J., 2009. Overview of the research activities and results at Puijo semi-urban measurement station. Boreal Environment Research 14, 576-590.

Portin, H., Komppula, M., Leskinen, A., Romakkaniemi, S., Laaksonen, A., Lehtinen, K.E.J., 2009. Observations of aerosol-cloud interactions at Puijo semi-urban measurement station. Boreal Environment Research 14, 641-653.

Twomey, S., 1977. The influence of pollution on the shortwave albedo of clouds. Journal of the Atmospheric sciences, 34, 1149-1152.

COLD SEASON PRECIPITATION ON THE TERRITORY OF VERHNIAYA VOLGA DURING THE LAST 25 YEARS

Bezrukova, N.A .[1], E.A. Stulov[1], V.V. Sokolov[2], O.V. Nikitina[2]

[1]Central Aerological Observatory, Dolgoprudny, Moscow Region, 141700
[2]"Nizhegorodsky CHMS-R", Roshydromet Department of the Volga Federal District, Russia

1. INTRODUCTION

Weather data for Nizhniy Novgorod and Kirov area from observational stations of Roshydromet Department of the Volga Federal District (VFD) for the period 1986-2009/10 have been analyzed to get the statistics of winter slipperiness events that endanger traffic. The number of road accidents during glaze and rime events, compared with the overall number, increases by 13 to16 % [3-5]. A technique has been developed to forecast glaze and rime formation on the road. Model climatic road charts have been constructed for the regions concerned. Using an executable code, standard Roshydromet network weather data has been analyzed to reveal the conditions leading to road slipperiness in winter. All the cases of slipperiness occurrence within the period concerned have been considered. The research fulfilled confirmed the tendency for winter warming in the region. During the last 25 years, the mean annual air temperature has been progressively growing mainly due to the increase of mean monthly temperatures in cold season.

2. RESEARCH REGION AND DATA

2.1. Weather network, motor roads, and initial data

The model climatic road chart of Nizhniy Novgorod Region builds upon the 1986-2009 weather observations on the VFD network. The Nizhniy Novgorod Center for Hydrometeorological Service (Nizhegorodsky CHMS-R) collected climatology and weather data from 18 ground stations in Nizhniy Novgorod Region and 20 ground stations in Kirov Region for the cold seasons of 1986-2009/10 and fulfilled data processing for 24-hour periods and standard weather observation times. Two e-databanks have been compiled to constitute a basis for the development of the climatic road model: Databank for routine weather observations (00, 03, 06, 09, 12 etc.) and Databank for diurnal data (processed 24-hour observations).

Corresponding author's address: Natalia A.Bezrukova, CAO, 3 Pervomayskaya Str., Dolgoprudny, Moscow Region, 141700, Russia. E-Mail: nataly_bez@yahoo.com

3. ROAD CLIMATOLOGY FOR THE CURRENT ENVIRONMENT CONDITIONS CHARACTERIZED BY INCREASED COLD SEASON TEMPERATURES

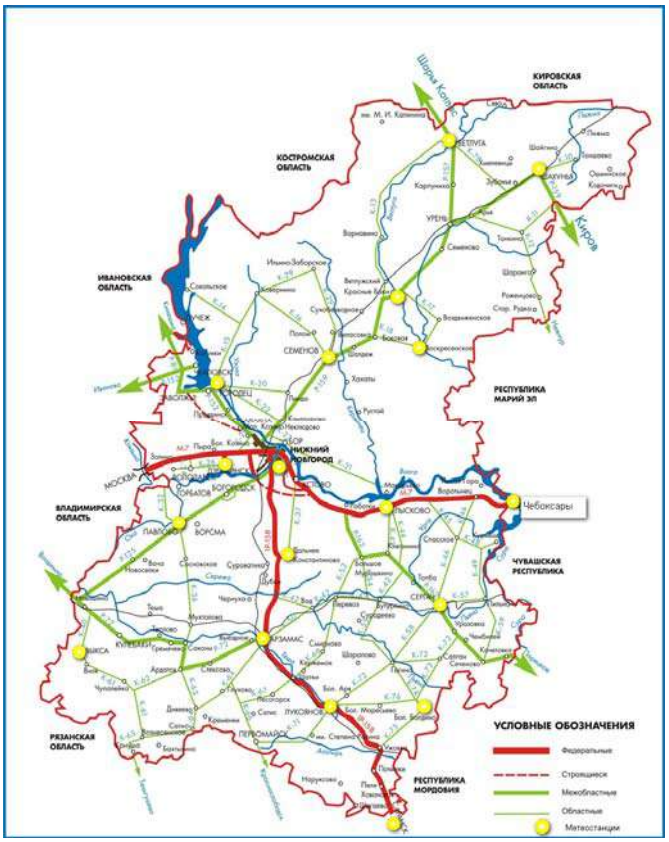

A map of motor roads for Nizhniy Novgorod Region. www.glavtransno.ru/

3.1. Cold season temperatures increasing

The air temperature changes observed at the VFD stations have been analyzed and compared with the mean climatic data (Fig. 1).

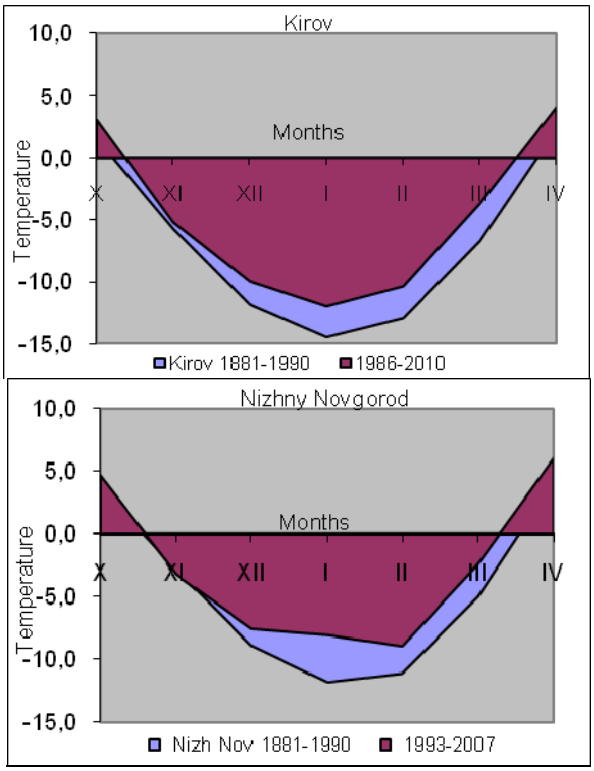

Fig. 1. Mean diurnal temperature increase in winter for 1993-2007 compared with the 1881-1990 mean climatic data [7].

Fig. 2 displays a linear approximation of the mean monthly temperatures for Lukoyanov station in the period from 1961 to 2009.

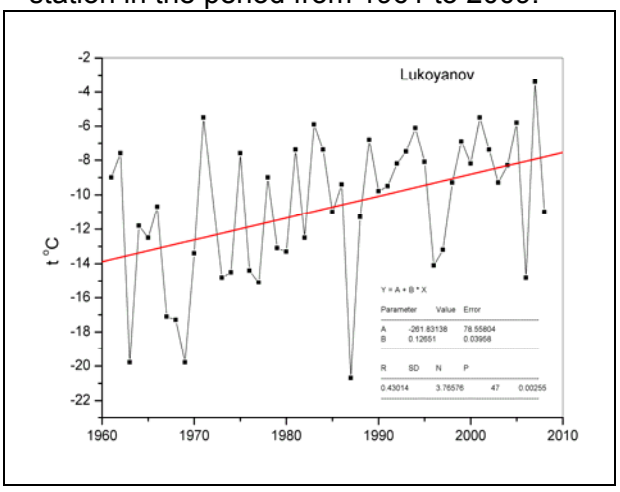

Fig.2. Mean monthly temperatures at Lukoyanov weather station in January.

During this 47-year period, the temperature increased from -14 to -7 °C. During the period 1993-2007, the linear mean monthly temperature approximation for January exhibited a rise by 2°C, from -9 to -7 °C, with average temperature at Lukoyanov station reaching a record mean -3°C value in January 2007, which is more like sites 300-400 km southward. This warming resulted in generally larger air moisture content in cold period, and thus in higher relative humidity and more frequent occurrence of precipitation, and slipperiness on motor roads in particular.

3.2. Winter air temperatures tending to pass over 0°C mark more frequently

It is but natural that with such a temperature record for January (Fig. 2), air temperatures at Lukoyanov station pass over 0°C much more often than in the early 1990s, to say nothing of the 1960s when such instances were only occasional.

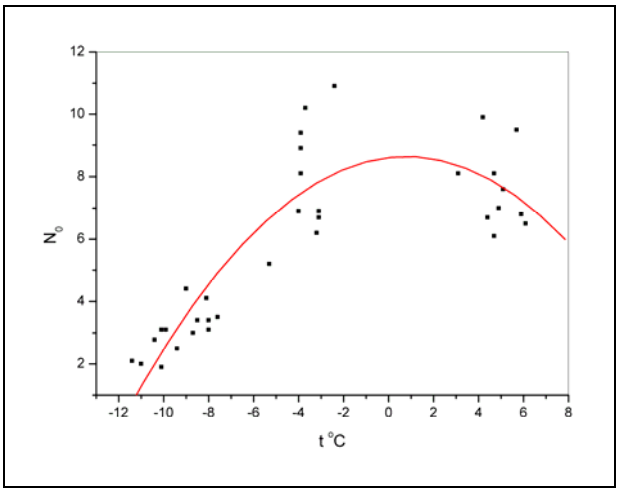

Fig.3. Mean frequency of temperature passes over 0°C toward negative temperatures depending on mean monthly temperatures at 5 stations: Arzamas, Kirov, Nizhniy Novgorod, Saransk, Cheboksary (1993 – 2007).

During three winter months in 1993-2007 period, air temperature in Nizhniy Novgorod passed over 0°C mark 12 times with the melting and freezing on road surface, which led to as frequent glazed frost formation. Within this period, air temperature in Nizhniy Novgorod Region in January was observed to pass over 0°C oftener, by 25-30% on average. The dependence of the number of temperature passes over 0°C on mean monthly temperature is established (Fig. 3), which is of practical use to planning road maintenance operations in this region.

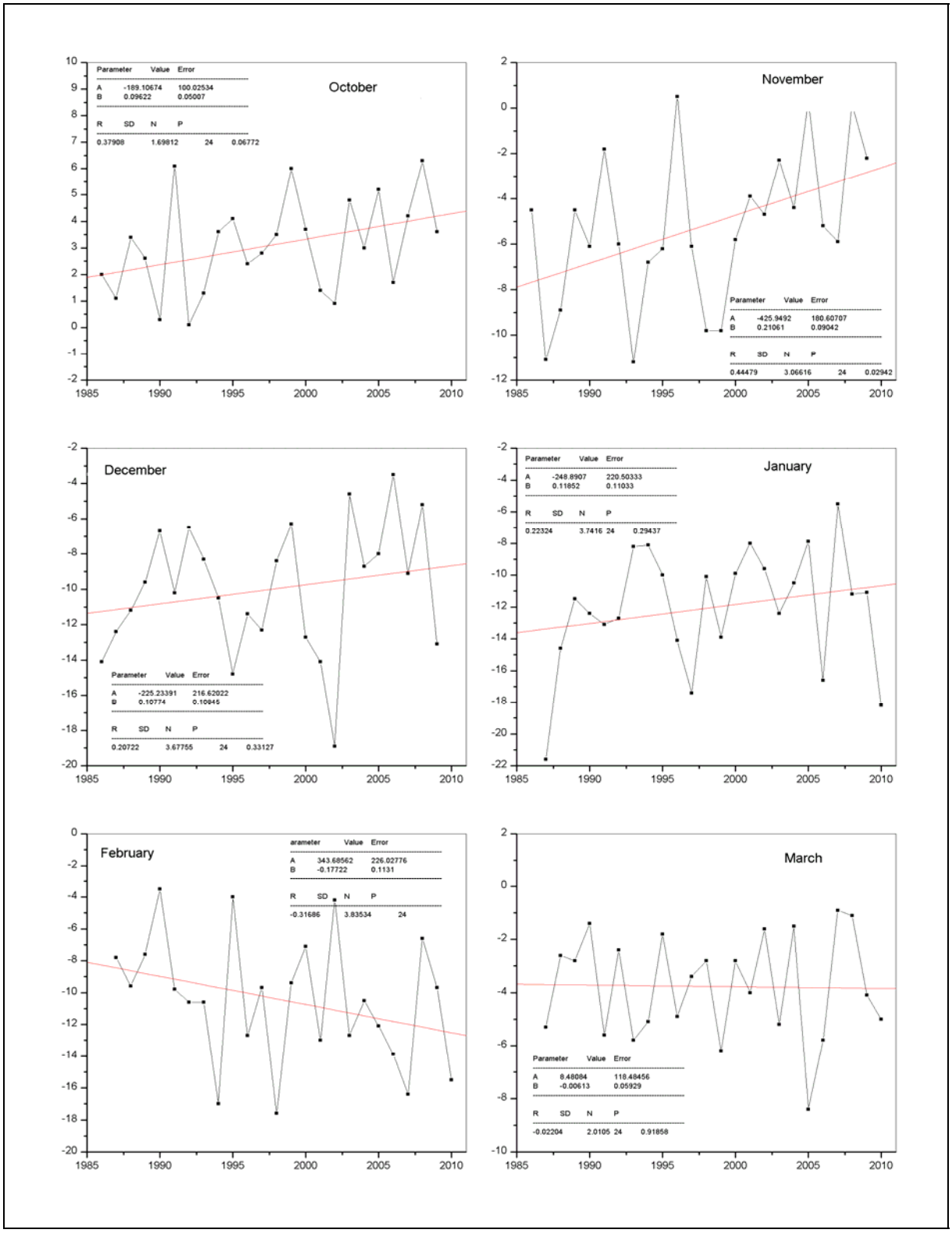

Fig.4. Dynamics of the mean monthly temperatures of cold period (Kirov, 1986-2010).

The mean monthly temperature dynamics during the cold months of 1986-2010 is presented in Fig. 4. Apparently, during the period from October to January including, the mean temperatures increased by 2-5 ^{0}C. The largest increase was observed in November (almost by 5 ^{0}C). In February, the temperature decreased a little. So, the period of continuously observed negative temperatures shifted to the second half of November.

3.3. Cold season precipitation increasing

Precipitation amount has been increasing with the variation of its mean monthlies decreasing each year since 1999. Hence more frequent hazardous packed snow events on the roads are observed. They are little dependent on local conditions, and generally cover large territories. Short-term warmings lead to snow melting and the formation of holes, thus ruining the pavement. Fig. 5 shows a linear approximation of the temperature variation in January for the period 1961-2009 at Lukoyanov weather station and a gradual increase of precipitation amount.

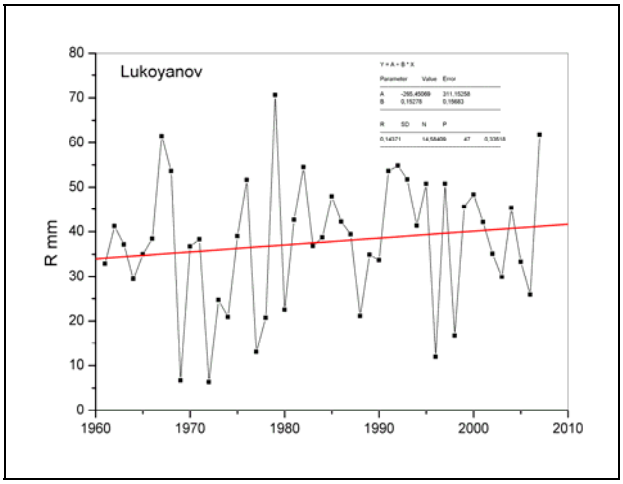

Fig.5. Precipitation variation for January in Lukoyanov station (Nizhniy Novgorod Region).

In Kirov Region, most weather stations report increased precipitation amount for the last two and a half decades (Fig. 6). This is observed in the north, the center, and southwest of the region, while in the southeast of the region (Vyatskie Polyany station), a small precipitation decrease is observed.

In November, December, January, and March, precipitation tends to increase over the last 24 years (Fig. 7). However, in February and October, a small precipitation decrease is observed. The most notable precipitation increase by approximately 25% over the last 50 years occurs in January (Fig.8). 90% of precipitation during three winter months (December, January, and February) and 67-75% during November and March occur at mean diurnal temperatures below 0°C. April and October account for about 20% of the total monthly precipitation at negative temperatures.

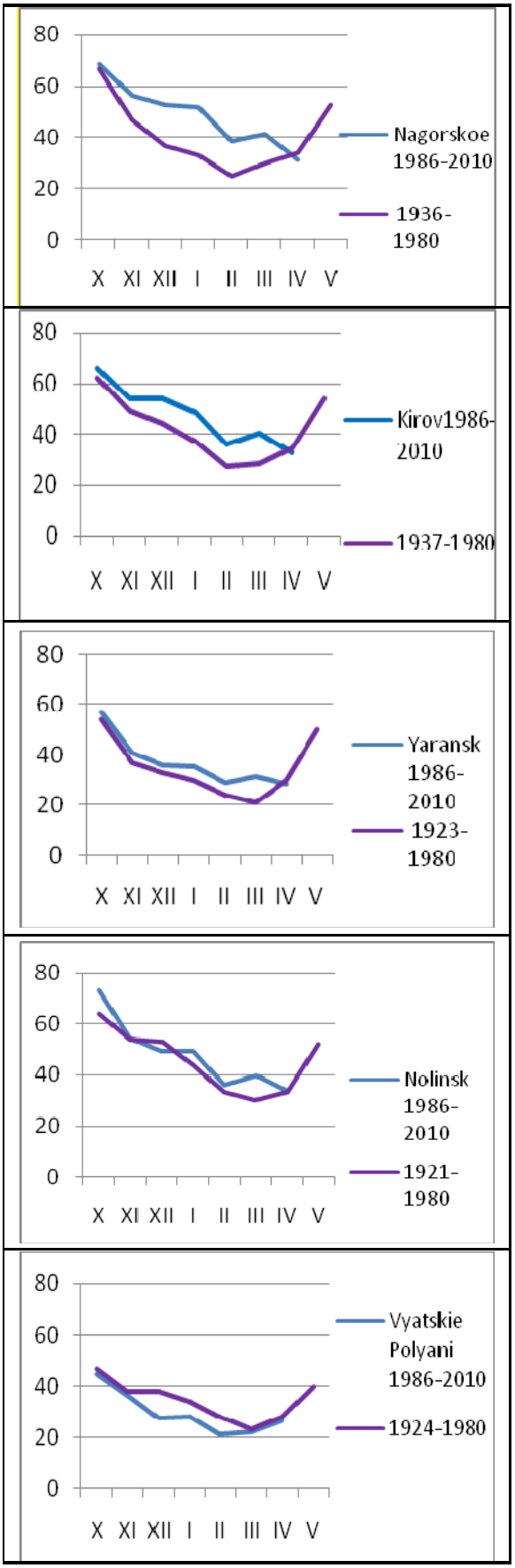

Fig.6. Mean monthly precipitation (mm) in winter for 1986-2010 (blue) compared with the 1921-1980 mean climatic data [7] (violet).

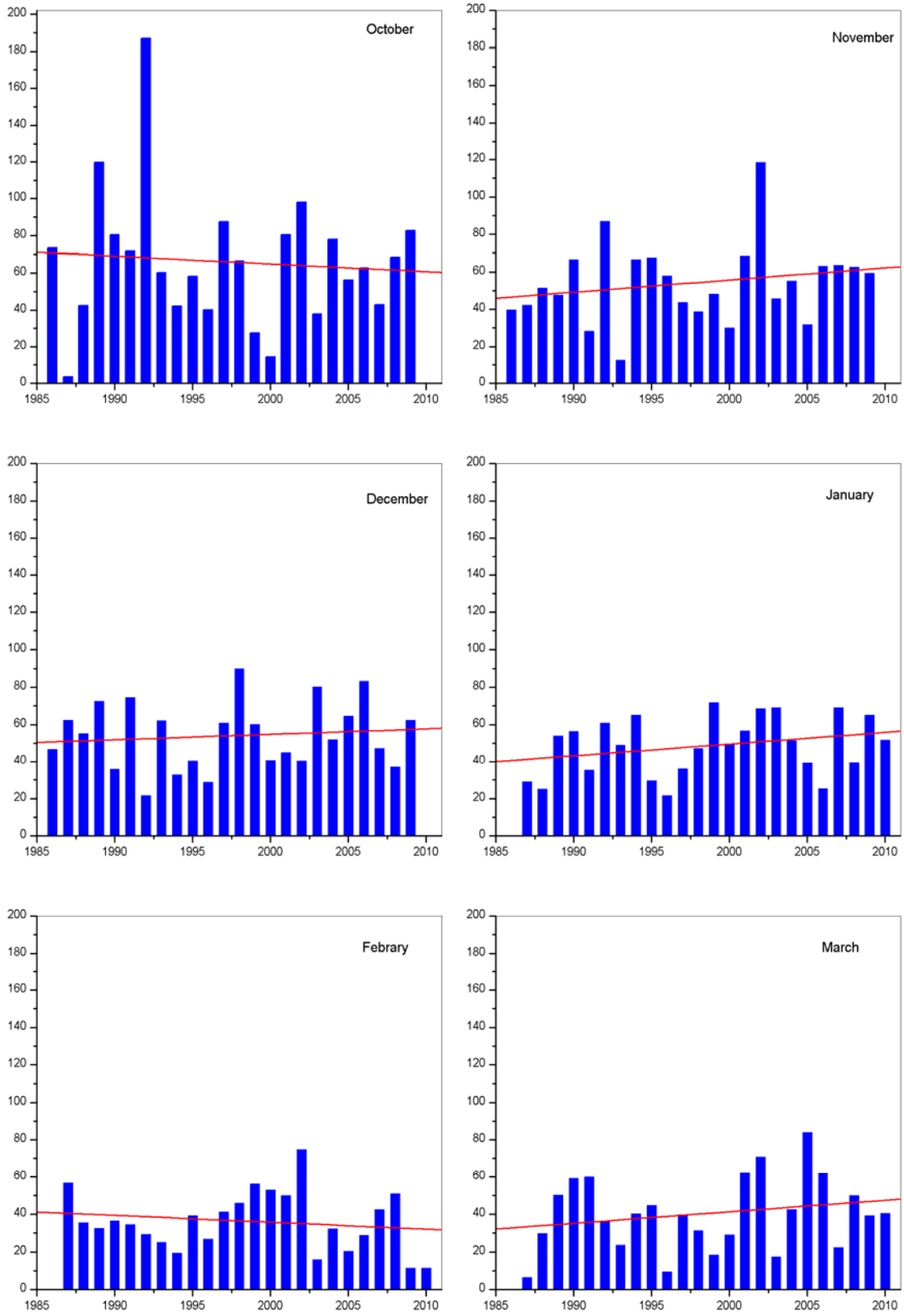

Fig.7. Dynamics of the mean monthly precipitation for cold period. (Kirov, 1986-2010).

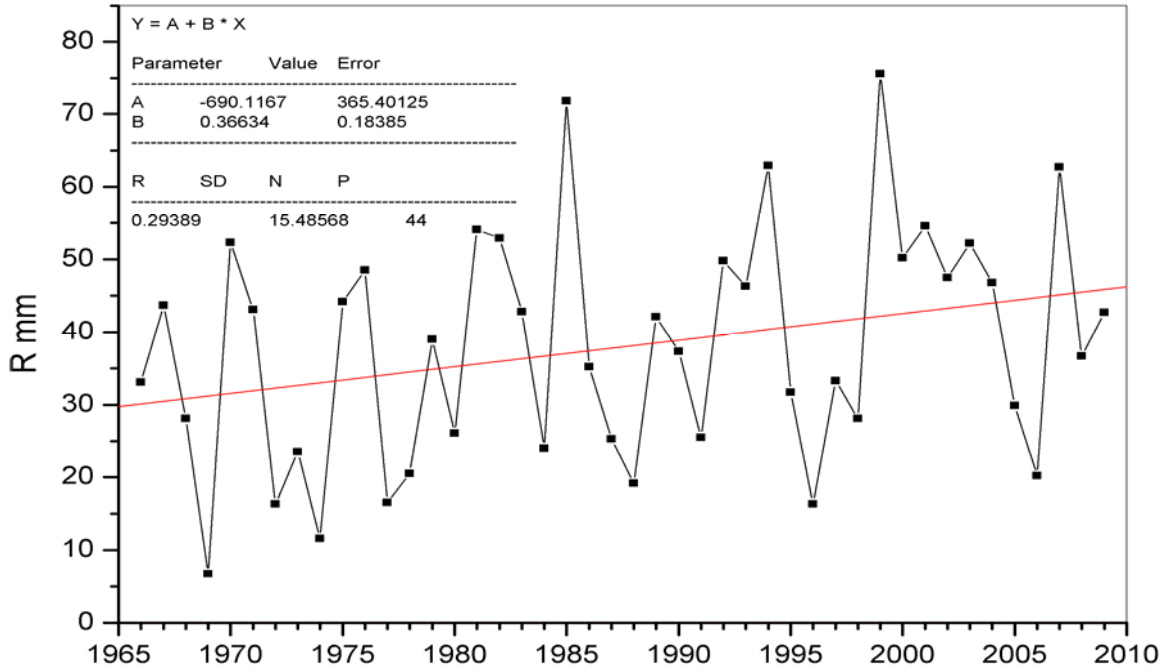

Fig. 8. Precipitation increase in January. Kumeny station (Kirov Region, 1966-2009)

3.4. Glaze and rime frequency increasing

Despite the disagreement between different authors on the tendencies in the occurrence of hazardous phenomena on the territory of the Russian Federation [1 , 2], it is commonly recognized that in Nizhniy Novgorod Region as well as in Ivanov and Vladimir Regions, Udmurtia, Chuvashia, and Krasnoyarsk Territory, the frequency of such hazardous events has been increasing. Fig. 9. presents the frequency of hazardous glaze and rime events for the last 14 years (by code CN-01).

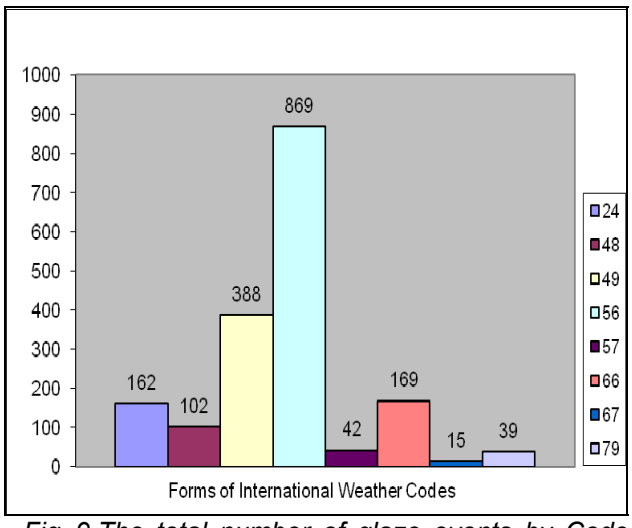

Fig. 9.The total number of glaze events by Code CN-01 for 18 stationsVFD for the period 1993-2007.

Most exposed to atmospheric icing are territories such as the steep downwind banks of the Volga, the highlands south and southeast of Arzamas, and Cheboksary Reservoir environs. One of the practically important regional climatic features directly affecting road conditions is the statistics of atmospheric icing and glaze and rime phenomena we designate in accordance with International Weather Code CN-01: 24, 48, 49, 56, 57, 66, 67, 79[1].

Most frequently, atmospheric icing is observed in Cheboksary and Lukoyanov, with less frequent icing events in Kirov, Nizhniy Novgorod, Voskresenskoye, Saransk, and Semenov. Table 1 shows the mean cold season frequency of glaze and rime events for Kirov and Nizhniy Novgorog Regions. Motor road sections with the highest frequency of icing are specially indicated on the climatic road charts. Southeast Route R-158 'Nizhniy Novgorod – Saransk' [6] is given as an example. The route lies across the territory very frequently exposed to glaze and rime (Fig.10).

[1] 24– freezing drizzle or rain между сроками наблюдений (гололед);
48 – transparent fog with rime deposition;
49 – dense fog with rime deposition;
56 – light freezing drizzle (glaze);
57 – moderate or heavy freezing drizzle (glaze);
66 –light freezing rain (glaze)
67 – moderate or heavy freezing rain (glaze);
79 – ice rain

Table 1a. Mean cold season frequency of glaze events for Nizhniy Novgorod Region (1986-2010)

№	Station	24	48	49	56	57	66	67	79	Σ
1	Arzamas	0.2	0.1	2.5	0.5	0	0.5	--	0.1	4
2	Bolshoe Boldino	0.8	0.9	3.8	2.2	0.2	0.4	0	0.1	8.5
3	Voskresenskoe	1	0.9	2.3	4.2	0.2	1	0.3	0.2	10.1
4	Vetluga	0.4	0	0.1	3.2	0.2	0.9	0	0.2	5
5	Viksa	0.3	0.5	1	2	--	1	--	0.1	4.8
6	Gorodets	0.8	0.5	1	2.7	0.2	0.5	0.2	0.3	6.2
7	Dalnee Konstantinovo	0.5	--	1.2	1.8	0	0.5	--	--	4
8	Dzerzhisk	0	0.1	0	0.1	0.1	--	--	0.3	0.7
9	Krasnie Baki	1.1	1.1	8.3	8	0.6	0.8	0	0.1	20.1
10	Lukoyanov	0.5	0.2	2	2.1	0.2	0.6	0	0.4	6
11	Liskovo	1.3	0.3	2.8	5	0.1	0.9	0	0.3	10.7
12	Nizhniy Novgorod	0.2	--	--	1.1	--	0.4	0	0.1	1.8
13	Pavlovo	0.7	0	0.5	2.9	0.1	1	0	0.3	5.5
14	Saransk	0.1	0.8	1.6	5.3	0.4	1.5	0.3	0.1	10.1
15	Semenov	1	1.1	1.7	5.9	0.6	1	0.3	0.1	11.9
16	Sergach	0.2	--	0.3	0.1	0.2	0.1	--	0.1	1
17	Cheboksary	1.1	1	5.8	7.7	0.5	1.5	0	0.1	17.8
18	Shahunia	0.5	0.9	2	5.3	0.1	0.7	--	0.4	10

Table 1b. Mean cold season frequency of glaze events for Kirov Region (1986-2010)

№	Station	24	48	49	56	57	66	67	79	Σ
1	Belaya Holunitsa	0,5	0,04	0	0,9	0	0,2	0	0,1	1,7
2	Verhneshimezhe	0,1	0,04	1,1	1,4	0,2	0,1	0	0,5	3,4
3	Vyatskie Poliani	0,4	1,9	11	1,7	0,04	0,6	0,04	0,1	15,7
4	Darovskoe	1,3	0,2	0,8	2,8	0,2	2,5	0,1	0,04	8,0
5	Kilmez	0,6	1,0	3,2	4,7	1,3	1,3	0,1	0,1	12,3
6	Kirs	1,2	0,3	0,7	9,7	0,04	1,0	0	0,1	13,0
7	Kotelnich	0,5	0,04	3,5	0,5	0,04	1,2	0	0	5,6
8	Kumeny	0,4	0,04	1,4	0,8	0	0,5	0,2	0,04	3,4
9	Lalsk	0,7	0	0	4,3	0,2	0,5	0,04	0,1	5,8
10	Murashi	0,4	0,2	1,5	1,5	0,2	0,3	0	0	4,1
11	Nagorskoe	0,5	0,5	1,2	1,6	0,1	1,5	0	0	5,4
12	Nolinsk	1,2	0,4	0,5	8,7	0,3	2,9	0	0,3	14,3
13	Oparino	2,4	0,2	0,1	10	0,1	1,0	0,04	0,1	13,9
14	Sanchursk	1,1	2,3	1,6	5	0,6	0,3	0	0,3	11,2
15	Uni	1,5	0,2	1,7	6,5	0,4	0,2	0,1	0,2	10,8
16	Urzhum	0,7	1,1	4,2	5,5	0,1	1,1	0,1	0,1	13,0
17	Falenki	0,2	0,3	2,5	0,8	0,2	0,3	0	0,04	4,3
18	Shabalino	0,2	0,1	2,3	1,7	0	0,7	0,04	0	5,1
19	Yaransk	0,5	1,1	3,3	1,3	0	1,2	0	0	7,4
20	Kirov	1,5	0,7	1,6	8,2	0,1	0,5	0	0,3	1,8

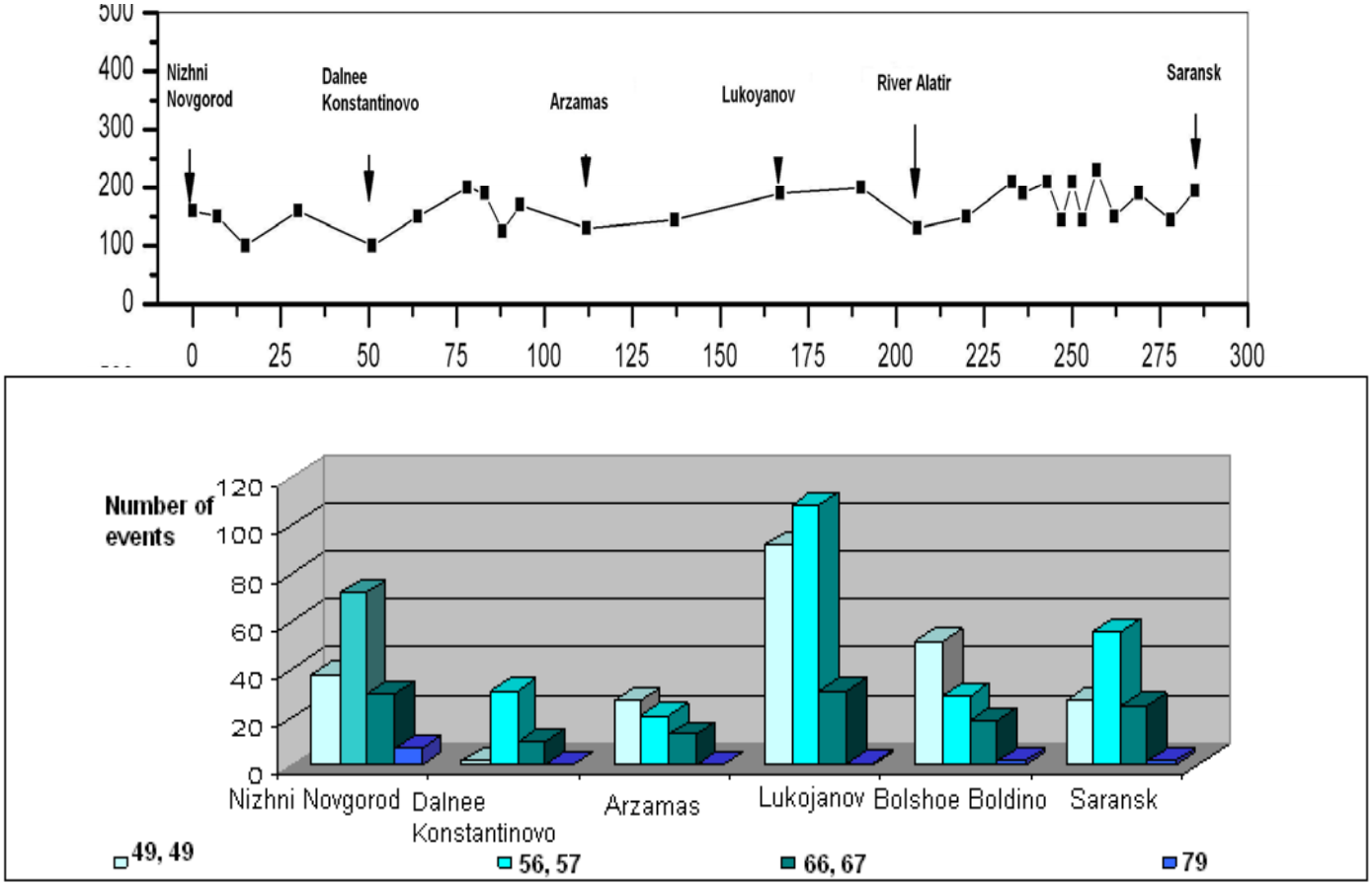

Fig. 10. Relief, m (upper) and total number of glaze events for VFD stations (for cold seasons 1993-2007) along the Regional Road No 158 (down).

4. RESUME

Observational data from ground-based weather network stations for the last 25 years are analyzed. A climatic statistical model of Verhniaya Volga area, exemplified by Nizhniy Novgorod and Kirov Regions, is compiled. Basic trends in cold season's weather parameters in these Regions are established, which testify to enhanced occurrence of glaze and rime events.

Ground observations during 47 years, from 1961 till 2007, and further on till 2010, show a maximum temperature rise from -14°C to -7°C at some of the stations. This rise resulted in generally higher air moisture content in cold seasons, higher relative humidity, and enhanced precipitation. During cold seasons (November, December, January, and March) precipitation tends to increase over the last 24 years. However, in February and October, a small precipitation decrease is observed. The frequency of hazardous events - slipperiness and icing of buildings and transport structures, as well as electric power lines – has increased.

These trends are clearly demonstrated by observations at the ground network stations. Now, the number of temperature passes over 0°C in January is on average larger by 25-30%.The dependence of this number on mean monthly temperature is obtained, which is also of practical importance. Now, air temperature in winter varies within the range of higher values, up to those above 0°C, and very often around 0°C when precipitation phase changes. Rising air temperature is followed by a growing number of passes over 0°C of the temperature of infrastructure elements.

Despite the opposite views of different authors on the tendencies in weather hazard occurrence across the territory of the Russian Federation, it is commonly recognized that in the Regions of Nizhniy Novgorod and Kirov, Ivanovo, Vladimir, and in some other territories the number of weather hazards, including those related with icing, is definitely increasing.

5. BILIOGRAPHY

1. Panfutova, Yu.A., N.A. Samoletova, O.D. Mokeyeva, and I.V. Romanova. Disastrous weather events on the flats of the Russian Federation. 2007. Proceedings MGO, No. 556, p.145-156. (In Russian).

2. Bedritsky, A.I., A.A. Korshunov, L.F. Khondozhko, and M.Z. Shaymordanov. 2004. Climatic system and provision for Russia's hydro-meteorological safety.– Meteorology and Hydrology, No.4, p. 120-129. (In Russian).

3. Enhancing protection against hazardous weather phenomena. 2002. Geneva, WMO, No. 936, 36 p. (In Russian).

4. Glukhov, A.T. Glaze formation conditions and motor traffic safety. In the book: The problems of the motor road network of Saratov Region and the ways of their solution. Materials of the Regional Science and Operation Conference, 16-17 May, 1996 (in 2 Parts). Part 1. Saratov State Technology University, 1996, p.72-75. (In Russian).

5. Vasiliev, A.P. Road conditions and motor traffic safety in unfavorable weather. Moscow, Transport, 1976, 224 p. (In Russian).

5. The Federal roads of Russia. 2008. Transportation service qualities and motor traffic safety. Statistics analysis collection. Rosavtodor, Moscow, 124 p. (In Russian).

6. Nauchno-prikladnoi spravochnik po klimatu USSR. Seria 3. Mnogoletnie Dannie, Part 1-6, Vipusk 29. Gidrometeoizdat, St-Petersburg, 1992. P. 582 (In Russian).

Acknowledgments

This report has been prepared under Themes # 8.85-1.7.51 of 2008-2011 R&D Plan within the framework of the Regional Program funded by Roshydromet.

The authors would like to thank the sponsors - WMO, IUGG, IAMAS and ICCP - for their financial support.

The authors are thankful to M.A. Khanchina for the adequate rendering of the contents of this paper in English.

A MODELING STUDY OF A WARM CLOUDS EXTREME EVENT IN SANTA CATARINA, BRAZIL

Theotonio Pauliquevis[1], Maria Assunção F. Silva-Dias[2], Henrique Barbosa[2]

[1]Universidade Federal de São Paulo, Diadema, Brazil (theotonio@gmail.com)
[2]Universidade de São Paulo, São Paulo, Brazil

1. INTRODUCTION

In 2008, November 21st-24th, the eastern portion of the Santa Catarina (SC) state in southern Brazil was subject to an extreme event of rain that lasted four days. Accumulated precipitation was ~ 700 mm, daily rain reached 280 mm and the total monthly rain was up to 1000 mm (INPE, 2009).

Beyond the serious social and economical consequences of this huge amount of precipitation, a surprising fact was the weak ability of models operational in Brazil by that time to forecast correctly the magnitude of the event. ETA model forecast indicated precipitation amount up to 200 mm for the period 20-24/november, as shown in Figure 1.

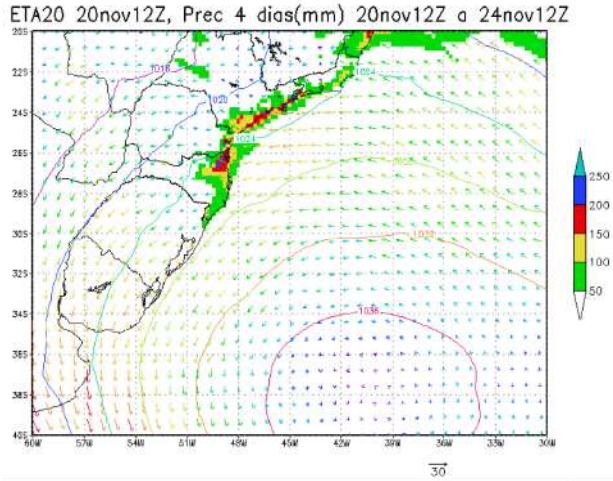

Figure 1: ETA model operational forecast (top) for total precipitation between 20-24/nov/2012.

From the synoptic point of view, the driver for this event was a stationary high pressure in the South Atlantic that advected very humid air masses from the ocean to the continent. Because the topography of the area is characterized by a mountain range following the coastline, the combination of these two facts resulted in very efficient formation of warm clouds with tops below 5000 m and precipitation due to the forced lifting of quasi-saturated air-masses from the ocean.

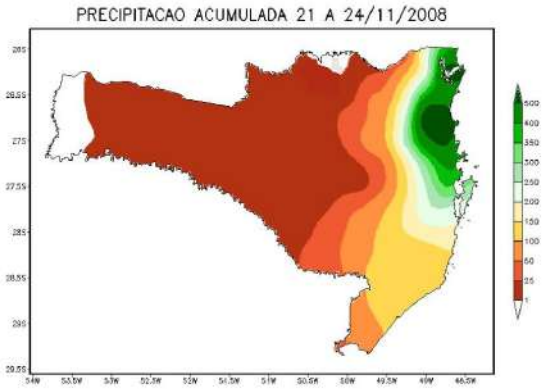

Figure 2: observed precipitation derived by pluviometers between 21-24/November/2008.

Another important feature of this event was that the 700 mm of rain did not precipitated in one or two storms. Instead, it was characterized by mid size but constant storm intensity. In Figure 3 it is shown the time series of the precipitation rate.

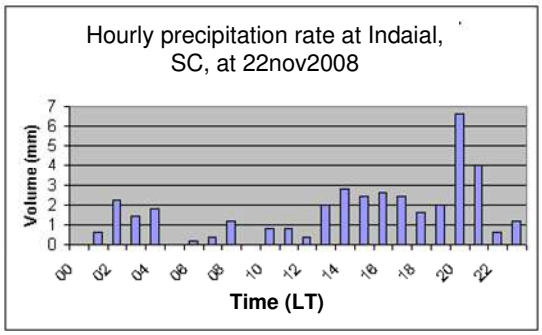

Figure 3: hourly mean precipitation observed at the city of Indaial, which is close to the maximum observed accumulated precipitation.

2. OBJECTIVE

The objective of this study was to investigate the ability of numerical models in correctly forecast events like this with respect to storm size and time-integrated volume of precipitation. In particular we tested how effective is the increase in spatial resolution (both in horizontal and vertical directions), different resolutions of topography, and the

employment of full microphysics for resolution about 2 km.

3. METHODOLOGY

The model employed in this study was the BRAMS Model (Brazilian developments on the Regional Atmospheric Modeling System) (Freitas et al., 2009), which is a tropicalized version of the RAMS Model (Pielke et al., 1992). The microphysics component is as described in Meyers et al. (1997).

Two kinds of simulations were performed. The first kind (type C simulation) focused on less vertical resolution and 2 nested grids with resolution 20km and 5km. First and second grids accounted, respectively, with 50 x 60 and 102 x 154 grid points. Grell convective parameterization (Grell and Dévényi, 2002) was turned on(off) for grid 1(2). First level in the vertical coordinate started with 120 m, with a vertical grid stretch ratio of 1.2 (maximum Δz = 1000m), in a total of 32 levels (top at 21 km). This configuration is more representative of the upper operational limit of most forecast centers, and we aimed to provide a somehow "control" configuration.

The second type of simulation (type F simulation) employed finer vertical resolution, (first level of 60, vertical stretching ratio of 1.15 (maximum Δz = 1000 m) and 37 levels (top at 18 km)). Simulations were performed with 1, 2 and 3 nested grids. Resolution was, respectively 40km, 10km and 2.5km.

We made different combinations with respect to topography and cumulus parameterization. One case was the "F1" simulation, where it was employed gradually enhanced topography. Thus, 1st/2nd/3rd grid were set to 10km/1km/200m topography, respectively. As an opposite case "F2" simulation was set to 10km resolution for topography in spite that grid points were smaller than it. The objective was to investigate the actual role of resolution of topography in the final results.

Cumulus parameterization (CP) was always turned "on" in the 1st (40km) and "off" in the 3rd (2.5km) grids. Three simulations were performed with respect to the effect CP "on" and "off" in the 2nd grid. In two of these cases simulation was performed only with 2 grids, and the third case we run 3 grids with CP "off" in the second grid to test whether it could affect the ability of microphysics module of the model in correctly generate rain in the 3rd grid. A fourth simulation, with CP "on" in 1st and 2nd grid and with 3 grids could not be run due to numerical instabilities generated during the run.

Simulation type	C	F1/F2
Simulated period	19nov2008_00Z 26nov2008_00Z	
Number of grids	1, 2	1, 2, 3
Grid points (per grid)	50 x 60 102 x 154	150 x 150 102 x 154 200 x 200
Spatial resolution (per grid)	20 km, 5 km	40 km, 10 km, 2.5 km
Vertical resol.: ΔZ_0, dZ ratio, ΔZ_{max}, n_{levels})	100 m, 1.2, 1000m, 32	60 m, 1.15, 500 m, 37
Time step	50s, 10s	50,12.5, 2.5
Topography resol.	10 km, 1 km	F1: 10km/1km/200m F2: 10km for all grids
Flag of cumulus parameterization	On/off	2 grids: on/off and on/on 3 grids: on/off/off
Input from borders	NCEP reanalysis	NCEP Reanalysis

Table 1: Configurations of the performed simulations. Type C (S) corresponds to Coarse (Fine) vertical resolution. Type F simulations can be separated in F1 type, with 10 km coarse topography for all grids, and F2, with finer topography for higher spatial resolution.

Bulk microphysics in BRAMS (and also in RAMS) is not grid selective, i.e., the same configurations apply to all grids. However, it is expected that it become more sensible at higher resolution (~5 km and less). In our case we employed the most prognostic as possible settings for microphysics. It means that starting from a fixed number of Cloud Condensation Nuclei (CCN) the model is able to calculate prognostic size and number distributions of liquid and ice phase hydrometeors, as well as mixing ratios (Meyers et al., 1997).

A general view of the simulations settings is shown in Table 1.

4. RESULTS

In Figure 4 it is shown the total precipitation for the entire simulated period. It is possible to see that type C simulations presented good agreement (Figures 4a and 4b). A good agreement was also achieved by type F simulation with 1 single grid. On the other hand, type F simulations with 2 and 3 grids reduced the total precipitation field in the target area, i.e. the SC state. Instead of it, is shifted the maximum precipitation to northern portions of the coast, and almost vanished precipitation in the SC coast.

This is an unexpected result, since it is expected that cloud mechanisms should be better represented with models working under higher spatial – specially vertical - resolution.

In Figure 5 it is shown the average field of cloud water mixing ratio in several heights for the 3rd grid in F1 and F2 simulations. It is possible to see that the model was able to create a cloud field over the target region. However, it is possible to see that most of cloud water was over the ocean, and not over the continent. It shows that not only the rain formation was harmed but also the cloud formation over the expected area.

Figure 6 shows vertical profiles of the different simulations. Relative humidity is shown in the first column. Simulation type C (1st line) shows a saturated profile from ground up to 3500 m, which means that model could represent very well the actual humidity profile that occurred during the target period.

5. DISCUSSION

The objective of this study was to figure out the reason for the fail in the correct forecast of this extreme event. The initial hypothesis was that the enhancement of spatial resolution – both in horizontal and vertical directions – would be enough to improve the representation of this convective event.

The results showed that a two-grids simulation, with inner grid resolution with $\Delta x = \Delta y = 5$km and $\Delta z_0 = 100$m represented the precipitation field much better than a three-grid simulation, with $\Delta x = \Delta y = 2.5$km and $\Delta z_0 = 60$m.
In fact, type C simulations resulted in a reasonable uniform precipitation field over the SC state coast line, as shown in Figures 4a (1ST grid) and 4b (2nd grid). Beyond that, type C simulations also correctly assigned the location of maximum accumulated precipitation, which is in the northern portion of the coast, around lat = -27S and lon = -49W as can be seen in the observed precipitation field (Figure 2). Further, it resulted in weekly precipitation volume up to 500 mm, which is quite close to the observed maximum.

The precipitation fields for type F simulation are displayed in Figures 4c-4f. The simulation with one grid (4c) agreed quite well with observed precipitation field presenting precipitation maxima up to 270 mm. It is also similar to the type C/1st grid simulation both in terms of spatial distribution and total precipitation.

Precipitation for the type F simulations with higher resolution is showed in figures 4d (2 grids) and 4e/f (3 grids). It is promptly realized that total precipitation is significantly reduced in the two cases.

With respect to the 2-grids simulation (Figure 4d) it is important to highlight that cumulus parameterization was activated, as well as microphysics. A possible explanation for this reduction in precipitation is the fact that CP is designed to work better in more coarse resolutions. In fact, the 2nd grid in the 2-grid simulation was set to 10km resolution. Several modeling studies have shown that the domain within the 1 – 10 km range is not ideal neither to CP or microphysics.

The same fields for the 3-grid simulations are shown in figures 4d-4f. The differences in these simulations are only due to the different resolution in the topography, which is finer (200m) in figure 4f.

Surprisingly, it did not improve the precipitation field. When compared to the 2-grid simulation, it was reduced even more.

A important feature of these 3-grid simulations is that CP was "off" in the 2nd grid, and possibly caused some influence in the 3rd grid yielding this low amount of rain. This hypothesis will be tested in a future simulation with CP "on" in 1st and 2nd grids.

All these observations are corroborated by the modeled vertical profiles, which are shown in Figure 6 for the location of the maximum measured precipitation (lat = 27S; lon = 49W). The first figures on the left correspond to relative humidity (RH). The first RH profile shows that the mean atmosphere was almost all the time saturated up to 4000m, which agrees with observational data like those ones shown in Figure 3, i.e., weak but constant rain. In the next plot (type F, 2nd grid) the profile is also saturated but reducing above 2000m. The scenario goes in the same direction for type F/3-grids/3rd grid profiles, which presented high RH but not saturated profiles. It means that microphysics module was unable to generate clouds.

The same analysis holds for the 2nd column plots (rainwater). With respect to rain efficiency (defined as the ratio rainwater/totalwater) the profiles are very similar, but it does not implicate in higher precipitation once total water was significantly smaller in type F cases. Snow profile (last column) was quite similar in all profiles.

6. CONCLUSION

This study investigated the effect of different settings of BRAMS regional model in its ability to correct forecast an extreme precipitation event in the Santa Catarina state in Brazil. Different resolutions were tested as grid point size, topography and selective activation of cumulus parameterizations in different grids. The results showed that higher resolution was not sufficient to improve the prediction in precipitation fields. Apparently the disabled cumulus parameterization in 2nd grid (type F simulation) induced a significant reduction in the 3rd grid ability to predict precipitation. Further simulations have to be performed to test this hypothesis.

ACKNOWLEDGMENTS

The authors acknowledge the financial support of FAPESP (Fundação de Amparo a Pesquisa do Estado de São Paulo). T.Pauliquevis specially acknowledge the grant number 2008/04463-7.

REFERENCES

INPE, Technical note: The November 2008 rain in Santa Catarina, 2009

Freitas, S. R., Longo, K. M., Silva Dias, M. A. F., Chatfield, R., Silva Dias, P., Artaxo, P., Andreae, M. O., Grell, G., Rodrigues, L. F., Fazenda, A., and Panetta, J.: The Coupled Aerosol and Tracer Transport model to the Brazilian developments on the Regional Atmospheric Modeling System (CATT-BRAMS) – Part 1: Model description and evaluation, Atmos. Chem. Phys., 9, 2843-2861, doi:10.5194/acp-9-2843-2009, 2009.

Grell, G.A. and D. Devenyi: A generalized approach to parameterizing convection combining ensemble and data assimilation techniques, Geoph. Res. Let., 29, NO 14.,10.1029/2002GL015311, 2002.

Meyers, M.P., R.L. Walko, J.Y. Harrington, and W.R. Cotton: New RAMS cloud microphysics prameterization. Part II: The two-moment scheme. Atmos. Res., 45, 3-39, 1997

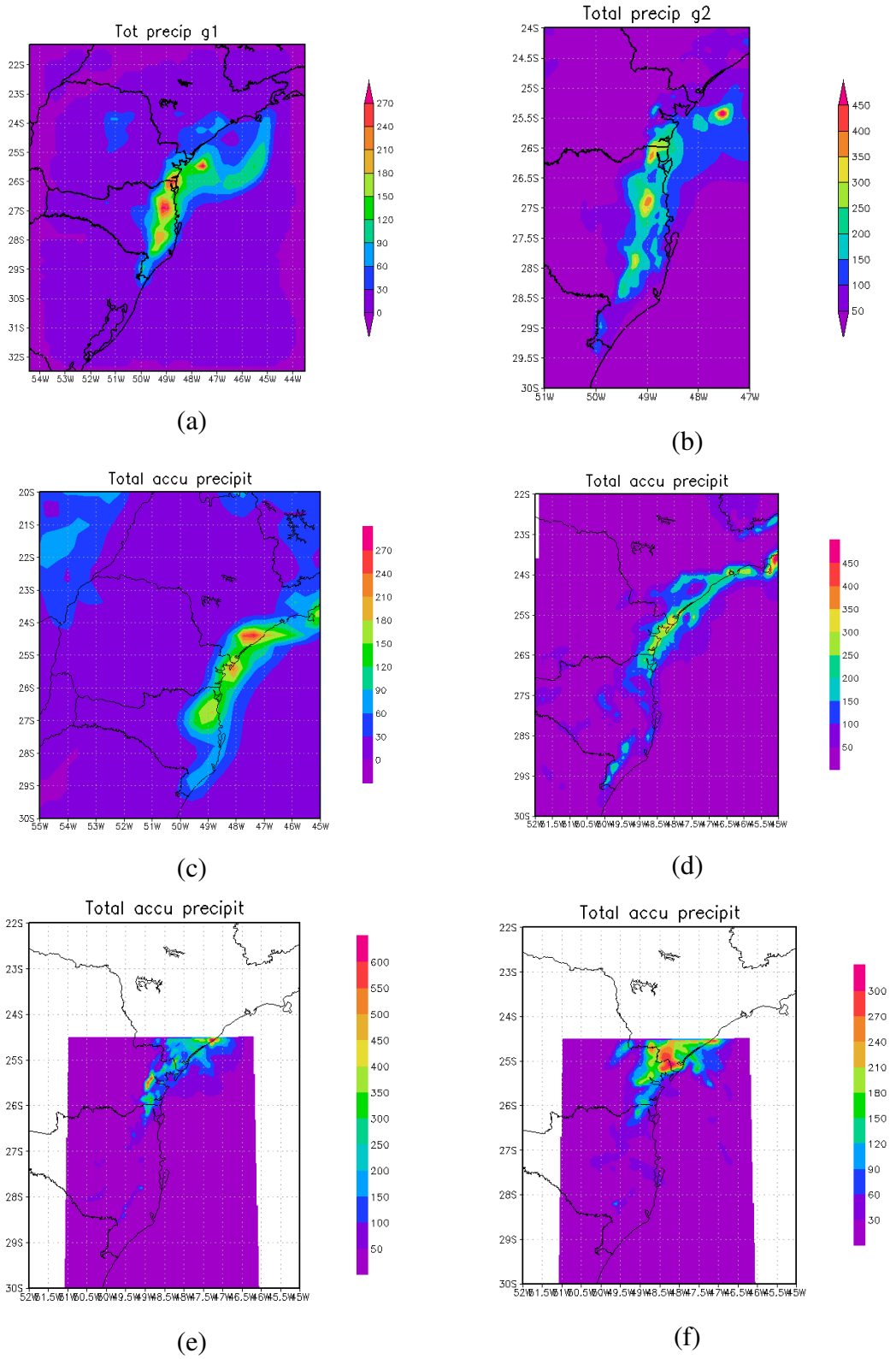

Figure 4: total surface precipitation at the end of each simulation type: (a) type C, one grid simulation (b) C, two grids 2, (c) F, one grid, (d) F, two grid, with cumulus parameterization (e) and (f) F, three grids, with difference in topography resolution being 10 km for all grids in (e), and 10km/1km/200m in (f).

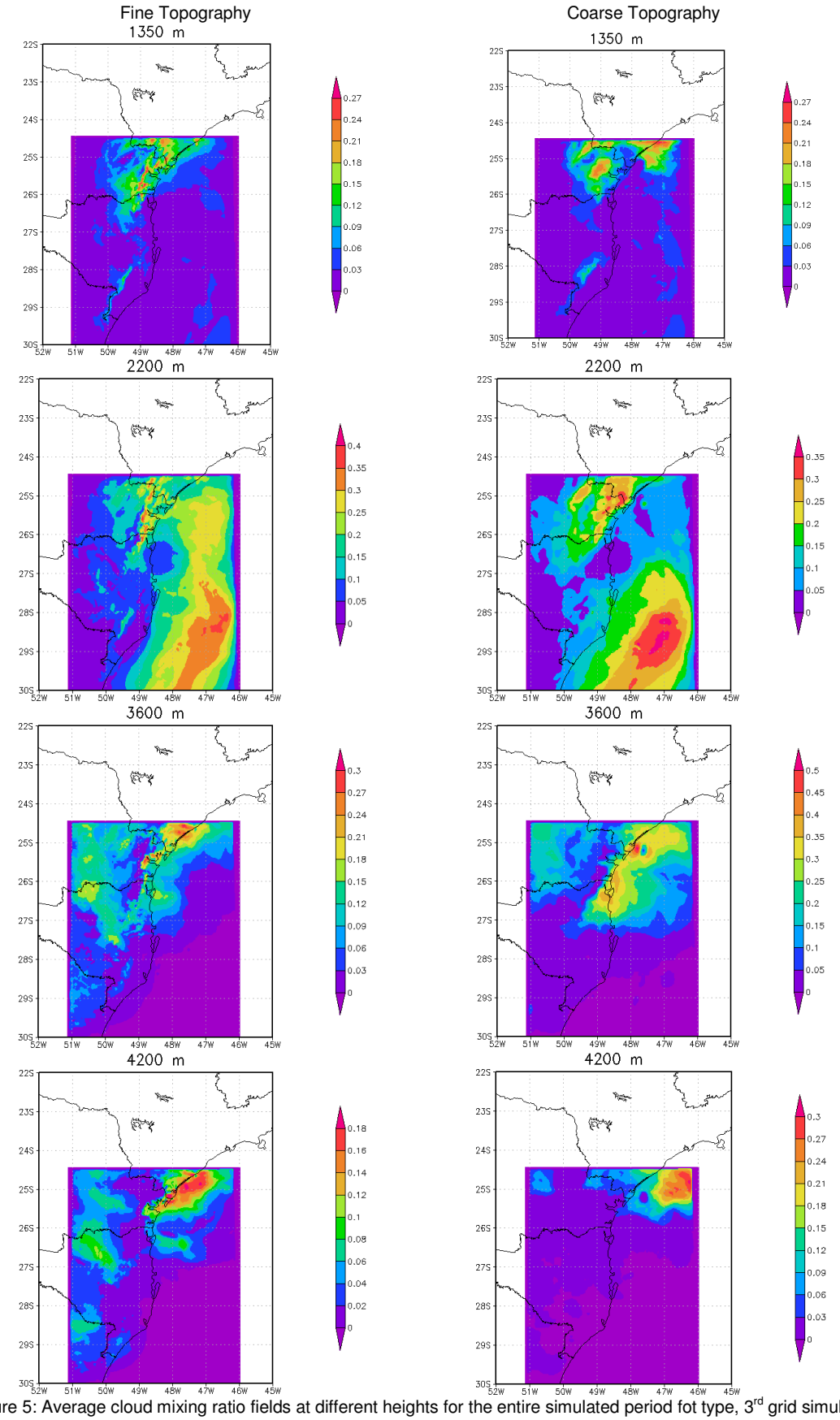

Figure 5: Average cloud mixing ratio fields at different heights for the entire simulated period fot type, 3rd grid simulation. Plots at left (F1) and right (F2) sides differ by the topography resolution, as described in Table 1.

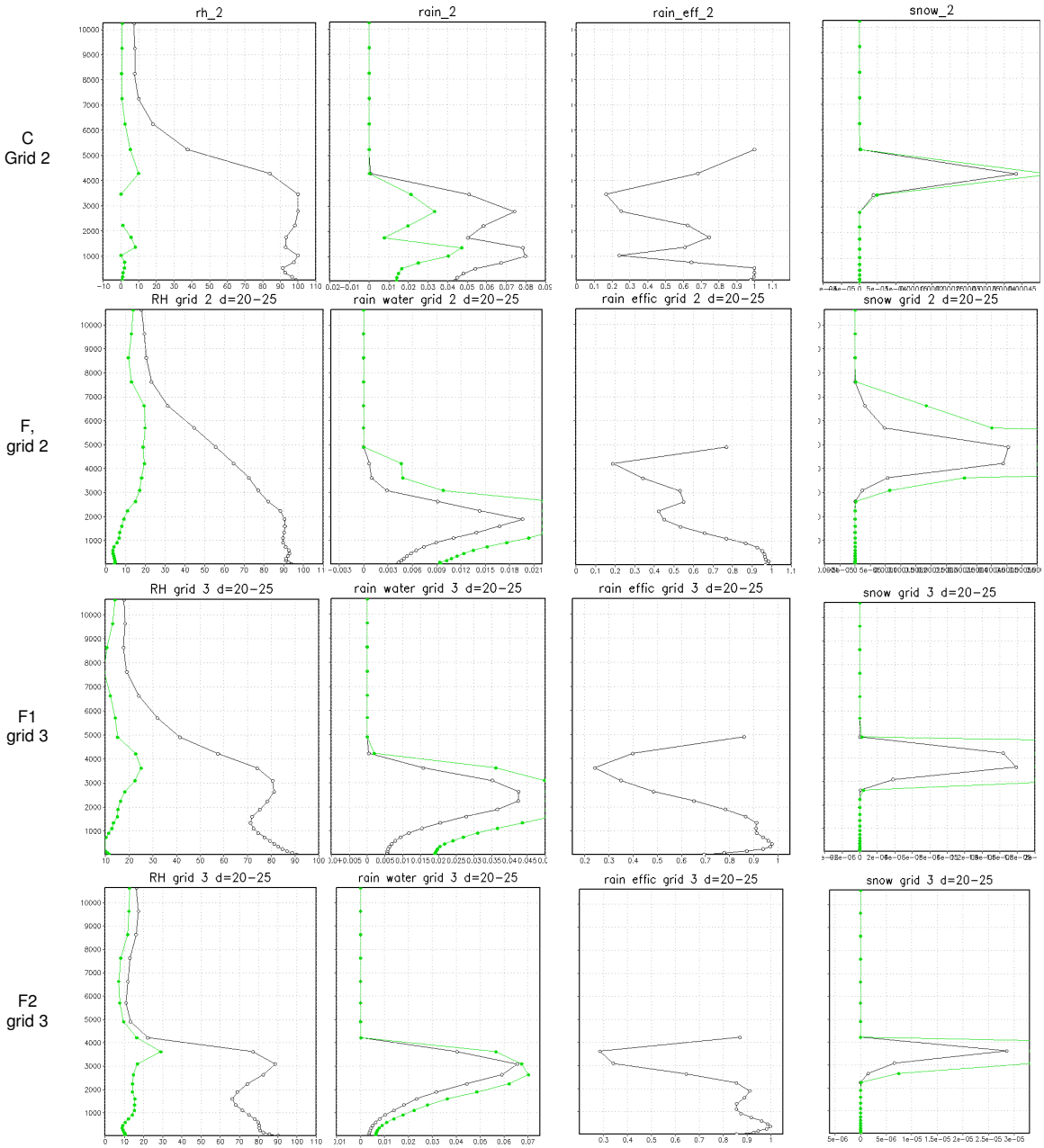

Figure 6: vertical profiles at Blumenau for the performed simulations. From left to right, plots correspond to Relative Humidity (RH), rain droplets mixing ratio (g/m^3), rain efficiency [rain/(cloud+rain)], and snow content (g/m^3).

SOL-GEL TRANSITION IN A MODEL OF WARM RAIN INITIATION BY TURBULENT COLLECTION

L. Alfonso
Universidad Autónoma de la Ciudad de México
Mexico City, 09790 México
Correspondence to:
lesterson@yahoo.com

G. B. Raga
Universidad Nacional Autónoma de México
México City, 04510 México

D. Baumgardner
Universidad Nacional Autónoma de México
Mexico City, 04510 México

ABSTRACT

A sol-gel transition is proposed here as a mechanism that forms the large droplets that are needed to trigger warm rain development in cumulus clouds. Warm rain in natural clouds is produced by the collision and coalescence of small droplets. By using a collection kernel enhanced by turbulence and a stochastic simulation method, the formation of a runaway droplet is modeled through the turbulent collection process. The model results show that the sol–gel transition (also called *gelation*) leads to the formation of a droplet with mass comparable to the mass of the initial system. The time when the sol-gel transition occurs is estimated with a Monte Carlo method when the parameter ρ (the ratio of the standard deviation for the largest droplet mass over all the realizations to the averaged value) reaches its maximum value. Moreover, we show that without turbulence, the sol-gel transition will not occur. In the context of theoretical cloud microphysics, gelation can be interpreted as the formation of the “lucky droplet” that grows at a much faster rate than the rest of the droplet population and subsequently becomes the embryo for raindrops.

1. INTRODUCTION

The formation process of large droplets, that triggers the production of rain in warm cumulus clouds, is one of the open problems in cloud physics. Various mechanisms have been proposed in the past (Pruppacher and Klett, 1997); however, there are still major gaps in our understanding of the rapid growth of cloud droplets across the size range of diameters from 10 to 50 μm. Some hypotheses explain the formation of these large droplets by enhanced condensation of water vapor molecules onto droplet embryos (Khain et al., 2000). Other

studies describe droplet coalescence as the important factor governing the evolution of the droplet spectrum at the early stages of cloud development, mainly by two mechanisms: i) the collision of large droplets growing on giant and ultra-giant nuclei and ii) the self-broadening of the droplet spectrum by collisions between cloud droplets. Regarding this second mechanism, it has been emphasized by experimental (Vohl et al., 1999) and theoretical studies (Pinsky et al.; 1999, 2000) that there is a significant acceleration of droplet growth rate by collisions in a turbulent flow, with collision efficiencies that can be up to 10 times larger than in the pure gravity case.

In this contribution we will focus on a model for the growth of cloud droplets by this second mechanism, i.e. turbulent collision-coalescence at an early stage of cloud development. We will show that this model reveals the sol-gel (defined below) transition and the formation of runaway droplets.

The kinetic collection or coagulation equation (hereafter KCE) has long been used to model the time evolution of droplet size distributions due to collection events. The discrete variant of this equation has the form (Pruppacher and Klett, 1997):

$$\frac{\partial N(i,t)}{\partial t} = \frac{1}{2}\sum_{j=1}^{i-1} K(i-j,j)N(i-j)N(j) - N(i)\sum_{j=1}^{\infty} K(i,j)N(j) \quad (1)$$

where $N(i,t)$ is the average number of droplets with mass x_i, and $K(i,j)$ is the coagulation kernel related to the probability of coalescence of two drops of masses x_i and x_j. In Eq. 1, the time rate of change of the average number of droplets with mass x_i is determined as the difference between two terms: the first that describes the average rate of production of droplets of mass x_i due to coalescence between pairs of drops whose masses add up to mass x_i, and the second that describes the average rate of depletion of droplets with mass x_i due to their collisions and coalescence with other droplets.

The collection process is stochastic in nature and therefore more accurately described by the master equation for the joint probability distribution $P(n_1, n_2, ..., n_k, ..., t)$ where $\bar{n} = (n_1, n_2, ..., n_k, ...)$ at time t. This equation has the form (Bayewitz et al., 1974):

$$\frac{\partial P(\bar{n})}{\partial t} = \sum_{i=1}^{N}\sum_{j=i+1}^{N} K(i,j)(n_i+1)(n_j+1)P(...,n_i+1,...,n_j+1,...,n_{i+j}-1,...;t)$$
$$+\sum_{i=1}^{N}\frac{1}{2}K(i,i)(n_i+2)(n_i+1)P(...,n_i+2,...,n_{2i}-1,...;t)$$
$$-\sum_{i=1}^{N}\sum_{j=i+1}^{N} K(i,j)n_i n_j P(\bar{n};t) - \sum_{i=1}^{N}\frac{1}{2}K(i,i)n_i(n_i-1)P(\bar{n};t) \quad (2)$$

The KCE can be obtained from Eq. 2 by taking the mean value of n_k:

$$\langle n_k \rangle = \sum_{\bar{n}} n_k P(\bar{n};t) \qquad (3)$$

and assuming (Bayewitz et al., 1974) that $\langle n_i n_j \rangle = \langle n_i \rangle \langle n_j \rangle$. In general, the average spectrum obtained from Eq. 1, and the ensemble averages spectrum obtained over different realizations of the stochastic collection process, are different. The solution to the KCE and the expected values calculated from the stochastic Eq. 2 are equal only if the covariances are omitted from the probabilistic model, as shown in Bayewitz et al., (1974) and Tanaka and Nakazawa (1993). When this condition is fulfilled, the deterministic solution provided by Eq. 1 corresponds to the average value of n_k over many realizations.

The first moment of the distribution of *N(i,t)* corresponds to the total mass (M_1) in the system and the second moment (M_2), defined as

$$M_2(t) = \sum_{i=1}^{N_d} x_i^{\,2} N(i,t) \qquad (4)$$

(where N_d is the number of drop categories or sizes of the discrete distribution) may become undefined, when the initial number of particles is small, or if *K(i,j)* increases sufficiently rapidly with x_i and x_j. In that case, the total mass of the system starts to decrease. This is usually interpreted to mean that a macroscopic, "runaway" particle has formed (known as a *gel*) and the system exhibits a phase transition (also called *gelation*). After this moment, the true averages calculated from the stochastic process will differ from the averages obtained from Eq. 1, and there is a transition from a system with a continuous droplet distribution to one with a continuous distribution *plus* a massive runaway droplet.

When the sol-gel transition occurs mass conservation is expected to break down. The gelation time, T_{gel} , is defined as the longest time such that the discrete model (1) has a solution with $M_1(t) \equiv M_1(0)$ for $t<T_{gel}$ and $M_1(t) < M_1(0)$ for $t>T_{gel}$, where M_1 is the total mass of the system. Analytical expressions for the gelation time only exists for very simple kernels; hence, as suggested in Inaba et al.,(1999), it should be estimated numerically by Monte Carlo simulations (Alfonso et al., 2008, 2010). The numerical algorithm of Gillespie (1975, 1976), which inherently incorporates all stochastic correlations, is used for the stochastic simulation in this work.

2. SIMULATION RESULTS FOR THE TURBULENT COLLECTION KERNEL

The gelation time, T_{gel}, can be estimated as the time when the maximum of the ratio, ρ, is reached. This ratio is defined as the standard deviation of the largest particle mass over all the realizations to its ensemble average, evaluated from the realizations of the stochastic process:

$$\rho = \sigma(M_{L1})/M_{L1} \qquad (5)$$

where M_{L1} is the ensemble mean of the mass of the largest droplet over all the realizations and the standard deviation for the largest droplet mass (σ) is calculated as:

$$\sigma(M_{L1}) = \sqrt{\frac{1}{K}\sum_{i=1}^{K}(M_{L1}^{i} - M_{L1})^2} \qquad (6)$$

In (6) M_{L1}^{i} is the largest droplet mass for each realization and K is the number of realizations of the Monte Carlo algorithm.

As previously mentioned the KCE (Eq. 1) has analytical solutions for only a few selected kernels such as the product kernel $K(i,j)=Cx_ix_j$. The validity of the KCE will break down once gelation occurs. We will demonstrate that the time when the ratio ρ (Eq. 5) reaches its maximum value is a good estimate of the gelation time T_{gel}. The calculations were performed for an initial, mono-disperse distribution of 100 droplets of 14 μm in radius (droplet mass 1.15×10^{-8}g), with C= $5.49\text{x}10^{10}$ cm^3 s^{-1} (Alfonso et al., 2008) in a volume of one cubic centimeter. This initial concentration is typical of maritime cumulus clouds and corresponds to a liquid water content of about 1.15 gm^{-3}. The time evolution of ρ was estimated from 1000 realizations (K=1000) of the Gillespie's (1975) Monte Carlo algorithm. The results of this simulation are displayed in Fig. 1 and we observe that the maximum of ρ (solid line) was obtained at τ=1335 s.

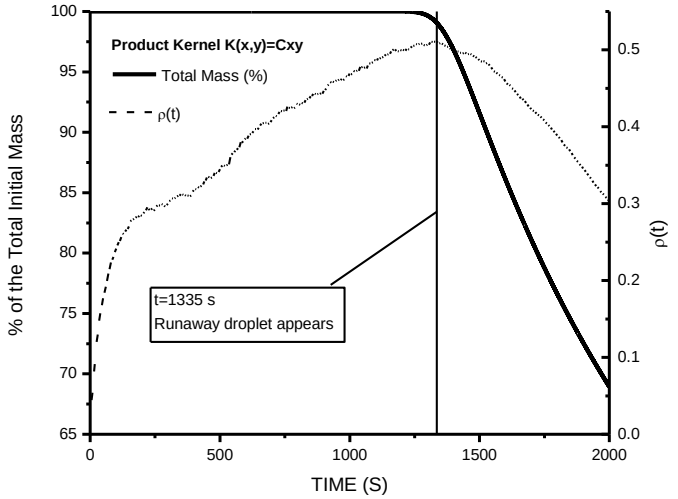

FIG. 1. Time evolution of the statistics ρ defined in Eq. 5 (dashed line and right axis) and the total mass (solid line and left axis) calculated from the numerical solution of the KCE. The results were obtained for the product kernel $K(x,y)=Cxy$, (C=5.49×10^{10} cm^3 g^{-2} s^{-1}).

Independently, the gelation time can be obtained analytically (Drake and Wright, 1972) from

$$M_2(\tau) = \frac{M_2(t_0)}{1 - CM_2(t_0)\tau} \quad (7)$$

$$T_{gel} = \left[CM_2(t_0)\right]^{-1} \quad (8)$$

and was found to be 1379 s, very close to the time when ρ reaches its maximum value. After this time, the largest droplet continues to grow by accretion of smaller droplets and the total mass M_1 predicted by the KCE starts to decrease (Wetherill, 1990) as seen in Fig.. 1. This indicates that the numerical method provides a reliable approximation of the gelation time.

For natural clouds collisions between droplets, under idealized, pure gravity conditions, are typically simulated with a collection kernel of the form:

$$K_g(x_i, x_j) = \pi(r_i + r_j)^2 \left|V(x_i) - V(x_j)\right| E(r_i, r_j) \quad (9)$$

The hydrodynamic kernel (Eq. 9) doesn't take into account the turbulence effects and considers that droplets with different masses (x_i and x_j and corresponding radii, r_i and r_j) have different settling velocities. In Eq. 9, the collision efficiencies $E(x_i, x_j)$ were calculated according to Hall (1980).

In turbulent air, the hydrodynamic kernel can be enhanced due to an increase in relative velocity between droplets (transport effect) and an increase in the collision efficiency (the drop hydrodynamic interaction). These effects were taken into consideration by implementing the turbulence induced collision enhancement factor $P_{Turb}(x_i, x_j)$ that is calculated in Pinsky et al. (2008) for a cumulonimbus cloud with dissipation rate, ε=0.1 $m^2 s^{-3}$ and Reynolds number, $Re_\lambda = 2\times10^4$, for cloud droplets with radii ≤ 21 μm. Consequently, the turbulent collection kernel has the form:

$$K_{Turb}(x_i, x_j) = P_{Turb}(x_i, x_j) K_g(x_i, x_j) \quad (10)$$

In the simulation for turbulent air, a system corresponding to a cloud volume of $1 cm^3$ and a bimodal droplet distribution was considered: 150 droplets of 10 μm in radius and another 150 droplets of 12.6 μm in radius, corresponding to a liquid water content (LWC) of 1.9 gm^{-3}. The behavior of the ratio ρ (Eq. 5) was evaluated from 1000 realizations of the Monte Carlo algorithm and, independently, the evolution of the total mass was obtained by solving the KCE (Eq. 1) numerically. Figure 2 shows that the total mass (expressed in % of the initial total mass), calculated numerically from the KCE, is no longer

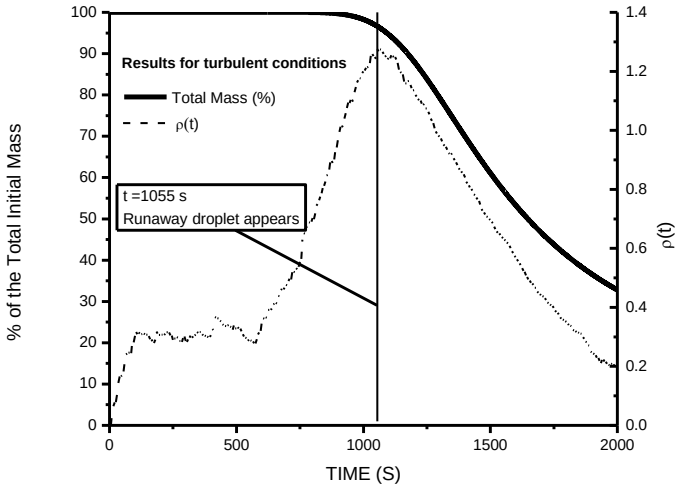

FIG. 2. Time evolution of total mass calculated from the numerical solution of the kinetic collection equation for turbulent collision coalescence (solid line and left axis) and the statistics ρ (dashed line and right axis) estimated from the Monte Carlo algorithm.

conserved after 1000 s. This time is very close to the time when the ratio ρ, determined from the Monte Carlo realizations, reaches its maximum (1055 s). Given that these results were obtained independently from the numerical solution of Eq. (1) and from the stochastic algorithm, this clearly indicates that the sol-gel transition and the formation of a runaway droplet took place around 1000 sec and that the ratio ρ can be used as an estimator of the gelation time when realistic turbulence collection kernels are used.

To emphasize the importance of the turbulence enhancement in the collection process, an additional simulation was performed for non-turbulent flow under the Earth's gravitational field with the same initial conditions. The total mass at the end of the simulation was found equal to 99.88% of the initial mass, illustrating mass conservation for this case.

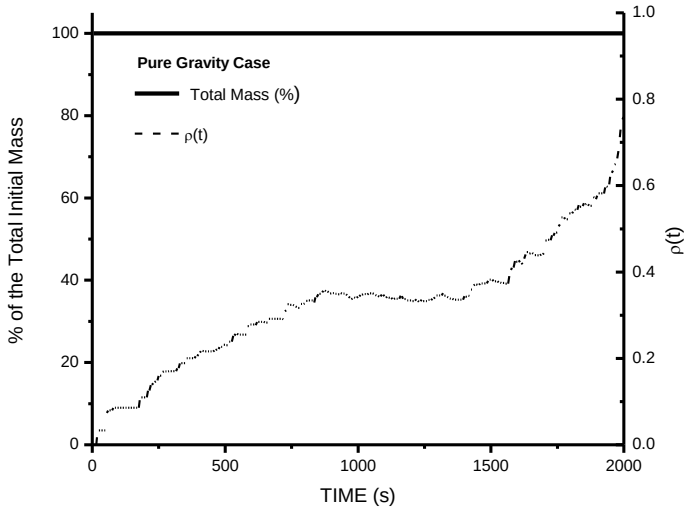

FIG. 3.Same as Fig. 2 but for the gravity only case.

Furthermore, the ratio ρ never reaches its maximum, confirming that the sol-gel transition does not take place under these conditions.

3. DISCUSSION AND CONCLUSIONS.

One of the outstanding problems in cloud physics is to explain the observations that show that raindrops can grow by condensation and collision-coalescence in times as short as 20 minutes. In order to form a

raindrop with a radius of 1mm in a warm cloud, a total of 10^5 droplets with radius of 10 μm must collide and coalesce. When droplets are small and of uniform size collisions between them are inefficient and collision events cannot occur at sufficient rates to produce raindrops until some of the droplets grow by condensation to a radius of about 20 μm. The appearance of a runaway droplet after a sol-gel transition is a possible mechanism that explains the rapid formation of raindrops.

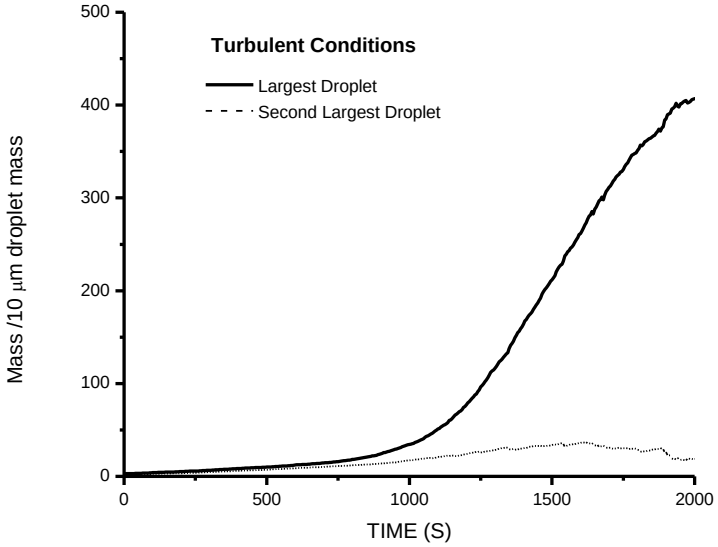

FIG. 4. Time evolution of the ensemble means over all the realizations for the largest (solid line) and second largest (dashed line) droplet masses (expressed in multiples of a 10μm droplet mass) for the turbulence case.

The stochastic process gives rise to a "lucky droplet" that grows more rapidly than the rest of the droplet population. To further clarify this point, we calculate the time evolution of the mass of the largest and second largest droplets as ensemble means over all the realizations. Figure 4 shows the results for the turbulent case, clearly indicating a significant gap between the mass of the largest and second largest droplets after 1000s. In contrast, the difference in mass in the non-turbulent, pure gravity case, shown in Fig.5, remains much smaller with no runaway behavior.

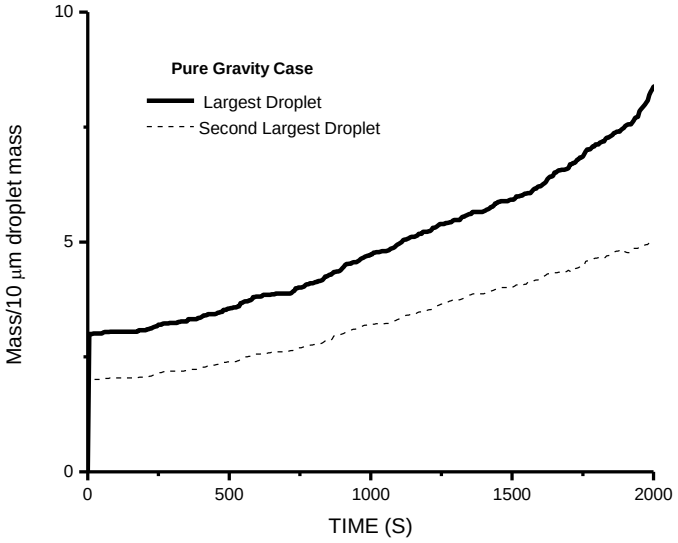

FIG. 5. Same as Fig. 4 but for the gravity only case.

The simulations under the turbulent conditions performed here include a collision enhancement factor for collisions between droplets with radii ≤ 21μm, so the role of turbulence in stochastically producing the runaway droplet is likely

underestimated in the present study. Since the nucleation and condensation processes are not yet included in this model, future developments will attempt to include the combined effect of turbulent collection and condensation (McGraw and Liu, 2003) on droplet growth.

4. ACKNOWLEDGMENTS

This study was partially funded by grants from the Consejo Nacional de Ciencia y Tecnología de Mexico (SEP-Conacyt 62071), (SEP-Conacyt 131879) and PAPITT-IN105811.

5. REFERENCES

Alfonso, L., Raga, G.B., Baumgardner, D.: The validity of the kinetic collection equation revisited. *Atmos. Chem. Phys*., 8, 969-982, 2008.

Alfonso, L., Raga, G.B., Baumgardner, D.: The validity of the kinetic collection equation revisited. Part II: Simulations for the hydrodynamic kernel, *Atmos. Chem. Phys*., 10, 6219-6240, 2010.

Bayewitz, M.H., Yerushalmi, J., Katz, S., and Shinnar, R.: The extent of correlations in a stochastic coalescence process, *J. Atmos. Sci*., 31, 1604-1614, 1974.

Drake, R.L., Wright, T.J. : The Scalar Transport Equation of Coalescence Theory: New Families of Exact Solutions, *J. Atmos. Sci*., 29, 548-556, 1972.

Gillespie, D.T.: An Exact Method for Numerically Simulating the Stochastic Coalescence Process in a Cloud, *J. Atmos. Sci*. 32, 1977-1989, 1975.

Gillespie, D.T.: A general method for numerically simulating the stochastic time evolution of coupled chemical reactions, *J. Comput. Phys*., 22, 403-434, 1976.

Hall, W.D.: A detailed microphysical model within a two-dimensional dynamic framework: Model description and preliminary results, *J. Atmos. Sci*., 37, 2486-2507, 1980.

Inaba, S., Tanaka, H., Ohtsuki, K., and Nakazawa, K.: High-accuracy statistical simulation of planetary accretion: I. Test of the accuracy by comparison with the solution to the stochastic coagulation equation, *Earth, Planets, and Space*, 51, 205-217, 1999.

Khain, A., Ovtchinnikov, M., Pinsky, M., Pokrovsky, A., Krugliak, H.: Notes on the state-of-the-art

numerical modeling of cloud physics, *Atmos. Res.* 55, 159- 224, 2000.

McGraw, R., Liu, Y.: Kinetic potential and barrier crossing: a model for warm cloud drizzle formation, *Phys. Rev. Lett.* 90, 018501, 2003.

Pinsky, M., Khain, A., Shapiro, M.: Collisions of small drops in a turbulentfFlow. Part I: Collisionefficiency. Problem formulation and preliminary results , *J. Atmos. Sci.* 56, 2585-2600, 1999.

Pinsky, M., Khain, A., Shapiro, M.: Stochastic effects of cloud droplet hydrodynamic interaction in a turbulent flow., Atmos. Res. 53, 131–169, 2000.

Pinsky, M., Khain, A., Krugliak, H.: Collisions of Cloud Droplets in a Turbulent Flow. Part V:Application of Detailed Tables of Turbulent Collision Rate Enhancement to Simulation of Droplet Spectra Evolution, *J. Atmos. Sci.* 65, 357–374, 2008.

Pruppacher, H.R., Klett, J.D.: Microphysics of clouds and precipitation, Kluwer Academic Publishers, 1997.

Tanaka, H., Nakazawa, K.: Stochastic coagulation equation and the validity of the statistical coagulation equation, *J. Geomag. Geoelecr*., 45, 361-381, 1993.

Vohl, O., Mitra, S.K., Wurzler, S.C., Pruppacher, H.R.: A Wind Tunnel Study of the Effects of Turbulence on the Growth of Cloud Drops by Collision and Coalescence, J. Atmos. Sci. 56, 4088-4099, 1999.

Wetherill, G.W.: Comparison of analytical and physical modeling of planetesimal Accumulation, *Icarus* 88, 336–354, 1990.

INVESTIGATION OF EFFECTIVE PEAK SUPERSATURATIONS IN LIQUID-PHASE CLOUDS AT THE HIGH-ALPINE SITE JUNGFRAUJOCH

Emanuel Hammer, Nicolas Bukowiecki, Zsófia Jurányi, Martin Gysel, Christopher Hoyle, Urs Baltensperger and Ernest Weingartner

Laboratory of Atmospheric Chemistry, Paul Scherrer Institut, Switzerland

1. INTRODUCTION

Climate models suffer from large uncertainties caused by aerosol/cloud feedbacks. An important aerosol parameter is the critical supersaturation (described by the Köhler theory), at which a particle forms a cloud droplet. This parameter depends on the particle's dry size and chemical composition. At ambient air conditions, the prevailing supersaturation determines the activation diameter of the particles (i.e. the diameter at which size a particle forms a cloud droplet). The highest supersaturation that a particle experiences in an ambient cloud, leading to a cloud droplet being formed from that particle, is the so-called effective peak supersaturation (SS_{peak}).

To date, no measurement device is available that is able to measure the SS_{peak} value within a cloud. Thus, the cloud peak supersaturation has to be retrieved indirectly from other measurements (e.g. Fors et al., 2011).

2. METHODS

In summer 2011, the Cloud and Aerosol Characterization Experiment (CLACE2011) was conducted at the high alpine research station Jungfraujoch (3580 m asl, Switzerland). Two different inlet systems were used to collect the total and interstitial aerosol separately. The in-cloud activation diameter was determined by comparing total and interstitial particle number size distributions, measured using two parallel scanning particle mobility sizer (SMPS) systems. The SS_{peak} value was then inferred by comparing the in-cloud activation diameter with the activation diameter, which was measured at different supersaturations with a cloud condensation nuclei (CCN) counter. The CCN counter was measuring the total aerosol in parallel to the SMPS systems and led to activation diameters at different supersaturations. The relationship between the in-cloud activation diameter and the one measured at different supersaturations can be explained with a power fit function for each CCNC-scan. Inserting the value of the ambient activation diameter into the power fit function leads to the SS_{peak}.

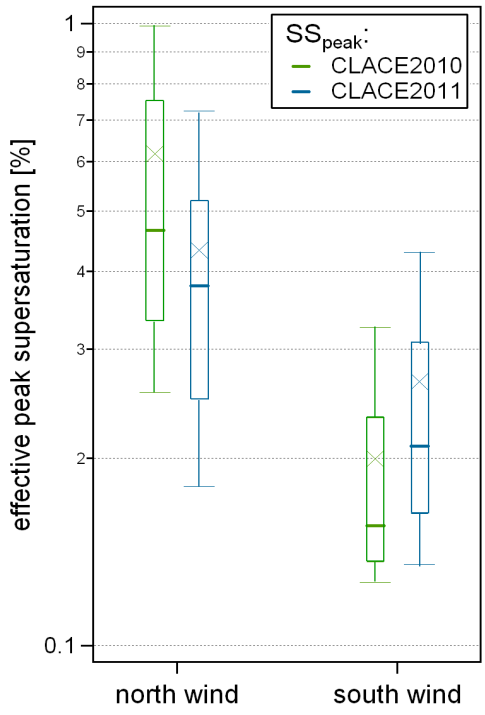

Figure 1. Effective peak supersaturation values distinguished by north and south wind conditions for CLACE2010 and 2011.

3. RESULTS

The analysis yielded SS_{peak} values between 0.04% and 1.62% (Percentiles and mean values are shown in Figure 1). While air masses coming from the north showed a

wide range of values, SS_{peak} values for air masses coming from the south were more constant at around 0.2%. This can most likely be explained by the different topography south and north of the Jungfraujoch causing different updraft velocities.

The CCN properties observed during CLACE agreed with a previous 17-month climatology of the CCN properties at the Jungfraujoch (Jurányi et al., 2011), indicating that the aerosol's hygroscopic properties during CLACE can be considered to be representative. Hence, this method can also be applied to earlier CLACE campaigns where no CCN counter had been used.

Currently, the influence of particle number concentration and size distribution on the SS_{peak} as a function of updraft velocity is being investigated in detail with a cloud box model.

A. BIBLIOGRAPHY

Fors, E.O., Swietlicki, E., Svenningsson, B., Kristensson, A., Frank, G. P., Sporre, M. (2011). *Atmos. Chem. Phys.* **11**, pp. 8343-8361.

Jurányi, Z., Gysel, M., Weingartner, E., Bukowiecki, N., Kammermann, L. and Baltensperger, U (2011). *J. Geophys. Res*. **116,** D10204

Acknowledgments

We thank the International Foundation High Altitude Research Stations Jungfraujoch and Gornergrat (HFSJG) for the opportunity to perform experiments on the Jungfraujoch. This work was supported by MeteoSwiss in the framework of the Global Atmosphere Watch program and the Swiss National Science foundation.

CHARGE MODULATION OF AEROSOL SCAVENGING (CMAS) CAUSING STORM INVIGORATION: POSSIBLE EFFECTS ON DOWNSTREAM BLOCKING AND EUROPEAN WINTER CIRCULATION

Brian A Tinsley
University of Texas at Dallas, USA Tinsley@UTDallas.edu

I. INTRODUCTION

A working hypothesis is presented that provides an explanation for correlations of high latitude winter storm vorticity changes with atmospheric inputs that change the ionosphere-earth electrical current density (J_z). The hypothesis is that the deposition by J_z of (unipolar) electric charge on droplets and aerosol particles (notably condensation nuclei - CCN) changes the rate of their in-cloud scavenging, so that on a timescale of one or more days the concentration of large CCN is reduced (by electro-scavenging) while the concentration of small CCN is increased (by electro-anti-scavenging). These processes (charge modulation of aerosol scavenging, or CMAS) affect atmospheric dynamics by the 'storm invigoration' process (Rosenfeld et al, 2008), as will be described in section IV.

II. CHARGE MODUALTION OF AEROSOL SCAVENGING

Initial results for electrically-induced changes in scavenging are given in a new model that includes Monte-Carlo simulation of scavenging by diffusion (Brownian motion) (Tinsley, 2010). Fig. 1 illustrates the different effects of electric charge for particles of different size – i.e., particles with different diffusion coefficients. With charge, the scavenging rate for small particles due to diffusion is decreased due to the long-range repulsion of the like charges on droplets and particles. For large particles the amount of diffusion is so small that without charge the near-Stokes flow carries the particle past the droplet, with a low scavenging rate coefficient. The long range repulsion has little effect due to the low mobility, and is cancelled by the short-range image attraction as the particle approaches the droplet.

Close to the droplet the short-range image electric force predominates, and this attractive force increases the collision rate. Thus for the larger particles the scavenging rate coefficient increases with charge.

III. MODELLING OF CMAS

Fig. 2 is an update of Tinsley (2010) for rate coefficients for in-cloud scavenging by droplets of radius (A) = 15 μm, with droplet charges (Q) of 200e, 100e, and 50e (e is the elementary charge) and particle charges (q) either 0e, 5e, 10e 20e or 50e, as a function of particle radius, from 0.002 μm to 3.75 μm. The rate for diffusive scavenging (zero charges) at 100% relative humidity (RH) is shown by the heavy curves; the analytic values (neglecting the intercept effect) by the black curve with Xs; the calculated values, taking it into account, by the grey curve with triangles. These lines coincide for particle radii less than about 0.1 μm. For the family of curves with Q = 100e, the curves for charges between 5e and 50e cross the zero charge line at a particle radius (a) of about 0.02 μm; thus defining a crossover radius (a_c) for which particles of radius smaller than a_c are dominated by electro-anti-scavenging for this combination of Q and A. The region of electro-scavenging for this Q and A is that with particle radii greater than this a_c. When Q is increased to 200e, a_c increases to about 0.05 μm, and when Q is decreased to 50e (not shown) a_c decreases to about 0.01 μm. We are in the process of parameterizing these variations of scavenging rate coefficient.

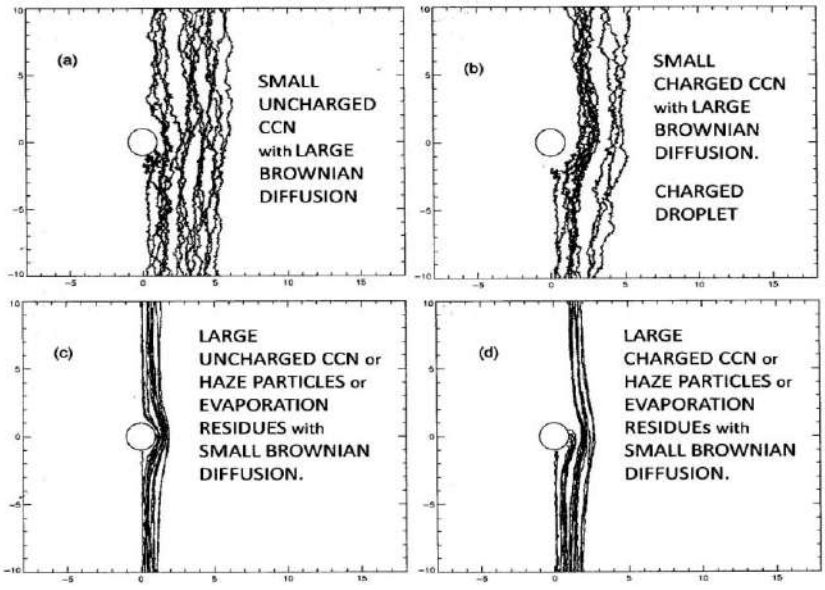

Figure 1. Monte-carlo simulations of effects on scavenging of aerosol particles by electric charges on particles and droplets. (a) and (c) represent uncharged particles, with no effect of any charge on the droplet. There is much scavenging for the small particles in (a) due to their Brownian diffusion, but very little in (c) for large particles with small diffusion. In (b) the small particles and droplets both have charges of the same sign, with the long-range repulsion between them reducing the Brownian scavenging rate. In (d) the large particles with charges are carried close enough to the droplet by the flow that the short-range image attraction increases the scavenging rate. From the model of Tinsley (2010).

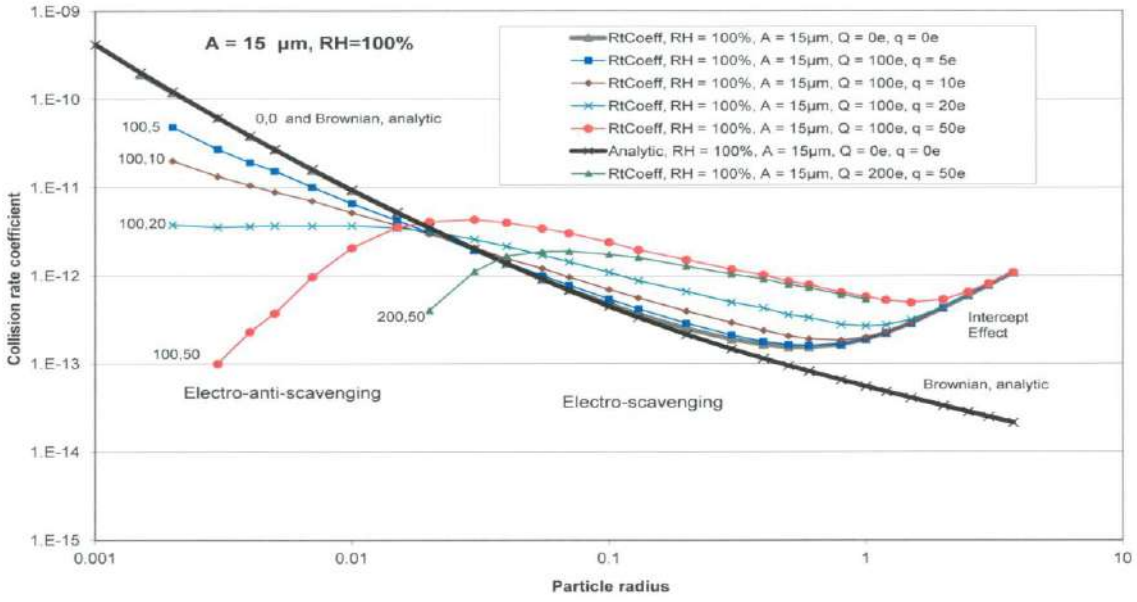

Figure 2. Collision rate coefficients for in-cloud scavenging of particles with radius 0.002 μm to 3.75μm, by droplets of radius15μm. The curves are labeled by droplet and particle charges (Q,q).

Fig. 3 shows new results using the Tinsley (2010) model for a droplet radius A = 3 μm, with *Q* either 50e and 25e for 100% *RH*, and particle charges which may be 0e, 2e, 5e,10e, 20e or 50e. In addition, curves for 95% *RH* for *q* of 0e and 10e are included. The value of a_c for *A* = 3 μm and *Q* = 25e is about 0.15 μm, and it increases to about 0.4 μm for *Q* = 50e.

For electro-scavenging the increase in scavenging rate coefficient depends approximately on q^2, and for electro-anti-scavenging the decrease in rate coefficient depends on the product Qq. From the models of cloud charging (Zhou and Tinsley, 2007; 2012) both the droplet and particle charges are proportional to J_z, so that the changes in both electro-scavenging and electro-anti-scavenging are proportional to the square of J_z.

IV. HIGH LATITUDE WINTER STORMS

In the environment of high latitude winter storms droplet and particle charges comparable to those in Figs 2 and 3 are expected in layer clouds, and also in convective clouds prior to the formation of ice owing to the transport in updrafts of unipolar charge from layers near the surface (Tinsley, 2012). The lifetime of CCN in a high latitude air mass is 1-10 days, depending on the amount of cloudiness present, with repeated scavenging episodes as air is processed multiple times through clouds.

It was shown by Rosenfeld et al. (2008) that increasing the concentration of CCN as in polluted air can invigorate a convective storm, by increasing the droplet concentration and reducing the average droplet size. This reduces the rate of coagulation of droplets and production of rain in updrafts, so that more liquid water is carried above the freezing level, where the increased release of latent heat of freezing invigorates the updrafts.

An additional way of reducing coagulation and rain production is by narrowing the CCN size distribution, which narrows (homogenizes) the droplet size distribution. This arises from electro-scavenging reducing the concentration of the largest CCN, which would otherwise be among the first to activate in the updraft and, because of their larger sizes, lead to the formation of large droplets. The reduction of rain production by this process also contributes to storm invigoration.

V. OBSERVATIONS OF CORRELATIONS OF VORTICITY WITH J_z

An increase in vorticity in winter cyclones accompanies the increase in updraft speed, as more low-level air is drawn into the cyclone. Correlations of increases and decreases of northern hemisphere winter storm vorticity with a number of solar and terrestrial inputs to the global electric circuit, that modulate the ionosphere-earth current density J_z have been reviewed by Tinsley (2008, 2012). Such localized increases in vorticity can be objectively assessed by use of the vorticity area index (VAI) introduced by Roberts and Olsen (1973) to measure the atmospheric area (in units of 10^5 km^2) where the absolute vorticity is above a given threshold (e.g., $24\times10^{-5}s^{-1}$). This index is obtained from global meteorological data sets such as ERA-40 and ERA-Interim. VAI reductions correlate with J_z reductions due to Forbush decreases in the galactic cosmic ray flux and with reductions in relativistic electron precipitation from the radiation belts. Vorticity increases correlate with J_z increases due to solar energetic particle precipitation into the atmosphere. These energetic space particles all vary on a timescale of one to several days, and effects of other inputs from solar activity (such as irradiance changes) can be ruled out because of their different time signatures.

Figure 4 is from a recent analysis of Tinsley et al. (2012) showing a superposed epoch analysis of winter northern hemisphere VAI, with the key days being proxies for the J_z minima; either the days of minima in relativistic electron flux precipitating into the stratosphere (third column) or the days of Earth crossings of the heliospheric current sheet (HCS).

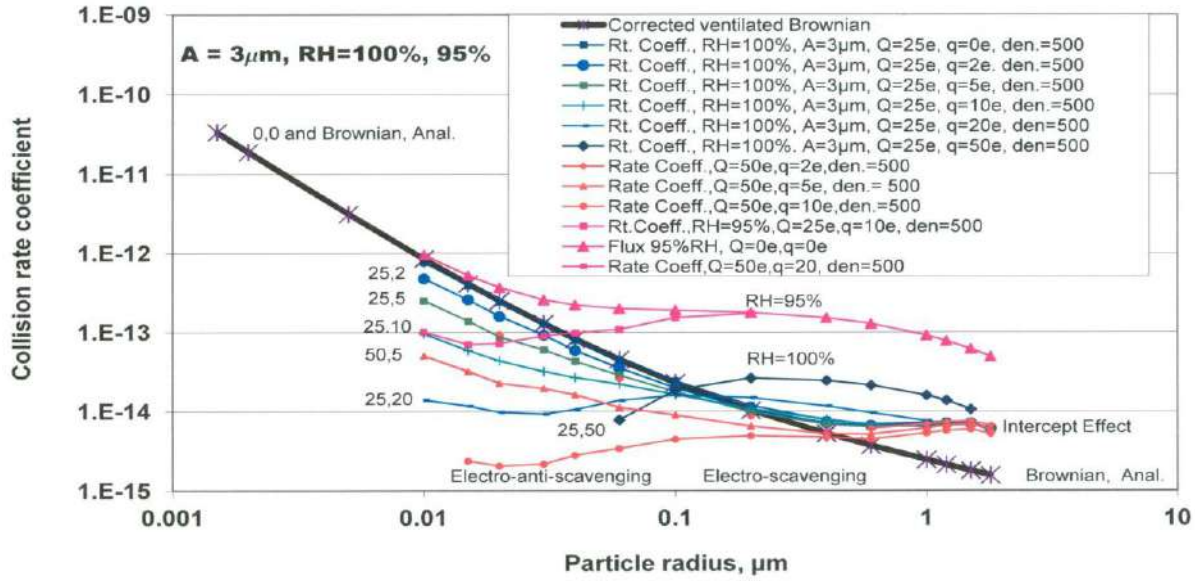

Figure 3. Collision rate coefficients for in-cloud scavenging of particles with radius 0.01 μm to 1.8μm, by droplets of radius 3μm. The curves are labeled by droplet and particle charges (Q,q).

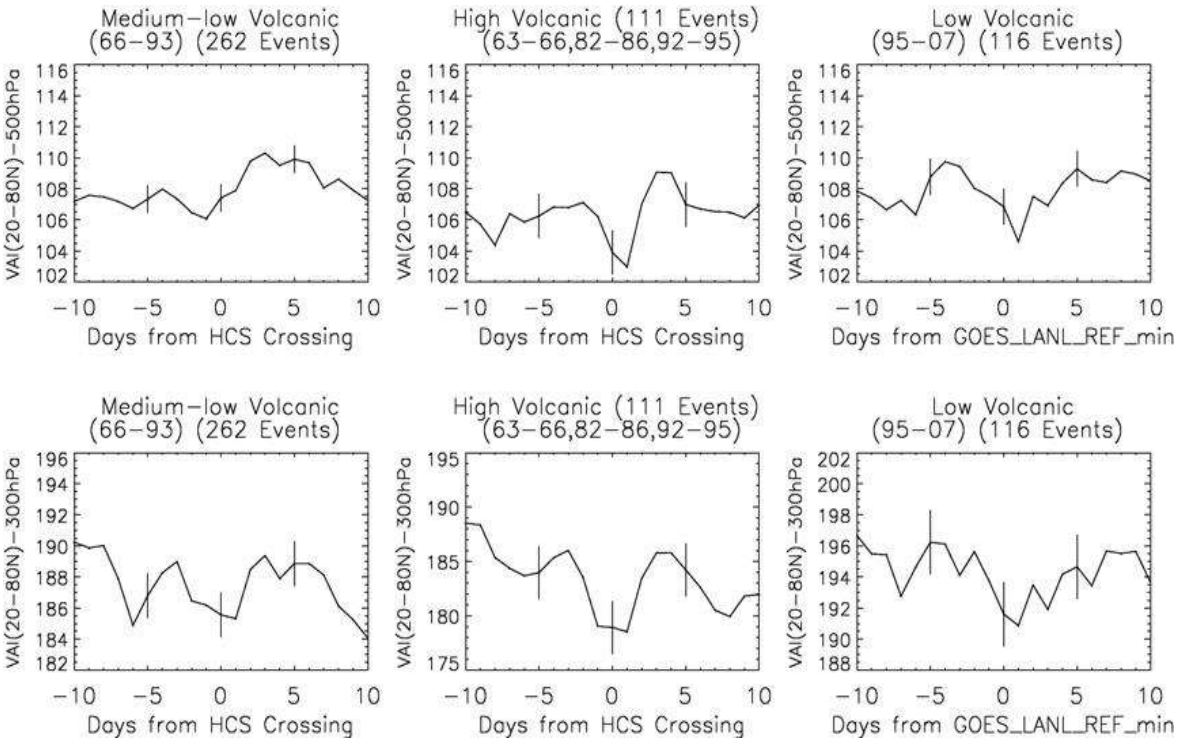

Fig. 4. Combined superposed epoch analyses of the VAI. The first column is the combined analyses for medium-low volcanic winters 1966–1993 using HCS crossings as key days. The second column is for all high volcanic stratospheric aerosol winters using HCS crossings as key days, and the third column is for the low volcanic years 1995–2007 using minima of the relativistic electron flux measured on the GOES and LANL satellites as key days. The top row of panels is for the VAI at 500 h Pa, and the bottom for 300 h Pa.

The analysis keyed to HCS crossings is in the first and second columns. The HCS crossings are associated with minima in relativistic electron precipitation. The top row of panels shows the VAI for 500 hPa pressure altitude, and the bottom row for 300 hPa. The first and third columns are for medium and low stratospheric sulfuric acid content, and the middle column is for a high content. The presence of sulfuric acid forming large cluster ions reduces the stratospheric conductivity so that the column resistance in the stratosphere is more sensitive to ionization produced by relativistic electron precipitation.

Other analyses have shown changes in the winter VAI with measured changes in J_z due to terrestrial sources; the day-to-day changes in the output of the low-latitude thunderstorm generators (Hebert et al., 2012). Also, the surface pressure changes measured within the polar vortices in the Antarctic and Arctic (Burns et al. 2008) are similarly associated with changes in the output of low-latitude thunderstorm generators.

VI. IMPLICATIONS FOR WINTER CIRCULATION CHANGES IN THE NORTH ATLANTIC, UK AND EUROPE

There are a number of consequences of increased vigor of updrafts in storm systems associated with increases in J_z. In winter cyclones where latent heat release is important (especially in Polar Lows) the reduction of rainfall allows more water to be carried to the upper troposphere, but it is not clear how much of this is retained rather than precipitated out by ice precipitation processes. More latent heat of fusion is deposited in the upper troposphere, and more ice melting at low altitudes provides more cooling the lower troposphere. The greater ice production with greater J_z is likely to be associated with more lightning, and there is some evidence for this for winter storms in the USA (Chronis, 2009).

Effects of J_z on storm invigoration are expected to be more important at longitudes where there is a strong land-sea temperature contrast in winter and strong cyclogenesis, (e.g., the Icelandic Low and Aleutian Low regions). The Icelandic Low region is centered at a higher geomagnetic latitude (~70°) than the Aleutian Low (centered ~ 50° gmlat.), and thus has a greater cosmic ray flux and greater mean J_z and a greater variation on the 11-year solar cycle than the Aleutian Low. The same processes which produce the vorticity responses to J_z on the day-to-day timescale as noted above are expected to operate on the 11-year timescale also. At solar cycle minimum there are increases in J_z of order 10% at high latitudes, with increases several times this amount at extended solar minima, such as occurred during the Maunder Minimum in 1650-1715. The very cold winters that occurred in that period have been attributed to enhance blocking in the Atlantic (Luterbacher et al. 2001) as have cold winters in recent (this century) deep solar minima (Lockwood et al. 2010), and some blocking has been reported for the weaker solar minima in the 20th century (Barriopedro et al., 2008). Thus we need to consider whether circulation changes in the North Atlantic, the UK and Europe during winters at decadal solar minima, are related to the decadal changes in J_z and increases in cyclonic vorticity in the Icelandic low region.

VII. OBSERVATION OF CIRCULATION CHANGES AT DECADAL SOLAR MINIMA

The possible consequences of decadal variation in CMAS producing decadal variations in North Atlantic-UK-European winter circulation regimes have been discussed by Tinsley (2012).

Increased cyclogenesis has been observed at decadal solar minima in the western side of the North Atlantic Ocean by Labitzke and van Loon (1989), and the resultant blocking explains the poleward deviation of storm tracks in the eastern side of the north Atlantic at solar minima since 1921, as shown by Brown and John (1979) with an update to 1989 given by Tinsley and Deen (1991). This is consistent with the reduction of zonal flow onto Europe at solar minima, and associated poleward component of the flow, as found by Venne and Dartt (1990) on the basis of 1959-1988 radiosonde observations. The era of these observations included some of the largest amplitude sunspot cycles on record, and also an unusually high content of anthropogenic aerosols at mid-high northern latitudes. The reduction of zonal winds (from about 6.5 m s-1 at solar maximum to about 3.5 m s-1 at solar minimum occurred for winters in the West phase of the QBO (quasibiennial oscillation of equatorial

stratospheric winds) which affects atmospheric dynamics at all latitudes, and as an upper boundary for tropospheric dynamics, may affect winter storm development. The reduction of average zonal winds was associated with more outbreaks of cold, dry, Arctic air onto the UK and Europe, which with less water vapor and less clouds is more transparent for longwave radiative cooling in winter, and maintains ice cover for enhanced ice-albedo feedback.

VIII. CONCLUSIONS

The working hypothesis for day-to-day winter storm vorticity changes due to the CMAS causing storm Invigoration is so far a qualitative hypothesis – the large quantitative uncertainty concerns whether the electric charges on CCN and droplets are large enough and widely enough distributed to affect the CCN and droplet size distributions sufficiently to cause the storm invigoration and the observed vorticity increases. This uncertainty could possibly be resolved with extensive measurements of J_z, CCN and droplet electric charges and the microphysics of rain and ice production in winter storm clouds over extended time intervals.

Work is in progress to parameterize the CMAS processes. Then there is a need to construct dynamic cloud models where the effects of electric charges are included in the microphysics. Work is needed to develop models to test the effect of changes in winter cyclone and Polar Low development on circulation changes in the North Atlantic Europe Region.

ACKNOWLEDGEMENTS

This work has been supported by the US National Science Foundation; Grants ATM0855351 and ATM0836171.

References.

Barriopedro, D., R. Garcia-Herrera and R. Huth, Solar modulation of the Northern Hemisphere winter blocking, J. Geophys. Res., 113, D14118, 2008.

Brown, G. M., and J. I. John, Solar cycle influences in tropospheric circulation, J. Atmos. Terr. Phys., 41, 43-52, 1979.

Burns, G. B., B. A. Tinsley, W. J. R. French, O.A. Troshichev and A.V. Frank-Kamenetsky, Atmospheric circuit influences on ground-level pressure in the Antarctic and Arctic, J. Geophys. Res. 113, D15112, 2008.

Chronis, T., Investigating possible links between incoming cosmic ray fluxes and lightning activity over U.S., J. Climate, 22, 5748-5754, 2009.

Hebert III, L., B. A. Tinsley and L. Zhou, Global electric circuit modulation of winter cyclone vorticity in northern high latitudes, in press, Adv. Space. Res., 2012.

Labitzke, K. and H. van Loon, Association between the 11-year solar cycle, the QBO and the atmosphere, Part III, Aspects of the association, J. Clim., 2, 554-565, 1989.

Lockwood, M., R. G. Harrison, T. Woolings and S. K. Solanki, Are cold winters in Europe associated with low solar activity? Environ. Res. Lett., 5, 024001, 2010.

Luterbacher, J., R. Rickli, E. Xoplaki, C. Tinguely, C. Beck, C. Pfister and H. Wanner, The late Maunder Minimum (1675-1715) – a key period for studying decadal scale climate change in Europe, Clim. Change 49, 441-462, 2001.

Roberts, W. O., and R. H. Olson, Geomagnetic storms and wintertime 300 mb trough development in the North Pacific – North America area, J. Atmos. Sci., 30, 135-140, 1973.

Rosenfeld, D., U. Lohman, G. B. Raga, C. D. O'Dowd, M. Kumala, S. Fuzzi, A. Reissell and M. O. Andrease, Flood or drought: how do aerosols affect precipitation, Science, 321, 1309-1313, 2008.

Tinsley, B. A., The global atmospheric electric circuit and its effects on cloud microphysics, Rep. Prog. Phys., 71, 066801, 2008.

Tinsley, B. A., Electric charge modulation of aerosol scavenging in clouds: rate coefficients with Monte-Carlo simulation of diffusion, J. Geophys. Res., 115, D23211, 2010.

Tinsley, B. A., A working hypothesis for connections between electrically-induced changes in cloud microphysics and storm vorticity, with possible effects on circulation, in press, J. Adv. Space Res., doi:10.1016/j.asr.2012.04.008, 2012.

Tinsley, B. A., and G. W. Deen, Apparent tropospheric response to MeV-GeV particle flux variations, a connection via electrofreezing of supercooled water in high level clouds?, J. Geophys. Res., 96, 2283-2296, 1991.

Tinsley, B. A., L. Zhou and W. Liu, The role of volcanic aerosols and relativistic electrons in modulating winter storm vorticity, in press, J. Adv. Space Res., doi:10.1016/j.asr.2011.12.019, 2012.

Venne, D. E., and D. G. Dartt, An examination of possible solar cycle-QBO effects in the northern hemisphere troposphere, J. Climate, 3, 272-281, 1990.

Zhou, L., and B. A. Tinsley, The production of space charge at the boundaries of layer clouds, J. Geophys. Res., 112, D11203, 2007.

Zhou, L., and B. A. Tinsley, Time dependent charging of layer clouds in the global electric circuit, in press, J. Adv. Space Res., doi:10.1016/j.asr.2011.12.018, 2012.

COMPLETE HAILSTONE PHYSICS

Roland List,
Department of Physics, University of Toronto, Toronto ON, Canada
roland.list@rogers.com

PURPOSE

The purpose of this paper is to present the new hailstone physics by the least number of variables, within their most probable ranges and in all combinations.

1. INTRODUCTION

Sixty years of extensive investigations of physical properties and behavior of hailstones by the author and his groups have produced new insights into heat and mass transfer, HMT, and growth of spherical hailstones. The six main variables of HMT are: air (t_A) and surface (t_S) temperatures, Reynolds number *Re*, cloud liquid water content W_f, net collection efficiency E_{NC} and ice fraction of the deposit I_f. The other variables affecting the HMT, relating to gyration, turbulence and roughness, can be combined into a constant K = 1.28 (List, 2012b). [Note that "mass transfer" only involves *diffusion* of water molecules and not *accretion* of particles such as droplets or drops.]. The heat components Q_i^* to conduction and convection, suffix CC, evaporation suffix E (hailstones always grow while evaporating, List 1963), heat added by the accreted cloud particles suffix CP; the sum serves to accommodate the latent heat of freezing, suffix F, resulting in

$$Q_{CC}^* + Q_E^* + Q_{CP}^* + Q_F^* = 0 \qquad (1)$$

In addition mass transfer *M** by accretion of cloud particles needs to be considered

$$M_{CP}^* = \frac{\pi}{2}\rho_H D^2 \frac{dD}{dt} = \frac{\pi}{4} E E_{NC} W_f V D^2, \quad (2)$$

which, in terms of the radial growth speed, is

$$V_R = \frac{dR}{dt} = 0.25\rho_w^{-1} E E_{NC} W_f V, \quad (3)$$

with ρ_H for hailstone density, *D* diameter of (spherical) hailstone, collection efficiency *E*, net collection efficiency E_{NC}, hailstone's radial growth speed V_R, hailstone fall velocity *V*.

There is another, very specific case (later specified as CASE 2), where the shedding occurs to such a degree that there is no formation of a water skin (Lesins & List, 1986). In that case V_R is limited to the degree the ice dendrites, growing at V_{IS}, keep catching up with the air-sponge interface (List, 1990), i. e.

$$V_{IS} = V_R. \qquad (4)$$

Where necessary other variables will be introduced. Note that all equations are in SI, while more appropriate units may be used in figures. The suffix i is often used to specify the magnitude of the quantity they are associated with. Thus i is the magnitude of the diameter, *D* in cm, the amount of liquid water, W_f, in g m^{-3}, and the fractional amount of the net accreted fractional ice content of *Y* [-]. Equations and figures are extracted from the papers by List (2012a and b).

2. AERODYNAMICS OF FREELY FALLING SPHERICAL HAILSTONES

2.1 Free fall

The basic physics is developed most easily by considering the free fall of spherical hailstones. By gedankenexperiment List (List and Abreu, 2008; List, 2010) established that it is a gyration about a horizontal (gyration) axis, with the spin axis moving on the surface of a cone with the hailstone center at its apex. This general motion produces spheroids (Kry and List, 1974a and b; Stewart and List, 1983), with the axis ratio dependent on the apex angle. If this angle is 90°, then the resulting body is a sphere. The consequence of such growth that is equal in all directions, is that ***the***

surface temperatures are the same everywhere.

Another important aspect is the drag coefficient C_D of rough spheres. Fortunately, List et al (1969) carried out such investigations, which also showed that the flow around a rough particle is always turbulent and, thus, supercritical – even for rough spheres with diameter as low as 0.5 cm.

What is not known for gyrating spheroids is the effect of spin and gyration rates on drag. However, considering that the surface speed of a 4 cm hailstone, spinning at 20 Hz, at -20C is 6.2% of the free fall speed, it is assumed that such an effect is of second order and can be neglected.

2.2 Turbulence

The group of the author extensively studied the effect of turbulence on the HMT, as affected by the particle roughness (Schuepp and List, 1969a and b; Schemenauer and List, 1972). It was suspected to be small because it would have to be created by the precipitation particles themselves. HMT studies with gyrating spheres (apex angle 60^o), however, showed that the combined effect of turbulence, gyration and roughness can be included in a correction factor of K = 1.28 (Zheng and List (1995).

2.3 Shape

Knowing that spherical hailstones in the diameter range 2-5 cm represent only 20% of all hailstones collected in ~27 samples by List (2012a), and ~70% were tri-axial ellipsoids, icing experiments were only carried out with gyrating spheroidal hailstones (from 1972 to 1995). The problems with that shape were already substantial because surface temperature differences of up to -6C were measured between pole and equator (List et al 1989). Thus, numerical models on the heat and mass transfer by conduction through the hailstone body had to be run in parallel with the experiments in order to compensate for the t_S difference. To base the HMT of spheroids and ellipsoids on spheres is more appropriate.

3. HAILSTONE GROWTH STAGES

The number of variables can be reduced by the introduction of three hailstone growth scenarios. They are: CASE 1, dry growth, and two categories with shedding. CASE 2 is shedding from wet surfaces not covered by water skins and CASE 3 represents shedding from surfaces covered by permanent water skins (Lesins and List, 1986; List, 2012a and b). In both cases the substrates consist of spongy ice (ice-water mixtures with I_f representing the fraction of ice). Surface supercooling is required in both cases. In CASE 2 it is very limited because growth is envisaged as a continuous advance of ice dendrites to the spongy-air interface that is supercooled to accommodate the growth rate. Assuming a maximum growth rate of 4 mm min^{-1} – as implied from radar observations – represents a maximum supercooling of -0.55C. For both CASES 1 and 3 a maximum supercooling to -40C seems possible - if no active ice nuclei were present (a limit that will later be rejected).

4. RANGE RESTRICTIONS

The parameter space occupied by the possible hail growth conditions can be minimized either by reducing the number of parameters or by a restriction of the ranges variables are allowed to cover. For dry growth, CASE 1, it is suggested to restrict the liquid water content to $1 \le W_f \le 3$ g m^{-3}, to be extended for wet growth, CASES 2 and 3, to ≤ 6 g m^{-3}; for diameters $0.5 \le D \le 8$ cm, and hailstone density $915 \le \rho_H \le 1000$ kg m^{-3}.

Before dealing with the HMT with the newest insights, the bounds for the surface temperature t_S had to be considered because they drastically affect all perceptions. Fig. 1 demonstrates the point with its four Panels. After selecting D and the environment air temperature t_A, coupled to height H and pressure p according to Beckwith (1960), the hailstones' fall speed can be calculated (Panel A). Panel B allows setting of the radial growth speed V_R according to (3), as determined further by the colliding (E) and net collected (E_{NC}) liquid water content. Panel D determines the gradient across the surface water skin, which is affected by the ice fraction I_f of the deposit [high I_f requires a high gradient]. Panel E provides the choices of combinations of surface temperature t_S and skin thickness d

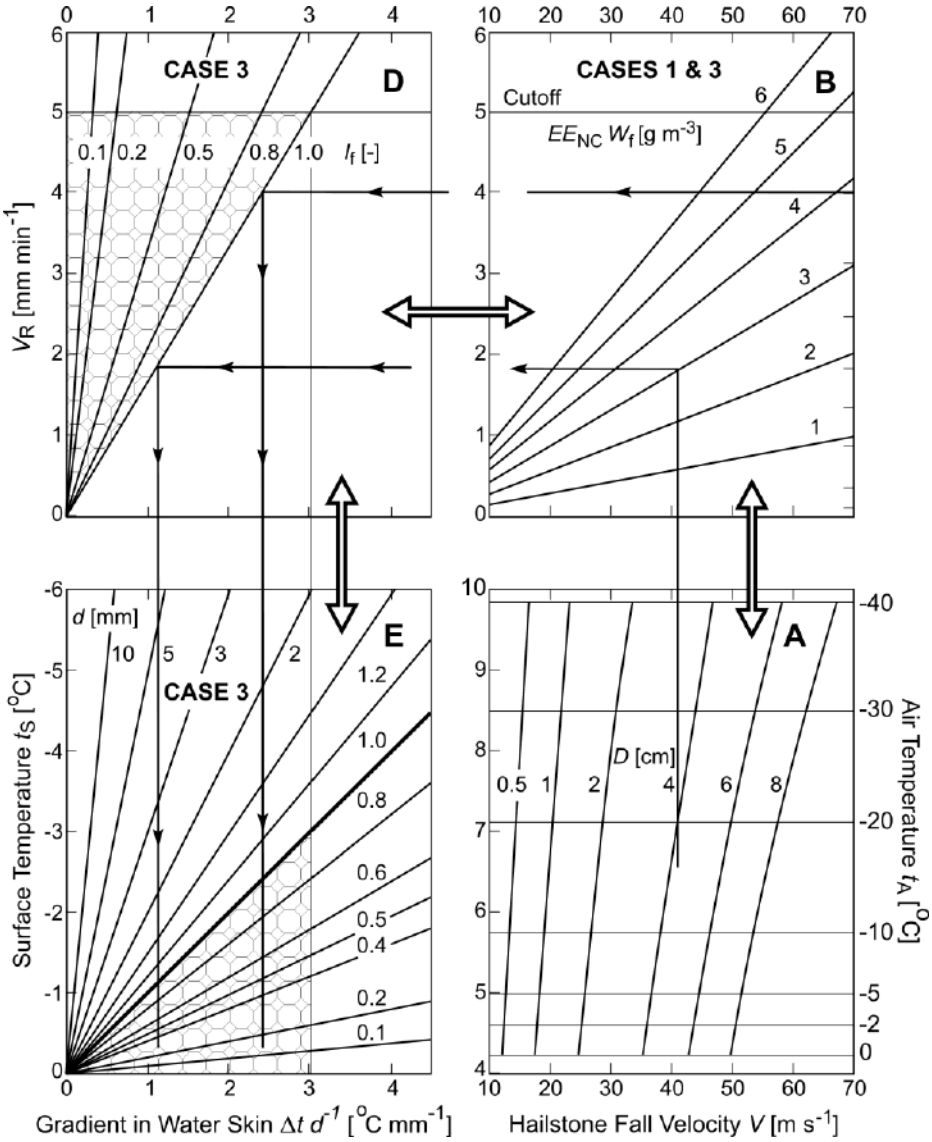

Fig. 1. CASE 3. Radial growth rates and water skin thickness of spherical hailstones of given diameter, freely falling in typical Denver hail cloud (Panel A); accreting cloud water (droplets and drops), resulting in a radial temperature gradient across the water skin (Pane D), followed by breakdown into gradient components surface temperature and water skin thickness (Panel E).

which form the temperature gradient across the water skin. While not actually measured, a limit of d = 1 mm could be suggested on the basis of experiments with spheroids. This would definitely limit t_S to >-3C, possibly even >-2C. Thereby consideration is given that E_{NC} at high I_f is also high, and not enough water is shed by the growing hailstones to maintain a high W_f. [At E_{NC} = 1, a (dry) CASE 1 would be established].

The reason why a high t_S-limit of -5C is suggested is to build in a large safety margin. It is also not known how the water skins behave under sphere growth conditions with an angular momentum that is minimal among the rotational hailstone bodies and may even represent a stabilizing factor.

5. HMT OF SPHERICAL HAILSTONES

5.1. *The variables X and Y*

Examination of the HMT equation (1) provides a surprising simplification, combined with a deeper insight into the physics. First, four of the original six variables can be reduced to two variables, namely

$$W_f\, Re^{1/2} = X, \qquad (5)$$

and

$$E_{NC}\, I_f = Y. \qquad (6)$$

X is the ratio of the diffusions of heat and mass over the accretion related terms. (5) and (6) express that the four original variables contained in them only enter the HMT eqns in tandem. However, *Re* in (5) is not an suitable variable because it depends on H or t_A. Therefore, it is being replaced by the H-independent variable D. This is done by considering the free fall relationship that connects D and V according to

$$V = \sqrt{\frac{4\, g\, \rho_H\, D}{3\, \rho_A C_D}}, \qquad (7)$$

with g standing for acceleration by gravity and ρ_A for air density. Thus

$$Re^{1/2} = \sqrt[4]{\frac{4 g\, \rho_H}{3 \rho_A C_D \upsilon^2}} \times D^{3/4} = F(\rho_A) \times D^{3/4}. \qquad (8)$$

In this way X in (5) is replaced by

$$X = F(\rho_A)\, W_f\, D^{3/4}. \qquad (9)$$

(8) provides the multiplier in the eqn for X.

(7) contains ρ_H and C_D, variables that can be considered constant because the errors are limited by the 4th root term of (8). The limits to hailstone density has been discussed above, while the drag coefficient for spheres of suitable roughness can be set at a supercritical $C_D = 0.5$. This is higher by a factor of 2 for $D = 0.5$ cm. However, the 4th root reduces the error from a factor of 2 to 20%. To further reduce the error a higher average C_D may be chosen. This was not done pending a reworking of the HMT for 0.5 ≤ D ≤ 1.0 cm.

The new insights are all consequences of using t_A-coupled fall velocities. (5) is exact, while the uncertainties of (8) seem acceptable, considering the gains in simplicity.

5.3. t_A-t_S-coupled Φ and Ψ

The eqn for X and Y takes the form

$$\Phi/X = Y - \Psi. \qquad (10)$$

Thereby Φ and Ψ are functions of t_A and t_S only and are of the form

$$\frac{\mathrm{K} \times \left[0.535\, k (t_S - t_A) + 0.511 D_{wa} L_{s.e} \frac{1}{R_w T_A} (e_S - e_A) \right]}{0.25 E\, L_f \upsilon} = \Phi \qquad (11)$$

and

$$\frac{c_w}{L_f}(t_S - t_A) = \Psi. \qquad (12)$$

(10) can be solved for X or Y, thus producing eqns of identical content.

Φ and Ψ are functions of t_A and t_S only. Thus, the auxiliary functions Φ and Ψ can be replaced by the surface and air temperatures, respectively. This represents a substantial improvement of the understanding of the following results. In summary, the solution to HMT is represented by four variables: X ($W_f\, Re^{1/2}$ or $F(\rho_A)\, W_f\, D^{3/4}$), Y ($E_{NC}\, I_f$), t_A and t_S.

6. SOLUTIONS TO HMT AND GROWTH EQUATIONS

6.1 The t_A-X domain

This Section will be used to display other solutions, in addition to CASE 3 in Fig. 1. The first diagram, Fig. 2, will juxtapose all three CASES of the variation of t_A with X for different t_S. Thereby, the range of solutions is highlighted by octagons, while the grey areas indicate regions limited by X_{L1} and X_{L3}, where $D \geq 0.5$ is required. CASE 1 shows dry growth with $t_S \leq 0$C. The region below the line $t_S = 0$C is forbidden. For CASES 2 and 3, the upper limit is extended from a W_f of 3 to 6 g m^{-3} or X_{L6}. The families of curves of fixed t_S are shifted parallel, while the ice fractions of the deposit are also given. For CASE 2 $t_S \geq -0.55$C, while for CASE 3 the possible conditions are within a band of $0 \geq t_S \geq -5$C. The X-ranges of D are indicated for CASE 2 by bars. The same bars also apply to CASE 3. Note that the range of X is CASE-dependent.

6.2 The V_R-t_S domain

Fig. 3 shows the radial growth velocities according to (3) for different surface temperatures at different t_A, W_f and

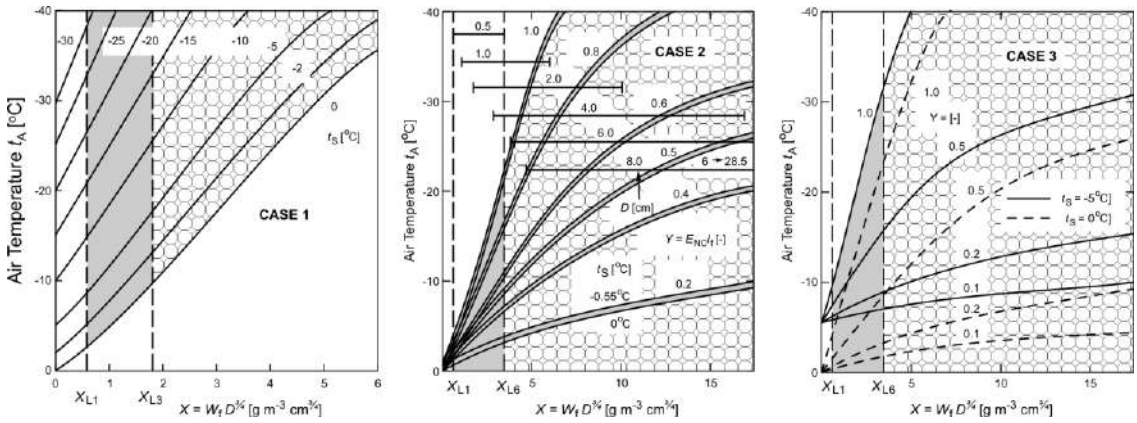

Fig. 2. The t_A-X domain; octagons indicate range of conditions, together with restricted grey area, limited by $X_{L1} < X < X_{L3}$ or X_{L6}, where $D \geq 0.5$ cm, with i giving W_f in g m^{-3}; no growth below X_{L1}. CASE 1: t_A dependence on X for different t_S, for dry growth. CASE 2: strong shedding of partial surface water skins, restricted to supercoolings within the thin grey bands $0 > t_S > -0.55$C, together with underlying sponginess of resulting deposits; drops shed from skins at $t_S \approx 0$C; bars indicating ranges for D_i and $1 \leq W_f \leq 6$ g m^{-3}. CASE 3: maximum supercooling -5C; for different Y (1, 0.5, and 0.2), for D_i range and W_f limits as in CASE 2.

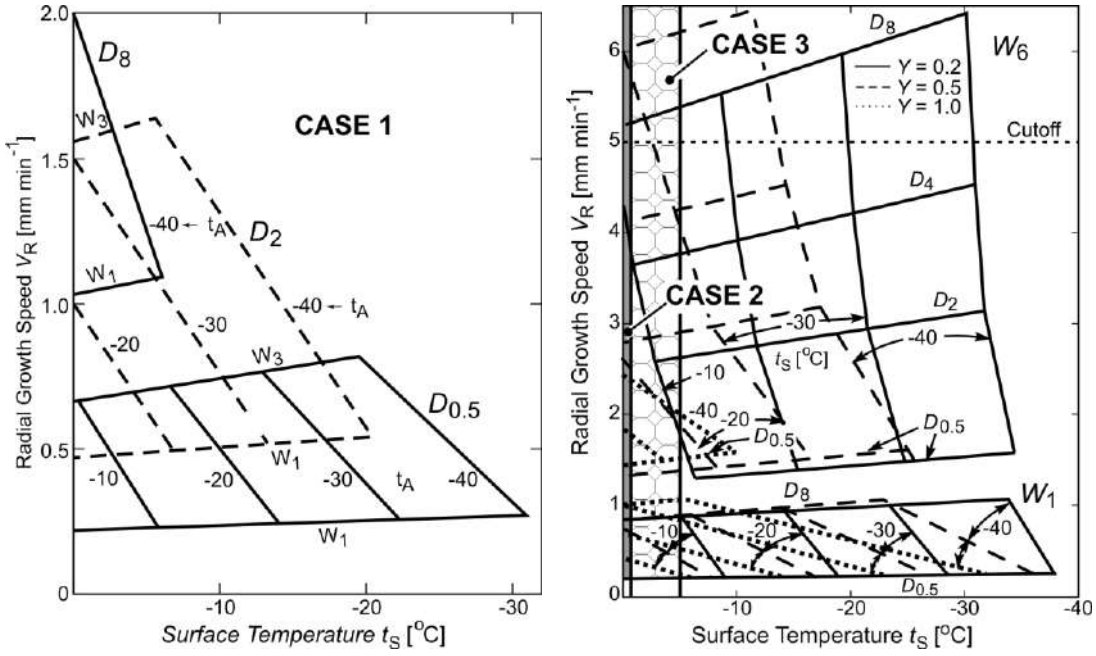

Fig. 3. CASE 1: V_R as function of surface temperature, for $D_{0.5}$, D_2 and D_8, different t_A and $W_1 \leq W_f \leq W_3$. CASES 2 and 3: ditto, but for two sets of trapezoids at W_1 and W_6 and different Y_i and D_i. CASE 2 in narrow grey band ($0 \leq t_S \leq -0.55$°C); CASE 3 in band >-5°C (octagons); highest V_R only possible under spongy growth, with highest speeds for $Y = 0.6$. Note difference in V_R scale between CASES.

D. The trapezoidal groups of CASE 1 are for different D_i and clearly show how increasing D increases the radial growth velocity. For D_8, the subscript giving the diameter in cm, the maximum V_R is 2 mm min^{-1}. The situation for CASES 2 and 3 is more complex because an additional variable enters: Y, the product of net collection efficiency and the ice fraction of the deposit. CASES 2 and 3, drastically show the cut of parameter space by limiting t_S to -0.55C (CASE 2) and -5C for CASE 3. The figure further shows an additional key result, namely that the highest V_R (limited by a cutoff at 5 mm min^{-1}) are reached for a $Y \leq 0.6$. It is known from the experiments with

gyrating spheroids by Garçia-Garçia and List (1992), Greenan and List (1995) and Zheng and List (1995) that high E_{NC} are normally connected to high I_f, i.e. they normally move up and down in parallel. In other words low Y means that both its components will be quite lower than unity for the above listed Y condition.

The 'active' parameter space for t_S is very limited because the possible surface temperatures do not extend to -40C. Nevertheless, it is considered important to see the patterns of the trapezoidal arrangements of D with t_A at different W_i. [The broken sides of the trapezoids are results of the linearization of basically smooth dependencies of D at fixed t_A.] Varying Y from $Y_{1.0}$ to $Y_{0.5}$ and $Y_{0.2}$ shows how the slopes of $D(t_A)$ change with the product of net collection efficiency and ice fraction in the growing spongy deposit. Of importance are the higher V_R for lower Y. To reach cutoff V_R values $Y \leq 0.6$.

7. SUMMARY AND COMMENTS

An outline has been given about growth and heat and mass transfer, HMT, of growing, spherical hailstones, supported by specific examples. For further details reference is made to List (2012a and b). The following points can be made:

1) The six HMT variables describing freely falling spherical hailstones, can be reduced to four by combining two pairs of old variables into two new ones, while the other two are functions of air and surface temperatures only.
2) A further reduction of the now four variables can be made by the classification of growth into three scenarios: CASE 1: dry growth; CASES 2 and 3: shedding from wet hailstones not covered by water skins, and shedding from hailstones covered by permanent water skins.
3) The range of growth conditions has been restricted to $0.5 < D < 8$ cm, $1 < W_f \leq 3$ g m^{-3} for CASE 1 and ≤ 6 g m^{-3} for CASES 2 and 3, and $915 \leq \rho_A \leq 1000$ kg m^{-3}.
4) The most drastic restrictions are for growth with shedding, with $0 \leq t_S \leq -0.55$C for CASE 2 and $0 \leq t_S \leq -5$C for CASE 3. CASES 2 and 3 are represented by one thin and one thicker surface temperature-band, respectively.
5) Growth was discussed for CASE 3 with permanent water skins, whereby the skin thickness was displayed with its dependence on surface temperature t_S and the temperature gradient across the skin. t_S can be directly related to X, thus proving links between all variables, old and new.
6) Other combinations of variables are represented in the t_A-X and V_R-t_S domains.
7) Growth of dry hailstones is substantially slower than in the shedding cases, while highest growth rates are achieved for CASE 3 with Y, the product of net collection efficiency and ice fraction of the deposit, being ≤ 0.6.

This work draws attention to shedding as initiator of a major hail-coupled warm rain process (Joe, 1982; Joe et al, 1980) that could be combined with the parameterization of drop interactions in warm rain by List et al (2008a and b). In many ways, the present work is also closely related to the exemplary CCOPE study described by Rasmussen and Heymsfield (1987a, b and c), which deals with the shed drops in terms of frozen hail embryos, while not addressing the shed drops as rain.

Acknowledgments

The author gratefully acknowledges the substantial contributions by the members of his two groups, in Davos 1052-1963, and at the University of Toronto (1963-2009). Without the enthusiasm and imagination of all the students, research associates, engineers and last but not least, the summer students, this work could not have been performed. The superb technical support by Mrs. Ana Susa and Mr. Raul Cunha was a key contributing factor. The American Meteorological Society is to be thanked for allowing copying figures and equations of List (2012a and b). The Physics Department of the University of Toronto provided the pleasant atmosphere for this work. Last but not least, the unwavering support by the Roland List Foundation was instrumental in the assembly of this 5-year synthesis.

8. BIBLIOGRAPHY

Beckwith, W. B., 1960: Analysis of hailstorms in the Denver network, 1949-1958. *Physics of Precipitation. Geophys. Monogr.,* No. 5, Amer. Geophys. Union, 348-358.

Garcia-Garcia, F., and R. List, 1992: Laboratory measurements and parameterizations of supercooled water skin temperatures and bulk properties of gyrating hailstones. *J. Atmos. Sci*. **49**, 2058-2073.

Greenan, B.J.W., and R. List, 1995: Experimental closure of the heat and mass transfer theory of spheroidal hailstones, *J. Atmos. Sci,,* **52**, 3797-3815.

Kry, P.R., and R. List, 1974a: Angular motions of freely falling spheroidal hailstone models. *Phys. Fluids*, **17**, No. 6, 1093-1102.

Kry, P. R., and R. List, 1974b: Aerodynamic torques on rotating oblate spheroids, Phys. Fluids, 17, 1087-1092.

Joe, P. J., 1982: The shedding of millimeter sized raindrops in simulated hail formation. PhD thesis, University of Toronto, pp. 306.

Joe, P. J., R. List and G.B. Lesins, 1980: Ice accretions, Part II: Rain production by icing assisted cloud water conversion. *J. Recherches Atmos*. **14**, 356-364.

Lesins, G.B., and R. List , 1986: Sponginess and drop shedding of gyrating hailstones in a pressure-controlled wind tunnel. *J. Atmos. Sci.*, **43,** 2813-2825.

List, R., 1963: General heat and mass exchange of spherical hailstones. *J. Atmos. Sci.*, **2**0, No. 3, 189-197.

List, R, 1990: The physics of supercooling of thin water skins covering gyrating hailstones. *J. Atmos. Sci.*, **47**, 1919-1925.

List, Roland, 2010: Hailstones, the main source of rain. Proc. 13th Conference on Cloud Physics, 28 June - 2 July 2010, Portland Oregon, American Meteorological Society, Paper 12.4, pp 8.

List, Roland, 2012a: New Hailstone Physics, Pt. I, Classification and Equations
J. Atmos. Sci., **70** (submitted)

List, Roland, 2012b: New Hailstone Physics, Pt. II, Growth and Heat and Mass Transfer
J. Atmos. Sci., **70** (submitted)

List, R., and D. Abreu, 2008: Shape evolution of growing hailstones as function of gyration parameters. Preprints, *Proceedings International Conference on Clouds and Precipitation,* Cancun, 7-11 July; on CD, paper P1.26. 7 p.

List, R., U.W. Rentsch, P.H. Schuepp and N.W. McBurney, 1969: The effect of surface roughness on the convective heat and mass transfer of freely falling hailstones. Preprints, *Proc. Sixth Conf. Severe Local Storms*, Chicago, Ill., 267-269.

List, R., F. Garcia-Garcia, R. Kuhn and B. Greenan, 1989: The supercooling of surface water skins of spherical and spheroidal hailstones. *Atmospheric Research*, **24**, 83-87.

List, R., C. Fung and R. Nissen, 2008a: Experiments on the pressure effect on collision and breakup of raindrops. *J. Atmos. Sci*., **66**, 2190-2203.

List, R., R. Nissen and C. Fung, 2008b: The parameterization and propagation of pressure effects on raindrop interactions in rainshafts. *J. Atmos. Sci*., **66**, 2204-2215.

Rasmussen, R. M., and A.J. Heymsfield, 1987a: Melting and shedding of graupel and hail. Part I: Model Physics. *J. Atmos.Sci.*, **44**, 2754-2763.

Rasmussen, R. M., and A.J. Heymsfield, 1987b: Melting and shedding of graupel and hail. Part II: Sensitivity Study. *J. Atmos.Sci.*, **44**, 2764-2782.

Rasmussen, R. M., and A.J. Heymsfield, 1987c: Melting and shedding of graupel and hail. Part III: Investigation of the role of shed drops as hail embryos in the I August CCOPE Severe Storm. *J. Atmos.Sci.*, **44**, 2783-2803.

Schemenauer, R.S., and R. List, 1972: Mass transfer measurements on models of snow crystals, conical graupel and small hail. *Proc. Intern. Cloud Phys. Conf.*, London, 60-61.

Schuepp, P.H., and R. List, 1969a: Mass transfer of rough hailstone models in flows of various turbulence levels. *J. Appl. Meteor*., **8**, No. 2, 254-263, 1969.

Schuepp, P.H., and R. List, 1969b: Influence of molecular properties of the fluid on simulation of the total heat and mass transfer of solid precipitation particles. *J. Appl. Meteor*., **8**, No. 5, 743-746.

Stewart, R.E., and R. List, 1983: Gyrational motions of disks during free fall. *Phys. Fluids,* **26**, 920-927.

Zheng Guoguang and R. List, 1995: Convective heat transfer of rotating spheres and spheroids with non-uniform surface temperatures. *Intern. J. Heat Mass Transfer*, **39**, 1815-1826.

The Role of Topography and Cold pool - Shear Interaction in Quasi-stationary Line-shaped Rainfall Systems over Shikoku Island Japan.

Takashi Unuma[1], Fumie Murata[2] and Tetsuya Takemi[3]

[1] Graduate School of Integrated Arts and Sciences, Kochi University, 5-1 Akebono-cho, Kochi, 780-8520, Japan,

[2] Faculty of Science, Kochi University, 5-1 Akebono-cho, Kochi, 780-8520, Japan,

[3] Disaster Prevention Research Institute, Kyoto University, Gokasho, Uji, Kyoto 611-0011, Japan.

1 Introduction

One of the precipitation systems that produce torrential rain in Japan is a quasi-stationary line-shaped (hereafter QSLS) rainfall system (Yoshizaki and Kato 2007). Many QSLS rainfall systems occur in the warm sector of extra-tropical cyclones whose centers move across the Sea of Japan. The high rainfall areas are found along the Pacific side of the Japanese archipelago. Shikoku Island along the Pacific is one of the high rainfall areas in Japan. QSLS rainfall systems are one of the factors that contribute to heavy rainfall in Shikoku Island. In particular, as one of the precipitation patterns that of Kubokawa - Kochi - Shigeto Line that often produce heavy rainfall in Shikoku Island (Unuma and Murata 2012). These precipitation patterns are similar location and strike to Kochi heavy rainfall that occurred in the 24 - 25 September 1998 as described by Yoshizaki and Kato (2007). Forecasters suggest that the topography and cold pool have some influences on the QSLS rainfall systems over Shikoku Island, but the mechanisms have not been examined. The occurrences of heavy rainfalls over complex orography have carried out in different parts of the world (Richard et al. 2007). The effects of cold pool due to the evaporation of rainfalls have been carried out observations in various regions such as the tropics and mid-latitude and idealized numerical simulations (LeMone et al 1998; Rotunno et al. 1988; Weisman and Rotunno 2004). However, these are intended for unstationary squall lines. There is less study that focused attention on QSLS rainfall systems.

We simulated Kubokawa - Kochi - Shigeto line that occurred on May 13th 2008, and this case was obtained by Unuma and Murata (2012). The purpose of this study is to numerically investigate mechanisms for the organization and maintenance of the QSLS rainfall systems over Shikoku Island with the use of the Weather Research and Forecasting (WRF) model.

2 Numerical setup

Version 3.1.1 of Advanced Research WRF (ARW-WRF) Model (Skamarock et al. 2008) was used to simulate QSLS rainfall systems. The computational domain is configured with three nested grids and the corresponding horizontal spatial resolutions are 12.5, 2.5 and 0.5 km, respectively(Figure 1, left). The domain sizes are 2187.5 km$\times$2250 km, 1125 km$\times$1125 km and 250 km$\times$250 km respectively. There are 55 levels in the vertical and the eta coordinate is stretched with Δ Z=40 m near the surface. We used Kain-Fritch cumulus parameterization only in the domain 1 and used Lin microphysical scheme the entire domains. We used YSU planetary boundary layer scheme in the two outer domains and use smagorinsky scheme in the domain 3. We used the JMA-MSM analysis data in the initial and boundary condition. We simulate 24 hours from the initial date of 03JST 13 May 2008.

3 Methods

The sensitivity experiments have all the same conditions as the control experiment expect the condition of terrains and make it a rule not to make the steep terrains in the sensitivity experiments (Table 1). To investigate the cold-pool shear interaction, we applied the analysis method of Weisman and Rotunno (2004) to this study. The cold-pool boundary is defined as a surface location where potential temperature is 290 K.

4 Results

4.1 Sensitivity experiments of topography

In order to investigate influences of the topography quantitatively, we calculated the total precipitation of two hours for the region of 100 km^2 of the location of QSLS rainfall systems, and also calculated the area of rainfalls (Figure 1, center). Using these outputs, we defined the area of rainfalls as ”the rate of the form of a line” and also defined the total precipitations as ”the rate of stationary”. Comparisons with CONTROL, NO-TOPO and NO-WEST, experiments of NO-TOPO and NO-WEST had less precipitation and less stationary. For the experiments of NO-EAST, the QSLS rainfall system was similar to CONTROL, although the rate of the form of a line was over 70 %. For the experiment of O-IMA, where only the mountain on the southwestern part of Shikoku Island (Imanoyama Mountain), the model-simulated QSLS rainfall system was reproduced, but rate of form of a line and the rate of stationary was nearly one-half (40 %

and 51 %). For the experiment of NO-NORTH, the model-simulated QSLS rainfall system was similar to CONTROL in terms of the rate of both the form of a line and stationary (76 % and 96 %) (Table 1).

4.2 Coldpool-Shear Interaction

Figure 1 shows temporal - spatial averaged vertical cross section in the direction that perpendicular to the QSLS rainfall systems for CONTROL (Figure 1, right). The shade and vector shows the entire mixing ratio (g/kg) and the wind vector (m/s) that was projected onto the vertical cross section respectively. The circulations between cold-pool and vertical wind shear were balanced, at the same time, QSLS rainfall systems were maintained.

5 Discussion

It is important that the topography of southern and western part of Shikoku Island in the experiment of NO-NORTH and NO-EAST. It suggests that the topography of the southwestern part of Shikoku Island is important to form the QSLS rainfall system in Shikoku Island. For CONTROL, the circulations between cold-pool and vertical wind shear were nearly balanced from the analysis of cold pool-shear interaction. It suggests that the QSLS rainfall systems are maintained by these circulations.

6 Acknowledgement

The JMA-MSM data is obtained from the Global Atmospheric Data of Kyoto University.

References

[1] LeMone, M. A., E. J. Zipser and S. B. Trier, 1998: The role of environmental shear and thermodynamic conditions in determining the structure and evolution of mesoscale convective systems during TOGA COARE. *Journal of the Atmospheric Sciences*, **55**, 3493-3519.

[2] Matsuo T., 1977: The Squall Lines in the Warm Sector in South-Shikoku District. *Tenki*, **24**, 97-104 (in japanese).

[3] Rotunno, R., J. B. Klemp and M.L. Weisman, 1988: A theory for strong, long-lived squall lines. *Journal of the Atmospheric Sciences*, **45**, 463-485.

[4] Weisman, M. L. and R. Rotunno, 2004:“ A Theory for Strong Long-Lived Squall Lines ” Revisited. *Journal of the Atmospheric Sciences*, **61**, 361-382.

[5] Yoshizaki M. and T. Kato, 2007: Metorology of Heavy rainfall and snowfall, Asakura shoten, 187pp (in japanese).

[6] Unuma, T. and F. Murata, 2012: Statistical Analysis of Quasi-stationary Line-shaped Rainfall Systems over Shikoku Island, Japan. *Tenki*, **59**, 119-125 (in japanese).

Table 1: The rate of the form of a line and stationary in each topography experiments.

Name of experiments	Rate of the form of a line	Rate of stationary	Details
CONTROL	1.0	1.0	–
NO-TOPO	0.0	0.0	No topography.
NO-EAST	**0.97**	**1.1**	No topography easter than Longitude of 133.5E.
NO-WEST	0.13	0.16	No topography wester than Longitude of 133.5E.
NO-NORTH	0.76	0.96	No topography norther than Latitude of 33.5N.
NO-SOUTH	0.69	0.73	No topography souther than Latitude of 33.5N.
ONLY-IMA	0.40	0.51	No topography exclude Imanoyama mountain.

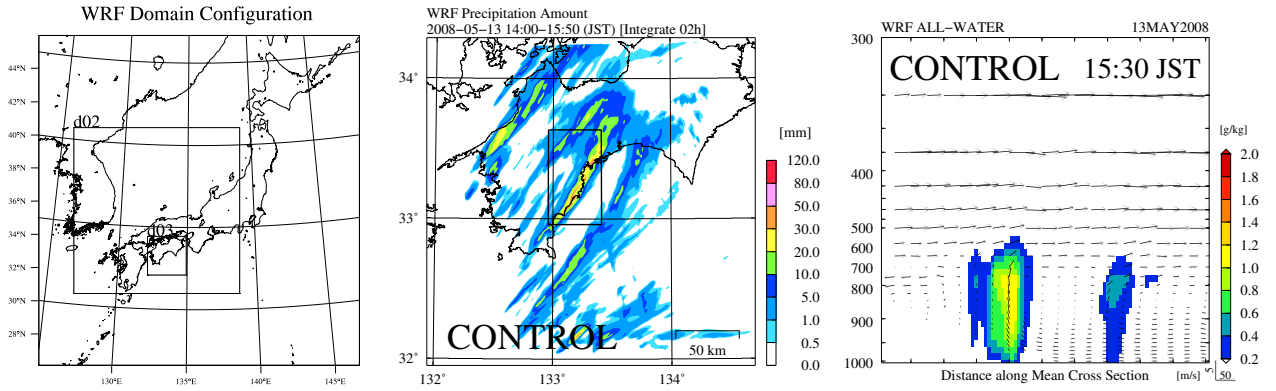

Figure 1: Computational domains for numerical simulations. (left). The simulated total rainfall from 14:00 to 15:50 in domain 3. Black rectangle indicates calculated domain for making Table 1 (center). Temporal - spatial averaged vertical cross sections in the direction that perpendicular to the QSLS rainfall systems in CONTROL. The shade and vector shows the entire mixing ratio (g/kg) and the wind vector (m/s) that was projected onto the vertical cross section respectively (right).

MODIFICATION AND TESTS OF PARTICLE PROBE TIPS TO MITIGATE ICE SHATTERING EFFECT

Alexei Korolev [1], Edward Emery [2], Kirk Creelman [3], Walter Strapp [1], Stewart Cober [1], George Isaac [1]

[1]*Environment Canada, Cloud Physics and Severe Weather Research Section, Canada;*
[2]*NASA Glenn Research Center, United States;*
[3]*Auriga Design Inc, Canada*

1. Introduction

Understanding the formation and evolution of small ice particles in clouds has been a long-standing problem in cloud physics. Debates around this problem extend well over three decades and began once optical particle size spectrometers became accepted instruments for airborne cloud particle sampling. Early airborne measurements suggested that in glaciated clouds the number concentration of ice particles is dominated by small particles with sizes less than 100μm. Small ice particles may play a significant role in radiation transfer and precipitation formation and their associated parameterizations have been included in many numerical climate and weather prediction models.

Characterization of ice particle concentration, sizes, and their habits is one of the primary objectives of experimental microphysical studies of cold clouds. Ice particles are effective sinks of water vapor and they can quickly grow into precipitation sized particles. Most liquid precipitation on the Earth goes through the ice phase before melting into rain or drizzle. The number concentration of ice particles is an important parameter determining the rate of conversion of liquid into ice in mixed phase clouds. Knowledge of the size distribution of ice particles is of great importance for numerical weather prediction and climate models. The results of airborne microphysical measurements of ice clouds are routinely used for verification of remote sensing instruments such as radar and lidar.

Most of our knowledge about the sizes and concentration of cloud ice particles has been obtained using airborne optical particle size spectrometers (Knollenberg 1976) which became widely available in the mid 1970s. Since that time, the amount of data describing the microphysics of ice clouds has been progressively increasing. One striking observation about ice clouds has been the omnipresence of small ice crystals with characteristic sizes less than 100μm (e.g. Heymsfield and Platt, 1984). It has been observed that the ice crystal number concentration is essentially always dominated by small ice particles (Fig.1 curve 1). Small ice particles in high concentrations have been observed in regions with undersaturated and supersaturated environments with respect to ice. Numerical simulations suggest that small ice particles should quickly grow to larger sizes in a supersaturated environment, or completely evaporate in a subsaturated environment, keeping the concentration of ice crystals D<100μm relatively low (Fig.1). In order to explain this high concentration of small ice particles, a number of mechanisms of ice multiplication in nature have been hypothesized. However, there is no experimental confirmation of any of these mechanisms, with the exception of that established by Hallett and Mossop (1974). The Hallett-Mossop mechanism is active only at relatively warm temperatures (between -5 and -8C), and it cannot explain the high concentration of small ice particles observed at lower temperatures.

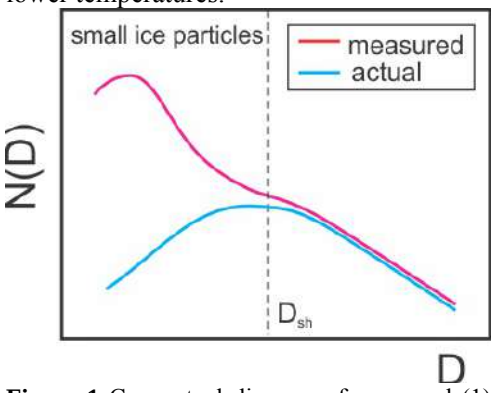

Figure 1 Conceptual diagram of measured (1) and presumed actual (2) size distributions of ice particles.

2. Hypothesis of shattering

One possible explanation for high concentrations of small ice particles is instrument-induced particle shattering. Prior to entering the instrument sample volume, an ice particle may impact the probe's upstream tips or inlet and shatter into small fragments, which may cause multiple artificial counts of small ice (Fig.2a). There have been a number of attempts

Corresponding Author: Alexei Korolev, Environment Canada, 4905 Dufferin Street, Toronto, Ontario, M3H5T4 Canada, e-mail: alexei.korolev@ec.gc.ca,

to quantify the effect of shattering from in-situ measurements (e.g. Gardiner and Hallett 1985; Gayet et al. 1996; Field et al, 2003, 2006; Korolev and Isaac 2005; Heymsfield 2007; McFarquhar et al. 2007; Vidaurre and Hallett 2009; Jensen et al. 2009). A review of these works can be found in Jensen et al. (2009). The estimates of the effect of shattering obtained in these studies varied in a quite wide range and resulted in large uncertainties.

Direct experimental support for the shattering hypothesis has been obtained with high speed video collected during dedicated tests by the NASA Glenn Research Center (GRC) at the Cox and Company wind tunnel, which will be described in section 4. The video technique provides only a qualitative characterization of the possible flow of shattered fragments from a larger particle breakup. However, for the first time, it has been documented that at aircraft speed ice particles bouncing off forward surfaces can travel several centimeters across the airflow before passing through the sample volume.

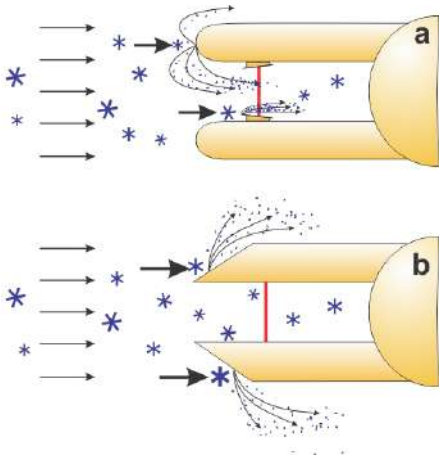

Figure 2. (a) Conceptual diagram of the effect of ice particle shattering and bouncing on the measurements of ice particles with the conventional probe tips. (b) The redesigned arm tips deflect ice particles away of the sample volume and result in mitigation of the shattering.

This work presents the efforts undertaken by Environment Canada in collaboration with NASA on the design of the particle probe arm tips, which are intended to mitigate the effect of ice shattering. The long standing problem of the ubiquitous existence of high concentrations of small ice particles in ice clouds has been studied using unique wind tunnel and in-situ aircraft measurements. The arm tips of the particle probes were modified by Environment Canada to deflect bouncing particles and to shed water away from the sample volume and optical field apertures (Fig. 2b) (Korolev 2011).

The first stage of the design work consisted of a sequence of iterations of modifications of mechanical design followed by the flow and particle bouncing simulations. The results of this work are described in section 3. During the second stage, the tips were tested at the Cox wind tunnel facility in ice particle and liquid conditions. Using high speed video recording, these tests were focused on two tasks: (a) identifying the frequency of ice particles bouncing towards the probe's sample area and (b) observing whether water would shed into the optical windows. The second stage of this work is presented in section 4. At the third stage the tips with the best performance were installed on the particle probes on the NRC Convair 580 and tested during the dedicated Airborne Icing Instrumentation Evaluation (AIIE) flight campaign in March-April 2009. The evaluation of the shattering effect was focused on the CIP, FSSP and OAP-2DC. The results of the AIIE project demonstrate that the contamination of particle size distributions by shattering is a significant problem for the airborne microphysical characterization of ice clouds. Shattering may contaminate the ice crystal size spectrum up to sizes of ~500 mm, particularly when large ice particles are present, resulting in an overestimation of the total number concentration of particles by up to a factor of 100. The main outcomes of the AIIE flight campaign (Korolev et al. 2011) are described in section 5. Section 6 presents the analysis of the existing data processing algorithms and their efficiency to filter out shattering events.

3. Flow and bouncing simulation

Computational fluid dynamics (CFD) simulations have been intensively used in the mechanical design and modification of probe arms and tips as a form of feedback regarding the quality of the airflow in the vicinity of the sample area of the probes. One of the main objectives was to design a set of probe tips with maximum uniformity and minimal disturbance to the air flow prior to entering the sample volume. The air flow disturbances related to convergence or divergence may result in the spatial sorting of particles with different aerodynamic sizes and, therefore, cause errors in measurements of particle concentration in different size bins. Acceleration and deceleration of the airflow in front of the

sample area may cause changes of the natural orientation of ice particles or an elongation of raindrops, which may be misleading in the particle habit recognition that is done from 2D imagery measured by the probes. T

he probe tip mechanical design optimization was a highly iterative process. After generating an initial 3D model of the tips based on conceptual design, the CFD simulation around the model was preformed. The results of the modeling were analyzed and modifications to the 3D model were applied if found to be necessary. Then, the CFD simulation around the modified model was performed again followed by one more repeated cycle of "design-simulation". The CFD simulations were conducted at different angles of attack, yaw, air speeds, temperatures and pressures. The CFD analysis was performed with the help of the Flow Simulation Tool in Solid Works software.

Below we show some results of the CFD simulations for the particle probes with standard and modified arms.

3.1 *Flow simulation*

Figure 3 shows the CFD simulations of the airflow at an airspeed of 100m/s, a pressure of 700mb and a temperature of 0C around the front part of the FSSP, OAP-2DC and CIP with standard[1] arms and tips. The diagrams in the central column depict the following changes: airspeed along the laser beam (Figs.3d, e, f); and along the line parallel to the airflow and passing through the center of the sample area (Figs.3g, h, i). Particles passing through the FSSP inlet tube experience deceleration and then acceleration before crossing the sample area (Figs.3g). The flow inside the tube has asymmetry caused by the knob mounted on one of the optical apertures (Figs.3g). The airspeed gradually decreases during its approach to the sample area of both OAP-2DC and CIP (Fig.3h, i). However, the airspeed along the sample volume of these probes increases from the center toward the arms. The ice particles passing close to the arms may experience aerodynamic stresses caused by the wind shear. This may cause aggregated ice particles with weak bonds such as aggregates of dendrites or needles to break apart.

[1] Hereafter, the term "standard" is referred to unmodified probes' configurations as they were built by manufacturers.

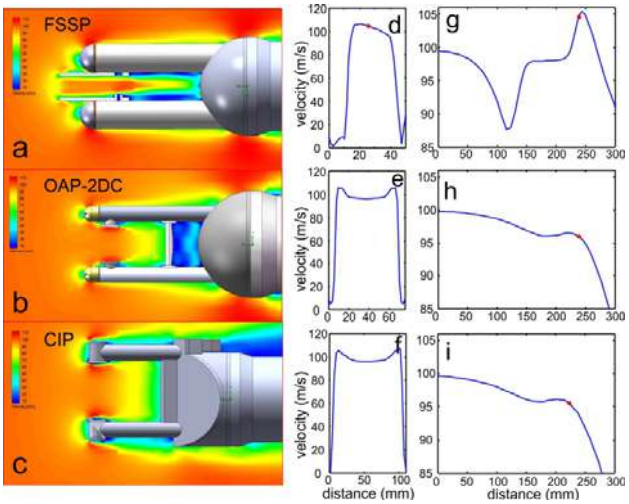

Figure 3. Simulations of the airflow at V=100m/s, P=700mb and T=0C around the particle probes FSSP (a), OAP-2DC (b) and CIP (c) having standard housing. Air velocity profile along the sample volume of FSSP (d); OAP-2DC (e), CIP (f). Center line air velocity upstream and downstream of the sample area (g); OAP-2DC (h), CIP (i). Red dots indicate the location of the sample volume. For OAP-2DC and CIP the sample volume on (e) and (f) is presented by the entire length of the beam between the arms.

Figure 4 shows a similar set of diagrams for the same conditions and the same type of instruments as in Fig.3, but with modified tips. The modified tips improved the uniformity of the airflow along the sample volume (Fig.4d, e, f). The airflow also becomes more uniform upstream the sample volume for the FSSP and OAP-2DC, and it varies less than 5%. The airflow upstream the CIP experiences deceleration and then acceleration within ±5%. The acceleration of the airspeed between the CIP arms is caused by the depression behind the tips resulting in the Venturi effect.

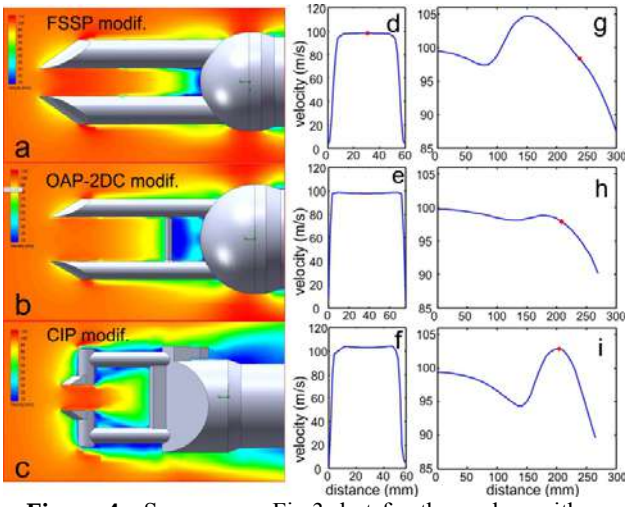

Figure 4. Same as on Fig.3, but for the probes with modified arm tips.

One of the tasks related to the modification of the tips was the protection of the optical windows from water shedding over the tip surface. Water might shed from the upstream lip onto an optical aperture, contaminate optics and eventually degrade measurements. A groove with angled edges around the open aperture was considered as one of the potential solutions of this problem. The shed water was expected to be trapped inside the groove and dumped out to the sides.

Figure 5 shows the flow trajectories over the surface of the tip upstream from the aperture and groove. The results of the CFD simulation suggest that the leading edge vortex sweeps the majority of the flow down and around the tip. The remainder, moves along the top surface of the tip, enters and is diverted by groove and then exits out through its sides corners. The wind tunnel tests described in section 4.3 confirmed the success of this design in protecting the optics from water contamination.

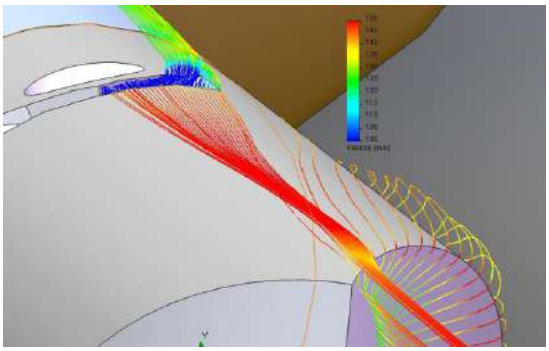

Figure 5. Simulations of the flow trajectories along the tip surface calculated from the CFD simulations. The flow analysis was performed for 150m/s, P=800mb and T=0C.

3.2 *Bouncing simulation*

A CFD simulation of bounced ice particles was performed to estimate the trajectory of deflected particles and to ascertain which regions of the sample area could potentially be contaminated by deflected ice particles. In simulation, the ice particles were assumed to be solid spherical balls having the density of ice. The restitution coefficient was estimated from the trajectories of ice particles deflected from the solid surface, which were obtained from the analysis of high speed videos recorded in the Cox and Company Wind Tunnel Facility. It was estimated that the normal coefficient of restitution (e_n) of ice particles generated in the wind tunnel varies from 0.55 to 0.85. Variation in this value is probably due to variations in individual particle shape, off-axis camera viewing angles and is further compounded by an unknown Tangential coefficient of restitution (e_t) between the machined, heated probe tip and the geometry of wind tunnel ice particles.

It should be noted that the restitution coefficient of ice particles grown through the water vapor diffusion process may be quite different from those generated in the wind tunnel by means of shaving solid ice blocks. The diffusion grown ice particles usually have lower bulk density due to developed branches and are more fragile as compared to those produced in the wind tunnel. Upon impact, such particles most likely shatter first and then bounce away. This results in a redistribution of the kinetic energy of the original particle into energy required for the particle fragmentation, heating, partial melting and kinetic energy of the bounced fragments. Therefore, the restitution coefficient of the individual fragments is expected to be lower than that for the case of bouncing without shattering. The analysis of the high speed video obtained in the wind tunnel tests showed that the interaction of the tunnel generated ice with a solid surface usually occurred without shattering. Although shattering events were observed in a number of cases.

Figure 6 shows the calculated trajectories of ice spheres with diameters 7μm, 12μm, and 20μm, bouncing from the FSSP inlet tube. The normal restitution coefficient during the bouncing simulation was assumed to be 0.85 The angle of attack for this simulation was 5 degrees. As seen from Fig.6 a large percentage of bounced particles enter the sample tube and pass through the sample volume of the probe. This is suggestive of the fact that the FSSP measurements in ice clouds may be contaminated by shattering and bouncing particles. As it will be shown in Section 6, the contamination of the FSSP measurements by ice particles is a serious issue.

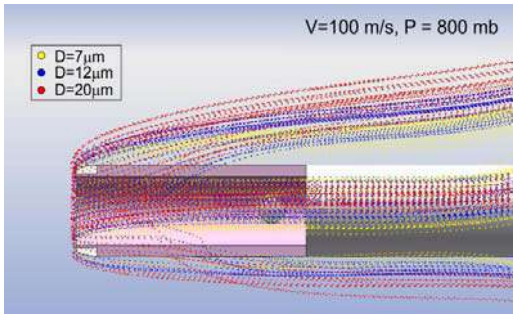

Figure 6. Simulation of bouncing of ice spheres with diameters 7μm, 12μm and 20μm from the FSSP inlet tube and angle of attack 5 degree. The diagram shows a crossection of the inlet tube.

In order to estimate the effect of ice particles bouncing from the OAP-2DC arms, the simulation of ice particles bouncing from a hemispherical head has been performed. The dimensions of the hemispherical head are the same as that for the OAP-2DC arm (see Figs.3b, 9a) although the anti-splashing guards installed on the OAP-2DC arm were not included in the simulation. The simulation assumed no particle shattering occurred and that the particle remains spherical throughout its flightpath. Figure 7 shows the trajectories of ice spherical particles after their impact with the surface of the hemispherical head. The simulation of trajectories along z-direction was discontinued at the location of the OAP-2DC sample volume z=4.5cm downstream from the tip of the head. As seen from Fig.7 that even in high pressures (P=1000mb, Fig.7a), bouncing ice particles with a D~50μm collectively covered the entire OAP-2DC sample volume, which has a length of 6.2cm.

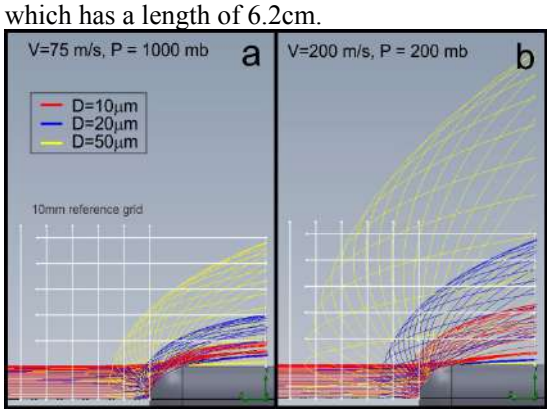

Figure 7. Simulation of the trajectories of ice spherical particles with different diameters after their impact with the hemispherical head. The calculations were performed for the restitution coefficient of 1.0, representing a perfect reflection thus giving a maximum limit of travel. The diameter of the hemispherical head is 2.5cm. The location of the OAP-2DC sample volume would be on the right side of the diagrams where the particle trajectories are terminated.

Figure 7 indicates that the travel distance of the particles across the airflow actually increases with an increase in the particle size and a decrease in the air pressure P. Figure 8 shows the maximum travel distance across the airflow L_{max} at z=4.5cm versus the pressure, calculated for different velocities V and different particle sizes. As seen from Fig.8 the curves $L_{max}(P)$ calculated from different airspeeds are grouped together, showing a weak dependence of L_{max} versus V. This result is suggestive of the fact that L_{max} primarily depends on particle size and air pressure (density) and that velocity has a minor effect on L_{max}.

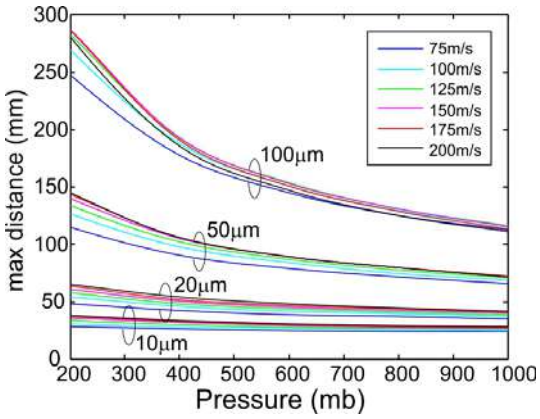

Figure 8. Simulations of the maximum travel distance across the airflow at the location z=4.5cm after particle bouncing from the hemispherical head with a diameter of 2.5cm. The distance z=4.5cm corresponds to the location of the OAP-2DC sample volume.

4. Wind tunnel tests

During the course of the modification of the probes arms and tips, a series of wind tunnel tests were performed. The main objectives of these tests were as follows:

(a) to evaluate the general performance of the probes after their modification;
(b) to characterize the effectiveness of the modified tips in mitigating shattering and to compare it with the originally designed ones;
(c) to characterize the effect of shedding water on optics contamination
(d) to determine the efficiency of the deicing heaters and their capability to keep the arms' surface in front of the sample area to free from ice build-up.

The present section will be focused mainly on objectives (b) and (c).

The tests were conducted in the Cox and Co. Wind Tunnel Facility. The characterization of the performance of the probe tips was conducted in both ice and liquid sprays. Most of the tests were conducted at an air speed of 80m/s. The performance of the modified probes was tested at two angles of attack: 0 degrees and 5 degrees.

4.1 *High speed video recording*

The characterization of the effectiveness of the tips in mitigating bouncing and shattering was conducted in ice sprays. The trajectories of the bouncing ice particles were recorded on a high speed video camera. Fig. 9 shows some example

images of ice particles bouncing from the standard OAP-2DC and CIP arm tips and the FSSP inlet tube. The high speed videos associated with these snapshots can be downloaded from (ftp://64.176.164.83/pub/bouncing_video).

The analysis of the high speed videos revealed that after bouncing from the OAP-2DC arm tips, the ice particles may travel several centimeters across the air flow, which results in the contamination of the entire sample area by shattered and bounced ice particles. This observation is in qualitative agreement with the prediction obtained from the bouncing simulation in section 3.2.

The CIP has saucer shaped tips with a sharp leading edge (Fig.9b). Such a shape results in a different bouncing pattern than the one for the OAP-2DC. Since the incident angle for the CIP tips remains approximately the same for all particles, they bounce from the surface at approximately the same angle in the plane passing through the sample area. As a result, the bounced particles form a relatively narrow cone of an ~20-30 degree angle which contaminates approximately 2-3cm of the sample area nearest to the tip (Fig.9b). The analysis of the high speed videos documented frequent instances when trajectories originated on the cylindrical part of the tip and ended up in the sample area. In other words, ice particles may bounce over the edge of the saucer tip. Since the travel distance increases with the decrease of the air density (section 3.2) it is anticipated that the contamination by particles coming from the cylindrical section of the probe tip will increase for the aircraft measurement, as compared to the wind tunnel tests conducted at P=1000mb.

Figure 9c shows a snapshot of the high speed video of the trajectories of ice particles bounced from the FSSP inlet tube. The illumination used for the high speed photography does not allow us to capture footage of particles entering the sample tube. However, the qualitative similarity between the trajectories of bouncing particles outside the inlet tube obtained from simulation (Fig.6) and the particles observed in the wind tunnel (9c) suggests that the results of the simulation on a qualitative level can be applied to the FSSP. The observed similarity between the wind tunnel observation and bouncing simulation suggests that ice particles bounce and pass through the sample volume of the probe similar to the conclusions obtained in the bouncing simulation.

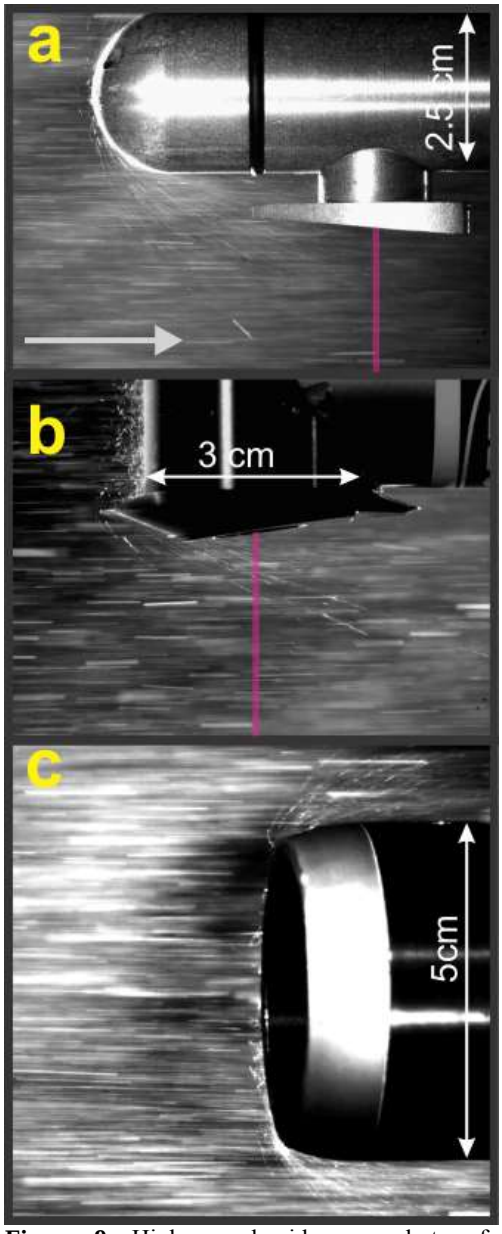

Figure 9. High speed video snapshots of the trajectories of ice particles bouncing from the arm tips of the CIP (a), OAP-2DC (b) and FSSP inlet tubes (c). Frames are from high speed videos taken in ice spays in the Cox Wind Tunnel at the airspeed of 80m/s, P=1000mb, T=-10C. Red areas in (a) and (b) highlight the sample volumes of CIP (a) and OAP-2DC (b) probes, respectively.

Analysis of the high speed video from the Cox and Company Wind Tunnel show that ice particles may bounce upstream from the airflow up to approximately 1cm. The picture in Fig.10 shows the trajectories of ice particles bouncing upstream to 8mm from the cylindrical tip of the CIP. As mentioned above, particle bouncing upstream will increase with the decrease of pressure.

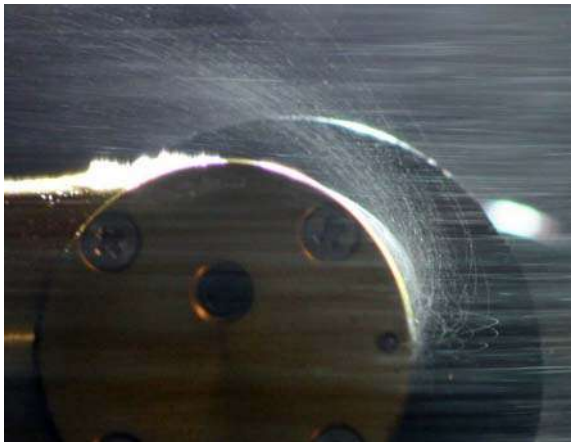

Figure 10. Snapshot of the trajectories of ice particles bouncing from the cylindrical surface of the CIP tip. Ice spay in the Cox Wind Tunnel, airspeed 80 m/s, *P*=1000mb, *T*=-10C

Figure 11 shows high speed video snapshots of ice particle trajectories around the modified tips for OAP-2DC and CIP at a zero degree angle of attack (Figs.11a,b) and a 10 degree angle of attack (Figs.11c,d). As seen in Figs.11a,b, trajectories associated with bouncing towards the sample volumes of these instruments are *not* observed here. The particles impacting the tips are deflected to the side opposite to the sensing area.

However, for a non-zero angle of attack, particles experiencing impact with the inner surface of the tips are deflected towards the sample areas. The snapshots of the cases with a 10 degree angle of attack are shown on Fig. 11c,d. As depicted, the airflow in this case is non-parallel to the inner surface of the tips and it is exposed to the impact with particles. After impact with this surface, particles bounce off or shed along this surface. It should be mentioned that most research airplanes do not fly with a 10 degree angle of attack. Such angle was selected for research purposes in order to exaggerate the effect of particle bouncing.

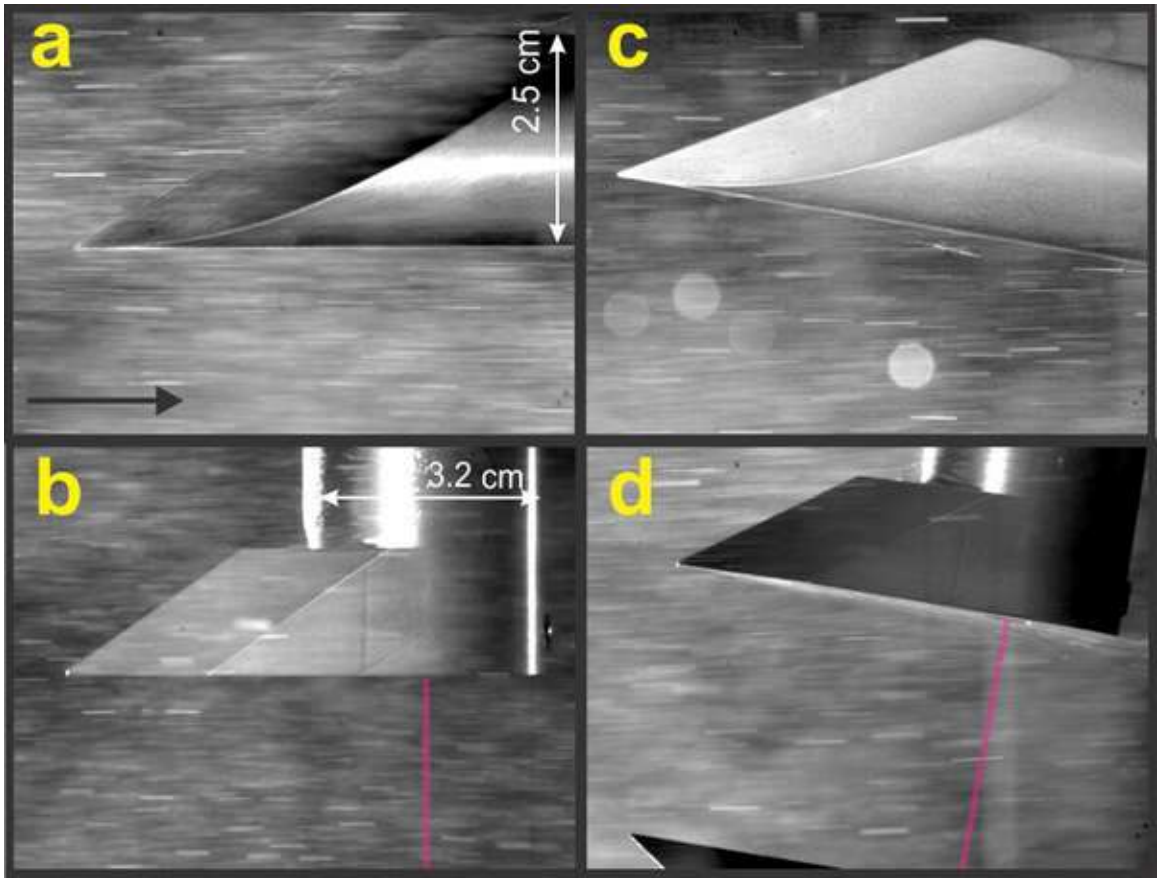

Figure 11. High speed video snapshots of the trajectories of ice particles bouncing from the modified arm tips of OAP-2DC (a,c) and CIP (b,d) at a 0 degree (a,b,) and a 10 degree (c,d) angle of attack. Frames are from high speed videos were taken in ice spays in the Cox Wind Tunnel at the airspeed of 80m/s, *P*=1000mb, *T*=-10C. Red areas in (b) and (d) highlight the sample volumes of CIP.

4.2. *Still photography*

Still photography of the illuminated sample volume exposed to the spray is another way to characterize the inhomogeneity of the particle flow across the probe's sensing area. This method is in many ways is similar to that used by the laser sheet technique. When particles pass through the illuminated sample volume they scatter light towards the camera. The amount of light received by the camera (intensity x exposure time) from each individual volume of the beam depends on the size of the particles in this volume, their concentration and their speed. For a uniform flow with a spatially homogeneous spray the brightness of the beam on the picture should remain constant. The non-uniformity of the beam brightness means that one of the following reasons, or their combinations, are currently present at the beam location: (a) inhomogeneity of particle sizes, (b) inhomogeneity of particle concentration and (c) non-uniform velocity along the sensing area.

Figure 12 shows still pictures of the OAP-2DC sample volume with standard tips. The pictures were taken during pne ice spray and three liquid sprays with the nominal mean volume diameters (MVD) 22μm, 40μm, 150μm. Depending on the spray, the time exposure of the camera varied from 2 to 10 seconds to get a statistically significant sample of particles passed through the sample volume and average the turbulent fluctuations of the air flow in the wind tunnel.

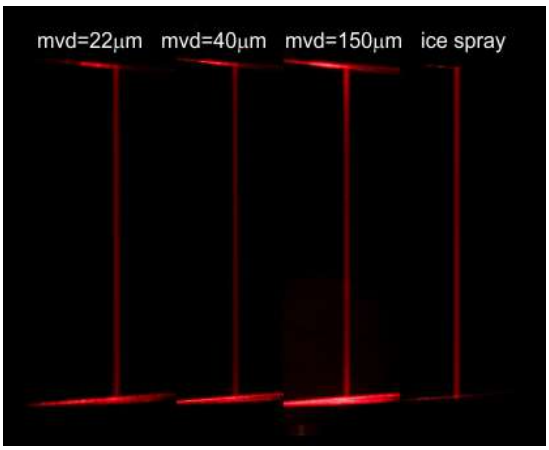

Figure 12. Still pictures of the OAP-2DC sample volume taken in three liquid and one ice spray at 80m/s

The distributions of the brightness along the sample volumes of the OAP-2DC and the CIP with standard and modified tips are shown in Figs 13 and 14. For all sprays, the brightness of the beam has a tendency to increase toward the edges of the sample area and, after passing its maximum, it may drop down near the walls of the arms. This observation is in general agreement with the analysis of the high speed video. For the liquid sprays, the brightness of the beam for the OAP-2DC and the CIP with standard tips (Figs.13a, 14a) increases with the increase of the droplet MVDs. This increase in brightness is most likely related to the splashing of large drops present in the sprays. For the probes with modified tips, the brightness of the beams appears to be essentially more uniform, although some inhomogeneities of the brightness are still present near the arms walls, indicating the disturbance of the flow and sprays by the upstream parts of the tips.

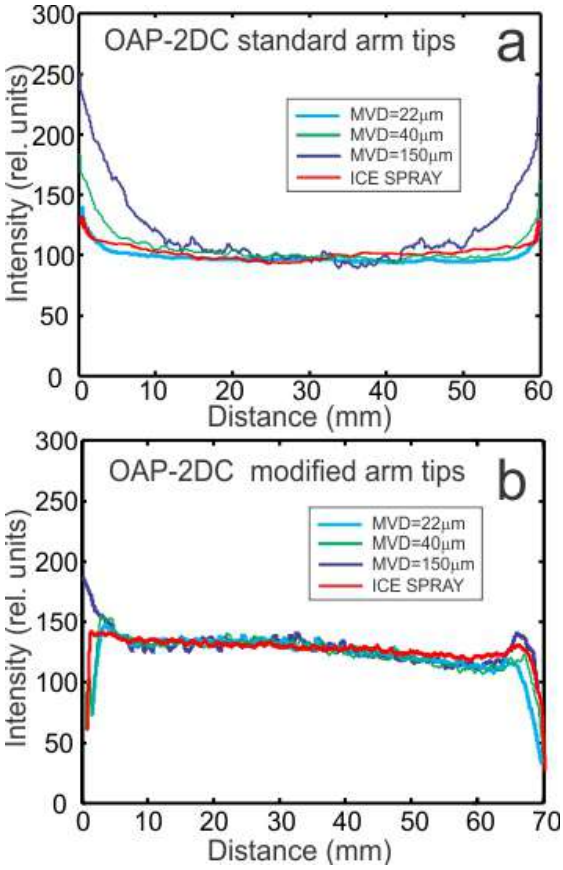

Figure 13. Intensity of the scattered light along the sample volume of the OAP-2DC with standard (a) and modified arm tips (b) calculated from the still pictures. The photographs of the beam were taken during three liquid sprays with MVD=22μm, 40μm, 150μm and ice spray. The airspeed was 80m/s.

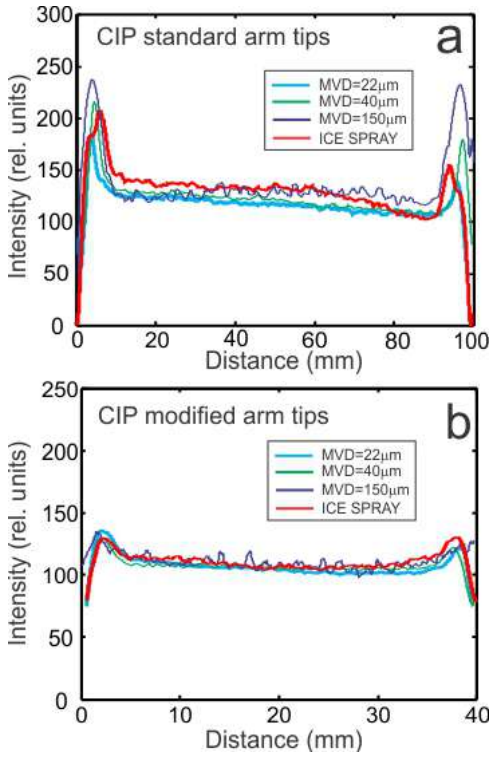

Figure 14. Intensity of the scattered light along the sample volume of the CIP with standard (a) and modified arm tips (b) calculated from the still pictures. The photographs of the beam were taken during three liquid sprays with MVD=22μm, 40μm, 150μm and ice spray. The airspeed was 80m/s.

4.3. *Shedding water*

Figure 15 shows a high speed video snapshot of the inner part of the modified tip with a V-shaped grove in front of the optical window. The probe was installed at a 10 degree angle of attack and exposed to a liquid spray with an air temperature above the freezing point. The streakers formed by shedding water appear in the section upstream the optical window. The shedding water trapped by the angular opening can be seen exiting on the side of the groove. The analysis of the videos with shedding water showed that the designed groove collects the shedding water, thus minimizing contamination of the optics by water.

5. Airborne Icing Instrumentation Evaluation (AIIE) flight campaign

The AIIE flight campaign focused on quantifying the effect of shattering on ice measurements, and better understanding the problem of small ice particles in clouds. To meet these objectives the following strategy was used: each probe-type was simultaneously flown side-by-side in its modified and standard configuration to quantify the effect of shattering by comparing the results from the modified and standard probes (Fig. 16) The suite of instruments installed on the aircraft is listed in Table 1. A total of thirteen research flights were conducted with modified/unmodified pairs in the vicinity of Ottawa during March-April 2009.

Several sets of modified arms and tips for OAP-2DC (8 sets), CIP (3 sets) and FSSP (3 sets) were designed and fabricated for the AIIE project. The inlet tube of the modified FSSP was removed and the original hemispherical tips were replaced with new designs. New tips were tested each flight. The first and the last research flights were conducted with all probes set in standard configuration to establish that the electronics and optics of each pair of probes produced equivalent measurements before and after modifications, and that their performances did not change during the flight campaign. The measurements of the pairs of OAP-2DCs, CIPs,

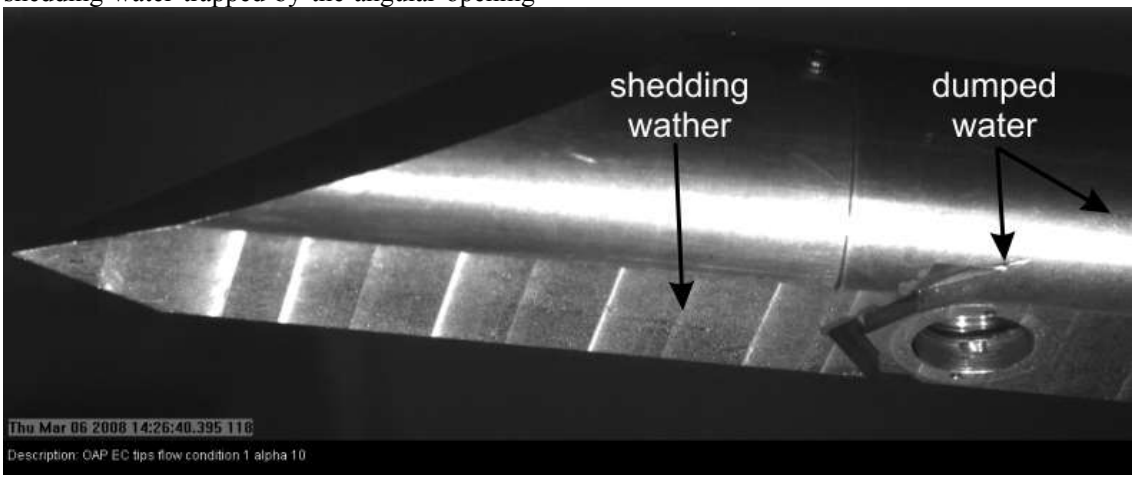

Figure 15. High speed video snapshots of the water shedding over the inner surface of the modified OAP-2DC tip. The shedding water is collected by the groove in front of the aperture and dumped on the side.

and FSSPs on these two flights were essentially identical for each pair of instruments, indicating that differences observed in other flights between the modified and standard probes were indeed due to the modifications and not to poor probe precision. The 2D-S tips were fabricated by SPEC in consulting with Environment Canada. Since only one 2D-S probe was flown, for the first part of the project it had standard tips, and for the second half modified ones.

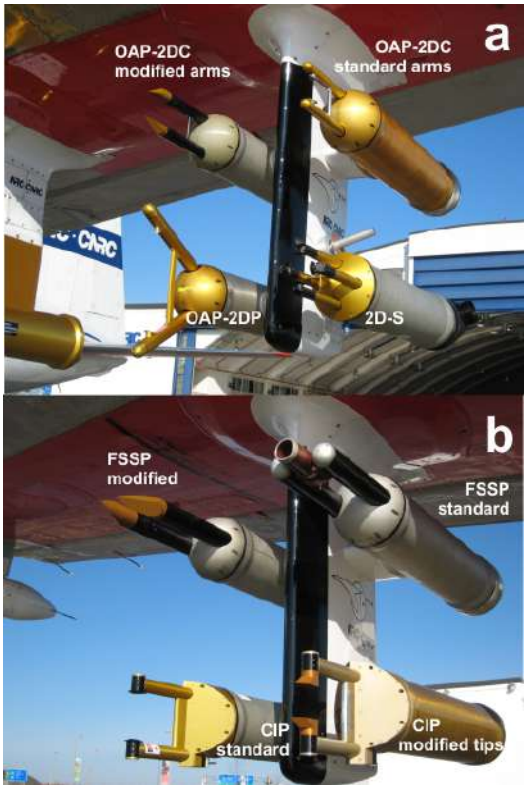

Figure 16. Cloud particle probes installed on the NRC Convair-580 during AIIE flight campaign. Pairs of the OAP-2DC (a), FSSP (b) and CIP (b) with modified and standard tips or inlets were mounted side by side on the same pylons. Such an installation enabled direct comparisons of the measurements of standard and modified probes and quantification of the effect of the ice shattering on the measurements.

The goal of each research flight was to evaluate the performance of each set of modified tips in a variety of cloud conditions with different ice particle habits, sizes, concentrations, and ice water contents. For this reason, the flights were deliberately conducted in deep precipitating glaciated cloud systems associated with frontal clouds. In such clouds the characteristic size of ice particles usually gradually changes from a minimum near the cloud top, to a maximum in the precipitation below the cloud base. Cloud sampling was conducted during spiral or porpoise ascent to maximum altitude (7.5km), and then descent to the minimum allowed altitude (usually 0.3-1.5km). In order to estimate the effect of air speed and angle of attack on the performance of standard and modified tips, a horizontal leg followed by pitch-up and pitch-down maneuvers were carried out on each flight at a pre-selected altitude.

The following examples show a dramatic reduction in the effect of shattering on the microphysical measurements using the modified tips and also by using shattering filtering algorithms.

6. Shattering by the FSSP

Fig. 17a shows comparisons of the particle concentration in ice and mixed-phase clouds measured by standard and modified FSSPs. In mixed-phase and liquid cloud regions the total particle number concentration measured by both FSSPs are in close agreement. Here, the presence of supercooled liquid is suggested by the increase of the Rosemount Icing Detector signal (Fig.17c) when LWC is sufficiently high, and/or by the appearance of 2D images typical for supercooled large droplets (SLD) with the occasional ice crystal image (Fig.18(1)). In ice clouds, outside these mixed-phase regions, the modified FSSP number concentration was 10^{-2} cm^{-3} or lower, whereas the standard FSSP concentration, with the inlet tube, varied between 1 cm^{-3} and 10 cm^{-3}. In these regions, the absence of liquid droplets is supported by a flat or decreasing Rosemount Icing Detector ramp voltage (Fig.17c) and the CIP particle imagery (Fig.18(2)) showing ice particles with no evidence of liquid droplets.

The total number concentrations from the FSSP in the mixed-phase regions in Fig.17a are quite low, which is often observed for clouds containing SLD. These concentrations are comparable to the concentrations of ice particles elsewhere measured by the standard FSSP in Fig. 17a. In this case, the standard FSSP is unable to distinguish mixed-phase cloud regions from ice regions due to artifacts in the ice regions. However, the modified FSSP shows only a very small signal in ice clouds, and in this particular case, can clearly identify liquid-containing cloud without other supporting measurements. This represents a potentially significant improvement of FSSP measurements in mixed phase clouds.

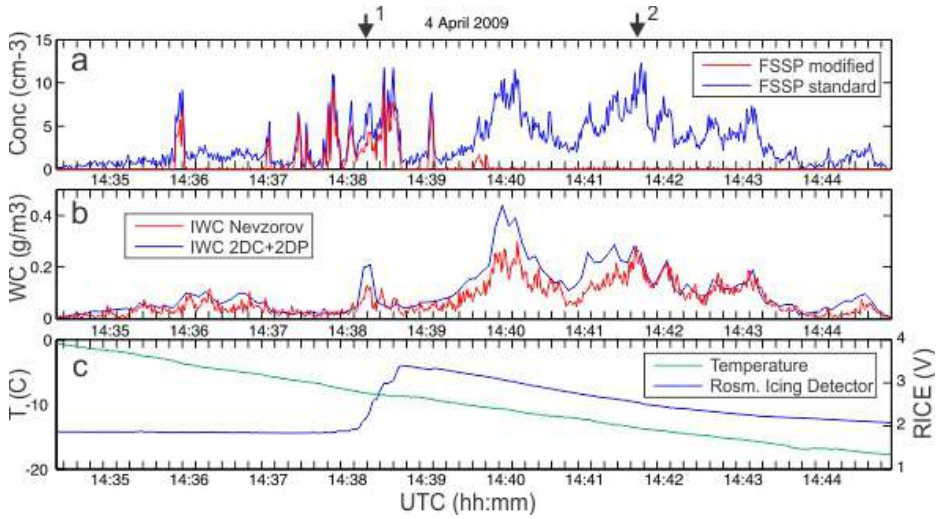

Figure 17. Time series of (a) cloud particle concentration measured by the modified and standard FSSPs; (b) IWC measured by the Nevzorov probe and calculated from the OAP- 2DC and 2DP images; (c) temperature and Rosemount Icing Detector (RID) signal. Arrows 1 and 2 at the top of (a) indicate the areas where the CIP particle images in Fig.6 have been sampled. The measurements were conducted on 08 April 2009, on the north-west side of Ottawa in glaciated frontal cirrostratus-nimbostratus cloud system. An increase of the RID ramp voltage between 14:37:40 and 14:39:00UTC indicates on a presence of cloud liquid water. Liquid clouds between 14:36:00 and 14:39:00UTC does not cause changes in the RID voltage since their LWC is below the RID sensitivity threshold (0.01g/m^3) and the air temperature is too warm (T>-4C) (Mazin et al. 2000).

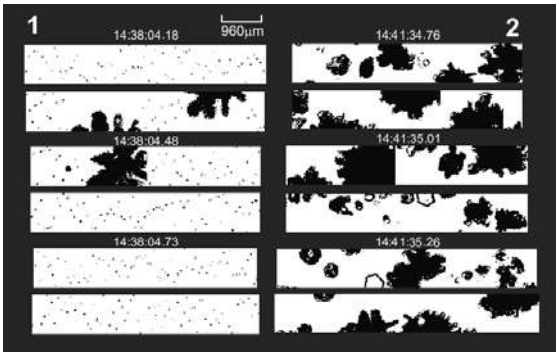

Figure 18. Cloud particle 2D images measured in the areas indicated by arrows "1" (mixed phase) and "2" (ice cloud) in Fig.17. The images were measured by CIP with the modified tips with 15μm pixel resolution.

Fig. 19 shows another case where, similar to the case in Fig 17, concentrations measured by standard and modified FSSPs agree well in mixed-phase and liquid clouds. In regions of ice cloud the particle concentration measured by the modified FSSP is again very low at ~ 10^{-2} cm^{-3}, but in a region of relatively high ice water content at 18:08, the standard FSSP concentration reaches 50 cm^{-3}. The existence of such high concentration of small ice particles may have an impact on precipitation formation and radiation transfer in ice clouds. The comparisons of Fig.19 suggest that the high concentration of small ice particles on the unmodified FSSP appears to be almost entirely artifact in this case.

Fig. 20 shows comparisons of the average size distributions measured by the standard and modified FSSPs for all ice (Fig. 20a), and liquid or mixed-phase (Fig 20b) clouds sampled during the AIIE project. The agreement is quite good in liquid and mixed-phase clouds (Fig. 20b), except for the larger sizes with D>30μm. Cober et al. (2001) showed that ice crystals in mixed phase clouds start to bias FSSP observed droplet spectrum at sizes >30μm, when the ice concentration exceeds 1l^{-1}. However, in ice clouds the ratio of the measured concentrations varies from 1.5 to 3 orders of magnitude depending on the droplet size (Fig. 20a).

Fig. 21 contains scatter diagrams of the 1-second total concentrations measured by both FSSPs in all ice (Fig 9a) and liquid/mixed phase (Fig 21b) clouds. Fig. 21a suggests that shattered particles dominate the unmodified probe number concentration in ice clouds. The two probes agreed very well in liquid/mixed phase clouds dominated by liquid droplets (Fig. 21b), indicating that the differences in ice clouds were not due to any fundamental electronic or optical response differences between the two probes, but rather were due to the lack of a sample tube and/or the modified tips on the modified probe. For all cases observed during the AIIE project, the particle number concentration measured in ice clouds by the standard FSSP exceeded the concentration of the modified one. Typically

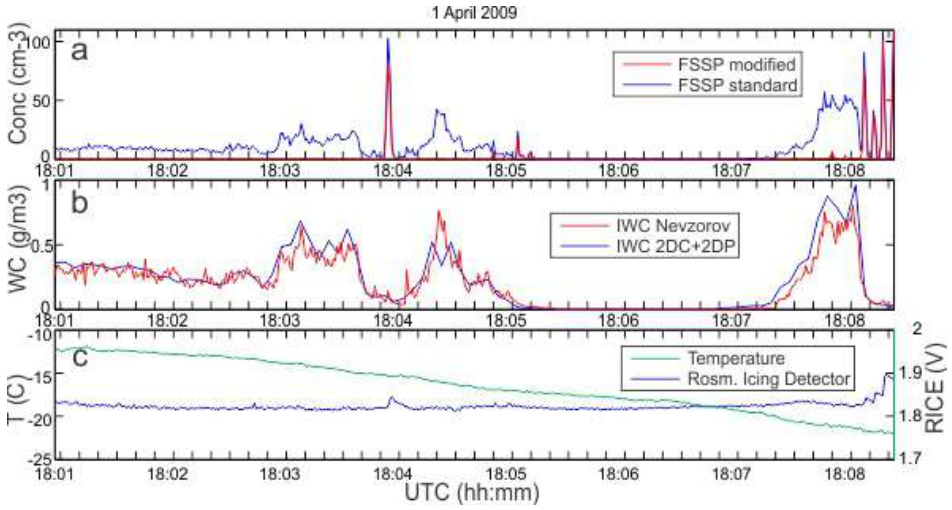

Figure 19. Time series of (a) cloud particle concentration measured by the modified and standard FSSPs; (b) IWC measured by the Nevzorov probe (deep cone) and calculated from 2D images; (c) temperature and Rosemount Icing Detector ramp voltage. The measurements were conducted on 01 April 2009, north-west of Ottawa, in ice clouds associated with a frontal system.

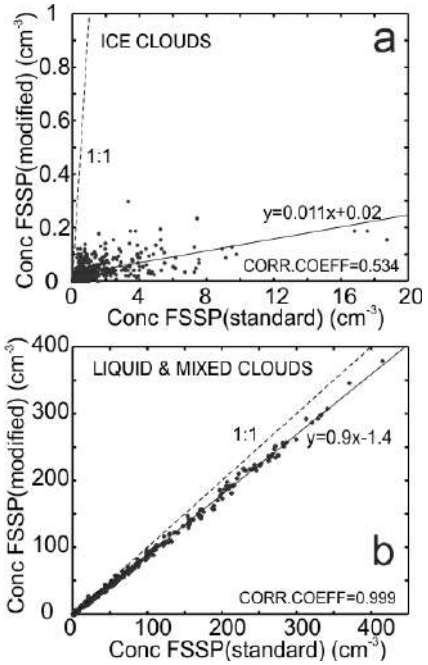

Figure 20. Scatter diagram of the cloud particle total number concentration measured by the standard and modified FSSPs in all ice clouds sampled during AIIE (a); and liquid and mixed phase clouds sampled on 08 April 2009 (b)

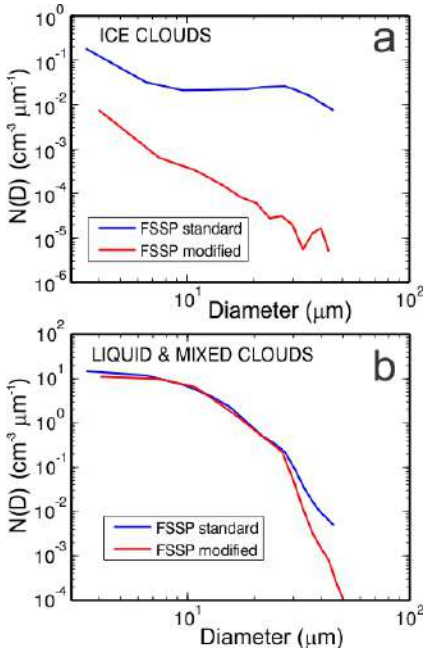

Figure 21. Size distributions measured by the standard and modified FSSP in (a) ice clouds and (b) liquid and mixed phase clouds, averaged over the entire AIIE flight data set.

the one-second concentration measured by the modified probe was $0.01cm^{-3}$ to $0.1cm^{-3}$, compared to $0.5cm^{-3}$ to $5cm^{-3}$ for the unmodified probe.

It is worth noting that the principle of the FSSP particle sizing is based on light scattering, and the size bin thresholds are calibrated for spherical water droplets. Scattering properties of non-spherical ice particles are quite different from that of liquid droplets. Fugal and Shaw (2009) attempted to establish ice size bin thresholds for the FSSP based on theoretical calculations of phase scattering functions for different ice particles. However, in the absence of laboratory confirmation of these results, FSSP measurements in ice clouds should be used with great caution, including those with the modified

7. Shattering by OAP-2DC, OAP-2DP, CIP and 2D-S

Figures 22 and 23 show comparisons of particle images measured in ice clouds by pairs of standard and modified OAP-2DCs and CIPs, respectively. It is evident that the probes with the standard tips in this case show a larger number of small particles not observed on probes with modified tips. Since we can conceive of no mechanism by which these modifications to the probes could have eliminated real particles, it is contended that these additional small particles must be the result of shattering.

A comparison of the total number concentrations measured by standard and modified OAP-2DCs and CIPs are shown in Figs. 24a and 24b, respectively. Concentrations measured by the probe with standard tips are in the range of 10s to 100s per liter, whereas the modified probe total concentrations are significantly lower. The difference becomes most pronounced in areas of the cloud with the largest particles (Fig. 24c, UTC 14:10-14:40).

Modified and standard probe particle size distributions are shown on Fig.25 for a ten minute period from the ice cloud shown in Fig. 25. The measurements were conducted in precipitating bullet-rosettes (Fig.22) formed high up. The size distributions, corrected for the shattering events, are also presented in Fig. 25, It appears that the effect of shattering is quite subtle above about 500 μm and increases dramatically towards smaller sizes. This shattering effect has a large impact on the small part of the size distribution, because the true concentration of small particles, for this case, is very low.

The effect of shattering can also be seen in the count distributions of interarrival times in Fig. 26. As discussed in the next section, the counts associated with the short interarrival time mode are dominated by shattering, (Field et al 2003, 2006). The ratio of the counts in the first mode to the total counts characterizes the shattering efficiency in terms of the particle counts. These ratios are included in Fig.26. The comparisons of the standard OAP-2DCs and CIPs (Fig.27a,b,c,d) indicate that the modified tips shatter significantly less. It also appears that OAP-2DP is less affected by shattering relative to other probes, likely due to the coarse pixel resolution and the configuration of the probes tips.

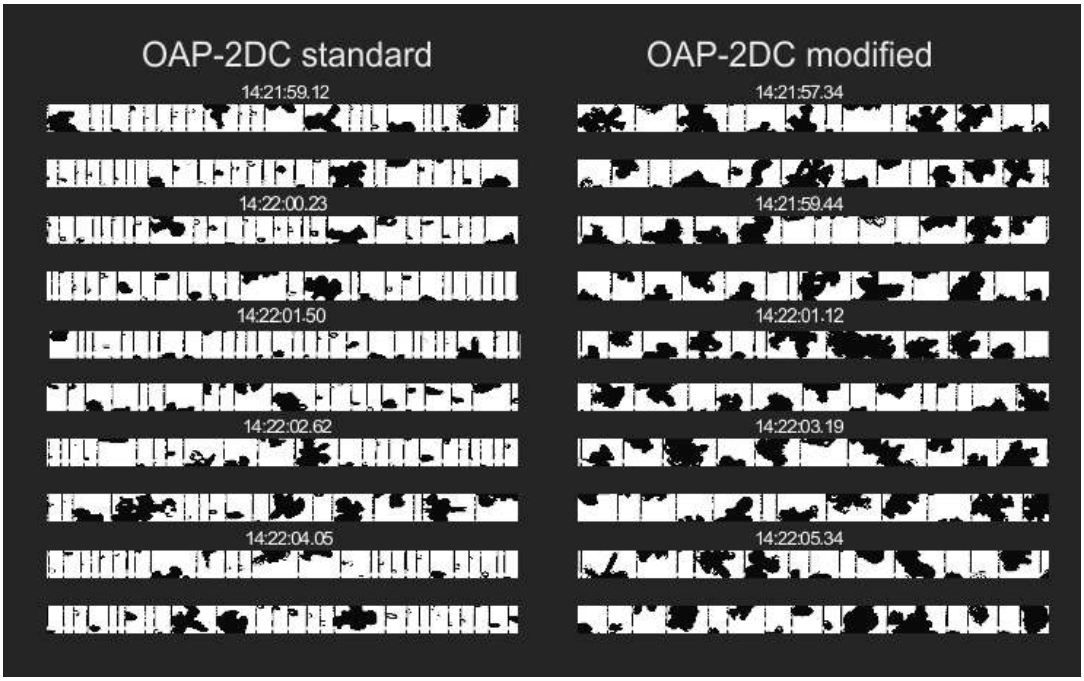

Figure 22. Comparisons of the ice particles images measured by two OAP-2DCs with the standard (left) and modified tips (right). The images on the left have many more small particles relative to those on the right. The majority of the small particles on the left result from the probe tip shattering. The pixel resolution of both OAP-2DCs is 25μm. The image sampling was conducted in frontal *Cs-Ns* cloud system in the vicinity of Ottawa, 08 April 2009, at P=690mb and T=-15C.

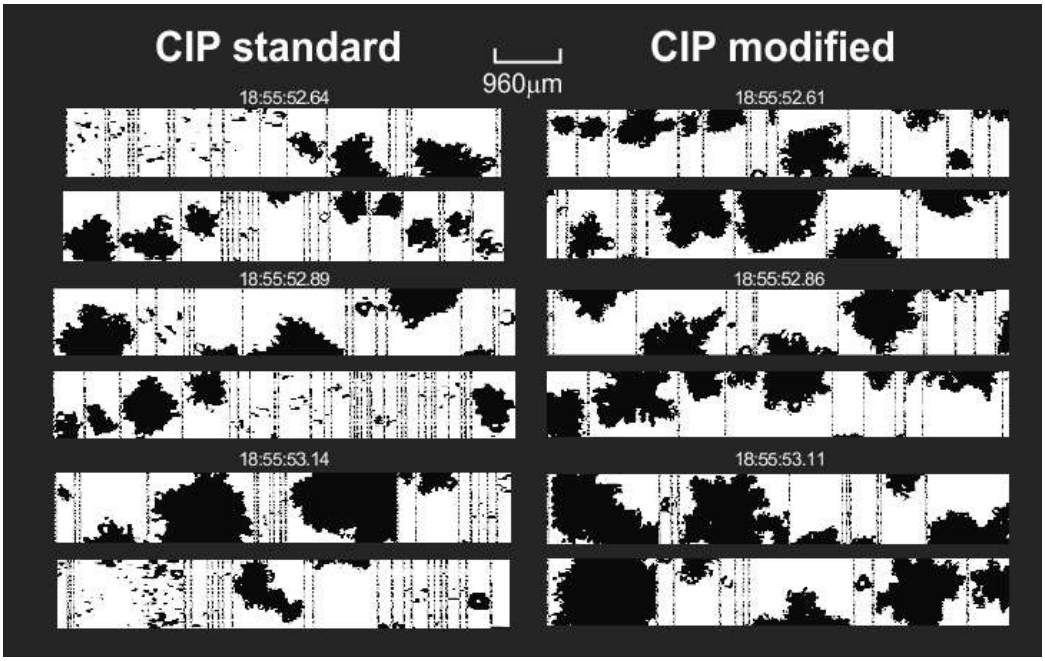

Figure 23. Comparisons of the ice particles images measured by two CIPs with the standard tips(left) and modified tips(right). The images on the left have many more small particles as compared to those on the right. The majority of the small particles on the left result from the probe tip shattering. The pixel resolution of both CIPs is 15μm. The image sampling was conducted in frontal Ns clouds in the vicinity of Ottawa, 01 April 2009, at *P*=580mb and *T*=-13C.

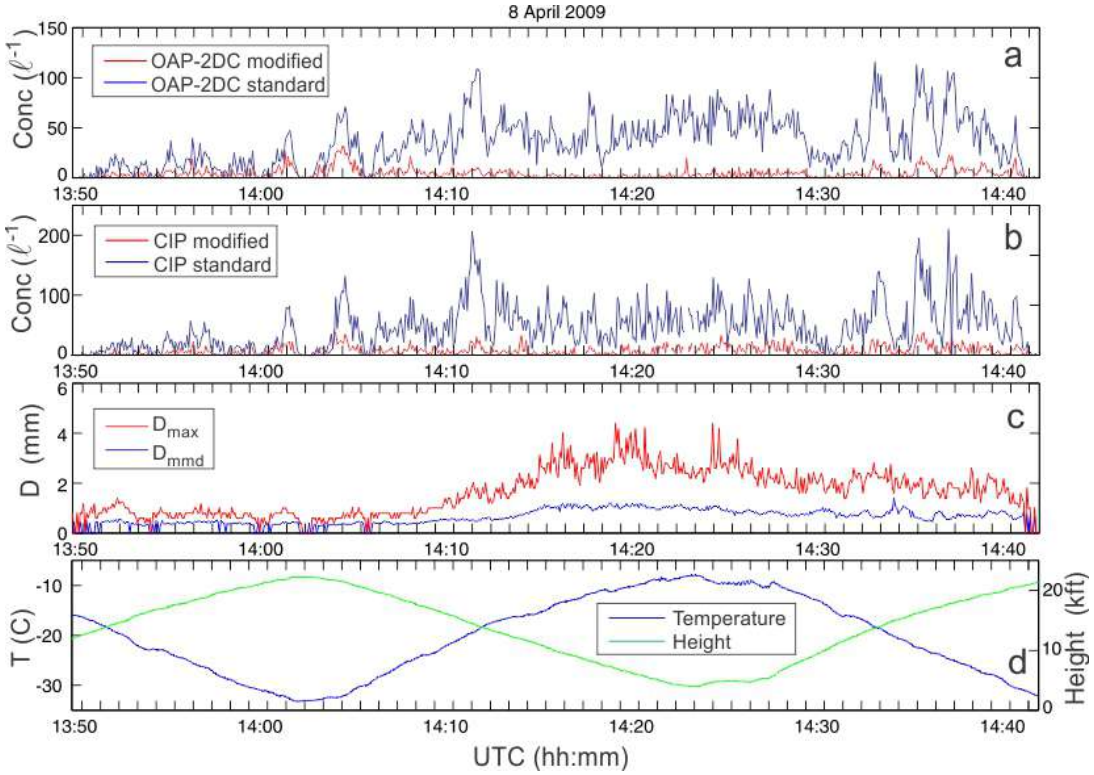

Figure 24. Time series of ice particle concentration measured in ice clouds by (a) two OAP-2DCs with the standard and modified arm tips; (b) two CIPs with the standard and modified arm tips; (c) maximum size D_{max} and median mass size D_{mmd}; (d) temperature and altitude. The measurements were conducted on 08 April 2009, north-west of Ottawa, in a glaciated frontal cirrostratus-nimbostratus cloud system.

Further analysis of a variety of cloud cases from the AIIE flights yields the important conclusion that the portion of the particle size range with diameters larger than ~300-500 μm appears insignificantly affected by shattering, whereas the smaller size range can be strongly contaminated in ice clouds (e.g. Fig. 25). Since the mass and radar reflectivity of typical size distributions measured in mid-latitude and Arctic clouds is usually associated with the larger particles, the IWC and radar reflectivity estimated from 2D particle images are significantly less affected by shattering than the number concentration in all AIIE data set.

The magnitude of the shattering effect on number concentrations for the OAP-2DC and CIP probes was found to depend on the particle size and habit. For size distributions with the maximum particle size of several millimeters the total number concentration during AIIE were greatly overestimated for the OAP-2DC. However, when maximum particle sizes were < 500μm, the difference in number concentrations is greatly reduced.

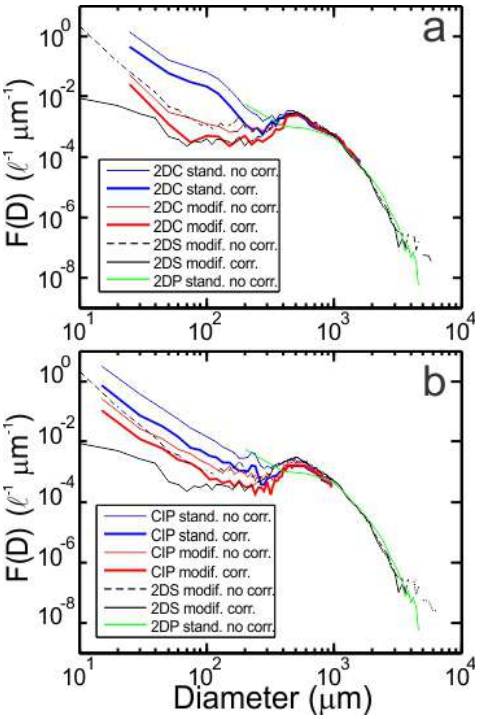

Figure 25. Comparisons of size distributions before and after inter-arrival time corrections, as measured by standard and modified OAP-2DCs (a) and CIPs (b). Size distributions measured by the modified 2D-S and standard OAP-2DP are shown on both (a) and (b). The results are for the large-particle region of Fig. 24. The size spectra were averaged over the time interval UTC 14:09:00 - 14:21:00.

Analysis of the high speed video obtained during the Cox wind tunnel experiments showed that at non-zero angle of attack ice particles may bounce from the inner surface of the modified arm tips and contaminate measurements with shattered particles (section 4.1). This is consistent with observations made during pitch up and down flight maneuvers during AIIE. Despite the fact that the modified tips can still shatter, the magnitude of the effect is still significantly smaller relative to standard tips

8. Efficiency of anti-shattering algorithms

Large data sets of OAP-2DC data collected by the community over the past thirty years have been used for parameterization of cloud microphysics for numerical weather and climate models and validation of remote sensing instruments. It has been shown here that the number concentrations of ice particles smaller than ~300-500 μm can be highly biased by small shattered fragments in clouds dominated by ice particles. This raises an important question: can the historical data be reanalyzed to filter out the data affected by shattering?

A number of different correction algorithms have been developed for identifying and filtering shattering events. Korolev and Isaac (2005) developed an algorithm based on the analysis of the image frames with fragmented particles. However, this algorithm has a limited efficiency due to low occurrence of the fragmented image frames (e.g. see Fig.27a).

One of the most effective algorithms uses the assumption that after impact a shattered particle forms a spatial cluster of closely-spaced fragments, most of which pass through a probe sample volume with inter-arrival times much shorter than natural particles (Cooper, 1977). The algorithm consists in determining the inter-arrival time between two successive particles Δt and comparing Δt with the cut off time τ. If $\Delta t < \tau$ then both particles are considered as a shattered artifact, otherwise they are accepted as intact particles. The cut off time τ is determined from the analysis of the frequency distributions of the inter-arrival times, as a time corresponding to the minimum between two distributions associated with the shattered and natural particles. If there distributions are well separated, their inter-arrival times can then be used for identification of shattering events (Cooper, 1977; Field et al. 2003, 2006; Baker et al. 2009).

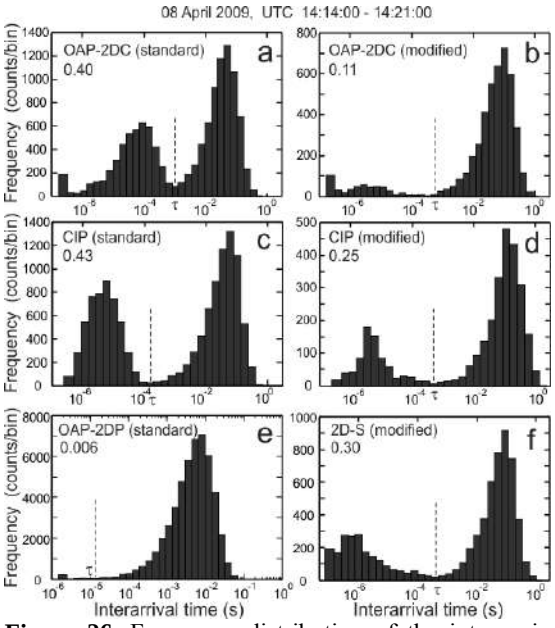

Figure 26. Frequency distribution of the inter-arrival time intervals for the standard and modified versions of OAP-2DC, OAP-2DP, CIP and 2D-S measured in the large-particle region of Fig. 24: 08 April 2009 UTC 14:14:00-14:21:00. The mode associated with the short interarrival time is assumed to result from shattered particles, whereas the natural particles are assumed to form the longer interarrival mode. The dotted lines show the cut off time (τ) used during data processing for filtering the shattered events. The numbers in the top left corners indicate the fraction of counts in the small inter-arrival mode (with $\Delta t<\tau$) to the total number of counts.

Inter-arrival time frequency distributions for the six imaging probes used in this study, measured in the large-particle region of the ice cloud of Fig. 24, are shown on Fig. 26. The distributions associated with short and long interarrival times have a small overlap area suggesting that they can be used to filter out shattered events. But how effective are these filtering algorithms? Even a small number of undetected small shatterers will contribute significantly to their concentration, due to the fact that the sample areas S of optical array probes with coherent light source is very small for small diameters ($S \propto D^2$; Korolev et al. 1998). The effectiveness of interarrival time filtering appears to vary from probe to probe, depending on the pixel resolution, response time of the electronics, shape of the tips and processing algorithm details. Filtered and unfiltered size spectra are compared in Fig. 25. At small sizes, concentrations of filtered size distributions for standard probes are still higher than those of the modified probes. This suggests that current filters for shattering for cases as in Fig.25 may be insufficient to eliminate all shattering artifacts, at least in the case of the OAP-2DC and CIP. This conclusion is supported by examining OAP-2DC and CIP

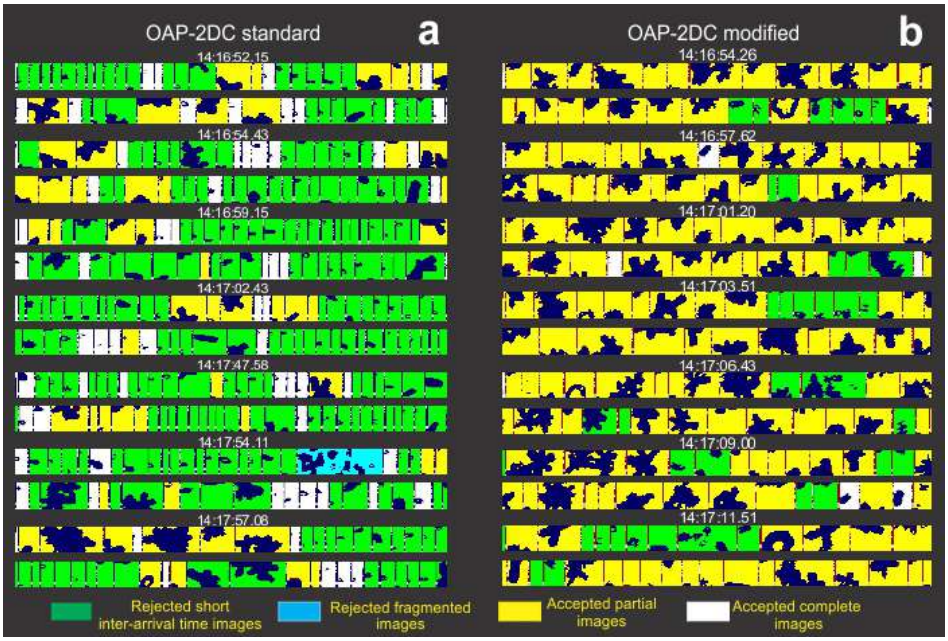

Figure 27. Example of the results of the image rejection/acceptance processing for the OAP-2DC with standard (a) and modified tips (b). Particles rejected due to interarrival time are highlighted in green; rejected multi-fragment images in blue; accepted partial images in yellow; accepted complete images in white. Most particles are rejected due to short interarrival time. However, some small images (presumably resulted from shattering) were accepted. At the same time many images which appear as intact were rejected due to interarrival time. This OAP-2DC image-set was sampled in the same cloud shown in Fig.24.

imagery, where artifacts can be observed to have characteristic elongated and out-of-focus images. In Fig.27, interarrival-time rejected and accepted images are color-coded for comparison. Although the algorithm rejects a large fraction of these artifact images, a significant fraction evades rejection. At the same time many images which appear as intact were rejected due to interarrival time (Fig.27a).

The explanation of the misidentification of the shattered and intact particles is related to the basic assumptions underlying the interarrival algorithm, which do not always hold up during measurements. The interarrival time algorithm is based on the following assumptions: (a) the shattered particles always pass through the sample volume in a form of spatially close clusters with $\Delta t < \tau$; (b) the number of particles in the shattered cluster is no less than 2; (c) the intact particles are spatially well separated from the shattered particles and they are not mixed up with each other (Fig.28a). In reality, the flow of shattered and intact ice particles through the sample volume frequently disobeys the above conditions, resulting in the failure of the inter-arrival algorithm. Thus, in many cases only one particle out of the ensemble of the shattered fragments is registered by the probe, while other group-fragments pass outside the sample volume (assumption b). Such particles are indistinguishable from the intact particles since $\Delta t > \tau$. It may also happen that the shattered and intact particles become mixed up in the view field of the probe and therefore they are identified as shattered since $\Delta t < \tau$ (assumption c). Examples of such cases can be found among the color-coded accepted and rejected images on Fig.27a. Figure 28a shows a conceptual diagram of the idealized conditions for the interarrival algorithm, and Fig.28b shows the situation which most likely occurs in real particle sampling.

Another problem of the inter-arrival algorithm is related to whether all shattered particles that pass through the sample volume, are registered by the probe. The shattered particles, whose sizes are below the sensitivity threshold of the probe, will not be detected. It may happen that only one particle of the shattered cluster is detected, whereas the rest particles are simply too small to be too small to be detected by the probe. The particles may also not be detected by the probe because of the low response time of the electronics. This will result in the violation of condition (b) and failure of the inter-arrival algorithm. This situation is most likely relevant to the OAP-2DP with a 200μm pixel resolution. As seen from Fig.25, most of the shattered particles are smaller than 200-300μm in size. Since the shattered particles have a higher probability to intersect the sample volume near the probe arms, they will appear out-of-focus and will not be detected by the 2DP electronics. On the contrary, the 2D-S has the highest pixel resolution (10μm) and the fastest response time, and therefore, it has a higher probability of identifying clusters of the shattered particles and filtering them out. This is consistent with the comparisons of the size distribution in Fig.25, showing that the modified and filtered 2D-S measurements provide the lowest concentrations at small sizes while agreeing well with other probes at larger sizes, suggesting that it has the best overall performance for eliminating shatterers. Lawson (2011) draws the same conclusion, although based on a single case comparison of the modified and standard 2D-S he concludes that for 2D-S, the inter-arrival time algorithm appears to be more effective than the modified tips.

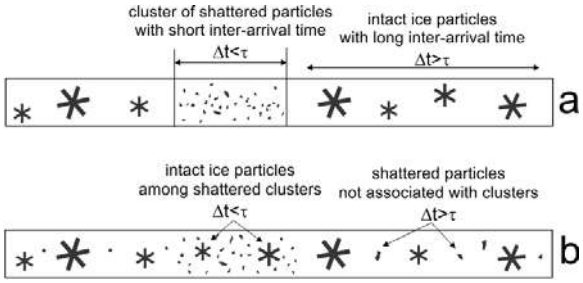

Figure 28. (a) An idealistic conceptual diagram of spatial separation of shattered and intact particles viewed by imaging probes. The inter-arrival time algorithm is based on this concept. (b) A more realistic concept of particle measurements, showing that shattered particles may appear as a single particle because they are not associated with other clustered fragments around it ($\Delta t > \tau$), and that intact particles may be mixed up within one cluster ($\Delta t < \tau$).

In summary, for the OAP-2DC and CIP probes, it is unlikely that the number concentration of particles less than 500μm can be fully corrected using interarrival time algorithms in cases strongly contaminated by shattering (e.g. Fig.25). At the moment, the 2D-S probe appears to provide the best results. Due to the higher resolution and faster response time of the 2D-S, datasets collected with its

standard tips are not as affected by shattering as the OAP-2DC and CIP data. All optical array probes still produce some concentrations at the smallest sizes which at the present time cannot be definitively stated to be real. Further probe enhancements and algorithm developments may prove to be productive. For standard versions of FSSP, with no interarrival time measurement capabilities, there are no known algorithms capable of recovering data contaminated by shattering.

A significant limitation for the antishattering algorithms has to do with cases with high concentrations of particles when the inter-arrival time of intact particles becomes comparable with the cut off time i.e. $\Delta t \sim \tau$. In this case, the distribution of long and short inter-arrival times are overlaid (Fig.29) and the separation of shattered and intact particles based on the comparisons of Δt and τ is hindered or impossible. Such cases are typical for clouds with naturally high concentrations of ice or for mixed phase clouds. Situations with minor overlaps of inter-arrival time distributions were discussed in Field et al. (2006).

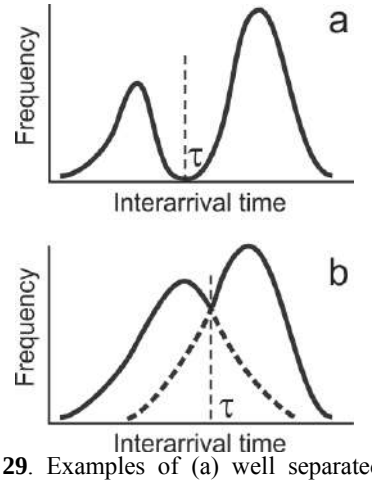

Figure 29. Examples of (a) well separated inter-arrival time frequency distribution, when the interarrival time algorithm is applicable, and (b) significantly overlapped inter-arrival time distributions. In the latter case, the inter-arrival time algorithm may result in large errors.

9. Concluding comments

The results of this study demonstrated that contamination of particle size distribution caused by shattering of ice particles on probe tips and inlets is a significant problem for airborne microphysical characterization of ice clouds. Further analysis of a variety of cloud cases from the AIIE flights yields the important conclusions:

(1) shattering can be significantly mitigated by using modified tips;
(2) flying modified and standard probes in pairs enables quantification of shattering effect on the measurements;
(3) the portion of the particle size range with diameters larger than ~500 μm is much less affected by shattering, whereas the smaller size range can be strongly contaminated in ice clouds;
(4) existing shattering algorithms are unable to filter out all shattering events from the measurements of OAP-2DC and CIP and in many cases they result in disregarding intact ice particles.

It is demonstrated that by modifying the probe tips and inlets, and by filtering in processing algorithms, the effects of shattering can be greatly reduced. Both methods are complimentary and should be used together for mitigation of shattering. For future flight campaigns, it is recommended that research groups adopt modified probe tips and apply algorithms to reduce the effect of shattering.

Numerical simulation of bouncing, analysis of high speed videos from the wind tunnel tests and the in-situ measurements collected during the AIIE project suggest that shattering, in a complex way, depends on air density, airspeed, angle of attack, shape and temperature of the tips, ice particle size and habit, and particle orientation at the moment of impact. Taking of all these effects into account in numerical models of shattering is a challenging problem. It is hindered by the lack of information about the rebound coefficient of ice, number and size of shattered fragments, angle of bouncing of shattered fragment and other factors.

Distributions of ice particles measured with the modified probes and corrected with existing algorithms can still be dominated by small ice particles. At the moment it cannot be determined whether this is real or a result of shattering and/or other factors. Other instrument problems and limitations (e.g. depth-of-field definition problems, out-of-focus images, image digitization, etc.) contribute additional uncertainty in the accuracy of small ice particle measurements. In order to address this important problem in cloud microphysics more efforts should be invested in eliminating shattering artifacts, and in improvement of small ice particle measurements in general.

Large sets of OAP-2DC data collected by the community over the past thirty years have been

used for parameterization of cloud microphysics for numerical weather and climate models and validation of remote sensing instruments. Much of these data are likely to have been contaminated by shattering artifacts and should be re-examined. This raises an important question: can the historical data be reanalyzed to filter out the shattering effect? To address this issue, the cloud physics community should undertake efforts to determine the limiting factors in using the historical data and identify possible ways of its retrieval. In this regard, a series of dedicated flight campaigns to study the effect of shattering and other problems related to the accuracy of ice measurement should be considered as one of the high priority issues for the cloud physics community.

Acknowledgements

This work was funded by Environment Canada, Transport Canada, the Federal Aviation Administration and NASA. Special thanks to Sara Lance (NOAA), Jorge Delgado (NOAA) and Dave Rogers (NCAR) for loaning their cloud particle probes for the AIIE project. We express our sincere gratitude to the NRC pilots Anthony Brown, John Aitken, and Tim Leslie for their outstanding support during the flight operations. The efforts of the NRC technicians in preparing and organizing the Convair-580 flights, and of the participants from DMT Inc. for their willingness and attempts to support the AIIE project, are greatly appreciated. A special thank you to the Cox and Company personnel and, in particular, to Adam Lawrence for such a high level of cooperation and support in operating the Cox wind tunnel facility. The NASA Glenn Research Center video group Vince Reich, Chris Lynch and Quentin Schwinn did an excellent job capturing high speed videos during the Cox wind tunnel tests. Brad Baker and Paul Lawson from SPEC Inc. are greatly appreciated for the support and analysis of the 2D-S data.

References

Cober, S.G., G.A. Isaac, A.V. Korolev and J.W. Strapp, 2001: Assessing cloud-phase conditions. *J. Appl. Meteor*., **40**, 1967-1983.

Cooper, W. A., 1977: Cloud physics investigation by the University of Wyoming in HIPLEX 1977. Bureau of Reclamation Rep. AS **119**, 321 pp.

Field, P.R., R. Wood, P.R.A. Brown, P.H. Kaye, E. Hirst, R. Greenaway, J.A. Smith, 2003: Ice particle interarrival times measured with a Fast FSSP. *J. Atmos. Oceanic Technol.*, **20**, 249-261.

Field, P. R., Heymsfield, A. J., and Bansemer, A.2006: Shattering and Particle Interarrival Times Measured by Optical Array Probes in Ice Clouds. *J. Atmos. Oceanic Technol.*, 23, 1357-1370

Fugal, J.P. and R. A. Shaw, 2009: Cloud particle size distributions measured with an airborne digital in-line holographic instrument *Atmos. Meas. Tech*., **2**, 259–271

Gardiner, B.A., and J. Hallett, 1985: Degradation of in-cloud forward scattering spectrometer probe measurements in the presence of ice particles. *J. Atmos. Oceanic Technol*., **2**, 171–180.

Gayet, J.F., Febvre, G. and Larsen, H. 1996: The reliability of the PMS FSSP in the presence of small ice crystals. *J. Atmos. Oceanic Techn*., **13**, 1300-1310.

Hallett J., and S.C. Mossop, 1974: Production of secondary ice particles during the riming process. *Nature*, **249**, 26-28

Heymsfield, A J., 2007: On measurements of small ice particles in clouds, *Geoph. Res. Lett*., **34**, L23812, doi:10.1029/2007GL030951

Heymsfield, A. J., and C. M. R. Platt, 1984: A parameterization of the particle size spectrum of ice cloudsin terms of the ambient temperature and ice water content. *J. Atmos. Sci.,* **41,** 846–855

Jensen, E. J., P. Lawson, B. Baker, B. Pilson, Q. Mo, A. J. Heymsfield, A. Bansemer, T. P. Bui, M. McGill, D. Hlavka, G. Heymsfield, S. Platnick, G. T. Arnold, and S. Tanelli, 2009: On the importance of small ice crystals in tropical anvil cirrus. *Atmos. Chem. Phys.,* **9**, 5519–5537

Knollenberg, R. G. 1976: Three new instruments for cloud physics measurements: The 2D-spectrometer probe, the forward scattering spectrometer probe and the active scattering spectrometer probe. *Preprints International Conf. on Cloud Physics*, Boulder, CO, Amer. Meteor. Soc., 554-561.

Korolev, A., *Probe Tips for Airborne Instruments Used to Measure Cloud Microphysical Parameters*, United States Patent No. 7,861,584, Issued: January 4, 2011, Owner: Her Majesty the Queen in

Right of Canada, as Represented by The Minister of Environment.

Korolev, A. V., Strapp, J. W., Isaac, G. A., 1998: Evaluation of the Accuracy of PMS Optical Array Probes. *J. Atmos. Oceanic Technol.*, **15**, 708–720.

Korolev, A. V., and G. A. Isaac, 2005: Shattering during sampling by OAPs and HVPS. Part 1: Snow particles. *J. Atmos. Oceanic Technol.,* **22,** 528–542.

Korolev AV, Emery EF, Strapp JW, Cober SG, Isaac GA, Wasey M, Marcotte D 2011. Small Ice Particles in Tropospheric Clouds: Fact or Artifact? Airborne Icing Instrumentation Evaluation Experiment. *Bull. Amer. Meteor. Soc.*, **92**: 967–973.

Lawson RP 2011. Effects of ice particle shattering on the 2D-S probe. *Atmos. Meas. Tech.*, **4**: 1361–1381.

Mazin, I.P., A. V. Korolev, A. Heymsfield, G. A. Isaac, and S. G. Cober, 2001: Thermodynamics of Icing Cylinder for Measurements of Liquid Water Content in Supercooled Clouds, *J. Atmos. Oceanic Technol.*, **18**, 543–558

McFarquhar, G. M., Um, J., Freer, M., Baumgardner, D., Kok, G. L., and Mace, G.: The importance of small ice crystals to cirrus properties: Observations from the Tropical Warm Pool International cloud Experiment (TWP-ICE), Geophys. Res. Lett., 57, L13803, doi:10.1029/2007GL029865, 2007.

Vidaurre and Hallett, 2009: Particle Impact and Breakup in Aircraft Measurement. *J. Atmos. Oceanic Technol.*, 26, 972–983

Table 1. List of instruments installed on the NRC Convair-580 during the AIIE project

Instrument	type	Measured parameter	owner
FSSP (PMS)	standard	droplet size distribution; 2-47μm; 15 size bins	EC
FSSP (PMS)	modified	droplet size distribution; 2-47μm; 15 size bins	NASA
OAP-2DC (PMS)	standard	25-800 μm; particle shadow- images at 25μm pixel resolution	EC
OAP-2DC (PMS)	modified	25-800 μm; particle shadow- images at 25μm pixel resolution	NCAR/EC
CIP (DMT)	standard	15-960 μm; particle shadow -images at 15μm pixel resolution	EC
CIP (DMT)	modified	15-960 μm; particle shadow- images at 15μm pixel resolution	NOAA
OAP-2DP (PMS)	standard	200-6400 μm; particle shadow- images at 200μm pixel resolution	EC
2D-S (SPEC)	standard or modified	10-1250 μm; particle shadow- images at 10μm pixel resolution	EC
Nevzorov (SkyTech)	standard	liquid and total water content; 0.005-2g/m^3	EC
Nevzorov (SkyTech)	modified	liquid and total water content; 0.005-2g/m^3	SkyTech
King probe (CSIRO)	standard	liquid water content; 0.01-3g/m^3	EC
CSI (DMT)	standard	total water content; 0.01-2.5g/m^3	EC
Extinction probe (EC)	standard	extinction coefficient 0.1-200km^{-1}	EC
Rosemount Icing Detector (Goodrich)	standard	rate of icing in supercooled liquid clouds	EC
LI-6262 (LI-COR)	standard	absolute humidity	EC
State parameters	-	P, T, TAS, longitude, latitude	NRC
Ka-band radar (SEA)	-	Radar reflectivity	EC
DAS M200 (SEA)	-	Data acquisition system	EC
DAS M300 (SEA)	-	Data acquisition system	EC

Calibrations and performance of the Cloud Extinction Probe

Alexei Korolev , Alex Shashkov , Howard Barker

Environment Canada, Cloud Physics and Severe Weather Research Section, 4905 Dufferin St., Toronto Ontario M3H 5T4, Canada

1. Introduction

Extinction coefficient is one of the fundamental microphysical parameters characterizing bulk properties of clouds. Knowledge of extinction coefficient is of crucial importance for radiative transfer calculations in weather prediction and climate models given that Earth's radiation budget (ERB) is modulated much by clouds. In order for a large-scale model to properly account for ERB, and perturbations to it, it must ultimately be able to simulate cloud extinction coefficient well. In turn this requires adequate and simultaneous simulation of profiles of cloud water content and particle habit and size. Similarly, remote inference of cloud properties requires assumptions to be made about cloud phase and associated single-scattering properties; of which extinction coefficient is crucial. Hence, extinction coefficient plays an important role in both application and validation of methods for remote inference of cloud properties from data obtained from both satellite and surface sensors (e.g. Barker et al. 2008).

While estimation of extinction coefficient within large-scale models is relatively straightforward for pure water droplets, thanks to Mie theory, mixed-phase and ice clouds still present problems. This is because of the myriad forms and sizes that crystals can achieve each having their own unique extinction properties. For the foreseeable future large-scale models will have to be content with diagnostic parametrization of crystal size and type. Before being able to provide satisfactory values needed for calculation of radiative transfer, however, they require the intermediate step of assigning single-scattering properties to particles. The most basic of these is extinction coefficient, yet it is rarely solution is to be able to measure measured directly and so verification of parametrizations is difficult. The obvious microphysical properties and extinction at the same time and for the same volume. This is best done by in situ sampling by instruments mounted on either balloon or aircraft. The latter is the usual route and the one employed here. Yet still, the problem of actually measuring extinction coefficient directly for arbitrarily complicated particles remains unsolved.

The following subsections document the history of attempts to directly measure cloud extinction, the current measurement device known as the Cloud Extinction Probe (CEP), specific problems with direct measurement of extinction coefficient, and the attempts made here to address these problems.

Corresponding Author: Alexei Korolev, Environment Canada, 4905 Dufferin Street, Toronto, Ontario, M3H5T4 Canada, e-mail: alexei.korolev@ec.gc.ca,

2. Background

The extinction process of a dispersed medium consisting of cloud particles suspended at random in the air can be described by the Beer-Bouguer law as

$$I = I_0 e^{-\beta(\lambda)L} \qquad (1)$$

where I_0 is incident light intensity, I is light intensity transmitted through the medium in the forward direction (i.e. parallel to the incident light), $\beta(\lambda)$ is volumetric extinction coefficient; and L is geometric distance between emitter and receiver.

Early attempts to use airborne extinctiometers for measurements of visibility in clouds go back to work by Kampe (1950) and Weickmann and Kampe (1953). The first airborne extinctiometer utilized the transmissiometric method. It consisted of incandescent lamp, collimator and a photocell for measuring light intensity. The source of light and the photocell were mounted on the wing and separated by a few metres. Zabrodsky (1957) built an airborne double

pass transmissiometer where light travelled to a retroreflector and back where it was then measured by a photodetector. Nevzorov and Shugaev (1972, 1974) built an advanced version of the double pass transmissiometer with improved stability and higher sensitivity. This was a successful design which allowed for the collection of a large data set of extinction coefficient for different types of clouds (Kosarev et al, 1976; Korolev et al. 2001). King and Handsworth (1979) built a single pass transmissiometer with an ultraviolet source of light generated by a germicidal lamp. Zmarzly and Lawson (2000) designed a multi-pass and multi-wavelength Cloud Extinctiometer. Gerber et al (2000) constructed a Cloud Integrated Nephelometer where the extinction coefficient was calculated from an arrangement of four Lambertian sensors, two of which had cosine masks.

In many studies cloud extinction coefficient was estimated from composite size distributions measured by several cloud spectrometers. Earlier measurements (Korolev et al. 1999) showed good agreement between extinction coefficient measured by a cloud transmissiometer and that derived from the PMS FSSP droplet size spectra. However, calculation of extinction coefficient from particle size distributions in ice and mixed phase clouds is subject to potentially large errors due to uncertainties related to the size-to-area conversion technique, shattering issues, and limited accuracy in measurements of concentration and sizes of ice particles smaller than approximately 100μm.

Despite the great influence of extinction coefficient on our ability to simulate radiation transfer for cloudy atmospheres and Earth's climate in general, probes that are capable of direct measurement of extinction coefficient have not become a part of conventional airborne microphysical instrumentation. The effort to fill this gap has been undertaken by Cloud Physics Research and the Severe Weather Section of Environment Canada (EC). The Cloud Extinction Probe (CEP) was designed and built in 2006 by EC for airborne measurement of cloud extinction coefficient (Korolev 2008) and has since operated successfully during several flight campaigns.

3. Principles of operations and description of CEP

The CEP utilizes the transmissiometric method. The principle of operation is based on having emission of visible light of known strength followed by its measurement after having traversed, and been attenuated by, a known volume. This method enables calculation of extinction coefficient from first principles based on the Eq.1. The CEP consists of an optical unit that combines a transmitter and receiver as well as a retroreflector. Figure 1 shows a general schematic of the optical unit. A collimated light beam is generated by an optical system consisting of a super-bright LED at wavelength λ=0.635μm (1), diffuser (2), condenser (3), pinhole (4), and objective (5). The beam travels from the optical unit to the retroreflector (6), and then returns the same distance back to the optical unit. Then, after passing though the objective and beam-splitter (7) its intensity is measured by a photodetector (8). The optical chopper (9) modulates the light beam and controls turning on and off the LED with the help of the optocouple (10). The optical chopper consists of a sequence of holes, dark areas and mirrors glued on its surface. During the first half of the period when the hole is opened, the LED is on, and the photodetector measures the intensity of transmitted light plus the background intensity (I_{tot}). During the second half of the period, when the hole is opened, the LED is off, and the photodetector measures the intensity of the

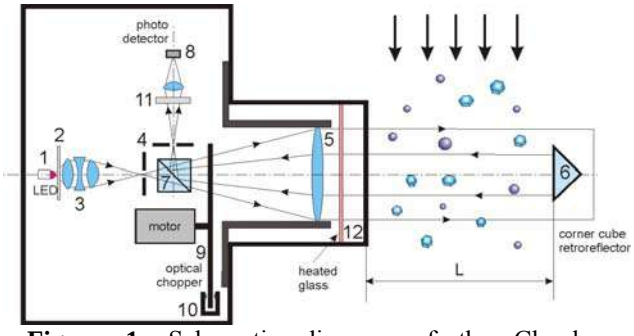

Figure 1. Schematic diagram of the Cloud Extinction Probe: (1) LED 0,635μm; (2) diffuser; (3) condenser; (4) pinhole; (5) objective; (6) cone cube retroreflector; (7) beamsplitter; (8) photodetector; (9) optical chopper; (10) optocouple; (11) bandpass filter; (12) front heated glass.

background light (I_{bkg}). During the first half of the period, when the hole is closed and the LED on, light is reflected from the mirrored surface. After passing though a beam-splitter the reflected light is measured by the photodetector (I_{norm}). This signal characterizes the intensity of the LED, and is used to normalize all other measured signals. During the second half of the period, when the chopper hole is closed, the LED is on and the beam hits the blackened surface of the chopper. In this case, the photodetector measures the signal (I_{int}) related to the light scattered inside the optical unit due to reflection from the optical surfaces and the different parts inside the probe's housing. The advantage of such a scheme is that it allows measurements of the intensities of the LED, background and attenuated light with the same photodetector. Utilizing of the above scheme minimizes the effect of changes of the photodetector sensitivity during flight (e.g. caused by temperature drift) on the measurements of the extinction coefficient.

The optical scheme was designed to produce a highly uniform collimated beam. The inhomogeneity of the light intensity across the beam does not exceed 2%. This minimizes the effect of vibration and mutual motion the optical unit and retroreflector with respect to each other during the flight operation. A similar approach has been used by Nevzorov and Shugaev (1974). The size of the retroreflector was chosen so that its displacement from the center of the beam in each direction at the distance of approximately 1cm does not affect the output signal.

Figure 2. Cloud Extinction Probe: optical unit (top); control box (bottom); retroreflector (right).

always stays inside the beam within the area of homogeneous light intensity, whereas the reflected beam always stays within the front lens area. This provides a stable output signal with a reduced sensitivity to aircraft vibration.

The CEP was designed to operate in all weather conditions. The optics of the probe are well heated to prevent fogging during rapid aircraft descent at vertical speed greater than 5m/s. The environment inside the optical unit is temperature controlled so that the instrument can operate at air temperatures as low as -60°C. Based on the flight tests the threshold sensitivity of the probe was found to be approximately 0.2 km^{-1}. The upper limit of the measured extinction coefficient is estimated to be no less than 200 km^{-1}.

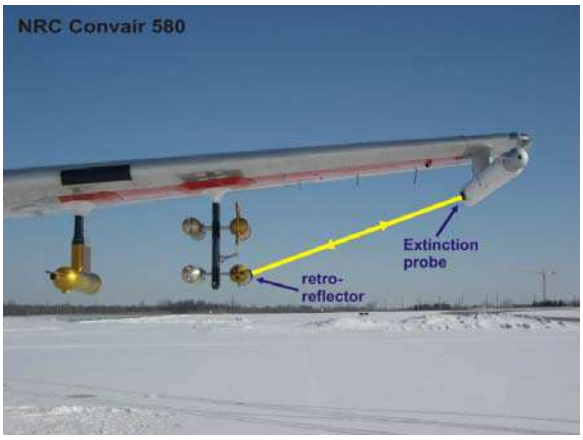

Figure 3. Installation of the Cloud Extinction Probe on the NRC Convair 580. The yellow line indicates the position of the beam under the wing.

The CEP was installed on the National Research Council (NRC) Convair 580. The optical unit was mounted inside the wing tip canister and the retroreflector inside a hemispherical cap at the rear side of a PMS probe canister (Fig.3). Distance between the optical unit and retroreflector was L=2.35m.

The sample area of the probe is defined by the length of the beam (L) and the diameter of the reflector (d=25mm) and is calculated as $S=Ld$. For the Convair-580 installation $S\approx0.06m^2$. At a typical airspeed of 100m/s, the corresponding cloud volume sampling rate is approximately $6m^3/s$. Assuming a decent sensitivity, the above sampling rate allows measurements of a statistically significant

extinction coefficient of ice particles with concentration of a few per cubic meter.

4. Objectives

Since the early 1950s it was recognized that the transmissiometric method is prone to contamination by photons passing through the receiving aperture that had been scattered into the near-forward direction. Hence, as long as one interprets the measured intensity of light as though it were unattenuated, extinction coefficient will be underestimated systematically through inversion of Eq. 1. Theoretical considerations (Gumprecht and Sliepevich 1953; Deepak and Box 1978) showed that the effect of forward scattering on the measured extinction coefficient depends on the angle of the receiving aperture (φ) and the scattering phase function of particles. Mie scattering calculations show that forward scattering is relatively weak for small particles and so in the case of small droplets underestimation of extinction coefficient will be small. Large particles, however, have strong forward scattering lobes that may result in significant underestimation of measured extinction coefficient. Theoretical calculations show that for large particles the relative error in extinction coefficient measurements approaches a factor of two.

Until now, due to the absence of calibrating standards, there have been no experimental techniques capable of estimating the errors in extinction coefficient measurements versus particle sizes. Gumprecht and Sliepevich (1953) attempted to utilize a set of monodisperse glass beads suspended in water to measure forward scattering. However, the accuracy of maintaining the constant bulk number concentration in the test cell was low. The number concentration is also affected by the rate of sedimentation for large glass beads. Environment Canada developed a technique and designed a laboratory installation for the CEP calibration. The main objective of this calibration is to obtain a calibration curve of the extinction efficiency Q versus particle size D, i.e. $Q(D)$. Due to the theoretical analysis (Deepak and Box 1978) the value of $Q(D)$ is supposed to vary between 2 for small particles and 1 for large particles. Knowledge of the function $Q(D)$ would allow one to make corrections to measured extinction coefficient when a particle size distribution is measured simultaneously with the CEP extinction coefficient.

Below is a description of the work to be performed within the frame of this project:

1. Design and fabricate a laboratory installation for the calibration of the CEP.
2. Perform laboratory calibrations of the CEP with the help of constant frequency dot arrays and glass beads. Based on the results of the calibrations determine corrections to measured extinction coefficient versus particle size.
3. Perform a theoretical analysis of the corrections to extinction coefficient.
5. Apply corrections deduced from laboratory calibrations to the CEP data set collected during the ISDAC flight campaign. Develop parameterization of extinction coefficient measured in ice clouds versus temperature.

6. Theoretical calculations of the effect of forward scatterints

In an attempt to better comprehend the nature of the observations, we constructed a numerical model of the extinctiometer. Rather than attempt to build an analytic approximation, it was decided that a Monte Carlo photon transfer-based solution would better serve our purposes in light of the complicated character of ice scattering phase functions. This subsection describes briefly the Monte Carlo technique.

To begin, 0.635 μm wavelength photon packets are emitted uniformly from the source lens travelling perpendicular to the lens toward the retroreflector. Distance to the first scattering event is computed as

$$d_s = -\frac{\ln R}{\beta} \qquad (2)$$

where R is a uniform random number between 0 and 1, and β is extinction coefficient (km^{-1}). Scattering angle is determined by first solving for θ_s as

$$R = \frac{1}{2}\int_0^{\theta_s} p'(\theta)\sin\theta\, d\theta, \qquad (3)$$

where $p'(\theta)$ is the azimuthally-averaged scattering phase function in which

$$\frac{1}{2}\int_0^{\pi} p'(\theta)\sin\theta\, d\theta = 1. \qquad (4)$$

This gives the deflection angle θ_s away from the incident ray. Then one solves for the azimuthal angle φ_s as

$$R = \frac{\int_0^{\varphi_s} p(\theta_s,\varphi)\, d\varphi}{\int_0^{2\pi} p(\theta_s,\varphi)\, d\varphi}, \qquad (5)$$

where $p(\theta_s,\varphi)$ is the full phase function given θ_s. If phase functions are azimuthally symmetric, as they are for spherical water droplets, (5) simplifies to

$$R = 2\pi\varphi, \qquad (6)$$

For this version of the model, aerosols and Rayleigh scatter are neglected. Moreover, it is assumed that particles can be represented as point scatterers and that $p(\theta,\varphi)$ and $p'(\theta)$ can be represented by far-field solutions (e.g., Mie theory for homogeneous spherical particles). This is a valid assumption given that cloud particles are generally expected to be small compared to most distances between scattering events and receiver (Mishchenko et al. 2006).

The possible fates of a photon are shown in Fig. 4. If a scattered photon strays outside the emitted column of light by more than 5 times the radius of the lens d it is considered to have exited the experiment. Note that detectable photons are not limited simply to those that get transmitted directly or undergo just a single forward scattering event (e.g., Deepak and Box 1978). Photons that undergo multiple scattering events, including backscatter, are detected too. These are, however, generally very minor contributions for values of β within the extinctiometer's reliable operating range. Hence, to a very good approximation the extinctiometer is effectively a single-pass device with separate source and receiver. Nevertheless, this Monte Carlo routine is fast, provides useful benchmarks, and, importantly, like most Monte Carlo treatments, can accommodate arbitrarily complicated, non-analytic scattering phase functions.

Let N_T and $N_R(\theta^*)$ be the numbers of photons emitted out and received at the lens of diameter d, respectively. In order for a photon to be received (i.e., detected) its angle of incidence relative to normal to the receiver's aperture has to be less than θ^*. For the experiments performed here, transmittance along the path from the source to the retroreflector, whose radius is r, and back is defined as

$$T'(\theta^*) = \frac{N_R}{N_T\left(\frac{r}{d}\right)^2}, \qquad (7)$$

Assuming Beer's Law for a collimated beam of light, and particles distributed entirely at random, the transmitted fraction of unattenuated photons is given by

$$T = \exp(-2L\beta), \qquad (8)$$

where L is distance (km) from source to retroreflector. However, because the receiver cannot discriminate scattered from completely unattenuated photons, if one tries to force Beer's Law onto (7), the implication is that

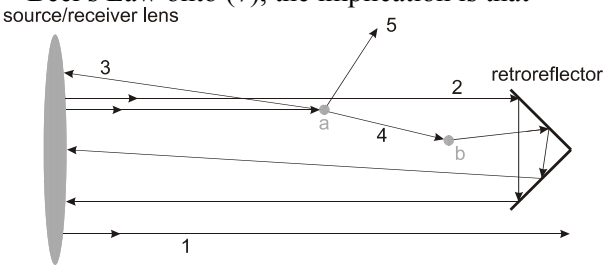

Figure 4 A collimated stream of photon packets gets emitted from the source/reciever lens toward the retroreflector. The fate of a packet can be: 1) emitted directly, or scattered, past the retroreflector and out of the experiment (all photons scattered behind the retroreflector are considered to be out of the experiment); 2) transmitted unattenuated to the retroreflector and back unattenuated to the receiver (true direct-beam transmittance); 3) scattered one or more times by particles into the receiver without interacting with the retroreflector; 4) scattered one or more times by particles into the retroreflector and back into the receiver (including scattering after encountering the retroreflector); 5) scattered by a particle, or the retroreflector, out of the experiment.

$$\beta(\theta^*) = -\frac{1}{2L}\ln\left(\frac{N_R}{N_T\left(\frac{r}{d}\right)^2}\right), \qquad (9)$$

which underestimates true extinction β; primarily because of single forward scattering events. Hence, by defining

$$T'(\theta^*) = \exp\{-2L\beta[1 - f(\theta^*)]\}, \qquad (10)$$

where $f(\theta^*)$ represents all contributions other than unattenuated direct-beam, the problem comes down to finding

$$f(\theta^*) = \frac{\beta(\theta^*)}{\beta}, \qquad (11)$$

In general, $f(\theta^*)$ will also depend on particle size D and type. If one assumes that single-scattering prevails and that the portion of the phase function that leads to scattered photons being detected does not depend on the location of the scattering event (i.e., small θ^*), and that backscattered photons are of no consequence, a very good approximation is obtained by

$$f(\theta^*) = \frac{1}{2}\int_0^{\theta^*} p'(\theta; r)\sin\theta\, d\theta, \qquad (12)$$

If these conditions are violated, or if scattering properties depend much on particle orientation, (12) could lead to untenable errors. Figure 5 shows, however, that for water spheres at small θ^* (i.e., small pin-hole apertures) and D less than about 500 μm (12) is extremely accurate.

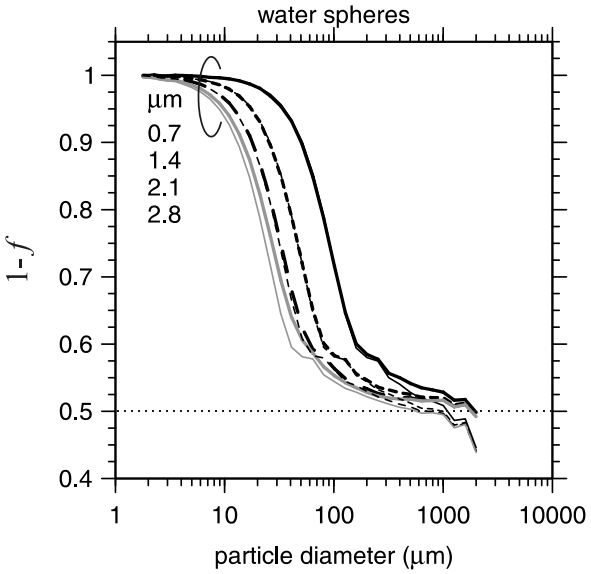

Figure 5 Extinction correction values 1-f, see (10), as determined by Monte Carlo simulation (heavy lines) and (12) (light lines) for water spheres and various pin-hole aperture sizes (as listed on the plot) as functions of particle diameter D.

7. Laboratory calibrations

6.1 Principle of transmissiometers calibrations

The essence of calibration of transmissiometers consists in transmitting the probes' beam through a media with a known particle dispersion and extinction coefficient, and then performing subsequent comparisons between the measured and known extinction coefficients. Such calibrations are hindered by the absence of calibrating standards. The main challenge in the calibrations is developing an environment with controlled particle size distribution and extinction coefficient. Until now there have been no known procedures for calibration of transmissiometers and for obtaining *Q(D)*.

In order to fill this gap, Environment Canada has developed a technique for the estimation of *Q(D)* from laboratory measurements. The principle of the calibration consists in passing the beam through a flat optical target with a known attenuating pattern. The extinction coefficient of the target is calculated from the attenuating pattern (e.g. Fig.9) and then compared with the measured one.

For the calibration purposes several types of targets have been used. The first types of targets consisted of a set of glass plates coated with a repeating pattern of (a) equally spaced opaque dots with known diameters *D,* and (b) six ended stars simulating stellar ice crystals. Such optical targets have predetermined area coverage (or area ratio) S/S_0, where S is total area of opaque dots covering area S_0. The intensity of the incident light I_0 and that passed through the target I are related as

$$\frac{I_0 - I}{I_0} = Q(D)\frac{S}{S_0} \qquad (13)$$

Such a technique enables estimation of Q for each individual target. Details of calculations of the function *Q(D)* are described in section 2.2.2.

The second types of optical targets were monodisperse glass beads randomly spread over the surface of a glass substrate. Calculation of the area ratio S/S_0 was deduced from the processing of microphotographs of the beads.

The third types of targets were particles with random shapes such as crystals of sugar or broken glass.

The results of the CEP calibrations by three types of targets are described in sections 2.2.4-2.2.7.

6.2 Calculation of instrumental scattering efficiency Q(D)

Consider the Beer law in the differential form for a medium consisting of monodisperse particles with the concentration n and thickness dz

$$dI = \sigma n I_0 dz \qquad (14)$$

where $dI = I_1 - I_0$ is the changes of the intensity of the light beam after passing though a medium; $\sigma = Qs$ is the scattering cross section of one particle; s is the geometric cross section of the particle; and Q is the extinction efficiency. The particle concentration n can be presented as $n = N/V = N/S_0 dz$, where N is the number of particles in the volume V; and S_0 is the cross section of the beam. Then substituting n and σ in Eq.14 yields

$$\frac{I_0 - I_1}{I_0} = Q\frac{S}{S_0} \qquad (15)$$

Here, $S = Ns$ is the total geometrical area of the particles.

For the double pass scheme (Fig.6a) light passes twice (forward and back) through the target. So, after the second pass the intensities of the incident and transmitted light are related as

$$\frac{I_1 - I}{I_1} = Q\frac{S}{S_0} \qquad (16)$$

Combining Eqs. 15 and 16 and excluding I_1 yields

$$Q = \frac{1 - \sqrt{\frac{I}{I_0}}}{\frac{S}{S_0}} \qquad (17)$$

During the calibrations two spatially separated targets (Fig.6b) were also used. For the case of two targets with the same dots, it can be shown that the intensities I/I_0 and area rations S/S_0 are related as

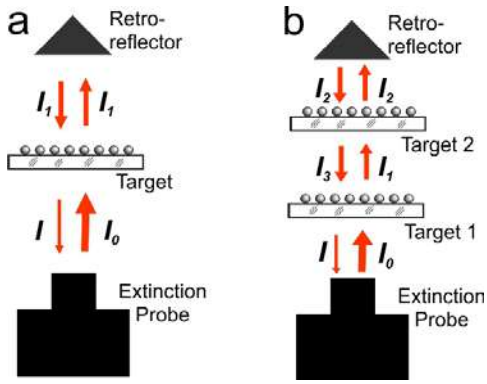

Figure 6. Scheme explaining calculation of the extinction efficiency from laboratory measurements for the cases of (a) one target and (b) two targets

$$Q = \frac{1 - \left(\frac{I}{I_0}\right)^{1/4}}{\frac{S}{S_0}} \qquad (18)$$

For the case of k targets I/I_0 and S/S_0 are related as

$$Q = \frac{1 - \left(\frac{I}{I_0}\right)^{1/2k}}{\frac{S}{S_0}} \qquad (19)$$

Eq.17 considers an ideal case assuming that the substrate is absolutely transparent and it does not attenuate light. In fact, the substrate reflects light in the backward direction and the material it is made of may absorb some fraction of light. This will result in a systematic bias in the measurements of the attenuation of the light. This effect was accounted for with the help of special transparent plates made of the same material as the target plates, but without dot arrays on its surface. In every session of measurements of the signal attenuation by the dot arrays, the beam attenuation by a blank glass plate was measured as well in order to estimate the effect of the substrate.

Figure 7 provides an explanation for the calculations of the effect of the substrate. In order to estimate the effect of the substrate, the target plate was considered as consisting of a "pure" coating and the glass substrate (Fig.7a).

The intensities of light transmitted through this system can be described by the following system of equations

$$\frac{I_0 - I_1}{I_0} = A \tag{20}$$

$$\frac{I_1 - I_2}{I_1} = Q\frac{S}{S_0} \tag{21}$$

$$\frac{I_2 - I_3}{I_2} = Q\frac{S}{S_0} \tag{22}$$

$$\frac{I_3 - I}{I_3} = A \tag{23}$$

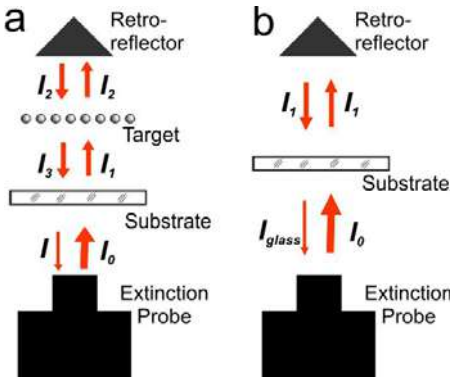

Figure 7. Scheme explaining calculation of the effect of the substrate of the attenuation of light by the target plate.

The effect of a substrate (Fig.7b) can be written as

$$\frac{I_0 - I_1}{I_0} = A \tag{24}$$

$$\frac{I_1 - I_{glass}}{I_1} = A \tag{25}$$

Solving the system Eqs. (20)-(25) yields

$$Q = \frac{1 - \sqrt{\frac{I}{I_{glass}}}}{\frac{S}{S_0}} \tag{26}$$

Eq.26 is similar to Eq.17 with only difference that I_o in Eq.17 is replaced by I_{glass} .

The values of I, I_{glass}, S/S_0 can be obtained from the measurements and thus yield estimates of Q from Eq.26. The physical meaning of Q calculated from Eq.26 should be interpreted as *"instrumental" extinction efficiency*. The instrumental extinction efficiency primarily depends on the receiving aperture of the transmissiometer. The objective of the laboratory studies described below, is to determine *Q(D)* and to estimate the feasibility of corrections depending on the type of cloud particles (ice or liquid) and their dispersion.

6.3 Laboratory installation

To achieve the calibration goals the following installation was designed and built in the laboratory facility of the Cloud Physics and Severe Weather Research Section. The picture of the laboratory installation is shown in Fig.8. The laboratory installation consisted of a vertically oriented frame with the CEP optical unit mounted on one end and a retroreflector on the other. The distance between the CEP and the retroreflector was the same as that on the NRC Convair 580 (2.30m). The optical targets were installed on a horizontal platform. The platform with the target was mounted on a set of rails, which enabled positioning of the targets in a vertical direction between the CEP and the retroreflector. The microphotography of the optical targets (e.g. glass beads) was conducted with the help of a high resolution CCD camera (Lumenera X32) attached to a microscope. The CCD matrix of the camera has 1216 x 1616 elements. However, micro-shifting technology utilized in this camera allowed images with a linear resolution four times higher resulting in images with 4864 x 6464 pixels. The microscope used in these calibrations has a long working distance

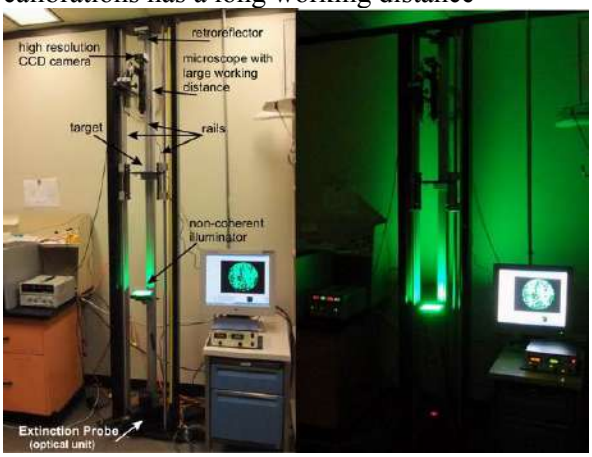

Figure 8. Laboratory installation used for the calibrations of the Cloud Extinction Probe

varying from 13mm to 89mm depending on the optical magnification. A set of high quality changeable Mitutoyo optics and zoom options provided high resolution imagery of micro-objects ranging in size from a few microns to a few millimetres. The microscope was mounted on a thee-positioning stage, which allowed it to be moved in and out of the CEP beam. As a result, it was possible to take microphotographs of the target and to measure light attenuation by the CEP without touching the optical target. This is important when working with glass beads, which can easily start moving over the substrate surface in case of minor vibrations.

Proper illumination is one of the critical components for obtaining high quality microscope imagery. A rectangular 10 x 10cm green LED array backlight (CCS Inc, Kyoto, Japan) provided a uniform diffuse illumination of the targets, without leaving hot spots. The backlight illuminator was mounted on a rail with a slider-lock, which could be positioned vertically in order to achieve the best quality of particle imagery depending on the microscope optics and magnification. The backlight illuminator holder design created the possibility of moving the illuminator in and out the CEP beam, in order to take microphotographs of the optical targets and measurements of the light intensity without any significant rearrangement of the installation.

6.4 Calibrations by constant frequency dots arrays

A set of custom made constant frequency dot arrays were manufactured (Applied Optics Inc.) for the calibrations of the CEP. The constant frequency arrays consist of 1mm thick glass plates coated with equally spaced blue chrome opaque dots with diameter *D* (Fig.9). The glass plates had an antiglare coating to mitigate reflection and increase transmittance. The distance between the centers of the dots in X- and Y-directions was the same and equal to 2*D*. As seen in Fig.9, the area coverage of the dot arrays is $S/S_0=\pi/16\approx0.196$. The calibrating set of dot arrays consisted of eight plates with dot diameters: 15μm, 31μm, 62μm, 125μm, 250μm, 500μm, 1000μm, 2000μm. The visual appearance of the plates is shown on Fig.10. The pictures if the glass plates with got array and the microphotographs of the dot arrays are shown in Figs.10 and 11, respectively.

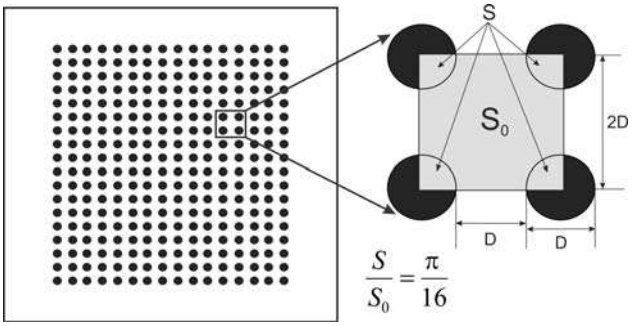

Figure 9. Dot arrays used for calibration of the Cloud Extinction Probe.

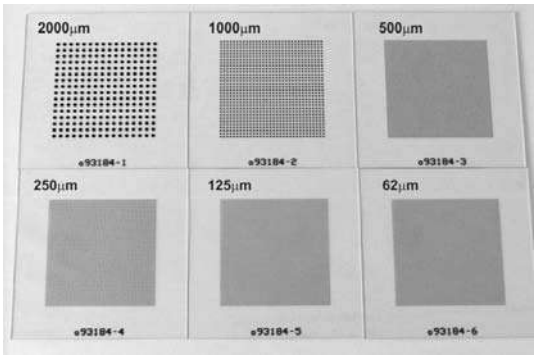

Figure 10. Custom made calibrating dot grids with different dot diameters. The area coverage of the dot arrays on each grass plate is the same: $S/S_0=\pi/16$.

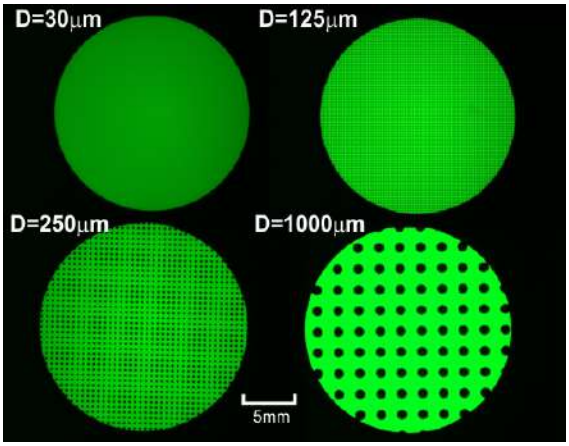

Figure 11. Microphotographs of the dot grids. The diameter of the field of view of the microscope is 20mm. All dot grids have the same area coverage: $S/S_0=\pi/16$.

The results of calibrations by the dot arrays are shown in Fig.12. It can be seen that extinction efficiency *Q(D)* approaches 1 for *D*>500μm, whereas for small dots *Q(D)* tends toward 2. Such behavior is in good agreement with the theoretical predictions described in section 2.1. The calibrations of the CEP were also performed with a double plate scheme as shown in Fig.6b. The obtained values of *Q(D)* agreed very well with that obtained for the single plate scheme (Fig.6a).

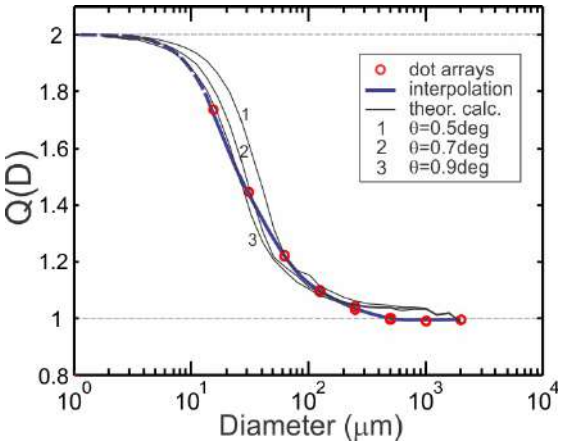

Figure 12. Instrumental extinction efficiency obtained from the CEP calibration by the dot arrays. Black solid curves are theoretical calculations of *Q(D)* for water spheres for different receiving aperture angles (section 2.1).

The best fit curve *Q(D)* for the dot arrays lies between the theoretical values calculated for the aperture angles θ=0.5deg and 0.9deg. The deviation from the theoretical predictions may be related to optical misalignment, e.g. the center of the pinhole 4 in Fig.1 is not centered with the optical axis, or other imperfections in the optical elements. Another explanation of this deviation may be related to the fact that the scattering phase functions of the opaque flat discs and those for transparent water spheres are different and, therefore, the theoretical calculations in section 2.1 are not directly applicable to the dot arrays.

The results in Fig.12 justify the approach used for the calibration of transmissiometers with the help of the dot arrays.

6.5 Calibrations by glass beads

Results of the CEP calibrations by opaque flat discs coated on the surface of the glass substrate were presented in the previous section. This approach raises a question about whether these results are applicable to cloud particles, which are essentially three-dimensional and transparent. The forward scattering of such particles may be quite different in comparison to opaque flat particles. Therefore, flat opaque and 3D transparent particles with the same linear sizes may have different instrumental extinction efficiencies *Q(D)*. To address this question, the CEP was calibrated by glass beads. The calibrations were done with monodispersions of glass beads (Thermo Inc.) having nominal diameters: 30 μm, 60 μm, 70 μm, 120 μm, 230 μm, 480 μm, 1000μm with standard deviations σ varying between 1% and 2%.

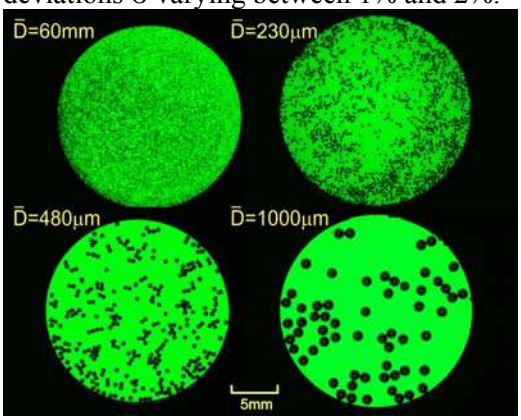

Figure 13. Examples of images of glass beads in the microscope's field of view.

Calibration by the glass beads consisted of a sequence of the following operations:

1. The calibration started from measurements of the intensity of the beam (I_{glass}) transmitted through a glass substrate installed in the center of the CEP beam.
2. Glass beads were positioned at random on the surface of the glass substrate. The surface of the substrate was limited by circular diaphragm with diameter 2cm. Figure 13 shows pictures of the glass beads with different diameters inside the 2cm diaphragm.
3. The intensity of beam *I* attenuated by the glass beads was measured by the CEP.

4. The microscope was moved in, and a microphotograph of the beads was performed. After the microphotograph was finished the microscope was moved out of the beam.
5. The beads were blown off the substrate and the background intensity I_{glass} was measured again.

Microscope magnification was selected according to bead size. That way images of the beads had no less that thirty pixels in diameter. Lower magnification would result in low image resolution and large errors in estimation of the area covered by the images of the beads. For small glass beads the microscope was set to a high magnification resulting in a small view field. At high magnification, the microscope view field was reduced thereby resulting in multiple pictures in order to cover the entire area of the 2cm diaphragm. Thus for glass beads with diameter from 30μm to 230μm the selected microscope magnification (1000pix/mm) required 35 frames in order to cover the entire area. For glass beads with diameter from 200μm to 2mm the microscope magnification was set low (230pix/mm), so that one image frame covered the entire diaphragm area.

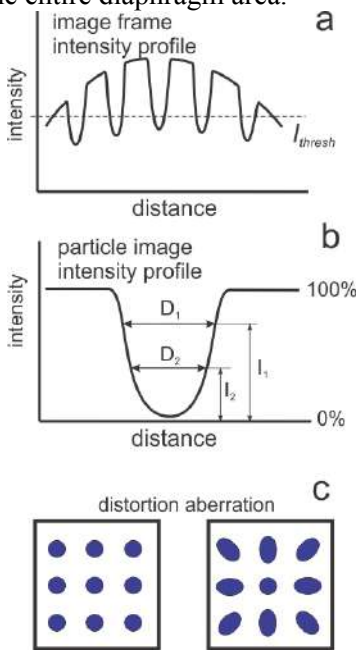

Figure 14. Explanation of different effects causing errors in sizing of images of particles: (a) inhomogeneity of background intensity; (b) different threshold intensity in conversion of grayscale into b/w image; (c) aberration of distortion.

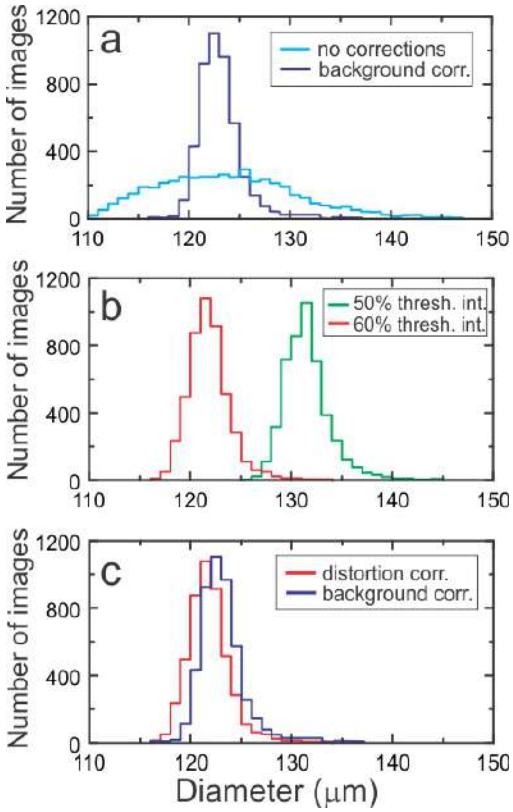

Figure 15. Contribution of different corrections on the reconstructed size distribution deduced from the analysis of the image frame of the 125μm dot grid. (a) corrections on the inhomogeneity of background intensity; (b) effect of the threshold intensity on image sizes; (c) effect of the distortion aberration corrections.

Despite the seeming simplicity, the processing of microphotography and calculation of the area coverage S/S_0 had several significant challenges. First, microscope images are prone to different optical aberrations, which result in the deformation of images of beads thus influencing estimation of their areas. The most significant of these aberrations contributing to the errors in S/S_0 is the distortion aberration. Figure 14c explains the effect of the distortion aberration which usually increases with decreasing microscope magnification; at high magnification the effect of distortion becomes insignificant. The effect of the distortion aberration also varies over the microscope's field-of-view, increasing towards the periphery.

Second, image size is sensitive to the threshold intensity level I_{thresh} selected for the

particle image sizing (Fig.14b). Thus, the size of the image increases with increasing I_{thresh}.

Third, background illumination intensity varies over the microscope's field-of-view, with intensity decreasing towards the outer edges. The non-uniform background intensity affects a change in particle image size depending on its position in the microscope's field-of-view. As such, if constant I_{thresh} is used for the entire image frame (Fig.14a), then after conversion of the grayscale image into black-and-white, the size of monodisperse particles in the center will be smaller than those in the periphery (Fig.14c).

The last two issues turned out to have the largest contribution to the accuracy of calculation of S/S_0 in the experimental setup. Figure 15 shows the effect of the three above issues on the calculation of particle size distribution for the case of a 125μm dot array.

In order to overcome these problems the following procedures were applied during image processing. The effect of the distortion aberration was accounted for with the help of the retrieval matrices C obtained from the microphotographs of the images of the dot arrays. The correction were applied with the help of Matlab function *imtransform(Im,C)* from the Image Processing Toolbox. This function applies spatial transformation of the image *Im* with the rule established in accordance with the correction matrix C.

The effect of the background illumination was accounted for by either: (1) normalizing the background intensity with the help of an image without beads; or (2) splitting the original image frame into 12 x 16 sub-frames and assuming that the background intensity within each sub-frame is constant. The first approach is very time consuming and requires significant computer resources and it was applied only for a single frame of measurements. For 35-frame cases the processing time of one set of microphotographs on a PC computer exceeds one day. The second approach was used for the cases with multi-frame measurements.

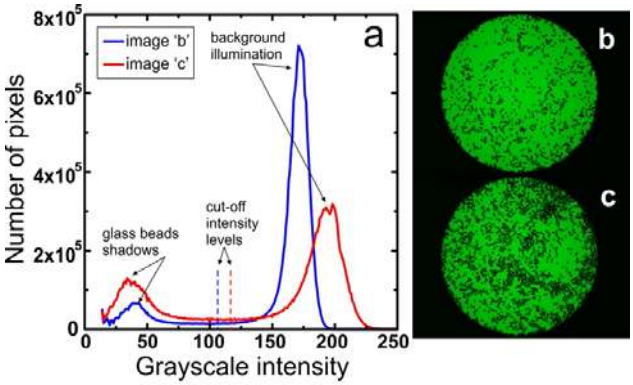

Figure 16. Determining of the cut-off level for conversion of a grayscale image into black-and-white for subsequent particle sizing and determination of particle area coverage.

The cut-off level for image sizing was determined as a middle point between the maxima corresponding to the background and particle shadows on the intensity distributions of all pixels in the grayscale image frame (or sub-frame). Figure 16 provides an explanation of the determination of the cut-off level of the image frames. Determination of the cut-off level this way corresponds to particle sizing at approximately 50% threshold intensity level.

The final tuning of the corrections described above and identifying cut-off levels was accomplished with the help of the microphotographs of the dot arrays. After applying the corrections, the accuracy in determining S/S_0 is estimated to be 5% to 10% depending on bead size and microscope magnification. If the corrections are not applied the systematic errors in calculations of S/S_0 may reach 30%.

The sequence of operations in processing and analysis of multi-frame microphotography of the substrate with the glass beads is shown in Fig.17. Finding common patterns in the neighboring image frames and subsequent frame concatenation was performed with a special program written in Matlab.

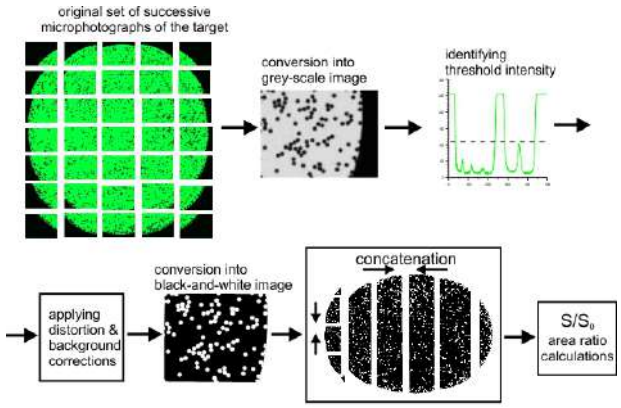

Figure 17. Sequence of procedures during image processing and calculation of S/S_0.

Figure 18 shows the results of the CEP calibrations for glass beads. The total number of calibration points is 75 for different sizes of glass beads. As seen from Fig.18 instrumental extinction efficiencies obtained for the glass beads are in good agreement with Q obtained for the dot arrays, which justifies the use of the constant frequency grids for the calibration of transmissiometers.

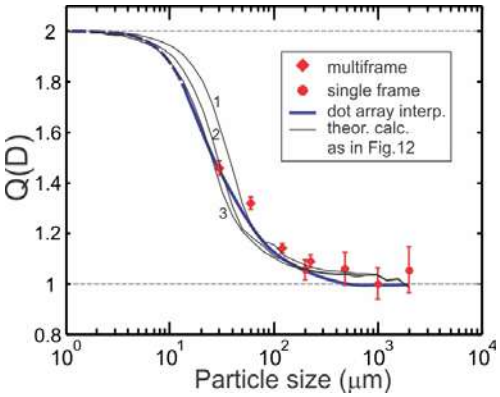

Figure 18. Instrumental extinction efficiency versus diameter calculated from the CEP calibrations for monodisperse glass beads.

6.6 Calibrations by constant frequency stellar grids

The results obtained in the previous two sections show the importance of the dispersion of the attenuating particles for the measured extinction coefficient. For example, for two sprays composed of particles with different sizes, but having the same total projected area, the *measured* extinction coefficient for the spray with the larger particles may be lower, than that of the smaller ones.

This raises a question about the role of characteristic sizes of elements composing a particle on the measured light attenuation. For example, if a 1mm size ice particle consists of an assembly of 100μm ice crystals, then will it attenuate light as a 100 μm or a 1mm particle? What are the elements composing a particle which determine its forward scattering? These questions are important for understanding what the characteristic size of non-spherical particle should be used upon applying corrections to measured extinction efficiencies.

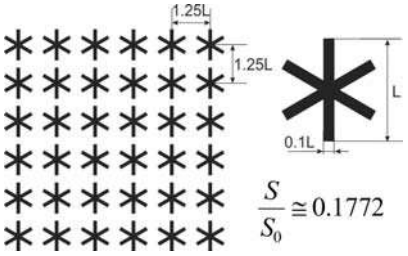

Figure 19. Arrangement of the stellar patterns on the "stellar" grids.

To address this question a set of custom made constant frequency arrays consisted of six ended stars were used. The six ended stellar shape was chosen because it is one of the common habits of ice crystals. Since the characteristic sizes of the fine structure of stellar branches are usually much smaller than the size of the particle, it is not clear what the attenuated properties of such particles would be. For this particular case, the thickness of the stellar branches was $0.1L$, where L is the length of the branch. Figure 19 shows the pattern of the custom made stellar arrays. Distance between the centers of the stars was $1.25L$, so the area ratio is S/S_0=0.1772. Three stellar arrays with sizes L=500μm, 1000μm and 2000μm were used. Microphotographs of the stellar arrays are shown in Fig.20.

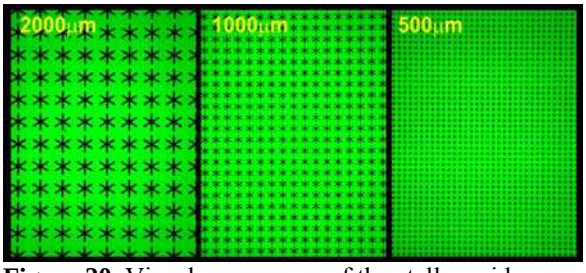

Figure 20. Visual appearance of the stellar grids under microscope

Figure 21 shows the instrumental extinction efficiency for the stellar habits. Since the considered objects have non-circular shapes, there may be several different definitions of their size. On the diagram in Fig.21 the values of Q were plotted versus four characteristic sizes: (1) maximum stellar dimension $D_{max}=L$, (2) effective size $D_{eff}=\sqrt{4S/\pi}$, (3) minimal size $D_{min}=0.1L$, which represent the width of the stellar branch; and (4) best fit size $D_{fit}=2D_{min}=0.2L$. As seen from Fig.21 utilizing D_{max} and D_{eff} results in overestimation of Q, whereas D_{min} would underestimate Q. However, $Q(D)$ obtained for dots would agree with that for stellar shapes for $D_{fit}=0.2L$. In other words, in terms of the attenuation measured by the CEP, a stellar particle with size L=500μm behaves like an opaque disc with D=100μm.

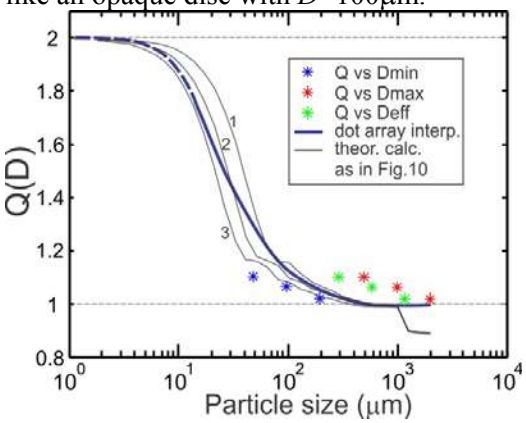

Figure 21. Instrumental scattering efficiency obtained from the CEP calibrations by stellar arrays with three different sizes L=500μm, 1000μm and 2000μm. Due to the ambiguity of the size definition of non-circular particles different sizes were applied to the stellar habits.

6.7 Calibrations by irregular shaped particles

Calibrations by the stellar arrays in section 2.2.6 suggests that the function $Q(D)$ for non-spherical particles (non-circular projected area) may be quite different from $Q(D)$ obtained for spherical particles. The reasons for these differences are related to the ambiguity of the definition of particle size for non-spherical particles and the difference in scattering functions of non-spherical and spherical particles. The following set of experiments attempts to identify feasibility of finding the size of non-spherical particle that would be universal for different habits for use in $Q(D)$ and thus used for corrections to extinction coefficient.

Crystals of sugar and broken glass particles were used as optical targets in order to simulate attenuation by cloud ice particles. Figure 22 shows two microphotographs of sugar crystals scattered over the glass substrate (left) and their corresponding distributions of X, Y, and D_{eff} (right). Here X and Y are randomly oriented Cartesian coordinates in the image plane during image processing. As seen from the diagrams in Fig.24 all three distributions and their modal sizes are in a good agreement with each other. The modal sizes for all three size definitions range from 600μm to 800μm. Figure 22 shows that all points $Q(D)$ are well grouped and are in good agreement with the results for dot arrays.

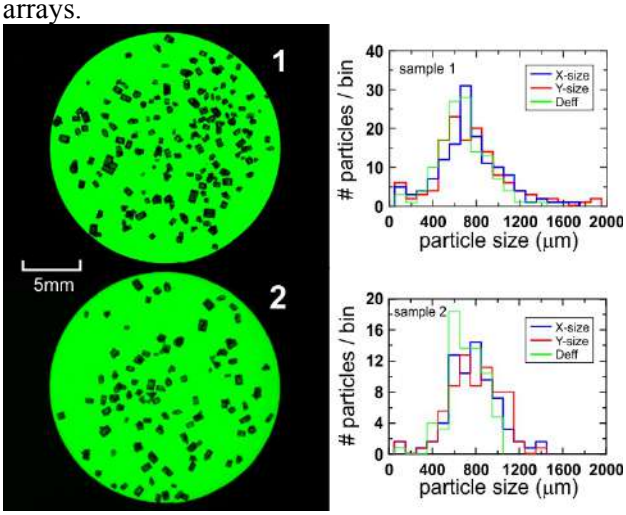

Figure 22. Microphotographs of sugar crystals (left) and corresponding distributions of X, Y, and D_{eff} sizes (right).

Figure 23 shows three microphotographs of broken glass particles (left) and corresponding distributions of X, Y, and D_{eff} sizes (right). The particles in cases 2 and 3 have transparent sections. Such transparent areas are typical for many types of ice crystals. Due to the transparent sections the effective size D_{eff} of the broken glass particles is smaller than D_x and D_y. However, for case 1 in Fig.23, all three size distributions agree since the particle images appear to be mostly without holes and transparent areas.

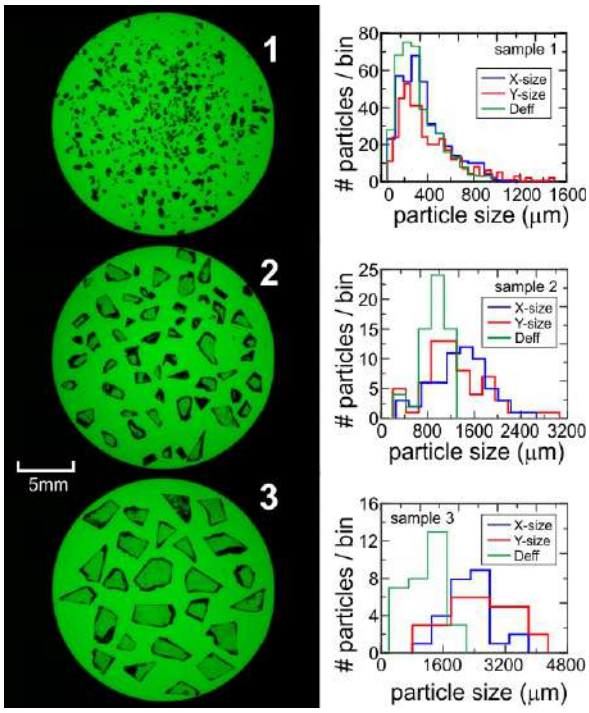

Figure 23. Microphotographs of broke glass particles (left) and corresponding distributions of *X, Y*, and D_{eff} sizes (right).

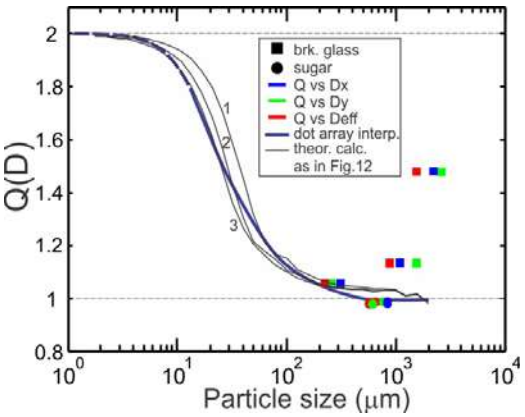

Figure 24. Instrumental scattering efficiency obtained from the CEP calibrations for sugar crystals and broken glass particles as shown in Figs.22 and 23.

Figure 24 shows that extinction efficiency for broken glass particles turned out to increase with increasing particle size. Such behaviour of *Q(D)* appears to be opposite to that for glass beads and dot arrays. For example, the scattering efficiency of 2-3mm glass particles would be the same as that for approximately 30μm glass beads or dots. It should be noted that the transparent sections of the images of the glass particles were not included in the calculations of S/S_0. A potential explanation of this may be related to the transparent sections in the broken glass imagery, since this is the only distinct difference with the previous targets. This may result in a flatter forward scattering lobe and increase of the instrumental scattering efficiency.

8. CEP measurements during ISDAC

The extinction coefficient measured by the CEP was calculated based on the Beer-Bouguer law as

$$\beta_{CEP} = -\frac{1}{2L}\ln\frac{I}{I_0} \qquad (27)$$

Here I and I_0 are the output signals which characterize the radiant fluxes transmitted in clouds and clear-sky, respectively. The intensity of the attenuated signal was calculated as $I=I_{tot}-I_{bkg}-I_{int}$; I_0 was determined the same as I but in a cloud-free atmosphere. The signals I_{tot}, I_{bkg} and I_{int} were normalized on the current values of I_{norm}.

7.1 Calculations of the extinction coefficient from FSSP and CDP measurements

In liquid clouds, the extinction coefficient was calculated from the FSSP droplet size distribution measured in fifteen size bins as

$$\beta_{FSSP} = \frac{\pi Q}{4}\sum_{j=1}^{15} n_j D_j^2 \qquad (28)$$

where n_i, D_i are concentration and diameter of droplets in the FSSP *i*-th size bin, and Q is extinction efficiency. Since the size of the FSSP measured droplets $D>>\lambda$, $Q \approx 2$ is a good approximation.

7.2 Calculations of the extinction coefficient from imaging probes

Extinction coefficient for ice clouds was calculated from Optical Array Probe (OAP) imagery. OAPs provide shadowgraphs of cloud particles that passed though the sample area of the probe (Fig.25a). In general, the OAP can be considered to be an extinctiometer, but instead of measuring attenuation of light integrated over the whole beam, it measures local attenuation associated

with the discrete binary images with shadow areas A_j (Fig.25b). Therefore, extinction coefficient can be calculated through the integration of the area shadowed by all particles $\sum A_j$ as,

$$\beta_{OAP} = \frac{Q}{LA_0}\sum_j A_j \qquad (29)$$

Here L is the distance between the OAP arms (Fig. 25b); A_0 is the total area covered by the probe's laser beam having width W and moving at speed U during time Δt, i.e. $A_0=WU\Delta t$. Substituting this expression into Eq.29 yields

$$\beta_{OAP} = \frac{Q}{LWU\Delta t}\sum_j A_j \qquad (30)$$

The direct area calculation (DAC) technique for estimating extinction coefficient is based on the following assumptions regarding OAP imagery: (1) the depth-of-field and the sample area width do not depend on particle size, i.e. the sample area of the probe stays constant for all particles; and (2) the shadow images represent geometrical shadows of cloud particles and so diffraction effects are neglected.

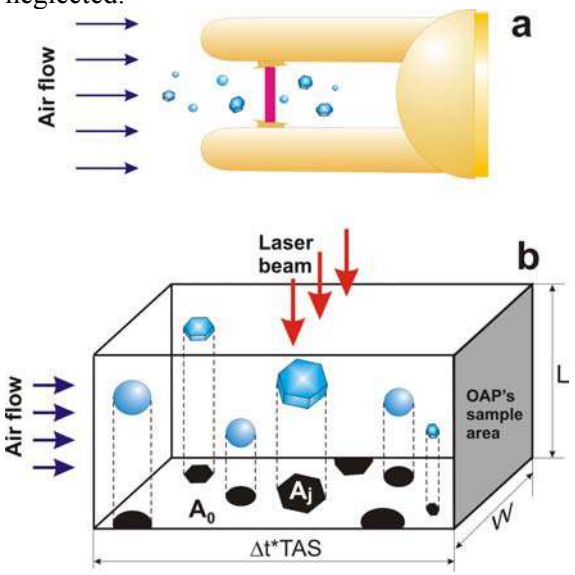

Figure 25. Conceptual diagram of calculation of extinction coefficient from OAP-2D imagery.

Assumption (1) is satisfied for particles with $D \geq 125\mu m$ for OAP-2DC and for particles with $D \geq 400\mu m$ for OAP-2DP, i.e. when the depth-of-field for these particles is larger than the distance between the arms. Korolev et al (1998) showed that the projected image area experiences several oscillations, when a particle moves from the object plane to the edge of the depth-of-field. The effect of particle distance on projected area decreases with increasing particle size. In other words the DAC technique is expected to work better for larger particles than for small ones. It should be mentioned that calculation of extinction coefficient from OAP-2DP/2DP imagery for ice clouds with large concentrations of ice particles (D<100μm) may result in significant underestimation of the extinction coefficient.

The DAC method gives more accurate estimation of the extinction coefficient, as compared to the alternative method based on the size-to-area conversion (STAC)

$$A=aD^b. \qquad (31)$$

Sources inaccuracy for the STAC method are related to uncertainty in the coefficients a and b for different particle habits. The STAC method also cannot be applied to partial images, and this significantly limits its use for particles with $D>W$.

7.3 Comparisons of the CEP and particle probe data in liquid clouds

Figure 26 shows time series of the extinction coefficient for a low-level stratiform deck sampled on flight#30 of the ISDAC project. The high frequency of cycling of the Rosemount Ice Detector (RICE) signal (Fig.26b) indicates that the cloud contained supercooled liquid water. Figure 26a shows that extinction coefficient measured by the CEP and that calculated from the FSSP and CDP varied from approximately 0 to 60km^{-1}. While this cloud layer also contained some ice particles, estimations from the OAP-2DC/2DP imagery suggest that for the most of the cloud extinction coefficient associated with ice is less than 0.5km^{-1}; much smaller than that for liquid regions. Therefore, this cloud layer can be considered as conditionally liquid and the effect of ice particles on extinction coefficient measured by the CEP, FSSP and CDP can be neglected.

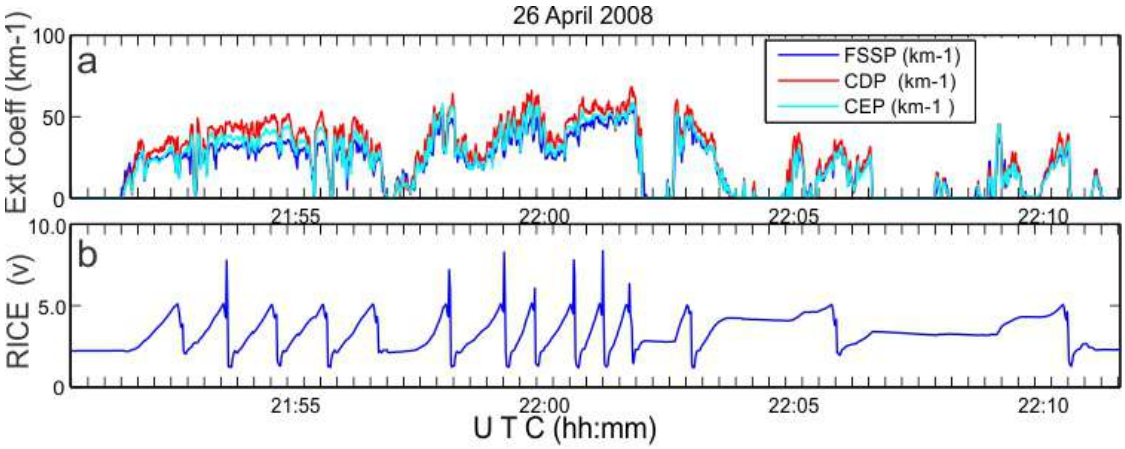

Figure 26. Time series of the measurements of extinction coefficient by the CEP and particle probes FSSP and CDP (a) and Rosemount Icing Detector signal (b). Measurements were made in a stratiform cloud deck during the ISDAC project in the Cape Barrow region, at 900<P<980mb; -11<T<-8C, flight #30, 26 April 2008

.

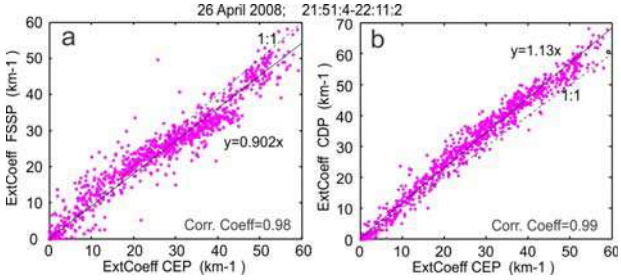

Figure 27. Scatter-diagrams of extinction coefficient measured by CEP and particle probes FSSP (a) and CDP (b) in liquid clouds on 26 April 2008 during the ISDAC project (Fig.26).

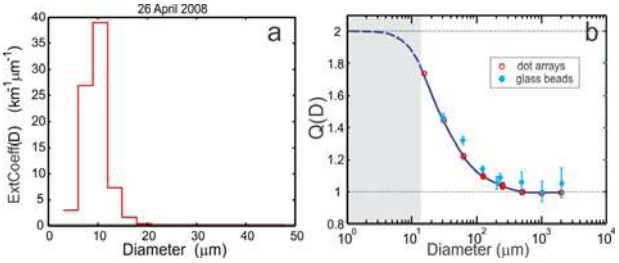

Figure 28. Distribution of extinction coefficient measured by FSSP and averaged over the time period corresponding to that shown in Fig.26 (a). Gray area indicates region of the instrumental extinction efficiency corresponding to the droplets mainly contributing to extinction coefficient based on (a).

Figure 27 shows scatter-diagrams between CEP, FSSP and CDP measurements of extinction coefficient. For liquid clouds the extinction coefficients measured by the CEP and particle probes FSSP and CDP agree reasonable well with each other. The scattering of the points does not exceed 15%. Such agreement is anticipated since as seen from Fig.28a the main contribution to extinction coefficient is made by droplets with D<15μm. The CEP instrumental extinction efficiency for such droplets is close to 2 (Fig.28b). Thus, results from in-situ measurements in liquid clouds provide good closure with laboratory experiments.

The results of comparisons airborne transmissometers and particle probes in liquid clouds similar to those shown in Figs.26,27 were also discussed in Korolev et al. (1999) and Korolev (2008)

7.4 Comparisons of the CEP and particle probe data in ice

Figure 29 shows spatial variations of extinction coefficient measured by CEP, OAP-2DC and OAP-2DP during a flight through As-Cs clouds. Extinction coefficients deduced from the 2D probes were calculated using DAC technique (Eq.30). Small variations of the RICE signal indicate the absence of liquid along the flight line (Mazin et al. 2001). This helps identify this cloud as glaciated. Images measured by the OAP-2DC shown in Fig.30b suggest that most ice particles were bullet rosettes with maximum sizes between 1mm and 2mm.

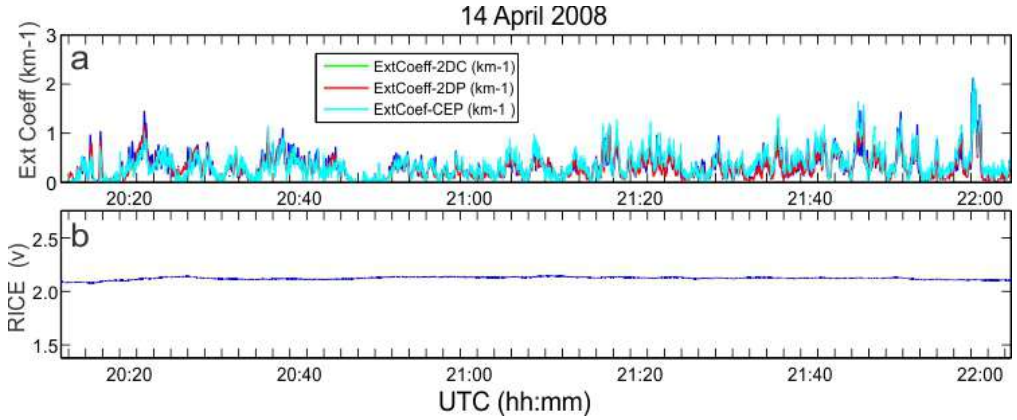

Figure 29. Time series of the measurements of extinction coefficient by the CEP and particle probes OAP-2DC and OAP-2DP (a) and Rosemount Icing Detector signal (b). The measurements were conducted in Cs-As clouds during the ISDAC project in the Cape Barrow region, at 540<P<680mb; -34<T<28C, on 14 April 2008.

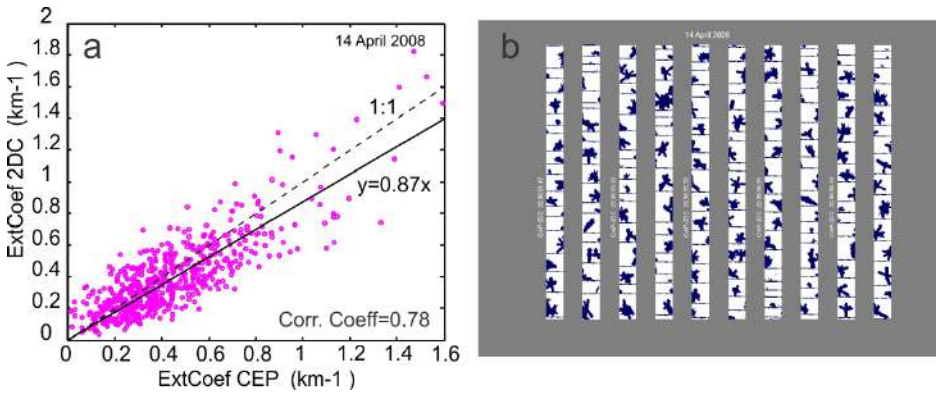

Figure 30. Scatter-diagrams of extinction coefficient measured by CEP and OAP-2DC (a) and particle images measured by OAP-2DC (b) for the time interval shown in Fig.29.

The scatter-diagrams in Fig.30a show good agreement between extinction coefficient measured by the CEP and that derived from the OAP-2DC. Figure 31a shows the distribution of extinction coefficient versus particle size averaged over the time period in Fig.29. The extinction distribution in Fig.31a was calculated based on the size-to-area conversion (Eq.31) applied to the measured particle size distribution. The distribution in Fig.31a suggests that extinction coefficient is mainly contributed to by particles larger than ~300μm. Laboratory calibration by opaque dots and glass beads suggest that the instrumental extinction efficiency *Q(D)* in this size range should be close to 1 as shown in Fig.31b. In this regard, it is anticipated that the extinction coefficient measured by the CEP should be approximately twice lower than that calculated from the imaging probes. However, the comparison between CEP and OAP values in Figs.29a and 30a suggest that the extinction coefficients measured by these two different techniques are in a quite good agreement.

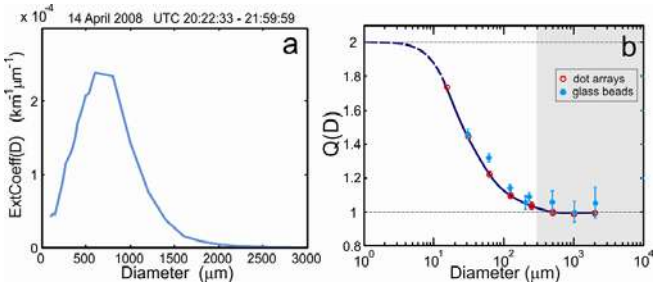

Figure 31. Distribution of extinction coefficient calculated from OAP-2DC and averaged over the time period corresponding to that shown in Fig.37 (a). Gray area on (b) indicates region of the instrumental extinction efficiency corresponding to the size range of ice particle mainly contributing in the extinction coefficient in (a).

Most of the extinction coefficient measurements conducted during the ISDAC for ice clouds were collected in optically thin clouds with β<2km^{-1}. These values of β are close to the threshold sensitivity of the CEP (0.2km^{-1}) and therefore they can be affected by noise. The following case shows measurements for ice clouds obtained during the C3VP project conducted in the southern Ontario during the cold season of 2006-2007 (Barker et al. 2008), with extinction coefficients up to 20km^{-1} . The diagrams in Figs. 40-41 show good agreement between extinction coefficient measurements by the CEP and imaging probes. Figure 41 shows that ice particles in this cloud were predominantly spatial dendrites. As in the previous case, ice particles with D>300μm provide the main contribution to extinction coefficient (Fig.42a).

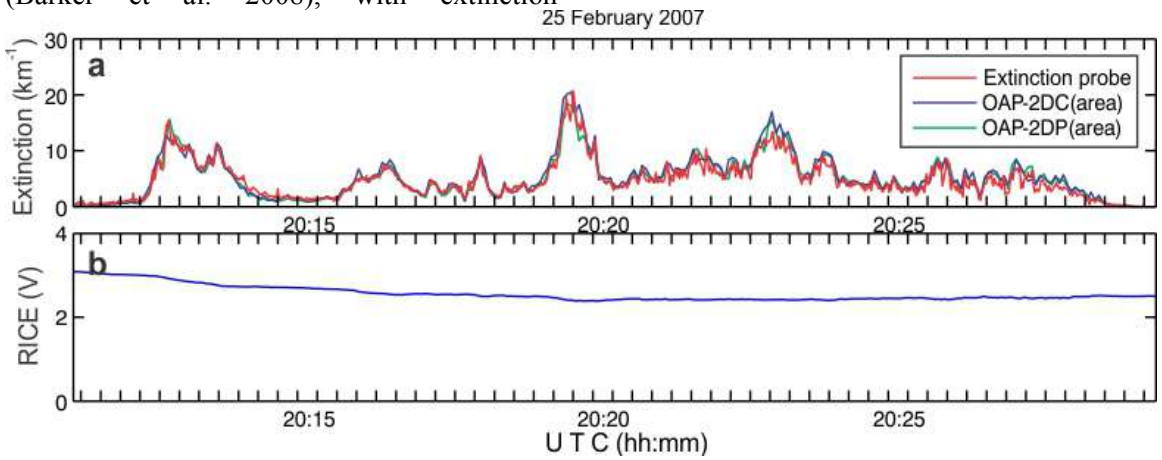

Figure 32. Time series of the measurements of the extinction coefficient by the CEP and particle probes OAP-2DC and OAP-2DP (a) and Rosemount Icing Detector signal (b). The measurements were conducted in Cs-As clouds during the C3VP project in the Ottawa region, at 500<P<580mb; -24<T<18C, on 25 February 2007.

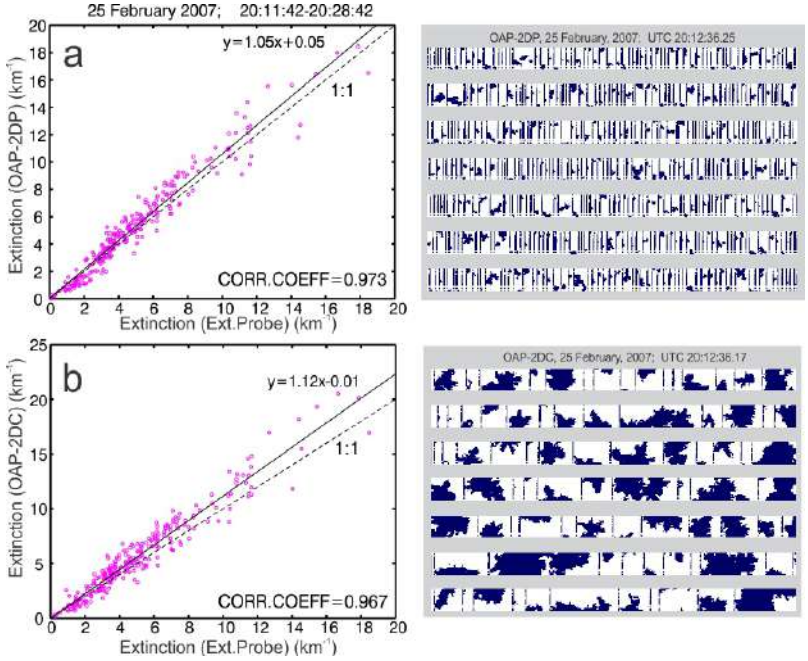

Figure 33. Scatter-diagrams of extinction coefficient measured by the CEP and OAP-2DC (a) and OAP-2DP (b) during the flight shown in Fig.32. Corresponding 2D images of the particles measured by the OAP-2DC and OAP-2DP are shown on the right.

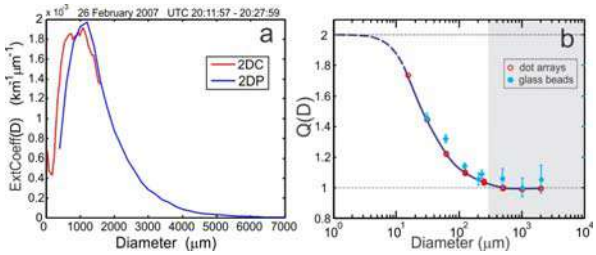

Figure 34. Distribution of extinction coefficient calculated from OAP-2DC/2DP and averaged over the time period corresponding to that shown in Fig.32. Gray area on (b) indicates region of the instrumental extinction efficiency corresponding to the size range of ice particle mainly contributing to extinction coefficient in (a).

9. Feasibility of corrections

8.1 Liquid clouds

The laboratory calibrations described in sections 2.2.4-2.2.5 suggest that CEP instrumental extinction efficiency Q is a unique function of D. This enables calculation of $Q(D)$ and the subsequent introduction of corrections to measured extinction coefficient.

Numerous prior measurements have shown that most liquid clouds consist of droplets with D<10μm. The contribution to extinction coefficient by droplets with larger D is expected to be small for the majority of liquid clouds. For droplets D<10μm extinction efficiency is close to 2 and so CEP inferences of extinction coefficient do not require corrections. However, for cases with larger droplets and precipitation, errors due to forward scattering may reach a factor of two and thus will require correction.

8.2 Ice clouds

It turned out that the agreement between extinction coefficient measured by the CEP and that deduced from the imaging probes is observed for the majority of sampled ice clouds. In all cases, ice particles with D>300μm are the main contributors to extinction coefficient (see Figs.31a, 34a). In the calculation of extinction coefficient from the imaging probe data in Eq.30 it was assumed that Q=2. However, laboratory calibrations by the dot arrays and glass beads suggest that for D>300μm, the CEP instrumental extinction efficiency $Q(D)$~1. Therefore, the CEP in-situ measurements of extinction coefficient in ice clouds and its comparisons with the imaging probes appear to contradict the laboratory calibrations. This is because agreement between CEP and imaging probes implies that $Q(D)$~2. The laboratory calibrations of extinction coefficient measured by CEP are expected to be roughly half those calculated from the imaging probes.

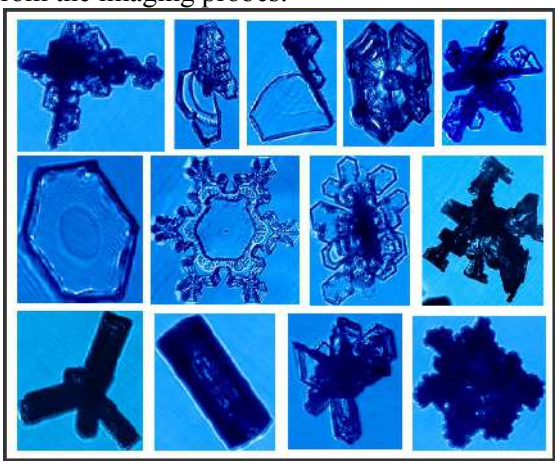

Figure 35. CPI imagery of ice particles.

Potential explanations of the agreement between extinction coefficients measured by the CEP and imaging probes may be related to: (a) underestimation of particle areas by the imaging probes; and (b) ice crystals scatter light in the forward direction in wider angles as compared to that for opaque discs and glass beads with the same linear dimensions.

Korolev et al (1998) showed that imaging probes with coherent illumination (OAP-2DC/2DP/2DG etc.) are susceptible to overestimation of the measured particle size and area. Therefore, the imaging probe measurements are likely to result in overestimation, rather than underestimation, of extinction coefficient. Thus explanation (a) does not seem a likely reason for the agreement in extinction coefficient measurements.

Figure 35 shows images of cloud ice particles with different habits. Many of these particles have transparent areas. The images of the particles clearly indicate that the dimensions of the distinct components forming an ice particle (e.g. internal inhomogeneities visible in transmitted light, features forming particle edges, etc) in some cases are much smaller than the linear dimensions of the entire particle. Therefore, it would be reasonable to hypothesize

that the forward scattering by such particles may be significantly affected by these small-scale features, thereby resulting in broadening of the forward scattering lobe. This effect would result in the increase of instrumental scattering efficiency *Q(D)* eventually approaching 2. This consideration is supported by the laboratory measurements of broken glass particles (section 2.2.7). Large glass particles with transparent parts had *Q(D)*>1 (Figs.23,24).

This consideration raises a series of important questions. First, whether ice particles scatter light like a conglomeration of small particles (Fig.36b) or like an opaque solid (Fig.36c)? Second, what is the effect of the transparent parts of the extinction coefficient? Third, how should the transparent parts be accounted for in extinction coefficient calculations stemming from imaging probe data?

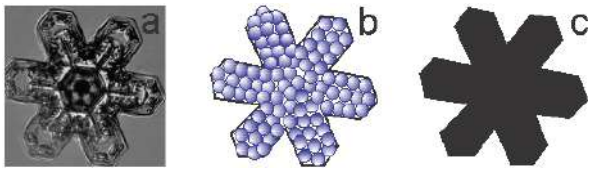

Figure 36. Image of a stellar ice particle showing multiple small-scale features in its internal structure (a). Representation of the ice particle in (a) as a conglomeration of small particles (b) and an opaque solid (c).

Laboratory experiments described in section 2.2 along with the frequently observed agreement between extinction coefficient measured by CEP and imaging probes, obtained from in-situ measurements, suggest that for ice particles *Q(D)* is an ambiguous function of *D*. In other words, information just about linear size *D* of an ice particle is insufficient to determine instrumental extinction efficiency *Q*. Ideally, a scattering function for ice particles would uniquely address this question. A potentially attractive approach seems to be that ice particle habit along with the particle size may provide a link to the scattering function and *Q*. However, infinite variety of particle shapes significantly hinders this approach, and even makes it impossible if one requires arbitrarily high accuracies.

9 Summary

The following outcomes have been obtained in the frame of this work:

(1) Laboratory calibrations of the CEP by dot arrays and glass beads showed that *Q(D)* can be considered as a unique function of *D*. This finding confirms that corrections of extinction coefficient measured in liquid clouds are feasible. The corrections of extinction coefficient can be made based on droplet size distributions measured by particle probes (e.g. FSSP, CDP) and the function *Q(D)* obtained from the laboratory calibrations.

(2) For most measurements in liquid clouds during the ISDAC project the contribution to extinction coefficient by droplets with *D*>15μm was relatively small and does not exceed 10-15%. Therefore, most CEP measurements do not require corrections due to forward scattering and thus can be used as reported.

(3) It appears that for the case of ice particles instrumental scattering efficiency *Q* is not a unique function of particle linear size. At this stage corrections of extinction coefficient measured in ice clouds does not seem feasible. Additional studies are required in this regard.

The Cloud Extinction Probe is a new instrument that lacks analogues among existing airborne instruments that attempt to measurement extinction coefficient. The set of experiments described in this work is a first attempt to characterize instrumental scattering efficiency *Q* from laboratory measurements. The set of tests and calibrations described in this report showed problems relevant to transmissiometeric technique. The results of this work, and the developed methodology, can be used as a starting point for further improvements to existing airborne transmissiometers.

The outcomes of this study bring up a series of important questions, which should be addressed in future studies:

(a) Do ice particles scatter light like conglomerations of small particles (Fig.36b) or like an opaque solid (Fig.36c)?

(b) What are the effects of the transparent parts of crystals on their extinction coefficient?

(c) How should the transparent parts of crystals be treated in extinction coefficient calculations from imaging probe data?

Acknowledgements
This work was funded by the US Department of Energy, DOE/SC-ARM-TR-105, Contract No 143648 and Environment Canada.

References

Barker, H. W., A. V. Korolev, D. R. Hudak, J. W. Strapp, and K. B. Strawbridge A. 2008: Comparison between CloudSat and Aircraft Data for a Multi-layer, Mixed-Phase Cloud System during C3VP. *J. Geophys. Res.* (submitted)

Deepak, A., and Box, M. A. 1978a Forward scattering corrections for optical extinction measurements in aerosol media. 1: Monodispersions. *Applied Optics*, **17**, 2900-2908

Deepak, A., and Box, M. A. 1978b Forward scattering corrections for optical extinction measurements in aerosol media. 1: Polydispersions. *Applied Optics*, **17**, 3169-3176

Gerber, H., Y. Takano,T. J. Garrett and P. V. Hobbs, 2000: Nephelometer Measurements of the Asymmetry Parameter, Volume Extinction Coefficient, and Backscatter Ratio in Arctic Clouds. *J. Atmos. Sci.,* **57**, 3021-3034

Gumprecht, R. O. and Sliepevich, C.M. 1953 Scattering light by large spherical particles. *J. Phys. Chem*. **57**, 90-95

Kampe, aufm, H.J., 1950: Visibility and Liquid Water in Clouds and in the Free Atmosphere. *J. Atmos. Sci.,* **7**, 54-57

King, W. D., and R. J. Handsworth, Total droplet concentration and average droplet sizes from simultaneous liquid water content and extinction measurements, *J. Appl. Meteorol.*, *18,* 940-944, 1979.

Korolev A. V., J. W. Strapp, and G. A. Isaac, A. N. Nevzorov, 1999: In situ measurements of effective diameter and effective droplet number concentration. *J. Geoph. Res.*, **27**, 3993-4003.

Korolev, A.V., G. Isaac, I. Mazin and H. Barker, 2001: Microphysical properties of continental stratiform clouds. *Quart. J. Roy. Meteor. Soc.,* **127**, 2117-2151

Korolev, A., 2008: New Airborne Extinction Probe. *International Conference on Clouds and Precipitation*, 7-11 Aug. 2008, Cancun, Mexico, CD P13.3

Kosarev, A. L., I. P. Mazin, A. N. Nevzorov, and V. F. Shugaev, 1976: Optical density of clouds. *Trans. Cent. Aerol. Obs.*, *124,* 44-110.

Mazin, I.P., A.V. Korolev, A. Heymsfield, G.A. Isaac, S.G. Cober, 2001: Thermodynamics of Icing Cylinder for Measurements of Liquid Water Content in Supercooled Clouds. *J. Atmos. Oceanic Techn.,* **18**, 543–558

Nevzorov A. N., and V. F. Shugaev, 1974: Aircraft cloud extinction meter. *Trans. of Cent. Aerol. Obs.*, **106,** 3-10.

Nevzorov A. N., and V. F. Shugaev, 1972: The use of integral parameters for study of cloud microstructure (in Russian), *Trans. Cent. Aerol. Obs.*, *101***,** 32-47.

Ruskin, R.R., 1974: The measurements of cloud elements: the use of transmission and scattering techniques to measure ice and water. *Proc. Symp. Measuremen of Cloud Elements*, W.D. Scott, Ed. NOAA, Tech Memo ERL WMPO-19, 117

Shifrin K.M. 1988 *Physical optics of ocean water*. Amer. Inst. of Physics, New York, pp285

van de Hulst, H. C. 1957 *Scattering of light by small particles*. Wiley, New York

Zabrodsky, G.M., 1957: Measurements and some results of study of visibility in clouds. in "*Study of clouds, precipitation and cloud electrification*" Gidrometeizdat, 131-134.

Zmarzly, P.M. and R.P. Lawson, 2000: An Optical Extinctiometer for Cloud Radiation Measurements and Planetary Exploration. Final Report submitted to NASA Goddard Space Flight Center in fulfillment of Contract NAS5-98032, September, 2000, 131 pp. (available from http://www.specinc.com/publications/Extinctiometer_Report.pdf)

Weickmann, H. K. and H. J. aufm Kampe, 1953: Physical properties of cumulus clouds. *J. Atmos. Sci.,* **10**, 204-211

A NEW MECHANISM OF DROPLET SIZE SPECTRA BROADENING DURING DIFFUSIONAL GROWTH

Alexei Korolev [1], Mark Pinsky [2], and Alex Khain [2]
[1]*Environment Canada, Cloud Physics and Severe Weather Research Section, Canada;*
[2]*The Hebrew University of Jerusalem, Department of Atmospheric Sciences, Jerusalem, Israel*

1. Introduction

The processes of droplet spectra broadening and warm rain initiation are one of the long-standing problems in cloud physics. In the early 1960's it was recognized that the observed droplet size distributions are, in fact, much broader than those predicted theoretically A theoretical consideration of the collective droplet growth in a frame of regular condensation showed that droplet size spectra is narrowing and diffusional droplet growth slows down during adiabatic ascend. One of the main challenges for this theoretical model lay in trying to explain the process of the formation of droplets D>40μm though the diffusion of water vapor in relatively shallow stratiform decks. Laboratory studies and theoretical analysis showed that the subsequent growth of such droplets may occur through the collision-coalescence process and would eventually result in precipitation formation. Since then, a number of hypotheses have been developed to explain large droplet formation at the condensational stage: giant and ultragiant CCN, stochastic condensation, entrainment and inhomogeneous mixing, preferential droplet concentration, etc. These hypotheses were discussed in great detail in a series of review papers by Beard and Ochs (1993), Vaillancourt and Yau (2000), Mazin and Merkulovich (2008), Devenish et al. (2012).

In the present study, we introduce another hypothesis on the process of droplet spectra broadening at the condensational stage. The essence of this mechanism consists of a sequence of mixing events between ascending and descending parcels. The ascending adiabatic parcel is enriched with supersaturated water vapor and has smaller droplets, whereas the descending parcel has undersaturated air but contains droplets with larger diameters. The mixing of such parcels may result in an enhanced growth of large droplets.

Corresponding Author: Alexei Korolev, Environment Canada, 4905 Dufferin Street, Toronto, Ontario, M3H5T4 Canada, e-mail: alexei.korolev@ec.gc.ca,

The rest of the paper is organized as follows: In section 2 the condensational processes in an adiabatic parcel undergoing vertical fluctuations with and without isobaric mixing are considered. Section 3 presents a consideration of the effects of thermodynamical and environmental parameters on the droplet spectra broadening that is formed during vertical fluctuations and mixing. Section 4 presents a discussion of the assumptions used in this study. The conceptual model of the droplet spectra broadening and precipitation initiation is discussed in Section 5.

2. Effect of fluctuations of vertical velocity on the droplet spectra formation

In the following sections, a number of simplifying assumptions have been made. The initial ensemble of droplets was considered to be monodisperse. The droplets were moved with the air and always remained inside of the cloud parcel until the moment of mixing. All processes inside the cloud parcels were treated as adiabatic until mixing with another parcel. The mixing process between the cloud parcels was considered isobaric. No activation of CCN, sedimentation and coalescence was allowed above the cloud base. The collective droplet growth and evaporation was considered in the frame of regular condensation, that is, the water vapor pressure and temperature fields at large distances from the cloud droplets are assumed to be uniform, and all droplets grow or evaporate under the same conditions. Furthermore, the radiation effects were ignored. It is recognized that these simplifications will mean that some of the quantitative results will not be directly applicable to real cloud systems. However, such simplifications allow us to build a theoretical understanding of the effect of in-cloud mixing on the droplet size distribution broadening that will aid us in attempting to construct a conceptual model of the droplet size spectra formation at the condensation stage and warm rain initiation. The effect of the simplifications stated above will be considered in more detail in Section 4.

a. No mixing

Figure 1 shows the modeled supersaturation (S), condensed liquid water mixing ratio (q), and droplet diameter (D) in a vertically oscillating adiabatic parcel with monodisperse droplets having a concentration of N=100cm^{-3}. The vertical fluctuations were set between levels z_1=515m and z_2=590m. The cloud parcel moved between these levels with a constant vertical velocity of $|u_z|$=1m/s. When the parcel reached one of those levels, the vertical velocity u_z changed its sign to the opposite. No mixing of the parcel with the cloud environment was allowed in this simulation. The trajectories of $S(z)$, $q(z)$ and $D(z)$ are shown in Fig.1 with thick lines, and represent a series of cycles of ascent and decent overlaid on top of one another. A detailed analysis shows that for this specific case, the changes in the trajectories of every additional cycle are negligibly small. Essentially, it means that the trajectories indicated by thick lines in Fig.1 represent the limit cycles of $S(z)$, $q(z)$ and $D(z)$. The rate of approach of the trajectories $S(z)$, $q(z)$ and $D(z)$ to their limit cycles is determined by the time of phase relaxation τ_p (e.g. Korolev and Mazin 2003), which characterizes the time of depleting or releasing water vapor by growing or evaporating cloud droplets.

$$\tau_p = (cND)^{-1} \qquad (1)$$

where c is the coefficient dependent on temperature T and air pressure P (hereafter, for variable notations see Appendix A). Since for this specific case $\tau_p \ll \tau_t$ the alignment of the trajectories $S(z)$, $q(z)$ and $D(z)$ with their limit cycles occurs within one turnover, here $\tau_t = 2\Delta z/u_z$ is the period of the vertical fluctuations.

The diagram in Fig.1c indicates that for an ensemble of monodisperse droplets the droplet size trajectories $D(z)$ are repeatedly passing though the same points during the cycling vertical fluctuations. In other words at each level the difference between the droplet size in ascending and descending parcels remains constant and does not change with time. This type of behavior is universal for both single phase and mixed phase clouds consisting of monodisperse liquid droplets and/or ice particles (Korolev and Field 2007). This brings up an important conclusion, that vertical fluctuations of adiabatic cloud parcels with no mixing *cannot* cause the broadening of the droplet size distribution. This conclusion is consistent with the earlier finding of Mazin and Smirnov (1969) and Bartlett and Jonas (1972).

For the following consideration it is important to note that at the same altitude z, the supersaturation in the ascending parcel is higher than that of the descending one, i.e.

$$S(z)\big|_{u_z>0} > S(z)\big|_{u_z<0} \qquad (2)$$

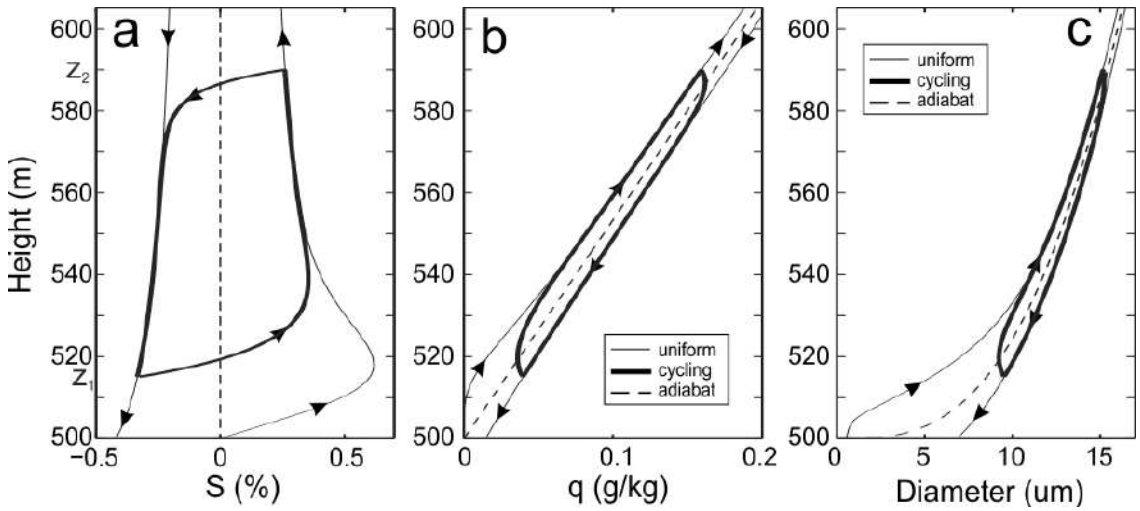

Figure 1. Numerical simulation of changes of supersaturation (a), mixing ratio of liquid water (b), and droplet diameter (c) formed during uniform ascent and descent (thin line) and cycling ascent and descent between z_1=515m and z_2=590m (thick line). For both cases the vertical velocity was $|u_z|$=1m/s. The droplets were assumed to be monodisperse with the number concentration N=100cm^{-3}. Initial condition at the cloud base: z_0=500m, S_0=0%, T_0=10C, r_{CCN}=0.04μm. Initial droplet size was considered to be equal to it its equilibrium size formed at r_{CCN}.

The supersaturation and condensed water content are related through the mass conservation law as (Pinsky et al., 2012).

$$S = A_1 z - A_2 q_w + C \qquad (3)$$

Therefore, for the ascending and descending parcels at the same altitude (z=const) Eq.(3) yields:

$$\Delta S = A_2 \Delta q \qquad (4)$$

Here, $\Delta S = S(z)\big|_{u_z>0} - S(z)\big|_{u_z<0}$ and $\Delta q = q(z)\big|_{u_z<0} - q(z)\big|_{u_z>0}$. Since $q \propto D^3$, then from Eq.(4) it follows that:

$$\Delta S = A_3 \Delta(D^3) \qquad (5)$$

Where: $\Delta(D^3) = D^3(z)\big|_{u_z<0} - D^3(z)\big|_{u_z>0}$

Eqs.(2) and (4) give the relationship between the condensed water in the ascending and descending parcels:

$$q(z)\big|_{u_z>0} < q(z)\big|_{u_z<0} \qquad (6)$$

Similarly Eq.(2) and (5) yield inequality:

$$D(z)\big|_{u_z>0} < D(z)\big|_{u_z<0} \qquad (7)$$

Thus, the condensed water content and droplet sizes in the ascending parcel are smaller than that of the descending one. Such behavior reversed for the supersaturation in Eq.(2)

The relationships between $S(z)$, $q(z)$ and $D(z)$ in ascending and descending cloud parcels described by inequalities in Eqs.(2), (6) and (7) are demonstrated in Fig.1.

b. In-cloud isobaric mixing

Consider vertical fluctuations of a cloud parcel under the same conditions as in Fig.1, with the only difference being that at the level z_1=515m, the descending parcel arriving to this level from z_2=590m (line CD in Fig.2a) mixes up with the parcel ascending through the cloud base (line AB in Fig.2a). Since the altitude of the cloud parcels at points B and D is the same, the mixing occurs isobarically. In the frame of this study, mixing is considered as a two step process consisting of (a) engulfing some fraction of air from a descending parcel into an ascending one, and then (b) mixing the entrained air with the recipient parcel. For simplicity, it is assumed that both parcels have a unit mass and that during mixing the μ-th mass fraction of the descending parcel entrains into the (1-μ)-th mass fraction of the ascending parcel. After mixing, the cloud parcel rises to the level z_2 and then descends back to the level z_1 where it mixes again with the ascending parcel arriving to this level though the cloud base. Then the process repeats.

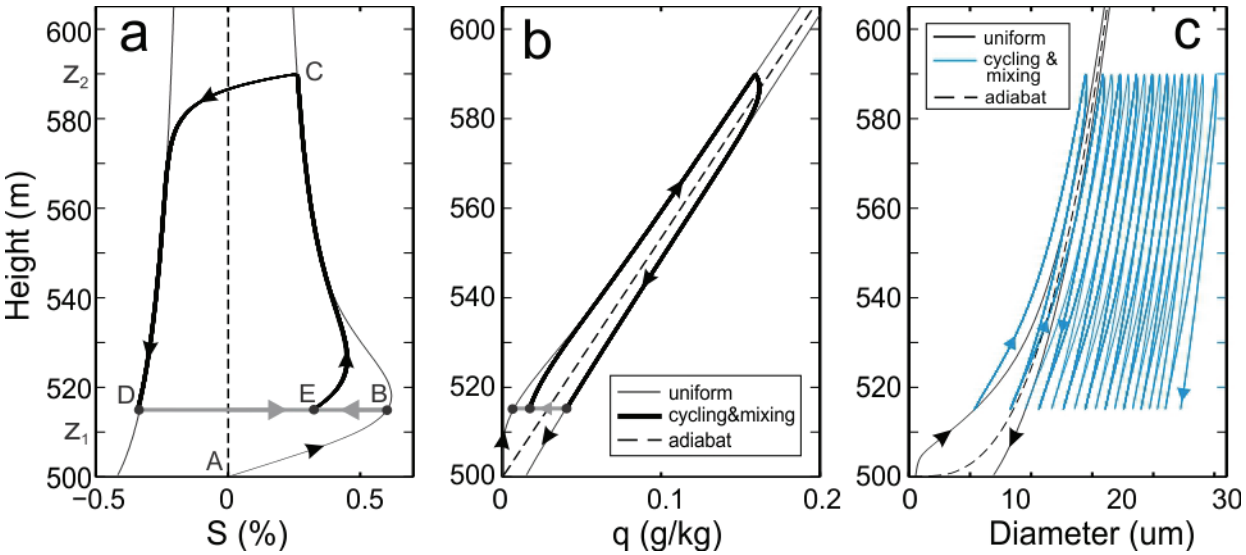

Figure 2. Same as in Fig.1 However, at level z_1=515 the descending parcel mixes with the cloud parcel ascending through the cloud base. After mixing the cloud parcel ascends to z_2=590m and descends back to z_1 and the process repeats. This repeated process for supersaturation (a) and liquid mixing ratio (b) forms limit cycles shown with thick lines, whereas, (c) the droplet size distribution experiences broadening. The number of cycles shown here is 9. The ratio of mixing of the parcels was μ=0.3.

As follows from Eqs.(2) and (7) the described process results in the entraining of undersaturated air from the descending parcel containing large droplets into the ascending parcel with supersaturated air and small droplets. Schematically this process is shown in Fig.3. The supersaturation S_m (point E in Fig.2a) resulting from the mixing of ascending and descending parcels satisfies the inequality (Appendix B):

$$S_2(z) \le S_m(z) \le S_1(z) \qquad (8)$$

where $S_1(z)$ and $S_2(z)$ are the supersaturation in points B and D, respectively (Fig.2a). It means that the supersaturation for the large droplets from the descending parcel *increases* after mixing, whereas for the small droplets in the ascending parcel the supersaturation *decreases* after mixing. Transferring large droplets from the undersaturated environment to the supersaturated one gives them an advantage in the diffusional growth as compared to the small ones. The large droplets sink the water vapor faster as compared to the smaller ones, therefore, the small droplets originated at the cloud base will experience lower supersaturation during ascent. Thus, the next ascent to z_2 and a subsequent descent to level z_1, large droplets will reach larger diameters, whereas small droplets will grow to even smaller diameters than those after the initial descent. Subsequent vertical fluctuations will result in a progressive increase of droplet sizes. Figure 2c demonstrates the increase of the droplets sizes during periodic vertical fluctuations with mixing at the level z_1.

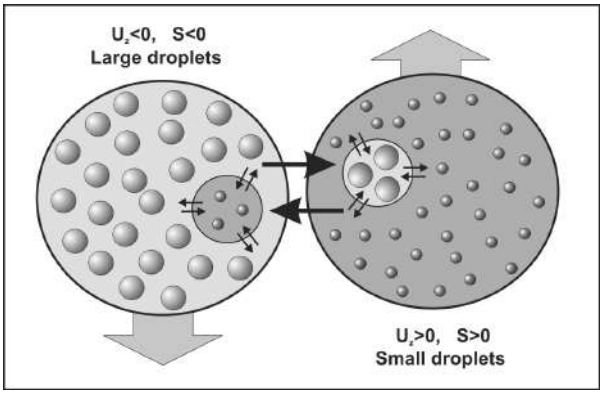

Figure 3. Conceptual diagram of isobaric mixing of ascending and descending cloud parcels.

It is important to note that periodic vertical fluctuations with mixing between parcels result in the formation of limit cycles for both $S(z)$ and $q(z)$ (Fig.2a,b). This type of behavior is similar to the case with no mixing in Fig.1ab. However, no limit cycles are formed for $D(z)$, if mixing takes place (Fig.2c).

For the case shown on Fig.2, during the first cycle, the ascending cloud parcel at z_1=515m consists of monodisperse droplets with $D_2 \approx 5.4\mu$m, whereas the descending parcel contains monodisperse droplets with $D_1 \approx 9.5\mu$m. After the first mixing, the droplet size distribution turns into a bimodal with the concentrations in the second and first modes $N_2 = (1-\mu)N$ and $N_1 = \mu N$, respectively (Fig.4a). After the second mixing the droplet size distribution becomes a tri-modal with sizes $D_3 \approx 5.4\mu$m $D_2 \approx 8.3\mu$m, $D_1 \approx 11.7\mu$m and concentrations $N_3 = (1-\mu)N$, $N_2 = (1-\mu)\mu N$, $N_1 = \mu^2 N$, respectively (Fig.4b). The sequence of transformations of the droplet size distribution during the first six cycles formed at z_1=515m is shown in Fig.4. The *k*-th cycle results in (*k*+1)-modal size distribution with the droplet number concentrations in the *j*-th mode:

$$N_j^{(k)} = \mu^k N \qquad (j=1) \qquad (9a)$$

$$N_j^{(k)} = (1-\mu)\mu^{k-j+1} N, \quad (2 \le j \le k+1) \qquad (9b)$$

where the superscript (*k*) denotes the cycle number. Summing $N_j^{(k)}$ in Eqs.(9a,b) yields that the droplet size distribution conserves its zero-th moment i.e. $\sum_{j=1}^{k+1} N_j^{(k)} = N$. In other words, during mixing the droplet number concentration always remains constant.

For vertical fluctuations *without mixing* the existence of the limit cycle for $D(z)$ means that for an arbitrary moment of time t_0

$$D(z, t_0 + \tau_t) - D(z, t_0) = 0 \qquad (10)$$

Eq.(10) means absence of the droplet size broadening. Integrating the equation of the droplet growth $\frac{dD}{dt} = \frac{AS_{eff}}{D}$ from t_0 to $t_0 + \tau_t$ yields:

$$D^2(t_0+\tau_t) - D^2(t_0) = 2A\int_{t_0}^{t_0+\tau_t} S_{eff}(t)dt \qquad (11)$$

Here, $S_{eff} = S + \left(1 - \frac{b}{D^3}\right)\exp\left(\frac{a}{D}\right)$ is the supersaturation corrected on the droplet salinity (Raoult's correction) and curvature (Kelvin's correction) (e.g. Rogers and Yau, 1976)

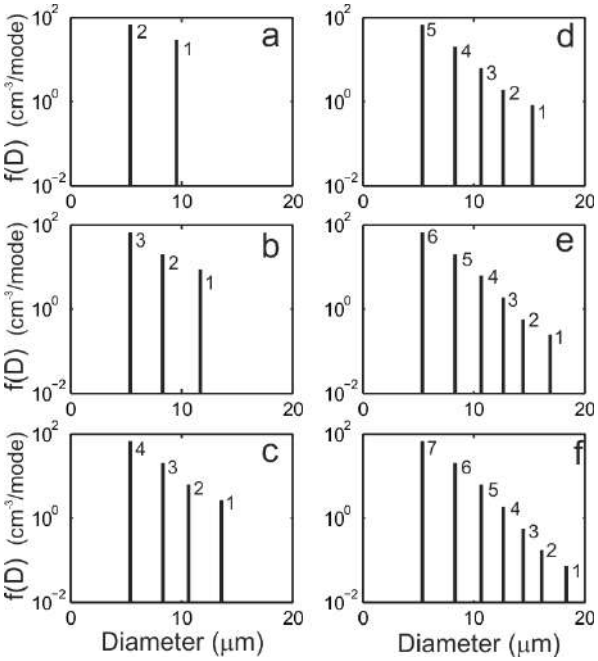

Figure 4. Progressive changes of the droplet size distributions at the level z_1=515m six successive cycles of ascents and descents with following mixing between descending parcel and the parcel ascending through the cloud base. The conditions correspond to those in Fig.2. The numbers indicate the mode numbers used in the text.

Substituting Eq.(10) in Eq.(11) gives:

$$\int_{t_0}^{t_0+\tau_t} S_{eff}(t)dt = 0 \qquad (12)$$

Eq.(12) indicates that for the case with no mixing the effective supersaturation averaged over one cycle is equal to zero, i.e $\overline{S}_{eff} = 0$.

For the case with mixing the limit cycle for $D(z)$ does not exist (Fig.2c), and as seen from Fig.4:

$$D_j(z, t_0+\tau_t) - D_j(z, t_0) > 0 \qquad (13)$$

Here, D_j is the droplet diameter of the *j*-th mode. Equating Eq.(11) and Eq.(13) gives:

$$\int_{t_0}^{t_0+\tau_t} S_{eff}(t)dt = \overline{S}_{eff}\tau_t > 0 \qquad (14)$$

Analysis of the results of numerical simulations suggests that the limit cycles exit for $\overline{S}_{eff}$, q and any moment of the droplet size distribution $N\overline{D^m}$. Specifically for the case of the effective supersaturation, the existence of the limit cycle for $\overline{S}_{eff}$ means that the area inside the contour $S_{eff}(z)$ remains constant with time, and therefore, $\overline{S}_{eff}$=const.

Eq.(11) allows for calculations of droplet diameters in the *j*-th mode after each cycle as:

$$D_j^{(k)} = \left(\left(D_j^{(k-1)}\right)^2 + 2A\overline{S}_{eff}\tau_t\right)^{1/2} \qquad (15)$$

Knowledge of $D_j^{(k)}$ Eq.(15) and $N_j^{(k)}$ Eq.(9) enables one to obtain the calculation of the evolution of the droplet size distribution. Thus, the problem of calculating the droplet size spectra for periodic fluctuations with μ=const can be reduced to finding the average of the effective supersaturation $\overline{S}_{eff}$ for one cycle, and calculating the term $\overline{dD^2} = 2A\overline{S}_{eff}\tau_t$ in Eq.(15).

Assuming that $\overline{S}_{eff}$ is the same for all droplets Eq.(15) gives a simple relationship between the droplet sizes in the *j*-th mode for the current and preceding cycles:

$$D_j^{(k)} = D_{j-1}^{(k-1)}, \qquad (3 \le j \le k+1) \qquad (16)$$

Eq.(16) means that with the exception of the first mode, the droplet size of the following mode in the next cycle repeats the size of the previous mode in the previous cycle. This behavior can be clearly seen in Fig.4, e.g. droplet diameter of the mode five formed after the fifth cycle (Fig.4e) is equal to the droplet diameter in the mode 4 formed after the fourth cycle (Fig.4d). The same type of repeated trajectories of $D_j^{(k)}$ are also demonstrated in Fig.2c.

3. Effect of different parameters of the droplet size distribution broadening

The purpose of this section is to examine the effects of different thermodynamical and environmental parameters on the efficiency of the broadening of the droplet size distribution. In particular, this section will be focused on how

droplet size spectra broadening is affected by: (a) elevation of the vertical fluctuations above the cloud base z, (b) spatial amplitude of the fluctuations Δz; (c) ratio of mixing μ; (d) droplet number concentration N, (e) vertical velocity u_z, (f) air temperature T; and (g) size of condensational nuclei r_{CCN}. These considerations are intended to help identify the most favourable conditions for droplet size broadening, and it aims to understand the mechanisms facilitating the warm rain initiation.

a. Effect of elevation over the cloud base

Figure 5 compares the droplet size spectra formed during the vertical fluctuations at two different altitudes, in a cloud with the cloud base at approximately 500m. The first size distribution was formed near the cloud base, when the cloud parcel fluctuations were limited to the range of $515<z<535$m, and the second one was fluctuating well above the cloud base at $780<z<800$m. Both droplet spectra were formed after ten vertical turnovers with the vertical amplitude Δz=20m and the ratio of mixing μ=0.3. The time required for the formation of both size distributions during the vertical fluctuations was approximately 6.7 minutes. As seen from Fig.5 the size distribution formed near the cloud base (curve 1) is essentially broader as compared to the one formed deep inside the cloud (curve 2).

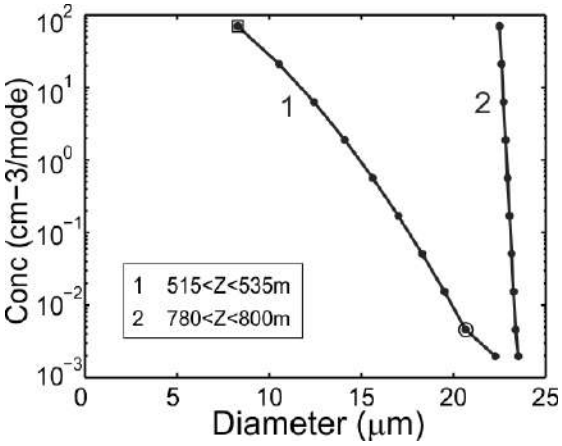

Figure 5. Comparisons of the droplet spectra formed during vertical fluctuations near the cloud base z_1=515m and z_2=530m and deep inside the cloud for z_1=780m and z_2=800m. The droplet size spectra were formed after ten turnovers with the vertical velocity $|u_z|$=1m/s and ratio of mixing μ=0.3. Initial conditions are the same as in Fig.1.

Figure 6 shows the trajectories of supersaturation $S(z)$ and $D(z)$ for the both cases. As seen from Fig.6a the trajectory $S(z)$ near the cloud base (curve 1) has a stronger asymmetry and a stronger bias toward positive values than the one that is elevated 300 meters above the cloud base. Therefore, it is anticipated that the $\overline{S}_{eff}$ and $\overline{dD^2}$ for the first case will be higher than for the second case, and that the size spectra broadening near the cloud base will be more efficient. This conclusion is in agreement with the dependences $\overline{S}_{eff}$ and $\overline{dD^2}$ versus z shown in Fig.7, which were obtained from the numerical simulations. As seen from Fig.7 both $\overline{S}_{eff}$ and $\overline{dD^2}$ have their maximum near the cloud base and then they rapidly decrease with the increase of z. This is suggestive of the fact that the maximum rate of the spectra broadening occurs in the vicinity of the cloud base, where the maximum of supersaturation is formed. Fig.7b also shows that the differences between $\overline{dD^2}$ calculated for the fluctuations with ΔZ >20m (curves 4, 5, and 6) are quite small. Therefore, increasing the amplitude of the vertical fluctuations beyond a certain threshold value Δz_s will not result in further broadening of the droplet size spectra.

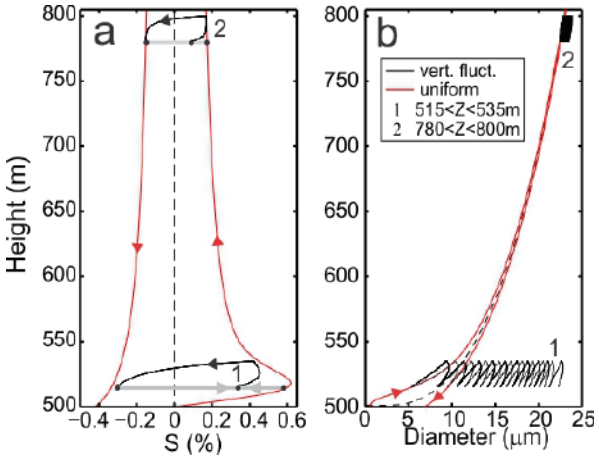

Figure 6. Vertical changes of supersaturation *S(z)* (a) and droplet diameter *D(z)* (b) obtained from the numerical simulation of droplet size spectra formed during vertical fluctuations at two levels above the cloud base (1) 515<z<535m and (2) 780<z<800m (see Fig.5). For both cases the vertical velocity was $|u_z|$=1m/s. Initial conditions are the same as in Fig.1.

As mentioned in the previous section, the droplet size spectra can be estimated from Eq.(15). As follows from Eq.(16) $D_{10}^{(10)} = D_2^{(2)}$, where $D_2^{(2)}$ and $D_{10}^{(10)}$ are the diameters of the 2nd and 10th modes, respectively, formed after the second and tenth cycles. The diameter $D_{10}^{(10)}$ is indicated on Fig.5 by an open square and it is equal to $D_{10}^{(10)} \approx 8.29$ μm. The diagram in Fig.7b gives $\overline{dD^2} \approx 42.47 \mu m^2$. Then, substituting $D_2^{(2)}$ and $\overline{dD^2}$ in Eq.(15) yields $D_2^{(10)} = \left(\left(D_2^{(2)} \right)^2 + n \cdot \overline{dD^2} \right)^{1/2} \approx 20.2$ μm formed after *n*=8 cycles. Eq.(9b) gives the concentration of droplets in the second mode after eight turnovers $N_2^{(10)} \approx 0.0046 cm^{-3}$. The numerical simulations give $D_2^{(10)} \approx 20.6$ μm and $N_2^{(10)} \approx 0.0046 cm^{-3}$, which are close to those found above, analytically. $D_2^{(10)}$ is indicated by a circle on Fig.5.

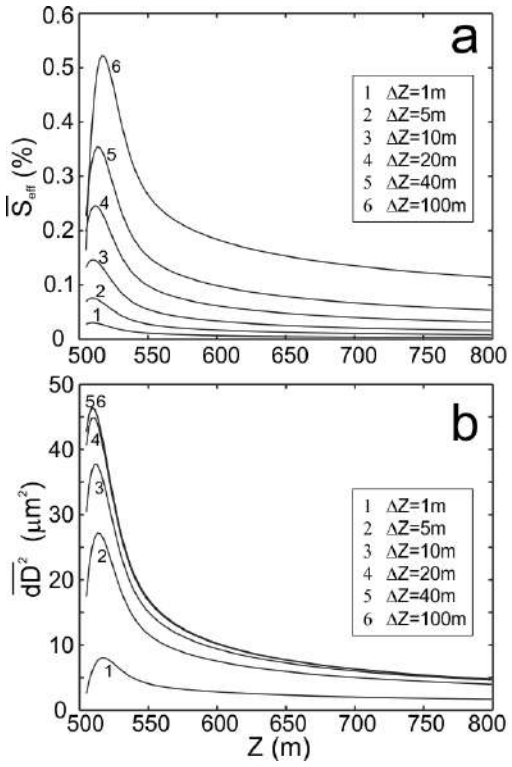

Figure 7. Changes of $\overline{S}_{eff}$ and $\overline{dD^2}$ versus altitude over the cloud base z. Both $\overline{S}_{eff}$ and $\overline{dD^2}$ are averaged over the period of one fluctuation τ_t and droplet size distribution.

b. Effect of amplitude of vertical fluctuations

Figure 8 shows droplet size distributions calculated for different amplitudes of the vertical fluctuations Δz =5m, 10m, 20m, and 30m in the vicinity of supersaturation maximum near the cloud base. The supersaturation maximum was located at $z_{max} \approx 18.1$m. Since the fluctuations had the same lower level z_1 =515m and different upper levels z_2, the size distributions were compared at z_1. As seen from Fig.8, the width of the droplet size spectra progressively increased, when Δz changed from 5m to 20m. However, an increase of Δz from 20m and 30m does not cause any significant increase of the spectra width. The numerical simulation showed no further broadening for Δz >30m in this case. The vertical amplitude, beyond which no increase of the broadening occurs will be referred to as the saturation amplitude Δz_s. The value of Δz_s is determined by the vertical distance, at which the trajectory of the limit cycle of $S(z)$ aligns with the supersaturation of the uniformly ascending parcel with no mixing. For a uniform ascent $\Delta z_s \propto u_z \tau_p$, where τ_p is the time of phase relaxation (Eq.(1)), determining the characteristic time of equilibrating supersaturation. The value of Δz_s depends on a number of parameters such as z_1, *N, D,* u_z, μ.

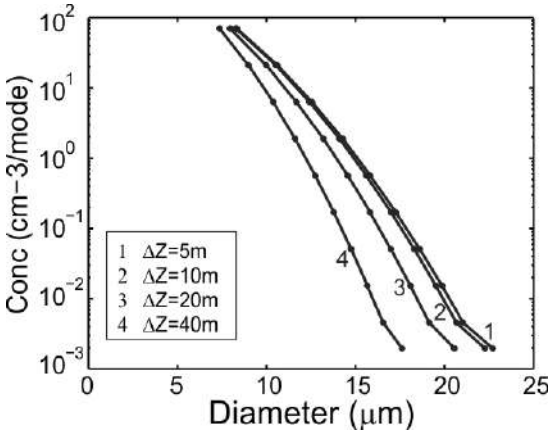

Figure 8. Comparisons of the modeled droplet size spectra formed for different amplitudes of the vertical fluctuations. All size distributions were formed at z_1=515m. Initial conditions are the same as in Fig.1.

Thus, Fig.9 shows the trajectories $S(z)$ for the cases Δz=5m and 30m associated with the formation of the size distributions in Fig.8. Despite the fact that for Δz=5m the supersaturation always remains positive (curve 1) the size spectra broadening is less efficient than the case of when Δz=30m. The low rate of broadening for Δz=5m is related to the short period of fluctuations τ_t, which result in a small decrement in the droplet diameter after each cycle.

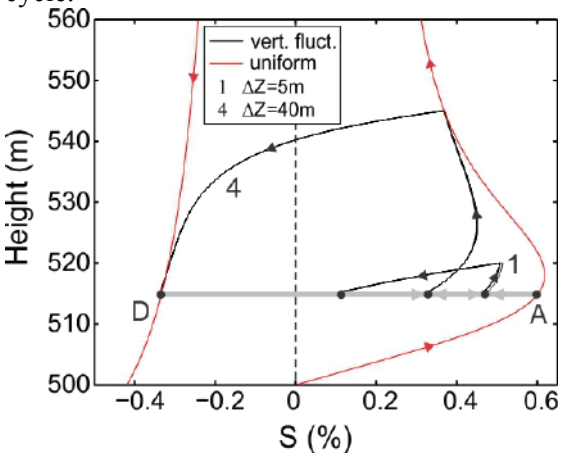

Figure 9. Vertical changes of supersaturation *S(z)* obtained from the numerical simulation of droplet size spectra formed during vertical fluctuations at two levels above the cloud base (1) 515<z<520m and (4) 515<z<545m (see Fig.8). For both cases, the vertical velocity was $|u_z|$=1m/s. Initial conditions are the same as in Fig.1.

Figure 10 shows the dependences of $\overline{S}_{eff}$ and $\overline{dD^2}$ versus Δz deduced from the numerical simulations. For the cases with $z_1 > z_{\max}$ (curves 2-5), the effective supersaturation $\overline{S}_{eff}$ is monotonically decreasing, whereas $\overline{dD^2}$ is monotonically increasing with the increase of Δz, i.e. $\overline{S}_{eff}$ and $\overline{dD^2}$ change in the opposite direction with respect to one another. Such behavior of $\overline{dD^2}$ is caused by its relation to $\overline{S}_{eff}$, i.e. $\overline{dD^2} \propto \overline{S}_{eff}\tau_t$, resulting in the fact that the decrease of $\overline{S}_{eff}$ is cancelled by the increase of the period of fluctuations τ_p with the increase of Δz.

For the cases with $z_1 < z_{\max}$ (curve 1), the effective supersaturation $\overline{S}_{eff}$ reaches a maximum near the cloud base and then monotonically decreases. The general behavior of $\overline{dD^2}$ is similar to the cases when $z_1 > z_{\max}$, i.e. it monotonically increases and then reaches saturation, although its value is higher than when $z_1 > z_{\max}$. Analysis of the dependence of $\overline{dD^2}$ on Δz and z showed that $\overline{dD^2}$ has maximum value when:

$$z_1 < z_{\max} < z_2 \qquad (17).$$

As seen from Fig.10b, at some point, $\overline{dD^2}$ reaches its saturation, so that $\overline{dD^2}$ remains constant with an increase of $\Delta z > \Delta z_s$. The saturation amplitude Δz_s changes from approximately 25m fluctuations near the cloud base (curve 1 in Fig.10b) to only a few meter fluctuations that occur far from the cloud base (curve 5).

As mentioned above, for $\Delta z > \Delta z_s$ the width of the size distribution formed after the same number of cycles – regardless of Δz – will remain the same. However, because the period of fluctuations τ_t increases with the increase of Δz, this means that the formation of the size distribution will take a longer time for the larger Δz. Therefore, the rate of broadening becomes less efficient with the increase of Δz. The analysis of the results of simulation showed that the rate of broadening has its maximum when $\Delta z \sim \Delta z_s$.

The above analysis suggests that there is an optimal amplitude and altitude for the vertical fluctuations when the maximum efficiency of the size distribution broadening can be reached: $z_1 < z_{\max} < z_2$ and $\Delta z \sim \Delta z_s$.

c. Effect of the ratio of mixing μ

Figure 11 shows comparisons of three droplet size spectra calculated for three different ratios of mixing μ=0.1, 0.5 and 0.9. The size spectra were formed after 6.7min of vertical fluctuation with 515<z<535m. As seen from Fig.11 the droplet size spectra are broader for smaller μ.

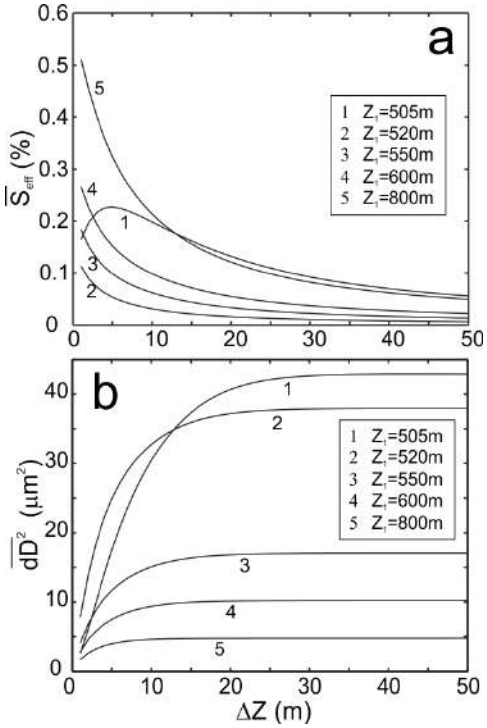

Figure 10. Changes of $\overline{S}_{eff}$ and $\overline{dD^2}$ versus the amplitude of the vertical fluctuations Δz. Both $\overline{S}_{eff}$ and $\overline{dD^2}$ are averaged over the period of one fluctuation τ_t and the droplet size distribution. Initial conditions are the same as in Fig.1.

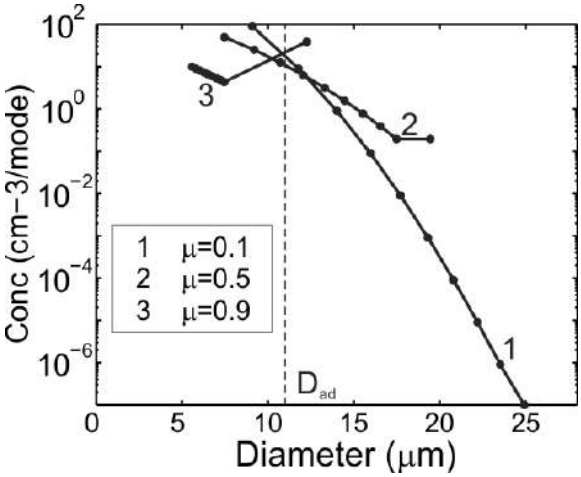

Figure 11. Comparisons of the droplet size spectra formed at 515m during the vertical fluctuations with different ratios of mixing μ. The rest of the conditions were the same as in Fig.1 and identical for all cases. The vertical dashed line indicates the adiabatic droplet size for a monodisperse size distribution.

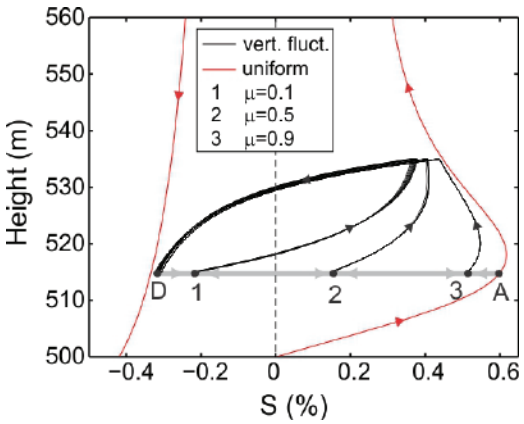

Figure 12. Vertical changes of supersaturation *S(z)* obtained from the numerical simulation of droplet size spectra formed during vertical fluctuations for different μ (see Fig.11). For both cases, the vertical velocity was $|u_z|$=1m/s. Initial conditions are the same as in Fig.1.

As seen from Fig.12 the initial supersaturation (points 1,2,3) resulting from the mixing of ascending (point A) and descending (point D) parcels increases with the decrease of μ. As a result the effective supersaturation $\overline{S}_{eff}$ increases with the decrease of μ. Therefore, droplets will grow to larger sizes after each cycle for smaller μ. However, as follows from Eq.(9a) the concentration of the droplets with maximum diameters decreases as μ^k. For the case μ=0.1 the concentration of large droplets after ten cycles grows small (10^{-7}cm^{-3}) and becomes too insignificant for cloud processes. For μ=0.5 droplets grow slower than in the previous case, however, their concentration is larger. For μ=0.9 the initial supersaturation is negative (point 3 in Fig.12). This case results in the evaporation of small droplets and the broadening of the droplet size distribution towards small sizes (curve 3 in Fig.11). It should be noted that cases with μ<0.5 result in the formation of bimodality, which becomes more pronounced for μ<0.2 (e.g. Fig.11). Figure 13 shows that both $\overline{S}_{eff}$ and $\overline{dD^2}$ decrease nearly linearly with the increase of μ.

Thus, the decrease of μ results in enhanced growth of large droplets, however, their concentration rapidly decreases after each mixing event. For small μ<0.1 the concentration of the large droplets becomes insignificant for any cloud processes after several mixing cycles.

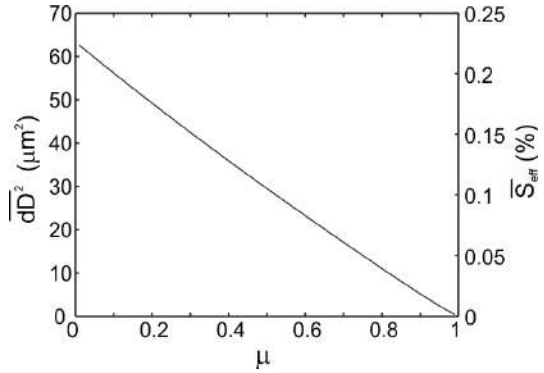

Figure 13. Changes of $\overline{S}_{eff}$ and $\overline{dD^2}$ versus the ratio of mixing μ. Both $\overline{S}_{eff}$ and $\overline{dD^2}$ are averaged over the period of one fluctuation τ_t and the droplet size distribution. Initial conditions are the same as in Fig.1.

d. Effect of droplet number concentration

Figure 14 illustrates the results of droplet size spectra simulation for four different concentrations. As it was shown in previous studies (e.g. Pinsky et al 2012) the supersaturation maximum $S_{\max}$ and its altitude over the cloud base $z_{\max}$ change as $N^{-1/2}$. Therefore, in order to achieve maximum efficiency of the size spectra broadening and to satisfy the condition in Eq.(17) the levels z_1 and z_2 should be adjusted in accordance with changes of $z_{\max}$ and N. To achieve this goal, the vertical fluctuations were set so that $z_1 = z_{\max}$ and Δz=20m. Under these conditions the duration of the size spectra formation remained the same for all cases.

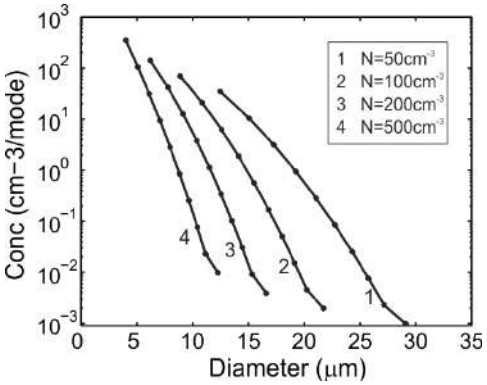

Figure 14. Comparisons of the modeled droplet size spectra calculated for the different droplet number concentrations. For all cases the vertical velocity was $|u_z|$=1m/s.The lower level and amplitude of the fluctuations were set $z_1=z_{\max}$ and Δz=20m. The rest of the conditions are the same as in Fig.1.

It appears that the number concentration has a significant effect on the broadening. As seen in Fg.14, after 6.7 minutes of vertical fluctuations and mixing, the droplet size spectra had a width of ΔD = 5.7μm, 9.5μm, 14.0μm and 19.5μm for the droplet number concentrations 500cm^{-3}, 200cm^{-3}, 100cm^{-3}, 50cm^{-3}, respectively. Thus, the width of the size spectra increase with the decrease of the droplet number concentration.

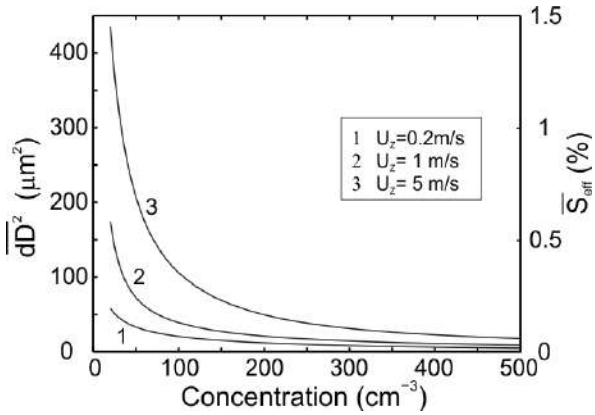

Figure 15. Changes of $\overline{S}_{eff}$ and $\overline{dD^2}$ versus droplet number concentration N calculated for three different vertical velocities. Modeling was preformed for $z_1=z_{\max}$ and Δz=20m. The rest of the conditions are the same as in Fig.1.

Figure 15 shows the dependence of $\overline{S}_{eff}$ and $\overline{dD^2}$ versus N for different u_z. As seen from Fig.15 both $\overline{S}_{eff}$ and $\overline{dD^2}$ rapidly increase below N=100cm^{-3}.

e. Effect of vertical velocity u_z

Figure 16 exhibits a set of comparisons of the droplet size spectra calculated for different velocities of the vertical fluctuations u_z. Both maximum supersaturation $S_{\max}$ and its altitude above the cloud base $z_{\max}$ depend on the vertical velocity as $S_{\max} \propto u_z^{3/4}$ and $z_{\max} \propto u_z^{3/4}$ (e.g. Pinsky et al 2012). Therefore, for the calculations of the size distributions in Fig.16 similar to the previous section the lower level of the vertical fluctuations, which was set at $z_1 = z_{\max}$. The vertical amplitude was selected to be $\Delta z \propto u_z$ in order to keep the same time duration required for the formation of the droplet size spectra and to facilitate their comparisons.

As seen from Fig.16, the vertical velocity has a strong effect on the droplet size spectra broadening and it increases with the increase of u_z. This conclusion is consistent with the diagram in Fig.17 showing an increase of both $\overline{S}_{eff}$ and $\overline{dD^2}$ with the increase of u_z.

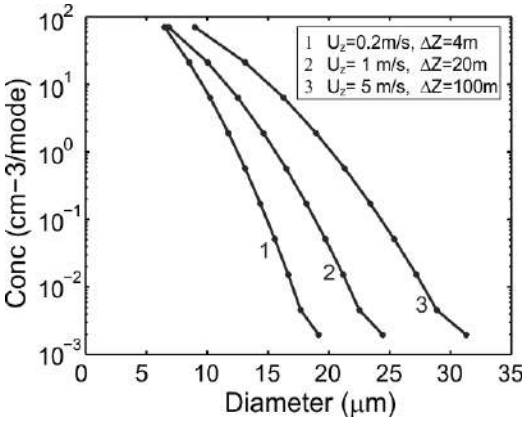

Figure 16. Comparisons of the modeled droplet size spectra formed for different velocities of vertical fluctuations. The lower level and amplitude of the fluctuations were set at $z_1=z_{\max}$ and Δz=20m. The rest of the conditions are the same as in Fig.1.

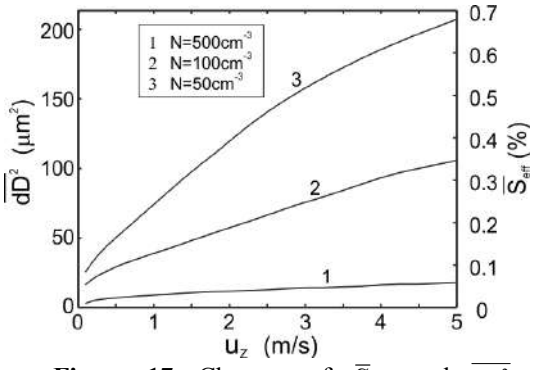

Figure 17. Changes of $\overline{S}_{eff}$ and $\overline{dD^2}$ versus vertical velocity u_z calculated for three different droplet concentrations. The lower level and amplitude of the fluctuations were set at $z_1=z_{\max}$ and Δz=20m. The rest of the conditions are the same as in Fig.1.

f. Effect of temperature T

Figure 18 depicts a set of comparisons of the droplet size spectra formed at 530m for five different temperatures at the cloud base -20C<T<20C. As seen from Fig.18, the effect of broadening increases with the increase of temperature. The rate of the broadening slows down with the increase of temperature. Such behavior is explained by the decrease of the rate of the growth of droplets due to the temperature dependence of the coefficient $A(T,P)$ in the droplet growth equation $D\frac{dD}{dt}=AS_{eff}$. The coefficient $A(T,P)$ monotonically decreases with the decrease of both temperature T and pressure P.

Figure 19 shows the dependencies of $\overline{S}_{eff}$ and $\overline{dD^2}$ calculated for three different z_1. Evidently, Fig.19 shows the effective concentration $\overline{S}_{eff}$ is monotonically decreasing with the decrease of T, whereas $\overline{dD^2}$ is monotonically increasing due to the compensation effect of the coefficient $A(T,P)$. Figure 19b also shows that $\overline{dD^2}$ decreases with the decrease of air pressure. Thus, the diagrams in Figs.18 and 19 are suggestive of the fact that the formation of liquid precipitation will be hindered with the decrease of temperature and air pressure. This conclusion is consistent with the low frequency of the observation of liquid precipitations from cold, high-altitude clouds.

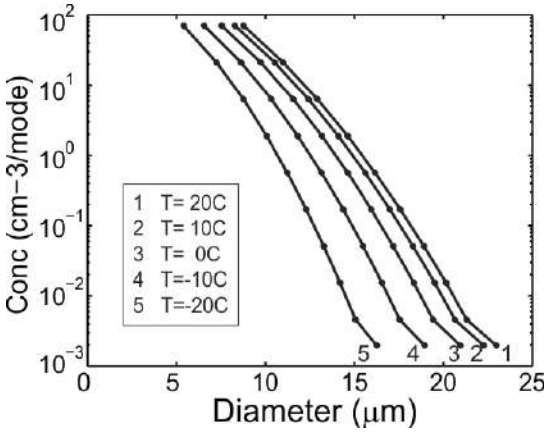

Figure 18. Comparisons of the modeled droplet size spectra calculated for different air temperatures. The rest of the conditions are the same as in Fig.1.

g. Effect of cloud condensational nuclei.

Figure 20 shows comparisons of the droplet size spectra calculated for different cloud condensation nuclei (CCN) on which the droplets were formed. The results of the calculations suggest that the droplet spectra width increases with the decrease of the CCN radius r_{CCN}. Such behavior is explained by the fact that the droplets with larger r_{CCN} have a higher rate of the water vapor depletion.

Therefore, the maximum supersaturation $S_{\max}$ formed near the cloud base will be lower for larger r_{CCN}. Lower supersaturation will result in the slowing down of the broadening of the size distribution formed during vertical fluctuations and mixing.

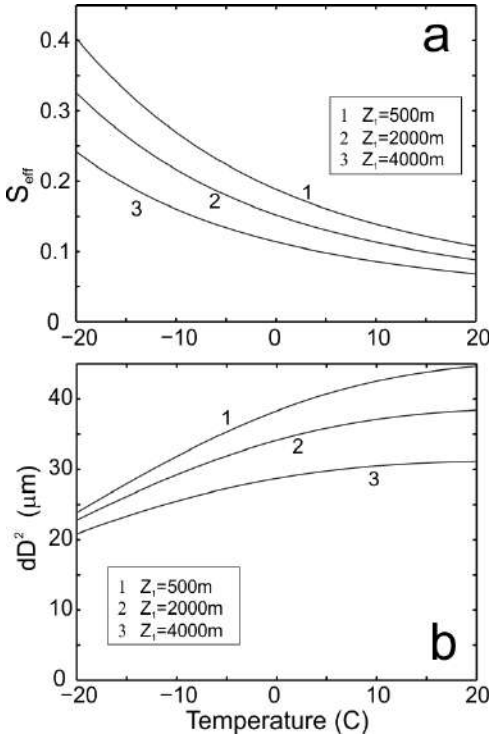

Figure 19. Changes of $\overline{S}_{eff}$ and $\overline{dD^2}$ versus vertical velocity u_z calculated for three different droplet concentrations. The lower level and amplitude of the fluctuations were set $z_1=z_{\max}$ and Δz=20m. The rest of the conditions are the same as in Fig.1.

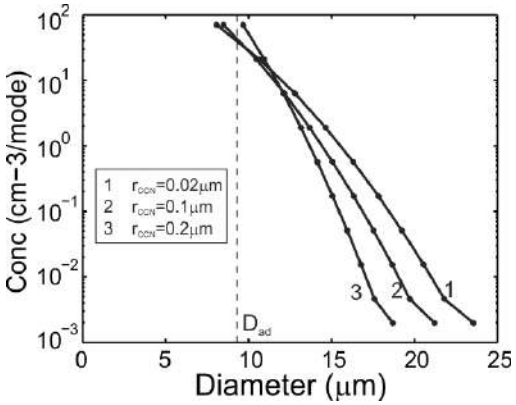

Figure 20. Comparisons of the modeled droplet size spectra calculated for different radii of CCN r_{CCN}, on which the droplets were formed. The rest of the conditions are the same as in Fig.1.

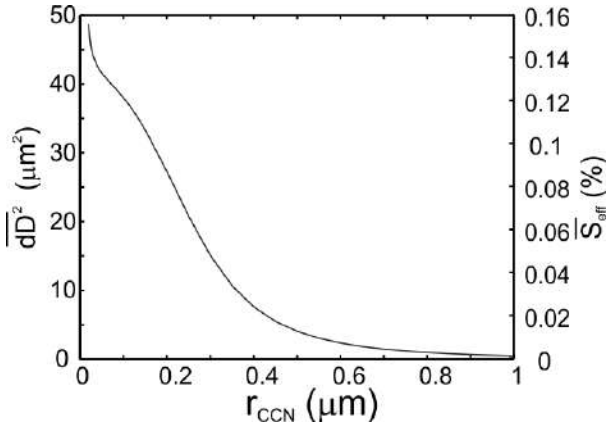

Figure 21. Changes of $\overline{S}_{eff}$ and $\overline{dD^2}$ versus CCN radius r_{CCN}, on which the droplets were formed. The rest of the conditions are the same as in Fig.1.

Figure 21 illustrates the dependencies of $\overline{S}_{eff}$ and $\overline{dD^2}$ versus r_{CCN}. As seen from Fig.21, the size of the CCN has a pronounced effect on the broadening as well as $\overline{S}_{eff}$ and $\overline{dD^2}$ which both increase with the decrease of r_{CCN}.

The obtained results suggests that droplet size spectra formed on smaller CCN will broaden faster than the spectra formed on larger CCN. This conclusion is the opposite of what was proposed in the frame of the hypothesis of the warm rain initiation by giant CCN, suggesting that the droplets formed on large CCN are subject of enhanced diffusional growth, which rapidly grow beyond 40μm.

4. Discussion

a. Turbulence

In the previous sections we discussed an idealized process of droplet size distribution broadening during vertical fluctuations accompanied by isobaric mixing. One of the critical assumptions made when describing turbulence was related to multiple turnovers of the turbulent eddy. It was assumed the a turbulent parcel may perform several up and down cycles without complete mixing and that it keeps the same vertical velocity $|u_z|$. For isotropic turbulence, the characteristic time of mixing of the cloud parcel with the spatial scale L is determined by $\tau_m = \left(L^2/\varepsilon\right)^{1/3}$, where ε is the turbulent energy dissipating rate. In

stratiform clouds, ε is typically 10^{-3} - 10^{-4} m^2 s^{-3} (e.g. MacPherson and Isaac, 1977; Mazin et al. 1984). For a cloud parcel with L~10m, the characteristic time of mixing τ_m in the order of 10^1-10^2 s. For a vertical velocity $|u_z|$~1m/s the lifetime of such a parcel will be limited by approximately one to two turnovers. Parcels with a smaller spatial scale will have a shorter lifetime. This may be a significant limitation of the hypothesis of broadening examined in this study. Based on the above consideration, the cloud parcel has to undergo 8 to 10 cycles of vertical fluctuations in order to reach the droplet spectra broadening sufficient for the beginning of the collision-coalescence process. Formation of such coherent structures in the cloud regions with isotropic turbulence is highly unlikely.

In order to overcome this problem, it is hypothesized that the existence of recirculating (coherent) turbulent eddies with the characteristic scale L~ 10^0-10^1m may be associated with the regular vertical updrafts. The recirculating vorticity may form at the interfaces of "updraft-still air" or an "updraft-downdraft" with the high velocity shear as a result of the Kelvin-Helmholtz instability. Existence of such structures was discussed by LeMone (1973). Obviously, the characteristics of turbulence in such cloud regions will be essentially non-isotropic. The lifetime of the coherent eddies will be determined by the existence time of the updraft at this level. During this time small scale recirculation can exist providing required recirculation of droplets.

The existence of the localized updrafts in stratocumulus clouds is supported by the dopplerized remote sensing observations (e.g. LeMone, 1973; Kollias and Albrecht, 2000; Pinsky et al 2008) and in-situ measurements (e.g. Lothon et al, 2004 Lenschov et al, 1980) and in numerical simulations (e.g. Khain and Ingel, 1995; Stevens et al, 1998)

b. Mixing

Another critical assumption used in the simulation of broadening has to do with the way the process of mixing in the numerical simulation is presented. In the numerical simulation mixing was considered as a process of instant engulfing of cloudy air and instant mixing with the recipient parcel. Based on the currently used concepts of turbulence (Broadwell and Breidenthal, 1982) mixing is a cascade of mass exchange between engulfing cloud volumes coming from opposite parcels into localized zones. The initially large-scale parcels break down into smaller ones due to turbulence. The turbulence stretches the interface between the engulfed volumes and exchanges the molecular diffusion across the increasing surface. The actual mixing of the engulfed volume is a molecular diffusion process that is most effective after the broken down volumes reduce to the Kolmogorov viscosity scale. The described process of mixing requires some time to mix up into a viscous state. This mixing time was not accounted in the present study. One of the consequences of neglecting the mixing time is that droplet size spectra broadening of may take a longer time than the time obtained in this study.

c. Radiation

Previous studies have shown that the radiation process plays important role in the formation and maintenance of stratiform clouds (e.g., Herman and Goody, 1976; Stevens et al., 2005). Cloud top cooling stimulates the formation of turbulent eddies and results in a formation of cloud top inversion, which stabilizes the cloud layer. The characteristic time of the radiation processes is of the order of tens of minutes and hours, which is significantly larger than the characteristic time of the droplet spectra broadening. Based on the discussions in the previous sections, the broadening presumably occurs near the cloud base, where the longwave radiation processes are usually smaller than that near the cloud top. Thus, it is anticipated that the radiation processes are not significant for the droplet size spectra broadening discussed in the frame of this study.

5. Conceptual model of the droplet spectra broadening

Based on the above consideration, the following conceptual model of the broadening of the droplet size spectra and initiation of warm precipitation is proposed here. The initial broadening occurs near the cloud base, where the cloudy air is enriched with supersaturated water vapor. The basic mechanism of the broadening consists in entraining of the undersaturated air

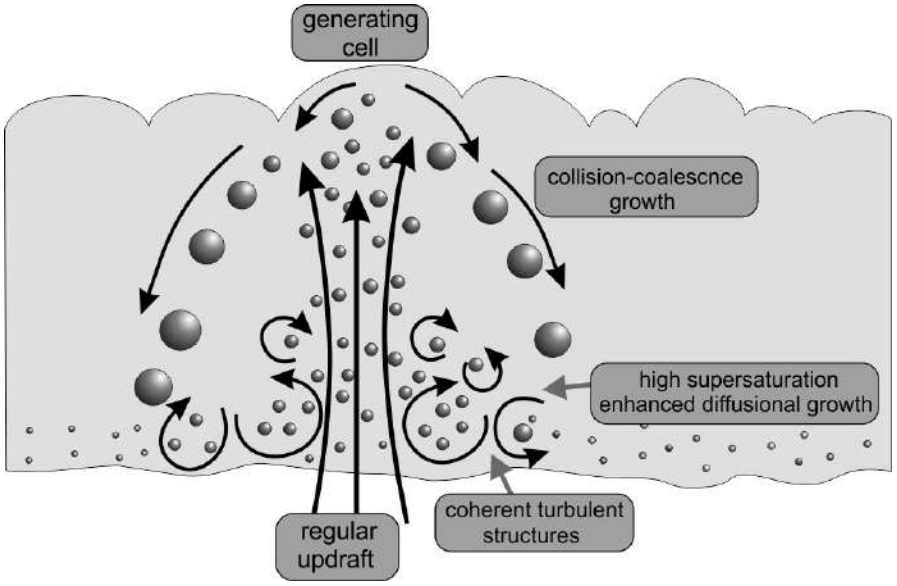

Figure 21. Conceptual diagram of precipitation formation in a stratiform cloud layer.

with larger droplets from a descending cloud parcel into an ascending parcel with high supersaturation and smaller droplets, which arrives to this level through the cloud base. The isobaric mixing of two parcels with a subsequent ascent enhances the rate of growth of large droplets versus the smaller ones. The repeated ascent-descent cycle, along with mixing broadens the size distribution by pumping supersaturated air into cloud parcels with depleted water vapor by means of mixing with ascending parcel containing supersaturated air.

The primary droplet size spectra broadening may occur in the coherent turbulent vortices, which may form at the interface of regular updrafts and still cloud air or downdrafts. The characteristic size of the coherent vortices required for the broadening ranges from a few meters to dozens of meters depending on the vertical velocity. After the primary broadening, the cloud parcels are engulfed by the regular updraft and then brought up to the cloud top. This will result in additional droplet growth, although the size distribution will experience narrowing. After ascending to the cloud top, some fraction of the droplets reach D>40μm. Such droplets will continue subsequent growth through the collision-coalescence process and may initiate precipitation formation. The illustration depicting this conceptual model is shown in Fig.21.

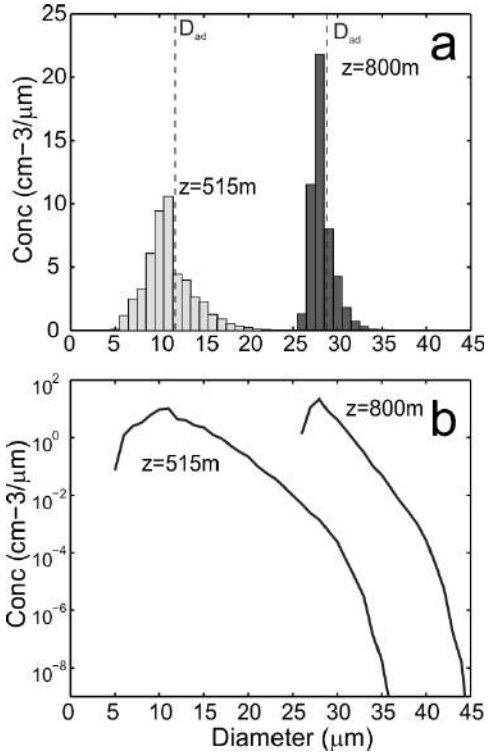

Figure 22. Average droplet size distribution formed as a result of multiple mixings of ascending and descending parcels t_1=9.8min; t_2=14.3min. The numerical simulation performed for μ randomly changes from 0 to 1 and vertical fluctuations 515m<z<535m. The rest of the conditions are the same as in Fig.1. The vertical dashed lines indicate the adiabatic diameter for monodisperse droplets having the same number concentration.

Figure 22 shows droplet size spectra averaged over number of droplets formed after vertical fluctuations with Δz=20m. During modeling the ratio of mixing μ was randomly changed from 0 to 1. Calculating the mixing using a random μ is more realistic as compared to μ=const used in the above simulations. The primary broadening occurred near the cloud base 515m<z<535m. As seen from Fig. 22a random μ results in broadening towards both large and small droplets, making the droplet size distribution appear similar to those observed in clouds. After the primary broadening near the cloud base, the parcel would uniformly ascend to z=800m. As seen from Fig.22b, the droplet size distribution near the cloud base contains droplets D~30μm with a concentration of N~1l^{-1}. The time required for the primary broadening is approximately 9.8 minutes. After lifting this parcel 300m these droplets grew up to D~40μm. At that point, the droplets reach the size sufficient for growth through the collision-coalescence process. The modeling time required for the secondary broadening (which includes the primary broadening time) was approximately 15 minutes.

6. Conclusions

In the frame of this study, we examined the effect of in-cloud isobaric mixing on the broadening of the droplet size distribution. With the help of a simple parcel model it has been demonstrated that vertical fluctuations with a characteristic scale of a few meters up to a few dozens of meters may broaden droplet size distribution within several minutes. The droplet size spectra broadening is most effective in the vertical fluctuations near the cloud base in the vicinity of maximum supersaturation, i.e. when $z_1 < z_{\max} < z_2$. Vertical fluctuation a few hundred meters above the cloud base does not result in any significant size distribution broadening. The effect of broadening is quite sensitive to the droplet number concentration N as well as the vertical velocity u_z and the broadening increases with the decrease N and the increase of u_z. It turns out that the effect of broadening is slowed down by a large CCN. Despite the fact that the mixing disturbs the adiabaticity of the individual parcels, it conserves mass and energy of the entire layer. As a result, the liquid water and temperature profiles remain adiabatic and wet-adiabatic, respectively.

The proposed mechanism of droplet size spectra broadening is also applicable in explaining the formation of droplets with D~40μm and a concentration of N~1l^{-1}, which is sufficient in initiating warm rain via the collision-coalescence process, and it does not require assumptions regarding the presence of giant CCN, stochastic condensation, or entrainment and inhomogeneous mixing. Although, it must be noted, these mechanisms may be complementary to that examined in this study.

The structure of turbulence and the existence of efficient small scale recirculation near the cloud base plays a critical role for the formation of large droplets and size distribution broadening. An increase of the amplitude of in-cloud recirculation, leading to droplet ascent toward the cloud top or to decent well below the cloud base, will decrease the efficiency or even completely cancel the effect of droplet broadening. Under the typical turbulent dissipation rate in stratocumulus clouds of 10 cm^2 s^{-3} (e.g., Siebert et al 2006; 2010a,b), vertical velocities are too weak to generate small scale recirculation near the cloud base. However, the droplet recirculation can be stimulated by either large eddies or embedded convection, observed in stratocumulus (Siebert et al. 2006; 2010). In both cases, the formation of intense small scale recirculation near the cloud base appears to be rare. Thus, in spite of the fact that the mechanism of large droplet formation discussed in the present study is very efficient, the conditions favorable for its initiation may not always be present in clouds. This is in agreement with observations that drizzle may form after several hours after the cloud formation. This is suggestive of the fact that the formation of drizzle in stratocumulus clouds may be associated with “lucky” air volumes, whose formation and transport to the cloud top is related to large eddies. The correlation between drizzle events and large eddies was observed by Stevens et al. (2005) and simulated by Mgaritz et al (2009).

We admit that the simplifications and assumptions used in the frame of this study may result in the overestimation of the effect of

broadening. In order to address this concern a more detailed analysis of the effect of turbulent fluctuations and mixing on the droplet size spectra broadening should be performed with the help of direct numerical simulation of the Navier-Stokes equations.

Acknowledgements

A. Korolev work is supported by Environment Canada. A. Khain and M. Pinsky are supported by the Office of Science (BER), US Department of Energy Award DE-SC0006788 and the Binational US-Israel Science Foundation (grant 2010446).

Appendix A. List of Symbols (not finished yet)

Symbol	Description	Units
A_1	$\frac{g}{R_a T}\left(\frac{L_w R_a}{c_p R_v T}-1\right)$	m^{-1}
A_2	$\frac{1}{q_v}+\frac{L_w^2}{c_p R_v T^2}$	-
c	$\frac{4\pi\rho_w}{\rho_a} A_2 A$	$m^2\ s^{-1}$
c_p	specific heat capacity of moist air at constant pressure	$J\ kg^{-1}K^{-1}$
C	constant	-
$\overline{dD^2}$	$2A\overline{S}_{eff}\tau_t$	m^2
D	diameter of droplets	m
D_v	coefficient of water vapor diffusion in the air	$m^2\ s^{-1}$
e	water vapor pressure	$N\ m^{-2}$
e_w	saturation vapor pressure above flat surface of water	$N\ m^{-2}$
g	acceleration of gravity	$m\ s^{-2}$
A	$\left(\frac{\rho_w L_w^2}{k_a R_v T^2}+\frac{\rho_w R_v T}{e_w(T) D_v}\right)^{-1}$	$m^{-2}\ s$
k_a	coefficient of air heat conductivity	$J\ m^{-1}s^{-1}K^{-1}$
L_w	latent heat for liquid water	$J\ kg^{-1}$
N	total concentration of liquid droplets	m^{-3}
$N_j^{(k)}$	concentration of droplets in the *j*-th mode formed after *k*-th cycle	m^{-3}
P	pressure of moist air	$N\ m^{-2}$
r_{CCN}	radius of CCN	m
R_a	specific gas constant of moist air	$J\ kg^{-1}K^{-1}$
R_v	specific gas constant of water vapor	$J\ kg^{-1}K^{-1}$
q	liquid water mixing ratio (mass of liquid water per 1kg of dry air)	-
q_v	Water vapor mixing ratio (mass of water vapor per 1kg of dry air)	-
S	e/e_w-1, supersaturation of water vapor	-
S_{eff}	$S+\left(1-\frac{b}{D^3}\right)\exp\left(\frac{a}{D}\right)$ efficient supersaturation	-
$\overline{S}_{eff}$	efficient supersaturation averaged over time period of vertical fluctuations	-
S_m	supersaturation resulting from mixing	-
$S_{\max}$	maximum supersaturation forming near the cloud base	-
T	temperature	K

t	time	s
u_z	vertical velocity	m s^{-1}
z	height over condensation level	m
z_1	altitude over the cloud base of lower limit of vertical fluctuations	m
z_2	altitude over the cloud base of upper limit of vertical fluctuations	m
$z_{\max}$	altitude over the cloud base corresponding to the supersaturation maximum	m
Δz	$z_2 - z_1$ amplitude of the vertical fluctuations	m
ε	turbulent energy dissipating rate	m^2 s^{-3}
μ	ratio of mixing	-
ρ_a	density of the air	kg m^{-3}
ρ_w	density of liquid water	kg m^{-3}
τ_m	characteristic time of mixing of turbulent parcel	s
τ_p	time of phase relaxation	s
τ_t	period of the vertical fluctuations	s

Appendix B

The supersaturation in the point E (Fig.2a) resulting from the mixing between the points B and D can be found as

$$S_m = \frac{e_m}{e_S(T_m)} - 1 \qquad \text{(B1)}$$

Here, $e_s(T_m)$ is the saturated water vapor pressure at temperature T_m, where T_m and E_m are the temperature and water vapor pressure, respectively, resulting from the mixing of two volumes (Korolev and Isaac, 2000)

$$T_m = \frac{\mu T_1 + a(1-\mu)T_2}{\mu + a(1-\mu)}; \qquad \text{(B2)}$$

$$e_m = P\left(\mu + \frac{e_2(p-e_1)}{p(e_1-e_2)}\right)\Bigg/\left(\mu + \frac{(p-e_1)}{(e_1-e_2)}\right); \qquad \text{(B3)}$$

$$a = \left(1 + \frac{c_{pv}R_a e_2}{c_{pa}R_v(p-e_2)}\right)\Bigg/\left(1 + \frac{c_{pv}R_a e_1}{c_{pa}R_v(p-e_1)}\right) \qquad \text{(B4)}$$

.

Here, here $T1$, $T2$ are the temperatures in first, second volumes, e_1, e_2 are the water vapor pressures in the first and second before mixing volumes, respectively; P is the moist air pressure (P=const during mixing); respectively; μ is the portion (ratio of mixing) of the first volume mixed with the $(1-\mu)$ portion of the second volume, both volumes having a unit mass of dry air, R_v, R_a, are the specific gas constants of water vapor and dry air, respectively, c_{pv}, c_{pa}, are the specific heat capacitance of water vapor and dry air at constant pressure, respectively.

If assume $p - e \approx p$ and $e_1 \approx e_2$ in Eqs. (B3) and (B4) then Eqs. (B2) and (B3) will turn into a simplified expressions for T_m and e_m, which can be found in e.g. Rogers (1976) or Bohren and Albreht (1998).

References

Bartlett, J. T., and P. R. Jonas, 1972: On the dispersion of the sizes of droplets growing by condensation in turbulent clouds. *Quart. J. Roy. Meteor. Soc.,* **98,** 150–164.

Beard, K. V. and Ochs, H. T. III, 1993:Warm-rain initiation: An overview of microphysical mechanisms. *J. Appl. Meteorol.*, **32,** 608–625.

Bohren, C. F., and C. H. Albrecht, 1998: *Atmospheric Thermodynamics.*Oxford University Press, 402 pp.

Broadwell JE, Breidenthal RE., 1982: A simple model of mixing and chemical reaction in a turbulent shear layer. *J. Fluid Mech.* **125**:397-410.

Devenish, B.J., P. Bartello, J-L. Brenguier, L.R. Collins, W.W. Grabowski, R.H.A. IJzermans, S.P. Malinovski, M.W. Reeks, J.C. Vassilicos, L._P. Wang and Z. Warhaft 2012: Droplet growth in warm turbulent clouds. *Q. J. Roy. Meteorol. Soc*. (in press)

Erlick C., Khain, **A. P.,** M. Pinsky and Y. Segal, 2005: The effect of turbulent velocity fluctuations on drop spectrum broadening in stratiform clouds. *Atmos. Res.* 75, 15-45.

Herman, G., and R. Goody, 1976: Formation and persistence of summertime Arctic stratus clouds, *J. Atmos. Sci*., **33,** 1537–1553

Khain, A. P**.,** and L. Kh. Ingel, 1995: Numerical modeling of interaction of a nonstationary divergent flow with convective processes in the boundary layer over the ocean. *Atmospheric and Oceanic Physics* ,v 31, 496-506.

Kollias P., and B. Albrecht, 2000: The turbulence structure in a continental stratocumulus cloud from millimeter-wavelength radar observations. J. Atmos. Sci., 57, 2417-2434.

LeMone, M. A., 1973: The structure and dynamics of horizontal roll vortices in the planetary boundary layer. *J. Atmos. Sci*., 30, p. 1077-1091

Lenschov, D.H., J.C. Wyngaard, W.T. Pennel, 1980: Mean –field and second moment budgets in a baroclinic, convective boundary layer. *J. Atmos. Sci*. 37, 1313-1326.

Lothon M, D. H. Lenschow, D. Leon, and G. Vali, 2004: Turbulence measurements in marine stratocumulus with airborne Doppler radar. *Quart. J. Roy. Met. Soc.* 999, 1-19.

MacPherson JI, Isaac GA., 1977: Turbulent characteristics of some Canadian cumulus clouds. *J. Appl. Met.* **16**:81-90.

Magaritz, L., M. Pinsky, Khain, A. P., O. Krasnov, 2009: Investigation of droplet size distributions and drizzle formation using a new trajectory ensemble model. Part 2: lucky parcels in non-mixing limit. *JAS, 66,* 781–805

Mazin I.P., and V.I. Smirnov, 1969: On the theory of cloud drop size spectrum formation by stochastic condensation. *Proceed. CAO*, **89**, 92-94 (in Russian).

Mazin, I.P. and V.M. Merkulovich, 2008: Stochastic condensation and its possible role in liquid cloud microstructure formation (Review). In *Problems of Cloud Physics,* Moscow, National Geophysical Committee, Russian Academy of Science, 263-295 (in Russian).

Korolev, A.V., 1995: The influence of suresaturation fluctuations on droplet size spectra formation. *J. Atmos. Sci.*, **52**, 3620-3634.

Korolev A., and I. Mazin, 2003: Supersaturation of water vapor in clouds. *J. Atmos. Sci*., **60**, 2957-2974.

Korolev, A.V., and P.R. Filed, 2007: The effect of dynamics on mixed-phase clouds: theoretical considerations *J. Atmos. Sci*., **65,** 66–86.

Lasher-Trapp SG, Cooper WA, Blyth AM. 2005. Broadening of droplet size distributions from entrainment and mixing in a cumulus cloud. *Q.J.R. Meteorol. Soc.* **131**:195-220.

Pinsky,M.B., and A.P.Khain, 2003: Fine structure of cloud droplet concentration as seen from the Fast-FSSP measurements. Part 2: Results of in-situ observations*, J. Appl. Meteor*., **42**, 65-73.

Pinsky , M. O. Krasnov, H. W. J. Russchenberg and A. Khain, 2010: Investigation of the turbulent structure of cloud topped boundary layer using Doppler radar. J. Appl. Meteorol and Climatology v. 49, Issue 6, pp. 1170-1190.

Pinsky, M, I.P. Mazin, A. Korolev, and A. Khain, 2012: Supersaturation and diffusional drop growth in liquid clouds. (*ibid*)

Rogers, R. R., 1976: *A Short Course in Cloud Physics.* Pergamon Press, 227 pp

Siebert H, K. Lehmann, and M. Wendisch, 2006: Observations of small-scale turbulence and energy dissipation rates in the cloudy boundary layer. *J. Atmos. Sci.*, **63**, 1451-1466.

Siebert, H., S. Gerashchenko, A. Lehmann, Gylfason, Lance Collins, Zellman Warhaft, 2010a: Towards the understanding the role of turbulence on droplets in clouds: In situ and laboratory measurements, and numerical modeling. *Atm. Res*. **97**, 426-437.

Siebert, H., R. A. Shaw, Z. Warhaft, 2010b: Statistics of Small-Scale Velocity Fluctuations and Internal Intermittency in Marine Stratocumulus Clouds. *J. Atmos. Sci.*, **67**, 262–273

Stevens, B, W.R. Cotton, G. Feingold, and C. Moeng, 1998: Large eddy simulations of strongly precipitating, shallow, stratocumulus-topped boundary layers. J. Atmos. Sci. 55, 3616-3638.
Stevens, B, W.R. Cotton, G. Feingold, and C. Moeng, 1998: Large eddy simulations of strongly precipitating, shallow, stratocumulus-topped boundary layers. J. Atmos. Sci. 55, 3616-3638.
Stevens, B., et al. (2005), Evaluation of large eddy simulations via observations of nocturnal marine stratocumulus, *Mon. Weather Rev*., **133**, 1443–1462.

THE INFLUENCE OF TEMPERATURE AND CLOUD DROPLETS ON THE GROWTH OF DENDRITIC SNOW CRYSTALS

Tsuneya Takahashi

Hokkaido Univ. of Education, Sapporo, 002-8502, Japan

1. INTRODUCTION

Snow crystals grow by vapor diffusion and play an important role in precipitation.

Laboratory studies of snow crystal habits have been carried out in static cloud chambers, in which ice crystals were grown on rabbit hair or fiber (Nakaya, 1954; Hallett and Mason, 1958; Kobayashi, 1961). These studies revealed that the crystal habit is determined mainly by temperature and that the complicated secondary features depend on the supersaturation of water vapor in air; however, the findings regarding the relationship of temperature and supersaturation with crystal shape vary slightly between the researchers.

In the atmosphere, snow crystals grow as they fall through a supercooled cloud. The effects of the fall as well as the water droplets surrounding the crystals, both of which serve to enhance mass and sensible heat transfer, have to be considered. Simulating snow crystal growth under free fall is necessary for further understanding the growth of snow crystals in a cloud.

To this end, vertical supercooled cloud tunnels in which a single snow crystal may be suspended freely and grown were developed. The growth of a snow crystal by vapor diffusion under free fall in a supercooled cloud environment with a liquid water volume of 0.1 g m^{-3} was successfully simulated for up to 30 min, and the characteristics of snow crystal growth during free fall were quantitatively investigated (Takahashi et al. 1991). Nevertheless, more data are needed to determine the detailed characteristics, including the snow crystal shape and the effect of cloud droplets surrounding the crystals.

We carried out detailed experiments on dendritic snow crystal growth for 10 min under isothermal and water-saturated conditions over a broader range of liquid water content than before. In this paper, we shall address the influence of temperature and cloud droplets on the growth of dendritic snow crystals in a cloud.

2. EXPERIMENTS

The present study was carried out in a vertical wind tunnel at Hokkaido University of Education in Sapporo, Japan, at an elevation of 5 m above sea level. In the tunnel, snow crystals could be suspended freely and grown in a vertical stream of artificially generated supercooled cloud by applying aerodynamical mechanisms for horizontal stability. A convergent configuration of the working/observation section provides excellent horizontal stability for crystal suspension.

Cloud droplets were continuously generated by an ultrasonic atomizer and supplied into the tunnel through a cloud chamber, where dense cloud was mixed and supercooled by cold air introduced by an air suction device. The turbulence was dampened in the chamber; the air was saturated with water; and the temperature and droplet concentration in the cloud became uniform.

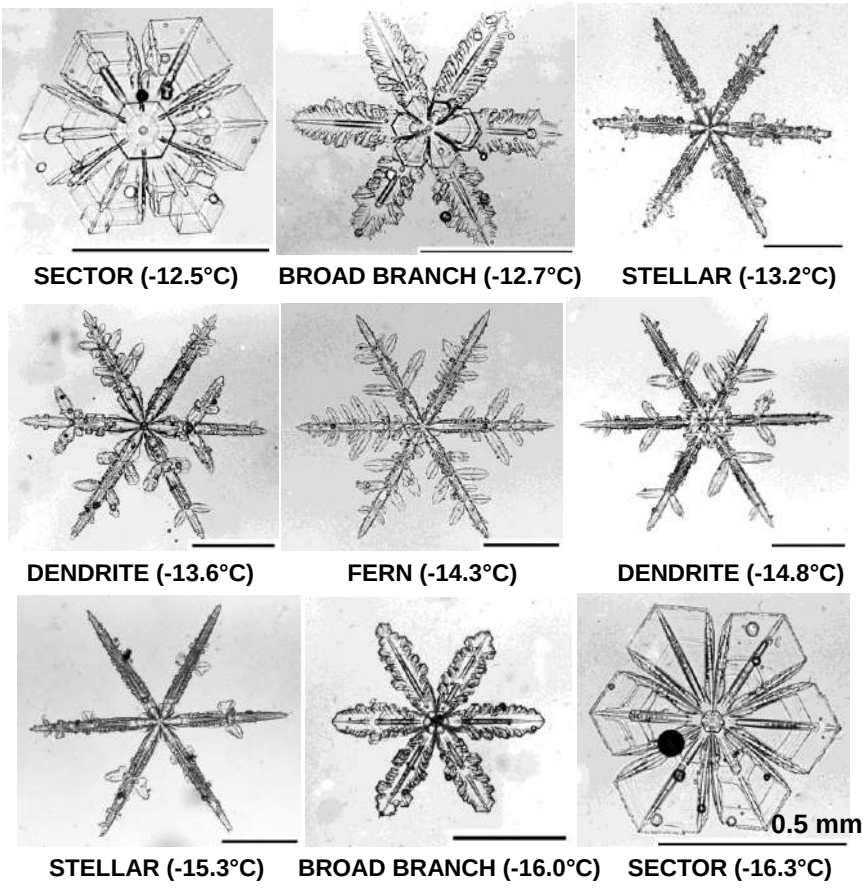

Fig. 1. Examples of snow crystals grown for 10 min
at temperatures between -12.3°C and -16.6°C.

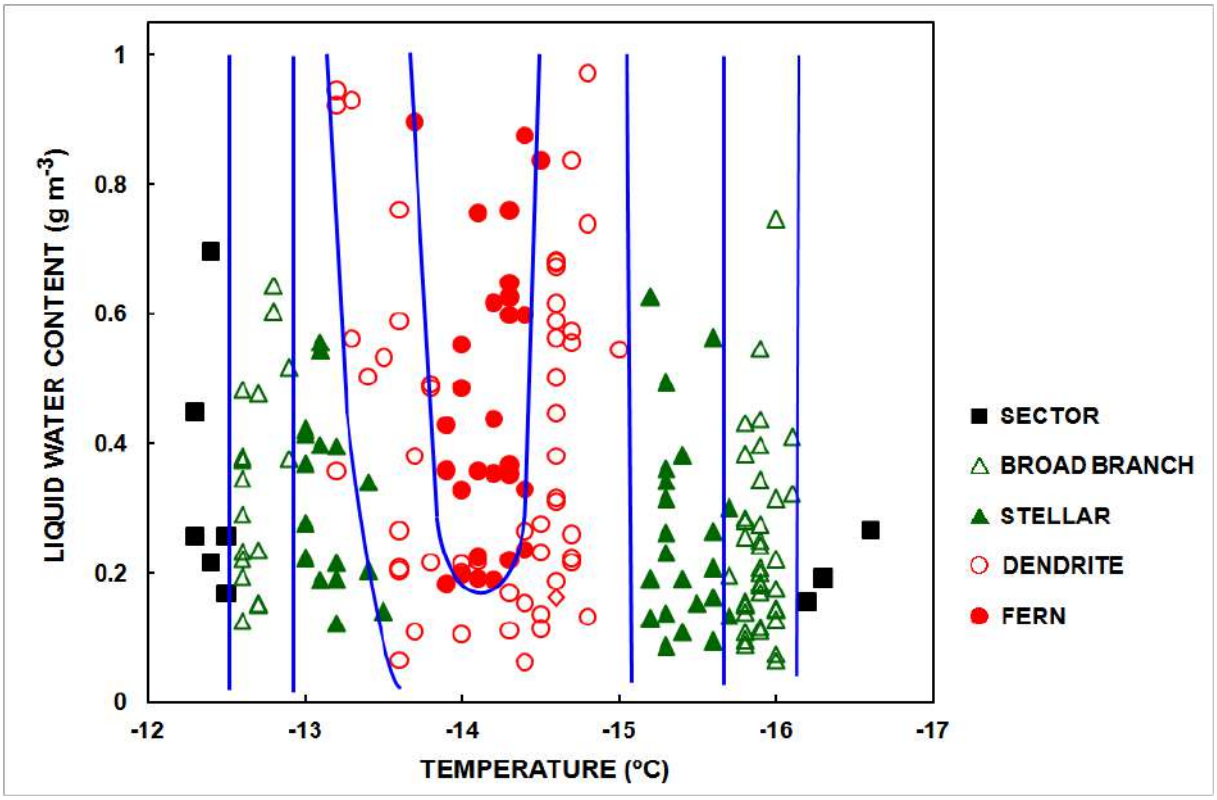

Fig. 2. The shape of a snow crystal as a function of temperature
and liquid water content for a growth time of 10 min.

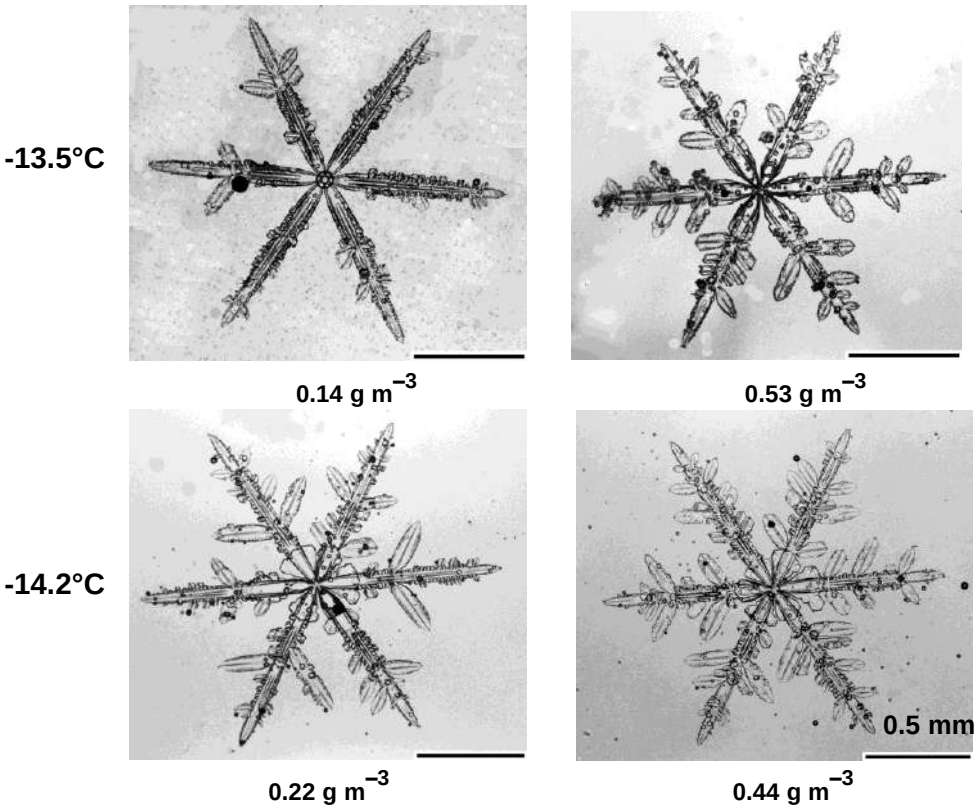

Fig. 3. Examples of snow crystals grown for 10 min at -13.4°C and -14.3°C for different liquid water content.

The cloud concentration was controlled by adjusting the applied voltage to an ultrasonic atomizer. The liquid water content of the cloud was calculated from the air temperature and the dew point of the air, determined by evaporating the cloud. The air temperature and dew point were continuously monitored by a thermister thermometer and a quartz dew point hygrometer, respectively. The cloud droplet size distributions were measured by an impaction method.

Experiments were carried out for a snow crystal growth time of 10 min under isothermal and water-saturated conditions from -12.3°C to -16.6°C with a constant liquid water content in the experimental range of 0.05 to 1 g m^{-3}.The probability of riming or developing spatial dendrites increased with the liquid water content. The crystals that were notably rimed or had spatial dendrites were excluded in this study. The average fluctuation in air temperature was 0.2°C for 10 min, which was half of the corresponding value in the study of Takahashi and Fukuta (1991). In addition, the maximum fluctuation in temperature was less than 0.2°C between 1 and 10 min of the growth time. The mean error in the liquid water content was less than 0.05 g m^{-3}; the content was calculated every minute between 2 and 10 min of the growth time and was averaged. The diameters of more than 60% of the droplets ranged from 5 to 10 μm, and the average diameter was approximately 8 μm; these parameters varied only slightly with the changes in the liquid water content.

3. RESULTS AND DISCUSSION

As shown in Figure 1, a sector (P1b), a

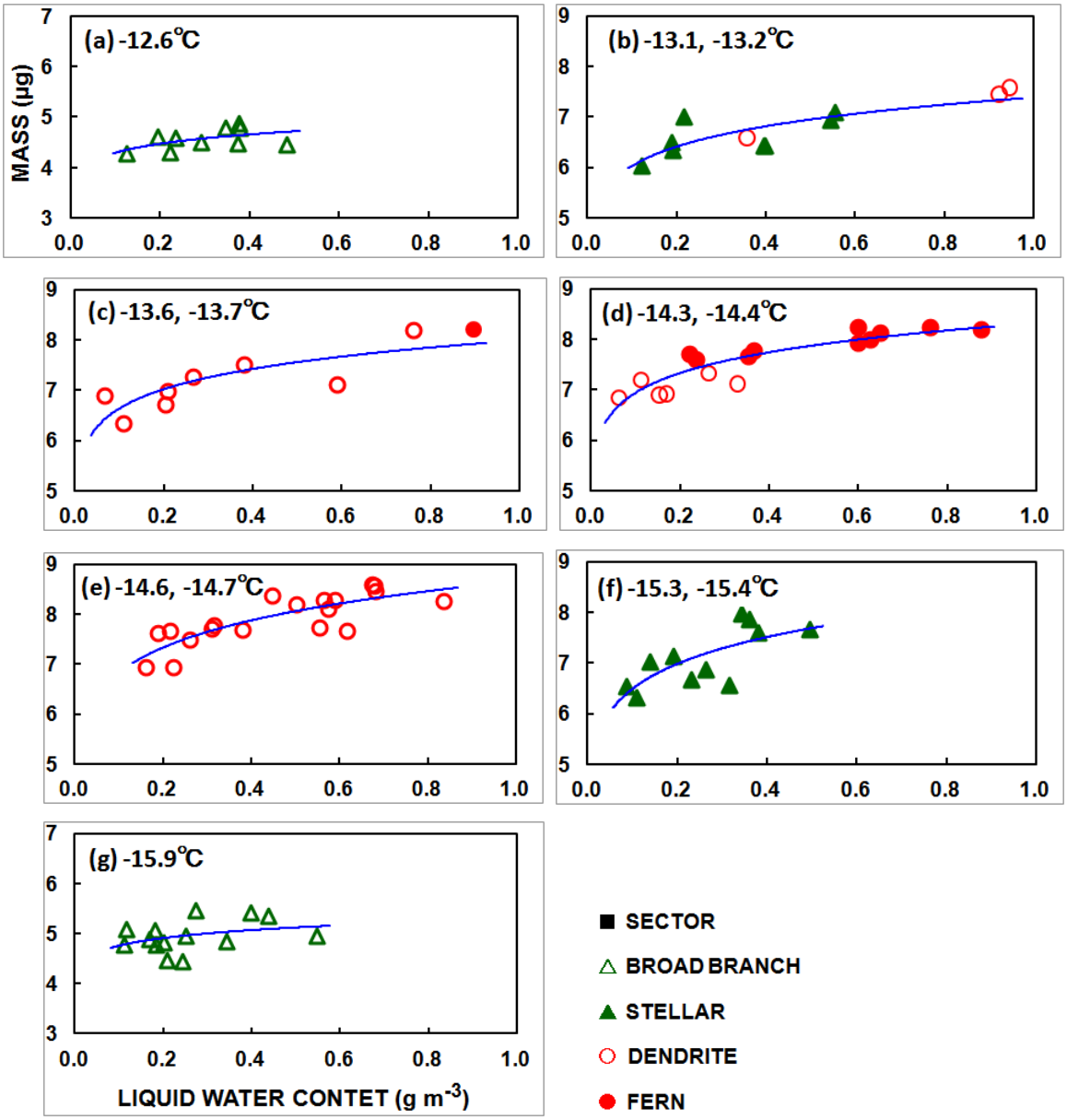

Fig. 4. Variation in crystal mass along the a-axis with changes in the liquid water content at various temperatures after 10 min of growth.

broad branch (P1c), a stellar (P1d), a dendrite (P1e), and a fern (P1f) were grown between -12.3°C and -16.6°C in the wind tunnel. Classification in the parentheses is after Magono and Lee (1966).

The variation in crystal shapes, formed over a wide range of liquid water content up to 1 g m^{-3} after 10 min of growth, are summarized in Figure 2. The following types of crystals were observed at different temperatures: a sector (>-12.5°C), a broad branch (-12.5°C to -12.9°C), a stellar (-12.9°C to -13.2°C), a dendrite (-13.2°C to -13.8°C), a fern (-13.8°C to -14.5°C), a dendrite (-14.5°C to -15.1°C), a stellar (-15.1°C to -15.7°C), a broad branch (-15.7°C to -16.1°C), and a sector (<-16.1°C). A dendritic snow crystal, comprised of a broad branch, a stellar, a dendrite, and a fern, was grown between -12.5°C to -16.1°C. Side branches developed between -13.3°C to -15.1°C, and fairly well between -13.8°C to -14.4°C. With the increase in the liquid water content, the stellar was transformed to a dendrite between -13.3°C and -13.6°C, and the dendrite, in turn, to a fern between

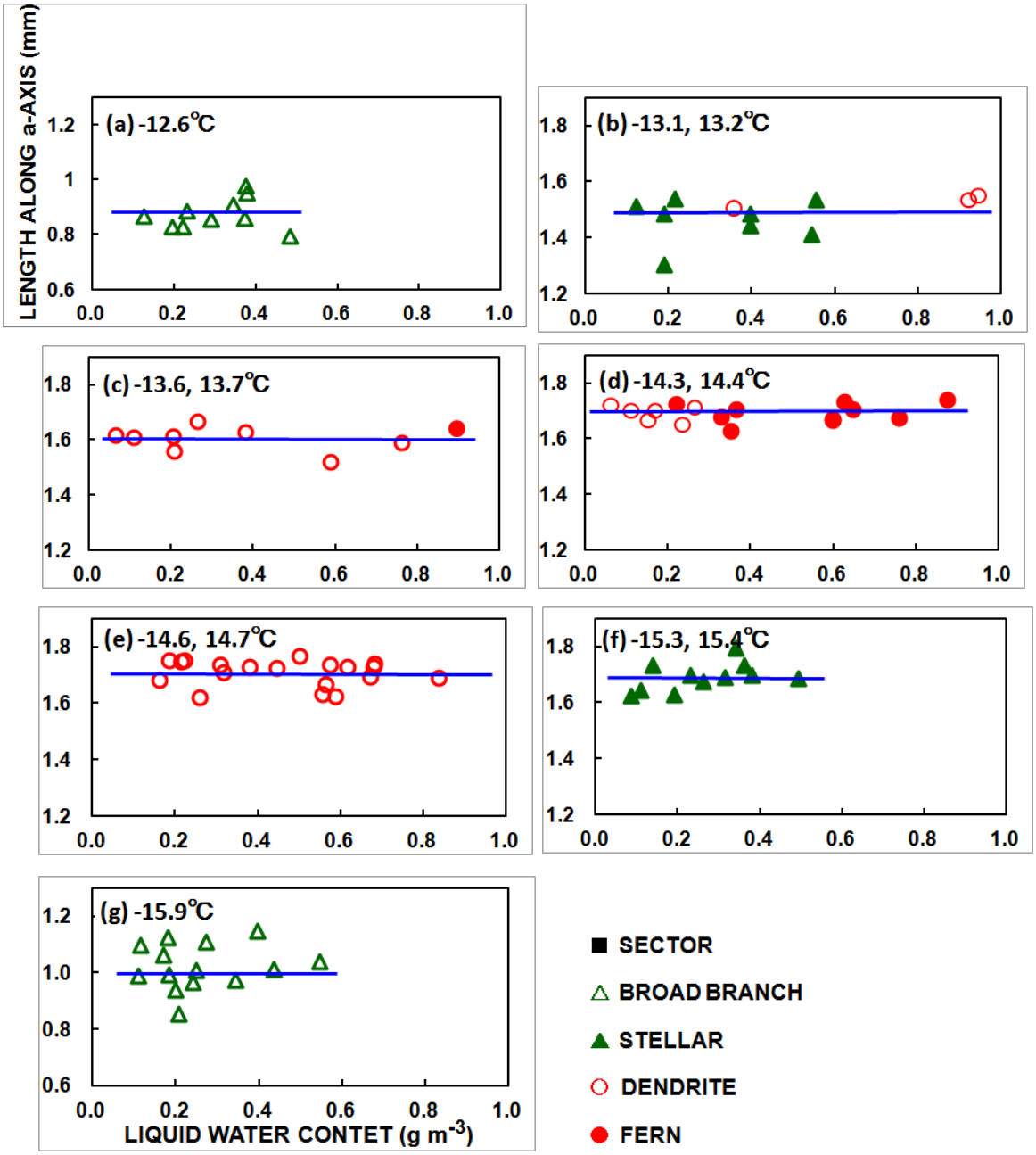

Fig. 5. Variation in crystal dimension along the a-axis with changes in the liquid water content at various temperatures after 10 min of growth.

-13.8°C and -14.4°C. The growth of side branches depends on the liquid water content, i.e., the amount of cloud droplets. Figure 3 shows examples of the changes in crystal shape. However, crystals grown at other temperatures retained their shapes spite of the increase in the liquid water content.

Figure 4 shows the changes in crystal mass with changes in the liquid water content at various temperatures: -12.6°C, -13.1°C to -13.2°C, -13.6°C to -13.7°C, -14.3°C to -14.4°C, -14.6°C to -14.7°C, -15.3°C to -15.4°C, and -15.9°C. At these temperatures, the changes in crystal mass in the liquid water content were expressed by a curve that was convex upward. This is most likely because the presence of cloud droplets in the vicinity of a snow crystal resulted in higher mass growth rates due to the steepening of both vapor density and temperature gradients; the rate of steepen-

ing was gradually slowed as the cloud became denser. At -12.6°C and -15.9°C, the effect was indistinct, and this is ascribed to the crystal dimensions being smaller at these temperatures than at other temperatures.

Marshall and Langleben (1954) found that the snow crystal growth rate is enhanced by a fog factor:

$$f_f = 1 + kC, \quad (1)$$

where

$$k = (3 W_L / \bar{r}_d^2)^{1/2}, \quad (2)$$

C, W_L, and $\bar{r}_d$ being the shape factor for a snow crystal, the liquid water content of a cloud, and the average radius of cloud droplets, respectively. For very thin plates,

$$C = a/\pi, \quad (3)$$

where a is the crystal dimension along the a-axis. The fog factor increases with the square root of the liquid water content of a cloud and with the crystal diameter. The fog effect also depends on cloud droplet size, as shown in eq. (1); the larger the droplet size, the smaller is the fog factor.

Figure 5 shows the changes in crystal dimension along the a-axis with changes in the liquid water content at various temperatures after 10 min of growth. The length of the snow crystals remained constant with increases in the liquid water content at all temperatures. The cloud droplets made little contribution to the growth along the a-axis; in other words, the fog factor contributed to the development of side branches and/or the increase in crystal thickness. The ventilation effect probably was the dominant cause of the growth of the tip of each primary branch.

4. CONCLUSIONS

Dendritic snow crystal growth was studied by using a vertical wind tunnel to simulate isolated snow crystal growth under free fall conditions in a supercooled cloud environment. Experiments were carried out for 10 min of growth with different liquid water content up to 1 g m^{-3} and between temperatures of -12.3°C and -16.6°C. The results and findings are summarized below:

1) The following types of crystals were observed at different temperatures: a sector (>-12.5°C), a broad branch (-12.5°C to -12.9°C), a stellar (-12.9°C to -13.3°C), a dendrite (-13.3°C to -13.8°C), a fern (-13.8°C to -14.4°C), a dendrite (-14.4°C to -15.1°C), a stellar (-15.1°C to -15.7°C), a broad branch (-15.7°C to -16.1°C), and a sector (<-16.1°C).

2) With increases in the liquid water content, stellar transformed to dendrites between -13.3°C and -13.6°C, and dendrites, in turn, to ferns between -13.8°C and -14.4°C.

3) The changes in the crystal mass in the liquid water content at various temperatures were expressed by a curve that was convex upward. The length of the snow crystals remained constant with increases in the liquid water content at all temperatures. The presence of cloud droplets in the vicinity of snow crystals resulted in higher mass growth rates due to the steepening of vapor density and temperature gradients, and thus contributed to the development of side branches and to the increase in crystal thickness.

REFERENCES

Hallett, J. and B.J. Mason, 1958: The influence of temperature and supersaturation on the habit of ice crystals grown from the vapour. *Proc. Roy. Soc. London*, A247, 440-453.

Kobayashi, T., 1961: The growth of snow crystals at low supersaturations. *Phil.*

Mag., **6**, 1363-1370.

Magono, C. and C. W. Lee, 1966: Meteorological classification of natural snow crystals. *J. Fac. Sci., Hokkaido Univ.*, Ser. VII, 2, 321.335.

Marshall, J. S., and M. P. Langleben, 1954: A theory of snow-crystal habit and growth. *J.Meteor.*, 11, 104-120.

Nakaya, U., 1954: *Snow crystals*. Harvard Univ. Press, 510 pp.

Takahashi, T., T. Endoh, G. Wakahama and N. Fukuta, 1991: Vapor diffusional growth of free-falling snow crystals. *J. Meteor. Soc. Japan*, 69, 15-30.

Phase Differences between Rainfall and Its Sources in the Tropical Deep Convective Regime: A Partitioning Analysis Based on Surface Rainfall Budget

Fan Ping [1]

Laboratory of Cloud-Precipitation Physics and Severe Storms (LACS)
Institute of Atmospheric Physics
Chinese Academy of Sciences
Beijing, China

Xiba Tang
Institute of Atmospheric Physics
Chinese Academy of Sciences
Beijing, China

Zhexian Luo
College of Remote Sensing
Nanjing University of Information Science and Technology
Nanjing, China

Revised in June 2011

Revised in September 2011

Revised parts are marked by blue ink.

[1] Corresponding author address: Dr. F. Ping, Laboratory of Cloud-Precipitation Physics and Severe Storms (LACS), Institute of Atmospheric Physics, Chinese Academy of Sciences, Beijing 100029, China
E-mail: pingf@mail.iap.ac.cn

Abstract

A partitioning scheme based on surface rainfall processes is applied to a lag correlation analysis between tropical rainfall and its sources in this study. The rainfall sources include convective available potential energy (*CAPE*), water vapor source (water vapor convergence plus surface evaporation), and net condensation (condensation and deposition minus evaporation of rain). The analysis is carried out using a 21-day TOGA COARE cloud-resolving model simulation data. Maximum model domain mean surface rainfall leads the minimum mean *CAPE* by 6 hours and is phase locking with the maximum mean net condensation mainly through the rainfall associated with water vapor convergence. Maximum mean surface rainfall lags the maximum mean water vapor source by 3 hours mainly through the rainfall associated with local atmospheric drying, water vapor divergence, and hydrometeor loss/convergence.

Keywords: Phase relation; convective available potential energy; surface rainfall; water vapor source, net condensation.

1. Introduction

Surface rainfall is associated with its sources including convective available potential energy (*CAPE*), water vapor source (water vapor convergence plus surface evaporation) in surface rainfall budget, and net condensation (condensation and deposition minus evaporation of rain) in cloud budget. The quasi-balance assumption between surface rainfall and its sources lays down the foundation for the development of cumulus parameterization in early years (e.g., Kuo 1965, 1974; Arakawa and Schubert 1974). Kuo (1965, 1974) considered water vapor convergence plus surface evaporation as the major rainfall source and assumed 95% of the source is consumed to produce surface rainfall and 5% of the source is used to moisten local atmosphere in his cumulus parameterization scheme. Arakawa and Schubert (1974) assumed that available potential energy produced by the large-scale processes is consumed to develop convection in their cumulus parameterization scheme. Although the maximum surface rainfall is phase locking with the maximum net condensation (e.g., Gao et al. 2005a), the minimum *CAPE* occurs a few hours after surface rainfall reaches a maximum (e.g., Xu and Randall 1998; Li 2009), and the maximum surface rainfall lags the maximum water vapor convergence by a few hours (e.g., Cui and Li 2011). These indicate actual deviations from quasi-balances between surface rainfall and *CAPE*/water vapor source. The release of unstable energy such as *CAPE* supports kinetic energy, whose perturbation component is associated with secondary circulation. The development of the secondary circulation and associated water vapor convergence lead to the onset and growth of cloud systems. As clouds growth, cloud microphysical processes such as collection, accretion, riming, and melting finally produce surface rainfall. Thus, the time needs for production of the

surface rainfall from the release of *CAPE*.

It must be pointed out that explicitly evaluating and understanding the phase difference between rainfall and its sources is necessary and important to develop and modify the cumulus parameterization schemes (e.g., Betts and Miller 1986; and Randall and Pan 1993).Current the cumulus parameterization schemes of weather and climate mode including the convection adjustment schemes and meso-sacle cumulus parameterization schemes (Anderson, Roymand, and Kain, 2007; Grandpeix, and Lafore, 2010) are adopted CAPE closure assumption, which need to explicitly deduce the convection adjustment time namely the phrase difference between rainfall and its sources. However as pointed out by Arakawa (2004), it exists some uncertainties in the cumulus parameterization schemes due to the assumption of unified clouds or the ensemble clouds. One feasible method of modified parameterization schemes is to design and develop individual convection adjustment time or the different phrase between the rainfall and its sources in allusion to individual cloud type. Other feasible method is that the statistical characteristics of individual cloud type can be described in the modified parameterization schemes. In fact, the progress on the cloud parameterization problem has been too slow and many researchers advocate a new approach that is very promising but also very expensive computationally (Randall, Arakawa and Grabow, 2003). One promising and relatively new option is to use cloud resolution models as tools to accelerate and otherwise optimize the process of cloud parameterization development. Hence, this research of the phase difference between rainfall and its sources will not only provide the

insight to evaluate and understand the interaction between individual cloud and the large-scale forcing, but also give the statistical characteristics of individual cloud type.

The phase difference between rainfall and its sources have been proved by the observation and the simulation. Munehisa (2008) used the Tropical rainfall Measuring Mission (TRMM) data during June-August 1998-2003 to investigate diurnal variations of rain and cloud systems over the tropics and midlatitudes. They found that the systematic shifts in peak time of convection relative to each sensor and the time differences of maximum frequency for TMI-PR and for VIRS-PR (TMI) are 2 and 3–6 h respectively. The sensors likely detect different stages in the evolution of convective precipitation, which would explain the phase difference. The PR directly detects near-surface rain. The TMI and VIRS observe deep convection and solid hydrometeors as the rainfall sources. Bowman (2005) used data rain gauges on ocean buoys and TRMM satellite measurements to analyze the climatological diurnal cycle of precipitation. They also found that the phase difference between the TMI and PR rainfall retrievals persist in the diurnal cycle. The phase differences also have been proved by the simulated results.

Li (2009) showed the maximum negative lag correlations between model domain mean *CAPE* and rainfall occurs around lag hour 6 in his 21-day cloud-resolving model experiment of the Tropical Ocean Global Atmosphere Coupled Ocean Atmosphere Response Experiment (TOGA COARE). The minimum mean *CAPE* lags mean and convective rainfall through the vapor condensation and depositions, water vapor convergence, and heat divergence whereas it lags stratiform rainfall via the transport of hydrometeor concentration from convective regions to raining stratiform regions, vapor condensation and depositions, water vapor storage, and heat divergence over raining

stratiform regions. The convective and stratiform rainfall separation scheme used in Li (2009) is mainly based on rain intensity (Tao et al. 1993). Other information such as vertical velocity and cloud mixing ratio is also use**d** to identify convective rainfall (Sui et al. 1994). Thus, such separation scheme may contain uncertainty. Shen et al. (2010b) developed a new rainfall separation scheme based on surface rainfall budget proposed by Gao et al. (2005a) in which eight rainfall types are identified through local atmospheric drying/moistening, water vapor convergence/divergence, hydrometeor loss/convergence or hydrometeor gain/divergence. Their preliminary results show that about 30% of convective rainfall is associated with water vapor divergence.

In this study, the rainfall separation scheme developed by Shen et al. (2010b) is applied to the analysis of the phase differences between surface rainfall and its sources (*CAPE*, water vapor source, and net condensation) in the tropical deep convective regime. The analysis of lag correlation is conducted using a two-dimensional (2D) cloud-resolving model experiment that is forced by the large-scale forcing derived from TOGA COARE. In the next section, the cloud model, forcing, and experiment are described. The results are presented in section 3. The summary is given in section 4.

2. Model, experiment, and methodlogies

Currently, cloud-resolving model is being incorporated into large-scale dynamic frameworks to facilitate the interaction between clouds and large-scale circulations in place of conventional parameterization (Emanuel and Raymond 1993) as an alternative approach (Raymond and Zeng 2005; Khairoutdinovet 2001).Not only the cloud-resolving

model explicitly resolves convective clouds and cloud system on fine spatial and temporal scales, but also its simulation can agrees well with the observation (Xu et al. 2002; Tao et al. 2003).In addition, the studies of the assimilation of the Geostationary Operational Environmental Satellites (GOES) imager observations into a cloud-resolving model have been made great processes and the modeled spatial distribution and short-term evolution of the ice cloud mass is significantly improved by the above assimilation method (Polkinghorne,2010,2011). Thus, the cloud-resolving model has been widely used in the researches of the cloud and precipitation processes as the reliable tools.

The 2D cloud-resolving model simulation data (Li et al. (2002a) are used in this study. Due to a small model domain of 768 km, the model is forced by zonally-uniform vertical velocity, zonal wind, and thermal and moisture advection based on 6-hourly TOGA COARE observations within the Intensive Flux Array (IFA) region (Zhang, personal communication, 1999) and hourly sea surface temperature (SST) at the Improved Meteorological (IMET) surface mooring buoy (1.75^{o}S, 156^{o}E) (Weller and Anderson 1996) from 0400 LST 18 December 1992 to 1000 LST 9 January 1993 (Fig. 1). The model simulation data have been used to study surface rainfall processes (Li et al. 2002b, c; Gao et al. 2005a; Zhou et al. 2006; Cui and Li 2006; Gao and Li 2010a; Shen et al. 2010a,b), precipitation efficiency (Li et al. 2002a; Sui et al. 2005, 2007b; Gao and Li 2011), vorticity vectors (Gao et al. 2004, 2005b; Cui 2008), effects of ice clouds on rainfall (Gao et al. 2006b), rainfall responses to large-scale forcing (Gao et al. 2006a; Gao and Li 2008b), cloud cluster (Ping et al. 2008), diurnal variations of tropical oceanic

rainfall (Gao et al. 2009; 2010b), convective and stratiform rainfall processes (Sui and Li 2005; Cui et al. 2007), and rainfall partitioning (Sui et al. 2007a; Shen et al. 2010b).

The model used in Li et al. (2002a) is the 2D version of the Goddard Cumulus Ensemble Model, which was originally developed by Soong and Ogura (1980), Soong and Tao (1980), and Tao and Simpson (1993) and was modified by Li et al. (1999). The model has prognostic equations of potential temperature, specific humidity, mixing ratios of five cloud species, and perturbation zonal wind and vertical velocity. The model also includes a set of cloud microphysical parameterization schemes from Rutledge and Hobbs (1983, 1984), Lin et al. (1983), Tao et al. (1989), Krueger et al. (1995), and interactive solar and thermal infrared radiation parameterization schemes from Chou et al. (1991, 1998) and Chou and Suarez (1994). The model uses cyclic lateral boundaries, and a horizontal domain of 968 km, a horizontal grid resolution of 1.5 km, 33 vertical levels, and a time step of 12 s. Detailed descriptions and discussions of the model, dynamic framework, and physics package can be found in Gao and Li (2008a).

Following Gao et al. (2005a) and Cui and Li (2006), the surface rainfall equation can be written as

$$P_s = Q_{WVT} + Q_{WVF} + Q_{WVE} + Q_{CM}, \quad (1)$$

where Q_{WVT} $(=-\frac{\partial[q_v]}{\partial t})$ is local vapor change, Q_{WVF} $(=-[\bar{u}^o \frac{\partial \bar{q}_v}{\partial x}]-[\frac{\partial(u' q_v')}{\partial x}]-[\bar{u}^o \frac{\partial q_v'}{\partial x}]-[w' \frac{\partial \bar{q}_v}{\partial z}])$ is water vapor convergence, Q_{WVE} is surface evaporation; Q_{CM} $(=-\frac{\partial[q_5]}{\partial t} -[u\frac{\partial q_5}{\partial x}]-[w\frac{\partial q_5}{\partial z}])$ is hydrometeor change /convergence; $q_5 = q_c + q_r + q_i + q_s + q_g$, q_c, q_r, q_i, q_s, q_g are mixing ratios of cloud

water (small cloud droplets), raindrops, cloud ice (small ice crystals), snow (density 0.1 g cm^{-3}), and graupel (density 0.4 g cm^{-3}), respectively; overbar is model domain mean, superscript "o" is imposed COARE data a prime denotes a perturbation from the zonal mean; $[()](=\int_{z_b}^{z_t}\overline{\rho}()dz)$ is mass integration. The surface rainfall equation (1) is derived through the combination of water vapor budget ($Q_{WVT}+Q_{WVF}+Q_{WVE}=Q_{NC}$) and cloud budget ($P_s=Q_{CM}+Q_{NC}$), where $Q_{NC}(=[P_{CND}]+[P_{DEP}]+[P_{SDEP}]+[P_{GDEP}]-[P_{REVP}]-[P_{MLTG}]-[P_{MLTS}])$ is the net condensation between vapor condensation ($[P_{CND}]$) and vapor deposition for the growth of cloud ice ($[P_{DEP}]$) and snow ($[P_{SDEP}]$) and graupel ($[P_{GDEP}]$) minus growth of vapor by evaporation of raindrop ($[P_{REVP}]$) and evaporation of liquid from graupel surface ($[P_{MLTG}]$), and evaporation of melting snow ($[P_{MLTS}]$). Following Shen et al. (2010b), hourly grid-scale rainfall simulation data are partitioned into eight rainfall types (TFM, TFm, tFM, tFm, TfM, Tfm, tfM, and tfm) (Table 1) and seven of them will be analyzed in this study because of negligible contribution of tfm to total rainfall.

To examine the phase difference between model domain mean surface rainfall (P_S) and its sources (*RS*), following Cui (2008) and Li (2009), the weighted lag correlation coefficients are calculated. Since model domain mean surface rain rate (P_S) can be partitioned into seven rainfall types (TFM, TFm, tFM, tFm, TfM, Tfm, tfM), the lag correlation coefficient between P_S and the mean rainfall source (*RS*) is determined by sum of the lag correlation coefficient between each rainfall type and *RS* weighted by the ratio of the standard deviation of each rainfall type to the standard deviation of the mean rainfall ($\frac{\sigma_{P_{Si}}}{\sigma_{P_S}}$)., i.e.,

$$C_{RS,P_S} = \sum_{I=1}^{7} WC_{RS,P_{SI}} \ , \tag{2}$$

$$WC_{RS,P_{SI}} = \frac{\sigma_{P_{Si}}}{\sigma_{P_S}} C_{RS,P_{SI}} \ . \tag{2a}$$

Since rainfall is associated with four rainfall processes (Q_{WVT}, Q_{WVF}, Q_{WVF}, Q_{CM}), the lag correlation coefficient between each rainfall type and *RS* is determined by sum of the lag correlation coefficient between the rainfall processes of each rainfall type and *RS* weighted by the ratio of the standard deviation of the rainfall processes to the standard deviation of the mean rainfall ($\frac{\sigma_{Q_J}}{\sigma_{P_S}}$). i.e.,

$$C_{RS,P_{SI}} = \sum_{J=1}^{4} WC_{RS,Q_J} \ , \tag{2b}$$

$$WC_{RS,Q_J} = \frac{\sigma_{Q_J}}{\sigma_{P_S}} C_{RS,Q_J} \ . \tag{2c}$$

In (2), σ_A is a standard deviation of A; $WC_{A,B}$ is a weighted lag correlation coefficient between *A* and *B*; P_S =(TFM, TFm, tFM, tFm, TfM, Tfm, tfM). Q=(Q_{WVT}, Q_{WVF}, Q_{WVF}, Q_{CM}).

3. Results

3.1 Rainfall versus CAPE

The calculation of lag correlation between model domain mean surface rain rate and the mean *CAPE* shows a negative lag correlation with the minimum of -0.331 at lag hour 6 (Fig. 2a and Table 2), which suggests that the maximum mean surface rainfall leads the minimum mean *CAPE* by 6 hour. A Student's t-test on the significance of the correlation coefficients is further conducted and a critical correlation coefficient at the

1% significant level is 0.113. Thus, this lag correlation is statistically significant. Although hourly observed rain rate is available, only 6-hourly observed temperature and water vapor profiles are available. Thus, this simulated lag correlation cannot be validated against observation. However, the correlation coefficient between simulated and observed rain rates is 0.45, which exceeds 1% significant level. The observed rain rate is derived by averaging over a 150x150 km^2 are, which is based on radar reflectivity data taken from the Massachusetts Institute of Technology Doppler radar and the TOGA radar located within the IFA region (Short et al. 1997).

Since the mean rainfall consists of eight rainfall types as indicated by the partitioning analysis based on surface rainfall budget (Shen et al. 2010b), the lag correlation between each rainfall type and the mean *CAPE* is calculated using (2) and (2a) to form weighted lag correlation coefficients. TfM (-0.090) shows a larger lag correlation with the mean *CAPE* than the other rainfall types do (Fig. 2b and Table 2), but the maximum TfM leads the minimum mean *CAPE* by 5 hours. Two other rainfall types (Tfm and tfM) associated with water vapor divergence have much smaller lag correlation coefficients than four rainfall types (TFM, TFm, tFM, and tFm) associated with water vapor convergence. The maxima of TFM, TFm, and tFm lead the minimum mean *CAPE* by 6 hours. Thus, these three rainfall types determine the 6-hour lead of the maximum mean rainfall to the minimum mean *CAPE*. Further calculations between rainfall processes for each rainfall type and the mean *CAPE* using (2b) and (2c) reveal that the maximum local atmospheric drying and the maximum water vapor convergence of TFM and TFm lead the minimum mean *CAPE* by 6 hours (Table 4a). The negative lag correlation between tFm and the mean *CAPE* is associated with that between water vapor

convergence of tFm and the mean *CAPE*. In TfM, the positive lag correlation between water vapor divergence and the mean *CAPE* is largely offset by the negative lag correlation between local atmospheric drying and the mean *CAPE*, which means that water vapor divergence leads to local atmospheric drying. As a result, the maximum hydrometeor loss/convergence leads the minimum mean *CAPE* by hour 5, which determines the 5-hour phase lead of the maximum TfM to the minimum mean *CAPE*.

The above phenomenon can be explained well by the physical mechanism. It is well known that the downdraft motion is incurred by the ascend motion and usually occurs after the convection starts. Since the water vapor divergence is associated with downdraft motion whereas the water vapor convergence is associated with the convection, the lag between the water vapor divergences and the precipitation is smaller than the water vapor convergence and the precipitation. This is the main reason that Tfm and tfM associated with water vapor divergence have much smaller lag correlation coefficients than four rainfall types (TFM, TFm, tFM, and tFm) associated with water vapor convergence. To study precipitation statistics over convective and stratiform regions, a hydrometeor loss/convergence and local atmospheric drying are associated with the convective precipitation whereas the hydrometeor gain/divergence and local atmospheric moistening is associated with the moistening environment and stands for the stratiform regions. Compared with stratiform region, convective regions have smaller the lag between the rainfall and its CAPE. This is the reason TfM shows a larger lag correlation with the mean *CAPE* than the other rainfall types do.

3.2 Rainfall versus water vapor source

Model domain mean surface rainfall is positively correlated with the mean water vapor source (water vapor convergence plus surface evaporation) with the maximum of 0.771 at lag hour -3 (Fig. 3a and Table 2). This indicates that the maximum mean surface rainfall lags the maximum mean water vapor source by 3 hours. Again TfM shows the largest lag correlation of 0.228 at lag hour -3 among the other rainfall types (Fig. 3b). Although the maximum tfM also lags the maximum mean water vapor source by 3 hour, its lag correlation coefficient is about one order of magnitude smaller than that of TfM. Thus, the phase difference between TfM and the mean water vapor source mainly determines that between the mean rainfall and the mean water vapor source. In TfM, the maximum local atmospheric drying lags the maximum mean water vapor source by 2 hours, whereas the maximum water vapor divergence lags the maximum mean water vapor source by 2 hours (Table 4b). Due to the fact that water vapor divergence dries local atmosphere, these two processes are largely offset, which only makes a small contribution to the phase difference between the mean surface rainfall and the mean water vapor source. Meanwhile, the maximum hydrometeor loss/convergence lags the maximum mean water vapor source by hour 3. Thus, the hydrometeor loss/convergence is responsible for 3-hour phase lag of maximum TfM to the maximum mean water vapor source.

The maximum TFM lags the maximum mean water vapor source by 4 hours, whereas the maxima of three other rainfall types (TFm, tFM, and tFm) associated with water vapor convergence lag the maximum mean water vapor source by 2 hours (Fig. 3b and Table 2). In TFM, all rainfall processes produce rainfall and rainfall covers small area (Shen 2010). The rain rate is the highest among all rainfall types. Thus, the

maximum of heaviest rainfall in TFM lags the maxima of other rainfall by 1-2 hours. The maximum water vapor convergence and the maximum hydrometeor loss/convergence lag the maximum mean water vapor source by 4 hours in TFM and by 2 hour in tFM (Table 4b). The maximum local atmospheric drying and the maximum water vapor convergence lag the maximum mean water vapor source by 2 hours in TFm and the maximum water vapor convergence lags the maximum mean water vapor source by 2 hours in tFm.

3.3 Rainfall versus net condensation

The Maximum model domain mean surface rainfall is in phase with the maximum mean net condensation with the maximum lag correlation of 0.931 at lag hour 0 (Fig. 4a and Table 2). The in-phase correlation between the maximum mean rainfall and the maximum mean net condensation is determined by the in-phase correlation between the maximum rainfall (TFM, TFm, tFM, and tFm) associated with water vapor convergence and the maximum mean net condensation (Fig. 4b and Table 2) mainly through the in-phase correlation between the maximum water vapor convergence and the maximum mean net condensation (Table 4c). The in-phase correlations between the maximum hydrometeor loss/convergence and the maximum mean net condensation in TFM and between the maximum local atmospheric drying and the maximum mean net condensation in TFm also contribute to the in-phase correlation between the maximum rainfall and the maximum mean net condensation for these two rainfall types.

The maximum TfM lags the maximum mean net condensation by 1 hour and their lag correlation coefficient is 0.272 (Fig. 4b and Table 2). In TfM, water vapor divergence leads to local atmospheric drying. As a result, the in-phase positive correlation between the maximum local atmospheric drying and the maximum mean net condensation is

largely offset by the in-phase negative correlation between the maximum water vapor divergence and the maximum mean net condensation. The maximum hydrometeor loss/convergence lags the maximum mean net condensation by 1 hour, which accounts for the 1-hour lag of the maximum TfM to the maximum mean net condensation.

4. Summary

The phase relation between tropical rainfall and its sources are examined through the lag correlation analysis on cloud-resolving model simulation data. The model is integrated for 21 days with the large-scale forcing from TOGA COARE. The rainfall separation scheme based on surface rainfall processes are applied to the lag correlation analysis. The major results include

- Maximum model domain mean surface rainfall leads the minimum mean *CAPE* by 6 hours though the rainfall (TFM) associated with local atmospheric drying, water vapor convergence, and hydrometeor loss/convergence, the rainfall (TFm) associated with local atmospheric drying, water vapor convergence, and hydrometeor gain/divergence, and the rainfall (tFm) associated with local atmospheric moistening, water vapor convergence, and hydrometeor gain/divergence. The maximum water vapor convergence of TFM, TFm and tFm leads the minimum mean *CAPE* by 6 hours.
- Maximum model domain mean surface rainfall lags the maximum mean water vapor source (water vapor convergence and surface evaporation) by 3 hours mainly though the rainfall (TfM) associated with local atmospheric drying, water vapor divergence, and hydrometeor loss/convergence. The maximum

hydrometeor loss/convergence of TfM lags the maximum mean water vapor source by hour 3.

- Maximum model domain mean surface rainfall is phase locking with the maximum mean net condensation through the rainfall associated with water vapor convergence. The maximum water vapor convergence of these four rainfall types is in-phase with the maximum mean net condensation.

The phase-locking between maximum mean rain rate (rainfall types with water vapor convergence) and maximum mean net condensation may break the lower limit (30 min) of the Ftitsch-Chappell scheme (Fritsch and Chappell 1980). This in-phase relation also implies that dramatic change can occur within very short time period when cloud microphysical processes produce rainfall. The largest negative 5-hour lag correlation coefficient between the mean *CAPE* and the rainfall type associated with local atmospheric drying, water vapor divergence, and hydrometeor loss/convergence (TfM) among seven rainfall types suggests importance of temporally varying local change of water vapor, which is a time-invariant of 5% in Kuo's scheme (Kuo 1965, 1974). The important role hydrometeor convergence plays in TfM is contradict to the assumption that complete condensation fallout does not allow the transport of hydrometeor concentration in cumulus parameterization (Emanuel and Raymond 1993).

Caution should be exercised with the applications of the results in this study because of two-dimensional model with large-scale forcing. It is necessary to conduct three-dimensional interactive model simulations to validate the results found by the two-dimensional forced modeling in this study.

Acknowledgements. The authors thank Dr. W.-K. Tao, NASA/GSFC, USA, for his two-dimensional cloud resolving model, Prof. M. Zhang, The State University of New York at Stony brook, USA, for his TOGA COARE forcing data, and three anonymous reviewers for their constructive comments. This work is supported by the National Key Basic Research and Development Project of China No. 2004CB418301, the National Natural Sciences Foundation of China under the Grants No. 40333028 and "Outstanding Oversea Scholars" project No.2004-1-5.

References

Anderson, C.J., R.W. Arritt, and J.S. Kain, 2007: An alternative mass flux profile in the Kain-Fritsch convective parameterization and its effects in seasonal precipitation. J. *Hydrometeorology*, 8(5), 1128–1140, doi:10.1175/JHM624.1

Arakawa, A., and W. H. Schubert, 1974: Interaction of a cumulus cloud ensemble with the large-scale environment. Part I. *J. Atmos. Sci*., **31**, 674-701.

Arakawa, A., 2004: The cumulus parameterization problem: Past, present, and future. *J. Clim.*, **17**, 2493–2525.

Bowman, Kenneth P., 2005: Comparison of TRMM Precipitation Retrievals with Rain Gauge Data from Ocean Buoys. *J. Climate*, **18**, 178–190. doi: 10.1175/JCLI3259.1

Betts, A. K., and M. J. Miller, 1986: A new convective adjustment scheme. Part II: Single column tests using GATE wave, BOMEX, ATEX and artic airmass data set. *Quart. J. Roy. Meteor. Soc.*, **112**, 692-709.

Chou, M.-D., and M. J. Suarez, 1994: An efficient thermal infrared radiation parameterization for use in general circulation model. NASA Tech. Memo. 104606, Vol. 3, 85pp. [Available from NASA/Goddard Space Flight Center, Code 913, Greenbelt, MD 20771.]

Chou, M.-D., D. P. Kratz, and W. Ridgway, 1991: Infrared radiation parameterization in numerical climate models. *J. Climate*, **4**, 424-437.

Chou, M.-D., M. J. Suarez, C.-H. Ho, M. M.-H. Yan, and K.-T. Lee, 1998: Parameterizations for cloud overlapping and shortwave single scattering properties for use in general circulation and cloud ensemble models. *J. Atmos. Sci*., **55**, 201-214.

Cui, X., 2008: A phase analysis of vorticity vectors associated with tropical convection. *Chin. Phys. B*, **17**, 2304-2310.

Cui, X., and X. Li, 2006: Role of surface evaporation in surface rainfall processes. *J. Geophys. Res.* **111**, D17112, doi: 10.1029/2005JD006876.

Cui, X., and X. Li, 2011: A cloud-resolving modeling study of short-term surface rainfall processes. *Meteor. Atmos. Phys.*, **111**, 1-11.

Cui, X., Y. Zhu, and X. Li, 2007: Cloud microphysical properties in tropical convective and stratiform regions. *Meteor. Atmos. Phys.*, **98**, 1-11.

Emanuel, K. A and D. J. Raymond, 1993: *The Representation of Cumulus Convection in Numerical Models*. *Meteor. Monogr.* No. 46, Amer. Meteor. Soc., 246 pp.

Fritsch, J. M., and C. F. Chappell, 1980: Numerical prediction of convectively driven masoscale pressure system. Part I: Convective parameterization. *J. Atmos. Sci.* **37**, 1722-1733.

Gao, S., and X. Li, 2008a: Cloud-resolving modeling of convective processes. 206 pp., Springer, Dordrecht.

Gao, S., and X. Li, 2008b: Responses of tropical deep convective precipitation systems and their associated convective and stratiform regions to the large-scale forcing. *Quart. J. Roy. Meteor. Soc.*, **134**, 2127-2141.

Gao, S., and X. Li, 2010a: Effects of time-dependent large-scale forcing, solar zenith angle, and sea surface temperature on time-mean tropical rainfall processes, *Meteor. Atmos. Phys.*, **106**, 95-105.

Gao, S., and X. Li, 2010b: Precipitation equations and their applications to the analysis of diurnal variation of tropical oceanic rainfall. *J. Geophys. Res.*, **115**, D08204, doi:10.1029/2009JD012452.

Gao, S., and X. Li, 2011: Can water vapor process data be used to estimate precipitation efficiency? *Q. J. Roy. Meteor. Soc.*, **137**, 969-978.

Gao, S., F. Ping, X. Li, and W.-K. Tao, 2004: A convective vorticity vector associated with tropical convection: A 2D cloud-resolving modeling study. *J. Geophys. Res.*, **109**, D14106, doi: 10.1029/2004JD004807.

Gao, S., X. Cui, Y. Zhu, and X. Li, 2005a: Surface rainfall processes as simulated in a cloud resolving model. *J. Geophys. Res.*, **110**, D10202, doi: 10.1029/2004JD005467.

Gao, S., X. Cui, Y. Zhou, X. Li, and W.-K. Tao, 2005b: A modeling study of moist and dynamic vorticity vectors associated with 2D tropical convection. *J. Geophys. Res.*, **110**, D17104, doi: 10.1029/2004JD005675.

Gao, S., F. Ping, and X. Li, 2006a: Tropical heat/water quasi-equilibrium and cycle as simulated in a 2D cloud resolving model. *Atmos. Res.*, **79**, 15-29.

Gao, S., L. Ran, and X. Li, 2006b: Impacts of ice microphysics on rainfall and thermodynamic processes in the tropical deep convective regime: A 2D cloud-resolving modeling study. *Mon. Wea. Rev.*, **134**, 3015-3024.

Gao, S., X. Cui, and X. Li, 2009: A modeling study of diurnal rainfall variations during the 21-day period of TOGA COARE., *Adv. Atmos. Sci.*, **26**, 895-905.

Grandpeix J-Y, Lafore JP. 2010. A density current parametrization coupled to Emanuel's convection scheme. Part I: the models. *Journal of the Atmospheric Sciences* **67**:

881–897.

Khairoutdinov, M. F., and D. A. Randall, 2001: A cloud-resolving model as a cloud parameterization in the NCAR CommunityClimate System Model: Preliminary results. *Geophys. Res. Lett.,* **28,** 3617–3620.

Krueger, S. K., Q. Fu, K. N. Liou and H.-N. S. Chin, 1995: Improvement of an ice-phase microphysics parameterization for use in numerical simulations of tropical convection, *J. Appl. Meteor.*, **34**, 281-287.

Kuo, H. L., 1965: On formation and intensification of tropical cyclones through latent heat release by cumulus convection. *J. Atmos. Sci.*, **22**, 40-63.

Kuo, H. L., 1974: Further studies of the parameterization of the influence of cumulus convection on large-scale flow. *J. Atmos. Sci.*, **31**, 1232-1240.

Li, X., 2009: Dominant physical processes associated with phase differences between surface rainfall and convective available potential energy, *J. Tropical Meteor.*, **15**, 148-154.

Li, X., C.-H. Sui, K.-M. Lau, and M.-D. Chou, 1999: Large-scale forcing and cloud-radiation interaction in the tropical deep convective regime. *J. Atmos. Sci*., **56**, 3028-3042.

Li, X., C.-H. Sui, and K.-M. Lau, 2002a: Precipitation efficiency in the tropical deep convective regime: A 2-D cloud resolving modeling study. *J. Meteor. Soc. Japan*, **80**, 205-212.

Li, X., C.-H. Sui, and K.-M. Lau, 2002b: Interactions between tropical convection and its embedding environment: An energetics analysis of a 2-D cloud resolving simulation. *J. Atmos. Sci.*, **59**, 1712-1722.

Li, X., C.-H. Sui, and K.-M. Lau, 2002c: Dominant cloud microphysical processes in a tropical oceanic convective system: A 2-D cloud resolving modeling study. *Mon. Wea. Rev.* **130**, 2481-2491.

Lin, Y.-L., R. D. Farley, and H. D. Orville, 1983: Bulk parameterization of the snow field in a cloud model, *J. Climate Appl. Meteor*., **22**, 1065-1092.

Ping, F., Z. Luo, and X. Li, 2008: Kinematics, Cloud microphysics, and spatial structures of tropical cloud clusters: A two-dimensional cloud-resolving modeling study. *Atmos. Res.*. **88**, 323-336.

Polkinghorne, Rosanne, Tomislava Vukicevic, K. Franklin Evans, 2010: Validation of Cloud-Resolving Model Background Data for Cloud Data Assimilation. *Mon. Wea. Rev.*, **138**, 781–795.

Polkinghorne, Rosanne, Tomislava Vukicevic, 2011: Data Assimilation of Cloud-affected Radiances in a Cloud-Resolving Model. *Mon. Wea. Rev.*, **139**, 755–773.

Randall, D. A., and D. M. Pan, 1993: Implementation of the Arakawa-Schubert cumulus parameterization with a prognostic closure. *The Representation of Cumulus Convection in Numerical Models, Meteor. Monogr.*, No. 46, Amer. Meteor. Soc., 137-144.

Randall, D., M. Khairoutdinov, A. Arakawa, and W. Grabowski, 2003: Breaking the cloud parameterization deadlock. *Bull. Amer. Meteor. Soc.,* **84,** 1547–1564.

Raymond, D. J. and X. Zeng, 2005: Modeling tropical atmospheric convection in the context of the weak temperature gradient approximation. *J. Roy. Soc.*, **131**, 1301-1320.

Rutledge, S. A., and P. V. Hobbs, 1983: The mesoscale and microscale structure and organization of clouds and precipitation in midlatitude cyclones. Part VIII: A model for the "seeder-feeder" process in warm-frontal rainbands, *J. Atmos. Sci*., **40**, 1185-1206.

Rutledge, S. A., and P. V. Hobbs, 1984: The mesoscale and microscale structure and organization of clouds and precipitation in midlatitude cyclones. Part XII: A diagnostic modeling study of precipitation development in narrow cold-frontal rainbands, *J. Atmos. Sci*., **41**, 2949-2972.

Shen, X., Y. Wang, N. Zhang, and X. Li, 2010a: Roles of large-scale forcing, thermodynamics, and cloud microphysics in tropical precipitation processes. *Atmos. Res.*, **97**, 371-384.

Shen, X., Y. Wang, N. Zhang, and X. Li, 2010b: Precipitation and cloud statistics in the deep tropical convective regime. *J. Geophys. Res.*, **115**, D24205, doi: 10.1029/2010JD014481.

Short, D. A., P. A. Kucera, B. S. Ferrier, J. C. Gerlach, S. A. Rutledge, O. W. Thiele, 1997: Shipboard radar rainfall patterns within the TOGA COARE IFA. *Bull. Amer. Meteor. Soc.*, **78**, 2817-2836.

Soong, S. T., and Y. Ogura, 1980: Response of tradewind cumuli to large-scale processes. *J. Atmos. Sci*., **37**, 2035-2050.

Soong, S. T., and W. K. Tao, 1980: Response of deep tropical cumulus clouds to mesoscale processes. *J. Atmos. Sci*., **37**, 2016-2034.

Sui, C.-H., and X. Li, 2005: A tendency of cloud ratio associated with the development of tropical water and ice clouds. *Terr. Atmos. Oceanic Sci*., **16**, 419-434.

Sui, C.-H., K.-M. Lau, W.-K. Tao, and J. Simpson, 1994: The tropical water and energy cycles in a cumulus ensemble model. Part I: Equilibrium climate. *J. Atmos. Sci.*, **51**, 711-728.

Sui, C.-H., X. Li, M.-J. Yang, and H.-L. Huang, 2005: Estimation of oceanic precipitation efficiency in cloud models. *J. Atmos. Sci.*, **62**, 4358-4370.

Sui, C.-H., C.-T. Tsay, and X. Li, 2007a: Convective stratiform rainfall separation by cloud content. *J. Geophys. Res.*, **112**, D14213, doi:10.1029/2006JD008082.

Sui, C.-H., X. Li, and M.-J. Yang, 2007b: On the definition of precipitation efficiency. *J. Atmos. Sci.*, **64**, 4506-4513.

Tao, W.-K., and J. Simpson, 1993: The Goddard Cumulus Ensemble model. Part I: Model description. *Terr. Atmos. Oceanic Sci.*, **4**, 35-72.

Tao, W.-K, J. Simpson, and M. McCumber, 1989: An ice-water saturation adjustment, *Mon. Wea. Rev.*, **117**, 231-235.

Tao, W.-K., J. Simpson, C.-H. Sui, B. Ferrier, S. Lang, J. Scala, M.-D. Chou and K. Pickering, 1993: Heating, moisture and water budgets of tropical and midlatitude squall lines: Comparisons and sensitivity to longwave radiation. *J. Atmos. Sci.*, **50**, 673-690.

Tao, W.-K., C.-L. Shie, R. Johnson, S. Braun, J. Simpson, and P. E. Ciesielski, 2003: Convective Systems over South China Sea: Cloud-Resolving Model Simulations. J. Atmos. Sci., 60, 2929-2956.

Weller, R. A., and S. P. Anderson, 1996: Surface meteorology and air-sea fluxes in the western equatorial Pacific warm pool during TOGA COARE. *J. Climate*, **9**, 1959-1990.

Xu, K.-M., and D. A. Randall, 1998: Influence of large-scale advective cooling and moistening effects on the quasi-equilibrium behavior of explicitly simulated cumulus ensembles. *J. Atmos. Sci.*, **55**, 896-909.

Xu, K.-M., M. Zhang, Z. A. Eitzen, S. J. Ghan, et al, 2005: Modeling springtime shallow frontal clouds with cloud-resolving and single-column models. *J. Geophys. Res.*, 110, D15S04, doi:10.1029/2004JD005153

Yamamoto, Munehisa K., Fumie A. Furuzawa, Atsushi Higuchi, Kenji Nakamura, 2008: Comparison of Diurnal Variations in Precipitation Systems Observed by TRMM PR, TMI, and VIRS. *J. Climate*, **21**, 4011–4028.

Zhou, Y., X. Cui, and X. Li, 2006: Contribution of cloud condensate to Surface rain rate. *Prog. Nat. Sci.*, **16**, 967-973.

Table Captions

Table 1 Summary of rainfall types. T and t represent local atmospheric drying and moistening, respectively. F and f represent water vapor convergence and divergence, respectively. M and m represent hydrometeor loss/convergence and gain/divergence, respectively.

Table 2 Maximum/minimum weighted lag correlation coefficients (*CORR*) and lag hours (*HOUR*) between (a) model domain mean *CAPE* and rainfall (b) (a) the mean of Q_{WVF}+Q_{WVE} and rainfall, and (c) the mean of Q_{NC} and rainfall.

Table 3 Critical weighted correlation coefficients at the 1% significant level for P_S, Q_{WVT}, Q_{WVF}, Q_{WVE}, and Q_{CM} and seven rainfall types.

Table 4 Maximum/minimum weighted lag correlation coefficients (*CORR*) and lag hours (*HOUR*) between (a) model domain mean *CAPE* and rainfall (b) (a) the mean of Q_{WVF}+Q_{WVE} and rainfall, and (c) the mean of Q_{NC} and rainfall. Comparison of Table 4 with table 3 shows that maximum/minimum weighted lag correlation coefficients generally exceed 1% significance level.

Table 1 Summary of rainfall types. T and t represent local atmospheric drying and moistening, respectively. F and f represent water vapor convergence and divergence, respectively. M and m represent hydrometeor loss/convergence and gain/divergence, respectively.

Type	Description
TFM	Water vapor convergence, local atmospheric drying, and hydrometeor loss/convergence
TFm	Water vapor convergence, local atmospheric drying, and hydrometeor gain/divergence
tFM	Water vapor convergence, local atmospheric moistening, and hydrometeor loss/convergence
tFm	Water vapor convergence, local atmospheric moistening, and hydrometeor gain/divergence
TfM	Water vapor divergence, local atmospheric drying, and hydrometeor loss/convergence
Tfm	Water vapor divergence, local atmospheric drying, and hydrometeor gain/divergence
tfM	Water vapor divergence, local atmospheric moistening, and hydrometeor loss/convergence
tfm	Water vapor divergence, local atmospheric moistening, and hydrometeor gain/divergence

Table 2 Maximum/minimum weighted lag correlation coefficients (*CORR*) and lag hours (*HOUR*) between (a) model domain mean *CAPE* and rainfall (b) (a) the mean of Q_{WVF}+Q_{WVE} and rainfall, and (c) the mean of Q_{NC} and rainfall.

	CAPE		Q_{WVF}+Q_{WVE}		Q_{NC}	
	CORR	*HOUR*	*CORR*	*HOUR*	*CORR*	*HOUR*
Mean P_S	-0.331	6	0.771	-3	0.931	0
TFM	-0.041	6	0.074	-4	0.084	0
TFm	-0.065	6	0.136	-2	0.185	0
tFM	-0.070	7	0.169	-2	0.191	0
tFm	-0.050	6	0.113	-2	0.144	0
TfM	-0.090	5	0.228	-3	0.272	-1
Tfm	-0.007	4	0.031	-2	0.039	0
tfM	-0.011	6	0.026	-3	0.031	-1

Table 3 Critical weighted correlation coefficients at the 1% significant level for P_S, Q_{WVT}, Q_{WVF}, Q_{WVE}, and Q_{CM} and seven rainfall types.

	P_S	Q_{WVT}	Q_{WVF}	Q_{WVE}	Q_{CM}
TFM	0.019	0.006	0.008	0.000	0.009
TFm	0.026	0.022	0.043	0.001	0.041
tFM	0.028	0.092	0.084	0.002	0.030
tFm	0.020	0.062	0.119	0.002	0.049
TfM	0.039	0.171	0.193	0.003	0.057
Tfm	0.008	0.049	0.032	0.001	0.015
tfM	0.006	0.005	0.006	0.001	0.015

Table 4 Maximum/minimum weighted lag correlation coefficients (*CORR*) and lag hours (*HOUR*) between (a) model domain mean *CAPE* and rainfall (b) (a) the mean of Q_{WVF}+Q_{WVE} and rainfall, and (c) the mean of Q_{NC} and rainfall. Comparison of Table 4 with table 3 shows that maximum/minimum weighted lag correlation coefficients generally exceed 1% significance level.

(a)	Q_{WVT}		Q_{WVF}		Q_{WVE}		Q_{CM}	
	CORR	*HOUR*	*CORR*	*HOUR*	*CORR*	*HOUR*	*CORR*	*HOUR*
TFM	-0.012	6	-0.013	6	-0.001	6	-0.016	4
TFm	-0.053	6	-0.105	6	-0.003	6	0.0095	6
tFM	0.235	9	-0.217	9	-0.006	8	-0.082	9
tFm	0.114	4	-0.282	8	-0.004	4	0.125	8
TfM	-0.279	9	0.314	9	0.008	5	-0.117	5
Tfm	-0.058	7	0.045	9	-0.002	4	0.012	4
tfM	0.008	6	0.012	6	-0.002	6	-0.029	6

(b)	Q_{WVT}		Q_{WVF}		Q_{WVE}		Q_{CM}	
	CORR	*HOUR*	*CORR*	*HOUR*	*CORR*	*HOUR*	*CORR*	*HOUR*
TFM	0.021	-5	0.025	-4	0.001	-3	0.028	-4
TFm	0.115	-2	0.244	-2	0.005	-2	-0.228	-2
tFM	-0.521	-2	0.483	-2	0.014	-3	0.193	-2
tFm	-0.320	-2	0.716	-2	0.009	-2	-0.292	-2
TfM	0.748	-2	-0.880	-2	0.020	-3	0.343	-3
Tfm	0.230	-2	-0.138	-1	0.006	-2	-0.068	-2
tfM	-0.022	-3	-0.027	-3	0.004	-3	0.071	-3

(c)	Q_{WVT}		Q_{WVF}		Q_{WVE}		Q_{CM}	
	CORR	*HOUR*	*CORR*	*HOUR*	*CORR*	*HOUR*	*CORR*	*HOUR*
TFM	0.022	-1	0.029	0	0.001	0	0.032	0
TFm	0.154	0	0.318	0	0.006	0	-0.292	0
tFM	-0.509	-1	0.482	0	0.014	-1	0.205	-1
tFm	-0.347	0	0.835	0	0.009	0	-0.353	0
TfM	0.817	0	-0.938	0	0.021	-1	0.386	-1
Tfm	0.246	0	-0.139	1	0.001	-2	-0.074	0
tfM	-0.023	-1	-0.029	-1	0.004	-1	0.079	-1

Figure Captions

Fig. 1 Time-height cross sections of (a) vertical velocity (cm s^{-1}), (b) zonal wind (m s^{-1}), and time series of (c) sea surface temperature (^{o}C) observed and derived from TOGA COARE for the 21-day period. Upward motions in (a) and westerly winds in (b) are shaded.

Fig. 2 (a) Lag correlation coefficient between model domain mean *CAPE* and mean surface rain rate (cross) and (b) weighted lag correlation coefficients between the mean *CAPE* and rain rate for the eight rainfall types. The lines with open circle, closed circle, open square, closed square, X, diamond, triangle, and open oval in (b) denote TFM, TFm, tFM, tFm, TfM, Tfm, and tfM, respectively.

Fig. 3 (a) Lag correlation coefficient between model domain mean of $Q_{WVF}+Q_{WVE}$ and mean surface rain rate (cross) and (b) weighted lag correlation coefficients between the mean of $Q_{WVF}+Q_{WVE}$ and rain rate for the eight rainfall types. The lines with open circle, closed circle, open square, closed square, X, diamond, triangle, and open oval in (b) denote TFM, TFm, tFM, tFm, TfM, Tfm, and tfM, respectively.

Fig. 4 (a) Lag correlation coefficient between model domain mean of Q_{NC} and mean surface rain rate (cross) and (b) weighted lag correlation coefficients between the mean of Q_{NC} and rain rate for the eight rainfall types. The lines with open circle, closed circle, open square, closed square, X, diamond, triangle, and open oval in (b) denote TFM, TFm, tFM, tFm, TfM, Tfm, and tfM, respectively.

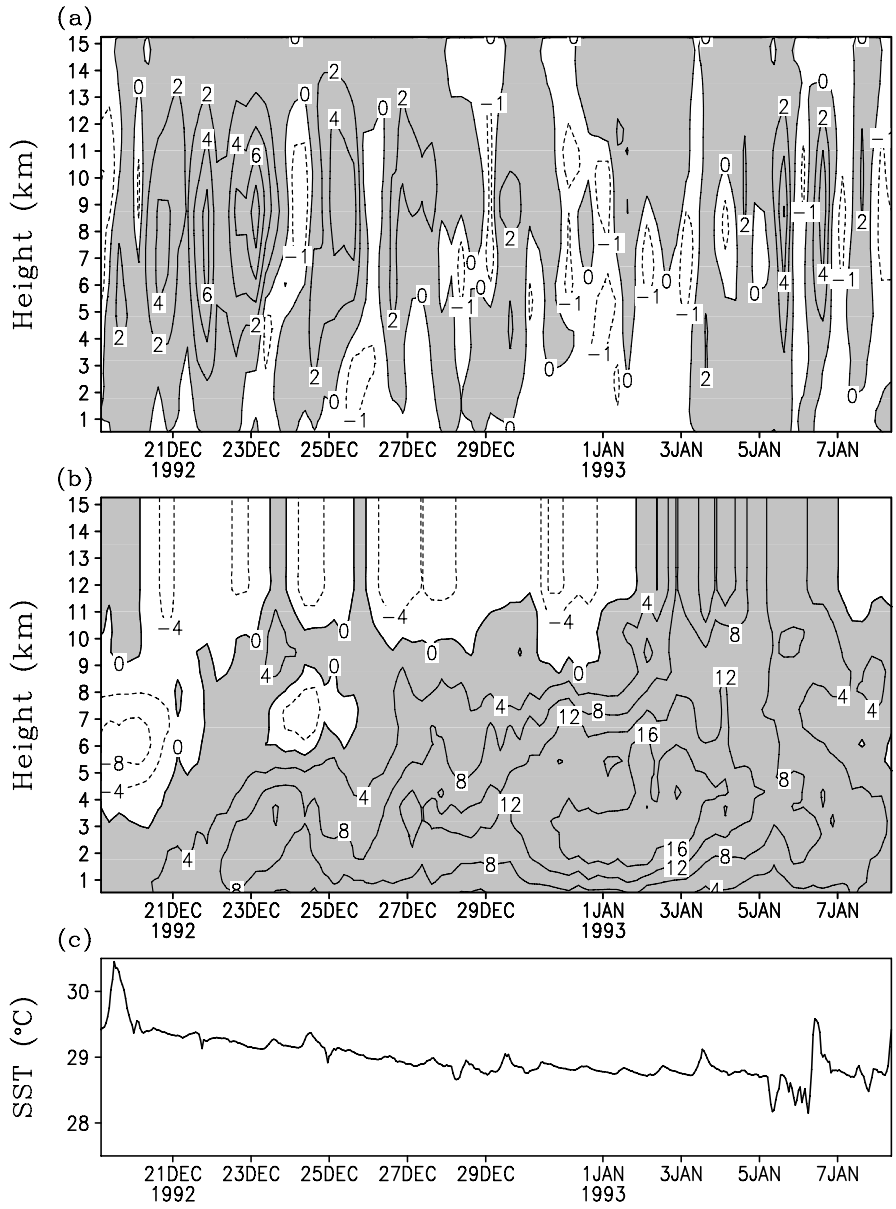

Fig. 1 Time-height cross sections of (a) vertical velocity (cm s^{-1}), (b) zonal wind (m s^{-1}), and time series of (c) sea surface temperature (^{o}C) observed and derived from TOGA COARE for the 21-day period. Upward motions in (a) and westerly winds in (b) are shaded.

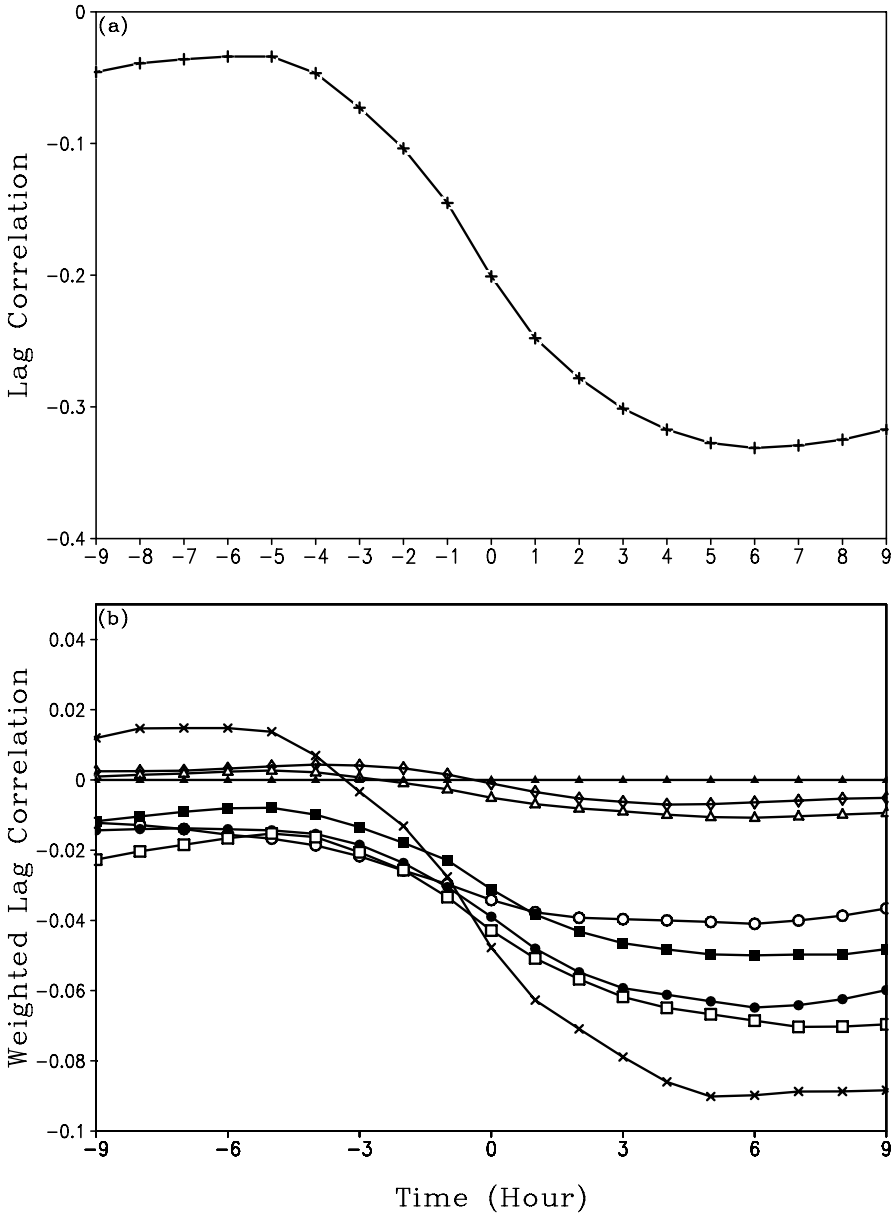

Fig. 2 (a) Lag correlation coefficient between model domain mean *CAPE* and mean surface rain rate (cross) and (b) weighted lag correlation coefficients between the mean *CAPE* and rain rate for the eight rainfall types. The lines with open circle, closed circle, open square, closed square, X, diamond, triangle, and open oval in (b) denote TFM, TFm, tFM, tFm, TfM, Tfm, and tfM, respectively.

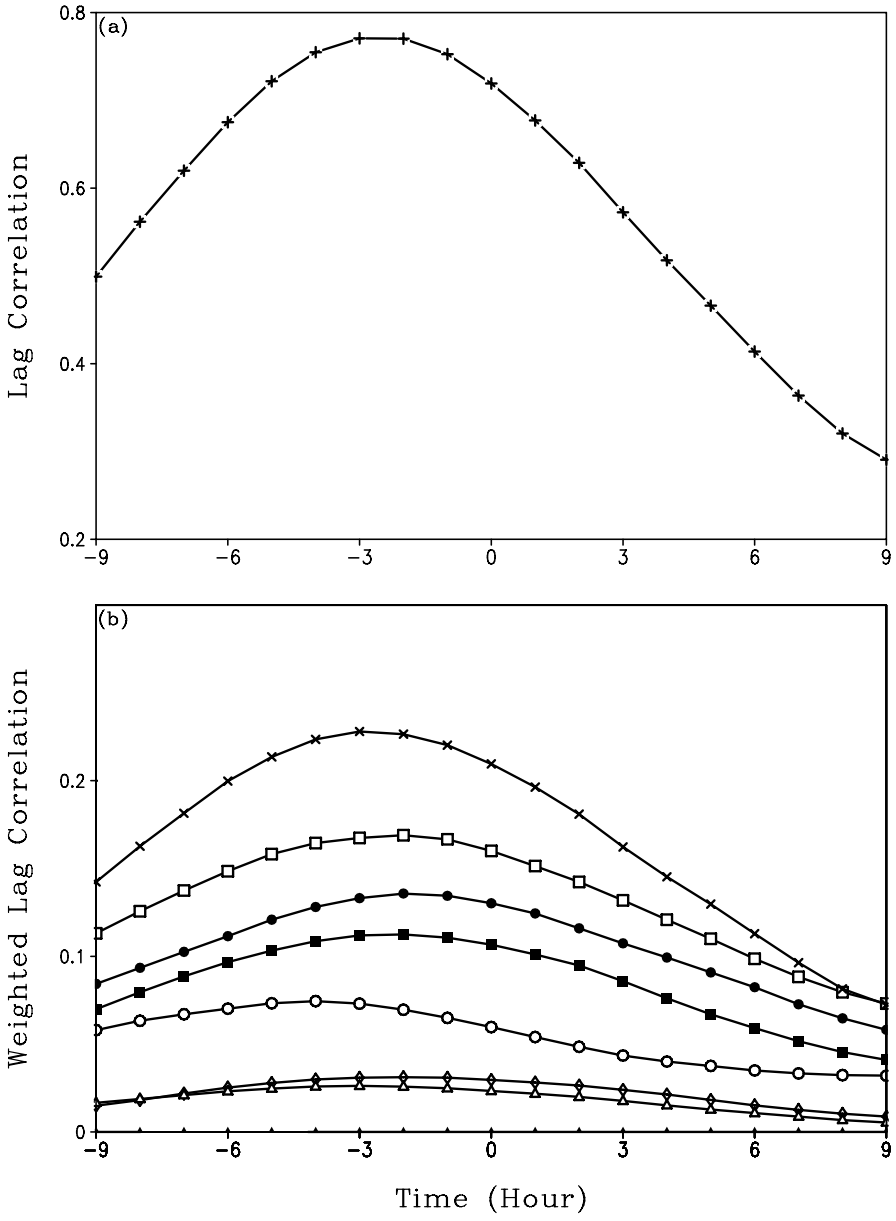

Fig. 3 (a) Lag correlation coefficient between model domain mean of $Q_{WVF}+Q_{WVE}$ and mean surface rain rate (cross) and (b) weighted lag correlation coefficients between the mean of $Q_{WVF}+Q_{WVE}$ and rain rate for the eight rainfall types. The lines with open circle, closed circle, open square, closed square, X, diamond, triangle, and open oval in (b) denote TFM, TFm, tFM, tFm, TfM, Tfm, and tfM, respectively.

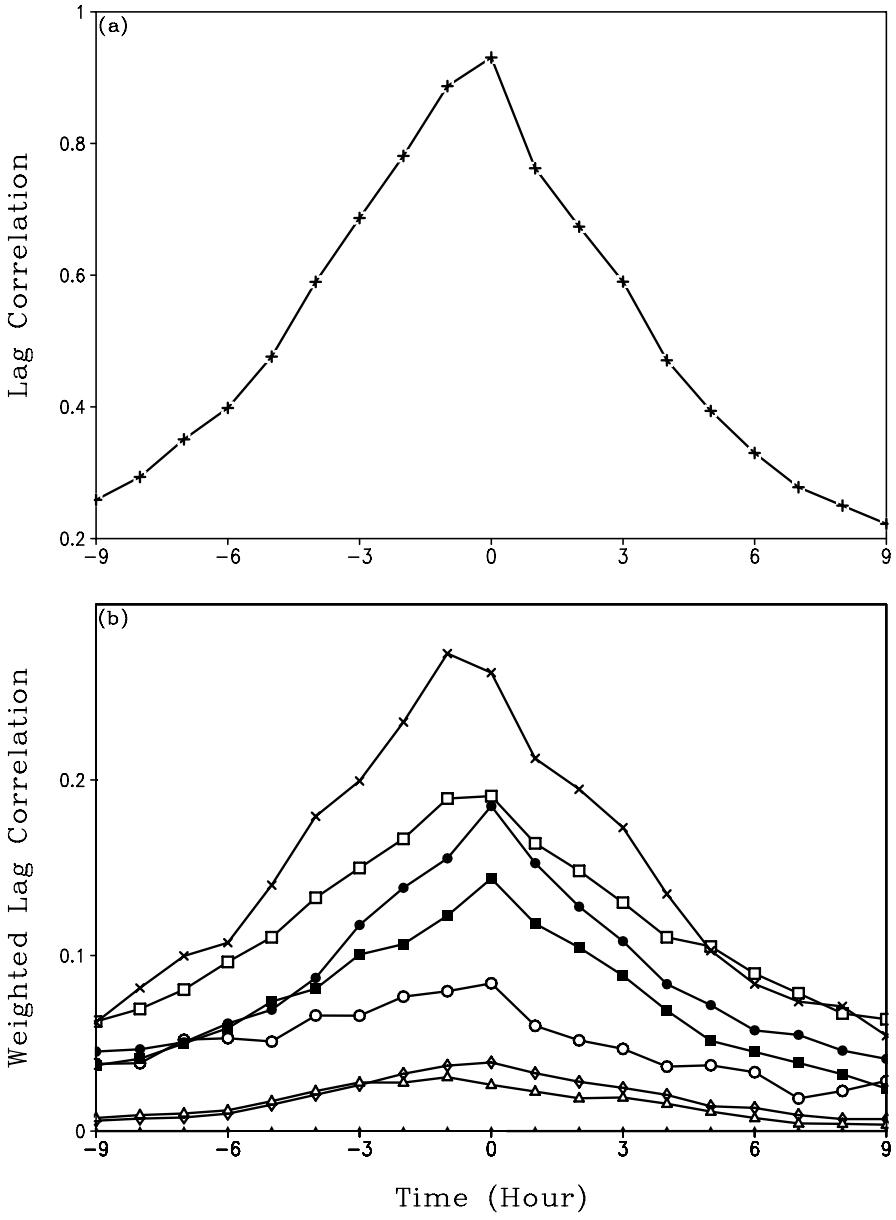

Fig. 4 (a) Lag correlation coefficient between model domain mean of Q_{NC} and mean surface rain rate (cross) and (b) weighted lag correlation coefficients between the mean of Q_{NC} and rain rate for the eight rainfall types. The lines with open circle, closed circle, open square, closed square, X, diamond, triangle, and open oval in (b) denote TFM, TFm, tFM, tFm, TfM, Tfm, and tfM, respectively.

OPTICAL MODELING OF CLOUD-ACTIVE SEA-SALT AEROSOL IN THE MARINE AND COASTAL ATMOSPHERE SURFACE LAYER

Kaloshin G.A.

V.E. Zuev Institute of Atmospheric Optics SB RAS,

1, Academician Zuev sq., Tomsk, Russia

gkaloshin@iao.ru

1. INTRODUCTION

The concentration and distribution of the aerosol is important for various optical remote sensing and environmental monitoring applications, understanding the Earth's radiative balance, studying cloud properties, etc. In the case when anthropogenic pollution is negligible the near-shore scattering extinction is greatly influenced by sea-salt aerosol fluxes from breaking waves and variations of relative humidity *RH*. The most essential factors affecting the ocean wave destruction are considered to be sea state, fetch, surface wind speed and tidal dynamics; it is also significantly modulated by amplitude of ocean swell, wave spectra and geometry of coastal line. Henceforth, the fetch is a length over open surface of water where wind can blow being uninterrupted by surrounding obstacles. Their impact on the boundary aerosol layer, being superimposed on the sea-salt aerosol generated by an open ocean, varies greatly with the meteorological parameters, such as wind speed [1].

Based on these facts the presented investigation seeks to contribute to a better understanding of visibility decrease and other optical effects of the atmospheric aerosol eventually aiming for a development of a robust algorithm for the aerosol extinction forecast. In the study we consider the coastal physical effects and ocean processes as functions of the wind speed, its direction, fetch, relative humidity (*RH*) and altitude above the sea level.

While taking into account the variability of marine and coastal aerosols, the paper focuses on the detailed description of the developed aerosol model (Sections 1, 2) and the optical properties of the aerosol (Section 3). In the last sections 4, 5 we discuss the developed algorithm and the comparison of our results calculated by the software product MaexPro (**M**arine **A**erosol **Ex**tinction **Pro**file) with available observational data and with the aerosol extinction results obtained by the software NAM (Navy Aerosol Model) and ANAM (Advanced Navy Aerosol Model) [2].

2. THE MICROPHYSICAL MODEL USED IN MAEXPRO

According to up-to-date representations [1], of the surface layer aerosol of the marine and coastal atmosphere, its microphysical and optical characteristics determine the aerosol extinction coefficients $\sigma(\lambda)$, in the same time essentially depending on the type of air mass parameter (AMP), the speed and the direction of the wind, the fetch and the relative humidity. Also it is highly sensitive to altitude structure, especially, in the range of the heights 0-30 meters.

The aerosol size distribution function (ASDF) dN/dr of the coastal aerosol microphysical model in the range of the particle's radii 0.01–100 μm may be expressed as a sum of four modified lognormal functions [3]. The choice of the particles sizes 0.01 – 100 μm is caused by the special attention to the wavelength band 0.2 - 14 μm where the aerosol extinction is of great practical interest, e.g. for the radiative transfer simulations. For the wave band the optical activity of the particles beyond the size range 0.01 – 100 μm is negligible [4].

The principal feature of the model is the parameterization of the amplitudes A_i and the widths C_i of the various modes as functions of fetch X and wind speed U. The approximation is based on the fit to the ASDF observed in Atlantic and Arctic Oceans, Mediterranean, Baltic and Norwegian Seas [5].

3. THE OPTICAL MODEL USED IN MAEXPRO

Thus, having obtained the aerosol size distribution and the refraction index as shown in [3] it is possible to calculate the aerosol scattering $\alpha(\lambda)$ and the extinction $\sigma(\lambda)$ values by means of the classical Mie solution assuming the spherically-shaped aerosol particles.

The aerosol substance is submitted as a combination of four materials: dry substance, sea salt and water. In the software MaexPro the real and imaginary parts of the complex optical index for the components of the aerosol particle substance have been taken from the empirical results [6] by means of the extrapolation in the wavelength band 0.2 – 14 μm sampled with the interval $\Delta\lambda$ = 0.001 μm.

4. THE OPTICAL ACTIVITY OF AEROSOL PARTICLES

It is common to think that the aerosol particles of the marine and coastal atmosphere in the range of diameters 0.1 – 10 μm are the most optical active for the sun radiation in the visible and near IR wavebands. Actually, for marine and coastal aerosols the approximation is not correct for many reasons. For example, our calculations based on the MaexPro model have revealed essential difference between the aerosol extinction spectra computed from the incomplete (0.1 – 10 μm) and the full range (Δr = 0.01 – 100 μm) of the particle sizes [4] as shown in Fig. 1.

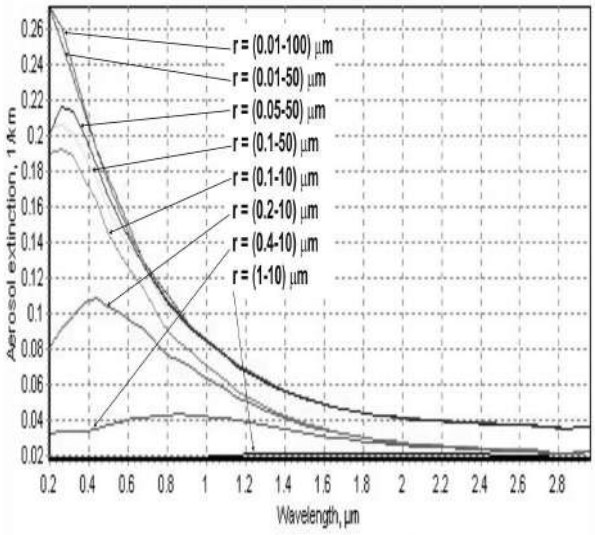

Fig. 1. The optical activity of the coastal aerosol particles of eight distinct particle size distributions similar to the experimental one, which was detected by a typical aerosol counters.

5. THE SPECTRAL TRANSPARENCY VS. METEOROLOGICAL PARAMETERS

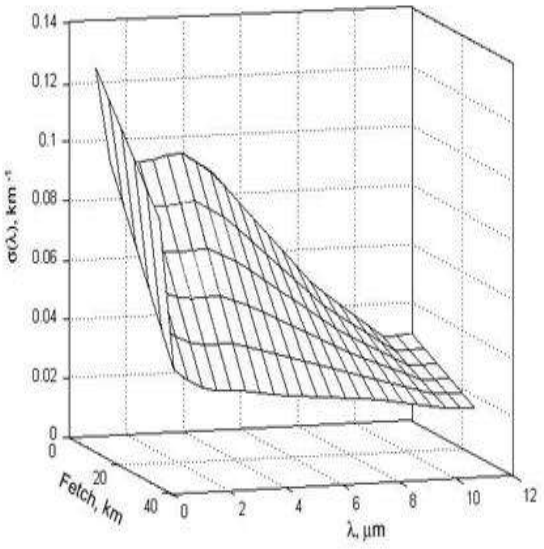

Fig. 2. The spectral aerosol extinction coefficient $\sigma(\lambda)$ vs. fetch *X*:
H = 20 m, *RH* = 75%, *U* = 3.3 m/s.

Fig. 2 evidences how significant is the dependence of the extinction spectra on the fetch parameter. It is clear from Fig. 2 that in the range of the small values of the fetch (3-10 km) the presented extinction spectra have a steep decline behavior that is typical for the coastal aerosol. With increasing fetch, the extinction spectra become almost uniform proper for the typical marine aerosols. It means that in the coastal environment the fetch can be used in the same way as the air mass parameter (AMP) [7].

The wind speed is another important factor determining the aerosol extinction spectra of the coastal zone. Our simulations reveal that the spectrum of $\sigma(\lambda)$ has a relatively slight gradient in the range of the average values of the wind speed and for the small values of the fetch. The spectrum becomes to be more distinguishable when the wind speed increases.

It is interesting to note that the MaexPro model used in our simulations allows us to observe computationally a so-called “dilution effect” of the sea-salt aerosol [8]. The effect is possible to explain assuming that the greater fetch values are related to the marine

conditions, and the smaller values of the fetch correspond to the coastal conditions.

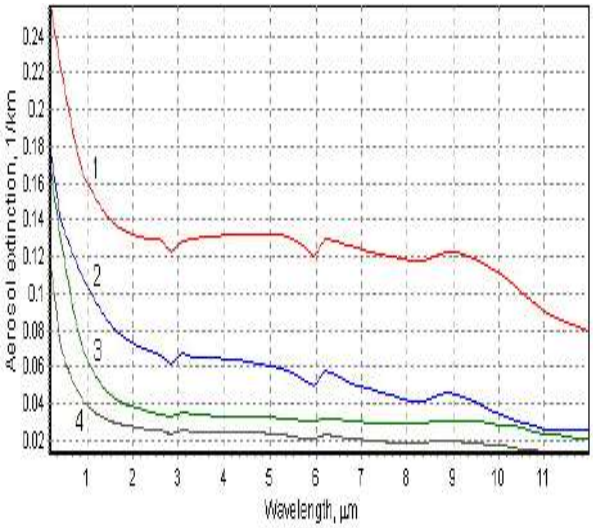

Fig. 3. The spectra of the aerosol extinction coefficients σ(λ) for different values of wind speed *U* and fetch *X* calculated by the code MaexPro: (1) *U* = 15 m/s and *X* = 30 km, (2) *U* = 3.5 m/s and *X* = 3 km, (3) *U* = 3.5 m/s and *X* = 30 km, (4) *U* = 15 m/s and *X* = 3 km.

On Fig. 3 a mutual influence of the fetch and wind speed on the spectral behavior of σ(λ) for the various wind speeds *U* and the fetch *X*, calculated by MaexPro is presented. Curve 1 and 3 show that at the greater fetch *X* = 30 km (marine conditions) with the growth *U* from 3.5 up to 15 m/sec σ(λ) also grows. Contrary to that, at the small fetch (curves 2, 4, coastal conditions) *X* = 3 km, with the increase of the wind speed *U* from 3.5 up to 15 m/sec we observe considerable decrease of σ(λ) in the spectral range of Δλ = 0.2-12 μm.

Fig. 4 plots the results of comparison between the aerosol extinction spectra σ(λ) calculated by the software MaexPro and the observational results received by IAO group [9] in the Black Sea coastal environment. σ(λ) in the 0.44–11.9 μm band was measured using a transmissometer with the spectral resolution of 0.3–0.4 μm. The experiment was conducted at a height of 4 meters above the sea surface, and the path length was 7.5 km. Meteorological sensors installed on the top of the receiver tower provided temperature, humidity, pressure and wind speed. Fig. 4 illustrates an agreement between the σ(λ) spectral behavior and the observational results received by IAO group [9] in the Black Sea coastal environment.

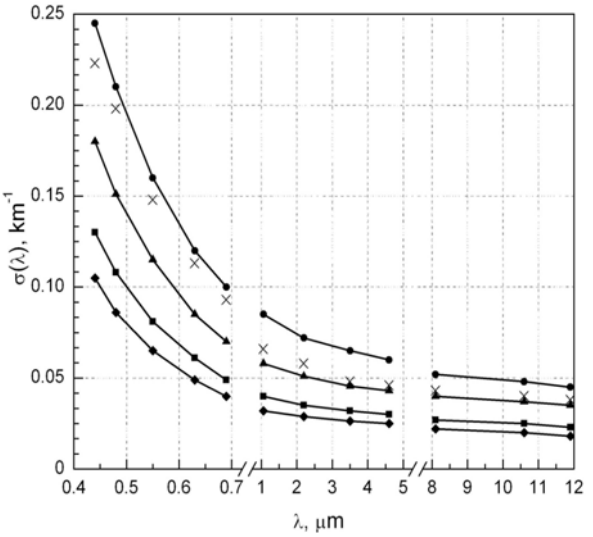

Fig. 4. The spectrum of σ(λ) at H = 4 m for X = 30 km, U = 3.3 m/s and for different RH: ♦ - RH = 66 %, ■ - RH = 75 %, ▲- RH = 85 %, ● - RH = 90 %; × - the observational results received by IAO.

6. CONCLUSIONS

Based on the comparison with the observational results, we can draw a conclusion, that the model MaexPro is capable to realistically describe the impact of the different factors, *viz.* - meteorological parameters, geometrical features of shoreline, wind mode and *etc*. To take into account air dynamics in the MaexPro model, the air mass parameter employed in NAM and ANAM, might be replaced by the fetch parameter. As a final result, the model is able to reproduce experimentally observed effects and regularities of the spectral and altitude profiles σ(λ) in the visible and IR wavelength bands.

REFERENCES

[1] Lewis, E.R., Schwartz S.E., [Sea Salt Aerosol Production: Mechanisms, Methods, Measurements, and Models - A Critical Review (Geophys. Monograph)], AGU, Washington, DC, (2004).

[2] Gathman, S.G., van Eijk, J. A.M., "Characterizing large aerosols at the lowest levels of marine atmosphere," Proc. SPIE 3433, 41-52 (1998).

[3] Piazzola, J., Kaloshin, G., "Performance evaluation of the coastal aerosol extinction code “MEDEX” with data from the Black Sea," J. Aerosol Science, 36(3), 341-359 (2005).

[4] Kaloshin G.A., Grishin I.A. An Aerosol Model of the Marine and Coastal Atmospheric Surface Layer // Atmosphere-Ocean, Vol. 49, № 2, P. 112 – 120(2011).
[5] Kaloshin, G.A., Shishkin, S.A., Serov, S.A., "The program package MaexPro for calculation atmospheric aerosol extinction in the marine and coastal surface layer," J. Opt. Tech., 74(6), 20-27 (2007).
[6] Kaloshin, G., Piazzola J., "Influence of the Large Aerosol Particles on the Infrared Propagation in Coastal Areas," Proc. 23rd Int. Laser Radar Conf.; Nara, Japan, 429-432 (2006).
[7] Volz, F.E., "IR index of atmospheric aerosol substances," Appl. Opt., 11, 755-759 (1972).
[8] Kaloshin, G.A., "Influence of wind conditions on aerosol extinction in the sea and coastal atmosphere surface layer," J. Atmos. and Oceanic Opt., 20(7), 571-576 (2007).
[9] Clarke, A.D., Kapustin, V.N., "The Shoreline Environment Aerosol Study (SEAS): A Context for Marine Aerosol Measurements Influenced by a Coastal Environment and Long-Range Transport," J. Atmos. and Ocean. Tech., 20(10), 1351-1361 (2003).
[10] Kabanov, M.V., Panchenko, M.V., Pkhalagov, Yu.A., Veretennikov, V.V., Uzhegov, V.N., and Fadeev, V.Ya., [Optical Properties of Coastal Atmospheric Hazes], Nauka, Novosibirsk, 201 (1988).
[11] Kaloshin G.A. Visible and infrared extinction of atmospheric aerosol in the marine and coastal environment // Appl. Optics. Vol. 50, № 14, P. 2124 – 2133(2011).

TURBULENT MIXING IN STRATOCUMULUS CLOUDS

L. Magaritz[1], M. Pinsky[1], A. Korolev[2] and A. Khain[1]
[1]Department of Atmospheric Sciences, The Hebrew University of Jerusalem, Israel
[2]Environment Canada, Toronto, Canada

1. INTRODUCTION

Turbulent mixing in clouds has long been a matter for investigation and interest and there are contradictory opinions concerning the role of mixing on microphysical cloud properties. In some studies effects of mixing are associated with entrainment of cloud free air from the surroundings (Baker; Latham 1979, 1982; Baker et al. 1980; Blyth et al. 1980; Cooper 2011). In these studies it is assumed that dilution and evaporation of small droplets near cloud edges can lead to formation of cloudy volumes with low concentration of droplets while containing mostly large droplets. These droplets can then grow to superadiabatic sizes and contribute to the formation of raindrops (theory of inhomogeneous mixing). In other studies (Khain et al. 2012; Paluch 1986; Prabha et al. 2011) it is shown that namely undiluted and slightly diluted air volumes contain maximum liquid water content with the widest droplet size distributions (DSD) containing the largest drops. These parcels are suspected to have the first raindrop formation. The effects of mixing on the structure and microphysical properties of stratocumulus clouds are even less known then in cumulus clouds. Hill et al. (2009) simulated the evolution of a stratocumulus cloud using a LES model in which mixing was described either traditionally using k-theory or with some additional corrections of droplet concentration required by the inhomogeneous mixing hypothesis. The results in both cases were indistinguishable from one another. Magaritz et al. (2009) simulated stratocumulus cloud evolution using a hybrid Lagrangian-Eulerian model of the boundary layer in which a great number of adjacent Lagrangian air parcels were advected by a turbulent-like velocity field obeying turbulent correlation laws. Drizzling and non-drizzling stratocumulus clouds measured during research flights were successfully reproduced in simulations with a non-mixing limit, i.e. in the absence of turbulent mixing between adjacent parcels. The parcels interacted only via droplet sedimentation. It was found that first drizzle droplets form in a small number of "lucky" parcels that started their trajectory near the surface and contained maximum humidity. Additional feature of the lucky parcels is that they spent significant time in clouds and have maximum liquid water content (LWC).

The simplified model used in the previous study did not include turbulent mixing between parcels, radiative cooling, surface fluxes or an inversion layer above the cloud. Under such assumptions, no penetration of drop free volumes into the cloud from the upper boundary took place. Such design could artificially decrease the role of mixing.

The purpose of this research is to investigate formation of microphysical and thermodynamical structure of a stratocumulus cloud and, in particular, the role of mixing in this evolution. Here we present the first part of the research that concentrates on the effects of turbulent mixing on macroscopic properties of stratocumulus clouds and the boundary layer (BL). Further research will include the analysis of the mixing process on the finer scales, mainly the droplet size distribution.

2. MODEL DESCRIPTION

New model configuration – an inversion layer

For this study a spectral bin microphysics hybrid Lagrangian-Eulerian model of a stratocumulus topped BL is used. The original version of the model is described in Pinsky et al. (2008) and Magaritz et al. (2009). The model is constructed from about 2000 adjacent parcels with typical linear size of 25m and 40m in different experiments. The parcels cover the entire computational area of 2500x1250m. Each parcel represents a "small cloud" and contains a detailed description of microphysical processes such as nucleation/de-nucleation, diffusion growth/evaporation and growth by collisions. In order to calculate diffusion growth of wetted aerosols (haze particles) a small time step of 0.01 s is used. Aerosol and drop distributions are calculated using a 500-bin mass grid within the 0.01 μm to 1000 μm radius range.

The parcels are advected in a turbulent-like velocity field. The velocity field is represented as a sum of a large number of harmonics with random time-dependent amplitudes. The field is horizontally statistically uniform and obeys the turbulent laws, among of which is the Kolmogorov -5/3 law, in agreement with available turbulent measurements in maritime BL. The intensity of turbulence in the velocity field is determined by the r.m.s. of vertical velocity fluctuations profile, $\sigma_w(z) = \left\langle w'^2 \right\rangle^{1/2}$, where w' are the fluctuations of vertical wind velocity and brackets indicate horizontal averaging (Magaritz et al. 2009; Pinsky et al. 2008). During the parcel motion some may cross the lifting condensation level and droplets form within them; these parcels now contain cloud droplets as well as wetted aerosols. The model's input includes initial profiles of temperature and humidity, an aerosol distribution and statistical properties of the velocity field taken from measurements.

The model has been substantially modified as compared to previous studies. Most prominently, in the new model version there are two types of interactions between the parcels: sedimentation which allows larger droplets that form to reach the surface as drizzle and turbulent mixing of temperature, humidity and droplets. Other modification implemented into the model included surface fluxes of moisture and temperature using well known aerodynamic formulas and radiation long wave cooling using two-stream approximation

Turbulent mixing between Lagrangian parcels has been implemented in the model following the procedure described in Pinsky et al. (2010). The mixing algorithm represents an expansion of k-theory to the case of mixing of non-conservative values such as DSD. Two options of mixing are available. The first option takes into account the change of drop size and corresponding latent heat release during mixing. In the second option there is no latent heat release during mixing and the mixing is referred to as passive or mechanical mixing. Characteristic mixing time depends on parcel size and on the distance between the parcel centers. The Richardson 4/3 law is used to calculate turbulent coefficients. A turbulent-like velocity field was constructed assuming the dissipation rate equal to 10 cm^2 s^{-3}. This value is typical of stratocumulus clouds under consideration (Siebert et al. 2006)

Simulations of a stratocumulus cloud under conditions close to those observed during the research flight RF01 of the DYCOMS-II field experiment (Stevens et al. 2003a) were carried out. The stratocumulus cloud measured during this flight was $\sim 300m$ thick, capped by a strong inversion and there was no drizzle measured at the surface. To reveal the role of turbulent mixing between

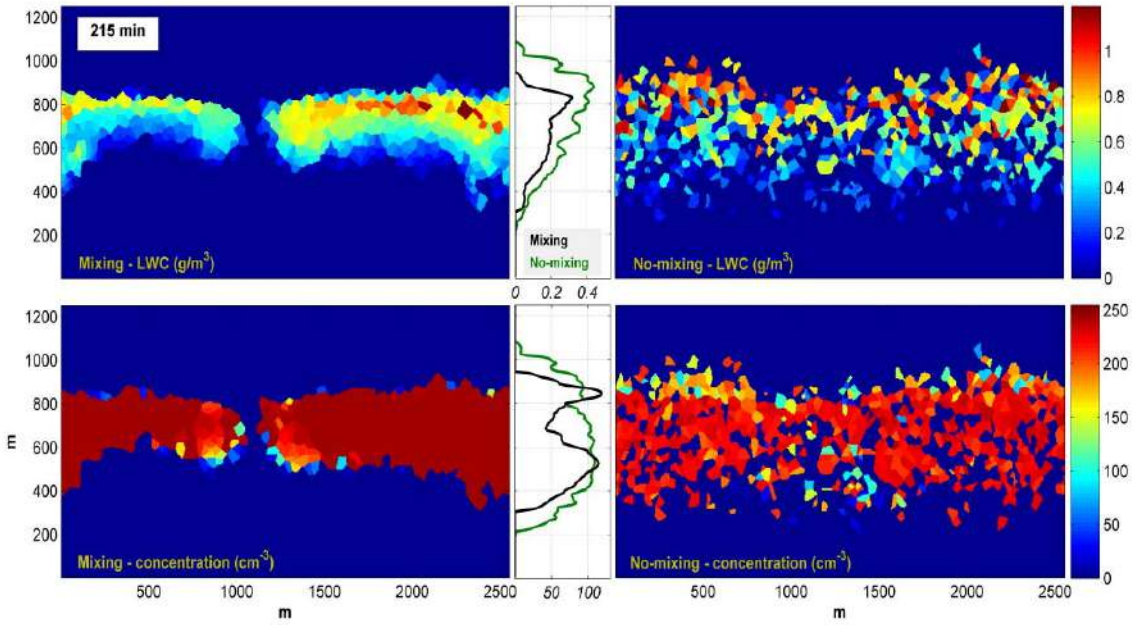

Figure 1. Fields of LWC (top) and droplet concentration (bottom) after 215 min of the model simulation in case of mixing (left panels) and when mixing is turned off (right panels). The profile of the standard deviation is plotted between the fields.

Largangian parcels, supplemental simulations were performed in which mixing was turned off. To investigate the effect of parcel size, special simulations with parcel size of 25 m have been performed.

3. RESULTS

a. Mixing and the geometric structure

The first impression concerning the effects of mixing on cloud structure can be derived from comparison of LWC (top) and concentration (bottom) fields in a simulations with (left panels) and without (right panels) mixing (Figure 1).

One can see a dramatic effect of mixing on cloud structure. In the no-mixing case the cloud layer contains many droplet free air volumes penetrating from the inversion layer. The mixing between the parcels leads to a more homogeneous cloud with a single area of reduced LWC. Transitions from cloudy and cloud-free zones are smoother in the mixing simulation. The LWC maximum is clearly located near the cloud top and the cloud base is relatively straight. In the no-mixing case the geometric extent of the cloud appears to be similar but the expected stratification of the LWC is harder to locate. It is interesting to note that the concentration in the mixing case seems homogeneous throughout the cloud except at the cloud edges. Such structure of droplet concentration and LWC are typical of stratocumulus clouds.

b. Mixing diagrams

For analysis of mixing the Paluch diagrams are often used (Burnet; Brenguier 2007; Paluch 1979). These diagrams express a relationship between conservative variables which do not change in adiabatic process, for instance, the total water content (q_t), a sum of water vapor content and CWC, and liquid water potential temperature (θ_l). On the Paluch diagram, a single point (q_t vs. θ_l) corresponding to an adiabatic volume will remain at the same place depending on the initial conditions in the parcel. Since mixing is a nonadiabatic process, a parcel that mixes with its surrounding will be indicated by a certain trajectory on the diagram. The stronger the mixing process is, the larger the shift of the parcel in the Paluch diagram will be.

Figure 2 compares the Paluch diagrams in cases with and without mixing. The difference between the diagrams is dramatic. In the no-mixing case parcels located initially at low levels, having high initial q_t and low θ_l can ascend to high levels keeping their place in the diagram. Similarly, parcels that were initially at upper levels move down to the surface keeping low q_t and high θ_l. As a result, the diagram indicates that the cloud structure is quite unrealistic. In the no-mixing diagram there is no stratification and separation of colors with height because each parcel remains at its initial place in the diagram at any height. In contrast, in case mixing is taken into account, clear height stratification of parcel properties arises. The ellipse in Figure 2 marks the cloud layer. The inversion layer is seen as a concentration of dry and warm points at the bottom of the diagram. These two regions on the diagram are connected by a "yellow-red" branch which represents the cloud top mixed layer. Parcels in this area are either entering the cloud layer from above, becoming cooler and more humid, or entering the inversion layer and drying out. The last area seen in the diagram is the subcloud layer. This area is formed by parcels located near the ocean surface and that obtain extra humidity and heat. Within the cloud layer the changes of θ_l and q_t are not large indicating that mixing creates a comparatively homogeneous cloud structure.

Figure 3 compares the Paluch diagrams for the cloud top and inversion layer calculated in the simulations with and without mixing with the Paluch diagram build using the observed data collected during Flight RF01. Mixing between the cloud air and inversion air can be seen as a nearly linear line in the diagram. Here the grey color represents parcels with low droplet concentration and the blue color indicates parcels with a concentration above 3cm^{-3}. One can see that simulations with mixing reproduce the observed mixing diagram quite reasonable. In the diagram obtained in the no-mixing simulation there is a large zone consisted of parcels with high q_t. These parcels ascended from the ocean surface to the upper cloud boundary. The comparison with observations indicates that such a diagram does not match observations, so *simulations without mixing cannot describe thermodynamics of the cloud topped BL properly.*

c. The effect of mixing on mean vertical profiles

Figure 4 shows vertical profiles of

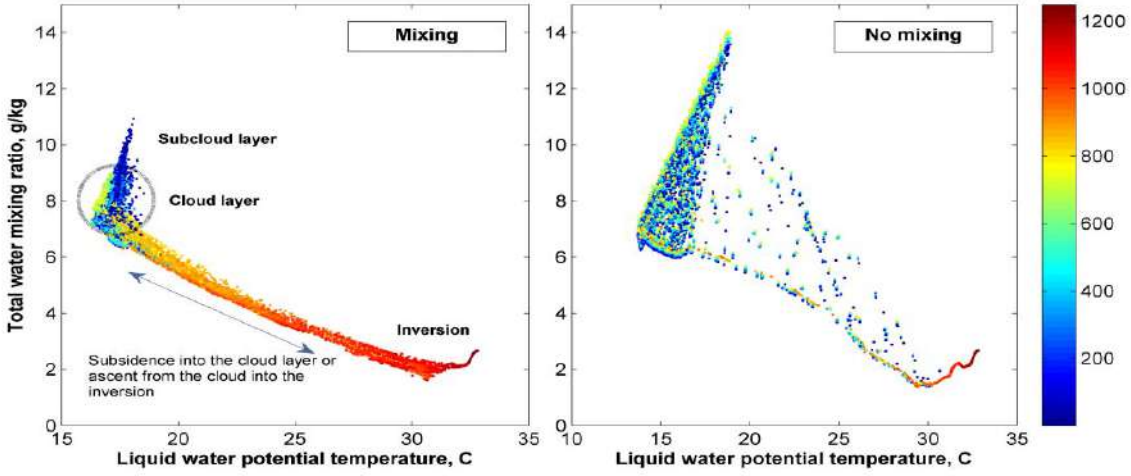

Figure 2. The Paluch diagrams for mixing (left) and no-mixing (right) simulations for the entire computational area. Each point indicates an air parcel during 160-200 min of the simulation. The color of the parcel indicates the height of the parcel.

horizontally averaged main microphysical and thermodynamical parameters. These profiles are in good agreement with the measurements during flight RF01. During RF01 the averaged total water content was $9g/kg$, and the LWC maximum at cloud was $0.7g/kg$ (Stevens et al. 2003b). Even though the fields presented in Figure 1 appear very different, the average profiles calculated from the two simulations do not show significant changes. The main affect of the mixing process in the average profile can be seen in the inversion layer, where the mixing leads to an increase in q_t and temperature above the inversion. Temperature and humidity profiles indicate formation of a well mixed BL, with dry adiabatic lapse rate below cloud base and moist adiabatic within the cloud layer. A strong inversion is seen above cloud layer. The LWC increases with height nearly linearly till a maximum of 0.6 gm^{-3} at the upper cloud boundary. Both this linear behavior and the value of the maximum are well simulated by the model. The value of LWC is close to adiabatic one. It is interesting to note that the concentration in the mixing case is homogeneous throughout the cloud except at the cloud edges. This is also a typical feature of stratocumulus clouds (Pawlowska et al. 2000)

The similarity of the mean profiles in the mixing and no-mixing cases may be attributed to the following. Latent heat release accompanies the mixing process when mixing occurs between parcels that are relatively different. The larger the difference, the more drops may change during the process and latent heat is released. Mixing within clouds should not be accompanied by significant latent heat release since the parcels mix into a similar environment, and so in the cloud layer mixing is mostly mechanical mixing between parcels. From these volumes the mean profile is calculated. In the no-mixing simulation the averaged values are determined as averaged over adiabatic parcels and droplet free volumes. These two procedures should produce similar values. A supplemental numerical simulation in which the latent heat release during mixing procedure was excluded was performed. The results were as in the mixing case. Thus, in the mixing simulations values in parcels represent mixtures of cloudy and penetrated air. But the mixture takes place in the same proportion as in case of simple horizontal averaging of non-interacting cloudy and drop-free volumes. In this way, horizontal averaging has to lead to similar results,

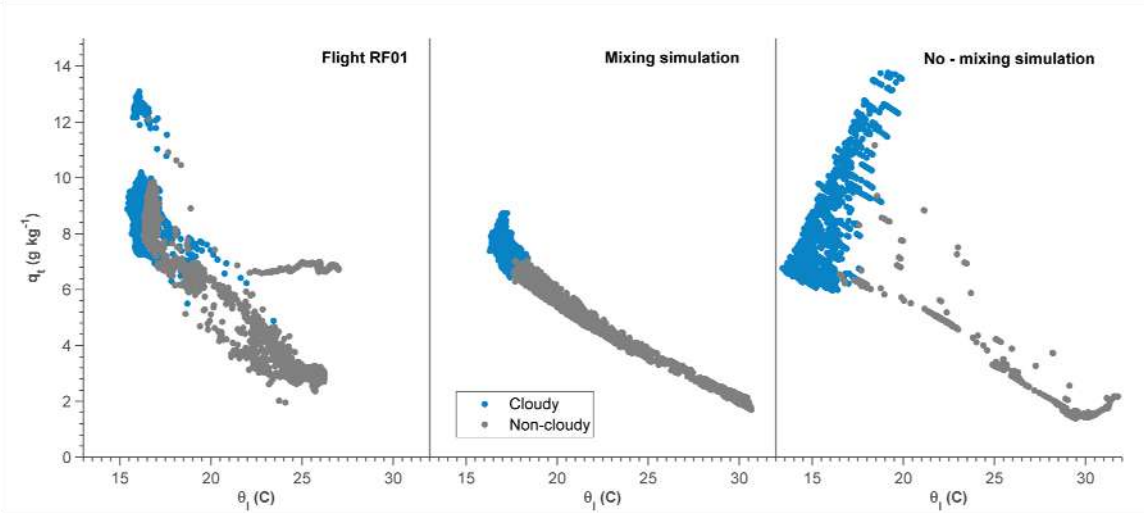

Figure 3 The Paluch diagrams for cloud top calculated in simulations with and without mixing with the Paluch diagram build using the observed data of RF01 (Stevens et al. 2003a). A concentration limit of 3cm^{-3} was used to separate between cloudy and non-cloudy parcels.

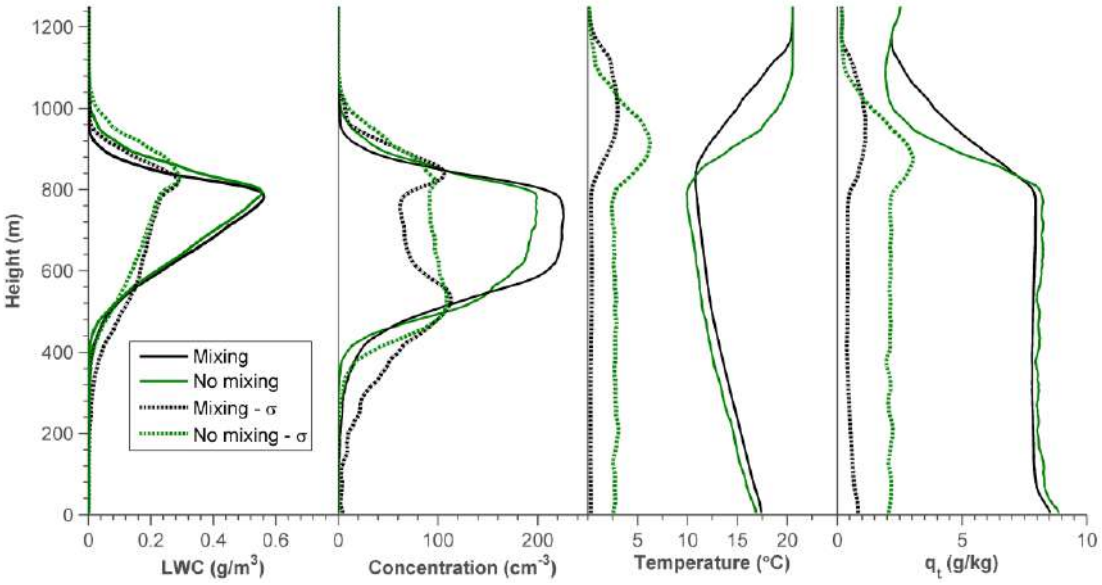

Figure 4. Vertical profiles of horizontally averaged LWC, droplet concentration, temperature and the total water content in simulations with and without mixing. Profiles are obtained by time averaging from 150-300 min. Also presented are the standard deviation profiles for these parameters (dashed)

even if particular values in the no mixing simulations may be unrealistic.

Note that similar situation takes place when performing in situ observations made with standard 1 Hz frequency. In these observations it is impossible to say whether results are obtained due to horizontal averaging of drop-free and cloudy volumes or by averaging of already mixed volumes. Only 1000Hz measurements show that most cloud volumes are mixed (to a variable degree) even at small scales (Gerber 2000; Gerber et al. 2008).

While the differences between vertical profiles of different microphysical and thermodynamic values in the mixing and no-mixing simulations is comparatively small , the difference in the vertical profiles of standard deviations of corresponding values is high (Figure 4). The variability of concentration, temperature and total water content values in the mixing case are much lower all over the BL. The largest variability in the mixing simulation takes place at the cloud boundaries. As seen in . , mixing leads to more distinguishable cloud boundaries by decreasing the variability both inside and outside the cloud layer. Variability in the no-mixing simulations is too large to be realistic. In the no-mixing simulation high variability is seen in the entire BL depth. For instance, standard deviation of humidity exceeds 2 g/m^3 all over the BL.

d. Correlation functions and other statistical characteristics

Figure 5 presents the correlation functions for several parameters in the mixing and no-mixing runs. These functions are calculated as the average between 150-300 min at the height of 750m. The correlation function for the vertical velocity is designed to have the observed correlation function. The correlation function of LWC and temperature from measurements are presented in Figure 6.

The correlation lengths for all parameters in the mixing case are considerably larger than the same functions in the no-mixing case. In the no-mixing simulation the correlation length is of the order of the linear size of the parcel, while in the mixing case it is determined by the physical process of mixing. The mixing case displays a correlation length of a few hundred meters, close to the correlation length of vertical velocity. The concentration has a shorter correlation

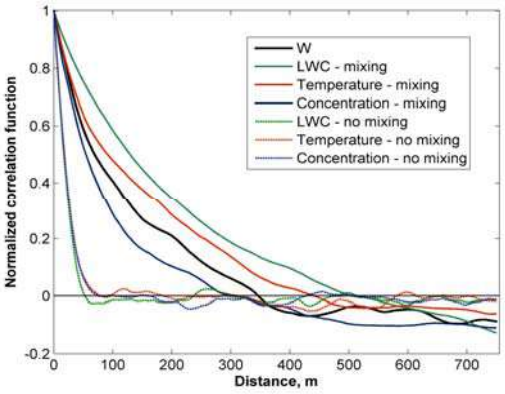

Figure 5. The correlation functions at 750 m for several parameters in the mixing and no-mixing simulations. The correlation functions are averaged between 150-300 min

length (~300 m). Differences in the correlation lengths are determined by the nature of the particular parameter. LWC is an integral parameter and is a result of the total effect of supersaturation on drop size. As such, the LWC will not respond to possible rapid changes in the vertical velocity. For this reason, the LWC and temperature have a correlation length which is larger than the correlation length of W. At the same time, droplet concentration is the most rapidly changing

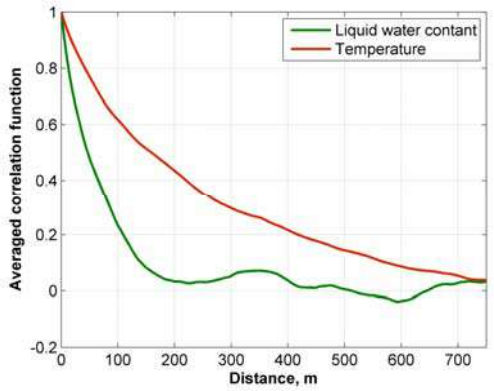

Figure 6. Averaged correlation functions in the cloud layer for LWC and temperature calculated from the data collected during RF01.

value. For instance, cloud nucleation is accompanied by an increase in concentration, or droplet evaporation caused by mixing may change droplet concentration at comparatively low variations of vertical velocity. The droplet concentration has a correlation length which is lower than the correlation length of W.

In order to support the conclusion that the correlation length is determined by the physical properties of the parameters a supplemental simulation was preformed. Here the linear size of the parcels was set at about half of what it was in the previous simulations, 25m. The correlation functions for the supplemental run are shown in Figure 7. One can see that correlation length in the no-mixing run is again in the order of the parcel size, while correlation lengths in mixing runs are comparable with those shown in Figure 5, i.e a few hundred meters. A comparison with correlation functions derived from observed data indicates a good agreement with mixing runs indicating that process of mixing is simulated realistically.

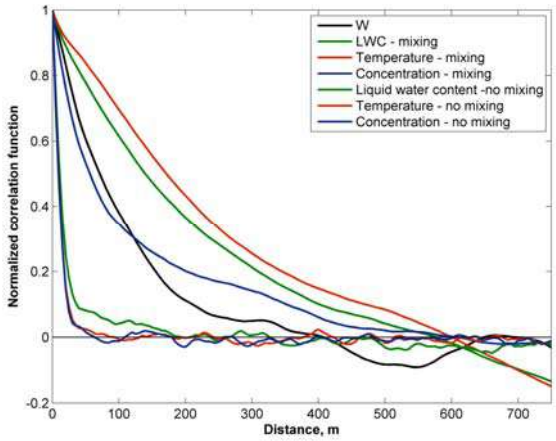

Figure 7. As in Figure 5 but for parcels with the linear size of 25m.

Figure 8 shows histograms of humidity and temperature in simulations with and without turbulent mixing between parcels. In these diagrams we again focus our attention to the cloud top and inversion layer, between 700-950 m. Entrained parcels are marked in yellow (parcels that at t=0 were located in the inversion layer).

The histograms quantitatively show the effects of mixing mentioned above in the analysis of the Paluch diagrams. Indeed, it is seen that in the no-mixing case humidity in some parcels remains extremely high (~15 g/m-3). These high values of humidity arise when parcels near the surface ascend into the cloud layer and transport the humidity within them to

the higher levels. In the mixing case parcels with high humidity share it with neighboring parcels in the process of turbulent mixing. At the same time, there are extremely dry parcels which were initially located at upper levels. These parcels have high temperature. Including the mixing process leads to formation of realistic distributions of humidity and temperature. The mixing decreases the number of extremely wet parcels as well as extremely dry ones. The temperature changes accordingly. The histograms plotted in Figure 8 indicate again that no-mixing clouds have unrealistic thermodynamical structure. For instance q can reach 16 g/m^3.

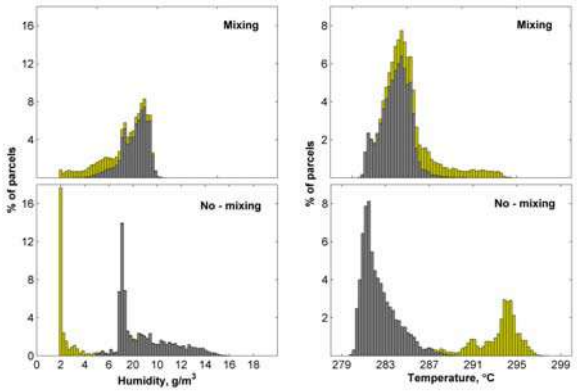

Figure 8. Histograms of humidity and temperature in simulations with and without turbulent mixing between parcels. Areas marked in yellow represent parcels that at t=0 min were in the inversion layer.

Figure 9 shows histograms of main microphysical parameters: LWC and droplet concentration. The histograms of LWC in both cases are similar, this can be attributed to the same range of variation of LWC in both cases: from zero to adiabatic value. However, histograms of droplet concentration in the two cases indicate dramatic difference. In the non-mixing limit the histogram depicts extremely high variability of drop concentration. Indeed, isolated adiabatic parcel can be either droplet free, or have different values of drop concentration depending on vertical velocity during CCN activation. Such concentrations may continuously change from low close to zero values to maximum values at highest vertical velocities. In case mixing is allowed there is a homogenization of concentration. This process explains the narrowing of the concentration histogram. The exception is parcels with very low droplet concentration in the mixing case. Analysis shows that these parcels are located at the cloud boundaries; some at cloud top, but mostly at cloud base or around areas of downdraft with reduced LWC (refer to Figure 1).

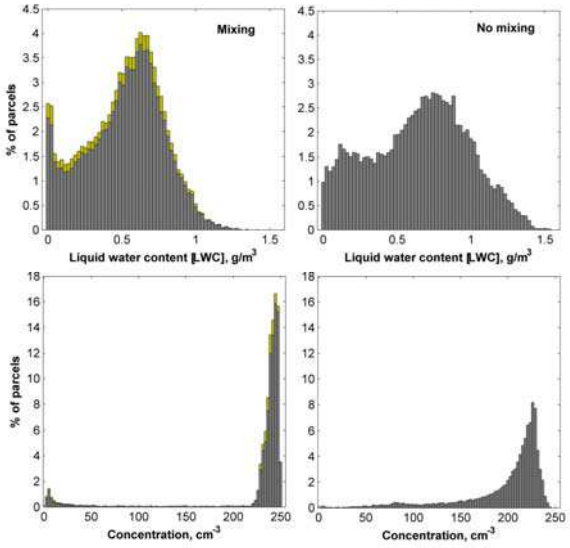

Figure 9. Histograms of main microphysical parameters: LWC and droplet concentration in simulations with and without turbulent mixing between parcels. Areas marked in yellow represent parcels that at t=0 min were in the inversion layer.

e. Comparison of DSD properties

Histograms of different parameters of the drop distribution are presented in Figure 10. For the mean radius the histograms are quite similar. There are slightly larger tails in the no-mixing case. The effective radius forms a narrow distribution with a maximum around 9 μm. In the no-mixing case there is a small tail of larger values.

Histogram of DSD width in the no-mixing case shows the existence of significant amount of very narrow DSD which can be attributed to the existence of droplet free volumes within the cloud. At the same time in the no-mixing case some spectra are especially wide. This effect

can be attributed to generation of small droplets due to incloud nucleation in parcels which contain large droplets. The mixing leads to formation of a more homogeneous distribution of DSD with respect to the DSD width. Mixing decreases the number of extreme values.

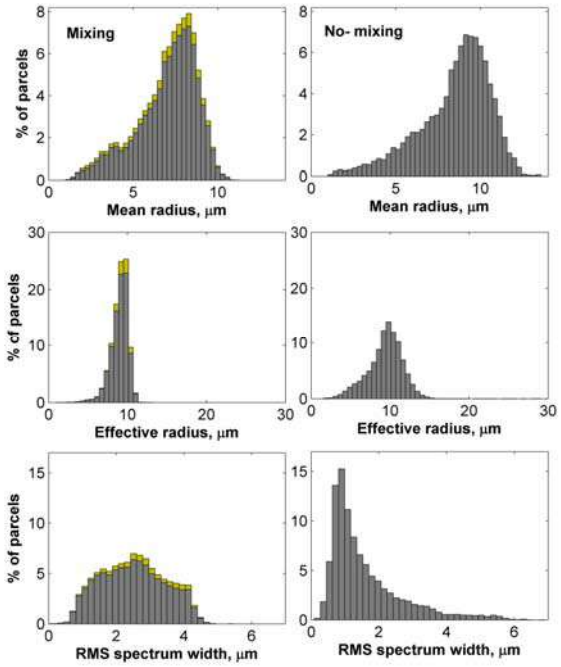

Figure 10. Histograms of mean radius, effective radius and spectrum width for mixing and no-mixing simulations. The histograms are calculated for the layer between 700-950 m.

f. Life time of parcels

One of the interesting questions arising with the problem of mixing is the characteristic time during in which an individual parcel keeps its identification. To evaluate this process several parcels that ascend from the ocean surface or penetrate the cloud from above were chosen. The specific feature of these parcels is that initially their properties substantially differ from those in surrounding parcels. During the mixing process, the parcel's properties become similar to its surrounding environment and the selected parcels lose their identity. The time period from when a parcel is selected and has a maximum difference from the adjacent parcels until it blends with its environment will be considered as the life time of a particular parcel.

Figure 11 shows several examples of time dependencies of the differences in q_t between the selected parcels and its environment. Each line in the figure represents a single parcel. Black lines represent parcels from the bottom of the BL, near the ocean surface. These parcels are most affected by the humidity fluxes and become more moist then their surrounding environment. Parcels marked in green were in the inversion layer and penetrate the cloud. These parcels have a deficit of q_t compared to the environment. One can see that the difference decreases to ~zero during 30-40 min. This time can be considered as the characteristic life time. Note that characteristic life time can be defined also as the time during which the initial difference in the parcel properties (say θ_l or q_t) decreases e-times. In this case the characteristic life time can be estimated as 15-20 min which is close to mixing time used in the mixing procedure introduced in the model and determined as: $\tau_{mix} = Cl^{2/3}\varepsilon^{-1/3}$. Where l is the mixing distance taken equal to the distance between parcel centers, ε is the dissipation rate, C=6 (Monin and Yaglom 1975).

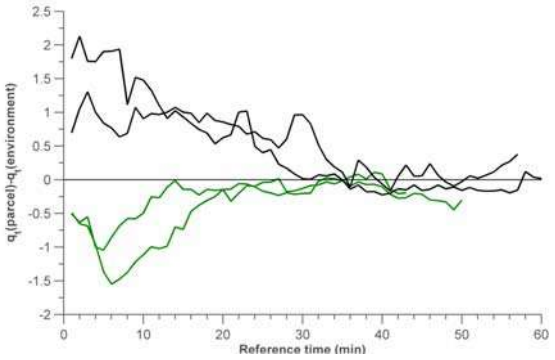

Figure 11. Time dependencies of the differences in total water content between selected parcels and the values averaged over adjacent parcels

g. Drizzle formation

Figure 12 shows time dependence of rain flux in simulations with and without mixing. One can see that rain flux is zero in all simulations during first 6 h of

simulation and remains quite small. These results agree with observations according to which clouds observed in RF01 were not drizzling ones. Nevertheless, there is clear tendency to formation of rainflux (large droplets) in simulations with mixing allowed. The mechanisms by which mixing fosters formation of drizzle will be analyzed in the future. It is possible that drizzle forms earlier in the mixing simulations because in the non-mixing simulations drizzle droplets during their fall cross droplet free dry volumes, where they evaporate and lose their ability to serve as drop-collectors. In simulations with mixing all parcels within the cloud are saturated and contain small droplets that can be collected by falling droplets.

We will check the conclusions derived by Magaritz et al. (2009) that drizzle forms first in parcels that ascend from the ocean surface, and spend significant time near cloud top, where LWC is maximum. Another hypothesis to test is that parcel recirculation creates droplets of different size because of non-reversability of droplet size in updrafts and downdrafts. The maximum difference in drop size should be observed near cloud base. Mixing of DSD at low levels can lead to DSD broadening at the lower levels where supersaturation reaches its maximum (Korolev et al 2012).

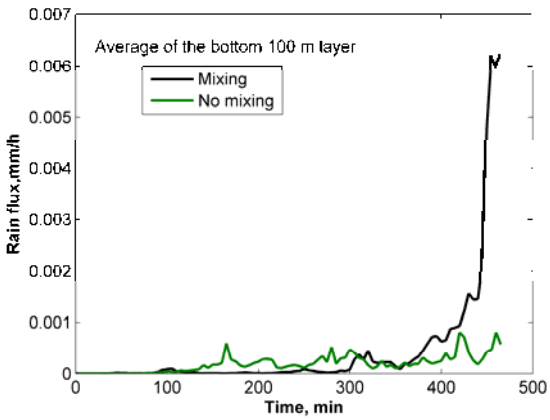

Figure 12. Rain flux in simulations with and without mixing.

4. DISCUSSION

The model reproduces realistically the thermodynamical and microstructure of stratocumulus clouds measured during flight RF01 as part of the DYCOMS-II field experiment. Mixing between parcels makes cloud base and cloud top more uniform and substantially increases the radius of correlation of liquid water content and other quantities. The mixing leads to formation of cloud stratification with the correlation length of few hundred meters. *Without mixing between parcels the thermodynamic and microphysical cloud structure become unrealistic and do not agree with observations.* The mixing process is important if one wishes to simulate stratocumulus clouds and the overlying inversion layer.

The horizontally averaged properties of the clouds, such as LWC do not change significantly between the mixing and non-mixing simulations. This result arises from properties of the mixing in the cloud layer. In this area adjacent parcels are similar and the mixing process does not involve release of latent heat. Mixing in this area is mostly mechanical and the result will be proportional to averaging of extreme adiabatic values. In the mixing case extreme values are eliminated and a more homogenous cloud is seen. Variability of all parameters in the mixing case is lower.

The life time of parcels is estimated by the time needed for specific parcels to lose initial difference in the properties. Such life time is estimated in the order of 40 min, i.e. quite large.

No drizzle was formed during RF01 and still the presented case may be used for the investigation of the first formation of rain drops. Numerical simulations indicate that mixing fosters drizzle formation. In the no-mixing case small amounts of drizzle sized drops reach the surface. These were not seen in the no-mixing case. The possible mechanisms of such effect will be analyzed in the future.

The question arises, if the no mixing runs lead to unrealistic cloud structure, why Magaritz et al. (2009) got realistic results in a non-mixing limit. The answer is somewhat paradoxical. Realistic results were obtained because of a simplifying assumption that the upper boundary of the computational area coincides with the upper cloud boundary. As a result, the entrainment of dry warm parcels from above was prohibited. Analysis of parcel tracks shows that most droplet free holes within clouds in the non-mixing case (Figure 1) arise due to penetration of dry parcels through the upper boundary. So, exclusion of such penetration in the study by Magaritz et al. (2009) led to increase in the correlation lengths, decrease in variability of thermodynamic and microphysical parameters and made results more realistic.

5. BIBLIOGRAPHY

Baker, M. B., and J. Latham, 1979: Evolution of Droplet Spectra and the Rate of Production of Embryonic Raindrops in Small Cumulus Clouds. *Journal of the Atmospheric Sciences*, **36,** 1612-1615.

——, 1982: A Diffusive Model of the Turbulent Mixing of Dry and Cloudy Air. *Quarterly Journal of the Royal Meteorological Society*, **108,** 871-898.

Baker, M. B., R. G. Corbin, and J. Latham, 1980: The influence of entrainment on the evolution of cloud droplet spectra: I. A model of inhomogeneous mixing. *Quarterly Journal of the Royal Meteorological Society*, **106,** 581-598.

Blyth, A. M., T. W. Choularton, G. Fullarton, J. Latham, C. S. Mill, M. H. Smith, and I. M. Stromberg, 1980: The influence of entrainment on the evolution of cloud droplet spectra: II. Field experiments at Great Dun Fell. *Quarterly Journal of the Royal Meteorological Society*, **106,** 821-840.

Burnet, F., and J. L. Brenguier, 2007: Observational study of the entrainment-mixing process in warm convective clouds. *Journal of the Atmospheric Sciences*, **64,** 1995-2011.

Cooper, W. A. L.-T., S. G. Blyth, A. M., 2011: Initiation of coalescence in a cumulus cloud: a beneficial influence of entrainment and mixing JO - Atmos. Chem. Phys. Discuss., **11,** 10557-10613.

Gerber, H., 2000: Structure of small cumulus clouds. *13th Intern. Conf. Clouds Precip.*, Reno, NV, 14-18 Aug, 105-108.

Gerber, H. E., G. M. Frick, J. B. Jensen, and J. G. Hudson, 2008: Entrainment, Mixing, and Microphysics in Trade-Wind Cumulus. *Journal of the Meteorological Society of Japan*, **86,** 87-106.

Hill, A. A., G. Feingold, and H. L. Jiang, 2009: The Influence of Entrainment and Mixing Assumption on Aerosol-Cloud Interactions in Marine Stratocumulus. *Journal of the Atmospheric Sciences*, **66,** 1450-1464.

Khain, A., T. V. Prabha, N. Benmoshe, G. Pandithurai, and M. Pinsky, 2012: Possible physical mechanism of linear relationship between drop concentration and the level of raindrop formation in cumulus clouds. *Journal of Atmospheric Sciences*, Submitted.

Korolev A., M.Pinsky , and A. Khain, 2012: A new mechanism of droplet size spectra broadening during diffusional grow**th**. 16 Conference on Clouds and Precipitation, Leipzig 29 July-3 Aug 2012.

Magaritz, L., M. Pinsky, O. Krasnov, and A. Khain, 2009: Investigation of Droplet Size Distributions and Drizzle Formation Using A New Trajectory Ensemble Model. Part II: Lucky Parcels. *Journal of the Atmospheric Sciences*, **66,** 781-805.

Monin, A.S. and Yaglom, A.M. 1975: "*Statistical Fluid Mechanics: Mechanics of Turbulence*", vol. 2, MIT Press. pp 874

Paluch, I. R., 1979: The Entrainment Mechanism in Colorado Cumuli. *Journal of the Atmospheric Sciences*, **36,** 2467-2478.

——, 1986: Mixing and the Cloud Droplet Size Spectrum: Generalizations from the CCOPE Data. *Journal of the Atmospheric Sciences*, **43,** 1984-1993.

Pawlowska, H., J. L. Brenguier, and F. Burnet, 2000: Microphysical properties

of stratocumulus clouds. *Atmospheric Research*, **55,** 15-33.

Pinsky, M., A. Khain, and L. Magaritz, 2010: Representing turbulent mixing of non-conservative values in Eulerian and Lagrangian cloud models. *Quarterly Journal of the Royal Meteorological Society*, **136,** 1228-1242.

Pinsky, M., L. Magaritz, A. Khain, O. Krasnov, and A. Sterkin, 2008: Investigation of Droplet Size Distributions and Drizzle Formation Using a New Trajectory Ensemble Model. Part I: Model Description and First Results in a Nonmixing Limit. *Journal of the Atmospheric Sciences*, **65,** 2064-2086.

Prabha, T. V., A. Khain, R. S. Maheshkumar, G. Pandithurai, J. R. Kulkarni, M. Konwar, and B. N. Goswami, 2011: Microphysics of Premonsoon and Monsoon Clouds as Seen from In Situ Measurements during the Cloud Aerosol Interaction and Precipitation Enhancement Experiment (CAIPEEX). *Journal of the Atmospheric Sciences*, **68,** 1882-1901.

Siebert, H., and Coauthors, 2006: Probing finescale dynamics and microphysics of clouds with helicopter-borne measurements. *Bulletin of the American Meteorological Society*, **87,** 1727.

Stevens, B., and Coauthors, 2003a: Dynamics and chemistry of marine stratocumulus - Dycoms-II. *Bulletin of the American Meteorological Society*, **84,** 579.

——, 2003b: Supplement to Dynamics and Chemistry of Marine Stratocumulus—DYCOMS-II. *Bulletin of the American Meteorological Society*, **84,** 593-593.

Acknowledgments

DYCOMS-II data used in this study was obtained from the NCAR EOL database. The study is supported by the Office of Science (BER), US Department of Energy Award DE-SC0006788 and the Binational US-Israel Science Foundation (grant 2010446).

RESOLUTION AND DOMAIN SIZE REQUIREMENTS FOR THE LARGE-EDDY SIMULATION OF PRECIPITATING TRADE WIND CUMULUS

AXEL SEIFERT[1], THIJS HEUS[2], MIRJANA SAKRADZIJA[2] AND BJORN STEVENS[2]

[1]Hans-Ertel Centre for Weather Research, Deutscher Wetterdienst, Hamburg, Germany
[2]Max Planck Institute for Meteorology, Hamburg, Germany

1. INTRODUCTION

Large-eddy simulation (LES) of shallow convection is an important tool to study cloud properties, the life cycle of clouds and the formation of rain, but the results can be sensitive to resolution and domain size. The present study provides a systematic evaluation to quantify the dependency of such large-eddy simulations on the chosen grid spacing and domain size. A focus of the analysis is on the impact of such choices on the cloud size distribution, cloud organization and the resulting precipitation amounts.

It is well know that the properties of the simulated clouds and the turbulent flow field depend on the choices regarding numerics, microphysics and turbulence closure (e.g., vanZanten et al. 2011). Previous studies have mostly quantified this for the statistics of the flow field and cloud properties like cloud fraction and liquid water path (Stevens and Seifert 2008; Matheou et al. 2011). Especially for cases which are close to the onset of precipitation, i.e., simulations which contain only a few clouds that do precipitate, the sensitivities are often large and the simulations are far away from being converged (Matheou et al. 2011). Our investigation aims to provide some guidelines for the simulation of such cases, i.e., to answer questions like: How important is domain size vs grid resolution? Are moister cases which rain more easily more robust than drier conditions? Is there a minimum domain size for cloud organization? How is the cloud size distribution and cloud organization affected by domain size and resolution? To quantify such sensitivities is a crucial step before the simulated cloud fields can be used to study cloud processes and develop improved parameterizations for large-scale models.

Corresponding author's address: Dr. Axel Seifert, Max-Planck Institut für Meteorologie, Bundesstr. 53, 20146 Hamburg, Germany. E-mail: axel.seifert@dwd.de

2. MODEL SETUP

We study trade wind cumulus cloud fields based on the composite RICO case as defined by vanZanten et al. (2011). This case is based on data from the Rain in Cumulus over the Ocean (RICO) field study and represents the average conditions during an undisturbed period between December 16 2004 and January 8 2005. As a variation of this standard GCSS RICO case we include also the setup of Stevens and Seifert (2008) which has as the only modification a somewhat moister cloud layer resulting in higher precipitation rates.

We apply a version of the UCLA LES (Stevens et al. 2005; Stevens 2007) similar to Seifert et al. (2010). The model solves prognostic equations for the velocity vector (u, v, w), the total water mixing ratio r_t, liquid water potential temperature θ_l, the mass mixing ratio of rain water r_r and the mass specific number of rain drops n_r. The cloud water mixing ratio r_c is diagnosed from r_t and the saturation mixing ratio r_s. We apply double periodic boundary conditions. For the advection of scalars we use an upwind-biased flux limiter scheme. The default bulk microphysical scheme of the UCLA LES model is the one from Seifert and Beheng (2001). Optionally the microphysics can be coupled to the sub-grid turbulence scheme of the LES to represent the turbulence effect on collision rates of droplets Seifert et al. (2010).

In all simulation the vertical extent of the domain is 4 km and the vertical grid spacing is either 20 m (for simulation with horizontal grid spacing of 20 m, 40 m or 80 m) or 25 m (all other simulations).

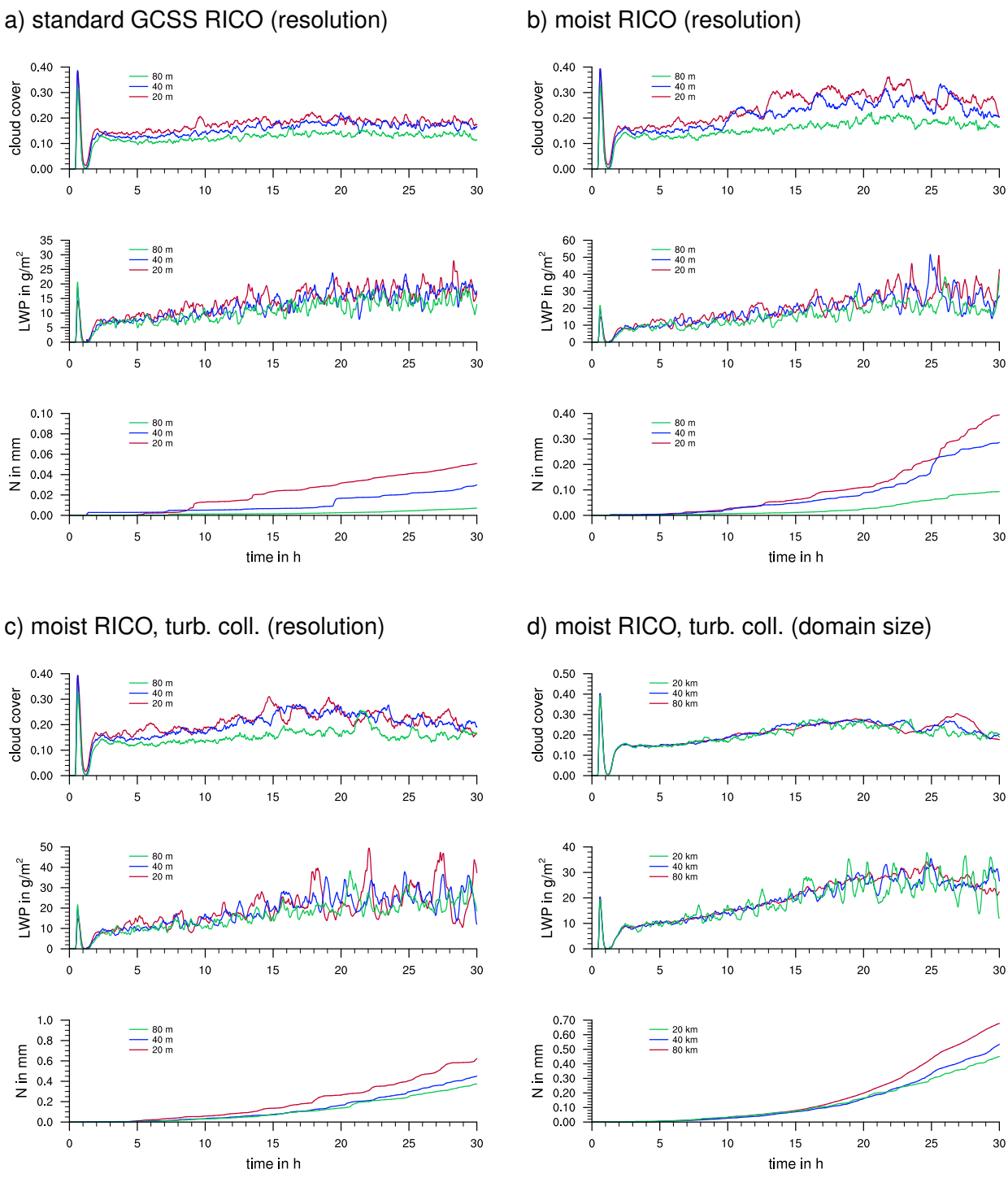

Fig. 1: Time series of cloud cover, liquid water path and accumulated precipitation N for different simulations of the RICO trade wind cumulus case. Resolution dependency of the standard GCSS RICO case (a), of the moist case (b), of the moist case with turbulence effects on collision rates (c), and the domain size dependency of the moist case with turbulence effects (d).

3. RESULTS

Figure 1 shows time series of the domain averaged cloud cover, liquid water path (LWP) and accumulated precipitation for different grid spacings (Figs. 1a,b,c) and domain sizes (Fig. 1d). Liquid water path is most robust to grid spacing and cloud cover does show some reasonable convergence, but the convergence for precipitation is not so obvious. For the standard RICO case precipitation increases quite dramatically with resolution, e.g., by roughly an order in magnitude between the coarsest grid (80 m) and the finest resolution (20 m). This shows that for this case the smallest scales represented by the model are crucial for precipitation formation. This is similar for the moist RICO case, but here some convergence can be seen. Taking into account turbulence effects on the collision rate increases the precipitation amounts by almost a factor of 2 and the simulations become somewhat more robust to grid spacing, although the convergence behavior seems odd as the 20 m simulation differs quite significantly from the other two runs. Corresponding to Fig. 1c, we show also the domain size dependency which proves that the precipitation increases with domain size and in the last 10 hours of the simulation the larger domain runs start to deviate from the small domain simulation.

This behavior is also summarized by Fig. 2 which shows the relative change in the precipitation rates compared to a reference simulation with a domain size L of 20 km and a grid spacing of $\Delta x = 40$ m. Here we have also included another set of simulations for the standard GCSS RICO case in which the numerical limiters in the upwind advection scheme have been turned off for liquid water potential temperature θ_l and total water q_t. This simulation does exhibit the strongest sensitivity to grid spacing. This could either mean it converges faster or that we get spurious precipitation from numerical noise. But even the run with limiter shows the strong increase in precipitation. In relative terms the moist case, and especially the moist case with turbulence effects, are more robust. This may be interpreted in the way that the standard GCSS case is very sensitive because the precipitation rates are very low and only a few clouds do actually precipitate. For the moister simulation which rain more

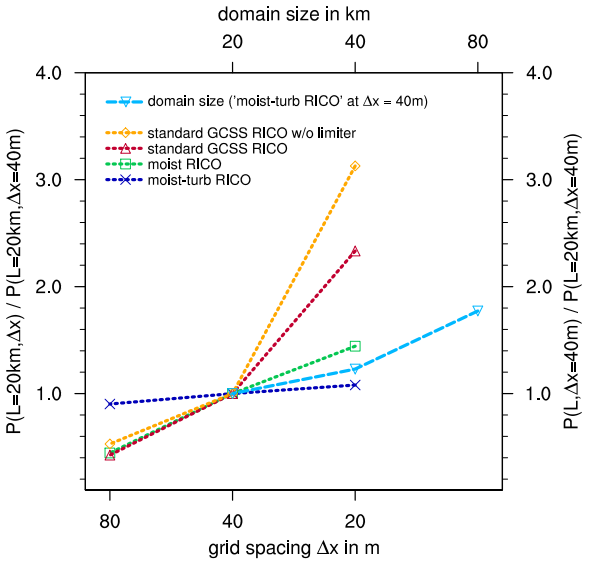

Fig. 2: Sensitivity of average precipitation rate (at 20-24 h simulation time) to grid spacing and domain size. All simulations for the resolution dependency use a 20 km domain size. Shown are 5 different sets of simulations: standard GCSS RICO without advection limiter on liquid water potential temperature θ_l and total water q_t (orange), standard GCSS RICO with limiters (red), the moist RICO case (green) and the moist RICO case with turbulence effects on collision rates (blue). The domain size dependency is only shown for the moist RICO case with turbulence effects on collision rates (light blue) at a grid spacing of Δx = 40 m.

readily the grid spacing become less important and domain size might actually become the limiting factor. Nevertheless, for all simulations the results are unsatisfactory in the sense that the strong sensitivities to the model setup remain either in grid spacing or in domain size.

There are two reasons for the strong sensitivity of the simulations to model setup: First, the rain formation by collision-coalescence is very sensitive to the liquid water content in the cloud and more vigorous and better resolved updrafts which support a higher liquid water content do lead to more precipitation. Second, higher resolution and larger domains favor organization of clouds in bigger clusters which also leads to the development of bigger clouds. The details of the mechanism that leads to organization are not yet well understood, but cold pools and/or the modulation of the subcloud layer moisture by precipitation seem to be key. Therefore the ability of the precipitating clouds to organize makes this a truly multiscale problem, because the organization which occurs on

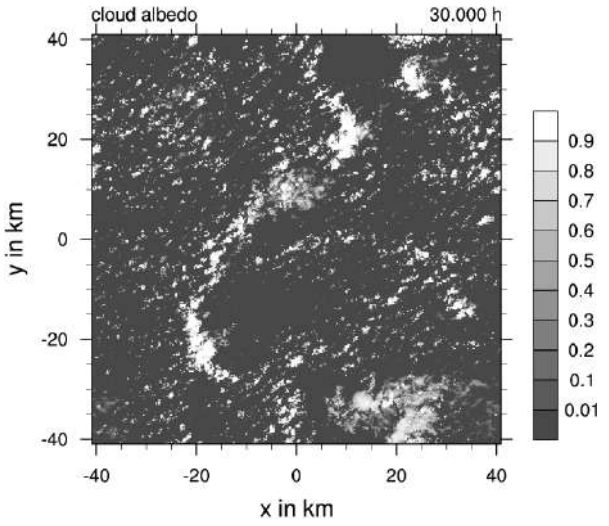

Fig. 3: Cloud albedo for a moist RICO case on a 80 km domain and with $\Delta x = 40$ m. Shown is the simulation result after 30 h.

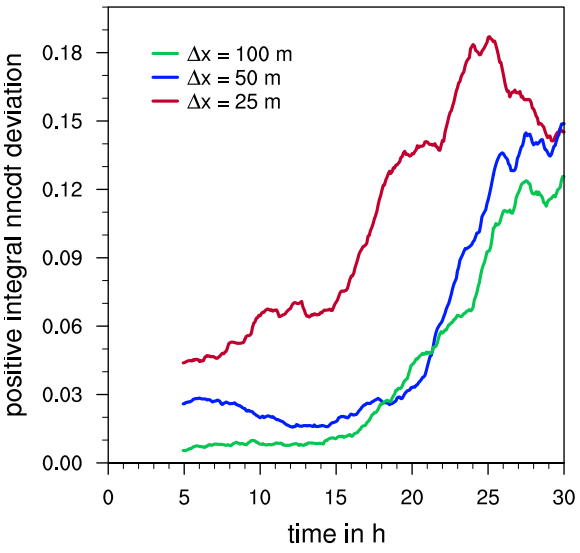

Fig. 4: Timeseries of the scalar clustering metric based on nearest neighbor distribution function. Higher values correspond to stronger clustering (clumping). Shown are results of the moist RICO case on a 25 km domain for different models resolutions.

the mesoscale depends in the rain formation which happens on the small scales (which are poorly resolved in LES). An example for organization on the mesoscale is Fig. 3 which shows the cloud albedo for the moist RICO case on a 80 km domain and with $\Delta x = 40$ m. On such a big domain the cloud field develops mesoscale organization, here in the form of mesoscale arcs quite similar to cloud fields as they were observed for the precipitating cases during RICO (Snodgrass et al. 2009).
Organization can, e.g., be quantified in terms of the nearest neighbor cumulative distribution function (NNCDF). To arrive at a scalar metric the average deviation from the NNCDF of a random cloud field is calculated following Nair et al. (1998). Figure 4 gives an example of such an analysis and proves that (a) the moist RICO case does develop some significant organization and (b) this organization depends on the grid spacing, e.g., at $\Delta x = 25$ m the organization develops several hours earlier than on the coarser grids. Note that domain size is also a crucial parameter for organization (not shown). Given the above it is clear that also the cloud size distribution will show a strong sensitivity to the model setup. Here we apply a 2D cloud tracking based on liquid water path and cloud cores. Figure 5 shows the cloud number densities of the moist RICO case for different model resolutions on a 25 km domain. For higher resolutions we find not only more small clouds, but the whole distribution shifts to smaller sizes. On the coarse grids the cloud size distribution shows a power law behavior similar to previous studies (Neggers et al. 2002), although without an evidence for a scale break. For the highest resolution the power law is less obvious, which can be explained by cloud organization forming more bigger clouds than expected for a power law. Again, this shows the complexity and richness in behavior of the precipitating shallow convection which makes this cloud regime a challenging problem for LES modeling and cloud parameterization.

4. CONCLUSIONS

We have performed a large set of large-eddy simulations for the RICO trade wind cumulus case. Our results confirm and extend the findings of Matheou et al. (2011) and show that the simulations are indeed very sensitive to the model setup, e.g., grid spacing and domain size. For example, cloud cover and precipitation rate tend to increase for higher resolution. In relative terms the sensitivity of the precipitation rate is strongest for the standard GCSS setup and decreases for the cases which rain more readily. This is easily understood as the standard GCSS case is just at the onset of precipitation and therefore most sensitive to any

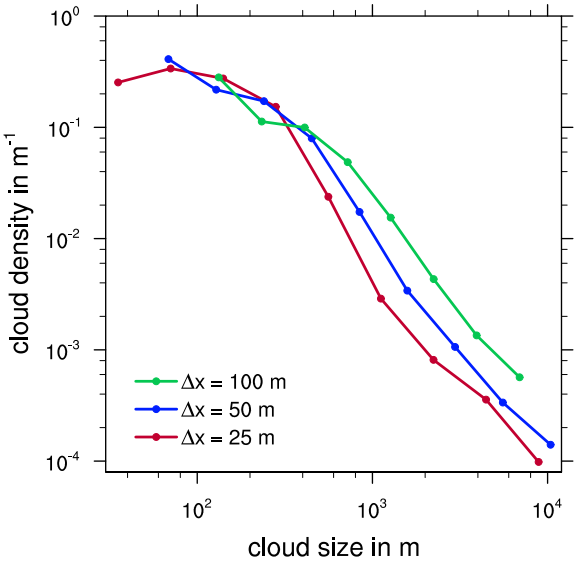

Fig. 5: Cloud size distribution for the moist RICO case on a 25 km domain for different models resolutions.

changes that affect precipitation formation. This simple fact might explain some of the large difference found in the GCSS model intercomparison.

Given currently available computers the model resolution is usually too coarse and the domains are almost always too small to achieve converged and statistically robust results for precipitating shallow convection. The problems are caused by the the multiscale nature of precipitating clouds: First, precipitation formation is very sensitive to the resolved liquid water content and the internal circulations within the clouds requiring grid spacing of $\mathcal{O}$(10 m), c.f. Heus et al. (2009). Second, precipitation causes cloud organization on mesoscales by the formation of cold pools or, in case of trade wind cumulus, moisture perturbations in the sub-cloud layer. This organization (clustering, clumping) occurs on scales of $\mathcal{O}$(10 km) and would require domain sizes of 100 km, i.e., converged behavior can only be expected on domains of 10.000$\times$10.000 grid points in the horizontal.

Acknowledgements: This research was carried out as part of the Hans Ertel Centre for Weather Research. This research network of Universities, Research Institutes and the Deutscher Wetterdienst is funded by the BMVBS (Federal Ministry of Transport, Building and Urban Development). We thank ECMWF and DWD for providing the supercomputing resources for this research.

References

Heus, T., C. F. J. Pols, H. J. J. Jonker, H. E. A. Van den Akker, and D. H. Lenschow, 2009: Observational validation of the compensating mass flux through the shell around cumulus clouds. *Quart. J. Roy. Met. Soc.*, **135**, 101–112.

Matheou, G., D. Chung, L. Nuijens, B. Stevens, and J. Teixeira, 2011: On the Fidelity of Large-Eddy Simulation of Shallow Precipitating Cumulus Convection. *Mon. Wea. Rev.*, **139**, 2918–2939.

Nair, U., R. Weger, K. Kuo, and R. Welch, 1998: Clustering, randomness, and regularity in cloud fields - 5. The nature of regular cumulus cloud fields. *J. Geophys. Res.*, **103**, 11363–11380, doi:10.1029/98JD00088.

Neggers, R., A. Siebesma, and H. Jonker, 2002: A multiparcel model for shallow cumulus convection. *J. Atmos. Sci.*, **59**, 1655–1668.

Seifert, A. and K. D. Beheng, 2001: A double-moment parameterization for simulating autoconversion, accretion and selfcollection. *Atmos. Res.*, **59-60**, 265–281.

Seifert, A., L. Nuijens, and B. Stevens, 2010: Turbulence effects on warm-rain autoconversion in precipitating shallow convection. *Quart. J. Roy. Met. Soc.*, **136**, 1753–1762.

Snodgrass, E. R., L. Di Girolamo, and R. M. Rauber, 2009: Precipitation Characteristics of Trade Wind Clouds during RICO Derived from Radar, Satellite, and Aircraft Measurements. *J. Appl. Met.*, **48**, 464–483.

Stevens, B., 2007: On the growth of layers of non-precipitating cumulus convection. *J. Atmos. Sci.*, **64**, 2916–2931.

Stevens, B., C. Moeng, A. Ackerman, C. Bretherton, A. Chlond, S. De Roode, J. Edwards, J. Golaz, H. Jiang, M. Khairoutdinov, M. Kirkpatrick, D. Lewellen, A. Lock, F. Muller, D. Stevens, E. Whelan, and P. Zhu, 2005: Evaluation of large-eddy simulations via observations of nocturnal marine stratocumulus. *Mon. Wea. Rev.*, **133**, 1443–1462.

Stevens, B. and A. Seifert, 2008: Understanding macrophysical outcomes of microphysical choices in simluations of shallow cumulus convection. *J. Met. Soc. Jap.*, **86**, 143–162.

vanZanten, M., B. Stevens, L. Nuijens, A. Siebesma, A. Ackerman, F. Burnet, A. Cheng, F. Couvreux, H. Jiang, M. Khairoutdinov, Y. Kogan, D. Lewellen, D. Mechem, K. Nakamura, A. Noda, B. Shipway, J. Slawinska, S. Wang, and A. Wyszogrodzki, 2011: Controls on precipitation and cloudiness in simulations of trade-wind cumulus as observed during RICO. *J. Adv. Model. Earth Syst.*, **3**.

MASS SPECTROMETRIC ANALYSIS OF INDIVIDUAL BIOLOGICAL PARTICLES – A RELATION BETWEEN CHEMICAL COMPOSITION AND ICE-NUCLEATION ACTIVITY?

B. Sierau[1], C. Oehm[2], O. Möhler[2], O. Stetzer[1], and C. Chou[1,3]

[1]ETH Zurich, Institute for Atmospheric and Climate Science, Universitätsstr. 16, 8092 Zürich, Switzerland
[2]Karlsruhe Institute of Technology, Institute for Meteorology and Climate, Hermann-von-Helmholtz-Platz 1, 76344 Eggenstein-Leopoldshafen, Germany
[3]now at: University of Hertfordshire, Science & Technology Research Institute, College Lane, Hatfield, Hertfordshire, AL10 9AB, United Kingdom

Presenting author email: berko.sierau@env.ethz.ch

1. INTRODUCTION

Aerosols of biological origin such as bacteria and spores are gaining increasing attention in the research field of cloud microphysics. Their ability to act as heterogeneous ice nuclei has been shown in various laboratory studies; however, their atmospheric relevance in aerosol-cloud interactions is debatable. This is partly due to the lack of understanding of the actual processes driving ice nucleation on biological particles (e.g. Möhler *et al.*, 2008), and the challenging identification of these particles in the field (Pratt *et al.*, 2009). Both objectives were tackled in the framework of the BIO06 campaign at the AIDA facility at the Karlsruhe Institute of Technology, Germany. The ice nucleation behavior of bacterial species such as *Pseudomonas syringae* and *Pseudomonas fluorescence* was studied with focus on differences in the physico-chemical properties between the individual, intact cells, bacteria strains and their residuals - a by-product from the aerosol production process. Additionally, cells coated with ammonium sulfate were investigated.

2. METHODS AND RESULTS

We present data on the chemical composition of coated and uncoated bacterial cells and their residues from single particle mass spectrometry measurements, and relate differences in the mass spectra to the observed ice nucleation activity.
A TSI Aerosol Time-of-Flight Mass Spectrometer (ATOFMS) was applied for this study featuring the chemical analysis of single particles. The ATOFMS uses laser ablation to evaporate and ionize the particles for mass spectrometric detection and allows a size resolved analysis of the particles' chemical composition, i.e. mass spectra from intact cells and their residues can be separated. Both were represented as two distinct modes in the measured size distribution as seen in *Figure 1*.

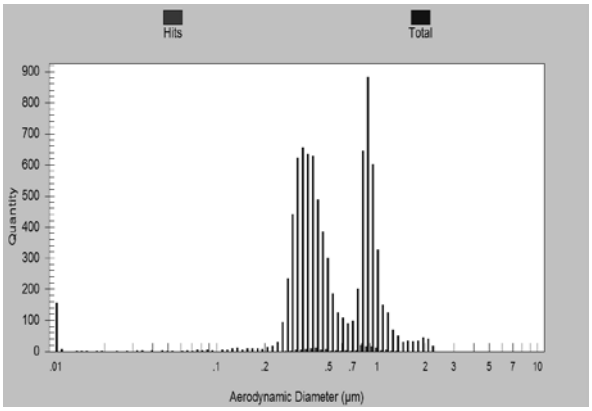

Figure 1. ATOFMS-measured aerodynamic size distribution of Pseudomonas syringae strain 32b74 bacterial cells (large mode) and cell residuals (small mode), color-coded by sized ("total") and analyzed ("hits") particles.

The elaboration of mass spectrometric "fingerprints" usable for the identification of bacteria by aerosol mass spectrometry is also a key aspect of this study. *Figure 2* exemplarily depicts an ATOFMS mass spectrum of *Pseudomonas syringae* cell of strain 13b2. The ions representing phosphate, potassium, and nitrogen-containing organic compounds are clearly visible and have been detected by the instrument. However, unidentified peaks

remain which have also been observed in ambient aerosols.
The chemical composition is linked to the ice nucleation activity of the different species, and the influence of ammonium sulfate coatings on the ice-nucleation behavior of the investigated particles is explored.

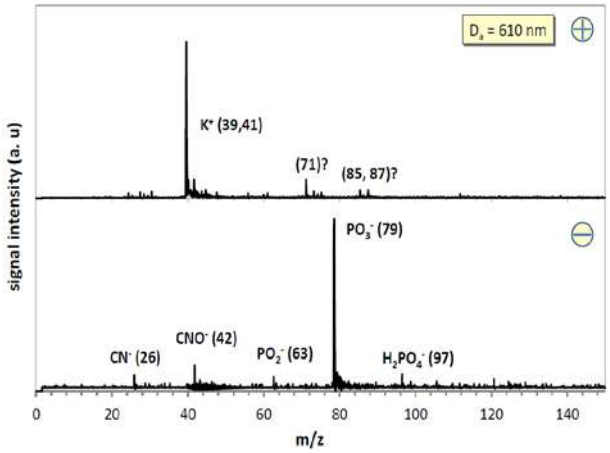

Figure 2. Mass spectrum of Pseudomonas syringae bacteria cell recorded by the ATOFMS. The most prominent, identified ion peaks are marked.

3. SUMMARY

The mass spectrometric signatures and ice nucleation behavior of bacterial species such as *Pseudomonas syringae* and *Pseudomonas fluorescence* were studied. The presented data on mass spectrometric measurements of biological particles helps explaining the ice nucleation process from the chemical point of view, but also provides valuable reference spectra for the mass spectrometric community. Reference spectra obtained with a single particle mass spectrometer are of high importance as this type of instrumentation is widely used for the online, in situ detection and identification of aerosols as well as ice crystal and cloud droplet residuals in field studies.

4. BIBLIOGRAPHY

O. Möhler *et al*. (2008) *Biogeosciences,* **5**, 1425-1435.
K. A. Pratt *et al*. (2009) *Nature Geosci.* **2**, 398-401.

Acknowledgements

The project was funded by EUROCHAMP Transnational Access (TA) contract no. E2-2011-03-02-0052 and the Swiss National Science Foundation.

A NUMERICAL MODELLING STUDY FOR THE ISSUES ON THE PLANNED AND INADVERTENT WEATHER MODIFICATION IN JAPAN

Akihiro Hashimoto and Masataka Murakami

Meteorological Research Institute, Japan Meteorological Agency

1. INTRODUCTION

The authors are developing the numerical model for the simulation of aerosol-cloud interaction to cover the issues on planned and inadvertent weather modification. The nucleation properties of aeolian dust and anthropogenic aerosol particles will be implemented using experimental results from the dynamic cloud chamber experiment in Meteorological Research Institute. The ice nucleation property of silver iodide (AgI) has been formulated as a function of temperature and humidity based on past experimental studies.

Preliminary result has been obtained from the simulation of the cloud seeding with AgI ground-based generator in mountain range.

2. NUMERICAL MODEL

Three dimensional cloud seeding model has been developed on the basis of Non-Hydrostatic Model of Japan Meteorological Agency (JMANHM, Saito et al. 2006). This model is able to simulate the cloud seeding operation and its effect on cloud and precipitation. Three types of seeding agent are available in the model; dryice pellet, LCO, and AgI. The seeding procedure can be choice from the two options from ground generators and an aircraft.

For the DIP and LCO seeding, nucleation ratio of 10^{13} ice crystals for the evaporation of 1 g of the seeding agent is assumed. For the AgI seeding, four types of nucleation mechanism; deposition, condensation freezing, immersion, and contact freezing are implemented.

3. NUMERICAL SIMULATIONS

In the cloud seeding simulation, double moment bulk microphysics is applied. The model domain covers the catchment of Okutone dam in Gunma prefecture, Japan. Five ground-based generators of LCO or AgI are deployed along the ridge of Uonuma hills about 30 km away to the northwest of the dam across the watershed, Echigo mountain range in the model domain. Initial time of the simulation is 12 UTC on 25 January 2008. Time integration is performed up to 9 hours.

4. RESULTS

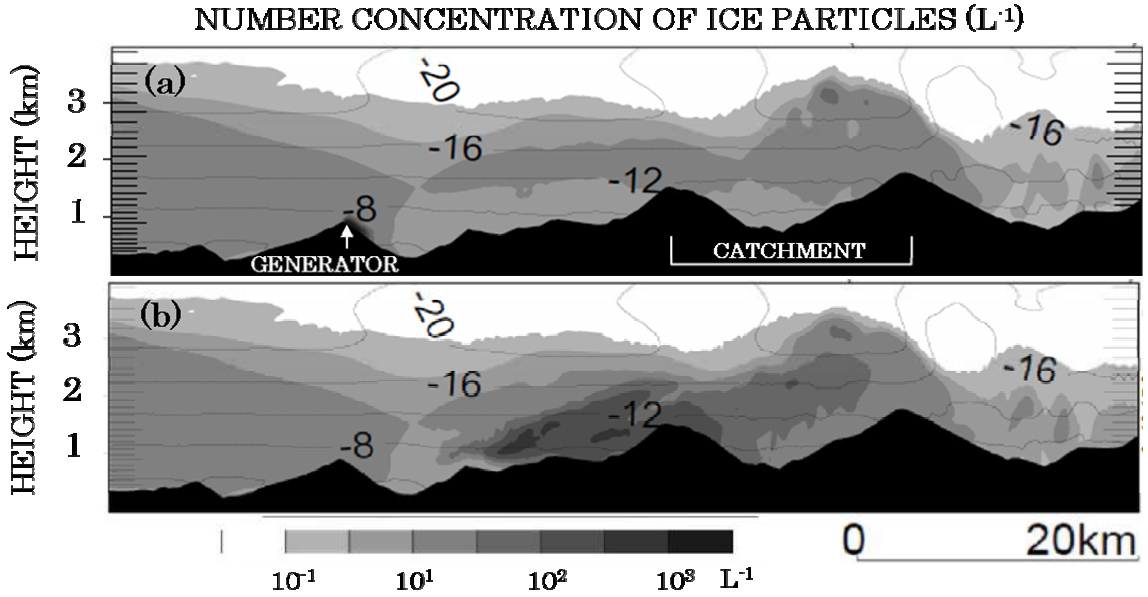

Figure 1. Distribution of number concentration of ice crystals (grey scale) one and half hour after the beginning of cloud seeding. Winter monsoon directs from the left to the right in the panels. Black contours indicate air temperature.

Figure 1a shows the distribution of number concentration of ice crystals one and a half hours after the cloud seeding started. In the case of LCO seeding, the artificially generated ice crystals immediately evaporate due to the downwind in the lee side of Ounoma hills. The number concentration of ice crystals over the catchment is same as in the simulation without seeding (not shown). In the case of AgI seeding, the seeded AgI particles are transported by air stream firstly without activation but keeping the ability of ice nuclei until they come to the spot where temperature and humidity meet the condition of activation. Finally, the seeding effect on the number concentration of ice crystals appears over the catchment (Fig. 1b).

5. SUMMARY

The LCO seeding is able to generate ice crystals immediately at the seeding site, if only the super-cooled cloud covers the seeding site. However the realization of seeding effect on the targeted area much depends on the topographic location of seeding site and the inherent meteorological conditions there. For the AgI seeding, the released seeding agent autonomously selects the location to activate according to the conditions of temperature and humidity. The realization of seeding effect is less dependent on the topographic location than in the case of LCO seeding.

Flexible strategy is desirable for a cloud seeding project in accordance with a situation to choice the type of seeding agent,

and the timing and location of seeding operation.

REFFERENCES

Saito, K., T. Fujita, Y. Yamada, J. Ishida, Y. Kumagai, K. Aranami, S. Ohmori, R. Nagasawa, S. Kumagai, C. Muroi, T. Kato, H. Eito, and Y. Yamazaki, 2006: The operational JMA non- hydrostatic mesoscale model. *Mon. Wea. Rev.,* **134,** 1266− 1298.

MICROPHYSICAL VERTICAL STRUCTURE OF THE MELTING LAYER IN MESOSCALE CONVECTIVE SYSTEMS

Christophe Duroure , Régis Dupuy , Olivier Jourdan , Marie Monier , Alfons Schwarzenboeck , Emmanuel Fontaine, W. Wobrock
Université Blaise Pascal Clermont-Ferrand, CNRS, Laboratoire de Météorologie Physique, 24 avenue des landais, 63000 Clermont-Ferrand, 63171 Aubière, France

1- Introduction

Within the frame of the Megha-Tropiques project, microphysical characteristics of the melting layer of some MCS have been observed using a complete set of imaging probes (2DS, CIP, PIP) mounted on the French research aircraft Falcon 20 during two measurement campaigns, one above the continent (2010 over West Africa) and another in 2011 above the Indian Ocean.

The vertical evolution of the shape of hydrometeors in the temperature range between -5℃ and +5℃ has been studied extensively. As a function of particle size, hydrometeor images are classified into *not melted, partially melted and completely melted* (drop) hydrometeor types.

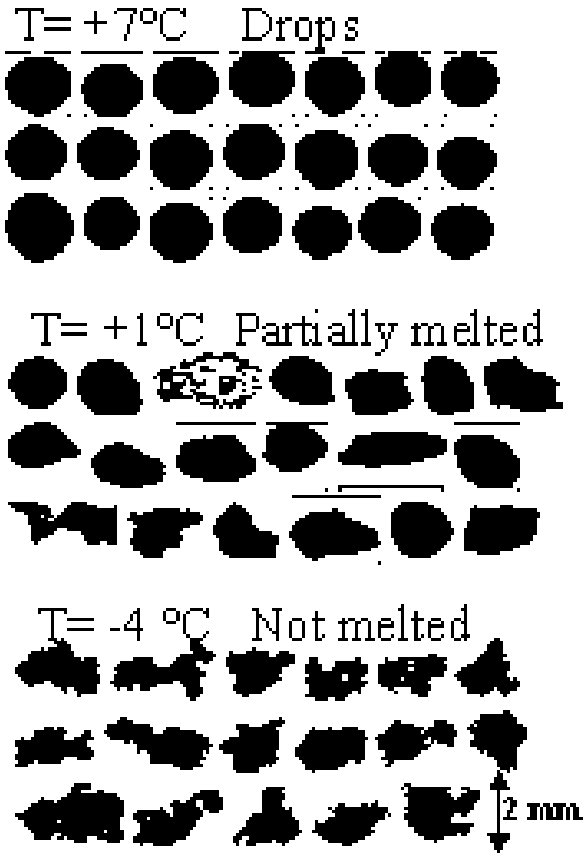

Fig. 1: Raw samples of hydrometeor images at three fixed pressure levels in a MCS melting layer (Niamey, Megha-tropique flight18). The three samples are from CIP imager (64 pixels of 25 µm size). No manual selections were made in this figure. Only complete particle images are used

This classification allows to statistically estimating the exact temperature of complete melting as a function of the size and shape of hydrometeors. The above experimental studies are compared to a simple thermodynamical model of melting, assuming mass-diameter relationships for the densities, terminal velocities, and ventilation coefficients of hydrometeors

2- Temperature envelope of melting

This semi-quantitative analysis distinguishing *non-melted, partially melted and completely melted particles*, is uses during aircraft soundings in order to estimate the range of the melting layer. For that purpose the method detects the first observed drop and the last observed non-completely melted hydrometeor of a given size at a given temperature. First results (see one case on the Fig. 2) show that for D=2mm the minimal envelope value (i.e. temperature for the occurrence of one drop) appears near +4℃. This value seems larger than results of thermodynamical parameterization (Planche, 2011, see comments in the conclusion).

The Fig. 2 shows the observation of completely melted hydrometeor (drops) diameter with the temperature during a

rapid descent through the melting region during flight 19 of Megha-Tropiques, 2010. Two analysis techniques are compared on this figure: 1) an automatic quasi-circular shape recognition of complete images with simple geometric criteria corresponding to the small symbols and 2), a manual selection of images recognized as droplets (even the incomplete ones) corresponding to the large symbols.
Two imaging probes where used for this analysis: Firstly, the CIP probe (pixel resolution of 25µm), corresponding to small crosses and large triangles, and secondly the PIP probe (pixel resolution 100µm), corresponding to small diamonds and large stars in Fig.2.

The envelope of the observations shows that the minimum temperature for a complete fusion varies relatively slowly with the hydrometeor diameter. There is no observation of drops larger than 1.5 mm for temperatures lower than +2℃ in this sample.

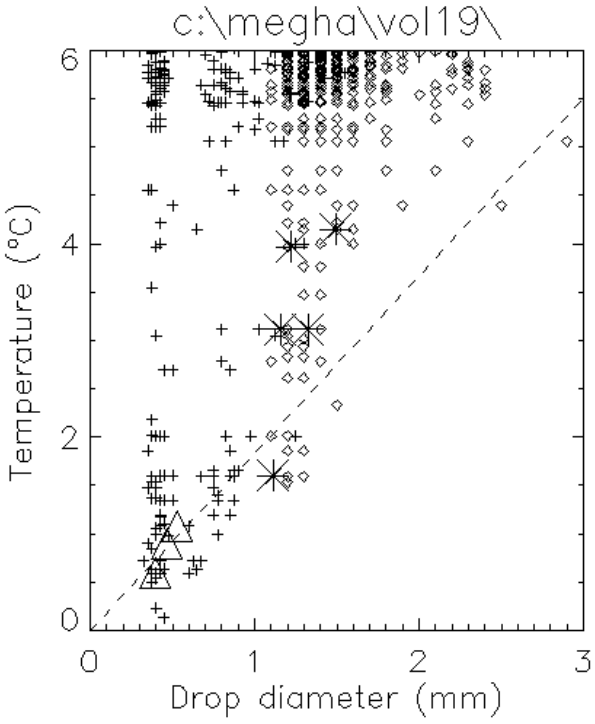

Figure 2: Envelope of the temperature and complete melting observations. Sounding in a MCS sampled over Niamey (Megha-Tropiques, Flight19).

3- Microphysics and temperature fluctuations in the melting layer

Flight legs at fixed pressure (and/or altitude) levels are used to quantify the small scale temperature fluctuations into the melting band. Each sample was collected over a horizontal distance of 180 m. In the warmer part of this melting layer (mean temperature of the leg equal to +7.3℃) large fluctuation of temperature were observed. These fluctuations with values up to 0.7℃ over a 10km scale (see Fig. 3) are larger than the turbulent fluctuation expected in a well mixed dry turbulent layer. The diabatic effects (evaporation of drops and fusion of ice) could be an explanation for these large fluctuations.

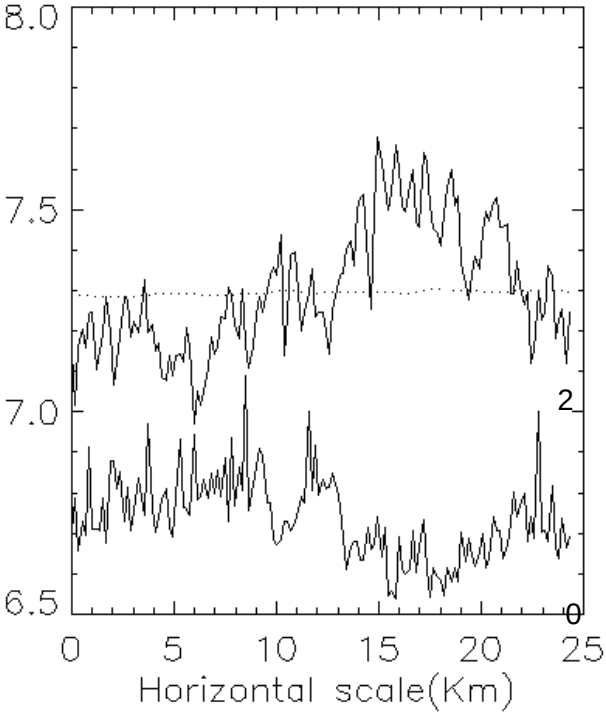

Fig. 3: Temperature fluctuations (in ℃) in a fixed pressure level near the low limit of melting band (upper graph). The dashed line gives the expected temperature determined under hydrostatic pressure conditions. Lower graph: concentration of large hydrometeors (mainly drop at this temperature level) of size larger than 1.3 mm (right Y axis in particle number/m^3).

For this case study the local temperature seems to have a negative correlation with the concentration of precipitating hydrometeors as shown on the figure 4.

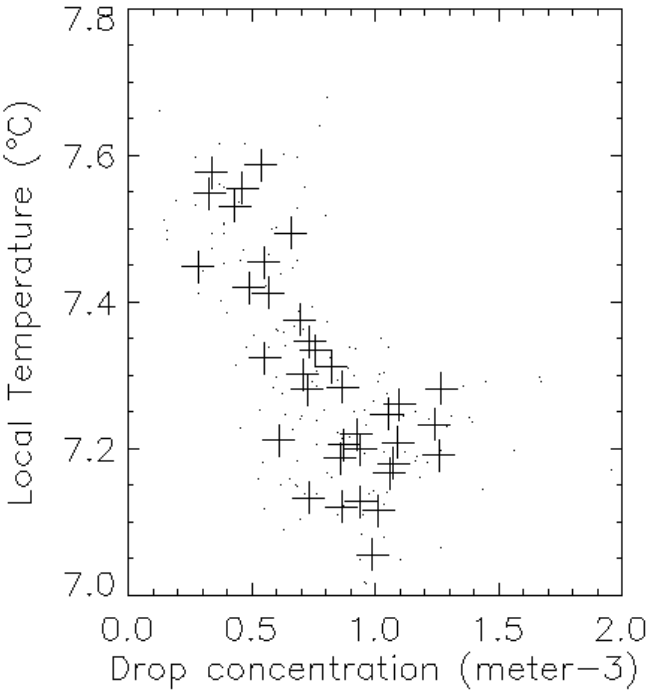

Fig. 4: Scatter plot of the local temperature versus local concentration of precipitation in the lower part of the melting layer (same case as the figure 3, mean temperature = +7.3 °C). Averages over 720 m are given by the big crosses, individual samples by the dots

4- Population roughness exponent

Within the 0°C to +2°C temperature range an important increase of the roughness exponent (i.e. the exponent of the power law when fitting the *perimeter - size* relationship), for hydrometeor sizes beyond one millimetre is observed. This latter observation could be interpreted as a rapid increase of the collection kernel of surface melted aggregates.

5- Conclusions

This preliminary study use only 2 of the 20 interesting cases sampled during the AMMA, MT1 and MT2 experiments.

A first result of this study is the possibility to measure the envelope of the melting band by imaging probes and so allow comparing the observations with exact modelling of the hydrometeor melting process.

The second result is the possible importance of small scale humidity fluctuations in the melting band. The humidity measured in this study (i.e. saturation all over the melting band) is not in agreement with the observed melting envelope. Model and cloud chamber experiments (Rasmussen and Pruppacher, 1981) have shown that non-melted hydrometeors of 2mm size do not occur in saturated air at +4°C. One possible explanation for this discrepancy can be the very intermittent water vapour field prevailing in a precipitating cloud layer (where saturation is expected only in the vicinity of the drop trajectories). In the future we need high resolution measurements of the humidity in order to confirm this hypothesis.

References:

Rasmussen R. and H. Pruppacher, 1982, A wind tunnel and theorical study of the melting behavior of atmospheric particles, J. Atmos. Sci., vol 39, pp 152-158

Planche Céline, Développement et évaluation d'un modèle tridimensionnel de nuage mixte à microphysique détaillée: Application aux précipitations orographiques. 2011, PhD thesis, Université Blaise Pascal, Clermont-Ferrand.

Acknowledgments:

Thanks to the SAFIRE team (INSU and Météo-France) for the Falcon20 data, special thanks to the pilots for good quality of altitude fixed legs.

Thanks to CNES for financial support of the aircraft measurements campaigns.

FINE-SCALE TURBULENCE AT THE EDGES OF TRADE WIND CUMULI

Jeannine Katzwinkel* and Holger Siebert*

**Leibniz-Institute for Tropospheric Research, Leipzig, Germany*

1 INTRODUCTION

Small-scale dynamics in clouds play an important role for the rain formation. This is especially true for trade wind cumuli, which are able to develop rain within a short time. Although, the analysis of trade wind cumuli started already in the mid 1940's (Stommel [1947]), the understanding of the complex dynamic system of shallow cumulus clouds is insufficient until now. One important role plays the entrainment process at the edge of cumuli, which was already pointed out by Squires [1958]. Updrafts in the cloud core and the negative compensation flows outside the clouds lead to significant horizontal wind shear at cloud edges. The following mixing of environmental and cloudy air results in evaporation of cloud droplets followed by negative buoyancy (Grabowski [1993]). The resulting small-scale turbulence at cloud edges can leads to shells around the cloud (so called humidity halos, Laird [2005]) or downdraft regions at cloud edges (so called "subsinding shell", Heus and Jonker [2008]). Latter is analysed within this paper based on highly-resolved measurements at the edges of trade wind cumuli. The measurements were performed with the helicopter-borne measurement payload ACTOS (Airborne Cloud Turbulence Observation System). In this paper, the relations between the intensity of the small-scale turbulence and the width and intensity of the "subsiding shell" are presented.

2 EXPERIMENTS

High-resolution measurements were performed intrade wind cumuli over Barbados during the CARRIBA (Cloud, Aerosol, Radiation and tuRbulence in the trade wInd regime over BArbados) campaign. The campaigns took place in November 2010 and April 2011. The low true airspeed (TAS) of ACTOS of $15 - 20$ m s^{-1} enables measurements with a spatial resolution down to cm scale, which cannot be reached by fast-flying research aircraft so far. The following analysis concentrates on data of thermodynamic and turbulent sensors, especially on: 3D wind vector measured with an ultrasonic anemometer of type Solent, temperature (T) measured with an UltraFast Thermometer (UFT), absolute humidity (a) measured with a dewpoint mirror and liquid water content (LWC) measured with a particle volume monitor (PVM-100A). Further informations concerning the instrumentation can be found in Siebert et al. [2006].
The data were collected over the sea near the east coast of Barbados. The flights consists of several profiles and horizontal legs, while the latter were used for the following analysis.

3 RESULTS AND DISCUSSION

The thermodynamic and turbulent properties of a single cloud passage are characterized as an example to illustrate the analysis method. The following cloud passage was recorded during the flight on April, 14th 2011 in an altitude of 1320 m. Its thermodynamic properties are shown in Fig. 1, whereby the cloud region is characterized by a LWC of maximum 1 g m^{-3}, a mean vertical wind velocity (w) of 2 m s^{-1}, a mean absolute humidity a of 15 g m^{-3} and a mean temperature T of 17 °C. In the environmental region w fluctuates around zero, a and T decrease to 13 g m^{-3} and 16.4 °C, respectively. The intensity of small-scale turbulence of this cloud is characterized by the energy dissipation rate $\overline{\varepsilon}_\tau$ in Fig. 2. Its calculation is based on the second-order structure function: $S^{(2)}(r') = \langle (w(r+r') - w(r))^2 \rangle_\tau \simeq 2\varepsilon_\tau^{2/3} (t' \langle U \rangle_\tau)^{2/3}$, where $\langle \cdot \rangle$ denotes the average over the integration time τ. Detailed information are given in Siebert et al. [2010]. In this case the local energy dissipation rate was calculated using a moving window including 100 samples ($\tau = 1$ s), which was shifted sample by sample. Inside the cloud $\overline{\varepsilon}_\tau$ reaches values in order of 10^{-2} m^2 s^{-3}, while $\overline{\varepsilon}_\tau$ decreases outside the cloud to values around 10^{-4} m^2 s^{-3} with some variability.
Figure 3 corresponds to the black box in Fig. 2 and gives a closer look into the details of the cloud edge.

The green line marks LWC, while the black line denotes $\overline{\varepsilon}_\tau$ and w is marked with the blue line. Based on $\overline{\varepsilon}_\tau$ and w we define two subsections at the cloud edge. The first region (hereafter called "cloud-free shear region") is marked with the red box and characterized by a sharp increase of $\overline{\varepsilon}_\tau$ and a decrease of w to its local minimum w_{min}. The width of this region is defined as dx_{down}. The second region (hereafter called "in-cloud shear region") is marked with the blue box starting at w_{min} and is limited by the first local maximum of w (w_{max}). This region is characterized by a significant horizontal wind shear of the vertical wind velocity ($S^2 = \left(\frac{dw}{dx}\right)^2$), which is marked with the orange line, and a slight increase of $\overline{\varepsilon}_\tau$. The horizontal wind shear S^2 is calculated based on the difference between w_{max} and w_{min} (dw) and the difference between the corresponding x values (dx). The spatial expansion of the in-cloud shear region dx, is somehow related to the maximum possible entraining eddy sizes at cloud edge. In this case, $dx \approx 10$ m is observed. With the observed mean $\overline{\varepsilon}_\tau$ we estimate a typical mixing time $\tau_m = \left(\frac{l^2}{\overline{\varepsilon}_\tau}\right)^{1/3} = 23$ s.

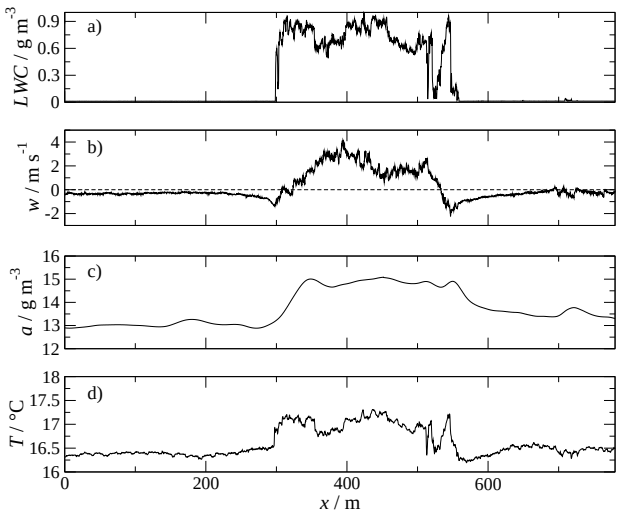

Figure 1: A single cloud passage of a horizontal flight of April, 14th 2012 is shown. Following thermodynamic properties are plotted: a) liquid water content (LWC), b) vertical wind velocity (w), c) absolute humidity (a) and d) temperature (T).

Based on the definition of the two subsections, 15 trade wind cumuli were analysed. Figure 4 deals with the small-scale turbulence in the in-cloud shear region. As a measure for the turbulence intensity inside this region we chose the 90% percentile of $\overline{\varepsilon}_\tau$ ($\overline{\varepsilon}_{\tau,90\%}$) instead of the maximum value of $\overline{\varepsilon}_\tau$ which may be biased by single peaks. The 90% percentile was calculated based on the probability density function of $\overline{\varepsilon}_\tau$. Its correlation with S^2 is shown in Fig. 4a. Furthermore, we define a normalized LWC_{norm}

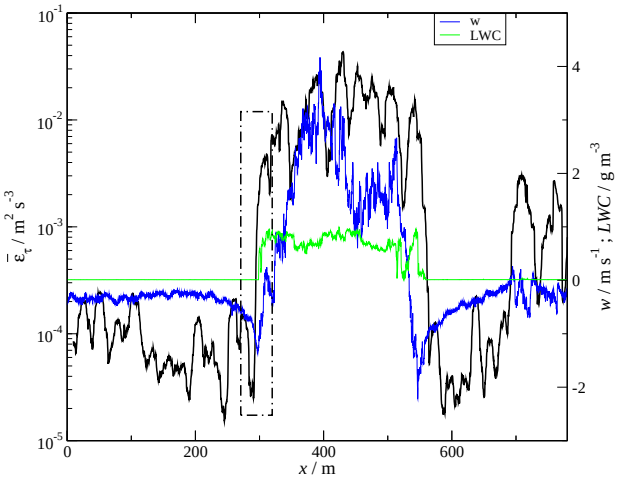

Figure 2: The local energy dissipation rate ($\overline{\varepsilon}_\tau$) of the same cloud passage as in Fig. 1 is marked with the black line. The blue line denotes the vertical wind velocity (w) and the green line shows the liquid water content (LWC). Both are used the identify the cloud edge, which is marked with the box.

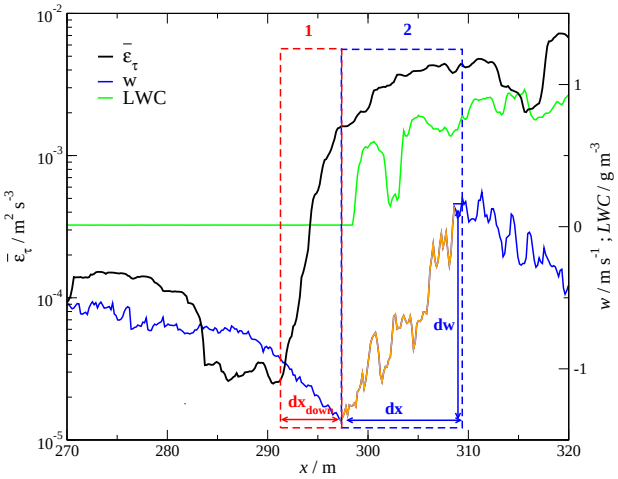

Figure 3: Local energy dissipation rate ($\overline{\varepsilon}_\tau$) given in black, vertical wind velocity (w) denoted by a blue line and liquid water content (LWC) marked by a green line are shown for the cloud edge marked in Fig. 2. The red box denotes the region with increasing small-scale turbulence and is called "cloud-free shear region". The width of this region is given by dx_{down}. The blue box marks the "in-cloud shear region", where the shear is denoted by the orange line and calculated with $S^2 = \left(\frac{dw}{dx}\right)^2$.

by dividing the observed LWC with the adiabatic value LWC_{ad} as a measure of mixing and diluting of cloudy air with subsaturated air at cloud edges. The adiabatic value is calculated using a mean cloud base of 500 m and the corresponding temperature at this height. The correlation plot of the arithmetic mean of LWC_{norm} and S^2 is shown in Fig. 4b, whereas Fig. 4c shows the correlation between w_{min} and $\overline{\varepsilon}_{\tau,90\%}$. The 90% percentile of $\overline{\varepsilon}_\tau$ increases with increasing S^2 and converges to values in order of 10^{-2} m^2 s^{-3} corresponding to observed in-cloud values. This indi-

cates that shear plays a major role in the production of turbulent energy in this region. However, with increasing turbulence the mixing process between environmental and cloudy air is enhanced and more cloud droplets evaporate. This is indicated by the correlation of LWC_{norm} and S^2 in Fig. 4b, where LWC_{norm} decreases with increasing shear. Increased evaporation leads to additional production of negative buoyancy, which will intensify the downdrafts. This is in agreement with the correlation between $\overline{\varepsilon}_\tau$ and w_{min} in Fig. 4c, where with increasing $\overline{\varepsilon}_{\tau,90\%}$ an increasing absolute value of w_{min} is observed. Furthermore, increasing downdrafts due to evaporation will add to an enhancement of the shear (see Fig. 4a and 4b).
In Fig. 5 the relationship between the small-scale turbulence in the in-cloud shear region and dx_{down} is analysed. In addition to $\overline{\varepsilon}_{\tau,90\%}$, we calculate further turbulence parameters as the local mixing length ($l = \frac{\sigma_w^3}{\overline{\varepsilon}_\tau}$) and the local mixing time τ_m averaged over the entire region of the in-cloud shear region. The local mixing length l is estimated based on the standard deviation of the vertical wind velocity, σ_w, estimated based on the detrended time series of w using the same moving window as for $\overline{\varepsilon}_\tau$. With the help of l the local mixing time is calculated.
Figure 5 shows an increase of $\overline{\varepsilon}_{\tau,90\%}$ with increasing dx_{down}, while l (Fig. 5b) and τ_m (Fig. 5c) decrease, indicating a more rapid mixing at cloud edges.

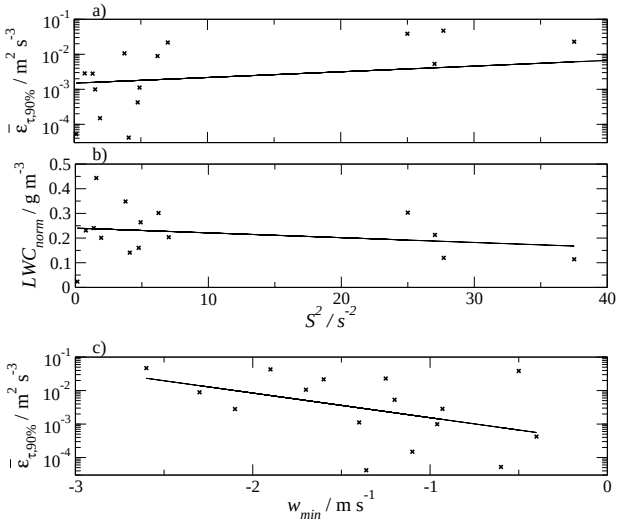

Figure 4: Correlations between properties at the edge of 15 cumuli are given for: a) horizontal wind shear of the vertical wind velocity (S^2) and the normalized liquid water content ($LWC_{norm} = \frac{LWC}{LWC_{ad}}$), b) S^2 and the 90% percentile of the energy dissipation rate $\overline{\varepsilon}_{\tau,90\%}$ and c) minimum vertical wind velocity w_{min} and $\overline{\varepsilon}_{\tau,90\%}$. The black lines denote the regression lines.

The observations indicate that the mixing process due to small-scale turbulence inside the in-cloud

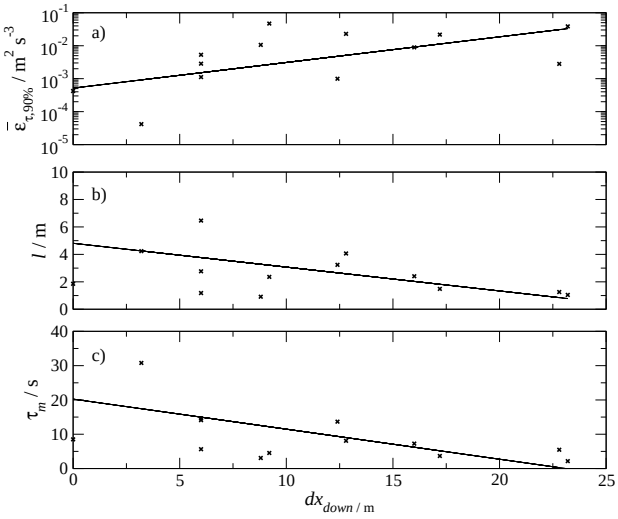

Figure 5: Correlations for the same 15 cumuli as in Fig. 4 are given between dx_{down} and a) $\overline{\varepsilon}_{\tau,90\%}$, b) mean local mixing length (l) and c) mean local mixing time (τ_m). The black lines denote the regression lines.

shear region significantly influences the cloud region where it leads to evaporation of cloud droplets and negative buoyancy. Furthermore, we observe a relationship between the in-cloud turbulence and the width of the cloud-free shear region: an increased width is observed for more intense in-cloud turbulence.
It should be kept in mind, that many different mixing processes do interact with each other and "cause and effect" may be difficult to distinguish with observations only. Numerical simulations might shed light on this problem. Moreover, the analysis is only based on cloud edges of 15 cumuli and further analysis is needed to investigate small-scale turbulence at cloud edges in more detail and more robust statistics.

References

W. W. Grabowski. Cumulus entrainment, fine-scale mixing, and buoyancy reversal. *Q. J. R. Meteorol. Soc.*, 119:935–956, 1993.

T. Heus and H. J. J. Jonker. Subsiding shells around shallow cumulus clouds. *J. Atmos. Sci.*, 65:1003–1018, 2008.

N. F. Laird. Humidity Halos Surrounding Small Cumulus Clouds in a Tropical Environment. *J. Atmos. Sci.*, 62:3420–3425, 2005. doi: 10.1175/JAS3538.1.

H. Siebert, H. Franke, K. Lehmann, R. Maser, E. W. Saw, Dieter Schell, R. A. Shaw, and M. Wendisch. Probing finescale dynamics and microphysics of clouds with helicopter-borne measurements. *Bull. Amer. Meteor. Soc.*, 87:1727–1738, 2006.

H. Siebert, R. A. Shaw, and Z. Warhaft. Statistics of small-scale velocity fluctuations and internal intermittency in marine stratocumulus clouds. *J. Atmos. Sci.*, 67:262 – 273, 2010.

P. Squires. Penetrative downdraughts in cumuli. *Tellus*, 10:381–389, 1958.

H. Stommel. Entrainment of air into a cumulus cloud. *J. Meteorol.*, 4:91–94, 1947.

GLOBAL DISTRIBUTION AND SPATIAL CONTEXT OF OPTICALLY THIN LIQUID WATER CLOUDS INVESTIGATED USING FIVE YEARS OF CALIOP-CALIPSO DATA

Abhay Devasthale[1] and Manu Anna Thomas[2]
[1]Atmospheric Remote Sensing Unit, Research and development department, Swedish Meteorological and Hydrological Institute (SMHI), Norrköping, Sweden
[2]Air Quality Unit, Research and development department, SMHI, Norrköping, Sweden
Correspondence: abhay.devasthale@smhi.se

1. Introduction

Clouds play an important role in the global radiation budget. Low level clouds have a special role in this context as they significantly reflect incoming solar radiation back to the space and produce the net cooling effect at the surface (Wood, 2012). These clouds mainly consist of liquid phase and occur in a range of spatial scales (Wood and Field, 2011). Apart from the radiation budget, they are also instrumental in regulating local thermodynamics and stability. In particular, our understanding of thin water clouds (TWC), processes governing their characteristics and their interactions with aerosols is limited in spite of their large coverage (Turner et al., 2007). The CALIOP-CALIPSO sensor allows their accurate characterization due to its high sensitivity to thin clouds.

The present study attempts to investigate following two aspects of these clouds.
a) Global and seasonal distribution.
b) The spatial context for these clouds. Here we try to understand if these clouds are the edges of or open cells/holes/depressions in the existing thick stratus/stratocumulus decks or whether they are independent systems themselves. Which type of clouds surround TWC pixels and to what spatial extend?

2. CALIPSO data and methodology

We used the standard 5 km Cloud Layer Product for the period June 2006 through May 2011 for the present study. The basic description of this data set along with algorithm theoretical basis for retrieving features, aerosol-cloud discrimination, optical depth, phase and cloud subtyping are explained in detail in various articles in the special issue of J. Atmos. Oceanic Tech. (2009) (Hu et al., 2009; Liu et al., 2009; Winker et al., 2009; Young and Vaughan, 2009).

We define thin water cloud (TWC) as a retrieval when a) cloud feature is retrieved with high confidence and b) cloud phase is deemed to be liquid, also with high confidence and c) layer optical depth is less than 3.0 and 4) CALIOP is able to fully penetrate cloud feature and 5) all other retrieved values are within physical limits (e.g. layer heights etc).

Once a TWC is detected, we further examine properties of other cloudy pixels along the distance of 100 km on the either side of the CALIPSO track to gain insights into its spatial context. We investigate following parameters as a function of distance from the TWC pixel; a) relative frequency of similar TWCs in the lowermost layer versus other cloud types, b) relative layer top height of neighbouring cloudy pixels, c) thermodynamic phase of neighbouring cloudy pixels, d) relative frequency of occurrence of cloud subtypes and e)

layered structure of neighbouring clouds.

3. Results and discussions

Fig. 1 shows the absolute frequency of occurrence of TWCs and their seasonality based on five years of data for nighttime conditions. Seasonal distribution shows highest frequency of TWCs during the JJA months. These clouds are prevalent over the Southern Oceans during all seasons. The higher latitudes in the Northern Hemisphere show strongest seasonality with highest frequency of occurrence during the JJA months.

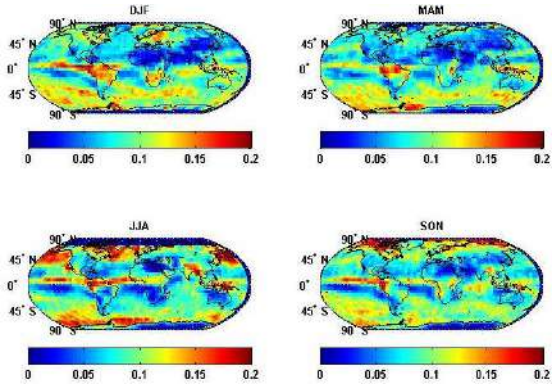

Fig. 1: Seasonal absolute frequency of TWCs.

It is clear from Fig. 2 that, whenever TWCs are encountered, in majority of the cases, neighbouring lowermost layers of clouds in the atmosphere are also of liquid phase and semi-transparent in the range of 100 km studied here. Fig. 3a further reveals that the majority of cloud top heights of neighbouring pixels lie within +/- 1 km relative to TWC top heights, although the tops are located at increasingly higher altitudes as the distance from the TWC pixel increases.
Even at 100 km scale, more than 30% of cloud tops are still within +/- 1 km relative to TWC top heights. The overwhelming majority of neighbouring pixels are assigned cloud subtype categories of low and medium level transparent clouds.

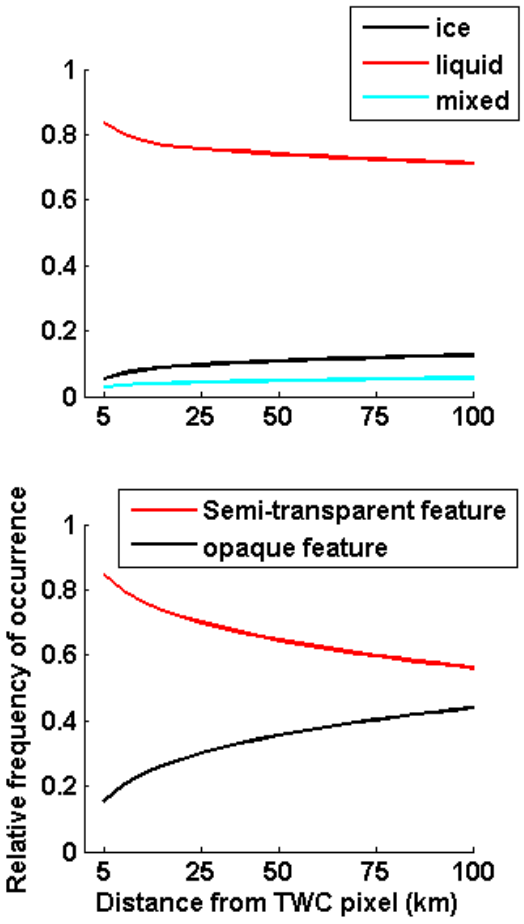

Fig. 2: Relative frequency of occurrence of neighbouring cloudy pixels from the lowermost layers as a function of distance from TWC for a) cloud phase and b) opacity. The study region is the Arctic (67N-82N, 180W-180E).

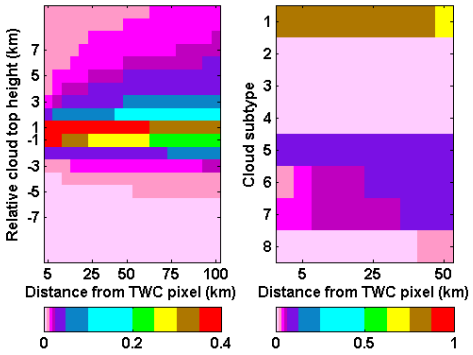

Fig. 3: a) Frequency of occurrence of lowermost cloud layer top heights relative to TWC as function of horizontal distance, b) Relative distribution of various cloud subtypes. 1 – Low overcast transparent, 2 – low overcast opaque, 3 – Transition stratocumulus, 4 – Low broken cumulus, 5 – Altocumulus transparent, 6 – Altocumulus opaque, 7 – Transparent cirrus, 8 – Opaque deep convective.

Due to brevity, only preliminary statistics for the Arctic region is currently presented in the extended abstract.

4. References

Hu, Y., and Coauthors, CALIPSO/CALIOP cloud phase discrimination algorithm. J. Atmos. Ocean. Tech., 26, 2293-2309 2009.

Liu, Zhaoyan, and Coauthors, 2009: The CALIPSO Lidar Cloud and Aerosol Discrimination: Version 2 Algorithm and Initial Assessment of Performance. J. Atmos. Oceanic Technol., 26, 1198–1213. doi: http://dx.doi.org/10.1175/2009JTECHA1229.1

Turner et al., Thin liquid water clouds: Their importance and our challenge, BAMS, 177-190, Feb 2007.

Winker, D. M., M. A. Vaughan, A. H. Omar, Y. Hu, K. A. Powell, Z. Liu, W. H. Hunt, and S. A. Young, Overview of the CALIPSO Mission and CALIOP Data Processing Algorithms. J. Atmos. Oceanic Technol., 26, 2310–2323, doi:10.1175/2009JTECHA1281.1, 2009.

Wood, R., Stratocumulus Clouds, Monthly Weather Review, 2012, e-View doi: http://dx.doi.org/10.1175/MWR-D-11-00121.1.

Wood, R., and P. R. Field, The distribution of cloud horizontal sizes, J. Clim., 24, 4800-4816, 2011.

Young, Stuart A., Mark A. Vaughan, 2009: The Retrieval of Profiles of Particulate Extinction from Cloud-Aerosol Lidar Infrared Pathfinder Satellite Observations (CALIPSO) Data: Algorithm Description. J. Atmos. Oceanic Technol., 26, 1105–1119. doi: http://dx.doi.org/10.1175/2008JTECHA1221.1

REGIONAL MODELLING OF THE TROPOSPHERIC MULTIPHASE SYSTEM USING COSMO-MUSCAT

R. Schrödner, A. Tilgner, R. Wolke

Leibniz Institute for Tropospheric Research, Leipzig, Germany

Presenting author email: roland.schroedner@tropos.de

ABSTRACT

The evaluation of multiphase chemistry versus overall tropospheric chemistry is challenging since microphysical and chemical processes occurring at different time scales within clouds are still poorly known. The coupled 3-D chemical transport model COSMO-MUSCAT was extended to consider cloud-chemical processes on the regional scale replacing the former aqueous phase parameterization. With the advanced model system, 2D-sensitivity-studies have been conducted for urban and remote environmental conditions. The comparison of two different mechanisms (simple inorganic and detailed organic mechanism CAPRAM) have revealed agreements but also interesting differences for important chemical subsystems. This is e.g. in the modelled HO_x budget and pH whereas the simple mechanism leads to always less acidic cloud droplets than CAPRAM. The difference in pH is consequently responsible for different regimes for the S(IV).

1. INTRODUCTION

Clouds play a major role in the atmosphere due to their influence on the Earth's radiative budget, on the hydrologic cycle and on the tropospheric chemical composition (e.g. Ramanathan et al., 2001). Cloud lifetime is driven by the dynamics of the atmosphere at the synoptic scale and, in close interaction, by microphysical processes (e.g. nucleation of cloud droplets and ice crystals, condensation and evaporation, collision/coalescence processes, freezing, sedimentation of hydrometeor) on the small scale. These processes depend on the chemical composition of particles and cloud droplets. In addition, microphysical processes redistribute chemicals among the various reservoirs: gaseous, particulate, liquid and ice phases. Clouds favour the development of "multiphase chemistry" since they are an ideal reaction medium for this: (1) clouds support very efficient photochemical processes inside droplets; (2) certain homogeneous chemical reactions within clouds can be usually faster than the equivalent reactions in the gas phase, and reactions such as those involving ionic species, can be important; (3) finally, interactions between the aqueous and solid phase can contribute additionally to chemical processes in clouds (for example dissolution of soluble particulate species)

The objective of the present study is, to enhance the 3D chemical transport model (CTM) COSMO-MUSCAT by implementation of cloud chemical processes. As this work is mainly model evaluation, only test simulations will be presented in the following.

2. MODEL DESCRIPTION AND SETUP

The model system COSMO-MUSCAT consists of the CTM MUSCAT (Wolke et al., 2004a) and the forecast model of the German Weather Service (DWD) COSMO (Schättler et al., 2008). Both models are coupled online where meteorological fields are provided by COSMO and are used by MUSCAT for transport and chemistry. The treatment of gas phase chemical processes and aqueous phase chemistry parameterization (by loss of certain gaseous compounds via wet scavenging) was already included. In this work, MUSCAT was extended to consider cloud-chemical processes (chemical aqueous phase reactions and phase transfer processes) in a regional scale model. Routines that compute chemical aqueous phase reactions and phase transfer

processes were implemented and integrated into MUSCAT replacing the former aqueous phase parameterization. Moreover, the numerical solver was adjusted to ensure numerical robustness and accuracy.

In the present work, the new model environment was tested in 2D with a stand-alone and a coupled model version (i.e. homogenous in y-direction). For the stand-alone-version MUSCAT was used with prescribed time independent meteorology, i.e. without coupling to the meteorological model. In that case, the cloud is like a reactor since it is the only area, where aqueous phase chemistry is taking place. Due to the prescribed meteorology, vertical mixing is only caused by diffusion to prevent transport in one vertical direction only. In the coupled system, air streaming over a mountain was simulated, which leads to a cloud evolving at the top of that mountain. Because of difficulties with numerical stability due to variable and inhomogeneous liquid water content (LWC) in the coupled system, a minimum LWC (0.01 g/m^3) was necessary. Figure 1 shows the spatial distribution of liquid water content (LWC) in the integration area (height vs. horizontal) for both model versions at high noon. Note, that the spatial resolution is different. The number of the monodisperse cloud condensation nuclei (which only are activated in the cloud) is prescribed and held constant at 300 cm^{-3} in the whole model area. Hence, the droplets are smaller at the edges of the clouds (and the "cloud-free" area with minimum LWC for the coupled system). The droplet radii vary from 2.0 to 7.5 µm. The photolysis rates are decreased up to 60% of the clear sky value under the cloud because of shading (Chang et al., 1987). In the model, particles are initiated with a total mass and given initial composition. The initial concentrations are uniform in x-direction. In z-direction the mixing ratio is held constant. During integration the initial composition of the air and the particles enter through the left boundary into the integration area and are transported by the wind field from the left to the right boundary. All simulations start at midnight at last 24 hours. To examine which differences the consideration of cloud chemical processes account for, the model runs have been performed using a gas-phase mechanism (RACM-MIM2ext, see Tilgner and Herrmann, 2010) in combination with two different aqueous phase mechanisms of different complexity, i.e. CAPRAM 3.0 red (C3.0RED; Deguillaume et al., 2009; detailed description of the oxidation of inorganics and organics up to C4), and INORG (Sehili et al., 2005; focussing on production of sulphate, no organics are treated). To give information on the behaviour of the aqueous phase chemistry in different chemical regimes, model simulations were performed for two different chemical environmental conditions (remote continental background and urban polluted), which differ in initial concentrations.

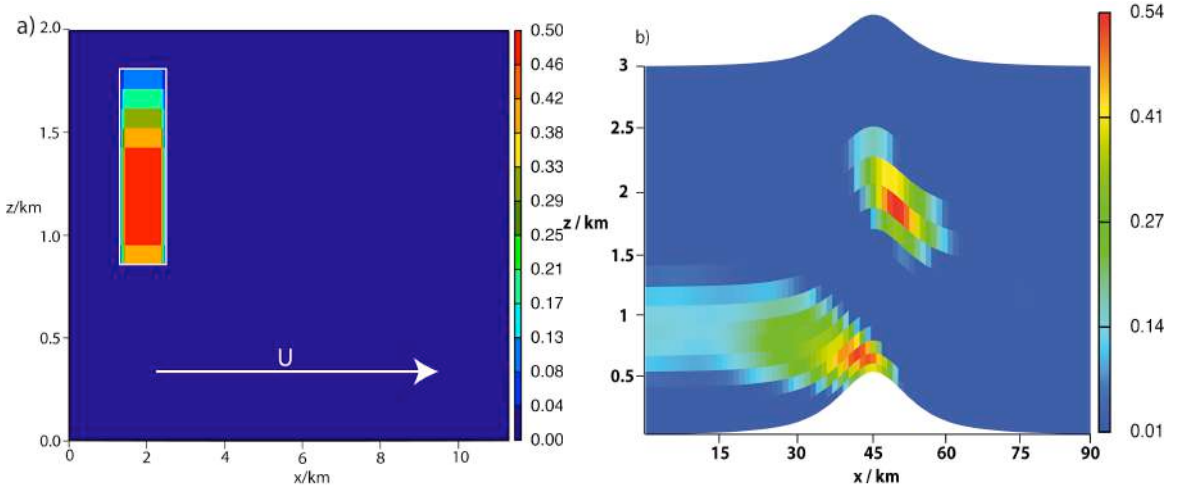

Figure 1. Liquid water content in gm^{-3} at high noon for a) stand-alone-version and b) coupled version.

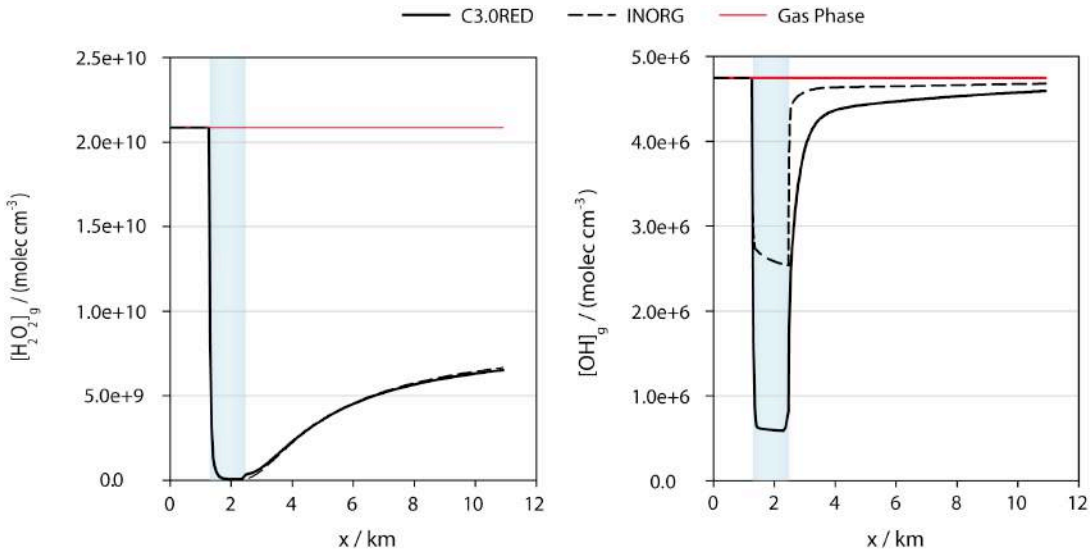

Figure 2. Simulated gas phase concentration of H_2O_2 and OH in urban environment at high noon for the stand-alone-version in molec cm^{-3}. The cloud passage is marked by the blue-shaded area.

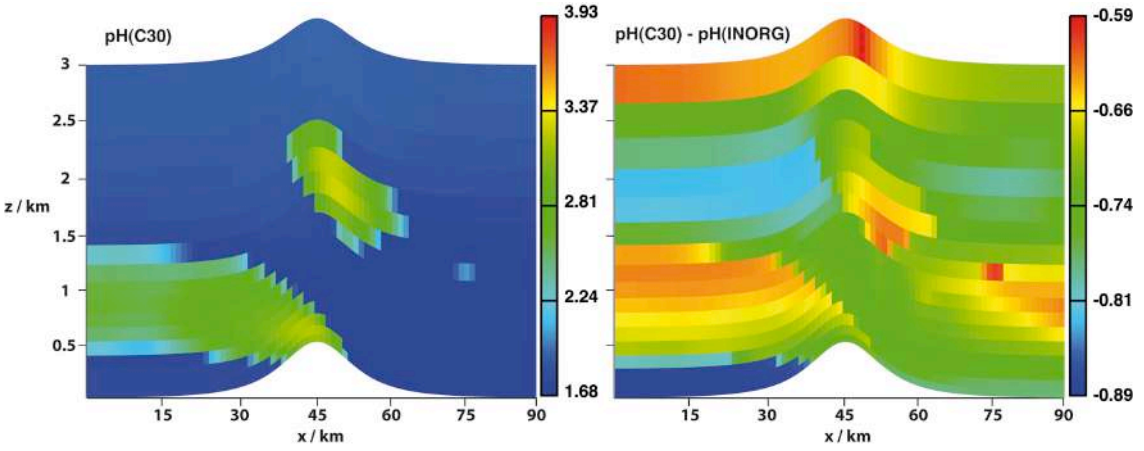

Figure 3. Simulated pH using C3.0RED and difference of pH between C3.0RED and INORG in the urban environment for the coupled model system at high noon.

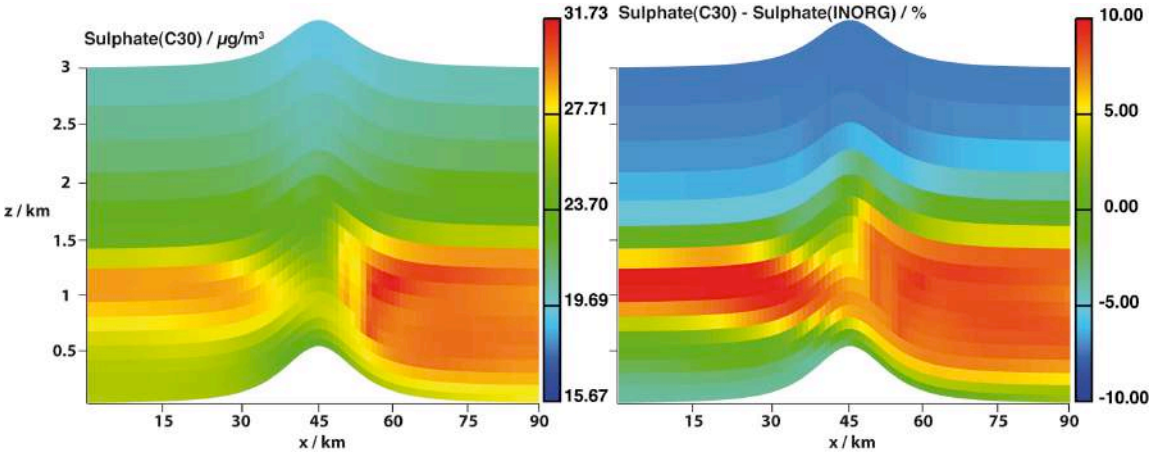

Figure 4. Simulated sulphate mass (µg m^{-3}) using C3.0RED and relative difference (%) of sulphate mass between C3.0RED and INORG in the urban environment for the coupled model system at midnight.

3. RESULTS AND DISCUSSION

For comparison of the chemical mechanisms, important chemical subsystems and parameters were investigated including e.g. major oxidants, the pH and sulphate. Due to the required minimum LWC differences for the gas phase between in-cloud and cloud-free area have not been investigated for the coupled model system. In Figure 2, plots of the gas phase concentrations of OH and H_2O_2 vs. the width of the model area in flow direction 1250 m above ground at high noon are presented in the urban environment for both aqueous phase mechanisms and a run without aqueous phase chemistry. All gas phase radical concentrations are depleted by about 90 % up to nearly 100 % during the cloud flow for the C3.0RED scenario in the urban environment. In the remote case, the reduction of radical concentrations is smaller (between 60 and 85 %). For INORG, there are higher radical concentrations in the gas phase (except for H_2O_2 in urban case). This is due to the fact, that their phase transfer and aqueous phase chemistry, especially the aqueous phase links between HO_x and H_2O_2 and transition metal ion chemistry, is not treated there. Thus, only shading effects and a reduced H_2O_2 concentration result in lower OH and HO_2 concentrations in the gas phase. After the cloud, new radicals are produced in the gas phase and are mixed by vertical diffusion. Even 8 km horizontally after the cloud, the concentration of OH and HO_2 are about 5-10% lower than in the pure gas phase run for both the urban and the remote environment for C3.0RED. In the INORG-scenarios, the gas phase concentration after the cloud is a little higher than computed using C3.0RED.

Hydrogen peroxide is strongly connected to OH and HO_2, highly soluble and an important S(IV) oxidant. Because a main target of INORG is the description of S(VI) production, both multiphase chemistry mechanisms result in similar H_2O_2 concentrations. The depletion in the gas phase in the cloud is 82% and nearly 100% for the remote and the urban environment, respectively. After the cloud, H_2O_2 is with a reduction of about 75% (urban) and 20% (remote) on a considerably lower level than in the pure gas phase run. This might be one explanation for the lower HO_x levels after the cloud.

In MUSCAT, the pH is calculated explicitly, i.e. the H+ concentration is calculated directly from the dissociation equilibria assuming electron neutrality conditions. The importance of pH is its ability to balance the aqueous phase equilibria. Consequently, in urban and remote cases, with different pH, other reaction paths might be of interest.

Figure 3 shows the pH for the urban environment in the coupled system (nearly same results for stand-alone-version) for C3.0RED. Additionally the difference between C3.0RED and INORG is plotted on the left of figure 3. The clouds with higher LWC have bigger droplets and hence higher pH. The average cloud pH for C3.0RED is about 2.8 and 5.5 in the urban and the remote environment, respectively. The INORG scenario is always less acidic. The average difference in pH between INORG and C3.0RED is 0.7 for the urban and 0.3 for the remote environment. This additional acidification using C3.0RED seems to be caused by the production of organic acids. The discrepancy in pH is slightly different in the stand-alone-version with higher differences for the remote scenario. An explanation cannot be given up to now, because reaction fluxes have not been observed, yet. Due to the differences in pH between C3.0RED and INORG, they result in different regimes for e.g. the S(IV)-oxidation.

In comparison to INORG, C3.0RED considers more reaction pathways to oxidize S(IV) to S(VI). Figure 4 shows the sulphate mass at midnight for C3.0RED for the urban scenario and the difference between C3.0RED and INORG. The structure of the clouds has not changed since high noon, but the sulphate production has flattened. As can be seen, in some areas C3.0RED produces more in other areas less sulphate compared to INORG (+/- 10 %). In the stand-alone-version, more sulphate was generally produced by INORG. However, these differences are smaller in the remote

environment. It can be expected that this is mostly due to shifts in the S(IV)-oxidation-regime caused by different cloud pH. But, also the minimum LWC restricts the interpretation of the simulated data. Future investigation of reaction fluxes will clarify these questions.

4. CONCLUSION

Aqueous phase chemical processes were implemented into the regional chemical transport model COSMO-MUSCAT. Test simulations were carried out in a stand-alone and a coupled model version. Treating realistic meteorological dynamics vs. prescribed meteorology leads to differences for investigated target species and parameters, such as pH and S(VI). Besides that, also the complexity of the aqueous phase chemistry is responsible for such differences. The more simple inorganic mechanism is always less acidic (up to +0.7 in pH) than the complex organic mechanism. That difference causes shifted chemical regimes for sub-mechanisms, which include dissociations, such as oxidation of S(IV) to S(VI). However, this shift in the S(IV)-oxidation is responsible for +/- 10% of total sulphate mass. No general difference occurs for sulphate between both observed mechanisms. Besides that, the behaviour of the major gas phase oxidants has been examined. When there is a cloud, gas phase concentrations of these species are depleted by 60 % up to 100 %, depending on the environmental conditions. For clean cases a bigger part of the oxidants remains in the gas phase. Interpretation of the data is difficult due to the complex chemistry and dynamical effects. Therefore, reaction studies will be investigated in the future work. Additionally, more sensitivity studies on chemical subsystems and numerical parameters will be conducted.

5. REFERENCES

Deguillaume, L., A. Tilgner, R. Schrodner, R. Wolke, N. Chaumerliac, and H. Herrmann, 2009. Towards an operational aqueous phase chemistry mechanism for regional chemistry-transport models: CAPRAM-RED and its application to the COSMO-MUSCAT model, J Atmos. Chem. 64, 1-35.

Ramanathan, V., P. J. Crutzen, J. T. Kiehl, and D. Rosenfeld, 2001. Atmosphere - Aerosols, climate, and the hydrological cycle. Science. 294, 2119-2124.

Schättler, U., G. Doms, and C. Schraff, 2008. A Description of the Nonhydrostatic Regional COSMO-Model Part VII: User's Guide, Deutscher Wetterdienst, Offenbach.

Sehili, A. M., R. Wolke, O. Knoth, M. Simmel, A. Tilgner, and H. Herrmann, 2005, Comparison of different model approaches for the simulation of multiphase processes. Atmospheric Environment. 39, 4403-4417

Tilgner, A. and H. Herrmann, 2010 Radical-driven carbonyl-to-acid conversion and acid degradation in tropospheric aqueous systems studied by CAPRAM. Atmospheric Environment, 44(40), 5415-5422

Wolke, R., O. Knoth, O. Hellmuth, W. Schröder, and E. Renner, 2004a. The parallel model system LM-MUSCAT for chemistry-transport simulations: Coupling scheme,parallelization and application, in Parallel computing: Software technology, algorithms, architectures and applications, pp. 363-370.

Effect of dilution on drop size distribution and rain formation

Thara Prabhakaran [1], Khain Alexander [2], Mark Pinsky[2], J. R. Kulkarni [1], B. N. Goswami [1]
[1]Indian Institute of Tropical Meteorology, Dr. Homi Bhabha road, India, Pune 411008, India
[2]The Hebrew University of Jerusalem, Department of Atmospheric Sciences, Jerusalem, Israel

Abstract: The relationship between the shape of droplet size distributions (DSD) and the level of cloud air dilution (measured as the adiabatic fraction) is investigated using observations obtained during the field experiment CAIPEEX in India. It is shown that nearly adiabatic cloudy volumes reach high levels till heights of 7 km. Dilution caused by entrainment and mixing leads to the formation of DSD with shapes nearly similar to those in adiabatic parcels, but with proportional decrease in liquid water content (LWC) and droplet concentration. As a result, the values of radii of DSD peaks as well as effective radii remain nearly unchanged along horizontal traverses in spite of strong changes in drop concentration. Largest droplets form in nearly adiabatic cloudy volumes containing the maximum LWC and drop concentration. It is hypothesized that these "lucky" volumes are the source of the first raindrops. This hypothesis allows explaining recently reported linear dependence of the height of first raindrop formation on droplet concentration.

1.Introduction

Observational (e.g. Rosenfeld and Gutman, 1994; Freud et. al., 2008; Freud et al, 2011; Prabha et al 2011) and numerical (e.g. Pinsky and Khain, 2002; Benmoshe et al 2012) studies show that rapid formation of raindrops in convective clouds begins when effective radius exceeds its threshold value ranged from about 11 to 15 μm depending on cloud type and droplet concentration. Freud and Rosenfeld (2011) found that dependence of the height of formation of first raindrops above cloud base nearly linearly increases with increasing droplet concentration. In simulations with the parcel model, the height of first rain drop formation was identified by the values of the mean volume radii corresponding to the threshold values of rain water mixing ratio. The linear dependence was found in observations for different environment conditions and in such different geographical locations as India and Israel. It suggests that this linear dependence (or nearly linear) is of general feature of deep convective clouds. Note that according to Freud and Rosenfeld (2011), the values of effective radii in developing cumulus clouds at the non-precipitating stage are close to the adiabatic values. Note that the nearly linear dependence of the distance above cloud base at which mean volume radius reaches its threshold value on drop concentration directly follows from the theory of diffusion drop growth in an ascending adiabatic parcel. Indeed, as Pinsky et al (2012) showed that the height of formation of first raindrops above cloud base D_p depends on droplet concentration at the cloud base supersaturation maximum as:

$$D_p \sim r_{v\_c}^3 N \qquad (1)$$

The linear dependence (1) is strictly valid within the range of heights of about ~1 km. At larger heights there is some deviation from the straight line because of temperature dependence of the proportionality coefficient on the thermodynamic parameters of air. In this study we address the question; "What is the role of entrainment and mixing in the formation of first raindrops?" by analyzing observational data during the Cloud Aerosol Interaction and Precipitation Enhancement Experiment (CAIPEEX).

Results of numerical simulations using spectral microphysics cloud model HUCM are presented to support observations.

2. CAIPEEX Observations

The details of measurements during CAIPEEX and instruments used are presented by Prabha et al (2011) and Kulkarni et al (2012) In the present study we used 11 observations of clouds in the very high polluted super continental conditions during premonsoon (especially in May) to the cleaner conditions during monsoon (June to September). Observations carried out over Pathankot (32.28 ^{o}N, 75.65 ^{o}E) on 24 and 28 May, Hyderabad (17.45 ^{o}N, 78.46 ^{o}E) 15-17 June, 20-22 June and Bareilly (28.22 ^{o}N, 79.27 ^{o}E) during 23-28 August are used. Over Hyderabad and over Bareilly observations are taken during the polluted dry conditions to the relatively cleaner and wet monsoon conditions. 22 June and 28 August showed cleaner conditions above the boundary layer. The cloud droplet probe (CDP; Droplet Measurement Technologies DMT) were used for cloud droplet size distributions in 30 bins between 2 and 50 µm, and derived parameters include liquid water content (LWC), droplet effective radius, cloud droplet number concentrations (CDNC), mean volume radius, etc. Aircraft Integrated Meteorological Measurement System **(**AIMMS) is used to register air temperature, relative humidity, and winds. Cloud condensation nuclei (CCN) concentration is measured using DMT CCN counter and necessary pressure corrections were applied. The subcloud observations of CCN were carried out with three (0.2%, 0.4% and 0.6 %) supersaturation settings. Passive Cavity Aerosol Spectrometer Probe (PCASP) is used for aerosol measurements (size distribution, effective radius and concentration). Aerosol data is considered only outside of clouds (cloud droplet number concentration; CDNC < 10 cm^{-3}) and are averaged for every 100 m level. All measurements are carried out at 1 Hz sampling frequency, i.e., averaged over approximately 100 m of horizontal distance. Cloud microphysics data during both ascent and descent through single deep convective clouds are used for the present analysis.

Results and discussion

Figure 1 shows the fraction of slightly diluted parcels (ADF>0.7) with height at each 200 m height intervals in the 11 cases from CAIPEEX. In the monsoon cloud of 22 June (fitted line) we may note some increase in the percentage of slightly diluted parcels with height. This increase is supposedly related to full dissipation of the smallest highly diluted cloud volumes. These observations suggest that there is at least up to 30-40 % of slightly diluted parcels in these cumulus clouds.

Figure 2 shows droplet concentration - mean volume radius relationships for air volumes with ADF > 0.7. Data is presented from 11 different cloud observations during CAIPEEX. These observations are taken from highly polluted conditions to the cleaner monsoon conditions during CAIPEEX.

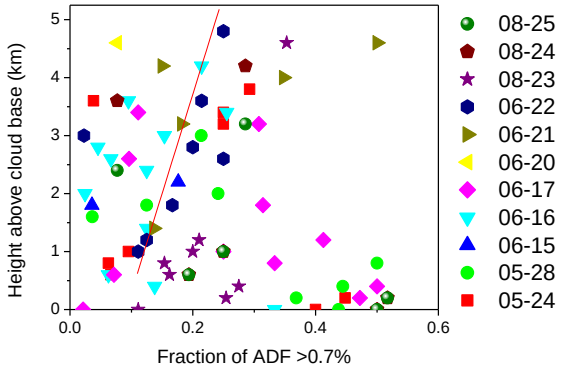

Figure 1. Fractional occurrence of less diluted cloudy parcels with height above cloud base

Accordingly, results of all flights combined together indicate that in these volumes droplet mass depends inversely on droplet concentration as in adiabatic parcels ascending from cloud base with different droplet concentrations. Thus, among a great number of diluted air volumes, there are slightly diluted volumes that indicate the behavior typical of adiabatic parcels ascending from cloud base. Based on these results, one may characterize three different

regimes in the data, one with highly polluted pre-monsoon cases with $r_v^3 < 500\ \mu m^3$, the polluted and the relatively clean cases with higher r_v^3.

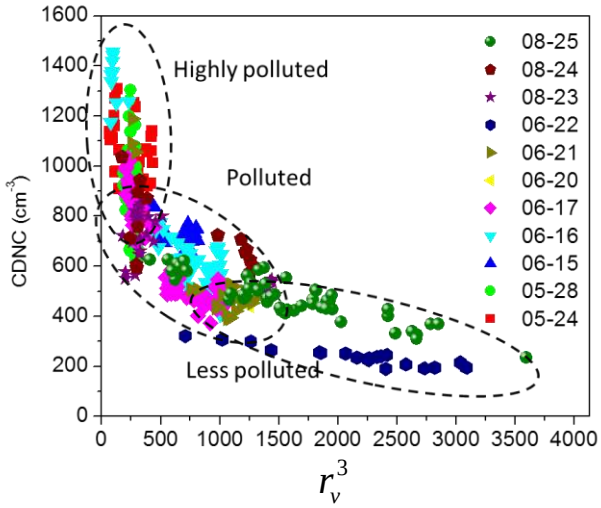

Figure 2. Relationship between cloud droplet number concentration (CDNC) and mean volume radius of highly polluted, polluted and less polluted conditions (legend shows date mm-dd) under conditions of ADF >0.7 %, excluding cloud base to 1 km above cloud base observations.

Figure 3 illustrates the relationship between the concentration of small (diameter less than 20 µm) droplets and the minimal diameter of 10 largest droplets (D10) as measured at the tail of DSD. All cloud base data has been screened out from this analysis. The color map used is for the ADF. Figure shows different types of clouds, in the top panel premonsoon polluted, transition to monsoon observed in the Peninsular India. On the bottom panel, observations from the Himalayan foothills region with premonsoon cloud, transition to monsoon are presented. Several points may be noted; D10 and concentration of small droplets is high in the cloud volumes with high ADF. It may be noted that the DSDs in slightly diluted parcels contain larger number of smallest cloud droplets and have high D10 (large droplets at the tail of DSD). It is reasonable to assume that dilution (low adiabatic fraction; ADF) decreases concentration of small droplets by evaporation, which is prevalent in both the premonsoon and monsoon clouds. The decrease in concentration is not taking place in all cases, but in general, dilution is accompanied by decrease in concentration. It may also be noted that maximum dilution corresponds to minimum droplet concentration. For instance, in premonsoon case (Figure 3d), all parcels with CDNC <500 cm^{-3} are diluted. It is reasonable to suppose that the minimum diameter of 10 largest drops characterizes the tail of largest droplets. The larger the minimum diameter, the longer the tail. Figure 3c (monsoon) shows that DSD in parcels with very low concentrations contain only large droplets: indeed if CDNC =10 cm^{-3}, all drops are large. These droplets may fall down by sedimentation like drizzle fall below cloud base through much diluted air.

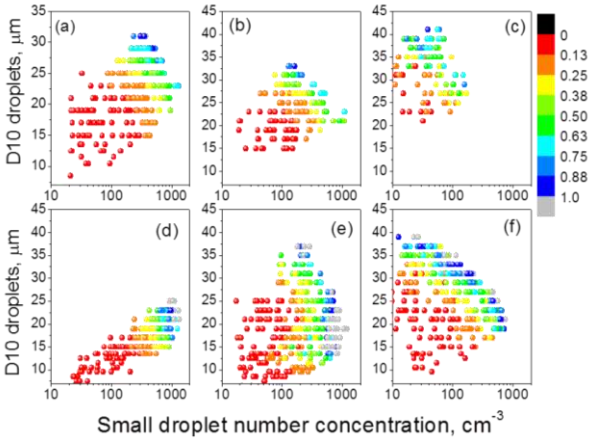

Figure 3. The relationship between minimum diameter of the 10 largest droplets in the DSD as measured in situ in premonsoon (a; 16 June), transition (b; 21 June), monsoon (c; 22 June), highly polluted premonsoon (d; 24 May), polluted monsoon (e; 23 August) and clean monsoon (f; 25 August) . Color scale indicates value of adiabatic fraction: blue circles indicate low diluted volumes; red circles indicate highly diluted volumes.

At higher droplet concentration DSD are narrower and D10 is small as the tail is shorter. Diluted volumes do not contain large drops. The tail is the largest (i.e. DSD has a long tail) only in weakly diluted volumes (50%) or even 90% of adiabatic value. So,

one can expect that the first raindrops form in these non-diluted parcels. For instance, at concentration of about 80 cm^{-3}, the largest droplets exceed 40 μm in diameter. It seems to be natural that the increase in concentration to 700 cm^{-3} (in non-diluted volumes) leads to the decrease in the size of the largest droplets to 20-25 μm in diameter. Low concentration means strong dilution and evaporation of droplets. As a result, maximum droplet diameters in diluted parcels are low. Non-diluted cloudy volumes (close to adiabatic ones) have larger LWC and no evaporation of droplets takes place. It leads to the fact that namely in these parcels droplets reach larger radii.

We used 2-D Hebrew University Cloud Model (HUCM) with grid spacing of 50 m to simulate deep mixed-phase convective clouds with characteristics similar to those in CAIPEEX 22 June. The model microphysics is based on equation system for size distribution functions for water drops, three types of ice crystals, aggregates, graupel and hail. Each size distribution is defined on mass grid containing 43 bins with doubling mass from one bin to the next one. Size distribution of aerosols (CCN) contains 43 bins with maximum radius of dry CCN of 2 μm. Turbulence is characterized by values of dissipation rate and the Taylor microscale Reynolds number. These parameters are calculated in course of model integration. Using these parameters, look-up tables of turbulent induced collision enhancement factors are applied to take into account effect of turbulence on collisions of cloud droplets. The detailed description of the model is presented in Benmoshe et al (2012).

Figure 4 shows fields of CWC, RWC, dissipation rate and mean volume radius near the top of developing convective cloud. Zone of cloud top contains three turrets. The mean volume radius reaches ≈9 μm in tops of the bubbles. Effective radius is equal to 9.8 μm at this height, which is in agreement with the observations in premonsoon clouds (Prahba et al 2011). Note that ratio $r_{eff} / r_v \approx 1.08 - 1.1$ in the model simulations coincides with the

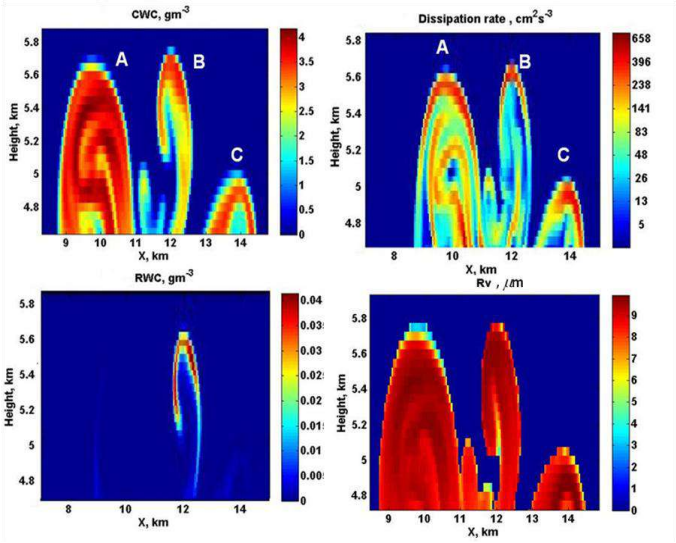

result of analysis of *in-situ* measurements

Figure 4. Fields of CWC, RWC, dissipation rate and mean volume radius near the top of the developing convective cloud simulated using HUCM.

(Freud and Rosenfeld 2011). Supplemental simulations of deep convective clouds under different aerosol conditions showed that this relationship between mean volume and effective radius is valid in deep cumulus clouds under wide range of aerosol loading.

First raindrops form near the top of decaying bubble B where high LWC is accompanied by enhanced turbulence. This result agrees well with that reported by Benmoshe et al (2012) where the formation of first rain drops in turbulent clouds was investigated in detail. Analysis of the structure of turrets shows that at the developing stage the turrets contain slightly diluted cores with LWC of ~3.5-4 gm^{-3} in the tops of these cores which reasonably agrees with the observations. In Fig. 4 turret A is developing, while turret B is decaying. The analysis of the history of formation and evolution of bubbles A, B and C shows that all bubbles begin developing from the same stream that starts developing from the cloud base. This stream then is separated giving raise to formation of

different bubbles (plumes, jets). The existence of the common source leads to the effect that in each bubble (especially near top of the ascending bubbles) contains large CWC comparatively close to adiabatic value. Bubble B develops first and the first raindrops are produced in the top of this bubble. First raindrops form in slightly diluted core near the top of developing turret A few minutes later (not shown) . After forming near cloud top, first rain drops spread along the edges of the bubbles where downdrafts take place. Thus, numerical simulations show that first raindrops form in slightly diluted zones near tops of turrets where turbulence is most intense and CWC is maximum. Since these zones are diluted only slightly, the drop concentration in these zones is larger than in the adjacent zones with lower CWC, but with the same mean volume or effective radii.

The value of mean radius (or effective radius) alone cannot determine the rain drop formation. Indeed, at low cloud water content (CWC) and low droplet concentrations formation of raindrops by collisions is hardly possible. Thus, the formation of drop size distribution with r_{eff} (or r_v) equal or exceeding their threshold values is necessary, *but not a sufficient condition* for raindrop formation. As shown by Freud and Rosenfeld (2011) collision kernel is proportional to $r_{eff}^{4.8}$. As follows from the stochastic collision equation, the collision rate is proportional to the product of collision kernel and square of droplet concentration. Taking into account that r_{eff} is nearly constant along the horizontal traverses (i.e. collision kernel is nearly the same), is natural to assume that efficient collisions with the first rain drops formation take place in air volumes with the maximum droplet concentration, i.e. with maximum CWC. Note that the role of CWC in rain formation is well recognized and used in many bulk parameterization schemes, where the rate of rain drop formation is proportional to CWC (e.g., Kessler 1969). This assumption means that first raindrops should form in the undiluted or slightly diluted volumes.

First raindrops form in a comparatively small number of "lucky" cloudy volumes (illustrated in Figure 3 from observations), several questions concerning the role of entrainment and mixing between cloudy and environment air should be addressed. Indeed, Figures 3 indicate that in the cloud experiencing mixing with environment, the largest droplets form in parcels with higher droplet concentration, which contradicts to the classical concept of aerosol effects on raindrop formation. The "classical" dependence of raindrop formation on aerosol concentration can be seen only by comparison of DSDs between undiluted (or between slightly diluted) volumes. The obvious validity of classical concept means that mixing and entrainment play, supposedly, a secondary role in the formation of first raindrops.

References

Benmoshe, N., M. Pinsky, A. Pokrovsky, and A. Khain (2012), Turbulent effects on the microphysics and initiation of warm rain in deep convective clouds: 2-D simulations by a spectral mixed-phase microphysics cloud model, J. Geophys. Res., 117, D06220, doi:10.1029/2011JD016603.

Freud, E., D. Rosenfeld, M. O. Andreae, A. A. Costa, and P. Artaxo, 2008: Robust relations between CCN and the vertical evolution of cloud drop size distribution in deep convective clouds. Atmos. Chem. Phys., 8, 1661–1675, 2008.

Freud E., D. Rosenfeld, D. Axisa, and J. R. Kulkarni, 2011: Resolving both entrainment-mixing and number of activated CCN in deep convective clouds. Atmos. Chem. Phys. Discuss., 11, 9673-9703

Freud, E., and D. Rosenfeld (2012), Linear relation between convective cloud drop number concentration and depth for rain initiation, J. Geophys. Res., 117, D02207, doi:10.1029/2011JD016457.

Kulkarni J.R., Maheshkumar R. S., Morwal S. B. , Padma kumari B., Konwar M., Deshpande C. G., Joshi R. R. , Bhalwankar R. V., Pandithurai, Safai P. D., Narkhedkar S. G., Dani K.K., Nath A., Sathy Nair, Sapre V.V., Puranik P. V., Kandalgaonkar S.S., Mujumdar V.R., Khaladkar R.M., Vijaykumar R., Prabha T.V. and Goswami B.N. (2012), Cloud Aerosol Interaction and Precipitation Enhancement Experiment (CAIPEEX): overview and preliminary results, Current Science, 102, February 2012, 413-425

Pinsky, M. and A. P. Khain, 2002: Effects of in-cloud nucleation and turbulence on droplet spectrum formation in cumulus clouds. Quart. J. Roy. Meteorol. Soc., 128, 1–33.

Pinsky M., I.P. Mazin, A. Korolev, and A. Khain, 2012: On the theory of cloud droplet diffusion growth, J. Atmos. Sci. (in revision)

Prabha, Thara V., A. Khain, R. S. Maheshkumar, G. Pandithurai, J. R. Kulkarni, M. Konwar, B. N. Goswami, 2011: Microphysics of Premonsoon and Monsoon Clouds as Seen from In Situ Measurements during the Cloud Aerosol Interaction and Precipitation Enhancement Experiment (CAIPEEX). J. Atmos. Sci., 68, 1882–1901.

Rosenfeld D. and G. Gutman, 1994: Retrieving microphysical properties near the tops of potential rain clouds by multispectral analysis of AVHRR data. Atmos. Res, **34**, 259-283.

Acknowledgement

The CAIPEEX project and IITM are fully funded by Ministry of Earth Sciences, Government of India, New Delhi. This research was supported by the Office of Science (BER), US Department of Energy Award DE-SC0006788 and the Binational US-Israel Science Foundation (grant 2010446). Authors acknowledge with gratitude that several scientists at IITM, their team effort and dedication made CAIPEEX a grand success.

Vertical oscillations in monsoon clouds during CAIPEEX and the origin of small droplets

Thara Prabhakaran 1, Alexander Khain 2, G. Pandithurai 1, J R Kulkarni 1, B N Goswami 1
1IITM, Dr. Homi Bhabha road, India, Pune 411008, India
2The Hebrew, University of Jerusalem, Department of Atmospheric Sciences, Jerusalem, Israel

Abstract: Cloud Aerosol and Precipitation Enhancement Experiment was conducted during 2009-2011 over the Indian subcontinent. Instrumented aircraft observations of cloud microphysics inside shallow and deep continental cumuli were conducted over different regions and with varying aerosol pollution. Significant downdrafts (with velocities exceeding 10 ms-1) were found to be a common feature of the deep convective clouds. The drop spectrum evolution in the monsoon clouds showed characteristics of well mixed conditions with lower adiabatic fraction compared to the premonsoon conditions. There are less mixed regions, close to adiabatic regions inside these monsoon clouds, which showed small droplets and bimodal spectra. The drop spectrum evolution in these regions is investigated with the help of quasi-steady supersaturation. Liquid water within these clouds was highly variable at any specific level.

Droplet size distributions in updrafts and downdrafts are compared. Droplets in the downdraft regions were found to be larger than those in the updraft regions. Among the possible mechanisms are: drop collisions and preferable settling of raindrops in cloud downdrafts. Another mechanism can be related to non-reversibility of diffusion/evaporation process during cloud volumes oscillation as suggested theoretically by Pinsky et al (2011).

Introduction: Typically, drop spectrum distribution (DSD) broadening has been explained by incloud nucleation. Mixing with environment was usually considered as the mechanism of decreasing droplet concentration. But in principle, it can lead to appearance of small droplets as a result of partial evaporation. The vertical oscillations represent another mechanism of DSD formation. Several of the seminal writings of Telford (Telford 1999; Telford and Chai, 1980; Telford and Wagner 1980; Telford and Wagner 1981; Telford et al., 1984) illustrated that such oscillations exist and considered those oscillations as a very important mechanism of DSD broadening. In these studies This mechanism was argued to be much more efficient as regards DSD broadening than "inhomogeneous" mixing. However, Telford supposed that air in downdrafts begins its sinking from cloud top with dry conditions above. According to Telford, the mixing and evaporation of droplets penetrated from the lateral boundaries to dry descending air lead to cooling and to further acceleration downward.

Telford and Wagner (1980) showed how mixing of dry air from cloud top may lead to oscillations inside the cloud through ‘cycling of the air up and down in the cloud’, leading to depletion of cloud liquid water mixing ratio as droplets of all sizes are influenced. They proposed that mechanism can further lead to the formation of large drops as the particles ascent in the updrafts. The changes in the DSD in such a case are less influenced by CCN, where they say that ‘maritime like DSD form in the continental cumuli’. We analyze two different deep convective clouds observed during the monsoon conditions with contrasting CCN concentrations and moisture conditions.

Data and methods: The unique cloud microphysical observations of continental deep convective clouds over the Indian subcontinent during the Cloud Aerosol Interaction and Precipitation Enhancement Experiment (CAIPEEX) are used in this study. CAIPEEX was conducted in two phases during 2009-2011. The experiment mainly focused the continental clouds during the monsoon season (June to September). Instruments and other details are presented by Prabha et al (2011) and Kulkarni et al (2012). The cloud droplet probe (CDP; Droplet Measurement Technologies DMT) were used for cloud droplet size distributions in 30 bins between 2 and 50 µm, and derived parameters include liquid water content (LWC), droplet effective radius, cloud droplet number concentrations (CDNC), etc. Aircraft Integrated Meteorological Measurement System **(**AIMMS) is used to register air temperature, relative humidity, and winds. Cloud condensation nuclei (CCN) concentration using DMT CCN counter (at 0.2, 0.4 and 0.6 % supersaturation cycles) and aerosol concentration with DMT Passive Cavity Aerosol Spectrometer Probe (PCASP) were also measured. Supersaturation inside the cloud is not directly measured. We found quasi-steady supersaturation based on Squires (1952) and Korolev and Mazin (2003) in the horizontal cloud passes at several heights to illustrate the associated changes in the drop size distributions.

Case studies: Cloud microphysics and AIMMS data during both ascent and descent through single deep convective clouds on horizontal transect at different heights are used for the present analysis. Two different cases from monsoon are considered, where 22nd June is a case from peninsular India after the monsoon onset over that region and 25th August case is over the Ganges Valley during the monsoon. The cloud base for 22nd June is 1950 m and for 25th August is 730 m. The cloud base droplet number concentration is 64±45 and 232±180 cm^{-3} and subcloud CCN concentration at 0.4% supersaturation is 469±133 and 2252±882 cm^{-3} respectively for the June and August case. The CCN estimated from the observed CCN spectra at 1% supersaturation for the two cases are 1655 and 4668 cm^{-3} and slope of CCN spectra (k parameter in the relation $N_{CCN}=N_oS^k$) are 1.028 and 0.57. Both cases have moist and polluted boundary layer. The boundary layer water vapor mixing ratio was 13.5 gkg^{-1} and 20 gkg^{-1}, respectively for the two cases. Both cases are characterized by large-scale moisture transport associated with the monsoon flow over the region. Precipitable water in the 22nd June case is 4.4 cm and for 25th August is 5 cm.

Results

Vertical velocity and adiabatic fraction**:** In Figure 1 we examine the near horizontal cloud passes at different heights in two of the monsoon clouds discussed earlier. Vertical velocity (Figure 1a color contour) for 22nd June shows that there are alternating regions in the cloud pass with updrafts and downdrafts which mimic the oscillatory nature described in Telford and Wagner (1980). This is seen throughout the cloud body, while the downdrafts are noted at the cloud top, they became stronger (up to -12 ms^{-1}) in the middle part of the cloud at 4.7 km (-1^oC). It is to be noted that updrafts are weaker than the downdrafts, more so for the adiabatic regions of the cloud. In the warm part of the cloud, updrafts and downdrafts are of similar magnitude in a horizontal transect (see for example in Figure 1a at 3.7 km). The downdrafts are also noted down to 2.4 km, but the origin of these downdrafts could not discerned. More adiabatic region (indicated by adiabatic fraction (ADF); contour line in Figure 1a) of the cloud is close to the centerline. The liquid water content in this region exceeded 2 gm^{-3} and effective radius was above 13 µm (Figure 2a).

In Figure 1b, the vertical velocity (with color contours) and ADF (contour line) for the 25 August case is presented. The downdrafts are not widespread in this case and are seen especially in the cold regions of the cloud.

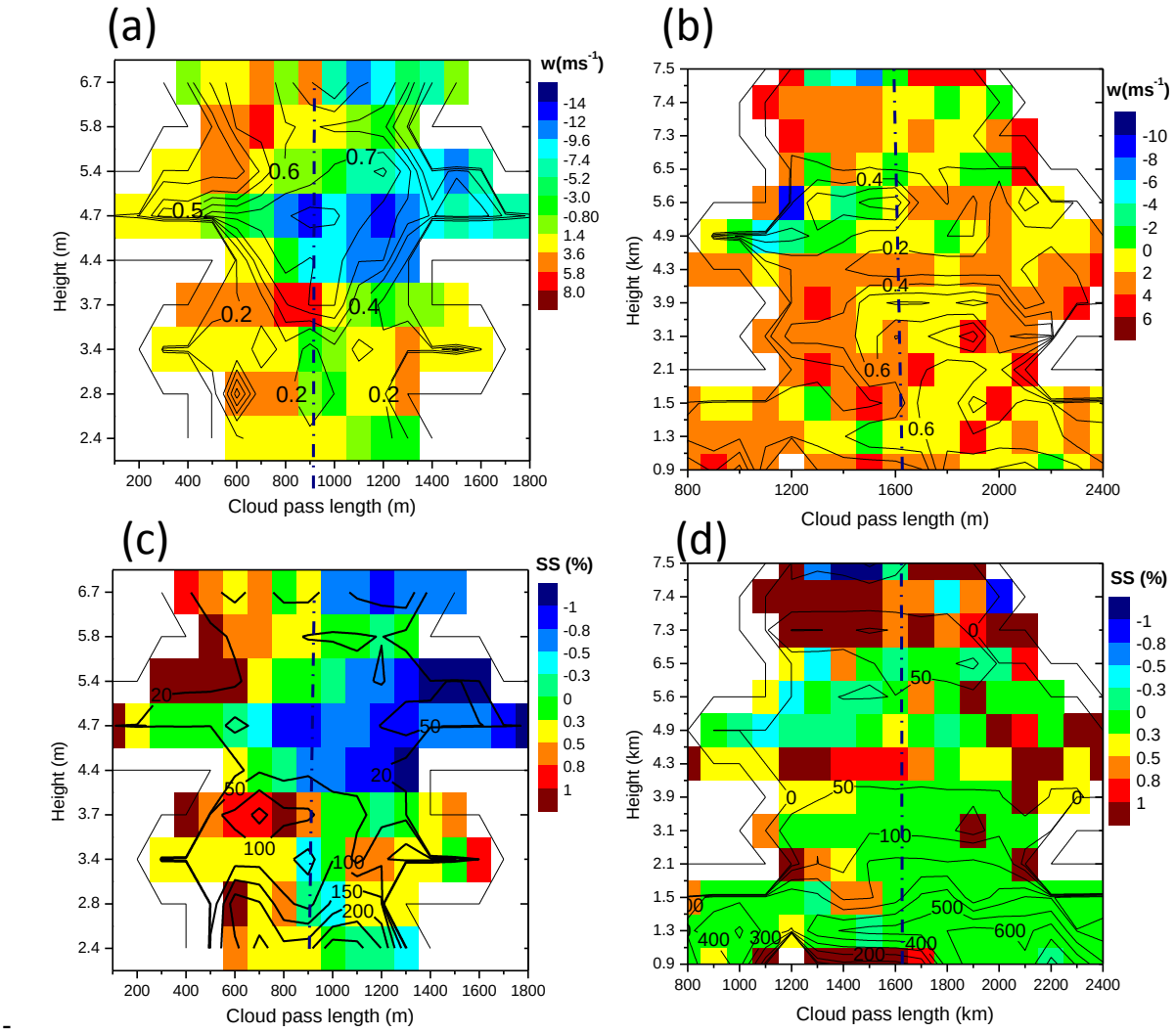

Figure 1. Incloud vertical velocity along horizontal cloud pass lengths inside monsoon cloud of 22nd June over peninsular India (a) and 25th August 2009 (b) over Ganges valley and quasi-steady supersaturation (c and d respectively) at different heights. Vertical (dash-dotted) line is approximate center of the cloud penetration. In (a) and (b), color contours are vertical velocity and black contour lines are adiabatic fraction (ADF). In (c) and (d) color contours are supersatuation and contour lines are for small droplet number concentration (<20 μm).

Aerosol effects seem to dominate in the warm region of the cloud with higher droplet concentrations. Updrafts dominate in the warm regions (2.1-4.3 km except for a few occasions below 2.1 km). The downdrafts are prevalent in the upper part of the cloud, also they are more concentrated in the adiabatic regions of the cloud. Unlike in the 22nd June case, the cloud is slightly more diluted and the gradient in ADF is not strong at the boundaries. The lowest 3.9 km is more adiabatic than the 22nd June case. The cloud base is shallow and high concentration of large droplets is formed at a low level, leading to the increase in the LWC (Figure 2b). The high aerosol/CCN concentration in

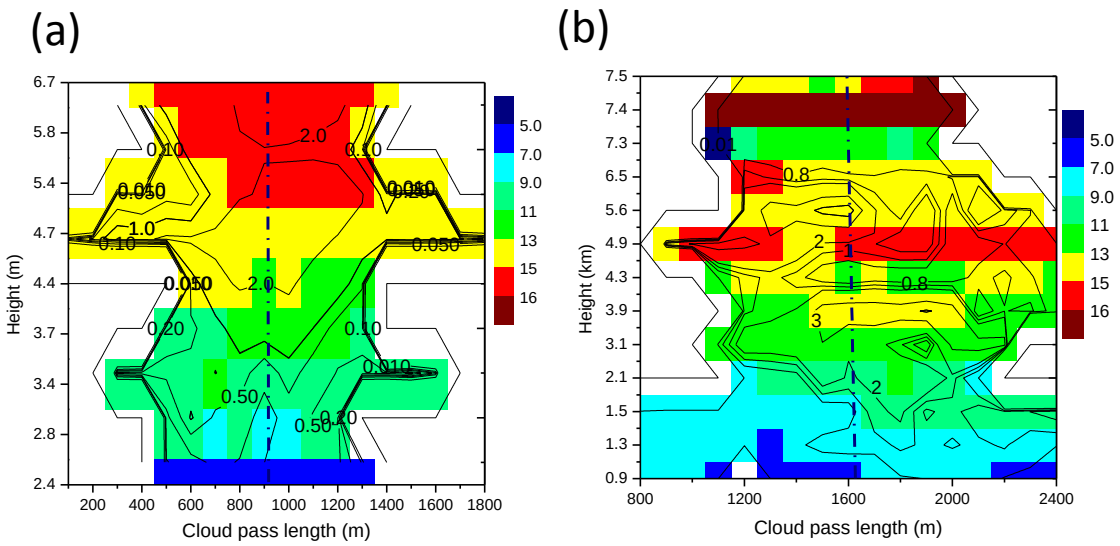

Figure 2 Cloud droplet effective radius (in color contours) and Liquid water content (in contour line) are indicated for 22nd June (a) and 25th August (b) case.

this case explains higher droplet concentrations; meanwhile the depth of the layer where larger droplets are observed is also related high moisture content in the boundary layer and to the low cloud base.

Quasi-steady supersaturation and small droplet number concentration: The quasi-steady supersaturation (color contour) and the number concentration of small droplets (contour line) showed in Figure 1c and 1d for 22nd June and 25 August indicates high concentration of small droplets in the supersaturated regions. In the 22nd June case, it may be noted especially at 3.7 km (6 ^{o}C) and 5.8 km (-6 ^{o}C) levels, indicating the incloud nucleation as illustrated in Prabha et al (2011). In the 25th August case, high supersaturation is more wide spread and that may also indicate isolated peaks in small droplet concentration at several places close to the center of cloud penetrations.

Large droplet concentration and drop diameter of DSD peak: Largest droplets are noted in more adiabatic regions of the cloud (Figure 3). This is in contrast to the findings of Blyth and Lantham (1985). They showed from aircraft observations that '*breadth of the DSD and the size of largest droplets in the spectrum were not systematically related to the degree of dilution'*. We note that concentration of largest droplets (Figure 3a for 22nd June and Figure 3b for 25 July case) indeed occur at locations where adiabatic fraction is high (Figure 1a and Figure 1b contour lines) for respective cases. This indicated that external dry air mixing did not affect the growth of cloud droplets in these clouds significantly. The entrainment mixing of dry air was pertained to the cloud lateral boundaries, where there are strong gradients in the ADF.

What mechanisms give rise to high concentrations of large droplets in the almost adiabatic supersaturated as well as subsaturated regions (negative supersaturation)? First probable mechanism is collisions of droplets in updrafts and successive downdrafts in the course of oscillations. Such mechanism was analyzed by Magaritz et al (2009, 2010) in parcel oscillations in stratocumulus clouds.

Second possible mechanism is related to process of diffusion growth/evaporation in

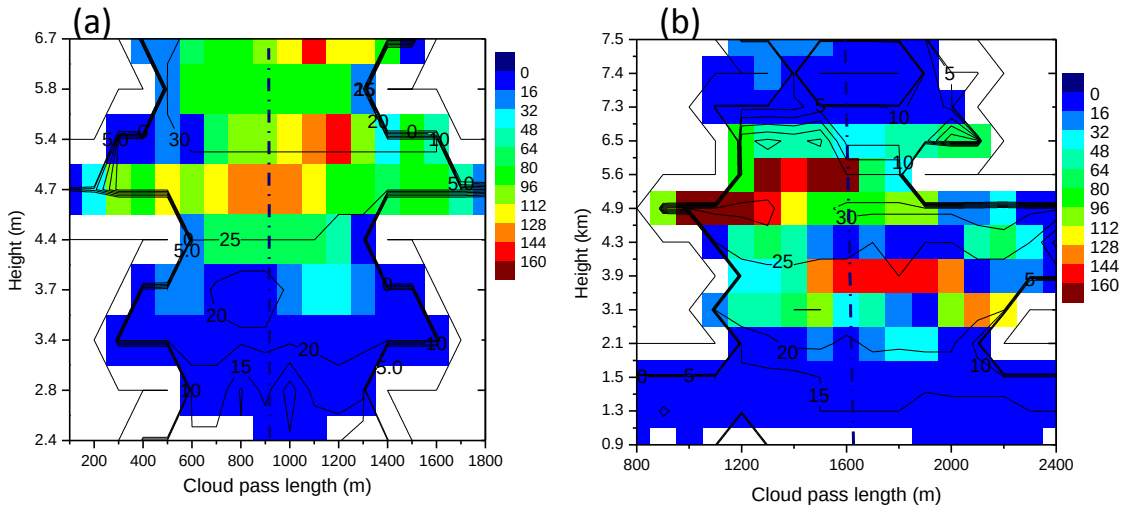

Figure 3 The concentration of cloud droplets in the 27-49 μm bins (in color contours) and the drop size in DSD peak (in contour line) are indicated for 22nd June (a) and 25th August (b) case.

oscillating adiabatic parcels. Pinsky et al (2011) showed that in vertically oscillating adiabatic parcels drop size during subsidence is a few μm larger than at the ascending branch of parcel track. The difference in drop size increases with increase in the difference in vertical velocities and toward the cloud base. Korolev et al (2012) showed that incloud mixing between DSD in descending and ascending branches may lead to efficient formation of large droplets. DSDs measured in updrafts and downdrafts at 5.4 km from 22nd June are shown in Figure 4.

Figure 4 shows a sample of horizontal flight pass through the convective cloud at 2 km above cloud base. The vertical velocity sampled with AIMMS probe at 1 Hz sampling interval, temperature, CDP effective radius and estimated quasi-steady supersaturation are shown. Droplet spectrum distribution (DSD) is also shown for the selected periods of updrafts and downdrafts. The DSD in the downdrafts show a bimodal distribution with 8 and 30 μm peaks. In the updraft region all sized droplets are noted between this bins showed higher droplet concentration compared to those in the downdrafts.

Note first that DSDs in updrafts and in downdrafts are quite similar. In both zones the DSD peaks are located at drop diameter of 31 μm (see also Figure 3a). In both zones CWC is linearly proportional to droplet concentration (Figure 5). Low statistics does not allow distinguishing the slopes in the relationships in updrafts and downdrafts. It seems that DSD in downdrafts contains larger mass of largest droplets. Figures 4 and 5 show that volumes with lower rate of dilution (i.e. larger droplet concentration) have larger LWC. The DSDs in such slightly diluted volumes are favorable for rain drop formation. The similarity of DSD shapes in updrafts and downdrafts and a similar rate of dilution (adiabatic fraction) (seen also from similarity of mean volume radii) suggests that the observed oscillations are incloud ones, so that downdrafts do not contain extra environment air as compared to updrafts.

The main difference in the DSD shapes in updrafts and downdrafts is in size range of small droplets. DSD in the updraft region contain a lot of small droplets forming, probably, due to incloud nucleation (see Prabha et al 2011 for more detail). Diffusion growth leading to faster growth of smaller droplets leads to formation of long smoothed tail in small droplet size range. The updraft region may also contribute some droplets that are freshly nucleated. While in the downdrafts there appears to be partial/total

evaporation of droplets that leads to formation of peak with radius lower than 20 μm. These droplets can be just haze particles. The effective radius changed very little (small increase) in these downdraft regions. One important aspect to note that large (27-49 μm bins) droplet concentration increased in this region (see Figure 3a), indicating that large-large droplet collisions were more important.

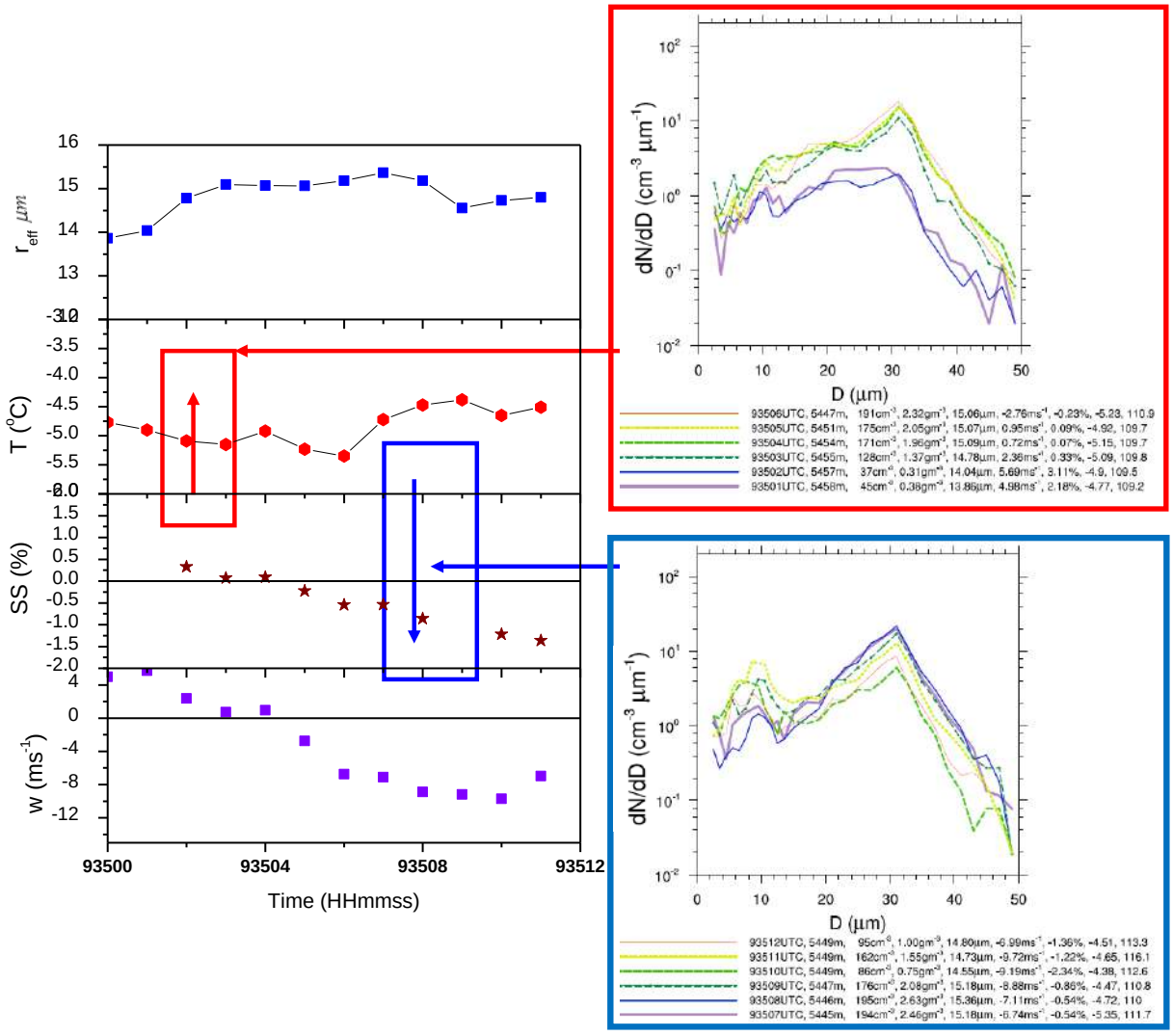

Figure 4. The variation of vertical velocity, quasi-steady supersaturation, temperature and effective radius during a horizontal pass at 5.4 km. The drop spectrum distribution (DSD) in the updraft and downdraft regions are shown on the right. The time, flight altitude, droplet concentration, LWC, effective radius, vertical velocity, the quasi-steady supersaturation, temperature (°C) and relative humidity (%) along aircraft traverses are presented in the right panel.

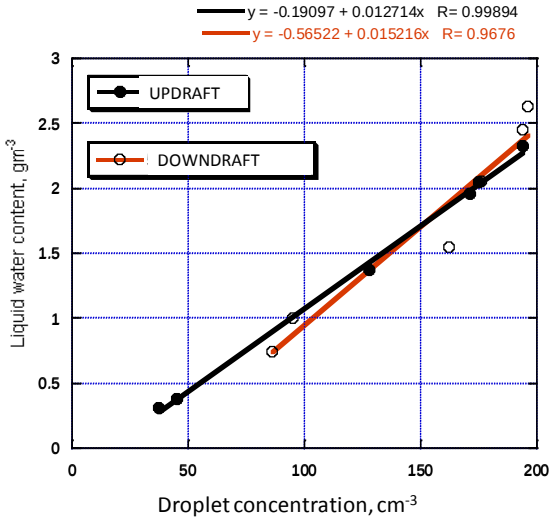

Figure 5. Relationships between LWC and concentration in updraft (black line) and downdrafts (red line).

Discussion and Conclusions

The unique measurements performed during the CAIPEEX allowed answer several important longstanding questions and to find new features in microphysical and dynamical structure of in deep convective clouds.

First, it was found that such clouds contain cores in which cloudy air is diluted only slightly. It was found that namely in these slightly diluted volumes contain the widest DSD with the largest LWC and droplet concentration.

Second, it was found that deep convective cloud contains zones of cloud downdrafts with air velocities that can exceed those in updrafts. These downdrafts were observed all over the clouds including the cloud core. Significant similarity in DSDs in updrafts and downdrafts was revealed. These DSDs are centered at the same drop size, in both zones LWC and droplet concentration are linearly related; and slopes of these relationships are close. The rates of dilution (adiabatic fraction) are also similar. DSDs in downdrafts contain, possibly, little more large droplets that can be explained by droplet collisions and by the non-reversibility of diffusion growth and evaporation in oscillating air volumes. Such similarity in DSDs allows us to suggest that downdrafts represent part of process of vertical oscillations of large air masses within clouds. Similar adiabatic fractions in updrafts and downdrafts suggest that downdrafts do not involve more surrounding air via entrainment than updrafts. This finding does not agree with the concept of downdraft formation proposed by Telford who assumed that downdrafts arise as a result of evaporation of droplets penetrating dry air volumes entrained the cloud through the cloud top. Mechanisms leading to downdrafts observed in the CAIPEEX require further investigation.

The role of downdrafts in the DSD broadening also requires special investigation. One can expect that downdrafts transport large drops toward cloud base. In case these downdrafts are replaced by updrafts, the large droplets will continue to grow, contributing to rain formation, and supposedly to formation of graupel. In studies by Telford important role of oscillations in clouds for rain formation was stressed.

Note also that downdrafts decrease the cloud averaged vertical mass flux. It is well known that mass flux in clouds is the main parameter to be calculated in the schemes of convection parameterization. It seems that dynamical and microphysical effects of downdrafts should be taken into account in cloud and large scale models.

References

Korolev, A. V., and I. Mazin, 2003: Supersaturation of water vapor in clouds. J. Atmos. Sci., 60, 2957–2974.

Korolev A.V, M. Pinsky, and A.P. Khain, 2012. A new mechanism of droplet size spectra broadening during diffusional growth. Extended abstract. 16-th Conference on Clouds and Precipitation,Leipzig,2012.

Kulkarni J.R., Maheshkumar R. S., Morwal S. B. , Padma kumari B., Konwar M., Deshpande C. G., Joshi R. R. , Bhalwankar R. V., Pandithurai, Safai P. D., Narkhedkar S. G., Dani K.K., Nath A., Sathy Nair, Sapre V.V., Puranik P. V., Kandalgaonkar S.S., Mujumdar V.R., Khaladkar R.M., Vijaykumar R., Prabha T.V. and Goswami B.N. (2012), Cloud Aerosol Interaction and Precipitation Enhancement Experiment (CAIPEEX): overview and preliminary results, Current Science, 102, February 2012, 413-425

Magaritz, L., M. Pinsky, Khain, A. P., O. Krasnov, 2009: Investigation of droplet size distributions and drizzle formation using a new trajectory ensemble model. Part 2: lucky parcels in non-mixing limit*. J. Atmos. Sci., 66,* 781–805

Magaritz L., M. Pinsky and Khain, A. P., 2010: Effects of stratocumulus clouds on aerosols in the maritime boundary layer. Atmos. Research, 97, 498-512.

Pinsky M., I.P. Mazin, A. Korolev, and A. Khain, 2011: Supersaturation and diffusional droplet growth in liquid clouds. J. Atmos. Sci. (in revision)

Prabha, Thara V., A. Khain, R. S. Maheshkumar, G. Pandithurai, J. R. Kulkarni, M. Konwar, B. N. Goswami, 2011: Microphysics of Premonsoon and Monsoon Clouds as Seen from In Situ Measurements during the Cloud Aerosol Interaction and Precipitation Enhancement Experiment (CAIPEEX). J. Atmos. Sci., 68, 1882–1901

Squires, P., 1952: The growth of cloud drops by condensation. I. General characteristics. Aust. J. Sci. Res., 5, 59–86.

Telford, J.W., 1999: Comments on "Droplet spectral broadening in marine stratus". J. Atmos. Sci., 56, 2261–2263.

Telford, J.W., and S. K. Chai, 1980: A new aspect of condensation theory. Pageoph, 118, 720-742.

Telford J. W. and P. B. Wagner 1981: Observations of condensation growth determined by entity type mixing, Pageoph, 119.

Telford J. W., T. S.Keck and S. K . Chai, 1984: Entrainment at cloud tops and the droplet spectra, J. Atmos. Sci. 41, 3170-3179.

Telford J. W. and P. B. Wagner 1980: The dynamical and liquid water structure of the small cumulus as determined from its environment, Pageoph, 118 (2), 935-952.

Acknowledgements

The CAIPEEX project and IITM are fully funded by Ministry of Earth Sciences, Government of India, New Delhi. A. Khain was supported by the Office of Science (BER), US Department of Energy Award DE-SC0006788 and the Binational US-Israel Science Foundation (grant 2010446).

Aerosol-Cloud-Precipitation interaction during CAIPEEX: a perspective from mixing in clouds

T. V. Prabha, S. Patade, N. Malap, S. Dipu, G. Pandithurai, R. S. Maheshkumar, Padmakumari B., M. Konwar, Morwal S., C. G. Deshpande, S. G. Narkhedkar, P.D. Safai, RR Joshi, R. Bhalwankar, K. K. Dani, A. Nath, Sathy Nair, V. V. Sapre, J. R. Kulkarni, B. N. Goswami
Indian Institute of Tropical Meteorology, Pune, India

Duncan A, C. Weeks, Roelof B.,
National Center for Atmospheric Research, Boulder, CO, USA

Abstract: Aerosol and cloud microphysical observations were conducted during the Cloud Aerosol and Precipitation Enhancement experiment (CAIPEEX) over the Indian subcontinent. The observations characterized highly polluted to clean aerosol regimes during the premonsoon dry conditions to moist monsoon conditions. These observations give a unique opportunity to investigate the role of pollution and humidity on the droplet spectral characteristics. A classification of data is carried out with the help of aerosol/cloud condensation nuclei concentration and water vapor mixing ratio in the boundary layer. Vertical variation of droplet concentration, liquid water content, spectral width and mean radius in widely varying pollution and thermodynamic environments during CAIPEEX is studied.

It is noted that droplet spectra in the supercontinental dry conditions was narrow with much less variation in the spectral width. However, as the monsoon progressed, both the mean radius and the spectral width increased. Recently several studies illustrate that increasing aerosols decreased precipitation in the dry environments, while in the moist environments; there was increase in precipitation and precipitation intensity. CAIPEEX results illustrate that monsoon clouds are 'marine like', however influenced by continental aerosols. Most revealing result is illustrated with an investigation on the effect of mixing and how the vertical variation of different cloud microphysical parameters is influenced for different cloud types in different aerosol regimes.

Introduction: Cloud Aerosol Interaction and Precipitation Enhancement Experiment (CAIPEEX) was the first campaign in India, focusing on the microphysics of premonsoon and monsoon clouds. An instrumented research aircraft was used in two phases during 2009-2011 monsoon seasons to document the aerosol and cloud microphysics with approximately 640 hours of *in situ* data. Details of the experiment and data and instruments can be found in (Prabha et al., 2011, Kulkarni et al., 2012, Nair et al., 2012) and at http://www.tropmet.res.in/~caipeex/

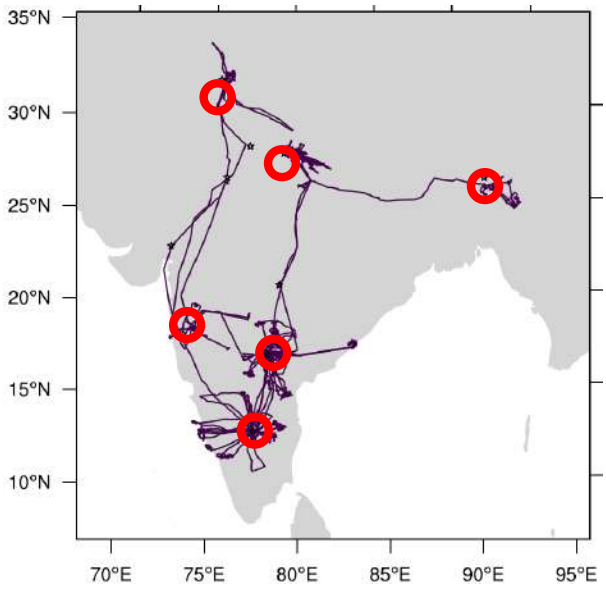

Figure 1. CAIPEEX Phase I flights used in this study.

In Phase I (2009), main observations over several places in India (Figure1) focused characterization of different cloud types and their microphysics and aerosol environments. During Phase II (2010-2011) data was collected from in the Peninsular India mainly investigating the continental clouds over the semi-arid, rain shadow region. Cloud microphysics observations of deep convective clouds up to 6 km above cloud base were carried out. These are unique continental cloud observations in the aerosol laden tropical land area. Data used in this study are from the premonsoon dry conditions to the moist monsoon conditions.

Results

An overview of observations during 2009 is presented in Figure 1. The boundary layer v component velocity is used as a measure of continental or maritime airmass. During the monsoon, strong positive v component is associated with moisture transport from Arabian Sea. The modification of airmass characteristics occur mainly from the northern continental air intrusions which are associated with negative v component. The boundary layer aerosol concentration showed a strong relationship with v velocity. The relative dispersion (ratio of spectral width and mean radius) 1 km above cloud base is shown in Figure 2b. Relative dispersion is used to make comparison between different cases as a normalized variable. Relative dispersion showed a strong dependence on the airmass characteristics. The spectral width and mean radius has a more complex relation with the airmass characteristics. The high relative dispersion are associated with maritime like observations and lower relative dispersion correspond to the cases that have a continental origin, which have low spectral width and mean radius.

The derived maximum reflectivity (dbZ) and average rain rate (mm/hour) are used to investigate the precipitation relationship with aerosols or moisture content in the boundary layer. It may be noted that the high aerosol dry regime is associated with widely varying maximum reflectivity and low rain rates.

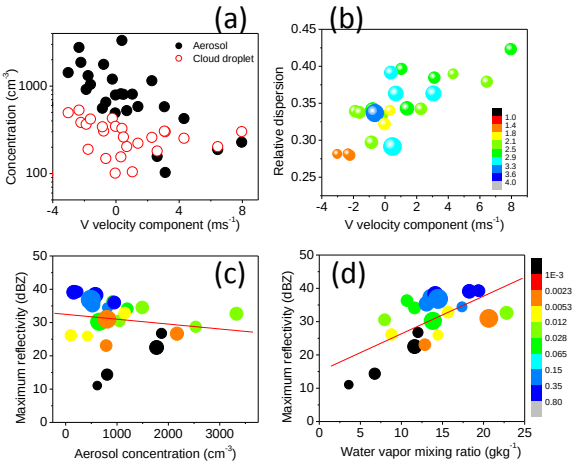

Figure 2. The relationship between the mixed layer v component of velocity and aerosol and cloud droplet number concentration (a), v component of velocity with relative dispersion (b, color is spectral width in μm and size of symbol is mean radius both at 1 km above cloud base). The relationship of maximum reflectivity with aerosol concentration (c) with boundary layer water vapor (d). The rain rate is shown in color and mean radius at 1 km above cloud base shown with size of symbols.

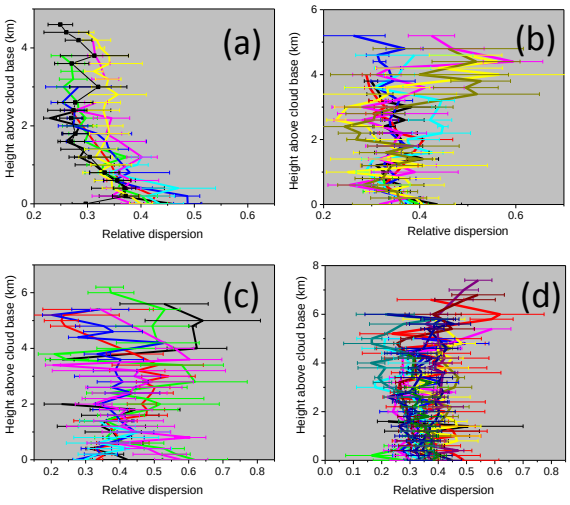

Figure 3. Vertical variation of relative dispersion for cloud observations of

premonsoon dry conditions (a), wet monsoon conditions (b), and coastal clouds during monsoon (c) and active monsoon conditions over land with intermediate level aerosols and water vapor content (d)

Wet, high aerosol regime showed higher (>25 dbZ) reflectivity and less rain rate. Clean wet conditions corresponding to marine and wet monsoon conditions have reflectivity >30 dbZ.The observations are classified to four categories depending on the moisture and aerosol conditions.

Miles et al (2000) gives a comprehensive list of droplet dispersion in marine and continental clouds, but no such observations in the continental cumulus/deep convective clouds were available except for a few cases from Gulf of Mexico Atmospheric Composition and Climate Study (GoMACCS) (Lu et al 2008) and the Large-Scale Biosphere-Armosphere Experiment in Amazonia (LBA) experiment (Andrea et al.,). Figure 3 shows vertical variation of relative dispersion in different classifications as pre-monsoon (a), monsoon wet conditions (b), coastal clouds during the monsoon (c) and active monsoon over land (d). Deep convective clouds up to a height of 6-7 km above the cloud base are presented. Relative dispersion (found from cloud droplet probe for 3-50 µm) was averaged at every 100 m height intervals and the standard deviation at each level is presented with error bars. In the premonsoon dry conditions, typical behavior of relative dispersion is maximum near the cloud base and a gradual decrease in relative dispersion with height is noted. A few cases show near constant values of relative dispersion beyond 1.5 km above cloud base.

In the monsoon clouds (Figure 3b) with wet conditions, the relative dispersion is much higher and varies significantly with height. It is interesting to note that the relative dispersion increases at higher levels in the deep convective clouds. This is attributed to increase in the spectral width and a relatively less change in the mean radius at those locations. The spectral broadening is explained with various processes and the incloud nucleation and droplet evaporation seem to be important in contributing to higher spectral width and the relative dispersion (Prabha et al., 2011). However, higher relative dispersion in these monsoon conditions at very low levels (1 km above cloud base) is notable. This could also be attributed to the initiation of collision coalescence at lower elevations in the cleaner monsoon clouds. Phase II observations during 2010-2011 constituted multiple cloud droplet probes and provide unique opportunity to study the collision coalescence processes in monsoon clouds. A sample of particle size distribution is presented in Figure 4 from different probes.

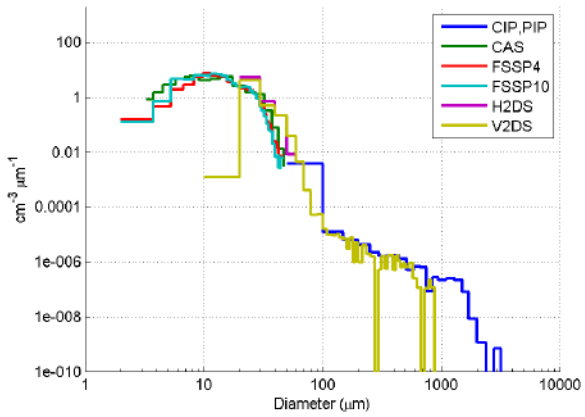

Figure 4. Droplet size distribution observed in a warm region of monsoon cloud at 3.7 km layer showing spectral broadening and precipitation formation within 1 km of the cloud base.

In the coastal (marine line) cloud observations (Figure 3c), more variations in the relative dispersion is noted at any specific level. Over the land during active monsoon, relative dispersion varies between 0.3 and 0.4 and it showed a slight increase with height or near constant values.

A strong negative correlation (-0.87) between water vapor mixing ratio in the boundary layer and adiabatic fraction (Figure 5a) is noted.

This showed that under highly moist conditions, clouds are well mixed and dry conditions they are mode adiabatic. There is some exceptions to these effects for clouds growing in highly polluted and moist environment.

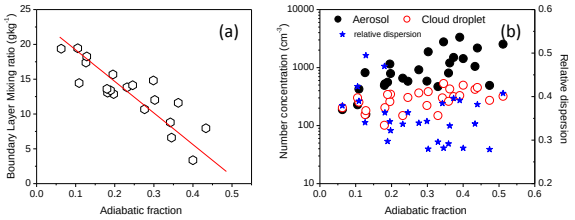

Figure 5. Dependence of adiabatic fraction and water vapor mixing ratio (a) number concentration of aerosol particles, cloud droplets, relative dispersion (b)

Figure 5b shows the dependence of various parameters and adiabatic fraction. It may be noted that less polluted clouds are highly mixed compared to the polluted clouds. This dependence is more due to strong relationship with the moisture content than the aerosol effect. The Phase II observations (not presented here) reconfirm these inferences.

References:

Andrea M.O, Rosenfeld D., Artaxo P., Costa A.A., Frank G.P., Longo K.M. and Silva-Dias M.A.F, Smoking rain clouds over Amazon, Science, 303, 1337-1342.

Kulkarni J.R, Maheshkumar R.S., Morwal S.B., Padma kumari B., Konwar M., Deshpade C.G., Joshi R.R., Bhalwankar R.V., Pandithurai, Safai P.D., Narkhedkar S.G., Dani K.K., Nath A., Sathy Nair, Sapre V.V., Puranik P.V., Kandalgaonkar S.S., Mujumdar V.R., Khaladkar R.M., Vijaykumar R., Prabha T.V., and Goswami B.N. (2012), Cloud Aerosol Interaction and Precipitation Enhancement Experiment (CAIPEEX): overview and preliminary results, current science, 102, February 2012, 413-425.

Lu, M. L., Feingold G., Jonsson H.H., Chuang P. Y., Gates H., Flagan R.C., and Seinfeld J.H., Aerosol-cloud relationship in continental shallow clouds, J. Geophys, Res,113, D15201, doi:10:1029/2007JD009354 (2008).

Miles, N.L., Verlinde, J., Clothiaux, E.E., 2000: Cloud droplet size distributions in lowlevel stratiform clouds. *J. Atmos. Sci.*, **57**, 295-311.

Nair Sathy, Sanjay J., Pandithurai G., Maheskumar R., S., Kulkarni J.R. (2010): On the parameterization of cloud droplet effective radius using CAIPEEX aircraft observations for warm clouds in India, Atmospheric Research, 108, May 2010, DOI:10:1016/j.atmosres.2012.02.002,104-114.

Prabha T.V., Khain A., Maheshkumar R.S., Pandithurai G., Kulkarni J.R, Konwar M., Goswami B.N. (2011), Microphysics of pre-monsoon and monsoon clouds as seen from in situ measurements during CAIPEEX, *J. Atmos. Sci.*, doi: 10.1175/2011 JAS3707.1, 1-60.

Acknowledgement

The CAIPEEX project and IITM are fully funded by Ministry of Earth Sciences, Government of India, New Delhi.

Global Assesment of Ice Nuclei Effects on Ice Cloud Formation using the NASA Goddard Earth Observing System (GEOS-5)

Donifan Barahona*[1, 2], Andrea Molod[1, 3], Andrew Gettelman[4], Julio Bacmeister[4], Hugh Morrison[4], and Athanasios Nenes[5]

[1]NASA GSFC, Greenbelt, MD, USA
[2]I.M. Systems Group, Rockville, MD, USA
[3]University of Maryland College Park, MD, USA
[4]National Center for Atmospheric Research, Boulder, CO, USA
[5]Georgia Institute of Technology, Atlanta, GA, USA

Aerosol emissions impact the formation of cirrus and mixed phase clouds by modifying the background concentration of ice nuclei (IN). In this work a new cloud microphysics scheme, including a novel ice nucleation framework, is implemented within the NASA Goddard Earth Observing System (GEOS-5) to study the effects of ice nuclei emissions on the global climate.

GEOS-5 is a state-of-the-art Earth system model regularly used for decadal predictions of climate, field campaign support, satellite data assimilation, and weather forecast [1]. In its current configuration GEOS-5 is capable of running at spatial resolutions as high as 3 km [2]. Recently a new microphysics cloud scheme [3, 4] has been implemented in GEOS-5 to account for the effects of aerosol-cloud interactions on climate. The new scheme links cloud properties (i.e., cloud particle number and effective size, condensate amount and cloud fraction) to formation conditions and aerosol characteristics using a two-moment (mass and number) approach and state-of-the-art aerosol activation and ice crystal formation parameterizations [5]. Activation of cloud condensation nuclei (CCN) is described using an analytical, physically-based parameterization [6]. Aerosol emissions and transport are modeled using the GOCART aerosol model [7]. Sea-salt, sulfate and organics are assumed to be CCN active.

1 ICE NUCLEATION FRAMEWORK

Along with the new microphysics and CCN activation schemes, a new physically-based ice nucleation framework was implemented in GEOS-5 [8, 9]. This scheme predicts the formation of ice crystals from homogeneous and heterogeneous ice nucleation accounting for subgrid scale dynamics, aerosol abundance and composition. Heterogeneous ice nucleation is described using the ice nucleation spectrum, which describes the formation of ice crystals by immersion, deliquesced-heterogeneous freezing (DHF), and deposition modes, and accounts for particle surface area and composition (and their variability across the aerosol population), droplet volume, supersaturation and tempera-

*Correspodence to: donifan.o.barahona@nasa.gov

ture.

Theoretical prediction of the ice nucleation spectrum from physical principles is typically challenging. Thus, empirical and semiempirical correlations that represent the main factors defining the ice crystal concentration are often used [9, 10, 11, 12]. This approach neglects the variability in ice nucleation properties within single aerosol species. Here a different, physically-based route is taken based on the ice nucleation probability dispersion theory [5]. Rather than trying to find the distribution of surface-specific properties like contact angle and active site density in an aerosol population, the theory defines an ice nucleation probability dispersion function (NPDF) describing the deviation in the number of ice germs per particle from the average of the population.

The ice crystal concentration, N_c, is then given by

$$N_\mathrm{c} = \sum_{i=1}^{N_\mathrm{T}} N_{a,i} \sum_{k=1}^{M_\mathrm{T}} \alpha_\mathrm{i,k} \left[1 - \mathcal{N}_{i,k}(\bar{\varphi}_{i,k}, \sigma_{\varphi i,k})\right] \tag{1}$$

where N_a is the aerosol number concentration, $\mathcal{N}(\bar{\varphi}, \sigma_\varphi)$ the Laplace transform of the NPDF, $\bar{\varphi}$, is the average number of ice germs per particle and, σ_φ, the ice nucleation dispersion coefficient in the population. The subscripts i and k indicate the i-th aerosol population and k-th nucleation mode, respectively. The factor $\alpha_\mathrm{i,k}$ is used to discriminate between ice nucleation modes. For example, above water saturation only immersion freezing is considered and $\alpha_\mathrm{i,imm} = 1$, and $\alpha_\mathrm{i,dep} = \alpha_\mathrm{i,dhf} = 0$. For water subsaturated regimes $\alpha_\mathrm{i,imm} = 0$ and a linear RH ramp is used to determine $\alpha_\mathrm{i,dep}$ and $\alpha_\mathrm{i,dhf}$, i.e., at low RH deposition dominates whereas for RH$\rightarrow$ 100%, $\alpha_\mathrm{i,dhf} \rightarrow 1$. $\mathcal{N}(\bar{\varphi}, \sigma_\varphi)$ typically follows a error function [5], however if more than one mechanism is involved in ice nucleation it may be a compositition of several functions. $\bar{\varphi}$ is calculated following classical

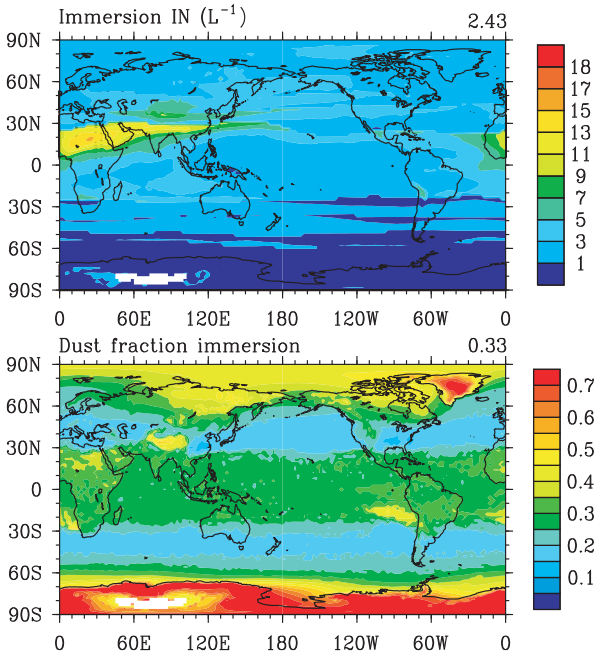

Figure 1: Spatial distribution (weighted by cloud fraction) of immersion IN from the GEOS-5 model

nucleation theory,

$$\bar{\varphi}_{i,k} = J_\mathrm{het,i,k} \tau_\mathrm{nuc} s_\mathrm{p,i} \tag{2}$$

where J_het is the heterogeneous nucleation rate coefficient calculated at the mean aerosol properties, s_p the particle mean surface area, and τ_nuc the nucleation timescale [5]. The new scheme is applied to describe ice nucleation on dust and soot IN for cirrus and mixed-phase regimes. The dispersion coefficients for each population and ice nucleation mode are obtained fitting laboratory and literature data.

2 RESULTS AND CONCLUSIONS

GEOS-5 was run for five years using a spatial resolution of 2° by 2.5° to assess the impact of dust and black carbon IN emissions on the formation of cirrus and mixed-phase clouds. It was found that in the cirrus regime dust IN emissions acting in the deposition mode domi-

nate ice crystal production in the midlatitudes of the Northern Hemisphere. In the Tropical regions soot deposition IN significantly affect the cirrus ice crystal concentration. At mixed-phase levels in the Northern Hemisphere soot and dust IN equally affect the freezing of cloud droplets. In fact, soot emissions make about 50% of the total immersion IN in the Tropics. The nucleation spectrum of soot however indicates that only a minor fraction of soot particles (below 1 in a 1000) freeze at mixed-phase levels but increases for lower temperature. This shows the importance of accounting for variability in ice nucleation properties within atmospheric models.

The effects of soot IN emissions on precipitation were also analyzed. Reducing soot emissions by 50% resulted in an increase in supercooled cloud fraction and a slight increase in precipitation due to increased accretion rates. The largest absolute change in precipitation occurred around the ITCZ likely from changes in global circulation brought about by changes in latent heat released at the mixed-phase levels. In a relative sense, precipitation near the source regions, i.e., North and South America, south east Asia and north Africa, was strongly affected. These changes resulted mostly from reduction in immersion freezing IN indicating that a physically-based treatment of ice nucleation variability may be required for reliable prediction of aerosol effects on ice clouds and climate.

References

[1] M. Rienecker, M. Suarez, R. Todling, J. Bacmeister, L. Takacs, H.-C. Liu, W. Gu, M. Sienkiewicz, R. Koster, R. Gelaro, I. Stajner, and J. Nielsen, *The GEOS-5 Data Assimilation System - Documentation of Versions 5.0.1, 5.1.0, and 5.2.0.*, vol. 27 of *echnical Report Series on Global Modeling and Data Assimilation.* Greenbelt, MD, USA: NASA Goddard Space Flight Center, 2008.

[2] W. Putman and M. Suarez, "Cloud-system resolving simulations with the nasa goddard earth observing system global atmospheric model (geos-5)," *Geophys. Res. Lett.*, vol. 38, no. 16, p. L16809, 2011.

[3] H. Morrison and A. Gettelman, "A new two-moment bulk stratiform cloud microphysics scheme in the community atmosphere model, version 3 (cam3). part i: Description and numerical tests," *J. Clim.*, vol. 21, no. 15, pp. 3642–3659, 2008.

[4] D. Barahona, A. Molod, J. Bacmeister, A. Nenes, A. Gettelman, and H. Morrison, "Implementation of two-moment cloud microphysics within the nasa goddard earth observing system model (geos-5)," *J. Geophys. Res.*, p. In preparation, 2012.

[5] D. Barahona, "On the ice nucleation spectrum," *Atm. Chem. Phys.*, vol. 12, no. 8, pp. 3733–3752, 2012.

[6] C. Fountoukis and A. Nenes, "Continued development of a cloud droplet formation parameterization for global climate models," *J. Geophys. Res.*, vol. 110, pp. D11212, doi:10.1029/2004JD005591, 2005.

[7] P. Colarco, A. da Silva, M. Chin, and T. Diehl, "Online simulations of global aerosol distributions in the nasa geos-4 model and comparisons to satellite and ground-based aerosol optical depth," *J. Geophys. Res.*, vol. 115, no. D14, pp. D14207–, 2010.

[8] D. Barahona and A. Nenes, "Parameterizing the competition between homogeneous and heterogeneous freezing in cirrus cloud formation. polydisperse ice nuclei," *Atmos. Chem. Phys.*, vol. 9, pp. 5933–5948, 2009.

[9] D. Barahona, J. Rodriguez, and A. Nenes, "Sensitivity of the global distribution of cirrus ice crystal concentration to heterogeneous freezing," *J. Geophys. Res.*, vol. 15, p. D23213, 2010.

[10] C. Hoose, J. Kristjansson, J.-C. Chen, and A. Hazra, "A classical-theory-based parameterization of heterogeneous ice nucleation by mineral dust, soot, and biological particles in a global climate model," *J. Atmos. Sci.*, vol. 67, pp. 2483–2503, 2010.

[11] B. Kärcher, J. Hendricks, and U. Lohmann, "Physically based parameterization of cirrus cloud formation for use in global atmospheric models," *J. Geophys. Res.*, vol. 111, pp. D01205, doi:10.1029/2005JD006219, 2006.

[12] X. Liu and J. Penner, "Ice nucleation parameterization for global models," *Meteorol. Z.*, vol. 14, no. 4, pp. 499–514, 2005.

TOWARD THE ASSESSMENT OF THE ROLE OF CLOUD TURBULENCE IN WARM RAIN DEVELOPMENT

W. W. Grabowski[1]*, A. A. Wyszogrodzki[1], L.-P. Wang[2], and O. Ayala[2]

[1]National Center for Atmospheric Research, Boulder, Colorado, USA
[2]Mechanical Engineering, University of Delaware, Newark, Delaware, USA

1. INTRODUCTION

Small cloud droplets grow efficiently by the diffusion of water vapor. They are able to grow efficiently by gravitational collisions only after their radius reaches a few tens of microns (Pruppacher and Klett 1997). In general, it is difficult to explain the rapid growth of cloud droplets in the size range from 15 to 50 μm in radius for which neither the diffusional mechanism nor the gravitational collision-coalescence mechanism is effective (i.e. the condensation-coalescence bottleneck). An open question is what drives the droplet growth through the bottleneck size range. The onset of drizzle-size drops ($\sim$ 100 μm) is still poorly understood, and this issue is regarded as one of unresolved problems of cloud physics. A related issue is the discrepancy between the width of observed and simulated size distributions of cloud droplets (Brenguier and Chaumat 2001). Several mechanisms have been proposed to explain the rapid development of rain in shallow convective clouds, including entrainment of dry environmental air into the cloud, effects of giant aerosol particles, turbulent fluctuations of the water vapor supersaturation, and turbulent collision-coalescence (Pruppacher and Klett 1997; Xue et al. 2008).

Here we focus on the effects of air turbulence on the growth of cloud droplets by collision-coalescence. The central issue is the magnitude of the enhancement of the gravitational collection kernel due to the air turbulence, and whether the enhancement can significantly impact rain initiation.

2. TURBULENT ENHANCEMENT OF THE COLLISION KERNEL

In this study, the impact of turbulent collisions on warm rain initiation is evaluated by comparing results obtained using the turbulent collection kernel and the traditional gravitational kernel. We apply the bin microphysics scheme as described in Grabowski and Wang (2009) and Grabowski et al. (2011) with 112 bins. Activation of cloud droplets follows Twomey's approach, see Grabowski et al. (2011) for details. The concentration of activated cloud droplets N is given by $N = N_o S^b$, where S is the supersaturation, and N_o and b are prescribed parameters selected to represent pristine CCN conditions (cf. Grabowski et al. 2011 and Wyszogrodzki et al. 2011).

The gravitational kernel without effects of turbulence is given by:

$$K_{ij} = E^g_{ij}\ \pi\ (r_i + r_j)^2\ |v^t_i - v^t_j| \quad , \qquad (1)$$

where E^g_{ij} is the collision efficiency of droplets with radii r_i and r_j in a quiescent background air, and v^t_i and v^t_j are their sedimentation (terminal) velocities. The gravitational kernel applies tabulated collision efficiencies given in Hall (1980) and terminal velocities of Beard (1976) as given by Pruppacher and Klett (1997).

The turbulent collection kernel combines the analytic parameterization of turbulent geometric collection kernel of Ayala et al. (2008b) with the collision-efficiency enhancement factor obtained from a hybrid direct numerical simulation (Wang et al. 2008). The turbulent collection kernel is expressed as

$$K_{ij} = K^0_{ij}\ E^g_{ij}\ \eta_E \quad , \qquad (2)$$

where the turbulent geometric collection kernel K^0_{ij} is obtained when droplet-droplet local aerodynamic interaction is not considered, in which case the disturbance flows induced by other droplets are excluded when the motion of a given droplet is solved. The collision efficiency of droplets in a quiescent background air E^g_{ij} is the same as in (1). The ratio of turbulent collision efficiency to E^g_{ij} is represented by the relative enhancement factor η_E, see Wang et al. (2005). The geometric collection kernel

* *Corresponding author address*: Dr. Wojciech W. Grabowski NCAR, PO Box 3000, Boulder, CO 80307; e-mail: grabow@ucar.edu.

K_{ij}^0 is given by the following kinematic formulation (Wang et al. 2005)

$$K_{ij}^0 = 2\pi R^2 \ \langle |w_r(r=R)| \rangle \ g_{ij}(r=R) \quad , \qquad (3)$$

where the radial relative velocity w_r is defined in terms of the center-to-center separation vector $\mathbf{r}$ (pointing from a droplet of radius r_j to a droplet of radius r_i), the velocity $\mathbf{V}_i$ of the r_i droplet, and the velocity $\mathbf{V}_j$ of the r_j droplet as $w_r = \mathbf{r} \cdot (\mathbf{V}_i - \mathbf{V}_j)/r$ with $r = |\mathbf{r}|$. $R \equiv r_i + r_j$ is the geometric collision radius. The additional factor g_{ij} is the radial distribution function which measures the effect of preferential concentration on the pair number density at separation $r = R$. Both $\langle |w_r| \rangle$ and g_{ij} in (3) are computed without local aerodynamic interaction. The kinematic formulations (2) and (3) have been validated against dynamic collision rates from direct numerical simulations (DNS), for both ghost droplets and aerodynamically-interacting droplets in a turbulent air flow, see Wang et al. (2005) and Ayala et al. (2008a).

Ayala et al. (2008b) developed parameterizations for both $\langle |w_r| \rangle$ and g_{ij}, guided by data from DNS. It should be noted that their parameterizations consider the effects of flow Reynolds number which cannot be fully represented by the hybrid DNS. For example, the parameterization for $\langle |w_r| \rangle$ makes use of velocity correlations that are valid for both the dissipation subrange and the energy-containing subrange of turbulence. The intermittency of small-scale turbulent fluctuations was incorporated into the model for g_{ij} following Chun et al. (2005). The detailed expression for K_{ij}^0 can be found in Ayala et al. (2008b). The enhancement factor η_E is interpolated from the hybrid DNS results reported in Wang et al. (2008) and depends on the flow dissipation rate.

Overall, the turbulent collection kernel depends of two parameters: the dissipation rate of the turbulent kinetic energy (TKE) ϵ and the root mean square (rms) fluctuation velocity U'. When applied locally in large eddy simulation (LES) model, the two have to be derived from model-predicted variables, the TKE in particular. In simulations discussed here, $\epsilon = c_\epsilon E^{3/2}/L$ (where E is TKE; $L = (\Delta x + \Delta y + \Delta z)/3$ with Δx, Δy, Δz denoting grid increments; and $c_\epsilon = 0.845$), and $U' = 2.02(\epsilon/4.0 \times 10^{-2})^{1/3}$ (SI units). The latter formula comes from assuming $U' = 2.02 \ \mathrm{m\,s^{-1}}$ for $\epsilon = 400 \ \mathrm{cm^2\,s^{-3}}$ and applying inertial range scaling for other values of ϵ. It is important to point out that derivation of the turbulent collection kernel based on local conditions makes the LES code run slower than in the case of the gravitational kernel. This is because the gravitational kernel can be precomputed during model initiation and used during model run. In contrast, the turbulent kernel needs to be derived at each model gridpoint and each model timestep.

Examples of the enhancement over the gravitational kernel were provided in previous publications and will not be shown here (see, for instance, Fig. 3 in Wang and Grabowski 2009 or Fig. 2 in Grabowski and Wang 2009). The impact on the drizzle/rain development assuming an initial spectrum of cloud droplets was previously documented in simulations of the evolution of the drop spectrum (e.g., Fig. 4 in Wang and Grabowski 2009) and in idealized rising parcel simulations of Grabowski and Wang (2009). Before applying the turbulent kernel in realistic LES cloud field simulations, an additional issue needs to be investigated. The problem is in the disparity of spatial scales represented in DNS and LES models. The DNS model, with the computational domain typically a small fraction of a cubic meter, simulates effects of small-scale turbulence only. The LES model, on the other hand, has the gridbox typically between 10^3 and 10^6 cubic meters and incorporates the effects of significantly larger range of scales. Because TKE dissipation rate is highly intermittent, the disparity between DNS domain size and LES gridbox needs to be accounted for. In a nutshell, the local (i.e., single gridbox) TKE dissipation rate predicted by the LES model corresponds to a large spectrum of dissipation rates at scales corresponding to the DNS domain size. However, an investigation of this issue documents that the dissipation rate intermittency leads to only minor modification of the mean kernel within the LES gridbox. In other words, applying the local LES dissipation rate gives approximately correct prediction of the turbulent kernel even if the effects of the small-scale dissipation rate intermittency are included.

3. CLOUD SIMULATIONS WITH TURBULENT COLLISION KERNEL

The model used in this study is the anelastic semi-Lagrangian/Eulerian model EULAG documented in Smolarkiewicz and Margolin (1997; model dynamics), Grabowski and Smolarkiewicz (1996; model thermodynamics), and Margolin et al. (1999; SGS turbulent mixing); see Prusa et al. (2008) for a recent review with comprehensive list of references. Implementation of the bin microphysics in EULAG was discussed in Wyszogrodzki et al. (2011), although only CCN activation and

condensational growth of cloud droplets was considered there.

As an initial example, we compare results from 2D simulations of a rising precipitating thermal as in Grabowski et al. (2010) applying either the gravitational collection kernel or the turbulent kernel corresponding to a constant dissipation rate of $\epsilon = 100$ cm^2 s^{-3}. In these simulations, the initially spherical bubble rises in the stably-stratified environment, produces cloud water as a result of water vapor condensation, and eventually drizzle and rain due to collisional growth of cloud droplets. Figure 1 compares evolutions of the averaged surface precipitation rate and surface rain accumulation from the two simulations. The figure shows that rain reaches the surface several minutes earlier in the case of the turbulent kernel. Moreover, the total rain accumulation is also significantly higher in the turbulent case. The former is anticipated because turbulence does lead to a faster formation of drizzle drops and thus more rapid development of precipitation as documented in bin simulations mentioned above. The latter effect is perhaps more surprising. Arguably, it can be understood as the effect of faster formation of drizzle drops in the turbulent case leading to washout of cloud condensate earlier in the cloud lifecycle, before the cloud starts to dissipate.

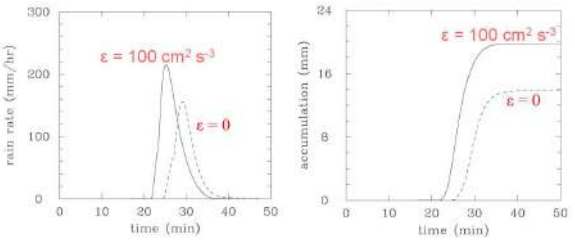

Figure 1: Evolution of the surface mean rain rate (left panel) and the total surface rain accumulation (right panel) in simulations of the 2D rising precipitating thermal. Solid and dashed lines are for turbulent and gravitational kernel, respectively.

The assumption of a constant in space and time dissipation rate in the rising thermal simulation discussed above is not realistic. Figure 2 compares results from three simulations of a cloud field following the shallow convection case based on BOMEX observations (Siebesma et al. 2003). In the first simulation, the collision-coalescence is excluded and only diffusional growth is considered as in Wyszogrodzki et al. (2011). The second simulation features growth by collision-coalescence applying the gravitational collection kernel. Finally, the third simulation applies turbulent kernel with the enhancement of droplet collisions based on local cloud conditions as described above. The figure compares CFADs (Contoured Frequency by Altitude Diagrams) of drop sizes in simulated clouds. Without collision-coalescence, CFAD of droplet sizes is relatively narrow, with the mean drop size increasing with height as expected. Including gravitation collision leads to a significant broadening of the CFAD in the upper parts of the cloud field as well as a shift towards larger radii. These are significantly enhanced when effects of turbulence are included in the third simulation.

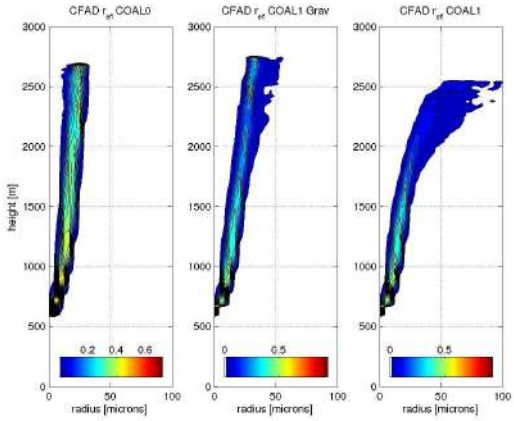

Figure 2: CFADs of the droplet radii in simulations of BOMEX shallow convective clouds. The left panel shows results from simulations without collision-coalescence. The middle and right panels show results from simulations applying gravitational and turbulent kernel, respectively.

4. SUMMARY

This paper presents preliminary results from sensitivity simulations that consider effects of cloud turbulence on the formation of drizzle and rain in shallow convective clouds. More extensive discussion of these results will be presented at the conference.

BIBLIOGRAPHY

Ayala, O., B. Rosa, L.-P. Wang, and W. W. Grabowski, 2008a: Effects of turbulence on the geometric collision rate of sedimenting droplets: Part 1. Results from direct numerical simulation. *New J. Physics*, **10**, 075015, doi:10.1088/1367-2630/10/7/075015.

Ayala, A., B. Rosa, and L.-P. Wang, 2008b: Effects of turbulence on the geometric collision rate

of sedimenting droplets: Part 2. Theory and parameterization. *New J. Physics*, **10**, 075016, doi:10.1088/1367-2630/10/7/075016

Beard, K. V, 1976: Terminal velocity and shape of cloud and precipitation drops aloft. *J. Atmos. Sci.*, **33**, 851-864.

Brenguier, J.-L. and L. Chaumat, 2001: Droplet spectra broadening in cumulus clouds. Part I: Broadening in adiabatic cores. framework. *J. Atmos. Sci.*, **58**, 628-641.

Chun, J., D. Koch, S. L. Rani, A. Ahluwalia, and L. R. Collins, 2005: Clustering of aerosol particles in isotropic turbulence. *J. Fluid Mech.*, **536**, 219-251.

Grabowski, W. W. and P. K. Smolarkiewicz, 1996: On two-time-level semi-Lagrangian modeling of precipitating clouds. *Mon. Wea. Rev.* **124**, 487–497.

Grabowski, W. W., and L.-P. Wang, 2009: Diffusional and accretional growth of water drops in a rising adiabatic parcel: effects of the turbulent collision kernel. *Atmos. Chem. Phys.*, **9**, 2335-2353.

Grabowski, W. W., O. Thouron, J.-P. Pinty, and J.-L. Brenguier, 2010: A hybrid bulk-bin approach to model warm-rain processes. *J. Atmos. Sci.*, **67**, 385-399.

Grabowski, W. W., M. Andrejczuk, and L.-P. Wang, 2011: Droplet growth in a bin warm-rain scheme with Twomey CCN activation. *Atmos. Res.*, **99**, 290-301.

Hall, W. D., 1980: A detailed microphysical model within a two-dimensional framework: Model description and preliminary results. *J. Atmos. Sci.*, **37**, 2486-2507.

Margolin, L. G., P. K. Smolarkiewicz, and Z. Sorbjan, 1999: Large-eddy simulations of convective boundary layers using nonoscillatory differencing. *Physica D*, **133**, 390-397.

Pruppacher, H. R., and J. D. Klett, 1997: *Microphysics of Clouds and Precipitation*, Kluwer Academic, 954 pp.

Prusa, J. M., Smolarkiewicz P. K., and A. A. Wyszogrodzki (2008), EULAG, a computational model for multiscale flows, *Computers & Fluids*, **37**, 1193-1207.

Siebesma, A. P., and Coauthors, 2003: A large eddy simulation intercomparison study of shallow cumulus convection. *J. Atmos. Sci.*, **60**, 1201-1219.

Smolarkiewicz, P. K., and L. G. Margolin, 1997: On forward-in-time differencing for fluids: An Eulerian/semi-Lagrangian nonhydrostatic model for stratified flows. *Atmos.-Ocean Special*, **35**, 127-152.

Wang, L. P., O. Ayala, S. E. Kasprzak, and W. W. Grabowski, 2005: Theoretical formulation of collision rate and collision efficiency of hydrodynamically-interacting cloud droplets in turbulent atmospheres. *J. Atmos. Sci.*, **62**, 2433-2450.

Wang, L.-P., O. Ayala, B. Rosa, and W. W. Grabowski, 2008: Turbulent collision efficiency of cloud droplets, *New J. Physics*, **10**, 075013, doi:10.1088/1367-2630/10/7/075013.

Wang, L.-P., and W. W. Grabowski, 2009: The role of air turbulence in warm rain initiation. *Atmos. Sci. Let.*, **10**, 1-8.

Wyszogrodzki, A. A., W. W. Grabowski, and L.-P. Wang, 2011: Activation of cloud droplets in bin-microphysics simulation of shallow convection. *Acta Geophysica (EULAG topical issue)*, **59**, 1168-1183.

Xue, Y., L. P. Wang, and W. W. Grabowski, 2008: Growth of cloud droplets by turbulent collision-coalescence. *J. Atmos. Sci.*, **65**, 331-356.

Acknowledgments.
This work was supported by the US National Science Foundation (NSF) through grants OCI-0904534 and OCI-0904449. Computer time at NCAR was provided by NSF MRI Grants CNS-0421498, CNS-0420873, and CNS-0420985; NSF sponsorship of the National Center for Atmospheric Research; the University of Colorado; and a grant from the IBM Shared University Research (SUR) program. The National Center for Atmospheric Research is operated by the University Corporation for Atmospheric Research (UCAR) under sponsorship of NSF.

THE PUERTO RICO AFRICAN DUST AND CLOUDS STUDY (PRADACS) – AEROSOL AND CLOUD MEASUREMENTS AT A CARIBBEAN TROPICAL MONTANE CLOUD FOREST

Carlos J. Valle Diaz [1,2], Elvis Torres Delgado [1,2], Felix Zurcher [1], Adriana Gioda [3], Taehyoung Lee [4], Jeffrey L. Collett, Jr. [4], Paul J. DeMott [4], Gavin McMeeking [4], Thomas Hill [5], Gary D. Franc [5], Myrelis Díaz Martínez [1,2], Elizabeth M. Fitzgerald [6], Melanie D. Zauscher [6], Luis A. Cuadra Rodríguez [6], Kimberly A. Prather [6,7], Johanna K. Spiegel [8], Werner Eugster [8], Stephan Mertes [9], Johannes Schneider [10], and Olga L. Mayol-Bracero [1,2*]

[1]Institute for Tropical Ecosystem Studies, University of Puerto Rico, San Juan, PR
[2]Department of Chemistry, University of Puerto Rico, San Juan, PR
[3]Department of Chemistry, Pontifical Catholic University of Rio de Janeiro, Rio de Janeiro, Brazil
[4]Department of Atmospheric Science, Colorado State University, Fort Collins, Co., USA
[5]University of Wyoming, Department of Plant Sciences, Laramie, Wyoming, USA
[6]Department of Chemistry and Biochemistry, University of California San Diego, La Jolla, CA
[7]Scripps Institution of Oceanography, University of California San Diego, La Jolla, CA
[8]Institute for Agricultural Sciences, ETH Zurich - Zurich, Switzerland
[9]Leibniz-Institute for Tropospheric Research, IFT - Leipzig, Germany
[10]Particle Chemistry Department, Max Planck Institute for Chemistry, Mainz, Germany

1. INTRODUCTION

The Saharan desert is the world's largest dust source and it is believed that it accounts for about half of the Aeolian material supplied to the world's oceans [Goudie and Middleton, 2003]. Desert dust particles in the atmosphere have a lifetime of hours to weeks, which allows long-range transport over thousands of kilometers [Jickells et al., 2005]. Saharan dust is well known to cross primarily the Atlantic Ocean and arrive to North America and the Caribbean [Usher et al., 2003].

Mineral dust is known to have both a direct and indirect effect on the climate system. Dust particles interfere directly with the radiative energy (scattering and/or absorbing incoming solar light), and indirectly by acting as cloud condensation nuclei (CCN) that can affect cloud processes [Seinfeld and Pandis, 2006; IPCC, 2007]. The magnitude of the effect mineral dust aerosols have on Earth's energy budget is still uncertain [IPCC, 2007]. Mineral dust uncertainties regarding their radiative forcing are still very large, and in order to quantify mineral dust impact on Earth's climate and ecosystems, it is essential to physically and chemically characterize those mineral dust particles. Several studies have focused on African dust close to the source; however, the small number of studies related to long-range transported African dust (LRTAD) only provided a limited understanding of LRTAD physical-chemical properties, how it might change during transport, and its possible impacts, for example, on climate, ecosystem, and public health.

Of special interest in our study is the impact LRTAD might have on climate. Coastal tropical regions and tropical islands are highly vulnerable to the Earth's changing climate [IPCC, 2007]. The Caribbean is an ideal place for this type of study since it receives African dust mainly during the summer months and it represents a grossly under-sampled region of great importance for tropical and global climate. In particular, the Caribbean island of Puerto Rico is desirable location for such a study since it harbors tropical montane cloud forests (TMCFs) exposed to the trade winds that may directly respond to dust inputs and changes in cloud and fog conditions. Measurements at the TMCF will allow the study of dust-cloud-climate interactions.

As part of the *Puerto Rico African Dust and Clouds Study* (PRADACS), collaborators from the USA and Europe aimed to test the hypothesis that if cloud properties are significantly modified by the presence of LRTAD events. Here we present preliminary results of our findings from measurements performed in summer 2011. During the summer of 2011, measurements of cloud properties such as liquid water content (LWC), droplet

effective radius (R_e), cloud droplet size distribution, pH, conductivity, and bulk chemical composition were performed.

2. METHODOLOGY

2.1 Sampling Site

LRTAD were sampled at Pico del Este (PE) (18°16' N, 65°45' W), in the Luquillo Experimental Forest (LEF), and part of El Yunque National Forest (EYNF). The LEF, administered by the USDA Forest Service and located in the windward eastern portion of the island, is one of the wettest areas on the island and in the region. PE, a TMCF at 1051 masl, is located 20 km southwest downwind of our control site at the natural reserve of Cabezas de San Juan, CSJ (18°22.85' N, 65°37.07' W) **(Figure 1)**. PE's elevation sits above the cloud condensation level thus facilitating the study of clouds without the need for aircraft and the related complexity and costs. The mean annual precipitation at PE is > 5000 mm/yr.

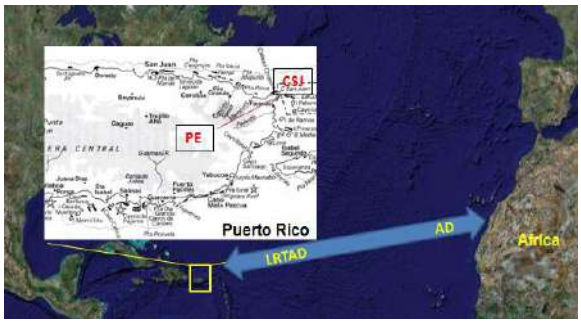

Figure 1: Image schematically showing the air carrying African dust across the Atlantic Ocean and arriving to Puerto Rico. A zoom of northeastern Puerto Rico is shown to see the air mass arriving at CSJ first, and then traveling downwind to PE, the site under study.

2.2 Sampling and Analysis

A series of online and offline instruments were used to determine the chemical, physical, and optical properties of the aerosols, cloud water, and rain water. With HYSPLIT back-trajectory analysis and SAL images, the origin of air masses at PE was determined in order to identify dust and non-dust events.

Cloud-water samples were collected using an aluminum version of the single-stage Caltech Active Strand Cloud Water Collector Version 2 (Al-CASCC2), and a size fractionating 2-stage collector (sf-CASCC). Rain water was collected using two rain samplers (bulk rain collector and a time-resolved automated precipitation collector).

All the samples for cloud and rain water were split for different analyses for the measurement of total organic carbon (TOC), total nitrogen (TN), dissolved organic carbon (DOC), proton nuclear magnetic resonance (^{1}H-NMR), ion chromatography (IC), inductively coupled plasma (ICP), S(IV), H_2O_2, and CH_2O.The details of sample handling and chemical analysis were adapted from previous work performed in our research laboratory [Gioda et al., 2008a; Gioda et al., 2008b; Reyes et al., 2009].

3. RESULTS AND DISCUSSION

3.1. pH and Conductivity

Both cloud water pH (**Figure 2A**) and conductivity (**Figure 2B**) are higher in the presence of dust showing its impact on cloud chemistry. The values of pH and conductivity in the 1st stage of the size fractionating cloud collector, relative to the 2nd stage, indicate a higher content of dust, which is consistent with the larger sizes of these particles and their reduced hygroscopicity; in effect requiring more water to serve as CCN. The concentration of the water-soluble ions is reduced for rain water compared to cloud water because rain droplets are larger and dilute the sample. This, in turn, translates to higher pH and lower conductivity than for the cloud water samples.

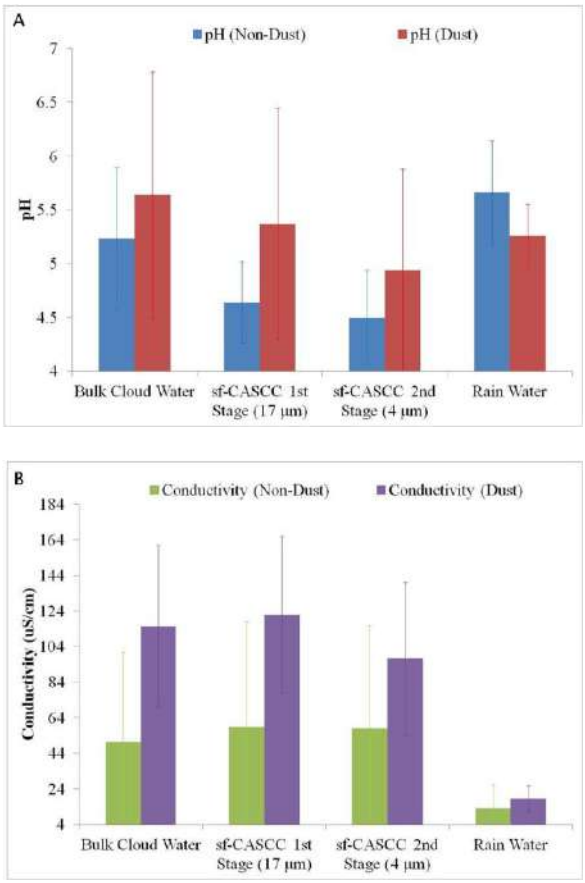

Figure 2(A-B): A) pH and B) conductivity of cloud water collected with the 2-stage sf-CASCC and the Al-CASCC2 (bulk), and rain water during the field measurements.

3.2 FM-100 DROPLET SPECTROMETER

Measurements of cloud properties such as liquid water content (LWC), droplet effective radius (R_e), and cloud droplet size distribution were performed with an FM-100 Fog Monitor from Droplet Measurement Technologies (Boulder, CO, USA). This instrument resolves the droplets in the range of 2 to 50 um in 40 size bins, from which the LWC and R_e can be computed. Results from the FM-100 suggest that long range transported dust can lead to more numerous, but smaller cloud droplets (around 8 um in average) in the TMCF at Pico del Este. However, total LWC appeared to be unaffected by this shift of droplet sizes. Hence, the effect of African dust on clouds appears to be similar to the anthropogenic aerosol effect; however, a detailed analysis of the aerosol data collected is needed to better understand the aerosol-cloud interactions.

3.3 PARTICLE MASS SPECTROMETRY

Online particle chemical analysis via particle mass spectrometry (Aircraft based Laser Ablation Mass Spectrometer - ALABAMA, and Aerosol Mass Spectrometer - AMS) were performed by collaborators from Germany. Single-particle size and chemistry of insoluble cloud residues was measured using aerosol time-of-flight mass spectrometry (ATOFMS). Sea-salt particles (Na^+, ss-Ca^{2+}) and dust particles (Fe, Ti, Mg, nss-Ca^{2+}) were detected. Anthropogenic influence was also detected as the presence of EC, a tracer for combustion processes.

Non-decreasing particle absorption of the drop residues was observed, although residual particle number decreased substantially during the dust event, implying that the absorption does not come from black carbon.

3.5 ICE-T

The potential of LRTAD as a source of ice nuclei was also studied during the Ice in Clouds – Tropical (ICE-T) experiment, with a goal of understanding ice formation processes in tropical cumuli. Real-time, aircraft-based measurements during ICE-T documented the structure of transported African aerosol layers and revealed a strong correlation between ice nuclei concentrations and dust. These were compared to those obtained on ground at PE.

4. CONCLUSIONS

Overall, differences in the studied physicochemical properties of aerosols and clouds during dust and non-dust events were observed. Our preliminary results show that LRTAD have an impact on the chemical and physical properties of aerosols and clouds at the tropical montane cloud forest of Pico del Este. Therefore, this type of study can develop a better understanding of the impact of African dust particles on clouds and climate to reduce the uncertainties in terms of their radiative forcing.

5. BIBLIOGRAPHY

Gioda, A.; O.L. Mayol-Bracero, F. Morales-García, J. Collett, S. Decesari, L. Emblico, M.C. Facchini, R.J. Morales-De Jesús, S. Mertes, S. Borrmann, S. Walter, J. Schneider. Chemical composition of cloud water in the Puerto Rican tropical trade wind cumuli. *Water, Air and Soil Pollut.* **2008**, pp doi:10.1007/s11270-008-9888-4.

Gioda, A.; O.L. Mayol-Bracero, F. Morales-García, G.J. Reyes-Rodríguez, G. Santos-Figueroa, and J. Collett, Jr. Water-soluble organic and nitrogen levels in cloud and rainwater in a background marine environment under influence of different air masses. *J. Atmos. Chem.* **2008**, pp doi:10.1007/s10874-009-9125-6.

Goudie, A.S., and N.J. Middleton. Saharan dust storms: nature and consequences. *Earth-Sci. Rev*. **2001**, *56*, pp 179-204.

Jickells, T.D., Z.S. An, K.K. Anderse, A.R. Baker, G. Bergametti, N. Brooks, J.J. Cao, P.W. Boyd, R.A. Duce, K.A. Hunter, H. Kawahata, N. Kubilay, J. laRoche, P.S. Liss, N. Mahowald, J.M. Prospero, A.J. Ridgwell, I. Tegen, and R. Torres. Global iron concentrations between desert dust, ocean biogeochemistry, and climate. Science. **2005**, *308*, pp 67-71.

Reyes-Rodríguez, G.J., A. Gioda, O.L. Mayol-Bracero, and J. Collett, Jr. Organic carbon, total nitrogen, and water-soluble ions in clouds from a tropical montane cloud forest in Puerto Rico. *Atmos. Environ*. **2009**, *43*, pp 4171-4177.

Seinfeld, J.H. and S.N. Pandis. Atmospheric Chemistry and Physics: From Air Pollution to Climate Change, 2nd Edition, John Wiley & Sons, Inc.: Hoboken, New Jersey and Canada, 2006.

Solomon, S.; D. Qin, M. Manning, Z. Chen, M. Marquis, K.B. Averyt, M. Tignor, and H.L. Miller. Climate Change 2007: The Physical Science Basis (Contribution of Working Group I to the Fourth Assessment Report of the Intergovernmental Panel on Climate Change), Cambridge University Press: Cambridge, United Kingdom and New York, NY, USA, 2007.

Usher, C.R.; A.E. Michel, V.H. Grassian. Reactions on mineral dust. *Chem. Rev*. **2001**, *103*, pp 4883-4839.

Acknowledgements

This project is funded by NSF AGS Grant 0936879. We also thank the Luquillo Long-Term Ecological Research Program for their support. Special thanks to the PRADACS team, the Institute for Tropical and Ecosystem Studies (ITES), the El Yunque National Forest, the Conservation Trust of Puerto Rico, the US Forest Service and Bill McDowell for the chemical analysis, and Ricardo Morales, Carlos Estrada, and Fred N. Scatena, for their help with the weather data and results. From ICE-T, P. DeMott and G. McMeeking acknowledge support from NSF grant AGS-1036028; and T. Hill and G. Franc acknowledge support from NSF grant ATM-0841542. Thank you also to laboratory members, family, and friends.

WRF-SBM SIMULATION UPON LPVEX FIELD CAMPAIGN FOR DEVELOPMENT OF THE SYNTHETIC GPM SIMULATOR

Takamichi Iguchi[1,2], Toshihisa Matsui[1,2], and Wei-Kuo Tao[2]
1. University of Maryland College Park ESSIC, College Park, Maryland, USA
2. NASA Goddard Space Flight Center, Greenbelt, Maryland, USA

1. INTRODUCTION

The next-generation Global Precipitation Measurement (GPM) mission will offer a global view of precipitation systems and enable accurate measurement of frozen precipitation and light rainfall. Analysis of mixed-phase precipitation structure including a melting layer is one of the important topics. The development of synthetic GPM simulator was proposed to support development of the retrieval algorithm that can handle multi-signals by the GPM core-satellite instruments. The synthetic GPM simulator is composed of 1) the instruments simulator, 2) ground validation (GV) measurements, and 3) GV-constrained cloud resolving simulation with spectral-bin microphysics (SBM). These three components are independently as well as dependently supporting various aspects of pre-launch GPM algorithm developments.

This presentation addresses GV-constrained simulations upon the Light Precipitation Validation Experiment (LPVEx) field campaign. This campaign was took place at the site in the vicinity of Helsinki, Finland during the autumn of 2010. Generally mixed-phase stratiform clouds with low-level melting layer were dominant over the area in the season. Two light rainfall events on Sep. 21 and Oct. 20, 2010 were simulated by the Weather Research and Forecasting (WRF) model coupled with SBM.

2. MODEL DESCRIPTION

The Advanced Research WRF (WRF-ARW) ver. 3.1.1 was coupled with the SBM part of the Hebrew University Cloud Model (HUCM) (Khain et al., 2011; Iguchi et al., 2012, submitted). The WRF-SBM was employed in 36-hours real-time simulations covering the targeted days using online 2-way grid nesting configuration for the two domains with the horizontal resolutions of 3 and 1 km.

The WRF-SBM explicitly provides three-dimensional prognostic fields of hydrometeor particle size distributions (PSD) and melting fraction of precipitable ice hydrometeors. Our GV simulator based on the Goddard Satellite Data Simulator Unit (G-SDSU) (Matsui et al., 2009) can translate the simulation output into various GV measurements, including multi-frequency radar reflectivities, disdrometors, and aircraft-based microphysics measurements.

3. RESULT

The C-polarization radar measurement during the field campaign provides the three-dimensional structure of clouds and

precipitation around the site (D. Moisseev, personal communication). The data can be used to evaluate the overall result of the WRF-SBM simulation through a direct comparison using the GV simulator. Figure 1 shows an example in the form of the contoured frequency diagram of the maximum radar reflecitivity (Zmax) and 0 dB echo-top height (Het). The observed 0 dB echo-top height ranges from 3 to 7 km, whereas the simulated height ranges from 1.5 to 2.5 km and from 3 to 6 km. The simulated structure tends to be lower than that in the observation. The simulation overestimates Zmax by approximately 5 dB.

We plan to offer a discussion of mixed-phase microphysics of the light rainfall events also with reference to aircraft and ground-based measurements.

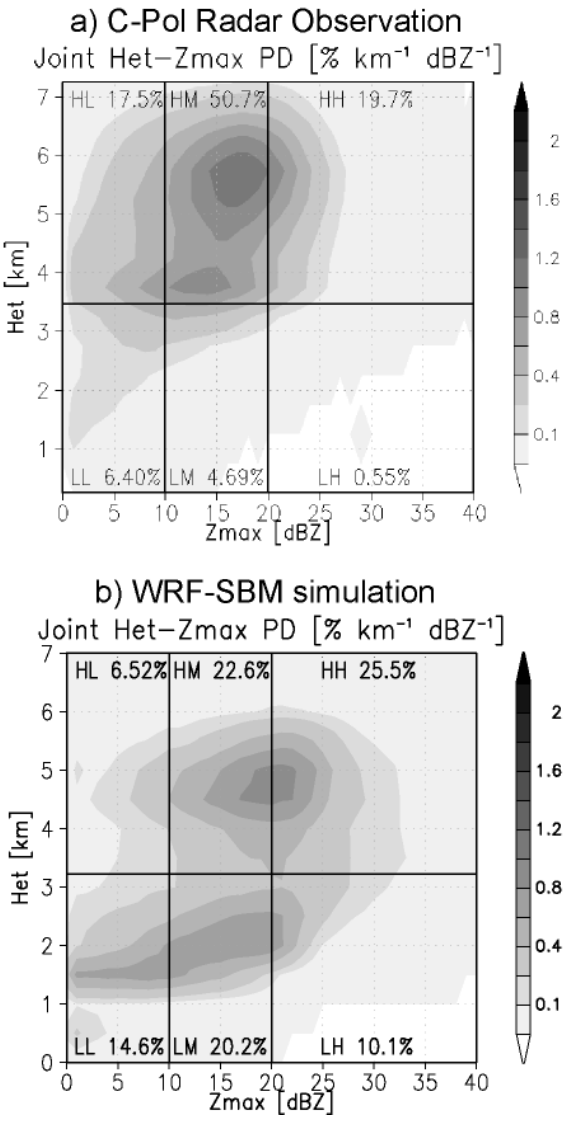

Fig. 1. Contoured frequency diagram of maximum radar reflectivity and 0dB echo-top height derived from (a) C-Pol radar measurement and (b) WRF-SBM simulation.

ACKNOWLEDGEMENTS

This research was supported by the NASA Precipitation Measuring Mission (PMM) and NASA Modeling Analysis Prediction (MAP).

REFERENCE

Iguchi et al. (2012), Numerical analysis using WRF-SBM for the cloud microphysical structures in the C3VP field campaign: Impacts of supercooled droplets and resultant riming on snow microphysics. J. Geophys. Res., submitted.

Khain et al. (2011), The role of CCN in precipitation and hail in a mid-latitude storm as seen in simulations using a spectral (bin) microphysics model in a 2D dynamic frame, Atmos. Res., 99, 129-146.

Matsui et al. (2007), Evaluation of long-term cloud-resolving model simulations using satellite radiance observations and multifrequency satellite simulators. J. Atmos. Oceanic. Technol, 26, 1261-1274.

UNDERSTANDING THE ELETRIFICATION PROCESS

Carlos A. Morales[1], Moacir Lacerda[2], Evandro M. Anselmo[1], João R. Neves[1], Rachel I. Albrecht[3]
1-Universidade de São Paulo, morales@model.iag.usp.br
2-Universidade Federal do Mato Grosso do Sul
3-Instituto Nacional de Pesquisas Espaciais

1. INTRODUCTION

According to the lightning distribution observed in South America by STARNET (Sferics Timing And Ranging NETwork, Morales et al., 2011), Brazil shows a diverse thunderstorm activity in its territorial extent. The onset of thunderstorm follows the summer time period in most of the southeast and central region, but in some northern regions it is possible to find two active periods, i.e., during the transition period (dry to wet season) and at the end of the raining season, Figure 1.

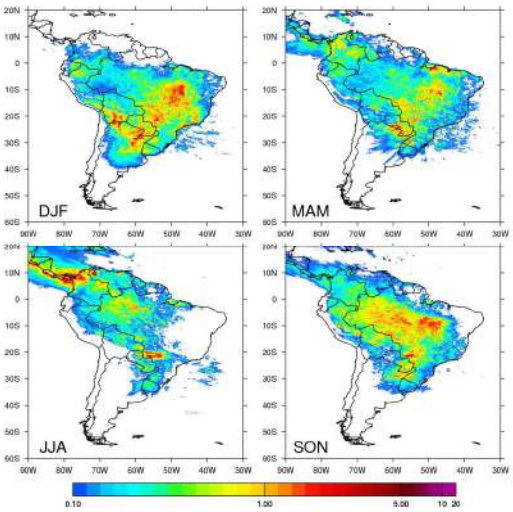

Figure 1. Mean seasonal lightning distribution (sferics/km^2) as observed by STARNET during 2009 through 2011.

These lightning features reveal regions that have more than 30 days per year with thunderstorm activity to more than 300 days and the lightning flash rate varies from 0.1 to more than 50 sferics/ km^2/year. In analyzing these maps, we find regions with higher thunderstorm activity that are not necessarily very electrically activate. For example Belém (northern part of Brazil) area presents than 250 days with thunderstorms but less than 10 sferics/km2/year, Fortaleza (northeast coast) has less than 50 days in a year with thunderstorms and a density less than 1 sferics/km2/year. São Paulo area though has around 100 days with thunderstorms but more than 16 sferics/km2/year. Thus this electrification behavior is most likely associated with the cloud and precipitation physics complexity among the different precipitation systems observed in Brazil.

In order to understand these particular characteristics, this study will focus on the precipitation measurements taken during the CHUVA field campaign in 2011 to explore some features that might aloud a better understanding of charging mechanisms.

2. CHUVA PROJECT and DATA SET

CHUVA (Cloud processes of tHe main precipitation systems in Brazil: A contribUtion to cloud resolVing modeling and to the GPM - GlobAl Precipitation Measurement) is a research project that aims to build a database that can describe the cloud processes of the main precipitating system in Brazil, in order to improve the satellite rainfall estimation. Moreover, this project is seeking to answer the following questions:

- How to estimate rainfall from warm clouds?
- What is the contribution of rain from warm clouds to the total precipitation in different regions of Brazil?
- How to improve both space and time precipitation estimation of rainfall over the continent for the GPM constellation?
- What are the average characteristics (3D - cloud processes) of the main regimes of precipitation in Brazil?
- What is the contribution of the aerosol in the process of formation of precipitation?
- What are the main surface and boundary layer processes in the formation and

maintenance of clouds?
• How cloud microphysics and electrification processes evolve during the cloud life cycle?
• How to improve precipitation estimation and cloud microphysics description by using conventional and polarimetric radar?

To elaborate the precipitation database that can answer these points, CHUVA prepared a series of 7 field campaigns that will be able to depict the main precipitating systems observed in Brazil, i.e., warm raining clouds, local convection, MCS, MCC, instability lines, and frontal systems.

Until the present moment, 3 field experiments have been realized: Fortaleza (April/2011), Belém (June/2011) and VALE-GLM (November-December/2011). Fortaleza is characterized mainly by warm rain process and maritime precipitating systems, Belém, maritime systems that trigger instability lines, while Vale do Paraíba (VALE-GLM) we find frontal systems, local convection, orographic systems and instability lines.

For this study, the thunderstorms are identified by the lightning measurements of STARNET while the electrical properties are done with the use of field mills that are measuring the vertical electrical field. The precipitation features are diagnosed by the Dual Polarimetric X-Band measurements performed during the 3 CHUVA field campaigns.

3. RESULTS

The daily and hourly lightning distributions along the 3 experiments are shown on Figure 2. It is possible to note that most of the thunderstorms were concentrated during 15-22 UTC, except in Fortaleza that had some episodes during night and early evenings. This daily cycle points to the influence of local convection in the thunderstorm triggering.

For the daily accumulations though, each location presented some different frequencies. Fortaleza, had less than 150 sferics per day, except the first lightning burst with almost 300 sferics per day. Belém in contrast was between 200 and 600 sferics per days and in Vale do Paraiba between 300 and 400 sferics/day. These results are intriguing since one would expect more lightning flashes at VALE than Belém due to its oceanic proximity and influence.

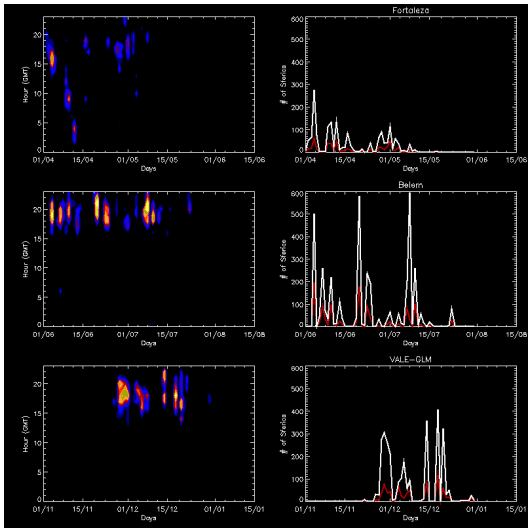

Figure 2. Hourly (left) and daily sferics accumulation during the 3 CHUVA field campaigns: Fortaleza (April/2011), Belém (June/2011) and VALE-GLM (November-December/2011).

In order to understand these differences, we selected some RHIs during the maximum lightning activity during the campaigns. Thus, Figures 3, 4 and 5 show radar reflectivity RHIs over specific azimuths where CHUVA had its super sites for Fortaleza, Belém and VALE-GLM field campaigns respectively. Those cross sections provide detailed information about the vertical structure of the storms sampled and will be used here as examples to understand the differences between the thunderstorms in each field campaign. Detailed analyses require other polarimetric variables and the match between lightning and field mill measurements.

Despite that, these RHIs can be used to seek some features among those thunderstorms. The time of these images correspond to the periods of maximum lightning activity. In all thunderstorms it is possible to see radar reflectivity values above 35 dBZ between the 5 and 7 km height, roughly the isotherm of 0 and -25

^{o}C). These values might indicate the presence of graupel, super cooled water droplets and other ice particles [Petersen et al. 2002] that are the ingredients for the non inductive charging process [Takahashi, 1978 ; Saunders and Brooks, 1992]

Although we find vertical developed towers at Fortaleza and Belém (14-15 km echotops) in comparison to VALE-GLM (< 12 km), the later had around 300 sferics/day against the others with less than 200 sferics/day. In contrast, the vertical electrical at Belém (~3 kV/m) is more intense than VALE (2 kV/m), which is a paradox when we compare to the frequency of lightning strokes. As STARNET measures mainly cloud to ground (CG) lightning, this result might indicate that Belém had more intra-cloud lightning than VALE.

As the electrical field depends on the magnitude of the charges and it is inversely proportional to the distance square, we would expect more charged particle at Belém than VALE. By looking the RHI cross sections (Figure 3-5), Belém and Fortaleza show much more liquid and ice content than VALE due to higher reflectivity values and vertical extend, thus higher electrical field. Due to these characteristics, we would expect several charge centers in the vertical among the maritime storms than the more continental storm that might be better represented by a dipole. The charge centers are highly dependent of hydrometeors development and interactions, and depending on the temperature and the terminal velocity (graupel, ice particles and super cooled water droplets), the hydrometeors might gain positive or negative charges. [Takahashi, 1978; Saunders and Brooks, 1992, Pereyra et al. 200]. So more charge regions would imply in more competition, thus more IC [MacGorman and Nielsen, 1991] opposite to a more defined dipole-tripole that might have more CGs.

In order to understand these mechanisms and the presence of different types of hydrometeors, polarimetric and Doppler measurements are required to evaluate the cloud microphysics and perhaps its temporal evolution.

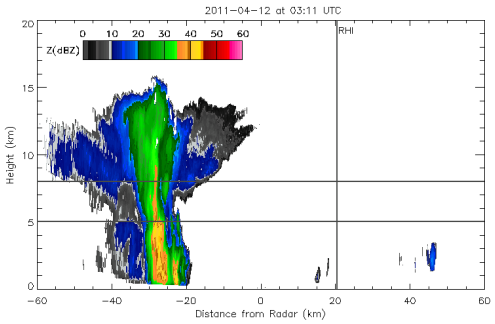

Figure 3. Radar reflectivity RHI for Fortaleza during April 12th at 03:11 UTC

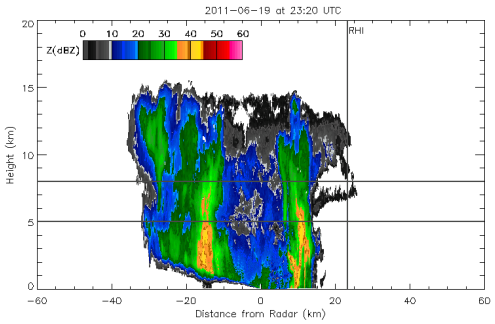

Figure 4. Radar reflectivity RHI for Belém during June 19th at 23:20 UTC

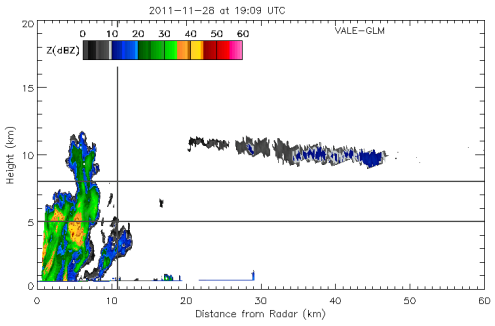

Figure 5. Radar reflectivity RHI for VALE-GLM during November 28th at 19:09 UTC.

Figure 6. Electrical vertical field at June 19, 2011 in Belém

Figure 7. Vertical electrical field at November 28th in Vale do Paraíba.

4. CONCLUSIONS

This study presented a preliminary analysis of some thunderstorms that developed in Brazil and were observed during the CHUVA field campaigns. The main interesting features found were: a) the vertical extent of the maritime (Belém and Fortaleza) thunderstorms that produced high electrical field (> 3 kV/m) but few lightning, the opposite to VALE-GLM storm that was shallower, had more lightning and the vertical electrical field was under 2 kV/m.

Although we only used radar reflectivity values, it seems that a competition between the charge regions might be responsible for the low frequency of CG at Belém and Fortaleza than at VALE.

Later studies will concentrate on the analyses of polarimetric and Doppler measurements to seek the hydrometeor identification and vertical movements, because the collision between graupel and ice particles on the presence of super cooled water droplets is the key mechanism for cloud electrification.

5. REFERENCES

Pereyra, R. G., E. E. Avila, N. E. Castellano, and C. P. R. Saunders, 2000:Alaboratory study of graupel charging. J. Geophys. Res., 105, 20 803–20 812.

MacGorman, D. R., and K. E. Nielsen, 1991: Cloud-to-ground lightning in a tornadic storm on 8 May 1996. *Mon. Wea. Rev.,* **119,** 1557–1574.

Morales, C.A., J.R., Neves,,E. Anselmo, 2012: Sferics Timing and Ranging Network – STARNET: Evaluation over South America, XIV International Conference on Atmospheric Electricity, August 8-12, 2011, Rio de Janeiro, Brazil

Saunders, C. P. R., and I. M. Brooks, 1992: The effects of high liquid water content on thunderstorm charging. *J. Geophys. Res.,* **97,** 14 671–14 676.

Takahashi, T., 1978: Riming electrification as a charge generation mechanism in thunderstorms. J. Atmos. Sci., 35, 1536–1548.

6. ACKNOWLEGEMENTS

This work is funded by FAPESP grant # 2009/15235-8 (CHUVA Project) and partly funded by CAPES-PROEX.

HIGH-RESOLUTION SIMULATION RESULTS OF KINEMATIC AND DYNAMIC COLLISION STATISTICS OF CLOUD DROPLETS

Bogdan Rosa[1], Hossein Parishani[2], Orlando Ayala[2], Lian-Ping Wang[2*], and Wojciech W. Grabowski[3]
[1]*Institute of Meteorology and Water Management - National Research Institute, 61 Podlesna St., 01-673 Warsaw, Poland*
[2]*Department of Mechanical Engineering, University of Delaware, Newark, Delaware 19716, U.S.A.*
[3]*Mesoscale and Microscale Meteorology Division, National Center for Atmospheric Research, PO Box 3000, Boulder, Colorado 80307-3000, USA*

1. INTRODUCTION

Collision-coalescence of cloud droplets is a necessary step for the development of warm rain, namely, the transformation of small cloud droplets into rain drops. Research in recent years has demonstrated that small-scale turbulent motion can enhance the collision rate of droplets by either enhancing the relative velocity and collision efficiency or by inertia-induced droplet clustering. Quantitative description of the effects of air turbulence remains challenging due to experimental difficulties in probing statistics at droplet scales and computational difficulties in simulating all relevant scales of the turbulent flow. In this study, we first address computational issues related to direct numerical simulations (DNS) of turbulent collision-coalescence. We continue to develop a hybrid DNS approach incorporating DNS of air turbulence, disturbance flows due to droplets, and droplet equation of motion, to quantify turbulent collision rate and collision efficiency of sedimenting inertial droplets. Highly scalable hybrid DNS simulations are developed to increase the range of scales or size of the computation domain so that most turbulence scales affecting droplet pair statistics can be faithfully represented. This makes it possible to perform simulations with background-flow Taylor microscale Reynolds number up to 500 and with up to 10 million droplets. We present results of dynamic and kinematic collision statistics (i.e., radial distribution function and relative velocity) from these high-resolution simulations. A key issue to be discussed is how these statistics vary with droplet size and flow Reynolds number.

2. METHODOLOGY

In recent years, direct numerical simulations (DNS) of multiphase flows have emerged as an important tool for studying collision-coalescence of cloud droplets. Spectral-based DNS provides accurate and quantitative representation of small-scale physical processes occurring in clouds. The rapid progress in both the numerical methods and availability of high-performance supercomputers allows DNS to address flows at a somewhat wider range of Reynolds numbers, thus its relevance to applications continues to grow.

The earlier DNS implementations for particle-laden turbulent flows were single-threaded applications designed for vector computers [1, 2]. They are limited to low Taylor-microscale flow Reynolds numbers (typically less than 100). As a result, only the dissipation ranges of energy spectra were adequately represented in the simulations. In addition, memory constraints did not allow tracking of a large number of particles, consequently collision statistics had large numerical and physical uncertainties.

The emergence of multiprocessor computers with shared memory model opens up new opportunities for developing multi-threaded codes. They allow higher grid resolutions to be handled at a reasonable wall-clock time. To develop multi-threaded codes, standard OpenMP parallel programming libraries must be employed. An important goal in this approach is to distribute uniformly tasks among different computing nodes. Assigning particular tasks to a processor is performed by loop splitting. Although the combination of shared memory computers with OpenMP libraries has a substantial advantage in code development, there are also several limitations. Firstly, both memory and number of processors are strictly dependent on machines and very limited. For example, each node in IBM Power 575 cluster (4064 POWER6 processors running at 4.7 GHz) has 32 processors and a maximum of 64GB memory. Secondly, the codes cannot scale well due to a bottleneck in CPU-to-memory connection. In terms of problem size, parallelization with OpenMP could efficiently handle problems up to 128^3 flow grid points with $O(10^5)$ droplets, yielding a maximum Reynolds number of $R_\lambda \sim 75$ [10].

Since 2003, clock frequencies of CPUs begun to stagnate or even decrease (due to energy constraints). The number of cores per CPU started to double every two to three years. Therefore, it was necessary to develop a new implementation suitable for computers with architecture based on distributed memory. The main difficulty in developing such codes is uniform distribution of tasks among processing units. In the simulation of droplet collision-coalescence in a turbulent flow, one must deal with two different approaches in a single simulation: Eulerian grid for turbulent flow and Lagrangian movement of droplets (particle tracking). Our first DNS implementation on a supercomputers with distributed memory was based on 1D domain decomposition and used MPI (Message Passing Interface) library for data communication. Scalability of the code (without droplet-droplet aerodynamic interaction) up to $O(100)$ cores has been presented in [4, 5]. This implementation was a significant step forward. It allowed utilizing a larger number of processors (up to the number of grid points in

*Corresponding author: Department of Mechanical Engineering, 126 Spencer Laboratory, University of Delaware, Newark, Delaware 19716-3140. Phone: (302) 831-8160; Fax: (302) 831-3619; Electronic mail: LWANG@UDEL.EDU

the decomposed direction), large memory size, and improved cache utilization, leading to a higher overall computational efficiency. In this paper we present an improved version of the code, which is based on two-dimensional (2D) domain decomposition (DD). The 2D DD implementation scales further the needed data communication, by employing a larger number of processors, and makes it possible to perform simulations at higher flow Reynolds numbers.

Figure 1 illustrates the concepts of 1D and 2D domain decompositions. The computational domain is decomposed along the directions perpendicular to gravity in order to minimize the number of droplets crossing the subdomain boundaries, MPI is used to communicate between the subdomains whenever the solution or data collection procedure requires data from non-local processors.

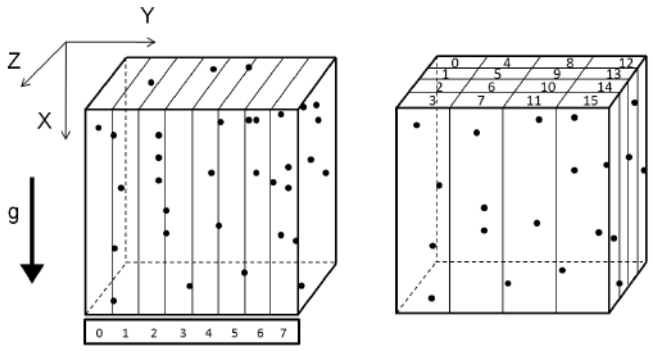

FIG. 1: Two spatial domain decompositions. Left: 8 subdomains in 1D decomposition, Right: 16 subdomains in 2D decomposition. Fluid nodes and droplets in each subdomain are assigned to an individual processor. In this figure 4 and 8 divisions are used for illustration purpose.

The basic ideas and algorithms for the hybrid DNS approach have been presented in [6]. Therefore, only a brief description of the approach is given here.

2.1 Flow simulation

The first step of the multiphase numerical simulation is to develop homogenous turbulent flow in a cubic domain with periodic boundary conditions. The flow is modeled by solving incompressible Navier-Stokes (N-S) equations:

$$\frac{\partial \mathbf{U}}{\partial t} = \mathbf{U}\times\omega - \nabla\left(\frac{P}{\rho}+\frac{1}{2}\mathbf{U}^2\right) + \nu\nabla^2\mathbf{U} + \mathbf{f}(\mathbf{x},t), \qquad (1)$$

$$\nabla\cdot\mathbf{U}(\mathbf{x},t) = 0. \qquad (2)$$

Here $\omega \equiv \nabla\times\mathbf{U}$ is the vorticity vector, P is the pressure, ρ is fluid density and ν is fluid kinematic viscosity (in our simulations ν is the air viscosity). To achieve a stationary turbulence, the flow is driven by the forcing term $\mathbf{f}(\mathbf{x},t)$ which is nonzero only for a few low-wave-number modes in Fourier space. Discretization of the domain is carried out by uniform division of the domain into N^3 grid points, where N is the number of grid points in each direction and takes the values of 2^n, n being a positive integer. The restrictions on N comes from the use of the fast Fourier transform (FFT) algorithm. At these grid points, the turbulent fluid velocity is computed in spectral space yielding the physical fluid velocity by inverse Fourier transform. Further mathematical details of the pseudo-spectral method is given in [1]. The use of spectral methods for HDNS has several advantages, such as the simplicity of forcing the turbulent flow and imposing periodic boundary conditions, and high computational accuracy. On the other hand, use of the spectral method involves significant computational complexity, and in the case of a parallel implementation, intense communication between processes due to FFT. So far, only a few 3D FFT implementations for distributed memory computers have been documented in the literature. For our previous DNS code based on 1D domain decomposition we used algorithm developed by Dmitruk *et al.* (2001) [8]. The new 2D DD implementation code utilizes a 2D DD implementation of 3D FFT. This new algorithm is based on standard FFTW (*www.fftw.org*) and sequence of parallel transpositions. Details of the new FFT algorithm are presented in [9].

2.2 Droplet tracking

Droplet tracking starts from the moment when the flow becomes statistically stationary. Droplets are initially introduced to the flow at random locations. To achieve a truly random distribution of their location, a single core creates random locations for all droplets in the domain. Then, the coordinates of the droplets are broadcasted to their host domains. This task is performed at the onset of the simulation and the cost is negligible compared to the full simulation.

Once the undisturbed fluid velocity $\mathbf{U}(\mathbf{Y}^{(k)}(t),t)$ is computed, droplets are advanced by solving their equation of motion which for the $k-$th droplet becomes:

$$\frac{d\mathbf{V}^{(k)}(t)}{dt} = -\frac{\mathbf{V}^{(k)}(t) - \left(\mathbf{U}(\mathbf{Y}^{(k)}(t),t) + \mathbf{u}^{(k)}\right)}{\tau_p^{(k)}} + \mathbf{g} \qquad (3)$$

$$\frac{d\mathbf{Y}^{(k)}(t)}{dt} = \mathbf{V}^{(k)}(t) \qquad (4)$$

where $\tau_p^{(k)} = 2\rho_p(a^{(k)})^2/9\mu$ is the Stokes inertial response time of the k-th droplet, μ is the air dynamic viscosity, $\mathbf{g}$ is the gravitational acceleration and $\mathbf{u}^{(k)}$ is the air perturbation velocity originating from the motion of surrounding droplets.

Two additional tasks have to be completed before equations 3 and 4 can be integrated. First, interpolation of the fluid velocity from the regular grid to the location of the droplets must be performed. Second, Stokes disturbance velocities $\mathbf{u}^{(k)}$ must be solved. The location and velocity of each droplet are advanced by integrating the equation of motion, with a fourth-order Adams-Moulton scheme (chapt. 16.7 in [12]) for droplet velocity and a fourth-order Adams-Bashforth scheme (chapt. 16.7 in [12]) for droplet location.

2.3 Velocity interpolation

Interpolation of the fluid velocity from the regular grid points to the droplet centers requires substantial computational effort. The interpolation is done for a large number of droplets at every time step. For parallel implementations based on spatial domain decomposition, the interpolation algorithm requires intensive communication between processes in order to obtain data from a sufficiently large volume surrounding every droplet. Therefore, optimization of this task is essential to obtain high computational efficiency. The size of the interpolation volume (and the number of grid points within) determines the cost of the interpolation. The size of the interpolation volume is specified by the order (thus the precision) of the interpolation method. Several different interpolation techniques have been developed in past, see a brief review of the commonly employed methods in [4].

We use 6-point Lagrangian interpolation in each spatial direction. For grid points near subdomain boundary, fluid velocities at 3 grid layers from right and top (or 2 grid layers from left and bottom) are required. As illustrated in Figure 2, data

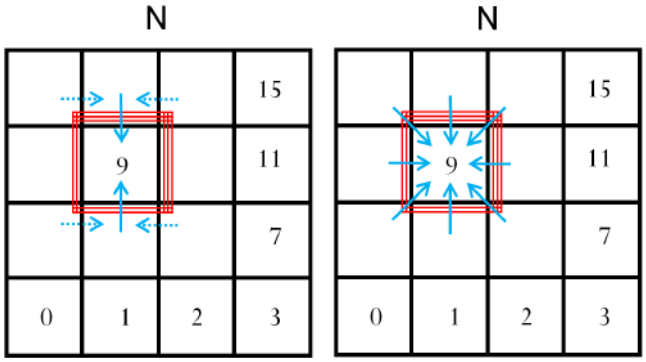

FIG. 2: Two different communication strategy for fluid velocity interpolation. Red lines show the layers of grid velocity data to be communicated. Left panel: Indirect communication. First, all subdomains communicate to right and left subdomains. The data of the corner subdomains is extracted and padded to the beginning and the end of local buffer matrix in the north and south subdomains. The buffered data is communicated form north and south subdomains altogether. Right panel: Direct communication. All data is communicated to and from 8 neighboring subdomains directly.

communication could be achieved in two different manners. The left panel shows an indirect (or successive) communication scheme where the grid velocity data is first communicated to the right and left. After the first communication is completed, the data of corner subdomains are extracted and buffered along with north and south subdomain data. The final communication step from north and south completes the data transfer. This scheme requires blocking in the first stage of communication. On the other hand, in the right panel of Figure 2, we show a direct communication scheme which is achieved by communicating data directly to and from neighboring subdomains. In this way all the communication could be performed at the same time without blocking.

Our experiments show that for the range of parameters and decomposition size we are interested in, there is only $\sim 1\%$ run-time difference between the two schemes. This shows that the communication overhead of the direct method compensates the blocking and extra copy time required for indirect scheme. In the rest of this paper, we will make use of the direct communication scheme (right panel of Figure 2) as we found its performance to be less machine dependent.

Halo zone in the 6-point Lagrangian interpolation method has similar or even larger thickness than the halo zones in other interpolation methods with comparable precision. Size of the halo has significant impact on computational efficiency. For algorithms with large halo, more time is consumed to transfer the data between nodes. The use of the Lagrangian interpolation in the new code is beneficial in the sense that our new results can be directly compared to the results obtain from the previous implementations in which the same interpolation method was used.

2.4 Aerodynamic interaction between droplets

If Stokes disturbance velocities of all N_p droplets in the system are superposed appropriately [7, 11], we will have a linear system for disturbance velocities $\mathbf{u}^{(k)}$ felt by the $k-$th droplet:

$$\mathbf{u}^{(k)} = \underbrace{\sum_{m=1}^{N_p}}_{m\neq k} \mathbf{u}_S\left(\mathbf{Y}^{(k)}(t)-\mathbf{Y}^{(m)}(t);a^{(m)},\mathbf{V}^{(m)}-\mathbf{U}(\mathbf{Y}^{(m)},t)-\mathbf{u}^{(m)}\right) \qquad k=1,2,...,N_p \tag{5}$$

where Stokes disturbance flow of the $k-$th droplet is:

$$\mathbf{u}_S(\mathbf{r}^{(k)};a^{(k)},\mathbf{V_p}^{(k)}) = \left[\frac{3}{4}\frac{a^{(k)}}{r^{(k)}}-\frac{3}{4}\left(\frac{a^{(k)}}{r^{(k)}}\right)^3\right]\frac{\mathbf{r}^{(k)}}{(r^{(k)})^2}(\mathbf{V_p}^{(k)}\cdot\mathbf{r}^{(k)})+ \left[\frac{3}{4}\frac{a^{(k)}}{r^{(k)}}+\frac{1}{4}\left(\frac{a^{(k)}}{r^{(k)}}\right)^3\right]\mathbf{V_p}^{(k)}. \tag{6}$$

Here particles with index m will be all particles neighboring the target particle with index k. In this paper, the terms particles and droplets are used interchangeably. The disturbance velocity acting on a given droplet depends on the background turbulent flow, as well as positions and velocities of all other droplets in the system. It is important to note that periodicity of the domain holds for particles and disturbance velocity $\mathbf{u}^{(k)}$ as well as for the flow.

Given $a^{(k)}, \mathbf{V}^{(k)}$, $\mathbf{Y}^{(k)}$ and $\mathbf{U}(\mathbf{Y}^{(k)},t)$ at a specified time t, (5) is a system of equations of $3N_p$ unknowns for the three components of the disturbance velocities $\mathbf{u}^{(k)}$ of the N_p droplets. The disturbance velocity at the location of each droplet is coupled with the disturbance velocities of all other droplets and the three spatial components of the disturbance velocity cannot be separated to form three independent smaller linear systems. Therefore, system (5) must be solved as a whole to yield the disturbance velocities $\mathbf{u}^{(k)}$. In our simulations, we use an efficient iterative scheme known as the generalized minimum residual algorithm GMRES [12] with pre-computation of coefficients to solve the system (5).

The solution of (5) could be significantly accelerated by truncating the aerodynamic disturbance flow of a droplet (with radius a) to some optimal distance $H_{trunc} \times a^{(k)}$. H_{trunc} is non-dimensional value, which could be determined by analysis of the statistical data from previous numerical experiments. As far as collision statistics are concerned, Ayala *et al.* (2007) [6] showed that one could truncate the summation in (5) and restrict the radius of influence of the disturbance flow. Their experiments showed that the computed collision efficiency is insensitive to H_{trunc} if $H_{trunc} > 35$. In the new implementation the truncation radius is set to $H_{trunc} = 50$ which is more conservative than $H_{trunc} = 35$.

To limit the data communication to the nearest neighbor subdomains, we assume that the truncation sphere of any individual droplet at most covers a volume belonging to immediate neighboring subdomains. Since, the droplet radii are in the range of 10 to 60 μm and are much smaller than the Kolmogorov length of the undisturbed flow, this assumption does not pose a severe restriction on the maximum number of cores. This assumption amounts to the upper bound on the number of subdomains in each decomposed direction, as:

$$N_{subd1} \leq \left[\frac{L_{box}}{H_{trunc} \times a_{max}} \right] \tag{7}$$

where N_{subd1} is the number of subdomains in a single decomposed direction, a_{max} is the maximum radius of the droplets in the system, L_{box} is the domain size in the decomposed direction and $[.]$ denotes the integer part of a real number.

2.5 Parallel implementation of droplet tracking

In our implementation, communication of data associated with droplets is implemented by proper use of droplet indices and careful rearrangement of droplet data when droplets are leaving or entering a subdomain. As shown in Figure 3, we have made data communication effective by creating a halo layer around each subdomain. The thickness of this halo region is preset based on the maximum truncation radius. At each time step, the required data of the droplets in this halo zone are communicated between neighboring subdomains to make data available to a host subdomain.

In order to efficiently locate the droplets and their immediate neighboring droplets inside the truncation sphere, we make use of cell-index method and the concept of linked lists [13]. This is numerically implemented by dividing the domain into small cells and keeping track of droplet indices inside each cell. This speeds up the process of finding neighbor droplets, without affecting the final results. To be able to track a specific particle over the whole domain, we also introduce the droplet global index. This global index is unique to each droplet and will be passed to host subdomain if droplet changes subdomain. The index also has another useful function, namely, it facilitates trajectory tracking of any selected droplet.

Particle motion between subdomains requires the transfer of migrating particle's data from the source subdomain to host subdomain. At each time step, after advancing the particle location, particles that need to migrate are detected, and their

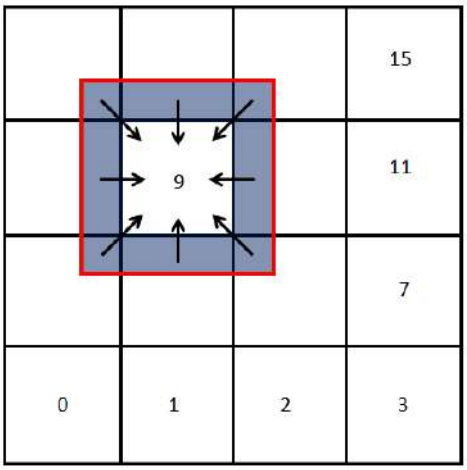

FIG. 3: Dark region around subdomain 9 shows the "halo region" in 2D domain decomposition. Particles' data in this region is made available for subdomain 9 via communications from 8 neighboring subdomains. Arrows indicate the direction of data communication.

data are stored in 8 different buffers depending on where their new location is. Then the buffered lists are communicated between source and host subdomains. Departed particles are removed from local particle list and arrived particles are added. In this step we take care of periodicity of the particles, so that particles which are moving the domain on one side are brought back to their host domain on the other side of the computational box. At this stage, another cell-index sorting is performed to locate and relate particles to their host cells.

3. PARALLEL PERFORMANCE

The scaling performance of different tasks in 1D and 2D decompositions are shown in Figure 4. The timing measurements are carried out for a benchmark problem of 2×10^6 droplets of radii 20 and 40 microns at 512^3 grid resolution. All measurements are carried out on NCAR's Bluefire machine with identical compiler and optimization settings. Measurements are averaged over 1000 time-steps of simulation.

We observed following behavior for 1D decomposition. All simulation tasks have an almost ideal scaling with the number of cores for small number of processors, but quickly start to saturate at about $N_{proc} = 64$. This suggests that 1D decomposition will not be the method of choice for larger problem sizes.

On the other hand, the 2D decomposition does not show any symptom of saturation up to 1024 cores suggesting that the 2D implementation is highly scalable. We note that the 2D domain decomposition code could not be run on small number of cores due to memory requirements. Unlike 1D decomposition, in 2D decomposition flow simulation is the bottleneck of computation. This is mainly the result of high cost of 3D FFT for large number of cores on a 2D decomposed domain.

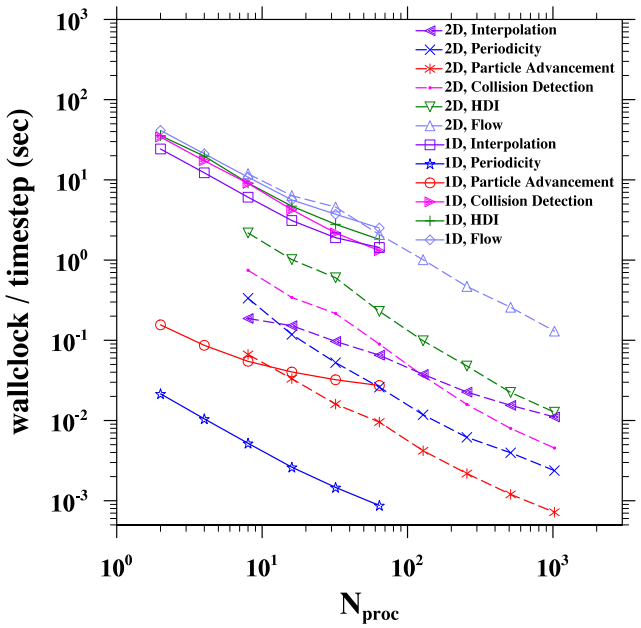

FIG. 4: Scalability of the major tasks in the HDNS code in terms of the total execution time

TABLE I: Flow parameters after reaching statistically stationary state (DNS units, grid size 256^3)

r.m.s fluctuating velocity	0.942 ± 0.012
Energy dissipation rate	0.398 ± 0.030
Reynolds number R_λ	151.4 ± 3.3
Resolution	1.091 ± 0.020
Skewness	-0.506 ± 0.006
Flatness	5.631 ± 0.178
Kolmogorov length η	$(8.628 \pm 0.162) \times 10^{-3}$
Kolmogorov time τ	$(5.727 \pm 0.215) \times 10^{-2}$
Kolmogorov velocity υ	0.150 ± 0.003
Transverse Taylor microscale	0.209 ± 0.006
Longitudinal int. length scale	1.059 ± 0.017
Eddy turnover time Te	2.241 ± 0.125
CFL	0.228 ± 0.016

4. SIMULATION RESULTS

In this section, we report the DNS results based on the 2D DD implementation. The results include characteristics of the background turbulent flow field, and kinematic and dynamic statistics related to collision-coalescence of noninteracting droplets. The numerical experiments are limited to self-collision (collision of the same-size droplets).

4.1 Background turbulent flow

The DNS simulation of the background turbulent flow, has been performed for the periodic box with $N = 256^3$ uniformly distributed grid points. To initialize the isotropic velocity field we used random phase algorithm with prescribed energy spectrum as in [14] (equation 2.5). Statistically stationary state is obtained by integrating the N-S equation and continuous injection of the kinetic energy to large-scale motions. To apply the energy we employ deterministic forcing scheme adopted from [15]. In this scheme, the energy levels of two inner shells ($0.5 < |\mathbf{k}| < 1.5$ and $1.5 < |\mathbf{k}| < 2.5$) are specified as constants and equal $E(1) = 0.309556$ and $E(2) = 0.356409$, respectively. The time step was chosen to ensure numerical stability, accuracy and high numerical performance. The spatial resolution of the simulation was monitored by the value $k_{max}\eta$, which should be greater than unity. On the other hand, this parameter ($k_{max}\eta$) should be kept close to unity in order to maximize turbulent Reynolds number R_λ. Table I lists the average values of key flow parameters obtained from the benchmark simulation.

In order to validate the new DNS code, one-dimensional energy spectrum has been computed and compared with reference simulations. Figure 5 shows the normalized energy spectrum computed in the current simulation and the spectra from the simulations performed using older version of the MPI code (1D domain decomposition). Additionally, the spectra from DNS are compared with experimental data measured in three different wind tunnel experiments [16–18]. In each of these experiments the turbulence was generated by specially designed grids. The measurement stations were located far from the turbulence-inducing grids, at the places where the flow was homogenous and isotropic. We chose the one-dimensional energy spectrum for comparison because this quantity can be directly measured in the wind tunnel. Moreover, 1D energy spectrum can be more accurately computed than for example the three-dimensional spectra, since the modes are more evenly distributed [1].

We conclude that, in the inertial subrange, all the experimental data agree very well with curves from numerical simulations.

4.2 Radial distribution function and relative velocity

Radial distribution function (RDF) is a measure of preferential concentration of droplets carried by the turbulent flow. Numerous efforts using different approaches, i.e., analytical [19, 20], numerical [21–26] and experimental [24], have been made in past to compute or measure the RDF. Most of the studies claim that the RDF satisfies power law

$$g(r) = c_0(\eta/r)^{f(St)}, \tag{8}$$

where the exponent $f(St)$ depends on the particles Stokes number.

The RDF together with radial relative velocity evaluated at contact, i.e., for nearly touching particles ($r = R$, $R = a_1 + a_2$) yields the kinematic collision kernel Γ^K.

$$\Gamma^K_{12} = 2\pi R^2 \langle |w_r|(r = R)\rangle g_{12}(r = R), \tag{9}$$

where the radial relative velocity w_r is defined in terms of the

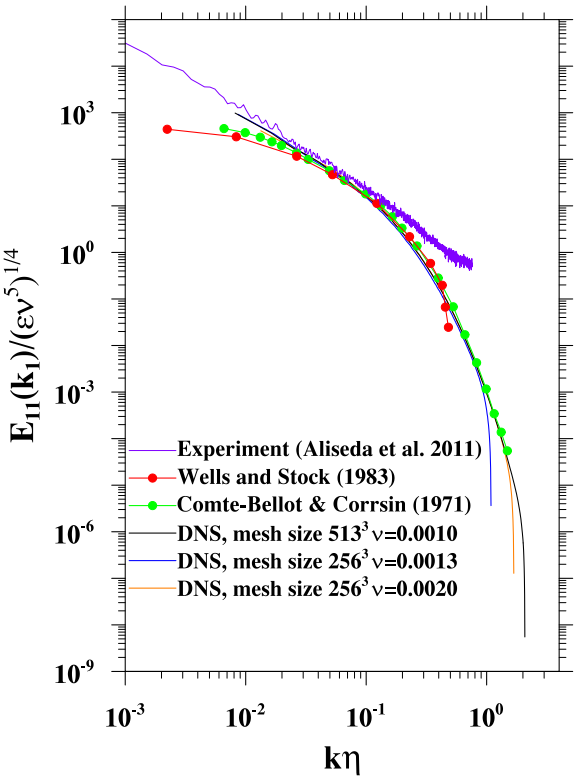

FIG. 5: Normalized 1D energy spectra of the simulated flows with different viscosity. The blue line corresponds to the simulation performed using the new (2D MPI) implementation. The figure displays also data from the three different wind tunnel experiments [16–18].

relative velocity **w** between two droplets with separation vector **r** as $w_r \equiv \mathbf{w}\cdot\mathbf{r}/|\mathbf{r}|$, with $r \equiv |\mathbf{r}|$.

The convenient method to compute the RDF on the fly in DNS simulations was proposed in [27, 28]. In the method, the RDF at contact ($r = R$) is computed directly from the definition

$$g_{ii}(r;t) = \frac{\mathrm{N_{pairs}}/\mathrm{V_s}}{N_i(N_i-1)/V_\mathrm{B}}, \qquad (10)$$

where $i = 1$ or 2 and N_{pairs} is the total number of pairs detected with separation distance (r) falling in a spherical shell of inner radius equal to $R-\delta$ and outer radius equal to $R+\delta$. Here δ is small fraction (1%) of R [27, 28]. V_s is the volume of the spherical shell, $V_s = 4\pi[(R+\delta)^3-(R-\delta)^3]/3$. N_i is the total numbers of a_i droplets, used in the simulation, V_B is the size of computational domain. $g_{ii}(r;t)$ is further averaged over time to obtain $g_{ii}(r=R)$. This method is relatively efficient and simple to implement but for very small droplets is not accurate. This, is due to the small number of events in which the droplets are located close to each other. Consequently the statistical uncertainty is large. Therefore, in this study we computed the RDF at $r = R$ using a more accurate method. In the first step, the RDF is computed in the usual manner as in [27] but for different separation distances. In the second step we fit the curve described by equation 8 to the discrete data. In order to perform the first step, we have to generalize definition of the RDF (equation 10) by new variable shell size, namely, the inner radius equal to $r-\delta$ and outer radius equal to $r+\delta$ where $r \in [R, 10R]$ is discretized into 180 equal-size bins. Although, the maximum of r can choose any arbitrary value larger than R, but computational restrictions (related to domain decomposition and amount of data to be sent and received between processes in parallel MPI code) do not allow r to be larger than a specific value. Ultimately, in our simulation r is restricted to $[R, 10R]$.

Similar to the RDF, relative velocity between droplet pairs has been computed.

In Figures 6 and 7 the radial distribution function and the relative velocity as a function of separation distance are presented. The kinematic parameters have been determined with 10 million droplets.

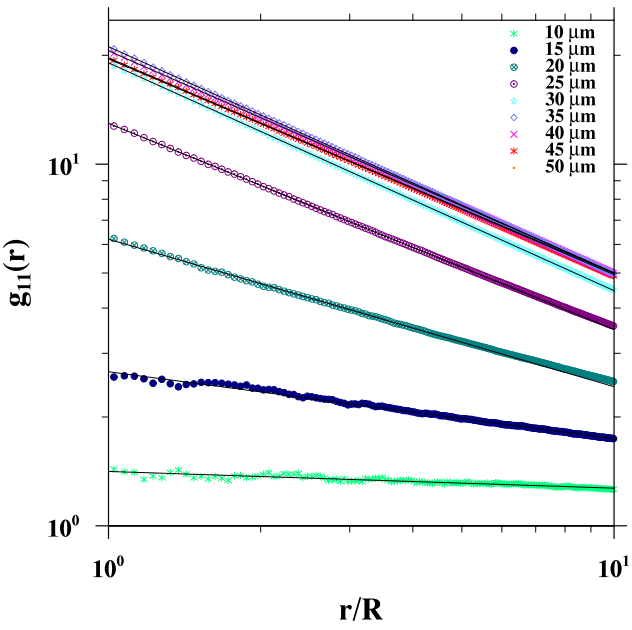

FIG. 6: Radial distribution function as a function of separation distance. Black lines represent the best exponential fit to the data.

The monodisperse pair statistics of nearly touching particles are shown in Figs. 8 and 9, along with results at other flow Reynolds numbers. For larger droplets, the pair statistics increase with the flow Reynolds number. However, for any given droplet size, there is a tendency of saturation, namely, the pair statistics eventually become insensitive to flow Reynolds number. This saturation for smaller droplets is reached at smaller flow Reynolds number, since the range of flow scales affecting the pair statistics is more limited for smaller droplets due to their smaller Stokes number.

Direct comparison of the three-dimensional RDF with the RDF measured in a wind tunnel is problematic. It is more convenient to measure experimentally the one-dimensional representation of the RDF function (assuming Taylor's hypothesis of frozen turbulence [17]). Therefore, in order to compare the RDF from two different approaches (numerical and experimental) special 1D version of the RDF has been computed. The methodology of computing the 1D RDF along with relationships between 1D and 3D representations is described in

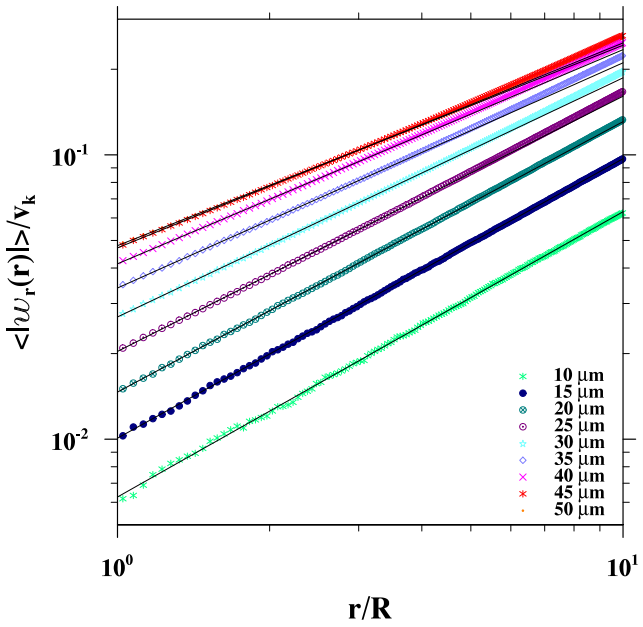

FIG. 7: Radial relative velocity as a function of separation distance. Black lines represent the best fit to the DNS data.

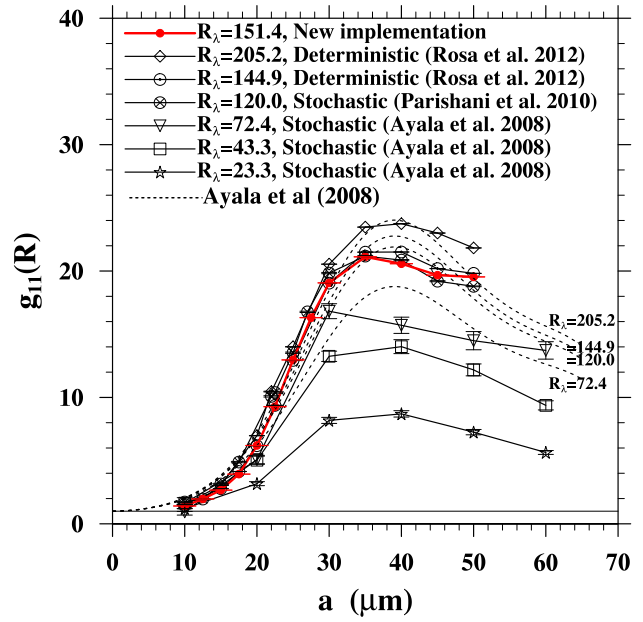

FIG. 8: Radial distribution function at contact ($r = R$) for monodisperse pairs as a function of droplet size for different values of flow Reynolds number. Dashed lines represent theoretical prediction from [29]. All simulations have been performed for energy dissipation ε = 400 cm^2/s^3.

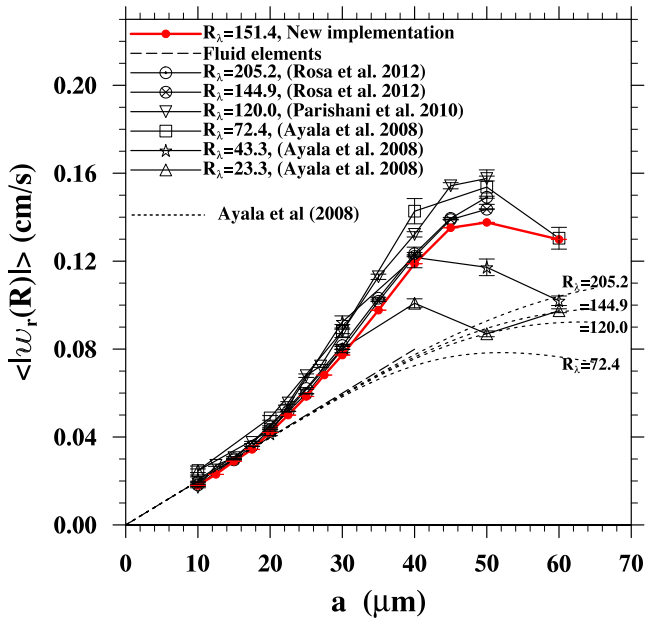

FIG. 9: Radial relative velocity normalized by Kolmogorov velocity at contact r = R for monodisperse pairs as a function of droplet size for different values of Reynolds number. Dashed lines represent theoretical prediction from formulas developed in [29]. All simulations have been performed for energy dissipation ε = 400 cm^2/s^3.

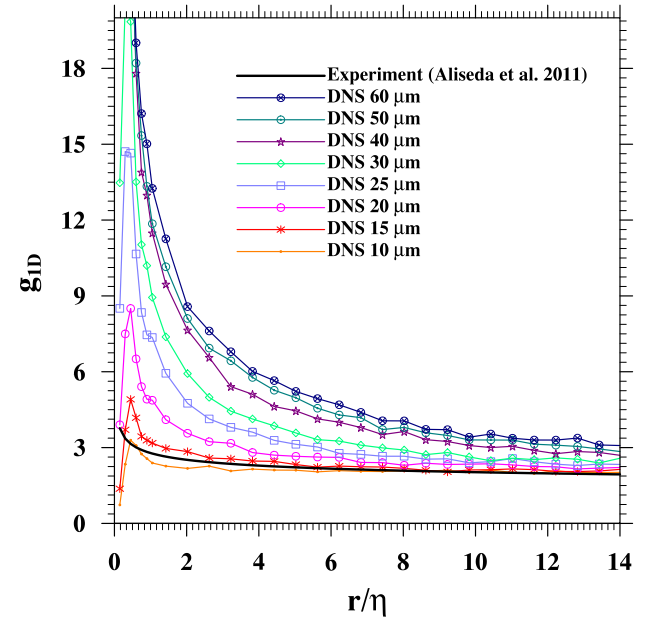

FIG. 10: 1D Radial distribution function computed in DNS. Black line represent 1D RDF measured in the wind tunnel [17]

[30]. In order to avoid problems typical for MPI codes such as the distribution of data in different memory blocks the most convenient way was to perform these calculations in a separate post-processing code.

Figure 10 shows that there is a quantitative agreement between 1D RDF computed in the numerical simulation and measured in wind tunnel. The comparison shows that the RDF, has a large peak at distances below the Kolmogorov length η of turbulence. At large separations relative to the integral length, the RDF shows slow decay to a unit value expected for a random distribution.

4.3 Dynamic and kinematic collision kernels

Here we demonstrate that the kinematic formulation of the collision kernel eq. 9, is consistent with the dynamic formulation. In the computation of the dynamic collision kernel, we employed the same method as in [10]. The collision events were detected during the simulation and the number of collisions was recorded in each time step. The mean and statistical uncertainty of the dynamic collision kernel were evaluated at the post-processing stage. The comparison has been performed for monodisperse collisions of sedimenting droplets with no aerodynamic interactions. For sedimenting inertial droplets the radial relative velocity and RDF are no longer spherically symmetric. Figure 11 presents comparison of kinematic and dynamic collision kernels computed in simulations at different Reynolds numbers and using different implementations. Clearly, the kinematic formulation agrees well with the dynamic kernel in all cases. We also conclude that the newly developed results agree with previous DNS, within statistical uncertainties. Additionally, the numerical

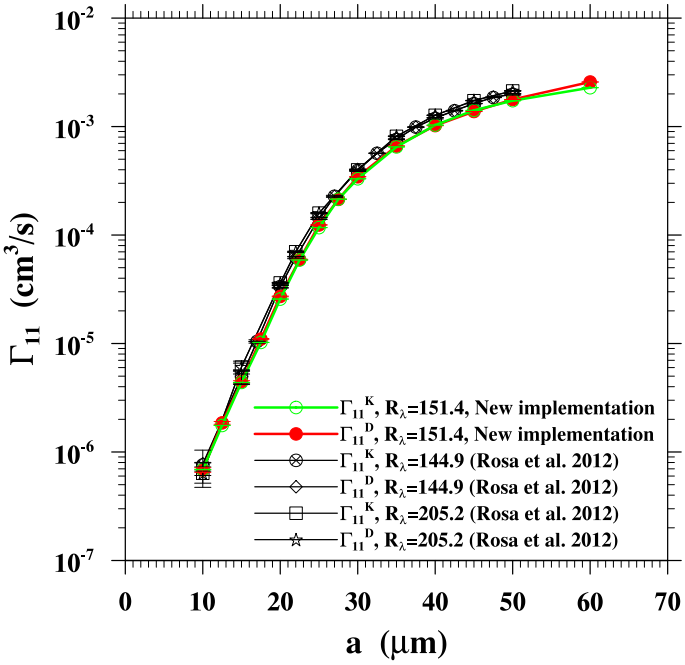

FIG. 11: Comparison of dynamic and kinematic collision kernels. The figure shows the results from different implementations.

values of kinematic collision kernel in cm^{3}s^{-1}, are tabulated in Table II. These tabulated values could be used to guide the development of theoretical parameterization of turbulent collision kernel.

5. SUMMARY AND CONCLUSIONS

In this paper, we reported on our recent efforts in developing high-resolution simulation of turbulent collision of cloud droplets. In order to perform high-resolution simulations, we have developed a novel parallel implementation of hybrid DNS, based on 2D domain decomposition. This new development enables us to conduct hybrid DNS with flow field solved at grid resolutions up to 1024^3 while simultaneously track up to $\sim 10^7$ aerodynamically-interacting droplets.

Using the 2D domain-decomposition hybrid DNS code, we then examined several important aspects of the DNS concerning turbulent collision-coalescence of cloud droplets. First, we showed that the structure of the background turbulent flow agree well both with previous DNS and experimental data. Then we computed radial distribution function and relative velocity for nearly touching particles. For these parameters we achieved good agreement with previous simulations and the theoretical prediction. Additionally, 1D RDF has been computed for a monodisperse system. Finally, kinematic and dynamic formulation of the collision kernel were shown to be consistent for sedimenting droplets.

Acknowledgments

This work was supported by the National Science Foundation (NSF) under grants ATM-0730766, OCI-0904534, OCI-0904449, and CRI-0958512. Computing resources are provided by National Center for Atmospheric Research (NCAR CISL-35751010, CISL-35751014, and CISL-35751015).

References

[1] L.P. Wang and M.R. Maxey, Settling velocity and concentration distribution of heavy-particles in homogeneous isotropic turbulence, *Journal of Fluid Mechanics*, 256:27–68, 1993.

[2] K.D. Squires and J.K. Eaton, Preferential concentration of particles by turbulence, *Phys. Fluids A*, 3:1169–1178, 1991.

[10] 0. Ayala, B. Rosa, L.P. Wang, and W.W. Grabowski, Effects of turbulence on the geometric collision rate of sedimenting droplets: Part 1. results from direct numerical simulation, *New J. Physics*, 10(075015), 2008.

[4] B. Rosa and L.P. Wang, Parallel implementation of particle tracking and collision in a turbulent flow, *Lecture Notes in Computer Science*, pages 388–397, 2010.

[5] B. Rosa, H. Parishani, 0. Ayala, L.P. Wang, and W.W. Grabowski, High-resolution simulation of turbulent collision of cloud droplets, *Lecture Notes in Computer Science*, pages 401–410, 2012.

[6] O. Ayala, W-W. Grabowski, and L.P. Wang, A hybrid approach for simulating turbulent collisions of hydrodynamically-interacting particles. *JCP*, 225:51–73, 2007.

[7] L.P. Wang, 0. Ayala, and W.W. Grabowski, Improved formulations of the superposition method, *J. of the Atmospheric Sciences*, 62:1255–1266, 2005.

[8] P. Dmitruk, L.P. Wang, W.H. Matthaeus, R. Zhang, and D. Seckel, Scalable parallel FFT for spectral simulations on a Beowulf cluster, *Parallel Computing*, 27(14):1921–1936, 2001.

[9] O. Ayala and L.P. Wang, Parallel implementation and scalability analysis of 3d fast fourier transform using 2d domain decomposition, *Parallel Computing* (Submitted), 2012.

[10] 0. Ayala, B. Rosa, L.P. Wang, and W.W. Grabowski, Effects of turbulence on the geometric collision rate of sedimenting

TABLE II: Comparison of dynamic and kinematic collision kernels $[cm^3/s]$. The values of $\delta CK_{dynamic}$ and $\delta CK_{kinematic}$ are the corresponding statistical uncertainties.

$a_i[\mu m]$	$CK_{dynamic}$	$\delta CK_{dynamic}$	$CK_{kinematic}$	$\delta CK_{kinematic}$
10	6.826×10^{-7}	3.311×10^{-8}	6.888×10^{-7}	2.346×10^{-9}
12.5	1.856×10^{-6}	5.381×10^{-8}	1.757×10^{-6}	4.207×10^{-9}
15	4.453×10^{-6}	8.556×10^{-8}	4.377×10^{-6}	6.457×10^{-9}
17.5	1.099×10^{-5}	1.308×10^{-7}	1.024×10^{-5}	1.232×10^{-8}
20	2.717×10^{-5}	2.143×10^{-7}	2.569×10^{-5}	4.365×10^{-8}
22.5	5.948×10^{-5}	3.257×10^{-7}	5.885×10^{-5}	7.347×10^{-8}
25	1.239×10^{-4}	4.652×10^{-7}	1.171×10^{-4}	1.134×10^{-7}
27.5	2.131×10^{-4}	6.212×10^{-7}	2.142×10^{-4}	1.256×10^{-7}
30	3.444×10^{-4}	8.642×10^{-7}	3.301×10^{-4}	2.303×10^{-7}
35	6.611×10^{-4}	1.221×10^{-6}	6.493×10^{-4}	3.873×10^{-7}
40	1.020×10^{-3}	1.670×10^{-6}	1.032×10^{-3}	6.676×10^{-7}
45	1.376×10^{-3}	1.960×10^{-6}	1.411×10^{-3}	9.701×10^{-7}
50	1.776×10^{-3}	2.722×10^{-6}	1.731×10^{-3}	1.516×10^{-6}
60	2.576×10^{-3}	3.762×10^{-6}	2.281×10^{-3}	1.824×10^{-6}

droplets: Part 1. results from direct numerical simulation, *New J. Physics*, 10(075015), 2008.

[11] H. Parishani, B. Rosa, W-W Grabowski, and L.P. Wang, Towards high-resolution simulation of turbulent collision of cloud droplets, *Proceedings of the 7th International Conference on Multiphase Flow, Tampa, Fl, USA*, 2010.

[12] W.H. Press, S.A. Teukolsky, W.T. Vetterling, B.P. Flannery, *Numerical Recipes in Fortran: The Art of Scientific Computing.* Cambridge University Press, (1992).

[13] M.P. Allen and D.J. Tildesley, *Computer Simulation of Liquids.* Oxford University Press, 385 pp. (1987).

[14] J.C. Isaza and L.R. Collins, On the asymptotic behaviour of large-scale turbulence in homogeneous sher-flow, *Journal of Fluid Mechanics*, 637:213–239, 2009.

[15] B. Rosa, H. Parishani, 0. Ayala, L.P. Wang, and W.W. Grabowski, Kinematic and dynamic pair collision statistics of sedimenting inertial particles relevant to warm rain initiation, *J. Phys.: Conf. Ser.*, 318, 072016, 2011.

[16] G. Comte-Bellot and S. Corrsin, Simple Eulerian time correlation of full- and narrow-band velocity signals in grid-generated, 'isotropic' turbulence, *J. Fluid Mech.*, 48:273-337, 1971.

[17] A. Aliseda, C. Bateson, O. Ayala, H. Parishani, L.-P. Wang, and B. Rosa, Experimental and Numerical investigation of a droplet-laden turbulent flow: preferential concentration due to turbulence and its influence on droplet collisions and growth, *64th Annual Meeting of the APS Division of Fluid Dynamics*, Volume 56, Number 18 (2011).

[18] M.R. Wells and D.E. Stock, The effects of crossing trajectories on the dispersion of particles in a turbulent flow, *J. Fluid Mech.*, 136:31–62, 1983.

[19] L.I. Zaichik, and V. M. Alipchenkov, Clustering of low-inertia particles in isotropic turbulence, *High Temperature*, 45:58–67, 2007.

[20] J.H. Chun, D.L. Koch, S.L. Rani, and A. Ahluwalia, Clustering of aerosol particles in isotropic turbulence, *Journal of Fluid Mechanics*, 536:219–251, 2005.

[21] G. Falkovich and A. Pumir, Intermittent distribution of heavy particles in a turbulent flow, *Physics of Fluids*, 16, L47–L50, 2004.

[22] G. Falkovich and A. Pumir, Sling effect in collisions of water droplets in turbulent clouds, *Journal of the Atmospheric Sciences*, 64:4497–4505, 2004.

[23] W.C. Reade and L.R. Collins, Effect of preferential concentration on turbulent collision rates, *Physics of Fluids*, 12:2530–2540, 2000.

[24] E.W. Saw, R.A. Shaw, S. Ayyalasomayajula, P.Y. Chuang, and A. Gylfason, Inertial Clustering of Particles in High-Reynolds-Number Turbulence, *Physical Review Letters*, PRL 100, 214501, 2008.

[25] L.R. Collins and A. Keswani, Reynolds number scaling of particle clustering in turbulent aerosols, *New Journal of Physics*, 6(119), 2004.

[26] J. Bec, L. Biferale, M. Cencini, A. Lanotte, S. Musacchio, and F. Toschi, Heavy particle concentration in turbulence at dissipative and inertial scales, *Physical Review Letters*, 98, 084502, 2007.

[27] L.P. Wang, A.S. Wexler, Y. Zhou, Statistical mechanical description and modelling of turbulent collision of inertial particles, *J. Fluid Mech.*, pages 117–153, 2000.

[28] Y. Zhou, A.S. Wexler, L.P. Wang, Modelling turbulent collision of bidisperse inertial particles, *J. Fluid Mech.*, 433:77–104, 2001.

[29] O. Ayala, B. Rosa, and L.P. Wang, Effects of turbulence on the geometric collision rate of sedimenting droplets. Part 2. Theory and parameterization, *New Journal of Physics*, 10, 2008.

[30] G.L. Holtzer and L.R. Collins, Relationship between the intrinsic radial distribution function for an isotropic field of particles and lower-dimensional measurements, *J. Fluid Mech.*, 459:93–102, 2002.

Re-examination on the performance of Continuous-Flow Diffusion-Chamber type Ice Nucleus Counter

Atsushi SAITO[1], Narihiro ORIKASA[1], Takuya TAJIRI[1], Katsuya YAMASHITA[1] and Masataka MURAKAMI[1]

[1]Meteorological Research Institute/ Japan Meteorological Agency, Tsukuba, Japan

1. INTRODUCTION

Water clouds, ice clouds and mixed phase clouds have different microphysical and radiative properties. It is well known that most precipitation in middle and high latitudes comes through cold rain process, where ice particles play an important role. The activation of ice nuclei is a dominant mechanism to produce ice particles in clouds. The understanding of spatial and temporal distributions and activation processes of natural ice nuclei are important for the improvement on precipitation forecast and climate change projection.

We have been conducting the experimental research by using Continuous Flow Diffusion Chamber type Ice Nucleus Counters (CFDC-INC) for identifying and quantifying the ice formation mechanisms as a part of the study on the indirect effects of aerosol particles on clouds and precipitation.

This paper describes the performance of CFDC-INC. We made a direct observation of cloud droplet formation immediately downstream of the growth section, and report on the accuracy of water saturation setting in the sample air. We also made a direct measurement of the interior surface temperature of the outer cylinder in the evaporation section, and report on valid ranges of the interior surface temperature of the evaporation section outer cylinder for IN measurements with CFDC-INC taking into account the theoretical consideration based on 1-D simulation of ice nucleation, growth and sublimation in the CFDC-INC.

[1]*Corresponding author's address:*
Atsushi SAITO, Meteorological Research Institute/ Japan Meteorological Agency, 1-1 Nagamine, Tsukuba, Ibaraki, 305-0052 Japan; E-mail: asaito@mri-jma.go.jp

2. APPARATUS DESCRIPTION

We built two Continuous Flow Diffusion Chamber type Ice Nucleus Counters (CFDC-INC) based on the design of Rogers et al. (1988, 2001) at Colorado State University, USA and improved them to operate automatically; one is for ground-based observation and another is for aircraft observation. Main improvements are

1) Decrease in heat inertia of inner cylinder, which makes more quick wall temperature control possible.
2) Automatic measurement of temperature and supersaturation spectrum of ice nuclei activation.
3) Automatic procedure to ice cylinder walls, which makes a fully-automated IN measurement possible.

Figure 1 shows a rack mount arrangement of MRI-CFDC1 instrument.

The Continuous Flow Diffusion Chamber (107cm in total length), which has the volume between two ice-coated concentric cylinders, are made of two sections; one is the growth section (49cm) occupying the upper part of chamber and another is the evaporation section (33cm) occupying the lower part of chamber. In the growth section it is possible to set temperature and humidity of the sample air by controlling two ice-coated wall temperatures, separately. Aerosol particles included in the sample air are activated as droplets and ice crystals and grow up further. In the evaporation section the outer cylinder has no-ice on the wall and is kept its temperature as close as possible to that in the growth section. This change in the boundary conditions makes the relative humidity in sample air lower than water saturation, forcing water droplets to evaporate. Ice crystals that survive the evaporation section are detected by optical particle counter at the outlet end of the chamber and counted as ice nuclei.

3. PERFORMANCE CALIBRATIONS

Because the chamber of CFDC-INC is made of two ice-coated concentric copper cylinders, we cannot observe inside of the chamber directly. Therefore the acquisition of the data, which are used to check the performance of CFDC-INC, has been difficult until now.

In our experimental procedures to measure IN activation spectrum in terms of supersaturation, we change wall temperatures of the inner and outer cylinders rather quickly. Therefore, it has been our concerns how rather quick change in wall temperatures influences the performance of the growth section and the evaporation section and IN measurement accuracy.

In addition, the possibility that ice crystals evaporate excessively due to the temperature rise in the evaporation section caused by heat invasion from the environment has been our another concern for a long time.

- **GROWTH SECTION**

To improve the quality of IN measurements, we re-examined a water saturation point in the sample airflow using an outer cylinder of evaporation section specialized for calibration purpose. The configuration of CFDC-INC with the outer cylinder is shown in figure 2. The water saturation point was examined by detecting the initial droplet formation in the sample airflow during an increase of saturation ratio. Figure 3 shows the relationship among temperature, SSi and SSw in sample air as a function of the warm and cold wall temperatures. The change in the position of sample air (the velocity profile of sample and sheath air) between the two cylinders were calculated by Rogers(1988) in consideration of viscosity, pressure, temperature and buoyancy. The cross marks indicate measurements of wall temperatures at the time when the initial droplet formation was detected from the observation window during the increase of saturation ratio.

The cross marks are distributed on the line of SSw=0 % or higher SSw up to several %. Taking into consideration a rather quick change in SSw (2-3 % min^{-1}) during the calibration procedure and a time delay in the detection of droplet formation, it may be said that the water saturation point produced in the real sample air is almost in agreement with that expected theoretically.

- **EVAPORATION SECTION**

We made a direct measurement of the interior surface temperature of the evaporation section. Figure 4 shows the temperature difference between the interior surface of the growth section outer cylinder and that of the evaporation section outer cylinder at different distance from the border of the growth and evaporation sections at different temperature settings at the ice saturation setting (left) and the water saturation setting (right). Because the temperature of the evaporation section outer cylinder is not controlled, but insulated from an environment to some extent, it was revealed that the interior surface temperature was higher than that of the growth section outer cylinder to a large extent. This suggested the possibility for ice crystals to evaporate in the evaporation section excessively.

We calculated the temperature and humidity fields in the evaporation section and growth/evaporation of droplets and ice crystals in CFDC-INC with the modified Rogers's model (1988) using the measured temperatures on the interior surface of evaporation section outer cylinder as a boundary condition. Figure 5 shows the changes in the temperature, SSi, SSw of the sample air and the ice crystal size that is calculated through growth and evaporation of activated particle. If there was a further temperature rise in the evaporation section, the ice crystal would evaporate much faster and become smaller than 2 μm and could not be detected as ice crystal.

We also examined the effect of the abrupt change in sample air temperature at the border of the growth and evaporation sections. The abrupt temperature change would produce a temporal increase (a few % at most) of relative humidity in sample air. The temporal increase of relative humidity in sample air could be suppressed by assuming a transient time of the abrupt temperature change to be 0.3 sec. or more.

Table 1 shows valid temperature ranges of the evaporation section outer cylinder to detect ice crystals activated through deposition nucleation mode with particle size detection threshold of 2μm when the initial ice crystal size and the transient time of the abrupt temperature change are assumed to

be 10^{-2}μm and 0.3 seconds. In addition, Table 2 shows valid temperature ranges to detect ice crystals activated through condensation-freezing nucleation mode under the same conditions as those in Table 1. It is seen that excessive evaporation of ice crystals does not occur by appropriately controlling the temperature of the evaporation section outer cylinder made of the polyvinyl chloride.

4. CONCLUSIONS

The water saturation point was examined by detecting the initial droplet formation in the sample airflow during the increase of saturation ratio. It appears that the water saturation point produced in the real sample air almost agreed with that expected theoretically.

With the temperature rise in the evaporation section, its influence on the evaporation of ice crystals is examined. The valid temperature ranges of the evaporation section outer cylinder for appropriate IN measurements with CFDC-INC are estimated theoretically and some improvement on the evaporation section is proposed.

ACKNOWLEGEMENTS

This study is supported by the Ministry of Education, Culture, Sports, Science and Technology of the Japanese Government under the program of the Grant in Aid for KAKENHI (23244095).

BIBLIOGRAPHY

Rogers, D. C., 1988: Development of a continuous flow thermal gradient diffusion chamber for ice nucleation studies. Atmos. Res., 22, 149-181.

Rogers, D. C., and et al., 2001: A continuous-flow diffusion chamber for airborne measurements of ice nuclei. J. Atmos. Ocean. Technol., 18, 725-741.

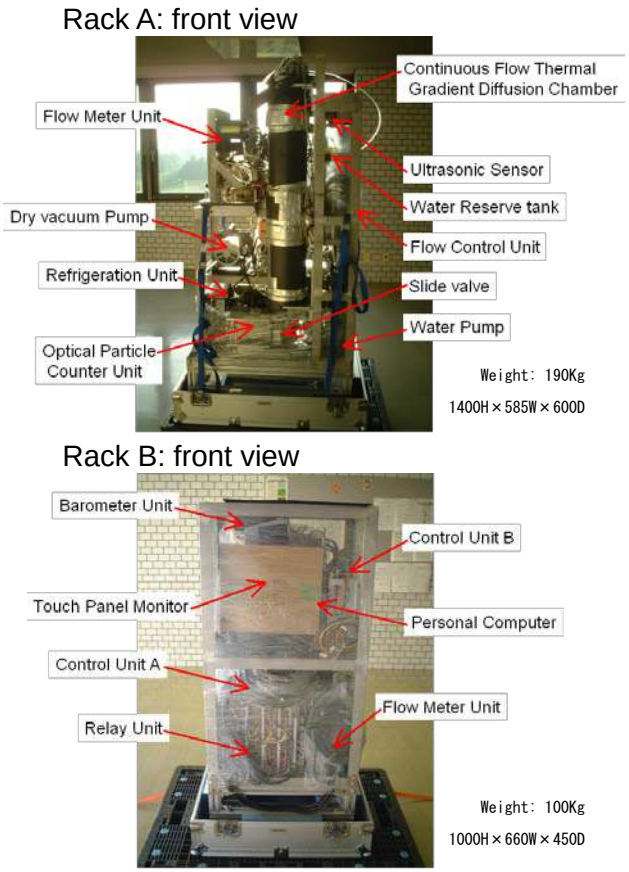

Figure 1. Rack mount arrangement for MRI-CFDC1 instrument.

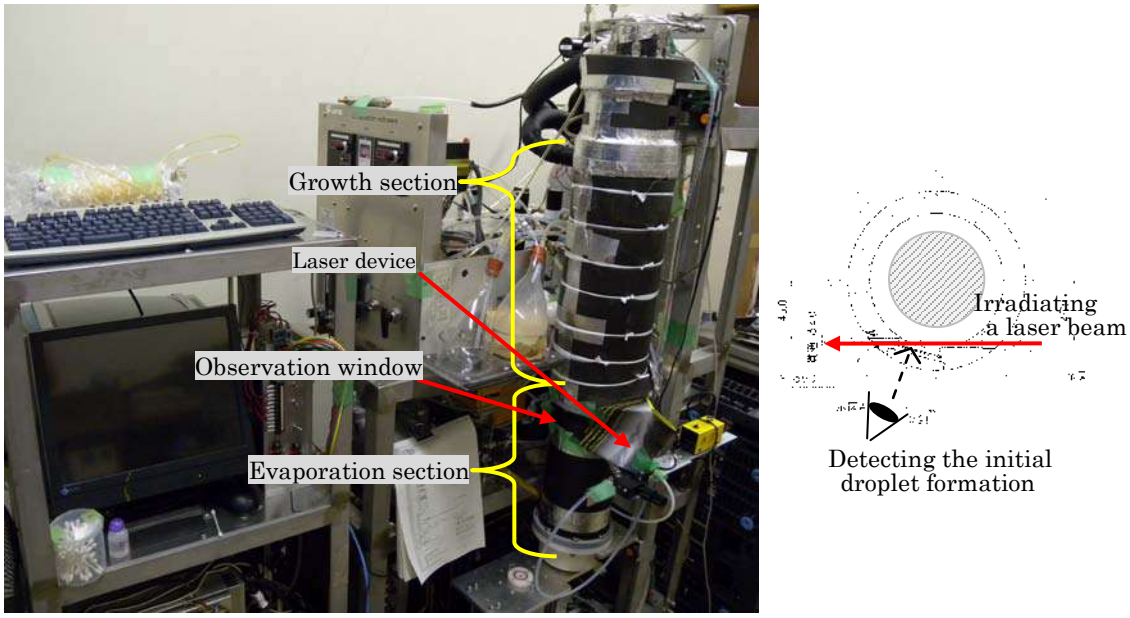

Figure 2. Photo of the CFDC INC with the evaporation section outer cylinder for the water saturation point calibration (left) and horizontal cross-section of the outer cylinder for the calibration (right).

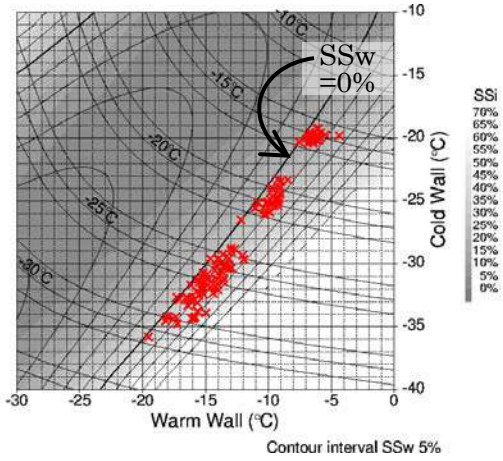

Figure 3. Relationship among temperature (line contour), SSi (shade contour) and SSw (line contour) in sample air as a function of the warm and cold wall temperatures. The cross marks indicate measurements of the wall temperatures at the time when cloud droplet formation was detected.

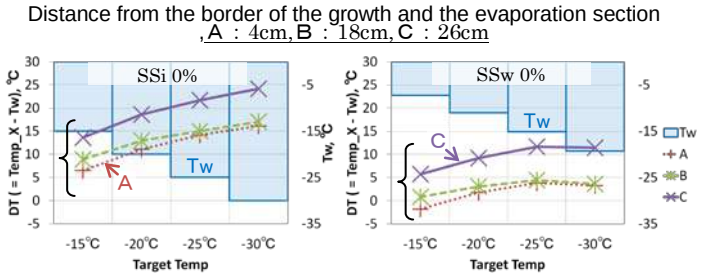

Figure 4. Temperature difference between the interior surface of the growth section outer cylinder and that of the evaporation section outer cylinder at different distance from the border of the growth and evaporation sections at the ice saturation setting (left) and the water saturation setting (right).

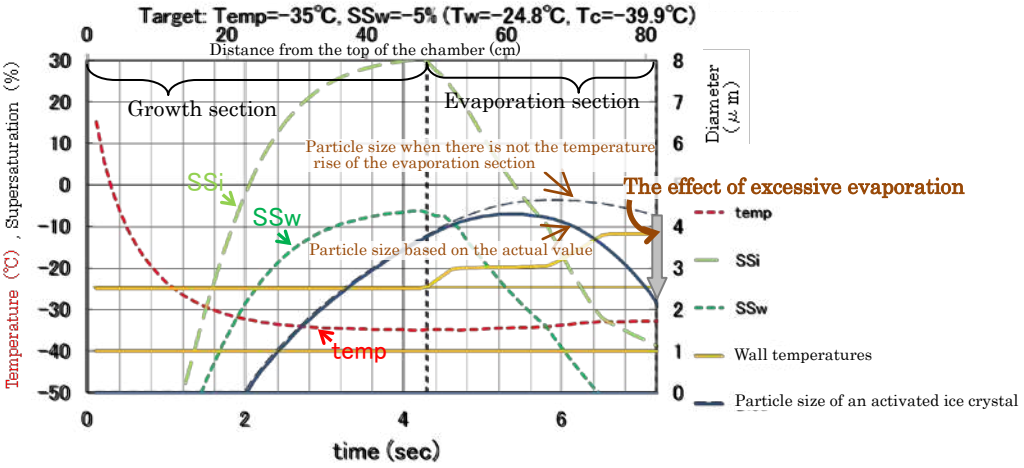

Figure 5. Temperature, SSi and SSw of the sample air and the ice crystal size as a function of travel time or distance from the top of the growth section (Target temperature and SSw are -35℃ and -5%).

Table 1. Valid temperature ranges of the evaporation section to detect ice crystals activated through deposition mode with particle size detection threshold of 2μm when the initial ice crystal size and the transient time are assumed to be 10^{-2}μm and 0.3 seconds,.

		Target temperature for ice nucleation with deposition mode							
		-5℃	-10℃	-15℃	-20℃	-25℃	-30℃	-35℃	-40℃
Target supersatulation (SSw)	−10%	−	−	invalid -11.3 -17.8	invalid -14.4 -23.7	-18 -18.0 -29.2	-23～-20 -21.9 -34.4	-27～-21 -26.0 -39.6	-31～-24 -30.3 -44.7
	−5%	−	invalid -5.9 -13.1	-10 -9.0 -18.9	-14～-12 -12.6 -24.4	-16～-12 -16.3 -29.7	-22～-15 -20.5 -34.8	-26～-15 -24.8 -39.9	-30～-19 -29.2 -44.9
	±0%	invalid -0.5 -8.4	-4 -3.5 -14.4	-7～-5 -7.1 -19.8	-10～-5 -10.8 -25.1	-15～-5 -14.9 -30.3	-19～-4 -19.1 -35.4	-23～-15 -23.5 -40.4	-28～-8 -27.9 -45.5
	+5%	−	-3～0 -1.8 -14.8	-7～0 -5.7 -20.2	-11～-1 -9.7 -25.3	-16～ -13.8 -30.4	-20～ -18.2 -35.4	-25～ -22.6 -40.6	-29～ -27.3 -45.4

※a valid temperature range of outer wall of evaporation section(upper),
a setting temperature of outer wall of growth section(middle),
a setting temperature of inner wall of growth section(bottom)

Table 2. Same as Table 1 except for ice crystals activated through condensation-freezing mode.

		Target temperature for ice nucleation with condensation-freezing mode							
		-5℃	-10℃	-15℃	-20℃	-25℃	-30℃	-35℃	-40℃
Target supersatulation (SSw)	±0%	invalid -0.5 -8.4	invalid -3.5 -14.4	invalid -7.1 -19.8	-11～-10 -10.8 -25.1	-15～-13 -14.9 -30.3	-19～-15 -19.1 -35.4	-24～-20 -23.5 -40.4	-28～-23 -27.9 -45.5
	+5%	−	-3～-1 -1.8 -14.8	-7～-2 -5.7 -20.2	-11～-3 -9.7 -25.3	-16～-3 -13.8 -30.4	-20～-6 -18.2 -35.4	-25～-11 -22.6 -40.6	-29～-17 -27.3 -45.4
	+10%	−	-3～+6 -0.3 -15.3	-7～+7 -4.3 -20.6	-11～ -8.4 -25.7	-16～ -12.8 -30.7	-20～ -17.2 -35.7	-25～ -21.7 -40.7	-29～ -26.4 -45.6

LABORATORY STUDIES OF ICE FORMATION BY SOOT AND MINERAL DUST PARTICLES

Takuya Tajiri[1*], Katsuya Yamashita[1], Atsushi Saito[1], and Masataka Murakami[1]

[1]Meteorological Research Institute, Tsukuba, Japan

1. INTRODUCTION

It is an urgent issue to unravel the entanglement of ice formation processes through multiple pathways and the susceptibility of ice nucleation associated with the variability of atmospheric aerosol components in mid-level mixed-phased clouds and upper-tropospheric ice clouds. The object at the outset of this study is to examine the ice formation ability of surrogates for atmospheric soot and mineral dust particles as heterogeneous and homogeneous ice nuclei (IN) in the temperature range of -15 to -50°C. At advanced stage, we will have comprehensive study to identify where ice crystals originate with their external mixing state.

MRI cloud simulation chamber is used to seize ice initiation and subsequent growth scenes for a variety of aerosol particles and atmospheric circumstances, and to quantify the activated fraction. Since the immersion and condensation freezing occur only after droplet formation has started, it is essential to know the ability of aerosol particles acting as cloud condensation nuclei (CCN) as well as IN to sufficiently realize the ice formation mechanism under conditions relevant to the atmosphere. The results on the potential role of these particles as CCN will be also reported in the companion presentation by Yamashita et al. at the conference (see details in extended abstracts on P. 10.6).

* *Corresponding author's address*: TAKUYA TAJIRI, Meteorological Research Institute, 1-1 Nagamine, Tsukuba, Ibaraki 305-0052, Japan; E-mail: ttajiri@mri-jma.go.jp

2. OVERVIEW OF THE STUDY

A schematic explanation of the key physical links between aerosol and cloud microphysical processes is depicted in Fig. 1. A quantitative description of the relation between physicochemical properties of aerosol particles and their ability to initiate cloud particles is a crucial subject for an improvement of numerical cloud model. To overcome the current lack of understanding on aerosol-cloud-precipitation interactions and to reduce the uncertainty in estimates of the aerosol indirect effects, we need to develop and propose novel physics-based equations that link aerosol particles and cloud particles from the experimental approaches.

Some of the nucleation mechanisms have been investigated with numerical models (e.g., Khain et al., 1999). According to Hoose et al. (2010), immersion freezing by mineral dust is found to be the dominant ice formation process, followed by immersion and contact freezing by soot from a global climate model implemented with an ice nucleation parameterization based on classical nucleation theory.

The outcome of numerical model simulations may provide insights into the functional aspects of the aerosol indirect effects; nevertheless many of the fundamental processes are still unclear. To reach better understanding on the immersion and condensation freezing of soot and mineral dust, the first necessary step is to get the ability of sample aerosol particles as not only IN but also CCN.

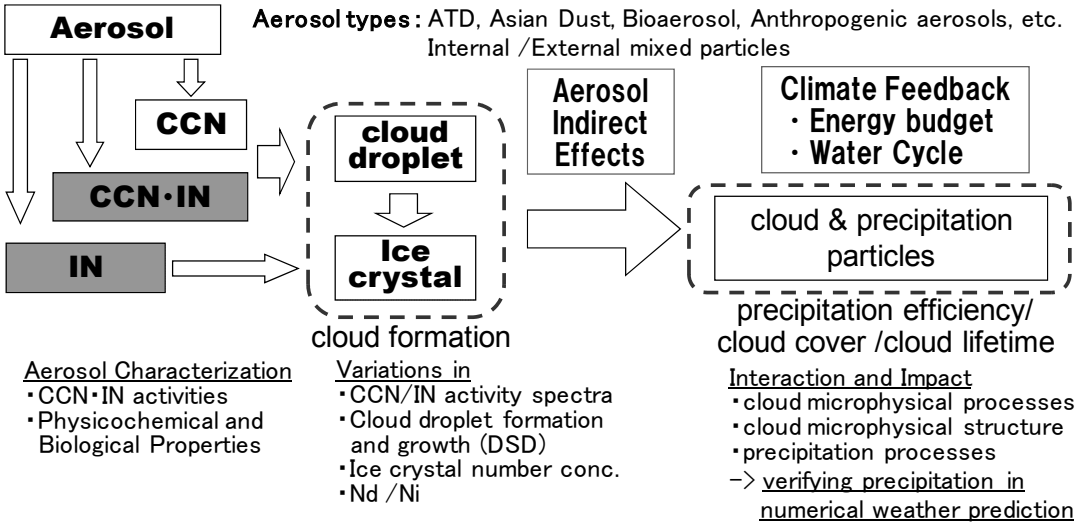

Fig. 1. Schematic diagram of aerosol-cloud-precipitation interactions.

From the above view points, the experimental apparatus and techniques in a variety of types are put into this study as shown in Fig. 2. In the laboratory, we have been investigating both CCN and IN ability by using the Cloud Condensation Nucleus Counter (DMT-CCNC) and the Continuous-Flow Diffusion-Chamber type Ice Nucleus Counter (CFDC-INC) developed at MRI (see extended abstracts of this conference on P. 10.7). Size distribution, activated fraction of CCN as a function of supersaturation with respect to water (SSw), hygroscopicity parameter (k), activated fraction of IN as a function of temperature and supersaturation with respect to ice (SSi) are available to evaluate the potential role of sample particles as IN. Then, for well-characterized particles from our own measurements, the experiments of ice formation using the MRI chamber can be conducted in each intensive experimental period. Detailed information of the MRI chamber for ice nucleation studies is described in detail by Tajiri et al. (2006). We will try to collect residual particles of ice crystals during the chamber experiments by operating the pumped counterflow virtual impactor (e.g., Matsuki et al., 2010) and the automated aerosol sampler (AAS-001WT, ARIOS) in near future.

3. EXPERIMENTAL METHODS

The soot particle was produced by a commercial graphite spark type generator (GNP2000, PALAS). The morphology, organic carbon to elemental carbon ratio, and optical properties of soot particles produced by such type of generator were comprehensively analyzed in AIDA studies (Saathoff et al., 2003; Schnaiter

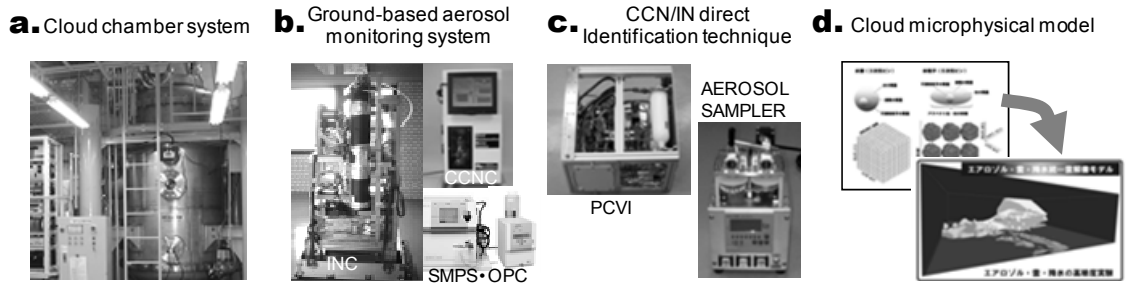

Fig. 2. Experimental apparatus and a parcel model with detailed cloud microphysics.

et al., 2003). We also tested Arizona Test Dust (ATD; Powder Technology Inc., Minnesota, USA) as a reference dust material, which can be used in other labs for comparison of results and methods of IN measurements. Detailed information was presented in Möhler et al. (2006). The dust particle was dispersed using the rotating brush type generator (RBG1000, PALAS) in dry synthetic air.

At the aerosol preparation and characterization, all aerosol samples were originally put into an aerosol buffer tank (4m^3 volume) via two cyclones (50% cutoff diameters of 2.5 μm and 1.0 μm; URG), and then supplied to aerosol, CCN and IN measurement instruments. The Scanning Mobility Particle Sizer spectrometer (SMPS; MODEL3936, TSI) and the optical particle counter (KC-01E, RION) were used for monitoring dry particle size distributions (PSDs) and number concentrations. The activated fraction of IN (the ratio of Nin/Ncn) was calculated from the CN concentrations (Ncn) measured with Condensation Particle Counter (CPC) and IN concentrations (Nin) measured with CFDC-INC as a function of temperature and SSw.

In the MRI chamber experiment, test aerosols stored in the buffer tank were introduced into the cloud chamber (1.4m^3 experimental volume) to attain a desired concentration followed by preconditioning of sample air in terms of temperature and humidity. At least during the pre-expansion initialization period, dry particle size distributions and number concentrations of test particles were measured by another SMPS and the Cloud Aerosol Spectrometer, which has a function to measure the forward and backward scattering particle by particle (CAS, DMT). In addition, the Welas OPC (Promo2000, PALAS) can detect particles as small as 1.0 μm.

Pre-set parameters such as the initial pressure, temperature and dewpoint temperature can be determined arbitrarily. The cloud formation experiments are performed on the principle of adiabatic expansions by synchronously controlling air pressure and wall temperature. The air pressure in the chamber can be decreased down to below 30hPa with a vacuum rate corresponding to updraft velocities of 0 to 30 m s^{-1}. The wall temperature, which has to catch up with the sample air temperature to minimize heat exchange, is capable to be cooled down to -100°C by circulating the coolant. The experimental difficulty is to continue cloud formations throughout a cloud layer (the entire duration of the ascent) without sedimentation of the hydrometeors to the bottom of the vessel and condensation of water vapor onto the chamber wall. We need to consider that accurate adiabatic expansions are realized for rather short time due to such effects.

The temperature control shifts from dry to moist adiabatic lapse rate after passing the Lifting Condensation Level (LCL), which are estimated from initial temperature, dewpoint temperature and pressure in advance. The actual LCL is optimally specified by comparing the key observational variables (temperature, relative humidity, mixing ratio, PSD, cloud droplets concentration, etc.) that are always monitored during the expansion.

The initial formation of cloud droplet (CCN activation) and the development of their size distribution (DSD) are properly measured by using the CAS, Welas OPC, Cloud Particle Imager probe (CPI, SPEC) and the laser scattering and depolarization measuring system (LSDMS, MRI). These devices for sensing cloud particles are also served to investigate the ice nucleation processes, so that Nin/Ncn of sample particles can be inferred from the cloud expansion experiments on performance basis.

In this paper, we mainly show the analyzed results of experimental data obtained from the CPI and the CAS, which provide us with the identification of IN activation, predominant temperature

zones of the initial ice crystal growth and the activated fraction of IN and a clue to discriminate the principal ice nucleation mode operating in each experiment.

4. RESULTS AND DISCUSSION

The PSDs of the sample particles inside the aerosol buffer tank are shown in Fig. 3. The soot and ATD particles prepared for the present experiments have peak diameters of 100 and 300 nm, respectively.

The activation spectra of pure soot and ATD from the CFDC-INC measurements are plotted in Fig. 4. At higher SSw region, larger fractions of the soot and ATD particles activate as IN and form ice crystals. No evidence has been found of any significant fraction of the soot activating above -38°C. Ice formation was detected only above water saturation at -38°C. Although the maximum activated fraction reached nearly 10^{-1}, homogeneous freezing assumably occurs above water saturation at lowest temperature so that it is not clear whether the immersion freezing nucleation on soot particles acts as efficient mechanism. ATD particles tend to induce ice nucleation at lower SSi. Differences, up to 10^{-1}, in the onset SSi have been observed at -38°C. The onsets of ice formation at temperatures up to -30°C occur on ATD through deposition nucleation below water saturation as seen in the activation spectra, thereafter the activated fractions in this temperature range were sharply and continuously increasing beyond water saturation. Condensation freezing is likely to attribute such change in the fractions above water saturation. But the discrimination of condensation freezing and deposition nucleation above water saturation is intractable in this measurement. Above -30°C, ice nucleation surely occurs above water saturation. At –20°C and -15°C, ice nucleation signals cannot be

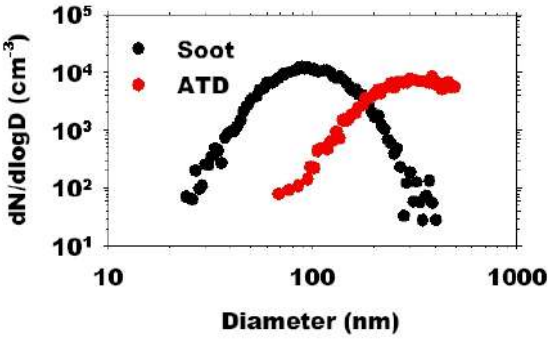

Fig. 3. PSDs of the soot and ATD particles measured with SMPS.

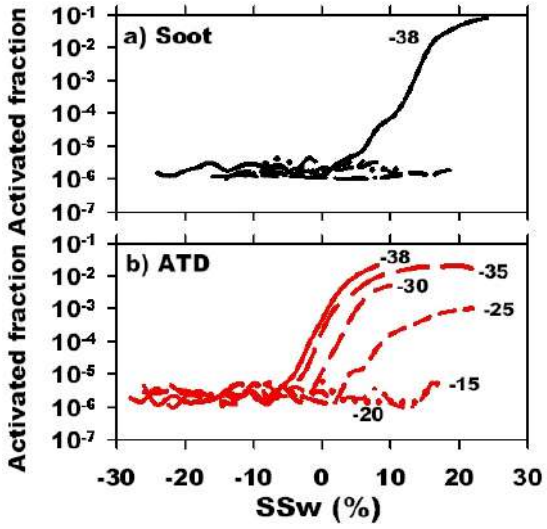

Fig. 4. Activation spectra of a) soot and b) ATD (activated fraction vs. SSw) for temperatures from −15°C to −38°C.

unambiguously distinguished. It might be thought that the measured activated fraction at high temperatures tends to be underestimated due to a possible evaporation of ice crystals in the lower part of IN counter.

A series of expansion experiments for soot particles was performed in order to acquire a dataset of their ice nucleating ability and to compare with the activation spectra from CFDC-INC measurements. The initial values of pressure and air temperature were set to 1000 hPa and 15°C respectively, and then the initial dewpoint temperature is varied from –10°C to -30°C. Pre-set adiabatic ascent rate was 5 m s^{-1} and was kept down to below -50°C. The activated fractions

obtained from the expansion experiments are depicted in Fig. 5. The numbers on the figure denote the programmed onset temperatures of cloud formation, i.e., the preset LCL temperatures (Tlcl-20, Tlcl-30, Tlcl-40), which usually deviate from the measured ones mostly due to an expense of water vapor onto the wall (frost formation). Delay of the actual condensation point (LCL) increases with decreasing the dewpoint temperature (typically a few degrees at dewpoint temperatures below –25°C). The expansion control doesn't always succeed in reaching the LCL due to the depletion of excess water vapor through depositional growth of ice crystals activated below water saturation and rather slow production of excess water vapor through the expansion, especially below -30°C. The activated fraction of soot particles measured with the CPI shows a three-step-like activation pattern at around –26°C, -33°C and -40°C for Tlcl-20 case (Fig. 5). The first step of ice nucleation did not significantly contribute to the activated fraction, but produced ice crystals whose number concentration barely exceeds the minimum detection limit. The droplet freezing may occur in this step, although cloud droplet formation and its interaction with soot particles are not clear yet. The next step is indicated more distinctly from the CPI and the CAS measurements. A possible interpretation of the second step ice nucleation is the deposition nucleation because uncoated soot particles act as deposition nuclei at low ice saturation ratios between 1.1 and 1.3 at this temperature range (e.g., Möhler et al., 2005). The last step is thought to correspond to the onset of immersion freezing nucleation, since the saturated fraction measured with the CAS is very close to that for the Tlcl-40 case. For the Tlcl-40 case, the expansion was conducted below water saturation so that homogeneous freezing could not be realized. The onset of ice formation for

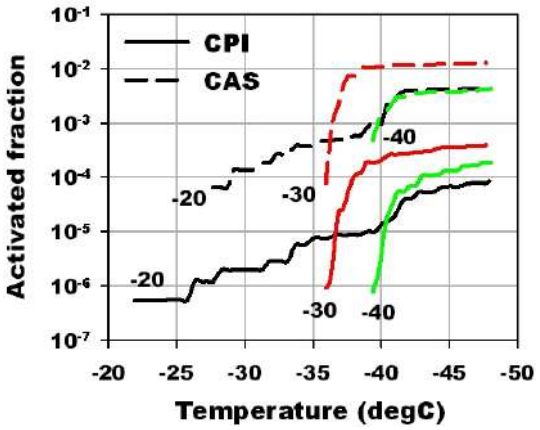

Fig. 5. Activated fraction of soot particles (activated fraction vs. temperature)

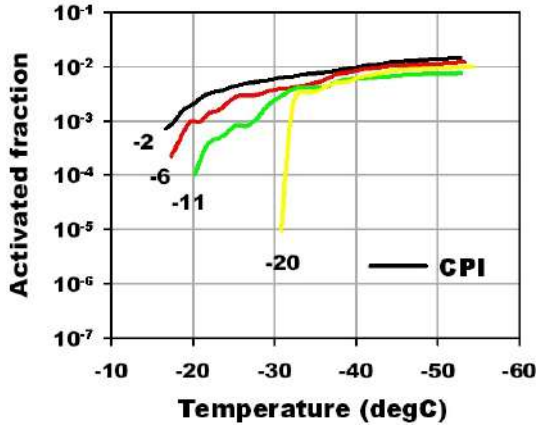

Fig. 6. Same as fig. 5., but for ATD.

the Tlcl-30 case was well below -35°C. The highest value of the activated fractions among 3 cases might result from homogeneous freezing of droplets formed on soot particles.

For ATD particles, we also carried out the sensitivity experiments in a similar way (Fig. 6). A remarkable feature is the similarity in the saturation of the activated fractions at colder temperatures, although the onset temperatures of ice formation and the contributions of individual mechanisms to the activated fractions are certainly different for different cases. According to the CFDC-INC measurements, at temperatures above -30°C, the ice initiation occurred only through the condensation freezing nucleation. Except for the Tlcl-20 case,

the activated fractions above -25°C are higher than those from CFDC-INC measurements and increase with increasing Tlcl. Therefore it is speculated that pre-existing droplets had affected ice nucleation in some way. The activated fractions abruptly increased at around -35°C except for the Tlcl-2 case, and gradually approached 10^{-2} beyond -35°C, which is comparable to the values obtained from the CFDC-INC measurements (about 10^{-1} of ATD particles activated). The result implies that ATD particles also act as the deposition nuclei.

5. SUMMARY

The cloud expansion experiments were conducted to examine the ice nucleation ability of pure soot and ATD particles as heterogeneous and homogeneous ice nuclei (IN) under conditions relevant to the atmosphere at temperatures between -15°C and -50°C. The ice initiation processes were examined in the air with the vacuum rate corresponding to the ascent rate of 5 ms^{-1} with different initial dewpoint temperatures (preset Tlcl). To identify the mechanism of ice initiation and to assess the IN ability of particles, the activated fractions of soot and ATD particles from the expansion experiments were compared with those from CFDC-INC measurements.

No evidence has been found of any significant fraction of the soot particles activating above -38°C from the CFDC-INC measurements although the cloud chamber experiments showed very low values of the activated fraction above -38°C. Ice formation was detected only above water saturation and at -38°C from the CFDC-INC measurements, which strongly suggests that homogeneous freezing occurred. However it is not clear whether the immersion/condensation freezing nucleation on soot particles acts as efficient mechanism at or slightly above water saturation and at temperatures warmer than -38°C.

Above -30°C, immersion/condensation freezing was the dominant ice nucleation mode for ATD particles at water saturation or slightly above water saturation. More than 10^{-3} of ATD particles activated. Below -30°C, ATD particles also act as deposition nuclei below water saturation.

REFERENCES

Hoose, C., J. E. Kristjánsson, J.-P. Chen, and A. Hazra, 2010: A Classical-Theory-Based Parameterization of Heterogeneous Ice Nucleation by Mineral Dust, Soot, and Biological Particles in a Global Climate Model. *J. Atmos. Sci.*, **67**, 2483–2503.

Khain A., A. Pokrovsky, and I. Sednev, 1999: Some effects of cloud-aerosol interaction on cloud microphysics structure and precipitation formation: Numerical experiments with a spectral microphysics cloud ensemble model. *Atmos. Res.*, **52**, 195-220.

Matsuki, A., A. Schwarzenboeck, H. Venzac, P. Laj, S. Crumeyrolle, and L. Gomes, 2010: Cloud processing of mineral dust: direct comparison of cloud residual and clear sky particles during AMMA aircraft campaign in summer 2006, *Atmos. Chem. Phys*., **10**, 1057-1069.

Möhler, O., S. Büttner, C. Linke, M. Schnaiter, H. Saathoff, O. Stetzer, R. Wagner, M. Krämer, A. Mangold, V. Ebert, and U. Schurath, 2005: Effect of sulfuric acid coating on heterogeneous ice nucleation by soot aerosol particles, *J. Geophys. Res.,* **110**, D11210.

Möhler, O., P. R. Field, P. Connolly, S. Benz, H. Saathoff, M. Schnaiter, R.

Wagner, R. Cotton, M. Krämer, A. Mangold, and A. J. Heymsfield, 2006: Efficiency of the deposition mode ice nucleation on mineral dust particles, *Atmos. Chem. Phys.*, **6**, 3007-3021.

Saathoff, H., O. Möhler, U. Schurath, S. Kamm, B. Dippel, and D. Mihelcic, 2003: The AIDA soot aerosol characterisation campaign 1999, *J. Aerosol Sci*., **34**(10), 1277– 1296.

Schnaiter, M., H. Horvath, O. Möhler, K. H. Naumann, H. Saathoff, and O. W. Sch öck, 2003: Uv-vis-nir spectral optical properties of soot and soot-containing aerosols, *J. Aerosol Sci.*, **34(**10), 1421– 1444.

Tajiri T., M. Murakami, N. Orikasa, A. Saito, and K. Kusunoki, 2006: Laboratory experiments of ice formation in cloud simulation chamber. *Proceedings of the 12th Conference on Cloud Physics of the American Meteorological Society*, 10-14 July, 2006, Madison WI. P2.53.

Three-Aircraft Measurements of the Microphysical Characteristics of Stratiform Cloud in Hebei Province: the Size Spectra and Microphysical Processes

Yang Jiefan[1], Lei Henchi[1], Hu Zhaoxia[1], Hou Tuanjie[1]

1. *Laboratory of Cloud-Precipitation Physics and Severe Storms Institute of Atmospheric Physics Chinese Academy of Sciences, Beijing* 100081

Abstract: By employing the three-aircraft measurements combined with radar and satellite images, the microphysical structures of a precipitus stratiform cloud caused by a westerly trough in Zhangjiakou City, Hebei Province on May 1, 2009 are analyzed in this paper, focusing on vertical distribution of PSD (particle size distribution) and the 2D imagery at a variety of altitudes and temperatures. In a closer examination of the shift in PSD, ice particle habits in the 2D imagery, and water content and number concentration of supercooled liquid droplet. The PSD generally appeared to conform to an exponential size distribution, with well-correlated linear fits between the log of the number concentration and particle diameter. Analyses of PSD parameters N_0 and λ show that three stages of particle growth according to the spectral trajectory is similar to previous studies. However, the positive shift in both N_0 and λ at temperature warmer than -8 ℃ in our study was likely caused by extension of supercooled droplet spectra.

Key words: Stratiform cloud, PMS, PSD, Ice crystal multiplication

1. Introduction

In the 1930s, Bergeron (1935), and Wegener and Findeisen (1938) proposed that when ice crystals and supercooled droplets coexist in a cloud, different super saturation rates near the surface of ice and liquid phase hydrometeor will lead to the preferential growth of ice particles by consuming supercooled droplets and further to the formation of precipitation particles. Since then, interest in ice particles in clouds has centered around three topics: their origins, their concentrations and their growth (Hobbs 1985). Precipitation formation mechanisms in different locations may differ dramatically from each other. When the cloud top reaches temperature lower than 0 ℃, ice develops and precipitation can develop through different microphysical processes; and the number concentration and size spectra of particles, both of which are key factors of cloud seeding with AgI, also vary dramatically at different synoptic backgrounds (Bruintjes 1999). Based on Braham (1986), the factors that hinder the research mainly lie in two aspects: the large scale variability and an incomplete understanding of the physical processes involved. The investigation thus should concentrate on microphysical processes of precipitation formation.

In last decades, airborne probes have been applied to facilitate the measurement of precipitation processes throughout storm systems, which can be found in many studies (Herzegh and Hobbs 1980, Lo and Passarelli 1982, Field 1999, and Heymsfield *et.al* 2002) where it is confirmed that the size spectra of particles change to adjust to such microphysical processes as deposition growth and aggregation, at various altitudes and temperatures within the precipitation system. Besides, it is shown in these studies

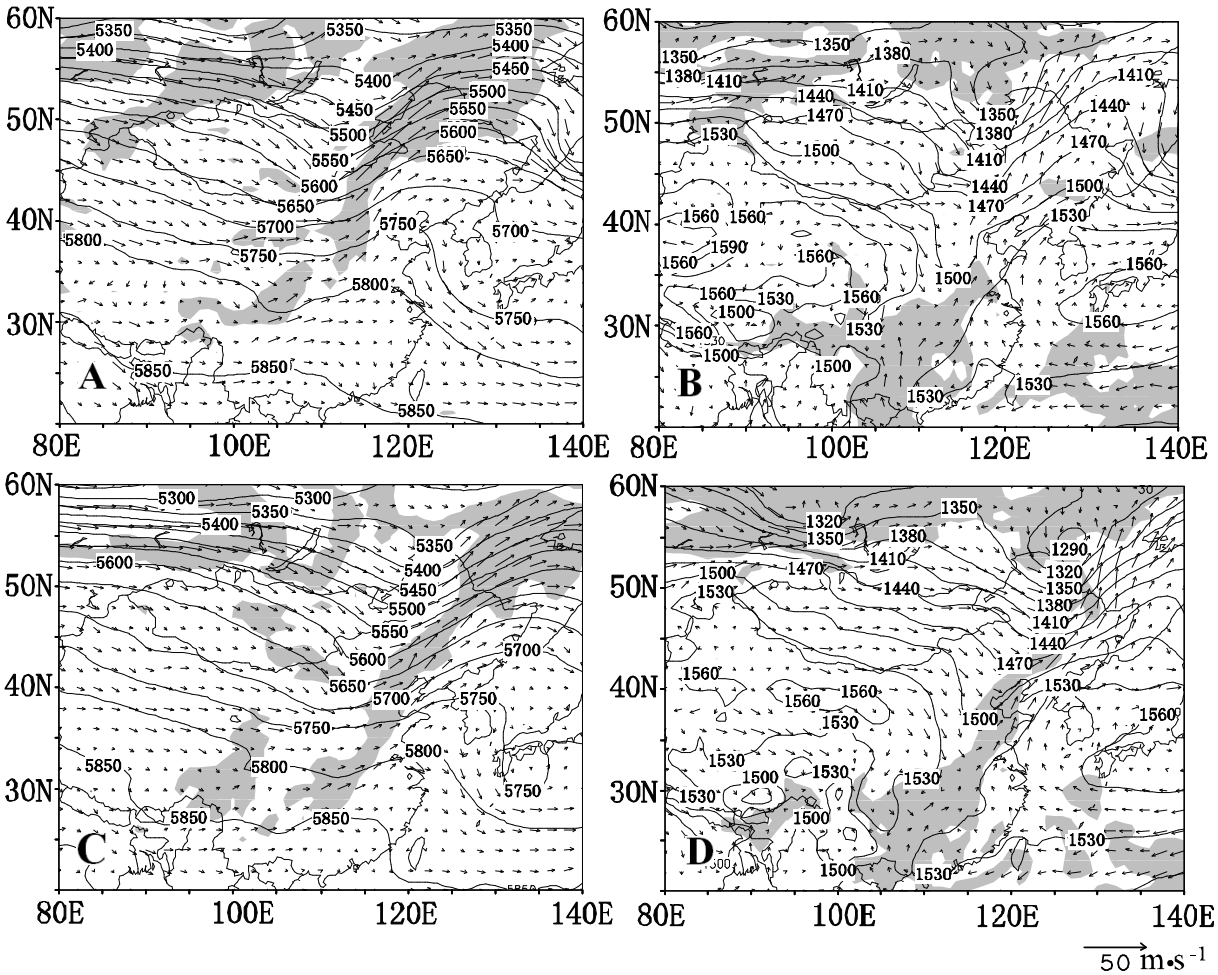

Fig.1. Synoptic conditions over North China on 1 May, 2009: (A) 500 hPa map for 0200 LST; (B) 850 hPa map for 0800 LST; (C) 500 hPa map for 0200 LST; (D) 850hPa map for 0800 LST. Heights of pressure surfaces in geopotential meters (solid line), shade areas for relative humidity >90%

that between particle size spectra and temperatures there exist correlations. In addition to information on particle size distribution, the 2D imagery probes (Lawson and Jensen 1998) also provide a further insight into particle shapes and habits.

In this paper, we investigate PSD collected by probes installed in three aircrafts manufactured by PMS and DMT Inc., in a westerly trough precipitation system in Zhangjiakou City, Hebei Province on May 1, 2009, during the field study of R&D of Key Technology and Equipment for Weather Modification.

In the subsequent sections, we will investigate the following aspects of precipitus stratiform: the vertical and horizontal distribution of size spectra of both liquid and ice/snow particles; the relationship between temperatures and ice crystal habits; the influences of different secondary ice enhancement processes; and the relationship between the concentration of ice particles and supercooled liquid particles. We also compare our findings with those prior investigations of spectra changes and particle imagery.

2. Synoptic situation

The observation data used in this section mainly involve surface rainfall and radar reflectivity, among which the surface rainfall was collected during the field study, and the observed radar reflectivity originally provided by LACS (Laboratory of Cloud-Precipitation Physics and Severe Storms, Institute of

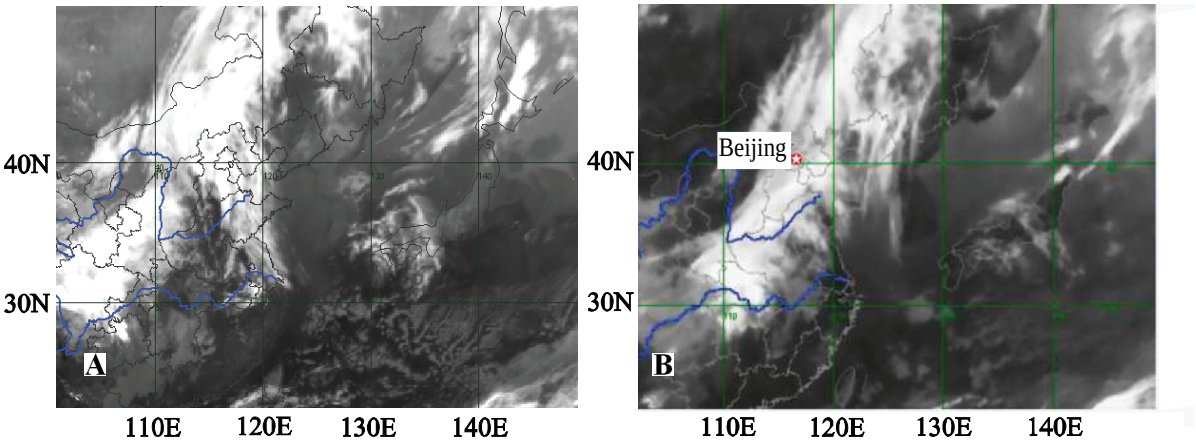

Fig.2. Visible cloud imagery from FY-2 satellite: (A) at 0000 LST; (B) at 0080 LST

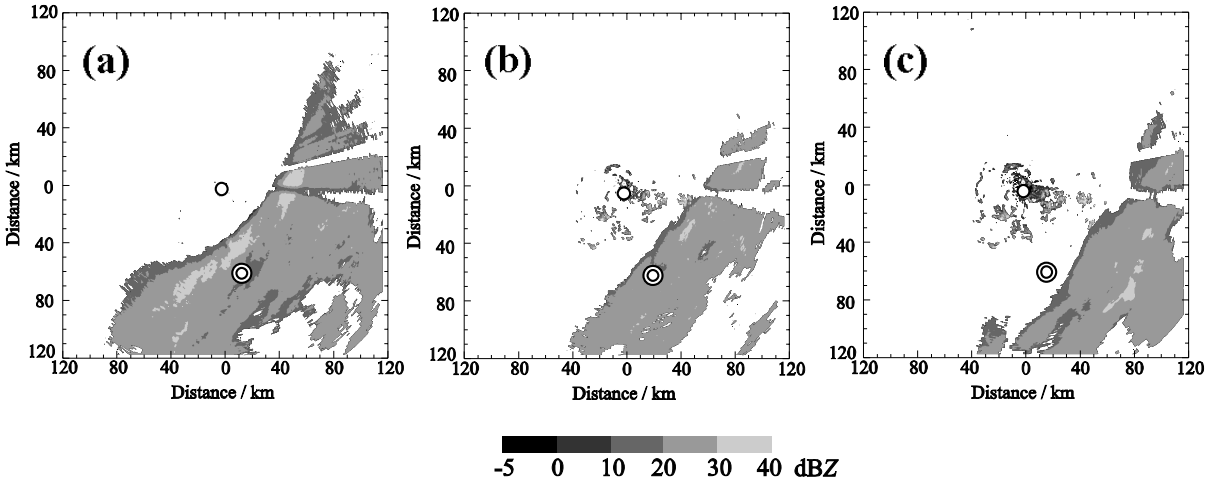

Fig.3. Plan position indicator (PPI) radar scan of reflectivity (dB*Z*) from X band vehicle-carried Doppler weather radar located in the suburbs of Zhangbei City on 1 May, 2009, black cycle indicate the radar location and the double cycle represent Zhangjiakou city: (a) at 0838 LST; (b) at 0911 LST; (c) at 0959 LST

Atmospheric Physics) was derived from base reflectivity scans of the vehicle-carried X-band Doppler weather radar located in the suburbs of Zhangbei City. The resulting products were binned into 5-dB*Z* intervals and the synoptic map was based on the NCAR reanalysis dataset with 1×1 grid resolution.

The synoptic situation on 1 May, 2009 over Zhangjiakou City was primarily influenced by a shallow upper level trough. This northeast-southwest oriented trough appeared in west Baikal Lake, mid Inner Mongolia and Hetao area on 500 hPa map for 0200 (all times LST). On the 850 hPa synoptic analysis for 0200LST in Fig.1b, water vapour was transported by the south warm wet airflow from Indo-China Peninsula to the westerly trough system. Influenced by a strong west wind back of the trough and northward subhigh displacement, the trough advanced through north Inner Mongolia and North China. At 0800 LST the 850 hPa chart depicts a closed cyclonic feature lying to North China (N45º, E128º), and Fig.1d unveils the orientation of the trough at 0800 LST.

As the 850-hPa westerly trough moved forward (Fig 1 D), satellite imagery in Fig.2 showed a broad cloud shield associated with this system, extending from Central China to Pacific coast. Most parts of Eastern China at 0000 LST were covered by a cloud band

TABLE 1 Aircrafts operated during the field study and the on board instruments

Aircraft	Instrument	Notes
Shanxi Y-12	DMT CDP	2~50μm
	DMT CIP	25~1550μm; 2D grey
	DMT LWC-100	Liquid water content 0.01~3.0 g m^{-3}
	DMT PIP	100~6200μm; 2D grey
	DMT CCN	0.75~10μm
	AIMMS20	Air speed, temperature and pressure
Beijing Y-12	DMT CAS	0.51~50μm
	DMT CIP	
	DMT PIP	
	DMT CCN	
	PCASP-100X	0.1~3.0μm
	AIMMS20	
Hebei Cheyenne-ⅢA	PMS FSSP-100-ER	Selectable 1~95μm
	PMS OAPDGA-2	25~1550μm
	PMS OAPDGB-2	100~6200μm
	DMT CCN	0.75~10μm
	PCASP-100X	0.10~3.0μm

along the Inner Mongolia – Central China and the relative humidity exceeded 90% on 850 hPa map. At 0800 LST, the cloud band moved to Northeast China – North China.

Fig.3 reveals the observed plan position indicator (PPI) of radar intensity from X-band vehicle-carried Doppler weather radar located in the suburbs of Zhangbei City on 1 May, 2009, during the period of 0838~0959 LST. It is quite obvious that the rainband was approximately parallel and oriented to axis SSW to NNE and moving at speed of 7.78 $m \cdot s^{-1}$ perpendicular to the rain band. And the considerable substructures contained in the rainband are cores with radar reflectivity exceeding 30 dB*Z*. This rain band, which was forced by a cloud front, play a significant role in producing precipitation over the study field from approximately 0800 LST 30 April until 1130 LST 1 May.

From 30 April, 2009 to 1 May, 2009 the precipitation rates were measured with rain gauges at 232 stations in Zhangjiakou City, among which the accumulated precipitation from 176 stations were greater than 5 mm and 78 stations exceeded 10 mm, with an average precipitation of 8 mm and the maximum of 13.6 mm in Chongli County.

3. Field study and instrumentation

R&D of Key Technology and Equipment for Weather Modification is mainly aimed to study microphysical processes of straitiform cloud in North China and build datasets for improvement of weather modification technologies. As is shown in Fig.4, the field study area covers: N 40º35', E 113º35'; N 40º35', E 115º30'; N 41º40', E 115º30'; N 41º40', E 113º50'. The field study made use of a full compliment of ground-based instrumentation (including radar measurements and precipitation measurements) to measure and investigate the precipitation system passing through the field study area. During the field study the aircrafts and instruments belonging to three different organizations are listed in TABLE 1. To study the precipitation growth at various levels within the stratiform cloud, the flight pattern within the precipitation event was designed to consist of vertical stacks of horizontal flight legs ranging from 50~120 km horizontally, 1~6 km in altitude, and 17~-19 ℃ in temperature. Detailed flight legs of three aircrafts are illustrated in Fig.4 and Fig.5.

On board instrumentation provided measurements of basic-state parameters (e.g. pressure, temperature and humidity) and important microphysical quantities (e.g. cloud liquid water content, ice particle concentration, particle size spectra, and particle imagery). In our study, The Hebei Y-12 equipped with a Particle Measuring

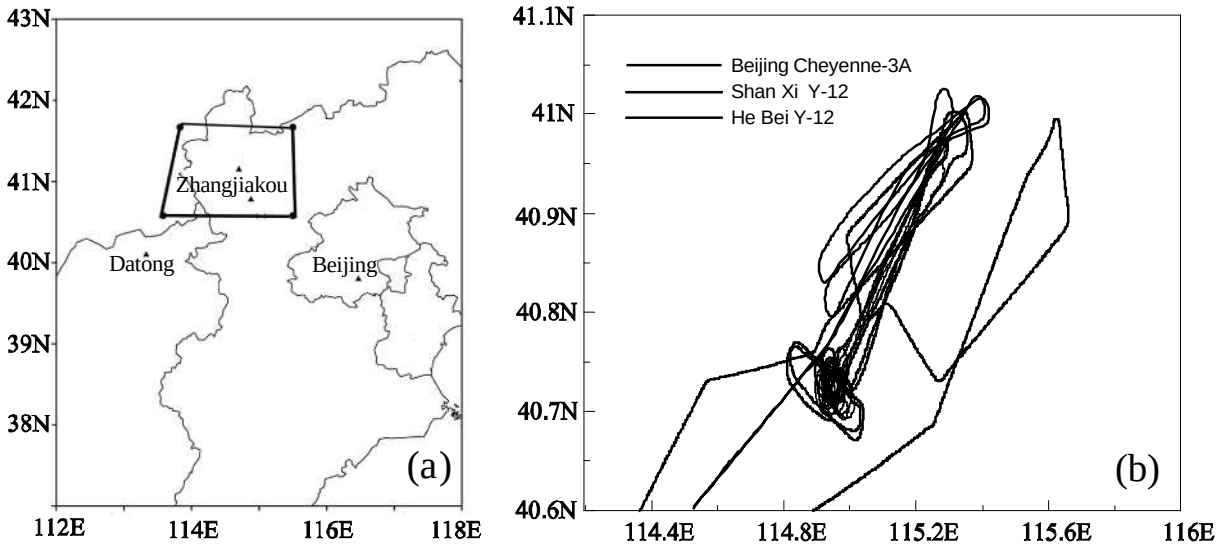

Fig.4. Field study area on 1 May, 2009: (a) study area in North China, the solid box for the region sampled by aircrafts; (b) flight tracks of three aircrafts

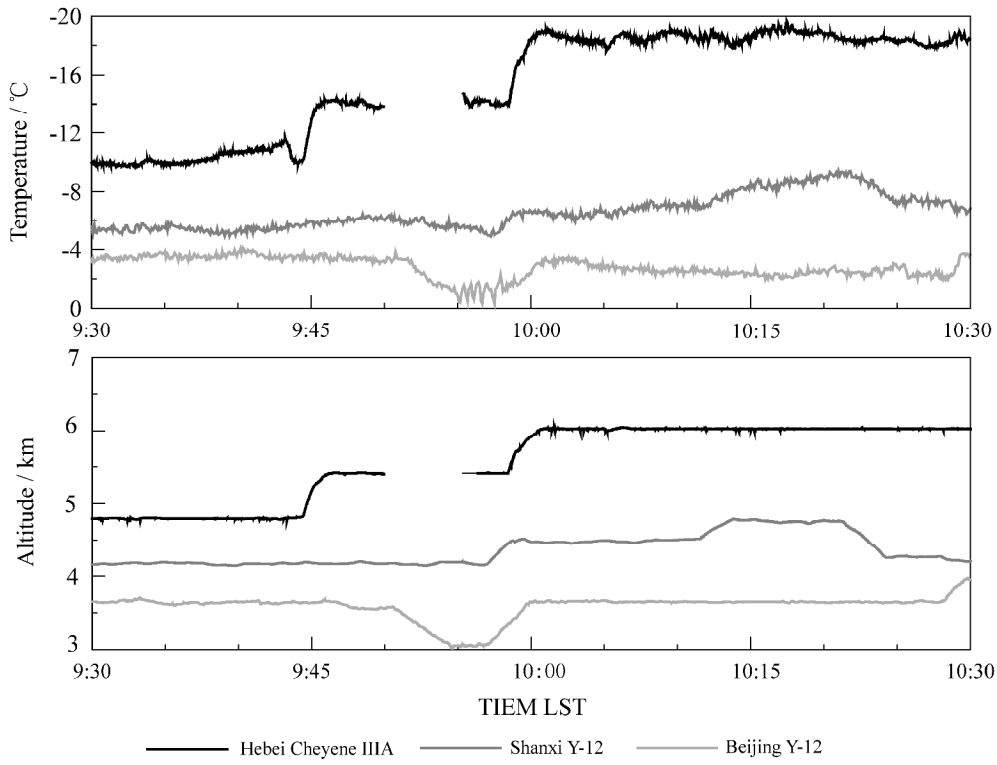

Fig.5. Variation of heights and temperatures with time from three aircrafts during field study

System. Inc.(PMS) Forward Scattering Spectrometer Probe (Fssp100; Knollenberg 1976), which sampled concentration and spectrum of cloud droplets with 2 <D< 47 μm, and PMS OAPDGA-2 (2DC) PMS OAPDGB-2 (2DP) probes for imaging particles with size range of 25~1550 μm and 100~6 200 μm respectively. The Shanxi Y-12 carried a Droplet Measurement Technologies. Inc. CIP probe (25~1550 μm) and PIP probe (100~6200 μm) for providing 2D-imageries, (DMT) CDP probe (2~50 μm) for cloud droplets. The Beijing Y-12 equipped with DMT PIP (100~6200 μm), and DMT Cloud, Aerosol and Precipitation Spectrometer (CAPS) which is a combination of CAS (0.51~50μm) and CIP (25~1550μm) probes. All the instruments with their arms vertically

aligned to allow imaging of particles (e.g. plates) oriented in the horizontal plane.

The aircrafts and instruments listed in TABLE 1 were provided by the following three organizations:

• Weather Modification Office, Beijing meteorology Bureau

• Weather Modification Office, Shanxi meteorology Bureau, Datong City, Shanxi Province

• Weather Modification Office, Hebei meteorology Bureau, Zhangjiakou City, Hebei Province

4. Methodology

Particle size spectra were collected by two Y-12s and Cheyenne-IIIA at each level during the field study on 1 May, 2009. The CAS measurements were analyzed over a size range from 2 to 50 μm in order to eliminate aerosol particles. The sample volume of the instruments was calculated by employing the reconstruction technique in Heymsfield and Parrish (1978). And to estimate LWC by the probe-derived particle size distribution of FSSP, CAS and CDP in our study it requires a summation of the form

$$LWC=\pi/6 \times \rho \times \sum D_i^3 \times n(D_i), \quad (1)$$

Where i is the number of discrete size bins in the particle size spectrum, $n(D_i)$ is the particle concentration in the ith bin, D_i is the mean diameter for each bin, and ρ is the density of water. Particles with 2<D<50 μm were considered as spherical liquid water.

Sample volume is defined as

$$V=SE \times TAS \times T, \quad (2)$$

where TAS is true air speed, T is the sample time, and SE is for the sample area.

The number concentration of particles is presented as

$$N=\sum n(D_i), \quad (3)$$

The particle size distribution is presented as

$$N(D_i) = n(D_i)/V \times \Delta d_i, \quad (4)$$

Calculating the number concentration and size spectrum from imaging instruments like CIP and PIP is different than calculating it from light scattering instruments like the CDP and CAS, this is because sample volume used to derived particle concentration depend on the particle size whereas it is

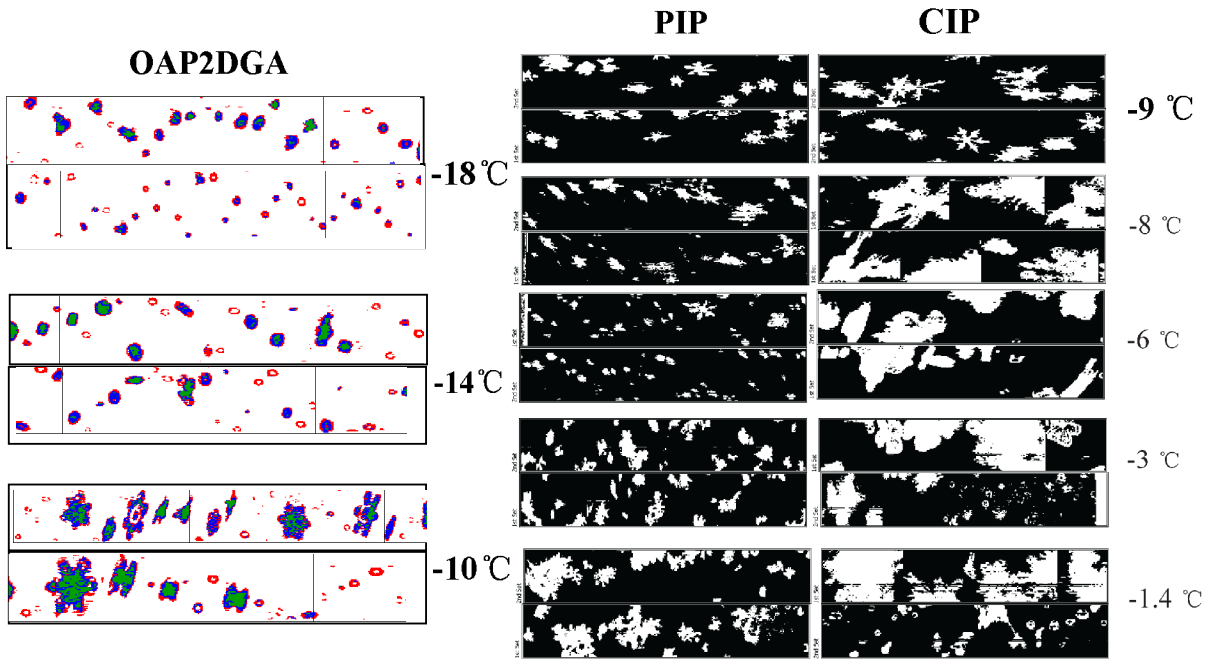

Fig.6. CIP and PIP images from Shanxi Province and Beijing City Y-12 (See TABLE 1) at different altitudes (the vertical bars for each CIP and PIP image are 1 550 μm and 6 200 μm respectively)

constant in scattering probes. The final calculation for sample volume of imaging probes is as follows:

$V = DOF_i \times TAS \times T \times (63-i) \times$[probe resolution], (5)

Where the DOF_i represents depth of field, which depends on mean radius of particles of size *i*th bin, the incident wavelength and an adjustment factor.

5. Microphysical structure of clouds

5.1 *Cloud liquid water*

For the 1 May 2009 case study, we use three sources (as mentioned in Section 2) for CLW measurements in situ measurements in the cloud band. The measurements of liquid water content (Fig.10), those plots show that the lower layers contained significant amounts of liquid water from penetration of cloud deck. Much lower liquid water values were observed at the top of the cloud (Hebei aircraft), exhibit considerable ranging from 0~0.01 g m^{-3}.

5.2 *Ice particle images analysis*

Recently, by analyzing a large dataset of particle imagery and particle size spectra collected by aircraft flying through stratiform precipitation system near the British Isles with Lagrangian descents, it is demonstrated in Field *et al*. (2000) that depositional growth alone is not responsible for the observed evolution, and the process of aggregation is chiefly responsible for the large-particle mode of bimodal ice size spectra.

In our study, for each flight level, CIP and PIP particle images were examined, and particles (both single crystals and components

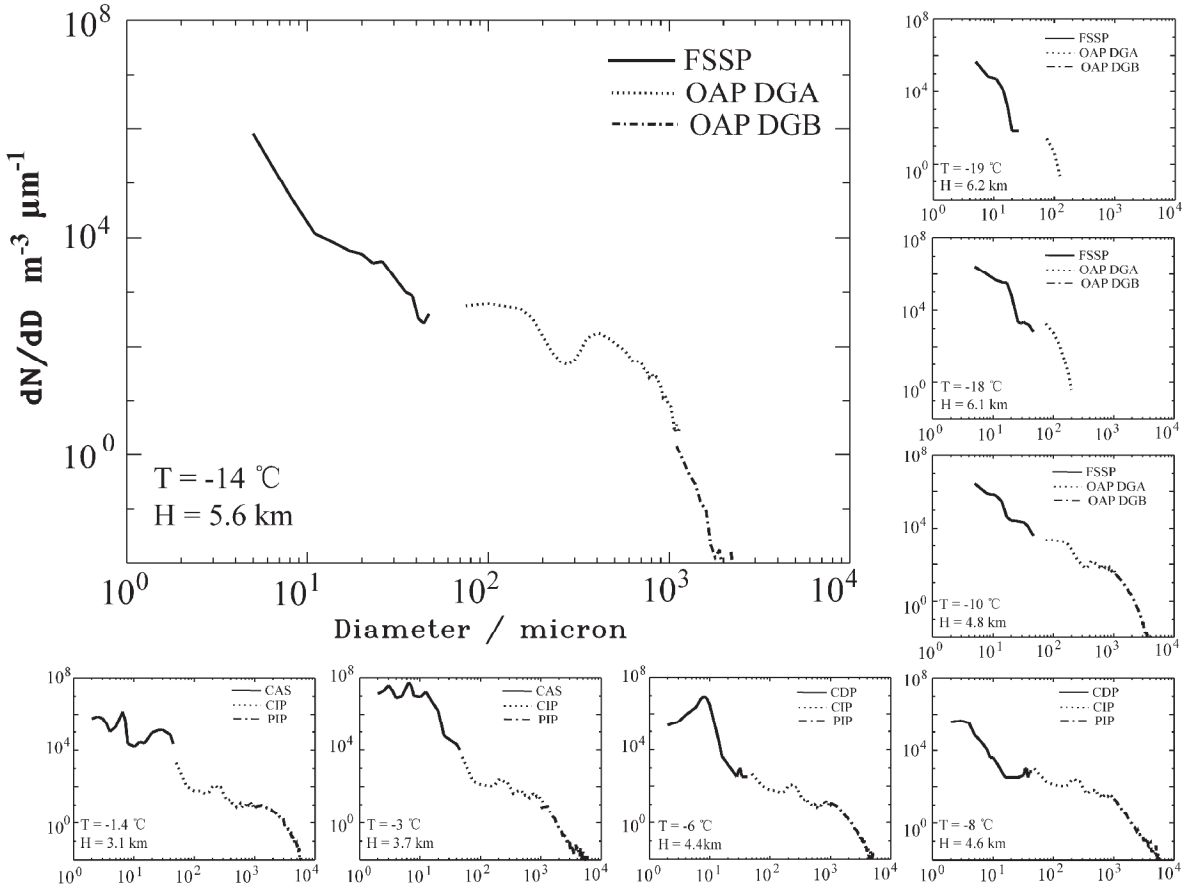

Fig.7. Spectra with CAS, CDP, CIP and PIP combined from Shanxi Province and Beijing City Y-12 (see TABLE 1); Particle size spectra normalized by bin-width are arranged vertically in terms of altitude and the altitudes.

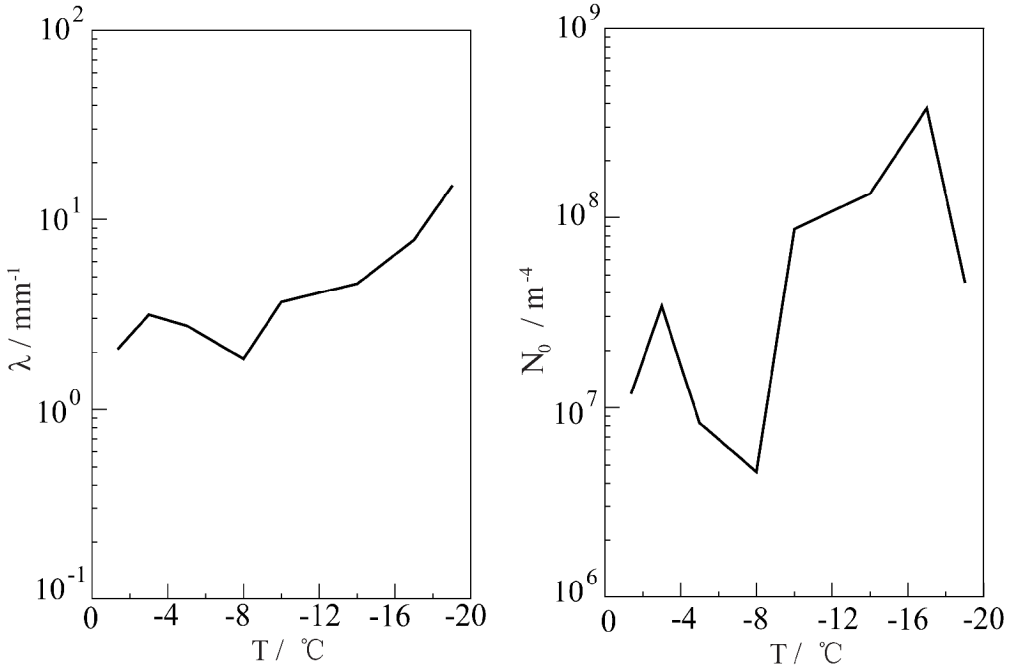

Fig 8 Ice particle size spectra parameters No (a) and λ (b) as a function of temperature

of aggregates) were classified by visual inspection (Wood 2008), and our observations of ice (snow) particles with 2D imagining airborne probes is that the vast of majority of

ice particles are identifiable as some regular type according to established classification schemes, such as Magono and Lee (1966).

Fig.6 shows CIP and PIP images obtained at different temperatures and altitudes from three aircrafts are similar to those in Field (1999, 2000) with a different Lagrangian descent. Particles become bigger as the temperature increases and eventually form rain drops under 0℃ isotherm of the cloud (not shown).

Along the upper flight legs (-18 ~14 ℃), OAP2DGA particle imageries indicated the cold type habit (ie. sectors, column, side planes) in the upper region of the rain band. Along the warmer level legs (-10 ~-8 ℃ in lower altitude), warm habit, such as transmit form (sector growing to dendritic form), dendritic crystals, aggregations of dendrites and some needle-like crystals, were observed in both CIP and PIP probes. Additionally, it appears that most of the images are irregular and not pristine in nature between the temperatures of 0~-8℃. Aggregation of dendrites; heavily rimed ice particle and spheres were observed. The apparent absence of pristine particles (e.g. columns, bullet rosettes or highly symmetrical crystals) suggests that aggregation and the riming process are the dominant growth mechanisms for ice particles in this temperature range.

5.3 ***Particle size distributions analysises***

In the early study of the size distribution of natural snowflakes by Gunn and Marshall (1958), it was deduced from ground observation of snowflakes that the particle size distribution followed an exponential form:

$$N_s(D) = N_o \exp(-\lambda D), \qquad (5)$$

where D is the diameter of a snowflake, and both N_o and λ depend on precipitation rate. Based on the dataset of Gunn and Marshall (1958), Sekhon and Srivastava (1970) did a further analysis along with other snowflake size distribution measurements and drew the conclusion that the exponential form adequately described the measurement, which is apparently crucial since it allows snow size distribution parameters to be represented in a relatively simple way in bulk microphysical schemes.

In previous studies (Lo and Passarelli 1982; Field and Heymsfield 2003) of wintertime precipitation, plots of N_0 and λ have been constructed, and it is found that the changing of spectra along altitude or temperature represents the adjustment to microphysical processes within the precipitation band. Following Lo and Passarelli (1982) particle growth falls into three stages according to spectral trajectory. In stage 1, deposition growth results in increase in N_0 and decrease in λ in values, as mass is added at all sizes across original size spectrum. Evolutions of spectra caused by aggregation leads to decrease in both intercept and slope in stage 2. This results from mass shifting from small to large sizes in the absence of additional growth. And collisional breakup is the mechanism for increase in both N_0 and λ in stage 3. Indicating a simultaneous increase in the number of small particles and decrease in the number of large particles.

Because our target clouds were precipitating, the typical size spectra of ice particles (ie, typical size mode varing from several hundred to several thousand micrometers) can't be well sampled by OAP2DGC or CIP alone, OAP2DGB and PIP was often more sensitive to the presence the large particle than was the OAP2DGA and CIP. In those situations, to ensure that the 2D-imagery probes provided the accurate size spectra, the ice PSDs was estimated from combination of probes with different sizing range. The ice concentrations from the two probes cross over each other at a critical diameters typically at 1 000 μm. In estimate the PSDs, the OAP2DGA (CIP)/OAP2DGB (PIP) PSD was used for diameters that were less/greater than the critical diameter, providing

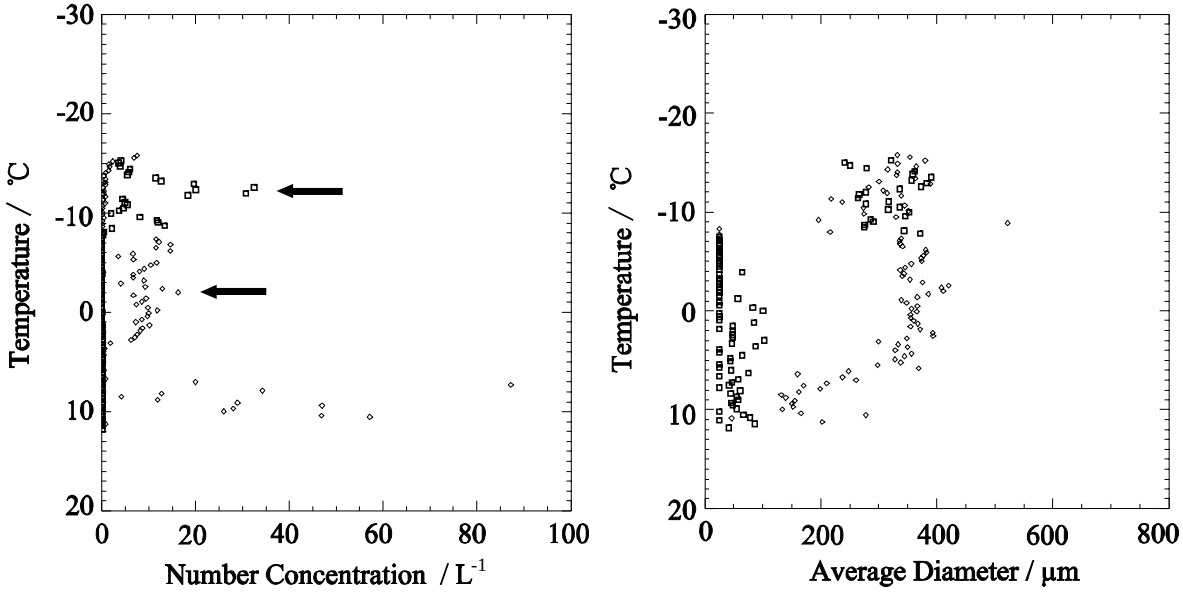

Fig.9. Average concentration (L^{-1}) and diameters (μm) of particles from CIP, square indicating the data collected by Shanxi Y-12, rectangles for Beijing Y-12 and black arrows for the two maximum concentrations from CIP

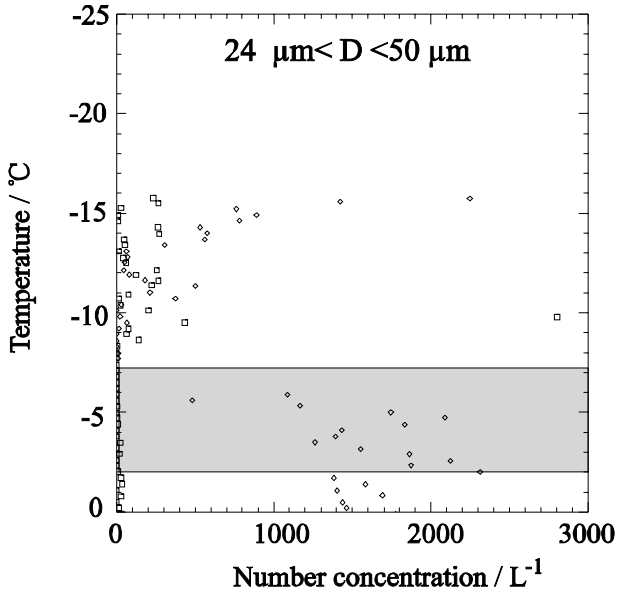

Fig.10. Average concentration (L^{-1}) of droplets with D>24 μm measured by Shanxi Province and Beijing City Y-12, shaded region indicating the occurrence of the rime-splintering process

a smooth and continuous PSD that is more accurate than using the OAP2DGA or CIP alone. Fig 7 shows the PSD from field study using the different probes measurements shows good agreements between the particles smaller that 1 mm measured by the OAP2DGA and CIP, and the particle larger than 1 mm measured by OAP2DGB and PIP.

Fig.7 is the combined spectra from the Shanxi and Beijing Y-12s and shows a satisfying coherence (within the limits of uncertainty) among the three probes at the interface. It is found that the *in situ* size spectra were well represented by an exponential fit of the form given by (5). According to Woods *et.al* (2008), the best fit line is defined here as $|r| > 0.95$ (r represents the relative coeffecience) within the size interval 200~6200 μm.

In accordance with Lo and Passarelli (1982), the changes of spectra in Fig.8 suggest

deposition growth is the primary mechanism that affects precipitation within -15~-10 ℃ although there are also some additional collisonal breakups indicated by the appearance of light rimed ice particles and low number concentration and water content of supercooled droplets. Within -10~-6.4 ℃ the ice/snow spectra change in a path similar to stage 2 growth in Lo and Passarelli (1982), which leads to decrease in both N_0 and λ. A closer examination of the shift in spectra within -6~-1.5 ℃ combined with the microphysical measurements of cloud water concentration and ice particle habit identification reveals the probability that secondary ice production through rime splintering is responsible for the simultaneous increase in N_0 and decrease in λ. The presence of both cloud droplets with D>24 μm (Fig.10) and heavy rimed graupels (Fig.6) further proves the probability that the spectra shift was caused by secondary ice production rather than by particle breakup since particles with D<1000 μm increase without the decrease in the number of large particles. Further discussion on those secondary ice production mechanisms will be covered in the next section.

Based on the analysis of the measurements taken by aircraft Piper-Aztec of France during the experiment of the Precipitation Enhancement Project organized by WMO in Spain in 1981, the study of Liu (1986) showed that in precipitation cloud the maximum concentration of ice particles occurred not only in the region of -3~-7 ℃ but also in the regions of -9~-12 ℃ and -16~-19. In our case, the two maximum concentrations existed in the regions of -10~-15 ℃ and -3~-5 ℃, which shares the same implication of different ice multiplication mechanisms within different temperature ranges as Liu (1986).

6. Horizontal distribution of particles and possible causes

However, the focus of our study mainly lies in secondary ice production mechanisms, including riming splinter and collisonal ice-ice breakup which are based on theories from laboratory studies (Vardiman 1978, Hallet 1976, Mossop 1978, Goldsmith 1976). And those theories can only be checked against field data indirectly by comparing theoretical predictions with measurable parameters (e.g. the required droplet size spectra, temperature, and presence of graupels) since the initial secondary ice particles produced by riming or collisonal breakup are too small to be detected in natural clouds.

6.1 *Fragmentation of ice crystal in -10~-15 ℃ temperature region*

The quantity of fragments generated by crystal collisions in cloud depends on the number of fragments produced per collision and collision frequency. Brewer and Palmer (1949) and Vardiman (1978) proposed that the fragmentation of delicate ice crystals may have an impact on the increase of ice particle concentrations in clouds. And Vardiman (1978) pointed out some interesting facts: (1) For plane dendrites, the greater the degree of rime, the greater the fragmentation; (2) Light-moderate rimed spatial crystals are the most effective crystal studies for generating fragments; (3) Graupels are surprisingly ineffective in generating fragment. Although unlike the riming-splinter mechanism, the criteria for ice enhancement by crystal fragmentation are less quantified in the laboratory, there are still some evidence of the contribution of ice fragment to ice enhancement in clouds (Hobbs, 1985, Liu 1986 and Chen 1987). For instance, Hobbs (1985) found that ice crystals were predominant near the top of stratiform clouds, and as the distance from the cloud top increases, the number of crystal fragments and aggregates grows with the maximum reaching 5 times of those measured near cloud top.

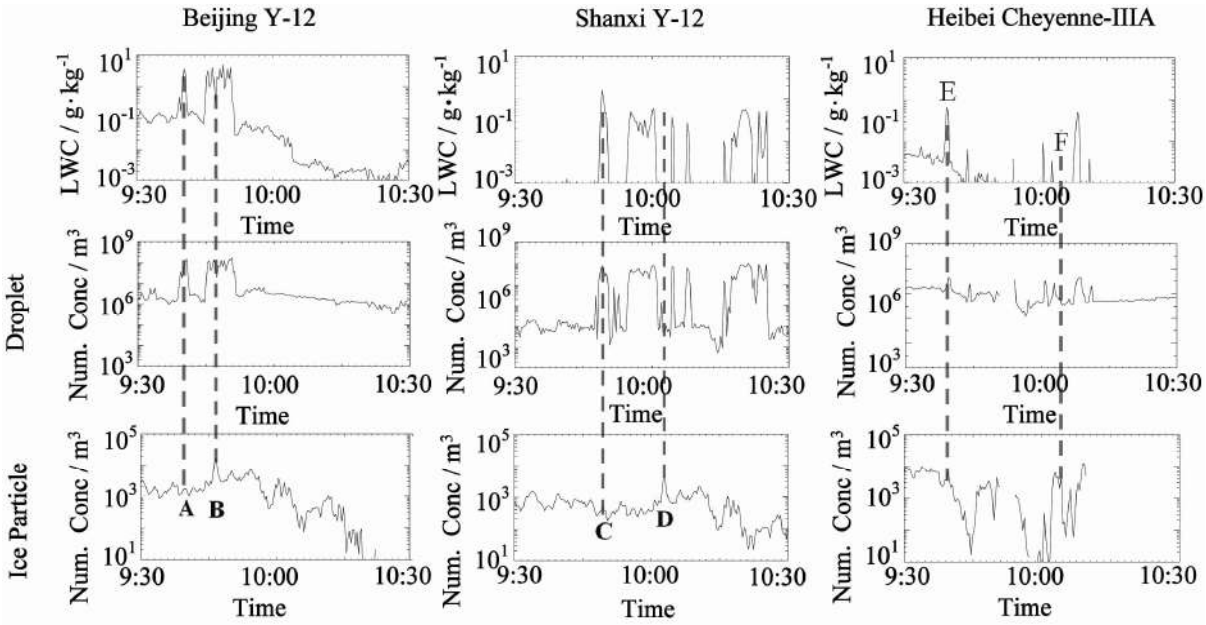

Fig.11. 30 sec average of LWC, number concentration of water droplet measured by FSSP, CAS and CDP; ice particles from on board probes including OAP2DGA and CIP, during 0930 LST and 1030 LST

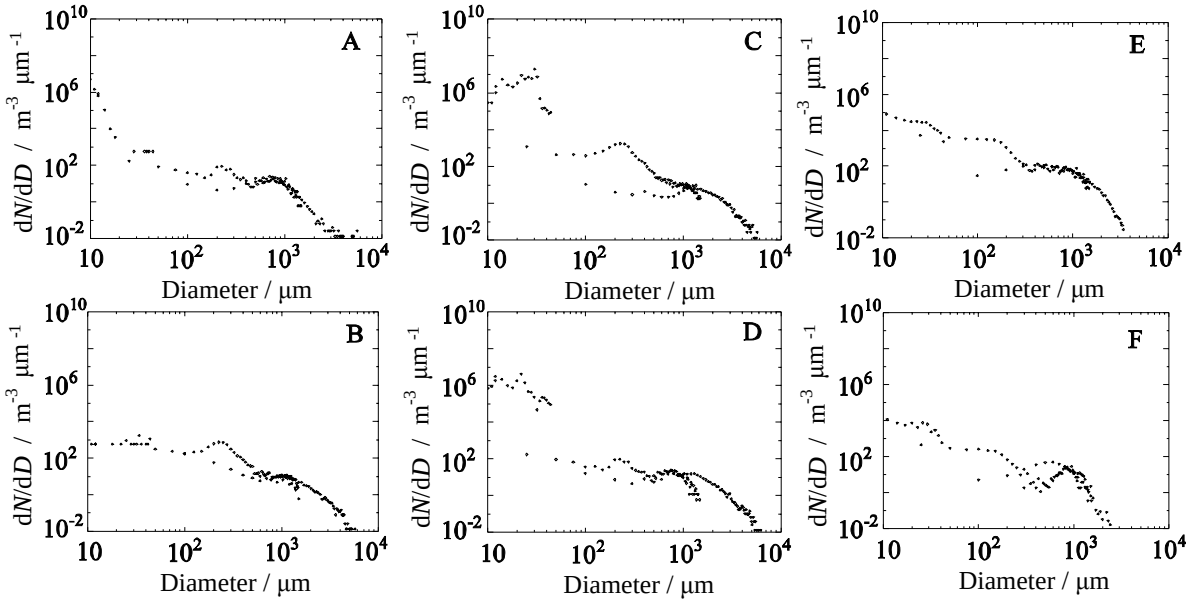

Fig.12. The combined size spectra of particles at the six points of A, B, C, D, E and F indicated in Fig.10

In our study, the shifting of particle spectra and the 2D imagery share the similar results to the theoretical studies of Vardiman (1978). In Fig.11 point C (I > 5 L^{-1}) and D (I <1 L^{-1}) in -10~-15 ℃ respectively represent the areas where the collision breakup mechanism is more sufficient and suppressive, and the combined spectra in vicinity of 300~400 μm show a greater growth at point C than that of point D. From the CIP 2D imagery (Fig.13) it can be seen that at point C there are mainly plane assemblages of sector and their aggregations which are lightly rimed, and needle-like ice particles which may be produced by secondary ice production, whereas at point D there are chiefly heavily rimed particles and graupels with undistinguished boundaries.

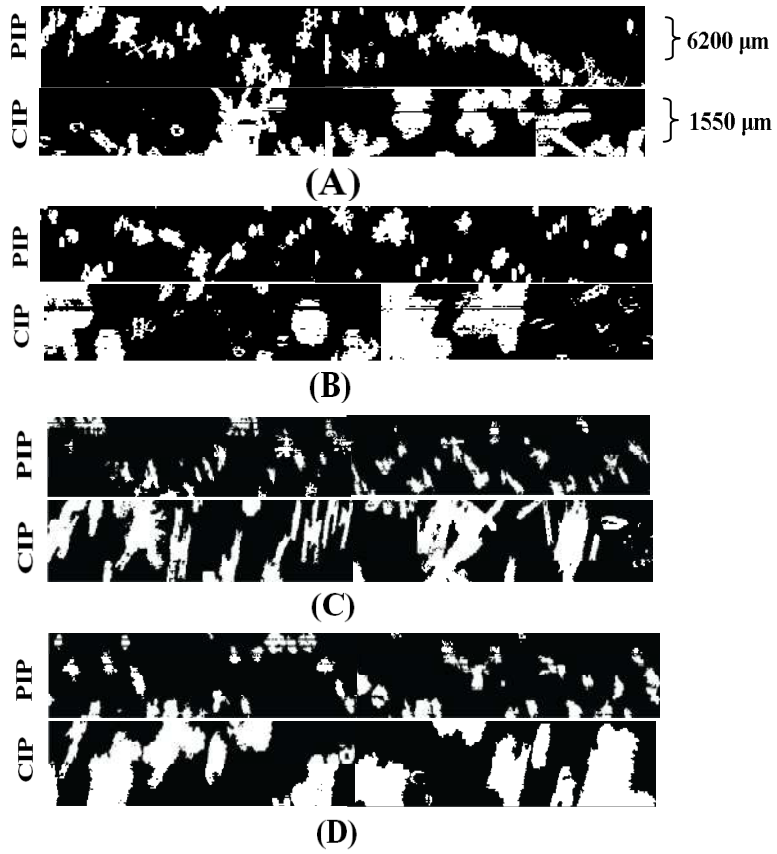

Fig.13. Two-dimensional cloud probe imagery of particles at the four points of A, B, C and D indicated in Fig.11

As mentioned above, the collision breakup mainly depends on the riming degree of ice crystals and ice habits. Measuring the average size distribution of accreted droplets for each of the five different crystal shapes from 84 single snow crystals, with different crystal shapes taken as the measured on photographs, Mosimann (1994) pointed out that two separated modes for planner and long columnar crystals peak at diameters of 20 and 60 μm. Ono (1969) and Harimaya (1975) found that the rimed spectrum for plate, broad branch and dendrite crystals is much narrower than that for columnar crystals, about 80% of the accreted droplets with D < 25 μm.

Since in our study the 2DC and 2DP suggested the planner ice particle was predominant in the region of -10~-15 ℃, and encouraged by the laboratory studies of Mosimann (1994), we attempt to unveil the relationship between intensity of ice-ice collision breakup and the riming degree by comparing ice crystals with water droplets with D<25 μm, and the comparison with the previous research is restricted for lack of studies on the number of accreted cloud droplets and fragments. In Fig.14 the relationship between number concentration of ice crystals and water droplets with D<25 μm, which is based on the finding of Mosimann (1994), indicates that when the concentration of cloud droplets with D<25μm is less than 1 cm^{-3}, the concentration of ice particles is directly proportional to the concentration of cloud droplets at this size range, and when the concentration of cloud droplets with D<25μm is more than 100 cm^{-3}, they are inversely proportional. However when the cloud droplet concentration with D<25μm is in the range of 1~100 cm^{-3} the relationship still remains uncertain for lacking sufficient data.

6.2 *Ice splinter production during riming in -3 ~ -8 ℃ temperature region*

Following the investigation of ice splinter production during riming by Macklin *et al* (1960),

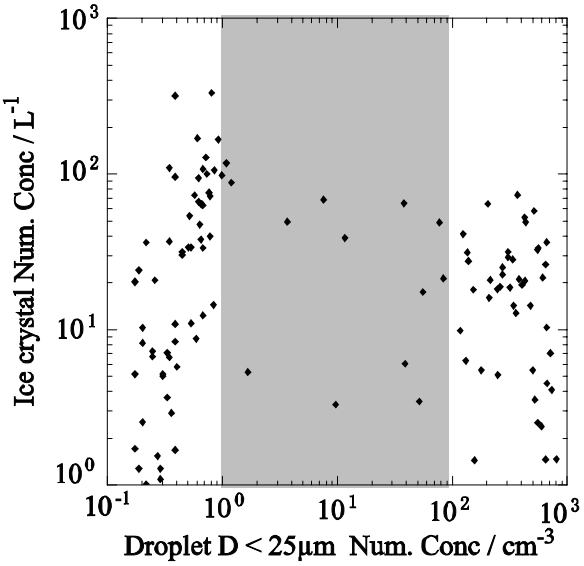

Fig.14. Ice concentration versus the concentration of cloud drops with D<25 μm within temperatures of -10~-15 ℃, measured by Shanxi Province Y-12; the shade area indicating the uncertain relationship between ice particles and water droplets

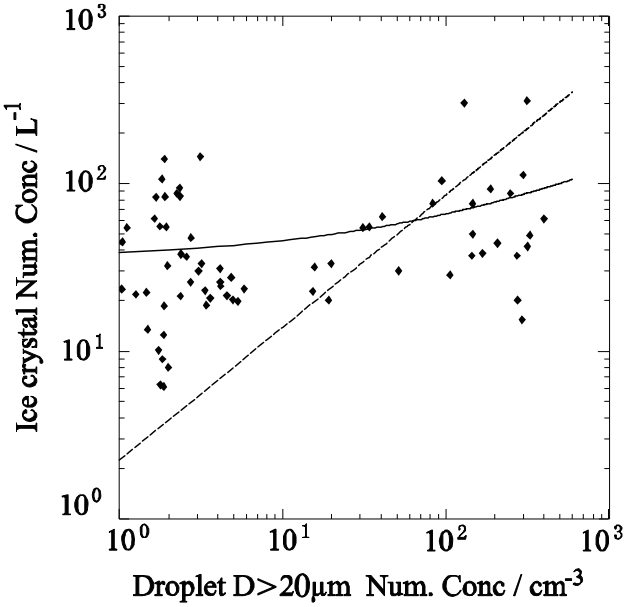

Fig.15. The ice concentration versus the concentration of cloud droplets with D>20 μm within temperatures of -3~-8 ℃, measured by Beijing City Y-12, the dash line indicating best fit line in cumulus clouds of Hobbs (1985), and the solid line representing the one in our study

Latham and Mason (1961) and Hallett and Mossop (1974), Hallett and Mossop (1978) further consolidated the mechanism for ice enhancement and indicated that small ice splinters are produced when supercooled droplets approximately > 23 μm in diameter impact at speeds > 1.4 m s^{-1} onto an ice surface at air temperature within -3~-8 ℃. The dataset of our horizontal flight during 0930 to 1030 LST proves the variation of ice particles and supercooled water droplets satisfies the original Hallett-Mossop criteria within 3~-8 ℃. Fig.11 A and B present the average cloud droplet spectra for low and high ice production areas, and high ice producers have broader droplet spectra than those of the low ones. For

example, the number concentration of droplets with D>23 μm at point A is much greater than that at point B. The CIP 2D imagery (Fig.13), which shows heavy rimed ice particles, graupels and large droplets at point B, also suggests the riming splinter process could be invoked in the area. Gordon and Marwitz (1986) introduced the possibility of secondary production by rime splintering as a potential reason for an increase in Ns and the relatively steady value of λ, implying that precipitation growth occurred equally at all particle sizes, and Fig.12 provides more obvious evidence of such shifts in ice particle size spectra.

Fig.15 unveils the relationship between ice particles and water droplets with D>20 μm. Since this plot isolates the dependence of ice particles on large cloud droplets, the slope in Fig.15 indicates that the production rate is proportional to the concentration of such droplets. According to Hobbs (1985), the effect of large droplets on ice concentration can also be proved by seeking correlations between *I* (ice particle concentration) and the concentration of cloud droplets exceeding a certain diameter. With the quantity (C_{20}) expressed in the unit of cubic centimeter and I_{max} in per liter, the best fit relationship between ice concentration and cloud droplets (D>20 μm) is

$$I_{max} = a\,(C_{20})^b, \quad (6)$$

in our study a=3.61, b=0.464 and the correlation coefficient *r*=0.641. Compared with the findings of Hobbs and Rango (1985), and Harris-Hobbs and Cooper (1987), on one hand, they share the similar relationship between ice crystal concentration and large droplets in cumuliform cloud, on the other hand, it is probable that as a result of less turbulence within the stratiform cloud, ice particles are less dependent on large cloud droplets in our case than in the mature and aging cumuliform cloud studied by Hobbs (1985) with coefficients a=2.25, b=0.79 with *r*=0.89 within cumulus. Compared with stratiform cloud, convective cloud has several features (e.g. higher collision frequency and more forceful collisions) that could make them very efficient in generating secondary particles by mechanical fracturing.

7. Conclusion

This study presents analysis of the size distribution and the 2D imagery observed by three air crafts fly horizontal legs at a variety of altitudes in a westerly wind trough precipitation system occurring in the field study of R&D of Key Technology and Equipment for Weather Modification. Based on the results, we can draw the conclusions that

(1). Similar to the study results of the precipitous stratiform cloud in Liu (1986), in our case it can be seen from the particle size distribution shift, the CIP and PIP 2D imagery and the ice particle concentration at different temperatures, the two maximum ice concentration regions (-10~-15 ℃ and -2~-5 ℃) could be invoked by two different ice multiplication mechanisms (i.e. collision breakup and H-M process).

(2). In the region of -10~-15 ℃, the main secondary ice production mechanism is planner crystal-crystal collision breakup, which leads to an increase in vicinity of 300～400 μm. The relationship between ice concentration and cloud droplets with D<25 μm unfolds two distinctive tendencies, i.e. when the concentration of cloud droplets with D<25 μm is less than 1 cm^{-3}, the concentration of ice particles is directly proportional to that of cloud droplets, and when the cloud droplet concentration is more than 100 cm^{-3}, the secondary ice production rate is suppressed. However when the cloud droplet concentration is in the range of 1~100 cm^{-3} the relationship still remains uncertain for lacking sufficient data.

(3). In our study, within the region of -3~-8 ℃, the riming splinter process is mainly responsible for secondary ice production. Compared with the findings in convective cloud, stratiform cloud in our study shares a similar

relationship between ice particle concentration and water droplets with D>20 μm. However, the number concentration of ice particles is less dependent on that of large water droplets than in cumulus cloud, and it is probably caused by less turbulence, lower collision frequency and less forceful collisions.

References

Bergeron, T., 1935: On the physics of cloud and precipitation. *Proc. Fifth Assembly U.G.G.I.*, Lisbon, 2,156-160

Braham, R. R.. Jr., 1986: Precipitation enhancement – A scientific challenge. Precipitation Enhancement – A Scientific Challenge, Meteor. Monogr., , *Amer. Meteor. Soc*., No. 43, 1~5

Hobbs, P.V., A. L. Rangno, 1985: Ice particle concentrations in clouds. *J.Atmos. Sci.*, 42, 2523~2546

Bruintjes, R. F., 1999: A Review of Cloud Seeding Experiments to Enhance Precipitation and Some New Prospects. *Bull. Amer. Meteor. Soc.,* 80, 806~820

Brewer, A. W., and H. P. Palmer, 1949: Condensation processes at low temperatures and the production of new sublimation nuclei by the splintering of ice. *Nature*, 164, 312~313

Liu Wenbao., 1986: The characteristics of ice crystal concentration distribution in cold cloud. *Plateau Meteorology*, 5: 53~61

Chen Wankui., 1987: The multiplication generated by dendritic snow crystals collision and aggregation. *J. Aca. Met. Sci (in Chinese)*., 2, 74~80

Findeisen, W., 1938: Die Kolloidmeteorologischen Vorgange beider Wiederschlagsbidung. *Met. Z*., 55,121~132

Field, P. R., 1999: Air craft observation of ice crystal evolution in altostratus cloud. *J. Atmos. Sci.*, 56, 1925~1941

Filed, P. R., 2000: Binmodal ice spectra in frontal clouds. *Q.* J. *R. Meteoml. Soc.,* 126, 397~392

Field, P. R., and A. J. Heymsfield. 2003: Aggregation and scaling of ice crystal size distribution. *J. Atmos. Sci*., 60, 544~560

Goldsmith, P., Gloster and C. Hume, 1976: The ice phase in clouds. *Preprints intern. Conf. on cloud physics*, Boulder, Amer. Meteor. Soc., 163~167

Gun, K. L. S., and J. S. Marshall, 1958: The distribution with size of aggregate snowflakes. *J. Atmos. Sci.*, 15, 452~461

Herzegh, P. H., and P. V. Hobbs, 1985: size spectra of ice particles in frontal clouds: Correlations between spectrum shape and cloud conditions. *Quart. J. Roy. Meteor. Soc*., 111, 463~477

Hallett, J., and S. C. Mossop, 1974: Production of secondary particles during the riming process. *Nature*, 249, 26~28

Harris-Hobbs, R. L., W. A. Cooper, 1987: Field evidence supporting quantitative predictions of secondary ice production rate. *J. Atmos. Sci.* 44: 1071~1081

Heymisfield, A. J., A. Bansemer, P. R. Field, S. L. Durden, J. L. Stith, J. E. Dye, W. Hall, and C. A. Grainger, 2002: observations and parameterizations of particle size distribution in deep tropical cirrus and stratiform precipitation clouds: Result from in situ observations in TRMM field campaigns. *J. Atmos. Sci*., 59: 3457~3491

Harimaya, T., 1975: The riming properties of snow crystals. *J. Atmos. Sci.,* 26, 522~531

Korolev, A., and B. Sussman, 2000: A technique for habit classification of cloud particles. *J. Atmos. Oceanic Technol*., 17, 1048~1057

Knollenberg. R. G., 1976: Three new instruments for cloud physics measurements: the 2-D spectrometer, the forward scattering spectrometer probe, and the active scattering aerosol spectrometer. *Preprint, Int. Conf. on cloud Physics*. Boulder, CO, Amer. Meteor. Soc.,

554~561

Lo, K, K., and R. E. Passarelli, 1982: The growth of snow in winter storm: an airborne observation study. *J. Atmos. Sci*., 39, 697~706

Latham, J., and B. J. Mason, 1961: Generation of electric charge associated with the formation of soft hail in thunderclouds. Proc. Roy. Soc., A260, 537~549

Lawson, P. R., and T. L. Jensen, 1998: Improved microphysical observation in mixed phase cloud. Preprints, Conf. on cloud Physics, Everett, WA, *Amer. Meteor. Soc*., 451~454

Mossop, S. C., 1976: Production of secondary ice particles during the growth of graupel by riming. *Quart. J. Roy. Meteor. Soc*., 102, 45~47

Macklin, W. C., E. Strauch and F. M. Ludlam, 1960: The density of hailstones collected from a summer storm. *Nubila*., 3, 12

Korolev, A, V., and I. P. Mazin., 1993: Zones of increased and decrease droplet concentration in straitifom clouds. *J. Appl. Met*. 32, 760~773

Mosimann, L., E. Weingartner and A. Waldvogel., 1994: An analysis of accreted drop sizes and mass rimed snow crystals. *J. Atmos. Sci*. 51, 1548~1558

Ono, A., 1969: The shape and riming properties if ice crystal in nature clouds. *J. Atmos. Sci*., 26, 138~147

Sekhon, R. S., and R. C. Srivastava, 1970: Snow size spectra and radar reflectivity. *J. Atmos. Sci*., 41: 299~307

Vardiman, L., 1978: The generation of secondary ice particles in cloud crystal-crystal collisions. *J. Atmos. Sci*., 35, 2168~2180

EFFECTIVENESS OF ASIAN DUST PARTICLES AS ICE NUCLEI IN OROGRAPHIC SNOW CLOUDS

Masataka Murakami, Narihiro Orikasa, Takuya Tajiri, Atsushi Saito and Katsuya Yamashita

[1]Meteorological Research Institute, Tsukuba, Japan

1. INTRODUCTION

Aerosol particles, which act as ice nuclei, determine ice crystal concentrations and affect precipitation forecast through precipitation efficiency. Also from the viewpoint of climate change study, it is pointed out that ice nuclei as well as cloud condensation nuclei modulate the coverage and life of clouds and precipitation distribution through radiation properties and precipitation efficiency, and affect climate projection 100 years later through consequent modulation of global energy and water cycle.

Studies on ice nuclei have been carried out for more than half a century. However there are many things to remain unsolved because of huge complexity in activation mechanisms of ice nuclei unlike a single process of CCN activation.

Dust particles has been thought to be representative ice nuclei for a long time. Ice nucleation ability of montmorillonite, kaolinite and volcanic ashes as well as dust particles have been investigated. As for dust particles from inland of Chine, Isono et al. (1959) investigated chemical and physical characteristics and ice nucleation ability by using electron microscopic techniques and filter method.

DeMott et al. (2003) measured ice nucleation ability of Saharan dust particles using CFDC IN counter and Sassen et al. (2003) observed clouds in dust storm by using depolarization lidar. Recently ice nucleation ability of dust particles have also been studied in AIDA chamber (Field et al., 2006; Möhler et al., 2006; Möhler et al., 2008a).

Possibility of internal mixing of dust particles with sea salt or sulfate particles during their transport is also suggested through electron microscopic analysis of dust particles fallen over the western part of Japan.

But there are no in-situ measurements of microphysical structures of clouds during dust storms. In this paper, effectiveness of Asian dust particles as ice nuclei is investigated through a modulation of ice crystal concentrations in orographic snow clouds observed by an instrumented aircraft, airborne measurements of ice nuclei concentrations and dynamic cloud chamber experiments of ice nucleation on dust particles.

2. AIRBORNE IN-SITU MESUREMENTS OF OROGRAPHIC SNOW CLOUDS DURING HEAVY DUST STORM

Field campaigns on orographic snow cloud study had been carried out around the

Corresponding author's address: Masataka MURAKAMI, Meteorological Research Institute, Tsukuba, Ibaraki 305-0052, Japan; E-Mail: mamuraka@mri-jma.go.jp.

Echigo Mountains in the central part of Japan. We had flown an instrumented aircraft for the consequent 6 winter seasons (Feb.-Mar. 1998, Feb.-Mar. 1999, Feb.-Mar. 2000, Feb.-Mar. 2001, Dec. 2001, and Dec. 2002) over the study area.

The instrumented aircraft was equipped with various kinds of cloud microphysics and ordinary meteorological instruments, including a gust probe to measure three components of wind relative to the ground, on the wing tip pylons and fuselage. Cloud microphysics instruments included FSSP, 2D-C, 2D-P, CAPS, PVM-100 and two KLWC-5 probes.

We had a dust storm event for two days in series (March 5 and 6, 2000). The typical concentration of aerosol particles larger than 2 μm during dust storms was several particles cm^{-3} and was 2 to 3 orders of magnitude greater than background concentrations ranging from 10^{-1} to 10^{-2} particles cm^{-3}.

The maximum concentrations of ice crystals during the heavy dust storm were about 100 particles L^{-1} in orographic clouds with top temperature of -20 C on the both days, which is half order of magnitude higher than the mean values of those for usual days without dust storm. Although the data points from the both days are located near the upper boundary of scattered data points, there are several data points from clouds without dust storm effects that show number concentrations as high as those on the dust event days (Fig.1).

This observation result suggests that dust particles act as efficient IN, and some particles other than dust particles also act as good IN.

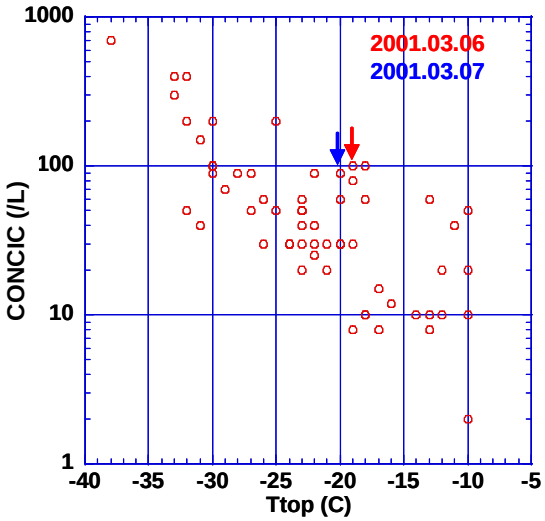

Fig. 1 Relation between the maximum number concentration of ice crystals and cloud top temperature obtained from aircraft observation data for 6 winter seasons from 1998 through 2003.

The total concentrations of dust particles may have been at least one order of magnitude higher than the observed concentrations of particles larger than 2 μm according to the past studies on Asian dust particles.

This means that one particle out of 100 to 1,000 particles is activated in orographic clouds during dust storm, which is much less effective as compared with experimental results by DeMott et al. (2003).

3. AIRCRAFT MEASUREMENTS OF IN CONCENTRATIONS

Recently we built an aircraft-version of CFDC IN counter and collected data in summer and winter seasons.

The results of aircraft measurements of IN concentrations made on March 5th, 2009 are presented as an example. Aircraft observation was made behind the extratropical low (Fig.

2a). IN measurements were made at -25 C and at water saturation or slightly water supersaturation.

We had a moderate dust storm, especially from 3 to 5 km. The concentrations of dust particles larger than 2 μm (measured with FSSP) were several tenths cm^{-3} and IN concentrations were about 100 particles L^{-1} (Fig. 2b).

Activated fraction of aerosol particles larger than 0.5 and 0.01 μm were 10^{-1} to 10^{-2} and 10^{-3} to 10^{-4}, respectively (Fig. 2c).

4. DYNAMIC CLOUD CHAMBER EXPERIMENTS OF ICE NUCLEATION ON DUST PARTICLES

The MRI cloud chamber was designed as an adiabatic-expansion-type cloud chamber, similar to CSU dynamic cloud chamber. We use the rotating brush disperser to generate dust particles and two-stage cyclones to remove large-size particles.

Figure 3 shows an example of experimental results; from top to bottom, time series of air pressure, wall and air temperatures and dewpoint temperature, relative humidity, particle concentrations measured with CAS, laser scattering intensity, and depolarization ratio. Two vertical dashed lines indicate the onset of cloud droplet formation and ice crystal formation. Ice nucleation started to occur at around -17 C.

Figure 4 shows number concentrations of large droplets (a) and ice crystals (b) measured with CPI, and number fractions of ATD larger than 0.5 μm activated as IN (c) as a function of air temperature. Very few particles already start to activate at around

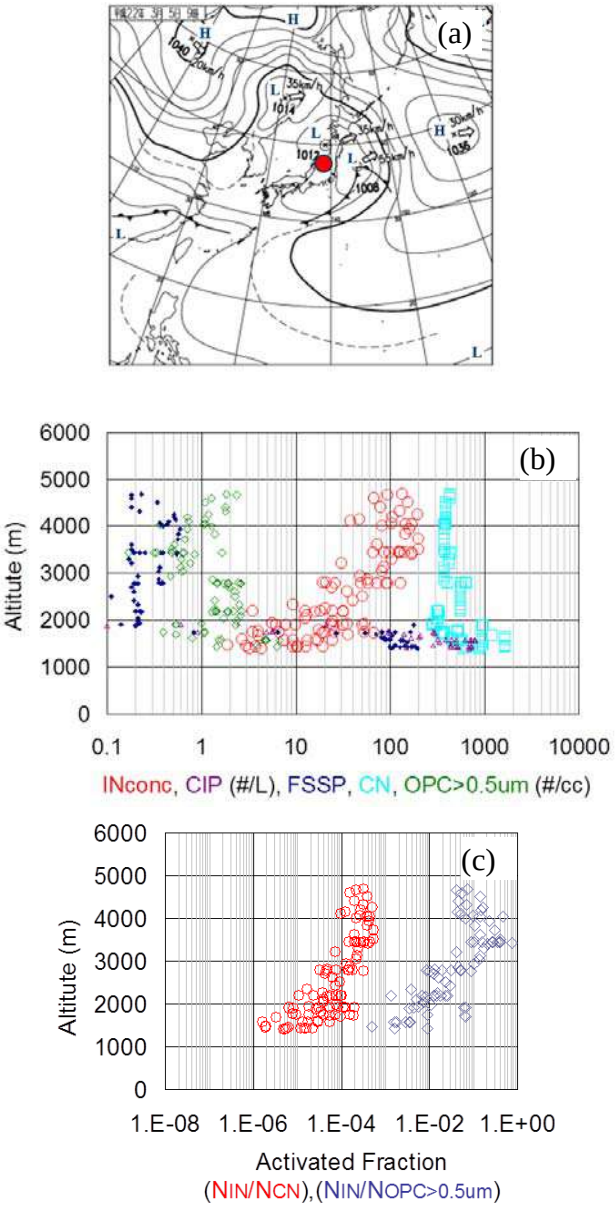

Fig. 2 Surface weather map at 0900 JST on 5 Mar. 2009 (a), vertical profiles of particle concentrations (b) and activated fractions of aerosol particles larger than 0.01 and 0.5 μm (c).

-10 C, but significant fractions (10-2 to 10-3) of ATD activate at around -17 C or colder temperatures.

Activated fractions are also dependent on

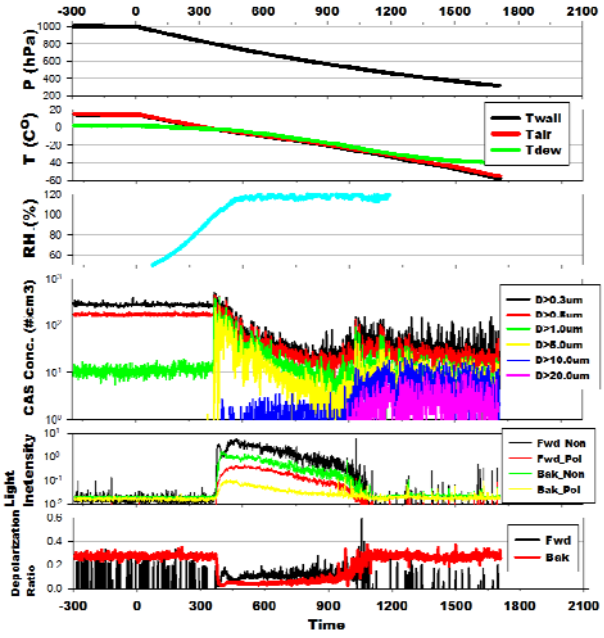

Fig. 3 Time series of air pressure, wall and air temperatures and dewpoint temperature, relative humidity, particle concentrations measured with CAS, laser scattering intensity, and depolarization ratio.

dewpoint temperature, namely temperatures of lifting condensation level, which determine the mean diameter of cloud droplets, and updraft velocity.

5. ACTIVATED FRACTION OF ATD AND ASIAN DUST

Figure 5 shows the relation between number concentrations of dust particles larger than 0.5 μm and IN concentrations. IN concentrations obtained from aircraft observations during moderate and light dust storms range from one to a few hundreds particles L^{-1} at -25 C, and the activated fractions of Asian dust particles are 10^{-3} to 10^{-1}. On the other hand, the activated fractions of ATD particles obtained from MRI chamber experiments and IN counter

Table 1 Initial conditions and ascent rate

Case	P [hPa]	T [℃]	Tdew [℃]
a	999.8	15.1	0.7
b	1000.0	15.9	-0.9
c	1000.0	14.9	-6.5
d	999.9	15.0	-6.2

Ascend Rate :
a, c : 5m/s b, d : 2m/s

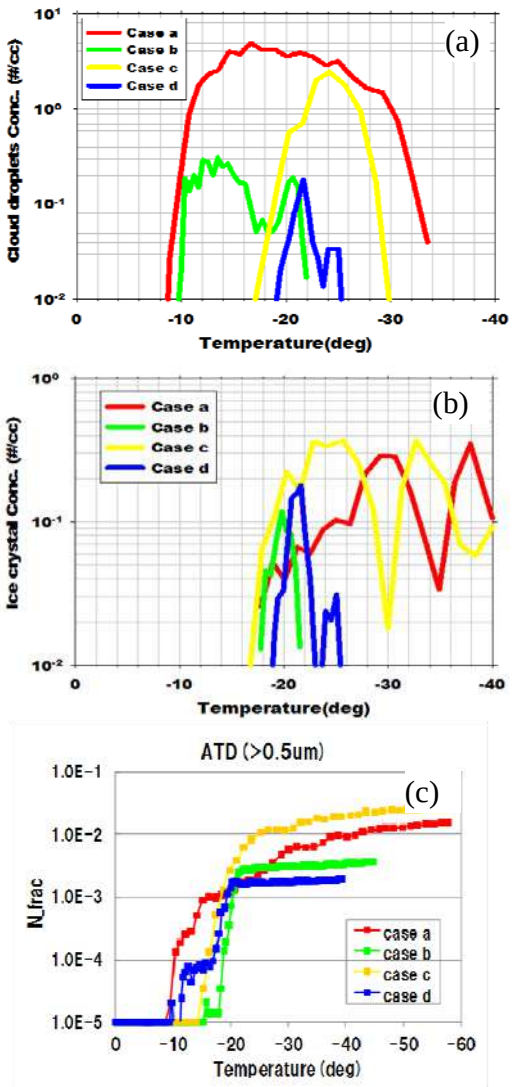

Fig. 4 Number concentrations of large droplets (a) and ice crystals (b) measured with CPI, and (c) activated fractions of ATD larger than 0.5 μm as a function of air temperature.

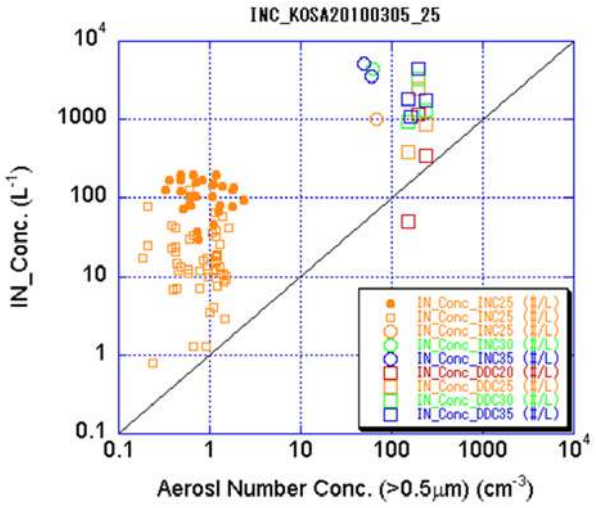

Fig. 5 Relation between number concentrations of dust particles larger than 0.5 μm and ice nuclei concentrations activated at -20 C (red), -25 C (orange), -30 C (green) and -35 C (blue) . All marks except for large square are for atmospheric aerosol particles and large square is for ATD.

measurements are almost the same and are 10^{-3} at -25 C to 10^{-1} at -35 C.

6. CONCLUSION

Aircraft observations of orographic snow clouds during heavy dust storms showed that ice crystal concentrations were ~100 particles L^{-1} in clouds with top temperature of -20 C, which is half order of magnitude higher than concentrations on no dust storm days. This observation result shows that dust particles indeed act as effective ice nuclei (IN), but some particles other than dust may also act as good IN. Activated fractions of Asian dust particles larger than 2 μm (measured with FSSP) were on the order of 10^{-2}. Activated fraction of Asian dust larger than 0.5 μm was estimated to be on the order of 10^{-3} assuming typical size distribution of dust particles over Japan.

Resent aircraft measurements of IN concentrations during light and moderate dust storms and MRI cloud chamber experiments on IN ability of Asian and Arizona Test Dust particles showed that activated fraction of particles larger than 0.5 μm ranged from 10^{-3} to 10^{-1} at -20 ~ -25 C, which is consistent with the maximum ice crystal concentrations observed by the instrumented aircraft during the heavy dust storm.

REFERENCES

DeMott P. J., K. Sassen, M. R. Poellot, D. Baumgardner, D. C. Rogers, S. D. Brooks, A. J. Prenni, S. M.Kreidenweis, 2003: African dust aerosols as atmospheric ice nuclei, *Geophys. Res. Lett.*, **30**, 1732,doi: 10.1029/2003GL017410.

Field, P. R., O. Möhler, P. Connolly, M. Krämer, R. Cotton, A. J. Heymsfield, H. Saathoff, and M. Schnaiter, 2006: Some ice nucleation characteristics of Asian and Saharan desert dust, Atmos. Chem. Phys., 6, 2991-3006.

Isono, K., M. Komabayasi, and A. Ono, The nature and origin of ice nuclei in the atmosphere, *J. Meteorol. Soc.Japan*, **37**, 211-233, 1959.

Möhler, O., P. R. Field, P. Connolly, S. Benz, H. Saathoff, M. Schnaiter, R. Wagner, R. Cotton, M. Krämer, A. Mangold, and A. J. Heymsfield, 2006: Efficiency of the deposition mode ice nucleation on mineral dust particles, Atmos. Chem. Phys., 6, 3007-3021.

Möhler, O., S. Benz, H. Saathoff, M. Schnaiter, R. Wagner, J. Schneider, S. Walter, V. Ebert, and S. Wagner, 2008: The effect of organic coating on the heterogeneous ice nucleation efficiency of mineral dust aerosols, Environmental Research Letters, 3(2), doi:10.1088/1748-9326/1083/1082/025007.

Sassen K., P. J. DeMott, J. M. Prospero, M. R. Poellot, 2003: Saharan dust storms and indirect aerosol effects on clouds: CRYSTAL-FACE results. *Geophys. Res. Let*t., **30** (12), 1633, doi: 10.1029/2003GL017371.

CAN BACTERIA WITH ICE FORMING ABILITIES IMPACT ON RAIN FORMATION IN A CONVECTIVE CLOUD?

M. Monier[1], A. Flossmann[1], M. Andraud[1], and the BIOCLOUD Team: N. Good[1], O. Möhler[2], C. Oehm[2], E. Attard[3], P. Amato[3], A.M. Delort[3], T. Koop[4], S. Borrmann[5], C. Morris[6]

[1] *Laboratoire de Météorologie Physique (LaMP), Université Blaise Pascal, OPGC/UMR-6016, Clermont-Ferrand, France*

[2] *Forschungszentrum Karlsruhe (FZK), Germany*

[3] *Institut de Chimie de Clermont-Ferrand (ICCF), Université Blaise Pascal, OPGC/UMR-6016, Clermont-Ferrand, France*

[4] *Bielefeld University, Germany*

[5] *Max Planck Institute for Chemistry, Mainz, Germany*

[6] *Plant Pathology Research Unit, INRA, Avignon, France*

1. INTRODUCTION

Biological matter is found in the atmosphere in the form of living or "dead" organisms. These aerosol particles of biological origin (ABO) represent about one fourth of the total aerosol particle number (Jaenicke, 2005). Some are known to be good ice nuclei like some bacteria species (Szyrmer and Zawadzki, 1997) and thereby may influence the life cycle of clouds and their precipitation. The focus of the collaborative French-German project BIOCLOUDS is to investigate and quantify the role of ABO particles in tropospheric clouds. Combining the partners' expertise in microbiology, aerosol-cloud microphysics, meteorology, and cloud modelling, the project aimed to (1) identify relevant species in cloud and precipitation water and, for comparison, in the aerosol outside clouds, (2) extract and culture relevant samples for laboratory investigations of CCN and IN properties, and, (3) make use of the new experimental results as input to cloud models in order to improve the formulation of microphysical processes for ABO in models and to more accurately assess the potential importance of these processes for cloud evolution.

Here, we present the first modelling studies, which investigate the critical ABO concentrations with IN capabilities to impact precipitation production of a convective system.

2. BIOCLOUD EXPERIMENTAL DATA

Cloud water was sampled at the summit of puy de Dôme. Bacteria strains in cloud water were identified. Strains were cultivated and the standard drop-freezing method (Vali, 1971) for testing their ice nucleation activity was used. The strains that were the most efficient to form ice were selected for more in-depth studies at the AIDA facilities of the KIT group. Three different campaigns were designed to test heterogeneous ice nucleation on bacteria. Living cells were suspended in pure water and sprayed in the AIDA and NAUA chambers. Adiabatic expansions in AIDA were realized to test their IN potential from -2 to -15°C. NAUA chamber was used for studying physical and chemical properties of the bacterial aerosol particles.

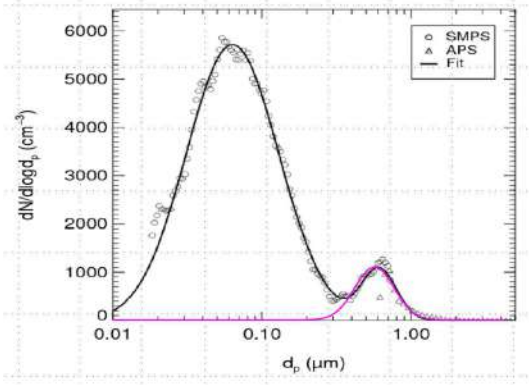

Fig.1: Number size distributions of *Pseudomonas syringae* cc242 suspended in the NAUA chamber measured with a SMPS and an APS instruments. The pink fit was used to initialize DESCAM model (see text).

After spraying and drying the bacterial suspension, during every experiment two different aerosol modes were observed; one example is shown in Figure 1. There, we see one mode with a smaller concentration and a diameter peaking at 0.6 µm that we assumed to be bacteria cells, and another mode, more important in number but with a smaller mean diameter that we assumed to be bacteria debris and residues of chemicals in the bacteria suspension.

Cloud condensation nuclei (CCN) properties of the particles were investigated with CCN chambers.

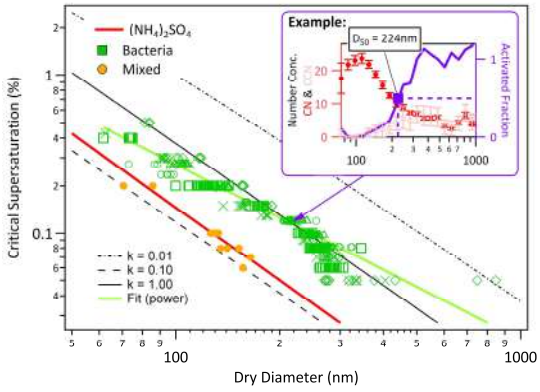

Fig.2: Derived critical supersaturation for the entire second campaign of Bioclouds as a function of the dry diameter of aerosolized particles. The upper right picture shows how each dots of the plot has been derived.

From the CCN studies, summarized in Figure 2, we can conclude that bacteria cells together with the smaller residuals APs, which are created during the suspension spraying, behave exactly like aerosol particles with a hygroscopicity corresponding to a kappa-value (κ) greater than 0.1. Bacteria cells are so big that, at relatively warm temperature (-2℃ to -10℃), with this hygroscopic behavior they likely act first as CCN before being involved in ice formation. Optical counters available in the AIDA chamber (PALAS/WELAS instruments) confirmed that liquid clouds were always formed before ice appearance. Subsequently, we assumed that the ice formation due to bacteria is associated with the heterogeneous mechanism of condensation following by freezing.

To determine the ice onset and the number of ice crystals, the assumption was made that each single particle exceeding 20 µm in diameter in the optical counters data is an ice crystal. Ratio of IN/cells varied depending on the strains used, but values as high as 8% were observed.

3. MODEL SET-UP

The model DESCAM (DEtailed SCAvenging Model) used in our study is coupled with the columnar dynamical framework described in Asai and Kasahara (1967). DESCAM is a microphysics model under development since the 1980s (Flossmann and Wobrock, 2010, and references herein). DESCAM is a detailed explicit microphysical model that prognoses evolution of humid aerosol particles, drops, and ice crystals number size distributions. The particularity of DESCAM is to follow explicitly the aerosol particle population but also the fate of the uptaken particles in the hydrometeors by means of additional mass density distribution functions for aerosol mass in each size bin for the aerosol particles, the drops, and the ice crystals. DESCAM is built to consider an external mixture of aerosol particles.

The simulations, we present here, are a sensitivity study to determine the critical concentrations and/or efficiency of bacteria with ice nucleation activity to impact convective precipitation. We used the convective case of CCOPE to conduct this study (Dye et al., 1986; Cloud Modeling Workshop at IRSEE, Germany, report n°139 of WMO). Dynamical set-up and initialization are described in Leroy et al. (2006).

We considered two different populations of aerosol particles, for both of

them the concentration profile is exponentially decreasing with a scaling height (i.e. 3km) until the top of the boundary layer and kept constant in the free troposphere. The background aerosol particles are distributed following the "continental" parameters of Jaenicke (1988) and the bacteria particles are log-normally distributed following observations in NAUA (Figure 1) with a mean diameter of 0.62 µm and a standard deviation of 0.13. Total concentration for these particles will vary. Background particles are set to an internal mixing of 80% of insoluble material and 20% of sulfuric acid.

In any microphysical processes, if one particle (humid AP, drops, or ice crystals) containing background particulate material coagulates with one containing bacteria cell, we assumed the resulting particles to contain bacteria.

To reproduce observations, the bacterial population is followed inside the drops and if the temperature is below -3℃, then 5% of the bacteria cells inside freeze the droplets. Background aerosol particles can form ice heterogeneously following the parameterization of Meyers et al. (1992) and homogeneously in the upper troposphere following Koop et al. (2000).

4. MODELLING RESULTS AND DISCUSSION

Figure 3 shows the development of the storm with no bacteria considered. Once warm air reaches the lifting condensation level (at 3km), condensation starts and updraft velocities rapidly increase up to 17 $m.s^{-1}$. A dense liquid cloud (more than 2 $g.m^{-3}$ of water) develops vertically and rises to an altitude where temperature is cold enough for homogeneous nucleation to occur. Then precipitations are generated and a strong downdraft is associated with it. (Note that the model considers the melting of hailstone as instantaneous).

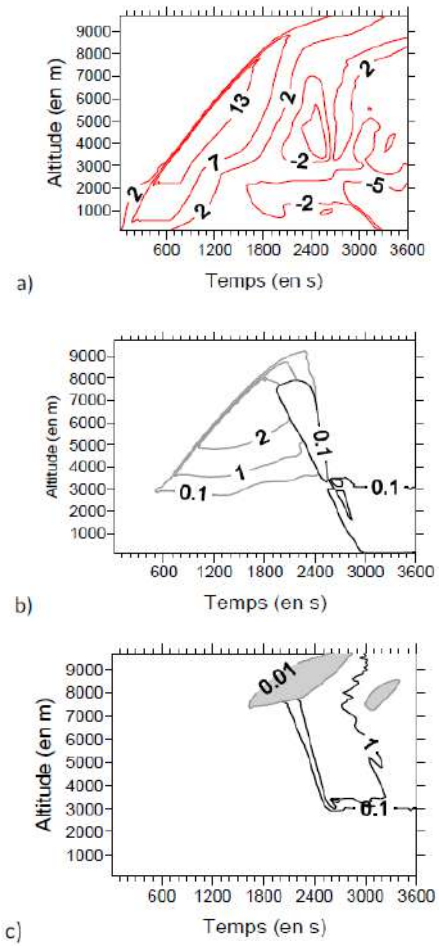

Fig.3: Vertical profiles as a function of time for: a) vertical velocity ($m.s^{-1}$), b) liquid water and c) ice water contents ($g.m^{-3}$).

The second species of biological aerosol particles is then introduced. Burrows et al. (2009) gave different concentrations of ABOs in air above different habitats; we chose to test the minimum, median and maximum of those concentrations. Values for those concentrations and the consequent rain production are given in the table below.

	Minimum	Median	Maximum
N_{ABO} (cm^{-3})	10^{-5}	0.102	0.840
Rain (mm)	1.3	2.0	1.5

The minimum concentration is very low and the quantity of rain reaching the ground is exactly the same than without any bacteria. Regarding the evolution of rain production in increasing ABOs, we remark first that an increase in the IN

population increase precipitation, but if ABO concentration exceed an optimum value then precipitation decreases again.

In the scenario of a warmer and more humid climate, ABO concentrations are expected to increase. With this in mind, we chose to also test the production of rain with an ABO concentration 10 times higher than the previous maximum. In this sensitivity study the production of rain reaching the ground was totally inhibited. Figure 4 shows the evolution of LWC with altitude for that run.

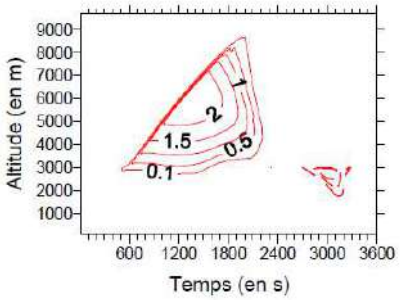

Fig.4: Vertical profile of liquid water content water contents ($g.m^{-3}$).

This figure 4 explains why too much ABOs can reduce rain. Comparing figure 4 and 3b, we notice that less liquid water reaches the “nest” of ice crystals at 9000 m of altitude, ice crystals being so few the rain production is not efficient. The change in LWC profile in the first 30 minutes is little and it can be explained because convection was not as strong as before. The ice formation on bacteria, near the cloud base at the beginning, induced very little precipitation that evaporated below the cloud base. The subsequent cooling is very small but strong enough to lower the convection considerably.

5. DISCUSSION

In this theoretical study, we investigated if the bacteria cells, which were isolated from cloud water sampled at the puy de Dôme mountain site and found in AIDA to be IN active through the condensation freezing mechanisms, could impact rain production in convective systems. It was found that if we increase slightly the IN population then rain is more important, but exceeding an optimum value will lower rain production.

This study remains preliminary since we need to include as accurately as possible the observations made during the last BIOCLOUDS campaign in Karlsruhe. We need also to point out that the modeling studies were performed in a columnar model. Therefore the sensitivity of the model on early precipitation that cools cloud base and lower convection could be overestimated. We have to repeat this study in 3D dynamical framework and include cases on stratiform precipitations.

5. REFERENCES

Asai T., and A. Kasahara, *J. Atmos. Sci.* **24** (1967) 487-596.

Burrows, S.M., W. Elbert, M.G. Lawrence, and U. Pöschl, *Atmos. Chem. Phys*., **9** (2009) 9263-9280.

Dye, J.E, J.J. Jones, W.P. Winn, T.A. Cerni, B. Gardiner, D. Lamb, R.L. Pitter, J. Hallet, and C.P.R. Saunders, *J. Geophys. Res.* **91** (1986) 1231-1247.

Jaenicke, R., 1988. Aerosol physics and chemistry. In: Fischer, G. (Ed.), Landolt-Boernstein: Zahlenwerte und Funktionen aus Naturwissenschaften und Tecknik, 4b, pp. 391–457.

Jaenicke, R. *Science*, **308**, (2005) 73.

Flossmann, A.I, and W. Wobrock, *Atmos. Res.* **97** (2010) 478-497

Koop, T., H. P. Ng, L. T. Molina, B. Luo, A. Tsias, and T. Peter *Nature,* **406 (2000)** 611–615.

Leroy, D., M., Monier, W. Wobrock, and A.I. Flossmann, *Atmos. Res.* **80** (2006) 15-45

Meyers, M. P., P. J. DeMott, and W. R. Cotton, *J. Appl. Meteor.,* **31, (1992)** 708–721.

Szymer W. and I. Zawadzki *Bull. Am. Meteorol. Soc.,* **78**, (1997) 209-228,

Vali G., *J. Atmos. Sci.* **28** (1971) 402-409.

Acknowledgements

The authors acknowledge with gratitude the financial support provided through the French-German joint research project BIOCLOUDS financed by DfG and CNRS/INSU.

SCHNEEFERNERHAUS AS A CLOUD-TURBULENCE RESEARCH STATION. PART 1: FLOW CONDITIONS AND LARGE-SCALE TURBULENCE

Stefan Risius[1], Haitao Xu[1], Hengdong Xi[1], Holger Siebert[2], Raymond Shaw[3], and Eberhard Bodenschatz[1]

1 Max Planck Institute for Dynamics & Self-Organization (MPIDS), 37077 Göttingen, Germany
2 Leibniz Institute for Tropospheric Research, 04318 Leipzig, Germany
3 Department of Physics, Michigan Technological University, Houghton, MI 49931, USA

1. INTRODUCTION

Cloud measurements are usually carried out with airborne campaigns that are costly and limited by weather conditions and low spatial resolution. Ground based measurements at elevated research stations therefore can play a complementary role. Using the meteorological data (wind speed, direction, temperature, humidity, visibility, etc.) collected by the German weather service (DWD) over the last 10 years and turbulence measurements recorded by multiple ultrasonic sensors (sampled at 10 Hz) during the past two years, we show that the Umwelt-forschungsstation Schneefernerhaus (UFS) located in the German Alps, at a height of 2650m, is a well-suited station for cloud-turbulence research. Analysis of the second and third order structure functions from the continuous recordings of ultrasonic sensors at UFS shows that the wind turbulence exhibits well-developed inertial ranges with Taylor micro-scale Reynolds numbers between 1500 and 3500. In spite of the complex topography of the UFS, the turbulence appears to be close to isotropic when evaluated with the so-called "Lumley-triangle".

2. GEOGRAPHY & ENVIRONMENT

UFS (47°25'00'' N, 10°58'46'' O) is located near the top of Zugspitze, the highest mountain of Germany (2962m above sea level). The southern flank of the mountain is covered with Germany's largest glacier, the Schneeferner, which is surrounded by a mountain arc that shields it from winds coming from north, west and south. The Schneeferner is unshielded towards the southeast where melt water streams run down the mountain. The mountain ridge on the west of the glacier is known as the Schneefernerkopf. Over a length of about 200 meters erosion has decreased its height significantly and the lowest point is about 175 meters lower than the Schneefernkopf summit. This part is known as the "wind hole", because it directs the wind over the glacier like a funnel (Engelbrecht, 2011). UFS is situated on the north side of the glacier and half way to the top of Zugspitze, at a height of about 2650 meters (see Fig. 1).

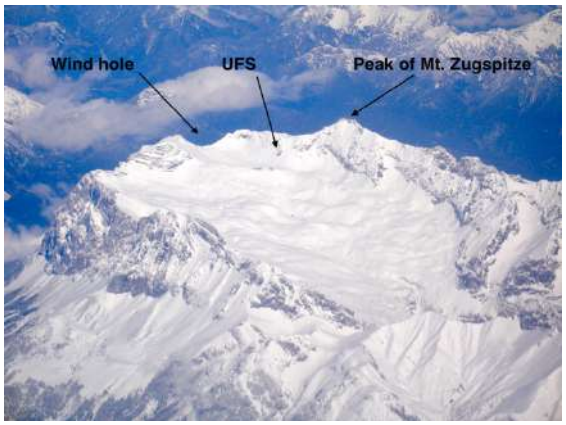

Figure 1. View of the Schneeferner valley from the southeast (Photo taken by Xtream, alpinforum.com Luftbilder Topic, 2009. http://www.alpinforum.com/forum/viewtopic.php?f=7&t=19048&start=50).

The weather at Zugspitze is mainly influenced by the westerlies, which are strong prevailing winds in the middle latitudes. The winds often carry great masses of moist air, leading to heavy precipitation on the northwest side of the Zugspitz massif. In addition to this, on about 60 days per year the weather is dominated by Foehn winds, which push against the massif from the south, resulting in relatively high temperatures during the winter times. The average

temperature during the "standard reference period" (1961-1990) was −4.8°C and the average precipitation was 2003 mm per year (Siebler, 2010). The lowest temperature recorded at Zugspitze was −35.6°C while the highest was 17.9°C (DWD, 2000). Figure 2 shows the local weather conditions at Zugspitze, averaged over the years 2000 – 2005 using observations data at UFS from the Deutscher Wetterdienst (DWD). As shown in the middle right panel, the research station is "in clouds" for about 25% of the time in July and August, which is promising for ground-based observation of cloud-turbulence interaction.

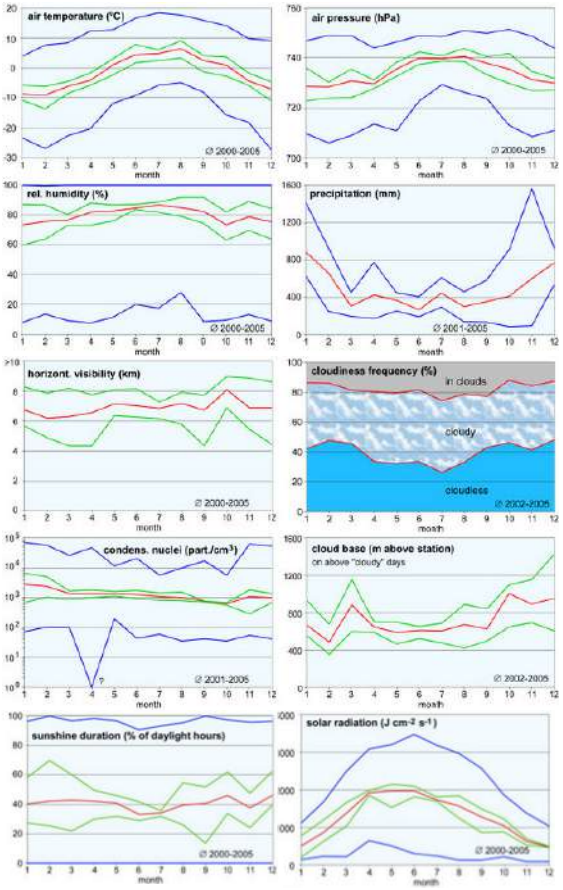

Figure 2. Local weather conditions at UFS, obtained from the 2000 – 2005 average of observations by the Deutscher Wetterdienst (DWD). Image courtesy of UFS (http://www.schneefernerhaus.de/en/wetterdaten/climatology.html).

3. FLOW CONDITIONS

UFS is a nine-story building, constructed into the southern flank of the Zugspitze (see Fig. 3).

Figure 3. Views of UFS from the south.

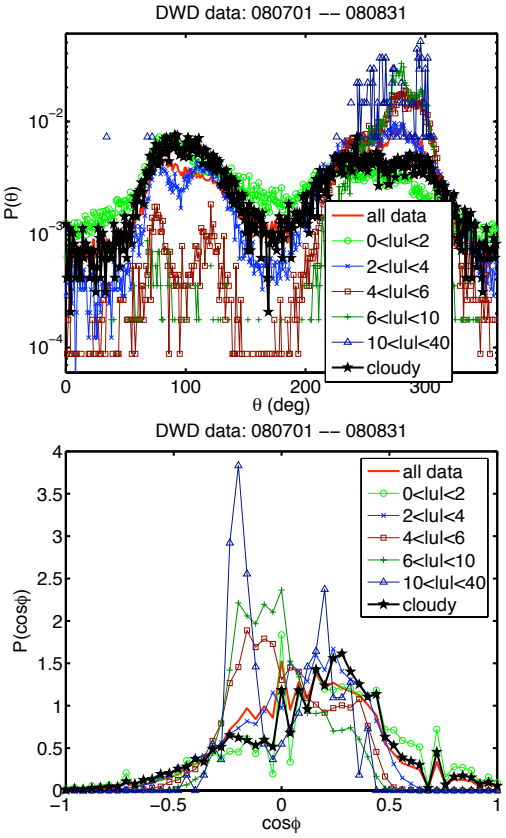

Figure 4. PDFs of wind directions in the horizontal (top panel) and the vertical (bottom panel) directions. θ=90° corresponds to wind from the east and θ=270° corresponds to wind from the west. $\cos\phi$<0 and $\cos\phi$>0 corresponds to wind from above and below, respectively. See text for "cloudy" conditions.

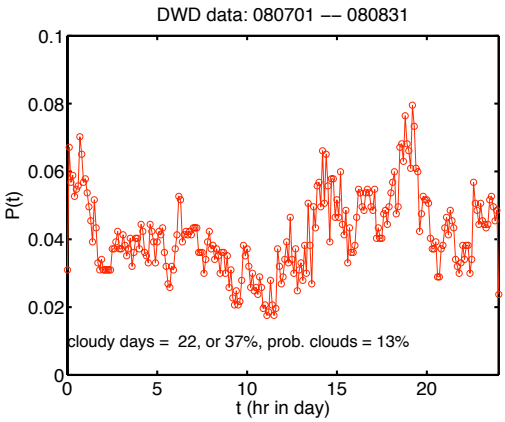

Figure 5. Probability of clouds covering UFS at given time of the day in July and August of 2008 (local time at UFS).

Due to the local topography, the winds measured at UFS are primarily in the east-west direction. For detailed analysis, we used the DWD data in July and August 2008. Figure 4 shows the probability density functions (PDFs) of the wind directions in the horizontal and vertical directions. The PDF around east or west winds are not the same, most likely due to the different topography on the two sides. Winds from the west have to pass along the mountain before reaching UFS and hence are influenced by the mountain flank, while east winds flow along the valley and are mostly free from the effect of the mountain. In Fig. 4, we also show the wind directions conditioned on the events with moist clouds, which we defined as when the relative humidity is above 99%, the temperature is above 0 degree C and the visibility is below 200m. It can be seen that clouds are usually associated with mild wind, especially for wind from the east. However, some strong west wind could also carry clouds, which are usually under severe weather conditions.

To access the chance of measuring clouds, we also checked the probability to have clouds during the time of a day, as shown in Figure 5. It can be seen that clouds are more likely to occur during the late afternoon and shortly after mid-night. A cross-correlation with wind conditions shows that the late afternoon clouds are often from the east, due to the condensation of moist evaporated from the valley by solar heating during the day. The mid-night clouds are often from the west, probably formed far away and then carried over by severe storms. It is therefore very interesting to compare these two types of clouds and the associated turbulence in future observations.

4. LARGE-SCALE TURBULENCE

Before carrying out cloud measurements, we first studied quantitatively the turbulent flows at UFS. We present here large-scale flow measurements. Analysis of small-scale turbulence is reported in an accompanying paper (Katzwinkel et al 2012).

Figure 6. The mast of ultrasonic wind sensors on the roof of UFS.

To measure large-scale turbulence, we installed 5 three-dimensional ultrasonic sensors (manufactured by Thies Clima, Germany) on a mast located on the round tower of the UFS (Figure 6). The sonic sensors are arranged in a configuration as tetrahedrons. The analysis shown here is from the measurements by the top sensor, which is approximately 6 m above the roof and 20 m away from the mountain. The sensors have been continuously recording wind velocities at 10 Hz since March 2010, of which we analyzed in detail the data between September and December 2010. From these recordings, we select the “steady” events that are defined as a

period between 1 and 2 minutes during which the fluctuations of wind around its mean is less than 25% of the mean. For these events, we used Taylor's frozen turbulence hypothesis to obtain spatial correlations and structure functions from the time series of velocity data measured by the top sensor. Using the integral scale L and the RMS velocity fluctuation u obtained from the velocity correlation, we estimate the Taylor micro-scale Reynolds number of the event using the isotropic relation (see, e.g. Pope 2001) as

$$R_\lambda = \sqrt{15uL/\nu}, \quad (1)$$

where ν is the kinematic viscosity of air at the given temperature. The integral scale we obtained is approximately 14 - 20 m and the range of R_λ is between 1500 and 3500.

Energy dissipation rate per unit mass ε is the most important quantity to characterize turbulence. For cloud studies, the energy dissipation rate of turbulence determines the other parameters of cloud droplets such as the Stokes number, the settling parameter, and the Froude number (Siebert et al, 2009). From the longitudinal and transverse second order velocity structure functions, we fit the inertial range scaling

$$D_{LL} = C_2(\varepsilon r)^{2/3} \quad (2)$$

and

$$D_{NN} = \frac{4}{3}C_2(\varepsilon r)^{2/3} \quad (3)$$

with a value of C_2=2.1 (see e.g., Pope 2001) to obtain the energy dissipation rates ε (Figure 7, top panel), which we then check against the measured third order structure function that has an exact scaling law

$$D_{LLL} = -\frac{4}{5}\varepsilon r \quad (4)$$

As shown in Fig. 7 bottom panel, Eq. (4) with the energy dissipation rates measured from the second order velocity structure functions agree with measurements within a factor of 2. We therefore take the averaged ε measured using Eqs. (2) and (3). The energy dissipation rate derived from the third order structure functions are more sensitive to noise and the inhomogeneity of the flow (Xu et al 2009). The energy dissipation rates determined in this way are in the range of 10^{-4} to 10^{-2} m^2/s^3.

With the measured values of ε, L, and u, we check the normalized dissipation rate

$$C_\varepsilon = \frac{\varepsilon L}{u^3}. \quad (5)$$

It has been found that the normalized energy dissipation rate C_ε is a constant of approximately 0.5 for a wide range of Reynolds numbers, including both laboratory flows and flows in the atmosphere (Burattini et al, 2005; Pearson et al, 2002; Sreenivasan, 1998). This observation has also been called the "zeroth law of turbulence", as Kolmogorov's hypotheses assume that the mean energy dissipation rate is independent of the viscosity at high Reynolds numbers (Frisch, 1995; Pearson et al., 2004).

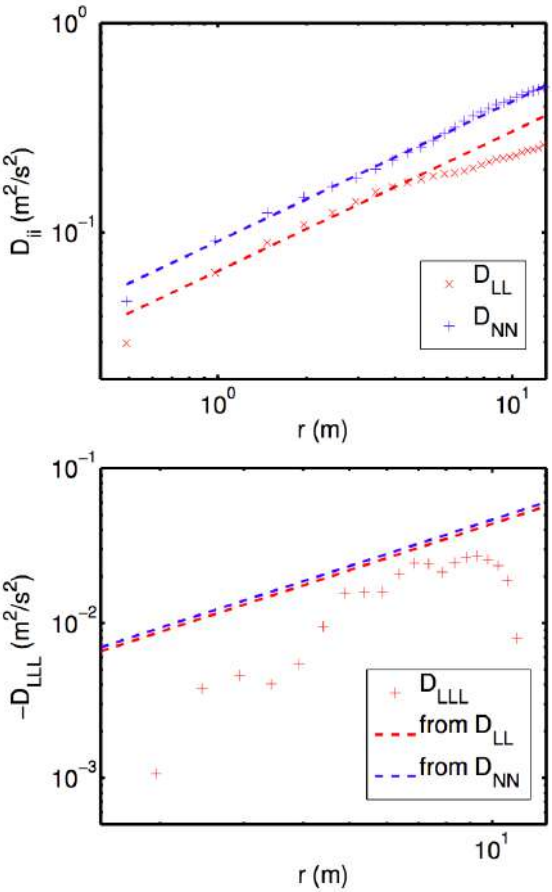

Figure 7. The second order (top panel) and the third order (bottom panel) velocity structure functions obtained from the ultrasonic sensor data. The dashed lines in the top panel are fits to Eqs. (2-4), which gives values of ε. Those are then used to plot Eq. (4) in the bottom panel.

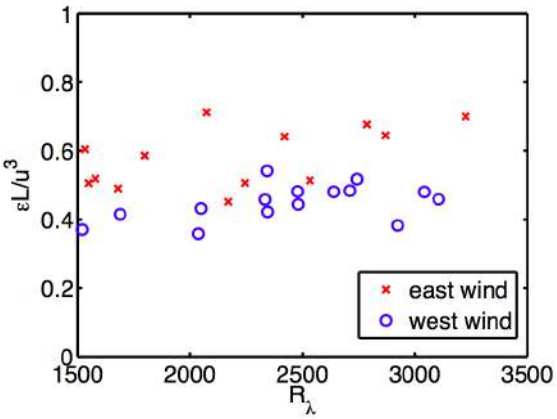

Figure 8. Normalized energy dissipation rates.

Figure 8 shows the current measurements of C_ε as a function of Reynolds number. In agreement with earlier measurements, a value of about 0.5 was found. It can also be seen that the value of C_ε depends weakly on the wind direction, which can be attributed to the different flow conditions of the east and the west wind. As described before, winds from the west are subject to stronger shear than winds from the east and larger shear could lead to a smaller value of the energy dissipation rate (Sreenivasan et al., 1995).

Finally, to access the deviation of the turbulent flow at UFS from the ideal isotropic conditions, we show the measured events on the so-called "Lumley triangle", which is the realizable region on the plane spanned by the two invariants of the deviatoric part of the Reynolds stress tensor (Schumann, 1977; Lumley & Newman, 1977; Pope, 2001). When mapped onto that plane, any realistic turbulent flow should lie within the Lumley triangle. The origin on that map represents the isotropic flows. The closer to the origin, the closer the flow is isotropic. As shown in Figure 9, the flows at UFS (for winds from the east) are anisotropic. As the Reynolds number increases, however, there is a trend for the flow to become more isotropic. We also compare the flows at UFS with two widely used laboratory turbulent flows, i.e, the von Kármán swirling flow between two counter-rotating disks (Voth et al, 2002) and the propeller-stirred turbulent flow within an icosahedra (Zimmermann et al, 2010; the apparatus is named the Lagrangian Exploration Module or LEM). The turbulent flows at UFS are less isotropic than the LEM flow, which is designed to achieve high homogeneity and isotropy (Zimmermann et al, 2010). On the other hand, the degree of isotropy of the UFS flows is comparable, and in many cases, even better than the von Kármán flows, especially as the Reynolds number increases. For winds from the west, the range of anisotropy is approximately the same as that of the east winds, but no clear change with Reynolds number can be observed. This is most likely due to the effect of shear as discussed before.

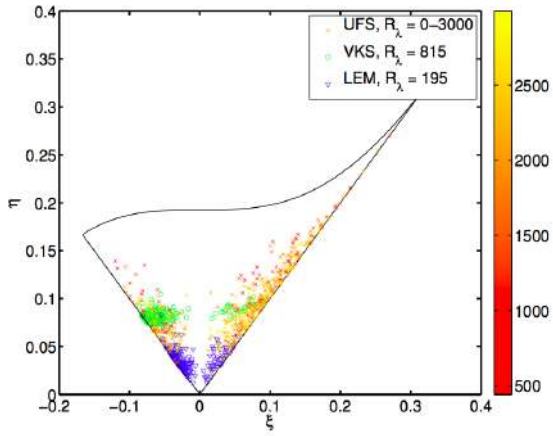

Figure 9. Mapping of the turbulent flows at UFS due to east winds on the Lumley triangle, in comparing with two laboratory flows: the von Kármán flows and the LEM flows. The symbols are color-coded with the Reynolds numbers of the flow, whose range is indicated by the colorbar.

5. CONCLUSIONS & FUTURE WORK

From our analyses of both meteorological data and the turbulent flow data, we can conclude that the research station UFS is suited for cloud-turbulence interaction studies. The flow turbulence at large scales are similar to other laboratory flows, especially for winds coming from the east, which are less influenced by the nearby mountain. In addition to the analyses of small-scale turbulence, we are also analyzing the spatial structures of the turbulence using the multi-point correlations obtained from simultaneous measurements of the 5 ultrasonic sensors. The results will be reported elsewhere.

6. BIBLIOGRAPHY

P. Burattini, P. Lavoie, R. Antonia 2005 On the normalized turbulent energy dissipation rate. Phys. Fluids, 17.

DWD 2000 Wetter und Klima - Deutscher Wetterdienst - Flächenpräsenz, http://www.dwd.de/zugspitze.

H. Engelbrecht 2011 Zugspitzplatt und Plattumrahmung. http://www.umweltgeol-he.de/WerdenfelserGeotope.Wetterstein.ZugspitzplattUndPlattumrahmung.htm.

U. Frisch 1995. Turbulence: The legacy of K. N. Kolmogorov. Cambridge University Press, Cambridge, UK.

J. Katzwinkel, T. Schmeissner, R. A. Shaw, H. Siebert, E. Bodenschatz, H. Xu 2012 Schneefernerhaus as a cloud-turbulence research station. Part 2: Cloud microphysics and fine-scale turbulence. Proc. ICCP'16, Leipzig, Germany.

J. L. Lumley and G. R. Newman 1977 The return to isotropy of homogeneous turbulence. J. Fluid Mech., 82:161.

B. R. Pearson, P. Krogstad, W. van de Water 2002 Measurements of the turbulent energy dissipation rate. Phys. Fluids, 14:1288.

B. Pearson, T. Yousef, N. Haugen, A. Brandenburg, P. Krogstad 2004 Delayed correlation between turbulent energy injection and dissipation. Phys. Rev. E, 70.

S. B. Pope 2001 Turbulent Flows. Cambridge University Press. Cambridge, UK.

U. Schumann 1977 Realizability of Reynolds stress turbulence models. Phys. Fluids, 20:721.

H. Siebert, S. Gerashchenko, A. Gylfason, K. Lehmann, L. Collins, R. A. Shaw, Z. Warhaft 2010 Towards understanding the role of turbulence on droplets in clouds: in-situ and laboratory measurements. Atmos. Res. 97:426.

D. Siebler 2010 Bestimmung von Größen- und Formfaktoren von Schnee anhand von Messungen am Schneefernerhaus. http://elib.dlr.de/63396/.

K. Sreenivasan, P. R. Viswanath, S. M. Deshpande, A. Prabhu 1995 The energy dissipation rate in turbulent shear flows. In Developments in Fluid Dynamics and Aerospace Engineering, Bangalore, India.

K. Sreenivasan 1998 An update on the energy dissipation rate in isotropic turbulence. Phys. Fluids, 10:528.

G. A. Voth, A. La Porta, A. M. Crawford, J. Alexander, E. Bodenschatz 2002 Measurement of particle accelerations in fully developed turbulence. J. Fluid Mech., 469:121.

H. Xu, N. T. Ouellette, H. Nobach, E. Bodenschatz 2009 Experimental measurements of Lagrangian statistics in intense turbulence. Proc. 11th European Turbulence Conference.

R. Zimmermann, H. Xu, Y. Gasteuil, M. Bourgoin, R. Volk, J.-F. Pinton, E. Bodenschatz 2010 The Lagrangian Exploration Module: An apparatus for the study of statistically homogeneous and isotropic turbulence. Rev. Sci. Instru., 81:055112.

Acknowledgements

We thank Dr. Szymon Malinowski, Dr. Alain Pumir, and Dr. Jörg Schumacher for helpful discussions during this work. We are grateful to Mr. Fabio Di Lorenzo, the engineering team led by Dr. Artur Kubitzek and Mr. Udo Schminke at MPIDS, to Dr. Till Rehm, Mr. Markus Neumann and the staff at UFS for their technical help in building and installing our instruments at UFS. Financial support from Max Planck Society, Leibniz Society, Deutsche Forschungsgemeinschaft (DFG) through the SPP 1276 Metström, and the EU COST Action MP0806 "Particles in Turbulence" are gratefully acknowledged.

INITIAL PART DISCUSSION OF CLOUD MERGER

Li Yanwei Niu Shengjie

Key Laboratory for Atmospheric Physics and Environment of China Meteorological Administration, Nanjing University of Information Science & Technology

Abstract: Though many cloud merging processes begin from the middle and lower parts of clouds, but the authors find that many merging processes begin from the middle and upper parts of clouds. Because of the important effect of cloud merger, the authors studied a merging process on 17 May 2005 using a cloud-resolving mesoscale model WRF (Weather Research and Forecasting Model). In this process, many mergers happened. Observation and simulation results show the process goes through three stages: (1) convective cells merging into a convective cloud; (2) convective clouds merging into a convective cloud cluster; (3) cloud clusters merging into a cloud system. The first and second stages of the merger process begin from the middle and lower parts, often between the young or developing clouds. The third stage of merger begins from the middle and upper parts, often between the mature cloud clusters. These two kinds of merging mechanisms are quite different, but both are related to shear of wind and updraft velocity. In this paper, the authors set forth these two kinds of mechanisms in detail.

Key words: numerical simulation, convective clouds merger, cloud clusters merger

1. INTRODUCTION

Merger of clouds plays an important role on evolution of clouds forming and precipitation process. A large amount of papers(Bennetts et al., 1982; Tian, 1991; Doernbrack, 1997; Knupp et al., 1998; Carey et al., 2000; Jirak et al., 2003;) have shown that Merger often happens between clouds or cloud clusters. Cloud merger is the expression of enlargement and enhancement of clouds, which has significant effect on genesis of precipitation system. In order to discuss the merger mechanism, many research deeply analyzed the merger process and environment condition using methods of observation and numerical simulation, most of essays（Tao et al., 1984; Ackerman et al., 1988; Westcott et al., 1989, 1994; Chu et al., 2000; Lee et al., 2006; Pozo et al., 2006; Danhong Fu et al., 2007）support a similar conclusion: Surface convergence and shear of wind is essential to merger. The genesis of merger processes are mainly because of the cold outflow of convective clouds, which inspires cloud bridges between nearby cells, and initial merger happens at lower part of the clouds.

We found through observation, however, sometimes merger initially develops from the lower part of clouds, while sometimes from the upper part. Merger initially from lower part often emerges in original stage or developing stage of cloud body, while the other ones often happens in mature stage. The above shows that there are different types of merger, which is not mentioned in

previous study. This type of merger is equally important in development of clouds, so that we choose a merger case in mountainous area of Southwest China to reveal this type of merger in a new sight of view.

2. INSTRUCTIONS ON THE OBSERVATIONS AND ANALYSIS OF THE CONVECTIVE CLOUDS MERGER PROCESS

This paper begins with case analysis, and a merger process happened in Southwest mountainous area (mainly in Guizhou Province) from May 17th-18th, 2005, is studied. The whole process experience Instruction of merger during development of clouds (Shown in Fig 3): at 22:50, May 17th, there are two larger convective clouds displaying in Guiyang radar pictures which merged by some small convective cells; at 00:00, May 18th, these two convective clouds continue to develop and merge small convective cells, and finally become two relatively larger convective cloud clusters; at 02:00, May 18th, these two cloud clusters finally get together as one wide-ranged precipitation system with long duration.

By comparing vertical section of radar echo patterns (shown in Fig1b~d), it found that merger can initially develop from lower part of clouds (Fig1b-c), as well as the upper part (Fig1d). Those processes which develop from lower level often happen between newly-generated cells. The clouds are developing and have short distance between each other. And those processes developing from upper part often happen between relatively large clouds. In this situation, each clouds is already has several column-like convective echoes, and with wide horizontal range.

3. PRELIMINARY ANALYSIS OF SIMULATION RESULTS

Using the mesoscale numerical model WRF simulation, the simulation results well reproduced the true phenomenon of mergers. The merger process is divided into three stages to discuss in this article.

(1)The first stage: convective cells merged into large clouds occurred from 260 to 310 min after the simulation. Under the condition of being close to each other, the nascent cumulus monomers merged into larger size of convective clouds. After merging, the original smaller scale of a few monomers formed a strong convective cloud of big scale and uniform flow field.

(2)The second stage: large convective clouds merged into convective cloud cluster, occurred from 310 to 450 min after the simulation. After the first stage of merging and forming a strong convective cloud, convective cells generated continuously around the convective cloud. Through mergers, the echo, and flow field were closely connected to the formation of a greater intensity and multiple internal convective cores in a mesoscale convective cloud.

(3) The third stage: convective cloud clusters merged into a wide range of precipitation cloud systems, which occurred in the simulation of 450 to 620 min. Through the first two stages of merging, two mature mesoscale convective cloud clusters formed. They were close and merged during the move. The flow field and the echo were

closely connected, and finally formed a precipitation system about 200 to 300 km length, bringing a wide range of long precipitation.

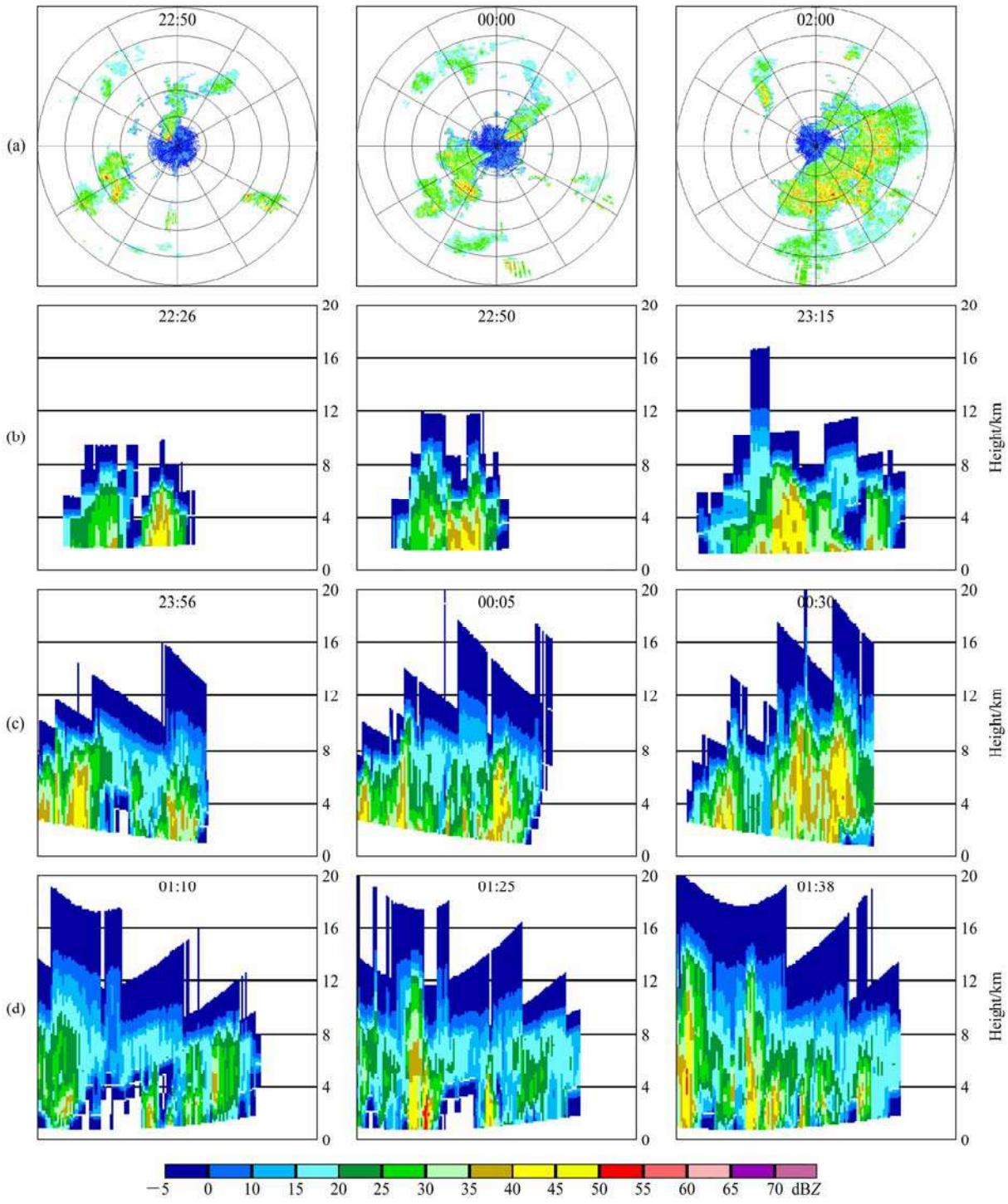

Fig.1 (a) PPI radar reflectivity of Guiyang at elevation 1.5°; (b) cloud merger process from the middle and lower part at azimuth 240°; (c, d) cloud clusters merger process from the middle and upper part at (c) azimuth 220°, (d) azimuth 90°. Color shading: radar echo

4. CONVECTIVE CELLS MERGED TO LARGE CONVECTIVE CLOUDS

4.1 THE MERGER PROCESS

At the beginning of the simulation (260~310 min), a large number of newborn

convective cells generated in turn from front to back along the direction of movement of the clouds, under the suitable weather condition of ground stationary front, vertical shear of wind and so on. In the process of moving, some of the close proximity of the convective cells merged. The numerical simulation results showed that the merger process between the clouds monomer was start from the middle and lower parts of the cloud body. In the process of merging, mature monomers were weakened and merged. On the contrary, newborn monomers were enhanced. At last, few monomers combined into a large convective cloud (Figure 2).

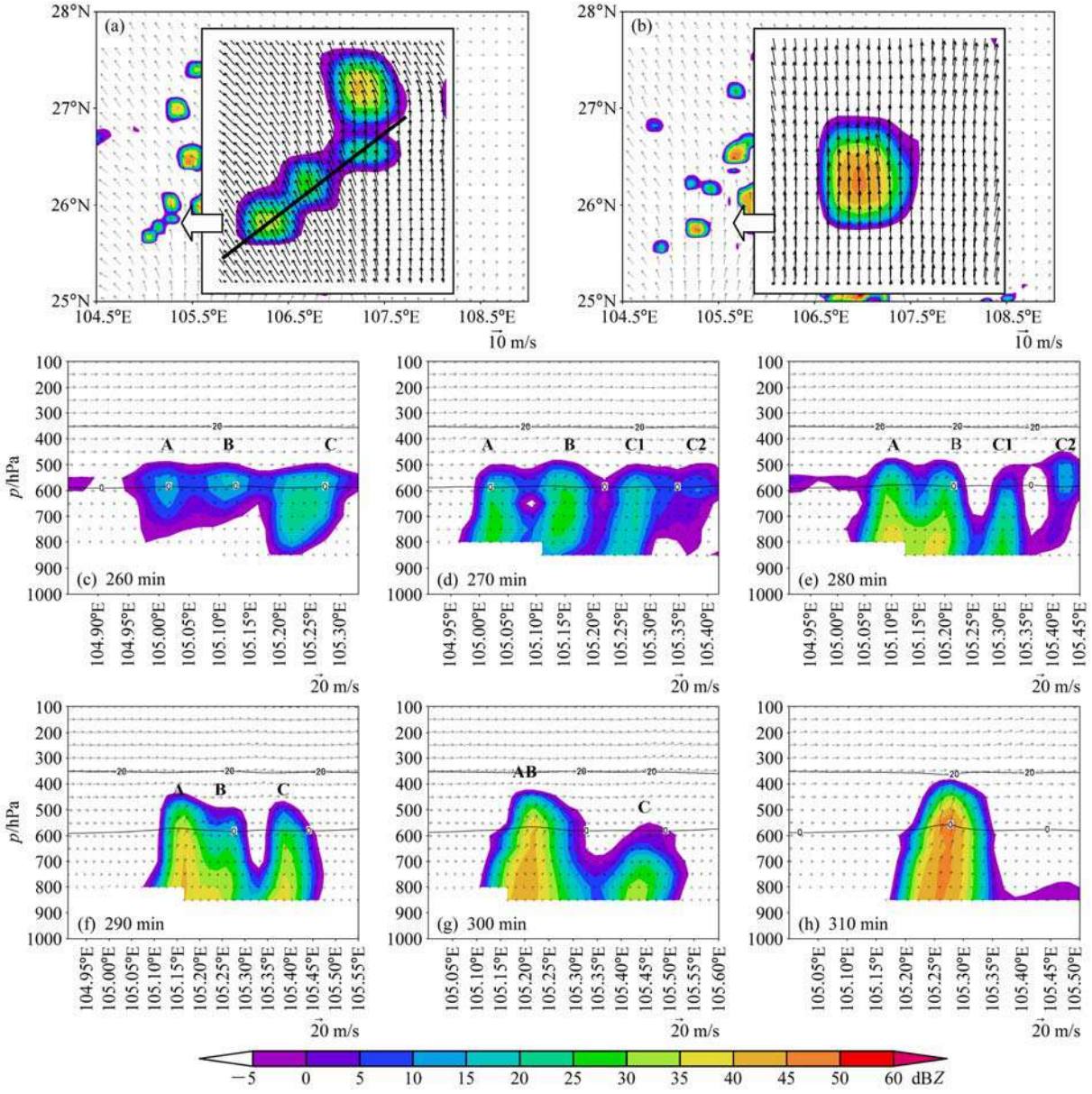

Fig.2 Radar echo (color shading) and wind vectors at 750 hPa at (a) 270 min and (b) 310 min, and (c-h) cross sections along the black line in Fig. 2a. The two horizontal lines denote 0 ℃ and −20 ℃ isotherms

4.2 DISCUSSION ABOUT MERGER POSITION

Calculated the vertical shear of wind value (the upper wind speed of each grid point minus the lower wind speed of each grid point), convective cells of the vertical shear of wind (Fig. 3) at 260 min showed the initial convective cells merge part (center) was precisely the smaller level vertical shear of wind. At the same time, this level was exactly the level of the strongest updraft inside several convective cells (Figure 2).

The cloud development process should possess two different developing tendencies simultaneously. On the one hand, the strong updraft of the cloud body, this means a strong upward trend of the cloud body, in other words a strong rising tendency. On the other hand, according to the physical meaning of the vertical shear of wind, when the vertical shear of wind gets larger, it means that the tendency for the cloud body rotation (or tilt) is relatively large and the cloud body has the development trend to rotate or tilt. These two trends both play an important role in the development of the cloud. The key is which of these two trends will play a leading role at different stages of development and merger.

For this stage of the merger, center was the initial part of merger. The updraft of this part was strong, which meant a greater rising tendency. Rising tendency in favor of the cloud body to further development, including height increase and broaden the horizontal scale. In the horizontal scale widening process, the rising tendency of clouds was very conductive to the expansion of the adjacent cloud rising area, like a "bridge" connected the adjacent cloud bodies, this article names it "dynamic cloud bridge". At the same time, the vertical wind shear at the merger position was precisely small, which meant that the cloud rotation tendency was quite weak in this layer, which lead to the conclusion that the rotation tendency played an unimportant role in the merger process of cloud bodies. Therefore, seems comprehensive, the cloud bodies' rotation tendency was weak but rising tendency was strong, formed a "dynamic cloud bridge" between adjacent monomers to connect others, and finally contributed to the overall merger. To 300 min, a few convective bubbles have been merged into a powerful convective cloud, the cloud body central level vertical shear of wind minimum. But the top of the cloud body vertical shear of wind very conducive to the further development of cloud.

Draw a conclusion, the initial merging part is related to the vertical shear of horizontal wind change and the velocity of updraft. Merge mechanism can be attributed to the connection of "dynamic cloud bridges", which promotes the monomers merge from the middle and lower part.

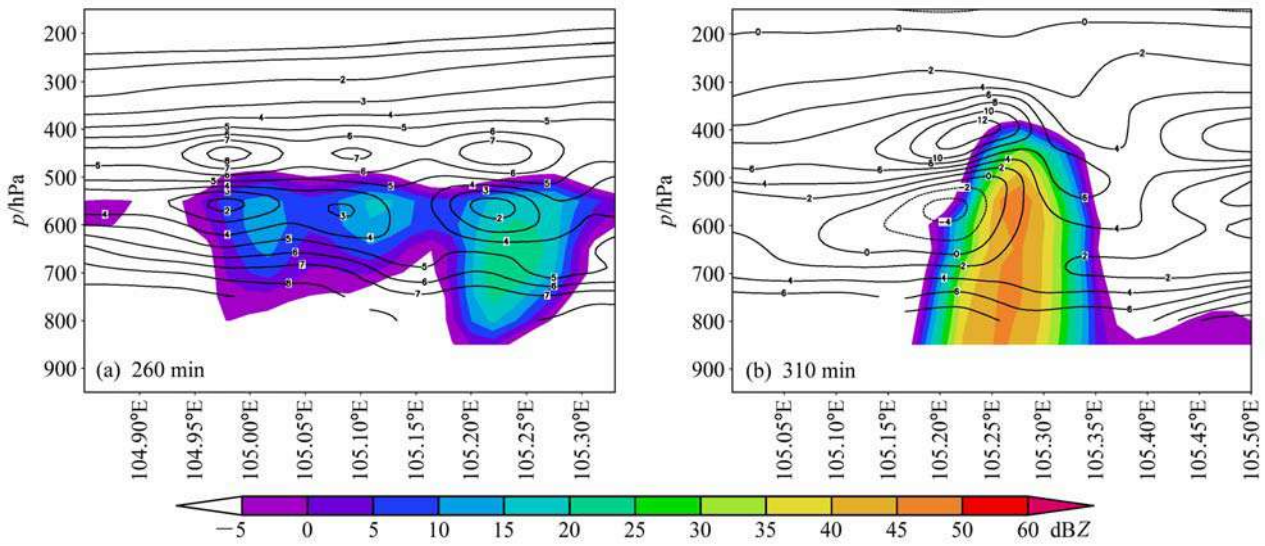

Fig.3 Vertical shear of wind (isolines, units: m/s) and radar echo (color shading) along the black line in Fig.2a

5 CONVECTIVE CLOUDS MERGED INTO CONVECTIVE CLOUD CLUSTERS

5.1 THE MERGER PROCESS

Through the first stage of the merger, a large cloud was formed. The convective cloud was affected by favorable weather situations and moisture conditions around the 850 hPa convergence line during the process of moving. Newborn convective cells generated and merged nearby continuously and finally formed a great strength of the convective clouds (Circle A in Figure 4a below). The same situation, the growing process (circle B in Figure 4a) was similar. Take Circle A (Figure 4) as an example to discuss the merging process of convective clouds to convective clouds cluster. Discovery: convective clouds merged into convective clouds cluster is from middle and lower part. This process is accompanied by the front of the convective center maturing and decaying in turn and then being merged, while the rear convective center developing and enhancing, and finally merging into strong convection convective clouds with a number of strong internal convective centers. If there are new up-coming convective clouds, the cloud will continue to develop.

Fig.4 (a) Radar echo (color shading) and wind vectors (m/s) at 750 hPa and (b-d) cross sections along the black line in Fig.5a. The two horizontal lines denote 0 ℃ and −20 ℃ isotherms

5.2 DISCUSSION OF THE MERGER LOCATION

The mechanism is same as the first stage merger. From the figure about the vertical shear of the wind speed when the convective clouds merged at 400 min (Figure 5) can we saw that, the level which had smaller vertical shear of horizontal wind basically corresponds to the initial position of the merger. The minimum shear value of 400 min and 450 min is 0 m / s, between about 600 to 650 hPa, and the position of merger was between 600 to 700 hPa. Meanwhile, the small vertical shear of wind height level is precisely the strongest updraft level among a few centers of convective

the convective center was weak but the rising tendency was strong, so the rising tendency plays a dominant role in the

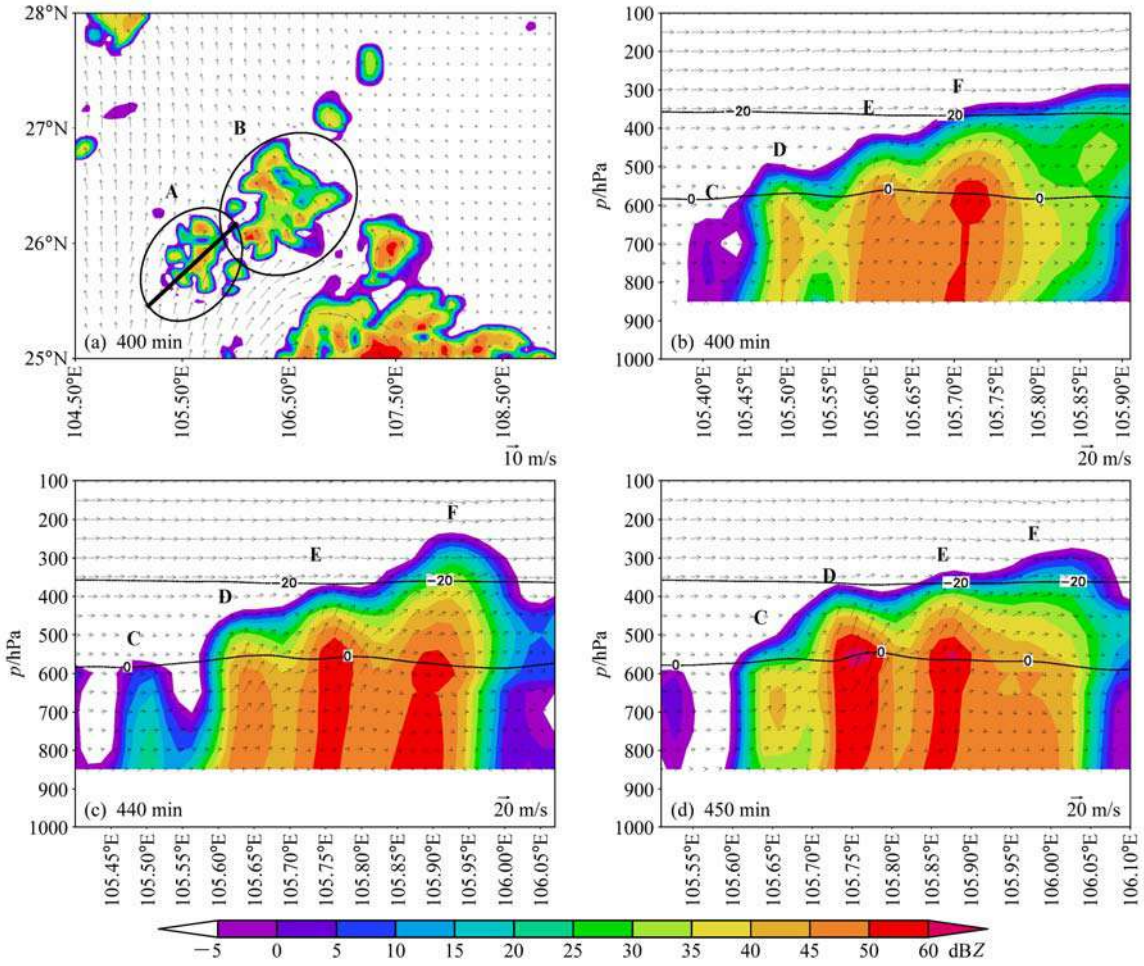

Fig.4 (a) Radar echo (color shading) and wind vectors (m/s) at 750 hPa and (b-d) cross sections along the black line in Fig.5a. The two horizontal lines denote 0 ℃ and −20 ℃ isotherms

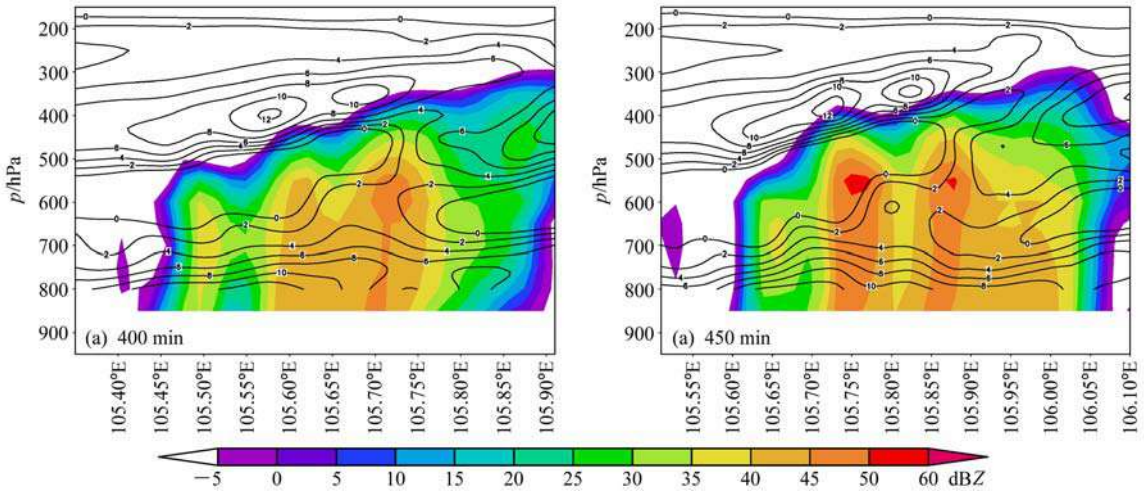

Fig.5 Same as in Fig.3, but along the black line in Fig.4a

cloud (Figure 4). The rotation tendency of merger process. This rising tendency is very conducive to the expansion of adjacent cloud rising areas, formed "dynamic cloud bridges" between convective clouds, "dynamic cloud bridges" made clouds connected, which finally resulted in their merger.

6 CONVECTIVE CLOUD CLUSTERS MERGED INTO A WIDE RANGE OF PRECIPITAION CLOUD SYSTEMS

6.1 MERGE PROCESS

Through the first two stages of the merger, convective clouds formed as the Circle A in Figure 6a. Similarly, in other areas of Guizhou Province, also appeared a lot of processes of the formation of convective clouds, such as circle B. When A and B the two clouds merged, resulted in the formation of a large-scale precipitation cloud system. The merging process was shown as Figure 6. The merger happened from 450 min. But it was strange that the merger of clouds started from the middle and upper part of the cloud this time (Figure 6).

6.2 DISCUSSION OF THE MERGER LOCATION

From vertical shear of wind of 460 min and 570 min (Figure 7), we can see that the initial position of the merger still corresponded to a small vertical shear of wind height level, but the merger mechanism was significantly different from the previous two phases.

At the initial height level of the merger, the velocity of the cloud updraft was significantly reduced than the previous two stages, which meant that the cloud body had little rising tendency. Although the tendency of the rotation of this part of the cloud was very weak (shear of wind is very small), cloud rising tendency of the body was very weak and so it was difficult to form a dynamic cloud bridge to connect others. But the shear of wind of the upper part clouds had large values, which meant that the upper part of clouds had a strong rotating tendency, therefore, the rotating tendency of the upper part of the clouds played a major role in the merger. The merger which the rotating tendency played a major role in was seen as the oblique ascending air flow formed by the oblique sinking divergence and outflow from the rear clouds cluster strengthened the convective development of the front of the cloud on the one hand. On the other hand, the difference between the horizontal velocities of the upper parts of the two cloud clusters promoted the merger. The merge mechanism can be attributed to that the rotating tendency of the clouds which caused by shear of wind promoted the merger.

7 SUMMARIES AND DISCUSSION

This paper summarized the basis of observed facts, by the numerical simulation of a case and detailedly analyzed the cloud merging process. Now the analyses of the results of the individual case are summarized as follows:

(1) The merger has gone through three stages: ① Convective cells merge to form large convective clouds; ② Convective clouds merge to form cloud clusters; ③ Cloud clusters merge to form a wide range of precipitation cloud system.

(2) Some initial part of the merger is the middle and lower part of clouds; some is the middle and upper part. The merging process which starts from the middle and lower part usually occurred in younger monomers. The merging process which starts from the middle and upper part usually occurred in large convective clouds.

(3) The initial part of the cloud merger is often close to the small vertical shear of

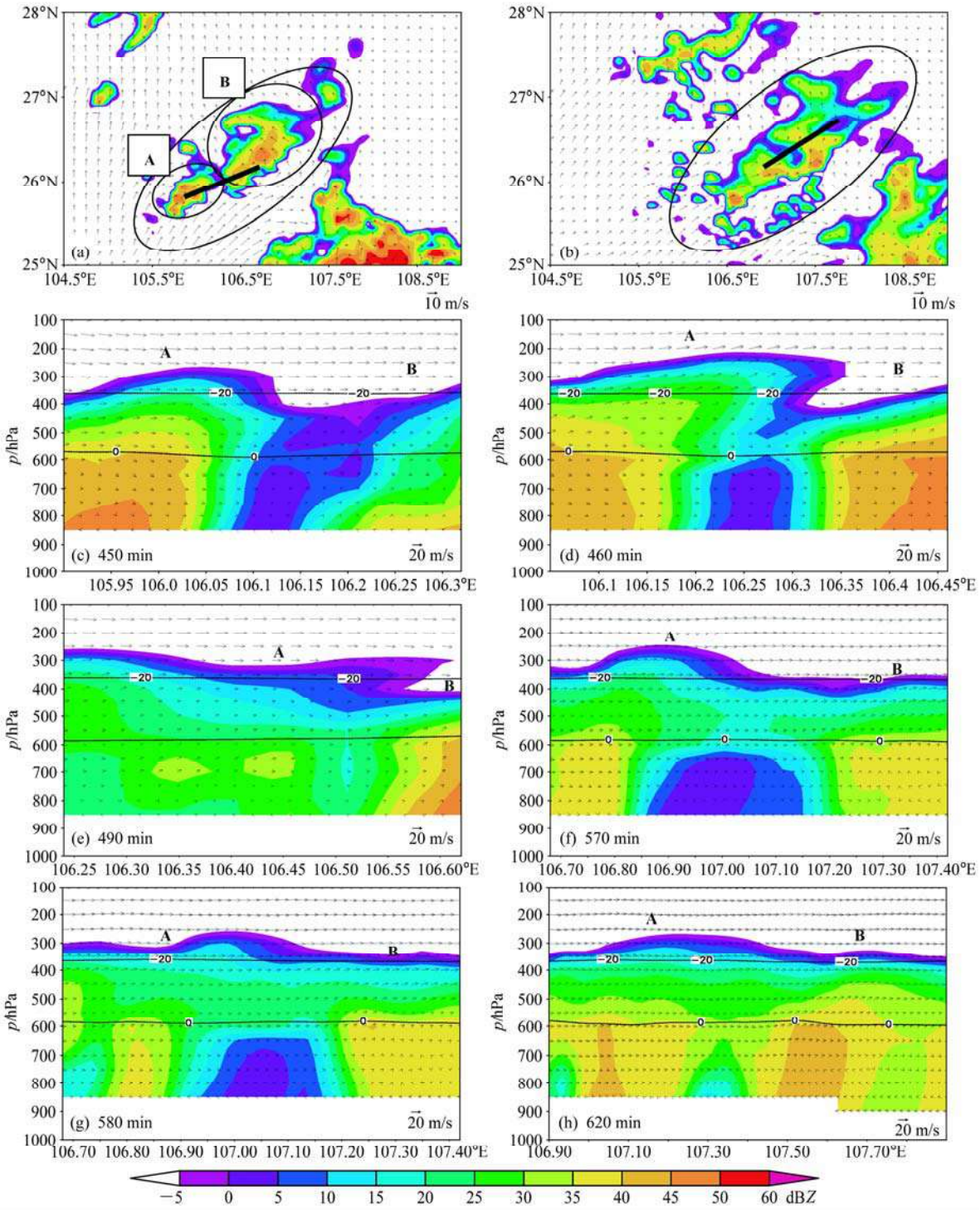

Fig.6　Radar echo (color shading) and wind vectors at 750 hPa　at (a) 460 min and (b) 600 min, and cross sections (c-e) along the black line in Fig.6a and (f-h) along the black line in Fig.6b. The two horizontal lines denote 0 ℃ and　−20 ℃ isotherms

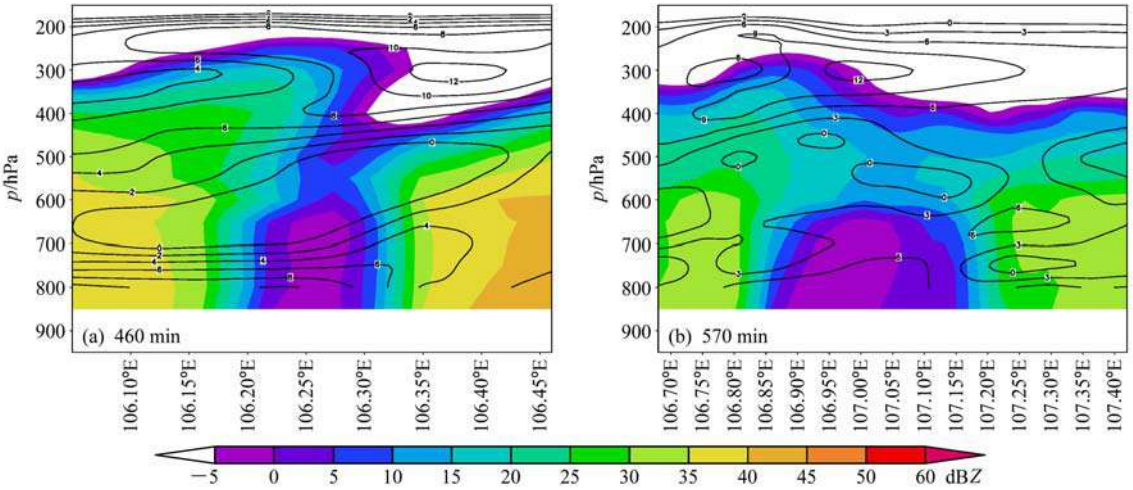

Fig.7 Same as in Fig.4, but (a) along the black line in Fig.7a and (b) along the black line in Fig.7b

wind height level. But the two merge mechanisms are different.

(4) “Upward tendency" and "rotating tendency" are two different tendencies in the cloud development. These two trends have played an important role in cloud development. The key is which one will play a leading role in the different stages of cloud development and merger.

(5) The merger starts from the middle and lower part is result from the weak rotating tendency (the small shear of wind) and the strong rising tendency (the large velocity of updraft) in the merging part. The weak rotating tendency and the strong rising tendency are very conducive to the expansion of adjacent cloud rising areas, thus creating a "dynamic cloud bridge" to connect the adjacent clouds, and to promote the merger and the development and enhancement of clouds.

(6) It is not possible to form a "dynamic cloud bridge” by the merger process which starts from the middle and lower part because of the weak rising tendency (the small velocity of updraft). But the strong rotating tendency caused by the big shear of wind in the upper part of clouds also promoted the merger. This kind of merger caused by rotation tendency is mainly manifested in two parts: on the one hand, the oblique ascending air flow formed by the oblique sinking divergence and outflow from the rear clouds cluster strengthens the convective development of the front of the cloud; on the other hand, the difference between the velocities of the two cloud clusters promote the merger of the rear cloud cluster and the front cloud cluster.

(7) In view of the importance and complexity of the merger process, the article studies on the analysis of an individual case and explore the phenomenon and the reasons for the merger in this process. In order to get more regularity results in future work, I will collect a large number of cases in different places for further researches.

8 REFERENCES

Ackerman B, Kennedy P C. 1988. On the merger of two small convective radar echoes[J]. Annalen der Meteorologie, 2(25): 440-442.

Bennetts D A, Bader M J, Marles R H. 1982. Convective cloud merging and its effect on rainfall[J]. Nature, 300(5887): 42-45.

Carey L D, Rutledge S A. 2000. The relationship between precipitation and

lightning in tropical island convection: a C-band polarimetric radar study[J]. Mon. Wea. Rev, 128(8): 2687-2710.

Chu C M, Lin Y L. 2000. Effects of orography on the generation and propagation of mesoscale convective systems in a two-dimensional conditionally unstable flow[J]. Journal of the Atmospheric Sciences, 57(23): 3817-3837.

Doernbrack A. 1997. Broadening of convective cells[J]. Quarterly Journal of the Royal Meteorological Society, 123(540): 829-847.

Fu D H, Guo X L. 2006. A cloud-resolving study on the role of cumulus merger in MCS with heavy precipitation [J]. Advances in atmospheric sciences, 23(6): 857–868.

Fu D H, Guo X L. 2007. The role of cumulus merger in a severe mesoscale convective system[J]. Chinese Journal of Atmospheric Sciences (in Chinese), 31(4): 635-644.

Jirak I L, Cotton W R, McAnelly R L. 2003. Satellite and radar survey of mesoscale convective system development[J]. Mon. Wea. Rev., 131(10): 2428-2449.

Knupp K R, Geerts B, Goodman S J. 1998a. Analysis of a small, vigorous mesoscale convective system in a low-shear environment. Part I: Formation, radar echo structure, and lightning behavior[J]. Mon. Wea. Rev, 126(7): 1812-1836.

Knupp K R, Geerts B, Tuttle J D. 1998b. Analysis of a small, vigorous mesoscale convective system in a low-shear environment. Part II: Evolution of the stratiform precipitation and mesoscale flows[J]. Mon. Wea. Rev, 126(7): 1837-1858.

Lee B D, Jewett B F, Wilhelmson R B. 2006a. The 19 April 1996 Illinois tornado outbreak. Part I: Cell evolution and supercell isolation[J]. Weather and Forecasting, 21(4): 433-448.

Lee B D, Jewett B F, Wilhelmson R B. 2006b. The 19 April 1996 Illinois tornado outbreak. Part II: Cell mergers and associated tornado incidence[J]. Weather and Forecasting, 21(4): 449-464.

Lei H C, Hong Y C, Zhao Z, et al. 2008. Advances in cloud and precipitation physics and weather modification in recent years[J]. Chinese Journal of Atmospheric Sciences, **32** (4) : 967～974

Lin Y L, Farley R D, Orville H D. 1983. Bulk parameterization of the snow field in a cloud model[J]. Journal of climate and applied meteorology, 22(6): 1065-1092.

Pozo D, Borrajero I, Marin J C. 2006a. A numerical study of cell merger over Cuba - Part I: implementation of the ARPS/MM5 models[J]. Annales Geophysicae, 24(11): 2781-2792.

Pozo D, Borrajero I, Marin J C. 2006b A numerical study of cell merger over Cuba - Part II: sensitivity to environmental conditions[J]. Annales Geophysicae, 24(11): 2793-2808.

Rutledge S A, Hobbs P V. 1984. The mesoscale and microscale structure and organization of clouds and precipitation in midlatitude cyclones. Ⅶ: A diagnostic modeling study of precipitation development in narrow cloud-frontal rainbands[J]. Journal of atmospheric Sciences, 41(20): 2949-2972.

Simpson J. 1980. On cumulus mergers[J]. Archiv fuer Meteorologie, Geophysik und Bioklimatologie, 29(1): 1-40.

Tian S C. 1991. Effect of merging of the convective cloud clusters on occurrence of heavy rainfall[J]. Advances in Atmospheric Sciences, 8(4): 499-504.

Tao W K, Simpson J. 1984. Cloud interactions and merging: numerical simulations[J]. J. Atmos. Sci., 41(19): 2901-2917.

Westcott N E, Kennedy P C. 1989. Cell development and merger in an Illinois thunderstorm observed by Doppler radar[J]. J. Atmos. Sci., 46(1): 117-131.

Westcott N E. 1994. Merging of convective clouds: cloud initiation, bridging, and subsequent growth[J]. Mon. Wea. Rev, 122(5): 780-790.

9 ACKNOWLEDGE

This work was supported jointly by the National Natural Science Foundation of China (Grant No. 40975086 and 40537034)

DEEP TROPICAL CONVECTION FORMING OVER THE CONTINENT AND OVER THE OCEAN : A COMPARISON OF THEIR DYNAMICS AND MICROPHYSICS BY MEANS OF DETAILED CLOUD MODELING

Wolfram Wobrock[1,2], Elise Drigeard[1,2], Emanuel Fontaine[1,2] and Andrea I. Flossmann[1,2]

[1]Clermont Université, Université Blaise Pascal, Laboratoire de Météorologie Physique, F-63000 Clermont-Ferrand, France

[2]CNRS, INSU, UMR 6016, LaMP, F-63177 Aubière, France

1. INTRODUCTION

This modeling study focuses on the understanding of the observations collected during the airborne experiments of MEGHA-TROPIQUES in August 2010 over the western part of the Niger and in Nov/Dec. 2011 over the Maldives. Measurements were mainly performed in mixed phase stratiform regions of deep convective clouds using the latest microphysical measuring techniques (2DS, CIP, PIP) allowing to observe droplet and ice crystal size spectra from 25 µm to 6mm. Significant differences in the microphysics of both cloud systems could be observed (Fontaine et al., this issue). The detailed cloud micro-physics model DESCAM was run to study the influence of the prevailing aerosol particles concentration on the observed hydrometeor spectra.

2. THE MODEL

The 3D model with detailed (bin-resolved) microphysics used herein couples the 3D non-hydrostatic model of Clark and Hall (1991) with the Detailed Scavenging Model DESCAM (Leroy et al., 2009; Flossmann and Wobrock, 2010) for the microphysical package. It follows 5 density distribution functions: the number distribution function for the aerosol particles $f_{AP}(m_{AP})$, for drops $f_d(m)$ and for the ice particles $f_i(m_i)$, as well as the mass density distribution function for aerosol particles in the drops $g_{AP,d}(m)$and in the ice crystals $g_{AP,i}(m_i)$.
A discussion of the different processes considered in the microphysics code can be found in Flossmann and Wobrock (2010), and the coupling with the 3-D code is discussed in Leroy et al (2009).

3. RESULTS

The dynamical model was set up for a horizontal domain of 614 x 614 km^2 with 2.4km grid resolution. The vertical domain reached up to 22 km and used a grid resolution of 250 m. ECMWF large scale data were used for initial and boundary conditions. The model was run for August 5, 2010 and compared to the airborne microphysical measurements.

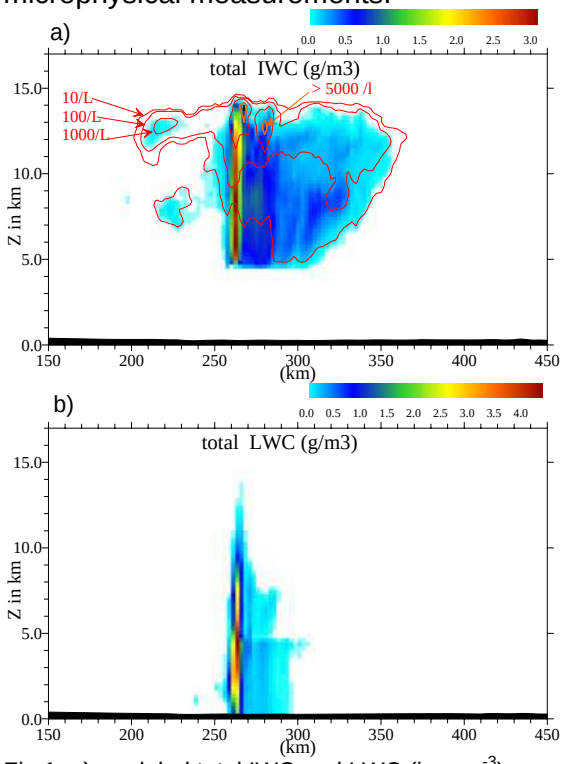

Fig.1: a) modeled total IWC and LWC (in g m^{-3})

Aerosol particle spectra needed for the cloud formation were taken from the airborne observations made during the AMMA experiment in summer 2006 (Matsuki et al., 2010). Figs.1a and b give a vertical cross section of the total IWC field (Fig.1a) and LWC field (Fig.1b) after 8 h of integration. The upper level cloud anvil

covers a region of 150 km while precipitation is restricted to a 40 km large field below. Maximum values of both parameters occur in the main convective core for the vertical cross section which was selected here. Thus, in altitudes from 5 to 8km total condensed water masses up to 7 g/m^3 can arise.
In the stratiform part the total water content doesn't exceed 1 g/m^3.
Fig.1b gives also the number concentration of ice crystals, which typically increases with altitude and is highest in levels below -30°C.

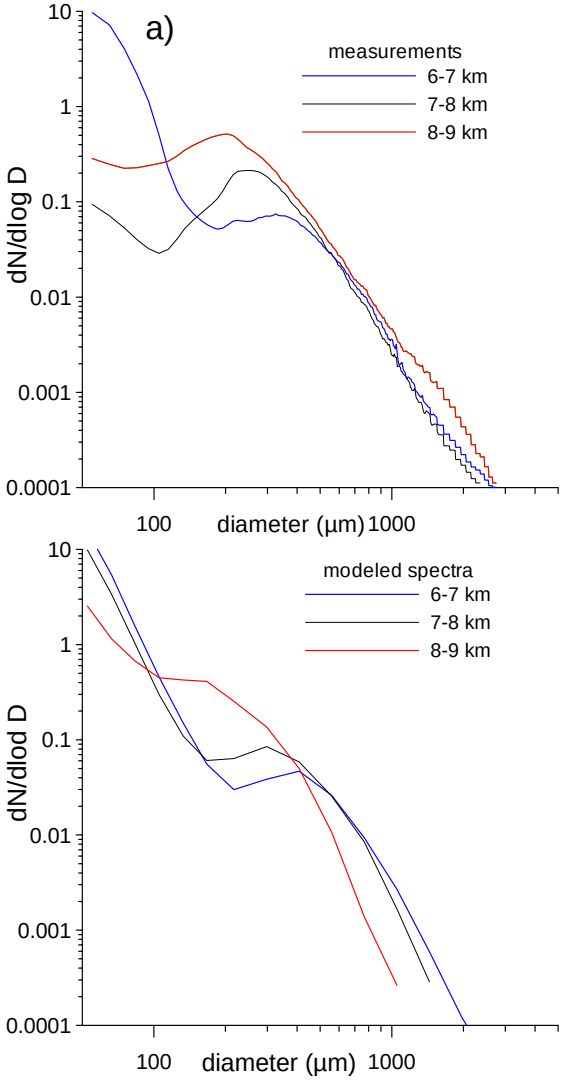

Fig. 2: observed (a) and simulated (b) hydrometeor spectra (in l^{-1}µm^{-1}) for 5 August 2010

In order to compare the model results with the microphysical measurements Figs. 2a and 2b display the observed and simulated hydrometeor spectra. Flight missions during the afternoon of 5 Aug. 2010 restricted to altitudes between 6 to 9 km. Fig. 2 thus presents the mean hydrometeor spectra observed in layers of 1 km depth ranging from 6 to 9 km. The mean observed spectra are calculated on the basis of 300 to 700 individual measurements in each layer. The mean modeled spectra use more than 3000 grid points but exclude grid points of the convective cores.
The comparison of observations and simulation shows that most observed features were met in the simulations. Main differences occur in the presence of large ice crystals above diameters above 1 mm, where the model underestimates large ice particles. Hydrometeor sizes below 100 µm, however, were overestimated by the model.
A special feature of all observed spectra in both campaigns (i.e. over Africa and over the Indian Ocean) is the presence of a size mode in the diameter range between 200 to 400 µm. In addition, it was also found that the number concentration in this mode typically decreases with altitude and at the same time its diameter shifts to larger sizes.
The presence of the large particle mode can also be detected in the simulation results. The analysis of the modeled spectra suggests an explanation for the presence of this mode. Fig.3 shows the individual spectra of water droplets and ice crystals as calculated independently by the model in a mixed phase cloud region.

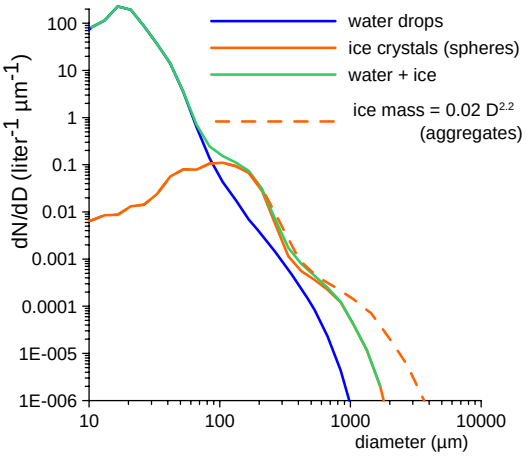

Fig. 3: modeled droplet and ice particle spectra in an altitude of 8 km

This illustration demonstrates that the presence of the large particle mode results from the ice crystals which were grown by water vapor deposition as well as by riming with small droplets to sizes in ranges of 200 µm. Droplet numbers for

sizes above 100 µm are only a few but many liquid drops are still present in the size reservoir below 100 µm.
As these small size categories are overestimated in the model results presented in Fig. 2b we can suggest that the stratiform cloud field still included too many convective elements.

4. CONCLUSIONS

The modeling allows reproducing a certain number of features observed during the MEGHA-TROPIQUES experiments. The observations obtained during the Niger campaign are almost completely analyzed and compare generally well with the model results. The observations of the Maldives campaign are currently analyzed and will be exploited and compared once available.

5. REFERENCES

Matsuki A. ;Schwarzenböck A.; Venzac H. ; Laj P. ; Crumeyrolle S. ; Gomes, L. 2010. Cloud processing of mineral dust: direct comparison of cloud residual and clear sky particles during AMMA aircraft campaign in summer 2006, Atmos. Chem. Phys. Vol. 10 , No. 3 , p. 1057-1069 http://www.atmos-chem-phys.net/10/1057/2010/ (EGU)

Clark, T.L. and W.D. Hall, 1991: Multi-domain simulations of the time dependent Navier-Stokes equation: benchmark error analysis of some nesting procedures. J. Comput. Phys., 92, 456-481.

Flossmann, A. I. and W. Wobrock, 2010: A review of our understanding of the aerosol – cloud interaction from the perspective of a bin resolved cloud scale modeling, Atmos. Res. doi:10.1016/j.atmosres.2010.05.008

Fontaine E., A. Schwarzenböck, N. Viltard, A.Protat, J. Delanoe, W. Wobrock, R. Dupuy and C. Gourbeyre, 2012: Overview of microphysical properties of Tropical convective clouds observed in 2010 and 2011 Megha-Trophiques campaigns over West Africa and the Indian Ocean. In: Proceedings of ICCP 2012, Leipzig, Germany

Leroy D., Monier, M.; Wobrock, W. ; Flossmann, A. I. 2006: A numerical study of the effects of the aerosol particle spectrum on the development of the ice phase and precipitation formation, Atmos. Res. Vol. 80 , No. 1 , p. 15-45 DOI 10.1016/j.atmosres.2005.06.007

Leroy, D., W. Wobrock and A. I. Flossmann, 2009: The role of boundary layer aerosol particles for the development of deep convective clouds: a high-resolution 3D model with detailed (bin) microphysics applied to CRYSTAL-FACE , Atmos. Res.; *DOI: 10.1016/j.atmosres.2008.06.001*

Planche, C., W. Wobrock, A.I. Flossmann, F. Tridon, J. VanBaelen, Y. Pointin et M. Hagen, 2010: The influence of aerosol particle number and hygroscopicity on the evolution of convective cloud systems and their precipitation: A numerical study based on the COPS observations on 12 August 2007; Atmos. Res. doi.:10.1016/j.atmosres.2010.05.003

Pruppacher H. R. and J.D. Klett, 1997 : *Microphysics of clouds and precipitation*. 2nd ed. Kluwer Academic, 954p.

6. ACKNOWLEDGEMENTS

The calculations for this study have been done on computer facilities of IDRIS, CNRS at Orsay and CINES in Montpellier, under the project 940180. The authors acknowledge with gratitude the hours of computer time and the support provided.

A COMPARISON OF AIRBORNE IN-SITU CLOUD MICROPHYSICAL MEASUREMENTS WITH GROUND C AND X BAND RADAR OBSERVATIONS IN AFRICAN SQUALL LINES

E. Drigeard[1], E. Fontaine[1], W. Wobrock[1], A. Schwarzenböck[1], E.R. Williams[2], F. Cazenave[3], M.Gosset[4], A. Protat[5] and J. Delanoë

[1] *Laboratoire de Météorologie-Physique, Université Blaise Pascal, OPGC/UMR-6016, Clermont-Ferrand, France*
[2] *Parsons Laboratory, Massachusetts Institute of Technology, Cambridge, Massachusetts, USA*
[3] *LTHE – Université Grenoble 1 /IRD/ CNRS, Grenoble France*
[4] *IRD / LTHE – CNRM / GMME / MOANA, Toulouse, France*
[5] *Center for Australian and Weather Climate Research, Melbourne, Australia.*
[6] *Laboratoire Atmosphère, Milieux, Observations Spatiales, Velizy, France*

1. INTRODUCTION

During the MEGHA-TROPIQUES experiment in August 2010 the French research aircraft Falcon 20 investigated mainly stratiform parts of deep convective systems in the western part of Niger, close to Niamey (2°W, 13.5°N). The focus of this experiment was the probing of the microphysical characteristics of mixed phase clouds from the melting level, typically around 4500m, up to 10500m. The operation of two precipitation radars provides the possibility to compare measured radar reflectivity with those calculated from the in-situ observations of the hydrometeor spectra.

2. INSTRUMENTATION

The aircraft was equipped with the latest microphysical measuring techniques (2DS, CIP, PIP) allowing to resolve droplet and ice crystal size spectra from 25 µm to 6 mm. The flight levels range between 3500 and 10500m allowing to detect warm cloud regions with precipitation up to 40 dBZ, melting layers, mixed phase regions and pure ice clouds with IWC up to 4-5 g m^{-3}.
On the Niamey airport the Doppler C Band radar of MIT (Russell et al., 2010) was operated and 30 km to the south-east the polarized Doppler X band radar (Xport) of LTHE/IRD (Gosset et al., 2010). The MIT radar covers a horizontal range of 150 km, the X band radar 135 km (see Fig.1). Both radars are using volumetric protocols, which give a 3D spatial distribution of the reflectivity every 10 minutes.

Fig.1 illustrates observations made on 13 August 2010 at 15:11 UTC by the Xport and MIT radars. Both radars give the same horizontal structure for the cloud and precipitation field. From Fig. 1a we can also see that the Xport radar allows

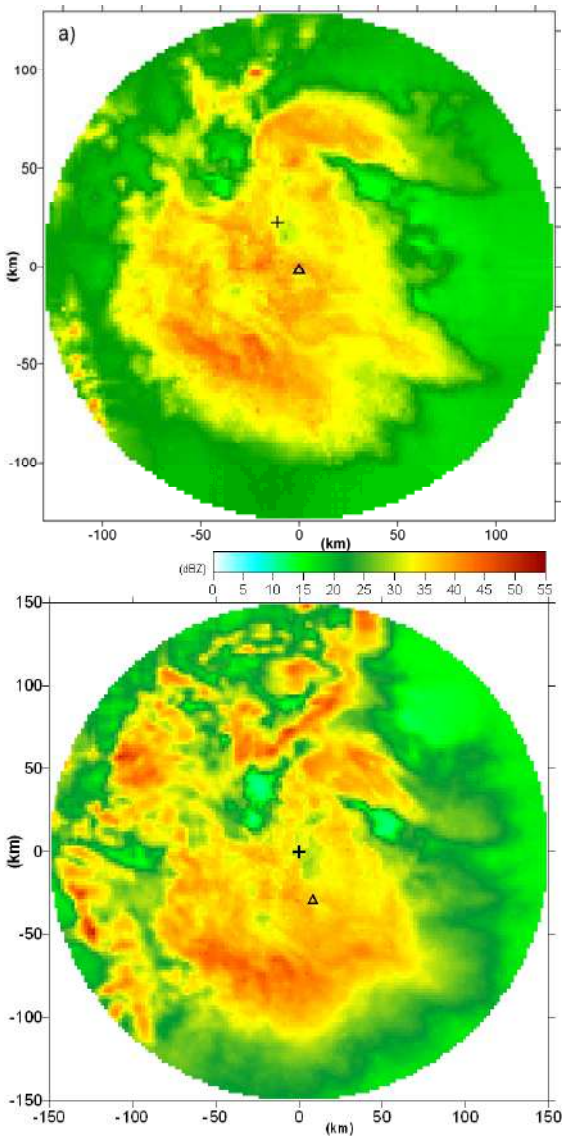

Fig. 1: a) LTHE/IRD Xport radar at 15:11, elevation 2.62°, b) MIT C band observation at 15:11 UTC, elevation 2.88°; the cross indicates the location of the C band, the triangle the X band radar

detecting reflectivity only in a range of 90 km. Thus, we restrict our analysis of the airborne measurements to distances of 90 km between Xport radar and aircraft.

3. CO-LOCALISATION OF AIRCRAFT AND RADAR

Different analysis techniques were developed to co-localize the aircraft position and the radar observations. Best results were found by using all 15 scans collected by the radars during an 8-10 minutes observational period. The functioning of the co-localization technique, which is based on the steady state hypothesis of the reflectivity field, is illustrated by the comparison of observed and calculated RHI scans given in Fig. 2.

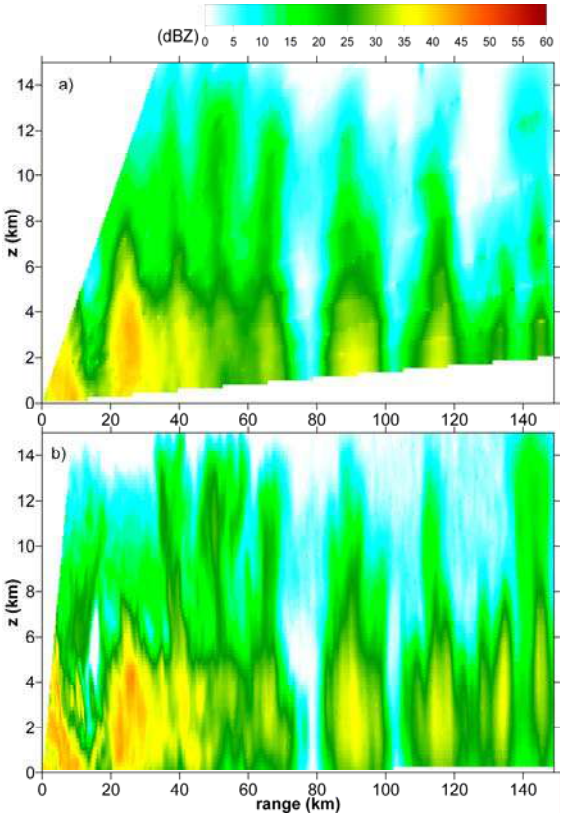

Fig.2: RHI scans for 13 August 2010 (azimuth direction 55°): a) re-calculated from the volumetric measurements (15 scans) performed from 13:20-13:28; b) RHI observed at 13:29.

Differences mainly occur for long-range distances from the radar as the vertical resolution becomes weak. A statistical analysis of the differences between the observed and the recalculated signals were performed on the basis of the vertically high resolved RHI scans (scanning 300 different elevations) of the MIT radar. From this analysis we found that the signals recalculated from the volumetric scans have a mean error of 3 dBZ. In a next step the co-localization technique was applied to determine radar MIT and Xport reflectivity prevailing at the position of the flying aircraft.

4. CALCULATING RADAR REFLECTIVIY FROM IN-SITU MICROPHYSICS

Fig.3b shows reflectivity calculated from the volumetric scans of MIT and Xport radar as well as aircraft height and its distance to the ground radars. One can easily detect that both radar signals differ in their absolute value. A closer analysis of their temporal evolution, however, demonstrates rather well that instantaneous changes such as sudden increases or decreases occur simultaneously in both signals confirming the functioning of our co-localization technique.

A description of the microphysical measurements performed on the Falcon-20 aircraft is given in Fontaine et al (2012a, this issue).

The microphysical measurements show that cloud particle spectra in altitudes above 5000m are dominated by graupel type ice particles with quite irregular shape (Fontaine et al., 2012b). In order to calculate the equivalent reflectivity Z_e from the observed hydrometeor number distribution the irregular form of the ice particles has to be taken into account. This was done by the use of a power mass law $m = \alpha D^{\beta}$ relating the observed equivalent particle diameter D with the hydrometeor mass m. In order to determine α and β Fontaine et al (2012a, this issue) uses in-situ measurements of the 95 GHz cloud radar Rasta (Protat et al, 2005) that was operated on the airborne platform as well. Reflectivity measured just above and below the aircraft was recalculated using Mie theory and the observed hydrometeor spectra. β was fixed to 2.1 accordingly to Westbrook et al (2004), while α was determined to match the calculated reflectivity with values measured by the cloud radar. α values were found to range between 0.001 and 0.1.

In order to determine also the reflectivity of MIT and Xport radars by means of the in-situ particle spectra the observed mass/diameter relationship $m=\alpha D^{\beta}$ was again applied. For these calculations of Z_e the Rayleigh approximation was used.

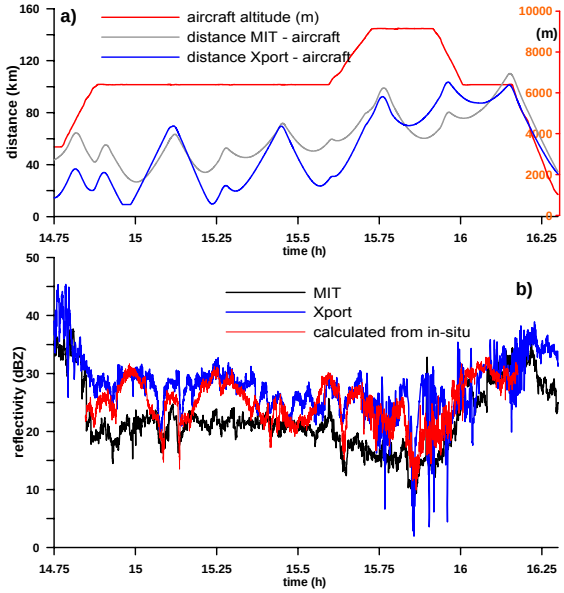

Fig.3: 13 Aug. 2010; a) flight altitude and distances from ground radars to the aircraft, b) MIT and Xport reflectivity co-localized with the aircraft. The red line shows the reflectivity calculated from the in-situ hydrometeor spectra.

The red line in Fig.3b illustrates the results of this analysis. The calculated reflectivity fits well the observations of the Xport radar while the MIT measurements still need some corrections.

Reflectivity was also calculated by assuming the observed particle sizes to be spherical and replacing the mass-diameter relationship by the classical D^6 approach. This method (not illustrated here), however, results in a reflectivity of more then 50 dBZ for the time period presented in Fig.3b.

4. CONCLUSIONS

The operation of two precipitation radars during the MEGHA-TROPIQUES campaign in Niger provided the possibility to compare measured radar reflectivity with those calculated from the in-situ observations of the hydrometeor spectra. Using Rayleigh approximation and a mass-diameter relationship for the observed hydrometeor spectra the calculated reflectivity fits well with the observations of the Xport radar. The difference with the MIT reflectivity is still under investigation.

5. REFRENCES

Fontaine E., A. Schwarzenböck, A. Protat, J. Delanoe, R. Dupuy, W. Wobrock, C. Duroure, and C. Gourbeyre, 2012a.; Determination of area-diameter and mass-diameter relationship from ice particle imagery in order to deduce IWC within tropical convective clouds. In: Proceedings of ICCP 2012a, Leipzig, Germany

Fontaine E., A. Schwarzenböck, N. Viltard, A.Protat, J. Delanoe, W. Wobrock, R. Dupuy and C. Gourbeyre, 2012b: Overview of microphysical properties of Tropical convective clouds observed in 2010 and 2011 Megha-Trophiques campaigns over West Africa and the Indian Ocean. In: Proceedings of ICCP 2012, Leipzig, Germany

Gosset M., E-P. Zahiri and S. Moumouni, 2010: Rain droplet size distribution variability and impact on X-band polarimetric radar retrieval: Results from the AMMA campaign in Benin. *Q.J.R. Meteorol. Soc*. 136: 190-208

Russel B., E.R. Williams, M. Gosset, F. Cazenave, L.Descroix, N. Guy, T. Lebel, A. Ali, F. Metayer and G. Quantin 2010: Radar/rain gauge comparisons on squall lines in Niamey, Niger for the AMMA. . *Q.J.R. Meteorol. Soc*. 136: 289-303

Protat A, Bouniol D, Delanoë J, May PT, Plana-Fattori A, Hasson A, O'Connor E, Görsdorf U, Heymsfield AJ. 2009. Assessment of CloudSat reflectivity measurements and ice cloud properties using ground-based and airborne cloud radar observations. *J. Atmos. Oceanic Technol.* **26**: 1717–1741.

Westbrook and Coauthors, 2004: A theory of growth by differential sedimentation, with application to snowflake formation. Phys.Rev. E, 70, 021403, doi:10.1103/ PhysRevE.70.021403.

6. ACKNOWLEDGEMENT

The authors would like to thank SAFIRE for operating the French Falcon 20 research aircraft during the two measurement campaigns. We are particularly grateful to CNES for funding both aircraft measurement campaigns within Megha-Tropiques

URBAN SNOWFALL FROM SLIGHTLY SUPERCOOLED FOG

Gary Lloyd[1], Jonathan Crosier[1], Paul Connolly[1], Thomas Choularton[1]

[1]School of Earth Atmospheric and Environmental Sciences, University of Manchester, Manchester, M13 9PL,
Keywords: urban fog, snow, anthropogenic aerosols, ice nuclei
Presenting author email: Gary.Lloyd@student.manchester.ac.uk

1. INTRODUCTION

The development of snowfall from shallow slightly supercooled cloud is a particular weather forecasting issue. During Autumn and Winter months snowfalls have been observed in urban areas of England during periods of slightly supercooled fog in the temperature range mostly between 0^{o}C and -5^{o}C. These snowfalls were originally recognised in the United States by Agee (1971) and Farn et al. (1978) but more recent work by Wood and Harrison (2009) reported events in a number of places in England, close to sources of industrial aerosol. Van den Berg (2009) presented a satellite image of the Netherlands after a period of freezing fog that revealed localised snowfalls downwind of industrial and urban areas, strengthening the events association with industrial aerosol.

2. MECHANISM

Manchester, England has experienced a number of events that have been recorded by the Whitworth Observatory Meteorological Station. The sequence of precipitation detected by the Disdrometer in Manchester during an event in December 2010 suggested a mechanism by which these snowfalls are produced. Initially primary heterogeneous nucleation of fog droplets by industrial aerosol occurs. These primary ice crystals grow and fall, riming as they do so. Anthropogenic Snowfall Events (ASE's) occur in temperatures around -5^{o}C. Riming in these temperatures is known to produce significant quantities of secondary ice splinters. This secondary ice production is likely to lead to an increase in ice crystal number concentrations, producing the snowfalls sometimes observed from urban fogs.

3. MODELLING

The purpose of current work is to gain a more comprehensive understanding of the microphysical processes that are leading to the formation of Anthropogenic Snowfall Events (ASEs). Secondly Ice particle production by the Hallett-Mossop process is thought to be key to the production of snowfall in many of these fogs. This process is explicitly included in Aerosol-Cloud and Precipitation Interaction Model (ACPIM). Here we use ACPIM to test the sensitivity of precipitation formation in a shallow, slightly supercooled fog to changes in variables such as temperature and primary ice nucleation

4. RESULTS

The implications of results from the investigation of slightly supercooled fog using ACPIM, together with in-situ measurements of ASEs from the Whitworth Observatory in Manchester will be presented.

5. BIBLIOGRAPHY

Agee, E.M. (1971) *Bull.Amer.Meteorology Society*. **52,** 557–560.

Farn, P., Parungo., Paul, A., Alee., Helmut, K. and Weickmann HK. (1978) *Geophysical Research Letters.* **5,** 515–517

Van den Berg W. (2008) *Weather.* **63,** 248

Wood, Curtis R and Harrison, R. Giles. (2009) *Weather.* **64,** 227-280

CHEMICAL COMPOSITION OF RAINWATER AND AEROSOL INTEGRATED-COLUMN PROPERTIES BEFORE AND AFTER RAINFALL AT SELECTED EUROPEAN SITES

R. Fraile[1], M. Sorribas[2], I. San Martín[1], A.I. Calvo[3], E. Alonso[4], M. Fernández-Raga[1], A. Castro[1]

[1]Department of Physics. University of León, León, 24071, Spain
[2]National Institute for Aerospace Technology (INTA), Huelva, Spain
[3]Centre for Environmental and Marine Studies (CESAM), University of Aveiro, 3810-193
[4]Center for Energy, Environmental and Technological Research (CIEMAT), Madrid, Spain

ABSTRACT

Precipitation processes are the primary mechanisms for transporting aerosol from the atmosphere to the Earth's surface. They are also the main process connecting aspects of climate and the quality of human life. The knowledge of these atmospheric mechanisms requires the coordination of operational long-term networks, such as EMEP and AERONET. We have used data from both sources to characterize the connection between rain and the scavenging of aerosols in Europe.

The main aims of this study are:

1) to analyze the chemical composition of the rainwater samples collected in several EMEP stations, studying intense rain episodes by means of a HYSPLIT back-trajectory analysis,

2) to study the influence of rain intensity on the variation of the sub- and super-micron aerosol size distribution by means of the aerosol integrated-column properties from AERONET sites.

Several European stations have been selected using as criteria the proximity between an EMEP station and an AERONET site. In the precipitation samples, Cl^-, NO_3^-, SO_4^{2-} Ca^{2+}, Mg^{2+}, Na^+ and K^+ concentrations were measured. From AERONET sites, aerosol optical depth (AOD), α-parameter and aerosol size distribution from inversion products will be presented.

RAINFALL MICROSTRUCTURE IN LEÓN, SPAIN (2006-2009)

M. Fernández-Raga[1], N. Pichel[1], A.I. Calvo[2], C. Tomás[3], C. Palencia[1], A. Castro[1], R. Fraile[1]

[1]Department of Physics (IMARENAB), University of León, León, Spain
[2]Centre for Environmental and Marine Studies (CESAM), University of Aveiro, Portugal
[3]Department of General and Atmospheric Physics. University of Salamanca, Spain

1. INTRODUCTION

The study of the parameters characterizing rain events and the modelization of their behavior constitute a complex task because of the local nature of rain and because it is impossible to compare two similar events (Ciach et al., 2007). As a result, research on climate focuses today on the distribution of rain in order to reveal how it affects the current and future weather in one particular place (Bartley et al., 2006).

A detailed knowledge of the physical characteristics of rain is essential in meteorological studies (rain formation, classification of rain events, etc.), in the hydrological study of reservoirs, in studying the washout processes of atmospheric aerosols, and also to determine the influence of rain on soil erosion processes or on the attenuation of the electromagnetic signals used in communication systems.

2. METHODOLOGY

The present study was carried out in the province of León, Spain. The geographic and climatic features of this area are described in detail in Fernández-Raga *et al.*, (2009). The precipitation data used for this study were collected by means of a disdrometer installed at the University of León, to the northwest of the city of León, Spain.

The study is based on the characterization of the physical parameters of the precipitation registered in the city of León over a period of nearly 4 years, from the 1st of March 2006 until the 30th of November 2009.

The laser disdrometer Thies (LPM) was used. This device provides a complete characterization of atmospheric precipitation (Fernandez-Raga et al., 2010) over a sampling area of 45.6 cm^2.

The atmospheric situations have been classified following Lamb's (1972) weather types. Jenkinson and Collison (1977) and Jones *et al.* (1993) have objectively defined the types of weather using indices based on the direction and vorticity of the geostrophic wind. This system has been successfully employed in many studies (Fernandez-Gonzalez et al., 2012).

Each weather type is described according to 6 variables computed from the atmospheric pressure measured daily at sea level at 16 different points over the Iberian Peninsula (Fernandez-Raga et al., 2010). Table 1 shows the 26 resulting weather types.

3. RESULTS

Table 2 shows the characteristics of the precipitation registered during the study period. Nearly one fourth of the sample are rain days.

The maximum intensities registered each day were studied and most of them were lower than 20 mm/h of rain per minute (Fig. 1). These maximum values did not depend on the time of day, except in the case of convective precipitation, which caused more intense rain after the warmest period of the day (Fig. 2).

Finally, a detailed study of the physical characteristics of the rain drops was carried out (number and size), classified by weather types. The results for the weather types with more than 1 rain day are shown in Table 3.

Table 1. Weather types according to Lamb's (1972) classification.

Weather type	*Acronym*
North	N
Northeast	NE
East	E
Southeast	SE
South	S
Southwest	SW
West	W
Northwest	NW
Anti-cyclonic	A
Cyclonic	C
Cyclonic north	CN
Cyclonic northeast	CNE
Cyclonic east	CE
Cyclonic southeast	CSE
Cyclonic south	CS
Cyclonic southwest	CSW
Cyclonic west	CW
Cyclonic northwest	CNW
Anti-cyclonic north	AN
Anti-cyclonic northeast	ANE
Anti-cyclonic east	AE
Anti-cyclonic southeast	ASE
Anti-cyclonic south	AS
Anti-cyclonic southwest	ASW
Anti-cyclonic west	AW
Anti-cyclonic northwest	ANW

The main results are the following:

- The most frequent weather types are A and NE, which account for 36% of the sample, a figure very similar to the one found by Fernandez-Gonzalez et al. (2012) for the period between 1948 and 2009, which is 34.7%.

Table 2. Main characteristics of rain in León (2006-2009).

Variable	
Days with rain > 0.1 mm	307
Average number of drops per day (m^{-2})	2.99 10^7
Average raindrop size (mm)	0.463

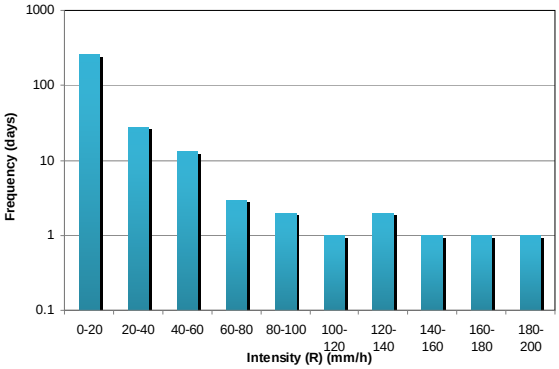

Fig. 1. Frequency of daily maximum rainfall intensity in León (2006-2009).

- The rainiest weather types are CW, CSW, SW, C and W, all with a likelihood of rain higher than 50%. Type CW causes rain in 2 out of every 3 days in which it prevails. The only types with no precipitation at all were types S and ASE.
- The weather types with the highest number of drops registered per day are ANE and SW.

As for the raindrop sizes, there are differences between the weather types. A more detailed analysis focused on the raindrop sizes registered with the anti-cyclonic weather types (A, AN, ANE, ANW, ASW, AW), which were later compared to the sizes found in cyclonic weather types (C, CE, CN, CNE, CNW, CS, CSW, CW).

The average size of the raindrops registered on anti-cyclonic days was 0.41 mm, whereas the raindrops registered on cyclonic days were somewhat larger (0.47 mm). This difference is more important than the standard deviation computed (0.04 mm).

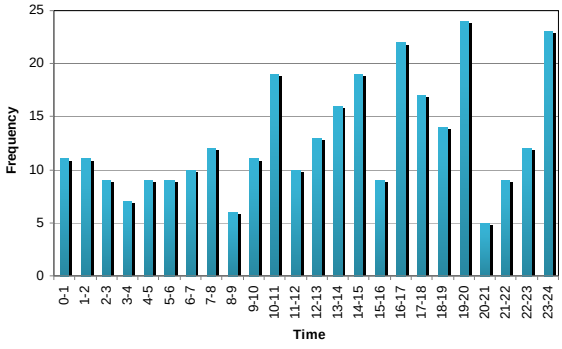

Fig. 2. Temporal distribution of daily maximum rainfall intensity.

Table 3. Physical characteristics of rainfall with each weather type causing more than one rain day.

Weather type	Days	Days with rain >0.1 mm	Raindrops / m^2 mean	Raindrops / m^2 std. dev.	Mean raindrop size (mm)
A	334	39	$2.79\ 10^7$	$3.12\ 10^5$	0.39
AE	27	1	-	-	-
AN	79	8	$2.49\ 10^7$	$1.20\ 10^5$	0.43
ANE	60	4	$4.55\ 10^7$	$3.67\ 10^5$	0.45
ANW	57	9	$1.43\ 10^7$	$5.52\ 10^4$	0.46
AS	6	1	-	-	-
ASE	11	-	-	-	-
ASW	21	2	$4.63\ 10^6$	$9.15\ 10^2$	0.50
AW	50	25	$3.62\ 10^7$	$1.82\ 10^5$	0.42
C	75	42	$3.78\ 10^7$	$2.29\ 10^5$	0.45
CE	11	3	$2.42\ 10^7$	$8.70\ 10^4$	0.52
CN	12	4	$3.66\ 10^7$	$1.31\ 10^5$	0.54
CNE	20	3	$1.52\ 10^7$	$6.56\ 10^4$	0.49
CNW	7	3	$2.44\ 10^7$	$4.40\ 10^4$	0.57
CS	7	2	$2.41\ 10^7$	$1.52\ 10^5$	0.53
CSE	5	1	-	-	-
CSW	12	7	$3.17\ 10^7$	$7.32\ 10^4$	0.55
CW	9	6	$2.81\ 10^7$	$8.77\ 10^4$	0.49
E	92	8	$1.33\ 10^7$	$8.76\ 10^4$	0.48
N	90	35	$2.67\ 10^7$	$1.36\ 10^5$	0.54
NE	158	10	$1.10\ 10^7$	$6.16\ 10^4$	0.48
NW	72	26	$2.57\ 10^7$	$1.63\ 10^5$	0.50
S	11	0	-	-	-
SE	27	3	$2.09\ 10^7$	$1.22\ 10^5$	0.43
SW	37	21	$5.30\ 10^7$	$2.54\ 10^5$	0.43
W	81	44	$2.98\ 10^7$	$9.12\ 10^4$	0.47

As far as the pure weather types are concerned, a similar study was carried out to compare the ones with a northern component (N, NE, NW) and the ones with a southern component (S, SE, SW). In the first group the average drop size is 0.52 mm, clearly larger than the average size of the drops registered on days with a weather type including a southern component, which was 0.43 mm.

4. BIBLIOGRAPHY

Bartley, R., Roth, C.H., Ludwig, J., McJannet, D., Liedloff, A., Corfield, J., Hawdon, A. and Abbott, B., 2006: Runoff and erosion from Australia's tropical semi arid rangelands: influence of ground cover for differing space and time scales. Hydrol. Process 20, 3317-3333.

Ciach, G.J., Krajewski, W.F. and Villarini, G., 2007: Product-error-driven uncertainty model for probabilistic quantitative precipitation estimation with NEXRAD data. J. Hydrometeor 8, 1325-1347.

Fernandez-Gonzalez, S., del Rio, S., Castro, A., Penas, A., Fernandez-Raga, M., Calvo, A.I., Fraile, R., 2012: Connection between NAO, weather types and precipitation in León, Spain (1948–2008). DOI: 10.1002/joc.2431

Fernandez-Raga, M., Castro, A., Palencia, C., Calvo, A.I., Fraile, R., 2009: Rain

events on 22 October 2006 in León (Spain): Drop size Spectra. Atmos. Res.: 93, 619-635.

Fernandez-Raga, M., Fraile, R., Keizer, J.J., Teijeiro, M.E.V., Castro, A., Palencia, Calvo, A.I., Koenders, J., Marques, R.L.C., 2010: The kinetic energy of rain measured with an optical disdrometer: An application to splash erosion. Atmos. Res.: 96, 225-240.

Jenkinson, A.F., Collison, F.P., 1977: An initial climatology of gales over the North Sea. Synoptic Climatology Branch Memorandum 62. Meteorological Office, Bracknell.

Jones, P.D., Hulme, M., Briffa, K.R., 1993: A comparision of Lamb circulation types with an objetive classification scheme. International Journal of Climatology 13, 655-663.

Lamb, H.H., 1972. British Isles weather types and a register of daily sequence of circulation patterns, 1861–1971. Geophysical Memoir 116. HMSO, London.

Acknowledgements

This study was partially supported by the Regional Government of Castile and León (Grants LE014A07 and LE039A10-2), and by the Spanish Ministry of Education (Grants TEC2007-63216 and TEC2010-19241-C02-01).

Z-R RELATIONSHIPS IN LOW-INTENSITY RAINFALLS

A. Castro[1], N. Pichel[1], M. Fernández-Raga[1], A.I. Calvo[2], O. Pujol[3], R. Fraile[1]

[1]Department of Physics (IMARENAB), University of León, Spain
[2]Centre for Environmental and Marine Studies (CESAM), University of Aveiro, Portugal
[3]Laboratoire d'optique atmosphérique. Université Sciences et Technologie de Lille, France

1. INTRODUCTION

Rainfall intensity *R* can be estimated by means of remote sensors. In the case of radars, this measurement is usually linked to back scattered power, in terms of reflectivity factor *Z* (Fraile and Fernandez-Raga, 2009). The relationship between reflectivity and precipitation intensity determines the type of precipitation (Hazenberg et al., 2011). This relationship is generally assumed to follow a power law (Marshall et al., 1955): $Z = a R^b$. The values *a* and *b* depend on the drop size spectra.

The non-unique *Z–R* relationship and the impossibility to measure drop size spectra directly make it very difficult to obtain exact measurements of intensity and accumulation rain by radar (Dutta et al., 2011).

Nevertheless, the values *a* and *b* may be obtained empirically computing Z and R from raindrop size distributions as observed by a disdrometer (Ulbrich and Lee, 1999).

Many researchers have studied the natural variation of *Z–R* relations because the type of precipitation provides information on where the drop formation processes occur and, therefore, where the heat exchanges take place in the atmosphere.

This paper aims at characterizing precipitation events in León, Spain, with intensities lower than 10 mm/h, from *Z-R* relations.

2. METHODOLOGY

The present study was carried out in the city of León, Spain. The geographic and climatic features of this area are described in detail in Fernández-Raga *et al.*, (2009). The precipitation data used for this study have been registered by a disdrometer installed at the University of León, to the north-west of the city of León.

The Thies laser disdrometer (Laser Precipitation Monitor) employed provides a complete characterization of atmospheric precipitation (Fernandez-Raga et al., 2010) over a sampling area of 45.6 cm^2.

The Z-R relationships were represented graphically for all the precipitation events with an intensity lower than 10 mm/h between 2006 and 2011. It was found that the typical curves sometimes split into two. Lamb's (1972) classification of weather types was used to study the meteorological conditions of these days.

Jenkinson and Collison (1977) and Jones *et al.* (1993) put forward an objective definition of weather types using as a starting point indices based on the direction and vorticity of the geostrophic wind. This methodology has been used successfully in many previous studies (Fernandez-Gonzalez et al., 2012).

Each weather type is determined according to 6 variables computed from the values for atmospheric pressure measured daily at sea level in 16 points covering the whole of the Iberian Peninsula (Fernandez-Raga et al., 2010). The 26 resulting weather types are listed in Table 1.

3. RESULTS

In each day, rainfall intensity R and reflectivity Z were determined and graphically shown every minute. It was

observed that for 28 days with precipitation rates of less than 10 mm/h, the dots split into two when *R* increased; this means that different types of Z-R relationships can be found the same day.

Figure 1 shows a few examples of Z-R relationships, one of each year in the study period. The figure also represents the curve that fits best all the dots. In the bottom left-hand corner are parameters *a* and *b* for each fit. It can be seen that the direct fit of the daily Z-R relationships would lead to a considerable error if the split into two was not taken into account.

The most common weather types of these low rainfall intensity days have been analyzed. It was found that these days do not usually occur in the summer (only 1 out of 28), and most days occur in winter (nearly half the sample).

As for the weather types, Table 2 shows that these days occur more often with types W, C, NW and SW. Three of these are among the rainiest weather types (CW, CSW, SW, C and W, with a likelihood of rain of more than 50%). However, this is not the case of NW, so we may say that the likelihood of splitting is not proportional to the likelihood of rain.

Table 1. Lamb's (1972) classification of weather types.

Weather type	Acronym
North	N
Northeast	NE
East	E
Southeast	SE
South	S
Southwest	SW
West	W
Northwest	NW
Anti-cyclonic	A
Cyclonic	C
Cyclonic North	CN
Cyclonic Northeast	CNE
Cyclonic East	CE
Cyclonic Southeast	CSE
Cyclonic South	CS
Cyclonic Southwest	CSW
Cyclonic West	CW
Cyclonic Northwest	CNW
Anti-cyclonic North	AN
Anti-cyclonic Northeast	ANE
Anti-cyclonic East	AE
Anti-cyclonic Southeast	ASE
Anti-cyclonic South	AS
Anti-cyclonic Southwest	ASW
Anti-cyclonic West	AW
Anti-cyclonic Northwest	ANW

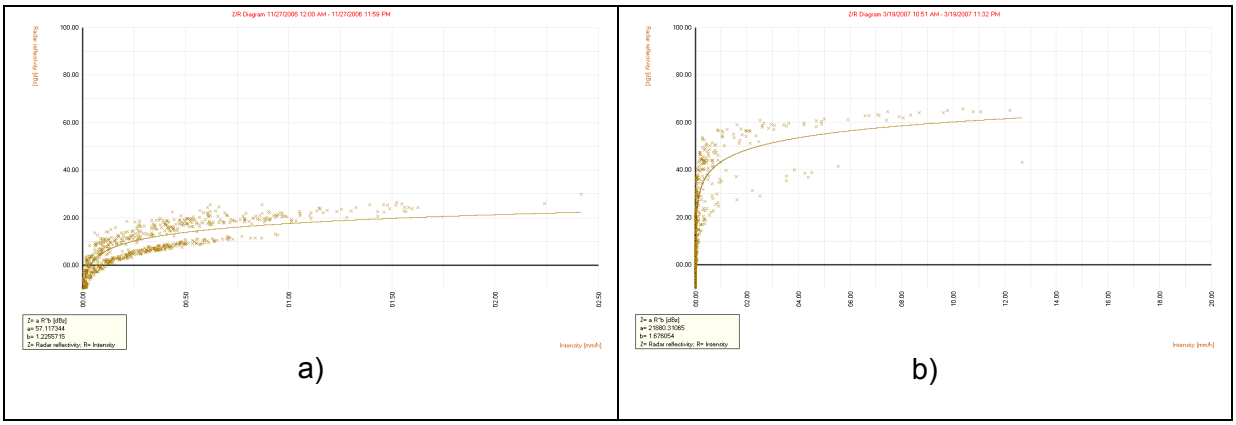

a) b)

Fig 1. Z-R relationships for the rain recorded: a) 27 November 2006 (weather type: SW); b) 19 March 2007 (weather type: N); c) 15 June 2008 (weather type: NW); d) 21 December 2009 (weather type: CSW); e) 12 January 2010 (weather type: SW) and f) 16 February 2011 (weather type: C).

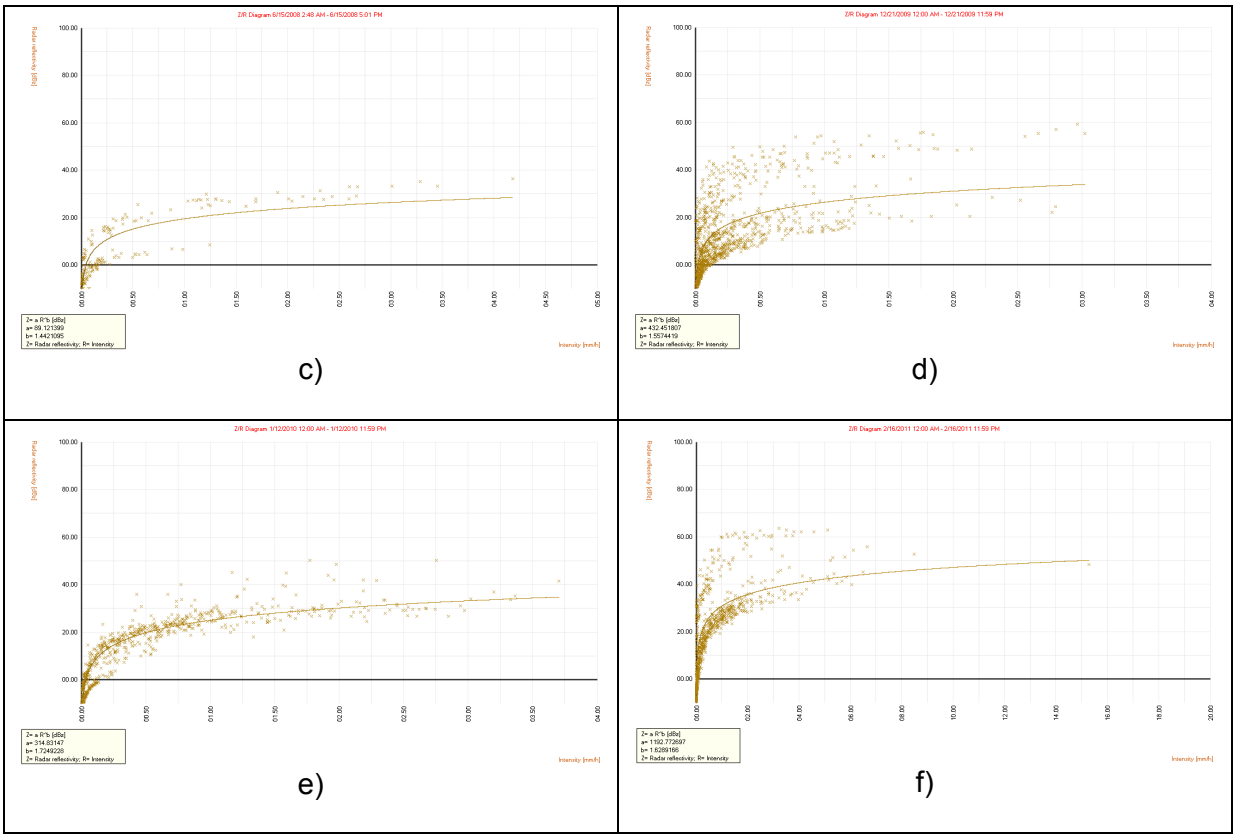

Fig 1. *(Continued)*.

Table 2. Frequency of the weather types with splitting in the Z-R relationships.

Weather type	N. of days
A	2
AN	1
ASW	1
C	4
CNW	1
CSE	1
CSW	2
N	2
NW	4
SE	1
SW	4
W	5

4. BIBLIOGRAPHY

Fernandez-Gonzalez, S., del Rio, S., Castro, A., Penas, A., Fernandez-Raga, M., Calvo, A.I., Fraile, R., 2012: Connection between NAO, weather types and precipitation in León, Spain (1948–2008). DOI: 10.1002/joc.2431

Fernandez-Raga, M., Castro, A., Palencia, C., Calvo, A.I., Fraile, R., 2009: Rain events on 22 October 2006 in León (Spain): Drop size Spectra. Atmos. Res.: 93, 619-635.

Fernandez-Raga, M., Fraile, R., Keizer, J.J., Teijeiro, M.E.V., Castro, A., Palencia, Calvo, A.I., Koenders, J., Marques, R.L.C., 2010: The kinetic energy of rain measured with an optical disdrometer: An application to splash erosion. Atmos. Res.: 96, 225-240.

Fraile, R., Fernandez-Raga, M. 2009: On a more consistent definition of radar reflectivity. Atmósfera 22(4), 375-385.

Hazenberg, P., Yu, N., Boudevillain, B., Delrieu, G., Uijlenhoet, R., 2011: Scaling of raindrop size distributions and classification of radar reflectivity–rain rate relations in intense Mediterranean precipitation. Journal of Hydrology 402, 179–192.

Jenkinson, A.F., Collison, F.P., 1977: An initial climatology of gales over the North Sea. Synoptic Climatology Branch Memorandum 62. Meteorological Office, Bracknell.

Jones, P.D., Hulme, M., Briffa, K.R., 1993: A comparision of Lamb circulation types with an objetive classification scheme. International Journal of Climatology 13, 655-663.

Lamb, H.H., 1972. British Isles weather types and a register of daily sequence of circulation patterns, 1861–1971. Geophysical Memoir 116. HMSO, London.

Marshall, J.S., Hitschfeld, W., Gunn, K.L.S., 1955. Advances in radar weather. Adv. Geophys. 2, 1–56.

Ulbrich, C.W., Lee, L.G. 1999: Rainfall measurement error by WSR-88D radars due to variations in Z–R law parameters and the radar constant. J. Atmos. Oceanic Technol. 16, 1017–1024.

ACKNOWLEDGEMENTS

This study was partially supported by the Regional Government of Castile and León (Grants LE014A07 and LE039A10-2), and by the Spanish Ministry of Education (Grants TEC2007-63216 and TEC2010-19241-C02-01)

INFLUENCE OF WILDFIRES AND RAIN ON AEROSOL SIZE DISTRIBUTION IN A RURAL AREA

E. Alonso-Blanco [1, 2], A. Castro [2], A.I. Calvo [3], I. San Martín [2], M. Fernández-Raga [2], R. Fraile [2]

[1]Center for Energy, Environmental and Technological Research (CIEMAT), Madrid, Spain
[2]Department of Physics (IMARENAB), University of León, 24071 León, Spain
[3]Centre for Environmental and Marine Studies (CESAM), University of Aveiro, 3810-193 Aveiro, Portugal

1. INTRODUCTION

The study of atmospheric particulate matter is crucial in our understanding of climate change on the Earth (Vergaz, 2001). The presence of particulate matter in the atmosphere triggers climate change. On the one hand, particles have a direct effect on the global radiative balance (IPCC, 2001; Calvo et al., 2010), altering the amount of radiation reaching or evading the Earth. On the other hand, many of these particles function as Cloud Condensation Nuclei (CCN) in the formation of raindrops and set off indirect atmospheric effects, such as an increased albedo.

Biomass burning is one of the main contributors of particulate matter to the atmosphere, releasing large amounts of particles and gases and altering the atmospheric composition. Many studies have analyzed the changes in aerosol size distributions due to wildfires, revealing an increase in the number of particles in the fine or accumulation mode (Reid and Hobbs, 1998; Remer et al., 1998; Alonso-Blanco et al., 2011).

The size of these particles is one of the most important parameters to characterize aerosols (Hinds, 1999), since it determines many of their properties. The aerosol size distribution and their lifetime in the atmosphere depend both on the sources and the sinks, as well as on the meteorological and physical-chemical processes they undergo (Ito, 1993; Castro et al., 1998; Suzuki and Tsunogai, 1988; Fraile et al., 2006).

Analyzing the changes in aerosol size distributions implies a detailed study of the weather conditions (Goméz-Moreno et al., 2011), the air masses, the dry deposition processes, such as the ones associated to the aerosol-precipitation interaction (Castro et al., 2010), and, finally, aerosol water absorption, i.e. hygroscopic growth.

This paper studies the influence of precipitation and wildfires on the number of aerosols and their size distributions, as well as the interaction between these particles and the ambient conditions and air masses crossing over the rural areas of the Iberian Peninsula in the summer months, when most of these particles are of biogenic origin, except in the case of wildfires or agricultural waste burning.

2. STUDY ZONE

In the summer months the province of Leon is seriously affected by wildfires in tree woodland areas and other areas. The study was carried out in Carrizo de la Ribera, a town in the middle of the province of Leon, Spain, to the northwest of the capital (Fig. 1). The town lies at 873 m on the terrace of the River Orbigo. It is a rural area with 2,554 inhabitants working mainly in agriculture.

The weather in Carrizo is controlled by a station installed there by the Spanish National Agency for Meteorology (42º 35´ N, 5º 39´ W). The area has a continentalized Mediterranean climate.

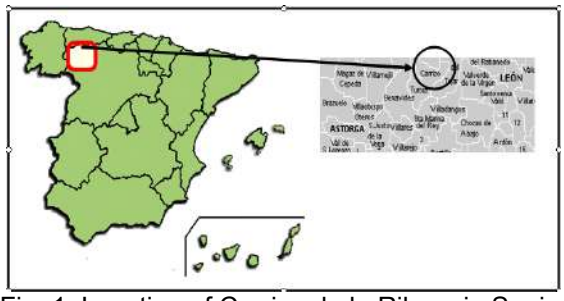

Fig. 1. Location of Carrizo de la Ribera in Spain.

3. MATERIALS AND METHODS

The aerosol size distributions were characterized by means of a laser *Passive Cavity Aerosol Spectrometer Probe, PMS Model PCASP-X* registering particle sizes between 0.1 and 10 μm in 31 channels. The device was installed in a field in Carrizo de la Ribera from June to September 2000. The ambient particle size spectrum was measured 8 times daily in this rural area. The measurements were carried out every 3 hours, and lasted 15 minutes each.

The probe was calibrated by the manufacturer using polystyrene latex particles of a known size. The refractive index of latex beads (1.59 – 0i) is different from that of atmospheric particles, resulting in an aerosol size distribution that is "latex equivalent".

The refractive index of the particles was estimated according to the relative humidity (in this study the values have ranged between 37% and 98%). The relative humidity of the ambient atmosphere affects the size and the complex refractive index of aerosols. Raw size bins were corrected applying a program based on Mie Theory (Bohrenm and Huffman, 1983) to the estimated refractive indices. Because this study was carried out in a rural area, the index used was m=1.52-0.00626i for a relative humidity of 50%. Data by Kim et al., 1990 have been used to estimate the refractive index for other humidity values. The humidity was corrected in each measurement by linear interpolation.

To compute the number of particles by unit of volume in each channel, a number of corrections had to be made. The flux value had to be corrected according to the altitude of the sampling site. Carrizo de la Ribera lies at an altitude of 873 m, so the correction factor was 0.905. The activity registered must also be considered, and the correction factor applied was 1/(1-0,052A), following the instructions of the manufacturer.

A weather station was installed next to the probe to register automatically data on pressure, temperature, humidity and wind every 30 minutes. A Davis weather station was also installed to record the amount of precipitation fallen in those months. The data on precipitation were also registered and stored automatically every 30 minutes.

In order to compare meteorological data and data on the particulate matter, it has been deemed necessary to use average and/or accumulative values (in the case of rain) of the 3 hours prior to the aerosol measurement.

In order to identify the type of weather associated to a particular synoptic situation a Circulation Weather Type classification (CWTs) was used based on Jenkinson and Collison (1977) and Jones et al. (1993). These procedures were developed to define objectively Lamb Weather Types (Lamb, 1972) for the British Isles. The daily circulation affecting the Iberian Peninsula is described using a set of Indices associated to the direction and vorticity of the geostrophic flow. The Indices used were the following: southerly flow (SF), westerly flow (WF), total flow (F), southerly shear vorticity (ZS), westerly shear vorticity (ZW) and total shear vorticity (Z). These Indices were computed using sea level pressure (SLP) values obtained for 16 grid points distributed around the Iberian Peninsula. This same classification has already been used for the Iberian Peninsula in previous studies on splash erosion (Fernandez-Raga et al., 2010) or aerosol size distribution in precipitation events (Castro et al., 2010).

The thermal inversions have been computed using data from soundings in La Coruña (43.36ºN, 8.41ºW, altitude 67 m), Madrid (40.50ºN, 3.58ºW, altitude 633 m) and Santander (43.48ºN, 3.80ºW, altitude 59 m) at 0000 UTC, provided by the University of Wyoming (http://weather.uwyo.edu/upperair/ sounding.html).

Back trajectories of 120 h (5 days) have been used, computed at 500 m, 1,500 m and 3,000 m AGL, using the HYSPLIT Model (*HYbrid Single-Particle Lagrangian Integrated Trajectory Model)* by NOAA (Draxler and Rolph, 2003). This was done to determine the source regions of the air

masses reaching the study zone. This study will be complemented by a description of the air masses.

The Department for the Environment of the regional government Junta de Castilla y León provided the database of all the wildfires registered in the province of León in the year 2000, including the district where the fire occurred, the date of detection and extinction (exact day and time), and the land area affected (in hectares), as well as the type of vegetation burnt.

This information was used to draw daily maps of the province of León showing the sites affected by wildfires.

The maps and the data on wind speed and wind direction obtained from the weather station next to the probe were used to determine which measurements might have been contaminated by the smoke plumes from the wildfires.

Because of the low time resolution of the measurements carried out by the probe (one measurement every 3 hours), there is usually only 1 contaminated measurement among the 8 ones carried out daily. However, several measurements were eventually contaminated in the case of large fires raging for more than 24 hours and with an affected area of >50 ha, under favorable wind conditions.

To identify the measurements that had been affected by the wildfires, we considered the distance to the sampling point, the wind speed and direction, and the time the smoke plume took to reach the probe. When all these parameters pointed towards the fact that a smoke plume from a wildfire containing aerosols was coming close to the probe, the evolution of the number of particles was analyzed in detail. The measurements with increases of more than 500% with respect to other measurements on the same day were considered as contaminated by the wildfires.

A previous study has been carried out on the influence of rain and wildfires in the number of atmospheric particles and their size distribution in the four months of the sampling campaign (June-September). This study will focus on what happened on the 25th, 26th and 27th of August 2000. A detailed analysis of the weather conditions and wildfires on those days has been carried out, with particular reference to the contamination they caused in the probe measurements.

On the 25th of August began a wildfire which affected the aerosol measurements of the 26th of August. On the 26th, two wildfires were active and there was a rain event; and on the 27th we observe the stabilization of the number of aerosols registered.

4. RESULTS AND DISCUSSIONS

4.1 METEOROLOGICAL STUDY: CIRCULATION WEATHER TYPES AND AIR MASSES

Table 1 shows the meteorological features of the 25th**,** 26th and 27th of August 2000. The average temperatures on these days are low: under 16ºC. This is due to the fact that the maximum temperatures were not very high, never exceeding 22ºC. The nocturnal temperatures were low and the proximity of the River Orbigo also contributed to these moderate temperatures.

The wind speed is low too, less than 2.1 m/s, and the relative humidity is around 70%. As a result, the smoke plumes move rather slowly.

The weather types on these days are cyclonic (C), northern and north-eastern hybrid anti-cyclonic (AN, ANE), i.e., the air masses reaching the Iberian Peninsula on these days are of maritime origin.

The back trajectories on the study days at three different altitudes (500, 1,500 and 3,000 m AGL) show that the air mass reaching the Iberian Peninsula on the 25th of August is of the tropical maritime type (mT). In contrast, on the 26th and 27th of August the air mass is a polar maritime one (mP), i.e., a cold air mass with a high relative humidity. On the 26th of August the back trajectories at 500 and at 1,500 m AGL come from Europe, but on the 27th they clearly come from the North Pole (Fig. 2).

Table 1. Meteorological study of the 25th, 26th and 27th of August 2000, with data on maximum, minimum and average temperatures, relative humidity, wind intensity and total precipitation registered.

Day	T_{max} (ºC)	T_{min} (ºC)	T_{av} (ºC)	HR (%)	Wind (m/s)	P_{total} (mm)
25th August 2000	21.3	8.9	15.3	61	2.1	0
26th August 2000	19.7	9.6	14.9	68	1.9	10.6
27th August 2000	21.3	4.9	13.4	67	1.3	0

a)

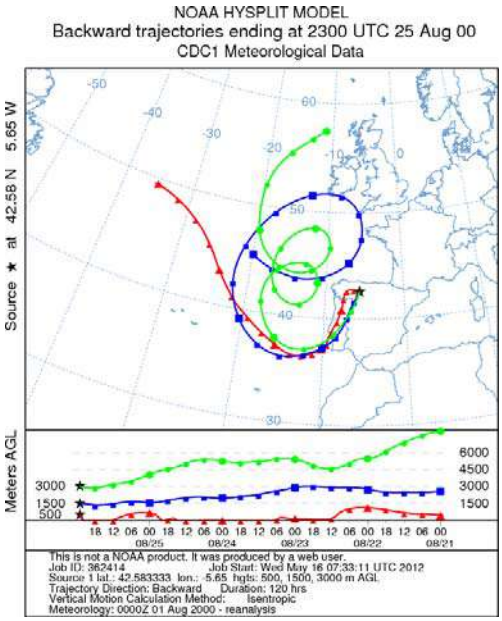

b)

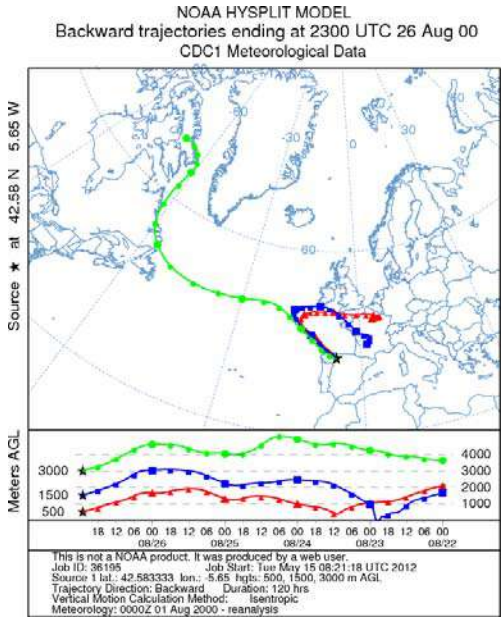

c)

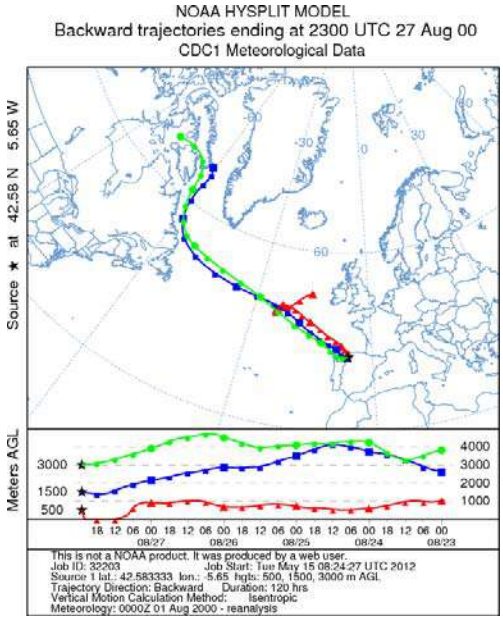

Fig. 2. Back trajectories for three different altitudes (500, 1500 and 3000 m) using the HYSPLIT model.

Table 2. Day, district and town where the wildfires occurred, distance to the sampling site, date of detection and extinction, land area burnt by type of vegetation (tree woodland, non-tree woodland and non-forest vegetation), and total land area burnt in the wildfires contaminating the aerosol measurements on the 26th and 27th of August 2000.

Day	District/ town	Distance to the sampling site (km)	First Detected		Date of Extinction		Area burnt (ha)			
			Day	Time (UTC)	Day	Time (UTC)	tree woodland	non-tree woodlad	non-forest vegetation	Total area burnt
25th August 2000	La Pola de gordón/Geras	35	25th August 2000	1647	26th August 2000	1315	0	15	0	15
26th August 2000	Benuza/ Llamas de Cabrera	69	26th August 2000	1325	26th August 2000	1757	10	20	0	30
26th August 2000	Benuza/ Sigüeya	73	26th August 2000	1330	27th August 2000	1800	0	3	37	40

Of the three study days, on the 25th and on the 27th radiative thermal inversions were registered in the soundings carried out in Madrid at 0000 UTC, at 46 and at 138 m (AGL), respectively. In addition, on the 25th there was also a subsidence thermal inversion at 324 m (AGL) in the sounding carried out in Santander at 0000 UTC.

4.2 CHARACTERIZATION OF THE WILDFIRES AFFECTING THE AEROSOL MEASUREMENTS

The province of León, Spain, has a land area of 15,581 km^2, and is the largest in the region of Castile and León. The confluence of Eurosiberian and Mediterranean climates results in varied landscapes and a number of micro-climates in the province. One important consequence is the high number of wildfires registered, and an important land area is affected by these fires. Most of the wildfires – around 90% - are of human origin, either caused accidentally or intentionally.

Table 2 shows the characteristics of the wildfires contaminating the aerosol measurements on the 26th and 27th of August.

On the 25th of August 2000 a wildfire begins in Geras, at about 35 km from the sampling area (Carrizo de la Ribera). This fire burns 15 ha of non-tree woodland. The fire starts at 1647 UTC and is extinguished at 1315 UTC on the 26th of August. It contaminated the measurement registered at 1300 UTC on the 26th.

On the 26th of August 2000 two wildfires are recorded simultaneously in the district of Benuza, with a distance of 5 km between each other. The first fire occurred in Llamas de Cabrera; it began at 1325 UTC and was extinguished at 1757 UTC on the 26th. The second fire began in Sigüeya at 1330 UTC and was extinguished at 1800 UTC on the 27th of August 2000. These two fires burnt a total land area of 70 ha: 10 ha of tree woodland, 23 ha of non-tree woodland, and 37 ha of non-forest vegetation. The two fires occurred at a distance of around 70 km from the sampling site. Both fires contaminated the measurement carried out at 1900 UTC on the 26th of August. Fig. 3 shows the maps with all the fires recorded in the province of León on the 25th and 26th of August 2000.

The three fires contaminating the probe began during the day. The fire in Geras lies to the north of Carrizo de la Ribera, and the fires in Llamas de Cabrera and Sigüeya lie to the west. All three districts are mountainous areas, with altitudes around 1,000 m and a great landscape value.

The smoke plumes of average wildfires may be carried by the wind over large distances. In this study, the three plumes move slowly towards the probe and are responsible for important increases in the number of aerosols registered on those days.

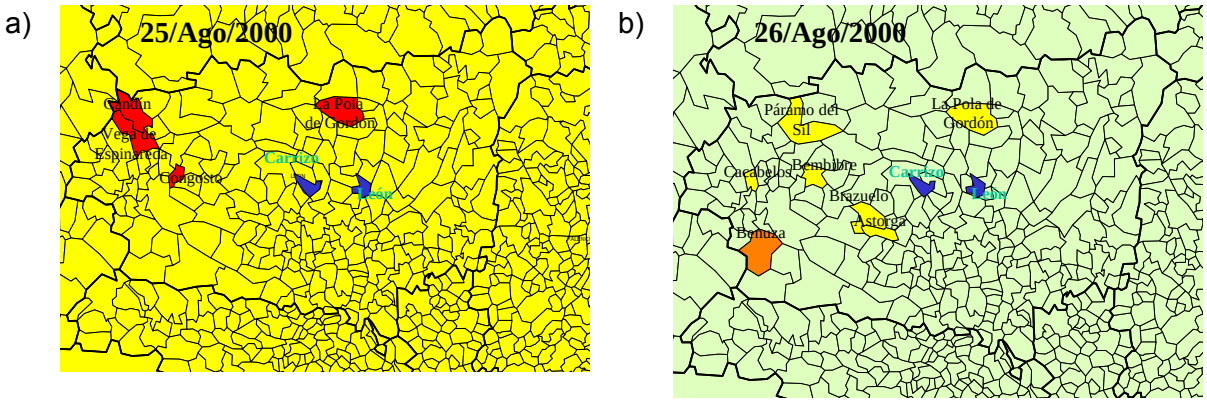

Fig. 3. Maps with the districts where wildfires were registered in the province of Leon, Spain, on the (a) 25th and (b) 26th of August 2000 (the probe was installed in Carrizo).

4.3 INFLUENCE OF WILDFIRES AND PRECIPITATION IN AEROSOL SIZE DISTRIBUTION

An analysis was carried out of the changes in the number of atmospheric particles and their size distribution, considering the wildfires occurring in nearby areas and whose smoke plumes were likely to reach the probe, and also the precipitation registered in the sampling site causing washout.

As for the number of particles, the average number registered in the measurements carried out before 1300 UTC on the 26th of August (and not affected by smoke plumes or precipitation of any type, according to our data) is of 1,200±200 particles cm^{-3} (Table 3).

In contrast, the measurement carried out when the smoke plume had already reached the probe, such as the one at 1300 UTC, shows an increase in the total number of particles by 600% when compared with the previous measurement, not contaminated by the wildfires.

Table 3. Total number of particles, CMD, and σ for the accumulation mode (f) and the coarse mode (c) of the number size Distribution and precipitation on the 25th, 26th and 27th of August 2000.

Day	Time (UTC)	Nº particles.cm^{-3}	Fine mode			Coarse mode			Precipitation (mm)
			N_f	CMD_f	σ_f	N_c	CMD_c	σ_c	
25th August 2000	2200	909	1197	0.10	1.65	1	1.00	1.40	0
26th August 2000	0100	1263	1856	0.13	1.61	1	1.00	1.40	0
	0400	1398	1992	0.12	1.59	4	1.00	1.60	0
	0700	1436	1491	0.13	1.53	2	1.10	1.60	0
	1000	957	988	0.13	1.52	1	1.00	1.45	0
	1300	6324	10692	0.10	1.45	1	1.00	1.40	0.4
	1600	573	679	0.14	1.48	1	1.00	1.50	10
	1900	9223	4048	0.12	1.50	1	1.20	1.50	0.2
	2200	800	521	0.20	1.25	34	0.32	1.40	0
27th August 2000	0100	1316	820	0.23	1.26	28	0.46	1.13	0
	0400	853	393	0.22	1.18	96	0.31	1.30	0
	0700	794	947	0.14	1.51	1	1.10	1.50	0
	1000	647	869	0.13	1.56	0	1.00	1.50	0

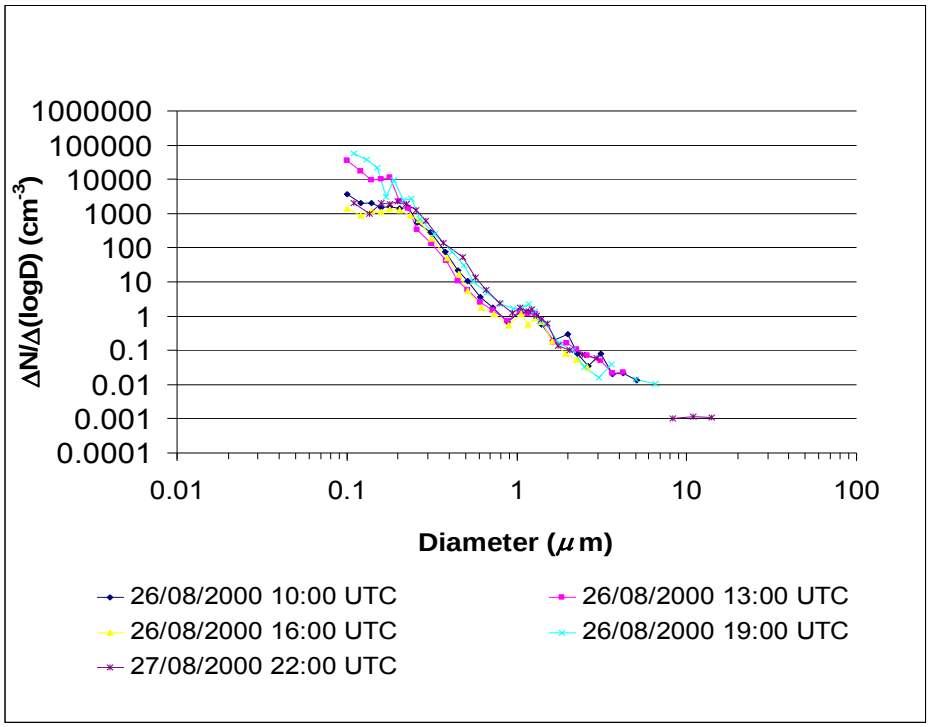

Fig. 4. Distributions of the size spectrum in the measurements contaminated by the wildfires and affected by the rain events, and in the measurements carried out immediately before and after the contaminated measurements on the 26th and 27th of August 2000.

Later, when the precipitation recorded in the three hours prior the aerosol measurement is of 10 mm (at 1600 UTC), we find a clear example of washout, with a decrease in the total number of particles of 90%, when compared with the previous measurement. Then, at 1900 UTC, the number of particles increases again by 1,500% because of the influence of the nearby fires.

After both phenomena (fires & rain) stop having an impact on the aerosol registers, from 2200 UTC on the 26th of August, the number of particles decreases again to an average value of 900±300 particles.cm^{-3}.

A decrease was observed in the CMD of the fine mode (CMD_f) in the measurements contaminated by the smoke plumes, when compared to the previous measurements (1300 UTC and 1900 UTC on the 26th of August) of around 20%. Once the plume moves away, the values tend to stabilize again in the measurement after the contaminated one.

The size distributions obtained by the PCASP-X have been found to be bimodal: they have a fine mode (0.1-1 μm) and a coarse mode (1-10 μm). In the measurements contaminated by the smoke plumes there was an increase in the number of particles in the fine mode (0.1-1 μm), mainly between 0.1 and 0.2 μm. This increase exceeded by 2,000% the values registered in previous measurements.

Figure 4 shows the size distributions of the measurements contaminated by the smoke plumes and the ones altered by rain.

The measurements carried out on the 26th of August at 1300 and 1900 UTC are contaminated by the wildfires in Geras, and by the ones in Llamas de Cabrera and Sigüeya, respectively. During the three hours prior to these measurements, the probes recorded 0.4 mm of rain at 1300 UTC and 0.2 mm at 1900 UTC. The small amount of rain fallen does not have any significant effect on the size distributions found.

In contrast, at 1600 UTC the amount of rain recorded in the three hours prior to the aerosol measurement is of 10 mm, and in this case the size distribution is different from the previous ones. We claim that this is due to the washout affecting mainly the smallest particles, the ones between 0.1 and 0.2 μm (comprised in the fine mode). The measurement carried out at 1600 UTC showed a decrease of 1,000% in this size range, when compared with the previous measurement.

The remaining size distributions in Figure 4 correspond to measurements not contaminated by wildfires and not affected by rain (the one at 1000 UTC on the 26th and the one at 2200 UTC on the 27th).

We have found that wildfires cause an increase in the number of atmospheric particles, mainly in the fine mode. It was also found that rain events play a role on aerosol records, resulting in a clear decrease in proportion with the intensity of the precipitation. In other words, the particle concentration and distribution in the atmosphere depends greatly on the sources and on the meteorological processes present at each point in time.

5. CONCLUSIONS

The wildfires registered in the areas close to the study zone have a clear influence on the number of particles recorded as well as on their size distribution. Increases of the total number of particles of up to 1,500% have been found in contaminated measurements. Most of this increase corresponds to the smallest fraction of the fine mode (0.1-0.2 μm). A decrease was found in the CMD_f of about 20% in the aerosol measurements contaminated by the smoke plumes. The values went back to normal once the plume moved away from the probe.

The simultaneous occurrence of rain causes aerosol washout, and the total number of particles decreases by up to 90%, when compared with measurements carried out before the rain event. Washout affects mainly particles with a size range between 0.1 and 0.2 μm.

The study of the role played by the weather and natural and/or anthropogenic phenomena in the composition of the atmosphere is a very complex task. Determining any feedbacks, synergies and conflicting processes between different events at a small scale may help us understand the evolution of atmospheric particulate matter at a larger scale and the changes undergone by this particulate matter during its lifetime.

6. BIBLIOGRAPHY

Alonso-Blanco, E. Calvo, A.I., Fraile, R., Castro, A, 2011. The influence of wildfires on aerosol size distributions in rural areas. *The Scientific World Journal*, **2012**, 13, Article ID 735697 doi:10.1100/2012/735697.

Bohren, C. F.and Huffman, D. R., 1983. Absorption and scattering of light by small particles. Wiley, New York.

Calvo, A. I., Pont, V., Castro, A., Mallet, M., Palencia, C., Roger, J.C., Dubuisson, P., Fraile, R., 2010. Radiative forcing of haze during a forest fire in Spain. *Journal of Geophysical Research- Atmospheres*. **115**, D08206, doi:10.1029/2009JD012172.

Castro A., Alonso-Blanco E., González-Colino M., Calvo A. I., Fernández-Raga M., Fraile R., 2010. Aerosol size distribution in precipitation events in León. Spain. *Atmospheric Research*. **96**, 421–435.

Castro, A., Marcos, J.L., Dessens, J., Sánchez, J.L., Fraile, R., 1998. Concentration of ice nuclei in continental and maritime air mases in León (Spain). *Atmospheric Research*. **47–48**, 155–167.

Draxler, R.R., Rolph, G.D., 2003. HYSPLIT (HYbrid Single-Particle Lagrangian Integrated Trajectory). Model access via NOAA ARL READY Website (http://www.arl.noaa.gov/ready/hysplit4.html). NOAA Air Resources Laboratory, Silver Spring, MD.

Fernandez-Raga, M., Fraile, R., Keizer, J.J., Varela-Teijeiro, M.E., Castro, A., Palencia, C., Calvo, A.I., Koenders, J., Marques, R.L., 2010. The kinetic energy of rain measured with an optical disdrometer: an application on splash erosion. *Atmospheric Research*. **96**, 225-240.

Fraile, R., Calvo, A.I., Castro, A., Fernández-González, D., García-Ortega E., 2006. The behavior of the atmosphere in Long-Range transport. *Aerobiologia*. **22**, 35–45.

Gómez-Moreno F.J., Pujadas M., Plaza J., Rodríguez-Maroto J.J., Martínez-Lozano P., Artinaño B., 2011. Influence of seasonal factors on the atmospheric particle number concentration and size distribution in Madrid *Atmospheric Environmental*. **45 (18)**, 3169-3180.

Hinds, WC. 1999. Aerosols technology: properties, behaviour and measurement of airborne particles, 2nd ed., New York: Wiley, 504.

IPCC: Climate Change 2001: The Scientific Basis. Cambridge University Press, Cambridge, 2001.

Ito, T., 1993. Size distribution of Antarctic submicron aerosols. *Tellus*. **45**, 145–159.

Jenkinson, A.F., Collison, F.P., 1977. An initial climatology of gales over the north sea. Synoptic Climatology Branch Memorándum, 62, Meteorological Office, London.

Jones, P.D., Hulme, M., Briffa, K.R., 1993. A comparison of Lamb circulation types with an objective classification scheme. *International Journal Climatology*. **13**, 655-663.

Kim, Young J. and Boatman, Joe F., 1990. Siza calibration corrections for the Active Scattering Aerosol Spectrometer Probe (ASASP-100X). *Aerosol Science Technology*. **12:3**, 665-672.

Lamb, H.H., 1972. British Isles weather types and a register of daily sequence of circulation patterns, 1861-1971. Geophysical Memoir 116, HMSO, London.

Reid, J. S. and Hobbs, P. V., 1998. Physical and optical properties of smoke from individual biomass fires in Brazil. *Journal Geophysical Research*. **103**, 32,013–32,031.

Remer, L. A., Kaufman Y. J., Holben B. N., Thompson A. M., and D. McNamara, 1998. Biomass burning aerosol size distribution and modeled optical properties. *Journal Geophysical Research*. **103(D24)**, 31,879–31,891.

Suzuki, T. and S. Tsunogai, 1988. Daily variation of aerosols of marine and continental origin in the surface air over a small island Okushin in Japan sea. *Tellus*. **40**, 42–49.

Vergaz, R. 2001. Caracterización de los aerosoles atmosféricos. *Óptica pura y aplicada*. **34**, 57-82.

ACKNOWLEDGMENTS

The authors wish to thank Miguel Angel Olguín from the regional government of Castilla y León for his help whenever required. Many thanks go to Dr. Laura López Campano for her co-operation and to Dr. Noelia Ramón for translating the paper into English. This study was supported by the Junta de Castilla y León (Grant LE039A10), and by the Spanish Ministry of Education (Grant TEC2010-19241-C02-01).

METEOROLOGICAL STUDY OF THE DEVASTATING LOCAL SEVERE STORMS OF BANGLADESH

Akter, Fatima and Ishikawa, Hirohiko
Disaster Prevention Research Institute, Kyoto University, Gokasho, Uji, Kyoto, 611-0011, JAPAN
Email: fatima_a@storm.dpri.kyoto-u.ac.jp; ishikawa@storm.dpri.kyoto-u.ac.jp

ABSTRACT

Local Severe Storms (LSS) are frequently occurring devastating meteorological phenomena, which occur in the pre-monsoon season (March – May) in Bangladesh. Locally induced these storms bring huge damages both in lives and properties in a very short time. Many of these LSSs are called as Nor'wester since the systems migrate from north-west to south-east. Violent LSS mainly the Nor'wester and tornado events that occurred in Bangladesh between 2000 and 2011 are analyzed using JRA-25 1.25 degree resolution reanalysis data provided by Japan Meteorological Agency (JMA). Surface and upper air analysis such as pressure, temperature, specific humidity and wind direction of successive 5 days prior and during each LSS event showed typical temporal course of synoptic environment.

The stability indices of Showalter Stability index (SSI), K-Index (KI),Total Index (TT), Lifted Index (LI), Bulk Richardson Number (BRN), BRN-Shear (BRNS), Convective Available Potential Energy (CAPE), Convective Inhibition (CIN), Storm Relative Helicity (SRH), Energy Helicity Index (EHI), Precipitable Water Content (PW), are calculated using JRA-25 reanalysis data and the response of these variables as for the occurrences of LSS are examined.

For years after 2008, the finer 20km resolution analysis data by using Global Spectral Model (GSM) of JMA are used. TTI value showed favorable for LSS occurrence but it also showed higher value in other regions and the value remained high after the event occurred. CAPE and EHI found favorable for the formation of LSS. The use of GSM 20km resolution data are found to be useful in identifying local features such as the dry-line which is said to have relation with initiation of severe local storm and the accompanying tornado. These data enables detailed representation of land/sea mask and topography and can identify the mechanism of LSS which could improve effective forecasts.

Keywords: Thunderstorms, Severe Storm, Instability, Tornado, Stability indices, Bangladesh disaster

1. INTRODUCTION

Every year the LSS of Bangladesh cause the highest death toll in the World. The annual death toll only from tornadoes in Bangladesh is about 179 deaths per year from the period of 1967-96 (Ono. Y, 2001). During the pre-monsoon season the severity and frequency of LSS occurrences are higher than the other months. In a study Yamane et al. (2010a) mentioned that 84% of total LSS are occurred in pre-monsoon season, the peak occurrence in April, then the frequency decreases sharply in the monsoon season, and again in the late monsoon season from September to October the frequency slightly increases by analyzing newspaper reports from 1990-2005. Violent deadliest Tornadoes are also reported mainly in April. Very few tornadoes have occurred before March and after May. (Newspaper report 1976-2005)

Total 10 LSS cases are taken between 2000 and 2011 those are reported as either tornadoes or severe thunderstorms in different months in Bangladesh, are analyzed using JRA-25 reanalysis data to understand their meteorological features. To

identify the general environmental conditions several objective analyses had conducted in this study. The Nor'wester and thunderstorms are very small scale phenomena and due to the unavailability of data very few detail studies addressing there mechanisms of development and evolution of genesis are found. The previous studies focusing on the dynamic and thermodynamic aspects of the initiation of LSS (Lohar and Pal, 1995), LSS propagation and modes of organization of Mesoscale Convective System (Dalal et al 2012) and lower and mid upper tropospheric features in initiation of Nor'westers (Ghosh et al 2008), but all the studies for the cases occurred in Northern India.

There are few studies about LSS formation, favorable environmental condition over Bangladesh and adjoining area. The favorable environmental settings found in pre-monsoon season are sufficient low level warm moisture flow from Bay of Bengal that influence the convection and also mid-upper moderate to strong westerly flow; often with westerly jet, (Weston, 1972; Prasad, 2006; Yamane and Hayashi; 2006) for LSS development. The detail thermodynamic condition of pre-monsoon season comparing convective parameters on severe local convective storms (SLCSD) and those on non-severe local convective storms (NSLCSD) are precisely analyzed (Yamane et al, 2010b; 2012) to show that thermal instability can discriminate between SLCSD and NSLCSD with statistical significance. Some studies also include preferred areas of LSS formation in Bangladesh (Peterson and Meheta, 1981; Yamane et al 2010a).

The physical process that is involved in the organization of LSS is rarely studied due to the unavailability of data. To analyze the mechanism of LSS development it is also important to know the effect of "dryline", that is a very narrow transition zone with a difference of mixing ratio of at least 12g/kg within 12 km, in Northern India and Bangladesh (Weston, 1972). To observe the dryline activity, and influence on LSS formation GSM 20km resolution data are used.

2. DATA AND METHODOLOGY

The JRA-25 re-analysis data are produced since 1979 by the Japan Meteorological Agency (JMA) and the Central Research Institute of Electric Power Industry (CRIEPI) (Onogi et al., 2007). The standard pressure level data are 1.25 degree in both longitude and latitude, and temporal resolution is six hours (00, 06, 12 and 18 UTC). The model level data with reference to terrain following model levels which has seven layers from the surface to 850 hPa are also available in 1.125 degree resolution. Analysis domain in the present study is 65˚-100 ˚ E and 5˚-29˚ N covering the south Asia region. The topographic height of the Gangetic plain and coastal area is very low - nearly sea level; whereas it gradually increases in the West and North.

JMA's Global Spectral Model (GSM) has very higher horizontal resolution – 0.1875 degrees, approximately 20 km – operational global model in the world. The initial field is to be used as fine grid analysis of global meteorology The available variables are wind (zonal and meridional), temperature, specific humidity, surface pressure and cloud water content. In the vertical, GSM has 60 layers up to 0.1 hPa. The vertical resolution is higher in the lower atmosphere for better simulation of the planetary boundary layer processes.

The major purposes of this study are to identify the dryline influences in the mechanism and development of LSS in Bangladesh. Severe thunderstorms of the Great Plains of United states in springtime months are greatly triggered by dryline. The studies focusing dryline importance in thunderstorm initiation (Reha,1966), the modes of severe storm development along the dryline (Bluestein and Parker, 1993) and mechanism of severe thunderstorms development along a dryline (Hane et al 1997) explaine how dryline influences on severe thunderstorm development in United States. Similar dryline environment is observed in pre-monsoon season over Bangladesh. So an initiative is taken to find the relationship of dryline in initiation of LSS in Bangladesh from this work.

3. RESULT AND DISCUSSION

3.1 SYNOPTIC CONDITION

Analyzing pre-monsoon seasons LSS events, the mean sea level pressure, temperature, specific humidity and wind, it is found that low level temperature is very high at the event occurrence day and there is sufficient moist warm Southerly/South-westerly wind flows from the Bay of Bengal to the land. The specific humidity level is very high all over Bangladesh. There are also dry warm westerly wind evident from the Indian high lands. Southerly/South-westerly tongue of warm moist wind from the Bay of Bengal is observed in those seasons and in most of the April cases southerly is much stronger than in March and May cases.

High Specific humidity is observed in the active cases of April and also strong horizontal gradient of Specific humidity is observed within a short distance of area that is sometime mentioned as dryline (Weston,1971). Westerly wind component is prominent at the upper air from 850hPa. High temperature is observed over Indian high lands and westerly warm advection is observed over Bangladesh at 850 hPa; Cold advection is observed at 500 hPa. At upper troposphere Westerly to North-westerly wind is prominent over Bangladesh.

All the pre-monsoon LSS events are observed in the late afternoon to evening hours. As the day advances low level temperature and specific humidity started to increase, which enhance the instability condition of the atmosphere to form the LSS.

3.2 MESOSCALE FACTORS

In estimating the possibility of the development of LSS atmospheric instability is a major determinant. A variety of instability indices are used to identify the LSS possibility. In this study several indices are computed using JRA-25 data. High instability are observed mainly in pre-monsoon cases. The critical values of some instability indices are examined for LSS occurrences in Bangladesh by Karmakar and Alam (1960).The critical values of all indices should be determined based on Bangladesh cases.

The KI values exceeding 28K indicates the likelihood of convection (Fuelbarg and Biggar, 1994). It shows higher values in the event occurrence day. Karmakar and Alam (1960) concluded that about 88% of the Nor'westers occurs when TTI ranges from 40 to 58. It is found above 60 in the most of the April cases.

The Lifted Index (LI) is a measure of the thunderstorm potential which takes into account the low level moisture availability and can be used as a predictor of latent instability. Karmakar and Alam (2006) studied a number of thunderstorm cases over Dhaka and concluded that thunderstorms are likely to occur over Bangladesh when LI ≤0 and, severe Nor'westers with tornadic intensity are possible when LI < -3 over Bangladesh. In this study LI values are found very low negative values.

Convective Available Potential Energy (CAPE) is an indicator of atmospheric instability. CAPE shows higher values in April case of LSS of tornadic intensity. CAPE are found high over the sea than the land. Potential Instability is larger over sea than the land (Yamane et al 2012)

The Energy Helicity Index (EHI) is the combination of the Storm Relative Helicity (SREH) and CAPE, and a measure of tornadic supercell. Rasmussen and Blanchard (1998) showed the EHI is highly correlated with the generation of supercells in the United States of America. Values of 1 or more are said to indicate a threat of tornadoes potential. There are no critical threshold values for Bangladesh to confirm or predict the occurrence of tornadoes of a violent intensity. EHI values more than 1 observed in all the cases.

Pricipitable water content (PW) is very high in the event occurrence day over Bangladesh indicating the increasing of water vapor in the lower level.

It is found that CAPE, LI, SSI and EHI are good measures for tornadic

outbreaks. Among them CAPE and EHI successfully pointed out the time and place of outbreaks in pre-monsoon season of Bangladesh. The performance of these indices are, however, low in other seasons.

3.3 ENVIRONMENTAL FACTORS

Besides the synoptic analysis and instability parameters some case specific environmental features are also important to understand the LSS development. In the United States mesoscale narrow boundary separates moist maritime tropical air masses of Gulf of Mexico from continental tropical dry air of the deserts in the western Great Plains during the warm season. This boundary has been referred to as “dry front” (Fujita 1958; Miller 1959), more popularly “dryline” (Rhea 1966). The similar landscape is observed in Bangladesh between the moist warm southerly wind from the Bay of Bengal and the dry wind from the Indian Highland; horizontal moisture gradients is created which associate with dryline(Fig: 3c).

On 20th March, 2005 a Tornado swept over the North-western part of Bangladesh (25°N 89°E). The devastation activity was started at 18.45 BST (local standard time) and lasting for 5 minutes only. The serious devastation of this tornado was in a stretch of 10 km in length and 1 km in width. According to Disaster Management Bureau (DMB) the loss of lives were 43, number of injured people 4688 and 8786 houses were damaged. Besides numerous trees, crop fields, educational and religious institutions, domestic animals, shops, electric lines and many other resources of individual and community were damaged or lost due to the tornado. The surface temperature, specific humidity and wind precisely indicate the presence of dryline (Fig1a).

The instability indices are calculated as: CAPE = 1300J/kg (Fig1b), EHI = 1.2(Fig1c), SRH = 150m^2/s^2, PW > 40kg/s^2, SSI= -2, TT = 60, LI = -3

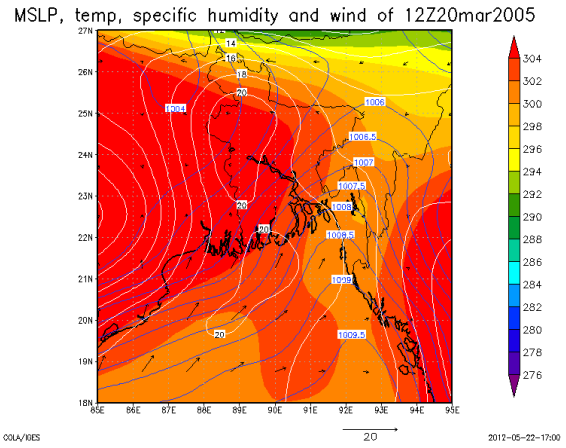

Fig: 1a Mean Sea level temperature (K), specific Humidity (g/kg) and wind (m/s) pattern of 12Z20mar2005

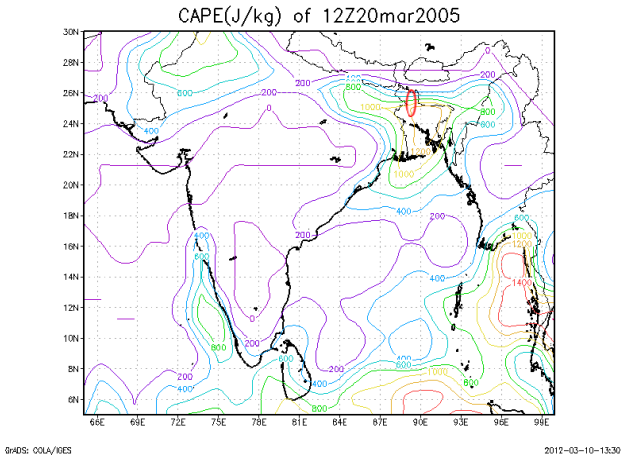

Fig: 1b CAPE (J/Kg) of 12Z20mar2005

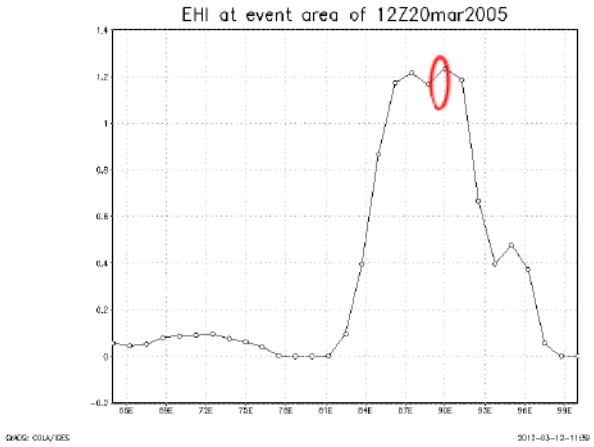

Fig: 1c EHI graph of 12Z20mar2005

14th April, 2004 a deadliest tornado occurred in Mymensingh and Netrokona districts in Bangladesh (24.5°N 90.5°E). The

devastating activities of tornado started at 19.41 BST (local standard time) and lasted for about 10 minutes. Wind speed was over 150 km/hr (41.67m/sec), the tornado track length was about 30 km and about 400-600 meters in width. It is reported that a 15 square kilometer area was devastated. The loss of lives are 66 , around 1700 people are injured and 23 villages affected, 3,000 houses damaged and many tube wells blown away, fish were killed in the water bodies and Numerous houses, school, shops and trees collapsed, roofs are blown away.

In this event the presence of dryline was also identifiable (Fig2a). The Instability parameters calculated as CAPE = 3400J/kg (Fig2b), EHI = 4(Fig2c), SRH = 250m^2/s^2, PW = 47kg/s^2, SSI = -2, TT = 60, LI = -3

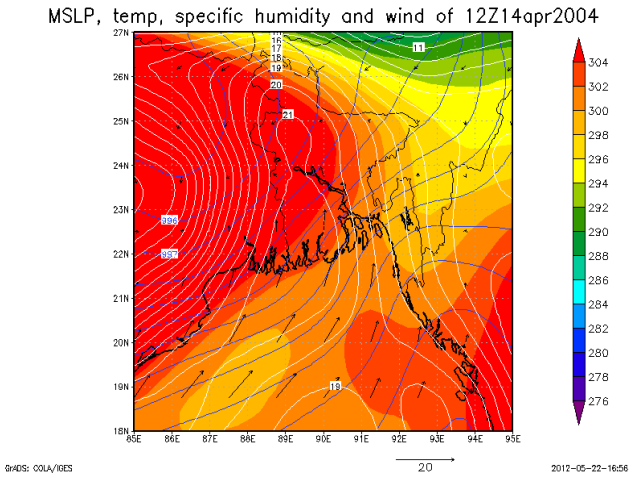

Fig: 2a Mean Sea level temperature (K), specific Humidity (g/kg) and wind (m/s) pattern of 12Z14apr2004

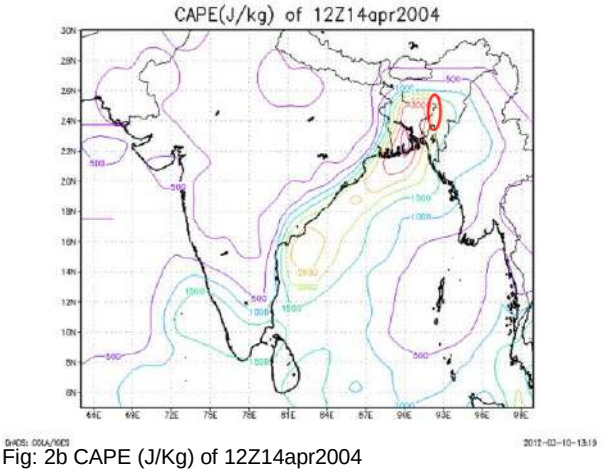

Fig: 2b CAPE (J/Kg) of 12Z14apr2004

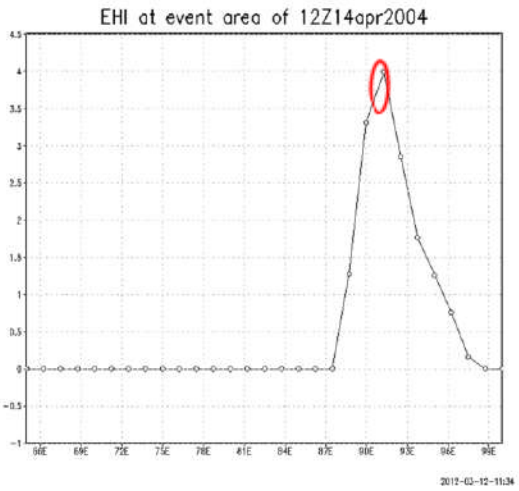

Fig: 2c EHI graph of 12Z14apr2004

There was a squall development over Bangladesh on 13th April, 2010 and continuous records of LSS were reported up to 15th April. On 13th there were several LSS events occurred in Rangpur, Bogra Syedpur in and around (25.5° N, 89° E). The surface analysis with GSM 20km resolution data has an added advantage to see the dryline. Very close Specific humidity lines observed near Bangladesh territory (Fig 3a). Sharp gradient of Specific Humidity is observed by graph (Fig 3b). The lower level convergence is also observed(Fig 3c).

The Instability parameters are calculated as CAPE = 3000J/kg (Fig:3d), EHI = 1.02, PW = 38kg/s^2, SSI = - 4.6,

LI = -6.25,

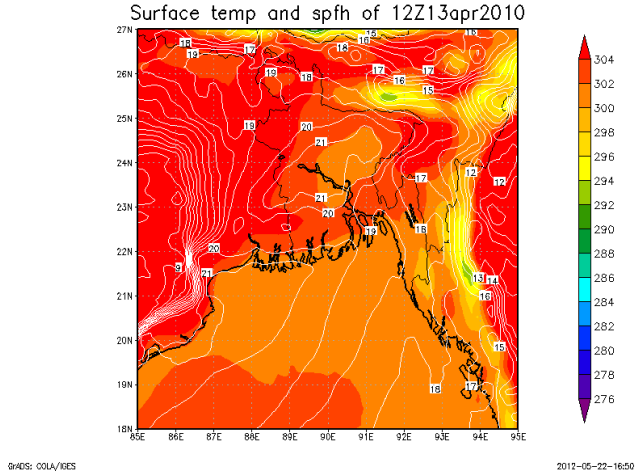

Fig: 3a Surface temperature (k) and specific humidity (g/kg) of 12Z13apr2010

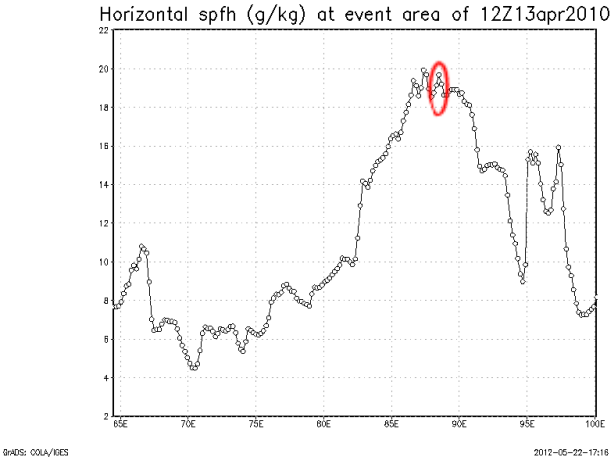

Fig: 3b Horizontal Specific humidity (g/kg) gradient of 12Z13apr2010

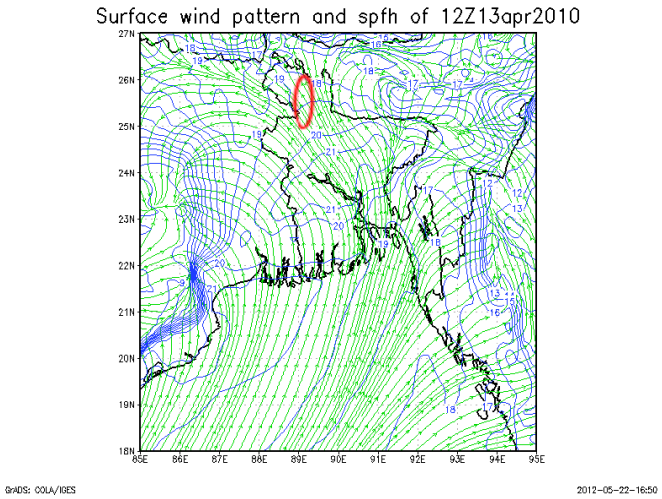

Fig: 3c Surface specific humidity (g/kg) and wind (m/s) of 12Z19apr2009

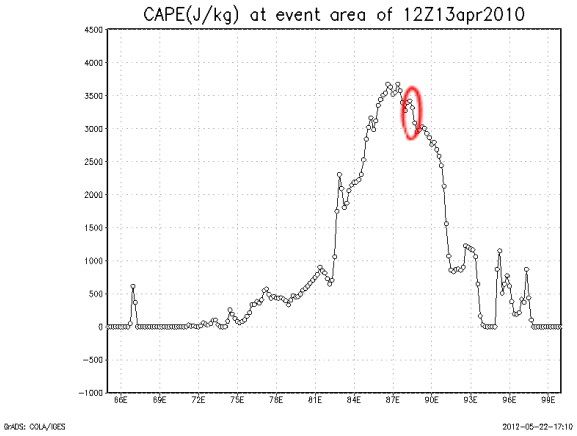

Fig: 3d CAPE (J/Kg) of 12Z19apr2009

The GSM analysis with 20km resolution would be a good tool to detail analysis of dryline and its influence on LSS development

4. CONCLUSION AND REMARKS

Bangladesh is one of the counties where severe local storms bring severe damages to the society. Because of the absence of dense observation network, storm research and forecasting are still in developing stage. We introduced a fine grid (20km resolution) JMA analysis to see the structure of background environment of LSS. Data seems appropriate to investigate key environmental features such as extended dry line, elevated boundary layer etc. Further detailed analyses with the data are to be continued.

5. REFERENCES

Bluestein, H.B. and S.S. Parker, 1993. Modes of isolated, severe convective storm formation along the dryline. Mon. Wea. Rev., 121, 1354–1372.

Dalal, S., Lohar, D., Sarkar, S., Sadhukhan, I., Debnath, G.C., 2012. Organizational modes of squall-type Mesoscale Convective Systems during premonsoon season over eastern India. Atmospheric research 106, 120-138

Fujita, T. T., 1958. Structure and movement of a dry front. Bull. Amer. Meteor. Soc., 39**,** 574–582.

Fuelbarg, H.E., Biggar, D.G., 1994. The preconvective environment of summer thunderstorms over the Florida Panhandle.Weather Forecast. 9, 316–326.

Ghosh A, Lohar D and Das J., 2008. Initiation of Nor'wester in relation to mid-upper and low-level water vapor patterns on METEOSAT-5 images. Atmos. Res. 87 116.135.

Hane, Carl E. and et al., 1997. Severe Thunderstorm Development in Relation to Along-Dryline Variability: A Case Study. Monthly Weather Review, vol.125.2, Pp 231-51

Karmakar, S. and M. Alam. 2006. Instability of the Troposphere Associated with Thunderstorms/nor'westers over Bangladesh during the pre-monsoon season. Mausam 57(4): 629-638.

Lohar, D and Pal, B., 1995. The effect of irrigation on pre-monsoon season precipitation over south West Bengal. India J. Climate, 8 (1995), pp. 2567–2570

Miller, R. C., 1959: Tornado-producing synoptic patterns. Bull.Amer. Meteor. Soc., 40**,** 465–472.

Mukhopadhyay P., Mahakur M., Singh H.A.K., 2009. Interaction of large scale and mesoscale environment leading to formation of intense thunderstorms over Kolkata Part I: Doppler radar and satellite observations. Journal of Earth System Science, 118, 441-46

Ono, Y., 2001. Design and adoption of household

tornado shelters to mitigate the tornado hazard in Bangladesh. PhD Dissertation, Kent State University

Onogi, K., J. Tsutsui, H. Koide, M. Sakamoto, S. Kobayashi, H. Hatsu-shika, T. Matsumoto, N.Yamazaki, H. Kamahori, K. Takahashi , S. Kadokura, K. Wada, K. Kato, R. Oyama, T.Ose, N. Mannoji, and R. Taira, 2007. The JRA-25 reanalysis. J. Meteor. Soc. Japan, 85, 369−432.

Peterson, R.E and K.C. Mehta, 1981. Climatology of Tornadoes of India and Bangladesh. Arch. Met. Geoph. Biokl., Ser.B, Vol. 29

Prasad K. 2006. Environmental and synoptic conditions associated with no'westers and tornadoes in Bangladesh – An appraisal based on numerical weather prediction (NWP) guidance products. 14th report of SAARC Meteorological Research Center, Dhaka, Bangladesh.

Rasmussen, E.N., Blanchard, D.O., 1998. A baseline climatology of sounding derived supercell and tornado forecast parameters. Weather Forecast. 13, 1148–1164.

Rhea, J. O., 1966: A study of thunderstorm formation along dry lines. J. Appl. Meteor., 5**,** 58–63.

Yamane, Y. and Hayashi, T., 2006. Evaluation of environmental conditions for the formation of severe local storms across the Indian subcontinent. Geophys. Res. Lett. 33, L17806..

Yamane Y, Hayashi T, Dewan AM, Fatima A. 2010a. Severe local convective storms in Bangladesh: Part 1. Climatology. Atmospheric Research 95: 400-406.

Yamane Y, Hayashi T, Dewan AM, Fatima A. 2010b. Severe local convective storms in Bangladesh: Part 2. Environmental conditions. Atmospheric Research 95: 407-418.

Yamane, Y., Hayashi, T., Kiguchi, M., Akter, F. and Dewan, A. M., 2012. Synoptic situations of severe local convective storms during the pre-monsoon season in Bangladesh. International Journal of Climatology,

Weisman, M.L., Klemp, J.B., 1982. The dependence of numerically simulatedconvective storms on vertical wind shear and buoyancy. Mon. Weather Rev. 110, 504–520.

Weston, K.J. 1972. The dryl-ine of Northern India and its role in cumulonimbus convection. Quarterly Journal of the Royal Meteorological Society 98 (417): 519–531

6. ACKNOWLEDGEMENTS

The JMA data used in this study was provided by way of ”Meteorological Research Consortium”, a framework for research cooperation of JMA and MSJ.

Supersaturation and diffusional droplet growth in liquid clouds

M. Pinsky[1], I.P. Mazin[2], A. Korolev[3], and A. Khain[1]

[1]Department of Atmospheric Sciences, The Hebrew University of Jerusalem, Israel
[2]Center for Earth and Space Research, George Mason University, Fairfax, Virginia
[3]Environment Canada, 4905 Dufferin St., Toronto, ON, M3H 5T4, Canada

Abstract

The process of collective diffusional growth of droplets in an adiabatic parcel is analyzed in the frame of the regular condensation approach. Closed equations for the evolution of liquid water content, droplet radius and supersaturation are derived from the mass balance equation centered with respect to the adiabatic water content. The analytical expression for the maximum supersaturation $S_{\max}$ formed near the cloud base is obtained here. Similar analytical expressions for the height $z_{\max}$ and liquid water mixing ratio $q_{\max}$ corresponding to the level where $S_{\max}$ occurs, have also been obtained. It is shown that all three variables $S_{\max}$, $q_{\max}$ and $z_{\max}$ are linearly related to each other and they all proportional to $w^{3/4}N^{-1/2}$, where *w* is the vertical velocity and *N* is the droplet number concentration. Universal solutions for supersaturation and liquid water mixing ratio are found here, which are independent of vertical velocity, droplet number concentration, temperature and pressure. The actual solutions for S and q can be obtained from the universal solutions with the help of appropriate scaling factors described in this study. The results obtained in the frame of this study provide a new look at the nature of supersaturation formation in liquid clouds. The outcomes of this work can be useful for the parameterization of cloud microphysical processes in cloud models especially for the parameterization of CCN nucleation.

1. Introduction

Description of the diffusional growth and evaporation of an ensemble of cloud particles is one of the fundamental tasks in cloud physics. The first analytical description of the condensation process of an ensemble of liquid droplets goes back to Squires (1952). A later, detailed theoretical analysis of the supersaturation equation was provided in the work of Kabanov et. al. (1971). The behavior of the supersaturation equation was analyzed in many studies (e.g. Twomey, 1959; Sedunov, 1965; Rogers, 1975; Fukuta, 1993; Khvorostyanov and Curry, 2009). Chen (1994) and Korolev and Mazin (2003) generalized this equation for a three phase system consisting of liquid droplets, ice particles and water vapor. The outcome of these works was an analytical description of supersaturation S in a vertically moving adiabatic cloud parcel.

The equation for water vapor supersaturation can be written in the form (e.g. Pruppacher and Klett, 1997):

$$\frac{dS}{dt} = A_1 \frac{dz}{dt} - A_2 \frac{dq_w}{dt} \qquad (1)$$

where $q_w(z)$ is the liquid water mixing ratio. For the sake of brevity in the forthcoming consideration we will refer to the liquid water mixing ratio q_w as water content. The first term in the right-hand side in Eq.(1) describes changes of

supersaturation of the moist air due to its adiabatic cooling or heating, whereas the second term describes the supersaturation changes caused by condensation or evaporation of water vapor by droplets.

Eq.(1) can be rewritten as (Korolev and Mazin 2003):

$$\frac{dS}{dt} = A_1 w - A_2 b N \bar{r} S \qquad (2)$$

where w is the vertical velocity; $\bar{r}$ is the average droplet radius; *N* is the droplet number concentration. In Eqs. (1-2) A_1, A_2 and b are coefficients dependent on temperature T and pressure P (hereafter, for variable notations see Appendix A). For the case when the temperature and pressure dependences of the coefficients A_1, A_2 and b are neglected and the droplet radii are assumed to be constant $\bar{r} = const$, Eq. (2) can be integrated analytically. In this case the solution $S(t)$ tends towards supersaturation:

$$S_{qs} = A_1 w \tau_p \approx \frac{A_1 w}{4\pi D N \bar{r}} \qquad (3)$$

The characteristic time of approaching of $S(t)$ to S_{qs} is determined by the time constant

$$\tau_p = \left(A_2 b N \bar{r}\right)^{-1} \approx \left(4\pi D N \bar{r}\right)^{-1} \qquad (4)$$

The case when $\bar{r} = const$ is usually referred to as *quasi-steady approximation*, S_{qs} as *quasi-steady supersaturation*, and τ_p as *time of phase relaxation*. The quasi-steady approximation plays an important role in cloud microphysics. During time τ_p the difference between initial supersaturation $S(t)$ and quasi-steady value S_{qs} decreases *e*-times. In cases when τ_p is small and does not exceed few seconds, the quasi-steady approximation can be effectively used for the estimation of the actual supersaturation in clouds, when the vertical velocity, droplet radii and concentration are known from measurements (e.g. Warner, 1968; Paluch and Knight, 1984; Politovich and Cooper, 1988; Prabha et. al., 2011). The rate of the droplet growth neglecting the surface tension and salinity corrections is described by the equation:

$$\frac{dr}{dt} = \frac{S}{Fr} \qquad (5)$$

where coefficient F depends on temperature and pressure. (2)

Substitution of Eq. (3) into Eq. (5) and successive integration leads to the linear dependence of droplet mass on height. According to this dependence droplet mass depends only on the distance between initial and final levels and does not depend on the ascend velocity (e.g. Khain et. al., 2000). The linear dependence between vertical velocity and supersaturation creates the major problem in explaining of droplet size distribution (DSD) broadening during the diffusion growth stage so that mechanisms allowing breaking such dependencies were looked for in many studies (e.g. Sedunov, 1974, Khivorostyanov and Curry, 1999).

Eq. (2) relates two time dependent variables $\bar{r}(t)$ and $S(t)$. Strictly speaking, the assumption that $\bar{r} = const$ (3) is not valid non-zero values of supersaturation result in changes in droplet size. The basis for this assumption is that when the droplets are large enough the characteristic time of changing of supersaturation, determined by the time of phase relaxation is much smaller than the characteristic time of changing of the droplet radius. This assumption is not justifiable for the cases with small droplets (e.g. in the vicinity of cloud base). In such cases a closed equation for supersaturation accounting droplet changes should be used.. Integrating the equation of the droplet growth and then substituting it into Eq. (2) yields a closed integro-differential equation with just one dependent variable:

$$\frac{dS}{dt} = A_1 w - A_2 b N S \left(\overline{r_0^2} + \frac{2}{F} \int_0^t S(t')dt' \right)^{1/2} \qquad (6)$$

This type of equation has been used for the analysis of CCN activation near cloud base (e.g. Twomey, 1959, Sedunov, 1974; Ghan et al., 1993, 1995; Bedos et al., 1996; Cohard et al., 1998; Abdul-Razzak et al., 1998; Abdul-Razzak and Ghan, 2000; Fountoukis and Nenes, 2005;

Khvorostyanov and Curry 2006; 2009; Shipway and Abel, 2010). In these studies approximate solution was looked for supersaturation cloud base maximum under different activation CCN spectra. Eq. (6) was also used in analysis of supersaturation behavior inside clouds by Korolev and Mazin, (2003).

In numerical models supersaturation and droplet sizes are calculated from a numerical integration of the relevant system of differential equations. If special precautions are not taken into account the errors in calculations of *S* and *r* may become overly large (Klaassen and Clark, 1985; Stevens et al., 1996; Grabowski and Morrison, 2008).

Closed equations for supersaturation and water content enabling its analytical treatment would be a great ease for the analysis of a general behavior of major cloud microphysical variables and development of parameterizations for numerical models. In the frame of this study we undertook efforts to derive such equations based on the water mass balance equation centered with respect to the adiabatic liquid water mixing ratio. The analysis of the obtained equations allowed (a) estimation of the range of droplet spectra broadening caused by fluctuations of supersaturation in a vertically moving adiabatic parcel; (b) find analytical expression for the maximum supersaturation and altitude of its formation above the cloud base; (c) demonstrate universality of the vertical profiles of supersaturation and water content.

The rest of study is organized as follows. In Section 2 equation of water balance as well as closed equations for supersaturation and cloud water content are derived and analyzed. In Section 3 the equation for supersaturation maximum near cloud base is derived and analyzed. In Section 4 it is shown that equations for supersaturation and liquid water content can be represented in universal non-dimensional form. In Section 5 the applicability of the approach to real cloud conditions is discussed. Conclusions can be found in Section 6.

2. Basic equations of the collective droplet growth

In the following sections we consider an ensemble of monodisperse droplets with concentration N and radii r in a vertically moving adiabatic parcel. It is assumed that the cloud droplets move with the air and stay inside the parcel beginning from cloud base. No sedimentation and coalescence is allowed. The collective droplet growth and evaporation will be considered in the frame of regular condensation, that is, the water vapor pressure and temperature fields at large distance from cloud droplets are assumed to be uniform, and all droplets grow or evaporate under the same conditions.

a. Water balance equation

The water mass balance equation derived in this section forms a basis for the entire analysis in the frame of this study.

Assuming the coefficient A_1 and A_2 are constant, the integration of Eq. (1) yields:

$$S = A_1 z - A_2 q_w + C \qquad (7)$$

where z is the height above cloud base. $C = A_2 q_{w0} + S_0$ is determined by the initial S_0 and q_{w0} at $z = 0$. Neglecting by the mass of water associated with the wetted CCN at the cloud base, it can be assumed $C = 0$ with the high accuracy.

In a moist adiabatic process, when the supersaturation adjusts to zero, $S(z) \equiv 0$, Eq.(7) yields changes of water content as:

$$q_{ad}(z) = q_{w0} + \frac{A_1}{A_2} z \qquad (8)$$

The variable $q_{ad}(z)$ in the subsequent discussion will be called “adiabatic” water content. Strictly speaking, all microphysical variables considered in the frame of this work are adiabatic due to the main assumption made at the beginning of this section. In order not to confuse $q_{ad}(z)$ with q_w, the term “adiabatic” will be applied only for the special case, when $S(z) \equiv 0$, and omitted for the cases, when $S \neq 0$.

The ratio $\beta_{ad} = A_1 / A_2$ in Eq. (8) is the adiabatic gradient of liquid mixing water ratio (e.g. Khrgian, 1969). As shown in Appendix

B the coefficients A_1 and A_2 are slow changing functions of T and P, the changes of β_{ad} remain small when z varies within few hundred meters (Appendix B). Therefore, the adiabatic water content with a high accuracy can be considered linearly related to altitude, if changes of *z* do not exceed few hundred meters. A more accurate equation for the adiabatic water content requires integration of the last term in Eq. (8) over dz (e.g. Korolev and Mazin, 1993).

In essence, Eq. (7) represents a water mass balance centered with respect to the adiabatic water content, i.e.

$$q_w + q_{sv} = q_{ad} + const \qquad (9)$$

where $q_{sv} = S/A_2$ is the mixing ratio of the supersaturated fraction of water vapor. In its traditional form, the equation of integral water balance in a vertically moving parcel is usually presented as $q_w + q_v = const$. As it is shown in the following section the mass balance equation in the form Eq. (7) enables deducing a set of equations describing microphysical parameters in a new form.

b.Supersaturation equation

This section presents derivation of a closed equation for supersaturation in a new form.

For an ensemble of monodisperse droplets with concentration N and radii *r*, water content can be written as

$$q_w = \frac{4\pi\rho_w}{3\rho_a} N r^3 \qquad (10)$$

Substituting Eq. (10) into Eq. (5) yields

$$\frac{dq_w}{dt} = BN^{2/3} S q_w^{1/3} \qquad (11)$$

where $B = \frac{3}{F}\left(\frac{4\pi\rho_w}{3\rho_a}\right)^{2/3}$. Then substituting q_w from the balance equation (7) into Eq. (11) leads to the equation for supersaturation

$$\frac{dS}{dt} = A_1 w(t) - B(A_2 N)^{2/3}(A_1 z(t) + C - S)^{1/3} S \qquad (12)$$

Eq. (12) can be rewritten for the independent variable z as:

$$\frac{dS}{dz} = A_1 - \frac{1}{w(z)} B(A_2 N)^{2/3}(A_1 z + C - S)^{1/3} S \qquad (13)$$

Eqs. (12) and (13) represent a new form of the supersaturation equation in comparison to its traditional form (e.g. Eq. (2)) introduced by Squires (1952) and its subsequent modifications. After several simple transformations Eq. (12) can be reduced to Eq. (2).

The supersaturation equation in the form of Eq. (13) is a closed differential equation with just one dependent variable. Other forms of closed equations for S were considered in Sedunov (1974), Korolev and Mazin (2003). However, the earlier representations of the closed supersaturation equations have integro-differential form, which are essentially more complex and more difficult for analysis, in comparison to Eq. (13).

Figure 1 shows comparisons of the supersaturation calculated from Eq. (13) and that deduced from a numerical integration of a full system of equations describing a collective droplet growth in adiabatic parcel. Eq. (13) was integrated assuming that the coefficients A_1, A_2 and B remain constant, whereas in the numerical model, the dependences of A_1, A_2 and B on T and P were accounted for. As seen from Fig.1, Eq. (13) accurately depicts the changes of supersaturation and it agrees well with the numerically modeled supersaturation. In this particular case the difference between the modeled supersaturation and that calculated from Eq. (13) does not exceed few percent. It should be noted that neglecting the dependences of the coefficient A_1, A_2 and B on T and P gives quite accurate solutions for S within the vertical scale of the order of few hundred meters. However, for the displacements Δz beyond one kilometer these dependences should be accounted for.

c. Limiting supersaturation

As seen from Fig.1 and Eq. (13) that after passing its maximum, the

supersaturation is monotonically decreasing with altitude towards

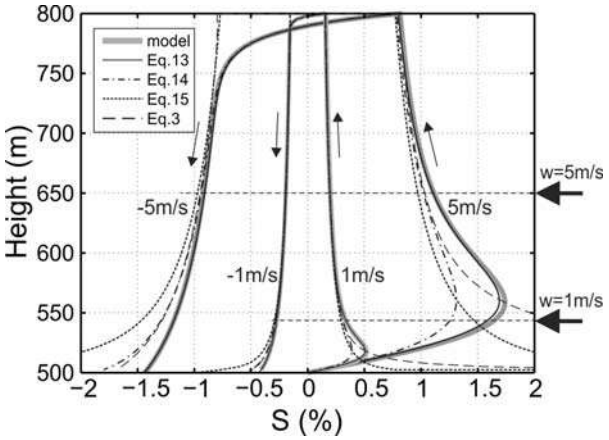

Fig 1. *Vertical changes of supersaturation in a cloud parcel ascending with and descending with* $w = \pm 5\,m/s$ *and* $w = \pm 1\,m/s$. *The droplet concentration is* $N = 100\,cm^{-3}$. *The supersaturation was calculated from numerical simulation of the collective droplet growth (solid gray); non-linear Eq. (13) (solid thin); linearized Eq. (14) (dashed-dotted); quasi-steady approximation by Eq. (3) (dashed); limiting approximation by Eq. (15) (dotted). Initial conditions are:* T_0*=10°C,* P_0*=950mb,* $S_0 = 0$, r_0*=0.01* μm. *The horizontal, bolded arrows on the right-hand side indicate the levels above which the condition in Eq. (18) is valid, and the quasi-steady approximation is justified.*

zero. Therefore, above some level, the supersaturation becomes $S << A_1 z + C$. At that point, S can be neglected inside the brackets on the right-hand side in Eq. (13). In this case, Eq. (13) can be linearized resulting in:

$$\frac{dS}{dz} = A_1 - B(A_2 N)^{2/3} \frac{(A_1 z + C)^{1/3}}{w(z)} S \quad (14)$$

Since S tends to zero with increasing of the distance above cloud base, the left hand term becomes much smaller than any of two terms on the right hand side. In this case, after neglecting the term $\frac{dS}{dz}$ in Eq. (14), it yields:

$$S_{\lim} = \frac{A_1 w(z)}{B(A_2 N)^{2/3}(A_1 z + C)^{1/3}} \quad (15)$$

Taking into account Eq. (7) and that $\beta_{ad} = A_1 / A_2$, at $C = 0$ Eq. (15) can be rewritten in a form

$$S_{\lim} = \frac{\beta_{ad} w(z)}{BN^{2/3} q_{ad}^{1/3}} = \frac{\beta_{ad}^{2/3} w(z)}{BN^{2/3} z^{1/3}} \quad (16)$$

Eq. (16) represents a limiting (or asymptotic) supersaturation forming in adiabatic cloud parcel. After substitution Eq. (10) into Eq. (16), it can be transformed into a form,

$$S_{\lim} = \frac{A_1 w}{A_2 b N r_{ad}} \quad (17)$$

Here r_{ad} is the adiabatic droplet radius related to the adiabatic water content q_{ad} as in Eq. (10). Eq. (17) coincides with the expression for the quasi-steady supersaturation Eq. (3), with the only difference, that the droplet radius r in Eq. (3) is replaced by its adiabatic value r_{ad} in Eq. (17). The analysis of derivations of Eqs. (3) and (15) shows that the aforementioned difference is a result of linearization applied in Eq. (14).

As seen from Eq. (16) for the case of uniform ascent, $S_{\lim}$ decreases with height as $z^{-1/3}$. Since $S_{\lim}$ approximates $S(z)$, then $S(z)$ changes as $z^{-1/3}$, as well. The same dependence $S(z)$ was obtained in Sedunov (1974) and Fukuta (1993), but in a much more challenging way.

Fig. 1 shows comparisons of the supersaturation calculated from the linearized Eq. (14) and the modeled one. As seen from Fig. 1 the linearized Eq. (14) approximates the exact solution well for $z > 30$m at w=1m/s and $z > 150$m at w=5m/s above the level of the supersaturation maximum. When these altitudes are translated into time required for the parcel to reach them, it turns out that this time remains approximately the same (i.e. 30s for this specific case). Eq. (14) also leads to a formation of a local supersaturation maximum near the cloud base, but this maximum is lower than that obtained from the numerical model.

Fig.1 also shows that the limiting supersaturation $S_{\lim}$ (Eq. (16)) asymptotically approaches $S(z)$ with altitude. Comparisons between S_{qs} (Eq. (3)) and $S_{\lim}$ (Eq. (16)) in Fig. 1 show that S_{qs} approaches $S(z)$ faster as compared to $S_{\lim}$. Such behavior is a result of using adiabatic values for liquid water or droplet radii in Eqs. (16) and (17) respectively.

The large deviation of S_{qs} from $S(z)$ near the cloud base in Fig.1 is a consequence of the limitations of the quasi-steady approximation. Indeed, according to Eq. (3) S_{qs} tends to infinity at cloud base since droplet size tends to zero. The condition of applicability of S_{qs} for estimation of supersaturation was presented by Korolev and Mazin (2003)

$$G\frac{|w|}{r^4N^2} << 1 \qquad (18)$$

Here, G is the coefficient dependent on P and T (see Appendix A). Inequality (18) was derived from the condition that droplet radius should not change significantly during time changes of supersaturation.

The horizontal, bolded arrows on the right hand side in Fig.1 indicate the altitude below which $G\frac{|w|}{r^4N^2} > 0.1$, i.e. the altitude below which condition (18) is not satisfied. In other words, the quasi-steady approximation is justified only above the levels indicated by the horizontal, bolded arrows corresponding to each velocity. As seen from Fig.1, below the indicated levels, the deviation of S_{qs} and $S_{\lim}$ from $S(z)$ is significant, whereas above these levels the agreement between S_{qs}, $S_{\lim}$ and $S(z)$ improves and the difference between them does not exceed 10%.

d. Water content and droplet radius equations

This section present derivation and analysis of a closed equation for water content.

After substituting the mass balance equation (7) into Eq. (11) a closed equation for q_w is obtained:

$$\frac{dq_w}{dz} = -\frac{BN^{2/3}}{w(z)}\left(A_2 q_w^{4/3} - (A_1 z + C)q_w^{1/3}\right) \qquad (19)$$

Analysis of Eq. (19) shows that, when height is large enough, then each of the two terms in the right-hand side become significantly larger than $\frac{dq_w}{dz}$. The balance between these two large terms leads to a linear dependence of q_w on height, so that for large z the solution of Eq. (19) is reduced to Eq. (8), i.e. when $q_w(z) = q_{ad}(z)$.

Eqs. (10) and (19) yield differential equations for the changes of *r*:

$$w(z)\frac{dr}{dz} = -\frac{4\pi A_2 \rho_w N}{3\rho_a F} r^2 + \frac{(A_1 z + C)}{Fr} \qquad (20)$$

At heights large enough, when *r* only slowly changes with height, solutions of Eq. (20) can be approximated by the adiabatic dependence:

$$r(z) = \left(\frac{3\rho_a (A_1 z + C)}{4\pi A_2 \rho_w N}\right)^{1/3} = \left(\frac{3q_{ad}(z)}{4\pi\rho_w N}\right)^{1/3} \qquad (21)$$

After substitution, Eq. (10) into Eq. (21) turns into a trivial equality $r(z) = r_{ad}(z)$.

Figure 2 shows the changes of water content and droplet sizes computed in Eqs. (19) and (20), respectively, for two different vertical velocities. The initial conditions were kept the same as for the case in Fig. 1. As seen from Fig. 2 the integration of Eqs. (19) and (20) provides a good agreement with q_w and *r*, respectively, calculated from the numerical model. Fig. 2a also shows the changes of the mixing ratio of the supersaturated or undersaturated fraction of water vapor q_{vs}. One can see that the deviation of r from the adiabatic value is largest near the cloud base, where the supersaturation is maximal and it decreases with increasing altitude. As it is

seen from Fig. 2 the deviation of q_w and r from q_{ad} and r_{ad}, respectively, increases with the increase of vertical velocities.

It is worth noting that S, q_w and r are irreversible in ascending and descending parcels. In ascending parcels supersaturation is positive ($S > 0$), whereas in descending parcels it is negative ($S < 0$). Substituting

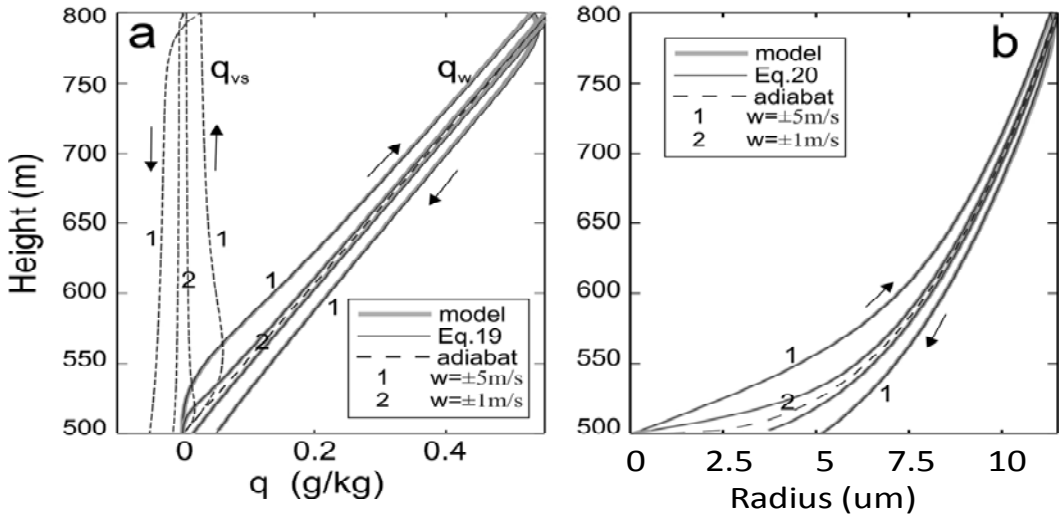

Fig. 2. *Vertical changes of (a) liquid water q_w Eq. (19) (solid lines) and supersaturated vapor q_{vs} mixing ratios (dashed lines) and (b) droplet radius calculated from Eq. (20). The calculations were performed from the vertical velocity w=±1m/s and ±5m/s. Arrows indicate calculations corresponding ascending and descending parcels. The initial conditions are the same as in Fig. 1.*

these inequalities into Eq. (7) yields the inequality $q_w(z)\big|_{w(z)>0} < q_{ad}(z)$ for ascending parcels and for descending parcels $q_w(z)\big|_{w(z)<0} > q_{ad}(z)$. It should be noted that the inequalities obtained above are valid at the time scales $t > \tau_p$. At shorter time scales they may be reversed. For example, in Fig.1, when the cloud parcel changed its direction from ascent to descent at h=800m, for some time ($t \sim \tau_p$) the supersaturation remained positive during its descent. From balance Eq. (7) it follows that $q_w(z)\big|_{w(z)>0} < q_w(z)\big|_{w(z)<0}$. It means that for the same altitude z, liquid water in ascending parcels is always lower that that in the descending ones. The same relationship refers to the droplet radii as well. The last inequality also follows from two inequalities presented above.

This type of behavior is a result of the delay of droplet growth response to the change in supersaturation. Droplets reach the maximum size in the upper point of the parcel ascent where supersaturation is zero or close to zero. If the release and absorption of the water vapor by the liquid droplets, in order to compensate supersaturation, were to occur instantly (i.e. $S \equiv 0$), then the condensational processes in ascending and descending parcels would be reversible and the above inequalities would turn into equalities.

The condensational inertia of the diffusional processes results in spatial inhomogeneities of the microphysical parameters. The horizontal fluctuations of

supersaturation can be estimated as the difference between S forming at the same altitude in the ascending and descending parcels, i.e. $\Delta S = S(z)\big|_{w(z)>0} - S(z)\big|_{w(z)<0}$. Substituting Eqs.(16) and (17) into this expression and assuming that $\Delta w = 2|w|$, yields

$$\Delta S = 2|S_{\lim}| = \frac{2\beta_{ad}^{2/3}|w|}{BN^{2/3}z^{1/3}} = \frac{2\beta_{ad}|w|}{bNr_{ad}} \qquad (22)$$

The spatial fluctuation of droplet radii can be estimated from the difference in the droplet radii cubes in ascending and descending parcels at the same altitude. Thus, substituting Eq. (7) into Eq.(10) with the following differentiating gives

$$\Delta\left(r^3\right) = \frac{3}{4\pi\rho_w A_2}\frac{|\Delta S|}{N} \qquad (23)$$

Assuming that $\Delta r << r$ Eq. (23) can be rewritten as

$$\frac{\Delta r}{r} = \frac{1}{3}\frac{|\Delta S|}{A_2 q_w} \qquad (24)$$

The ratio $\frac{\Delta r}{r}$ can be used as a surrogate for the variation coefficient, which usually referred to as droplet size spectrum relative dispersion and is equal to the ratio of DSD width σ_r to the mean radius $\overline{r}$. In clouds the variation coefficient changes from approximately 0.1 to 0.6. In-situ observations suggest no significant changes of the variation coefficient with height (Politovich, 1993; Martin et. al., 1994; Prabha et. al., 2011).

The ratio $\frac{\Delta r}{r}$ in Eq. (24) was used for estimation of the difference of potential supersaturation in cloud parcels required to obtain a variation coefficient obtained from in-situ observations in different clouds. The estimations presented in **Table. 1** are performed for $\frac{\Delta r}{r} = 0.2$.

As seen from Table 1, the values of $|\Delta S|$ required to get such variation coefficient are much higher than the characteristic values of supersaturation existing in clouds. Thus, for the vertically moving adiabatic parcels having the same initial conditions, the diffusional growth and evaporation of droplets cannot explain formation of broad DSD usually observed in clouds.

Cloud type	N, cm^{-3}	q_w, gm^{-3}	r, μm	$\lvert\Delta S\rvert$, %
Deep maritime Cu (Andreae et al., 2004)		**2.0**	**16.8**	**28.9**
Maritime stratocumulus (e.g., Martin et al, 1984; Stevens et al, 2003; 2005; Magaritz et al., 2009)	**100**	**0.5**	**10.6**	**7.2**
Weak stratocumulus (Stevens et al, 2003, 2005)	**100**	**0.2**	**7.8**	**2.9**
Deep continental Cu (Andreae et al, 2004; Prabha et al, 2011)	**1000**	**3**	**8.9**	**43.2**

Tab. 1. *Difference in supersaturation needed to obtain spectrum dispersion equal to 0.2. The parameters used in the table are chosen according to the references presented.*

Earlier the same conclusion was obtained by Mazin and Smirnov (1969) and Bartlett and Jonas (1972).

In case of vertical oscillations the ratio $\frac{\Delta r}{r}$ may serve as a measure of non-reversibility of microphysical parameters in adiabatic cloud parcels experiencing cycling ascents and descents. Estimations of the value of the ratio $\frac{\Delta r}{r}$ show that it reaches its maximum near the cloud base, where it can reach significant values. This effect is clearly seen in Fig. 2. At levels above the cloud base supersaturation maximum $\frac{\Delta r}{r}$ typically does not exceed 0.1. Substituting Eq. (22) into Eq. (24) yields an estimate of the droplet radii fluctuations

$$\Delta r = \frac{2|w|}{3A_2^2 bNz} = \frac{\rho_a \beta_{ad} |w|}{2\pi\rho_w A_2 bN^2 r_{ad}^3} \qquad (25)$$

For the constant altitude z Eq. (9) yields the relationship between fluctuations of liquid water and mixing ratio of the supersaturated vapor as $\Delta q_w = -\Delta q_{vs}$. Therefore, fluctuations Δq_w can be estimated as $\Delta q_w = \frac{2}{A_2}|S_{\lim}|$ (Korolev, 1995).

e. Vertical changes of the phase relaxation time

The coefficient in front of S in the right hand side of Eq. (12) has a meaning of inverse phase relaxation time (see Eq. (4)). Bringing up the similarity of Eq. (2) and Eq. (12), one can conclude that the expression $B(A_2N)^{2/3}(A_1z(t)+C-S)^{1/3}$ in Eq. (12) has the same meaning as in Eq.(2), i.e. an inverse phase relaxation time:

$$\tau_{pr}^{-1} = B\left(A_2N\right)^{2/3}\left(A_1z + C - S\right)^{1/3} \qquad (26)$$

The value of τ_{pr} in Eq. (26) coincides with τ_p from Eq. (4), for the case of monodisperse droplets i.e. when $\bar{r} = \bar{r}_3$, where $\bar{r}_3$ is the mean cubic radius of droplets.

Assuming $C = 0$ and substituting Eq. (16) into Eq.(26) yields

$$\tau_{pr}^{-1} = B\left(A_2N\right)^{2/3}\left(A_1z - \frac{\beta_{ad}^{2/3} w(z)}{BN^{2/3} z^{1/3}}\right)^{1/3} \qquad (27)$$

For the altitudes $z >> S/A_1$, when the second term in the brackets can be neglected, Eq. (27) turns into

$$\tau_{pr}^{-1} = B\left(A_2N\right)^{2/3}\left(A_1z\right)^{1/3} \qquad (28)$$

Figure 3 shows changes of τ_{pr} versus the height of cloud parcels with different droplet concentrations ascending through a cloud base with w=1m/s calculated from Eq. (27). The dashed portions of the curves in Fig. 3 indicate the regions where the condition in Eq. (18) for the quasi-steady approximation is not satisfied. The solid portion of the curves with a good approximation follows $z^{-1/3}$ law as in Eq. (28).

3. Maximum of supersaturation

An important feature of Eq. (13) is that it allows for the estimation of the supersaturation maximum $S_{\max}$ and the height $z_{\max}$ corresponding to the level, where

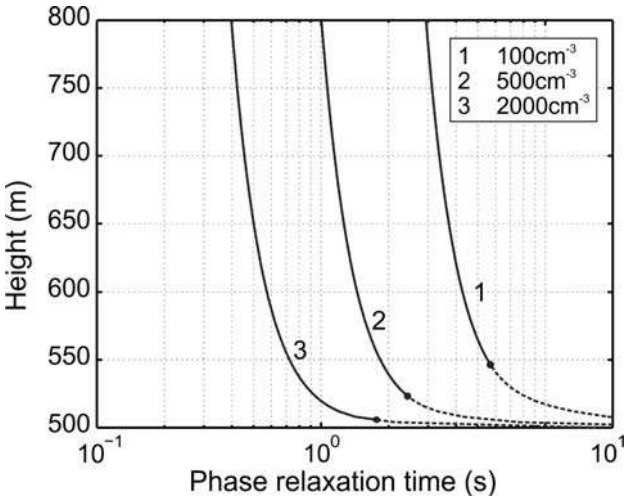

Fig. 3 *Changes of $\tau_{pr}(z)$ calculated from Eq. (27) for cloud parcels ascending w=1m/s and having different concentrations. The initial conditions are the same as in Fig.1.*

$S_{\max}$ occurs. For simplicity, assume $C = A_1q_0 + S_0 = 0$. Then introduce a non-dimensional altitude $h = A_1z$ and a non-dimensional parameter

$$R = \frac{BN^{2/3}A_2^{2/3}}{wA_1} = \frac{3}{FA_1w}\left(\frac{4\pi\rho_w NA_2}{3\rho_a}\right)^{2/3}.$$

Using new variables, Eq. (13) can be rewritten in the form

$$\frac{dS}{dh} = 1 - R(h-S)^{1/3}S \qquad (29)$$

with the initial condition $S\big|_{h=0} = 0$ at the cloud base.

An inspection of Eq. (29), suggests, that the solution $S(h)$ depends on the sole parameter R. The condition $\left.\frac{dS}{dh}\right|_{h=h_{\max}} = 0$ in Eq. (29) yields an expression relating $S_{\max}$ and $h_{\max}$:

$$1 - R(h_{\max} - S_{\max})^{1/3} S_{\max} = 0 \qquad (30)$$

Figure 4 shows the dependences $S_{\max}(R)$ and $h_{\max}(R)$ calculated from the numerical solutions of Eq. (29) for different *R*.

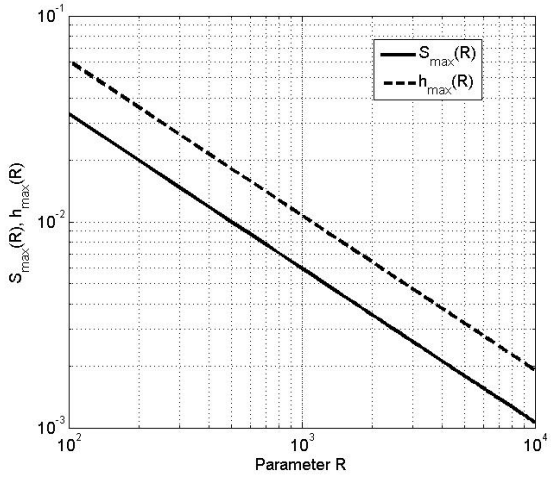

Fig. 4. *Dependences* $S_{\max}(R)$ *and* $h_{\max}(R)$.

Analyses of the results of the calculations shows that $S_{\max}(R)$ and $h_{\max}(R)$ obey the power law with high accuracy. Therefore, looking for a solution to Eq. (30) in a form $S_{\max}(R) \propto R^{\alpha}$ and $h_{\max}(R) \propto R^{\alpha}$ one can get:

$$S_{\max}(R) = C_1 R^{-3/4};\ h_{\max}(R) = C_2 R^{-3/4};$$
$$z_{\max}(R) = \frac{C_2}{A_1} R^{-3/4} \qquad (31)$$

where coefficients $C_1 = 1.058$ and $C_2 = 1.904$ were obtained from the diagram in Fig. 4. It should be noted that the value of the coefficients C_1 and C_2 are linked just to the type of the differential equation Eq. (29) and they are not related to any physical variables (i.e. T, P, N, w, etc).

Substituting R and Eq. (7) in Eqs. (31) enables deriving the dependences of $S_{\max}$, $h_{\max}$ and $q_{\max}$ versus droplet concentration and vertical velocity:

$$S_{\max} = C_1 \left(\frac{FA_1}{3}\right)^{3/4} \left(\frac{3\rho_a}{4\pi\rho_w A_2}\right)^{1/2} w^{3/4} N^{-1/2} \quad (32)$$

$$z_{\max} = C_2 A_1^{-1/4} \left(\frac{F}{3}\right)^{3/4} \left(\frac{3\rho_a}{4\pi\rho_w A_2}\right)^{1/2} w^{3/4} N^{-1/2} \quad (33)$$

$$q_{\max} = \left(\frac{C_2}{C_1} - 1\right) \left(\frac{FA_1}{3}\right)^{3/4} \left(\frac{3\rho_a}{4\pi\rho_w A_2^3}\right)^{1/2} w^{3/4} N^{-1/2} \quad (34)$$

Eqs. (32) to (34) show that all three variables $S_{\max}$, $h_{\max}$ and $q_{\max}$ are proportional to $w^{3/4} N^{-1/2}$. The conclusion that $S_{\max} \propto w^{3/4} N^{-1/2}$ was also obtained by Fukuta (1993), although in his study unjustified assumptions have been applied when deriving this relationship. As a result, in Fukuta (1993) the coefficients C_1 and C_2 are missed in formulations for $S_{\max}$ and $t_{\max}$ (equivalent of $z_{\max}$).

Eqs. (32) to (34) allow important conclusion about the universal nature of the following rations:

$$\frac{S_{\max}}{A_1 z_{\max}} = \frac{C_1}{C_2} = 0.556;$$
$$\frac{S_{\max}}{A_2 q_{w\ \max}} = \frac{C_1}{C_2 - C_1} = 1.25 \qquad (35)$$

In other words, $S_{\max}$, $z_{\max}$ and $q_{\max}$ are linearly related to one another. This finding was verified with the help of a numerical simulation of the droplet growth in the ascending adiabatic parcel. The diagrams in **Figure 5** show that the modeled relationships between $S_{\max}$, $z_{\max}$ and $q_{\max}$ follow Eq. (35) with high accuracy for a wide range of vertical velocities w and droplet number concentrations N, which occur in the tropospheric liquid clouds.

One of the interesting features of the initial stage of the cloud formation, which follows from Eqs. (35), is that at the level of supersaturation maximum, 45% of potentially

condensed water exists in liquid phase, whereas the remaining 55% exists in a form of supersaturated vapor.

4. Universal profiles for supersaturation and water content

Substitution of Eq. (7) into Eq. (29) yields a dimensionless equation for water content:

$$\frac{dQ}{dh} = R(h - Q)Q^{1/3} \qquad (36)$$

Here $Q = A_2 q_w$ is the dimensionless water content. The dimensionless equations for S and Q (Eqs. (29) and (36) respectively) in a form dependent on just one coefficient, along with the linear relationships of Eqs. (35) are suggestive of the existence of universal equations for S and q_w.

Thus, introducing new variables

$$S^* = SR^{3/4}, h^* = hR^{3/4}, Q^* = QR^{3/4} \qquad (37)$$

and then substituting them into Eqs.(29) and (36) yields normalized equations for S and q_w, which do not contain any parameters

$$\frac{dS^*}{dh^*} = 1 - (h^* - S^*)^{1/3} S^* \qquad (38)$$

$$\frac{dQ^*}{dh^*} = \left(h^* - Q^*\right) Q^{*1/3} \qquad (39)$$

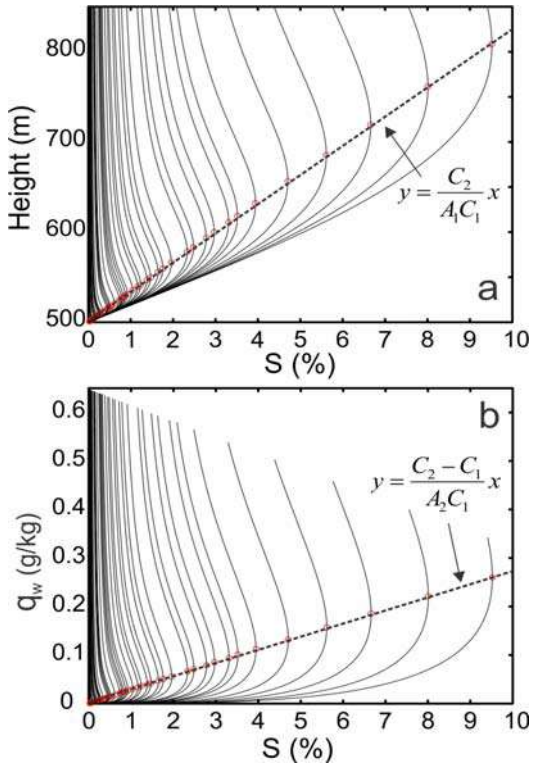

Fig. 5. *Modeled dependences (a) $S(z)$ and (b) $S(q)$ calculated for various combinations of vertical velocities of ascending parcel and droplet number concentrations from the respective ranges $0.01m/s \le w \le 10m/s$ and $10cm^{-3} \le N \le 1000cm^{-3}$. The red circles indicate the locations of $S_{\max}$. The calculations were performed for the initial conditions: T_0=10°C, P_0=950mb, $S_0 = 0$, r_0=0.01 μm.*

The solutions $S^*(h^*)$ and $Q^*(h^*)$ are universal and valid for any droplet concentration, vertical velocity, temperature and pressure. **Figure 6** shows the behavior of universal $S^*(h^*)$ and $Q^*(h^*)$.

As seen from Fig. 6 the maximum of supersaturation $S^*_{\max} = C_1$ and altitude $h^*_{\max} = C_2$ remains constant. In order to obtain an actual $S(z)$, $q_w(z)$ for specific w, N, T and P the normalized solutions $S^*(h^*)$ and $Q^*(h^*)$ should be scaled using $S_{\max}$, $q_{\max}$

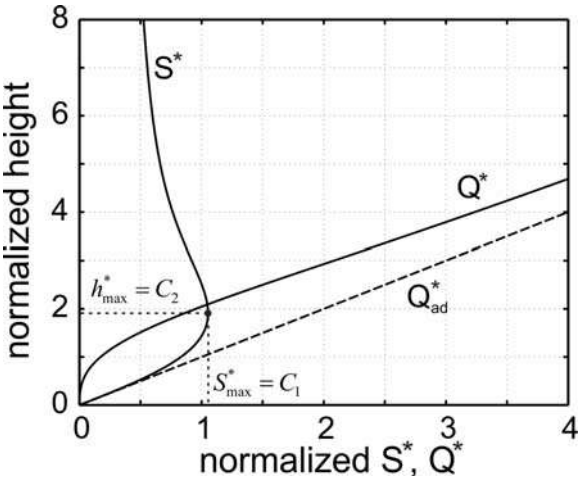

Fig. 6. *Normalized supersaturation and liquid mixing ratio versus normalized height.*

and $h_{\max}$ from Eqs. (31) to (34) and the corresponding definitions of Q and h. For the new variables normalized adiabatic water content is

$$Q^*_{ad} = h^* \qquad (40)$$

It should be noted that Eqs. (38) and (39) are dependent, and each can be derived from the other using the mass balance equation (7) written in the normalized from as

$$S^* + Q^* - h^* = 0 \qquad (41)$$

The existence of universal profiles of supersaturation and water content reflect, supposedly, the existence of deep laws of diffusional droplet growth.

5. **Applicability of the approach to real cloud conditions**

There are few simplifications underlying the derivation of the equations describing changes of supersaturation, water content and droplet size. The purpose of this section is to consider consequences and limitations in use of the obtained equations related to three most significant of those simplifications.

The first simplification is related to the assumption that the coefficients A_1, A_2 and F in Eqs.(1) and (5) are constant and their dependences of T and P were neglected. As it was discussed in section 2b this assumption provides an accurate solutions for S, q and r with a few percent accuracy for vertical motion within the several hundred meters.

The second simplifications was related to neglecting corrections in the droplet curvature and salinity in the droplet growth equation Eq.(5) A more accurate treatment of the diffusional droplet growth requires accounting this corrections and it yields an equation (e.g. Pruppacher and Klett, 1997)

$$r\frac{dr}{dt} = \frac{1}{F}\left(S - S_{eq}\right) = \frac{1}{F}\left(S - \frac{A}{r} + \frac{Er_N^3}{r^3}\right) \qquad (42)$$

where r_N is the dry radius of soluble fraction of aerosol, that plays a role of a cloud condensation nuclear (CCN); and A, E are the coefficients (see Appendix 1). In Eq. (42) $S_{eq}(r)$ is the equilibrium supersaturation (Kohler equation)

$$S_{eq}(r) = \frac{A}{r} - \frac{Er_N^3}{r^3} \qquad (43)$$

Substituting Eq. (42) in Eq. (13) instead of Eq. (5) yields

$$\frac{dS}{dz} = A_1 - \frac{1}{w}B(A_2N)^{2/3}(A_1z + C - S)^{1/3}(S - S_{eq}) \qquad (44)$$

Using the balance equation Eq. (7) one can represent droplet radius and then equilibrium supersaturation as a function of z and S, i.e. $S_{eq} = S_{eq}(z, S)$ and thus, closing Eq. (44).

Figure 7 shows vertical changes of supersaturation calculated for monodisperse CCN with radii of 0.02 and 0.1 μm. Vertical profiles of $S_{eq} = S_{eq}(z, S)$ for these cases are presented in Fig.7 as well.

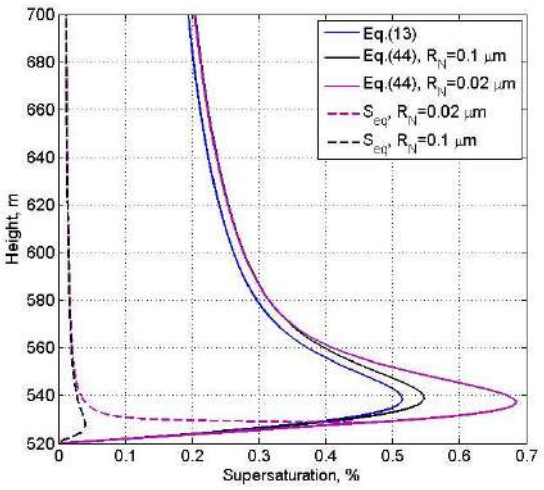

Fig. 7. *Vertical profiles of supersaturation and equilibrium supersaturation calculated for monodisperse CCN with radii 0.02 μm and 0.1 μm. The profile of supersaturation neglecting the corrections on the droplet curvature and salinity calculated from Eq. (13) is also presented.*

For large CCN the correction of the salinity cancels the correction of the curvature, which result in that $S_{eq} << S_{\max}$ and vertical profiles of supersaturation calculated using Eq. (13) and Eq. (44) turn out to be close to each other. For small CCN, the correction

on curvature dominates over the correction on salinity, which results in large maximum of S_{eq} near the cloud base and more significant difference in solutions of Eq. (13) and Eq. (44) at the level of $S_{\max}$. Above level of maximum supersaturation ($z>z_{max}$) the difference between the solutions of Eq. (13) and Eq. (44) decreases. Since the chemical term in expression for S_{eq} is proportional to r^{-3}, and the curvature term is proportional to r^{-1}, for $z>>z_{max}$ the corrections on salinity become small and the changes of S_{eq} will be mainly determined by the curvature term. In other words for $z>>z_{max}$ *S(z)* becomes insensitive to CCN and its changes can be accurately described by Eq.(13).

In order to estimate the effect of curvature and salinity on $S_{\max}$ and $z_{\max}$ we introduce the residual supersaturation $\tilde{S} = S - S_{eq}$ and non-dimensional height $\tilde{h} = A_1 z - S_{eq}$. Similar to Eq. (30) the equation for supersaturation maximum can be written in the form

$$1 = R(\tilde{h}_{\max} - \tilde{S}_{\max})^{1/3}\tilde{S}_{\max} \qquad (45)$$

The solution of Eq. (45) has the same form as that for Eq. (31), i.e.

$$\tilde{S}_{\max}(R) = C_1 R^{-3/4};\ \ \tilde{h}_{\max}(R) = C_2 R^{-3/4} \qquad (46)$$

Eqs. (46) yield

$$S_{\max} = C_1 R^{-3/4} + S_{eq}(z_{\max});$$
$$h_{\max}(R) = C_2 R^{-3/4} + S_{eq}(z_{\max}) \qquad (47)$$

where $S_{eq}(z_{\max})$ is the value of S_{eq} at $z = z_{\max}$. Thus for a more accurate estimation of $S_{\max}$ and z_{max} one should introduce corrections in Eqs. (31-32) represented by the second terms in right hand side of Eq. (47) calculated for aerosol radius r_N. Note that this correction becomes significant when CCN size spectrum consists only of small CCN.

The third simplification is related to utilizing the monodisperse model of size distribution. To estimate the limitations of this simplification a set of numerical simulations with the parcel model described by Pinsky and Khain (2002) were conducted. The main feature of the model is an accurate descriptions of diffusional growth of wetted aerosols and droplets. To describe the DSD of particles (non-activated aerosols and droplets) 2000 mass bins are used within the range from 0.01 μm to 2000 μm. The grid has resolution 0.001 μm for small particles and it gradually decreases down to 8 μm for large particles. Such resolution is sufficient fro explicit description of the process of separation of all particles into growing droplets and non-activated wetted aerosols. Accordingly, process of droplet nucleation is treated directly without using any parameterization procedures. To describe the diffusion growth, a non-regular grid with a variable set of masses is used. The masses related to corresponding bins are shifted with time according to the equation of diffusion growth. Correspondingly, no remapping is applied, i.e. no artificial spectrum broadening is introduced when droplet growth by diffusion is calculated. The time step of 0.005 s was used to calculate diffusion growth of drops and aerosol particles. The size distribution CCN is a sum of three log-normal modes, representing small, intermediate and larger aerosol particles (Respondek et. al., 1995). Simulations were performed for the vertical velocities of 1, 3 and 5 m/s. The total CCN concentration was selected such way in order to produce droplet concentrations of approximately 100, 200 and 500 cm^{-3}.

(46)

(47)

The main purpose of this examination is to identify the limitations of the universality of the supersaturation presentation described by Eq. (31), i.e. the applicability of the approach in a more general case of polydisperce CCN.

Figure 8 (left) shows vertical profiles of supersaturation calculated using the bin model. One can see that the profiles

resemble those plotted in Fig. 1 and Fig.5a. For instance, $S_{\max}$ and $z_{\max}$ are related linearly (dashed line). The normalized profiles are plotted in right panel of Fig. 8. One can see that the separation of the normalized profiles turned out to be low justifying the proposed approach. The difference between the normalized values of supersaturation at the level of supersaturation maximum is less than 5-10% for most simulations. The exception is the case with low vertical velocity of 1 m/s and high droplet concentration of 500 cm^{-3}. However, even in the latter case the maximum of the normalized supersaturation is located at nearly the same normalized height, what was obtained using Eq. (31) for monodisperse case. The obtained dispersion between the curves is largely the effect of the curvature and chemical terms as in the monodisperse case. Note that the case with low vertical velocity and high droplet concentration is not typical of real clouds.

The closeness of the supersaturation profiles calculated for the monodisperse and

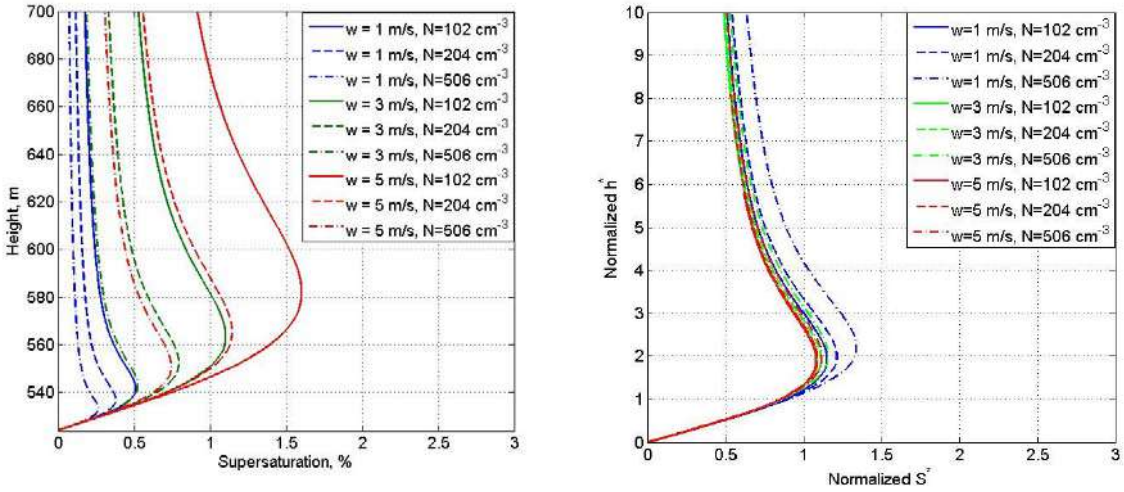

Fig. 8. *Left: Vertical profiles of supersaturation calculated using the parcel model (Pinsky and Khain, 2000) with explicit calculations of aerosols activation and of diffusion drolpet growth. Right: The same supersaturation profiles calculated in the normalized form (see text)*

polydisperse size distributions can be interpreted in the way that supersaturation profile is determined by "equivalent" CCN with large sizes. **Figure 9** shows the dependencies of minimal, mean, mean volume and effective radii of aerosols on concentration of CCN activated at w=1 m/s (left) and 3 m/s (right). One can see that in spite of the fact that along large CCN, small CCN are also activated, the mean volume radius of activated CCN is about of 0.2 μm. One can introduce effective or equivalent CCN size of monodisperce CCN in such a way that effect of CCN of this size on supersaturation and drop concentration is equivalent to that of polydisperse CCN. It is reasonable to assume that the effective CCN size is close to the mean volume radius of activated CCN. In this case, we can conclude that the effect of curvature and chemical terms is not substantial in real CCN spectra and that the effect of polydisperse CCN on supersaturation can be approximated using the approach developed in the present study. The exception is the case when CCN size distribution contains only small CCN. Thus, the proposed method and corresponding conclusions are applicable to a wide range of conditions in real clouds.

It should be toted, that simplified equation for diffusional growth Eq.(5) was used in many studies for calculation of supersaturation maximum (Twomey1959;

Ghan et al., 1993, 1995; Bedos et al., 1996; Cohard et al., 1998; Abdul-Razzak et al., 1998; Abdul-Razzak and Ghan, 2000; Fountoukis and Nenes, 2005; Shipway and Abel, 2010). The difference with our approach is that in these studies the simplified equation was used to describe diffusion growth of droplets after nucleation, i.e. at some height above cloud base, which is quite small for "equivalent" CCN size.

Conclusions

The main outcomes of this study can be formulated in the following way:

1. A new form of the closed equations for supersaturation, water content and droplet radii were obtained (i.e. Eqs.(13), (19), (20)) based on the consideration of the water mass balance equation centered with respect to the adiabatic liquid water mixing ratio.

2. An analytical expression for the supersaturation maximum $S_{\max}$ forming in the vicinity of the cloud base has been obtained here. Similar expressions for the height $h_{\max}$ and liquid water mixing ratio $q_{\max}$

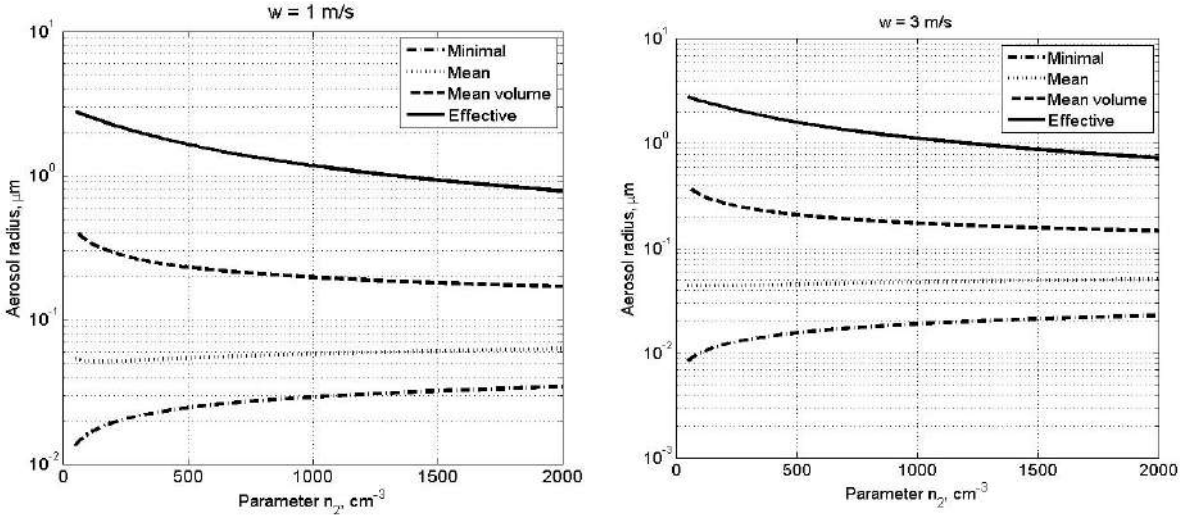

Fig. 9. *Dependencies of minimal, mean, mean volume and effective radii of aerosols on CCN concentration in the second CCN mode at w=1 m/s (left) and 3 m/s (right).*

corresponding to this level of $S_{\max}$ were obtained here as well. It is shown that the values of all three variables $S_{\max}$, $h_{\max}$ and $q_{\max}$ are linearly related to each other and are all proportional to $w^{3/4}N^{-1/2}$.

3. The approach developed in the frame of this study enabled obtaining universal solutions for supersaturation $S^*(h^*)$ and liquid water mixing ratio $Q^*(h^*)$. These solutions are independent of *w, N, T* and *P*. The actual solutions $S(z)$ and $q_w(z)$ can be obtained from $S^*(h^*)$ and $Q^*(h^*)$ using scaling coefficient from Eqs. (37).

The results obtained in this study provide a new look at the nature of supersaturation formation in liquid clouds. The findings of this work open the door for an entirely new way of parameterization of cloud microphysical processes and specifically for the parameterization of CCN nucleation in cloud models. The first step in this direction is done in study by Pinsky et. al. (2012).

Acknowledgements:

This research was supported by the Office of Science (BER), US Department of Energy Award DE-SC0006788 and the Binational US-Israel Science foundation (grant 2010446)

Appendix A. List of Symbols

Symbol	Description	Units
A	$\frac{2\sigma_w}{\rho_w R_v T}$	m
A_1	$\frac{g}{R_a T}\left(\frac{L_w R_a}{c_p R_v T}-1\right)$	m^{-1}
A_2	$\frac{1}{q_v}+\frac{L_w^2}{c_p R_v T^2}$	-
B	$\frac{3}{F}\left(\frac{4\pi\rho_w}{3\rho_a}\right)^{2/3}$	$m^2\ s^{-1}$
b	$\frac{4\pi\rho_w}{F\rho_a}$	$m^2\ s^{-1}$
c_p	specific heat capacity of moist air at constant pressure	$J\ kg^{-1}K^{-1}$
C_1	1.058 constant coefficient	
C_2	1.904 constant coefficient	
D	coefficient of water vapor diffusion in the air	$m^2\ s^{-1}$
E	$\frac{\nu_a \Phi_a \delta_s M_w \rho_a}{M_{sol}\rho_w}$	-
e	water vapor pressure	$N\ m^{-2}$
e_w	saturation vapor pressure above flat surface of water	$N\ m^{-2}$
g	acceleration of gravity	$m\ s^{-2}$
G	$\frac{2A_1}{A_2^2 b^2 F}$	$m\ s^{-1}$
F	$\left(\frac{\rho_w L_w^2}{k_a R_v T^2}+\frac{\rho_w R_v T}{e_w(T) D}\right)$	$m^{-2}\ s$
h	$A_1 z$, dimensionless height	-
h^*	$hR^{3/4}$ normalized dimensionless height	-
k_a	coefficient of air heat conductivity	$J\ m^{-1}s^{-1}K^{-1}$
L_w	latent heat for liquid water	$J\ kg^{-1}$
M_w	Molecular weight of water	$kg\ mol^{-1}$
N	concentration of liquid droplets	m^{-3}
P	pressure of moist air	$N\ m^{-2}$
r	liquid droplet radius	m
R	$\frac{3}{FA_1 w}\left(\frac{4\pi\rho_w N A_2}{3\rho_a}\right)^{2/3}$	-
R_a	specific gas constant of moist air	$J\ kg^{-1}K^{-1}$
R_v	specific gas constant of water vapor	$J\ kg^{-1}K^{-1}$
q_{ad}	adiabatic liquid water mixing ratio	-
$q_{\max}$	liquid water mixing ratio formed at the level corresponding to the supersaturation maximum	-
q_v	water vapor mixing ratio (mass of water vapor per 1 kg of dry ai	-
q_{vs}	mixing ratio of supersaturated fraction of water vapor	-

	(mass of water vapor per 1 kg of dry air)	
q_w	liquid water mixing ratio (mass of liquid water per 1kg of dry air)	-
Q	$A_2 q_w$ dimensionless liquid water mixing ratio	-
Q^*	$QR^{3/4}$ normalized dimensionless liquid water mixing ratio	-
Q^*_{ad}	dimensionless adiabatic liquid water mixing ratio	-
S	$e/e_w - 1$, supersaturation over water	-
$S_{\lim}$	limited supersaturation of water vapor	-
$S_{\max}$	maximum supersaturation forming near the cloud base	-
S^*	$SR^{3/4}$ normalized supersaturation	-
T	temperature	K
t	time	s
w	vertical velocity	m s^{-1}
z	height over condensation level	m
$z_{\max}$	height corresponding to the supersaturation maximum	-
Δq_w	spatial fluctuation of liquid water mixing ratio	kg m^{-3}
Δr	spatial fluctuation of droplet radius	kg m^{-3}
ΔS	spatial fluctuation of supersaturation	kg m^{-3}
δ_s	Soluble fraction of aerosol particle	-
Φ_a	Osmotic coefficient	
ρ_a	density of the air	kg m^{-3}
ρ_w	density of liquid water	kg m^{-3}
σ_w	surface tension of water-air interface	Nm^{-1}
τ_p	time of phase relaxation	s

Appendix B

Figure A1 shows the temperature dependence of coefficients F, A_1, A_2 and β_{ad} for three different air pressures. As seen, the changes of the coefficients F and A_2 are relatively slow at positive temperatures and they change relatively fast below -20C. The coefficient A_1 is nearly insensitive to pressure and its slope remains approximately constant in the entire temperature range of -30C<*T*<30C. The analysis of the diagrams in Fig.A1 suggests that the temperature and pressure dependencies of the coefficients F, A_1, A_2 and β_{ad} with an accuracy higher than 10% can be neglected for vertical displacements of the order of a few hundred meters at T>0C and a few tens of meters at T<-20C assuming the moist adiabatic changes of temperature.

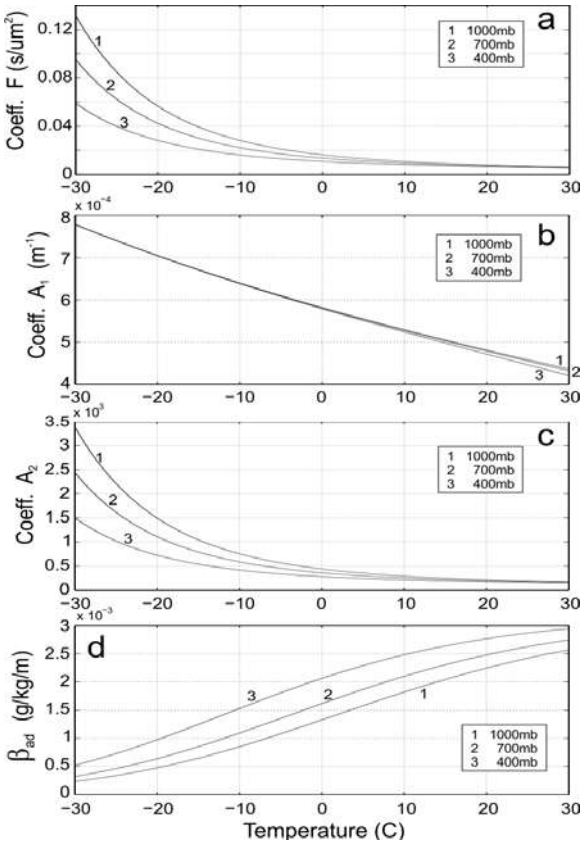

Fig. A1. *Temperature dependence of coefficients (a)* F *, (b)* A_1*, (c)* A_2 *(d) and adiabatic gradient of liquid mixing ratio* β_{ad} *calculated for different air pressures.*

References

Abdul-Razzak H. and S.J. Ghan, 2000: A parameterization of aerosol activation 2. Multiple aerosol types, *J. Geophys. Res.* **105** (D5), 6837–6844.

Abdul-Razzak H., S.J. Ghan and C. Rivera-Carpio, 1998: A parameterization of aerosol activation 1. Single aerosol type, *J. Geophys. Res.* **103** (D6), 6123–6131.

Andreae, M.O., D. Rosenfeld, P. Artaxo, A.A. Costa. G.P. Frank, K.M. Longlo, and M.A.F. Silva-Dias, 2004: Smoking rain clouds over the Amazon. *Science*, **303**, 1337-1342.

Bartlett, J. T., and P. R. Jonas, 1972: On the dispersion of the sizes of droplets growing by condensation in turbulent clouds. *Quart. J. Roy. Meteor. Soc.,* **98,** 150–164.

Bedos C., K. Suhre, and R. Rosset, 1996: Adaptation of a cloud activation scheme to a spectral-chemical aerosol model. *Atmos. Res*., **41**, 267-279.

Cohard J.M., J.P. Pinty and C. Bedos, 1998: Extending Twomey's analytical estimate of nucleated cloud droplet concentrations from CCN spectra, *J. Atmos. Sci.*, **55**, 3348-3357.

Devenish, B.J., P. Bartello, J-L. Brenguier, L.R. Collins, W.W. Grabowski, R.H.A. IJzermans, S.P. Malinowski, M.W. Reeks, J.C. Vassilicos, L._P. Wang and Z. Warhaft 2012: Droplet growth in warm turbulent clouds. *Q. J. Roy. Meteorol. Soc*. (in press)

Fukuta, N., 1993: Water supersaturation in convective clouds. *Atmos. Res*. **30**, 105-126.

Fountoukis C., and Nenes A., 2005: Continued development of a cloud droplet formation parameterization for global clime models. *J. Geophys. Res.* **110,** D11212

Ghan S.J., C. C. Chuang, and J.E. Penner, 1993: A parameterization of cloud droplet nucleation. Pt.1: single aerosol type. *Atmos. Res.,* **30**, 197-221.

Ghan S.J., C. C. Chuang, R. C. Easter, and J.E. Penner, 1995: A parameterization of cloud droplet nucleation. Pt. 2: multiple aerosol types. *Atmos. Res*., **36**, 39-54.

Grabowski, W. W. and H. Morrison, 2008: Toward the mitigation of spurious cloud-edge supersaturation in cloud models. *Mon. Wea. Rev.*, **136**, 1224–1234.

Kabanov A. S., Mazin, I.P., and Smirnov V. I., 1971: Supersaturation of water vapor in clouds. *Proc. of Central Aerologic Observatory*, **95**, 50-61 (in Russian)

Khain, A. P., M. Ovtchinnikov, M. Pinsky, A. Pokrovsky, and H. Krugliak, 2000: Notes on the state-of-the-art numerical modeling of cloud microphysics. *Atmos. Res.* **55**, 159-224.

Khrgian, A.Kh., 1969: Physics of the Atmosphere. Gidrometeoizdat, Leningrad, p.647.

Khvorostyanov V.I. and J.A. Curry,1999: Toward the Theory of Stochastic Condensation in Clouds. Part I: A General Kinetic Equation. J. Atmos. Sci., 56, 3985-3996

Khvorostyanov V.I. and J.A. Curry, 2006: Aerosol size spectra and CCN activity spectra: reconciling the lognormal, algebraic, and power laws. *J. Geophys. Res.*, **111**, D12202.

Khvorostyanov V.I. and J.A. Curry, 2009: Parameterization of Cloud Drop Activation Based on Analytical Asymptotic Solutions to the Supersaturation Equation, *J. Atmos. Sci*., **56**, 1905-1925

Klaassen, G. P., and T. L. Clark, 1985: Dynamics of the cloud environment interface and entrainment in small cumuli: Two dimensional simulations in the absence of ambient shear. *J. Atmos. Sci.,* **42,** 2621–2642.

Korolev A., and I. P. Mazin, 1993: Zones of increased and decreased droplet number concentration in stratiform clouds. *J. Appl. Meteor.,* **32,** 760–773.

Korolev A. V. 1995: The influence of supersaturation fluctuations on droplet spectra formation. *J. Atmos. Sci.,* **52,** 3620-3634.

Korolev A., and I. Mazin, 2003: Supersaturation of water vapor in clouds. *J. Atmos. Sci*., **60**, 2957-2974.

Magaritz L., Pinsky M., Krasnov O., and Khain A. 2009: Investigation of droplet size distributions and drizzle formation using a

new trajectory ensemble model. Part II: Lucky parcels. *J. Atmos. Sci*., **66**, 781-805.

Martin G.M., D. W. Johnson and A. Spice, 1994: The measurements and parameterization of effective radius of droplets in warm stratocumulus clouds. *J. Atmos. Sci.,* **51**, 1823-1842.

Mazin, I.P. and V.M. Merkulovich, 2008: Stochastic condensation and its possible role in liquid cloud microstructure formation (Review). In a book "*Some problems of Cloud Physics" Collected papers*, Memorial issue dedicated to Prof. S.M. Shmeter, Moscow, National Geophysical Committee, Russian Academy of Science, 2008, 263-295 (in Russian).

Paluch, I. R., and Ch. A. Knight, 1984: Mixing and evolution of cloud droplet size spectra in vigorous continental cumulus. *J. Atmos. Sci.,* **41,** 1801–1815.

Pinsky, M. and A. P. Khain, 2002: Effects of in-cloud nucleation and turbulence on droplet spectrum formation in cumulus clouds. *Quart. J. Roy. Meteorol. Soc.*, **128**, 501–533.

Pinsky M., A. Khain, I. Mazin and A. Korolev, 2012: Analytical estimation of droplet concentration at cloud base. *J. Geophys. Res.* (in revision)

Politovich, M. K., and W. A. Cooper, 1988: Variability of the supersaturation in cumulus clouds. *J. Atmos. Sci.,* **45,** 1651–1664.

Politovich, M. K., 1993: A study of the broadening of droplet size distribution in cumuli*, J. Atmos. Sci.*, **50**, 2230-2244.

Prabha T., Khain, A. P., B. N. Goswami, G. Pandithurai, R. S. Maheshkumar, and J. R. Kulkarni, 2011: Microphysics of premonsoon and monsoon clouds as seen from in situ measurements during the Cloud Aerosol Interaction and Precipitation Enhancement Experiment (CAIPEEX). *J. Atmos. Sci*. **68**, 1882-1901.

Pruppacher, H. R., and J. D. Klett, 1997: *Microphysics of Clouds and Precipitation.* Kluwer Academic, 976 pp.

Respondek, P.S., A.I. Flossmann, R.R. Alheit and H.R. Pruppacher 1995: A theoretical study of the wet removal of atmospheric pollutants: Part V. The uptake, redistribution, and deposition of (NH4)2SO4 by a convective cloud containing ice. *J. Atmos. Sci.* **52**, 2121–2132.

Rogers, R. R., 1975: An elementary parcel model with explicit condensation and supersaturation. *Atmosphere,* **13,** 192–204.

Sedunov, Yu. S., 1965: Fine cloud structure and its role in the formation of the cloud spectrum. *Atmos. Oceanic Phys.,* **1,** 416–421.

Sedunov, Yu. S., 1974: *Physics of Drop Formation in the Atmosphere.* John Wiley & Sons, 234 pp.

Shipway B.J. and S.J. Abel, 2010: Analytical estimation of cloud droplet nucleation based on an underlying aerosol population. *Atmos. Res.*, **96**, 344-355.

Squires, P., 1952: The growth of cloud drops by condensation. *Aust. J. Sci. Res.,* **5,** 66–86.

Stevens, B., R. L. Walko, W. R. Cotton, and G. Feingold, 1996: The spurious production of cloud-edge supersaturations by Eulerian models. *Mon. Wea. Rev.*, **124**, 1034–1041.

Stevens, B, and Coauthors, 2003: On entrainment rates in nocturnal maritime stratocumulus. *Quart. J. Roy. Meteorol. Soc*. **129**, 3469-3492.

Stevens, B, G and COAUTHORS, 2005: Evaluation of large-eddy simulations via observations of nocturnal marine stratocumulus. *Mon. Wea. Rev*., **133**, 1443-1455.

Twomey, S., 1959: The nuclei of natural cloud formation. II The supersaturation in natural clouds and the variation of cloud droplet concentrations. *Geofis. Pura.Appl.,* **43**, 243-249.

Vaillancourt, P. A., M. K. Yau, and W. W. Grabowski, 2001: Microscopic approach to cloud droplet growth by condensation. PartI: Model description and results without turbulence. *J. Atmos.Sci.,* **58,** 1945–1964.

Warner, J., 1968: The supersaturation in natural clouds. *J. Rech. Atmos.,* **3,** 233–237.

ESTIMATION OF SNOWFALL RATE DERIVED FROM LASER DISDROMETER DATA

Hiroyuki Konishi [1], Naohiko Hirasawa [2] and Masaaki Ishizaka [3]

[1] *Osaka Kyoiku Univ., JPN*

[2] *National Institute of Polar Research(NIPR), JPN*

[3] *National Research Institute for Earth Science and Disaster Prevention(NIED), JPN*

1.INTRODUCTION

This study attempts to provide better methods to measure amount of solid precipitation accurately by using a disdrometer which measures sizes and fall velocities of all precipitation particles passing through the laser beam. Compared with raindrops, the shape of snow particles is complicated and since the density of snow particles are not constant, it is difficult to presume each mass of particles from one dimension size. However, since the mass of each precipitation particles become large as size and fall velocity become large, it is expected that the mass of each particles would estimated by the function of two variables, particle diameter and fall speed. This indirect measurement of the amount of snowfall was compared with other direct measurement of snowfall from the result performed simultaneous observation of snowfall.

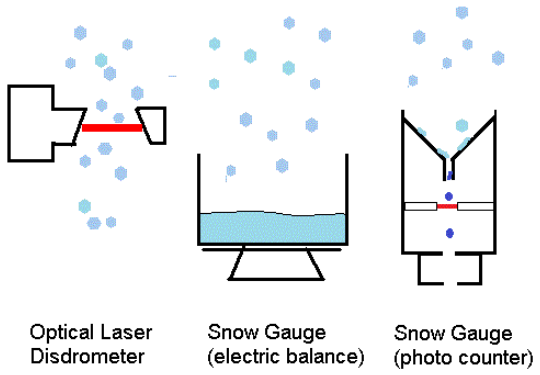

Fig.1. Outline of instruments to measure the snowfall rate.

2. INSTRUMENTS AND METHODS

The measurements of snowfall were tested in two winter seasons 2009/2010 for wet snow at Nagaoka/central part of Japan and 2010/2011 for dry snow at Kitami/northern part of Japan. To reduce the influence by a strong wind, all the measuring instruments were installed into the protection net with a height of 5m against wind.

The laser-optical disdrometer (SE－LP5411) can measure the particle horizontal sizes between 0.16 to 8 mm into 22 ranks, and velocities of between 0.2 and 20 m/sec into 20 ranks. This disdromater also shows the precipitation rate by unknown method. Preliminary observation shows that the value of precipitation rate was quite reliable for rain, but unreliable for snow. Then, new methods were required to estimate the snowfall rate more precisely.

The mass of precipitation particles classified each rank was decided to Interpolate the relation for earlier work between the particle diameter and fall speed and/or between the particle diameter and the mass for various precipitation particles (e.g. Atlas et al. (1973), Heymsfield and Kajikawa (1987), Kajikawa et al. (1996)). Total amount of precipitation was calculated from the sum of the mass of each particle.

The presumption of the mass for each particle was tested for simultaneous observation by other two types of snow gauges for comparison. One measures the

weight of accumulated snow in a bucket by using an electric balance and another counts the number of water drops falling into snow gauge after heating by using the photo-counter. The main advantage of the former is its ability to measure the snowfall rate most exactly, however, the gauge cannot have measured for long time without manual helps because of overflow of accumulated snow in a bucket in case of heavy snowfall. On the other hand, the advantage of the latter is its ability to measure continuously without maintenance like normal tipping bucket rain gauge for rain, however, the gauge cannot measure correctly without evaporation in case of weak snowfall. The outline of instruments was depicted in Fig.1.

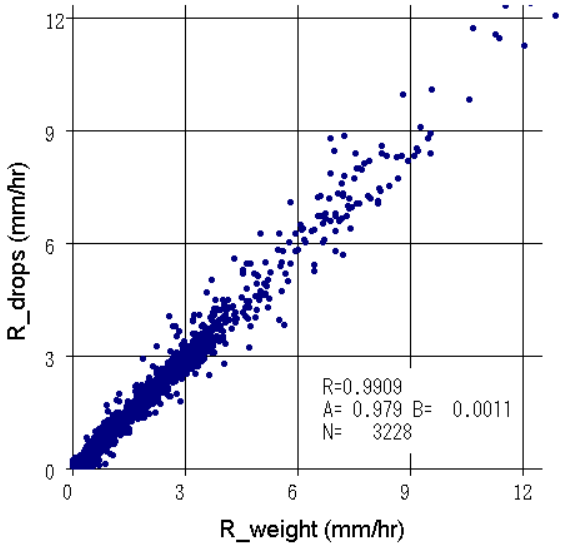

Fig. 2. Comparison of snowfall rate by two different snow gauges. R=0.99, a=0.98

3. RESULTS and DISCUSSION

The comparison with 5 minutes average snowfall rate measured at Nagaoka for wet snow by two different snow gauges was shown in Fig.2. The figure shows that the both observed value was almost equal and a correlation coefficient was almost 1 and the both snow gauges were sufficiently reliable. Since the observation time was much more longer than by photo counter type than electric balance type, It decided to compare the snowfall rate estimated from the laser didrometer data and that of measured by the snow gauge using the photo counter.

Figure 3 shows the comparison of 5 minutes snowfall rate at three different temperature ranges from left to right in the figure, -2 to -1, 1 to 2 and 5 to 6 °C respectively, which means the different types of precipitation particles as snowflake

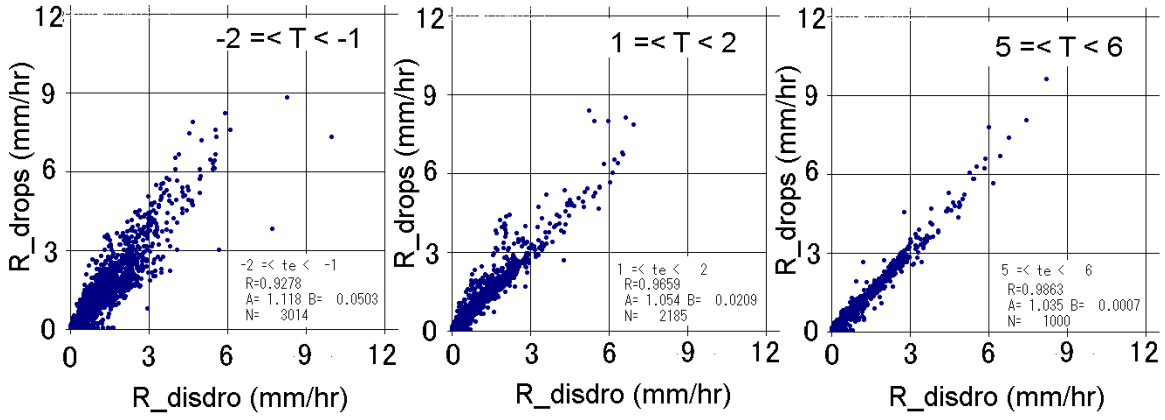

Fig.3. Comparison of 5 minutes snowfall rate at three different temperature ranges. Left : -2 to -1 °C, R=0.93, a=1.12, mainly snowflake aggregates, Middle: 1 to 2 °C, R=0.97, a=1.05, sleet, Right: 5 to 6 °C, rain, R=0.99, a=1.04.

aggregates, sleet and raindrops respectively. The correlation coefficient exceeded 0.9 and the inclination of regression line was almost 1.0 in any temperature. It turned out that the estimation of the amount of precipitation by using the method to sum up the mass of particles for each rank measured by laser disdrometer was quite good. At compared with initial unknown method for solid precipitation, the correlation coefficient increased from 0.84 to 0.93 and the inclination of regression line changed from 0.68 to 1.11 close to 1.

Since it was shown that the sum of the mass decided for each rank measured by the disdrometer was almost equal to the amount of precipitation measured by snow gauge, It can be possible to estimate the apparent density for every rank, assuming the precipitation particles are sphere. Figure 4 shows the averaged apparent density for each particle size summed every 10% relative humidity. The figure shows the apparent density for 4 temperature ranges from upper left to lower right, -1 to 0, 1 to 2, 3 to 4, 5 to 6 °C respectively. At below the melting point, the density was as small as 0.1 g/cm^3, so that the precipitation particles are considered to be the snowflake aggregates except for small size. Above the melting as relative humidity and temperature was higher. At the melting process, the snow particles became snow-like sleet in case of lower humidity, however, it became rain-like sleet in case of higher humidity. Such a difference was confirmed by the results of our observation although it was already shown in the earlier work (Matsuo et al. (1981). In case of the temperature was 5 °C or more, the apparent density became large about 0.9 g/cm^3 for every particle size and relative humidity so that the precipitation

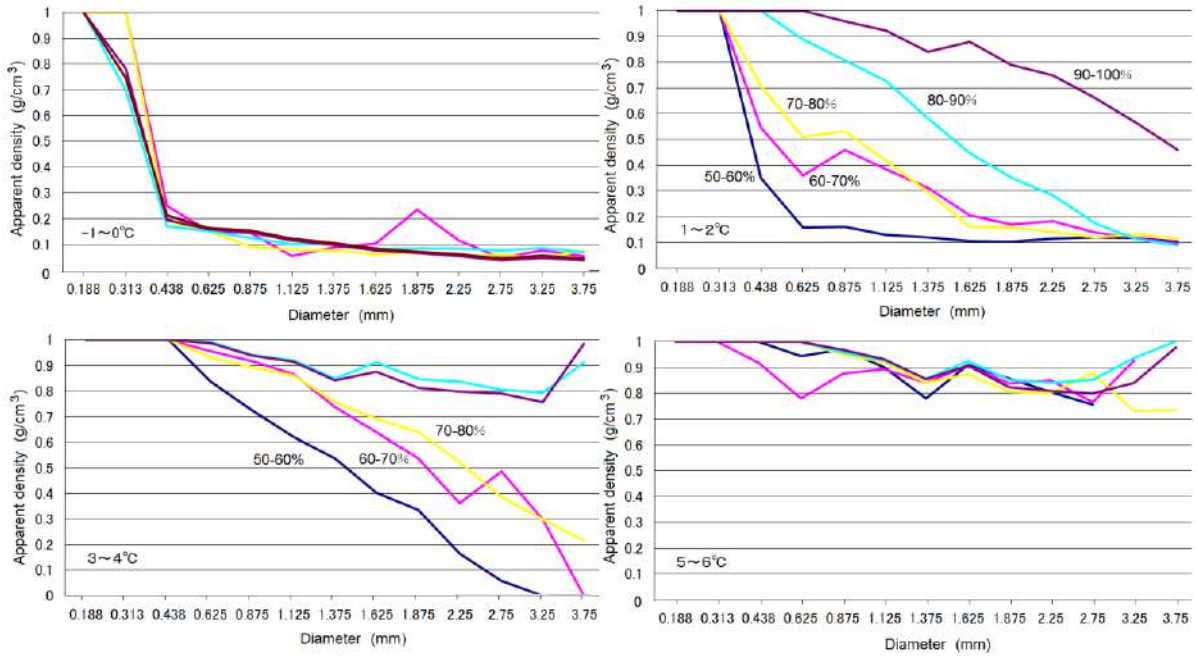

Fig.4. Apparent density of precipitating particles averaged for every particle size summed every 10% relative humidity. Upper left: -1 to 0 °C, snow, Upper right: 1 to 2 °C, sleet, Lower left: 3 to 4 °C, sleet, Lower right: 5 to 6 °C, rain.

particles are considered to be the rain drops.

5. CONCLUDING REMARKS

Snowfall observation was performed using one optical laser disdrometer and two snow gauges, and the better method of presuming snowfall was considered. As a result, it turned out that the method of presuming mass from the particle diameter and fall speed of each particle can estimate the snowfall rate precisely using the laser disdrometer. Moreover the apparent density of precipitation particles was also evaluated for various temperature and humidity conditions. It is confirmed that the snow particles tend to melt easily at higher humidity than lower humidity at above the melting point.

REFFERENCES

Atlas, D., R. C. Srivastava and R. S. Sekon, 1973: Doppler radar characteristics of precipitation at vertical incidence. *Rev. Geophysics. Space physics.*, 11, 1-35.

Heymsfield, A. J., and M. Kajikawa, 1987: An Improved Approach to Calculating Terminal Velocities of Plate-like Crystals and Graupel. *J. Atmos. Sci.*, 44, 1088–1099

Kajikawa M., S. Taniguchi and S. Ito, 1996: Relationship between the fall velocity of snowflakes and the shape of their component crystals., *Seppyo*, 58(6), 455-462. (In Japanese with English abstract)

Matsuo T., Y. Sasyo and Y. Sato, 1981: Relationship between types of precipitation on the ground and surface meteorological elements, *J. Meteor. Soc. Japan*, 59, 462-476.

MEASUREMENT OF COLLECTION EFFICIENCIES BETWEEN AEROSOL PARTICLES AND MILLIMETRIC DROPS

Arnaud Quérel[1], Pascal Lemaitre[1], Marie Monier[2], Emmanuel Porcheron[1], Andrea Flossmann[2]

[1]IRSN, BP68 91190 Gif-sur-Yvette, France

[2] *LaMP, Université Blaise Pascal - CNRS - OPGC, 24 avenue des Landais, Aubière, France*

1. INTRODUCTION

The nuclear industry is not entirely prevented from a potential accident with loss of containment and release of radioactive aerosol particles into the atmosphere.

To predict the consequences of this kind of radioactive release, a profound understanding of the aerosol particles scavenging is necessary, in order to anticipate with utmost possible precision the ground contamination and the air pollution dispersion of radioactive particles.

Among all mechanisms implied in the aerosol particles deposition, we focused on the scavenging of particles by the rain, also called “washout” or below-cloud scavenging.

This particular mechanism can be described as a function of collection efficiencies between aerosol particles and drops, depending of relative humidity and the size of the involved objects.

An experimental setup called BERGAME was built to measure a large range of previously unmeasured collection efficiencies. These newly measured collection efficiencies can, then, be introduced, e.g., into the DESCAM model (Flossmann and Wobrock, 2010) to improve the modeling of the aerosol particle scavenging by the rain.

The DESCAM model and the results obtained with the collection efficiencies newly measured are described in the poster P8.35 “The aerosol particles scavenging by rain performed by the DESCAM model” by the same authors.

2. DETERMINATION OF THE REGION OF INTEREST

The washout modeled by DESCAM needs a database of collection efficiencies. These data are relatively well known for drops smaller than 0.8 mm (Wang and Pruppacher, 1977). But, for larger drops, the calculation of the collection efficiencies fails, mainly due to the fall speed of drops (the airflow around the drop is no more laminar) and to the oscillations of the drop

shape (Szakáll *et al.*, 2010). Then, the modeling of the impaction of aerosol particle by a drop is not possible any more.

The main mass of the rain drop size distribution is widely located in drops with diameters larger than one millimeter. We will, thus, focus on the role of these drops for below cloud particle scavenging below.

DESCAM can be used to estimate the importance of theses size ranges for washout. It allows computing the mass of particles collected by drops as a function of their diameter (Figure 1). For a drop size distribution centered around 0.9 mm, the drops which collect the most important mass of particles are centered around 2.2 mm. This is mainly due to fact that the larger drops reach the ground first, and therefore meet a higher density of particles than the smaller drops, that come later and meet an already depleted air.

We concluded that the range of drops involved in a significant washout is between 1 and 5 mm.

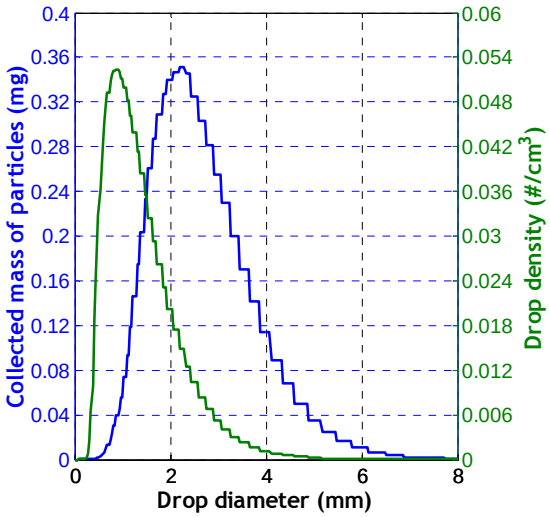

Figure 1: Collected mass of particles by class and drop density as a function of the drop diameter

The same approached is used to determine the range of particles involved in the washout. The mass of particles scavenged as a function of their diameter is shown in Figure 2. Here, using the Jaenicke particle size distribution "continental" (Hobbs, 1993), the range of particles involved mainly in the washout appears to be between 0.1 and 10 µm.

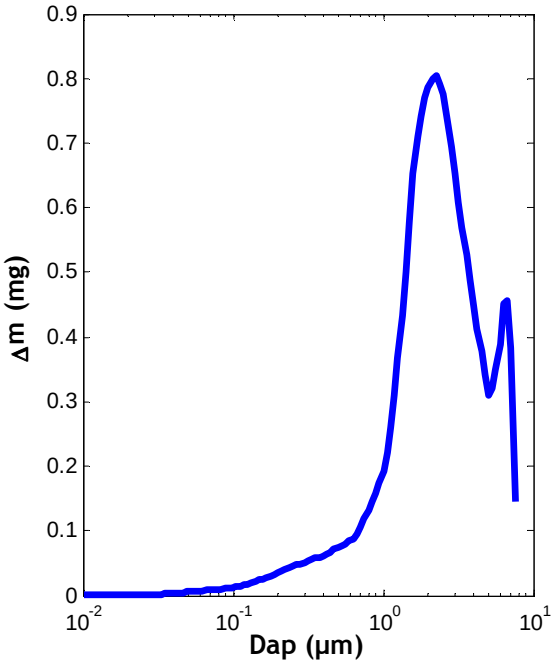

Figure 2: Mass of particles scavenged as a function of their diameters

Only few experimental measurements of collection efficiencies have been done inside these ranges (Lai *et al.*, 1978, Pranesha and Kamra, 1997). And the washout modeling is very sensitive to these collection efficiencies data (see poster P8.35 of this conference for details).

3. BERGAME EXPERIMENT

In order to determine these collection efficiencies, the BERGAME experiment was built. BERGAME is a French acronym meaning "*Facility to study the aerosol*

scavenging and to measure the collection efficiency".

BERGAME consists of three mains parts. The first one is a drop generator (stable in frequency and stable in generated drop diameter). The drops accelerate in a shaft of ten meters in height, high enough to reach their terminal velocities (Wang and Pruppacher, 1977). The third part is an aerosol particle containment of one meter in height, where the collection efficiencies measurements are performed.

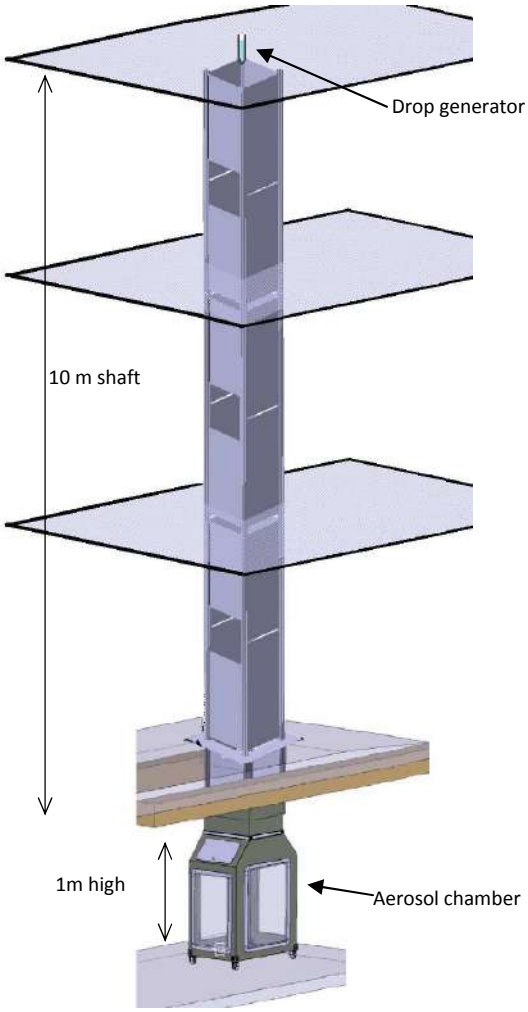

Figure 3: Sketch of BERGAME facility

Drops are collected after their path through the aerosol chamber and the mass of aerosols collected is measured.

Fluorescein powder is dissolved in water, then this liquid is atomized and the droplets produced are dried, producing fluorescein aerosol particles. The droplets are created by an ultrasonic generator: a ceramic vibrates at 500 kHz or 2400 kHz (depending on the apparatus used), creating a fog of mono-dispersed droplets. Also, the resulting distribution of particles of fluorescein is almost mono-disperse. The Fluorescein particles are collected by the falling drops during their path through the chamber. Finally the drops are collected after their path through the aerosol chamber and analysed with an appropriate fluorimeter. This instrument sends UV light through the collected liquid (between 100 and 250 drops), and the intensity of the fluorescent light is measured. As the fluorescence intensity is proportional to the fluorescein concentration, the fluorescein aerosol mass collected by drops is determined. The lowest measurable concentration is 5.10^{-11} g/cm^3.

It is necessary to know the number and the size of particles in the aerosol chamber. The particle size distribution measurements are performed with an Electrical Low Pressure Impactor (ELPI, Marjamäki *et al.* [7]) and an Aerodynamic Particle Sizer (APS TSI-3321). The APS has a better resolution (52 channels against 12), but its range of measurement is only between 0.5 and 20 µm. Thus, the ELPI is used to measure particles smaller than 0.5 µm.

The mass density of particles inside the aerosol chamber is determined by a sample on filters. Air is sampled through a HEPA filter, then the filter is withdrawn and the mass of fluorescein collected by the filter is determined. Knowing the flow and the duration of the sample, the mass density of fluorescein in the aerosol chamber is calculated.

Knowing the particle size (d_{AP}, measured with the ELPI or APS), the aerosol mass density in the chamber ($\rho_{Air,\,fluo}$ obtained by sample on filters), the mass density of fluorescein collected in the drops ($\rho_{D,\,fluo}$), the height of the aerosol chamber (H), the drop size (D_D measured by shadowgraphy) and the relative humidity (RH) it is possible to determine the collection efficiency. The Equation 1 represents the ratio between the mass collected and the mass of particle in the volume crossed by a drop during its fall.

Equation 1

$$E\left(D_D, d_{AP}, RH\right) = \frac{2\,\rho_{D,\,fluo}\,D_D}{3H\,\rho_{Air,\,fluo}}$$

4. COLLECTION EFFICIENCIES MEASURED

177 collection efficiencies are measured, mainly for drops of diameter of 2.0 and 2.6 mm and for particles between 0.3 and 3.5 µm.

The 2 mm drops results are compared to the Lai *et al.* (1978) results (Figure 4), and we observe a good agreement between the both measurements.

But very strong differences appear between these new measurements and the DESCAM data and the Slinn model (1978) (which is mainly used to model the aerosol scavenging of the rain, Volken *et al.* (1993)).

The original DESCAM data overestimate the collection efficiency for particles larger than 1 µm (up to a ten factor) and the minimum of collection efficiency in not existing for the drops larger than 1 mm. Therefore, there appears a large underestimation for particles smaller than 0.5 µm.

At the opposite, the Slinn model underestimates the collection efficiency for particles larger than 1 µm. Furthermore, the minimum of collection efficiency is located around particles of 0.1 µm, while the measurements located the minimum around 0.8 µm.

Therefore, the DESCAM data of collection efficiencies have been modified (Figure 4).

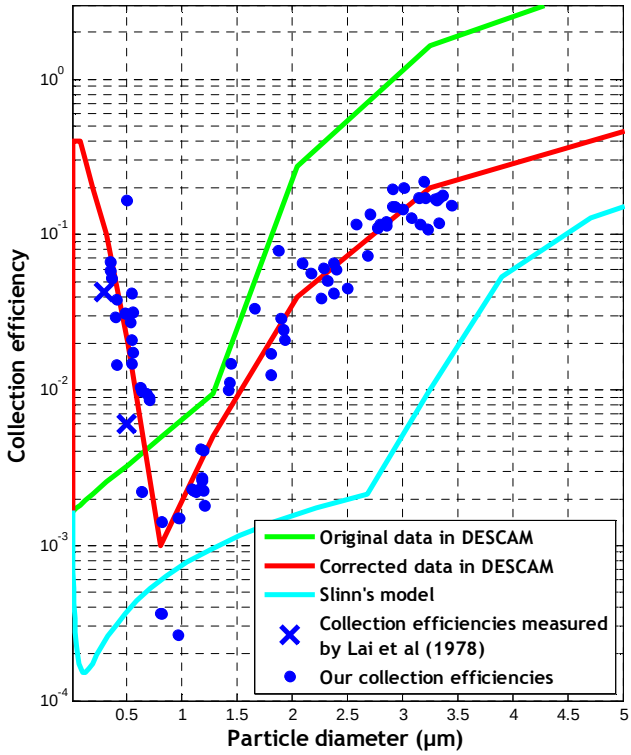

Figure 4: Collection efficiencies measured in BERGAME for drops of 2 mm

Wang and Pruppacher (1977) insist on the importance of the relative humidity to the collection efficiency. Therefore the influence of the relative humidity is tested too (**Figure 5**).

There doesn't seem to be an influence of the relative humidity for drops of 2 mm and particles around 1 µm. This issue should

be investigated for different particles and drops sizes in the future.

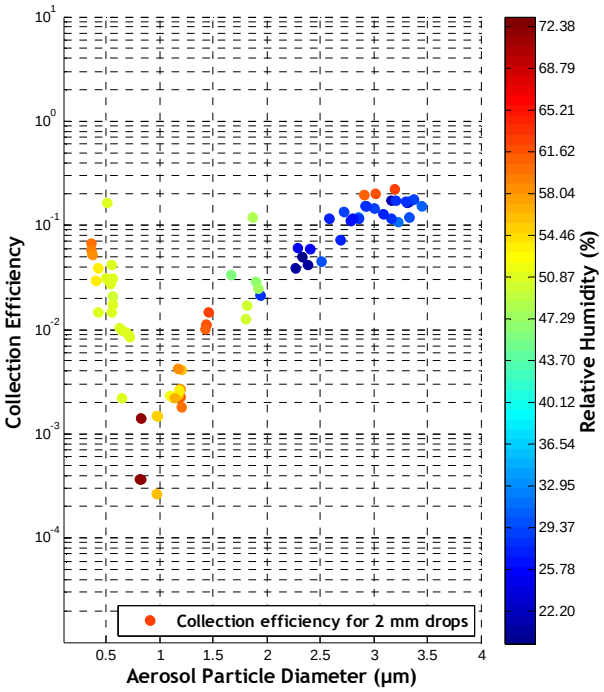

Figure 5: Collection efficiency for 2 mm drops for relative humidities between 20 % and 80 %

CONCLUSION

Particles between 0.1 and 10 µm and drops between 1 and 5 mm are the most important for the calculation of washout. A free fall shaft and an aerosol chamber have been designed and built to measure these collection efficiencies.

Although we have only studied the collection efficiencies for drops of 2 and 2.6 mm and particles between 0.3 and 4 µm, significant differences with respect to the collection efficiencies previously known are observed.

These new collection efficiencies are then used with the DESCAM model (see poster P8.35), despite the fact that not yet all the region of interest are explored.

Therefore the collection efficiencies for other drop size, particles size and humidities must be measured to complete this study, and to obtain a much better modeling of the aerosol particle scavenging by rain below the cloud.

REFERENCES

Flossmann A.I., Wobrock W., 2010, “A review of our understanding of the aerosol-cloud interaction from the perspective of a bin resolved cloud scale modeling”. *Atmos. Res.,* Vol. **97**, No. 4, pp. 478-497

Lai K., Dayan N., Kerker M., 1978, “Scavenging of Aerosol Particles by a Falling Water Drop”, *J. Atmos. Sci.*, **35**, pp. 674-682.

Marjamäki M., Keskinen J., Chen D-R, Pui D.Y.H., 2000, “Performance evaluation of the electrical low-pressure impactor (ELPI)”, *J. Aerosol Sci.*, **31**(2), pp. 249-261.

Pranesha T.S., Kamra A.K., 1996, “Scavenging of aerosol particles by large water drops 1”, Neutral case. *Journal of Geophysical Research*. **101**(18), pp. 23 373-23 380.

Slinn W.G.N., 1977, “Some approximations for the wet and dry removal of particles and gases from the atmosphere”. *Water, Air, and Soil Pollution*, **7** (4), pp. 513-543.

Szakáll M., Mitra S.K., Diehl K., Borrmann S., 2010, “Shapes and oscillations of falling raindrops — A review”. *Atm. Res*., Vol. **97**, pp. 416-425

Volken, M., Schumann, T., 1993, “A critical review of below-cloud aerosol scavenging, results on mt. Rigi”, *Water, Air, and Soil Pollution*, **68**(1-2), pp 15-28.

Wang P.K., Pruppacher, H.R., 1977, “An experimental determination of the efficiency with which aerosol particles are collected by water drops in subsatured air”, *Journal of the Atmospheric Sciences*, **34**, pp. 1664-1669.

THE AEROSOL PARTICLES SCAVENGING BY RAIN PERFORMED BY THE DESCAM MODEL

Arnaud Quérel[1], Marie Monier[2], Andrea Flossmann[2], Pascal Lemaitre[1], Emmanuel Porcheron[1]

[1]IRSN, BP68 91190 Gif-sur-Yvette, France

[2] *LaMP, Université Blaise Pascal - CNRS - OPGC, 24 avenue des Landais, Aubière, France*

1. INTRODUCTION

The nuclear industry is not entirely prevented from a potential accident with loss of containment and release of radioactive aerosol particles into the atmosphere.

To minimize the consequences of this kind of radioactive release, a profound understanding of the aerosol particles scavenging is necessary, in order to predict with utmost possible precision the ground contamination and the air pollution dispersion of radioactive particles.

Among all mechanisms implied in the aerosol particles deposition, we focused on the scavenging of aerosol particles by the rain, also called “washout” or below-cloud scavenging.

The simulation of the aerosol particles scavenging by rain is performed with the DESCAM model.

As a first step, the sensitivity of the aerosol scavenging to the collection efficiencies database changes is tested. It is shown that a profound knowledge of the collection efficiencies is mandatory to determine, e.g., the masse of aerosol particles still into the atmosphere after a rain event.

Then, to calculate a realistic below cloud scavenging, DESCAM needs a reliable dataset of collection efficiencies for drops and aerosol particles involved in washout. These data was newly obtained with the help of BERGAME experiment, which was constructed in particular to measure these data.

The results obtained by these new collection efficiencies are explored.

The ranges of particles and drops studied, the experimental setup and the results obtained are described in the poster P8.32 **“**Measurement of collection efficiencies between aerosol particles and millimetric drops” by the same authors.

2. BRIEF DESCRIPTION OF THE DESCAM MODEL

DESCAM (DEtailed SCavening Model, Flossmann and Wobrock 2010) is a detailed cloud model. It uses explicit microphysics scheme to forecast the number size distributions of the liquid droplets and the aerosol particles at mesoscale.

DESCAM exists in 1.5, 2 and 3 dimensions. In our study the 1.5D version is suitable because able to study the aerosol scavenging and fast enough to perform sensitivity tests.

The version 1.5D uses a bi-cylindrical geometry. The microphysical phenomena are calculated in the inner cylinder.

DESCAM details 6 spectra: the drop size distribution, the wet particle size distribution, the ice crystal size distribution, and three additional distributions that give for each particles bin size, the mass of aerosol material contained within.

These detailed spectra allow an in-depth following of the particles scavenging by the rain.

In order to determine the region of interest, the sensibility of the model and to focus on the washout, DESCAM is simplified. The temperature is always positive (no ice), there is no vertical velocity in the column, and no in-cloud processes. The rain size distribution is a simple Marshall and Palmer (1948) shape maintained constant at 1000 m in altitude that washout atmosphere below. The atmosphere is initially loaded with particles that have a size distribution prescribed as by Jaenicke (continental background; Hobbs, 1993).

3. SENSIBILITY OF THE DESCAM MODEL TO THE COLLECTION EFFICIENCY DATABASE

As it is described in the poster P8.32, the collection efficiencies for particles between 0.1 and 10 µm and drops between 1 and 5 mm are the most important for the calculation of washout.

We also noted that the collection efficiencies in these ranges are not well known. As a consequence, DESCAM database of collection efficiencies is widely extrapolated and approximated for these size ranges.

The calculation of the below cloud scavenging is done as a function of collection efficiencies, to determine the sensitivity of the model to this parameter.

We test the increase by a factor of ten of the collection efficiencies for the drops of 2 mm diameter. Only the collection efficiency of this drop size is modified, the collection efficiencies remain the same for the other drops bins. The multiplication by ten is selected following Pranesha and Kamra's (1996) work. Indeed, the Pranesha and Kamra's works were published later than the initial database creation and there are strong differences between their experimental measurements and the DESCAM database of collection efficiencies (e.g. for drops of 4.8 mm and particles of 3.8 mm, Pranesha and Karma measure a collection efficiency of 0.06, while DESCAM database gives to us 1.7).

The main result obtained is shown in Figure 1 that gives the mass of particles deposited to the ground by rain for the two different datasets, the original and the modified.

The mass of scavenged particles calculated with the help of the modified database is 22 % more important than the masse of particles scavenged calculated with the original collection efficiencies database.

Therefore, a relatively small modification in the DESCAM database of collection efficiencies can bring an important variation to the calculation of the deposited mass of particles on the ground.

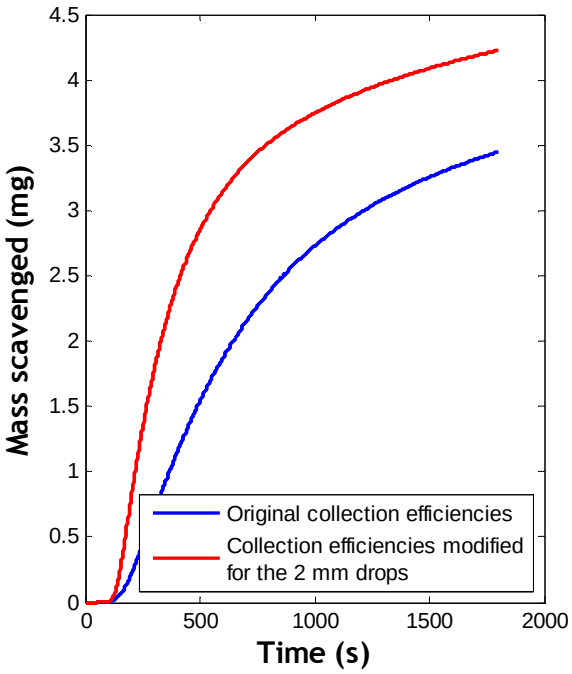

Figure 1: Mass of particles scavenged as a function of time for two different collection efficiencies database

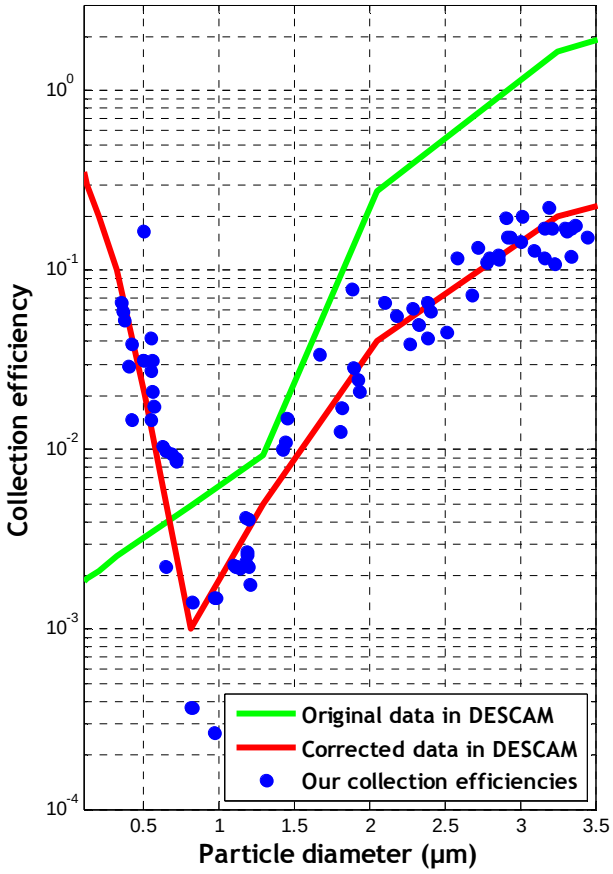

Figure 2: Collection efficiencies measured in BERGAME for drops of 2 mm

4. THE NEW COLLECTION EFFICIENCIES DATABASE

As detailed in the poster P8.32, 177 measurements of collection efficiencies were performed, allowing an important improvement of the database.

The original DESCAM dataset overestimates the collection efficiency for particles larger than 1 µm (up to a factor of ten) and the minimum of collection efficiency in not existing for the drops larger than 1 mm. Therefore, there appears a significant underestimation for particles smaller than 0.5 µm (see **Figure 2**). The new collection efficiencies database corrects these issues.

Unfortunately, the entire region of interest concerning the washout has not been explored due to experimental restrictions. **Figure 3** highlights the location of our collection efficiencies measurements inside the DESCAM database. Thus, the collection efficiencies are measured only for drops of 2.0 and 2.6 mm and for particles between 0.3 and 3.5 µm.

The other collection efficiencies in DESCAM are generally not modified when the database was altered. However, in addition to the collection efficiencies measured, we extrapolated the collection efficiencies to the particles between 0.1 and 0.3 µm and between 3.5 and 10 µm. For the drops, extrapolations are done for drops of diameter of 1.3 mm and 3.2 mm.

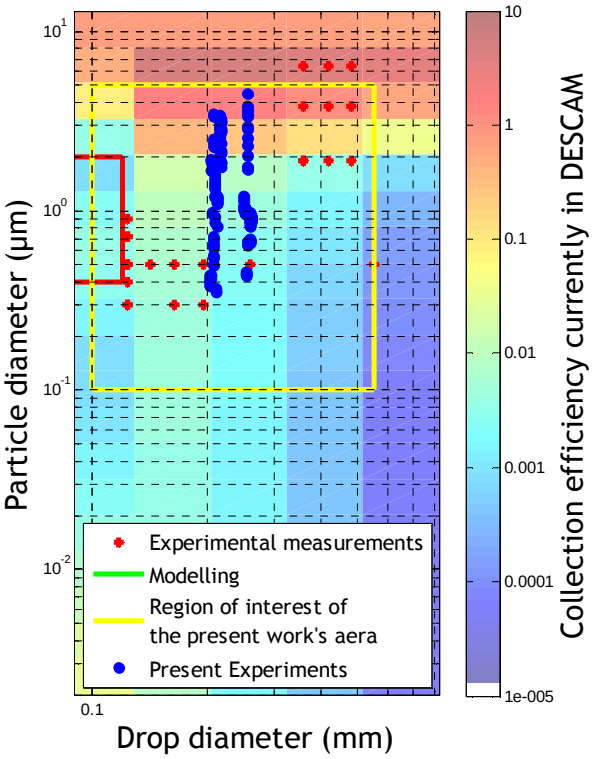

Figure 3: Representation of the database of collection efficiencies

5. APPLICATION TO THE CCOPE CASE

CCOPE (Dye *et al*, 1986) is a very well instrumented experiment, which follows the evolution of a small thunderstorm that occurred in southeastern Montana in 1981.

The CCOPE case is very useful to test the cloud formation models. DESCAM was already compared to the CCOPE measurements, and this case yielded a significant amount of rain formation and an important rainfall rate.

For this simulation, DESCAM is not simplified. All the microphysics processes are active in the modeling.

The calculations are done with the both collection efficiencies database.

There are two different kinds of particles for both computations. The first type is distributed at the start of the simulation, it represents the continental background. This aerosol is lifted by the airflow (Figure 4, Figure 5) and used as condensation nuclei for the droplet forming. This aerosol undergoes the rainout (scavenging inside the cloud) and later the washout, when the raindrops created in the cloud finally fall through the layer of particles still present in the lower troposphere. Flossmann (1998) founds that 70 % of the mass of particle reaching the ground comes from the rainout and therefore only 30 % by the washout.

Thus, there is not a large difference of particles mass scavenged between both computations, with only 14 % more mass scavenged with the new collection efficiencies database.

A second type of aerosol particles was used to simulate a release of particles a few minutes before the onset of rain. This plume represents a potential radioactive release consecutive to a potential nuclear accident. The aerosol particles are uniformly distributed into de first kilometer of the atmosphere with a Jaenicke particle size distribution (Hobbs, 1993).

In this case, the particle scavenging is only due to washout. The new efficiencies scavenge 33 % more than the original data.

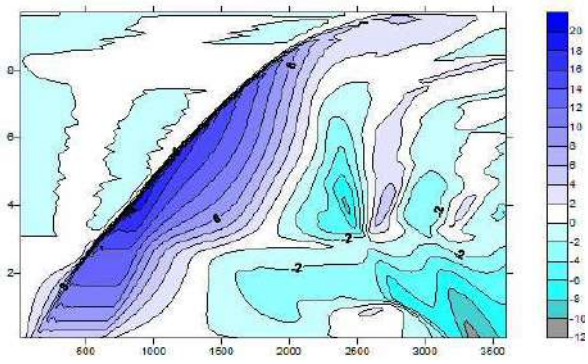

Figure 4: Vertical wind velocity (m/s)

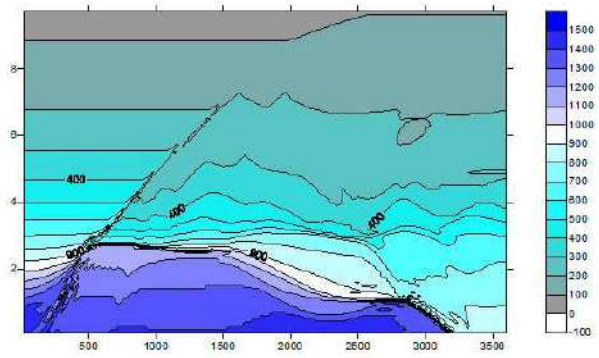

Figure 5: Aerosol number concentration (type 1) in the air (#/cm^3)

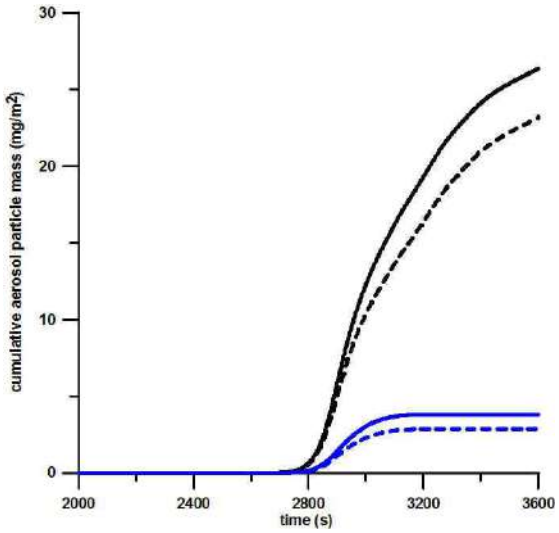

Figure 6: Evolution of aerosol deposition by rain (black: type 1; blue: type 2); solid line: new efficiencies, dashed lines: old efficiencies); new efficiencies scavenge 14% more of background particle mass and 33% more of plume particle mass.

CONCLUSION

These first results highlight the importance of an accurate knowledge of drop aerosol collection efficiencies in order to assess the potential cleaning effect of a rain event after an accidental release of particle pollution.

The large difference obtained with only some corrections in the matrix of collection efficiencies confirms the great significance of the measurement of collection efficiencies for drops larger than one millimeter. Thus, we need to continue these measurements to reach an accurate modeling of the washout.

These last calculations confirm the great importance of the distribution of the plume. If the release is far away from the rain and the pollution enters the cloud updraft region, the rainout will take the main part of the scavenging. But, if the rain is close to the release (therefore with a plume below the cloud), the washout takes the main part in the particles scavenging. In this case, the presented results are very encouraging to continue our investigations and to extend the measurements of collection efficiencies to other drop sizes, and finally to complete the database of collection efficiencies.

REFERENCES

Dye, J. E., J. J. Jones, W. P. Winn, T. A. Cerni, B. Gardiner, D. Lamb, R. L. Pitter, J. Hallett, and C. P. R. Saunders (1986), “Early Electrification and Precipitation Development in a Small, Isolated Montana Cumulonimbus”, *J. Geophys. Res.*, **91**(D1), 1231–1247

Flossmann, A.I., Wobrock W., 2010, “A review of our understanding of the aerosol–cloud interaction from the perspective of a bin resolved cloud scale modelling”, *Atmos. Res.,* **97**(4), pp 478-497.

Hobbs P.V., 1993, “Aerosol-Cloud-Climate Interactions”, *Academic Press Inc.*

Pranesha T.S., Kamra A.K., 1996, “Scavenging of aerosol particles by large water drops 1”, Neutral case. *Journal of Geophysical Research*. **101**(18), pp. 23 373-23 380.

PARTICLE INTER-ARRIVAL TIME ANALYSIS AND SHATTERING REMOVAL OF 2D-STEREO PROBE DATA AT HIGH SAMPLING SPEEDS AND HIGH PARTICLE CONCENTRATIONS IN MESOSCALE CONVECTIVE SYSTEMS

R. Dupuy, C. Duroure, A. Schwarzenboeck
CNRS / Université Blaise Pascal Clermont-Ferrand 2 / Observatoire de Physique du Globe de Clermont Ferrand / Laboratoire de Météorologie Physique, 24, avenue des Landais, 63171 Aubière, France

1. INTRODUCTION

During 2010 and 2011, two aircraft measurement campaigns within the frame of the Mégha-Tropiques project allowed performing more than 20 research flights. Amongst other probes, the 2D-S imaging probe has been installed under the wing of the French Falcon 20 aircraft. Due to the high speed of the aircraft and the strong meteorological and therefore specific microphysical conditions encountered in the mesoscale convective system (MCS), the limits of the probe sampling capabilities (true air speed up to 200 m/s and high concentrations of particles) have been reached. Due to the rapid response of the probe, we have been able to remove large percentages of shattered ice crystals, using particle inter-arrival time analysis (PITA).

2. DESCRIPTION OF PITA

The principle of PITA is described in Field and al. (JAOT 2006). It is based on the assumption that particles are uniformly distributed in the cloud. This assumption implies that the cloud particle inter-arrival time distribution follows a Poisson law which can be described with the following equation:

$$\frac{d\,P(\Delta t)}{d\,ln(\Delta t)} = \frac{\Delta t}{\tau}\, e^{-\frac{\Delta t}{\tau}}$$

where P(Δt) is the probability of a given inter-arrival time (Δt) and τ is the inter-arrival time mode.

PITA consists in analyzing the inter-arrival time probability through fitting of Poisson law distributions to the inter-arrival time mode(s) observed. The analysis is performed only when hydrometeors larger than 100 µm are present.
The second step of PITA then consists in analyzing the mode(s) fitted with Poisson laws. In case that a second Poisson law distribution with very small inter-arrival times is observed, then it has to belong to the particles produced by shattering. This assumption is correct as long as there is a good mixing in the cloud and the sample used for PITA is not too large.
In an ideal case, we obtain two separate modes as shown in figure 1.

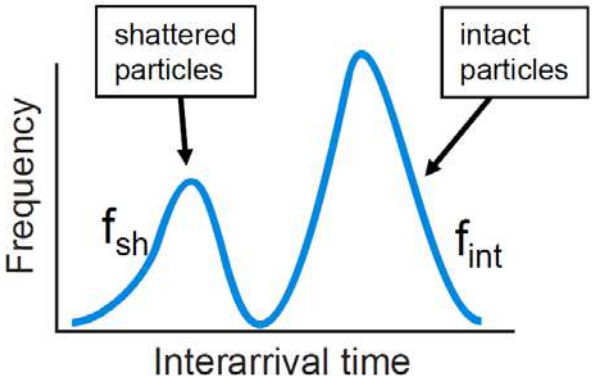

Figure 1: ideal case of cloud hydrometeors inter-arrival time frequency distribution (from Korolev et al., 2010).

In the worst case scenario, when the mode of intact particles and the mode of shattered particles are too close together, it is almost impossible to differentiate shattered from intact particles (see figure 2).

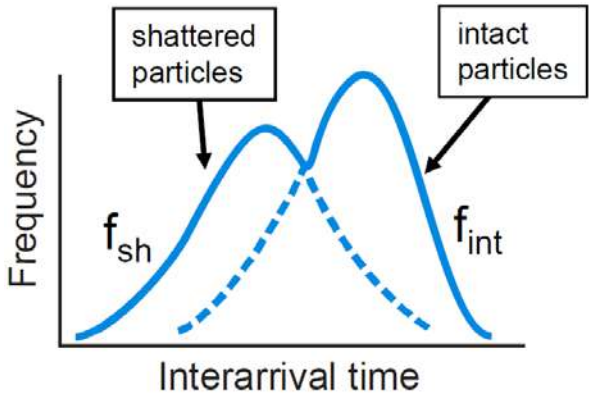

Figure 2: worst case of cloud hydrometeors inter-arrival time frequency distribution (from Korolev et al., 2010).

3. PITA APPLIED TO 2D-S

A PITA method applied to 2D-S measurement was presented recently by Lawson (2011). This method tests each particle, whether it stems from shattering or not, using criteria derived from the Poisson law. These criteria are calculated for the mean inter-arrival time over 10000 particles and constants based on experience. This approach makes PITA faster in order to apply the method to every single particle.

In this study, a different approach is presented. In particular, we do not use a priori experimental constants as done by Lawson for the calculations.

We chose to fit directly Poisson law distributions onto the particle inter-arrival time frequency distribution. Therefore, the free mpfit toolbox for IDL has been used (http://www.physics.wisc.edu/~craigm/idl/).

Also, we chose to use a sample length of 2000 particles for the PITA analysis, which is (i) sufficiently large to obtain an adequate fit of the Poisson law distribution(s) and (ii) small enough to assure a rather good homogeneity of the cloud microphysical properties.

We present here four examples of inter-arrival time distributions in order to demonstrate the advantages of the presented algorithm.

On figure 3 can be seen a case close to ideal as defined on figure 1. In this case, the algorithm finds a good fit of two Poisson law distributions. However, there is still an overlap between the shattered particles mode and the intact one. The advantage of the fit is to obtain the threshold (blue line) of inter-arrival time above which we are sure we will not have any shattered particles. On top of that, we also obtain a good estimation of the number of intact particles discarded when we remove all the particles under that threshold. As we are in a homogenous case (one mode of intact particles), we can apply an adjustment factor to the whole size spectrum obtained with particles kept by the PITA.

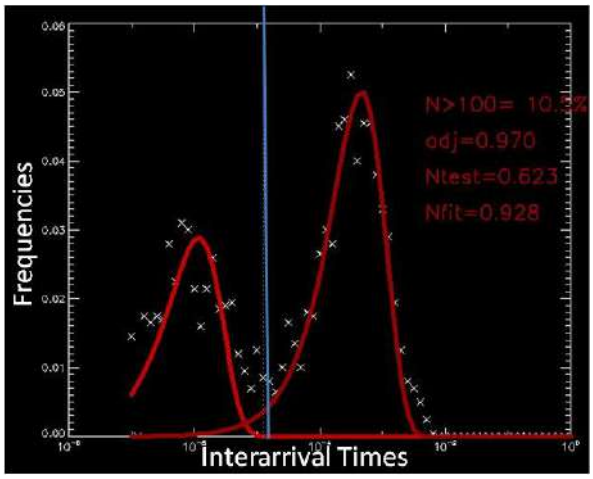

Figure 3: Inter-arrival time frequency distribution. Ideal case with 10.5% of particules over 100 µm (N>100) and an adjustement factor (adj) of 0.97.

Figure 4 and 5 show two very different cases with respectively high concentrations of small particles and high fractions of large particles. In both cases, no satisfying Poisson law distribution can be fitted on the smallest inter-arrival times corresponding to the shattered particles. Yet, we can still see the right side of a Poisson law distribution, which is all we need in order to obtain the threshold between shattered and intact particles. To do so, in this case, the algorithm fits an exponential curve (i.e. $\exp(-\Delta t/\tau)$) to the lowest inter-arrival times. Since the intact particle mode is still fully defined, we can obtain the adjustment factor.

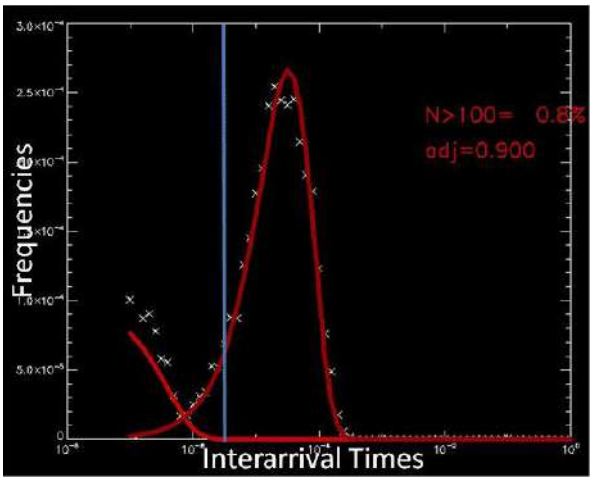

Figure 4: Inter-arrival time frequency distribution. High concentration case with 0.8% of particules over 100 µm and an adjustement factor of 0.9.

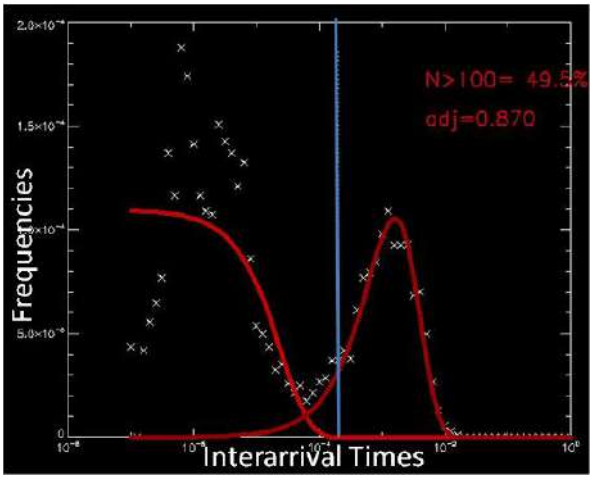

Figure 5: Inter-arrival time frequency distribution. Large particles case with 49.5% of particules over 100 µm and an adjustement factor of 0.87.

The last two examples (Figure 5 and 6) also show why the algorithm presented here does not need a priori parameters and thus, seems to be more inoffensive than the one described in Lawson (2011). As Lawson's algorithm is based on parameters extracted from the Poisson law, they are most likely to be flawed if the poisson law distribution for the shattered particles is not fully defined. In Lawson's paper, it is not said if it is why there are empirical constants. Indeed, they could be useful to weight shattered particles distributions not fully defined. Under this assumption, these constants still need to be changed for each sample tested with PITA as the measurable fraction of the mode of shattered particles defined on the inter-arrival time frequency distribution varies as well.

Regarding our algorithm, there are some problematic cases where the shattered particles cannot be removed efficiently from the intact ones. The most obvious ones correspond to the worst case scenario shown on figure 2 where the two modes are closely merged and cannot be separated, without removing also a very significant fraction of still intact particles. We consider that when removing more than 35 % of intact particles (which equals an adjustment factor lower than 0.65), the algorithm failed.

Another problematic case is presented in Figure 6. This example presents two coexisting Poisson law distributions of intact particles, despite the reduced sample length for PITA analysis of only 2000 particles. The coexistence of two hydrometeor populations may occur for example in convective cloud systems where strong updrafts induce a mixing of high concentrations of small hydrometeors (less than 100 µm) with larger preexisting ones. In this case, the algorithm can find the threshold and the adjustment factor, but applying this factor to more than one mode of intact particles is wrong. Indeed, the cloud portion sampled is no longer homogenous and it is not possible to separate the particles from both intact particles inter-arrival time modes.

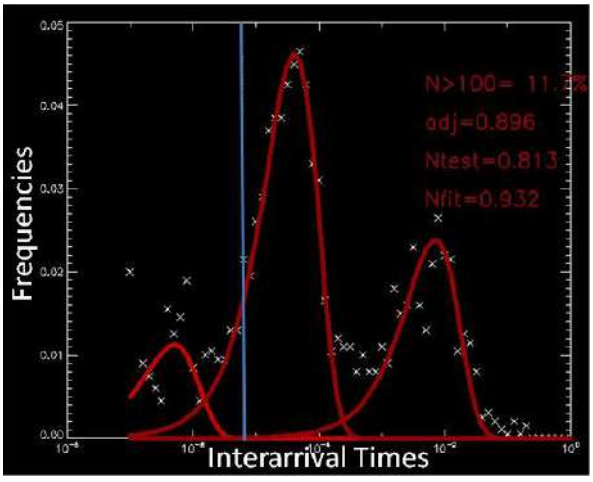

Figure 6: Inter-arrival time frequency distribution. Inhomogenous cloud case with 11.7% of particules over 100 µm and an adjustement factor of 0.896.

So far, these problematic cases (Figure 2 and Figure 6 cases) were not encountered often (less than 5 % of the 2000 particle samples for the strongest episode). Still, we are improving our algorithm and will show new results during the presentation.

4 IMPACT OF PITA ON PARTICLE SIZE SPECTRUM

An example of the impact of the shattered particles removal with PITA on particle size spectrum (PSD) is shown in figure 7. The two important points to notice are that:

1) there no significant impact in number of particle removal for particles beyond 250µm in diameter;
2) PITA shattering removal induces a decrease of concentration by a factor of 5 to 8 for sizes smaller than 150 µm.

These two points translate well what occurs during the shattering of large particles on the probe tips, where a small quantity of large particles is capable of producing a huge quantity of smaller particles.

The presented results demonstrate a satisfying response of the PSD to PITA shattering removal. Yet, the work is continuing to make the presented algorithm still more reliable. More results will be presented during the presentation.

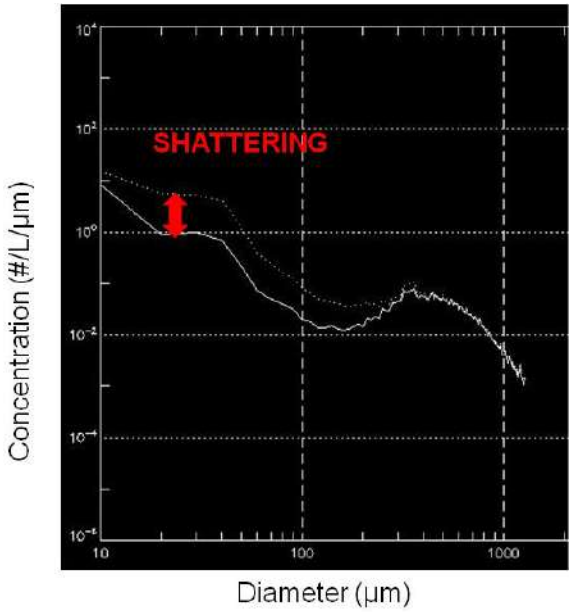

Figure 7: Particle size spectrum obtained in a MCS with 2 million particles before (dotted line) and after (solid line) removal of the shattered particles with PITA.

BIBLIOGRAPHY

Field, P. R., A. J. Heymsfield, A. Bansemer, 2006: Shattering and Particle Interarrival Times Measured by Optical Array Probes in Ice Clouds. *J. Atmos. Oceanic Technol.*, **23**, 1357–1371.

Korolev A., G. McFarquhar, P. Lawson, J.-F. Gayet, M. Kramer, A. Heymsfield, D. Rogers, C. Twohy, O. Stetzer, The effect of ice bouncing and shattering on the performance of airborne cloud microphysical instrumentation, Workshop for In Situ Airborne Ice Cloud Instrumentation Seaside, June 23-24, 2010.

Lawson R. P., Effects of ice particles shattering on the 2D-S probe, Atmos. Meas. Tech., 4, 1361–1381, 2011

Acknowledgements

The authors would like to thank SAFIRE for operating the French Falcon 20 research aircraft during the two measurement campaigns. We are particularly grateful to CNES for funding the aircraft measurement campaigns within Megha-Tropiques and for partially funding the 2D-S probe.

ICE FORMATION IN ALTOCUMULUS CLOUDS

M. Simmel[1], J. Bühl[1], A. Ansmann[1], and I. Tegen[1]

[1]Leibniz Institute for Tropospheric Research, Permoserstraße 15, 04318 Leipzig, Germany

1. INTRODUCTION

Primary ice formation in low and mid-level clouds is mainly caused by heterogeneous freezing occuring up to temperatures as warm as -10 °C to -15 °C. Ice formation at these relatively warm temperatures requires (at least partly) insoluble aerosol particles such as biological material or mineral dust acting as ice nuclei (IN) in different modes (e.g., immersion freezing, contact freezing). However, the relative importance of the different primary ice forming processes are not yet clear, and generally, the mixed phase is rather poorly understood.

A second topic is how the thermodynamically instable coexistence of the liquid and the solid phase after the formation of the first ice particles can be conserved. The study of Korolev and Field (2008, later named KF2008) discussed the conditions for which cloud droplet nucleation can take place within a pure ice cloud. The two necessary and sufficient conditions are that a certain threshold of vertical velocity has to be exceeded as well as a certain threshold vertical displacement (see Fig. 1).

2. MODEL STUDIES

A Langrangian box model with spectral mixed-phase microphysics SPECS (Simmel and Wurzler, 2006, Diehl et al. 2006) is applied to expand the theoretical studies of KF2008, namely where they have restricted themselves to monodisperse drop and ice particle distributions, sperical ice particles, neglect of ventilation effects on particle growth, and sedimentation.

SPECS originally assumes the ice particles to be spherical. However, to study the influence of the shape (and the ventilation effects) on particle growth and the coexistence of ice and liquid water, the ice particle shape parameterization (empirical mass-dimension and projected area-dimension relationships) of Morrison and Grabowski (2008) was applied using a constant bulk rimed fraction since riming was neglected within this study.

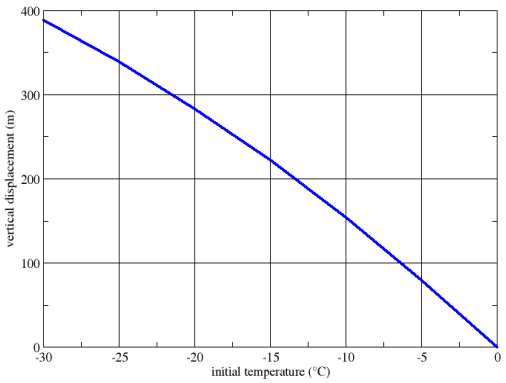

Fig. 1: Theoretical threshold for vertical displacement to reach saturation w.r.t. liquid water from initial saturation w.r.t. ice depending on temperature (cp. KF2008, Fig. 3).

The model was initialized with saturation w.r.t. ice at a height of 5000 m asl. The parcel is driven by a vertical harmonic oszillation $w(z) = w_0 \sin(2\ t\ w_0 / Z_0)$ with the maximum vertical velocity w_0 (varies between 0.1 and 5 m/s; not all cases shown) and the cloud extension Z_0=1000 m. Initially, 1 ice particle per liter with an equivalent radius of 10 µm is given.

Fig. 2 shows several cycles of ups and downs of the air parcel. In the first cycle, drop nucleation takes place at about 300 m above cloud base (cp. Fig. 1). Ice particles grow not only in the updraft but also at least partly in the downdrafts on the expense of the liquid phase. Throughout the cycles, the location of droplet nucleation is shifted further upwards. A quasi steady state is reached after about 8 cycles for this configuration.

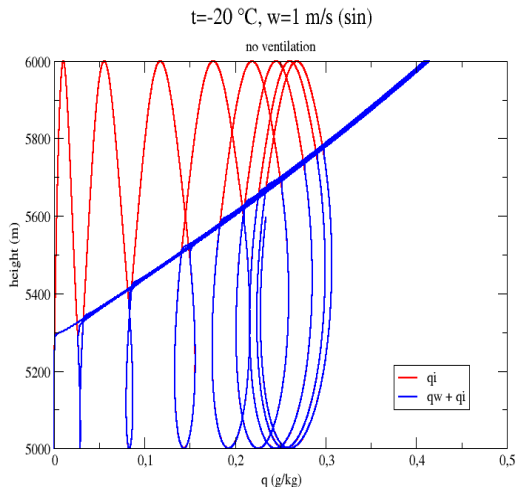

Fig. 2: Ice (red) and ice+liquid (blue) water mixing ratios for an initial temperature T_0=-20 °C and w_0=1 m/s.

If the ventilation effect is taken into account additionally (Fig. 3) no liquid phase can be observed. This is due to the much faster growth of the ice particles which inhibits supersaturation w.r.t. water and, therefore, droplet nucleation. Quasi steady state is reached within the first cycle.

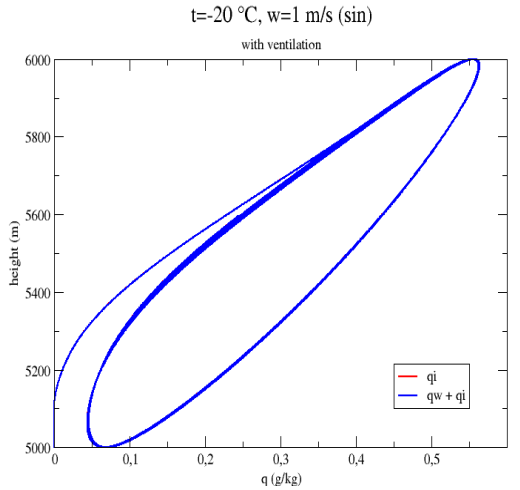

Fig. 3: The same as in Fig. 2 but with ventilation effect.

If the vertical velocity is enhanced by a factor of 5 (w_0=5 m/s, Fig. 4) enough water vapour is avaiable to form droplets despite the fast ice article growth due to ventilation, however, the quasi steady state is reached after 3 cycles and more ice mass is formed compared to Fig. 2. At least for the Ac cases observed (see e.g. Fig. 6), such high vertical velocities did not occur.

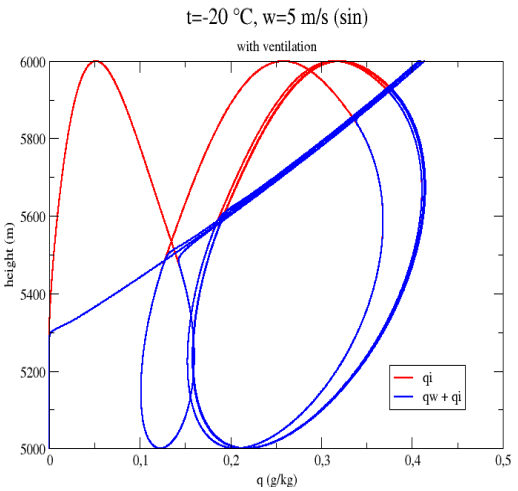

Fig. 4: The same as in Fig. 3 but with w_0=5 m/s.

Sedimentation should be an important sink for the ice particles and, therefore, should enhance droplet formation and the liquid phase. However, the only (very crude) possibility to 'model' sedimentation in a parcel model is to remove particles exceeding a certain terminal fall velocity (here 1 m/s) at a certain rate. Fig. 5 shows that all ice particles are removed within the first updraft cycle and that the following cycles form pure liquid clouds (since no further primary ice formation is described).

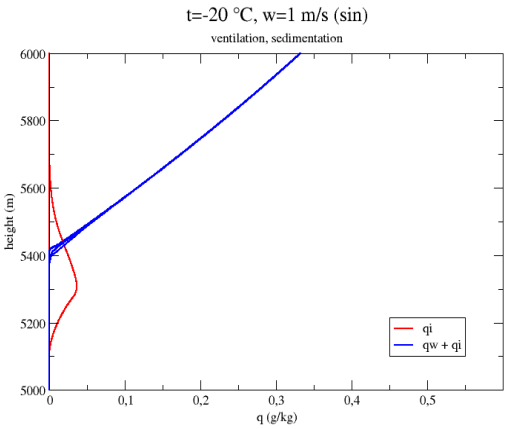

Fig. 5: The same as in Fig. 3 but with 'sedimentation'.

3. OBSERVATIONS

A set of altocumulus cloud cases observed by lidar over Leipzig (aged, processed and unprocessed dust), Morocco (pure, unprocessed dust) as well as Cape Verde (processed dust) can be used to study cloud evolution including ice and drop formation.
The observed clouds typically occur at about 3000 to 5000 m height and at temperatures

of about -10 °C to -15 °C with typical vertical velocities of about +/-1 m/s. Some of the observed clouds consist entirely of liquid water, some of them are glaciated producing virgae, which gives a nice spectrum of different cases to work out the controlling parameters.

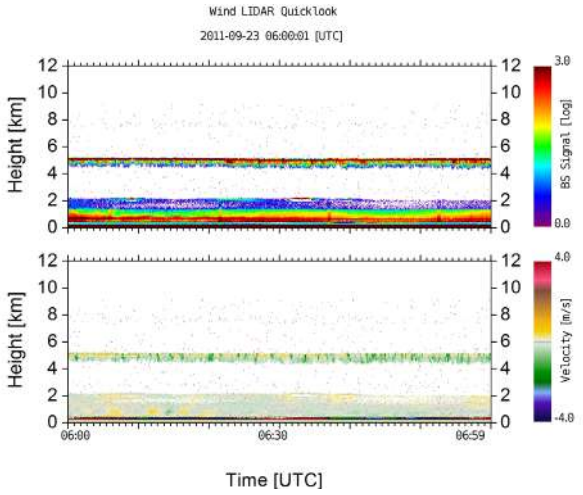

Fig.6: Example of Ac LIDAR observation above Leipzig. Note the vertical velocity fluctuations between about +/-1 m/s.

4. CONCLUSIONS

The present study examines the question of coexistence of solid and liquid water following the work of KF2008 and trying to extend it at certain points. The main topics of KF2008 remain valid, however, it seems that neglect of the ventilation effect could lead to a large overestimation of the liquid phase for realistic ice particle concentrations, despite the initially small ice particles. Sedimentation of the larger ice particles could counteract these effects. However, a parcel model is too limited to answer this question and total ice particle depletion makes it necessary to explicitly describe primary ice nucleation.

Droplet formation in a preexisting ice cloud is a competition of water vapour depletion by the ice particles and the availability of water vapour due to the rising air parcel. The ruling parameters can be divided into two groups: The microphysical ones cover mainly the ice particle characteristics (number size distribution, shape, description of microphysical processes), but also the aerosol particles serving as potential CCN for cloud droplet formation. The second group consists of the (thermo-)dynamical parameters such as vertical velocity, temperature, and (initial) relative humidity.

5. BIBLIOGRAPHY

Diehl, K., M. Simmel, and S. Wurzler, 2006. Numerical sensitivity studies on the impact of aerosol properties and drop freezing modes on the glaciation, microphysics, and dynamics of clouds. J. Geophys. Res., 111, D07202, doi:10.1029/2005JD005884.

Korolev, A. and P. R. Field, 2008. The effect of dynamics on mixed-phase clouds: Theoretical considerations. J. Atm. Sci. 65, 66-86.

Morrison, H. and W. W. Grabowski, 2008. A novel approach for representing ice microphysics in models: Description and tests using a kinematic framework. J. Atm. Sci. 65, 1528-1548.

Simmel, M. and S. Wurzler, 2006. Activation and condensation in sectional cloud microphysical models. Atm. Res. 80, 218-236.

Acknowledgements

This work is part of the the project UDINE (**U**p- and downdrafts and **D**rop and **I**ce **N**ucleation **E**xperiment: Lidar observations and modeling of tropical and mid-latitude altocumulus). UDINE is supported by the DFG (Deutsche Forschungsgemeinschaft) under contract AN258/15-1.

LARGE-EDDY SIMULATIONS OF STRATOCUMULUS TO CUMULUS TRANSITION

Marcin J. Kurowski[1] *, Dorota Jarecka[2], Hanna Pawlowska[2] and Wojciech W. Grabowski[3]
[1]Institute of Meteorology and Water Management - National Research Institute, Warsaw, Poland
[2]Institute of Geophysics, Faculty of Physics, University of Warsaw, Poland
[3]National Center for Atmospheric Research, Boulder, Colorado, USA

1. INTRODUCTION

The vast fields of subtropical marine stratocumulus off the western coasts of continents are known for their persistent existence. In these regions, the large-scale subsidence associated with Hadley circulation provides favorable conditions for the formation of strong inversion, which separates moist and cool stratocumulus-topped boundary layer (STBL) from dry and warm free atmosphere above. A quasi-steady equilibrium of the STBL results from a subtle balance between subsidence and mass exchange (*i.e.* small-scale entrainment) around the inversion. A faithful representation of a brake-up of solid cloud deck and its subsequent transition to cumulus field is of a great importance to the Earth's radiative budget as the process leads to a significant change in the planetary albedo. However, the fidelity with which the contemporary mesoscale/climate atmospheric models reconstruct the transition is still insufficient. It suffers from our poor understanding of a complex nature of the processes involved as well as their multi-scale coupling. The progress is also conditioned by both temporarily and spatially limited observational data while explicit representation of all scales in the models is far beyond their capabilities.

The large-eddy simulations (LES) are one of basic tools that helps to our understanding of large-Reynolds number atmospheric flows. With an explicit representation of only the largest and most energetic scales this approach substantially reduces complexity of the problems found in atmospheric modeling. In spite of its great usefulness, the question remains to what extend this approach is consistent with the observations and what the main obstacles are in accurate LES modeling of stratocumulus to cumulus transition. These issues are partially being addressed in the EUCLIPSE project. In the project, a model intercomparison study was designed based on ASTEX observations (Bretherton et al., 1999). University of Warsaw participates in the project with the anelastic nonhydrostatic model EULAG (see e.g. Prusa et al., 2008). The model, a well-established research fluid flow solver, is widely used in various atmosphere-related problems ranging from small-scale turbulence to planetary flows. In this study, the focus is on modification of the solver to LES modeling of a multi-hour evolution of the Sc to Cu transition.

* *Corresponding author*: e-mail: mkuro@igf.fuw.edu.pl

2. SETUP OF THE EXPERIMENT

The numerical experiment is based on the data collected during the ASTEX Lagrangian field campaign. The initial profiles correspond to a shallow (700 m-deep) boundary layer that includes 400 m-deep cloud layer, capped with a fairly sharp inversion (temperature jump of 5.5 K over 50 m). The sea surface temperature (SST) increases gradually over time, from 290.4 K to 294.7 K over 40 hours. The large-scale subsidence evolves as well, decreasing by a factor of five compared to the initial value. Evolution of the SST and large-scale subsidence mimics Lagrangian drift of the air column towards the equator observed during the field project.

The uniform horizontal grid length is 35 m while stretched grid is applied in the vertical. The vertical grid length decreases from 15 m near the surface to 5 m in the upper part of domain, starting to compress around the initial cloud top height. The domain size is $4.48 \times 4.48 \times 2.4$ km^3 (*i.e.* $128 \times 128 \times 400 \approx 6.5 \times 10^6$ grid points), and periodic lateral boundaries are assumed. The computations last 40 hours starting at 00:00 UTC.

3. ADAPTATION OF THE MODEL

To develop atmospheric LES model capable in realistic simulation of diurnal cycle of precipitating STBL, a set of modules was modified or added to EULAG. The most important changes are reported in this section.

a. Radiation

Two different radiation schemes were examined in the experiment. First, the simplified long-wave radiative cooling (Stevens et al., 2005) was implemented along with a short-wave radiation from the Dutch Atmospheric Large Eddy

Simulation (DALES) model (Heus et al., 2010). This approach, however, was found to be insufficient in the long-term simulations. The solutions were strongly sensitive to a set of parameters proposed in Stevens et al. (2005); it was difficult to balance both radiative cooling and large-scale subsidence above the inversion; and gradual smoothing of the temperature inversion was observed. All those effects are relatively small but errors accumulate in time. After about 10 h their contribution to the solution is noticeable. Since the analyzed case is sensitive to the radiative effects, we decided to implement full radiation scheme. The radiation schemes comes from CCM2 climate model (Hack at al., 1993). The scheme works in extended vertical domain (up to 48km) and employs a pressure coordinate system. Since the radiation is computationally expensive, radiative fluxes are calculated once every two minutes and remain unchanged until the next calculation. A more expensive time interval of one minute was also tested, but the results were only a few percent different in terms of the domain averaged liquid water path and entrainment velocity.

b. Large-scale subsidence

As in other models, implementation of the large-scale subsidence is based on the upstream advection scheme. Subsidence velocity results from the integration of the continuity equation applying evolving horizontal divergence. The large-scale subsidence is assumed constant above 1600 m.

c. Subgrid-scale mixing

The subgrid-scale turbulent transport is one of the key processes that affect the entrainment velocity and thus development of STBL. Too intense entrainment of dry and warm air from a free atmosphere leads to excessive dilution of stratocumulus and its premature decay. On the other hand, too little entrainment suppresses development of the whole layer and postpones transition from Sc to Cu. To find setup suitable for this case, two different subgrid-scale schemes (SGS) were examined, namely, Smagorinsky (1963) or Schumann (1991), the latter based on the subgrid-scale turbulent kinetic energy (TKE) closure. Although both schemes are commonly used in LES modeling, the choice of basic parameters, such as the Prandtl number (Pr) or the turbulent mixing length (Λ), is uncertain. This is because the schemes were originally developed for dry convection with the grid-box aspect ratio of one. In contrast, model grid-boxes are strongly non-uniform in the EUCLIPSE setup, boundary layer is moist, and the essential subgrid-scale processes occur within a thin stably-stratified inversion layer rather than across neutrally stratified layer below. We selected $Pr = 1$ and $\Lambda = \Delta z$. The former is typical for stable stratification and the latter corresponds to the vertical gridlength.

d. Surface fluxes

Surface sensible and latent heat fluxes are calculated applying a prescribed value of the drag coefficient (here $C_d = 0.0014$) and depend on both the flow and the sea surface conditions, namely

$$F = -C_d|U|(q - q_{surf}), \tag{1}$$

where F is the flux; U is the near-surface flow velocity; q represents either the water vapor mixing ratio (for the latent heat flux) or the temperature (for the sensible heat flux) right above sea surface; and q_{surf} denotes the surface value (the sea surface temperature or the saturated water vapor mixing ratio corresponding to the surface temperature).

e. Microphysics

To represent processes of drizzle formation in stratocumulus, we first examined a bulk parameterization of Kessler (1969) warm rain initiation, which is commonly used in LES modeling of convective clouds. The scheme assumes linear dependence of autoconversion rate on the excess of cloud water (q_c) over a given threshold (q_{tr}). Since the value of a threshold is rather arbitrary, a set of different q_{tr} was tested. A strong sensitivity of the results to q_{tr} was found, especially for extreme values of the domain averaged liquid water path (LWP). For instance, the maximum LWP of 160 g/m^2 was simulated for $q_{tr} = 0.68$ g/kg, whereas 170 g/m^2 for $q_{tr} = 0.70$ g/kg. This is because Sc is almost uniform and the cloud water mixing ratio closely follows adiabatic profile within each column, with q_c increasing almost linearly with altitude. Therefore, arbitrary definition of q_{tr} imposes also arbitrary level above which drizzle formation is allowed.

To improve representation of the autoconversion, two other parameterizations, namely, Berry and Reinhardt (1974) and Khairoutdinov and Kogan (2000; hereafter KK2000), were examined. They both operate on mean volume radius of the cloud water rather than explicit value of the cloud water mixing ratio. The former scheme is often applied in simulations of convective clouds, whereas the latter was proposed for LES models of STBLs.

The use of Berry and Reinhardt (1974) scheme resulted in a very intense drizzle initiation along with a rapid fallout of precipitation. For instance, reduction of the initial LWP by more than 30% during the first four hours was simulated. Furthermore, sensitivity of the results to the parameters describing cloud droplet spectrum (*e.g.*,

the spectral dispersion) was fairly weak and it could not reverse the strong negative LWP trend.

The final microphysical setup is based on KK2000 drizzle parameterization. Because the KK2000 is designed for a double-moment bulk microphysics scheme (i.e., predicting both the concentrations and mixing ratios of cloud droplets and drizzle drops), we assumed a constant droplet concentration (100 per cc) for the autoconversion and accretion, and a constant sedimentation velocity of 0.72 m/s for drizzle sedimentation. Further improvements applying the double-moment scheme are being considered.

3. RESULTS OF THE SIMULATIONS

A large number of simulations, including many sensitivity studies, was performed to examine and adjust each element of the model. The results of that part were shortly described in previous section. Here, we present and discuss the solution provided by EULAG for the final setup.

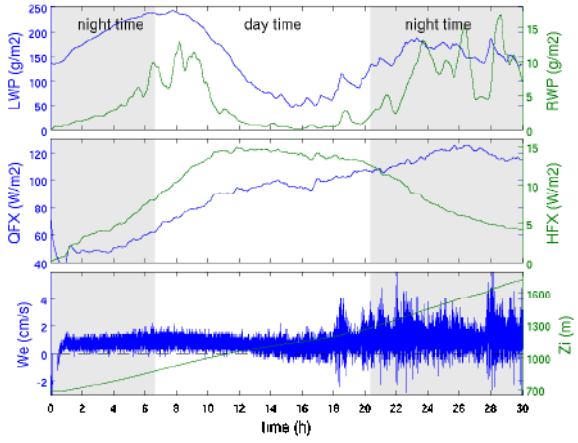

Figure 1: Time evolution of the domain averaged scalars: LWP, RWP, QFX, HFX, We and Zi (see text for details).

A typical development of STBL is shown in Fig. 1. The figure shows evolution of the of the following domain averaged scalars: the liquid water path (LWP), rain water path (RWP), surface sensible heat flux (HFX), surface latent heat flux (QFX), inversion height (Z_i), and entrainment velocity (We). During the night, the longwave radiative cooling combined with relatively large surface latent heat flux ($45-50$ W/m^2) leads to a gradual increase of LWP. As a result, RWP increases to more than 10 g/m^2 shortly after a sunrise (around 06:40). During the day, solar radiation reverses that trend because the cloud layer is heated throughout its entire depth. After 16 hours, LWP and RWP both reach their minima of 50 g/m^2 and 0.5 g/m^2, respectively. With weakening solar heating, LWP and RWP begin to increase again. Entrainment velocity is positively correlated with changes of LWP because a slower growth of the boundary layer depth is observed for a thinner cloud. During the second night, the cloud layer becomes less uniform, and the amplitude of We fluctuations as well as LWP and RWP all increase. After 30hrs, the STBL depth is already twice as large as the initial one.

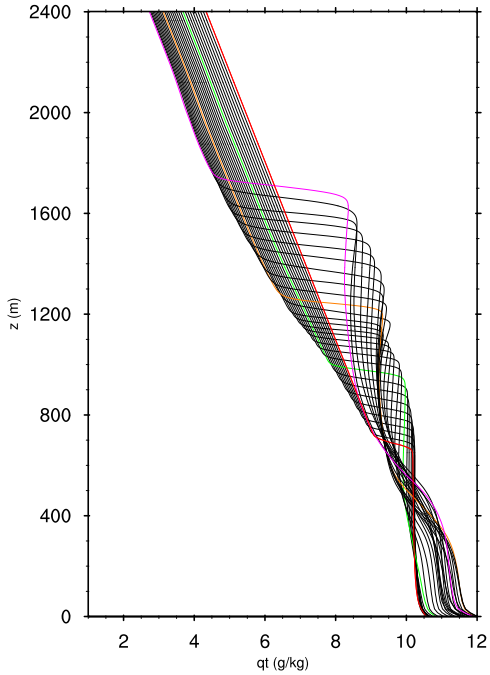

Figure 2: Hourly averaged mean profiles of the total water mixing ratio for 30 h of simulation. Each profile represents one hour (1 h - red, 10 h - green, 20 h - orange, 30 h - magenta).

To better understand the evolution of STBL, a set of hourly averaged vertical profiles is shown in Figs. 2-6. The profiles of q_t (Fig. 2) and θ_l (Fig. 3) document drying and warming of the free atmosphere by the large-scale subsidence. As the subsidence weakens with time, the radiative cooling begins to prevail over the subsidence after about 20 hours and the free-atmospheric temperature tendency turns to negative. The initially well-mixed STBL is affected by the buoyancy production at the layer top (negative, due to radiative cooling) and the layer bottom (positive, due to surface fluxes). These are responsible for the generation of downdrafts and updrafts, which in turn enhance turbulence and vertical mixing across the STBL. Although STBL remains well mixed in θ_l, continuous supply of water vapor from the ocean, as well as precipitation and drying of the STBL top, all lead to the decoupling observed in q_t and also $< w'w' >$ (Fig. 4). The difference between mean q_t at the height of 200 m and 1200 m after 30 h is more than 2 g/kg (around 20%).

Fig. 5 shows evolution of the cloud water (q_c) profiles. For Sc, the cloud remains close

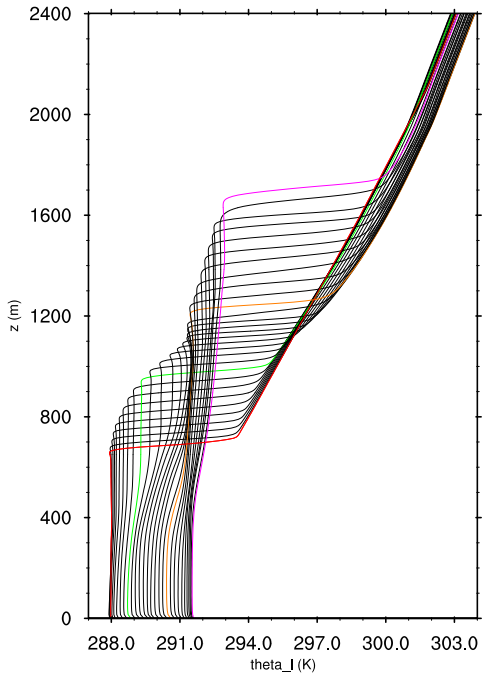

Figure 3: Hourly averaged mean profiles of the liquid water potential temperature for 30 h of simulation. Each profile represents one hour (1 h - red, 10 h - green, 20 h - orange, 30 h - magenta).

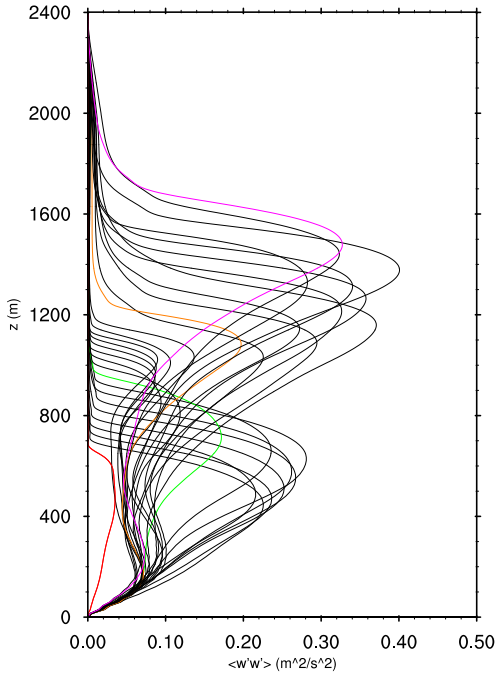

Figure 4: Hourly averaged profiles of the $< w'w' >$ for 30 h of simulation. Each profile represents one hour (1 h - red, 10 h - green, 20 h - orange, 30 h - magenta).

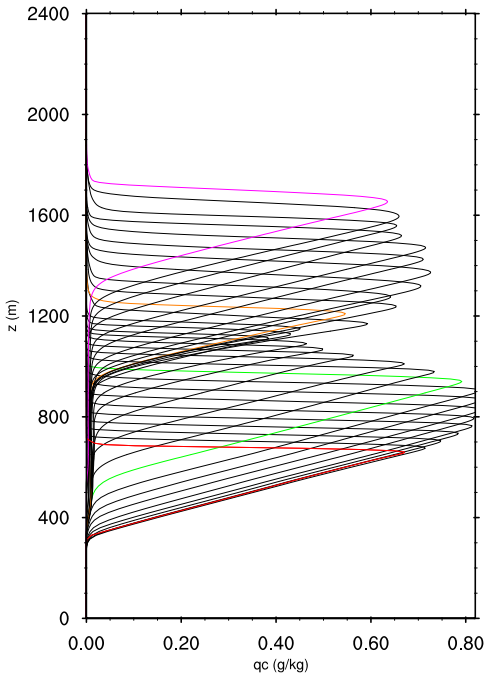

Figure 5: Hourly averaged mean profiles of the cloud water mixing ratio for 30 h of simulation. Each profile represents one hour (1 h - red, 10 h - green, 20 h - orange, 30 h - magenta).

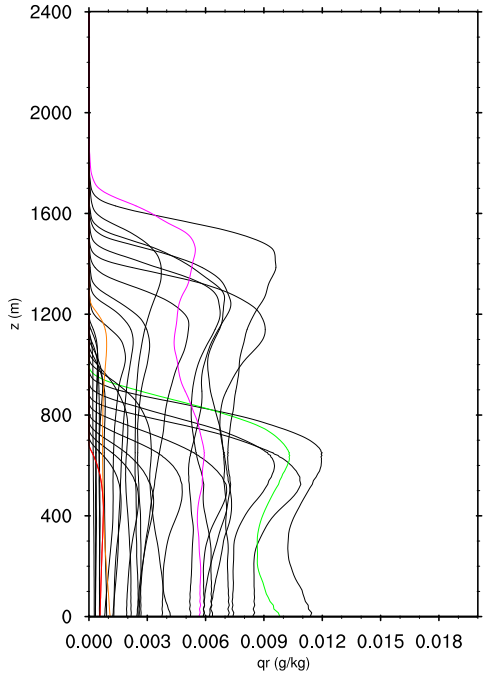

Figure 6: Hourly averaged mean profiles of the rain water mixing ratio for 30 h of simulation (1 h - red, 10 h - green, 20 h - orange, 30 h - magenta).

to adiabatic at all times due to efficient mixing within the STBL. The mean cloud top height follows the evolution of inversion level, but the cloud base rises only about 250 m after 30 h. The cloud layer below stratocumulus, with mean q_c values of just a few hundredths of g/kg or less, represents a field a scattered shallow convective clouds that forms during the course of the simulation. The

sub-layer of broken Cu thickens in time and at the end represents about 50% of the cloud field depth.

Evolution of the drizzle mixing ratio profiles is shown in Fig. 6. The maximum of the drizzle water is observed at 11 h (0.012 g/kg). Although the autoconversion is less efficient at later hours, the second night is characterized by similar RWP values as during the first night time. This is because precipitating water falls out from a much larger altitude as the top of STBL systematically increases in time.

4. SUMMARY AND CONCLUSIONS

In this study, modifications of the anelastic nonhydrostatic model EULAG to LES setup designed for simulating Sc to Cu transition was presented along with many-hour simulation results. The STBL evolution is characterized by a continuous increase of its depth and a gradual decoupling of its internal structure. A sub-layer of broken Cu develops beneath close-to-solid St. According to the results of sensitivity tests, radiation, microphysics and subrid-scale transport at the cloud top all play vital role in the simulation, and their interactions strongly affect evolution of the boundary layer. When simulating cloud-top radiative cooling, a full radiation scheme has demonstrated its clear advantage over a simplified approach, especially for multi-day simulations. The microphysical schemes, commonly used in Cu modeling, turned out to produce too much precipitation when used for the representation of drizzle. The most realistic results were obtained for Sc-oriented microphysics, full radiation scheme, and relatively small mixing length used in subgrid-scale turbulent transport scheme. Results of subsequent studies will be presented at the conference.

5. REFERENCES

Bretherton, C. S., S. K. Krueger, M. C. Wyant, P. Bechtold, E. van Meijgaard, B. Stevens, and J. Teixeira, 1999: A GCSS boundary-layer cloud model intercomparison study for the first ASTEX Lagrangian experiment. *Bound.-Lay. Meteor.*, **93**, 341-380.

Berry, E. X., and R. L. Reindhart, 1974: An analysis of cloud drop growth by collection. Part II. Single initial distributions. *J. Atmos. Sci.*, **31**, 1825-1831.

Hack, J. J., B. A. Boville, B. P. Briegleb, J. T. Kiehl, P. J. Rasch, D. L. Williamson, 1993: Description of the NCAR Community Climate Model (CCM2), *NCAR Technical Note*, NCAR/TN-382+STR

Heus, T., C. C. van Heerwaarden, H. J. J. Jonker, A. Pier Siebesma, S. Axelsen, K. van den Dries, O. Geoffroy, A. F. Moene, D. Pino, S. R. de Roode, and J. Vila-Guerau de Arellano, 2010: Formulation of the Dutch Atmospheric Large-Eddy Simulation (DALES) and overview of its applications. *Geosci. Model Dev.*, **3**, 415-444.

Kessler, E., 1969: *On the Distribution and Continuity of Water Substance in Atmospheric Circulations. Meteor. Monogr.*, No. 32, Amer. Meteor. Soc., 84 pp.

Khairoutdinov, M., and Y. Kogan, 2000: A new cloud physics parameterization in a large-eddy simulation model of marine stratocumulus. *Mon. Wea. Rev.*, **128**, 229-243.

Prusa, J. M., P. K. Smolarkiewicz, and A. A. Wyszogrodzki, 2008: Eulag, a computational model for multiscale flows. *Comp. and Fluids*, **37**, 1193-1207.

Smagorinsky, J., 1963: General circulation experiments with the primitive equations. *Mon. Wea. Rev.*, **91**, 99-164.

Schumann, U., 1991: Subgrid length-scales for large-eddy simulation of stratified turbulence. *Theor. Comput. Fluid Dyn.*, **2**, 279-290.

Stevens, B., and Co-authors, 2005: Evaluation of large-eddy simulation via observations of nocturnal marine stratocumulus. *Mon. Wea. Rev.*, **133**, 1443-1462.

Acknowledgements

The authors would like to express sincere gratitude to Swiss National Computing Center and National Center for Atmospheric Research for providing computational resources. The National Center for Atmospheric Research is operated by the University Corporation for Atmospheric Research under sponsorship of the National Science Foundation. The technical support from Johan van der Dussen is also gratefully acknowledged.

This work has been funded by the European Commission 7th Framework programme project EUCLIPSE, contract no. 244067.

CONVECTION AND PRECIPITATION UNDER VARIOUS STABILITY AND SHEAR CONDITIONS: NUMERICAL EXPERIMENTS FOR MESOSCALE CONVECTIVE SYSTEMS

Tetsuya Takemi
Disaster Prevention Research Institute, Kyoto University, Uji, Kyoto, Japan

1. INTRODUCTION

The structure and intensity of mesoscale convective systems (MCSs) are strongly regulated by their environmental conditions such as horizontal wind, temperature, and moisture. These environmental conditions are determined by synoptic-scale and/or larger-scale meteorological settings that develop in various climates ranging from the Tropics, sub-Tropics, mid-latitude regions, and arid/semi-arid regions. Because of the diversity of the climates over the globe, the meteorological settings that host mesoscale convective phenomena have a wide variety which is characterized by the horizontal and vertical distribution of wind, temperature, and moisture. Although a large number of studies have investigated the various aspects of MCSs in a certain specific region of the world, much less number of studies compared the characteristics of MCSs that develop in different climate regions.

A significant difference between tropical and midlatitude convection is found for vertical velocities. Zipser and LeMone (1980) showed that the size and intensity of updrafts and downdrafts are significantly weaker in the tropical system than in the midlatitude one by comparing their observations with the data from the Thunderstorm Project. Lucas et al. (1994) suggested that the weaker vertical velocities in the Tropics are due to smaller buoyancy that is attributed to more effective water loading and entrainment, and they identified the midlatitude soundings as large buoyancy and the tropical sounding as small buoyancy. The importance of buoyancy profiles has been pointed out by a number of studies (e.g Takemi and Satomura 2000, Takemi 2010).

The purpose of this study is to investigate the sensitivity of the structure and intensity of MCSs to the vertical profiles of temperature and moisture that represent tropical, oceanic and midlatitude, continental environments. A special focus for the environmental conditions is given to the vertical distribution of convective available potential energy (CAPE) that is determined by the temperature and moisture profiles. For the present purpose, we use the Weather Research and Forecasting (WRF) model/the Advanced Research WRF (ARW) version to perform a set of numerical experiments for MCSs under various temperature, moisture, and shear conditions in an idealized model setup. Squall lines are specifically examined as a representative mode of MCSs. This study is a part of the series of the studies conducted by the present author (Takemi 2006; 2007a; 2007b; 2010).

Corresponding author address:
Tetsuya Takemi, Disaster Prevention Research Institute, Kyoto University, Uji, Kyoto 611-0011, Japan
E-mail: takemi@storm.dpri.kyoto-u.ac.jp

2. MODEL AND EXPERIMENTAL SETUPS

The numerical model used in this study is the WRF/ARW model Version 3.1.1 (Skamarock et al. 2008). The model is configured for performing numerical experiments in idealized settings. The base-state atmosphere is horizontally homogeneous, and uni-directional shear is assumed.

The grid resolutions of the experiments are 500-m spacing in the horizontal directions and 116 vertical levels in the computational domain of 300 km (east-west) by 60 km (north-south) by 23 km (vertical). The physics processes included in the present idealized experiments are only cloud-microphysics (Goddard warm-rain and ice-phase parameterization) and turbulent mixing (Deardorff TKE scheme). The lateral boundary conditions are periodic at the north and south boundaries and open at the east and west boundaries. The lower boundary is free slip, while the upper boundary is rigid with a Rayleigh-type damping layer.

The thermodynamic profiles are given by a tropical sounding for a squall line over the tropical western Pacific (Trier et al. 1996) as a tropical, oceanic environment (TROPICS), and by an analytical sounding for mid-latitude supercells (Weisman and Klemp 1982) as a mid-latitude, continental environment (MIDLAT). The MIDLAT conditions are further divided as a moist type (the original Weisman-Klemp humidity profile, referred to as MIDLATM) and a dry type (reduced humidity from the Weisman-Klemp profile, referred to as MIDLATD). These thermodynamic conditions are characterized by the same CAPE value for the surface air parcel but by different CAPE distribution for elevated parcels above the surface level. On the other hand, five types of wind shear are examined: 5 m/s difference in the 0-2.5-km layer or in the 2.5-5-km layer; 15 m/s difference in the 0-2.5-km layer or in the 2.5-5-km layer; and 15 m/s difference in the 0-5-km layer. For each thermodynamic profile (TROPICS, MIDLATM, MIDLATD), these five shear profiles are defined. Furthermore, the initial disturbances are given by both warm and cold linear-type thermal aligned in the north-south direction. The set of experiments initialized by the warm line thermal is referred to as W-type, while that initialized by the linearly oriented cold pool is as C-type. Taking into account the different initialization, we perform five sets of experiments (TROPICS-W, TROPICS-C, MIDLATD-W, MIDLATD-C, MIDLATM-W) with five different shear profiles. Thus, the total number of experiments is 25. The integration time period for each experiment is 6 hours.

3. RESULTS

We compared the structure and intensity of the simulated MCSs in different conditions in terms of means and variability of precipitation intensity, vertical velocities, updraft fractional areas, and the relevant properties. The temporal and spatial mean precipitation intensity (which is the same as the accumulated precipitation) generally increases with the increase in temperature lapse rate (Fig. 1).

CAPE for the surface air parcel

distinguishes the intensity of MCSs if the lapse rates among the different conditions are similar. A critical impact on the MCS intensity is related to the vertical distribution of CAPE for elevated parcels above the surface (mainly within the PBL depth). The CAPE distribution is closely tied to the lapse rate in the troposphere as well as the moisture content in the boundary layer. The role of the shear profile in determining the MCS intensity becomes more significant in drier conditions by counteracting cold pools through the Rotunno-Klemp-Weisman mechanism. The sensitivity to the initial disturbances is less significant in moister environments. An interesting result is found for the maximum instantaneous precipitation intensity: the maxima increases with the decrease in lapse rate. There may be an optimal lapse rate for developing precipitation maxima.

4. REMARKS

We conclude that temperature lapse rate in the convectively unstable troposphere is useful in comparing the characteristics of MCSs that occur in various stability and shear conditions. An implication of this study is that precipitation characteristics in a future climate under global warming may be explained by the static stability (Takemi et al. 2012; Takemi 2012). It is suggested that stability diagnosis for the climate simulation data should be useful for examining the variation of precipitation characteristics in the simulated climates.

5. ACKNOWLEDGMENTS

This work is supported by the grant under Strategic Programs for Innovative Research (SPIRE)-Field 3 “Projection of Planet Earth Variations for Mitigating Natural Disasters”. I appreciate the supports made by Dr. Kazuo Saito at Meteorological Research Institute in coordinating the research project.

6. REFERENCES

Lucas, C., E. J. Zipser, and M. A. LeMone, 1994: Vertical velocity in oceanic convection off tropical Australia, J. Atmos. Sci., 51, 3183-3193.

Skamarock, W. C., J. B. Klemp, J. Dudhia, D. O. Gill, D. M. Barker, M. G. Duda, X. Y. Huang, W. Wang, and J. G. Powers, 2008: A description of the Advanced Research WRF Version 3. NCAR Tech. Note, 475, 113 pp.

Takemi, T., 2012: Projected regional-scale changes in atmospheric stability condition for the development of summertime convective precipitation in the Tokyo metropolitan area under global warming. Hydrol. Res. Lett., 6, 17-22.

Takemi, T., 2010: Dependence of the precipitation intensity in mesoscale convective systems to temperature lapse rate. Atmos. Res., 96, 273-285.

Takemi, T., 2007a: Environmental stability control of the intensity of squall lines under low-level shear conditions. J. Geophys. Res., 112, D24110.

Takemi, T., 2007b: A sensitivity of squall-line intensity to environmental static stability under various shear and moisture conditions. Atmos. Res., 84, 374-389.

Takemi, T., 2006: Impacts of moisture profile on the evolution and organization of midlatitude squall lines under various

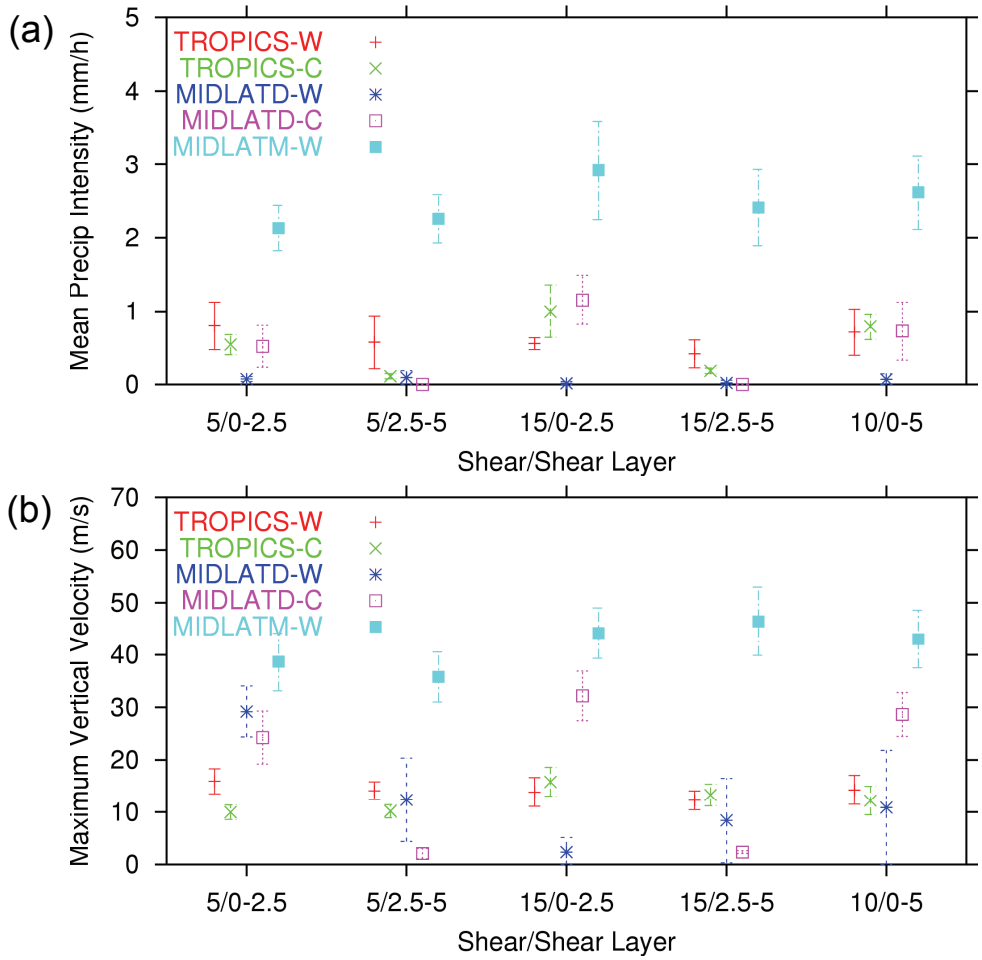

Fig. 1: (a) Mean precipitation intensity (mm h^{-1}) and (b) maximum vertical velocity in the computational domain for the various shear conditions in various stability conditions.

shear conditions. Atmos. Res., 82, 37-54.

Takemi, T., and T. Satomura, 2000: Numerical experiments on the mechanisms for the development and maintenance of long-lived squall lines in dry environments. J. Atmos. Sci., 57, 1718-1740.

Takemi, T., S. Nomura, Y. Oku, and H. Ishikawa, 2012: A regional-scale evaluation of changes in environmental stability for summertime afternoon precipitation under global warming from super-high-resolution GCM simulations: A study for the case in the Kanto Plain. J. Meteor. Soc. Japan, 90A, 189-212.

Weisman, M.L., and J. B. Klemp, 1982: The dependence of numerically simulated convective storms on vertical wind shear and buoyancy. Mon. Wea. Rev., 110, 504-520.

Zipser, R. J., and M. A. LeMone, 1980: Cumulonimbus vertical velocity events in GATE. Part II: Synthesis and model core structure, J. Atmos. Sci., 37, 2458-2469.

CALCULATED AND EXPERIMENTAL REGULARITIES OF CLOUD MICROSTRUCTURE FORMATION AND EVOLUTION

N.P. Romanov, V.G. Eran'kov

Institute of Experimental Meteorology, FBSI RPA 'Typhoon'

4 Pobedy Street, 249038, Obninsk, Kaluga region, Russian Federation

Tel.: +7(48439) 71540

Fax: +7(48439) 40910

E-mail: vernik@typhoon.obninsk.ru

1. INTRODUCTION

Studying of the processes of cloud and fog microstructure formation during their initiation plays an important role in the understanding of the mechanisms of the microstructure formation and interaction of the drops formed with the environmental pollutants. The connection of a cloud microstructure with atmospheric aerosol composition influences the climate forming conditions. Of importance is also the problem of precipitation enhancement at cloud modification with hygroscopic agents. But up to the present, there is no generally accepted mechanism of experimentally observed in natural conditions rather broad cloud spectra [1], because the mechanism of regular condensation does not explain this aspect. In the monograph by Yu.S. Sedunov [2] devoted to the initial stage of condensation it is shown that within the frameworks of the theory of regular condensation at a constant rate of updraft the drop spectrum becomes narrower with altitude.

In the same way, by analyzing dominant estimations for the Junge condensation nuclei (CN) the regularities of cloud drop spectra were obtained. These are the exponential function of maximum oversaturation and the concentration of the drops formed unambiguously connected with it on the velocity of updraft and CN concentration. Corresponding expressions for the exponents are given. In the next work [3, part 2] broad drop spectra, formed due to evaporation of fine drops, were obtained for high concentrations of CN (HC). But this result has not been analyzed from the physical viewpoint and was not considered later on. In the recently published work [4], with the use of a numerical model of regular condensation confirmed is the dependence, obtained in [2], of drop concentration on the velocity of air mass updraft, and its corrected dependence on CN concentration is given. The dependence of drop concentration on air mass temperature and pressure is given as well. But the author limited himself by the case of small concentrations (SC) at which the cloud drop concentration formed at the initial moment remained constant at a further updraft. In the works by foreign authors the attempts to find a solution of the problem are likely to be stopped. In the work by Khvorostyanov V.I. and J. A.

Curry [5] the same dependences are studied for three kinds of spectra: the exponential, log-normal and algebraic ones. For the determination of the drop concentration without defining parameters of their spectra one can find a set of parameters for CN spectra in the paper by N. Kivekas et al. [6]. In all the works mentioned above the case of high CN concentrations, that must result in qualitative changes of the mechanism of drop spectrum formation, has not been practically studied. The effect of air mass temperature on the regularities of cloud drop spectra has not also been studied (with the exception of [4]).

To eliminate these gaps, the present paper presents a cycle of numerical studies for the initial stage of the condensation process made in the frameworks of the theory of regular condensation. For this purpose the author constructed a numerical model of regular condensation, the description of which together with the calculation results for different concentrations of CN and temperatures at a constant velocity of air mass updraft are given in the first part of the present paper. There are also given the results of numerical simulations of cloud microstructure evolution at ceasing of updraft and at varying modes of updraft and downdraft and analyzed the possibilities to describe the calculated spectra with the analytic expressions.

The second section gives a comparison of calculated regularities with the experimental results of cloud spectra formation in the Big Aerosol Chamber.

2. CALCULATED REGULARITIES OF CLOUD SPECTRA FORMATION

2.1. BASIC RELATIONSHIPS AND GENERAL PATTERN OF CALCULATION SPECTRA FORMATION

For studying calculated regularities of cloud spectra formation we shall limit ourselves by a two-parametric inverse power distribution of the condensation nuclei over their equivalent radii r_c.

$$F(r_c) = C_c \frac{(\nu - 1)}{r_{c0}} \left(\frac{r_c}{r_{c0}} \right)^{-\nu} \qquad (1)$$

where C_c determines the number of particles with $r_c > r_{c,0}$ per 1 mg of air.

This distribution is transformed at a 100% humidity into an equilibrium distribution over the radii r_w of CN covered with water being droplets of a salt particles dissolved in water [2]

$$F(r_w) = C_c \frac{(\nu_w - 1)}{r_{w,0}} \cdot \left(\frac{r_w}{r_{w,0}} \right)^{-\nu_w} \qquad (2)$$

Under an approximation of the equality of the surface tension δ and the solution density ρ with the corresponding characteristics of pure water, the value of r_w is determined by the number of salt molecules n_c multiplied by the Van't-Hoff factor i_c with the relationship [7]

$$\nu_w = \frac{2\nu + 1}{3} \qquad r_w^2 = \frac{3 m_w R_w T}{8\pi\sigma_w} i_c n_c \qquad (3)$$

Here m_w is the mass of a water molecule, T is temperature, R_n is the gas constant of water vapor.

The use of distribution (3) makes it possible to avoid the numerical procedure of

studying the process of dry CN transformation at increasing relative humidity of air. For calculating the processes of drop formation the CCN interval chosen is separated into n channels with an equal number of CCN in them, that is not necessarily to be an integer. At a growth of a drop the number of salt molecules in it remains constant, and its growth depends on the precipitation of the number of water molecules at increasing relative humidity f. The Van't-Hoff factor is considered constant, the distribution of salt is homogeneous. The formulae for drop growth are taken from the monograph [2] at introduction of oversaturation δ=lnf. The value of vapor molecules accommodation is taken equal to 0.98.

At the first stage during the time interval Δt is determined by the variation of thermodynamic parameters due to the air mass updraft. At the second stage an increment of mass that occurred during this time is calculated for every nucleus. Then, the value of *f* is corrected for the total growth of mass on drops. It has been stated experimentally that stable results of calculations were obtained at Δh = 1 cm and n ≥ 100. Here, it appeared that, depending on the CN concentration, two different modes of cloud spectra formation can be realized. They will be named the regime of small (SC) and high (HC) concentrations. The difference of these regimes is illustrated by the curves in figure 1, where for the process of air mass updraft with the velocity of 1 m/s to the height of 30 m and at its further evolution at a ceased updraft presented are the trajectories of drop growth (1a and 1b) at the separation of the whole spectrum into 100 channels, and in figure 1c – the trend of the drop concentration C_g(1/mg), δ(%) and a relative breadth rb.

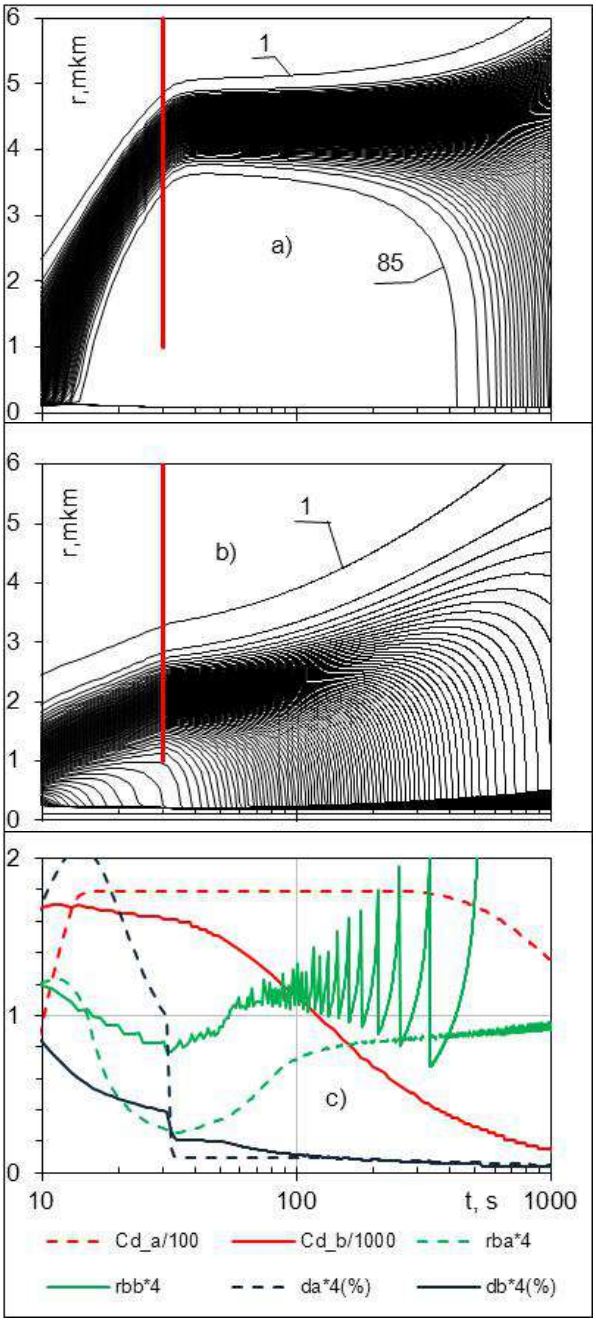

.

Figure 1. Trajectories of drop growth (a, b) and (c) - the trend of drop spectrum integral characteristics (Cd, d≡δ and rb): a) in the mode of SC – $C_c=10^2$ mg^{-1}; b) in the mode of HC – $C_c = 10^4$ mg^{-1}, v = 1 m/s, ν=5, T=20°C, n = 100.

The red vertical lines in figures a and b indicate the moments of updraft termination t = 30 s, and the numbers near the trajectories correspond to the ordinal number of channels. From figure 1a the process of growing drops separation from CCN covered with water at the moment of maximum oversaturation at the 16 second is distinctly seen. For the case shown in figure 1b the concept of 'a drop' is dimmed because in the spectrum different from stationary sizes of CN covered with water both growing and evaporating drops are present. Therefore, all the drops covered with water of non-stationary sizes or exceeding any size (in this case it is 0.4 micrometer) can be considered as drops.

2.2. APPROXIMATION OF CALCULATED SPECTRA

When studying the spectra the main problem is in their adequate presentation in the form of particular analytic expressions. As such we tested the Lifshitz spectrum f_{lif} [8,9], gamma-distribution f_γ, log-normal distribution f_L, Smirnov distribution f_S [10] and a possibility to use a combination of algebraic expressions.

Here it appeared that the spectrum f_{lif} coincides with the calculated one only for the appropriate for this spectrum value of rb≈0.215. The analytic distributions f_γ, f_S, f_L give a qualitative difference as compared with the calculated spectra. It is in a slower decrease in the large drop spectrum fraction and a quicker increase in a small-droplet spectrum fraction. The choice of expressions in the form of the power law with the index from 2.6 to 3 in the left-hand side and the inverse power law with the index from 8 to 11 in the right-hand side wings and a parabolic one in the spectrum center showed that such an approach can satisfactorily describe the calculated spectra. But the choice of corresponding parameters is very time-consuming.

To find appropriate relationships for describing the calculated spectra we used dissymmetric shifted $f_{\gamma m}$ $f_{\gamma m}$ and f_{SKm} distributions obtained at replacing the value of r by the value of (r_{max}-r+<r>). Below, we write these expressions for normalized by unity distributions in a dimensionless form with the use of the value of u=r/<r> and the location of a maximum of the approximation function u_m

$$f_{\gamma m}(u) = \frac{\mu^{\mu+1}}{\Gamma(\mu+1)}(u_m - u + 1)^{\mu} \exp(-\mu(u_m - u + 1)) \quad (4)$$

$$f_{Sm}(u) = \frac{(k)^{k-1}}{\Gamma(k-1)} \cdot (u_m - u + 1)^{-k} \exp\left(-\frac{k}{u_m - u + 1}\right) \quad (5)$$

Both these distributions are the functions of one parameter u_m and the second parameters μ and k, correspondingly. Maxima of these functions do not depend on the value of u_m.

The dispersion of the spectra with spectra with the use of moments of function M(n) is expressed their application in the form of

$$\sigma^2 = \int_0^{\infty} (r - \bar{r})^2 f(r) dr = \bar{r}^2 \left(\frac{M(2)M(0)}{M^2(1)} - 1 \right)$$

A relative breadth spectrum is determined by the ratio rb=σ/<r>

The values of u_m and sg obtained after

calculations or experiments can be used for determining the parameters of μ and k in the approximation spectra. But at a corresponding comparison it appeared that the calculated value δ strongly depends on the behavior of f(u) on their wings, where an measurement or calculation errors can be significant. It also appeared that for an adequate description of spectra more reasonable is the agreement of measured and approximated spectra in the location of a maximum and its value. But we failed to obtain an analytic expression for the dependence of μ and k on max f(u). Therefore we propose to use for this the following approximation expressions.

$$\mu = 6{,}9 \cdot \max \mathrm{f(u)}^{1{,}92} - 0{,}7$$

$$k = 7{,}1 \max f(u)^{1{,}79} \qquad (6)$$

We shall also write an expression for the non-parametric distribution $f_{\gamma m}$ with rb≈0.215 that pretends to be an asymptotic distribution.

$$f_{lif}(u) = \begin{cases} \dfrac{3^4 e}{2^{\frac{5}{3}}} \dfrac{u^2 \exp\left(-\dfrac{1}{1-2u/3}\right)}{(u+3)^{\frac{7}{3}}\left(3/2-u\right)^{\frac{11}{3}}}, & u < u_0 = \dfrac{3}{2} \\ 0, & u > u_0 = \dfrac{3}{2} \end{cases} \qquad (7)$$

The results of comparison of calculated and approximation spectra are given in figure 2 a and b for typical moments (the time is given in the legend) of the air mass updraft cycle with the velocity of 1 m/s to the height of 30 m and its further evolution at this height.

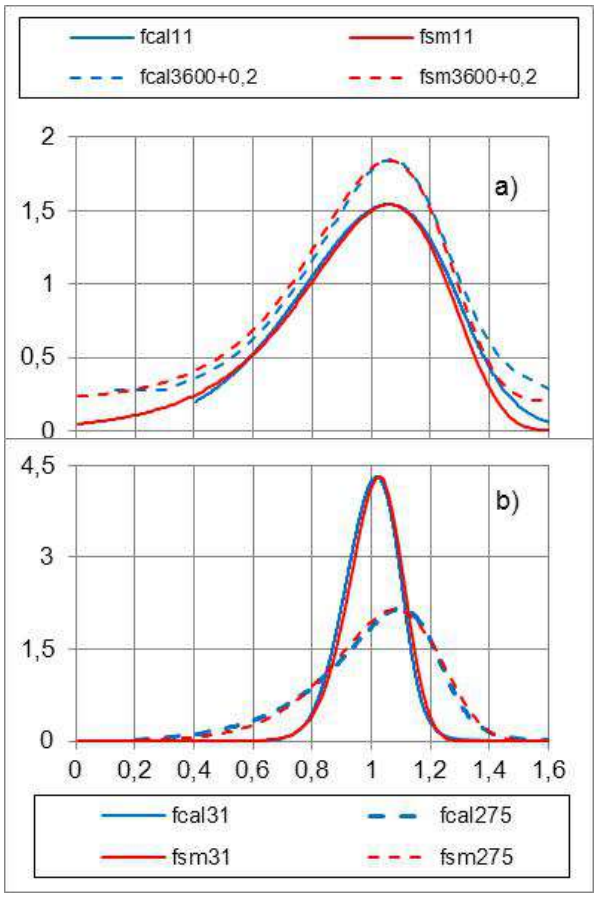

Figure 2. Comparison of calculated f_{cal} and f_{sm} for the time moments a) 11 and 3600 s after the beginning of the process and b) 30 s (termination of updraft) and 275 s (the moment of reaching rb=0.215).

After comparison at other updraft heights, the CCN concentrations and other parameters it appeared that $f_{\gamma m}$ и f_{Sm} describe rather well the calculated spectra in the range of 0.2<u<1.4 both at the stage of their formation at an air mass updraft and the stage of their evolution at a constant altitude. The first one is better at spectra approximation for large CCN concentrations and the second – for small CCN concentrations. The difference noted at u>1.4 can be eliminated by using the inverse power law for this part.

2.3. APPROXIMATION RELATIONSHIPS FOR INTEGRAL PARAMETERS OF THE INITIAL STAGE OF CONDENSATION

The studies of maximum oversaturation δ_m and other parameters on the updraft velocity u, CCN concentration and the index v, air mass temperature Ti and pressure ρ were performed at the subdivision (separation) into 1000 intervals.

Studied were the ranges of u = 0.1 ÷ 10 m/s, C_c = 100 ÷ 10000 at $r_{w,0}$=0.1 μm, ν from 4 to 8, *Tc* = -10 ÷ +30°C и ρ = 0.8 ÷ 1.25 atm. As a result, it appeared that at SC δ_m can be approximated via the following relationships:

$$\delta_м(C_c,u,T)=\delta_{m0}(T)\left(\frac{C_c}{C_{c0}}\right)^{-x}\left(\frac{u}{u_0(T)}\right)^{y}$$

$$y=\frac{1.05}{(\nu+1)^{2/3}} \qquad x=\frac{1}{\nu+1}$$

$$u_0(T,C_{c0}=100)=0.82+0.009T_c$$

$$\delta_{m0}(T,C_{c0}=100)=0.62-0.005T_c$$

(8)

The height of the updraft h_m at which δ_m is attained is practically proportional to δ_m and is determined by the relationship similar to (4). Let us write this relationship in the form of

$$h_m(C_c,u,T)=h_{m0}(T)\left(\frac{C_c}{C_{c0}}\right)^{-x}\left(\frac{u}{u_{h0}(T)}\right)^{y}$$

(9)

where the exponents x and y are determined by formulae (8), and the values of h_{m0} (20^0C) = 10 m and u_{h0} (20^0C) = 0.42 m/s at C_c = 100 mg^{-1}.

At the heights h=2_{hm} and 3_{hm} drop liquid content makes 80 and 90% as compared with (relative to) the thermodynamic one, correspondingly. Note that for the mode of SC an approximation error (9) does not exceed the units of percent. The character of the above-mentioned dependences at the transition to the mode of HC is not considered in this paper.

The analytic regularities for the drop concentration Cd(1/mg) for the mode of SC can be obtained by integration over δ from 0 to δ_m of the nucleus distribution function over oversaturations (8). But for the errors from there not to be included here, an approximation for the drop concentration was obtained on the basis of its own calculations. It has the form of:

$$C_d=C_{d0}\left(\frac{C_c}{C_{cd}}\right)^{s}\left(\frac{u}{u_{d0}}\right)^{q} \qquad s=\frac{\nu+5}{3(\nu-1)}$$

$$q=0.707\frac{\nu-1}{(\nu+1)^{2/3}}-0.01(\nu-3.5)$$

$$C_{d0}(T)=114+0{,}4T_c$$

$$u_{d0}(T)=0.26+0.07T_c$$

C_{d0} = 200 (mg^{-1}).

(10)

To conclude this part we shall note that in our calculations the dependence of the above-mentioned parameters on ρ has not been found in the above range.

2.4. EVOLUTION OF CLOUD PARAMETERS AT A CONSTANT HEIGHT

A calculated character of integral parameters behavior at a constant temperature depending on the conditions of their formation at an ascending air mass illustrated in figure 3 a, b and c.

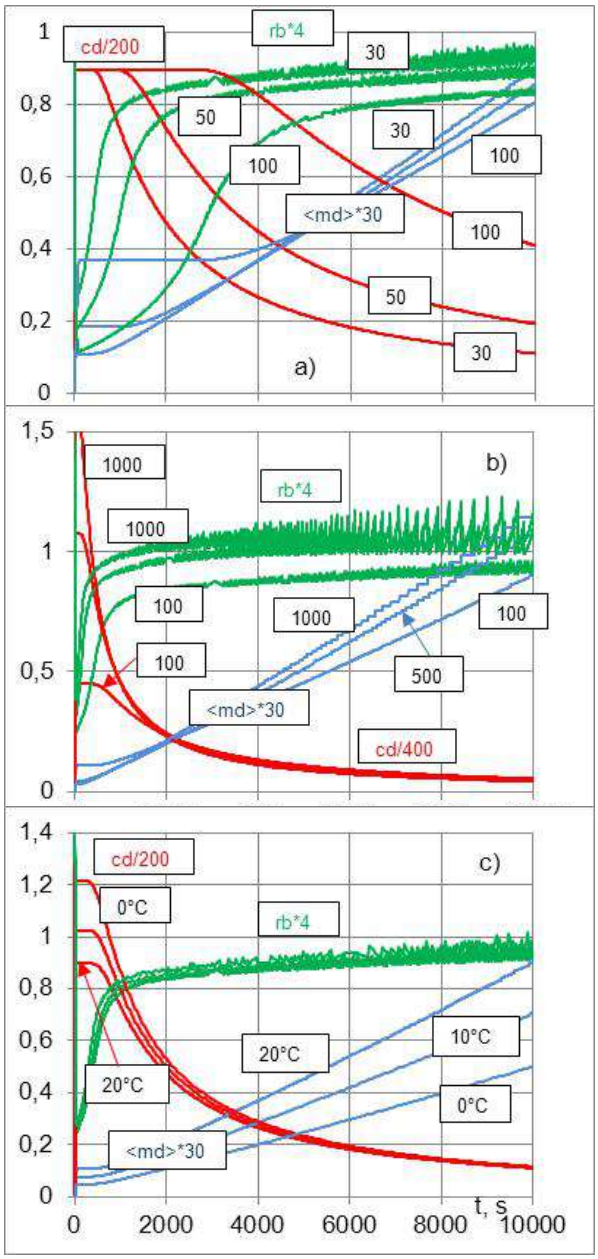

Figure 3. Dependence (v = 1 m/s) of an average drop mass <m_d> (10^{-10}g), C_d(mg^{-1}) and relative breadth rb on time at different a) updraft heights, (T=20°C, C_c=500), b) CCN concentrations (h=30 m, T=20°C) and c) temperatures (h=30 m, C_c=500). The multipliers of the values are indicated in the figure.

From the figures it is seen that in some time after the air mass ascent ceased depending on the value of h the growth of the drop average mass starts to acquire a linear regularity with time counted from the moment t_0 of ascent termination. This coefficient weakly depends on the updraft height ((drop liquid content) and increases noticeably with a growing CCN concentration and temperature increase. Considering only the dependence on temperature and taking into consideration the range of the value of *a* changes at varying h and C_c, this dependence can be written in the form of

$$\overline{m}_d(t) = a(T,h,W_T)t$$

$$a \cong (1 \div 2)\cdot 10^{-10}(1+0{,}05T_c)\ \text{(g/s)} \quad (11)$$

The moment when the regularity t_{as} comes into action strongly depends on the initial width of spectra and may last several hours at rb≈0.01

2.5. FORMATION OF BIMODAL DROP SPECTRA

A fast growth of updraft velocity can result in the appearance in the spectrum the drops of the second kind. An illustration of such a condition is given in figure 4, where for two CCN concentrations given are the trajectories of particle sizes at an increase of updraft velocity by 5 times.

The condition for the appearance of the second mode v2 ≥5. v1 does not practically depend on the n the environmental conditions and the velocity v1. For a cloud medium remaining for some time at a constant height, the appearance of the second mode is possible at the updraft velocities of v≈0.2 m/s.

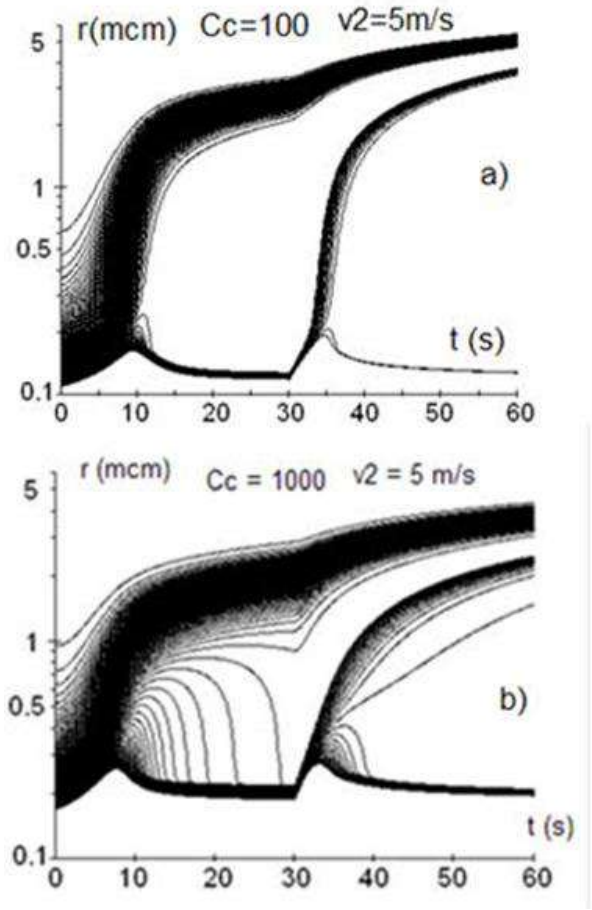

Figure 4. Trajectories of particles at a strong growth of updraft velocity v1 = 1 m/s at moment t = 30 s, T = 20^0C, ν = 5

Note that at slow cyclic altitude variations the law of growth of an average drop mass at a fixed level does not change.

3. EXPERIMENTAL STUDIES OF CLOUD MICROSTRUCTURE FORMATION IN ARTIFICIAL FOG CHAMBER

3.1 DESCRIPTION OF AN EXPERIMENT

Experimental studies of regularities of cloud spectra formation and transformation were performed in the BAC of IEM [11] (cylinder of the height of 18 and diameter of 15 m) where an air mass updraft was simulated by dropping excessive pressure created earlier. The Chamber is equipped with the temperature and humidity sensors with the use of standard instrumentation and drop spectra with the help of a photo-electric meter (counter) FIROK operating in the range of cloud drop radii from 0.35 to 50 micrometer.

A change of updraft equivalent velocity is ensured by the change of pressure dropping rate and was determined by the relationship.

$$\frac{1}{p}\frac{dp}{dt} = -\frac{g}{R_e T}u$$

The conditions of isothermality were ensured by a termination of the process of pressure dropping at equal temperature in the Chamber and the temperature of its walls. The composition of CN was determined by their content in the environmental air. CN spectra and composition was not controlled, but the stability of their characteristics was checked by the reproducibility of characteristics of cloud drop spectra formed under similar conditions of pressure dropping.

3.2. EXPERIMENTAL RESULTS AND COMPARISON WITH THE CALCULATED DATA

Some experimental results obtained with the use of the BAC were reported at the 13-th Conference on Cloud Physics [12] without a comparison with the calculation data. The present paper gives new results with a corresponding comparison.

At the first stage studied was a dependence of cloud drop concentration on the equivalent velocity of air mass updraft. It appeared that the experimental points coincide best of all with the calculated ones at ν=5, Cc=10^4(1/mg). Such high concentrations of

condensation nuclei are explained by the fact that the air is pumped into the chamber from the height of only 20 m. The formation of spectra at such CCN concentration occurs in the GC mode. Therefore, in the experiments in BAC no narrow spectra were observed. Their form is stabilized in some time. The dependence of cloud parameters on time connected with drop spectra is shown in figure 5.

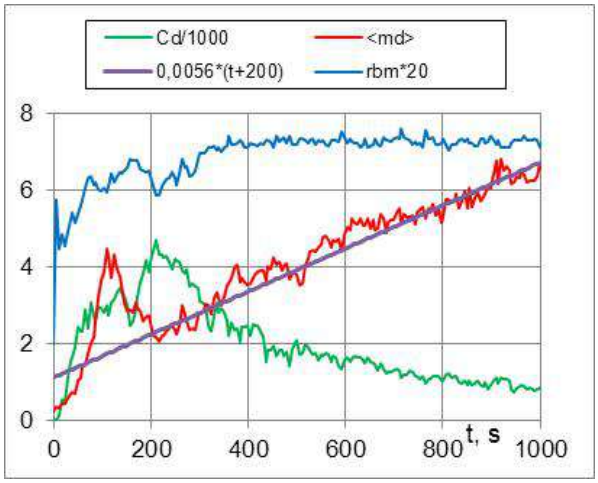

Figure 5. Dependence of $C_d(cm^{-3})$, rb, $<m_d>$(microgram) and its approximation by the linear law for a cycle of updraft to the altitude of 200 m and a further evolution of the cloud medium. t = 200 s is the time of the discharge termination. The data are multiplied by the coefficients from the legend. An average temperature of the process is equal to 20^0C.

In the same figure for an updraft cycle to 200 m with the velocity of 1 m/s (after which the air temperature in the chamber becomes equal to the wall temperature) shown is the curve of an average drop mass, their concentration and a relative width of spectra depending on time. From the figure it is seen that the relative spectrum width changes little during the whole process. The average drop mass grows linear just after the updraft termination with the growth coefficient that is almost twice as that in the calculated relationship (11). The observation of spectra form made during the process showed its sufficient stability. A comparison of spectra in this experiment and a special experiment with cleaning the air from aerosols is shown in figure 6.

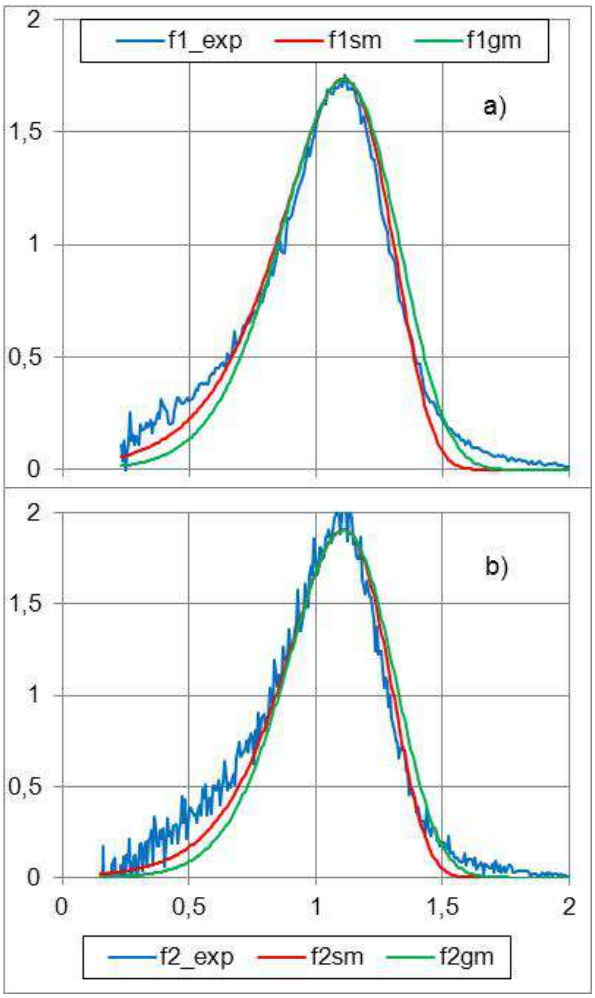

Figure 6. Comparison of an experimental f_{exp} and approximation f_{sm} and f_{gm} spectra with u_m=1,1 for the conditions a) without cleaning (<r>5.1 micrometer, C_d = 80 cm, k = 21, μ = 19) and b) with the cleaning of the air medium (<r> = 8 micrometer, C_d = 30 cm^{-3}, k=25, μ=23).

From the comparison it is seen that for the approximation of the experimental spectra most reasonable is the function f_{sm}. Without taking into consideration the differences in the range of small values of u, we shall note that at u>1.4 the experimental spectra are a little greater than the approximation ones. It is higher for the spectrum a) than for the spectrum b). Such an excess was noted for the calculated spectra as well. This phenomenon needs a more thorough investigation in the nearest future.

The experiments with the formation of the second mode demonstrated that for the updraft velocities v1 = 0.3 – 1 m/s the appearance of the second mode was noted at v2 = (4.5 – 5)v1, that corresponds to the calculated values of this relationship. For cloud spectra after 10 min of evolution at a constant temperature the appearance of the second mode was noted at v = 0.2 m/s, that qualitatively agrees with the calculated results obtained. Figure 7 is an illustration of spectra formation and transformation.

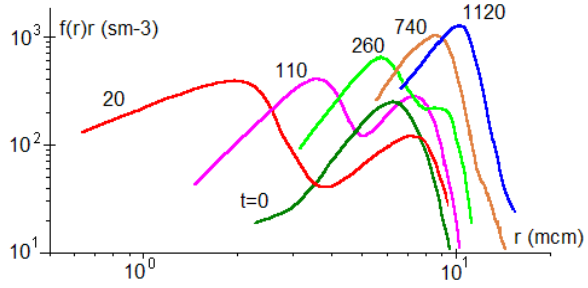

Figure 7. Formation of the second mode at the updraft velocity of 0.2 m/s after fog evolution at a constant height (temperature). The numbers at the curves indicate time in seconds from the updraft beginning.

From this figure it is seen that already at the 20-th second of the updraft beginning a fine-drop spectrum fraction is formed. The after the 280-th second the spectrum becomes a bimodal one. Later both modes merge.

4. CONCLUSIONS

A numerical model has been constructed, that makes it possible at a preset CN spectrum to calculate the process of drop spectrum formation at any variations of air mass updraft equivalent velocities. Based on the calculations with this model two approximation formulae applicable for the description both of narrow and broad cloud spectra are proposed. The main conclusions obtained with the model are supported by experiments performed in the Big Aerosol Chamber of SI “RPA ‘Typhoon’.

On the basis of these conclusions one can estimate the properties of natural clouds spectrum formation as:

— Broad spectra in natural clouds can be explained both by a high concentration of CN and the evolution of cloud microstructure under stationary meteorological conditions.

— Multi-modality of natural cloud spectra can be caused by fluctuations of air mass vertical motions.

— The factor of additional modes formation at vertical fluctuations of cloud layer even at the velocities of several tenths of m/s can result in a significant spectrum broadening in nature and stimulate coagulation processes in clouds.

— The spectra of natural fogs measured by the author [12, 13] have the form that is

described by the direct (mirror) shifted (displaced) distributions of the form of (4 and 5) proposed by us. It is likely that such a description is suited for the spectra of natural objects.

5. BIBLIOGRAPHY

1. I.P. Mazin, V.N. Merkulovich. Stochastic condensation and its possible role in the formation of cloud drop microstructure (review). Problems of cloud physics. Collection of articles in the memory of S.M. Shmeter, Moscow, 2008, p. 217-267.
2. Yu.S. Sedunov. Physics of liquid-drop phase formation in the atmosphere. Leningrad. Gidrometeoizdat, 1972,208 pp.
3. E. L. Alexandrov, N.V. Klepikova, Yu.S. Sedunov. Some results of cloud drop spectra formation. Parts I and II. Trudy IEM, issue, 12 (31), 1976. Moscow. Gidrometeoizdat. p. 19-53.
4. Drofa A.S. Formation of cloud microstructure during hydroscopic seeding. Izvestiya, Atmospheric and Oceanic Physics, 42, 326-336, 2006.
5. V.I. Khvorostyanov, J.A.Curry. Kinetics of Cloud Drop Formation and Its Parameterization for Cloud and Models. J. Atmos. Sci., 2008, V65, N 9, p. 2784 – 2802.
6. N. Kivekas, V.-M. Kerminen, T. Anttila, H. Korhonen, H. Lihavainen, M. Komppula, M. Kulmala. Parameterization of cloud droplet activation using a simplified treatment of the aerosol number size distribution. Journal of Geophysical Research, 2008, v. 113, p. 1-9.
7. N.P. Romanov. On an analytic presentation of Van'-Hoff's factor for water solutions of strong electrolytes. Izvestiya RAS. Fizika atmosfery I okeana. 2005. V. 41. No. 5. p. 702-714.
8. I.M. Lifshitz, V.V. Slyosov. On the kinetics of oversaturated solid solution diffusion decay. ZETF, 1958, V. 35, issue 2 (8), p. 479-492.
9. D.I. Busygina, A.S. Kabanov. An effect of temperature variations on condensation growth in clouds. Trudy IEM, issue 8 (46), 1974. Moscow. Gidrometeoizdat, p. 15-41.
10. V.I. Smirnov. About of the approximation of empirical distributions on a size clouds drops and other aerosol particles. Izvestiya AN USSR. Fizika atmosfery i okeana., 1973, v 9, No.1, p. 54-65.
11. Romanov, N. P. and Zhukov, G. P Thermodynamic Relations for a Fog Chamber, Russ. Meteorol.and Hydrol., 2000, No. 10, pp. 27-37.
12. N. P. Romanov. Experimental investigation of the processes of formation and evolution of natural and artificial fogs microstructure. 13th International Conference on Clouds and Precipitation. 14-18 August 2000, Reno Area, Nevada USA
13. N.P. Romanov. Some characteristics of fog in the center of European territory of Russia in October 1987. Meteorologiya i gidrologiya. 1990, No. 4. p. 63-68.

ENTRAINMENT IN UNBROKEN STRATOCUMULUS

Hermann Gerber[1], Glendon Frick[2], and Szymon Malinowski[2]
[1] Gerber Scientific, Reston, VA 20190, USA
[2] Naval Research Laboratory, Washington, D.C. 20375, USA
[3] University of Warsaw, Warsaw 02-093, Poland

1. INTRODUCTION

In July and August of 2008 the POST (Physics of Stratocumulus Top) field study was held off the California Coast to again investigate the entrainment process in unbroken stratocumulus (Sc). This study was motivated by the earlier DYCOMS-II stratocumulus entrainment study also of unbroken stratocumulus off the California Coast (Stevens et al., 2003a). DYCOMS-II was a useful learning experience on how to measure entrainment into Sc, since it was found that the horizontal width of entrained parcels was smaller than the mounting separation of the probes on the C-130 aircraft used during DYCOMS-II, and that the probes were mounted too far from the 5-hole gust probe on the aircraft nose. These factors likely affected entrainment flux (F_e) and velocity (w_e) estimates, with the latter varying as much as a factor of four as measured with 4 co-located independent probes on the C-130 (Gerber et al, 2005; Falloona et al. 2005), making comparisons with model predictions difficult (Stevens et al., 2003b).

The aircraft chosen for POST was the fully-instrumented Twin Otter (TO) from Naval Post Graduate School (CIRPAS, Center for Interdisciplinary Remotely Piloted Aircraft Studies). Figure 1 gives a head-on photo and sketch of the TO where only the closely co-located probes related to the present study are shown. The UFT (Ultra-Fast Temperature; Haman et al., 2001; Haman et al., 2007) probe, the PVM (liquid water content (LWC), and effective radius; Gerber et al., 1994), and three probes for measuring the vapor mixing ratio (q_v) are mounted on a hard-point ring close to the nose of the aircraft that also has on it 5 holes for the gust probe. The UFT and PVM data was collected at 1000 hz. However, given the ~0.5 m separation the two probes the data was averaged to 50 hz yielding horizontal incloud resolution in the cloud of ~1 m at the TO speed of ~50 m/s. This resolution is consistent with the smallest entrainment scales observed during DYCOMS-II, and provides for the first time the opportunity to look at the microphysics and thermodynamics of individual entrained parcels.

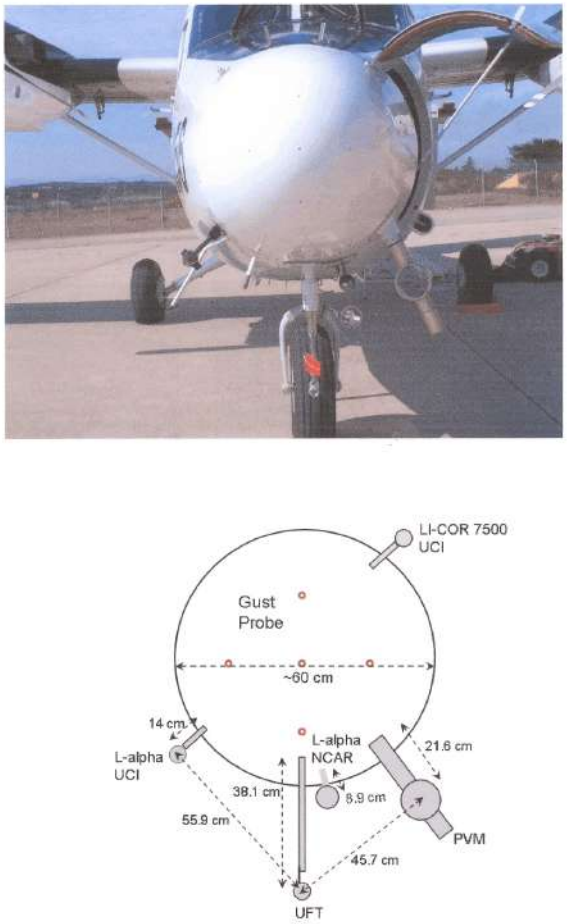

Fig. 1 - Head-on view of the CIRPAS Twin Otter (TO) research aircraft showing the locations of the UFT and PVM probes, and the q_v probes which surround the 5-hole UCI gust probe on the aircraft's nose.

The following briefly describes the measurements of w_e made during POST, the limitations found in making such measurements, the role of wind shear and mixing at cloud top, the contribution of evaporating LWC to the cooling observed in the entrained parcels, and the predictions of CTEI (cloud-top entrainment

instability) and mixture fraction analysis. For greater detail see Gerber et al. (2012).

2. TWIN OTTER FLIGHT PATHS

Seventeen flights of the TO were flown out of the airport in Marina, CA located just North of Monterey. The ferry portion of most flight took the TO ~150 km WNW of Monterey Bay at which point a horizontal quasi-Lagrangian zig-zag pattern was flown so that the mean downwind location of the TO matched the mean wind speed in the Sc. A NEXSAT satellite image shown in Fig. 2

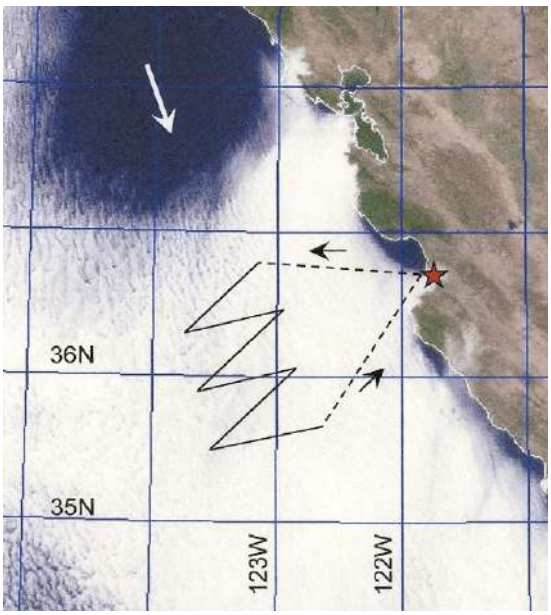

Figure 2 - Early evening NexSat satellite image of the CA coast and Pacific Ocean showing a sketch of the Twin Otter aircraft horizontal flight track for flight TO3. The white arrow shows the prevailing wind in the Sc.

illustrates a typical horizontal flight path. This path is for TO flight TO3 where a rapidly advancing area of Sc dissipation likely caused by strong shear and mixing at Sc top is seen.

The typical vertical flight path of the TO is illustrated in Fig. 3 for flight TO10. The vertical path for each TO flight concentrated on performing "saw-tooth" like profiles ranging from ~100-m above to 100-m below Sc top in order to investigate the processes associated with entrainment. In between each set ("pod") of porpoise-like profiles (Hill et al., 2012) the TO descended to near the sea surface for flux

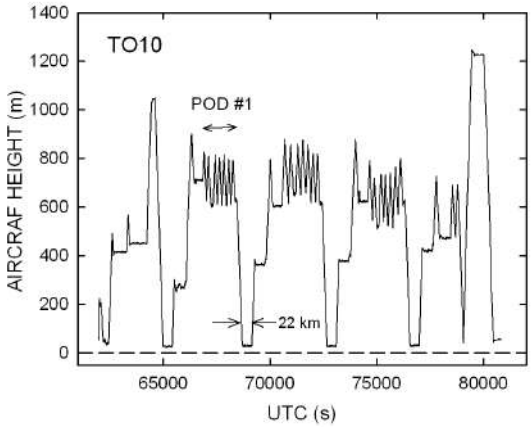

Figure 3 - Vertical flight path of the Twin Otter during flight TO10. Pods represent series of porpoises from 100-m above cloud top to 100-m below cloud top.

measurements. Horizontal legs were also flown just below cloud base and in the cloud for the same purpose. At least one higher profile was also included.

3. ENTRAINMENT MEASUREMENTS

The classical "flux-jump" equation (Lilly, 1968) often used for estimating the average entrainment velocity is given by

$$w_e = \langle w \times \phi \rangle / \Delta\phi \qquad (1)$$

where w is the vertical velocity, ϕ is the scalar conserved during entrainment, and $\Delta\phi$ is the jump of the scalar across the inversion separating Sc top from the free atmosphere. The numerator of Eq. (1) is termed the entrainment flux (F_e); and the brackets indicate an average.

POST provided an opportunity to evaluate the application of Eq. (1). Three factors are considered: 1) The jump of the scalar is strong (as indicated by the title of Lilly's paper). 2) The entrainment flux is linear with

respect to height below Sc top to permit extrapolation of *Fe* to Sc top where w_e is calculated. 3) Entrained parcels descend in the Sc.

The scalar used in this study is the total water mixing ratio q_t. Factor No. 1) is not met for all POST flights causing large uncertainties for the value of w_e. On occasion moist layers are found adjacent to Sc top making the denominator of Eq. (1) quite small. Further, it is difficult to find the upper limit of the jump for several flights. Factor No. 2 is not met by several POST flights where F_e changes rapidly near Sc top; see the example in Fig. 4. This

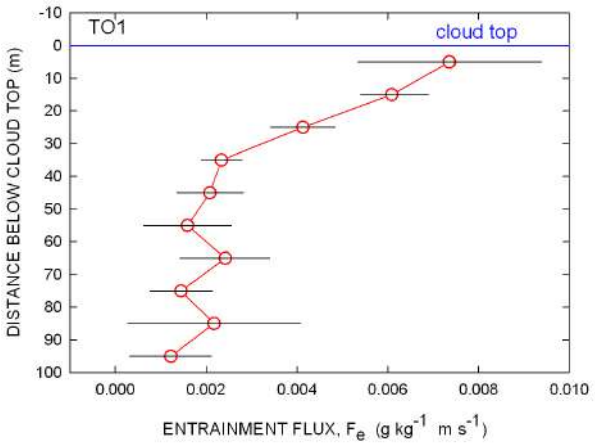

Figure 4 - Entrainment flux, F_e as a function of distance below cloud top for flight TO1 showing the non-linearity of the flux with height.

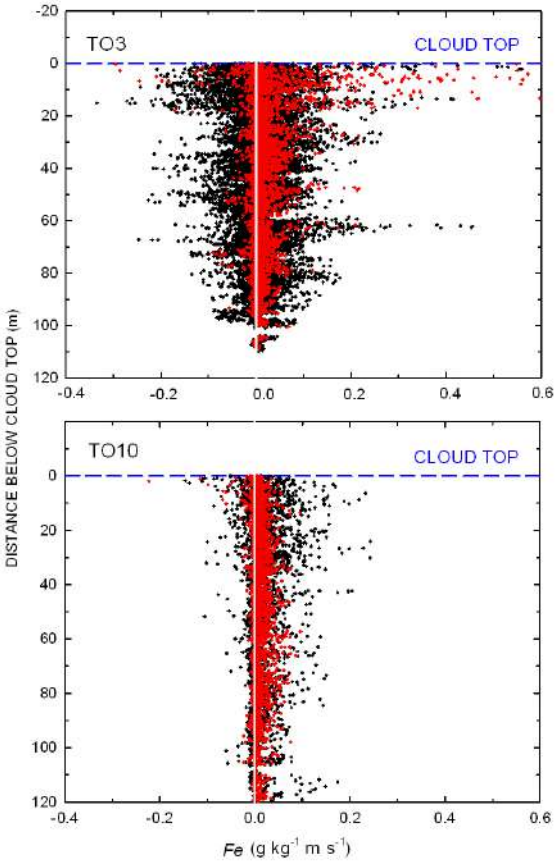

Figure 5 - Entrainment flux F_e as a function of distance below cloud top for flights TO3 and TO10; red is the flux from q_v and black is the flux contribution from LWC. The pattern for TO3 indicates strong mixing of the entrained parcels.

behavior occurs for several daylight flights (about half of the total POST flights are daylight flights) as well as for one night-time flight.This result has implication on previous attempts to determine w_e from measurements made lower in the Sc. The observations dealing with factor No. 3 are surprising in that entrained parcels not only descend in the Sc but also ascend. This is likely caused by mixing at Sc top where entrained parcels are fragmented by the turbulence. Figure 5 shows an example of this effect for flights TO3 and TO10 where a positive LWC contribution to *Fe* indicates entrained parcels with depleted LWC that are descending.

The method applied here to estimate w_e uses a variation of the flux-jump method where conditional sampling is used to identify the entrained parcels. The "indicator variable" (Khalsa, 1993) used for this identification are the high rate LWC measurements. Figure 6 shows an example of picking out the entrained parcels which uses the assumption that the sharp deviations of LWC from a approximately steady LWC background are the entrained parcels. Given that the q_t scalar needs both LWC and q_v in the entrained parcels, q_v is calculated by applying the Clausius-Clapeyron equation and assuming that q_v is equivalent to the saturation mixing ratio. This approach is necessary since the q_v probes on the aircraft nose were unable to provide fast data.

Figure 7 shows the calculated values of w_e for the POST flights as a function of the wind shear measured just above cloud top. The

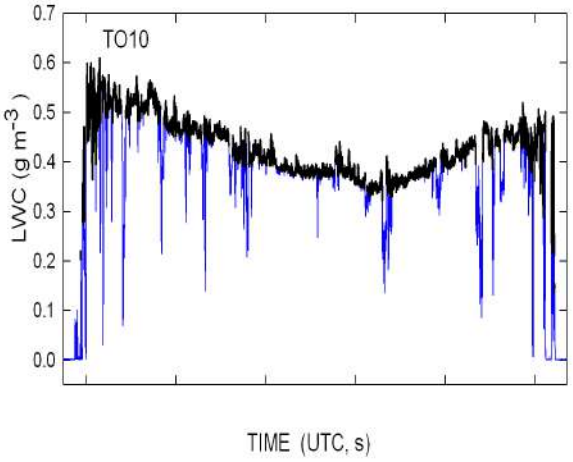

Figure 6 - High rate LWC measurements for one porpoise into the Sc from flight TO10 showing the background LWC values (black) and the location of the entrained parcels identified by conditional sampling (blue).

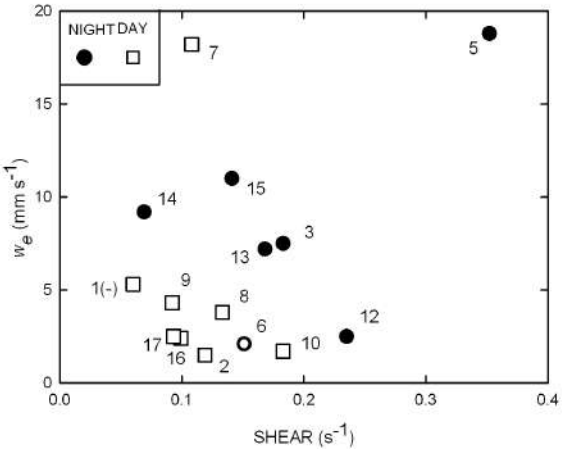

Figure 7 - Average entrainment velocity for all Sc POST flights (numbered) as a function of wind shear measured above cloud top. A higher overcast existed for night flight TO6.

correlation between the two parameters is poor suggesting that wind shear does not enhance entrainment by a significant degree. For a different result see Wang et al. (2008). Correlations made between w_e and other parameters measured on the aircraft (not shown) also give poor correlations).

4. MICROPHYSICS

An expanded segment of Flight TO is shown in Fig. 8 where temperature deviations from a slowly varying temperature background are compared to locations (red) identified as entrained parcels. The correlation between the temperature deviations and the entrained parcels is strong,

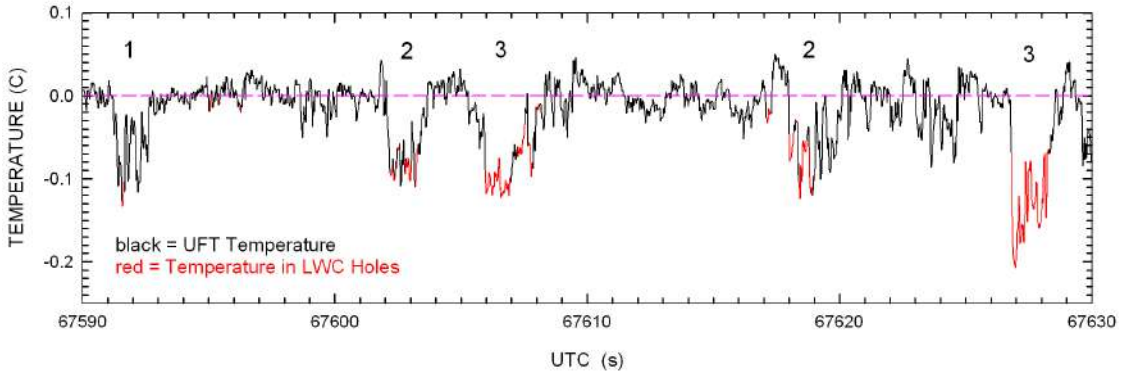

Figure 8 - Expanded segment of flight TO10 showing negative temperature deviations from the background temperature (black) and the location of the entrained parcels identified by conditional sampling of the LWC data (red); 1-m resolution data. See text for explanation of the numbers.

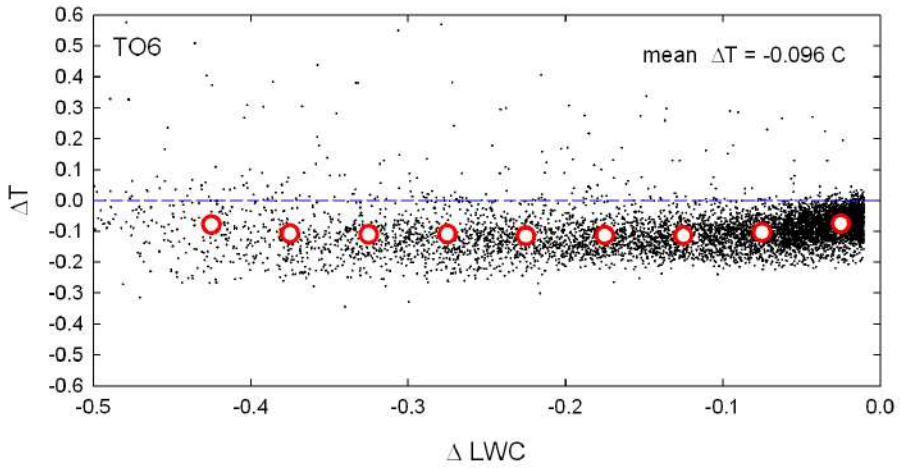

Figure 9 - Change of temperature in the entrained parcels as a function of depleted LWC in the entrained parcels for flight TO6. The red circles indicate average values.

which is also the case in the other POST flights except in some flights near Sc top. The numbers in Fig. 8 indicate how much of the segments with temperature deviation are filled with entrained parcels. Note that the number 1 indicates empty segments, 2 indicates partially filled segments with entrained parcels, and 3 indicates fully filled. Also the segments with temperature deviation are usually broader than the entrained parcels. The lack or partial presence of entrained parcels in the reduced temperature segments suggests that cooling due to droplet evaporation in the entrained parcels is minimal, and that the cooling must be due to radiative cooling. This behavior is observed both for daytime and nighttime flights.

Another way to illustrate the cooling effects is shown in Fig. 9 for flight TO6 where the temperature change in the reduced temperature segments is related to the decrease of LWC found in the segments. Mixture fraction analysis predicts the largest buoyancy reversal for POST flight TO6 with a decrease in temperature of several tenths of one degree. If cooling due to LWC evaporation plays a significant role it should show up in Fig. 9 as an increase in the loss of LWC for an increase in the cooling. The cooling in Fig. 9 is nearly constant again suggesting a minimal role for evaporative cooling and a major role for radiative cooling.

Using equations given in Stevens (2002) for mixture fraction analysis of "saturated buoyancy perturbations" the predicted temperature change resulting from mixing cloudy air near Sc top with free atmospheric air above the inversion is calculated for all POST flights and shown in Fig. 10 compared to the average observed temperature change in the entrained parcels.

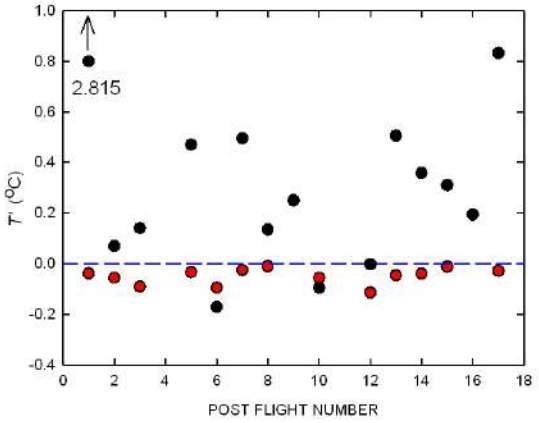

Figure 10 - The observed average change (red) in temperature T' in the entrained parcels and the predicted temperature change (black) in the parcels using mixture fraction analysis.

The correlation in Fig. 10 is poor, with the predicted temperatures changes generally indicating warming due to the mixing, and with the observed temperatures changes showing

slight cooling or near isothermal mixing. Calculation of CTEI for all the flights also suggests that most flights should show warming in saturated mixtures.

A key assumption in mixture fraction analysis and CTEI calculations is that cloudy air near Sc top mixes with air from the free atmosphere above the inversion. The observations in POST suggest that this assumption does not hold, and that cloudy air mixes with pre-conditioned inversion air caused by detrainment of sensible heat and evaporation of cloud water as proposed earlier (Gerber et al., 2002, 2005). While the predictive equations must be correct, they need to use much smaller jumps consistent with the pre-conditioning to explain the lack of cooling in the entrained parcels due to LWC evaporation; see Malinowski et al. (2012) for further discussion of this topic.

5. CONCLUSIONS

1) The application of the "flux-jump" approach to estimate the entrainment velocity (w_e) requires a linear entrainment flux below cloud top which is not always observed in the POST Sc.

2) The jump of the conserved scalar (q_t) across the inversion, needed to estimate w_e, is often difficult to determine in the Sc, as has been also noted in previous studies. This leads to significant uncertainty in w_e.

3) The aircraft measurement of entrainment flux [(numerator of Eq. (1)] gives more robust numbers than the jump measurements and should be used for model inter-comparisons.

4) All POST flights show wind shear above cloud top, with some showing strong shear and mixing causing significant droplet evaporation.

5) Cooling in segments of cloud which have a high correlation with entrained parcels is caused primarily by radiative cooling and at most by a minimal amount by LWC evaporation.

6) Entrained parcels appear to be nearly buoyancy neutral and fill various portions of radiatively cooled parcels and with an unknown mechanism.

7) Effective radius in entrained parcels is nearly constant compared to unaffected cloud suggesting that mixing is either inhomogeneous or homogenous if the entrained air is pre-conditioned to be moist and near isothermal. The latter appears to be the case for POST Sc.

8) Predictions of CTEI and buoyancy changes (mixture fraction analysis) are incorrect for POST Sc because of wind shear and mixing at Sc top, and because the predictions make use of entire jumps across the inversion rather than jumps that are a fraction of the entire jumps.

9) The observations show that moisture flux goes both ways across the cloud-top interface. Theory is missing to include this phenomena likely caused by wind shear, mixing, and droplet evaporation.

10) Another field study of unbroken Sc is recommended with a longer observation period than for POST. More flights with better meso-scale coverage is desired.

11) POST data is available that are suitable for high-resolution inter-comparisons between LES and measurements (see http://www.eol.ucar.edu/projects/post/).

6. ACKNOWLEDGMENTS

POST was a collaborative effort of about two dozen participants. All are thanked for their efforts. Haf Jonsson the TO chief scientist and Mike Hubbell the TO pilot have special thanks for making the POST experience at CIRPAS outstanding and a pleasure. H. Gerber, G. Frick, and S. Malinowski were supported by NSF for the POST field study (ATM-07355121).

7. REFERENCES

Faloona, I., D. H. Lenschow, T. Campos, B. Stevens, M. C. VanZanten, B. Blomquist, D.

Thornton, A. Bandy, and H. Gerber, (2005): Observations of entrainment in Eastern Pacific marine stratocumulus using three conserved scalars. *J. Atmos. Sci., 62*, 3268-3285.

Gerber, H., B. G. Arends, and A. S. Ackerman, (1994): New microphysics sensor for aircraft use. *Atm. Res., 31*, 235-252.

Gerber, H., S. P. Malinowski, J.-L. Brenguir, and F. Burnet, (2002): On the entrainment process in stratocumulus clouds. *Proc. 11th Conf. On Cloud Physics*, Ogden, UT, Amer. Meteor. Soc., CD-ROM, paper JP7.6

Gerber, H., S. P. Malinowski, J.-L. Brenguier, and F. Burnet, (2005): Holes and entrainment in stratocumulus. *J. Atmos. Sci., 62*, 443-459.

Gerber, H., G. Frick, S. Malinowski, H. Jonsson, D. Khelif, and S. Krueger, (2012): Entrainment in unbroken stratocumlulus. *J. Geophys. Res., Atm*., submitted.

Haman, K. E., S. P. Malinowski, B. Strus, R. Busen, and A. Stefko, (2001): Two new types of ultra-fast aircraft thermometer. *J. Atmos. Oceanic Technol., 18*, 117-134.

Haman, K. E., S. P. Malinowski, M. J. Kurowski, H. Gerber, and J.-L. Brenguier, (2007): Small scale mixing processes at the top of a marine stratocumulus - A case study. *Quart. J. Roy. Meteor. Soc., 133*, 213-226, doi10.102/qj.5.

Hill, S., S. Krueger, H. Gerber, and S. Malinowski, (2012): Entrainment and mixing in stratocumulus-topped boundary layers during POST. *Extended abstract in 16th ICCP*; paper P.2.40.

Khalsa, S. J. S., (1993): Direct sampling of entrainment events in a marine stratocumulus layer. *J. Atmos. Sci., 50*, 1734-1750.

Lilly, D. K., (1968): Models of cloud-topped mixed layers under a strong inversion. *Quart. J. Roy. Meteor. Soc., 94*, 292-309.

Malinowski, S., K. Nurowska, M. Kopec, W. Kumala, H. Gerber, and D. Khelif, (2012): Turbulent inversion and entrainment into stratocumulus toped boundary layer. *Extended abstract in 16th ICCP*, paper P.2.12.
.

Stevens, B., (2002): Entrainment in stratocumulus toped mixed layers. *Quart. J. Roy. Meteor. Soc., 128*, 2663-2690.

Stevens, B., and Coauthors, (2003a): Dynamics and chemistry of marine stratocumulus - DYCOMS II. *Bull. Amer. Meteor. Soc., 84*, 579-593.

Stevens, B., and Coauthors, (2003b): On entrainment rates in nocturnal marine stratocumulus. *Quart. J. Roy. Meteor. Soc., 129*, 3469-3493.

Wang, S., J.-C. Golaz, and Q. Wang, (2008): Effect of intense wind shear across the inversion on stratocumulus. *Geophys. Res. Lett., 35*, L15814, doi:10.1029/2008GL033865.

IMPROVED THERMOMETER FOR HIGH-RESOLUTION AIRBORNE MEASUREMENTS

Wojciech Kumala[1], Paweł Klimczewski[2], Szymon P. Malinowski[1],
Kamil Kwiatkowski[1], Karol Wędołowski[2], Jacek Kopeć[1]

[1]University of Warsaw, Faculty of Physics, Institute of Geophysics, Pasteura 7, 02-093 Warsaw, Poland
[2]University of Warsaw, Faculty of Physics, Institute of Theoretical Physics, Hoża 69, 00-681 Warsaw, Poland

1.INTRODUCTION

A prototype miniature thermometer UFT-2 was developed from the former Ultra Fast Thermometer UFT(Haman et al., 1997, 2001). It is aimed at very high resolution airborne measurements in clear air as well as in clouds. The sensing element is an ultra-thin resistive wire (1.25 µm in diameter). Tests with alternative, more robust, thin film resistive sensor are on the way. The sensing element is placed behind a 0.25mm thick and 4mm long rod that protects it from cloud droplets and ice crystals. The whole thermometer has no moving parts, is thinner than a pencil, and potentially may be integrated with cloud droplet sensors like FFSSP or CDP. Miniaturization of the sensor results in lower flow distortions and reduced aerodynamic noise compared to previous UFT thermometers . This improvement was confirmed both in preliminary test flights and in numerical simulations of the airflow around the sensor head. Frequency response of UFT-2 reaches 10kHz in flight conditions, corresponding to ~2mm spatial resolution. In order to collect data from such a fast sensor, a small autonomous acquisition system (DAS) recording on a memory flash card up to 200000 of 16-bit samples per second was built. UFT-2 together with dedicated DAS form small, battery powered package which can be easily adopted on various aircraft, including UAS. To fully characterize the prototype UFT-2 more tests with different sensing elements and under various atmospheric and flight conditions are needed.

2. DESIGN

A significant modification of the UFT geometry was introduced, in order to avoid moving parts which are difficult to certify on a research aircraft. Rotatable anti-droplet shield was replaced by a fixed protecting rod. Studies of the airflow around fixed anti droplet shield lead to the conclusion that the fixed sensor should be smaller: the Reynolds number Re of the flow behind the rod had to be reduced to diminish wake effects.

The new sensor is 34mm long and 4mm wide. The anti-droplet protecting rod has a diameter of 0.25mm and is placed 0.75mm in front of the sensing element. Such geometry, should ensure satisfactory protection of the sensing element from wetting by cloud droplets and hitting by ice crystals. At the typical airspeed of 100m/s flow around the rod is characterized by Re~1600 (Re~800 at 50m/s). At this values of Re pressure fluctuations (and consequently temperature fluctuations) in the vortices shedding from the rod are reduced.

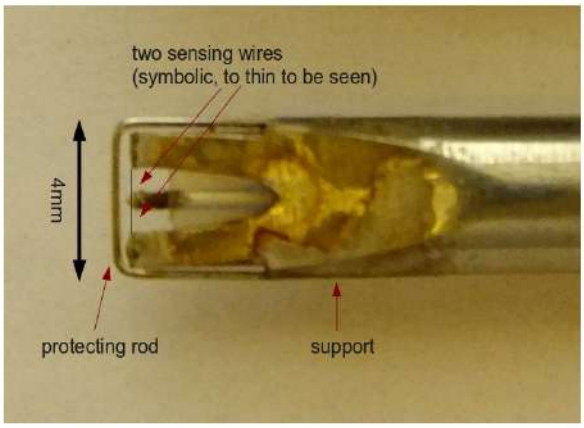

***Fig.1**. Prototype UFT-II – sensor head.*

As in former UFT's, the sensor is a thermoresistive thin and long cylinder. It is spanned between the central core coaxial cable connector and external supports. Symmetric collection of the signal prevents external electromagnetic interferences. A photograph of the prototype of the new UFT-2 with no moving part is presented in Fig.1.

3. MANUFACTURING

After a series of laboratory tests of various materials and assembly techniques, a following construction of the sensor was chosen:

- sensor shell, 34mm long, made of stainless steel (AISI 304) tube of external diameter of 4mm with 1.6mm duct for isolated central conductor;

- coaxial cable (Habia flexiform 405 FJ) to collect signal from the sensing element;

- protecting rod of stainless steel (AISI 321), 0.25mm in diameter, located 0.75mm in front of sensing resistive wires;

- sensing platinum wires,1.25μm in diameter, or metalized glass fibers 5μm in diameter;

A Wollaston technique is adopted to apply fine wires as sensing elements. Wollaston wire: 25μm thick silver shell with the inner platinum core 1.25μm in diameter, is soldered with Au80/Sn20 alloy to the supports. After soldering it is etched in 60% nitric acid in order to remove silver shell.

In alternative version a 5μm thick fiberglass cylinder of is soldered with indium to the support. Then it is metalized with gold using Quorum Technologies Q150R sputter coater to achieve resistance of about 50Ω at 20°C (Fig.2).

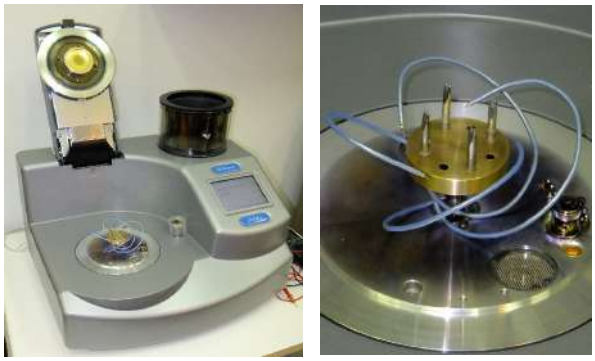

Fig.2*. Four UFT-2 senors ready for coating with gold in a special clamp in sputter coater.*

A series of 10 prototype UFT-2 sensors was built for the laboratory and flight tests. These sensors are prepared to work with a modified (changed resistors) bridge/amplifier system originating at UFT-M thermometers.

UFT-2 sensors' stability and linearity were tested in laboratory. In course of tests readings from UFT-2 sensors in thermally stable environment were compared to standard PT-100 thermometer.

Laboratory tested specifications of the new UFT-2 with the dedicated data acquisition system are the following:

- temperature dependence: 0.15Ω/K
- sensitivity : 21mV/K

Due to differences between the sensors resulting from manufacturing, sensitivities of individual sensors may differ from this value by less than 10%.

Selected sensors were tested in a laminar wind tunnel at the airspeeds up to 40m/s. No significant effects of vortex shedding was observed, but it occurred that platinum sensing wires are very delicate and break easily.

3.1. A/D CONVERTER AND DATA ACQUISITION SYSTEM.

UFT thermometers are characterized by a very good frequency response, (Haman et al., 1997, Rosa et al., 2005) which requires sampling frequencies exceeding 10000 samples per second. Available research aircrafts are not equipped in data acquisition systems (DAS) ensuring proper recording of UFT signals. Experience with commercially available data acquisition systems onboard research aircraft is that the records were affected by electromagnetic noise from radio, radar and avionic systems (Kumala et al., 2010). A new, dedicated compact DAS was designed and manufactured in order to complete construction of the UFT-2.

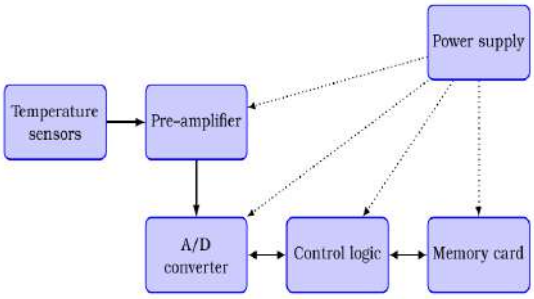

Fig.3. *Block diagram of the complete UFT-2: sensing elements, amplifiers and data acquisition system (DAS).*

The dedicated UFT-2 DAS is completely autonomous and records signals on a static memory card. Signals are measured with MAX1167, low noise 16-bit A/D converter. MAX1167 output results in continuous data stream at rate up to 4.8 Mbps. Proper reception of such data stream requires

appropriate hardware. Therefore AT91SAM7S256, 32 bit micro-controller with ARM7 core was chosen.

Except for CPU and memories which are common in this class of devices, AT91SAM7S256 contains few additional hardware units. Two fast serial transmitters (SPI, SSC) and direct memory access unit (DMA) were used to transfer data between ADC and memory card. PWM unit was used to generate control signals for ADC. Due to utilization of these hardware blocks AT91SAM7S25 processing power was enough to control device. Block diagram of the firmware of the UFT-2 DAS is shown in Fig. 4.

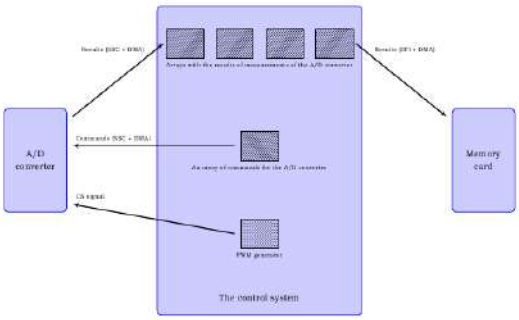

Fig.4. *Logic diagram of the UFT-2 DAS*.

DAS firmware is responsible for the initialization of the hardware subsystems and saving read data to the memory card. A/D converter uses two sets of arrays in RAM.

1. A single array store the configuration of individual measurements. The contents of the array is filled by software. Thus one have possibility to set customized configuration (the number of channels, sequence of measurements) by modifying the firmware.

2. Four arrays store results of measurements. Results are written periodically to the subsequent arrays with use of DMA unit. Set of arrays works as buffer and ensures enough time to rewrite these data to memory card.

The measurement results are finally stored on the MMC memory card. Maximum capacity of the card is 4 GB and provides nearly four hours of data recording at a speed of 100,000 measurements/sec. MMC memory card is controlled by the micro-controller using SPI unit.

A series of laboratory tests aimed at the verification of the performance of UFT-2 DAS were performed. A special effort was made to ensure that there is no signal leakage, no critical system failure or that no data is lost.

Laboratory-confirmed technical specification of the system is:

- maximum total sampling frequency 200 kS/s,
- four channels with sampling frequency up to 50kS/s per channel,
- resolution: 0.075mV (3mK),
- recording on MMC card of 4GB capacity.

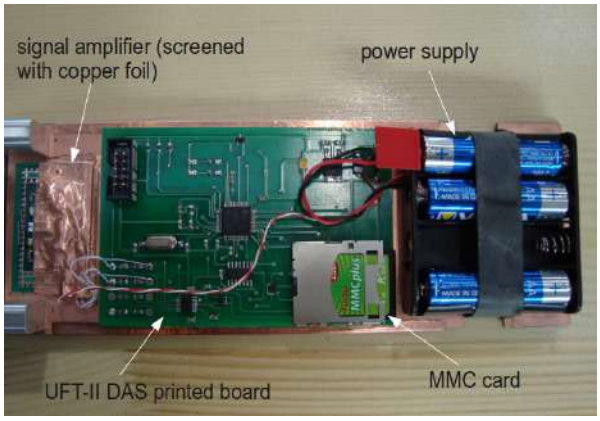

Fig.5. *UFT-2 electronics.*

A complete electronics of the prototype UFT-2 is shown in Fig.5.

4. TESTS IN FLIGHT.

Field tests of the UFT-2 with the dedicated DAS were performed in course of EUFAR-DENCHAR field campaign with the Enviscope Learjet aircraft, on 23/05–1/06 2011, in Höhn, Germany. Enviscope designed and built dedicated UFT-2 housing, capable to hold two UFT-II senors, amplifiers and the dedicated DAS (Fig.6.). It was mounted outside the measurement container under the right wing of the Learjet aircraft. (Fig.7).

In course of flight campaign one of ultrafine (1.25μm thick) wires was substituted by a resistor (fake sensor) in order to test amplifiers and data acquisition system.

The amplifiers and data acquisition system worked flawlessly in all research flights from the boundary layer up to stratosphere. In contrary, ultra-fine wires occurred delicate and broke in course of flights on this fast jet aircraft. Additional improvements are necessary in order to make the sensor robust, additional flight tests with thin film coated fiberglass sensors are necessary.

Nevertheless, enough data to characterize basic sensor performance was collected.

Fig.6. *Two UFT-II thermometers with housing designed and built by Enviscope in course of DENCHAR field intercomparison campaign.*

Fig.7. *UFT-2 in housing attached to the container under the left wing of Learjet aircraft.*

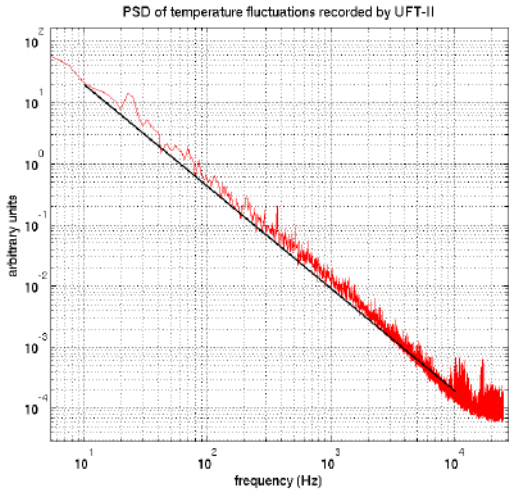

Fig.8. *Power spectral density of temperature fluctuations recorded with the UFT-2.*

In Fig. 8 power spectral density of temperature fluctuations in the atmospheric boundary layer recorded in a first phase of one of research flights. It can be seen that the record is free from the aerodynamic noise resulting from vortex shedding to frequencies up to 10 kHz. The relative amplitude of the noise is substantially smaller compared to the UFT-F sensors (c.f. Fig. 4 in Kumala 2010). Also, practically no signal damping (drop below -5/3 line) can be noticed for frequencies as high as 5kHz.

5. NUMERICAL TESTS

A large number of numerical experiments was performed in order to characterize flow around UFT-2. Transient direct numerical simulations were performed with the OpenFOAM® (Weller et al., 1998) code. The initially uniform, structured, hexagonal mesh was refined and deformed in such a way that it fitted a digital model of the UFT-2 geometry. In the region behind the rod cells had size between $(0.0012\text{mm})^3$ and $(0.05\text{mm})^3$. In some simulations the mesh with increased resolution was used in order to examine mesh-sensitivity of the results.

The numerical model solved incompressible Navier-Stokes equations using the PISO algorithm implemented in the so-called pisoFOAM solver. The equations were discretized using the finite volume method with the second order accuracy. The second order accurate Crank-Nicolson scheme was used to perform stable integration in the time domain. The time step used in most cases was equal to 4e-7s which resulted in the maximal value of the Courant number slightly below 3. The length of the time step was the main factor which influenced the large amount of computational time required by the simulations.

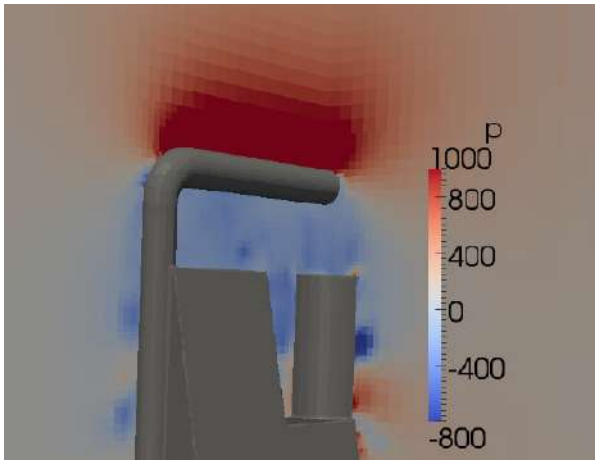

Fig.9. *A snapshot of pressure fluctuations behind the sensing rod at TAS 70m/s. Value of the pressure is given in Pascals divided by the air density.*

In all simulations uniform velocity of 70m/s was used as a inlet boundary condition along with a no-slip boundary condition at the surface of the thermometer.

Exemplary results of simulations are illustrated in Figs 9-13. In all the figures

sensor location is not shown (the sensor spanned the region between the middle cylinder and the sides, see Fig. 1).

Fig. 9 shows that the sensor is located in the area of slightly reduced pressure behind the rod.

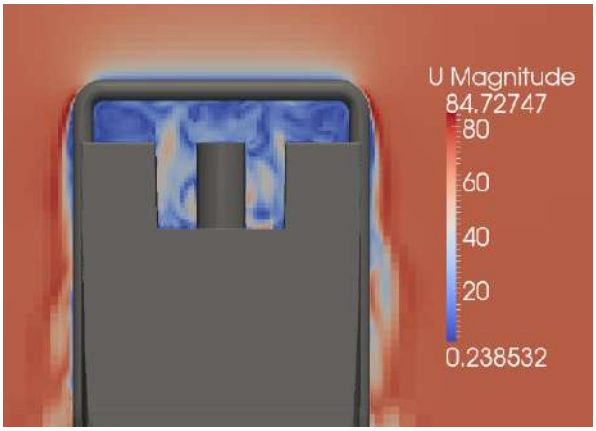

Fig.10. *A snapshot of air velocity magnitude in the plane of symmetry.*

Fig. 10. presents magnitude of air velocity around the senor. It can be seen, that in the position of sensing element velocity is reduced from 70m/s TAS down to 30-50m/s.

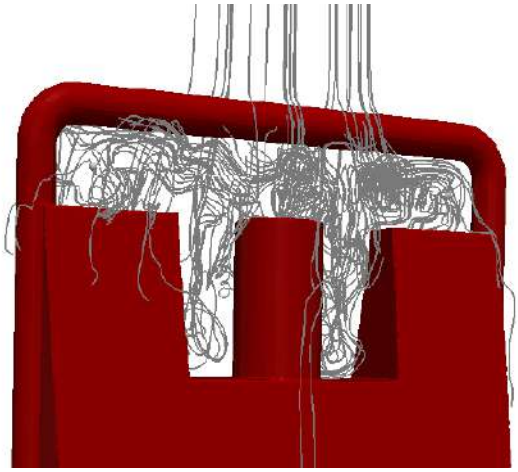

Fig.11. *Streamlines indicating recirculation of the flow behind the rod and escaping after recirculation. Air represented by these streamlines gets to the measurement volume – location of the sensing element*

Figs 11 and 12 show streamlines: few of them are trapped in a wake of the rod, and escape the wake after some recirculations (Fig. 11), while most of them flow around the sensor head. (Fig.12).

Reduction of velocity behind the rod and some recirculation should effect in reduction of the frequency response of the senor. This effect is shown in Fig.13, in which simulation of a sharp front of passive scalar advected with a flow is simulated and response of a modeled sensing element is investigated.

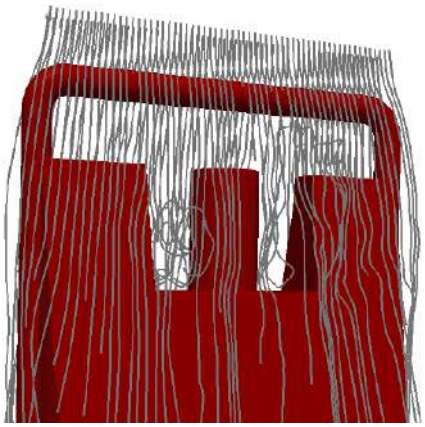

Fig.12*. Streamlines indicating airflow around the senor head. Air represented by these streamlines cannot be in contact with the sensing element.*

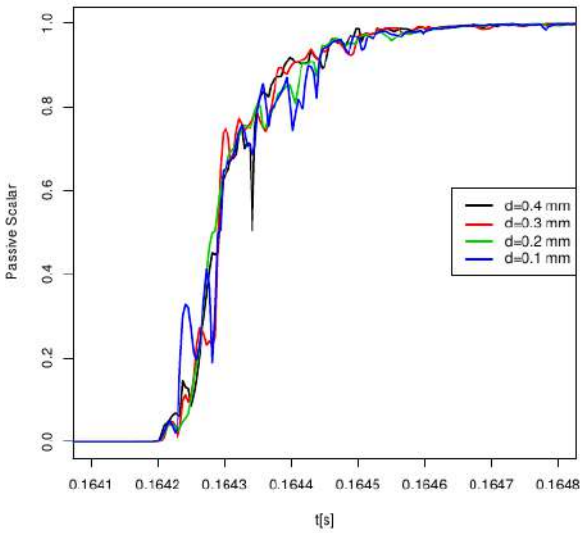

Fig.13. *Response of the "synthetic" sensing element placed 0.75mm behind the protecting rod to the step-like passive scalar (e.g. temperature) jump in the flow.*

Presented curves refer to value of the passive scalar collected from four points uniformly distributed along the sensing element. It is shown, that the disturbance of the flow and some recirculation behind the rod slightly reduce frequency response of the senor. In effect after 0.0002s sensing element can recover about 80% of initial passive scalar jump. The same simulation was performed with the mesh resolution twice as large as for results presented above, showing almost the same response of the sensing element.

The estimated response time better than 0.0002s is in agreement with the PSD of temperature fluctuation shown in Fig. 8,

where some damping of frequencies above 5kHz can be noticed.

Acknowledgments:

This research was funded as a part of Joint Research Activity JRA-1 in frames of the EUFAR EU FP-7 project nr 227159 supported by Polish Ministry Of Science matching fund 1283/7. PR UE/2010/7.

References:

Haman, K.E., A. Makulski, S. P. Malinowski, and R. Busen, 1997: A new ultrafast thermometer for aiborne measurements in clouds. *J. Atmos. Oceanic Technol.*, **14**, 217–227.

Haman, K.E., S.P. Malinowski, B.D. Struś, R. Busen and A. Stefko, 2001: Two new types of ultrafast aircraft thermometers, *J. Atmos. Ocean. Technol.*, **18**, 117-134.

Kumala, W., K. E. Haman, M. Kopec, and S. P. Malinowski, 2010: Ultrafast thermometer UFT-M and high resoltution temperature measurements in Physics of Stratocumulus Top (POST). 13th AMS Conference on Cloud Physics 28 June–2 July 2010, Portland, OR USA, http://ams.confex.com/ams/pdfpapers/170832.pdf

Rosa B., Bajer K.; Haman K.E.; Szoplik T., 2005: Theoretical and experimental characterization of the ultrafast aircraft thermometer: Reduction of aerodynamic disturbances and signal processing. *J. Atmos. Ocean. Technol.*, **22**, 988-1003.

Weller H. G., Tabor G., Jasak H., Fureby C., 1998: A tensorial approach to computational continuum mechanics using object-oriented techniques. *Computers in Physics* **12**, 620–631

TURBULENT INVERSION AND ENTRAINMENT INTO STRATOCUMULUS TOPPED BOUNDARY LAYER

Szymon P. Malinowski[1], Marta K. Kopeć[1], Wojciech Kumala[1], Katarzyna Nurowska[1]
Hermann Gerber[2], DjamalKhelif[3]

[1]University of Warsaw, Faculty of Physics, Institute of Geophysics, Pasteura 7, 02-093 Warsaw, Poland
[2]Gerber Scientific Inc., Reston, VA, USA.
[3]Department of Mechanical & Aerospace Engineering and Earth System Science, University of California Irvine, CA, USA.

1. INTRODUCTION

Exchange processes between stratocumulus and free troposphere above have been intensively investigated in many research campaigns (see e.g. Albrecht et al. (1988), Lenshow et. al. (1988), Stevens et al. (2003), Bretherton et al. (2004)). Despite the fact that marine stratocumulus is a relatively simple system: almost plain-parallel, warm cloud occupying the upper part of the well mixed boundary layer above a homogeneous flat surface, understanding entrainment into the stratocumulus topped boundary layer (STBL) is limited. Consequently, estimates of the entrainment velocity are ambiguous (e.g. Stevens (2002), Gerber et al. (2005), Faloona et al. (2005), Lilly (2008)). Data from in-situ measurements (e.g. Caughley et al. (1982), Nicholls (1989), Lenshow et. al. (2000), Rode and Wang (2007)) and results of numerical simulations (e.g. Moeng et.al. (2005), Yamaguchi and Randall (2008)) clearly indicate that top of the stratocumulus is located below the capping inversion and does not touch the free troposphere. In between there is so-called entrainment interface layer, EIL, of thickness varying from few meters to few tens of meters Gerber et al., (2002), Haman et al. (2007), Kurowski et.al., (2009). Data from the majority of field campaigns and numerical simulations are of too poor resolution to infer about details of this layer. In this note we present two cases of very different structures of stratocumulus top, capping inversion and EIL, documented by means of very high spatial resolution measurements of temperature and liquid water content. Analyzed airborne data were collected in course of Physics of Stratocumulus Top (POST) research campaign performed in 2008 Gerber et al. (2010, 2012). The present document is structured in a following way: information of POST and key instruments are in section 2, data from two contrasting cases TO10 and TO13 are described in section 3 and discussed in section 4.

2. POST: PHYSICS OF STRATOCUMULUS TOP RESEARCH CAMPAIGN

Physics of Stratocumulus Top (POST) was a research campaign held in the vicinity of Monterey Bay in July and August 2008. High-resolution in-situ measurements with CIRPAS Twin Otter research aircraft were focused on a detailed study of processes occurring at the interface between the STBL and the free troposphere. The aircraft was equipped to measure thermodynamics, microphysics, dynamics and radiation.

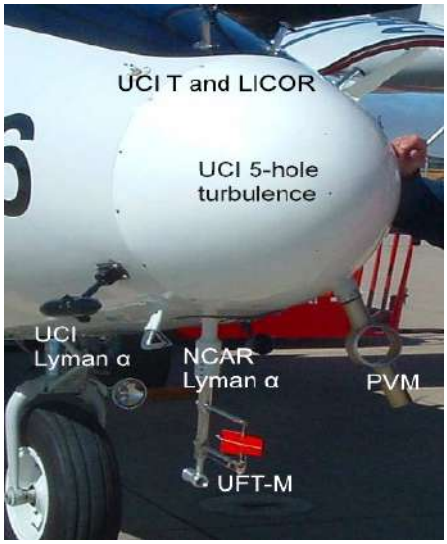

Figure 1. Radome of CRPAS Twin Otter research aircraft with fast-response instruments used in POST.

Adopted flight strategy was aimed at collection of data from the cloud-top region, accompanied by information on fluxes in various levels of STBL and vertical profiles of thermodynamic and dynamic parameters allowing to characterize lower atmosphere

for the purpose of Large Eddy Simulations. Of key interest was cloud top, sampled in course of porpoises across EIL, as shown in Fig.3 of Gerber et al. (2010). In this study we focus on a fine-scale measurements collected with the UFT-M thermometer Kumala et al. (2012), Particulate Volume Monitor PVM-100 Gerber et al. (1994), and other fast-response instruments collocated in close proximity around the radome of the aircraft (Fig.1). The finest resolution PVM and UFT-M data discussed here are of 1000Hz sampling frequency, which corresponds to ~5.5cm spatial resolution at 55m/s true airspeed (TAS) of Twin Otter. Other fast response sensors provided 100Hz and 40Hz (55cm and 1.4m spatial resolution) measurements of three components of turbulent velocity fluctuations and humidity. Data are freely available from the POST database maintained by by National Center of Atmospheric Research Earth Observation Laboratory, http://www.eol.ucar.edu/projects/post/.

Preliminary analysis of collected data performed by Gerber et al. (2010, 2012) allowed to distinguish between ”classical” and ”nonclassical” cases. Out of 17 research flights performed in course of campaign, 6 were characterized as ”classical” and 9 as ”non-classical”. In the following we analyze details of EIL structure in ”classical” TO10 case and ”non-classical” TO13 in order to understand similarities and differences between the cases.

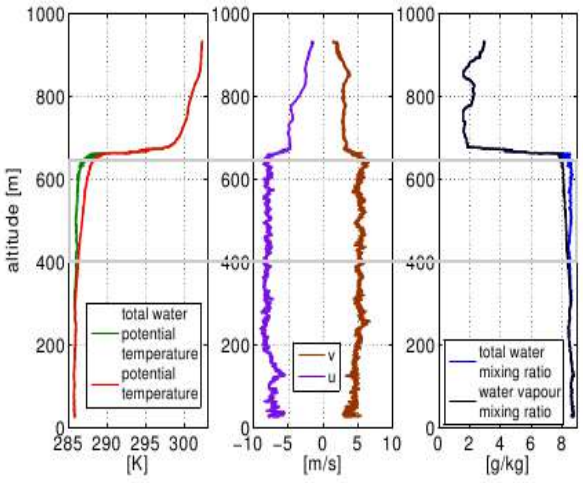

Figure 2. Vertical profiles of potential temperatures,mixing ratios and components of horizontal wind characteristic for TO10 research flight. Cloud layer marked with a gray box.

3. TWO CASES: TO10 AND TO13 FLIGHTS

3.1. CLASSICAL CASE TO10

Flight TO10 was performed on 2008/08/04, 17:15-22:15 UTC. It was a daytime flight (local time was UTC -7h) in a fairly uniform cloud field (c.f. satellite images in POST database). Typical sounding, taken in course of TO10 (Fig.2), shows a sharp liquid water potential temperature θ_l jump (10K) in ~30m thick layer above the cloud top, accompanied by a rapid drop of water vapor mixing ratio and a substantial wind shear (~4m/s for each component of wind velocity).

In Fig.3 records of temperature *T*, liquid water content *LWC*, pressure corrected altitude h, water vapor mixing ratio *r* and fluctuations of three components of velocity (*u,v,w*) in course of typical descend into the cloud deck are presented. Three black vertical lines discriminate between the layers of substantially different properties. The first one, corresponding to the left part of the plot is a free troposphere (FT) above the inversion. Temperature, water vapor mixing ratio and velocity records are smooth, fluctuations are small.

The first black line set at 67726s (659m altitude) marks the end of FT layer. After the marker temperature decreases, fluctuating rapidly. Velocity records show presence of a substantial wind shear and turbulence. Temperature jump of ~8K is recorded in ~13m thick layer on a horizontal distance of ~550m. Such temperature drop, wind shear and turbulence are common features for all porpoises in this flight, suggesting existence of a characteristic Turbulent Inversion Sub-Layer (TISL) above the cloud top. It is worth noticing, that vapor pattern not always mirrors that of *T*. Increased humidity spots, indicating former mixing events (detrainment), are present in FT above TISL.

2nd marker, set at 67736s (644m altitude), indicates entrance into a first blob of a cloud (*LWC*>0). Later aircraft penetrates through a series of cloudy and clear filaments. Inside the last ones a remarkable (amplitude ~2°C) temperature fluctuations are present. Horizontal velocities indicate continuing wind shear, slightly weaker than in TISL. Turbulent velocity fluctuations are increased. Intertwined cloudy and clear air filaments are recorded on a distance of ~800m in ~30m thick layer. This region is named a Cloud Top

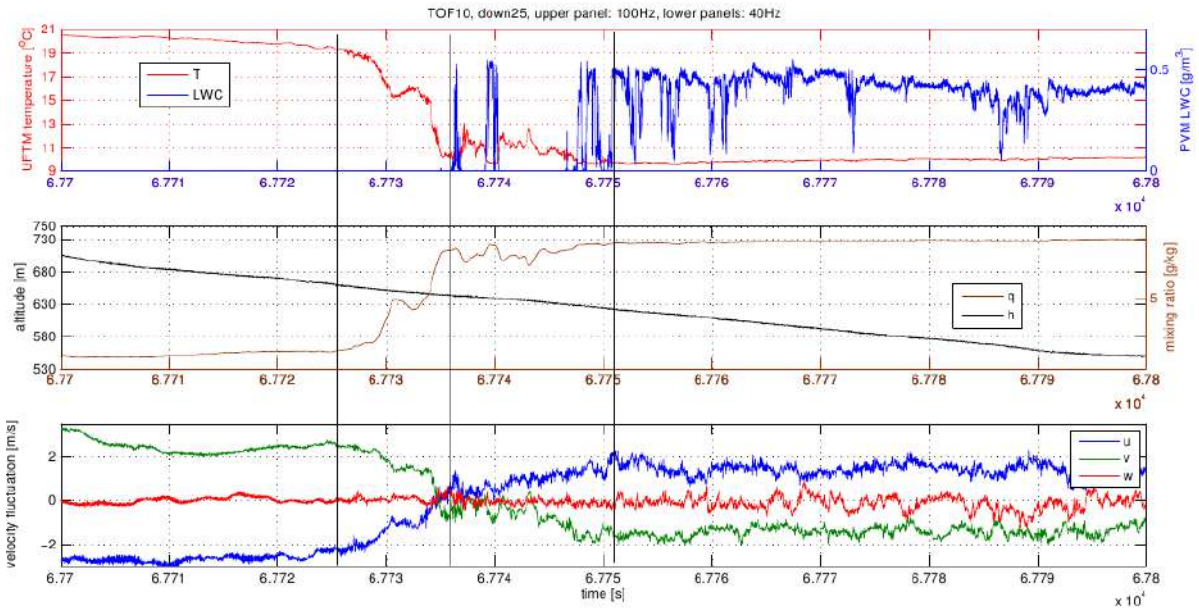

Figure 3. Temperature T, liquid water content LWC, water vapor mixing ratio q and velocity fluctuations (mean value substracted) in course of descend (h-altitude) into the stratocumulus cloud deck. Three black vertical lines mark borders between the free troposphere, the inversion, the cloud mixing layer and the cloud top.

Mixing Sub-Layer (CTMSL). CTMSL together with TISL forms the Entrainment Interface Layer, EIL.

The rightmost black mark at 67751s (628m altitude) indicates entrance into the cloud top layer (CTL). There are remarkable fluctuations of *LWC* inside CTL, but its value at 100Hz (55cm spatial resolution) record is everywhere above 0. Temperature fluctuations are small, typically of 0.2°C, in contrast to that in CTMSL where they exceed 2°C. Velocity fluctuations are still large, especially of a vertical component.

In Fig.4 three expanded segments of 1000Hz *LWC* and *T* records from CTMSL are presented in order to demonstrate character of small-scale *T* and *LWC* fluctuations. It can be seen that locally, in cloudy filaments, *LWC* approaches 0.6gm^{-3} , i.e. the maximum value across the whole cloud depth. These filaments are cold, of temperature ~9.8°C, characteristic for the CTL. Some cloudy filaments with depleted LWC are warmer, of temperatures 10.2-10.6°C. Fluctuations of *LWC* in CTMSL are steeper than fluctuations of *T*. Sometimes (e.g. at 67736.8s) a shift

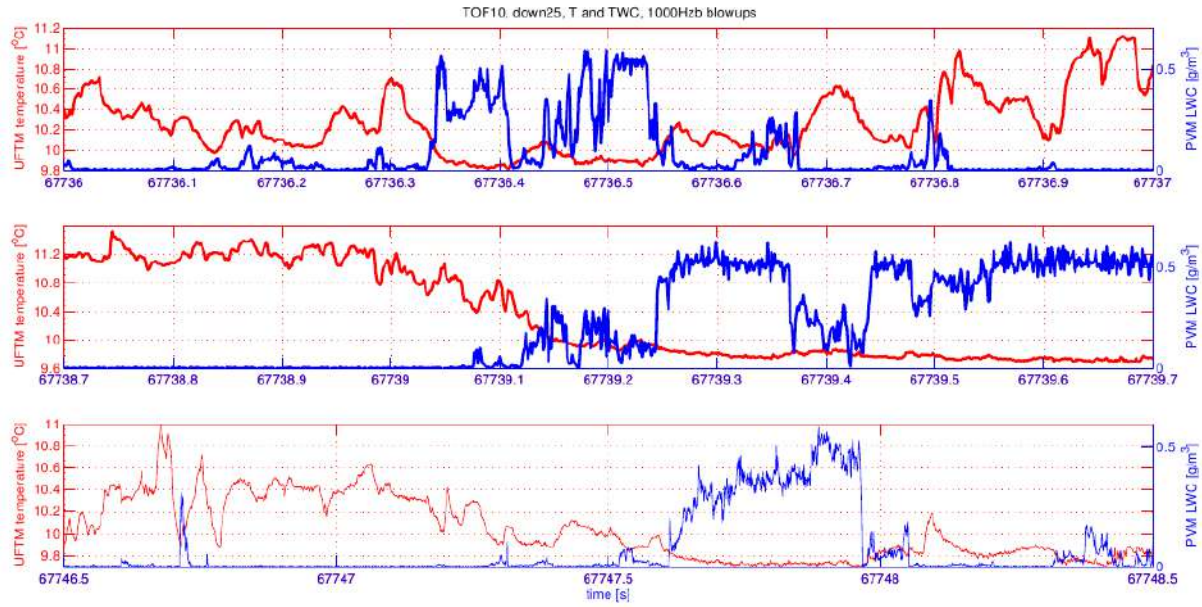

Figure 4. Full 5.5cm resolution (1000Hz) blow-ups of T and LWC fluctuations in the cloud mixing layer. Time corresponds to that in Fig.3. Two upper panels show 1s (55m long) segments, the bottom one shows 2s (110m long) segment.

between *LWC* and *T* peaks can be noticed, most likely effect of different location of PVM and UFT sensors.

Vertical profiles of LWC across CTMSL and CTL from 12 consecutive typical penetrations are presented in Fig.5. Each dot corresponds to LWC averaged over 1.4m long distance (40Hz data). In most subplots the maximum *LWC* increases linearly with height, suggesting presence of parcels lifted (almost) adiabatically from the cloud base, (c.f. Pawlowska et.al., (2000), Gerber (1996)). Parcels with reduced *LWC* most often appear in CTMSL, in CTL depleted *LWC* is less common and indicates presence of ”cloud holes” (Gerber et al. (2005), Kurowski et.al. (2009), Malinowski et al. (2012)), parcels of negative buoyancy, formed in course of mixing and evaporative cooling at the cloud top, slowly descending across the cloud deck.

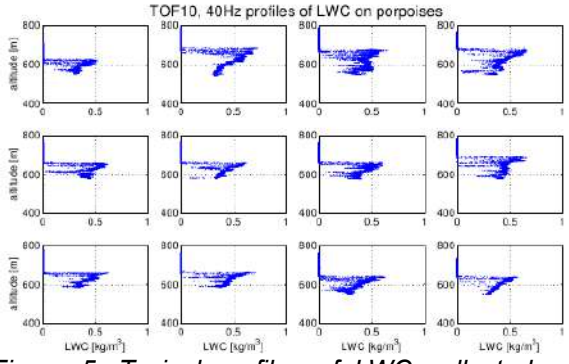

Figure 5. Typical profiles of LWC collected on porpoises in TO10 flight. Each data point corresponds to 1.4m long average (40Hz data). Four consecutive profiles are shown in each row. Successive rows are from different flight legs in order to illustrate LWC profiles for the the whole flight.

3.2. NON-CLASSICAL CASE TO13

Conditions during evening flight TO13, performed 2008/08/09, 00:58-06:00 UTC were different, as illustrated in Fig.6. While the total jump of θ_l between the middle of the mixed layer and the ~1000m altitude is comparable to TO10 case (~10K), a sharp inversion above the cloud top has a temperature jump of no more than ~4K. θ_l and total water profiles are tilted from vertical across the upper part of the cloud. This suggests that the cloud top is not a part of the mixed atmospheric boundary layer.

Humidity profile in Fig.6 shows almost saturated layer (or blob?) at ~750m height. Wind jump in the cloud top region is smaller than in TO10 case and a shear layer is significantly deeper, its bottom correlates with the top of the mixed boundary layer.

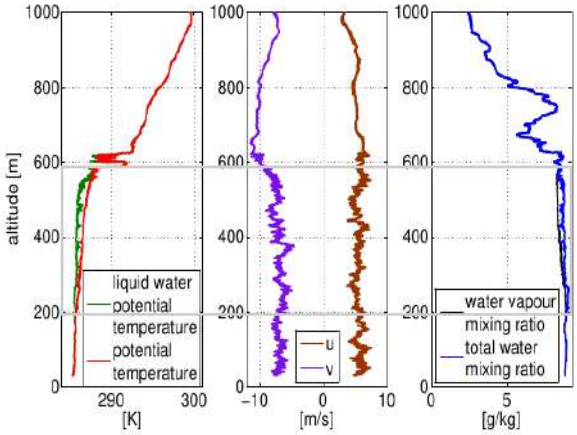

Figure 6. As in Fig.2, but for TO13 flight.

In Fig.7 100Hz series of *T*, *LWC*, *r* and velocity fluctuations in typical penetration of the cloud top are presented. In contrast to TO10 case (c.f. Fig.4), *T, r* and velocity fluctuations are present in FT above EIL. Line discriminating between FT and TISL is set at 14746s (altitude of 599m), marking beginning of the sharp inversion associated with a wind shear (*v* velocity component only). Patterns of *T* and *v* before the marker suggest wavy engulfment of FT air into TISL.

A first blob of cloudy air (14751s, 591m height) marks beginning of CTMSL. There are increased velocity fluctuations associated with this parcel and successive cloud blobs. Later, till 14772s (down to 554m altitude) *T*, *r* and *LWC* vary. Except for the first cloudy filament, *LWC* in CTMSL does not exceed 0.25gm^{-3} , which is substantially less than the maximum *LWC* in cloud top region. This suggests that cloud filaments in this region do not contain adiabatic parcels originating at the cloud base. Humidity in both cloud and clear air filaments approaches the saturation value.

A marker discriminating between CTMSL and CTL is set in a point in which *LWC* jump correlates with drop of *T* and *r*. Right to this point there are remarkable fluctuations of *LWC* and of all velocity components, but no more systematic increase of *v* (end of wind shear layer). Across the whole depth of EIL (between 599m and 554m) temperature changes by less than 2.5K, *v* velocity component changes by ~4m/s and, paradoxically, water vapor mixing ratio

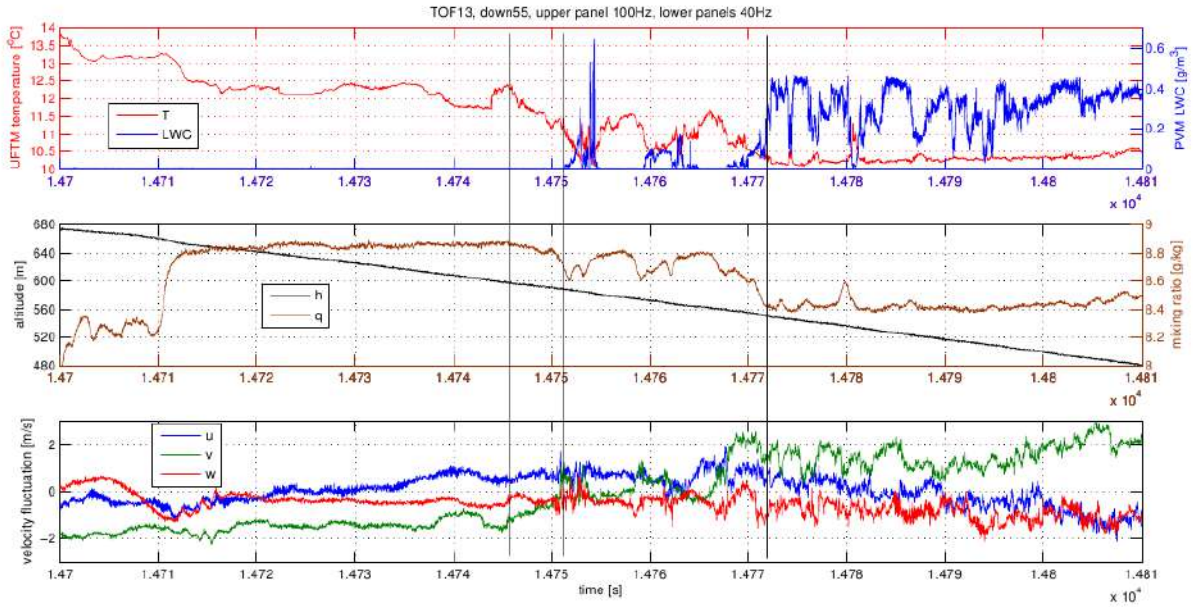

Figure 7. As in Fig.3, but for TO 13 flight.Figure 3.

increases with height, indicating that the whole EIL is close to saturation.

Fig.8 shows 1000Hz blow-ups of *T* and *LWC* fluctuations in CTMSL. Microscale picture of cloud-clear air mixing clearly differs from that in TO10 (c.f. Fig.5). Regions of *LWC*<0.1g/m^3 accompanied by temperature fluctuations of ~0.5K are common. Sharp ramps in temperature record suggest very narrow interfaces between the filaments of various temperatures. Such ramps, common within both: cloudy and clear air filaments were not observed in TO10 case.

In Fig.9 twelve consecutive vertical profiles of LWC in are presented in a similar manner as in Fig.6. Differences between these figures are striking. In TO10 maximum LWC in CTL and CTMSL in 100m thick layer at the cloud top increases with height, in TO13 it decreases or is constant. Several panels indicate that in a layer below 100-150m from the cloud top the maximum LWC shows pattern typical to that in the mixed layer: a linear increase of maximum LWC with the altitude.

It is worth of mentioning, that structure of stratocumulus top in TO13 is not unique. It resembles closely e.g. clod top from RF08B case of FIRE I research campaign (c.f. Fig 6 in Rode and Wang (2007)).

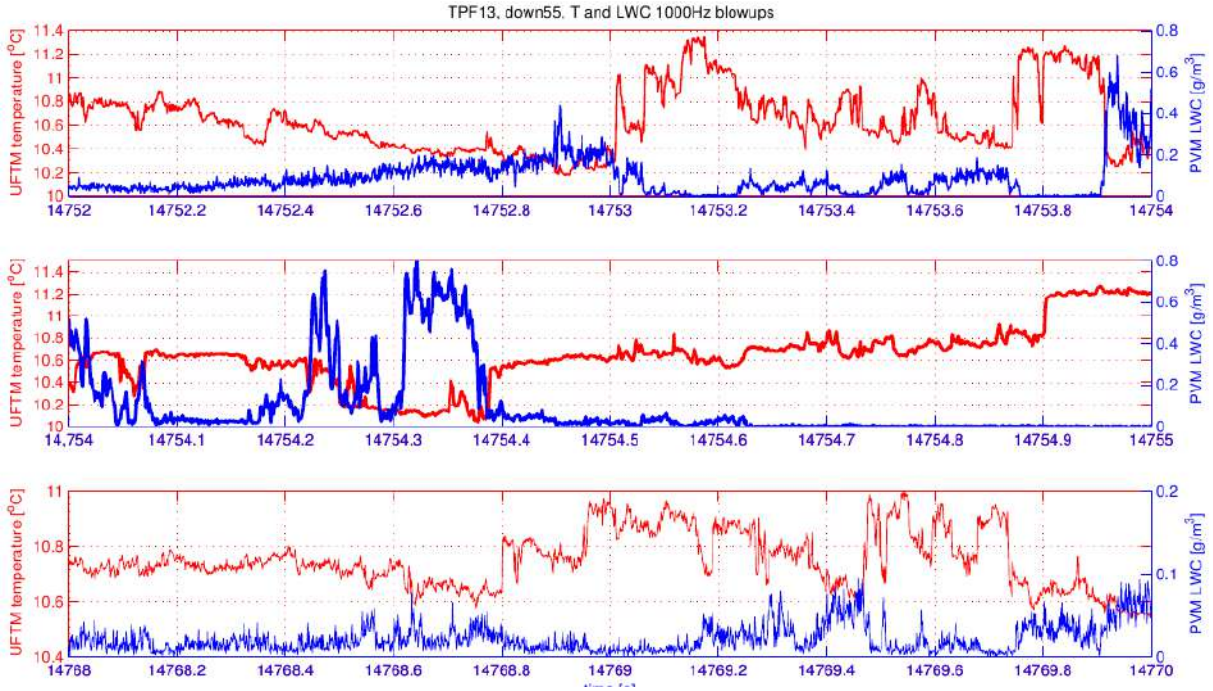

Figure 8. As in Fig.4, but for TO 13 flight. Panels 1 and 3 show 2s (110m long) segments, in the middle panel1s (33m long) segment is presented.

4. DISCUSSION

Differences in thermodynamical and dynamical properties of the cloud tops between TO10 and TO13 cases were reflected in visual appearance of stratocumulus top. Observers on board noticed ”classic stratocumulus layer” in course of TO10 flight, while in course of TO13 they reported ”cloud tops looking like moguls”.

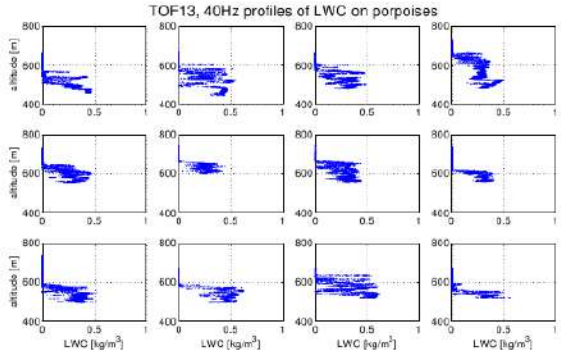

Figure 9. As in Fig.5, but for TO13 flight.

Nature of these differences requires additional analysis. Consider crude estimates of turbulence parameters in consecutive layers and sublayers of the cloud top region (Table 1), based on few penetrations in each case.

TOF10	RMSV	Ri	$\frac{L_C}{L_O}$	TOF13	RMSV	Ri	$\frac{L_C}{L_O}$
FT	0.15	3.9	2.8	FT	0.20	3.9	2.8
TISL	0.49	0.20	0.30	TISL	0.36	0.28	0.38
CTMSL	0.42	0.60	0.68	CTMSL	0.78	0.34	0.44
EIL	0.63	0.39	0.49	EIL	0.72	0.47	0.57
CTL	0.50	-	-	CTL	0.53	-	-

Table 1. Typical properties of turbulence in consecutive layers of the cloud top in TO10 and TO13.

Rows: FT-free troposphere, TISL- turbulent inversion sublayer, CTMSL- cloud top mixing sublayer, CTL- cloud top layer, EIL: entrainment interfacial layer.

Columns: RMSV- root mean square velocity in m/s, Ri- bulk Richardson number, L_C – Corrsin scale, L_O – Ozmidov scale.

Root mean square velocity (RMSV) fluctuations were calculated using low-pass filtered velocity (10Hz cutoff frequency) in order to damp the instrumental noise. Bulk Richardson number was estimated from 1 Hz data across ~50m thick layer of FT, and the whole depths of TISL, CTMSL and EIL using the following formula:

$$Ri = \frac{\frac{g}{\theta_l}\left(\frac{\Delta \theta_l}{\Delta z}\right)}{\left(\frac{\Delta u}{\Delta z}\right)^2 + \left(\frac{\Delta v}{\Delta z}\right)^2} \qquad (1)$$

where g is gravity acceleration, $\Delta\vartheta_l$, Δu and Δv are jumps of liquid water potential temperature and horizontal velocity components across the layer of thickness of Δz.

Vertical gradients are affected by the way data were collected. Almost horizontal flight path (typical inclination 2 degrees) and inevitable horizontal variability of temperature and wind are cause of this problem. In particular, CTMSL as seen in Figs. 3 and 6, may not appear on vertical profiles from. e.g. dropsondes. Thickness of this sublayer is just a ”first guess” estimate of the amplitude of cloud top fluctuations on a horizontal distance of few km.

Keeping above in mind, a simplified dynamical picture of cloud top region in both, such different cases, is surprisingly similar. Free troposphere is dynamically stable (Ri≈4), with the minimum values of RMSV in all the investigated layers. TISL, CTMSL and the whole EIL are characterized by values of Ri close to the critical (which, according to different sources varies in a range 0.2–1.0). Minimum value of Ri seems to be characteristics of TISL. All the penetrations seen by the authors so far confirm that TISL is turbulent, despite the maximum static stability across this layer. SiA border between non-turbulent FT and turbulent TISL is always sharp, no gradual increase of velocity fluctuations is observed. CTL begins at the level where horizontal velocity gradient vanishes. Similar properties of EIL, collected from helicopter-borne instrumented platform ACTOS were reported by Katzwinkel et al., (2011).

Estimates of Ri and RMSV across whole EIL are more reliable than across the sublayers. Despite the uncertainties, turbulent properties of EIL as diagnosed from Ri are similar in both cases. This can be explained analyzing the length scales associated with the turbulence. The first one, Corrsin scale, is a scale above which eddies are deformed by the shear and can be expressed as:

$$L_C = \sqrt{\frac{\epsilon}{S^3}} \qquad (2)$$

In the above S is velocity shear across the EIL and ε is the turbulent kinetic energy dissipation rate. Ozmidov length scale is a scale above which eddies are deformed by a stable stratification in EIL and is expressed as:

$$L_C = \sqrt{\frac{\epsilon}{N^3}} \quad (3)$$

where N is Brunt-Vaisala frequency across the EIL. While we do not know ε in both cases (estimates from the power spectra of velocity on short flight segments are not reliable), we can estimate the ratio of Corrsin and Ozmidov scales:

$$\frac{L_C}{L_O} = \left(\frac{N}{S}\right)^{\frac{3}{2}} = Ri^{\frac{3}{4}} \quad (4)$$

The last equation shows link between the scale ratio and Ri which can be interpreted in a following way: production of turbulence by the shear and across EIL and its damping by the buoyancy across EIL coincides. Ri in range 0.3-0.5 in statically stable turbulent mixing layers is widely reported in the literature (see review by Peltier and Caulfield (2003)), direct numerical simulations of Smyth and Moum (2000) (c.f. Fig 6 therein), of Brucker and Sarkar (2007) (Fig.7 therein) and of Pham and Sarkar (2010) (Fig. 2B therein); consequently show Ri in range 0.3-0.5 in the stratified shear layer in agreement with the laboratory experiments reviewed by Peltier and Caulfield (2003) and with our estimates. More interestingly, Peltier and Caulfield (2003) discuss details of the mechanism which drives mixing across stratified shear layer: overturning of densities in Kelvin-Helmhols billows leading to secondary convective instability across the layer which determine mixing efficiency. What differs Sc cloud top mixing region from stable mixing layers reviewed in the literature is the effect of evaporative cooling in course of mixing, leading to nonlinear effects in buoyancy of mixed parcels. Relative humidity RH of FT in TO10 case is 0.12, while in TO13 it reaches 0.92. In both cases CTL is saturated containing small, typical for stratocumulus clouds, amounts of LWC. Mixing diagram for TO10 case closely resembles that from RF01 of DYCOMS II experiment (c.f. Fig. 11 in Kurowski et.al. (2009)). For dry troposphere parcels containing FT fraction χ<0.12 in mixing event are negatively buoyant, and mixtures of FT fraction χ<0.11 are saturated after completion of mixing. This means, that diluted cloudy parcels of χ<0.12 are likely to be removed from CTML by negative buoyancy.

In contrary, for TO13 case, mixing across inversion cannot produce negative buoyancy. High RH of entrained FT air and small temperature difference between FT and CTL cause that evaporative cooling in course mixing is weak, which only marginally affects buoyancy (density). Additionally, mixtures of as high fraction of clear air as χ<0.7 are still cloudy. In consequence, most of the mixed parcels maintain diluted cloud water and remain close to the level where mixing occurred, which leads to formation of a layer with reduced LWC below the inversion.

5. CONCLUSIONS

1. Inversion capping stratocumulus layer is turbulent.

2. Exchange between FT and CTL is governed by turbulent mixing across EIL. Thickness of EIL results from dynamic adaptation of thickness of the shear layer to temperature (density) and wind jumps between CTL and FT. Adaptation means maintaining the Richardson number close to its critical value.

2. Despite similarities in dynamics of exchange process across EIL, existence or non-existence of cloud top entrainment instability leads to substantial differences of the Sc top structure. When thermodynamic conditions allow CTEI, mixed parcels which are negatively buoyant they are removed from CT region due to negative buoyancy. For high RH of FT, preventing from CTEI, mixed parcels often remain cloudy and buoyancy sorting prevents them from sinking. They remain in the cloud top region below inversion.

Acknowledgments: *This research was supported by the National Science Foundation with the grant ATM-0735121 and by the Polish Ministry of Science and Higher Education with the grant 186/W-POST/2008/0. We thank all POSTers and CIRPAS for the excellent collaboration during the field campaign. The manuscript was written in Kavli Institute for Theoretical Physics at UC Santa Barbara in course of "Nature of Turbulence" program, SPM acknowledges support from KITP.*

References:

Albrecht, B.A., Randall, D.A., Nicholls, S. (1988), Observations of marine stratocumulus clouds during fire,Bull.Amer.Meteor.Soc., 69, 618–626.

Bretherton, C.S., Uttal, T., Fairall, C.W., Yuter, S.E.,Weller, R.A., Baumgardner, D., Comstock, K., Wood. R., Raga, G.B. (2004), The Epic 2001 Stratocumulus Study, Bull.Amer.Meteor.Soc., 85, 967–977.

Brucker, K.A., Sarkar, S. (2007), Evolution of an initially turbulent stratified shear layer, Phys.Fluids, 19, 1050105.

Caughey, S. J.,Crease, B. A., Roach, W. T. (1982), A field study of nocturnal stratocumulus: II. Turbulence structure and entrainment, Q.J.Roy.Meteor.Soc., 108, 125–144.

Faloona, I., Lenschow, D.H, Campos T., Stevens, B., van Zanten, M. (2005), Observations of Entrainment in Eastern Pacific Marine Stratocumulus Using Three Conserved Scalars, J.Atmos.Sci., 62, 3268–3285.

Gerber, H., Arends, B.G., Ackerman, A.S. (1994), A new microphysics sensor for aircraft use, Atmos.Res., 31, 235–252.

Gerber, H. (1996), Microphysics of Marine Stratocumulus Clouds with Two Drizzle Modes, J.Atmos.Sci., 53, 1649–1662.

Gerber , H., S.P. Malinowski, J.-L Brenguier, and F. Burnet (2002): On the entrainment process in stratocumulus clouds. *Proc. 11th Conf. On Cloud Physics*, Ogden, UT, Amer. Meteor. Soc., CD-ROM, paper JP7.6

Gerber, H., Frick, G., Malinowski, S.P., Brenguier, J-L., Burnet, F. (2005), Holes and entrainment in stratocumulus, J.Atmos.Sci., 62, 443–459.

Gerber, H., Frick, G., Malinowski, S.P., Kumala, W., Krueger, S. (2010), POST-A New Look at Stratocumulus, 13th Conference on Cloud Physics, Portland, OR, 2010, American Meteorological Society http://ams.confex.com/ams/pdfpapers/170431.pdf

Gerber, H., Frick, G., Malinowski, S.P, Jonsson H., Khelif D., Krueger S. (2012): Entrainment in Unbroken Stratocumulus. submitted to J.Geophys. Res.

Haman, K.E., Malinowski, S.P., Kurowski, M.J., Gerber, H., Brenguier, J-L. (2007), Small scale mixing processes at the top of a marine stratocumulus - A case study, Q.J.R.Meteorol.Soc., 133, 213–226.

Katzwinkel, J., H. Siebert, and R. A. Shaw. (2011), Observation of a self-limiting, shear-induced turbulent inversion layer above marine stratocumulus. Boundary-Lay. (13p) Meteorol., DOI: 10.1007/s10546-011-9683-4

Kumala, W., Haman, K.E., Kopec, M.K., Malinowski, S.P. (2012), Ultrafast Thermometer UFT-M: High Resolution Temperature Measurements During Physics of Stratocumulus Top (POST), in preparation to Atmos Meas.Tech.

Kurowski, M.J., Malinowski, S.P., Grabowski, W.W. (2009), A numerical investigation of entrainment and transport within a stratocumulus-topped boundary layer, Q.J.R.Meteorol.Soc., 135, 77–92.

Lenschow, D. H., Paluch, I.R., Brandy, A.R, Pearson, R., Kawa S.R, Weaver C.J., Kay, J.G, Thornton D.C., Driedger A.R., (1988), Dynamics and Chemistry of Marine Stratocumulus (DYCOMS) Experiment, Bull.Amer.Meteor.Soc., 69, 1058–1067.

Lenschow, D.L., Zhou, M., Zeng, X., Chen, L., Xu, X., (2000), Measurements of fine-scale structure at the top of marine stratocumulus, Boundary Layer Meteorol., 97, 331–357.

Lilly, D. K. (1968) Models of cloud-topped mixed layers under a strong inversion, Q.J.R.Meteorol.Soc., 94, 292–309.

Lilly, D. K. (2008), Validation of a mixed-layer closure. II: Observational tests, Q.J.R.Meteorol.Soc., 134, 57–67.

Malinowski, S.P., Haman, K.E, Kopec M.K., Kumala, W., Gerber H.E., Krueger, S.K (2010),Small scale variability of temperature and LWC at Stratocumulus top , 13th Conference on Cloud Physics, Portland, OR, 2010, American Meteorological Society http://ams.confex.com/ams/pdfpapers/171260.pdf

Moeng C-H., Stevens B., Sullivan PP. (2005), Where is the interface of the stratocumulus-topped PBL?, J. Atmos. Sci., 62, 2626–2631.

Nicholls, S. (1989), The structure of radiatively driven convection in stratocumulus, Q.J.R.Meteorol.Soc., 115, 487–511.

Pawlowska, H., Brenguier, J-L., Burnet, F. (2000), Microphysical properties of

stratocumulus clouds, Atmos.Res., 55, 15–23.

Peltier, W.R., Caulfield C.P. (2003), Mixing Efficiency in stratified shear flows.Annu.Rev.Fluid.Mech., 35, 135–167.

Pham, H.T., Sarkar, S. (2010), Transport and mixing of density in a continuously stratified shear layer.J.of.Turbulence, 11, 1–23.

Roode, S.R., Wang, Q. (2007), Do stratocumulus clouds detrain? FIRE I data revisited, Boundary-Layer Meteorol., 122, 479–491.

Smyth, W.D., Moum, J.N. (2000), Length scales of turbulence in stably stratified mixing layers, Phys.Fluids, 12, 1327–1342.

Sorbjan, Z. (2010), Gradient-based scales and similarity laws in the stable boundary layer, Q.J.R.Meteorol.Soc., 136, 1243–1254.

Stevens, B. (2002), Entrainment in stratocumulus-topped mixed layers, Q.J.R.Meteorol.Soc., 128, 2663-2690.

Stevens, B., Lenschow, D.H., Vali, G., Gerber, H., Bandy, A., Blomquist, B., Brenguier, J-L., Bretherton, C. S., Burnet, F., Campos, T., Chai, S., Faloona, I., Friesen, D., Haimov, S., Laursen, K., Lilly, D.K., Loehrer, S.M., Malinowski, S.P., Morley, B., Petters, M.D., Rogers, D.C., Russell, L., SavicJovcic, V., Snider, J.R., Straub, D., Szumowski, M.J., Takagi, H., Thornton, D.C., Tschudi, M., Twohy, C., Wetzel, M., van Zanten, M.C. (2003), Dynamics and chemistry of marine stratocumulus - Dycoms II, Bull. Amer. Meteorol.Soc., 84, 579–593.

Stevens B., Moeng C.H., Ackerman A.S., Bretherton C.S., Chlond A., De Roode S., Edwards J., Golaz J.C., Jiang H.L., Khairoutdinov M., Kirkpatrick M.P., Lewellen D.C., Lock A., Muller F., Stevens D.E., Whelan E., Zhu P. (2005), Evaluation of large-Eddy simulations via observations of nocturnal marine stratocumulus, Mon. Wea. Rev., 133, 1443–1462.

Wang, S., Golaz, J.-C., Wang, Q. (2008), Efect of intense wind shear across the inversion on stratocumulus clouds, Geophys.Res.Lett., 35, L15814.

Yamaguchi, T., Randall, D.A., (2008), Large-Eddy Simulation of Evaporatively Driven Entrainment in Cloud-Topped Mixed Layers, J. Atmos. Sci., 65, 1481–1504.

Yamaguchi, T., Randall, D.A., (2012), Cooling of entrained parcels in a large-eddy simulation. J.Atmos. Sci., 69, 1118-1136.

LIDAR INVESTIGATION OF AEROSOL PARTICLE SIZE DISTRIBUTION UNDER CUMULUS BASE

T. Stacewicz[1], M. Posyniak[2], S.P. Malinowski[2], A.K. Jagodnicka[1], S. Sitarek[3], S. Arabas[1]

[1]Institute of Experimental Physics, Faculty of Physics, Warsaw University, ul. Hoża 69, 00-681 Warsaw, Poland

[2]Institute of Geophysics, Faculty of Physics, Warsaw University ul. Pasteura 7, 02-093 Warsaw, Poland

[3]Institute of Applied Optics, ul Kamionkowska 18. 03-805 Warsaw, Poland

1. INTRODUCTION

In the updraft, below the base of convective cloud the boundary layer aerosol becomes hydrated due to increase of relative humidity in adiabatic lift. Cloud Condensation Nuclei (CCN) are activated and small droplets are formed. In 1959 Twomey [1] elaborated model of this process that is still considered a valid one. The refined and improved versions of this approach are widely used for numerical modeling of convective processes, [2, 3] and to elucidate in-situ measurements [4]. There are, however, many uncertainties related with the details of droplet formation, particularly important in context of indirect aerosol influence on the radiative forcing [5]. Remote retrievals of vertical profiles of the aerosol size distribution can help in better understanding of the microphysical processes at the cloud base. Here we present a technique to investigate CCN activation and preliminary phase of droplet growth at base of convective cloud using multiwavelength lidar. It combines on a natural technique of aerosol particle size distribution (APSD) retrieval described in [6] and additional information on CCN activation from Twomey model [1].

Briefly the method consists in assumption of APSD function in a predefined form with several free parameters. In particular, for our three wavelength lidar we chose a bimodal combination of lognormal functions. The aerosol is assumed to consist of spheres of known refractive index. Such conditions are well fulfilled for the hygroscopic aerosol at high relative humidities close to the cloud base and for small cloud droplets. Using Mie approach [7] we calculate backscattering coefficient $\beta_\lambda(z)$ and total scattering coefficient $\alpha_\lambda(z)$ for each wavelength λ in a range of distances z from the lidar located at z_0. After substitution of obtained parameters to a set of lidar equations :

$$L_\lambda(z) = A_\lambda \beta_\lambda(z) \exp\left[-2\int_{z_0}^{z} \alpha_\lambda(x)dx\right], \qquad (1)$$

the range corrected calculated signals $L_\lambda(z)$ are compared to the measured ones.

Direct substitution of extinction and backscattering coefficients into (1) ensures that APSD remains as the only unknown function in the system of equations. Application of the minimization procedure provides an opportunity to get the optimal parameters characterizing the predefined APSD distribution. The method does not require knowledge of lidar ratio.

2. LIDAR, EXPERIMENT AND SIGNALS REGISTERED UNDER CUMULUS CLOUD

Construction of the lidar used in observations of Cumulus base was described elsewhere [6, 8]. Briefly, in the optical transmitter pulsed Nd:YAG laser generates the beams at 1064, 532 and 355 nm. The energy of the light pulses reaches 100 mJ, the repetition rate is 10 Hz. In the optical receiver a Newtonian telescope with the mirror of 400 mm in diameter and focal length equal 1200 mm is used. The return light pulses, collected by the telescope, are spectrally separated by a polychromator and registered in relevant channels, corresponding to consecutive wavelengths. The signals from the photomultipliers installed at each channel are digitized by 12-bit A/D converters.

Lidar data analyzed in this study were

collected in Warsaw on 30. 08. 2008. On this day fair weather cumuli were developing in a mass of marine polar air advecting from north in peripheries of the Scandinavian high pressure system. The laser beams were sent vertically, pointing at clouds drifting above the lidar station. Cloud base height was increasing in course of measurements. Moreover, wind shear caused that clouds were tilted and signature of clouds in lidar profiles was observed at altitudes in a range from 1400 to 2000 m.

Fig.1 presents an example of range-corrected lidar profiles from the region classified as a cloud base. These profiles were obtained by averaging over 300 laser shots (30 s) and over 9 m long segments along the beam.

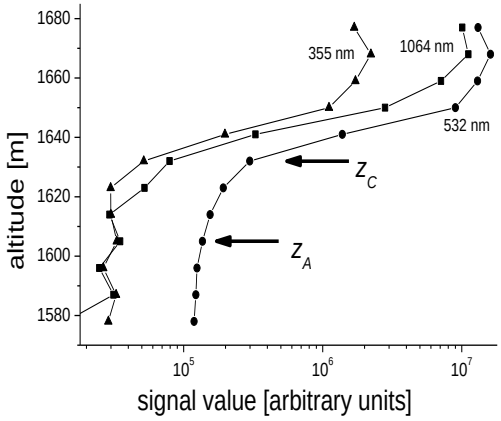

Fig. 1*. Example of range corrected lidar signals in vicinity of the cumulus cloud base. z_A and z_C denote the activation and the condensation altitudes respectively*

In general, presented profiles are typical for the lidar signals at the cloud base, as reported e.g. in [9] and [10]. At the altitudes below 1.6 km (i. e. more than 40 m below the cloud base) the signals are weak, which indicates that the light is scattered by aerosol consisting of small particles. For these altitudes the technique of retrieval, described in [6] was applied in its generic form. Beginning from 1605 m (the lower arrow in Fig. 1) all three signals increase. That indicates the enhanced scattering due to hygroscopic aerosol particle size growth. The corresponding height is denoted z_a, and is considered a signature of activation of CCN beginning. In this region we change the retrieval algorithm using additional information, i.e. Twomey's model of CCN activation in adiabatic parcel. Its details are described in the next section.

Above the signal maximum (1670 m) lidar returns are strongly affected by multiple light scattering. Consequently, the signals above the maximum are not analyzed.

In course of measurements about 65 three wavelength profiles with cloud signature was collected. 12 of them was classified as pointing into the cloud base within the whole averaging period. For all 65 “cloudy” profiles a modified retrieval accounting for CCN activation and droplet growth was applied, but the statistical analysis of retrieval was performed separately for “cloud base” and “cloud side” cases, in order to look for differences. By principle the method should work for uniform cloud bases only.

3. PARCEL MODEL CALCULATIONS OF CCN ACTIVATION

Starting from the activation altitude, z_a (method of z_a determination is described in the next part) a simple model of CCN condensation and droplet growth, based on adiabatic parcel approach was used to provide additional information on vertical profiles of the particle distributions. Calculations of the evolution of CCN and droplet size distributions were performed with the accurate and efficient numerical code described in [11].

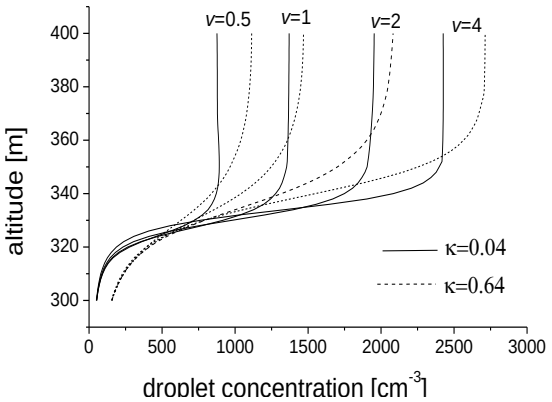

Fig. 2. *Effective radius as a function of relative altitude for various lift speed v [m/s] and hygroscopity coefficient κ.*

Thermodynamic conditions were taken from the atmospheric sounding from 12 UTC from nearby (~25 km north) Legionowo (WMO

123740). Typical well mixed boundary layer was observed. Aerosol evolution in updraft was calculated using κ-Koehler approach [12]. Computations were done for constant updraft velocities at the cloud base ranging from 0.1 to 4.0 m/s and two values of κ: 0.04 (non-hygroscopic aerosol) and 0.64 (hygroscopic aerosol). Example results, shown in Fig. 2, indicate that to the first approximation number of the activated particles increases with the updraft velocity, while the depth of activation zone depends on the hygroscopicity of aerosol.

The initial modal distribution of aerosol retrieved from the lidar profile analysis below z_a was taken for the calculations. The starting level for all model runs was about 350 m below cloud base, and the simulations were stopped after reaching 500 m above the starting level. The following conclusions were drawn from the parcel model:

a) In the range of investigated updraft velocities and for hygroscopity parameter from 0.04 (non-hygroscopic aerosol) to 0.64 (highly hygroscopic aerosol), the particles of dry radius which exceeds r_{min}=100±20 nm, are activated and grow into cloud droplets. Thus the droplet number concentration in cloud can be estimated from the integration of the right part of the APSD at the activation level z_a :

$$N_A = \int_{r_{\min}}^{\infty} n(r)dr \qquad (2)$$

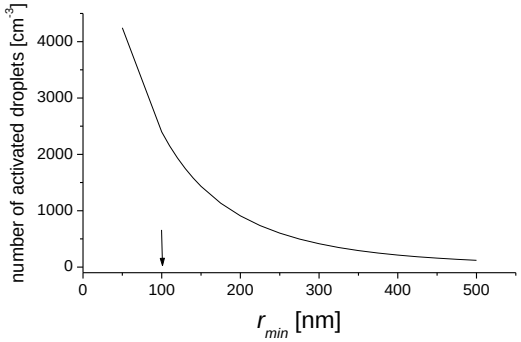

Fig. 3. *Number of activated particles as a function of r_{min}. The arrow indicates r_{min} value.*

The value of N_A as a function of r_{min} is presented in Fig. 3. While in this preliminary study the initial APSD is determined with precision of 50 % and the r_{min} with precision 20 %, the estimated droplet number concentration in investigated clouds is N_A = 2400±1000 cm^{-3}, which is the value expected in polluted urban area.

b) Starting from the activation altitude z_A activated droplets constitute the Gaussian distribution. Its amplitude increases with height due to growing number of activated droplets. Median radius of the mode r_0 and its width σ remains constant: r_0≈1000 nm, σ≈500 nm

c) For the particles smaller than r_{min} the APSD remains unchanged.

d) At the altitude z_c, all hygroscopic particles of dry radii $r>r_{min}$ become activated. Further growth (for $z>z_c$) of activated droplets takes place due to the condensation. It can be expressed by increase of the median radius of Gauss mode with the constant amplitude.

4. RETRIEVAL OF APSD IN UPDRAFT

Basing on the above conclusions a modified algorithm for retrieval of APSD in updraft under cumulus base consists of the following steps:

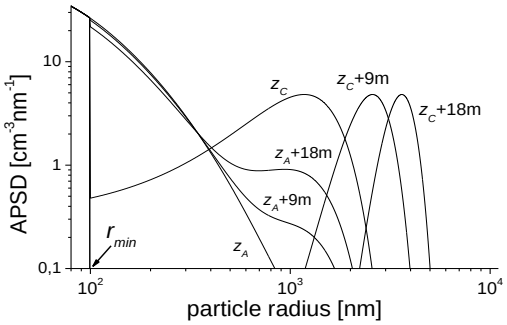

Fig. 4. *Changes of Aerosol Particle Size Distribution with altitude, starting from activation altitude z_A for and consecutive altitudes to the condensation altitude z_C and above.*

a) An initial guess of z_a altitude.

The first guess is an altitude above which a systematic increase of all three lidar signals is observed. At this level the APSD function, which was determined for $z<z_a$, is divided in two parts: for $r<r_{min}$ it persists in its initial form while for $r \geq r_{min}$ a Gaussian mode containing N_a particles is generated. Then the backscattering and total scattering coefficients ($\beta_\lambda(z)$ and $\alpha_\lambda(z)$) are calculated for each wavelength λ with Mie approach [7]. Using the formula (1) the range corrected

lidar signals $L_\lambda(z)$ are found and compared to the measured ones. Fit provides the opportunity to determine the amplitude of the Gauss mode.

b) Since the determination of z_a is ambiguous, the procedure is repeated starting from the neighboring altitudes (z_A±9 m *etc*.). The smoothness of increase of the Gauss mode amplitude with the altitude is evaluated for each level.

After such iteration procedure the activation altitude is finally determined. The following evolution of the modeled aerosol particle size distribution within the activation range $z_A<z<z_c$ are shown in Fig. 4.

c) Above the condensation altitude z_c the increase of the lidar signals (Fig. 1) result from the condensational growth of activated droplets, i.e. by the increasing median radius r_0 at the constant number concentration N_A. Comparison of synthetic lidar signal calculated using this assumption to the measured one provides opportunity to determine r_0 for each altitude.

Within these consecutive steps the size distribution function *n(r,z)* for each observed altitude can be determined (Fig. 4) and used e.g. to calculate the effective radius of droplets expressed by:

$$r_{eff}(z) = \frac{\int r^3 n(r,z) dr}{\int r^2 n(r,z) dr} \qquad (3)$$

5. RESULTS AND DISCUSSION

Figs. 5 and 6 present statistics of lidar retrievals of activation/condensation at the cloud base. Due to the variability of cloud base heights their altitude was normalized to z_C for each lidar profile.

It can be seen, that the cases classified as “cloud base” are characterized with a smaller spread of activated droplets number and of the effective radius than the cases classified as “cloud side”. This confirms that usage of parcel model of droplet growth is useful in the retrieval procedure.

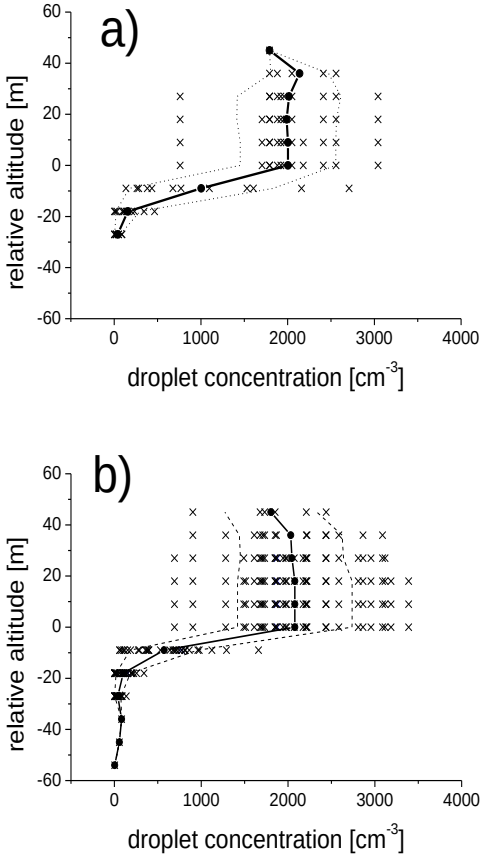

Fig. 5. *Number of activated droplets as a function of the relative altitude (z_c=0) retrieved for profiles classified as “cloud base” (a) and “cloud side” (b)*

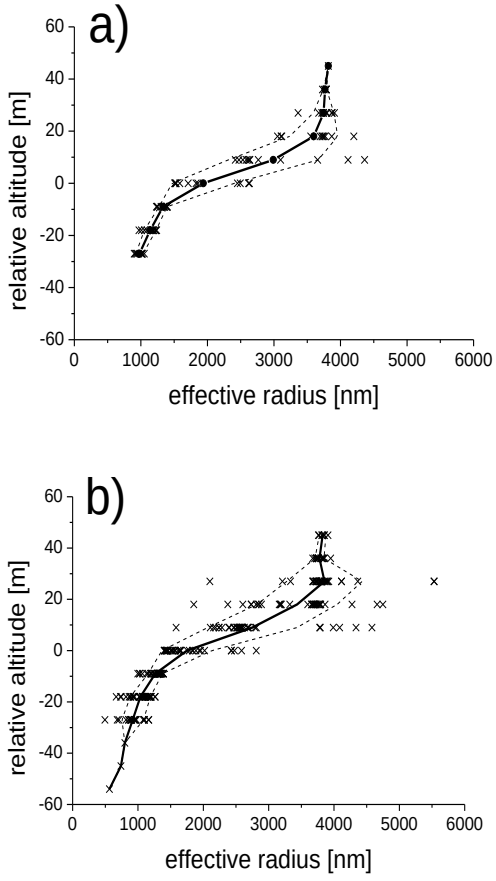

Fig. 6. *Effective radius as a function of relative altitude (z_c=0) in profiles classified as “cloud base” (a) and “cloud side” (b)*

Decrease of N_A and fluctuations of r_{eff} at the topmost end of “cloud base” profiles are the effects of low-number statistics (only few shots reach this level). On the other hand similar effect is visible in the profiles classified as “cloud side”. This suggests the artifacts due to secondary scattering, which means that two topmost points should be rejected.

A sharp tilt in N_a at z=0 and constant N_a above is the effect of retrieval assumptions, not of non-hygroscopic aerosol (c.f. N_a profiles from parcel model in Fig.2.). Comparison of Figs 2 and 5 suggests that the most probable updraft speed at the cloud base is ~2 m/s.

In summary we may conclude that:

a) Information from parcel model of activation and condensational growth of cloud droplets can be used to estimate the cloud droplet number concentration N_a at the cloud base from multiwavelength lidar signals.

b) Additionally, the method allows estimating vertical profile of the effective radius of cloud droplets at the cloud base.

c) Comparison of measured lidar profiles at the cloud base to lidar profiles calculated theoretically with the parcel model allows to estimate updraft velocity for a given dry APSD functional shape and hygroscopicity.

5. ACKNOWLEDGEMENTS

This work was supported by Polish Ministry of Higher Education and Science with the statutory funds for research (2011/12) Faculty of Physics of University of Warsaw, (Institutes of Experimental Physics and of Geophysics) as well as of Institute of Applied Optics.

6. REFERENCES

[1]. Twomey S. and H. B. Howell. 1965. “The Relative Merit of White and Monochromatic Light for the Determination of Visibility by Backscattering Measurements.” *Applied Optics* 4: 501-506.

[2]. Khvorostyanov, V. I. and J. A. Curry. 1999. "A Simple Analytical Model of Aerosol Properties with Account for Hygroscopic Growth 1. Equilibrium Size Spectra and Cloud Condensation Nuclei Activity Spectra." *Journal of Geophysical Research D: Atmospheres* 104 (D2): 2175-2184.

[3]. Celani, A., A. Mazzino, and M. Tizzi. 2008. "The Equivalent Size of Cloud Condensation Nuclei." *New Journal of Physics* 10: 16.

[4]. Colón-Robles, M., R. M. Rauber, and J. B. Jensen. 2006. "Influence of Low-Level Wind Speed on Droplet Spectra Near Cloud Base in Trade Wind Cumulus." *Geophysical Research Letters* 33 (20): L20814.

[5]. McFiggans, G., P. Artaxo, U. Baltensperger, H. Coe, M. C. Facchini, G. Feingold, S. Fuzzi, et al. 2006. "The Effect of Physical and Chemical Aerosol Properties on Warm Cloud Droplet Activation." *Atmospheric Chemistry and Physics* 6 (9): 2593-2649.

[6]. Jagodnicka, A. K., T. Stacewicz, G. Karasiński, M. Posyniak, and S. P. Malinowski. 2009. "Particle Size Distribution Retrieval from Multiwavelength Lidar Signals for Droplet Aerosol." *Applied Optics* 48 (4): B8-B16.

[7]. Bohren, C. F. and D.R Huffman. 1999. “Absorption and Scattering of Light by Small Particles.” *John Wiley & Sons, New York*.

[8]. Jagodnicka, A. K., T. Stacewicz, M. Posyniak, and S. P. Malinowski. 2009. "Aerosol Investigation with Multiwavelength Lidar." *Proceedings of SPIE* 7479: 747903.

[9]. Apituley, A., A. Van Lammeren, and H. Russchenberg. 2000. "High Time Resolution Cloud Measurements with Lidar during CLARA." *Physics and Chemistry of the Earth, Part B: Hydrology, Oceans and Atmosphere* 25 (2): 107-113.

[10]. Boers, R., H. Russchenberg, J. Erkelens, V. Venema, A. Van Lammeren, A. Apituley, and S. Jongen. 2000. "Ground-Based Remote Sensing of Stratocumulus Properties during CLARA, 1996." *Journal of Applied Meteorology* 39 (2): 169-181.

[11]. Arabas, S., and H. Pawlowska. 2011. “Adaptive method of lines for multi-component aerosol condensational growth and CCN activation.” *Geoscientific Model Development* 4**:** 15-31.

[12]. Petters, M. D. and S. M Kreidenweis, 2007 “A single parameter representation of hygroscopic growth and cloud condensation nucleus activity”, *Atmos. Chem. Phys.*7, 1961-1971, doi:10.5194/acp-7-1961-2007,

CLOUD EFFECTS ON AEROSOL OPTICAL PROPERTIES

Leskinen, Ari[1], Arola, Antti[1], Portin, Harri[1,2], Romakkaniemi, Sami[2], Hyvärinen Antti-Pekka[3], Laaksonen, Ari[2,3], Lehtinen, Kari E.J.[1,2] and Komppula, Mika[1]

[1]Finnish Meteorological Institute, Kuopio Unit, P.O.Box 1627, FI-70211, Kuopio, Finland
[2]University of Eastern Finland, Department of Applied Physics, P.O.Box 1627, FI-70211, Kuopio, Finland
[3]Finnish Meteorological Institute, Research and Development, P.O.Box 503, FI-00101 Helsinki, Finland

Keywords: atmospheric aerosols, aerosol optical properties, aerosol-cloud interactions, cloud scavenging

1. INTRODUCTION

According to the Intergovernmental Panel on Climate Change the direct effect of aerosols to radiative forcing is still highly uncertain (IPCC, 2007). The direct effect arises from light extinction by aerosol particles, i.e. due to the combined effect of aerosol light scattering and absorption. Evaluation of the direct effect's magnitude is complicated, because these properties depend on the wavelength of the incident light and the angular distribution of the scattered light, which, in turn, depends, e.g., on the size, concentration, and chemical composition of the aerosol particles. Particles that contain sulfate, nitrate, and organic carbon predominately scatter light, and particles that contain black carbon absorb it. Furthermore, internal mixing (e.g., of organics and black carbon) may dramatically influence the aerosol optical properties.

Aerosol particles exit the atmosphere, e.g., by activating into cloud droplets, which subsequently fall down, or being scavenged by the falling rain droplets. The degree of activation depends largely on the aerosol size but also on its chemical composition (Dusek et al., 2006). For example, fresh soot is generally hydrophobic and therefore inhibits activation, whereas sulphurous compounds are hygroscopic. Furthermore, the scavenging efficiency in clouds is enhanced by aging of organic species and subsequent mixing (Sellegri et al., 2003).

In this work we present aerosol optical properties during three cloud events. Our analysis is based on long-time measurements of aerosol scattering and absorption coefficients at Puijo in Kuopio, Finland (Leskinen et al., 2009; Leskinen et al., 2012). We inspect the cloud effects on aerosol optical properties in different conditions with or without emissions from local pollutant sources.

2. MEASUREMENT SITE

The Puijo measurement station (Leskinen et al. 2009) on the top of an observation tower (62°54’34’’ N, 27°39’19’’ E, 306 m above sea level, 224 m above the surrounding lake level) near the town of Kuopio (population 97000) in Eastern Finland, has provided continuous data on aerosol-cloud interactions since 2006. Since then the station has been covered by clouds 15 % of the time. The optimal months for investigating low-level clouds are from September to November (Portin et al., 2009).

We categorize the Puijo measurement station as a semi-urban measurement station, because there are local pollutant sources (traffic routes, residential areas, industrial plants) in a particular sector (0–245°) seen from the Puijo tower, whereas the remaining sector (245–360°) represents a "cleaner" sector with almost no local sources. This enables studying the properties of freshly emitted aerosol (e.g., sulphurous compounds from a nearby paper mill or black carbon from combustion sources) and aged long-range transported aerosols. Furthermore, the elevated location enables studies of the interaction of aerosols with low-level clouds (Portin et al., 2009).

3. INSTRUMENTATION

By using a special twin inlet setup (total and interstitial inlets) and a switching valve system we are able to separate the total aerosol from the interstitial (unactivated) particles. The total air inlet has the same construction as that used and designed by Weingartner et al. (1999), who reported that the cut-off size of the inlet is 40 µm when the wind speed is below 20 m/s, which is the case most of the time at Puijo. The large cut-off size allows both cloud droplets and unactivated interstitial aerosol particles to enter the sampling line. The inlet is heated, which makes the water evaporate from the droplets, leaving only the cloud condensation nuclei as a residual aerosol. This way it is possible to study the aerosol properties as it would be outside of the cloud. The interstitial inlet has a PM_1 impactor (cut-off size 1 µm), which prevents cloud droplets from entering the sampling line. When a cloud is present, this inlet samples only the interstitial aerosol. We use a valve system to switch the sampling lines for the measurement devices every 6 minutes.

We measured the aerosol scattering coefficients at 450, 550, and 700 nm by using an integrating nephelometer (TSI Model 3563). The nephelometer illuminates the sample volume from the side and detects the light scattered by the aerosol particles and gas molecules in the sample with a photomultiplier tube over an angle of 7–170°. The sample flow in the nephelometer was 8.0 l/min. The nephelometer calibration was checked periodically (every three months) with pure carbon dioxide and filtered air. The data collection frequency in the nephelometer was 1 minute.

We measured the aerosol absorption with a multi-angle absorption photometer (Thermo Model 5012 MAAP). The MAAP determines aerosol light absorption by illuminating a particle-loaded filter with 637 nm (Müller et al., 2011; 670 nm according to the manufacturer) light and measuring simultaneously the radiation passing through the filter. It compensates light scattering from the filter, which improves the aerosol absorption measurement considerably. The flow rate through the MAAP was 5.0 l/min. We performed periodic checks and flow calibrations for the instrument. We collected the MAAP data every 1 minute.

4. DATA PROCESSING

We analyzed the aerosol scattering and absorption coefficients during the cloud events that took place between October 5, 2010 – December 5, 2011. We inspected each 6-minute cycle between two consecutive valve switchings. In order to exclude unstable data due to possible flow disturbances in the instruments caused by the valve switching, we ignored the first and the last minute of the cycle and calculated 4-minute averages for each cycle.

We calculated the single scattering albedo (SSA), which is defined as the ratio of the scattering coefficient to the extinction coefficient (the sum of the scattering and absorption coefficients), at 637 nm. For this, the scattering coefficient at 637 was calculated by using the Ångström power law. The SSA can be used to determine whether an aerosol layer in the atmosphere causes net heating or cooling.

5. RESULTS

During a cloud event the scattering and absorption values for unactivated particles compared to those for the activated particles are sometimes smaller and sometimes not. In two cases on October 8–9, 2010 (Figure 1) the decrease was stronger for the scattering than for absorption. The stronger decrease in scattering results in a decrease in the single scattering albedo (SSA). During the two cloud events the SSA dropped from its initial value of 0.80–0.85 to as low as 0.4–0.5, on an average (Figure 1). A similar, but not as intensive, decrease in the SSA was observed by Berkowitz et al. (2011) in a foggy situation.

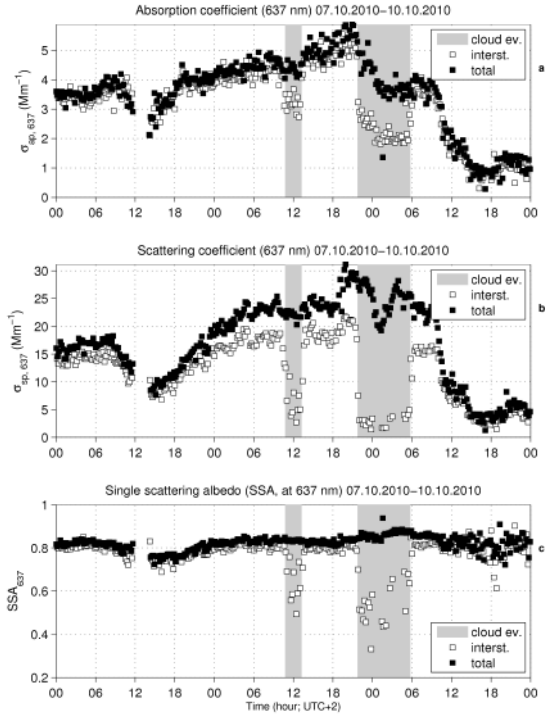

FIGURE 1. The (a) total scattering coefficient at 637 nm, (b) absorption coefficient at 637 nm, and (c) single scattering albedo at 637 nm (SSA637) of total and interstitial aerosol particles at Puijo in October 7–11, 2010, when two cloud events took place.

The scavenging is less efficient when the wind blows from the direction of local pollutant sources (the first cloud event in Figure 1) than when it blows from a cleaner sector with no local sources (the second cloud event in Figure 1). A similar observation was done by Sellegri et al. (2003) who concluded that the scavenging efficiency in clouds is enhanced by aging of organic species and subsequent mixing.

When the wind blows from a larger residential area during a cloud event on September 27, 2011 (Figure 2), the absorption does not change much but the scattering by the interstitial particles drops below the detection

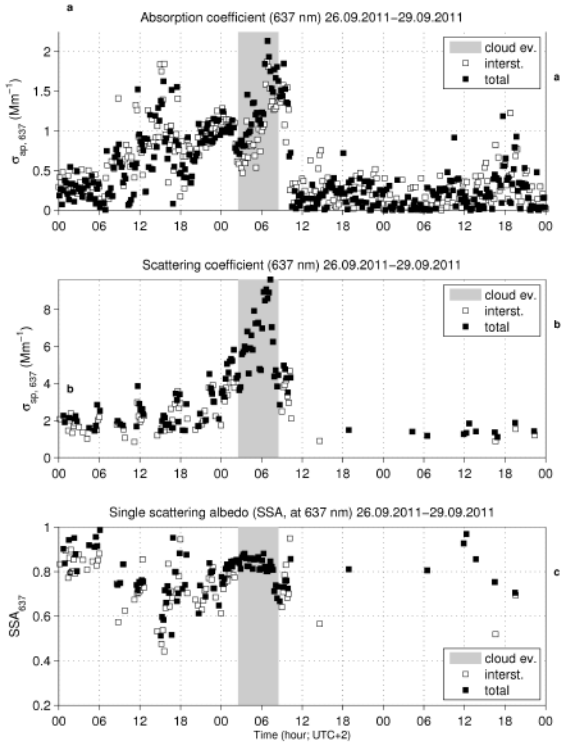

FIGURE 2. A cloud event in September 27, 2011. Please see the caption of Figure 1 for explanations.

limit of the nephelometer. This might be due to the fact that the absorbing material resides in the size fraction that does not activate into cloud droplets and that the scattering material is in the activated fraction.

6. FURTHER ANALYSES

Here we have presented the changes in the aerosol optical properties during three cloud events. Our data set with the total and interstitial aerosol lines separated during the 14-month period (October 5, 2010 – December 5, 2011) consists of altogether ~50 cloud events. The analysis of all these cloud events will be published in a forthcoming paper, which is under preparation. Also, we will analyse more aerosol mass spectrometry data in order to strengthen our knowledge about the role of the chemical composition of the aerosol particles in their activation into cloud droplets.

7. ACKNOWLEDGEMENTS

We acknowledge the financial support for instrumentation by the European Regional Development Fund (ERDF).

REFERENCES

Berkowitz, C.M., Berg, L.K., Yu, X.-Y., Alexander, M.L., Laskin, A., Zaveri, R.A., Jobson, B.T., Andrews, E., Ogren, J.A., 2011. The influence of fog and airmass history on aerosol optical, physical and chemical properties at Pt. Reyes National Seashore. Atmospheric Environment 45, 2559-2568.

Dusek, U., Frank, G.P., Hildebrandt, L., Curtius, J., Schneider, J., Walter, S., Chand, D., Drewnick, F., Hings, S., Jung, D., Borrmann, S., Andreae, M.O., 2006. Size Matters More Than Chemistry for Cloud-Nucleating Ability of Aerosol Particles. Science, 312, 1375-1378.

IPCC 2007. Climate change 2007: The physical science basis. Intergovernmental panel on Climate Change, Cambridge University Press, New York.

Leskinen, A., Portin, H., Komppula, M., Miettinen, P., Arola, A., Lihavainen, H., Hatakka, J., Laaksonen, A., Lehtinen, K.E.J., 2009. Overview of the research activities and results at Puijo semi-urban measurement station. Boreal Environment Research 14, 576-590.

Leskinen, A., Arola, A., Komppula, M., Portin, H., Tiitta, P., Miettinen, P., Romakkaniemi, S., Laaksonen, A., Lehtinen, K.E.J., 2012. Seasonal cycle and source analyses of aerosol optical properties in a semi-urban environment at Puijo station in Eastern Finland. Atmospheric Chemistry and Physics Discussions, 12, 4719-4754.

Müller, T., Henzing, J.S., de Leeuw, G., Wiedensohler, A., Alastuey, A., Angelov, H., Bizjak, M., Collaud Coen, M., Engström, J. E., Gruening, C., Hillamo, R., Hoffer, A., Imre, K., Ivanow, P., Jennings, G., Sun, J.Y., Kalivits, N., Karlsson, H., Komppula, M., Laj, P., Li, S.-M., Lunder, C., Marinoni, A., Martins dos Santos, S., Moerman, M., Nowak, A., Ogren, J.A., Petzold, A., Pichon, J.M., Rodriquez, S., Sharma, S., Sheridan, P.J., Teinilä, K., Tuch, T., Viana, M., Virkkula, A., Weingartner, E., Wilhelm, R., Wang, Y.Q., 2011. Characterization and intercomparison of aerosol absorption photometers: result of two intercomparison workshops. Atmospheric Measurement Techiques, 4, 245-268.

Portin, H., Komppula, M., Leskinen, A., Romakkaniemi, S., Laaksonen, A., Lehtinen, K.E.J., 2009. Observations of aerosol-cloud interactions at Puijo semi-urban measurement station. Boreal Environment Research 14, 641-653.

Sellegri, K., Laj, P., Dupuy, R., Legrand, M., Preunkert, S., Putaud, J.-P., 2003. Size-dependent scavenging efficiencies of multicomponent atmospheric aerosols in clouds, Journal of Geophysical Research, 108, D11, 4334.

Weingartner, E., Nyeki, S., Baltensperger, U., 1999. Seasonal and diurnal variation of aerosol size distributions (10 < D < 750 nm) at a high-alpine site (Jungfraujoch 3580 m asl). Journal of Geophysical Research, 104, 26809-26820.

EXPERIMENTAL ASSESSMENT OF THE IMPACT OF THE VERTICAL CLOUD STRUCTURE ON RADIATION

S. Placidi[1], C.L. Brandau[1], D.P. Donovan[2], R.A. Roebeling[3] and H.W.J. Russchenberg[1]

[1] Delft University of Technology, Delft, The Netherlands
[2] KNMI, Royal Netherlands Meteorological Institute, De Bilt, The Netherlands
[3] EUMETSAT, Darmstadt, Germany

1. ABSTRACT

In this work, we evaluate and assess the impact of the in-cloud vertical structure of liquid water clouds on radiation.

Two retrieval techniques, from surface and from satellite, are used in order to describe the vertical variation of the cloud microphysical properties.

The EarthCARE SIMulator is used to carry out the radiative transfer calculations needed to perform the surface radiation closure experiment and to simulate synthetic satellite observations.

We present a case study referring to a stratocumulus cloud observed during the COPS campaign in Germany in order to introduce the methodology and illustrate the results of this experiment.

For this case, the radiation closure experiment at the surface shows that the considered vertical cloud models can represent the irradiances with bias within 5 W/m^2. The satellite algorithm retrieves the best cloud properties for the cloud modeled with constant properties in height.

2. INTRODUCTION

The microphysical and optical properties of liquid water clouds are essential parameters for the quantification of the surface radiation budget since they have strong impact on the absorption and scattering processes within the clouds. The representation of clouds and their interactions with radiation in the meteorological and climate models and in the satellite retrieval algorithms are still treated in a simplistic way, due to the large variability in the relevant cloud properties at small and large scales, favoring the occurrence of errors and uncertainties in the model predictions. Accurate observations and retrievals of cloud properties and their spatial and temporal variations are hence required to overcome these uncertainties. The synergy of ground-based detailed observations with high temporal resolution enables the study of the effects of the assumptions on the vertical structure of the liquid water clouds on the surface radiation budget.

The radiation closure experiment of clear and cloudy sky provide the opportunity to assess the accuracy of the measurements techniques and retrieval algorithms of cloud properties in order to estimate the cloud impact on the Earth's energy budget [Brandau et al., 2010; Wang et al., 2011].

We use the synergy of the ground-based sensors and various cloud models to derive the profiles of the microphysical and optical properties of liquid water clouds.

Three different cloud models for the vertical variation of the in-cloud properties are assumed in order to evaluate the impact of the different profiles on the radiation at surface and at the top-of-atmosphere.

The retrieved profiles forming the observed cloud are input into a satellite simulator which calculates the surface (SFC) irradiances and the Top-Of-

Atmosphere (TOA) reflectances. The radiative closure experiment is performed by comparing the simulated surface irradiances with the surface irradiances measured by the pyranometer.

The simulated TOA reflectances are input into a satellite cloud properties retrieval algorithm in order to analyze the impact of the different cloud models on the satellite derived cloud properties.

3. METHODOLOGY

The presented work makes use of a broad source of data, models and retrieval techniques in order to assess the impact of the assumptions on the cloud vertical structure on radiation at surface and at top-of-atmosphere and on the satellite retrieved cloud properties.
Figure 1 shows a diagram of the steps followed in this work.

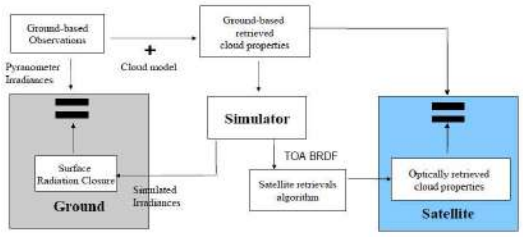

Figure 1 Block diagram of the methodology

Ground-based observations from cloud radar, lidar ceilometer and microwave radiometer (MWR) belonging to the ARM Mobile Facility (AMF) deployed in Germany during the COPS campaign are used together with a cloud model describing the vertical variation in the cloud to retrieve the profiles of the microphysical and optical properties.

The retrieved profiles of liquid water content (LWC) and cloud effective radius (Re) are ingested into the European Space Agency (ESA) EarthCARE SIMulator (ECSIM) [Voors et al, 2007], in order to re-create the observed cloud scene and run the radiative transfer model.

The simulated shortwave broadband surface irradiances are compared with the collocated surface irradiances measurements of the pyranometer in order to perform the radiation closure experiment. Simultaneously, the top-of-atmosphere bidirectional reflectances distribution functions (BRDFs) for visible and near-infrared channels are also calculated and used in the Cloud Physical Properties [Roebeling et al., 2006] satellite retrieval algorithm by the Royal Netherlands Meteorological Institute (KNMI-CPP). The KNMI-CPP retrieved cloud properties are compared with the same properties derived from the ground-based retrievals in order to perform the cloud properties closure.

During the two closure experiments, for radiation and for cloud properties, we use three different cloud models describing the vertical variation into the observed cloud.
The closure experiments will help in evaluating the impact of the in-cloud vertical variation on radiation and on the satellite retrieved properties.

3.1 The surface retrieval algorithm

The retrieval method relies on a combination of the cloud radar reflectivity, the estimated MWR-LWP and on the cloud geometrical thickness from the lidar and the cloud radar. These observations are used as input data for three vertical cloud models to retrieve profiles of the LWC, the droplet concentration, the effective radius, the optical extinction and the optical depth [Brandau, 2012].

Figure 2.a and 2.b show the averaged profiles of the liquid water content (LWC) and the effective radius (Re) retrieved from the surface observations of the selected water cloud case. In the Vertical Uniform (VU) cloud model, the cloud layer mean droplet radius is uniformly distributed over the cloud layer thickness while the Scaled-Adiabatic

Stratified (SAS) and Homogeneous Mixed (HM) cloud models parameterize the vertical profiles of the effective droplet radius in consideration of possible impacts of the cloud dilution.

The SAS cloud model accounts for the entire range of mixing processes available in the atmosphere by a constant reduction in the particle size with height compared to the pure adiabatic stratified growth.

In case of the HM cloud model, the impact of mixing is associated with the observed vertical variation in the radar reflectivity profile, which is attributed to changes in the mean particle size. The cloud models are described in detail in Brandau, 2012.

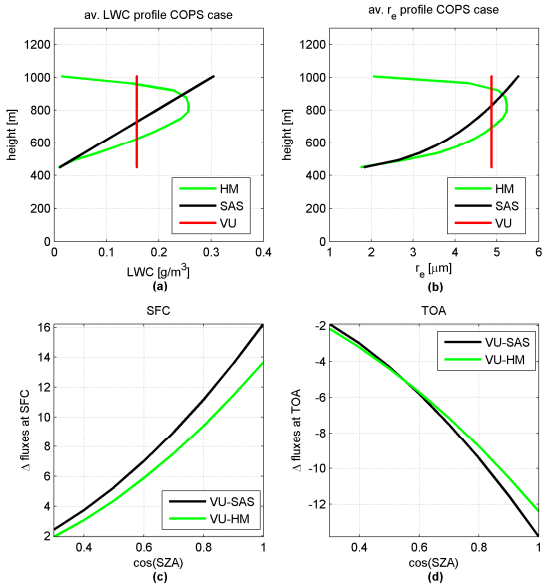

Figure 2 Example of the three cloud models for the averaged LWC (a) and Re (b) during COPS case. Plot of the fluxes differences between VU and the SAS and HM cloud models for different solar zenith angles at surface (c) and top-of-atmosphere (d).

The retrieved profiles presented in figure 2.a and 2.b correspond to the averaged profiles during the study case and are used as input for the EarthCARE SIMulator to analyze the impact of the different vertical structure on the SFC and TOA radiative fluxes. Plots 2.c and 2.d show the differences between the presented VU and the HM and SAS models with respect to the Sun zenith angle (sza) for the simulated radiative fluxes at surface and at the top-of-atmosphere, respectively. Differences for the fluxes in W/m^2, in both cases, increase with higher values of the cosine of sza, where the income solar radiation is largest.

3.2 The EarthCARE SIMulator

The EarthCARE SIMulator (ECSIM) is the end-to-end satellite mission simulator developed by the European Space Agency in order to completely simulate the EarthCARE (Earth Cloud-Aerosols-Radiation Explorer) mission.
It is able to simulate the four sensors onboard the EarthCARE satellite, such as the 94GHz Cloud Profiling Radar, the Atmospheric LIDar, the MultiSpectral Imager and the BroadBand Radiometer, by means of forward and instrument models, retrieval algorithms and scattering libraries [Donovan et al., 2008].

ECSIM creates a tridimensional cloud scene from information on the profiles of LWC and Re, on the thermodynamic status of the atmosphere and on the surface albedo. The forward and instruments models are run on this three-dimensional "realistic" scene [Placidi, 2012].

In this paper, we only use outputs from the Indipendent Pixel Approximation radiative transfer model as the broadband shortwave surface irradiances and the TOA BDRFs at 0.6 μm and 1.6 μm channels.

3.3 The satellite retrieval algorithm

The KNMI-CPP is developed at KNMI as meteorological satellite retrieval algorithm to derive cloud, precipitation and radiation products and it is part of the EUMESAT satellite application facility for climate monitoring (CM-SAF).

The cloud properties, optical thickness (τ) and effective radius (Re), are retrieved with the KNMI-CPP satellite retrieval by iterative comparing the simulated/observed reflectances at visible (0.6 μm) and near-infrared (1.6 μm) wavelengths with pre-calculated reflectances simulated with the Doubling-Adding KNMI (DAK) radiative transfer model. DAK is developed for line-by-line and/or monochromatic multiple scattering calculations at UV, visible and near-infrared wavelengths for narrow and broad bands in an horizontally homogeneous (plane parallel) cloudy atmosphere using the doubling-adding method [De Haan et al., 1987]. The liquid water path – LWP is consequently retrieved assuming a vertically uniform cloud with a constant vertical profile of the cloud water content, hence with the following formula, where ρ is the density of water :

$$LWP = \frac{2}{3} \rho \ \tau \ \mathrm{Re}$$

4. THE CASE STUDY

We present a case study in order to illustrate the methodology followed in this project and to present the results.
In order to fulfill the goal of this project there is the need of having accurate observations of the overcast atmosphere from different and complementary sensors.

We choose to study a case of overcast sky observed by the ARM Mobile Facility during the COPS campaign in Germany in October 24th, 2007. Figure 3 shows the plots of the best estimates of the sensor measurements for this case, the 94 GHz cloud radar reflectivity (3.a), the MWR - LWP (3.b) and the pyranometer shortwave (SW) irradiances (3.d).

These plots show the presence of an overcast sky with stratocumulus cloud with a thickness of about 500 m and liquid water path ranging between 10 and 200 g/m^2. Plot 3.d shows the trend of the shortwave irradiance at surface which becomes close to zero at about 1600 UTC due to the Sun zenith and azimuth angles.

The same cloud scene is re-created in ECSIM using the retrieved profiles of the LWC and Re along with the atmospheric thermodynamic status measured by the radiosondes and the actual surface albedo.

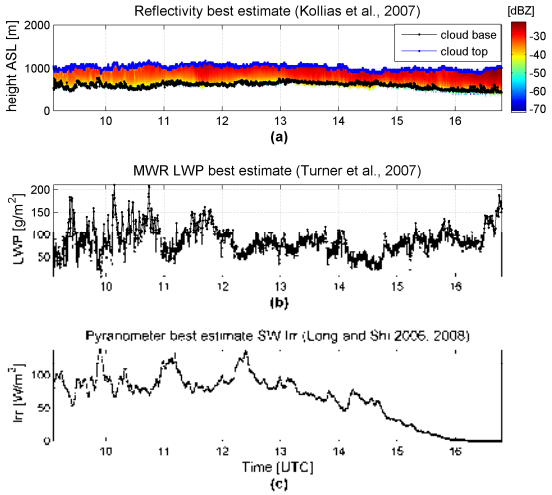

Figure 3 Best estimates of the ARM instruments observations for the study case: Radar reflectivity (a), MWR LWP (b) and SW irradiances (c)

4.1 IMPACT AT SURFACE

The plots in the columns of figure 4 show the results of the radiation closure experiment at surface for the three different vertical cloud models, Vertical Uniform (VU), Scaled-Adiabatic Stratified (SAS) and Homogeneous Mixed (HM), respectively. The three rows from top-down show the time-series, scatter plots and histograms of the differences between the simulated and the observed surface irradiances.

The three cloud models can correctly reproduce the radiation at surface in terms of variability showing correlations of about 85% and in terms of magnitude. In fact, the average bias between the simulated irradiances and the measured one is below 5 W/m^2 for all the three models. However, for this study

case, the vertical uniform model represent best the magnitude of the surface irradiances, in fact, the difference between the simulated and the observed ones is about 0.2 W/m^2. The standard deviations are around -16 W/m^2.

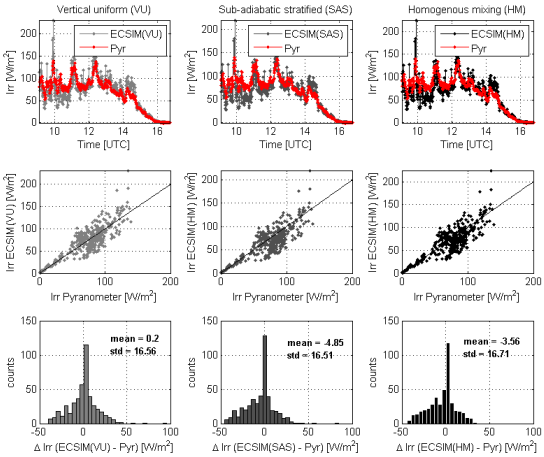

Figure 4 The simulated and observed surface shortwave irradiances for the three vertical cloud models (columns) are compared with the timeline (first row), scatterplots (second row) and histograms of their differences (third row).

4.2 SATELLITE CLOUD PROPERTIES

After evaluating the impact of the vertical cloud model on surface radiation, we analyze the impact on the satellite retrieved cloud properties. The KNMI-CPP retrieves optical thickness, effective radius and liquid water path assuming the cloud to be vertically uniform (VU).

Figure 5 and figure 6 show the scattering plots and the histograms, respectively, for the three vertical models in the columns and for the three cloud properties in the rows, optical thickness (τ), effective radius (Re) and liquid water path (LWP).

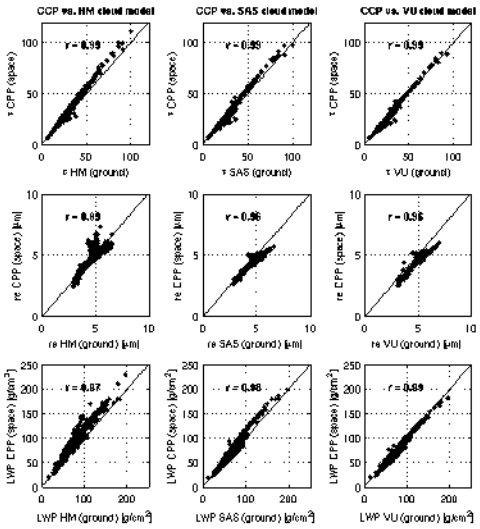

Figure 5 Scatter plots of the original and the satellite retrieved cloud properties (top-down: optical thickness, effective radius, liquid water path) for the three vertical cloud models (columns).

The satellite algorithm can correctly retrieve the cloud properties for the three models with some differences in the magnitude. Correlations above 96% between the KNMI-CPP and the original cloud properties are obtained for optical thickness and liquid water path, while for the effective radius they are slightly lower.

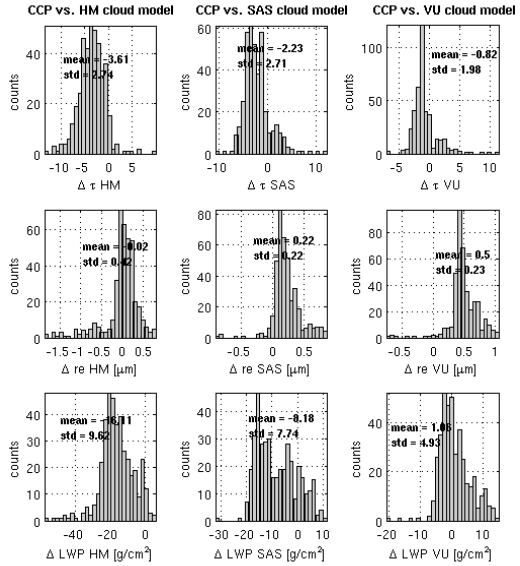

Figure 6 Histograms of the differences between the retrieved and the original cloud properties for the three vertical cloud models. (same as figure 5)

The histograms show that the differences between the retrieved and the original cloud properties are not large for optical thickness and effective radius for all the three models, even if the VU model shows the best closure. Liquid water path, instead, presents large differences for the HM and SAS models, while it is correctly retrieved for the VU model.

The best closure for the VU model is expected since the cloud model in the satellite retrieval algorithm is the same as the one used to retrieve the ground-based properties.

5. CONCLUSIONS

A methodology to asses the impact of the assumptions about the vertical structure of the liquid water clouds on radiation by means of surface radiation closure has been introduced. Furthermore, the impact of the assumptions about the in-cloud vertical structure with respect to satellite retrieval algorithm is also presented.

The EarthCARE SIMulator is the fundamental tool for this research because it allows to compute the radiative transfer model calculations on the three-dimensional realistic cloud scene.

For this case, the three vertical cloud models are able to reproduce the observed surface irradiances with small biases.

The closure for the satellite derived cloud properties also shows that the satellite algorithm can correctly reproduce the properties for all the three cloud models.

The optical thickness, being an integrated quantity is not strongly influenced by the vertical model. The effective radius is also not influenced by the cloud model, due to the use of the 1.6 μm channel for the retrieval. This channel, in fact, observes the radiation coming from within the cloud, where the differences for the effective radii in the three models are low.

The satellite retrieval of liquid water path is related to the assumptions of the vertical distribution of water in the cloud. The satellite LWP retrieval assumes a VU cloud and in fact, retrieves the LWP for the VU cloud model with the smallest differences.

Future works will focus on the use of synthetic cloud profiles and the impact on the radiation and satellite retrieved properties with respect to different Sun zenith angles and for more cloud cases.

Acknowledgements

The ground-based data were obtained from the Atmospheric Radiation Measurement (ARM) program sponsored by the U.S. Department of Energy, Office of Science, Office of Biological and Environmental Research, Climate and Environmental Sciences Divisions.

The cloud boundaries and reflectivity data from the ground-based measurements are WACR_ARSCL value added products from Kollias et al.,2007.

The best estimate shortwave irradiance retrieval from Long and Shi, 2006, 2008 is part of the Radiative Flux Analysis methodology which is the result of many years of research by Dr. Charles N. Long.

We thank Dr. K. Ebell from University of Cologne for providing the data for the atmospheric thermodynamic status.

REFERENCES

Brandau C.L., 2012: “Retrieval of liquid water cloud properties from ground-based remote sensing observations”, TU Delft PhD dissertation, in progress

Brandau, C.L., H. W. J. Russchenberg, W. H. Knap. 2010: Evaluation of ground-based remotely sensed liquid water cloud properties

using shortwave radiation measurements, Atmos. Res., doi:10.1016

De Haan, J. F., P. Bosma, and J. W. Hovenier, 1987: The adding method for multiple scattering calculations of polarized light,J. Astron.Astrophys., **183**, 371-391.

Donovan D.P., Voors, R.H., van Zadelhoff, G.-J. and Acarreta, J.R., 2008: ECSIM Models and Algorithms Document

Kollias, P., Clothiaux, E. E., Miller, M. A., Luke, E. P., Johnso,n K. L., Moran, K. P., Widener, K. B. and Albrecht B.A., 2007: The Atmospheric Radiation Measurement Program Cloud Profiling Radars: Second-Generation Sampling Strategies, Processing, and Cloud Data Products. J. Atmos. Oceanic Technol., 24, 1199–1214

Long, C. N. and Y. Shi, (2006): The QCRad Value Added Product: Surface Radiation Measurement Quality Control Testing, Including Climatologically Configurable Limits, Atmospheric Radiation Measurement Program Technical Report, ARM TR-074, 69 pp., Available via http://www.arm.gov.

Long, C. N., and Y. Shi, (2008): An Automated Quality Assessment and Control Algorithm for Surface Radiation Measurements, TOASJ, 2, 23-37, doi: 10.2174/1874282300802010023.

Placidi, S., 2012: “New techniques for monitoring water clouds” , TU Delft PhD dissertation, in progress

Roebeling, R.A., A.J. Feijt, and P. Stammes, 2006: Cloud property retrievals for climate monitoring: implications of differences between SEVIRI on METEOSAT-8 and AVHRR on NOAA-17, J.Geophys. Res., **11**

Turner, D. D., Clough, S. A., Liljegren, J. C., Clothiaux, E. E., Cady-Pereira, K., and K. L. Gaustad, 2007: Retrieving liquid water path and precipitable water vapor from Atmospheric Radiation Measurement (ARM) microwave radiometers. IEEE Trans. Geosci. Remote Sens., 45, 3680-3690, doi:10.1109/TGRS.2007.903703.

Voors, R., Donovan D.P., Acarreta J.R., Eisinger M., Franco R., Lajas D., Moyano R., Pirondini F., Ramos J., and Wehr T., 2007: ECSIM: the simulator framework for EarthCARE, Proc. SPIE 6744

Wang, P., W. H Knap and P. Stammes. 2011: Cloudy-sky shortwave radiative closure for a Baseline Surface Radiation Network site. J. Geophys. Res, 116, D08202, doi:10.1029/2010JD015141

The Development and Evaluation of the Explicit Cloud Physical Schemes for AREM Model

You-Ping XU[1], Wei CHENG[1], Ru-Cong YU[1], Guo-Xiong WU[1], Hui XIAO[2], and Rui CHENG[1]

1. State Key Laboratory of Numerical Modeling for Atmospheric Sciences and Geophysical Fluid Dynamics (LASG), Institute of Atmospheric Physics，Chinese Academy of Sciences , Beijing 100029, China

2. Laboratory of Cloud-Precipitation Physics and Severe Storms, Institute of Atmospheric Physics, Chinese Academy of Sciences, Beijing 100029, China

1. INTRODUCTION

Physical conditions which result in clouds and rains are key ingredients in the formation and maintain mechanisms of the precipitation. The physical processes of clouds and rains play significant roles in the occurrence and development of mesoscale disaster weather systems. Because clouds are extremely complex phenomena, treatments of cloud and precipitation processes in numerical model are usually simplified. Only the water vapor was considered in the early model whose grid resolution was low, whereas the condensate water substance was treated "implicitly" as estimated by atmosphere temperature and humidity. Such sort of simple treatment, however, would directly influence the accuracy of rainfall forecast in numerical models because of its poor ability in reflecting the actual variation of clouds and precipitation.

Along with the increasing of the grid resolution of numerical model, the recognition of the cloud and precipitation processes is quickly enhancing in the model. It is then more and more important to describe the detailed processes of the cloud and precipitation explicitly in the model. Therefore, the development and improvement of explicit cloud forecast schemes merged into numerical model increasingly receive considerable attentions and become an important choice in improving the capability of precipitation forecast .

Based on AREM (Advanced Regional Eta-coordinate Model, Ru-Cong YU, You-Ping XU, 2004), we establish a water-bearing numerical framework and design explicit warm and cold cloud predicting schemes under this framework. In order to evaluate the reasonableness and improvement of the new developed cloud predicting schemes, the numerical experi-ments using this water-bearing framework are carried out and the simulation of typical heavy rain processes are compared among different cloud predicting schemes.

2 . DESCRIPTION OF THE WATER-BEARING AREM

AREM is a mesoscale numerical prediction model based on original REM's framework, which is developed by the State Key Laboratory of Numerical Modeling for Atmospheric Sciences and Geophysical Fluid Dynamics (LASG) of Institute of Atmospheric Physics (IAP) , Chinese Academy of Sciences(CAS). AREM has shown good capabilities in simulating heavy rainfall in East Asian monsoon region. To further improve its forecasting capability of mesoscale disastrous weather, this study focuses on the development and evaluation of the cloud physical scheme for AREM. The AREM's water-bearing numerical framework is established and explicit warm-cloud predicting scheme (BW scheme) and explicit cold-cloud predicting scheme (BC scheme) are designed.

2.1 The Water-bearing Framework in AREM

The treatment of cloud and precipitation processes was relatively simple in original version of AREM, which only included large-scale saturated condensation (hereafter referred to as NC scheme) and Betts-Miller wet convection adjustment. In order to develop explicit cloud forecast scheme in AREM, the prediction equations of water substances such as cloud water, cloud ice, rain and snow are introduced. The load of condensate water substances floating in the air and the effects on water vapor density variation are considered in the dynamical framework. The specific water-bearing prediction equations in AREM are as follows:

（1） Basic Dynamical Framework

$$\frac{\partial U}{\partial t} = -\sum_{m=1}^{3} L_m(U) - f^* V - P_{edx} + D_{H,u} + D_{V,u} \quad (1)$$

$$\frac{\partial V}{\partial t} = -\sum_{m=1}^{3} L_m(V) + f^* U - P_{edy} + D_{H,v} + D_{V,v} \quad (2)$$

$$\frac{\partial \Pi}{\partial t} = -\sum_{m=1}^{3} L_m(\Pi) + S\left(C_0 + \frac{R\Pi Q_{ed}}{C_P^* P}\right)\left(\frac{1}{P\eta}\Omega^{(1)} + \Omega^{(2)}\right) + D_{H,T} + D_{V,T} + \frac{PRL}{C_0 C_p^*}(\dot{\mathrm{H}}_{\mathrm{L}} + \dot{\mathrm{H}}_{\mathrm{S}}) \quad (3)$$

$$\frac{\partial P^2}{\partial t} = -\frac{1}{\eta_s}\int_0^{\eta_s} D_{xy}\, d\eta \;;\; \int_{\eta_2}^{\eta_1}\left(\frac{\partial P^2}{\partial t} + D_{xy}\right) d\eta = P^2(\dot{\eta}_2 - \dot{\eta}_1) \quad (4)$$

$$\frac{\partial \Phi}{\partial \eta} = -C_0 \frac{S\Pi Q_{ed}}{P\eta} \quad (5)$$

$$\dot{\eta}\big|_{\eta=0;\eta_s} = 0 \quad (6)$$

where,

$$P_{edx} = P\frac{\partial \Phi}{a\sin\theta\partial\lambda} + SC_0\Pi Q_{ed}\frac{\partial \ln P^2}{a\sin\theta\partial\lambda} \quad (7)$$

$$P_{edy} = P\frac{\partial \Phi}{a\partial\theta} + SC_0\Pi Q_{ed}\frac{\partial \ln P^2}{a\partial\theta} \quad (8)$$

$$Q_{ed} = (1 + 0.608q_v)\left(1 + \frac{q_w + q_i + q_r + q_s}{1 + q_v}\right)^{-1} \quad (9)$$

$$C_p^* = (1 + 0.81q_v)C_p \quad (10)$$

$$\eta = \sigma \bullet \eta_s; \eta_s = \frac{p_{rf}(Z_s) - p_t}{p_{rf}(Z_b) - p_t}; \sigma = \frac{p - p_t}{p_s - p_t}; P = \sqrt{(p_s - p_t)/\eta_s} \quad (11)$$

$$U = Pu; V = Pv; \Pi = \frac{PRT}{C_0}; S = \frac{p - p_t}{p} = \eta\Big/\left(\eta + p_t/p^2\right); \quad (12)$$

$$L_1(F) = \frac{1}{2a\sin\theta}\left(2\frac{\partial Fu}{\partial\lambda} - F\frac{\partial u}{\partial\lambda}\right) \quad (13)$$

$$L_2(F) = \frac{1}{2a\sin\theta}\left(2\frac{\partial Fv\sin\theta}{\partial\theta} - F\frac{\partial v\sin\theta}{\partial\theta}\right) \quad (14)$$

$$L_3(F) = \frac{1}{2}\left(2\frac{\partial F\dot{\eta}}{\partial\eta} - F\frac{\partial\dot{\eta}}{\partial\eta}\right) \quad (15)$$

$$\Omega^{(1)} = -\int_0^{\eta} D_{xy} d\eta \tag{16}$$

$$\Omega^{(2)} = V\frac{\partial \ln P^2}{a\partial\theta} + U\frac{\partial \ln P^2}{a\sin\theta\partial\lambda} \tag{17}$$

$$D_{xy} = \frac{1}{a\sin\theta}\left(\frac{\partial PV\sin\theta}{\partial\theta} + \frac{\partial PU}{\partial\lambda}\right) \tag{18}$$

$$\dot{\eta} = \frac{d\eta}{dt} = \frac{\partial\eta}{\partial t} + u\frac{\partial\eta}{a\sin\theta\partial\lambda} + v\frac{\partial\eta}{\partial\theta} \tag{19}$$

$$f^* = 2\omega\cos\theta + \left(ctg\theta \Big/ a\right)u \tag{20}$$

$$C_0 = \left[\frac{R^2\tilde{T}}{g}\left(\frac{g}{C_P} + g\frac{d\tilde{T}}{d\tilde{\phi}}\right)\right]^{1/2} \tag{21}$$

Where , C_P^* is the specific heat at a constant pressure of moisture air, and C_P is the specific heat at a constant pressure of day air. q_v , q_w , q_i , q_r q_s are the mixing ratioes of water vapor, cloud water, cloud ice, rain and snow respectively. R is gas constant. C_0 is the constant gravity wave speed of the standard atmosphere. u , v , T and ϕ are the zonal wind, meridional wind, departures of temperature and geopotential from their "standards" respectively. a and ω are the radius of the Earth and angular velocity of the Earth's rotation. (λ,θ,η) are the common surface spherical coordinates. t is the time coordinates, z_b is the base elevation defined so as to include gentle slopes of surface topography, $p_{rf}(z)$ is a reference pressure as a function of z , p_t , p_s and p are the pressure of model top, surface pressure and air pressure, respectively. $\dot{H}_L$ is the latent and sensible heat rate during the phase transformation of water substances, $\dot{H}_R$ is atmosphere radiative heating rate, ρ is dry air density, $\tilde{T}$, $\tilde{\phi}$ are the temperature and geo-potential of "standards atmosphere", g is gravity accelerated velocity.

（2）Water Substance Forecasting Equations

All sorts of water substance mixing ratio are regarded as forecast quantities to establish water substance forecasting equations in the water-bearing framework of AREM. The specific forms are as follows:

$$\frac{\partial Q_v}{\partial t} = -HA(Q_v) - VA(Q_v) + P^2 P_V \tag{22}$$

$$\frac{\partial Q_w}{\partial t} = -HA(Q_w) - VA(Q_w) + P^2 P_W \tag{23}$$

$$\frac{\partial Q_i}{\partial t} = -HA(Q_i) - VA(Q_i) + P^2 P_I \tag{24}$$

$$\frac{\partial Q_r}{\partial t} = -HA(Q_r) - VA(Q_r) + P^2 P_R - g\frac{\partial(\rho_d q_r W_R)}{\partial\eta} \tag{25}$$

$$\frac{\partial Q_s}{\partial t} = -HA(Q_s) - VA(Q_s) + P^2 P_S - g\frac{\partial(\rho_d q_s W_S)}{\partial\eta} \tag{26}$$

where ,

$$HA(F) = \frac{1}{a\sin\theta}\left(\frac{\partial Fu}{\partial\lambda} - \frac{\partial Fv\sin\theta}{\partial\theta}\right) \tag{27}$$

$$VA(F)=\frac{\partial F\dot{\eta}}{\partial \eta} \tag{28}$$

$$Q_v = P^2 q_v, Q_w = P^2 q_w, Q_i = P^2 q_i; \tag{29}$$

$$Q_r = P^2 q_r, Q_s = P^2 q_s; \tag{30}$$

In the above equations, some parameters have been explained before, and will not repeat here. The new parameters include: P_V is water vapor generation rate in the processes of cloud changes, namely water vapor source and sink term. P_W is cloud water generation rate in the processes of cloud changes, namely cloud water source and sink term. P_I is cloud ice generation rate in the processes of cloud changes, namely cloud ice source and sink term. P_R is storm water generation rate in the processes of cloud changes, namely storm water source and sink term. P_S is snow generation rate in the process of cloud changes, namely snow source and sink term. W_R is mass weighted mean descend terminal velocity of raindrop, and W_S is mass weighted mean descend terminal velocity of snow.

2.2 Cloud Microphysics Process Framework

This paper introduces two cloud micro-physics schemes. One is explicit warm cloud forecast scheme (hereafter referred to as BW scheme) considering three categories of water substances and six types of cloud micro-physical processes (i.e., condensation, evaporation, agglomeration and coagulation of cloud water and rainwater). The BW scheme is a simplified one which treat the cloud in the atmosphere only as liquid cloud (i.e., warm cloud). The other is explicitly cold cloud forecast scheme (hereafter referred to as BC scheme) considering five categories of water substances, i.e., the cloud water, rain, cloud ice, snow and water vapor.The BC scheme is a more complex one which provided more detailed description of clouds and precipitation of mixed phase microphysical processes, which considers 25 kinds of cloud microphysical processes. Table 1 gives the meaning of the 25 kinds of cloud physical processes and the symbols of their water substance conversion rates. The symbols with * are the cloud physical processes which are considered in both the BC and the BW schemes. Figure 1 and Figure 2 show the framework for the conversion of cloud physical processes of the BW and the BC schemes, respectively.

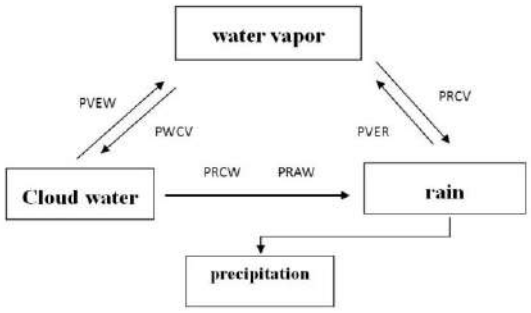

Fig 1 The basic framework of warm cloud microphysical processes (BW scheme)

Table1 The meaning of cloud physical processes and the symbols of water substance phase changes

Symbol	Meaning	Symbol	Meaning
PIAR	Accretion of rain by cloud ice	PSAW	Accretion of cloud water by snow
PIDV	Depositional growth of cloud ice	PSCI	Autoconversion of cloud ice to form snow
PIDW	Depositional growth of cloud ice at expense of cloud water	PSDV	Depositional growth of snow
PIFW	Homogeneous freezing of cloud water to form cloud ice	PSFI	Transfer rate of cloud ice to snow through growth of Bergeron process embryos
PINT	Initiation of cloud ice	PSFW	Bergeron process (deposition and riming)—transfer of cloud water to form

			snow
PRAI	Accretion of cloud ice by rain	PVER*	Evaporation of rain
PRAS	Accretion of snow by rain	PVES	Evaporation of melted snow
PRAW*	Accretion of cloud water by rain	PVEW*	Evaporation of cloud water
PRCV*	Condensational growth of rain	PVSI	Sublimation of cloud ice
PRCW*	Autoconversion of cloud water of form rain	PVSS	Sublimation of snow
PRMS	Melting of snow to form rain	PWAS	Accretion of snow by cloud water
PSAI	Accretion of cloud ice by snow	PWCV*	Condensation of water vapor to form cloud water
PSAR	Accretion of rain by snow	PWMI	Melting of cloud ice to form cloud water

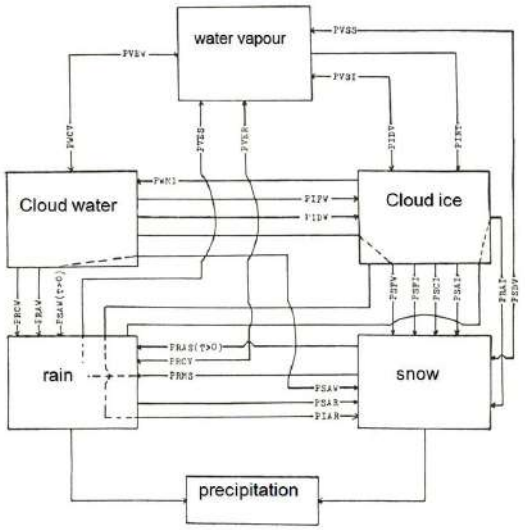

Fig2 The basic framework of cold cloud microphysical processes (BC scheme)

2.3 difference calculus of water substance treatment

To ensure that the advection transport of all kinds of condensate water substance is positive definite and conserved, a two-step shape-preserving positive definite advection scheme is applied here in the advection calculation of condensate water substance (Ru-Cong YU,1994,1995)

To guarantee positive definite in the vertical differential calculation of the rain, snow and other rainfall substances, the following difference computation formats in calculating the rainfall speed is used:

The forecast equations (25) and (26) of rain and snow water substances can be written as a general form when considering the vertical convection and fall speed:

$$\frac{\partial Q}{\partial t} = -VA(Q) - \frac{\partial \rho_d gqW}{\partial \eta} \tag{31}$$

Where, the spatial and temporal difference can be written as :

$$Q_k^{t+\Delta t} = Q_k^t - \Delta t\left[VA(Q) + \delta_\eta(\rho_d gqW)\right]_k^t \tag{32}$$

the difference operator above is

$$\delta_\eta F_k \equiv F_{k+\frac{1}{2}} - F_{k-\frac{1}{2}} \tag{33}$$

In order to guarantee the positive definite of rainfall substances, the vertical fall speed must agree with the following law :

$$\frac{\Delta t}{\Delta \eta}(\rho_d gqW)^t_{k+\frac{1}{2}} \le Q_k^t - \Delta t\left[VA_k(Q) - \frac{1}{\Delta \eta}(\rho_d gqW)_{k-\frac{1}{2}}\right]^t \tag{34}$$

so,

$$Q_k^{t+\Delta t} = \begin{cases} Q_k^t - \Delta t\left[VA_k(Q) + \dfrac{1}{\Delta \eta}\delta_\eta(\rho_d gqW)\right]_k^t & \text{If formula 34 is right} \\ 0 & \text{If formula 34 is wrong} \end{cases} \tag{35}$$

3 . RESULTS OF NUMERICAL EXPERIMENTS

To investigate the prediction results of AREM after the introduction of explicit cloud prediction schemes, we design three groups of numerical forecasting experiments as AREM_NC, AREM_BW and AREM_BC, , which uses the original NC scheme and the new BW scheme and BC scheme, respectively. The three groups of experiments base on the same conditions except cloud and precipitation physics schemes. The numerical experiments adopts the model with horizontal resolutions of 37km and 15km and vertical resolution of 32 layer with top at 10hPa. The initial condition uses the observations based on the objective analysis of NCEP reanalysis. To ensure the representation of the experiments, three different types of typical rainstorm cases in Chinese flood season are chosen as the object of study. The three cases were the heavy rain process with fast mobility occurred on August 24 to 25 2002, in Huang-Huai River Valley (short for CASE1), continuous heavy rainfall process occurred on June 12 to13 2008 in South China's Guangdong and Guangxi province (short for CASE2) and heavy rainfall appeared after the "Phoenix" landed in the eastern China on July 30 to 31 2008 (short for CASE3) .

Figures 3a, b and c show respectively the 24-hour precipitation forecasts and the comparison with observation in the three groups of numerical experiments namely CASE1, CASE2, CASE3. In general, the forecast results of BW scheme and BC scheme are better than NC scheme, as they can overcome the unreasonable phenomenon such as the scattered rainfall, the "stay" of the moveable heavy rainfall systems which appears in the NC scheme. For the continuous stable heavy rain system (such as CASE2), the forecast results of BC scheme is similar to those in BW scheme, whereas for the fast moved storm system (such as CASE1), BC scheme is different with the BW scheme. The results of BC scheme is more detailed and accurate in predicting the center, the strength and evolution of the storm than BW scheme. It is indicated that to describe the physical processes of clouds and precipitation in detail, especially the ice phase physical processes, can efficiently improve the prediction of the rain drop zone, movement and strength.

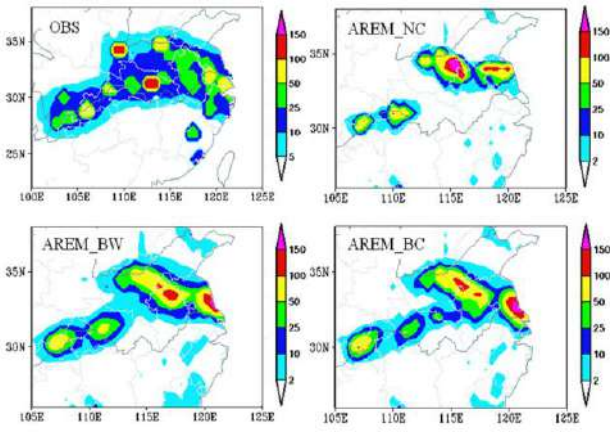

Figure 3a The observed and 24-hour forecasted rainfall distributions in three experiments during August 24-25 in 2002 (CASE1).

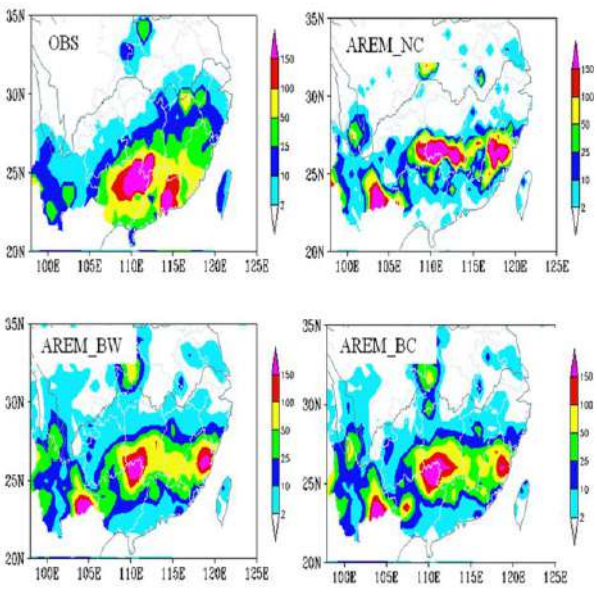

Figure 3b Same as Figure 3a but for June 12-13 in 2008 (CASE2)

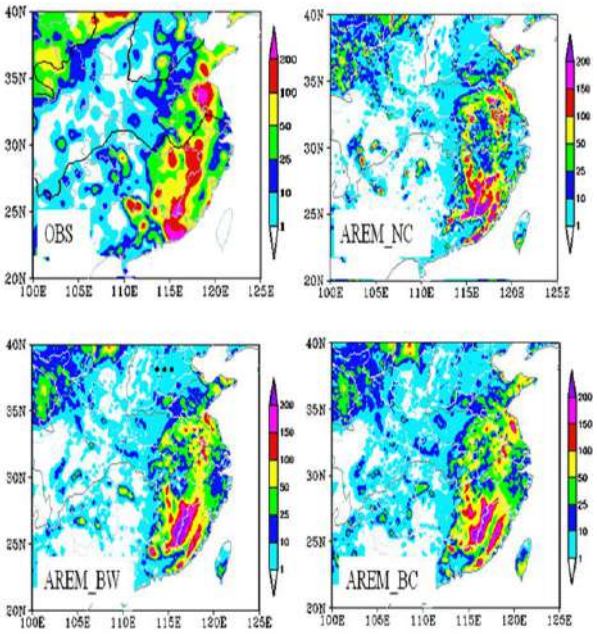

Figure 3c Same as Figure 3a but for July 30-31 in 2008 (CASE2)

Why does explicit cloud scheme better improve the forecast of rainfall and the mesoscale system? The preliminary reason is explored by the analysis of atmospheric structures in the numerical results among the three different schemes. Figure 4 gives the zonal section of vertical speed along the 25° N, which are the 12-hour forecast (July 30, 20 o'clock) of the BC, BW and NC schemes in CASE3.

It can be seen that though the vertical speed in the heavy rain center in BC scheme is not larger than NC and BW scheme, the BC scheme favors the development of ascending motion, and spread throughout the whole atmosphere. Although the vertical speed of NC scheme is strong in the low-level, the altitude of ascending motion is not very high. Figure 5 shows the stream field and the water substance advection of BC, BW and NC schemes at 300 hPa level with 12-hour forecast of CASE3. It can be seen that in the downstream of high level flow above the storm center, the positive advection of water substance occur in all three schemes. But by comparing the results of the three schemes (Figures 5b ~ d) , it is found that the differences of positive advection intensity and its extension area of the water substance are fairly large. As at the typhoon rainstorm center in the south of China, the extension range and the value of the positive advection to the downstream are larger in the BC scheme and BW scheme, whereas very small in the NC scheme. Therefore, the explicit cloud forecast scheme can not only improve the vertical distribution of water substance and atmospheric heating, but also improve obviously the advection processes of water substance, so as to effectively improve the ability of the heavy rains forecast.

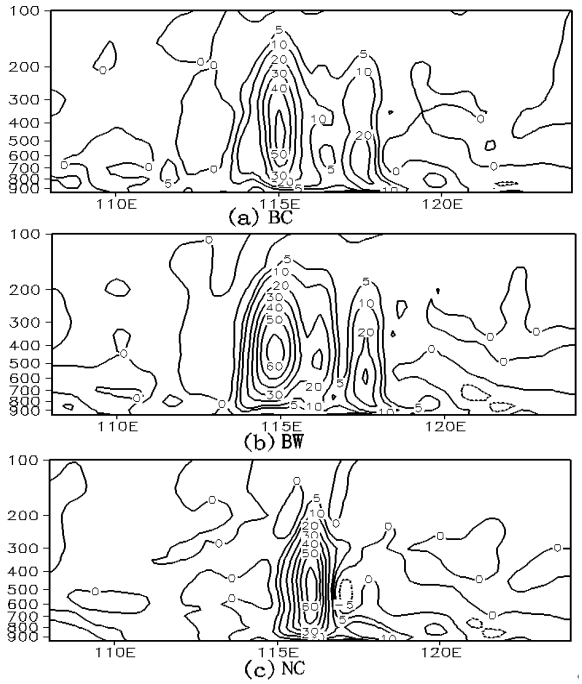

Figure 4 Zonal section of 12-hour forecasted (July 30, 20 BJT) vertical speed (unit: $10^{-3}hPa/s$) along the 25° N for BC, BW and NC schemes in CASE3. The initial hour is 08 BJT.

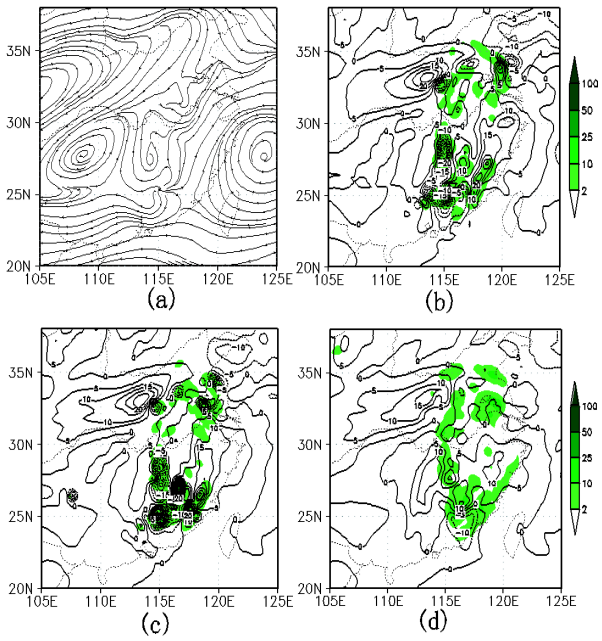

Fig.5 The stream field and the water substance advection (unit: 10-8kg·kg-1·s-1) field of BC, BW and NC schemes for the 12-hour forecast at 300 hPa of CASE3. The shadings are corresponding hourly rainfall (unit: mm). The initial hour is 08 BJT, July 30 in 2008.

4 . MAIN CONCLUSIONS

The paper briefly introduced the water-bearing framework of AREM model and two kinds of explicit cloud schemes (BW and BC schemes). The forecasting of three typical heavy rainfall cases in Chinese flood seasons are compared among three experiments, namely AREM_BC, AREM_ BW and AREM_NC. The influences of different cloud physical schemes to the improvement of numerical forecast capability of heavy rainfall are evaluated by analyzing the rainfall, mesoscale systems and cloud structures.some conclusions are: the new developed BC and BW explicit cloud schemes in AREM can evidently improve the heavy rainfall forecasting and reasonable capability to forecast the clouds. the explicit cloud forecast schemes have better capability in forecasting the occurrences, development and moving path of mesoscale systems compared to the saturated condensation scheme (NC scheme). The forecasting of heavy rainfall area, location of rainfall centers and their remotion are also remarkably improved in explicit schemes. Besides, because of the more complicated physical processes of clouds and precipitation are involved in the BC scheme, especially the ice-phase physical processes, it show more detailed and accurate forecasting capabilities of cloud and precipitation compared to the BW scheme.

Acknowledgments. The authors want to thank Dr. Hao-Ming Cheng of Chinese Academy of Meteorological Science for his help in plotting and analyzing forecast results and the improvement of the original manuscript.

REFERENCES

Acker, T., L. Buja, J. Rosinski, et al. 1996: "User's Guide to NCAR CCM 3." NASA(19980137458).

Asai, T. 1965: "A numerical study of the air-mass transformation over the Japan Sea in winter." J. Meteor. Soc. Japan 43: 1-15.

Betts, A. and M. Miller 1986: "A new convective adjustment scheme. Part I: Observational and theoretical basis." Quart. J. Roy. Meteor. Soc 112(473): 677-692.

Betts, A. K. and C. Jakob 2002: "Evaluation of the diurnal cycle of precipitation, surface thermodynamics, and surface fluxes in the ECMWF model using LBA data." Journal of Geophysical Research Atmospheres 107: 8045.

Kessler, E. 1969: "On the Distribution and Continuity of Water Substance in Atmospheric Circulation. Meteor. Monogr., 32." Amer. Meteor. Soc 10(32): 84.

Kristjaasson, J. 1992: "Initialization of cloud water in a numerical weather prediction model." Meteorology and Atmospheric Physics 50(1): 21-30.

Li, k. 2002: "Simulating on Heavy Rains along the Yangtze River by AREM." The First China-Japan Workshop on Heavy Rainfall Experiment and Study.

Li, Y., R. Yu, Y. Xu, et al. 2005: "AREM simulations of cloud features over eastern China in February 2001." Advances in Atmospheric Sciences 22(2): 260-270.

Lin, Y., R. Farley and H. Orville 1983: "Bulk parameterization of the snow field in a cloud model." Journal of Applied Meteorology 22(6): 1065-1092.

Liu, G. and Y. Fu 2001: "The characteristics of tropical precipitation profiles as inferred from satellite radar measurements." Journal of Meteorological Society of Japan 79(1): 131-143.

Mesinger, F. 1981: "Horizontal advection schemes of a staggered grid¡ªAn enstrophy and energy-conserving model." Monthly Weather Review 109(3): 467-478.

Mesinger, F. 1984: "A blocking technique for representation of mountains in atmospheric models." Rivista di Meteorologia Aeronautica 44(1-4): 195-202.

Pruppacher, H. and J. Klett 1978: "Microphysics of Clouds and Precipitation, 714 pp." D. Reidel, Dordrecht.

Orville, H. and F. Kopp 1977: "Numerical simulation of the life history of a hailstorm." Journal of the Atmospheric Sciences 34(10): 1596-1618.

Reisner J , Rasmussen R M. Bruintjes R T. 1998: Explicit forecasting of supercooled liquid water in winter storms using the MM5 mesoscale model. Qurt . J . Roy. Meteor. Soc. , 124 : 1071 - 1107

Rucong, Y. 1994: "A two-step shape-preserving advection scheme." Advances in Atmospheric Sciences 11(4): 479-490.

Rucong, Y. 1995: "Application of a shape-preserving advection scheme to the moisture equation in an E-grid regional forecast model." Advances in Atmospheric Sciences 12(1): 13-19.

Sun, J., X. Zhang, L. Qi, et al. 2005: "An analysis of a meso-¦Â system in a mei-yu front using the intensive observation data during CHeRES 2002." Advances in Atmospheric Sciences 22(2): 278-289.

Wang, Y. 2002: "An explicit simulation of tropical cyclones with a triply nested movable mesh primitive equation model: TCM3.

Part II: Model refinements and sensitivity to cloud microphysics parameterization." Monthly Weather Review 130(12): 3022-3036.

Wu, G. and S. Chen 1985: "The effect of mechanical forcing on the formation of a mesoscale vortex." Quart. J. Roy. Meteor. Soc 111: 1049-1070.

Xia, D. and Y. Xu (1995). A Grid-Nested, Water-Bearing, N-Level Primitive Equation Model and Its Operational Forecasting Experiments.

Xia, D. and Y. Xu 1998: "The water-bearing numerical model and its operational forecasting experiments part I: the water-bearing numerical model." Advances in Atmospheric Sciences 15(2): 221-232.

Xu, Y., D. Xia and Y. Qian 1998: "The water-bearing numerical model and its operational forecasting experiments part ii: The operational forecasting experiments." Advances in Atmospheric Sciences 15(3): 321-336.

Yu, R. 1993: "A Regional Numerical Prediction Model and its Simulation on the Heavy Rainfalls along the Yangtze River." International Conference on Mesoscale Convective Systems and Heavy Rainfall/Snowfall in East Asia. October 29-31, 2002, Tokyo, Japan.

Yu, R., Y. Xu, T. Zhou, et al. 2007: "Relation between rainfall duration and diurnal variation in the warm season precipitation over central eastern China." Geophysical Research Letters 34(13): L13703.

Zhao, Q., T. Black and M. Baldwin 1997: "Implementation of the cloud prediction scheme in the Eta Model at NCEP." Weather and forecasting 12(3): 697-712.

Zhou, T., R. Yu, H. Chen, et al. 2008: "Summer precipitation frequency, intensity, and diurnal cycle over China: A comparison of satellite data with rain gauge observations." Journal of Climate 21(16): 3997-4010.

EVALUATION OF HEAVY RAINFALL FORECASTS OVER THE NORTHERN ANDES CORDILLERA IN COLOMBIA BY EXPLICIT AND IMPLICIT PARAMETERIZATION SCHEMES

Gerardo de J. Montoya G. and Alejandro Uribe

National University of Colombia

1. INTRODUCTION

The Andes Cordillera is the longest continental mountain range in the world. It is a continual range of highlands along the western coast of South America. This range is about 7,000 km long, about 200 km to 700 km wide, and of an average height of about 4,000 m. The Andes extend from north to south through seven South American countries: Venezuela, Colombia, Ecuador, Peru, Bolivia, Chile and Argentina (first panel in figure 1).

The climate in the Andes varies greatly depending on latitude, altitude, and proximity to the sea. Temperature, atmospheric pressure and humidity decrease in higher elevations. The southern section of the Andes is rainy and cool, the central Andes are dry. The northern Andes are typically rainy and warm, with an average temperature of 18 [1]in Colombia.

The northern Andes, particularly in Colombia (second and third panels in figure 1), are characterized by intense and extreme rainfall events, which cause devastating phenomena such as flash-floods and landslides. Therefore, improving the Quantitative Precipitation Forecast QPF over this region could prevent large loss of life and economical damage to homes and businesses on a yearly basis.

The two main approaches to tackle the problem of cloud formation and precipitation in numerical weather prediction (NWP) models are the *explicit or microphysical scheme* (ES) and the i*mplicit or Cumulus Parameterization Scheme* (CPS). The first one takes into account the discrete structure of cloud and precipitation, whereas, the later represents an interaction between large

[1] Corresponding author address:
Gerardo Montoya Universidad Nacional de Colombia, depto Geociencias, Cra 30 No 45-03, Bogota, Colombia
E mail: gdmontoyag@unal.edu.co

scale environment and an ensemble of cumulus clouds (Yanai et al., 1973, Arakawa and Schubert, 1974).

Traditionally, the CPS has been used in unstable grid points and the ES in stable grid points. It has also been documented that for grid-scales greater than 10km, the CPS must be used; for grid-scales between 10 to 6 km both schemes (CPS and ES) could be used simultaneously and for grid-scales less that 4 km the ES is enough to capture the effects of atmospheric convection (Molinary and Dudek, 1992, Weisman e.a 1997, Belair and Mailhot 2001). Generally, CPS tends to smooth and to diffuse spatially simulated precipitation, whereas the ES scheme tends to overestimate it (Belair and Mailhot 2001, Clark, e.a., 2007)

The main objective of this study is to investigate the degree of accuracy for which both the ES and the CPS simulate the observed rainfall over the Northern Andes Cordillera in Colombia. To do so, several numerical experiments were performed over this complex topography (third panel in figure 1) by using the Weather Research Forecast (WRF) model. The skill for model-predicted (forecast skill) rainfall, for both schemes, was estimated by using a new methodology, which might be cataloged as object oriented (Weisman 2008) or event oriented (Baldwin & Lakshmivarahan, 2003) technique.

The remainder of this paper is organized as follows. Section 2 describes the numerical experiments and observations. Section 3 follows with the methodology used in this study. Results are discussed in section 4. Section 5 presents the conclusions.

2. NUMERICAL EXPERIMENTS AND OSERVATIONS

In this study, observed and model-predicted rainfall are compared to evaluate the forecast skill rainfall of the WRF model. The spatial domain of the study is the northwestern part of Colombia, which is located approximately between the latitudes 4°N to 10°N and the longitudes 72°W to 78°W (third panel of figure 1). This geographical coverage presents a complex topography including three ramifications (the western, the central and the eastern branches) of the Andes Cordillera and the Magdalena Valley.

The observed rainfall data in this study is obtained from the Measured Colombian Rain Gauge Data, which has about 700 stations over the region under study.

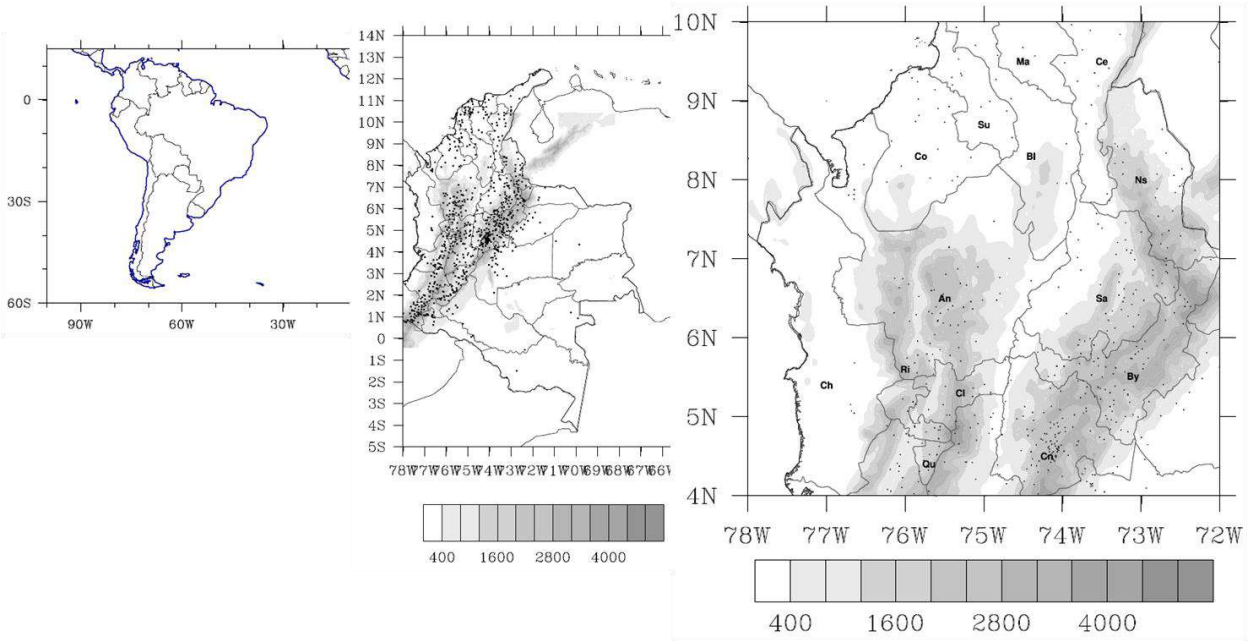

Fig.1. The Domain of the experiment (rightmost panel). Topography is shaded and rain gauge station network is represented with dots. State abbreviations are: An-Antioquia, Bl-Bolivar, By-Boyaca, Cl-Caldas, Ch-Choco, Ce-Cesar, Co-Cordoba, Cu-Cauca, Cn-Cundinamarca, Qu-Quindio, Ma-Magdalena, Ns-Norte de Santander, Ri-Risaralda,Sa-Santander, Su-Sucre.

To obtain the model-predicted rainfall, the WRF model was run for three different configurations as described in Table 1.

Table 1. Configuration of the experiments

Kain-Fritsch +WCM6	Morrison Only
10 km grid size	5km grid size
With WRFDA	With WRFDA
	With WPS only

In the first numerical experiment, both the CPS - Kain-Fritsch and WCM6 schemes were used with 10km grid-resolution and data assimilation (WRFDA). In the second experiment, the ES Morrison scheme was used with 5km grid-resolution and data assimilation. Finally, in order to investigate the effect of initial data, a third experiment was performed without WRFDA and the Morrison scheme.. Each numerical simulation was initialized with data from the National Center of Environmental Prediction (NCEP).

Each forecast output is produced up to 36-hour, but due to the model spin up, only the last 24-hour of accumulated rainfall was compared against the observations. To compare the observed and model-predicted rainfall, the

observed data was interpolated to the model grid using Cressman method. The case study corresponds to October 29, 2011.

3. **METHODOLOGY**

Previous studies by Ebert and McBride (2000), Baldwin and Lakshmivarahan, (2003), Clark et al., (2007), Davis et al., (2006), Weisman et al. (2008) indicate that the traditional grid point based statistical forecast verification technique presents problems at high grid resolutions (simulation of small convective systems). This is because it penalizes small displacements of these systems. As an attempt to solve this issue, the above mentioned authors propose an alternative approach, the object oriented method. The basic idea of this method is as follows: For an extreme rainfall event, the aim of this method is to determine which forecast areas (characterized, for instance, by a maximum precipitation exceeding a threshold value) have counterparts in the observations and vice versa (which observed areas are forecasted).

In this paper a similar approach is used but, instead of the Equitable Treat Score ETS (Clark & Chen, 2007)) or Critical Success Index CSI (Davis et al. 2006) in this work a matching and a false alarm indexes are applied separately. Succinctly, the method used here is as follows: 1) Both the observed and the simulated domains are divided into sub domains (equal squares of 100x100km each one) 2). In each square, the maximum precipitation exceeding a threshold value is searched in both domains (observed and modeled). In this investigation, a heavy rain event is characterized by a threshold value of 80 mm/day, 3). Two skill measures are defined; the Matching Probability (MP) and the False Alarm Probability (FP). The MP is calculated as

$$MP = \frac{FM}{NO} \qquad (1)$$

Where, *FM* is the number of predicted-matched with observed areas and *NO* is the total number of observed areas with heavy precipitation. Note that $FM \leq NO$ because the number of predicted-matched areas is less than the observed. The MP index determines the observed areas that have counterpart in the simulated areas. On the other hand, the FP is calculated as

$$FP = \frac{NS-FM}{NS} \qquad (2)$$

Where, *NS* is the total number of simulated areas exceeding the threshold value (80mm). Note that also *FP* ≤ 1. The FP index determines the predicted areas that exceed matched areas. In other words, the areas predicted as false alarms.

4. RESULTS AND DISCUSSION

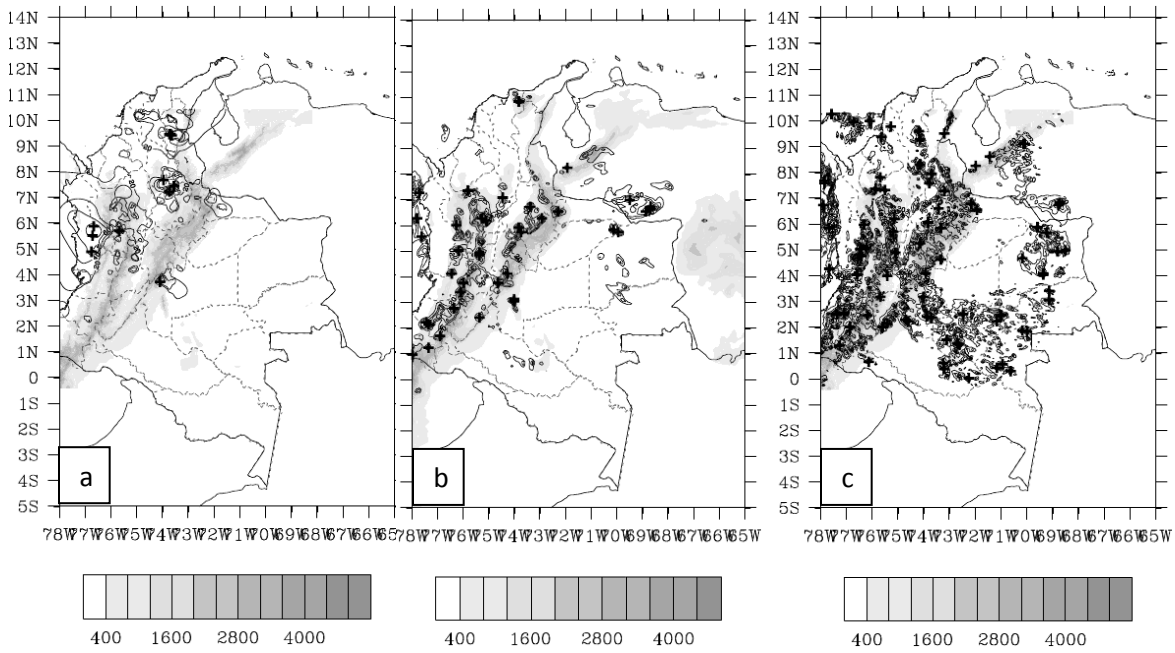

Fig. 2 Observed (a) and simulated daily precipitation by the KF (b) and Mo (c), schemes. The precipitation is contoured every 20mm. The symbol "+" identifies precipitation maxima exceeding 80mm.

Figure 2a shows the observed daily rainfall, and Figures 2b and 2c show the model-simulated rainfall for two different parameterization schemes. From figure 2a is clear that the precipitation occurs mostly to the west of western branch of the Andes Cordillera, over the valleys between the mountains, and a small amount over the mountains. On the other hand, Figures. 2b and 2c indicate that the model-simulated rainfall is mostly over the mountains. It is also clear that the model-simulated rainfall by both schemes overestimates the observations. As it is indicated by Celeste et al., (2001), the overestimation over mountains is a common shortcoming of the numerical models. Overestimation of rainfall also

occurs over the oceans, however, no comparison was made over this area because there are not rain gauge observations over there.

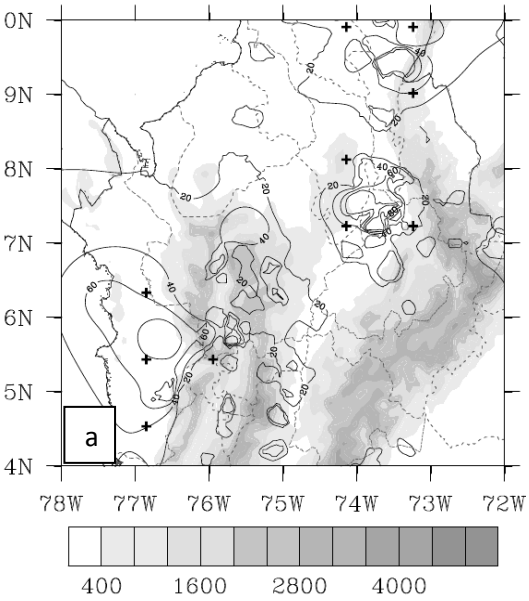

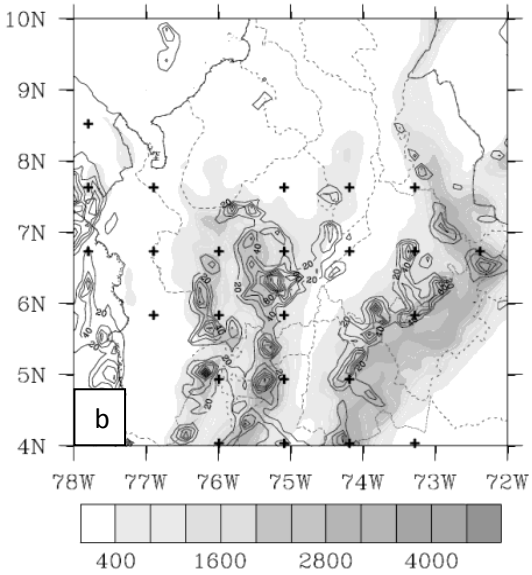

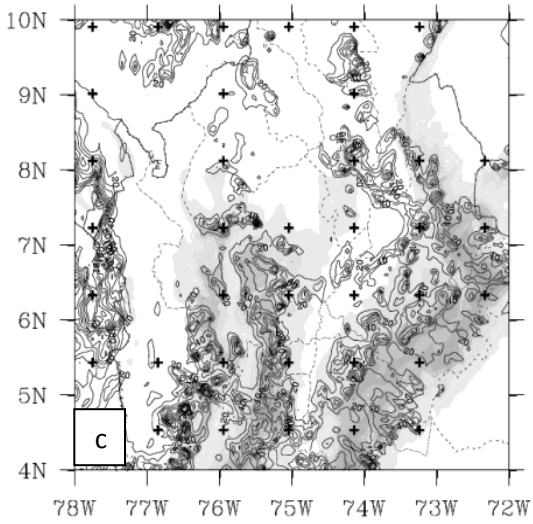

Fig.3. Illustration of the skill methodology. (a) observed (b) simulated with KF and (c) with Mo schemes. The "+" symbol is plotted in the center of each area and indicates that this area has maximum precipitation > 80mm (the maximum value is not showed). contours are every 20mm. Topography is shaded.

The methodology used for the calculation of skill measures is illustrated in Fig. 3. In this Figure the "+" symbol indicates the areas having maximum precipitation > 80mm. This is valid, because according to our methodology, the maximum value is representative for any point of the considered area. Thus, there is not a + for areas where the maximum precipitation does not exceed 80mm.

It can be seen from Fig. 3, that Mo scheme overestimates, whereas KF underestimates precipitation. This result is also shown in column bar graphic (Fig. 4).

In this figure, the observed maximum per area, exceeding 80mm is shown in blue and the corresponding for these areas maximum simulated are showed for the Mo (red) and KF (Yellow) schemes. It can be seen that the Mo overestimates whereas KF underestimates the observed precipitation.

This tendency to the overestimation (underestimation) by the Mo (KF) schemes, can be appreciated more clearly in bias (simulated – observed) (see Figure 5).

Table 2 summarizes the results for matching and false alarm probabilities. In this table results for the simulation without WRFDA is also included

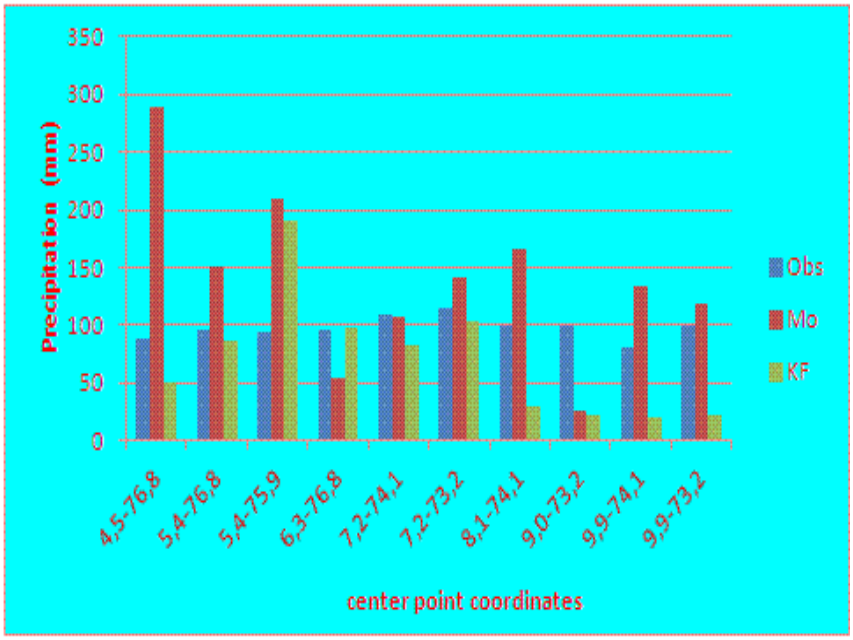

Fig.4. Observed maximum per area precipitation (blue) exceeding 80mm and correspondingly maximum simulated for these areas, by Mo (red) and KF (yellow) schemes.

According to Fig. 4, there are 10 observed areas with maximum precipitation exceeding the threshold value. From these areas, 8 areas are matched by the Mo and 5 by the KF scheme. Thus, the matching probability MP (see Eq.1) is 0.8 for Mo and 0.5 for KF schemes. This is a good result, for the Mo scheme. However, the number of simulated areas by this scheme with maximum precipitation exceeding 80mm

are 41, which gives a false alarm probability of 0.8 (see Eq. 2).

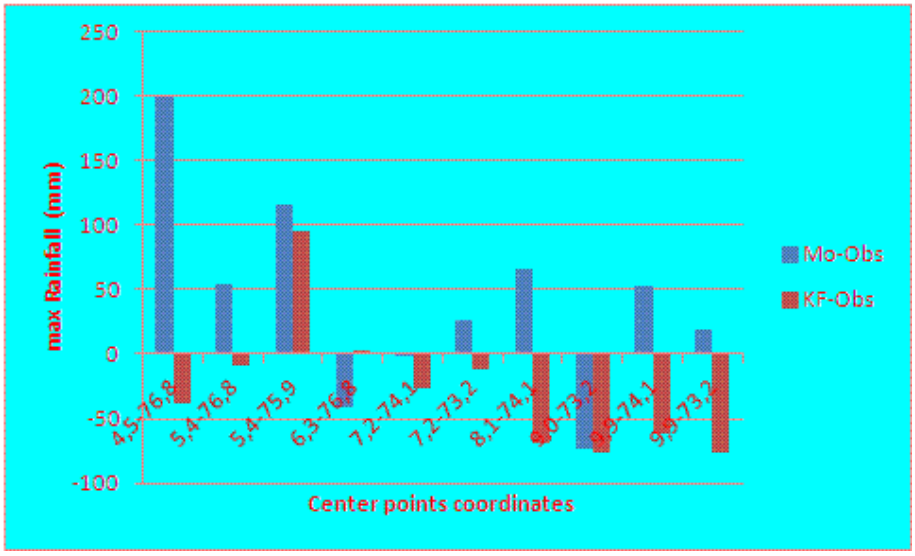

Fig.**5. As in Fig. 4 but for bias (simulated – observed) by the Mo (blue) and KF (red) Schemes**

Table 2. results for matching and false alarm probabilities

	Obs	KF	Mo	Mo without WRFDA
Areas with max >80mm	10	39	41	38
Matched areas		5	8	7
MP		0.50	0.80	0.70
FP		0.87	0.80	0.82

Obviously, a good forecast should have high matching probability MP and low false alarm probability FP. The explicit scheme Mo has MP of 80% which is a good result in comparison with the obtained low ETS in (Clark et al., 2007) or CSI in (Davies et al., 2006, see fig. 6 in this paper). However, Mo also has a high FP. We suppose that this high FP is associated with over prediction produced by Explicit schemes.

Although, the high FP represents a disadvantage, the separation of the skill measure into MP and FP allows to the end user, to involve other meteorological information (synoptic or modeled) to reduce the number of false alarms. For instance, taking into account that any convective parameterization tends to over predict precipitation over the mountains, for regions with complex topography as Colombia thus, looking at convergence – divergence behavior at

greater scales over the mountains, some of false alarms can be discarded.

According to table 2, the convective parameterization KF has a lower MP and also little higher FP in comparison with Mo. This fact makes the convective parameterization no suitable for predicting heavy rain events. The results with the run without supplementary data assimilation (WRFDA) are better than of KF results but a little worse than Mo with WRFDA. Although, it is well known to modelers, this result shows to the decision makers, the adding value that can be obtained if the observation network is improved.

5. CONCLUSIONS

In this study, we evaluated the heavy rainfall forecasts over the northern Andes Cordillera in Colombia by explicit (ES) and implicit (CPS) parameterization schemes. The comparison between these schemes was performed by an object-based verification methodology. Our results indicate that the ES generates better results than the CPS.

The separation of the skill measure into matching probability and false alarm seems to be a very promising procedure, since it allows to the end user to involve alternative synoptic or modeled information in order to discard false alarms and to improve the final decision about the forecast.

It is important to point out that our results were related to a particular case study. A more robust conclusion about the effectiveness of this methodology can be achieved by a more extensive statistical analysis involving many other case studies. This task is currently on the way.

Acknowledgments. This work was done during the sabbatical leave research of the first author, and was supported by the national university of Colombia, we also thanks to Colombian Met service (IDEAM), NCEP for supplying the local and initial data respectively and a reviewer for improving the manuscript.

REFERENCES

Arakawa, A., & W.H. Schubert, 1974: Interaction of a cumulus cloud ensemble with large –scale environment. Part I. J. Atmos., Sci., **31**, 674-701.

Baldwin, M. E., and S. Lakshmivarahan, 2003: Development of an events-oriented verification system using data mining and image processing algorithms. Preprints, *Third Conf. on Artificial Intelligence*

Applications to Environmental Science, Long Beach, CA, Amer. Meteor. Soc., CD-ROM, 4.6.

Belair, S., and Mailhot, J. 2001: Impact of horizontal resolution on the numerical simulation of a mid latitude squall line: Implicit versus explicit condensation. Monthly Weather Review, **129**, 2362-2376.

Celeste et al., 2001 S.A. Celeste, M. Seluchi, C. Campetella, and L. Ferreira, 2001, Error Evaluation of NCEP and LAHM regional model daily forecasts over Southern South America, *Weather and Forecasting* **16** (2001), pp. 697-712.

Davis, C., B. Brown, and R. Bullock, 2006: Object-based verification of precipitation forecasts. Part I: Methodology and application to mesoscale rain areas. *Mon. Wea. Rev.,* **134,** 1772–1784

Ebert, E:E., and J.L. McBride 2000:Verification of precipitation in weather systems: determination of systematic errors. J. of Hydrol., 1-24.

Clark, A.J., W.A. Gallus Jr. and T.C. Chen 2007: Comparison of the Diurnal Precipitation Cycle in Convection-Resolving and Non-Convection-Resolving Mesoscale Models. Mon. Wea. Rev. **135**, 3456- 3473.

Molinari, J. and M. Dudek 1992: Parameterization of convective precipitation in mesoscale numerical models: a critical review. Mon. Wea. Rev. **120**, 326-343

Weisman, M. L., W. C. Skamarock, and J. B. Klemp, 1997: The resolution dependence of explicitly modeled convective systems. *Mon. Wea. Rev.,* **125,** 527–548.

Weisman, M. L., C. Davis, W. Wang, K. W. Manning & J. B. Klemp 2008: Experiences with 0–36-h Explicit Convective Forecasts with the WRF-ARW Model. Wea and Forecasting, **23**, 407-437.

Yanai, M., Esbensen, S., and Chu, J.-H., 1973: Determination of bulk properties of tropical clouds cluster from large-scale heat and moisture budgets. Journal of the Atmospheric Sciences, **30**, 611-627.

Zhang, D.L., E.-Y. Hsie & M.W. Moncrieff, 1988: A comparison of explicit and implicit prediction of convective and stratiform precipitation weather systems with meso – β- scale numerical model. Quart J. Roy Meteor. Soc., **114**,31-60

THE FEATURES OF CLOUD OVERLAPPING IN EASTERN ASIA AND THEIR EFFECT ON CLOUD FORCING

Zhang Hua[1], Peng Jie[2,3,1], Jing Xianwen[1,2], Li Jiangnan[4]

1 Laboratory for Climate Studies of CMA, National Climate Center, Beijing, China
2 Chinese Academy of Meteorological Sciences, Beijing, China
3 Nanjing University of Information Science and Technology, Nanjing, China
4 Canadian Center for Climate Modeling and Analysis, University of Victoria, Victoria, BC, Canada

1 INTRODUCTION

The accurately description of cloud and cloud radiation process in climate models are important aspects to improve their modeling ability and can decrease the uncertainty of cloud radiative feedback greatly. In simulation of cloud radiative process in climate model, the uncertainty in cloud vertical overlapping treatment is one of the biggest barriers, how to treat multiple cloud overlap vertically have great influence on radiative heating (or cooling) rate, whereas the heating rate of cloud influences not only the development of cloud, but the radiation balance in the atmosphere and at the surface as well.

In most of GCMs, the commonly used hypothesis of cloud overlapping is maximum, random overlapping or the combination of both, respectively, Generally speaking, the above three overlapping schemes are characterized by fixed expression and not flexible and unable to represent the true cloud overlapping which varies temporally and spatially.

By adding an adjustable overlapping parameter, Hogan and Illingworth (2000) assumed the actual total cloud amount is between maximum overlapping and random overlapping, which is called the general overlapping hypothesis, making the expression of cloud overlapping flexible and adjustable. The overlapping parameters exhibit an exponential distribution, and hence obtained a parameter—decorrelation depth（L_{cf}*） that can remove the dependence of cloud vertical structure on model vertical resolution effectively. The observing study of decorrelation depth is still at the initial stage, and it is necessary to conduct relevant study over China region by using available datasets from satellite.

We use the datasets of solar polar orbit satellite-CloudSat launched (by UTC) on April 28, 2006, and combining with Stochastic Cloud Generator (SCG), to analyze temporal and spatial variation of decorrelation depth over Eastern Asia.

2 DESCRIPTION AND PROCESSING OF THE CloudSat DATA

In this paper, the level 2 productions of 2B-GEOPROF and 2B-GROPROF-Lidar are mainly used. We determines the existence of clouds within each pixel according to figure 1.

Figure 2 shows the five study regions over Eastern Asia divided according to local climatic characteristics, so there are totally six regions if plus the whole Eastern Asia.

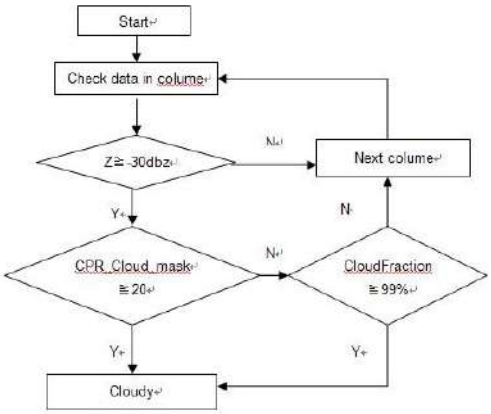

Fig. 1 The schematic of cloud determination

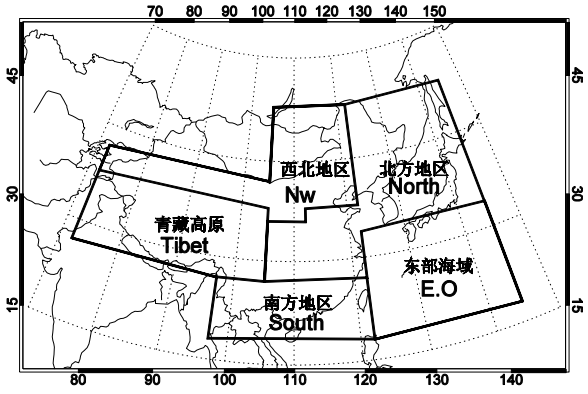

Fig. 2 The schematic of regional divisions in this work

3 METHOD

3.1 Scheme description

For GCM could not distinguish the cloud smaller than the model resolution, cloud geometrical position (include vertical overlapping) within any model grid region can be decided by generating sub-grid cloud structure based on the information from model grid.

Recently, a new 3D sub-grid cloud scheme named Stochastic Cloud Generator (SCG) has been developed, which can generate 3D sub-grid cloud structure based on the cloud profile (cloud cover, water/ice content) and cloud overlapping hypothesis, therefore it is very useable to study L_{cf}.

When using SCG, three initial conditions need to be set: cloud overlapping scheme, vertical profile of cloud amount and the value of L_{cf}, then the SCG can generate cloud in 3D sub-grid structure, so that we can obtain the total cloud amount for the 3D structure regions. Here the vertical profile is obtained from CloudSat data, and we choose the new general overlapping scheme in this work. By setting L_{cf} increasingly, SCG can generate different cloud structure and different total cloud amount. Therefore, we obtained a functional relationship between cloud amount and L_{cf}-- $C(L_{cf})$. When $C(L_{cf}^*)$ equal to the total cloud amount from CloudSat data, L_{cf}^* is then considered to be the scale parameter that correctly describing cloud overlapping there.

3.2 Approach to obtain L_{cf}^*

Firstly, we chose the sub-domain that range from 33.482 °N: 98.732 °E to 34.441 °N: 98.461 °E within orbit 03609 at January, 2007. The total cloud amount of the sub-region was 0.85 according to the CloudSat data, the cloud amount vertical profile was also calculated (see figure 3 (a)), and was input into SCG; L_{cf} was changed from 0.1 km to 10 km with the interval of 0.1 km, by generation of different cloud amount through SCG, the function $C(L_{cf})$ was obtained (see figure 3 (b)).

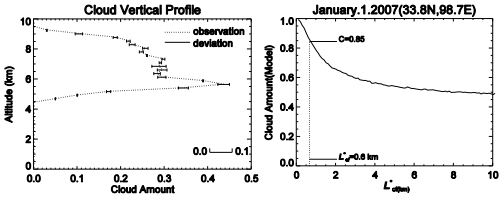

(a) (b)

Fig. 3(a) Differences of cloud amounts between SCG and observations at different altitudes, (b) cloud function as L_{cf} ($C(L_{cf})$) at sub-region of (33.48 °N: 98.73 °E, 34.44 °N: 98.46 °E）.

4 RESULTS AND DISCUSSIONS

4.1 Decorrelation length

Figure 4 provides the average value of L_{cf}* as the function of the cloud amount of sub-regions at 4 seasons and 6 study regions.

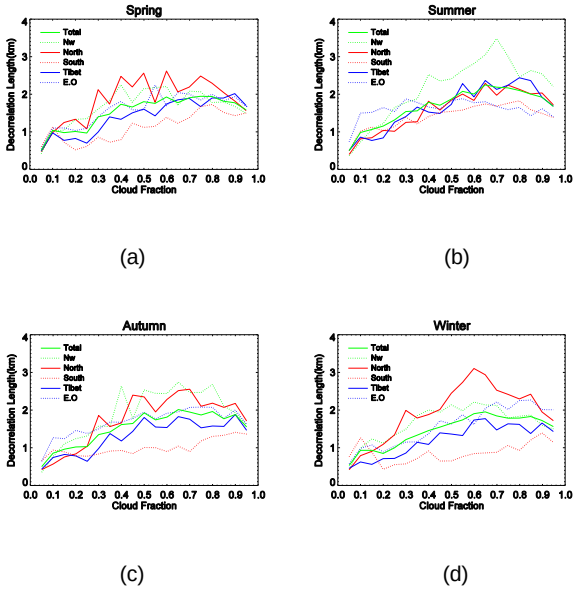

Fig. 4 The mean value of L_{cf}^{*} as functions of cloud amount for 6 regions in (a) Spring, (b) Summer, (c) Autumn, and (d) Winter.

4.2 Sensitivity Test of cloud radiative forcing to L_{cf}* value

After the geographical distribution and seasonal varies of L_{cf}* were calculated and analyzed, we will then discuss the influence of setting different value of L_{cf}* on the simulation of cloud radiation in GCM, especially on cloud radiative forcing.

Figure 5 shows the longwave cloud radiative forcing (CRF) in winter (January), 2000. Figure 5 (a) is the result of setting L_{cf}*=2 km, while Figure 5 (b) is the difference between setting L_{cf}*=1 km and L_{cf}*=2 km and the 5 (c) is the difference between setting L_{cf}*=3 km and L_{cf}*=2 km. While the shortwave CRF shows similar difference (figures are ignored), which indicate that the CRFs are greatly sensitive to the decorrelation length, especially for several main monsoon regions.

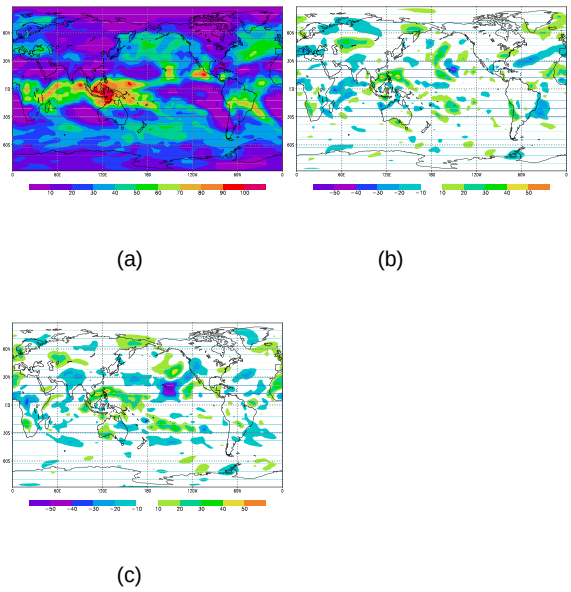

Fig.5 (a) Long wave CRFs in January 2000 (unit: W/m^2) when L_{cf}*=2 km; (b) the difference of CRFs between L_{cf}*=1 km and L_{cf}* =2 km; and (c) the difference of CRFs between L_{cf}*=1 km and L_{cf}*=3 km.

5. CONCLUSIONS

(1) The decorrelation length in six study regions are mostly within 0-3 km, by dividing decorrelation length according to the cloud amount in sub-regions, its peak appears near the sub-regions with cloud amount between 0.6 and 0.8, the average is 2.5.

(2) The spatial varies of L_{cf}*. L_{cf}* of North and Nw in higher latitudes is larger than that of Tibet and South in lower latitudes generally, while E.O and Total are between them. With the cloud amount in sub-regions change from 0 to 1.0, the difference of L_{cf}* between its maximum and its minimum in six regions ranges from 0 to 1.6 km, 0 to 2 km, 0 to 1.7 km and 0 to 2.4 km in four seasons, respectively.

(3) The seasonal varies of L_{cf}*. The L_{cf}* in Total and Nw, Tibet which located in western

area of East Asia have maximum value in summer, smaller values in spring and autumn, and minimum value in winter; whereas the L_{cf}* of E.O and North located in east regions of Eastern Asia have maximum value in winter, smaller values in spring and autumn, and minimum in summer.

(4) Setting the value of L_{cf}* to 2 km can result in an error of 15% in average cloud amount, which then has great influence on the CRFs.

(5) L_{cf}* has significant influence on longwave and shortwave CRFs, especially in several main monsoon regions and western area of East Asia where the absolute peak values are up to 40-50 W m^{-2}, indicating it is necessary to provide accurately parameterization of L_{cf}* with geographical and seasonal change, which needs to be done in the next.

Acknowledgements

This work was financially supported by National Natural Foundation of China (41075056), National Basic Research Program of China (2011CB403405), and the Public Meteorology Special Foundation of MOST (Grant No. GYHY201106022).

EXPLICIT SIMULATION OF ELECTRIFIED CLOUDS: FROM IDEALIZED TO REAL CASE STUDIES

Jean-Pierre PINTY [1], Christelle BARTHE [2], Eric DEFER [3],
Evelyne RICHARD [1] and Michel CHONG [1]

[1]Laboratoire d'Aérologie, CNRS, Université Paul Sabatier, Toulouse, France
[2]Laboratoire de l'Atmosphère et des Cyclones, Saint-Denis, La Réunion, France
[3]Laboratoire d'Etude du Rayonnement et de la Matière en Astrophysique, Paris, France

1. INTRODUCTION

The electrification of clouds is a natural phenomenon that can be studied and observed in many ways: networks of detectors to count and to map the lightning flashes, but also field mills and even induction rings to record the local evolution of the electric field and to sample the electrical charge carried by the raindrops, respectively. These observations are precious to understand the physical processes that drive the electrical properties of the clouds. They are absolutely essential to evaluate the electrical schemes which still contain many uncertainties in the description of the cloud charging processes and in the charge neutralization rates by means of intermittent cloud discharges.

The explicit simulation of the electrification of real meteorological precipitating cloud systems remains difficult for three reasons at least. First, meaningful experiments need to reproduce the good timing and location of the convective clouds to compare with flash network maps. Second, the requirement of high horizontal resolution (the kilometric scale and better) is necessary to simulate both the flow structure inside deep convective clouds prone to electrification processes and the morphological structure of the lightning flashes. Consequently, kilometer-scale simulations of real electrified clouds must be achieved on large enough horizontal grid systems to cover areas commensurate with the scale at which meterological analyses are available (tens of km). In this context, a multiprocessor computing environment is the rule and a fully parallelized coding of the electrification module, which is specially uneasy to achieve for the lightning flash algorithm, is a demanding task. Third, real case simulations imply complex terrain conditions and the need of terrain following-coordinates. So even if orographic flows can be resolved accurately in this case, the computation of the electric field components needs a fast-converging iterative algorithm while distortions of the coordinates impose to revise the lightning flash algorithm that otherwise would operate nicely with traditional cartesian coordinates.

Very few three-dimensional (3D) models with a complete cloud electrification scheme (Helsdon et al, 2002; Mansell et al., 2002; Barthe and Pinty, 2007) are available to explore the sensitivity of the physical mechanisms that regulate the electrical state of the clouds. A recurrent weakness of these models however, is their limitation to investigate idealized deep convective cases with a poor comparison to electrical data. This is in contrast with the present study which attempts to simulate for the first time the electrical properties of real orographic clouds and furthermore to compare maps of the simulated flash rates to network observations. This goal could be achieved after a profound revision of CELLS, the electrification scheme of MesoNH (Barthe et al., 2012).

2. CELLS: THE ELECTRICAL SCHEME OF MESONH

The cloud resolving model MesoNH (see `http://mesonh.aero.obs-mip.fr/mesonh/`) is able to simulate real meteorological events at high resolution on large domains with complex terrain. Since the code is fully vectorized and efficiently parallelized, the 3D evolution of cloud systems at one kilometer resolution is currently simulated on large grids with hundreds of points in each horizontal direction.

2.1 Electrical charges

The electrification scheme integrates the evolution of bulk charge densities (q_x in C kg^{-1} of dry air) which are closely related to the mixing ratio (r_x in kg kg^{-1}) of the microphysical species x (cloud droplets, rain, pristine ice crystals, snow/aggregates, graupel and hail). The evolution of the concentrations of positive (n_+) and negative (n_-) free ions is considered to reproduce the screen charges and to close carefully the electrical charge budget when the cloud particles and the hydrometeors (the main electrical charge carriers) evaporate or sublimate.

The non-inductive charge separation mechanism due to rebounding collisions between small unrimed and bigger rimed ice particles, is the crucial process to consider. For each colliding event, the polarity and the quantity of separated charge is given as a function of the temperature and the liquid water content (Takahashi, 1978) or riming rate (Saunders et al., 1998). This concerns only three types of collision: pristine ice-snow, pristine ice-graupel and snow-graupel. In addition, electrical transfer rates (T_x^q) due to the microphysical evolution of the particles are included in proportion of the mixing ratio and the electrical charge, i.e. $T_x^q = (q_x/r_x) \times T_x^r$ where the mass transfer rates T_x^r are provided by the microphysical scheme.

2.2 Electric field

The electric field ($\vec{E}$) is diagnosed at each time step and after the charge rearrangement following a flash. Multiple flashes are allowed in a single model timestep. $\vec{E}$ is the solution of the Gauss equation forced by the total volume charge density $\tilde{q}_{tot} = \rho_{dref} q_{tot}$

$$\epsilon_a \nabla \cdot \vec{E} = \tilde{q}_{tot} = \rho_{dref} [\sum_x q_x + |e|(n_+ - n_-)] \quad (1)$$

with $\epsilon_a = 8.85$ pF m^{-1}, the air permittivity and $|e| = 1.602 \times 10^{-19}$ C, the elementary electric charge. The integration of Eq.(1) is done using a pseudo electric potential V' defined by $\tilde{\rho}\, \vec{\nabla} V' = -\vec{E}$ so that the diagnostic "pressure equation" analog in MesoNH is recovered:

$$\epsilon_a GDIV(\tilde{\rho}\, GGRAD(V')) = \tilde{q}_{tot} \quad (2)$$

$GDIV(GGRAD)$ is the generalized divergence(gradient) operator in a terrain-following coordinate system, and $\tilde{\rho} = \rho_{dref} \times J$ is the local mass of dry air (J, the Jacobian of the coordinate transform, equals the grid-box volume). As a result, the optimized elliptic pressure solver of MesoNH can be used to get V' from Eq. 2 but with mixed boundary conditions. The solver is based on an iterative conjugate-residual algorithm with a "flat Laplacian" preconditioner. $\vec{E}$ is obtained by applying the $GGRAD$ operator to V'.

2.3 Lightning flashes

The lightning flash scheme is widely based on observed morphological characteristics of the flashes as described in Barthe and Pinty (2007) and in Barthe et al. (2012) for the adaptation of the code to parallel computing.

Flashes are composed of a bidirectional leader phase (extending vertically upward and downward from the triggering point) followed by a probabilistic branching phase to simulate the horizontal spread of the flash in electrically charged zones. A flash is triggered when $||\vec{E}||_{max} > E_{trig}$ where $E_{trig} = 167 \times 1.21 \exp(-z/8.4)$ with altitude z in km, is the breakdown field. The leader propagates vertically until $||\vec{E}||$ drops below 15 kV m^{-1}. A branching algorithm selects the gridpoints to form the ramifications of the flash. The number N of these gridpoints at a distance d from the triggering point, is assumed to follow a fractal law (Niemeyer et al, 1984):

$$N(i) = \frac{L_\chi}{L_{mean}} i^{\chi - 1} \quad (3)$$

with L_{mean}, the mean mesh size (m), L_χ, a characteristic length scale (m), and χ, the fractal dimension ($2 < \chi < 3$ according to Petrov and Petrova (1993). The running integer $i = NINT(d/L_{mean})$[†], varies from $i_{min} = 0$ to i_{max}. The index i_{max} corresponds to the maximum distance where branching is possible in the electrically charged zone defined by $q_{tot} > 0.2$ nC kg^{-1}. Because most of the time there are more possible fitting grid points at distance i than necessary, the $N(i)$ flash grid point locations are chosen at random. The constraint of code parallelization (Barthe et al, 2012) imposes an important simplification that disregards any connection condition be-

[†] $NINT$ is an intrinsic Fortran function which rounds its argument to the Nearest INTeger

tween grid points selected at successive distance $i-1$, i, $i+1$, etc.

The total charge q_{tot} in excess of $q_{neut} = 0.1$ nC kg^{-1} along the lightning channel is neutralized. In the case of intra-cloud (IC) flashes, a charge correction is applied to all the flash grid points to ensure the total charge neutrality (MacGorman et al, 2001) before the redistribution of net charge at grid points. This constraint does not apply to cloud-to-ground (CG) discharges which are selected when the tip of the downward branch of the leader reaches an altitude below 2 km above ground level.

3. THE HEAVY PRECIPITATING CASE OF 6-8 SEPT. 2010

On 6 September, 12 UTC, the synoptic situation was characterized by an elongated trough extending from from West of Greenland to North of Spain. In the low-level, the Cévennes region remained under the influence of a persistent and convectively unstable low-level moist flow blowing from the Mediterranean Sea towards the Massif Central leading to heavy precipitation and an intense electrical activity.

The MesoNH model was run at 1 km horizontal resolution for 54 hours over a large domain of 384×384 km^2 with 50 vertical levels encompassing the South-East of France. "AROME"[‡] analyses at 2.5 km were used to initialize MesoNH (6 Sept. 2010 at 00 UTC) and to feed the lateral boundary conditions which were updated every 3 hours.

Fig. 1 displays the amount of rainfall produced by the model and the raw non-gridded rain gauge data between 7 and 8 Sept. 2010 taken at 06 UTC. The agreement is quite good along the Cevennes ridge (peak value is 273 mm in "Ardeche" while MesoNH gives ∼300 mm but at the right location). This high resolution experiment leads us to conclude that the model was able to catch the location and timing of the cloud system that developed over the Cevennes ridge. The consistency of the simulation invites us to restart the model (7 Sept. at 12 UTC) for a 6 hour simulation of the electrical properties of the precipitating system using CELLS and Takahashi's diagram to compute the charge separation rate.

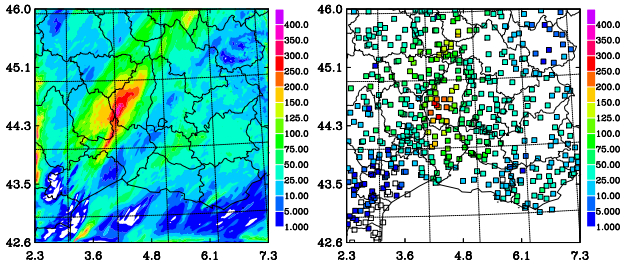

Figure 1: 24 hour amount of precipitation for the 7-8 Sept. 2010 at 06 UTC, (right) simulated by MesoNH, and (left) observed by the raingauge network.

In the following, a detailed cross-section of the electrical charge density and maps of the electric field and the flash rate are selected to illustrate briefly the results of the MesoNH simulation once the CELLS module is activated.

A detailed vertical structure of the electrical charges is shown in Fig. 2 along a South-North cross-section taken at 16 UTC and one third from the left of the domain of simulation. The total ice mixing ratio (black contours) and the rain mixing ratio (red contours) are superimposed with the bulk electric charge density, ranging between ±2 nC kg^{-1}, of cloud ice, snow-agregates, graupel and rain, according to Figs 2a-d order. The cloud ice and the graupel are mainly positively charged while snow particles are electrically negative. This charge arrangement is inverted around $z \sim 6.5$ km according to the temperature-polarity reversal of non-inductive charging diagram of Takahashi (1978). The raindrops drain mostly positive charges which obviously come from the melting of the graupel but some negative charges, brought by an earlier melting of the snow particles, are also visible. As a result, the polarity of the raindrops reaching the ground can be viewed as a tracer of the origin of the drops. As graupel is falling faster than snow, the raindrops should be first positively charged then negatively charged along this precipitating event. The total charge density obtained by summing the individual charges plotted in Fig. 2, leads to an electrical tripole structure (not shown here).

[‡]AROME: Applications de la Recherche à Opérationnel à Méso-Echelle, is the operational high resolution weather prediction model of Météo-France

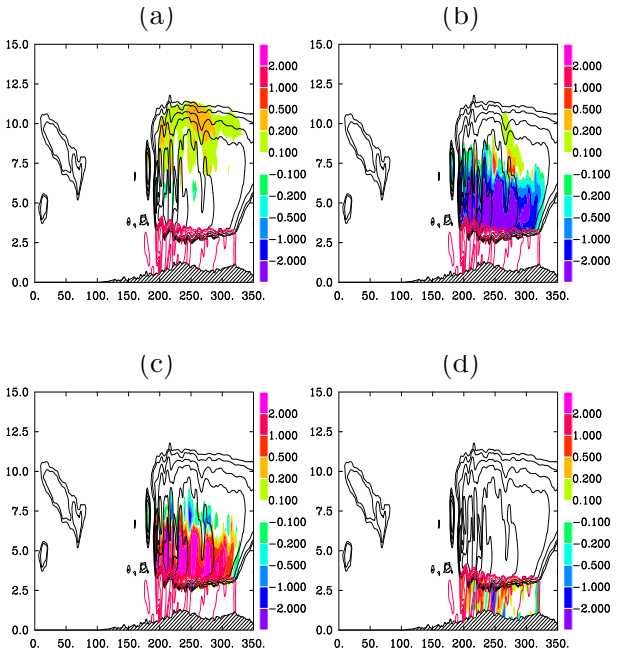

Figure 2: South-North cross-section located at one third of domain of simulation starting from the West, displaying the electric charges (in nC kg^{-1}) carried by (a) pristine ice crystals, (b) snow-aggregates, (c) graupel and (d) raindrops for 7 September 2010 at 16 UTC. The mixing ratio of the total ice condensate (black) and of the rain (red) is superimposed (contour intervals are 0.1, 0.2, 0.5, 1.0, 2.0 and 5.0 g kg^{-1}).

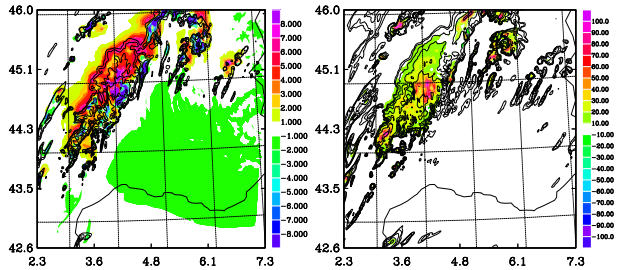

Figure 3: Instantaneous vertical electric field component (colored area) and total condensate mixing ratio (solid contours) at first model level (left) and at z=4km (right) for 7 Sept. 2010 at 16 UTC. The condensate mixing ratio contours are 0.1, 0.2, 0.5, 1.0, 2.0 and 5.0 g kg^{-1}. The E_z ranges are in kV m^{-1}.

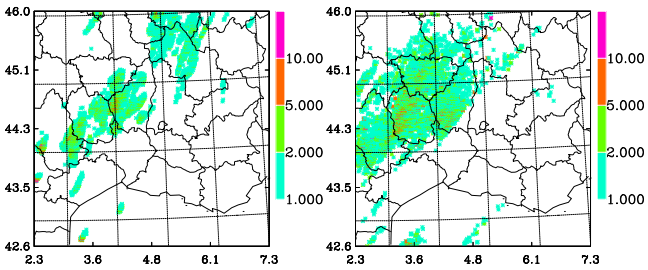

Figure 4: Map of flash density (in flash/km^2) simulated by the 6 hour run of MesoNH (left) and recorded by the LInet network (right).

The vertical component E_z of the electric field is plotted in Fig. 3. At the first model level ($\sim$ 30 m AGL), E_z is in the range of $\pm$ 10 kV m^{-1} and shows a complex structure under the main precipitating cloud system. At very low levels, E_z is sensitive to the electrical charge brought by the raindrops. Tens of km away from the leading edge of the heavy precipitating system, the electrification of the cloud is still detectable ($E_z > 1$ kV m^{-1}). The wide area in green in the South-East part of the domain corresponds to the negative fair-weather electric field which dominates away from the electrified cloud cells. At 4 km ASL, the structure of E_z is well organized with a peak value of 100 kV m^{-1} ($E_{trig} \sim 120$ kV m^{-1} at the same altitude). The E_z contour fits with the geometry of the clouds while young cells (according to the main southern flow) are not electrified.

The microphysical state of the clouds and all the other prognostic fields (e.g. the vertical velocity, etc...) are initialized from a "restart" file produced by a precedent run performed without cloud electrification. In absence of spin-up, the clouds become electrified very rapidly. For instance, the first flash is triggered after 144 s of simulation only.

During the 6 hour run, MesoNH produced 10 143 flashes. This number of flash can be compared to the 12 368 strokes observed by LInet and 12 513 strokes detected by ATDnet over the same area and for the same interval of time. Note that several strokes can be related to a single flash.

Fig. 4 shows at 1 km resolution, the horizontal distribution of the total flashes produced by MesoNH (here the horizontal location of the triggering point is considered) and the same for the observed LInet strokes. One can notice that the simulated areas of high flash rate (> 5 flash/km^2) are well reproduced by the model. This result is due to the good location of the simulated electrified clouds as previously observed, but also due to the realistic microphysical development of the ice phase which is absolutely essential for the cloud electrification processes.

4. CONCLUSIONS

This work demonstrates the feasability of simulating explicitly electrified clouds in the context of real flows and for demanding conditions: kilometer scale resolution, large computational domain and presence of orography. This context corresponds to the envisioned simulation project of the next coming HyMeX experiment (SOP 1.1) which will take place in the same area between late Summer and end of Fall 2012 (see `http://www.hymex.org/`). The bulk comparison between the simulated flashes and the data of two flash detection networks reveals the strong need of a reference dataset with a high degree of detection capability of the total flashes. To this goal, the HyMeX experiment will benefit from the deployment of high resolution additional networks, a Lightning Mapping Array (LMA) (Krehbiel et al., 2000) detector and possibly, a high resolution LInet network (Höller et al., 2009), to capture all the discharge events. Moreover, it is also worth to consider the economical measurement of the electrical charge of the raindrops by induction rings in several places. We hope that with the help of high value wind and humidity analyses and the access to the many verifying cloud and precipitation data (radar, instrumented aircrafts, disdrometers and raingauges), the electrical activity of the precipitating systems over the Cévennes area will be investigated in great details for a complete evaluation of the representation of the charging processes and lightning flash scheme in the CELLS module of MesoNH.

6. REFERENCES

Barthe, C. and J.-P. Pinty, 2007: Simulation of a supercellular storm using a three-dimensional mesoscale model with an explicit lightning flash scheme.*J. Geophys. Res.,* **112**, doi:10.1029/2006JD007484.

Barthe, C. and coauthors, 2012: CELLS v1.0: updated and parallelized version of an electrical scheme to simulate multiple electrified clouds and flashes over large domains. *Geophys. Mod. Dev.,* **5**, 167-184.

Helsdon, J. H. and coauthors 2002: An examination of the convective charging hypothesis : Charge structure, electric fields, and Maxwell currents.*J. Geophys. Res.,* **107**, doi:10.1029/2001JD001495.

Höller H. and coauthors, 2009: Lightning characteristics observed by a VLF/LF lightning detection network (LINET) in Brazil, Australia, Africa and Germany. *Atmos. Chem. Phys.,* **9**, 7795-7824.

Krehbiel, P. and coauthors 2000: Lightning mapping observations in Central Oklahoma. *EOS Trans. AGU,* **81**, 21-25.

Lafore J.Ph. and coauthors, 1998: The Meso-NH atmospheric simulation system. Part I: adiabatic formulation and control simulations. *J. Ann. Geophysicae.,* **16**, 90-109.

Niemeyer L., Pietronero L., and H. J. Wiesmann, 1984: Fractal dimension of dielectric breakdown. *Phys. Rev. Let.,* **12**, 1033-1036.

MacGorman D.R., J. M. Straka, and C. L. Ziegler, 2001: A lightning parameterization for numerical cloud model. *J. Appl. Meteor.,* **40**, 459-478.

Mansell, E. R. and coauthors, 2002: Simulated three-dimensional branched lightning in a numerical thunderstorm model.*J. Geophys. Res.,* **107**, doi:10.1029/2000JD000244.

Petrov, N. I. and G. N. Petrova, 1993: Physical mechanisms for intracloud lightning discharges. *Technical Physics,* **44**, 472-475.

Saunders, C. P. R., and S. L. Peck: Laboratory studies of the influence of the rime accretion rate on charge transfer during crystal/graupel collisions.*J. Geophys. Res.,* **103**, 13949-13956.

Takahashi, T., 1978: Riming electrification as a charge generation mechanism in thunderstorms. *J. Atmos. Sci.,* **35**, 1536-1548.

Acknowledgements

The authors thank Prof-Dr Hans-Dieter Betz, University of Munich, Germany and Drs Alec Bennett and Melanie Collins, Met Office, UK for kindly providing us with LInet and ATDnet data, respectively. We also thank Météo-France for the access to the "AROME" analyses and for formatting the raingauge data of the studied event.

TRACKING, ANALYSIS, AND NOWCASTING OF CUBAN CONVECTIVE CELLS AS SEEN BY RADAR: FIRST RESULTS

S. Novo*, D. Martínez, and O. Ledesma
Centro de Física Atmosférica, Instituto de Meteorología, La Habana, Cuba
*Now at: Centro de Ciencias de La Atmósfera, UNAM, México
Email to: sadielnovo@gmail.com

1. INTRODUCTION

The province of Camaguey and its surroundings are an almost flat region in the eastern part of Cuba. It is frequently affected by thunderstorms during the afternoon and evening of the rainy season, from May to October. These systems produce a high proportion of the total annual precipitation in the region and are frequently responsible for severe weather reports. Consequently, there is considerable interest in gaining a better understanding of the storm properties and the means to prevent the damages they cause.

This work describes the implementation and validation of an objective methodology for storm cell tracking and nowcasting, which only uses radar reflectivity data as input. The methodology is applied to the statistical characterization of convective storms in Camaguey. Section 2 describes the data and methodology utilized. In Section 3, distributions of storm properties are presented and compared with other reports. Evaluation of the system performance is discussed in Section 4, and some conclusions, limitations and future work developments are highlighted in Section 5.

2. DATA AND METHODOLOGY

The Camaguey radar (S-band) is located at a height of 160 masl at 21.38°N, 77.85°W. It is a modernized Russian MRL-5 with antenna control and product generation fully automated (Perez *et al.*, 1999; Peña *et al.*, 2000). Figure 1 shows the study area around the radar position, including topography.

During the 2007 rainy season, radar observations with high temporal resolution (5 min) were taken in Camaguey, as one of the main tasks of the Randomized Experiment of Cold Cloud Seeding in Extended Areas that has taken place in that province since 2005 (Martinez *et al.*, 2007).

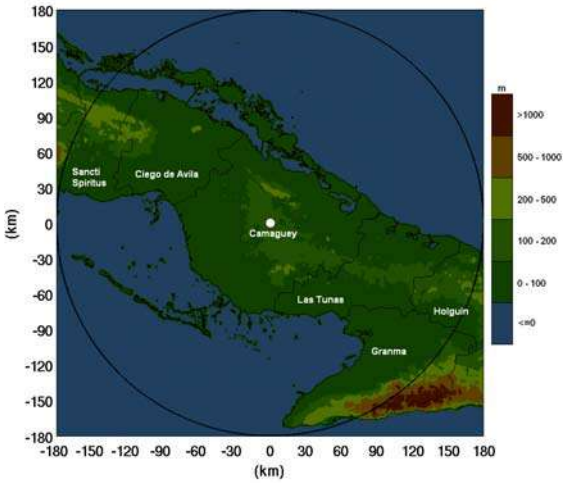

Fig. 1. Study area with topography.

Each radar volumetric observation was composed by 16 PPI scans at elevation angles between 0.5° and 21.2°. For each PPI scan there were 256 radials at 1.4° in azimuth and each radial comprised 1500 sample bins at 300 m length to a maximum range of 450 km. Thirteen days with active convection were selected for this study on a semi-random basis depending on data availability and trying to include a wide range of events. The observing period each day is shown in Table 1. The sample was composed of a total of 2076 radar scans at 5-min intervals. Another shorter sample of 1238 radar scans (not shown) taken during the rainy seasons of 2005 and 2006 was chosen in the same way for comparison. All the observations were pre-processed with Vesta software (Perez *et al.*, 1999; Peña *et al.*, 2000; Rodriguez *et al.*, 2005) to obtain two-dimensional maps of main radar products inside a radius 180 km around the radar position. The cell resolution was 1.5 km. Table 2 shows the radar products that served as input to the storm identification algorithm.

Table 1. Sample of radar data.

Date	Observation period (LT)
24 Aug 2007	12:20 – 20:00
27 Aug 2007	12:00 – 22:45
30 Aug 2007	12:00 – 22:15
31 Aug 2007	12:00 – 21:05
10 Sep 2007	12:00 – 23:55
11 Sep 2007	12:00 – 00:00*
15 Sep 2007	12:00 – 08:00*
17 Sep 2007	13:30 – 07:00*
18 Sep 2007	12:10 – 08:00*
22 Sep 2007	12:00 – 22:15
27 Sep 2007	12:00 – 08:00*
28 Sep 2007	18:20 – 08:00*
4 Oct 2007	12:00 – 23:20

*Final hour on next day

Table 2. Radar products for storm identification and analysis.

Name	Code	Range
Maximum reflectivity	ZM	10-70 dBZ
Height of ZM	H	1-20 km
Echo top (10 dBZ)	T	1-20 km

For storm identification and tracking we follow Handwerker (2002, hereafter referred as H02), but we use here the ZM matrices. In the H02 method, regions of precipitation are discriminated from the background using a first threshold of reflectivity. Within each of the regions thus obtained, the convective cells are defined through the use of a second threshold, which depends on the maximum reflectivity in the region. In this work the first threshold was chosen to be 25 dBZ (H02 used 35 dBZ) with the aim of detecting the storms as early as possible. After the first dissection of the radar image, a second threshold is defined as the maximum reflectivity inside each precipitating region minus 10 dBZ. Each storm will then be formed by contiguous pixels (connectivity = 4) that exceed this second threshold, provided that the maximum reflectivity inside the storm is 35 dBZ or higher and the storm covers an area of at least 3 pixels (6.75 km2). This means that the storm area depends on the maximum reflectivity inside the first dissected region and it will surround its most intense part. This procedure allows the discrimination of storm cells inside large thunderstorm clusters.

After the identification of storm cells, their instantaneous properties are calculated and saved for further analysis. To estimate the translation velocity of each storm, its previous positions are utilized, assigning to them different weights according to their age (as in H02). For each location in a given scan, the algorithm estimates the future location by using its estimated velocity and the time lag between scans. The new real location for each storm is assumed to be in the vicinity of its estimated location, and is taken as the nearest one to the forecast position, providing the distance between the two points is less than certain threshold (taken here as 4.5 km). If the storm under inspection is newly formed, then the averaged velocity of all other storms present in the previous scan is used. If there are no previous scans (typical at the start of tracking when there are only very few storms) then the next position is taken as the nearest one if the velocity between the two points does not exceed 15 m/s. This procedure results in the temporal association between the storms through the scans, and two new properties are saved into the storm table: the instantaneous velocity and direction of motion for each storm. Storm tracks are considered continental if more than ¾ of its lifetime is spent over land, otherwise, maritime.

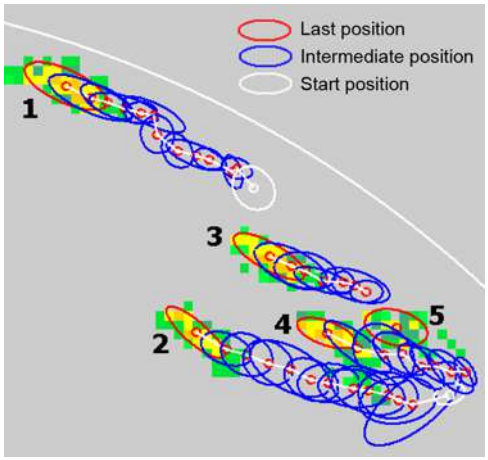

Fig. 2. Storm tracking during 1 h on 10 Sep 2007.

Figure 2 shows an example of storm tracking during the first hour on 10 September 2007. Only the backward trajectories of the storms detected in the last scan (1300 h) are shown. Storms #1 and 2 lasted 1 h, while storms #3 and 4

lasted at least 30 min, and storm #5 is a new cell. Figure 3 shows all the storm tracks registered on the same day from 1200 to 1600 h. Notice that the storms were moving mainly between W and WNW. For comparison, the mass-weighted mean wind velocity between the surface and 300 hPa obtained from the available sounding at 0700 h on 10 September 2007 was (30.2 km/h, 275°).

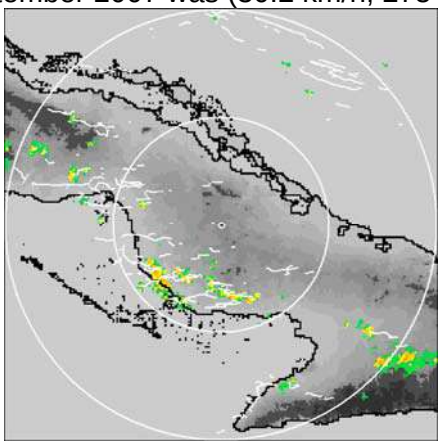

Fig. 3. Storm tracks observed between 1200 and 1600 on 10 Sep 2007.

Once each storm has an instantaneous velocity assigned for every time step, it is possible to extrapolate its movement into the future to forecast its position. This is done by a straight line to the last up to ten positions of each track. As in the algorithm used by SCIT (Johnson *et al.*, 1998), equal weight is given to every previous position.

3. STORM PROPERTIES

The spatial distribution of storm frequency for all the 2076 volumetric scans is shown in Figure 4. Each grid square represents a 30x30 km^2 area and the frequency corresponds to the number of times the centroid of a storm lied within the same square. The three main zones of maxima observed coincide with the reports of Lecha *et al.* (1994) and Alvarez (2006) for the spatial distribution of rainstorms from three-hourly surface data, although in those reports the relative importance of each maximum slightly varies between them and in relation to the obtained here.

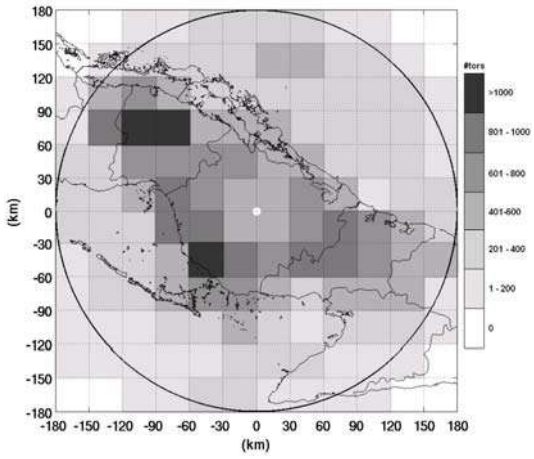

Fig. 4. Spatial distribution of storm frequency.

For each storm, the time at the middle of its lifetime was taken as representative of its time of occurrence. The diurnal variation in the frequency of mean time of occurrence between noon and midnight (Fig. 5) shows that convection reaches its maximum activity at 1600 h over land, while convection over the sea is low. After this time, convection over the sea begins to increase monotonically, surpassing the land activity near 2000 h and reaching its maximum at 2200 h when it begins to decrease but remains higher than land activity up to the end of the day. The diurnal convection maximum at 1600 h has also been observed by Núñez *et al.* (1999) and Alvarez (2006), although none of these studies discriminated between land and sea, nor did they note the lower nocturnal maximum mainly due to convection over the sea.

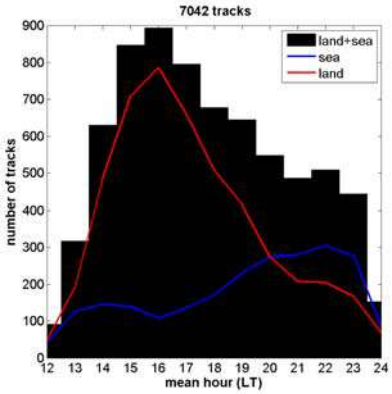

Fig. 5. Diurnal variation in the frequency of storm occurrence.

The frequency of the total duration of storms (Fig. 6) shows the typical exponential decay distribution reported in other studies (Cruz, 1973; Dixon &

Wiener, 1993; Handwerker, 2000). Only 211 (land: 114, sea: 97) from 5159 storm tracks last more than 1 h (4.1%). The average lifetime of a storm cell was roughly 19 min. The inner plot in Fig. 6 refers the fraction of storms in each group, land or sea, separately. Both curves are quite similar each other, which indicates a low influence of terrain (land or sea) on the number of convective cells with the same lifetime in the study region. Fig. 7 indicates that the life cycle of a storm cell and its maximum reflectivity are correlated. The maximum reflectivity reached by different groups of storm duration is displaced to higher values when the duration increases. This has also been reported by Handwerker (2000) for storms in Germany. Mean values for the distributions in Fig. 7 are, in the same ascending order as duration groups: 42.9, 46.0, 47.3 and 48.8, all in dBZ.

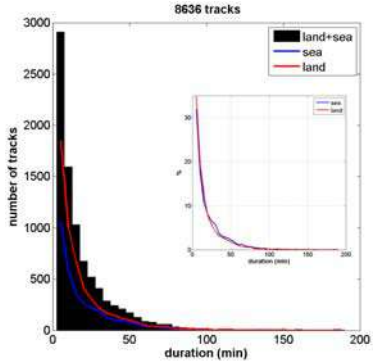

Fig. 6. Distribution of storm total duration.

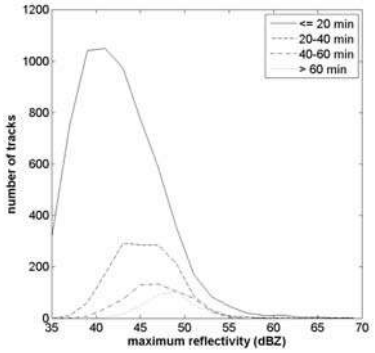

Fig.7. Distribution of maximum reflectivity for different duration ranges.

The frequency distribution of the maximum area reached by storms during their life cycle (not shown) also follows an exponential decay curve, which has been reported by Cruz (1973), Dixon & Wiener (1993) and Potts *et al.* (2000). The mean value was 48 km^2 and more than 95% of storms reached areas below 150 km^2.

The frequency distribution of the maximum reflectivity (Fig. 8) is slightly positively skewed with skewness 0.5 and kurtosis 3.7. The mean and median coincide in 44 dBZ, which is close to the median of 43 dBZ reported by Potts et al. (2000) for Sydney storms. About 88% of storms reached maximum reflectivities below 50 dBZ. The inner graph in Fig. 8 shows that storms over land are relatively more frequent than storms over the sea for maximum reflectivities in excess of 47 dBZ, which indicates higher intensities of storms over land.

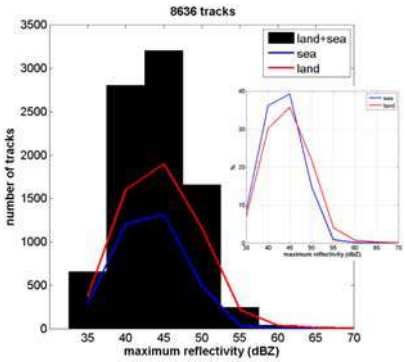

Fig. 8. Distribution of maximum reflectivity.

Fig. 9 shows that the maximum top (10 dBZ) more frequently reached by storms was 10 km, with almost the same contribution from land and sea storms (~900 each) for this height. Mean and median values for the distribution are 9.8 and 9.6 km, respectively. This compares with a median of 9.7 km for Venezuelan storms (Cruz 1973). Mean values for land and sea storms in Fig. 9 are 9.6 and 10.2 km, respectively. In addition, the inner graph indicates the much higher percent that represents the storms over the sea with tops between 7 and 14 km inside their group, when compared to the same portion in the group of storms over land. Only for tops beyond 14 km, the relative percent of storms over land is slightly higher. Distributions of maximum reflectivity for different groupings of storm height are shown in Fig. 10. The correlation between maximum top and maximum reflectivity reached by storms during their lifetimes is evident. Potts et al. (2000) found a similar relationship for storms around Sydney, Australia. The mean values for the distributions in Fig. 13 are: 42.3, 42.4, 45.1 and 48.5 dBZ.

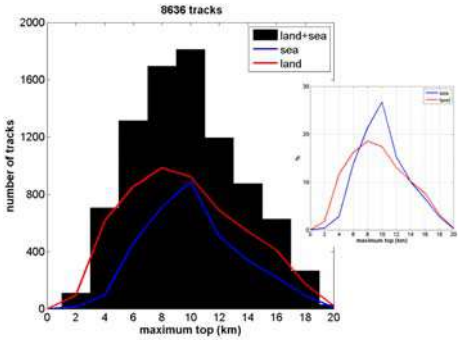

Fig. 9. Frequency distribution of maximum top height of storms.

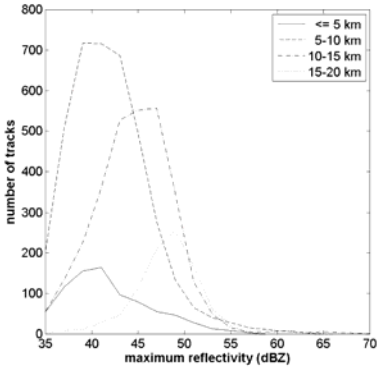

Fig. 10. Distribution of maximum reflectivity for each height group.

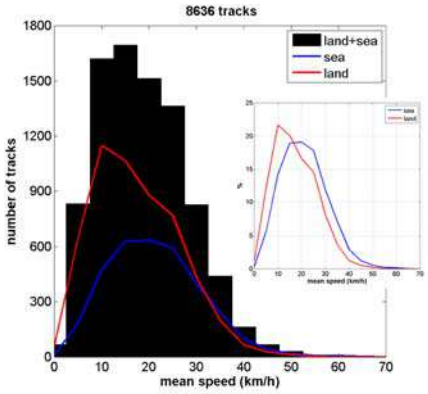

Fig. 11. Distribution of storm mean speed.

The frequency distribution of storm mean speed (Fig. 11) indicates that storms were moving more frequently over land with a mean speed around 10 km/h, while storms over sea were moving more at a mean speed around 20 km/h. Besides that, the fraction of the sea storms that were moving at mean speeds above 16 km/h was superior to those over land with the same range of velocity, as indicated by the inner plot in the same figure. Both results are consistent with the lower friction of the sea surface.

The frequency distribution of storm track mean direction of movement is depicted in Fig. 12. The bulk of tracks (71 %) moved westward on average, between 225° and 315°, with the maximum around 270° (W). This is consistent with the predominant trade winds in the southern side of the North Atlantic Subtropical High during August-October over eastern Cuba.

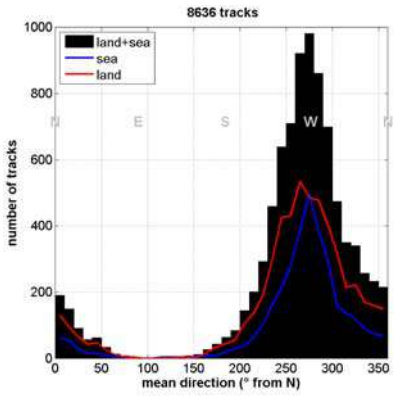

Fig. 12. Frequency distribution of storm track mean direction of movement.

There were two days without sounding information (31 Aug and 4 Oct). If they are not considered in the analysis, the mass-weighted mean wind vector obtained from the rest of the tracks is (16.2 km/h, 274°). This compares well with the mean wind vector in the surface-300 hPa layer calculated from the available soundings: (14.6 km/h, 273°), which indicates that most of the storms were moving close to the mean wind.

4. PERFORMANCE EVALUATION

To assess the skill of the tracking algorithm, results were compared with those determined subjectively. Three days with different degrees of convective activity (in relation with the number of storms by image) and different environmental conditions (in relation with the predominant wind speed) were selected and the comparison was carried out during 6 hours of storm tracking each day. The temporal assignments detected subjectively were called “the true set” and those detected by the tracking algorithm were called “the objective set”. The total number of hits, misses, and false alarms were determined, and with them the probability of detection (POD), the false alarm rate (FAR) and the critical success index (CSI).

Table 3 shows the performance statistics for the three cases analyzed. The tracking algorithm performs best for a day with the least number of cells by image, strong predominant wind speed and the least number of merge/split events (not shown). This result was expected because the algorithm performs best tracking isolated storms moving with the wind. However, the worst performance was on 27 August, a day with strong wind and a relatively low number of cells by image, when compared with 4 October. This was linked to a great amount of merge/split events that took place during this day. In Table 3, CSI values are similar to POD because of the low FAR values. In average POD=0.88, FAR=0.02 and CSI=0.86, comparing well with other reports, as shown in Table 4.

Table 3. Performance statistics for tracking.

Day	Cells/imag	Wind	POD	FAR	CSI
27 Aug	21	Strong	0.84	0.02	0.83
10 Sep	16	Strong	0.93	0.01	0.91
4 Oct	30	Weak	0.87	0.02	0.85

Table 4. Performance statistics in other reports (DW93 is Dixon & Wiener 1993; KN05 is Kyznarova & Novak 2005; H02 as above). A ? symbol means not reported value.

Author	Cells/image	Wind	POD	FAR	CSI
H02	16	?	0.90	0.04	0.87
H02	19	?	0.93	0.09	0.85
H02	27	?	0.87	0.07	0.81
DW93	?	?	0.91	0.13	0.80
KN05	25<?<30	Weak	0.89	0.08	0.83
KN05	~20	Strong	0.92	0.06	0.87
KN05	~20	Strong	0.93	0.06	0.88

As a comparison, Table 4 shows the cell tracking results from several authors. The higher FAR values are supposed to be a consequence of some fails in the merge/split detection algorithm included in those tracking systems. As some of these authors mention (Handwerker 2002; Kyznarova & Novak 2005), most of the merge/splits events are artificial products of reflectivity core identification. However, none of these authors check the performance of the merge/split detection algorithm. By contrast, Johnson et al. (1998) did not include merge/split detection in the SCIT algorithm and reached higher values of POD (95% in average, nothing is said about FAR or CSI).

The tracking algorithm here evaluated does not include the detection of merge/splits. It is then remarkable that, on average, the CSI values in this study compare very well with those in Table 4.

To assess the performance of storm motion nowcasting, forecast and actual locations were compared (at the time of the forecast). The distance between each pair of locations was calculated, and the results for different lead times were averaged to find the mean forecast error. This was done for forecast lead times up to 60 min. All the observation periods during the thirteen days of 2007 were included in the analysis. Table 5 shows the results. As comparison, the results from Johnson et al. (1998) for the same forecast lead times are included in parenthesis. The larger mean forecast errors in Johnson et al. (1998) could be caused by the type of thunderstorms they analyzed, mainly severe. However, the results in Table 5 are encouraging.

Table 5. Performance of storm motion nowcasting. In parenthesis results from Johnson *et al*. 1998.

Forecast time (min)	Number of cells in sample	Mean forecast error (km)
5	30773 (898)	1.8 (2.0)
15	17300 (498)	3.7 (5.0)
30	8272 (227)	6.7 (9.9)
45	3955 (109)	9.8 (15.2)
60	1826 (55)	12.8 (22.8)

Mean forecast error was also calculated for an independent sample of 12 days from the 2005-2006 rainy seasons. For a lead time of 60 min in a sample of 612 cells, the mean forecast error was 11.6 km, which is similar to 12.8 in Table 5.

5. SUMMARY AND CONCLUSIONS

An algorithm has been presented and validated, which automatically detects and tracks convective cells and provides a forecast for their location. The algorithm only uses radar reflectivity data as input and has been applied to the analysis of Cuban convective storms during 13 days of the 2007 rainy season. Some preliminary results were obtained for the Camaguey province and its surroundings, and are summarized here.

The spatial distribution of storms in the

region of study has two maxima toward the center of the Cuban island and a third one along the south coast of Camaguey. All of them reflect the interaction between the general circulation driven by the North Atlantic Subtropical High and the local sea-breeze circulation over Cuba, and have been reported before.

The diurnal cycle of convection shows the highest activity around 1600 h over land, and a much lower secondary maximum around 2200 h when land breeze produces convergence over the sea.

Storm properties like total duration, maximum area and maximum reflectivity show the typical distributions reported in the literature. The distribution of maximum top is similar to the one reported for northern Venezuela, with the highest contribution from storms with heights between 8 and 10 km, both over sea and over land.

The motion of storms over land is more frequent at mean speeds around 10 km/h, whereas the maritime storms move faster with a mean around 20 km/h. Mean direction of movement preferred by storms is westward between 250° and 300°.

Both the total duration and the height of 10-dBZ storm top are shown to be clearly correlated with the maximum reflectivity reached by storms. Other storm properties like maximum area and mean speed can be also correlated with maximum reflectivity, but this needs further study.

The performance evaluation for 6 h during three days with different degrees of convective activity and environmental conditions shows that, on average, the tracking algorithm performs well for 86% of the time. This compares well with tracking algorithms elsewhere. However, the inclusion of an effective merge/split detection algorithm can improve considerably the tracking skill.

The performance evaluation of storm motion nowcasting shows encouraging results, with a mean error in the forecast position of 12.8 km for a forecasting time of 60 minutes. Similar results were found for an independent sample of 12 days during the 2005-2006 rainy season.

The tracking and nowcasting system described in this article is currently been tested in Cuba with the high temporal resolution radar data from the Randomized Convective Cold Cloud Seeding Experiment under way (Martinez et al., 2007) during summer. An adapted version has been also used for tracking and analyzing large convective areas during the same experiments (Novo et al., 2008). The analysis of larger datasets from different regions will provide useful information about the climatology of convective activity in the country, as well as local detailed studies about the properties of severe storms.

6. REFERENCES

Alvarez L. 2006. Estudio de la localización espacial de las tormentas eléctricas en Cuba y su tendencia. Ph.D. Thesis, 170 pp. Centre for Atmospheric Physics, Institute of Meteorology, La Habana, Cuba.

Cruz LA. 1973. Venezuelan rainstorms as seen by radar. J. Appl. Meteorol. 12: 119-126.

Dixon M, Wiener G. 1993. TITAN: Thunderstorm identification, tracking, analysis, and nowcasting – A radar-based methodology. J. Atmos. Ocean. Technol. 10: 785-797.

Handwerker J. 2000. Studying the life cycles of convective cells in the upper Rhine valley. In 30th International Conference on Radar Meteorology, Munich, Germany, 19-24 July, session 12A, paper 6.

Handwerker J. 2002. Cell tracking with TRACE3D – a new algorithm. Atmos. Res. 61: 15-34.

Johnson JT, MacKeen PL, Witt A, Mitchell ED, Stumpf GJ, Eilts MD, Thomas KW. 1998. The storm cell identification and tracking algorithm: an enhanced WSR-88D algorithm. Weather Forecast. 13: 263-276.

Kyznarova H., Novak P. 2005. Development of cell-tracking algorithm in the Czech Hydrometeorological Institute. In Proceedings of World Weather Research Program Symposium on

Nowcasting and Very Short Range Forecasting, Toulouse, France, 5-9 September, pp 6-11.

Lecha LB, Paz LR, Lapinel B (eds.). 1994. El clima de Cuba. Editorial Academia, La Habana, Cuba, 186 pp.

Martinez D, Perez CA, Koloskov B, Korneev VP, Petrov V, Gamboa F., Novo S. 2007. Randomized convective cold cloud seeding experiment in extended areas in Cuba (EXPAREX). In Proceedings of 9th WMO Scientific Conference on Weather Modification, Antalya, Turkey, 22-24 October, pp 92-95.

Novo S, Martinez D, Perez CA, Koloskov B, Gamboa F. 2008. Radar tracking method for cloud seeding experimental units over Cuba. In 15th International Conference on Clouds and Precipitation, Cancun, Mexico, 7-11 July 2008, session P-13, paper 37.

Nuñez O, Gonzalez A, Cordoba L, Rego J, Perez M, Valdes R. 1999. Caracterización macroscópica de las nubes sobre Cuba a partir de la información de radar. Final Report of the Radar Group, 74 pp. Institute of Meteorology, La Habana, Cuba.

Peña A, Rodriguez O, Perez M, Naranjo R, Fernandez L, Barreiras A, Martinez A, Rodriguez MD. 2000. Modernization of the Cuban weather radar network. Phys. Chem. Earth PT B 25: 1169-1171.

Perez M, Rodriguez O, Peña A, Naranjo R, Fernandez L, Barreiras A, Martinez A, Rodriguez MD. 1999. Reengineering MRL-5 for the Cuban weather radar network. In Proceedings of 29th International Conference on Radar Meteorology, Montreal, Quebec, Canada, 12-16 July. American Meteorological Society: Boston, MA, pp 811-814.

Potts RJ, Keenan TD, May PT. 2000. Radar characteristics of storms in the Sydney area. Mon. Weather Rev. 128: 3308-3319.

Rodriguez O, Fernandez L, Naranjo R, Barreiras A, Peña A, Diez M, Pozas W, Aguiar M, Perez J. 2005. The Cuban weather radar network: current status and trends. In 32nd International Conference on Radar Meteorology, Albuquerque, NM, USA, 24-29 October. American Meteorological Society: Boston, MA, session P10R, paper 9.

OVERVIEW OF MICROPHYSICAL PROPERTIES OF TROPICAL CONVECTIVE CLOUDS OBSERVED IN 2010 AND 2011 MEGHA-TROPIQUES CAMPAIGNS OVER WEST AFRICA AND THE INDIAN OCEAN.

E. Fontaine[1], A. Schwarzenboeck[1], A. Protat[2,3], N. Viltard[3], M. Gosset[4], J. Delanoe[3], R. Dupuy[1], W.Wobrock[1], C. Duroure[1], C. Gourbeyre[1].

[1] Laboratoire de Météorologie Physique, Clermont-Ferrand, France.
[2] Center for Australian and Weather Climate Research, Melbourne, Australia.
[3] Laboratoire ATmosphère, Milieux, Observations Spatiales, Velizy, France.
[4] IRD / LTHE – CNRM / GMME / MOANA, Toulouse, France.

1. INTRODUCTION.

Detailed information on the property of ice phase hydrometeors (crystal density and size) has emerged as a strong need to improve and validate the rain restitutions from BRAIN (Viltard et al., 2006) algorithm within the Megha-Tropiques project. The ice phase is parameterized in BRAIN by a Particle Size Distribution (PSD) and a density which depends on the type of particles. Namely three types are implemented: dense particles (hail), moderately dense particles (graupel) and light particles (snow). The mass-diameter relationship can be set according to various values found in the literature or can be set as a constant for a given class of particles.

Two measurement campaigns have been performed in order to capture correctly the properties of these cloud particles and thus, to improve the existing parameterization implemented in BRAIN. The study covers cases of continental (2010 over West Africa, MT1) and oceanic convection (2011 over the Indian Ocean, MT2) over the Tropical belt, in order to demonstrate most eminent differences in continental and oceanic ice cloud microphysics.

2. INSTRUMENTATION.

The ice microphysics study presented here will primarily give an overview of the microphysical cloud data from state of the art instrumentation mounted during two measurement campaigns on the French Falcon 20 (FF20) research aircraft operated by SAFIRE (Service des Avions Français Instrumentés pour la Recherche en Environnement). The in situ instrumentation mounted on the FF20 during the MT1 campaign consisted of the imaging probes 2D-S, CIP (Cloud Imager Probe), and PIP (Precipitation Imager Probe) as well as the cloud droplet spectrometer FSSP-100. Moreover, the cloud Doppler radar RASTA (Protat et al., 2009) was used to measure the reflectivity (or backscattering energy) of the hydrome-

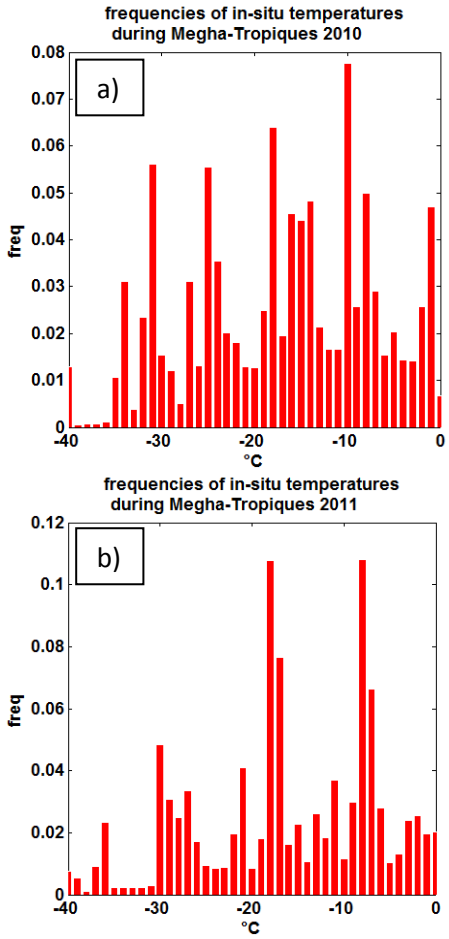

Figure 1: Histograms of the temperatures measured during the Megha-Tropiques campaigns. a) Niamey, Niger, above the African Continent in August 2010. b) Gan, Maldives above the Indian Ocean, in November/December 2011.

teors at 95GHz above and below the FF20 aircraft. The basic thermodynamical and dynamical parameters such as temperature, pressure, and vertical velocity were recorded routinely on the aircraft along its trajectory.

For the MT2 campaign the CIP array probe used during MT1 has been replaced by a cloud particle imager CPI. In addition, a Nevzorov probe has been added to the instrumentation on the FF20 to measure the in-situ condensed water content (CWC).

Figure 1 illustrates the in-situ temperatures encountered during the two campaigns. Temperatures included here cover the range between -40℃ and 0℃. The maximum occurrences during MT1 have been observed for temperatures near -30℃, -25℃, -20℃, and -10℃. During MT2 the temperatures of maximum occurrences were somewhat similar with maximum occurrences of temperatures near -30℃, -20℃, and -10℃, however, temperatures below -30℃ have been barely encountered in contrast to MT1.

In general, the FF20 did not enter the deep convection cores of the MCS systems, in particular not over the continent. Approximately 75% of the data points of measured vertical velocity have been found in the velocity interval of -0.5m/s to 0.5m/s (figure 2). The cloud systems encountered during MT1 were essentially extended MCS systems. During MT2 a first smaller period of the campaign experienced somewhat extended cloud systems (up to MCS size), whereas during the second period of MT2, the cloud systems were especially comprised of smaller isolated convection systems. The updrafts in the oceanic systems were less violent for comparable reflectivities, when compared to the continental convection. Over the ocean the pilots accepted easily to cross the systems without restrictions.

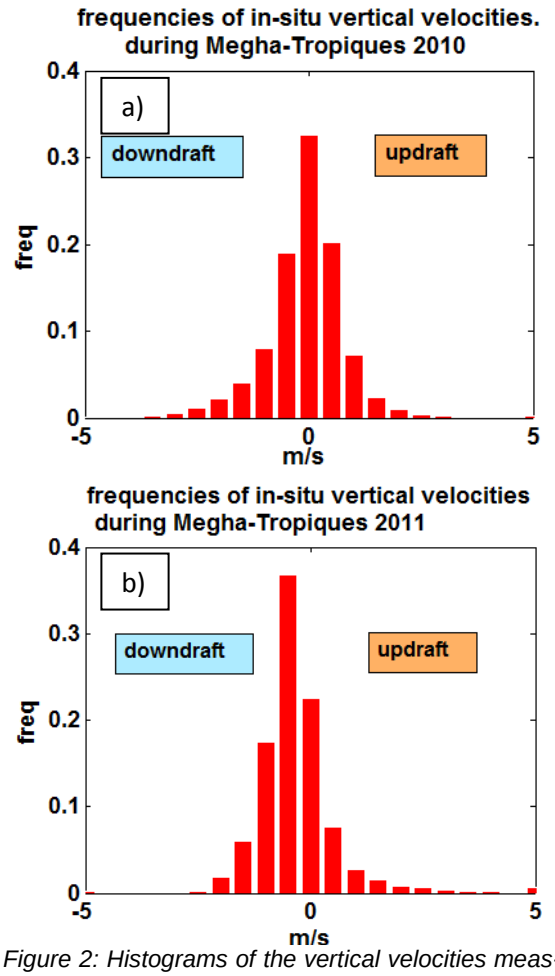

Figure 2: Histograms of the vertical velocities measured during the Megha-Tropiques Campaigns. a) Niamey, Niger, above the African continent in August 2010. b) Gan, Maldives above the Indian Ocean, in November/December2011.

3. INTERCOMPARISON OF CLOUD MICROPHYSICAL PROPERTIES (CONTINENTAL & OCEANIC CLOUDS).

Particles recorded by the particle imagers were classified, both as a function of their maximum length (D_{max}) and as a function of the equivalent diameter of a disc corresponding to the crystal surface (D_{eq}). The 1Hz composite particle size distribution (PSD) has been derived, combining PSD (in Dmax or Deq) of individual probes used during each flight. For this study, composite PSD were built for flights 15,17,18,19, 20 of MT1 from the size-restricted individual PSD of 2DS, CIP and PIP. For MT2 the composite PSD for flights 45, 46, 49 and 50 were build from the individual PSD of 2DS and PIP probes.

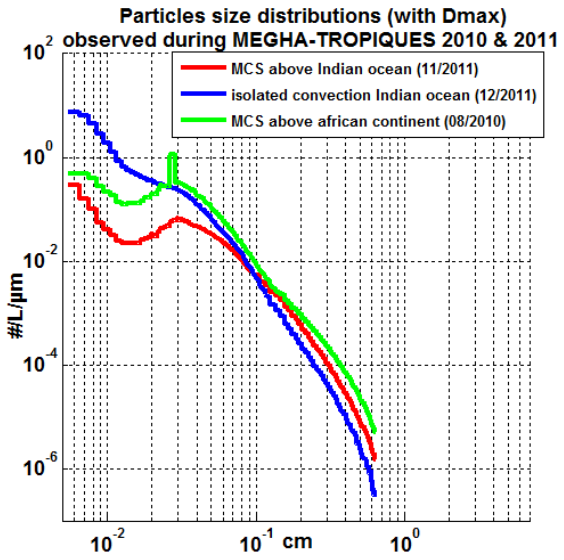

Figure 3: Trends of particles size distributions as a function of D_{max} of the particles measured during the two measurement campaigns of Megha-Tropiques. Flights included in the category "MCS above African continent" are flight numbers 15, 17, 18, 19, and 20 of MT1. The category "isolated convection above the Indian Ocean" averages PSD from flight numbers 49 and 50 of MT2 (December 2011). Finally flight numbers 45 and 46 are included in the category "MCS above Indian Ocean" (November 2011).

The averaged composite PSD have been calculated separately for each flight and subsequently averaged over all flights of the same category of cloud systems. Therefore the available microphysical data from FF20 flights have been grouped in three different categories corresponding to different synoptic features as there are: (i) MCS (Mesoscale Convective System) above African continent, (ii) MCS above Indian Ocean, and (iii) isolated convection above the Indian Ocean (figure 3). Averaged PSD for the two types of MCS (category (i) and (ii)) are similar in shape, however with higher total concentrations of sub-millimeter crystals and larger sizes of super-millimeter crystals for the continental PSD as compared to the oceanic PSD. Compared to both MCS type PSD, the averaged PSD of isolated oceanic convection reveals much higher concentrations of smallest ice particles and also significantly smaller sizes of the entire crystal population.

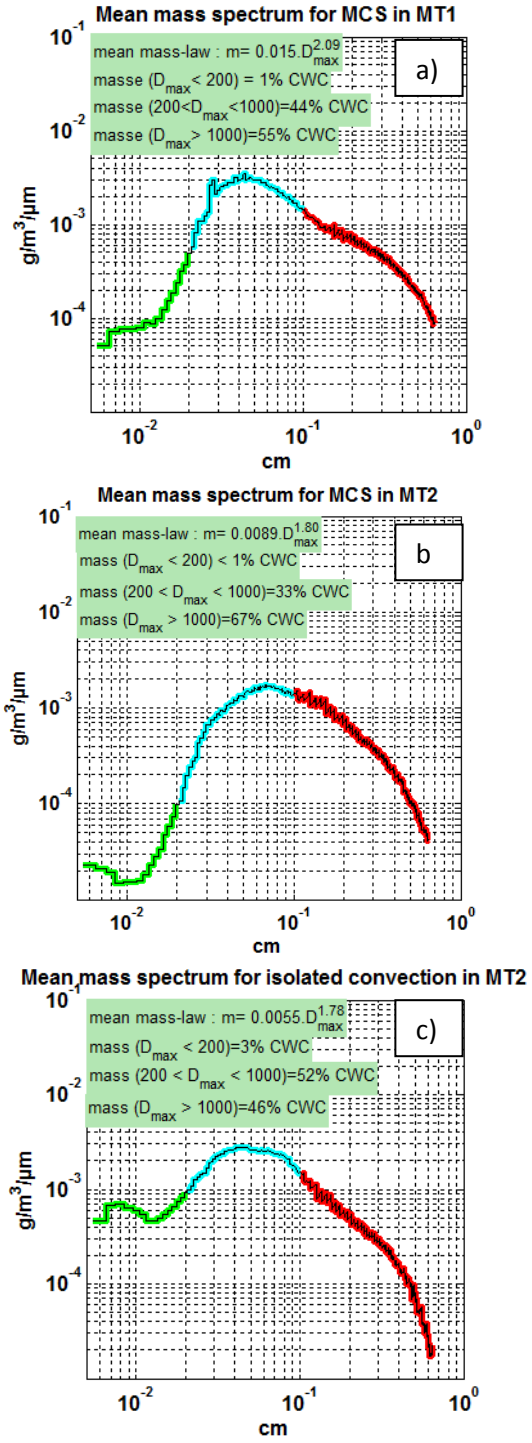

Figure 4 : Mean mass spectrum calculated with the mass-diameter relationships constrained by the reflectivity measured by RASTA and the simulated reflectivity from the composite PSD and area-diameter relationships. The fraction of the mass size distribution of particles with diameters smaller than 200µm is underlined in green, the range between 200µm and 1000µm in blue the super-millimeter particles in red.

It appears (figure 4), that the mean mass-diameter relationship deduced by constraining simulated reflectivity from particle size distributions with measured

reflectivities from the Doppler radar RASTA (95 GHz) (see Fontaine et al, 2012b, this ICCP issue), is greater for MCS observed above the African continent ($m=0.015D_{max}^{2.09}$) than for oceanic MCS systems and isolated convection ($m=0.009D_{max}^{1.80}$ and $m=0.0055D_{max}^{1.78}$), respectively. Figures 4a, 4b , and 4c illustrate that, on average, super-millimeter particles (with D_{max} beyond 1mm) comprise a mass fraction of 55% in the continental MCS compared to 67% and 46% in oceanic MCS and isolated convection systems, respectively.

Particles shown in figures 5a and 5b have been chosen within identical temperature ranges. Whereas figure 5a is an extract of the PIP catalogues for MT1, figure 5b presents an extract of particles sampled during MT2. Particles have been selected, if the particle surface is larger than 1000 pixels for MT1. Since the 1000 pixel criteria didn't produce counts for the MT2 clouds, the threshold has been set to 500 pixels for MT2.

In order to connect findings from figures 3, 4, and 5 we have seen larger and somewhat higher concentrated super-millimeter particles in continental MCS as compared to oceanic MCS. Since we stated above that super-millimeter mass comprises 55% of the total cloud particle mass in the continental MCS, compared to 67% in the oceanic MCS, this means that the relative mass contribution of sub-millimeter particles to the total particle mass is more important for continental MCS (44%) than it is for oceanic MCS (33%).

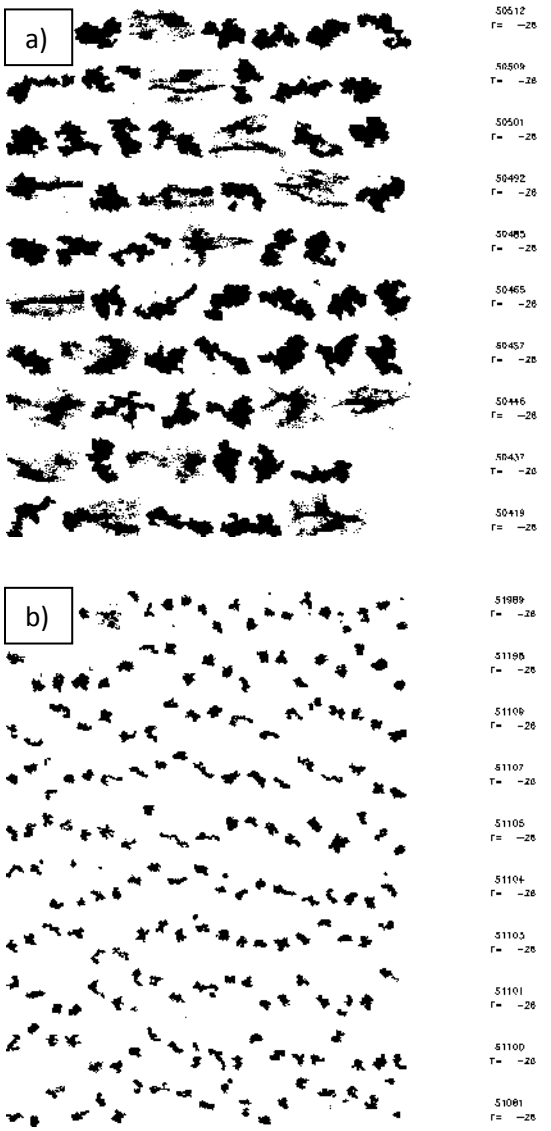

Figure 5: Extract of particle catalogue recorded by the PIP. At the end of each line temperature and arrival time in second after midnight of the last particle is shown. Particles have been selected if their surfaces in pixels are larger than a threshold of 1000 pixel for MT1 (figure 5a) and 500 pixel for MT2 (figure5b)

In general, the mean density of the cloud particles is larger in continental MCS (MT1) than in oceanic MCS (MT2). Whereas it is not possible to clearly classify the particle shapes in the continental MCS (shapes somewhere between graupel and aggregates), in the oceanic MCS much more pristine (rosettes, columns, sideplanes, etc…) ice can be found.

An important conclusion is that for observed oceanic convection the growth of the cloud particles is much more dominated by vapor diffusion, as compared to the

more violent continental convection. Thus, cloud particle aggregations that lead to very large particles in the continental convection are somewhat limited in oceanic convection.

4. REFERENCES.

E. Fontaine, A. Schwarzenboeck, A. Protat, J. Delanoe, R. Dupuy, W. Wobrock, C. Duroure, C. Gourbeyre. Determination of area-diameter and mass-diameter relationships from ice particle imagery in order to deduce IWC within tropical convective clouds. In Proceedings of ICCP 2012a, Leipzig, Germany.

Protat A, Bouniol D, Delanoë J, May PT, Plana-Fattori A, Hasson A, O'Connor E, Görsdorf U, Heymsfield AJ. 2009. Assessment of CloudSat reflectivity measurements and ice cloud properties using ground-based and airborne cloud radar observations. J. Atmos. Oceanic Technol. 26: 1717–1741.

Viltard, N., Burlaud, C., Kummerow, C.D., 2006. Rain Retrieval from TMI Brightness Temperature Measurements Using a TRMM PR–Based Database. Journal of Applied Meteorology and Climatology 45, 455–466.

Acknowledgements:
The authors are particularly grateful to CNES for funding the aircraft measurement campaigns within the Megha-Tropiques project. We would like to thank SAFIRE for operating the French Falcon 20 research aircraft during the two campaigns.

DETERMINATION OF AREA-DIAMETER AND MASS-DIAMETER RELATIONSHIPS FROM ICE PARTICLE IMAGERY IN ORDER TO DEDUCE IWC WITHIN TROPICAL CONVECTIVE CLOUDS.

E. Fontaine[1], A. Schwarzenboeck[1], A. Protat[2,3], J. Delanoe[3], N. Viltard[3], R. Dupuy[1], W. Wobrock[1], C. Duroure[1], and C. Gourbeyre[1].

[1] Laboratoire de Météorologie Physique, Clermont-Ferrand, France.
[2] Center for Australian and Weather Climate Research, Melbourne, Australia.
[3] Laboratoire ATmosphère, Milieux, Observations Spatiales, Velizy, France.

1. INTRODUCTION.

The presented study is performed within the Megha-Tropiques (MT) project. Megha-Tropiques is a French-Indian satellite devoted to improve our knowledge on the understanding of the processes linked to the tropical convection. The relevant instrument on the satellite for cloud studies is the MADRAS microwave imager with 9 frequencies (18,7 GHz to 157 GHz). Two aircraft measurement campaigns (MT1 over West Africa in 2010 and MT2 over the Indian Ocean in 2011) have been performed with the French Falcon 20 in order to improve cloud microphysics parameterization and precipitation retrievals from the satellite data. The presented study is using solely MT1 data. Onboard the French Falcon aircraft, the French Doppler radar RASTA (Radar Aéroporté et Sol de Télédétection des propriétés nuAgeuses; with a frequency of 95GHz: Protat & Al, 2009), the Cloud Imaging Probe (CIP), the Precipitation Imaging Probe (PIP) and the 2D Stereo (2DS). In situ CWC mass has not been measured directly. After image data processing two types of composite particle size distributions (hereafter PSD) have been derived. The representation of PSD is given as a function of the equivalent diameter of a disc corresponding to the crystal surface (hereafter Deq), the second type of PSD is presented as a function of the maximum length of the particle (Dmax). Both PSDs are calculated for a 1 s and 10 s time resolution (PSD are handled in 10 µm bin resolution from 50µm to 6400µm).

Determining the mass of a particle is very difficult when its shape is not known. Baker and Lawson, (2006) presented a relationship between particle mass and geometric parameters derived from 2D particle images. Schmitt and Heymsfield (2010) showed that the fractal dimensions of aggregates are related with their mass.

The estimation of IWC in MCS systems over West Africa presented in this study is based on two slightly different approaches of IWC retrieval from simultaneous analysis of in situ cloud particle imagery and radar reflectivity measured at 95GHz with the cloud Doppler radar RASTA.

2. METHOD USED TO RETRIEVE THE MASS-DIAMETER RELATIONSHIP.

The reflectivity at 95 GHz is usually calculated, assuming the mass of the ice particles. Thus, our purpose is to estimate the mass-diameter relationship which produces the smallest deviations (equation 2) between the measured radar reflectivity (Z_{95GHz}) and the equivalent reflectivity (Z_{Mie}) calculated from the mass-diameter power law (equation 1). The diameter D stands either for the equivalent or the maximum diameter. In the present study the maximum error (cf. equation 2) has been set to 5%.

$$m(D) = \alpha D^{\beta} \qquad \text{(eqn. 1)}$$

$$error\ (\%) = 100. \left| \frac{Z_{95GHz} - Z_{Mie}}{Re_{95GHz}} \right| \qquad \text{(eqn. 2)}$$

The equivalent reflectivity at 95 GHz can be calculated as shown in the equation 3, where *Ki* and *Kw* are the dielectric constants for ice and water. The PSD is represented with *n(D)* and the Mie scattering effect is described by the function *f(D)*. However, this formula is difficult to implement, since the Mie scattering effect cannot be described by a simple equation. Therefore, to calculate properly the equivalent reflectivity we use an algorithm, where the Mie theory is applied on a sphere with a homogenous mixture of ice and air. The mixture is related to the mass-diameter law by the fact that the ice fraction is proportional to the mass of the ice in the particle divided by its mass if the particle would only consist of ice.

$$Ze_{95GHz} = \left|\frac{Ki}{Kw}\right|^2 . \sum_D n(D).m(D)^2.f(D)$$

(eqn. 3)

The calculation is performed in two different ways: Either we fix the β exponent to be equal to 2.1 (for example) or we calculate the β exponent as a function of the exponent of an area-diameter relationship (to be derived from particle images) of the crystals. Thus, either β is a constant, or it is a function of the 2D images recorded by the in situ imagers (2DS, CIP, PIP). In order to characterize a falling particle in the atmosphere, Heymsfield and Miloshevich, (2003) and Mitchell (1996) use the area $S_\perp$ and the aspect ratio A_r (which is the area of the particle projected normal to the flow ($S_\perp$) divided by the area of a circumscribing disc).

$$A_r = \frac{S_\perp}{\frac{\pi}{4}Dmax^2} \quad \text{(eqn. 4)}$$

$$S_\perp = \gamma . Dmax^\sigma \quad \text{(eqn. 5)}$$

In this study we consider that the diameter-area law is equal to ($S_\perp$). The Diameter-area law could be explained as the expected area (or mean area) for a given maximum length *(Dmax)*. An example of a diameter-area law is given in figure 1 and has been calculated using all particle images in a time interval of 10 seconds for one arbitrary flight of the MT1 campaign. We can see that the relationship between the mean area and the maximum length is well fitted with a power law.

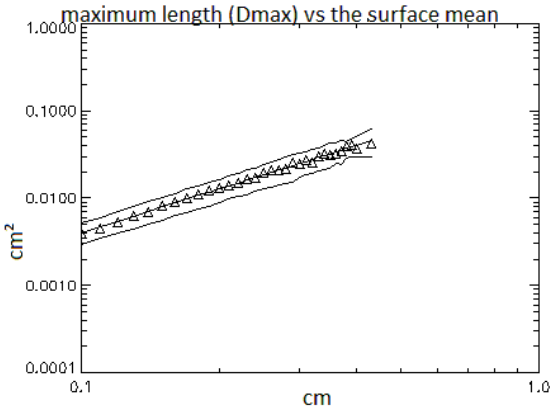

Figure 1. Example of relationship for crystal mean area as a function of the maximum length for an ice crystal population of more than 200 analyzed crystals within a time period of 10 seconds. The particles have been recorded by the PIP probe.

The diameter-area law shown in this figure has been calculated for 2D images recorded by the PIP probe in the size interval 1000µm and 6400µm. The calculated mean areas are represented by triangular symbols and the line corresponds to the fitted power law. The line above and below the data points represents one standard deviation.

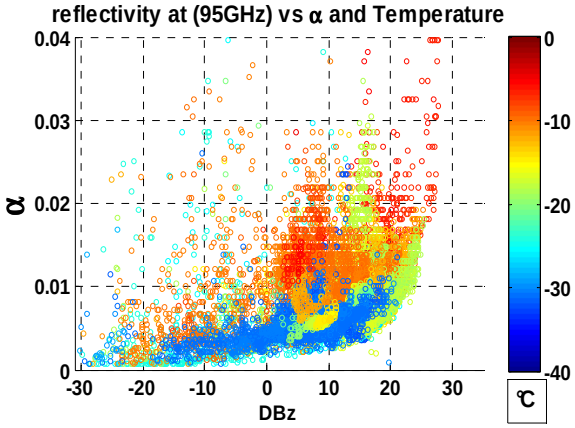

Figure 2. Scatter plot of the reflectivity versus α of the mass-diameter law. Each point corresponds to 1 second of measurement data of flights 15, 17, 18, 19, 20 of the MT1 campaign and its color represents the measured in situ temperature.

3. RESULTS.

In this first part of the results, we show findings obtained when fixing β equal to 2.1. In figure 2, the calculated coefficient α of the power law is plotted as a function of the reflectivity measured by RASTA. The temperature measured in the corresponding cloud volume is color coding the data points. We can see that there is some temperature dependency in this figure. Low values of α are particularly found for low temperatures, which is of course the result of having chosen a constant exponent β, independently of the temperature and related to the clouds microphysics.

A reason to study area-diameter relationships from particle imagery is also to compare the in situ findings to the terminal velocity of the hydrometeors deduced from the reflectivity measured by the radar RASTA. Since area-diameter relationship is varying during a flight and since the area-diameter law of the particles is strongly influenced by the specific ice microphysics, different relationships between the β exponent of the mass-diameter law and the σ exponent from the area-diameter law have been tested. Figures 3 and 4 present the results obtained with the dataset from the MT1 campaign. The mass-diameter laws are calculated for the flights 15, 17, 18, 19, 20 with a time integration of 10 seconds. The PSD used have been built as a function of the equivalent diameter Deq and the area-diameter law has been calculated using the 2D images monitored with the PIP probe. In figure 3 we can see the relationship between the condensed water content (equation 6; CWC) and the measured reflectivity (Z_{95GHz}). The data points are color coded with measured temperature. The resulting relationship is a power low which is influenced by the temperature (equation 7). For a given reflectivity, CWC increases with decreasing temperature. We can also conclude that a given CWC produces lowest reflectivities for lowest temperatures.

$$CWC = \sum_D n(D).m(D) \qquad \text{(eqn. 6)}$$

$$CWC = C_{cwc}(T).{Z_{95GHz}}^{A_{cwc}(T)} \quad \text{(eqn. 7)}$$

The subsequent relation in equation 8 resumes what is presented in figure 4. α is written as a power law of β and with C_m and A_m both depending upon temperature. Overall, β increases (for given α) with increasing temperature T, whereas α increases with decreasing T (for given β).

$$\alpha = C_m(T).\beta^{A_m(T)} \qquad \text{(eqn. 8)}$$

Finally figure 5 shows the impact on CWC retrievals when applying 6 different mass-diameter relationships. The figure is a zoom of 15 minutes of calculations for one exemplary flight (flight number 19). It shows results obtained with 4 different relationships between σ (from the area-diameter law) and β (from the mass-diameter law) calculated for PSD expressed in terms of the maximum length Dmax and the area-diameter law calculated from the PIP probe (maximal length between 1000µm to 6400µm). To these four curves are added two curves. In one of these two curves CWC is calculated for PSDs expressed in terms of the equivalent diameter Deq with data from the PIP probe, whereas in the other curve CWC is calculated for Dmax, however for CIP data (maximal length between 500µm to 1600µm) derived area-diameter relationships.

The results of these 6 curves are rather similar and somewhat independent of the relationship between σ and β, independent of the probe used for the area-diameter relationship and thus, the range of the particles used to calculate that relationship, and independently of the parameters (Dmax or Deq) of 2D images used to classified the particles to build up the PSD.

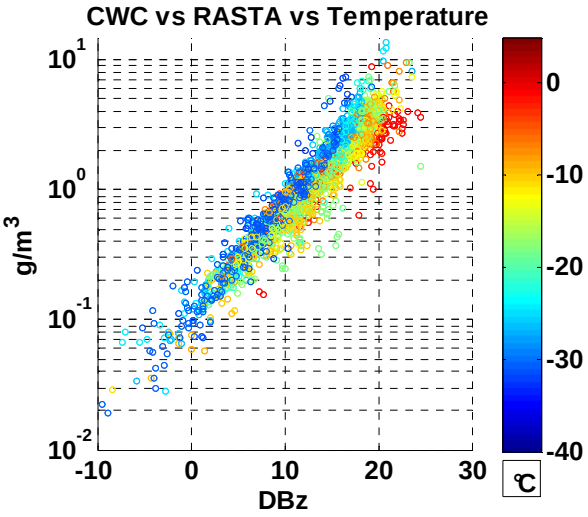

Figure 3. Scatter plot of the CWC versus the reflectivity at 95 GHz measured by RASTA. Each point corresponds to 10 seconds of measurement data of flights 15, 17, 18, 19, 20 of MT1 and its color shows the in-situ temperature.

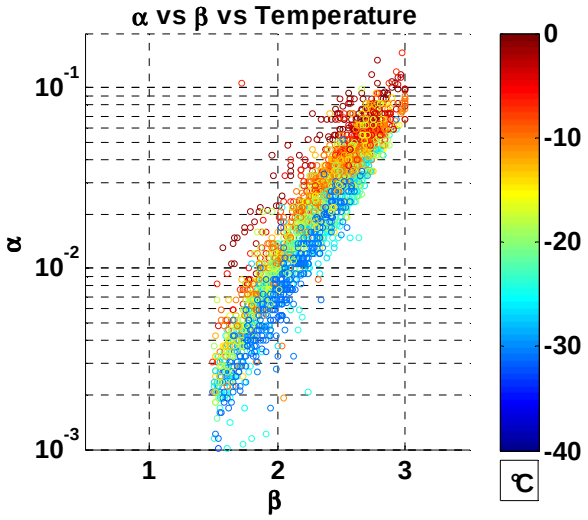

Figure 4. Scatter plot of α versus β from the mass-diameter law $m=\alpha D^{\beta}$. Each point corresponds to 10 seconds of measurement data of flights 15, 17, 18, 19, 20 of MT1 and its color shows the temperature in-situ.

5. CONCLUSION.

To resume figures 3, 4, 5, we can state that the mass-diameter relationship is significantly influenced by the temperature. CWC calculated from the RASTA radar reflectivities using the Mie theory and applying different relationships for the mass-diameter relation, the results are approximately the same, if all m(D) relations have been constraint by the radar reflectivities. In fact, for any given value of β, α can be calculated to fit to the function given in equation 8. It is important to give the variations of the area-diameter law to the mass-diameter law. It seems that the area-diameter law is influenced by the temperature and some further parameters. More studies have to be performed in order to understand how the area-diameter law varies in clouds, and what are the most significant physical parameters controlling the calculation of the area-diameter law.

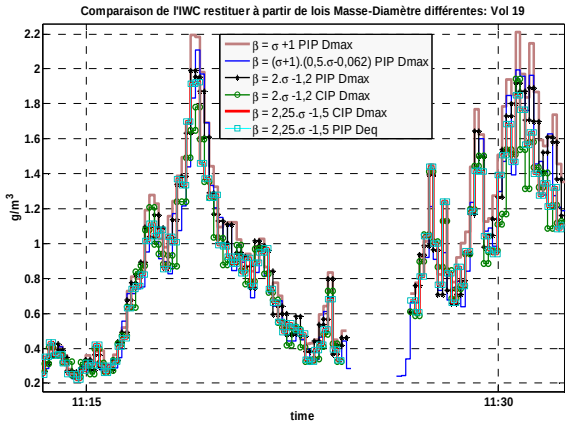

Figure 5 : CWC calculations for 6 different mass-diameter relationships, all laws have been constraint by the radar reflectivities.

6. REFERENCES.

Baker, B., Lawson, R.P., 2006. Improvement in Determination of Ice Water Content from Two-Dimensional Particle Imagery. Part I: Image-to-Mass Relationships. Journal of Applied Meteorology and Climatology 45, 1282–1290.

Heymsfield, A.J., Miloshevich, L.M., 2003. Parameterizations for the Cross-Sectional Area and Extinction of Cirrus and Stratiform Ice Cloud Particles. Journal of the Atmospheric Sciences 60, 936–956.

Lawson, R.P., Baker, B.A., 2006. Improvement in Determination of Ice Water Content from Two-Dimensional Particle Imagery. Part II: Applications to Collected Data. Journal of Applied Meteorology and Climatology 45, 1291–1303.

Mitchell, D.L., 1996. Use of Mass- and Area-Dimensional Power Laws for Determining Precipitation Particle Terminal Velocities. J. Atmos. Sci. 53, 1710–1723.

Protat A, Bouniol D, Delanoë J, May PT, Plana-Fattori A, Hasson A, O'Connor E, Görsdorf U, Heymsfield AJ. 2009. Assessment of CloudSat reflectivity measurements and ice cloud properties using ground-based and airborne cloud radar observations. J. Atmos. Oceanic Technol. 26: 1717–1741.

Schmitt, C.G., Heymsfield, A.J., 2010. The Dimensional Characteristics of Ice Crystal Aggregates from Fractal Geometry. Journal of the Atmospheric Sciences 67, 1605–1616.

Acknowledgements:

The authors are particularly grateful to CNES for funding the aircraft measurement campaigns within the Megha-Tropiques project. We would like to thank SAFIRE for operating the French Falcon 20 research aircraft during the two campaigns.

QUANTIFICATION OF DRIZZLE FRACTION USING LARGE EDDY SIMULATION MODEL OUTPUT - THE MULTI-PURPOSE OF THE EARTHCARE SIMULATOR

Igor Stepanov, Simone Placidi and Herman Russchenberg

Delft University of Technology, Delft, The Netherlands

1 INTRODUCTION

Earth's low altitude, warm, layered clouds play a major role in the climate system, reflecting back a large amount of the incoming shortwave radiation from the Sun. Stratocumulus (Sc) clouds are typical representatives of such type of clouds. They cover vast areas, extensively spreading in horizontal direction, having a considerable impact on the radiation budget.

To look into the process of the Sc structure variability and evolution, retrievals of the microscale cloud properties are used. These can be related back to the large scale processes that consequently onset due to a change in the microscale. One of such chain of events is the growth of cloud droplets via process of diffusion until a critical size is achieved, from where process of collisions and coalescense takes over, forming light drizzle drops. This type of feedback could lead to development of pockets of open cells (Stevens et al., 2005), also changing the cloud radiative properties.

Drizzle onset process regarding such clouds is of great importance to comprehend the cloud evolution and its impact on the radiation budget. To analyze the consequence chain this microphysical process holds on a large scale, a modified version of the EarthCARE mission Simulator (ECSIM) is used here to ingest cloud scenes from a Large Eddy Simulation (LES) model, represented with microphysical output. Full description of the LES model used is given in Heus et al., 2010. Recreated scenes in ECSIM were used in order to generate realistic observations for ground-based radar instrument.

2 RADAR OBSERVATIONS IN DRIZZLE CATEGORIZATION

Previous studies have shown presence of drizzle is very common in water clouds (Fox and Illingworth, 1997). Issue with proper quantification of drizzle is that the retrieved radar reflectivity when profiling clouds does not match the cloud structure identically, when drizzle is present. This offset happens due to increased sensitivity of radar reflectivity (proportional to the power of six of the cloud droplet radius) to large cloud drops, which are usually located near the bottom of the clouds. These, however do not contribute analogously to the water content of the cloud itself. For this reason drizzle droplets dominate the radar reflectivity, obscuring the retrieval interpetation. A method initially created by Krasnov and Russchenberg 2002., and used later in Khain et al. 2008., further analyzed the relationship between radar reflectivity (Z) and liquid water content (LWC). It distinguishes 3 categories of drizzling clouds: ``the cloud without drizzle fraction'', ``the cloud with light drizzle'' and ``the cloud with heavy drizzle'', derivated using radar retrievals. Such method adopted categorization of Z-LWC relationship from previous studies (Baedi et al., 2000; Fox and Illingworth 1997; Sauvageot and Omar, 1987 and Atlas, 1954). This technique encouraged extensive classification and potential in improving the microphysical retrieval algorithms.

3 METHODOLOGY

The EarthCARE satellite mission is scheduled to be launched in 2015. The payload will consist of 4 instruments onboard: a $94GHz$ cloud profiling radar, a high spectral resolution lidar at $353nm$, a broadband radiometer and a multispectral imager. ECSIM is a tool developed as a part of the mission development process in order to simulate the complete mission instrument observations. It consists of scene creation, orbit, forward, instrument and retrieval models. Put together, they simulate how EarthCARE measurements would be. Extensive description of models and algorithms

ECSIM employs can be found in the documentation by Donovan et al., 2008. In our simulation, one output from LES model was used to create a cloud scene used as input in ECSIM. LES was utilized to reproduce Sc clouds observed during the Atlantic Stratocumulus Transition Experiment (ASTEX) campaign. Input information read in from LES output contained liquid water content values stored in the centre of each model grid box. Resolution of the cloud scene is $50m$ and $15m$ in horizontal and vertical direction, respectively. Scene domain size is $25.6km$ x $25.6km$ in horizontal, and $2.75km$ in vertical direction.

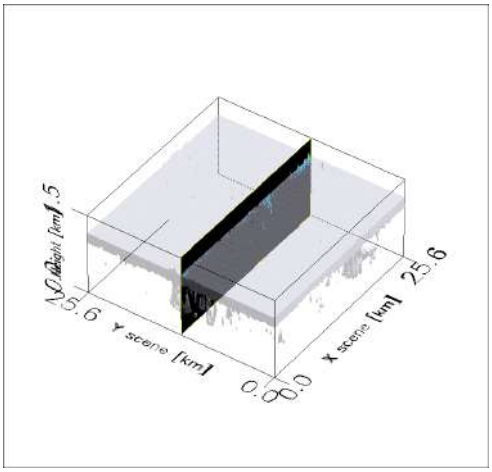

Figure 1: 3D view of the LES cloud scene used as input in ECSIM.

4 LES to ECSIM parametrizations

In the process of parameterizing the droplet size ditribution, number concentration (N) was assumed a fixed value in order to calculate droplet effective radius. In order to study drizzle, four different simulations were run with N shifted towards lower (consequently resulting in higher droplet effective radius values of the cloud scene) and higher (lower effective radius) N values, keeping the LWC values unmodified. Values used for N were 10, 50, 100 and $150cm^{-3}$. These are several of the suitable values to use, as they were observed during the ASTEX campaign measurements (Wood, 2000). Droplet size distribution was modeled by choosing a generalized gamma distribution (Hu and Stamnes, 1993).

$$N(r) = \frac{N}{R_m}\frac{1}{\Gamma(g)}(\frac{r}{R_m})^{\Gamma-1}exp(-\frac{r}{R_m}), \quad (1)$$

where r is the particle radius, R_m is the mode radius, N is the number concentration and g is the width parameter. To recreate the cloud scene in ECSIM we used liquid water content, effective radius values and a fixed value of the distribution shape parameter (g), for liquid water clouds. LES model gives information solely on LWC, meaning effective radius had to be calculated. The effective radius of cloud droplets was subsequently determined, according to equations (2) and (3):

$$R_m = (\frac{3q_l}{4\pi\rho N})^{\frac{1}{3}} \quad (2)$$

$$r_{eff} = \frac{4}{3}(g+2)R_m, \quad (3)$$

where q_l stands for liquid water content and r_{eff} for effective radius.

The ``*equivalent radar reflectivity*'' for $3GHz$ is calculated from the ECSIM radar forward model, and then related to other - user specified frequency values. It represents a value related to the power of the backscattered coefficient at the radar wavelength β_{rad} as:

$$Z_e = \frac{\lambda_{rad}^4}{\pi^5}\frac{1}{|K_w|^2}4\pi\beta_{rad}, \quad (4)$$

where

$$K_w = \frac{n_w^2 - 1}{n_w^2 + 2}, \quad (5)$$

and n_w is the complex index of refraction of water at $3GHz$ at a fixed temperature ($20\,°$C so that $|K_w|^2 = 0.92$. λ_{rad} is the radar wavelenght.

The hardware configuration profile used was a $32GHz$ cloud profiling radar with parameters:

-Pulse Repetition Frequency: $6800Hz$
-Vertical resolution: $25m$
-Antenna diameter: $1.75m$
-Pulse length: $100m$
-Power: $29.5W$

Figure 1 shows a three-dimensional overview of the cloud scene used in this case study. Vertical axis is exaggerated by a factor of 10 to emphasise the variability of the cloud shape in both vertical and horizontal direction.

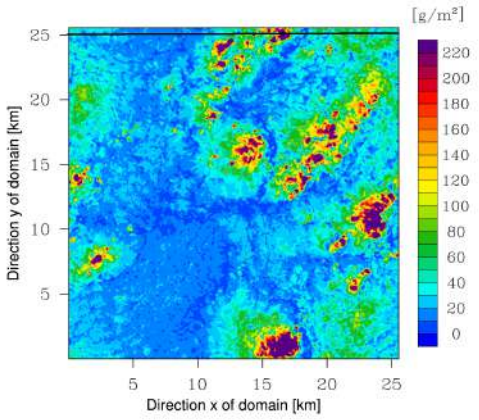

Figure 2: Liquid Water Path of the cloud scene.

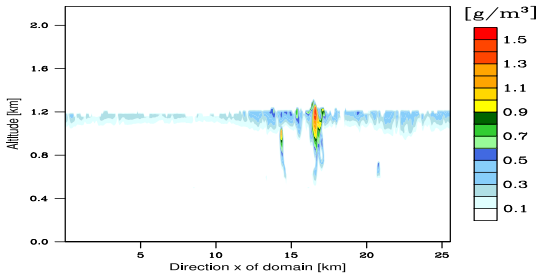

Figure 3: Liquid Water Content vertical crossection of the scene at y=25km.

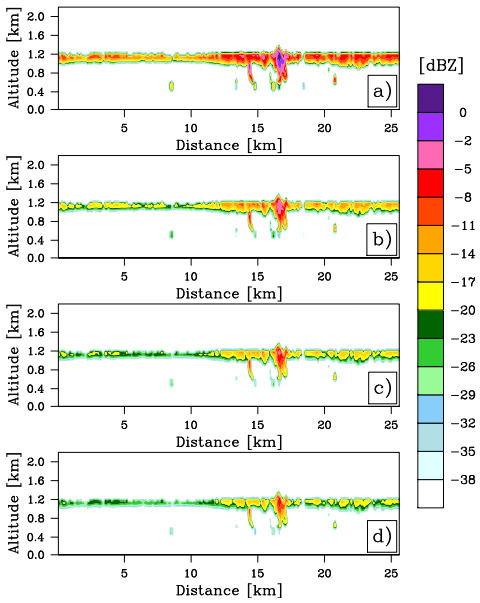

Figure 4: 32GHz Radar reflectivity profile for different NC values: $a) N = 10, b) N = 50, c) N = 100, d) N = 150$ (in cm^{-3})

5 RESULTS

To select a vertical crossection of the cloud scene for instrument runs, liquid water path (LWP) profile (Figure 2) was used to locate a single track along the LES modeled domain that reveals high variability in LWP. The location used is $y = 25km$, which generated a $25.6km$ along-track profile. The track where the radar instrument slice was created is indicated on Figure 2 with a black horizontal line.

Radar instrument model output for four different values of N is shown as four vertical profiles on Figure 4.

Direct comparison of the LWC for the chosen crossection and retrieved radar reflectivity measurement are shown in Fig.3 and Fig.4. A strong spatial correlation of high LWC and radar relectivity values is present. From formulation of effective radius calculation (Eqs. (2) and (3)) it is clear this correlation comes directly from relationship of effective radius values to the radar retrievals.

As both are integrated values, relationship (shown on Fig.5) between the integrated radar reflectivity and LWP (*red scatterers*) indicate a

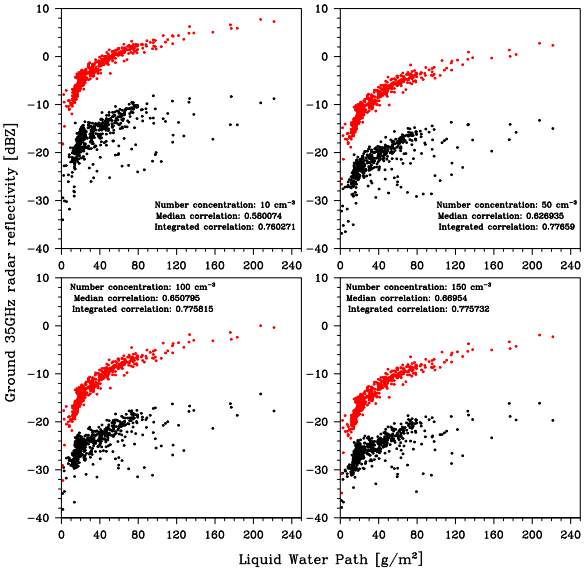

Figure 5: Relationship of median and integrated reflectivity simulated retrievals with collocated Liquid Water Path values.

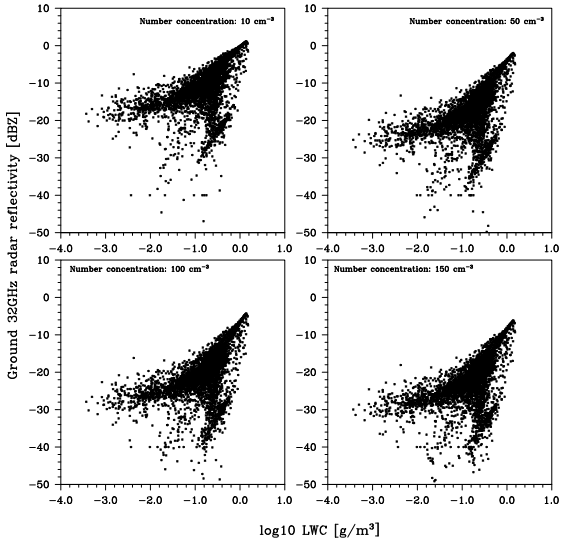

Figure 6: Relationship of of Radar Reflectivity and Liquid Water Content for 4 different NC values.

pattern that remains consistent for all four N parametrizations. Median reflectivity relationship with LWP (*black scatterers*), gives a relationship with lower correlation, however stable for all N values. Dispertion of reflectivity values has shifted for different N values due to inverse relationship with effective radius, thus retrieving higher reflectivities for lower N and opposite for higher N values.

Taking the aforementioned approach as in Krasnov and Russchenberg 2002., ECSIM simulated retrievals combined with LES data have merited a Z-LWC relationship, indicating the same character used in their categorization of drizzle presence (Fig.6).

6 CONCLUSION

The method of utilizing ECSIM for ground based studies of remote sensing using modeled cloud structure in terms of drizzle, appears to be valid and gives confidence for future studies. With such infrastructure in place, next step is combining a ground based elastic backscatter lidar instrument simulations with both modeled and observed cloud scenes.

Classification of observed patterns in Sc sheets using combined ECSIM generated radar-lidar profiles should merit drizzle categorization for a given cloud scene. This information is planned to be related to passive satellite imagers, in order to create a classification of drizzle categories, observed with such intruments as well. This part of the research would be implemented via ECSIM, using the satellite mode for the simulation and the same cloud scenes - profiling them from above and using the ground module. Simulated observations from the ground are used due to its high spatial and temporal resolution capability, compared to the satellite module. Capturing high drizzle variability within the cloud and further influence it has on the cloud evolution is to be established using the aformentioned simulation infrastructure. The final product would establish a capability of tracking the drizzle fraction and its variability using passive satellite imagers alone, that would allow further insight on the large scale observations and study of the drizzle impact on the Sc clouds mutation.

Acknowledgements Authors of this paper would like to thank TU Delft Research Group *Clouds, Climate and Air Quality* and Johan van der Dussen for providing the LES model data and generous assistance in adaptation of the data.

References

[1] Atlas, D., 1954: The estimation of cloud content by radar. *J. Meteor.,* **11**, 309-317.

[2] Baedi, R. J. P., J. J. M. de Wit, H. W. J. Russchenberg, J. P. V. Poiares Baptista, 1999: Alternative algorithm for correcting FSSP measurements, *Proc. Int. workshop CLARE '98*, ESA-ESTEC, 123-127.

[3] Donovan, D., Voors, R. H., van Zadelhoff, G.-J. and Acarreta, J .-R., “ECSIM Model and Algorithms Document”. ESTEC Contract: 20003/06 /NL/FF, (2006).

[4] Fox, N. I. and A. J. Illingworth, 1997: The retrieval of stratocumulus cloud properties by ground-based cloud radar. *J. Appl. Meteor.,* **36**, 485-492.

[5] Heus T., C. C. van Heerwaarden, H. J. Jonker, A. Pier Siebisma, S. Axelsen, K. van den Dries, O. Geoffroy, A. F. Moene, D. Pino, S. R. de Roode, J. Vila-Guerau de Arellano (2010), Formulation of the Dutch Atmospheric Large-Eddy Simulation (DALES) and overview of its applications, *Geosci. Model, Dev., 3*, 415-444.

[6] Hu, Y. X., and K. Stamnes, An accurate parameterization of the radiative properties of water clouds suitable for use in c limate models, *J. Clim., 6*, 728-742, 1993

[7] Khain, A., M. Pinsky, L. Magaritz, O. Krasnov, H. W. J. Russchenberg, 2008: Combined Observational and Model Investigations of the Z–LWC Relationship in Stratocumulus Clouds. *J. App l. Meteor. Climatol.*, **47**, 591–606.

[8] Krasnov, O.A., and H. W. J. Russchenberg, 2002: The Relation B etweenthe Radar to Lidar Ratio and the Effective Radius of Dro plets in Water Clouds: An Analysis of Statistical Models and O bserved Drop Size Distributions. In *Proc. 11th AMS Conf. on Cloud Physics, Ogden, Utah, USA, 3-7.06.2002.*

[9] Sauvegeot, H. and J. Omar, 1987: Radar reflectivity of cumulus clouds. *J. Atmos. Oceanic Technol.,* **4**, 264-272.

[10] Stevens, B., G. Vali, K. Comstock, R. Wood, M. C. van Zanten, P. H. Austin, C. S. Bretherton, and D. H. Lenschow, 2005: Pockets of open cells and drizzle in marine stratocumulus. *Bull. Amer. Meteor. Soc.,* **86**, 51-57.

AEROSOL PROCESSING BY DRIZZLING STRATOCUMULUS
A MODELLING STUDY USING A NOVEL PARTICLE-BASED APPROACH

Sylwester Arabas*, Anna Jaruga, and Hanna Pawlowska

Institute of Geophysics, Faculty of Physics, University of Warsaw, Poland

1 INTRODUCTION

In this paper we discuss simulations performed within the framework of the 8th WMO Cloud Modelling Workshop to be held in Warsaw prior to the ICCP. The modelled system, outlined in the next section, is intended for studying aerosol processing by a drizzling stratocumulus (model set-up following the workshop's "case 1" by Grabowski and Xue, 2011).

Presented simulations are performed with a newly developed modular modelling tool for cloud and precipitation research, which is briefly introduced in section 4. In the discussed simulations we couple a 2D kinematic (prescribed-flow) cloud model, a particle-based aerosol-cloud-precipitation microphysics module, and a positive-definite non-oscillatory advection transport scheme. The employed particle-based microphysics scheme is being developed following the description of the Super-Droplet Method (SDM) of Shima et al. (2009). Being a particle-based method, SDM retains information on the cloud condensation nuclei (CCN) properties throughout the whole lifecycle of a particle making it a suitable tool for aerosol processing research.

2 MODELLED SYSTEM

The employed prescribed-flow 2D kinematic framework is a reimplementation of the one of Szumowski et al. (1998, one of the set-ups of the 4th WMO Cloud Modelling Workshop). It is built upon the assumption of stationarity of the dry air density field $\rho_d(z)$. It is further assumed that the heat and moisture are transported without any interaction with the flow. The dry air carrier flow field is defined by a constant-in-time stream function $\psi(x,z)$ such that the velocity components are prescribed as $u = {}^{-\partial_z\psi}/_{\rho_d(z)}$, and $w = {}^{\partial_x\psi}/_{\rho_d(z)}$. Here, the definition of $\psi(x,z)$ is the same as in Rasinski et al. (2011, Eq. 2). The model equation system consists of two advection equations for potential temperature θ and water vapour mixing ratio r:

$$\begin{cases} \partial_t(\rho_d r) + \nabla\cdot(\vec{v}\rho_d r) = \rho_d S_v \\ \partial_t(\rho_d \theta) + \nabla\cdot(\vec{v}\rho_d \theta) = -\rho_d S_v \cdot f(T,p,r) \end{cases} \tag{1}$$

where $\vec{v} = (u, w)$ is the velocity field, S_v is the sink/source of water vapour due to condensation/evaporation, and f is the rate of change of potential temperature with respect to water vapour mixing ratio.

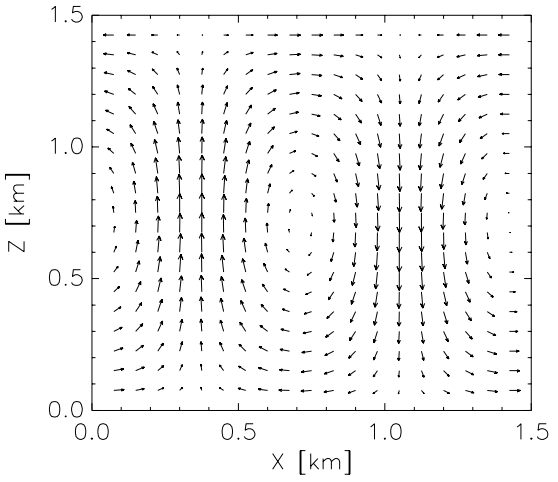

Figure 1: The constant-in-time velocity field used in the presented simulations (plotted values are multiplied by the dry air density).

The initial profiles of both θ and r are defined in the workshop set-up as constant with altitude, resulting in supersaturation with water vapour to be reached in the top quarter of the domain height, where the cloud deck is formed. The velocity field used in the simulations is depicted in Figure 1. It mimics an eddy-pair spanning the whole (periodic) domain, and thus covering an updraft and a downdraft region. For detailed set-up parameters consult Grabowski and Xue (2011).

Equations (1) may be developed in a variety of ways to cover representation of aerosol, cloud and

*Correspondence to: Sylwester Arabas, Pasteura 7, 02-093 Warsaw, Poland. E-mail: sarabas@igf.fuw.edu.pl

Paper presented at the 16th International Conference on Clouds and Precipitation ICCP-2012, Leipzig, Germany

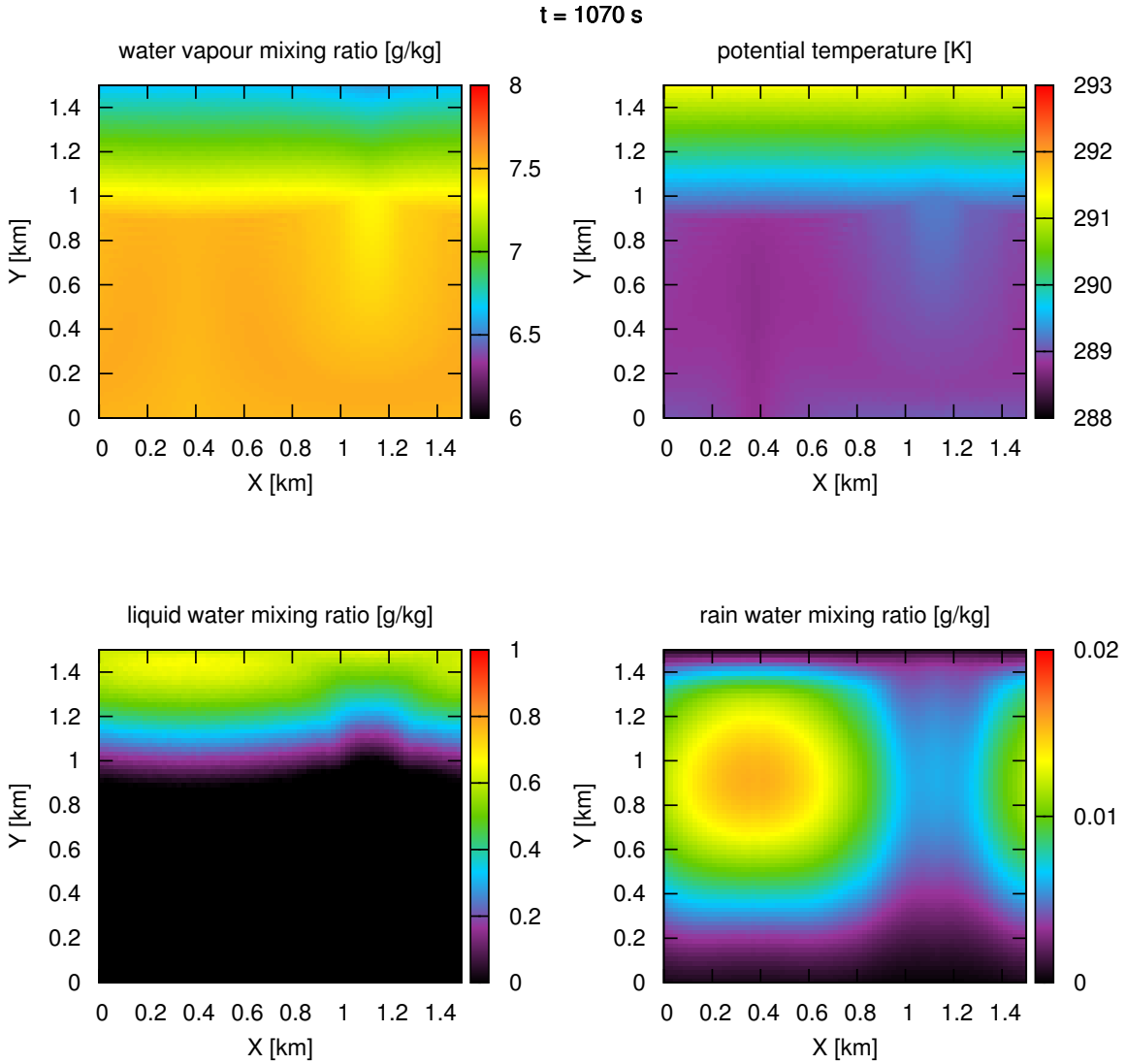

Figure 2: A snapshot of the model state after a quasi-stationary state is reached in a simulation with bulk microphysics (Kessler-type parameterisation with the autoconversion threshold set to 0.0005).

precipitation processes. A common simplest way is the so-called bulk microphysics, in which the two equations are supplemented by a transport equation for liquid water mixing ratio, and the condensation process is modelled following the assumption that any supersaturation/subsaturation resulting from the advection of heat and moisture instantly triggers condensation/evaporation of liquid water. A minimal set-up allowing to simulate drizzle formation in a bulk cloud model needs further extension by adding a transport equation for rain water mixing ratio, and parameterising source/sink terms representing transformations of liquid water into rain, and sedimentation of the rain water. Figure 2 presents simulation results from a bulk-microphysics simulation using the Kessler parameterisation implemented following Grabowski and Smolarkiewicz (1996, e.g. eqs 5a-d therein). It depicts the key features of the model set-up: the cloud deck at the upper part of the domain, and the drizzle maximum of rain water mixing ratio collocated with the updraft (where the precipitation fall speed is balanced with the carrier flow vertical velocity).

3 AEROSOL REPRESENTATION

A bulk simulation such as show in Figure 2 does not provide any information on the size spectrum of cloud and precipitation particles. Models that do cover representation of the size spectrum of particles may be divided into those representing the evolution of the size spectra in an Eulerian (bin-resolved) or Lagrangian (particle-based) manner. The Lagrangian approach is aptly suited for simulations focused on aerosol processing as it

offers the possibility to assign any number of persistent parameters to each modelled particle (in particular, the CCN physicochemical parameters). Furthermore, since the type of residual nuclei for each droplet in the model is known and retained throughout the simulation, representation of the process of evaporation of droplets to form aerosol particles may be implemented through the same mechanism as CCN activation and drop growth. In the present study we use an implementation of a Lagrangian microphysics representation referred to as the Super-Droplet Method (SDM, Shima et al., 2009). The formulation of SDM assumes no distinction between aerosol, cloud, drizzle and rain particles. Each modelled particle represents a multiplicity of real-world particles of the same properties. In SDM all particles are subject the same set of processes including advection by the flow, gravitational sedimentation, diffusional growth and evaporation, and collisional growth. In the present study, the so-called κ-Köhler parameterisation (Petters and Kreidenweis, 2007) is used to represent aerosol chemical composition.

Figure 3 shows an example snapshot of the distribution of super-droplets (top panel) as well as cloud and aerosol particles they represent (middle and bottom panels, respectively) before the onset of precipitation. The super-droplet distribution depicted in the top panel is uniform across the domain with small fluctuations stemming from the random initial placement of particles. The cloud droplet concentration plot reveals the location of cloud base, and shows that the model predicts roughly constant concentration of droplets within the cloud. The fact that the super-droplet dry radii are assigned randomly during model initialisation, contributes to the fluctuations of cloud droplet concentration. Finally, the plot of aerosol concentration reveals that the model captured the depletion of aerosol number in the upper part of the domain due to conversion to cloud droplets.

Further developments to the particle-based microphysics module are on the way and these will be the basis for simulations to be carried out and analysed during the WMO workshop.

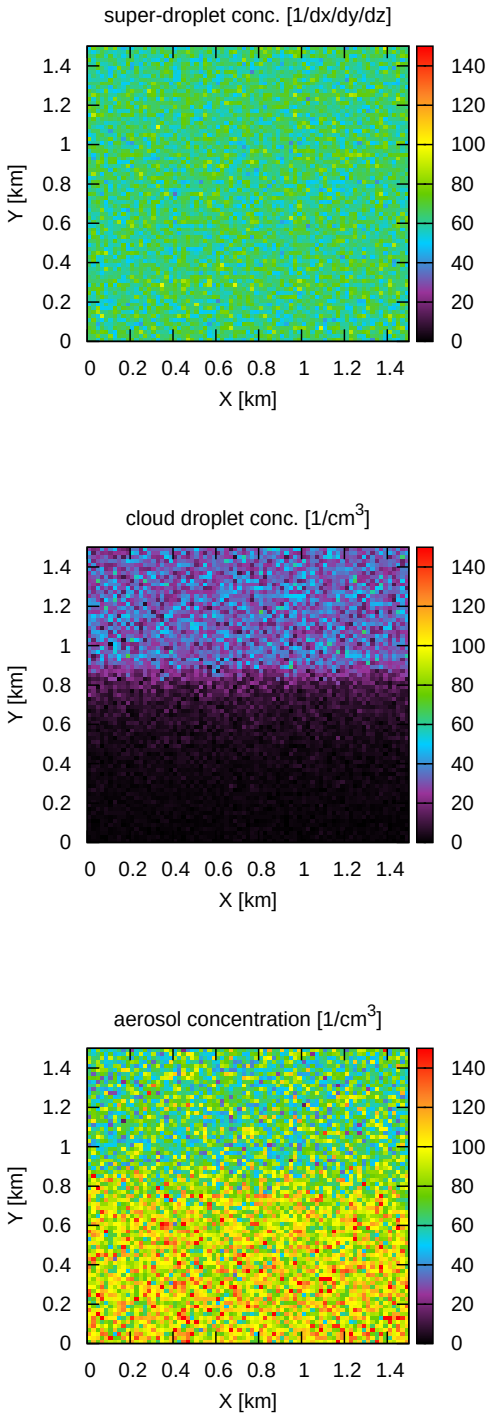

Figure 3: A snapshot of the model state before the onset of precipitation in a simulation with particle-based microphysics. The top panel depicts concentration of super-droplets per volume of a single grid box. The middle and bottom panels depict distribution of cloud and aerosol number concentration per unit volume (i.e. different unit than in the top panel). Differentiation of cloud and aerosol particles was done using a size threshold of 1 μm in diameter. All particles were assumed to be composed of pure sodium chloride.

4 MODEL IMPLEMENTATION

The simulations for the present study are performed using a new cloud modelling tool – *icicle* – being developed at the University of Warsaw. The project aim is to develop a reliable, maintainable and auditable tool for studying cloud microphysical processes.

The model is implemented employing modern coding techniques in C++11. Model architecture features full separation of numerics-

related (e.g. integration algorithms), physics-related (e.g. aerosol composition parameterisations), and technical aspects (e.g. parallel computing, data input/output) of the model logic. A substantial part of computations is delegated to pre-existing free and open source libraries.

The program is structured as a versatile solver for systems of transport equations – its functionality is not limited to the presented application to a 2D kinematic prescribed-flow set-up (as of the time of writing the abstract, the model is capable of performing simulations covering flow dynamics within an isentropic framework, and further extensions are planned). The flagship feature of *icicle* is the newly built object-oriented implementation of the MPDATA advection scheme of Smolarkiewicz (2006, and earlier works of the author). MPDATA is a positive-definite scheme with small implicit diffusion. Present implementation covers the so-called non-oscillatory option of MPDATA (so-called Flux Corrected Transport scheme), as well as treatment of source/sink terms using the improved Euler scheme (a second-order Runge-Kutta type scheme). In context of the presented results, the MPDATA is employed to accurately represent moisture and heat transport within the domain (i.e. solving equations 1).

The implementation of model components corresponding to the Eulerian calculations are based upon the Blitz++ library which employs the *expression template* technique to achieve high performance of array operations not scarifying code readability or object-oriented structure (see e.g. Veldhuizen and Jernigan, 1997; Iglberger et al., 2012, and references therein).

The Lagrangian component of the model (i.e. the Super-Droplet engine) is built upon the Thrust library (Hoberock and Bell, 2010) what allows execution of the same code on multiple parallel architectures including general-purpose GPUs (via CUDA) and multi-core CPUs (via OpenMP). The implemented particle-based scheme for cloud microphysics is well suited for running in a set-up where the Eulerian computations are carried out on a CPU, and the Lagrangian computations are delegated to a GPU. That is due to the low data exchange rate between these two components (in particular, there is never a need to transfer the state of all super-droplets to the Eulerian component residing in the main memory – only the aggregated size spectrum parameters defined per each grid box are needed). Furthermore, the fact that each super-droplet, be it aerosol, cloud or rain particle, is subject to the same set of processes that are mathematically expressed using ordinary differential equations make the algorithm readily parallelisable on a GPU.

Where applicable, the Boost.Units library (Schabel and Watanabe, 2008) is used to perform zero-overhead analysis of the code at compile time ensuring unit correctness of physically meaningful expressions in the code.

Particle tracking logic and the drop growth equation solver for the particle-based microphysics module, as well as the saturation adjustment procedure in the bulk microphysics module are implemented using the ODEINT package of Ahnert and Mulansky (2011) which is compatible both with Boost.units and Thrust.

Employment of numerous third-party libraries, and the modular code structure reduces the source code volume, increases code readability and auditability, and simplifies maintenance including documentation updates. The employed object-oriented programming techniques including runtime polymorphism allow modifying virtually all simulation parameters via command-line options (i.e. at runtime – without the need to modify and recompile the source code). The spectrum of command-line program options range from floating point precision, through parallelisation mechanism type, to advection scheme, and finally to microphysics representation type (i.e. bulk or particle-based) and parameters (e.g. autoconversion threshold value or the number of super-droplets and the assumed chemical composition and size spectrum of aerosol).

Source code and documentation development is hosted in a public source code repository at: **http://github.com/slayoo/icicle/**. Anyone is welcome to use and develop the model under the terms GNU GPL license.

5 SUMMARY AND OUTLOOK

Presented material summarises our preparations for the upcoming WMO Cloud Modelling Workshop. The aim of the workshop's "case 1" described herein is to explore the evolution of the aerosol size spectrum in the vicinity of drizzling stratocumulus cloud.

Presented simulations were carried out using a newly developed 2D prescribed-flow kinematic cloud model with detailed treatment of aerosol, cloud and precipitation microphysics. Basing a cloud model on a simple 2D kinematic framework for mimicking typical air motion scenarios in a cloud allows (and limits) one to study cloud microphysical processes decoupled from cloud dynamics. Such approach results in a computationally cheap yet still insightful set-up of potential use in (i) development and testing of cloud-processes parametrisations for larger scale models, (ii) studying such processes as cloud pro-

cessing of aerosols, and (iii) developing remote-sensing retrieval procedures involving detailed treatment of cloud microphysics.

The key findings from the workshop simulations as well as a summary of the model development status will be reported during ICCP.

Acknowledgements

Thanks are due Piotr Smolarkiewicz and Wojciech Grabowski (NCAR) for their continuous assistance in the development of *icicle*. SA thanks Shin-ichiro Shima (University of Hyogo, Japan) for introducing to particle-based simulations. *Icicle* development is funded by the Polish National Science Centre grant no. DEC-2011/01/N/ST10/01483.

References

Ahnert, K. and Mulansky, M.: ODEINT - Solving ordinary differential equations in C++, in: AIP Conf. Proc., vol. 1389, pp. 1586–1589, doi: 10.1063/1.3637934, 2011.

Grabowski, W. and Smolarkiewicz, P.: Two-time-level semi-lagrangian modeling of precipitating clouds, Mon. Weather Rev., pp. 487–497, doi:10.1175/1520-0493(1996)124<0487:TTLSLM>2.0.CO;2, 1996.

Grabowski, W. and Xue, L.: CCN processing by a drizzling stratocumulus: warm-rain microphysics case, URL `http://www.rap.ucar.edu/~gthompsn/workshop2012/case1/`, 2011.

Hoberock, J. and Bell, N.: Thrust: a parallel template library, URL `http://www.meganewtons.com/`, 2010.

Iglberger, K., Hager, G., Treibig, J., and Rüde, U.: Expression templates revisited: a performance analysis of current methodologies, SIAM J. Sci. Comput., 34, C42–C69, doi:10.1137/110830125, 2012.

Petters, M. and Kreidenweis, S.: A single parameter representation of hygroscopic growth and cloud condensation nucleus activity, Atmos. Chem. Phys., 7, 1961–1971, doi:10.5194/acp-8-6273-2008, 2007.

Rasinski, P., Pawlowska, H., and Grabowski, W.: Observations and kinematic modeling of drizzling marine stratocumulus, Atmos. Res., 102, 120–135, doi: 10.1016/j.atmosres.2011.06.020, 2011.

Schabel, M. and Watanabe, S.: Boost.Units: Zero-overhead dimensional analysis and unit/quantity manipulation and conversion, in: Boost Library Documentation, (available at `http://www.boost.org/doc/libs/`), 2008.

Shima, S., Kusano, K., Kawano, A., Sugiyama, T., and Kawahara, S.: The super-droplet method for the numerical simulation of clouds and precipitation: A particle-based and probabilistic microphysics model coupled with a non-hydrostatic model, Quart. J. Roy. Meteor. Soc., 135, 1307–1320, doi:10.1002/qj.441, 2009.

Smolarkiewicz, P.: Multidimensional positive definite advection transport algorithm: An overview, Int. J. Numer. Meth. Fluids, 50, 1123–1144, doi: 10.1002/fld.1071, 2006.

Szumowski, M., Grabowski, W., and Ochs III, H.: Simple two-dimensional kinematic framework designed to test warm rain microphysical models, Atmos. Res., 45, 299–326, doi:10.1016/S0169-8095(97)00082-3, 1998.

Veldhuizen, T. and Jernigan, M.: Will C++ be faster than Fortran?, in: Scientific Computing in Object-Oriented Parallel Environments, edited by Ishikawa, Y., Oldehoeft, R., Reynders, J., and Tholburn, M., vol. 1343 of *Lect. Notes Comp. Sci.*, pp. 49–56, Springer Berlin / Heidelberg, doi:10.1007/3-540-63827-X_43, 1997.

COARSE PARTICLE AND ICE CRYSTAL CONCENTRATIONS IN THE NORTHERN AND SOUTHERN SUBTROPICAL MIDDLE TROPOSPHERE

J.R.Snider[1], D.Zhang[1], Z.Wang[1], D.Leon[1], G.Sever[1] and P.Field[2]

[1]University of Wyoming, Department of Atmospheric Science

[2]Met Office, Exeter, UK

ABSTRACT

Satellite-based climatologies reveal that mineral dust aerosol increases from south to north across the intertropical convergence zone. The south-to-north aerosol gradient, combined with the propensity of mineral dust to nucleate ice at a relatively warm temperature, indicate that cloud properties within the tropics and subtropics could be impacted. A statistical investigation of the south-to-north aerosol contrast was conducted by analyzing coarse mode aerosol concentration measurements, a surrogate for mineral dust, sampled above a southern hemisphere and a northern hemisphere subtropical marine boundary layer. Coarse mode concentrations were obtained from an optical particle counter operated on the NCAR C-130 during two summer-season projects (VOCALS and ICET). The coarse particle concentration values were also input into the DeMott et al. (2010) parameterization and ice nuclei concentrations were derived. The temperature-dependence of ice nucleus activity was evaluated and compared to a satellite-based ice crystal retrieval. The potential for refining the retrieval, based on a comparison of the derived-IN and retrieved-crystal assessments, is discussed.

1 - INTRODUCTION

This paper investigates the occurrence of mineral dust particles, within the subtropical middle troposphere, and their propensity to nucleate ice crystals within clouds. Our work is motivated by the recognition that crystal abundance influences cloud microstructure, cloud dynamics and the Earth's infrared and visible energy budgets. Predicting these impacts, and how they respond to changing aerosol abundance, and changing aerosol particle chemistry, remains a challenge.

We examine two sources of information. The first is airborne measurement of coarse particle concentration, a surrogate for mineral dust, obtained during the VOCALS (southeastern Pacific region) and ICET (Caribbean region) field experiments. We define coarse particles as those with an optical diameter larger than 0.5 μm. The coarse particle measurements were obtained from a model 300 forward scattering spectrometer probe (FSSP300) (Snider and Petters, 2008). Particle sizing is based on laboratory calibrations employing test particles with refractive index equal to 1.59. The second comes from ice crystal concentrations derived using space-based measurements of radar reflectivity and lidar backscatter. The basis for that retrieval is Zhang et al. (2010) and Zhang et al. (2012).

The Zhang et al. retrieval selects clouds with top temperatures colder than 0 ^{o}C and with radar reflectivity profiles extending less than a few kilometers downward from a liquid cloud top. As in Zhang et al. (2012), we refer to this cloud subset as supercooled stratiform clouds (SSC).

2 – DATA SELECTION

2a. – COARSE PARTICLE CONCENTRATION

We analyzed coarse particle measurements from an externally-mounted FSSP300 operated on the NCAR C-130 during VOCALS (November 2008) and ICET (July 2011). Coarse particle concentration, atmospheric state (dew point temperature and pressure) and precipitation (2DC), all sampled at 1 Hz, were analyzed. Since we are interested in coarse particles that can impact ice abundance within supercooled stratiform clouds (SSCs), only the low-temperature subset of the VOCALS and ICET records, corresponding to the altitude of SSC formation (P~500 hPa) were selected for analysis. The subset we selected corresponds to measurements made at altitude greater than 3 km (msl). This subset defines the free-tropospheric samples. Further selection was performed by considering coincident cloud liquid water content (FSSP300) and two-dimensional optical array probe (OAP) measurements. Our criterion is that the current datum, and samples proceeding and following the current datum, are associated with a cloud liquid water content (LWC) less than 0.01 g/m^3 and OAP concentration less than 0.1 per liter. Measurements satisfying both the altitude selection and selection against cloud (and precipitation) are identified as free-tropospheric and cloud-free.

For evaluating the derived ice nucleus concentration, we assume the airborne measurements of dew point temperature (T_{dp}) and pressure (P) to define the thermodynamic state that the sampled air parcels would form SSCs. The free-tropospheric and cloud-free samples were binned into four T_{dp} intervals: -10/-15, -15/-20, -20/-25 and -25/-30 ^{o}C. Results are presented in Sec. 3a.

2b. – RETRIEVED ICE CRYSTAL CONCENTRATION

Selection of SSC scenes containing ice crystals starts with the CALIOP lidar and CloudSat radar vertical profiles from the NASA A-Train satellite constellation (Zhang et al., 2010; Zhang et al., 2012). A relatively narrow interval of attenuated backscatter coefficient (0.2 sr^{-1} km^{-1} to 0.5 sr^{-1} km^{-1}), retrieved by CALIOP at cloud top, a relatively flat cloud top, and the absence of radar echo reaching the ground (or ocean), are three properties of accepted scenes. Another attribute is a radar reflectivity (Z_e) greater than the expectation for a drizzle-free stratiform cloud. This expectation is based on a parameterized Z_e-LWC relationship and the adiabatic assumption (Zhang et al., 2010). These four criteria qualify a scene as a stratocumulus. Scenes with cloud-top temperature less than 0 ^{o}C define the SSC subset.

The value of Z_e retrieved from the top-most 500 m of these clouds, and the associated temperature, are the measurements we used to retrieve the ice crystal concentration. A temperature-dependent 1-D ice growth model was used to generate fall trajectories for crystals nucleated at cloud top (Zhang et al., 2012). By varying the modeled concentration of ice crystals, and formulating a model-predicted radar reflectivity, the value of the latter that best approximates the cloud-top Z_e was the constraint used to retrieve the concentration of ice crystals (N_{XT}).

3 - RESULTS

3.a - COARSE PARTICLE CONCENTRATION

We begin this analysis with coarse particle concentrations, measured by the FSSP300, at the ambient atmospheric state. In post processing, these were converted to a common standard state. Properties used in the extrapolation are the ambient measurements (coarse concentration, T_{dp} and P) and the standard state values 273 K and 1013 hPa. Extrapolated coarse particle concentrations ($N_{0.5}$) are reported as a count per standard cubic centimeter ($sccm^{-1}$).

The number of free-tropospheric/cloud-free samples is $4.0x10^4$ and $4.9\ x10^4$, and the averaged coarse particle concentrations are 0.3 and 1.0 $sccm^{-1}$ for VOCALS and ICET, respectively. In Figures 1a-1b we present frequency distributions of coarse particle concentration. The larger averaged concentration for ICET, and the local maximum at ~20 $sccm^{-1}$ (Fig. 1b), seem indicative of the stronger mineral dust source in the northern hemisphere. To investigate this we used retrievals from the upward-looking Wyoming Cloud Lidar (WCL). Specifically, we used received power, sensed with phase perpendicular to the transmitted pulse, and depolarization – the perpendicular-to-parallel signal ratio - to pick "dust-free" samples from the free-tropospheric and cloud-free ICET set. This resulted in an average concentration consistent with that found in VOCALS (0.3 $sccm^{-1}$). A comparison of these two ICET selections is shown in Figures 1b-1c. From this we conclude that the presence of dust is a factor which distinguishes the ICET and VOCALS regions, consistent with aerosol climatologies (e.g., Liu et al., 2008). However, it needs to be recognized the frequency of occurrence of dust is low, in our ICET data set, as indicated by the fact that the number of samples decreases by only 20% ($4.9\ x10^4$ to $3.9\ x10^4$) between Figs. 1b and 1c. Furthermore, our conclusion is tentative because a classification of the VOCALS data set, using data derived from the WCL, is presently not available.

3.b - DERIVED ICE NUCLEI CONCENTRATION

In this section we analyze ice nuclei concentrations derived using the free-tropospheric/cloud-free sets from VOCALS and ICET. Figures 2a-2d were constructed using the ice nuclei parameterization of DeMott et al. (2010). We symbolize the nuclei concentrations as N_{IN} and express them as a count per standard liter, consistent with DeMott et al. Each set of aircraft measurements ($N_{0.5}$, T_{dp} and P) were input to the parameterization and nuclei concentrations were calculated. Average nuclei concentrations increase from approximately 0.2 per standard liter (SL^{-1}), for the -10/-15 ^{o}C interval, to 1.2 SL^{-1} for -25/-30 ^{o}C. Quite surprisingly, the VOCALS and ICET averages are comparable (Fig. 2d), or the VOCALS averages are larger (Figs. 2a-2c). The number of samples selected ranged from 0.2 x10^4 (Fig. 2c, VOCALS) to 1.1 x10^4 (Fig. 2a, ICET).

Nuclei frequency distributions were also derived using the dusty samples selected from free-tropospheric/cloud-free ICET set, but that result is not presented. Because of the overall tendency for dust to be detected at an altitude smaller than our free-tropospheric threshold (3 km), only the -10/-15 ^{o}C dew point interval has a non-zero number of dusty samples. In this particular instance the number of samples is 0.2 x10^4. For that set of ICET values the average nuclei concentration is 0.6 SL^{-1} – compared to the VOCALS -10/-15 ^{o}C dew point interval, a factor of two larger – so there is evidence for dust influencing nuclei abundance but only for data classifying the -10/-15 ^{o}C dew point interval.

3.c - RETRIEVED ICE CRYSTAL CONCENTRATION

Frequency distributions for the retrieved crystal concentration, segregated by cloud-top temperature, are presented in Figs. 3a-3d. The retrieved concentrations are from the ICET region and for the summer months of June, July and August (2006 to 2010). The number of selected cloud scenes is 0.2 x10^4. The number of free-tropospheric cloud scenes selected for the summertime VOCALS region is substantially smaller (results not shown). In Figs. 3a-3d we also present the derived-IN concentration frequency distributions. These are reproduced from Figs. 2a-2d so that a comparison can be made between the retrieved-crystal and derived-IN concentrations for the Caribbean region.

Ignoring the warmest temperature bin (-10/-15 ^{o}C), and focusing on Figs. 3b-3d, we see that both the retrieved-crystal and derived-IN concentrations increase inversely with temperature. That increase is evident both in the modes of the distributions and in the displayed averages. Better quantitative agreement between the retrieved and derived values will result once we extrapolate the retrieved-crystal concentrations to the reference state used for the derived-IN values. Also not accounted for are scenes with cirrus overlaying a SSC and the possibility that some of the crystal retrievals, particularly those

classifying in the -10/-15 ^{o}C bin, are invalid because of the presence of supercooled drizzle (Zhang et al., 2010).

4 - CONCLUSIONS

We have presented coarse particle, derived ice nuclei and retrieved crystal concentration assessments for two subtropical free-tropospheric regions during summer. The occurrence of dust events within the north region (ICET, Caribbean), and their effect on coarse particle concentrations, is apparent in our analysis. We are confident that conclusion will be strengthened once we are able to evaluate the lidar assessments of dust in the south region (VOCALS, southeast Pacific). With regard to the satellite-based retrieval of ice crystal concentration, the investigations of Zhang et al. (2012), and this study, show that there is potential, yet both call for further refinement. That work is ongoing.

5 - ACKNOWLEDGEMENTS

This research was supported by the NSF under award AGS-1034858.

6 - BIBLIOGRAPHY

DeMott, P.J., A.J.Prenni, X.Liu, S.M.Kreidenweis, M.D.Petters, C.H.Twohy, M.S.Richardson, T.Eidhammer and D.C.Rogers: Predicting global atmospheric ice nuclei distributions and their impact on climate, Proc. of the National Academy of Sciences, USA, 107, 11217–11222, 2010

Liu, D., Z.Wang, Z.Liu, D.Winker and C.Trepte, A height resolved global view of dust aerosols from the first year of CALIPSO lidar measurements, J.Geophys.Res., 103, doi:10.1029/2007JD009776, 2008

Snider, J.R. and M.D.Petters, Optical particle counter measurement of marine aerosol hygroscopic growth, Atmos. Chem. Phys., 8, 1949-1962, 2008

Zhang, D., Z.Wang and D.Liu, A global view of midlevel liquid-layer topped stratiform cloud distribution and phase partition from CALIPSO and CloudSat measurements, J. Geophys. Res, 115, doi:10.1029/2009JD012143, 2010

Zhang, D., Z.Wang, J.R.Snider, M.Deng, M.Zhao, A.Heymsfield, D.Liu and J.Fan, Quantifying dust's impact on ice generation in supercooled stratiform clouds by combining remote sensing and in situ measurements, presented at the 16th International Conference on Clouds and Precipitation, Leipzig, Germany, 2012

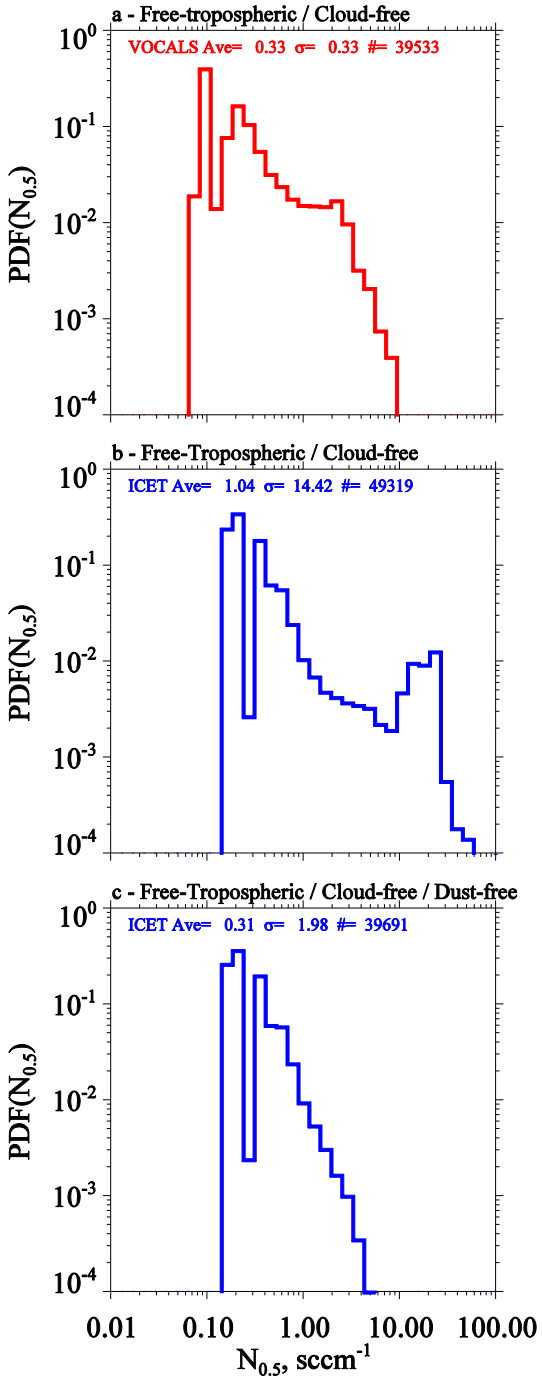

Figure 1 – Coarse particle concentration frequency distributions. a) free-tropospheric and cloud-free conditions in VOCALS (southeast Pacific); b) free-tropospheric and cloud-free conditions in ICET (Caribbean); c) free-tropospheric, cloud-free and dust-free conditions in ICET. See text for details.

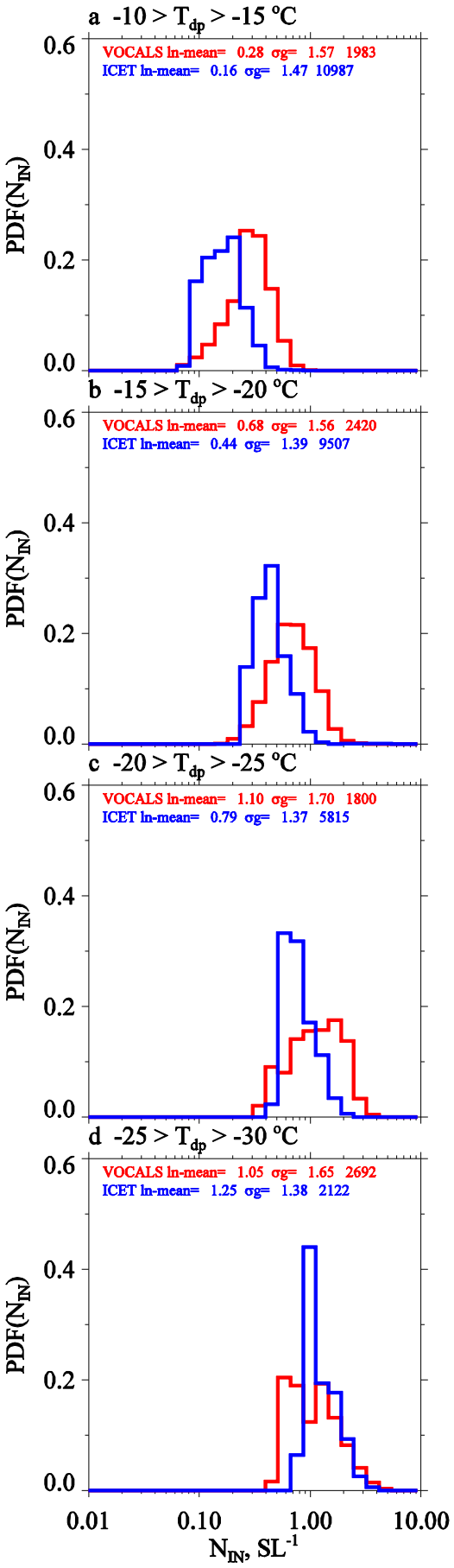

Figure 2 – Derived ice nuclei concentration frequency distributions. The free-tropospheric/cloud-free sets, from VOCALS (southeast Pacific) and ICET (Caribbean), are presented. See text for details.

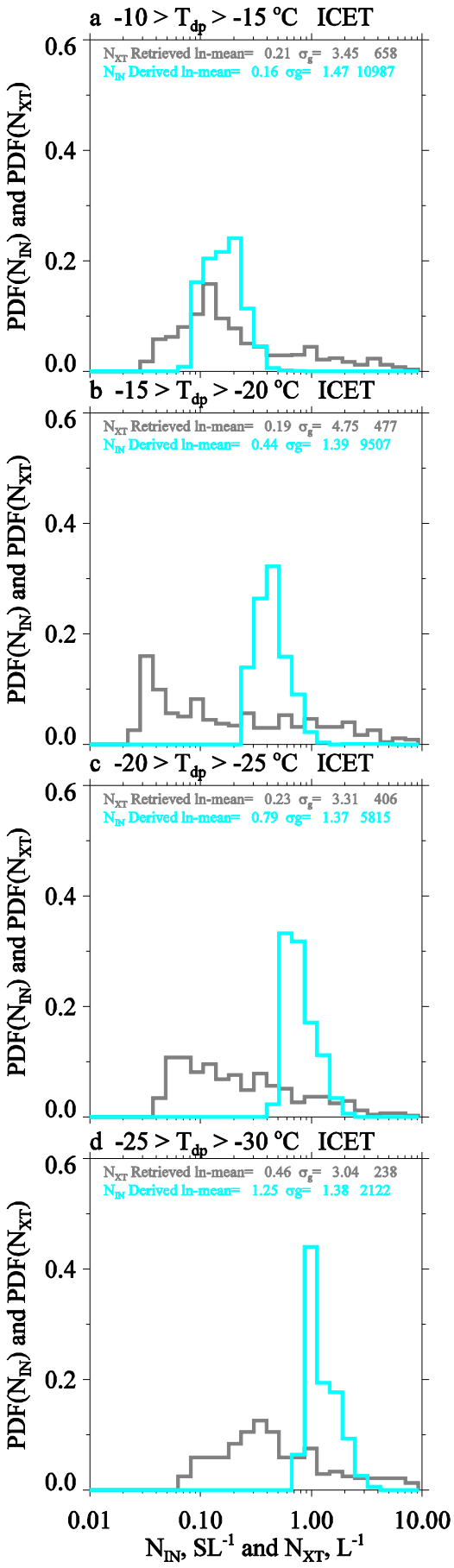

Figure 3 – Derived ice nuclei concentration frequency distributions from ICET (Caribbean). These distributions are reproduced from Figure 2. Also presented (gray), are retrieved ice crystal concentration distributions. The retrieval is based on five years of satellite measurements, from the Caribbean basin (June, July and August).

MID-TROPOSPHERIC SUPERCOOLED LIQUID WATER OBSERVATION CONSISTENT WITH NUCLEATION INDUCED BY A MOUNTAIN LEE WAVE

Fabio Madonna[1], Felicita Russo[2], Randolph Ware[3,4], and Gelsomina Pappalardo[1]

[1]Istituto di Metodologie per l'Analisi Ambientale, CNR, Tito Scalo , Potenza, Italy.
[2]Istituto di Scienze dell'Atmosfera e del Clima CNR, Via Gobetti 151, 40129, Bologna, Italy.
[3]Radiometrics Corporation, 2840 Wilderness Place Boulder, CO 80301.
[4]Cooperative Institute for Research in the Environmental Sciences, Boulder, CO 80309.

1. ABSTRACT

A case study relative to the observation of liquid water in an apparently cloudless atmosphere is presented. Microwave radiometer profiler observations on 14 April 2008 in Boulder, Colorado, USA, showed an increase in the liquid water path with values higher than 0.05 mm and a corresponding relative humidity saturation from 4.75 to 6.75 km above the ground level in profiles retrieved using a neural network algorithm. The reported scenario shows the presence of a mountain lee wave passing through a stable atmosphere in the temperature time series. The passage of the wave, in agreement with the E/NE upper level wind direction calculated by the North American Model (NAM), induced a rapid adiabatic expansion and a following compression of the atmosphere that generated strong humidity pulses with high relative humidity variations from dry to supersaturated conditions and the activation of nucleation of supercooled liquid droplets.
The present analysis provides an example of the existence of supercooled liquid water in the mid-troposphere related to a wave activity that occurred in a sky condition classifiable as "clear" and describes an atmospheric scenario consistent with the observation of the so-called twilight zone. This might also indicate a probable physical connection between the atmospheric wave activities and the presence of the twilight zone.

2. INTRODUCTION

From a thermodynamic standpoint, condensation of water in the atmosphere can occur under different conditions. The formation of cloud droplets in the atmosphere occurs by means of heterogeneous nucleation where aerosols act as condensation nuclei (CCN) reducing to 1 – 2 % the supersaturation ratio required for water vapour to liquid water phase transition [Pruppacher, 1995].
The lowest temperature at which supercooled liquid droplets exist for times longer than a fraction of seconds depends on the drop size [Rosenfeld et al., 2000], but evidence of the existence of supercooled liquid water droplets down to –40°C, obtained using ground based, airborne and satellite observations, is reported in literature [e.g. Sassen et al., 1988]. Supercooled water layers formed from supercooled water droplets represent a severe hazard for aircraft operations because they can lead to ice accretion on the wings. Moreover, radiative fluxes at the Earth's surface are very sensitive to small integrated liquid water (ILW) changes if clouds with LWP values < 50 g/m^2 are present [Turner et al., 2007].
In this work, we present an interesting case study relative to the observation of an unexpected increase in integrated liquid water retrieved on 14 April 2008 by an MP-3000A microwave profiler operating in Boulder, CO, USA [Madonna et al., 2010]. The observations showed an increase of the atmospheric liquid water content in apparently cloudless sky conditions and the corresponding supersaturated conditions retrieved using a neural network profiling algorithm [Solheim et al., 1998].
In the next section, the observations collected with the MP-3000A are reported and discussed.

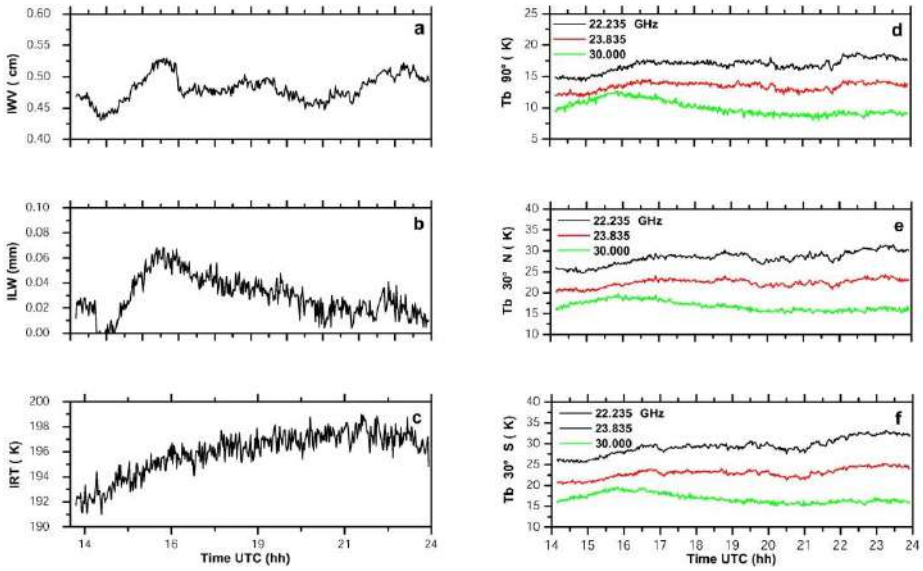

Figure 1: Time series of the integrated water vapour (a), integrated liquid water (b), zenith infrared temperature (c), 22.235, 23.835 and 30 GHz brightness temperatures observed at 90 deg (d), 30 deg elevation north (e) and 30 deg elevation south (f) measured by the MP-3000A microwave profiler on 14 April 2008 at Boulder.

3. OBSERVATION AND DISCUSSION

On 14 April 2008, the MP-3000A microwave radiometer profiler operational in Boulder (105.25W, 40.02N, 1635 m a.s.l.) observed an unexpected amount of liquid water from 15:00 to 21:00 UTC even though no evidence of the presence of clouds is provided by an infrared thermometer (9.6-11.0 μm) included in the profiler system. From a meteorological point of view, this event is difficult to be precisely identified but we expect to have observed some kind of haze. The liquid water path was retrieved using 27 neural net inputs including 7 upper V-band at 90 deg elevation, 7 V-band and 5 K-band data at 30 deg elevation north and south (NS), plus 58.8 GHz data at 9.45 and 19.35 deg NS, and 58.8 plus 57.288 GHz data at 41.85 deg NS. The combination of angle scanning and zenith observations can improve the upper tropospheric relative humidity retrieval. In fact, for stratified atmospheric conditions the radiometer observes twice as much integrated vapour and liquid water at 30 deg elevation and it is therefore twice as sensitive to small ILW variations. The integrated water vapour (IWV) and the LWP time series from 14:07 to 23:58 UTC on 14 April 2008, and the corresponding zenith infrared temperature observation are shown in Figure 1. The LWP time series (Figure 1b) shows a significant increase after 15 UTC with peak values higher than 0.05 mm between 16:04 and 17:16 UTC. Infrared temperature measurements, reported in Figure 1c, by the infrared thermometer (IRT) are lower than 200 K along the whole time series and thus consistent with cloudless sky conditions. In Figure 1, the time series of the 22.234, 23.834 and 30 GHz brightness temperatures (Tb) measured by the MP-3000A at the 90 deg, 30 deg elevation north and south for the considered period are also reported. These frequencies are located in 22 GHz water vapour resonance band and, in particular, the 30 GHz frequency is the nearest of the MP-3000A to a window spectral region and therefore the most sensitive to the LWP variations.

The time series of temperature, water vapour density and relative humidity, reported in Figure 2, shows the presence of humidity peaks in the upper troposphere

with the occurrence of saturation conditions in a vertical region extending from about 4.75 to 6.75 km a.g.l. that corresponds to the period when the increase in the ILW is observed. The supersaturation condition observed about from 16:00 to 17:30 UTC follows a time period characterized by values of the relative humidity lower than 50% and by an increase of temperature in the considered region of about 4 K at all levels higher than 3 km a.g.l. However a wave activity with upper troposphere humidity pulses with RH within 60 % is still observable also on 15 April.

The rapid and unstable event observed in Boulder could be caused by the passage of an atmospheric mountain lee wave observable both in the time series of the temperature and relative humidity profiles. The passage of the wave, in agreement with the E/NE upper level wind direction calculated by the North American Model (NAM), induced a rapid adiabatic expansion and a following compression of the atmosphere that generated strong humidity pulses with high relative humidity variations from dry to supersaturated conditions. The formation of supercooled liquid droplets in an apparent clear sky could refer to the observation of the so-called “twilight zone” [Koren et al., 2007; Pust et al., 2008], described as a region characterized by evaporating cloud fragments and enhanced aerosol with, therefore, intermediate conditions between clear and cloudy sky. This region generates a continuum of cloud optical depth evidencing the existence of cloud fragments down to very small optical depths, even lower than the aerosol background levels [Charlson et al., 2007]. The absence of “visible” clouds has been also verified using the images a sky webcam located about 1 km north of the radiometer site (available at http://www.eol.ucar.edu/webcam/img_viewer.html). The presented case study shows that the passage of an atmospheric mountain lee wave in a stable atmosphere could be responsible for the occurrence of high supersaturated conditions in the free troposphere and lead to the growth of droplets in a supercooled environment. The unstable humidification and evaporation processes generated by the wave passage are consistent with the thermodynamic scenario typically observed in a twilight zone.

The NAM numerical model has been also investigated. There is no evidence of this event even though its horizontal resolution is 12 km and the observed event is extended on a sufficiently large horizontal domain as revealed by the microwave scanning elevation measurements used for the retrieval of ILW, as described in this section.

The presented case study shows an interesting scenario where the adiabatic expansion and compression processes induced by a mountain lee wave passing through a stable atmosphere are able to generate supersaturated conditions and formation of small supercooled liquid droplets in low concentration. This might also indicate a probable physical connection between the mountain lee wave activities and the presence of the twilight zone. This analysis provides interesting remarks for the atmospheric modelling community considering that small amounts of supercooled liquid water are particularly interesting both for climatological and meteorological studies [Dupont et al., 2008].

In addition, the presented case study confirms the high sensitivity of the microwave profiling to supercooled liquid water (of particular interest for modelling), the capability of the method to detect the effect of lee waves on the thermodynamic state of the atmosphere, and its sensitivity to events on small temporal scales.

BIBLIOGRAPHY

Charlson, R.J., A.S. Ackerman, F.A.-M. Bender, T.L. Anderson, and Z. Liu (2007), On the climate forcing consequences of the albedo continuum between cloudy and clear air. *Tellus*, 59B, 715-727, doi:10.1111/j.1600-0889.2007.00297.x.

Dupont J.C., M. Haeffelin, and C.N. Long (2008), Evaluation of cloudless-sky periods detected by shortwave and longwave algorithms using lidar measurements, *Geophys. Res. Lett., 35*(10), doi:10.1029/2008GL033658.

Koren, I., L. A. Remer, Y. J. Kaufman, Y. Rudich, and J. V. Martins (2007), On the twilight zone between clouds and

aerosols, *Geophys. Res. Lett. 34*, L08805, doi:10.1029/2007GL029253.

Madonna, F., F. Russo, R. Ware, and G. Pappalardo (2009), Mid-tropospheric supercooled liquid water observation consistent with nucleation induced by a mountain lee wave, Geophys. Res. Lett., 36, L18802, doi:10.1029/2009GL039545.

Pruppacher, H. R. (1995), A new look at homogeneous ice nucleation in supercooled water drops, *J. Atmos. Sci., 52,* 1924–1933.

Pust, N. J., and J. A. Shaw (2008), "Digital all-sky polarization imaging of partly cloudy skies," Applied Optics, 47, No. 34, H190-H198.

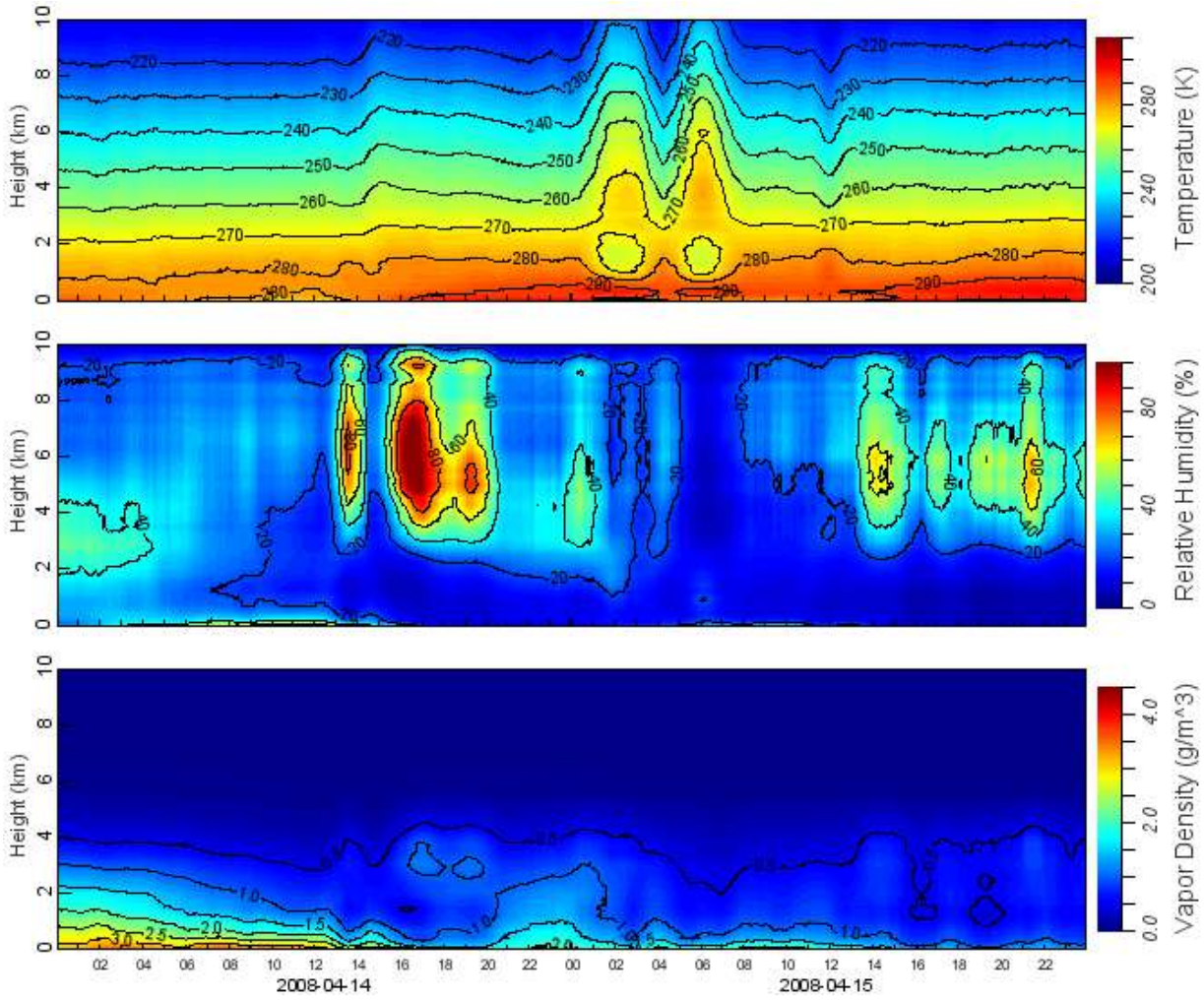

Figure 2: Time series of the vertical profiles of temperature (upper panel), relative humidity (middle panel) and water vapour mixing ratio (lower panel) up to 10 km above the ground level retrieved by the microwave profiler MP-3000A from 00 UT on 14 April 2008 at Boulder to 24 UT on 15 April 2008.

Rosenfeld, D. & Woodley, W. L. (2000), Deep convective clouds with sustained supercooled liquid water down to -37.5 °C, *Nature. 405*, 440-441.

Sassen, K. (1985), Highly supercooled cirrus cloud water: confirmation and climatic implications, *Science, 227*, 411-413.

Solheim, F., J. Godwin, E. Westwater, Y. Han, S. Keihm, K. Marsh and R. Ware (1998), Radiometric Profiling of Temperature, Water Vapor, and Cloud Liquid Water using Various Inversion Methods, Rad. Sci., 33, 393-404.

Turner, D.D et al. (2007), Thin liquid water clouds: Their importance and our challenge, *Bull. Amer. Meteor. Soc., 88*, 177-190.

Acknowledgements

The authors gratefully acknowledge NOAA Air Resources Laboratory (ARL) for the

provision of the NAM model (http://www.arl.noaa.gov/ready.html) used in this publication. The authors also wish to acknowledge the NCAR Atmospheric Technology Division for providing images from their sky webcam at Foothills laboratory.

A diffusion chamber design to study effects of temperature, ambient pressure and water vapour saturation on the fine structure of ice crystals using scanning electron microscopy

Georg Ritter, Evelyn Hesse, Paul H. Kaye and Zbigniew Ulanowski*

Center for Atmospheric & Instrumentation Research (CAIR), School of Physics, Maths and Astronomy, University of Hertfordshire, Hatfield, AL10 9AB, United Kingdom

1 INTRODUCTION

Understanding radiation transport in high altitude clouds is of great importance to improve our knowledge of the Earth's climate system, as the high altitude cloud system plays a significant role in the Earth's radiation budget. It is currently the biggest source of uncertainty in the understanding of the radiative forcing [10].

To understand the role of cirrus clouds and their contribution to the radiative forcing, depends on better understanding the morphology, genesis and the life cycle of the water ice particles present in these clouds and also in mixed phase clouds. Bulk shape, size and surface roughness of the crystals have profound effects on the light scattering characteristics of cirrus clouds[5, 18] and a more detailed understanding of the microphysical properties of small (<50 µm) ice crystals will not only allow to improve the precision of weather and climate models but also allow to increase the precision of cloud remote sensing and will help understand cloud feedback in general.

Computational studies found that changes in the microphysical properties of the crystal surfaces can change the asymmetry parameter g greatly [17]. Laboratory measurements of smooth and rough ice crystal analogues found the g parameter to be 0.8 and 0.63, respectively for visible wavelengths [14]. This shows that the rough variants in this example might back reflect nearly twice as much solar radiation as their smooth counterparts.

In situ measurements of ice crystal surface details are complicated by the limitations of optical cloud probes flown on aircraft. Optical resolution, the large required sample volumes and fragility of the crystals, which break up at instrument inlets, are examples of these limitations [4, 2, 11].

An instrument that is not limited by the optical resolution and ice crystal breakup is the latest version of Small Ice Detector Mk. 3 (SID-3) an improved version based on SID-2 [3]. It uses light scattering patterns to detect and classify crystals down to a size of 1 µm through comparison with the Ray Tracing with Diffraction on Facets (RTDF) scattering model [1]. In situ data acquired with SID-3 during flying campaigns add to already existing evidence that ice crystals with non smooth surfaces can occur in significant proportions [12]. Other evidence is the absence of atmospheric halos [17, 13] and the shape of phase functions [9].

In this manuscript we describe the experimental setup used in our ongoing effort to add to the understanding of the influence of temperature, ambient pressure and water vapour saturation on the development of details of ice crystal surfaces. Water ice crystal growth from the vapour phase is studied using scanning electron microscopy.

Scanning electron microscopy, has been previously used to image water ice crystals, snow flakes and to investigate ice nucleation and sublimation (e.g. in [15, 8, 16, 19, 7]). In some of these experiments, samples were frozen and maintained at very low temperatures. Other studies reported on ice grown inside the microscope's specimen chamber by passing a stream of water vapour over a

*Corresponding author: Joseph Z. Ulanowski (z.ulanowski@herts.ac.uk)

cold growth surface or by filling the specimen chamber with water vapour.

Our approach is to use a small closed ice diffusion chamber inside the microscope's specimen chamber to create and influence the crystal growth conditions. Crystals are grown on a cold surface inside this chamber.

2 METHODS

A scanning electron microscope (JEOL Carryscope jcm-5700) is used for imaging. The microscope is equipped with a low pressure (environmental scanning, ESEM) option which allows imaging of specimens at pressures between 1 and 100 Pa using a semiconductor backscattered electron detector. At higher pressures the electrons' mean free path is reduced and a small distance between specimen and the detector is essential for imaging.

To study crystal growth from the vapour phase, a well defined water vapour environment is required. Attempts to introduce and maintain a well defined water vapour environment in the specimen chamber proved to be technically too problematic, as this would have required major changes to the microscope's vacuum system. Therefore, a second smaller chamber is placed inside the microscope's main specimen chamber (Fig. 2.1). This diffusion chamber (~23 g Cu, ~170 µl chamber volume) is closed with a ~0.5 mm opening at the top to allow electron beam entry. The top lid is formed by a semiconductor back scattered electron detector in form of a photo diode mounted on a ceramic substrate (custom design, Centronic, UK), from which the imaging signal is derived after amplification.

An amount of ~0.5 ml ultrapure water (18.2 MOhm cm, Neptune, Purite, UK) is frozen at the bottom of the chamber prior to specimen chamber evacuation and forms the source ice that acts as the water vapour source. The desired growth surface material can be attached, the chamber closed and inserted into the specimen chamber.

The water vapour pressure inside the diffusion chamber depends on the source ice temperature, which is at the same temperature as the chamber. The chamber itself is temperature controlled by a standard

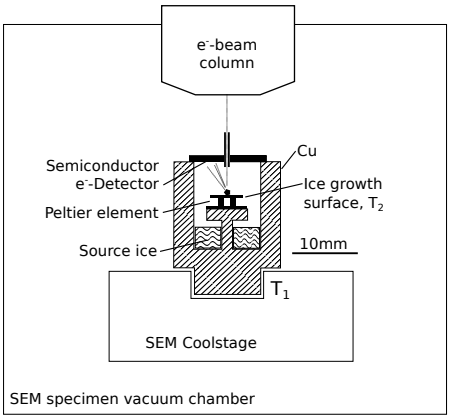

Figure 2.1: Experimental setup using a small diffusion chamber placed inside the SEM specimen chamber, with a small opening to allow electron beam entry containing a cold crystal growth surface (scale bar for diffusion chamber only).

water cooled Peltier specimen cooling stage providing ±0.2 C temperature stability at a ±1.5 C accuracy (ULTRA Coolstage, Deben, UK) over a temperature range from -50 to 50 C. Because of the high heat load the chamber presents through radiative and convective losses, chamber temperatures down to -40 C can be achieved at present.

The water vapour pressure is derived using the expression given in Murphy and Koop [6] and the pressure of the microscope specimen chamber is set (in 1 Pa steps) to a pressure found to minimize outflow of vapour out of the diffusion chamber for the selected temperature. With the temperatures achievable, this allows to access a pressure range from 20 to 100 Pa. Extending this range is subject to improvements. The specimen chamber pressure is monitored using an additional independent pressure gauge (Barocell 655 100 Pa, Edwards Vacuum, UK), which provides an accuracy of ±(0.15 of reading+1 Pa).

Inside the diffusion chamber, a Peltier element (<1.35W, 4x4 mm surface) controls the temperature of the cold ice crystal growth surface. A pair of thermocouple junctions in differential configuration is used to measure the temperature difference between the growth surface and the water vapour source. One junction of the thermocouple is frozen into the

source ice, the other is glued into a kerb of the Peltier element cold surface. The signal is conditioned and fed digitally through the specimen chamber to the outside (Thmod-I^{2}C, Hygrosens, DE).

Temperatures, the specimen chamber pressure and the Peltier supply voltage are recorded using a microcontroller based interface we developed and programmed. This allows to read the values using the SCPI[1] protocol from a separate PC which is used for time stamping the measurements and recording them to disk as well as controlling the specimen chamber pressure and the diffusion chamber temperature. The sensor readings and the timebase are also transmitted via Ethernet to the microscope's imaging system PC, where they are received by software written to superimpose the data onto the live video feed, which itself is archived. In this way, every single video frame carries a precise time stamp and sensor readings.

A typical experiment is run as follows: The diffusion chamber bottom is filled with deionized water, a source ice temperature is selected and the diffusion chamber cooled to this value. This freezes the water into the source ice. At this stage it is also possible to use different ice growth surface materials, for example by freezing them to the peltier ceramic substrate. So far copper and the peltier's ceramic surface have been used. The detector is mounted and the specimen chamber closed and evacuated to the pressure matching the water vapour pressure over ice. After contrast and focus alignment, ice growth can be initiated by changing the ice growth surface's temperature. We find that it is possible to make observations over several hours before the source ice ist lost.

3 PRELIMINARY RESULTS

Imaging with water vapour present in the specimen chamber is challenging: The signal quality is degraded due to collisions of the beam electrons with the gas. Especially, at higher pressures (100 Pa) this means images can only be obtained using beam acceleration voltages greater than >12 keV. Image signal integration time and the time scales at which crystals form or change mean that fast changes can only be observed in realtime under conditions that do allow imaging at high (video) frame rates.

We also find that effects on the ice through the electron beam's deposited energy can be limited by selecting slow scan rates or by taking frames at intervals, blanking the beam inbetween.

Some features of ice crystal growth, such as roughening of surfaces during sublimation, local vapour transport (ice crystals growing at the expense of others) and differences in ice crystal morphology have been successfully observed (Fig. 3) and are subject to further studies. Improvements of the experimental parameter and measurement are also subject of ongoing work.

4 CONCLUSION

We have demonstrated a temperature controlled diffusion chamber design that allows *in situ* imaging of small water ice crystals grown on different substrates using scanning electron microscopy. The ice crystals can be grown from a frozen ice water vapour source at different temperatures and pressures and imaged using a backscattered electron detector forming the top of the chamber. Electron beam entry is through a ~0.5 mm sized hole in the detector. Some preliminary images showing crystal growth under different conditions are presented.

5 ACKNOWLEDGEMENTS

This work was supported by NERC grant NE/I020067/1.

References

[1] A. J. Clarke, E. Hesse, Z. Ulanowski, and P. H. Kaye. A 3D implementation of ray tracing combined with diffraction on facets: Verification and a potential ap-

[1] Standard Commands for Programmable Instruments

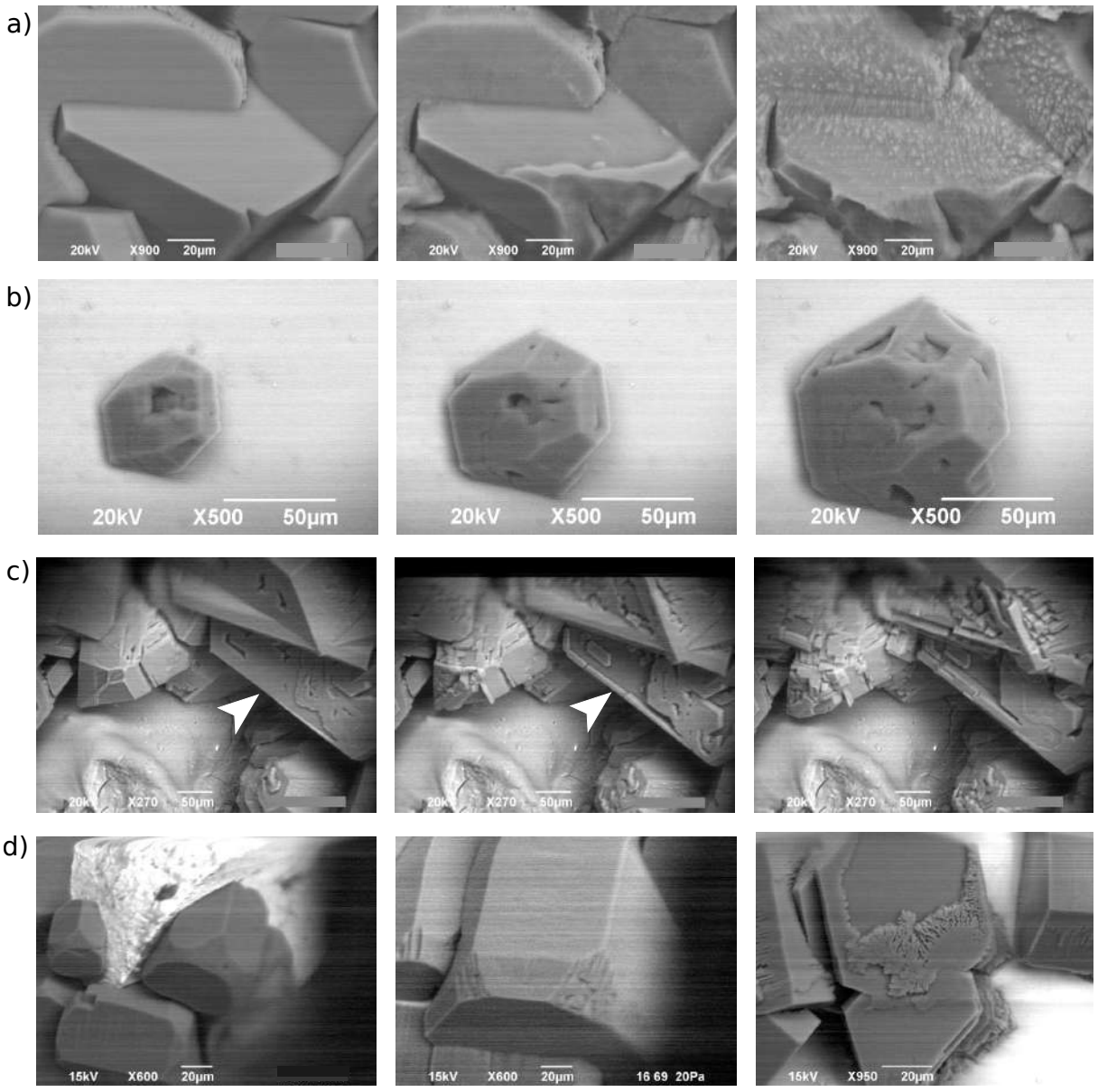

Figure 3.1: Ice growth and sublimation effects: Surface roughening through fast sublimation, T_{srcice}=-40 C (a), crystal growth at T_{srcice}=-25 C on siliconized glass (b), formation of macroscopic steps (c) and fast grown crystals on Cu (bottom (d) left and middle) and an interesting morphology during growth found in a different experimental run (bottom (d) right).

plication. *J. Quant. Spectrosc. Radiat. Transfer.*, 1001-3:103–114, 2006.

[2] P. J. Connolly, M. J. Flynn, Z. Ulanowski, T. W. Choularton, M. W. Gallagher, and K. N. Bower. Calibration of the cloud particle imager probes using calibration beads and ice crystal analogs: The depth of field. *J. Atmos. Oceanic. Technol.*, 24 11:1860–1879, 2007.

[3] R. Cotton, S. Osborne, Z. Ulanowski, E. Hirst, P. H. Kaye, and R. S. Greenaway. The ability of the small ice detector (SID-2) to characterize cloud particle and aerosol morphologies obtained during flights of the FAAM BAe-146 research aircraft. *J. Atmos. Oceanic*, 27:290–303, 2009.

[4] P. Field, A. Heymsfield, and A. Bansemer. Shattering and particle interarrival times measured by optical array probes in ice clouds. *J. Atmos. Oceanic Technol.*, 23: 1357–1371, 2006.

[5] Q. Fu. A new parameterization of an asymmetry factor of cirrus clouds for climate models. *J Atm Sci*, 62:4140–4151, 2007.

[6] D. M. Murphy and T. Koop. Review of the vapour pressures of ice and supercooled water for atmospheric applications. *Q. J. Roy. Meteorol. Soc.*, 131:1539–1565, 2005.

[7] W. C. Pfalzgraff, R. M. Hulscher, and S. P. Neshyba. Scanning electron microscopy and molecular dynamics of surfaces of growing and ablating hexagonal ice crystals. *Atmos. Chem. Phys.*, 95:20739–20763, 2009.

[8] W. Rosenthal, J. Saleta, and J. Dozier. Scanning electron microscopy of impurity structures in snow. *Cold Reg. Sci. Technol.*, 471-2:80 – 89, 2007.

[9] V. Shcherbakov, J.-F. Gayet, B. Baker, and P. Lawson. Light scattering by single natural ice crystals. *J. Atm. Sci.*, 635: 1513–1525, 2006.

[10] S. Solomon, D. Qin, M. Manning, Z. Chen, M. Marquis, K. Averyt, M. Tignor, and H. Miller, editors. *Contribution of Working Group I to the 4^{th} Assessment Report of the Intergov. Panel on Climate Change*. Cambridge Univ. Press, 2007.

[11] Z. Ulanowski, P. Connolly, and M. Flynn. Using ice crystal analogues to validate cloud ice parameter retrievals from the cpi ice spectrometer. In *In Proc. 14 Int. Conf. Clouds Precip.*, 2004.

[12] Z. Ulanowski, P. Kaye, E. Hirst, and R. Greenaway. Light scattering by ice particles in the earth's atmosphere and related laboratory measurements. In *Electromagagnetic and Light Scattering XII, International conference Helsinki*, 2010.

[13] Z. Ulanowski. Ice analog halos. *Appl. Opt.*, 4427:5754–5758, 2005.

[14] Z. Ulanowski, E. Hesse, P. H. Kaye, and A. J. Baran. Light scattering by complex ice-analogue crystals. *J. Quantit. Spectr. Rad. Transf.*, 100:382–392, 2006.

[15] D. Waller, D. J. Stokes, and A. M. Donald. Improvements to a cryosystem to observe ice nucleating in a variable pressure scanning electron microscope. *Rev. Sci. Instrum.*, 7910:103709, 2008.

[16] W. P. Wergin, A. Rango, J. Foster, E. F. Erbe, and C. Pooley. Low temperature scanning electron microscopy of irregular snow crystals. *Microsc. Microanal.*, 8: 722CD–723CD, 2002.

[17] P. Yang, G. W. Kattawar, G. Hong, P. Minnis, and Y. Hu. Uncertainties associated with the surface texture of ice particles in satellite-based retrieval of cirrus clouds - part i: Single-scattering properties of ice crystals with surface roughness. *IEEE Trans. Geosci. Rem. Sens.*, 467:1940–1948, 2008.

[18] P. Yang, Z. Zhang, G. W. Kattawar, S. G. Warren, B. A. Baum, H. lung Huangand Yong X. Hu, D. Winkerand, and J. Iaquinta. Effect of cavities on the optical properties of bullet rosettes: Implications for active and passive remote sensing of ice cloud properties. *J. Appl. Meteorol.*, 47:2311–2330, 2008.

[19] F. Zimmermann, M. Ebert, A. Worringen, L. Schütz, and S. Weinbruch. Environmental scanning electron microscopy (ESEM) as a new technique to determine the ice nucleation capability of individual atmospheric aerosol particles. *Atmos. Env.*, 4137:8219–8227, 2007.

EVALUATION OF CLOUD MICROPHYSICS ABOUT VERTICAL PROPERTIES OF CLOUD SYSTEMS IN A CLOUD RESOLVING SIMULATION USING SATELLITE SIMULATORS

Woosub Roh[1] and Masaki Satoh[1,2]
[1]Center for Climate System Research, the University of Tokyo,
[2]JAMSTEC

1. INTRODOCTION

Mesoscale convective systems in a tropical open ocean region play important roles for energy balance and precipitation. Cloud resolving models (CRMs) with a horizontal grid spacing of a few kilometers is one of useful tools to study mesoscale convective systems. As computational power increase, it is possible to simulate global cloud systems with a few kilometers. Miura et al. 2007 had global cloud resolving simulations using Nonhydrostatic Icosahedral Atmospheric Model (NICAM, Satoh et al. 2008) and reproduced cloud systems of the Madden-Julian Oscillation (MJO) event.

CRMs have many uncertainties in physical schemes like microphysics. Satellite observations have been used to evaluate tropical cloud properties of CRMs. It is useful to compare simulated radiance with observed radiance, because it is possible to use same size distribution assumption for both of a numerical model and satellite simulator. Matsui et al., 2009 proposed an evaluation method referred as the TRMM Triple-Sensor Three-Step Evaluation Framework (T3EF) based on joint diagrams and Contoured Frequency by Altitude Diagrams (CFADs) using observed and simulated measurements radiance.

One moment bulk microphysics schemes have used in high resolution experiments for efficiency of computation. One of well-known bias of 1 moment bulk is strong reflectivities in high altitude. It was originated from setting of N_0 of an exponential function in the size distribution of precipitating particles. N_0 is related to mean diameter and number concentration. There are several observations of N_0 of snow about dependency of temperature and inverse of a mean diameter (Heymsfield et al 2002). It is difficult to apply to make a parameterization using observation results, because dependency of lambda and temperature has also temporal and spatial variation. So we use simple physical model of snow in order to make a parameterization. A snow growth model could reproduce relationships with lambda, temperature, and N_0. It is based on combined moment conservation equations and a steady state height dependent model, which considered with advection, diffusion and aggregation term.

$$N(D) = N_0 \exp(-\lambda D) \qquad (1)$$

N(D) is number concentration unit volume having diameter D.

Size distribution of hydrometers is related to terminal velocity, collection and deposition/ sublimation term in a microphysics scheme. So we consider the how to affect to precipitation and cloud structures by parameterization of a size distribution.

In this study, we evaluate the horizontal and vertical structure of MCS between satellite data and NICAM using satellite simulator and investigate parameterizations of snow and graupel size distribution on vertical distribution of radar reflectivity in TRMM signals based on T3EF. We consider the problems of bulk microphysics schemes using satellite data and effects on cloud structures.

2. EXPERIMENTAL DESIGN

NICAM simulations are performed from 00 UTC 1 January to 00 UTC 6 January 2007. The actual analysis was made for the period of from 00 UTC 2 to 00 UTC 6 January for evaluations. We focused on the MCS systems over middle of tropical Pacific Ocean. The central point of the simulation is 180E on the equator and analysis domain is 10S-10N and 170E-170S. We used the stretched grid system (Tomita et al. 2008a), and the minimum horizontal grid is set to 3.5km. Most of the horizontal grid spacing is less than 5 km. The total number of vertical levels is 40.

We prepared the sensitivity tests for parameterizations of N_0 for snow and graupel. The integration time is 24 hours from 06 UTC 2 to 06 UTC 3 January.

The microphysics scheme in this study is the six-water categories single moment bulk scheme including cloud water, cloud ice, snow and graupel for hydrometeors (NSW6; Tomita et al. 2008b) which is based on the scheme by Lin et al. 1983.

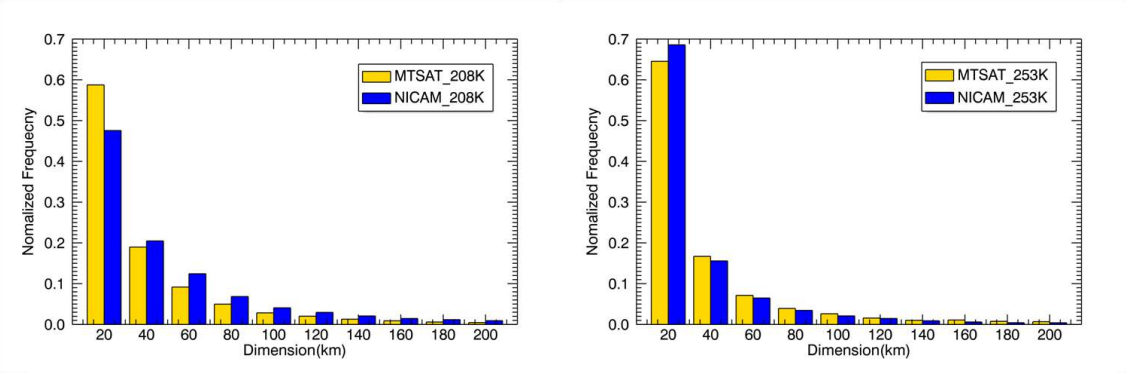

Figure 1. Histograms of cloud size of T_{BB} for deep convection defined by 208K and 253K. The size in abscissa is defined as square root of area.

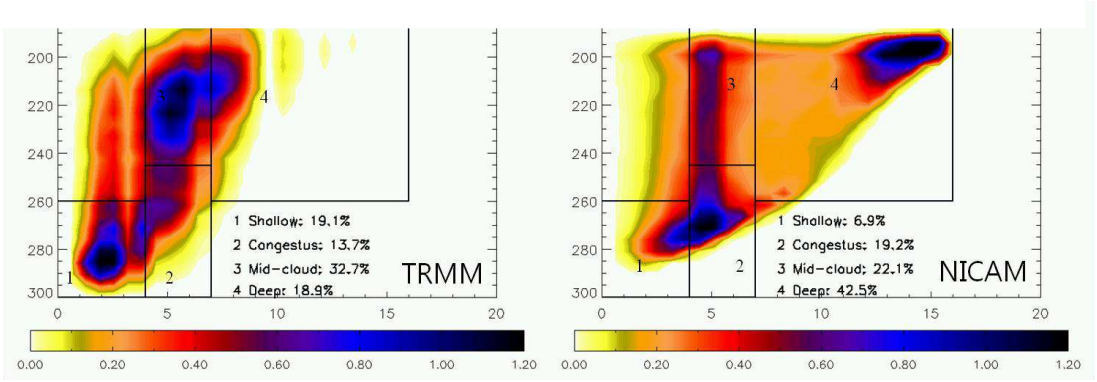

Figure 2. The joint histograms of PR echo-top height (x axis) and IR TBB (y axis) between TRMM (left side) and NICAM (right side)

3. SATELLITE DATA AND SIMULATOR

We used equivalent blackbody temperature (T_{BB}) of the infrared channel of 11 um of the Japanese geostationary meteorological satellite (MTSAT-1R) in order to evaluate the cloud size of MCS. We selected two threshold temperature, 208K and 253K based on Inoue et al. 2008. TRMM PR 13.8 Ghz attenuation corrected reflectivity (2A25) were used. We simulated corresponding infrared brightness temperature, radar reflectivity of NICAM using the Satellite Data Simulation Unit (SDSU, Masunaga et al. 2010).

A snow growth model (SGM) developed by Mitchell et al. 2006 was used for evaluation of snow parameterization. It is based on the conservation equation of number concentration and radar reflectivity. We did not consider the nucleation process in this study.

4. RESULTS

NICAM has good agreement of cloud size distributions of 253K MCS systems, but the size of deep convective clouds of 208K is larger than MTSAT data (Figure 1). We found there are schematic bias related joint diagram such as higher echo top height (Figure 2). We focus on improvement of the biases about higher echo top height in the joint diagram. We found the size distribution parameter for snow and graupel had some impact on the location of high frequency of echo top height (Figure 3). The variation of size depending on mass is small in the constant N_0. For example, small N_0 reproduce larger particle of precipitating cloud systems. It is also related to vertical motion. There is difference of intensity of convection between ocean and continents. In the case over ocean, it is not enough to transport large ice particle in the upper troposphere than continent. So only small particle and water vapor exist over 10km. Ice particles grow with deposition and aggregation. Our single bulk microphysics scheme could not explain the lower precipitating top height and continuous transition from small ice particle to large snow category, because constant N_0 is assumed for strong updraft deep convective system over continent area or multitude. We introduce the size snow and graupel's distribution parameterization with N_0 based on the observation and SGM. We could reduce frequency of higher echo top height.

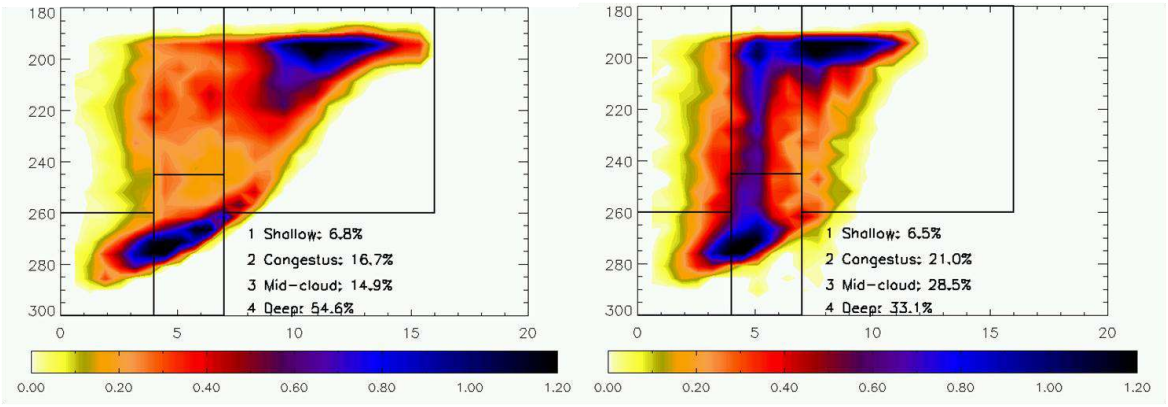

Figure 3. Sensitivity tests for consideration of temperature dependency of only snow's N_0 (left), and temperature and lambda dependency for snow and graupel based on observation and SGM (right).

BIBLOGRAPHY

Heymsfield, A. J. et al. 2002. "Observations and parameterizations of particle size distributions in deep tropical cirrus and stratiform precipitating clouds: Results from in situ observations in TRMM field campaigns". J. Atmos. Sci. 59 (24): 3457–3491.

Lin, Y. L, R. D Farley, and H. D Orville. 1983. "Bulk parameterization of the snow field in a cloud model." Journal of Applied Meteorology 22(6): 1065–1092.

Masunaga, H., M. Satoh, and H. Miura. 2008. "A joint satellite and global cloud-resolving model analysis of a Madden-Julian Oscillation event: Model diagnosis." J. Geophys. Res 113.

Matsui, T. et al. 2009. "Evaluation of long-term cloud-resolving model simulations using satellite radiance observations and multifrequency satellite simulators." Journal of Atmospheric and Oceanic Technology 26(7): 1261–1274.

Masunaga, H. et al. 2010. "Satellite Data Simulator Unit (SDSU): A multi-sensor, multi-spectral satellite simulator package." Bul. Am. Meteorol. Soc.

Mitchell, D.L. et al. 2006. "A new snow growth model with application to radar precipitation estimates" Atmos. Re. 82(2006): 2–18.

Satoh, M. et al. 2008. "Nonhydrostatic icosahedral atmospheric model (NICAM) for global cloud resolving simulations." J. Compu. Phys. 227(7): 3486–3514.

Miura, H., Satoh, M., Nasuno, T., Noda, A.T., Oouchi, K., 2007. "A Madden-Julian oscillation event realistically simulated by a global cloud-resolving model." Science 318(5857): 1763.

Satoh, M., T. Matsuno,T., H. Tomita, H. Miura, T. Nasuno, S. Iga, 2008. "Nonhydrostatic icosahedral atmospheric model (NICAM) for global cloud resolving simulations." Journal of Computational Physics 227(7): 3486–3514.

Tomita, H. 2008a. "A Stretched Icosahedral Grid by a New Grid Transformation." Journal of the Meteorological Society of Japan 86(0): 107–119.

Tomita, H. 2008b. "New Microphysical Schemes with Five and Six Categories by Diagnostic Generation of Cloud Ice." Journal of the Meteorological Society of Japan 86(0): 121–142.

LACROS — LEIPZIG AEROSOL AND CLOUD REMOTE OBSERVATIONS SYSTEM

Patric Seifert, Ronny Engelmann, Ulla Wandinger, Albert Ansmann, Dietrich Althausen, Birgit Heese, Johannes Bühl, Jörg Schmidt, Anja Hünerbein, Andreas Macke

Leibniz Institute for Tropospheric Research, Permoserstr. 15, 04318 Leipzig, Germany
E-mail: seifert@tropos.de

1. INTRODUCTION

During the last decade active remote sensing of with lidar revealed notable insights into aerosol–cloud interaction processes. At Leibniz Insitute for Tropospheric Research IfT, Leipzig, Germany one key topic investigated is the relationship between aerosol properties and heterogeneous freezing temperature in clouds. One of the main conclusions of these studies is that heterogeneous ice formation at temperatures between -40 and 0 °C is considerably driven by the amount and type of aerosol particles that act as ice nuclei [*Kanitz et al.*, 2011]. Saharan dust was found to enhance ice formation at comparably high temperatures of around -10 °C [*Seifert et al.*, 2010]. However, aerosol–cloud interaction studies solely based on lidar techniques are restricted to scenarios with optically thin cloud layers. Optically thick clouds cannot be penetrated by the laser beam of the lidar. Hence, lidar alone is not capable of documenting aerosol–cloud interaction processes in their full vertical extent.

The large number of unsolved questions concerning the interaction between aerosol particles and clouds and corresponding indirect effects on precipitation and radiative transfer demand new measurement strategies to resolve the atmospheric processes involved. In this regard, obtaining synergistic information about cloud and aerosol properties from multi–instrument and hence multi–sensor observations is a key approach to overcome the current lack of knowledge. Motivated by these needs, the novel mobile multi–instrument platform Leipzig Aerosol and Cloud Remote Observations System — LACROS — has been set up at IfT.

2. INSTRUMENTATION

LACROS comprises a unique set of active and passive remote-sensing instruments which are to a large extent containerized and available for application in field campaigns. The instruments of LACROS are shown in Fig. 1. In 2011, the 35-GHz cloud radar MIRA-35 and the microwave radiometer HATPRO have been integrated. The active-remote-sensing branch now spans the wavelength range from the UV to microwave radiation which is covered with multiwavelength-Raman-polarization lidar (Multiwavelength Tropospheric Raman lidar for Temperature, Humidity, and Aerosol profiling — MARTHA, [*Mattis et al.*, 2002], Backscatter Extinction Ratio Temperature, Humidity Lidar — BERTHA, [*Althausen et al.*, 2000], Portable Lidar System — Polly$^{\mathrm{XT}}$ [*Althausen et al.*, 2009]) , high-spectral-resolution lidar (BERTHA), a ceilometer CHM 15kx, a Doppler lidar (WiLi,*Engelmann et al.* [2008]), and the cloud radar. The Spectral Aerosol Extinction Measurement System (SAEMS) provides spectrally resolved extinction coefficients of aerosols at 15 m above ground. Passive instrumentation which helps to interpret the active remote measurements consists of an Aerosol Robotic Network (AERONET) Sun photometer [*Holben et al.*, 2001], the microwave radiometer HATPRO [*Rose et al.*, 2005] that includes also two infrared radiometers, and an all-sky imager. Meteorological surface data and radiosondes are available in addition. It is planned to become part of the Baseline Surface Radiation Network (BSRN, *Ohmura et al.* [1998]) that aims at obtaining quality-assured surface radiation measurements. For the determination of precipitation properties an optical disdrometer records the velocity and size distribution of falling hydrometeors in the size range from 0.1 to 10 mm at 4 m above ground.

In addition to the ground-based remote sensing instrumentation, IfT is acquiring growing expertise in the managenemt and analysis of spaceborne observations with passive sensors as the Spinning Enhanced Visible Infrared Imager (SEVIRI) aboard the Meteosat Second Generation (MSG) satellite or the Moderate Resolution Imaging Spectroradiometers (MODIS) aboard the Terra and Aqua satellites.

3. FIELDS OF APPLICATION

The available lidar systems measure the optical and microphysical properties of aerosols and optically thin clouds, vertical winds within aerosol layers and at cloud base, as well as temperature and humidity profiles. The integration of the cloud radar into LACROS overcomes the limitation of the lidar systems to observe only cloud-free and thin-cloud (cirrus, altocumulus) scenarios. It enables extensive insights into the microphysical and dynamical processes of thick stratiform and convective clouds, and thus the investigation of droplet activation and precipitation formation in convective cloud systems. This achievement will facilitate novel links between atmospheric measurements,

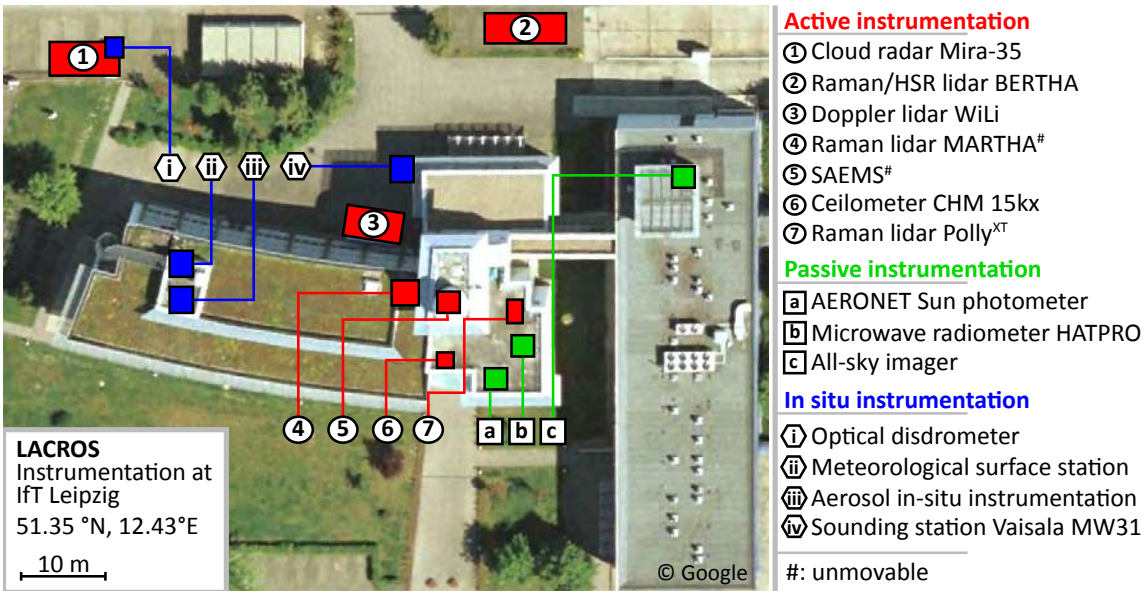

Figure 1. Instrumentation of LACROS at IfT. Besides MARTHA (4) and SAEMS (5) all instruments are mobile or at least available in a mobile version.

laboratory studies, and modeling activities. The future application of LACROS concentrates on four main subjects:

1. Investigation of heterogeneous ice–formation processes by exploiting co–located remote–sensing observations of aerosol and cloud radiative and microphysical properties.

2. Instrument validation and development of algorithms and new measurement techniques for ground–based cloud and aerosol microphysics retrieval in the frame of the Aerosols, Clouds, and Trace gases Research InfraStructure Network (ACTRIS). Here, activities currently concentrate on the development of the dual–field–of–view lidar technique [*Schmidt et al.*, 2012] to derive cloud droplet size information and on retrievals of aerosol microphysical properties from combined lidar and Sun photometer measurements. In this context, the CLOUDNET algorithms [*Illingworth et al.*, 2007] have been implemented at IfT. CLOUDNET already provides a framework for the determination of cloud microphysics from remote-sensing observations, but further extensions are needed to improve reliability and availability.

   The steadily growing number of spaceborne sensors for cloud and aerosol characterization also implies a need for ground–based observing stations that provide data sets for the validation of the derived products. Also, the combination of ground-based and spaceborne measurements may allow to reduce the uncertainties in the retrieval of cloud and aerosol microphysical properties.

3. Deployment during field campaigns in key regions of atmospheric research. LACROS is already scheduled for the deployment in field campaigns at Barbados and in Jülich, Germany, which will both take place in 2013.

4. MEASUREMENT EXAMPLE

Figure 2 provides insight into the measurement capabilities of LACROS. Shown is the observation of an ice-precipitating altocumuls layer that occurred at heights from 4.5 to 6 km or -3 to -15 °C, respectively, between 0100 and 0140 UTC on 26 August 2011. The measurements were performed with the Raman lidar MARTHA (a,b), cloud radar MIRA-35 (c-e), Doppler lidar WiLi (f), and microwave radiometer HATPRO (g). Fig. 2 (h) shows the infrared brightness temperature measured at 10.8μm with SEVIRI. The lidar measurements of the 1064-nm range-corrected signal (a) and the 532-nm depolarization ratio (b) indicate that the cloud layer was topped with an optically thick, about 200 m deep liquid-water layer. Beneath the liquid-water layer, ice crystals were precipitating. The amount of liquid water present in the top layer is derived from measurements of HATPRO (g, black line). The total amount of water vapor available in the atmospheric column is provided as well (g, green line). No liquid-water layer is indicated in the cloud radar measurements (c-e), because the radar is much more sensitive to the larger ice crystals due to the long wavelength of 0.8 cm of the emitted signal. This also explains the differences in the

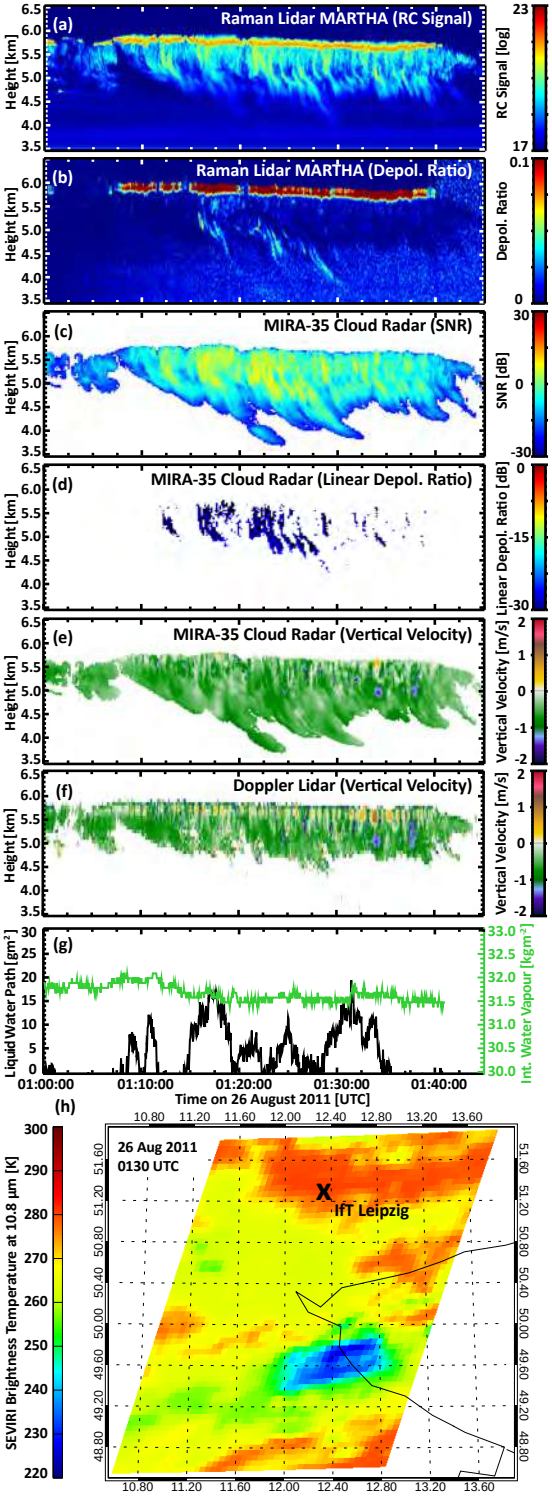

Figure 2. Combined LACROS observation of an ice-precipitating altocumulus layer on 26 August 2011. Shown are measurements of MARTHA (a,b), MIRA-35 (c-e), WiLi (f), HATPRO (g), and SEVIRI (h); RC Signal — range-corrected signal, SNR — signal-to-noise ratio.

observed vertical velocities between MIRA-35 (e) and the Doppler lidar (f). In the liquid layer, WiLi is sensitive to the motion of the numerous small water droplets whereas MIRA-35 already detects the fall velocity of the larger ice crystals. Below the liquid layer, the vertical velocities measured with both systems are similar. The rather high brightness temperature (f) measured by SEVIRI above Leipzig indicates that the cloud layer was obviously optically thin. The effective brightness temperature of around 280 K represents an intermediate temperature that lies between the ones at ground ($T \approx 290$ K) and in the cloud layer (258 K$<T<$270 K).

Further analysis of the measurement would reveal the lidar-derived optical and microphysical properties of the aerosol particles present at cloud level from which the number of cloud condensation nuclei and ice nuclei could be estimated. Spectral information from the radar signal and velocity data would yield information about the size distribution of the scattering hydrometeors.

REFERENCES

Althausen, D., D. Müller, A. Ansmann, U. Wandinger, H. Hube, E. Clauder, and S. Zörner (2000), Scanning 6–wavelength 11–channel aerosol lidar, *Journal of Atmospheric and Oceaniv Technology*, *17*, 1469–1482.

Althausen, D., R. Engelmann, H. Baars, B. Heese, A. Ansmann, D. Müller, and M. Komppula (2009), Portable Raman lidar Polly^{XT} for automated profiling of aerosol backscatter, extinction, and depolarization, *Journal of Atmospheric and Oceanic Technology*, *26*, 2366–2378.

Engelmann, R., U. Wandinger, A. Ansmann, D. Müller, E. Žeromskis, D. Althausen, and B. Wehner (2008), Lidar observations of the vertical aerosol flux in the planetary boundary layer, *Journal of Atmospheric and Oceanic Technology*, *25*, 1296–1306.

Holben, B. N., et al. (2001), An emerging ground–based aerosol climatology: Aerosol optical depth from AERONET, *Journal of Geophysical Research*, *106*, 12,067–12,098, doi: 10.1029/2001JD900014.

Illingworth, A. J., et al. (2007), Cloudnet — continuous evaluation of cloud profiles in seven operational models using ground–based observations, *Bulletin of the American Meteorological Society*, *88*, 883–898.

Kanitz, T., P. Seifert, A. Ansmann, R. Engelmann, D. Althausen, C. Casiccia, and E. G. Rohwer (2011), Contrasting the impact of aerosols at northern and southern midlatitudes on heterogeneous ice formation, *Geophysical Research Letters*, *38*, L17802, doi:10.1029/2011GL048532.

Mattis, I., A. Ansmann, D. Müller, U. Wandinger, and D. Althausen (2002), Dual–wavelength

Raman lidar observations of the extinction–to–backscatter ratio of Saharan dust, *Geophysical Research Letters*, *29*, 1306, doi: 10.1029/2002GL014721.

Ohmura, A., et al. (1998), Baseline Surface Radiation Network (BSRN/WCRP): New precision radiometry for climate research, *Bulletin of the American Meteorological Society*, *79*, 2115–2136, doi:10.1175/1520-0477(1998)079<2115:BSRNBW>2.0.CO;2.

Rose, T., S. Crewell, U. Löhnert, and C. Simmer (2005), A network suitable microwave radiometer for operational monitoring of the cloudy atmosphere, *Atmospheric Research*, *75*, 183–200, doi:10.1016/j.atmosres.2004.12.005.

Schmidt, J., U. Wandinger, A. V. Malinka, and J. Bühl (2012), Determination of cloud microphysical properties with dual–field–of–view Raman lidar measurements, in *Reviewed and revised papers presented at the 26th International Laser Radar Conference (ILRC), 25–29 June, Porto Heli, Peloponnesus, Greece, edited by the Organizing Committee of the 26th ILRC*.

Seifert, P., A. Ansmann, I. Mattis, U. Wandinger, M. Tesche, R. Engelmann, D. Müller, C. Pérez, and K. Haustein (2010), Saharan dust and heterogeneous ice formation: Eleven years of cloud observations at a central European EARLINET site, *Journal of Geophysical Research*, *115*, D20201, doi:10.1029/2009JD013222.

THE ROLE OF EVAPORATION AND CLOUD TOP ENTRAINMENT INSTABILITY IN AIRCRAFT SEEDING EXPERIMENTS OF SUPERCOOLED STRATUS CLOUDS

Chris J. Walcek
State University of NY at Albany

1. INTRODUCTION

The most convincing evidence that cloud seeding can induce cloud transformations involve aircraft flying at the tops of stratiform clouds inducing cloud dissipation by dispensing seeding agents such as dry ice pellets or silver iodide.

Fig. 1 shows a photograph of a seeded cloud that appears in many meteorology textbooks. The accepted explanation assumes that seeding induced ice particle nucleation, followed by glaciation of the supercooled cloud to larger falling snow, which then fell out of the dissipated cloud region.

Fig. 1. "Racetrack" cloud dissipation pattern photographed 24 minutes after a B17 aircraft completed flying the pattern immediately above cloud top at 2070m ASL for 13 minutes at a speed of 76 m/s. The temperature at the top of this 700-m thick cloud was -5.6 ˚C. The longer sides of the oval shape are about 29 km long, and the path cleared is 2-3 km wide. Crushed dry ice pellets with diameter 5-10 mm were dispensed through a small hole in the B17 floor at a rate of 480 g/km. Picture was taken at 11:21AM local time on 24 Nov 1948 over Utica NY. Note that dissipated cloud did not penetrate to cloud base, even though the entire depth of the cloud was < 0˚C.

Here an alternate explanation of aircraft-induced dissipation of stable clouds is proposed that does not involve ice. As shown in Fig. 2, while flying, aircraft produce a significant downwash (~10-50 m/s) immediately below their airframe, and also generate a substantial turbulent wake.

Fig. 2. Downwash and vortex pair below a B-777-200 aircraft (mass ~145000 kg) flying immediately above a 150 m thick cloud while approaching London Gatwick airport at 7AM local time on 10 July 2006. Surface temperature was 16˚C. Aircraft was descending through 0.61 km altitude at a speed of ~108 m/s. Photograph courtesy of Steve Morris photographer, who was positioned ~9 km in front of the approaching aircraft at the surface, using a 840mm telephoto lens. Cloud in this viewing area was reported to completely dissipate 20 minutes after the photograph was taken.

Thus, if an aircraft is flying just above cloud top, then dry air from above the cloud is forced into the cloud. Here we suggest that the wake disturbance shown in Fig. 2 simply grows to the pattern shown in Fig. 1 primarily via cloud evaporation. Turbulent mixing of dry air into a cloud can under many conditions trigger an unstable sequence of evaporation, cooling and downdrafts that can dissipate wide swaths of stable cloud via the mechanism of cloud top entrainment instability (CTEI). The dynamics of this mechanism are the reverse of the seeding process. Freezing will heat a cloud, while

evaporation of the same water mass can induce comparable or greater cooling, due to the large latent heat of evaporation.

The potential impacts of aircraft turbulence and downwash-induced evaporation have been neglected or poorly accounted for in all past explanations of cloud seeding. While both seeding/ice formation and evaporation can be occurring in seeded clouds, it is suggested here that the dynamical effects of induced CTEI can under many conditions dominate the cloud dissipation process at the tops of supercooled clouds. Here the mechanism of aircraft downwash is reviewed, and CTEI is described, followed by a discussion of evaporation and its effects on past cloud seeding experiments.

2. DOWNWASH

During flight, aircraft generate a wake of considerable turbulence due to aerodynamic drag, and also produce a net downward displacement of air ("wake downwash") while generating lift. This downwash consists of a pair of horizontal vortices that descend through stagnant air, dissipating below the aircraft flight altitude within a few minutes. Fig. 2 shows a picture of a descending vortex pair below a commercial aircraft.

Aircraft produce lift by accelerating air over the tops of the wings relative to the air flowing under the wings. Air is then diverted down under and aft of the wings. Newton's third law dictates that while flying, the force of gravity on the plane is balanced by an upward lift force generated by the wings. The "equal and opposite" lift force consists of a flux of air accelerated down below the wings

$$m_{plane} g = m_{air} \frac{dw}{dt} = \frac{dm_{air}}{dt} w \qquad (1)$$

Here m_{plane} is the aircraft mass (kg), and g is the gravitational acceleration. m_{air} is the mass of air pushed down (kg), w is the impulse downward vertical velocity of air induced by the wings immediately below and behind the wings (m/s). The mass flux of air pushed down per unit time (dm_{air}/dt, $kg_{air}\ s^{-1}$) is the product of the air density (ρ_{air}), the accelerated vertical velocity perturbation, and the horizontal area under the wings/airframe (A_{wing}) being pushed down

$$\frac{dm_{air}}{dt} = A_{wing} \rho_{air} w \qquad (2)$$

Substituting (2) into (1), the downward impulse velocity below a flying airplane is

$$w = \sqrt{\frac{m_{plane} g}{A_{wing} \rho_{air}}} \qquad (3)$$

The wing area of the B-17 aircraft that generated the flight track shown in Fig. 1 is 132 m^2, and its empty mass is 16400 kg. Using an air density of 1 kg/m^3 yields downward velocities immediately below the seeding aircraft of 35 m/s.

As downward-moving rotating cylinders of wake vortex air descend through stagnant air, local shear-induced turbulent mixing will cause drag and turbulent entrainment that slows and ultimately stops the downward propagation. Using a semi-empirical model validated with flight observations, Greene (1986) shows that wake effects can penetrate 2-8 wingspans below the aircraft before dissipation, and the ultimate vertical displacement is strongly influenced by atmospheric stability.

Clearly a downwash of this magnitude, along with any turbulence generated by the aircraft itself ("parasitic drag"), will produce turbulence that is several orders of magnitude more intense than any naturally-occurring ambient turbulence that might be present near the tops of supercooled clouds in stable environments.

3. ENTRAINMENT INSTABILITY

As turbulent downwash air shown in Fig. 2 descends into a cloud, the warmer dry air will mix with the cloudy air, evaporating condensed cloud water. Lilly (1968) proposed that statically stable clouds could be potentially unstable if there were a negative gradient of equivalent potential temperature in a cloudy environment. Under certain conditions, warm dry air mixed into a cloud can produce sufficient evaporation to make mixtures colder than the unmixed cloudy air, thus generating negative buoyancy. Under these conditions there is a potential for a positive feedback between mixing creating negatively buoyant air, which induces more mixing propagating the process. Yamaguchi and Randall (2008)

describe the history and physics of the CTEI mechanism. This instability will not always be

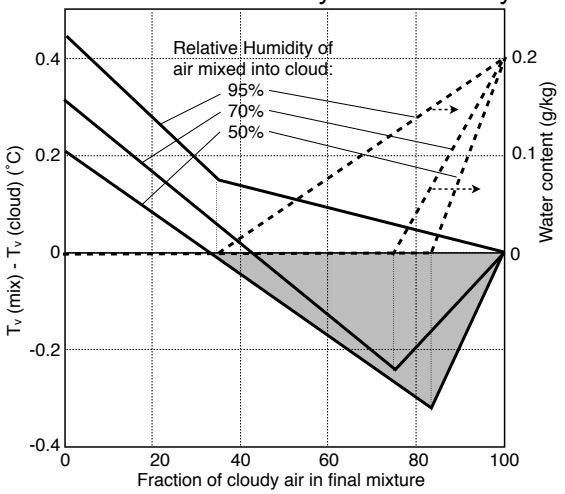

Fig. 3. Virtual temperature difference (solid lines) and liquid water content (dashed lines) of mixtures of air 0.4 ˚C warmer mixed with a cloud containing 0.2 g/kg water at -5.6 ˚C, 790 hPa (Fig. 1 conditions). Coldest mixtures occur at mixing fraction where all condensed water evaporates and final mixture Rh is 100%.

released if there is no triggering mechanism. Usually the tops of supercooled stratiform clouds exist in statically stable environments with relatively little ambient turbulence, and there is no triggering mechanism. The aircraft-induced turbulence and wake vortices below an aircraft shown in Fig. 2 can provide precisely the trigger necessary to release CTEI.

Any evaporation will induce cooling in proportion to the amount of water evaporated during the mixing process

$$c_p(T_i - T_{mix}) = L\,(q_{li} - q_{lmix}) \qquad (4)$$

Where c_p is the heat capacity of air (1004 J/˚K/kg), and L is the latent heat of liquid evaporation (2.5×10^6 J/kg). T_i and q_{li} are initial estimates of the temperature and liquid water content of a mixture of cloudy and clear air, calculated by linearly scaling with the mixing proportions of the clear and cloudy air

$$q_{li} = q_{lcld} f_{cld} \qquad (5)$$

$$T_i = T_{cld} f_{cld} + T_{env}(1 - f_{cld}) \qquad (6)$$

Where f_{cld} is the fraction of cloud air in the mixture, and q_{lcld}, T_{cld} and T_{env} are the water content and temperature of the cloud and environment before mixing. These initial estimates will generally not be saturated, and if unsaturated mixtures form, cloudwater will quickly evaporate, bringing the mixture to saturation, but if all water evaporates, the mixture will equilibrate at a relative humidity below 100%.

Calculating the amount of cooling using Eq. (4) that can occur during mixing requires iterative methods due to the exponentially relationship of final mixture temperature and saturation water mixing ratio.

Fig. 3 shows the calculated temperature difference of mixtures of cloudy and clear air vs. the mixing fraction of cloudy air in the final mixture for conditions that might be typical of the stable clouds shown in Figs. 1-2, and a 10-100 m downward adiabatic displacement of clear air into the cloud.

Fig. 3 shows that if 95% Rh dry parcels are mixed into a cloud, none of the mixtures with the surrounding cloud will be negatively buoyant. In contrast, at a relative humidity of 50 or 70%, well over half of the possible mixing fractions are negatively buoyant. The coldest negatively buoyant mixtures are produced at precisely the mixing point where all cloudwater in the mixture evaporates, leaving the mixture at 100% Rh. The maximum cooling that can be produced is comparable in magnitude to the positive stable temperature difference between the unmixed dry parcel and cloud. Without mixing (f_{cld}=0), dry parcels pushed down into a cloud by aircraft downwash will experience a strong upward-directed restoring buoyancy force. However, with mixing and evaporation, a downward acceleration can be produced, amplifying the initial downward impulse of air into the cloud. Under these conditions, it would be possible to trigger a positive feedback process whereby evaporation induces cooling, which generates more downward-directed air that mixes and evaporates cloudwater, propagating the cycle of cloud-top entrainment instability.

Further calculations similar to those shown in Fig. 3 quantify the temperature and humidity regimes where CTEI effects should occur near the tops of clouds. Negatively buoyant unstable conditions occur below a threshold relative humidity, and as the temperature difference (ΔT) of dry air pushed into a cloud increases, this Rh threshold decreases. For a 1 ˚C temperature difference, which for the conditions shown on Fig. 1 corresponds to a adiabatic displacement of about 170m (if the

measured ∂T/∂z in the cloud -4˚C/km extends above cloud top), the Rh of the dry air pushed into the cloud must be below about 80% in order to generate negatively buoyant mixtures and trigger cloud top instabilities.

4. DISSIPATION PROPAGATION

4a: Heating due to freezing: It is well recognized that in order to explain the relatively wide areas (1-2 km shown in Fig. 1) affected by seeding along a narrow track (Fig. 2), a dynamic positive feedback mechanism that propagates the initial wingspan-scale microphysical or dynamical disturbance must occur, causing the wingspan-wide (~10-40 m) initial disturbance to grow in size by a factor of 100 or more in a 20-30 minute period.

For seeding-induced glaciation, it has been assumed that a turbulent mechanism driven by latent heat released during freezing is responsible for generating positively buoyant parcels, generating more turbulence that mixes ice nuclei into the neighboring ice-free cloud, thus propagating the cycle of freezing, heating & turbulence.

The heating associated with freezing a supercooled cloud is proportional to the amount of liquid frozen and the vapor excess over ice saturation:

$$c_p \Delta T_{heat} = L_f (q_l) + L_s \Delta q_v \qquad (7)$$

where L_f and L_s are the latent heat of liquid freezing (3.21 x 10^5 J/kg) and sublimation (vapor to ice, 2.84 x 10^6 J/kg), and Δq_v is the difference between the initial liquid-saturated water vapor pressure minus the final vapor saturated with respect to ice.

Fig. 4 shows the warming induced by freezing a supercooled cloud containing 0.2 g/kg liquid water as a function of temperature below freezing at three different heights (pressures) in the atmosphere. The warming must be calculated iteratively since the saturation vapor pressure is exponentially related to the warmer cloud temperature that results from the freezing. The lower heating curve shown in Fig. 4 shows the contribution of the warming due to liquid freezing only, showing that the freezing of liquid contributes only a small fraction to the potential warming. The maximum heating occurs at -18 to -14 ˚C,

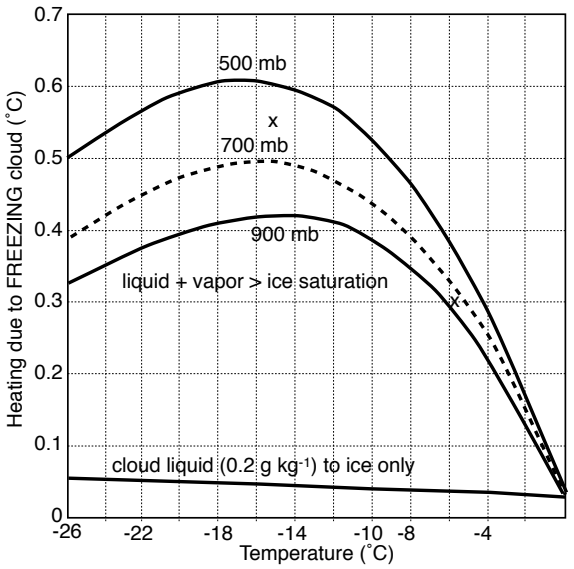

Fig. 4. Warming induced by condensation/ freezing of a supercooled liquid cloud vs. cloud temperature below freezing. Calculated assuming initial water content is 0.2 g/kg for three different pressure levels.

and except for temperatures very close to freezing, a vast majority of the heating is due to direct vapor deposition into ice and therefore the heating is proportional to the saturation vapor pressure difference between ice and liquid, and relatively insensitive to cloud liquid water content. This suggests that clouds are not even necessary for seeding to accomplish these effects, and supercooled clouds only tell where the atmosphere is likely saturated with respect to liquid.

4b: Cooling due to evaporation: In contrast, cloudwater evaporation will produce cooling in proportion to the amount of water evaporated. Fig. 5 plots the maximum cooling that can occur when just all the water is evaporated in a mixture of cloudy and clear air by mixing cloudy air with drier and hotter environmental air pushed into the cloud from above. The temperature plotted here is the coldest temperature shown on Fig. 3.

Fig. 5 shows that the potential cooling associated with evaporation is nearly linearly sensitive to the condensed water content, with higher water content clouds producing more cooling. This behavior differs from the heating due to glaciation shown in Fig. 4, where heating is largely insensitive to the cloud water content.

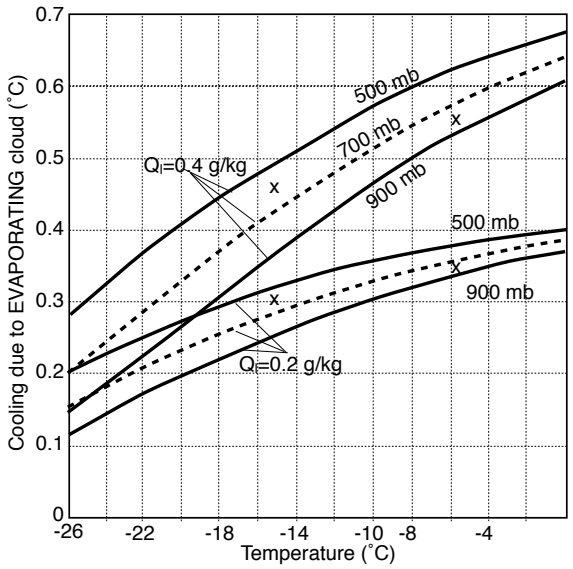

Fig. 5. Cooling induced by evaporating a liquid cloud containing 0.2 g/kg liquid at three different pressure levels.vs. cloud temperature. Dry air mixed into cloud is assumed to be 0.2 ˚C warmer at 65% Rh.

Fig. 5 also shows that the evaporative cooling effect increases with temperature. Therefore if cloud tracks are observed at temperatures near or above freezing, then the likely mechanism is evaporation and not freezing effects associated with aircraft-cloud interactions.

4. DISCUSSION

The above calculations suggest that the evaporation effects of turbulent mixing of dry air forced into a cloud by aircraft downwash can be significant. The evaporative cooling and release of cloud top entrainment instability under the appropriate conditions could play a major role in the observed dissipation of clouds that are influenced by aircraft flying near them. One prediction of this hypothesis is that this mechanism should occur whenever aircraft fly within a few 100m above cloud top and CTEI instability criterion are satisfied across the cloud top interface. The numerous aircraft-induced cloud effects shown in Heymsfield et al. (2010) are consistent with this hypothesis of CTEI-induced effects.

In order to assess the potential for CTEI, it is necessary to perform relatively high vertical resolution measurements of the temperature, humidity, and cloudwater content throughout the depth of the downwash-influenced region below a flying aircraft. Such measurements have not been reported in past cloud seeding experiments.

Heymsfield et al., (2010; 2011)'s explanation of aircraft-induced cloud dissipation implies that only aircraft flying WITHIN a cloud would induce cloud dissipation. The explanation proposed here works best for aircraft flying above but very close to cloud top, as long as CTEI criteria are satisfied. If aircraft that are not actively seeding can produce these dissipated cloud tracks while flying slightly above cloud top, then the mechanism is likely CTEI-triggered.

In the original project reports documenting the cloud seeding experiments of the 1940s-1950s, there were scattered observations of ice formation, and several visual reports suggesting no evidence of ice in dissipated cloud regions. Many cloud seeding experiments do not routinely monitor conditions under seeding tracks, and there are occasional observations from above which showed reflections from sunlight off the seeded paths that are characteristic of sunlight glinting from ice crystals (Schaefer 1950a). When no ice was observed, it was assumed to have fallen away from dissipated clouds as snow/precipitation from the seeded regions. An alternate explanation of no observed ice would be that evaporation was the primary mechanism dissipating the clouds beneath seeding tracks.

Ice nucleation could be occurring during aircraft seeding operations, but it is suggested here that effects associated with ice formation would be superimposed and possibly even overwhelmed by evaporation effects associated with CTEI.

Another factor suggesting that seeding effects could be much smaller than CTEI effects relates to the differences in the cloud volume initially impacted by either the seeding agents or the downwash turbulence. During dry ice seeding experiments, the dry ice was crushed into pellets with a diameter of about 1 cm. The pellets were dispensed through a small hole in the floor of the seeding aircraft at rates of less than 1-2 lbs per mile (280-560 g/km). The horizontal linear distance between individual dry ice pellets as they fell through

the cloud deck is thus about 5-6 meters. Any individual falling dry ice pellet will initially only influence an area 1-2 meters at most around its fall path (~1-4 m^2, viewed from above). In contrast, the wake downwash area experiencing evaporation will span the entire vortex width, approximately the aircraft wingspan. Therefore, around each falling dry ice pellet, the wake vortex evaporation area will be the product of the downwash width (32 m) and the pellet spacing (5.6m) = 179 m^2, an area 10-100 times greater than the area affected by each dry ice pellet seed. Clearly, downwash effects will dominate the initial impacted cloud area if the downwash wake penetrates into the top of a cloud while the seeding aircraft flies above cloud top.

Another observation in support of this evaporation mechanism of cloud dissipation is evident in Fig. 1. Note that the cloud is only dissipated over a finite depth. According to the freezing-seeding explanation, ice formation within a supercooled cloud should unstably propagate wherever ice forms and falls. The dry ice pellets themselves should fall a considerable vertical distance into the cloud before subliminating. If precipitation-sized ice particles were produced, they should induce phase change throughout their descending path and clear the cloud all the way to the freezing level or through to cloud base if the entire cloud is below freezing. For the “racetrack” cloud shown in Fig. 1, the entire cloud depth (0.7km) was below freezing, and yet dissipation only occurs in a restricted region near cloud top. One outcome of the CTEI mechanism is that any CTEI-induced turbulence will only propagate downward a finite distance into the cloud, since downward moving air warms along a moist or dry adiabat as it descends further. If the cloud is stably stratified (usually the case), any cooled descending parcels will eventually warm to the cloud temperature at a distance of several hundred meters at most, depending on the amount of evaporative cooling initiating the CTEI, and on the stability of the air below the cloud top.

5. EXPERIMENT SUGGESTIONS

For future cloud seeding investigations, an experimental protocol that would ascertain the importance of seeding-freezing relative to mixing-evaporation would be to simply stop the seeding for specified portions of the flight track and ascertain the differences between the seeded and unseeded portions of the flight track.

For dry ice seeding, a single dry ice particle could be dropped into a supercooled cloud from a high enough distance above cloud top to ensure that no downwash affects the cloud layer. According to the seeding-freezing mechanism, a 1-2 mile wide hole should develop. In the unpublished notes and reports of past cloud seeding trials, there were records of “single point” dry ice seeding drops with ambiguous results.

Another important measurement that would unambiguously ascertain whether CTEI evaporation effects are occurring would be to measure temperatures within and across the dissipated seeded track with a high time/space-resolution probe. According to the seeding/freezing dissipation mechanism, only air warmer than the surrounding cloud should be measured in the dissipated cloud region. In contrast, according to the downwash mixing/evaporation mechanism proposed here, regions that are colder than the surrounding cloud should be measured at some points in the dissipated/evaporated cloud area if CTEI criteria are satisfied.

Another fallout of this mechanism would be that the cloud effects induced by aircraft would be significantly influenced by the height at which the aircraft flies above cloud tops. At higher heights above cloud top, generally warmer and drier air mixes into the cloud, and the magnitude of the evaporation response should change.

Another prediction of this hypothesis would be that this mechanism should work even for clouds that are warmer than 0˚C and satisfy CTEI instability criterion. If a flight track is found at temperatures >0˚C, then obviously any mechanism involving freezing cannot explain the cloud dissipation. Therefore it would be prudent to observe stratiform cloud decks that are above freezing in regions of aircraft traffic for these “canal tracks” as aircraft fly over. Similarly, cirrus clouds composed entirely of ice particles would also be susceptible to CTEI,

since clouds composed of frozen or liquid water have similar potential to evaporate when mixed with warmer air as aircraft fly above. However, as shown in Fig. 5, the intensity of any CTEI effects should diminish with decreasing temperature.

Both the CTEI mechanism and the seeding-induced cloud dissipation processes are turbulence-scale processes. Thus, relatively high vertical resolution (1-10s of meters) measurements would be required of the condensed water content, temperature and relative humidity across the cloud top layer and into the cloud-free area above a cloud in order to fully document the turbulent propagation effects associated with either evaporation or freezing. It would be valuable to measure turbulent properties within seeding/dissipation tracks, and additional measurements of microphysical phase using another aircraft flying through a seeded cloud would be extremely valuable, however, these measurement aircraft would be introducing another downwash turbulent artifact into the system.

6. CONCLUSION

Aircraft flying within and above clouds "vertically-stirs" or "seeds" clouds with turbulence, and this turbulent downwash can have a significant impact if the gradients of temperature, relative humidity and condensed water content satisfy well-established cloud top entrainment instability (CTEI) criterion. If CTEI criterion are satisfied near cloud top, then aircraft downwash can trigger an unstable evaporation process that could propagate laterally to considerable horizontal distances away from a flight track, driven by the cooling associated with cloud evaporation and dissipation. There are many obvious and simple-to-perform experiments of this proposed hypothesis that warrant further investigation. While phase change and ice formation has been observed in some cloud seeding experiments, the effects associated with evaporation have been neglected in past explanations of cloud seeding. If this evaporation mechanism occurs as aircraft fly close to the tops of stratiform clouds, then current and past meteorology textbooks describing cloud seeding provide only a partial explanation of the physics and dynamics of the observed dissipation.

REFERENCES

Greene, G. C., 1986: An approximate model of vortex decay in the atmosphere. J. Aircraft. 23, 566-573.

Heymsfield, A. J., G. Thompson, H. Morrison, A. Bansemer, R. M. Rasmussen, P. Minnis, Z. Wang and D. Zhang, 2011: Formation and spread pf aircraft-induced holes in clouds. Nature 333, 77-81.

Heymsfield, A. J., P. C. Kennedy, S. Massie, C. Schmitt, S. Want S. Haimov, and A. Rangno, 2010: Aircraft-Induced hole punch and canal clouds. Bull. Amer. Meteor. Soc. 91, 753-766.

Lilly, D. K., 1968: Models of cloud-topped mixed layers under a strong inversion. Quart. J. Roy. Meteor. Soc., 94, 292–309.

Schaefer, V. J., 1950a: The effects produced by seeding supercooled clouds with dry ice and silver iodide. Centenary Proceedings of the Royal Meteorological Society, 42-50.

Yamaguchi, T., and D. A. Randall, 2008: Large-eddy simulation of evaporatively driven entrainment in cloud-topped mixed layers. J. Atmos. Sci., 65, 1481-1504.

Acknowledgements. The author is grateful to Dr. Duncan Blanchard, who flew on many of the original 1940s-era seeding missions, and provided invaluable advice and commentary. Also Geoffrey P. Williams, Archivist at the University at Albany Library Special Collections and Archives, provided valuable assistance in browsing through mountains of archival notes and reports from the Vincent Schaefer collection.

SCALE (IN)DEPENDENCY OF STATISTICAL CLOUD COVER PARAMETERIZATIONS

VERA SCHEMANN[1], BJORN STEVENS[1], VERENA GRÜTZUN[1] AND JOHANNES QUAAS[2]

[1]Max Planck Institute for Meteorology, Hamburg, Germany
[2]Institute for Meteorology, University of Leipzig, Leipzig, Germany

1. INTRODUCTION

The parameterization of cloud processes and cloud cover is known to be a main reason for uncertainties in recent global climate models and their simulations (Randall et al. 2007). Even though different parameterizations are using varied approaches, they all rely on information about the subgrid scale variability of total water mixing ratio. The more complex and detailed the parameterizations are getting, the more important the right subgrid scale variability becomes.

In the new generation of global climate models the possibility to use grid refinement methods gets more important. This leads to a new challenge for parameterizations. It is no longer feasible to tune parameterizations to certain resolutions. The aim has to be to develop parameterizations which adjust automatically to different grid sizes. Those parameterizations should be able to manage a consistent transition from today's global scale ($\mathcal{O}(100\,\mathrm{km})$) up to cloud resolving scales ($\mathcal{O}(1\,\mathrm{km})$).

One possible kind of parameterizations with the potential to adjust to different scales is the approach of statistical parameterizations. The statistical parameterizations are using higher moments of total water mixing ratio to describe a distribution inside a gridbox. In this study we will evaluate the variance of total water mixing ratio with respect to scale dependency.

2. STATISTICAL CLOUD COVER SCHEMES

Our research and study is based on the idea of a prognostic statistical cloud cover scheme by Tompkins (Tompkins 2002). In this framework a beta distribution is used as probability density function (PDF) of total water mixing ratio. To define the shape of a beta distribution four parameters are needed. For the calculation of these parameters the mean values of total water and cloud water mixing ratio, a shape controlling condition and two additional prognostic equations for skewness and variance are used.

There is still ongoing discussion if it is feasible to use a prognostic skewness, (e.g. (Klein et al. 2005)) but for almost all statistical parameterizations the variance plays an important role. For this reason we will focus in this study on the variance.

The sources and sinks of total water mixing ratio variance are the physical processes of convection (c), turbulence (t) and microphysics (m). With this we can write the prognostic equation for the variance of total water mixing ratio (r_t) in the following way:

$$\frac{\partial \overline{r_t'^2}}{\partial t} = \left(\frac{\partial \overline{r_t'^2}}{\partial t}\right)_{\mathrm{c}} + \left(\frac{\partial \overline{r_t'^2}}{\partial t}\right)_{\mathrm{t}} + \left(\frac{\partial \overline{r_t'^2}}{\partial t}\right)_{\mathrm{m}}$$

In the current formulation for the variance (Tompkins 2002) only convection and turbulence are considered.

Ideally, through the coupling to other parameterizations the cloud cover scheme would get information about the resolution and be adapted to different grid sizes.

Our aim is to evaluate the prognostic equation of variance with respect to scale adaptivity. This might be used as a first step for the evaluation of the whole statistical cloud cover scheme. But before we can start with the evaluation of the prognostic subgrid-scale variance we need to collect more information about the scaling behaviour of the variance of total water mixing ratio.

In this study we present a detailed evaluation of the distribution of variance of total water mixing ratio to different scales, based on high resolution model data.

Corresponding author's address: Vera Schemann, Max Planck Institute for Meteorology, Bundesstr. 53, 20146 Hamburg, Germany. E-mail: vera.schemann@zmaw.de

3. DATA

We evaluated the data of three different models. The data with the highest resolution is produced by the UCLA Large-Eddy-Simulation (LES) model ((Stevens et al. 2005), (Stevens et al. 1999) and (Stevens and Seifert 2008)). We investigated two different cases - one stratocumulus case (CGILS s12) with a 25 m resolution and one cumulus case (CGILS s6) with a 100 m resolution. As an representative for numerical weather prediction models we picked the COSMO model (Baldauf et al. 2011) from the german weather service (Deutscher Wetterdienst) in a setup for Germany (DE, 2.8 km resolution) and for Europe (EU, 7 km resolution). The general circulation models are in our study represented by the ECHAM6 model (Stevens et al. 2012) in two different resolutions, the T63 and the T127. We constrain the data to the region around the equator (30° North - 30° South) to have gridboxes of equal size.

4. METHOD

The power density spectrum of a certain quantity provides information about the distribution of the variance to different wavenumbers. The total resolved variance is equal to the integral of the power density spectrum over all wavenumbers.

With a Fast Fourier Transformation (FFT) of the two dimensional horizontal field of total water mixing ratio (r_t) we calculated the two dimensional power spectrum for every level and every timestep. After transformation to polar coordinates we integrated over the angles to receive a one dimensional power spectrum which is only depending on the radius, that is the effective wavenumber.

For the comparison of data from different models we need to look at a quantity which is independent of the chosen wavenumber discretization. This is reached by calculating a density through division by the width of the wavenumber bins ($\Delta k = k_{n+1} - k_n$).

The resulting one dimensional power density spectrum shows the distribution of the variance of total water mixing ratio over different scales. All calculations are done for every timestep and every level.

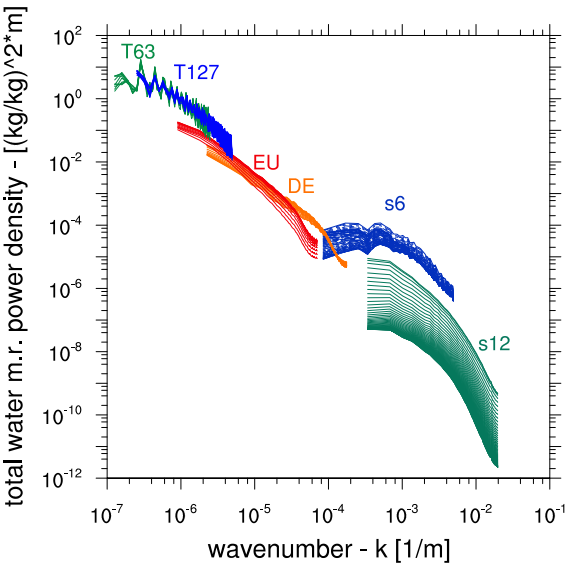

Fig. 1: Time averaged power density spectrum. Different lines of the same color show different height level, only level in the cloud layer are shown. For the labeling of the different models see section 3.

The highest and lowest wavenumbers for every datasets are influenced by numerical effects and domain size effects. The intermediate wavenumbers are less influenced and thus are thought to be more robust. Due to this reason we are focusing our evaluation on an intermediate subrange of the considered wavenumber space.

To evaluate the different power density spectra, we assume, that we can approximate them by a power law of $\sim k^{\alpha}$, where k is the wavenumber and α the power law exponent. As a last step we fit the power law exponent for every timestep and every level to this subrange of wavenumber space with a least square algorithm.

5. RESULTS

The time averaged power density spectra of the three different models can be seen in Fig. 1. All data sets show a clear scaling of the variance of total water mixing ratio. From the largest until the smallest scales we can see a consistent behaviour with regard to slope and height.

In Fig. 2 the subrange of the wavenumber space can be seen, which is considered in this evaluation and where the power law is assumed to be valid. Besides the consistent scaling this figure shows, that with the used datasets not the whole wavenumber space

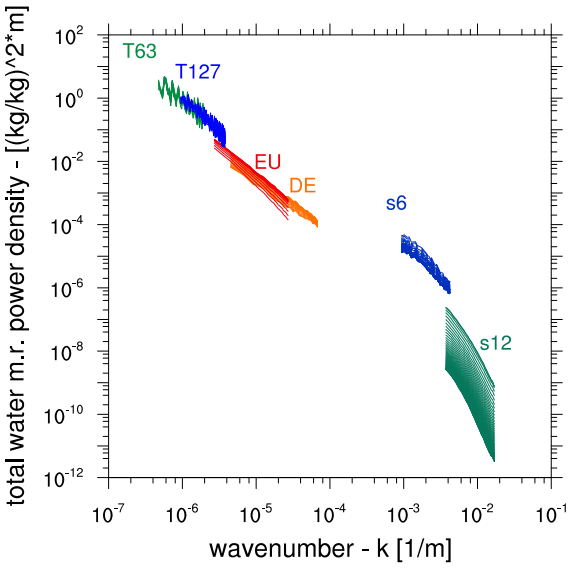

Fig. 2: Time averaged power density spectrum. Different lines of the same color show different height level, only level in the cloud layer are analyzed. Due to numerical issues only intermediate wavenumbers are shown in this figure and considered during the evaluation. For the labeling of the different models see section 3.

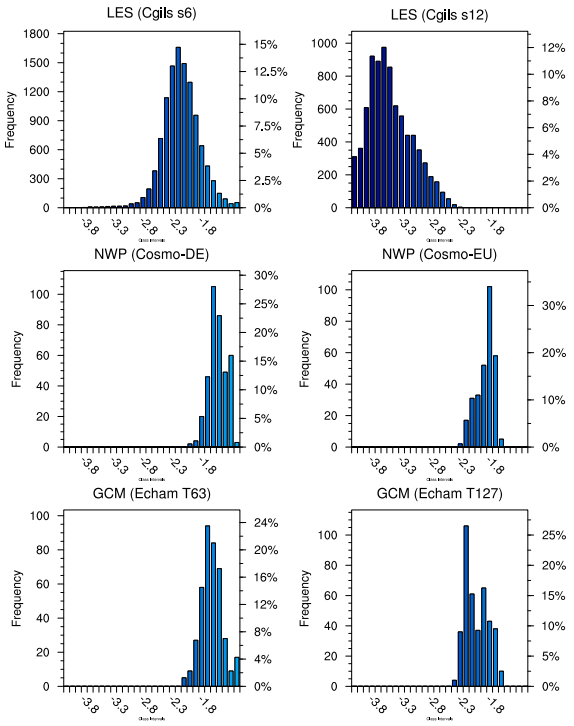

Fig. 3: Distributions of power law exponents, calculated by least square fit to a certain range (see Fig. 2).

Data	Mean
LES s6	-2.3
LES s12	-3.6
Cosmo-DE	-1.7
Cosmo-EU	-2.0
ECHAM6 T63	-1.8
ECHAM6 T127	-2.2

Table 1: Mean values of power law exponents. The exponents are calculated by least square fit to a certain range (see Fig. 2).

could be covered. To get a more continuous spectrum we will need datasets with high resolution and large domains in the future.

The impression of a consistent scaling gets confirmed if we look at the distribution of power law exponents in Fig. 3. For the general circulation model ECHAM6 and the numerical weather prediction models COSMO-DE and COSMO-EU the distributions are narrow and look relatively similar. Also the mean values (Tab. 1) confirm this impression and show a consistent scaling of around -2 for both models.

For both LES cases the calculated mean values are larger than -2 and the distributions show a different behaviour too. With a mean value of -3.6 especially the stratocumulus case differs clearly from the other values. This might be explained by the specific simulated physical situation. The power spectrum for this case gives evidence, that in a stratocumulus environment the variance is mainly resolved by larger scales. For the cumulus case the mean value of power law exponents (-2.3) is lower and this might be explained by a more uniform distribution of variance to different scales. Also the smaller scales contribute to the production of variance of total water mixing ratio.

6. CONCLUSIONS AND OUTLOOK

The general circulation model ECHAM6 and the numerical weather prediction model COSMO-DE and COSMO-EU show a consistent power law behaviour around -2 (Fig. 3 and Tab. 1). This value can be used to evaluate the

prognostic variance equation of the statistical cloud cover scheme. If the parameterization is used on different resolutions, the subgrid scale variance should show a power law scaling behaviour with an exponent around -2.

The broader spread of exponents produced by the two different LES cases supports the use of a prognostic equation for the variance. A purely diagnosed or even extrapolated variance might ignore the influence of certain physical processes.

A statistical cloud cover scheme with a prognostic variance equation coupled to other physical parameterizations has the potential to take physical processes into account and reproduce a varying scaling behaviour. But in the global and temporal mean, we should force the subgrid-scale variance to follow a power law with an exponent close to -2.

Acknowledgements: This research was funded by the Deutscher Wetterdienst as part of the extramural research program.

References

Baldauf, M., A. Seifert, J. Foerstner, D. Majewski, M. Raschendorfer, and T. Reinhardt, 2011: Operational convective-scale numerical weather prediction with the cosmo model: Description and sensitivities. *Mon. Wea. Rev.*, **139**, 3887 – 3905, doi:10.1175/MWR-D-10-05013.1.

Klein, S. A., R. Pincus, C. Hannay, and K.-M. Xu, 2005: How might a statistical cloud scheme be coupled to a mass-flux convection scheme? *J. Geophys. Res.*, **110**, doi:10.1029/2004JD005017.

Randall, D., R. Wood, S. Bony, R. Colman, T. Fichefet, J. Fyfe, V. Kattsov, A. Pitman, J. Shukla, J. Srinivasan, R. Stouffer, A. Sumi, and K. Taylor: 2007, Climate models and their evaluation. *Climate Change 2007: The Physical Science Basis. Contribution of Working Group I to the Fourth Assessment Report of the Intergovernmental Panel on Climate Change*, S. Solomon, D. Qin, M. Manning, Z. Chen, M. Marquis, K. Averyt, M.Tignor, and H. Miller, eds., Cambridge University Press, Cambridge, United Kingdom and New York, NY, USA., chapter 8.

Stevens, B., M. A. Giorgetta, E. Roeckner, T. Mauritsen, T. Crueger, H. Schmidt, E. Manzini, M. Esch, S. Rast, S. Kinne, L. Kornblueh, and R. Pincus, 2012: Echam6: Model and climate. in preparation.

Stevens, B., C.-H. Moeng, A. S. Ackerman, C. S. Bretherton, A. Chlond, S. de Roode, J. Edwards, J.-C. Golaz, H. Jiang, M. Khairoutdinov, M. P. Kirkpatrick, D. C. Lewellen, A. Lock, F. Mueller, D. E. Stevens, E. Whelan, and P. Zhu, 2005: Evaluation of large-eddy simulations via observations of nocturnal marine stratocumulus. *Mon. Wea. Rev.*, **133**, 1443–1462.

Stevens, B., C.-H. Moeng, and P. P. Sullivan, 1999: Large-eddy simulations of radiatively driven convection: sensitivities to the representationi of small scales. *J. Atmos. Sci.*, **56**, 3963–3984.

Stevens, B. and A. Seifert, 2008: On the sensitivity of simulations of shallow cumulus convection to their microphysical representation. *J. Meteorol. Soc. Japan*.

Tompkins, A. M., 2002: A prognostic parameterization for the subgrid-scale variability of water vapor and clouds in large-scale models and its use to diagnose cloud cover. *J. Atmos. Sci.*, **59**, 1917–1942.

CASE STUDY OF 'FIRST ECHO' BEHAVIOR ASSOCIATED WITH CUMULONIMBUS DEVELOPMENT OBSERVED BY KA-BAND DOPPLER RADAR IN THE KANTO REGION, JAPAN

Namiko Sakurai[1], Koyuru Iwanami[1], Takeshi Maesaka[1], Sin-ichi Suzuki[1], Shingo Shimizu[1], Ryohei Misumi[1], Dong-soon Kim[1], and Masayuki Maki[1]

[1] National Research Institute for Earth Science and Disaster Prevention (NIED), Japan

1. ABSTRACT

Simultaneous observations of cumulonimbi by a Ka-band Doppler radar (KaDR) and an X-band polarimetric Doppler radar (MP-X) were performed during the summer of 2011 in the Kanto region, Japan to study the process of cumulonimbus initiation and development. A cumulonimbus developed in the mountainous western part of the Kanto region on the morning of 18 August 2011, and its initiation and development were observed by the KaDR and the MP-X. We labeled each echo newly detected in a range height indicator (RHI) or plan position indicator (PPI) scan as a 'first echo (FE)'. In the developing stage, FEs occurred one after another, and the echo top height and maximum reflectivity of each individual echo gradually increased. The maximum echo top height of the cumulonimbus grew to 12 km. In the beginning of the developing stage, no echo was detected by the MP-X for more than 25 minutes. After the FE was detected by the MP-X and as the cumulonimbus developed, the time lag between FE detection by the KaDR and the MP-X tended to be smaller. In the first half of the developing stage, the FEs appeared between 2 and 5 km in height. In contrast, the appearance height of FEs stepped up to between 5 and 12 km in the second half of the developing stage. These results suggest that the ascent of appearance height of FE is one of key factors in the prediction of deep convection that may cause local heavy rainfall.

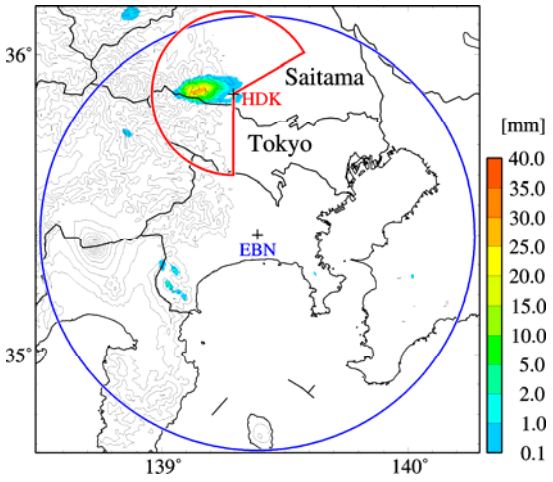

Figure 1. Locations of a Ka-band Doppler radar (KaDR) installed at Hidaka city and an X-band polarimetric Doppler radar installed at Ebina city (MP-X) (cross marks). Observation ranges were 30 km (KaDR) and 83 km (MP-X) (circles). Rainfall amount from 10:30 to 12:30 JST on 18 August 2011 is shaded. Elevation contours are depicted every 300 m.

2. INTRODUCTION

Localized heavy rainfall, one type of local severe weather, has been occurring with increasing frequency in the Tokyo Metropolitan Area, Japan (Sato and Takahashi, 2000). The localized heavy rainfall resulting from the sudden development of isolated thunderstorm often causes disasters such as flash floods and traffic congestion. In some locations of the Tokyo Metropolitan Area, bearable rainfall rate is less than 50 $mmhr^{-1}$ (Bureau of Urban Development

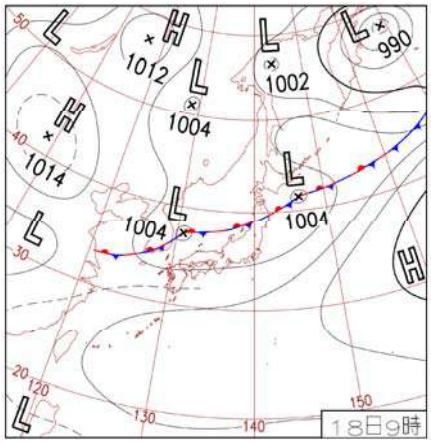

Figure 2. Surface weather map at 09:00 JST on 18 August 2011.

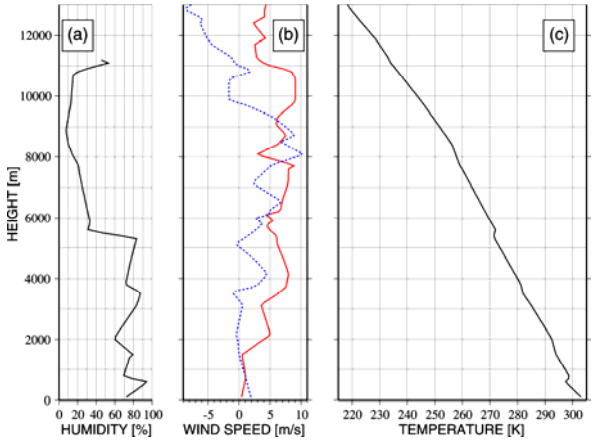

Figure 3. Sounding profiles of relative humidity (a), horizontal wind (b), and temperature (c) observed at Tateno at 09:00 JST on 18 August 2011. Solid red line (dashed blue line) in (b) indicates zonal wind (meridional wind).

Tokyo Metropolitan Government, 2007). A localized heavy rainfall associated with a thunderstorm occurred on 5 August 2008, making more than 80 mm of 1-hour accumulated rainfall in maximum. The localized heavy rainfall caused five deaths and the flooding of 34 houses above floor level in the Chiyoda, Shinjuku, and Bunkyo wards of Tokyo (Bureau of General Affairs of Tokyo Metropolitan Government 2008). To mitigate such disasters, it is necessary to develop a technique for the early detection and prediction with high accuracy of localized heavy rainfall.

Millimeter-wavelength radar is a useful tool for observing the initiation and early developing stage of cumulonimbi because it has higher sensitivity and higher spatial resolution than those of conventional weather radars (S-, C-, and X-band radars; centimeter-wavelength radars). However, there is only one previous study of the initiation and development of a cumulonimbus cloud using a vertically pointing W-band radar with 3 mm wavelength in the Kanto region in Japan (Kobayashi et al., 2011). The National Research Institute for Earth Science and Disaster Prevention (NIED) of Japan set up the Ka-band Doppler radar (KaDR) at Hidaka city, Saitama prefecture, Japan, and carried out simultaneous observations of cumulonimbi with an X-band polarimetric Doppler radar installed at Ebina city (hereafter called MP-X) in August 2011 (Fig. 1). The KaDR's observation area is one of the areas with highest frequency of thunderstorms within the Kanto region during the summer season (Saito and Kimura, 1998). On the morning of 18 August 2011, a cumulonimbus cloud developed within the observation range of the KaDR, and we succeeded in observing the cloud from initiation to developing stage using the KaDR and from developing to dissipation stage using the MP-X. The objective of this study is to describe the process of initiation and development of the cumulonimbus cloud observed on 18 August 2011 by using the KaDR and MP-X data. We investigated the time variation of the cumulonimbus cloud such as echo top height and echo intensity associated with the cumulonimbus development using mainly the KaDR data.

3. OBSERVATION AND DATA DESCRIPTION

The NIED KaDR, which is track-mounted Ka-band Doppler radar (Iwanami et al., 2001), was installed at Hidaka (HDK) in Saitama prefecture, Japan at the end of July, 2011 (Fig. 1). The period of intensive observation by the KaDR was 1 to 26 August 2011. The KaDR operated at 35.35 GHz, had a beam width of 0.28◦, a pulse width of 0.5 μs, a Nyquist velocity of 8.5 ms^{-1}, and the observation range of 30 km (Fig. 1). Nearly

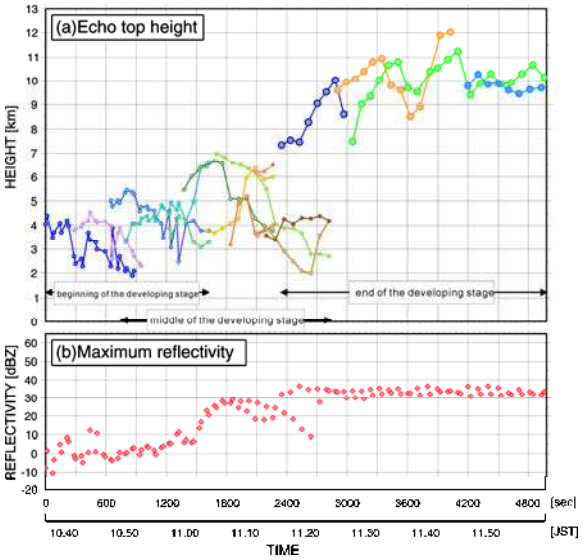

Figure4. Time series of echo top height (a) and maximum reflectivity (b) of a cumulonimbus observed by the KaDR in the developing stage on 18 August 2011. Echo top height of identical echo is connected by same colored line in (a). Left end of horizontal axis corresponds to 10:36:56 JST, when RHI scan started.

the entire observation area for the KaDR was contained within the observation area of MP-X (Fig. 1). A sensitivity of reflectivity signal of the KaDR was −23 dBZ at 10 km range. In this study, reflectivity data were used for analysis after the attenuation correction by using the relationship between the reflectivity factor and specific attenuation calculated by Iwanami et al. (2005).

The KaDR's observation method is as follows. To detect the initiation of a cumulonimbus cloud, a sector plan position indicator (PPI) scan at three elevation angles (7.3°, 10.5° and 14.9°) was conducted. The three angles were chosen so as to detect efficiently the initiation of a cumulonimbus cloud between 2 and 4 km in height and between 10 and 20 km in range. Kobayashi and Inatomi (2003) reported that the first radar echo of summer thundercloud often occurs between 2 and 4 km in height in southern Kanto region including the observation area of the KaDR using X-band radar data. Once a radar echo was detected, the scan strategy was changed: the sector PPI scans were stopped and range height indicator (RHI) scans toward the detected echo were started, although a sector PPI scan was inserted after every two or four RHI scans to obtain the position of the radar echo. This scan strategy, combining RHI and sector PPI scans, was continued until the radar echo decayed and dissipated or the radar echo left the observation area of the KaDR.

The MP-X performed sector scans to collect data of the cumulonimbus cloud after its radar echo was detected by the KaDR. The sector scans had a 60° azimuthal width and 17 elevation angles from 0.7° to 15.6°. The time resolution of the sector volume scan was 2 minutes and the observation range of the MP-X was 83 km (Fig. 1). The MP-X has a pulse width of 0.5 μs and beam width of 1.3°. Reflectivity (Z_H) data of the MP-X were corrected for rainfall attenuation using the relationship between specific attenuation and specific differential phase (K_{DP}) derived from differential propagation phase (Φ_{DP}) data (Maesaka et al. 2011) and used for analyses in this study.

4. RESULTS AND DISCUSSION

Figures 2 and 3 show a surface weather map and sounding profiles at Tateno at 09:00 Japan Standard Time (JST = UTC + 9 hours) on 18 August 2011, respectively. On that day, there was a stationary front in the northern part of Japan, but no synoptic disturbances in the Kanto region, and warm and humid air moved into the Kanto region near the surface. Relative humidity between the surface and 5.5 km was relatively high, but was low above 5.5 km (Fig. 3a). A westerly wind was dominant from the surface to 13 km (Fig. 3b). The convective available potential energy (CAPE) was 2028 Jkg^{-1}, the lifted condensation level (LCL) was about 750 m, and the level of free convection (LFC) was about 2400 m.

A radar echo was first detected at a height of about 3.8 km at 10:32:13 JST by the KaDR. Following radar echoes occurred one after another in the same part of the mountainous area.

Each radar echo gradually developed and migrated eastward. The reflectivity and the dimensions of latter radar echoes became larger than those of former radar echoes. The maximum reflectivity attained to 60.2 dBZ, as observed by the MP-X at 11:50:21 JST (figure not shown). The radar echo passed over the KaDR site at around 12:15 JST, left observation area, and then decayed. The MP-X observed the last radar echo at around 12:24 JST (figure not shown). The total rainfall amount between 10:30 and 12:30 JST is shown in Fig. 1. The maximum rainfall amount was 29 mm observed about 12 km west of the HDK site.

Evolution of the cumulonimbus cloud was investigated by the time series of its echo top height and maximum reflectivity during the developing stage from 10:36:56 to 11:59:56 JST (Fig. 4). Echo top height increased with time in three steps (Fig. 4a). In the beginning of the developing stage (0 to 1620 sec), convective activity was considered shallow because the echo top height was from 2.0 to at most 5.5 km. In the middle of the developing stage (720 to 2880 sec), the maximum echo top height of each identical echo reached to from 4.5 to at most 7.0 km. In the end of the developing stage (2340 to 4980 sec), the echo top became higher than 7.5 km and maximum height attained to 12 km. Similarly, maximum reflectivity increased with time in three steps corresponding to the time series of echo top height (Fig. 4b). In the beginning of the developing stage, the maximum reflectivity was about 0 dBZ on average and increased slowly. In the middle of developing stage, the maximum reflectivity sharply increased and had a peak at 30 dBZ. In the end of the developing stage, the maximum reflectivity was about 35 dBZ on average and had little change. This is much lower than the reflectivity observed by the MP-X (60.2 dBZ at maximum at 11:50:21 JST) in the end of the developing stage. It is considered that the difference occurred because raindrop size in

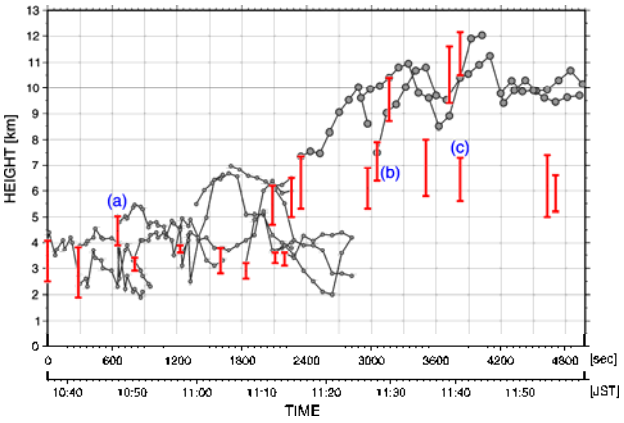

Figure5. Time series of top and bottom of first detected radar echo (red) and echo top height (gray) of a cumulonimbus observed by the KaDR in the developing stage on 18 August 2011. The echo top height of the cumulonimbus is same with that of Fig. 4a. Left end of horizontal axis corresponds to 10:36:56 JST, when RHI scan started. FEs labeled as (a)-(c) correspond to FEs in Fig. 6(a)-(c).

cumulonimbus cloud grew large enough to exist in the Mie scattering region for Ka-band frequency.

The time lag between the first detection of radar echo by the KaDR and the MP-X was also investigated. The KaDR and MP-X first detected an echo at 10:32:13 and 10:57:37 JST, respectively. Thus the time lag of the first detection of radar echo was 25 min 24 sec in the the developing stage of the cumulonimbus. The radar echo was observed about 20 (60) km from the KaDR (MP-X). The minimum detectable intensity of the KaDR and the MP-X was −16.4 dBZ (about 20 km) and 11.9 dBZ (about 60 km), respectively. Furthermore we labeled an echo newly detected in an RHI or PPI scan as a ‘first echo (FE)’. Time lag was estimated for each FE by comparing sector PPI data observed by the KaDR and the MP-X. The time lag tended to be smaller as convection developed: the lags were 08 min 59 sec and 07 min 59 sec in the middle period, compared with 02 min 28 sec in the final period of the developing stage.

Figure 5 shows the height range of the FE observed by RHI scans by the KaDR. The top and bottom height for the FE is shown. The FEs appeared in two height regions. In the first half of the developing stage (including the beginning and first half of the middle stage), the FEs were observed between 2 and 5 km in height. In the second half of the developing stage (including the second half of the middle stage and the end stage), the FEs were observed between 5 and 12 km in height. The height of the FE was low during shallow convection and jumped in the second half of the developing stage. The process of first echo development is shown in Fig. 6. The FEs appeared near or side an old echo (Fig. 6). The appeared FE developed separately (Fig. 6a) or merged with an old echo (Fig. 6b and c). It should be noted that the FE activated the old echo in the second half of the developing stage (Fig. 6b and c).

Figure 3c shows a temperature profile (T) observed at Tateno at 09:00 JST on 18 August 2011. There were stable layers at around 0.8, 1.8, 3.8, 5.5, and 8.1 km. $\Delta T/\Delta z$ of the each layer was smaller than moist adiabatic lapse rate (Ohno, 2001). Two of them at around 0.8 and 5.5 km were temperature inversion layers, and they are extremely stable layers. It is well known that the height of convective activity relates to that of inversion layer (Nodzu et al., 2006). In the beginning of the developing stage, development of echo top height was suppressed by the stable layer at around 5.5 km (Fig. 4a). Convective activity broke through the stable layer in the first half of the developing stage, and echo top height in the second half of the developing stage reached at higher altitude than that in the first half of the developing stage. Similarly, we investigated a relationship between the height of FE and that of stable layer. In the first half of the developing stage, the height of the FE concentrated between 2 and 5 in height, and most of echo top heights of the FEs were located just below 4 km, where a stable layer existed. In the second half of the developing stage, the height of the FE

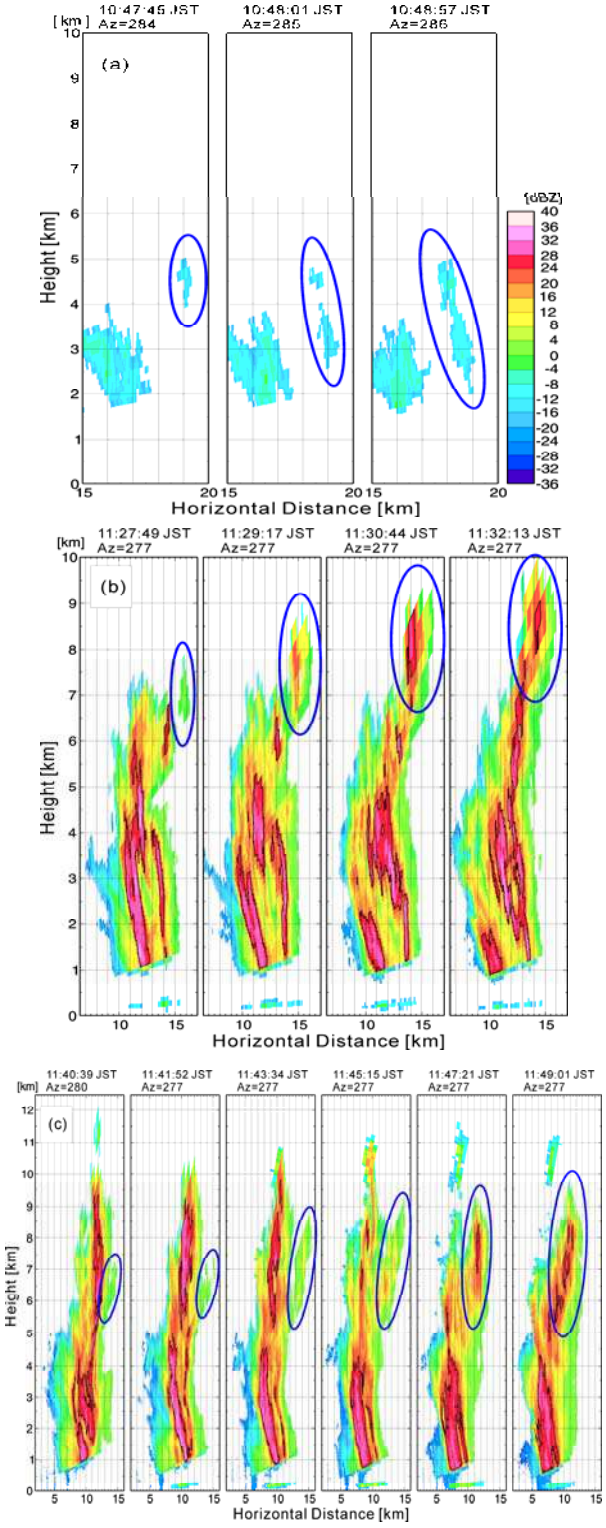

Figure6. Vertical cross-sections of reflectivity observed by RHI scan by the KaDR on 18 August 2011. The blue ovals indicate positions of FE and its following echoes.

concentrated between 5 and 8 km, where stable layers existed. Stronger updraft makes FE at higher altitude (Markowski and Richardson, 2010). It is considered that updrafts became strong associated with the development of convection, which made FEs at higher altitude in the second half of developing stage. Thus, it was cleared that echo top height and the height of FE well corresponded to the height of stable layers. However, the reason why the height of FE related with that of stable layer is unknown. To clear the mechanism of FE appearance, an accumulation of case study and an investigation on process of cloud microphysics using numerical model such as bin microphysics model will be necessary.

5. SUMMARY

Intensive observation of cumulonimbi with a Ka-band Doppler radar (KaDR) and an X-band polarimetric Doppler radar (MP-X) was conducted in the western Kanto region, Japan in August 2011. Using the KaDR with high sensitivity and high spatial resolution, we could observe the initiation and development of a cumulonimbus cloud on 18 August 2011. On the morning of this day, a cumulonimbus cloud emerged in the mountainous western part of the Kanto region, and at the location of maximum rainfall delivered a total of 29 mm. From the analysis with the KaDR and MP-X data, three points about the developing stage of cumulonimbus cloud were described in this paper.

1. The echo top height and maximum reflectivity developed in three steps. In the beginning of the developing stage, convection was shallow and reflectivity is weak. The MP-X could not detect any echo of the cumulonimbus cloud in the beginning of the developing stage. In the middle of the developing stage, the echo top height and reflectivity increased, and the MP-X first detected an echo. In the end of the developing stage, echo top height and reflectivity became higher than those in the middle period. The maximum echo top height exceeded 12 km in height in the end of the developing stage.

2. The time lag between first detection of radar echo by the KaDR and the MP-X became smaller as the cumulonimbus cloud developed.

3. The height of the FE was concentrated in two regions. In the first half of the developing stage, the FE was observed between 2 and 5 km in height; however, the FE was observed between 5 and 12 km in height in the second half of the developing stage.

The term ‘first echo’, has often used for the first detected echo of a cumulonimbus cloud by radar (Braham Jr., 1958; Kobayashi and Inatomi, 2003), although when used in this sense the term provides no useful information for identifying a cloud with the potential to be a large cumulonimbus. In contrast, by defining the newly detected echo in a cumulonimbus cloud as the ‘first echo’ (as in the present study), we propose to utilize the variation of first echo height to identify a cloud that would grow through deep convection such as a cumulonimbus. In the present study, we showed the effectiveness of the KaDR for the early detection of a cumulonimbus cloud. Because we presented only a single case study, it is necessary to perform additional case studies in order to obtain a comprehensive understanding of the process of cumulonimbus cloud development.

REFERENCES

(1) Braham Jr., R., 1958: Cumulus cloud precipitation as revealed by radar -Arizona 1955. J. Meteor., 15, 75-83.

(2) Iwanami, K., R. Misumi, M. Maki, T. Wakayama, K. Hata, and S. Watanabe, 2001: Development of a multiparameter radar system on mobile platform. Proc. 30th Conf. on Radar Meteor., 104-106.

(3) Iwanami, K., Y. Chono, T. Harimaya, J. Testud, M. Maki, R. Misumi, and S.-G. Park, 2005: Retrieval of vertical rain rate profile by

dual-frequency radar data. Proc. 32th Conf. on Radar Meteor., 104-106.

(4) Kobayashi, F., and N. Inatomi, 2003: First radar echo formation of summer thunderclouds in southern Kanto, Japan. J. Atmos. Electricity, 23, 9-19.

(5) Kobayashi, F., T. Takano, and T. T, 2011: Isolated cumulonimbus initiation observed by 95-GHz FM-CW radar, X-band radar, and photogrammetry in the Kanto region, Japan. SOLA, 7, 125-128.

(6) Maesaka, T., M. Maki, K. Iwanami, S. Tsuchiya, K. Kieda, and A. Hoshi, 2011: Operational rainfall estimation by X-band MP radar network in MLIT, Japan. Proc. 35th Conf. on Radar Meteor., 12-18.

(7) Markowski, P., and Y. Richardson, 2010: Mesoscale meteorology in midlatitudes. Wiley, 430 pp.

(8) Nodzu, M., S. Ogino, Y. Tachibana, and M. D. Yamanaka, 2006: Climatological description of seasonal variations in lower-tropospheric temperature inversion layers over the Indochina peninsula. J. Climate, 19, 3307-3319.

(9) Ohno, H., 2001: Thunderstorm and meso scale meteorology. TOKYODOSHOTEN, 309pp (in Japanese).

(10) Saito, T., and F. Kimura, 1998: Diurnal variation of convective precipitation in Chubu-Kanto area in the summer. Tenki, 45, 541-549.

(11) Sato, N., and M. Takahashi, 2000: Long-term changes in the properties of summer precipitation in the Tokyo area. Tenki, 47, 643-648.

SENSITIVITY OF AEROSOL INDIRECT EFFECTS TO IN SPECTRUM IN MIXED-PHASE CLOUDS OF GLOBAL CIRCULATION MODELS

Ricardo Morales Betancourt [1], Athanasios Nenes [1,2], Donifan Barahona [3], Dongmin Lee [4,5], Lazaros Oreopoulos [5]

[1]School of Earth and Atmospheric Science, Georgia Institute of Technology, Atlanta, Georgia, USA
[2]School of Chemical and Biomolecular Engineering, Georgia Institute of Technology, Atlanta, Georgia, USA
[3]NASA Goddard Space Flight Center / GESTAR, NASA GSFC, Greenbelt, Maryland, USA
[4]USRA Goddard Earth Sciences Technology and Research Columbia, Maryland, USA
[5]NASA Goddard Space Flight Center, NASA/GSFC Greenbelt, Maryland, USA

1. INTRODUCTION

Adequate estimates of aerosol indirect effects in mixed-phase and cold clouds requires of parameterizations of microphysical processes that are strongly based on physical principles. In particular, a parameterization of the ice nucleation process capable of capturing the competition between different freezing mechanism, as well as to respond to changes in the chemical nature and size of the aerosol substrate is necessary for the study of aerosol effects on precipitation, and in the optical properties of ice bearing clouds. The recent Barahona and Nenes (2009) ice nucleation parameterization, which is capable of handling any IN spectra to describe heterogeneous freezing in its competition with homogeneous freezing, is well suited to test the response of simulated cloud fields to changes in the IN spectra. Tests with three different IN spectra were performed in the single column mode of GEOS-5, with the objective of getting insightful information on the complete response of a cloud field to changes in the description of ice nucleation.

2. SIMULATION EXPERIMENTS

The simulation experiments were carried out using the Microphysics of Clouds with Relaxed Arakawa-Schubert and Aerosol-Cloud interaction (McRAS-AC) *[Sud and Wlaker 1999, Sud and Lee 2007]*, driven by the Goddard Earth Observing System Model, version 5 (GEOS-5). The lateral forcing fields to the 72 pressure levels in the atmospheric column of GEOS-5 are prescribed from assimilated 4D observational data. For the purpose of this study, we used the forcing from the TWP-ICE intensive observation period (IOP), derived by the Atmospheric Radiation Measurement (ARM) program. It includes data from January 17 to February 12, 2006.

Three well known IN spectra were utilized in the Barahona and Nenes (2009) ice nucleation parameterization framework to describe the availability of IN for heterogeneous nucleation. These IN spectra are the *Phillips et al., 2008* (PDA08), *Meyers et al., 1992* (MY92), and *Barahona and Nenes, 2009* (BN-CNT), based on classical nucleation theory.

3. RESULTS AND DISCUSSION

Despite the large differences in the predicted IN concentration by different IN spectra (which can differ by a factor of 100 to 1000), the results show large similarities in the cirrus cloud regime between all the schemes tested, in which ice crystal concentrations were within a factor of 10 regardless of the parameterization used. This similarity is the result of the competition between homogeneous and heterogeneous freezing. Schemes that predict low IN concentrations will be dominated by homogeneous nucleation (e.g., the BN-PDA08), while schemes with higher IN concentrations will transition from homogenous to heterogeneous freezing as a function of temperature (Fig 1).

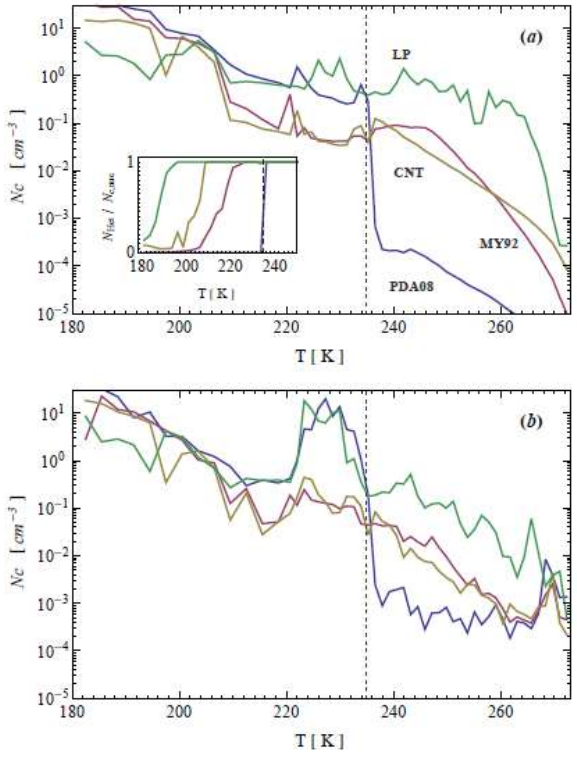

Figure 1- (a) Average number of nucleated ice crystals as a function of temperature for the simulations considered in this study. The inset is the fraction of crystals nucleated heterogeneously (b) Average number concentration of ice crystals as a function of temperature. The vertical dashed line marks the homogeneous freezing temperature threshold

In mixed-phase clouds there are some persistent differences in cloud particle number concentration and size, as well as in cloud ice fraction, ice water mixing ratio, and ice water path. In this regime, the imprint of the IN spectra was found to be much larger, since the buffering effect of homogeneous freezing is not present.

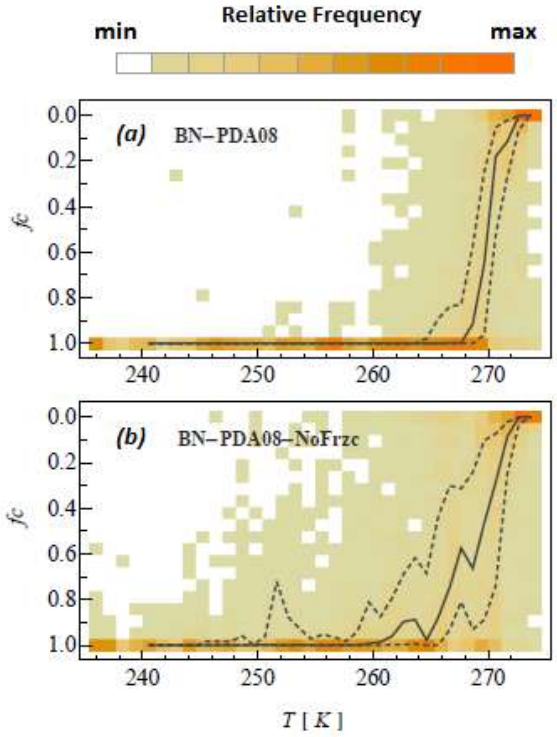

Figure 2 – Relative frequency of column-cells with a given ice-fraction as a function of the cell mean temperature. (a) for a simulation with the PDA08 spectrum and (b) for a simulation with the same spectrum, but in which contact freezing was neglected.

However, contact freezing of cloud droplets with mineral dust aerosol, contributed to transfer liquid to ice efficiently in the mixed-phase clouds, so that on average, the clouds were fully glaciated at T = 260 K, irrespective of the ice nucleation parameterization used (Fig 2). Only when contact freezing was neglected, did the simulated ice fractions exhibit a

dependence on the IN spectrum. This confirm the action of contact freezing as to buffer the impact of the IN spectrum in the partitioning of cloud condensate. Similarly, contact freezing contributed to the number of ice crystals (on average 10^{-4} cm^{-3}), providing a lower bound for ice crystal concentration (Fig 1).

Comparison of simulated ice water path to available satellite derived observations was also performed, finding that all the schemes tested were in good agreement with observations.

Sensitivity of the observed cloud fields performed in Single Column Model simulations with different IN spectrums suggest that the imprint of the IN spectrum in the simulated cloud fields is buffered by other processes, resulting in relatively similar fields even in simulations with considerably different nucleation schemes. Full GCM simulations are necessary to investigate further impacts of the ice nucleation on the radiation fields and possible feedbacks that cannot be observed in the SCM simulations.

4. BIBLIOGRAPHY

Barahona, D., and A. Nenes (2009), Parameterizing the competition between homogeneous and heterogeneous freezing in cirrus cloud formation: polydisperse ice nuclei, *Atmos. Chem. Phys.*, 9, 5933-5948

Liu, X., and J. E. Penner (2005), Ice nucleation parameterization for global models, *Meteo. Z.*, 14(4), 499-514

Meyers, M., P. J. DeMott, and W. R. Cotton (1992), New primary ice-nucleation parameterizations in an explicit cloud model, *J. Appl. Met.*, *31*, 708–721

Phillips, V. T. J., P. J. DeMott, and C. Andronache (2008), An empirical parameterization of heterogeneous ice nucleation for multiple chemical species of aerosol, *J. Atmos. Sci.*, *65*, 2757–2783

Sud, Y. C., and D. Lee (2007), Parameterization of aerosol indirect effect to complement McRAS cloud scheme and its evaluation with the 3-year ARM-SGP analyzed data for single column models, *Atmos. Res.*, *86*, 105–125.

Sud, Y. C., and G. K. Walker (1999), Microphysics of clouds with the Relaxed Arakawa-Schubert scheme (McRAS). Part I: Design and evaluation with GATE phase III data, *J. Atmos. Sci.*, *56*, 3196–3220

Acknowledgments

R. Morales-Betancourt acknowledges the JCET/NASA Graduate Summer Research Program in Earth Sciences. A. Nenes acknowledge support from DOE contract DE-SC0007145 and NASA ACMAP contract NNX08AK50G. D. Barahona was supported by the NASA Modeling, Analysis, and Prediction program under WBS 802678.02.17.01.07.

CORRECTING UNDERPREDICTION BIASES IN AUTOCONVERSION RATES IN WARM BOUNDARY LAYER CLOUDS BY INCLUDING SUBGRID VARIABILITY OF CLOUD DROPLET NUMBER CONCENTRATION

Ricardo Morales Betancourt [1], Athanasios Nenes [1,2], Donifan Barahona [3], Xiaohong Liu [4]

[1]School of Earth and Atmospheric Science, Georgia Institute of Technology
Atlanta, Georgia USA
[2]School of Chemical and Biomolecular Engineering, Georgia Institute of Technology
Atlanta, Georgia, USA
[3]NASA Goddard Space Flight Center / GESTAR, NASA GSFC
Greenbelt, Maryland USA
[4]Pacific Northwest National Laboratory, Atmospheric Sciences & Global Change Division,
Richland, USA

1. INTRODUCTION

A physically based description of subgrid scale variability of moist processes in Global Circulation Models (GCM) is an important requirement for achieving realistic representations of cloud properties and processes. Neglect of this subgrid variability can lead to important biases in cloud amount, liquid water content, and precipitation. Even sophisticated cloud microphysical schemes, which account for subgrid variability of in-cloud water content, fail to account for the subgrid variability of cloud droplet number concentration (CDNC) and the subsequent induced variability on effective radius and autoconversion rate. In this work, a simple scheme to include subgrid variability of CDNC was tested in an AGCM model framework, using the Community Atmospheric Model version 5 (CAM5). This scheme uses the link between cloud-scale updraft velocity and CDNC, provided by physically based activation parameterizations, to map variability in updraft (derived from turbulent kinetic energy), into variability in CDNC, and this is also propagated to other microphysical parameters (effective radius, and autoconversion rate). Under a Gaussian PDF of updrafts, adequate for warm boundary layer clouds, these corrections can be included with minimal computational cost, avoiding explicit integrations over the PDF.

2. MODEL CLOUD MICROPHYSICS

The cloud microphysics module of CAM-5 is described in *Morrison and Gettelman [2008]*, MG08 hereafter. MG08 is a 2-moment scheme that tracks liquid water, ice, and snow. The partial cloudiness scheme is that of *Zhang et al., [2003]*. Statistical treatment of the subgrid variability in moist processes has been shown to be of fundamental importance for partial cloudiness schemes.

One of the salient features of the MG08 microphysics is the inclusion of a statistical description of the in-cloud variability in the mixing ratio of liquid water, *ql*. It assumes, based on satellite observations of stratiform clouds, that the variations in *ql* follow a gamma distribution, with mean equal to the average in-cloud liquid water content for the grid cell, and with a prescribed relative dispersion. This pdf is then used to average all the process rates in the cloud scheme that depend on *ql*, including autoconversion and accretion rates, as well as the sedimentation velocity of hydrometeors.

This method results in an enhancement of each process by a different factor, which depends on the dispersion chosen for the gamma distribution, i.e., the relative dispersion of the distribution can be considered as a tuning parameter, but the nature of each physical processes transform it into process-specific tuning parameter.

In this work we incorporate into MG08 a similar approach developed by *Morales and Nenes [2010],* in which in-cloud variability of CDNC, and its impact on autoconversion rate is accounted for. This method uses physically based activation parameterization (which depends on the updraft velocity w), as the physical link to map variability on *w* into variability of CDNC. MG08 uses the activation routine of *Abdul-Razzak and Ghan [2000]*. In this approach, an analytical approximation in the integration of the activation rate is used, allowing the numerical integration to be replaced by a single evaluation of the activation parameterization.

The effect of this scheme is that instead of considering a monodisperse distribution of in-cloud CDNC, the distribution of CDNC is polydisperse. The contribution of the low-CDNC end of the distribution is amplified in processes with a strong dependence on droplet number, N_d. Such is the case of autoconversion rate, described in MG08 with the *Khairoutdinov and Kogan [2000]* parameterization, which depends on CDNC as $N_d^{-1.79}$. Therefore, including subgrid scale variability on CDNC with the method proposed here will cause an increase in autoconversion rate due to the presence of pockets of low droplet number concentration which promote pockets of enhanced autoconversion.

3. SIMULATION EXPERMENTS

The Morales and Nenes (2010) approach is incorporated into the MG08 microphysics by assuming that the dispersion in the distribution of in-cloud CDNC comes solely from the activation process. Two five-year simulations in CAM5 forced with climatology SST and present-day aerosol emissions were performed. The CTL simulation uses the default microphysics; while the VAR01 simulation was included the Morales and Nenes (2010) approach applied to autoconversion rate, but is otherwise identical to the CTL experiment. The precipitation rate for the CTL simulation for DJF is shown in Figure 1, together with the cloud amount.

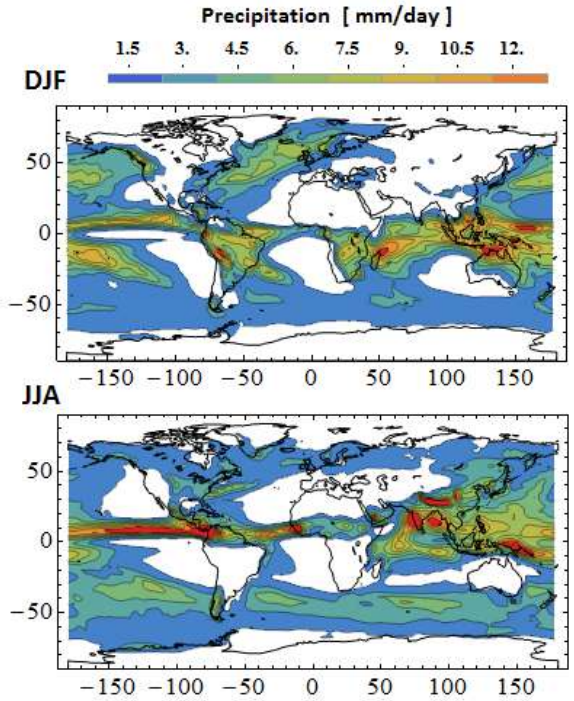

Figure 1. Precipitation pattern for northern hemisphere winter (DJF) and summer (JJA) for the CTL simulation experiment.

4. RESULTS AND DISCUSSION

The resulting modification translated into an enhancement of autoconversion rate in

warm stratiform clouds, by up to a factor of four. This change will cause an increase in the drizzle rate, but because this is will impact only the stratiform clouds in the model, total precipitation should not be greatly impacted. This was confirmed by the simulations results, in which a marginal decrease in mean precipitation rate from 2.33 mm/day in CTL, to 2.31 mm/day in VAR01. However, the changes should cause differences in the vertical structure as well as in the spatial distribution of the simulated clouds, by altering the distribution of heat in the atmospheric column through the modification of the latent heat release associated with drizzle evaporation. Difference maps for precipitation between CTL and VAR01 are shown in Figure 2, for the northern hemisphere winter and summer months.

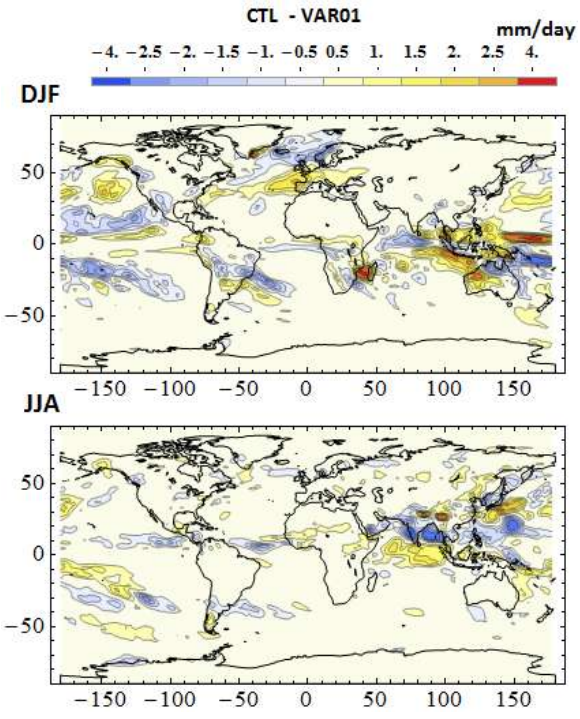

Figure 2. Difference in surface precipitation between CTL and VAR01 experiments

.

5. BIBLIOGRAPHY

Abdul-Razzak, H., and S. J. Ghan (2000), A parameterization of aerosol activation 2. Multiple aerosol types, *J. Geophys. Res.*, 105, D5, 6837-6844

Fountoukis, C., and A. Nenes (2005), Continued development of a cloud droplet formation parameterization for global climate models, *J. Geophys. Res.*, *110*, D11212

Khairoutdinov, M. F., and Y. Kogan, 2000: A new cloud physics parameterization in a large-eddy simulation model of marine stratocumulus. Mon. Wea. Rev., 128, 229–243.

Morales, R., and A. Nenes (2010), Characteristic updrafts for computing distribution-averaged cloud droplet number and stratocumulus cloud properties, *J. Geophys. Res.*, 115, D18220

Morrison, H., and A. Gettelman (2008), A new two-moment bulk stratiform cloud microphysics scheme in the community Atmosphere Model, Version 3 (CAM3). Part I: Description and numerical tests, *J. Climate*, 21, 3642-3659

Zhang, M., W. Lin, C. S. Bretherton, J. J. Hack, and P. J. Rasch, 2003: A modified formulation of fractional stratiform condensation rate in the NCAR Community Atmosphere Model (CAM2). *J. Geophys. Res.,* **108,** 4035

Acknowledgements

R. Morales Betancourt acknowledges support from an Alternate Sponsored Fellowship from the Pacific Northwest National Laboratory.

BACTERIAL ICE NUCLEI EFFECTS ON CLOUD RADIATIVE PROPERTIES INFERRED BY THE BRAMS MODEL

Costa, Tassio S.[1], Gonçalves, Fábio L. T.[1]; Yamasoe, Marcia A.[1], Martins, Jorge A.[2]; Silva Dias, M. A. F. [1]; Morris, Cindy E. [3]

[1]Dept. of Atmospheric Sciences, IAG/USP/Brazil
Rua do Matão 1226, zip 05508090, São Paulo , SP, Brazil
[2] Universidade Tecnológica Federal do Paraná, 86036-370, Londrina, PR, Brazil
[3] INRA, UR407 Pathologie Végétale, F-84140 Montfavet, France.

1. ABSTRACT

In the last years, a surge of research has been focusing on the role that microorganisms can play in cloud processes. Certain bacteria may constitute the most active ice nuclei found in the atmosphere and might have some influence on the formation of crystals in clouds. This study investigates the bacterial concentrations acting as ice nuclei through cloud numerical simulations using the *Brazilian Regional Atmospheric Model System*. The numerical simulations were developed in order to investigate the effect on the amount of rainwater as a function of bacterial ice nuclei concentrations with different scenarios (classified as S2 to S4 scenarios) corresponding to a maximum of 10^2 to10^4 IN bacteria per liter of cloud water plus the RAMS default (classified as the S5 scenario). Additionally, two other scenarios were included: without any IN (S1) and the sum of RAMS default and S4 scenarios (classified as S6). The chosen radiosonde data was for March 3rd, 2003, typical summertime in São Paulo City which presents a strong convective cell. The results show a decrease from 3% to 8% of reflected solar radiation at the top of the atmosphere (280 to 3000 nm) for scenarios S2, S3, S4 and S6, compared to S5 (BRAMS default) and an increase from 13 to 16% in infrared upward irradiance (3000 to 30000 nm) in the same scenarios S2, S3, S4 and S6, compared to S5. Therefore, the scenarios where bacteria act as IN in the warmer temperatures, show an important impact on cloud structures (such as cloud top height and albedo).

2. INTRODUCTION

Airborne microorganisms were found in the atmosphere for the first time in the XIX century. Since then, many studies on airborne fungi have been carried out to investigate atmospheric concentrations and compositions and their impact on the environment such as involvement in cloud

physic processes. Airborne bacteria can act as cloud condensation nuclei and some airborne bacterial and fungal species are able to act as ice nuclei and therefore induce rainfall in moderate climates and cause frost on crops (Schnell & Vali, 1973). Therefore, Schnell & Vali (1973, 1976) came to the conclusion that *P. syringae* is active as an ice nucleus because these bacteria produce a protein on their outer membrane that is one of the most active of the naturally-occurring ice nuclei (IN), and because freezing of cloud water is a critical step for rainfall over major parts of the earth (Sattler *et al.* 2001; Ariya & Amyot 2004; Diehl *et al.* 2000 and, Hamilton & Lenton, 1998). These bacteria are widely distributed across the planet, survive airborne dissemination up to the clouds and fall out with precipitation. On the other hand, the ice nuclei activity (INA) of fungi has received little attention where Pouleur et al. (1992) reported that the species *Fusarium* can freeze water at around -1.0^{o}C and -2.5^{o}C. Recently, according to Amato *et al.* (2005), the total bacterial count in clouds reached about 3x10^{4} cells.m^{-3} of cloud volume (1x10^{5} cells L^{-1} of cloud water).

On the other hand, cloud properties are quite important to the energy balance of the terrestrial atmosphere, holding infrared radiation from the surface as well as partially scattering and reflecting solar radiation through albedo. Solar radiation is the main external energy source for Earth's climate. It promotes atmospheric motions in our planet, turning it into a complex and dynamic system. Atmospheric constituents may interact with radiation by processes of emission, absorption and reflection/scattering. Here clouds act as one of the main modulators of the radiative balance, in addition to exerting a primary role in Earth's hydrological cycle. But despite their importance, clouds are still involved in processes that are among the least known by the scientific community (IPCC, 2007).

A numerical study using climatic models has shown representative low and medium cloud albedo (assuming clouds as black bodies) of 77% and 82%, respectively, inducing a cooling effect. High clouds, on the other hand, mainly composed of ice, showed 10% of solar albedo and 48% of emissivity, suggesting a greenhouse affect (Liou, 2002).

Studies have shown that bacteria may efficiently act as ice nuclei (Yankofsky *et al.*, 1981), which might influence cloud properties. Recent studies considering bacteria as ice nuclei agree that under typical bacterial concentrations no significant effect is found in a global scale (Hoose, Kristjásson and Burrows, 2010; Sesartic, Lohmann and Storelvmo, 2011), but local and regional effects have to be further studied, especially under high bacterial concentrations.

In this investigation, we used a high-resolution configuration of the Brazilian Regional Atmospheric Modeling System (BRAMS). The RAMS model utilizes the full set of non-hydrostatic, Reynolds-averaged primitive equations (Tripoli and Cotton, 1982). The Brazilian version of the RAMS is the result of changes incorporated by Brazilian users in recent years, which include a simple photochemical and a soil moisture scheme. Validation of the BRAMS for use in Amazon region simulations is presented by Freitas et al. (2009). The cloud microphysics in BRAMS is described by Martins et al (2009) based on Walko et al. (1995) and Meyers et al. (1997). This article's main goal is to investigate the role of the concentration of ice nucleation-active bacteria in cloud properties using the BRAMS cloud modeling and its consequences on the radiation budget using an atmospheric radiative transfer code.

2. METHODOLOGY

2.1 BRAMS modeling

The main BRAMS modeling is based on Gonçalves et al. 2012 which numerical simulations were developed in order to investigate the effect of IN concentrations on the total amount of rainwater in the integrated vertical column and on rainfall. Homogeneous initializations were performed and simulations carried out for a time interval of 3 hrs, Heating and wetting at the center of the grid were introduced after 10 minutes of simulation, mimicking a low level forcing in order to develop a convective cell. This low level forcing was applied according to Gonçalves et al. (2008). The chosen temperature and humidity profiles to initiate the model were taken from a radiosonde on March 3rd, 2003, which is typical for summertime at São Paulo City (-43.66 ° longitude, -23.59 ° latitude). The objective of the simulations is to analyze the effect of the IN concentrations on the BRAMS modeled cloud properties and precipitation.

In these simulations, bacteria act only as IN as it follows in the next section.

2.2 Ice nucleation modeling

Based on the model characteristics described above, six numerical experiments were run in order to analyze the effects of IN concentrations on modeled cloud properties, precipitation and electrification. These simulations considered a series of ice nucleation parameterizations as shown in Figure 1. In the first numerical experiment (S1) the model was run in the homogeneous nucleating mode only. In this case, a small group of water molecules take on a crystal lattice structure due to random motions. After the initial crystal structure was established, it grew throughout the entire water droplet. The homogeneous nucleation followed the parameterization proposed by DeMott et al. (1994) and was applied in the

temperature range from -50°C to -30°C (the value at -50°C was then applied to colder temperatures). In the second numerical experiment (S2 scenario), homogeneous nucleation occurred and IN concentration was assumed to follow 100,000 times less than the total population of bacteria where temperature range of -12°C to -2°C. Only a fraction of total bacteria can act as IN (Morris et al., 2008), therefore it was set to 1000 INA per L of cloud water (see Figure 1, for S3 scenario). As no observational data were available at temperatures colder than -12°C, the IN concentration for -10°C was used, as illustrated in Figure 1. Therefore, the number of nucleated ice crystals at a certain time (*t*) was also based on Morris et al. (2008). The *P. syringae* IN concentrations were assumed homogeneous over the whole model domain (vertical and horizontal) at the beginning of the simulation (t = 0) with no changes after the simulation started, there is no depletion of IN. The bacteria concentrations, in these scenarios, induced ice formation, as indicated in Figure 2. Time step is given in 2 minute.

The third and fourth numerical experiments were the same as S2, but the initial IN concentration profiles were 10 (S3) and 100 (S4) times the value of S2. The last numerical scenario (S5) is the one that represents RAMS' default parameterization, and it includes a variety of physical mechanisms: homogeneous nucleation (as in scenario S1); deposition nucleation and condensation-freezing nucleation (Meyers et al., 1992); contact freezing nucleation (Cotton et al., 1986). S6 presents IN concentration summing up the S5 (RAMS default) and S4 scenario, with bacteria acting as IN. It must be pointed out that S5 and S6 scenarios based on the RAMS ice nucleation parameterization were used as reference cases. Secondary ice production, based on the Hallett-Mossop theory (Cotton et al., 1986), is included in all scenarios. *P. syringae* bacterial concentrations are based on Amato et al. (2005, 2007), where we adjusted a polynomial equation to the observed values from -12°C to -2°C. It should be noted that the BRAMS default ice nucleation parameterization (S5) does not allow nucleation warmer than -8°C. The concentration of IN with bacteria follows exactly the IN concentration for normal RAMS and BRAMS defaults, i.e., there is no change in time by other processes as it is normally used for those models.

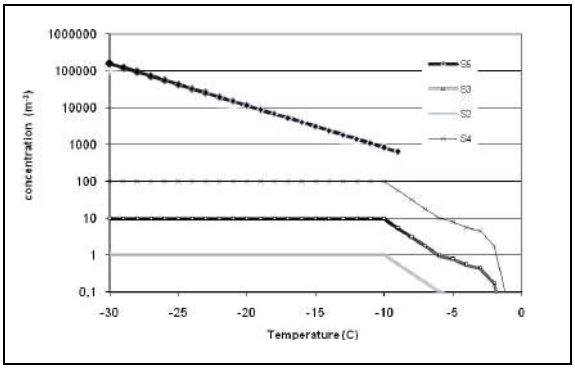

Figure 1. Ice nuclei concentration profiles (m^{-3}), where 10 bacteria per m^3 corresponds to 1000 IN bacteria per L of cloud water (S2 scenario), for different numerical scenarios involving the bacterium *P. syringae* (S2, S3, S4) and BRAMS default parameterization (S5). Scenario S6 is performed summing up S4 and S5.

2.3 Cloud radiative properties:

Input data:
Radiative simulations were performed using the libRadtran (Mayer and Kylling, 2005) atmospheric radiative transfer. Cloud parameters input are the vertical profiles of: i. liquid water and ice effective radius; ii. liquid water and ice content. These input parameters were obtained from BRAMS, considering the different bacterial loads as already described. BRAMS provides among its cloud properties the size distribution, concentration and mixture ratio of the following hydrometeors: a) cloud droplets; b) rain; c) pristine; d) snow; e) aggregates; f) graupel and g) hail. It provides also temperature, density and vertical velocity. Each output is provided in a vertical profile extending from 1000 hPa to 50 hPa every 50 hPa. The hydrometeor size distributions were converted to effective radius through the following relation:

$$r_{eff} = \frac{\int_0^\infty \pi \cdot r^3 \cdot n(r) dr}{\int_0^\infty \pi \cdot r^2 \cdot n(r) dr}$$

For simulations in the radiative transfer code, cloud droplets have been considered for the liquid phase hydrometeors. Snow, pristine and aggregates were taken into account for the ice phase through an average of effective radius and content weighted by the hydrometeor concentration. The remaining hydrometeors have been neglected, since they do not contribute significantly to rativive transfer simulations in comparison to the others.

Vertical profiles of temperature and density from BRAMS were also used as input for libRadtran. Surface albedo was set as urban type from the libRadtran library.

Simulated solar albedo (280 to 3000 nm) and thermal emission (3000 to 30000 nm), both at top of atmosphere, have been evaluated. The two streams method was used in the simulations.

3. RESULTS

Figures 2 and 3 show the solar and infrared irradiances in $W.m^{-2}$, for the different simulations, S1 to S6, in the center of the convective cell, at the time when the most vigorous vertical motions occurred inside the cloud. Figure 2, the light colors present the differences between simulations

and S5, RAMS default, where the S4 has the highest difference, 8%. It must be notified that S4 and S6 have the highest bacterial concentrations. The difference between S4 and S6 is that the last one has also the RAMS default and S4 has only the bacterial default.

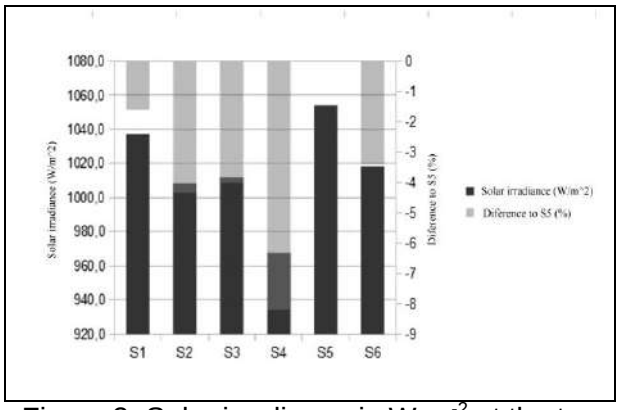

Figure 2. Solar irradiance in W.m^{-2} at the top of the atmosphere

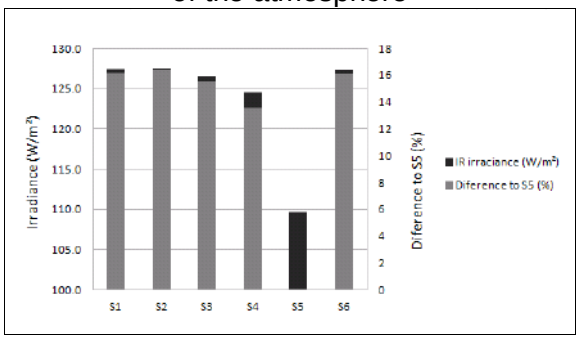

Figure 3. Infrared at the top of the atmosphere in W.m^{-2}**.**

Figure 3 presents infrared results, where there are also differences from 13 to 16%. S4 simulation presents a difference of 13% against the RAMS default S5 and S6 presents the highest difference of 16%. Therefore, when bacterial concentrations are taken into account, significant differences are observed in comparison to the RAMS default.

4. Conclusions

The results of this work suggest that, the presence of biological ice nuclei active at relatively warm temperatures, and in particular the bacterium *P. syringae,* can induce and modify cloud ice, which in turn induces changes in its radiative structures. As it was shown in Gonçalves et al. (2012) for other cloud structures and lightning, the (B)RAMS default should be modified. Future works should consider modifying the default parameters (-8^{o}C) to explore deeper convective storms in other realistic contexts that involve more detailed parameterization of the hydrometeor concentrations.

Therefore, the results show a decrease from 3% to 8% of reflected solar radiation at the top of the atmosphere (280 to 3000 nm) for scenarios S2, S3, S4 and S6, compared to S5 (BRAMS default) and an increase from 13 to 16% in infrared upward irradiance (3000 to 30000 nm) in the same scenarios S2, S3, S4 and S6, compared to S5. Therefore, the scenarios, where bacteria act as IN in the warmer temperatures, show an important local impact on cloud structures and microphysics, which consequently alters the local radiation fluxes.

5 REFERENCES

Ariya P.A. and Amyot M. New directions: The role of bioaerosols in atmospheric chemistry and physics.

Atmospheric Environment 38: 1231–1232, 2004.

DeMott, P. J., M. P. Meyers, W. R. Cotton. Parameterization and impact of ice initiation 755 processes relevant to numerical model simulations of cirrus clouds. *J. Atmos. Sci. 51*, 77-90, 1994.

Diehl, K., Matthias-Maser S., Mitra, S.K., and Jaenicke R. Laboratory studies on the ice nucleating ability of biological aerosol particles in condensation freezing, immersion freezing and contact freezing modes. *J. Aerosol Sci.* 31, S70-S71, 2000.

Gonçalves, F. L.T., Martins, J.A., Albrecht, R.I., Morales, C.A.,Silva Dias, M.A.F., Morris, C.E., Effect of bacterial ice nuclei on the frequency and intensity of lightning activity inferred by the BRAMS model. *Atmos. Chem. And Phys. Discussion forum.* doi:10.5194/acpd-11-1-2011.

Hamilton, W.D., Lenton, T.M. Spora and Gaia: how microbes fly with their clouds. *Ethology, Ecology and Evolution*, 10, 1-16, 1998.

Martins, J. A., M. A. F. Silva Dias, and F. L. T. Gonçalves. Impact of biomass burning aerosols on precipitation in the Amazon: A modeling case study. *J. Geophys. Res*., 114, 1, 1-68, 2009.

Martins, J. A. and M. A. F. Silva Dias. The impact of smoke from forest fires on the spectral dispersion of cloud droplet size distributions in the Amazonian region *Environ. Res. Lett*. 4, 015002 doi: 10.1088/1748-9326/4/1/015002, 2009.

Meyers, M. P., R. L. Walko, J. Y. Harrington, and W. R. Cotton. New RAMS cloud microphysics parameterization. Part II: The two-moment scheme, *Atmos. Res., 45*, 3-39, 1997.

Morris CE, Georgakapoulos D, Sands D.C. Ice nucleation active bacteria and their potential role in precipitation. *J Phys IV, France* 121, 87-103, 2004.

Morris, C. E., D. C. Sands, M. Bardin, R. Jaenicke, B. Vogel, C. Leyronas, P. A. Ariya, and R. Psenner. Microbiology and atmospheric processes: research challenges concerning the impact of airborne micro-organisms on the atmosphere and climate. *Biogeosciences* 8,17-25, 2011.

Morris, C. E., D. C. Sands, J. L. Vanneste, J. Montarry, B. Oakley, C. Guilbaud, and C. Glaux. Inferring the evolutionary history of the plant pathogen *Pseudomonas syringae* from its biogeography in headwaters of rivers in North America, Europe and New Zealand. *mBio* 1(3): e00107-10-e00107-20, 2010.

Hoose, C.; Kristjásson and Burrows S.,. How important is biological ice nucleation in clouds on a global

scale? Environ. Res. Lett. 5 (2010) 024009.

Liou, K. N. An Introduction to Atmospheric Radiation. Second Edition. International Geophysics Series, volume 84. 2002. P. 480.

Morris, C. E., D. C. Sands, B. A. Vinatzer, C. Glaux, C. Guilbaud, A. Buffière, S. Yan, H. Dominguez, and B. M. Thompson. The life history of the plant pathogen *Pseudomonas syringae* is linked to the water cycle. *ISME Journal* 2, 321-334, 2008.

Mayer, B., Kylling, A.: Technical note: The libRadtran software package for radiative transfer calculations - description and examples of use. Atmos. Chem. Phys., 5, 1855-1877, 2005.

Pouleur, S., Richard, C., Martin, J.G., Antoun, H. Ice Nucleation Activity in *Fusarium acuminatum* and *Fusarium avenaceum App. Environ. Microbiol*. 58:2960-2964, 1992.

Sattler, B., Psenner R., Puxbaum, H. and Limbeck, A. Clouds as habitat and seeders of active bacteria. Proc. SPIE-*The International Society for Optical Engineering 4495 (Instruments, Methods, and Missions for Astrobiology IV*), 211-222, 2002.

Sesartic, Lohmann and Storelvmo. Bacteria in the ECHAM5-HAM global climate model. Atmos. Chem. Phys. Discuss., 11, 1457–1488, 2011.

Schnell, R.C. & Vali, G. World-wide source of leaf decomposing vegetation. *Nature*, 236, p.163-165, 1973

Solomon, S., D. Qin, M. Manning, Z. Chen, M. Marquis, K.B. Averyt, M. Tignor and H.L. Miller (eds.). IPCC Climate Change 2007: The Physical Science Basis : Contribution of Working Group I to the Fourth Assessment Report of the Intergovernmental Panel on ClimateChange.Cambridge University Press, Cambridge,UK and New York, NY, USA, 996 pp

Tripoli, G. J., and W. R. Cotton. The Colorado State University three-dimensional cloud mesoscale model, Part I: General theoretical framework and sensitivity experiments*, J. Rech. Atmos*., 16, 185-220, 1982.

Walko, R., W. R. Cotton, M. P. Meyers, and J. Y. Harrington. New RAMS cloud microphysics parameterization. Part I: The single-moment scheme. *Atmos. Res.,* 38, 29-62, 1995.

Yankofsky, S. A., Z. Levin, T. Bertold, N. Sandlerman, 1981: Some Basic Characteristics of Bacterial Freezing Nuclei.J. Appl. Meteor.,20, 1013–1019

ROUGH AND IRREGULAR ICE CRYSTALS IN MID-LATTITUDE CLOUDS

Z. Ulanowski[1], P.H. Kaye[1], E. Hirst[1], R.S. Greenaway[1] and R. Cotton[2]

[1] Centre for Atmospheric and Instrumentation Research, University of Hertfordshire, Hatfield AL10 9AB, UK. Email: z.ulanowski@herts.ac.uk
[2] Met Office, Fitzroy Road, Exeter EX1 3PB, UK

1. INTRODUCTION

Cloud feedbacks are the largest source of uncertainty in climate models. In particular, uncertainties exist concerning the radiative forcing of clouds containing ice crystals, most notably cirrus. Indeed, whether cirrus clouds warm or cool the Earth's surface depends on ice crystal morphology. Reducing this uncertainty requires detailed *in situ* characterization of cloud particles. Also, detailed knowledge of the scattering properties of cloud particle types is needed for accurate retrieval of cloud microphysical properties from remote sensing. One of the main barriers to achieving these goals is the inability of cloud probes to determine the contribution of small ice crystals (that is crystals smaller than about 50 μm) to the total distribution. This is partly due to their inability to resolve the geometric structure of small ice crystals because of the conflicting demands of high optical resolution and large sample volume (Ulanowski et al. 2004, Connolly et al. 2007, Kaye et al. 2008).

There is also growing evidence, largely indirect, that atmospheric ice crystals have shapes departing from idealized geometries based on perfect hexagonal prisms (Garrett 2008, Baran 2012). Korolev et al. (2000) concluded that the majority of ice particles in mid-latitude stratiform clouds observed during several campaigns were of irregular shape. Best fits to data obtained by Lampert et al. (2009) in Arctic ice cloud were consistent with deeply rough hexagonal ice crystals. Gayet et al. (2011) found prevalent particles with imperfect or complex shapes at trailing edge of mid-latitude frontal cirrus. Measurements using the Polar Nephelometer (Shcherbakov et al. 2006) indicated that the surface of Antarctic ice crystals was deeply rough. It is important in this context that particle roughness can dramatically alter the scattering properties of ice crystals. For example, it can significantly reduce the asymmetry parameter (Yang et al. 2008, Ulanowski et al. 2006). Roughness may also account for the relative rarity of ice halos (Ulanowski 2005). Therefore it is important to quantify fine detail of ice crystal geometry, currently largely beyond the reach of imaging cloud probes, although there are indications that a new generation of probes using incoherent light may be able to resolve at least some of the detail (Schön et al. 2011).

It is possible to circumvent the optical resolution limitations of imaging probes by acquiring light scattering "patterns" instead of images. Such patterns can be obtained from relatively large sample volumes, as there is no sharply-defined image plane to limit resolution. Several light scattering cloud probes, jointly known as Small Ice Detectors (SID) have been developed over the last decade at the University of Hertfordshire. Successive models obtain scattering patterns with progressively higher angular resolution. The earlier designs rely on multi-element detectors measuring mainly the azimuthal scattering, while the most recent, collectively known as SID-3, acquire high-resolution two-dimensional (2D) scattering patterns (Kaye et al. 2008). 2D scattering patterns offer high potential for detailed particle characterization. It is possible to recover the shape, size and orientation of small ice particles by comparing such patterns to models such as the Ray Tracing with Diffraction on Facets (RTDF) scattering model (Clarke et al. 2006, Kaye et al. 2008). Ice particle roughness can also be obtained, as evidenced by experimental patterns from ice analogue crystals with smooth and rough surfaces, which show distinct differences: while the former have sharp, well-defined bright arcs and spots, the latter have much more random, "speckly" appearance, but with greater azimuthal symmetry (Ulanowski et al. 2006). Here we focus on the application of 2D scattering patterns to retrieving the roughness ice particles encountered in mid-latitude cirrus and mixed phase clouds.

2. METHODS

First *in situ* cloud data from the SID-3 probe was obtained during the Met Office CONSTRAIN campaign in Scotland in Feb. 2010 with another case in south England in

Sept. 2010. SID-3 was flown in a PMS-style canister on the FAAM research aircraft. The probe has “open” geometry similar to SID-2, to minimize ice particle shattering. Particle triggering, incident illumination (532 nm wavelength laser beam) and sample volume definition are also similar to SID-2 (Cotton et al. 2010). However, the main detector of SID-3 is an intensified CCD camera with a nominal resolution of 780 by 582 pixels (Kaye et al. 2008). The camera produces 2D scattering patterns from single particles at rates up to 30 per second, depending on configuration. Receiving optics collect the scattered light over an annulus covering scattering angles from 6° to 25°, sufficient to encompass the 22° halo scattering from ice prisms, but with the central low-angle area obscured by a beam stop.

Image texture can be quantified using statistical measures, e.g. the gray-level co-occurrence matrix (GLCM), which deals with spatial relationships of pairs of gray values of pixels. Previously, GLCM was applied to retrieving surface roughness from laser speckle images (Lu et al. 2006). Initially, four GLCM features were chosen: contrast, correlation, energy and homogeneity. In addition, image entropy and two measures relating to image brightness distribution, rather than texture, were examined: the ratio of root-mean-square (RMS) brightness to its standard deviation (*RMS*/*SD*, Jolic et al. 1994), and kurtosis. The measures were calculated for 2D patterns from a range of test particles: smooth and rough ice analogues, and mineral dust grains and correlated with a semi-quantitative measure of particle roughness. We also examined the sensitivity of the same measures to potential bias sources, including image noise, particle size, shape and orientation, and detector gain. Various image normalization and averaging schemes were compared too, and the chosen one involved scaling mean image brightness to 10 on the 0 - 255 scale.

Energy was found to have the strongest correlation with roughness and robustness with respect to the potential bias sources of all the GLCM measures. It is relevant that the GLCM energy also shows good correlation with surface roughness and is most robust with respect to variation of "the setup configuration, the position, and the orientation of the surface to be measured" in the context of laser speckle (Lu et al. 2006). Similar performance characterized the remaining measures, entropy, *RMS*/*SD* and kurtosis, but different measures showed sensitivity to different sources of bias. For example, entropy was slightly sensitive to gain and particle size. A combined feature was therefore defined, composed of the most robust measures, energy *E*, *RMS*/*SD* and the logarithm of kurtosis *K*, as follows:

$$RMS/(200SD) - 10E - \log(K)/5 + 0.7.$$

The combined roughness measure is weighted so that individual measures contribute to it approximately equally and it is centred on zero for the particles examined, with approximate bounds of ±1.

Scanning electron microscopy (SEM) images of test particles were taken using JEOL-5700 environmental SEM. Images of ice were obtained in the presence of water vapour in the SEM chamber. Ice was allowed to grow on a metal substrate on a Deben Ultra Peltier-cooled cold stage.

3. RESULTS AND DISCUSSION

Fig. 1 shows a typical selection of scattering patterns from ice particles from the flight campaign, in comparison with test particles. Both cirrus and mixed phase patterns are qualitatively similar to the rough rosette pattern. The roughness measures were calculated for a random selection of several hundred patterns from marine cirrus and mixed phase flights, as well as one cirrus flight in a continental airmass – the frequency distributions of the combined roughness measure are shown in Fig. 2. Roughness measures were also calculated for a range of test particles, including ice analogue crystals (Ulanowski et al. 2006) and mineral dust grains, all representing a range of surface roughness – the results are given at the bottom of Fig.2, with example test particles shown in Fig. 3. It can be seen that smoother test particles correspond to the tails of the roughness distributions, which are better represented by the rougher particles in the selection. Scattering from ice analogue rosettes very similar to those used here was previously characterized using a levitation technique. It was found that the transition from smooth to rough geometry for these large crystals lowered the asymmetry parameter from 0.81 to about 0.63 (Ulanowski et al. 2006). It is worth noting that such a large change corresponds to almost doubling the reflectivity of a cloud composed entirely of such particles.

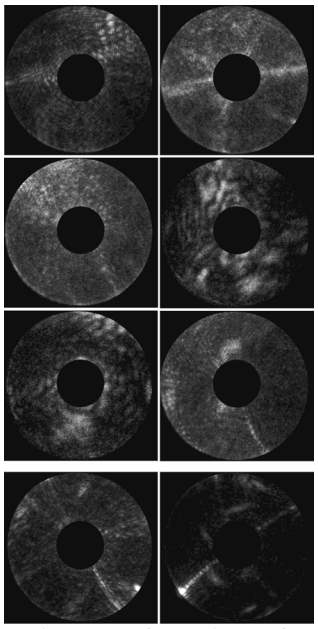

Fig. 1. Top 3 rows show 6 randomly selected SID-3 patterns from ice particles during mixed phase (left) and marine cirrus (right) flights, compared to patterns from ice-analogue rosettes with moderately rough (bottom left) and smooth surfaces (bottom right).

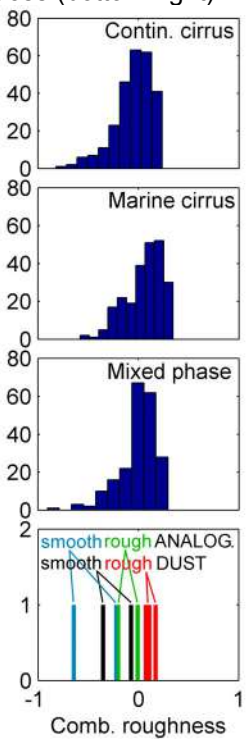

Fig. 2. Distributions of combined roughness measure from 2D SID3 patterns in continental cirrus, marine cirrus and mixed phase flights, compared to test particle roughness.

It is interesting to observe that, while rough particles dominated in all three cloud types, marine cirrus and mixed phase clouds were similar, but cirrus in a continental, polluted airflow had lower roughness. We speculate that this is due to higher concentration of ice nuclei in the last case. High-resolution cloud modeling shows that lower ice supersaturations can be found in continental than in marine cases (Flossmann and Wobrock 2010). This raises the possibility that the observed roughness may be the outcome of faster ice growth.

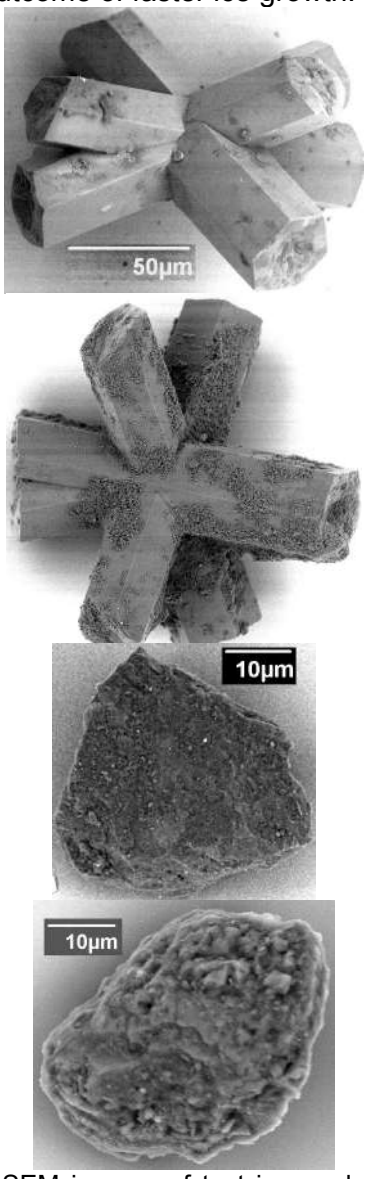

Fig. 3. SEM images of test ice analogues and mineral dust grains with roughness measure shown in Fig. 2. Max. dimension and combined roughness are given, top to bottom: 150 µm rosette –0.22, 160 µm rosette –0.01, 41 µm dust -0.07, 47 µm dust 0.17. The scattering patterns from the rosettes are shown in Fig. 1.

Roughness was similar in growth and sublimation zones of cirrus. This suggests that the currently prevailing view that ice crystals merely become rounded as they sublimate (Nelson 1998) may be incorrect. Indeed, laboratory experiments show that ice surfaces can become rough during fast sublimation (Cross 1969, Pfalzgraff et al. 2010,Ritter et al. 2012). Sublimating ice

crystals seen at high resolution is shown Fig. 4. While rounded crystals are frequently observed using imaging cloud probes, optical resolution limitations conceal fine detail associated with roughness (Ulanowski et al. 2004, Connolly et al. 2007).

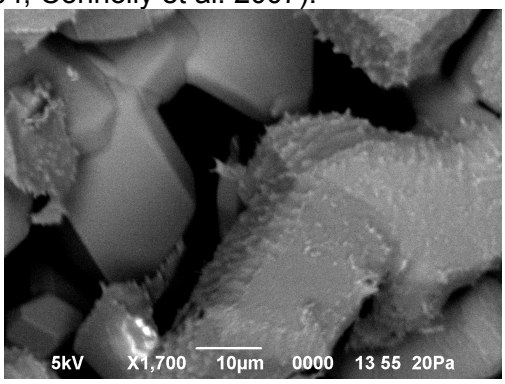

Fig.4. Scanning electron microscopy image of ice crystals sublimating near –40°C. Note that surfaces deeper within the sample, where subsaturation is expected to be weaker (due to lower temperature and/or higher local water vapour pressure), remain smooth while the exposed surfaces are rough.

4. CONCLUSIONS

SID-3 probe was flown on the FAAM aircraft in mid-latitude clouds. Unlike most earlier results from cloud chambers, where SID-3 2D scattering patterns typically displayed characteristics attributable to idealized geometric crystal shapes, the majority of the cloud patterns showed random, "speckly" appearance. Lab experiments show that this is typical of particles with rough surfaces or complex structure. Quantitative comparison of lab and cloud data was done using pattern texture measures, originally developed for surface roughness analysis using laser speckle. The results are consistent with the presence of strong roughness in the majority of cirrus and mixed phase cloud ice crystals, at levels similar to those found in rough ice analogue and mineral dust particles used for reference. Similar roughness was found in the growth and sublimation zones of cirrus, suggesting that roughness can be maintained or possibly even reinforced by sublimation. Slightly weaker roughness was present in cirrus in polluted airmass of continental origin than in marine cirrus, possibly as an indirect outcome of higher concentrations of ice nuclei in the former.

5. BIBLIOGRAPHY

Baran A. J.: From the single-scattering properties of ice crystals to climate prediction... Atm. Res. doi: 10.1016/j.atmosres.2012.04.010, 2012.

Connolly P.J., Flynn M.J., Ulanowski Z. et al.: Calibration of 2-D imaging probes… J. Atm. Oceanic Technol. 24, 1860-79, 2007.

Cotton R., Osborne S., Ulanowski Z., et al.: The ability of the Small Ice Detector (SID-2)... *J. Atm. Oceanic Technol.* 27, 290–303, 2010.

Cross J.D.: Scanning electron microscopy of evaporating ice. Science 164, 174-5, 1969.

Flossmann A.I. & Wobrock W.: A review of our understanding of the aerosol-cloud interaction... Atm. Res. 97, 478-97, 2010.

Gayet J.F., Mioche G., Shcherbakov V. et al.: Optical properties of pristine ice crystals... Atm. Chem. Phys. 11, 2537-44, 2011.

Garrett T.J.: Observational quantification of the optical properties of cirrus cloud. Light Scattering Reviews 3, Springer, 3-26, 2008.

Jolic K.I., Nagarajah C.R. & Thompson W.: Non-contact, optically based measurement of surface... Meas. Sci. Technol. 5, 671-84, 1994.

Kaye P.H., Hirst E., Greenaway R.S. et al.: Classifying atmospheric ice crystals by spatial light scattering, Opt. Lett. 33, 1545-7, 2008.

Korolev A., Isaac G.A. & Hallett J.: Ice particle habits in stratiform clouds: Q. J. R. Meteor. Soc. 126, 2873-902, 2000.

Lampert A., Ehrlich A., Dörnbrack A. et al.: Microphysical and radiative characterization of a subvisible midlevel Arctic ice cloud… Atm. Chem. Phys. 9, 2647–61, 2009.

Nelson J.: Sublimation of ice crystals. J. Atm. Sci. 55, 910-19, 1998.

Schön R., Schnaiter M., Ulanowski Z. et al.: Particle habit imaging using incoherent light… J. Atm. Oceanic Technol. 28, 493-512, 2011.

Shcherbakov V., Gayet J.F., Jourdan O. et al.: Light scattering by single ice crystals of cirrus clouds, Geophys. Res. Lett. 33, L15809, 2006.

Lu R.S., Tian G.Y., Gledhill D. & Ward S.: Grinding surface roughness measurement... Appl. Opt. 45, 8839-47, 2006.

Pfalzgraff W.C., Hulscher R.M. & Neshyba S.P.: Scanning electron microscopy and molecular... Atm. Chem. Phys. 10, 2927–35, 2010.

Ritter G., Ulanowski Z., Hesse E. & Kaye P.H.: A diffusion chamber design to study effects of temperature, ambient… This conference, 2012.

Ulanowski Z., Connolly P., Flynn M. et al.: Using ice crystal analogues…. Proc. 14 Int. Conf. Clouds Precip., Bologna, 1175-8, 2004.

Ulanowski Z., Hesse E., Kaye P.H. & Baran, A.J.: Light scattering by complex ice-analogue crystals. J. Quantit. Spectr. Rad. Transf. 100, 382-92, 2006.

Yang P., Kattawar G.W., Hong G. et al.: Uncertainties associated with the surface texture of ice particles.... IEEE Trans. Geosci. Remote Sens., 46, 1940-57, 2008

Acknowledgements

This work was supported by the UK NERC grants NE/E011225/1 and NE/I020067/1.

Marine cold air outbreaks in a general circulation model: Climatology and convection

Verena Grützun*[1], Axel Seifert[2], and Bjorn Stevens[1]

[1]Max Planck Institute for Meteorology, Hamburg, Germany
[2]Hans-Ertel Centre for Weather Research, Deutscher Wetterdienst, Hamburg, Germany

May 22, 2012

Abstract

Today's global and weather prediction models approach the convective greyzone, i.e., convective motions are explicitely representable, but convection is still not entirely resolved. Statistical assumptions underlying convection schemes become unreliable. The Working Group on Numerical Experimentation (WGNE) of the World Meteorological Organisation proposed case studies on marine cold air outbreaks (MCAOs) to better understand how skilful traditional convection schemes are on these scales. MCAOs are an often overlooked but highly interesting example of cloud topped marine boundary layers. Boundary layer depth increases with distance from land due to heating from the ocean surface and exhibits a variety of cloud structures such as cloud streets, stratocumulus and open cells. There is evidence that systematic biases particularly related to the momentum transport in regions of MCAOs play a major role for errors in the model forecast. As a first step, we investigate how well MCAOs are represented in the global circulation model ECHAM6. Heat fluxes from ocean to atmosphere, boundary layer depth and cloudiness retrieved from the model are compared to data from ERA-interim and satellite offering insight to general shortcomings of the model. At a later stage, we will perform large eddy simulations of a selected case. By this we gain detailed information about the statistics of clouds, heat and mass fluxes, which are important components of convection schemes.

1 INTRODUCTION

Maritime cold air outbreaks (MCAOs) are among the most challenging problems for numerical forecast models. Not only a high momentum transport of the cold air mass from the polar regions is involved, but also a high convective activity once the cold air reaches beyond the cold surface such as an ice or snow covered land, and is transported over the warm land or ocean. Latent and sensible heat fluxes strongly increase, and strong vertical motion is induced by heating from the surface. Due to the low temperature inversion being characteristic for an MCAO the convection is mostly shallow, and the cloudiness has a life cycle through stratus or sea fog where the cold air first reaches the warm surface, via cloud streets

*Corresponding author, verena.gruetzun@zmaw.de

towards open and closed cellular convection.

The representation of convection is problematic for today's numerical atmospheric models. Depending on the resolution of the model, convection is either not resolved at all (global circulation models), partly resolved (most numerical forecast models) or completely resolved (e.g. large eddy simulation (LES) models). In the coarse resolution of the global models, convection is parametrized using more or less accurate and sophisticated statistical assumptions about convective plumes and their characteristics such as moisture and temperature (e.g. Tiedtke, 1989, as a basic but groundbreaking scheme). While the statistical assumptions are well justified in the coarse global models, they break down at higher resolutions. Most numerical weather prediction (NWP) models by now work in that "greyzone" of convection, i.e., on the kilometer scale, where the statistics is not justified anymore but the convection is not entirely resolved yet.

MCAOs, being an interesting and challenging phenomenon for models in themselves, also provide an ideal testbed for investigating and improving convection parametrizations due to their strong convection and richness in cloud regimes. Taking part in the initiative "Greyzone" of the Working Group on Numerical Experimentation (WGNE) of World Meteorological Organization (WMO) and World Climate Research Programme (WRCP) which tackles the limits of convective parametrizations with regard to their applicability on different model scales we put our focus on the study of MCAOs in global models and at a later stage in LES simulations. As a first step, we present climatologies of MCAOs in ERA-interim (Berrisford et al., 2009; Dee et al., 2011) and compare model results from the global model ECHAM6 (Stevens et al., 2012). In the following, we first define a new index for the identification of MCAOs in the data, then we will show climatologies as found in ERA-interim data and compare them with two ECHAM6 runs, one employing climatological sea surface temperatures (SSTs) and one employing a coupled interactive ocean model.

2 DETECTING MARITIME COLD AIR OUTBREAKS

The main process going on in a MCAO is cold air being transported over a warm surface. Therefore Bracegirdle and Gray (2008) found that the difference in potential temperature between the surface layer and the 700 hPa layer is a good quantity to identify the event. An index basing on temperature is both, physically reasonable and also intuitively understandable, thus we follow the basic idea of Bracegirdle and Gray (2008) with a few changes. Firstly, we consider 700 hPa as too high to serve as a reference temperature, since MCAOs and their characterisic inversion heights are typically much lower than that. Since an analysis of the various CMIP5[1] models is planned, we use the lowest default output level for the CMIP5 runs, which is 850 hPa. We thus ignore the fact, that the low airmass is influenced by the heat fluxes from the ground (Bracegirdle and Gray, 2008) and is not independent of its time over the warm ocean anymore. We consider it more realistic to use the actual cold air mass as a reference and not the air above it, and also to include the effects of warming of the air mass during the MCAO's life time. Secondly, as the lower reference, we decided to use the skin temperature which directly influences the heat fluxes towards the atmosphere.

Our index, G, is thus a modified lower tropospheric stability $LTS_{850\,\mathrm{hPa,sfc}}$, and it is defined by

$$G \equiv LTS_{850\,\mathrm{hPa,sfc}} = \theta_{850\,\mathrm{hPa}} - \theta_{\mathrm{sfc}}, \qquad (1)$$

[1]CMIP5 - Coupled Model Intercomparison Project Phase 5, `http://cmip-pcmdi.llnl.gov/cmip5/`

where $\theta_{850\,\mathrm{hPa}}$ is the potential temperature at 850 hPa and θ_{sfc} is the potential temperature calculated with the skin temperature and the surface pressure. This index has the dimension K, and is in the order of $\sim 10^0 - 10^1$ K. Since ist is so closely related to LTS, here also a low index means a low stability, high convective activity and high surface heat fluxes.

3 RESULTS

Data basis

The data we use as a reference to build up a climatological database for MCAOs over the North Atlantic are ERA-interim reanalysis data (Berrisford et al., 2009; Dee et al., 2011) from the years 1989-2005. We only use the winter seasons, where MCAOs normally occur, and calculate the daily averages from 6 hourly data. To reduce the amount of data and to make a comparison with CMIP5 models, especially ECHAM6, possible, the ERA-interim data are coarse grained to T63, which corresponds to a spatial resolution of about 180 km at the equator. The ECHAM6 data we use are from CMIP5. We use an AMIP run, which employs climatological SSTs and a run which includes a coupled ocean model ("historical run"). The ECHAM6 data are already stored on a T63 grid, but we extract the winter seasons of 1989-2005 and use daily averages of the data, too.

ERA-interim climatology

We first look at the frequency of occurrence of MCAOs in ERA-interim. One drawback of the defined index is that no clear threshold exists with which MCAOs can be identified. This, however, is the case in previous studies, too (e.g. Kolstad et al., 2009; Vavrus et al., 2006), and it is a matter of discussion in which way the threshold is best set.

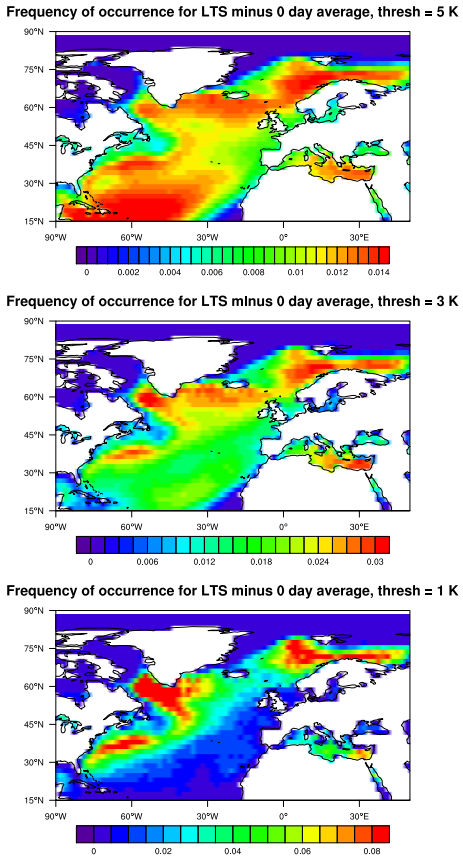

Figure 1: Frequency of occurrence of detected MCAOs over the North Atlantic using dfferent detection thresholds, below which an event is counted as an MCAO. Top: $G = 5$ K, middle: 3 K, bottom: 1 K.

Fig. 1 shows the frequency of occurrence of MCAOs detected by different thresholds in ERA-interim. An event is counted as MCAO when the index G falls below that threshold. The expected regions for MCAOs most clearly show for the low threshold of 1 K. Chosing an even lower threshold does not change the picture too much, since the distribution of G is strongly skewed towards high values and falls off towards low values quickly (Fig. 2). Chosing too low a threshold will finally result in not detecting any occurences. For the comparison

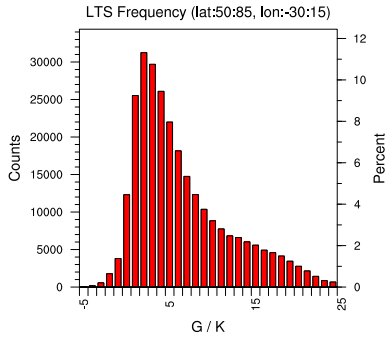

Figure 2: Distribution of the index G over the North Atlantic region, years 1989-2005, winter seasons.

of the CMIP5 data with ERA-interim we chose the threshold 1 K for now.

ECHAM6 and ERA-interim

Fig. 3 shows the corresponding frequencies of occurrences from ECHAM6 with climatological sea surface temperatures (top) and from ECHAM6 with a coupled ocean model (bottom). Except for the Southern part of the gulf stream the regions where MCAOs are frequent are reasonably well captured. It is not clear yet if the missing occurences there are due to a misrepresentation of the SSTs or due to a systematic bias in the atmospheric part in the model. South of greenland the two ECHAM6 runs differ, and the coupled model shows a smaller area where MCAOs occur. This is due to a slightly wrong meridional overturning circulation in the coupled run, which causes a cold bias south of Greenland.

Fig. 4 illustrates joint histograms of the MCAO index G and the surface heat fluxes. As mentioned before, the fluxes increase with decreasing index, since the index is closely related to LTS, giving us confidence that we found a physically meaningful index. Generally the fluxes are slightly higher in ECHAM6 and the range of G is slightly smaller. Also, the distribution is broader in ECHAM6. However, the

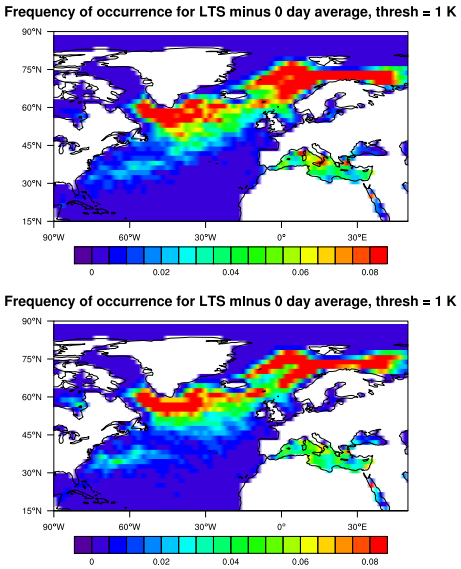

Figure 3: Frequency of occurrence of detected MCAOs ($G = 1$ K), ECHAM6 with climatological SSTs (top) and with a coupled ocean model (bottom).

agreement between the two data sets is quite satisfactory. The results so far build a the basis for assessing the specific characteristics of MCAOs and for identifying potential misrepresentation of momentum transport or convection in ECHAM6.

4 CONCLUSIONS

MCAOs are a challenge for current NWP models due to their high momentum transport and the high convective activity they induce. Through their variety and their life cycle of cloudiness they also build and ideal testbed for some important parts of convection parametrizations. As a first step to investigate the limitations and drawbacks of current convection parametrizations we investigate how well MCAOs are represented in global models. We have defined an index to identify MCAOs and created climatologies from ERA-

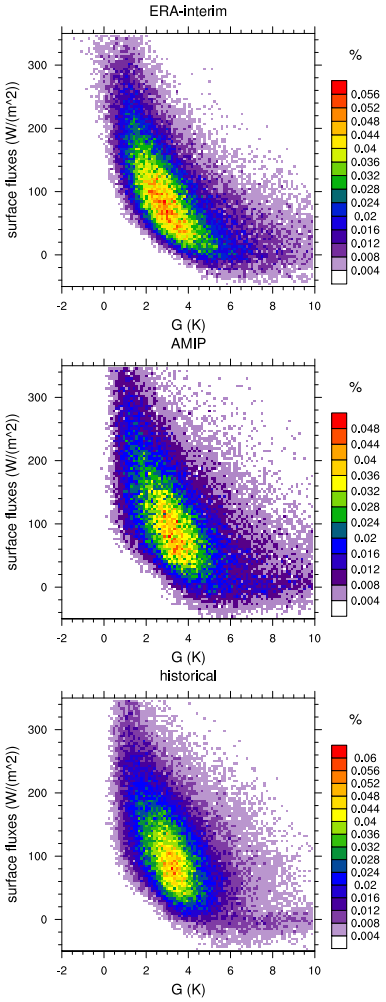

Figure 4: Joint histograms of surface heat fluxes and MCAO index G, top: ERA-interim, middle: AMIP run, bottom: coupled ocean run.

interim data. First comparisons with data from ECHAM6 runs show promising results: the joint distribution of surface heat fluxes and index are similar, though the one resulting from ECHAM6 is generally slightly broader. Though most of the regions where MCAOs are detected in ERA-interim are also present in ECHAM6, some areas are missing and point to potential flaws in the model such as a misrepresented meridional overturning circulation in the coupled model.

Basing on the results so far, we will compile typical characteristics of MCAOs through conditional averaging of, e.g., cloudiness, vertical profiles of wind, temperature and humidity, and mean heat fluxes. With this composite structure we can judge better how well models do represent MCAOs and may be able to identify potential problems in the models. Also we can guide further high resolution modeling of idealized MCAOs. The combination of large- and small-scale modeling will finally lead to a better understanding of the limitations of convective parametrizations and offers a great potential to improve them.

This research was carried out as part of the Hans Ertel Centre for Weather Research. This research network of Universities, Research Institutes and the Deutscher Wetterdienst is funded by the BMVBS (Federal Ministry of Transport, Building and Urban Development).

References

Berrisford, P., D. Dee, K. Fielding, M. Fuentes, P. Kållberg, S. Kobayashi, and S. Uppala (2009). The ERA-Interim archive Version 1.0. Technical report, European Centre for Medium Range Weather Forcasts.

Bracegirdle, T. and S. Gray (2008). An objective climatology of the dynamical forcing of polar lows in the Nordic seas. *Int. J. Climatol. 28*, 1903–1919.

Dee, D. P., S. M. Uppala, A. J. Simmons, P. Berrisford, P. Poli, S. Kobayashi, U. Andrae, M. A. Balmaseda, G. Balsamo, P. Bauer, P. Bechtold, A. C. M. Beljaars, L. van de Berg, J. Bidlot, N. Bormann, C. Delsol, R. Dragani, M. Fuentes, A. J. Geer, L. Haimberger, S. B. Healy, H. Hersbach, E. V. Hólm, L. Isaksen, P. Kållberg,

M. Köhler, M. Matricardi, A. P. McNally, B. M. Monge-Sanz, J.-J. Morcrette, B.-K. Park, C. Peubey, P. de Rosnay, C. Tavolato, J.-N. Thépaut, and F. Vitart (2011). The ERA-Interim reanalysis: configuration and performance of the data assimilation system. *Q. J. R. Meteorol. Soc. 137*, 553–597.

Kolstad, E. W., T. J. Bracegirdle, and I. A. Seierstad (2009). Marine cold-air outbreaks in the North Atlantic: temporal distribution and associations with large-scale atmospheric circulation. *Clim. Dyn 33*, 187–197.

Stevens, B., M. A. Giorgetta, E. Roeckner, T. Mauritsen, T. Crueger, H. Schmidt, E. Manzini, M. Esch, S. Rast, S. Kinne, L. Kornblueh, and R. Pincus (2012). Echam6: Model and climate. in preparation.

Tiedtke, M. (1989). A comprehensive mass flux scheme for cumulus parameterization in large-scale models. *Mon. Wea. Rev. 117*, 1779–1800.

Vavrus, S., J. E. Walsh, W. L. Chapman, and D. Portis (2006). THE BEHAVIOR OF EXTREME COLD AIR OUTBREAKS UNDER GREENHOUSE WARMING. *Int. J. Climatol. 26*, 1133–1147.

HOW DO SUBCLOUD THERMALS GROW TO BECOME SHALLOW CUMULUS CLOUDS?

Thijs Heus*

1. INTRODUCTION

What does it take for a subcloud thermal to become a shallow cumulus cloud? We study this question using Large-Eddy Simulations (LES). By tracking a decaying tracer emitted at the surface, individual subcloud thermals are followed through their lifetime without making any assumption on the thermodynamical properties of the thermal. As it turns out, the virtual potential temperature of thermals that become clouds is indistinguishable from the virtual potential temperature of thermals that remain unsaturated. Only when looking at the two-dimensional probability density function (pdf) of humidity and liquid water potential temperature, a clear separation between dry and moist thermals can be found. This holds true for both maritime as well as continental cases. However, the liquid water potential temperature of thermals varies strongly with the Bowen ratio: Continental situations require thermals to be warm to be buoyant enough to reach the lifting condensation level. For maritime thermals, the water vapor excess is sufficient to cause thermals to be positively buoyant, and a lower temperature in the thermals is preferable for cloud formation, since this lowers the local lifting condensation level.

2. EXPERIMENTAL SETUP

LES experiments have been performed using UCLALES (Stevens et al., 2005) on a $25.6 \times 25.6 \times 4\mathrm{km}$ domain with a $50\mathrm{m}$ resolution in all directions. Two different cases of shallow cumulus convection have been analyzed, both following the specifications of their respective intercomparison studies: The maritime Rain In Cumulus over the Ocean (RICO) case (vanZanten et al., 2011), with a Bowen ratio $B = 0.05$ and the continental ARM Southern Great Planes case (Brown et al., 2002) with a Bowen Ratio of $B = 0.28$.

2.1 *Cloud and thermal selection*

Life cycle and tracking studies of shallow cumulus clouds in LES have been performed in recent years by visual cherry-picking (e.g. Zhao and Austin, 2005; Heus et al., 2009), or in a more automated manner (Dawe and Austin, 2012). These studies have in common that the definition of 'cloud' is an area of non-zero cloud water content q_l in 3D space and time that is continuously connected. To account for splitting and merging events, through which otherwise separate clouds can become connected, Dawe and Austin (2012) used a more sophisticated approach that excludes collisions of clouds where the two cloud cores remain separate. To track the subcloud layer thermal, they use a decaying scalar C as introduced by Couvreux et al. (2010):

$$\left.\frac{\partial C}{\partial t}\right|_{\text{decay}} = -\frac{C}{\tau_0} \tag{1}$$

with $\tau_0 = 1800s$ sufficiently close to the typical time scale of the boundary layer, and the scalar surface flux

$$\left.\overline{w'C'}\right|_{surf} = \text{cst} \tag{2}$$

as the boundary condition. Since the scalar has no real physical meaning, the actual value of the scalar (and of its surface flux) is irrelevant. A grid cell $\mathbf{x}$ is defined as being part of the thermal Conditional Sampling CS if its scalar value is more than 1 standard deviation over the slab average:

$$\mathbf{x} \in \text{CS if } \frac{C(\mathbf{x}) - \overline{C}(z)}{\sigma_C(z)} > 1 \tag{3}$$

This method of defining the thermal does not rest on implicit structural assumptions of the thermal, like a buoyancy or velocity structure, but essentially only assumes that the parcel of air has been connected to the surface recently.

While the method by Dawe and Austin (2012) allows us to do automated tracking fast enough to produce a statistically reliable ensemble of clouds, the time dependent nature of cloud tracking still poses some severe practical limitations. Since the tracking occurs off-line, i.e., as a post processing step after the LES simulation, storing all the necessary data quickly becomes an issue. One could of course pursue to do (most of) the tracking on line, thus limiting the necessary output, but this would be a complicated effort because of the necessity to keep information of previous time steps in memory, as well as by considerations of parallelization. Therefore, we assume that all cloudy points in a single LES column belong the same cloud. If that is the case, only the projected cloud cover needs to be tracked, and the size of the dataset deflates with typically 2 orders of magnitude. By additionally saving the local cloud base and top heights, we can reconstruct the geometry of the cloud field up to a sufficient degree.

Given these additional constraints, a data set of a few simulated days on a domain of tens of kilometers requires in the order of 50 GB of memory, making it possible to quickly browse through the data set on a large memory node. The smallest clouds and thermals, with an accumulated size of less than 10 grid cells are being discarded from the ensemble. Subcloud thermals are required to be connected to the surface at some point in time. A thermal is connected to a cloud if at some location in space and time the thermal top is higher than the cloud base at the

* *Corresponding author address:* Thijs Heus, Max-Planck Institute for Meteorology Atmosphere in the Earth System, Bundesstrasse 53, 20146 Hamburg, Germany

same position. Note that this does not mean that all of the air of this thermal will flow into the cloud.

The main focus in this study lies on the investigation of the deviations of scalar quantities ϕ from the horizontal mean, averaged over the subcloud layer (sc) or the cloud layer (cld):

$$\phi'_{sc}(x,y,t) = \frac{1}{cb}\int_0^{cb} \phi(x,y,z,t) - \overline{\phi}(z,t)dz \qquad (4)$$

$$\phi'_{cld}(x,y,t) = \frac{1}{ct-cb}\int_{cb}^{ct} \phi(x,y,z,t) - \overline{\phi}(z,t)dz \qquad (5)$$

where ct is the top of the highest cloud, and cb the lowest cloud base. While there are fluctuations in these levels over time, the assumption being made here is that the fluctuations from the mean will be relatively small, unless a cloud is involved.

3. RESULTS

As a first visual inspection, figure 1 shows $xz-$cross sections of both the RICO (left) and ARM (right) case. Isolines display thermals (red), clouds (blue), and rain (black), while the background color denotes the deviation from horizontal mean for liquid water potential temperature (top) and total water content (bottom). From figure 1, cloudy columns and thermals overlap well, and often connect. There is however some difference in the humidity and temperature excess of the thermals: While in both RICO and ARM the thermals show an excess of moisture, a temperature deficiency is visible for the RICO thermals. The ARM case, with the relatively stronger sensible heat flux, still shows a temperature excess in the thermals.

In figure 3, the probability density function of the subcloud buoyancy θ_v is shown. From this figure it is clear that although the thermals tend to occupy the higher end of the θ_v-pdf, the spread is considerable, and only marginally buoyant air can easily be part of a thermal. Therefore, more information can be obtained by looking at the joint pdf of humidity and temperature (figure 3). In these graphs, the qualitative result from figure 1 is confirmed: for both ARM and RICO, the thermal pdfs are substantially different from the overall subcloud pdf, but the direction in which the thermal pdf is shifted depends on the case. In figure 3, the blue isolines depict the thermals that are connected to a cloud, and the red isolines depict the thermals that are never connected to a cloud, the so called dry thermals. The grey lines depict isolines of buoyancy (dashed) or lifting condensation level (dotted). An increase in buoyancy with respect to the mean subcloud layer is what is necessary to become a thermal, and in both RICO and ARM a thermal then needs to be more moist to reach its lifting condensation level and to become a cloud. Up to a Bowen ratio of ≈ 0.08, and this includes most maritime conditions, the latent heat flux is the dominant contributor to the subcloud layer buoyancy. For higher Bowen ratios this is no longer true, and the interplay between humidity and temperature becomes more complicated. This is also illustrated by the

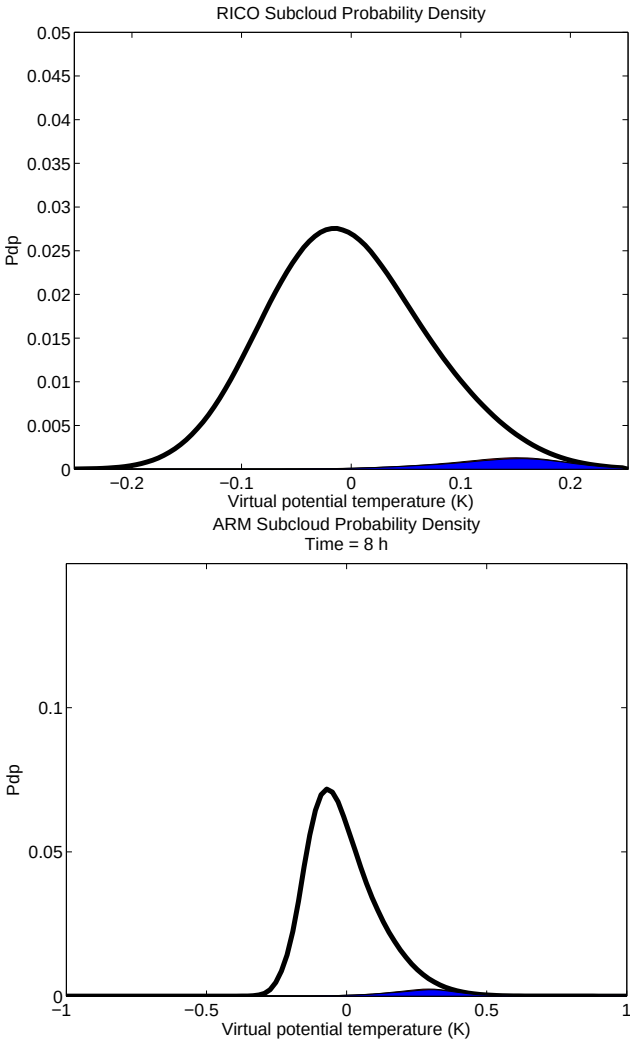

FIG. 2: Probability Density Function for the subcloud virtual potential temperature in RICO (top) and for the 8th hour of ARM (bottom). The colored area denotes the thermals, the black line is the rain formation.

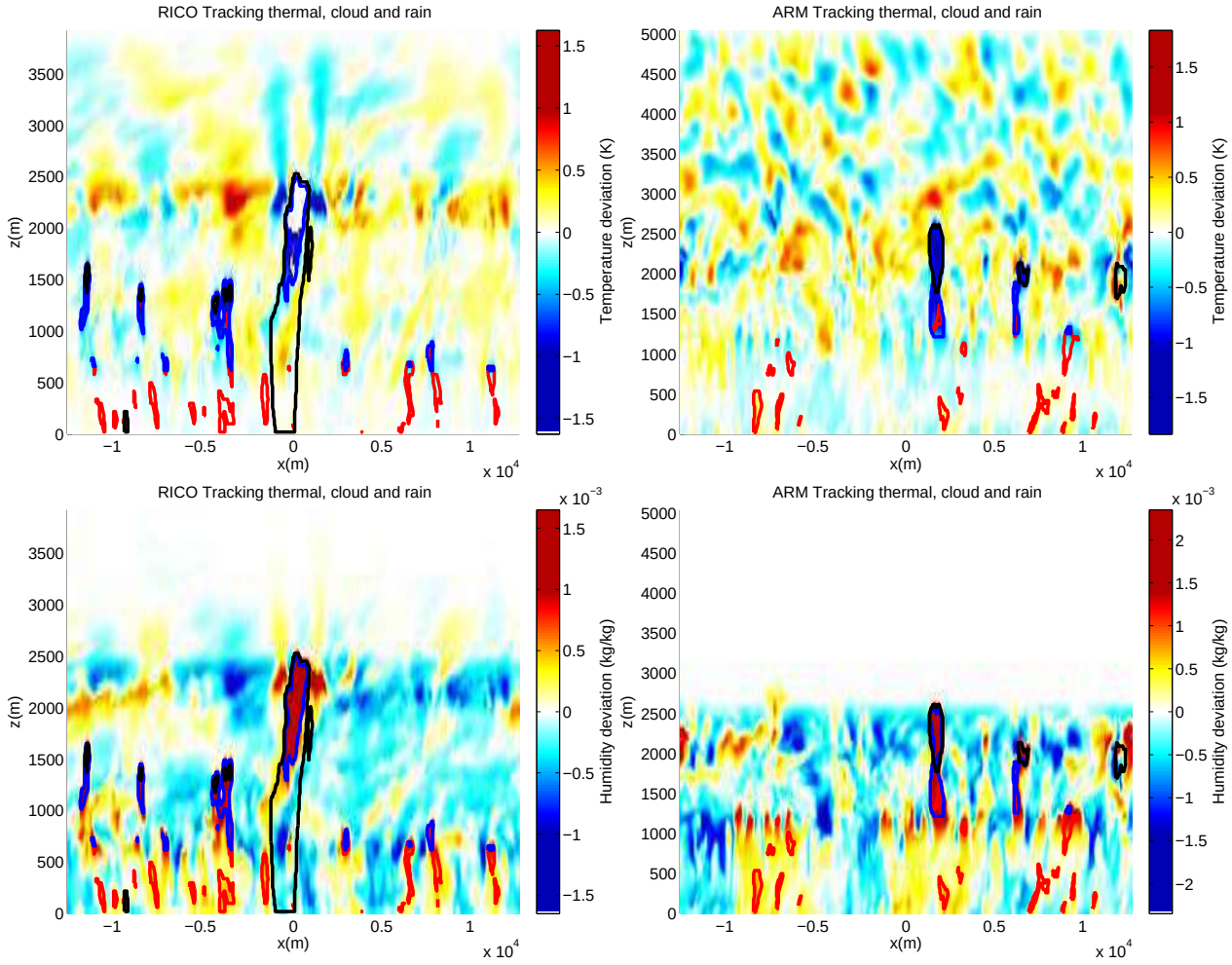

FIG. 1: Crosssections of the RICO (left) and ARM (right) simulations. Isolines display thermals (red), clouds (blue), and rain (black), while the background color denotes the deviation from horizontal mean for liquid water potential temperature (top) and total water content (bottom).

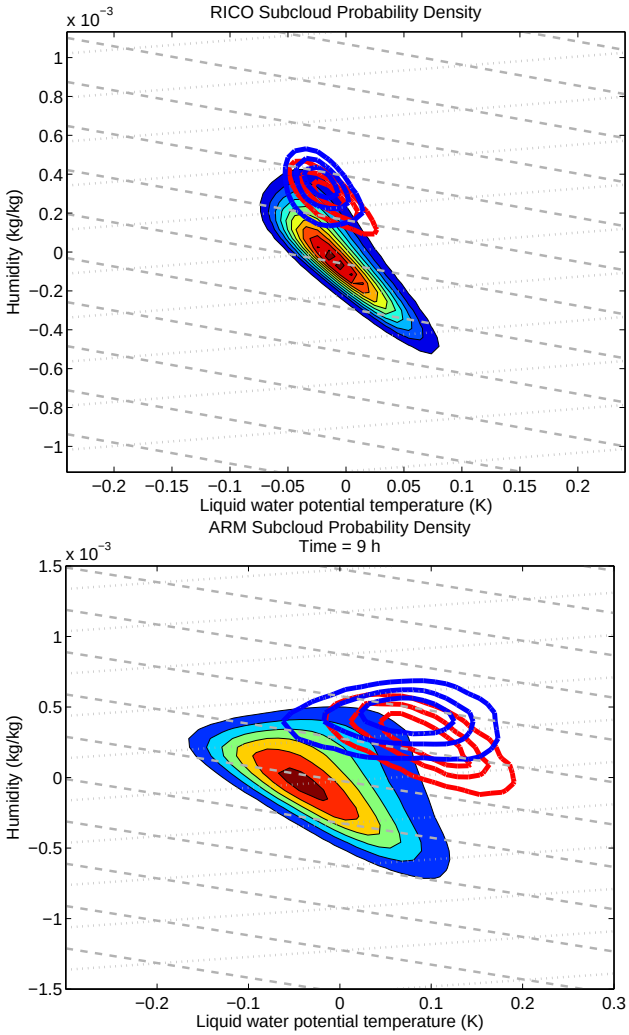

FIG. 3: Joint pdfs for the subcloud temperature fluctuations versus the subcloud humidity fluctuations. For RICO (top) and for the 9th hour of ARM (bottom). The colored area denotes the entire sub cloud layer, the red lines denote the pdf of the thermals that are not connected to clouds; the blue lines denote the pdf of thermals that are. Grey dashed lines are isolines of buoyancy; dotted lines are isolines of lifting condensation level.

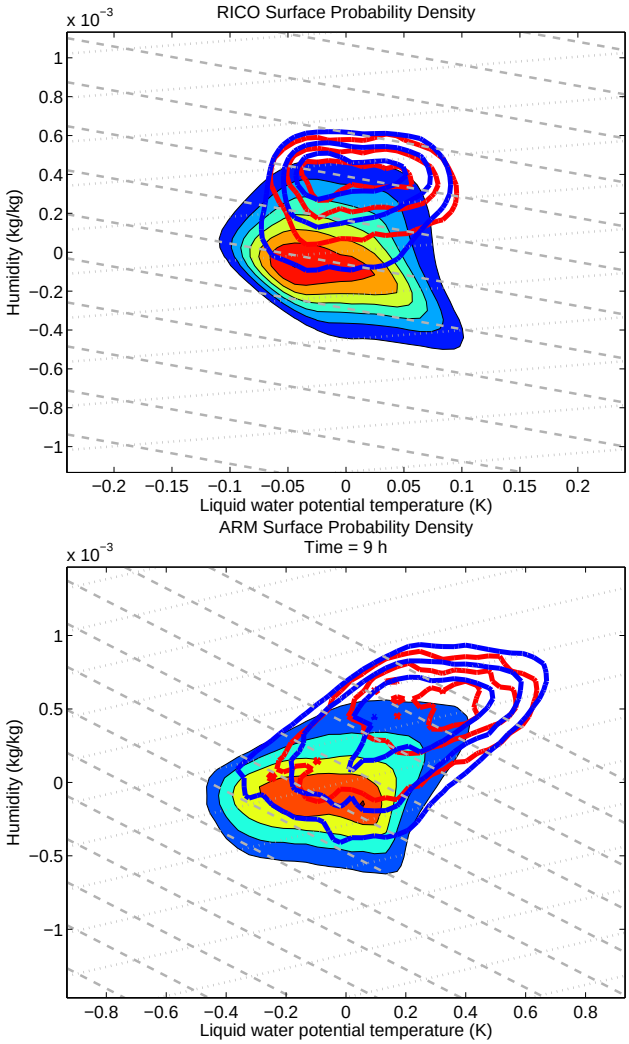

FIG. 4: As in figure 3, but for the instantaneous values at 100m above the surface.

strong anticorrelation between temperature and moisture in RICO, something that is less well observed in ARM. According to de Roode et al. (2004), an anticorrelation on larger scales between temperature and moisture is a necessary requirement for keeping the length scales of buoyancy limited, while the length scales of temperature and moisture grow. This in turn may have its impact on the size of thermals and of the resulting clouds.

Many thermal based cloud parameterizations, such as Neggers et al. (2010), base their cloud (base) properties on the values of the surface values of the buoyancy. Figure 4 shows similar joint pdfs as figure 3, but now with the instantaneous fields at 100m above the surface. While these pdfs already show some separation of the thermal values from the mean surface values, the

4. CONCLUSIONS

This study shows that the birth of subcloud layer thermals, and the production of clouds from those thermals, is an essentially multi-variate process where temperature and moisture both play there parts. Taking into account the details of the sub cloud layer may lead to a better understanding of the closure assumptions of many cloud schemes, such as the cloud base mass, heat and moisture fluxes. Whether or not these subcloud details actually result in bigger clouds is an open question. As Dawe and Austin (2012) argues, the correlation of scalar quantities between the cloud layer and the subcloud layer may be low, but the size of thermal when arriving at the cloud base can be of importance in determining cloud size and entrainment rates later on.

ACKNOWLEDGMENTS

This research was carried out as part of the Hans Ertel Centre for Weather Research. This research network of Universities, Research Institutes and the Deutscher Wetterdienst is funded by the BMVBS (Federal Ministry of Transport, Building and Urban Development).

REFERENCES

Brown, A. R., R. T. Cederwall, A. Chlond, P. G. Duynkerke, J. C. Golaz, M. Khairoutdinov, D. C. Lewellen, A. P. Lock, M. K. MacVean, C.-H. Moeng, R. A. J. Neggers, A. P. Siebesma, and B. Stevens, 2002: Large-eddy simulation of the diurnal cycle of shallow cumulus convection over land. *Quart. J. Roy. Meteor. Soc.*, **128**(582), 1075–1093.

Couvreux, F., F. Hourdin, and C. Rio, 2010: Resolved versus parametrized boundary-layer plumes. part i: A parametrization-oriented conditional sampling in large-eddy simulations. *Boundary-layer meteorology*, **134**(3), 441–458.

Dawe, J. and P. Austin, 2012: Statistical analysis of an LES shallow cumulus cloud ensemble using a cloud tracking algorithm. *Atmos. Chem. Phys*, **12**, 1101–1119.

de Roode, S. R., P. G. Duynkerke, and H. J. J. Jonker, 2004: Large-eddy simulation: How large is large enough? *J. Atmos. Sci.*, **61**(4), 403–421.

Heus, T., H. J. J. Jonker, H. E. A. Van den Akker, E. J. Griffith, M. Koutek, and F. H. Post, 2009: A statistical approach to the life-cycle analysis of cumulus clouds selected in a Virtual Reality Environment. *J. Geophys. Res.*, **114**, D06208.

Neggers, R., A. P. Siebesma, and T. Heus, 2010: The KNMI Parameterization Testbed. *Bulletin of the American Meteorological Society* in preparation.

Stevens, B., C. H. Moeng, A. S. Ackerman, C. S. Bretherton, A. Chlond, S. De Roode, J. Edwards, J. C. Golaz, H. L. Jiang, M. Khairoutdinov, M. P. Kirkpatrick, D. C. Lewellen, A. Lock, F. Muller, D. E. Stevens, E. Whelan, and P. Zhu, 2005: Evaluation of large-Eddy simulations via observations of nocturnal marine stratocumulus. *Mon. Wea. Rev.*, **133**(6), 1443–1462.

vanZanten, M., B. Stevens, L. Nuijens, A. Siebesma, A. Ackerman, F. Burnet, A. Cheng, F. Couvreux, H. Jiang, M. Khairoutdinov, et al., 2011: Controls on precipitation and cloudiness in simulations of trade-wind cumulus as observed during RICO. *Journal of Advances in Modeling Earth Systems*, **3**(6), M06001.

Zhao, M. and P. H. Austin, 2005: Life cycle of numerically simulated shallow cumulus clouds. Part I: Transport. *J. Atmos. Sci.*, **62**, 1269–1290.

What controls the structure of rain in shallow cumulus convection?

Anna Jaruga*[1], Louise Nuijens[2], and Hanna Pawlowska[1]

[1]Institute of Geophysics, Faculty of Physics, University of Warsaw
[2]Max Planck Institute for Meteorology, Hamburg

1 INTRODUCTION

Shallow convection is a key process that maintains the structure of the lower troposphere in the trades (Stevens, 2005). Through the vertical transport of heat and moisture fluxes, shallow convection links the planetary boundary layer with the free troposphere and hence influences the global circulation.
Due to the enormous range of scales important for shallow convection (ranging from the cloud microphysics, to forcings due to the global circulation), understanding shallow convection process remains a challenging problem. The process of rain formation, interactions between aerosols and rain structure and the influence of rain on the cumulus field are good examples of open questions linked with shallow convection (VanZanten et al., 2011).

A very commonly used approximation of shallow cumulus convection assumes no precipitation throughout the whole cloud life-cycle. Indeed, for a typical shallow cumulus cloud fraction of 10%, precipitation is of an order of magnitude smaller. On the other hand it contributes up to 50% of the total precipitation in trade wind region (Nuijens et al., 2009) and therefore could be important in understanding the whole shallow convection process.

To fully understand precipitation processes it is important to measure the intensity of rain (rain-rate) over a wide area. Because of that, meteorological radars are frequently used. Common meteorological radars measure reflectivity (Z) (a quantity proportional to drop diameter to the power six) whereas rain-rate (R) is a function of the drop diameter cubed.

In this study we will focus on characterising the structure of rain in shallow cumulus convection in terms of reflectivity and rain-rate. The aim is not to derive a parametrisation for retrieval of rain-rate from reflectivity measurements, but rather to try to depict the great variability in Z and R measurements and to understand the physics behind it. Due to the great variance in observed data we will not focus on single rain events or specific time period, but rather apply statistical approach in analysing data from a long period of time.

2 INSTRUMENTS

Barbados Cloud Observatory is a remote measurement platform stationed at the Island of Barbados (`http://barbados.zmaw.de/`). The site is located at the east coast of the island, allowing to study nearly unperturbed maritime trade wind shallow convection. The site is operational since April 2010 and provides continuous time series of measurements.

In this study we will use data obtained from the Micro-Rain Radar (MRR) (`http://www.metek.de/`). It is a vertically pointing radar located at Barbados Cloud Observatory. It measures the fall velocity of rain-drops (with diameters of 0.25 mm up to few centimeters). Using those measurements vertical profiles of rain-drop sizes from close to the surface up to 3 km can be derived. Thanks to those measurements, both Z and R profiles can be calculated independently. This allows to explore the dependence of Z-R relationships on different parameters.

*Correspondence to: Anna Jaruga, Pasteura 7, 02-093 Warsaw, Poland. E-mail: ajaruga@igf.fuw.edu.pl

3 ANALYSIS

Let N be the density of size distribution of rain drops, D their diameter and v their terminal fall velocity. Then reflectivity (Z) and rain-rate (R) can be calculated as follows:

$$Z = \int_0^\infty N(D) D^6 \mathrm{d}D \qquad (1)$$

$$R = \int_0^\infty N(D) D^3 v(D) \mathrm{d}D \qquad (2)$$

In practice, when retrieving Z and R from MRR measurements the integration from 0 to ∞ over the whole drop size distribution changes into the sum over all rain-drop sizes that can be detected by the Micro-Rain Radar.

The idea to describe rain in terms of reflectivity and rain-rate originates from practical aspects of studying meteorological radar data. This method also enables to look more into the structure of rain. As seen in equations (1) and (2) reflectivity is a function of higher statistical moment than rain-rate. Therefore, reflectivity is more connected to bigger rain drops, whereas rain-rate, as a function of the third statistical moment, is more linked to the areas with the biggest rain water content. The maximum of Z and R is not necessarily collocated in space in a given rain event. Profiles of Z and R of a given rain event carry interesting information about the microphysical structure of rain, but the interpretation of such data is very difficult (Steiner et al., 2004).

Dataset analysed in this study consists of all rain detections observed at Barbados Cloud Observatory from April 2010 till April 2011. MRR data were averaged over 1 minute time period. Rain detection algorithm used in this study recognises as rain any MRR detection of reflectivity greater than 0 dbZ and of vertical length greater than 400 m.
Figure 1 presents 2-dimensional histogram of reflectivity vs rain-rate from all rain detections from constructed dataset. X axis represents 10 times logarithm of measured reflectivity [dbZ] and y axis represents logarithm of rain-rate [mm/h]. The black line marks one of available parametrisations that could be used for calculating rain-rate from reflectivity (as in (Nuijens et al., 2009)). Vertical lines located in the bottom left hand corner of the plot are an artifact resulting from the lack of accuracy of MRR measurements for very small rain-rates.

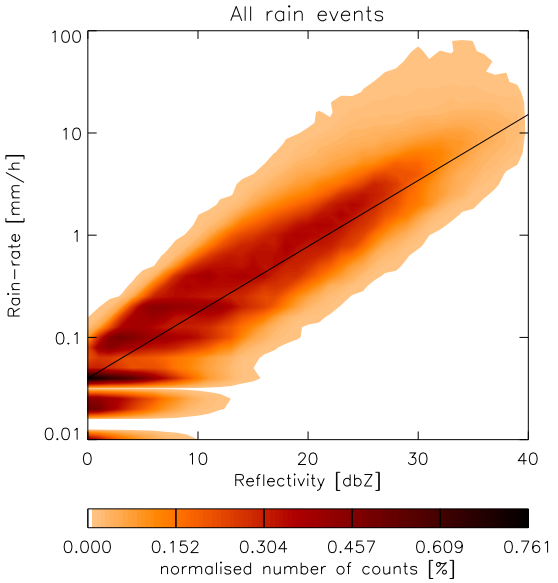

Figure 1: Contour plot of 2-dimensional histogram of reflectivity vs rain-rate. X axis represents 10 times logarithm of reflectivity, y-axis represents rain-rate, plotted in logarithmic scale. Colors represent number of counts in each histogram bin normalised by the total number of counts. Black line represents Z-R parametrisation used for calculating rain-rate from shallow convective clouds. The dataset consists of all rain detections measured between April 2010 and April 2011.

The most striking feature of figure 1 is a very big scatter of Z and R. For a given Z the variability in R reaches one order of magnitude. It is interesting to see such a great variance, but it also points out that calculation of rain parameters based solely on reflectivity should be treated with caution.

One of the reasons causing such variability is that figure 1 shows rain events from shallow convection as well as bigger meteorological systems passing over the Island of Barbados. Designing a criterion to discriminate between different types of rain based only on MRR measurements is difficult. A poor man approximation for that criterion could be the time span of a given rain event. Although such criterion eliminates rain events too long to be caused by shallow convective clouds, it doesn't discard rain detections from big rain systems with center further away from MRR.

Taking into account the number of occurrences of rain events of a given time-span, obtained median rain event lasts 4 minutes. The 25^{th} and 75^{th} percentile are rain events lasting 2 minutes and 10 minutes respectively. The interpretation of such results is not straightforward, since we can't measure the total time-span of a given rain event but only the time when it is above Micro-Rain Radar. Also, the center of rain event doesn't necessarily pass directly above MRR, hence the measurements can be biased toward shorter time-spans. Nevertheless, such small time durations show that short rain events are the most frequent ones, creating a constant background of short rain showers caused by shallow convective clouds.

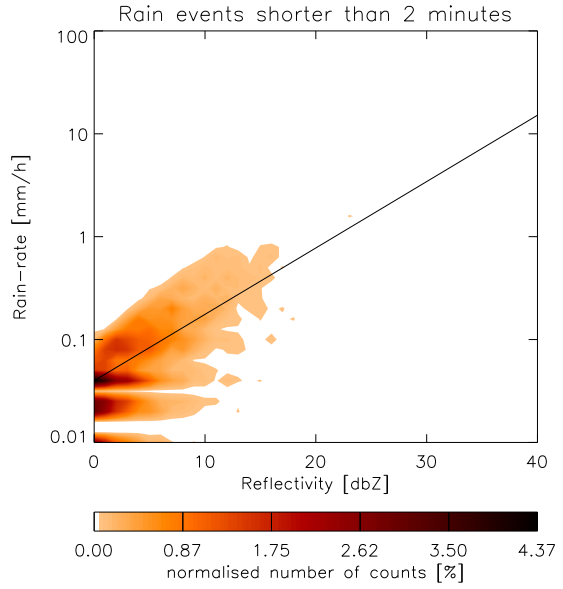

Figure 2: Contour plot of 2-dimensional histogram of reflectivity vs rain-rate. X axis represents 10 times logarithm of reflectivity, y-axis represents rain-rate, plotted in logarithmic scale. Colors represent number of counts in each histogram bin normalised by the total number of counts. Black line represents Z-R parametrisation used for calculating rain-rate from shallow convective clouds. The dataset consists of all rain detections from April 2010 until April 2011 of time-span shorter than 2 minutes.

Figures 2, 3 and 4 present 2-dimensional histograms of reflectivity vs rain-rate divided by the time-span of rain events. As a cutoff value for a given figure, the values of 25^{th} and 75^{th} percentile of rain event time-span were taken.
It is clear that longer rain events more frequently achieve bigger reflectivities and rain-rates. But more interestingly, for shorter rain events the area of the maximum occurrence of rain-rate

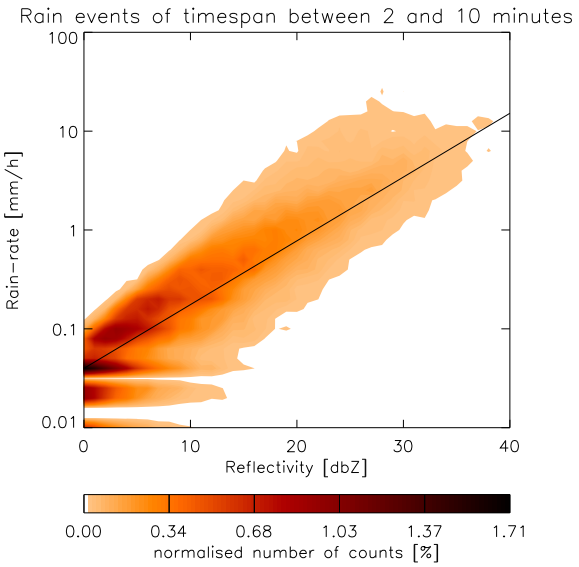

Figure 3: Contour plot of 2-dimensional histogram of reflectivity vs rain-rate. X axis represents 10 times logarithm of reflectivity, y-axis represents rain-rate plotted in logarithmic scale. Colors represent number of counts in each histogram bin normalised by the total number of counts. Black line represents Z-R parametrisation used for calculating rain-rate from shallow convective clouds. The dataset consists of all rain detections from April 2010 until April 2011 of time-span longer than 2 minutes but shorter than 10 minutes.

for a given reflectivity is more narrow and tends towards higher rain-rates (compare figures 3 and 4). In terms of microphysical structure of rain it could point that for a given rain-rate, short rain events consist of bigger amount of smaller rain drops, whereas longer rain events tend to have wider size distribution spectrum including some bigger rain drops.

Even after restricting the analysis to rain events of duration shorter than 10 minutes, the scatter between Z and R is still significant. One of the causes of such behavior is that Z-R relationship differs basing on the vertical location within rain event, as well as the time that has passed from the actual onset of precipitation within the cloud. It is caused by the fact that rain-drops of different sizes have different terminal fall velocities. At the early stages of precipitation all rain drops are located within the cloud. Then, as the rain event develops, the biggest rain drops are the first to start falling below cloud base. Finally, at the late stages of precipitation the majority of rain drops is located below the cloud base. One can think about this

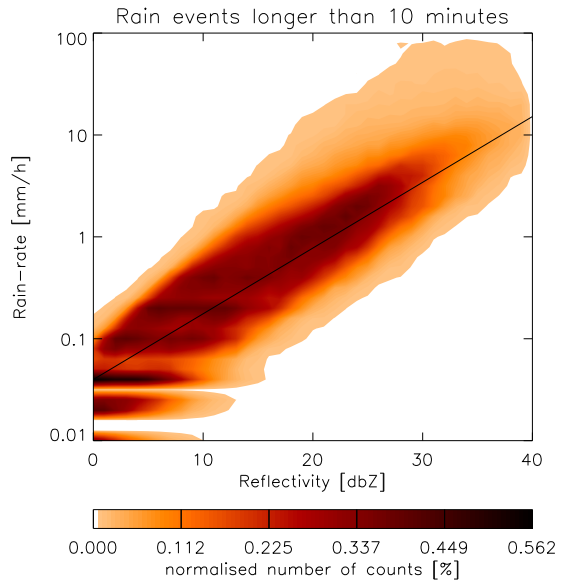

Figure 4: Contour plot of 2-dimensional histogram of reflectivity vs rain-rate. X axis represents 10 times logarithm of reflectivity, y-axis represents rain-rate. Colors represent number of counts in each histogram bin normalised by the total number of counts. Black line represents Z-R parametrisation used for calculating rain-rate from shallow convective clouds. The dataset consists of all rain detections from April 2010 until April 2011 of time-span longer than 10 minutes.

behaviour as rain life-cycle. Temporal changes of relative location of maximum of Z and R within rain event influence the Z-R relationship.
Another cause of observed variability in rain structure is the variability in initial cloud droplet size distribution caused either by the variability in aerosol spectrum or by the macrophysical factors (such as humidity profile). Although aerosol-cloud-rain interactions are very interesting, untangling aerosol influence from rain life-cycle and macrophysical effects is difficult.

It is worth stressing that presented decomposition of time-span of rain events was made basing on the frequency of the occurrence and not the total duration of rain events. Although short rain events are the most frequent, their contribution to the total precipitation time within a year is small. - The total time of rain from rain events longer than 10 minutes (75^{th} percentile) is nearly 3 times longer than from rain events shorter than 10 minutes (376 hours in one year and 131 hours in one year respectively)

4 SUMMARY AND OUTLINE

Preliminary results presented in the previous section show that trade wind convective clouds are able to produce rain showers of considerable magnitude and great variability in their microphysical structure.

As shown in previous section, focusing only on short rain events (presented in figures 2 and 3) narrows the scatter between Z and R, but observed variability is still big. Using the same framework as presented above, in the further study we will investigate the influence of other parameters on the structure of rain in shallow convection . We will focus on vertical structure of reflectivity and rain rate as well as the effects of rain life-cycle. We will also try to link the MRR measurements with other instruments operating at Barbados Cloud Observatory and look for connections between rain structure and some microphysical (aerosols) or macrophysical (humidity) factors. Further findings will be reported at the ICCP.

Acknowledgements

AJ thanks International Max Planck Research School on Earth System Modelling for funding my stay at Max Planck Institute for Meteorology, Hamburg, Germany.

References

Nuijens, L., Stevens, B., and Siebesma, A.: The Environment of Precipitating Shallow Cumulus Convection, J. Atmos. Sci., 66, 1962–1979, 2009.

Steiner, M., Smith, J., and Uijlenhoet, R.: A Microphysical Interpretation of Radar Reflectivity-Rain Rate Relationship, J. Atmos. Sci., 61, 1114–1131, 2004.

Stevens, B.: Atmospheric Moist Convection, Annu. Rev. Earth Planet. Sci., 33, 605–643, 2005.

VanZanten, M., Stevens, B., Nuijens, L., Siebesma, A., Ackerman, A., Burnet, F., Cheng, A., Couvreux, F., Jiang, H., Khairouidinov, M., Kogan, Y., Lewellen, D., Mechem, D., Noda, A., Shipway, B., Slawinska, J., Wang, S., Wyszogrodzki, A., and Nakamura, K.: Controls on precipitation and cloudiness in simulations of trade-wind cumulus as observed during RICO, J Adv Model Earth Syst., 3, 2011.

TROPICAL CLOUD PROCESSES : FIRST RESULTS FROM CHUVA PROJECT.

L. MACHADO[*], A. CALHEIROS[*], E. MATTOS[*], I. COSTA[*], D. VILA[*], R. ALBRECHT[*], C. MORALES[+], C. ANGELIS[*], M. SILVA DIAS[+], G. FISCH[#].

** INPE/CPTEC, BRAZIL*
+ USP/IAG, BRAZIL
 # DCTA/IAE, BRAZIL

ABSTRACT

CHUVA is a project that will carry out seven field experiments to investigate the different precipitation regimes in Brazil. The objective of the field campaign is to collect information about the cloud processes of the main precipitating systems over Brazil to evaluate and improve quality precipitation estimation and the knowledge of cloud microphysical process. The project intend to cover different types of precipitation regimes, but the main focus are the warm clouds, the analysis will be performed considering the microphysical and precipitation evolution during the cloud life cycle and the development of thunderstorms. Four field campaigns have already been realized in the following places: Alcantara (MA), Fortaleza (CE), Belem (PA) and Vale do Paraíba (SP). The first three campaign were held in tropical region, on the coast, from the Amazonia to the semi-arid in the Northeast Brazil. The fourth campaign was held in a valley between two mountains, around 100 km far from the ocean. This campaign was jointed with the GOES-R Geostationary Lightning Mapper - pre-launch algorithm validation. 3-D Lightning Mapping Array, LINET, high speed digital video, X-Dual-Pol radar, Micro Rain Radar, disdrometer and several others instruments were employed during all the rainy season. This study describes the preliminary results for these experiments. A description of the cloud liquid water and DSD as function of the region, rain rate and cloud type, the cloud processes changes during the life cycle, some examples of the electrification process and reflectivity and ZDR profiles are described.

1- Introduction

The Cloud processes of the main precipitation systems in Brazil: A contribution to cloud resolving modeling and to the GPM (CHUVA Project) is a project designed to measure the cloud processes of the main precipitating systems in Brazil to improve precipitation estimation from satellite over land and the knowledge of cloud microphysics. CHUVA is designed to measure from typical warm clouds on the tropical coastal systems up to cold fronts and large MCCs in the Brazil extra tropics.

The Precipitation estimation has been noticeably improved by the TRMM satellite and consequently the development of new algorithms (Adler et al., 2001; Huffman et al., 2007). However, precipitation estimation over land still has several deficiencies because it is indirectly estimated (Berg et al., 2006) and precipitation from warm clouds is barely retrieved (Liu and Zipser, 2009). Warm clouds can significantly contribute to the total rainfall in a tropical region mainly near the coast. For instance, during November last year 600 mm was precipitated in two days in Southeast Brazil from warm clouds, but most of the precipitation estimation algorithms showed only a very small amount of precipitation. It is very important to quantify the amount of precipitation from warm clouds that is not being considered in satellite based climate datasets and it is likely possible that for some regions it corresponds to the majority of the precipitation amount. The description of the cloud processes and precipitation from warm clouds is one of the main focus of the CHUVA project.

Stephens and Kummerow (2007) stated that assumptions on the vertical cloud and precipitation structures as well as the details of ice particle properties and

size distributions are a dominant source of uncertainties in the estimation of precipitation. They consider that a better definition of the atmospheric state and the vertical structure of clouds and precipitation are needed to improve the information extracted from satellite observations. Battaglia et al (2011) using CHUVA dataset, collected in Alcantara, observed large amount of liquid water reaching the saturation of ADMIRAI at 10.7 GHz, the authors describes this feature was observed for the first time at this frequency.
The main source of information comes from the X-POL radar. Schneebeli et al. (2012) describes the radar data processes and the first results from Fortaleza campaign.
This work intends to present the CHUVA project, how to access the dataset and some preliminary results.

2 - Field Campaigns

Chuva field campaign has been realized in 4 different regions. The first one occurred in Alcântara, Maranhão State, located at around -2 latitude, in a semi arid region on the coastal of Atlantic Ocean. This campaign was held in March 2010. The second Campaign was realized in Fortaleza during the March and April 2011. Fortaleza, in the Ceará State, is also located in the coastal of Atlantic at around -3.7 latitude. The third Campaign was held in Belem, in the coastal of Amazonas region, this experiment occurred in June 2011. A dense GNSS network was operated during the campaign. The fourth campaign, started in November 2011 and ended in March 2012, occurred in Paraíba Vale, latitude -23. This campaign was jointed with GLM (Geostationary Lightning Mapper) and had a strong lightning component, including an important array of LMA (Lightning Mapping Array) instruments. Figure 1 shows a descriptive location of each of these campaign. All campaigns were realized during the rainy season of the specific region.

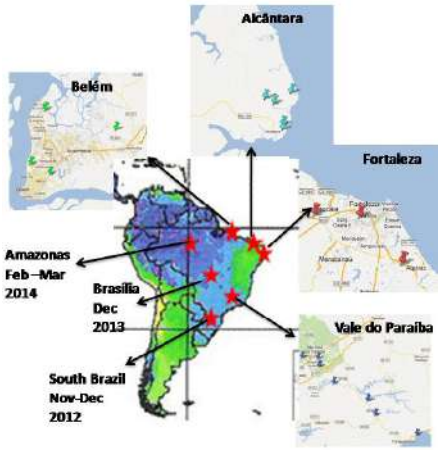

Figure 1: Location and date of the CHUVA field Campaigns.

The campaigns had nearly the same measurement strategy, a X-POL radar operated with a strategy between 6 and 10 minutes with comprise a volscan and RHI over the main site. The main site was distant between 10 and 20 km, and was equipped with several disdrometers, MRR, microwave radiometers (MP3000), raingauges, surface station, soil moisture, radiosonde, field mill and several others ancillary instruments. All campaigns had an intensive period were a triangle of radiosonde releases 4 radiosondes/day. The list of the instruments as well the description of each campaign can be accessed by the following URL: http://chuvaproject.cptec.inpe.br/portal/en/index.html.

3- Data Access

The CHUVA data has open access, all data in friendly formats can be accessed through the following URL: http://chuvaproject.cptec.inpe.br/projetochuva/acesso?language=en. Users need to fill the form to receive a password to access the database. Data is distributed by field campaign. Using the CHUVA Web page, users can have specific description of each campaign, including weather reports, instruments description and responsible.

4 - Preliminary results

A large effort was done during this last year running the field campaigns and organizing and pre-processing the database. However, some interesting results are showing the potential of these data to improve knowledge of the cloud processes of the main precipitation systems in Brazil. The studies are covering the following areas: numerical models, cloud microphysics, nowcasting, atmospheric electricity, mesoscale, boundary layer and precipitation from satellite estimation. This work will show some examples of the results been obtained by some of these areas.

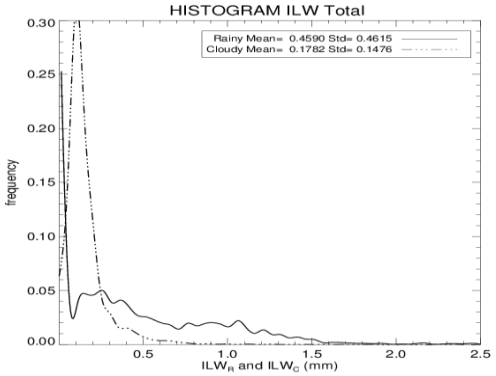

Figure 2: Cloud and rain Integrated liquid Water (ILW) for Alcântara, Fortaleza, Belém and Vale do Paraíba.

Figure 2 shows the cloud liquid water obtained from the MP3000 radiometer (Surface-based passive microwave and infrared remote sensing at 35 Channels in 22.00 – 30.00 GHz and 51.00 – 59.00 GHz). Using the periods without rain (raingauge) and eliminating the periods 3 hours before the end of rain (to eliminating possible cases of wet radome) the ILW was computed using the radiometrics neural network calculations. For the rain ILW calculations we have used the MRR (Micro rain radar - 24 GHz). For this calculations Alcantara was not included because the MRR was used jointed with the ADMIRAI radiometer (Battaglia et al, 2011). The ILW for rain cases were computed integrating from cloud base up to 600 meters below the zero degrees, to eliminate the brightness band effect in the ILW calculations. This calculations were applied only for the cases when the raingauge, co-located with the MRR, indicated rain events larger than 1 mm. Calculations for rainfall types is been processed.

Using an radar adapted version of a cloud tracking methodology called ForTraCC (Vila et al, 2008) we have followed rainfall structures using the CAPPI at 3km. The rainfall structures shows very distinct behavior for clouds and rainfall cells merged inside the mesoscale cloud structures. For Fortaleza, results shows that 80% of the rain cells have life cycle and size smaller than 42 minutes and 40 km^2. Figure 3 shows the distribution of size and lifecycle duration for Fortaleza campaign.

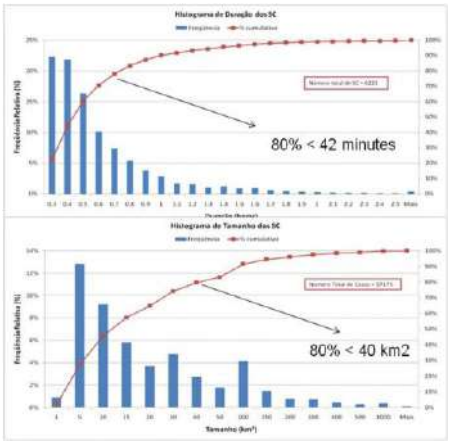

Figure 3: life cycle duration and size distribution of rain cells in Fortaleza Campaign.

At the present time, data is been processed and intercompared. Figure 4 is an example of the comparison between disdrometers, raingauge, MRR and X-pol precipitation measurement/estimation. It is clear in this Figure the differences between the different instrument and estimation methodologies. The same procedure is been applied for different satellite rainfall estimation. Warm clouds is been particularly investigated in these studies.

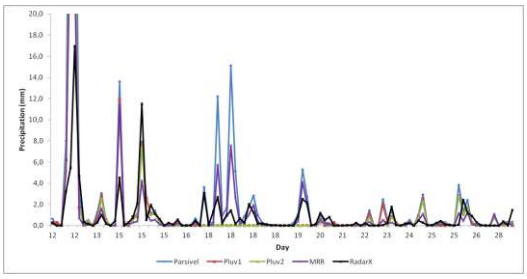

Figure 4: Fortaleza Campaign, rainfall estimation/measured by two co-located raingauge, disdrometer, MRR and X-Pol radar.

Several studies is been carried but it is still in initial phase. The CHUVA VALE-GLM campaign, has just finished (March 2012). The data collected has a strong potential to improve the knowledge of atmosphere electricity. The combination of measurements of total lightning activity, lightning channel mapping, and storm microphysics can contribute to improve nowcasting and the understanding of thunderstorms and lightning. Figure 5 shows an example of a thunderstorm day measured by the LMA. The combination of dual Polarization information profiles with the vertical distribution of flashes, described from ground-based 3-D total lightning mapping networks and coincident with overpasses of microwave radiometers open an opportunity to understand the formation of electricity processes inside the clouds and develop algorithms using satellite data.

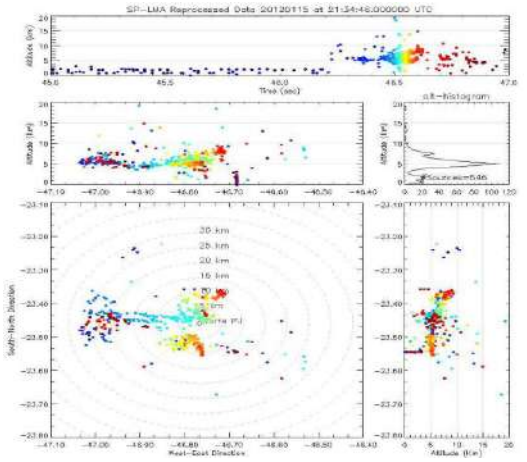

Figure 5: Example of the LMA data for a thunderstorm case in Paraiba Vale during 20 December 2011 at 21:34 UTC.

5- Conclusions

CHUVA Project is the first effort to create a regional database describing the cloud processes in Brazil. Results are still preliminary, however, the 59 papers submitted to the First CHUVA Workshop, in May 2012, highlight the strong effort being done and the potential research to improve the cloud processes knowledge, nowcasting and precipitation estimation by satellite and radar in South America. Each region show a typical space/time scale of cloud organization, however, DSD, cloud liquid water seen to have a much more dependence of the cloud type than regionally.

6- Acknowledgements

This research was support by FAPESP Grant 2009/15235-8.

7- References

Adler, R.F., Kidd, **C**., Petty, G., Morissey, M., Goodman, H.M. (2001). Intercomparison of Global Precipitation Products: The Third Precipitation Intercomparison Project (PIP–3). *Bulletin of the American Meteorological Society:* Vol. 82, No. 7, pp. 1377–1396

Battaglia,A.,P. Saavedra, C. Morales, and C. Simmer: Understanding three-dimensional effects in polarized observationswith the ground-based ADMIRARI radiometerduring the CHUVA campaign. Journal of Geophysical research, VOL. 116, D09204, 2011

Berg, W., T. L'Ecuyer, and C. Kummerow, 2006: Rainfall Climate Regimes: The Relationship of Regional TRMM Rainfall Biases to the Environment. *J. Appl. Meteor. Climatol.*, **45**, 434–454.

Huffman, G.J., R.F. Adler, D.T. Bolvin, G. Gu, E.J. Nelkin, K.P. Bowman, Y. Hong, E.F. Stocker, and D.B. Wolff, 2007: The TRMM Multisatellite Precipitation Analysis (TMPA): Quasi-Global, Multiyear, Combined-Sensor Precipitation Estimates at Fine Scales. *J. Hydrometeor.*, **8**, 38–55.

Liu, C., and E.J. Zipser, 2009: “Warm Rain” in the Tropics: Seasonal and Regional Distributions Based on 9 yr of TRMM Data. *J. Climate*, **22**, 767–779.

Stephens, G.L. and Kummerow, C. D. 2007. The Remote Sensing of Clouds and Precipitation from Space: A Review. J. Atmos Science, 64, 3742-3765

Schneebeli,M., J. Sakuragi, T. Biscaro, C. F. Angelis, I. Carvalho da Costa,C. Morales, L. Baldini, and L. A. T. Machado: Observations of tropical rain with a polarimetric X-band radar: first results from the CHUVA campaign. Atmos. Meas. Tech. Discuss., 5, 1717–1761, 2012

Vila, D., Machado, L. A. T., Laurent, H., Velasco, I.: Forecast and Tracking the evolution of cloud clusters(ForTraCC) using satellite infrared imagery: Methodology and validation. Weather and Forecasting. , v.23, p.233 - 245, 2008.

ICE NUCLEATION PROPERTIES OF SOIL DUST PARTICLES

Isabelle Steinke[1]*, Ottmar Möhler[1], Alexei Kiselev[1], Monika Niemand[1], Harald Saathoff[1], Martin Schnaiter[1], Julian Skrotzki[1], Emre Toprak[1], Corinna Hoose[1], Matthias Hummel[1], Roger Funk[2], Thomas Leisner[1,3]

[1] Institute for Meteorology and Climate Research - Atmospheric Aerosol Research, Karlsruhe Institute of Technology, Germany

[2] Leibniz Centre for Agricultural Landscape Research, Müncheberg, Germany

[3] Institute of Environmental Physics, University of Heidelberg, Germany

1 INTRODUCTION

Aerosol particles exert a significant influence on clouds [1] with mineral dust particles and sea salt residuals being the most abundant aerosol species in terms of mass [2, 3]. However, the composition of atmospheric aerosol is strongly dependent on regional source patterns. Laboratory studies and in-situ measurements have explored the different pathways through which aerosols influence both warm, liquid clouds and ice clouds. Mineral dust particles emitted from arid and desert areas have been identified as potentially efficient ice nuclei under many atmospheric conditions [4, 5]. These mineral dust particles consist mainly of silicates such as kaolinite and quartz. In contrast to these silicate-rich mineral dust particles, soil dust from agricultural areas also contains major amounts of biological components such as plant debris, fungi and bacteria. Some of these biological agents (such as bacteria) have been found to nucleate ice at even higher temperatures than mineral dusts [6, 7, 8]. Thus, it has been proposed that soil dust from agricultural area can act as a very efficient ice nucleus species [9] and thus may have a regional impact on clouds.

In this study the relevance of biological agents for the ice nucleation effiency of soil dust particles is investigated with laboratory measurements at the AIDA cloud chamber facility (KIT, Karlsruhe, Germany). From these measurements a preliminary parameterization for immersion freezing of soil dust particles is developed. Estimated emission fluxes from the COSMO-ART model will be used to calculate upper limits for the contribution of soil dust particles to the global ice nuclei burden.

2 EXPERIMENTAL RESULTS

At the AIDA cloud chamber facility (KIT, Karlsruhe, Germany) the interaction between aerosol particles and clouds is investigated unter atmospherically relevant conditions because the AIDA chamber simulates the ascent of an air parcel through the quasi-adiabatic expansion of humid air within the vessel. Our measurements cover a temperature range from 263 K to 223 K which corresponds to the regime of tropospheric mixed-phase and cirrus clouds.

For a sample from an agricultural area near Karlsruhe, the ice nucleation efficiency was measured and compared to mineral dusts from desert regions.

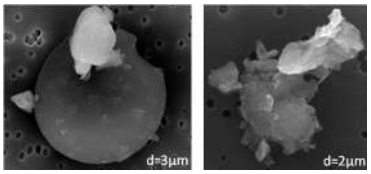

Fig. 1: Electron microscope (ESEM) images of soil dust particles

*isabelle.steinke@kit.edu

Fig.1 shows microscope images of soil dust particles which occur as single particles and complex agglomerates. Biological agents in soil dust particles have been qualitatively investigated by cultivating soil dust on agar plates and by using fluorescence microscopy to visualize dead and living bacteria attached to soil dust particles.

Fig. 2: Agar plate with AIDA filter sample of soil dust particles after cultivation at 20°C (courtesy of A. Rieder)

After dispersion of the soil dust sample within the AIDA chamber, a filter sample was taken and incubated at 20°C on an agar medium. After a day, a close coverage with numerous bacteria colonies is visible (Fig.2) which indicates the presence of viable organisms on the soil dust particles. Fluorescence microscopy images confirm this finding and also show that not only living, but also dead bacteria are attached to the surface of soil dust particles (Fig.3).

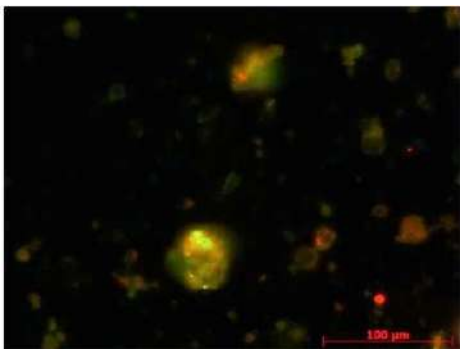

Fig. 3: Fluorescence microscopy image of several soil dust particles with dead (red fluorescence) and living (green fluorescence) bacteria (courtesy of A. Rieder)

The ice nucleation efficiency of the soil dust particles is quantified by the ice-active surface site density n_s which is given by the ratio between the measured ice crystal concentration n and the total aerosol surface A [10]. The ice-active surface site density depends on temperature and saturation over ice. We found indications that for immersion freezing as well as for deposition nucleation the ice nucleation efficiency might be enhanced for organic-rich mineral dust particles in comparison to mineral dusts from desert areas. Exposing the soil dust samples to a higher temperature (T=100°C) leads to a reduction of the ice nucleation efficiency in immersion freezing mode as can be seen from the decrease in ice-active surface site density (Fig.4). This reduction in ice nucleation efficiency might be related to destroying the protein structures of biological agents.

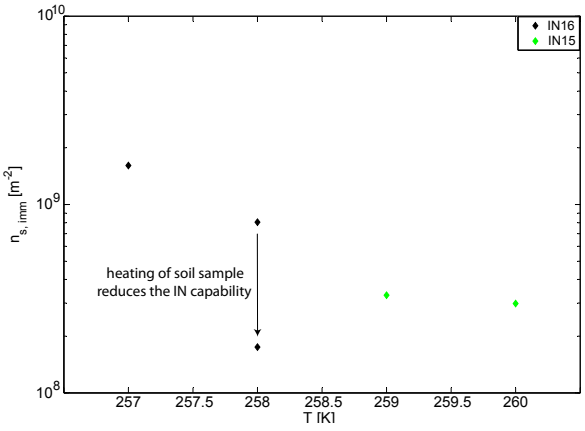

Fig. 4: Reduction of ice nucleation efficiency by heat treatment of soil dust sample

3 OUTLOOK

In future studies, further results from ice nucleation experiments with soil samples from several geographic regions (such as Argentina) will be presented. Also, the elemental composition of the samples and the population of viable organisms will be investigated.

From the measured ice-active surface site densities a parameterization can be derived which expresses the expected ice crystal concentration as a function of aerosol surface area, tem-

perature and saturation over ice. For estimating the contribution of soil dust particles to the global atmospheric ice nuclei burden this parameterization will be applied to the COSMO-ART model where ice nuclei concentrations can be diagnosed from the emission fluxes of aerosol particles. Dust from agricultural areas is emitted by dry exposed soil surfaces and during tillage activities. Currently, the emission fluxes from these sources are not very well quantified. Within this work we will present first estimates for the maximum emissions of soil dust particles and the corresponding ice nuclei concentrations.

Further measurements are needed in order to establish a closer link between biological soil dust components and the average ice nucleation efficiency. Also, in-situ measurements which confirm the presence of soil dust particles in the atmosphere are currently not available. These measurements will also be needed to constrain further refined ice nuclei calculations estimated with COSMO-ART.

REFERENCES

[1] H. R. Pruppacher and J. D. Klett. *Microphysics of clouds and precipitation*. Atmospheric and oceanographic sciences library; 18. Kluwer, Dordrecht, 2. rev. and enl. edition, 1997.

[2] I. Tegen and I. Fung. Modeling of mineral dust in the atmosphere: Sources, transport, and optical thickness. *Journal of Geophysical Research*, 99:D11, 1994.

[3] U. Pöschl. Atmospheric aerosols: Composition, transformation, climate and health effects. *Angewandte Chemie International Edition*, 44(46):7520–7540, 2005.

[4] M. Niemand, M. Möhler, B. Vogel, H. Vogel, C. Hoose, P. Connolly, H. Klein, H. Bingemer, P. DeMott, J. Skrotzki, and T. Leisner. A particle-surface-area-based parameterization of immersion freezing on desert dust particles. *Journal of the Atmospheric Sciences*, 2012.

[5] O. Möhler, P. R. Field, P. Connolly, S. Benz, H. Saathoff, M. Schnaiter, R. Wagner, R. Cotton, M. Krämer, A. Mangold, and A. J. Heymsfield. Efficiency of the deposition mode ice nucleation on mineral dust particles. *Atmospheric Chemistry and Physics*, 6(10):3007–3021, 2006.

[6] A. J. Prenni, M. D. Petters, S. M. Kreidenweis, C. L. Heald, S. T. Martin, P. Artaxo, R. M. Garland, A. G. Wollny, and U. Pschl. Relative roles of biogenic emissions and Saharan dust as ice nuclei in the Amazon basin. *Nature Geoscience*, 2:402–405, 2009.

[7] V. T. J. Phillips, C. Andronache, B. Christner, C. E. Morris, D. C. Sands, A. Bansemer, A. Lauer, C. McNaughton, and C. Seman. Potential impacts from biological aerosols on ensembles of continental clouds simulated numerically. *Biogeosciences*, 6(6):987–1014, 2009.

[8] O. Möhler, D. G. Georgakopoulos, C. E. Morris, S. Benz, V. Ebert, S. Hunsmann, H. Saathoff, M. Schnaiter, and R. Wagner. Heterogeneous ice nucleation activity of bacteria: new laboratory experiments at simulated cloud conditions. *Biogeosciences*, 5(5):1425–1435, 2008.

[9] F. Conen, C. E. Morris, J. Leifeld, M. V. Yakutin, and C. Alewell. Biological residues define the ice nucleation properties of soil dust. *Atmospheric Chemistry and Physics*, 11(18):9643–9648, 2011.

[10] P. J. Connolly, O. Mhler, P. R. Field, H. Saathoff, R. Burgess, T. Choularton, and M. Gallagher. Studies of heterogeneous freezing by three different desert dust samples. *Atmospheric Chemistry and Physics*, 9(8):2805–2824, 2009.

APPLYING AN MCMC INVERSE MODELLING METHOD TO ASSESS AEROSOL-TO-DROPLET SPECTRUM CLOSURE USING THREE DIFFERENT CLOUD PARCEL MODELS

Daniel Partridge*[1,2], Sylwester Arabas[3], and Hanna Pawlowska[3]

[1]Atmospheric Physics Clarendon Laboratory, Department of Physics, University of Oxford, UK

[2]Bert Bolin Centre for Climate Research, Stockholm University, Sweden

[3]Institute of Geophysics, Faculty of Physics, University of Warsaw, Poland

1 INTRODUCTION

In order to assess the impact of aerosols on clouds in the climate system, it is crucial to understand the underlying physical processes governing cloud-aerosol interactions. The difficulty in untangling relationships among aerosols, clouds and precipitation has been partly attributed to the inadequacy of existing tools and methodologies (Stevens and Feingold, 2009). Numerous cloud-aerosol modelling sensitivity studies have been conducted (e.g. Feingold, 2003; Rissman et al., 2004; Chuang, 2006) however, few have used detailed statistical methods to investigate the global sensitivity of a cloud model to input aerosol parameters (Anttila and Kerminen, 2007; Partridge et al., 2012). Global sensitivity analysis considers parameter changes over the entire multi-dimensional parameter domain. This generally leads to different, but more reliable results because parameter sensitivities in non-linear models of complex systems typically vary considerably over the feasible space of solutions.

Current parameterisations used to estimate cloud microphysical properties in many large-scale models (GCM) are usually based upon some form of parcel model theory (Hsieh et al., 2009). The current parametric uncertainty inherent in these cloud parameterisations propagates through to global estimates of the aerosol indirect effect calculated using a GCM. The ultimate test for prognostic parameterisations and cloud models is the comparison of their predictions against comprehensive in-situ data. Hence, these parameterisations are typically compared against adiabatic cloud parcel models for a range of input aerosol/meteorological conditions as well as in-situ observations of droplet number concentration (Snider et al., 2003; Fountoukis et al., 2007; Hsieh et al., 2009, and references therein). These studies typically focus on the cloud spectral properties, e.g. the droplet number concentration, whilst few closure studies have investigated the effects of the entire droplet size distribution (aerosol-cloud droplet spectrum closure). One approach in which both a global sensitivity analysis and aerosol-cloud droplet spectrum closure can be performed in one single integrative framework for the investigation of cloud-aerosol interactions is to embrace an Bayesian inverse modelling framework (Partridge et al., 2012).

To achieve this Partridge et al. (2012) coupled an adiabatic cloud parcel model to a Markov Chain Monte Carlo (MCMC) algorithm, and invoked posterior probability density functions of the cloud model input parameters used to describe the meteorological and aerosol physiochemical conditions. This not only provides an estimate of the optimal parameter values, but also a sample set of the underlying (posterior) uncertainty. This distribution contains important information about parameter sensitivity and correlation (interaction), and can be used to produce confidence intervals on the model predictions, allowing us to in a statistically robust manner provide a measure of the discrepancy between the model and in-situ measurements of cloud droplet size distributions as a function of the calibration parameters. Hence, a key advantage of embracing inverse modelling for aerosol-cloud closure studies is that it allows for the simultaneous assessment of both the adiabatic cloud model input parameters and predicted droplet spectra. The combination of a cloud parcel model, MCMC inverse modelling and aerosol and cloud measurements provides an integrative framework that is compatible with cloud droplet activation parameterisations used in GCMs. The framework can be applied to cloud parcel models of varying complexity, hence MCMC provides an efficient test bed for developing and validating cloud-droplet activation parameterisations that contribute to the representation of the indirect effect in GCMs.

*Correspondence address: Daniel Partridge, Atmospheric Physics Clarendon Laboratory, Parks Road, Oxford, OX1 3PU, UK. E-mail: Daniel.Partridge@physics.ox.ac.uk

Paper presented at the 16th International Conference on Clouds and Precipitation ICCP-2012, Leipzig, Germany

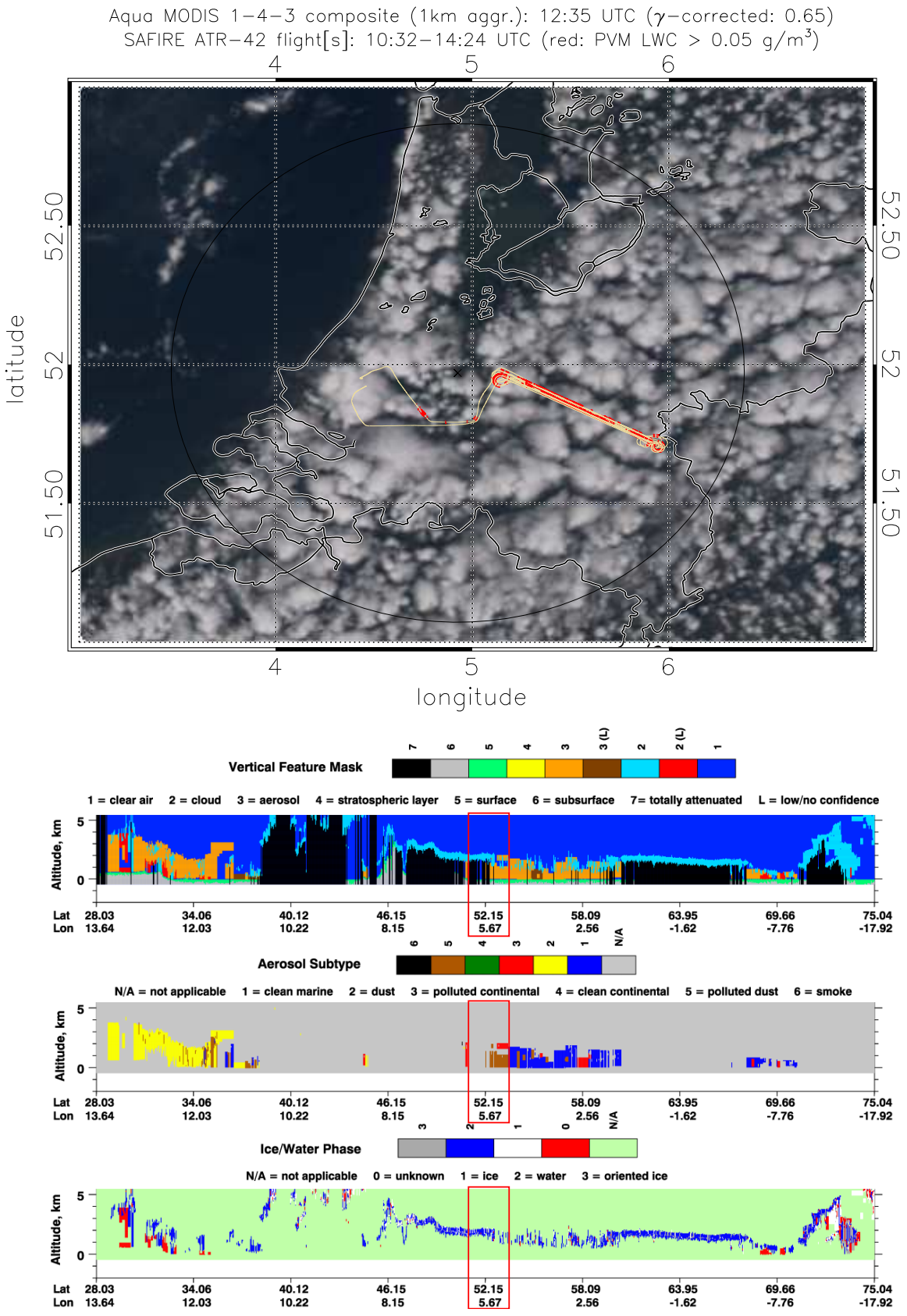

Figure 1: **Top:** True-colour composite from MODIS granule with IMPACT RF55 trajectory overlaid. (satellite overpass concurrent with the flight). Cloud penetrations indicated with red colour. The black circle has a radius of 100 km and is centred around the location of the KNMI meteorological observatory in Cabauw, The Netherlands (location indicated with a black cross). **Bottom:** Summary of CALIPSO products for an overpass concurrent with the IMPACT Rf55 research flight (2008-05-19 12:32:20.3 – 12:45:48.9 UTC). Red rectangles indicate approximately when/where the research flight has taken place. Aircraft data courtesy of Météo-France CNRM/GMEI/TRAMM. Satellite data courtesy of NASA.

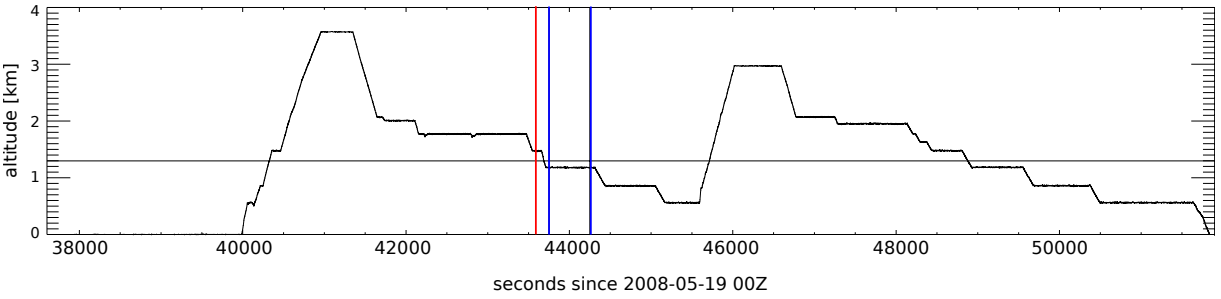

Figure 2: Top: RF55 trajectory in time/altitude coordinates with the estimated cloud-base height indicated with vertical line at 1.3 km, and the vertical bars denoting the flight leg which was chosen for analysing vertical velocity measurements and SMPS aerosol size distribution.

The goal of this study is to apply this methodology to measurements of cumuli over land in a polluted air mass for three different adiabatic cloud parcel models, that of that of Roelofs and Jongen (2004); Arabas and Pawlowska (2011) and Tunved et al. (2010). We will then examine the posterior parameter distributions from the MCMC simulations to ascertain the suitability of cloud parcel models to comprehensively describe convective clouds under adiabatic conditions, whilst concurrently investigating the global parameter sensitivity, and interaction within the adiabatic cloud parcel model. The results herein will be presented for one of the three adiabatic cloud parcel models under investigation (Arabas and Pawlowska, 2011).

2 METHOD

In this cloud-aerosol inverse analysis, the cloud parcel model is calibrated by iteratively changing input values of the meteorological and aerosol physiochemical parameters (calibration parameters) until the simulated droplet spectra match the measured spectra (calibration data) as closely and consistently as possible. Bayesian inference represents a mathematically rigorous approach to parameter estimation. This statistical method treats the calibration parameters as random variables with a joint (but yet unknown) posterior probability distribution. MCMC represents an efficient sampling method for the approximation of the posterior distribution within a limited number of model evaluations. The posterior distribution is the product of the prior distribution and the likelihood function. The prior distribution defines our knowledge about the parameters. The likelihood function $L(\theta|\mathbf{Y})$ provides a diagnostic measure of how well the model fits the data. It essentially measures the distance between the model predictions and corresponding observations.

Mathematically, the model calibration problem can be formulated as follows: Let $\tilde{\mathbf{Y}} = \mathbf{\Phi}(\mathbf{X}, \theta) = \{\tilde{\mathbf{y}}_\mathbf{1}, \ldots, \tilde{\mathbf{y}}_\mathbf{n}\}$ denote predictions of the model Φ with observed input variables X and model parameters θ. Let, $\mathbf{Y} = \{y_1, \ldots, y_n\}$ represent observations of the droplet size distribution (where n corresponds to the resolution – number of FSSP size bins). Real world observations of the cloud droplet size distribution considered herein typically exhibit heteroscedasticity, i.e. the measurement error varies dynamically with the magnitude of the data. Thus, in the likelihood function for the heteroscadastic case used in this study the error residuals (difference between the model-predicted and measured droplet number concentration in each size bin) need to be normalised with the measurement error to ensure statistically optimal estimates of the calibration parameters as follows,

$$L(\theta|\mathbf{Y}) = \prod_{i=1}^{n} \frac{1}{\sqrt{2\pi\sigma_i^2}} \left[-\frac{1}{2}\sigma_i^{-2}(y_i - \Phi(X_i, \theta))^2 \right] \quad (1)$$

where σ denotes the standard deviation of the measurement error.

In this study we couple adiabatic cloud parcel models to a state of the art self-adaptive DiffeRential Evolution Adaptive Metropolis algorithm (DREAM) (Vrugt et al., 2009). A detailed description of the inverse framework between the coupling of an adiabatic cloud parcel model and an MCMC algorithm can be found in Partridge et al. (2012).

3 OBSERVATIONAL DATA

3.1 Overview of atmospheric conditions

The methodology outlined in section 2 is tested on a polluted case study from the EUCAARI IMPACT[1] campaign in which measurements were performed in- and outside the cloud layer. The observational data used to initialise the parcel models comes from in-situ measurements on board the French ATR-42 research aircraft during the EUCAARI-IMPACT field campaign. More detailed information on the ATR-42 instrumentation used in this campaign can be found in Crumeyrolle et al. (2010, sec. 2.2) and Crumeyrolle et al.

[1]European Integrated Project on Aerosol Cloud Climate Air Quality Interactions – Intensive Measurement Period at Cabauw Tower

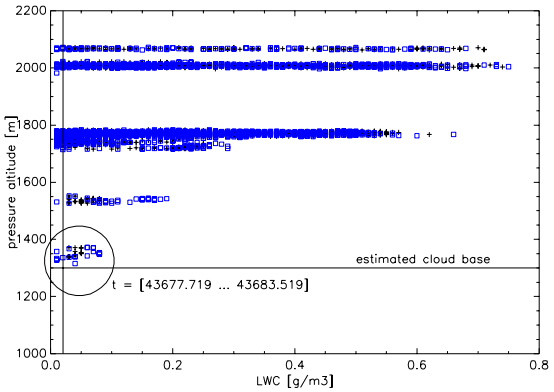

Figure 3: Scatter plot of LWC values measured by the FSSP-100 (blue symbols) and PVM-100A (black symbols) during the flight leg 41000–44000 (in seconds since midnight, consult Fig. 2).

(2012, sec. 2). Present analysis covers data gathered during the research flight number 55 (RF55) that took place on May 19th 2008 in the vicinity of the KNMI meteorological observatory in Cabauw, The Netherlands. The flight trajectory is depicted in Figure 1 (top panel) in longitude/latitude coordinates, and in Figure 2 in time/altitude coordinates. Figure 1 provides an overview of the atmospheric conditions during RF55 as measured by the Aqua and the CALIPSO satellite instruments. The aircraft probed a relatively uniform deck of convective clouds with depths of few hundred meters. These were ice-free clouds, formed in a polluted air mass. The cloud base height was approximately at 1300 m (estimated by analysing measured liquid water content (LWC) profiles, cf. Fig. 3).

3.2 Calibration data

A flight leg during which the FSSP-100 probe recorded cloud droplet size spectra within 100 meters from the cloud base was selected for further analysis (encircled region in figure 3, all spectra recorded within the 43677–43683 period in seconds since midnight UTC, and highlighted in time in Fig. 2 with red vertical lines). These droplet size distributions were filtered so that we only kept those associated with positive updraft velocity. The resultant set of 13 size spectra (mean spectrum depicted in Fig. 4) is defined as our calibration data to be compared with output from the parcel-model at the altitude of 1350 metres (about 50 metres above cloud base).

3.3 Calibration parameters

In this study the calibration parameters are the updraft velocity, lognormal distribution parameters describing the aerosol size spectrum, and soluble mass fraction. The remaining input parameters (temperature, pressure, humidity) are held fixed in the MCMC procedure. The values of these fixed parameters were picked from within the range of values observed at the altitude of 1000 m (the starting altitude for all model runs) by selecting a combination matching the estimated adiabatic cloud base at 1300 m.

A constant-level leg flown below cloud base was selected for analysis of aerosol characteristics and vertical velocity measurements – the variable calibration parameters used as parcel model input parameters to be calibrated by the MCMC algorithm. The chosen period (43750–44250 s) is depicted in Figure 2 with blue vertical lines.

The 5th and 95th percentiles of measured data for each calibration parameter are used to define the prior range of the parameter for the MCMC procedure. The prior range should represent the variability in our measurements during the observation period and provides the range over which DREAM is allowed to search for the parameter values giving the best fit to the calibration data.

For vertical velocity measurements (gust probe integrated in the nose of the aircraft, 5Hz sampling) a gaussian curve was fitted to the frequency distribution of measured values, and the 5th and 95th percentiles were calculated analytically from the part of the distribution corresponding to positive values only (Fig. 4).

A lognormal fitting was applied to each cloud aerosol size distribution measurement from the same flight leg from the SMPS instrument. The 5th, 95th percentiles for the lognormal parameters describing the Aitken, accumulation and course modes were calculated. The preliminary analysis presented herein covers the accumulation mode number concentration (Fig 4). In this first test we simplify the chemistry and define it as a two-component scheme consisting of either a soluble component, (here represented by the chemical properties of ammonium bisulphate (NH_4HSO_4), or an insoluble component, black carbon (represented by the chemical properties of black carbon, (BC). We then define the final calibration parameter describing the soluble mass fraction and its prior range of: 0.20 – 1.00.

4 RESULTS

Overall, the adiabatic cloud parcel model can successfully match the observed droplet size spectra for IMPACT flight RF55 when initialised with calibration parameter values within the prior range. The discrepancy between the mean measured and mean model-predicted droplet size spectra is shown in Figure 4. It confirms that the MCMC algorithm successfully converges.

The droplet size distribution that corresponds to the maximum a-posteriori (MAP) value represents the closest agreement between the simulated and observed droplet distributions. The MAP value is simply the point in the MCMC sample for which the likelihood function, $L(\theta|\mathbf{Y})$ (Eq. 1) was maximised (hence corresponding to the calibration parameter values within the pos-

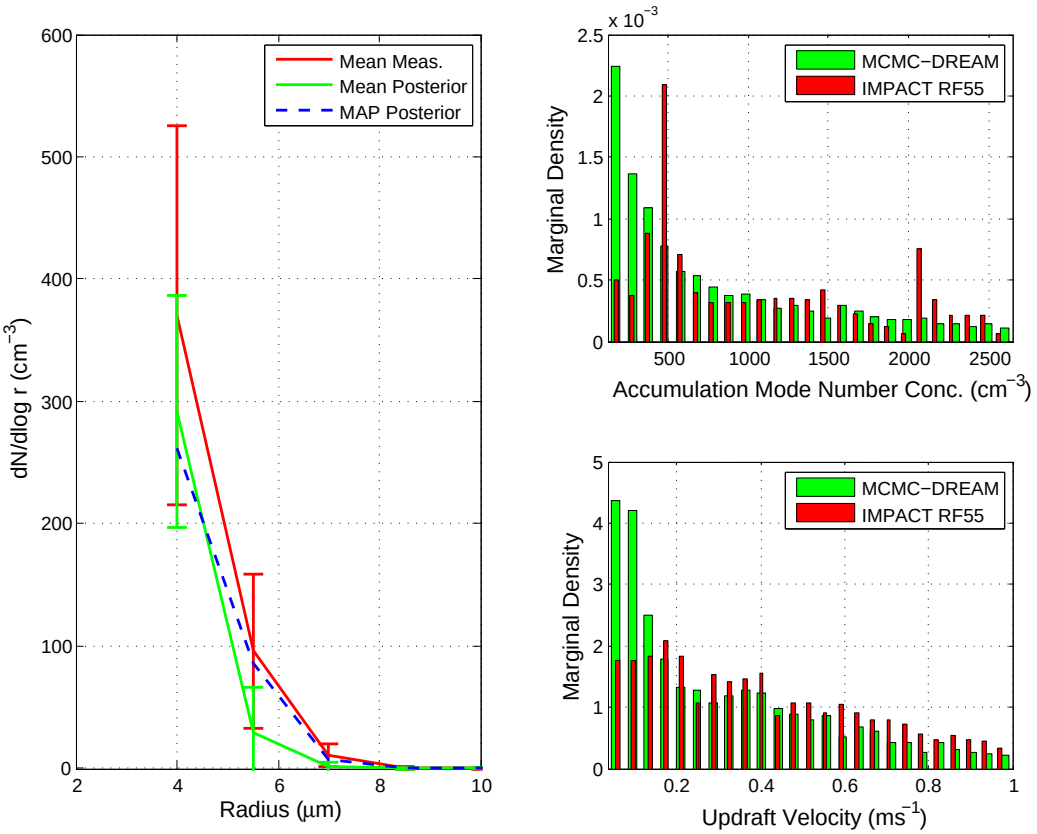

Figure 4: **LEFT**: The simulated and measured $dN/d\log r$ droplet size distribution for the flight leg (43677–43683 s) during RF55. We present the mean and standard deviation of the calibration data for each cloud case as well as the corresponding model predicted mean and standard deviation of the posterior distribution, and overlay the droplet size distribution that corresponds to the MAP value. **RIGHT**: Histograms of the marginal distributions for the number concentration of the accumulation mode (TOP) and updraft velocity (BOTTOM) with corresponding observations from flight leg (43750– 44250 s). Posterior parameter samples and measurements for each parameter normalised to provide a marginal density with integral of 1.

teriori distribution that provided the closest fit to the calibration data).

The difference between the mean and the MAP droplet spectra reflects the averaging over all the simulated droplet size distributions associated with the different posterior parameter values. The mean value thus reflects an "overall" droplet distribution and illustrates the broadening effects of running multiple simulations with variable calibration parameter values in the same way that previous studies have calculated an "overall" droplet distribution from the superposition of droplets distributions associated with a probability density function (PDF) of the updraft velocity (Hsieh et al., 2009; Morales and Nenes, 2010).

The concurrent fit to the calibration parameters is provided for two parameters known to be important for controlling the number of droplets activated, the updraft velocity and number concentration of the accumulation mode aerosol. These are presented alongside the observations in Figure 4. The respective marginal density is the probability distribution of the variables under investigation and provides us with counts of the calibration parameters values over their posterior distribution range, thus providing the shape of the posterior distribution (Partridge et al., 2012). The scale and orientation of the inferred posterior parameter distributions provide important diagnostic information about the structure of the adiabatic cloud parcel model under investigation. It is evident that the posterior distribution for both of these calibration parameters depart from a normal distribution as the probability density is forced to accumulate at the parameter bounds. This suggests the model structure provides a reasonable representation of the processes controlling droplet activation as they mimic the shape of the measurement spectra of these two parameters.

In addition the posterior distribution contains the required information to assess the importance (sensitivity) of individual parameters, and their cross-correlation. A marginal distribution that extends over the entire prior ranges is indicative for poor parameter sensitivity. On the contrary, if the histogram is well defined with narrow ranges, then this parameter is important for the parcel model to accurately represent the calibration data. Thus, the reduction in uncertainty of the posterior distribution compared to the prior is a simple and useful diagnostic to assess parameter sensitivity.

For this polluted continental aerosol environ-

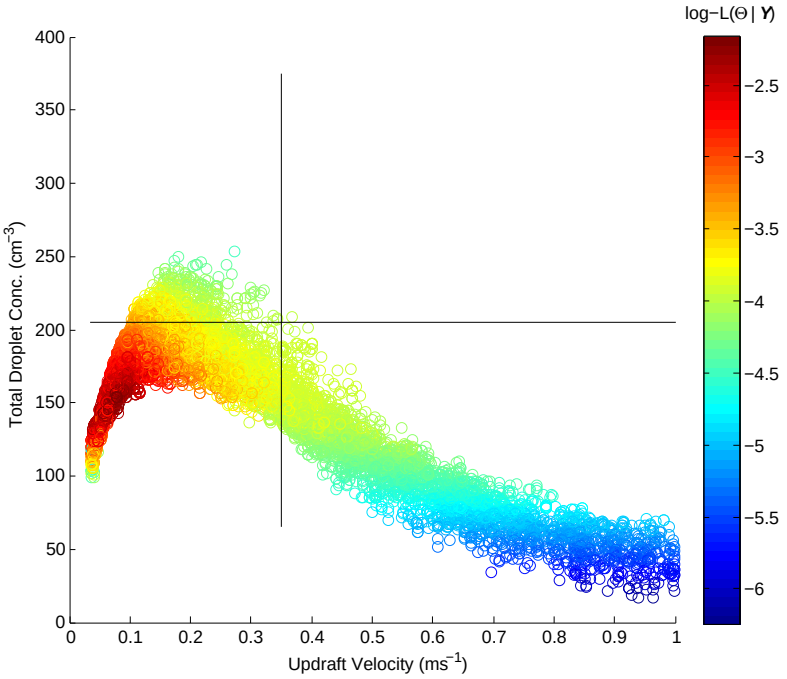

Figure 5: Scatterplot of the posterior samples of the updraft velocity versus cloud droplet number concentration. Colour represents the log-likelihood value that corresponds to each sample of the updraft velocity stored in the posterior distribution. Black vertical and horizontal lines represent the 5th to 95th percentile range of measurements observed during the selected flight legs of RF55 (see text for details).

ment these two parameters are not well defined, illustrating significant parameter variation across the posterior range. This indicates that for these calibration parameters there is a wide range of possible aerosol size distributions that can be considered optimal for the given environmental conditions. Similar results were found for the sensitivity of the remaining aerosol physiochemical parameters. The low sensitivity to aerosol physiochemical properties for this polluted cloud is in accordance with previous studies as the environment was not CCN limited (Anttila and Kerminen, 2007; Partridge et al., 2011, 2012).

To examine the shape of the posterior distributions in more detail and assess parameter interaction, correlation coefficients were calculated between different calibration parameters and the likelihood function. A strong correlation was found to exist between the updraft velocity and likelihood function, which we will therefore focus on. The relationship between the updraft velocity and corresponding model predictions of the total droplet concentration stored within the posterior distribution is presented in Fig. 5. The variation in droplet number concentration represents the range of predicted droplet spectra (Fig.4) that provide the closest match to the observations. This is in accordance with previous studies which have found that different droplet concentrations in near adiabatic cloud samples that provide a close match to the range of observations can only result from variations of the strength of cloud-base updraft that affects the number of nucleated droplets (Pawlowska et al., 2006). Thus in order to capture the range of measured droplet size distributions along this flight leg (measurement range illustrated by the black lines in the figure) it is necessary to account for the below cloud variability in updraft velocity and parameterise this accurately in GCMs (Hoose et al., 2010; Pringle et al., 2009; Golaz et al., 2011).

5 SUMMARY AND OUTLOOK

- We have provided a description of how an MCMC inverse modelling approach can be used to provide droplet spectra closure, global parameter sensitivity and parameter correlation in a single integrative framework.

- It has been demonstrated that an adiabatic cloud parcel model coupled to an MCMC algorithm can successfully represent measured droplet size distributions above the cloud base of polluted cumuli measured during the IMPACT campaign.

- Future work will involve a more in depth analysis of the posterior distributions of the remaining parameters in relation to the observations. Further simulations will be performed for different cloud cases as well as increasing the complexity of the chemistry analysis of the modelling framework by including in the prior ranges the statistics of the below cloud chemistry data based on aerosol mass spectroscopic measurements.

Acknowledgements

This work acknowledges flights performed by the SAFIRE ATR-42 team within the framework of EUCAARI (European Integrated project on Aerosol Cloud Climate and Air Quality interactions, No. 036833-2). The authors acknowledge S. Crumeyrolle and A. Schwarzenboeck for providing the aerosol observational data for RF55.

References

Anttila, T. and Kerminen, V.-M.: On the contribution of Aitken mode particles to cloud droplet populations at continental background areas – a parametric sensitivity study, Atmos. Chem. Phys., 7, 4625–4637, 2007.

Arabas, S. and Pawlowska, H.: Adaptive method of lines for multi-component aerosol condensational growth and CCN activation, Geosi. Model Dev., 4, 15–31, 2011.

Chuang, P. Y.: Sensitivity of CCN activation to kinetic parameters, J. Geophys. Res., 111, D09 201, 2006.

Crumeyrolle, S., Manninen, H. E., Sellegri, K., Roberts, G., Gomes, L., Kulmala, M., Weigel, R., Laj, P., and Schwarzenboeck, A.: New particle formation events measured on board the ATR-42 aircraft during the EUCAARI campaign, Atmos. Chem. Phys., 10, 6721–6735, 2010.

Crumeyrolle, S., Schwarzenboeck, A., Sellegri, K., Burkhart, J. F., Stohl, A., Gomes, L., Quennehen, B., Roberts, G., Weigel, R., Roger, J. C., Villani, P., Pichon, J. M., Bourrianne, T., and Laj, P.: Overview of aerosol properties associated with air masses sampled by the ATR-42 during the EUCAARI campaign (2008), Atmos. Chem. Phys. Discuss., 12, 9451–9490, 2012.

Feingold, G.: Modeling of the first indirect effect: Analysis of measurement requirements, Geophys. Res. Lett., 30, 1997, 2003.

Fountoukis, C., Nenes, A., Meskhidze, N., Bahreini, R., Conant, W., Jonsson, H., Murphy, S., Sorooshian, A., Varutbangkul, V., Brechtel, F., Flagan, R., and Seinfeld, J.: Aerosol-cloud drop concentration closure for clouds sampled during the International Consortium for Atmospheric Research on Transport and Transformation 2004 campaign, J. Geoph. Res., 112, D10S30, 2007.

Golaz, J.-C., Salzmann, M., Donner, L., Horowitz, L., Ming, Y., and Zhao, M.: Sensitivity of the aerosol indirect effect to subgrid variability in the cloud parameterization of the GFDL Atmosphere General Circulation Model AM3, J. Climate, 24, 3145–3160, 2011.

Hoose, C., Kristjansson, J., Arabas, S., Boers, R., Pawlowska, H., Puygrenier, V., Siebert, H., and Thouron, O.: Parameterization of in-cloud vertical velocities for cloud droplet activation in coarse-grid models: analysis of observations and cloud resolving model results, in: Proc. of the 13th AMS Conference on Atmospheric Radiation, Portland, Oregon, USA, 2010.

Hsieh, W. C., Nenes, A., Flagan, R., Seinfeld, J., Buzorius, G., and Jonsson, H.: Parameterization of cloud droplet size distributions: Comparison with parcel models and observations, J. Geophys. Res., 114, D11 205, 2009.

Morales, R. and Nenes, A.: Characteristic updrafts for computing distribution-averaged cloud droplet number and stratocumulus cloud properties, J. Geoph. Res., 115, D18 220, 2010.

Partridge, D., Vrugt, J., Tunved, P., Ekman, A. M. L., Struthers, H., and Sorooshian, A.: Inverse modelling of cloud-aerosol interactions – Part 2: Sensitivity tests on liquid phase clouds using a Markov chain Monte Carlo based simulation approach, Atmos. Chem. Phys., pp. 2823–2847, 2012.

Partridge, D. G., Vrugt, J. A., Tunved, P., Ekman, A. M. L., Gorea, D., and Sorooshian, A.: Inverse modeling of cloud-aerosol interactions ?? Part 1: Detailed response surface analysis, Atmos. Chem. Phys., 11, 2011.

Pawlowska, H., Grabowski, W., and Brenguier, J.-L.: Observations of the width of cloud droplet spectra in stratocumulus, Geophys. Res. Lett., 33, L19 810, 2006.

Pringle, K. J., Carslaw, K. S., Spracklen, D. V., Mann, G. M., and Chipperfield, M. P.: The relationship between aerosol and cloud drop number concentrations in a global aerosol microphysics model, Atmos. Chem. Phys., 9, 4131–4144, 2009.

Rissman, T., Nenes, A., and Seinfeld, J.: Chemical amplification (or dampening) of the Twomey effect: Conditions derived from droplet activation theory, J. Atmos. Sci., 61, 919–930, 2004.

Roelofs, G. J. and Jongen, S.: A model study of the influence of aerosol size and chemical properties on precipitation formation in warm clouds, J. Geophys. Res., 109, D22 201, 2004.

Snider, J., Guibert, S., Brenguier, J.-L., and Putaud, J.-P.: Aerosol activation in marine stratocumulus clouds: 2. Köhler and parcel theory closure studies, J. Geophys. Res., 108, 2003.

Stevens, B. and Feingold, G.: Untangling aerosol effects on clouds and precipitation in a buffered system, Nature, 461, 607–613, 2009.

Tunved, P., Partridge, D. G., and Korhonen, H.: New trajectory-driven aerosol and chemical process model Chemical and Aerosol Lagrangian Model (CALM), Atmos. Chem. Phys., 10, 10 161–10 185, 2010.

Vrugt, J. A., Ter Braak, C. J. F., Diks, C. G. H., Robinson, B. A., Hyman, J. M., and Higdon, D.: Accelerating Markov chain Monte Carlo simulation by differential evolution with self- adaptive randomized subspace sampling, Int. J. Nonlin. Sci. Num., 10, 273–290, 2009.

RADAR FORWARD OPERATOR FOR VERIFICATION OF CLOUD RESOLVING SIMULATIONS FOR THE COSMO MODEL

Dorit Epperlein[1], Yuefei Zeng[1] and Ulrich Blahak[2]

[1]Institute for Meteorology and Climate Research, Karlsruhe Institute of Technology (KIT)
[2]German Weather Service (Deutscher Wetterdienst, DWD)

1 INTRODUCTION

Weather radar systems provide unique information on dynamical and microphysical characteristics of cloud structures and precipitation with a high temporal and spatial resolution. The new weather radar network of the German Weather Service (Deutscher Wetterdienst, DWD) will soon comprise 17 C band dual polarisation Doppler radar systems evenly distributed throughout Germany for complete coverage. Figure 1 shows the location of all 17 radar stations in Germany. They will measure the radar observables reflectivity, radial wind and polarisation parameters in three dimensions and with a temporal resolution of 5 minutes.

The DWD runs the non-hydrostatic limited area numerical weather prediction model of the Consortium for Small Scale Modeling (COSMO), called “COSMO model” (formerly “Lokal Modell” LM) [1],[2]. COSMO is a cooperation of 7 European national meteorological services including the German Weather Service. More information on COSMO can be found on the webpage: `http://www.cosmo-model.org`

Up to now radar data are not used in the COSMO model, except within the framework of latent heat nudging and for a simple nudging method of the radial wind. However, future applications are planned to make better use of radar data within an upcoming new LETKF data assimilation system. Since the model is also used for higher resolution cloud resolving studies using a modern two-moment bulk scheme [3], the radar data can be used together with the output of the COSMO model in the context of data assimilation as well as model and cloud microphysics verification.

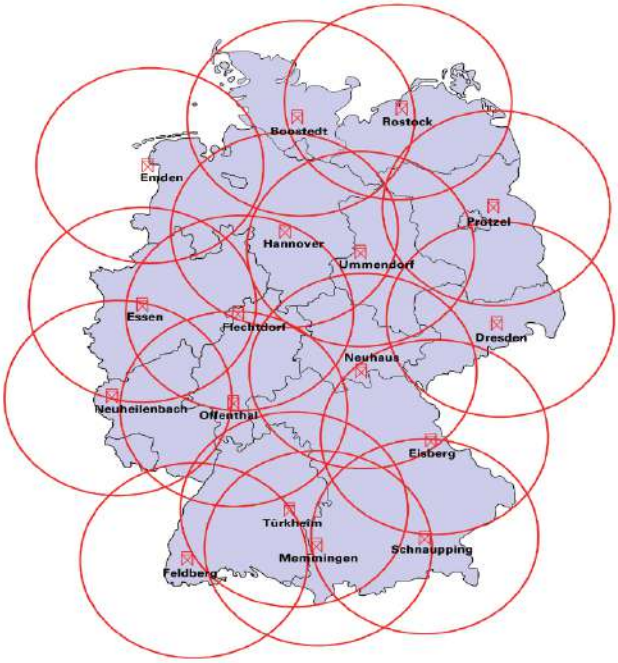

Figure 1: The new radar network of the German Weather Service (Deutscher Wetterdienst, DWD): 17 radar stations throughout Germany provide complete coverage.

In order to enable comparisons between measured data and numerically modeled data a radar forward operator that calculates the radar observables from the prognostic output of the COSMO model has been developed. The design of the forward operator and first results will be described in the following.

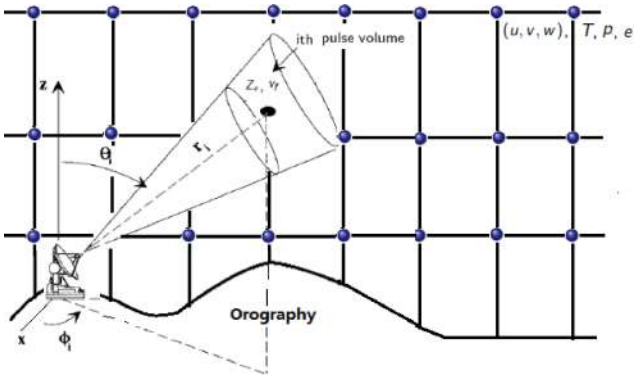

Figure 2: Radar beam vs. model grid: Radar data (reflectivity Z_e, radial wind v_r) are measured in the "radar system" with radial distance r_i, azimuth ϕ_i and elevation θ_i. Prognostic variables of the model (3d wind components (u, v, w), temperature T, pressure p, vapour pressure e) are given on the model grid (marked by blue dots).

2 RADAR FORWARD OPERATOR

Radar observations (radial wind, reflectivity, polarisation parameters) differ from the prognostic variables (wind, temperature, hydrometeors,...) of the model and cannot directly be compared to each other. The radial wind is defined as the one-dimensional component of the wind vector projected along the radar beam. Reflectivity is a measure for the echo contribution of scattering particles and allows conclusions to be drawn about e.g. the precipitation rate. Polarisation parameters give information about type and shape of the hydrometeors (variation from spherical shape). Reflectivity and polarisation parameters reflect in a sense only a sum over all hydrometeors with limited information on their partitioning. Another problem in comparing radar data and model output is the different coordinate systems of the radar beam (spherical) on the one hand and the model grid (cartesian) on the other hand. Figure 2 shows a conceptual sketch of the radar beam compared to a simplified model grid. The measured radar data refer to the "radar system" which is given in radial distance r, azimuth ϕ and elevation Θ. Starting from the prognostic output of the model given on a model grid the aim of the radar forward operator is to simulate the radar variables in the same coordinate system as a "real" radar would measure them. Several additional physical processes and important radar measuring characteristics/errors at different levels of complexity are taken into account, which is described in detail below. The Operator was created in a comprehensive and modular design and hence by subsequent neglect, simplification and/or approximation of single physical effects, the "best" balance between computational efficiency and physical accuracy can be investigated.

An overview of the schematic structure of the radar forward operator is shown step-by-step in Figure 3. As already stated, the operator uses the prognostic variables of the COSMO model given on the model grid. The main quantities needed for further calculations are the three-dimensional wind components (u, v, w), temperature T and information on hydrometeors. Depending on the microphysical bulk scheme we distinguish between cloud droplets, cloud ice, raindrops, snow, graupel using its mass densities $\{q_c, q_i, q_r, q_s, q_g\}$ in case of the one-moment scheme and hail as sixth type of precipitation particle using the mass densities and the number densities of all six hydrometeor classes in case of the two-moment scheme [3], [4], [5].

As a start the temperature dependent refractive index m of the particles is calculated. Here one can choose between different formulas of approximation for water and ice. Special emphasis is given to melting particles composed of a mixture of ice, water and air depending on the degree of melting (see e.g. [6], [7], [8]).

Now the radar reflectivity η can be calculated on the model grid,

$$\eta(r, \phi, \theta) = \int_0^\infty \sigma_b(D, m) N(D, r, \phi, \theta) dD$$

with σ_b backscattering cross section, N particle size distribution and D diameter of the particles. And hence the equivalent radar reflectivity factor Z_e is given as

$$Z_e(r, \phi, \theta) = \eta(r, \phi, \theta) \frac{\lambda^4}{\pi^5 |K_{w,0}|^2}$$

with λ wavelength of the radar and $K_{w,0}$ reference value of the dielectric constant of water. The computation of σ_b can be based either on full Mie scattering theory or with more efficient formulas employing the Rayleigh approximation together with simple approximations for the refractive index. Afterwards a summation over all types of hydrometeors still has to be done.

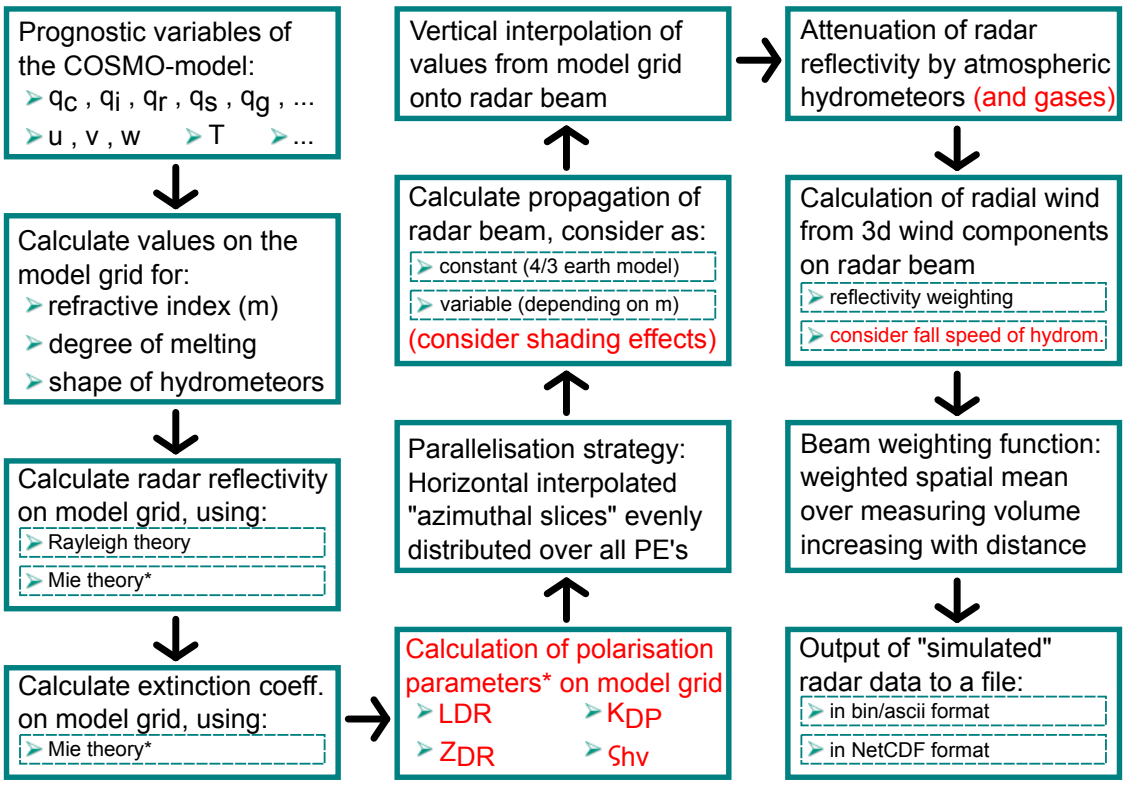

Figure 3: Conceptual flow chart of the full comprehensive and modular radar forward operator including all important physical processes. Red means not implemented yet and * indicates calculations where lookup tables are required due to computational complexity.

Using the same rationales as for the reflectivity the extinction coefficient Λ can be calculated

$$\Lambda(r,\phi,\theta) = \int_0^\infty \sigma_{ext}(D,m) N(D,r,\phi,\theta) dD$$

with σ_{ext} extinction cross section including side scattering effects and absorption. Note that the calculation of σ_{ext} requires the use of Mie theory. One further remark on this point: Compared with the simpler and more efficient Rayleigh approximation, calculations using Mie theory are very demanding and computationally expensive. Optimisation of the computation of Mie scattering can be done by means of lookup tables which are currently being implemented.

Since the radar forward operator has to work on parallel supercomputer architectures, parallelisation techniques also have to be considered for good computational efficiency. One strategy is to divide the radar volume in “azimuthal slices” and distribute them evenly in a way that each computing processor gets about equal work to do. This is necessary to achieve good load balancing and avoid idle times of single processors.

In the next step the propagation of the radar beam is calculated considering beam bending due to atmospheric refraction. This can either be done once –assuming as constant in time– using the 4/3 earth approximation (to save numerical effort) or for every radar time step depending on the variable refractive index as a function of temperature, pressure and vapour pressure. Shadowing by orographic obstacles can be additionally taken into account but is not fully implemented by now. Afterwards the values of reflectivity, extinction and model wind can be interpolated trilinearly onto the radar beam.

Knowing the path of the radar beam to the scattering particles, the attenuation of the radar beam due to atmospheric hydrometeors and gases can be calculated. Using the extinction coefficient Λ, the so-called two-way attenuation coefficient l_N^{-2} is defined as:

$$l_N^{-2} = \exp\left(-2\int_0^{r_0} \Lambda(r,\phi,\theta) dr\right)$$

with r_0 distance of the scattering particle to the radar. To get the attenuated reflectivity (Z_a), Z_e has to be multiplied by l_N^{-2}.

The radial wind is easily calculated from the wind components, that are now given in the coordinate system of the radar beam. Additionally, a reflectivity weighting and the fall speed of the hydrometeors can be taken into account.

At this point, all radar observables are given on the radar beam lying on a single line along the beam axis. For the increasing pulse volume with distance (see Figure 2) a Gaussian beam weighting function can be employed. This was implemented using a Gauss-Legendre quadrature with a selectable number of integration points. More details can be found in [9].

Finally a few words on polarisation parameters: At the moment, they have not been implemented in the operator but it is planned for the near future to include at least some polarimetric moments, possibly by means of the program SynPolRad by Pfeifer et al. [10]. However, the computation of the polarisation parameters will drastically increase the runtime of the forward operator and hence again lookup tables depending on temperature, mass densities and the shape of the hydrometeors (including canting angle distributions and axis ratios of the spheroids as a function of size) are mandatory.

3 FIRST RESULTS

Having all relevant processes implemented, the nearly complete radar forward operator embedded in the COSMO model can be tested in its present state. This has been done on the NEC SX-9 vector-parallel supercomputer of the DWD. First simulations were conducted using an idealised test case, a convective system triggered by a warm bubble along the lines of Weisman and Klemp [11]. At first, one radar station was simulated with a resolution of 130 range bins of 1 km in radial direction, 20 elevations and $360 \times 1^\circ$ azimuths in a temporal resolution of 5 min. For the model the horizontal grid spacing has been chosen to 1 km with a time step of 6 s. The operator was tested with the different adjustments which have been explained in the previous section. Some of the results are shown in Figure 4 for the reflectivity after two hours of model run. Two different radar wavelengths were chosen to represent radar systems typically used for weather surveillance (5.5 cm$\Leftrightarrow$C band and 3.0 cm$\Leftrightarrow$X band). The results in the first column have been obtained by applying Rayleigh scattering in combination with an approximation of the hydrometeors refractive index described by Oguchi [8]. Compared with Mie scattering shown in the second column, the Rayleigh calculation becomes inaccurate at high values of reflectivity due to the presence of partially melted large graupel. The third column shows the same Mie calculation but additionally considering attenuation by hydrometeors. One can see a big influence of this effect increasing towards smaller wavelengths. All other aspects of the operator, like, e.g., refractive beam bending depending on the actually simulated model temperature, pressure and humidity, and smoothing with the beam weighting function have also been successfully tested.

The next step in testing the operator has been to simulate true meteorological situations and more than one radar station. One example of such a simulation run is shown in Figure 5 for the 04.09.2011, comparing pseudo-composites of the 16 current DWD radar stations of both simulated and measured radar reflectivities, in this case a simple plot of all the 1.5 degree constant elevation scans (PPI, plan position indicator). Thus, reflectivity often shows “jumps“ at intersections of radar boundaries because of the different scan altitudes. This simulation run serves to demonstrate the technical functionality, and virtually any number of radar stations can be simulated within one COSMO-model run on supercomputer architectures. The run time of the radar operator was less than 10% of the total model run time using the same configurations for all radars as described above for the idealised experiments and using Rayleigh theory.

4 CONCLUSION AND OUTLOOK

First simulations done with the current version of the radar forward operator show good results so far. However, the program is still under development, a few processes have to be completed and some polarimetric moments need to be implemented (see red indications in Figure 3). More work has to be invested in making the computations more efficient.

The application of the radar forward operator enables comparisons between simulated and measured radar data for interesting case studies (e.g. of convective hail cells), using for example the CFAD (contoured frequency by alti-

tude diagram) method, which compares vertically stratified areal statistics. Thus, hints and conclusions about the representation of microphysical processes within the model system can be drawn, which is an important step for further improving cloud microphysical schemes.

BIBLIOGRAPHY

[1] G. Doms, U. Schättler: A Description of the Nonhydrostatic Regional COSMO Model. Part I: Dynamics and Numerics (Model Documentation (2002))

[2] M. Baldauf et al.: Operational Convective-Scale Numerical Weather Prediction with the COSMO Model: Description and Sensitivities (Mon. Wea. Rev. 139 (2011) 3887-3905)

[3] A. Seifert, K.D. Beheng: A two-moment cloud microphysics parameterization for mixed-phase clouds. Part 1: Model description (Meteor. and Atmos. Phys. 92 (2006) 45-66)

[4] H. Noppel et al.: A Two-Moment Cloud Microphysics Scheme with Two Process-Separated Modes of Graupel (12th AMS Conference on Cloud Physics, Madison, Wisconsin, (2006))

[5] U. Blahak: Towards a Better Representation of High Density Ice Particles in a State-of-the-Art Two-Moment Bulk Microphysical Scheme (15th ICCP, Cancun, Mexico, (2008))

[6] J.C. Maxwell Garnett: Colours in metal glasses and in metallic films (Proc. of the Royal Society of London A203 (1904) 385-420)

[7] D.A.G. Bruggemann: Berechnung verschiedener physikalischer Konstanten von heterogenen Substanzen. I. Dielektrizitätskonstanten und Leitfähigkeiten der Mischkörper aus isotropen Substanzen (Annalen der Physik 416(7) (1935) 636-664)

[8] T. Oguchi: Electromagnetic wave propagation and scattering in rain and other hydrometeors (Proc. IEEE 71(9) (1983) 1029-1078)

[9] U. Blahak et al.: Radar Forward Operator for Data Assimilation and Model Verification for the COSMO Model (35th Conference on Radar Meteorology, Pittsburgh, Pennsylvania, (2011))

[10] M. Pfeifer et al.: A Polarimetric Radar Forward Operator for Model Evaluation (J. Appl. Meteor. Climatol. 47 (2008) 3202-3220)

[11] M.L. Weisman, J.B.Klemp: The dependence of numerically simulated convective storms on vertical wind shear and buoyancy (Mon. Wea. Rev. 110 (1982) 504-520)

[12] T. Hengstebeck, private communication

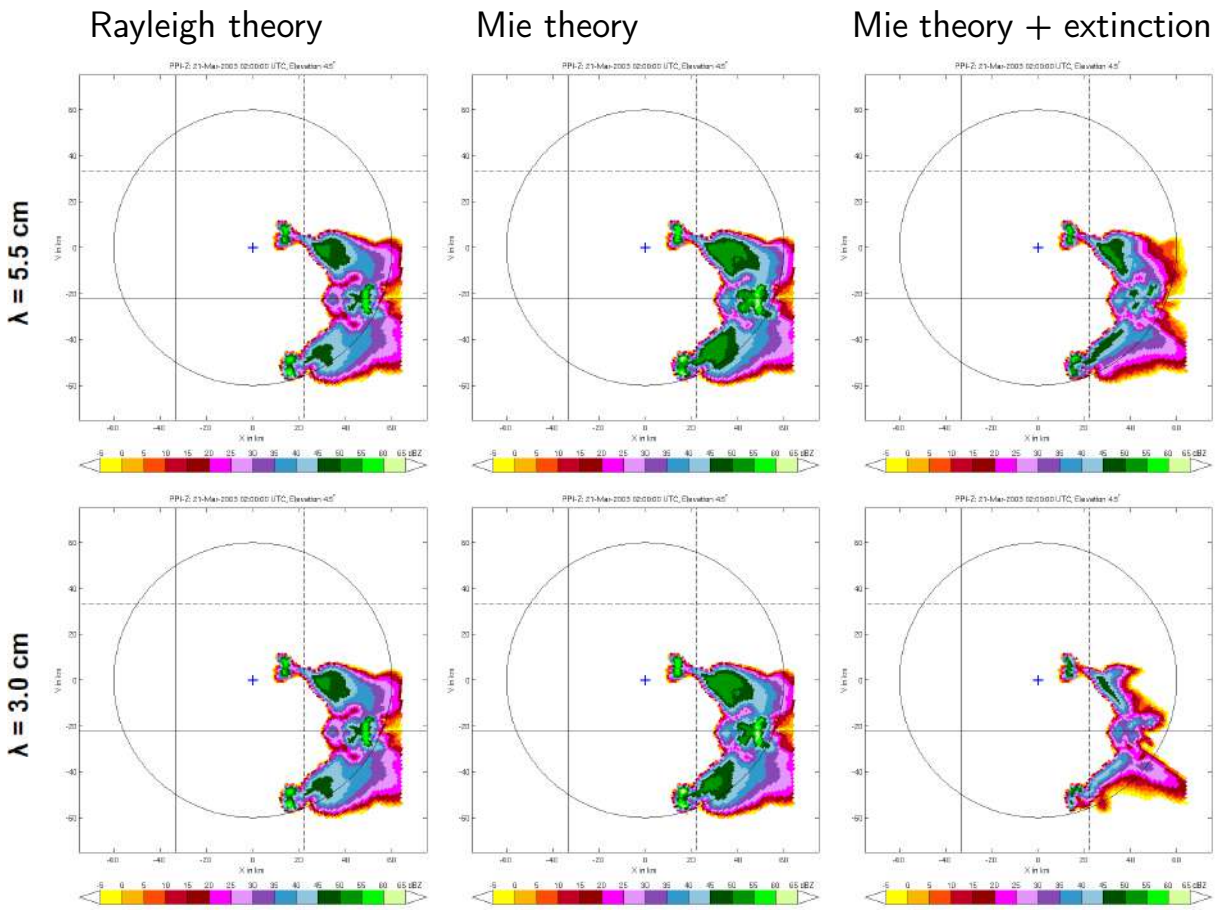

Figure 4: Simulations using the radar forward operator: radar reflectivities of an idealised test case.

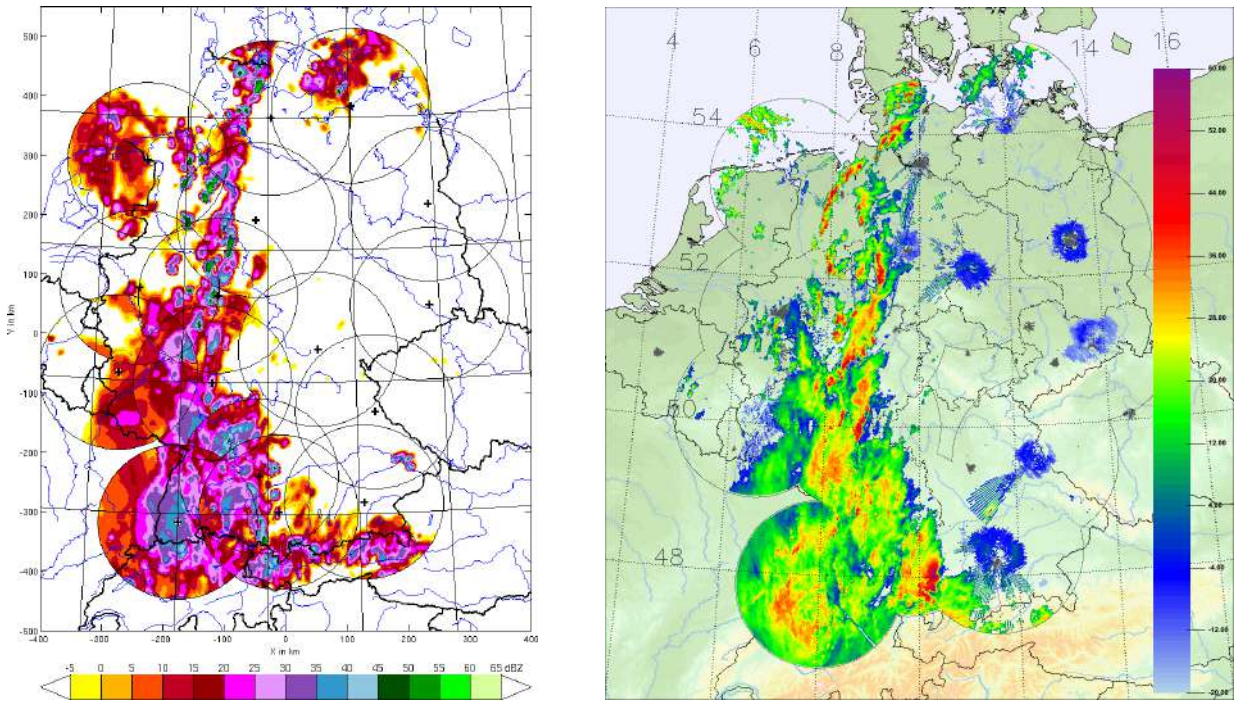

Figure 5: Radar composite with 16 radar stations of a real synoptical situation, date: 04.09.2011, time: 3:30 pm. Left: radar data simulated using the forward operator. Right [12]: radar data measured by the 16 current radar stations of DWD.

THE ENTRAINMENT INTERFACE LAYER OF STRATOCUMULUS-TOPPED BOUNDARY LAYERS DURING THE POST FIELD CAMPAIGN

Samantha A. Hill,[1] Steven K. Krueger,[1] Hermann Gerber,[2] and Szymon P. Malinowski[3]
[1]University of Utah, Salt Lake City, Utah, USA
[2] Gerber Scientific Inc., Reston, Virginia, USA
[3] University of Warsaw Institute of Geophysics, Warsaw, Poland

1. INTRODUCTION

The fine-scale cloud structure near the top of Stratocumulus-Topped Boundary Layers (STBLs) has remained unexplored for many years due to limitations in aircraft and technology. This cloud top region in marine stratocumulus (Sc) is especially of interest because processes taking place there are believed to govern the behavior and persistence of the cloud decks that form at the top of these boundary layers. Small-scale cloud-top processes influence physical characteristics of these cloud layers, such as albedo, which currently plays a major role in keeping the earth's climate cooler than it would be in their absence due to the high amount of incident solar radiation marine Sc cloud decks reflect back to space (Bretherton 1997; Klein and Hartmann 1993). Thus, marine STBLs play an important role in Earth's radiation balance and climate (Hartmann 1992). Furthermore, studies have shown that uncertainties in the behavior of Sc clouds inhibit the accurate prediction of future climate change (Bony et al. 2006; Wyant et al. 2006). Therefore, largely due to their potential influence on climate, and due to the fact that little is understood about the small-scale processes that influence the behavior of these clouds, STBLs have remained a central topic in cloud physics research.

Our results are based on high-resolution aircraft data from the Physics of Stratocumulus Top (POST) field campaign that took place during July and August of 2008 off the coast of Monterey, California. A major focus of POST was sampling the fine-scale structure of the entrainment interface layer (EIL), the transition layer between the top of the cloudy mixed layer and the free troposphere. Consequently, a major result of our work is an approximation of the location and extent of the EIL for a subset of flights during POST. Using total water mixing ratio and liquid water potential temperature, we calculated the mixing fraction. This quantity is an indicator of the degree of mixing a parcel has undergone. We focused on five research flights during POST: two in the day, and three in the evening. Further, we used a mixing fraction analysis to calculate the warming and cooling due to radiative processes and phase changes near cloud top. For all of the flights analyzed, we find a clearly defined EIL, and that the effects of radiation and phase changes on net heating or cooling within the EIL are comparable. Our results support the idea that entrainment involves a buoyancy-sorting process in which mixtures with various fractions of free-atmosphere and mixed-layer air are produced in the EIL, but only those parcels with neutral or negative buoyancy relative to the mixed layer are entrained.

2. FLIGHT PATHS AND SELECTING DATA

With the EIL being a primary focus of the POST project, vertical flight plans were specially designed to collect data from within the EIL, and from the regions transitioning into, and out of, the EIL. These flightpaths were comprised of three (sometimes four) sections of repeated "sawtoothing" through the cloud deck, meaning the aircraft would dip down into the cloud layer, and then once in the cloud layer, would rise back up above the cloud layer. This pattern was repeated several times within a section of the flight path. Also, level legs were flown near the surface, in-cloud, and just below the cloud layer for later calculation of fluxes. An example of a typical vertical flight path is shown in Figure 1.

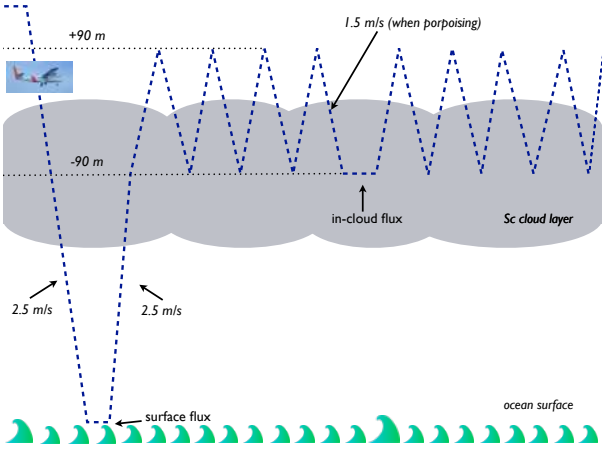

Figure 1: Diagram of a section of a typical vertical flight path during POST.

Simultaneously, in the horizontal, the flight path was prescribed as well, in an attempt to sample consistent parcels of air. Instead of simply flying down the coast or maintaining a straight path within the Sc layer, the pilot was assigned to fly a quasi-Lagrangian flight path, meaning the aircraft would follow the general flow of the surrounding atmosphere while sampling as much as possible from the same parcel of air, resulting in an overall zig-zag pattern. An example of the horizontal quasi-Lagrangian flight path from Research Flight 10 is shown in Figure 2.

Most of the data collected during POST were gathered by high-rate, fast-response probes at a frequency of 1000 Hz. However, to accommodate LI-COR vapor data, which was taken at a lower frequency of just 40 Hz., the 1000 Hz. data sets were averaged to 40 Hz. using matrix techniques in Matlab. Data from the aircraft cabin instrumentation were used for calculations involving ambient air pressure and height data. As the recording frequency for the cabin instruments was only 10 Hz., these data were interpolated to 40 Hz. using Matlab interpolation functions.

As previously mentioned, each flight included sections of "porpoising" in and out of the cloud layer, as well as horizontal legs for calculating fluxes. The analyses included here mainly focus on studying the extent and structure of the EIL; therefore, they focus on the portions of each flightpath that were comprised of these porpoises, and

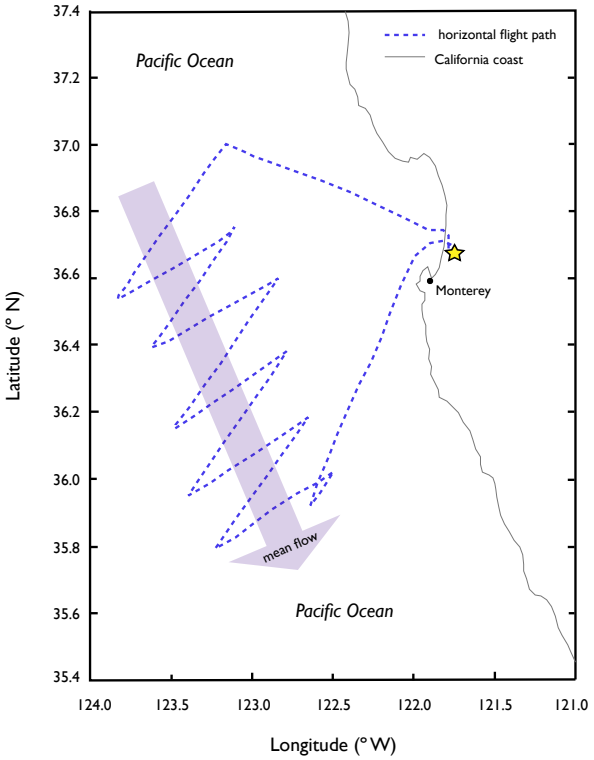

Figure 2: A typical horizontal flightpath during POST.

the data used for these analyses are solely those data points from within the porpoising sections of the flightpath. These groups of repetitive porpoises during each flight were named "pods." In most cases, each flight contained three pods comprised of at least five porpoises each. Most results of the following analyses are in the form of results from pods of a given flight.

3. CONSERVED VARIABLES AND MIXING

The use of conserved variables to investigate mixing between two thermodynamically distinct types of air within clouds has been employed in several studies (Burnet and Brenguier 2007; Paluch 1979). Specifically, this type of analysis has proven useful to study parcels in the midst of entrainment as dry and warm free-tropospheric air mixes with cool and moist cloudy air. Moist conserved variables, such as total water mixing ratio (q_t), are important for these analyses because they are conserved quantities under moist adia-

batic processes, and will remain constant, regardless of the altitude of the parcel in the atmosphere. For two parcels of different types of air undergoing mixing, a conserved variable, such as q_t, of the new mixture will be a linear combination of the q_ts of the original parcels, weighted by the mass contribution of each original parcel to the mass of the resultant mixture:

$$q_{t,mix} = (1 - \chi) * q_{t,a} + \chi * q_{t,b}, \qquad (1)$$

where $q_{t,a}$ is the total water mixing ratio of the first parcel, and (1-χ) is the fraction of unit mass contributed to the final mixture from the first parcel, while $q_{t,b}$ is the total water mixing ratio of the second parcel, and χ is the fraction of unit mass contributed to the final mixture from the second parcel.

Due to this linear characteristic of mixing for conserved variables, all possible mixing states for a resultant mixture between the initial, distinct states of the two original parcels lie on a straight line connecting a point representing the original mixing state of the first parcel, and a point representing the original mixing state of the second parcel. This is called a mixing line.

For studying mixing near the top of Sc clouds, one pure mixing state is taken to be the cloudy layer at the top of the STBL, and the second pure mixing state is taken to be the free troposphere overlying the STBL. VanZanten and Duynkerke (2002) suggest a method for using a conserved variable called mixing fraction to study radiative and phase change effects on temperature near the top of a Sc layer. Mixing fraction is a measure of the amount of one type of air mixed into a parcel of a second type of air, and is calculated using ratios and differences in q_t for the two types of air.

Locating mixing events at the top of the STBL during POST first required defining pure mixing states in and above the boundary layer. Moist, turbulent, cloud-layer air was defined as one such mixing state, and dry, warm, free-troposphere air from above the inversion was defined as a second pure state. The mixing of these two pure states was then used to study the properties of the EIL.

First, it was necessary to select and use variables that are conserved under both dry adiabatic and moist adiabatic processes due to the presence of moisture in both vapor and liquid phases throughout circulations within the mixed layer. The two moist conserved variables selected for this analysis were q_t (which remains constant though moisture may change from the vapor state to the liquid state, or visa versa), and liquid water potential temperature (Θ_l). An example of a mixing line from one pod of a daytime flight during POST is shown in Figure 3, with density of points expressed via color-coding. In this figure, one can see that most points are located at either endpoint of the mixing line in either one of the pure mixing states, but many parcels are located on the mixing line in between the pure states, in various stages of the mixing process. Data points that have been shifted to the right or left of the mixing line show the effects of radiative heating or cooling on parcels within the EIL.

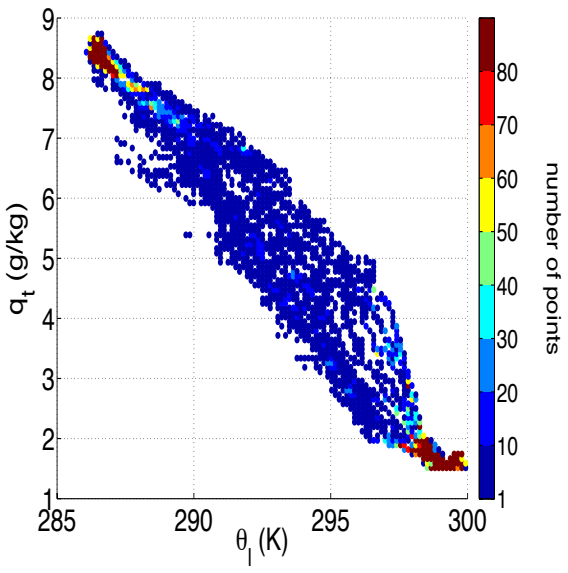

Figure 3: Mixing line from one pod of a daytime flight, when the aircraft was porpoising in and out of the cloudy mixed layer.

4. MIXING FRACTION

The conserved variables q_t and Θ_l were used to calculate a third conserved quantity, mixing

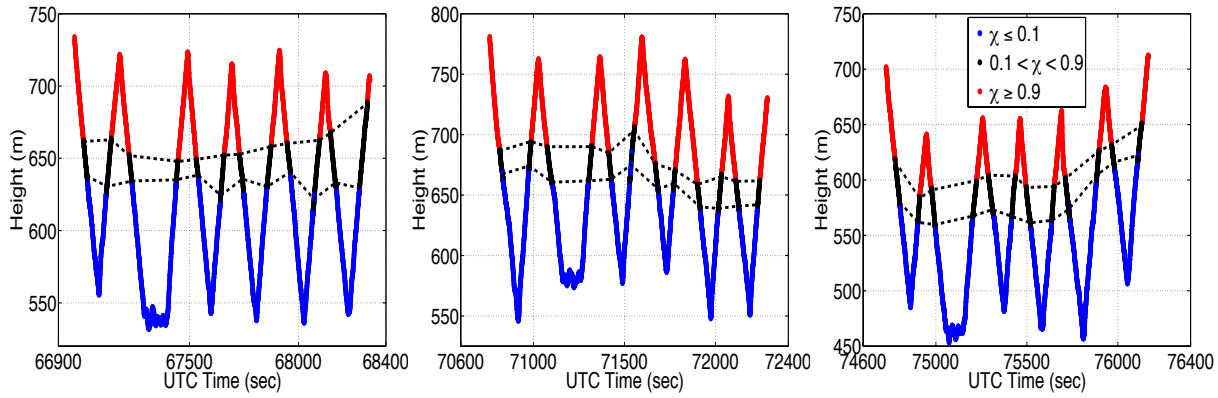

Figure 4: Flightpath characterized by mixing fraction. Black points are characteristic of a layer of mixing between the overlying free atmosphere (red points) and the underlying cloudy mixed layer (blue points).

fraction, for each point along the flight path.

In this case, mixing fraction is defined to be the fractional amount of free-tropospheric air mixed into a parcel of pure cloudy mixed-layer air. Values of mixing fraction range between 0 and 1, with a mixing fraction of 0 meaning no free-tropospheric air has been mixed into the parcel of cloudy air, and therefore representing a parcel of completely pure cloud-layer air. Conversely, a mixing fraction of 1 represents a parcel comprised completely of free-tropospheric air.

Following the methodology of vanZanten and Duynkerke (2002), mixing fraction was computed using the following equation:

$$\chi = \frac{\delta q_t}{\Delta q_t} \tag{2}$$

where

$$\delta q_t = q_{tm} - \overline{q_{t2}}, \tag{3}$$

and

$$\Delta q_t = \overline{q_{t1}} - \overline{q_{t2}}. \tag{4}$$

In the equations above, q_t represents total water mixing ratio, a subscript of 1 represents a pure free-tropospheric value, a subscript of 2 represents a pure cloudy mixed-layer value, a subscript *m* refers to the mixed parcel, and an overbar indicates an average over the given layer (cloudy mixed layer or free troposphere). In general, Δq_t is the jump in total water mixing ratio across the inversion at cloud top, and δq_t is the local fluctuation in total water mixing ratio.

Calculating mixing fraction for each point along the porpoising sections of the flightpath allowed for the region near the top of the mixed layer to be plotted in a new way, now characterized by mixing fraction. Values with a mixing fraction of at least 0.9 were taken to be values characteristic of pure free-tropospheric air, and were plotted in red; values with a mixing fraction of 0.1 or less were taken to be characteristic of pure cloud layer air, and were plotted in blue; finally, points with mixing fraction values between those two extremes were taken to be characteristic of parcels in the midst of mixing processes, and were plotted in black. The result, for all flights analyzed, was a clearly defined layer of black points, bordered on the top by red points (the free troposphere), and on the bottom by blue points (the cloudy mixed layer). This result indicates a relatively clearly defined layer of mixing between two pure states of the atmosphere, and is our best approximation for the location and extent of the EIL during POST. Three pods of a daytime flight from POST, characterized by mixing fraction, are shown in Figure 4.

5. EIL RESULTS

To calculate EIL thickness over the course of a flight, the EIL bottom height was subtracted from the EIL top height for each porpoise within the pods of each flight. Those thicknesses were then averaged over all pods within a given flight to produce our best estimate of EIL thickness over an entire flight. Averages of EIL thickness for each of the five analyzed flights are given in Table 1.

For all five flights, individual instances of EIL thickness of several tens of meters were most common. While there were a few instances of extremely thick EILs, they were much less common, and there was only one instance of an especially thin EIL under 10 meters using our mixing fraction technique for defining the EIL.

Table 1: Flight averages of EIL thickness for RF10, RF11, RF12, RF14, and RF16.

Flight	Avg. EIL Thickness (m)
RF10 (daytime)	31.8
RF11 (evening)	43.8
RF12 (evening)	47.0
RF14 (evening)	76.2
RF16 (daytime)	82.5

6. EFFECTS OF RADIATION AND PHASE CHANGES

Relative contributions of radiation and phase changes to a net heating or cooling within the EIL was calculated from moist conserved variables and our new variable, mixing fraction. To calculate the cooling within the EIL due to radiation, we again followed the methodology from vanZanten and Duynkerke (2002):

$$(\delta\Theta_l)_{rad} = \delta\Theta_l - \chi\Delta\Theta_l \tag{5}$$

where, as with mixing fraction, a subscript of 1 indicates a free troposphere value, a subscript of 2 indicates a cloud layer value, *m* refers to the mixed parcel, and an overbar indicates an average over the given layer.

$$\delta\Theta_l = \Theta_{lm} - \overline{\Theta_{l2}} \tag{6}$$

is the local fluctuation in liquid water potential temperature, and

$$\Delta\Theta_l = \overline{\Theta_{l1}} - \overline{\Theta_{l2}} \tag{7}$$

is the jump in liquid water potential temperature across the inversion at cloud top.

The calculation of cooling/warming within the EIL due to phase changes was accomplished using the following equation, also from vanZanten and Duynkerke (2002):

$$(\Theta_v)_{phase} = (\frac{L_v}{c_{pd}} - 1.61\overline{\Theta_{l2}})(q_{lm} - [1-\chi]\overline{q_{l2}}) \tag{8}$$

where L_v is the latent heat of vaporization, c_{pd} is the specific heat of dry air at constant pressure, χ is mixing fraction, and the definitions of subscripts and overbars remain the same as for previous equations. In this equation, however, an estimate of the average liquid water mixing ratio of pure cloudy mixed-layer air is required ($\overline{q_{l2}}$). To make a reliable approximation for this quantity, a saturation adjustment code was used, with inputs of pressure, temperature, and vapor mixing ratio from the aircraft data. The code calculated a saturation adjusted value for each point along the flightpath, which were used in the above equation to calculate the relative contribution of phase changes to net heating or cooling within the EIL.

Next, maximum, minimum, and mean values of warming and cooling for binned values of mixing fraction were calculated for temperature effects due to both radiation and phase changes. For these calculations, mixing fraction values were binned over all mixing fractions found within the EIL (0.1-0.9), with a bin width of $\Delta\chi = 0.1$. Mean $(\delta\Theta_l)_{rad}$ and $(\delta\Theta_v)_{phase}$ values were then calculated for each bin, and plotted as a function of mixing fraction, revealing a profile of the effects of radiation and phase changes across the EIL. Plots of these profiles, as well as temperature effects due to mixing, for (a) a daytime flight, and (b) an evening flight are shown in Figure 5.

For daytime RF10, on average, net warming due to radiation occurs in the EIL across all mixing

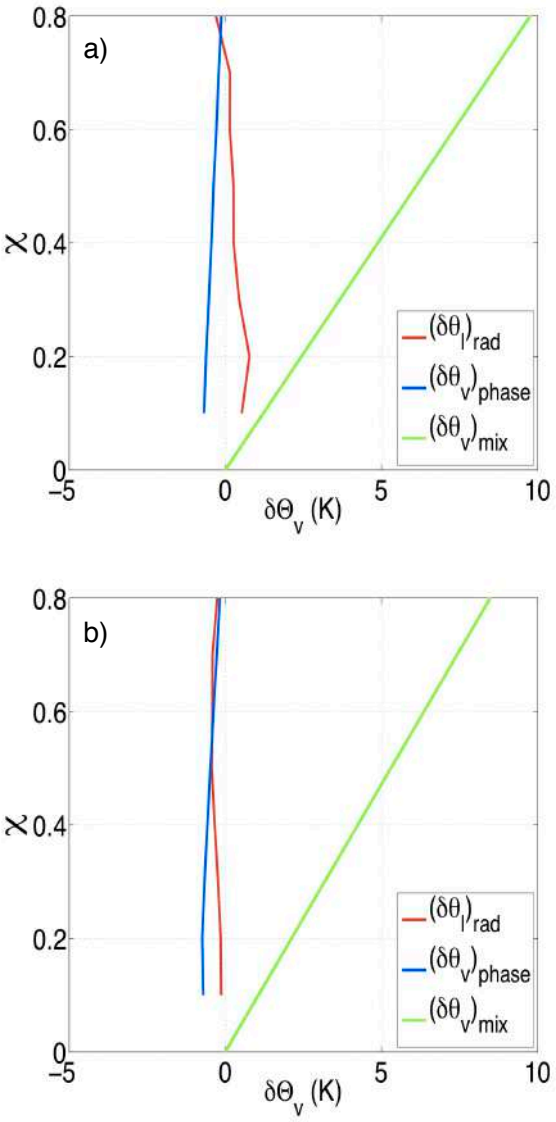

Figure 5: Effects of radiation and phase changes for mixing fractions within the EIL for (a) RF10, a daytime flight, and (b) RF12, an evening flight.

fractions. Evening RF12 exhibits slight cooling due to radiation in the EIL on average, on the same order of magnitude.

Daytime RF10, as well as evening RF12, exhibit net cooling due to phase changes within the EIL across all mixing fraction values, on average. This highlights the effects of evaporative cooling near the top of the cloudy mixed layer, and within the EIL, regardless of the time of day.

For all analyzed flights, magnitudes of heating and cooling in the EIL due to radiative effects and due to phase changes are comparable, on average. However, as expected, the effects of mixing on heating and cooling within the EIL are much more substantial than those due to radiation or phase changes.

Based on our calculations of mixing fraction, we find a well-defined, substantial EIL between the cloudy mixed layer and the free troposphere for all flights analyzed. Within this EIL, the effects of radiation and phase changes on net heating or cooling near cloud top are of comparable magnitude. These results support the idea that there exists a region between the free troposphere and the cloudy mixed layer of STBLs that has properties intermediate between those of the overlying atmosphere and those of the boundary layer. Our intermediate values of mixing fraction located at altitudes in between the altitude of the free troposphere and the altitude of the boundary layer suggest that this region is also one containing parcels at different stages in the mixing process.

ACKNOWLEDGMENTS. This material is based upon work supported by the National Science Foundation under Grant No. ATM-0735118, and by the National Science Foundation Science and Technology Center for Multi-Scale Modeling of Atmospheric Processes, managed by Colorado State University under cooperative agreement No. ATM-0425247.

REFERENCES

Bony, S., et al., 2006: How well do we understand and evaluate climate change feedback processes? *J. Climate*, **19** (**15**), 3445–3482.

Bretherton, C.S., 1997: Convection in stratocumulus-capped atmospheric boundary layers. In *The Physics and Parameterization of Moist Atmospheric Convection*, R.K. Smith, ed., Klumer Publishers, 127–142 (peer-reviewed book chapter).

Burnet, F. and J.-L. Brenguier, 2007: Observational study of the entrainment-mixing

process in warm convective clouds. *J. Atmos. Sci*, **64**, 1995–2011.

Hartmann, D. L, M. E. Ockert-Bell, and M. L. Michelsen, 1992: The effect of cloud type on earth's energy balance - global analysis. *J. Climate*, **5**, 1281–1304.

Klein, S. A. and D. L. Hartmann, 1993: The seasonal cycle of low stratiform clouds. *J. Climate*, **6**, 1588–1606.

Paluch, I.R., 1979: The entrainment mechanism in Colorado cumuli. **36**, 2467–2478.

vanZanten, M. C., and P.G. Duynkerke, 2002: Radiative and evaporative cooling in the entrainment zone of stratocumulus - the role of longwave radiative cooling above cloud top. *Bound.-Layer Meteor.*, **102**, 253–280.

Wyant, M.C., C.S. Bretherton, J.T. Bacmeister, J.T. Jiehl, I. M. Held, M. Zhao, S. A. Klein, and B.A. Soden, 2006: A comparison of tropical cloud properties and responses in GCMs using mid-tropospheric vertical velocity. *Climate Dyn.*, **27**, 261–279.

MODEL OF CRYSTALLIZATION OF SUPERCOOLED DROPLETS OF AQUEOUS SOLUTIONS

Vladimir V. Chukin, Anastasija S. Platonova
Russian State Hydrometeorological University, Saint-Petersburg, Russia
chukin@meteolab.ru

1. INTRODUCTION

Crystallization of supercooled droplets of water and aqueous solutions play an important role in the formation of upper air clouds, which have a significant influence on Earth's climate by scattering and absorption of solar and terrestrial radiation.
The phase state of upper layer clouds is mostly determined by the homogeneous mechanism of ice nuclei formation. In the lower and middle troposphere, ice crystals appear mainly due to the heterogeneous mechanism of ice nuclei formation on the surface of foreign particles in a volume of supercooled droplets. Recent experimental data suggest that heterogeneous crystallization can play a significant role in the formation of crystals in the upper troposphere.
Model of homogeneous and heterogeneous crystallization of supercooled droplets of aqueous solutions is described in the report.

2. ICE NUCLEATON RATE

In our model we suggest to estimate rate of homogeneous and heterogeneous ice nuclei formation in supercooled droplets of solutions using the classical expression for calculation of ice nuclei rate formation in pure water but taking into account presence of soluble.
The basis of the proposed model is the assumption of the constancy of the ice nucleation rate while temperature changes by law like dependence of ice melting temperature T_0 on water activity a_w:

$$T_0 = 273.16 + 103.6 \ln(a_w) + 15.6 \ln^2(a_w) + 54.1 \ln^3(a_w).$$

We have introduced an empirical parameter with dimension of temperature, taking into account the effect of solutes and temperature on formation of ice nuclei in the droplets of aqueous solutions:

$$T' = 273.16 + 103.6 \ln(1 - a_w + a_w^*) + 15.6 \ln^2(1 - a_w + a_w^*) + 54.1 \ln^3(1 - a_w + a_w^*),$$

where

$$a_w^* = \exp\left[15.8 + \frac{25301.6 - 5018.9 \ln(T)}{T} - \frac{399755.4}{T^2}\right]$$

This parameter depends on temperature and water activity as schematically shown in Figure 1.

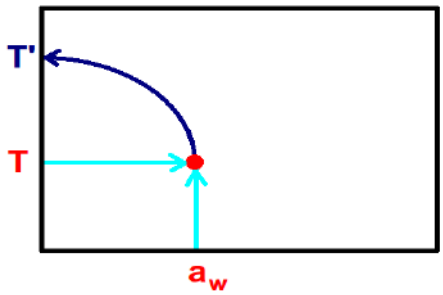

Fig. 1. Parameter T' dependence on temperature and water activity

So, this way makes possible to use classical expression for homogeneous ice nucleation rate

$$J_{wi}^{gom} = J_0^{gom} \exp\left(\frac{-\Delta G_{max}^{gom} - \Delta G_{act}}{k T'}\right),$$

$$\Delta G_{max}^{gom} = \frac{16 \pi m_w^2 \sigma_{wi}^3}{3 \rho_i^2 L_{wi}^2 \ln^2\left(\frac{T_0}{T'}\right)}$$

and for heterogeneous ice nucleation rate

$$J_{wi}^{get} = J_0^{get} \exp\left(\frac{-\Delta G_{max}^{get} - \Delta G_{act}}{k T'}\right),$$

$$\Delta G_{max}^{get} = \frac{\pi \alpha^2 m_w^{2/3}}{\rho_w^{2/3} L_{wi} \ln\left(\frac{T_0}{T'}\right)}.$$

To characterize the properties of the substrates in the droplets of supercooled aqueous solutions we use the so-called specific linear energy α. Calculated values of α are presented in Table 1.
These data show that substrates like AgI have the lowest values of the specific linear energy.

Table 1. Specific linear energy

Substrate	α (J/m)
$C_{16}H_{33}OH$	$5.75 \cdot 10^{-12}$
AgI	$5.98 \cdot 10^{-12}$
$C_{25}H_{51}OH$	$7.39 \cdot 10^{-12}$
$C_{30}H_{61}OH$	$7.53 \cdot 10^{-12}$
$C_{25}H_{51}OH$	$7.73 \cdot 10^{-12}$
Nanodekanol	$7.84 \cdot 10^{-12}$
$C_{30}H_{61}OH$	$7.91 \cdot 10^{-12}$
$C_{17}H_{35}OH$	$8.96 \cdot 10^{-12}$
Montmorillonite	$1.03 \cdot 10^{-11}$
SiO_2	$1.04 \cdot 10^{-11}$
Kaolinite	$1.06 \cdot 10^{-11}$
OAD	$1.20 \cdot 10^{-11}$

3. CRYSTALLIZATION TEMPERATURE

Numerical simulation of crystallization temperature dependence on the water activity of an aqueous solution carried out and compared with experimental data (Bertram, 2000; Larson, 2006; Koop, 2000; Zuberi, 2002; Zobrist, 2006; Cantrell, 2006). The simulation data confirms that the increase in the concentration of dissolved substances in water leads to a significant decrease in the rate of formation of nuclei and, consequently, the crystallization of drops of the solution occurs at lower temperatures (see Fig. 2 and Fig. 3).

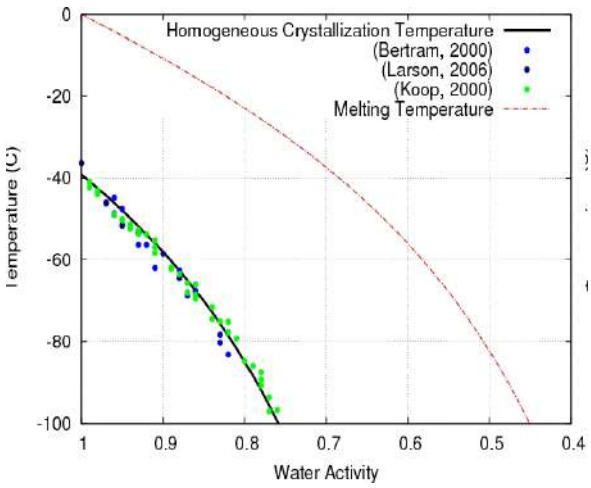

Fig 2. Homogeneous Crystallization Temperature of Droplets of Aqueous Solutions

a)

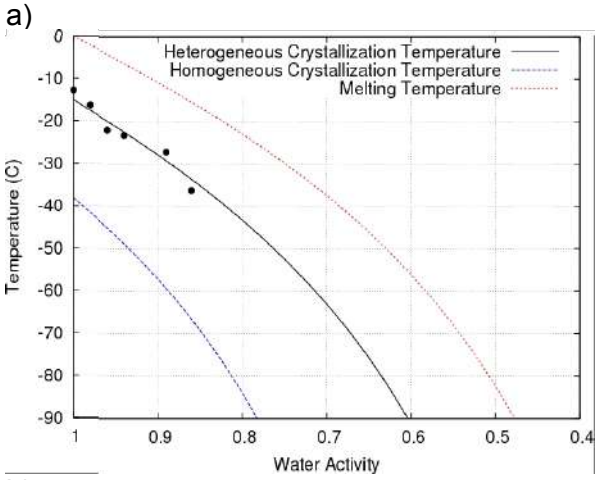

b)

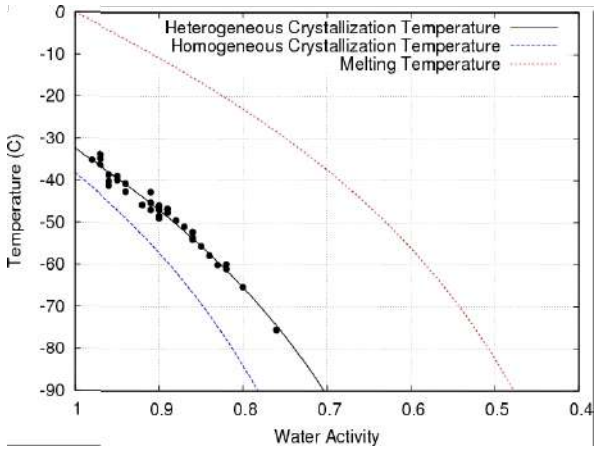

c)

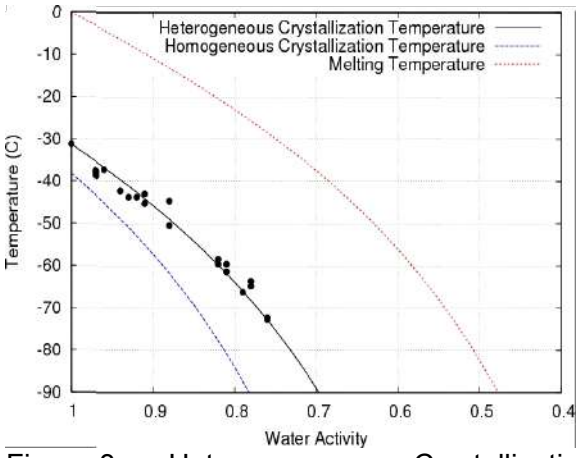

Fig. 3. Heterogeneous Crystallization Temperature of Droplets of Aqueous Solutions: NaCl / C17H35OH (a), (NH4)2SO4 / Kaolinite (b), (NH4)2SO4 / Montmorillonite (c)

Dependence of the heterogeneous crystallization temperature on specific linear energy shows that nucleus of crystallization on the surface of the substrates are flat (see

Fig. 4).

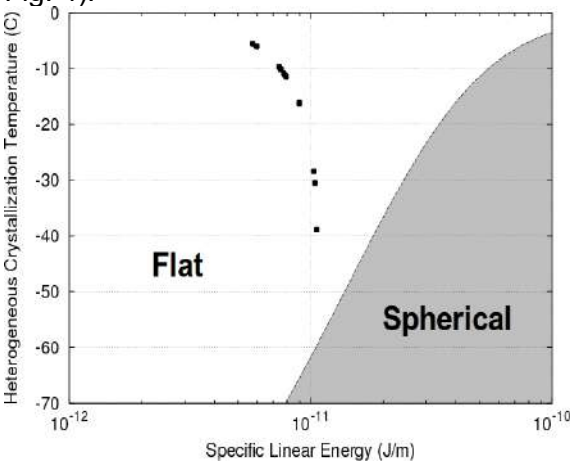

Fig. 4. Heterogeneous Crystallization Temperature as a function of Specific Linear Energy

The accuracy of the crystallization temperature calculation was estimated for the crystallization model (CM), activity model (AM), labmda model (LM). Results of calculation of root mean square errors are presented in Table 2.

Table 2. RMS Errors of Crystallization Temperature Calculation

Solution / Substrate	AM	LM	CM
NaCl / $C_{17}H_{35}OH$	0.8	0.9	0.8
NaCl / $C_{25}H_{51}OH$	1.6	1.0	1.2
NaCl / $C_{30}H_{61}OH$	1.7	1.1	1.2
$(NH_4)_2SO_4$ / $C_{16}H_{33}OH$	1.4	1.5	1.4
$(NH_4)_2SO_4$ / $C_{25}H_{51}OH$	1.9	1.5	0.9
$(NH_4)_2SO_4$ / $C_{30}H_{61}OH$	2.7	1.4	1.7
$(NH_4)_2SO_4$ / Kaolinite	0.5	0.5	0.2
$(NH_4)_2SO_4$ / Montmorillonite	0.9	1.2	0.5
$(NH_4)_2SO_4$ || NaCl || H_2SO_4 / OAD	0.4	0.6	0.3
$NaCH_3CO$ || LiCl || K_2CO_3 / AgI	0.9	1.0	0.7
$(NH_4)_2SO_4$ || NaCl / Nanodekanol	0.5	0.5	0.5
$(NH_4)_2SO_4$ || H_2SO_4 / SiO_2	0.5	0.6	0.5

Accuracy of suggested model is comparable to empiric models one, but our model is more universal because additionally considers dependence on such parameters as cooling rate and surface properties of substrates which in real atmosphere changes significantly and cannot be regarded as constant.

4. CONCLUSION

Calculation results of homogeneous and heterogeneous crystallization temperatures describes experimental data with enough accuracy for practical purposes. This fact allows to recommend the usage of suggested formulas for numerical modeling of microphysical processes in clouds.

5. BIBLIOGRAPHY

Bertram, A.K., T. Koop, L.T. Molina and M.J. Molina, 2000: Ice formation in $(NH_4)_2SO_4$-H_2O particles, J. Phys. Chem. A., 104, 584–588.

Cantrell, W. and C. Robinson, 2006: Heterogeneous freezing of ammonium sulfate and sodium chloride solutions by long chain alcohols, Geoph. Res. Lett., 33, L07802.

Koop, T., B. Luo, A. Tsias and T. Peter, 2000: Water activity as the determinant for homogeneous ice nucleation in aqueous solution, Nature, 406, 611–614.

Larson, B.H. and B.D. Swanson, 2006: Experimental Investigation of the Homogeneous Freezing of Aqueous Ammonium Sulfate Droplets, J. Phys. Chem. A., 110, 1907–1916.

Zobrist, B., 2006: Heterogeneous ice nucleation in upper tropospheric aerosols, Dissetration for the degree of Doctor of Natural Sciences, Zurich, 135.

Zuberi, B., A.K. Bertram, C.A. Cassa, L.T. Molina and M.J. Molina, 2002: Heterogeneous nucleation of ice in $(NH_4)_2SO_4$–H_2O particles with mineral dust immersions, Geophys. Res. Lett., 29, 142-1–142-4.

Acknowledgements

This investigation was made under the Grant of the Federal Target Program “Scientific and Pedagogical Staff of Innovative Russia” for Russian State Hydrometeorological University, Russia. One of the authors of this contribution acknowledges with gratitude the financial support provided by IUGG, IAMAS and WMO for the participation at the ICCP.

AGGREGATION GROWTH OF SNOWFLAKES OBSERVED BY RADAR AND GROUND-BASED PARTICLE VIDEO IMAGER

Dmitri Moisseev [1], Susanna Lautaportti [1], Larry Bliven [2], V. Chandrasekar [1,3,4], and Markku Kulmala [1]

[1] Dep. of Physics, University of Helsinki
[2] GSFC/Wallops Flight Facility, NASA
[3] Colorado State University
[4] Finnish Meteorological Institute

1. INTRODUCTION

Weather radar quantitative precipitation estimation (QPE) in snowfall is notoriously difficult. Radar observations depend on phase, size, shape, and density of precipitating particles. Variability in these physical properties is one of the major error sources in quantitative snowfall estimation with radar. The physical properties of ice precipitation are governed by growth mechanisms, i.e. water vapour deposition, aggregation and riming processes. One approach, to limit this variability, is to divide winter precipitation according to hydrometeor classes, such as aggregates, crystals, rimed particles, as inferred from dual-polarization radar observations. Despite the successful application of fuzzy logic hydrometeor classification algorithms [Liu and Chandrasekar, 2000; Straka et al., 2000, Lim et al., 2005] to summer time precipitation , there have been a very limited success in using them in winter precipitation. As the experience has shown, polarimetric radar signatures are not very different for many types of ice particles, i.e. aggregates and rimed ice particles [Plummer et al., 2010]. This is seriously affecting the ability of dual-polarization classification to improve quantitative radar observations of snowfall.

The goal of this work is not to explain measured properties of populations of hydrometeors present in a radar volume. Instead, we focus on growth processes, and study vertical and spatial structure of polarimetric radar observations of precipitation to infer dominating growth mechanisms, namely vapour deposition and aggregation.

In this study, we have analyzed several winter storms from years 2009 and 2010 using coinciding measurements of University of Helsinki C-band dual-polarization and vertically pointing Doppler radars. During the winter season 2010-2011 Light precipitation Validation Experiment extended observation period took place. During the EOP the University of Helsinki precipitation measurement site instrumentation was augmented with 2D-video disdrometer and snow particle imager (PVI). PVI measurements of a snowfall event are also used in this study.

2. MEASUREMENT SETUP

Data collected in two snowfall events that took place in the Greater Healsinki area, on March 3, 2009 and December 5, 2010 are used in this work. The measurements were carried out using University of Helsinki Kumpula radar and a transportable Doppler radar. Kumpula radar is a C-band polarimetric weather radar located at the top of Department of Physics building (60°12.26' N, 24°57.78' E). The radar is positioned 59 m above the mean sea level and 30 m above the ground level. The transportable Doppler C-band weather radar used in this study is stationed 32 km to the north (azimuth 11.8 degrees) of Kumpula radar in the city of Järvenpää (60°29.07' N, 25°4.91' E). The radar is positioned 53 m above the mean sea level about 3 meters above the ground level. There is a clear line of sight between the radars.

For all measurements, the transportable radar was operating in a Doppler spectral mode with the antenna pointing to the zenith. Doppler spectra were collected every 10 s. At the same time, Kumpula radar was performing range-height indicator (RHI) scans over the transportable radar. These scans were repeated every two minutes. Given the measurement geometry, the Kumpula radar beam is about 500 m wide at

Figure 1. PVI installation at the University of Helsinki precipitation measurement site in Järvenpää.

the location of the transportable radar and the lowest beam height is 350 m. The range resolution of the transportable radar is 100 m.

Kumpula radar is a dual-polarization weather radar that operates either in the simultaneous transmission and receiving (STAR) mode [Doviak et al., 2000] or in the cross-polarization mode. In this study, measurements collected in the STAR mode are used. These measurements include observations of reflectivity, Zh, differential reflectivity, Zdr, co-polar correlation coefficient and differential phase. The presented analysis mainly focuses on reflectivity and differential reflectivity measurements.

During the winter 2010-2011 particle video imager (PVI) was deployed in Järvenpää. The PVI captures video of falling snow, by processing which one can estimate particle size distributions as well as analyze images of falling particles. In Fig. 1 the PVI setup is shown.

3. RESULTS

Lo and Passarelli [1986] have observed that a little amount of liquid water is often present in the atmosphere even when temperatures are below freezing. Using lidar observations, Hogan et al. [2003] have shown that more than 30 % of ice clouds at temperatures between -10 to 0 C and more than 10 % at temperatures between -20 to -10 C contain a considerable amount of liquid water. Depending on liquid water content (LWC), supercooled droplet sizes and temperature, different ice growth mechanisms take place. In cases of low LWC, diffusional crystal growth and consecutive aggregation typically occur. Higher water contents are favorable for riming growth.

Diffusional growth and aggregation (March 3, 2009)

On March 3, 2009 the main cyclone centre was moving from over Iceland towards Scotland. The snowfall in Finland was related to a through in the cyclone's eastern edge forming a tongue of warmer air mass moving eastwards from the Baltic Sea. The surface wind was blowing from SSE until the gradual change between 14 and 15 UTC to a out-westerly wind. The radar wind soundings showed winds blowing from SSE below 500 m, and slight clockwise turning with increasing height to flow from SW at 5 km level. Maximum winds of about 20 m/s in this layer was observed by radar at around 2 km level from SSW. Temperature in Järvenpää rose gradually during the event from -5 to -0.5 degrees C, in the first denser snowfall the temperature was from -4 to -3 degrees C.

The snowfall event has lasted for 7 hours, starting at 5 UTC and continuing until 12 UTC. The observed snow ratio is close to 10:1 and indicates presence of mainly unrimed particle. During this event, high Zdr valued bands at altitudes of 3-3.5 km, 1-2 km and 0-0.5 km were visible. In those bands, Zdr values larger than 1 dB and in some instances exceeding 4 dB were observed. These high values indicate presence of horizontally aligned non-spherical particles, such as dendrites, needles or other types of ice crystal [Straka et al., 2000]. Typically Zdr values that do not exceed 0.5 dB were present below (or between) the bands. Those values are characteristic for low density aggregates. In Figure 1 (A1-A3) measurements taken at 7.54 UTC are shown. Differential reflectivity bands at altitudes of 3 km and just below 0.5 km are visible. The 12 UTC Jokioinen sounding exhibit temperatures of approximately -15 C and -5 C for these bands respectively.

Simultaneous Doppler and dual-polarization radar observations, presented in Figure 2 and Figure 4, show that high Zdr layer located between 3 and 3.5 km corresponds to a change in the mean Doppler velocity from 0.5 to 1 m/s. By comparing central and left panels in Figure 2 A, one can also see that higher Zdr regions appear to correspond to lower reflectivity values. A closer analysis show that this observation is not entirely complete.

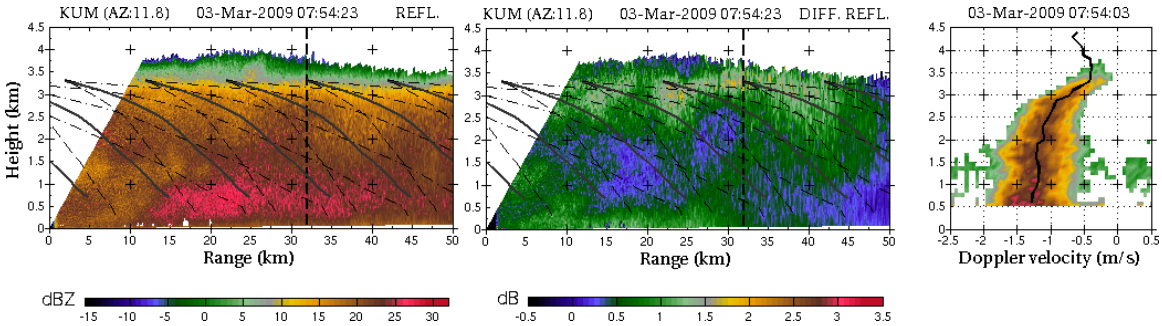

Figure 2. RHI and Doppler spectra observations of a snow storm that took place on March 3, 2009. The left two panels show reflectivity and differential reflectivity measurements. The left panel shows doppler spectra observations. RHI observations were carried out by University of Helsinki Kumpula radar and Dopppler spectra are from vertically pointing Doppler radar located in Järvenpää, 32 km to the north of Kumpula.

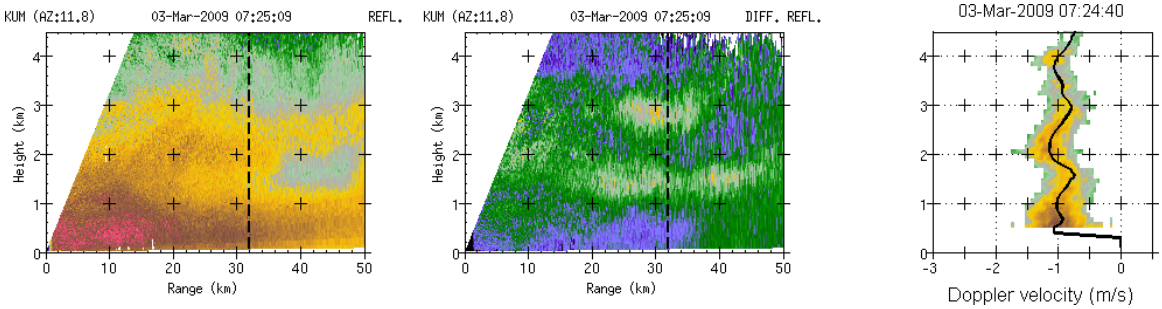

Figure 3. Same as Fig. 2 only the measurements collected at 0725 UTC on March 3, 2009. In this figure there are two clearly visible bands at altitudes of 1.5 and 3 km.

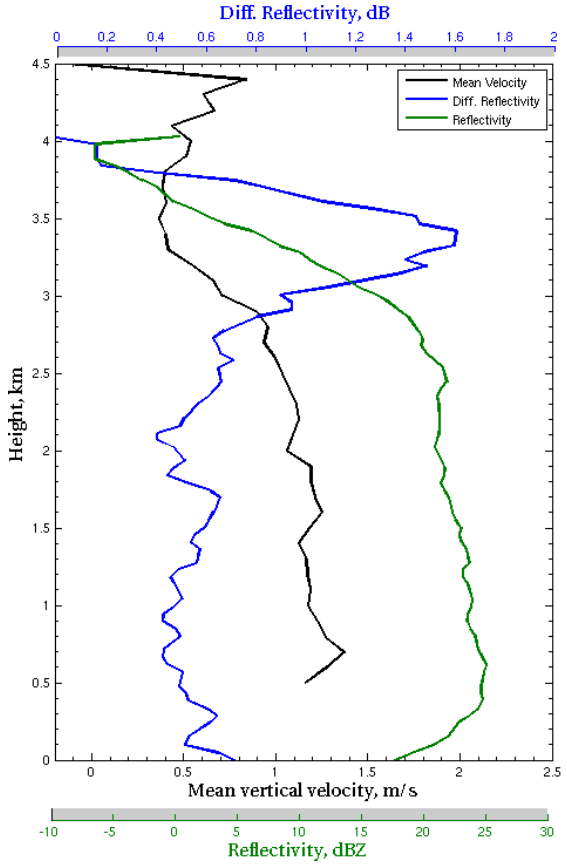

Figure 4. Profiles of reflectivity, differential reflectivity and vertical Doppler velocity, calculated from measurements presented in Fig. 3.

Observations presented in those figures can be split into three regions starting from the echo top at about 4 km altitude and continuing to the ground. The analysis, presented here, refers to the observations taken above the Doppler radar, namely 32 km from Kumpula radar.

- The first region, located between 4 and 3.5 km above the ground, is characterized by a rapid growth of both Zdr and Zh. Differential reflectivity and reflectivity grow at rates of roughly 2 dB/km and 20 dBZ/km respectively. At the same time the mean Doppler velocity remains aproximetly constant and equal to 0.5 m/s.
- The second region, located between 3.5 and 3 km above the ground, is characterized by a continuing rapid growth of reflectivity while differential reflectivity is rapidly decreasing. The differential reflectivty reached its maximum at the altitude of 3.5 km. At the same altitude the mean vertical velocity begin to increase, at a rate of more than 1 ms-1 / km, and reaches a value of about 1 m/s at 3 km above the ground.

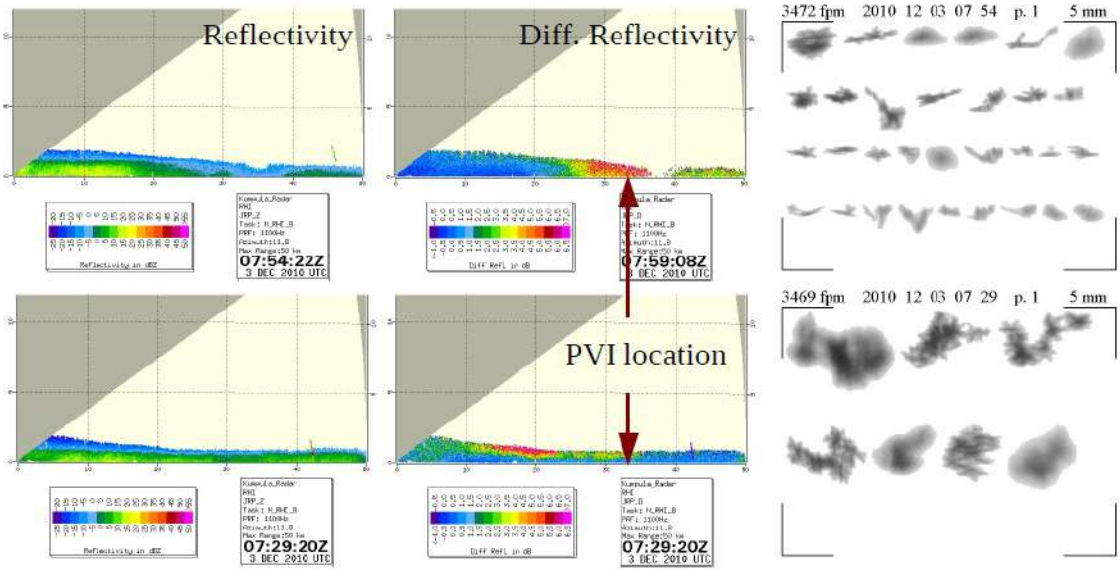

Figure 5. Observations of a Zdr band touching the ground and corresponding particle images as recorded by the PVI.

- The rapid growth of reflectivity and mean velocity ceases at about 3 km above the ground. From this altitude and to the ground, reflectivity increases at a rate of about 2.5 dBZ/km, mean velocity changes at a rate of 0.15 ms-1 / km and differential reflectivity stays more or less constant at a value of 0.5 dB.

Our initial explanation of the presented observations is presence of two snow growth processes. The first stage of snow growth is characteristic of the diffusional crystal growth. It is difficult to definitely prove whether there was a supercooled liquid water layer present, as was observed by Hogan et al. [2002]. Our preliminary modeling results using a simple diffusional growth model [Rogers and Yau, 1996; pp 159] with different crystal types (P1b, P1d, and P1e; [Pruppacher and Klet, 1997]) support this conclusion, however, there is some uncertainty due to different mass-diameter relations reported in literature. Growth of these particles explains increase in Zdr and initial increase in reflectivity. At the later stage, aggregation of these particles starts to play more and more important role, that explains further increase in reflectivity and rapid change in the observed fall velocity. At the last stage, aggregation dominates the growth process. This pattern is similar to the aggregation observed by Lo and Passarelli [7]. The main weakness of this this explanation is that radar signatures of ice crystals are easily masked by larger aggregates.

As can be seen in Fig. 3 in some events multiple Zdr bands are clearly visible. In those cases lower band is observable even though aggregates formed in the upper band are falling through it. It appears that those Zdr bands cannot be explained solely by presence of ice crystals, since it woul be reasonble to expect that those would be masked by falling aggregates.

On December 3, 2010 observations of a Zdr band that was touching the ground were collected in Järvenpää. A sample of those measurments is shown in Fig. 5. One can see from the figure that in both cases, where the Zdr band is a loft and where it is touching the ground, the observed particles are aggregates. Only in the case where high differential reflectivity values are at the ground, the observed particles are snowflake aggregate embryos consisting of few ice crystals. In the other case, the aggregates are more mature and consist of many crystals. The aggregate embryos are highly oblate and have horizontal size comparable to one of a more mature aggregate. Therefore, the aggregate embryos should have radar cross sections of approximately the same magnitude as mature aggregates. Meanwhile due to their oblateness the differential reflectivity values produced by such particle should be comparable to ones of crystals. Results of scattering calculations using Rayleigh approximation are shown in Fig. 6 and 7 confirm our proposition.

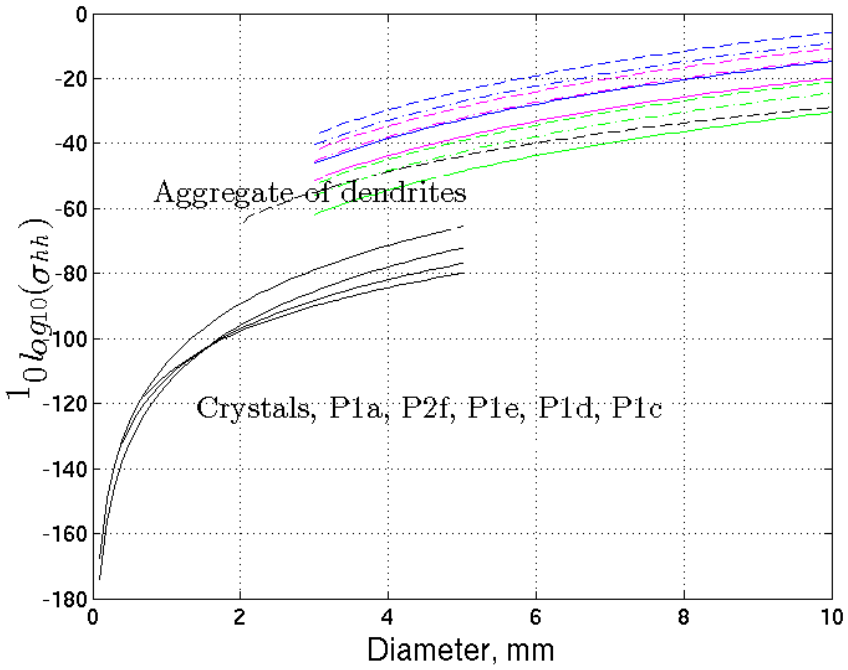

Figure 6. Radar cross section for different particle types. Solid black lines depict gross sections of ice crystals, dashed line represents RCS of aggregate of dendrites, color lines show cross sections of aggregate embryos calculated for different axis ratios (0.1, 0.2 and 0.3) and densities.

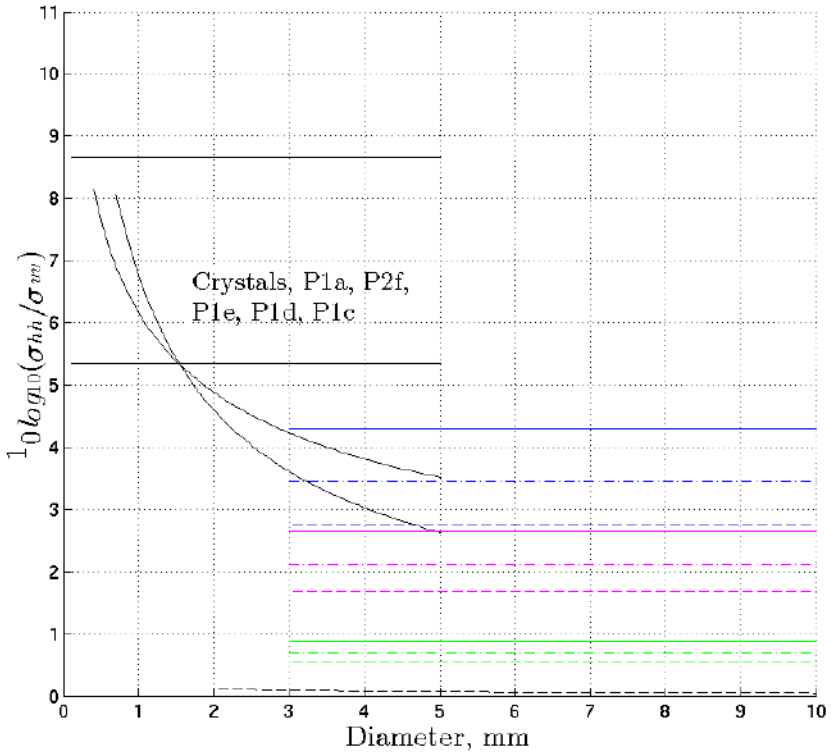

Figure 7. Same as Fig. 5 only for ratio of hh and vv cross sections.

Conclusions

Radar observations of high differential reflectivity (Zdr) bands and corresponding specific differential bands (Kdp) in winter storms and ice clouds were reported in literature. The reported observed Zdr values vary from 1 to 8 dB. Just below those bands Zdr values smaller than 1 dB are observed. The Kdp maximum is typically reached 100-200 meters below the Zdr maximum, in the area of low Zdr. The main explanation of those bands is that they are caused by scattering of radio waves from ice crystals rapidly growing in a presence of supercooled water. During the Light Precipitation Validation Experiment that took place in Helsinki in the fall 2010, we have collected a large number of observations of winter storms with such bands. In several cases the bands extended to the ground. Those observations have shown that the high Zdr observations are not caused by pristine ice crystals, but rather by aggregate embryos consisting of small number of monomers. Those aggregate embryos are very oblate and have horizontal dimensions comparable to the more mature aggregates. The modified explanation of the observed radar bands is that high Zdr and Kdp are caused by oblate aggregate embryos and not solely by pristine ice crystals. The importance of this observation is that firstly it completely explains the radar observations. Secondly, it provides an insight into initial stages of aggregation. Because observed embryos are very oblate one can conclude that initial aggregation is mainly caused by relative horizontal movements of ice crystals. Thirdly, a combination of Zdr and Kdp observations shows not only the onset of aggregation but also how rapidly embryos are converted to the mature aggregates.

References

Doviak, R.J., V. Bringi, A. Ryzhkov, A. Zahrai, and D. Zrnić (2000), Considerations for Polarimetric Upgrades to Operational WSR-88D Radars. *J. Atmos. Oceanic Technol.*, *17*, 257–278.

Gourley J, P. Tabary, J. Parent du Chatelet (2006), Data Quality of the Meteo-France C-Band Polarimetric Radar. *J. Atmos. Oceanic Technol., 23*, 1340-1356.

Hogan, R. J., P. R. Field, A. J. Illingworth, R. J. Cotton and T. W. Choularton (2002), Properties of embedded convection in warm-frontal mixed-phase cloud from aircraft and polarimetric radar, *Quart. J. Roy. Meteorol. Soc., 128*, 451-476.

Hogan, R. J., A. J. Illingworth, E. J. O'Connor and J. P. V. Poiares Baptista (2003), Characteristics of mixed-phase clouds - 2. A climatology from ground-based lidar, *Quart. J. Roy. Meteorol. Soc., 129***,** 2117-2134.

Lim, S., V. Chandrasekar, and V. N. Bringi (2005), Hydrometeor classification system using dua-lpolarization radar measurements: Model improvements and in situ verification, *IEEE Trans. Geosci. Remote Sens., 43*, 792–801.

Liu, L., V. Bringi, V. Chandrasekar, E. Mueller, and A. Mudukutore (1994) Analysis of the Copolar Correlation Coefficient between Horizontal and Vertical Polarizations. *J. Atmos. Oceanic Technol.*, ***11,*** 950–963.

Liu, H., and V. Chandrasekar (2000), Classification of Hydrometeors Based on Polarimetric Radar

Measurements: Development of Fuzzy Logic and Neuro-Fuzzy Systems, and In Situ Verification, *J. Atmos. Oceanic Technol., 17*, 140–164.

Lo K. K., and R. E. Passarelli, Jr. (1982), The growth of snow in winter storms: an airborne observational study, *J. Atmos. Sci., 39*, 697-706.

Locatelli, J. D. and Hobbs, P. V., (1974), Fall speed and masses of solid precipitating particles. *J. Geophys. Res.*, *79*, 2185-2197.

Mitchell, D. L., R. Zhang and R. L. Pitter (1990), Mass-dimensional relationships for ice particles and the influence of riming on snowfall rates, *J. Appl. Meteor.*, *29*, 153-163.

Plummer D.M., S. Göke, R. M. Rauber, L. Di Girolamo (2010), Discrimination of mixed- vs. ice-phase clouds using dual-polarization radar with application to detection of aircraft icing regions. *J. Appl. Meteor. Climat.: In Press.*

Spek, A. L. J., C. M. H. Unal, D. N. Moisseev, H. W. J. Russchenberg, V. Chandrasekar, and Y. Dufournet (2008), A New Technique to Categorize and Retrieve the Microphysical Properties of Ice Particles above the Melting Layer Using Radar Dual-Polarization Spectral Analysis. *J. Atmos. Oceanic Technol., 25*, 482-497.

Straka, J.M., D.S. Zrnic, and A.V. Ryzhkov (2000), Bulk Hydrometeor Classification and Quantification Using Polarimetric Radar Data: Synthesis of Relations, *J. Appl. Meteor., 39*, 1341–1372.

Zawadzki I., F. Fabry and W. Szymer (2001), Observations of supercooled water and secondary ice

generation by a vertically pointing X-band Doppler radar, *Atmos. Res., 59-60,* 343-359.

Zrnic, D.S., and A.V. Ryzhkov (1999): Polarimetry for Weather Surveillance Radars. *Bull. Amer. Meteor. Soc.*, ***80***, 389–406

THUNDERSTORM CHARACTERISTICS OF SUMMER PRECIPITATING SYSTEMS DURING CHUVA-GLM VALE DO PARAIBA FIELD CAMPAIGN

Rachel I. Albrecht[1*], Carlos A. Morales[2], Evandro M. Anselmo[2], João R. Neves[2], Enrique Mattos[1], Thiago Biscaro[1], Luiz A. T. Machado[1]

[1] Centro de Previsão de Tempo e Estudos Climáticos (CPTEC)
Instituto Nacional de Pesquisas Espaciais (INPE)

[2] Instituto de Astronomia, Geofisica e Ciências Atmosféricas (IAG)
Universidade de São Paulo (USP)

*rachel.albrecht@cptec.inpe.br

1. INTRODUCTION

CHUVA (**C**loud processes of t**H**e main precipitation systems in Brazil: A contrib**U**tion to cloud resol**V**ing modeling and to the GPM (Glob**A**l Precipitation Measurement)) is a project that will carry out seven field experiments to investigate the different precipitation regimes in Brazil. The objective of these field experiments is collect detailed information about the different precipitation regimes found in Brazil and their associated physical processes in support of the GPM program. This information will improve the quality of precipitation estimation and the knowledge of cloud microphysical processes of several different types of convective systems in Brazil, from warm clouds and local thunderstorms to squall lines, frontal and mesoscale convective systems. For more details on the CHUVA experiment see Machado et al. (2012) and http://chuvaproject.cptec.inpe.br/.

The fourth field experiment was conducted in southeast Brazil, at Vale do Paraiba and São Paulo metropolitan region from November-2011 through March-2012. To depict precipitating weather systems, CHUVA uses a XPOL Doppler Radar, 2 MiniRain Radars, 6 disdrometers, 10 rain gauges, 1 microwave radiometer MP3000, 1 Lidar, a GPS network for water vapor retrievals. This particular experiment was called CHUVA-Geostationary Lightning Mapper (GLM) Vale do Paraiba and in addition to characterize the precipitating systems observed in Southeast Brazil it also collected lightning proxy data for the upcoming geostationary lightning imagers (GOES-R GLM and MTG LI) using 10 lightning locating systems (LLS) (LMA, LINET, TLS200, ENTLN, RINDAT, STARNET, WWLLN, GLN, ATDnet, GLD360), high-speed cameras, and the TRMM-LIS satellite. Figure 1 shows the distribution of CHUVA-GLM Vale field experiment.

CHUVA-GLM provided a comprehensive database of thunderstorm development and characteristics for the first time in Brazil, where a large variety of cloud systems were sampled: cold fronts, squall lines, the South Atlantic Convergence Zone (SACZ) and local convective systems. Microphysical characteristics (such as hydrometeor identification and ice/water mass) of these summer 2011-2012 precipitating systems can be inferred from the X-Pol and 3 operational S-band radars, and the LLS provide detailed information about the storms electrical activity (such as charge centers and lighting propagation processes).

The Sao Paulo Lightning Mapping Array (SPLMA) was deployed at the metropolitain region of Sao Paulo city using 12 sensors in a baseline of 15-20km. The Lightning Mapping Array was developed by the New Mexico Institute of Mining and Technology (Rison et al. 1999), based on the Lightning Detecting and Ranging (LDAR) system developed to be used at the NASA Kennedy Space Center (Maier et al. 1995). The LMA system locates the peak source of impulsive VHF radio signals from lightning in an unused television channel by measuring the time-of-arrival of the magnetic peak signals at different receiving stations in successive 80 μs intervals. Hundreds of sources per flash can be detected in space and time, allowing a three-dimensional (3-D)

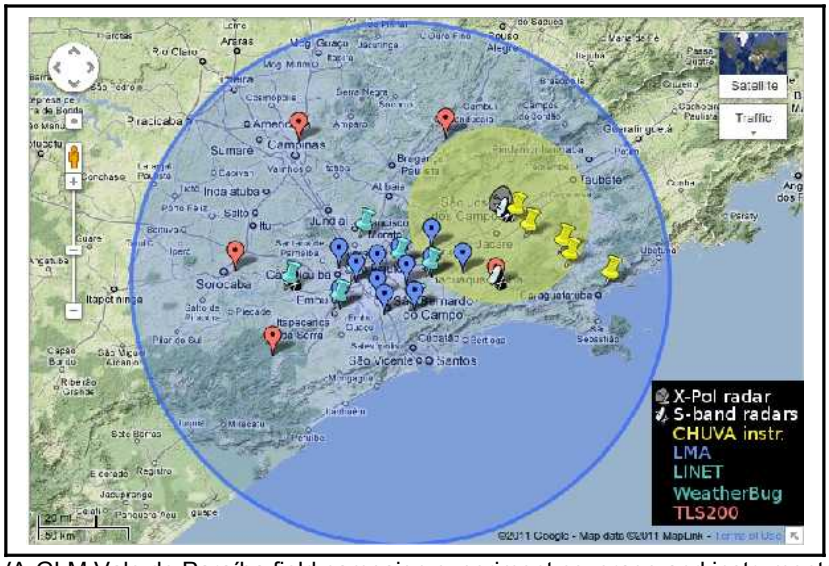

Figure 1 – CHUVA-GLM Vale do Paraíba field campaign experiment coverage and instruments. Blue, pink and cyan pins represent the 4 total (intracloud and cloud-to-ground)lightning deployed for this experiment. Yellow pins are the CHUVA sites with disdrometers, pluviometers, radiometers, lidars, etc.The yellow circle is the Dual-Pol X-band radar 50km coverage area, and the blue circle is the SPLMA 250km coverage.

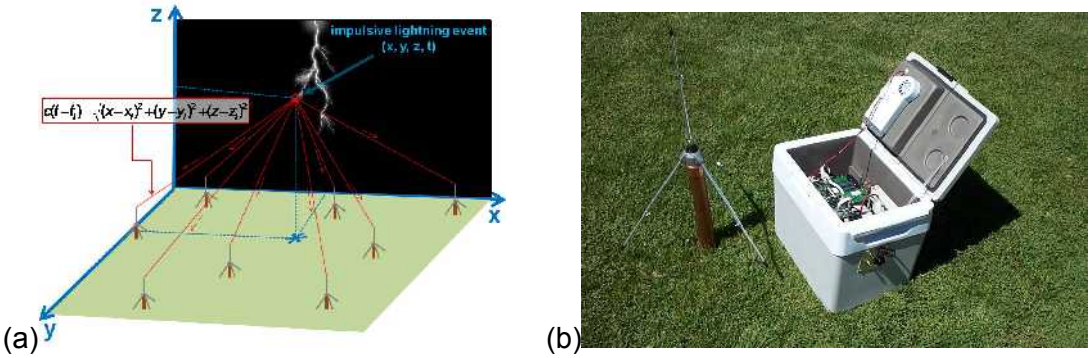

Figure 2 – (a) Illustration of the time-of-arrival technique used by the LMA system. The times (t_i) when a signal is detected at N≥4 stations are used to solve for the 3D source location (x, y, z, t) of the impulsive breakdown processes associated with a discharge. (b) Portable LMA station electronic box and antenna.

Figure 3 – Snapshots of a video testimony from the 07 January 2012 hailstorm and flooding in Guarulhos, SP, Brazil. (http://www.youtube.com/watch?v=9Y3AEZzK-9k)

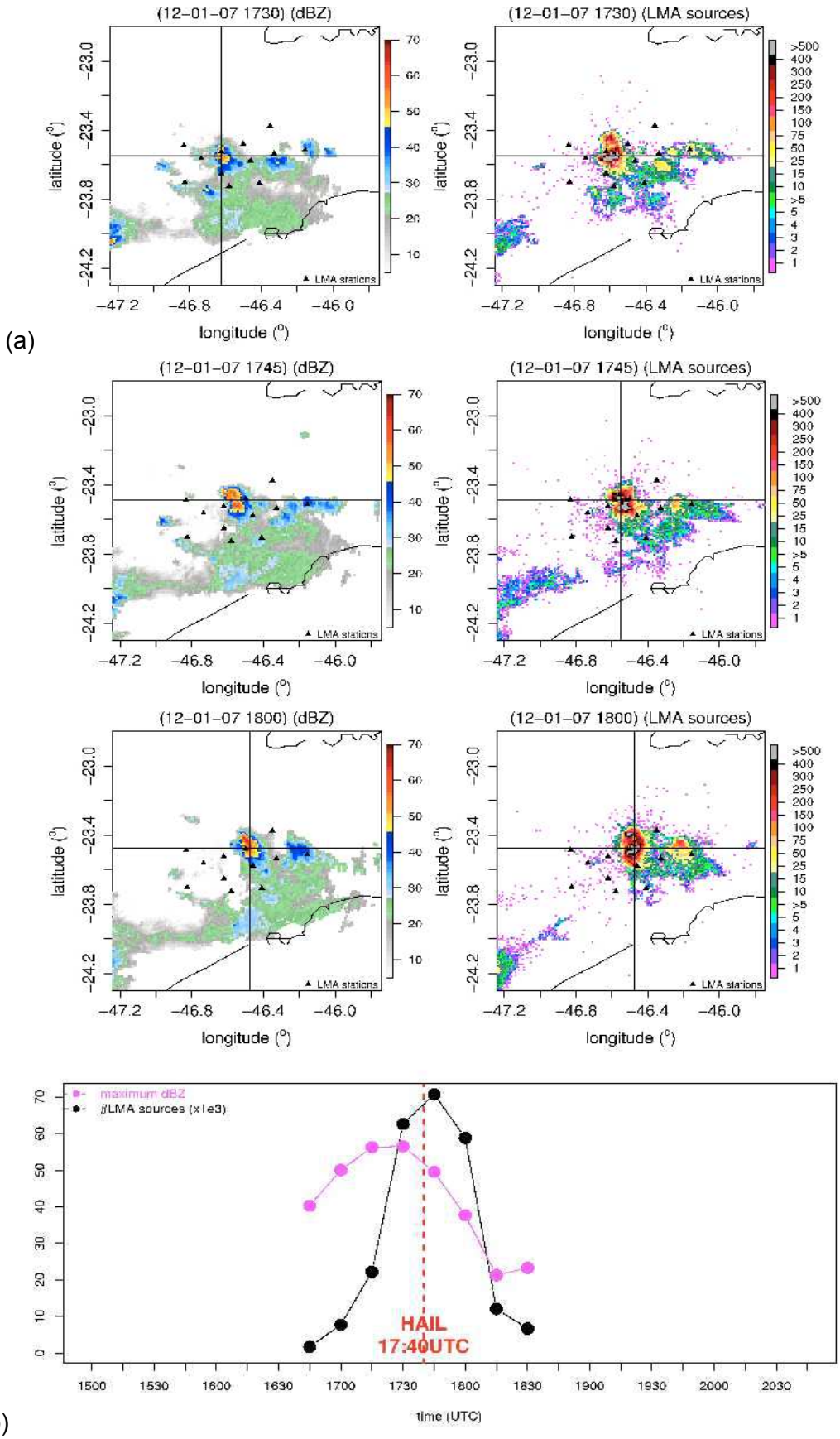

Figure 4 – (a) Radar reflectivity (dBZ) CAPPI at 3km height and LMA lightning source density (number of sources in 1x1 km grid), and (b) time evolution of the maximum reflectivity and number of LMA lightning sources of the severe storm cell that produced hail and flooding in Sao Paulo and Guarulhos on 07 January 2012. The vertical and horizontal lines at (a) indicate the location of maximum at (b).

lightning map to be constructed with nominally<50 m error within 150 km (Goodman et al. 2005). Figure 2a illustrates the time-of-arrival approach used in the LMA system. Global Positioning System (GPS) receivers at each station provide both accurate signal timing and station location knowledge required to apply this approach. Figure 2b is a picture of a portable LMA station hardware.

2. PRELIMINARY RESULTS

From November 2011 to March 2012, several severe weather cases were observed during this experiment, where hail, damage winds and flooding were reported over the metropolitan area of Sao Paulo City and across state of Sao Paulo. Localized and a few organized convective systems were responsible for hail precipitation from pea to tennis ball sizes. Brazil national weather service does not hold an official weather phenomena reporting database. Therefore, during this field experiment we had collected severe weather reports based on city of Sao Paulo Civil Defense service, media news (newspaper and TV) and internet searching from social network reports. Up to the time that this manuscript was written, we had identified 24 hail and damaging wind reports over the metropolitan area of Sao Paulo.On 07 January 2012 a convective system produced pea sized hail and flooding in Sao Paulo and Guarulhos, SP. Guarulhos the hailstorm lasted for about 15 minutes from 15:40 to 15:55 local time (1740 1755 UTC). Several video testimonies from this hail and flooding event can be found on the internet (Figure 3). Figure 4 shows a sequence of the operational S-band radar reflectivity and the SPLMA lightning source density. This convective system initiated southwest of Sao Paulo city and traveled troughout Sao Paulo and Guarulhos with reflectivity above 40 dBZ from 14:00 LST to 18:00 LST, reaching values as high as 59 dBZ at 15:15 LST when hail was reported downtown Sao Paulo. Half an hour later hail and flooding was repoted in Guarulhos when a maximum of LMA sources was observed (Figure 4). This maximum of lighting sources is known as “lightning-jump” and has been associated with severe weather, including tornados (Schultz et al., 2009; among others). Figure 5 shows the accumulated LMA source density plot in a latitude-longitude, latitude-height and longitude-height views. It can be seen that the lightning activity had two major regions of sources at ~7 and 10 km of height, where

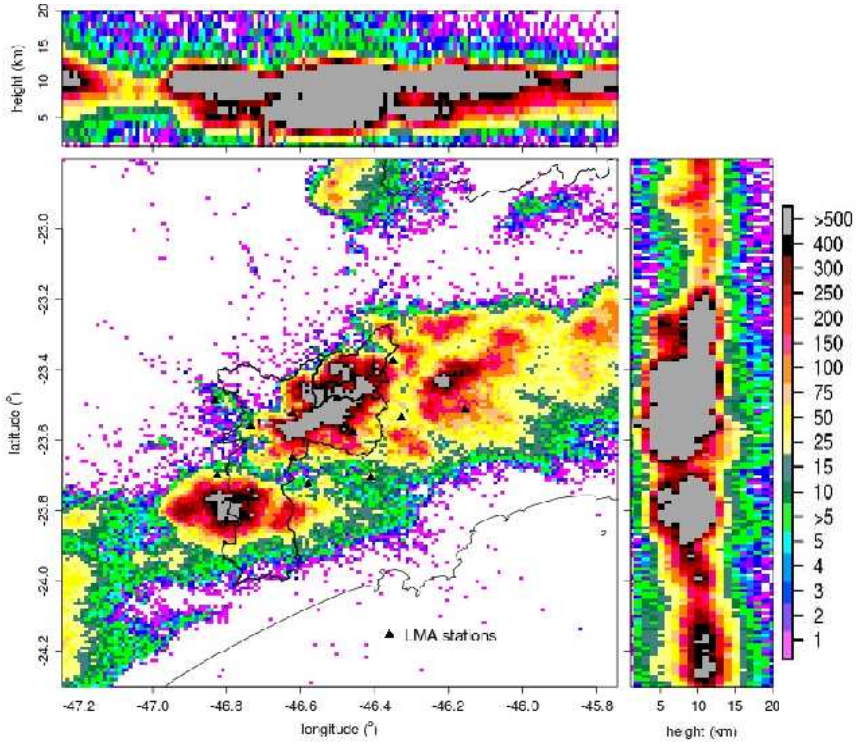

Figure 5 – Accumulated LMA lightning source density (number of sources in 1x1 km grid) from 07 January 2012 13:00-18:59 LST (1500-2059UTC) at a plan (latitude-longitude) view, as well as latitude-height and longitude-height views. Black solid lines indicate Sao Paulo and Guarulhos city boundaries.

mixed ice phase collision rebounding of ice particles occur and thunderstorm electrical charge centers are built. It can also be seen that thunderstorms extended up 18 km of height (LMA source density >5 in Figure 5).

A lightning-jump was observed during all the severe weather reported. This feature is a useful tool for warning issues. Moreover, the SPLMA map in detail all the convective-core cells of the thunderstorms in near real time. The last 10 minutes of SPLMA lightning data was updated to the CHUVA nowcasting website (SOS, Machado et al., 2012) every 5 minutes, giving the civil defense, management organizations, power companies and the public in general real time information about convection and lightning threat.

3. CONCLUSIONS

The total lightning information provided during the CHUVA-GLM Vale do Paraiba field campaign showed that lightning channel mapping and detailed information on the locations of cloud charge regions. The real-time availability of LMA observations contributed a lot and supported improved weather situational awareness for the mission execution as well for civil defense warnings and nowcasting. The measurements obtained from SPLMA provided for the first time total lightning measurements in conjunction with Meteosat SEVIRI observations, which is the proxy data for the future GOES-R Advanded Baseline Imager. Proxy data for the GLM sensor will be developed using the SPLMA generating a unique and valuable proxy data sets for both GLM and ABI sensors in support of several on-going research investigations, and nowcasting tools.

REFERENCES

Goodman, S. J., and co-authors (2005): The North Alabama Lightning Mapping Array: Recent severe storm observations and future prospects. Atmos. Res., 76, 423-437.

Machado, L. A. T., A. Calheiros, E. Mattos, I. Costa, D. Vila, R. Albrecht, C. Morales, C. Angelis, M. Silva Dias, G. Fisch (2012): Tropical Cloud Processes : First Results from CHUVA Project. Proceeding of the 16th International Conference on Clouds and Precipitation (ICCP2012), 30 July – 03 Augst 2012, Leipzing, Germany. (*this issue*)

Maier, L., C. Lennon, T. Britt, and S. Schaefer (1995): LDAR system performance and analysis, in Proceedings of the International Conference on Cloud Physics, Am. Meteorol. Soc., Boston, Mass., Dallas, Tex., Jan 1995.

Rison, W., R. J. Thomas, P. R. Krehbeil, T. Hamlin, and J. Harlin (1999): A GPS-based three-dimensional lightning mapping system: Initial observations in central New Mexico, Geophys. Res. Lett., 26, 3573– 3576.

Schultz, C. J., W. A. Petersen, L. D. Carrey (2009): Preliminary Development and Evaluation of Lightning Jump Algorithms for the Real-Time Detection of Severe Weather. J. Appl. Meteorol. Climatol., 48, 2542-2563.

PARAMETERIZATION OF TURBULENT COLLISION STATISTICS OF CLOUD DROPLETS

L.-P. Wang[1*], O. Ayala[1], H. Parishani[1], B. Rosa[2], W. W. Grabowski[3], and A.A. Wyszogrodzki[3]
[1]*Department of Mechanical Engineering, University of Delaware, Newark, Delaware 19716, U.S.A.*
[2]*Institute of Meteorology and Water Management - National Research Institute, 61 Podlesna St., 01-673 Warsaw, Poland*
[3]*Mesoscale and Microscale Meteorology Division, National Center for Atmospheric Research, PO Box 3000, Boulder, Colorado 80307-3000, USA*

Quantitative parameterization of turbulent collision of cloud droplets represents an important topic in cloud physics as, under certain conditions, air turbulence can significantly enhance the collision rate and collision efficiency, relative to the levels determined by the gravitational sedimentation alone [1]. Turbulent collision of cloud droplets affects the droplet size distribution, autoconversion rate, and rain initiation time, therefore an accurate parameterization is essential to the development of better large-scale weather and climate models.

Quantitative understanding of turbulent collision of cloud droplets in recent years is derived primarily from direct numerical simulations (DNS) of turbulent collision of inertial particles, where the dynamics of both small-scale turbulence and inertial particles are accurately represented. The unique advantage of DNS is that the *dynamic* collision kernel and the *kinematic* pair statistics relevant to the collision rate can be simultaneously obtained [2], a capability that is still out of reach in physical experiments. A major result from DNS is the generalized kinematic formulation of turbulent geometric collision kernel

$$K_{12}^t = 2\pi R^2 \langle |w_r(r=R)| \rangle g_{12}(r=R), \qquad (1)$$

where $R = a_1 + a_2$ is the geometric collision radius for two colliding droplets of radii a_1 and a_2, w_r is the radial relative velocity (RRV) at contact which combines the differential sedimentation and turbulent transport, and g_{12} is the radial distribution function (RDF) or pair-distribution function that quantifies the effect of local droplet clustering on the average pair density. This kinematic formulation has been validated against DNS dynamic collision kernel. It forms the basis for theoretical parameterization of collision kernel.

The radial relative velocity w_r includes contributions from differential sedimentation, effect of local fluid shear, and effect of particle differential acceleration which is the major source of analytical difficulty. The differential acceleration contains both contribution from local fluid acceleration and memory effect due to finite droplet inertia.

Inertial particles tend to accumulate in local regions of low vorticity and high strain rate due to an inertial bias or the centrifugal effect. Since local collision rates are proportional to the second moment of local droplet concentrations, the preferential concentration may significantly increase local pair density as measured by RDF g_{12}. The value of g_{12} depends on the levels of clustering of the two droplet sizes and the spatial correlation of the droplet concentrations. While there have been a large body of theoretical studies of inertia-induced particle clustering (most for non-sedimenting initial particles), no rigorous theory exists to predict RDF for bidisperse finite-size sedimenting droplets.

Another issue concerns the collision efficiency of cloud droplets. Turbulence alters the distributions of angle of approach and relative velocity for colliding droplets, thus the turbulent collision efficiency is usually higher than the gravitational collision efficiency [3].

Existing parameterizations of these statistics are of the main concern here. Most studies tend to address only a subset of the pair statistics. A systematic effort to parameterize the turbulent geometric collision statistics was made in Ayala et al. [4], and turbulent collision efficiencies from DNS have been documented in Wang and Grabowski [5]. It has been shown that turbulence can enhance the gravitational collision kernel by a factor of 2 to 3 at flow dissipation rate of $\varepsilon = 100\ cm^2/s^3$, and 4 to 5 at $\varepsilon = 400\ cm^2/s^3$ (see Fig. 2 in [6]). Typically, the turbulence effect on collision efficiency is primarily responsible for the enhancement associated with different droplet sizes (i.e., small a_2/a_1), while the clustering (g_{12}) is mainly responsible for the enhancement for nearly equal sizes ($a_2/a_1 \sim 1$).

Several other parameterizations have also been published. Falkovich et al. [7] developed a semi-analytical kernel that includes the effects of clustering of droplets and local fluid acceleration due to cloud turbulence; they concluded that turbulence has a significant effect on the geometric collision kernel for droplets of radii from 20 to 60 μm. A similar parameterization appeared in Derevyanko et al. [8] where a model for the enhancement factor due to droplet clustering, applicable to arbitrary droplet Stokes numbers, was proposed. Franklin [9] suggested an empirical parameterization based on the DNS data in Franklin et al. [10] of turbulent geometric collision kernel. A limitation of her parameterization is that the flow Reynolds number was assumed to match the conditions in DNS, rather than to cloud conditions. Onishi et al. [11] provided a parameterization of turbulent geometric collision for monodisperse cloud droplets, focusing on the effect of gravity on the radial relative velocity.

Using a hybrid direct numerical simulation (DNS) tool, we are generating new simulation data of dynamic and kinematic collision statistics at higher flow Reynolds numbers and computational domain sizes (see [12]), with increasing accuracy for a wide range of droplet sizes. The main purpose of this talk is to compare the simulation data with existing analytical models in order to identify the current model limitations, and to develop a more accurate theoretical parameterization

*Corresponding author: Department of Mechanical Engineering, 126 Spencer Laboratory, University of Delaware, Newark, Delaware 19716-3140. Phone: (302) 831-8160; Fax: (302) 831-3619; Electronic mail: LWANG@UDEL.EDU

of turbulent collision kernel. Additional considerations will be given to the effect of flow intermittency that is not fully considered in the hybrid DNS. Using a PDF description of the locally volume-averaged flow dissipation rate, we study the impact of dissipation intermittency on the average collision kernel. Our results suggest that the average effect of intermittency is not significant since collision is a binary interaction and its average statistics are governed by low-order (i.e., second-order) statistical moments. A related issue to be discussed is how to incorporate the effects of sub-grid variations in the parameterization of turbulent collision kernel within large-eddy simulation models of cloud dynamics.

References

[1] Grabowski WW, Wang L-P. 2013. Growth of cloud droplets in a turbulent environment, *Annu. Rev. Fluid Mech.* , to appear.

[2] Wang L-P, Rosa B, Gao H, He G-W, Jin G-D. 2009. Turbulent collision of inertial particles: point-particle based, hybrid simulations and beyond. *Int. J. Multiphase Flow* 35:854–67

[3] Wang L-P, Ayala O, Rosa B, Grabowski WW. 2008. Turbulent collision efficiency of heavy particles relevant to cloud droplets. *New J. Phys.* 10:075013

[4] Ayala O, Rosa B, Wang L-P. 2008b. Effects of turbulence on the geometric collision rate of sedimenting droplets: Part 2. Theory and parameterization. *New J. Phys.* 10:075016.

[5] Wang L-P, Grabowski WW. 2009. The role of air turbulence in warm rain initiation. *Atmos. Sci. Lett.* 10:1-8

[6] Grabowski WW, Wang LP. 2009, Diffusional and accretional growth of water drops in a rising adiabatic parcel: effects of the turbulent collision kernel. *Atmos. Chem. Phys.* 9:2335–53

[7] Falkovich G, Fouxon A, Stepanov MG. 2002. Acceleration of rain initiation by cloud turbulence. *Nature* **419**: 151–154.

[8] Derevyanko S, Falkovich G, Turitsyn S. 2008, Evolution of non-uniformly seeded warm clouds in idealized turbulent conditions. *New J. Phys.* 10:075019.

[9] Franklin CN. 2008. A Warm Rain Microphysics Parameterization that Includes the Effect of Turbulence. *J. Atmos. Sci.* 65:1795-815

[10] Franklin CN, Vaillancourt PA, Yau MK. 2007. Statistics and parameterizations of the effect of turbulence on the geometric collision kernel of cloud droplets. *J. Atmos. Sci.* 64:938–954

[11] Onishi R, Takahashi K, Komori S. 2009. Influence of gravity on collisions of monodispersed droplets in homogeneous isotropic turbulence. *Phys. Fluids* 21:125108

[12] Rosa B, H. Parishani H, Ayala O, Wang L-P, Grabowski WW. 2012. High-resolution simulation results of kinematic and dynamic collision statistics of cloud droplets. This ICCP proceedings

EVALUATING STATISTICAL CLOUD SCHEMES - WHAT CAN WE GAIN FROM GROUND BASED REMOTE SENSING?

Verena Grützun*[1], Johannes Quaas[2], and Felix Ament[3]

[1]Max Planck Institute for Meteorology, Hamburg, Germany
[2]University of Leipzig, Leipzig, Germany
[3]University of Hamburg, Hamburg, Germany

May 22, 2012

Abstract

A correct representation of clouds in global circulation models (GCMs) is challenging and yet crucial. Clouds have a great influence on both, the hydrological cycle and the radiation budget of the earth. Statistical cloud schemes offer a great potential to realistically simulate clouds across the scales. However, the evaluation of these schemes is challenging. Satellite data give comprehensive horizontal information about the overall cloud cover but lack horizontal resolution and accuracy of the retrievals. Ground based remote sensing measurements have this high vertical resolution and more accuracy. We investigate the opportunity of using long term ground based remote sensing measurements to assess cloud related quantities, especially their statistical distribution moments, for the evaluation of statistical cloud schemes. By using high resolution modelling as a virtual reality, we show that higher statistical moments are not straight forward to get but need probabilistic approaches.

*Corresponding author, verena.gruetzun@zmaw.de

1 INTRODUCTION

Statistical cloud schemes (e.g. Tompkins, 2002) gain popularity. Atmospheric models call for more flexible resolutions including local grid-refinements and scale adaptivity, which a statistical cloud scheme, given it works correctly, can grant. These schemes rely on a horizontal subgrid-scale distribution of the total water, sometimes joint with the temperature or vertical wind distribution. Higher moments of this distribution are prognostic and sources and sinks for them are modeled basing on physical processes such as turbulence, convection and micropysics. The total water distribution is then mainly used to calculate the cloud coverage within a gridbox. However, it also offers sub-cloud variability which can be used for the calculation of radiation and the autoconversion process.

Though in principle statistical cloud schemes offer a sophisticated and promising approach for the modeling world, the effects of the physical processes on higher distribution moments such as variance and skewness can only be estimated and parametrized. These parametriza-

tions are often rather crude. While the cloud coverage itself not so much depends on the specific details of the distribution, radiation and autoconversion do and a detailed evaluation of the statistical schemes is desirable.

The overall outcome, the cloud cover, can be gained comparably easily from satellites and hints at potential flaws in the model. An evaluation on the process level, however, is very difficult, since it would need the full high resolution 3D information about the total water in the atmosphere. But measurements can only give us either a high horizontal resolution without a decent vertical one (e.g., satellites), or a high vertical resolution without the horizontal one (e.g., ground based remote sensing). While air crafts are lying somewhere in between and can offer insights about specific height levels they still do not offer the horizontal coverage but only line measurements through the atmosphere. The best statistics we therefore expect from long-term ground-based measurements such as stationary microwave profilers.

We investigate in the following the potential of ground based remote sensing data with a high time and vertical resolution to evaluate the total water distribution modeled by statistical cloud schemes. We do so by using the "perfect model approach", i.e., we use the same model run to create entirely consistent horizontal statistics and time series of a vertical profile at a specific point in the model.

2 MODEL DATA

For our investigations we use the COSMO-DE model (Baldauf et al., 2011) of the Deutscher Wetterdienst (German Weather Service, DWD) in its operational setup. The model domain covers whole Germany and a few surrounding areas, and the spatial resolution is about $2.8 \times 2.8\,\mathrm{km}^2$ ($0.025° \times 0.025°$). The vertical resolution is about 20 m at the bottom of the atmosphere up to about 1 km at the top of the atmosphere with 51 height levels. We simulate the 16th June 2009, which was a day with stratiform clouds and some precipitation in middle and in the South of Germany. This model run is our "virtual reality" and we create consistent data sets in the following way: Firstly, we define our "true spatial total water distribution" by the global model ECHAM6's (Stevens et al., 2012, T63 resolution) grid box around Hamburg. This means that we look up the boundaries of that box in terms of longitude and latitude and then take all COSMO-DE grid points to gain the spatial statistics. This is what a perfectly working statistical cloud scheme should see. Secondly, we put a "virtual lidar" at a certain point, say Hamburg, in that box and save the vertical profile of that point with a high time resolution of 25 s. Fig. 1 shows the model domain, the ECHAM6 box and the COSMO-DE gridpoint of Hamburg.

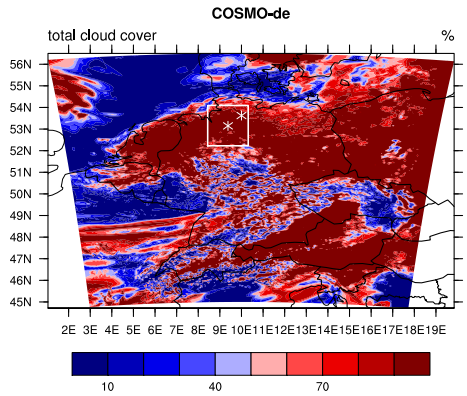

Figure 1: COSMO-DE model domain and cloud cover after 10 h of the simulation. The box marks the ECHAM6 box used for retrieving the spatial statistics ("true distribution"), and the asterisks mark Hamburg and the middle point of the box.

The idea now is that we can translate the statistics over that time series, which corresponds to a line measurements through the

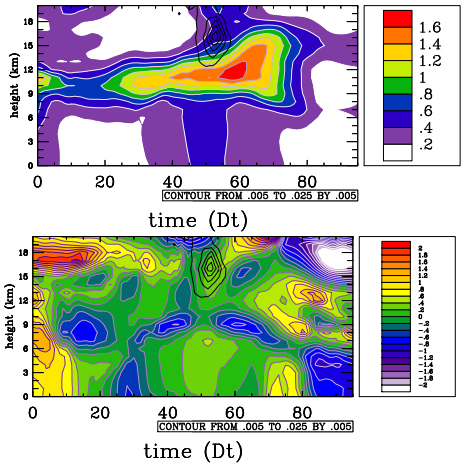

Figure 2: Variance (top) and skewness (bottom) of the total water distribution as gained from the spatial statistics. Black contours mark liquid cloud water. This is what a perfect statistical cloud scheme would see.

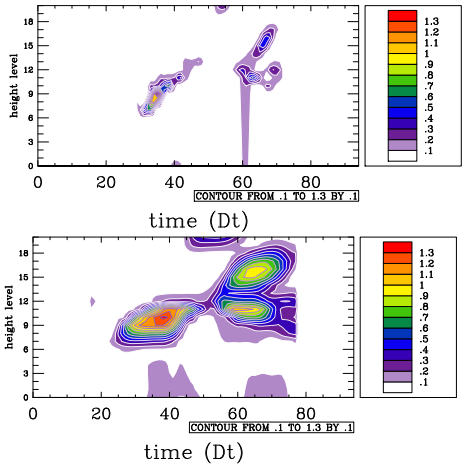

Figure 3: Variance gained from temporal data, time frame 500 s (top) and 2000 s (bottom).

global box, to the spatial statistics by using the wind speed. For the mean values of the distribution this is frequently done, but can we also retrieve the higher moments variance and skewness?

3 RESULTS

The spatial output of our simulation is 15 minutes, thus we get spatial statistics with the same resolution. To gain the statistics from the high resolution time series we define a time frame at each hight level and shift the frame with a time step of 15 minutes through the time series. Thus we get temporal statistics each 15 minutes. It is desirable that the statistics match, though we are aware that ergodicity is not necessarily given at each location. However, since long-term measurements from the ground are the best data we can get we investigate their potential and what we can actually gain.

Fig. 2 shows the spatial statistics gained from the box corresponding to the global model ECHAM6. This is our truth, which a perfect statistical cloud scheme should see, and which we ideally also find in the temporal data.

The great challenge is to find the right length of the time frame so that it corresponds to the model grid box. We experiment with different time frames. Fig. 3 shows the variance gained from the temporal statistics, i.e., from our virtual measurement we would like to use to evaluate our cloud scheme. It is strongly visible and also logical that the retrieved variance much depends on the time frame chosen. We find that the statistics does not get stable and that the time evolution of the total water too much disturbs it to be compared with the true spatial statistics. However, at least the general shape of the variance in the time height slice shows some similarities to what we would like to see.

Fig. 4 shows the same but for the skewness instead of the variance. We note that this higher moment is even more sensitive to the time frame, and that large errors occur, in quantity and also in sign. On a positive note, we might detect the same boundary layer height in both plots.

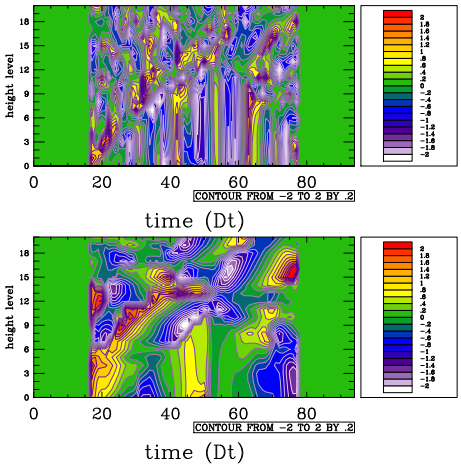

Figure 4: Same as fig. 3, but for skewness.

We find that the direct way of comparing time and spatial statistics does not work, the time evolution of the data is too strong and does not lead to a stable statistics which can be compared with the "snapshots" of the spatial distribution. We will propose a new method basing on conditional sampling of the distribution which might help to better assess an evaluation of statistical cloud schemes.

4 CONCLUSIONS

Statistical cloud schemes employing a spatial total water distribution gained importance in the last few years since they potentially work scale-adaptive and also offer the possibility to predict sub-cloud variability of the water. However, the distribution is difficult to predict and the equations are not easy to close, thus a detailed evaluation on the process level is necessary to make sure the parametrization works correctly. High resolution 3D data is scarce, though, and we have to use what we can get to assess the statistics.

We have investigated the potential of long-term ground-based remote sensing data to gain information about the statistics and find that a direct comparison is not leading to the desired results. The time evolution of the data is too strong and ergodicity is not given. We argue that the results are probably better if the same analysis was done in a more stable region than the midlatitudes, such as the trades.

We developed a new ensemble method based on conditional sampling of the total water distributions which might solve the problem partly. This method, however, needs very long time series in the order of years, and only proves the correctness of the model with a certain probability. The method will be presented in more detail on the poster.

This work was funded by the Cluster of Excellence "Integrated Climate System Analysis and Prediction" (CliSAP) of the University of Hamburg.

References

Baldauf, M., A. Seifert, J. Foerstner, D. Majewski, M. Raschendorfer, and T. Reinhardt (2011). Operational convective-scale numerical weather prediction with the cosmo model: Description and sensitivities. *Mon. Wea. Rev. 139*, 3887–3905.

Stevens, B., M. A. Giorgetta, E. Roeckner, T. Mauritsen, T. Crueger, H. Schmidt, E. Manzini, M. Esch, S. Rast, S. Kinne, L. Kornblueh, and R. Pincus (2012). Echam6: Model and climate. in preparation.

Tompkins, A. (2002). A Prognostic Parameterization for the Sub-Scale Variability of Water Vapor and Clouds in Large Scale Models and Its Use to Diagnose Cloud Cover. *J. Atmos. Sci. 59*, 1917–1942.

SCHNEEFERNERHAUS AS A CLOUD-TURBULENCE RESEARCH STATION. PART 2: CLOUD MICROPHYSICS AND FINE-SCALE TURBULENCE

J. Katzwinkel[1], T. Schmeißner[1], R. A. Shaw[1,2], H. Siebert[1]*, E. Bodenschatz[3], and H. Xu[3]
[1]Leibniz Institute for Tropospheric Research, Leipzig, Germany
[2]Department of Physics, Michigan Technological University, Michigan, USA
[3]Max Planck Institute for Dynamics and Self Organization, Göttingen, Germany

1. INTRODUCTION

Measurements of detailed interactions between turbulence and cloud processes are challenging. Airborne measurements allow for the most flexibility in going to the clouds of interest, but sample times are limited and measurements are inherently Eulerian in nature. We have investigated the suitability of making cloud measurements from a mountaintop research station, with the aim of characterizing the fine-scale turbulence and cloud microphysical properties. From a ground-based station it is possible to measure for extended periods of time and it also becomes feasible to perform Lagrangian measurements. The context of this study specifically addresses cloud-turbulence interactions. Here we present high spatial resolution measurements liquid water content, droplet diameter, and turbulent velocity and temperature fluctuations were made at the Environmental Research Station (UFS) Schneefernerhaus, taken in summer and fall 2009, and again in summer 2011. The measurements are analyzed and interpreted in a manner similar to data recorded in cumulus and stratocumulus clouds by the ACTOS platform Siebert et al. (2006a) in order to compare the two approaches.

The UFS is located in the German Alps near the top of Zugspitze (4725'00" N, 1058'46" E), the highest mountain in Germany (2962 m above sea level). The station is situated on the north side of the glacier and near the top of Zugspitze, at a height of about 2650 meters. The UFS is a nine-story building, constructed into the southern flank of the Zugspitze, and it experiences frequent immersion in clouds (see Fig. 1). Due to the local topography, the winds measured at UFS are primarily in the east-west direction. An analysis of the meteorological and large-scale turbulence conditions is given in the companion paper by Risius et al. (2012). The near uniformity of wind direction is a significant advantage for measurements because it allows instruments to be pointed in one direction (e.g., see Fig. 2).

Figure 1: View of the UFS embedded in clouds. The arrow shows the location of the microphysical and fine-scale turbulence instrumentation during the 2009 experiment.

*siebert@tropos.de

2. EXPERIMENT DESCRIPTION

Measurements of fine-scale turbulence and cloud microphysical properties in a Eulerian reference frame were performed from a fixed 3 m height mast with various measurement instruments (cf. Fig. 2). The mast was situated on the 9th-floor measurement platform during the first campaign (August, 3 - 22, 2009). The ultrasonic anemometers (hereafter called"sonics") at the mast were orientated westward during both measurement periods.

The exact setup of the mast with the heights of the individual sensors is shown in Fig. 2. Two sonics of Solent HS type manufactured by Gill Ltd, Lymington, UK were fixed in a height of 1.80 m and 2.55 m above the terrace, respectively. The measurement of the three-dimensional wind velocity vector and the virtual temperature are based on transit time measurements of ultrasonic pulses traveling between two transducers (for one velocity vector component) with and against the wind. The temporal resolution of the sonics is 100 Hz whereas the measuring resolution of the wind velocity is $\triangle u = 0.01 \mathrm{m\,s^{-1}}$ and $\triangle T = 0.01 \mathrm{K}$, respectively (see Siebert and Muschinski (2001) for more details uf the Solent HS.

An ultra-fast thermometer (UFT) and a one-component hot-wire anemometer were fixed at a height of 2.20 m. The UFT is based on a 2.5 μm resistance wire protected against droplet impaction (cf. Haman et al. (1997)) and the hot-wire anemometer is a constant temperature anemometer (Comte-Bellot (1976)). Both instruments are sampled with 1kHz.

Cloud microphysical variables were also measured from the mast. A particle volume monitor (PVM-100A, see Gerber (1991)) is positioned beside the UFT to measure the liquid water content (LWC) and the particle surface area (PSA). The intensity of laser light diffracted by a cloud droplet ensemble in a given measurement volume is related to the absolute volume concentration due to a transmission filter in front of the detector.

The one-dimensional velocity of individual cloud droplets is measured with a MSE Laser-Doppler Anemometer (LDA) positioned below the PVM. The measurement is based on the Doppler-shifted light scattered from moving cloud droplets and the resolution is 1 - 2 $\mathrm{cm\,s^{-1}}$ (Abbiss et al. (1974)). The Phase-Doppler Interferometer for Cloud Turbulence (PICT) is located at a height of 1.50 m above ground. Based on light scattering interferometry of individual droplets, droplet diameter and a single component of the droplet velocity vector can be determined (Chuang et al. (2008)).

In addition to our sonic measurements the German Weather Service (DWD) performs measurements with a sonic at the UFS. The measurements are taken on the 7th-floor measurement platform with a fixed mast (cf. Fig. 1). The sonic is located at the top of the mast in about 4 m above ground. In addition meteorological parameter as temperature, relative humidity, precipitation, etc. and surface ozone, carbon monoxide and methane are measured routinely (www.schneefernerhaus.de/ufs.htm).

3. DATA ANALYSIS

3a. *Sonic Measurements: Mean Flow Characteristics*

Figure 3 shows a one-hour long time series of the wind velocity $U = \sqrt{u^2 + v^2 + w^2}$ and the wind direction d, here u, v, and w are the velocity vector components in the sonic frame. During this period, the U ranges from nearly 0 to 13 $\mathrm{m\,s^{-1}}$ with a mean value of $\overline{U} = 4.2\ \mathrm{m\,s^{-1}}$ and a standard deviation of $\sigma_U = 1.9\ \mathrm{m\,s^{-1}}$. The prevailing wind direction was 300°.

In the next step, the velocity vector was transformed in such a way that the vector component u is directed into the mean flow direction and $< v >=< w >= 0$. From these new data set the integral length scale $\mathcal{L}$ was estimated by integrating the auto-correlation function ρ_{u_i} of the velocity vector components u_i:

$$\mathcal{L}_i = \mathcal{T}_i \cdot \overline{u} = \int_0^{\tau_m} \rho_{u_i}(\tau) d\tau \cdot \overline{u}.$$

In Fig. 4 all three functions are plotted for both sonics including an estimate of the three $\mathcal{T}$ scales and the corresponding length scales $\mathcal{L}$, for integration an upper limit of $\tau_m = 80\ s$ was

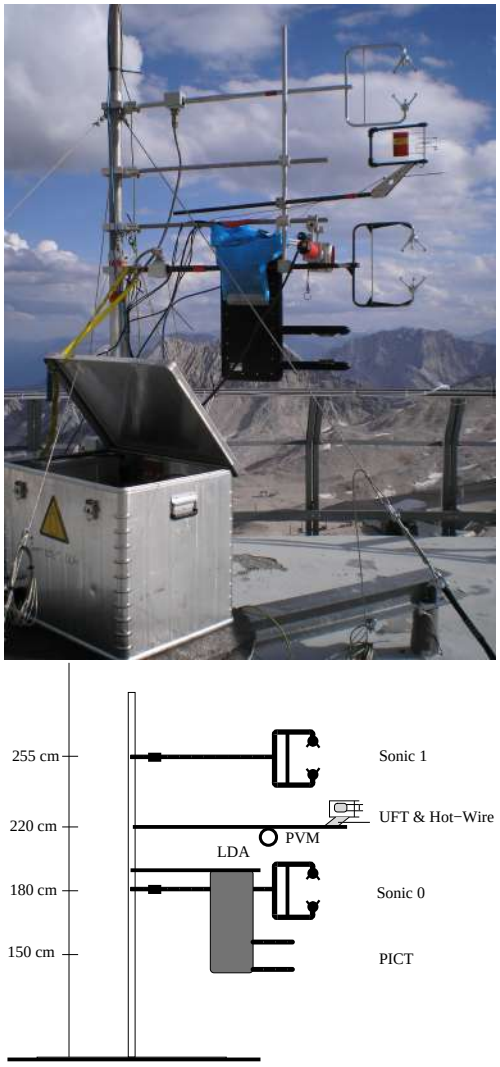

Figure 2: (a) Measurement instrumentation on 9th-floor measurement platform of the UFS during the campaign in August 3 - 22, 2009. The mast is equipped with two sonics, ultra-fast thermometer (UFT), one-component hot-wire anemometer, laser-Doppler anemometer (LDA), particle volume monitor (PVM) for liquid water content measurements, and a phase-Doppler interferometer for cloud turbulence measurements (PICT). (b) A schematic of the mast indicating the different instrument heights.

used. We estimate for both horizontal components $\mathcal{L}_{u,v} \approx 40$ to 70 m and for the vertical $\mathcal{L}_w \approx 5$ to 10 m. The higher values always correspond to the measurements of the upper sonic. Since the large-scale cut-off wavelength

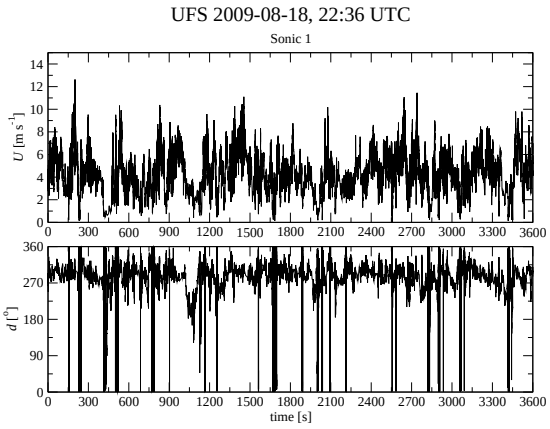

Figure 3: Time series of horizontal wind velocity $U = sqrtu^2 + v^2 + w^2$ and wind direction d. Data were measured with the upper sonic (S1) about 2.55 m above surface. Wind speed ranges from nearly 0 to 13 $\mathrm{m\,s^{-1}}$ with a mean wind speed of $\overline{U} = 4.2\,\mathrm{m\,s^{-1}}$ and a standard deviation σ_U = 1.7 $\mathrm{m\,s^{-1}}$.

λ of quasi-isotropic turbulence is a function of measurement height z_i ($\lambda = 4z_i$, see Muschinski and Roth (1993)) we find $\mathcal{L}_w \approx \lambda = 10$ m with $z_i = 2.5$ m for the upper sonic.

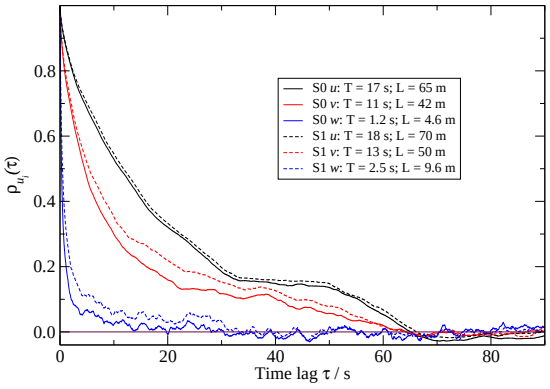

Figure 4: Auto-correlation functions $\rho(\tau)$ of the longitudinal wind velocity component u, the transversal component v, and the vertical component w. The integral time and length scales are estimated by integrating over $\rho(\tau)$ in the range $\tau \in [0; 70\,\mathrm{s}$ where $\tau = 70$ s is the time where $\rho = 0$ the fist time.

In Fig. 5 the one-dimensional power spectral density functions $S(f)$ (hereafter called "spectra") are plotted for all three components and both sonics S1 and S2. For the inertial subrange, classical turbulence theory predicts

$$S(f) = \frac{2\pi}{\overline{u}} \alpha \varepsilon^{2/3} f^{-5/3}, \qquad (1)$$

with α is a universal constant (≈ 0.5) and ε is the turbulent energy dissipation per unit mass. The factor $\frac{2\pi}{\overline{u}}$ is due to the conversion of the spectrum from wavenumber to frequency space. In the upper panel of Fig. 5 the spectra are multiplied by the frequency f to estimate the cut-off frequency f_c where the spectra deviates from the -2/3-slope for smaller frequencies i.e., for larger spatial scales. This is obvious for the w component at $f_c \approx 0.7$ Hz ($\lambda = \overline{u}/f_c \approx 7$ m) due to the limited measurement height. Therefore, for the vertical component the spectra for the lower sonic S0 are always below the values for the upper sonic S1 for $f < f_c$. At frequencies close to the Nyquist frequency $f_{Ny} = 50$ Hz the spectra of the horizontal components began to flatten which is most likely due to noise or an Aliasing effect. For the vertical component the spectra drop-off due to line averaging effects which become significant for spatial scales of $L' \approx \pi L \approx 45$ cm where $L = 15$ cm is the separation of the transducers of the sonic. The spectra S_w start to drop off around 10 Hz which corresponds to a spatial scale of 40 cm which is close to L'. Due to different spectral transfer functions for the horizontal and vertical components this line averaging effect is most pronounced for S_w.

In the lower panel of Fig. 5, the spectral ratios of the transversal to longitudinal components are plotted. For local isotropic turbulence theory predicts in the inertial subrange

$$S_v/S_u = S_w/S_u = 4/3.$$

For S_v/S_u, the ratio is close to one for $f > 0.1$ Hz which corresponds to the integral time scale $\mathcal{T}$. The ratio S_w/S_u is close to the predicted ratio of 4/3 for $f > 1$ Hz which compares well with the estimated $\mathcal{T}$. For frequencies above around 10 Hz the drop-off for all components is due to the reasons discussed above for the spectra. It has to be pointed out that the exact value of the spectral ratios for atmospheric conditions is the topic of current discussion, see Biltoft (2001)

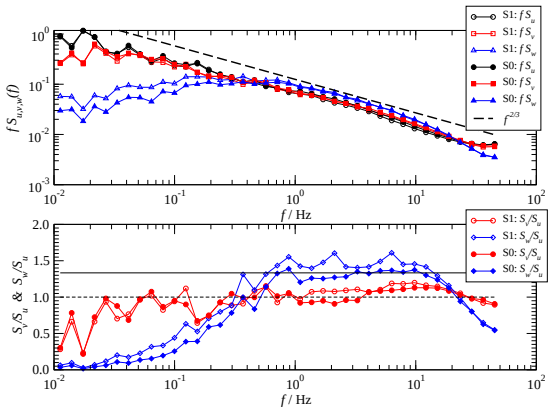

Figure 5: Upper panel: Power spectral density functions $S_{u_i}(f)$ of the three wind vector components u, v, and w of the lower sonic (S0) and uper sonic (S1). The spectra are multiplied with the frequency f to emphasize the inertial subrange scale which is characterized by a $-2/3$-slope. The wind vector was transformed in such a way that $< v >=< w >= 0$ and u is along the mean wind direction. Lower panel: Spectral ratios S_v/S_u and S_w/S_u. A 4/3 ratio is plotted for reference, indicating the value predicted by classical theory for isotropic turbulence.

Wind tunnel measurements and classical theory predicts that the distribution of velocity fluctuations in homogeneous and local isotropic turbulence are nearly Gaussian with slightly negative skewness and a kurtosis of around 3.2 or so. In Fig. 6 the probability density functions (PDF) of the normalized velocity components $(u_i - < u_i >)/\sigma_{u_i}$ are presented. For reference, a Gaussian distribution is added. The horizontal components are close to Gaussian with some deviations for $(u_i - < u_i >)/\sigma_{u_i} > +-3$ but the vertical components exhibit increased tails most pronounced for $(u_i - < u_i >)/\sigma_{u_i} < 2$. The reason for that is unknown...

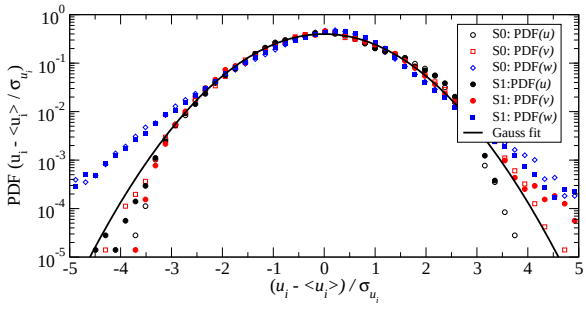

Figure 6: PDFs of normalized velocity components $(u_i - < u_i >)/\sigma_{u_i}$ for the upper sonic (S1) and the lower sonic (S0). A Gaussian fit is given as reference.

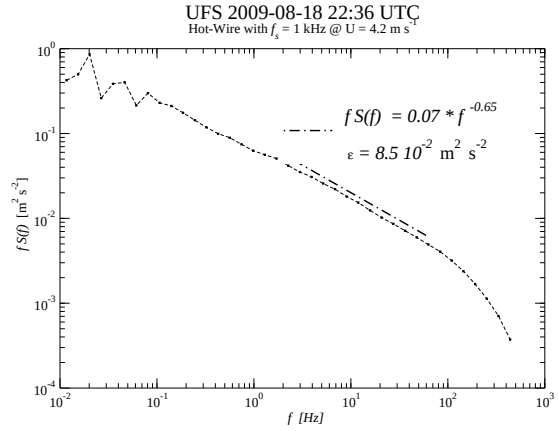

Figure 7: Power spectrum derived from a one-hour record of one-component hot-wire data. From an inertial sub-range fit (see dot-dashed line), a mean energy dissipation rate of $\overline{\varepsilon} \approx 8.5 \cdot 10^{-2}\,\mathrm{m^2\,s^{-3}}$ was estimated.

3b. *Hot-Wire Measurements: Fine-Scale Turbulence*

In order to characterize the mean flow and the small-scale statistics hot-wire data were analyzed. The data set consists of a one-hour long record sampled at $f_s = 1$ kHz. which means a spatial resolution of about 4 mm. In Fig. 7 the one-dimensional spectrum $f \cdot S_u(f)$ is plotted. The spectrum shows a nice inertial subrange scaling in the frequency range of 3 to 60 Hz. A linear fit was applied for that region yielding a slope of -0.65 which is close to the theoretical value of -2/3. For frequencies below 3 Hz, the spectrum is slightly more flatten, the reason is unknown. With Eq. 1 a mean $\varepsilon = 8.5{\cdot}10^{-2}\,\mathrm{m^2 s^{-3}}$ was estimated. For $f > 100$ Hz the spectrum drops off due to dissipation effects.

An alternative method to estimate the mean energy dissipation rate is the use of two relationships based on $n-$th order structure functions $S_u^{(n)} =< (u(x) - u(x+r))^n >$:

$$S^{(2)}(r) = \left(2\varepsilon^{2/3}\right) r^{2/3}, \qquad (2)$$

and

$$S^{(3)}(r) = -\frac{4}{5}\varepsilon r. \qquad (3)$$

Both functions are plotted in Fig. 8 together

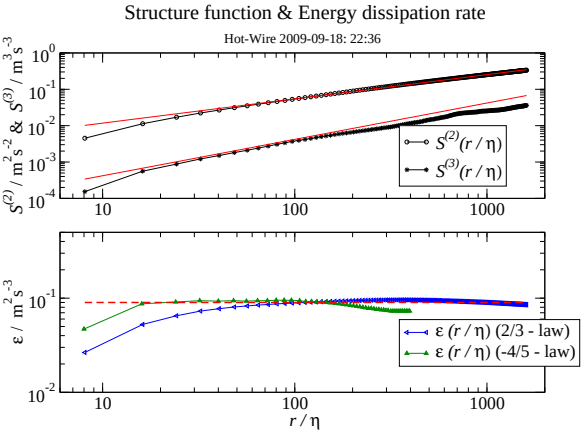

Figure 8: 2nd- and 3rd-order Structure functions derived from hot-wire measurements with 1 ms time resolution (upper panel) and compensated structure functions indicating the energy dissipation rate ε as a function of r/η.

with their compensated form from which we estimate a mean $\varepsilon = 8.8 \cdot 10{-}2\,\mathrm{m^2 s^{-3}}$ which is in good agreement with the value derived from the spectrum. The resulting Kolmogorov scale is $\eta = \left(\nu^3/\varepsilon\right)^{1/4} \approx 0.4$ mm.

With the mean ε, a typical eddy length scale

$l \propto u'^3/\overline{\varepsilon} \approx$ 50 m which is also consistent with our previous estimate of the integral length scale. With a variance of $\sigma^2 \approx 2.5\,\mathrm{m}^2\,\mathrm{s}^{-2}$ we estimate a Taylor-Reynolds number of $\sim 10^4$, a typical value also found in free atmospheric cumulus clouds (Siebert et al. 2006b).

3c. *Cloud Microphysics*

Measurements of cloud droplet size distributions show a variety of conditions typical at the UFS, and here just two representative examples are shown. On August 11, 2009 the UFS was exposed to relatively intermittent, thin clouds for several hours, of which a 40-minute time period was selected. On October 26, 2009 the UFS was embedded in thick clouds for an extended period of time, and a 100-minute time series of homogeneous coverage was selected. The temporal evolution of the cloud droplet size distribution is shown in Fig. 9. The August 11 period is dominated by extremely small cloud droplets, with intermittent bursts of droplets with diameter of approximately 8 to 12 μm, representative of microphysical conditions in small cumulus or thin stratocumulus clouds, either just in the process of formation, or during dissipation. The October 26 period shows a much more symmetric size distribution with a mean-diameter mode varying between 12 and 14 μm. Time averaged probability density functions for the two periods are shown in Fig. 10. Immediately striking are the pronounced exponential large-droplet tails. It is apparent especially in the October 26 example that some mechanism for large droplet production is likely present, given the small but significant number of droplets with diameters above 25 μm.

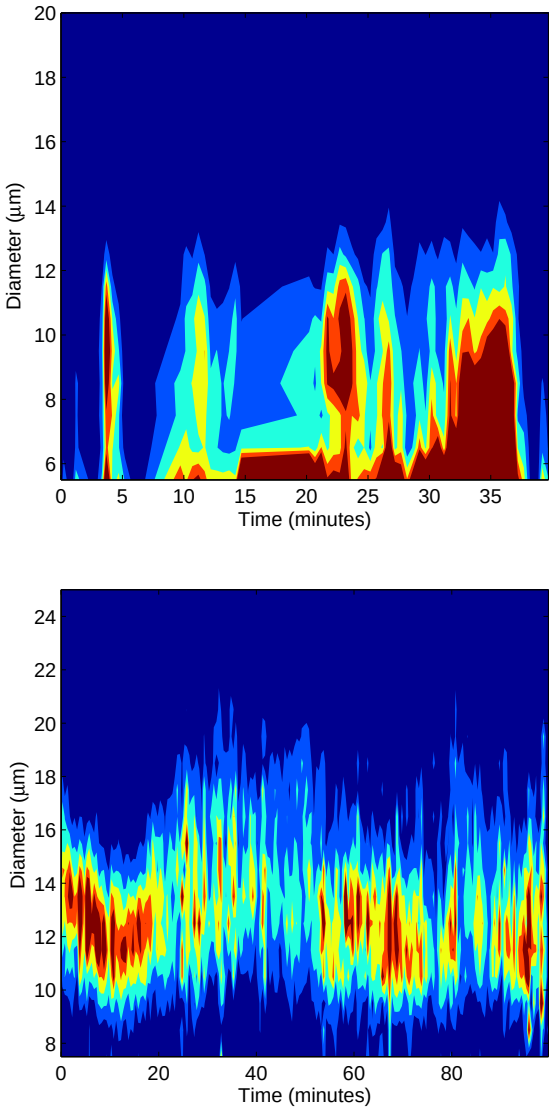

Figure 9: Temporal evolution of the cloud droplet size distribution during a 40-minute time period on August 11, 2009 (top) and a 100-minute period on October 26, 2009 (bottom). The size distributions were measured by the phase-Doppler interferometer (PICT).

The microphysical conditions sampled in these two examples are quite representative of those measured in free clouds. We may also consider what part of the dimensionless parameter space they lie in respective to droplet inertia and sedimentation effects. Taking a representative droplet diameter of $d \approx 10$ μm and a turbulent energy dissipation rate of $\varepsilon \approx 0.1$ m^2 s^{-3} yields a droplet Stokes number of approximately $St \approx 0.03$ and a settling parameter of $Sv \approx 0.09$, both of which are within the range of values reported for typical convective clouds Siebert et al. (2010). Further analysis, accounting for the lognormal nature of ε, will allow for more detailed comparison with the results of Siebert et al. (2010) for small cumulus and stratocumulus clouds.

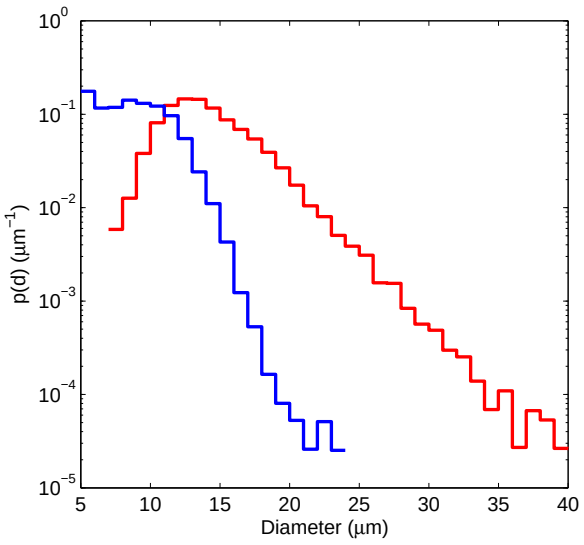

Figure 10: Estimated probability density functions for droplet diameter measured during the same time periods as in Fig. 9: August 11, 2009 (blue) and October 26, 2009 (red). The pdfs are plotted in log-linear coordinates to make clear the exponential large droplet tails.

4. SUMMARY

High spatial resolution measurements of liquid water content, droplet diameter, and turbulent velocity and temperature fluctuations were made at the Environmental Research Station (UFS) Schneefernerhaus in summer and fall 2009, and again in summer 2011. Hotwire velocity measurements are analyzed to provide second-order structure functions in cloudy and cloud-free conditions, as well as PDFs of local turbulent kinetic energy dissipation rate. Results are consistent with the assumption of statistically stationary and isotropic turbulence on the spatial scales of relevance to cloud microphysical processes. Time series of droplet number density, liquid water content, temperature, horizontal and vertical wind, and local energy dissipation rate, as well as averaged cloud droplet size distributions, are compared with measurements of boundary-layer-topped cloud properties from prior ACTOS (Airborne Cloud Turbulence Observation System) field projects. Comparisons of relevant dimensionless parameters for droplet inertial effects, the Stokes number and the settling parameter, show similar ranges as in "free" clouds, suggesting that the mountain top station is a reasonable location for making measurements of cloud-turbulence interactions that would be difficult to obtain from an airborne system.

Acknowledgement We thank Mr. Thomas Conrath for help with logistical aspects of the experiment and to Mr. Matthew Beals and Ms. Amanda Shaw for help with data processing. We are grateful to Mr. Markus Neumann and the staff at UFS for their technical help at UFS. Financial support from Leibniz Society, Max Planck Society, Deutsche Forschungsgemeinschaft (DFG) through the SPP 1276 Metstrm, the EU COST Action MP0806 "Particles in Turbulence," and through the US National Science Foundation (NSF grant AGS-1026123) are gratefully acknowledged.

References

Abbiss, J., T. Chubb, and E. Pike, 1974: Laser Doppler anemometry. *Optics Laser Technology*, **6**, 249–261.

Biltoft, C. A., 2001: Some thoughts on local isotropy and the 4/3 lateral to longitudinal velocity sprectrum ratio. *Boundary-Layer Meteorol.*, **100**, 393–404.

Chuang, P. Y., E. W. Saw, J. D. Small, R. A. Shaw, C. M. Sipperley, G. A. Payne, and W. Bachalo, 2008: Airborne phase doppler interferometry for cloud microphysical measurements. *Aerosol Sci. and Technol.*, **42**(8), 685 – 703.

Comte-Bellot, G., 1976: Hot-wire anemometry. *Annual Review of Fluid Mechanics*, **8**(1), 209–231.

Gerber, H., 1991: Direct measurement of suspended particulate volume concentration and far-infrared extinction coefficient with a laser-diffraction instrument. *Appl. Opt.*, **30**, 4824–4831.

Haman, K. E., A. Makulski, S. P. Malinowski, and R. Busen, 1997: A new ultrafast thermometer for airborne measurements in clouds. *J. Atmos. Oceanic Technol.*, **14**, 217–227.

Muschinski, A., and R. Roth, 1993: A local interpretation of Heisenberg's transfer theory. *Contr. Atmos. Phys.*, **66**, 335–346.

Risius, S., H. Xu, H. Xi, H. Siebert, R. A. Shaw, and E. Bodenschatz, 2012: Schneefernerhaus as a cloud-turbulence research station. Part 1: Flow conditions and

large-scale turbulence. *Proc. ICCP'16*, Leipzig, Germany.

Siebert, H., H. Franke, K. Lehmann, R. Maser, E. W. Saw, R. A. Shaw, D. Schell, and M. Wendisch, 2006a: Probing finescale dynamics and microphysics of clouds with helicopter-borne measurements. *Bull. Amer. Meteor. Soc.*, **87**, 1727–1738.

Siebert, H., S. Gerashchenko, A. Gylfason, K. Lehmann, L. Collins, R. A. Shaw, Z. Warhaft, 2010: Towards understanding the role of turbulence on droplets in clouds: in-situ and laboratory measurements. *Atmos. Res.*, **97**, 426–437.

Siebert, H., K. Lehmann, and M. Wendisch, 2006b: Observations of small scale turbulence and energy dissipation rates in the cloudy boundary layer. *J. Atmos. Sci.*, **63**, 1451 – 1466.

Siebert, H., and A. Muschinski, 2001: Relevance of a tuning-fork effect for temperature measurements with the Gill Solent HS ultrasonic anemometer-thermometer. *J. Atmos. Oceanic Technol.*, **18**, 1367–1376.

OBSERVATIONS OF CLOUD DROPLET SIZE DISTRIBUTIONS ON MICROPHYSICALLY RELEVANT SCALES

Matthew Beals[1]*, **Jacob P. Fugal**[2], **Raymond A. Shaw**[1],
Scott Spuler[3], **Jeff Stith**[3], **and Teresa Campos**[3]
[1]Atmospheric Sciences Program, Michigan Technological University
[2]Max Planck Institute for Chemistry
[3]Earth Observing Laboratory, National Center for Atmospheric Research

1. MOTIVATION

Microphysical interactions between cloud droplets occur over a range of temporal and spatial scales, but at least the local diffusive interactions that govern condensation growth or evaporation occurs on scales ranging from the droplet size to tens of centimeters. For instance, entrainment of dry air into clouds strongly influences their microphysical properties as well as their depth and lifetime. The thermodynamic equilibrium state after dilution and evaporation can be reached through a variety of microphysical pathways, such as uniform evaporation of all droplets in the diluted volume, or the complete evaporation of a subset of droplets. These pathways are described as homogeneous and inhomogeneous mixing, respectively, and the concept has generated an active debate in the several decades since it was formulated (Latham and Reed 1977; Baker et al. 1984). We refer to the scales over which droplets can interact as "microphysically relevant." One question that has been of particular interest is whether inhomogeneous mixing is capable of generating large droplets, which presumably could later contribute to the initiation of precipitation.

The argument, in its idealized form, is that upon dilution and total evaporation of a subset of droplets, the remaining droplets (which experienced no evaporation) subsequently experience less competition for vapor and therefore reach larger sizes compared to the droplets in more crowded, undiluted neighboring volumes. Whether actual clouds exhibit such behavior was questioned early on (Paluch and Knight 1986), but in later work it has been recognized that one basic limitation is the ability to sample cloud volumes at relevant scales (Paluch and Baumgardner 1989; Burnet and Brenguier 1987; Lehmann et al. 2009). Paluch and Baumgardner (1989) illustrate the essential concept in their Figure 6, and Burnet and Brenguier (1987) explicitly discuss the ambiguities introduced as a result of spatial averaging. For example, if a broad size distribution containing both large and small droplets is measured, does it represent the actual size distribution existing at the fine scales, or is it a sampling of locally narrow distributions with different mean values?

The main problem is that measurements of the cloud droplet size distribution are typically made from single droplet counting instruments that require averaging over distances of tens or hundreds of meters to achieve statistically reliable samples. In this contribution we address the assumption directly through measurements of cloud droplet size distributions from microphysically relevant volumes. The measurements were made with the Holographic Detector for Clouds (Holodec), which flew aboard the NCAR C130 during the IDEAS4 project in October 2011. Data presented here are from flights through small cumulus over northern Colorado and southern Wyoming. In what follows we first describe the Holodec instrument with a focus on

*mjbeals@mtu.edu

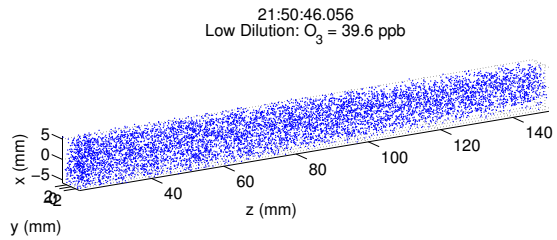

(a) Low Dilution: $O_3 = 39.6\ ppb$, 2347 total particles

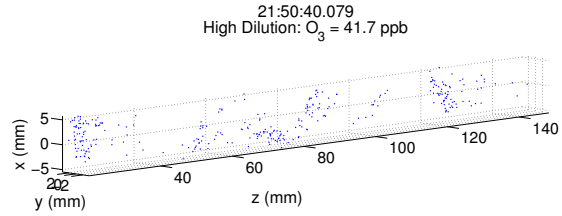

(b) High Dilution: $O_3 = 41.7\ ppb$, 312 total particles

Figure 1: Scatter plots of particle positions for low (top) and high (bottom) diltuion cases.

its ability to measure microphysically relevant, or 'local' size size distributions, and we then use this ability to investigate the microphysical response to mixing and dilution.

2. LOCAL SIZE DISTRIBUTIONS

The Holographic Detector for Clouds (Holodec), version II, utilizes digital in-line holography to make instantaneous measurements of particles residing in a $20\ cm^3$ volume of cloud air. Holograms are recorded at a rate of 3.3 per second, yielding approximately a $0.07\ Ls^{-1}$ sample rate: the volume sample rate is comparable to single-particle instruments, but the sampled volumes are microphysically local, with the longest axis of the volume having a dimension of approximately 15 cm. The ability of digital holography to make measurements of cloud microphysical parameters has been demonstrated previously by Fugal and Shaw (2009), but those measurements were made with an earlier version of the instrument that lacked the resolution to fully resolve the cloud droplet size distribution. The current instrument, however, has a theoretical lower particle resolution of approximately $6\ \mu m$ and an upper limit of several mm (Spuler and Fugal 2011), so complete droplet size distributions, with the exception of recently activated droplets, can be sampled.

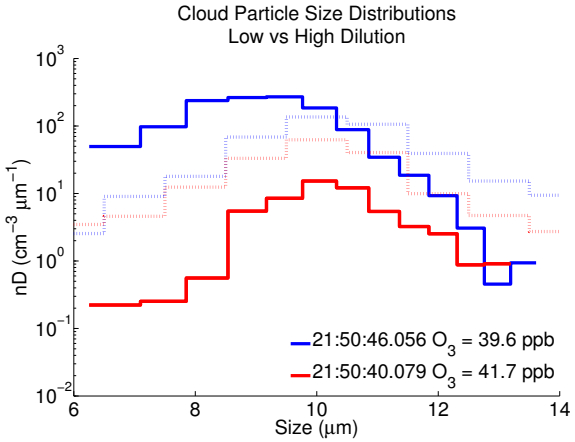

(a) Size distributions for two cases shown in figure 1. Solid lines indicate Holodec II data and dashed lines indicated CDP data.

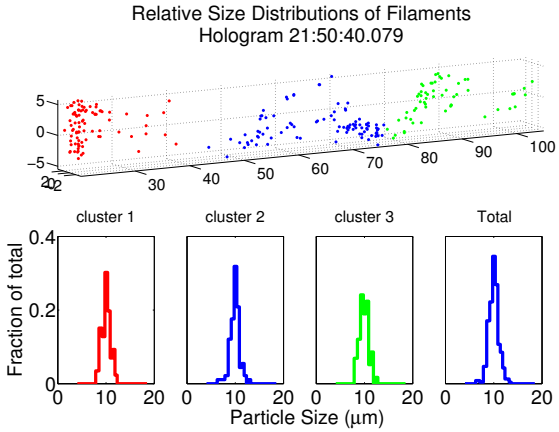

(b) Relative size distributions of individual filaments observed in hologram 21:50:40.079. Size distributions represent fraction of particles in the size bin relative to the number of partilces in the filament.

Figure 2: Analysis of size distributions for high and low dilution cases. Holodec II distributions (solid lines) indicate a preference for large drops in the dilute case; an observation missed by the CDP (dashed lines). Inspection of the individual filaments found in the highly dilute case indicate that small scale, filament-relative size distributions are very similar to the large scale distribution for the entire sample volume.

Unlike single particle counting probes, the sample volume size of the Holodec II is large enough that each hologram represents a sta-

tistically significant population of cloud particles. This eliminates the necessity to combine multiple volumes to obtain accurate size distributions and number densities and allows each hologram to stand alone as a discrete, microphysically independent volume. The dimensions of the sample volume are also similar to characteristic microphysical length scales in typical clouds, capturing a snapshot of the complete process. Examples of two cloud volumes are shown in Fig. 1. The volume shown in Fig. 1a is from a relatively undiluted section of cloud and contains approximately 2000 droplets. Figure 1b shows a cloud volume that has undergone significant entrainment and dilution, with filaments of cloud mixed with clear air evident even on the centimeter scale. Droplet size distributions are shown for the individual filaments in Fig. 2b. The nature of the mixing in this cumulus cloud is further discussed in Section 3.

Time series of variables such as liquid water content and number density can be computed from local samples and compared against those calculated by continuously-sampling instruments. Figure 3 compares number densities (Fig. 3a) and liquid water content (Fig. 3b) calculated from Holodec data to values retrieved from the CDP and king probe (respectively). The CDP (Cloud Droplet Probe) is a forward scattering cloud particle spectrometry probe capable of sizing individual particles. The king probe is a hot-wire liquid water probe capable of measuring the total mass of water striking the sensing element. Both plots show reasonable agreement over the length of the pass with only a few regions (e.g. 21:50:55) of noticeable disagreement. Due to the differences in sampling techniques between the two instruments discrepancies are anticipated, and only under statistically stationary conditions can a careful comparison be made.

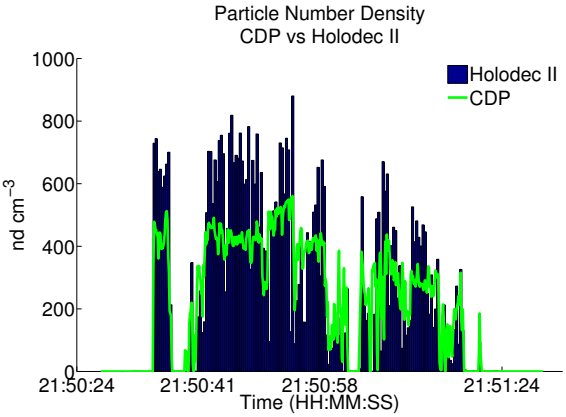

(a) CDP vs Holodec II number density

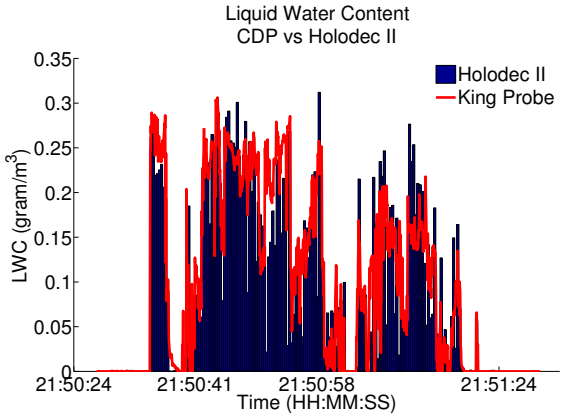

(b) King Probe vs Holodec II LWC

Figure 3: Comparison of parameters computed from Holodec II holograms to data recorded by other instruments during the same time period.

3. MICROPHYSICAL RESPONSE TO CLOUD DILUTION

As discussed in section 1, entrainment of dry air has been hypothesized to result in increased populations of large droplets in clouds. Figure 2a explores this question by comparing size distributions computed from two holograms; one taken in a dilute region (solid red) and one from an undilute (solid blue) region. The figure illustrates that for these two samples, the dilute volume not only has a larger mean diameter but is also significantly skewed to the right, with concentrations equalling and even exceeding those of the undilute sample in the largest size ranges. This is consistent with the large-drop hypothesis; the dilute volume does contain a larger proportion of large drops in comparison to undilute cloud.

It is also worth noticing the size distributions for the same time periods made by the CDP. Each trace is computed from a $0.1\ s$ sample, rep-

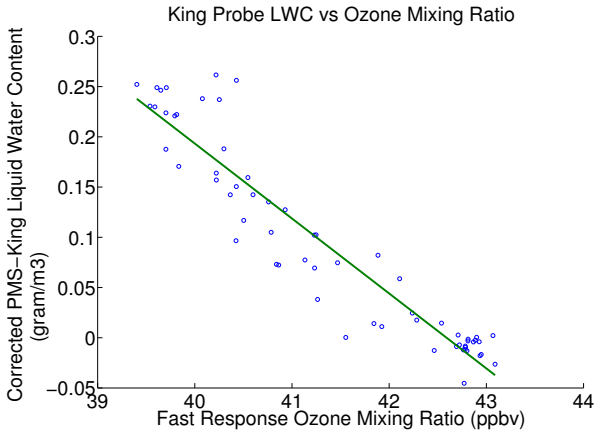

(a) Comparison of king probe liquid water content vs ozone mixing ratio. The linear correlation between liquid water content and ozone mixing ratio indicates that ozone mixing ratio is representative of cloud dilution.

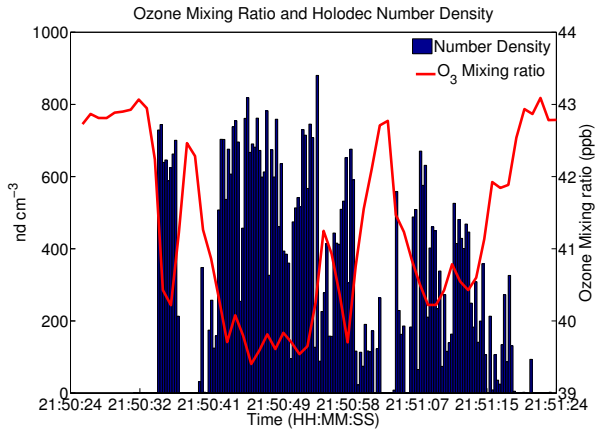

(b) Ozone mixing ratio as a function of time compared to Holodec II number densities. Ozone levels are the highest before and after cloud penetration with lowest values observed around 21:50:49, corresponding with an unmixed core.

Figure 4: Ozone mixing ratio compared to liquid water content and particle number density. Panel (a) illustrates correlation between LWC and ozone mixing ratio, indicating its usefullness as a metric in estimating cloud dilution. Panel (b) illustrates the correlation between ozone and dilution. Elevated values of ozone in the initial penetration (just after 21:50:32) and in the latter half of the pass indicate the presence of entrained environmental air, suggesting various levels of dilution should be observed.

resenting a total sample volume similar to the Holodec's, albeit averaged over $\sim 10\ m$. The CDP data is shown in dashed lines following the same color convention. It is immediately evident that the CDP size distributions do not show a large difference between the two samples, except for a near uniform decrease in total number density for the dilute case. This is very likely a result of spatial averaging, including diluted and undiluted regions of cloud. The CDP data also shows a uniform decrease in the large-drop tail of the distribution in the diluted sample; a direct contradiction to the Holodec data.

It is difficult to determine unambiguously the exact nature of the discrepancy between the Holodec and CDP size distributions. As pointed out earlier, each size distribution for the CDP is averaged over $\sim 10\ m$ of cloud, which would smooth out the fine structure observed in Fig. 1b. Another possible explanation is the coincidence effect studied in detail by Lance et al. (2010) in which multiple small droplets in the CDP sample volume are counted as single, larger droplets. This tends to decrease total counts and shift size distributions toward larger particles, a trend observed between the two blue lines.

To study the effects of dilution on drop size distributions on a larger scale, ozone mixing ratio is used as a tracer for environmental air following Pearson and Weaver (1989). The utility of ozone as a tracer for dilution is further explored in Fig. 4. Regardless of the type of mixing (homogeneous or inhomogeneous), diluted regions of cloud should exhibit lower liquid water contents than undiluted regions. The observed inverse relationship between (King probe) liquid water content and ozone mixing ratio (Fig. 4a) illustrate that regions of dilute air correspond to higher levels of ozone, confirming its utility as a tracer.

When ozone mixing ratio is plotted against cloud particle number density (figure 4b), regions with varying levels of dilution are observed. The expected inverse relationship between ozone and environmental air is observed in both the regions of clear air before and after the pass, as well as the relatively low concentrations in the region near 21:50:49 indicating a relatively unmixed core. The higher levels of ozone observed at cloud edge as well as in the latter half of the pass (after 21:50:58) indicate the presence of increasing levels of mixing within the cloud.

Figure 5 shows probability distributions for

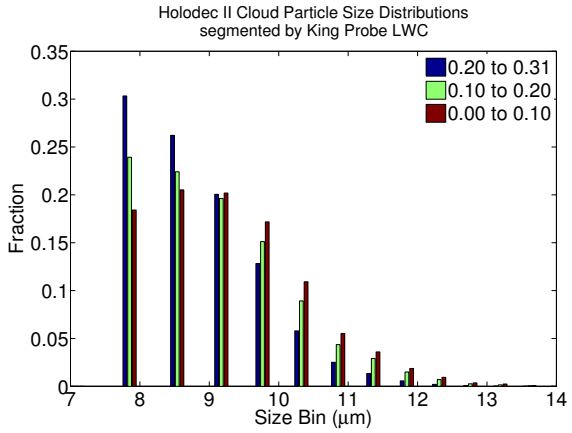

(a) Cloud droplet size distributions as a function of liquid water content

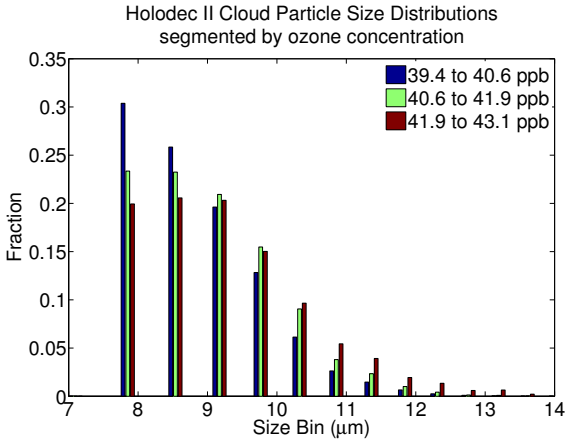

(b) Cloud droplet size distributions as a function of ozone mixing ratio

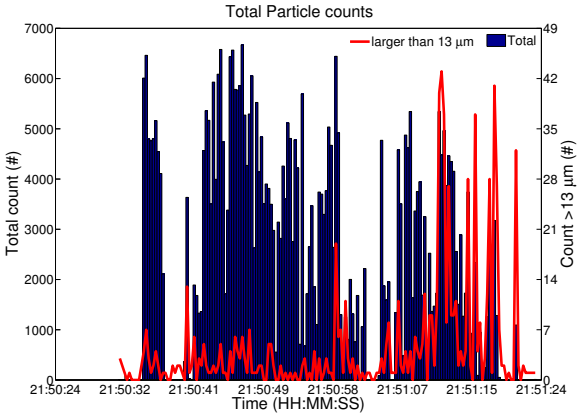

(c) Total particle counts (blue bars) plotted with total counts of particles greater than $13\ \mu m$ (red line). Large particle counts correlate well with ozone mixing ratio (figure 4) indicating that dilution is correlated with their formation.

Figure 5: Cloud droplet size distributions for regions of cloud segmented by liquid water content (a) and ozone mixing ratio (b). Plot (a) shows the presence of large drops mainly in regions with low liquid water, while regions of high liquid water are dominated by smaller drops. Using ozone mixing ratio as a tracer for environmental air suggests that regions with large drops are correlated with regions of high dilution. This is supported by panel (c), showing total counts of particles greater than $13\ \mu m$ peaking in regions of expected high dilution

droplet diameter for relatively undiluted and diluted regions of cloud, as determined by liquid water content and ozone mixing ratio (top and bottom panels respectively). For simplicity, three different dilution levels are displayed. The distributions show a clear tendency for large droplets to be preferentially located in diluted regions of cloud. This can also be seen in Fig. 5c, where a time history of droplets with diameters greater than 13 μm is shown. Again, there is a clear tendency for large droplets to be located in heavily diluted regions of cloud. It is interesting to note that when an analogous plot as in Fig. 5 is created using CDP size distributions (not shown), the opposite pattern is observed; the tendency is for larger droplets to be located in undilute clouds. This is again suggestive that the coincidence problem discussed above extends from the single samples in Fig. 2a to the global population.

This brings us back to the holograms and size distributions shown in Figs. 1 and 2. The undiluted and diluted distributions in Fig. 2a are consistent with strong inhomogeneous mixing and subsequent growth leading to an increase in the mean diameter as well as the large droplet tail. By further subdividing the diluted volume into an analysis of individual cloudy filaments, as is shown in Fig. 2b, we indeed see a striking consistency with the inhomogeneous mixing hypothesis. Even at centimeter scales the droplet size distributions are essentially identical to each other and show little or no evidence of a small droplet tail resulting from evaporation. The transition from inhomogeneous to homogeneous mixing (Lehmann et al. 2009) is expected to occur at scales on the order of $l^* = (\varepsilon\tau_p^3)^{1/2}$, where ε is the turbulent kinetic energy dissipation rate (per unit fluid mass), and $\tau_p \approx (2\pi n\mathcal{D}d)^{-1}$ is the phase relaxation time (here, $\mathcal{D}$ is the diffusion coefficient of water vapor in air, taking into account modifications of latent heat release during droplet growth or evaporation). Taking $n \approx 500$ cm^{-3} and $d \approx 10$ μm, as well as $\varepsilon \approx 10^{-3}$ m^2 s^{-3} obtained from estimates from the second order velocity structure function, a transition length scale of $l^* \approx 6$ cm is obtained. Considering that the homogeneous mixing limit is not expected to emerge until length scales significantly less than l^*, the local microphysical behavior observed in Fig. 2b is not unreasonable.

4. SUMMARY

Cloud particle volumes measured by the Holodec instrument during the IDEAS4 campaign are analyzed to study cloud particle size distributions on microphysically relevant scales. Holodec measurements are unique in that each sample represents a statistically significant, "microphysically local" volume of cloud, allowing for the study of particle interactions. One fifty second pass through a cumulus cloud is selected to study the variations in cloud particle size distributions due to cloud dilution from entrainment and subsequent mixing.

Regions of high and low dilution are determined from this pass via analysis of liquid water content and ozone mixing ratio: elevated ozone mixing ratios correspond to regions of entrainment and dilution. From this, dilute and undilute regions of the cloud are identified. Analysis of single holograms identified as dilute and non-dilute show a larger mean diameter and large-diameter tail for the dilute case, suggesting the creation of larger drops through inhomogeneous mixing processes. This observation is not seen in size distributions recorded by the CDP for the same areas, potentially due to spatial averaging and the known coincidence problems. Individual size distributions computed for filaments found in the dilute case show little variation in statistics, further bolstering the inhomogeneous argument.

Holograms from the entire pass are divided up into three levels of dilution based on measured liquid water content and ozone mixing ratio. It is found that dilute regions of the cloud tend to have a larger mean diameter and enhanced large-diameter tail than non-dilute regions. When total counts of particles larger than 13 μm are compared against dilution, it is observed that regions undergoing the strongest mixing tend to contain the largest number of large particles.

The scientific conclusions drawn here are

based on a small sample size, but they serve to illustrate the new window that Holodec provides into local microphysical variability. Comparing droplet size distributions obtained through spatial averaging and through local sampling by Holodec will lead to improved understanding of mixing and entrainment, which are known to occur on spatial scales extending all the way to the dissipation range (mm-scales).

Acknowledgement This research was supported by the Office of Biological and Environmental Research of the U.S. Department of Energy as part of the Atmospheric Radiation Measurement Climate Research Facility, and by the U.S. National Science Foundation (AGS-1026123).

References

Baker, M. B., R. E. Breidenthal, T. W. Choularton, and J. Latham, 1984: The effects of turbulent mixing in clouds. *J. Atmos. Sci.*, **41**, 299–304.

Burnet, F. and J.-L. Brenguier, 1987: Observational study of the entrainment-mixing process in warm convective clouds. *J. Atmos. Sci.*, **64**, 1995–2011.

Fugal, J. P. and R. A. Shaw, 2009: Cloud particle size distributions measured with an airborne digital in-line holographic instrument. *Atmos. Meas. Tech.*, **2**, 259–271.

Lance, S., C. A. Brock, D. Rogers, and J. A. Gordon, 2010: Water droplet calibration of the cloud droplet probe (cdp) and in-flight performance in liquid, ice and mixed-phase clouds during arcpac. *Atmos. Meas. Tech.*, **3 (6)**, 1683–1706.

Latham, J. and R. L. Reed, 1977: Laboratory studies of the effects of mixing on the evolution of cloud droplet spectra. *Quart. J. Roy. Meteor. Soc.*, **103**, 297–306.

Lehmann, K., H. Siebert, and R. A. Shaw, 2009: Homogeneous and inhomogeneous mixing in cumulus clouds: Dependence on local turbulence structure. *J. Atmos. Sci.*, **66**, 3641–3659.

Paluch, I. R. and D. G. Baumgardner, 1989: Entrainment and fine-scale mixing in a continental convective cloud. *J. Atmos. Sci.*, **46**, 261–278.

Paluch, I. R. and C. A. Knight, 1986: Does mixing promote cloud droplet growth? *J. Atmos. Sci.*, **43**, 1994–1998.

Pearson, R. and C. J. Weaver, 1989: Ozone conservation and entrainment in cumulus congestus. *J. Atm. Sci.*, **46**, 2031–2043.

Spuler, S. and J. Fugal, 2011: Design of a digital, in-line, holographic imaging system for airborne measurement of clouds. *App. Optics*, **50**, 1405–1412.

Development of Ice Hydrometeors in a Tropical Oceanic Deep Convective Cloud System

Paul T. Willis
NOAA/HRD/CIMAS CIMAS/U Miami
4301 Rickenbacker Causeway
Miami, Florida 33149, United States

1.0 INTRODUCTION

Most of the observations which indicate a large discrepancy between observed ice particle concentrations and expected ice nucleus concentrations have been observed in cumulus clouds, and usually in the presence of large drops. Consequently the subject cloud of this study should be well suited to the study of primary, and secondary, ice development.

Rangno and Hobbs (1991) discussing their observations of high concentrations of ice particles in many clouds at fairly warm temperatures (~-10C), state that in particular maritime cumulus clouds, and some continental clouds, containing drizzle drops, or larger raindrops, show a propensity for high ice particle concentrations. In fact most of the observations which indicate large discrepancies between observed ice particle concentrations and measured, or expected, ice nucleus concentrations have been in convective clouds, and usually in the presence of large drops (Mossop (1974), Koenig (1963). The production of secondary ice particles (ice multiplication) is usually invoked to explain these observations, but secondary ice processes require the development of proto ice (primary ice). It is the purpose of this study to explore the development of the requisite proto ice in a cloud system that also displays copious secondary ice development.

A deep convective cloud system was profiled with the instrumented NASA DC-8 on 20 Aug 2006. Cloud microphysical data were obtained on five transects within 23 min., nominally at +11C, -2Cto-3C, -11C, -21C, and -34C. The focus of this study is tracing the development of ice in this cloud system - from the arrival at 0C of parcels in updrafts with developed warm rain distributions, to the copious ice hydrometeor concentrations observed at cold anvil levels in this deep convective cloud. Particular attention is here focused on the development of first ice, and ice multiplication in the layer from -3C to-11C.

2.0 DATA

Data from numerous instruments are utilized in this study, but the primary analysis is of the imaging probe data – in particular from the SPEC 2DS imaging probe which has a resolution near 10um from an 128 element photodiode array. In addition to the state parameters the high resolution air motions, particularly the vertical winds from the NASA AMES MMS provide a framework for the analysis of the microphysical data in this study. The diode laser hygrometer DLH from NASA Langley provides high resolution relative humidity measurements in the cloud system. The DC8 aircraft instruments are summarized at: http://airbornescience.nsstc.nasa.gov/namma/instruments.html#dlh Two soundings from dropwindsondes were obtained in the environment of the subject cloud.

3.0 ORGANIZATION OF CONVECTIVE ELEMENTS BY VERTICAL WIND SHEAR

The vertical shear of the horizontal wind exerts a strong influence on the organization of convective clouds in the tropics. It is a fairly common observation that new cloud turret growth occurs preferentially on the upshear flank of a cloud system (Cotton and Anthes 1989)). This organization affects several scales from the freshest thermals, or updraft pulses, which occur on the upshear flank of an individual cloud, to a mesoscale organization of individual clouds within a convective cloud system. We see both of

these organizations in the subject deep convective cloud in this study.

The cloud sampling transects with the DC-8 aircraft were made nominally aligned with the general shear vector. Figure 1 is a radar profile showing the general shear of the cloud system upshear on the north, to the downshear anvil on the south. It can be seen that the shear creates slope of the precipitation cells, and presumably the slope of the updrafts as well.

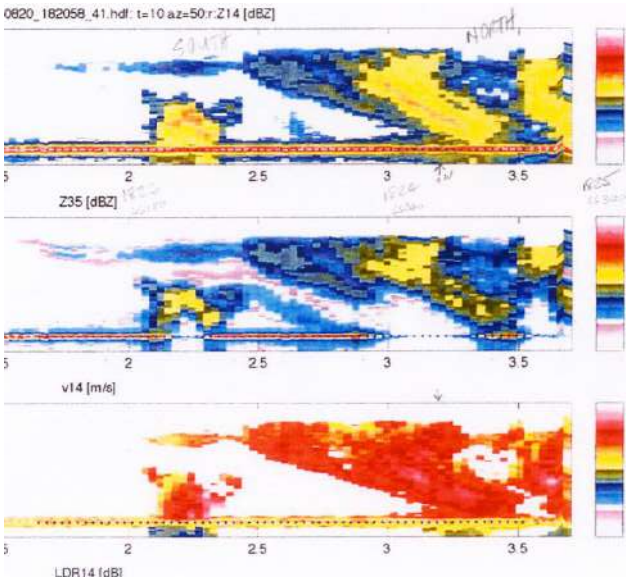

Figure 1 Radar profile showing general organization of cloud by shear

The distributions of the high resolution vertical winds measured on three cloud transects (T=-2C, -11C, and -21C) are shown in Figure 2. The combined distribution of these three transects is also plotted. This sample was limited to times that are within the visible cloud boundaries. Within the cloud boundaries the median updraft velocity is very close to +1 m/s on the combined sample and on individual transects. We can't tell from this data set what the lifetimes of an individual cloud updraft are; but, it is pretty clear that over the 23 minutes of sampling a fairly similar distribution of updraft is occurring somewhere within this cloud. These updrafts are not steady state, but they are

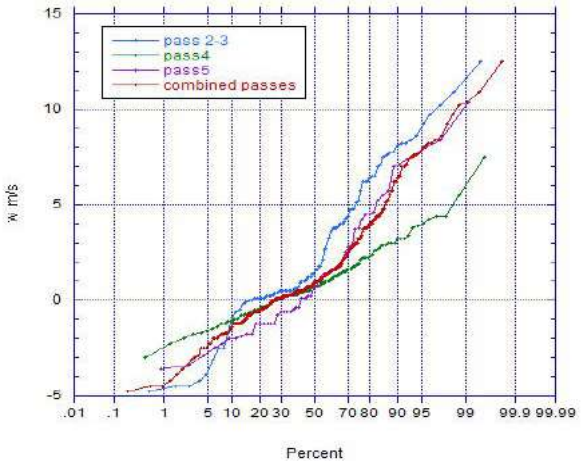

Figure 2 Distributions of vertical winds (w) for 3 sampling transects and the combined distributions.

features that are at least quasi steady for periods of the order of ten minutes.

4.0 CLOUD MICROPHYSICS AND DYNAMICS

This deep convective cloud is characterized by a very deep layer of developed warm rain. Consequently, the active updrafts arrive at the level where T=-2C (basically the freezing level) with a developed high water content warm rain drop size distribution. These warm rain distributions are formed by balance (or interplay between collision coalescence growth, and collision breakup due to collisions between medium to large raindrops with slightly smaller drops due to their difference in terminal velocity. The largest sizes that arrive at the freezing level are those sizes that the updraft velocity can loft to that level (updraft velocity > drop terminal velocity). In these deep convective clouds considerable rainout has occurred below the freezing level. This is apparent from radar data from this cloud (Fig. 1), and from radar data from similar deep convective clouds with deep layers of warm rain throughout the tropics, and subtropics.

At levels just above the freezing level the terminal velocity of a 0.5 mm raindrop is 2.6 m/s, and a 4mm raindrop 11.33 m/s. So, the active updrafts in this cloud pretty well bracket the range of raindrop terminal velocities. This very important to the ice development of this cloud in the layer from T=-2C to T=-11C.

A very large fraction of the total aerosol from cloud base air, as well as from air later entrained into cloudy parcels in the updraft, is immersed in these raindrops at T=-2C. The relevant mechanisms are condensation on cloud droplets near cloud base, as well as subsequent coalescence of raindrops and cloud droplets continually forming in the updrafts, and scavenging capture of aerosol by sweep out of cloudy volumes by raindrops falling relative to the updrafts, and downdrafts. Thus, virtually all of the soluble aerosol, and a large part of the insoluble aerosol, is immersed in these raindrops arriving at the freezing level.

Figure 3a shows the vertical wind (w), and the relative humidity w/r to water for the transect at T=-2C. In this figure upshear is to the right, and downshear to the left. There are two active updraft regions of cloud on this transect, and both display relative humidities above water saturation. There are some missing humidity data around 65720s. Figure 3b shows the SPEC 2DS concentrations of cloud droplets in two size ranges, and the concentrations of rain drops in two size ranges. The concentration of small (<25um) cloud droplets is 30-60 cm-3, and the concentration of cloud droplets (D (25-105um)) is 10-19 cm-3. In this all water transect the an otherwise unedited sample showing the raindrops and the small cloud droplets sampled in their environment. Each strip has a vertical dimension of 1.28 mm. small cloud droplets are virtually absent outof the active updraft regions

Figure 3c shows what 2DS images look like in an all water warm rain active updraft sectionof the cloud. These samples have had only obvious artifacts (splashes, etc.) removed, and are The small solid droplets are in the depth of field of the sample, butthe characteristic donuts are not. Under the uni-modal laser illumination used in this, and other imaging probes, any particle image out of the depth of field collapses to this donut shape. These are images of real particles, but out of focus. A method is used in the data reduction to reconstruct the actual sizes of these particles. This pass at T=-2C is all water, with the exception of the downdraft region near 65700 which displays some ice images (not shown).

Now that we established that the updrafts at T=-2C are all water with high concentrations of large drops, we will explore what happens after the cloud parcels transit through the critical region from this level to T=-11C. Figure 4a shows the vertical wind (w) and the rh w/r to water for the transect at T=-11C. Here upshear is to the left, and downshear to the right.
The rh w/r to water trace touches the 100% line in the active updrafts, but is not as high as in figure 3a. This transect is just above the needle ice multiplication region (-3C to -8C) and in the column growth region. It is still a region of supercooled droplets and considerable riming. The upshear regions of active updraft are still characterized by high concentrations of supercooled cloud water droplets, even though the humidity measurement only shows two incursions above 100% relative humidity with respect to water.

Figure 4b contains plots of the concentrations of medium to large hydrometeors 405-805 um, and >805 um, and <25 um and 25-105 um cloud droplets. On this transect the cloud is more continuous, but still divides into two areas, or entities. The concentrations of the two sizes of cloud droplets are 80/cm3 and 10 cm-3 in the extreme upshear edge updraft, then 30 cm-3 and 5 cm-3 in the further downshear but active updrafts, then very much lower in the regions just downshear of the active updrafts. The concentration of large hydrometeors (>805 um) are about 2/liter uniformly across the transect. The concentration of 405-805 um hydrometeors are 40-50 /liter in the active updraft regions but then peak at 70-80 in the regions downshear of the active updraft regions.

Figure 4c,4d, 4e, and 4f show a sequence of 2DS image data samples across this transect. First of all the large hydrometeors are all ice on this entire transect, and appear to be recently frozen but rimed drops. The characteristic semicircle shape of a drop that shattered on freezing are fairly common among the large hydrometeors. There is evidence of coalescence of these frozen drops, which is consistent with warm drop surface temperatures. The image samples

on the extreme upshear edge show drizzle size liquid drops, so there is some small amount of liquid making it through this layer. In the active updraft regions there is evidence of supercooled cloud droplets, presumably the result of new condensation in the active updrafts. But, in between and downshear of these active updrafts; lo and behold there are copious concentrations of columns. Any evidence of supercooed water droplets is gone, and the concentration of columnar ice very high (Fig. 4e). The surface of the large graupel in these regions displays evidence of columnar growth on the surface of the graupel (Fig.4e middle). This clear evidence of ice multiplication, consistent in principle with the scenario outlined by Hallet and Mossop (1974)

The two right panels of figure 4f are from a transect of T=-21C and clearly show dendritic growth spicules on the surface of this large graupel. Mechanical collision fracture of such hydrometeors could easily be a source of additional ice particles at colder cloud temperatures.

5.0 FREEZING DROPS AND PROTO ICE

Figures 4c through 4e strongly suggest that the proto ice particles in this cloud are frozen drops riming by collecting supercooled liquid cloud droplets made available in the active upshear updrafts. In Fig 5a the measured vertical winds (w)from this transect of parcels arriving at(T=-2C) has been added to the terminal velocities of a range of raindrop sizes (0.3mm to3mm). In the figure it can be seen that only in the active updrafts are any hydrometeors moving up in this cloud. Everywhere else raindrops of all sizes are moving down is space. And in the active updrafts they are moving up at a velocity of w minus their terminal velocity. Figure 5b is a plot of only the up part of curve and on the right ordinate axis is indicated the time it would take raindrops of various sizes to rise through (transit) a 500m vertical layer. Of course this assumes a steady state vertical wind, or at least a quasi-steady updraft structure. This is not strictly applicable because the cloud is a very active dynamic changing entity. Even though the structure is not steady state the vertical wind distributions are stable and the lifetime of the updrafts probably have a lifetime of the order of at least 10 minutes. The concept is that raindrops (hydrometeors) move through a layer at w – Vt. Thus when the w approximately equals Vt, the motion in space is very slow and those hydrometeors have a long residence time in a layer. The data of this study show that this is a very common occurrence in this cloud, and indeed probably in most maritime convective clouds.

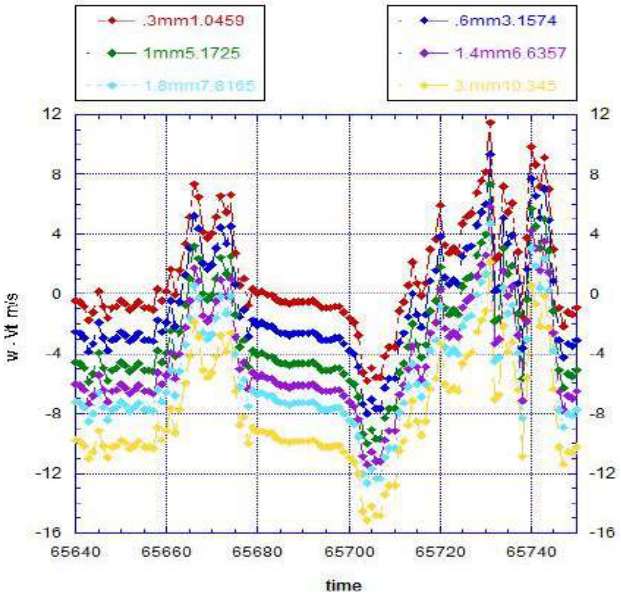

Figure 5a Vertical wind minus terminal velocity for a range of rain drop sizes

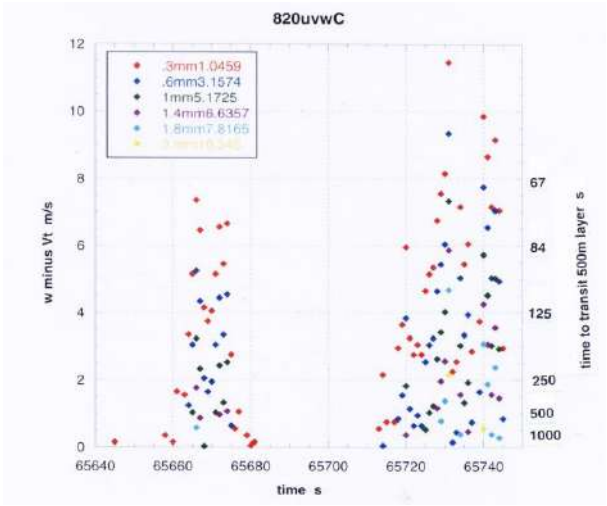

Figure 5b Time to transit a 500m layer – moving up through ice multiplication zone

This concept has significant ramifications for the freezing of rain drops. I submit that any place and any time in for example the -2C to -11) in this cloud, or any similar cloud, that the updraft velocity (w) is of the same order as the raindrops terminal velocity, those hydrometeors will have a significant dwell time in that temperature stratum.

The ramifications for freezing are that due to the long residence time, the temperature equilibration of the drop with it's environment has a long time, and also the transfer of latent heat from the surface of the freezing drop also has a long time. Likewise, the ice nucleation of the drop has a long time. So, now nucleation can be by immersion freezing, contact freezing, etc. as the time constraints are considerably relaxed.

The ramifications for secondary ice production are also profound. Say, a riming frozen drop (graupel or ice pellet) has a terminal velocity that just matches w in the updraft; the rate of riming is controlled entirely by Vt, and even though the hydrometeor is stationary inspace and stays at a constant environment temperature, this frozen drop will rime at a collision rate determined by Vt times it's cross sectional area. The time spent by a riming hydrometeor in the layer -3C to_8C could be very long, and that the collision rate is controlled by Vt regardless of the w, has profound implications for secondary ice production by Hallett-Mossop.

This concept of long residence time explains many of the observations in this cloud, eg. all large hydrometeors at the -11C level appear to be frozen drops. Also, the observation that parcels in slightly more aged weaker updraft regions of the cloud contain evidence of a secondary ice production mechanism. Portions of the cloud system at -11C have very high concentrations (~100/l) of columnar crystals, consistent with an Hallet-Mossop secondary ice production mechanism.

Summarizing the ice development in this cloud between -2C and -11C, the first ice development is frozen drops. These drops rime heavily in the active updrafts in the -3C to -8C layer. These smaller crystals grow rapidly to columns and populate slightly aged regions of the cloud at -11C. Ice needles were not observed, but this could be that the instrument was not capable, or that the cloud was not observed at-5C.

N. BIBLIOGRAPHY

Cotton and Anthes, 1989: Storm and Cloud Dynamics, Academic Press, San Diego
Hallett and Mossop, 1974: Nature **249**, 26-28
Koenig, 1963: 1963: J Atmos Sci **20**, 29
Mossop, 1976: Q J Roy Met Soc, **102**, 45-47
Rangno and Hobbs, 1991: Q J Roy Met Soc, **117**, 497, 207-242
Willis, 1984: J Atmos Sci, **41**:9 1648

Acknowledgements

We wish to acknowledge Dr. Ramesh Kakar, the NASA Weather Focus Area Lead and

Program Manager for Atmospheric Dynamics at NASA Headquarters, who was the NAMMA mission director

I wish to acknowledge Dr. Andrew J Heymsfield, NCAR who was responsible for the NAMMA microphysics project and who is a co-author on a collaborative publication in progress

We wish to acknowledge Dr. Glenn Diskin who was responsible for the NASA Langley Diode Laser Hygrometer data.

We wish to acknowledge Dr. T Paul Bui who was responsible for the NASA AMES MMS high resolution vertical wind data

We wish to acknowledge Dr. Paul Lawson who was responsible for the SPEC 2DS data

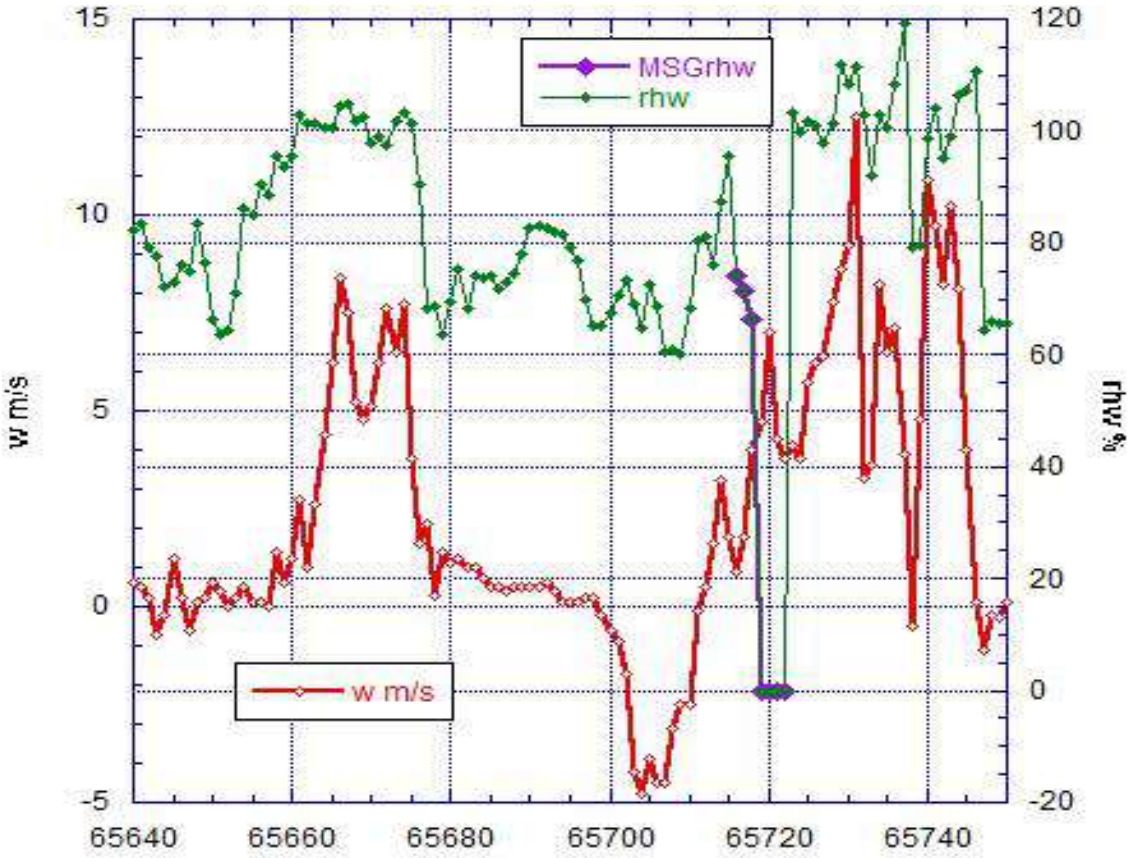

Figure 3a Vertical winds for cloud transect 2-3 at T=-2C and the relative humidity w/r to waterUpshear is to the right and downshear to the left. There are missing rhw data near 65720s.

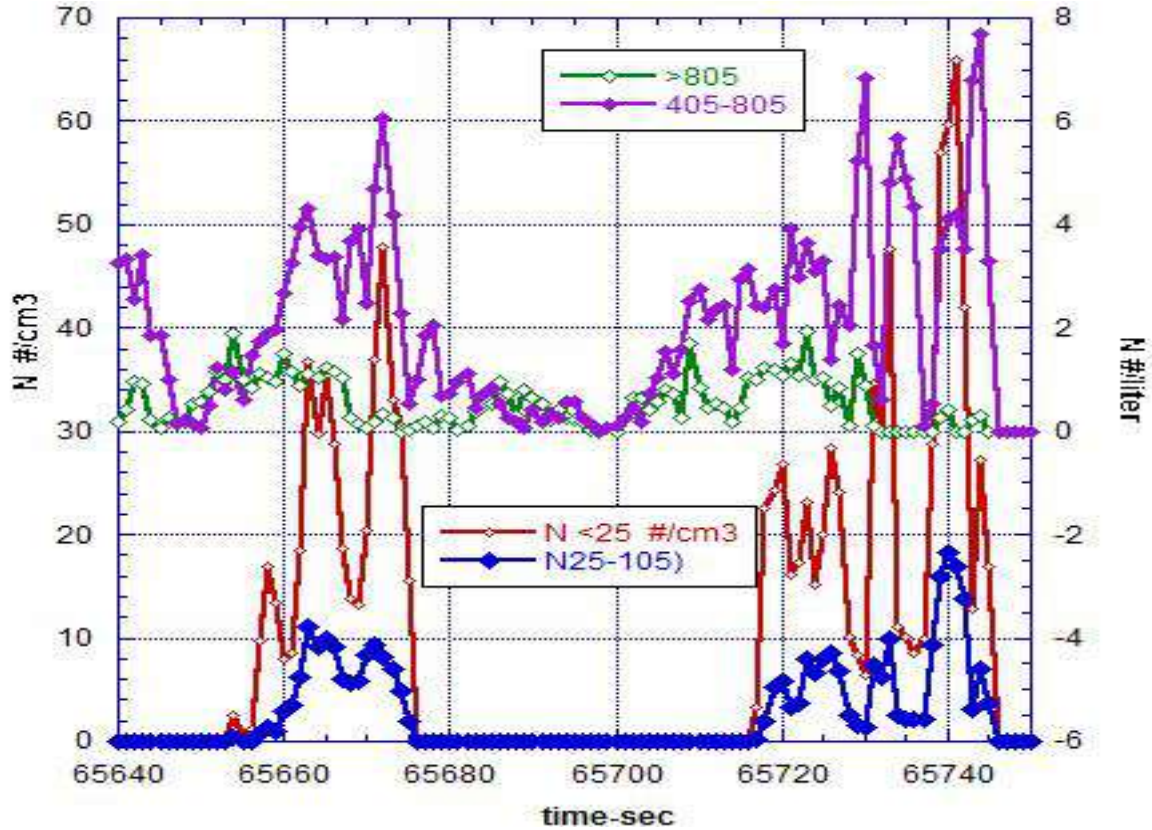

Figure 3b Concentrations of cloud droplets D<25 um, and D 25-105 um; and rain drops D> 805 um and D 405-805 um

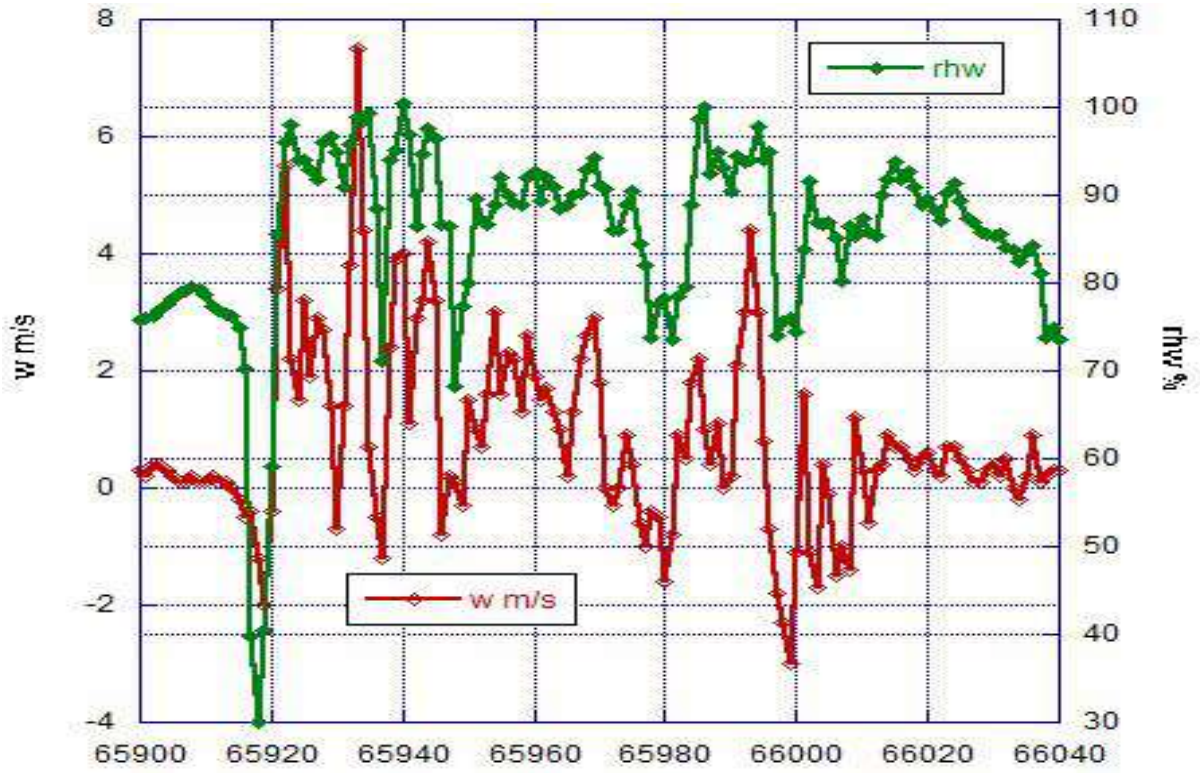

Figure 4a Cloud 4 transect at T=-11C, vertical wind and relative humidity w/r to water

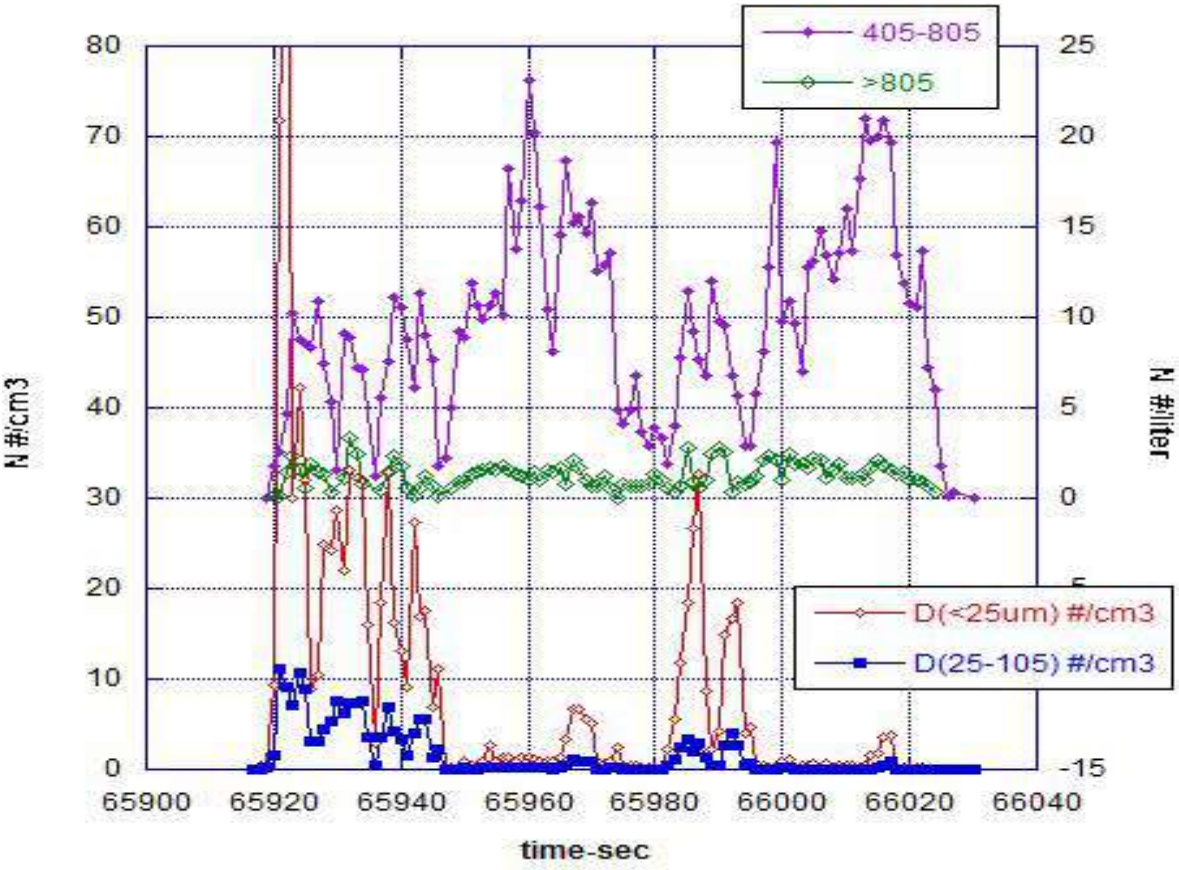

Figure 4b Concentrations of cloud droplets D<25 um, and D 25-105 um; and large hydrometeors D> 805 um and D 405-805 um.

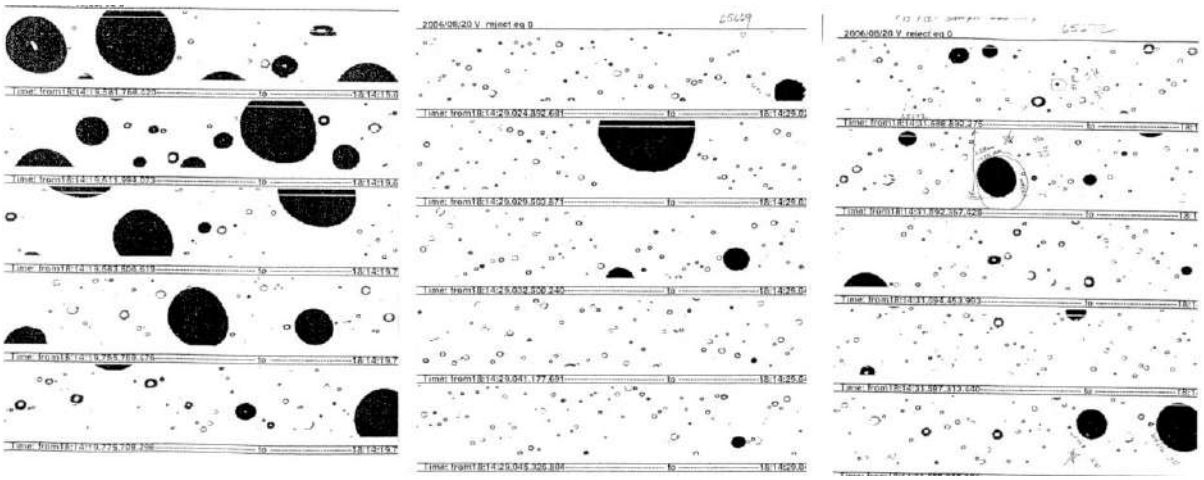

Figure 3c Cloud 2-3 transect 2DS image samples at 65659s, 65669s, 65672s, illustrating images in all rain at T=-2C. Size is indicated by horizontal bars which are dimension of 1.28 mm apart.

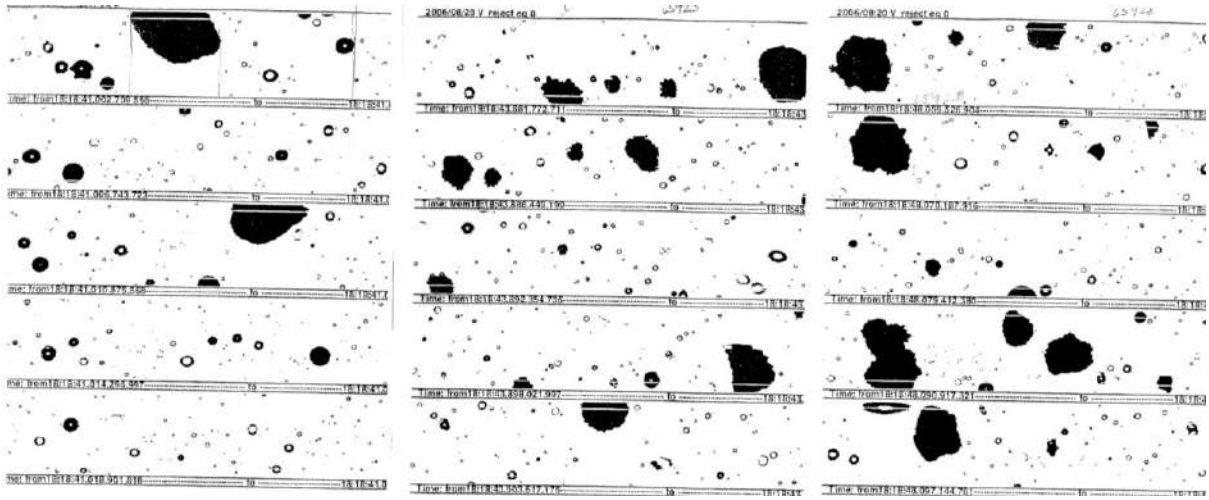

Figure 4c Cloud 4 transect 2DS image samples at 65921s, 65923s, 65928s, illustrating images in upshear active updrafts at T=-11C. Size is indicated by horizontal bars which are dimension of 1.28 mm apart.

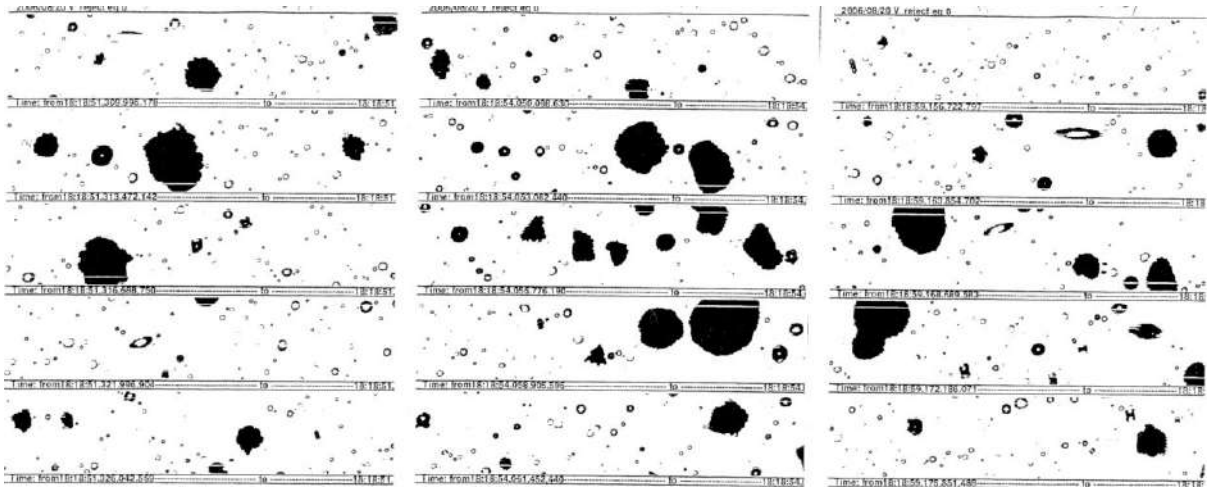

Figure 4d Cloud 4 transect 2DS image samples at 65931s, 65934s, 65939s, further illustrating images in upshear active updrafts at T=-11C. Size is indicated by horizontal bars which are dimension of 1.28 mm apart.

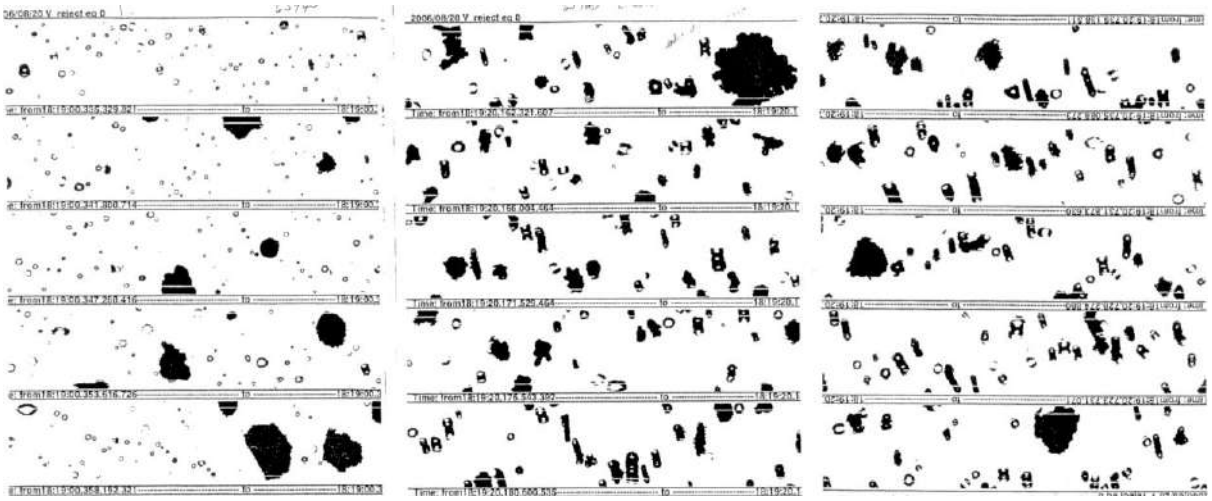

Figure 4e Cloud 4 transect 2DS image samples at 65940s, illustrating images in active updrafts at T=-11C and transition to columns in images at 65960s, 65961s. Size is indicated by horizontal bars which are dimension of 1.28 mm apart.

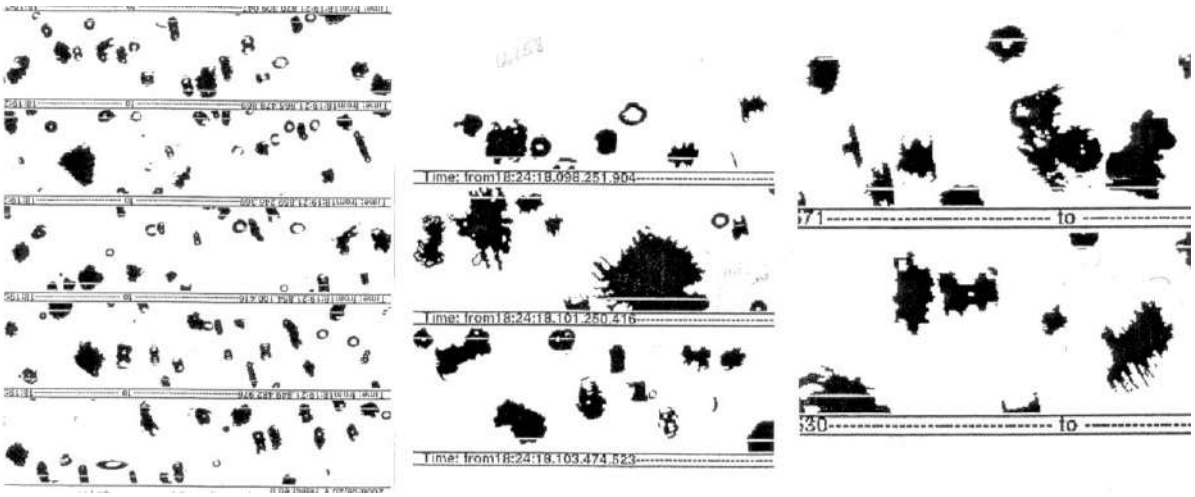

Figure 4f Cloud 4 transect 2DS image sample at 65961s, further illustrating images in column region, and images from cloud transect 5 at T=-22C illustrating dendritic growth spicules on graupel in images at 66258s. Size is indicated by horizontal bars which are dimension of 1.28 mm apart.

ON THE THUNDERSTORMS MORPHOLOGY OBSERVED IN SOUTH AMERICA

Evandro M. Anselmo[a], Carlos A. Morales[a]

[a] *Institute of Astronomy, Geophysics and Atmospheric Science of USP, São Paulo-SP, 05508-090, Brazil*

1. INTRODUCTION

Since the launch of TRMM satellite, it has been possible to evaluate the 3D structure of precipitation in the tropics by the means of the Precipitation Radar (PR) and the liquid and ice content in the column by the TRMM Microwave Imager (TMI) (Kummerow et al., 1998). With the use of the Lightning Imaging Sensor (LIS) on board TRMM (Christian et al., 1992) it has been possible to identify and quantify the thunderstorms in the tropics. For example, Cecil et al. (2005) found approximately 6 million storms that were classified into 5 categories according to their lightning severity. 97.6% of them presented weak radar reflectivity echoes, weak microwave brightness temperature signatures and low lightning flashes ($<$ 1 flashes.min-1). Over the continent, 10-15% of the storm presented lightning, while over the ocean only 1% (Toracinta and Zipser, 2001; Zipser et al., 2006). Petersen and Rutledge (2001) inspected the 3D precipitation structure associated with thunderstorms observed in the continent and ocean over 22 regions, and found that maritime system do not vary considerably, but the more continental storms were associated with some variability above the freezing level.

This work is a preliminary study that aims to analyze the 3D vertical precipitation structure of the thunderstorms observed by the TRMM-PR and LIS over the South America. In this article, the 3D structure is evaluated in respect to the number of events detect in each lightning flash to seek some understanding that might explain why there flashes with more or less strokes.

2. METHODOLOGY

To depict the thunderstorms in South America, this study combines TRMM PR and LIS measurements, such that for every event detected by LIS, coincident 2A25 radar reflectivity profiles were extracted during the period of 1998 and 2010. The dataset were bounded by 10N-40S and 91-30W, covering mainly South America and part of Central America.

As LIS detects the momentary brightness changes in the clouds associated with the emission that results from the dissociation, excitation and recombination of atmospheric constituents, in response to occurrence of lightning (Christian et al., 1992), several lightning parameters are used to characterize a lightning stroke: Events - single pixels that exceed the LIS threshold; Groups - clusters of contiguous events within a frame; Flashes - clusters of groups within 330 ms and 5 km; Areas - clusters of flashes. For this study, we use LIS lightning flashes that are used to define the lightning position and the number of events within the flash to evaluate the severity of the thunderstorm.

Based on the lightning positions (latitude and longitude), we extracted the nearest ($<$5km) 2A25 radar reflectivity profile, the respective rain classification (Convective, Stratiform or others), and the number of groups and events associated with each lightning flash. Based on this approach it was possible to built a database of 1.375,478 radar reflectivity profiles that were associated with lightning flashes. According to the 2A25 rain type classification, 71% of those profiles were convective and 17% stratiform, while the remaining 12% were classified as “others”.

Email address: evandro@model.iag.usp.br (Evandro M. Anselmo)

Later, the vertical profiles were grouped in event groups of 1-2, 3-5, 6-9, 10-17 and greater then 17. Each event class had a relative frequency of approximately 20%. Thus, with correspondent event profiles we created 2D histograms, known as CFADs , (Yuter and Houze Jr., 1995). The histograms were binned in 1 dBZ intervals for radar reflectivity factor and 0.25 km in altitude. Finally, the histograms were normalized by the altitude and cumulative distributions for each CFAD were evaluated as well.

3. RESULTS

The first step to explore the morphology of South American thunderstorms will be related to the number of strokes on a single flash as determined by LIS algorithm. In principal, more strokes per flash would imply in higher charge densities in the column, i.e., more charged particles. In theory the return stroke lowers most of the charges from the first charge center and if the neutralization does not happen, sub sequent (dart leader) strokes would lower the remaining charges from the first center or at high levels. Therefore, more strokes per flash could be related to some thunderstorm severity, simply because charge density is related to hydrometeor type and concentration. As consequence, the profiles were sorted according to the number of events and the main precipitation characteristics are summarized on the panels of Figure 1 and Table 1.

As the number of strokes increases, the profiles become more convective, i.e., starting at 51% with 1-2 strokes up to 80% for more than 17 events, Table 1. It is also important to note that there is an increase of more than 20% just from 1-2 class to 3-5 strokes. Convective profiles are usually associated with more ice aloft, graupel, ice particles and super-cooled water droplets in the mixed zone (0 to -20°C) and higher rain volumes. Therefore, this convective nature would imply that higher stroke rate might be related to the strength of the thunderstorm. In this sense, the profiles should reveal some of these features.

To better explore the 2D histograms (CFADs), cumulative distributions were computed for each altitude and regions with same cumulative frequencies were plotted. By doing this exercise it is easier to determine the position of the 50% probability (median) or the extremes. Figure 1 shows these normalized radar reflectivity CFADS for all the 5 stroke classes as a function of height. The black line in each plot corresponds to the median value.

By inspecting the regions that represent the cumulative frequencies of 30 to 70% (40% of the sample), orange contours, Figure 1, it is possible to note a shift on the vertical profiles as the number of strokes increase. For instance at lower levels (below 4km) and at the mixed/middle region (5-7km) we find an enhancement of both the rain volume and ice/graupel/super cooled water droplets particles. At higher levels, above 7 km, the distribution gets narrow and little bit more intense. Table 1 presents a summary of the radar reflectivity intervals for each of the 5 event classes.

Table 1 – Radar reflectivity interval for a cumulative frequency of 30-70% for different stroke classes and heights. The last two columns show the convective and stratiform fraction for each stroke class.

stroke cls.	7-9Km [dBZ]	5-7Km [dBZ]	2-3Km [dBZ]	Cv [%]	St [%]
1-2	22-32	24-35	30-40	51	19
3-5	23-33	27-37	33-41	73	16
6-9	24-32	27-37	33-42	76	15
10-17	24-32	27-37	33-42	78	15
$>$17	24-31	27-36	34-42	80	15

For the profiles that had more than 3 strokes, it is possible to observe that the regions of 30-70% cumulative distribution are getting narrow at higher altitude and to a less extent at surface. As the number of strokes increase, the distributions are tightening towards the median value with height. This narrowing might indicate the presence of one to few ice species in contrast to broaden distributions. As a consequence, the electrification process might become more efficiency if those particles collide with the graupel in the layer below.

Despite that, it is also observed that at 2-3 km height, the radar reflectivity increases as the number of strokes raises and the contrary is observed at 7-9 km height. This pro-

file bounce could be attributed to the efficient hydrometeor growth. The ice particles aloft collide with the graupel and super cooled droplets, so both accretion and aggregation can take place simultaneously. In fact, we do see an increase in radar reflectivity that might be related to the appearance of large graupel and ice splitting between 5 and 7 km height. As the particles melt and become water we do observe a precipitation enhancement near the 0°C isotherm and between 2 and 3 km height.

Finally, Figure 2 shows the lightning distribution and density of the flashes with the different strokes classes. The southern part of Brazil and northern Argentina presents the highest frequency of flashes with one and two strokes, Figure 2a coincide with the regions that had the most intense thunderstorms (Cecil et al., 2005). This region is affected by Mesoscale Convective Complex (MCC) and frontal systems that besides having a lot of lightning discharges are known to have more than 50% of stratiform precipitation.

By increasing the number of strokes, Figure 2b-c-d, more thunderstorms are presented on the central and northern part of Brazil, but to higher stroke density ($>$ 18 strokes/flash), mainly Argentina and Colombia show signification distributions. Central and northern areas of Brazil have the occurrence of both Mesoscale Convective Systems (MCS) and localized convection and depending on the season some of these systems are more frequent and are more continental and convective, which is consistent with the results on Table 1.

4. CONCLUSIONS

The vertical profiles associated with flashes that had 1-2 strokes presented the most variabilibity in comparison with the more intense lightning. This variability was more evident at 5 km height, region where we would expect the interaction between ice particles, graupel and super-cooled water droplets and consequently the charge electrification region. Despite the fact that the vertical radar reflectivity profiles presented great variability for the weak flashes (1-2 strokes), these profiles showed a strong signature of less dense ice particle aloft and were concentrated in southern Brazil and northern Argentina. This region is known to have MCCs and frontal systems and could explain the low values of convective profiles found, since it prevails the stratiform profiles.

As the number of strokes increase, the radar reflectivity profiles enhanced in magnitude, specially between 2-3 km and to less extent at high altitudes. And most importantly, the radar reflectivity distribution got narrow with height which implies in a reduction of the number of ice species. Therefore, enhancing the collision and charge transferring that can explain the higher concentration of strokes.

5. ACKNOWLEDGEMENTS

This work is funded by CNPq grant number 140842/2011-0 and partly funded by CAPES-PROEX.

References

Cecil, D., Goodman, S., Boccippio, D., Zipser, E., Nesbitt, S., 2005. Three years of trmm precipitation features. part i: Radar, radiometric, and lightning characteristics. Mon. Wea. Rev. 133, 543–566.

Christian, H. J., Richard, J. B., J., G. S., 1992. Lightning Imaging Sensor (LIS) for the Earth Observing System. Marshall Space Flight Center, Alabama, nASA Technical Memorandum TM-4350.

Kummerow, C., Barnes, W., Kozu, T., Shiue, J., Simpson, J., 1998. The tropical rainfall measuring mission (trmm) sensor package. J. Atmos. Oceanic Technol. 15, 809–817.

Petersen, W., Rutledge, S., 2001. Regional variability in tropical convection: Observations from trmm. Journal of climate 14 (17), 3566–3586.

Toracinta, E. R., Zipser, E. J., 2001. Lightning and ssm/i-ice-scattering mesoscale convective systems in the global tropics. J. Appl. Meteor. 40, 983–1002.

Yuter, S. E., Houze Jr., R. A., 1995. Three-dimensional kinematic and microphysical evolution of florida cumulonimbus. part ii: Frequency distribution of vertical velocity, reflectivity, and differential reflectivity. J. Appl. Meteor. 123, 1941–1963.

Zipser, E., Cecil, D., Liu, C., Nesbitt, S., Yorty, D., 2006. Where are the most intense thunderstorms on earth? Bull. Amer. Meteor. Soc. 87, 1057–1071.

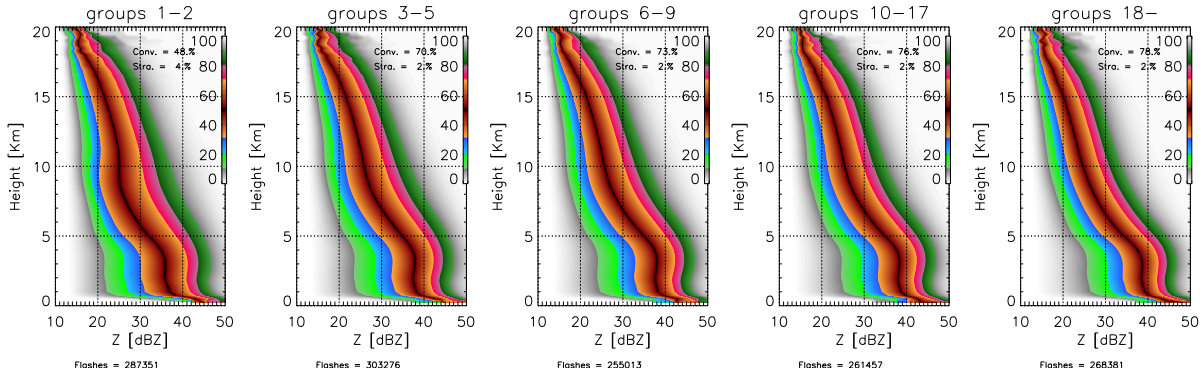

Figure 1: Cumulative distributions of the normalized radar reflectivity CFADs as a function of height for 1-2, 3-5, 6-9, 10-17 and $>$ 17 events per flash. The black line indicates the median value (50%).

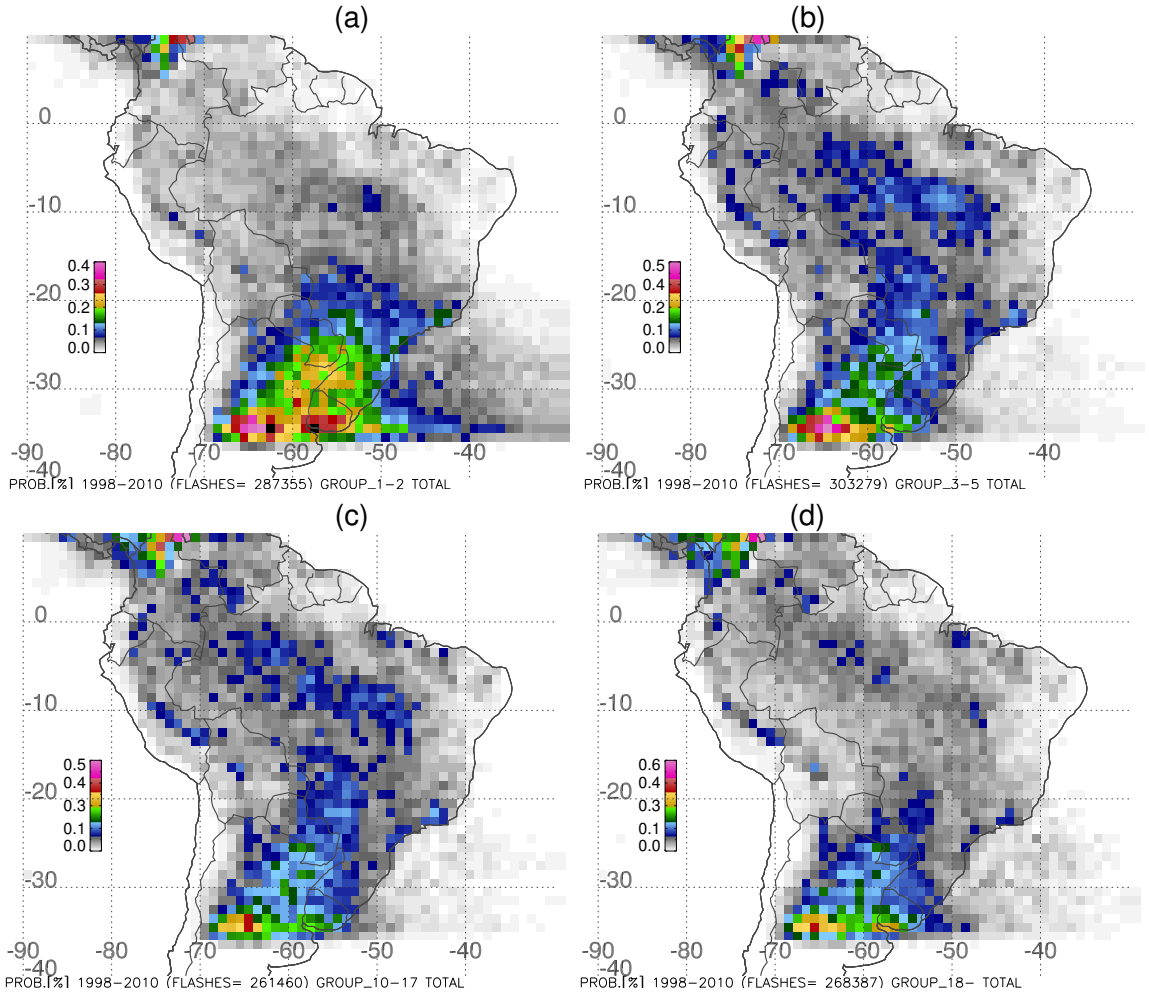

Figure 2: Spatial distribution of the flashes that that 1-2, 3-5, 10-17 and more than 18 strokes. The colors represent the relative frequency of occurrence.

ESTIMATING THE MAGNITUDE OF ELECTRIC CHARGE INSIDE ISOLATED CONVECTIVE CLOUDS.

Moacir Lacerda[2], Carlos Morales[1],Evandro Anselmo[1],Joao Neves[1],Rachel Albrecth[3], Marco Ferro[4],

Moacir Lacerda <moacirlacerda@gmail.com>

[1]University of Sao Paulo, Atmospheric Science, Rua do Matao, 1226, Sao Paulo, Sao Paulo, 05508-090, Brazil ; [2]Federal University of Mato Grosso do Sul, Physics, Centro de Ciências Exatas e Tecnologia – CCET-PGTA, Campo Grande, Mato Grosso do Sul, 79070-900, Brazil ; [3]Instituto Nacional de Pesquisas Espaciais (INPE), Divisão de Satélites e Sistemas Ambientais (DSA/CPTEC), Rodovia Dutra, km40, Cachoeira Paulista, Sao Paulo, 12630-000, Brazil [4]IAE (Instituto de Aeronáutica e Espaço) – Praça Mal. Eduardo Gomes, 50 Vila das Acácias, 12.228-904 – São José dos Campos –Sp-Brazil

1. INTRODUCTION

The use of coulomb's law to study cloud structure is not new. It was employed by Jacobson and Krider, (1976) and Livingston and Krider (1978) to study the electric cloud structure of thunderstorm by using electric field network in Florida.

During November and December a network of electric field mill and data of a polarimetric radar (X-band) were used to infer the cloud structure of thunderstorms. We tried to find a isolated small thunderstorm to simplify the problem of using coulomb's law (Stolzenbourg et al 1998, Stolzenburg, and Marshall, 1994).

The approach used was to solve the inverse problem (Tarantola, 1987) of coulomb's law. This is not a trivial problem and requires the knowledge of the region were the electric charges could be, inside the thundercloud. This optimizes the computational effort because it localize the seed for start the solution of z coordinate too close of the true region. Radar images gives that seed.

2. METHODOLOGY

It was installed a network of electric field mill close to a polarimetric radar in São José dos Campos. Four sensors with distance varying between 1 to 2 km were installed (See Table 1). In figure 1 we see the localization of this network and the Radar, represented as a white circle with black concentric circunferences centered in a position marked as XPOL. In Figure 1 (a), we see the representation of the network and radar image. The scale of colors represents the reflectivity of the radar. In Figure 1 (b) we represent the detailed image of radar with concentric circles with radius multiple of 10 km.

The thunderstorm occurred at 19:30 GMT and was monitored by several equipments, like LINET, STARNET, LMA, BRASILDAT.

Table 1. Localization of sensor

Site - name	latitude	longitude
Meteorology (INPE) - met	-23.211283	-45.860278
Batalhão e Infantaria da Aeronáutica (BINFA)- bin	-23.209431	-45.880862
Aeroport - aer	-23.224739	-45.862521
Pequenópolis School - peq	-23.201461	-45.873773

A sequence of images like that presented at figure 1 and b were mounted at every six minutes and were used to estimate the coordinate x and y of the electrically active region of cloud (reflectivity greater than 40 dBZ).

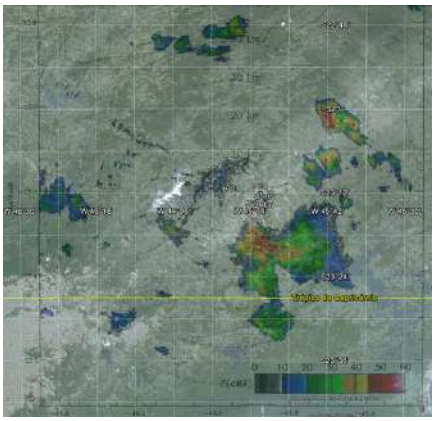

(a)

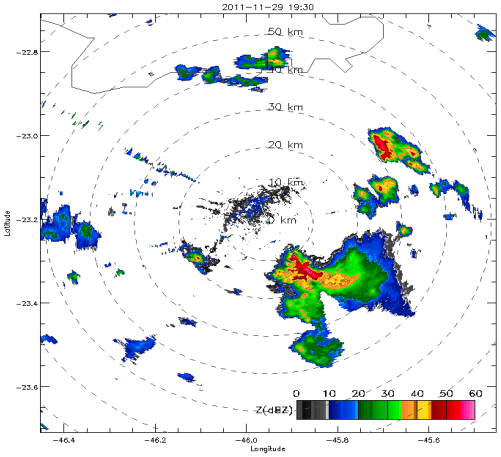

(b)

Figure 1. a) representation of network and radar position in a georeferenced map; b) the radar reflecitivy associated to the thunderstorm of 29 nov 2011 at 19:30 GMT is shown right down.

The coordinate z of the charge centers were chosen between 2000 and 10000, and calculations of electric charge q at every center were performed by using

$$\mathbf{q} = (\mathbf{R}^T.\mathbf{R})^{-1}.\mathbf{R}^T.\mathbf{E} \qquad \text{eq (1)}$$

where

$$Rij := 2k \cdot \frac{(zj - zi)}{\left[(xj - xi)^2 + (yj - yi)^2 + (zj - zi)^2\right]^{\frac{3}{2}}}$$

eq (2)

R is a *i* x *j* matrix and *i* refers to the position of sensor on ground and *j* to the charge center and $k = (1/4\pi\varepsilon_o)$ with ε_o being permissivity of vacuum; **q** is a *i* x 1 matrix and **E** is a *j* x 1 matrix of measurements.

Then we used the calculated electric structure to recalculate electric field on ground, Ec_i, by using

$$Ec_i = \Sigma_{ij} (R_{ij} \square q_j) \qquad \text{eq.(3)}$$

and compare the measured electric field at every field mill with that calculated one, by using

$$\eta = Ec_i/E_j \qquad \text{eq (4)}$$

maintaining $0 \leq \eta \leq 0.1$.

We arbitrarily adopt the dipolar structure. The results are presented in next section.

3. RESULTS AND DISCUSSION

Figures 2, 3 and 4 shows the fit of the curve for 5 points.

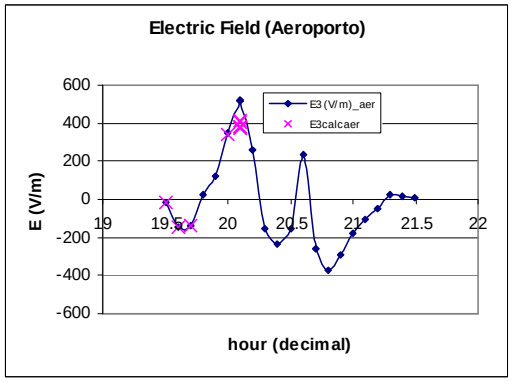

Figure 2. Measured E_i (line) versus Calculated Ec_i (x) at Aeroporto position.

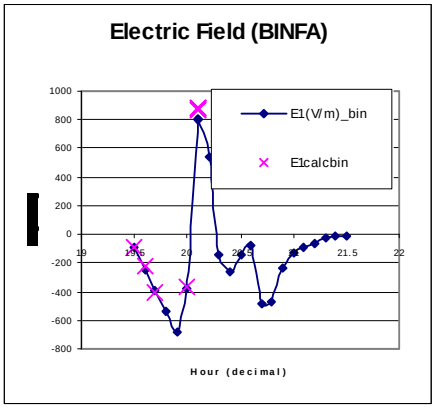

Figure 3 . Measured E_i (line) versus Calculated Ec_i (x) at BINFA position.

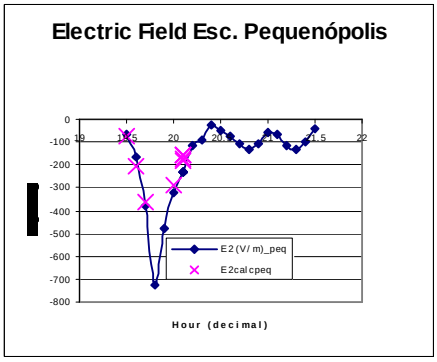

Figure 4. Measured E_i (line) versus Calculated Ec_i (x) at Escola Pequenópolis position.

The two points that were not fitted between those points of figures 2, 3 and 4 correspond to situations where it was not possible to localize precisely charge center's in radar image.It would be very difficult to find a solution that could be physically reasonable with only few measurements. The last point was poorly fitted because of the same difficulty, and several essay were proceeded. The cloud was already too complicated to get a reasonable solution.

4. CONCLUSIONS

We used data of dense electric field mill network (distance between sensors ~ 1.5 km) and data of polarimetric radar to investigate the electrical structure inside a thunderstorm cloud occured in 29 november 2011. The main conclusions are:

1. The inverse problem of Coulomb's law is a reasonable tool to find the structure of charges inside the cloud (position and magnitude of electric charges).
2. Temporal data of three sensors (BINFA, Esc. Pequenópolis and Aeroporto) were reasonably fitted by the recalculated electric field.
3. Results show a cloud with inverted dipole with electric charge varying between -13 C and -78 C (heigth from 4800 to 7900 m), and 15 C up to 54 C (height from 2800 to 5000) for negative and positive centers respectively.

5. ACKNOWLEGMENT. To CNPq for financial support Proj. 151997/2010-1. To FAPESP projeto CHUVA , 2009/15235-8. To Marco Antonio Ferro (IAE), Carina Schumann (INPE) and Coronel da Aeronáutica Peres, Sgt. Aleixo, Sgt. Faustino (BINFA) and all personnel of CTA and INPE that helped us during installation and operation of network.

6. REFERENCES

-Jacobson, E. A., Krider, E. P., Electrostatic Field Changes Produced by Florida Lightning, Journal of Geophysics Research, p. 103, jan 1976.

- Livingston, M. J., Krider, E. P., Electric Fields Produced by Florida Thunderstorms, Journal of Geophysical Research, Vol 83, n. C1, jan 1978.

- Stolzenburg, M., W. D. Rust, and T. C. Marshall (1998), Electrical structure in thunderstorm convective regions 2. Isolated storms, J. Geophys. Res., 103 (D12), 14,079–14,096, doi: 10.1029 /97JD03547.

- Stolzenburg, M., Marshall, T. C., Testing models of thunderstorm charge distributions with Coulomb, s law, Journal of Geophysical Research,V. 99, N. D12, p.p. 25921-25932, Dec, 1994.

- Tarantola, A., Inverse Problem Theory, methods for data fitting and model parameter estimation, Elsevier, 1987

ON SIMULATED TRADE-WIND CUMULUS COLD POOL

Zhujun Li[1], Paquita Zuidema[1], and Ping Zhu[2]
[1] Rosenstiel School of Marine and Atmospheric Science, University of Miami, Miami, Florida, USA
[2]Department of Earth and Environment, Florida, International University, Miami, Florida, USA

1. INTRODUCTION

The trade wind region is of great research interest for its significant share in the planetary radiation budget (Medeiros et al. 2008), and its role in fueling the atmosphere overturning circulation (Tiedtke et al. 1988). The trade wind cumulus convection is important for moistening and deepening the boundary layer (Stevens 2005). Various literature has contributed to representing the development of non-precipitating trade wind cumulus (Betts 1975, Albrecht et al. 1979), however, the precipitating trade wind cumulus is less studied due to the difficulties in representing the precipitation process.

Previous studies have assessed the precipitation efficiency of the precipitating trade wind cumulus from observations (Short and Nakamaru 2000, Snodgrass et al. 2009, Nuijens et al. 2009), and tested the sensitivity of the precipitation process to the environmental forcing and aerosol conditions (Stevens and Seifert 2008, Xue et al. 2008, Nuijens and Stevens 2012). Zuidema et al. (2012) documented cold pools–the region of drier and colder (negative buoyant) air relative to the environment–that associated with convections reaching 4-5 km and precipitating at rates exceeding 2 mm hr^{-1}, during Rain in Cumulus over the Ocean (RICO) experiment. Their analysis highlighted multiple impacts on the boundary layer that related to the evolution of cold pool, such as the presence of multiple inversions within the cloud-free zones, and the recovery of the surface air temperature with little accompanying change in the surface moisture. Inspired by the observational analysis, we seek to address these leading scientific questions with a modeling study: How much do the surface fluxes account for the increase in cold pool stable layer mean buoyancy? How much impact does the cold pool generated mechanical lifting have on the convective triggering, at different stage of the convection? We answer these questions using a nested WRF simulation, focusing on selected 4 cases for cold pool recovery process study, and another 1 case for cold pool invigorating convection study.

2. DESCRIPTION OF WRF SIMULATION

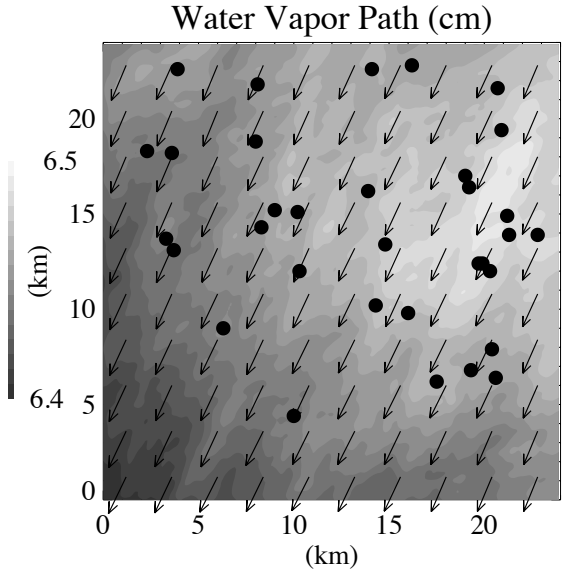

Figure 1 The location of 33 simulated cold pool at their initial stage as marked by closed black circle on top of the mean water vapor path of the day (shaded contours). Arrows indicate mean wind direction at 10 m.

We use the Weather Research and Forecasting model (WRF) to simulate 30 hours period during RICO, from 0000 UTC 19 January 2005 to 0600 UTC 20 January 2005 (allow first six hours for model spin-up). This day was selected because it has been previously analyzed (Abel and Shipway, 2007; Snodgrass et al. 2009). The National Centers for Environmental Prediction (NECP) reanalyses of 1 degree resolution available in every 6-hour is used to supply the initial and lateral boundary conditions for this simulation. Thompson scheme (Thompson et al. 2008) is used for cloud microphysics, and the sea surface temperature (SST) is prescribed from the NCEP Global Tropospheric Analyses and updated every 6 hours. One parent domain and four two-way nested domain that centered at 61.7◦W 18◦N were configured with nesting ratio of 1:3. The nested domain simulation allows the model to

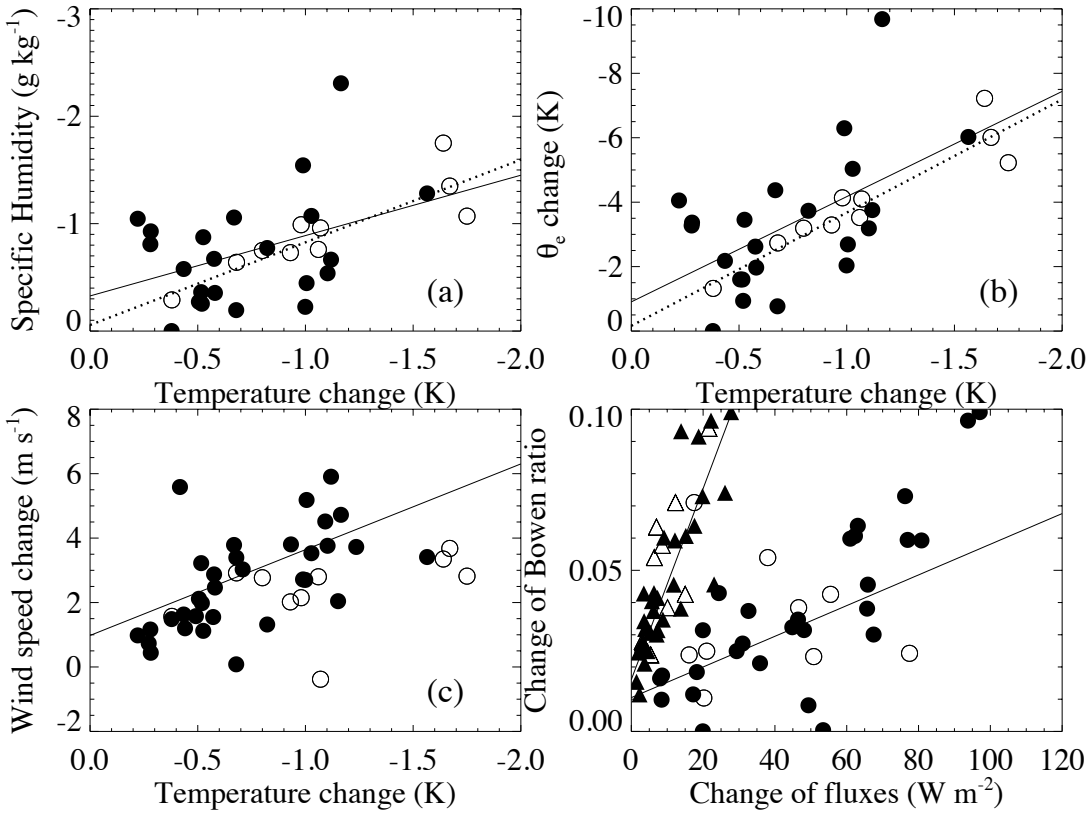

Figure 2 For 33 cold pool cases from WRF simulation (closed circles and triangles), and 37 cases from RICO observation (open circles and triangles): maximum change of surface water vapor mixing ratio, θe, and surface wind speed plotted as function of the maximum change of temperature at 2 m (for simulation); the change of surface sensible, latent heat fluxes plotted against the change of Bowen ratio. Solid (dotted) lines indicate the linear square fit of data from the simulation (observation).

explicitly resolve turbulent scale processes in the innermost domain, while also reacting to realistic large scale forcing imposed on the parent domain and transported inwardly. The results from the innermost domain are analyzed in this study. The innermost domain has 241×241 mesh grid, horizontal resolution of 100 m, and vertical resolution varies from 6.5 to 200 m below 4 km.

3. VALIDATE THE SIMULATION WITH OBSERVED COLD POOL PROPERTIES

Under the influence of a dissipated cold front, the boundary layer condition was presumably more pronounced on the day of 19 January 2005, nevertheless, the observation has reported precipitating convections all below the melting level (Zuidema et al. 2012). Therefore, the cold pools of this day are still representative of the cold pools generated by warm rain process during the observational period from 9 January to 24 January. The domain has low level northeasterly mean wind on this day, and in total 33 shallow convection cold pools, which are identified by their surface temperature depression (Figure 3). Despite the subtle change in gradient of mean water vapor path, the cold pools are favorably located at the side of higher mean water vapor path. To acquire analogous result as the ship measurement documented in Zuidema et al. (2012), we select one grid point on each cold pool propagation path, and calculate the maximum change in surface property on this grid point while the cold pools passes over, using the surface property of the time right before the onset of surface rain as reference. The surface changes in temperature, specific humidity, wind speed, sensible and latent heat fluxes, and Bowen ratio are similar for the simulated and observed (from 16 days) cold pools (Figure 2). The ratio between the change in surface specific humidity/θ_e and temperature is slightly lower in the simulation than observation, with the simulated results being more scattered. This may be due to the cold front disturbances within the simulated short period of 24 hours. Also, similar to observation, the simulated change of Bowen ratio is more sensitive to the change of sensible heat flux than latent heat flux.

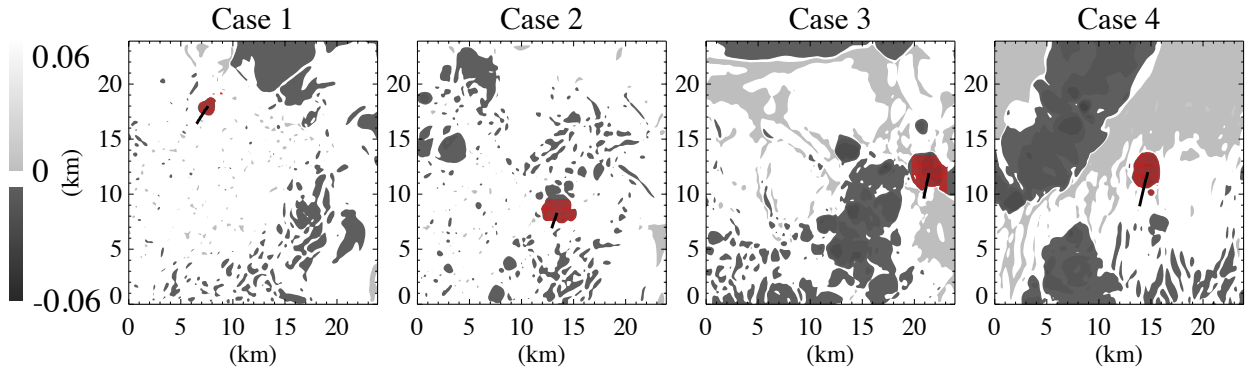

Figure 3 The surface negative (dark shaded) and positive (light shaded) buoyancy field of 4 cases at the beginning of the interested period. The cold pool surface region is stippled in red. Solid line indicate the path that the center of the cold pool propagates during the period of interest.

4. COLD POOL BOUNDARY LAYER RECOVERY

The cold pool is "a region or 'pool' of relatively cold air surrounded by warmer air". In order to trace the change in mean buoyancy of the cold pool stable layer, we identify the cold pool size and average depth by the interface of neutral buoyancy. Where the buoyancy is calculated from the temperature and water vapor mixing ratio relative to the mean, plus liquid loading, following Weisman and Rotunno (2004). Within the identified cold pool volume, the buoyancy is negative.

Case Number	1	2	3	4
Average Diameter (km)	2.2	2.9	4.0	3.9
Average Depth (m)	141	219	224	147
Average LHF (W m^{-2})	81	78	112	112
Average SHF (W m^{-2})	5.8	6.5	10.3	10.7

Table 1 Characteristics of the 4 cases averaged over the period of interest.

In this section, we study the period with no precipitation upon the cold pool, so to focus on the recovery process of the cold pool stable layer, and exclude the intensification of cold pool due to precipitation. We examine the evolution of 4 such cold pool cases (Figure 3) from the time when the mean cold pool buoyancy begins to increase, to the time the cold pool surface area reaches the maximum size. The 4 cases have average diameter from 2.2 to 4.0 km that is significantly smaller than observed cold pools, implying faster recovery than the observation.

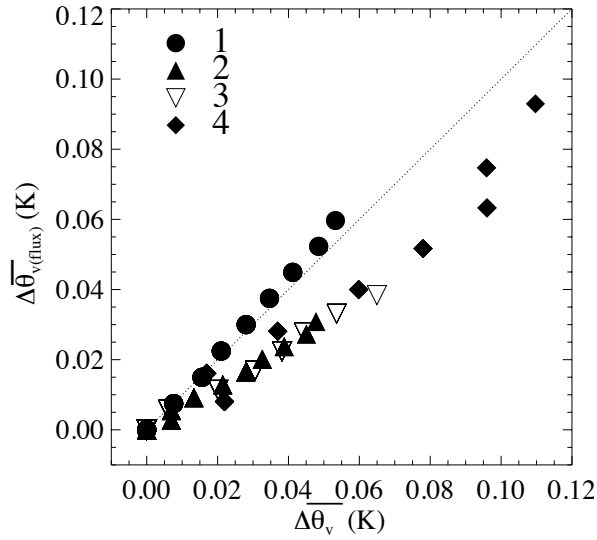

Figure 4 $\Delta\overline{\theta}_v$ and $\Delta\overline{\theta}_{v(flux)}$ of entire cold pool volume at different time (1 minute interval). Different symbols represent for 4 cases.

The surface fluxes and turbulent mixing with the environment are considered the two main processes of cold pool boundary layer recovery (Ross et al. 2004). To distinguish between these two mechanisms, we calculate the accumulated increase of mean cold pool buoyancy due to the surface fluxes at each time step ($\Delta\overline{\theta}_{v(flux)}$), and compare the results with model simulated values at corresponding times ($\Delta\overline{\theta}_v$). Both $\Delta\overline{\theta}_{v(flux)}$ and $\Delta\overline{\theta}_v$ equal to 0 in the beginning, and increase with time (Figure 4). For case 2, 3, and 4 that have $\Delta\overline{\theta}_{v(flux)}$ less than $\Delta\overline{\theta}_v$, the difference between the two represents the least mean buoyancy change caused by the mixing with environment. It can be estimated that the mixing process accounts for about 30% to 40% of the total cold pool recovery for

these 3 cases. While in case 1, the surface fluxes are sufficient to account for the total change in mean buoyancy.

Cold pool that has greater exposure relative to its volume recovers faster. For example, case 4 is similar to case 1 in average depth, but much larger in average size, resulting in faster increase of $\Delta\overline{\theta}_v$. For case 3 and 4 that have similar averaged size and surface fluxes, the recovery of case 4 is still faster, because case 4 is much shallower.

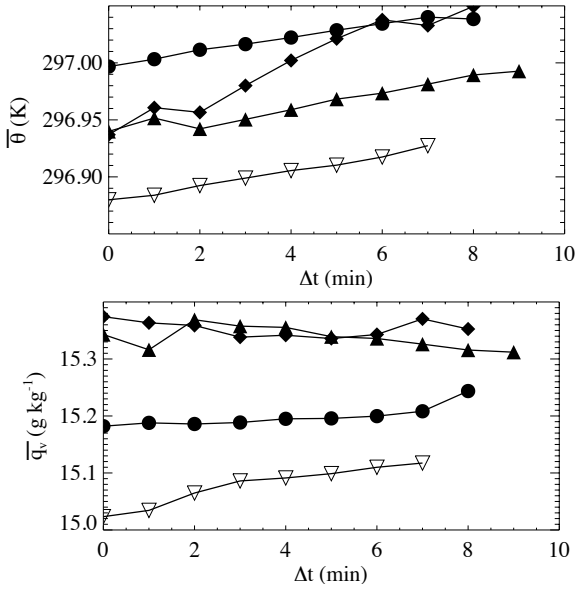

Figure 5 The mean temperature (upper panel) and water vapor mixing ratio (bottom panel) of the 4 cold pool cases at each time step after the increase of mean cold pool buoyancy. Symbols represent different cases as in Figure 4.

The mean temperature and humidity of the cold pool change in different ways during the recovery process. While all cases have cold pool mean temperature increases continuously with time, the mean humidity change is inconsistent among cases (Figure 5). This is similar to the observations during RICO (Zuidema et al. 2012). Since the surface fluxes enhance both the temperature and humidity, the decrease in humidity must due to the contribution from the mixing with drier environmental air. Therefore, in general, the mixing process enhances mean buoyancy of the cold pool mainly by enhancing the mean cold pool temperature.

5. INVIGORATION OF CONVECTIONS AT COLD POOL FRONT

It is often observed in the trade wind region that new convections form ahead of the existing one, creating the updraft and downdraft pair following the leading part of the convection. While in theory the lidar-derived air velocity cannot be clearly separated from the hydrometeor motions, an updraft region at the front of the convection is still clearly shown in an observed example from 19 January (Figure 6). The low level convergence at the cold pool front can generate updraft, thus invigorate the convection. However, it is rather difficult to judge from the observation that whether the updraft is merely generated by positive buoyancy, or with the help of horizontal convergence. We focus on one simulated case (from 1500 to 1540 UTC) that is accompanied with precipitation through its lifetime, to evaluate how much of the mean positive vertical velocity at the cold pool front is due to the convergence.

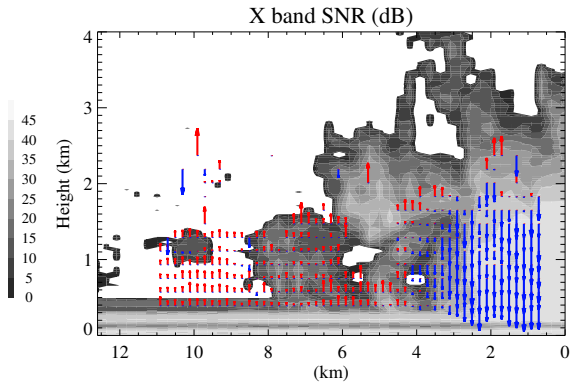

Figure 6 RICO ship based X-band radar SNR (shaded contours) and lidar observed vertical velocity (positive in red arrow, negative in blue arrow). Distance on x axis is converted from the time, ship speed and wind speed, increasing along the mean wind direction.

Left column in Figure 7 shows the updraft at the front boundary of the cold pool, with the maximum mean low level convergence located roughly at the middle of x axis. Since the horizontal velocity along the propagation direction is much larger than the cross wind, the convergence in the cross wind direction is omitted. We estimate the convergence generated vertical velocity ("Conv w" in right panels, Figure 7) by calculating the difference between the horizontal wind averaged over the left 1 km and right 1 km shown in the plot. The result is compared with the simulated vertical velocity averaged horizontally over 1 km range centering at the middle of x axis ("Ave w" in right panels, Figure 7). The rate of

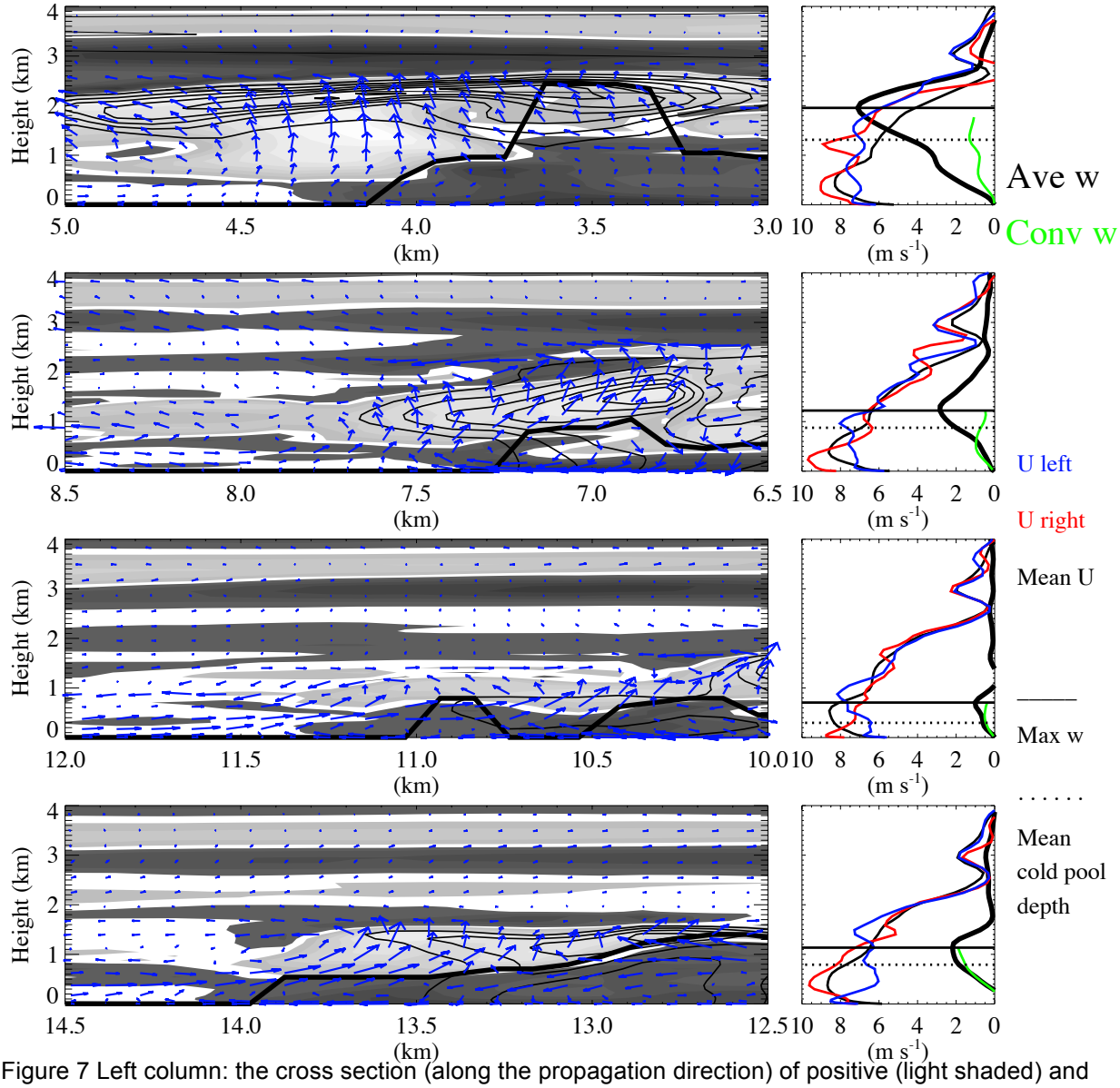

Figure 7 Left column: the cross section (along the propagation direction) of positive (light shaded) and negative (dark shaded) buoyancy, and wind vectors with the hori- zontal mean subtracted from the horizontal component (blue arrow) from 2111 to 2129 UTC (top to bottom) with 6 minute interval. The cold pool volume is outlined in thick black contour. The x axis value increases along the mean wind direction.

Ave w increasing with height is enhanced at the level of positive buoyancy when the convection is still active, indicating the importance of buoyancy generating vertical velocity at this stage of convection (top two panels Figure 7). The convergence generated vertical velocity becomes prominent at later stage of the convection, shown as the significantly reduced difference between Ave w and Conv w (two bottom right panels, Figure 7). At 2123 and 2129 UTC, the cold pool substitutes the sub-cloud layer with negative buoyant air, suppressing the generation of low level positive buoyant updraft (two bottom left panels, Figure 7) The revival of Ave w from 2123 to 2129 UTC, which is mostly contributed by the convergence (two bottom right panels, Figure 7), indicates that the convergence is able to support updraft even without the help of positive buoyancy.

6 CONCLUSIONS

In this abstract, we present part of our detailed study on simulated trade wind cumulus cold pools, from their recovery process to their influence on the related convections. The limited case studies we have examined to date suggest that, the surface fluxes can account for large portion

of the cold pool buoyancy recovery. The recovery is faster for expansive and shallow cold pools (e.g., case 4). The mixing process enhances the mean cold pool buoyancy mainly by increasing the temperature. The mean positive vertical velocity generated by cold pool front convergence becomes more prominent toward the later stage of the convection. This is due to the suppression of low level positive buoyancy by cold pool stable layer, as the cold pool front propagates ahead of the convection.

REFERENCES

[1] Albrecht, B.A., A.K. Betts, W.H. Schubert, and S.K. Cox, 1979: A model of the thermodynamic structure of the trade-wind boundary layer. Part I: Theoretical formulation and sensitivity tests. J. Atmos. Sci., 36, 73–89

[2] Abel, S. J., B. J. Shipway, 2007: A comparison of cloud-resolving model simulations of trade wind cumulus with aircraft observations taken during RICO Q. J. Roy. Meteor. Soc., 133, 781–794.

[3] Betts, A. K., 1975: Parametric interpretation of trade-wind cumulus budget studies. J. Atmos. Sci., 32, 1934–1945.

[4] Medeiros, B., B. Stevens, I. Held, M. Zhao, D. L. Williamson, J. Olson, and C. S. Bretherton, 2008: Aquaplanets, climate sensitivity and low clouds. J. Climate, 21, 4974–4991.

[5] Moeng, C.H., Shen, S., Randall, D.A, 1992: Physical processes within the nocturnal stratus- topped boundary layer. J. Atmos. Sci., 49, 23842401.

[6] Nuijens, L., B. Stevens, and A. P. Siebesma, 2009: The environment of precipitat- ing shallow cumulus convection. J. Atmos. Sci., 66, 1962–1979.

[7] Nuijens, L., and Stevens, B., 2012: The influence of wind speed on shallow marine cumulus convection. J. Atmos. Sci., 69, 168–184.

[8] Ross, A. N., A. M. Tompkins, D. J. Parker, 2004:Simple models of the role of surface fluxes in convective cold pool evolution. J. Atmos. Sci., 61, 1582–1595.

[9] Stevens, B., 2005: Atmospheric moist convection. Ann. Rev. Earth Planet. Sci., 33, 605–643.

[10] Stevens, B. and A. Seifert,2008: Understanding macrophysical outcomes of micro- physical choices in simulations of shallow cumulus convection. J. Meteorol. Soc. Japan , 2006, 143–162[11] Short, D. A., and K. Nakamura, 2000: TRMM radar observations of shallow pre- cipitation over the tropical oceans. J. Climate, 13, 4107–4124.

[12] Snodgrass, E. R., L. D. Girolamo, and R. M. Rauber, 2009: Precipitation characteristics of trade wind clouds during RICO derived from radar, satellite, and aircraft measurements. J. Appl. Met. Clim., 48, 464–483.

[13] Tiedtke, M., W. Heckley, and J. Slingo, 1988:Tropical forecasting at ECMWF: The influence of physical parameterization on the meanstructure of forecasts and analyses. Q. J. R. Meteorol. Soc., 114, 639–664.

[14] Thompson, G., P. R. Field, R. M. Rasmussen, W. D. Hall, 2008: Explicit forecasts of winter precipitation using an improved bulk microphysics scheme. part II: imple- mentation of a new snow parameterization. Mon. Wea. Rev., 136, 5095–5115.

[15] Weisman, M.L., and R. Rotunno, 2004: A theory for strong long- lived squall lines revisited. J. Atmos. Sci., 61, 361–382.

[16] Xue, H., G. Feingold and B. Stevens, 2008: Aerosol Effects on Clouds, Precipitation, and the Organization of Shallow Cumulus Convection. J. Atmos. Sci., 65, 392–406

[17] Zuidema, P., Z. Li, R. Hill, L. Bariteau, B. Rilling, C. Fairall, W. A. Brewer, B. Al- brecht and J. Hare, 2012: On trade-wind cumulus cold pools. J. Atmos. Sci., 69, 258–277.

STUDY OF THE ASSOCIATION OF ENVIRONMENTAL PARAMETERS WITH ECHO TOP HEIGHTS OF MESOSCALE CONVECTIVE SYSTEMS

[1]Devajyoti Dutta, [1]Sanjay Sharma, [2] R. M. Gairola

[1]Department of Physics, Kohima Science College, Jotsoma, Nagaland, 797002, India

[2]Meteorology and Oceanography Group, Space Application Centre, Ahmedabad, 380015, India

INTRODUCTION:

Rain height is an important parameter which has wide applications in meteorology and satellite communication. It is the height of the top of the rain column above the mean sea level. Strength of convective systems is measured by many parameters and one of them is rain height. The vertical precipitation profiles reflects dynamical and microphysical process in clouds (Zipser and Lutz 1994). By studying maximum radar reflectivity profiles of convective cells in MCSs, Zipser and Lutz (1994) pointed out that profile shape between land and oceanic cells shows significant difference in accordance to different strength of the updrafts. Vertical profiles of reflectivity (rain height) is used to estimate the profiles of radiative and latent heating. Several studied are carried out to investigate the impact of variability of tropical precipitation profiles on microwave brightness temperature (Fu and Liu, 2001; Liu and Fu 2001; Petersen and Rutledge 2001). Rain height is also an input parameter to get path length for attenuation and volume for backscatter.

Studies on precipitation profiles have been mainly based on surface radar observations in field experiments. The first space borne precipitation radar (PR), an active microwave instrument aboard the Tropical Rainfall Measuring Mission (TRMM) satellite, was designed to measure rain and its vertical structures over the both tropical oceans and continents. TRMM PR directly observes the rain-top height inside cloud. More recently airborne and space borne sensors have provided information for large to global scales (Geerts, and Dejene, 2005; Geerts and Dawei,, 2004; Heymsfield, et al. 2000; Hirose and Nakamura, 2002).

In the present work an attempt has been made to develop an Artificial Neural Network (ANN) based technique to estimate rain Echo Top Height for 20 dBZ reflectivity threshold (ETH_{20dBZ}) with the help of environmental convective parameters for mesoscale convective systems (MCSs). For the present study the 2A25 data product of TRMM-PR and NCEP reanalyzed data set are utilized. The considered atmospheric parameters are (i). Convective Available Potential Energy (CAPE) (ii). Convective Inhibition (CIN) (iii). Wind Shear at lower height (1 to 5 km) (SH1) (iv). Wind Shear at upper height (5 to 9 km) (SH2) and (v).Perceptible Water at Surface (PW).

For present study nadir looking beam of PR is utilized to estimate $ETH_{20\ dBZ}$ and within a system maximum value of $ETH_{20\ dBZ}$ is considered.. Precipitating system is considered as MCSs when they are characterized by an area of at least 2000 km^2 bounded by PCT_{85} value of 250 ^0K, with a minimum value of PCT_{85} in it ≤ 225 ^0K (Mohr and Zipser, 1996). To collocate the data points of TRMM-PR pixels with NCEP reanalyzed data set (Kalnay 1996)

observation time from TRMM-PR and centre of mass of MCSs are matched with nearest time slot and grid point of reanalysed data set (with a temporal resolution of 6 hrs and spatial resolution of 2^0 x 2^0 grid size).

3. METHODOLOGY:

The overall methodology consist of two subsection namely (i).To study of the data characteristics (ii). Estimation of ETH_{20dBZ} by using ANN technique

3.1 Data characteristics

The characteristics of input and output data are studied in terms of maximum and minimum value of each parameter along with the mean and standard deviation. These parameters are provided in Table -1 . These values are conditional in the sense that atmospheric parameters are taken only for those days when a MCS is detected. A correlation analysis is carried out for two cases. For first case, CC is estimated between input atmospheric parameters and ETH_{20dBZ}. The estimated CC values are provided in Table 2 The magnitude of the CC is varying in the range of 0.40 – 0.53. The maximum and minimum correlation of the atmospheric parameters with rain height is observed for CAPE and PW respectively. For second case CC amongst the input variable is estimated. The estimated CC values are also provided in Table 2 It is observed that except for CAPE- SH1, CAPE- SH2 and CAPE- CIN , the CC is ≤ .29, which indicates that majority of the input variables are independent to each other.

Table -1

	Min	Max	Mean	Std
CAPE ($J\ Kg^{-1}$)	20	1700	1121	285
CIN ($J\ Kg^{-1}$)	10	1045	540	138
SH1 ($m\ sec^{-1}$)	0.3	17.5	7.1	5.48
SH2 ($m\ sec^{-1}$)	0	16.8	6.6	5.92
PW ($Kg\ m^{-2}$)	17.3	63.8	43.11	8.10
ETH_{20dBZ} (Km)	3.8	19.6	9.5	2.66

Table - 2

Correlation Coefficient Matrix

	$ETH_{20\ dBZ}$	CAPE	CIN	SH1	SH2	PW
ETH	1.00	0.53	-0.50	0.49	0.46	0.40
CAPE	0.53	1.00	-0.63	0.41	0.31	0.29
CIN	-0.50	-0.63	1.00	-0.14	-0.11	-0.22
SH1	0.49	0.41	-0.14	1.00	0.24	0.22
SH2	0,46	0.31	-0.11	0.24	1.00	0.11
PW	0.40	0.29	-0.22	0.22	0.11	1.00

3.2 Estimation of ETH_{20dBZ} by using an ANN technique

An ANN is trained by taking into account the five identified environmental parameters as an input and ETH_{20dBZ} as an output. The data set is divided into two parts. One part consists of 80% data points which is utilized for training purpose and the remaining 20% is utilized for a validation purpose. The different network architectures are trained in MATLAB tool box based on Levenberg-Marquardt back propagation algorithm. The networks with the following architecture comes out to be good enough to trace the nonlinear relation of atmospheric parameters versus Rain Height . The architecture is provided in the format of : no. of nodes in input layer - no. of node in 1st hidden layer – no. of nodes in 2nd hidden layer – no. of nodes in output layer.

RAIN_HEIGHT : 5-25-15-01

The weight matrices is developed for global minima. The developed weight matrices are utilized to estimate rain height for a given set of input values Performance of a rain height estimation methodology is examined with error statistics in terms of RMSE, Bias and CC with respect to observed values.

4. RESULTS AND CONCLUSION:

A scatter plot for a observed and ANN estimated rain height for training and validation data set is shown in figure 1 (a, b) respectively. Similarly a scatter plot for independently observed and ANN estimated rain height is shown in figure.1(c) The error statistics is provided in the respective figure panels. For an independent testing of the algorithm, the CC is 0.71 The results are encouraging. Further work is in progress to incorporate the all types of precipitating systems.

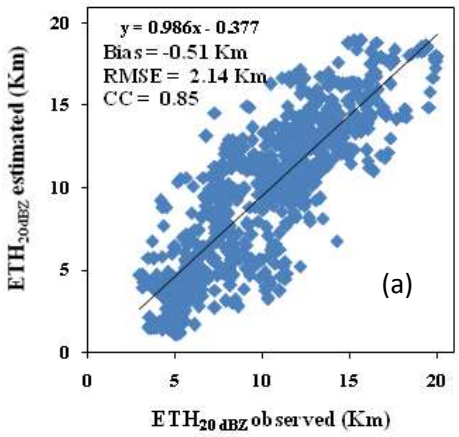

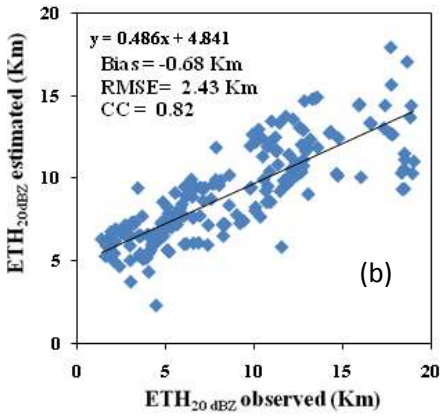

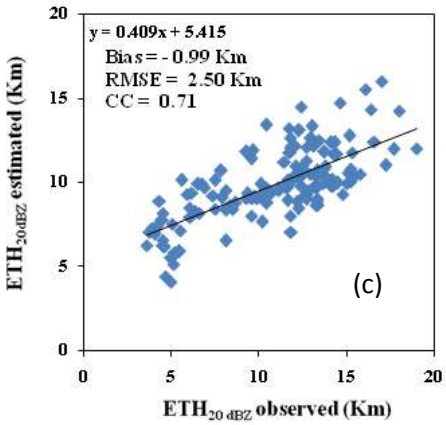

Fig 1: Scatter plots for Observed and estimated ETH 20 dBZ for (a) training set (b) validation set and (c) testing set

ACKNOWLEGEMENT:

The financial support from Indian Space Research Organization (ISRO) to carry out the work is thankfully acknowledged. The TRMM data, downloaded from the web site (http://www.trmm.chpc.utah.edu) of University of Utah, PMM science, is thankfully acknowledged. The downloaded 20th Century Reanalyzed data products of *NOAA/OAR/ESRL PSD, Boulder, Colorado, USA, from their web site at* http://www.esrl.noaa.gov/psd/ *is thankfully acknowledged.* One of the authors acknowledges with gratitude the financial support provided by IUGG, IAMAS and WMO for the participation at the ICCP.

REFERENCES:

Fu Y, G. Liu, 2001, The variability of tropical precipitation profiles and its impact on microwave brightness temperature as inferred from TRMM data, *J Appl. Meteor.*, Vol. 40, pp. 2130-2143.

Geerts, B., Dawei, Y., 2004 (a). Classification and characterization of tropical precipitation based on high resolution airborne vertical incidence radar . Part –I; Classification, J. Appl. Meteor., 43, 1554-1566.

Geerts, B., Dejene, T., 2005. Regional and diurnal variability of the vertical structure of precipitation systems in Africa based on space borne radar data. J. Climate. 18, 893-916.

Heymsfield, G.M., B. Geerts and L. Tian, 2000: TRMM precipitation radar reflectivity profiles as compared with high resolution airborne and ground based radar measurements, J. Appl. Meteor., 39, 2080-2102.

Hirose, M., K. Nakamura, 2002: Spatial and seasonal variation of rain profiles over Asia observed by space borne precipitation radar, J. Climate, 15, 3443-3458.

Iguchi T, Kozu T, Mrneghini R, Awaka J & Okamoto K, 2000: Rain profiling algorithm for the TRMM precipitation radar, *J Appl. Meteor(USA)*, 39, 2038.

Kalnay, E., M. Kanamitsu, R. Kistler, W. Collins, D. Deaven, L. Gandin, M. Iredell, S. Saha, G. White, J. Woolen, Y. Zhu, M. Chelliah, W. Ebisuzaki, W. Higgins, J. Janowiak, K. C. Mo, C. Ropelewski, J. Wang, A. Leetma, R. Reynolds, R. Jenne, and D. Joseph, 1996, The NCEP/NCAR 40-year reanalysis project. *Bullet. Amer. Meteor. Soc.*, Vol. 77, pp. 437-471.

Liu, G., Fu, Y. The characteristics of tropical precipitation profiles as inferred from satellite radar measurements, J. Meteor. Soc. Japan 79, 131-143, 2001.

Mohr, K. I. and E. J., Zipser, , 1996 : Mesoscale convective system defined by their 85GHz ice scattering signature: size and intensity comparison over tropical oceans and continents, Mon. Wea. Rev., 124, 2417-2737.

Petersen, W. A, and S. A. Rutledge, 2001, Regional variability in tropical convection: Observations from TRMM, *J. Climate*, Vol. 14, pp. 3566–3586.

Zipser E. J., and K. R. Lutz, 1994, The vertical profile of radar reflectivity of convective cells: A strong indicator of storm intensity and lightning probability?, *Mon. Wea. Rev*., Vol. 122, pp. 1751-1759.

Cloud Physics and UFOs, a Historic-Modern Note

Roland List,
Department of Physics, University of Toronto, Toronto ON, Canada M5S 1A7
roland.list@rogers.com,

1. Introduction

At the ICCP in Cancun, 2008, the author has tried to question the crash of a UFO in Roswell, N.M., in 1947, with a great story involving the cloud physicists Charles Moore and Paul MacCready and their adventure of deliberately flying into a thunderstorm with a balloon. They were supposed to have run into severe icing and had to throw all cloud physics equipment over board to slow the decent. Charley and Paul obviously survived. In that descent phase the balloon was flattened and looked like a flying saucer, enhanced by a ring of icing. It was a good story, but only partially true because it was not related to Roswell and occurred later. In the meantime, I learned about a book of the Roswell incident, co-authored by Charles Moore (a very close friend of Bernie Vonnegut). The book is entitled *"UFO Crash at Roswell, the genesis of a modern myth"* by B. Saler, C. A. Ziegler and C. B. Moore, published by the Smithsonian Institution (*sic!*).

In the 50ties and 60ties the US Air Force followed the many "observations" of UFOs through its highly secret Committee working on "Project Blue Book" (Google!). The purpose of this undertaking was: 1) to determine if UFOs were a threat to national security, and 2) to scientifically analyze UFO-related data. One of the big atmospheric physicists of that time, James E. McDonald from the University of Arizona in Tucson, was a member of that committee. At the beginning only about 70% of the events could be explained by physical phenomena – as I learned directly from Jim during an after-diner talk at an AMS meeting. The rate of unexplainable events was given as 701 out of 12618 sightings or 5.56%, according to the final report "Project Blue Book", with its top secret documents that were made public some years ago. Later, Jim got humiliated by Members of Congress, labeling him as a believer in the existence of UFOs. While Jim's end was tragic, it was not related to the UFO stories.

2. The Players

Prof. Charley Moore was a pioneer in exploration of the atmosphere by balloon and was a key contributor to launching instruments to measure meteorological components. One of the major research areas he had been later involved was atmospheric electricity and the movement of charges on the outer surfaces of clouds.

Dr. Paul MacCready, who joined Charley Moore on a balloon flight into a thunderstorm and barely got out because of icing, also deserves recognition as one of the world's top engineers, who started with a degree in aeronautical engineering – and won the world soaring championship. When I asked him how he did it, he responded that he developed an instrument which allowed him to optimally change from one thermal to the next. [Rick can Tuttenhooft, # 3 in that championship took me up for a spin with Doyne Sartor's sailplane (Doyne was a reknowned Cloud Physicist at NCAR, who had previously owned that sail plane) and taught me to properly fly it - with the help of a ping pong ball attached to the plane's nose].

The next big achievement of Paul came as an inspiration in a sleepless night when he mentally solved the problem of manpowered flight. He then built a plane with light carbon fiber materials. All members of his family flew the "Gossamer Albatross", including grandmother. However, it took the stamina of a bicycle racer to keep it aloft long enough, first to fly a figure eight around two poles 1 miles apart – which netted him the first Kremer prize. That venture was then followed by the incredible crossing of the English Channel. With pride Paul told me that, seven months after the initial idea, the "Gossamer Albatross" was

hanging next to Lindberg's Sprit of Saint Louis (the plane of the first trans-Atlantic flight).

Paul MacCready was also a cloud physicist and had a company doing weather modification and air pollution work. He was a prime mover in the quest for a hailstorm penetrating armored aircraft, the T28, and pushed the idea of using drones in the exploration of clouds. Why do I mention him here? Paul also *built* saucer-like flying objects, which, with TV camera equipped, could be used for surveillance in big halls.

Prof. James E. MacDonald, see above.

3. The Facts

At the UFO "crash" remnants of a radar reflector and balloon material were found. It was from a contract to NYU for constant level balloons. Charles Moore was the project manager. Due to the Cold War secrecy was high and the truth was hidden for a long time. The ufologists made hay out of this "crash" after 1970.

4. The Myth

The creation of the story of the landing of aliens in Roswell, N.M., is similar to Carl Spitteler`s Noble Prize-winning story "Olympian Spring" (1919). In the story the flatfooted inhabitants of a swamp deeply disliked the beautiful Apollo and the gorgeous Aphrodite driving the sun wagon across the sky. The ugly flat-footers also wanted a sun-god, but one who spewed fire and brimstone and, most importantly, also stank. In building a new vehicle, the 'flatties' realized that they needed the support and admiration of the masses to kotow the new sun god. So they created a new religion and appointed a high priest. So what is new in ufology?

Fig.1. UFO on transit to Roswell, N.M., Alien spacecraft from Back Bench comic strip.

It is the wish of mankind to believe in something full of wonders and mysteries, something supernatural - and what is better than a belief in aliens who have experiences capabilities and powers far beyond ours. Like modern fairytales. The imagination is boundless. It is a credit to Cloud Physics that our strange broken tools and instruments have started such a wild cult.

ABSORPTION OF SOLUBLE TRACE GASES BY ATMOSPHERIC NANOAEROSOLS

Tov Elperin[a,*], Andrew Fominykh[a], Boris Krasovitov[a], Alexey Lushnikov[b]

[a] *Department of Mechanical Engineering, The Pearlstone Center for Aeronautical Engineering Studies,Ben-Gurion University of the Negev, P.O.Box 653, 84105 Israel*
[b] *Karpov Institute of Physical Chemistry, 10, Vorontsovo Pole, 105064 Moscow Russia*

Abstract

We investigate mass transfer during absorption of atmospheric trace soluble gases by a single droplet whose size is comparable to the molecular mean free path in air at normal conditions. It is assumed that the trace reactant diffuses to the droplet surface and then reacts with the substances inside the droplet according to the first order rate law. Our analysis applies a flux-matching theory of transport processes in gases and assumes constant thermophysical properties of the gases and liquids. We derive an integral equation of Volterra type for the transient molecular flux density to a liquid droplet and solve it numerically. Numerical calculations are performed for absorption of sulfur dioxide (SO_2), dinitrogen trioxide (N_2O_3) and chlorine (Cl_2) by liquid nanoaerosols accompanied by chemical dissociation reaction. It is shown that during gas absorption by nanoaerosols the kinetic effects play significant role, and neglecting kinetic effects leads to significant overestimation of the soluble gas flux into a droplet during all the period of gas absorption.

Keywords: nanoaerosol, gas absorption, diffusion, free molecular flow, soluble gas, chemical dissociation reaction

1. INTRODUCTION

Atmospheric aerosols are directly emitted into the atmosphere from natural or anthropogenic sources or can be formed in the atmosphere through nucleation of gas-phase species. Aerosol nucleation events produce a large fraction of atmospheric aerosols. New particle formation occurs in two distinct stages, i.e., nucleation to form a critical nucleus and subsequent growth of the critical nucleus to a larger size ($>$2 – 3 nm) that competes with capture and removal of the freshly nucleated nanoparticles by coagulation with pre-existing aerosols (Zhang et al., 2012). In the continental boundary layer, there are frequent observations of the formation of ultrafine aerosol particles accompanied by the subsequent growth (Kulmala et al., 2004). Gas absorption of soluble trace atmospheric gases by the liquid atmospheric aerosol particles including ultrafine particles plays an important role in climate and atmospheric chemistry.

The consequence for the aerosol climate forcing is that the cooling can be intensified with increasing atmospheric amount of water-soluble trace gases such as $\mathrm{HNO_3}$, counteracting the warming effect of the greenhouse gases (Krämer et al., 2000). Scavenging of atmospheric gaseous pollutants by cloud droplets is a result of gas absorption mechanism (Pruppacher & Klett, 1997; Flossmann, 1990). Gas scavenging of highly soluble gases by atmospheric water droplets includes absorption of HNO_3, H_2O_2, H_2SO_4, HCl and some other gases. The sources of these gases in the atmosphere are briefly reviewed in Seinfeld & Pandis (2006) and Hayden et al. (2008). Soluble gas absorption by noncirculating droplets was investigated experimentally by Taniguchi & Asano (1992) where conditions of noncirculation for falling liquid droplets were determined by employing water droplets with Sauter mean diameter equal to 0.185, 0.148 and 0.137 mm.

Gas absorption by stagnant liquid droplets in the presence of inert admixtures when both phases affect mass transfer was analyzed by Clift et al. (1978),

*Corresponding author: elperin@bgu.ac.il

pp. 54-55. Scavenging of soluble gases by single evaporating droplets was studied by Elperin et al. (2007, 2008).

All aforementioned works considered the trace gas absorption in the continuous limit, where Fick's law relates the flux and the concentration gradient of reactant. Recently some studies attempt to describe the reactant transport in the gaseous phase in the free–molecular and the transition regimes, where the droplet size is less than or comparable to the mean free path of the molecules in the gaseous phase. Comprehensive reviews of the results and approaches can be found in Seinfeld & Pandis (2006), Clement (2007), Pöschl et al. (2007) and Lushnikov (2012). The existing attempts to describe the transitional and free–molecule regimes encounter some difficulties in formulating the boundary conditions to the transport equations. For example, Vesala et al. (2001) used the diffusion equations and a microscopic boundary condition for describing the reactant transport toward the particle surface. The rigorous approach requires solution of the full transport problem including the reactant transport in the gaseous phase and gas–liquid interface by solving the Boltzmann kinetic equation and the diffusion–reaction equation inside the droplet. To the best of our knowledge this approach was not applied as yet.

In this study we employ a different approach for describing gas uptake by nanodroplets. We modify the flux–matching approach of Lushnikov & Kulmala (2004) by including the in–particle chemical transformations of the reactant molecules. The results are applied for considering the trace gases scavenging by atmospheric aerosols.

Let us assume that the reactant molecules (A–molecules) move toward the droplet which captures them. The further fate of reactant molecules depends on the results of chemical reactions inside the particle. Let us denote by $n_\pm$ the concentrations of A–molecules right outside (n_+) or right inside (n_-) the particle surface. Clearly these concentrations $n_\pm$ depend on the nature of physicochemical processes at the surface and inside the particle. Let n_∞ be the number density of A–molecules far from the particle. It is commonly accepted that the concentration difference $n_\infty - n_+$ drives a flux of A–molecules towards the particle surface. The mass of the particle begins to increase and its chemical composition changes. The rate of change of the number of A–molecules inside the particle is equal to the total flux J, i.e. the total number of molecules deposited per unit time at the particle surface minus the rate of consumption of molecules A by chemical reaction inside the particle. Some fraction of A–molecules is assumed to escape from the particles. In steady–state conditions the flux J can be written as

$$J = \alpha(a)(n_\infty - n_+)\,, \tag{1}$$

where $\alpha(a)$ is the capture efficiency and a is the particle radius. Clearly, capture efficiency α depends on the mass accommodation coefficient S_p. The latter is defined as the probability for an A–molecule to stick to the particle after a single collision. Since the interface and in–particle processes determine the value of n_+ Eq. (1) can be rewritten as follows (Lushnikov, 2012):

$$J = \frac{\alpha(a) n_\infty}{1 + \alpha(a)\psi(a, J)}\,, \tag{2}$$

where $\psi(a, J)$ is a function depending on the nature of the chemical reaction. In the case of the first–order chemical reaction the function ψ is independent of J. An example of such function is given below. If, however, the chemical reaction inside the particle is of the higher order, then J is a solution of the transcendent equation (2). Note that we did not yet specify the functions $\alpha(a)$, $\psi(a, J)$, and Eq. (2) contains only n_∞. The information on the processes at the surface and inside the particle is carried by the function $\psi(a, J)$. Hence, Eq. (2) is quite general. All further approximations concern the values of the uptake efficiency $\alpha(a)$ and the reaction function $\psi(a)$.

2. DESCRIPTION OF THE MODEL

2.1. Preliminary remarks

The characteristic times of changes of the number density of reactant A in gaseous and liquid phases differ by several orders of magnitude. In particular, the relaxation time inside the micrometer-sized droplet is $\tau_L \propto a^2/D_L \simeq 10^{-3}$ s, where $D_L \simeq 10^{-5}$ cm^2/s denotes the diffusivity of the reactant molecules in the liquid phase. The relaxation time in the gaseous phase can be estimated as $\tau_G \propto a/v_T \simeq 10^{-8}$ s, where v_T is the mean thermal velocity of the reactant molecules, $v_T \simeq 10^2$ m/s. Here one can use the free molecular estimate because the droplet size is of the order of the mean free path of the reactant molecule. Following Seinfeld & Pandis (2006) the characteristic time of diffusion in a

gaseous phase, corresponding to the time required by gas-phase diffusion to establish a steady-state profile around a particle, can be alternatively estimated as $\tau_G \propto a^2/D_G \simeq 10^{-8}$ s. As can be seen from these estimates, the characteristic time of diffusion in a gaseous phase, τ_G , is much smaller than the characteristic time of diffusion in the liquid phase, τ_L, which is required for a saturation of the droplet by soluble gas (i.e., $\tau_G \ll \tau_L$). Therefore for the large values of t ($t \gg \tau_G$) it is reasonable to assume that concentration profile in a gaseous phase in the transitional regime and the flux attain their quasi-steady state values (Wagner, 1982) and are determined by Eq. (1) (or in more general form by Eq. (2)).

The molecular mean free path in air at normal conditions is $\ell \approx$ 65 nm , i.e., it is comparable to the sizes of the nanometer droplets. This implies that the motion of the reactant molecules cannot be described as the Fickian diffusion, and one must apply the Boltzmann kinetic theory. However, solving the Boltzmann equation analytically or numerically is a formidable task.

The idea to apply the flux–matching approach in the aerosol kinetics was pioneered by Fuchs (1964). His reasoning was quite simple. At large distance from the droplet the reactant transport can be described by the diffusion equation. In the vicinity of the droplet at the distances of the order of ℓ or less the collisions with the carrier gas do not hinder the reactant transport. Consequently, inside the region $a < r < R \propto \ell$ (R is referred to as the radius of the limiting sphere) the reactant molecules move in the free molecule regime. The value of R must be found from different consideration. Fuchs & Sutugin (1971) proposed to determine this value from the numerical solution of the BGK equation (see e.g., Sahni, 1966). An improved version of the Fuchs interpolation formula (Fuchs, 1964) was obtained by Loyalka (1982) in near continuum regime by solving Boltzmann equation using momentum method.

2.2. Trapping efficiency

The latest modification of the Fuchs theory (Lushnikov & Kulmala, 2004; Lushnikov, 2012) includes the solution of the diffusion equation with a fixed flux J in the diffusion zone $r > R$, the solution of the collisionless Boltzmann equation in the free molecular zone $r < R$, and determining the radius of the limiting sphere from the condition of equality of the fluxes in both zones. The expression for $\alpha(a)$ was found by Lushnikov & Kulmala (2004) for $n_+ = 0$ and $S_p = 1$:

$$\alpha(a) = \frac{2\pi a^2 v_T}{1 + \sqrt{1 + \left(\frac{a v_T}{2D_G}\right)^2}}\,, \tag{3}$$

where D_G is the reactant diffusivity in the carrier gas. The extension of this formula to the case $n_+ \geq 0$ and $S_p \leq 1$ reads (for details see Lushnikov, 2012):

$$\alpha(a) = \frac{S_p \pi a^2 v_T}{1 + \frac{S_p}{2}\left[\sqrt{1 + \left(\frac{a v_T}{2D_G}\right)^2} - 1\right]}\,. \tag{4}$$

The radius R of the limiting sphere is found from the condition of the equality of flux in the diffusion region to the flux from in free molecular region. This condition yield the radius of the limiting sphere (Lushnikov, 2012; Lushnikov & Kulmala, 2004):

$$R = \sqrt{a^2 + \left(\frac{2D_G}{v_T}\right)^2}. \tag{5}$$

It must be noted that R is independent of S_p and n_+. The spherical surface with the radius R separates between the zones of the free–molecular and the continuous flow regimes. The value of $2D_G/v_T$ is of the order of ℓ, the reactant molecule mean free path. Hence, if $a \simeq \ell$ or less, then the radius R is of the order of $R \simeq \ell$.

The concentration profile of the reactant $n(r)$ in the gaseous phase inside the limiting sphere $a < r < R$ is continuous at $r = R$ together with its first derivative and is given by the following formula (Lushnikov & Kulmala, 2004):

$$\frac{n(r) - n_+}{n_\infty - n_+} = \left(1 - \frac{\alpha(a)}{4\pi D_G R}\right)\frac{b(r)}{b(R)} \tag{6}$$

where

$$b(r) = 1 - \frac{S_p}{2}\left(1 - \sqrt{1 - \frac{a^2}{r^2}}\right). \tag{7}$$

Outside the limiting sphere at $r \geq R$

$$\frac{n(r) - n_+}{n_\infty - n_+} = 1 - \frac{\alpha(a)}{4\pi D r}\,. \tag{8}$$

Note that the number density $n(a)$ is always larger than n_+. The formula for the concentration jump at

the particle surface reads (Lushnikov, 2012):

$$\Delta_a = n(a) - n_+ = (n_\infty - n_+)\left(1 - \frac{\alpha(a)}{4\pi D_G R}\right)\frac{b(a)}{b(R)}. \quad (9)$$

Inspection of Eq. (4) shows that when $av_T/2D_G \gg 1$, $\alpha(a) = 4\pi a D_G$ and Eq. (4) recovers the Maxwell's equation for the molecular flux in the continuum regime J_c:

$$J_c = 4\pi a D_G (n_\infty - n_+). \quad (10)$$

In Fig. 1 we showed the dependence of the ratio J/J_c vs. Knudsen number Kn for differen values of the accommodation coefficient S_p (S_p was assumed to be 0.1, 0.2, 0.5 and 1.0 and $D_G \simeq 10^{-5}$ m^2/s). As can be seen from this plot the role of the kinetic effects can be significant for the $Kn \gtrsim 0.1$. Comparison of mass transfer rates as function of Kn

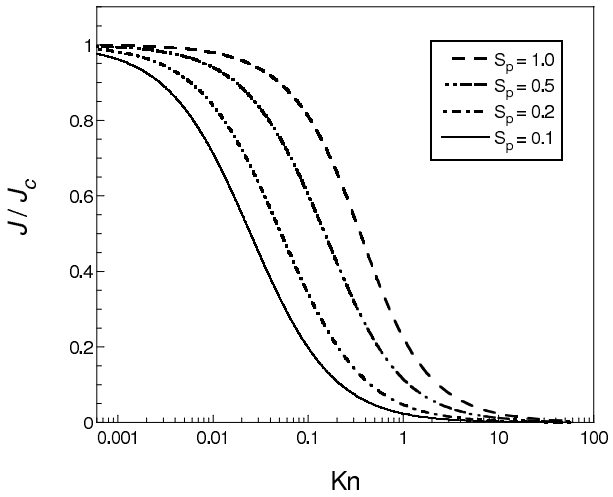

Figure 1: Ratio of the molecular flux to the molecular flux in a continuum regime, J/J_c , as a function of Knudsen number Kn.

predicted by different theories (Fuchs, 1964; Fuchs & Sutugin, 1971; Loyalka, 1982; Lushnikov & Kulmala, 2004) are shown in Fig. 2. As can be seen from Fig. 2 all approaches yield approximately the same results for small Kn numbers, $Kn \lesssim 0.1$, and for $Kn \gtrsim 10$.

2.3. Inner diffusio–reaction equation

Consider now the effect of the first order chemical reaction, e.g., chemical reaction dissociation, inside the droplet on the reactant flux towards the droplet.

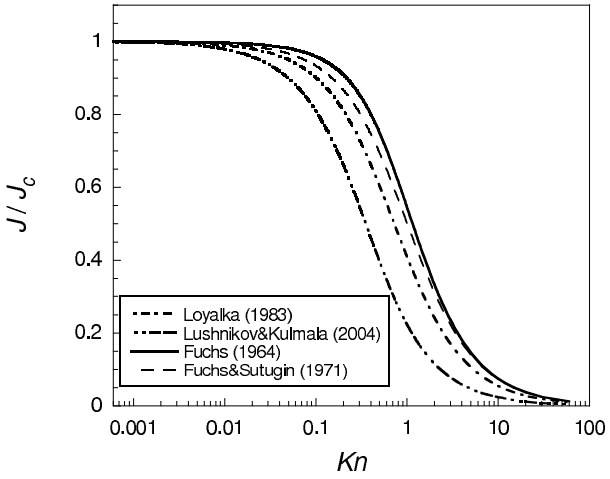

Figure 2: Ratio of the molecular flux to the molecular flux in a continuum regime, J/J_c , as a function of Knudsen number Kn: —— - Fuchs (1964); – – – - Fuchs & Sutugin (1971); – · – - Loyalka (1982); – ·· – - Lushnikov & Kulmala (2004). Accomodation coefficient $S_p = 1$.

Neglecting recombination the number density of reactant molecules inside the particle $n_L(r,t)$ is governed by the linear diffusion–reaction equation:

$$\frac{\partial n_L}{\partial t} = D_L \Delta n_L - \lambda n_L, \quad (11)$$

where $n_L = n_L(r,t)$ is the number density of reactant molecules inside the particle, D_L is the reactant diffusivity in the liquid phase, and λ is the dissociation rate. Equation (11) must be supplemented with the initial condition,

$$n_L(r,0) = 0 \quad (12)$$

(no reactant inside the droplet at $t = 0$)and the boundary conditions:

$$\left.\frac{\partial n_L(r,t)}{\partial r}\right|_{r=0} = 0 \quad (13)$$

and

$$j(t) = -D_L \left.\frac{\partial n_L(r,t)}{\partial r}\right|_{r=a}, \quad (14)$$

where $j = j(t)$ is the flux density $j = J/(4\pi a^2)$, J is the total flux.

Equation (11) with the initial and boundary conditions (12) – (14) can be solved by the method of separation of variables (see Appendix A). The result is the concentration profile $n_L(r,t)$ as a linear functional of $j(t)$. Substituting the determined concentration distribution $n_L(r,t)$ into the boundary condition,

Eq. (14), yields the integral equation of Volterra type (Apelblat, 2008) for $j(t)$:

$$j(t) = \frac{\alpha(a)}{4\pi a^2}\left[n_\infty - \mathcal{H}\int\limits_0^t S(t-t')j(t')dt'\right], \quad (15)$$

where

$$S(\xi) = 2\sum_{n>0} e^{-[D_L(\mu_n/a)^2+\lambda]\xi} + 3e^{-\lambda\xi} \quad (16)$$

and μ_n is the infinite set of the roots of the following transcendental equation:

$$\mu = \tan(\mu)\,. \quad (17)$$

Equation (15) can be rewritten in the dimensionless form for the dimensionless flux $j^*(\tau) = j(t)4\pi a^2/\alpha(a)n_\infty$, $\tau = D_L t/a^2$:

$$j^*(\tau) = 1 - g(a)\int\limits_0^\tau S^*(\tau-\tau')j^*(\tau')d\tau', \quad (18)$$

where $g(a) = \dfrac{3\alpha(a)\mathcal{H}}{4\pi a D_L}$ and

$$S^*(\tau-\tau') = e^{-\mathrm{D}a(\tau-\tau')}\left[1 + \frac{2}{3}\sum_{n=1}^{\infty} e^{-\mu_n^2(\tau-\tau')}\right]. \quad (19)$$

In Eqs. (18) and (19) $D\mathrm{a} = \lambda a^2/D_L$ is Damkohler number, $\mathcal{H} = (H_A\mathcal{R}T)^{-1}$ and H_A is Henry's law constant, $\mathcal{R}$ is universal gas constant and T is the temperature in the gaseous phase.

3. NUMERICAL METHOD

For the solution of the integral equation Eq. (18) we use the method based on the approximation of the integral in Eq. (18) using some quadrature formula:

$$\int_a^b F(x)\,dx = \sum_{j=1}^{n} A_j F(x_j)\,dx + R_n(F)\,, \quad (20)$$

where $x_j \in [a,b]$, $j = 1,2,...,n$, A_j are the coefficients associated with a family of quadrature rules and $R_n(F)$ is a corresponding residuum. Taking successively $x = x_i$ $(i = 1,...,n)$ and using the quadrature formula after discarding the terms $R_n(F_i)$ $(i = 1,...,n)$ we obtain the following system of linear algebraic equations:

$$j_i^* - g(a)\sum_{j=1}^{n} A_j S_{ij}^* j_j^* = 1 \quad (i = 1,...,n). \quad (21)$$

Using the unequally spaced mesh with an increment $h_i = \tau_i - \tau_{i-1}$, $i = 2,...,n$ and applying the trapezoidal integration rule Eqs. (21) yield the following recurrence equations:

$$\begin{aligned} j_1^* &= 1 \\ j_2^* &= \frac{1 + \dfrac{h_2}{2}K_{21}j_1^*}{1 - \dfrac{h_2}{2}K_{22}} \\ j_i^* &= \frac{1 + \dfrac{h_2}{2}K_{i1}j_1^* + \displaystyle\sum_{j=2}^{i-1}\left(\frac{\tau_{j+1}-\tau_{j-1}}{2}\right)K_{ij}j_j^*}{1 - \dfrac{h_i}{2}K_{ii}} \quad (i = 3,...,n) \end{aligned} \quad (22)$$

Equations (22) are valid in the case when $h_i \neq \dfrac{2}{K_{ii}}$.

In the numerical calculations we spaced the mesh points adaptively using the following formula:

$$\tau_i = \tau_1 + (\tau_N - \tau_1)\left[1 - \cos\left(\frac{\pi}{2}\frac{i-1}{N-1}\right)\right], \quad (i = 1,2,...,N)\,. \quad (23)$$

In Eq. (23) N is the chosen number of mesh points, τ_1 and τ_N are the locations of left and right boundaries of time interval, respectively.

4. RESULTS AND DISCUSSION

Using the suggested model the calculations were performed for sulfur dioxide (SO_2), dinitrogen trioxide (N_2O_3) and chlorine (Cl_2) absorption by water aerosol particles. In order to validate our model we compared the results obtained using the suggested model with the results obtained in our previous study for large droplets ($Kn \ll 1$)(see e.g., Elperin et al., 2008). The calculations were performed for the SO_2 absorption by a non–evaporating water droplet of 10 μm in radius. The concentration of sulfur dioxide in ambient air was assumed to be 0.01 ppm. The calculations showed that the time of the complete saturation of droplet by sulfur dioxide estimated using the suggested model is $\approx$ 0.08 s, while the time of complete saturation of droplet by sulfur dioxide estimated

using our previous model is $\approx$ 0.1 s. These calculations demonstrate that the results obtained by both models are in fairly good agreement.

The results of calculation of the total mass flux of sulfur dioxide as a function of time are shown in Figs. 3 and 4. The calculations were performed for various radii of water aerosol particle (from 0.5 μm to 1.0 μm, $0.07 \lesssim Kn \lesssim 0.14$, see Fig. 3 and from 50 nm to 100 nm, $0.7 \lesssim Kn \lesssim 1.42$, see Fig. 4).

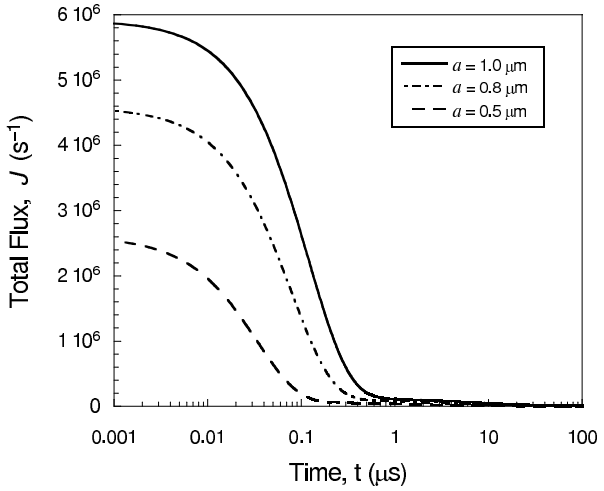

Figure 3: Total molecular flux of sulfur dioxide as a function of time (droplet radii a = 1.0, 0.8 and 0.5 μm)

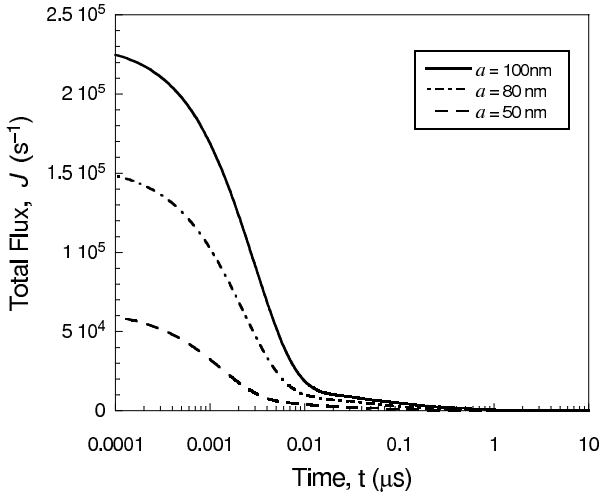

Figure 4: Total molecular flux of sulfur dioxide as a function of time (droplet radii a = 100.0, 80.0 and 50.0 nm)

As can be seen from these plots for small and moderate size droplets the flux of absorbate decreases rapidly at the initial stage of gas absorption and approaches asymptotically zero at the final stage of the process. The vanishing flux of the absorbate implies the stage of saturation of droplet by gas.

The results of calculation of the dimensionless flux $j^*(\tau) = j(t)4\pi a^2/\alpha(a)n_\infty$ as a function of dimensionless time $\tau = D_L t/a^2$ for different gases such as sulfur dioxide, chlorine and dinitrogen trioxide are shown in Fig. 5. Larger values of mass flux at the later stages of gas absorption for N_2O_3 in comparison with SO_2 and Cl_2 absorption can be explained by large values of the constant of chemical reaction for N_2O_3 gas absorption in water ($\lambda_{N_2O_3} = 1.2 \cdot 10^4$ s^{-1}, $\lambda_{SO_2} = 10^{-3}$ s^{-1}, and $\lambda_{Cl_2} = 13.3$ s^{-1}).

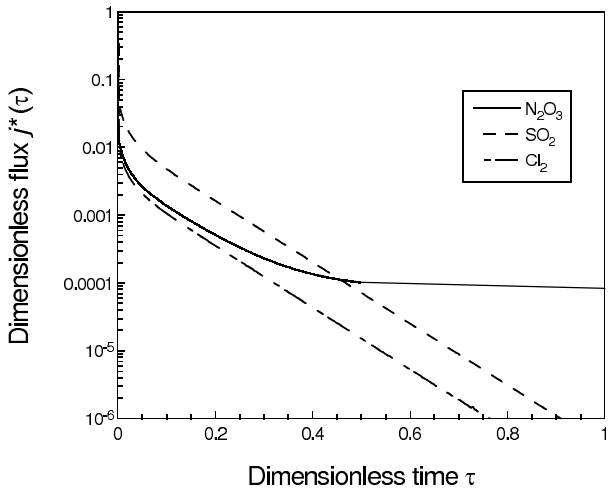

Figure 5: Dimensionless molecular flux density $j^*(\tau)$ as a function of dimensionless time τ (radius of the droplet R = 100 nm).

Intensive depletion of the dissolved gaseous N_2O_3 in a water droplet due to chemical reaction leads to the decrease of N_2O_3 concentration in the bulk of a water droplet and to increase of the concentration gradient at the interface in a liquid phase. These both factors increase mass transfer coefficient in a droplet and increase the driving force of mass transfer in liquid.

As it was mentioned above in the case of large droplets ($Kn \ll 1$) the capture efficiency (see Eqs (3) and (4)) can be expressed by $\alpha(a) = 4\pi a D_G$. Consequently the flux of soluble gas in a gaseous phase is expressed by equation similar to Maxwell's equation (see Eq. (10)). In Fig. 6 we showed the results of calculation of the dimensionless flux $j^*(\tau)$ of sulfur dioxide as a function of the dimensionless time τ. It was assumed that concentration of sulfur dioxide in a gaseous phase is equal to 1 ppb, tem-

perature in a gaseous phase 298 K and radius of water nanoparticle is equal to 10 nm. The dashed line presents the results of calculation when the capture efficiency was calculated using Eq. (4). In our calculations we assumed that the accommodation coefficient $S_p = 1$.

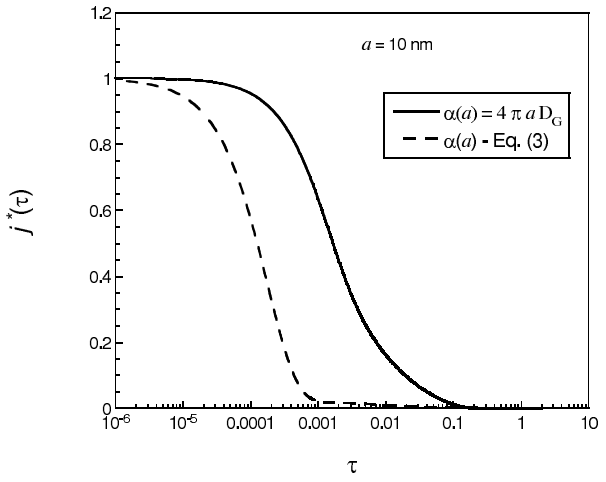

Figure 6: Dimensionless molecular flux density $j^*(\tau)$ as a function of dimensionless time τ (plane line – $\alpha(a) = 4\pi a D_G$, dashed line – $\alpha(a)$ calculated using Eq. (3)).

The solid line present the results of calculation without using the kinetic approach, and thereby the capture efficiency was assumed to be equal $\alpha(a) = 4\pi a D_G$. As can be seen from these plots neglecting kinetic effects in the case of gas absorption by nanoaerosols can lead to the essential overestimation of mass flux.

Dependence of the average concentration of soluble sulfur dioxide in a droplet vs. time is shown in Figs. 7 and 8.

Calculations were performed for water droplets with the radii 0.5, 0.8 and 1 μm (Fig. 7) and for water droplets of radii 5, 10 and 20 nm (Fig. 8). In these calculations we employed the kinetic approach by using Eq. (4) for the capture efficiency $\alpha(a)$ with $S_p = 1$. In Fig. 9 the dependence of average concentration of SO_2 in a droplet vs. time was calculated using the kinetic approach (solid lines) and neglecting kinetic effects (dashed lines). Calculations were performed for the droplets with the radii 10 and 5 nm. As can be seen from these plots neglecting kinetic effects leads to the significant overestimation of concentration of the dissolved gas in a droplet during all the period of gas absorption. Clearly, when the duration of gas absorption $t \to \infty$, both approaches yield

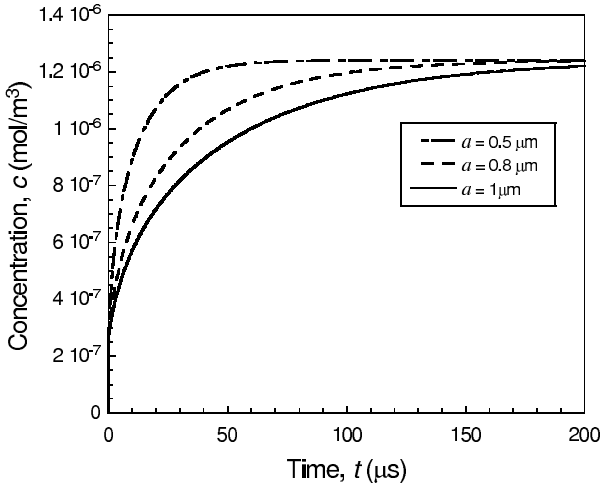

Figure 7: Concentration of the dissolved SO_2 in the bulk of a droplet as a function of time (radii of a droplet 0.5, 0.8 and 1.0 μm).

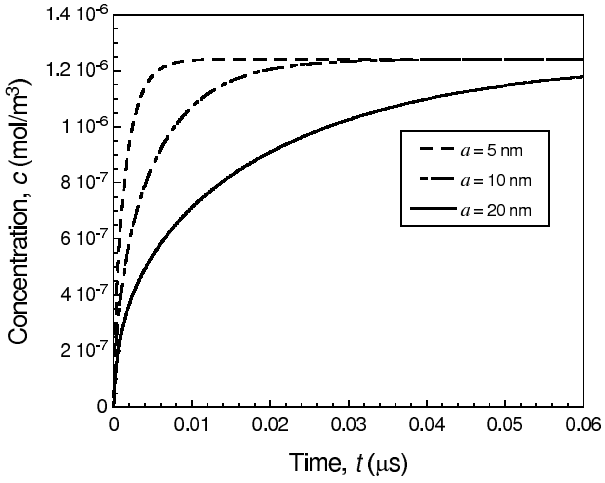

Figure 8: Concentration of the dissolved SO_2 in the bulk of a droplet as a function of time (radii of a droplet 5.0, 10.0 and 20.0 nm).

the same result for the magnitude of the dissolved gas concentration.

5. CONCLUSIONS

In this study we developed a model for absorption of soluble trace gases by nanoaerosols taking into account dissociation reaction of the first order in a liquid phase. In the case when radius of the particle is comparable with the mean free path transport of reactant molecules cannot be described by Fickian diffusion. However, application of the flux-matching theory allowed using transient diffusion equation with

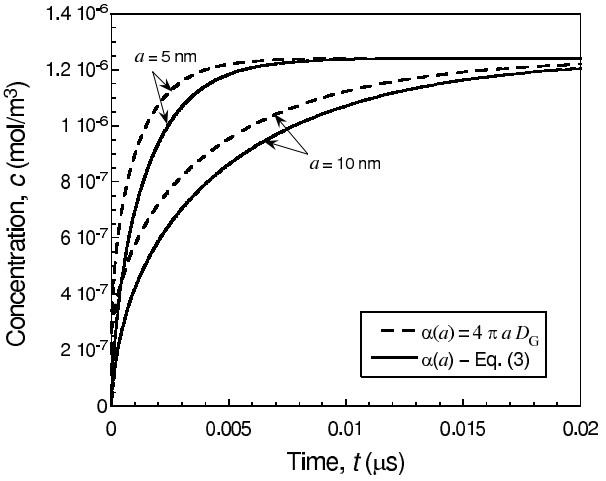

Figure 9: Effect of Knudsen layer on temporal evolution of concentration of the dissolved SO_2 for droplets with the radii 5.0 and 10.0 nm.

the kinetic boundary conditions for the description of gas absorption by nanoaerosols. Transient diffusion equation was solved analytically by the method of separation of variables. We derived linear integral equation of Volterra type for the transient mass flux to a liquid droplet. Integral equation was solved numerically by the method based on the approximation of the integral using the quadrature formula with unequally spaced mesh.

The comparison of the suggested model with our earlier model developed for gas absorption by large droplets ($Kn \ll 1$) (see, Elperin eta al., 2008) showed that both models yield the same time of complete saturation of a large droplet by the soluble gas.

Using the suggested model we studied absorption of sulfur dioxide (SO_2), dinitrogen trioxide (N_2O_3) and chlorine (Cl_2) by water nanoaerosol. It is showed that enhanced depletion of the dissolved N_2O_3 gas in a water droplet due to chemical reaction leads to the decrease of N_2O_3 concentration in the bulk of a water droplet and to the increase of the concentration gradient at the gas–liquid interface. Consequently, the flux of dinitrogen trioxide into a droplet is higher than the fluxes of sulfur dioxide and chlorine at later stages of gas absorption.

It was demonstrated that neglecting kinetic effects leads to the significant overestimation of the soluble gas flux into a droplet during all the period of gas absorption.

Appendix A. DERIVATION OF THE INTEGRAL EQUATION OF VOLTERRA TYPE FOR THE MOLECULAR FLUX DENSITY

Here we give the details of derivation of Eq. (15). Let us first remove j from the boundary condition (14). To this end let us introduce the new unknown function $C(r,t)$:

$$n_L = C(r,t) - \frac{j(t)r}{D_L}. \tag{A.1}$$

Substituting Eq. (A.1) into Eq. (11), and taking into account that in spherical coordinates the Laplacian $\Delta r = 2/r$ we obtain the following equation for $C(r,t)$:

$$\frac{\partial C}{\partial t} = D_L \Delta C + \frac{r j_t}{D_L} - \frac{2j}{r} - \lambda C + \frac{\lambda j r}{D_L}\,, \tag{A.2}$$

with the following boundary conditions

$$\left.\frac{\partial C}{\partial r}\right|_{r=a} = 0 \tag{A.3}$$

and

$$\left.\frac{\partial C}{\partial r}\right|_{r=0} = \left.\frac{j}{D_L}\right|_{r=0}\,. \tag{A.4}$$

Substitution

$$C(r,t) = \frac{\chi(r,t)}{r} \tag{A.5}$$

reduces Eq. (A.2) to

$$\frac{\partial \chi}{\partial t} = D_L \frac{\partial^2 \chi}{\partial r^2} - \lambda\chi - 2j + \frac{1}{D_L}(r^2 j_t + \lambda j r^2)\,. \tag{A.6}$$

The boundary conditions to Eq. (A.6) read:

$$\left.\frac{\partial \chi}{\partial r}\right|_{r=a} - \left.\frac{\chi}{r}\right|_{r=a} = 0 \tag{A.7}$$

and

$$\chi|_{r=0} = 0. \tag{A.8}$$

Let us introduce the eigenfunctions

$$\frac{d^2\phi_n}{dr^2} = -\kappa^2 \phi_n\,, \tag{A.9}$$

where the boundary conditions to the equation (A.9) are the same as for χ, i.e., given by Eqs. (A.7) – (A.8):

$$\left.\frac{\partial \phi_n}{\partial r}\right|_{r=a} - \left.\frac{\phi_n}{r}\right|_{r=a} = 0\,, \qquad \phi_n|_{r=0} = 0. \tag{A.10}$$

Then the solution of the Eq. (A.9) reads:

$$\phi_n = u_n \sin(\mu_n \frac{r}{a}) \,, \tag{A.11}$$

where $\mu = \kappa a$ is the infinite set of the roots of the characteristic equation:

$$\mu = \tan(\mu) \,. \tag{A.12}$$

The roots μ_n of the Eq. (A.12) can be calculated numerically and are as follows $\mu_1 = 4.4934, \mu_2 = 7.7253, \mu_3 = 10.9041, \mu_4 = 14.0662, \mu = 17.2208$ etc. The orthogonality condition for eigenfunctions reads:

$$\int_0^a \phi_n \phi_m dr = \delta_{nm} \tag{A.13}$$

where δ_{nm} is the Kronecker delta. Equation (A.13) allows to determine the normalization constant u_n:

$$u_n^2 = \left(\int_0^a \sin^2(\mu_n \frac{r}{a}) dr \right)^{-1} = \frac{2}{a \sin^2 \mu_n} \,. \tag{A.14}$$

The eigenvalue $\mu_n = 0$ (which is also the solution of Eq. (A.12)) and the respective eigenfunction require a special consideration. Solution of Eq. (A.9) for $\mu_n = 0$ reads:

$$\phi_0(r) = u_0 r \,, \tag{A.15}$$

where the normalization constant u_0 is determined from Eq. (A.13):

$$u_0 = \sqrt{\frac{3}{a^3}} \,. \tag{A.16}$$

Let us now look for the solution to Eq. (A.6) in the following form:

$$\chi(r,t) = 2\Psi_0(t)\phi_0 + \sum_{n>0} \Psi_n(t)\phi_n(r) \,, \tag{A.17}$$

where the coefficient 2 appears due to double degeneration of the eigenvalue $\mu_n = 0$. Equation for Ψ_n reads:

$$\frac{d\Psi_n}{dt} = -\sigma_n \Psi_n + \frac{1}{D_L}(j_t + \lambda j) b_n - 2 j a_n \,, \tag{A.18}$$

where

$$\sigma_n = \lambda + D_L \left(\frac{\mu_n}{a}\right)^2, \qquad a_n = u_n \int_0^a \sin\left(\mu_n \frac{r}{a}\right) dr,$$
$$b_n = u_n \int_0^a r^2 \sin\left(\mu_n \frac{r}{a}\right) dr \tag{A.19}$$

and

$$\sigma_0 = \lambda, \qquad a_0 = u_0 \int_0^a r dr = \frac{1}{2}\sqrt{3a},$$
$$b_0 = u_0 \int_0^a r^3 dr = \frac{1}{4}\sqrt{3a^5}. \tag{A.20}$$

For $n > 0$ we obtain:

$$\Psi_n(t) = \frac{b_n j(t)}{D_L} - \left(\left(\frac{\mu_n}{a}\right)^2 b_n + 2a_n \right) \int_0^t j(t') e^{-\sigma_n (t-t')} dt' \tag{A.21}$$

and

$$\Psi_0(t) = \frac{b_0 j(t)}{D_L} - 2a_0 \int_0^t j(t') e^{-\lambda (t-t')} dt' \tag{A.22}$$

for $n = 0$. The number density of molecules A inside the particle near the surface reads:

$$n_-(a,t) = \frac{\chi(a,t)}{a} - \frac{j(t) a}{D_L} \,. \tag{A.23}$$

Now let us determine χ from Eq. (A.17). Noting that

$$\sum_{n \geq 0} b_n \phi_n(a) = \frac{a^2}{4} \tag{A.24}$$

and

$$\left(\left(\frac{\mu_n}{a}\right)^2 b_n + 2a_n \right) \phi_n(a) = 2 \quad n > 0 \,, \tag{A.25}$$

$$\left(\left(\frac{\mu_n}{a}\right)^2 b_n + 2a_n \right) \phi_n(a) = 3 \quad n = 0 \,, \tag{A.26}$$

Eq. (A.17) and Eq. (A.23) yield:

$$n_-(a) = -2 \sum_{n>0} \int_0^t e^{-\sigma_n (t-t')} j(t') dt' - 3 \int_0^t e^{-\lambda (t-t')} j(t') dt'. \tag{A.27}$$

According to the Henry's law $n_+ = \mathcal{H} n_-$. Using the equation for the flux density

$$j(t) = \frac{1}{4\pi a^2} \alpha(a) (n_\infty - n_+) \tag{A.28}$$

we arrive at the following integral equation of Volterra type for $j(t)$:

$$j(t) = \frac{\alpha(a)}{4\pi a^2} \left[n_\infty - \mathcal{H} \int_0^t S(t-t') j(t') dt' \right] , \tag{A.29}$$

where the kernel $S(t-t')$ is given by the following formula:

$$S(\xi) = 2\sum_{n>0} e^{-[D_L(\mu_n/a)^2+\lambda]\xi} + 3e^{-\lambda\xi}\,. \qquad \text{(A.30)}$$

References

Apelblat, A., 2008. Volterra Functions, Nova Science. NY. 360 p.

Clement, C.F., 2007, Mass transfer to aerosols, in the book Environmental chemistry of aerosols, ed. by I. Colbeck, Wiley Interscience, 49 – 89.

Clift, R., Grace, J.R., and Weber, M.E., 1978. Bubbles, Drops and Particles. Academic Press. NY. 380p.

Elperin, T., Fominykh, A., and Krasovitov, B., 2007. Evaporation and condensation of large droplets in the presence of inert admixtures containing soluble gas. Journal of the Atmospheric Sciences 64, 983 – 995.

Elperin, T., Fominykh, A., and Krasovitov, B., 2008. Scavenging of soluble gases by evaporating and growing cloud droplets in the presence of aqueous-phase dissociation reaction. Atmospheric Environment 42, 3076 – 3086.

Flossmann, A.I., 1998. Clouds and pollution. Pure and Appl. Chem. 70, No. 7, 1345 – 1352.

Fuchs, N.A., 1964. In: Davies CN (ed) The mechanics of aerosols. MacMillan, New York.

Fuchs N.A., Sutugin, A.G., 1971. Highdispersed aerosols. In: Hidy GM, Brock JR (eds) Topics in current aerosol research, vol 2. Pergamon, Oxford, pp 1 - 60.

Hayden, K.L., Macdonald, A.M., Gong, W., Toom-Sauntry, D., Anlauf, K.G., Leithead, A., Li, S.M., Leaitch, W.R., and Noone,K., 2008. Cloud processing of nitrate. Journal of Geophysical Research 113, D18201, doi:10.1029/2007JD009732.

Krämer M., Beltz, N., Schell, D., Schütz, L., Sprengard-Eichel, C., and Wurzler, S., 2000. Cloud processing of continental aerosol particles: Experimental investigations for different drop sizes. J. Geophys. Res. 105, No.D9, 11739 – 11752.

Kulmala, M., Vehkamäki, H., Petäjä, T., Dal Maso, M., Lauri, A., Kerminen, V.-M., Birmili, W., McMurry, P.H., 2004. Formation and growth rates of ultrafine atmospheric particles: a review of observations. Aerosol Science 35, 143176.

Loyalka, S.K., 1982. Condensation on a Spherical Droplet, II, Journal of Colloid and Interface Science 87, No. I, 216–224.

Lushnikov, A.A., 2012. Nanoaerosols in the atmosphere. Chapter 3 in Bychkov, V., Golubkov G., and Nikitin A., (eds) The Atmosphere and Ionosphere. Elementary Processes, Discharges and Plasmoids. Physics of Earth and Space Environment. DOI 10.1007/978-94-007-2914-83, Springer.

Lushnikov, A.A., and Kulmala, M., 2004. Flux–matching theory of particle charging, Physical Review E70, 046413(1 – 9).

Pöschl, U., Rudich, Y., and Ammann, M., 2007, Kinetic model framework for aerosol and cloud surface chemistry and gas–particle interactions — Part 1: General equations, parameters, and terminology. Atmospheric Chemistry and Physics 7, 5989 – 6023.

Pruppacher, H.R., and Klett, J.D., 1997. Microphysics of Clouds and Precipitation, 2nd edn., Kluwer Academic Publishers, Dordrecht, 955 pp.

Sahni, D.C., 1966. The effect of black sphere on the flux distribution of an infinite moderator, J. Nuclear Energy 20, 915 – 920.

Seinfeld, J.H., and Pandis, S.N., 2006. Atmospheric Chemistry and Physics. From Air Pollution to Climate Change. Second ed. John Wiley & Sons, NY. 1225p.

Taniguchi, I., and Asano, K., 1992. Experimental study of absorption of carbon dioxide from carbon dioxide-air gas mixture by water spray. J. Chem. Eng. Japan 25, 614 – 616.

Vesala, T., Hannemann, A.U., Luo, B.P., Kulmala, M., and Peter, Th., 2001. Rigorous treatment of time-dependent trace gas uptake by droplets including bulk diffusion and surface accommodation. Aerosol Sci. 32, 843 – 860.

Wagner, P.E., 1982. Aerosol Growth by Condensation. Chapter 5, pp. 129 – 178, in Aerosol Microphysics, II: Chemical Physics of Microparticles, edited by W. H. Marlow, Springer, Berlin.

Zhang, R., Khalizov, A., Wang, L., Hu, M., and Xu, W., 2012. Nucleation and Growth of Nanoparticles in the Atmosphere. Chemical Reviews 112, 1957 – 2011.

ANALYSIS OF THE MICROPHYSICAL STRUCTURES OF FOG DURING THE PARISFOG PROJECT

F. Burnet[1], L. Gomes[1], M. Haeffelin[2], J.-C. Dupont[3] and T. Elias[4,2]

[1] Météo-France/CNRS, CNRM/GAME, Toulouse, France
[2] Institut Pierre Simon Laplace/CNRS, Palaiseau, France
[3] Institut Pierre Simon Laplace/UVSQ, Palaiseau, France
[4] HYGEOS, Lille, France

1. INTRODUCTION

The occurrence and development of fogs result from the nonlinear interaction of competing radiative, thermodynamic, microphysical and dynamical processes and the forecasting of their life cycle still remains a challenging issue.

To better understand relationships between such processes field campaigns are carried out at the SIRTA observatory in the Paris suburb area (France). During these experiments state of art measurements of particle size distribution were performed in addition to a suite of active and passive remote sensing instruments and in situ sensors deployed to monitor the vertical thermodynamic structure of the surface layer and the dynamic conditions.

A strength of the instrumental set up deployed for the PreViBOSS project (2010-2013) is the in situ measurement of fog particles at ambient humidity. These data are investigated here to document the fog microphysical properties and to study the evolution of these properties along the fog life cycle.

2. DATA ANALYSIS

The FM-100 Fog-Monitor from DMT is a single particle counter that provides the size distribution of droplet from ~2 to 50 µm in diameter. A PVM-100 from Gerber Scientific Inc. provides the liquid water content (LWC) and the particle surface area (PSA) over the same size range. Finally a Palas-2000 from Welas measures the size distribution of particles from 0.4 to 40 µm in diameter. These instruments were installed side by side on a scaffolding at 2.5 m AGL and operated on 24/7 during wintertime from Oct 1st to March 31st .

Eighty-two fog events occurred during winters 2010 and 2011. However due to laser failures only 21 events were sampled by the FM-100, half of them during Nov 2011. Acording to the Tardif and Rasmussen (2007) classification, most of them are radiation fogs (60%) and stratus-lowering fogs (20%).

Corresponding author's address:
Frédéric Burnet, Météo-France, CNRM/GMEI/MNPCA
42 av. Coriolis, 31 057 Toulouse Cedex 01, France.
E-Mail: frederic.burnet@ meteo.fr

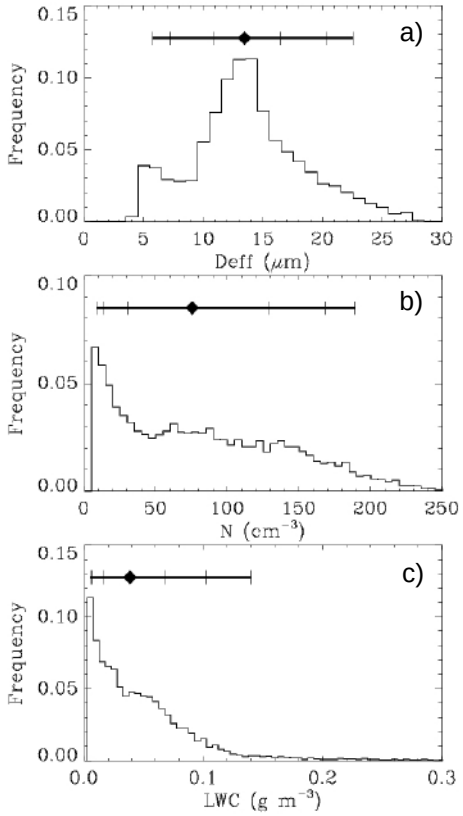

Fig. 1: Frequency distribution for the 21 fog events of (a) effective diameter (D_{eff}), (b) total droplet number concentration (N) and LWC. Median values (diamond) and percentiles 5,10,25,75,90 and 95 % (ticks on the error bar) are also indicated.

Note however that over all the fog events the proportion of each of these fog type is about 40% as already reported in Haeffelin et al. (2010) for a previous experiment.

For each fog case the 1 Hz size distribution measured by the FM-100 is cumulated every minute to derive the effective diameter (D_{eff}), total droplet number concentration (N) and LWC values. The frequency distributions computed by using samples with N > 5 cm^{-3} of all the cases, are shown in Fig. 1 for each microphysical parameter: 9757 samples have been used that represents about 163 hours of fog.

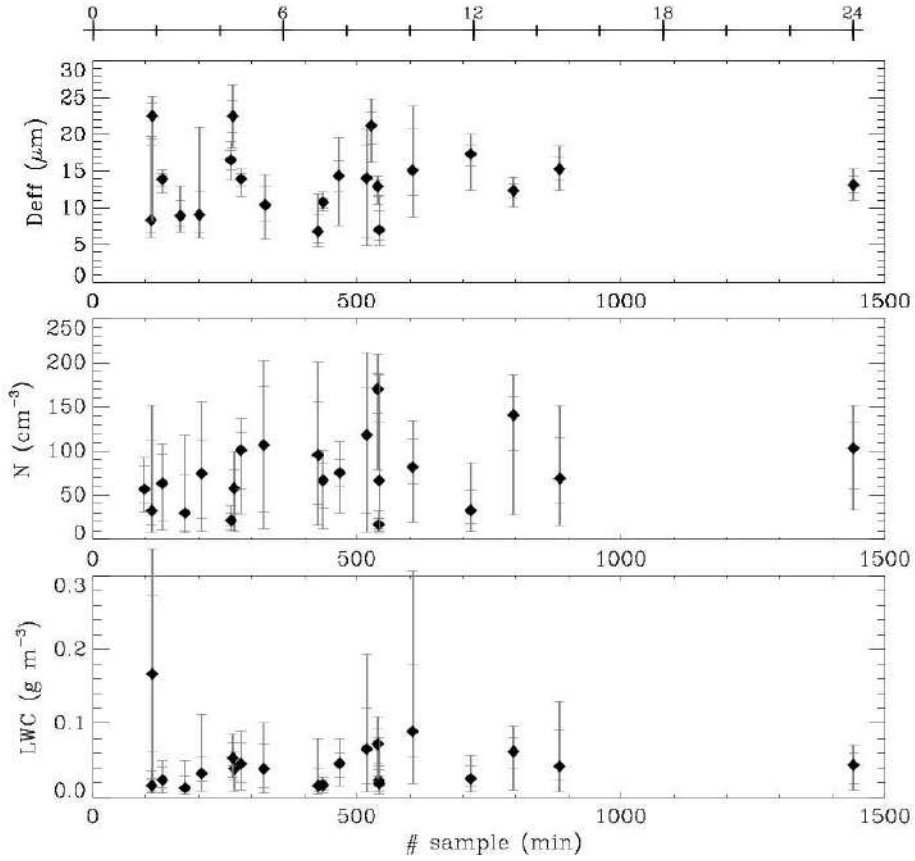

Fig. 2: Statistics of the microphysical parameters of the 21 fog cases represented by the median (diamond) and percentiles 10,25,75 and 90 % of the frequency distribution (ticks on the error bar) of, from top to bottom: D_{eff}, N and LWC, as function of the number of the one minute samples. The scale on the top indicates the corresponding cumulated duration in hours.

The distributions of LWC and N are similar to those reported in Gultepe et al (2009) (their Fig. 17) but for the ocean fog cases (FRAM-L). The shape of the LWC distribution exhibits an exponential decrease but the median value (0.038 g m^{-3}) is slightly larger. The frequency of N is roughly constant from 50 to 150 cm^{-3}. But the proportion of low values is larger, with 25% of the values < 30 cm^{-3}, and then the median is 75.5 cm^{-3} that is in between the values reported in Gultepe et al (2009) for the land (~50 cm^{-3}) and for the ocean (~90 cm^{-3}) fog cases. In contrast the D_{eff} distribution exhibits a different shape with a pronounced mode around the median value (13.5 µm) and a second mode around 6 µm.

The comparison of the distributions for each fog event reveals that there is a significant variability among the cases. This is illustrated in Fig 2 where the statistics are reported as function of the sample number. This latter is used here as a proxy of the fog duration but note that the real duration of the event could be longer when the fog is intermittent. Most of the events have duration between 1h30 and 10h. Only one case lasted about 24h but during Nov 2011 some consecutive events are separated by just a few hours.

Median values of LWC range from 0.012 to 0.089 g m^{-3}, except one case that reaches 0.168 g m^{-3}, but most of them (15 over 21) are < 0.05 g m^{-3}. Concentration values encompass also an order of magnitude from 17 to 170 cm^{-3}. This variability is reflected on the droplet size with D_{eff} values that range from 6.9 to 22.3 µm.

The shape of these distributions is also highly variable. For D_{eff} for example, it can be very narrow with mean and 25^{th}-75^{th} percentile interval of 10.8±1.31 µm, or in contrast very broad as 14.1±12.56 µm with a bimodal shape.

The time evolution of the microphysical parameters follow very different behaviours depending on the events. But at this stage no systematic trend along the fog life cycle was pointed out.

Median values of N are reported in Fig. 3-a as function of LWC for each cases. Various values of N are observed for a given LWC illustrating the diversity of the dataset. While liquid water production is mainly controlled by radiative cooling, the number of fog droplets depends on

the aerosol properties (size distribution and chemical properties). Once droplets have been formed during the activation they compete for the available water : the less numerous they are, the larger the size they can reach by water vapour diffusion growth. Fig 3-b shows indeed that median values of D_{eff} decrease as the concentration values increase, reflecting the expected inverse relationship between the size and the number of droplets, but only for D_{eff} > ~12 µm. For cases with lower D_{eff} values however the concentration remains surprising low with values less than ~100 cm^{-3}. Fig 3-c reveals that LWC values of such samples are also rather low. Lack of available water could obviously limit the droplet growth. But since LWC depends on the cube of the droplet size, this factor alone could hardly explain the observed discrepancy.

Comparison with measurements from the PVM reveal however noticeable differences. This is illustrated on Fig 4 that shows scatterplots of LWC and D_{eff} for three fog events. PSA comparisons are not shown here but they follow the same trend as LWC. Fig 4-a indicates a good agreement between both instruments. In contrast Fig 4-b-c reveal large discrepancies with LWC values from the FM-100 much lower and larger than the PVM ones for cases on 17/11/10 and 20/11/11, respectively. A bias on D_{eff} appears on Fig 4-b. The disagreement for low values of D_{eff} is more pronounced on Fig 4-c where median values are 8.05 and 12.56 µm, for FM-100 and PVM data, respectively. All the cases that exhibits too low values of D_{eff} on Fig. 3-b show similar comparisons. It is then likely that the FM-100 underestimates the smallest values of D_{eff} in such cases.

Examples of particle size distributions are displayed on Fig. 5. They reveal that the Palas underestimates the concentration of the large particles that confirms the assumption of Elias et al. (2009). In contrast the FM-100 underestimates the droplet counts in the first two size classes. Otherwise Fig 5 attests a nice overlap of both spectra.

These size distributions were sampled at different stages of the fog event on 19/11/10. At 03:00:00 UTC a few hours before the onset of fog, the spectrum is mainly composed of submicronic deliquesced aerosols. Between 05:00:00 and 05:30:00 the visibility at 3 m AGL slightly decreases from ~2 to 1.3 km. Spectra show a huge increase of the concentration of particles around 1 µm and a mode of droplets > 10 µm diameter has also appeared. After 05:30:00, as the visibility drops down below 300 m, both probes indicates a third mode around 5 µm and a large increase of the concentration of the largest droplets. Finally during the mature stage where the visibility remains below than 160 m, concentration of the mode of the smallest particle has decreased while both the others have increased by a factor of ten. Such a bimodal size distributions with most of the mass concentrated in the large drop mode are typical of fog (Wendish et al 1998, Gultepe et al 2009).

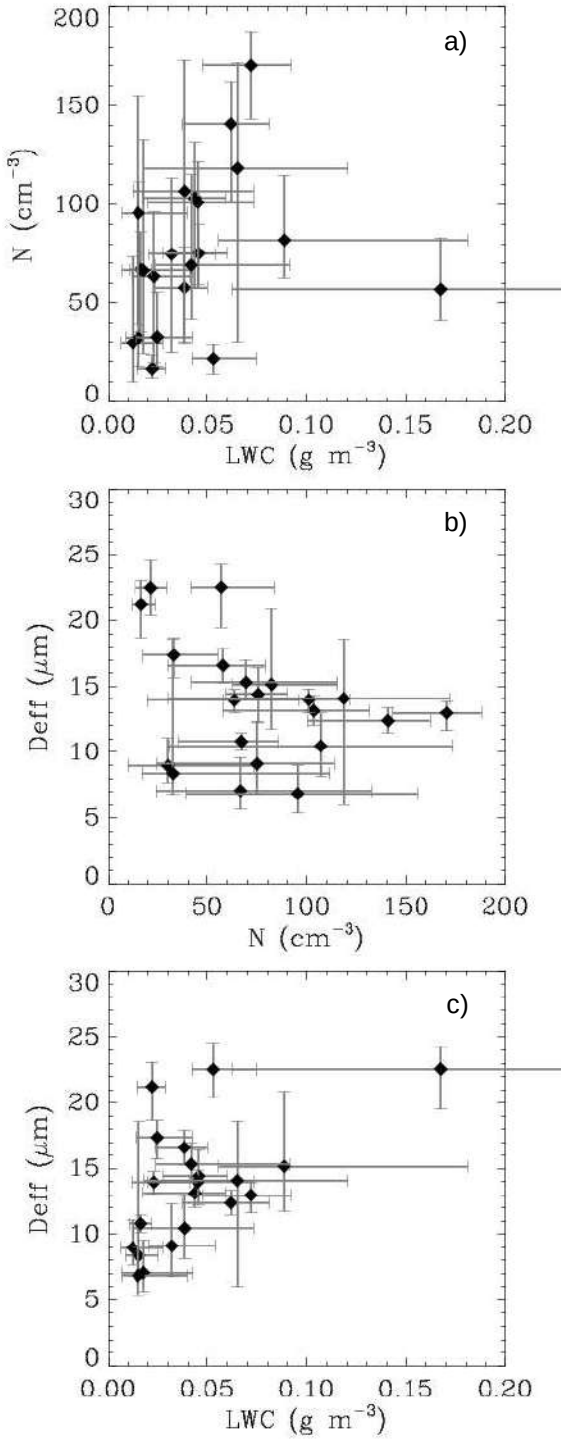

Fig. 3: Scatterplots of the median values of each cases. a) N vs. LWC, b) D_{eff} vs. N and c) D_{eff} vs LWC. Error bars correspond to the 25th-75th percentile intervals.

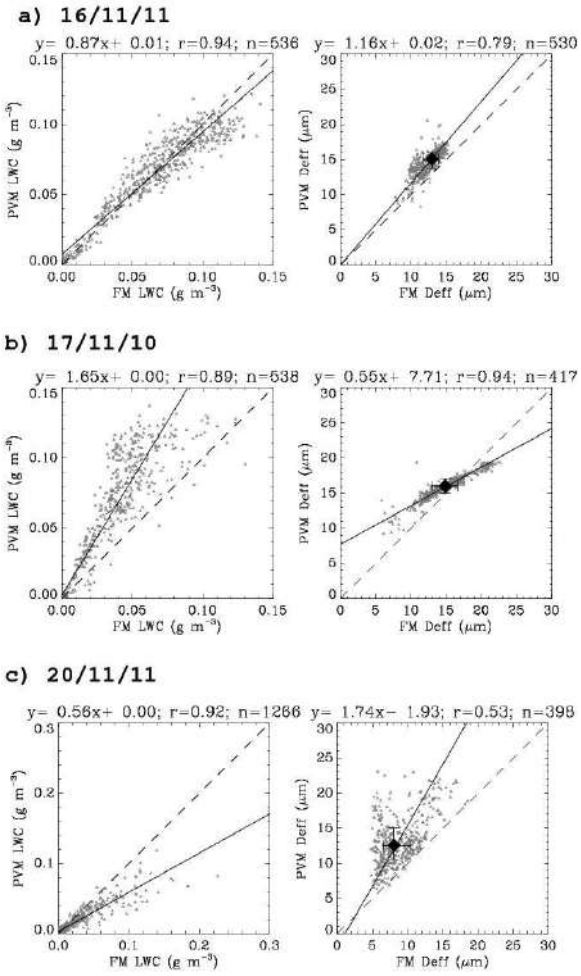

Fig. 4: PVM vs FM-100 measurements of LWC (left) and D_{eff} (right) for three fog events. One to one (dashed) and linear regression (continuous) lines are overlaid on the one minute samples. On the Deff panel median values (diamond) and 25^{th}–75^{th} percentile intervals are also shown

4. SUMMARY

Microphysical measurements collected during 21 wintertime fog events have been examined to document their properties. Statistics of the droplet number concentration, LWC and effective diameter derived from the FM-100 particle size distribution show a large variability of their characteristic values among the different cases, as well as various evolutions of these properties during the fog life cycle.

Comparisons between FM-100 and PVM measurements however reveal noticeable differences depending on the events, with estimations of LWC that range in a factor of two. A bias appears on D_{eff} comparisons under some circumstances which leads to a substantial underestimation of the FM-100 compared to the PVM when droplets are small. Reasons for this bias is not clear yet and further investigations are needed to validate the dataset. However the agreement is excellent for some cases.

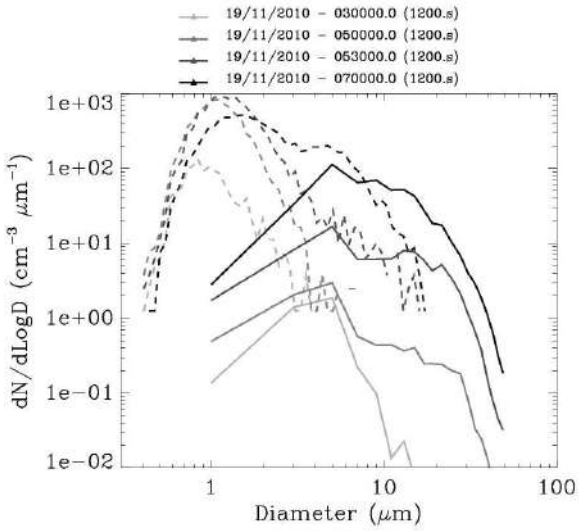

Fig. 5: Particle size distributions as measured with the Palas (dashed) and with the FM-100 (continuous) during the fog event on 19/11/2010. Each spectra is an average over 20 minutes starting at time as indicated on the legend.

Finally, analysis of size distributions shows that the FM-100 underestimates the droplets number in the two first size bins and confirms that the Palas underestimates the concentration of the larger droplets. Otherwise the overlap is very nice and the evolution of both spectra during the fog life cycle are consistent suggesting that this instrumental set up is well suited to study the impact of aerosols on the fog life cycle.

5. ACKNOWLEGMENTS

The authors acknowledge the SIRTA team for the technical support during the campaigns. Funding for this work was provided by Météo-France, MINEFI and DGA through the PreViBOSS project.

6. REFERENCE

Elias, T., and Coauthors, 2009: Particulate contribution to extinction of visible radiation: Pollution, haze, and fog. *Atmospheric Research*, **92**,443-454,Doi:10.1016/j.atmosres.2009.01.006.

Gultepe, I., and Coauthors, 2009: The Fog Remote Sensing and Modeling Field Project. *Bull. Amer. Meteor. Soc*., **90**, 341–359. doi:10.1175/2008BAMS2354.1

Haeffelin, M., and Coauthors, 2010: PARIFOG shedding new light on fog physical processes, *Bull. Amer. Meteor. Soc*., **91**, 767-783. doi:10.1175/2009BAMS2671.1.

Tardif, R., and R. M. Rasmussen, 2007: Event-based climatology of fog in the New York City region. *J. Appl. Meteor. Climatol.*, **47**, 1681-1703.

Wendisch, M., and Coauthors 1998: Drop size distribution and LWC in Po Walley Fog. *Contr. Atmos. Phys.*, **71**, 87-100.